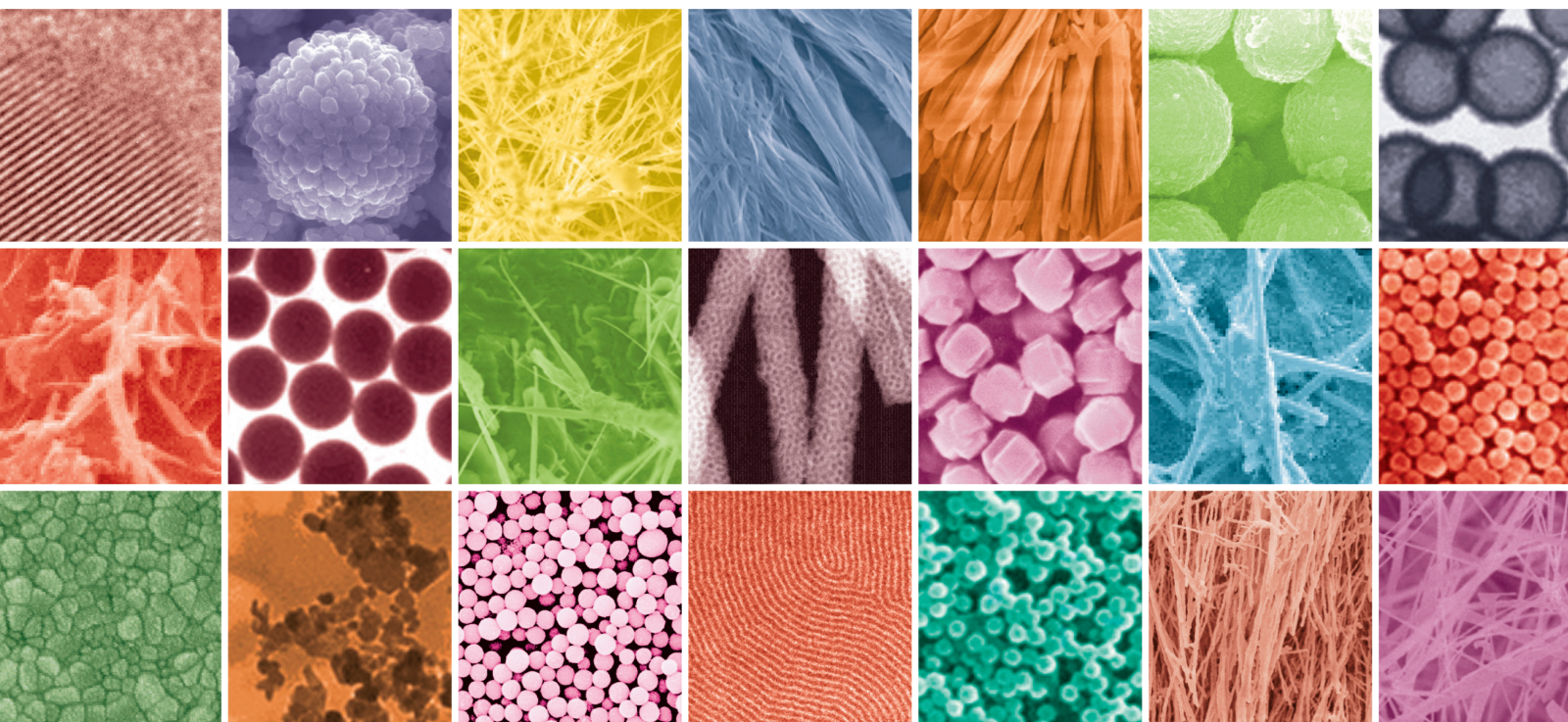# Functional Nanomaterial-based Flexible Electronics

Lead Guest Editor: Awais Ahmad
Guest Editors: Runwei Mo and Pandiyarasan Veluswamy

Functional Nanomaterial-based Flexible Electronics

Functional Nanomaterial-based Flexible Electronics

Lead Guest Editor: Awais Ahmad
Guest Editors: Runwei Mo and Pandiyarasan Veluswamy

Sherine Obare , USA
Abdelwahab Omri , Canada
Dillip K. Panda, USA
Sakthivel Pandurengan , India
Dr. Asisa Kumar Panigrahy, India
Mazeyar Parvinzadeh Gashti , Canada
Edward A. Payzant , USA
Alessandro Pegoretti , Italy
Oscar Perales-Pérez, Puerto Rico
Anand Babu Perumal , China
Suresh Perumal , India
Thathan Premkumar , Republic of Korea
Helena Prima-García, Spain
Alexander Pyatenko, Japan
Xiaoliang Qi , China
Haisheng Qian , China
Baskaran Rangasamy , Zambia
Soumyendu Roy , India
Fedlu Kedir Sabir , Ethiopia
Lucien Saviot , France
Shu Seki , Japan
Senthil Kumaran Selvaraj , India
Donglu Shi , USA
Muhammad Hussnain Siddique , Pakistan
Bhanu P. Singh , India
Jagpreet Singh , India
Jagpreet Singh, India
Surinder Singh, USA
Thangjam Ibomcha Singh , Republic of
Korea
Vidya Nand Singh, India
Vladimir Sivakov, Germany
Tushar Sonar, Russia
Pingan Song , Australia
Adolfo Speghini , Italy
Kishore Sridharan , India
Marinella Striccoli , Italy
Andreas Stylianou , Cyprus
Fengqiang Sun , China
Ashok K. Sundramoorthy , India
Bo Tan, Canada
Leander Tapfer , Italy
Dr. T. Sathish Thanikodi , India
Arun Thirumurugan , Chile
Roshan Thotagamuge , Sri Lanka

Valeri P. Tolstoy , Russia
Muhammet S. Toprak , Sweden
Achim Trampert, Germany
Tamer Uyar , USA
Cristian Vacacela Gomez , Ecuador
Luca Valentini, Italy
Viet Van Pham , Vietnam
Antonio Vassallo , Italy
Ester Vazquez , Spain
Ajayan Vinu, Australia
Ruibing Wang , Macau
Magnus Willander , Sweden
Guosong Wu, China
Ping Xiao, United Kingdom
Zhi Li Xiao , USA
Yingchao Yang , USA
Hui Yao , China
Dong Kee Yi , Republic of Korea
Jianbo Yin , China
Hesham MH Zakaly , Russia
Michele Zappalorto , Italy
Mauro Zarrelli , Italy
Osman Ahmed Zelekew, Ethiopia
Wenhui Zeng , USA
Renyun Zhang , Sweden

Contents

Contents

Contents

Contents

Contents

Contents

Hindawi

Retraction

Retracted: Application and Equipment of Preparation Technology of Ferroelectric Thin Film Materials in Sports Industry

Journal of Nanomaterials

This article has been retracted by Hindawi following an investigation undertaken by the publisher [1]. This investigation has uncovered evidence of one or more of the following indicators of systematic manipulation of the publication process:

(1) Discrepancies in scope

(2) Discrepancies in the description of the research reported

(3) Discrepancies between the availability of data and the research described

(4) Inappropriate citations

(5) Incoherent, meaningless and/or irrelevant content included in the article

(6) Peer-review manipulation

The presence of these indicators undermines our confidence in the integrity of the article's content and we cannot, therefore, vouch for its reliability. Please note that this notice is intended solely to alert readers that the content of this article is unreliable. We have not investigated whether authors were aware of or involved in the systematic manipulation of the publication process.

Wiley and Hindawi regrets that the usual quality checks did not identify these issues before publication and have since put additional measures in place to safeguard research integrity.

We wish to credit our own Research Integrity and Research Publishing teams and anonymous and named external researchers and research integrity experts for contributing to this investigation.

The corresponding author, as the representative of all authors, has been given the opportunity to register their agreement or disagreement to this retraction. We have kept a record of any response received.

References

[1] Y. Xu, "Application and Equipment of Preparation Technology of Ferroelectric Thin Film Materials in Sports Industry," *Journal of Nanomaterials*, vol. 2022, Article ID 9480475, 13 pages, 2022.

Hindawi

Retraction

Retracted: Application Effect Analysis of a Nanotube Combined with Orthopedic Exercise Rehabilitation Therapy in the Treatment of Patients with Knee Arthritis

Journal of Nanomaterials

This article has been retracted by Hindawi following an investigation undertaken by the publisher [1]. This investigation has uncovered evidence of one or more of the following indicators of systematic manipulation of the publication process:

(1) Discrepancies in scope
(2) Discrepancies in the description of the research reported
(3) Discrepancies between the availability of data and the research described
(4) Inappropriate citations
(5) Incoherent, meaningless and/or irrelevant content included in the article
(6) Peer-review manipulation

The presence of these indicators undermines our confidence in the integrity of the article's content and we cannot, therefore, vouch for its reliability. Please note that this notice is intended solely to alert readers that the content of this article is unreliable. We have not investigated whether authors were aware of or involved in the systematic manipulation of the publication process.

In addition, our investigation has also shown that one or more of the following human-subject reporting requirements has not been met in this article: ethical approval by an Institutional Review Board (IRB) committee or equivalent, patient/participant consent to participate, and/or agreement to publish patient/participant details (where relevant).

Wiley and Hindawi regrets that the usual quality checks did not identify these issues before publication and have since put additional measures in place to safeguard research integrity.

We wish to credit our own Research Integrity and Research Publishing teams and anonymous and named external researchers and research integrity experts for contributing to this investigation.

The corresponding author, as the representative of all authors, has been given the opportunity to register their agreement or disagreement to this retraction. We have kept a record of any response received.

References

[1] J. Zhang and Z. Xing, "Application Effect Analysis of a Nanotube Combined with Orthopedic Exercise Rehabilitation Therapy in the Treatment of Patients with Knee Arthritis," *Journal of Nanomaterials*, vol. 2022, Article ID 1275250, 9 pages, 2022.

Retraction

Retracted: Application Value Analysis of Nanooptical Materials in Martial Art Single-Kick Protective Equipment

Journal of Nanomaterials

This article has been retracted by Hindawi following an investigation undertaken by the publisher [1]. This investigation has uncovered evidence of one or more of the following indicators of systematic manipulation of the publication process:

(1) Discrepancies in scope

(2) Discrepancies in the description of the research reported

(3) Discrepancies between the availability of data and the research described

(4) Inappropriate citations

(5) Incoherent, meaningless and/or irrelevant content included in the article

(6) Peer-review manipulation

The presence of these indicators undermines our confidence in the integrity of the article's content and we cannot, therefore, vouch for its reliability. Please note that this notice is intended solely to alert readers that the content of this article is unreliable. We have not investigated whether authors were aware of or involved in the systematic manipulation of the publication process.

In addition, our investigation has also shown that one or more of the following human-subject reporting requirements has not been met in this article: ethical approval by an Institutional Review Board (IRB) committee or equivalent, patient/ participant consent to participate, and/or agreement to publish patient/ participant details (where relevant).

Wiley and Hindawi regrets that the usual quality checks did not identify these issues before publication and have since put additional measures in place to safeguard research integrity.

We wish to credit our own Research Integrity and Research Publishing teams and anonymous and named external researchers and research integrity experts for contributing to this investigation.

The corresponding author, as the representative of all authors, has been given the opportunity to register their agreement or disagreement to this retraction. We have kept a record of any response received.

References

[1] S. Yu, "Application Value Analysis of Nanooptical Materials in Martial Art Single-Kick Protective Equipment," *Journal of Nanomaterials*, vol. 2022, Article ID 2714874, 8 pages, 2022.

Hindawi

Retraction

Retracted: Electrospinning of Nanofiber-Based Materials and Application of the Technology to Lower Extremity Joint Exercise Rehabilitation

Journal of Nanomaterials

This article has been retracted by Hindawi following an investigation undertaken by the publisher [1]. This investigation has uncovered evidence of one or more of the following indicators of systematic manipulation of the publication process:

(1) Discrepancies in scope

(2) Discrepancies in the description of the research reported

(3) Discrepancies between the availability of data and the research described

(4) Inappropriate citations

(5) Incoherent, meaningless and/or irrelevant content included in the article

(6) Peer-review manipulation

The presence of these indicators undermines our confidence in the integrity of the article's content and we cannot, therefore, vouch for its reliability. Please note that this notice is intended solely to alert readers that the content of this article is unreliable. We have not investigated whether authors were aware of or involved in the systematic manipulation of the publication process.

In addition, our investigation has also shown that one or more of the following human-subject reporting requirements has not been met in this article: ethical approval by an Institutional Review Board (IRB) committee or equivalent, patient/participant consent to participate, and/or agreement to publish patient/participant details (where relevant).

Wiley and Hindawi regrets that the usual quality checks did not identify these issues before publication and have since put additional measures in place to safeguard research integrity.

We wish to credit our own Research Integrity and Research Publishing teams and anonymous and named external researchers and research integrity experts for contributing to this investigation.

The corresponding author, as the representative of all authors, has been given the opportunity to register their agreement or disagreement to this retraction. We have kept a record of any response received.

References

[1] J. Ma and S. Baek, "Electrospinning of Nanofiber-Based Materials and Application of the Technology to Lower Extremity Joint Exercise Rehabilitation," *Journal of Nanomaterials*, vol. 2022, Article ID 6437728, 8 pages, 2022.

Retraction

Retracted: Application of Nanoscaffold Material Combined with Exercise Rehabilitation Therapy in the Treatment of Athletes with Hip Injuries

Journal of Nanomaterials

This article has been retracted by Hindawi following an investigation undertaken by the publisher [1]. This investigation has uncovered evidence of one or more of the following indicators of systematic manipulation of the publication process:

(1) Discrepancies in scope
(2) Discrepancies in the description of the research reported
(3) Discrepancies between the availability of data and the research described
(4) Inappropriate citations
(5) Incoherent, meaningless and/or irrelevant content included in the article
(6) Peer-review manipulation

The presence of these indicators undermines our confidence in the integrity of the article's content and we cannot, therefore, vouch for its reliability. Please note that this notice is intended solely to alert readers that the content of this article is unreliable. We have not investigated whether authors were aware of or involved in the systematic manipulation of the publication process.

In addition, our investigation has also shown that one or more of the following human-subject reporting requirements has not been met in this article: ethical approval by an Institutional Review Board (IRB) committee or equivalent, patient/participant consent to participate, and/or agreement to publish patient/participant details (where relevant).

Wiley and Hindawi regrets that the usual quality checks did not identify these issues before publication and have since put additional measures in place to safeguard research integrity.

We wish to credit our own Research Integrity and Research Publishing teams and anonymous and named external researchers and research integrity experts for contributing to this investigation.

The corresponding author, as the representative of all authors, has been given the opportunity to register their agreement or disagreement to this retraction. We have kept a record of any response received.

References

[1] M. Xiang, F. Cao, J. Peng, and G. Bai, "Application of Nanoscaffold Material Combined with Exercise Rehabilitation Therapy in the Treatment of Athletes with Hip Injuries," *Journal of Nanomaterials*, vol. 2022, Article ID 6582511, 12 pages, 2022.

Retraction

Retracted: Meta-Analysis of the Main Components of Nanophotodynamics Combined with Traditional Chinese Medicine in the Treatment of Tumors

Journal of Nanomaterials

This article has been retracted by Hindawi following an investigation undertaken by the publisher [1]. This investigation has uncovered evidence of one or more of the following indicators of systematic manipulation of the publication process:

(1) Discrepancies in scope

(2) Discrepancies in the description of the research reported

(3) Discrepancies between the availability of data and the research described

(4) Inappropriate citations

(5) Incoherent, meaningless and/or irrelevant content included in the article

(6) Peer-review manipulation

The presence of these indicators undermines our confidence in the integrity of the article's content and we cannot, therefore, vouch for its reliability. Please note that this notice is intended solely to alert readers that the content of this article is unreliable. We have not investigated whether authors were aware of or involved in the systematic manipulation of the publication process.

Wiley and Hindawi regrets that the usual quality checks did not identify these issues before publication and have since put additional measures in place to safeguard research integrity.

We wish to credit our own Research Integrity and Research Publishing teams and anonymous and named external researchers and research integrity experts for contributing to this investigation.

The corresponding author, as the representative of all authors, has been given the opportunity to register their agreement or disagreement to this retraction. We have kept a record of any response received.

References

[1] Y. Liu, Y. Li, and Y. Wen, "Meta-Analysis of the Main Components of Nanophotodynamics Combined with Traditional Chinese Medicine in the Treatment of Tumors," *Journal of Nanomaterials*, vol. 2022, Article ID 4552356, 14 pages, 2022.

Retraction

Retracted: Relationship between Urban Landscape Design and Ecological Environment Protection in the Application of Environmental Protection and Renewable New Energy Materials

Journal of Nanomaterials

This article has been retracted by Hindawi following an investigation undertaken by the publisher [1]. This investigation has uncovered evidence of one or more of the following indicators of systematic manipulation of the publication process:

(1) Discrepancies in scope

(2) Discrepancies in the description of the research reported

(3) Discrepancies between the availability of data and the research described

(4) Inappropriate citations

(5) Incoherent, meaningless and/or irrelevant content included in the article

(6) Peer-review manipulation

The presence of these indicators undermines our confidence in the integrity of the article's content and we cannot, therefore, vouch for its reliability. Please note that this notice is intended solely to alert readers that the content of this article is unreliable. We have not investigated whether authors were aware of or involved in the systematic manipulation of the publication process.

In addition, our investigation has also shown that one or more of the following human-subject reporting requirements has not been met in this article: ethical approval by an Institutional Review Board (IRB) committee or equivalent, patient/participant consent to participate, and/or agreement to publish patient/participant details (where relevant).

Wiley and Hindawi regrets that the usual quality checks did not identify these issues before publication and have since put additional measures in place to safeguard research integrity.

We wish to credit our own Research Integrity and Research Publishing teams and anonymous and named external researchers and research integrity experts for contributing to this investigation.

The corresponding author, as the representative of all authors, has been given the opportunity to register their agreement or disagreement to this retraction. We have kept a record of any response received.

References

[1] S. Wu, X. Yu, Y. Cao, and G. Wang, "Relationship between Urban Landscape Design and Ecological Environment Protection in the Application of Environmental Protection and Renewable New Energy Materials," *Journal of Nanomaterials*, vol. 2022, Article ID 6360300, 13 pages, 2022.

Retraction

Retracted: Athletes' Ankle Injury Features and Rehabilitation Methods Based on Internet Big Data

Journal of Nanomaterials

This article has been retracted by Hindawi following an investigation undertaken by the publisher [1]. This investigation has uncovered evidence of one or more of the following indicators of systematic manipulation of the publication process:

(1) Discrepancies in scope

(2) Discrepancies in the description of the research reported

(3) Discrepancies between the availability of data and the research described

(4) Inappropriate citations

(5) Incoherent, meaningless and/or irrelevant content included in the article

(6) Peer-review manipulation

The presence of these indicators undermines our confidence in the integrity of the article's content and we cannot, therefore, vouch for its reliability. Please note that this notice is intended solely to alert readers that the content of this article is unreliable. We have not investigated whether authors were aware of or involved in the systematic manipulation of the publication process.

In addition, our investigation has also shown that one or more of the following human-subject reporting requirements has not been met in this article: ethical approval by an Institutional Review Board (IRB) committee or equivalent, patient/participant consent to participate, and/or agreement to publish patient/participant details (where relevant).

Wiley and Hindawi regrets that the usual quality checks did not identify these issues before publication and have since put additional measures in place to safeguard research integrity.

We wish to credit our own Research Integrity and Research Publishing teams and anonymous and named external researchers and research integrity experts for contributing to this investigation.

The corresponding author, as the representative of all authors, has been given the opportunity to register their agreement or disagreement to this retraction. We have kept a record of any response received.

References

[1] X. Li and M. Kang, "Athletes' Ankle Injury Features and Rehabilitation Methods Based on Internet Big Data," *Journal of Nanomaterials*, vol. 2022, Article ID 7904739, 9 pages, 2022.

Hindawi

Retraction

Retracted: Garment Digital Design Method Oriented to the Production Process of Graphene-Modified Nylon Knitted Fabric

Journal of Nanomaterials

This article has been retracted by Hindawi following an investigation undertaken by the publisher [1]. This investigation has uncovered evidence of one or more of the following indicators of systematic manipulation of the publication process:

(1) Discrepancies in scope

(2) Discrepancies in the description of the research reported

(3) Discrepancies between the availability of data and the research described

(4) Inappropriate citations

(5) Incoherent, meaningless and/or irrelevant content included in the article

(6) Peer-review manipulation

The presence of these indicators undermines our confidence in the integrity of the article's content and we cannot, therefore, vouch for its reliability. Please note that this notice is intended solely to alert readers that the content of this article is unreliable. We have not investigated whether authors were aware of or involved in the systematic manipulation of the publication process.

Wiley and Hindawi regrets that the usual quality checks did not identify these issues before publication and have since put additional measures in place to safeguard research integrity.

We wish to credit our own Research Integrity and Research Publishing teams and anonymous and named external researchers and research integrity experts for contributing to this investigation.

The corresponding author, as the representative of all authors, has been given the opportunity to register their agreement or disagreement to this retraction. We have kept a record of any response received.

References

[1] Z. Zhou, "Garment Digital Design Method Oriented to the Production Process of Graphene-Modified Nylon Knitted Fabric," *Journal of Nanomaterials*, vol. 2022, Article ID 6114483, 13 pages, 2022.

Retraction

Retracted: Health Screening and Promotion System Based on Disease Prevention

Journal of Nanomaterials

This article has been retracted by Hindawi following an investigation undertaken by the publisher [1]. This investigation has uncovered evidence of one or more of the following indicators of systematic manipulation of the publication process:

(1) Discrepancies in scope

(2) Discrepancies in the description of the research reported

(3) Discrepancies between the availability of data and the research described

(4) Inappropriate citations

(5) Incoherent, meaningless and/or irrelevant content included in the article

(6) Peer-review manipulation

The presence of these indicators undermines our confidence in the integrity of the article's content and we cannot, therefore, vouch for its reliability. Please note that this notice is intended solely to alert readers that the content of this article is unreliable. We have not investigated whether authors were aware of or involved in the systematic manipulation of the publication process.

In addition, our investigation has also shown that one or more of the following human-subject reporting requirements has not been met in this article: ethical approval by an Institutional Review Board (IRB) committee or equivalent, patient/participant consent to participate, and/or agreement to publish patient/participant details (where relevant).

Wiley and Hindawi regrets that the usual quality checks did not identify these issues before publication and have since put additional measures in place to safeguard research integrity.

We wish to credit our own Research Integrity and Research Publishing teams and anonymous and named external researchers and research integrity experts for contributing to this investigation.

The corresponding author, as the representative of all authors, has been given the opportunity to register their agreement or disagreement to this retraction. We have kept a record of any response received.

References

[1] F. Zheng, J. Zheng, M. Han, Y. Wei, and L. Shi, "Health Screening and Promotion System Based on Disease Prevention," *Journal of Nanomaterials*, vol. 2022, Article ID 4540935, 13 pages, 2022.

Retraction

Retracted: Realization of a Noncontact IC Chip with Embedded Ferroelectric Memory in an Auxiliary Timing Device for Sports Games

Journal of Nanomaterials

This article has been retracted by Hindawi following an investigation undertaken by the publisher [1]. This investigation has uncovered evidence of one or more of the following indicators of systematic manipulation of the publication process:

(1) Discrepancies in scope
(2) Discrepancies in the description of the research reported
(3) Discrepancies between the availability of data and the research described
(4) Inappropriate citations
(5) Incoherent, meaningless and/or irrelevant content included in the article
(6) Peer-review manipulation

The presence of these indicators undermines our confidence in the integrity of the article's content and we cannot, therefore, vouch for its reliability. Please note that this notice is intended solely to alert readers that the content of this article is unreliable. We have not investigated whether authors were aware of or involved in the systematic manipulation of the publication process.

Wiley and Hindawi regrets that the usual quality checks did not identify these issues before publication and have since put additional measures in place to safeguard research integrity.

We wish to credit our own Research Integrity and Research Publishing teams and anonymous and named external researchers and research integrity experts for contributing to this investigation.

The corresponding author, as the representative of all authors, has been given the opportunity to register their agreement or disagreement to this retraction. We have kept a record of any response received.

References

[1] J. Chen, "Realization of a Noncontact IC Chip with Embedded Ferroelectric Memory in an Auxiliary Timing Device for Sports Games," *Journal of Nanomaterials*, vol. 2022, Article ID 9933084, 12 pages, 2022.

Hindawi

Retraction

Retracted: Facile and straightforward synthesis of Hydrazone derivatives

Journal of Nanomaterials

This article has been retracted by Hindawi following an investigation undertaken by the publisher [1]. This investigation has uncovered evidence of one or more of the following indicators of systematic manipulation of the publication process:

(1) Discrepancies in scope

(2) Discrepancies in the description of the research reported

(3) Discrepancies between the availability of data and the research described

(4) Inappropriate citations

(5) Incoherent, meaningless and/or irrelevant content included in the article

(6) Peer-review manipulation

The presence of these indicators undermines our confidence in the integrity of the article's content and we cannot, therefore, vouch for its reliability. Please note that this notice is intended solely to alert readers that the content of this article is unreliable. We have not investigated whether authors were aware of or involved in the systematic manipulation of the publication process.

Wiley and Hindawi regrets that the usual quality checks did not identify these issues before publication and have since put additional measures in place to safeguard research integrity.

We wish to credit our own Research Integrity and Research Publishing teams and anonymous and named external researchers and research integrity experts for contributing to this investigation.

The corresponding author, as the representative of all authors, has been given the opportunity to register their agreement or disagreement to this retraction. We have kept a record of any response received.

References

[1] N. U. Ain, T. M. Ansari, M. R. H. Shah Gilani et al., "Facile and straightforward synthesis of Hydrazone derivatives," *Journal of Nanomaterials*, vol. 2022, Article ID 3945810, 6 pages, 2022.

Retraction

Retracted: Application and Optimization of Wing Structure Design of DF-2 Light Sports Aircraft Based on Composite Material Characteristics

Journal of Nanomaterials

This article has been retracted by Hindawi following an investigation undertaken by the publisher [1]. This investigation has uncovered evidence of one or more of the following indicators of systematic manipulation of the publication process:

(1) Discrepancies in scope
(2) Discrepancies in the description of the research reported
(3) Discrepancies between the availability of data and the research described
(4) Inappropriate citations
(5) Incoherent, meaningless and/or irrelevant content included in the article
(6) Peer-review manipulation

The presence of these indicators undermines our confidence in the integrity of the article's content and we cannot, therefore, vouch for its reliability. Please note that this notice is intended solely to alert readers that the content of this article is unreliable. We have not investigated whether authors were aware of or involved in the systematic manipulation of the publication process.

Wiley and Hindawi regrets that the usual quality checks did not identify these issues before publication and have since put additional measures in place to safeguard research integrity.

We wish to credit our own Research Integrity and Research Publishing teams and anonymous and named external researchers and research integrity experts for contributing to this investigation.

The corresponding author, as the representative of all authors, has been given the opportunity to register their agreement or disagreement to this retraction. We have kept a record of any response received.

References

[1] F. Li, S. Zhang, and W. Cheng, "Application and Optimization of Wing Structure Design of DF-2 Light Sports Aircraft Based on Composite Material Characteristics," *Journal of Nanomaterials*, vol. 2022, Article ID 6967016, 10 pages, 2022.

Corrigendum

Corrigendum to "Local Dimming Algorithm of Automotive LCD Instrument Based on Otsu and Maximum Entropy"

Tianfu Liu and **Chunqiu Tang**

School of Mechanical and Electrical Engineering, Wuhan University of Technology, Wuhan 430070, Hubei, China

Correspondence should be addressed to Tianfu Liu; ltf999@whut.edu.cn

In the article titled "Local Dimming Algorithm of Automotive LCD Instrument Based on Otsu and Maximum Entropy" [1], Figures 2–9 have been replaced within the article due to legal reasons. As a result of this the change to the sample figures, Table 3 has also been revised and updated within the article. This does not affect the conclusions of the article.
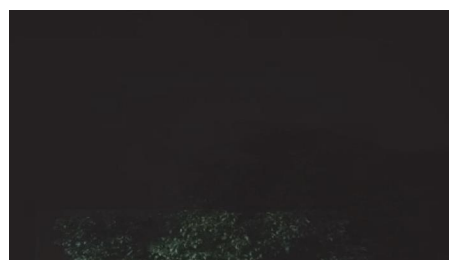
FIGURE 2: Block effect simulation diagram.
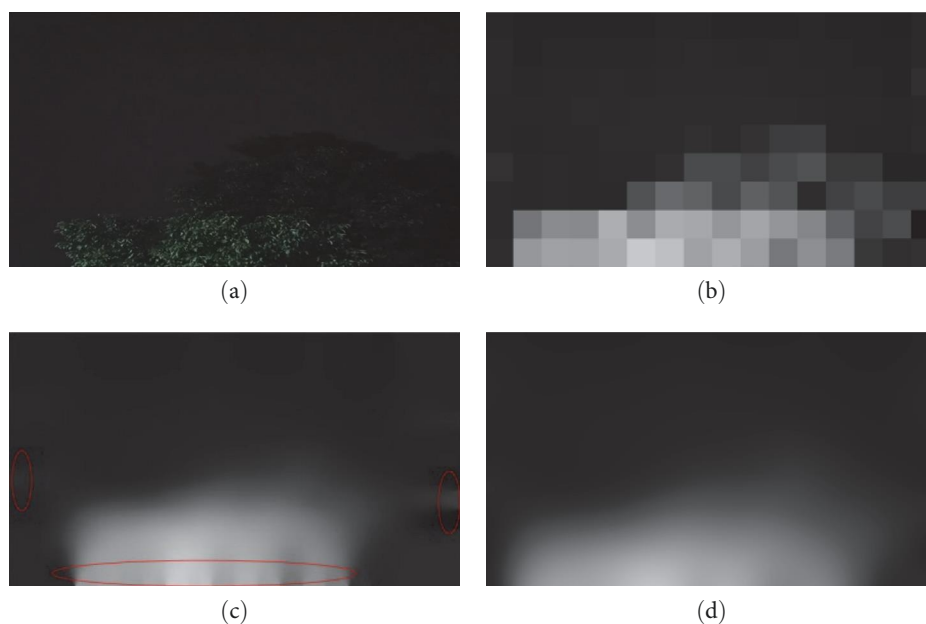
FIGURE 3: Effect comparison of backlight smoothing algorithm: (a) original image; (b) backlight image; (c) traditional BMA; (d) improved BMA.
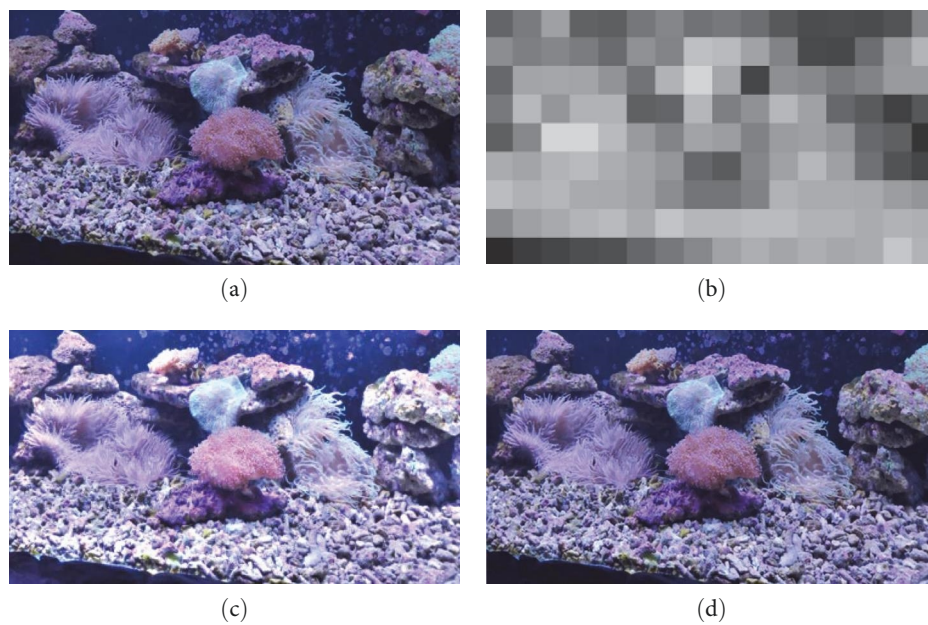
FIGURE 4: Effect comparison of pixel compensation algorithm: (a) original image; (b) backlight image; (c) traditional pixel compensation; (d) improved pixel compensation.
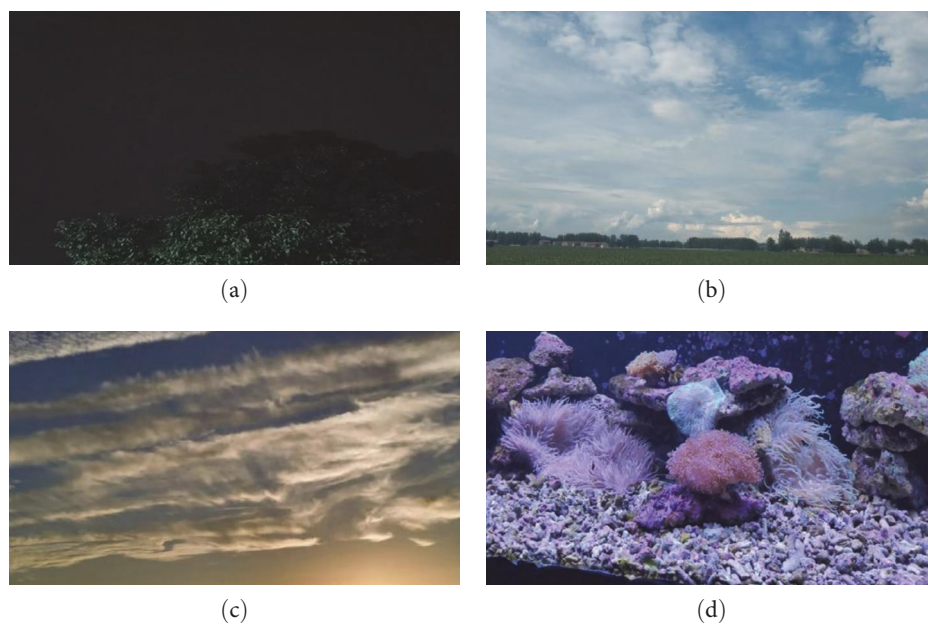
FIGURE 5: Sample image: (a) low brightness; (b) high brightness; (c) low contrast; (d) high contrast.
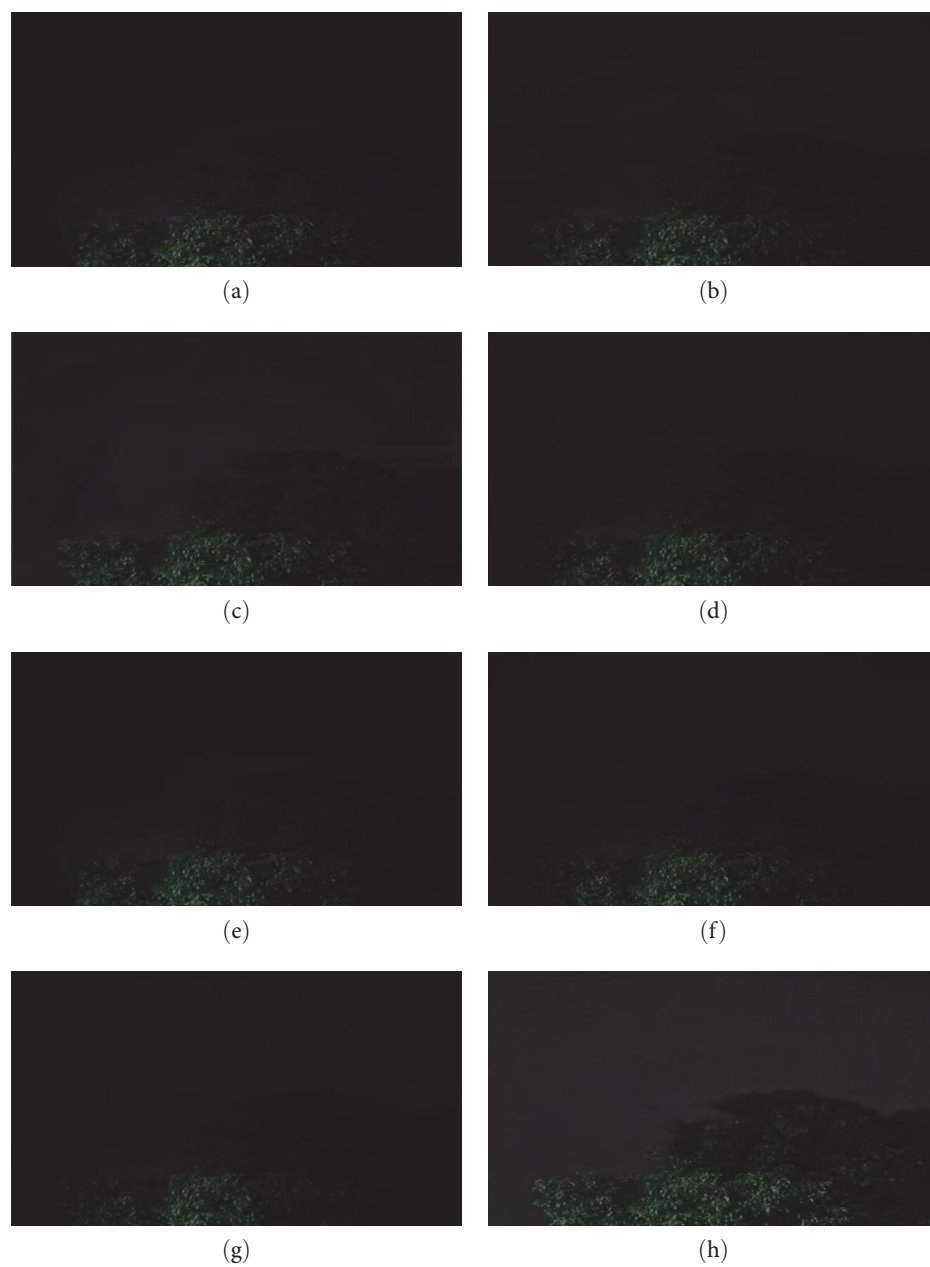
FIGURE 6: Low brightness image simulation diagram: (a) max; (b) average; (c) sqrt; (d) SD; (e) ECM; (f) CDF; (g) IMF; (h) new.

Figure 7: High brightness image simulation diagram: (a) max; (b) average; (c) sqrt; (d) SD; (e) ECM; (f) CDF; (g) IMF; (h) new.
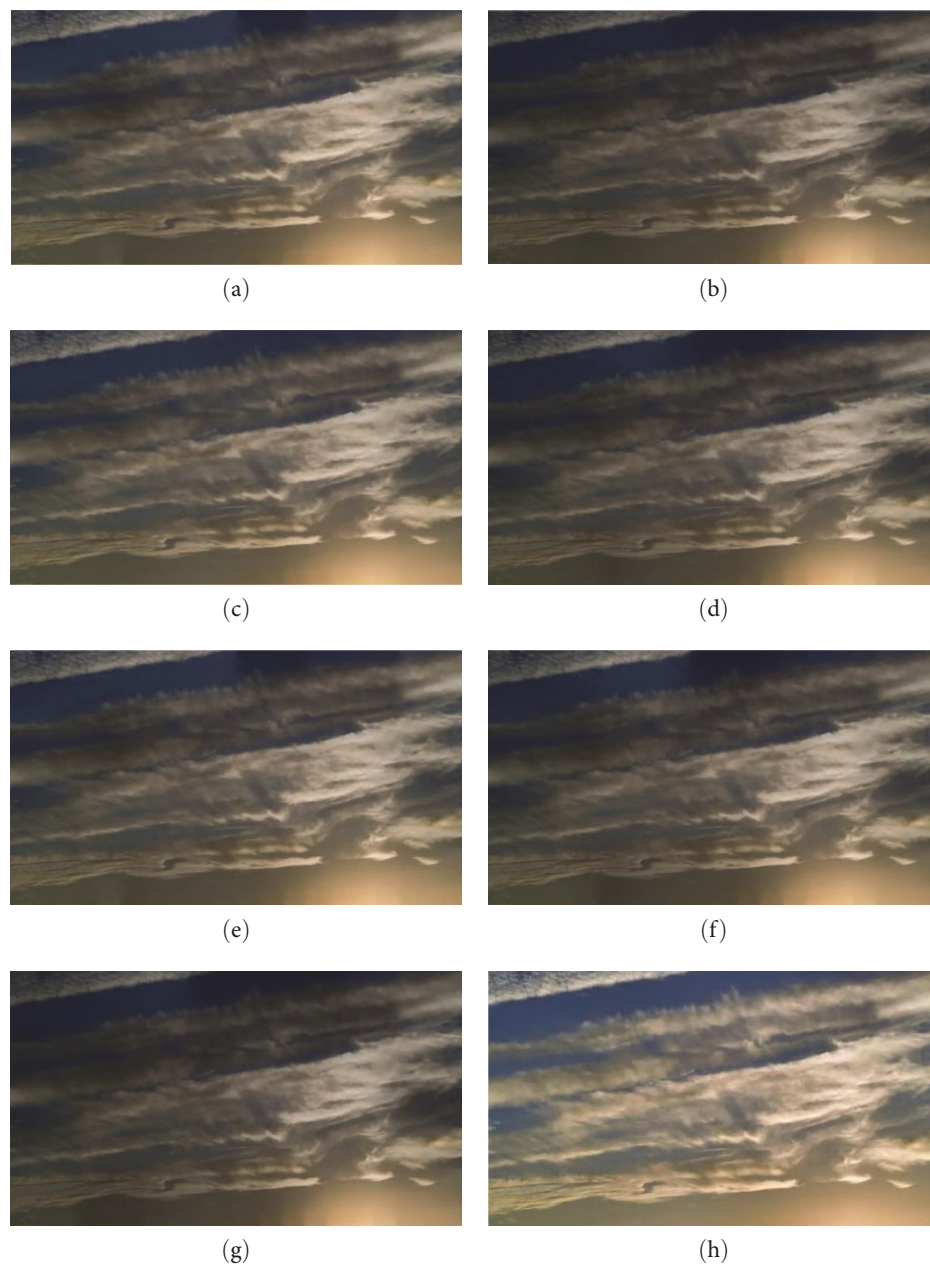
FIGURE 8: Low contrast image simulation diagram: (a) max; (b) average; (c) sqrt; (d) SD; (e) ECM; (f) CDF; (g) IMF; (h) new.
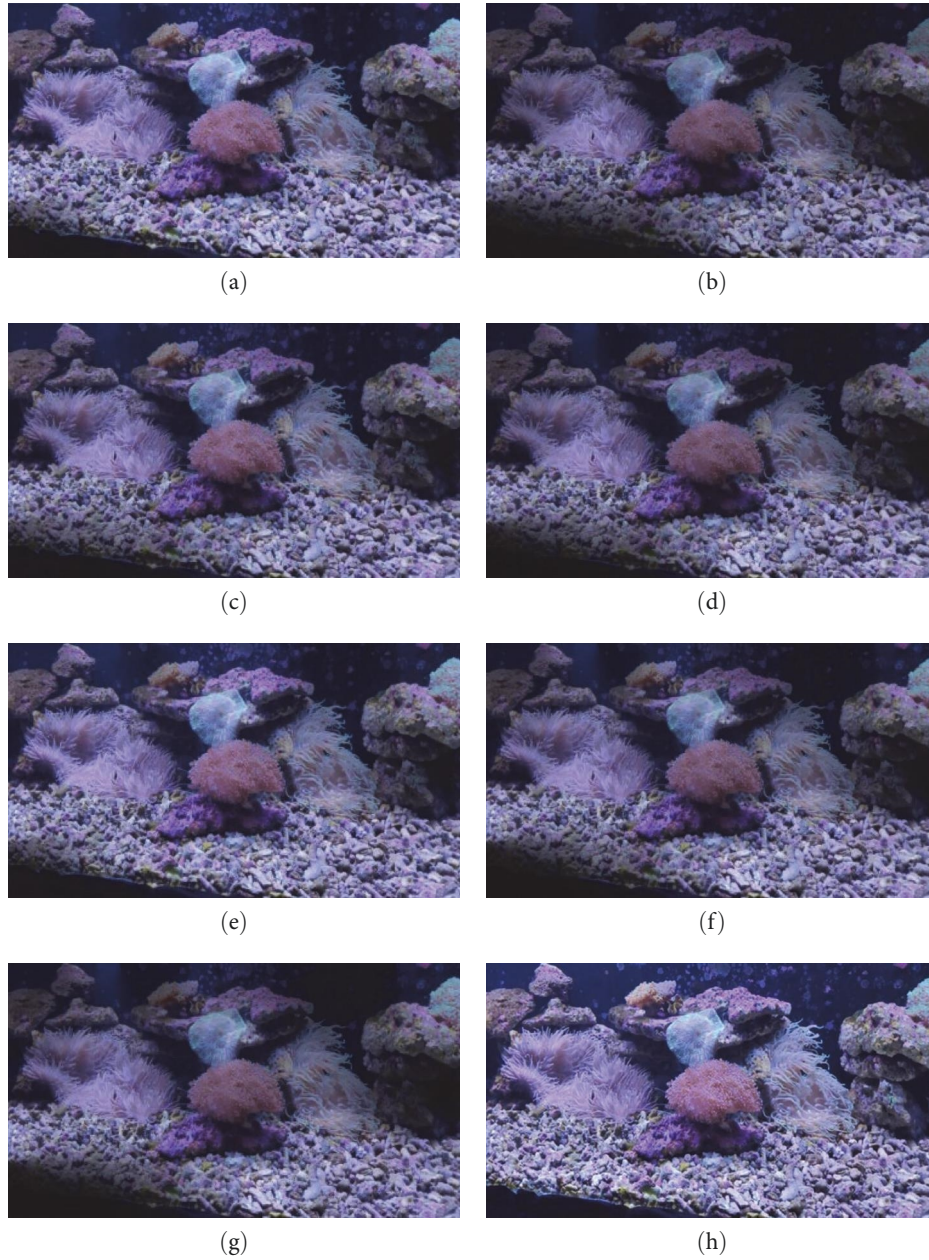
FIGURE 9: High contrast image simulation diagram: (a) max; (b) average; (c) sqrt; (d) SD; (e) ECM; (f) CDF; (g) IMF; (h) new.

TABLE 3: Objective evaluation results.

Algorithm	Low brightness				High brightness				Low contrast				High contrast			
	SER	OFR	CR	SUM	SER	OFR	CR	SUM	SER	OFR	CR	SUM	SER	OFR	CR	SUM
Max	65	80	60	70.71	70	80	68	68.73	70	80	80	77.20	75	80	80	78.33
Average	85	50	70	63.38	80	80	85	83.16	80	62	80	69.17	80	80	85	81.92
Sqrt	65	65	50	60.34	70	80	72	71.26	70	74	70	72.40	75	85	80	79.74
SD	80	60	60	64.09	70	80	80	76.33	70	70	80	71.19	75	85	85	81.66
ECM	70	70	60	66.89	70	80	75	73.16	70	74	80	73.60	75	85	80	79.74
CDF	80	70	60	68.94	70	80	80	76.33	70	71	80	71.80	75	85	80	79.74
IMF	85	55	80	68.91	70	80	85	79.50	80	62	80	69.17	75	85	85	81.66
New	85	85	70	80.34	80	80	85	83.16	80	82	80	81.20	80	85	85	83.33

References

[1] T. Liu and C. Tang, "Local Dimming Algorithm of Automotive LCD Instrument Based on Otsu and Maximum Entropy," *Journal of Nanomaterials*, vol. 2022, Article ID 5244088, 9 pages, 2022.

Retraction

Retracted: Relationship between Urban Landscape Design and Ecological Environment Protection in the Application of Environmental Protection and Renewable New Energy Materials

Journal of Nanomaterials

This article has been retracted by Hindawi following an investigation undertaken by the publisher [1]. This investigation has uncovered evidence of one or more of the following indicators of systematic manipulation of the publication process:

(1) Discrepancies in scope
(2) Discrepancies in the description of the research reported
(3) Discrepancies between the availability of data and the research described
(4) Inappropriate citations
(5) Incoherent, meaningless and/or irrelevant content included in the article
(6) Peer-review manipulation

The presence of these indicators undermines our confidence in the integrity of the article's content and we cannot, therefore, vouch for its reliability. Please note that this notice is intended solely to alert readers that the content of this article is unreliable. We have not investigated whether authors were aware of or involved in the systematic manipulation of the publication process.

In addition, our investigation has also shown that one or more of the following human-subject reporting requirements has not been met in this article: ethical approval by an Institutional Review Board (IRB) committee or equivalent, patient/participant consent to participate, and/or agreement to publish patient/participant details (where relevant).

Wiley and Hindawi regrets that the usual quality checks did not identify these issues before publication and have since put additional measures in place to safeguard research integrity.

We wish to credit our own Research Integrity and Research Publishing teams and anonymous and named external researchers and research integrity experts for contributing to this investigation.

The corresponding author, as the representative of all authors, has been given the opportunity to register their agreement or disagreement to this retraction. We have kept a record of any response received.

References

[1] S. Wu, X. Yu, Y. Cao, and G. Wang, "Relationship between Urban Landscape Design and Ecological Environment Protection in the Application of Environmental Protection and Renewable New Energy Materials," *Journal of Nanomaterials*, vol. 2022, Article ID 6360300, 13 pages, 2022.

Hindawi

Research Article

Relationship between Urban Landscape Design and Ecological Environment Protection in the Application of Environmental Protection and Renewable New Energy Materials

Shengnan Wu [1], **Xiwen Yu,**[1] **Yejun Cao,**[1] **and Guangrong Wang**[2]

[1]*School of Arts and Media, Hefei Normal University, Hefei, 2230061 Anhui, China*
[2]*HeFei Golden Sun Energy Technology Co., Ltd., Hefei, 2230041 Anhui, China*

Correspondence should be addressed to Shengnan Wu; wsn230@hfnu.edu.cn

With the economic growth in recent years, urban construction has also developed rapidly. In developing countries, the pursuit of rapid development has also brought about huge energy consumption, energy shortage, and environmental pollution. It is urgent to find and develop renewable energy. In order to understand the role of renewable energy materials in urban landscape design and ecological environment protection, replace nonrenewable materials with renewable energy materials, and reduce urban pollution, we analyze the available energy for buildings in urban areas and optimize the allocation of various available resources. Energy, improve energy efficiency, so as to save energy, protect the environment, and coordinate the development of energy, economy, and environment. Renewable energy is also known as alternative energy, sustainable energy, or nontraditional energy. It is energy that can be obtained from nature and can be replenished naturally. Experimental results prove that the energy required for traditional material consumption is much higher than the consumption of renewable energy, and its range is more than 50%. Renewable energy can replace the role of nonrenewable energy. This article hopes to stimulate more relevant architects to think about this subject through the research and analysis of renewable energy.

1. Introduction

The rational use of renewable resources such as solar energy, geothermal energy, and bioenergy in urban buildings will contribute to the sustainable development of urban energy, economy, and environment. Through the analysis of the available energy in urban buildings, rationally optimizing the distribution of various available energies and improving energy efficiency, the goals of energy conservation, environmental protection, and coordinated development of energy, economy, and environment can be achieved. With the development of the new era, the concept of sustainability has gradually penetrated into the hearts of the people, and the design of gardens must also develop with the trend of the times. Starting with the functionality of the garden, to a certain extent, make the garden a purification system for the urban environment and play a role in buffering air pollution. Therefore, on this basis, the design of urban gardens must be highly coordinated with

the planning of related cities, and the different functions of gardens should be brought into play according to the content of urban planning. Therefore, it is necessary to study the design of urban building energy system and coordinate the available energy distribution of various buildings from the urban planning level. In this way, the sustainable use of energy can be ensured, the utilization of energy can be maximized, and the urban ecologicalization can be realized.

Renewable energy collection embedded system is a technology that uses renewable energy to have the characteristics of wide distribution, sustainable collection, and low cost, and to efficiently collect and store renewable energy while replacing a single battery as the energy supply unit of the embedded system. However, in terms of energy harvesting and storage, the technology is still affected by environmental changes and the limitations of traditional energy storage technologies, resulting in irregular and unpredictable input energy in the energy harvesting process, energy conversion, and high energy consumption

of the energy storage system. The development and utilization of new energy and renewable energy are the basic requirement for implementing the scientific development concept and building a resource-saving and environment-friendly society. It is an urgent need to adjust the energy structure, save energy and reduce emissions, and reasonably control the total energy consumption. At the same time, it is also an important way to protect the ecological environment, deal with climate change, develop the rural economy, and cultivate strategic emerging industries. This paper aims to explore the relationship between urban landscape design and ecological environmental protection in the application of environmental protection and renewable new energy materials, in order to make a certain contribution in this regard, so as to inspire more relevant architects to think about this topic.

For sustainable development, experts at home and abroad have conducted many studies. Samadi P is concerned about the load dispatching and power trading issues in systems with high penetration of renewable energy (RER). The game theory method is used to simulate the interaction and excess generation between users. The simulation results show that the proposed algorithm reduces the user's energy expenditure. The proposed algorithm also promotes the use of RER by encouraging users to consume excess power locally instead of reinjecting it into the grid [1]. Yang P formulated the cost minimization problem of storage and power generation planning, while considering the initial investment cost and operation/maintenance cost, and proposed a distributed optimization framework to overcome the difficulties caused by the large-scale optimization problem. The results will help to make decisions about energy storage and power generation capacity planning in future decentralized grids with high renewable penetration rates [2]. Rezaei R's model focuses on the unified theory of technology acceptance and use (UTAUT), which is extended to study the factors that influence the intention to use renewable energy. Using the structural equation model's multiple techniques and adding attitude variables as mediating variables in the model, it was found that the predictive ability of the model increased by 19%, providing evidence for five mediation paths in the cognitive process of renewable energy use intentions [3]. Wu Y considered cost-effective energy dispatch for residential smart grids equipped with centralized renewable energy. Quantify the best use of renewable energy to achieve a trade-off between the system-wide benefits of using renewable energy and the related costs due to its fluctuation; evaluate how the fluctuation of renewable energy affects its optimal development. A distributed algorithm with high computational efficiency is proposed to determine the best use of renewable energy and related energy scheduling decisions [4]. Rahim S conducted a comparative evaluation of the performance of home energy management controllers designed based on heuristic algorithms, introduced general demand-side management (DSM) architecture, and used a combination model of time-of-use electricity prices and inclined block rates for energy pricing. The simulation results show that all the designed energy management models have significantly achieved our goals and proved to be a cost-effective solution to improve the sustainability of the smart grid [5]. The purpose of the Athari M H study is to use an optimized fuzzy logic controller (FLC) to examine the impact of time-varying power prices on the performance of the energy storage components of the grid-connected hybrid renewable energy system (HRES). Considering that the grid electricity price has a considerable impact on the performance of the energy storage components running on the grid-connected HRES, because the weekly and daily optimized FLC results in less working hours of fuel cells and electrolyzers, and less SOC fluctuations [6]. The Dogan E empirical study analyzed the impact of actual income, renewable energy consumption, nonrenewable energy consumption, trade opening, and financial development on CO2 emissions in the first few countries listed in the EKC model. It is found that by using CADF and CIPS unit root tests, the analyzed variables become stable at the first-order difference, and the analyzed variables are cointegrated by using the LM bootstrap cointegration test. The increase in renewable energy consumption, trade opening, and financial development reduced carbon emissions, while the increase in nonrenewable energy consumption contributed to the level of emissions [7]. These studies provide a lot of reference for this article, but due to insufficient relevant research data and old research methods, the conclusions of the research cannot convince most people.

The innovations of this paper are as follows: (1) The concept, technical principles, and characteristics of regional building energy planning are analyzed. On this basis, the method of urban regional building energy planning is studied, and the basis of urban regional building energy planning is proposed. (2) Through analysis and evaluation, the available amount of conventional energy and renewable resources in urban areas can be obtained, which can provide strong data support for the comprehensive planning of urban building energy, thereby promoting energy, economic, and sustainable development. (3) Use the urban building energy planning method proposed in this paper to carry out energy planning for new urban buildings, combining theoretical research with practical engineering cases.

2. Research and Use Methods of Renewable New Energy Materials

2.1. Renewable New Energy. Renewable energy is also called alternative energy, sustainable energy, or nontraditional energy. It is energy that can be obtained from nature and can be supplemented naturally, such as wind energy, solar energy, hydro energy, geothermal energy, biological energy, and ocean energy. [8]. The main reasons why humans use renewable energy are as follows. The advancement of science and technology has made such energy more "easy to use." Fossil energy is limited, not only will its price increase day by day, but it will eventually run out. Certain renewable energy sources (e.g., wind, hydro, and solar) do not emit greenhouse gases (e.g., carbon dioxide) and therefore do not increase the risk of the greenhouse effect. To improve energy supply security, reduce reliance on imported fossil fuels, and meet the demand for sustainable energy. As a clean energy source, renewable energy is environmentally friendly and sustainable. However, along with its advantages, the use of renewable energy is still limited due to some disadvantages.

(a) Renewable resources   (b) Non-renewable resources
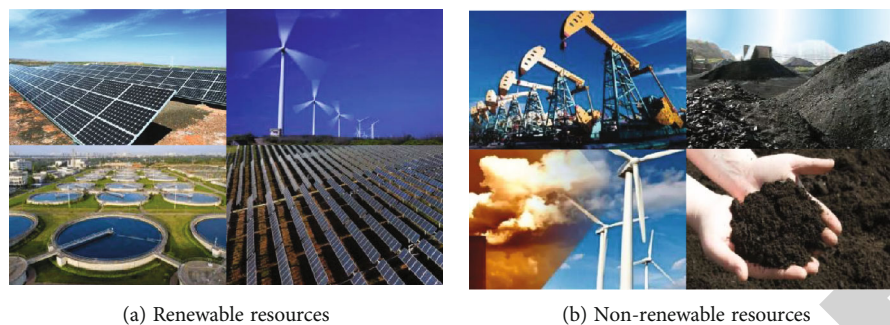
Figure 1: Renewable and nonrenewable resources.

First of all, one of the main disadvantages is climate dependence, because these energies continue to exist in different geographical spaces, so the available energy changes in the order of magnitude all the time [9]. The solution at this stage is to apply multiple forms of renewable energy hybrid collection technology to enable the energy collection system to continuously collect energy from the natural world. The second disadvantage is that the energy collection efficiency is low, and the energy collection cost is high. In addition to geothermal energy collection, compared with traditional energy collection technology, the cost of renewable energy collection is much higher than that of traditional energy collection systems. Therefore, reducing the cost of renewable energy collection and improving energy utilization efficiency are key issues. The third is technology development and commercialization. Nowadays, some high-efficiency, stable, and sustainable collection technologies for renewable energy are still under development [10]. Practice has proved that renewable energy can not only provide clean alternative energy, but more importantly, it can also stimulate the development of related industries such as equipment manufacturing. It is an effective way to speed up the transformation of economic development mode and the adjustment of economic structure in the post-international financial crisis period.

Renewable energy harvesting application technology mainly includes five parts: energy harvesting, electric energy conversion, electric energy transmission, electric energy storage, and electric energy use. Due to the frequent and unpredictable changes of renewable energy, the collected energy cannot be directly supplied to the load. Therefore, the collected energy needs to be rectified or stored to supply power to the load [11]. The main function of the regenerative energy storage system (ESS) and energy management system (EMS) is that in addition to efficient storage of the collected energy, it can also play a role in "shaving peaks and filling valleys" to reduce energy fluctuations and slow down the load caused by fluctuations. The energy management system includes data acquisition and monitoring system, automatic power generation control and economic dispatch control, power system state estimation, safety analysis, and dispatcher simulation training system. Renewable resources and nonrenewable resources are generally shown in Figure 1:

In the analysis of the energy storage process, the part of the object or space that is delineated in order to determine the research object is called the energy storage system. It includes energy and matter input and output, energy conversion, and storage equipment. Energy storage system (ESS) can be divided

into physical energy storage, chemical energy storage, and electromagnetic energy storage in terms of characteristics and methods. Among them, flywheel technology, pumped water energy storage, and compressed air energy storage technology belong to physical energy storage; superconducting and supercapacitors are electromagnetic energy storage technologies; lead-acid, lithium ion, sodium sulfur, and liquid batteries are electrochemical energy storage technologies [12, 13]. Small-scale low-power storage technologies are mainly lithium-ion batteries, lead-acid batteries, and super capacitors. Traditional ESS is mainly based on lead-acid batteries and lithium-ion batteries. Energy storage systems often involve multiple energies, multiple devices, multiple substances, and multiple processes. They are complex energy systems that change over time and require multiple indicators to describe their performance. Commonly used evaluation indicators include energy storage density, energy storage power, energy storage efficiency, energy storage price, and impact on the environment. With the development of ESS technology, people are paying more and more attention to supercapacitor technology. Table 1 shows the comparison of the characteristics of three energy storage devices.

The role of the EMS is to protect, detect, and control the ESS to ensure the safe and efficient operation of the ESS and to extend the service life of the ESS. The main functions of EMS include protection functions, state and parameter estimation, and energy balance and redistribution functions between single cells [14].

With the development of China and the further improvement of people's living standards, people have higher and higher requirements for the comfort of the indoor thermal environment of residential buildings, which will lead to a further increase in the energy consumption of residential buildings [15]. Currently, urban energy, economic, and environmental issues have become issues of concern to the world. How to use energy reasonably, improve the overall energy efficiency of urban buildings, optimize the energy distribution of urban buildings, and protect the urban environment on which mankind depends for survival is a long-term interest issue in the world today.

2.2. Renewable Energy Collection. We conduct research on traditional wind energy collection, solar energy collection, and storage technologies. The structure, parameters, and their mathematical models and equivalent circuits of energy conversion devices will be analyzed separately [16]. At the same time, the I-V curve and P-V curve of solar energy collection

TABLE 1: Comparison of characteristics of three energy storage devices.

	Lead-acid batteries	Lithium ion battery	Super capacitor
Energy density (Wh/kg)	25-55	85-300	5-55
Power density (W/kg)	25-55	160-500	$699 - 10^5$
Cycle life (times)	<499	499-3000	$>10^6$
Cell voltage (V)	1-2	2-3	3-5
Equivalent internal resistance (Ω)	<1	<1	<0.01
Self-discharge	High	Low	Generally
Safety	Generally	Lower	High
Environmentally destructive	Higher	Generally	Lower
Market	Saturation	Develop	Great potential

and the Cp-λ, Cp-ω characteristic curves of wind energy collection are listed for the model.

Wind energy is a kind of available energy provided to human beings due to the work done by air flow and belongs to renewable energy. The kinetic energy of air flow is called wind energy. Wind energy harvesting includes energy conversion devices (WT) and control systems. In wind energy collection technology, accurate modeling of wind energy conversion devices is particularly important. Because in order to efficiently collect and transform wind energy, MPPT is required. The MPPT technology is inseparable from an accurate wind energy conversion device model. The WT mechanical energy collection model is as follows:

$$P_m = \frac{1}{2} p\pi r^3 v^3 C_p, \tag{1}$$

where P_m is the mechanical power (W), r is the radius of the WT blade, v is the wind speed, and C_p is the power coefficient. Expressed by the tip speed ratio function C_p, the relationship between the power factor and the tip speed ratio is shown in the following formula:

$$C_p(\lambda, \beta) = c_1[c_2\partial - c_3\beta]e^{-c6\partial} + c7\lambda, \tag{2}$$

$$\partial = \left(\frac{1}{\lambda + 0.05\beta}\right) - \left(\frac{0.025}{1 + \beta^3}\right), \tag{3}$$

where λ is the tip speed ratio and β is the blade pitch angle because the constant parameters are different for different WTs. For the convenience of research, suppose the blade pitch angle β of WT is 0. Therefore, the maximum mechanical power at a given wind speed P max is:

$$P\text{ max} = \frac{1}{2} p\pi r^3 v^3 C_p(\lambda_{opt}), \tag{4}$$

$$\lambda_{opt} = \frac{rw}{v} \longrightarrow w_{opt} = \frac{\lambda_{opt} v}{r}. \tag{5}$$

The above formula can be rewritten as:

$$P_{max} = \frac{1}{2} p\pi r^5 \frac{C_{pma}x}{\lambda_{opt}^3} * \frac{\lambda_{opt}^3 v^3}{r^3}, \tag{6}$$

$$K_{opt} = \frac{0.5p\pi r^5 C_{p\text{ max}}}{\lambda_{opt}^3}. \tag{7}$$

From the above reasoning, the relationship between the power coefficient and the tip speed, as well as the relationship between the power and the angular speed of the rotor, can be obtained.

Figure 2 is a schematic block diagram of the wind energy collection system. The control system can sample the motor speed ω and output voltage, current, and power. Then, the system will calculate the maximum power point. If the output power of the WT needs to be adjusted, the control system can adjust the WT gearbox or control the DC-DC circuit to achieve MPPT.

Solar energy is produced by the fusion of hydrogen and helium atoms inside the sun to release huge nuclear energy, which is the radiation energy from the sun. The vast majority of human energy needs come directly or indirectly from the sun. Solar energy collection technology is similar to wind energy collection technology and also requires mathematical modeling of energy harvesting devices, and at the same time depicting output characteristic curves and MPPT strategy design based on mathematical models [17]. Different from wind energy harvesting, the solar energy output energy waveform changes more slowly. Therefore, the output voltage of the device can be regarded as direct current and does not require AC-DC rectification.

After the PV device is made, it needs to be packaged. The package structure mainly includes the front plate, solar cell, sealing layer, back plate, protective frame, and junction box [18]. The front panel can increase the mechanical strength and rigidity of the PV. It should be noted that the front panel must have good penetration and low reflectivity for light with wavelengths from 350 nm to 1200 nm; the back panel provides physical protection for the PV and can pass through the back panel. Surface reflection improves the efficiency of PV. We use the single diode model to describe the characteristics of the
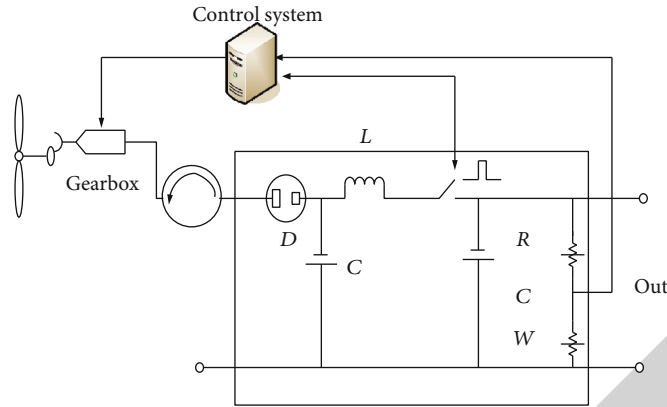
Figure 2: Wind energy collection system.
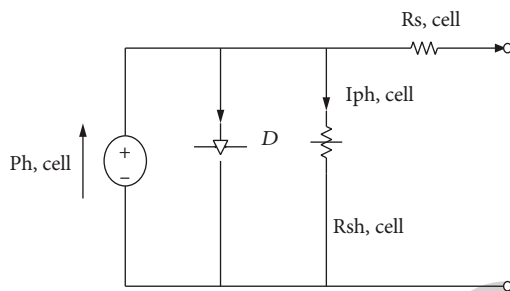
Figure 3: PV equivalent circuit diagram.

photovoltaic cell, and the PV equivalent circuit is shown in Figure 3:

According to Kirchhoff's first law definition [19], the battery output current satisfies the formula:

$$I = I_{\text{ph,cell}} - I_{d,\text{cell}} - I_{R_{\text{sh,cell}}}. \tag{8}$$

In order to determine the volt-ampere relationship of the PV cell, it is necessary to determine the parameters such as the sum of the cell. The function relationship between the induced current of the PV cell equivalent circuit and the irradiance and temperature is shown in the formula.

In order to determine the volt-ampere relationship of the PV cell, it is necessary to determine the parameters such as the sum of the cell. The function relationship between the induced current of the PV cell equivalent circuit $I_{\text{ph,cell}}$ and the irradiance and temperature is shown in the formula:

$$I_{\text{ph,cell}} = \frac{G}{G_{\text{ref}}}(I_{\text{sc,ref}} + K_i \Delta T), \tag{9}$$

where V is the output voltage of the PV cell and T_{ref} is the output current of the PV cell. The current absorbed by the internal resistance of the PV cell equivalent circuit G_{ref} is as follows:

$$I_{d,\text{cell}} = I_{s,\text{cell}} \exp\left[\left(\frac{V + I_{R_{s,\text{cell}}}}{n V_{\text{th,cell}}}\right) - 1\right], \tag{10}$$

where V is the output voltage of the PV cell and I is the output current of the PV cell. The current absorbed by the internal resistance of the PV cell equivalent circuit is as follows:

$$I_{R_{\text{sh,cell}}} = \frac{\left(V + I_{R_{s,\text{cell}}}\right)}{R_{\text{sh,cell}}}, \tag{11}$$

where $I_{\text{sh,cell}}$ is the shunt resistor of the PV cell. Saturation current of PV battery diode:

$$I_{s,\text{cell}} = I_{\text{sref,cell}}\left[\frac{T}{T_{\text{ref}}}\right]^3 \exp\left(\frac{q R_q}{n K}\right). \tag{12}$$

For any given $x \in X$, there is a uniquely determined $\mu A(\text{x}) \in [0, 1]$ membership function value corresponding to it, and the fuzzy set can be expressed as:

$$\mu \tilde{A}(x): X \longrightarrow [0, 1]. \tag{13}$$

Generally, the expression of fuzzy sets is as follows:

$$\tilde{A} = \frac{\mu_{\tilde{A}}(x_1)}{x_1} + \frac{\mu_{\tilde{A}}(x_2)}{x_2} + \cdots + \frac{\mu_{\tilde{A}}(x_n)}{x_n}. \tag{14}$$

This method of representation is also called Zadeh notation. It can also be expressed in ordinal notation:

$$\tilde{A} = \{(x_1, \mu_{\tilde{A}}(x_1)), (x_2, \mu_{\tilde{A}}(x_2)), \cdots, (x_n, \mu_{\tilde{A}}(x_n))\}, \tag{15}$$

Or, use vector notation:

$$\tilde{A} = \{\mu_{\tilde{A}}(x_1), \mu_{\tilde{A}}, \cdots, \mu_{\tilde{A}}(x_n)\}. \tag{16}$$

The definition of the distance function is as follows: For all $\vec{x}_1 \in \Gamma$

$$d\left(\vec{x}\right) = \min\left(\left|\vec{x} + \vec{x}_1\right|\right). \tag{17}$$

(a) Back pressure steam turbine unit process

(b) Pumping condensing unit
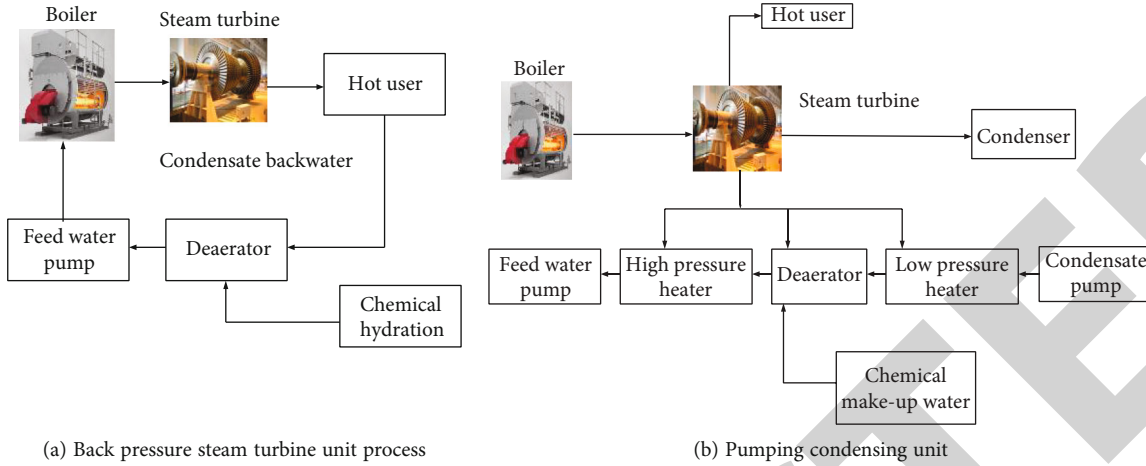
Figure 4: Typical process of two groups of units.

From the definition, when the unknown point is on the boundary, the function value is 0. Find the nearest point on the boundary and mark the nearest point, the value of the distance function is

$$d\left(\vec{x}\right) = \left|\vec{x} - \vec{x}c\right|. \tag{18}$$

From the definition of the distance function, the specific definition of the signed distance function is:

$$\phi\left(\vec{x}\right) = d\left(-\vec{x}\right) = 0, \quad \vec{x} \in \Gamma$$
$$\phi\left(\vec{x}\right) = -d\left(\vec{x}\right) \qquad \vec{x} \in \psi. \tag{19}$$

The signed distance function is a subset of the implicit function and has all the properties of the implicit function discussed in the previous section. Using the signed distance function can simplify many level set methods for dealing with implicit functions.

$$Z_i = T^T (x_{nm} - f \notin R^n). \tag{20}$$

When solar and wind energy are sufficient, that is, the collected energy is greater than the energy consumed by the equipment, in order to avoid energy loss and maximize the use of the collected energy, it is necessary to store the excess energy [20]. Due to the irregular, unpredictable, and serious environmental impacts of the output power of solar and wind energy collection systems, the ESS of the collection system is mostly multicell cascade. This increases the difficulty of monitoring the battery module [21].

2.3. Regional Planning of Urban Landscape Design. Urban landscape is a broad, comprehensive, and difficult to define profession in architecture. A city is a complex organism, and housing and architecture should be the main body of it, complemented by a space environment other than architecture. The two together are called urban landscape.

Table 2: Changes under different voltages and currents.

Experimental parameters	Parameter value
Charge switching frequency	1 khz
Circuit PWM modulation pulse frequency	400 khz
Buck mode input voltage range	5 V-25 V
Buck mode input current range	0-1.5 A
Buck mode output voltage	5 V
Boost mode input voltage	3 V-12 V
Boost mode input current range	0-5 A
Boost mode output voltage	15 V

Landscape planning refers to the activities of comprehensively determining and arranging the nature, scale, development direction, main content, infrastructure, comprehensive spatial layout, construction staging, and investment estimation of landscape construction projects. Urban garden planning is a complex and important project. Certain principles must be followed to achieve good results. The construction of gardens on the basis of following the corresponding principles can achieve a multiplier effect with half the effort. Urban landscape refers to the natural landscape beauty inherent and created by the landscape function in the human settlement environment. It can make the city have natural landscape art and make people feel comfortable and happy in urban life. Generally speaking, urban landscape design needs to follow the following principles:

(1) The principle of function. The main function of urban gardens is to maintain the physical and mental health of residents and protect the local natural ecology. Humans and nature are the two key points of garden construction and cannot be ignored

(2) The principle of economy and efficiency. There is no doubt that economy is the foundation of garden construction, and efficiency is the driving force of

TABLE 3: Different energy harvesting classifications.

Energy harvesting technology	Equivalent internal resistance	Output voltage (V)	Output power	Conversion efficiency
Electromagnetic induction technology	25-450	0-13	0.1-0.5 W	35%-50%
Gear transmission technology	50-200	0-8	0.1-1.3 W	20%-35%
Piezoelectric ceramic technology	50-280	0-30	10 mW-30 mW	80%-85%
RF receiving technology	5 k-45 k	0-0.5	0.002 mW-0.1 mW	5%-15%
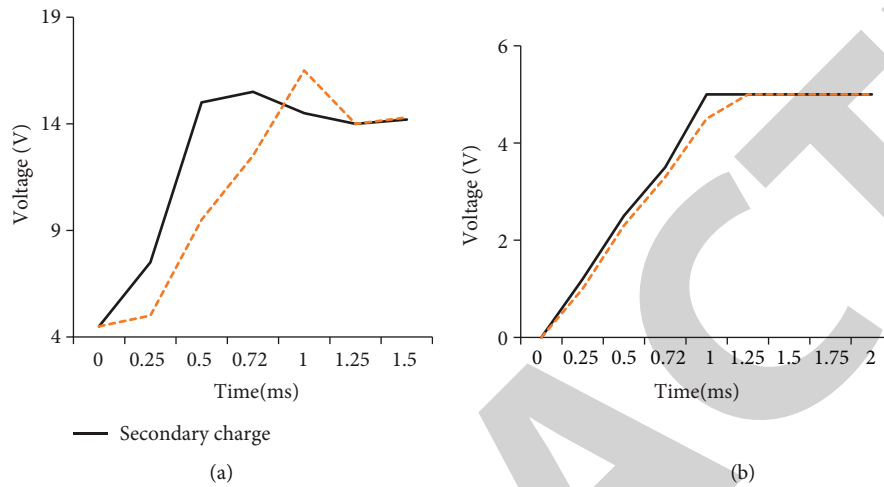
FIGURE 5: Changes in step-up and step-down.

garden construction. How to achieve economy and efficiency is a key issue that relevant departments and units should think about

(3) The principle of recycling and regeneration. As the concept of sustainable development gains roots in the hearts of the people, recycling and regeneration have become the focus of urban development. We must not only make good use of the recycling and regeneration functions of nature, but also must protect these functions. Nature's gifts to us are never infinite, and if we abuse them uncontrollably, the consequences will be disastrous

How to comprehensively utilize the energy resources available in the region is the key to the energy planning of urban buildings. It is particularly necessary to consider advanced and reasonable comprehensive utilization technologies of energy resources in the regional building energy planning and to rationally configure various resource supply systems. The back pressure steam turbine unit refers to the steam turbine unit that directly supplies the steam of the steam turbine to heat users for heating, and this unit corresponds to the condensing unit [22]. The exhaust steam condensing unit has holes in the appropriate position, and the steam turbine condensing unit that releases part of the steam for heating is called the exhaust steam condensing unit. The steam extraction method of this unit is divided into two types: adjustable exhaust and nonadjustable exhaust. Provide thermal users with adjustable output, and the system uses nonadjustable output. The typical flow of the unit is shown in Figure 4.

The heat, power, and cold cogeneration system is based on the basic idea of cascade utilization of energy, uses natural gas as fuel, and uses natural gas-burning equipment such as micro internal combustion engines, gas internal combustion engines, and small gas turbines. The waste heat generated after the high-temperature exhaust gas is used for heating in winter, cooling in summer, or supplying domestic hot water [23]. The system makes full use of high-temperature exhaust gas and increases system efficiency to 80%, thereby saving a lot of time. Compared with the central power generation-long-distance power transmission, the natural gas heat-electricity-cooling three-electric system significantly improves the overall energy efficiency. For example, the current output efficiency of large power plants is about 30%-40%. If the cogeneration system is used for waterfall energy utilization, the efficiency of the power supply system can be increased by about 40% compared with the conventional power generation system. At about 80%, there is no transmission loss problem.

District cooling technology can also use rivers and lakes, sea water, urban sewage, or steam produced by thermal power plants as cold and heat sources. Combining the actual situation of the urban area, the Dalong Lake and the hot water pipeline of the thermal power plant can be used. Therefore, the regional cooling in the urban area is suitable for heating pipelines and the surrounding areas of rivers and lakes. The application object is the density of buildings and the larger plot ratio. At the same time, with the application of a large temperature difference and a small flow energy supply system, the pipe diameter of the entire system can be reduced, and the

Table 4: Energy conservation in the region.

Type	New increment				Cumulative amount			
	Installed capacity (ten thousand KW)	Average annual power generation (100 million kWh)	Annual average emission reduction (ten thousand tCO$_2$)	Annual average standard coal quantity (ten thousand tce)	Installed capacity (ten thousand KW)	Average annual power generation (100 million kWh)	Annual average emission reduction (ten thousand tCO$_2$)	Annual average standard coal quantity (ten thousand tce)
Hydropower	195	64	407	195	799	253	1555	839
Wind power	1049	216	1521	647	1699	615	2301	863
Solar energy	487	74	578	227	499	76	280	228
Biomass energy	29	4	30	15	30	4	30	15
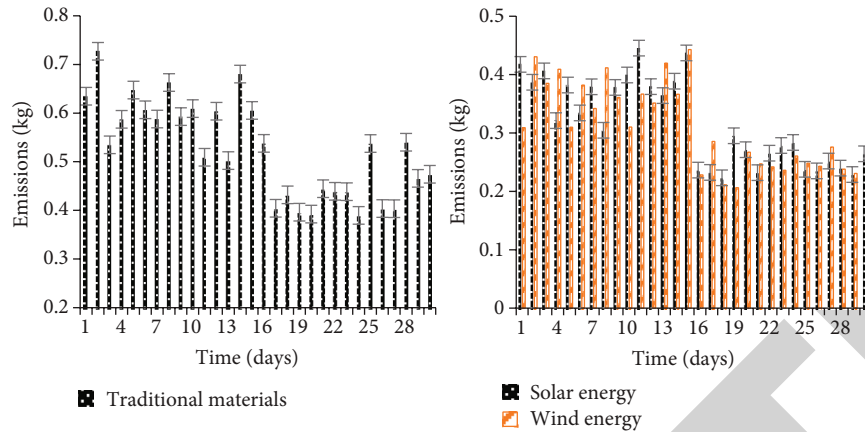
Figure 6: Comparison chart of carbon emissions statistics.
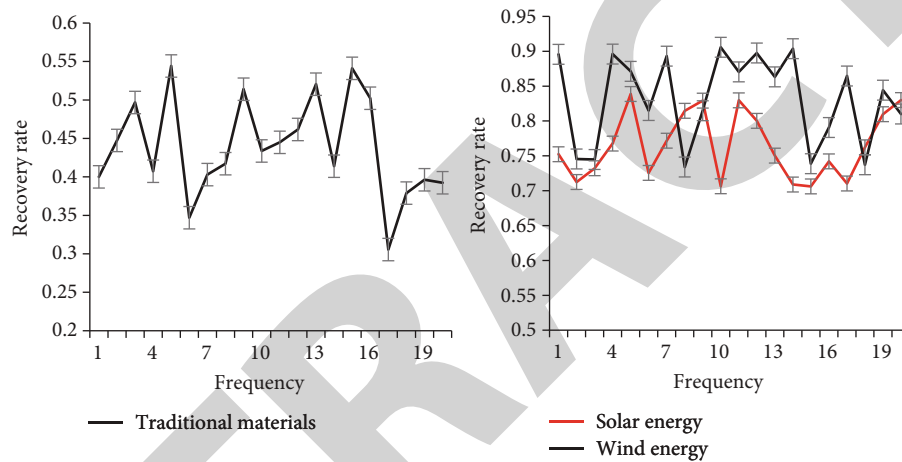
Figure 7: Recycling ratio of different materials.

flow rate of the water pump can be reduced, thereby saving operating costs and initial equipment investment. Therefore, through the combination with district cooling technology, initial investment and operating costs can be saved [24].

3. Experiments and Results of Renewable New Energy Materials

3.1. Energy Changes. In the experiment, we first display the collected energy conversion efficiency and make statistics on the changes under different voltages and currents. The results are shown in Table 2:

It can be seen that in this experiment, the input voltage range of the step-down mode is 5 V-25 V, the output voltage is 5 V, and the output current range is 0A-1.5A; the input voltage range of the step-up mode is 3 V-12 V; and the output voltage range is 5 V-25 V.

The capability classification of different energy harvesting technologies is shown in Table 3:

We compare the two-stage charge pump with the single-stage boost. Under the same experimental conditions, when the two-stage charge pump and the single-stage boost/buck circuit rise from 4.5 V to 15 V and from 24 V to 5 V, apply

the voltage simulated by OrCAD—the time results are shown in Figure 5, where Figure 5(a) is boost and Figure 5(b) is buck:

It can be seen that when the buck/boost topology circuit is used alone for voltage regulation, as the horizontal axis voltage rises, the conversion efficiency decreases almost linearly. The secondary voltage regulating circuit added with the charge pump will slow down the decline of the conversion efficiency of the circuit at the mode switch by changing the mode of the charge pump voltage regulation [25].

3.2. Comparison before and after Transformation. The ultimate goal of developing new energy is to realize the sustainable development path of low energy consumption, high energy efficiency, less pollution, and diversified energy supply for economic and social development. We calculate the carbon emission reduction and energy saving of new energy and renewable energy in the region, and the results are shown in Table 4:

We compare new energy materials using wind and solar energy with traditional materials. By comparing their carbon dioxide emissions, recycling capacity, time cost, and energy consumption, we first make statistics on carbon emissions, and the results are shown in Figure 6:

Figure 8: Time required to produce materials.

Figure 9: Virtual city image.

As can be seen from the figure, in the time shown for the production of materials, the average time required for materials produced by traditional methods is about 0.6 h, while the average value of wind energy and solar energy is about 1 h. This is due to the requirements of solar and wind energy for climate. Higher, the display is not stable, which also causes the traditional method to produce materials faster than renewable energy. We use environmentally friendly materials to plan the city, and the virtual image is shown in Figure 9:

At present, the environment in which we live has become worse due to energy consumption, and people have gradually realized the importance of protecting the environment. Therefore, we have compared the energy consumed by different materials, and the results are shown in Figure 10.

It can be clearly seen that the energy required for the consumption of traditional materials is much higher than that of renewable energy, which is more than 50% higher. This is also due to the different production methods of the materials. Regarding the role that different materials can play in urban landscape design, we have compared the existing data and obtained relevant results. The results are shown in Figure 11.

It can be seen that in the eyes of most people, traditional materials have been more and more questioned due to their serious damage to the environment. People's pursuit of environmentally friendly materials and renewable energy has become more and more urgent. Advantages, it has become more and more people's first choice [26].

4. Discussion

Carbon dioxide and other greenhouse gas emissions are causing global climate change, posing a serious threat to human survival and sustainable economic and social development. Therefore, climate change is not only an environmental issue, but also a development issue.

By analyzing and researching the energy planning concepts, technical principles and characteristics of building regional energy planning, it is concluded that the building regional energy planning mainly includes the setting of

It can be seen from the comparison of the figure that in the comparison of the carbon emissions of different materials within one month, the carbon emissions of traditional materials are much greater than that of solar and wind energy, with an average daily emissions of about 0.4, which is twice as high as that of solar and wind energy. Many, great damage to the environment, needs to be changed.

We have carried out statistics on the recycling capacity of different materials, conducted multiple simulations, and took the average value for comparison. The results are shown in Figure 7:

It can be seen that the current recycling rate of materials is not ideal, especially in traditional materials, the recycling rate is about 35%, while for renewable energy, the recycling rate can reach about 85%, which greatly improve the protection of the environment.

We have made statistics on the time required after each piece of material is produced. Of course, due to the lack of relevant technology, our statistical time is only fuzzy time and not very accurate. The statistical results are shown in Figure 8:

Figure 10: Different materials consume energy.
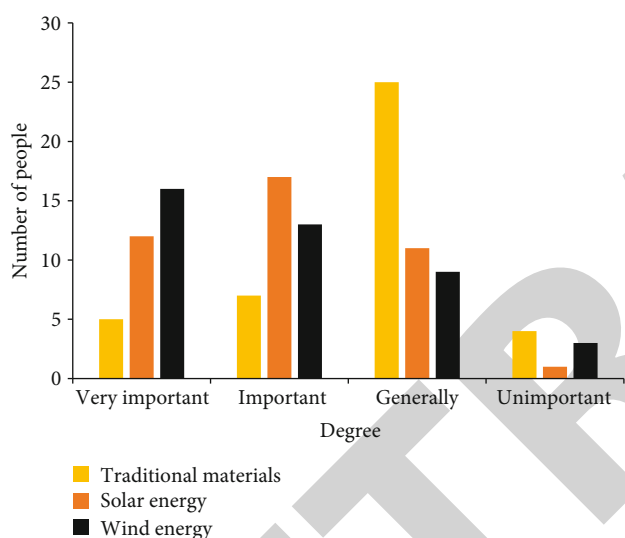
Figure 11: The importance of different energy sources.

regional energy-saving strategic goals. Determine the available energy resources and the development of energy construction in the region. And forecasting the energy load of the region, select the appropriate energy system and technical route, and evaluate the energy utilization rate of the regional energy system and the possible impact on the environment.

In the field of architectural planning, how to rationally arrange the location of buildings and plants to achieve natural ventilation and natural lighting, and in a single building, how to integrate solar energy, solar cells, solar water heaters, range hoods, biogas, and geothermal heat to make rational use of ground-floor dwellings are all issues that need to be considered. In this regard, this paper proposes some technical solutions by adopting the method of software-assisted analysis. Among them, the key to passive design is to handle the relationship between the building and the environment and nature, plan and overall design in the plot, and choose the appropriate building layout and courtyard shape, and the environmental elements such as plants and ponds must be reasonably matched with the building.

For natural ventilation, the key is to organize the ventilation channels and vents; for natural lighting, the building's shading system and day lighting system must follow the angle and track of the sun. These are all used in traditional residences, especially in the planning of new residential districts, and they should be planned and laid out in detail. For the use of energy, priority is given to selecting renewable energy sources, such as solar energy, biogas energy, and geothermal energy. Solar energy is abundant, and solar power generation is now mainly used in areas where there is no grid, and it needs to be popularized due to its high cost. Solar water heaters have a big trend and can be used in engineering and construction applications, but they still face many challenges.

Generally speaking, the use of renewable energy in daily life has been very extensive, and various energy sources have their own application ranges and limitations. In order to make the effective use of renewable energy, various energy sources should complement each other in the application. This article analyzes the device and packaging structure of the PV cell and then in-depth study of the equivalent circuit model of the PV cell. According to the PV cell equivalent circuit model, the mathematical model and power-voltage output characteristic curve of the PV cell are derived. In this way, based on the output characteristic curve and mathematical model of the PV cell, the PV cell can be controlled by MPPT to obtain the maximum output power.

5. Conclusion

At present, most countries in the world have realized the importance of a good and environmentally friendly living environment to people, and have begun the ecological construction and design of modern human settlements, and have achieved some results, solving the problem of satisfying people's living conditions. Quality requirements, so in the contemporary human settlement environment, we should see the ecological philosophy and spiritual connotation of traditional residential buildings, which in many aspects show its advanced and modern concept of ecological environmental protection. Fully use and use it for reference to the modern living environment, and build a modern residential area suitable for modern people

with a good ecological environment, energy saving, and intelligent. This is also our long-term pursuit of the modern living environment. Of course, the research in this article also has its shortcomings. The article only considers the comparison of solar energy and wind energy to renewable energy, and does not give more introduction to other environmentally friendly energy sources. The design of energy harvesting does not meet the design requirements. Therefore, in future research, this paper will design a self-starting system for the energy harvesting system to further improve the efficiency of energy harvesting. According to the characteristics of wind and solar hybrid energy harvesting, a dedicated energy harvesting controller chip is designed to reduce the energy consumption of the energy harvesting circuit, reduce the circuit volume, and improve the efficiency of energy harvesting. However, due to the limitation of time and technology, we did not further discuss the design of urban garden landscape. We will also conduct in-depth discussions in the follow-up, in order to make certain contributions in this regard.

Data Availability

No data were used to support this study.

Conflicts of Interest

There is no potential conflict of interest in this study.

Acknowledgments

References

[1] P. Samadi, V. Wong, and R. Schober, "Load scheduling and power trading in systems with high penetration of renewable energy resources," *IEEE Transactions on Smart Grid*, vol. 7, no. 4, pp. 1–1, 2017.

[2] P. Yang and A. Nehorai, "Joint optimization of hybrid energy storage and generation capacity with renewable energy," *IEEE Transactions on Smart Grid*, vol. 5, no. 4, pp. 1566–1574, 2014.

[3] R. Rezaei and M. Ghofranfarid, "Rural households' renewable energy usage intention in Iran: extending the unified theory of acceptance and use of technology," *Renewable Energy*, vol. 122, pp. 382–391, 2018.

[4] Y. Wu, V. K. N. Lau, D. H. K. Tsang, L. P. Qian, and L. Meng, "Optimal energy scheduling for residential smart grid with centralized renewable energy source," *IEEE Systems Journal*, vol. 8, no. 2, pp. 562–576, 2014.

[5] S. Rahim, N. Javaid, A. Ahmad et al., "Exploiting heuristic algorithms to efficiently utilize energy management controllers with renewable energy sources," *Energy & Buildings*, vol. 129, pp. 452–470, 2016.

[6] M. H. Athari and M. M. Ardehali, "Operational performance of energy storage as function of electricity prices for on-grid hybrid renewable energy system by optimized fuzzy logic controller," *Renewable Energy*, vol. 85, pp. 890–902, 2016.

[7] E. Dogan and F. Seker, "The influence of real output, renewable and non-renewable energy, trade and financial development on carbon emissions in the top renewable energy countries," *Renewable & Sustainable Energy Reviews*, vol. 60, pp. 1074–1085, 2016.

[8] U. Al-Mulali, I. Ozturk, and S. A. Solarin, "Investigating the environmental Kuznets curve hypothesis in seven regions: the role of renewable energy," *Ecological Indicators*, vol. 67, pp. 267–282, 2016.

[9] J. B. Geng and Q. Ji, "Technological innovation and renewable energy development: evidence based on patent counts," *International Journal of Global Environmental Issues*, vol. 15, no. 3, pp. 217–219, 2016.

[10] A. Ghafoor, T. U. Rehman, A. Munir, M. Ahmad, and M. Iqbal, "Current status and overview of renewable energy potential in Pakistan for continuous energy sustainability," *Renewable & Sustainable Energy Reviews*, vol. 60, pp. 1332–1342, 2016.

[11] R. M. Ferdous, A. W. Reza, and M. F. Siddiqui, "Renewable energy harvesting for wireless sensors using passive RFID tag technology: a review," *Renewable & Sustainable Energy Reviews*, vol. 58, pp. 1114–1128, 2016.

[12] G. Ferruzzi, G. Cervone, L. D. Monache, G. Graditi, and F. Jacobone, "Optimal bidding in a day-ahead energy market for micro grid under uncertainty in renewable energy production," *Energy*, vol. 106, pp. 194–202, 2016.

[13] A. Kamjoo, A. Maheri, A. M. Dizqah, and G. A. Putrus, "Multi-objective design under uncertainties of hybrid renewable energy system using NSGA-II and chance constrained programming," *International Journal of Electrical Power & Energy Systems*, vol. 74, no. 1, pp. 187–194, 2016.

[14] W. Chen, X. Wu, L. Yao, W. Jiang, and R. Hu, "A step-up resonant converter for grid-connected renewable energy sources," *Transactions of China Electrotechnical Society*, vol. 30, no. 6, pp. 3017–3029, 2016.

[15] R. Hosseinalizadeh, H. G. Shakouri, M. S. Amalnick, and P. Taghipour, "Economic sizing of a hybrid (PV–WT–FC) renewable energy system (HRES) for stand-alone usages by an optimization-simulation model: case study of Iran," *Renewable & Sustainable Energy Reviews*, vol. 54, pp. 139–150, 2016.

[16] V. Bertsch, M. Hall, C. Weinhardt, and W. Fichtner, "Public acceptance and preferences related to renewable energy and grid expansion policy: empirical insights for Germany," *Energy*, vol. 114, pp. 465–477, 2016.

[17] Y. Shu, Z. Zhang, and J. Guo, "Study on key factors and solution of renewable energy accommodation," *Zhongguo Dianji Gongcheng Xuebao/Proceedings of the Chinese Society of Electrical Engineering*, vol. 37, no. 1, pp. 1–8, 2017.

[18] A. Gasparatos, C. Doll, M. Esteban, A. Ahmed, and T. A. Olang, "Renewable energy and biodiversity: implications for

Review Article

Pertinence of Textile-Based Energy Harvesting System for Biomedical Applications

Shriya V. Iyer,[1] **Jyothis George,**[1] **Suhasini Sathiyamoorthy,**[2] **Rohini Palanisamy** [ID],[3]
Abhijit Majumdar,[4] **and Pandiyarasan Veluswamy** [ID][1,3]

[1]*SMart and Innovative Laboratory for Energy Devices (SMILE), Indian Institute of Information Technology Design and Manufacturing (IIITDM) Kancheepuram, Chennai 600127, India*
[2]*Department of Electronics and Communication Engineering, SRM Institute of Science and Technology, Kattankulathur, 603203 Tamil Nadu, India*
[3]*Department of Electronics and Communication Engineering, Indian Institute of Information Technology Design and Manufacturing (IIITDM) Kancheepuram, Chennai 600127, India*
[4]*Department of Textile and Fibre Engineering, Indian Institute of Technology Delhi, New Delhi 110016, India*

Correspondence should be addressed to Rohini Palanisamy; rohinip@iiitdm.ac.in
and Pandiyarasan Veluswamy; pandiyarasan@iiitdm.ac.in

In the era of technological advancements in healthcare and medicine, monitoring of health status and treatment conditions has been made convenient by the development of various categories and forms of biomedical sensors. They have been incorporated within watches and mobile phones and can be worn as stand-alone based on user preference. However, the longevity, cost, and sustainable functionality have impeded its adoption within the population. In this review article, we have introduced a concept of bridging the textile industry and biomedical sensors to yield a self-powered biomedical system that operates on textile-based energy harvesters. Textile-based wearable systems have been compared to E-skin-based systems. The energy released by different actions in human motion has been quantified along with insights on its effective utilization in the form of energy harvesters in the subsequent sections. Information on designing such a textile-based system with schematics has been done. This review focuses on the development and connection of textile-based energy harvesters to existing models of biomedical sensors.

1. Introduction

Traditionally, hospitals with state-of-the-art instruments and patient monitoring facilities have taken precedence when an individual needs aid with diagnosis, treatment, operation, or postoperative care. Monitoring of an individual's vital organs/systems, such as heart rate, body temperature, and ECG, has been done in the presence of a doctor within a hospital or a doctor's office room. It is also well known that the treatment of certain medical conditions that necessitate intensive care units (ICU) is expensive not only for the patient but also for the hospital because they must invest in the upkeep of medical equipment such as blood pressure cuffs, oxygen saturation meters, thermometers, breathing, and urinal tubes [1, 2]. Even when the patient is shifted from an ICU room to a general care unit, the majority of the equipment is shifted as well for postoperative monitoring. However, various tubes and needles on the patient body, even after surgery for the monitoring of the vitals, cause a great deal of pain and discomfort as by this stage, the effect of anesthesia given during the operation wears off. This prompted the health-care professionals in the medical field to raise the need for an effective and less expensive setting for the patient's treatment. Consequently, the integration of nanotechnology, medical, and electronics had opened ways to develop biomedical devices with outstanding

features of drug delivery, real-time health monitoring of physiological parameters, and even the recording of nerve stimulation [3]. This gave birth to the smart health monitoring systems that possessed sensors for obtaining medical information from the patient connected to them that can sometimes wirelessly transfer real-time details to the monitor of the health-care professional were known as portable biomedical devices, which revolutionized the health-care system. With the boom of material science and miniature technology, biomedical devices could also be implanted or attached to the skin (wristwatches/smart bandages).

Medical treatments, on the other hand, can sometimes last for months, and in other cases, the patient may need to make the device a permanent part of their life. For such long-term use, biomedical devices had to be built with large batteries, which resulted in substantial models that required frequent replacement, as well as increased consumer discomfort. Moreover, this psychologically creates a negative impact on the wearer's mind reminding them of the particular medical condition, which has clinically proven to impede recovery rates. Additionally, the apparent visibility of such devices implanted or attached to the skin is hard to miss for an onlooker who quickly identifies the wearer to be a patient or sick, which no wearer finds appealing as for most people their treatment tends to be a matter of privacy. These limitations of traditional biomedical devices have undoubtedly raised the need to develop a self-sustaining power system for a biomedical device to counter the need for frequent replacement of batteries.

The progress of fabrication technology and biocompatibility has seen the textile industry contributing to the biomedical field in intensely effective ways. Due to the material advancements made, biosensors can now be integrated into textiles to make wearable clothes for people [4]. This textile-based system processes and transmits the biosystemic data with vital information directly to the health professional, thus solving the psychological impact of wearing visible biomedical devices and increasing the mental as well as emotional wellbeing, therefore overall benefitting the health of the individual. Textile-based biomedical devices also possess the ability to not only harvest but also self-generate energy.

In this review paper, we aim to emphasize the importance of these textile-based energy harvesters. We begin by highlighting the different categories of wearable health devices and elaborate on the unique features of human motion to understand the energy generated from a human body. This will be followed by the various textile-based energy harvesting systems for application in the biomedical field and an overview of self-powering textile-based wearable systems. The relevant information will be summarized in the final section of this review.

2. Different Types of Wearable Biomedical Devices [WBD]

2.1. E-Skin-Based WBD. Electronics that possess an excellent ability to stretch and showcase elasticity/flexibility with a certain extent of self-healing capabilities are referred to as electronic skin. These are popularly used in the field of prosthetics development, artificial intelligence, robotics, and now even in health monitoring systems [5–8]. E-skin-based WHC devices mimic the capabilities of the human skin and try replicating its function towards external environmental stimuli such as heat, pressure, and temperature.

E-skin, also known as artificial electronic skin, comprises sensors and actuators that receive the biosystemic information and convert it into a form of signal that can be processed, communicate the information, and self-powered. The regions of the skin on which these components are put; biocompatibility and ability to stretch in response to the demands of human mobility, as well as comfort and lightweight for the user with a reasonable shelf life, are all factors in the material selection process. Biofluid-proof materials are required in some instances. The overall device performance of such WBD pertains to the type of materials and substrates used, dimensional structures incorporated into the design, signal processing units, overall architecture, and design formed and size of the storage units. The appeal of E-skin-based WBD devices to potential wearers ultimately depends on functionality but is also more influenced by cost and esthetic appearance.

Typical substrates used for making flexible E-skin-based WBD include a wide variety of polymers segregated and chosen based on Young's modulus (for flexibility) and degradation temperature (transition temperature, T_g) in addition to the factors mentioned in the above paragraphs (refer to Table 1). These include poly-dimethyl-siloxane (PDMS), poly-ethyleneterereph-thalate (PET), poly-ethylene-napthalate (PEN), poly-ether-sulfone (PES), poly-ether-ether-ketone (PEEK), polycarbonate (PC), and polyimide (PI) [9–15]. In some cases where the transparency of the appearance of the device needs to be altered, liquid crystal polymer and eco-flex are also utilized as substrate materials that are opaque and translucent in nature [16–18]. Figure 1 illustrates the different types of such WBD devices used in the health-care system.

A key component in these WBDs is the range of sensors used. Sensors tend to make or break the entire functionality of the device [11, 12]. The different types of sensors used are demonstrated in Figure 2.

The interaction of the biotic and abiotic components, as well as a robust interface between them, is the key focus for E-skin-based or any skin-based implants [19, 20]. From a manufacturing standpoint, Ray et al. [21] emphasized the necessity of biointegrated devices for health monitoring to be user-specific. There must be excellent compatibility of the implant-/skin-based devices with the texture of the skin, size of the body part, and lifestyle of the wearer. One of many drawbacks of such an approach is the utilization of gel-based adhesive sensors in the manufacturing of skin-based biomedical devices that cause skin irritation. Moreover, large-scale manufacturing of such a technology cannot dwell into the user-specific details; thus, the end product might be of comfort to some but discomfort to others. Apart from this, the dynamic nature of the human biology system that is in continuous contact with rapidly evolving environments poses a significant challenge to the performance of

TABLE 1: Substrates used to develop E-skin-based WBD.

Substrate material	$T_d(^0C)$	σ $Wm^{-1}K^{-1}$	Transparency	Young's modulus Pa	References
PDMS	150	0.15-0.17	Transparent	0.3-3 M	[9–13]
PET	120	0.15-0.24	90% transparent	2800-3100 M	[9, 14, 15]
PEN	160	0.15	87% transparent	2500 M	[9, 14–16]
PES	190	0.18	89% transparent	2400-2800 M	[10, 14, 15]
PEEK	240	0.25	NA	3600 M	[10, 14]
PC	150	0.19	92% transparent	2400 M	[15]
PI	>300	1.3	30%-60% transparent	2500 M	[10, 14]
Liquid crystal polymer (LCP)	>350	0.3	Opaque	NA	[17]
Ecoflex	NA	NA	Translucent	0.027-0.029 M	[18–20]
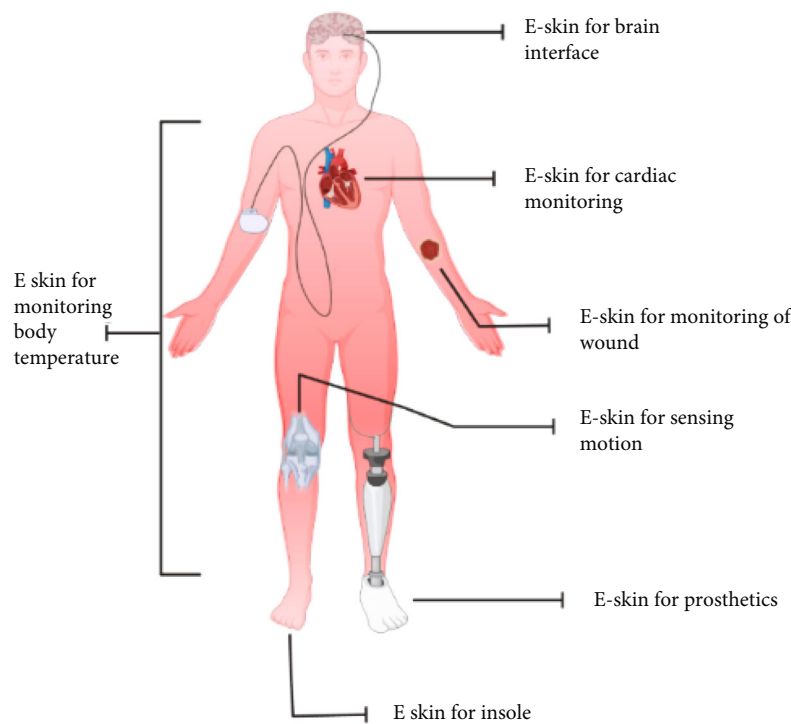
FIGURE 1: Showcases the various forms of E-skin-based WBD system application.
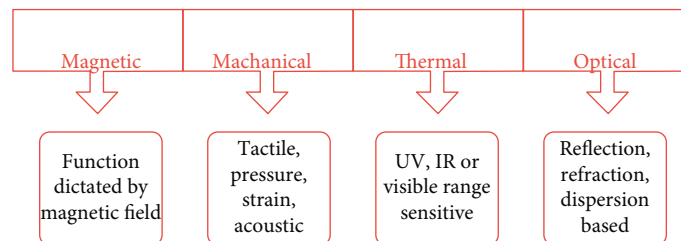
FIGURE 2: Different types of sensors applied in E-skin-based WBD.

these devices. Moreover, they do not provide continuous health data (real time), making it hard for the health professional to determine the disease onset, which is attributed to the limited power from batteries requiring replacements. This naturally creates the need to develop a counter mechanism that can record and transmit continuous biosystemic data without causing discomfort and involving replacements of batteries. The interconnection between textile-based WBD (parent system) with textile-based energy harvesters as power supply unit is the proposed solution in our work.
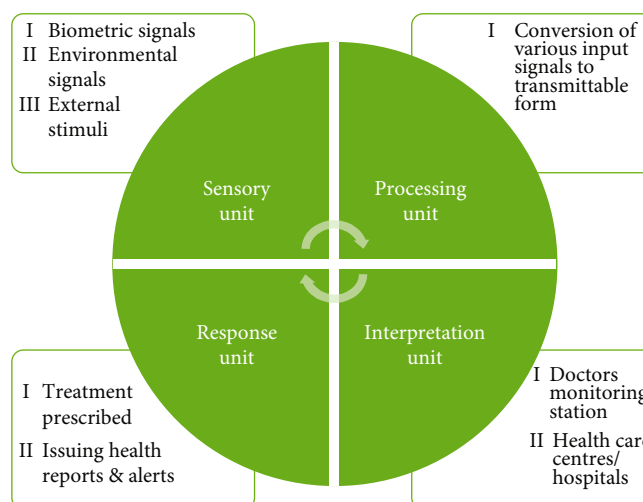
FIGURE 3: Patient-oriented textile-based WBD.

2.2. Textile-Based WBD. Textile-based wearable biomedical devices (WBD) had been the invention that was born out of necessity on the battlefield. The concept of an "intelligent garment" was developed since people's lives depend on immediate medical attention, which is not always possible in a war zone. Primary objectives were to constantly monitor the vital organs of the soldier/wearer with additional features of military benefit including enemy weaponry knowledge by measuring the penetration of bullets on the garment. A group of doctors residing on the military base camp was sent the information directly transmitted from the garment, thus enabling constant monitoring. Smart textiles were born as a result of this concept gaining traction in the fields of material science, electronics, and medicine.

As clothes are worn at all times by people of all age groups, making these clothes, the source of medical information has gained monumental appeal from the biomedical professionals. Unlike noninvasive (electronic skin) and invasive (implants) counterparts that result in psychological stigmatization and discomfort in terms of physical wearability and technical drawbacks as highlighted in the above section, the textile-based health monitoring system provides the wearer with mental, psychological, and overall well-being. This is mainly achieved due to the easy incorporation of energy harvesters into the framework design of smart textiles.

From the customer/patient point of view, the functioning of smart textile is as simple as wearing a new shirt. The functionality of such a patient-oriented biomedical invention is summarized in Figure 3.

The sensory unit constitutes arrays of wearable sensors integrated within or onto the textile because the textile is made up of flexible fiber. This allows for the gathering of biomechanical data to be done without interruption while taking into account the natural or movement-induced deformation that occurs in humans. Based on the type of stimuli, sensors could be piezoelectric, capacitive, resistive, and triboelectric, which will be explained later in this review.

Research and development of low-dimensional electronic systems have made it possible to integrate various components onto various substrates and, more importantly, textile products. Simultaneous research into the deposition of coatings onto fibers to synthesize conductive materials/polymers has backed up the former. Further research has now enabled these conductive materials to function as actuators and transducers, which are crucial components of the processing unit shown in Figure 3.

We have taken this one step further and categorized smart textiles into three broad categories, namely, active, passive, and very active smart textiles. Passive smart textiles are believed to be the primitive of the group as these only possess the capacity to make changes to their properties based on stimuli. Optical fibers are popular inventions that come under this category.

Active materials, on the other hand, are the next generation of materials capable of making decisions about how to react to external stimuli. However, the convergence of the textile industry and biomedical field took place on the development grounds of third-generation smart textiles. These not only could sense and make decisions but also configure themselves based on the stimuli, thus opening opportunities to monitor health via apparel and clothing, known as very active smart textiles.

Furthermore, the interpretation and response unit is nearly identical to that of an E-skin-based WBD, with the exception of the level of monitoring, which is not continuous in an E-skin-based WBD due to battery and energy requirements.

Modern society is showing signs of becoming more health conscious. The demand to have a constant update on health and having control over it has pushed even the biggest telecom companies, IT industry, and brands to incorporate health applications within mobile phones and gadgets to make them more appealing. However, these are not built to provide disease onset information, postoperative care, or well-rounded health information. Many medical professionals find data from such devices unreliable due to the vulnerability of glitches.

Thus, the goal of this review is to emphasize the necessity of using the human body as a source of energy and

storing it in order to power the WBD, which can only be truly effective with a textile-based approach. The following section will comprehend this approach better by highlighting the enormous amount of energy that can be harnessed from various parts of the human body.

3. Underutilized Marvel: The Human Motion

The calculations of energy given out by the different body parts have been provided by Riemer and Shapiro [22] in their comprehensive work. Our human body per day releases energy equivalent to 20 kilograms of AA batteries with 2500 mAh each, approximately around 800-850 in number. Thermal and movement centered activities are a common outlet for such energy expenses. We can eradicate the adversities associated with modern technology that lack the convenience of long-haul usage attributed to exhaustible power sources/batteries by harvesting this unexploited energy source to power electronics.

The energy to perform human motion is gained from biomolecules such as carbohydrates, proteins, and fats. Energy converted from them by our body for utilization (specific energy) is 35 to 100 times more than the batteries used in the present day, according to Rome, L. C [23]. However, more than 70% of the energy consumed is released towards the atmosphere, thus bringing the mechanical efficiency of the body to less than 30%, validated by Vélez Día and Moreno Gutiérrez [24] in their study. Another reason why the marvel of human motion needs to be explored is to harness all the wasted energy.

According to studies, when a person moves freely, such as during running, energy is generated in various parts of the body. The data in Table 2 depicts this energy in terms of power.

Ultimately, these energies are born and released by the muscles involved in the respective motion. Therefore, to effectively harvest the energy, it is vital to consider the muscular phases—positive muscle work and negative muscle work. These phases occur during a single act of motion.

Any work done by muscles to generate motion is considered the positive phase of work of the muscle and the termination of the motion is the negative phase, in which energy is absorbed to perform this task. Eminent works of Riemer and Shapiro [25] and Alexander [26] validated that the contraction of muscle fibers due to the application of torque at the muscle joint in the same direction of the angular velocity results in motion constituting the positive phase. However, an energy harvester present at this phase to extract the energy developed here would increase the minimum energy required to perform the task, also known as metabolic cost. The body would have to exert more energy to perform the same task which would lead to a detrimental effect on health; therefore, knowing which energy to harvest is crucial. On the other hand, the negative phase involves the opposite of the former. Therefore, an energy harvester placed at this point would hamper no natural motion. Additionally, more energy harvesting can be performed in the regions where the human body gives off energy to the environment.

TABLE 2: Energy expenditure by various parts of the body.

Body movement	Energy released (W)
Elbow	0.78 W
Finger motion	6.9-19 mW
Shoulders	1.34 W
Breathing band	0.83 W
Hip	7.2 W
Knee	33.5 W
Ankle	18.9 W
Heel strike	<10 W
Blood pressure	<1 W

The heat generated from the human system, according to Carnes, if quantified, amounts to around 100 W, which is released towards the surroundings is underutilized. Thermo-electrical generators can only make use of sensible heat and not latent heat. The temperature difference is the main driving force for sensible heat, and occasions such as sweat evaporation harbor in latent heat. Consider the movement of the arms, the first motion is related to the movement of the elbow (between the forearm and upper arm), and the second motion is related to the upper arm and humorous bone involving the changes in the movement of the shoulder. It was recorded for an average male subject, and the percentage of negative work was between 35-40% for the elbows and 60-63% for the shoulders. An average of 2.2 W of power was generated just by casual walking in these regions, quantified by Winters [27] and his research team.

The most common act of carrying a heavy load on the shoulder may be a bag among children or military troupe or lifting heavy bags of groceries since the power generated as negative work is going to increase for both arm and shoulder. This concept is also called the center of mass motion. In efforts to simplify, it can be best understood as quantifying the energy from a relative motion between the bag and the person carrying it. Research has shown that for each kilogram, 1 W of energy could be available for usage. Thus, the region of shoulders could have energy harvesters, and hands could have special gloves possessing them. This energy could power up WBD that serves monitoring purposes for the upper body in addition to the energy dissipated as heat.

Heel strike, for instance, while walking, occurs each time when the heel strikes the ground. Fair to say, the higher the distance between the heel and the ground higher the energy release. This means that jumping, jogging, and other activities can provide more energy release than walking at a casual pace. Shorten [28], a researcher engaged in quantifying energy loss during heel strike, relied on a previous study [25] that showed energy loss occurs when walking towards the sole. More than 10 J of energy loss occurred based on his calculations when his heel struck the ground. This energy, if harvested, could provide power to the biosensors in WBD. The amount of energy harvested depends on the area of contact from where the loss takes place. In this case of heel strike, socks and shoes are the only two things that
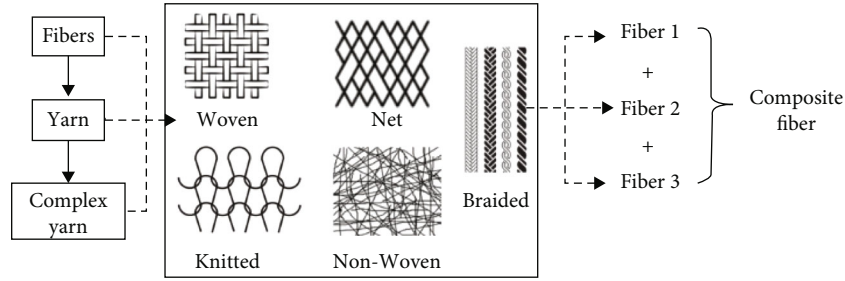
Figure 4: Variations in fabric development.

provide continuous and maximum contact. Socks and soles of shoes developed with energy harvesters could be materialized through the merging of the textile industry and electronics. Not only can it harvest, but when connected to WBD can provide sustainable livelihood for the long haul as it could probably serve as an inexhaustible source of power to the biomonitoring devices, thus enlightening the importance of developing textile-based energy harvesters. As mentioned in earlier sections, textile products and apparel are the most effective since they are the only components with the most considerable contact with the skin and human body. As a result, establishing a link between textile-based energy harvesters and wearable biomedical devices is the most natural strategy for addressing contemporary difficulties and the key to revolutionizing the biomedical-electronics industry.

4. World of Smart Textile

4.1. Birth and Development of Fabrics.
The textile industry has come far from producing fabrics, polymers, and apparel merely for esthetic needs. In the age of personalized health care, personal attire has become the primary medium to deliver medical services. Textiles have been well known to outperform traditional electronics in terms of stretchability and comfort. Modernization has enabled the textile industry to enter an entirely new genre of application by utilizing various techniques to impart functional qualities to their polymers.

A textile-based monitoring system, as explained earlier, requires sensing and transducing functions; these capabilities can be built into the system either by coating it on the textile and using it as the substrate or by using a polymer that itself has transducing capabilities, thus earning itself the name of smart textile. It is essential to understand the hierarchy of processes involved in fabric development. A piece of fabric is an amalgamation of individual fibers (yarn) interconnected in various manners such as knitting, weaving, net formation, tufted, and nonwoven. Additionally, the evolution of composite fabrics enables the fabrication of multi-functional fabrics, formed when two or more types of fabric are interconnected. The following Figure 4 showcases the various forms of fabric development for a clearer understanding [29].

The coating of functional materials (sensing and transducing) can occur during the lower dimensional stage of the hierarchy and, in the final, thus being more flexible than traditional electronics. However, one must keep in mind that each fabric structure has its own properties and will serve a specific application better than others. Therefore, the choice must be based on the common ground where the application meets the properties offered by the polymer.

The geometrical properties of a fiber are its area of cross section and length; the chemical properties of a fiber are determined by its reactivity/inertness to alkaline and acidic environments; and the physical properties of a fiber are determined by the crystallography of the polymer used to make it. Tracton's [30] and Luo and Van Ooij's [31] elaborative works provide insightful light on this aspect. The final performance of the coated polymer will depend on the interfacial reaction (between the surface of coating and the surface of fiber) as the surface chemistry will also determine the nature of bonds formed between the coating layer and fiber and dictate the reversibility of the process.

4.2. Designing.
The process and approach to designing are quite different from the traditional method of printing electrical components onto a circuit board. This variation is attributed to the versatility of textiles. As explained above, it is a very application-based approach.

The first step must be to realize what is the expected function of the smart textile and the degree of wearability (ranges from static to fully wearable). Based on step one, the substrate, fabric structure, sensing, and transducer-coating materials should be decided which becomes step 2. During the coating process, it is extremely crucial to obtain a uniform layer of coating. Cover factor C and power factor (PF) must be calculated according to Equations (1) and (2). According to Tracton and colleagues' paper, the penetration of the coating into the fiber is calculated using

$$C = \left(w * d_w + f * d_f - w * f * d_w * d_f \right), \tag{1}$$

where w is the number of warp threads per inch, f is the filling threads per inch, d_w is the diameter of warp in inches, and d_f is the diameter of the filling yarn in inches.

$$\text{PF} = \frac{\text{Fabric Density}}{\text{Fiber Density}} = \frac{W * V_{\text{Fabric}}}{W * V_{\text{Fiber}}} = \frac{V_{\text{Fiber}}}{V_{\text{Fabric}}} \tag{2}$$

In the scenario of nonuniform coating, micro-cracks formation probability increases, leading to overall deformations. Moreover, the optimal functioning of the sensor is

inversely proportional to the nonuniformity of the coating. Therefore, proper adhesion of the coating, as well as its uniform thickness, plays a prime role. Mechanical, chemical, and plasma-based surface modifications can aid in ensuring the same. The research of Luo and Van Ooij is an excellent resource for learning more about surface modification techniques. In step 3, the chosen transducing material will determine the kind of power source and the system would need to function. In step 4, the data transferring system must be finalized. In addition, since the necessity for textile-based energy harvesters has been established in previous sections, step 5 is an extra step indicated by this study, which is to introduce connections between the parent system and an energy harvester that can aid in the constant supply of energy. Finally, in step 6, testing of the entire set-up must be performed.

4.3. Textile-Based Energy Harvesters. Textile-based energy harvesters provide numerous advantages over standard batteries in various biomedical devices already in use, including unlimited capacity, convenience, low maintenance, and no need for battery replacement. There are undeniably a slew of concerns at the individual, technical, and environmental levels that are driving the shift to textile-based energy harvesters. These energy harvesters make use of the energy that is wastefully released by the human body (mentioned in section III). On an average day, inclusive of all the activities performed by a normal individual, the biomechanical energy sums up to approximately 70 W. Thus, being able to utilize this and use it as a source of power for smart textiles rather than regular batteries is an intriguing, environmentally benign, and sustainable option that deserves careful consideration. Textile-based energy harvesters like smart textiles follow a similar process of fabrication. These harvesters can sense and transform energy from one form to another. They come in a variety of shapes and sizes, depending on the type of energy they convert or transform.

4.3.1. Triboelectric Energy Harvester. Mechanical energy expensed by the body is the leading source for the generation of electricity. It is an amalgamation of two processes: triboelectrification (resultant of the physical contact between two materials with varied electron affinity) and electrostatic induction (the potential difference that is created when two opposite charge carrying materials are separated). The shift towards miniature technology has shown property enhancement as the size of materials shifts from the macro-micro-nanoscale. This section will focus on energy harvesting triboelectric nanogenerators (TENGs). In 2012, Wang and his team introduced this concept and demonstrated its capabilities. Many notable research works have also showcased the advantages offered by TENGs [32–37]. TENGs can potentially harvest energy from sound, wind and vibrations. Furthermore, its fabrication involves materialistic diversity, thus aiding in choosing the material as specific as the application demands.

Zou et al. [38] have proved, and the TENGs can be made of materials such as cotton, wool, silk, artificial fiber, rubber, and polyurethane. As explained in Section 4, fabrics can be coated with various functional materials. Therefore, bridging the two concepts gives birth to a textile-based triboelectric energy harvester [39, 40]. A common concern with textile-based biomedical systems is washability. This concern was washed away by Ning et al. [41] who worked on a textile-based TENG that could generate a peak voltage of about 1050 V by measuring the friction within the clothes during everyday activities. They used nanofiber with high hydrophobic properties to impart the convenience of washing. The nanofiber was then woven into a nonwoven textile substrate via a shuttle flying process, and they have shown that a simple fabric (lab coat) can be incorporated with such a functionalized polymer fiber to generate electricity (Figure 5).

Their work intends to showcase the importance of bridging the merits of textile-based energy harvesters to solve the predicament faced by textile-based WBDs. In their work, they used electricity to power 54 LEDs. By replacing the LEDs with an inlet with a textile-based WBD system, we can have a sustainable long-lasting energy source that will ultimately enable continuous monitoring of vitals.

Zhou et al. [42] proved that using functional fiber inserted into textile could aid physiological monitoring using the power it generated in a newly published study. A combination of nylon fabric (positive) and polyester (negative) served as the source for triboelectrification with a conductive silver fiber fabric at the center. These textile-based TENGs developed by team Zhou et al. [43] were breathable, washable, and convenient, and they went on to produce alternating current by exploiting the energy expense at the arm joints during elbow movement. These composite fibers can feed in energy to textile-based WBDs, as shown in Figure 6.

When the principle behind the different forms of textile-based energy harvesting is understood, this enables the conjunction of two other energy harvesting systems as well. Interconnection between the two energy harvesting systems and material compatibility with textile manufacturing processes must be well understood before undertaking such a feat. To guide the reader towards understanding the same, we have highlighted the works of Chen et al. Chen et al. [44], in their work, explained the energy harvesting from not only mechanical sources but also solar at the same time. Another important highlight of their research was the interconnection technique used to connect the two different energy harvesters. They developed two modules, one being the module that harnesses energy from incident radiation of the sun, hence photovoltaic, and the second being the triboelectric/TENG, which harnesses power from the friction in the body motion, the action of wind blowing, vibrations, and deformations.

This was achieved using a polymer fiber-based solar cell and interlacing two polymer fibers with varied electron affinity to generate a triboelectrification effect. Another important aspect to note is that they ensured all the chosen polymer-fiber/electrodes were compatible for industrial textile processing. Figure 7 shows the interlayer distinction of one such fabric-based TENG in the form of a yarn.

Within the photovoltaic module, the ZnO/dye becomes the interface region where electrons and holes get separated due to the energy from incident sunlight, forming electron-
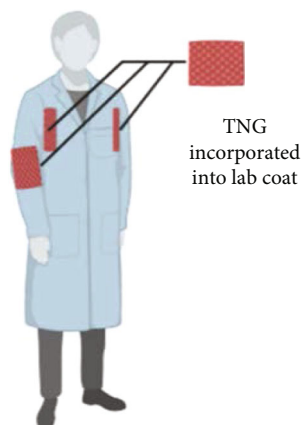
FIGURE 5: Application of lab coat.

Washable
TNG for
arm joint
energy
extraction
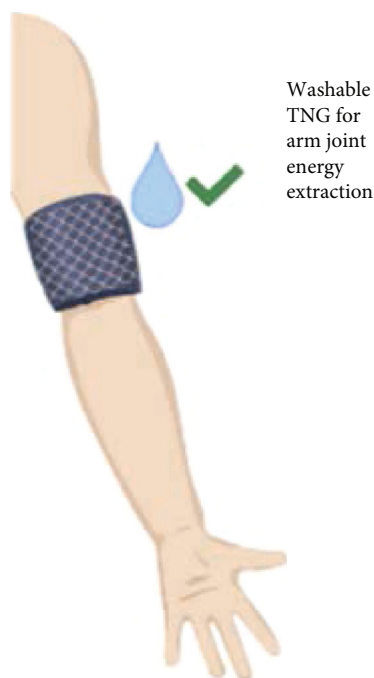
FIGURE 6: Arm joint energy exploitation by washable TENG.

☐ Mn   ☐ CuI
☐ ZnO/Dye   ☐ Cu
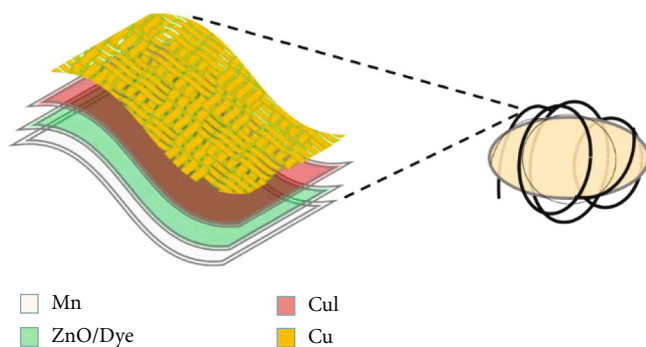
FIGURE 7: Fabric-based TENG in yarn form.

hole pairs. The wire-shaped counter electrode acts as a collector for holes, while electrons move through the semiconductor's conduction band. They are then collected at the photo anode, thus generating electricity from solar energy. Within the TENG module, the two PTFE strips are placed adjacently and interlaced with the copper electrode. When any deformations occur, mechanical excitation causes the two PTFE strips to come into contact, followed by deformation removal, resulting in a backflow of electrons between the electrodes, eventually leading to the current generation, as seen in Figure 8.

Both the independent modules were interconnected by counter electrodes, and copper was used as the common electrode. The interconnection procedures and materials used are explained in the same work. Moreover, the interlacing and other processes are also presented as visual aids/videos for the reader in their supplementary information. Thus, this work showcases the vast potential of such hybrid textiles possessing more than one energy harvesting system. The electricity generated from their hybrid textile was significant enough to charge a cell phone and an electronic watch under ambient conditions. If in a similar manner, this power generated could be connected to a textile-based WBD (parent system), this could lead to a fully self-powered textile-based biomedical device.

4.3.2. Piezoelectric Energy Harvesting. Piezoelectricity is the term for the generation of electricity by converting mechanical energy to electrical energy through the use of a specific material and motions involving any compression-based deformations (from the human body's perspective), whether caused by movements, the wind, or being struck/squeezed. Thus, most wearable electronics possess a piezoelectric component within their design. Textile-based piezoelectric energy harvesting similarly will possess a patch of piezoelectric material at the location of the source of mechanical energy [45–50]. Just as TENGs for triboelectric generators, here for piezoelectric energy harvesting, we have piezoelectric nanogenerators (PENGs). Polyvinylidene fluoride (PVDF) is the most commonly utilized material component for textile-based PENG because it is easy to incorporate into a fabric substrate [51, 52].

For a personalized health monitoring system, such a fabric-based patch can be directly attached or incorporated into the textile, with the help of interconnections, and the energy generated from the PENG module can be utilized to power the textile-based WBD (parent system) [53, 54]. Qin et al. [55] developed ZnO-based PENG on a Kevlar fiber by hydrothermal process. Since the fiber is coated with ZnO utilizing a fiber and twisted layer, the force created by stretching can be determined as illustrated in Figure 9. Tetraethoxysilane was utilized as a mechanical strengthening component, and the whole structure generated a voltage of 2.2 V with a current of 60-120 nA. This fabric-based PENG could be used to detect heartbeat and extract energy from it to create power under low-frequency biomechanical energy conditions.

Yang et al. [56], in their works, explored a similar application of employing ZnO nanowires for textile-based PENG.
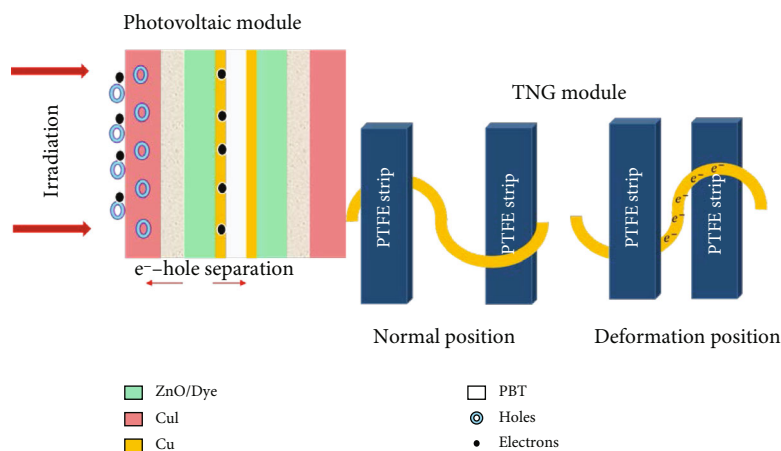
Figure 8: Electricity generation in photovoltaic module and triboelectric module.
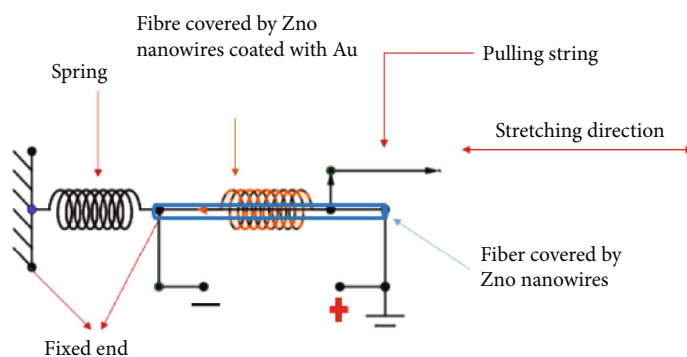
Figure 9: Fiber-based PENG.

They were able to produce an oscillating voltage up to 50 mV during the action of stretching and releasing. An ultrahigh piezoelectric voltage of 0.79 Vm $N − 1$ was developed by Chen and his team. They synthesized lead zirconate titanate (PZT) fibers via sol-gel technique, and a layer of polydimethylsiloxane (PDMS) was coated on it. On the application of pressure, the strain created flowed through the PZT fiber and passed the PDMS to generate charges during their testing. They suggested that by using more efficient piezoelectric material to coat a fiber substrate, the output voltage of 1.63 V that was observed could be improved. Further to harness the energy from a human arm, Zhang et al. developed a woven fabric generator of $BaTiO_3$-PVC composite fiber, which produced a voltage of 1.9 V. Gu et al. [57] further added to this research where they explained vertically aligned PENGs yield more voltage. In their work, a voltage of around 209 V was generated. This was a huge leap in the PENG research. Such high output, if interconnected to a textile-based WBD, could promote the shift towards a self-powering health monitoring system.

Thus, it is logical to say that in order to produce flexible textile-based PNG, the two electrodes used for PENG must be flexible and fibrous, or else attaching to the human body may not be a comfortable fit. We would like to highlight the work of Ji et al. [58] and the team, as they developed a yarn-based PENG in the form of a core-shell structure. There were two conductive threads used, an inner layer (inner electrode) and an outer layer (outer electrode). The piezoelectric nanofiber BNT-ST/PVDF was wound around the inner electrode. The core-shelled piezoelectric yarn/nanofiber was braided with two strands of conductive thread (outer electrode). For interested readers who wish to understand the synthesis process of BNT-ST/PVDF nanofibers, it has been elaborately explained in Ji et al.'s works.

This specific structural integration of components leads to improved performance and durability as it is sensitive towards bodily deformations. The core-shelled piezoelectric yarn, which was braided with the electrodes, was then directly stitched onto fabric to yield the final textile-based PENG. When this textile-based PENG was tested, the output voltage was found to be 50 kPa. Their work investigated that the voltage variation is based on the length of the PENG patch stitched, the stitching interval between the yarns and the pattern of stitching. Thus, these factors must be considered as prime factors to evaluate the voltage output with precision. They are able to introduce this patch in gloves and elbow region as a guard, and a considerable amount of power can be generated as a result of stretching and bending of these parts as illustrated in Figure 10.

Thus, if a shirt with textile-based WBD is developed, it could incorporate these PENG patches at the source of deformations, with proper interconnections between different
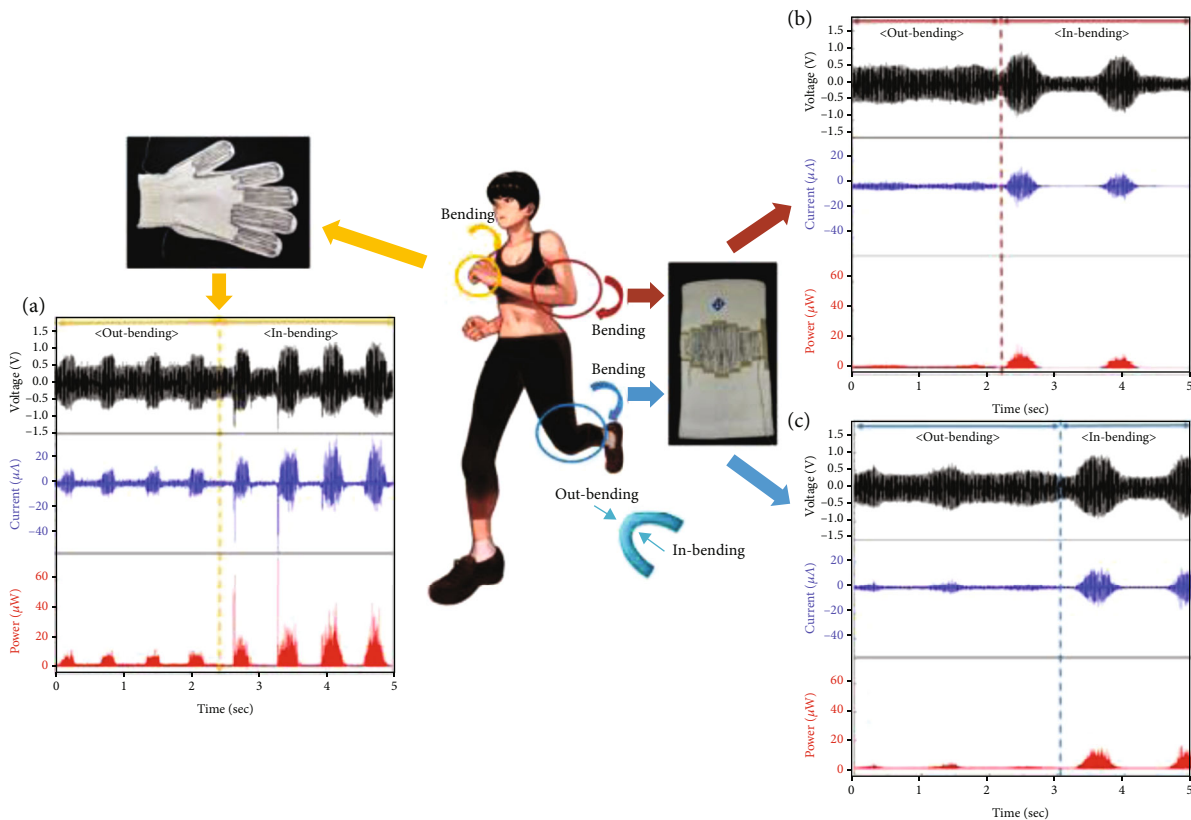
FIGURE 10: Application of textile-based PENG.

modules, as shown by Chen et al. in their study. It may self-generate the power required to run the device without the need for batteries to be replaced.

4.3.3. Thermoelectric Energy Harvesters. Thermoelectric energy harvesting systems have gained attention primarily because of their working principle. It functions based on the heat released by the human body and the temperature gradient of the environment. It requires no additional deformations or body movements or external sources of energy such as sunlight. A thermoelectric energy harvester generally possesses two sides: cold and hot (refer to Figure 11). The hot side, which is between the rough skin surface and smooth thermoelectric element, generates thermal contact resistance. Subsequently, on the cold side, the heat is released via convection. Normally, this region needs to have a high surface area for higher convection. To incorporate the thermoelectric materials onto textile, a preferred polymer is poly (3, 4- ethylenedioxythiophene): poly (styrene sulfonate) (PEDOT: PSS). This is a type of conductive polymer complex. The main advantage of this polymer complex is the ease with which it can be transformed into a full-fledged textile-based system. Coating and spinning are the two main methods that facilitate this incorporation.

In previous research works, both in-plane and out-of-plane devices based on thermoelectric polymer-based textiles have been explored. Du et al. [59] coated cotton with PEDOT: PSS and used a silver wire. The cotton strip was
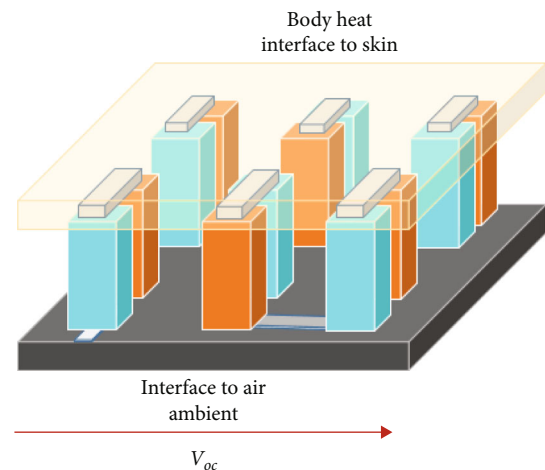
FIGURE 11: Wearable thermoelectric module.

35 mm x 5 mm, and it produced a maximum power output of 12.16 nW. Using vapor deposition, p-doped PEDOT-Cl was deposited onto cotton for an out-of-plane thermoelectric device by Allison et al. [60]. The power generated was around 4.5 nW.

In the most recent research work, Lund et al. [61] and the team have developed eight thermocouples whose each leg pair generates 2.3 nW per degree at a gradient of temperature 65 K with an overall power output of 1.2 microwatts. The highlight of this research is not only the high power
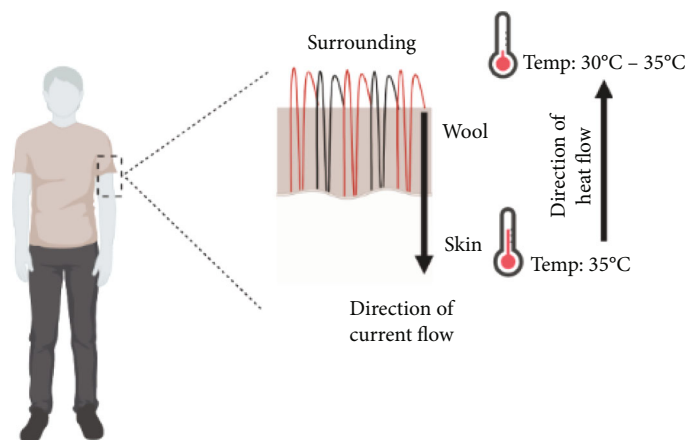
Figure 12: Embroidery into wool fabric and current generation.

output but the compatibility of their textile-based thermo-electric material with the existing textile manufacturing processes for large-scale applications. This group has also created plain and dyed conductive polymer rolls that are wash and wear-resistant and ready to be woven and sewn.

Another intriguing finding from their research is the use of conducting paste as an interface between thermocouples to lower component contact resistance. To generate the out-of-plane layout, they perform embroidery by hand to hold the different layers of wool fabric in place, as shown in Figure 12. Wool fabric was chosen for its comfort and ability to generate a temperature gradient. Therefore, when this textile-based thermoelectric energy harvesting system is worn in low-temperature conditions, the body becomes the hot region, and the external environment becomes the cold; thus, the heat will flow from hot to cold region, which results in the production of electricity, as shown in Figure 12. With such research happening, in our review, we would like to highlight once again the importance of creating a link between textile-based energy harvesters and textile-based biomedical wearable devices. This could revolutionize the field of health monitoring systems forever, as the main drawback of traditional biomedical devices can be addressed.

5. Conclusion

An increasingly health-conscious and convenience-driven culture has prompted the convergence of technology and medicine. As a result, a variety of invasive and noninvasive wearable devices that can capture biosystemic data have been developed, and they have proven to be useful in disease diagnosis and detection. However, their effective acceptance by wearers/patients has been hampered by their performance life-span, wearability, expense, and comfort. Furthermore, its psychological impact has been identified as a contributing factor in slow recovery rates. Fortunately, with the advancement in miniature technology and the textile industry, this new fusion can be the solution to the predicaments faced by traditional wearable devices. The solution lies in bridging textile-based wearable biomedical devices

with textile-based energy harvesters which can provide the continuous source of power that can be generated from the wasteful energy released by various human motions using source-specific textile-based nanogenerators. Therefore, we hope to plant a seed of thought in the minds of the readers and researchers about the importance of textile-based energy harvesters and their vast but less explored potential.

Conflicts of Interest

The authors declare that they have no conflicts of interest.

Acknowledgments

References

[1] S. Park and S. Jayaraman, "Smart textile-based wearable bio-medical systems: a transition plan for research to reality," *IEEE Transactions on Information Technology in Biomedicine*, vol. 14, no. 1, pp. 86–92, 2010.

[2] M. Anderson, "What are the components of a patient monitoring system? ATL Technology," 2020, https://atltechnology.com/blog/components-of-patient-monitoring-systems/.

[3] Y. Zhang, J. Ding, B. Qi et al., "Multifunctional fibers to shape future biomedical devices," *Advanced Functional Materials*, vol. 29, no. 34, p. 1902834, 2019.

[4] S. M. A. Iqbal, I. Mahgoub, E. Du, M. A. Leavitt, and W. Asghar, "Advances in healthcare wearable devices," *NPJ Flexible Electronics*, vol. 5, no. 1, 2021.

[5] S. J. Benight, C. Wang, J. B. H. Tok, and Z. Bao, "Stretchable and self-healing polymers and devices for electronic skin," *Progress in Polymer Science*, vol. 38, no. 12, pp. 1961–1977, 2013.

[6] A. dos Santos, E. Fortunato, R. Martins, H. Águas, and R. Igreja, "Transduction mechanisms, micro-structuring techniques, and applications of electronic skin pressure sensors: a review of recent advances," *Sensors*, vol. 20, no. 16, p. 4407, 2020.

[7] H.-H. Chou, A. Nguyen, A. Chortos et al., "A chameleon-inspired stretchable electronic skin with interactive colour changing controlled by tactile sensing," *Nature Communications*, vol. 6, no. 1, p. 8011, 2015.

[8] T. Someya and M. Amagai, "Toward a new generation of smart skins," *Nature Biotechnology*, vol. 37, no. 4, pp. 382–388, 2019.

[9] J. Mark, *Polymer Data Handbook*, Oxford University Press, New York, 1999.

[10] M. C. Bélanger and Y. Marois, "Hemocompatibility, biocompatibility, inflammatory and in vivo studies of primary reference materials low-density polyethylene and polydimethylsiloxane: a review," *Journal of Biomedical Materials Research*, vol. 58, no. 5, pp. 467–477, 2001.

[11] B. A. Grzybowski, S. T. Brittain, and G. M. Whitesides, "Thermally actuated interferometric sensors based on the thermal expansion of transparent elastomeric media," *The Review of Scientific Instruments*, vol. 70, no. 4, pp. 2031–2037, 1999.

[12] T. N. Tran, J. A. Heredia-Guerrero, B. T. Mai et al., "Bioelastomers based on cocoa shell waste with antioxidant ability," *Advanced Sustainable Systems*, vol. 1, no. 7, article 1700002, 2017.

[13] D. Sun, *Characterization of Medical Grade Poly-Dimethylsiloxane as Encapsulation Materials for Implantable Microelectromechanical Systems*, Case Western Reserve University, 2014.

[14] A. Nathan, A. Ahnood, M. T. Cole et al., "Flexible electronics: the next ubiquitous platform," *Proceedings of the IEEE*, vol. 100, pp. 1486–1517, 2012.

[15] J.-g. Liu, H.-j. Ni, Z.-h. Wang, S.-y. Yang, and W.-f. Zhou, "Colorless and transparent high–temperature-resistant polymer optical films–current status and potential applications in optoelectronic fabrications, in: optoelectronics-materials and devices," in *Optoelectronics - Materials and Devices*, IntechOpen, 2015.

[16] M. Kaltenbrunner, T. Sekitani, J. Reeder et al., "An ultra-lightweight design for imperceptible plastic electronics," *Nature*, vol. 499, no. 7459, pp. 458–463, 2013.

[17] C. J. Lee, S. J. Oh, J. K. Song, and S. J. Kim, "Neural signal recording using microelectrode arrays fabricated on liquid crystal polymer material," *Materials Science and Engineering C*, vol. 24, no. 1-2, pp. 265–268, 2004.

[18] M. Irimia-Vladu, P. A. Troshin, M. Reisinger et al., "Environmentally sustainable organic field effect transistors," *Organic Electronics*, vol. 11, no. 12, pp. 1974–1990, 2010.

[19] P. Boonvisut and M. C. Çavuşoğlu, "Estimation of soft tissue mechanical parameters from robotic manipulation data," *IEEE/ASME Transactions on Mechatronics*, vol. 18, no. 5, pp. 1602–1611, 2013.

[20] E. Series, *Super-soft, addition cure silicone rubbers, smooth-on*, 2015.

[21] T. R. Ray, J. Choi, A. J. Bandodkar et al., "Bio-integrated wearable systems: a comprehensive review," *Chemical Reviews*, vol. 119, no. 8, pp. 5461–5533, 2019.

[22] R. Riemer and A. Shapiro, "Biomechanical energy harvesting from human motion: theory, state of the art, design guidelines, and future directions," *Journal of Neuroengineering and Rehabilitation*, vol. 8, no. 1, p. 22, 2011.

[23] L. C. Rome, L. Flynn, E. M. Goldman, and T. D. Yoo, "Generating electricity while walking with loads," *Science*, vol. 309, no. 5741, pp. 1725–1728, 2005.

[24] D. Vélez Día and S. S. Moreno Gutiérrez, "Biomechanics and motor control of human movement," *XIKUA Boletín Científico de La Escuela Superior de Tlahuelilpan*, vol. 1, no. 1, 2013.

[25] J. Ortiz, *Wearable technologies*, Intech Open, Rijeka, Croatia, 2018.

[26] R. M. Alexander, "Biomechanics and motor control of human movement. David A. Winter," *The Quarterly Review of Biology*, vol. 66, no. 1, pp. 106–106, 1991.

[27] A. D. Winter, E. A. Patla, S. J. Frank, and E. S. Walt, "Biomechanical walking pattern changes in the fit and healthy elderly," *Physical Therapy*, vol. 70, no. 6, pp. 340–347, 1990.

[28] M. R. Shorten, "The energetics of running and running shoes," *Journal of Biomechanics*, vol. 26, pp. 41–51, 1993.

[29] L. M. Castano and A. B. Flatau, "Smart fabric sensors and e-textile technologies: a review," *Smart Materials and Structures*, vol. 23, no. 5, article 053001, 2014.

[30] A. A. Tracton, *Coatings Technology Handbook*, Taylor & Francis, 2006.

[31] S. Luo and W. J. Van Ooij, "Surface modification of textile fibers for improvement of adhesion to polymeric matrices: a review," *Journal of Adhesion Science and Technology*, vol. 16, no. 13, pp. 1715–1735, 2002.

[32] Z. L. Wang, L. Lin, J. Chen, S. Niu, and Y. Zi, "Harvesting body motion energy," in *Triboelectric Nanogenerators*, pp. 207–236, Springer, Switzerland, 2016.

[33] J. Y. Park, M. Salauddin, and M. S. Rasel, "Nanogenerator for scavenging low frequency vibrations," *Journal of Micromechanics and Microengineering*, vol. 29, article 053001, 2019.

[34] F. Yi, Z. Zhang, Z. Kang, Q. L. Liao, and Y. Zhang, "Recent advances in triboelectric nanogenerator-based health monitoring," *Advanced Functional Materials*, vol. 29, no. 41, article 1808849, 2019.

[35] F. Invernizzi, S. Dulio, M. Patrini, G. Guizzetti, and P. Mustarelli, "Energy harvesting from human motion: materials and techniques," *Chemical Society Reviews*, vol. 45, no. 20, pp. 5455–5473, 2016.

[36] Z. L. Wang, "Triboelectric nanogenerators as new energy technology for selfpowered systems and as active mechanical and chemical sensors," *ACS Nano*, vol. 7, no. 11, pp. 9533–9557, 2013.

[37] J. Chen, *Triboelectric Nanogenerators*, Georgia Institute of Technology, Atlanta, GA, USA, 2016, http://hdl.handle.net/1853/54956.

[38] Y. Zou, V. Raveendran, and J. Chen, "Wearable triboelectric nanogenerators for biomechanical energy harvesting," *Nano Energy*, vol. 77, p. 105303, 2020.

[39] K. Parida, G. Thangavel, G. Cai et al., "Extremely stretchable and self-healing conductor based on thermoplastic elastomer for all-three-dimensional printed triboelectric nanogenerator," *Nature Communications*, vol. 10, no. 1, p. 2158, 2019.

[40] T. He, Q. Shi, H. Wang et al., "Beyond energy harvesting-multi-functional triboelectric nanosensors on a textile," *Nano Energy*, vol. 57, pp. 338–352, 2019.

[41] C. Ning, L. Tian, X. Zhao et al., "Washable textile-structured single-electrode triboelectric nanogenerator for self-powered wearable electronics," *Journal of Materials Chemistry A*, vol. 6, no. 39, pp. 19143–19150, 2018.

[42] Z. Zhou, S. Padgett, Z. Cai et al., "Single-layered ultra-soft washable smart textiles for all-around ballistocardiograph, respiration, and posture monitoring during sleep," *Biosensors and Bioelectronics*, vol. 155, p. 112064, 2020.

[43] T. Zhou, C. Zhang, C. B. Han, F. R. Fan, W. Tang, and Z. L. Wang, "Woven structured triboelectric nanogenerator for wearable devices," *ACS Applied Materials & Interfaces*, vol. 6, no. 16, pp. 14695–14701, 2014.

[44] J. Chen, Y. Huang, N. Zhang et al., "Micro-cable structured textile for simultaneously harvesting solar and mechanical energy," *Nature Energy*, vol. 1, no. 10, 2016.

[45] W. Deng, T. Yang, L. Jin et al., "Cowpea-structured PVDF/ZnO nanofibers based flexible self-powered piezoelectric bending motion sensor towards remote control of gestures," *Nano Energy*, vol. 55, pp. 516–525, 2019.

[46] B. Yang and K.-S. Yun, "Piezoelectric shell structures as wearable energy harvesters for effective power generation at low-frequency movement," *Sensors and Actuators A: Physical*, vol. 188, pp. 427–433, 2012.

[47] E. Nilsson, L. Mateu, P. Spies, and B. Hagström, "Energy harvesting from piezoelectric textile fibers," *Process Engineering*, vol. 87, pp. 1569–1572, 2014.

[48] D. Matsouka, S. Vassiliadis, and D. V. Bayramol, "Piezoelectric textile fibres for wearable energy harvesting systems," *Materials Research Express*, vol. 5, no. 6, article 065508, 2018.

[49] E. Yang, Z. Xu, L. K. Chur et al., "Nanofibrous smart fabrics from twisted yarns of electrospun piezopolymer," *ACS Applied Materials & Interfaces*, vol. 9, no. 28, pp. 24220–24229, 2017.

[50] W. Zeng, X.-M. Tao, S. Chen, S. Shang, H. L. W. Chan, and S. H. Choy, "Highly durable all-fiber nanogenerator for mechanical energy harvesting," *Energy & Environmental Science*, vol. 6, no. 9, p. 2631, 2013.

[51] F. Mokhtari, G. M. Spinks, C. Fay et al., "Wearable electronic textiles from nanostructured piezoelectric fibers," *Advanced Materials Technologies*, vol. 5, no. 4, p. 1900900, 2020.

[52] F. Mokhtari, Z. Cheng, R. Raad, J. Xi, and J. Foroughi, "Piezofibers to smart textiles: a review on recent advances and future outlook for wearable technology," *Journal of Materials Chemistry A*, vol. 8, no. 19, pp. 9496–9522, 2020.

[53] Z. L. Wang, "From nanogenerators to piezotronics—A decade-long study of ZnO nanostructures," *MRS Bulletin*, vol. 37, no. 9, pp. 814–827, 2012.

[54] Z. L. Wang and J. Song, "Piezoelectric nanogenerators based on zinc oxide nanowire arrays," *Science*, vol. 312, no. 5771, pp. 242–246, 2006.

[55] Y. Qin, X. Wang, and Z. L. Wang, "Microfibre-nanowire hybrid structure for energy scavenging," *Nature*, vol. 451, no. 7180, pp. 809–813, 2008.

[56] R. Yang, Y. Qin, L. Dai, and Z. L. Wang, "Power generation with laterally packaged piezoelectric fine wires," *Nature Nanotechnology*, vol. 4, no. 1, pp. 34–39, 2009.

[57] L. Gu, N. Cui, L. Cheng et al., "Flexible fiber nanogenerator with 209 V output voltage directly powers a light-emitting diode," *Nano Letters*, vol. 13, no. 1, pp. 91–94, 2013.

[58] S. H. Ji, Y.-S. Cho, and J. S. Yun, "Wearable core-shell piezoelectric nanofiber yarns for body movement energy harvesting," *Nanomaterials*, vol. 9, no. 4, p. 555, 2019.

[59] Y. Du, K. F. Cai, S. Z. Shen et al., "Multifold enhancement of the output power of flexible thermoelectric generators made from cotton fabrics coated with conducting polymer," *RSC Advances*, vol. 7, no. 69, pp. 43737–43742, 2017.

[60] L. K. Allison and T. L. Andrew, "A wearable all-fabric thermoelectric generator," *Advanced Materials Technologies*, vol. 4, no. 5, p. 1800615, 2019.

[61] A. Lund, Y. Tian, S. Darabi, and C. Müller, "A polymer-based textile thermoelectric generator for wearable energy harvesting," *Journal of Power Sources*, vol. 480, article 228836, 2020.

Research Article

Properties and Modification of Bismuth-Layered Structure Ferroelectric Materials and Application in Sports

Guorong Jiang (ID)

School of Sports, Jiujiang University, Jiujiang, 332005 Jiangxi, China

Correspondence should be addressed to Guorong Jiang; 2021001548@poers.edu.pl

Bismuth-layered oxides are a very important class of ferroelectric materials. Due to their special structure, they have outstanding features in many aspects, such as high Curie temperature, large spontaneous polarization, polarization stability to temperature, high voltage resistance, low dielectric loss, and excellence. Due to its antifatigue properties, the system is very suitable for applications in nonvolatile random access memory and high-temperature sensors. The purpose of this paper is to study the application of the performance and modification of bismuth-layered ferroelectric materials in sports scientific research. Proposed the combination of new materials and sports scientific research projects. This article uses sample analysis and (the comparative experiment method is a method to compare the experimental group and the control group to illustrate the superiority of the experiment) comparative experiment methods, sets up an experimental group and a control group, summarizes the algorithm rules through the study of the microscopic properties of nanomaterials, and designs a numerical simulation program. The experimental results in this article show that after receiving hyperbaric oxygen recovery in the first week, the heart rate of the experimental group subjects has a significant change, which is significantly lower than the initial value ($p < 0.05$), from 58.0 to 53.0, The higher pressure oxygen had a very significant drop before recovery, from 62.9 to 53.0. In the second week and the third week, the heart rate index decreased significantly after 1 hour of hyperbaric oxygen recovery ($p < 0.01$), from 54.3 to 49.3 and 56.1 to 52.4, respectively. After the fourth week of intensity training, the heart rate increased significantly from the initial value ($p < 0.05$), from 49.6 to 55.2. After 1 hour of hyperbaric oxygen recovery, there was a significant decrease compared with before the hyperbaric oxygen recovery ($p < 0.05$), dropped from 55.2 to 53.1. Illustrate the success of the experimental results. It also completed the subject of interaction and combination of the performance and modification of bismuth-layered ferroelectric materials in sports scientific research.

1. Introduction

In a certain temperature, the ferroelectric material exhibits the characteristics of spontaneous polarization when there is no external electric field, and its polarization may have multiple directions. When an electric field is applied, the polarization direction changes with the change of the electric field. Generally, after the temperature exceeds a certain value, the spontaneous polarization of the ferroelectric material will disappear, and the ferroelectric material will become paraelectric. The transition between ferroelectricity and paraelectricity is called ferroelectric phase transition. Many physical properties of crystals at this temperature are different from usual, and the temperature of this transition is the Curie point of ferroelectrics. In addition to spontaneous polarization, the hysteresis loop is also an important way to observe whether a crystal is a ferroelectric. Research shows that the polarization intensity and direction of the crystal will exhibit a dielectric characteristic different from ordinary materials with the applied electric field. Ferroelectric materials are special electrolytes and have been extensively studied. It has a variety of polarization modes, which have different effects at different frequencies, so that the dielectric spectrum of different materials is very different. From the microscopic mechanism, it can be attributed to two different types: (1) displacement type and (2) order and disorder type. Frequency-tunable materials have potential applications in the fields of frequency selection,

absorption, imaging, and biology. Certain elements are sensitive to temperature changes. Doping these elements in ferroelectric materials can affect its dielectric properties. Ferroelectric materials are widely used in subject interaction due to their unique properties.

Multiferroic materials with ferromagnetism and ferroelectricity are mainly concentrated in transition metal (rare earth element) oxides, mainly due to their complex electronic structures and competing interactions. These competitions include charge, spin, orbital, and lattice degrees of freedom, which are more easily regulated by external means (such as electric field, magnetic field, and stress). At the same time, multiferrocity requires that the d or f orbitals of transition metals or rare earth elements must be partially filled with local electrons, and through exchange interactions between local moments, magnetic order (time reversal broken) is caused. On the other hand, for ferroelectric materials, in order to induce spontaneous polarization (spatial inversion broken), empty d orbitals are required. Few systems can meet these two requirements at the same time, so there are very few multi-iron materials in nature. According to the microscopic sources of different iron-containing properties, multicore materials can be divided into different types, and the magnetic properties of materials can generally be divided into paramagnetic, antiferromagnetic, and ferromagnetic. When the magnet is lower than the Curie temperature, it is ferromagnetic; when it is higher than the Curie temperature, it is macroscopically paramagnetic. Adjacent magnetic atoms have different magnetic coupling results, leading to different magnetic orientations, leading to different magnetic step settings. In the rectangular perovskite system, ferromagnetism (FM), the magnetic orientation of all its atoms is the same. For diamagnetism, there are four different magnetic orientations, namely, A-type diamagnetism (A-AFM): the orientation of the magnetic order of the atoms in the plane is the same, and the magnetic order of the atoms in the plane is opposite. Diamagnetic C-type (C-AFM): the magnetic order of atoms in the plane is diamagnetic order, and the magnetic order of atoms in the plane is diamagnetic. The magnetic order between the outer atoms is the same. Antimagnetic G (G-AFM): the magnetic sequence of the nearest neighbor is opposite. E-AFM: the magnetic orientation of diamagnetism is along the AC plane, and individuals with the same magnetic orientation are saw-shaped.

From 1935 to 1938, Basheer et al. discovered that the simple structure of potassium dihydrogen phosphate (KDP) and many of its isomorphic crystals are also piezoelectric, and all have high room temperature electromechanical coupling coefficients. But they did not propose the concept of piezoelectric effect [1]. The piezoelectric effect was first discovered in quartz crystal by Nie et al. in 1880. Its discovery led to the rapid development of piezoelectric devices and piezoelectric materials. However, due to time constraints, their research did not further analyze other media and materials related to the piezoelectric effect [2]. In 1954, Ketwong et al. discovered the quasihomomorphic phase boundary (MPB) of Pb $(Zr,Ti)O_3$(PZT) system solid solution. The ferroelectric near MPB has excellent dielectric and piezoelectric properties, and it is close to $BaTiO_3$

ceramics. The high electromechanical coupling coefficient has made piezoelectric materials widely used, but their research stopped here, and the ferroelectricity of subsequent perovskite structure compounds was not found [3].

The innovations of this paper are as follows: (1) in the research content, the macroscopic research method, the transfer matrix method, is selected to study the microstructure characteristics of the crystal. The characteristic matrix is used to express its interaction with electromagnetic waves. (2) The $Bi_4Ti_3O_{12}$ crystal was selected as the bismuth-layered ferroelectric material in this article. The crystal has stable properties, relatively good ferroelectricity, and convenient preparation. (3) The research and introduction of the ferroelectric polarization value have been carried out, making the concept of perfecting the text clear.

The new materials adopted in this article are combined with traditional sports scientific research to meet the needs of subject interaction.

2. Performance and Modification of Bismuth-Layered Structure Ferroelectric Materials and Application Methods in Sports Scientific

2.1. Ferroelectricity. The ferroelectric system is a substance that has spontaneous polarization after transitioning from a high-temperature phase to a low-temperature phase, and its polarization direction can be reversed by an external electric field [4]. Many properties of ferroelectric systems are similar to ferromagnets. For example, electric polarization (P) corresponds to magnetization (M), electric field (E) corresponds to magnetic field (H), and electric displacement (D) corresponds to magnetic flux density (B) [5]. At the same time, ferroelectric materials can form domains, and their polarization and electric displacement exhibit electric hysteresis loop behavior in the applied electric field. Therefore, ferroelectric materials can be used for data storage. Research has found that ferroelectric materials can also be used as capacitors, because the concentration of charge density in ferroelectric materials will cause them to have a high dielectric constant [6].

The early work of ferroelectric materials mainly focused on Rochelle salt, $KNa(C_4H_4O_6)\cdot4H_2O$. Although the research of Rochelle's salt has established many basic properties of ferroelectric materials, the complex structure and the large number of atoms in each cell make it difficult to give a microscopic theory to clarify ferroelectricity from an experimental point of view [7]. At present, the widely studied ferroelectric system is the perovskite structure oxide ABO3. The ideal perovskite structure is characterized by a cation (B) with a small particle radius, in the center composed of an anionic oxygen octahedron, and the particle radius. The larger cation (A) is at the apex of the primitive cell [8]. The relatively simple structure of perovskite allows researchers to study its ferroelectric properties in detail and have a deeper understanding of the basic principles of ferroelectricity [9].

Table 1 is an introduction to 32 crystallographic point groups.

TABLE 1: 32 crystallographic point groups.

T	Th	O	Td	Oh		
C4	S4	C4h	D4	C4v	D2d	D4h
D2	C2v	D2h				
C2	Cs	C2h				
C1	Ci					
C3	S6	D3	C3v	D3d		
C6	C3h	C6h	D6	C6v	D3h	D6h

Symmetry determines whether the system is ferroelectric. Among the 32 crystallographic point groups, 11 crystallographic point groups have a center of symmetry (centrosymmetric); that is, they do not have ferroelectricity; in the remaining 21 point groups, the O point group does not have ferroelectricity. The remaining 20 all show piezoelectric effect, but only 10 point groups have its specific polarity direction [10].

2.2. Preparation Technology. The traditional solid-phase melting process is used to manufacture bismuth-coated ceramic powder. The uniformity of the powder is low, and the melting temperature is high [11]. It is difficult to obtain ceramic samples with high density and excellent performance [12]. In recent years, some liquid chemical methods, such as sol-gel method, hydrothermal synthesis method, and other powder preparation methods, have gradually attracted the attention of scientific researchers [13]. The use of liquid chemical methods to manufacture ceramic powder can achieve molecular-level mixing between the various components of the material [14], with high product purity, large powder specific surface area, and high ceramic fusion temperature, which can also be reduced to a certain extent. The sol-gel method was used to prepare ceramic powder $(K_{0.16}Na_{0.84})_{0.5}Bi_{4.5}Ti_4O_{15}$ (KNBT) [15], and the phase structure and electrical properties were studied. Studies have found that when the composition temperature is 500°C, single-phase KNBT ceramic powder can be formed, and the Curie temperature of the ceramic sample is 659°C [16], which is higher than the Curie temperature of KNBT ceramic prepared by traditional methods. The ferroelectric ceramics of the $SrBi_4$-$xCexTi_4O_{15}$ system can also be successfully prepared by the sol-gel method. The study found that all ceramic samples formed a typical phase structure with a bismuth layer, and the Curie temperature of the samples was above 500°C [17]. In short, the use of different powder preparation techniques will definitely have different effects on the structure and performance of ceramic samples [18]. This liquid chemical method can prepare ceramic powder with uniform particle size and large specific surface area. However, the cost of raw materials used in this type of process is high, the experimental process is complicated, and the organic solvent used in the reaction process is toxic and difficult to achieve. Batches of lead-free bismuth piezoelectric ceramics have a wide range of applications in industrial production and can be used in the research of this article [19].

Lead-free dual-structure piezoelectric materials are widely used in the research of ferroelectric thin films and devices due to their fatigue resistance and high-temperature Curie characteristics [20]. However, due to the limitation of its own structure, it is difficult to effectively improve the two-level performance of ceramics, ferroelectric properties, and piezoelectric properties [21, 22]. The physical and chemical properties of materials are determined by the structure of the material, and the structure of the material is related to the composition of the material. Therefore, replacing the composition and structure of ceramic crystals with doping is an effective measure to improve the electrical properties of bismuth ceramics [23, 24]. This type of method has low preparation cost and simple process and is suitable for a wide range of applications [25]. At present, the doping modification methods of bismuth lead-free piezoelectric ceramics mainly include A-site substitution, B-site substitution, and additive modification [26].

2.3. Transfer Matrix Method. The matrix transmission method (TMM) is a method that combines the knowledge of Maxwell's equations (It is a set of partial differential equations established by British physicist James Clark Maxwell in the 19th century to describe the relationship between electric field, magnetic field, charge density, and current density.) and optical matrices to calculate the transmission and reflection propagation of electromagnetic waves in multiple layers of different media structures. The propagation of electromagnetic waves in the intermediate layer is considered to be the superposition of incident electromagnetic waves and reflected electromagnetic waves. The tangent continuous state of the electromagnetic field is satisfied at the limit of each intermediate layer, and its interaction with electromagnetic waves can be represented by a characteristic matrix. Assuming that the field vectors on both sides of the dielectric layer are EI and HI and EII and HII, the relationship between them can be linked by the characteristic matrix:

$$\begin{bmatrix} E_1 \\ H_1 \end{bmatrix} = M \begin{bmatrix} E_{11} \\ H_{11} \end{bmatrix}. \tag{1}$$

For interface I,

$$\left\{ \begin{array}{l} E_1 = E_{i1} + E_{r1} = E_{t1} + E'_{r2} \\ H_1 = H_{i1} \cos \theta_{i1} - H_{r1} \cos \theta_{i1} \end{array} \right\}. \tag{2}$$

In the same way, in interface II,

$$\left\{ \begin{array}{l} E_{II} = E_{i2} + E_{r2} = E_{r2} + E'_{r3} \\ H_{II} = H_{i2} \cos \theta_{i2} - H_{r2} \cos \theta_{i2} \end{array} \right\}. \tag{3}$$

The thickness of the medium nb is b (that is, the distance between the interfaces I and II), and the formula of

the transmission field E_{t1} on the interface I and the incident field E_{i2} of the interface II is shown in

$$\begin{cases} E_{t1} = E_{t10} e^{-i(k_x x + k_z z)} \big|_{z=0}, \\ E_{t2} = E_{t10} e^{-i(k_x x + k_z z)} \big|_{z=b} = E_{t1} e^{i\delta_b}. \end{cases} \tag{4}$$

The phase difference when the electromagnetic plane wave crosses the two interfaces perpendicularly is

$$\delta_b = -k_z h_b = -\frac{\omega}{c} n_b b \cos \theta_b. \tag{5}$$

The same goes for

$$E'_{r2} = E_{r2} e^{i\delta_b}. \tag{6}$$

Organize to get

$$\begin{cases} E_1 = \cos \delta_b E_{\mathrm{II}} - \dfrac{1}{\eta_b} \sin \delta_b H_{\mathrm{II}}, \\ H_1 = -i\eta_b \sin \delta_b E_{\mathrm{II}} + \cos \delta_b H_{\mathrm{II}}, \end{cases} \tag{7}$$

where

$$\eta_b = \sqrt{\frac{\varepsilon_0}{\mu_0}} \sqrt{\frac{\varepsilon_r}{\mu_0}} \cos \theta_b. \tag{8}$$

In matrix form, there are

$$\begin{bmatrix} E_1 \\ H_1 \end{bmatrix} = \begin{bmatrix} \cos \delta_b & -\dfrac{1}{\eta_b} \sin \delta_b \\ -i\eta_b \sin \delta_b & \cos \delta_b \end{bmatrix} \begin{bmatrix} E_{\mathrm{II}} \\ H_{\mathrm{II}} \end{bmatrix}. \tag{9}$$

The characteristic matrix of any dielectric layer j is

$$M_j = \begin{bmatrix} \cos \delta_j & -\dfrac{i}{\eta_j} \sin \delta_j \\ -i\eta_j \sin \delta_j & \cos \delta_j \end{bmatrix}. \tag{10}$$

For the case in TTE mode, where

$$\begin{cases} \delta_j = -\dfrac{\omega}{c} n_j h_j \cos \theta_j, \\ n_j = \sqrt{\dfrac{\varsigma_0}{\mu_0}} \sqrt{\dfrac{\mu_j}{\varepsilon_j}} \cos \theta_j. \end{cases} \tag{11}$$

In the case of TM mode, the other formulas are the same, but the key variables are replaced:

$$n_j = \sqrt{\frac{\mu_0}{\varepsilon_0}} \sqrt{\frac{\mu_j}{\varepsilon_j}} \cos \theta_j. \tag{12}$$

For multilayer media, it can be applied layer by layer, then:

$$\begin{bmatrix} E_1 \\ H_1 \end{bmatrix} = M_1 M_2 \cdots M_{N-1} M_N \begin{bmatrix} E_{N+1} \\ H_{N+1} \end{bmatrix} = \begin{bmatrix} A & B \\ C & D \end{bmatrix} \begin{bmatrix} E_{N+1} \\ H_{N+1} \end{bmatrix}. \tag{13}$$

The transmittance T, reflectance R, and absorptance A are

$$\begin{cases} T = |t|^2, \\ R = |r|^2, \\ A = 1 - T - R. \end{cases} \tag{14}$$

Among them,

$$\begin{cases} \delta_a = -\dfrac{\omega}{c} n_a a \cos \theta_a, \\ \delta_b = -\dfrac{\omega}{c} n_b b \cos \theta_b, \\ \eta_a = \sqrt{\dfrac{\varepsilon_0}{\mu_0}} \sqrt{\dfrac{\varepsilon_0}{\mu_0}} \cos \theta_a, \\ \eta_b = \sqrt{\dfrac{\varepsilon_0}{\mu_0}} \sqrt{\dfrac{\varepsilon_0}{\mu_0}} \cos \theta_b. \end{cases} \tag{15}$$

In summary, the introduction of the transmission matrix method is complete, and the experiment is ready to begin.

3. Performance and Modification of Bismuth-Layered Structure Ferroelectric Materials and Application Experiments in Sports Scientific

3.1. Preparation and Application of $Bi_4Ti_3O_{12}$ Powder. $Bi_4Ti_3O_{12}$ material has a low forbidden band width and photocatalytic activity, and its absorbable spectral range can be extended to the visible light range through the method of nanomaterialization or doping modification of the material. This plays an important role in improving the utilization of sunlight. In addition, it is a typical ferroelectric material with good ferroelectric and piezoelectric properties. In this chapter, $Bi_4Ti_3O_{12}$ powder is prepared by hydrothermal method, and the role of hydrothermal temperature in the preparation process is discussed. The key work of this chapter is to apply ultrasound and light to $Bi_4Ti_3O_{12}$ powder at the same time. It is expected that ultrasound can be used to activate the piezoelectric properties of bismuth titanate, to achieve polarization of bismuth titanate powder, and to improve its photocatalytic efficiency.

In this paper, $Bi_4Ti_3O_{12}$ powder is prepared by hydrothermal method. The preparation process can be divided into three steps: preparation of hydrothermal reaction precursor, hydrothermal reaction, and heat treatment of hydrothermal product. Among them, bismuth nitrate is used as

TABLE 2: The main drugs needed for the experiment.

Reagent name	Specification	Manufacturer
Bismuth nitrate	Analytically pure	Sinopharm
Tetrabutyl titanate	Analytically pure	Sinopharm
Ethylene glycol monomethyl ether	Analytically pure	Sinopharm
Glacial acetic acid	Analytically pure	Coron
Acetylacetone	Analytically pure	Sinopharm
Disodium ethylenediaminetetraacetate	Analytically pure	Sinopharm
Tert-butanol	Analytically pure	Sinopharm

TABLE 3: Basic situation of the athlete group.

Group	Number	Average age	Average height	Average weight	Main item 5/10 km	Marathon	Sport level International master	Master
Athlete	130	23.1	169.29	55.53	91	31	43	79
Male athlete	65	24.27	174.98	61.48	46	15	11	50
Female athlete	65	20.84	163.53	49.48	45	16	32	29

TABLE 4: Basic situation of the control group.

Group	Number	Average age	Average height	Average weight
Control	130	21.53	173.4	63.99
Male	65	20.29	174.95	69.23
Female	65	19.96	163.03	56.97

the titanium source, tetrabutyl titanate is used as the bismuth source, and 3 mol/L NaOH solution is used as the mineralizer for the hydrothermal reaction. First, 30 mL of glacial acetic acid and 30 mL of ethylene glycol methyl ether are mixed, and then, 9.7 g of bismuth nitrate is added to form solution A; then, 5.10 g of tetrabutyl titanate is dissolved in 20 mL of ethylene glycol methyl ether to form solution B. Finally, solution B was slowly added to solution A, and an appropriate amount of ethylene glycol methyl ether was added to prepare a 0.05 M bismuth titanate sol. After drying the sol, a dry gel is obtained, and the dry gel is ground and dissolved in a mineralizer to prepare a hydrothermal reaction precursor. After the preparation of the hydrothermal precursor is completed, the hydrothermal precursor solution is put into the reaction kettle and put into the oven for hydrothermal reaction. Through literature research and consideration of experimental safety, three hydrothermal temperature points of 160°C, 180°C, and 200°C that do not exceed 200°C are selected for the experiment, and the holding time is 24 h.

The main experimental drugs are shown in Table 2.

3.2. Objects of Experiments. The subjects of this study are divided into the excellent long-distance runner group (case) and the general population control group (control group).

The basic situation of the outstanding long-distance runner group is shown in Table 3.

The athletes and ordinary personnel in this experiment were taken from two classes in a major physical education department and a certain electrical engineering department

with the same basic situation, each with 130 students as samples.

The basic situation of the control group is shown in Table 4.

3.3. Test Instrument and Test Index. The equipment used in the exercise capacity test is hyperbaric oxygen equipment, 0.035 MPa, and the maximum working load is 0.05 MPa.

In the HRV test, the omega wave test and analysis system are used to collect signals, and Excel is used for index calculation. Use the SPSS24.0 software statistical package to perform statistical processing on the data. $p < 0.05$ indicates a significant difference.

4. Application of the Performance and Modification of Bismuth-Layered Ferroelectric Materials in Sports Scientific

4.1. Influence of $Bi_4Ti_3O_{12}$ on the Quiet Heart Rate of Middle and Long Distance Runners. Figure 1 shows the initial value of heart rate in the experimental group during the experimental period, before the recovery of hyperbaric oxygen, and the change of resting heart rate after 1 hour of recovery.

After receiving hyperbaric oxygen recovery in the first week, the heart rate of subjects in the experimental group changed significantly from the initial value ($p < 0.05$), from 58.0 to 53.0, before the higher oxygen pressure was restored. There has been a very significant drop, from 62.9 to 53.0. In the second week and the third week, the heart rate index decreased significantly after 1 hour of hyperbaric oxygen
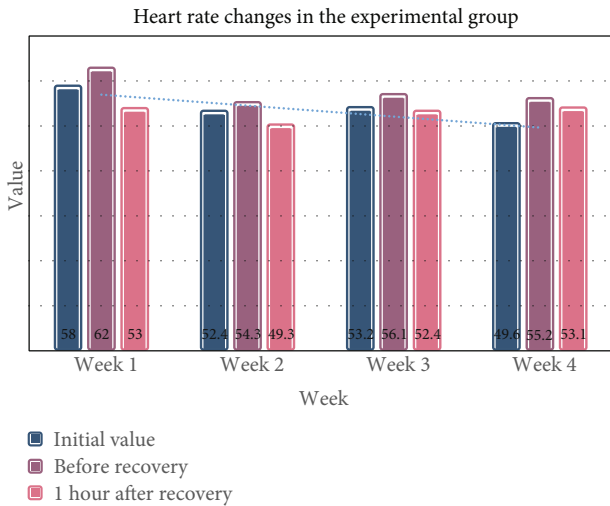
Figure 1: Heart rate changes in the experimental group.
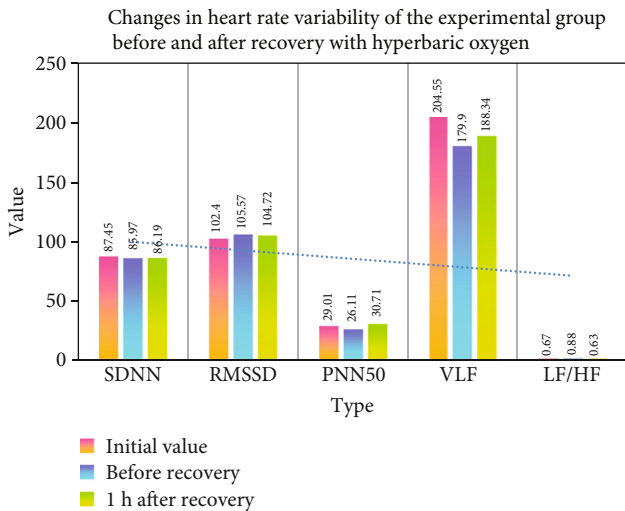
Figure 2: Changes in heart rate variability of the experimental group before and after recovery with hyperbaric oxygen in the first week.

recovery ($p < 0.01$), from 54.3 to 49.3 and 56.1 to 52.4, respectively. After the fourth week of intensity training, the heart rate increased significantly from the initial value ($p < 0.05$), from 49.6 to 55.2. After 1 hour of hyperbaric oxygen recovery, there was a significant decrease compared with before the hyperbaric oxygen recovery ($p < 0.05$), dropped from 55.2 to 53.1.

The changes in heart rate variability of the experimental group before and after recovery using hyperbaric oxygen in the first week are shown in Figure 2.

It can be seen that there is no significant change in the time domain indicators of heart rate variability.

The initial value of the experimental group in the second week, before the recovery of hyperbaric oxygen, and the change of heart rate variability index after the recovery of hyperbaric oxygen for 1 hour are shown in Figure 3.

In the second week, the time domain indicators SDNN, RMSSD, and PNN50 of the experimental group showed a
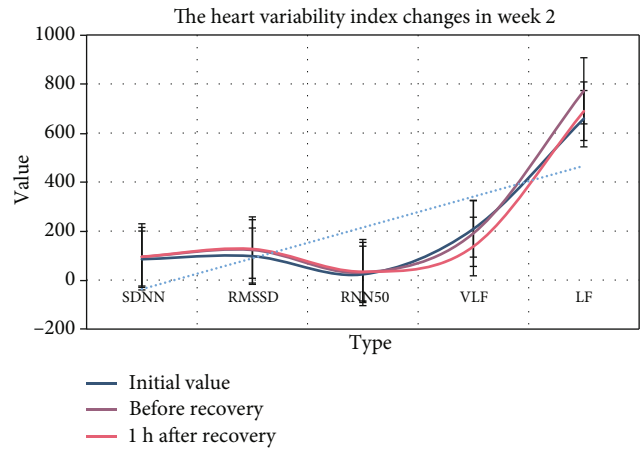
Figure 3: The initial value of the experimental group in the second week, before the recovery of hyperbaric oxygen, and the change of heart rate variability index after 1 hour of hyperbaric oxygen recovery.
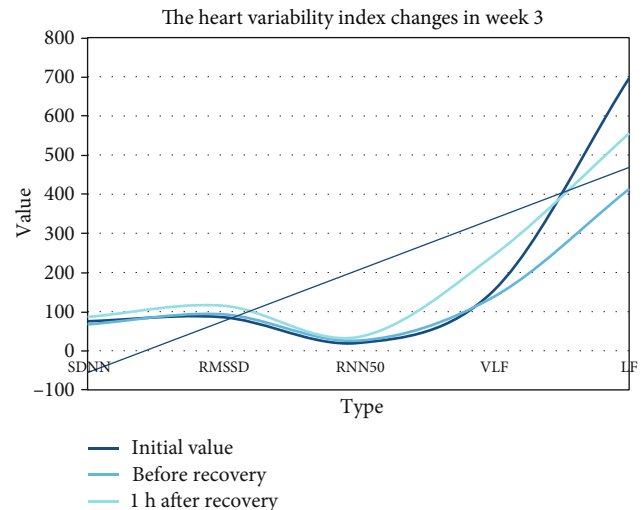
Figure 4: The initial value of the experimental group in the third week, before the recovery of hyperbaric oxygen, and the change of heart rate variability index after the recovery of hyperbaric oxygen for 1 hour.

slight upward trend from the initial value before the hyperbaric oxygen recovery and 1 h after receiving the hyperbaric oxygen recovery, but there was no significant difference. One hour after the recovery of hyperbaric oxygen, the change before the recovery of higher pressure oxygen was not obvious. The VLF in the frequency domain indicators of the subjects decreased sequentially, but there was no significant difference. The change of HF and LF is not obvious.

The initial value of the experimental group in the third week, before the recovery of hyperbaric oxygen, and the change of heart rate variability index after the recovery of hyperbaric oxygen for 1 hour are shown in Figure 4.

It can be seen from the above table that in the time domain index, the initial value of PNN50, the value before hyperbaric oxygen recovery, and the value after hyperbaric
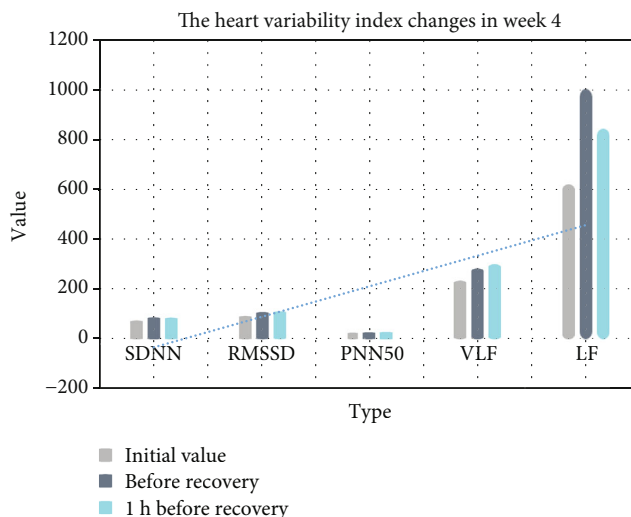
Figure 5: The heart variability index changes in week 4.

Table 5: The experimental group did not apply hyperbaric oxygen for two weeks during the observation period to restore the changes in heart rate variability.

Heart rate variability index	First week of observation period	Second week of observation period
SDNN	85.12	70.80
RMSSD	85.65	81.54
PNN50	22.04	19.99
VLF	305.77	209.38
HF	165.13	1095.35
LF	817.80	537.79
HF/LF	1.17	1.35

Table 6: The calculated ferroelectric polarization of ABX_3 perovskite halide compounds.

System	Px	Py	Pz	Ptot
MASncl$_3$	-8.68	0.94	9.58	12.96
MASnBr$_3$	8.03	8.67	-15.08	19.16
MASnI$_3$	-3.78	0.00	15.63	16.08
MAPbCl$_3$	4.01	4.59	-11.48	13.00
MAPbBr$_3$	-3.38	-3.60	11.70	12.70
MAPbI$_3$	2.68	2.68	13.52	14.03
FASnC$_{13}$	3.30	-4.64	-13.85	14.98

Px refers to the microscopic component of the material on the x-axis.

oxygen recovery 1 h showed a sequential upward trend, and the initial value after 1 h hyperbaric oxygen recovery appeared compared with the initial value. There was a significant increase ($p < 0.05$), from 19.93 to 35.12, and the RMSSD value also showed an upward trend, but there was no significant change. In the frequency domain indicators, both VLF and LF showed a downward trend and then an upward trend. HF showed a sequential upward trend, but there was no significant difference. LF/HF showed a downward trend, but it did not appear significant.

The initial value of the experimental group in the fourth week, before the recovery of hyperbaric oxygen, and the change of heart rate variability index after the recovery of hyperbaric oxygen for 1 hour are shown in Figure 5:

In the time domain index, the value of RMSSD in the experimental group was higher after 1 hour of hyperbaric oxygen recovery, and there was a significant increase ($p < 0.05$), from 108.91 to 111.70, while the changes in SDNN and PNN50 were not very obvious and not significant. In the frequency domain parameters of the subjects, HF increased significantly ($p < 0.05$) from 1354 to 1683 after receiving hyperbaric oxygen treatment for 1 hour than before hyperbaric oxygen recovery. LF also increased from the initial value before hyperbaric oxygen recovery. After

TABLE 7: Estimated Rashba parameters for organohalide perovskites.

| | Er | | Ke | | aR | |
	VB	CB	VB	CB	VB	CB
MASncl$_3$	7.19	182.38	0.04	0.16	0.37	2.28
MASnBr$_3$	18.87	143.52	0.03	0.09	1.28	3.29
MASnI$_3$	28.44	99.45	0.04	0.06	1.56	3.12
MAPbCl$_3$	7.81	113.41	0.02	0.09	0.65	2.56
MAPbBr$_3$	25.88	120.30	0.04	0.08	1.28	3.01
MAPbI$_3$	72.62	136.01	0.08	0.08	1.86	3.50
FASnC$_{I3}$	8.62	142.97	0.0.3	0.13	0.49	2.18

TABLE 8: Crystal information and refinement conditions of $Bi_4Ti_3O_{12}$ at room temperature.

Atom	Site	X	y	z	100Uiso/A2	Occupancy
Bil	4a	0.25	0.7726 (14)	0	0.95	0.505
Lal	4a	0.25	0.7726 (14)	0	0.95	0.495
Bi2	8b	0.244 (9)	0.7266 (9)	0.21672 (8)	1.05	0.757
La2	8b	0.244 (9)	0.7266 (9)	0.21672 (8)	1.05	0.243
Bi3	8b	0.248 (8)	0.7804 (8)	0.10695 (10)	1.09	0.952
La3	8b	0.248 (8)	0.7804 (8)	0.10695 (10)	1.09	0.018
Ti1	8b	0.252 (19)	0.257 (4)	0.0586 (4)	0.19	0.75

receiving treatment for 1 hour, the trend of AIDS decreased, but there was no significant change.

In the fifth and sixth weeks, the experimental group stopped hyperbaric oxygen during the observation period and resumed the initial value of the heart rate on the week, as shown in Table 5.

The subjects' various time-domain indicators have declined, but there is no significant difference, and there is little change. The values of VLF and LF have a downward trend, HF does not change significantly, and LF/HF rises, but there is no significant difference. SDNN is an indicator of heart rate variability; generally, it is greater than 100.

4.2. Iron Polarization Value. The ferroelectric polarization value is zero for the antiferroelectric structure ($\lambda = 0$), and the subsequent trend shows that a nonmonotonic line increases with λ. The nonmonotonic behavior as a lambda function is common in the case of organic-inorganic hybrid compounds. At the same time, the components of the total ferroelectric polarization vector and the modulus of the vector are calculated by the first principles, as shown in Table 6.

The estimated Rashba coefficient in organic halide perovskite is shown in Table 7.

4.3. $Bi_4Ti_3O_{12}$ Microstructure and Ferroelectric Properties. Table 8 is the crystal information and refinement conditions of $Bi_4Ti_3O_{12}$ at room temperature.

It can be seen from the table that the contribution of the total spontaneous polarization of $Bi_4Ti_3O_{12}$ is better, and the ferroelectricity is increased. It shows that the phase reversal does come from signal polarization reversal and ferroelectric behavior, which is higher than 0.26 nm in OPP mode.

5. Conclusions

The experimental results show that the performance and modification research of the bismuth-layered ferroelectric material proposed in this paper is applied in sports scientific research. Compared with the current traditional sports scientific research, due to the use of a new type of bismuth-layered ferroelectric material, as a result, the effect of scientific research is better. After athletes use the material for long-distance running assistance, all data and performance have increased significantly. The observation effect is better, the data collection is more accurate, and it is more convenient for sports-assisted scientific research personnel and researchers to judge and test. In this paper, sample collection method, comparison experiment method, and transmission matrix method are used to design a method to calculate the transmittance and reflectance of electromagnetic wave propagation in multilayer different media structures by combining the knowledge of Maxwell's equation and matrix optics. And the changes in heart rate variability before and after 4-week recovery with hyperbaric oxygen in the control and experimental groups were also tested. The experimental results showed that after receiving hyperbaric oxygen recovery in the first week, the heart rate of the experimental group subjects changed significantly, which was significantly lower than the initial value ($p < 0.05$), from 58.0 to 53.0. There was a very significant drop before hyperbaric oxygen recovery, from 62.9 to 53.0. In the second week and the third week, the heart rate index decreased significantly after 1 hour of hyperbaric oxygen recovery ($p < 0.01$), from 54.3 to 49.3 and 56.1 to 52.4, respectively. After the fourth week of intensity training, the heart rate increased significantly from the initial value ($p < 0.05$), from 49.6 to 55.2. After 1 hour of

hyperbaric oxygen recovery, there was a significant decrease compared with before the hyperbaric oxygen recovery ($p < 0.05$), dropped from 55.2 to 53.1. It illustrates the success of the experiment results after the ferroelectric material is used in sports scientific research. It also completed the subject of interaction and combination of the performance and modification of bismuth-layered ferroelectric materials in sports scientific research. The shortcomings of this article are as follows: (1) use long-distance running as the basis of the subject for research and does not consider sports such as long jump and various ball sports. In future research, the research content can be gradually improved and expanded to more sports items. (2) Among the research materials in this article, due to the limitation of experimental site and funding, only the research on $Bi_4Ti_3O_{12}$, a layered bismuth ferroelectric material, has been carried out. In future research, efforts can be made to find bismuth-layered ferroelectric materials with cheaper prices, better experimental results, and ferroelectric properties more in line with experimental requirements. (3) Due to time and space constraints, this article only conducted a 4-week training for the two groups to collect heart rate indicators. In future research, the experimental time and interval length can be extended to ensure the scientific reliability of the experimental results.

Data Availability

No data were used to support this study.

Conflicts of Interest

There is no potential conflict of interest in this study.

References

[1] M. A. Basheer, G. Prasad, G. S. Kumar, and N. V. Prasad, "Raman and electrical studies on $Bi_2SmTiNbO_9$ ceramics," *Ferroelectrics*, vol. 517, no. 1, pp. 75–80, 2017.

[2] R. Nie, J. Yuan, and J. Zhu, "Influence of co-modification with tungsten and tantalum on the crystal structure and electrical properties of bismuth titanate ceramics," *Journal of Materials Science Materials in Electronics*, vol. 30, no. 15, pp. 14445–14455, 2019.

[3] P. Ketwong, P. Kidkhunthod, and P. Pookmanee, "Effect of ethanol assistance on chemical structure of ferroelectric bismuth vanadate via solvothermal method," *Integrated Ferroelectrics*, vol. 175, no. 1, pp. 9–17, 2016.

[4] Z. Liu, A. R. Paterson, H. Wu, P. Gao, W. Ren, and Z. G. Ye, "Synthesis, structure and piezo-/ferroelectric properties of a novel bismuth-containing ternary complex perovskite solid solution," *Journal of Materials Chemistry C*, vol. 5, no. 16, pp. 3916–3923, 2017.

[5] E. V. Ramana, N. V. Prasad, D. M. Tobaldi et al., "Effect of samarium and vanadium co-doping on structure, ferroelectric and photocatalytic properties of bismuth titanate," *RSC Advances*, vol. 7, no. 16, pp. 9680–9692, 2017.

[6] T. Obayashi, M. Kobune, T. Matsunaga et al., "Effects of Pt sacrificial layer on microfabrication in layered bismuth-based fer-

[7] H. Maleki, "Photocatalytic activity, optical and ferroelectric properties of $Bi_{0.8}Nd_{0.2}FeO_3$ nanoparticles synthesized by sol-gel and hydrothermal methods," *Journal of Magnetism& Magnetic Materials*, vol. 458, no. 1, pp. 277–284, 2018.

[8] S. N. Das, S. Pradhan, S. Bhuyan, R. N. Choudhary, and P. Das, "Modification of relaxor and impedance spectroscopy properties of lead magnesium niobate by bismuth ferrite," *Journal of Electronic Materials*, vol. 46, no. 3, pp. 1637–1649, 2017.

[9] Y. Zhang, M. Yuan, B. Jiang, P. Li, and X. Zheng, "Effect of mesoporous structure on $Bi_{3.25}La_{0.75}Ti_3O_{12}$ powder for humidity sensing properties," *Sensors& Actuators B Chemical*, vol. 229, no. 2, pp. 453–460, 2016.

[10] X. Chen, F. Huang, Z. Lu et al., "Influence of transition metal doping (X=Mn, Fe, Co, Ni) on the structure and bandgap of ferroelectric $Bi_{3.15}Nd_{0.85}Ti_2X_1O_{12}$," *American Political Science Review*, vol. 54, no. 2, pp. 948–979, 2017.

[11] X. Chen, F. Huang, Z. Lu et al., "Influence of transition metal doping (X=Mn, Fe, Co, Ni) on the structure and bandgap of ferroelectric $Bi_{3.15}Nd_{0.85}Ti_2X_1O_{12}$," *Journal of Physics: D Applied Physics*, vol. 50, no. 10, article 105104, 2017.

[12] M. Hasan, M. A. Hakim, M. A. Basith et al., "Size dependent magnetic and electrical properties of Ba-doped nanocrystalline $BiFeO_3$," *AIP Advances*, vol. 6, no. 3, pp. 2–8, 2016.

[13] G. Hernandez-Cuevas, J. R. Leyva Mendoza, P. E. García-Casillas et al., "Effect of the sintering technique on the ferroelectric and d_{33} piezoelectric coefficients of $Bi_{0.5}(Na_{0.84}K_{0.16})_{0.5}TiO_3$ ceramic," *Journal of Advanced Ceramics*, vol. 8, no. 2, pp. 278–288, 2019.

[14] E. D. Politova, G. M. Kaleva, N. V. Golubko et al., "Specific features of the structure and properties of high-temperature oxide materials based on bismuth sodium titanate," *Crystallography Reports*, vol. 63, no. 2, pp. 266–270, 2018.

[15] L. X. Chen, C. Xu, X. L. Fan, X. H. Cao, K. Ji, and C. H. Yang, "Study on leakage current, ferroelectric and dielectric properties of BFMO thin films with different bismuth contents," *Journal of Materials Science: Materials in Electronics*, vol. 30, no. 8, pp. 1–7, 2019.

[16] I. Soibam and M. A. Devadatta, "Optimisation and the effect of addition of extra bismuth on the dielectric and optical properties of bismuth ferrite (BFO)," *Materials Today Proceedings*, vol. 5, no. 1, pp. 2064–2073, 2018.

[17] R. A. Golda, A. Marikani, and E. J. Alex, "Effect of ceramic fillers on the dielectric, ferroelectric and magnetic properties of polymer nanocomposites for flexible electronics," *Journal of Electronic Materials*, vol. 50, no. 6, pp. 3652–3667, 2021.

[18] L. Thansanga, A. Shukla, N. Kumar, and R. N. Choudhary, "Study of effect of Dy substitution on structural, dielectric, impedance and magnetic properties of bismuth ferrite," *Journal of Materials Science: Materials in Electronics*, vol. 31, no. 13, pp. 10006–10017, 2020.

[19] A. Panda, R. Govindaraj, R. Mythili, and G. Amarendra, "Formation of bismuth iron oxide based core–shell structures and their dielectric, ferroelectric and magnetic properties," *Journal of Materials Chemistry C*, vol. 7, no. 5, pp. 1280–1291, 2019.

[20] C. Aydin, H. Aydin, M. Taskin, and F. Yakuphanoglu, "A novel study: the effect of graphene oxide on the morphology, crystal structure, optical and electrical properties of lanthanum ferrite based nano electroceramics synthesized by hydrothermal

roelectric thin films," *Transactions of the Materials Research Society of Japan*, vol. 45, no. 2, pp. 31–34, 2020.

method," *Journal of Nanoscience and Nanotechnology*, vol. 19, no. 5, pp. 2547–2555, 2019.

[21] N. A. Zhuk, S. V. Nekipelov, D. S. Beznosikov, L. V. Rychkova, M. V. Yermolina, and B. A. Makeev, "Magnetic properties and NEXAFS-spectroscopy of Co-doped ferroelectric ceramic $Bi_5Nb_3O_{15}$," *Letters on Materials*, vol. 9, no. 4, pp. 405–408, 2019.

[22] D. Ruth, L. Venkidu, and B. Sundarakannan, "Structure–property relation to enhance the piezoelectric and ferroelectric properties in $(Na_{0.5}Bi_{0.5})$ TiO_3-based non-MPB lead-free piezoelectric ceramics," *Journal of Materials Science: Materials in Electronics*, vol. 29, no. 7, pp. 5433–5438, 2018.

[23] S. Chakraborty, S. Mukherjee, and S. Mukherjee, "Effect of yttrium doping on the properties of bismuth ferrite: a review," *International Journal of Semiconductor Science& Technology*, vol. 8, no. 2, pp. 23–32, 2018.

[24] G. Parida and J. Bera, "Effects of CuO additive on ferroelectric and dielectric properties of Nb doped $SrBi_8Ti_7O_{27}$ ceramics," *Journal of Materials Science Materials in Electronics*, vol. 27, no. 5, pp. 5309–5314, 2016.

[25] A. Klr, B. Ds, and A. Db, "Gamma irradiation induced structural, electrical, magnetic and ferroelectric transformation in bismuth doped nanosized cobalt ferrite for various applications," *Materials Research Bulletin*, vol. 110, no. 10, pp. 126–134, 2019.

Hindawi

Retraction

Retracted: Application Effect Analysis of a Nanotube Combined with Orthopedic Exercise Rehabilitation Therapy in the Treatment of Patients with Knee Arthritis

Journal of Nanomaterials

This article has been retracted by Hindawi following an investigation undertaken by the publisher [1]. This investigation has uncovered evidence of one or more of the following indicators of systematic manipulation of the publication process:

(1) Discrepancies in scope
(2) Discrepancies in the description of the research reported
(3) Discrepancies between the availability of data and the research described
(4) Inappropriate citations
(5) Incoherent, meaningless and/or irrelevant content included in the article
(6) Peer-review manipulation

The presence of these indicators undermines our confidence in the integrity of the article's content and we cannot, therefore, vouch for its reliability. Please note that this notice is intended solely to alert readers that the content of this article is unreliable. We have not investigated whether authors were aware of or involved in the systematic manipulation of the publication process.

In addition, our investigation has also shown that one or more of the following human-subject reporting requirements has not been met in this article: ethical approval by an Institutional Review Board (IRB) committee or equivalent, patient/participant consent to participate, and/or agreement to publish patient/participant details (where relevant).

Wiley and Hindawi regrets that the usual quality checks did not identify these issues before publication and have since put additional measures in place to safeguard research integrity.

We wish to credit our own Research Integrity and Research Publishing teams and anonymous and named external researchers and research integrity experts for contributing to this investigation.

The corresponding author, as the representative of all authors, has been given the opportunity to register their agreement or disagreement to this retraction. We have kept a record of any response received.

References

[1] J. Zhang and Z. Xing, "Application Effect Analysis of a Nanotube Combined with Orthopedic Exercise Rehabilitation Therapy in the Treatment of Patients with Knee Arthritis," *Journal of Nanomaterials*, vol. 2022, Article ID 1275250, 9 pages, 2022.

Research Article

Application Effect Analysis of a Nanotube Combined with Orthopedic Exercise Rehabilitation Therapy in the Treatment of Patients with Knee Arthritis

Jie Zhang[1] and Zhongyou Xing [2]

[1]*Physical Education Teaching and Research Section, Zhumadian Preschool Education College, Zhumadian, 463000 Henan, China*
[2]*College of Physical Education, Xuchang University, Xuchang, 461000 Henan, China*

Correspondence should be addressed to Zhongyou Xing; 11992005@xcu.edu.cn

Knee arthritis is one of the common diseases with the highest incidence in osteoarthrosis, which seriously affects people's health, and as the patient's medical history prolongs, the pain degree becomes more and more serious. In recent years, with the rapid development of nanotechnology, its application scope has gradually been involved the medical field. The application of nanotube-targeted drugs to treat osteoarthritis can repair bone to a certain extent and relieve patient pain symptom. Sports rehabilitation therapy, as an important nursing method in orthopedic treatment, can improve the patient's body recovery ability and enhance the therapeutic effect of surgery. Based on this, this article proposes the application research of a nanotube combined with exercise rehabilitation therapy in the treatment of patients with knee arthritis. The research carried out in this article is mainly divided into three parts: the first part is the research of titanium dioxide nanotubes in orthopedic treatment, studying the diameter and drug loading of nanotubes, research on how to target the damaged bone tissue and release drugs, and discussing the tissue compatibility and safety of nanotubes to the human body; the second part is the study on exercise rehabilitation therapy in orthopedic treatment and study on how to exercise properly to enhance the patient's body recovery; the third part is clinical investigation and research, according to the observation group in contrast with the indicators of the control group to draw conclusions. The results of this experiment show that in the clinical treatment of knee arthritis surgery, in the analysis of postoperative patients, the scores of the three groups of patients before treatment were relatively low, with scores ranging from 5 to 8, but the scores of the observation group were significantly higher than those of the first and second groups. The observation group ranged from 7 to 10. The joint scores of the observation group gradually increased at 1 week and 2 weeks after treatment. The increase in functional score was more pronounced. For patients with a longer medical history, perform appropriate helping exercises. Titanium dioxide nanotubes have good antibacterial properties as an endoplant and good histocompatibility with human bones. In the observation group combined with exercise therapy, various complications such as pain, swelling, and muscle atrophy were relatively small, allowing the patient to speed up the recovery of various body functions.

1. Introduction

As one of the human organs, bones have important functions that many other organs do not have, such as maintaining body posture, exercising, and supporting muscles and organ tissues. Degenerative osteoarthritis, also known as osteoarthritis, degenerative arthritis, senile arthritis, and hypertrophic arthritis, is a degenerative disease caused by

aging, obesity, strain, trauma, congenital abnormalities of joints, joint degeneration of articular cartilage, and joint edge and subchondral bone-reactive hyperplasia caused by many factors such as deformity. Osteoarthritis [1] is a kind of synovial arthritis, which is very common in clinical treatment, and knee osteoarthritis [2, 3] has the highest incidence. It is more common in middle-aged and elderly people and occurs in weight-bearing joints and joints with

more activities (such as the cervical spine, lumbar spine, knee joint, and hip joint). Excessive weight bearing or use of these joints can promote degenerative changes. At the onset, symptoms include cartilage damage, joint pain, infection, and a prolonged medical history. Relevant investigations have shown that every year, more than one million arthritis patients undergo implant repair [4] and related knee joint surgery. Some patients undergo a series of complications such as internal infections after the surgery, which leads to implantation failure. A second operation is required. Curing OA can only slow symptoms or delay the progression of the disease. OA treatment methods are divided into surgical treatment and nonsurgical treatment. Relieving or eliminating pain and controlling the development of inflammation are the main methods for the treatment of OA at present. With the continuous development of tissue engineering and materials science, researchers have used nanoparticles as drug carriers to inhibit the inflammatory response and promote cartilage repair in OA patients. Therefore, in order to solve a series of problems that may arise, it is a common method to use therapeutic drugs to treat bone diseases. It is a common method to transport the therapeutic drugs to the damaged bone tissue through a certain carrier. Because the composition and function of bone tissue are quite different from other human tissues, especially in cases of fracture, trauma, or cancer with impaired blood supply, the effect of medication is not good.

Infection of the implant site in orthopedic treatment [5, 6] is one of the most difficult complications in orthopedic surgery, ranging from delaying the treatment cycle and increasing treatment costs to amputation or death due to infection. There are generally two reasons for orthopedic prosthesis infection: firstly, bacterial adhesion [7] forms a biofilm on the surface of the implant, which hinders the body's immune response and the killing effect of antibiotics on bacteria. Secondly, because the implant material has poor biocompatibility and cannot form a firm bond with human bone, the fiber layer of the implant osseointegration interface will reduce the local resistance of the host. Therefore, finding nanomaterials with excellent antibacterial properties [8] is of great value for reducing the infectivity of internal implants and prolonging the service life and promoting the development of high-end orthopedic implants with independent intellectual property rights. In the nursing process before and after orthopedic surgery, rehabilitation training is an important part of fracture recovery treatment and the effect of independent exercise is unmatched by other treatment methods. It can enhance the recovery effect of the patient's function, which is very conducive to the recovery of the patient's body, and greatly reduces the postoperative mortality and disability rate of the patient. Based on this, nanotubes combined with exercise rehabilitation therapy [9–11] have great application potential in the treatment of knee arthritis. As a plant medicine carrier in orthopedics, it has a good clinical effect and has great potential for improving the clinical treatment of knee arthritis. However, for the research on knee arthritis injury caused by nanotubes and exercise rehabilitation therapy, the definition and thinking of traditional

exercise therapy have not been removed, so that the two cannot be well combined.

Nanomaterials are widely used in energy, materials, biology, medicine, and other fields due to their superior physical and chemical properties. With the development of materials science, osteoarthritis has been developed and its focus is on repair and reconstruction. Finding materials with good human tissue compatibility, strong mechanical properties, and strong antibacterial ability has always been a difficult point in orthopedics. As a newly developed material, TiO_2 nanotubes [12, 13] have better human tissue compatibility and strong anti-infection performance than commonly used orthopedic materials such as stainless steel, titanium alloy, polyethylene, and ceramics. In addition, by changing the diameter of the nanotube, the thickness of the tube wall, the length of the tube, and the amount of drug loaded, the damaged bone tissue can be targeted and the drug can be released, which has a long-lasting antibacterial effect of the implant. In addition, its nanopore morphology [14] can be suitable for a variety of cell adhesion and growth, achieving good compatibility with human tissues [15]. On this basis, as an important integrated treatment, nursing staff must develop a corresponding rehabilitation exercise plan for the patient. And according to the degree of disease and medical history of orthopedic patients, the patients are arranged for corresponding preoperative and postoperative exercises. Compared with injection of DEX or CDMP-1 alone, intra-articular injection of CDMP-1 and DEX-loaded discoid lipid nanoparticle DLNPs can significantly reduce the levels of inflammatory factors in serum and synovial tissue of knee arthritis and can significantly reduce the levels of inflammatory factors in knee arthritis. Promote the repair of damaged cartilage, and delay or avoid the occurrence of joint replacement surgery. This study suggests that the discoid lipid nanoparticles loaded with synergistic drugs with sustained release have broad development space in clinical practice [16].

The research carried out in this paper is mainly divided into three parts: the first part is the research of titanium dioxide nanotubes in orthopedic treatment. Titanium dioxide nanotubes are another form of TiO_2. Because nanotube nanofilms have a relatively large surface area ratio, so, it has a high adsorption capacity and can achieve compatibility with human tissues, especially the addition of other equipment to the nanotubes for assembly into advanced nanomaterials, which will improve all aspects of the performance of titanium dioxide to a certain extent. In this paper, TiO_2 nanotubes are used as antibacterial drugs and growth factor carriers to study the application of knee arthritis; the second part is the study of sports rehabilitation therapy in orthopedic treatment. Rehabilitation exercises for orthopedic patients can reduce postoperative pain, eliminate swelling in the surgical area and surrounding areas, avoid various complications such as muscle atrophy, and enable patients to speed up the recovery of various body functions. In the orthopedic nursing process, the nursing staff should pay close attention to the various indicators of the patient's body and do a good job in the communication between the doctor and family members and the content of family care. The self-

confidence of recovery must be established for the patient, so that the patient's sports rehabilitation can be realized. The third part is the clinical investigation and research part. Investigate the therapeutic improvement degree, clinical effect, and patient satisfaction of titanium dioxide nanotubes as a new nanomaterial in the treatment of knee arthritis. This article will discuss in detail the advantages and disadvantages of nanotechnology and explore the feasibility of nanotechnology combined with sports rehabilitation therapy to treat knee arthritis. In this paper, the efficacy, clinical effect and patient satisfaction of titanium dioxide nanotubes as a new nanomaterial in the treatment of knee arthritis were investigated. This article will discuss in detail the advantages and disadvantages of nanotechnology and explore the feasibility of combining nanotechnology with the rehabilitation of knee arthritis [17].

2. Treatment of Knee Arthritis Based on Titanium Dioxide Nanotubes

The TiO_2 nanotube materials prepared in orthopedic research are often prepared using the surface layer of pure titanium or titanium alloy. Observing the TiO_2 nanotube under an electron microscope, it can be found that it is composed of a large number of uniform tubular structures. Each tubular structure is hollow in the middle, the top is open, and the bottom is closed. The specific surface area of the entire tubular structure is large and porous. This is a special structure used for drug carrier adsorption. The research of TiO_2 nanotubes in orthopedics can be divided into two aspects: one is to study the biocompatibility of TiO_2 nanotubes, that is, to study bone fusion and bone growth, and to study the application of TiO_2 nanotubes as antibacterial drug carriers, including drug load, anti-infection, and antitumor. Related studies have found that TiO_2 nanotubes can resist the adhesion of bacteria and the surface layer of nanotubes with a diameter of 80 nm can resist the adhesion of bacteria and promote the production of biofilms. Because of this feature, it can reduce the risk of infection for patients, so it is a new type of simple antibacterial nanomaterial.

2.1. Biocompatibility of TiO_2 Nanotubes

2.1.1. Research on Histocompatibility. TiO_2 nanotubes have a special structure that promotes bone formation. The frosted surface of the nanotube is conducive to cell adhesion, cell proliferation, and cell diffusion. Its structure diagram is shown in Figure 1.

It can be seen in Figure 1 that it has the following characteristics:

(1) Compared with traditional titanium, the growth capacity of osteoblasts on the surface of nanotubes is increased by 200%–300%, which can greatly improve the activity of osteoblasts and the deposition of materials on the surface of bone cells

(2) Previous studies have shown that the enhancement of bone formation ability on the surface of nanotubes is related to the diameter of nanotubes. The diameter
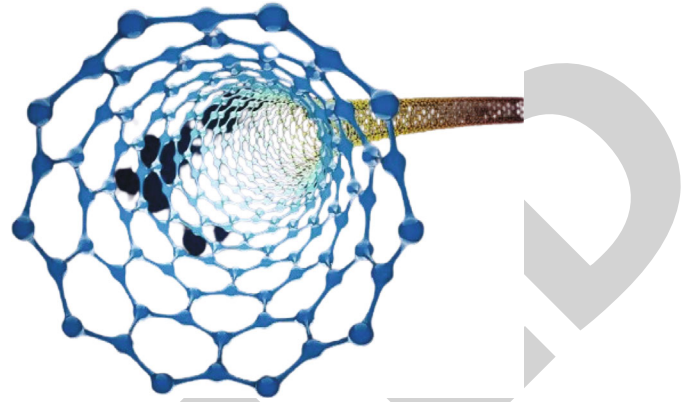
FIGURE 1: Structure diagram of titanium dioxide nanotubes.

of TiO_2 nanotubes can significantly promote the adhesion and proliferation of osteoblasts, thereby affecting the differentiation and proliferation of osteoblasts. When the diameter of the nozzle is about 30 nm, it is conducive to cell adhesion; when the diameter is 100 nm, the cell adhesion begins to decrease. Under this condition, the proliferation of osteoblasts and the increase of alkaline phosphatase activity begin to accelerate. When the diameter is between 30 nm and 100 nm, TiO_2 nanotubes are very suitable for osseointegration surgery

(3) The biocompatibility of titanium nanoparticles' surface layer with osteoblasts is quite good, which can cause the nanomaterials to merge with primitive bone cells, boosting the stability of the interior components [18]

(4) The special structure of nanotubes not only promotes bone fusion but also eliminates the body's immune rejection response

(5) The research on nanotubes is limited and not comprehensive enough

2.1.2. Research on Improving Biocompatibility with Growth Factors. TiO_2 nanotubes can use the combination with growth factors to enhance bone formation and promote tissue compatibility. The TiO_2 nanotube array can be used as a carrier to achieve bone cell fusion of human bone. Relevant studies have shown that the combination of TiO_2 nanotube array and bone morphogenetic protein can greatly promote the differentiation of stem cells into bone cells in the human body, resulting in better surgical results. However, although TiO_2 nanotubes can improve the adhesion and activity of fibroblasts, no studies have shown that TiO_2 nanotubes can promote the adhesion and growth of fibroblasts [19].

2.2. Application of TiO_2 Nanotubes as Drug Carriers

2.2.1. Loaded Silver (Ag). Silver has been widely used as an antibacterial substance a long time ago, and its antibacterial mechanism is more complicated. In recent years, with the production of nanosilver, silver as an antibacterial drug has become more and more popular. Due to its good electrical

conductivity, nanosilver particles occupy an extremely important position in the field of microelectronics. The surface effect and quantum size effect of nanosilver particles also make them have some special uses, such as surface-enhanced Raman applications and medical applications [20]. Silver nanoparticles have a large surface area, so they can be in contact with microorganisms. They can attack bacteria and release a substance to damage the cell wall, which can effectively kill bacteria. The study found that the antibacterial activity after loading silver was significantly higher than that of the control titanium surface and the nonsilver nanotube surface and it had no adverse effect on the adhesion and growth of bone cells. Zhao et al. found that the surface layer of titanium dioxide nanotubes containing silver nanoparticle bubbles immersed in AgNO solution can effectively kill early bacteria and effectively inhibit bacterial adhesion. However, it is worth noting that Ag+ may also cause cell toxicity in humans, especially in areas where Ag+ may accumulate. Therefore, it is necessary to deeply study the regulation of the nanotube structure and the release control of silver and other metal ions.

2.2.2. Contains Antibiotics. TiO_2 nanotubes are used as a powerful carrier to release antibacterial drugs, thereby forming a local receptor system on the bone surface. The research results of Popa et al. showed that lyophilization of gentamicin into TiO_2 nanotubes can resist the growth of bacteria to a certain extent and will not affect the adhesion, proliferation, and proliferation of osteoblasts near the nanotubes. Differentiation. Research by Gulati et al. found that a titanium rod with a diameter of 70 mm was placed in a TiO_2 nanotube in a PBS solution, and it was found that the drug was released slowly within 6 hours before the rapid release and the drug was released with zero-order kinetics. The above two-stage drug release stage shows that TiO_2 nanotubes meet the needs of targeted drug release. In addition, in order to delay the release time of the drug and achieve long-term antibacterial effect, the TiO_2 nanotube drug carrier can be covered with a polymer coating and the drug release can be controlled by a slow speed.

2.2.3. Containing Antimicrobial Peptides. Antibacterial peptides (AMPs) are a kind of peptides, composed of no more than 50 amino acids. This is an antibiotic and is unlikely to develop resistance. Related studies have shown that the use of vacuum-assisted physical adsorption technology to fill antimicrobial peptides into TiO_2 nanotubes can achieve targeted effective sterilization and inhibit bacterial adhesion and the release kinetics of nanotubes is closely related to the crystal type. Nitric oxide (NO), also known as an endothelial relaxing factor, can relieve the body's vascular tension, and by producing some substances, it destroys the bacterial cell membrane and DNA, thereby producing antibacterial effects. Smith et al.'s experimental research on animal implantation showed that the NO release system with titanium dioxide nanotubes as a carrier was discussed. The surface of titanium dioxide nanotubes can significantly reduce the surrounding NO level, fibrous tissue thickness, and macrophage concentration. Therefore, the NO release

system using titanium dioxide nanotubes as a carrier needs further research and demonstration. In addition, the combination of antibacterial drugs albumin and quaternary ammonium salts with titanium dioxide nanotubes must be further studied for verification. So far, more than 1200 antimicrobial peptides have been identified. The antibacterial peptides were loaded onto the titanium dioxide nanotubes by physical methods to study the antibacterial ability of the antibacterial peptides against Gram-positive bacteria and *Staphylococcus aureus*. After 2 hours of cultivation, the antibacterial peptides on the surface of the nanotubes can destroy bacteria and reduce the number of bacteria.

2.2.4. Antibacterial Agent. Gentamicin in the antibacterial inner plant coating is a broad-spectrum antibiotic that has been extensively studied and is more sensitive to *Staphylococcus aureus*. Related studies have found that 80 nm nanotubes loaded with gentamicin have better antistaphylococcal effects than nanotubes without gentamicin. Compared with traditional titanium sheets, TiO_2 with or without gentamicin can significantly facilitate cell adhesion, proliferation, and differentiation of adult bone. Gallium nitrate is a new type of antibacterial agent. The gallium ions formed by ionization can strongly resist the production of iron ions, thereby inhibiting the metabolic activity of bacteria. Gallium nitrate can resist the production of *E. coli* and the accumulation of *E. coli*. The titanium gallium nitrate plate was immersed in the serum and incubated at 36°C. Antibacterial activity can be maintained for up to 30 days. Therefore, implants coated with gallium nitrate can resist the reproduction of bacteria on its surface.

2.2.5. Contains Antitumor Drugs. Because of the larger specific surface area and better surface activity of TiO_2 nanotubes, a large number of researchers have studied in vitro the filling, release, and anticancer effects of doxorubicin and 5-fluorouracil on TiO_2 nanotubes. The physical adsorption method can be used to fill doxorubicin into the TiO_2 nanotubes, and the pH value can be adjusted by adjusting the release solution. Corresponding in vitro experiments show that the best loading time is 12 hours, and the total release rate of doxorubicin is greater than 75%. Nanotubes loaded with uracil have very good drug release kinetics and selective killing ability to cancer cells. In summary, TiO_2 nanotubes are promising anticancer drug carriers.

2.3. Problems with TiO_2 Nanotubes. At present, although a large number of studies have been conducted on TiO_2 nanotubes at home and abroad, there are still deficiencies in clinical application treatment, so there is no generally recognized stable application. TiO_2 nanotubes have better human histocompatibility and strong anti-infective properties. At present, the preparation of uniform and stable nanotubes requires a lot of material research. The study of TiO_2 nanotubes in knee arthritis is mainly limited to in vitro studies, so it is impossible to specifically express the specific conditions in vivo. The coating and drug loading of TiO_2 nanotubes are incomplete in terms of drug loading, targeted drug release, and stability. Based on this, although the

research on TiO_2 nanotubes is not thorough enough, the preparation process of TiO_2 nanotubes is less complicated and less harmful to the human body, has large drug loading, and has good antibacterial properties. It is a promising orthopaedic implant material with great potential value.

3. Research on Sports Rehabilitation in Knee Arthritis

In the nursing process before and after orthopedic surgery, rehabilitation training is an important part of fracture recovery treatment and the effect of independent exercise is unmatched by other treatment methods. It can enhance the recovery effect of the patient's function, which is very conducive to the recovery of the patient's body. Through postinjury rehabilitation training, the body's energy metabolism can be balanced, preventing weight gain and shortening the time required to resume exercise after injury [21].

3.1. Necessity of Sports Health Treatment in the Treatment of Knee Arthritis. Symptoms of knee stiffness usually occur after knee surgery, which will greatly affect the patient's walking posture and reduce the subjective well-being of life. Relevant studies have shown that the incidence of knee stiffness after knee surgery is 10% to 16%. However, proper exercise, light stretching, and regular walking can significantly reduce the occurrence of knee stiffness. This article studies the effect of sports rehabilitation therapy on knee stiffness. It is found that good therapeutic effects have been obtained in the early rehabilitation training investigation of patients with knee stiffness.

This study selected 60 patients with knee stiffness after surgery, including 38 males and 22 females, with an average age of 47 years. The patients were divided into three groups according to the order of admission.

3.2. Method. Group 1 uses common knee joint treatment clinical methods and conventional medical care, group 2 uses TiO_2 nanotubes to carry antibacterial drugs for knee arthritis treatment and conventional medical care, and group 3 uses TiO_2 nanotubes to carry antibacterial drugs for knee arthritis treatment and professional sports rehabilitation therapy, among which group 1 and group 2 are used as the control group and group 3 is used as the observation group. Before rehabilitative training, their body will experience different pain conditions; the specific method is as follows:

(1) Psychological counseling

In the course of rehabilitation training after knee arthritis surgery, the patient's confidence in recovery plays an important role in the recovery of the disease. Because of the stiffness of the knee, the flexion and extension of the patient are restricted to a certain extent, which greatly affects the quality of life of the patient, and the patient often feels a decrease in inner happiness. Therefore, nurses should pay close attention to the patients actively and give them a certain degree of psychological counseling, so that the patients can control their emotions and have an optimistic and confident attitude towards recovery. In addition to eliminating the patient's dependence on psychological surgery and equipment, we should also actively cooperate with nursing staff to carry out functional exercises.

(2) Pain care

Patients with stiff knees will experience pain after surgery, which is the main reason that affects the recovery of patients. Before the anesthesia effect disappears, advance recovery training is required. During exercise, an analgesic pump can be used to reduce the pain caused by exercise. After the analgesic pump is relieved, analgesic drugs can be taken immediately to reduce pain and accelerate the recovery of knee joint function.

(3) Actively exercise

From the patient's activity ability, guide and encourage the patient to exercise actively and tell the patient not to rush to achieve the immediate effect of overexercising, but to exercise patiently and confidently, so as to promote fracture recovery.

(4) Dynamic auxiliary physical therapy

For patients with a long medical history, appropriate assistance exercises should be carried out. Because the patient has not recovered well, he cannot carry out voluntary exercise training and needs to rely on others to carry out exercises within a certain range of strength. Only in this way can the health recovery of the illness be achieved. Therefore, the nurse or family member must provide some help to the patient, especially when lying down [22].

(5) Massage

For patients with stiff knee joints, caregivers should actively tell their family members to massage the biological part of the patient's muscles. Massage can promote blood circulation and increase the blood supply to the osteoarthritis surgery site, reduce muscle swelling and pain, and improve patient satisfaction with nursing. However, it is worth noting that during exercise, the strength of the massage should be adjusted to avoid secondary injuries. The intensity should not be too high; otherwise, the exercise effect will be difficult to achieve.

The observation group adopted the above nursing methods, while the control group adopted methods (1), (2), and (3). The postoperative active and assisted activity records of the control group and the observation group are shown in Table 1. The autonomous and assisted movement ranges of the two groups of patients have been expanded. However, the movement angle of the observation group was significantly higher than that of the control after recovery. ($P < 0.05$).

3.3. Evaluation Index. The range of flexion motion between the maximum flexion and the maximum elongation of the

TABLE 1: The range of physical activity of the three groups of patients.

Group	Before recovery		After recovery	
	Autonomous range of motion	Power range of motion	Autonomous range of motion	Power range of motion
Group 1	61.65	68.32	77.14	92.17
Group 2	63.47	72.16	87.42	101.42
Group 3	69.21	75.85	98.18	110.26

knee joint before and after nursing was measured, and the active and passive angles of the knee joints in the two groups were evaluated.

The simple life scale is used to assess the quality of life of patients after surgery. The indicators include physical pain, limb stretching, mental health, social activities, and overall health. 10 points in the score is the upper limit; the higher the score, the better the patient's quality of life. The quality of life scores of the observation group was higher than that of the control group in all indicators. Therefore, it can be concluded that, compared with ordinary nursing care, the addition of specialized exercise therapy intervention after surgery can effectively speed up the recovery of knee joint function and not only improve the patient's quality of life during illness but also make the patient recover better and better. At the same time, from the perspective of the patient, the communication between the doctor and the patient is increased and the patient's satisfaction with the treatment is improved. The postoperative quality of life of the patients was assessed by observing various indicators.

3.4. Statistical Methods. SPSS statistical software can analyze the relationship between single variables and multiple variables. The chi-square test was used to compare the incidence of intraoperative and postoperative complications and the rate of stone clearance. The factors with statistical significance ($P < 0.05$) were used as independent variables and whether blood transfusion treatment was used as the dependent variable. The t-test was used for comparison between groups. When $P < 0.05$, it is considered statistically significant. The chi-square test formula is as follows:

$$\chi^2 = \sum_{i=1}^{k} \frac{(f_i - np_i)^2}{np_i}. \tag{1}$$

Among them, χ^2 is the test statistic, n is the number of experiments, and f_i is the group frequency.

3.5. Advantages of Sports Health Treatment. In the course of rehabilitation training after knee arthritis, the patient's confidence in recovery plays an important role in the recovery of the condition:

(1) Because of the stiffness of the knee, the patient's flexion and extension are restricted to a certain extent, which greatly affects the patient's quality of life. The caregiver and family members massage some of the patient's muscles. Massage can promote blood circulation and improve the osteoarthritis surgery site. Blood supply can reduce muscle swelling and pain and stiffness

(2) Normal nursing includes effective methods such as psychological counseling, pain nursing, massage, and adding exercise fixation belts. The observation group's nursing involves professional sports rehabilitation and rehabilitation projects. In the process, rehabilitation training is an important part of fracture recovery treatment and the effect of independent exercise is unmatched by other treatment methods. It can enhance the recovery effect of the patient's function, which is very conducive to the recovery of the patient's body, and greatly reduces the postoperative mortality and disability rate of the patient

(3) During training, attention should be paid to alleviating the pain of the patient, such as early recovery training before the effect of anesthesia disappears. During exercise, an analgesic pump can be used to reduce the pain caused by exercise. After the analgesic pump is relieved, analgesic drugs can be taken immediately to reduce pain and accelerate the recovery of knee joint function

Because the number of research subjects in this study is small, the results of the survey have certain flaws. If the number of researchers is expanded, I believe that more valuable research results can be obtained.

4. Survey Results and Analysis

In this study, 60 patients with knee stiffness after surgery were selected as the research objects, including 38 males and 22 females, with an average age of 47 years. According to the order of admission, the patients were divided into an observation group and two control groups. Among them, age, gender, and knee stiffness are the characteristics of this experiment, which are important factors that determine the degree of nanomaterials for knee injury repair.

Group 1 adopts common knee joint treatment clinical methods and routine medical care, group 2 adopts TiO_2 nanotubes to carry antibacterial drugs for knee arthritis treatment and routine medical care, and group 3 adopts TiO_2 nanotubes to carry antibacterial drugs for knee arthritis treatment and professional sports rehabilitation therapy, among which group 1 and group 2 are used as the control group, and group 3 is used as the observation group. Specific investigation and research found that among the three groups compared, the observation group had higher scores of physical pain, physical function, mental health, social function, and overall health compared with the control group. It can be seen that rehabilitation nursing intervention is more effective than conventional nursing. Promote the recovery of knee joint function, improve the quality of daily life, and help patients return to normal home and work life better and faster.
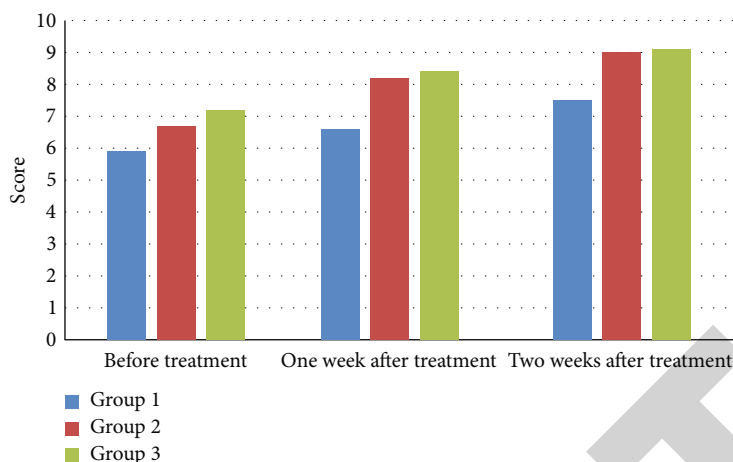
Figure 2: Comparison of knee joint activity scores before and after treatment in the three groups.
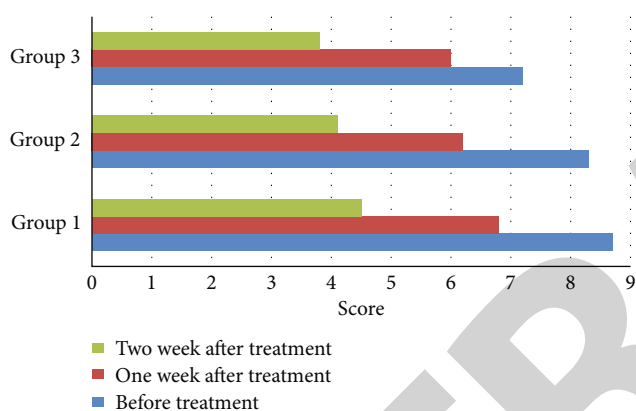
Figure 3: Comparison of pain scores before and after treatment in the three groups.

It can be seen in Figure 2 that the knee joint activity scores of the three groups before and after treatment are significantly different. The scores of the three groups of patients before treatment were relatively low, but the scores of the observation group were significantly higher than those of groups 1 and 2. The joint scores of the observation group gradually increased one week and two weeks after treatment. The functional score increased more significantly. For patients with a long medical history, carry out appropriate help exercises. Because the patient has not recovered well, he cannot carry out voluntary exercise training and needs to rely on others to carry out exercises within a certain range of strength. Therefore, the nurse or family member must provide some help to the patient, especially when lying down. Patients with stiff knees will experience pain after surgery, which is the main reason that affects the recovery of patients. Before the anesthesia effect disappears, advance recovery training is required. During exercise, an analgesic pump can be used to reduce the pain caused by exercise. After the analgesic pump is relieved, analgesic drugs can be taken immediately to reduce the pain and accelerate the recovery of knee joint function, so the observation group can achieve a healthy recovery from the disease. Therefore, compared with patients without nanomaterials to heal knee joints and conventional treatment, patients after using nanotubes and exercise rehabilitation therapy are more effective for knee arthritis recovery.

It can be seen in Figure 3 that the pain scores of the three groups before and after treatment are significantly different. Before the treatment, the scores of the three groups of patients were relatively low but the scores of group 3 were significantly higher than those of groups 1 and 2. The pain scores of one week and two weeks after treatment were significantly reduced. Compared with the control group, the observation group's pain score decreased more obviously. The use of the sports fixation belt device is customized for patients with special conditions. The exercise fixation belt used for postoperative recovery can reduce the swelling of the patient's body, help restore the patient's muscle strength, accelerate the patient's nerve to touch recovery, and enhance the patient's ability to take care of themselves. Before the anesthesia effect disappears, advance recovery training is required. During exercise, an analgesic pump can be used to reduce the pain caused by exercise. After the analgesic pump is relieved, analgesic drugs can be taken immediately to reduce the pain and accelerate the recovery of knee joint function.

It can be seen in Figure 4 that the scores of pains, mental health, social function, and swelling of the three groups before and after treatment have obvious differences. The scores of various indicators of the observation group are significantly higher than those of the control group. In the course of rehabilitation training after knee arthritis surgery, the patient's confidence in recovery plays an important role in the recovery of the disease. Because of the stiffness of the knee, the flexion and extension of the patient are restricted to a certain extent, which greatly affects the quality of life of the patient, and the patient often feels a decrease in inner happiness. Therefore, nurses should pay close attention to the patients actively and give them a certain degree of psychological counseling, so that the patients can control their emotions and have an optimistic and confident attitude towards recovery.

It can be seen in Figure 5 that all the study subjects are very satisfied with the preoperative and postoperative care.
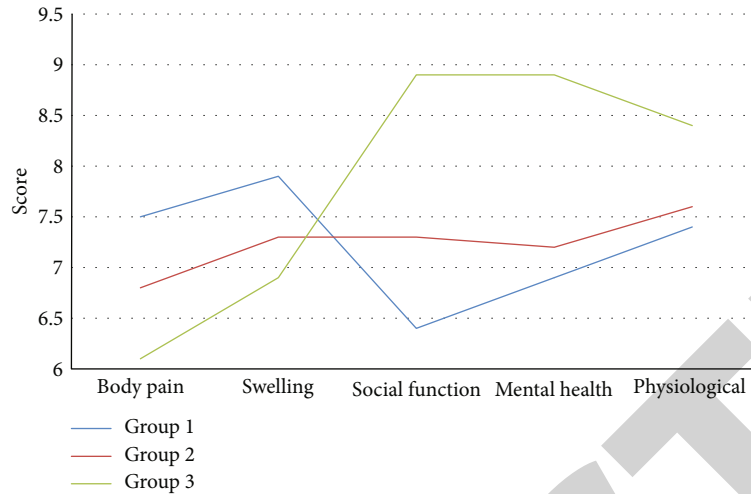
Figure 4: Comparison of quality of life scores before and after treatment in the three groups.
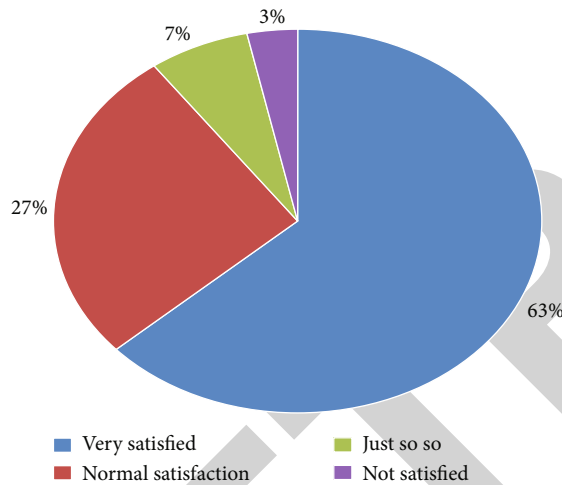
Figure 5: Patient satisfaction with surgery.

The patient's critical period is 24 hours after the operation. The nursing staff carefully observe the changes in the patient's physical signs. The patient will be tested every half an hour after the operation. If any abnormality is found, please inform the doctor for proper treatment in time. After the vital signs are stable, test once every 2 hours. When the patient was conscious, the nursing staff did the first time to tell the patient the news of the success of the operation and actively guided the family members to master some of the contents and methods of nursing, which greatly helped the patient to relieve the pressure and improve the family's understanding of nursing work. In addition, nurses observe the color and volume of the urinary tube and nephrostomy tube at regular intervals and make a record; for patients with knee stiffness, the nurse should actively tell the family to massage the patient's biological muscles, which can promote blood circulation. Increasing the blood supply to the osteoarthritis surgery site can reduce muscle swelling and pain and improve patient satisfaction with nursing care.

5. Conclusions

Osteoarthritis is a type of synovial arthritis, which is very common in clinical treatment, and knee osteoarthritis has the highest incidence. In recent years, TiO_2 nanotubes, as a newly developed material, have better human tissue compatibility and strong anti-infection performance than commonly used orthopedic materials such as stainless steel, titanium alloy, polyethylene, and ceramics. In addition, by adjusting the diameter and drug loading of the nanotubes, the damaged bone tissue can be targeted and the drug can be released and the internal implantation has a long-lasting antibacterial effect. Sports rehabilitation therapy combined with important nursing methods in orthopedic treatment can enable patients to speed up the recovery of various body functions. In this paper, the research of titanium dioxide nanotubes in orthopedic treatment is carried out and how the diameter and drug loading of TiO_2 nanotubes affect the recovery of damaged cells, as well as the tissue compatibility and safety of nanotubes to the human body. At the same time, a comprehensive analysis of the enhancement of exercise rehabilitation therapy to the patient's physical recovery ability is also carried out. Clinical investigation and analysis showed that according to the assessment of the simple life scale, the postoperative quality of life, social activities, mental health, and physical function of the observation group were higher than those of the control group. The movement of nanomaterials is of great importance in research in many fields of medicine, which are used as drug carriers, antibacterial drugs, anticancer drugs, and smart targeted drugs. In summary, in the clinical treatment of knee arthritis surgery, titanium dioxide nanotubes have good antibacterial properties as an endoplant and good histocompatibility with human bones. In the observation group combined with exercise therapy, various complications such as pain, swelling, and muscle atrophy were relatively small, allowing the patient to speed up the recovery of various body functions. At the same time, nurses should actively pay attention to patients and give patients a certain degree of

Hindawi

Research Article

Investigation on Mechanical Durability Properties of High-Performance Concrete with Nanosilica and Copper Slag

Raj Kumar,[1] Suganya Natarajan,[2] Rahul Singh,[3] Vinod Singh Rajput,[3] Ganesh Babu Loganathan,[4] Sanjeev Kumar,[5] T. Sakthi,[6] and Akter Meem Mahseena [7]

[1]Department of Mechanical Engineering, Swami Keshvanand Institute of Technology, Management and Gramothan, Jaipur, Rajasthan 302017, India

[2]Department of Civil Engineering, Sri Sairam Engineering College, -600 044, Chennai, Tamil Nadu, India

[3]Department of Mechanical Engineering, Engineering College, Nowgong, Madhya Pradesh 471201, India

[4]Department of Mechatronics, Faculty of Engineering, Tishk International University-Erbil, Kurdistan Region 44001, Iraq

[5]Department of Civil Engineering, Graphic Era Deemed to Be University, Bell Road, Clement Town, 248002 Dehradun, Uttarakhand, India

[6]Department of Mechanical Engineering, National Engineering college, KR, Kovilpatti, Nagar, Tamil Nadu, India

[7]Department of Electrical and Electronic Engineering, Daffodil International University, Ashulia, Savar, Dhaka-1207, Bangladesh

Correspondence should be addressed to Akter Meem Mahseena; mahseena33-919@diu.edu.bd

Mineral admixtures are frequently utilized as cement substitution materials in high-performance concrete (HPC), and so many studies have explored the influence of mineral admixtures on the rheological behavior of HPC. Investigations were done to examine the impact of nanosilica less than 100 nm on HPC by substituting copper slag at a fixed substitution of forty percent for fine aggregate. Concrete samples were cast by substituting cement with nanosilica at (0.5, 1, 1.5, 2, 2.5, and 3) percentages. Examinations on mechanical properties and durability were done on specimens. The above tests demonstrated an increase in water demand because of the increase in the nanosilica substitution percentage. Mechanical and durability properties were improved at a larger rate with the incorporation of nanosilica. The outcomes indicated that colloidal nanosilica is an effective material that enhances the microstructure and acts as a catalyst for pozzolanic activity. The incorporation of nanosilica improves the strength up to two percentage substitution level.

1. Introduction

HPC on the other hand is a concrete that is proved to give good strength as well as good durability. HPC has been generally utilized across the globe for the past thirty years. Compressive strength might differ from 50 to 200 MPa. Notwithstanding strength requisites, durability properties are essential in producing high-performance concrete. Consequently, it is important to utilize large amounts and worth resources to convene up above prerequisites. Aggregates comprise around 70 to 80 per cent of the volume of the concrete, and thus, there is fast growth in the utilization of normal aggregate worldwide. The industrialization has

prompted the creation of tremendous waste materials and side effects that leads to ecological issues. Hence, there is a vital requirement to discover and use substitute materials for aggregates by using waste materials and results utilizing no characteristics change that prompts a maintainable and better environment alongside specialized benefits. There is an enhancement in strength property of HPC while mineral admixtures are utilized since fractional replacement to concrete because of fortifying of the interfacial transition zone. These days, the utilization of nanomaterials in concrete is acquiring significance attributable to their improved property in the hardened and non-hardened conditions of concrete because of its particular superficial region. The

materials utilized in nanosize are nanosilica, nano-TiO_2, nano-Fe_2O_3, nano-Al_2O_3, and carbon nanotubes/strands. Among all the nanomaterials, nanosilica is the most generally used material in concrete due to pore filling impact [1]. A limited quantity of nanosilica, typically at 0 to 5 percentage substitution, is sufficient for enhancement in HPC. The addition of nanosilica speeds up the hydration cycle and responds with (CaOH2), creates more amounts of (C-S-H), and improves the mechanical properties. Cement combined with nanosilica brings a compact microstructure with a smaller quantity of calcium hydroxide crystals. Pozzolanic reactivity is faster in concrete when nanosilica is added up to three percentages. Substitution of nanosilica in concrete resulted in increased mechanical properties [2–5] and development in tensile strength [6] and improvement in abrasion resistance compared to conventional concrete to a significant stage. Research on permeability properties of nanosilica concrete proved that there is a decrease in absorption properties compared to conventional concrete [2, 6]. Substitution of nanosilica with GGBS resulted in prolonged hydration speed [7]. The increase of nanosilica content in concrete revealed decreased chloride particle entrance. Nanosilica addition worked on the compressive strength because of the speed increase of hydration [8–10]. The high amount of waste glass powder with nanosilica is made conceivable in concrete [11]. The adverse consequences of sludge inclusion in setting time and mortar strength provisions could be repaid by utilizing nanoparticles [12, 13]. The inclusion of nanoparticles could increase the strength of concrete by 15 to 20 percentages [14]. Additionally, nanosilica particles work on exhibition sludge combinations in tile creation with a decrease in water assimilation and expansion to wear [15]. The ($CaOH_2$) formed at some point in hydration to form added (C-S-H) gel. In this manner, nanosilica goes about as the focus of nucleation because of its high surface region, hence speeding up the hydration [16]. Likewise, expanding how much nanosilica brings about agglomeration forestalling the uniform appropriation of nanosilica particles inside the mortar because of its high explicit surface energies. In this manner, the enhancement of mechanical properties is diminished by increasing the nanosilica content. Nanosilica could absorb other Ca^{+2} particles and reduce the convergence of calcium particles, speeding up the disintegration of C_3S, which expands the pace of hydration successfully [17]. Adding colloidal nanosilica is more straightforward and effective than incorporating powdered content [18, 19]. The vast majority of examinations reduced the investigation of the properties of substitution of nanosilica in concrete. A couple of exploration was completed to decide concrete's mechanical properties and porousness with nanosilica. Numerous analysts announced extraordinary and incongruous ideal amounts of nanosilica alongside a few strange impacts, which need a lot of fixations in additional exploration [1, 11–17]. The ideal amount of nanosilica should show up for every material separately. The usage of waste produced from industry is the major challenge confronted today because of the removal cost and potential contamination issue. The above issue can be resolved or even disposed of alongside the accomplishment of asset protection, assuming that it is proficiently utilized. Fayalite slag is a derivative acquired during the refining process of copper. Fayalite slag tracks down its utilization in sandblasting, cutting devices, rail line counterweight, blacktop asphalt, and concrete [20]. Many kinds of exploration were done to concentrate on the conceivable outcomes of utilizing waste materials as fractional/complete substitution of concrete [21]. The utilization of copper slag as a replacement for fine aggregates further develops strength and durability parameters at similar usefulness. At the same time, superplasticizer is a vital fixing in HPC prepared by copper slag to give great functionality and better consistency. The utilization of Fayalite slag in concrete clinker formation and the impacts of copper slag on the properties of concrete have been examined by numerous analysts [22–24]. A few works detailed the mechanical properties of concrete prepared using fayalite slags substitution for sand, and crushed stones show more development than ordinary cement [25–27]. For each huge load of copper delivered, roughly 2.2 to 3 tons of slags were created according to a logical estimate. According to the review in 2010, copper slag creation was assessed by around 30 tons everywhere. Copper slag is a throwaway material that gives probable, natural, specialized, and financial advantages in concrete and cement.

Improvement of nanosilica based on HPC is relied upon to decrease cement utilization meant for environment conservation and economic benefits [1]. Even though there is not much information on adding nanoparticles in concrete, less consideration has been made on the importance of nanosilica in concrete. Additionally, it creates an interest in concrete innovation and is relied upon to work on the mechanical properties. The impact of copper slag as a partial substitution for sand on high-performance concrete was examined by different researchers [25–27]. As a primer work, an ideal amount of copper slag to be utilized in the research was examined and found as forty percentage substitutions is the perfect material for fine aggregate substitution. Here, the examination is reached out to explore the impact of the addition of nanosilica on HPC at consistent slump where copper slag is consolidated as a fractional substitution.

2. Materials

OPC 53 grade was utilized, and the specific gravity of the same is 3.15. River sand with a specific gravity of 2.67 and fineness modulus of 2.92 was utilized, and copper slag was used as a substitution material. The chemical properties of copper slag are displayed in Table 1. Polycarboxylic ether-based superplasticizer with a specific gravity of 1.09 and pH more noteworthy than 6. Chloride concentration under 0.25 percentage was utilized in this research. Colloidal nanosilica have a specific gravity 1.32, and pH 9.5 was used. Standard consistency and setting time tests were performed in concrete with nanomaterials at different substitution levels. XRD investigation of nanosilica has shown that a wide summit shifted between 15° and 30° was acquired by mixtures in nanostructure and amorphous nature shown in Figure 1.

Table 1: Chemical properties of copper slag, cement, and nanosilica.

Materials	Weight (percentage)
Silicon dioxide	26.72
Aluminum oxide	0.25
Ferric oxide	69.33
Calcium oxide	0.16
Sodium carbonate	0.6
Manganese oxide	0.25
Copper oxide	1.3
Titanium dioxide	0.5
Specific gravity (cement)	3.11
Initial setting (cement)	30 minutes
Final setting time (cement)	450 minutes
Specific surface area (m^2/gm) (nanosilica)	206
pH value (nanosilica)	4.3
Silica content (nanosilica)	99.9
Carbon content (nanosilica)	0.08
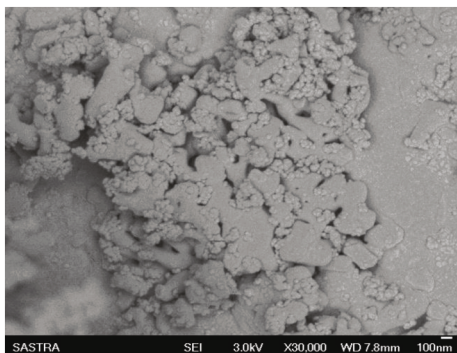
Figure 1: SEM of nanosilica.

2.1. Experimental Study. The experimental study is divided into two stages; initially, the percentage of copper slag is optimized with water-reducing admixtures. These cement matrix cubes of $70 \times 70 \times 70$ mm were cast with copper slag substitution of 0, 10, 20, 30, 40, and 50 percentages by weight of fine aggregate. Due to the lower water binder ratio, cement mortar cubes with superplasticizer results were improved than cubes without superplasticizer. Based on compressive strength, the ideal substitution of copper slag used for fine aggregate is 40%. The second stage of the study involves the study of the impact of nanosilica substitution for cement in mortar cubes. For this study, mortar cube of $70 \times 70 \times 70$ mm was cast by stable 40% of copper slag as substitution and nanosilica of 0.5, 1, 1.5, 2, and 2.5 and percentage by weight of cement with w/b 0.32 and constant rate of superplasticizer of 0.5 percentage. The cast cubes were tested for compressive strength at 3, 7, 28, 56, and 90 days.

Further, ACI [27] technique for mix proportioning was taken to show up at the orientation mix extent for M60 grade of concrete. Seven mixes of concrete at various doses of colloidal nanosilica N0, N0.5, N1, N1.5, N2, N2.5, and

N3 correspondingly (0, 0.5, 1, 1.5, 2, 2.5, and 3) weight fraction of cement were ready for workability between twenty-five to fifty mm with forty percentage substitution. The w/b proportion for all mix replacements was reserved at 0.32. The water-reducing admixture content was changed in each mix with the goal that the drop is kept up with at the required range, and details are shown in Table 2.

2.2. Casting and Testing of Specimens. The ingredients are mixed in a dry state. Later, nanosilica with water is added to get the uniform scattering of nanoparticles. The mixed matrix was filled in three layers, and compaction was done with the vibrating table. Slump properties of the concrete matrix were studied to understand the influence of nanosilica inclusion in the slag concrete. The samples were covered and were kept at room temperature until the demolding period. The samples were then demolded after twenty-four hours. The curing process is done till the required period and tested at the expected age. Cube of size $100 \times 100 \times 100$ mm were casted to determine the compressive strength of the samples at three, seven, twenty-eight, fifty-six, and ninety days. Cylinder specimens of size 150×300 mm were cast to find the split tensile strength of concrete. Rapid chloride penetration test was conducted on cylinders of size 100×50 mm, where the samples were placed in the cell, with liquid storage on every face. To perform the test, one cylinder was placed in the solution of sodium chloride with 3% concentration and the other with the solution of sodium hydroxide. The quality of electric current travelled through the concrete are measured by keeping potential variation of 60 V DC for 6 hours. Overall charges transferred (Coulomb) are closely connected to the specimen's chloride ion penetration. To perform the sorptivity test, 100×100 mm cubic samples set over the steel network in tub of water and bottom portion are submerged to five-millimeter depth. The other faces of the specimen are fixed such that it is saturated for 40 mm from the lower part such that progression of water is made from base surface.

3. Results and Discussions

3.1. Impact of Nanosilica on Strength Properties of Cement Mortars. From Figure 2, it is clear that the strength of the cement matrix with 2% nanosilica has higher strength than the control specimen. The improvement in three-day compressive strength was 26.88, 53.82, 81.54, 99.62, 96, and 85.52 percentage for N0.5, N1, N1.5, N2, N2.5, and N3 correspondingly than the control sample N0. Many outcomes have centered on the outstanding exposition in the premature strength. Moreover, the prime objective of pozzolanic material is strength advancement and decrease of pore size appropriation; based on this. The strength development is obtained up to 2% addition of nanosilica, which decreases the compressive strength [28]. The strength increase for the N2 mix is 22.9 and 14 percentages at the twenty-eight and ninety days correspondingly. In comparison, strength increases for the N3 mix diminished to 13.5 and 6.9 percentages at twenty-eight and ninety days. Samples with high nanosilica content experience excessive self-drying and

TABLE 2: Mix design properties.

Properties	Mix designation						
	N0	N0.5	N1	N1.5	N2	N2.5	N3
Cement (kg/m^3)	518	514	510	508	505	503	500
Colloidal nanosilica	0	4	8	10	13	15	18
Fine aggregate (kg/m^3)	350	350	350	350	350	350	350
Water (kg/m^3)	150	150	150	150	150	150	150
Copper slag (kg/m^3)	240	240	240	240	240	240	240
Coarse aggregate (kg/m^3)	1130	1130	1130	1130	1130	1130	1130
Super plasticizer (percentage)	0.42	0.42	0.43	0.45	0.5	0.55	0.55
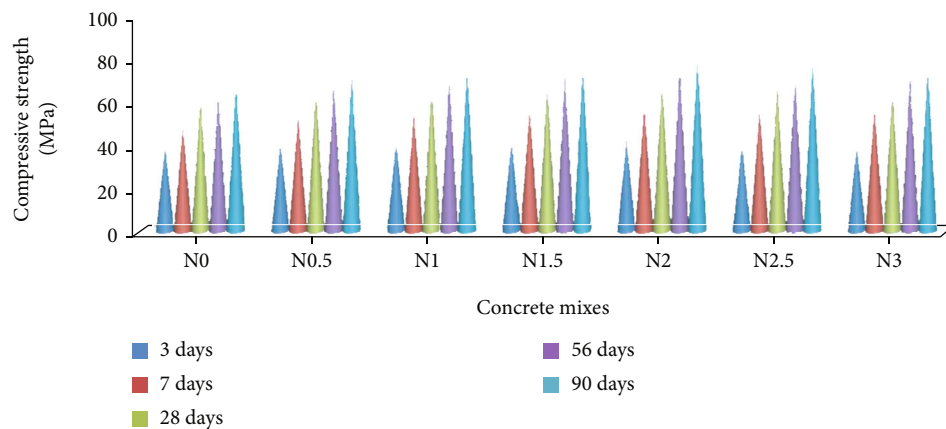
FIGURE 2: Impact of nanosilica on compressive strength properties of concrete containing copper slag.

breaking, and this can be by changing water and superplasticizer content [29–32]. Development in compressive strength by adding nanosilica came about because of both densification and filler impact of interfacial transition zone [33].

3.2. Impact of Nanosilica on Workability. Incorporating copper slag enhances workability because of its shiny surface, and less water absorption is shown in Figure 3. In any case, a higher level of copper slag incorporation brings bleeding due to the incorporation of nanosilica. Water particles are promptly drawn at nanosilica because of their elevated explicit surface region and larger reactivity. In this way, the consistency of the mix was expanded, bringing about a decline in usefulness upon the substitution of nanoparticles. To prevail over this problem, the quantity of superplasticizer was altered. Research on the impact of the substitution of nanosilica on cement concluded that incorporating nanomaterials to cementitious mixes decreases workability because of timely relations between the nanomaterials and cementitious matrix [34].

3.3. Impact of Nanosilica on Strength Properties of Concrete Containing Copper Slag. Results obtained from the samples are shown in Figures 4 and 5. Differences in compressive strength are noted because of the incorporation of nanosilica in slag concrete at 3, 7, 28, 56, and 90 days. The blends N0.5, N1, N1.5, N2, N2.5, and N3 improved compressive strength of 41.2, 57.5, 76.7, 90, 76.4, and 73.6 percentages corre-

spondingly as for the control mix. A similar pattern was seen on any remaining long periods. It was seen that the compressive strength upgraded up to two percentage of nanosilica substitution and afterwards declined to some extent. The more prominent utilization of calcium hydroxide is seen in the early ages because of the improved hydration. The outcome obtained is profitable for nanosilica substitution of two percentages by weight of cement. Hydration items fill the pores between the concrete in this manner, shortcutting the penetration of water to the unhydrated particles and bringing down the strength gain beyond two percentage substitution of nanosilica. It was found that the improvement in ninety-day compressive strength was 7.1, 12.8, 22.8, 27.9, 22.2, and 18.7 percentages for N0.5, N1, N1.5, N2, N2.5, and N3 mixes correspondingly compared to the control specimen. An increase in strength is recognized in the way that calcium hydroxide liberated during the process of hydration is used by nanosilica, bringing about higher strength at early ages. Additionally, the results of hydration fill the pores and make them denser. Mix N2 shows the greatest strength obtained at the entire period, and the proportion of addition in compressive strength concerning twenty-eight days was higher.

Figure 5 shows the difference of split tensile strength owing to the incorporation of nanosilica at entire ages. Samples of N0.5, N1, N1.5, N2, N2.5, and N3 increased 4.2, 9.9, 15.6, 17.8, 14.5, and 12.1 correspondingly by reference to the control sample at three days. Seven days, strength obtained
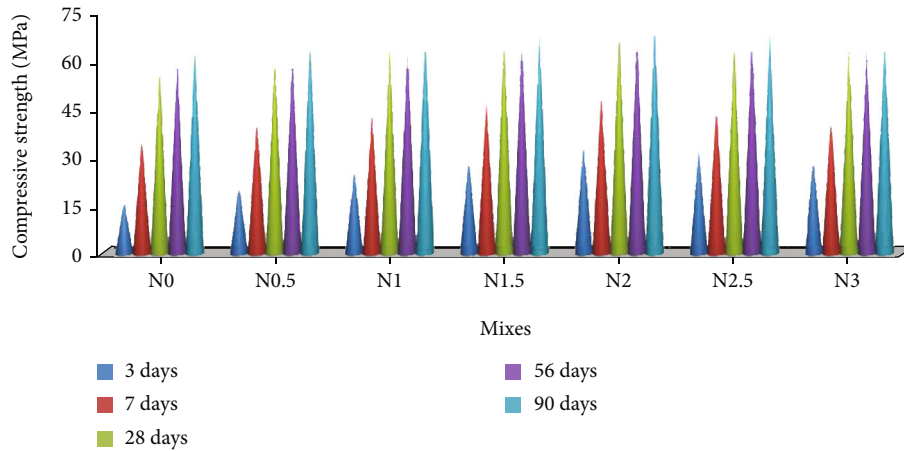
FIGURE 3: Impact of nanosilica on cement mortar strength.
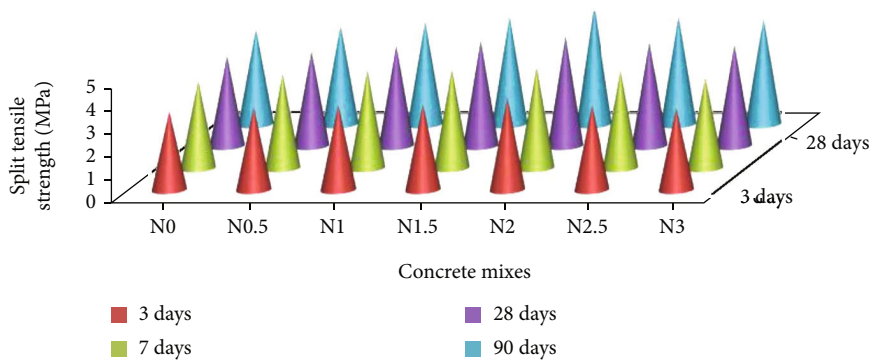
FIGURE 4: Impact of nanosilica on split tensile strength properties of concrete containing copper slag.
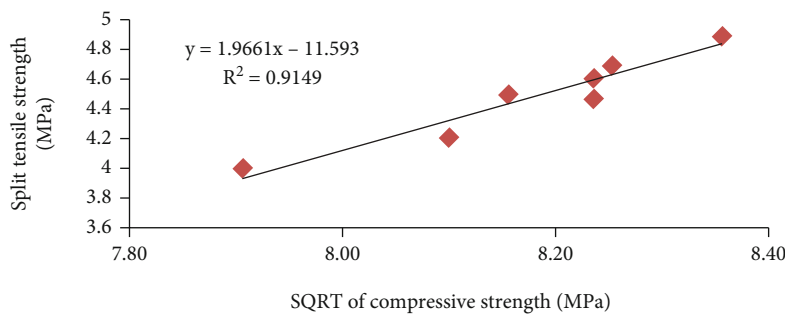
FIGURE 5: Relation between SQRT of compressive strength and splitting tensile strength.

was 4.8, 11.3, 17.3, 22.5, 19, and 15.4 percentages correspondingly for $N0.5$, $N1$, $N1.5$, $N2$, $N2.5$, and $N3$ compared with the control specimen. The improvement in strength was found to be 7.8 to 26.3 and 7.9 to 27.4 percentages for nanosilica mixes correspondingly than the control sample at twenty-eight and ninety days. This phenomenon is primarily due to a stronger attachment between the aggregate and cement matrix.

The reduction in mechanical properties with more prominent than two percentage of nanoparticle substitution is accredited to the explanation that the number of nanopar-

ticles is larger. On this junction, nanosilica is a replacement material for cement utilized for filling the pores yet does not engage in the hydration cycle.

3.4. Impact of Nanosilica on Chloride Ion Penetration. The capacity of concrete to oppose the access of chloride particles is an important constraint in deciding the service life of steel in concrete in marine conditions. It is likewise critical to research the conduct of cement containing substitutions like copper slag concerning protection from chloride particle infiltration. The rapid chloride penetration results of

TABLE 3: Impact of nanosilica on chloride penetration.

Parameters	Charge passed (Coulombs 28 days)	Chloride penetration	Charge passed (Coulombs 90 days)	Chloride penetration
$N0$	1140	Low	1155	Low
$N0.5$	1138	Low	990	Extremely low
$N1$	1050	Low	920	Extremely low
$N1.5$	980	Extremely low	850	Extremely low
$N2$	820	Extremely low	702	Extremely low
$N2.5$	910	Extremely low	788	Extremely low
$N3$	955	Extremely low	824	Extremely low

nanosilica with a forty percentage aggregate substitution by copper slag at twenty-eight and ninety days are shown in Table 3. It was noticed that every mix contained a small vulnerability towards chloride. Values of Coulombs were reduced by substituting nanosilica up to two percentages demonstrating that the concrete became denser—further addition of nanosilica results in small enhancement in Coulomb. The above perspective has been shown in the compressive strength result from which it very well may be presumed that concrete shows more protection from chloride ion penetration than different mixes. In this research, it was seen that concrete with nanosilica showed extremely low chloride particle penetration compared with other concretes. The decrease in chloride particle entrance might be because of the fuse of round particles like nanosilica and copper slag, which brought about the improvement of the molecule. Coulomb charges passed at ninety days are low compared to twenty-eight days due to dense microstructure.

3.5. Impact of Nanosilica on Sorptivity. The main strength of water suction is capillary pressure [35]. The sorptivity coefficient is a significant boundary to forecast the life of a structure [35]. Substitution of nanosilica quantity from zero to two percentages causes a reduction in the sorptivity esteem by 44.3 and 57.8 percentages at twenty-eight and ninety days correspondingly. Being extremely fine particles, nanomaterials fill up the pores in concrete, consequently decreasing the capillary pores.

4. Conclusions

Based on the experimental investigation on utilization of nanosilica in concrete with forty percentage of copper slag as fine aggregate substitutions, the following conclusions have arrived:

(i) As the quantity of nanosilica was raised to three percentages, the consistency was improved while the setting time was reduced because of the increased hydration rate. The nanosilica inclusion has increased the compressive strength of concrete containing forty percent copper slag as a weight fraction for fine aggregate compared to the control mix. The strength increment was observed up to

two percent of nanosilica substitution, beyond which the strength decreases

(ii) The highest strength properties were found in concrete containing copper slag in the samples containing two percentages of nanosilica. The above reaction brings about higher creation of calcium silicate hydrate gel. Further addition of nanosilica results in higher quantity than the amount of free lime and directly affects the pozzolanic activity. It very well may be acknowledged that the ideal nanosilica substitution is two percentage

(iii) Rapid chloride penetration test containing nanosilica in concrete was exceptionally low at twenty-eight and ninety days. The charges passed were not exactly aligned with the control specimens

(iv) Sorptivity results of concrete containing nanosilica and copper slag decrease with an increment in nanosilica content because of the consolidated activity of pore filling impact. The highest decrease in sorptivity values was seen in mixes with two nanosilica percentages

Data Availability

The data used to support the findings of this study are included in the article.

Conflicts of Interest

The authors declare that there is no conflict of interest regarding the publication of this article.

References

[1] L. P. Singh, S. R. Karade, S. K. Bhattacharyya, M. M. Yousuf, and S. Ahalawat, "Beneficial role of nanosilica in cement based materials - a review," *Construction and Building Materials*, vol. 47, pp. 1069–1077, 2013.

[2] M. H. Zhang and H. Li, "Pore structure and chloride permeability of concrete containing nano-particles for pavement," *Construction and Building Materials*, vol. 25, no. 2, pp. 608–616, 2011.

[3] S. Riahi and A. Nazari, "Compressive strength and abrasion resistance of concrete containing SiO2 and CuO nanoparticles

in different curing media," *Science China Technological Sciences*, vol. 54, no. 9, pp. 2349–2357, 2011.

[4] H. Li, M. H. Zhang, and J. P. Ou, "Abrasion resistance of concrete containing nano-particles for pavement," *Wear*, vol. 260, no. 11-12, pp. 1262–1266, 2006.

[5] A. Nazari and S. Riahi, "RETRACTED: The effects of SiO$_2$ nanoparticles on physical and mechanical properties of high strength compacting concrete," *Composites Part B:Engineering*, vol. 42, no. 3, pp. 570–578, 2011.

[6] K. S. Ali, V. Mohanavel, M. Ravichandran, S. Arungalai Vendan, T. Sathish, and A. Karthick, "Microstructure and mechanical properties of friction stir welded SiC/TiB2 reinforced aluminum hybrid composites," *Silicon*, vol. 14, no. 7, pp. 3571–3581, 2022.

[7] A. Nazari and S. Riahi, "RETRACTED: Splitting tensile strength of concrete using ground granulated blast furnace slag and SiO$_2$ nanoparticles as binder," *Energy and Buildings*, vol. 43, no. 4, pp. 864–872, 2011.

[8] S. Kaliappan, R. Saravanakumar, A. Karthick et al., "Hourly and day ahead power prediction of building integrated semitransparent photovoltaic system," *International Journal of Photoenergy*, vol. 2021, Article ID 7894849, 8 pages, 2021.

[9] M.-H. Zhang, J. Islam, and S. Peethamparan, "Use of nanosilica to increase early strength and reduce setting time of concretes with high volumes of slag," *Cement and Concrete Composites*, vol. 34, no. 5, pp. 650–662, 2012.

[10] R. Naveenkumar, M. Ravichandran, V. Mohanavel et al., "Review on phase change materials for solar energy storage applications," *Environmental Science and Pollution Research*, pp. 1–42, 2021.

[11] K. S. Elango, D. Vivek, G. Krishna Prakash, M. J. Paranidharan, S. Pradeep, and M. Prabhukesavaraj, "Strength and permeability studies on PPC binder pervious concrete using palm jaggery as an admixture," *Materials Today: Proceedings*, vol. 37, no. 2, pp. 2329–2333, 2021.

[12] D. Vivek, K. S. Elango, R. Saravanakumar et al., "Effect of nano-silica in high performance concrete," *Materials Today: Proceedings*, vol. 37, no. 2, pp. 1226–1229, 2021.

[13] A. Hmidet, U. Subramaniam, R. M. Elavarasan et al., "Design of efficient off-grid solar photovoltaic water pumping system based on improved fractional open circuit voltage MPPT technique," *International Journal of Photoenergy*, vol. 2021, Article ID 4925433, 18 pages, 2021.

[14] M. Choolaei, A. M. Rashidi, M. Ardjmanda, A. Yadegari, and H. Soltanian, "The effect of nanosilica on the physical properties of oil well cement," *Materials Science and Engineering: A*, vol. 538, pp. 288–294, 2012.

[15] V. Rajendran, H. Ramasubbu, K. Alagar, and V. K. Ramalingam, "Performance analysis of domestic solar air heating system using V-shaped baffles–an experimental study," *Proceedings of the Institution of Mechanical Engineers, Part E: Journal of Process Mechanical Engineering*, vol. 235, no. 5, pp. 1705–1717, 2021.

[16] K. Sobolev, I. Flores, R. Hermosillo, and L. Torres-Martinez, "Nanomaterials andnanotechnology for high-performance cement composites," *Proceedings of ACI Session on Nanotechnology of Concrete: Recent Developments and Future Perspectives*, vol. 254, pp. 93–120, 2008.

[17] L. Chen and D. Lin, "Applications of sewage sludge ash and nano-SiO$_2$ to manufacture tile as construction material," *Construction and Building Materials*, vol. 23, no. 11, pp. 3312–3320, 2009.

[18] F. Kontoleontos, P. E. Tsakiridis, A. Marinos, V. Kaloidas, and M. Katsioti, "Influence of colloidal nanosilica on ultrafine cement hydration: physicochemical and microstructural characterization," *Construction and Building Materials*, vol. 35, pp. 347–360, 2012.

[19] Y. Qing, Z. Zenan, K. Deyu, and C. Rongshen, "Influence of nano-SiO$_2$ addition on properties of hardened cement paste as compared with silica fume," *Construction and Building Materials*, vol. 21, no. 3, pp. 539–545, 2007.

[20] I. Campillo, J. S. Dolado, and A. Porro, *High-performance nanostructured materials for construction, The Proceeding of the First International Symposium onNanotechnology in Construction (NICOM1)*, Scotland, UK, Paisley, 2007.

[21] J. Sridhar and D. Vivek, "Influence of non-biodegradable wastes on mechanical properties of concrete – a neural network approach," in *IOP Conference Series: Materials Science and Engineering*, vol. 1025no. 1, p. 012007, Vizianagaram, India, November 2021.

[22] K. S. Elango, R. Gopi, R. Saravanakumar, V. Rajeshkumar, D. Vivek, and S. V. Raman, "Properties of pervious concrete - a state of the art review," *Materials Today: Proceedings*, vol. 45, pp. 2422–2425, 2021.

[23] F. Pacheco-Torgal and S. Jalali, "Nanotechnology: advantages and drawbacks in the field of construction and building materials," *Construction and Building Materials*, vol. 25, no. 2, pp. 582–590, 2011.

[24] C. Shi and J. Qian, "High performance cementing materials from industrial slags – a review," *Resources, Conservation and Recycling*, vol. 29, no. 3, pp. 195–207, 2000.

[25] P. Jaishankar and D. Vivek, "Behaviour of nano silica in tension zone of highperformance concrete beams," in *IOP Conference Series: Earth and Environmental Science*, vol. 80, p. 01202, Tirumalaisamudram, Thanjavur, India, March 2017.

[26] S. Venkat Raman, S. Elavarasan, K. S. Elango et al., "Comparative study on axial compressive behaviour of CFST and externally wrapped CFRP columns," in *IOP Conference Series: Materials Science and Engineering*, vol. 1145no. 1, p. 012015, Coimbatore, India, March 2021.

[27] C. Rajendra Prasath, D. Vivek, K. S. Elango, and R. Dharmaraj, "Experimental investigations on flexural behaviour of self compacting concrete beam with silica fume," in *IOP Conference Series: Materials Science and Engineering*, vol. 1145no. 1, p. 012101, Coimbatore, India, March 2021.

[28] D. Vivek, J. Sridhar, K. S. Elango et al., "Axial compressive behaviour of concrete filled steel tubular column," in *IOP Conference Series: Materials Science and Engineering*, vol. 1145no. 1, p. 012017, Coimbatore, India, 2021.

[29] C. Shi, C. Meyer, and A. Behnood, "Utilization of copper slag in cement and concrete," *Resources, Conservation and Recycling*, vol. 52, no. 10, pp. 1115–1120, 2008.

[30] K. S. Elango, R. Gopi, C. Jayaguru, D. Vivek, R. Saravanakumar, and V. Rajeshkumar, "Experimental investigation on concrete beams reinforced with basalt fiber reinforced polymer bars," *Materials Today: Proceedings*, vol. 45, pp. 2426–2429, 2021.

[31] K. S. Elango, P. R. Remya, D. Vivek, R. Gopi, V. Rajeshkumar, and R. Saravanakumar, "Strength and durability studies on ficus exasperata leaf ash concrete," *Materials Today: Proceedings*, vol. 37, no. 2, pp. 999–1002, 2021.

[32] G. Miruthun, D. Vivek, P. R. Remya, K. S. Elango, R. Saravanakumar, and S. Venkatraman, "Experimental investigation on strengthening of reinforced concrete beams using GFRP laminates," *Materials Today: Proceedings*, vol. 37, no. 2, pp. 2744–2748, 2021.

[33] K. S. Al-Jabri, M. Al-Jabri, S. K. Al-Oraimi, and A. H. Al-Saidy, "Copper slag as sand replacement for high performance concrete," *Cement and Concrete Composites*, vol. 31, no. 7, pp. 483–488, 2009.

[34] S. Caliskan and A. Behnood, "Recycling copper slag as coarse aggregate: hardenedproperties of concrete," in *Proceedings of Seventh International Conference onConcrete Technology in Developing Countries*, pp. 91–98, Kuala Lumpur, Malaysia, 2004.

[35] V. Rajeshkumar, K. S. Elango, D. Vivek, S. Anandaraj, C. Vinodhini, and P. Kamalakannan, "Experimental investigation of organic waste ash in concrete," in *IOP Conference Series: Materials Science and Engineering*, vol. 1145no. 1, p. 012018, Coimbatore, India, March 2021.

Hindawi

Retraction

Retracted: Application and Equipment of Preparation Technology of Ferroelectric Thin Film Materials in Sports Industry

Journal of Nanomaterials

This article has been retracted by Hindawi following an investigation undertaken by the publisher [1]. This investigation has uncovered evidence of one or more of the following indicators of systematic manipulation of the publication process:

(1) Discrepancies in scope

(2) Discrepancies in the description of the research reported

(3) Discrepancies between the availability of data and the research described

(4) Inappropriate citations

(5) Incoherent, meaningless and/or irrelevant content included in the article

(6) Peer-review manipulation

The presence of these indicators undermines our confidence in the integrity of the article's content and we cannot, therefore, vouch for its reliability. Please note that this notice is intended solely to alert readers that the content of this article is unreliable. We have not investigated whether authors were aware of or involved in the systematic manipulation of the publication process.

Wiley and Hindawi regrets that the usual quality checks did not identify these issues before publication and have since put additional measures in place to safeguard research integrity.

We wish to credit our own Research Integrity and Research Publishing teams and anonymous and named external researchers and research integrity experts for contributing to this investigation.

The corresponding author, as the representative of all authors, has been given the opportunity to register their agreement or disagreement to this retraction. We have kept a record of any response received.

References

[1] Y. Xu, "Application and Equipment of Preparation Technology of Ferroelectric Thin Film Materials in Sports Industry," *Journal of Nanomaterials*, vol. 2022, Article ID 9480475, 13 pages, 2022.

Research Article

Application and Equipment of Preparation Technology of Ferroelectric Thin Film Materials in Sports Industry

Yali Xu [ID]

School of Physical Education, Jiangxi University of Chinese Medicine, Nanchang, 330004 Jiangxi, China

Correspondence should be addressed to Yali Xu; 18409484@masu.edu.cn

With the rapid development of the integrated circuit industry, ferroelectric thin film materials and technologies have become increasingly important. Ferroelectric materials have been widely used in aerospace, information storage, artificial intelligence, microelectromechanical, wearable devices, and other fields. Traditional sports is an important carrier of traditional culture. It contains the sports cultural resources created and precipitated by the Chinese nation for thousands of years, and all sectors of society are also paying great attention to this. Under the background of the market economy system and the major premise of the vigorous development of the cultural industry and sports industry, industrialization is obviously the inevitable choice for traditional sports to break through the difficulties and seek development, and it will also promote the further inheritance and promotion of traditional sports. The complex combination causes its performance to decrease or even fail. Therefore, it cannot cause foresee losses and disasters. It has important application value and significance to master the performance changes and mechanisms of ferrous film materials under different adding environments. This paper takes ferroelectric $Pb(Zr_{0.52}Ti_{0.48})O_3(PZT)Bi_{3.15}Nd_{0.85}Ti_3O_{12}(BNT)$ as the research object, proposes the preparation of sol coating for thin film materials, and studies the preparation parameters PZT of the sol electric ferroelectric method. Electrical method and BNT electrical film properties affect iron and physical experiments on the properties of iron. The influence of the best sol-iron coating method on the electrical properties of PZT and BNT films is the ferroelectric properties of the 700°C layer of high-temperature gas, 10-layer PZT films, and 8-layer BNT films. The elasticity and elastic moduli of PZT and BNT films are 66.8 MPa and 99.6 MPa and 159.3 GPa and 189 GPa, respectively; the elastic coefficients of PZT and BNT films are 15.4×10^{10} N/m^2 and 18.4×10^{10} N/m^2, and their elastic coefficients $|e31|$ decrease with accompanying increase in swallowing. And with the disease of reading and writing field strength, as the speed becomes faster and slower, the carriers have more time to move to the brain wall, so the intensity is also intuitive. It has strong practicability and feasibility to popularize the material and manufacture the equipment of the current sports equipment club.

1. Introduction

Intel and IBM jointly launched a 45-nanometer processor chip in 2007, using high-dielectric constant hafnium dioxide to replace the previous silicon dioxide gate insulating layer, which solves the leakage that occurs as the processor becomes smaller. This technological invention has brought historical changes to the IT industry, and the research on hafnium dioxide has also kicked off an upsurge. With the progress of people's research work, hafnium dioxide has been widely used in the fields of electronics, optics, and so on. In 2006, Setter mentioned in a review of ferroelectric thin film materials, characteristics, and applications that ferroelectric field effect transistors (FeFET) will be used as a fast, low-energy, and nonvolatile storage technology for a long time in the future. In these devices, information will be permanently stored in the gate insulating layer in the form of polarization state and can be read nondestructively in the form of a threshold voltage change. Although as early as 1974, Wu had put forward the concept of ferroelectric field effect transistor experimentally, but for a long time, there are still many difficulties in practical application. For

example, it is difficult to obtain materials with strong stability. This is mainly due to the thermodynamic mismatch of known ferroelectric materials such as lead zirconate titanate (PZT), strontium bismuth tantalate (SBT), and strontium titanate (STO) on silicon. In addition, because silicon has a very small band step, in order to obtain low leakage current devices, thick film and precious metal electrodes must be used. In order to improve the stability of direct contact between ferroelectric materials and silicon, many methods such as the introduction of buffer layers have been tried, but these methods have reduced the scalability of such devices. To make matters worse, when the buffer layer is introduced, the existence of a higher depolarization field will degrade the information storage capacity. Therefore, in order to obtain a highly reliable ferroelectric field effect transistor, a new ferroelectric material with semiconductor compatibility is urgently needed. The ferroelectric thin film material proposed in this paper can satisfy this point. Although, in recent years, the traditional sports industry has gradually attracted the attention of people from all walks of life and has achieved certain results, but compared with the industrialization of most modern sports events, there is still a big gap. Especially in the context of the new era, how traditional sports can seize the economic and cultural double stilts to move forward steadily and realize the real industrialization of traditional sports requires further theoretical and practical discussions.

Through the investigation of the high dielectric constant gate insulating layer material, it can be found that only a few metal oxides have both semiconductor compatibility and sufficient energy band gap, and hafnium dioxide is one of them. Hafnium dioxide is an inorganic substance and an oxide of hafnium element. It is a white solid at room temperature and pressure, insoluble in water, insoluble in hydrochloric acid and nitric acid, and soluble in concentrated sulfuric acid and hydrofluoric acid. However, for a long period of time in the past, it is generally believed that hafnium dioxide does not have a noncentrosymmetric crystal structure, so hafnium dioxide cannot be a good ferroelectric material. However, many experiments in recent years have shown that hafnium dioxide-based ferroelectric thin film materials with ferroelectric properties can be obtained by controlling the material structure by methods such as doping and stress clamping. This is of great significance for the development of the next generation of ferroelectric memory that is compatible with semiconductor processes, can be miniaturized, and has low power consumption. In addition, the anti-irradiation ability of ferroelectric materials in extreme working environments has made them always regarded as one of the choices of aerospace-grade chip materials. However, after reaching a certain radiation dose, the performance of memory based on traditional ferroelectric materials will drop sharply. Therefore, research on the anti-radiation ability of ferroelectric hafnium dioxide devices has also become very important. This research has laid the foundation for us to explore the connotation and essence of industrialization. In terms of industrialization paths, cultural industrialization paths and sports industrialization paths have always been the focus and hotspot of research, providing reference for the research on traditional sports industrialization paths.

For structures with conductive oxide (IrO_2) and metal (Pt) top electrodes, Brewer et al. studied the influence of gamma radiation on the dielectric and piezoelectric response of $Pb[Zr_{0.52}Ti_{0.48}]O_3$(PZT) thin film stacks. When exposed to 2.5 Mrad (Si)60Co gamma radiation, the sample usually shows degradation of various key dielectric, ferroelectric, and electromechanical responses. However, the low-field, relative permittivity εr is largely unaffected by the irradiation of samples with two types of electrodes. The sample with the Pt top electrode showed a significant degradation of the remanent polarization and the overall piezoelectric response, as well as the shrinkage of the polarization hysteresis curve and the generation of multiple peaks in the dielectric constant-electric field curve after radiation. However, samples with oxide electrodes are largely unaffected by the same radiation dose, and any change in functional characteristics is less than 5%. The results show the radiation-induced changes in the number of defects or defect energy in the PZT with a metal top electrode. However, they did not consider the change and particularity of the dielectric constant of the PZT film after radiation, and there are still errors in the experiment [1]. Ferroelectric perovskite oxides are a promising photosensitive layer for photovoltaic applications due to their very high stability and the solar energy conversion mechanism associated with ferroelectrics they replace, which may lead to very high efficiency. One of the biggest challenges so far is to reduce their band gap to the visible light region while maintaining ferroelectricity. In order to solve these two problems, Pamela et al. replaced Fe with Co cations to carry out the elemental composition engineering of $BiFeO_3$ as a means to adjust the characteristics of transition metal-oxygen bonds. They formed an epitaxial, pure phase, and stable $BiFe_{1-x}Co_xO_3$ film through solution treatment, $x \leq 0.3$, and the film thickness is as high as 100 nm. Importantly, the band gap can be adjusted from 2.7 eV to 2.3 eV after cobalt substitution while enhancing ferroelectricity. As a proof of concept, unoptimized vertical devices have been fabricated, and it is gratifying that the electrooptic response in the visible light region of the Co-substituted. However, his method of substituting Co cations for Fe to reduce the band gap is not of high value for enhancing ferroelectricity, and further research is needed [2]. Shin and Son deposited epitaxial Bi_2FeMnO_6 (BFMO) film on Nb-doped $SrTiO_3$ (Nb:STO) substrate by pulsed laser deposition. X-ray diffraction confirmed that the 100 nm thick BFMO film has relatively high tetragonality, with a high cla ratio of 1.04. The BFMO film has low leakage current, good ferroelectric properties and an enhanced remanent polarization of about 25.0 μC/cm~2. Compared with conventional ferroelectric films (such as $PbTiO_3$ films), BFMO films have a larger ferroelectric domain structure due to their high domain wall energy. However, they did not make a detailed study on the ferroelectric fatigue of Nb-doped BFMO film, and there are still insufficient studies on the ferroelectric properties of BFMO film [3].

The innovation of this paper is to improve the preparation method of traditional ferroelectric thin film materials.

The sol-gel method is used to prepare ferroelectric thin films. It has precise composition control, easy adjustment, low annealing temperature, and easy to produce large-area thin films. It also has good ferroelectric properties for the prepared ferroelectric thin film. In addition, the research of this paper can also put forward suggestions for improving the equipment manufacturing and equipment production in the sports industry and provide a novel research direction for the development of sports.

2. Preparation and Performance Analysis of Ferroelectric Thin Film Materials

2.1. Ferroelectric Materials. Materials, information, and energy are the three pillars of human civilization, and materials are the material basis for the improvement of human production and living standards. The research, development, and application of new materials are the cornerstone of promoting social and technological progress. Since Schmid defined multiferroic materials in 1994 [4, 5] (referring to a class of materials with more than one ferroelectric sequence parameter for single-phase materials), the definition of multiferroic materials has been continuously broadened. At present, it is considered that the four basic order parameters of multiferroic materials are electric dipole moment, magnetic moment, elastic moment, and spin pole moment [6] (see Figure 1). That is to say, a multiferroic material is a material that has two or more basic ferroelectric characteristics (including ferroelectricity, antiferroelectricity, ferromagnetism, antiferromagnetism, and ferroelasticity). Multiferroic materials have unique physical and magneto-electric application functions, such as polarization reorientation or induction of ferroelectric phase transition under the action of a magnetic field and magnetization reorientation or induction of ferromagnetic phase transition under the action of an electric field. So they have emerged in many cutting-edge technology applications, such as sensors, energy converters, signal generation and processors, filters, information storage, and microwave devices. The research of multiferroic materials continues to attract the attention of many scholars and has become one of the key subjects of condensed matter physics and material science research [7, 8].

Multiferroic materials are mainly divided into two types: one is a single-phase multiferroic material, and the other is a composite multiferroic material. Single-phase multi-iron materials are represented by $BiFeO_3$ and $TbMnO_3$. $BiFeO_3$ has ferroelectricity and antiferromagnetism at room temperature. $TbMnO_3$ has a large magnetoelectric coupling coefficient but a low Curie temperature. In 1972, Van Suchtelen et al. proposed a mixed preparation method of ferroelectric phase and ferromagnetic phase, which is composed of ferroelectric materials and ferromagnetic materials in different combinations. There are currently three types of structures of 0-3, 1-3, and 2-2 [9, 10], which are characterized by a relatively high Curie temperature, a large magnetoelectric coupling coefficient, and performance far higher than single-phase materials and are available for selection. Because of
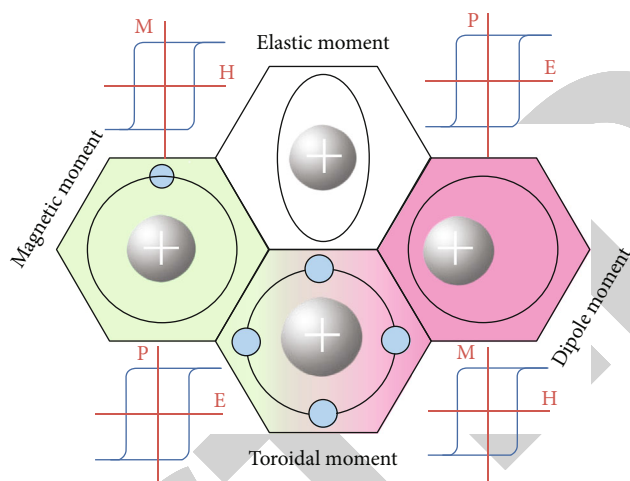
Figure 1: Multi-iron coupling order parameter.

this, composite multiferroic materials have become one of the hotspots in the research of multiferroic materials.

The essential feature of ferroelectric materials is the existence of spontaneous polarization, and the spontaneous polarization can change with the change of electric field [11], which is why the name of ferroelectric materials comes from. There is a hysteresis relationship between the polarization intensity of the ferroelectric material and the electric field intensity. When the polarization strength of the ferroelectric material increases, the electric field strength of the material does not increase immediately but changes only after a certain period of adaptation, as shown in Figure 2:

Ferroelectric thin films have good properties, such as ferroelectricity, piezoelectricity, pyroelectricity, electro-optics, and nonlinear optics [12, 13], and can be widely used in microelectronics, optoelectronics, integrated optics, and microelectronic mechanical systems. Other fields are currently one of the frontiers and hotspots of high-tech research [14].

After nearly a century of development, ferroelectric materials have formed five major types of structural systems: perovskite type, lithium niobate type, bismuth-containing layered, pyrochlore type, and tungsten bronze type structure system [15, 16]. Perovskite-type ferroelectrics are currently the most widely used, perfect perovskite structure, usually expressed by ABO_3. At present, the main research is barium titanate ($BaTiO_3$), lead titanate ($PbTiO_3$), and other representative perovskite-type ferroelectric materials, as well as their performance research such as A/B and AB position ion substitution [17, 18].

2.2. Test and Characterization Methods of Thin Film Materials and Development Overview. In recent years, the application of ferroelectric thin film materials has gradually increased. In the aerospace, automotive, and sports industries, ferroelectric thin film materials have potential applications. With the maturity of the preparation process of ferroelectric thin film materials, the performance of this material has been greatly improved. Its piezoelectric effect, pyroelectric effect, electro-optic effect, and acousto-optic
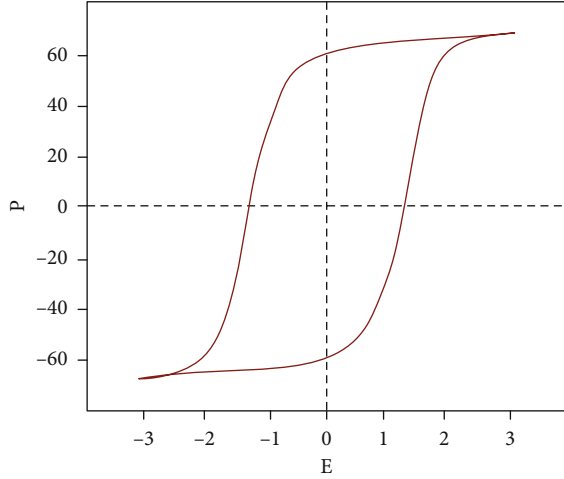
Figure 2: Hysteresis loop diagram of ferroelectric materials.

effect have been developed relatively maturely. And the cost has been greatly reduced, so its application fields have been expanded, and it can be used to manufacture precision parts for microwave circuit plug-ins and turbocharged propulsion. There are also reports on their applications in the sports industry and electronic fields. In the sports industry, the use of nanomaterials to develop volleyballs that do not touch water and dust is more conducive to the promotion of sports activities. Performance characterization (detection and evaluation) is particularly important for the future application of materials. It is not only related to the correct evaluation of materials but also lays the foundation for the design and application of materials. The detection and evaluation of materials has a wealth of content, such as the detection and analysis of key issues such as elastic modulus, plastic strain, fracture toughness, and fatigue [19, 20]. At present, the application scope of ferroelectric thin film and magneto-electric composite thin film involves all aspects of functional thin film materials and devices. It is represented by applications in the fields of microelectromechanical systems, sensors, detectors, and information storage. It is constantly advancing social progress and changing people [21]. Therefore, it is indispensable to understand the mechanical parameters of thin film materials such as elastic modulus, Poisson's ratio, residual stress, fatigue strength, and fracture strength before designing and manufacturing new materials and devices. The mechanical properties of thin film materials directly affect the quality of new materials and devices. The traditional testing methods are mostly suitable for bulk materials, which poses great challenges to the mechanical parameter testing of microcomponents and functional thin-film devices [22, 23].

2.3. Application of Ferroelectric Thin Film. In previous studies, significant progress has been made in the preparation of ferroelectric thin films, the synthesis of multilayer films, performance, testing, microstructure, and the integration of ferroelectric thin films into heterostructures [24]. The discovery of $SrBi_2Ta_2O_9$ (SBT) makes FRAM very suitable for its excellent fatigue resistance, excellent storage perfor-

mance, and low leakage current. However, the use of ferroelectric thin films is not limited to ferroelectric memories [25]. Utilizing the dielectric, ferroelectric, piezoelectric, electrostatic, pyroelectric, optical, electro-optical, and other properties of ferroelectric film, its application is extended to separation devices [26]. In this way, the main application of ferroelectric film in the memory of multilayer capacitors, nonvolatile ferroelectric dynamic random access memory (NVFRAM), smart cards, infrared detectors, infrared sensors and inverters, etc., will be extended. According to the physical results, the application of ferroelectric thin film can be classified as shown in Table 1.

New applications of ferroelectric thin films are still being proposed, such as the use of iron thin films such as laser disks, microwave waveguides, solar cell energy storage capacitors compatible with solar cells, and powerful electron emission sources [27].

2.4. Methods of Fatigue Characteristics of Ferroelectric Capacitors. The relationship between temperature and fatigue rate, when the temperature rises, the fatigue rate also rises rapidly. It can be expressed as

$$T(A) = T_0 \times [1 - R(S) \times \log A]. \tag{1}$$

Among them, T_0 is the initial residual polarization, $T(A)$ is the residual polarization after reading and writing, and $R(S)$ is a temperature-dependent phase.

$$\varepsilon_d \mu R(S) = A \times \exp\left[-\frac{B_a}{k_b T}\right]. \tag{2}$$

Among them, B_a is the activation energy, T is the temperature in Kelvin, K_B is the Boltzmann constant, and A is a proportional coefficient.

In this study, similar electrical performance characterization was performed on the devices before and after fatigue, and the modified SE model was used to fit the measured current under low field. The following can be drawn:

$$\text{In}\left(\frac{R_{SE}}{T^{2/3}}\right) = \text{In}(D(S)) - \frac{A}{\text{DT}}\left[\left(\sqrt{\frac{AB}{4\pi\varepsilon_0^2\varepsilon_d\varepsilon_{st}}}\right) - b\sqrt{V}\right], \tag{3}$$

$$D(S) = 2a\left(\frac{2\pi m_{\text{eff}} d}{h^2}\right)^{3/2}\mu E, \tag{4}$$

$$b = \sqrt{\frac{a^2 N_{\text{eff}}}{8\pi\varepsilon_0\varepsilon_d B}}, \tag{5}$$

$$\log\left(\frac{R_{\text{PF}}}{E}\right) = \frac{\left[-a\left[\varphi_t - (aE/\pi\varepsilon_d\varepsilon_0)^{1/2}\right]\right]}{D_B T \ln 10} + \log(B), \tag{6}$$

where m_{eff} is the effective mass of electrons, D_B is Boltzmann's constant, h is Planck's constant, μ is the mobility of carriers in the film, E is the applied field strength, φ_B is the barrier height at the interface, φ_t is the bound energy

TABLE 1: Application of ferroelectric thin film.

Performance	Main components
Dielectric	Capacitors, dynamic random access memory (DRAM)
Piezoelectricity	Surface acoustic wave (SAW) devices, miniature piezoelectric motors, miniature piezoelectric actuators
Pyroelectricity	Pyroelectric detector and array
Ferroelectricity	Ferroelectric random access memory (FRAM)
Electro-optic effect	Optical modulator, optical waveguide
Acousto-optic effect	Acousto-optic deflector
Photorefractive effect	Optical modulator, optical holographic memory
Nonlinear optical effect	Optical frequency doubler

level in the material, ε_0 is the dielectric constant in vacuum, ε_d is the dynamic dielectric constant of the ferroelectric material in the infrared region, ε_{st} is the static dielectric constant of the ferroelectric material, and N_{eff} is the depletion layer at the cross section charge density, including bound charge and shallow ions. B is the remanent polarization of the ferroelectric material, S is the applied voltage, and A is the unit point charge. The improved SE model takes into account the influence of polarization at the metal-ferroelectric-metal interface on the maximum field strength. If the ferroelectric polarization is not taken into account, the calculated Schottky barrier will be much lower than the actual one.

The next step will be to discuss the situation in the low field. According to the improved SE model, the magnitude of the tunneling current mainly depends on the free carriers of the injected metal passing through the Schottky barrier of the ferroelectric layer interface. The larger the actual value of the Schottky barrier, the smaller the value of the tunneling current. Here, first define the "significant" barrier 6:

$$\sigma_{ie} = \sigma_b - \sqrt{\frac{aB}{4\pi\varepsilon_0^2\varepsilon_d\varepsilon_{st}}}. \tag{7}$$

The value at each voltage can be obtained by fitting the slope of the straight line.

The Seebeck effect, as the most basic theoretical basis for ferroelectric performance, was first discovered by Seebeck in 1821. When two different materials are connected end to end into a closed loop, two connection points are formed. The two connection points are made by certain means. If the temperature difference is formed at the position, then an electric current is formed in the closed circuit. It can be expressed by a formula:

$$G_{iu} = \alpha_{ab}(C_1 - C_2), \tag{8}$$

where α_{ab} is the thermoelectromotive force rate. For the same material, when it approaches zero, α_{ab} can be regarded as a constant, which is named Seebeck coefficient, namely,

$$\alpha_{ab} = \lim_{\nabla C} \frac{G_{iu}}{\nabla C} = \frac{d\nu_{iu}}{dc}. \tag{9}$$

In a certain period of time, the change in heat at the connection point in the entire closed loop, that is, the transfer of heat is proportional to the current, and the ratio of the change in heat at the connection point Rt to the current I in unit time R_d is

$$\frac{R_d}{Rt} = \pi I, \tag{10}$$

where π is the Peltier coefficient, the unit is V, and its magnitude is related to the material and voltage of the closed loop.

The Thomson effect, which is a secondary thermal effect, when a current flows through a uniform conductor with a temperature gradient, in addition to generating Joule heat related to resistance, the conductor also absorbs or releases heat. This effect of absorbing or releasing heat is called the Thomson effect. It has a small heat absorption and release and is reversible, so it is very difficult to measure and easily confused with Joule heating.

$$\frac{R_d}{Rt} = \tau I\left(\frac{R_t}{t}\right). \tag{11}$$

The three do not exist independently of each other but are inseparable from the mutual influence of the three of the same substance. The relationship between them is

$$\pi_{ab} = \alpha_{ab}C, \tag{12}$$

$$\frac{d\alpha_{ab}}{dC} = \frac{\gamma_a - \gamma_b}{C}. \tag{13}$$

It can be seen that the three-point iron effect is reversible, and the Joule heat generated by the internal resistance of the material corresponding to it is irreversible.

The thermoelectric conversion device can directly convert heat energy and electric energy, and it provides a scalable, reliable, and environment-friendly energy conversion method. The conversion efficiency of the thermoelectric conversion device can be determined:

$$\lambda = \frac{P_e - P_o}{P_e} \times \frac{\sqrt{1 + ZP} - 1}{\sqrt{1 + ZP} + (P_e/P_o)}, \tag{14}$$

where P_e and P_o are the temperature of the hot and cold ends of the ferroelectric material and the ZP value is a dimensionless thermoelectric figure of merit. It is the decisive factor that determines whether the thermoelectric material can be widely used. Its size can be defined as

$$ZP = \frac{\delta^2}{d},\tag{15}$$

where P is the average temperature, which reflects the electrical transport characteristics of the thermoelectric material, and d is the thermal conductivity, which reflects the heat transport characteristics of the material.

2.5. Ferroelectric Thin Film Materials in Sports. At present, ferroelectric thin film materials are widely used in sports measurement sensors. It has both piezoelectricity and mechanical properties of soft film. Pressure sensors made with it can be used to detect human body signals such as pulse and heart sounds. The pulse and heart sound signal carries important physiological parameter information of the human body. Through effective processing of the signal, the waveform and the number of heart rate can be accurately obtained, which can provide a reliable basis for physical fitness measurement. In addition, sensors made of ferroelectric thin-film materials have a large frequency response range, pyroelectric effect, and other characteristics and have great application potential. In terms of vibration detection, it is mainly used in music pickup, machine condition monitoring, bearing wear, fan airflow, rope breakage, etc., as an accelerometer in acceleration detection and in nondestructive testing. When it appears in the form of a sensor array, it can also be used to monitor human movement, sports scoring, switches, and microphones. With the improvement of the production process of ferroelectric thin film materials, the continuous decline of production costs, and the continuous development and in-depth research in various aspects, it is reasonable to believe that the application prospects of ferroelectric thin film materials in the sports industry must be very broad.

3. Preparation of Ferroelectric Thin Film

3.1. Film Preparation Method. Although the pulsed laser deposition (PLD) film-making technology has only a history of more than 50 years, it is a promising manufacturing technology with distinct advantages and disadvantages. The main advantages are as follows: (1) the element measurement ratio of the film material and the target material can be consistent under appropriate conditions. (2) It can prepare many inorganic thin film materials such as refractory materials, metals, semiconductors, insulators, and some organic thin film materials. (3) Multilayer films, heterogeneous films, etc., can be prepared, and the target change is convenient and flexible. (4) It is convenient to adjust the deposition parameters and growth rate, the deposition temperature is low, and the film quality is high. The disadvantages are also obvious: the uniformity of the film formation is poor, the formation of a large area film is difficult, and mass production and preparation cannot be carried out.

The sputtering method started in 1940 and developed rapidly with the rise of the semiconductor industry and was officially born in the 1970s. Its advantages are mainly reflected in the following: (1) the film-forming temperature is usually lower than 500°C; it is compatible with microelectronics technology and can be used to make devices. (2) The prepared film is of good quality without pinholes and cracks. (3) The crystallization performance is good, and an epitaxial single crystal film can be obtained. The main disadvantages are slow film growth rate, long preparation time, deviation of film composition and target material, etc.

Metal organic chemical meteorological deposition (MOCVD) uses metal organic compounds as the material source for chemical vapor deposition. After more than 30 years of development, it has been relatively perfect. The method can precisely control the composition and thickness of the thin film; it is easy to produce a large-area film, the deposition temperature is low, and the uniformity and repeatability of the prepared thin film are high. However, due to the high toxicity of raw materials and the high cost of materials and equipment, the application scope of MOCVD is limited.

The sol-gel method uses inorganic metal salts or metal alkoxides prepared with liquid chemical reagents as solvents and alcohol solutions as solvents, and the two are mixed. After a series of hydrolysis, carbonization, and carbonization reactions, they are transparent and uniform. Use different methods. The precursor solution is aged; then, the precursor solution matures to polymerize and gel the solute; finally, the gel is dried and baked to remove organic compounds and obtain a thin film material. The processing equipment requirements are simple and easy to apply. The chemical uniformity is good and can reach the molecular level. The stoichiometry is accurate, quantitative and uniform doping can be achieved, the doping range is wide, the manufacturing temperature is low, and it is compatible with semiconductors. The sol-gel method also has certain limitations. The alkoxides that can be selected are limited, expensive, and easy to pollute the environment; during the drying process, organic matter volatilizes and cracks occur; when different materials are prepared, it is difficult to control the changes in process parameters. The above four methods for preparing ferroelectric thin films have their own advantages and disadvantages, and they need to be selected according to different needs. The bulging sample is a self-clamping free film, which is prepared by chemical etching in the later stage. At the same time, it is necessary to quickly prepare a film sample with good uniformity and stable performance. These differences indicate that the preparation method also has a certain impact on the performance of the material.

In Table 2, various properties under different preparation processes are compared. It can be seen that the film prepared by the sol-gel method has higher remanent polarization, and it also has the smallest coercive field and the largest dielectric constant. It reached 0.8 and 46, respectively. These indicators are important because a higher

TABLE 2: Comparison of film properties under different preparation methods.

	PLD	Sputtering	MOCVD	Sol-gel
2Pr (C/cm^2)	49	23	27	29
Rectify the field (MV/cm)	1.2	0.9	2.1	0.8
Dielectric constant	44	31	24	46

residual polarization means a larger read and write window, a smaller coercive field means lower power consumption, and a higher dielectric constant means smaller leakage. Therefore, this paper chooses the sol-gel method as the method of preparing the film.

3.2. Preparation of Sol-Gel Film

3.2.1. Experimental Supplies. The chemicals used in the experiment are shown in Table 3.

During the reaction process, a certain chelating agent (acetylacetone) is added to the solution to control the polycondensation rate and hydrolysis rate of the alkoxide while also keeping the titanium and zirconium ions in a stable state to obtain a uniform gel. After adding a certain amount of acetic acid, it can not only adjust the pH of the solution but also act as a catalyst.

Pt metal has stable properties and low diffusion performance and can prevent mutual diffusion between interfaces. The atomic weight of platinum is 195.078, which is slightly smaller than that of gold, and the atomic number is 78, which belongs to the transition metal. Therefore, Pt thin film is selected as the bottom electrode of the substrate. At the same time, the Ti film is selected as the buffer layer connecting SiO_2/Si to enhance the bonding strength of the Pt layer. The substrate used in the experiment was provided by Peking University Microelectronics, and the structure from top to bottom was $Pt/Ti/SiO_2/Si/SiO_2$, as shown in Figure 3. The total thickness is 500 μm, the thickness of the Pt layer is 150 nm, the thickness of the Ti layer is 20 nm, the thickness of the SiO_2 layer is 20 μm, and the preferred orientation of the Pt layer is (111).

3.2.2. PZT Film Preparation. For the preparation of PZT film precursor, the selected composition ratio is Pb:Zr:Ti $= 1.15 : 0.52 : 0.48$, which is near the quasihomotype phase boundary. An excess of 15% of lead is used to suppress the formation of oxygen vacancies caused by lead volatilization during annealing. The preparation steps of the PZT precursor solution are as follows:

(1) Use an electronic balance to weigh out 3.774 g lead acetate, 2.009 g zirconium nitrate, and 1.500 g butyl titanate. Dissolve zirconium nitrate and butyl titanate in ethylene glycol methyl ether solution and stir evenly. Add 3 to 5 drops of acetylacetone to the butyl titanate solution as a stabilizer

(2) Lead acetate is relatively insoluble, so after it is dissolved in ethylene glycol methyl ether, it is heated in a hot water bath while stirring on a magnetic stir-

rer. The temperature is set to 60°C, and it is completely dissolved and placed at 120°C. Dry in a vacuum drying oven (model DZF-6020) for 5~10 min to remove crystal water, and then add a little glacial acetic acid after cooling to room temperature

(3) Slowly dissolve the zirconium nitrate solution in the lead acetate solution, stir it evenly, and then add the butyl titanate solution to the mixed solution to form a light yellow precursor solution

(4) Add a proper amount of ethylene glycol methyl ether to adjust the concentration of the precursor solution to 0.3 mol/L, and add a proper amount of formamide to prevent the prepared film from cracking. After continuous stirring for 8-10 h, aging for 4-7 days, the solution is a light yellow transparent liquid without precipitation, and the preparation is complete. The flow chart is shown in Figure 3

3.2.3. Preparation of BNT Film. The preparation of BNT film precursors is relatively simple, and the preparation steps are as follows:

(1) According to the stoichiometric ratio of $Bi_{3.15}Nd_{0.85}Ti_3O_{12}$, weigh appropriate amounts of nitric acid ($Bi(NO_3)_3 \cdot 5H_2O$) and neodymium nitrate ($Nd(NO_3)_3 \cdot 6H_2O$), of which bismuth nitrate is weighed 10% more to make up Bi element volatilization loss during subsequent processing

(2) Place the weighed sample in a clean beaker, add 5 mL of glacial acetic acid and 4 mL of ethylene glycol methyl ether to the beaker, respectively, and place it on a magnetic stirrer and stir (the solution is purple), which is the A solution

(3) In another clean beaker, add 4 mL of ethylene glycol methyl ether and 4 drops of acetylacetone, stir appropriately to make the mixture even. After peeling the skin on the electronic balance, add a certain weight of butyl titanate ($C_{16}H_{36}O_4Ti$) solution to the beaker to form solution B

(4) After stirring the A and B solutions for 5-10 minutes, slowly add the A solution to the B solution to obtain a mixed solution (wine red), and adjust the concentration to 0.01 mol/L. Stir on a magnetic stirrer for 5 to 8 hours, and a light yellow BNT precursor will be obtained. Let it stand for 4 to 7 days to age the solution. If no precipitation appears, the preparation is complete. The schematic diagram of the process is shown in Figure 4

After the preparation of the precursor solution is completed, the preparation of the film can be carried out. The spin-coating preparation process is carried out in an ultraclean room, which has a grade of 10,000. The homogenizer is a KW-4B homogenizer produced by Beijing Saidecase Electronics Co., Ltd. When the film is prepared by the spin

TABLE 3: Summary of experimental drugs.

Drug name	Molecular formula	Purity	Molar mass (g/mol)
Zirconium nitrate	$Zr(NO_3)_4 \cdot 5H_2O$	Analytically pure	425.16
Lead acetate	$(CH_3COO)_2Pb \cdot 3H_2O$	99.1%	383.25
Butyl phthalate	$C_{16}H_{36}O_4Ti$	98.7%	351.67
Neodymium nitrate	$Nd(NO_3)_3 \cdot 6H_2O$	98.5%	328.16
Bismuth nitrate	$Bi(NO_3)_3 \cdot 5H_2O$	99.3%	491.38
Ethylene glycol monomethyl ether	$C_3H_8O_2$	99%	77.41
Acetylacetone	$C_5H_8O_2$	98%	101.79
Formamid	CH_3NO	Analytically pure	48.35
Acetic acid	CH_3COOH	Analytically pure	62.83
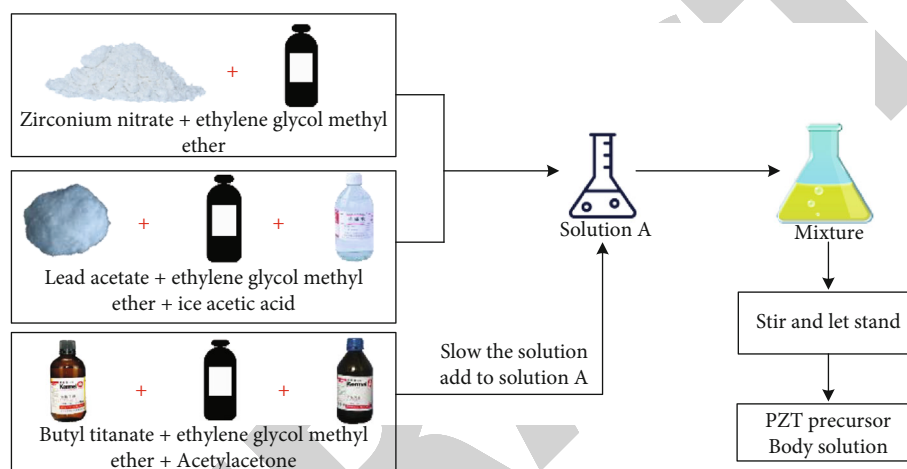
FIGURE 3: Schematic diagram of the preparation process of PZT precursor solution.
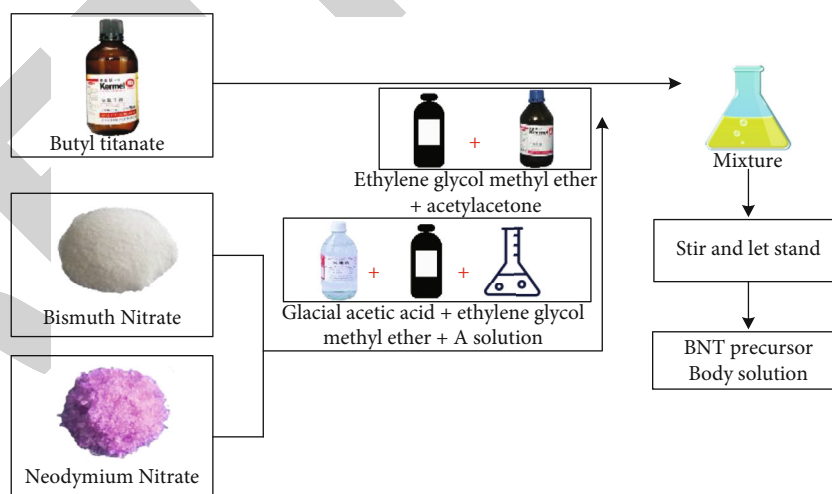
FIGURE 4: Schematic diagram of the preparation process of BNT precursor solution.

coating method, the effect of the parameter setting of the homogenizer on the performance of the film is mainly reflected in the uniformity of the film, and the annealing process mainly controls the ferroelectric properties of the film, such as the size and orientation of the crystal grains, and the defects in the film.

After many experiments and comparisons with other documents, the spin coating process parameters are set to low speed 400 r/s and high speed 4000 r/s, and the spin coating time is 10 s and 40 s, respectively. The air humidity in the ultraclean room is controlled between 39% and 48%, the temperature is changed between 17.4 and 22.2°C, and the
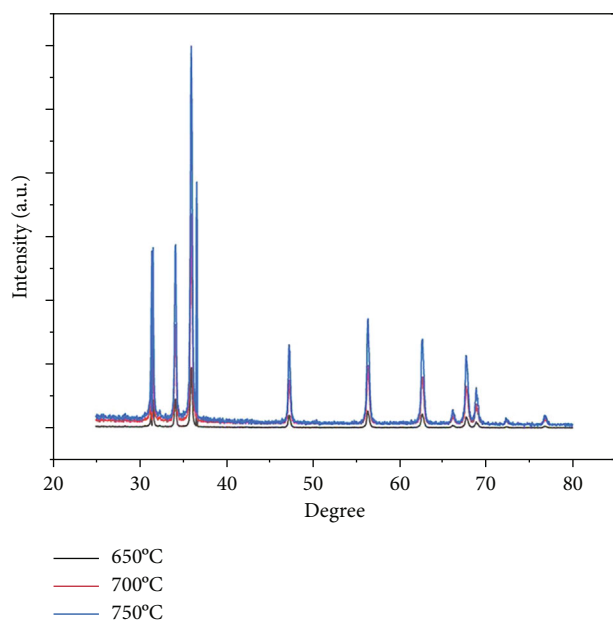
Figure 5: XRD pattern of PZT film under air and oxygen annealing atmosphere.

Figure 6: Ferroelectric thin film C-V test.

humidity and temperature remain basically unchanged during a single spin coating. The rapid annealing process is divided into three small stages: the first stage is drying, and 18 s is heated from room temperature to 180°C and maintained for 300 s; the second stage is pyrolysis, and 20 s is heated from 180°C to 400°C and maintained for 300 s; the third stage is annealing, and 20 s is heated from 400°C to 700°C and kept for 600 s; that is, a complete annealing is completed.

When the spin coating reaches the desired thickness, the annealing process is completed, and the film preparation is completed. The Ni layer in the Ni/PZT composite film is sputtered by the MIS800 multifunctional ion beam magnetron sputtering composite coating equipment. The sputtering voltage is 2 kV, the current is 50 mA, and the sputtering time is 20 min. The thickness is about 100 nm, and then, a 5-10 nm Ag layer is covered on the surface of the nickel layer as a protective layer to prevent oxidation of the nickel layer.

4. Influence of Preparation Parameters on the Ferroelectric Properties of PZT Thin Films

4.1. Effect of Annealing Environment on the Ferroelectric Properties of PZT Thin Films. When annealing at the same temperature, the environment of the sample can also affect the intrinsic properties of the film, and the difference in oxygen partial pressure will produce different effects. Figure 5 shows the XRD pattern of the PZT film under annealing environment.

Annealing in air has a low oxygen partial pressure, and there are usually more oxygen vacancies generated during annealing, resulting in more defects in the film; the existence of defects will increase the leakage current of the film, reduce the polarization of the film, and reduce the residual polariza-
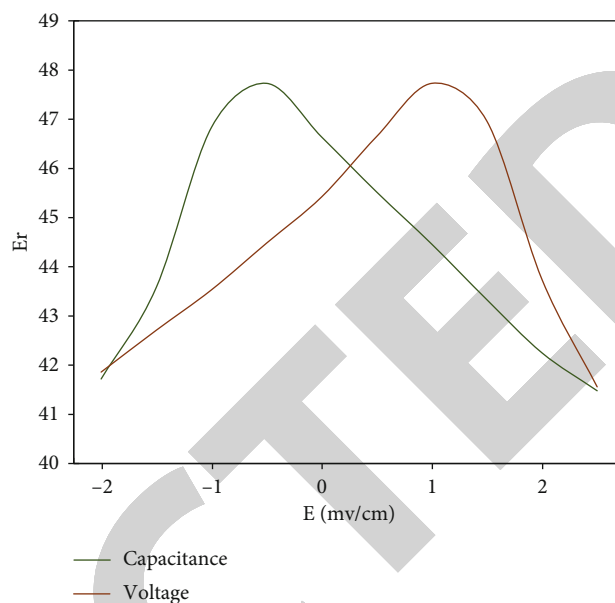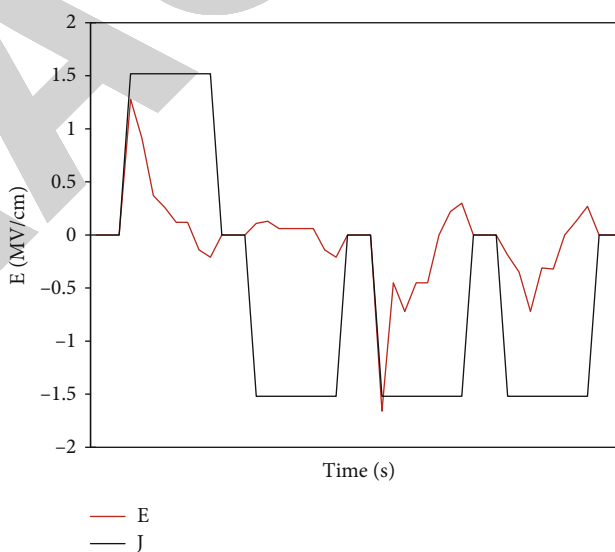
Figure 7: PUND test displacement current result.

tion. The value becomes smaller; at the same time, the increase of defects makes the clamping effect more significant and inhibits the reversal of the ferroelectric domain, and the electrical domain reversal is difficult; that is, the electric coercive field of the ferroelectric film becomes larger. Annealing in an oxygen atmosphere significantly increases the oxygen partial pressure ratio, inhibits the generation of oxygen vacancies, and reduces the number of internal defects in the film, making the film denser and improving the ferroelectric properties.

4.2. Structure and Conductivity of Ferroelectric Thin Films. First, the structure and ferroelectric properties of the prepared ferroelectric thin film were characterized.
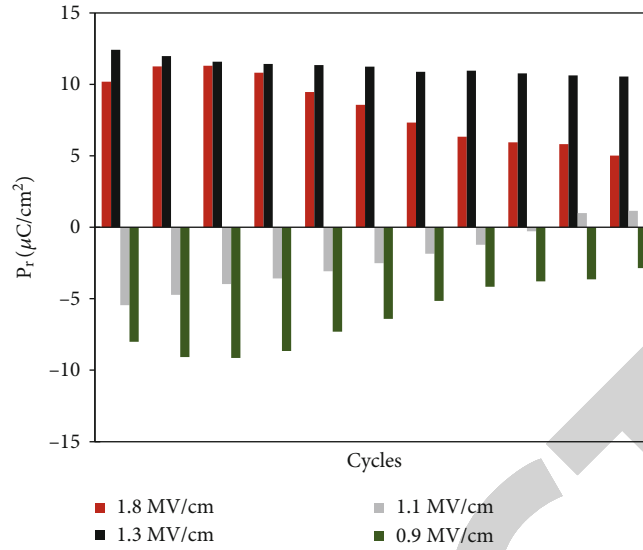
FIGURE 8: The relationship between the residual polarization intensity and the number of reads and writes under different pulse amplitudes.
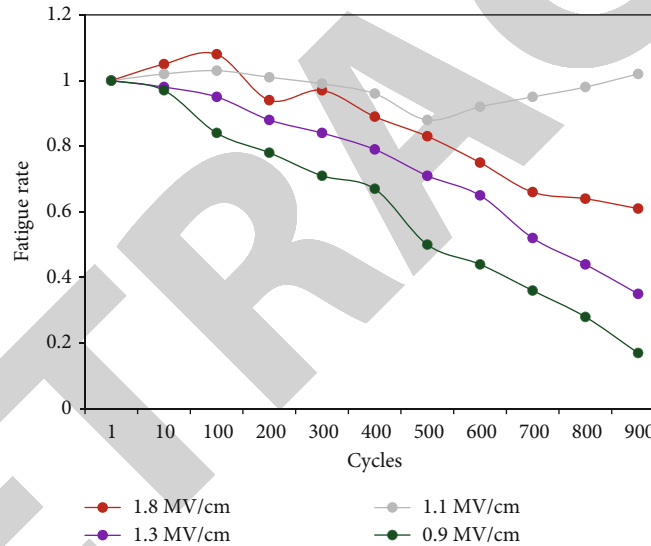
FIGURE 9: Normalized results of fatigue rate under each pulse amplitude.

Figure 6 shows the capacitance-voltage test of the prepared 15 nm thick sample. The electrode area of the test device is $30\,\mu$m $\times 30\,\mu$m, the applied field strength range is ± 3 MV/cm, and the test frequency is 50 kHz. From the figure, you can see a "butterfly-shaped" CV curve unique to ferroelectric materials. Two obvious "bulges" can be observed around ± 0.8 MV/cm, which is a characteristic of ferroelectric capacitors. The reason is that the movement of the domain wall near the coercive field will increase significantly.

Figure 7 shows the displacement current during the PUND (positive up, negative down) test. A polarization current of about 0.1 A cm^{-2} can be observed at the rising edge of the first positive pulse and the falling edge of the third pulse, which is also one of the current characteristics of ferroelectric materials.

4.3. Fatigue Characteristics Analysis of Ferroelectric Capacitors.
In PZT-based ferroelectric capacitors, there have been many reports that the rate of device fatigue is closely related to pulse width, pulse amplitude, and temperature. These characteristics are related to various fatigue mechanisms such as domain wall pinning, redistribution, and injection of oxygen vacancies.

In this experiment, the fatigue characteristics of the device were also characterized under these different experimental conditions. The first research is the relationship between fatigue characteristics and pulse amplitude. The frequency of the pulse is fixed at 0.91 MHz, as shown in the inset in Figure 8; the amplitude of the pulse varies from 0.8 MV·cm^{-1} to 1.8 MV·cm^{-1}, as shown in Figure 8. In the literature, hafnium dioxide-based ferroelectric materials will have the characteristic of "wake-up" in the polarization

TABLE 4: Comparison of device performance indicators under different irradiation doses.

Dose(ions/cm^2)	Dielectric constant	Coercive field (MV/cm)	2Pr (μC/cm^2) (at 2.5 MV/cm)	2Pr (μC/cm^2) (at 1.3 MV/cm)	2Pr after cycling (μC/cm^2) (at 1.3 MV/cm)		
					Mean values	Range	Percentage
Initial state	39.4	1.12/-0.68	24.9	13.9	1.5 ~ 5.5	2.75	23%
5×10^{13}				12.6	2.1 ~ 8.8	4.66	36%
10^{14}	39.2	1.19/-0.56	24.4	11.4	3.6 ~ 10	4.78	54%
$5 * 10^{14}$				10.7	1.6 ~ 8.4	5.52	43%
10^{15}	38.8	1.07/-0.59	23.6	9.8	1.2 ~ 6.6	3.24	26%

intensity during the first 200 reads and writes; that is, the polarization intensity will first increase with the increase in the number of reads and writes. This phenomenon has also been observed in this experiment. When the reading and writing field strength is 1.8 MV·cm^{-1}, the residual polarization intensity increases from 12 μC·cm^{-2} to 13 μC·cm^{-2} after reading and writing 200. It was also at this moment that fatigue began to occur. When the reading and writing field strength is reduced to below 1.3 MV·cm^{-1}, the "wake up" phenomenon disappears, and the device shows fatigue characteristics directly from the beginning of reading and writing. When the reading and writing field strength decreases from 1.8 MV·cm^{-1} to near 0.9 MV·cm^{-1} of the material coercive field, the fatigue rate increases significantly.

Figure 9 normalizes the fatigue rate under various field strengths ($P(N)/P0$, where $P(N)$ represents the residual polarization after reading and writing N times and $P0$ represents the initial residual polarization of the device). It can be seen very clearly that as the reading and writing field strength decreases, the fatigue rate of the device is gradually increasing.

In this paper, the fatigue characteristics are studied, and it can be seen that the device is more likely to exhibit fatigue characteristics at a voltage close to the coercive field. Therefore, in order to better study the characteristics of fatigue characteristics under proton irradiation, in this chapter, we have carried out fatigue tests on the device near the coercive field, and we can see that the fatigue has a tendency to first improve and then decrease.

Table 4 summarizes the changes of various ferroelectric properties under irradiation. It can be seen that the dielectric constant, the coercive field, and the residual polarization under 2.5 MV·cm^{-1} only slightly changed. Irradiation even has an inhibitory effect on fatigue. In general, the performance of devices based on ferroelectric thin films does not change significantly under proton irradiation.

5. Conclusions

Ferroelectric thin film materials can greatly improve the overall performance of sports facilities, improve sports equipment, improve the quality of new equipment, and promote athletes to obtain excellent results. Therefore, the application of ferroelectric thin film materials to sports will have a lasting high-quality impact on the sports industry. Ferroelectric thin film materials have great potential and can improve all aspects of sports. Sports activities require

specific equipment and equipment, as well as the material texture and design of the equipment, which play a vital role in the development of sports. The application of ferroelectric thin film materials in the sports industry is mainly reflected in two aspects: one is the application in sports infrastructure, such as the construction of sports venues, sports equipment, sports clothing, and sports biology. The second is the application in sports equipment, such as enhanced golf, tennis, swimming, racing, and cycling. The core part of sports industrialization refers to the industrial phenomenon that a certain sports event takes competition activities as the leader, achieves a high degree of marketization, and forms a considerable economy of scale, thus presenting an industrial phenomenon. Such industrialization has played a decisive role in the development of sports. The extension of sports industrialization refers to the industrialization of all sports-related departments. They will promote the development of sports, but they are not decisive. The industrialization of sports is the same as the socialist modernization construction in China. Its foothold can only be based on the national conditions. The industrialization of sports can only give full play to its own advantages and adapt to the requirements of the socialist market economy only if it conforms to the national conditions. Its basic feature is that the industrialization of sports is a direction for China to deepen the reform of sports. It is the process of sports from a closed system run by the state to an open system run by the state and society. What needs to be emphasized is the social and economic benefits of sports. In this paper, PZT and BNT ferroelectric films were prepared by sol-gel method, and PZT and BNT were used as the research objects to study the influence of sol-gel method preparation parameters on the properties of PZT and BZT ferroelectric films. When the annealing temperature increases, the degree of crystallization of the film increases. When the film is annealed in an oxygen atmosphere, the oxygen partial pressure increases, reduces the oxygen vacancy concentration, suppresses the occurrence of defects, and improves its ferroelectric properties. The increase of film thickness can increase the average size of crystal grains, reduce the internal stress of the film, and also improve the ferroelectric properties of the film. When annealed in an oxygen atmosphere at 700°C and a thickness of 10 layers, the ferroelectric properties of the PZT film are the best. The BNT film has the best ferroelectric performance when it is annealed in an oxygen atmosphere at 700°C, and the thickness is 8 layers. Then, using electrical characterization and other methods to study its fatigue

mechanism and anti-irradiation performance, it is concluded that the occurrence of the ferroelectric film fatigue process is closely related to the magnitude of the applied field strength, the frequency of read and write pulses, and the temperature, and these characteristics all point to the main fatigue mechanism caused by charged carrier injection. The performance of the device is stable under proton irradiation, and the fatigue characteristics are even improved. This paper studies the excellent performance characteristics of ferroelectric thin films that can be used in the optical and sensing sports industry. Sensors made of ferroelectric thin film materials have sufficient sensitivity and accuracy to perform online in-body monitoring and are widely used in the sports industry. However, there are still some shortcomings in the research of this paper. Although the mechanism of ferroelectric thin film fatigue is proposed in this paper, the improvement of fatigue has not been achieved. It is hoped that this problem that hinders commercial application can be completely solved in future work. And in future research work, I will propose methods for ferroelectric material optimization from more perspectives based on existing technologies and methods and continuously improve the quality and efficiency of research work.

Data Availability

No data were used to support this study.

Conflicts of Interest

There is no potential conflict of interest in this study.

References

[1] S. J. Brewer, C. Z. Deng, C. P. Ca Llaway, M. K. Paul, K. J. Fisher, and R. Q. Rudy, "Effect of top electrode material on radiation-induced degradation of ferroelectric thin film structures," *Journal of Applied Physics*, vol. 120, no. 2, p. 024101, 2016.

[2] M. Pamela, S. Mateusz, and G. Jaume, "Band gap tuning of solution-processed ferroelectric perovskite $BiFe_{1-x}Co_xO_3$ thin films," *Chemistry of materials: a publication of the American Chemical Society*, vol. 31, no. 3, pp. 947–954, 2019.

[3] H. W. Shin and J. Y. Son, "Large ferroelectric domain structures of epitaxial Bi_2FeMnO_6 thin films on Nb-doped $SrTiO_3$ substrates," *Journal of Materials Science*, vol. 28, no. 20, pp. 15302–15305, 2017.

[4] L. X. Chen, C. Xu, X. L. Fan, X. H. Cao, K. Ji, and C. H. Yang, "Study on leakage current, ferroelectric and dielectric properties of BFMO thin films with different bismuth contents," *Journal of Materials Science: Materials in Electronics*, vol. 30, no. 8, pp. 7704–7710, 2019.

[5] V. Georgiou, D. Veksler, J. T. Ryan, J. P. Campbell, P. R. Shrestha, and D. E. Ioannou, "Highly efficient rapid annealing of thin polar polymer film ferroelectric devices at sub=glass transition temperature," *Advanced Functional Materials*, vol. 28, no. 8, p. 1704165, 2018.

[6] R. K. Kotnala, G. S. Arya, J. Yogiraj, and N. S. Negi, "Strain-induced structural, magnetic and ferroelectric properties of heterostructure BST–NZFO nanocomposite thin film at room temperature," *Bulletin of Materials Science*, vol. 40, no. 4, pp. 623–630, 2017.

[7] F. Zhen, J. Deng, J. Wang, Z. Liu, P. Yang, and J. Xiao, "Ferroelectricity emerging in strained (111)-textured ZrO_2 thin films," *Applied Physics Letters*, vol. 108, no. 1, p. 012906, 2016.

[8] F. Zhen, J. Chen, and J. Wang, "Ferroelectric hafnium dioxide-based materials for next-generation ferroelectric memories," *Journal of Advanced Dielectrics*, vol. 6, no. 2, pp. 1153–1156, 2016.

[9] J. Shan, Y. Tang, X. Zhao, T. Wang, Z. Duan, and F. Wang, "Growth and electrical properties of epitaxial $0.7Pb(Mg_{1/3}Nb_{2/3})O_3-_{0.3}PbTiO_3$ thin film by pulsed laser deposition," *Journal of Materials Science Materials in Electronics*, vol. 29, no. 8, pp. 6779–6784, 2018.

[10] S. Sharma, P. Saravanan, O. P. Pandey, and P. Sharma, "Grain size distribution dependent magnetic and ferroelectric properties in sol–gel driven $BiFeO_3$ thin films," *Journal of Materials Science Materials in Electronics*, vol. 27, no. 6, pp. 5909–5915, 2016.

[11] N. Lee, J. Lee, T. Ryu, Y. Kim, Y. Lansac, and Y. H. Jang, "Doping graphene with ferroelectric β-PVDF polymer film: density functional theory calculation and molecular dynamics simulation," *Science of Advanced Materials*, vol. 6, no. 11, pp. 2422–2427, 2014.

[12] L. Xie, L. Li, C. A. Heikes, Y. Zhang, Z. Hong, and P. Gao, "Giant ferroelectric polarization in ultrathin ferroelectrics via boundary-condition engineering," *Advanced Materials*, vol. 29, no. 30, p. 1701475, 2017.

[13] T. Iamsasri, J. Guerrier, G. Esteves et al., "A Bayesian approach to modeling diffraction profiles and application to ferroelectric materials," *Journal of Applied Crystallography*, vol. 50, no. 1, pp. 211–220, 2017.

[14] C. Le Paven, R. Benzerga, A. Ferri, D. Fasquelle, V. Laur, and L. Le Gendre, "Ferroelectric and dielectric study of strontium tantalum based perovskite oxynitride films deposited by reactive rf magnetron sputtering," *Materials Research Bulletin*, vol. 96, no. 2, pp. 126–132, 2017.

[15] A. P. Chen, W. Lin, J. Chen, and Y. P. Feng, "Thickness and ferroelectric polarization influence on film magnetic anisotropy across a multiferroic material interface," *ACS Applied Materials and Interfaces*, vol. 12, no. 39, pp. 44317–44324, 2020.

[16] L. P. Zhang, Z. L. Lv, J. P. Cao, G. L. Zhao, and Y. Jiang, "Enhanced ferroelectric and photoelectric properties in lead-free $Bi_{1.07}FeO_3$-modified $K_{0.5}Na_{0.5}NbO_3$ thin films," *Journal of Materials Science: Materials in Electronics*, vol. 32, no. 47, pp. 2051–2060, 2021.

[17] P. P. Biswas, C. Thirmal, S. Pal, M. Miryala, M. Murakami, and P. Murugavel, "The composition and poling-dependent photovoltaic studies in ferroelectric $(Bi_{1-x}Sr_x)(Fe_{1-x}Ti_x)O_3$ thin films," *Journal of Materials Science: Materials in Electronics*, vol. 31, no. 2, pp. 1515–1523, 2020.

[18] T. Carlier, M. H. Chambrier, A. D. Costa, F. Blanchard, and A. Ferri, "Ferroelectric state in an α-Nd_2WO_6 polymorph stabilized in a thin film," *Chemistry of Materials*, vol. 32, no. 17, pp. 7188–7200, 2020.

[19] A. I. Stognij, N. N. Novitskii, S. A. Sharko et al., "On the visualization of the magnetoelectric coupling region for a thin ferromagnetic layer on a ferroelectric substrate," *Inorganic Materials*, vol. 55, no. 3, pp. 284–289, 2019.

[20] W. Xiao, C. Liu, Y. Peng, S. Zheng, and Y. Zhou, "Thermally stable and radiation hard ferroelectric $Hf_{0.5}Zr_{0.5}O_2$ thin films

Research Article

Preparation and Properties of Functional Materials Based on Digital Light Processing 3D Printing

Weiping Deng ![ORCID],[1] Deqiao Xie,[2] Fuxi Liu,[1] Lida Shen,[1,3] Zongjun Tian,[1,3] and Yang Yang[4]

[1]*College of Mechanical and Electrical Engineering, Nanjing University of Aeronautics and Astronautics, Nanjing, 210016 Jiangsu, China*
[2]*College of Energy and Power Engineering, Nanjing University of Aeronautics and Astronautics, Nanjing 210016, Jiangsu, China*
[3]*National Key Laboratory of Science and Technology on Helicopter Transmission, Nanjing University of Aeronautics and Astronautics, Nanjing, 210016 Jiangsu, China*
[4]*General Manager of Huaxin New Material (Zhuzhou) Co., Ltd, Zhuzhou, 412000 Hunan, China*

Correspondence should be addressed to Weiping Deng; wpdeng@nuaa.edu.cn

3D printing, known as the "new industrial revolution," has set off an upsurge in the scientific and technological field in recent years, and 3D printing of digital light processing technology has even improved the performance and efficiency of 3D printing. This technology uses the projection principle to form; no matter the size of the workpiece, the forming speed is not affected. It uses very cheap lamp radiation, the system has no injection-molded components, there is no nozzle clogging problem of traditional molding systems, and maintenance costs are greatly reduced. In this paper, based on digital light processing 3D printing technology, light-curing reactive functional materials commonly used in digital light processing 3D printing are prepared. In the past, most of these materials were imported. In this paper, by adjusting the DLP technology, a water-soluble photocurable reflection material is constructed, a method for shaping the reaction material. It conducts experiments on the preparation and performance research of water-soluble photocurable reaction materials through formulation and process optimization. It prepared a water-soluble photocurable reactive functional material and compared it with traditional imported materials. Due to the characteristics of UV curing and good mechanical properties and water solubility, it provides a new idea for the preparation of 3D printing-related functional materials.

1. Introduction

Digital light processing (DLP) refers to digitally processing an image signal and then projecting it to the desired point. In 3D printing, because of its high-precision casting technology, it can achieve excellent performance in material, detail, and surface material casting.

Nowadays, there are many types of 3D printing materials, the common ones are ABS, PLA, and Nylon. There are many more, such as resins under DLP/SLA molding technology and metals (such as aluminum, iron, steel, silver, gold, and titanium) for industrial-grade models, ceramics, etc. There are also various materials with special properties, such as magnetic materials, conductive materials, wood-like materials, elastic materials, and hard materials like concrete,

special inks for bio-3D printing. These materials are suitable for different application fields and show their own characteristics, and 3D printing of functional materials is also included in this category.

Functional materials refer to materials with excellent electrical, magnetic, optical, thermal, and other functions and special physical, chemical, and biological effects, which can complete the mutual transformation of functions, and are mainly used to construct various functions. Because 3D printing has the advantages of short manufacturing cycle, high molding precision, and customization, the technology is widely used in many aspects, and printing materials are the key. Among them, the vacancy of photocurable reactive functional materials as supporting materials has affected the development of digital light

processing 3D printing technology in China. In this paper, with digital light processing technology as the core, a water-soluble photocurable 3D printing reactive material was prepared and studied. This is of great significance for the development of digital light processing technology 3D printing and related functional materials. The innovation is that it can make up for the current situation of relying on imports of this material and play a certain reference role in promoting the development of related materials in China.

2. Related Work

Due to the increasing popularity of 3D printing, 3D printing-related technologies are becoming an emerging core competitiveness. Huang and Lin combined the "Conceive, Design, Implement, Operate" (CDIO) framework with 3D printing tangible to propose a novel technical thinking [1]. Xu et al. developed a framework to study the innovation capabilities of multilayer innovation ecosystems involving science, technology, and business subecosystems. They selected China's 3D printing ecosystem as a case study, in addition to analyzing the interplay between the science, technology, and business layers [2]. Vanderburgh et al. highlighted recent advances in 3D printing of tissue-engineered structures. They defined it as the layer-by-layer fabrication of a part guided by digital information in a 3D computer-aided design file. In this structure, they recapitulated the physical and cellular properties of the tissue microenvironment and it was used to study disease progression mechanisms and screen drugs [3]. Xu et al. proposed a combination of 3D scanning and cement mortar-based 3D printing for developing a new process for replicating decorative parts of historic buildings. The process was traditionally labor-intensive and expensive to build, but they developed and presented a layered algorithm for model slicing and an improved scanline algorithm for nozzle paths [4]. Ho et al. prepared stereolithography (STL) format computer models and contrast-enhanced CT of 3D printed models for 3D printing in the medical field. Their proposed 3D-printed model, generated from a strong and flexible plastic material, successfully replicated the anatomical details of the aortic structure and pathology [5]. The printability of the materials used in extrusion-based 3D printing was one of the most important properties, especially when manufacturing objects of architectural complexity. However, this parameter is affected by several factors (temperature, composition, and additives), which makes comprehensive evaluation and classification challenging. Kim et al. evaluated the printability of food inks for 3D food printing applications by systematically adjusting dimensional stability testing, handling performance evaluation, and shear rheology testing using edible hydrocolloids as reference materials. Thus, a high-quality solution is proposed [6]. To date, most printable thermoset materials suffer from complex processes, poor thermodynamic properties, and slow printing speeds. Wang et al. developed a photosensitive composite ink for fast photocuring printing, which has a good auxiliary role for 3D printing under digital light processing [7].

However, the photosensitive composite ink they developed is lacking in the accuracy of 3D printing and is prone to errors in more complex model processing tasks, so it still needs to be improved before it is widely used.

3. Technical Setup and Material Preparation Method of 3D Printing Based on Digital Light Processing

DLP 3D printing based on digital light processing mainly uses DMD chips developed by TI. It uses a high-pixel digital light processor (DMD) optomechanical to project model slices to solidify liquid photopolymer layer by layer [8]. In a DLP projection system, the core element is its DMD chip. The DMD chip can deflect the microscope to different angles to complete the light modulation [9]. The size of the DMD micromirror is generally $7.6\,\mu m$, the minimum is $5.4\,\mu m$, and the maximum is $13.6\,\mu m$. There are two types of arrangement: square arrangement and rhombus arrangement. In order to facilitate the deflection of the mirror, there is a certain gap between the arrays, so the actual size of the chip and the projection size are not only determined by the size of the mirror [10]. Figure 1 shows the layout of the lower exposure 3D printing system and DMD chip lens.

3.1. DLP Technology Adjustment. When DLP technology is applied to 3D printing, the reflectivity and diffraction performance of the DMD chip microprocessor can be affected due to the higher photoresponse of the photoinitiator in the photosensitive material to higher energy light. The energy rate of the system also has an effect [11]. Excessive use of light energy can cause excessive system losses, fail to reach projection targets, or even damage equipment. Therefore, the reflectivity of the DMD chip in different light zones, as well as in the DMD window, will be the main estimate.

According to the DMD chip guidance given by TI, DMD chips suitable for visible light, ultraviolet light, and near-infrared wavelengths also have different energy utilization rates for different light wavelengths under different human radiation angles, as shown in Figure 2.

The DMD window is optimized by coating for the wavelength of 420~700 nm in the visible light band to improve the transmission efficiency. The ultraviolet band is optimized for the light wavelength of 355~400 nm, and the optimized effect is shown in Figure 3.

In 3D printing applications, the typical wavelengths used by DLP technology are 355 nm and 405 nm, mainly determined by the light source [12]. The optimization effect of visible light band and ultraviolet light band in Figure 3 shows that the DMD chip for ultraviolet band should be used as the core of the system. It ensures that the system has a high light energy consumption rate. If the visible light region DMD chip is used, the system loss will increase. If the wavelength of the light source is 355 nm, the utilization rate is only 70%, and the waste of system energy is huge [13]. After completing the above settings, it can print the material. The specific process is shown in Figure 4.
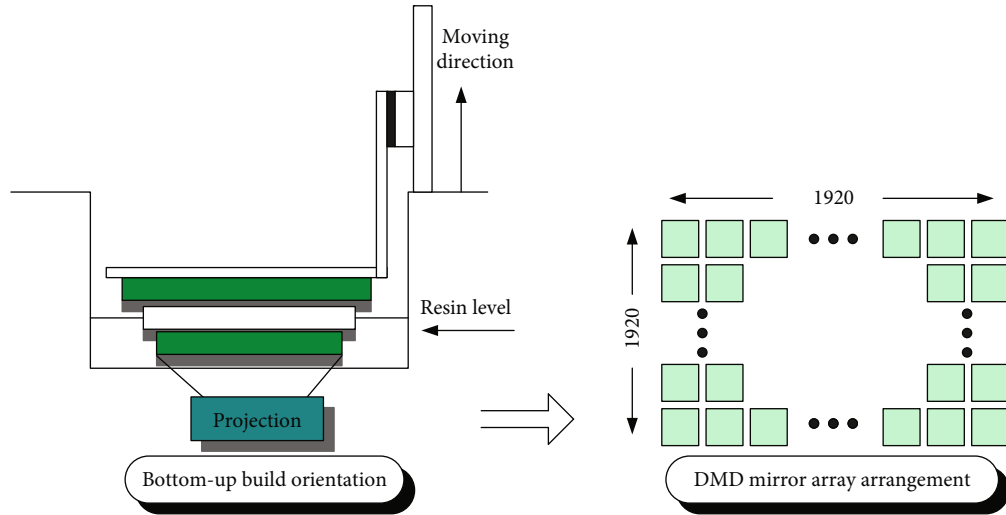
FIGURE 1: Layout of the lower exposure 3D printing system and DMD chip lens.
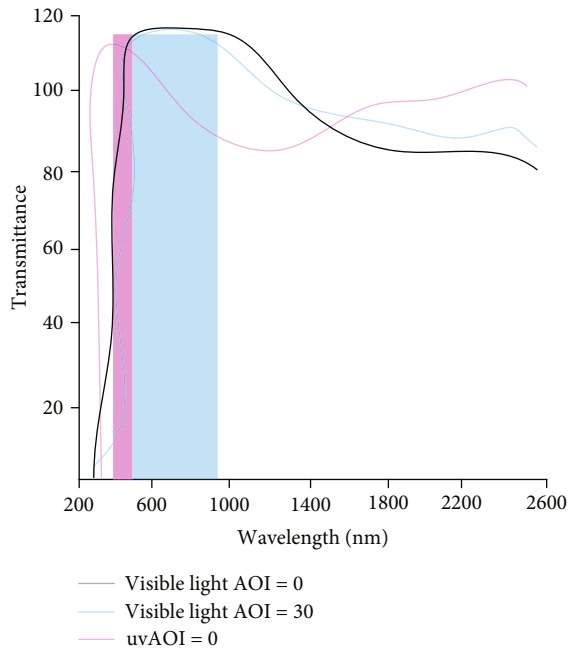
FIGURE 2: Energy utilization curve of DMD chip at different wavelengths.

After understanding the working principle and operation process of DLP technology, the next article will introduce the curing and molding mechanism of the functional materials to be prepared. It studies the effect of process conditions on the properties of the material before and after curing to determine the optimal formulation of the material. This provides a certain theoretical basis and practical methods for the localization of digital light processing 3D printing materials.

3.2. Construction Principle of Water-Soluble Photoreactive Materials. Light-curing 3D printing materials are composed of a solid material and a support material. The material

responsible for building the solid part of the part is called the solid material. It directly affects the molding accuracy and surface quality of solid parts and is a key functional material for photocuring 3D printing [14]. The composition of the material includes prepolymer, monomer, and photoinitiator, as shown in the following formula. The polymerization cross-linking reaction allows the liquid resin to form a cured product in a very short time:

$$
\begin{aligned}
X - Y &\xrightarrow{\text{hv}} \left(\frac{X}{Y}\right), \\
\left(\frac{X}{Y}\right) \cdot &\longrightarrow X \cdot + Y.
\end{aligned}
\tag{1}
$$
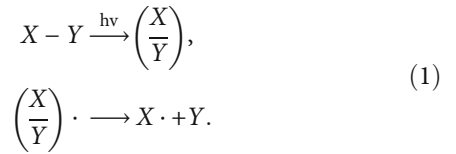
It abstracts hydrogen atoms from hydrogen atom donors such as prepolymers and active monomers, such as photoinitiator ITX, to make them active free radicals. After the previous step is completed, as shown in the following formula, the polymerization and cross-linking reaction is further initiated.

$$
\begin{aligned}
X &\xrightarrow{\text{hv}} X, \\
X \cdot &\xrightarrow{RH} XH + R.
\end{aligned}
\tag{2}
$$
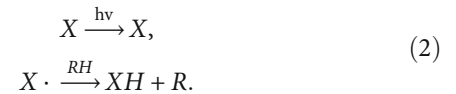
The photocurable reactive materials mainly include three stages of chain initiation, chain growth, and chain termination [15].

(1) Chain initiation

The photoinitiator (I) absorbs light energy under the irradiation of a UV lamp. It transitions from the ground state to the excited state, forming active radicals (R). The active free radical then undergoes an addition reaction with the monomer (M) to form a monomer free radical, as shown
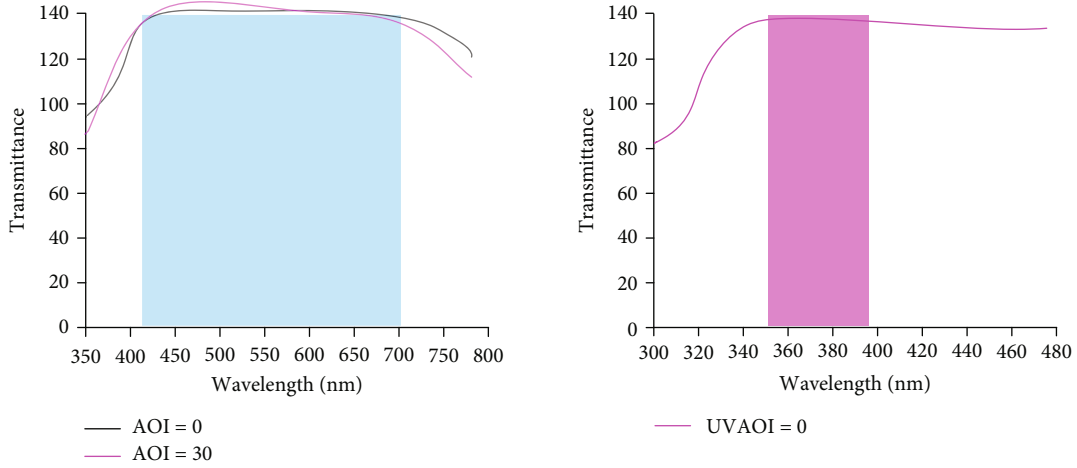
FIGURE 3: Optimization effect diagram of visible light band and ultraviolet light band.

in the formula:

$$I \xrightarrow{\text{hv}} R,$$
$$R \cdot + M \xrightarrow{\text{hv}} (R - M). \tag{3}$$
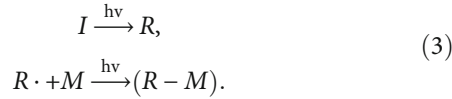
(2) Chain growth

The above process is repeated continuously, so that active radicals and monomers are rapidly added to form macromolecules. Light-curing printing materials change from liquid to solid:

$$(R\text{-}M)_n \cdot + M \xrightarrow{\text{hv}} (R - M - M)_n \cdot \tag{4}$$
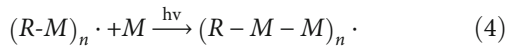
(3) Chain termination

Common chain terminations include disproportionation termination and coupling termination. With the continuous progress of the chain growth reaction, the content of free radicals in the chain increases continuously, and the photo-curing reaction ends [16].

3.3. Curing and Characterization of Reactive Materials

(1) Viscosity

The viscosity of the reactive material is measured according to the specified standard. It puts an appropriate amount of liquid reaction material into the barrel of the digital viscometer and then puts the barrel into a constant temperature water tank. It uses a No. 21 rotor to measure the viscosity of the reaction material at different temperatures [17].

Viscosity is an important process parameter characterizing the jetting properties of photocurable 3D printing support materials, which determines whether the reactive material can be smoothly and steadily ejected from the noz-

FIGURE 4: DLP printing process.

zle [18]. It is subjected to shearing force. It simplifies the injection process, and the viscosity of the reaction material is shown in the formula:

$$\tau = F|A,$$
$$D = \left(\frac{dx}{dz}\right)|dt, \tag{5}$$
$$\eta = \tau|D.$$

τ is the shear stress, F is the shear force, A is the area where the shear force acts, and D is the shear rate. dx/dz is the shear deformation, dt is the shear force action time, and η is the viscosity of the reaction material.

(2) Surface tension

It measures the surface tension of the reactive material. It puts an appropriate amount of liquid temperature-sensitive reactive material sample into the barrel of the automatic surface tensiometer and then puts the barrel into a constant temperature water tank. It chooses the platinum plate method to test the surface tension of the reaction material at different temperatures. The specific process is as follows:

$$P = \text{mg} + L\gamma(\cos\theta) - sh\rho g. \tag{6}$$

(3) Volatilization rate

It adds the reaction material to the beaker. The mass of the beaker is M_0, and the total mass after adding the reaction material is M_1. After being placed at different temperatures for different times, it measured a total mass of M_2. The volatilization rate α of the reaction material is calculated as follows:

$$\alpha = \frac{M_1 - M_2}{M_1 - M_0}. \tag{7}$$

(4) Curing shrinkage

Under the condition of 25°C, it uses the ZMD-2 electronic densitometer to measure the density of the reaction material before curing and the density of the cured product, and the curing shrinkage can be calculated by the formula:

$$\Delta = \frac{\rho_1 - \rho_0}{\rho_0}. \tag{8}$$

(5) Solubility

It cuts the cured product of the reaction material to obtain a sample with a size of $10 \times 10 \times 4\,\text{mm}^3$. The mass of the sample is called M_0, and the sample is soaked in distilled water of different temperatures for a certain period of time. It takes a filter paper with a quality of M_1 for filtration and puts the filter paper and the sample into a vacuum drying oven for drying, and the quality after drying is M_2. Then, the reaction material solubility S is calculated by the following formula:

$$S = \frac{M_0 - (M_2 - M_1)}{M_0}. \tag{9}$$
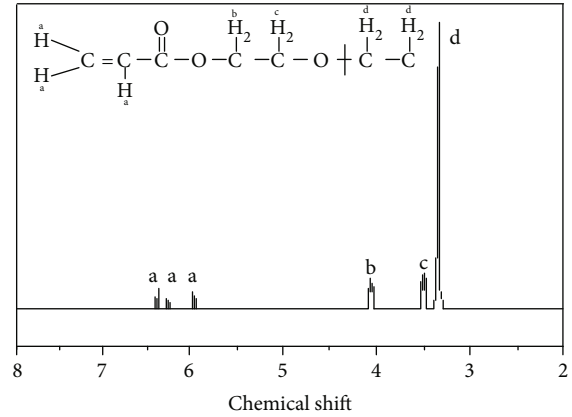
FIGURE 5: 1H NMR spectrum of single-end hydroxyl PEGmA.

The photocuring reaction process of the photocurable monomer is as follows:

$$R \xrightarrow{\text{violetray}} R,$$
$$R\cdot + mPEG400DA \longrightarrow R - PEG400DA_m,$$
$$R\cdot + R - PEG400DA_m \cdot \longrightarrow R - PEG400DA_m - R,$$
$$R - PEG400DA_m \cdot + R - PEG400DA_m \cdot \longrightarrow R - PEG400DA_m - R. \tag{10}$$
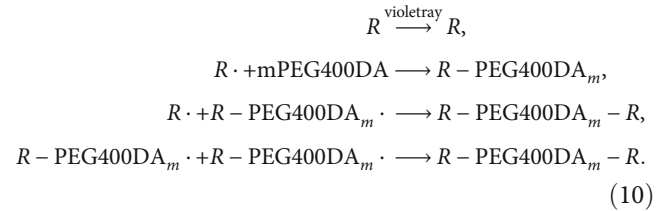
R is a photoinitiator, R is a free radical, and PEG400DA is polyethylene glycol 400 diacrylate.

Surface tension is also an important process parameter for light-cured 3D printing reaction materials, which determines whether the reaction materials can be smoothly and stably ejected from the nozzle [19]. During jet printing, the reactive material droplets have a tendency to automatically shrink into spherical shapes. The air resistance and the change of the mass of the reaction material droplets are ignored, and the force of the reaction material is simplified. The surface tension of the reactive material is shown in the formula:

$$\alpha = \frac{\omega}{\gamma}. \tag{11}$$

In the formula, α is the surface area of the new surface, ω is the work done when the new surface is generated, and γ is the surface tension coefficient.

3.3.1. Experiments on the Preparation and Performance of Water-Soluble Photocurable Reactive Materials. Before the experiment, the water-soluble photocurable monomer must first be provided for the preparation of the water-soluble photocurable 3D printing reaction material. Single-ended hydroxyl PEGmA, also known as polyethylene glycol acrylate monoester, has good UV curing properties. Because of its special molecular structure, PEGmA and its cured products have good water solubility and can be easily removed by water gun [20]. In addition, PEGmA has the advantages of nontoxicity and low volatilization rate. Therefore,

TABLE 1: Basic formula of water-soluble photocurable 3D reactive materials.

Materials	PEGmA	Polyethylene glycol	369	ITX	Other agents
Proportion of the 1st blend/wt%	75	12	2	2	9
Proportion of the 2nd blend/wt%	65	12	2	2	8
Proportion of the 3rd blend/wt%	43	6	2	1	7
Proportion of the 4th blend/wt%	22	6	1	1	6
Proportion of the 5th blend/wt%	15	3	1	1	4
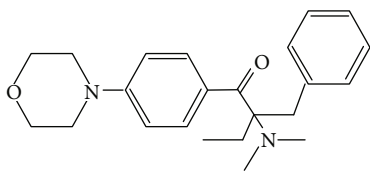
FIGURE 6: Schematic diagram of the structure of photoinitiator 369.
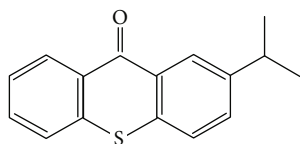
FIGURE 7: Schematic diagram of the structure of the photoinitiator ITX.

PEGmA provides a new idea for the preparation of water-soluble photocurable reactive materials. However, it is currently difficult to purchase pure PEGmA in the market, and the domestic synthesis process and purification method of PEGmA are not mature, and there is no commercial PEGmA, so it is necessary to make PEGmA.

3.4. Synthesis and Purification of Single-Ended Hydroxyl PEGmA. It firstly adds a certain amount of reactant polyethylene glycol into a 250 ml container equipped with a thermometer, a constant pressure dropping funnel, a water separator, and a condenser. In the flask, it heated the mixture to 60°C with magnetic stirring. After the p-toluenesulfonic acid and hydroquinone were completely dissolved, the temperature was raised to 120°C. It continues to magnetically stir for 10 to 15 minutes, and after no bubbles are produced, it filters. The filtered product was added to a rotary evaporator, distilled under reduced pressure, and toluene was removed to obtain a crude product of PEGmA.

It uses a pipette to, respectively, measure a certain amount of reaction solution and distilled water (mass ratio 1 : 10) into a conical flask, add indicator phenolphthalein, and mix evenly. It is titrated to a reddish color with standard NaOH solution, shaken, and the end point of the titration is that the red color does not fade within 30 seconds. It records the amount of NaOH solution consumed and calculates the acidity and esterification of the sample.

The formula for calculating acidity is as follows:

$$AV = \frac{CVMr}{m_s}. \tag{12}$$

In the formula, AV is the acidity value of the sample; C is the mass concentration of the standard NaOH solution; V is the volume of the NaOH solution consumed when the titration reaches the end point; Mr is the relative molecular mass of NaOH; m_s is the mass of the sample taken.

The calculation of the degree of esterification of the esterification reaction is as follows:

$$DE = \frac{A_i - A_t}{A_i}. \tag{13}$$

Among them, DE is the esterification degree of the sample; A_i is the initial acidity value of the sample; A_t is the acidity value of the sample measured at a certain time.

Figure 5 is the 1H NMR spectrum of single-ended hydroxyl PEGmA. It can be seen from Figure 5 that, compared with pure polyethylene glycol, characteristic peaks appear at the chemical shifts of 5.8-6.5 in the hydrogen spectrum of single-end hydroxyl PEGmA, corresponding to the 3 Hs of the terminal alkenyl group. The characteristic peaks at chemical shifts 4.2-4.4 correspond to the 2 Hs on the carbon atom of the ester group and the 2 Hs on the methylene group connected to the terminal hydroxyl group. It has characteristic peaks at chemical shifts of 3.6-3.8. The characteristic peaks at chemical shifts of 3.5 to 3.6 correspond to 82 Hs in the oxyethane structure of the monoester, which indicates that the oxyethane structure (ether chain structure) of polyethylene glycol is not destroyed. In conclusion, the esterification reaction of polyethylene glycol and acrylic acid occurred to generate single-end hydroxyl PEGmA. The peak shape in the figure is sharp, and there are few impurity peaks, which proves that the purity of the monoester is high.

3.5. Preparation of Reactive Photocurable 3D Printing Materials. Single-end hydroxyl PEGmA has excellent UV curability and can be cured quickly under the action of photoinitiator. And its cured product has good water solubility and mechanical properties, which can support the molding of solid materials [21]. After it has been formed, the PEGmA cured product can be removed by flushing with a water gun. Therefore, PEGmA meets the performance of water-soluble functional materials, which provides a new idea for the preparation of water-soluble photocurable 3D printing materials. In this section, on the basis of the synthesized water-soluble PEGmA as the photocurable monomer, a new type of water-soluble functional material, reactive photocurable 3D printing functional material, was prepared. It analyzes the influence of monomers, types, and contents

Table 2: The volatilization rate of reaction materials containing 75 wt% PEGmA in different environments.

Storing time	8	16	24	32	40	48	56	64	72
Wet environment	0.18	0.24	0.29	0.33	0.48	0.40	0.59	0.60	0.69
Dry environment	0.15	0.23	0.26	0.29	0.38	0.39	0.49	0.56	0.68
Hot environment	0.28	0.33	0.39	0.47	0.51	0.55	0.62	0.68	0.72
Cold environment	0.01	0.12	0.2	0.35	0.38	0.52	0.64	0.65	0.68
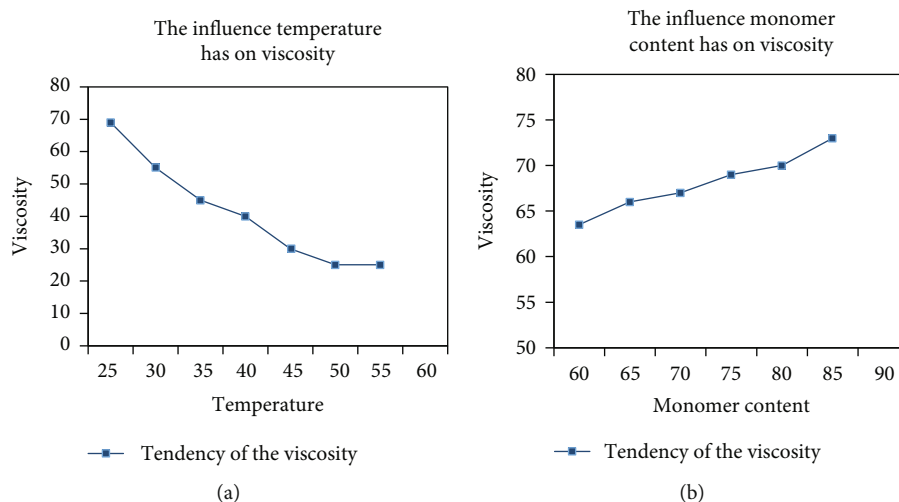
Figure 8: Effect of temperature and monomer content on viscosity of reaction material.

of photoinitiators on the properties of the material, studies the preparation process of the material, and analyzes its curing and forming mechanism. It finalizes the optimal formulation of water-soluble photocurable 3D reactive materials. The basic formula is shown in Table 1.

It formulates photoinitiator 369 and ITX, polyethylene glycol, and photocurable monomer PEGmA into a clean beaker. It was stirred with a magnetic stirrer until the photoinitiator 369 and ITX were completely dissolved. It is then added with the inhibitor according to the formula, and stirring is continued until the inhibitor is completely dissolved. When it forms a transparent and uniform solution 1, it needs to be sealed for later use. 369 is a photoinitiator with high sensitivity range and high UV absorption, which belongs to the cleavage type photoinitiator [22].

369 is often used to initiate free radical photopolymerization and is light yellow powdery crystal. Its structural formula is shown in Figure 6.

ITX is a highly efficient hydrogen abstraction photoinitiator, which is light yellow crystalline powder. Its pseudonym is isopropylthioxanthone, and its structural formula is shown in Figure 7.

369 is not only a cleavage free radical photoinitiator, but also a hydrogen-donating polymer photoinitiator, which can donate hydrogen to the hydrogen abstraction initiator ITX. Therefore, 369 is often compounded with ITX as a coinitiator, which can improve the initiation efficiency [23]. The volatilization of some components in the reaction material not only affects the performance of the reaction material but also causes pollution to the environment and harm to

the human body. Therefore, the volatilization rate is also a factor that must be considered for the reaction material.

Table 2 shows the volatilization rates of the reacted materials with a monomer concentration of 75 wt% stored at 55°C in different environments for different times. It can be seen from Table 2 that after the reaction material was stored at 55°C for 72 h, the volatilization rate was only 0.72% in the highest case. Therefore, the reactive functional material has good long-term spraying stability and can meet the requirements of long-term spraying.

3.6. Properties of Water-Soluble Photocurable Reactive Materials before Curing. As mentioned above, viscosity is an important process parameter that determines whether the reaction material can be smoothly and stably ejected from the nozzle. If the viscosity is too high, the required shear force is too large, and the reaction material will not be ejected from the nozzle smoothly. If the viscosity is too low, it is easy to cause ink leakage, thus affecting the molding quality and accuracy [24]. Therefore, the reactive material should have a suitable viscosity to ensure the smooth progress of photocuring 3D printing. The suitable viscosity range in this experiment is 10~25 mPa·s. There are many factors that affect viscosity, but the most important are temperature and monomer content.

A photocurable reaction material with a monomer content of 75 wt% was prepared, and the effect of temperature on the viscosity of the reaction material was studied. At the same time, the photocurable monomer PEGmA was prepared into reaction materials with contents of 60 wt%,

The influence temperature has on viscosity

● Tendency of the surface tension

The influence monomer content has on viscosity

● Tendency of the surface tension
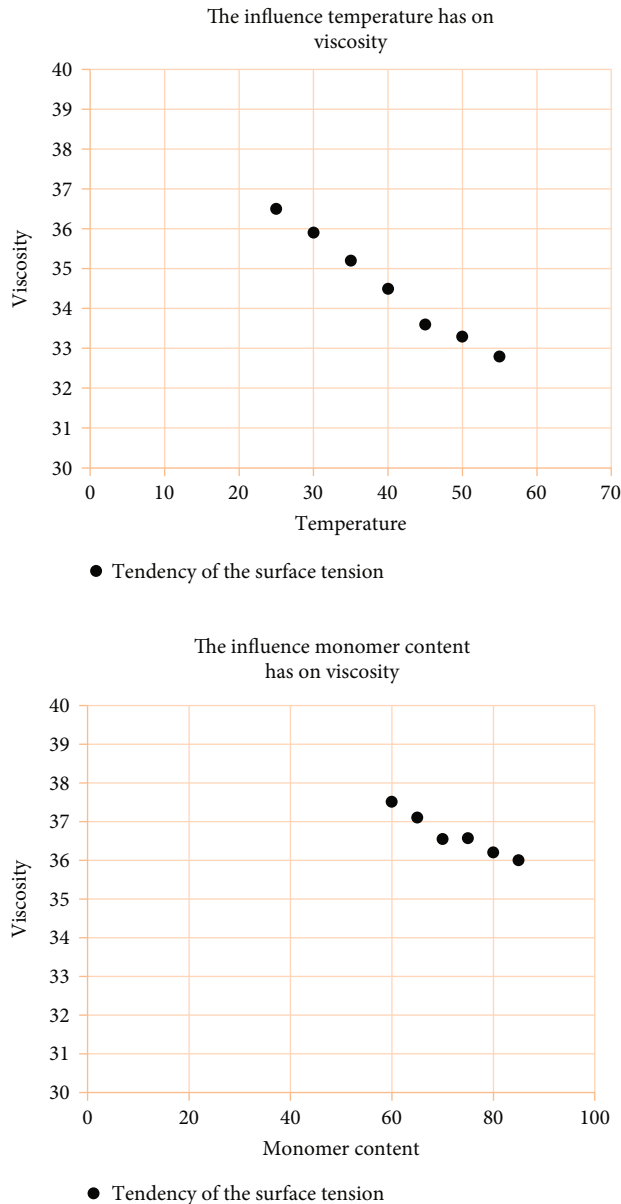
FIGURE 9: Effect of temperature and monomer content on the surface tension of reactive materials.

65 wt%, 70 wt%, 75 wt%, 80 wt%, and 85 wt%, respectively, and the effect of monomer content on the viscosity of the reaction material was studied. The results are shown in Figure 8.

It can be seen from Figure 8(a) that describing the effect of temperature on the reaction material, as the temperature increases, the viscosity of the reaction material gradually decreases, but the decreasing range gradually decreases. When the temperature reaches the interval of 45-60 degrees, the viscosity tends to be stable around 30. This is because the temperature increases, the intermolecular distance in the reaction material solution increases, the interaction force weakens, the resistance decreases, and the viscosity decreases. However, when the temperature is too high, the activity of the monomers in the reaction material solution increases, and a curing reaction is likely to occur. This causes the viscosity of the reaction material to rise sharply, and the solidified product of the reaction material is likely to cause clogging of the nozzle and damage the nozzle.

At the same time, Figure 8(b) shows that the viscosity of the reaction material increases gradually with the increase of the content of photocurable monomers. This is because when the content of the photocurable monomer is low, the effect of monomer molecules is weak. Each monomer molecule can be considered to exist individually, so the viscosity of the reactive material is low. However, when the monomer content is high, the intermolecular interactions of the monomers also increase significantly. At this time, the monomers no longer exist alone but exist in the solution in the form of aggregates. This in turn increases the viscosity of the solution, affecting the jetting process and part quality. Therefore, the content of monomers should be controlled to ensure the working stability of light-curing 3D printing.

Surface tension is also an important process parameter that determines whether the reaction material can be smoothly and stably ejected from the nozzle. The surface tension of the reactive material is too high, the required voltage exceeds the upper limit, and the reactive material cannot be ejected. If the surface tension is too low, the reactive material cannot form effective droplets, which affects the molding quality and accuracy. Therefore, the reaction material should have a suitable surface tension to ensure stable ejection of the reaction material. The suitable surface tension range in this experiment is 25~35 mN/m. It mainly studies the effect of temperature, monomer content, and leveling agent content on the surface tension of reactive materials [25, 26].

It prepares reactive materials with a monomer content of 75 wt% and studies the effect of temperature on the surface tension of reactive materials. It prepared the photocurable monomer PEGmA into reactive materials with contents of 60 wt%, 65 wt%, 70 wt%, 75 wt%, 80 wt%, and 85 wt%, respectively. It studies the effect of monomer content on the surface tension of reactive materials. The results are shown in Figure 9.

It can be seen from Figure 9 that with the increase of temperature, the surface tension of the reaction material gradually decreases. When the temperature exceeds 80, the surface tension drops below 36. This is because as the temperature increases, the intermolecular distance in the solution increases, the intermolecular interaction force weakens, and the surface tension decreases accordingly. But when the temperature is too high, the monomer is easy to solidify and block the nozzle. Therefore, a suitable working temperature can reduce the surface tension of the reaction material and ensure stable work. It can be seen from Figure 9 that with the increase of the content of the photocurable monomer, the surface tension of the reaction material decreases, but the decrease is smaller. This is because the pure PEGmA monomer has a low surface tension of only 32.667 mN/m. The surface tension of the solvent polyethylene glycol is as high as 57.13 mN/m. The higher the monomer content, the higher the viscosity of the reaction material. The lower the thermal stability, the easier it is to
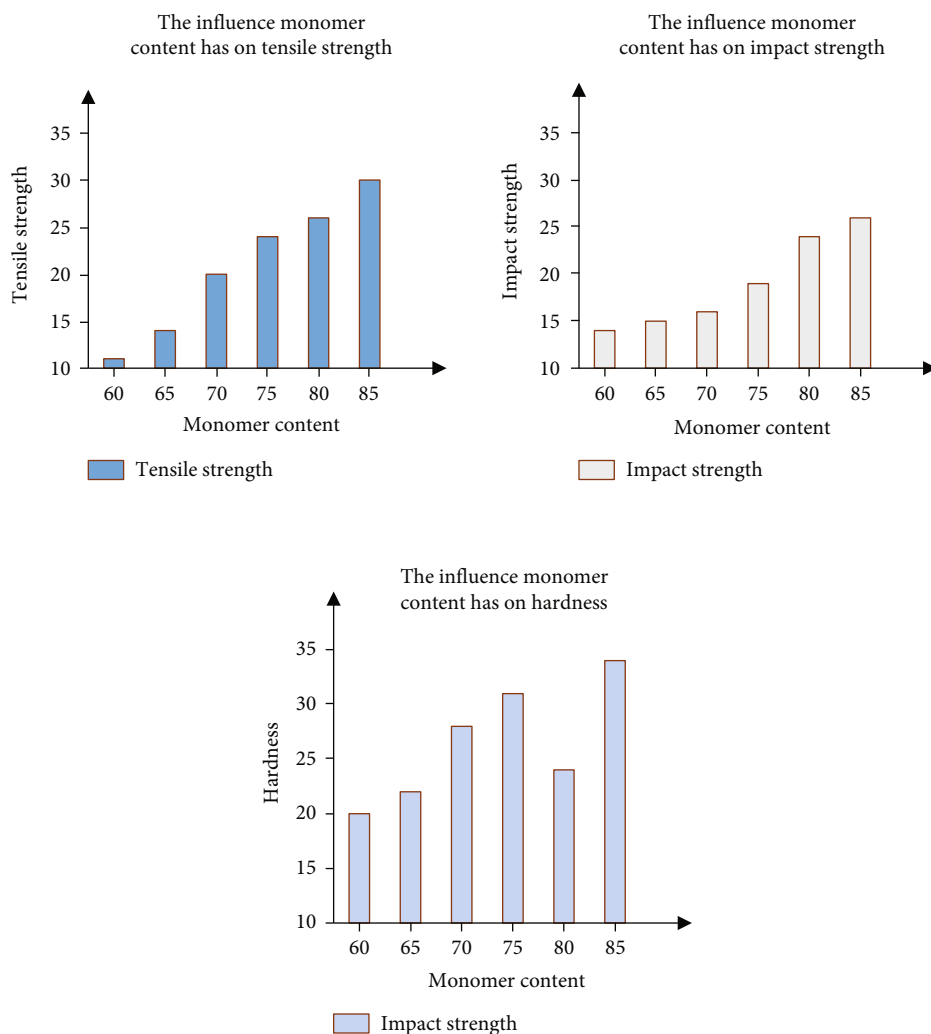
FIGURE 10: Effect of monomer content on surface tension, impact strength, and hardness of reactive materials.

TABLE 3: Effect of monomer content on hardness under different conditions.

Photocurable monomer content/wt%	60	65	70	75	80	85
Hard/HA	29	33	38	42	48	53
Soft/SA	14	18	20	29	30	39
Medium/MA	23	20	25	34	32	43

cure in advance and block the nozzle. Therefore, the higher the monomer content, the lower the solvent content, which is more conducive to the reduction of surface tension. The surface tension of the reactive material cannot be lowered by substantially increasing the monomer content [27].

3.7. Properties of Water-Soluble Photocurable Reactive Materials after Curing. There are many factors that affect the curing shrinkage of reactive materials. In this section, the effects of the content of photocurable monomers on the curing shrinkage and mechanical properties (tensile strength, impact strength, and hardness) of reactive materials are studied. It was prepared as reactive materials with monomer contents of 60 wt%, 65 wt%, 70 wt%, 75 wt%,

80 wt%, and 85 wt%, respectively. At 25°C, it studies the effect of photocurable monomer content on curing shrinkage of reactive materials.

It can be seen from Figure 10 that the higher the content of the photocurable monomer, the higher the tensile strength, impact strength, and hardness of the reaction material. This is because the photocurable monomer forms a three-dimensional space network structure after curing, which has higher mechanical properties and greater hardness. This in turn gives the reactive material suitable mechanical properties to aid in solid material shaping. Therefore, the higher the monomer content, the highest mechanical properties of the reactive material. In addition, under the influence of different environments, the reactive

TABLE 4: Comparison of this material with Fullcure705 and stig3.

Material types	Viscosity/ mPa·s	Tensile strength/mN/m	Volatilization rate/%	Curing shrinkage/%	Hardness/ HA	Solubility/ %
Material of this article	49.85	37.64	0.2	3.74	41	80.12
Fullcure705	71.51	33.45	0.39	0.88	26	78.6
stig3	70.49	30.88	0.51	0.66	31	69

materials are still stable. Table 3 shows the effect of monomer content on hardness under different conditions.

3.8. Performance Comparison of Water-Soluble Photocurable 3D Printing Reactive Materials and Traditionally Used Foreign Materials. In this section, the performance data of the water-soluble light-curing 3D printing materials obtained by the experiment are compared with the performance of the traditional imported commonly used materials Fullcure705 and stig3, as shown in Table 4.

It can be seen from Table 4 that the viscosity of the water-soluble photocurable reactive materials prepared in this paper is the lowest compared with the imported photocurable reactive materials Fullcure705 and stig3. It is only 49.85 mPa·s, which is beneficial to the stable ejection of the reaction material. Moreover, the surface tension is high, reaching 37.64 mN/m, which is beneficial to assist the molding of solid materials. In other properties, the solubility is as high as 80.12%, which is beneficial to the water washing and removal of the reaction material, which is also the key performance of the reaction material. And its volatilization rate is low, only 0.2%, and its mechanical properties are as high as 41HA. This is beneficial to ensure the ejection stability of the reaction material and assist the molding of the solid material. Compared with all key data, the reaction materials prepared in this paper have better comprehensive properties and are more suitable as functional materials for digital light processing 3D printing.

4. Conclusions

In this chapter, using the synthesized single-end hydroxyl PEGmA as a photocurable monomer, using its UV-curing properties and the water solubility of the cured product, and using polyethylene glycol, 369, and ITX coinitiators as raw materials, a kind of PEGmA was prepared. In addition, the curing molding mechanism and water-solubility characteristics of the material were also analyzed, the influence of each component of the material and the molding process conditions on the properties before and after curing were studied, and the optimal formulation of the water-soluble light-curing reactive material was optimized and determined. Finally, by comparing the prepared functional materials with the traditional imported materials, it is found that the materials prepared in this paper have better performance in various key indicators. In the future, the author hopes to optimize the formulation of this material through more experiments, so that it can be prepared in batches and can be used in more places.

Data Availability

Data are included within the manuscript.

Conflicts of Interest

There is no potential conflict of interest in this study.

References

[1] T. C. Huang and C. Y. Lin, "From 3D modeling to 3D printing: development of a differentiated spatial ability teaching model," *Telematics & Informatics*, vol. 34, no. 2, pp. 604–613, 2017.

[2] G. Xu, Y. Wu, T. Minshall, and Y. Zhou, "Exploring innovation ecosystems across science, technology, and business: a case of 3D printing in China," *Technological Forecasting & Social Change*, vol. 136, pp. 208–221, 2017.

[3] J. Vanderburgh, J. A. Sterling, and S. A. Guelcher, "3D printing of tissue engineered constructs for in vitro modeling of disease progression and drug screening," *Annals of Biomedical Engineering*, vol. 45, no. 1, pp. 164–179, 2017.

[4] J. Xu, L. Ding, and P. E. D. Love, "Digital reproduction of historical building ornamental components: From 3D scanning to 3D printing," *Automation in Construction*, vol. 76, pp. 85–96, 2017.

[5] D. Ho, A. Squelch, and Z. Sun, "Modelling of aortic aneurysm and aortic dissection through 3D printing," *Journal of Medical Radiation Sciences*, vol. 64, no. 1, pp. 10–17, 2017.

[6] H. W. Kim, H. Bae, and H. J. Park, "Classification of the printability of selected food for 3D printing: Development of an assessment method using hydrocolloids as reference material," *Journal of Food Engineering*, vol. 215, pp. 23–32, 2017.

[7] L. Wang, F. Zhang, Y. Liu, S. Du, and J. Leng, "Photosensitive composite inks for digital light processing four-dimensional printing of shape memory capture devices," *ACS Applied Materials and Interfaces*, vol. 13, no. 15, pp. 18110–18119, 2021.

[8] P. Upex, P. Jouffroy, and G. Riouallon, "Application of 3D printing for treating fractures of both columns of the acetabulum: benefit of pre-contouring plates on the mirrored healthy pelvis," *Orthopaedics & Traumatology: Surgery & Research*, vol. 103, no. 3, pp. 331–334, 2017.

[9] B. Bhushan and M. Caspers, "An overview of additive manufacturing (3D printing) for microfabrication," *Microsystem Technologies*, vol. 23, no. 4, pp. 1117–1124, 2017.

[10] C. Paredes, F. J. Martínez-Vázquez, A. Pajares, and P. Miranda, "Co-continuous calcium phosphate/polycaprolactone composite bone scaffolds fabricated by digital light processing and polymer melt suction," *Ceramics International*, vol. 47, no. 12, pp. 17726–17735, 2021.

[11] J. Xiao, Y. Jia, D. Liu, and H. Cheng, "Three-dimensional printing of SiCN ceramic matrix composites from preceramic

polysilazane by digital light processing," *Ceramics International*, vol. 46, no. 16, pp. 25802–25807, 2020.

[12] J. Zhang, L. Wei, X. Meng, F. Yu, and S. Liu, "Digital light processing-stereolithography three-dimensional printing of yttria-stabilized zirconia," *Ceramics International*, vol. 46, no. 7, pp. 8745–8753, 2020.

[13] J. R. Raney, B. G. Compton, J. Mueller, T. J. Ober, and J. A. Lewis, "Rotational 3D printing of damage-tolerant composites with programmable mechanics," *Proceedings of the National Academy of Sciences of the United States of America*, vol. 115, no. 6, pp. 1198–1203, 2018.

[14] R. P. Aquino, S. Barile, A. Grasso, and M. Saviano, "Envisioning smart and sustainable healthcare: 3D Printing technologies for personalized medication," *Futures*, vol. 103, pp. 35–50, 2018.

[15] I. A. Malik, M. Mirkhalaf, and F. Barthelat, "Bio-inspired "jigsaw"-like interlocking sutures: Modeling, optimization, 3D printing and testing," *Journal of the Mechanics and Physics of Solids*, vol. 102, pp. 224–238, 2017.

[16] R. J. Huang, Q. G. Jiang, H. D. Wu et al., "Fabrication of complex shaped ceramic parts with surface-oxidized Si3N4 powder via digital light processing based stereolithography method," *Ceramics International*, vol. 45, no. 4, pp. 5158–5162, 2019.

[17] D. Xue, Y. Wang, and D. Mei, "Multi-step exposure method for improving structure flatness in digital light processing-based printing," *Journal of Manufacturing Processes*, vol. 39, pp. 106–113, 2019.

[18] B. Peng, Y. Yang, K. Gu, E. J. Amis, and K. A. Cavicchi, "Digital light processing 3D printing of triple shape memory polymer for sequential shape shifting," *ACS Materials Letters*, vol. 1, no. 4, pp. 410–417, 2019.

[19] Y. Z. Yu, J. R. Lu, and L. Jing, "3D printing for functional electronics by injection and package of liquid metals into channels of mechanical structures," *Materials & Design*, vol. 122, pp. 80–89, 2017.

[20] P. Shakor, J. Sanjayan, A. Nazari, and S. Nejadi, "Modified 3D printed powder to cement-based material and mechanical properties of cement scaffold used in 3D printing," *Construction and Building Materials*, vol. 138, pp. 398–409, 2017.

[21] M. J. Ryan, D. R. Eyers, A. T. Potter, L. Purvis, and J. Gosling, "3D printing the future: scenarios for supply chains reviewed," *International Journal of Physical Distribution & Logistics Management*, vol. 47, no. 10, pp. 992–1014, 2017.

[22] T. Birtchnell, T. Bohme, and R. Gorkin, "3D printing and the third mission: the university in the materialization of intellectual capital," *Technological Forecasting & Social Change*, vol. 123, pp. 240–249, 2017.

[23] F. Naddeo, A. Naddeo, and N. Cappetti, "Novel "load adaptive algorithm based" procedure for 3D printing of lattice- based components showing parametric curved micro-beams," *Composites Part B Engineering*, vol. 115, pp. 51–59, 2017.

[24] S. Liu, Y. Li, and N. Li, "A novel free-hanging 3D printing method for continuous carbon fiber reinforced thermoplastic lattice truss core structures," *Materials & Design*, vol. 137, pp. 235–244, 2018.

[25] X. Xu, D. Shahsavari, and B. Karami, "On the forced mechanics of doubly-curved nanoshell," *International Journal of Engineering Science*, vol. 168, article 103538, 2021.

[26] X. Xu, B. Karami, and D. Shahsavari, "Time-dependent behavior of porous curved nanobeam," *International Journal of Engineering Science*, vol. 160, article 103455, 2021.

[27] L. Zeng, J. Shi, J. Luo, and H. Chen, "Silver sulfide anchored on reduced graphene oxide as a high-performance catalyst for CO_2 electroreduction," *Journal of Power Sources*, vol. 398, pp. 83–90, 2018.

Research Article

Dynamic Response Characteristics of the Electric Domain Structure of Ferroelectric Materials to the Surrounding Rock Structure of a Heavy-Duty Railway with a Small-Clearance Crossing Tunnel

Xiaotian Hao[1,2] and Hailong Wang [1,3]

[1]School of Traffic and Transportation, Shijiazhuang Tiedao University, Shijiazhuang, 050043 Hebei, China
[2]School of Urban Construction Engineering, Chongqing Technology and Business Institute, Chongqing 400052, China
[3]School of Civil Engineering, Hebei University of Architecture, Zhangjiakou, 075000 Hebei, China

Correspondence should be addressed to Hailong Wang; bhxt196346@cqtbi.edu.cn

At present, the world-wide heavy-haul transportation technology of cargo trains has developed rapidly. Heavy-haul railway transportation has received extensive attention due to its large capacity, high efficiency, and low transportation costs. In order to understand the role that ferroelectric materials can play in the dynamic response of a heavy-duty railway surrounding rock structures in crosstunnels, this article introduces the domain structure of ferroelectric materials, derives the calculation method of the dynamic response of the surrounding rock structure, simulates the dynamic response characteristics through the corresponding formula, and analyzes the changes of the heavy-duty railway in the presence and absence of water. The situation was analyzed. The research results found that the increase of axle load will increase the bending moment of the invert structure. When the axle load is 30 t, the V-class surrounding rock is the most unfavorable working condition and the bending moment value of the invert structure is the largest at this time. When the added value of contact pressure is generally around 6.5 kPa, the railway as a whole can maintain a stable state.

1. Introduction

With the continuous improvement of my country's railway network, "passenger high speed" and "freight heavy duty" have become the two important directions of today's railway development. The structural stress forms and disease characteristics of heavy-duty railway tunnels are very different from those of ordinary railway tunnels. The bottom of the tunnel is the foundation that bears the load of trains and structures. Coupled with the effect of geological factors such as groundwater, the diseases at the bottom of the tunnel are particularly prominent, manifesting as lining cracks, venting and sinking of the basement, external squeezing of the side ditch, and mud and mud. Damage to the tunnel bottom causes a decrease in the safety reserve of the tunnel structure in terms of strength, rigidity, and stability. These diseases not only endanger driving safety and deteriorate driving conditions but also increase tunnel maintenance costs and shorten tunnel service life.

Ferroelectric materials have some very excellent properties, such as dielectric properties. Ferroelectric materials include layered ferroelectric ceramics, relaxor ferroelectric ceramics, and antiferroelectric ceramics. When there is an external electric field, the positive and negative charges inside the ferroelectric material will shift to a certain extent, which will cause the charge centers to no longer overlap, and the so-called dipoles will appear. The applied electric field can drive the polarization direction of the dipole to move in the direction of the applied electric field, resulting in dielectric polarization. If we place a uniform dielectric

between the two poles of a capacitor, under the polarization of this dielectric, the capacitance value of the capacitor will increase several times compared with the capacitance value of the vacuum medium. This property is called dielectric. Ferroelectrics have the characteristics of large dielectric constant and obvious nonlinear effects. The spontaneous polarization of ferroelectric materials originates from the electric dipole generated by the noncoincidence of the positive and negative charge centers inside the unit cell. Perovskite structure ferroelectrics are currently the most widely studied, simplest, and most representative ferroelectric materials.

For the related applications of ferroelectric materials and the characteristics of railway dynamic response, experts at home and abroad have done a lot of research. In order to study the mechanism behind the collapse evolution, Xiao et al. conducted in situ microseismic (MS) monitoring in the left main/auxiliary power house. The temporal and spatial characteristics of stress-structure-controlled collapse are summarized and introduced. These methods provide a consistent set of results, that is, tensile fracturing is the most active rock mass fracturing mechanism in the evolution of stress-structure-controlled collapse. In addition, the evolution of microseismic activity during the development of the study collapse was also obtained. The results provide a direct case history, which will help predict and support stress-structure-controlled collapse disasters and help excavate deep-buried caves on site [1]. He et al. proposed an innovative roof-cutting and pressure-relief technology in response to the complex construction technology and high roadway construction costs in the traditional technology of retaining lanes along the goaf. A number of mechanical models of the "surrounding rock structure-roadside support" were established, and the design formulas for the support resistance of each roadway were obtained. The results show that through presplitting blasting, the lower foundation roof falls enough to better support the upper roof, thereby limiting the rotation deformation of the upper roof and reducing the impact load of the roof fracture [2]. Yan et al. deal with several types of inclination rail defects by simulating the acceleration system installed on the locomotive and theoretically study the feasibility of monitoring the inclination rail joint defects. The quantitative relationship between the axle box acceleration characteristics (peak) and the rail defects was determined by simulation. Therefore, the proposed method combines defect analysis and comparison with theoretical results, will enhance the ability of long-term monitoring and evaluation of the track system, and provide a more sensible preventive track maintenance strategy [3]. Cai et al. comprehensively studied the new track dynamics behavior of a polyurethane foam-cured ball in heavy-duty railway tunnels. First, based on the multibody system dynamics theory and finite element method, a dynamic model of the vehicle-track-tunnel interaction system is established. Then, the dynamic effect of the polyurethane foam-cured road ast track on the train and surrounding infrastructure is calculated and compared with the dynamic effect of the traditional road ast track [4]. In order to study the adaptability of cement-modified expansive soil as a filling material for heavy-duty railway subgrades, Cai et al. carried out different

axle loads, trains, speeds, and service environmental conditions based on the test section of the cement-modified expansive soil subgrade of the Menggan Railway. The results show that the dynamic parameters decay linearly along the depth and lateral direction of the subgrade in the same infill structure layer. The dynamic stress attenuation at the bottom of the subgrade surface is about 49%, and the dynamic stress attenuation at the bottom of the lowest subgrade is 76% [5]. Based on the train longitudinal dynamics theory and the vehicle-track coupling dynamics theory, Liu et al. established a heavy-duty train-track coupling dynamics model considering the longitudinal, lateral, and vertical forces of the coupler and traction system. The inspection conditions and mechanical properties of the locomotive under traction and braking conditions are analyzed, and the process and extent of the influence of traction, braking force, and coupler force on the locomotive performance are studied, and the theoretical model is verified by train [6]. The focus of Holder et al.'s research is the laboratory characterization of the lateral load path through the Skl-type fastening system using new instrument technologies that are subjected to heavy freight rail loading conditions. The investigation of the performance of the fastener system includes the evaluation of the lateral load distribution through the superstructure of the track and the evaluation of the single fastener system. The observations of this study will help the railway industry to improve the design of fastener systems and develop mechanical track structure design methods [7]. These studies have provided some references for this article, but due to certain problems in related research methods and data, the results of the experiment have not been accepted by the public.

The innovation of this article is that the article puts forward the theoretical calculation method of the surface load of the ballast bed based on the measured data combined with the existing specifications and the research results at home and abroad according to the characteristics of the ballast bed and the wheel-rail action mode. The elastic layered system is used to derive the elastic mechanics analytical solution of the surface load of the invert structure, which is an elastic foundation beam. The model and the load structure model provide the initial conditions of the load.

2. Response Characteristic Analysis Method

2.1. Ferroelectric Materials. A ferroelectric material is a kind of dielectric material. It has spontaneous polarization in two or more directions within a certain temperature range, and its spontaneous polarization will occur with the direction and magnitude of the external field (common electric field, temperature field). When the ferroelectric is below the critical temperature, it will transform from the paraelectric phase to the ferroelectric phase. This critical temperature is the Curie temperature (CT) [8, 9]. Figure 1 shows the change in the crystal structure of a ferroelectric material with a perovskite structure from a paraelectric phase to a ferroelectric phase. The general formula of perovskite is ABO_3: A and B are metal ions, and O is oxygen ion. Above the Curie temperature, the perovskite ferroelectric material has a cubic
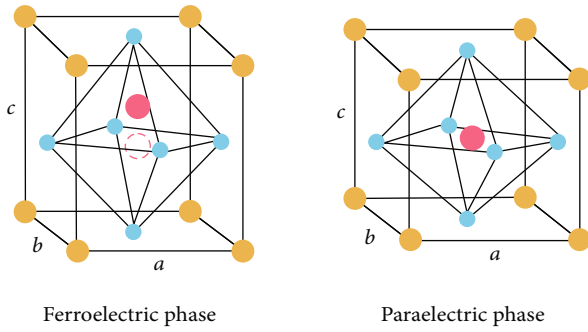
FIGURE 1: The crystal structure from the paraelectric phase to the ferroelectric phase of the perovskite structure.

FIGURE 2: Schematic diagram of hysteresis loop of ferroelectric material.

crystal structure. At this time, the positive and negative charge centers coincide and the ferroelectric material is in a nonpolarized state, that is, the paraelectric phase; when the temperature drops below the Curie temperature, the atoms in the unit cell will move the ferroelectric material. Due to the different displacements of the positive and negative ions, the positive and negative charge centers no longer overlap, resulting in an electric dipole moment. Polarization refers to the electric dipole moment per unit volume, that is, at the Curie temperature. The following ferroelectric materials exhibit ferroelectricity in the macroscopic view [10].

As a kind of dielectric material, a ferroelectric material has other characteristics besides showing ferroelectricity, such as dielectric, piezoelectricity, pyroelectricity, photoelectric effect, acousto-optic effect, and optical transition effect [11]. These different characteristics also make ferroelectric materials have a wide range of applications. In the application of ferroelectric materials, ferroelectric memory uses the polarized bistable state for information storage, so it has the advantages of nonvolatile, fast reading and writing, fatigue resistance, radiation resistance, etc. and is considered to be one of the most potential new types of memory at present; ferroelectric memory has been commercialized [12]. The hysteresis loop of ferroelectric materials is shown in Figure 2.

Important parameters such as spontaneous polarization CP, remanent polarization OP, coercive field BG, and ferroelectric loss can be obtained by measuring the hysteresis loop. It is precisely because of these advantages that ferroelectric memory has been widely used in both civilian and military fields [13, 14]. Ferroelectric memory is currently the only new-generation memory that has been widely used, and its advantages and application areas are shown in Figure 3.

Ferroelectric memory allows designers to write data to nonvolatile memory faster and more frequently and at a lower price. The failure of the ferroelectric thin film is caused by the abnormal evolution of the ferroelectric single domain. The essential reasons for determining ferroelectric domains and domain flipping are the microstructure of ferroelectric thin films such as lattice defects, interface terminal types, and oxygen vacancies [15]. With the miniaturization and high integration of ferroelectric memory, the size of ferroelectric thin films in the thickness direction is close to
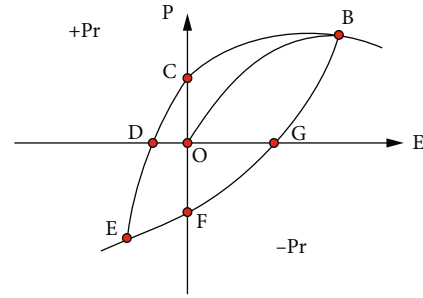
the nanometer scale and the polarization/domain structure and evolution are increasingly restricted by the abovementioned factors.

2.2. Heavy-Duty Railway Tunnel Structure. The tunnel bottom structure is the main load-bearing structure of heavy-duty railway tunnels, and the load size is mostly determined based on the experience of ordinary railway tunnels. The accurate theoretical calculation method can quickly calculate the dynamic load on the surface of each structural layer and determine the initial load conditions of the calculation model, which has important guiding significance for the design of heavy-duty railway tunnels [16].

Based on the force mode of the track bed structure of the heavy-duty railway tunnel under the action of sleepers, a calculation method for the dynamic load on the sleeper bottom surface is proposed, that is, the static axle load/wheel weight is converted to the dynamic axle load/wheel load according to the train speed, combined with the contact area of the sleeper bottom surface. The additional value threshold of the dynamic load caused by the train is calculated.

$$\sigma = \frac{P * (1 + \beta v)}{BL}, \tag{1}$$

where σ is the stress, P is the static axle load, and β is the dynamic impact coefficient, also known as the velocity influence coefficient.

The dynamic load on the surface of the track bed structure is calculated according to formula (1), which is different from the actual "saddle-shaped" or "triangular" load distribution on the surface of the track bed structure. The error is compensated [17]. Table 1 compares the calculated results of formula (1) with the measured dynamic load threshold on the surface of the track bed structure.

According to D'Alembert's principle, the dynamic differential equation of the structure can be obtained as follows:

$$[M]\{\ddot{\phi}\} + [C]\{\dot{\phi}\} + [K]\{\phi\} = [F(t)]. \tag{2}$$

Among them, M stands for the mass matrix, C stands for the damping matrix, K stands for the stiffness matrix, and ϕ stands for displacement.

Regarding the formula as a constant coefficient differential equation, the displacement of the structure can be used
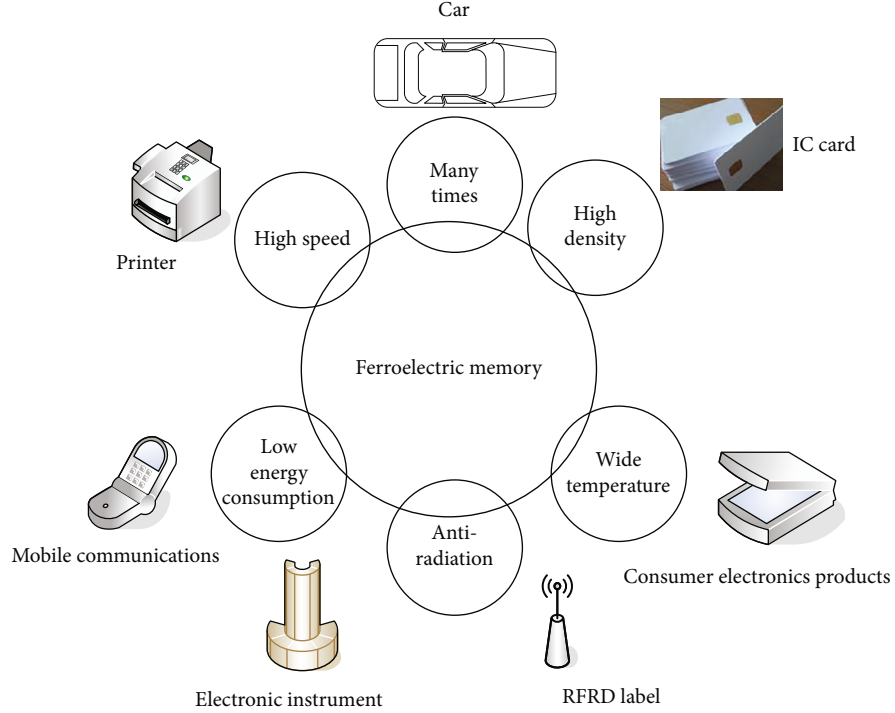
Figure 3: Ferroelectric memory application.

Table 1: Comparison of calculation results and formulas.

Surrounding rock level	Train axle weight (ton)	Tunnel form	Cumulative dynamic load threshold	Formula calculated value
III	26	Single-line ballastless	81.6	425.44
		Double-line ballast	143.2	425.44
			125.6	425.44
IV	26		129.5	425.44
	29	Two-wire ballastless	163.3	532.74
V	26		120.1	425.44
	29		164.1	532.74

to approximate the velocity and acceleration of the structure through a finite difference expression. One of the most effective solutions is the central difference method. The method assumes

$$\{\phi\} = \frac{1}{\Delta t^2}\left(\{\phi_{t-\Delta t}\} - 2\{\phi\} + \{\phi_{t+\Delta t}\}\right),$$
$$\{\phi_t\} = \frac{1}{2\Delta t}\left(\{-\phi_{t-\Delta t}\} + \{\phi_{t+\Delta t}\}\right). \tag{3}$$

Based on the abovementioned formula, we can get

$$\left(\frac{1}{\Delta t^2}[M] + \frac{1}{2\Delta t}\right)\{\phi_{t+\Delta t}\} = [F(t)] - \left([K] - \frac{2}{\Delta t^2}M\right). \tag{4}$$

The theoretical basis of the finite element method is the

weighted residual method and the variational method. The weighted margin method commonly used is the configuration method, the least square method, the moment method, and the Galerkin method, among which the Galerkin method is the most widely used. The variational method is aimed at solving the continuum problem. For the function of the unknown function, there are

$$\Pi = \int_\gamma F\left(u, \frac{\partial u}{\partial k}\right)d\gamma + \int_\gamma E\left(u, \frac{\partial u}{\partial x}\right)d\Gamma. \tag{5}$$

In the formula, u is an unknown function, F is a specific operator, and E is a specific operator.

Next, the discrete unit is determined, the finite element is divided, and the displacement interpolation function is determined. The matrix form is generally

$$u = \begin{pmatrix} u \\ v \end{pmatrix} = \begin{pmatrix} N_i \, 0 \\ 0 \qquad N_i \end{pmatrix} \begin{bmatrix} Ni & 0 & Nj \\ 0 & Ni & 0 \end{bmatrix} = [Ni, Nj, Nm] a^c. \tag{6}$$

In the formula, N is the interpolation function matrix and a^c is the nodal displacement matrix.

According to the element displacement obtained in the previous step, the stress-strain equation of each element can be solved according to the geometric and physical equations and the stress-strain matrix is obtained as follows:

$$\varepsilon = \begin{pmatrix} \varepsilon_x \\ \varepsilon_y \\ \varepsilon_{xy} \end{pmatrix} = Lu = LN a^e = [Bi, Bj, Bm] a^e = B a^e,$$

$$\sigma = \begin{pmatrix} \sigma_x \\ \sigma_y \\ \sigma_{xy} \end{pmatrix} = D\varepsilon = DB a^e = S a^e, \tag{7}$$

$$S = DB = D[B_i, B_j, B_m] = [S_i, S_j, S_m].$$

In the formula, B is the strain matrix, L is the differential operator, S is the stress matrix, and D is the elastic matrix.

Based on the principle of virtual work, the stiffness matrix equation is established as follows:

$$\{F\}^e = [K]^e \{u\}^e. \tag{8}$$

In the formula, $\{F\}^e$ is the vector of the concentrated force on the nodes of the element, $[K]^e$ is the element stiffness matrix, and $\{u\}^e$ is the displacement vector of the element nodes.

The stepwise integration method is a kind of direct integration method. It uses finite difference instead of the derivative of displacement γ'' with γ'' respect to time and expresses the sum with the combination of displacements to obtain the recurrence formula of each time interval and then obtain the response of the entire time history. The content of the method is as follows:

γ' and γ'' can be expressed by displacement γ:

$$\gamma'' = \frac{1}{\Delta t^2} (\delta_{t-\Delta t} - 2\delta_t + \delta_{t+\Delta t}),$$

$$\gamma' = \frac{1}{2\Delta t} (-\delta_{t-\Delta t} + \delta_{t+\Delta t}). \tag{9}$$

The recurrence formula of the stepwise integration method is as follows:

$$\left(\frac{1}{\Delta t^2} M + \frac{1}{2\Delta t} C \right) \delta_{t+\Delta t} = Qt - \left(K - \frac{2}{\Delta t^2} M \right) \delta_t. \tag{10}$$

The definition of the distance function is as follows for all $\vec{x}_1 \in \Gamma$:

$$d(\vec{x}) = \min \left(\left| \vec{x} + \vec{x}_1 \right| \right). \tag{11}$$

From the definition, when the unknown point is on the boundary, the function value is 0. Find the closest point on the boundary and mark the closest point and the value of the distance function is

$$d(\vec{x}) = \left| \vec{x} - \vec{x}c \right|. \tag{12}$$

From the definition of the distance function, the specific definition of the signed distance function is

$$\phi(\vec{x}) = d(-\vec{x}) = 0, \quad \vec{x} \in \Gamma,$$

$$\phi(\vec{x}) = -d(\vec{x}), \quad \vec{x} \in \psi. \tag{13}$$

The signed distance function is a subset of the implicit function and has all the properties of the implicit function discussed in the previous section [18]. Using the signed distance function can simplify many level set methods for dealing with implicit functions.

$$Z_i = T^T (x_{nm} - f \notin R^n. \tag{14}$$

Meet the orthogonal normalization condition, namely,

$$b_j^T b_k = \delta_{jk}, \tag{15}$$

in which, at the time, $j = k$, $\delta_{jk} = 1$; otherwise, $\delta_{jk} = 0$.

$$X'_{ij} = d + BB^T (X_{ij} - d) = d + BZ_j. \tag{16}$$

The formula is inverse transformation. In actual operation, due to the influence of noise data or different transformation methods, there are errors between them, as shown as follows:

$$\varepsilon_j = X_{ij} - X'_{ij} = X_{ij} - d - BB^T (X_{ij} - d). \tag{17}$$

The vibration load caused by train operation is generally a small amplitude load, and the shield tunnel lining and surrounding rock generally only undergo elastic deformation under the action of the train vibration load [19].

2.3. Heavy-Duty Railway. Chloride ions corrode the steel bars, resulting in the continuous loss of the effective cross-sectional area of the steel bars, and the load-bearing capacity is obviously reduced. The corrosion of the steel bars causes the rust expansion effect, causing the concrete protective layer to crack. The continuous development of the cracks also accelerates the corrosion of chloride salts and reduces the bearing capacity of the concrete. Chloride ions invade the reinforced concrete structure and severely reduce the bonding force between the steel bar and concrete, which will cause the steel bar and concrete to not work together normally [20, 21]. Therefore, the corrosive effect of chloride

ions is one of the main reasons that affect the service life of reinforced concrete structures.

Among the diseases of heavy-duty railway tunnels, the most frequent occurrence is water seepage diseases. Water leakage is the most common disease in well-known railway tunnels and has less harm to the tunnel structure. Therefore, the number of diseases at the bottom of the tunnel is ranked second, which is sufficient to explain the heavy-duty railway tunnels. The problem of the disease at the bottom of the tunnel is particularly prominent, which indicates that the bottom of the tunnel is the main place where the disease of the heavy-duty railway tunnel occurs. The conditions of the disease at the bottom of the tunnel are shown in Figure 4.

From the point of view of the location of the disease, different diseases occurred in the upper arch wall structure and the lower tunnel bottom structure of the heavy-duty railway tunnel [22]. Comparing the disease rates of passenger-cargo railway tunnels and heavy-duty railway tunnels, the disease rate of heavy-duty railway tunnels is much higher than the average disease rate of the whole road tunnel, indicating that the high disease rate of heavy-duty railway tunnels is its primary feature [23].

Because the heavy-duty train runs on continuous rails, the train vibration load generated by the interaction between the heavy-duty train and the rail is continuous in space and time. Then, the discrete fastener system distributed at a certain interval in the track structure converts the continuous excitation load on the upper part into multiple vertical excitation loads that act on specific positions of the track structure and then transfer them to the concrete track bed, and then, the track bed is transferred to the shield segment tunnel, and finally, the load is transferred to the soil layer [24]. Among them, under the action of the vibration load of the heavy-duty train, the vibration load curve of each fastener system can be obtained from the actual measurement situation [25].

Based on the vertical dynamics analysis model of the subway train in the shield tunnel, the vibration load of the subway train required for the similar model test is realized by applying a vertical excitation load on the position of the fastener on the concrete track bed and through multiple excitations. The device applies the fastener load at a certain time interval to simulate the effect of the train.

3. Response Characteristic Experiment and Results

3.1. Foundation Beam Calculation. Single-track heavy-duty railway tunnels and double-track heavy-duty railway tunnels are usually only equipped with the floor structure under the condition of level II surrounding rock. Therefore, this example is based on the Winkel foundation beam theory to analyze the single-track and double-track heavy-duty railways of level II surrounding rock. The internal force calculation of the tunnel was the floor structure. The internal force solution of the calculation model for the slab structure of the class II surrounding rock single-track tunnel under the action of 27 t axle load is shown in Table 2.

The theoretical calculation of the bending moment and shear force of the calculation model of the elastic foundation beam bottom plate of the single-track tunnel is shown in Table 3.

We list the converted concentrated loads corresponding to the characteristic points on the surface of the invert structure of the single-track tunnel under the condition of the 27 t axial load of the III-level surrounding rock. The boundary constraint conditions of the invert structure are considered in accordance with the consolidation, and the internal forces of the invert structure under different concentrated loads are solved. The overlay is shown in Table 4.

Then, the internal force of the invert structure under the action of concentrated force is solved and listed in Table 5.

It can be seen that the concentrated load of F1~F5 will cause the bending moment value of the corresponding characteristic point to increase. After the internal force is superimposed, it is found that the bending moment value of the single-track tunnel invert structure under the symmetrical load is also symmetrically distributed and the bending moment value at the center of the line maximum.

3.2. Dynamic Response Characteristic Analysis. Since the left amplitude of the surface load of the invert structure is larger than the right amplitude as a whole, the structural bending moments show the same regularity. The bending moment theory of the invert structure is obtained by summing the bending moments under the action of the equivalent 7 concentrated loads of the 27 t axle load calculated. We compare the theoretical calculation solution of the bending moment of the invert structure corresponding to different working conditions with the measured data, and the results are shown in Figures 5 and 6.

The measured data show that the decrease of surrounding rock conditions and the increase of axle load will increase the bending moment of the invert structure. When the axle load is 30 t, the V-level surrounding rock is the most unfavorable working condition and the bending moment value of the invert structure is the largest at this time. For the lateral distribution of the bending moment of the inverted arch structure, the value of the bending moment of the heavy-duty line, that is, the left line and the right rail position, is the largest and gradually decreases with the increase of the lateral distance. There is a certain error in the analysis of the bending moment under the most unfavorable conditions. According to the most unfavorable principle, it is considered that the calculation method of the curved elastic foundation beam can be applied to the design of the invert structure of the double-track heavy-duty railway tunnel.

The change curve of the additional value $\triangle P$ of the contact pressure of the no. 1 measuring point at the bottom left of the center line and the no. 2 measuring point below the center line with and without water is shown in Figure 7.

It can be seen that when the surrounding rock at the bottom of the tunnel is in anhydrous conditions, the additional value of contact pressure $\triangle P$ below the center line fluctuates at about 6.5 kPa and the additional value of contact pressure on the left and right side $\triangle P$ is stable at about 5.8 kPa but the

Side ditch blocked by coal ash

Lining water leakage

Mud and mud

Basal subsidence
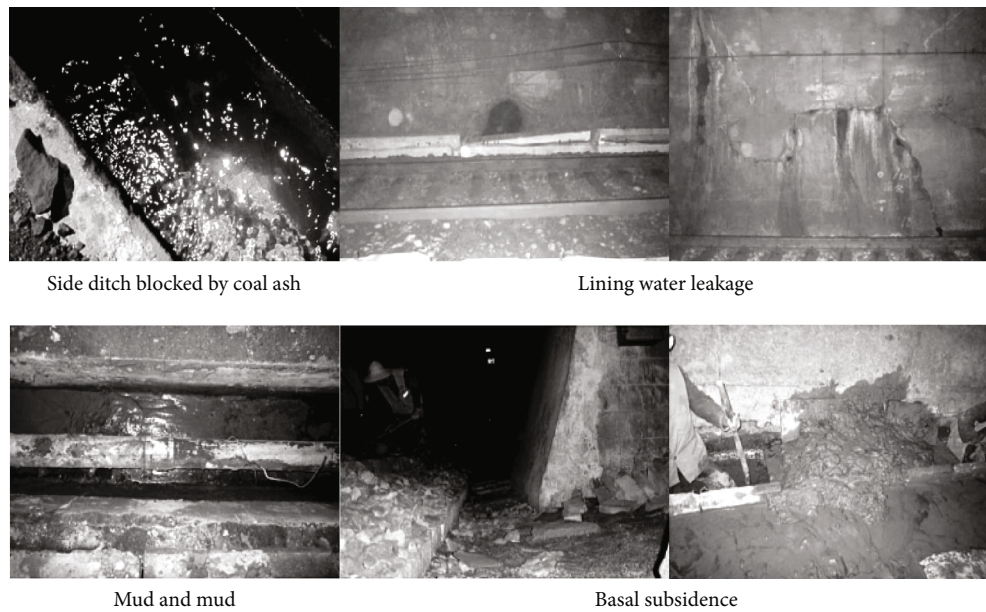
FIGURE 4: Classification of diseases in heavy-duty railway tunnels.

TABLE 2: Calculating model of the slab structure of the single-track tunnel in surrounding rock.

Internal solution	Feature location	q1-q2 load section		q2-q3 load section	
		Uniform load	Triangular load	Uniform load	Triangular load
	Left sulcus	−11.13	−1.76	−4.01	−0.64
	Line left rail	3.72	0.74	0.41	0.11
Bending moment (KN∗m)	Line center	4.44	1.02	4.44	1.02
	Right track	0.41	0.11	3.72	0.74
	Right sulcus	−4.01	−0.64	−11.13	−1.76
	Left sulcus	−30.06	−3.31	−3.62	−0.52
	Line left rail	−9.02	−2.17	−5.21	−1.07
Shear force (kM)	Line center	5.44	1.09	−5.43	−1.09
	Right track	5.22	1.07	9.02	2.19
	Right sulcus	3.62	0.52	30.06	3.31

TABLE 3: Moment and shear force calculation model for elastic foundation beam bottom plate of single-track tunnel.

Axle load	Internal solution	Left sulcus	Line left rail	Line center	Right track	Right sulcus
27 t	Bending moment (KN∗m)	−17.87	5.21	10.25	5.21	−17.87
	Shear force (kM)	−37.73	−16.71	0	16.71	37.73
30 t	Bending moment (KN∗m)	−18.54	6.46	11.46	6.46	−18.45
	Shear force (kM)	−40.31	−17.01	0	17.01	40.31

TABLE 4: Characteristic points of single-track tunnel invert structure.

Serial number	Feature point location	C0	C1	C2	C3	C4	Bending moment (KN∗m)
1	Left sulcus	$-1.17E-03$	$1.17E-03$	$-1.42E-03$	$-2.56E-03$	$2.76E-03$	1.53
2	Line left rail	$-2.41E-03$	$2.41E-03$	$-3.01E-03$	$5.14E-03$	$-5.44E-03$	4.31
3	Line center	$-2.62E-03$	$2.62E-03$	$-3.16E-03$	$-5.58E-03$	$-6.01E-03$	8.08
4	Right track	$-2.41E-03$	$2.41E-03$	$-3.01E-03$	$-5.58E-03$	$-5.44E-03$	4.31
5	Right sulcus	$-2.62E-03$	$2.62E-03$	$-3.16E-03$	$-5.58E-03$	$-6.01E-09$	1.53

TABLE 5: Calculation results of bending moment of surrounding rock invert structure.

Serial number	Feature point location	F1	F2	F3	F4	F5
1	Left sulcus	4.71	16.65	21.48	−2.01	−2.25
2	Line left rail	1.77	2.34	3.31	1.54	0.77
3	Line center	1.38	2.03	8.08	2.03	1.38
4	Right track	0.77	1.54	4.31	2.34	1.77
5	Right sulcus	0.76	1.02	1.63	1.86	1.29

(a) Level IV surrounding rock 27 t axle load

(b) Level IV surrounding rock 30 t axle load
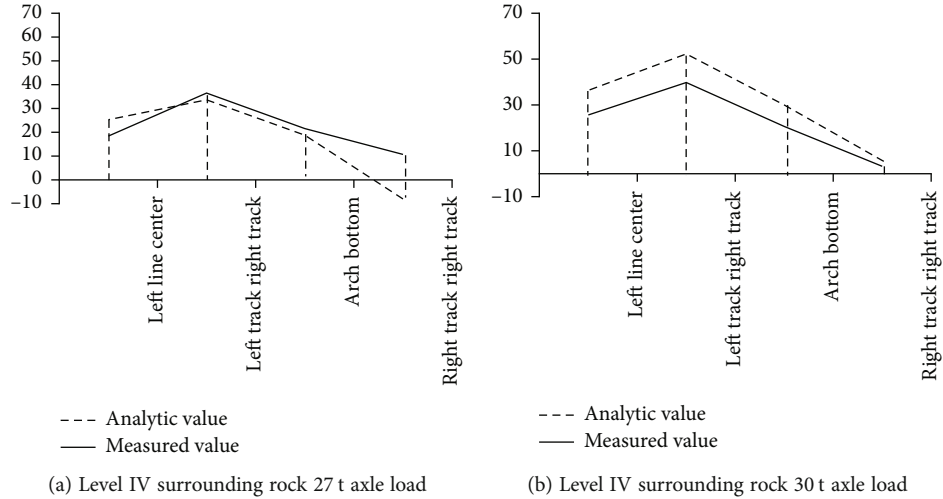
FIGURE 5: Bending moment of invert structure of class IV heavy-duty railway tunnel.

overall situation is relatively stable. The additional value of the contact pressure below the center line is slightly reduced compared with that below the center line, indicating that the effect of the excited vibration load below the center line is more obvious than that of other positions.

In order to understand the role of the domain structure of ferroelectric materials, we compare the elastic energy, depolarization energy, and various abilities of the ferroelectric material domain structure and the railway surrounding rock structure under traditional materials. The comparison result is shown in Figure 8.

It can be seen in Figure 8 that after comparing the elastic properties of different materials, it can be seen that the elastic properties of traditional materials vary greatly, and as the number of uses increases, their elastic properties must show a certain degree. In the case of ferroelectric materials, the elastic performance is much better than that of traditional materials and the increase rate is about 30%.

We compare the depolarization energies of the two materials, and the results are shown in Figure 9.

As can be seen, in the comparison of the depolarization energy of traditional materials and ferroelectric materials, the depolarization energy of traditional materials is much higher than that of ferroelectric materials and as the number of tests increases. The depolarization energy of traditional materials shows an upward trend, while the trend of ferroelectric materials shows a downward trend.

We compare the various abilities of the two materials, and the results obtained are shown in Figure 10.

It can be seen that for the supernatural power of materials, the difference between ferroelectric materials and traditional materials is not much. In this simulation test, there is no obvious difference between the values obtained by the two. This shows that ferroelectric materials have no special advantage over traditional materials in terms of abilities.

4. Discuss

4.1. Surrounding Rock Structure.
Based on a variety of research methods such as the on-site large-scale in situ vibration test, long-term remote monitoring, theoretical derivation, numerical simulation, and data investigation, the dynamic characteristics, load theoretical calculation methods, calculation models, and fatigue damage evolution laws of heavy-duty railway tunnel structures are carried out. The dynamic response and stress distribution characteristics of different structural parts of heavy-duty railway tunnels are clarified.

The heavy-duty railway tunnel is divided into two major structural parts, the upper arch wall structure and the lower tunnel bottom structure, to analyze the dynamic response and stress distribution characteristics, respectively. The increase of the axle load of the heavy-duty train, the decrease of the surrounding rock conditions, and the decrease of the

(a) V-class surrounding rock 27 t axle load

(b) V-class surrounding rock 30 t axle load
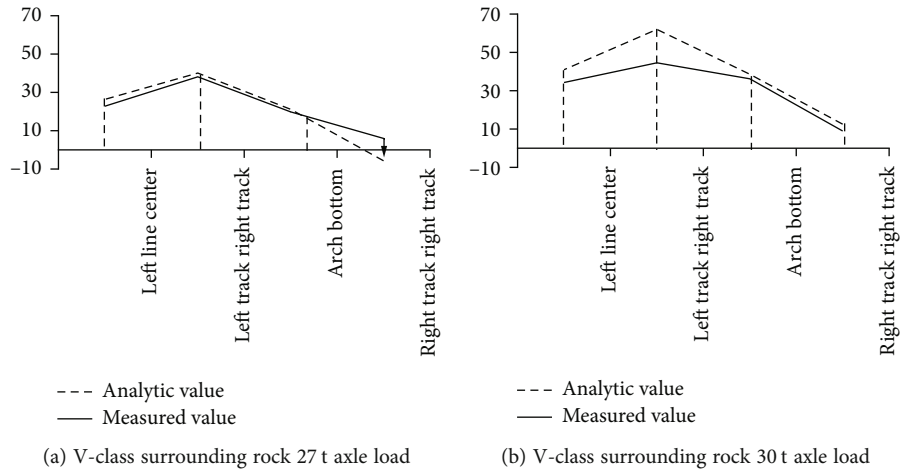
FIGURE 6: Bending moment of invert structure of V-class surrounding rock heavy-duty railway tunnel.
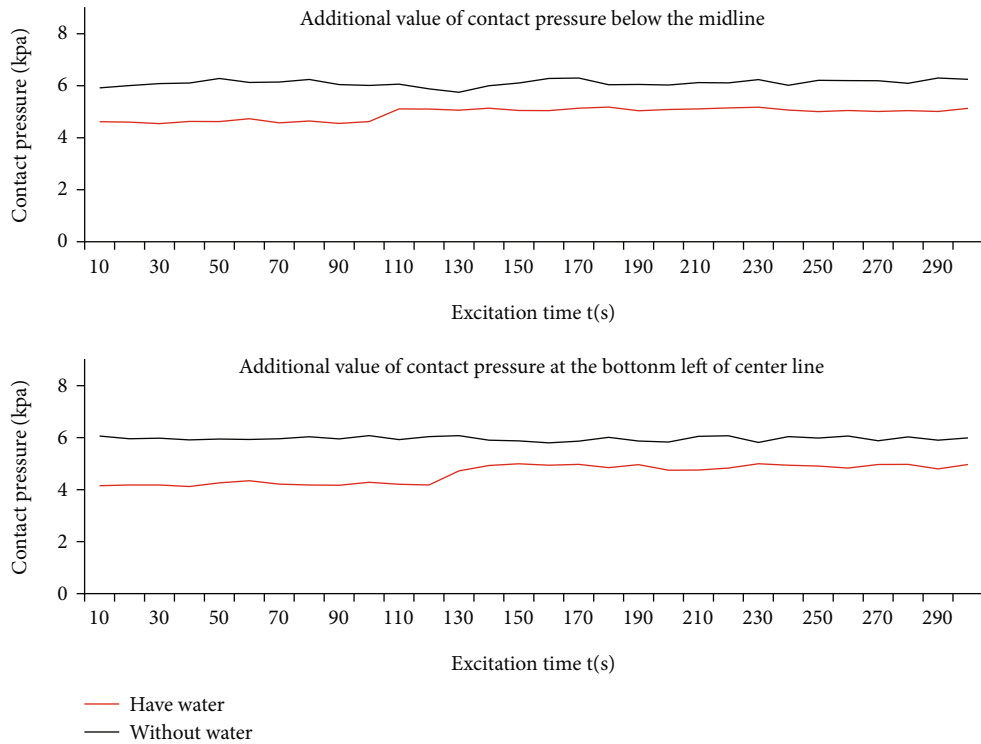
FIGURE 7: Pressure changes at the measuring point below the center line.

distance from the train load acting position will increase the dynamic load increment on the surface of the structure and the internal force of the structure.

The dynamic response and stress distribution characteristics of the arch wall structure are clarified: single- and double-line tunnels and ballastless and ballasted tunnel arch wall structures have similar dynamic load distribution laws under various working conditions and under the most unfavorable working conditions (class V) (surrounding rock, 30 t axle load). The maximum power increment does not exceed 5%, which is less affected by the power of heavy-duty trains.

The surface load distribution and vertical transmission laws of the various structural layers of the heavy-duty railway tunnel bottom structure are clarified: (1) the heavy-duty train load gradually decreases with the increase of the vertical depth during the transmission of the tunnel bottom structure, and the track bed structure has a large rigidity and a filling layer. The large thickness has a buffer effect on the dynamic load. When the dynamic load is transmitted to the surface of the surrounding rock, there has been a significant attenuation but the maximum power increase of the single-track tunnel is still 38.26% and 9.6% of the double-
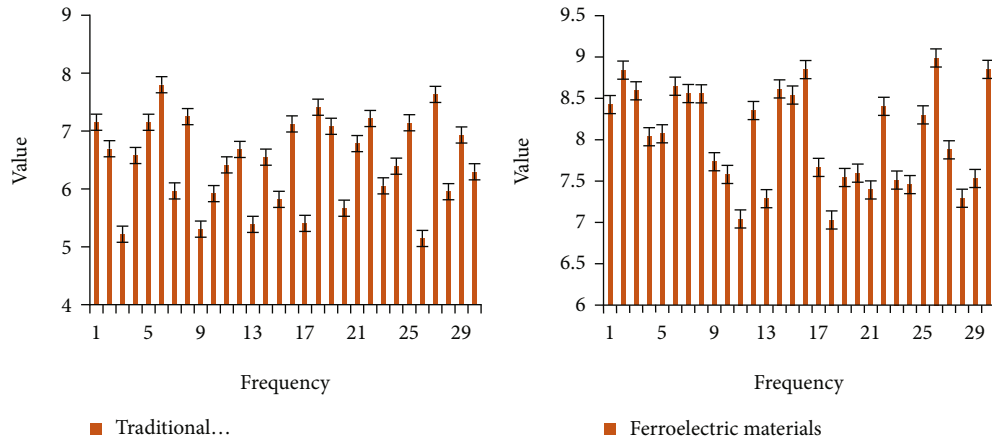
FIGURE 8: Comparison of elastic properties of different materials.
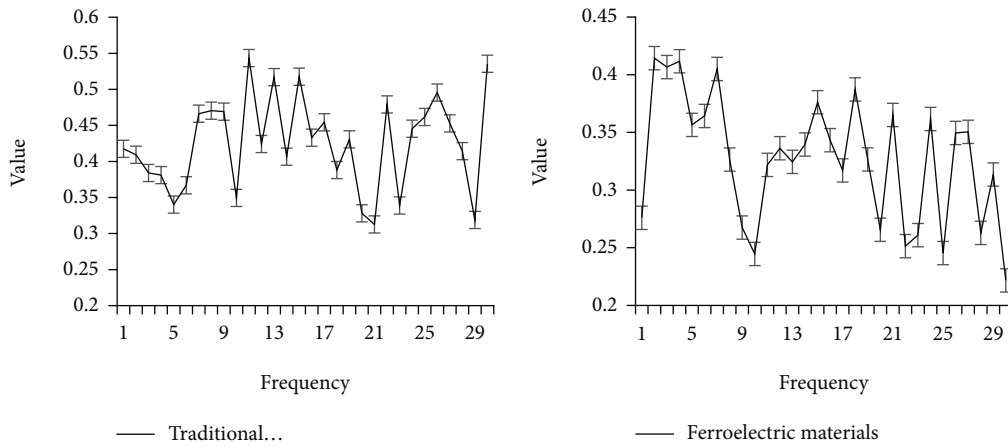
FIGURE 9: Comparison of depolarization energy.
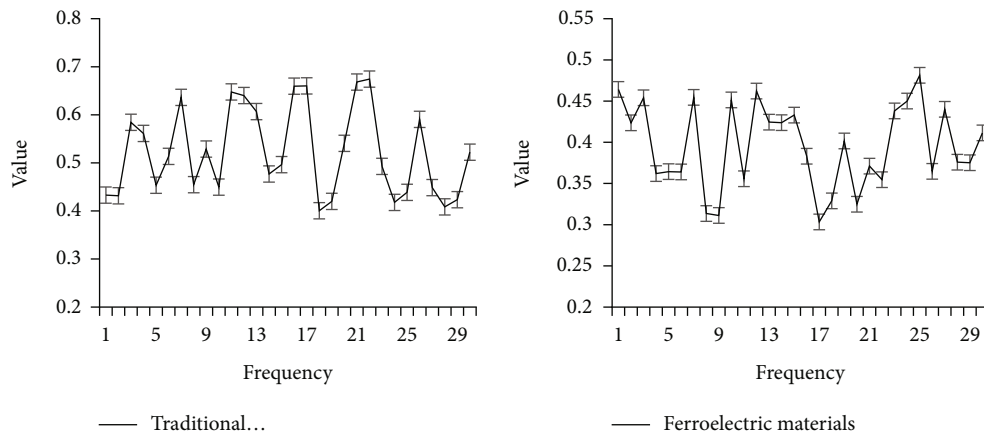
FIGURE 10: Comparison of various abilities.

track tunnel is much higher than the arch wall structure. Therefore, the dynamic impact of the heavy-duty train on the tunnel structure is mainly focused on the structure at the bottom of the tunnel. (2) In the single-track heavy-duty railway tunnel, due to the symmetry of the structure, the lateral distribution of the additional train load on the surface of each structural layer at the bottom of the tunnel is in a "triangular" distribution, which is represented by the largest line center and gradually attenuates with the increase of the lateral distance. (3) In double-track ballasted and unballasted heavy-duty railway tunnels, the dynamic load distribution on the surface of the track bed, the surface

of the invert, and the surface of the surrounding rock shows that the dynamic effect of the train is mainly concentrated on the position of the track of the heavy-duty line. There is a difference in the dynamic load distribution on the surface of the two types of ballast beds. The surface of the filled layer of the ballastless bed is "saddle shaped," and the ballast bed has a "triangular" load, and the dynamic load value of the ballast bed is higher than that of the ballastless bed. (4) The influence rate of the axle load on the dynamic increase of the tunnel bottom structure is up to 33.5%~48.2%, and the influence rate of surrounding rock conditions is up to 19.7%~24.3%. Therefore, axle load is the main factor affecting the dynamic response of the tunnel bottom structure.

4.2. Ferroelectric Materials. Ferroelectric materials are widely used in the manufacture of modern electronic devices due to their excellent dielectric properties, piezoelectric properties, and polarization reversibility. The microstructure of ferroelectric materials determines the macroscopic properties of ferroelectric materials to a certain extent, and the simulation of their microstructure is of great significance in material design. At present, the traditional phase field method used to calculate and simulate ferroelectric materials has limitations such as many material parameters, energy potential wells, and unobvious symmetry, which seriously hinder ferroelectric materials, especially the microstructure of new ferroelectric materials.

This paper establishes a theoretical framework for nontraditional phase field simulation of tetragonal and orthogonal ferroelectric phases. Based on the characteristic function of the ferroelectric material variant, use it as the phase field simulation sequence parameter to construct the anisotropic properties of the ferroelectric variant, which presents a multipotential well structure, and use it to replace the traditional phase field method to describe higher-order polynomials in ferroelectric materials. Using the anisotropic properties of ferroelectric variants to replace the polynomial of the internal energy of the traditional phase field method, an unconventional phase field method suitable for tetragonal and orthogonal phase ferroelectric domain structures has been developed. The nontraditional phase field method requires few parameters and can also describe the multipotential well structure of the ferroelectric material variant, and the potential well structure is obvious and the symmetry is obvious.

5. Conclusion

This study found that under different axle loads and surrounding rock conditions, the fatigue damage of the tunnel bottom structure of the single- and double-track heavy-duty railway tunnel is significantly higher than that of the arch wall structure and it is mainly concentrated in the position of the heavy-duty line track and decreases with the increase of depth. The track position of the infill structure began to show damage after 50 years of operation and developed downward; when the operation time exceeds 100 years, the fatigue damage of the inverted structure and the damage of the infill structure are connected. The fatigue damage of the single-track tunnel is always symmetrical, while the

double-track tunnel expands to the bottom of the side trench structure half of the heavy-duty line. Of course, there are some shortcomings in the research of this paper. The data studied in this paper are basically based on simulation results, and no real field investigation has been carried out. In the collected data, the factors that may damage the track in the tunnel are not considered. Completely, the experiments in this article cannot draw very perfect conclusions. This also requires that in today's research, we need to increase the scope of data and conduct real data investigations in order to obtain better research results.

Data Availability

No data were used to support this study.

Conflicts of Interest

There is no potential conflict of interest in this study.

References

[1] Y. X. Xiao, X. T. Feng, G. L. Feng, H. J. Liu, Q. Jiang, and S. L. Qiu, "Mechanism of evolution of stress-structure controlled collapse of surrounding rock in caverns: a case study from the Baihetan hydropower station in China," *Tunnelling and Underground Space Technology*, vol. 51, pp. 56–67, 2016.

[2] M. He, S. Chen, Z. Guo, J. Yang, and Y. B. Gao, "Control of surrounding rock structure for gob-side entry retaining by cutting roof to release pressure and its engineering application," *Zhongguo Kuangye Daxue Xuebao/Journal of China University of Mining and Technology*, vol. 46, no. 5, pp. 959–969, 2017.

[3] Q. S. Yan, M. Spiryagin, Q. Wu, C. Cole, and W. H. Ma, "Feasibility in assessing the dipped rail joint defects through dynamic response of heavy haul locomotive," *Transportation*, vol. 26, no. 2, pp. 96–106, 2018.

[4] X. Cai, Y. Zhong, X. Hao, Y. Zhang, and R. Cui, "Dynamic behavior of a polyurethane foam solidified ballasted track in a heavy haul railway tunnel," *Advances in Structural Engineering*, vol. 22, no. 3, pp. 751–764, 2019.

[5] Y. Cai, L. Xu, W. Liu, Y. Shang, N. Su, and D. Feng, "Field test study on the dynamic response of the cement-improved expansive soil subgrade of a heavy-haul railway," *Soil Dynamics and Earthquake Engineering*, vol. 128, p. 105878, 2020.

[6] P. Liu, K. Wang, and D. Zhang, "Influence of traction and braking operation on wheel-rail dynamic interaction for heavy haul locomotive," *Zhongguo Tiedao Kexue/China Railway Science*, vol. 38, no. 2, pp. 96–104, 2017.

[7] D. E. Holder, M. V. Csenge, Y. Qian, M. S. Dersch, J. R. Edwards, and B. J. van Dyk, "Laboratory investigation of the Skl-style fastening system's lateral load performance under heavy haul freight railroad loads," *Engineering Structures*, vol. 139, pp. 71–80, 2017.

[8] Y. Ogawa, B. Hu, C. M. Orofeo et al., "Domain structure and boundary in single-layer graphene grown on Cu(111) and Cu(100) films," *Journal of Physical Chemistry Letters*, vol. 3, no. 2, pp. 219–226, 2012.

[9] J. L. Coleman, C. Bolisetti, and A. S. Whittaker, "Time-domain soil-structure interaction analysis of nuclear facilities," *Nuclear Engineering & Design*, vol. 298, pp. 264–270, 2016.

[10] X. Xu, M. Fu, Z. Xu, and Z. Chen, "A new lever-type variable friction damper for freight bogies used in heavy haul railway," *Journal of Modern Transportation*, vol. 24, no. 3, pp. 159–165, 2016.

[11] W. R. Liu, D. Y. Wang, K. Gao, and Z. W. Huang, "Design of distributed cooperative observer for heavy-haul train with unknown displacement," *IET Intelligent Transport Systems*, vol. 11, no. 4, pp. 239–247, 2017.

[12] Y. Zhang, C. Li, Z. Yu et al., "Comparative test on shape and material of rail used for heavy haul railway of 30 t axle load," *Zhongguo Tiedao Kexue/China Railway Science*, vol. 39, no. 2, pp. 10–17, 2018.

[13] B. Hu and Z. Luo, "Life-cycle reliability-based assessment of internal stability for mechanically stabilized earth walls in a heavy haul railway," *Computers and Geotechnics*, vol. 101, pp. 141–148, 2018.

[14] T. Reis, E. D. A. Lima, F. Bertelli, and A. A. dos Santos Junior, "Progression of plastic strain on heavy-haul railway rail under random pure rolling and its influence on crack initiation," *Advances in Engineering Software*, vol. 124, pp. 10–21, 2018.

[15] J. Dong, Z. H. Wu, X. Li, and H. Y. Chen, "Dynamic response and pile-soil interaction of a heavy-haul railway embankment slope reinforced by micro-piles," *Computers and Geotechnics*, vol. 100, pp. 144–157, 2018.

[16] G. Duan, L. Chen, Y. Z. Li, and R. He, "Optimisation on empty trains distribution with time window in heavy haul railway," *International Journal of Computing Science and Mathematics*, vol. 9, no. 3, pp. 273–286, 2018.

[17] K. Smith, "Heavy-haul: navigating the digital railway in Narvik," *International Railway Journal*, vol. 59, no. 7, pp. 4–4, 2019.

[18] D. Zhang, K. Wang, W. Zhai, and P. Liu, "Effect of unsupported sleepers on the wheel/rail dynamic interaction on heavy-haul railway lines," *Zhendong yu Chongji/Journal of Vibration and Shock*, vol. 36, no. 18, pp. 1–7, 2017.

[19] L. Zhaohui, M. Yifei, S. Li, and Y. Zhiwu, "Experimental study on fatigue behavior of 8 m low-height reinforced concrete plate-girder of heavy-haul railway," *Journal of Central South University*, vol. 48, no. 9, pp. 2550–2558, 2017.

[20] D. Wang, J. Zhao, Q. Peng, and X. Wang, "Optimization of train combination schemes at marshalling station in loading end of heavy haul railway," *Tiedao Xuebao/Journal of the China Railway Society*, vol. 39, no. 6, pp. 10–19, 2017.

[21] H. Wang, T. Fang, Y. U. Xiaoqiang, H. Cao, and J. Guo, "The excavation scheme optimization of beside river interchange ramp unsymmetrical loaded foundation pit," *Journal of Railway Science and Engineering*, vol. 60, no. 2, pp. 64–66, 2016.

[22] A. Rahmati, L. Faramarzi, and M. Darbor, "Erratum to: squeezing rock conditions at phyllite-slate zone in Golab water conveyance tunnel, Iran: a case study," *Journal of Central South University*, vol. 24, no. 11, pp. 2745–2745, 2017.

[23] M. T. Semper and R. Bowersox, "Tripping of a hypersonic low-Reynolds-number boundary layer," *AIAA Journal*, vol. 55, no. 3, pp. 1–10, 2017.

[24] T. Toulkeridis, F. Rodríguez, N. A. Jiménez et al., "Causes and consequences of the sinkhole at El Trébol of Quito, Ecuador – implications for economic damage and risk assessment," *Natural Hazards and Earth System Sciences*, vol. 16, no. 9, pp. 2031–2041, 2016.

[25] V. D. H. Frank and K. Juchnevic, "The significance of the underground experience: selection of reference design cases from the underground public transport stations and interchanges of the European Union," *Tunnelling and Underground Space Technology incorporating Trenchless Technology Research*, vol. 55, pp. 176–193, 2016.

Hindawi

Research Article

Influence of New Energy Materials on Dynamic Interaction between Surrounding Rock and Structure of Heavy-Duty Railway in Small Clearance Crossing Tunnel

Xiaotian Hao[1,2] **and Hailong Wang** [1,3]

[1]*School of Traffic and Transportation, Shijiazhuang Tiedao University, Shijiazhuang, 050043 Hebei, China*
[2]*School of Urban Construction Engineering, Chongqing Technology and Business Institute, Chongqing 400052, China*
[3]*School of Civil Engineering, Hebei University of Architecture, Zhangjiakou, 075000 Hebei, China*

Correspondence should be addressed to Hailong Wang; bhxt196346@cqtbi.edu.cn

In the rapid development of urban traffic, the small clearance interchange tunnel has always been a difficult problem for heavy-duty railways, so special requirements are also put forward for materials. Bainite steel with excellent comprehensive mechanical properties is considered to replace traditional high manganese, the best material for steel. This article first improves the process of the material and analyzes the structural dynamics of the material through different isothermal cooling to analyze the different performances of the material on the heavy-duty railway. Using traditional theoretical data analysis, theoretical data calculation, numerical analysis simulation, and on-site engineering monitoring technical means is to complement the construction of the soft rock underground tunnel in the subway section at the intersection of the small clear distance line to the existing surrounding rock tunnel wall in the section. The degree of deformation affects the change law, and the related technical issues of engineering control are analyzed. Finally, the control measures of full-face grouting reinforcement with steel flower pipes and the final construction plan of constructing the left line, right line, and undercut section in sequence are proposed. FLAC numerical simulation software was used to complete the feasibility evaluation of the control measures for the deformation of the ground and lining induced by the construction of the cross tunnel. The results show that the maximum deformation of the ground surface is reduced by 35.4% compared with no control measures, and the longitudinal deformation range of the ground surface and the vault is reduced by 28.9%.

1. Introduction

Throughout the world of underground cities, the smooth utilization, development, and comprehensive utilization of public space in underground cities have been rapidly developed and gradually become an effective and important way to effectively solve the serious crisis of underground resources and local soil ecological environment pollution in various underground cities. After our country has entered the 21st century, our country's underground and aboveground urban rail transportation vehicle transportation system infrastructure has initially entered a new stage of rapid, healthy, and orderly development. According to statistics, as of the end of 2016, a total of 30 major large- and medium-sized cities in northern mainland China have completed and opened underground and aboveground urban rail transit automobile public transportation, a total of 133 operating subway lines, and a total of annual operating subway line mileage. The maximum length is 4152.8 kilometers, of which the cumulative operating mileage of Beijing Metro in 2016 was 3168.7 kilometers, accounting for 76.3%. Construction of Nanning Metro began in 2011, and Line 1 was opened

for operation in September 2016. Up to now, Nanning has planned 8 lines, including 187 stations, 22 transfer stations, and 4 vehicle lines.

With the continuous increase in the depth of underground space excavation and planned mileage, the number of stations and transfer stations will also continue to increase, and the cross construction of two or more tunnels will become increasingly apparent. In addition, due to the dense high-rise buildings in the urban areas of our country and the developed subway underground tunnel transportation network, the building pile foundations, municipal tunnel pipelines, underground tunnel structures, and other ancient buildings during the construction of subway underground tunnels have formed the use of space in the urban newly built subway tunnels. Large space restrictions cannot be avoided by design. Therefore, the probability of overlap between new tunnels and existing tunnels is greatly increased. However, the continuous construction of the existing new building tunnels will cause great disturbance to the surrounding building stratum structure, causing three or even four times of large stress between the existing new tunnel and the structural stratum, causing the existing new tunnel and steel structure stratum to occur the stress adds a large internal force and stratum deformation, causing sudden surface deformation values, and there is a major construction risk. Excessive deformation of the tunnel may directly cause the main structure of the existing domestic road tunnels to fail to fully meet the road operation safety requirements, and the ground will also have depressions. When severely damaged, road operations and traffic safety accidents will occur directly and cause great operational safety hazards. In order to ensure the safe and smooth operation of our country's urban rail network transportation, how to effectively supervise, control, and accurately evaluate the direct impact of the delayed construction of urban new railway tunnels on the existing urban new tunnels has gradually become a key academic research topic today.

At present, the research on the influence of new energy materials on the dynamic interaction between the surrounding rock and structure of the heavy-duty railway tunnel with a small clear interval is mainly in these directions. Yanowitz et al. layered the dolomite and rock limestone together and performed a separate downgrading modulus treatment. There was a problem that the dolomite rock surrounding rock model hierarchical modulus was low. According to the surrounding rock model ED (China Dynamics Yang) for tunnel engineering along the Chengdu-Chongqing Railway Modulus classification and quantitative model classification processing system, the dolomite surrounding rock is separately downgraded, which solves the problem of low dolomite surrounding rock model classification modulus, but the materials targeted in this direction are relatively limited [1]. Correa et al. established a three-dimensional numerical prototype virtual statistical model of the length of the subway tunnel based on the various geological surrounding rock deformation risk conditions in the domestic subway tunnel site engineering design and the results of this research, and calculated the collapse of the base layer of the domestic subway exit tunnel through the tunnel numerical prototype

simulation, the design process of the surrounding rock deformation during the construction, and the analysis of the deformation process of the base layer of the subway tunnel. After the design is completed, the exit tunnel of the existing domestic subway tunnel station exit tunnel and the newly built foreign existing domestic expressway Yangtze River Bridge station tunnel subway base collapsed surrounding rock statistics on the relatively large risk of construction deformation due to the collapse of the arch bottom. It is concluded that there may be a high-strength plasticity metro tunnel arch underneath part of the area under the subway arch of the newly built domestic existing expressway station tunnel, and there may be a greater risk of deformation of the surrounding rock when the base of the subway tunnel collapses. There is a certain amount of simulated data [2]. In the actual construction design stage of the railway elevated tunnel project, Yamada et al. formulated practical and feasible overall construction technology according to the actual construction situation of the weak layer and the horizontal hard rock layer in the railway tunnel, in order to effectively ensure the entire tunnel construction design project. Quality and safety are effectively guaranteed, and a detailed discussion of how the overall construction technology of the horizontal hard rock layer of the tunnel should be applied in the actual railway tunnel engineering construction design process is given, but the research is too theoretical [3]. Liu et al. conducted a comprehensive analysis of the movement measurement of the local stress and deformation of the surrounding rock structure of 8 underground tunnels located in 12 shallow and deep buried sections of the underground tunnel, and analyzed the tunnel surroundings of each section of the shallow tunnel under the shallow and deep buried section of the underground tunnel. The research and analysis results of the local movement and deformation of the rock structure's overall movement law are compared and analyzed in depth. The research and analysis of the overall local deformation movement law of the surrounding rock structure of each section of the underground tunnel is divided into the first rapid movement displacement of the surrounding rock of the underground tunnel-rapid movement displacement stable deformation—slow motion displacement stabilizes deformation—fast displacement stabilizes four different process stages. Through the simulation of the statistical numerical comprehensive analysis of the tunnel FLAC3D, the method of supporting treatment of the advanced and late construction conditions and the supporting method of the advanced and late construction treatment and the supporting method of the advanced construction support and the advanced construction treatment method of the underground tunnel are analyzed in depth. The overall local deformation of the rock structure is directly affected by the movement, and this analysis has not kept up with the background of the times [4]. Rynning et al. take the tunnel underneath the surrounding rock of the railway bridge section as an example. It conducts on-site monitoring through the deformation of the surrounding rock and performs necessary numerical simulations. Through statistical analysis of the experimental results, it can be seen that in the process of randomly excavating objects, the displacement of the object

section near the face of the object changes greatly, the maximum and minimum of the vertical square displacement are at an arch, and the maximum and minimum horizontal displacements are it is in an arched waist, and the material requirements of this research are too low [5]. Sonntag, Based on the situation of a large-scale railway branch tunnel in the planning, construction and design stage, Sonntag D studied the classification of surrounding rock and analyzed and guided the construction design and planning of the railway tunnel in combination with the thickness variation of the tunnel surrounding rock and the influence of related factors. At the same time, it provides an important reference and evaluation basis for the construction evaluation of similar tunnel projects, but the data used is not representative [6]. Sorgenfrei and Tsatsaronis take the railway sandy tunnel deep-buried railway single-track tunnel railway surrounding rock tunnel as the key object of the subject research; through the numerical statistical measurement and analysis of the measured railway load data of the railway surrounding rock tunnel, the research establishes the railway based on the BQ numerical calculation index. The numerical calculation and analysis method of the measured load of the surrounding rock, but the application range of this method for calculating the measured load of surrounding rock is too narrow [7].

The two materials used in the main test materials in this paper are the new Si-Mn-Cr series low- and medium-sized carbon fiber low-alloy steel developed by Xihua University. The low-alloy steel is heated under air-cooled and high-pressure conditions. Bainite without activated carbonized substance, through the contact fatigue strength test of the roller rolling gear, the direct influence of the smooth difference between the roller load and the gear rolling on the rolling contact fatigue test performance of the alloy steel used in the switch fork machine of the heavy-duty high-speed railway in China is studied. And further analyze the structure, phase, fracture morphology, and hardness change law and explore the fatigue damage mechanism and fatigue performance of heavy-duty railway frog steel. Using traditional theoretical data analysis, theoretical data calculation, numerical analysis simulation and on-site engineering monitoring combined technical means is to construct the soft rock underground tunnel in the subway section at the intersection of the small clear distance line to the existing soft rock tunnel wall in the section. The degree of deformation affects the change law, and the related technical issues of engineering control are studied in depth.

2. Overview of the Close Construction of Subway Tunnels

2.1. Classification of Close Construction of Subway Tunnels. The primary technical problem that the direct technical construction of underground construction projects must face in the near future is that the close construction of new underground constructions may have a certain impact on the original air stability performance of the underground construction structure, breaking the original balance mode. The main reason for the impact of this change is closest to the essence. The continuous construction of the new sur-rounding rock project may cause the stress system in the solid surrounding rock to redistribute again and again, which directly leads to a series of surrounding rock mechanical and physical behaviors. This force characteristic is related to many factors such as engineering and hydrogeological conditions, engineering construction sequence, spatial position relationship, and construction method, such as loading, unloading, horizontal, vertical, and spatial different effects under different conditions [8, 9].

Generally, the construction when the new construction is adjacent to the existing construction and the construction of the new construction may adversely affect the normal function use of the existing construction is called the near construction. When the new construction and the existing construction are both tunnel constructions, those that meet the above conditions can be defined as the adjacent construction of the tunnel construction. From the perspective of the construction location relationship of the grounding space, the construction location of the short-distance grounding of the tunnel can be divided into three kinds of construction location spatial relations: one-way parallel, overlapping, and two-way crossing [10, 11].

2.1.1. Side Wear. When a new tunnel passes through an existing tunnel, the surrounding rock and stratum are disturbed due to the construction of the new tunnel, and the surrounding rock of the existing tunnel will also relax. Therefore, the load on the lining of the existing tunnel will increase. The lining structure will undergo a certain tensile deformation to the new tunnel side, and biased pressure may occur. In subway engineering, the side-crossing problem mostly belongs to section crossing or the foundation pit crossing existing tunnel.

2.1.2. Underwear. When the newly built tunnels on both sides pass through the lower intersection of the existing tunnels on both sides, the two tunnels are in a downward crossing relationship. With the continuous excavation of the two newly built line tunnels, the interlayer lining space structure of the existing line tunnels may also continue to sink. At the same time, due to the excessive settlement of the tunnel, it is very likely that the gradient is unevenly distributed. The main reason is the change in the positional relationship of the interlayer space structure of the two tunnels. If the location is different, the excessive settlement may cause the track structure variation. The settlement value is too large to exceed the tunnel management standard, resulting in the temporary suspension of trains along the line.

2.1.3. Put on. When the new tunnel crosses the upper part of the existing tunnel, the two tunnels are in an upward pass relationship. With the excavation of new tunnels, due to the unloading effect of the soil, the existing tunnels will undergo vertical uplift deformation, which may be unevenly distributed. If the deformation is too large, it will also bring safety hazards to the safe operation of the train.

According to the way of crossing, it can be divided into three types: up, down, and side. Underpass mainly refers to crossing the existing sections, stations, buildings, bridges,

pipelines, railways, highways, etc.; upward crossing mainly refers to new projects crossing existing sections and underground pipelines; side crossing can refer to new projects crossing pile foundations or parallel tunnels, and their structural relationships are shown in Figure 1.

Here is a basic classification according to the characteristics of the tunnel force conditions under different force elements of the remote connection time, space, and remote connection construction method, which can be roughly divided into two newly built simultaneous tunnels in the short-distance and long-distance period. Two or more new tunnels are short-distance close to each other during the construction of two basic force types [12, 13].

The highway design requires that the new construction of the existing highway tunnel is connected with the new existing tunnel and the new highway tunnel is connected in coordination with the new construction of the existing highway tunnel according to the highway design requirements. The connection of the newly built highway tunnel also occupies the relationship between the space distance and the location of the tunnel as well as the mobile rate. It is subdivided into three cases: parallel tunnels, overlapped tunnels, and interlaced tunnels, as shown in Table 1.

Two or more new tunnels will be constructed at the same time at a close distance. According to the spatial position relationship between the new tunnel and the neighboring existing tunnels, Table 2 further subdivides them into three cases: parallel tunnels, overlapping tunnels, and intersecting tunnels [14, 15].

2.2. Zoning of the Impact Degree of Close-Up Construction. According to different classifications of close-range construction of subway tunnels, the influence degree of construction is also different. The extent of the impact of the construction of a new project in the underground project on the surrounding existing projects varies depending on the spatial position and can be expressed by the degree of proximity. At present, there are few researches on the adjacent tunnel engineering at home and abroad, and most of them are based on a scattered specific project summary, lacking systematic rules. The earliest method to study the construction of short-distance connection engineering is Japan. Due to the small land area in Japan, in order to make full use of the existing underground resources, there are many application cases of new tunnel connection engineering in the construction of short-distance connection engineering. Promulgated the "Guidelines for the Close-up Construction of Existing Railway Tunnels", which has carried out a more comprehensive and systematic theoretical explanation of the research on the problems of the construction of the short-distance connection engineering tunnels, and has directness in solving the construction problems of the existing underground railway tunnels. This paper comprehensively analyzes and considers various factors such as the building scale, construction design plan, geological space movement relationship between the structures, engineering, and ground hydrogeological objective conditions of different newly built tunnel projects, so that the construction of different newly built projects can be compared to the different

existing railways. The direct impact caused by the performance of the structure is of different severity and can be divided into four categories: the more specific and intangible impact consideration scope, the attention consideration scope, the consideration scope of measures taken when necessary, and the careful consideration scope, as shown in Table 3.

When a new line traverses an existing line, the division of its proximity is shown in Figure 2.

For the construction of two or more crossing tunnels, it is necessary to consider both the lateral impact range of the new tunnel construction on the existing tunnel and the longitudinal impact range that may be affected. The vertical and horizontal impact range of the existing tunnel by the new tunnel is shown in Figure 3.

When the longitudinal oblique line of the new tunnel in the existing tunnel overlaps with the area where the weak damage of the existing tunnel is weakly damaged and the damage is doubled, the intensity of the tunnel longitudinal oblique line overlaps again. If the landslide strength of the existing newly built new tunnel is weak and the damage affects the damage hazard again and the longitudinal slash of the tunnel overlaps again, then the strength of the newly built longitudinal landslide of the existing tunnel is the weak damage effect. The area of damage hazard is divided into the intensity range, and at the same time, the part of the intensity influence range is still not necessary to separately focus on the comprehensive consideration of the strength rupture effect of the newly built transverse landslide of the existing tunnel [16, 17].

Regarding the new longitudinal landslide, it can be divided according to the range of damage intensity. The format of the strength impact division criteria can be redetermined according to the Moore-Coulomb strength division criteria format and the potential longitudinal landslide strength fracture cross section of the newly built longitudinal landslide. The oblique angle of the fracture cross section is generally $45° + \varphi/2$. Among them, the division scope of the hazard zone for the strength damage of the newly built longitudinal tunnel can be divided according to the longitudinal oblique line of the newly built tunnel and the existing tunnel in which the transverse oblique line of the new tunnel overlaps the longitudinal oblique line on the main axis. The line position is redivided to increase the 2D intensity influence division range (D is the equivalent diameter of the newly built tunnel). Among them, 2D is the depth range involved in the oblique line deformation of the ground outside the included angle of the tunnel fracture [18, 19]. In the same way, the $45° + \varphi/2$ stratum oblique line from the top of the existing domestic newly built tunnel intersects the longitudinal and horizontal axis of the domestic newly built existing tunnel structure, which can be used to determine that the existing domestic tunnel structure of the affected vertical axis intersects the construction scope of the new tunnel, as shown in Figure 4.

For the specific nearby construction of underground engineering, the size of the existing tunnel and the newly built tunnel and the design distance between the two are known. According to the Moore-Coulomb failure criterion,
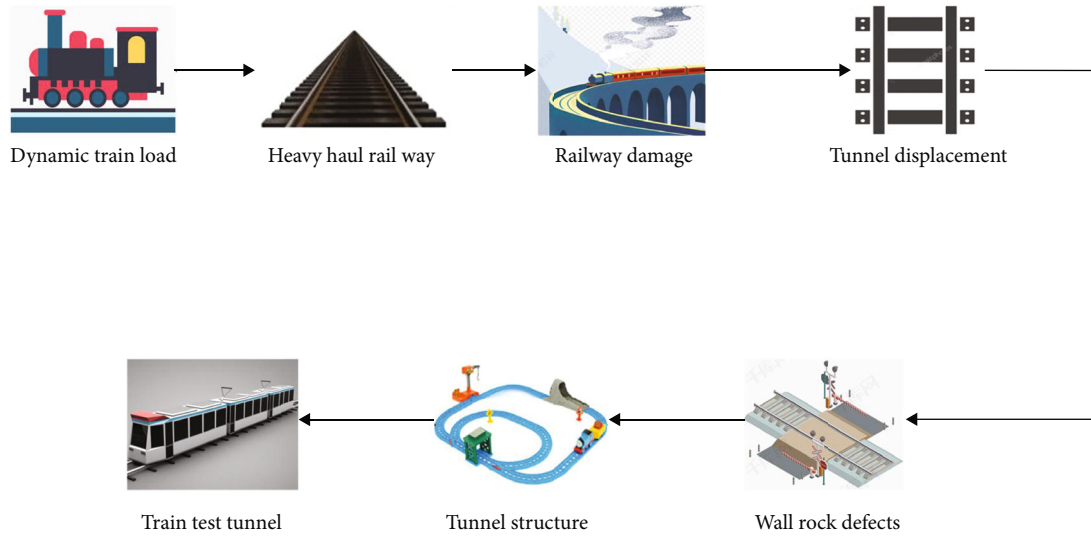
FIGURE 1: Analysis of the relationship between the various structures of the railway tunnel.

TABLE 1: Construction classification and engineering application of new tunnels adjacent to the existing tunnels.

Engineering applications	Type
When constructing new tunnels in parallel with the existing tunnels and planning new subway lines	Tunnel side by side
Due to the space conditions, the two tunnels must be built on top of each other	Tunnel overlap
Due to space constraints, the two tunnels must be constructed in a staggered way	Tunnel staggered
Pass through the existing tunnel from the upper or lower part of the existing tunnel. It is a transfer node for multiple lines	Tunnel crossing

TABLE 2: Construction classification and engineering application of two or more new tunnels at the same time.

Engineering applications	Type
Due to conditions, the two tunnels were constructed in parallel to the left and right at a short distance. Usually, the two tunnels are mostly uplink and downlink	Side by side tunnel
Due to conditions, the two tunnels were constructed in close distance and overlapped with the upper and lower ones, which are more common in the upper and lower lines of the tunnel	Tunnels overlap up and down
Due to conditions, the two tunnels were built diagonally and staggered at close distances.	Tunnel diagonally staggered
Due to conditions, the space of the two tunnels is twisted and cross-constructed, which is mostly seen in the simultaneous construction of two subway lines or the positional relationship between the main line and the vehicle line	Tunnel space cross torsion

TABLE 3: Division and measures of proximity.

Proximity division	Divide content	Measure content
No influence	Do not consider the scope of the impact of new construction on the existing structure	Generally do not take corresponding measures
Pay attention to the scope	Usually no adverse effects but a certain range	Usually by adopting appropriate construction methods, based on the monitoring data during construction combined with the allowable values of displacement and deformation of the existing structure, comprehensively determine whether to take other measures

the impact range of the nearby construction can be determined. The close construction of shield tunnels and general undercut tunnels has similar rules [20, 21].

For a shield tunnel, along tunneling direction, the cutterhead pushing pressure and cutterhead excavation have a disturbance influence zone on the front soil. When there are
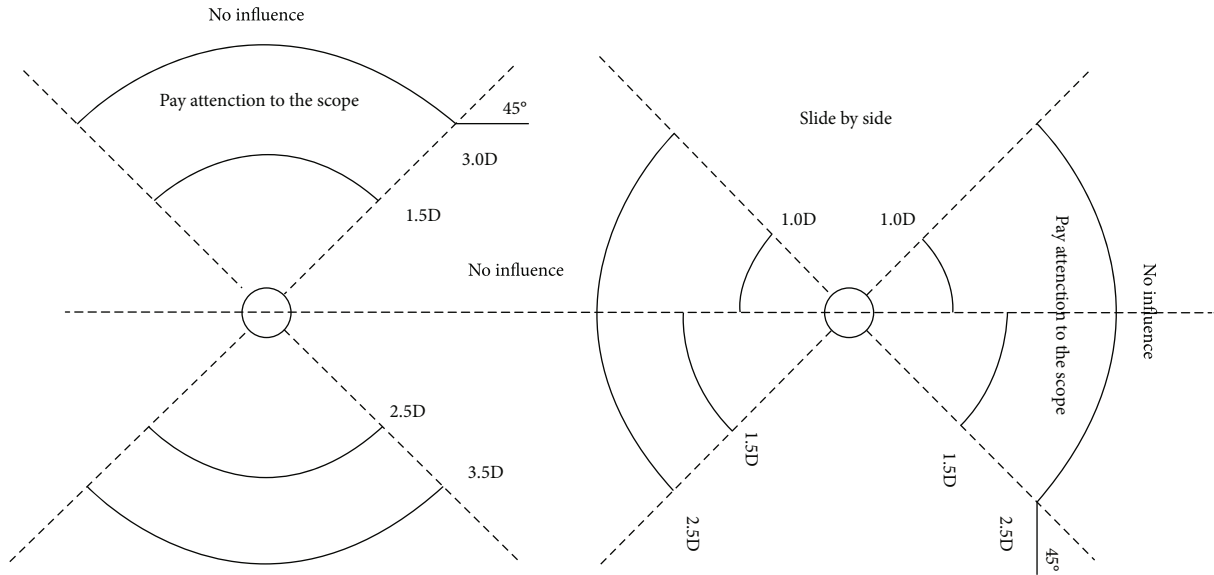
FIGURE 2: Dividing the proximity of a new tunnel through an existing tunnel.
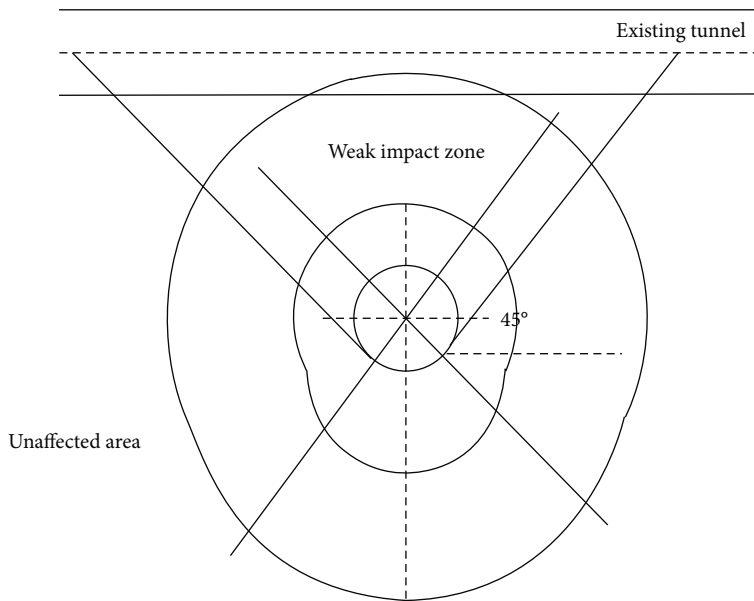
FIGURE 3: The existing tunnels affected by the construction of new tunnels.

existing structures in this influence zone, it is the approach construction. This process is the shield which passes through the affected zone. At this time, the main moving soil body in front is generally set to the pressure control state of the compressed moving soil, and it can directly face the direction of the upper shield tunnel construction area to introduce another shield tunnel that is tangent to the existing shield tunnel of the upper shield. The longitudinal shear of $45° - \varphi/2$ with the height of the tunnel horizontal plane passes through the line of the failure zone. At this time, when the existing tunnel of the upper shield machine intersects with the shear failure zone in a straight line, it can be directly considered that the existing tunnel of the upper shield machine

has entered a larger area that passes through the influence zone [22, 23]. In the same way, introduce a horizontal shear line that is tangent to the existing shield tunnel passing downward and is $45° - \varphi/2$ to the horizontal plane of the tunnel to pass through the failure zone. When the lower shield tunnel has an existing shield tunnel and when the tunnel and this line have not been sheared and intersected, it can be directly considered that the existing tunnel of the upper shield has entered a larger area that passes through the influence zone, as shown in Figure 5.

2.3. Analysis of Risk Factors in the Existing Tunnel Engineering. Urban subway tunnel construction has a great
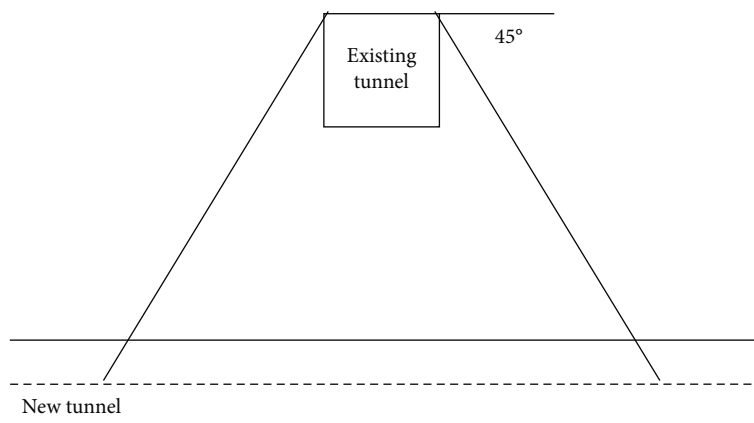
Figure 4: Construction scope of new tunnels affecting the existing tunnels.

impact on the surrounding environment. The deformation of the existing tunnels mainly depends on the engineering and hydrogeological conditions of the tunnel, the characteristics of the new tunnel, the characteristics of the existing tunnel, and the spatial relationship between the new tunnel and the existing tunnel. Among them, engineering hydrogeology is particularly important, which is an uncontrollable factor. The spatial position relationship between new tunnels and the existing tunnels is extremely sensitive to the deformation of the ground and lining [24, 25].

Whether it is a new underground tunnel project or an existing tunnel project, it is in a complex hydrogeological environment. Taking Nanning as an example, the Quaternary stratum in Nanning area mainly includes fill, silty clay, silt, silt sand, medium-coarse sand, round gravel, and pebbles; the lower bedrock is mostly soft rock, such as mudstone and siltstone . The cohesive force of silty clay is 20~65 kPa, the internal friction angle is 5~15°, and the characteristic value of foundation bearing capacity is 90~220 kPa; the cohesive force of silt clay is 15 kPa, the internal friction angle is 10°, and the characteristic value of foundation bearing capacity is 120 kPa. Among them, the characteristic value of foundation bearing capacity indicates the maximum allowable foundation pressure of the building foundation, and if the pressure exerted by the foundation on the foundation is greater than this value, excessive deformation may occur [26].

In this paper, the length of the shield machine is considered to be 9 m. Considering the larger model, the excavation distance is 3 m each time, that is, two ring segments. In the process of shield tunneling, in order to maintain the stability of the excavation surface, it is necessary to adjust the soil pressure inside the shield machine's soil bin from time to time. In the actual construction process, the supporting pressure is 0.25 MPa. During the excavation of the soil of each section of the tunnel, a supporting force of 0.25 MPa was added to the face of the tunnel at the same time. When the shield machine enters the hole completely, the relevant commands are compiled according to the process shown in Figure 6 until the shield machine exits the hole [27].

On the one hand, the impact of the construction of the new project on the existing subway tunnel is mainly trans-mitted through the deformation of the interlayer soil. On the other hand, the physical and mechanical properties of the stratum in which the existing subway structure is located also have a greater impact on the stratum deformation induced by construction disturbance, and the deformation will be transferred to the existing structure. Therefore, the deformation of the soil between the newly built tunnel and the existing tunnel during continuous failure is directly related to the deformation value of the existing structure. In areas with better stratum conditions, the structural deformation of the existing subway tunnels induced by the construction of new tunnels is small, while in areas with poor soil mechanical properties, rich water content, and high groundwater levels, due to the self-excavation of the new tunnel construction, poor stability, resulting in increased stratum deformation, and due to poor stratum mechanical properties, the existing subway structure will deform even more [28].

3. The Impact of New Energy Materials on the Dynamics Analysis of Heavy-Haul Railways

3.1. Changes in the Performance of Steel Used in Heavy-Duty Railway Frogs. After different heat treatment processes, the hardness of steel used on the plosive of heavy-duty railway is improved to some extent compared with that of the original sample. At the same temperature of austenite steel integrated treatment, the maximum hardness of the iron alloy steel used on the frog of heavy-duty high-speed railway train after air cooling is about 47.4 HRC, the highest hardness of the steel used after heat treatment of isothermal boiler is next, and the lowest iron hardness of the steel used after furnace cooling is about 42.3 HRC. This is mainly because the iron alloys used in China's high-speed railways cannot be rapidly cooled, and the heat dissipation is slow, and the heat dissipation performance of metal alloys and metal elements such as carbon atoms and iron is poor. The rich carbon sulphide austenite will rapidly diffuse and transform to other carbon-rich alloy martensite, which will increase the super-heated and undercooled saturation of the structure of the rich carbon alloy martensite, and improve the solid activity and insolubility of the carbon contained in the steel during
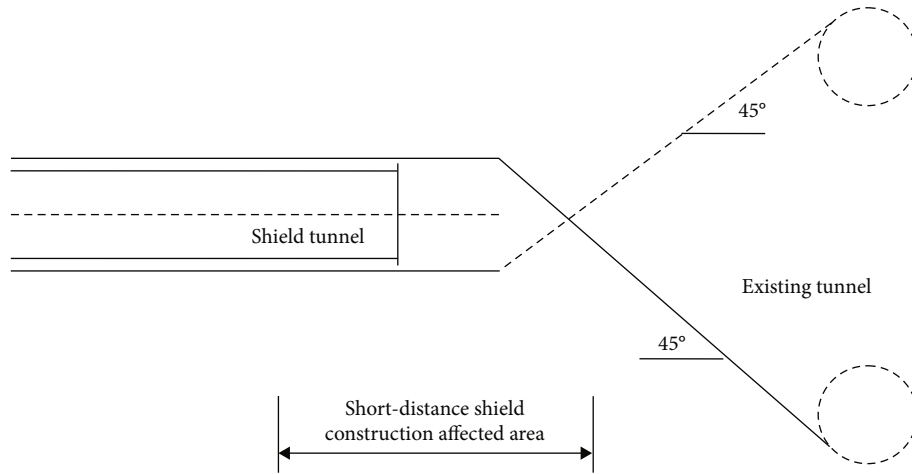
FIGURE 5: Schematic diagram of shield tunneling through adjacent affected area.
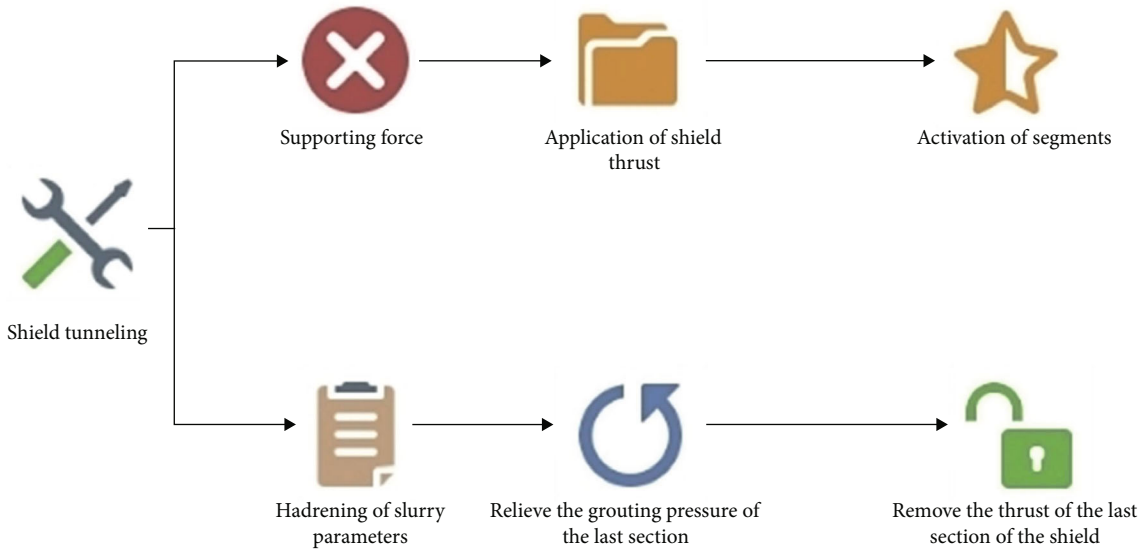
FIGURE 6: Shield tunnel simulation method.

the reaction of the main carbon-generating martensite heating process. In addition, the supercooling diffusion rate of the iron and steel used on all types of train vehicle frog of heavy-duty China high-speed railway is larger in air cooling, and the steel generated by carbon mixture in steel species has more understrip bainite, so the supercooling hardness of steel is the highest. Since the steel in China's high-speed railway has the slowest cooling diffusion rate in the furnace, the cooling diffusion of carbon and other metal alloys is insufficient, and the steel stays in the high-temperature environment for a long time during the cooling process, so the hardness is extremely small. The change rule of hardness of steel sample used on heavy-duty railway frog after heat treatment is shown in Figure 7.

When heat treatment is performed under isothermal conditions, some metal alloys and nonmetallic carbons in iron and steel used in frog vehicles for heavy-duty China high-speed railway frog vehicles and train-mounted iron

and steel have low thermal diffusivity and heat dissipation reaction capacity under isothermal conditions. It is not possible to directly carry out high-temperature thermal diffusion for a long period of time or short distance in the residual undercooled and overheated austenite. Bainite will grow in the carbon-depleted zone containing a small amount of residual undercooled or warm and overheated high-temperature austenite at the grain boundary temperature. In nucleus, with the growth of bainite, the content of metal elements such as Si hinders the rapid precipitation of metal carbides in the grain boundary temperature, which is more conducive to the continuity of the high-temperature cold-hot reaction of the grain boundary. The metal steel of steel has better compression resistance and impact toughness; however, when heat treatment is performed at a higher grain boundary temperature isothermally or heat treatment at a temperature, the heavy load capacity of China's high-speed rail will vary. The carbon content of some steel with
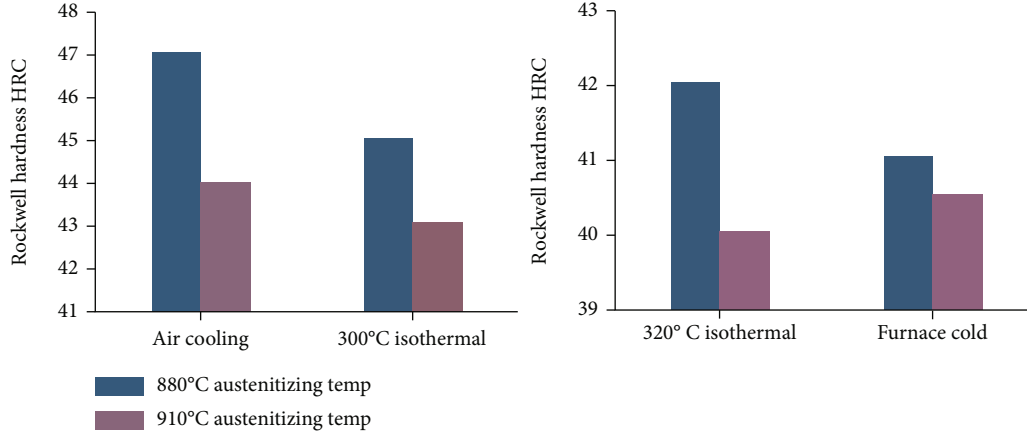
FIGURE 7: The effect of heat treatment on the hardness of heavy rail frog steel.

a small amount of residual supercooled and superheated austenite metal elements may also increase significantly, so its impact toughness can be improved. For the same cooling method, increasing the austenitizing temperature will increase the impact toughness value of heavy-duty railway bainitic steel. This is mainly because they increase the temperature of the two-austenite carbon gas compound, the energy diffusion between the two elements of carbon and metal alloys is more complete, the carbon content in the austenite increases and the stability is enhanced, and the final amount retained austenite. The increase makes the impact toughness increase to a certain extent. Compared with the traditional high manganese steel, the steel used in heavy-haul railway has to go through more processes and be made more complex, so its performance will be stronger. Figure 8 shows the influence of heat treatment on the impact toughness of bainitic steel used in heavy-duty railway frogs.

3.2. Dynamic Analysis of Heavy-Duty Trains. Heavy-haul train generally refers to a kind of a super-long and overweight freight train which is organized by large special trucks and pulled by two or more machines on the transportation line where the freight volume is concentrated. Heavy-haul trains have large load capacity. There are a large number of trains. The primary task of high-speed railway bridge research is to determine the impact of train operation on the substructure. This has always been the focus and difficulty of engineering research. At present, there are two main methods. The first is to use structural dynamics to establish train and substructure and the overall coupled dynamic equation of the track, but due to the many factors involved in the train-track coupled dynamic equation, it is difficult to solve the equation and it is difficult to apply it to practical engineering. The second is to directly fit the train load expression considering factors such as vehicles and tracks. However, there are many factors that affect the operation of high-speed trains, so it is difficult to determine an accurate expression that considers all influencing factors, but it is possible to obtain simplified expressions that can be applied to engineering problems. At present, there are mainly two train load simulation methods: the first kind of

track vibration acceleration is regarded as a random process, and the acceleration data is transformed into a force model by a data transformation method; the other is based on the excitation caused by track irregularity and a comprehensive consideration of vehicle and track factors for load fitting.

The differential equation of vehicle dynamic balance can be expressed as follows:

$$
\begin{aligned}
m_2 y_1 + c(y_1 - y_0) + k(y_1 - y_0) &= 0, \\
y_r &= y_1 - y_0, \\
m_2 y_r + c y_2 + k y_r &= -m_2 y_0.
\end{aligned}
\tag{1}
$$

Using the D'Alembert principle, the interaction force between the wheel and rail is as follows:

$$
P(t) = (m_1 + m_2)g + (m_1 + m_2)y_0 + m_2 y_r.
\tag{2}
$$

The idea of the track measured acceleration method is mainly based on the random vibration load model. By treating the environmental vibration induced by the train as a random process, the track measured acceleration data can be expressed in the following complex series:

$$
\begin{aligned}
x(t) &= 2 \sum_{k=1}^{(N/2)-1} |C_K| \cos (k w_0 t + \beta_k), \\
C_K &= \frac{1}{N} \sum_{n=0}^{N-1} x(t_k) \exp \left(-i \frac{nk\pi}{N} \right).
\end{aligned}
\tag{3}
$$

Assuming that the orbital vibration is a Gaussian stochastic process with a zero mean value, the following trigonometric expression of acceleration can be obtained through numerical changes:

$$
x(t) = 2 \sum_{k=1}^{(N/2)-1} a_k \cos (k w_0 t) + b_n \sin (k w_0 t).
\tag{4}
$$
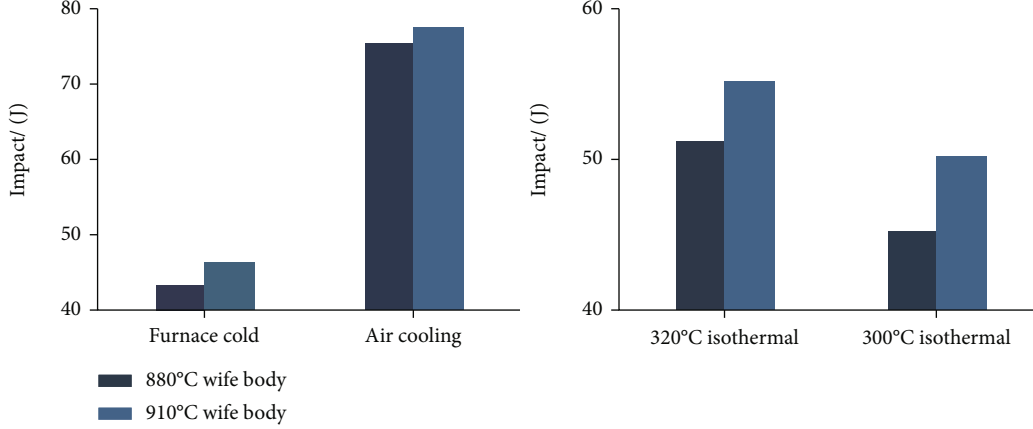
FIGURE 8: The effect of heat treatment on the impact toughness of steel used in heavy-duty railway frogs.

In the above formula,

$$a_k = C_K + \overrightarrow{C_K},$$
$$b_n = i\left(C_K + \overrightarrow{C_K}\right), \quad (5)$$
$$w_0 = \frac{2\pi}{N\Delta t},$$

where a_k represents the change amplitude of a numerical value, b_n represents the acceleration, and w_0 represents the period of track vibration.

Incorporating Equation (4) into the dynamic balance differential equation, ignoring the influence of transient response, the following load excitation model can be obtained as follows:

$$P(t) = (m_1 + m_2) + \sum_{k=1}^{(N/2)-1} \left[(m_1 + m_2)A_K - k^2 w_0^2 m_2 P_2\right]. \quad (6)$$

At present, the main method of statistics is to accurately analyze and describe the unevenness of the electric locomotive running track at the same time through the high-frequency density function statistics of the random power sequence amplitude of the electric locomotive running track irregularity and the random density power spectrum high-frequency density function statistical method. Electric locomotive running track uneven smooth random density power sequence spectrum high-frequency amplitude value density function calculation in the function of the statistical method is a general high-frequency spectrum random power amplitude density calculation function statistics that can use uniform value and square value to be accurate. Analyzing and describing the data characteristics of the random power sequence spectrum and the mathematical structure of the random frequency spectrum, many developed countries have preliminarily determined the functions in the calculation of the high-frequency density function of the random power sequence spectrum along with the uneven running track of their electric locomotives.

$$w_1 = D(i,j), w_{k-1} = D(O,P), I - O \le 1, J - P \le 1,$$
$$I - O \le 1, J - P \le 1. \quad (7)$$

The main constraint optimization problem is defined as the following formula:

$$\text{minLPELM} = \frac{1}{2}\|\alpha\|^2 + C\frac{1}{2}\sum_{i=1}^{n}\|\gamma_i\|^2. \quad (8)$$

The constraints are as follows:

$$h(x_i)\alpha = t_i^T - \gamma_i^T, \quad i = 1, \cdots, n. \quad (9)$$

The optimization problem encountered can be transformed into the following equation:

$$\alpha = H^T\varphi, \varphi_i = C\gamma_I, h(x_i)\alpha - t_i^T + \gamma_i^T = 0, \quad i = 1, \cdots, n, \quad (10)$$

where T is the Lagrange multiplier matrix. The final output weight α is calculated as the following formula:

$$\alpha = H^T\left(\frac{I}{C} + HH^T\right)^{-1}T. \quad (11)$$

Therefore, the output function of the extreme learning machine can be defined as the following formula:

$$f(x_j) = h(x_i)H^T\left(\frac{I}{C} + HH^T\right)^{-1}T, \quad j = 1, \cdots, n. \quad (12)$$

It is fitting to obtain the following power spectra of track irregularity:

$$S_V(\Omega) = \frac{KA_\alpha\Omega_c^2}{\Omega^2(\Omega^2 + \Omega_c^2)},$$
$$S_c(\Omega) = \frac{4KA_v\Omega_c^2}{\Omega^2(\Omega^2 + \Omega_c^2)(\Omega^2 + \Omega_s^2)}. \quad (13)$$

3.3. Forces on the Structure of the Tunnel Bottom under the State of Vacant Surrounding Rock. In underground rock engineering, the surrounding rock mass whose stress state changes due to excavation is called surrounding rock. There are roughly two kinds of relationships between ore bodies and surrounding rocks: there are significant differences in fabric and content of useful components between ore bodies and surrounding rocks, and the contact boundary is clear, such as the relationship between vein filling ore bodies and surrounding rocks. In this study, indoor model tests and finite element numerical simulations are used to study the process of underground water erosion on the surrounding rock at the bottom of the heavy-duty railway tunnel during the operation period due to the dynamic load of heavy-duty trains, and quantitatively analyze the voids. The change law of contact pressure and the transmission characteristics of earth pressure under the condition of the tunnel excavation process were monitored for the clearance convergence of the lining structure of the typical section of the left and right shield tunnels, as shown in Table 4.

The above research is based on indoor model tests to qualitatively study the process of underground water erosion on the surrounding rock at the bottom of the heavy-duty railway tunnel structure due to the dynamic load of heavy-duty trains during the operation period. The following quantitative analysis of the contact pressure during the erosion process and the transmission characteristics of earth pressure is as follows: the change curve of the additional value ΔP of the contact pressure at the bottom left of the center line, the bottom left of the center line, the bottom of the center line, the second point, and the bottom right of the center line, the point 3, when there is water and no water, and the additional value ΔP change curve.

The following can be seen from Figure 9:

(1) When the surrounding rock at the bottom of the tunnel is in anhydrous conditions, the additional value of contact pressure ΔP below the centerline fluctuates around 6.5 kPa, and the additional value of contact pressure on the left and right sides ΔP is stable at around 5.8 kPa, but the overall situation is relatively stable. The additional value of the contact pressure below the left and right sides of the center line is slightly reduced compared with that below the center line, indicating that the effect of the excited vibration load below the center line is more obvious than other positions

(2) When the surrounding rock at the bottom of the tunnel is in a water-rich condition, the additional value ΔP of the contact pressure at the three measuring points under the floor is lower than the ΔP when there is no water, which indicates that the water body between the structure and the surrounding rock is to a certain extent play a role in buffering the excitation load. After 100 s of excitation, ΔP began to rise and gradually stabilized at about 5.5 kPa at 100 s. The initial contact pressure value ΔP on the left and right sides of the center line is about 4.5 kPa, and after a period of excitation, it starts to increase and finally stabilizes at about 5.0 kPa, with a change value of about 0.5 kPa

Therefore, on the whole, the stress of the tunnel bottom structure in the state of empty surrounding rock is relatively stable, although there are different pressures in different positions. But the overall fluctuation is not big.

4. Experimental Results and Analysis

4.1. Comparative Analysis of Ground Surface Measurement and FLAC Simulation Data. FLAC (Fast Lagrangian Analysis of Continua) is a continuum mechanics analysis software developed by Itasca Company. It is an internationally used professional analysis software for geotechnical engineering. It has powerful calculation functions and extensive simulation capabilities, especially in the analysis of large deformation problems. Combining the layout of the measuring points, this paper selects four sections of 172, 175, 178, and 182 to analyze the measured data on the surface. The specific data is shown in Figure 10.

It can be seen from Figure 10 that the measured data has 2 to 3 large settlements depending on the time. Taking section 182 as an example, the tunnel face of the left-line shield tunnel reaches the measuring point, and a large area of settlement occurs on the ground surface with the largest settlement. The value is located directly above the center of the tunnel, and the surface settlement value is still increasing the next day, which is mainly due to the disturbance of the surrounding soil by the construction gap and the shield machine. On July 15th, the right-line shield tunnel was excavated to the location of the measurement point. At this time, the measurement point directly above the center of the left-line shield was still growing. After 7 days, the shield machine was far away from the measurement point, and the maximum surface settlement was at above the center of the right-line shield tunnel, and its value is 26.1 mm. On October 21, the face of the undercut tunnel has completely passed through the section of the measurement point. Since the left and right shield tunnels are both within the affected area of the undercut tunnel, the ground surface around the left and right shield tunnels has changed again. Settlement occurred again. As the net distance between the left-line tunnel and the right-line tunnel is slightly smaller than that of the undercut tunnel, the increase at this stage is not large.

The final maximum surface settlement is located directly above the center of the excavated tunnel, its value is 46.8 mm, and the maximum value obtained by simulation is 42.05 mm. Because of the damage of the measuring point of the 178 sections, only the surface settlement induced during the construction of the tunnel is shown in the figure, so the deformation value is much smaller than the final simulated settlement value. The development law of the ground surface in the simulation has been verified in the actual measurement, but its value still has a certain deviation compared with the actual measurement. The actual measurement data is slightly larger than the simulated value. The main reasons for the difference are as follows:

TABLE 4: Convergence and deformation of the overpass tunnel to the existing left-line shield tunnel.

Section position (m)	$y = 12$	$y = 27$	$y = 51$	$y = 75$	$y = 87$
After the left-line shield is completed (mm)	7.59	7.85	8.12	9.12	12.52
After the right-line shield is completed (mm)	8.02	8.15	8.23	9.23	11.52
After digging is completed (mm)	7.56	7.86	8.62	7.99	12.56
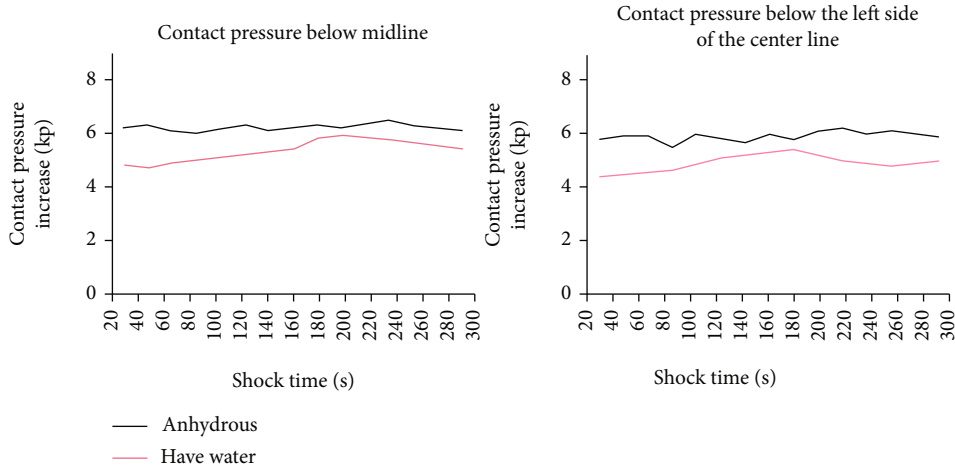
FIGURE 9: The change curve of the additional value ΔP of the contact pressure below the center line and the left side.
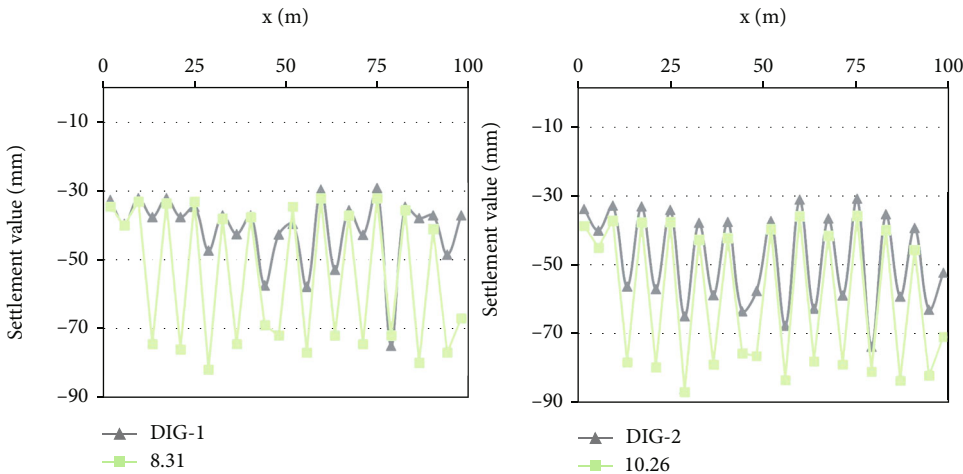
FIGURE 10: Surface deformation law of cross section.

(i) The problem of groundwater was not considered in the simulation. For undercut tunnels, water-free operation must be ensured, and the ground settlement induced by the lowering of the water level is very large

(ii) The creep effect of rock and soil is not considered in the simulation

(iii) The uncertainty of the load on the upper part of the ground. The dynamic load of vehicles has a greater impact on the deformation of the ground. In the simulation, the ground load is considered as a uniform load, and the operation of heavy-duty vehicles will inevitably increase the settlement of the ground

(iv) The rock and soil are heterogeneous, because the thickness and mechanical parameters of the rock and soil body at each section will have a certain difference, and the rock and soil are treated according to the same thickness of each section during the simulation

In the simulation, the soil layer is considered as waiting for homogeneity, and the ground load is simplified as a heap load, so the simulation results in the uniform and smooth

curve. The measured data are all nonsmooth broken line segments. The measured value is slightly larger than the simulated value on the whole, and the error is about 20%. The measured data of individual points is smaller than the simulated value. However, the deformation development law of the simulated curve and the measured curve is more consistent. For surface subsidence, the maximum value is not directly above the intersection, but at the almost parallel position of the three tunnels. The measured maximum value is 46.8 mm. The excavation of three tunnels is disturbed, so the surface deformation is relatively large.

4.2. Experimental Data Analysis

(1) Based on the results of numerical simulation of this project, reasonable construction methods and supporting measures for this project are given. That is, within the affected area of the upper and lower crossing sections, the left and right main line shield tunnels shall be constructed first, and then, the construction of the crossing section of the outbound line shall be continued. The undercut tunnel adopts a horseshoe-shaped composite lining structure, a comprehensively advanced small pipe presupport, and a step (reserved core soil) method for tunnel construction. Three control methods are put forward through advanced geological exploration, full-face grouting of steel flower pipes, stratum reinforcement, and strengthened inspection and monitoring, and the grouting range and grouting parameters of steel flower pipes are given

(2) Lagrange algorithm is very suitable for simulating large deformation problems. FLAC adopts the explicit finite difference scheme to solve the governing differential equation of the field and applies the mixed element discrete model, which can accurately simulate the yield, plastic flow, and softening to large deformation of materials, especially in the fields of elastic-plastic analysis of materials, large deformation analysis, and simulation of construction process. The FLAC analysis results show that the use of steel flower pipe grouting reinforcement is more obvious for controlling surface deformation than tunnel vaults and convergence. Among them, the maximum deformation of the ground surface is 35.4% less than that without reinforcement measures. The longitudinal deformation range of the ground surface and the vault is reduced by 28.9% compared with no reinforcement measures

5. Conclusion

This paper systematically analyzes and summarizes the large degree of risk impact, the characteristics of the stress conditions, and the degree of deformation of the tunnel through the construction of the subway and railway tunnels under different construction methods. It focuses on the analysis of various factors that affect the safety risks of the new subway tunnel project crossing the new existing subway tunnel

proximity project. The main factors are the existing railway engineering and the tunnel hydrogeological environmental conditions, the existing subway tunnel engineering status, and the new subway tunnel engineering status. There are four main aspects of the relationship between crossing the newly built subway tunnel and the three-dimensional space connection position of the existing subway tunnel. The steel of the railway tunnel frog bainite plate in the heavy load engineering of the tunnel is in the process of material compression processing due to the continuous change of dislocations and the combination and entanglement to form multiple dislocation cells, which hinder the slippage of dislocation cells. The steel processing hardness of the bainite plate gradually doubled from 450 HV to 608 HV, showing obvious work hardening and smoothness. The FLAC analysis results show that the use of steel flower tube grouting reinforcement is particularly obvious for controlling the surface and the tunnel vault. After the reinforcement measures were taken, the maximum deformation of the ground surface was reduced by 35.4%, and the influence of the deformation of the ground surface and the vault along the axial direction of the tunnel was reduced by 28.9%. Finally, the method is used to carry out dynamic numerical simulation during the construction phase of the tunnel with a small clear distance to analyze the stability of the surrounding rock of the tunnel. Due to the complex construction process of the small clear distance tunnel, in the numerical simulation modeling process, the boundary between the upper and lower steps is regarded as the boundary layer of soil and rock, and the grouting of the leading small pipe is equivalent to the entity, without considering the groundwater and actual working conditions. The impact of this coupling on the model in this paper can be further considered in future research.

Data Availability

No data were used to support this study.

Conflicts of Interest

There is no potential conflict of interest in this study.

References

[1] J. Yanowitz, R. L. Mccormick, and M. S. Graboski, "In-use emissions from heavy-duty diesel vehicles," *Environmental Science & Technology*, vol. 34, no. 5, pp. 729–740, 2000.

[2] A. X. R. Corrêa, S. Cotelle, M. Millet, C. A. Somensi, T. M. Wagner, and C. M. Radetski, "Genotoxity assessment of particulate matter emitted from heavy-duty diesel-powered vehicles using the *in vivo Vicia faba* L. micronucleus test," *Ecotoxicology & Environmental Safety*, vol. 127, pp. 199–204, 2016.

[3] H. Yamada, R. Hayashi, and K. Tonokura, "Simultaneous measurements of on-road/in-vehicle nanoparticles and NOx while driving: actual situations, passenger exposure and secondary formations," *Science of the Total Environment*, vol. 563-564, pp. 944–955, 2016.

[4] Z. C. Liu, K. B. Yu, J. Tian, Y. Q. Han, S. L. Qi, and P. K. Teng, "Influence of rail pressure on a two-stage turbocharged heavy-duty diesel engine under transient operation," *International Journal of Automotive Technology*, vol. 18, no. 1, pp. 19–29, 2017.

[5] I. Rynning, V. M. Arlt, K. Vrbova et al., "Bulky DNA adducts, microRNA profiles, and lipid biomarkers in Norwegian tunnel finishing workers occupationally exposed to diesel exhaust," *Occupational & Environmental Medicine*, vol. 76, no. 1, pp. 10–16, 2019.

[6] D. Sonntag and J. Gretz, "Planetary gears for heavy-duty operation," *Tunnel*, vol. 38, no. 1, pp. 38–43, 2019.

[7] M. Sorgenfrei and G. Tsatsaronis, "Detailed exergetic evaluation of heavy-duty gas turbine systems running on natural gas and syngas," *Energy Conversion and Management*, vol. 107, pp. 43–51, 2016.

[8] P. Mendoza-Villafuerte, R. Suarez-Bertoa, B. Giechaskiel et al., "NO_x, NH_3, N_2O and PN real driving emissions from a Euro VI heavy- duty vehicle. Impact of regulatory on-road test conditions on emissions," *Science of the Total Environment*, vol. 609, pp. 546–555, 2017.

[9] D. C. Quiros, J. Smith, A. Thiruvengadam, T. Huai, and S. Hu, "Greenhouse gas emissions from heavy-duty natural gas, hybrid, and conventional diesel on-road trucks during freight transport," *Atmospheric Environment*, vol. 168, pp. 36–45, 2017.

[10] D. C. Quiros, A. Thiruvengadam, S. Pradhan et al., "Real-world emissions from modern heavy-duty diesel, natural gas, and hybrid diesel trucks operating along major California freight corridors," *Emission Control Science & Technology*, vol. 2, no. 3, article 44, pp. 156–172, 2016.

[11] A. Walker, "Future challenges and incoming solutions in emission control for heavy duty diesel vehicles," *Topics in Catalysis*, vol. 59, no. 8-9, pp. 695–707, 2016.

[12] C. Huang, S. Tao, S. Lou et al., "Evaluation of emission factors for light-duty gasoline vehicles based on chassis dynamometer and tunnel studies in Shanghai, China," *Atmospheric Environment*, vol. 169, pp. 193–203, 2017.

[13] W. Hilsdorf, C. A. De Mattos, and C. De, "Principles of sustainability and practices in the heavy-duty vehicle industry: a study of multiple cases," *Journal of Cleaner Production*, vol. 141, pp. 1231–1239, 2017.

[14] C. Song, C. Ma, Y. Zhang et al., "Heavy-duty diesel vehicles dominate vehicle emissions in a tunnel study in northern China," *Science of the Total Environment*, vol. 637-638, pp. 431–442, 2018.

[15] K. Huang, S. Duan, S. Zhen, R. Xu, and Y. Xue, "Modeling and analyses of heavy-duty truck dynamics based on system constraints," *Zhongguo Jixie Gongcheng/China Mechanical Engineering*, vol. 28, no. 4, pp. 478–485, 2017.

[16] C. V. Preble, T. E. Cados, R. A. Harley, and T. W. Kirchstetter, "In-use performance and durability of particle filters on heavy-duty diesel trucks," *Environmental Science & Technology*, vol. 52, no. 20, pp. 11913–11921, 2018.

[17] C. Ruehl, J. D. Smith, Y. Ma et al., "Emissions during and real-world frequency of heavy-duty diesel particulate filter regeneration," *Environmental Science & Technology*, vol. 52, no. 10, pp. 5868–5874, 2018.

[18] D. Zhang, K. Wang, W. Zhai, and P. Liu, "Effect of unsupported sleepers on the wheel/rail dynamic interaction on heavy-haul railway lines," *Journal of Vibration and Shock*, vol. 36, no. 18, pp. 1–7, 2017.

[19] J. Zhang, J. Hua, Z. Sun, M. Yin, Y. Jiang, and Y. Gui, "Shield tunneling in large size cobble and boulder strata: rock-breaking mechanism and engineering application," *China Civil Engineering Journal*, vol. 50, no. 2, pp. 88–96, 2017.

[20] A. Wilson, "Oscillating devices for airway clearance in people with cystic fibrosis: a Cochrane review summary," *International Journal of Nursing Studies*, vol. 88, no. 32, pp. 165-166, 2018.

[21] I. Jorgensen, Y. Zhang, B. A. Krantz, and E. A. Miao, "Pyroptosis triggers pore-induced intracellular traps (PITs) that capture bacteria and lead to their clearance by efferocytosis," *Journal of Experimental Medicine*, vol. 213, no. 10, pp. 2113–2128, 2016.

[22] Z. Jie and W. Qi, "Modeling and simulation of a frictional translational joint with a flexible slider and clearance," *Multibody System Dynamics*, vol. 38, no. 4, pp. 367–389, 2016.

[23] C. Gao, Z. Lin, B. Jurado-Sánchez, X. Lin, Z. Wu, and Q. He, "Stem cell membrane-coated nanogels for highly efficient in vivo tumor targeted drug delivery," *Small*, vol. 12, no. 30, pp. 4056–4062, 2016.

[24] L. Craggs, J. Taylor, J. Y. Slade et al., "Clusterin/apolipoprotein J immunoreactivity is associated with white matter damage in cerebral small vessel diseases," *Neuropathology and Applied Neurobiology*, vol. 42, no. 2, pp. 194–209, 2016.

[25] P. C. Lee, M. Kamel, A. Nasar et al., "Lobectomy for non-small cell lung cancer by video-assisted thoracic surgery: effects of cumulative institutional experience on adequacy of lymphadenectomy," *The Annals of Thoracic Surgery*, vol. 101, no. 3, pp. 1116–1122, 2016.

[26] Y. Zhao, C. Bai, C. Xu, and L. K. Foong, "Efficient metaheuristic-retrofitted techniques for concrete slump simulation," *Smart Structures and Systems*, vol. 27, no. 5, pp. 745–759, 2021.

[27] Y. Zhang, W. Ni, and Y. Li, "Effect of siliconizing temperature on microstructure and phase constitution of $Mo\text{-}MoSi_2$ functionally graded materials," *Ceramics International*, vol. 44, no. 10, pp. 11166–11171, 2018.

[28] Z. Dingcheng, M. Xie, M. Hamadache, M. Entezami, and E. Stewart, "An adaptive graph Morlet wavelet transform for railway wayside acoustic detection116965," *Journal of Sound and Vibration*, vol. 529, 2022.

Hindawi

Retraction

Retracted: Health Screening and Promotion System Based on Disease Prevention

Journal of Nanomaterials

This article has been retracted by Hindawi following an investigation undertaken by the publisher [1]. This investigation has uncovered evidence of one or more of the following indicators of systematic manipulation of the publication process:

(1) Discrepancies in scope

(2) Discrepancies in the description of the research reported

(3) Discrepancies between the availability of data and the research described

(4) Inappropriate citations

(5) Incoherent, meaningless and/or irrelevant content included in the article

(6) Peer-review manipulation

The presence of these indicators undermines our confidence in the integrity of the article's content and we cannot, therefore, vouch for its reliability. Please note that this notice is intended solely to alert readers that the content of this article is unreliable. We have not investigated whether authors were aware of or involved in the systematic manipulation of the publication process.

In addition, our investigation has also shown that one or more of the following human-subject reporting requirements has not been met in this article: ethical approval by an Institutional Review Board (IRB) committee or equivalent, patient/participant consent to participate, and/or agreement to publish patient/participant details (where relevant).

Wiley and Hindawi regrets that the usual quality checks did not identify these issues before publication and have since put additional measures in place to safeguard research integrity.

We wish to credit our own Research Integrity and Research Publishing teams and anonymous and named external researchers and research integrity experts for contributing to this investigation.

The corresponding author, as the representative of all authors, has been given the opportunity to register their agreement or disagreement to this retraction. We have kept a record of any response received.

References

[1] F. Zheng, J. Zheng, M. Han, Y. Wei, and L. Shi, "Health Screening and Promotion System Based on Disease Prevention," *Journal of Nanomaterials*, vol. 2022, Article ID 4540935, 13 pages, 2022.

Research Article

Health Screening and Promotion System Based on Disease Prevention

Fangjiang Zheng,[1] Jie Zheng,[2] Mingxia Han,[3] Yanqiang Wei,[4] and Lili Shi [5]

[1]*Publicity Department, Gansu Provincial Hospital of Traditional Chinese Medicine, Lanzhou, 730050 Gansu, China*
[2]*Department of Nursing, The Third People's Hospital of Gansu Province, Lanzhou, 730050 Gansu, China*
[3]*Children's Rehabilitation Department, Gansu Province Hospital Rehabilitation Center, Lanzhou, 730000 Gansu, China*
[4]*Key Laboratory of Remote Sensing of Gansu Province, Northwest Institute of Eco-Environment and Resources, Chinese Academy of Sciences, Lanzhou 730000, China*
[5]*Public Health and Nosocomial Infection Management Division, Gansu Provincial Hospital of Traditional Chinese Medicine, Lanzhou, 730050 Gansu, China*

Correspondence should be addressed to Lili Shi; 18409158@masu.edu.cn

With the rapid development of modern medical technology, more and more clinicians use computerized medical images as the main diagnostic basis. At the same time, the generation of massive medical image information promotes the development of medical image management. Aiming at the above two problems, a medical image reporting system based on physical examination is designed and implemented, in which the medical image reporting system is an independent and complete system including login, registration, appointment, triage and doctor workstation (inquiry, report editing, and report printing), and other modules. Using the methods of literature review, expert interview, case analysis, and rational analysis, combined with nanotechnology research, this paper takes urban population health as the starting point and health promotion as the background. As the basis of systematic comparison, the theory, position, and function of health promotion are discussed in detail. Among them, Chinese Center for Disease Control and Prevention, World Health Organization, and Subscriber Data Center are the collection sites for the literature data mentioned in this article. With the construction of healthy towns and the development of social movements, the establishment of healthy sports to improve health promotion system aims to help sports play an important role in promoting healthy development. The results show that the average scores of step test for boys and girls in the test are 72.97 and 68.77, respectively, while the average scores of distance running in the national physique monitoring are 66 and 63. Therefore, in the newly established scoring standard, the step test scores of boys with 66 points are 72, while those of girls with 66 points are 68.

1. Introduction

Health promotion is a global strategy initiated by the World Health Organization (WHO), aiming at solving major challenges related to human health due to the speed of action. Using health promotion in urban planning is about creating a healthy city. The concept of health promotion aims to raise public awareness, encourage citizens to cooperate with local governments and social organizations, and create a series of effective health and environmental support, services, and interventions that affect human health, so as to achieve the purpose of health promotion. Urbanization is the general trend of the development of modern human society and the objective and inevitable result of the development of social productive forces. In the 2015 edition of the World Population Situation Report, it is estimated that in 2015, the urban population of the world will reach 54.4%, and that of developed countries will reach 81.6%. Today, when building a well-off society in an all-round way, China has entered a period of rapid urbanization, and it is estimated that the

level of urbanization will reach 50% in 2010. Rapid urbanization has brought about a series of changes. On the one hand, with the rapid development of urban construction, especially industrial towns, it is faced with overcrowding, homelessness, water shortage, and food insecurity, as well as many social, health, environmental, and other problems. Social problems such as environmental pollution are more and more important problems affecting human health. On the other hand, in the era of urban development, with the emergence of modern science and technology, the working and living conditions of urban residents have undergone earth-shaking changes. The intensification of social competition, the quickening pace of life, the improvement of intelligence, and the reduction of physical labor, the low grain output, and food shortage make people more vulnerable.

In view of the severe challenges brought by the urbanization process to human health, in order to ensure the sustainable development of cities and embody the concept of "people-oriented" urban development, the World Health Organization recommends that people in cities live a healthy life on a global scale. At present, many cities are building health promotion systems to build a healthy and harmonious affluent society, while the economy is growing rapidly. According to the concept of the World Health Organization, the importance of a healthy city means "ensuring the development of healthy life and work" to serve the broad masses of the people. To become an organic combination of healthy people, healthy environment, and society necessary for development, it must be suitable for the healthy development, growth, and enjoyment of human life.

Traditionally, health check-ups are usually done manually. Heavy business, insufficient statistics, poor management, and many other shortcomings are the result of human activities or complete lack of goal setting. Because of the extensive use of computer technology in disease management, the use of environment becomes more and more difficult for health promotion management. In the past, medical records and medical certificates were all paper, and many other medical records contained the results of medical examinations. This kind of storage system takes up a lot of space, and data is easy to be decomposed and lost. Importantly, it is difficult for Chinese Center for Disease Control and Prevention (CDC) to make statistical analysis and make effective use of medical information. The results of statistical analysis provide information for CDC's decision-making. Due to the rich experience in management follow-up and management and the rapid development and progress of network and computer technology, the use of advanced network and computer technology in medical care has become the inevitable status quo of the development of physical research methods. Using computer software for medical research can save a lot of people and property. It is necessary to know the authenticity of medical records, functional test results, other diagnostic criteria, and medical evidence of professionals, as well as the principles, information, and conditions of managing physical examination. The document is being worked out and will continue to study the medical information physical examination work. It is meaningful to build this part of Subscriber Data Center (SDC) knowledge.

2. Related Work

In the related fields of nanotechnology and health promotion, experts at home and abroad also have many research achievements. Mihail et al. discussed the progress of nanotechnology development since 2000, the achievements in the past ten years, and the global opportunities in research, education, innovation, and social achievements by 2020 [1]. Reis and Damgé thought that only through nanoparticles or biochips can nanoparticle-mediated materials be delivered to plants and advanced biosensors for precision agriculture [2]. The research of Falagan-Lotsch et al. introduced a new method of breast cancer nanodrugs based on active targeting. This method uses a multifunctional inorganic nanoplatform with biomedical relevance [3]. The research goal of Lee et al. was to provide a comprehensive overview of oil-water separation by nanotechnology and organic chemistry and to raise awareness of the environmental problems of water purification by nanotechnology [4]. Lisa et al. thought that although the side effects of medical interventions are well known and widely investigated, the possible unexpected effects of health promotion interventions are rarely discussed in the research [5]. These systems studied by Hors-Fraile et al. can be used to create tailor-made health interventions, thus reducing the cost of health care and fostering a healthier lifestyle among people [6]. However, due to the incomplete data of nanoanalysis, there are some controversies about the methods used in these studies, resulting in the related results not being recognized by the public.

3. Nanotechnology-Based Medical Examination Reporting System

This topic is a series of medical examination management system software developed based on Microsoft data. The software needs to be implemented in several stages, from registration to medical certificate issuance, changing the way of completing some work ahead of schedule, improving work efficiency, and simplifying workflow and product distribution [7]. Through large-scale data analysis, extensive analysis, and investigation, it is easy to generate reports such as quality statistics, turn data into useful information in decision-making, and provide faster decision-making suggestions for decision makers [8].

Individual nanoparticles such as nanotubes and nanorods have only one direction of electron motion left in it. Individual nanoparticles include nanoparticles, nanotubes, nanorods, and nanoviruses. Two-dimensional nanomaterials and three-dimensional nanoparticles are represented by nanoparticles, nanostructures, nanoceramics, and nanobodies. Nanocomposites are the most widely used materials today. From the point of view of morphology and structure analysis, nanoscale materials with one or more dimensions are called nanoparticles [9]. When nanoparticles are reduced
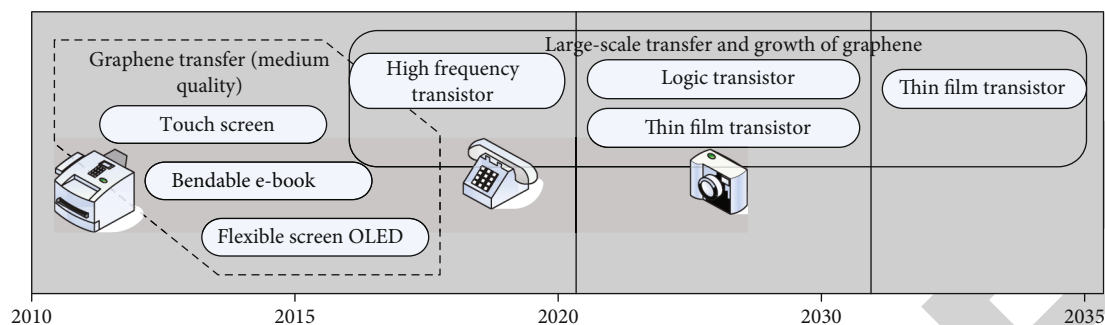
FIGURE 1: Timing diagram of graphene application in displays and electronics.
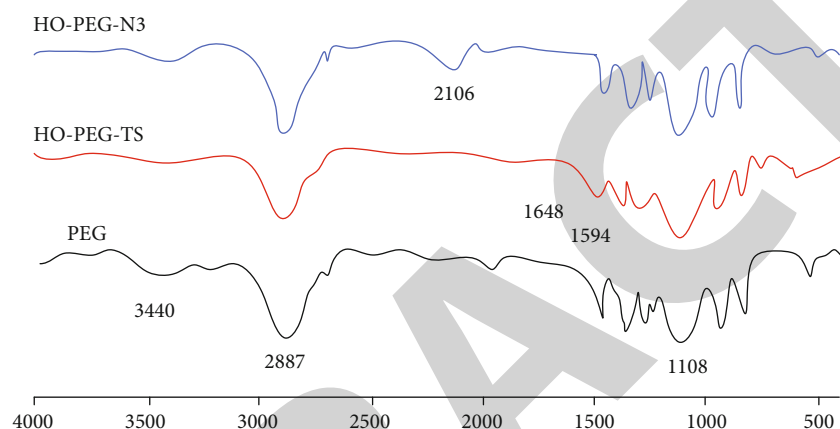
FIGURE 2: FT-IR spectra of PEG, HO-PEG-OTs, and HO-PEG-N3.

to the atomic or molecular level, materials show many specific effects, such as topological effect, dielectric reduction, large size, small size, and macroscopic quantum tunneling effect. Among the core materials, nanoparticles exhibit special physical and chemical properties such as optics, electricity, magnetism, mechanics, and heat. Different from the conventional properties in nanobelts and chemical converters, it can open the energy gap of graphene and increase the transmission current management ratio. Graphene is expected to be used in more industries in the near future [10]. Figure 1 shows the application schedule of graphene in displays and electronic devices.

In this paper, the change of PEG structure was detected and characterized by FT-IR spectra. The analysis of PEG, HO-PEG-OTs, and HO-PEG-N3 in this paper can help to understand the structure and display process of medical imaging system. Figure 2 shows the FT-IR spectra of PEG, HO-PEG-OTs, and HO-PEG-N3, respectively. Among them, 3440 cm-1, 2887 cm-1, and 1108 cm-1 are the O-H telescopic vibration absorption peaks of PEG, C-H telescopic vibration absorption peaks of methylene, and C-O telescopic vibration absorption peaks, respectively [11, 12]. In contrast, the FT-IR spectrum of HO-PEG-Ts not only has the characteristic absorption peak of PEG but also has two characteristic peaks of benzene ring skeleton vibration at 1648 cm-1 and 1594 cm-1. At the same time, the absorption peak of O-H stretching vibration at 3440 cm-1 obviously weakened, which indicated that the hydroxyl group at one end of

PEG successfully reacted with p-toluenesulfonyl chloride to form p-toluenesulfonate. In the FT-IR spectrum of HO-PEG-N3, two peaks at 1648 cm-1 and 1594 cm-1 disappeared, but the characteristic absorption peak of azide group appeared at 2106 cm-1. It shows that the tosyl group of HO-PEG-Ts is replaced by azide group [13].

The amino group at the end of DSPE reacts with PEG modified by chloroformate to obtain DSPE-PEG conjugate. Its characterization was mainly carried out by FT-IR and nuclear magnetic resonance. Infrared contrast is shown in Figure 3. In the infrared spectrum of DSPE-PEG, the characteristic peaks of DSPE (2887 cm-1 and 2851 cm-1) and PEG (1111 cm-1) appeared. Therefore, we can judge that DSPE-PEG long-acting phospholipid was successfully synthesized, and its nuclear magnetic resonance further proved the structure of the compound. Among them, the peak at the chemical shift of 0.86 ppm is the methyl peak of DSPE, 1.23 ppm is the methylene peak of DSPE alkyl chain, and 3.51 ppm is the characteristic peak of polyethylene glycol.

Up to now, micronanomaterials can be derived from fiber structures such as ceramics and polymers, spherical structures, and tubular structures. However, the most common product of electrospinning is fiber structures. At present, there are two shortcomings in electrospinning technology: most fibers are nonwoven fabrics. The voltage required for the electrospinning process is very high. To expand the application of fiber in microelectronic devices, people have invented and developed many methods,
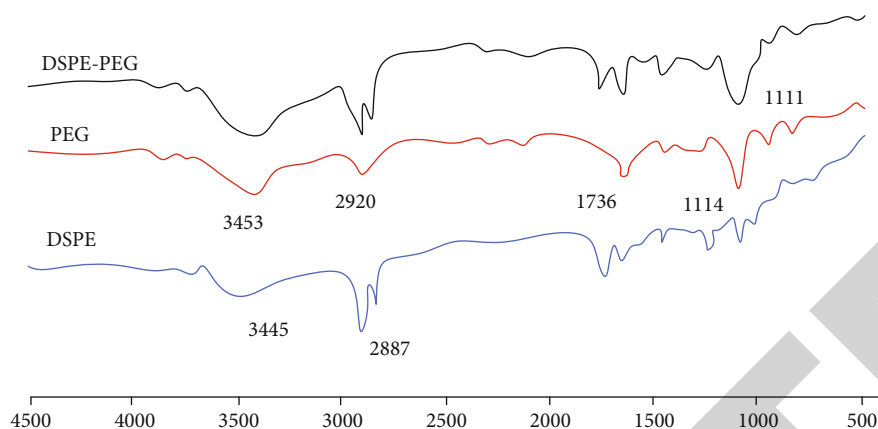
FIGURE 3: FT-IR spectra of PEG, DSPE, and DSPE-PEG.
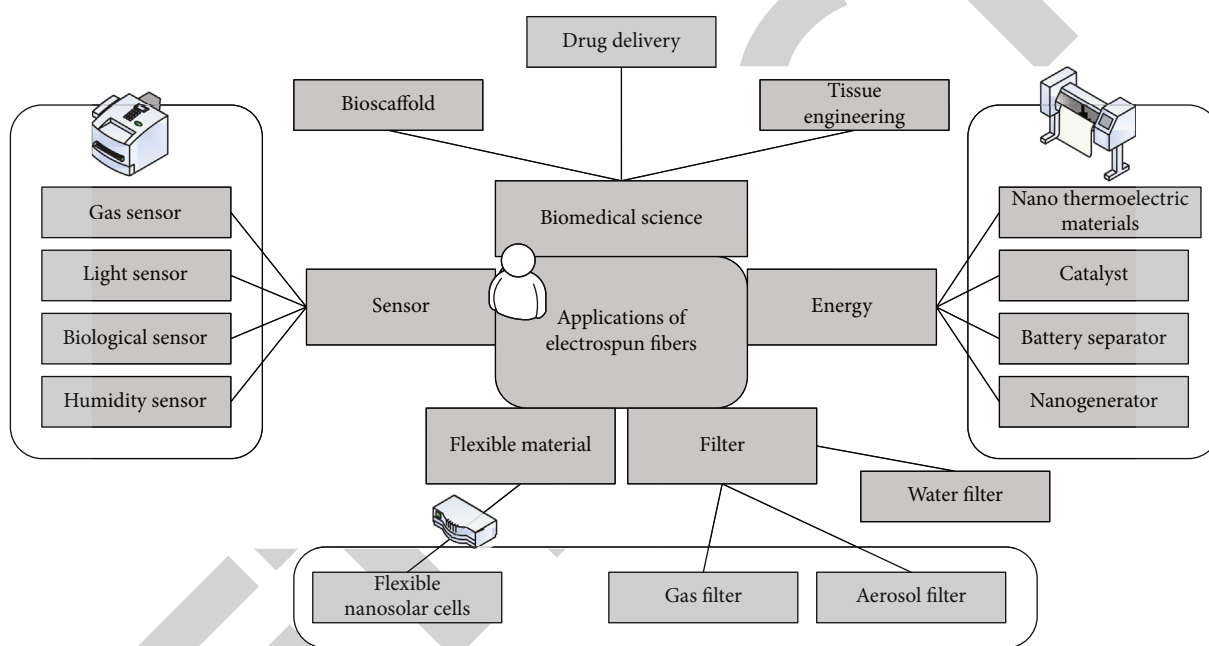
FIGURE 4: Various application areas for electrospun fibers.

including parallel double-electrode collection method and magnetic field electrospinning, to prepare micronanofibers [14]. By controlling the above experimental parameters, fibers with different morphologies such as coaxial structure, beaded structure, porous structure, red blood cell structure, ribbon structure, patterned fiber structure, spider web structure, and array structure can also be obtained [15]. Nonwoven fabric fiber is the most common fiber morphology. Electrospun fibers play an important role in the fields of sensors, filtering devices, tissue scaffolds, implant coating films, and wound dressings. As shown in Figure 4, there are many application fields of electrospun fibers [16].

Up to now, there are many methods to prepare nanomaterials, such as vacuum condensation method, ball milling method, chemical vapor deposition method, hydrothermal method, sol-gel method, spraying magnetron method, nanoprinting method, electrostatic spinning method, and template method. Sequential or random nanostructures can be

obtained by these methods. These electrothermal technologies can produce long-sized nanofibers with uniform diameters and different compositions. Fibers can be organic or inorganic [17, 18]. The method has the characteristics of simple operation process and wide application. According to the physical state of nanomaterials, it can be divided into gas phase method, liquid phase method, and solid phase method. In recent years, hydrothermal method, magnetron spraying method, chemical vapor deposition method, and electric drying method have been adopted. Nanotechnology has attracted much attention because of its simple tools, low cost, high efficiency, and convenience. With the progress of science and technology, people have a deeper understanding of nanomaterials, and the application of nanomaterials in people's lives is also more extensive [19].

In today's society, which has stepped into the post-Moore era, devices are gradually developing towards the fields of multifunction, miniaturization, and flexible

wearable. As a representative, ZnO (ZnO) is a semiconductor material of group II-IV direct band gap compounds. It can be used as a display interface module for medical imaging systems. It is an ideal material for developing ultraviolet detectors, blue-ultraviolet light emitting devices, and blue laser. In addition, compared with Si, GaAs, and InP, ZnO has higher breakdown electric field, thermal conductivity, electron saturation rate, and radiation resistance due to its unique wide bandgap structure [20]. It is ZnO that has these excellent properties at the same time, which has aroused extensive research by researchers. ZnO fiber has special crystal structure, wide band gap, high breakdown electric field, high thermal conductivity, high electron saturation rate, high radiation resistance, and so on and has many excellent properties, which can emit blue-violet light. As a typical representative of the third generation semiconductor, ZnO has a very wide application prospect. For example, it can be used in blue LED, photodetector, flexible nanosolar cell, nanopiezoelectric material, ZnO arrester, and tester and can also be used to prepare ZnO carriers. In addition, it can also be used to make facial masks. Figure 5 shows the application picture of ZnO [21].

However, these methods can only prepare ZnO thin films and short nanowires, which greatly limits the preparation of ZnO-based devices. Compared with other technologies, electrospinning technology has its unique advantages. For example, the device is simple, the cost is low, the applicable materials are wide, the modification is strong, the fiber morphology is diverse, and the specific surface area is large. In addition, it can prepare ultrathin fibers and long continuous fibers. Ce-ZnO prepared by electrospinning is spun. Long filiform ones have the advantages of large specific surface area, especially suitable for sensing applications and so on. In the literature on the properties and applications of electrostatically woven nanofibers, the application of electrospinning ZnO nanofibers is also very extensive, among which the representative applications are shown in Table 1.

PVDF has five different crystal phases, of which β phase has the best piezoelectric properties. In the process of electrospinning, the parameters such as voltage, polymer solution pushing speed, and boiling point of solvent are closely related to the formation of β phase PVDF. In order to study the influence of PVDF nanofiber membranes on the output performance of devices, it prepared a series of PVDF nanofiber membranes with different parameters and assembled them into devices for performance testing. Table 2 summarizes the parameters of these different samples. The definitions and dimensions of ZnO and PVDF are explained in the texts of Tables 1 and 2, and the display modules in the subsequent system architecture design are better constructed. Among these parameters, it changed the voltage and spinning time of electrospinning, and other constant parameters can be seen in the experimental part. When the spinning voltage is 12 KV, the α phase peak at 18.4° and 26.7° shifts to the β phase peak at 20.6°, showing an obvious broad peak at 20.1. This shows the transformation of PVDF from α phase to β phase during spinning. The output voltage results also show that when the voltage is 12 KV, the output
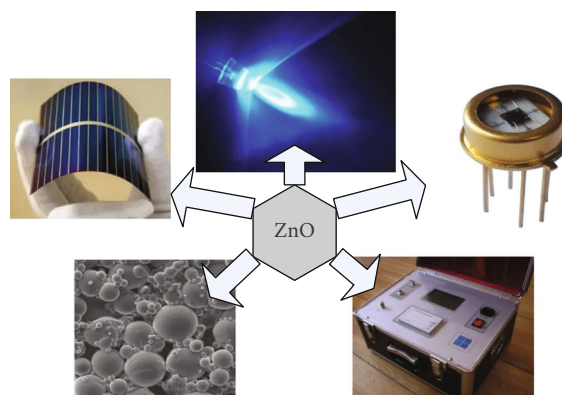
FIGURE 5: Application picture of ZnO.

value is the largest. In addition, the film thickness is also an important parameter that affects its output performance. As we know, for friction nanogenerators, the smaller the film thickness, the better the device output performance, while for piezoelectric devices, the increase of film thickness in a certain range is beneficial to the device output performance. Therefore, it is very important to find an optimal film thickness for PVDF film used as both friction material and piezoelectric material. PVDF nanofiber membranes with different thicknesses were prepared by controlling the spinning time. The thickness of PVDF film increases with the extension of spinning time. When the PVDF thickness is 145.3 μm, the maximum output voltage of 98 V is obtained. Therefore, the best preparation conditions are as follows: spinning voltage 12 KV and spinning time 2 h.

Figure 6 shows the XRD patterns of the prepared pure ZnO and cerium-doped ZnO nanofibers, which reflect the crystalline characteristics of pure ZnO and cerium-doped ZnO nanofibers. The clear diffraction pattern has higher peak position and narrower half-peak width, which indicates that pure ZnO and cerium doped ZnO have good crystallinity. XRD spectrum shows that pure ZnO nanofibers have hexagonal wurtzite structure (observed by JCPDS36-1451); the 2θ values of the strong diffraction peaks are 31.77°, 34.42°, and 36.26°, respectively; and the corresponding diffraction planes are (100), (002), and (101), respectively. Compared with pure ZnO, the diffraction peak of CeO2 (JCPDS34-0394) appears at the crystal plane (111) of 2θ = 28.55° after cerium doping. Moreover, by comparing the XRD profiles of pure ZnO and cerium-doped ZnO, it can be seen that the peak position of cerium-doped ZnO has a small angle (~0.31degree) shift. The radius of cerium atom is larger than that of zinc atom, which will make the crystal lattice of ZnO larger. According to Bragg formula, the lattice parameters are related to the interplanar spacing d. With the increase of atomic radius, the diffraction peak shifts to a small angle. It shows that cerium ions are successfully doped into the crystal lattice of ZnO. XRD results show that the synthesized nanofibers are the mixed phase of hexagonal ZnO and cubic cerium oxide. In XRD pattern, except Ce element, there are no other peaks. Therefore, the prepared sample is a combination of high-purity hexagonal ZnO and cubic ceria.

TABLE 1: Diameters, properties, and applications of electrospun ZnO-based nanofibers.

Material	Fiber diameter/nm	Performance	Application
Cu-ZnO	100	HRP2 protein detection limit is 10 μg/ml	Biological sensor
ZnSe/ZnO	200	Short circuit current density 6.60 mA/cm^2. Maximum power conversion efficiency of 1.24%	Solar battery
ZnO/CNFs-PA	150	At a current density of 200 mAg-1, the capacity is 702 mAhg-1	Lithium ion battery
CuO-ZnO	312 183	The maximum adsorption capacity of Congo red dye is 126.4 mg/g	Shows significant antibacterial activity against Staphylococcus aureus
ZnO/PVA	200	Detection limit for NO2 is 10 ppm	Sensor
PVDF-HFP/Co-ZnO	300	Maximum output voltage 2.8 V	Nanogenerator
ZnO/Al2O3/AuNPs	200	Detection limits of 0.19 μM and 15.0 μM for tea phenol and hydroquinone, respectively	New sensor (detection of tea phenol and hydroquinone)
TMCNF/ZnO	200	Ultrafast cycling stability (452 mA hg−1 after 500 cycles)	Lithium ion battery
PA6/PPy/ZnO	80	Urea detection limit is 0.011 mg DL−1	Biological sensor
ZnO/PU	250	Improve photocatalytic efficiency	Organic pollutant degradation and wastewater purification

TABLE 2: Dimensions of PVDF nanofibers electrospun with different process parameters.

Sample	Applied voltage (KV)	Applied time (h)	Diameters of nanofibers (nm)	Thickness of the film (μm)
1	10	1	180	68
2	12	1	160	68
3	14	1	152	68
4	16	1	122	68
5	18	1	123	68
6	12	0.5	160	37
7	12	1.5	160	97
8	12	2	160	145
9	12	3	160	189

Although the physical conditions of different materials are different, the thermal conduction modes are different due to different compounds. There are also significant differences in thermal conductivity. However, in different states of matter, one thing is similar, that is, heat in matter is transferred by collision and particles. The thermal conductivity κ of all solids can be directly expressed as the thermal conductivity of atomic gas as a thermal conductor, namely,

$$K = \frac{1}{3} Cv\Lambda. \tag{1}$$

Among them, C represents thermal conductivity of the solid per unit volume. V represents the average velocity of hot carrier movement per unit volume. Λ represents the mean free path of hot carrier movement per unit volume.

$$f = \frac{1}{e^{hwIk} - 1}, \tag{2}$$

$$U = \sum_{i=1}^{3N} \frac{hw}{e^{hwIK_BT} - 1}. \tag{3}$$

Assuming that the number of vibration modes of the crystal with a given polarization mode is $D(\omega)d\omega$ in the frequency range of $\omega + d\omega$, the formula can be changed into integral form:

$$U = \int \frac{hw}{e^{hwIk_BT} - 1} D(w)dw, \tag{4}$$

$$C = \frac{dU}{dT} = \frac{3Vh^2}{2\pi^2 v^3 k_B T^2} \int_0^{wD} \frac{w^4 e^{hw/r}}{(e^{hw/r} - 1)^2} dw. \tag{5}$$

The relaxation time of phonon scattering is a function $\tau(\omega)$ related to phonon frequency. According to the empirical formula of scattering probability of inverse scattering between phonons, impurity scattering, and boundary scattering, the relaxation time of inverse scattering can be obtained as follows:

$$\tau_{umkl}^{-1} = B_1 w^2 T \exp\left(\frac{-B_2}{T}\right), \tag{6}$$

$$\tau_{imp}^{-1} = A_1 w^4, \tag{7}$$
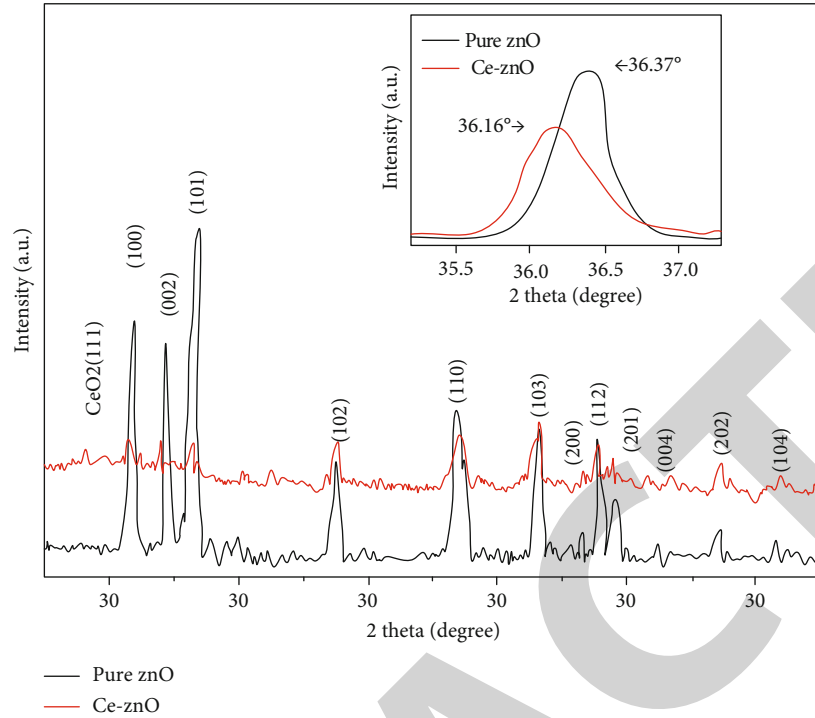
FIGURE 6: XRD patterns of pure ZnO and Ce-ZnO nanofibers, the inset is an enlarged view of the (101) diffraction plane.

$$\tau_{bdy}^{-1} = \frac{v_g}{L}, \tag{8}$$

$$\tau_{tol}^{-1}(w, T, L) = \tau_{umkl}^{-1}(w, T) + \tau_{imp}^{-1}(w) + \tau_{bdy}^{-1}(L), \tag{9}$$

$$\Lambda_{eff}^{-1}(w, T, L) = \Lambda_{umkl}^{-1}(w, T) + \Lambda_{imp}^{-1}(w) + \Lambda_{bdy}^{-1}(L). \tag{10}$$

The longitudinal acoustic lattice wave (LA) and the transverse acoustic lattice wave (TA) are not distinguished, and the thermal conductivity of germanium at low temperature is well predicted. Callaway model considers isotope impurity scattering, inverse scattering, normal scattering, and boundary scattering, respectively; and the expression of relaxation time is

$$\tau_C^{-1} = \tau_I^{-1} + \tau_U^{-1} + \tau_N^{-1} + \tau_b^{-1}, \tag{11}$$

$$Aw^4 + B_U T^3 w^2 + B_N T^3 w^2 + \frac{c}{L}, \tag{12}$$

$$Aw^4 + (B_U + B_N) T^3 w^2 + \frac{c}{L}. \tag{13}$$

Holland model is an extension of Callaway model. Different relaxation time approximations are adopted, so that the calculated results can accord with the experimental results at high temperature. The formula for calculating the thermal conductivity of Holland mode is

$$K_H = K_L + K_T, \tag{14}$$

$$KL = \frac{1}{3} \int_0^{\theta r/T} \frac{C_L T^3 x^4 e^x (e^x - 1) dx}{\tau_L^{-1}}, \tag{15}$$

$$KT = \frac{2}{3} \int_0^{\theta r/T} \frac{C_L T^3 x^4 e^x (e^x - 1)^{-2} dx}{\tau_L^{-1}}. \tag{16}$$

This indicates the contribution of the two transverse acoustic lattice waves TA to the thermal conductivity. When Holland model calculates the relaxation time, the thermal conductivity of LA is integrated in the whole frequency range:

$$\tau_L^{-1} = \frac{v_b}{FL + Aw^4 + B_L w^2 T^3}, \tag{17}$$

$$\tau_T^{-1} = \frac{v_b}{FL + Aw^4 + B_T w T^4 (w < w_1)}, \tag{18}$$

$$\tau_T^{-1} = \frac{v_b}{FL} + Aw^4 + B_T w T^4 + \frac{B_{TU} w^2}{\sinh x(w1 < w < w2)}. \tag{19}$$

The SW potential of silicon contains a two-body potential term and a three-body potential term, and the specific expression is

$$u_3(r_i, r_j, r_k) = \varepsilon \lfloor h(r_{ij}, r_{ik}, \theta_{jik}) + h(r_{ji}, r_{jk}, \theta_{jik}) + h(r_{ki}, r_{kj}, \theta_{ikj}) \rfloor. \tag{20}$$

It can be seen from the above that such formulas related to thermal conductivity can help the construction of the LCD display interface in the health promotion system.

TABLE 3: Segmentation results of the segmentation model.

Soccer-men	Number of people	Soccer-women	Number of people	Yoga-male	Number of people	Yoga-female	Number of people
Cluster 1	66	Cluster 1	31	Cluster 1	24	Cluster 1	52
Cluster 2	29	Cluster 2	19	Cluster 2	17	Cluster 2	38
Cluster 3	20	Cluster 3	15	Cluster 3	15	Cluster 3	23
Cluster 4	11	Cluster 4	12	Cluster 4	10	Cluster 4	15
						Cluster 5	10
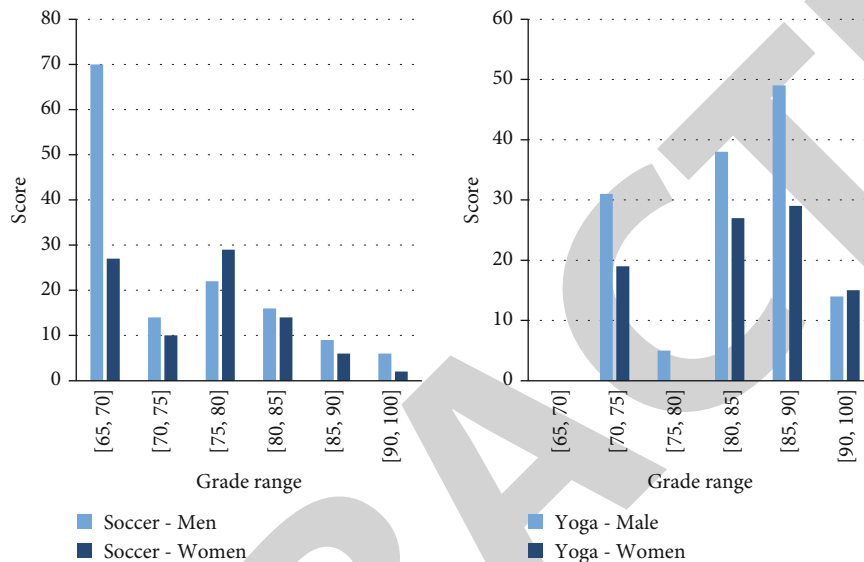
FIGURE 7: Number distribution of grade predictions.

4. Health Promotion System Experiment

Two common items, football and yoga, were selected in the experiment. Through nanotechnology, health promotion and health examination decision-making are studied. The former focuses on the quality of endurance and strength, while the latter focuses on the quality of practicing soft keys. The subjects were 137 males and 90 females. The hypothesis of this study is that students with higher endurance and strength qualities are more likely to get high scores in football matches, while students with flexible choice qualities are more likely to get good results in yoga activities. The main purpose of the experiment in this section is to establish the performance prediction model of health promotion and predict the results of these two items for the theme experiment to verify the accuracy of the hypothesis. It randomly selects the historical data of 136 men and 77 women in a football project and 66 men and 138 women in a yoga project to build the performance prediction models of the two projects. Through correlation analysis, it is found that the test indexes with higher correlation coefficient with football performance are step test and long standing jump. The test index with higher performance correlation coefficient of yoga is forward flexion, which is consistent with the results of the questionnaire. When building the partition model, the four data sets are divided into 4, 4, 4, and 5 subsets, respectively. To verify the health promotion model, Table 3 shows the division of the subdivision model.

On this basis, a performance prediction model is established for each subset of men's soccer, women's soccer, yoga men, and yoga women. The physical fitness data of these students have been used to verify the model. Of the four data sets, only one, two, and three made accurate predictions, with the accuracy rates of 99.2, 95.5, and 97.8%, respectively. The physical health data of 37 males and 90 females were included in the prediction model with the same degree to predict the performance of each student in health promotion activities. The results are shown in Figure 7. Therefore, the result of achievement prediction is consistent with the level of students' physical quality.

From the comparison of events, the expected performance of yoga events is higher than that of football events, because students' soft back quality is better than endurance and strength quality. From the comparison of men and women, the performance of women's football is better than that of men's football. Although men are usually less flexible than women, their yoga performance is not inferior to that of women. The reason may be that the gender orientation in football and yoga is obvious. Teachers will take care of disadvantaged gender groups and give them higher scores. This has a certain influence on the results of the health promotion system under nanotechnology. The results of data standardization are shown in Figure 8 and Table 4.

There are 1, 2, 3, and 4 categories. In terms of male or female, the degree of similarity is similar to normal distribution. The more equal the classification of boys, the greater
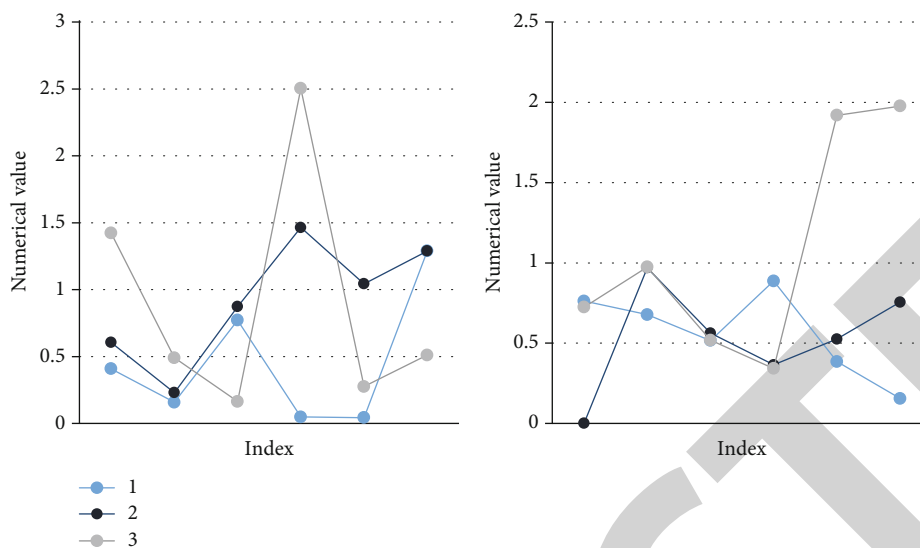
Figure 8: Sample data normalization.

Table 4: Effects of nanosystems on health promotion.

	Z height	Z weight	Z lung capacity	Z balance ability	Z body composition	Z cardiovascular
Male						
1	0.81401	0.85614	0.12564	0.36451	1.31456	0.53122
2	1.61914	1.03153	0.25612	0.24561	0.08312	0.23641
3	0.40257	0.95212	0.23152	1.13212	0.42312	1.05641
4	1.21362	0.22314	2.32212	1.61251	0.64652	0.51312
5	2.63296	0.22315	0.38515	0.16965	1.06315	2.84165
6	1.82162	2.54512	0.56123	0.05561	3.31322	0.51233
7	0.00214	0.95451	1.75123	0.26341	0.75612	0.26452
Female						
1	0.13564	0.45612	0.54522	0.39231	0.56123	0.75562
2	1.34561	0.15532	0.72131	1.00324	0.59221	0.75562
3	1.36123	0.28512	1.12356	0.15633	0.35121	1.65612
4	0.75132	2.35612	0.43221	0.34551	2.61521	0.75612
5	0.35641	0.69122	0.00656	0.67512	0.27512	0.75612
6	0.94512	1.24562	1.54233	0.54512	0.68963	0.75612
7	0.75212	1.23136	0.86312	0.34752	1.30312	1.95612

the difference between girls. The figure clearly shows the number of each type and the difference between the sexes. This is important because the classification and analysis of the variable table can be used to evaluate whether the type is reasonable. After the differential function is detected, the formula $Xi = (X1i, X2i, X3i, X4i, X5i, X6)$ is normalized. To obtain the required difference, it is necessary to compare it with the value of Y and classify the scores according to the rules. In this study, boys are used as case studies. According to the boys of four classes, five data sets of 20 people were selected, and the first data was normalized (Figure 9).

Then discriminate and predict the data (as shown in Figure 10).

First of all, according to the different data units of the training samples, this paper is dedimensioning, that is, stan-

dardization. Then, SPSS software is used to quickly cluster the standardized data. Finally, Fisher linear discriminant function is obtained, and the classification model is constructed. In Figures 9 and 10, the probability of dividing men and women is 99.3% and 99.2%, respectively, which indicates that the distribution model has a high probability of distribution results. Finally, according to the existing samples' 1, 2, 3, and 4 categories, this cycle is obtained, and a total of 20 model cycles are tested by the difference program. The correct rate was 99.5%. As long as the six types of information and their corresponding numerical values are standardized and modeled, the model can be inspected. Moreover, the six indicators proposed in this study have not been combined with the research. Samples measure the internal characteristics of the human body. Based on the
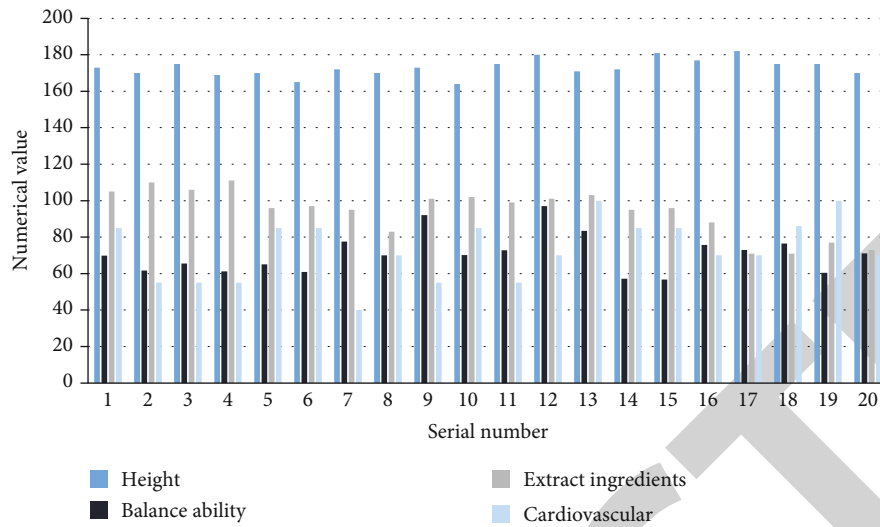
Figure 9: Standardization of sample data to be tested.
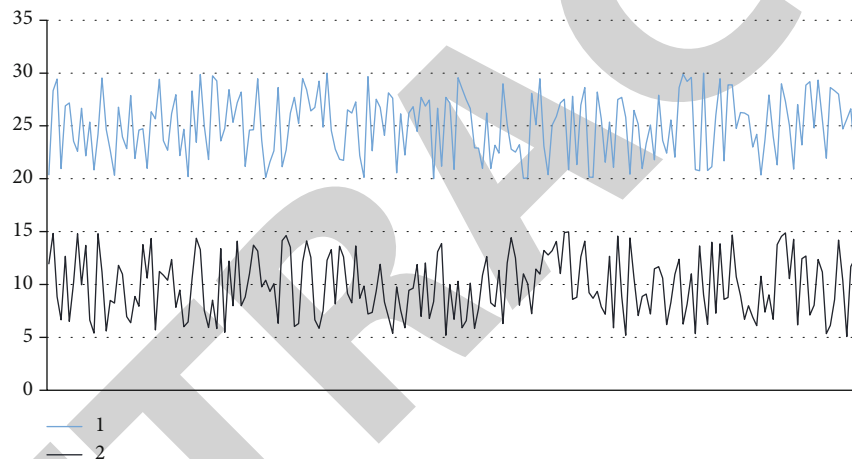
Figure 10: Sample prediction results.

intelligent health promotion service system, the corresponding index data of human body can be measured by simple instrument operation. It not only simplifies the process of obtaining test data but also reduces human error, which provides important scientific and technological support for studying physical health. Through the above data analysis, it can know that the physical health of boys is evenly distributed, which accords with normal distribution, while that of girls is unevenly distributed, showing a trend of two-level differentiation. As the social rhythm continues to accelerate, the pressure on students becomes more and more. For a long time, it has formed bad living habits, such as excessive intake of fat and calories. In addition, the structure of food is not very reasonable, and there is a lack of adequate physical exercise, which leads to physical deterioration, great influence on physical health and polarization. This needs attention. Therefore, it must pay more attention to the problems of physical health and adopt practical and feasible countermeasures to further improve the physical health in the actual process. This model can be used to comprehen-

sively evaluate the physical health of individuals and groups. In the process of applying this model, it is only necessary to standardize all kinds of index values actually measured by each individual into the corresponding model for calculation, so that the physical health level of an individual or a group can be obtained. The establishment of the grading model avoids the score according to each item in the standard. It then uses the weight to calculate the total score in this complicated process. To some extent, this simplifies the operation procedures, achieves the goal of simplicity, and then makes the evaluation results very clear and effective.

5. Discussion

Through the analysis of the model of the article, the article constructs the health promotion system from the aspects of physical quality, skills, and shape; tests the physical health data; realizes real-time analysis; and gives warnings. The early warning mechanism accurately provides health

information and is supplemented by early warning statement. This kind of early warning statement is predictive, and if individuals are allowed to develop continuously, physical health may be damaged. According to the warning statement, targeted prevention and exercise can effectively avoid this kind of future harm. The health examination management system introduced in this paper is based on the actual application requirements of the physical examination institute of the Center for Disease Control and Prevention. It is developed by Delphi and SQL server 2000. Through the comprehensive application of data analysis, data encryption, software reuse and other technologies, and information maintenance, it perfectly shows the modular design idea, and at the same time, it integrates the management mode of modern CDC physical examination center into it. The system has the characteristics of strong practicability, good real-time, high work efficiency, and easy data maintenance, which has brought higher economic benefits and good social reflection to the physical examination of center for disease control.

This paper designs the input module and physical examination and perspective module. The result is automatically judged. Single-particle imaging and single-particle spectroscopy based on the optical properties of metal nanoparticles, with nanoscale spatial resolution and millisecond temporal resolution, have become important tools for studying the behavior and function of biomolecules at the single-cell level. It uses bar code to scan and input the whole process, which simplifies unnecessary time in work. It provides users with a variety of flexible access methods. Customized human search object function, powerful demand function, and statistical analysis function help users easily understand daily tasks and problems and calculate relevant information. Data from the health screening system have been analyzed and evaluated by nanotechnology and medical promotion verification data, providing detailed data of disease prevention. The advantages of this system include developing a suitable C/S search engine, which is convenient and fast to use, improving the efficiency, improving the running speed of SDC, and realizing the verification data to test the physical form. It improves the speed and efficiency of data retrieval, the sorting of selection and record results, the sorting of people and laboratories, and the combination of physical screening software and verification tools to ensure that data will not be lost. It simplifies the workflow of SDC, improves performance, and provides detailed information during data analysis. Due to the limitation of resources, time, hardware, or other conditions and the standardization of medical information disclosure, there is no integration between the standardization of CDC management model and the standardization of information system model, and the system still has a lot of room for development. Even if there is relatively complete physical examination data, more detailed data mining research is needed. The system design should also fully consider the future upgrade and expansion of the system to promote the integration of the existing system and the proposed system. This system only realizes the interface with some inspection instruments, and it needs to reserve interfaces for other system equipment.

In view of vital capacity and cardiovascular index, according to relevant research, the vital capacity and maximum oxygen uptake of human body are closely related to body weight, height, body surface area, chest circumference, and sitting height. Therefore, according to different gender, age, race, region, and different types of sports groups or individuals, comparing and analyzing this index of vital capacity, and carrying out quantitative analysis on it, it can objectively reflect the differences among different individuals and carry out evaluation. Body mass index, the individual's fatness, and thinness directly affect the level of physical health. One of the criteria to measure the individual's weight is the height and body mass index (BMI). According to the BMI value, it can know the fat and thin level of individual figure. Therefore, the new early warning indicators in this paper still retain the height and weight indicators, body composition, and balance index. Body composition includes internal indexes related to physical health level, such as bone density and muscle. It can reflect the existing level of each index inside the body of the tested person and the ability of balance and coordination. Balance ability is to analyze the individual balance ability through the completion result of a given action. If the two indexes of body composition and balance ability are too low, early warning is needed so as to exercise pertinently and improve the physical health level.

6. Conclusion

Health promotion is the process of improving the health status of different groups of people. It improves people's lifestyle by means of sports intervention. It promotes the formation of healthy sports knowledge, improves the sports environment, and improves the quality of life. Health promotion system is a service and safety system that can provide sports health services for people, improve sports health, promote environmental conditions, meet the scientific needs of human health, and improve people's quality of life and health level. The goal system of sports promotion is to form healthy sports knowledge, including the formation of sports positive attitude, sports true values, and emotional sports positive experience. Sports lifestyle includes reasonable sports lifestyle, colorful sports activities, and sports content. The formation of a healthy sports environment includes the development of sports facilities, the formation of a strong institutional network, the formation of a good sports atmosphere, and other components. Health promotion action system includes raising residents' awareness of sports, encouraging residents to improve sports, shaping sports lifestyle, and improving sports environment. The safety system of sports promotion includes organizational guarantee, talent guarantee, fund guarantee, and facility guarantee. This is the guarantee for the smooth operation of the sports health promotion operation system and the realization of the sports health promotion purpose. Community organization network is an organization and operation organization that cooperates with sports health promotion association, individual community sports association, and community sports associations led by various committees

to promote community health. This paper basically realizes the medical image transmission and storage system based on ultrasonic equipment. However, there are still some problems in this system due to various reasons such as short development time and insufficient manpower. Therefore, in order to become a mature and stable system and put it into hospital use, it should continue to improve the problems existing in the system. The following aspects need to be completed. The encryption algorithm involved in the system only refers to the method of regular expression matching when the user logs in. Therefore, there are not many encryption algorithms used in the system, which leads to the low security performance of the system. Therefore, the following work needs to study the knowledge related to software encryption. The encryption algorithm is used in the programming that the system needs to be encrypted to improve the security of the system to prevent malicious damage by illegal personnel. The system needs to generate standard DICOM files for the transmission and storage of medical images, such as images collected by video acquisition card, patient basic information, examination information, and diagnosis information. The analysis and format conversions of DICOM files are involved when the patient history examination needs to consult DICOM files. In order to realize the above two aspects, this paper uses the executable file in DCMKT. However, the files in DCMKT are not flexible enough to realize the system functions accurately. Therefore, in the following work, it is necessary to reduce the reference to the executable files in DCMTK and fully grasp the DICOM protocol. Using c++ programming language to develop DICOM can accurately realize the functions required by the system. The actual use of the hospital needs to be integrated with the hospital information system, health examination information management system, and other information systems. Due to the lack of actual installation test in the hospital, this system has poor compatibility and can only be used as an independent system. Therefore, in the following work, according to the HIS system and health examination information management system of the hospital, the data interface between medical image reporting system and HIS system and health examination information management system is designed and implemented, so that the medical image reporting system can exchange data with HIS system and health examination information management system.

Data Availability

No data were used to support this study.

Conflicts of Interest

The authors declare that there are no conflicts of interest regarding the publication of this article.

Authors' Contributions

Fangjiang Zheng and Jie Zheng are co-first author.

References

[1] M. C. Roco, C. A. Mirkin, M. C. Hersam, and C. S. Alrokayan, "Nanotechnology research directions for societal needs in 2020," *Journal of Nanoparticle Research*, vol. 13, no. 3, pp. 897–919, 2011.

[2] C. P. Reis and C. Damgé, "Nanotechnology as a promising strategy for alternative routes of insulin delivery," *Methods in Enzymology*, vol. 508, pp. 271–294, 2017.

[3] P. Falagan-Lotsch, E. M. Grzincic, and C. J. Murphy, "New advances in nanotechnology-based diagnosis and therapeutics for breast cancer: an assessment of active-targeting inorganic nanoplatforms," *Bioconjugate Chemistry*, vol. 28, no. 1, pp. 135–152, 2017.

[4] C. H. Lee, B. Tiwari, D. Zhang, and Y. K. Yap, "Water purification: oil–water separation by nanotechnology and environmental concerns," *Environmental Science Nano*, vol. 4, no. 3, pp. 514–525, 2017.

[5] L. Gugglberger, E. Flaschberger, and F. Teutsch, "Side effects of health promotion: an example from Austrian schools," *Health Promotion International*, vol. 32, pp. 157–166, 2017.

[6] S. Hors-Fraile, O. Rivera-Romero, F. Schneider et al., "Analyzing recommender systems for health promotion using a multidisciplinary taxonomy: a scoping review," *International Journal of Medical Informatics*, vol. 114, pp. 143–155, 2018.

[7] E. Deng, W. Kang, and Y. Zhang, "Design optimization and analysis of multicontext STT-MTJ/CMOS logic circuits," *IEEE Transactions on Nanotechnology*, vol. 14, no. 1, pp. 169–177, 2015.

[8] C. A. Mirkin, T. J. Meade, and S. H. Petrosko, "Nanotechnology-based precision tools for the detection and treatment of cancer," *Anticancer Research*, vol. 35, no. 10, pp. 481–501, 2017.

[9] Y. Weng, J. Liu, S. Jin, W. Guo, X. Liang, and Z. Hu, "Nanotechnology-based strategies for treatment of ocular disease," *Acta Pharmaceutica Sinica B*, vol. 7, no. 3, pp. 281–291, 2017.

[10] M. Natan and E. Banin, "From nano to micro: using nanotechnology to combat microorganisms and their multidrug resistance," *FEMS Microbiology Reviews*, vol. 41, no. 3, pp. 302–322, 2017.

[11] G. Song, L. Cheng, and Y. Chao, "Emerging nanotechnology and advanced materials for cancer radiation therapy," *Advanced Materials*, vol. 29, no. 32, article 1700996, 2017.

[12] M. Bathe and P. Rothemund, "DNA nanotechnology: a foundation for programmable nanoscale materials," *MRS Bulletin*, vol. 42, no. 12, pp. 882–888, 2017.

[13] Y. F. Dufrêne, T. Ando, R. Garcia et al., "Imaging modes of atomic force microscopy for application in molecular and cell biology," *Nature Nanotechnology*, vol. 12, no. 4, pp. 295–307, 2017.

[14] D. Mcmanus, S. Vranic, and F. Withers, "Water-based and biocompatible 2D crystal inks for all-inkjet-printed heterostructures," *Nature Nanotechnology*, vol. 12, no. 4, pp. 343–350, 2017.

[15] R. Okada, K. Suzuki, and Y. Ito, "Profiles of advanced hepatic fibrosis evaluated by FIB-4 index and shear wave elastography in health checkup examinees," *Renal Failure*, vol. 29, no. 8, pp. 967–972, 2007.

[16] K. Nawata, Y. Sekizawa, and M. Kimura, "Evaluation of blood pressure control medicines using health and medical checkup

Research Article

Structure Optimization of Carbon Nanotubes Based on Swarm Intelligence Algorithm and Evolutionary Computation

Defei Liu [ID]

Center for Studies of Education and Psychology of Ethnic Minorities in Southwest, Southwest University, Beibei, 400715 Chongqing, China

Correspondence should be addressed to Defei Liu; swldf@mau.edu.mk

Swarm intelligence algorithm is an emerging evolutionary computing technology, which has become the focus of more and more researchers. It has a very special connection with artificial life, especially evolutionary strategies and genetic algorithms. The swarm intelligence algorithms you see include genetic algorithm, particle swarm optimization algorithm, and ant colony algorithm. This part of the content has been supplemented in the article. Evolutionary computing is a group-oriented random search technology and method produced by simulating the evolutionary process of organisms in nature. Evolutionary computing is based on natural selection strategy: survival of the fittest, elimination of the unfit, and individuals with large fitness values have a higher survival probability than individuals with small fitness values. The purpose of this paper is to study the structure optimization of carbon nanotubes based on swarm intelligence algorithm and evolutionary computation. It is expected to optimize the structure of carbon nanotube materials with the help of intelligent evolution algorithm, so that it can be used in more fields. In this paper, the preparation process and principle of carbon nanotube-based gas sensors are studied, and the preparation process of the side-heated gas sensor is selected. This paper focuses on the strain sensing performance of carbon nanotubes, analyzes various parameters that characterize the sensing performance, and proposes feasible technical routes for improvement, optimization and improvement. The experimental results in this paper show that when different proportions of oxides are added, the tensile strength of carbon nanotube materials is increased by about 8%, and the elastic modulus is increased by up to 40%. After adding CNFs, the tensile strength increased by up to 18%, and the elastic modulus increased by up to 50%.

1. Introduction

With the continuous advancement of science and technology, polymer materials are more and more widely used in daily life, and with the high requirements for the performance of polymer materials, this problem was not solved until the emergence of nanopolymers. Polymer materials are materials based on polymer compounds, materials composed of compounds with relatively high molecular weight, including rubber, plastics, fibers, and polymer-based composite materials. Polymers are the form of life. In fact, every advance of human society is closely related to the development of new materials. In the 21st century, with the continuous development of science and technology, the understanding of human beings is constantly expanding, and the exploration of nanomaterials has promoted the development of human beings in a deeper direction. Since the end of World War II, optimization computing has been widely introduced and used in the scientific community. Since optimization algorithms already have the advantage of effectively dealing with complex problems that are difficult to solve by traditional methods, these algorithms and designs are sought after as soon as they are published. The optimization algorithm can use the mathematical modeling method to convert the actual problem into an optimization problem and convert the optimization problem into a standard optimization model. It has a simple structure and flexible calculation and can solve many complex problems.

How to combine the swarm intelligence algorithm with evolutionary computing and carbon nanotube structure optimization is the problem to be explored in this paper.

With the increase of function dimension, traditional optimization methods cannot solve complex function optimization problems well. The evolutionary algorithm that simulates the biological evolution process can get a set of solutions in one run. This main advantage is introduced into the optimization problem, which effectively solves many complex optimization problems. The swarm intelligence optimization algorithm has good heuristics, parallelism, and distribution and can solve complex function optimization problems well, save resources, and improve efficiency.

Based on the work of genetic operator impact analysis, this paper proposes GPs based on edit distance 1 and 2 population diversity control, respectively. The influence of genetic operators in GP on the population and its diversity is analyzed and compared, and the correlation between population diversity and individual fitness is explored.

2. Related Work

With the development of the times, more and more people conduct research on optimization calculation. Bhattacharjee and Sarmah attempt algorithmic advantage to solve combinatorial problems. In the improved version of CSA, the local randomized wandering repair operator is used. And in the improved version of FA, variable distance shifts for local search are applied. The firefly algorithm is proposed by simulating the natural phenomenon of firefly swarming activities in nature at night. In the swarming activities of fireflies, each firefly communicates with its companions for food and courtship by emitting fluorescein. The efficiency of the proposed algorithm is demonstrated through experiments using a large number of benchmark problem examples [1]. Ntouni et al. proposed a robust iterative optimization algorithm based on standard particle swarm optimization (PSO) techniques called acceleration-assisted PSO (A-APSO). He implemented the A-APSO algorithm to evaluate the detector weights. The results show that the error performance is better than the weight values evaluated by the PSO algorithm when A-APSO weights are used [2]. Gao et al. proposed a protein structure prediction method. He used three different structural evolution methods, including an improved particle swarm optimization (PSO) algorithm, random perturbation, and fragment replacement, to update the protein structure while keeping the secondary structure unchanged. The high success rate and the accuracy of the results demonstrate the reliability of the method [3]. Zhong et al. proposed to extend the multidimensional similarity space region with group similarity and firstly used the optimal value of the iterative clustering function as the clustering quality index. In addition, he also proposed the fuzzy high-order hybrid clustering (F-HOHC-SIS) algorithm, which can effectively control the convergence speed and reduce the computation time, while improving the anti-interference capability [4]. In cloud environments, various meta-heuristics can be used to solve scheduling problems that fall under the NP-complete problem. Two of the funda-

mental goals of computer science are to discover algorithms that can be shown to perform well and yield optimal or suboptimal solutions. Heuristics, on the other hand, try to provide one or all goals at a time. Tabaghchi proposes task scheduling algorithms to reduce the idle time of virtual machines while achieving load balancing and reducing the running time. According to the results obtained, he reduced the manufacturing time and energy consumption using the proposed algorithm [5]. Son et al. proposed an optimization method to design radar absorbing structures made of fiber-reinforced plastic structures. In the optimized design, the objective function is set to maximize the absorption bandwidth of the X-band stealth. The results confirmed that using the S-FSM not only the electromagnetic performance of the samples could be detected but also the defects caused by the manufacturing process [6]. Ahmadi et al. describe the optimization of parameters involved in the production of nanofibers. Single-walled carbon nanotubes were used to improve the mechanical properties. The results show that the concentration has a greater effect on the fiber diameter than other parameters in PAN and PAN/CNT nanofibers. However, excessive CNTs have a negative effect on elongation and modulus due to the aggregation of CNTs within the nanofibers. The results showed that the PAN nanofibers have an amorphous structure compared to the conventional PAN nanofibers [7]. Lu et al. proposed carbon nanotube bucky paper as a sensing layer in composite materials. Bucky paper is a special kind of carbon nanotube thin layer, which looks very similar to ordinary carbon fiber paper. People also call it "Bucky paper." It is made of only one-fifty thousandth of a human hair, made of molecular weight. The experimental results show that the resistance temperature coefficient of the bucky paper is related to the curing behavior of the resin, and a critical value of the resistance temperature coefficient is determined. In addition, by monitoring and optimizing the curing parameters, the properties of the composites can indeed be improved [8]. Although these theories have analyzed the optimization calculation and carbon nanotube structure to a certain extent, the combination of the two is insufficient and not practical.

3. Swarm Intelligence Algorithm and Evolutionary Computation for Carbon Nanotube Structure Optimization Methods

3.1. Overview of Carbon Nanotubes. Since the 1990s, carbon nanotubes have been paid attention to by scientists. Unlike other materials, carbon nanotubes have two different structures, so carbon nanotubes have many applications in many fields. Carbon nanotubes have two structures, single-walled carbon nanotubes, and multiwalled carbon nanotubes. Single-walled carbon nanotubes can be regarded as hollow cylinders made of a layer of graphite curled, while multiwalled carbon nanotubes are composed of a group of coaxial graphene. In the development of carbon nanometers, its electrical properties have received extensive attention [9, 10]. Nanomaterials are materials with nanoscale structures, which can be divided into zero-dimensional

nanomaterials and one-dimensional nanomaterials according to their specific dimensions. It has been asserted that when people can arrange and combine substances on a very small scale, they will obtain various novel materials [11, 12]. The change in properties caused by the ratio of the number of atoms on the surface of the particle to the total number of atoms increases sharply as the particle size decreases. For example, when the particle diameter is 10 nm, the particle contains 4000 atoms, and the surface atoms account for 40%; when the particle diameter is 1 nm, the particle contains 30 atoms, and the surface atoms account for 99%. Nanomaterials have attracted attention as a potential dielectric material, and most of the current research on this material focuses on the effect of nanoceramic doping on the dielectric properties of ceramics [13]. The electronic properties of metallic carbon nanotubes are not sensitive to the chemical environment, but its electrical conductivity is very superior. It can be used as a wire, and its electrical conductivity far exceeds that of copper, while the internal electronic properties of semiconducting carbon nanotubes are affected by the environment and other substances. In the traditional manufacturing process, the oxide surface is usually coated on the ceramic surface by chemical means. This method can reduce the loss and increase the energy storage density, but since the oxide is a nonferroelectric, the ferroelectric properties of the ceramic itself will interfere [14, 15]. In order to meet the use of nanomaterials in defense and communication, we usually incorporate dopants into the original materials to modify their defects. This method has a good effect and has been widely used in the storage field. In use, it is found that when the doping substances reach a certain limit, the dielectric and ferroelectric properties of ceramics will exhibit relaxation ferroelectric phenomena [16, 17]. The application of nanoceramic materials in capacitors requires a stable dielectric temperature. This is achieved by adding rare earth elements. This method can inhibit the growth of crystal grains and can also obtain dense and fine powders. Figure 1 is an image of nanopowders. This material can be fired into high-density ceramics [18, 19].

Until the end of the last century, the first International Conference on Nanoscience and Technology was held in the United States, which formally combined theoretical research with contemporary science and technology, marking the official birth of nanotechnology [20]. When the size of the material is at the nanometer level, the number of atoms on the surface of the material will increase dramatically, which will far exceed the number of ordinary materials, and the chemical activity of the material will be greatly increased at this time. At the same time, nanomaterials are equal to or smaller than the wavelength of light wave, de Broglie wavelength, and coherence length of superconducting state, and the periodic boundary of the material is destroyed, resulting in "novel" optical, electrical, magnetic, acoustic, and thermodynamic properties. In addition, nanomaterials also have quantum size effects and macroscopic quantum tunneling effects. These unique characteristics provide conditions for the wide-scale application of nanomaterials. With the continuous and in-depth development of theory and practice, nanostructures that are not called sys-

tems have been established. With the maturity of application, the uniqueness of nanomaterials plays a pivotal role in the fields of biotechnology and advanced manufacturing. Figure 2 is a schematic diagram of common nanomaterials.

3.2. Overview of Optimization Calculations. With the continuous development of the production economy, the scale of computation involved is increasing, especially in the fields of management and engineering. With the continuous development of computer technology, and in order to reduce the complexity of the calculation, the optimization calculation came into being. In essence, optimization refers to the use of certain rules to meet the needs of users.

Evolutionary computing is a stochastic optimization method that simulates the genetic mechanism of the animal kingdom. It has the idea of "survival of the fittest." Therefore, when using evolutionary thinking to solve target optimization problems, genetic operations and natural selection become its important components. Evolutionary algorithms iteratively generate multiple solutions to each problem during the optimization process and continue to generate better solutions. The optimization function is called the fitness function. Each solution is called an individual, and all individuals in each generation form a group. The fitness value of individuals in each group is different. With iteration, better individuals are obtained through certain evolutionary strategies, such as crossover and mutation. When the algorithm terminates, the individual with the best fitness value in the entire population is selected as the solution to the problem. Figure 3 shows the basic structure of the optimization calculation.

Evolutionary algorithm is a random search method. Compared with other enumeration techniques and heuristic search techniques, the global optimal solution probability of this problem is higher. The evaluation information of the objective function is used to make it actionable and general. It is concise in form, can be operated with massively parallel computers, and can be easily combined with other methods. At present, evolutionary computing mainly includes genetic algorithm, evolutionary strategy, and evolutionary planning. Genetic algorithm refers to the population of solution sets, and the population is composed of several individuals encoded by genes. In essence, genetic algorithm is an optimization algorithm, which is a random search algorithm that uses the idea of natural selection and biological evolution to search for the optimal solution in the search space.

$$\min \{g(a)|a \in Q\}. \tag{1}$$

Formula (1) represents the function expression of the function optimization model, where a represents the decision variable, $g(a)$ represents the objective function, and Q represents the spatial subset.

$$\min g(a).\text{st} * p(a) \geq 0. \tag{2}$$

Formula (2) represents the decision variable inequality.

$$Q = \{a \in W^s | p(a) \geq 0\}. \tag{3}$$
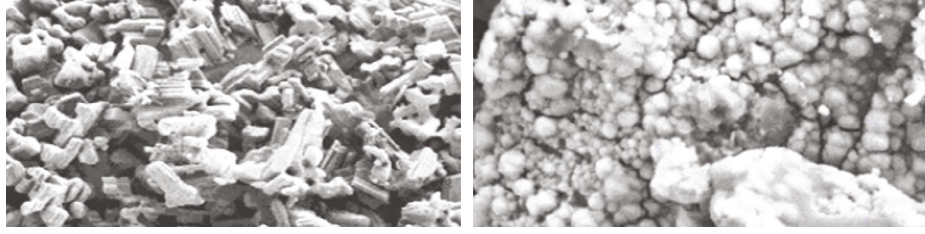
Figure 1: Nanopowder image.
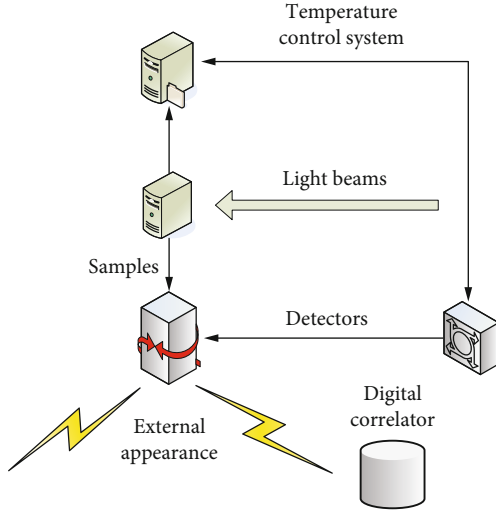
Figure 2: Common nanomaterial quiz structure.

Formula (3) represents the feasible region of the decision solution, which is the set of all solutions in layman's terms.

In order to get the optimal solution for the region, we need to optimize the model.

$$\forall a \in QI \left\{ a \in W^s \middle| \sqrt{\sum (a_1 - a*)^2} < a \right\}. \tag{4}$$

When formula (4) is satisfied $g(a*) \leq g(a)$, we say that the model has an optimal solution. Figure 4 shows the basic flow structure of the algorithm.

$$\beta = \frac{T_{\max} - T_{\min}}{2^p - 1}. \tag{5}$$

Formula (5) represents the precision of binary encoding, among them, T represents the range of values, and p represents the length of the encoded symbol.

$$k = T_{\min} + \left(\sum_{o=1}^{p} w_o * 2^{o-2} \right) * \frac{T_{\max} - T_{\min}}{2^p - 1}. \tag{6}$$

Formula (6) represents the decoding function expression when the encoded length is k.

$$\begin{cases} f_p = w_p, \\ f_p = w_{p+1} \oplus w_p, \end{cases} \tag{7}$$

$$\begin{cases} w_p = f_p, \\ w_p = w_{p+1} \oplus f_p. \end{cases} \tag{8}$$

Formulas (7) and (8) represent binary codes under different Gray codes.

In the genetic algorithm, we usually use the fitness function to judge the situation of the individual. The fitness function satisfies the generality, so the calculation steps can be reduced in the actual use process.

$$\text{Fitness}(g(a)) = g(a). \tag{9}$$

Formula (9) represents the functional expression of the maximal optimization problem.

$$\text{Fitness}(g(a)) = -g(a). \tag{10}$$

Formula (10) represents the functional expression for the minimal optimization problem.

Computers have been developing and progressing continuously since their appearance in 1946 and have been fully used in various fields of social production. Although the development is very rapid, the production needs of human beings are also expanding, and the traditional computing performance cannot meet the current development needs, so high-performance computing came into being. With the ever-increasing demand for computing power, high-performance computing is also evolving. The current research directions of high-performance computing include cluster computing, network computing, cloud computing, and FPGA-based reconfigurable heterogeneous computing [21]. The initial high-performance computing focused on the computing field, but with the continuous improvement of high-performance computing, high-performance computing has basically become an essential means of research, and high-performance computing can be seen in various fields. From computers, minicomputers to mainframes, the development and replacement of computers are fast, but they still cannot meet the needs of computing. Scientific computing, network computing, terminal computing, cloud computing, supercomputing, intelligent computing, GPU computing
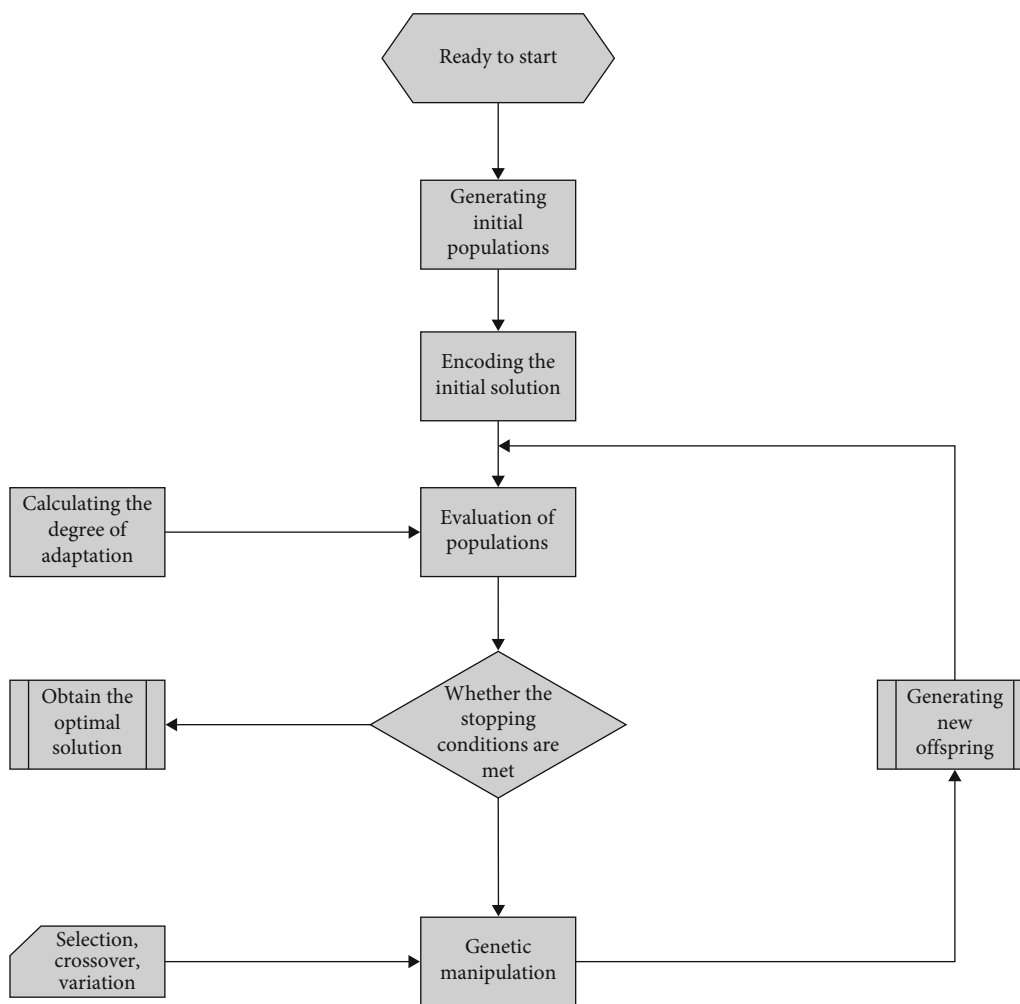
FIGURE 3: Basic framework of genetic algorithm.
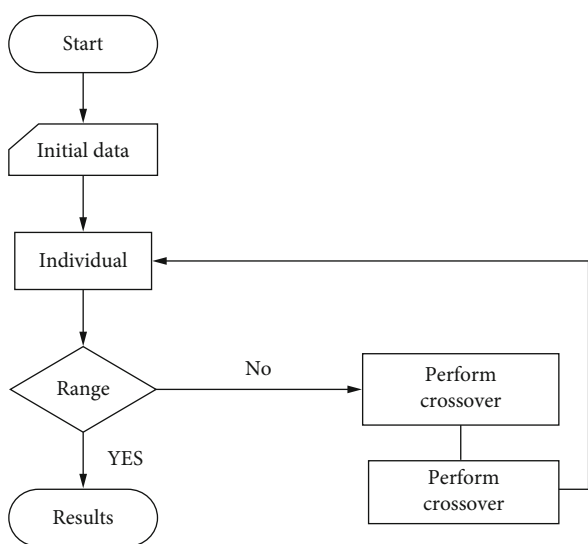
FIGURE 4: Model algorithm flow demonstration

and other computing modes, concepts, technologies, and applications dominate the progress and development of science and technology. Quantum computing, brain-like computing, borderless computing, human-machine-object ternary fusion computing, data-intensive computing, etc. have brought computing into the era of diversity. Although high performance computing has many advantages, the issues affecting the development of high performance computing are power consumption, energy efficiency ratio, energy saving, ecological environment and industrialization, performance and scalability, reliability and fault tolerance, application efficiency and applicability, efficient management, and low threshold operation [22, 23].

Figure 5 is a schematic diagram of a high-performance scientific computing cluster architecture.

China's research on high-performance computing is relatively late, and the pace of research has been officially started since the advent of China's first shared storage multiprocessor system. The Dawning 400A, developed in 2004, has entered the top ten in the world in computing power. In 2017, the world's first optical quantum computer that surpassed the early classical computers was born. The successful
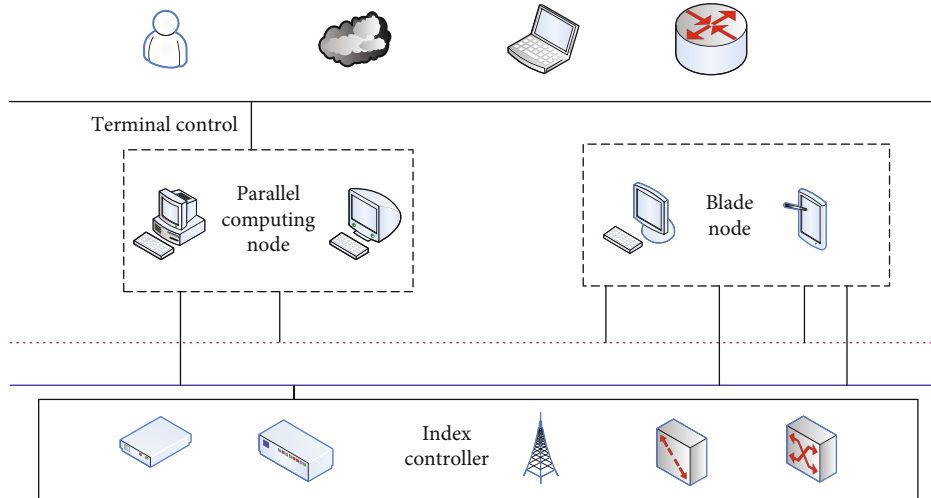
FIGURE 5: High-performance scientific computing cluster architecture.
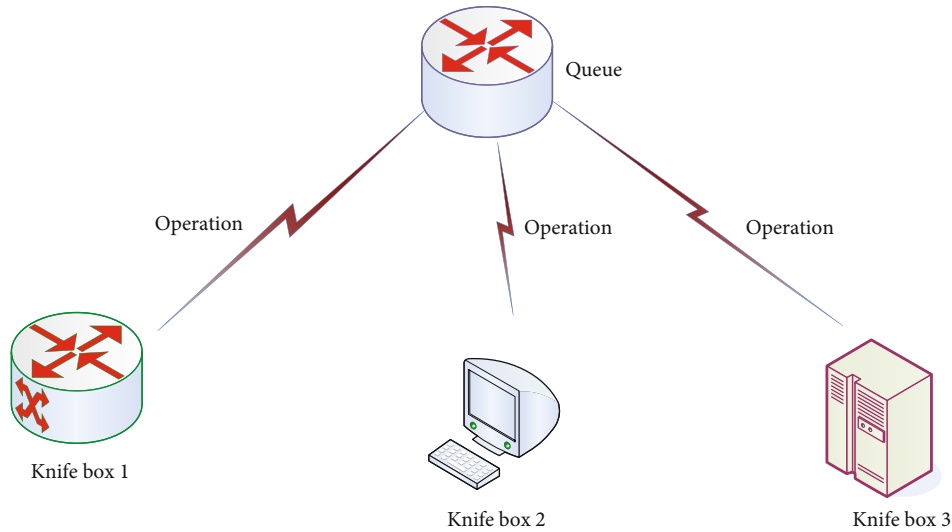
FIGURE 6: High-performance computing architecture.

development of the E-class system in 2018 shows that China's computing level has entered the forefront of the world and occupies a very important position in the field of high-performance computing. Figure 6 is a schematic diagram of a high performance computing architecture.

GC-MS is an analytical instrument that can obtain a set of chronological data during the experiment. During the experiment, the target object is composed of t parts, then each component is 1, 2, 3 ... n; the specific function expression is as follows:

$$W_1 = W_{11}, W_{12}, \Lambda W_{1M}, \tag{11}$$

$$W_2 = W_{21}, W_{22}, \Lambda W_{2M}, \tag{12}$$

$$W_N = W_{N1}, W_{N2}, \Lambda, W_{NM}. \tag{13}$$

Among them, W stands for different components.

Introducing the above formula into a matrix, it can be simplified to

$$W = \begin{pmatrix} W_{11}, & W_{12}, & \Lambda & W_{1M} \\ W_{21}, & W_{22}, & \Lambda & W_{2M} \\ \Lambda & \Lambda & \Lambda & \Lambda \\ W_{N1}, & W_{N2}, & \Lambda & W_{NM} \end{pmatrix}. \tag{14}$$

If the matrix is the distribution of n mixtures during the experiment; then, it can be represented by a two-

dimensional matrix. Each row represents a time point, and each column represents the distribution status. The specific function expression is as follows:

$$E = \begin{pmatrix} E_{11}, & E_{12}, & \Lambda & E_{1N} \\ E_{21}, & E_{22}, & \Lambda & E_{2N} \\ \Lambda & \Lambda & \Lambda & \Lambda \\ E_{U1}, & E_{U2}, & \Lambda & E_{UN} \end{pmatrix}. \tag{15}$$

Among them, E represents a two-dimensional matrix.

$$Q_K(C) = \frac{2}{R(c)} \sum_{k=1}^{n} N_{uk} * Y_{uk}. \tag{16}$$

Among them, Q represents the set of indicators, and $Q_K(C)$ represents the indicators under point C.

$$\alpha(C) = \int_M^1 \left(Q_K(C) - \frac{1}{m} \sum_{k=1}^{m} Q_K(C) \right)^3. \tag{17}$$

Among them, according to $0 < Q_K(C) \leq 1$, $0 \leq \alpha(C) < 0.57$ can be obtained.

$$\beta(C) = 1 - 2 * \alpha(C). \tag{18}$$

Among them, according to $0 \leq \alpha(C) < 0.57$, $0 \leq \beta(C) \leq 1$ can be obtained.

$$QW_j(c,r) = \frac{1}{\sqrt{c}} \int_{-\infty}^{+\infty} j(r)\chi * \left(\frac{w-t}{c} \right) dw. \tag{19}$$

Among them, $QW_j(c,r)$ is the wavelet coefficient, $\chi(w)$ is the wavelet basis function, and $j(r)$ is the analysis signal.

$$L_V = W \, \mathrm{diag}\left(s_{(v)} \right) D^U + Q_v, \quad v = 1, 2, \Lambda, V. \tag{20}$$

Among them, L stands for cubic matrix, W stands for pure chromatogram, and D stands for pure mass spectrum.

4. Swarm Intelligence Algorithm and Evolutionary Computation for Carbon Nanotube Structure Optimization Experiment

4.1. Experimental Material Parameters. Materials are the material basis for human survival and the symbol of human material civilization. Materials are the backbone of modern science and technology. At the same time, the progress of science and technology has put forward higher requirements for materials. The structural optimization of carbon nanotube materials explored in this paper is expected to bring infinite possibilities for development through the optimization of material structure. The material parameters involved in this paper are as follows.

TABLE 1: Mechanical parameters of composite materials.

Grain size	Volumetric fraction 6%			Volumetric fraction 10%		
	A (GPa)	B (GPa)	c	A (GPa)	B (GPa)	c
10	4.52	1.68	0.32	5.23	1.93	0.35
11.3	4.47	1.65	0.31	5.22	1.9	0.35
12.4	4.45	1.65	0.32	5.2	1.87	0.33
13.24	4.43	1.63	0.32	5.17	1.85	0.34
14.8	4.4	1.61	0.31	5.13	1.83	0.33

TABLE 2: Nanoparticle unit cell elastic stiffness matrix.

Z (GPa)	1	2	3	4	5
1	6.98	5.32	5.01	-0.31	-0.05
2	7.63	6.31	5.21	-0.04	1.37
3	6.31	4.74	6.97	1.43	0.39
4	5.02	5.25	3.28	0.41	1.39
5	-0.41	-0.03	-0.15	0.039	0.52

TABLE 3: Matrix action energy.

Grain size	Volume	Energy is 5%	Energy is 10%	5% energy per unit volume	10% energy per unit volume
10	4258	-304	-402	-0.09	-0.015
11.27	6512	-501	-456	-0.08	-0.06
12.3	7365	-536	-526	-0.07	-0.03
13.2	8964	-648	-614	0.06	-0.054
14.1	10254	-712	-715	-0.043	0.048

TABLE 4: Single cell model and single cell mechanical properties.

Performance	PI	Volumetric fraction 5%	Volumetric fraction 10%
Young's modulus	4.15	4.6	4.79
Volume	5.4	5.87	7.43
Lamé constant	4.62	4.71	6.25
Shear modulus	1.53	1.63	1.71
Poisson's ratio	0.35	0.36	0.37

As can be seen from the data in Table 1, assuming that the diameter of the nanoparticles is 10 nm and the thickness of the interface layer is 10 nm, when the volume of the nanoparticles increases continuously, the elastic modulus of the material will also change and show a certain linear law. When the diameter of the nanoparticle is 11.3 nm and the volume fraction is 6%, its elastic modulus is 0.31, and when the volume fraction is 10%, its elastic modulus is 0.35. When the diameter of the nanoparticle is 12.4 nm and the volume fraction is 6%, its elastic modulus is 0.32, and when the volume fraction is 10%, its elastic modulus is 0.33. When the diameter of the nanoparticle is 13.24 nm and the volume
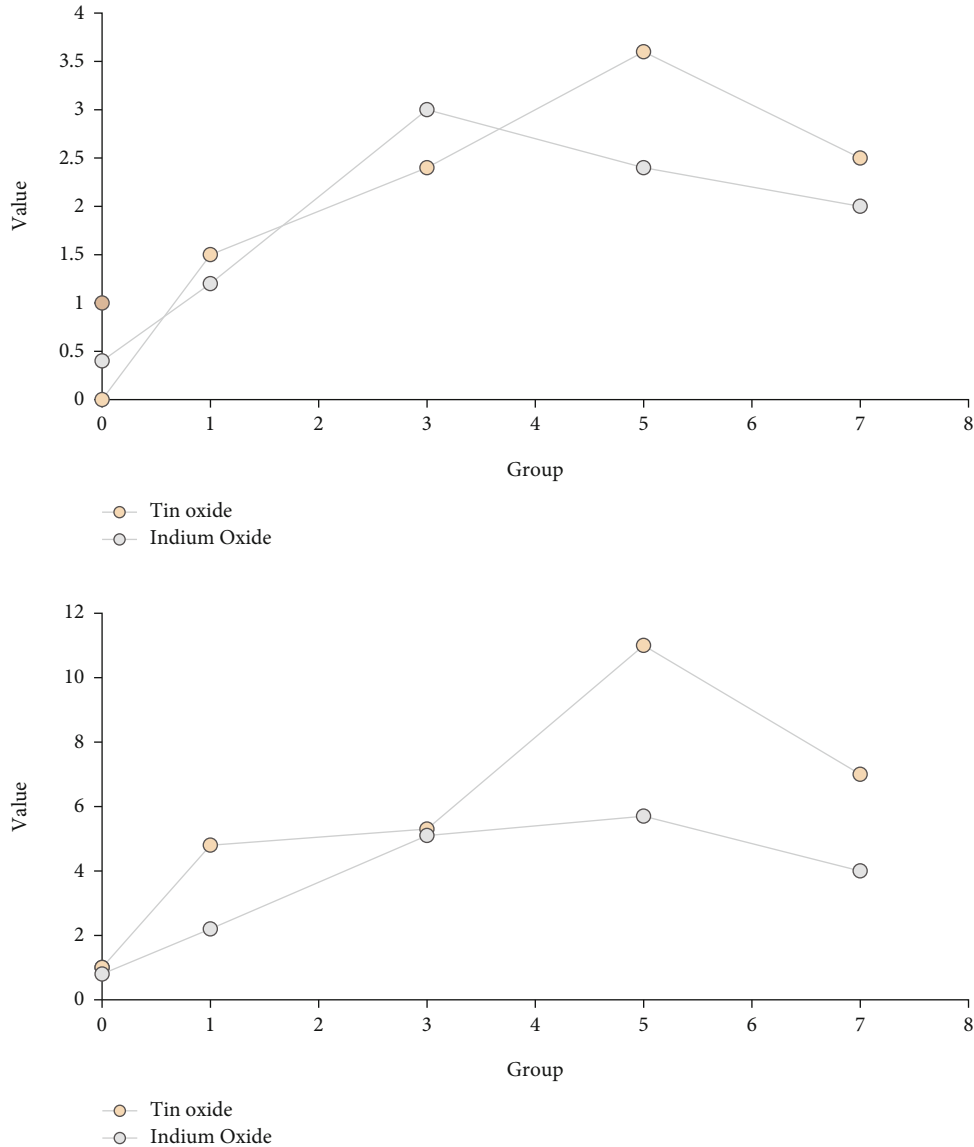
FIGURE 7: Doping concentration vs. sensitivity curve of carbon nanotubes.

fraction is 6%, its elastic modulus is 0.32, and when the volume fraction is 10%, its elastic modulus is 0.34. When the diameter of the nanoparticle is 14.8 nm and the volume fraction is 6%, its elastic modulus is 0.31, and when the volume fraction is 10%, its elastic modulus is 0.33. According to the data, when the particle diameter increases, the elastic modulus decreases and the change trend is relatively gentle.

According to the data in Table 2, there are many factors that affect carbon nanomaterials, and anisotropic materials are used in the experiment. However, according to the data in Table 2, the values of many materials can be regarded as zero, and there are also many materials whose values are relatively close under certain conditions. In fact, when determining the range of particle variation, the number of atoms increases at a certain rate, and when the volume fraction of nanoparticles is 6%, the number of unit cells

surges, and the number of filled molecular chains also increases rapidly.

4.2. Correlation between Material Structure and Matrix. Nanocomposites consist of filler particles, a polymer matrix, and an interface between the two. In order to explore the relationship between the properties and energy of nanomaterial structures, it is necessary to perform single-point energy calculations to obtain the interaction energy between the two.

According to the data in Table 3, when the nanoparticles embedded in the unit cell are enlarged, the number of atoms around them will also increase, and the number of nonbonded pairs between the nanomaterial structure and the matrix will also increase, so the interaction between the two also increases. When the diameter of the material is 10 nm and the volume is 4285, the energy ratios are -0.09
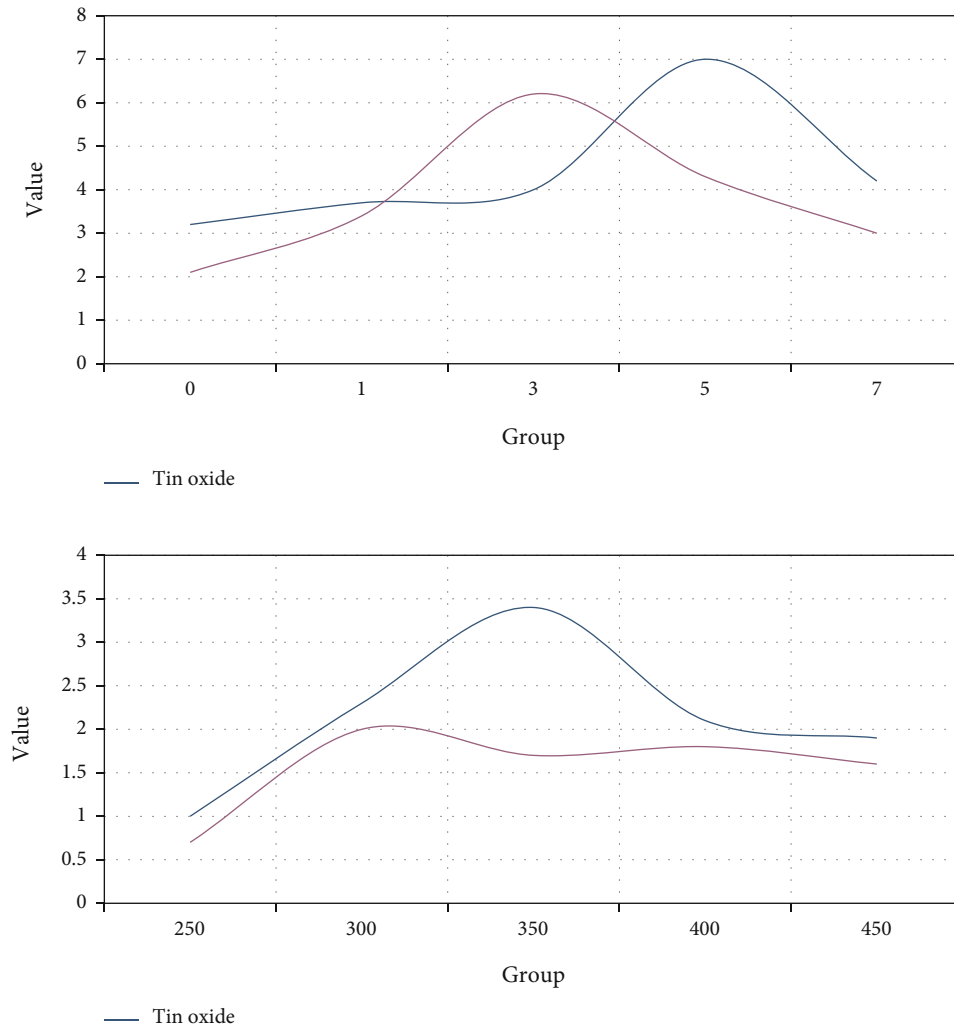
FIGURE 8: Curves of operating temperature versus sensitivity.

and -0.015 in different cases, respectively. When the diameter of the material is 11.27 nm and the volume is 6512, its energy ratios are -0.08 and -0.06 under different conditions, respectively. When the material has a diameter of 12.3 nm and a volume of 7365, its energy ratios are -0.07 and -0.03 under different conditions, respectively. When the diameter of the material is 13.2 nm and the volume is 8964, its energy ratios are 0.06 and -0.054 under different conditions, respectively. When the diameter of the material is 14.1 nm and the volume is 10254, its energy ratios are -0.043 and 0.048 under different conditions, respectively. According to this data, the qualitative correlation between the elastic properties of nanomaterials and the action energy is also related to the volume of nanoparticles. When the diameter of nanoparticles increases, the body-to-surface ratio decreases, resulting in a decrease in the number of nonbonded pairs, weakening the interaction energy, and reducing the elastic modulus of the composite.

4.3. Single-Cell Model and Single-Cell Mechanical Properties. Combined with molecular dynamics, this experiment simu-lates the mechanical properties of nanomaterials, explores the effects of nanoparticles and volume, and explores the relationship between the number of nanoparticles and the properties of composite materials.

According to the data in Table 4, when the PI of the nanomaterial is 4.15 and the volume fraction is 5%, the Young's modulus of the material is 4.6, and when the volume fraction is 10%, the Young's modulus of the material is 4.79. When the PI of the nanomaterial is 5.4 and the volume fraction is 5%, the Lame constant of the material is 4.71, and when the volume fraction is 10%, the Lame constant of the material is 6.25. When the PI of the nanomaterial is 1.53 and the volume fraction is 5%, the shear modulus of the material is 1.63, and when the volume fraction is 10%, the shear modulus of the material is 1.71. When the PI of the nanomaterial is 0.35 and the volume fraction is 5%, the Poisson's ratio of the material is 0.36, and when the volume fraction is 10%, the Poisson's ratio of the material is 0.37. According to this data, the Young's modulus, shear modulus, Lame constant, and volume of the composites all increased when nanoparticles were added to the material.
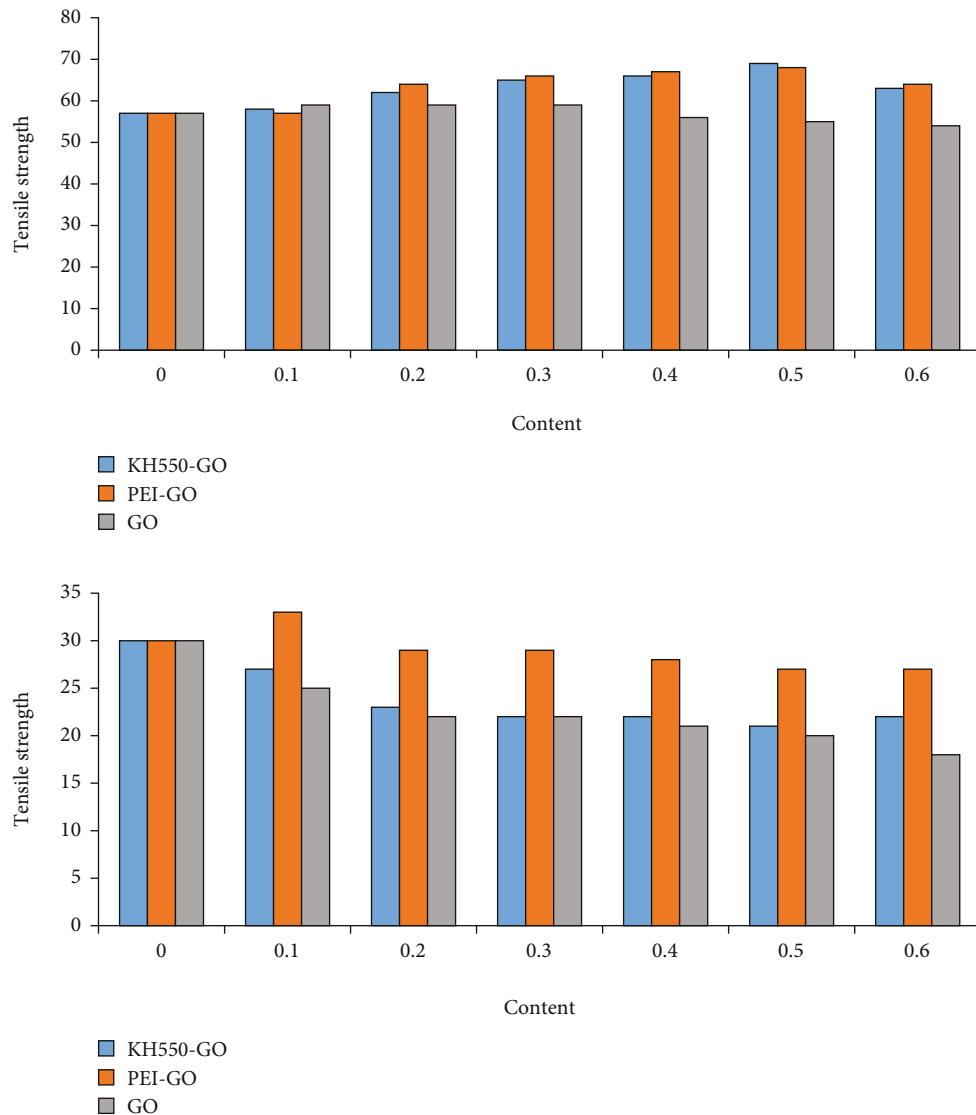
FIGURE 9: Schematic diagram of the secondary mechanical properties of the composite material.

And the data show that the difference becomes more obvious with the increasing volume, but the Poisson's ratio does not change much.

5. Swarm Intelligence Algorithm and Evolutionary Computation for Structure Optimization of Carbon Nanotubes

5.1. Gas Sensitivity of Carbon Nanotubes. Sensors are an important tool in modern technology. Gas sensitivity is an important branch of sensors that can detect different gases. Therefore, gas sensors are widely used in food and medical fields. Based on this, in order to find out the optimal doping concentration of carbon nanotubes for the two metal oxides, we analyzed them as follows.

According to the data in Figure 7, in order to explore the doping concentration of carbon nanotubes to different oxides, we analyzed the nanomaterials at different tempera-

tures. When the experimental temperature is 150 degrees Celsius, the sensitivity of tin oxide is 0, and the sensitivity of indium oxide is 0.4 in the case of dopant. When the doping content of tin oxide is 1%, the sensitivity of the sensor is 1.5, and when the doping content of indium oxide is 1%, the sensitivity of the sensor is 1.2. When the doping content of tin oxide is 3%, the sensitivity of the sensor is 2.4, and when the doping content of indium oxide is 3%, the sensitivity of the sensor is 3. When the doping content of tin oxide is 5%, the sensitivity of the sensor is 3.6, and when the doping content of indium oxide is 5%, the sensitivity of the sensor is 2.4. When the doping content of tin oxide is 7%, the sensitivity of the sensor is 2.5, and when the doping content of indium oxide is 7%, the sensitivity of the sensor is 2. According to the data, when the doping content of tin oxide is 5%, the sensitivity of the sensor is the best, and when the doping content of indium oxide is 3%, the sensitivity of the sensor is the best.
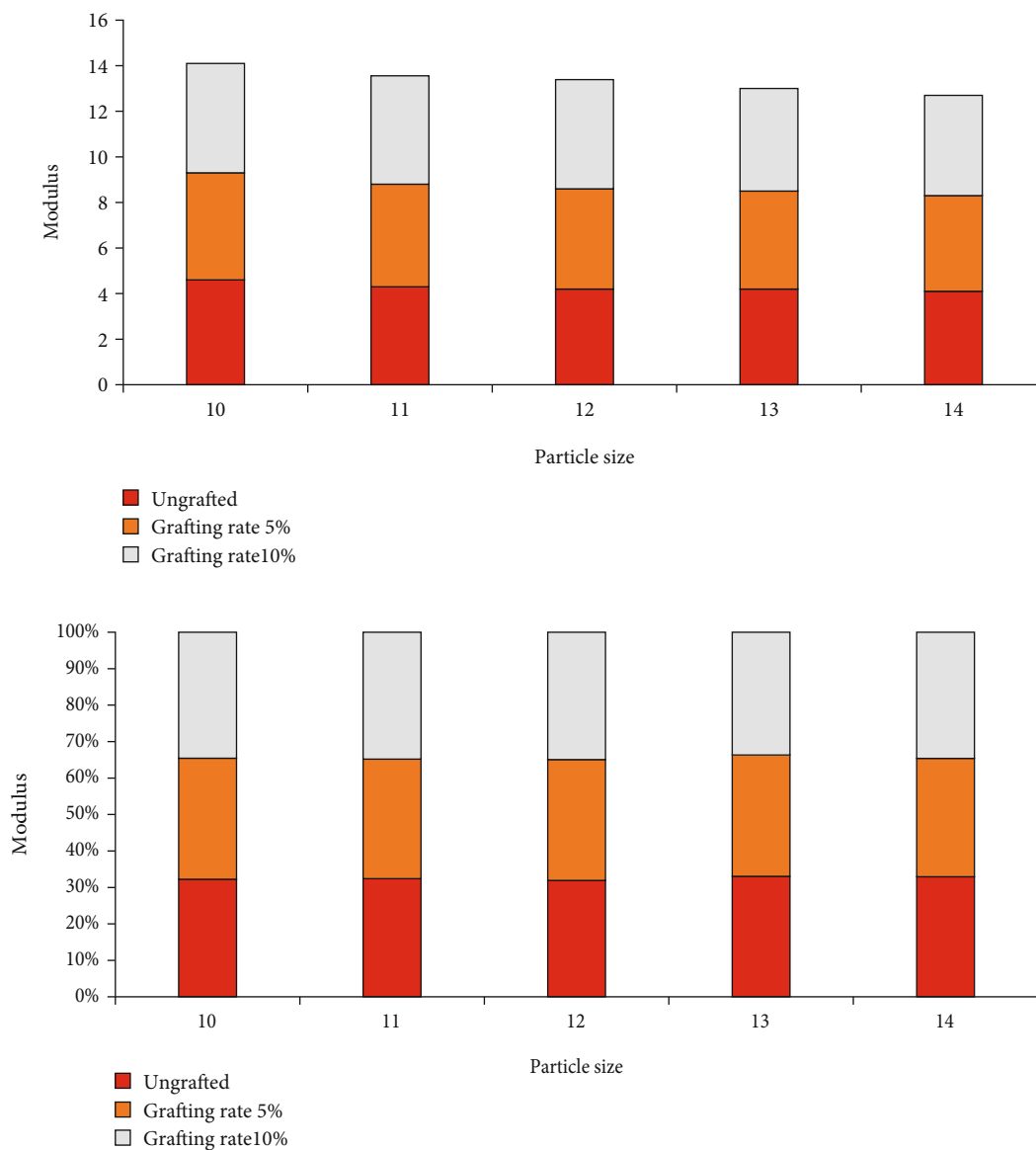
Figure 10: Schematic diagram of the relationship between composite material modulus and particle size.

When the experimental temperature is 250 degrees Celsius, in the case of dopant, the sensitivity of tin oxide is 1, and the sensitivity of indium oxide is 0.8. When the doping content of tin oxide is 1%, the sensitivity of the sensor is 4.8, and when the doping content of indium oxide is 1%, the sensitivity of the sensor is 2.2. When the doping content of tin oxide is 3%, the sensitivity of the sensor is 5.3, and when the doping content of indium oxide is 3%, the sensitivity of the sensor is 5.1. When the doping content of tin oxide is 5%, the sensitivity of the sensor is 11, and when the doping content of indium oxide is 5%, the sensitivity of the sensor is 5.7. When the doping content of tin oxide is 7%, the sensitivity of the sensor is 7, and when the doping content of indium oxide is 7%, the sensitivity of the sensor is 4. According to the data, when the doping content of tin oxide is 5%, the sensitivity of the sensor is the best, and when the doping content of indium oxide is 5%, the sensitivity of the sensor is the best.

According to the data in Figure 8, when the experimental temperature is 350 degrees Celsius, in the case of dopant, the sensitivity of tin oxide is 3.2, and the sensitivity of indium oxide is 2.1. When the doping content of tin oxide is 1%, the sensitivity of the sensor is 3.7, and when the doping content of indium oxide is 1%, the sensitivity of the sensor is 3.4. When the doping content of tin oxide is 3%, the sensitivity of the sensor is 4, and when the doping content of indium oxide is 3%, the sensitivity of the sensor is 6.2. When the doping content of tin oxide is 5%, the sensitivity of the sensor is 7, and when the doping content of indium oxide is 5%, the sensitivity of the sensor is 4.3. When the doping content of tin oxide is 7%, the sensitivity of the sensor is 4.2, and when the doping content of indium oxide is 7%, the sensitivity of the sensor is 3. According to the data, when the doping content of tin oxide is 5%, the sensitivity of the sensor is the best, and when the doping content of indium oxide is 3%, the sensitivity of the sensor is the best.

According to the experimental data, the sensitivity of carbon nanotubes changes differently at different temperatures. The sensitivity of tin oxide is the best at 350 degrees Celsius, and the sensitivity of indium oxide is the best at 300 degrees Celsius.

5.2. Performance of Carbon Nanotube Materials. According to Figure 9, the tensile strength, elongation, and Young's scale of the original nanomaterials all decreased to varying degrees, mainly due to the structural defects induced by the agglomerates in the matrix, resulting in a decrease in the mechanical energy of the nanomaterials. The improved agglomerates show an initial decrease in energy, allowing them to be more uniformly dispersed in the matrix, while improving the interfacial interaction with the matrix. From a macroscopic point of view, the elastic modulus is a measure of the resistance of an object to elastic deformation. From a microscopic level, as long as it is a factor that can interfere with the strength of the inspection, it can affect the elastic modulus.

According to the data in Figure 10, after the nanoparticles are modified, the Young's modulus and shear modulus of the composite have increased to varying degrees. And according to Figure 10, it can be seen that with the increase of the graft ratio, there will be an increasing trend, and at the same time, the performance of the composite material will decrease with the increase of the drop of nanoparticles.

6. Conclusions

With the development of science and technology, people's production needs are increasing, and traditional computing power cannot meet the needs of production. Therefore, optimal computing has become a current research hotspot. With the gradual deepening of people's understanding of natural science, more and more materials are produced. The purpose of this paper is to study the structure optimization of carbon nanotubes based on swarm intelligence algorithm and evolutionary calculation. Although this paper discusses the structure and optimization calculation of carbon nanotubes, there are still shortcomings: when the single-objective particle swarm optimization algorithm solves high-dimensional complex problems, it is still easy to fall into the local optimal solution, and the convergence accuracy still has a large room for improvement.

Data Availability

No data were used to support this study.

Conflicts of Interest

There is no potential conflicts of interest in this study.

References

[1] K. K. Bhattacharjee and S. P. Sarmah, "Modified swarm intelligence based techniques for the knapsack problem," *Applied Intelligence*, vol. 46, no. 1, pp. 1–22, 2017.

[2] G. D. Ntouni, A. E. Paschos, and V. M. Kapinas, "Optimal detector design for molecular communication systems using an improved swarm intelligence algorithm," *Micro & Nano Letters*, vol. 13, no. 3, pp. 383–388, 2018.

[3] P. Gao, S. Wang, J. Lv, Y. Wang, and Y. Ma, "A database assisted protein structure prediction method via a swarm intelligence algorithm," *RSC Advances*, vol. 7, no. 63, pp. 39869–39876, 2017.

[4] W. Zhong, D. Tan, and X. Peng, "Fuzzy high-order hybrid clustering algorithm for swarm intelligence sets," *Neurocomputing*, vol. 314, no. NOV.7, pp. 347–359, 2018.

[5] S. Tabaghchi, "Priority-based task scheduling method over cloudlet using a swarm intelligence algorithm," *Cluster Computing*, vol. 23, no. 2, pp. 663–671, 2019.

[6] D. S. Son, J. M. Hyun, and J. R. Lee, "Optimization of the design of radar-absorbing composite structures using response surface model with verification using scanning free space measurement," *Composite Structures*, vol. 186, pp. 106–113, 2018.

[7] Z. Ahmadi, S. Ravandi, F. Haghighat, and F. Dabirian, "Enhancement of the mechanical properties of PAN nanofiber/carbon nanotube composite mats produced via needleless electrospinning system," *Fibers and Polymers*, vol. 21, no. 6, pp. 1200–1211, 2020.

[8] S. Lu, C. Zhao, and Z. Lu, "Real time monitoring of the curing degree and the manufacturing process of fiber reinforced composites with a carbon nanotube buckypaper sensor," *RSC Advances*, vol. 8, no. 39, pp. 22078–22085, 2018.

[9] W. Wang, J. Xu, Y. Zhang, and G. Li, "First-principles study of electronic structure and optical properties of silicon/carbon nanotube," *Computational Chemistry*, vol. 5, no. 4, pp. 159–171, 2017.

[10] L. Yan, L. Li, X. Ru et al., "Core-shell, wire-in-tube and nanotube structures: carbon-based materials by molecular layer deposition for efficient microwave absorption," *Carbon*, vol. 173, no. 11, pp. 145–153, 2021.

[11] R. A. Shutilov, V. L. Kuznetsov, and S. I. Moseenkov, "Vacuum-tight ceramic composite materials based on alumina modified with multi-walled carbon nanotubes," *Materials Science and Engineering*, vol. 254, pp. 114508.1–114508.10, 2020.

[12] D. Ma, Y. Wang, and L. Zhang, "Parameter optimization on the compressed polypyrrole/carbon nanotube composite electrode for capacitive deionization," *Desalination & Water Treatment*, vol. 85, pp. 84–91, 2017.

[13] Q. Zaib and F. Ahmad, "Optimization of carbon nanotube dispersions in water using response surface methodology," *ACS Omega*, vol. 4, no. 1, pp. 849–859, 2019.

[14] Y. Nakazato, D. Kawachino, Z. Noda, J. Matsuda, A. Hayashi, and K. Sasaki, "SnO2-supported electrocatalysts on various conductive fillers for PEFCs," *ECS Transactions*, vol. 80, no. 8, pp. 897–906, 2017.

[15] E. S. Kudinova, E. A. Vorobyeva, N. A. Ivanova, V. V. Tishkin, and O. K. Alekseeva, "A magnetron sputtering method for the application of the Ni catalyst for the synthesis process of carbon nanotube arrays," *Nanotechnologies in Russia*, vol. 15, no. 11-12, pp. 715–722, 2020.

[16] D. Jean, S. Jessl, and K. Saeed, "Continuous flow chemical vapour deposition of carbon nanotube sea urchins," *Nanoscale*, vol. 10, no. 16, pp. 7780–7791, 2018.

[17] H. M. Park, S. M. Park, and S. M. Lee, "Automated generation of carbon nanotube morphology in cement composite via

data-driven approaches," *Composites*, vol. 167, pp. 51–62, 2019.

[18] B. Peng, M. Annamalai, S. Mothes, and M. Schröter, "Device design and optimization of CNTFETs for high-frequency applications," *Journal of Computational Electronics*, vol. 20, no. 6, pp. 2492–2500, 2021.

[19] S. Dereli, "A novel approach based on average swarm intelligence to improve the whale optimization algorithm," *Arabian Journal for Science and Engineering*, vol. 47, no. 2, pp. 1763–1776, 2022.

[20] M. Ali, "Large-scale structural optimization using a fuzzy reinforced swarm intelligence algorithm," *Advances in Engineering Software*, vol. 142, no. Apr., pp. 102790–102790.13, 2020.

[21] X. Xue and Y. Wang, "Using memetic algorithm for instance coreference resolution," *IEEE Transactions on Knowledge and Data Engineering*, vol. 28, no. 2, pp. 580–591, 2016.

[22] A. Ali, "A proposed AI-based algorithm for safety detection and reinforcement of photovoltaic steel," *Journal of Intelligent Systems and Internet of Things*, vol. 4, no. 1, pp. 41–55, 2021.

[23] M. Z. A. A. Kadir, M. Algrnaodi, and N. Ahmed, "Optimal algorithm for shared network communication bandwidth in IoT applications," *International Journal of Wireless and Ad Hoc Communication*, vol. 2, no. 1, pp. 33–48, 2021.

Hindawi

Research Article

Relevant-Based Feature Ranking (RBFR) Method for Text Classification Based on Machine Learning Algorithm

V. Durga Prasad Jasti [ID],[1] **Guttikonda Kranthi Kumar,**[1] **M. Sandeep Kumar,**[2]
V. Maheshwari,[2] **Prabhu Jayagopal,**[2] **Bhaskar Pant,**[3] **Alagar Karthick,**[4]
and M. Muhibbullah [ID][5]

[1]*Department of Computer Science and Engineering, VR Siddhartha Engineering College, Vijayawada,*
 Andhra Pradesh 520007, India
[2]*School of Information Technology and Engineering, Vellore Institute of Technology, Vellore, Tamil Nadu 632014, India*
[3]*Department of Computer Science and Engineering, Graphic Era Deemed to Be University, Bell Road, Clement Town,*
 248002 Dehradun, Uttarakhand, India
[4]*Renewable Energy Lab, Department of Electrical and Electronics Engineering, KPR Institute of Engineering and Technology,*
 Coimbatore, 641407 Tamil Nadu, India
[5]*Department of Electrical and Electronic Engineering, Bangladesh University, Dhaka 1207, Bangladesh*

Correspondence should be addressed to V. Durga Prasad Jasti; prasadjasti2018@gmail.com

High dimensionality of the feature space is one of the problems in the field of text classification. Identification of optimal subset of features can optimize text classification process in terms of processing time and performance. In this paper, we propose a novel Relevant-Based Feature Ranking (RBFR) algorithm which identifies and selects smaller subsets of more relevant features in the feature space. We compared the performance of the RBFR against other existing feature selection methods such as balanced accuracy measure, information gain, Gini index, and odds ratio on 3 datasets, namely, 20 newsgroup, Reuters, and WAP datasets. We have used 5 machine learning models (SVM, NB, kNN, RF, and LR) to test and evaluate the proposed feature selection method. We found that the performance of the proposed feature selection method is 25.4305% times more effective than the existing feature selection methods in terms of accuracy.

1. Introduction

Massive amount of information is generated and pushed into the digital world every second through various sources such as web pages, blog contents, eBooks, social media contents, and review documents. As the content is increasing day by day, it becomes difficult to convert the content into an organized form which causes many problems such as difficult in searching and lack of summarization. Automatic text classification is one of the way to efficiently organize the documents. Supervised machine learning models such as support vector machines (SVM) [1], Naïve Bayes (NB) [2], k nearest neighbor (kNN) [3], random forest (RF) [4],

and logistic regression (LR) [5] are very efficient in organizing content into one or more topics (or classes). There are wide applications of machine learning in the field of text classification such as spam detection [6], sentimental analysis [7], and topic classification [8].

There are three stages in text classification known as preprocessing, feature selection, and final classification. The preprocessing stage is responsible for formatting and removing useless words. Stop word removal, stemming, and text representations are few task performed in the preprocessing stage. Stop word removal eliminates useless symbols such as "is," "was," "that," and punctuation marks. Stemming is responsible for converting all the derived words into its root

form (e.g., "running" is converted to "run," and "walked" is converted to "walk"). Word representing formats the document into usable text. Features are identified in this stage. There are many text representations such as Bag-of-Words (BoW) [9] and n-gram [10].

A feature is the indivisible atomic unit in a text document. A text corpus may contain many documents $D = \{d_1, d_2, d_n\}$. Each document contains m number of unique features, and the entire text corpus contains k number of unique features such as $F = \{f_1, f_2, \cdots, f_k\}$. As the number of documents increases, the corresponding feature size also increases which increases the classification complexity, increases time, and decreases the accuracy. Hence, an optimal subset of F should be found to represent the document much better and increase the classification performance. The total number of subset possibility is $2^k - 1$ (excluding the null set), so it is not practically possible to brute force all the combinations; thus, there are various feature selection algorithms which are aimed at finding out the optimal combinations in much easier way.

There are three types of feature selection methods known as filter based, wrapper based, and embedded based [11]. Filter-based methods are model independent which picks the features based on statistical methods like correlation and chi-square. Filter-based methods are faster than the other two types but it cannot identify the dependency between the features. Wrapper-based methods are model dependent that means for each model, separate sets of features are selected. Wrapper-based methods use an evaluation strategy to pick the optimal subset. The embedded-based method combines both the filter based and wrapper based. Wrapper-based methods inherit both the positives and negatives of filter and wrapper based.

In this paper, we propose a filter-based feature selection method called as Relevant-Based Feature Ranking (RBFR) algorithm which identifies the most important features and removes irrelevant features from the feature space. The proposed method first ranks all the features according to two metrics known as true positive rate (TPR) and false positive rate (FPR). Then, the features from top TPR are picked; within the chosen list, the features with high FPR are removed. The list is appended by the common features selected by odds ratio (OR), information gain (IG), and chi-square feature selection methods. We have compared the proposed method with well-known standard feature selection methods such as balanced accuracy, OR, IG, and Pearson correlation. The main contributions are listed as follows:

(i) To develop a filter-based feature selection method which is able to pick the most important features that could describe the target class better

(ii) To identify and eliminate overlapping or weak features that poorly represent the target class

(iii) To utilize the merits of other filter-based methods to pick correct features

The above-mentioned contributions are aimed at picking the high rich features that could represent the target class

better than the other features; additionally, the error in the selected features should be identified and removed to increase the performance. Moreover, the high features selected by other filter-based methods are also utilized in the feature selection process.

The rest of the paper is organized as follows. Section 2 briefs the literature related to feature selection. Section 3 contains the working of the proposed algorithms. Section 4 presents the experimental results and the comparison with existing machine learning models and with other existing works. Finally, the conclusion is present in Section 5.

2. Related Works

In this section, we brief the recent works in the field of feature selection in text classification and list out the comparison, merits, and limitations.

A research work done by [12] proposes a feature selection method that uses correlation between each feature to the class. They have strengthened the positive features and weakened the negative features. A margin-based feature selection is implemented to increase the performance of the classification. They have evaluated their proposed filter-based method in thirteen datasets and showed the superiority over existing feature selection methods.

Feature selection can also be done in many stages. A work by [13] proposes a three-stage feature selection. In the first stage, they have incorporated particle swarm optimization to search for optimal features in the feature space. The second stage, the redundant features are found and removed from the selected features. The last stage is used to measure each feature for their significance; if the measure is too low, they are deleted from the feature space. Thus, one stage for selecting the features and two stages for removing irrelevant features are used.

The feature selection proposed by [14] focuses on selecting features in two decision levels. In the first level, they have used learners to find the relevant features. The filtration of learners is done to find the high confident learners. The elected learners are allowed to vote in the second level to pick the most relevant features among the feature space.

Clustering is used for grouping features and picking the relevant features in a work proposed by [15]. The redundancy and relevancy problems are solved by the clustering algorithm. A sorting algorithm is used which arranges all the features in the clustering space. Correlation is the main metric used in the sorting algorithm to rank all the features.

An embedded based feature selection was proposed by [16] for classification on Twitter review. As it combines both filter and wrapper methods, it eliminates the semantic problem. Transfer learning is used along with filter-based methods such as information gain, Pearson's correlation, and wrapper-based methods such as expectation maximization. A weight-based deep learning model is implemented to test the performance of the proposed method.

The irrelevant and redundant features present in the text corpus create a negative impact in text classification. A hybrid filter-based feature selection introduced by [17] combines principal component analysis and information gain. In

their experiment, they found that their proposed feature selection method reduces the dimension of data significantly by picking the correct feature subset thus reducing the training time.

A comparison of feature selection was done by [18]; they have used seven filter-based methods, two wrapped-based methods, and one embedded-based method to test the significance of the classification. Three models artificial neural network, support vector machine, and random forest were used in their experiment. Several combinations of feature selection and classifiers are made, and the most appropriate subset is found based on the training performance.

Instance selection is the method of selecting/removing instance. Reducing the number of instances is also one of the methods to increase the performance of the classification. Ensemble methods are also popular in feature selection such as in [19] where the authors have used both feature selection and instance selection. Three-feature selection algorithms along with instance selection are used in their experiment. Two ensemble-based techniques are used in the experiment.

Redundancy and dependency identification is generally good in filter-based methods [20]; a work [21] shows that mutual information feature selection is effective in finding correlation between the features and the target class. When it comes to the fuzzy-based environment, the mutual information like other filter-based methods is weak in calculating correlation and dependencies. They adopted a fuzzy independent classification on a fuzzy-based data space; then, based on the proportion of classification error, they adjust the fuzzy-based feature selection.

Feature selection is optimized by using genetic programming as mentioned in [22]. A hybrid feature selection is done by merging multiple filter-based feature selection methods. A feature construction algorithm is utilized to optimize the selected features. Nine datasets were used in their experiment, and the comparison shows that the feature construction algorithm is effective (Table 1).

From the above-mentioned literature, the feature selection needs lots of improvement, especially when considering the relevancy. Thus, we propose a feature selection which is able to extract the relevant features which improves the efficiency of the text classification.

2.1. Few Existing Feature Selection Methods.
This section presents an overview of three popular feature selection filter-based methods.

2.1.1. Information Gain.
Information gain [28] is a supervised feature selection methods which is used to rank the feature according to the word's contribution based on its presence or absence in a particular set of text inputs [29]. IG is calculated as

$$IG = -\sum_{i=1}^{m} P(c_i) \log P(c_i) + P(t) \sum_{i=1}^{m} P(c_i|t) \log P(c_i|t) P(\bar{t})$$
$$\cdot \sum_{i=1}^{m} P(c_i|\bar{t}) \log P(c_i|\bar{t}), \tag{1}$$

where m represents the total number of target classes. If binary classification is used then m value is 2. $P(C_i)$ denotes the probability of class i. $P(t)$ is the probability of the word t when t is present in the document, and similarly, $P(\bar{t})$ represents the probability of the word t when t is absent in the document. $P(c_i|t)$ and $P(c_i|\bar{t})$ are the conditional probabilities.

2.1.2. Chi-Square.
Chi-square [30] is the test of independence of a feature with the target class. It is used to measure how much a term is diverged from its dependent class [31]. CHI is calculated using the formula shown as follows:

$$CHI = t\big(tp, (tp + fp) + ve_{prob} + t\big(fn, (fn + tn) + ve_{prob}\big)$$
$$+ t\big(fp, (tp + fp) - ve_{prob)} + t(tn, fn + tn) - ve_{prob}\big). \tag{2}$$

The symbols $+ve_{prob}$ and $-ve_{prob}$ represent the probability of the positive class and the negative class, respectively.

2.1.3. Pearson Correlation.
Pearson correlation is one of the good statistical measures to test the dependence of a feature towards the target class [32]. It is unaffected by overfitting [33]. It is calculated by the formula as described as follows:

$$PC = \frac{Cov(X, Y)}{\sigma X \sigma Y}. \tag{3}$$

The existing feature selections have lots of problems such as lack of representation of class unique features, problems in removing the unless and common features, and unable to perform negativity test.

2.2. Overall Drawbacks in Existing Feature Selection Methods.
Feature selection is done to reduce the dimensionality of features in the dataset. Good features need to be identified to separate the classes. As the number of features increases, the complexity of the classifier is also increased; this creates a need for better feature selection methods [34].

Most existing feature selection methods use a weighted method such as frequency and distribution; these feature selection methods fail to pick the class unique features; that is, when one feature is very specific to one class or few classes, that feature is very important for a classifier to determine the class as the classifier feels very easy to identify the class.

Another problem in the feature selection is many methods rely on positive test; that is, if a feature is present, then an appropriate class can be identified; however, negativity test is also one of the powerful methods to eliminate weak candidates in the classification. There are only limited methods for the negativity test.

Combining two or more feature selection methods lets the classifier enjoys the advantages of multiple feature selection methods. The existing methods are least focused on ensembling. Hence, by the use of ensemble technique, the performance of feature selection can be improved.

TABLE 1: Comparison of recent works related to imbalanced classification.

Reference	Technique	Methodology	Comments
[23]	Extreme gradient boosting	Time-, frequency-, and spatial-based features were extracted by the proposed algorithm. Random forest is used for classification.	Correlation in time-based features can be improved. Embedded FS can be incorporated.
[24]	Orthogonal least squares	The authors have improved the speed of fetching the best features using orthogonal least squares. They have compared mutual information and other embedded methods.	Multiple correlation coefficient and the canonical correlation coefficient can be improved when feature generation and instance generation methods are used.
[25]	Centroid mutation-based search	A set of features which can represent a strong convergence to a set of classes is identified. This increases the position of classification margin and reduces the error.	The noisy features can be identified and removed before finding the strong convergence.
[26]	Balanced pointwise mutual information	A deep learning model is employed in Twitter text classification. Special characters like emoji are used as features to classify tweets.	Spam detection can be implemented to increase the accuracy.
[27]	Term weighting	Most of the feature selection methods just use frequency. The authors used category information as additional metric to select features for classification.	Semantics information can degrade the performance of the classification.

3. Relevant-Based Feature Ranking Algorithms

Feature selection is one of the important steps in text classification. The existing problem in ranking features is lack of identification of dependence. A good feature is identified by the following characteristics:

(i) A feature present in only one class is uniqueness, and it helps to identify the class correctly

(ii) A feature present in all the classes is not a good sign to identify a class

(iii) A feature is absent in one or more classes is also uniqueness, and it helps in negativity test

Consider a sample dataset as described in Table 2. There are two classes; one class is representing the topic astronomy, and other class is representing the topic society. Let us take the feature "planet" which is a unique feature in the topic 1; similarly, the feature "marriage" is a unique feature for the topic 2. The words "people" and "life" are present in both the topics. The ACC2 ratings are displayed in the last column; it is noted that for the unique feature "planet" and the nonsignificant feature "life" have the same rating, which is not a good sign for the classification. Hence, the rating methodology should be optimized to select the rich features.

The proposed feature selection algorithm takes this ranking problem in consideration and is aimed at assigning a rank based on its relevance towards the target class. If the feature represents the class fully, then high weight is given; similarly, when the feature is present in almost all the classes, then it is less likely that the proposed algorithm will pick this particular feature. The RBFR algorithm works in the following steps:

(1) Rank the features based on TPR-FPR

TABLE 2: Problems in feature selection.

Feature	Class 1	Class 2	TRP	FPR	Accuracy measure (ACC2)
Planet	5	0	0.5	0	0.5
People	1	2	0.1	0.2	0.1
Life	9	4	0.9	0.4	0.5
Marriage	0	9	0	0.9	0.9

(2) Within the list, remove the features with low FPR

(3) Merge three filter-based FS algorithm selected features

(4) Rank the features based on class unique weights

The feature ranks are given based on four metrics known as true positive (TP), true negative (TN), false positive (FP), and false negative (FN), which are defined as follows:

(i) TP: if a feature is present in the positive class

(ii) TN: if a feature is absent in the positive class

(iii) FP: if the feature is present in the negative class

(iv) FN: if the feature is absent in the negative class

The rich features for each class are determined by the ACC2 (TPR-FPR) [35], but there are high chances that the negative features are also selected alone with the rich features. Hence, a second level filtration on the basis of FPR could remove the weakly represented features.

3.1. Feature Selection Methods. To increase the rate of representation, three popular feature selection methods, namely, information gain, chi-square, and Pearson correlation, are

---

Input: F= set of features in the text corpus
Output: S – top N rich features
Begin:
1 **For each** f **in** F
2   TPR score = $TP/TP + FN$
3   FPR score = $FP/TN + FP$
4   L = {top k_1 features with high TPR-FPR score}
5 **For each** f **in** L
6   **If** FPR(f)<TH **then**
7   Remove f from L
8   F1 = top N features from IG = $-\sum_{i=1}^{m} P(c_i) \log P(c_i) + P(t) \sum_{i=1}^{m} P(c_i|t) \log P(c_i|t) + P(\bar{t}) \sum_{i=1}^{m} P(c_i|\bar{t}) \log P(c_i|\bar{t})$
9   F2 = top N features from CHI = $t(tp, (tp + fp) + ve_{prob}) + t(fn, (fn + tn) + ve_{prob}) + t(fp, (tp + fp) - ve_{prob)} + t(tn, fn + tn) - ve_{prob}$
10   F3 = top N features from Pearson Correlation
11   Common Features = $(F1 \cap F2) \cup (F1 \cap F3) \cup (F2 \cap F3)$
Return $L \cup Common\ Features$

ALGORITHM 1: RBFR.

used to extract features. If a feature is selected by at least two of the feature selection methods, then that feature is also selected as per equation (4) for classification.

$$F = (F1 \cap F2) \cup (F1 \cap F3) \cup (F2 \cap F3). \qquad (4)$$

$F1$, $F2$, and $F3$ in equation (4) represent the features selected by information gain, chi-square, and Pearson correlation, respectively. The details of the feature selection algorithms are briefed in the following subsections.

3.2. Class Unique Features. A feature is important based on how it represents the class. If a feature is present in only one class, then the feature is very important because it is very unique to a class. Similarly, if a feature is present across many classes, then it is very less important. After the second level of filtrations, a unique weight is calculated for each feature. This weight is based on the occurrence of a feature across various classes. Consider Table 3 which displays feature wise and class wise frequency, where $F_{i,j}$ represents the frequency of feature i in the class j. The first step is to remove the less class wise frequent term as per the condition in

$$\sum_i \sum_j F_{i,j} > \frac{\sigma}{n}. \qquad (5)$$

The average of all frequency count is calculated, and the first step is to remove all the entries which have the frequency less than the average frequency. Then, an inverse class frequency is calculated to find out whether a feature is common or rare. A term which is very important is then filtered using a threshold value as described in equation (6), where $|C|$ is the total number of classes in the classification. $F(c)$ represents the number of classes the feature f represent.

$$Threshold(f) = TF * \log \left(\frac{|C|}{|F(c)|} \right). \qquad (6)$$

TABLE 3: Feature weights.

Feature	Class 1	Class 2	Class 3	Class 4
1	$F_{1,1}$	$F_{1,2}$	$F_{1,3}$	$F_{1,4}$
2	$F_{2,1}$	$F_{2,2}$	$F_{2,3}$	$F_{2,4}$
3	$F_{3,1}$	$F_{3,2}$	$F_{3,3}$	$F_{3,4}$

TABLE 4: Dataset description.

#	Dataset name	Number of documents	Number of features
1	Reuters [36]	1504	2886
2	WAP [37]	1560	6852
3	20 newsgroup [38]	18828	17425

3.3. Machine Learning Models. The proposed feature selection algorithm is tested using five machine learning models which are briefed in the following subsections.

3.3.1. k Nearest Neighbor. kNN is the machine learning models that finds distances between each instance. When a new sample or instance needs to be classified, the kNN finds the k closest neighbors from the instance, and the target class is found by majority voting. Some statistical methods are used to fix the value of K before starting the classification. It is better to fix the value of K as odd number. kNN is called as lazy classifier because it does nothing in the training phase; the distance calculation and the majority voting are done only in the classification phase.

3.3.2. Naïve Bayes. One of the most used classifiers in the field of text classification is Naïve Bayes. This model works with the probability concept of Bayes theorem. NB groups the instances based on similarity and determines the class of the new sample based on how much it is related with each class.

3.3.3. Support Vector Machines. Support vector machines are the most used classifier in the text classification domain.

TABLE 5: Performance in Reuters.

Feature selection	kNN			NB			SVM			RF			LR		
	P	R	F	P	R	F	P	R	F	P	R	F	P	R	F
CHI	52	55	56	83	60	70	11	67	19	81	96	88	89	78	83
ACC2	56	79	66	77	89	86	60	90	72	83	96	89	73	93	82
NDM	71	80	75	86	90	88	78	96	86	83	77	80	75	86	80
IF	76	67	71	81	98	89	97	85	91	95	87	91	94	84	89
GI	89	88	88	85	74	79	93	81	87	62	94	75	52	71	60
RBFR	64	95	76	93	97	95	94	84	89	95	92	93	91	89	90

TABLE 6: Performance in WAP.

Feature selection	kNN			NB			SVM			RF			LR		
	P	R	F	P	R	F	P	R	F	P	R	F	P	R	F
ACC2	38	32	35	88	86	87	54	67	60	82	99	90	58	97	73
CHI	83	91	87	87	94	90	94	75	83	94	84	89	7	14	9
NDM	60	88	71	65	94	77	25	22	23	93	47	62	75	87	81
GI	98	74	84	90	84	87	83	93	88	91	98	94	83	52	64
IF	80	88	84	92	87	89	88	96	92	93	97	95	91	81	86
RBFR	91	95	93	94	95	95	86	89	87	97	98	97	68	71	69

TABLE 7: Performance in 20 newsgroup.

Feature selection	kNN			NB			SVM			RF			LR		
	P	R	F	P	R	F	P	R	F	P	R	F	P	R	F
ACC2	98	64	77	87	94	90	67	70	68	92	91	91	82	86	84
CHI	93	79	85	92	90	91	79	79	79	95	94	94	77	72	74
NDM	97	78	86	92	60	73	92	96	94	74	79	79	59	57	58
GI	81	91	86	99	95	97	91	98	94	95	92	92	80	40	53
IF	90	86	88	84	93	88	86	86	86	96	96	96	95	58	72
RBFR	98	90	94	91	91	91	98	97	97	95	96	96	44	64	52

SVM can classify both linear as well as nonlinear data. A support vector is an end point in each class. The SVM model fixes a linearly separatable margin between the class; this margin is used to classify the instances.

3.3.4. Random Forest.
RF is an ensemble-based classifier. The RF uses multiple decision tree. The number of DT is fixed before the start of classification. Each decision tree receives unique set of input and trained separately. Then, the output of each DT is used in majority voting to determine the final class.

3.3.5. Logistic Regression.
LR is a special type of classifier that is used to classify linear data. LR constructs a margin which separates the classes. The new instances are assigned a class based on the position where it resides with respect to the margin.

4. Results and Discussion

We have used three benchmark datasets for evaluating our proposed feature selection algorithm. Table 3 contains the descriptions of all datasets.

4.1. Dataset Description. The three datasets contain different instances, number of classes, and number of features as shown in Table 4. We have taken random 2500 features from each dataset for our experiment.

4.2. Performance Evaluation. In order to test the performance of our proposed feature selection algorithm, we have used four standard metrics: accuracy, precision, recall, and F1-score. The formulas for calculating all the metrics are shown as follows:

$$\text{Accuracy} = \frac{TP + TN}{TP + TN + FP + FN},$$

$$\text{Precision} = \frac{TP}{TP + FP},$$

$$\text{Recall} = \frac{TP}{TP + TN},$$

$$\text{F1-Score} = 2 * \frac{\text{Precision} * \text{Recall}}{\text{Precision} + \text{Recall}}.$$

(7)

All the documents are preprocessed; stemming and stop word removal are done before the classification; also, a
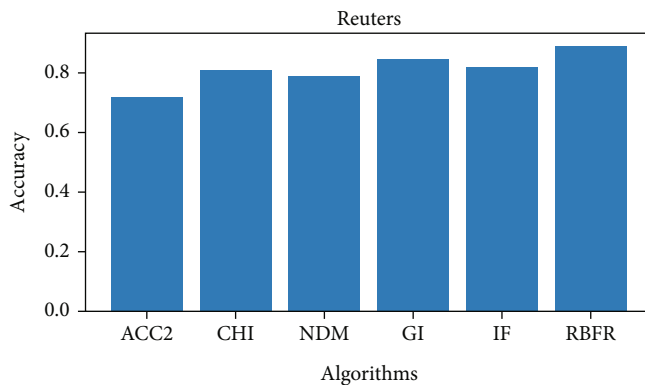
Figure 1: The accuracy comparison of kNN in Reuters dataset.
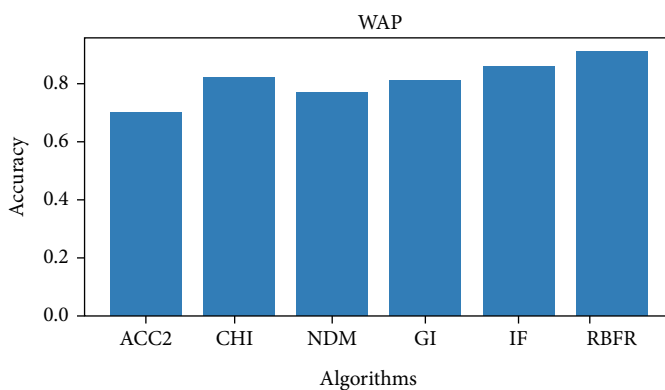
Figure 2: The accuracy comparison of kNN in WAP dataset.
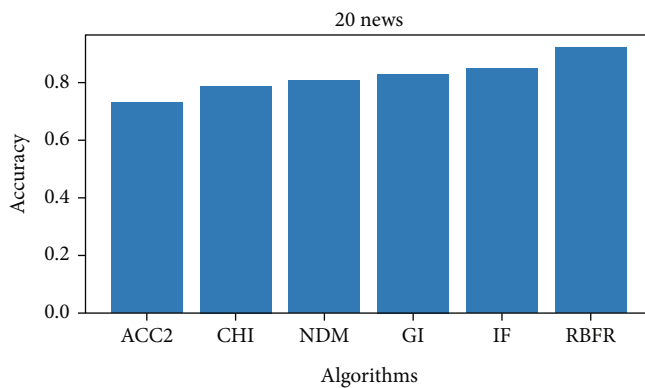
Figure 3: The accuracy comparison of kNN in 20 newsgroup dataset.

Table 8: Accuracy comparison.

Model	Two stage [39]	Noun based [40]	RBFR
LR	81.79%	74.91%	87.01%
kNN	85.94%	76.48%	89.6%
SVM	87.12%	81.44%	92.13%
NB	90.31%	87.8%	93.96%
RF	88.32%	88.91%	92.47%
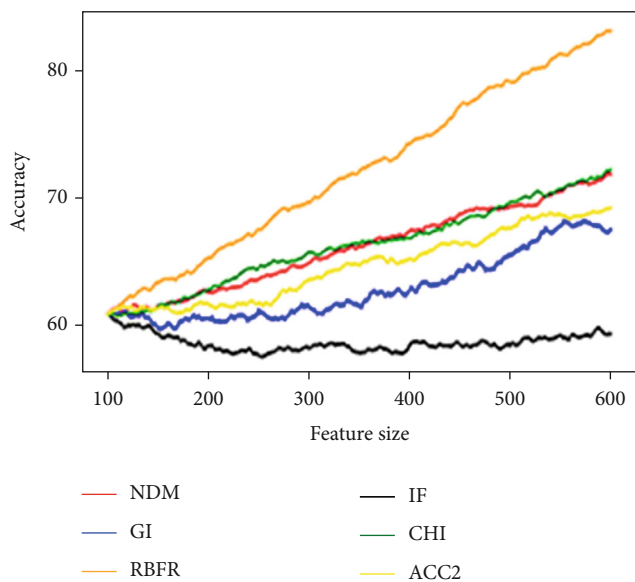
(a)
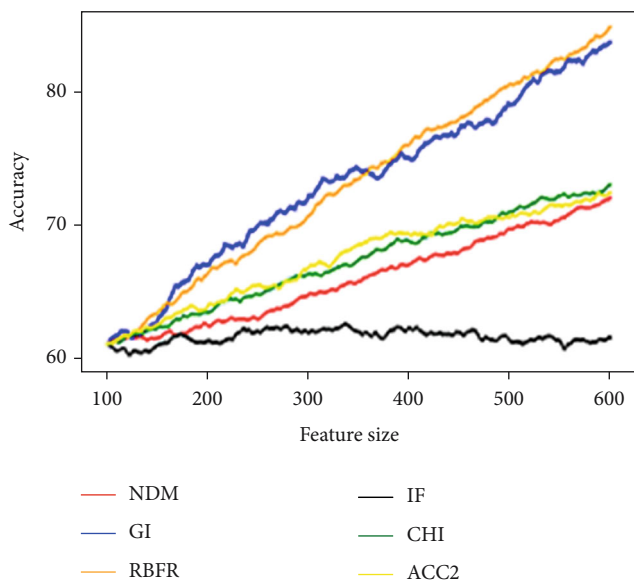
(b)
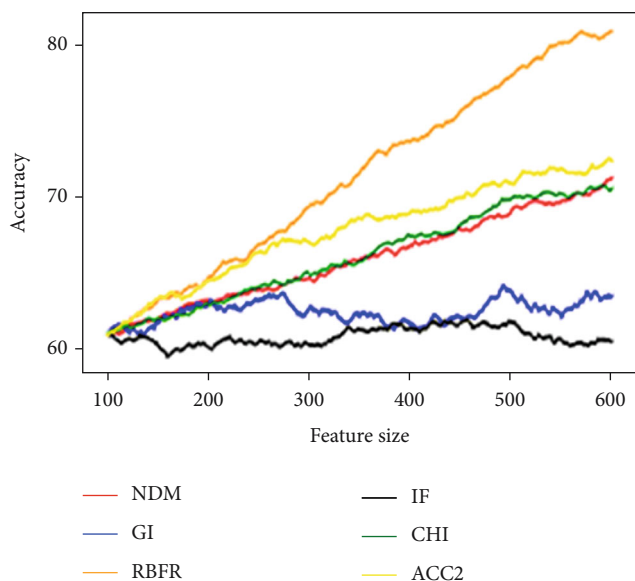
(c)
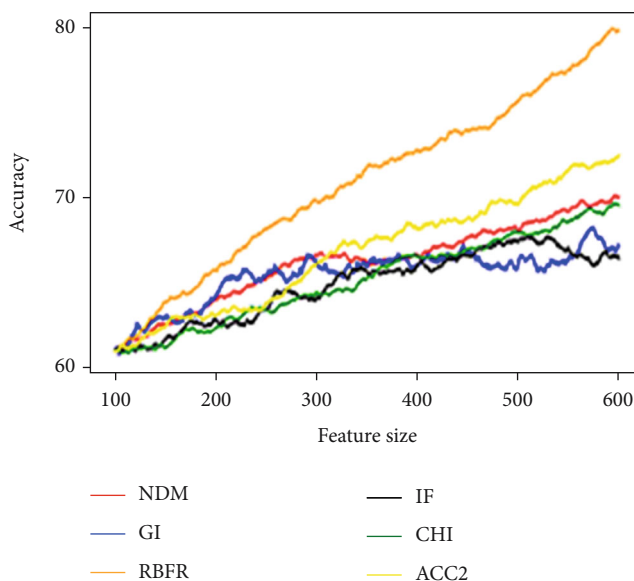
(d)

FIGURE 4: Continued.

(e)
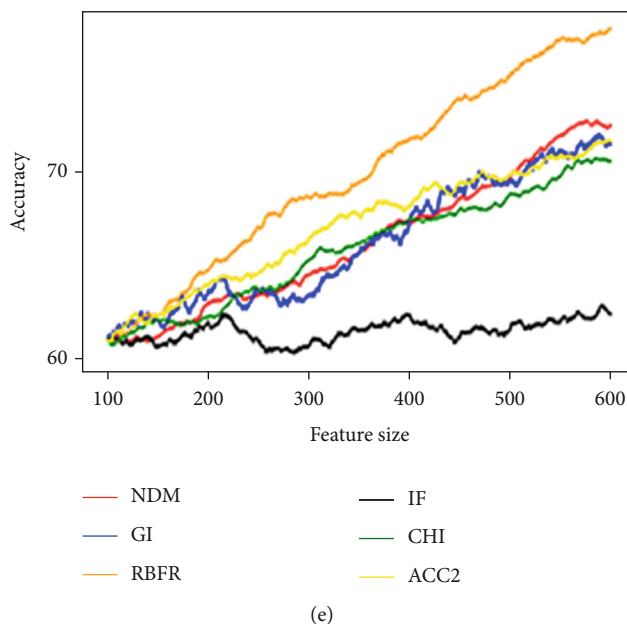
FIGURE 4: The accuracy comparison when the number of features changes: (a) kNN classifier; (b) LR classifier; (c) NB classifier; (d) SVM classifier; (e) RF classifier.

second level of filtering is done by identifying the frequent words. The frequent words are features that are present in almost every document. The datasets are divided as per 10-fold validation.

The characteristics of the features that are selected by a feature selection algorithm can be analyzed to test the effectiveness of the feature selection algorithm. If unique features are selected and high rank is given to those features, then it is more likely that the performance of the classification will be good. Similarly, if irrelevant features are assigned higher ranks, then that will cause very poor performance in classification. The proposed feature selection method removes the high false rates thus provides a way to rank good feature. This is one of the reasons for the good performance of each classifier. Along with the ranking, the RBFR also considers top selected features from three well-known filter-based methods, and the common features present in them were selected. The precision, recall, and F1 comparison are shown in the Tables 5–7 for the datasets Reuters, WAP, and 20 newsgroups, respectively.

From the performance comparison tables, it is clear that the RBFR method identifies the rich features present in the corpus and ranks them higher than the irrelevant features. Precision is one of the good measures to judge a classification. It indicates the quality of positive predictions. The RBFR has higher precision in majority cases while compared with other feature selection methods.

The ensemble of three filter-based feature selection increases the chance of selecting high rich features. As the selected features contain high level features, the classification using RBFR method is much higher than the classification done by other feature selection algorithms. Figures 1–3 display the accuracy of kNN in the three datasets. We have compared our proposed feature selection algorithm with other two works, and Table 8 shows the comparison.

The participation of multiple number of features in the process of classification is one of the important stages as it is not only responsible for increasing the efficiency of classification but also reduces the presence of simultaneous information redundancy. To solve the problems which affect the classification performance, the number of features should be selected optimally. If the feature size is very high, it increases the time of training rapidly; also if the size is too small, the accuracy becomes very low. Hence, the optimal number of features is determined by linearly increasing the number of features and stop when the performance degradation is observed.

In our experiment, we noticed that the optimal feature size is 600; after that, the accuracy of the classifiers seems to reduce. Among the classifiers, random forest seems to have increased accuracy even after 600; this is because the random forest can reduce the dimensionality by branching over the data. Up to 1400, the random forest classifier produces acceptable accuracy.

From Figure 4, it can be seen that among the existing feature selection methods, our proposed method outputs better performance in terms of accuracy, and SVM classifier produces the best accuracy when the number of features is 600. From the analysis, it can be found that as the number of features increases, there is a positive fluctuation in the classification performance. This is because, more sufficient knowledge can be derived in the training stage to improve the accuracy of the classification. Information duplication may arise when the number of features is increased too much; hence, an optimal count is preferred.

The number of neighbors plays a critical role in classification. From Figure 5, it can be observed that as the number of
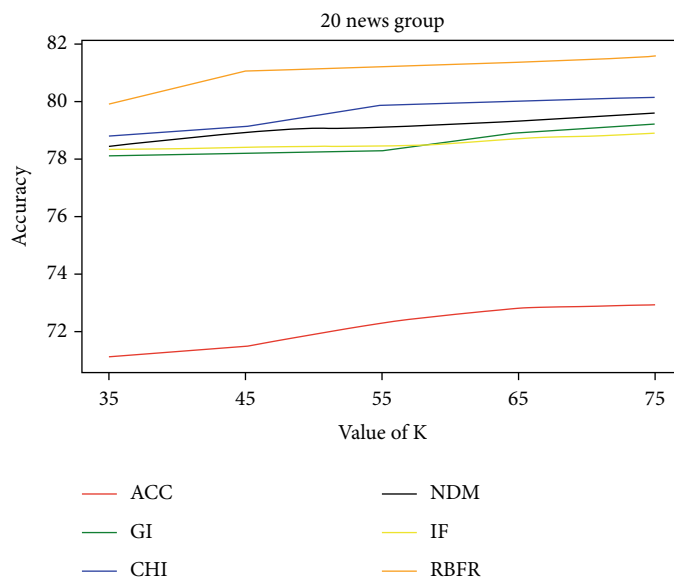
(a) Dataset 20 newsgroup
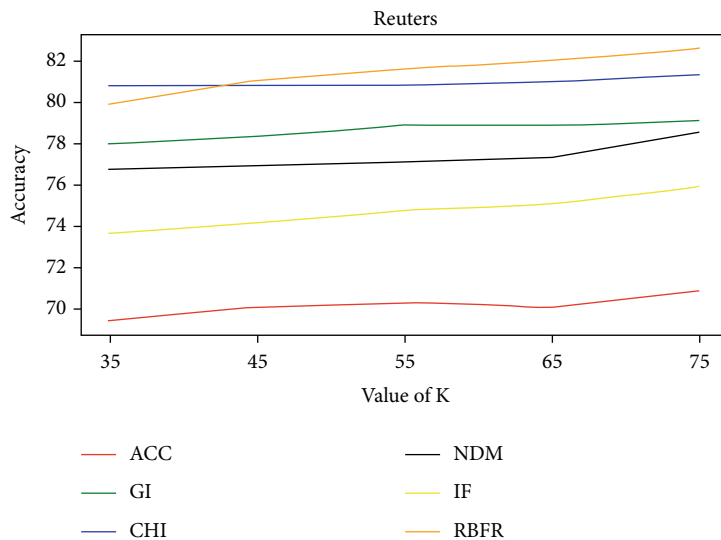
(b) Reuters

Figure 5: Continued.

WAP
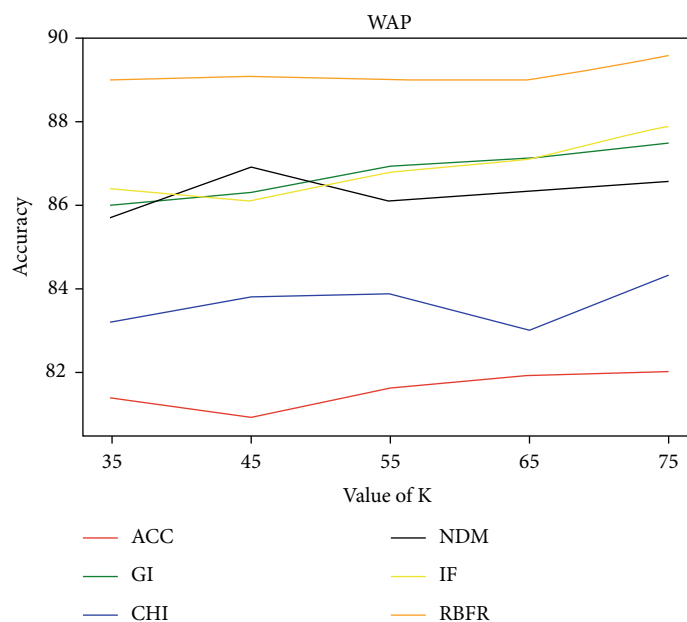
(c) WAP

FIGURE 5: The accuracy comparisons when different numbers of neighbors were considered in all three: (a) datasets 20 newsgroup; (b) Reuters; (c) WAP.

neighbor's increases, the performance also increases, but after 75, the classifier stabilizes. The proposed feature selection produces better results than the other feature selection methods because the removal of noise and redundant features.

5. Conclusions

Feature selection is one of the important stages in improving the performance of text classification. The existing feature selection methods can identify rich features present in the text corpus, but still lots of irrelevant features are also selected which degrades the performance of the text classification. In this work, we propose a ranking-based feature selection model which can identify and eliminate the irrelevant features from the selection set. We have implemented the proposed feature selection model in three datasets and compared with five existing filter-based feature selection methods, namely, ACC2, NDM, CHI, GI, and IG. The machine learning models used for classification were kNN, SVM, NB, LR, and RF. The experiment result shows that NB outperforms the classification task with 93.96% accuracy. In future work, we aim to rank the features based on its semantics and implement deep learning-based classification.

Data Availability

The data used to support the findings of this study are included within the article.

Conflicts of Interest

The authors declare that there is no conflict of interest regarding the publication of this article.

References

[1] A. A. A. Ali and S. Mallaiah, "Intelligent handwritten recognition using hybrid CNN architectures based-SVM classifier with dropout," *Journal of King Saud University-Computer and Information Sciences*, vol. 34, no. 6, pp. 3294–3300, 2022.

[2] K. M. El Hindi, R. R. Aljulaidan, and H. AlSalman, "Lazy fine-tuning algorithms for naive Bayesian text classification," *Applied Soft Computing*, vol. 96, article 106652, 2020.

[3] Z. Chen, L. J. Zhou, X. Da Li, J. N. Zhang, and W. J. Huo, "The Lao text classification method based on KNN," *Procedia Computer Science*, vol. 166, pp. 523–528, 2020.

[4] A. Mohammed and R. Kora, *An Effective Ensemble Deep Learning Framework for Text Classification*, Journal of King Saud University-Computer and Information Sciences, 2021.

[5] T. H. J. Hidayat, Y. Ruldeviyani, A. R. Aditama, G. R. Madya, A. W. Nugraha, and M. W. Adisaputra, "Sentiment analysis of Twitter data related to Rinca Island development using Doc2-Vec and SVM and logistic regression as classifier," *Procedia Computer Science*, vol. 197, pp. 660–667, 2022.

[6] Y. Li, X. Nie, and R. Huang, "Web spam classification method based on deep belief networks," *Expert Systems with Applications*, vol. 96, pp. 261–270, 2018.

[7] K. Rakshitha, H. M. Ramalingam, M. Pavithra, H. D. Advi, and M. Hegde, "Sentimental analysis of Indian regional languages on social media," *Global Transitions Proceedings*, vol. 2, no. 2, pp. 414–420, 2021.

[8] K. E. Daouadi, R. Z. Rebaï, and I. Amous, "Optimizing semantic deep forest for tweet topic classification," *Information Systems*, vol. 101, article 101801, 2021.

[9] A. Palanivinayagam and S. Nagarajan, "An optimized iterative clustering framework for recognizing speech," *International Journal of Speech Technology*, vol. 23, no. 4, pp. 767–777, 2020.

[10] E. Zhu, J. Zhang, J. Yan, K. Chen, and C. Gao, *N-gram Mal-GAN: evading machine learning detection via feature n-gram*, Digital Communications and Networks, 2021.

[11] D. Jain and V. Singh, "Feature selection and classification systems for chronic disease prediction: a review," *Egyptian Informatics Journal*, vol. 19, no. 3, pp. 179–189, 2018.

[12] L. Sun, T. Wang, W. Ding, J. Xu, and Y. Lin, "Feature selection using Fisher score and multilabel neighborhood rough sets for multilabel classification," *Information Sciences*, vol. 578, pp. 887–912, 2021.

[13] D. Paul, A. Jain, S. Saha, and J. Mathew, "Multi-objective PSO based online feature selection for multi-label classification," *Knowledge-Based Systems*, vol. 222, article 106966, 2021.

[14] F. BenSaid and A. M. Alimi, "Online feature selection system for big data classification based on multi- objective automated negotiation," *Pattern Recognition*, vol. 110, article 107629, 2021.

[15] A. Hashemi, M. B. Dowlatshahi, and H. Nezamabadi-pour, "An efficient Pareto-based feature selection algorithm for multi-label classification," *Information Sciences*, vol. 581, pp. 428–447, 2021.

[16] M. Selvapriya and G. M. Priscilla, "Integrated feature selection (IFS) algorithm and enhanced weight based convolutional neural network (EWCNN) for social emotion classification," *Materials Today: Proceedings*, 2021.

[17] E. O. Omuya, G. O. Okeyo, and M. W. Kimwele, "Feature selection for classification using principal component analysis and information gain," *Expert Systems with Applications*, vol. 174, article 114765, 2021.

[18] J. Chong, P. Tjurin, M. Niemelä, T. Jämsä, and V. Farrahi, "Machine-learning models for activity class prediction: a comparative study of feature selection and classification algorithms," *Gait & Posture*, vol. 89, pp. 45–53, 2021.

[19] C. F. Tsai, K. L. Sue, Y. H. Hu, and A. Chiu, "Combining feature selection, instance selection, and ensemble classification techniques for improved financial distress prediction," *Journal of Business Research*, vol. 130, pp. 200–209, 2021.

[20] W. Qian, C. Xiong, and Y. Wang, "A ranking-based feature selection for multi-label classification with fuzzy relative discernibility," *Applied Soft Computing*, vol. 102, article 106995, 2021.

[21] Z. Ruijie, X. Ying, J. Shuaichen, and L. Yonghe, "Patent text modeling strategy and its classification based on structural features," *World Patent Information*, vol. 67, article 102084, 2021.

[22] J. Dai and J. Chen, "Feature selection via normative fuzzy information weight with application into tumor classification," *Applied Soft Computing*, vol. 92, article 106299, 2020.

[23] J. Ma and X. Gao, "A filter-based feature construction and feature selection approach for classification using genetic programming," *Knowledge-Based Systems*, vol. 196, article 105806, 2020.

[24] T. Thenmozhi and R. Helen, "Feature selection using extreme gradient boosting Bayesian optimization to upgrade the classification performance of motor imagery signals for BCI," *Journal of Neuroscience Methods*, vol. 366, article 109425, 2022.

[25] S. Zhang and Z. Q. Lang, "Orthogonal least squares based fast feature selection for linear classification," *Pattern Recognition*, vol. 123, article 108419, 2022.

[26] E. H. Houssein, E. Saber, A. A. Ali, and Y. M. Wazery, "Centroid mutation-based search and rescue optimization algorithm for feature selection and classification," *Expert Systems with Applications*, vol. 191, article 116235, 2022.

[27] Z. Ahanin and M. A. Ismail, "A multi-label emoji classification method using balanced pointwise mutual information-based feature selection," *Computer Speech & Language*, vol. 73, article 101330, 2022.

[28] F. Shen, X. Zhang, R. Wang, D. Lan, and W. Zhou, "Sequential optimization three-way decision model with information gain for credit default risk evaluation," *International Journal of Forecasting*, vol. 38, no. 3, pp. 1116–1128, 2022.

[29] P. Jagadeesan, K. Raman, and A. K. Tangirala, "A new index for information gain in the Bayesian framework*," *IFAC-Papers OnLine*, vol. 53, no. 1, pp. 634–639, 2020.

[30] N. Peker and C. Kubat, "Application of chi-square discretization algorithms to ensemble classification methods," *Expert Systems with Applications*, vol. 185, article 115540, 2021.

[31] S. Bahassine, A. Madani, and M. Kissi, "An improved Chi-sqaure feature selection for Arabic text classification using decision tree," in *2016 11th International Conference on Intelligent Systems: Theories and Applications (SITA)*, pp. 1–5, IEEE, 2016.

[32] B. Kalaiselvi and M. Thangamani, "An efficient Pearson correlation based improved random forest classification for protein structure prediction techniques," *Measurement*, vol. 162, article 107885, 2020.

[33] M. Baak, R. Koopman, H. Snoek, and S. Klous, "A new correlation coefficient between categorical, ordinal and interval variables with Pearson characteristics," *Computational Statistics & Data Analysis*, vol. 152, article 107043, 2020.

[34] P. Ashokkumar and S. Don, *Link-based clustering algorithm for clustering web documents*, ASTM International, 2018.

[35] A. Rehman, K. Javed, and H. A. Babri, "Feature selection based on a normalized difference measure for text classification," *Information Processing & Management*, vol. 53, no. 2, pp. 473–489, 2017.

[36] "Reuters dataset," https://archive.ics.uci.edu/ml/datasets/reuters21578+text+categorization+collection.

[37] "WAP dataset," http://glaros.dtc.umn.edu/.

[38] "20 news group dataset," http://qwone.com/~jason/20Newsgroups/.

[39] P. Ashokkumar, S. G. Shankar, G. Srivastava, P. K. Maddikunta, and T. R. Gadekallu, "A two-stage text feature selection algorithm for improving text classification," *ACM Transactions on Asian and Low-Resource Language Information Processing*, vol. 20, no. 3, pp. 1–19, 2021.

[40] G. Siva Shankar, P. Ashokkumar, R. Vinayakumar, U. Ghosh, W. Mansoor, and W. S. Alnumay, "An embedded-based weighted feature selection algorithm for classifying web document," *Wireless Communications and Mobile Computing*, vol. 2020, 10 pages, 2020.

Hindawi

Research Article

Preparation of SnO₂-Based Composite Gas-Sensitive Material and Its Effect on the Membrane Treatment Process of Volatile Organic Compounds

Youping Shou, Junjie Zhao ⓘ, and Jianzhe Qiao

Tianjin Research Institute for Water Transport Engineering, M.O.T., 300000 Tianjin, China

Correspondence should be addressed to Junjie Zhao; 631406010214@mails.cqjtu.edu.cn

Semiconductor oxide-sensitive materials can be divided into n-type materials and p-type materials according to this characteristic. The carriers in n-type materials are mainly electrons, which are formed by the existence of a large number of oxygen vacancies in the material's crystal lattice. Common n-type materials include SnO_2, In_2O_3, and ZnO. This article is aimed at studying the effect of SnO_2-based composite gas-sensitive materials on the treatment process of volatile organic compounds. In this paper, the biomembrane method, the ultrafiltration membrane transmembrane pressure difference method, and the chemical reaction activity analysis method in the membrane treatment detection method are proposed, and then, the empirical kinetic model for the preparation of SnO_2-based composite gas-sensitive materials is established, and the TPU nanometer is analyzed. The cross-sectional scanning of the composite material explored the effect of the curing agent content on the SnO_2-based composite gas-sensitive material and analyzed the mechanical properties of the material. The experiment in this article uses 15 orders of magnitude of mechanics, which improves the scientific nature of the article. The experimental results show that the material modification has a better improvement effect on the film treatment process of volatile organic compounds.

1. Introduction

1.1. Background. With the development and progress of society, the population of urban areas has expanded, the flow of motor vehicles has increased, and chemical products have increased, but they have strong chemical activity. Some VOCs are also highly toxic and have certain hazards to the atmospheric environment and organisms. Affected by changes in the intensity of emission sources and traffic activities, VOCs exhibit regular daily and seasonal changes. The literature shows that there is a significant seasonal variation in the concentration of VOCs, which reaches the highest value in winter and drops to the lowest value in summer. Due to the low temperature in winter and the increase in coal consumption for heating, the increased VOC emissions increase the concentration level in the atmosphere, and the high temperature in summer reduces the consumption of coal and other energy sources. At the same time, high temperature promotes the elimination of some VOCs in the

atmosphere and reduces the level. In addition, in the chemical plant area, VOCs are greatly affected by changes in temperature. Olefin compounds such as isoprene are mainly derived from the natural emissions of plants, and their changes show significant characteristics of plant emissions. However, none of these methods can fundamentally solve the volatility problem of volatile organic compounds such as styrene.

1.2. Significance. For the detection of harmful gases, there are currently two methods: large analytical instruments and gas sensors. Although large-scale analytical instruments have the advantages of accurate and high-precision gas detection, they cannot be the main method for gas detection due to their high price, inconvenience to carry, and inability to complete rapid detection. For more than half a century, through the continuous efforts of scientists, the application of semiconductor oxide sensors in real life has become more and more extensive. At the same time, the nanofiber

material has the advantages of uniform thickness and good morphology consistency, which reduces the influence of the morphology on the gas-sensing properties and facilitates the comparison of the gas-sensing properties of different materials. However, semiconductor gas sensors still have a series of problems such as inaccurate gas detection and poor accuracy. Therefore, it is necessary to develop high-performance gas sensors to complete the detection of the types and concentrations of harmful gases.

1.3. Related Work. Volatile organic compounds are an important air pollutant and have a huge destructive effect on the human living environment. Zheng et al.'s research is aimed at evaluating the efficiency of removing volatile organic compounds (VOC) from process gases in the eastern Polish food industry plant, which produces high-quality animals (geese, ducks, and pigs) and vegetable fats using two phases: method combined with biological purification and membrane separation. The research was conducted on a semitechnical scale and compared the effects of traditional and two-stage biological filtration under the same process conditions. The concentration of VOC in the process gas is measured by a multigas detector. In addition, the temperature and humidity of the gas are determined by a thermal anemometer under the filter bed, followed by two different types of filling materials (a mixture of stumps and bark, and a mixture of stumps, bark, and compost: European Union and Poland national standard methods) and two kinds of membranes (using three-layer semipermeable membrane fabrics with different air permeability and water tightness) were analyzed [1]. VOC (volatile organic compounds) are mainly produced in workplaces or laundry shops using spray paint processes or organic solvents. Large-scale plasma treatment of exhaust gas under industrial or municipal conditions requires a high-efficiency plasma conversion process at a high processing speed, that is, a large volume flow. Due to the use of plasma processing steps, the integration of the plasma unit into the existing system puts forward requirements for pipeline system compatibility and minimum pressure drop. The innovative rotating electrode sliding arc plasma device described in this article can meet these conditions. The system consists of propeller-shaped high-voltage electrodes in a grounded metal pipe. The design of the high-voltage electrode eliminates the pressure drop inside the air system. In contrast, the plasma device itself can drive exhaust gas with a tube diameter of 20 cm at a volume flow rate of up to 300 cubic meters per hour. They are composed of various forms of hydrocarbons. Because of their low concentration, they are diluted in the atmosphere, so it is difficult to burn directly with traditional burners. In this research, Sun et al. proposed a new form of VMDC (volume matrix dump) burner to process this low-calorie VOC gas. The burner configuration combines the characteristics of a plasma burner, dump burner, and volume matrix burner. Therefore, VMDC is configured to ensure sufficient decomposition temperature and residence time for stable flame formation and VOC decomposition. [2]. Although wood-based panels release harmful formaldehyde, they are still widely used. In order to protect humans

from exposure to formaldehyde, we have successfully produced particle board by surface treatment of wood fibers and the use of unsaturated polyester resin (UP) as a formaldehyde-free binder. Phenolic (PF) aqueous solutions are used to treat wood particles to make them more compatible. Wan et al. inspected whether the mechanical properties of particleboard meet the national standard and M-1 level (ANSI A208.1-1999). The water absorption test confirmed the dimensional stability of FF particleboard. The performance of PF-treated FF particleboard is several times better than that of untreated FF particleboard. In addition, the effect of PF treatment on the adhesion of wood particles and UP interface was also studied by SEM, DMTA, and contact angle measurement. The results confirmed that PF treatment improved the interfacial adhesion between UP and wood particles [3]. Although his experimental studies have improved the interfacial adhesion between UP and wood particles, the adhesion is still insufficient.

1.4. Innovation. This paper introduces the curing kinetic parameter algorithm of unsaturated polyester resin, membrane processing detection method, chemical reaction activity analysis method, and other methods and then constructs the empirical kinetic model of unsaturated polyester resin, the preparation of cellulose nanocrystals, and study on the apparent kinetics of curing of unsaturated polyester resin and finally analyze the cross-sectional scan of the TPU nanocomposite, explore the effect of curing agent content on the gel time of unsaturated polyester resin, and analyze the mechanical properties of the material. According to the conclusions obtained after the comparison, the mechanism of the enhanced gas sensing properties of the composites and the mechanism of the conductivity type transition were analyzed.

2. Experimental Method

2.1. Gas Sensor Production. The experiment mainly uses hollow ceramic tubes to prepare indirectly heated gas sensors for gas sensitivity testing [4]. There are two ring electrodes in the middle of the ceramic tube, and each ring electrode leads out two pins. Put the metal oxide sensitive material prepared after the experiment into a mortar, add an appropriate amount of deionized water to it, and grind for 15-20 minutes, so that the sensitive material and deionized water are fully mixed to obtain a paste with good uniformity material [5, 6]. Use a brush to evenly coat the polished material on the middle part of the two electrodes of the ceramic tube, and the thickness should cover the electrodes. After drying at room temperature, put the coated ceramic tube in the muffle furnace, raise it to 300°C at a rate of 2°C/min, keep it for 120 minutes, and then lower it to room temperature at a rate of 3°C/min to ensure that the material is firmly attached to the electrode surface [7]. Pass the heating wire in the middle of the processed ceramic tube, weld the heating wire and the ceramic tube to the hexagonal base, aging in the air at a temperature of 300°C for 1 week, and then obtain a gas sensor that can be tested [8].

The static test system consists of air distribution box, DC power supply, A/D data acquisition card, and computer. The volume of the gas distribution box is 50 l, which is mainly used to prepare the required concentration of gas. The DC power supply is used to provide stable voltage, test voltage, and heating voltage for the gas sensor. The A/D data acquisition card (model USB7360B) is mainly used to convert the analog signal obtained by measuring the voltage of the sensitive element into a digital signal and then upload it to the computer for analysis by the software in the computer.

Since the VOC gas in this experiment is obtained through the vaporization of the corresponding organic solution, a heating crucible is equipped in the gas distribution box, which is to accelerate the evaporation of organic gas, and it is equipped with a gas exchange device and a test circuit [9]. During the test, the relationship between the volume V of the organic liquid to be injected and the gas concentration c in the gas distribution box is as shown in the formula:

$$\frac{p * w\% * v}{M} = \frac{V * c}{22.4 * (273 + T)/273}. \tag{1}$$

After simplification, you can get

$$v = \frac{V * c * M * 273}{(273 + T) * 22.4 * p * w\%}. \tag{2}$$

In the formula, M represents the molar mass of the gas to be tested, p represents the density of the organic liquid, $w\%$ represents the mass fraction of the component to be tested in the organic liquid, V represents the volume of the test chamber, and T is the temperature of the test chamber. For p-type materials, the expression of the response value S of the gas

$$S = \frac{Rg}{Ra} = \frac{Ug(10 - Ua)}{Ua(10 - Ug)}. \tag{3}$$

For n-type materials, the gas response value S can be expressed as

$$S = \frac{Ra}{Rg} = \frac{Ua(10 - Ug)}{Ug(10 - Ua)}. \tag{4}$$

In the formula, Ua and Ug are the voltage values of the tested component measured by the static test system in air and organic gas, respectively.

2.2. Membrane Treatment and Detection Method

2.2.1. Ultrafiltration Membrane Transmembrane Pressure Difference Method.
The experiment uses the change of transmembrane pressure difference as the basis for evaluating the fouling rate of the ultrafiltration membrane, and the transmembrane pressure difference is monitored online by a pressure gauge [10]. The detected water quality data includes the turbidity, SDI, and CODMn of the incoming and outgoing water of each processing unit. The surface morphology

changes of ultrafiltration membranes under different operation modes are analyzed.

In order to explore the pollution mechanism of ultrafiltration under different pretreatment conditions, the experiment refers to the Darcy resistance model [11] and analyzes each part of the resistance generated during the ultrafiltration process. The formula is as follows:

$$J = \frac{\Delta p}{\mu (R_m + R_f + R_c)} = \frac{\Delta p}{\mu R_t}. \tag{5}$$

Each resistance can be calculated by the following formula:

$$R_m = \frac{\Delta p}{\mu j_{iw}}, \tag{6}$$

$$R_f = \frac{\Delta p}{\mu j_{iw}} - R_m, \tag{7}$$

$$R_c = \frac{\Delta p}{\mu j} - (R_m + R_f), \tag{8}$$

where j_{iw} is the initial membrane water flux, $m^3/(m^2 \cdot h)$ and j is the membrane water flux after pollution, $m^3/(m^2 \cdot h)$.

Membrane treatment ultrafiltration technology has broad prospects in the treatment of volatile gases, sewage, drinking water, and surface water due to its own advantages. Based on the current problems of ultrafiltration, this research studies the pollution mechanism of ultrafiltration membranes to alleviate membrane pollution and reduce the cost of ultrafiltration. It also compares and analyzes the current commonly used pretreatment methods to find out suitable pretreatment methods such as Figure 1 shows the ultrafiltration device and its simple schematic diagram.

2.3. Chemical Reaction Activity Analysis Method.
Although the content of VOCs in the atmosphere is small, they can undergo a series of chemical reactions with oxidants such as OH radicals, HO_2 radicals, and O_3 in the atmosphere and play an important role in the elimination of atmospheric oxidants, thereby affecting the global OH radicals Distribution. On the other hand, VOCs can interact with NOx in the atmosphere and have an important impact on the formation of tropospheric ozone on a regional or even global scale. VOCs and ozone and other photochemical oxidation products can endanger the health of exposed people. VOCs have high volatility and also have characteristics such as permeability and lipophilicity. Most of the aromatic compounds are toxic and harmful substances. Due to the high lipophilicity, these compounds will enter the human body through respiration and be enriched. People who are exposed to these low-concentration toxic and harmful pollutants for a long time will produce chronic hazards. This hazard is often difficult to attract people's attention. These pollutants mainly irritate the eyes and nasal mucosa through contact with the respiratory mucosa, resulting in chronic bronchitis and asthma. Physiological dysfunctions such as lung cancer and

Industrial ultrafiltration device

Principle of ultrafiltration

Laboratory ultrafiltration device

Collection device

Nitrogen pressurized bottle
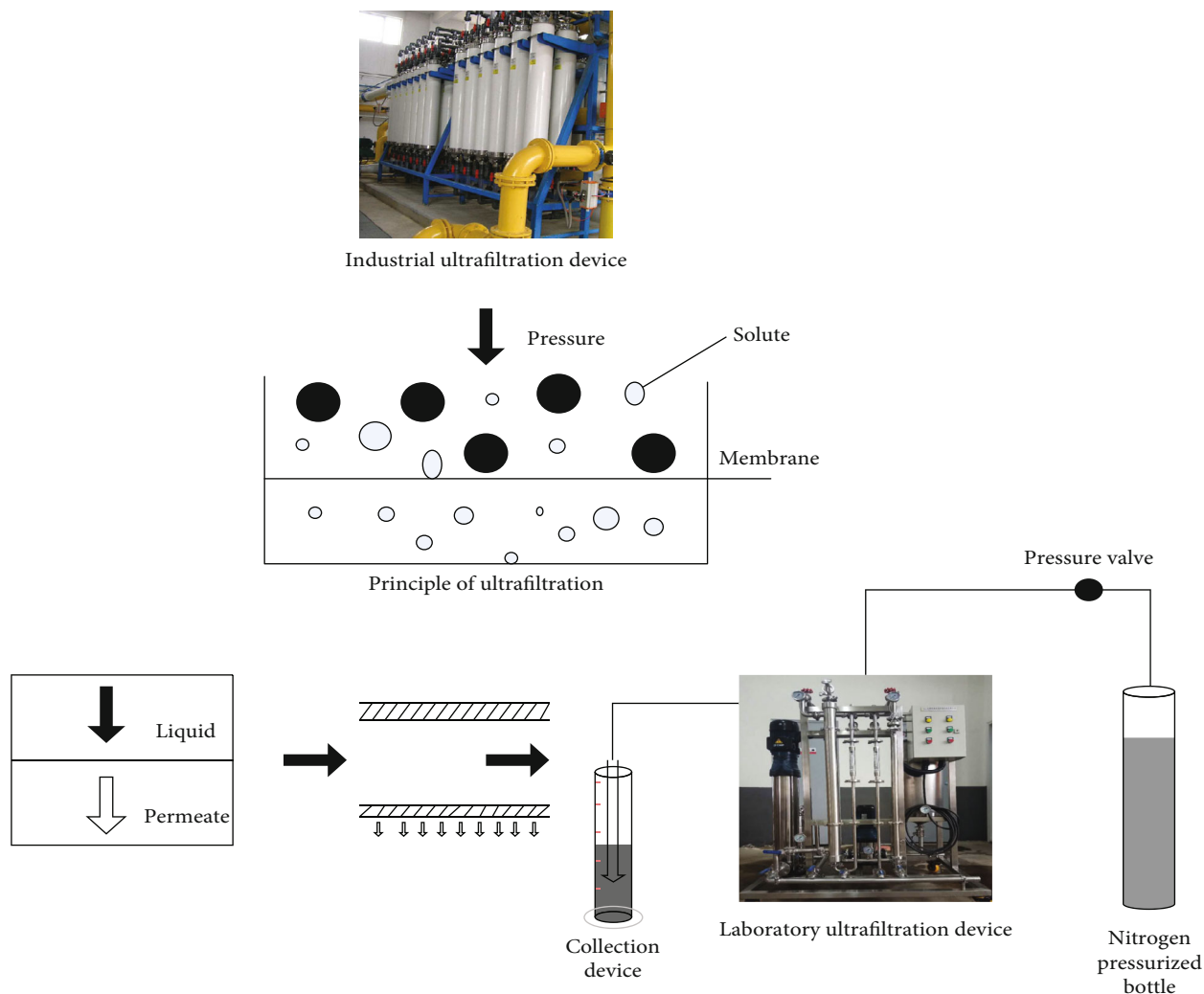
FIGURE 1: Ultrafiltration experimental device and principle.

lung cancer aggravate the condition of hypertension and heart disease.

At present, there are two main methods used to measure the reactivity of VOCs and their contribution to ozone production: First, the reactivity of VOCs species is expressed as

$$L_i^{\text{OH}} = [\text{VOCs}]_i \times K_i^{\text{OH}}. \tag{9}$$

Calculate the reactivity of each component of VOCs and then add the LiOH of each species in the component:

$$L^{\text{OH}} = \sum [\text{VOCs}]_i \times K_i^{\text{OH}}, \tag{10}$$

$$\Phi_{\text{ofp}} = \xi_{\text{MIR}} \times \rho(c_2 - c_{12}). \tag{11}$$

2.4. Performance Indicators of Gas Sensors. The performance of the gas sensor is mainly judged by the following aspects: the response value of the gas sensor, the working temperature, the selectivity, the response-recovery time, the stability, etc.

The response of the gas sensor to the gas to be measured will be affected by temperature, because the gas to be measured requires a certain amount of energy to react on the surface of the gas sensor [12, 13]. When the temperature is too low, the energy provided is too little, which will result in too little gas to be measured on the surface of the sensor, resulting in a relatively low response value; when the temperature is too high, it will lead to waste of energy and even damage to the device [14]. At a specific temperature, the sensitive element will show the maximum response value of the gas to be measured, and this temperature is usually called the optimal working temperature of the element. A lower optimal working temperature or even room temperature operation is one of the necessary conditions for a sensor with good performance [15, 16].

Selectivity is obtained by comparing the response value of the sensor to a specific gas with the response value of other gases [17]. It is known that the sensitive element will respond to a variety of gases when working at the optimal operating temperature, which will cause errors in the measurement. Therefore, it is necessary to prepare components with good selectivity.

(a)

(b)
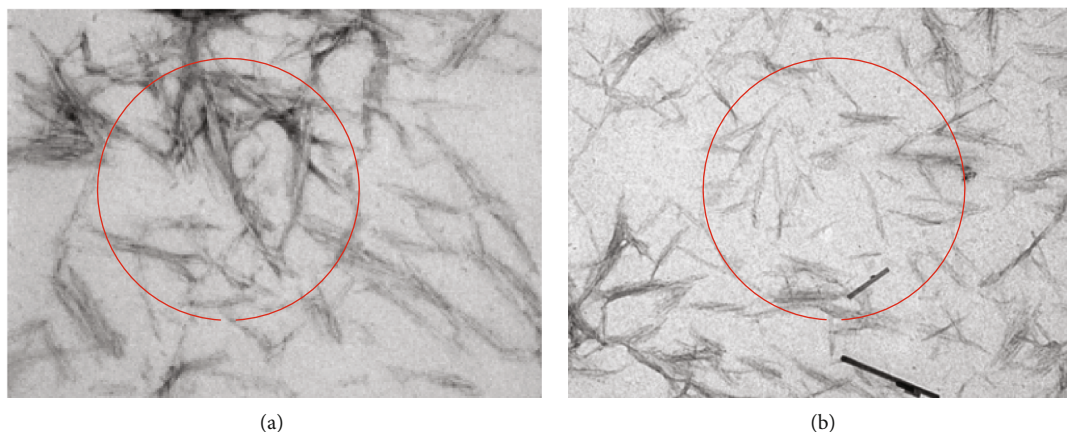
FIGURE 2: Transmission electron microscopy (TEM) photo of cellulose nanocrystals (a) 70,000 times magnification and (b) 40,000 times magnification.
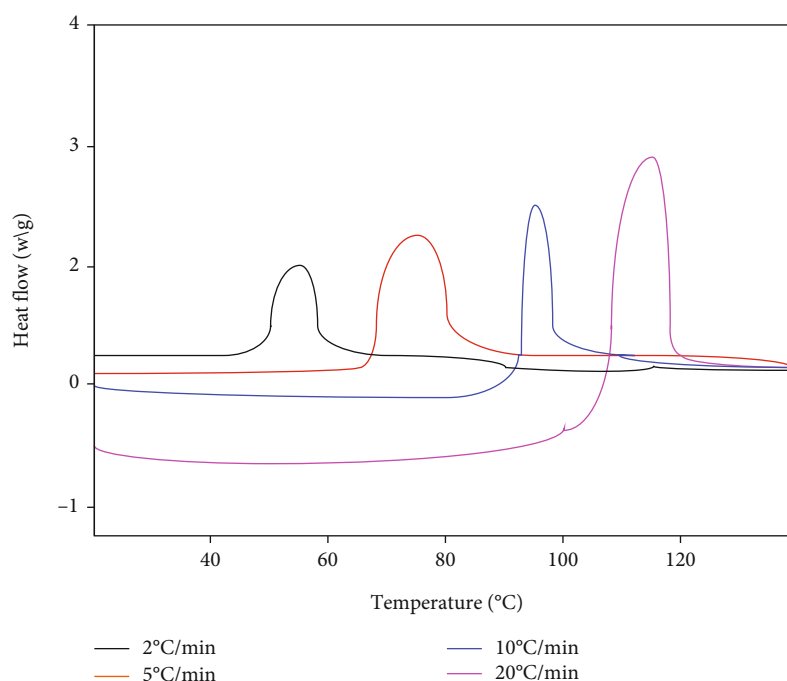
FIGURE 3: DSC curves of composite gas-sensitive materials at different heating rates.

TABLE 1: Characteristic temperature of DSC curve (°C).

B (°C/min)	Ti (°C)	Tp (°C)	Tf (°C)
2	46.8	54.5	62.5
5	65.1	73.1	81.2
10	76.9	91.0	107.2
20	82.6	100.8	125.7

TABLE 2: Composite gas-sensitive material curing kinetics data.

B (°C/min)	Tp (°C)	Tp (K)	$1/Tp$	$-\ln \beta/T^2_P$	$\ln \beta$
2	54.5	327.6	$3.053 * 10^{-3}$	10.890	0.693
5	73.1	346.3	$2.888 * 10^{-3}$	10.085	1.609
10	91.0	364.2	$2.746 * 10^{-3}$	9.493	2.303
20	100.8	374.0	$2.671 * 10^{-3}$	8.853	2.996

When it comes into contact with the gas to be measured, it takes a certain time for the sensitive element to reach the maximum response value [18]. The time when the initial state reaches 90% of the maximum response value is usually defined as the response time; similarly, when it is separated from the gas to be measured, the sensitive element needs to be restored. It takes a certain time to restore to the original state. Usually, the time from the maximum response value to 10% of the maximum response value is defined as the recovery time. Shortening the response-recovery time is helpful for continuous detection, so the response-recovery time is also an important parameter of the gas sensor.
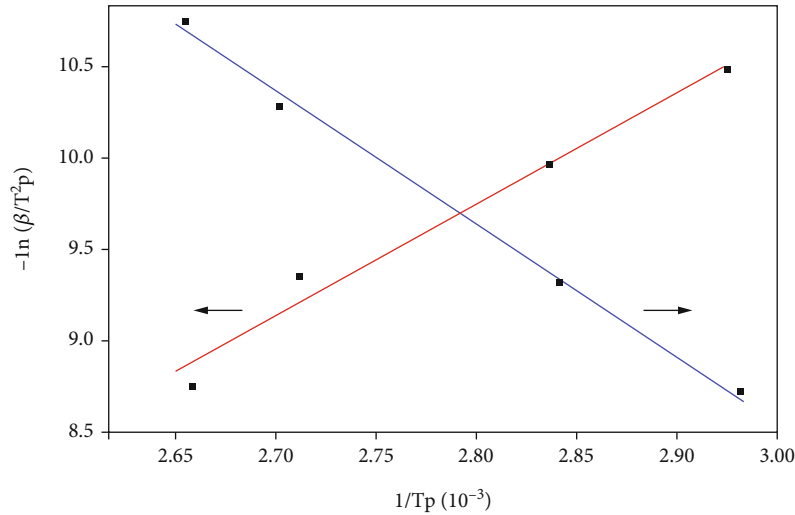
FIGURE 4: ln $(\beta/T^2_p) \sim 1/Tp$ and ln $\beta \sim 1/Tp$ of the curing reaction of composite gas-sensitive materials.
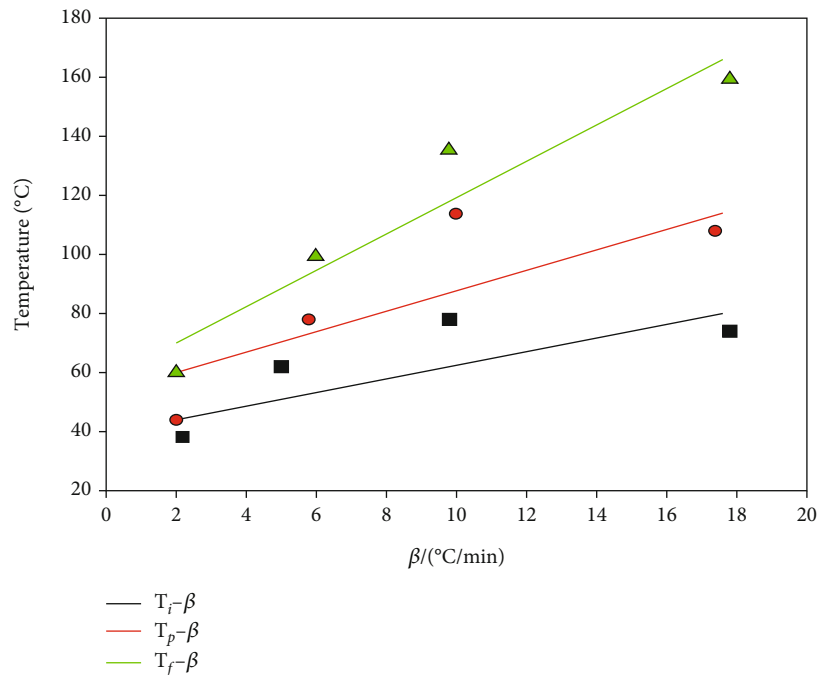
FIGURE 5: The relationship between T and β.

If the gas sensor is used for a long time or stored for a long time, its internal structure will change, causing the resistance to drift when measuring gas [19]. This will cause problems such as a decrease in the response value, which will affect the accuracy of the measurement. Therefore, stability is the decisive factor for whether the gas sensor can be applied in real life. The performance of these sensors is mainly determined by the characteristics of sensitive materials. Therefore, in order to make a gas sensor with good performance, it is necessary to prepare a sensitive material with good characteristics.

For gas sensors, sensitive materials with good characteristics must be prepared. The gas-sensing characteristics of

sensitive materials are mainly determined by factors such as the composition of the material, the morphology of the material, the porosity of the material, the size of the grain size of the material, and the specific surface area of the material. Therefore, improving the gas-sensing properties of sensitive materials can be achieved through physical modification and chemical modification.

3. Experimental Inquiry

3.1. Establishment of an Empirical Kinetic Model of Unsaturated Polyester Resin. The curing kinetics of unsaturated polyester resins can be roughly divided into two
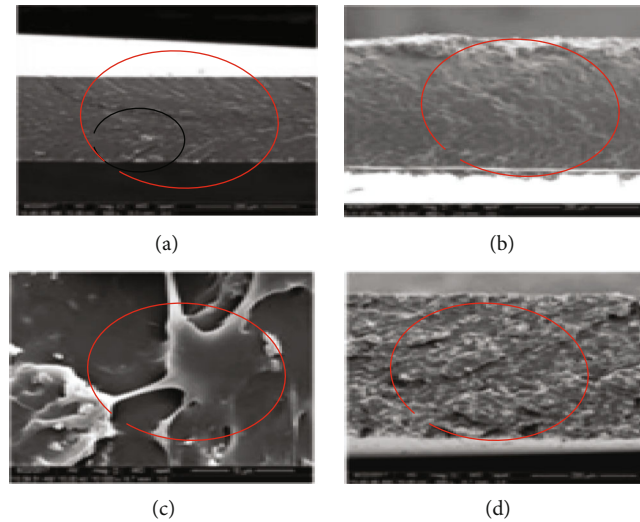
FIGURE 6: (a) GO/TPU, (b) GOE/TPU, (c) GOS/TPU, and (d) cross-sectional SEM image.

categories: empirical kinetic models and mechanism kinetic models [20]. The former does not consider the specific reaction process between the reactants, but a curing kinetic model equation established by mathematical simulation of a series of kinetic parameters measured through experiments during the curing reaction process. The latter is a curing kinetic model based on the principle of free radical polymerization. Unsaturated polyester resins include chain initiation, chain extension, and chain termination during the curing process, which are related to each other, and the reaction is difficult to stay in a certain way. In the first stage, with many parameters, it is difficult to get a suitable model. Therefore, empirical kinetic models are more commonly used to analyze the curing kinetics of unsaturated polyester resins.

The kinetic model of the n-order reaction model of unsaturated polyester resin is expressed as

$$\frac{d_a}{d_t} = kn(1-a)^n. \tag{12}$$

Curing reaction rate equation:

$$\frac{d_a}{d_t} = An(1-a)^n \exp\left[-\frac{E}{RT}\right]. \tag{13}$$

The expression of the autocatalytic model is

$$\frac{d_a}{d_t} = (_1 + k_2 a^m)(1-a)^n, \tag{14}$$

where k_1 is the reaction rate constant when $t = 0$ and k_2 is the reaction rate constant when $t > 0$, and both conform to the Arrheriu formula. m and n are the reaction order. Generally, it is assumed that the reaction order is 2 (i.e., $m + n = 2$). Equation (14) is widely used to describe the autocatalytic model of isothermal curing behavior of epoxy resin; afterwards, Ahmed et al. [21] did further research on Equa-

tion (14) and found that when $k_1 = 0$, it can be better used to study the isothermal curing kinetics of unsaturated polyester resin; the equation is as follows:

$$\frac{d_a}{d_t} = k_2 a^m (1-a)^n. \tag{15}$$

For this equation, there are also many application examples. Researchers have studied the curing kinetics of unsaturated polyester resin/composite initiation system and BMC materials and found that the selection of Equations (9)–(15) can well describe the curing reaction of unsaturated polyester resin.

3.2. Preparation of Cellulose Nanocrystals

3.2.1. Extraction of Cellulose Nanocrystals. According to related literature, cellulose nanocrystals (CNs) are extracted from cotton linters by sulfuric acid acidolysis. The specific steps are as follows: disperse 20 g of cotton linters in 175 ml with a concentration of 30% (*v/v*) sulfuric acid solution. The stirring was continued for 6 hours at a speed of 100 rpm at 60°C. After the reaction, the residual sulfonic acid groups on the surface of CNs were removed. Finally, freeze-dry at a low temperature of -50°C for more than 3 days. The CNs from which the distilled water has been removed are ground to obtain a white powder.

3.2.2. The Acetylation Process of Cellulose Nanocrystals. Weigh 5 g of CNs in 100 ml of anhydrous pyridine to ultrasonically disperse for 15 min to obtain a CNs suspension. Place it in a three-necked flask. Then, prepare a mixed solution of 25 ml of acetic anhydride and 20 ml of anhydrous pyridine. Add the acetic anhydride pyridine solution dropwise to the CN pyridine suspension through a separatory funnel to carry out the acetylation reaction. The acetylation process is carried out in a three-necked flask by condensing reflux. React at 400 rpm for 5 h at °C. After the reaction, the product in the three-necked flask was poured into 1 l of
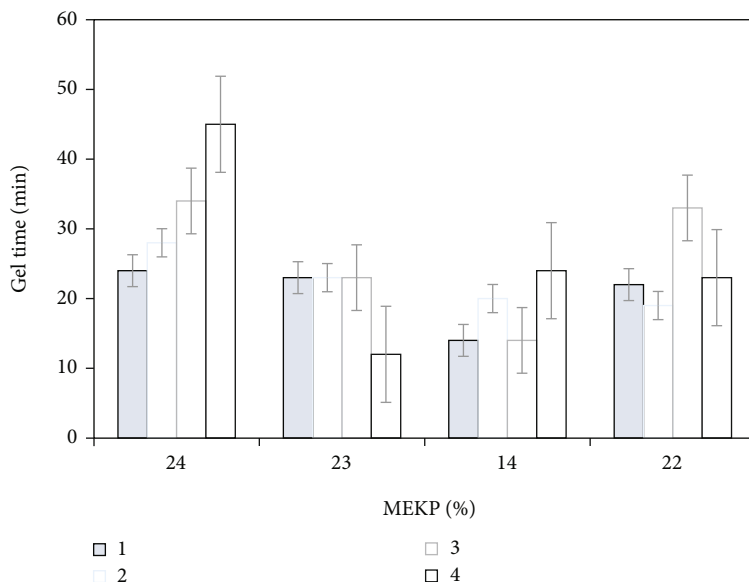
FIGURE 7: The effect of the amount of curing agent on the time of the composite gas-sensitive material was studied.
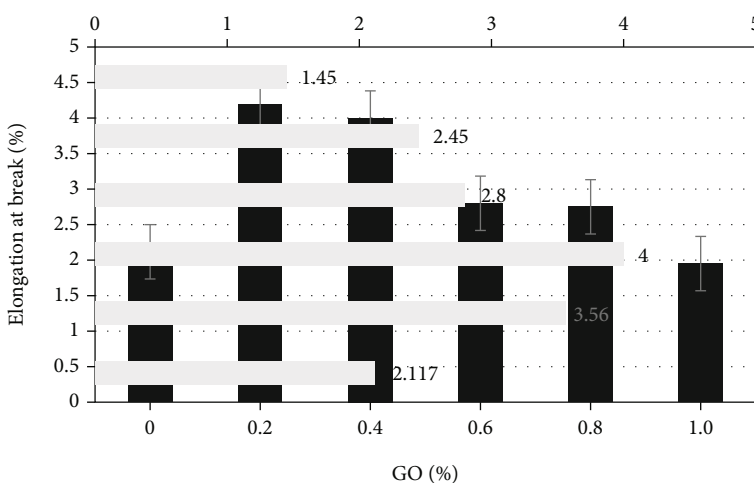
FIGURE 8: Comparison of elongation at break of graphene oxide/hydroxylated carbon nanotubes synergistically modified composite gas-sensitive materials.

TABLE 3: Mechanical properties of the composites.

Sample	Tensile strength (MPa)	Flexural modulus of elasticity (MPa)	Elongation at break (%)
0	38.42	2020.95	2.117
0.1	57.05	1678.46	4.189
0.25	53.31	1547.16	3.983
0.5	44.68	1721.01	2.896
0.75	45.96	1843.57	2.774
1	34.69	1931.86	1.951

distilled water to terminate the reaction, and the cellulose nanocrystals were precipitated, washed three times with acetone centrifugal precipitation, and then washed three times with distilled water. Then, it was dialyzed in distilled water

for 12 hours, and finally, the acetylated cellulose nanocrystals were freeze-dried, and the freeze-dried acetylated cellulose nanocrystals were ground to obtain a white powdery product (ACN).

Figure 2 shows a transmission electron microscopy (TEM) image of cellulose nanocrystals (CNs), using sulfuric acid hydrolysis to remove the amorphous areas in the linters cellulose and successfully extract CNs. After observation, the extracted CNs have a rod-like nanomorphology structure. The length of CNs was measured with the Image-Pro software to measure the average size length: length $L = 310.1 \pm 47.8$ nm and width $D = 18.9 \pm 6.2$ nm.

3.3. Study on the Apparent Kinetics of Curing of Unsaturated Polyester Resin. When using the DSC method to solve the curing kinetic parameters of the SnO_2-based composite
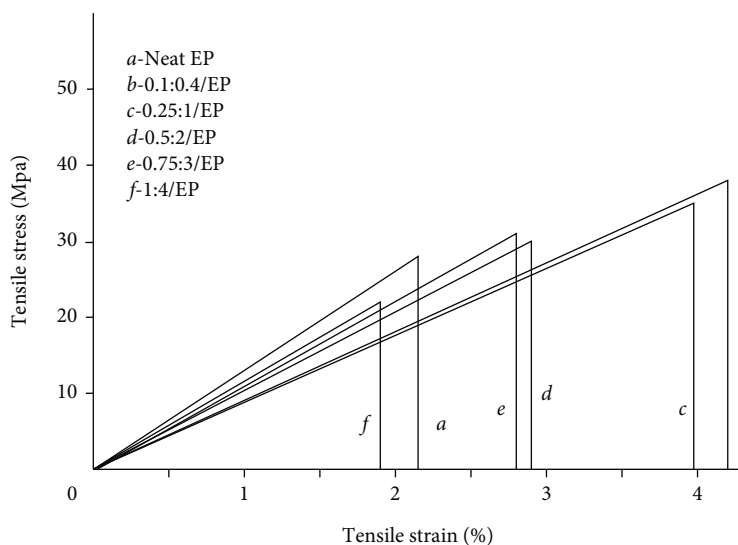
FIGURE 9: Stress-strain curve of graphene oxide/hydroxylated carbon nanotubes synergistically modified composite gas-sensitive material.

gas-sensitive material, it is necessary to test the DSC curves at different heating rates. The test result is shown in Figure 3.

In order to study the curing reaction kinetics of SnO_2-based composite gas-sensitive materials, it is necessary to solve the kinetic parameters such as the apparent activation energy (E) and reaction order (n) of the gas-sensitive materials and use the curing kinetic equation to describe the parameters and curing conditions. Table 1 shows the characteristic temperature (°C) of the DSC curve. Table 2 shows the curing kinetics data of the gas-sensitive material.

As shown in Figure 4, in order to achieve the above goal, linear fitting of the above known points can be obtained: $-\ln \beta/T^2_P \sim 1/Tp$ has a slope of $5.111 * 10^3$ and an intercept of -4.683, then $E/R = 5.111 * 10^3$, $\ln (AR/E) = 4.683$, so that the activation energy of DHEM50-1 resin system $E = 42.48$ kJ/mol, frequency factor $A = 5.523 * 10^5$. By linear fitting, it can be known that the slope of $\ln \beta \sim 1/Tp$ is $-5.81 * 10^3$, then $E/nR = 5.81 * 10^3$, since E has been obtained, substituting can be obtained $n = 0.880$.

Using the DSC method to solve the kinetics of composite gas-sensitive materials , the curing characteristic temperature of composite gas-sensitive materials can be preliminarily estimated. The relationship between temperature T and heating rate β is $T = C + B\beta$ (°C).

Use T-β to plot and get three different straight lines through linear fitting. As shown in Figure 5, when $\beta = 0$, the temperature of the composite gas-sensitive material is 51.5°C, the curing temperature is 57.8°C, and the postcuring temperature is 62.8°C. The above experiment test has no other fillers, and the dosage is small. Therefore, in actual production, it needs to be adjusted according to different situations.

4. Material Performance Analysis

4.1. Sectional Scanning Analysis of TPU Nanocomposite.
The fracture surface morphology of TPU and its composites was analyzed. Figure 6 shows the fracture SEM images of GO/TPU, GOE/TPU, GOS/TPU, and GOES/TPU composites with a filler content of 2 wt%. From Figures 6(a) to 6(d), it can be seen to varying degrees that the fracture surface has begun to become rough, with wrinkles and gullies appearing, which indicates that there is a strong interface interaction between the nanoparticles and the matrix. In addition, the composite material in Figure 6(d) is the roughest, and it is magnified to observe that GOES nanoparticles prepared by the stitching effect of EDA and SiO2 coating can effectively improve the mechanical properties of TPU. This shows that this unique stitched and multisize graphene-based material helps to enhance the interface interaction between the filler and the matrix.

4.2. The Effect of Curing Agent Content on the Time of Composite Gas-Sensitive Materials.
Figure 7 shows the effect of curing agent content on the time of the composite gas-sensitive material. It can be seen from Figure 7 that when the composition ratio, temperature, and other conditions of the composite gas-sensitive material remain unchanged, with the increase of the initiator MEKP and the accelerator TZ-9, the time of the composite gas-sensitive material gradually shortens, and the time decreases gradually. This is because the amount of initiator methyl ethyl ketone peroxide added is greater than the amount of accelerator cobalt salt added, so the greater the amount of initiator added, the more initial free radicals generated per unit time of methyl ethyl ketone peroxide, and the increase of initial free radicals can be accelerated resin free radical reactions; these reactions are exothermic reactions, which will increase the temperature of the system and accelerate the reaction rate again; however, the reaction rate of the composite gas-sensitive material cannot be increased indefinitely. This is mainly because the content of double bonds in the composite gas-sensitive material is limited, and these double bonds can only react with a limited number of free radicals. Therefore, when the initiator content increases again, the

composite gas-sensitive material time will be shortened, but the downward trend will decrease. When the initiator MEKP in the DHEM50-1 composite gas-sensitive material is added in the amount of 0.8-2 wt%, the time of the DHEM50-1 composite gas-sensitive material is in the range of 19-28 min.

4.3. Mechanical Properties. As shown in Figure 8 in conjunction with Table 3, the elongation at break and tensile strength of the material first increase and then decrease.

Figure 9 shows the tensile strength curve of GO-MWCNTs/EP material. Combined with the data in Table 3, it can be seen.

As shown in Figure 9, on the other hand, in the GO/EP system, when the GO content is 0.25 wt%, the mechanical properties of the material are the best, while in the GO-MWCNTs/EP system, when our GO content is reduced from 0.25 wt%. When it reaches 0.1 wt%, it can be seen from the graph that MWCNTs decreases with the decrease of GO content. The above experiments all show that the content of GO will enhance the material to a certain extent and is beneficial to the performance of the material.

5. Conclusions

The environmental effects of volatile organic compounds in the atmosphere are mainly manifested in their strong chemical activity. These active substances can participate in atmospheric chemical reactions, change the chemical properties of the atmosphere, and then change the air quality. This article mainly discusses the influence of composite gas-sensitive materials on the treatment process of volatile organic compounds exhaust gas membrane. It is hoped that effective treatment methods can be explored to reduce the emission and absorption of volatile organic compounds, so as to achieve the purpose of protecting the environment and improving human health. The double bond of the composite gas-sensitive material can undergo free radical polymerization with the double bond in the double bond monomer molecule as the crosslinking component under light conditions and form a more complex three-dimensional network structure under thermal initiation conditions. Combination of volatile organic compounds reduces pollution emissions. However, as far as the current situation is concerned, the technology is not perfect enough, and further research and development are needed. There are many ways to improve the gas sensing properties. The influence of the composite materials formed by doping on the gas sensing mechanism is relatively complicated. The relationship between the heterostructures composed of different materials and the gas sensing properties needs to be further studied.

Data Availability

No data were used to support this study.

Conflicts of Interest

The authors declare that they have no conflicts of interest.

References

[1] Z. Zheng, M. C. Cox, and B. Li, "Surface modification of hexagonal boron nitride nanomaterials: a review," *Journal of Materials ence*, vol. 53, no. 1, pp. 66–99, 2018.

[2] M. Sun, J. Ma, Y. Zeng, and Z. Liu, "Surface modification-the booster for application of magnetic nanomaterials," *Gongneng Cailiao/Journal of Functional Materials*, vol. 49, no. 4, pp. 04032–04039, 2018.

[3] E. Wan, L. Y. Heng, and M. Arip, "Surface modification of cellulose nanomaterial for urea biosensor application," *Sains Malaysiana*, vol. 47, no. 5, pp. 941–949, 2018.

[4] Z. Xiong, M. Shen, and X. Shi, "Zwitterionic modification of nanomaterials for improved diagnosis of cancer cells," *Bioconjugate Chemistry*, vol. 30, no. 10, pp. 2519–2527, 2019.

[5] O. V. Chudina, A. V. Eletskii, E. V. Terent'ev, and G. S. Bocharov, "Steel surface modification with carbon nanomaterial using concentrated energy flows," *Metal Science and Heat Treatment*, vol. 60, no. 5-6, pp. 367–372, 2018.

[6] Y. Niu and W. Hong, "Dielectric nanomaterials for power energy storage: surface modification and characterization," *ACS Applied Nano Materials*, vol. 2, no. 2, pp. 627–642, 2019.

[7] L. A. Urkhanova, S. A. Lkhasaranov, and S. L. Buyantuev, "Modification of cement and concrete with carbon nanomaterials, obtained by plasma method," *International Journal of Civil Engineering and Technology*, vol. 9, no. 1, pp. 652–656, 2018.

[8] N. P. Dikiy, A. N. Dovbnya, Y. V. Lyashko, E. P. Medvedeva, D. V. Medvedev, and I. D. Fedorets, "Modification of nanomaterial by radiation," *Problems of Atomic Science and Technology*, vol. 105, no. 5, pp. 83–87, 2016.

[9] X. Xu, Q. Zhou, N. Song, Q. Ni, and L. Ni, "Kinetic analysis of isothermal curing of unsaturated polyester resin catalyzed with tert-butyl peroxybenzoate and cobalt octoate by differential scanning calorimetry," *Journal of Thermal Analysis and Calorimetry*, vol. 129, no. 2, pp. 843–850, 2017.

[10] F. Tong and H. Ding, "numerical simulation and experiment of hardening behaviors in unsaturated polyester resin artificial marble blocks under microwave radiation," *IEEE Transactions on Plasma Science*, vol. 44, no. 10, pp. 2485–2492, 2016.

[11] Z. H. Dai, Q. Li, Z. W. Chen et al., "Reactive diluent derived from ferulic acid for the preparation of a fully biobased unsaturated polyester resin," *ACS Sustainable Chemistry & Engineering*, vol. 8, no. 47, pp. 17379–17386, 2020.

[12] G. W. Lee, K. Kim, C. J. Yoon, S. Yoon, and J. H. Choi, "Development of braille block for visually-impaired persons using unsaturated polyester resin," *Materials Today: Proceedings*, vol. 3, no. 2, pp. 99–103, 2016.

[13] M. Barcikowski, W. Krolikowski, and S. Lenart, "Microstructures of unsaturated polyester resins modified with reactive liquid rubbers," *Polimery*, vol. 62, no. 9, pp. 650–657, 2017.

[14] A. N. Johari, M. R. Ishak, Z. Leman, M. Z. M. Yusoff, and M. R. M. Asyraf, "Influence of CaCO3 in pultruded glass fiber/unsaturated polyester resin composite on flexural creep behavior

using conventional and time-temperature superposition principle methods," *Polimery*, vol. 65, no. 11-12, pp. 46–54, 2020.

[15] E. E. Al-Obeidi, M. M. Uonis, and M. A. Al-Jubouri, "Leverage of cigarette ash powder concentrations on the alternating bending fatigue of unsaturated polyester resin," *International Journal of Advanced Research*, vol. 8, no. 11, pp. 675–682, 2020.

[16] M. Farsane, L. Soufia, A. Anouar, S. Chah, S. Dagdag, and M. Bouzziri, "Experimental evaluation of the curing of unsaturated polyester resin at various amounts of methyl ethyl ketone peroxide, cobalt octoate and porcelain powder," *Revista de Chimie-Bucharest-Original Edition*, vol. 71, no. 10, pp. 58–66, 2020.

[17] V. Geaman, M. A. Pop, I. Radomir, A. Semenescu, B. Florea, and O. R. Chivu, "The influence of thermal behaviour to composites based on cotton tissue and unsaturated polyester resin," *Materiale Plastice*, vol. 57, no. 1, pp. 197–201, 2020.

[18] C. E. Odoala, I. O. Igwe, S. N. Okonkwo, and I. P. Oragwu, "Evaluation of mechanical properties of unsaturated polyester resin composite tiles of granite quarry dust filler," *International Journal of Scientific and Engineering Research*, vol. 11, no. 7, pp. 1737–1745, 2020.

[19] P. Wang, T. Yao, Z. Li et al., "A superhydrophobic/electrothermal synergistically anti-icing strategy based on graphene composite," *Composites Science and Technology*, vol. 198, p. 108307, 2020.

[20] N. Martin, F. Smarandache, and S. Broumi, "PROMTHEE plithogenic Pythagorean hypergraphic approach in smart materials selection," *International Journal of Neutrosophic Science*, vol. 13, no. 1, pp. 52–60, 2021.

[21] A. A. Elngar and S. I. El-Dek, "Novel artificial face mask based nanofibers with special intelligent engineered nanocomposite against Covid-19," *Journal of Cybersecurity and Information Management*, vol. 5, no. 2, pp. 21-22, 2020.

Research Article

Application of Nanoscale Microparticle Technology in Medical Imaging Diagnosis and Treatment

Jingzhe Li [ID]

College of Nursing, Hebi Polytechnic, Hebi, Henan, China 458030

Correspondence should be addressed to Jingzhe Li; 2111820011@e.gzhu.edu.cn

Nanotechnology is an alternative material manufacturing technology, and the research field involves a broad field of modern technology, especially in the field of high-end manufacturing. Nanotechnology is a technique for studying the properties and applications of materials with structural dimensions in the range of 1 nanometer to 100 nanometers. Medical imaging refers to the technology and processing process of obtaining internal tissue images of the human body or a certain part of the human body in a noninvasive way for medical treatment or medical research; the acquired image can be further processed to restore the original image that was not clear enough to highlight some characteristic information in the image. The appearance of medical imaging has promoted the development of the medical field. The purpose of this paper is to study the application of nanoscale microparticle technology in medical imaging diagnosis and treatment. It is expected that the combination of nanotechnology and medical imaging will improve the accuracy of medical imaging diagnosis. This paper mainly introduces the general methods and technologies of technical development of medical imaging instruments and briefly shows the process of data and image analysis. The experimental results in this paper show that when other conditions remain unchanged, the image quality will change when the quality factor of the image changes. When the image quality is 60%, the image transmission rate is about 5.5FPS, which is relatively stable and can be used in the medical field.

1. Introduction

With the continuous rise of science, all fields of society have developed rapidly, and scientific research has reached the level of microscopic molecules, providing new possibilities for scientific research. The development and popularization of medical imaging technology and the substantial improvement of computer computing power have greatly promoted the development of medical image processing technology. With the continuous development of nanotechnology, a large number of nanomaterials appear in the field of social production and are widely used in the biological field. When nanobiology develops to a certain technology, nanomaterials can be used to make nanobiological cells with recognition ability, and the biomedicine of cancer cells can be absorbed and injected into the human body, which can be used for targeted killing of cancer cells. With the improvement of living standards, people pay more and more attention to their own health. How to combine nanotechnology and medical imaging technology to improve the level of medical diagnosis is a problem that should be considered at present. Since the development of medical imaging, in addition to X-ray, there are other imaging technologies. In terms of information application, image files and image digitized files can be exchanged and viewed, and the medical digital image transmission protocol technology has been developed.

The combination of medical imaging and nanotechnology can accurately extract images of lesions, reduce manual workload, improve image extraction speed, and make diagnosis results more accurate. Combining multiple imaging modes to achieve complementary advantages of each imaging mode is of great significance in biomedical imaging.

The combination of the two further enhances the digitization of hospitals and drives the development of the biomedical industry.

In this paper, an evaluation version of the X-ray medical imaging diagnostic instrument is designed, which provides the conditions for the secondary development to realize the digital acquisition and diagnosis of medical imaging data. In this paper, an image compression algorithm based on adaptive truncation coding is proposed, which solves the problem that excessive coding of unimportant coefficients brings workload to image compression.

2. Related Work

The broad application of nanotechnology in the biological field provides the possibility for the development of the medical field. Image-guided core needle biopsy is an important tool in the treatment of musculoskeletal tumors. Although the diagnostic yield and accuracy of this procedure are high, nondiagnostic results may occur. Nondiagnostic CNB results can cause unnecessary anxiety and can lead to repeat biopsies and delays in treatment. The Chinese name of CNB is fine needle biopsy, which refers to taking biopsies from the body for pathological examination, that is, observing cell morphology and the relationship between cells under a microscope. Lin et al. believe that understanding the radiological and histological factors that affect the diagnostic rate of CNB in musculoskeletal lesions can help radiologists select lesion sites for biopsy and help manage physician and patient expectations for biopsy results. Informing radiologists about the factors associated with low diagnostic rates during CNB of musculoskeletal lesions can improve diagnostic rates, demonstrating that this technique can be used in diagnosis [1]. Medical imaging is the foundation of child care, and much of the field of medical imaging relies on ionizing radiation: radiography, fluoroscopy, CT, and nuclear imaging. Frush and Sorantin believe that many considerations for this imaging of children differ in terms of appropriate radiation use, other factors that determine examination quality, opportunities for participation and education through the Internet, and translation of research work. Given these needs, it is imperative to explore the contribution of the pediatric radiology community and its impact, especially in improving the value of children's care [2]. Exposure to low-dose radiation has increased exponentially due to the influx of diagnostic imaging and medical procedures that use radiation, and this set dose limit essentially limits the use of medical radiation for diagnosis due to public health concerns. Low-dose radiation refers to ionizing radiation with a low energy transfer linear density at a dose of 100 mSv and below, and its main health risk is random effects. Rpsgt investigated radiation exposure concerns in the form of a retrospective review of previous experimental studies and an observational evaluation of the health effects of low-dose radiation. These studies show that high doses of ionizing radiation have toxic effects and increase cancer risk. Furthermore, the limitations of radiation in medical imaging are based on the assumption that the health risk of low-dose radiation is a linear extrapolation of high-

dose radiation [3]. Mobile devices and software now have sufficient computing power, speed, and complexity to interpret radiology examinations in real time. Venson et al. conducted a multivariate user study exploring image-based diagnostic capabilities using mobile devices and traditional workstations. Using CT, MRI, and radiographic datasets, they performed a task analysis between subjects, showing that for images from emergency mode, a mobile interface can provide accurate interpretation and rapid response, which may benefit patient healthcare [4]. As technology nodes shrink below 45 nm, high power issues have become a major disadvantage of CMOS logic circuits. Emerging spintronic nanodevice-based hybrid memory logic architectures have recently been investigated to overcome these issues. Deng et al. conducted a research on the architecture design of multicontext hybrid STT-MTJ/CMOS logic structure. Experimental results show that their advantages and disadvantages depend on the application being addressed. Finally, they also propose some design considerations and strategies to further optimize its reliability performance [5]. Breast cancer is a leading cause of suffering and death in women. The limitations of current diagnostic and therapeutic approaches have led to new strategies that positively impact survival and quality of life in breast cancer patients. Falagan-Lotsch et al. present an emerging approach based on actively targeted breast cancer nanomedicines. This approach uses a multifunctional inorganic nanoplatform with biomedical relevance, and nanotechnology offers real possibilities for reducing breast cancer mortality through early cancer detection, more precise diagnosis, and more effective treatment with minimal side effects [6]. The spread of antibiotic resistance and the growing prevalence of biofilm-associated infections are driving the need for new approaches to treating bacterial infections. Nanotechnology offers an innovative platform for addressing this challenge and even has the potential to manage infections involving multidrug-resistant (MDR) bacteria. Michal and Ehud summarize recent advances in the field of antimicrobial nanomedicines over the past few years and describes their unique properties, modes of action, and activities against MDR bacteria and biofilms and discusses biocompatibility and commercialization [7]. With the development of nanotechnology, there has been great interest in using nanomedicine strategies to enhance the radiation response of tumors. Nanomaterials containing high-Z elements to absorb radiation rays (such as X-rays) can act as radiosensitizers, depositing radiant energy within tumors and enhancing therapeutic efficacy. Song et al. believe that nanoscale carriers are capable of delivering therapeutic radioisotopes into tumors for internal RIT or delivering chemotherapeutic drugs to synergistically combined chemoradiotherapy. As revealed by recent studies, the tumor microenvironment can be modulated by various nanomedicine approaches to overcome hypoxia-related radioresistance. The tumor microenvironment means that the occurrence, growth, and metastasis of tumors are closely related to the internal and external environment of tumor cells. It not only includes the structure, function, and metabolism of the tumor tissue but also is related to the internal environment (nuclear and
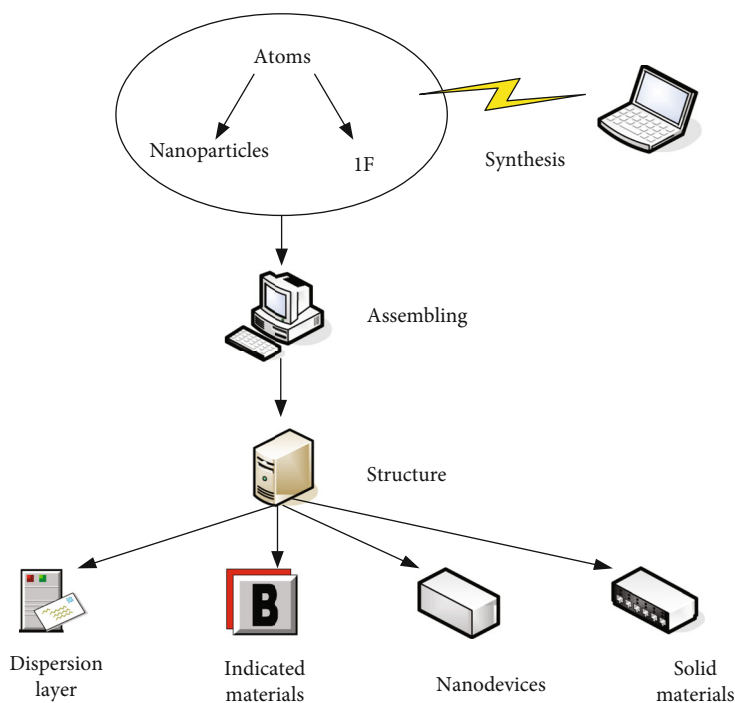
FIGURE 1: Nanomaterial structure.

cytoplasmic) of the tumor cell itself [8]. Although these theories describe nanotechnology and medical imaging, they are rarely combined and are not practical.

3. Nanotechnology and Medical Imaging Diagnostic Methods

3.1. Overview of Nanotechnology. Nanomaterials are materials with nanoscale structures, which can be divided into zero-dimensional nanomaterials and one-dimensional nanomaterials according to their specific dimensions. It has been asserted that when people can arrange and combine substances on a very small scale, they will obtain various novel materials [9, 10]. The change in properties caused by the ratio of the number of atoms on the surface of the nanocrystal particles to the total number of atoms increases sharply with the decrease of the particle size. For example, when the particle diameter is 10 nm, the particle contains 4000 atoms, and the surface atoms account for 40%; when the particle diameter is 1 nm, the particle contains 30 atoms, and the surface atoms account for 99%. Until the end of the last century, the first International Conference on Nanoscience and Technology was held in the United States, which formally combined theoretical research with contemporary science and technology, marking the official birth of nanotechnology [11]. When the size of the material is in the nanometer level, the number of atoms on the surface of the material will increase dramatically, which will far exceed the number of ordinary materials, and the chemical activity of the material will be greatly increased [12]. At the same time, nanomaterials are equal to or smaller than the wavelength of light wave, de Broglie wavelength and coherence length of superconducting state, and the periodic

boundary of the material is destroyed, resulting in "novel" optical, electrical, magnetic, acoustic, and thermodynamic properties. In addition, nanomaterials also have quantum size effects and macroscopic quantum tunneling effects. These unique characteristics provide conditions for the wide-scale application of nanomaterials [13, 14]. Macroscopic quantum tunneling is one of the fundamental quantum phenomena, that is, when the total energy of a microscopic particle is less than the height of the potential barrier, the particle can still pass through the potential barrier. With the continuous and in-depth development of theory and practice, relatively systematic nanostructures have been established at present. With the maturity of application, the uniqueness of nanomaterials plays a pivotal role in the fields of biotechnology and advanced manufacturing [15, 16]. Nanorobots are the most tempting content in the application of nanotechnology in the medical field. They can act as miniature doctors in biomedical engineering and solve problems that are difficult for doctors to solve with traditional techniques. Figure 1 shows the nanomaterial structure.

Since the introduction of carbon fiber in the 1960s, it has become one of the widely used materials for composite materials due to its excellent characteristics such as high strength and high modulus and is widely used in the fields of structural materials and high-temperature materials, and it has the effect that other materials cannot match [17]. With the development of nanotechnology, researchers have applied nanotechnology to composite materials, specifically carbon fibers, and made them into new nanoreinforced materials. The material plays a pivotal role in the modification of polymer-based materials. In terms of specific functions, polymer-based materials have the advantages of two
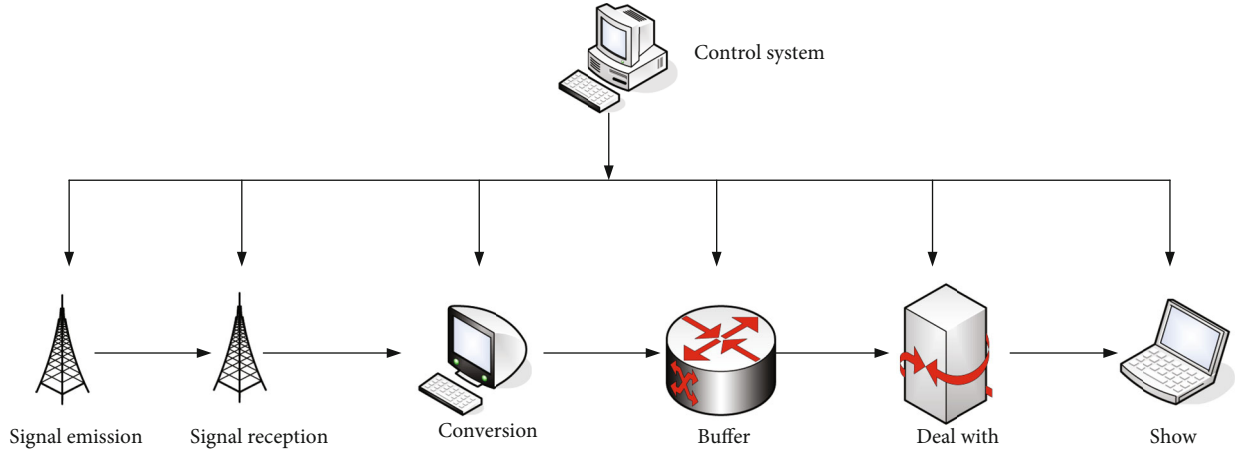
FIGURE 2: Ultrasonic flaw detector structure.

types of polymer materials, so they are nanocomposite materials with special performance materials [18, 19].

In the middle of the last century, the emergence of new substances made nanomaterials develop by leaps and bounds. In the subsequent gradual development, with the continuous exploration of theories by researchers, the scope of application of nanomaterials has become more and more extensive [20]. In recent years, the continuous improvement of science and technology has forced the upgrading of traditional materials. Traditional scientific and technological materials have been unable to meet the requirements of modern technology due to various functional limitations. New nanomaterials have a lot of room for development. From the offline situation, the entire nanomaterials are still in their infancy, and the follow-up development is still very violent. The focus of the first stage of development is to accurately control the number of atoms below 100. The second stage is the production of nanostructured substances, in which nanostructured substances and nanocomposites reach practical levels. In the third stage, it will be possible to mass-produce complex nanostructured substances. At this stage, although researchers choose different nanomaterials for experiments, so far there is no satisfactory result. In short, nanomaterials are very important functional materials, and the research and application of their properties still require continuous research and exploration [21, 22].

3.2. Image Processing Technology. Image processing refers to the process of analyzing images using computer technology [23]. Images are the basic tools for perception of the world and an important source of information for us. The subject of this article is the diagnosis and treatment of medical imaging. In the medical field, we often use imaging techniques, such as common B-ultrasound images and electrocardiograms [24, 25]. Therefore, it is necessary to focus on the research of image processing technology. Figure 2 shows the structure of the common ultrasound system.

In order to understand the information conveyed by the image, we need to collect data on the entire image. For the images collected by B-ultrasound, we need to process the

B-ultrasound images because of external environmental interference during the acquisition process.

$$h(a) = k(a) * g_q + f_s. \tag{1}$$

Formula (1) represents the noise model, $k(a)$ represents the original image, $h(a)$ represents the actual image, and f_s represents the noise.

$$h(a) = k(a) * g_q. \tag{2}$$

In the process of image processing, if the various points of the image are connected, the diagnostic information can be more accurate. In this case, we define the functional expression of the digital image as

$$g(a, b) = \begin{bmatrix} g(1, 1) & g(1, 2) & \cdots & g(1, n) \\ g(1, 2) & g(2, 2) & \cdots & g(2, n) \\ & & \vdots & \\ g(n, 1) & g(n, 2) & g(n, n) \end{bmatrix}, \tag{3}$$

where (a, b) represents a floating image point.

$$S_g(a, b) = y\big(S_g(g(a, b))\big). \tag{4}$$

$S_g(a, b)$ represents the gray value of the target point, g represents the displacement function of the image, and y represents the change function of the pixel value. The premise of pixel value transformation is spatial transformation, but this transformation does not occur in all cases. Figure 3 is a schematic diagram of image space conversion. When it changes, the function expression can be described as

$$S_g(a, b) = S_g(g(a, b)). \tag{5}$$

When formally transforming the image space, we need to determine the transformation process, especially the parameter transformation. We need to find the corresponding relationship
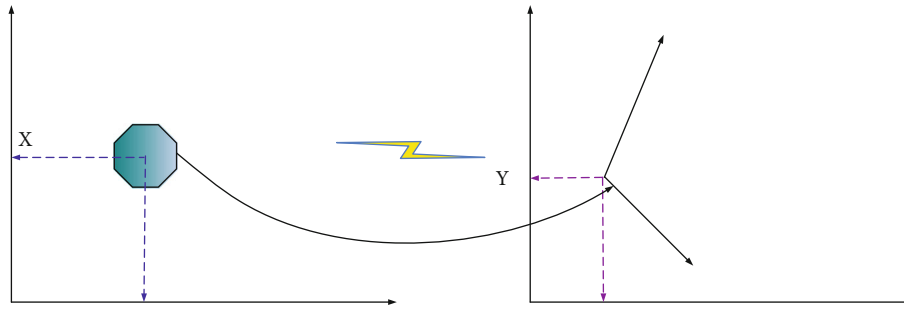
FIGURE 3: Principle of spatial transformation.
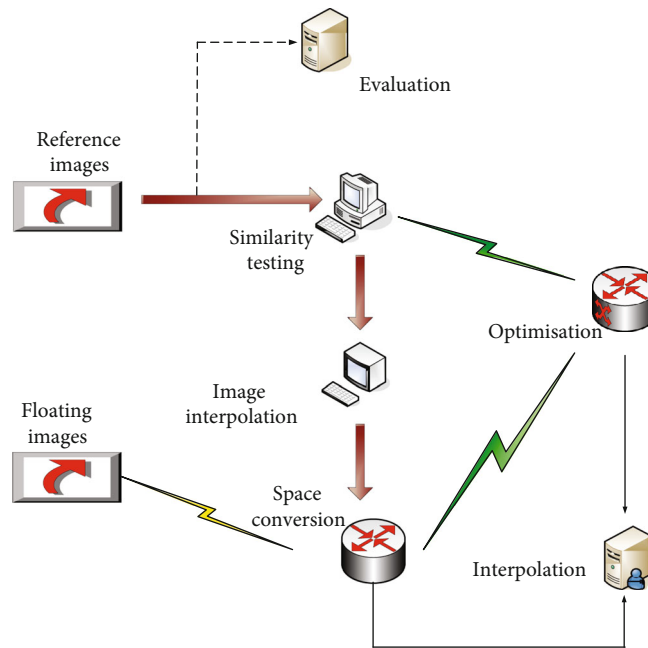
FIGURE 4: Image conversion process.

between the parameters. The main operation process is shown in Figure 4.

Entropy was originally used to represent the energy distribution in thermodynamics, and it has also made some progress in the medical field in recent years. We define its function expression as

$$F(a) = -q \sum_{i=1}^{m} k_i, \ln(k_i) \qquad (6)$$

Among them, $\sum_{i=1}^{m} k_i = 1$, when $k1 = k2 = k3 = \cdots km$, F takes the maximum value.

$$Q(a) = \int_0^1 \left(Q_{\text{int}}(a) + Q_{\text{image}}(a) \right) dc, \qquad (7)$$

where $Q_{\text{int}}(a)$ represents the internal energy, and its form is as follows:

$$Q_{\text{int}}(a) = \frac{1}{4} \left(\chi(c) |a'(c)|^3 + \eta(c) |a''(c)|^3 \right). \qquad (8)$$

Among them, $\chi(c)$ and $\eta(c)$ represent the weight coefficient.

In the process of image processing, entropy is mainly used to distinguish the foreground color and the background color. The main basis for distinguishing the foreground color and the background color is the gray value, and there is a big difference in the distribution of the gray value between the two. We express the expression of gray value as follows:

$$D_1(a) = -q \sum_{i=0}^{q-1} k_i \ln(k_i), \qquad (9)$$

$$k(i) = \frac{g(i)}{\sum_{j=0}^{q-1} g(i)}. \qquad (10)$$

Among them, $g(i)$ is the gray value function, q is a constant, and $k(i)$ represents the gray value range of 0–1.
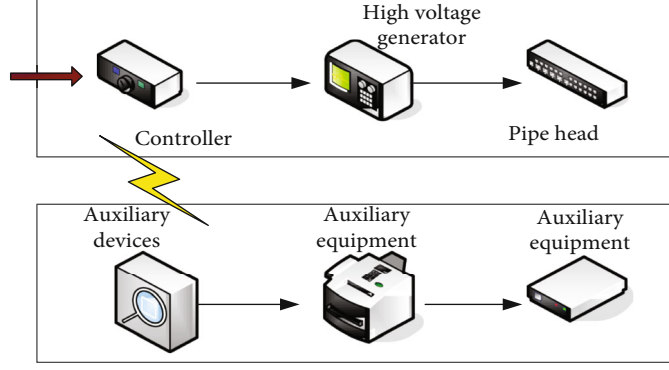
FIGURE 5: "X-ray" working principle.
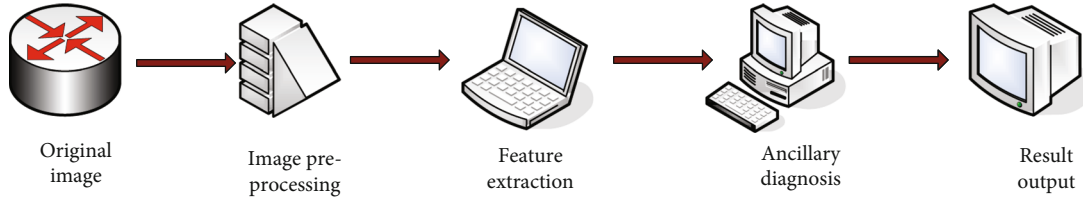
FIGURE 6: Image processing and diagnosis process.

The entropy of the part greater than the threshold q is expressed as

$$D_2(a) = -q \sum_{i=q}^{255} k_i \ln (k_i), \tag{11}$$

$$k(i) = \frac{g(i)}{\sum_{j=q}^{255} g(j)}. \tag{12}$$

Among them, $g(i)$ represents the gray value function, q is a constant, and $k(i)$ represents the gray value range in q-255.

The sum of the two entropies is

$$D(a) = D_1(a) + D_2(a). \tag{13}$$

When $D(a)$ is the largest, the threshold a is the maximum entropy threshold, that is, the threshold that distinguishes the foreground color from the background color.

$$\hat{Q} = s * \bar{Q} + d * Q. \tag{14}$$

Formula (14) represents a filtering algorithm, which can suppress the formation of noise. $\hat{Q}$ represents the image gray value, and Q represents the pixel gray value.

$$h(a, b) = \frac{\sum_{cd} t(c, d) u(a, b, c, d)}{\sum_{cd} u(a, b, c, d)}, \tag{15}$$

$$u(a, b, c, d) = \exp \left[-\left(\frac{(a-c)^3 + (j-d)^3}{\chi} + \frac{\|t(a, b) - u(c, d)\|}{\chi} \right) \right], \tag{16}$$

where χ represents the standard deviation of the intensity of the Gaussian function and formulas (15) and (16) represent the double filtering algorithm.

$$WY(a)(b) = \sum_p t(b, k) a(k) \tag{17}$$

Among them, $t(b, k)$ represents the weight coefficient, and a and b represent the pixels.

$$f(o, p) = \sum \|t(o) - u(p)\|_i^3, \tag{18}$$

$$f(o, p) = \sum k(j) \left(t(o_j) - u\left(p_j\right) \right). \tag{19}$$

i represents the standard deviation of the Gaussian function, and the value of $k(j)$ is determined according to the specific Gaussian function.

Smoothing the image is a very common technique. The gray value is calculated by calculating the weighted average value of the pixel points. The weighted average value is its core content, which is defined as

$$y(a) = \frac{u}{\partial \sqrt{2\pi}} e^{-(a-\varepsilon)^2 / 2\partial^2}. \tag{20}$$

Among them, the expected value of the Gaussian distribution is ε, the standard deviation is ∂, and the standard Gaussian distribution is $\varepsilon = 0, \partial = 1$.

In practical processing, we often use Gaussian blurred two-dimensional Gaussian distribution density distribution function, and its expression is expressed as

TABLE 1: Comparison of simulation results of PSNR image processing.

Simulation metrics	Category				
	1.2	0.9	0.6	0.3	0.1
Bayes threshold	52.93	52.03	48.72	47.22	42.63
Hard threshold	41.56	39.74	37.24	35.19	31.29
Soft threshold	37.01	36.28	34.71	32.47	28.31

TABLE 2: Comparison of simulation results of MMSIM image processing.

Simulation metrics	Category				
	1.2	0.9	0.6	0.3	0.1
Bayes threshold	0.998	0.995	0.992	0.989	0.984
Hard threshold	0.993	0.984	0.977	0.964	0.943
Soft threshold	0.982	0.982	0.973	0.947	0.921

$$H(a, b) = \frac{1}{2\pi\lambda^2} e^{-\left(a^2 + b^2\right)/2\lambda^2}, \tag{21}$$

where λ represents the standard deviation.

3.3. Overview of Medical Imaging Equipment. Science benefits the world. With the continuous development of science and technology, medical technology is also constantly improving, and various medical imaging equipment has begun to be used in the medical field [26]. The "X-ray" we often hear is a typical imaging device. Due to the difference in tissue density and thickness of the human body, the X-ray measurement that passes through the inspected part will be absorbed to different degrees due to the difference in tissue density and thickness, and the final effect on the screen or film will be displayed as images with different degrees of blackening due to different measurement. In the mid-1890s, scientists discovered a ray that was invisible to the naked eye but had strong penetrating power during experiments. After continuous exploration, it is found that the ray can examine the internal mechanism of the object and display the outline of the internal organs. We can analyze and judge its health status through images [27, 28]. The working principle of "X-ray" is shown in Figure 5.

In order to save the image for a long time and use it more conveniently, we transmit the medical image information to the monitor, and the doctor can use the network to share the image resources and improve the work efficiency. At the same time, doctors can compare different imaging data of patients on the same device to improve the accuracy of diagnosis [29, 30]. When the image resources can be extracted on the device, the main purpose is to perform feature extraction; the purpose is to quantitatively analyze the lesion characteristics extracted in the first step, such as the size, density, and morphological characteristics of the lesion. At this time, we abandon the way of storing image data in the past, which saves management expenses to a certain extent, and at the same time facilitates access. Figure 6 shows the image processing and diagnosis flow [31].

TABLE 3: Imaging-related indicators.

Group	1	2	3	4
Number	65	60	80	70
Angle of abduction (°)	41	38	42	39
Proportion (%)	85	90	88	89
Anteversion angle (°)	22	18	17	19
Proportion (%)	76	88	87	89

TABLE 4: Image evaluation index analysis.

Projects		Clarity	Resolution
Group 1	Experimental group	17	0.9
	Original image	11	1.3
Group 2	Experimental group	16	0.9
	Original image	11	1.3

4. Application Experiments in Medical Imaging Diagnosis and Treatment

4.1. Image Processing Data. The image examination performed by the patient in the hospital must be processed to obtain the information transmitted by the image, and the doctor can prescribe the right medicine according to the information. The most important thing in image processing is to remove noise and signal effects. In fact, different thresholding will give different results, so I was able to experiment with images for different threshold ranges.

According to the data in Table 1, we have conducted experiments with different threshold processing schemes. First, we set the compression index as PSNR. When the noise parameter is 1.2, the Bayes threshold is 52.93, the hard threshold is 41.56, and the soft threshold is 37.01. When the noise parameter is 0.9, the Bayes threshold is 52.03, the hard threshold is 39.74, and the soft threshold is 36.28. When the noise parameter is 0.6, the Bayes threshold is 48.72, the hard threshold is 32.74, and the soft threshold is 34.71. When the noise parameter is 0.3, the Bayes threshold is 37.22, the hard threshold is 35.19, and the soft threshold is 32.47. When the noise parameter is 0.1, the Bayes threshold is 42.63, the hard threshold is 31.29, and the soft threshold is 28.31. According to the data, when different noise parameters are selected, the obtained image effects are different. Generally speaking, the larger the set range, the higher the threshold simulation index.

According to the data in Table 2, we set the compression index as MMSIM to conduct experiments with different threshold processing schemes. When the noise parameter is 1.2, the Bayes threshold is 0.998, the hard threshold is 0.993, and the soft threshold is 0.982. When the noise parameter is 0.9, the Bayes threshold is 0.995, the hard threshold is 0.984, and the soft threshold is 0.982. When the noise parameter is 0.6, the Bayes threshold is 0.992, the hard threshold is 0.977, and the soft threshold is 0.973. When the noise parameter is 0.3, the Bayes threshold is 0.989, the hard threshold is 0.964, and the soft threshold is 0.947. When the noise parameter is 0.1, the Bayes threshold
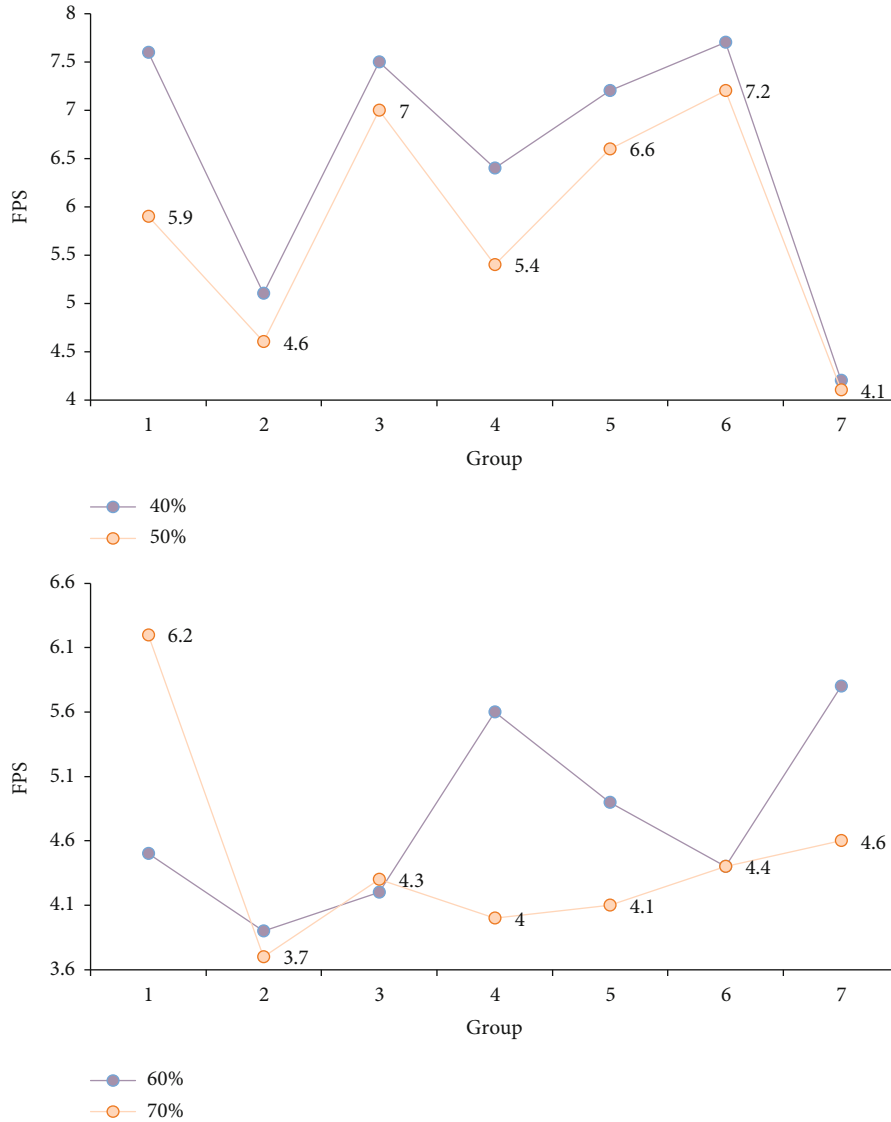
FIGURE 7: Different transmission image quality factor-MPR frame rate test results.

is 0.984, the hard threshold is 0.943, and the soft threshold is 0.921. According to the data, the optimal parameters can be selected according to different requirements during image noise reduction.

4.2. Imaging-Related Indicators. With the continuous development of science and technology, medical technology is also constantly improving. The development of imaging technology has promoted the progress of medical level. Based on this, we have briefly analyzed the relevant indicators of imaging. The details are as follows.

According to the data in Table 3, the abduction angle of the first group is 41°, the proportion in the safe area is 85%, the anteversion angle is 22°, and the proportion in the safe area is 76%. The second group had an abduction angle of 38°, 90% in the safe zone, and an anteversion angle of 18°, which was 88% in the safe zone. The third group had an abduction angle of 42°, 88% in the safe zone, and an anteversion angle of 17°, which was 87% in the

safe zone. The fourth group had an abduction angle of 39°, 89% in the safe zone, and an anteversion angle of 19°, which was 89% in the safe zone.

4.3. Image Evaluation Metrics. After image processing, it needs to be evaluated; we usually use resolution and sharpness. In order to explore the effect of image processing, we compare and analyze the indicators of the processed image and the original image. The details are as follows.

According to the data in Table 4, we have conducted two sets of experiments when evaluating the image quality, and the clarity of the original image has reached level 11, and its resolution is 0.9. The first group of processed images has a sharpness of 17 levels and a resolution of 0.9. The second group of processed images has a sharpness of 16 levels and a resolution of 0.9. According to the data, the sharpness of the processed image is obviously improved, but the resolution is decreased, but in actual situation, it does not affect the diagnosis result. It can be
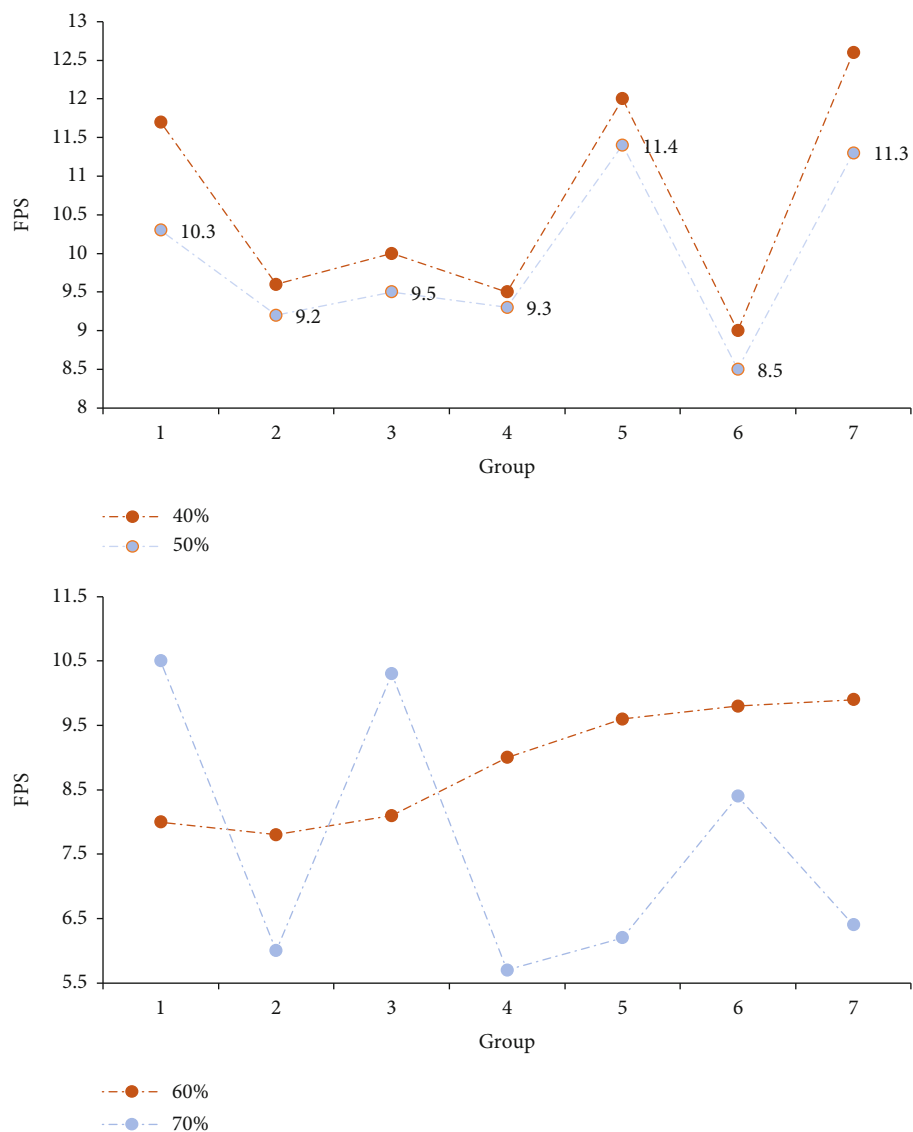
FIGURE 8: Different transmission image quality factor-DVR frame rate test results.

seen that the processed image is helpful for medical diagnosis [32].

5. Application Analysis of Medical Imaging Diagnosis and Treatment

5.1. Transmission Image Quality Factor System Performance Evaluation. Image quality is an important factor affecting doctors' diagnosis results, and the dynamic adjustment of image quality factors during image transmission has an important impact on image quality. When the user zooms and rotates the image, the original quality of the image will be reduced. For this reason, we briefly analyze the quality factor of image transmission. The details are as follows.

According to the data in Figure 7, we have carried out experimental analysis on the quality factor MPR frame rate in different ranges. At this time, the network environment of image transmission, network morbidity and image output device are all the same. In this case, we found that

when the quality factor is 40%, the image transfer rate is 7.6FPS for the first time, 5.1FPS for the second time, and 7.5FPS for the third time. The image transmission rate of the fourth time is 6.4FPS, the image transmission rate of the fifth time is 7.2FPS, the image transmission rate of the sixth time is 7.7FPS, and the image transmission rate of the seventh time is 4.2FPS. When the quality factor is 50%, the first image transfer rate is 5.9FPS, the second image transfer rate is 4.6FPS, and the third image transfer rate is 7FPS. The image transmission rate of the fourth time is 5.4FPS, the image transmission rate of the fifth time is 6.6FPS, the image transmission rate of the sixth time is 7.2FPS, and the image transmission rate of the seventh time is 4.1FPS. According to the data, the smaller the image quality factor is, the larger the image transmission rate is generally, but the image transmission rate will fluctuate during the same type of transmission process.

In order to prevent the chance of the experimental data, we used different quality factors to carry out the comparison
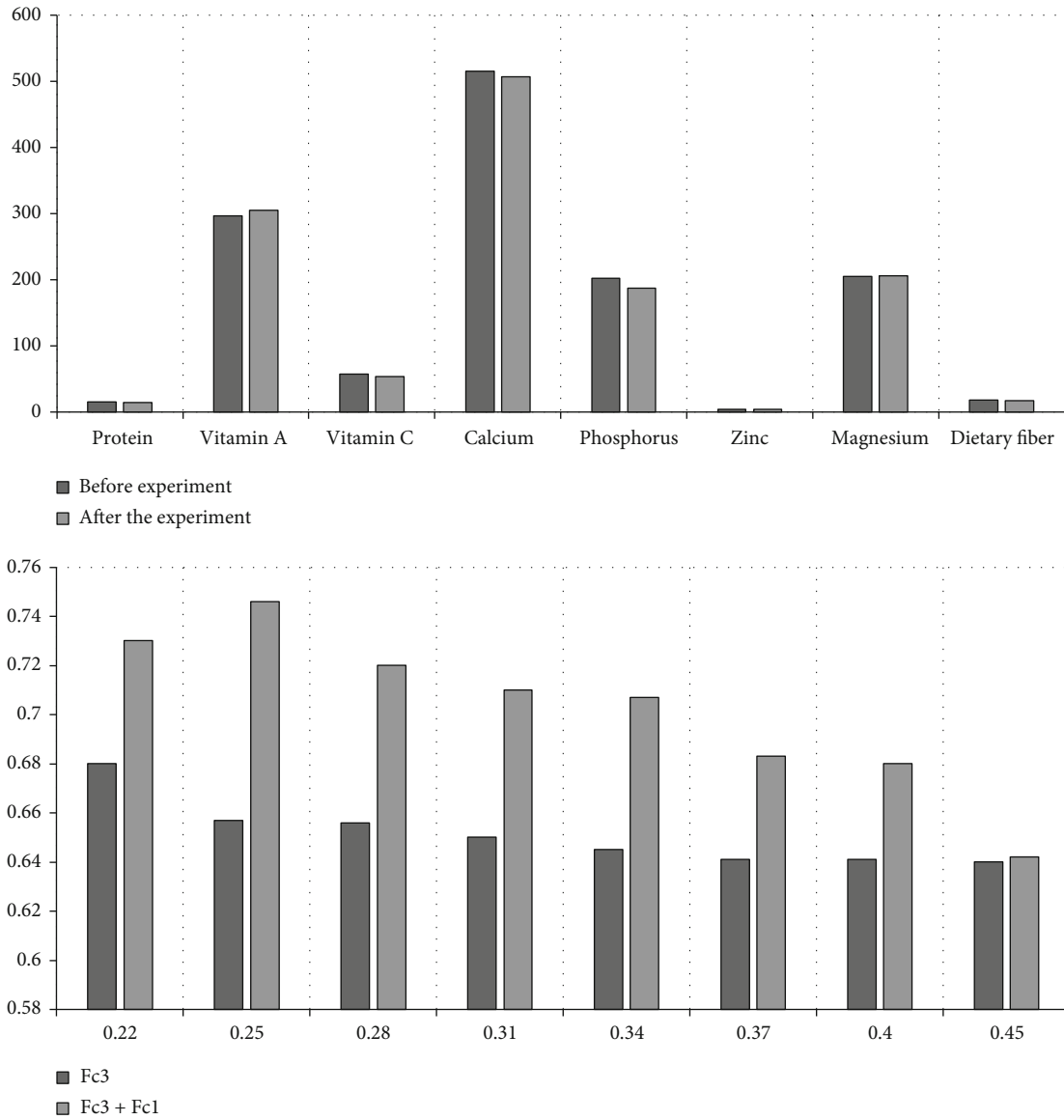
FIGURE 9: Image performance analysis.

experiment again. According to the trend of the experimental data, when the quality factor is 70%, the first image transmission rate is as high as 6.2FPS, and the subsequent transmission rate drops sharply. When the quality factor is 60%, its image transfer rate remains the same as in the previous experiment. It can be seen that the smaller the image quality factor is, the larger the image transmission rate is generally, but when the quality factor is 60%, the level is relatively middle [33].

According to the data in Figure 8, we have conducted experimental analysis on the quality factor of DVR frame rate in different ranges. At this time, the network environment of image transmission, network morbidity and image output device are all the same. In this case, we found that when the quality factor is 40%, the image transfer rate is 11.7FPS for the first time, 9.6FPS for the second time, and 10FPS for the third time. The image transmission rate of the fourth time is 9.5FPS, the image transmission rate of

the fifth time is 12FPS, the image transmission rate of the sixth time is 9FPS, and the image transmission rate of the seventh time is 12.6FPS. When the quality factor is 50%, the first image transfer rate is 10.3FPS, the second image transfer rate is 9.2FPS, and the third image transfer rate is 9.5FPS. The image transmission rate of the fourth time is 9.3FPS, the image transmission rate of the fifth time is 11.4FPS, the image transmission rate of the sixth time is 8.5FPS, and the image transmission rate of the seventh time is 11.3FPS. According to the data, the smaller the image quality factor, the larger the image transmission rate, but the image transmission rate will fluctuate during the same type of transmission, which is the same as the MPR frame rate test result.

Similar to the DVR frame rate experiment, we conducted a second experimental comparison of DVR frame rate measurements. According to the data results, when the quality factor is 70%, the fluctuation of the image transmission rate
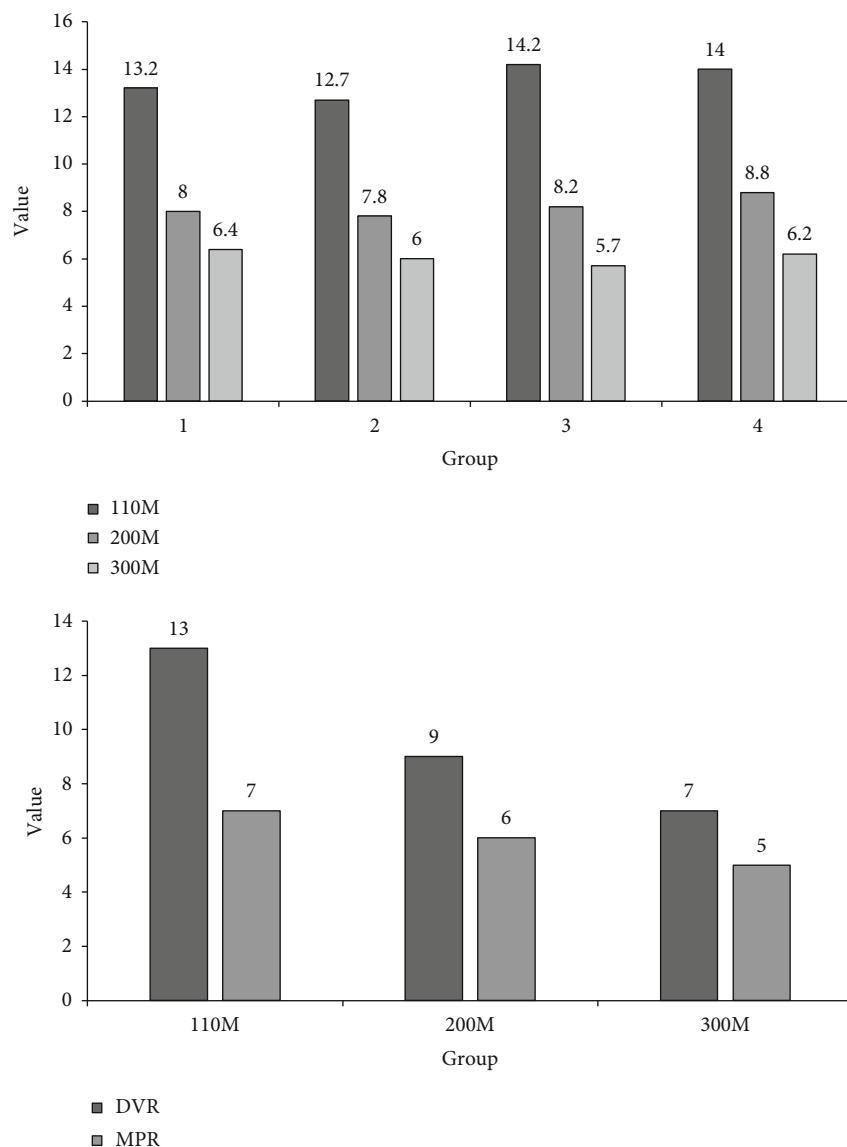
Figure 10: Image size data evaluation.

is too large, which is not suitable for image transmission. Secondly, according to the data, it can be found that when the quality factor is 60%, the fluctuation of the image transmission rate is small, which is suitable for image transmission.

5.2. Image Processing Performance Analysis. With the continuous development of imaging technology, medical imaging examination has become an indispensable inspection method in hospitals, providing strong support for clinical diagnosis and diagnosis. In order to explore the performance of image processing, we analyzed different situations of the image, as follows.

According to the data in Figure 9, this experiment retrieves the validity of medical images. When the usage rate of Fc1 was 22%, the image efficiency rate was 70%, and when the usage rate was 25%, the image efficiency rate was 69%. When the usage rate is 28%, the image efficiency rate is

68%, and when the usage rate is 31%, the image efficiency rate is 67.3%. When the usage rate is 34%, the image efficiency rate is 67%, and when the usage rate is 37%, the image efficiency rate is 60%. When the usage rate of Fc2 was 22%, the image efficiency rate was 68%, and when the usage rate was 25%, the image efficiency rate was 68.3%. When the usage rate is 28%, the image efficiency rate is 68.1%, and when the usage rate is 31%, the image efficiency rate is 67%. When the usage rate is 34%, the image efficiency rate is 66.5%, and when the usage rate is 37%, the image efficiency rate is 60%. According to this data, there is no significant difference in the imaging efficiency between Fc1 and Fc2.

When the usage rate of Fc3 was 22%, the image efficiency rate was 68%, and when the usage rate was 25%, the image efficiency rate was 65.7%. When the usage rate is 28%, the image efficiency rate is 65.6%, and when the usage rate is 31%, the image efficiency rate is 65%. When the usage

rate is 34%, the image efficiency rate is 64.5%, and when the usage rate is 37%, the image efficiency rate is 64.1%. When the combined use rate of Fc1 and Fc3 was 22%, the imaging efficiency rate was 73%, and when the utilization rate was 25%, the imaging efficiency rate was 74.6%. When the usage rate is 28%, the image efficiency rate is 72%, and when the usage rate is 31%, the image efficiency rate is 71%. When the usage rate is 34%, the image efficiency rate is 70.7%, and when the usage rate is 37%, the image efficiency rate is 68.3%. From this data, it can be seen that when Fc1 and Fc3 are used in combination, the imaging efficiency is greatly improved.

5.3. Image Size Data Evaluation. In addition to the transmission rate and the image quality factor, the image quality is also related to the size of the image itself. For this reason, we have analyzed images of different sizes. The details are as follows.

According to the data in Figure 10, we have conducted quality assessment on images of different data sizes. When the image is 110 M, the frame rate of the first test of the image is 13.2FPS, and the frame rate of the second test of the image is 12.7FPS. The frame rate of the third test of the image is 14.2FPS, and the frame rate of the fourth test of the image is 14FPS. When the image is 200 M, the frame rate of the first test of the image is 8FPS, and the frame rate of the second test of the image is 7.8FPS. The frame rate for the third test of the image was 8.2FPS, and the frame rate for the fourth test of the image was 8.8FPS. When the image is 300 M, the frame rate of the first test of the image is 6.4FPS, and the frame rate of the second test of the image is 6FPS. The frame rate for the third test of the image was 5.7FPS, and the frame rate for the fourth test of the image was 6.2FPS. When the size of the image data is the same, the DVR and MPR transmission rates of the images are quite different. According to the data, the size of the image data has a great influence on the image quality.

6. Conclusions

With the continuous progress of science and technology, the combination of science and technology and medical treatment has become the general trend. The continuous development of nanotechnology provides conditions for the development of the medical field. The purpose of this paper is to study the application of nanoscale microparticle technology in medical imaging diagnosis and treatment. It is expected that the combination of nanotechnology and medical imaging will improve the accuracy of medical imaging diagnosis. Although this paper has carried out some research on this basis, there are still some problems: the image processing method is very successful in the edge detection of the low-frequency part of the image, and the scale factor can be accurately calculated, but the sensitivity to the high-frequency part of the image is weak.

Data Availability

No data were used to support this study.

Conflicts of Interest

There is no potential conflict of interest in this study.

References

[1] Y. C. Lin, J. S. Wu, and J. W. Kung, "Image guided biopsy of musculoskeletal lesions with low diagnostic yield," *Current Medical Imaging Reviews*, vol. 13, no. 3, pp. 260–267, 2017.

[2] D. P. Frush and E. Sorantin, "Radiation use in diagnostic imaging in children: approaching the value of the pediatric radiology community," *Pediatric Radiology*, vol. 51, no. 4, pp. 532–543, 2021.

[3] S. Rpsgt, "Eliminating the stigma: a systematic review of the health effects of low-dose radiation within the diagnostic imaging department and its implications for the future of medical radiation," *Journal of Medical Imaging and Radiation Sciences*, vol. 51, no. 4, pp. 662–670, 2020.

[4] J. E. Venson, F. Bevilacqua, J. Berni, F. Onuki, and A. Maciel, "Diagnostic concordance between mobile interfaces and conventional workstations for emergency imaging assessment," *International Journal of Medical Informatics*, vol. 113, no. -MAY, pp. 1–8, 2018.

[5] E. Deng, W. Kang, and Y. Zhang, "Design optimization and analysis of multicontext STT-MTJ/CMOS logic circuits," *IEEE Transactions on Nanotechnology*, vol. 14, no. 1, pp. 169–177, 2015.

[6] P. Falagan-Lotsch, E. M. Grzincic, and C. J. Murphy, "New advances in nanotechnology-based diagnosis and therapeutics for breast cancer: an assessment of active-targeting inorganic nanoplatforms," *Bioconjugate Chemistry*, vol. 28, no. 1, pp. 135–152, 2017.

[7] M. Natan and E. Banin, "From nano to micro: using nanotechnology to combat microorganisms and their multidrug resistance," *FEMS Microbiology Reviews*, vol. 41, no. 3, pp. 302–322, 2017.

[8] G. Song, L. Cheng, and Y. Chao, "Emerging nanotechnology and advanced materials for cancer radiation therapy," *Advanced Materials*, vol. 29, no. 32, article 1700996, 2017.

[9] M. Bathe and P. Rothemund, "DNA nanotechnology: a foundation for programmable nanoscale materials," *MRS Bulletin*, vol. 42, no. 12, pp. 882–888, 2017.

[10] L. B. Naves, C. Dhand, J. R. Venugopal, L. Rajamani, S. Ramakrishna, and L. Almeida, "Nanotechnology for the treatment of melanoma skin cancer," *Progress in Biomaterials*, vol. 6, no. 1-2, pp. 13–26, 2017.

[11] D. Jasinski, F. Haque, D. W. Binzel, and P. Guo, "advancement of the emerging field of RNA nanotechnology," *ACS Nano*, vol. 11, no. 2, pp. 1142–1164, 2017.

[12] D. Lin, Y. Liu, and C. Yi, "Reviving the lithium metal anode for high-energy batteries," *Nature Nanotechnology*, vol. 12, no. 3, pp. 194–206, 2017.

[13] P. Senellart, G. Solomon, and A. White, "High-performance semiconductor quantum-dot single-photon sources," *Nature Nanotechnology*, vol. 12, no. 11, pp. 1026–1039, 2017.

[14] E. C. Yusko, B. R. Bruhn, O. M. Eggenberger et al., "Real-time shape approximation and fingerprinting of single proteins using a nanopore," *Nature Nanotechnology*, vol. 12, no. 4, pp. 360–367, 2017.

[15] C. Y. Chen, C. M. Wang, H. H. Li, H. H. Chan, and W. S. Liao, "Wafer-scale bioactive substrate patterning by chemical lift-off

lithography," *Beilstein Journal of Nanotechnology*, vol. 9, no. 1, pp. 311–320, 2018.

[16] L. Wang, M. Boutilier, P. R. Kidambi, D. Jang, N. G. Hadjiconstantinou, and R. Karnik, "Fundamental transport mechanisms, fabrication and potential applications of nanoporous atomically thin membranes," *Nature Nanotechnology*, vol. 12, no. 6, pp. 509–522, 2017.

[17] M. Hadjidemetriou and K. Kostarelos, "Evolution of the nanoparticle corona," *Nature Nanotechnology*, vol. 12, no. 4, pp. 288–290, 2017.

[18] F. Pi, Z. Hui, and L. Hui, "RNA nanoparticles harboring annexin A2 aptamer can target ovarian cancer for tumor-specific doxorubicin delivery," *Nanomedicine: Nanotechnology, Biology, and Medicine*, vol. 13, no. 3, pp. 1183–1193, 2017.

[19] M. Holzinger, R. Haddad, and A. Maaref, "Amperometric biosensors based on biotinylated single-walled carbon nanotubes," *Journal of Nanoscience & Nanotechnology*, vol. 9, no. 10, pp. 6042–6046, 2009.

[20] Y. Weng, J. Liu, S. Jin, W. Guo, X. Liang, and Z. Hu, "Nanotechnology-based strategies for treatment of ocular disease," *Acta Pharmaceutica Sinica B*, vol. 7, no. 3, pp. 281–291, 2017.

[21] C. A. Mirkin, T. J. Meade, and S. H. Petrosko, "Nanotechnology-based precision tools for the detection and treatment of cancer," *Anticancer Research*, vol. 35, no. 10, pp. 481–501, 2017.

[22] C. P. Reis and C. Damgé, "Nanotechnology as a promising strategy for alternative routes of insulin delivery," *Methods in Enzymology*, vol. 508, no. 508, pp. 271–294, 2017.

[23] C. H. Lee, B. Tiwari, D. Zhang, and Y. K. Yap, "Water purification: oil–water separation by nanotechnology and environmental concerns," *Environmental Science Nano*, vol. 4, no. 3, pp. 514–525, 2017.

[24] J. S. Duhan, R. Kumar, N. Kumar, P. Kaur, K. Nehra, and S. Duhan, "Nanotechnology: the new perspective in precision agriculture," *Biotechnology Reports*, vol. 15, no. 15, pp. 11–23, 2017.

[25] M. C. Roco, C. A. Mirkin, M. C. Hersam, and C. S. Alrokayan, "Nanotechnology research directions for societal needs in 2020," *Journal of Nanoparticle Research*, vol. 13, no. 3, pp. 897–919, 2018.

[26] Group, SFR-IA and French Radiology Community, "Artificial intelligence and medical imaging 2018: French Radiology Community white paper," *Imaging*, vol. 99, no. 11, pp. 727–742, 2018.

[27] X. Yi, H. Li, and A. Hcc, "Clinical placements for undergraduate diagnostic radiography students amidst the COVID-19 pandemic in Singapore: preparation, challenges and strategies for safe resumption," *Journal of Medical Imaging and Radiation Sciences*, vol. 51, no. 4, pp. 560–566, 2020.

[28] B. Jppa, E. Alcd, and G. Lbf, "Tomorrow's medical imaging builds on today's foundations - prevention, care and innovation at the service of patients: a program for radiology and medical imaging-ScienceDirect," *Diagnostic and Interventional Imaging*, vol. 101, no. 3, pp. 123–125, 2020.

[29] D. Mcrobbie, "Both sides now: diagnostic imaging medical physics in two hemispheres," *Australasian Physical & Engineering Sciences in Medicine*, vol. 40, no. 2, pp. 269–272, 2017.

[30] C. L. Ramanujam, D. Han, and T. Zgonis, "Medical imaging and laboratory analysis of diagnostic accuracy in 107 consecutive hospitalized patients with diabetic foot osteomyelitis and partial foot amputations," *Foot & Ankle Specialist*, vol. 11, no. 5, pp. 433–443, 2018.

[31] Jabbar Abed Eleiwy, "Characterizing wavelet coefficients with decomposition for medical images," *Journal of Intelligent Systems and Internet of Things*, vol. 2, no. 1, pp. 26–32, 2021.

[32] I. Mohammed, "Alghamdi, neutrosophic set with adaptive neuro-fuzzy inference system for liver tumor segmentation and classification model, International Journal of Neutrosophic," *Science*, vol. 18, no. 2, pp. 174–185, 2022.

[33] F. Q. Kareem and A. M. Abdulazeez, "Ultrasound medical images classification based on deep learning algorithms: a review, Fusion: Practice and Applications," vol. 3, no. 1, pp. 29–42, 2021.

Hindawi

Research Article

A New Type of Nanomaterial Traditional Martial Arts Training Body Protector with Buffering Effect

Zengli Li [ID] **and Jinxiang Zhao** [ID]

Sports Department, Hebei Academy of Fine Arts, Shijiazhuang, 050700 Hebei, China

Correspondence should be addressed to Jinxiang Zhao; zhaojinxiang@hbafa.edu.cn

With the development of people's living standards, the growing prosperity of the motherland, the traditional culture has been paid more and more attention, and traditional martial arts as a part of traditional culture is not only good for viewing but also strengthens the body, so it has been loved by many people. Traditional martial arts training is a high-collision, injury-prone sport, and making a good buffer protector can improve the safety of martial arts trainers and reduce the concept or degree of injury to athletes. Nanomaterials are materials produced by nanotechnology that are extremely small in one-dimensional, two-dimensional, or even three-dimensional directions, and are several nanometers long in at least one direction. The purpose of this paper is to study a new type of nanomaterial with buffering effect, so as to understand the actual protective effect of body protectors made of this material on martial arts trainers. In this paper, a net-like plant fiber nanobuffer material is proposed, and the relevant mechanical experimental tests are carried out on the material. According to static tensile experiments, the mesh nanofiber material can withstand a pressure of 1.2 million Pa under 90% strain, while ordinary fiber materials can only withstand a pressure of 700 thousand Pa under 80% strain. And the resilience of the mesh nanofiber material reaches 1.8 mm/s, while the maximum of ordinary fiber material is only 0.6 mm/s, which means that the protective gear made of mesh nanofiber material can significantly improve the stress bearing capacity of the protective gear and improve the rebound effect.

1. Introduction

With the development of science, technology, and industry, nanomaterials have become important materials used in many fields, and the protective ability of nanomaterials has become a concern in all kinds of intense sports or training venues. Especially in the training of martial arts, trainers will be subjected to various shocks, and the degree of shock is also different. These shocks will lead to changes in the trainer's athletic state, and serious injuries will lead to fractures of athletes. In order to minimize the injury of personnel during the training process, it is necessary to select appropriate buffer nanomaterials as body protectors to achieve the effect of buffering and antiseismic, so as to protect the trainers and avoid serious injuries to the trainers during the training process. Generally, an appropriate buffer pad is added to the protective gear to absorb the impact energy of the outside world on the product, so as to achieve the buffer effect and protect the trainer. The foam material used

to reduce shock and vibration during martial arts training is the buffer. The whole product and package are called protective gear, and the buffer material in the buffer system plays a decisive role. The function of martial arts is not only limited to fighting but also has dance, art, technology, maintenance, health, governance, and other categories. However, due to historical reasons and social development factors, traditional martial arts have developed to today, and its functions have included fitness, health preservation, competition, and fighting. The most common ones are performance and display [1].

In martial arts training, the buffer material plays a very important role in protecting the human body and can greatly avoid personal injury. Therefore, it is very necessary to conduct in-depth research on buffer materials. For the research on protective gear of nanomaterials, some scholars have published relevant academic articles on it. Among them, Jung et al. identified potential nucleophiles that could be incorporated into PIMs by quantitatively comparing the

reactivity of multiple small-molecule nucleophile scaffolds as organophosphate scavengers. Jung et al. provided new insights into PIM as a reactive material for CWA decontamination and its potential use in protective gear [2]. Heinze and Carastan investigated the effects of fumed silica content, ultrasonic energy used during silica particle dispersion, and humidity during storage to analyze the performance changes of STF. In stable samples, water uptake results in a substantial loss of maximum viscosity. Humidity on the sample reduces the overall viscosity but does not prevent the sample from turning into a gel if the parameters used cause the STF to become unstable. Shearing STF reduces its maximum viscosity, more so in higher viscosity samples [3]. Cerium oxide nanoparticles (CeNPs) have been shown to have antioxidant capacity. However, their efficiency in scavenging reactive oxygen species (ROS) and their underlying mechanisms remain unclear. Filippi et al.'s study found that ceria nanoparticles (CeNPs) and nanorods (CeNRs) exhibited stronger scavenging activity than OH generation in phosphate-buffered saline (PBS) and alternative lung fluid (SLF). These insights are important for understanding the redox activity of cerium nanomaterials and providing clues to the role of CeNPs in biological and environmental processes [4]. Rzayev highlighted the ability of molecular bottle brushes as highly tunable building blocks for the creation of nanostructured materials through molecular templating, solution polymerization, and melt self-assembly. Rzayev also highlighted recent achievements in the synthesis of discrete nano-objects, micellar structures, and periodic nanomaterials from bottlebrush copolymers and briefly discussed future opportunities in this field of polymer science [5]. Zheng et al. first described the mode of action of silver nanoparticles (Ag NPs) in disrupting bacterial cell outer membranes and their intracellular components, then allowing them to exhibit broad-spectrum antibacterial effects. Zheng et al. next invented an emerging high-efficiency antibacterial agent, ultrasmall silver nanoclusters (Ag NCs). Ag NCs are ultrasmall NPs with core size less than 2 nm, and they contain 'countable' Ag atoms as cores and protected by a certain number of organic ligands. The atomically precise properties of Ag NCs provide a good platform for designing and manipulating Ag NCs at the atomic level to achieve optimized antibacterial efficacy, which is also beneficial for antibacterial mechanism research [6]. The effects of adding anatase nano-TiO_2, nano-SiO_2, etc. on the crystallization and morphology of C-S-H were systematically studied by Li H experiments. Further characterization was carried out by microscopy to investigate the effect of nanomaterials on the C-S-H morphology. Different nanomaterials have different C-S-H morphologies. Pure CSH is sheet-like structure, nano-TiO_2 is CSH and rod-like structure, nano-SiO_2 is CSH and particle agglomeration, and C-S-H and GO or CNT form a C-S-H structure grown on a template [7]. Although the above studies have promoted the research and application of nanomaterials to a certain extent, most of them are in the field of theoretical chemical reactions, and there are relatively few physical analyses of the buffering properties of nanomaterials. Therefore, this paper has important value and significance for the research on the body protector of buffer type nanomaterials.

The innovations of this paper are as follows: A new type of mesh plant fiber nanomaterial is proposed as a buffer protector, which has better buffer performance and can protect the key body parts of traditional martial arts trainers. And the relevant mechanical experiments were carried out on the nanomaterials, and the specific data obtained were used as the basis to make the results more credible.

2. Based on Buffered Nanomaterials

2.1. Buffered Nanomaterials

2.1.1. Nanotechnology and Nanomaterials

(1) Definition

The so-called nanotechnology refers to the general term of the manufacturing technology whose processing accuracy or processing size is one order of magnitude. The lattice spacing of metal crystal lattices is about 1 to 100 nanometers, so the precision of nanofabrication has reached the limit. Nanotechnology includes a variety of advanced science and technology, such as nanomaterials, nanofabrication, nanotribology, nanometer measurement, nanocontrol, nanoelectronics, nanomicroscopy, nanobiology, and a number of high-tech groups. Among them, bionanotechnology is a bottom-up molecular self-assembly strategy, and molecular components will spontaneously organize into stable structures [8, 9]. A schematic diagram of nanotechnology is shown in Figure 1.

Nanomaterials are materials that have at least one dimension in three-dimensional space on the nanometer scale (1-100 nm), nanomaterials are the basic units built around them. This corresponds to a dense scale of about 10 to 1000 atoms [10, 11].

(2) Characteristics of nanomaterials

Nanomaterials are some low-dimensional materials, and nanomaterials can be single crystal, polycrystalline, crystal structure, quasicrystalline or amorphous phase, glassy, metal, ceramic, oxide, or composite material [12, 13]. The manufacturing methods of nanomaterials include general artificial methods, artificial nanomaterials, reduction of single-phase products, heat treatment, and natural nanomaterials. Table 1 shows the characteristics of nanomaterials with different diameters.

(3) Classification

Nanomaterials can be mainly divided into nanoceramics, bulk, fibers, and powder materials according to their properties, as shown in Figure 2.

There is also a particularly familiar nanomaterial: nanomembranes, which are often used in cellphone screens or filters. Nanofilms are divided into particle films and dense films. Particle films are thin films of nanoparticles with very small gaps between them [14, 15]. The dense film is a thin film having a dense film layer with a particle size of nanometer scale. Nanomembrane can be used for gas catalysis (such
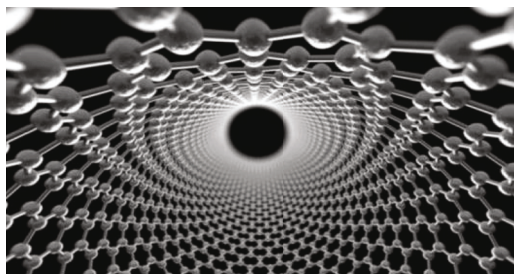
Nanotechnology

The science and technology of making substances with single atoms and molecules, and studies the properties and applications of materials with a structure size in the range of 1to100 nanometers
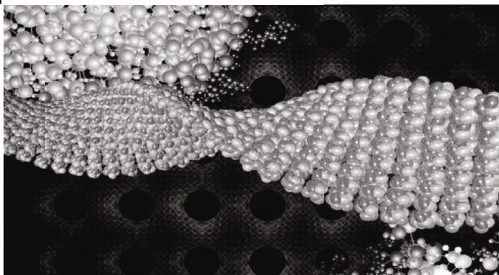
FIGURE 1: Schematic diagram of nanotechnology. Image source: https://www.sohu.com/a/415689238_120779191.

TABLE 1: Characteristics of nanomaterials with different diameters.

Diameter/ nm	Total number of atoms N	Percentage of the surface atoms
1	30	100
5	4000	40
10	30000	20
100	3000000	2

as automobile exhaust gas treatment) materials, filter materials, high-density magnetic recording materials, photosensitive materials, flat panel display materials, superconducting materials, etc. [16], as shown in Figure 3.

(4) Application fields of nanotechnology

At present, nanotechnology is widely used in many industrial, medical, energy, environmental protection, home and military fields, as shown in Figure 4.

2.1.2. Buffer Material. Buffer materials, as the name suggests, are elastic materials with a cushioning effect. At present, most of the research on cushioning materials is in the aspects of colloid, cotton, wool, leather, plant fibers, and mixed cushioning materials. The more typical ones are foamed polyethylene, foamed aluminum, cardboard fibers, etc., as shown in Figure 5. As a new type of environmental protection material, foamed polyethylene is more and more widely used in many fields, which has attracted the attention of many researchers on its cushioning, protection, and other properties. Due to its special electromagnetic shielding performance, sound insulation performance, sound absorption performance, energy absorption performance, vibration isolation, and damping performance, foamed aluminum materials are widely used in military equipment, shipbuilding, trains, automobiles, tunnel engineering, construction, and other industries. Waste paper fiber belongs to plant fiber,

so the basic principle of using it as the main raw material to prepare buffer material is the same as the current domestic and foreign researchers using plant fiber to prepare buffer material. In both of them, the fiber material is mixed with other additives, and foaming is formed by the action of the foaming agent [17, 18].

The chemical theory of a plant fiber, the concept of liquid foaming, and the associated theory of surface chemistry are used to produce the network structure of the reticulated plant fiber material [19]. The key is to first use the pressure difference between the inside and outside of the bubble to form a cavity inside the material, that is, to "squeeze" the space out of the solution, while "squeezing" the space, let the fibers adsorb around the bubble and gather into "arches." In order to make the material have the necessary physical and mechanical properties, the fibers should be connected, and before this, the "arch" fibers must be "oriented." Under the combined action of hydrogen bonds and adhesives, an effective and stable connection between fibers is formed. When the solution is excluded, it becomes an ultralightweight material with a plant fiber network structure that meets various properties. Figure 6 is a schematic diagram of the internal structure of the material similar to the "truss structure." The truss in the truss structure refers to the truss beam, which is a latticed beam structure. The truss structure is often used in public buildings such as large-span workshops, exhibition halls, gymnasiums, and bridges. Since most of them are used in the roof structure of buildings, trusses are usually also called roof trusses [20]. Plant fibers constitute "truss members," and the connection points between fibers with rubber compound constitute "truss nodes" [21].

2.2. Traditional Martial Arts. Traditional martial arts is a wonderful flower in Chinese history. It is deeply rooted in the fertile soil of Chinese culture. After thousands of years of development and precipitation, it is an important part of Chinese culture. Chinese martial arts can survive for thousands of years and maintain an active development trend. It is

Nano powder also known as ultrafine powder, generally refers to powder or particles with particle size below 100 nanometers

Nanofibers refers to a wire-like material with a diameter on the nanometer scale and a large length

(a)

Nano-block a nano-grain material obtained by high-pressure molding of nano-powder or controlled crystallization of metal liquid

Nano ceramics using nano-powder to modify existing ceramics, by adding or generating nano-scale particles, whiskers, wafer fibers, etc. into the ceramics, the grains, grain boundaries and the combination between them all reach the nano-level

(b)

Figure 2: Common Nanomaterials. (a) Nanopowders and fibers. (b) Nanobulk and nanoceramic. Image source: http://www.ex-dna.com/a/news/company_news/151.html. Image source: http://www.520730.com/wanwuzhi/shoucang/530333.html.

Dense film

Particle film
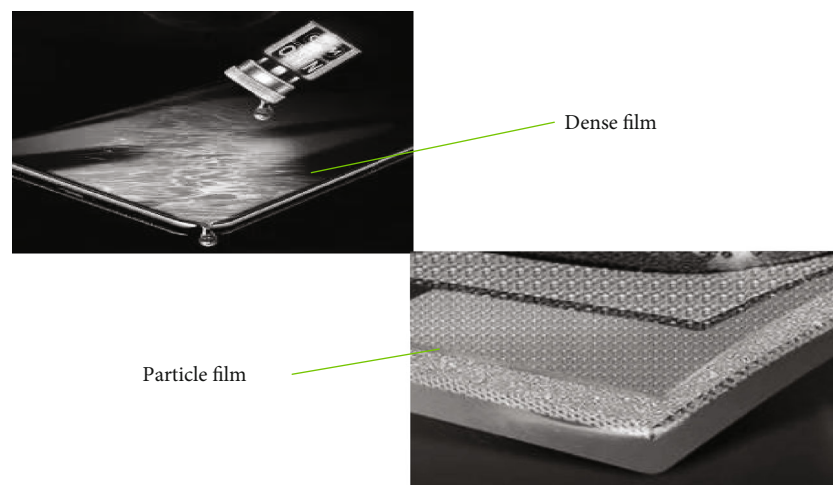
Figure 3: Nanofilm. Image source: https://www.smzdm.com/p/13577501/.
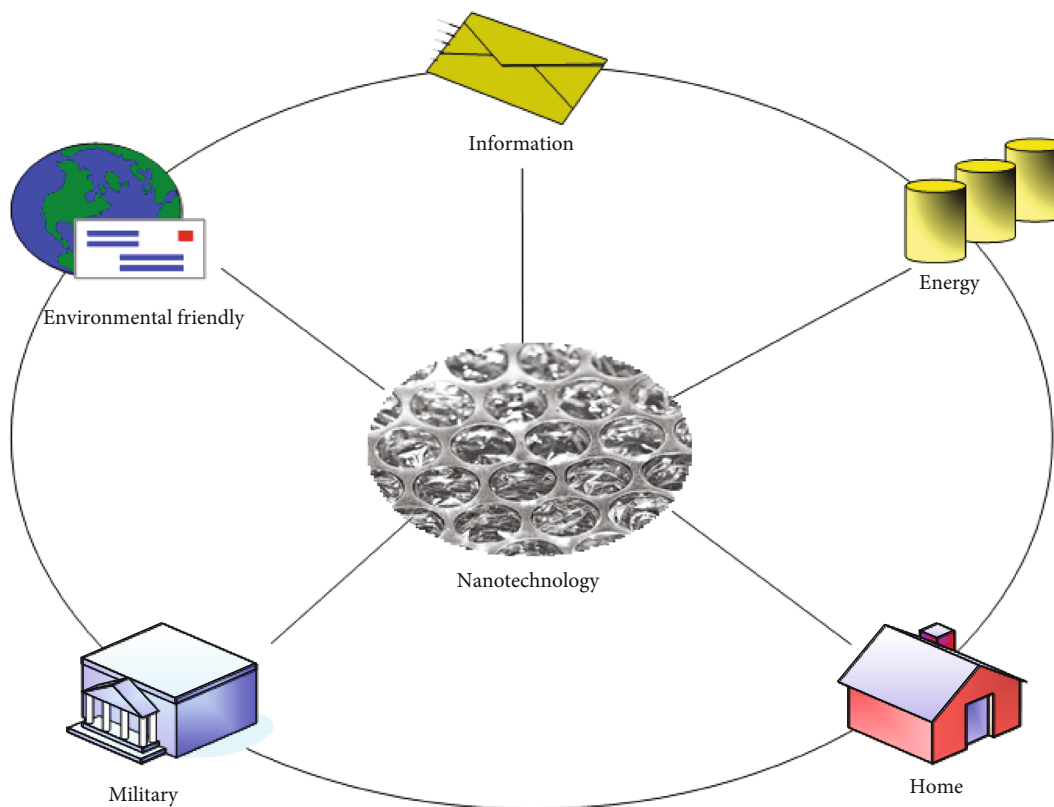
Figure 4: Applications of nanotechnology.
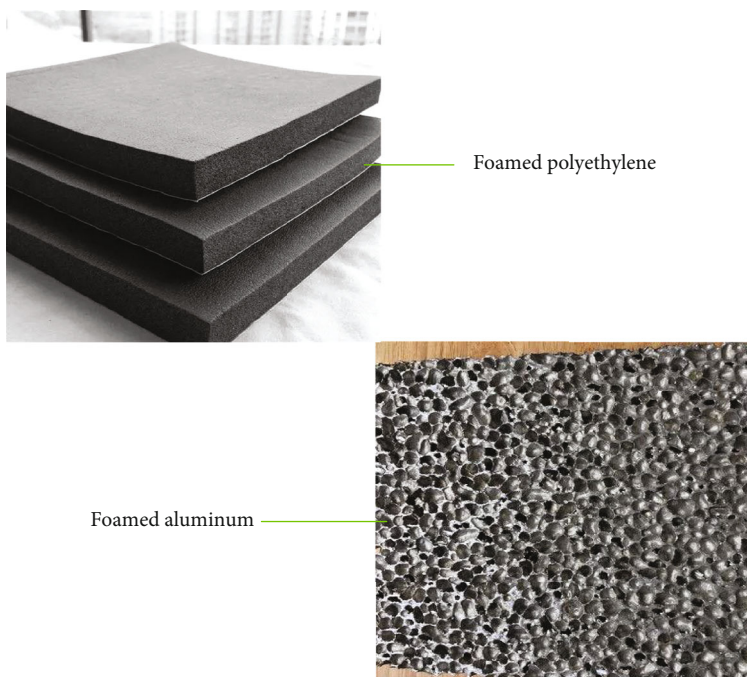
Figure 5: Buffer material. Image source: https://www.foodjx.com/chanpin/5042386.html.

fundamentally because it has rich traditional cultural connotations inside. However, in modern times, with the emergence and rapid development of Chinese competitive martial arts, the traditional connotation of martial arts has gradually become blurred, and especially the fighting ability, which is the essence of martial arts, has gradually faded out of people's
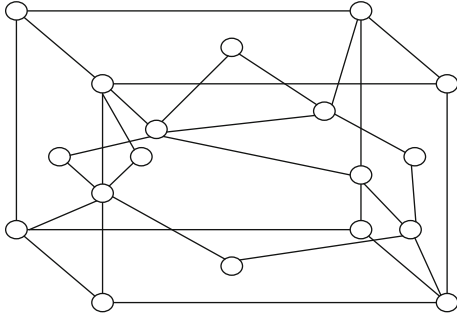
FIGURE 6: Schematic diagram of the internal structure of the mesh fiber material of the "truss structure."

attention, which has greatly misled people's understanding of martial arts. Due to the requirements of "high, difficult, new, and beautiful" put forward by competitive sports, in order to pursue the ranking and performance of the competition, traditional martial arts also excessively pursue the elegant movements and ignore the cultivation of its exercises, which has led to the fading of the cultural connotation of traditional martial arts. Figure 7 shows two traditional martial arts well known in China [22].

Tradition is to standardize and model a certain materialized spirit, so that living life can be condensed into rigid concept. It also restricts the life and practice of future generations, and becomes an example of their words and deeds. A "tradition" must have the following characteristics to be called a tradition. First, it has a long time span (time characteristics), and secondly, it has strong spatial binding force (regional characteristics), and thirdly, there are specific audiences (population characteristics). Traditional martial arts can be defined as follows: Chinese national fighting sports with a long history of development before modern China, with certain regional characteristics and practice crowds. Martial arts is a national sports event produced under the background of Chinese farming society, with tactical movements as the main content, routines, exercises, and fighting as forms of expression, focusing on both internal and external training. In terms of its time logic, traditional martial arts mainly refers to the martial arts before the old China, and it is the folk martial arts in the cold weapon era of ancient China. However, people only define traditional martial arts by time, which largely confuses the value and function characteristics of traditional and nontraditional martial arts. According to the value of martial arts, traditional martial arts and competitive martial arts correspond, but this ignores the existence of military martial arts, and only distinguishes them from the perspective of Western sports, and limits the value of traditional martial arts to the category of sports. Therefore, traditional martial arts exist not only in ancient times but also in modern times. It is developed by working people's long-term practice and accumulation. It has far-reaching implications and a long history. It takes traditional Chinese culture as the theoretical basis and takes offensive and defensive skills as the main purpose of activities. It combines physical fitness, self-defense, entertainment, and aesthetics, and it is a physical exercise with strong national traditional characteristics

[23]. Table 2 is a comparison of the force methods of different types of boxing in traditional martial arts, and Table 3 is a comparison of the force methods of different boxing methods of the same type.

From Tables 2 and 3, it can be seen that for different martial arts, their moves are different, the force is also different, and the parts of the force used in battle and the strength and parts of the blow are different. Therefore, it is necessary to wear protective gear for important parts of the human body to prevent serious injury.

2.3. Body Protector. According to the relevant regulations of the General Administration of Sports of the People's Republic of China, the national and provincial competition rules for traditional martial arts include head guards, clothing, leg guards, guards, thin belts, and mouth guards. When these basic protective gears are used, none of them can participate in the competition, and they must pass the security check before the competition and stamped with the seal before they can be used during the competition. However, judging from the current domestic competition scene, protective gear and other equipment are rarely used. One team member believes that the protective gear will affect the performance and when the level of confrontation reaches a certain level, the protective gear basically cannot protect the participants, and the protective gear does not really play its role. At the same time, female martial arts athletes will use some protective gears in the competition process and daily training of athletes in order not to damage the body. Figure 8 shows several common body protective gears.

3. Static Tensile Experiments of Nanobuffer Materials

3.1. Mechanical Model of Nanobuffer Material. According to the compression characteristics of the buffer material, a set of modulus can be used to characterize its linear elastic properties, that is,

$$\frac{E^*}{E_s} = C_1 \left(\frac{\rho^*}{\rho_s}\right)^2. \tag{1}$$

Among them, E^* is the elastic mode of the cushioning material, E_s is the elastic mode of the matrix, ρ^* is the density of the cushioning material, and ρ_s is the density of the matrix. C_1 is the scale factor.

$$\frac{G^*}{E_s} = C_2 \left(\frac{\rho^*}{\rho_s}\right)^2. \tag{2}$$

Among them, G^* is the shearing die of the buffer material and C_2 is the proportional coefficient.

In the nonbombing phase,

$$\frac{\sigma_{e1}{}^*}{E_s} = C_3 \left(\frac{\rho^*}{\rho_s}\right)^2. \tag{3}$$

FIGURE 7: Traditional martial arts. Image source: http://www.changjunwenhua.com/pic_detail.php?cid=2&id=48.

TABLE 2: Comparison of different types of force in traditional martial arts.

Fist name	Fist for example	Fist boxing method for example	Hard way
Straight-line boxing	Forward punch	South boxing: lunge step double punch boxing	Straight impact strength
Long curve boxing	Swing	Split boxing: a lotus hand	Curve whip
Short curve boxing	Hook	Fanzi fist: a wild horse running groove	Short-range impact

TABLE 3: Comparison of force methods of the same type of traditional martial arts and different styles of punches.

Boxing	Example action (punch punch)	Hard way
Eight extremes boxing	Hold the fist	In the storage of strength, cross-strength, a word to support strength
Taijiquan	Cover hands and punch with arm	Long storage strength, wrapped silk strength, elastic strength
Nanquan	Single butterfly step punch	Short storage strength, long inch strength, drill strength

FIGURE 8: Several common body protectors. Image source: https://shi222.sm160.com/Company/OfferDetail/1-000-7754-861.html.

Among them, σ_{e1}^* is the elastic limit of the buffer material and C_3 is the proportional coefficient.

For plastic buffer materials, the ultimate strength is

$$\frac{\sigma_{p1}^*}{\sigma_{ys}} = C_4 \left(\frac{\rho^*}{\rho_s}\right)^{3/2}. \tag{4}$$

Among them, σ_{p1}^* is the collapse limit of the buffer material and σ_{ys} is the yield strength of the matrix.

For a two-dimensional closed-cell buffer material, when it is compressed, its stress is:

$$\sigma = \sigma_{ys} \left[C_1 \left(\frac{\rho^*}{\rho_s}\right)^{3/2} + C_2 \frac{\rho^*}{\rho_s} \right]. \tag{5}$$

Equipment name	Model	Performance
Electronic balance	MP200-II	Capacity 180 g/0.02 g
Oven	Universal	$1 m^3$ 5 kw
Digital microscope	US MOTICDMEB5	1.3 million pixel objective lens: oil lens 100x eyepiece 5x
Environmental scanning electron microscopy	Netherlands XL30 ESEM-TMP	The resolution is 25 cm under 1KV voltage
Fourier infrared spectrometer	American Nicoli 360 intelligent	4000-400 cm^{-1}
Compression box	2	According to packing cushion material creep characteristics
Blender	7312-I	Manufactured by experimental method

The relationship between porosity and density is

$$P = \left(1 - \frac{\rho^*}{\rho_s}\right) \times 100\%. \tag{6}$$

Substitute into the previous formula to get

$$\sigma = \sigma_{ys}\left[C_1(1-P)^{3/2} + C_2(1-P)\right]. \tag{7}$$

That is to say, the porosity is inversely proportional to the strength of the buffer material.

For a buffer material, its ability to absorb energy can be expressed as

$$W = \int_0^\varepsilon \sigma d\varepsilon. \tag{8}$$

In formula, W is the absorption force per unit volume and ε is the strain.

Its ideal energy absorption efficiency is

$$I = \frac{1}{\sigma_{\max}} \int_0^\varepsilon \sigma d\varepsilon. \tag{9}$$

For the constitutive formula of the nanobuffer material, the constitutive relation of ben'gou materials mentioned in this paper is a mathematical model, which is an abstract reflection of the macroscopic properties of materials. One of the core tasks of studying the mechanical properties of materials is to establish constitutive equations that can describe the mechanical responses of materials under various loads. The parameters of the material constitutive equation are determined by a certain range of strain rate and temperature experiments, and the correctness of the constitutive equation can be verified by comparing the predicted value of the constitutive equation with the experimental results; it can be expressed as

$$\sigma = f(\varepsilon, \varepsilon^*, T). \tag{10}$$

For its mechanical properties, it can be expressed as

$$\sigma = (A + B\varepsilon^n)(1 + Cln\varepsilon^*)(1 - T^m). \tag{11}$$

The compressive stress-strain constitutive relation for the buffer material is

$$\sigma = E_0 f(\varepsilon). \tag{12}$$

In formula, E_0 is the initial modulus, $f(\varepsilon)$ is the shape function, and it has

$$f(\varepsilon) = \varepsilon\varphi(\varepsilon) = \varepsilon(a\varepsilon^{-p} + b\varepsilon^q). \tag{13}$$

If the factor of strain rate is introduced, and $f(\varepsilon)$ is regarded as the series, the constitutive relation is

$$\sigma_c = E_0(\varepsilon^*)f(\varepsilon). \tag{14}$$

In formula,

$$E_0\,\varepsilon^*) = k\varepsilon^*,$$
$$f(\varepsilon) = \sum_{i=0}^{10} A_i\varepsilon^i. \tag{15}$$

Considering that the strain rate factor is related to the strain, the more complete constitutive formula is obtained as

$$\sigma_c = M(\varepsilon, \varepsilon^*)f(\varepsilon),$$
$$M(\varepsilon, \varepsilon^*) = \left(\frac{\varepsilon^*}{\varepsilon_0^*}\right)^{n(\varepsilon)}. \tag{16}$$

In formula, ε_0^* is the static strain rate and $n(\varepsilon)$ is a linear function:

$$n(\varepsilon) = a\varepsilon + b. \tag{17}$$

3.2. Static Tensile Test. In this paper, the nanobuffer material within a certain density range is selected for stress testing at different strain rates. The density range is between 1 and 20 nanometers. The test conditions are as follows: temperature $T = 20°C$, relative humidity 75%, and the load is gradually increased to the limit on the test sample along the thickness direction at a speed of 10 mm/min. The experimental equipment is shown in Table 4.
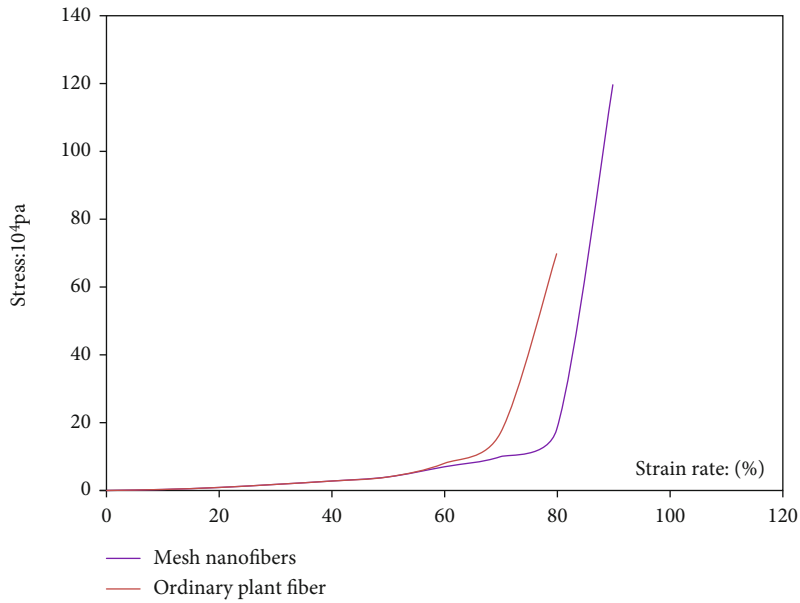
FIGURE 9: Stress comparison of buffer materials.
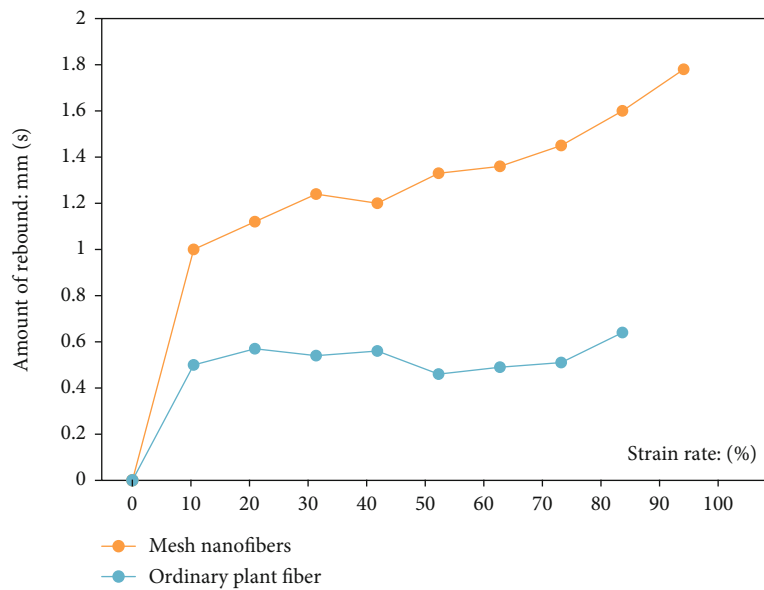
FIGURE 10: Comparison of resilience performance of cushioning materials.

The basic process of this paper is first to stretch and test the test sample according to the experimental equipment in Table 4. The stretching method is to gradually increase the load and record the stretched length of the buffer material in the process and then calculate the strain diagram according to the equation and then slowly withdraw the recovery length of the material and then calculate the rebound curve of the material according to the equation.

The strain curve is obtained according to the previous constitutive formula, and compared with the common fiber material, the results are shown in Figures 9 and 10.

According to Figure 9, it can be seen that the mesh nanofiber material can withstand a pressure of 1.2 million Pa under 90% strain, while the ordinary fiber material can only withstand a pressure of 700 kPa under 80% strain. It can be seen that the use of mesh nanofiber materials can significantly improve the bearing capacity of stress. According to Figure 10, it can be seen that the resilience of the meshed nanofiber material is significantly higher than that of ordinary fiber materials. Under 90% strain, its resilience reaches 1.8 mm/s, while the maximum of ordinary fiber materials is only 0.6 mm/s. It can be seen that the mesh nanofiber

material can significantly improve the stress bearing capacity of the protective gear and improve the rebound effect.

4. Discussion

Although the experiments in this paper have specific evidence that the mesh nanofiber material can significantly improve the stress bearing capacity of the protective gear and improve the rebound effect. However, there are still some shortcomings:

(1) In practice, some buffer materials will rupture due to too fast drying or excessive external force during the drying process, or due to too slow drying, small bubbles will merge into large bubbles, which will affect the shape of the space inside the material. And it will cause internal stress defects and thus affect the strength of the sample, which should be strengthened on the drying process

(2) It is recommended to conduct further research on the microscale of the pores of the buffer material and the size of the truss structure

(3) The recovery performance and compressive stress performance of cushioning materials with different densities will be different. Further experiments are needed to analyze the cushioning and resilience performance of materials under different densities, and verification tests should be carried out for this material

(4) In this paper, only the resilience and compressive stress of the buffer material are tested, and some characteristics of the buffer material need to be further discussed and studied

5. Conclusions

In the abstract, this paper first gives an overview of the overall content of the full text and then introduces the background of traditional martial arts in the introduction and introduces the protective effect of buffered nanomaterial protective gear on martial arts trainers. Then, the innovation points of this paper are summarized, and some related researches are listed in the related work part, so as to understand the current situation of the related content of this paper. Then, in the theoretical research part, the definition, characteristics, classification, and application fields of buffer nanomaterials are first introduced, and then, the relevant content of buffer materials is introduced, and the characteristics of traditional martial arts and the force application methods of different martial arts are introduced. Then, introduce the related content of body protector. Finally, the stress bearing performance and resilience performance of the mesh nanofiber material and ordinary fiber material are tested by mechanical experiments. It is concluded that the mesh nanofiber material can significantly improve the stress bearing capacity of the protective gear and improve the rebound effect, which can better provide safety protec-

tion for traditional martial arts trainers. In the future development, nanomaterials will be more and more widely used, such as the addition of nanoparticles to the martial arts protective ware of textile and chemical fiber products, which can remove flavor and sterilization. Although the chemical fiber material is strong, but there are annoying electrostatic phenomenon, adding a small amount of metal nanometer particles can eliminate the electrostatic phenomenon.

Data Availability

The data that support the findings of this study are available from the corresponding author upon reasonable request.

Conflicts of Interest

The authors declare that they have no conflicts of interest.

References

[1] B. Liu and S. E. Skrabalak, "ACS materials letters at 1.5 years," *ACS Materials Letters*, vol. 3, no. 1, pp. 134-135, 2021.

[2] D. Jung, P. Das, A. Atilgan, P. Li, and O. K. Farha, "Reactive porous polymers for detoxification of a chemical warfare agent simulant," *Chemistry of Materials*, vol. 32, no. 21, pp. 9299–9306, 2020.

[3] D. A. Heinze and D. J. Carastan, "The influence of fumed silica content, dispersion energy, and humidity on the stability of shear thickening fluids," *Rheologica Acta*, vol. 59, no. 7, pp. 1–14, 2020.

[4] A. Filippi, F. Liu, J. Wilson et al., "Antioxidant activity of cerium dioxide nanoparticles and nanorods in scavenging hydroxyl radicals," *RSC Advances*, vol. 9, no. 20, pp. 11077–11081, 2019.

[5] J. Rzayev, "Molecular bottlebrushes: new opportunities in nanomaterials fabrication," *ACS Macro Letters*, vol. 1, no. 9, pp. 1146–1149, 2012.

[6] K. Zheng, M. I. Setyawati, D. T. Leong, and J. Xie, "Antimicrobial silver nanomaterials," *Coordination Chemistry Reviews*, vol. 357, pp. 1–17, 2018.

[7] H. Li, T. Du, H. Xiao, and Q. Q. Zhang, "Crystallization of calcium silicate hydrates on the surface of nanomaterials," *Journal of the American Ceramic Society*, vol. 100, no. 7, pp. 3227–3238, 2017.

[8] X. Liu, F. Zhang, X. Jing et al., "Complex silica composite nanomaterials templated with DNA origami," *Nature*, vol. 559, no. 7715, article 332, pp. 593–598, 2018.

[9] Y. Chen, Y. Yi, and B. Xu, "Mesoporous carbon nanomaterials induced pulmonary surfactant inhibition, cytotoxicity, inflammation and lung fibrosis," *Journal of Environmental Sciences*, vol. 62, no. 12, pp. 100–114, 2017.

[10] S. T. Ha, S. Rui, and J. Xing, "Metal halide perovskite nanomaterials: synthesis and applications," *Chemical Science*, vol. 8, no. 4, pp. 2522–2536, 2017.

[11] H. Sadegh, G. Ali, V. K. Gupta et al., "The role of nanomaterials as effective adsorbents and their applications in wastewater treatment," *Journal of Nanostructure in Chemistry*, vol. 7, no. 1, article 219, pp. 1–14, 2017.

[12] K. Garner, S. Suh, and A. A. Keller, "Response to comments on "assessing the risk of engineered nanomaterials in the environment: development and application of the nanoFate model","" *Environmental Science & Technology*, vol. 52, no. 9, pp. 5511–5511, 2018.

[13] M. Abbas, Q. Zou, and S. Li, "Self-assembled peptide- and protein-based nanomaterials for antitumor photodynamic and photothermal therapy," *Advanced Materials*, vol. 29, no. 12, pp. 1605021.1–1605021.16, 2017.

[14] L. Yan, L. Tian, and X. Tan, "Synthesis, properties, and applications of black titanium dioxide nanomaterials," *Science Bulletin*, vol. 62, no. 6, pp. 431–441, 2017.

[15] W. Lu, Q. Xiong, and X. Fei, "2D nanomaterials based electrochemical biosensors for cancer diagnosis," *Biosensors & Bioelectronics*, vol. 89, Part 1, pp. 136–151, 2017.

[16] Y. Zhang, W. Ni, and Y. Li, "Effect of siliconizing temperature on microstructure and phase constitution of Mo-MoSi$_2$ functionally graded materials," *Ceramics International*, vol. 44, no. 10, article S0272884218307004, pp. 11166–11171, 2018.

[17] X. Zhang, Q. Yan, E. B. Hassan, J. Li, Z. Cai, and J. Zhang, "Temperature effects on formation of carbon-based nanomaterials from kraft lignin," *Materials Letters*, vol. 203, pp. 42–45, 2017.

[18] R. Kumar, A. Umar, and G. Kumar, "Antimicrobial properties of ZnO nanomaterials: a review," *Ceramics International*, vol. 43, no. 5, pp. 3940–3961, 2017.

[19] G. Bo, L. Chang, H. Chenglong et al., "Effect of Mg and RE on the surface properties of hot dipped Zn–23Al–0.3Si coatings," *Science of Advanced Materials*, vol. 11, no. 4, pp. 580–587, 2019.

[20] O. Suárez-Iglesias, S. Collado, P. Oulego, and M. Díaz, "Graphene-family nanomaterials in wastewater treatment plants," *Chemical Engineering Journal*, vol. 313, pp. 121–135, 2017.

[21] H. Xiao and S. Liu, "2D nanomaterials as lubricant additive: a review," *Materials & Design*, vol. 135, pp. 319–332, 2017.

[22] F. Lu and D. Astruc, "Nanomaterials for removal of toxic elements from water," *Coordination Chemistry Reviews*, vol. 356, pp. 147–164, 2018.

[23] D. Cassano, S. Pocoví-Martínez, and V. Voliani, "Ultrasmall-in-nano approach: enabling the translation of metal nanomaterials to clinics," *Bioconjugate Chemistry*, vol. 29, no. 1, pp. 4–16, 2018.

Research Article

Fiber Bragg Grating Smart Material and Structural Health Monitoring System Based on Digital Twin Drive

Zhen Lei [ID],[1] **Liang Zhu** [ID],[2] **Youliang Fang,**[3] **Chunjie Niu,**[3] **and Yunpeng Zhao**[3]

[1]*Hebei Province Civil Engineering Monitoring and Evaluation Technology Innovation Center, Hebei University, Baoding, 071002 Hebei, China*
[2]*School of Cyber Security and Computer Science, Hebei University, Baoding, 071002 Hebei, China*
[3]*College of Civil Engineering and Architecture, Hebei University, Baoding, 071002 Hebei, China*

Correspondence should be addressed to Zhen Lei; leizhen@hbu.edu.cn and Liang Zhu; zhu@hbu.edu.cn

The damage self-diagnosis function puts forward higher requirements for the research and development of intelligent structural health monitoring, and in most cases, it is necessary to monitor the load first, especially the monitoring of the impact load. The development of smart materials and structures is based on advanced sensing systems. In order to achieve this purpose, a high-speed demodulation system based on fiber grating with double long period grating is studied, and then, a damage self-diagnosis system based on fiber grating is constructed. The system can realize the strain distribution and impact load monitoring of the structure. After quantitative analysis of the signal, an advanced information identification method is used to realize the impact load location. This paper focuses on the data preprocessing process of bridge health monitoring. In view of the characteristics of high data complexity, large amount of data, and many noise components in the process of structural monitoring, this paper adopts basic data cleaning for the original data set, including data dimensionless and missing value processing. Based on the digital twin technology, the composition of the digital twin KNN model of bridge swivel construction monitoring and management is analyzed, and the digital twin system architecture of bridge swivel construction monitoring and management is built. The function display of the monitoring platform, including setting a variety of permission login modes, displaying BIM model, geographic information, and weather environment; monitoring data entry and addition, deletion, and modification; data chart analysis and export; and email warning, to verify the feasibility of the application of digital twin technology in bridge monitoring, and the advantages of the intelligent monitoring system are obtained. The strain error is found to be less than $15.48\,\mu\varepsilon$ in the research, which is within the range of the fiber grating. This method can effectively monitor and forecast these distributed, nonlinear, strongly coupled, multivariable, and time-varying complex structures. By monitoring bridges, the original monitoring data of bridges can be obtained, and scientific research data and analysis services can be provided. In particular, the damage caused by shock and vibration is monitored, so that the accumulation of damage can be detected before it threatens the safety of the structure, so that the damaged structure can be repaired in time to ensure the safe operation of the structure.

1. Introduction

With the development and progress of technology, a complete digital twin system is built from the perspective of bridge swivel construction monitoring and management and interacts with other digital twin systems to realize the interconnection of everything. The digital twin system of bridge swivel construction monitoring and management includes five levels: user domain, digital twin, measurement and control entity, real physical domain, and cross-domain functional entity. Digital twin is a simulation process integrating multidisciplinary, multiphysics, multiscale and multiprobability by making full use of physical model, sensor update, operation history, and other data to complete the mapping of physical entities

in virtual space, so as to reflect the whole life cycle process of physical entities.

A structural health monitoring system is an important application direction of intelligent structure, which has attracted more and more people's attention. In the process of bridge swivel construction, monitoring technology is used to ensure the smooth progress of the swivel process and the safety of the swivel construction, and to provide data support for decision-making at each stage. At the same time, it can detect the bridge structure, compare the monitoring data with the previous calculation results, and check each other to ensure the quality of the structure. According to the monitoring results, the design and construction process of the swivel bridge can be optimized. In addition, the data obtained from the construction monitoring can supplement the bridge construction data, improve the bridge life cycle data, and provide an important basis for the later bridge operation and maintenance [1].

In this paper, the sensing model of the uniform period fiber grating and its Fourier transform demodulation theory are studied, and the transmission response characteristics of the uniform period fiber grating are deduced according to the coupled mode theory. In the process of bridge operation, in order to ensure the safety performance and durability of long-span bridges, we need to monitor the health of bridge structures, establish a real-time and smooth network monitoring system, understand the health status of bridge structures, and ensure their normal work and operation. According to the calculation results and monitoring element analysis, sensor model, and using BIM technology, the measurement point layout and early warning mechanism design of the background swivel bridge monitoring scheme are carried out. According to the characteristics of bridges spanning high-speed railways when rotating, a bridge-building comprehensive information model is established. According to the characteristics of the swivel construction of the bridge spanning high-speed railway, combined with the background engineering, the swivel balance system is studied, which is used to adjust the unbalance of the cantilever end during the bridge swivel process, ensure the stability of the swivel process, and improve the construction safety.

2. Related Work

Digital twins are increasingly being introduced into the fields of Internet technology and industrial technology. Fiber Bragg grating (FBG) sensors and extrinsic fiber Fa-Per (EFPI) sensors are two very promising fiber optic sensors in the field of structural health monitoring. Xiaodan designed a virtual training platform for carrier-based aircraft approach and landing based on virtual reality technology. He adopts a distributed architecture, introduces each node of the system in detail, then gives a method for real-time communication using reflective memory technology, and introduces the logical relationship and integration of three dynamic modules [2]. Ye et al.'s accurate assessment of wind characteristics and wind-induced structural responses during typhoons is of great significance for bridge design and safety assessment. He proposed an angular linear approach based on the expectation maximization (EM) algorithm for probabilistic modeling of field-measured

wind properties [3]. Sarmadi et al. believe that environmental changes are a major challenge in bridge health monitoring because bridges are more prone to such changes than other civil structures. To address this challenge, they propose a new machine learning approach for early damage detection under environmental changes through clustering, a new damage metric, and an innovative method for selecting an appropriate number of clusters. Estimating reliable alert thresholds is another important challenge for early damage detection by most machine learning methods. On this basis, they propose a new probabilistic method for estimating alarm thresholds using extreme value theory and goodness-of-fit measures. Their major contributions include proposing a new damage metric suitable for clustering-based algorithms for decision making, an innovative cluster selection algorithm for dealing with environmental variability and improving damage detectability, and a new probabilistic method for threshold estimation [4]. Nguyen et al. introduced a new method for diagnosing structural damage based on changes in the mechanical parameters of materials. First, they integrated viscoelastic models into structural damage detection and diagnosis. Therefore, the model defines the mechanical properties of the material by two parameters, the elastic modulus and the coefficient of viscosity. Hooke's model is linear, while viscoelasticity is nonlinear and therefore more accurately reflects reality. Second, they exploited the amplitude and frequency of the vibrational signals and determined their relationship to mechanical parameters that detect structural changes. Based on theoretical analysis and experimental results, their research is more effective and general than previous studies. Simultaneous monitoring of structural changes using different parameters enabled the study to collect more appropriate data compared to previous studies [5]. A structural health monitoring system is one of the important application methods of intelligent structure. The digital twin will have an unignorable impact on the construction industry, and it will become the core engine for the transformation and development of the construction industry. The combination of digital twin and BIM technology will provide a digital model of the city for the government cloud platform based on image scanning, which will cover all high-voltage power grid lines, sewage systems, water supply and drainage systems, highways, traffic control systems, and all interconnected locations in the city. BIM is a building information modeling technology, which is a data-based tool used in engineering design, construction, and management. It is used to describe computer-aided design based on three-dimensional graphics, object-oriented, and architecture.

3. Fiber Bragg Grating Smart Materials and Structural Health Monitoring System Method

3.1. Fiber Bragg Grating Sensor Configuration. The grating sensor refers to a sensor that uses the principle of grating moire to measure displacement. The configuration of fiber Bragg grating sensors can be studied in terms of the number of sensors and the spatial layout of sensors. The spatial distribution of the sensors can adopt various sensor distribution

methods such as equidistant distribution, proportional distribution, and mixed distribution, which should be comprehensively determined in combination with various factors such as specific test objects, clamping methods, and loading methods. Therefore, in the subsequent test process, different sensor distribution designs will be adopted for specific test objects.

Regarding the configuration of the number of sensors, the number of sensors that can achieve wavelength division multiplexing for a single channel mainly depends on the bandwidth of the light source and the dynamic range of the measured parameters. Therefore, when determining the number of grating points on a single fiber string, the demodulation limit of the fiber grating demodulator and the actual strain of the measured object should be considered. The specific ideas are as follows.

First, the wavelength variation range of a single grating is calculated according to the strain variation range and grating strain sensitivity of a single grating monitoring point:

$$\Delta\lambda = K_\varepsilon \cdot \varepsilon. \tag{1}$$

In the formula, ε is the strain value of the ith grating point and K_ε is the strain sensitivity of the ith grating point.

Assuming that there are n grating points to be measured on a single-fiber grating string, on this basis, the wavelength variation range of all grating points on the channel of the fiber grating string is calculated [6]:

$$\Delta\lambda = \Delta\lambda_1 + \Delta\lambda_2 + \cdots + \Delta\lambda_n = \sum (K_\varepsilon \cdot \varepsilon). \tag{2}$$

In order to prevent the wavelength signals from aliasing during the measurement of grating points of adjacent wavelengths, the working range of a single grating measured point can be expressed as [7]:

$$\Delta\lambda = K_\varepsilon \cdot \varepsilon + \lambda \tag{3}$$

If n measured grating point on a single-fiber grating string can work normally without wavelength aliasing, then [8]

$$\Delta\lambda = \Delta\lambda_1 + \Delta\lambda_2 + \cdots + \Delta\lambda_n = \sum (K_\varepsilon \cdot \varepsilon + \lambda). \tag{4}$$

Then, the measurement range λ_n of the n sensors is [9]

$$\lambda_n = \Delta\lambda = \sum (K_\varepsilon \cdot \varepsilon + \lambda). \tag{5}$$

If the maximum measurement range of a single channel of the fiber grating demodulator is $\lambda_{\max}$.

$$\lambda_n \leq \lambda_{\max}, \tag{6}$$

$$n \leq \frac{[\lambda_{\max} - \sum (K_\varepsilon \cdot \varepsilon + \lambda)]}{\lambda_h}. \tag{7}$$

Assuming that the strain range measured by each grating sensor is ε, the above formula can be further simplified as [10]

$$n \leq (K_\varepsilon \cdot \varepsilon + \lambda). \tag{8}$$

Therefore, the maximum number of grating sensors that can be connected in series on each channel of the fiber grating demodulator can be calculated by the above formula [11].

3.2. KNN Algorithm. The mechanism of the KNN algorithm applied to the analysis of bridge monitoring data can be summarized as follows: when the model obtains a new detection data sample point, KNN can classify it according to the nearest known sample points of the sample point. Due to such classification characteristics, this paper uses this as a theoretical basis to design a bridge loss judgment model to classify the monitoring data of the bridge, so as to indicate the monitoring data of the bridge in a healthy state and a damaged state [12].

The basic steps of the KNN algorithm:

Input data set:

$$T = \{(x_1, y_1), (x_2, y_2), (x_3, y_3), \cdots, (x_n, y_n)\}, \tag{9}$$

where x_n represents a feature vector of the instance [13].

Output: the category to which instance x belongs.

According to the selected distance metric formula, find the k instance points closest to x in the data set, and the set of these K points is called the k neighborhood $N(x)$ of x.

According to the classification rule in the k neighborhood of x, the majority votes the classification category y of x:

$$y = \mathrm{argmax}_c \sum x \in N(x) I(y = c). \tag{10}$$

In the above formula, I is the indicator function, that is, when $y = c$, $I = 1$; otherwise, it is 0 [14].

At time t, the input layer inputs the bridge high-finesse time series data, and the state of each unit of the input layer at this time [15]:

$$U(t) = [u_1(t), u_2(t), \cdots, u_m(t)]^T. \tag{11}$$

When new data is input, the algorithm will update the state $x(t)$ of the storage layer and the update rule [16]:

$$x(t + 1) = wx(t) + w^{\mathrm{in}} u(t + 1). \tag{12}$$

After the node state update of the storage layer is completed, the node state matrix is obtained [17]

$$y = f^{\mathrm{out}} \left(\int w^{\mathrm{out}}(t) dt \right), \tag{13}$$

where w^{out} is the weight matrix of the output layer, and f^{out} is the activation function of the output layer.

Let

$$K_1 = \frac{L_0}{L_1},$$
$$K_2 = \frac{A_0}{A_1}. \tag{14}$$

It can get [18]

$$\varphi_1 = \frac{K_1 K_2}{K_1 + K_2 - 1},$$
$$\varphi_0 = K_\varphi \varphi_0.$$

(15)

Bridge construction monitoring is a general term for all the work that provides technical support for the realization of bridge design requirements through construction process simulation analysis, on-site monitoring and error identification and prediction, and feedback control. Bridge construction monitoring should include monitoring calculation, construction monitoring and data analysis, and feedback mechanism. The monitoring calculation includes design compliance calculation, presimulation calculation, and real-time simulation calculation. Construction monitoring includes stress (internal force) monitoring, linear monitoring, temperature monitoring, and monitoring of necessary environmental factors.

3.3. Structural Design of Digital Twin Bridge Health Structure Safety Monitoring System.
The digital twin bridge health structure safety monitoring system roughly includes two parts:

(1) Sensor and demodulation equipment system: sensors are divided into preembedded sensors from the installation stage, such as concrete embedded strain gauges, embedded crack gauges, and earth pressure gauges. Surface sensors, such as beam surface strain sensors, expansion joint displacement sensors, accelerometers, and inclinometers, were used. The demodulation equipment system is basically divided into static and dynamic monitoring. The static monitoring is second-level monitoring, which is collected at a certain interval, and the dynamic monitoring is about 100 Hz, the vibration data of the bridge is collected in real time

(2) Monitoring center system: the monitoring center is mainly to improve the efficiency, scientificity, rationality, and traceability of management, to achieve rational allocation of resources, and to reduce human errors. The system can be divided into two parts, data acquisition and transmission system and system integration. The data acquisition and transmission system integrates the sensor data in a unified manner, collects it centrally, and completes the software protocol connection with the system integration system. The system integration system is mainly used to assist the bridge management center, which roughly includes the following functional modules, manual inspection and maintenance management module, comprehensive early warning safety assessment module, and management center database management module

3.4. Hardware System Design of Digital Twin Bridge Health Structure Safety Monitoring System.
The hardware part of the digital twin bridge health structure safety monitoring system mainly consists of three parts:

(1) Sensor system: it consists of sensors with various functions and special components distributed on the bridge structure. The sensors are divided into embedded sensors and surface-mounted sensors

(2) Data acquisition system: the data acquisition system is divided into data acquisition and auxiliary devices. The data acquisition system is composed of demodulation equipment, acquisition equipment, acquisition computer, sensor optical cable, cable network, etc., which are arranged inside the bridge junction or on the bridge deck. At present, there are about a dozen types of sensors, and it also indicates that there are more than a dozen different types of demodulators. The auxiliary system consists of the equipment in the field and the monitoring center to assist the normal operation of the above system, including the cabinet, the chassis, the power supply module, the uninterruptible power supply system, and the lightning protection system

(3) Data processing system: process various sensors into digital signals for easy identification, package data, and connect to the system integration module. The hardware system design of the digital twin bridge health structure safety monitoring system is shown in Figure 1

3.5. Software Module Design of Digital Twin Bridge Health Structure Safety Monitoring System.
The overall architecture diagram of the software part of the digital twin bridge health structure safety monitoring system mainly covers the following contents:

(1) The sensor data acquisition, protocol transmission, and other related support services involved in each sensor measurement subsystem

(2) The centralized acquisition function of each sensor subsystem

(3) The relationship between the central database subsystem and other systems and the flow of related data

(4) The functional connection between the user interface subsystem, the structural warning and evaluation subsystem, the manual inspection auxiliary subsystem, and the user terminal. The system of the digital twin bridge health structure safety monitoring system software is shown in Figure 2

3.6. Bonding Process of Fiber Grating Sensor and Measured Structure.
The surface-mount packaging method is usually based on the preset optical fiber sensing layout, and the corresponding fiber grating sensing points are arranged on the surface of the monitored point of the structure, and the grating sensor is fixed with the help of a protective adhesive layer. The operation is convenient and simple, and it will not destroy the initial structural state of the measured object and will not cause too much influence on the strain transmission efficiency and sensitivity of the fiber grating sensor. In the actual
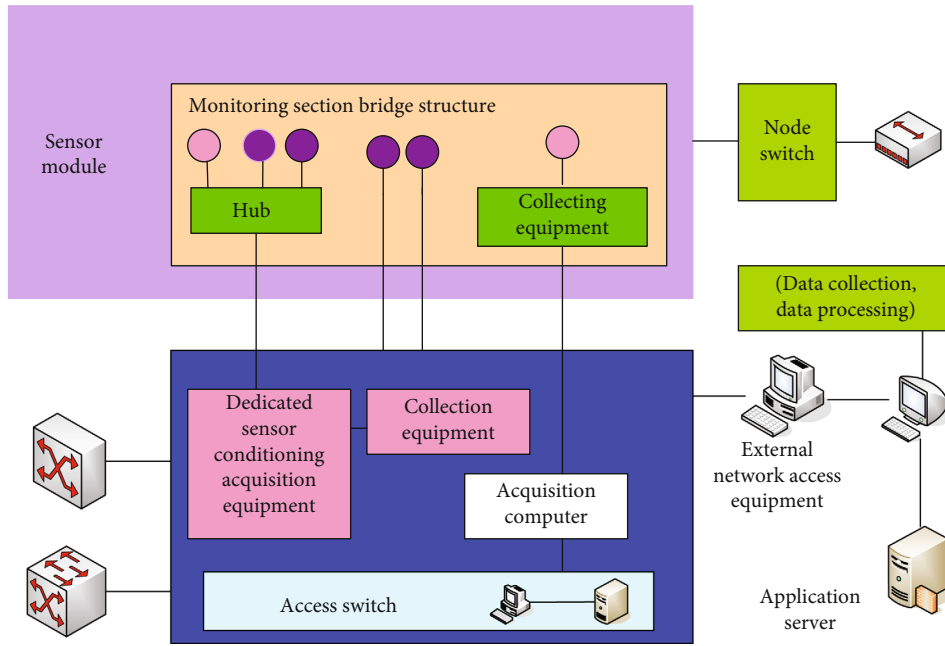
FIGURE 1: Hardware system design of digital twin bridge health structure safety monitoring system.
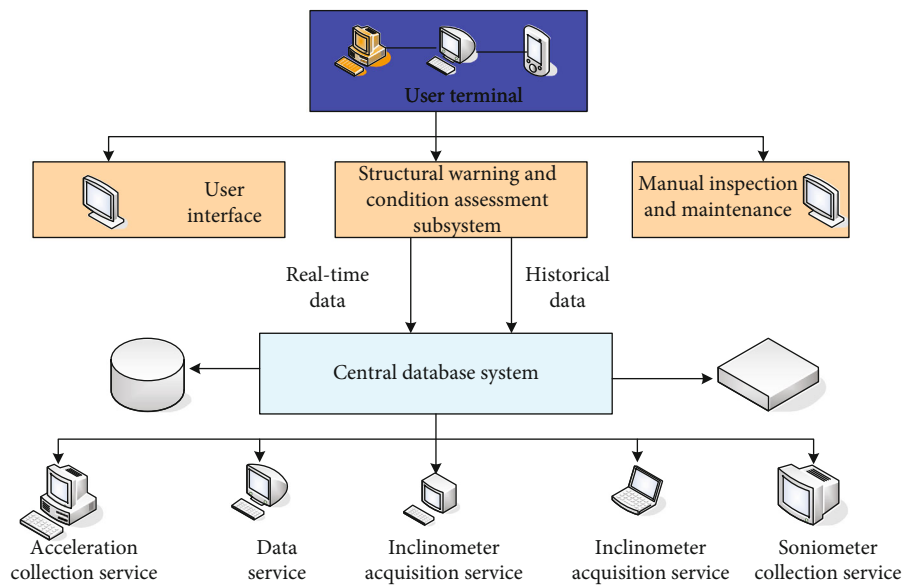
FIGURE 2: Software modules of the digital twin bridge health and structural safety monitoring system.

operation process, on the one hand, it is necessary to select an appropriate bonding method to fix the fiber grating to ensure its fit with the monitored point on the surface of the structure, and at the same time to protect the fiber grating from being damaged. On the other hand, it is necessary to select a reasonable amount of bonding material to reduce the influence on the strain transfer efficiency of the sensor after the fiber grating sensor is bonded to the structure. Based on the above discussion, the bonding process of the fiber grating sensor and the structure can be carried out according to the following steps: first, according to the preset optical fiber hybrid multiplexing network, the number and layout of the sensors required for

the test are planned. Grating sensors with different center wavelengths are selected and connected in series to form a fiber grating string, the connection is spliced by an optical fiber fusion splicer, and a metal sleeve is added at the fusion connection to protect the fusion point from breaking. Secondly, in order to ensure more sufficient contact between the grating sensor grid area and the structure, the grating sensor with the coating layer removed is selected, the grating grid area is laid on the monitored point corresponding to the structure, and a certain prestress is preapplied before gluing, to remove the residual stress that may be introduced in the process of fabrication and coating layer filtering in the grating gate
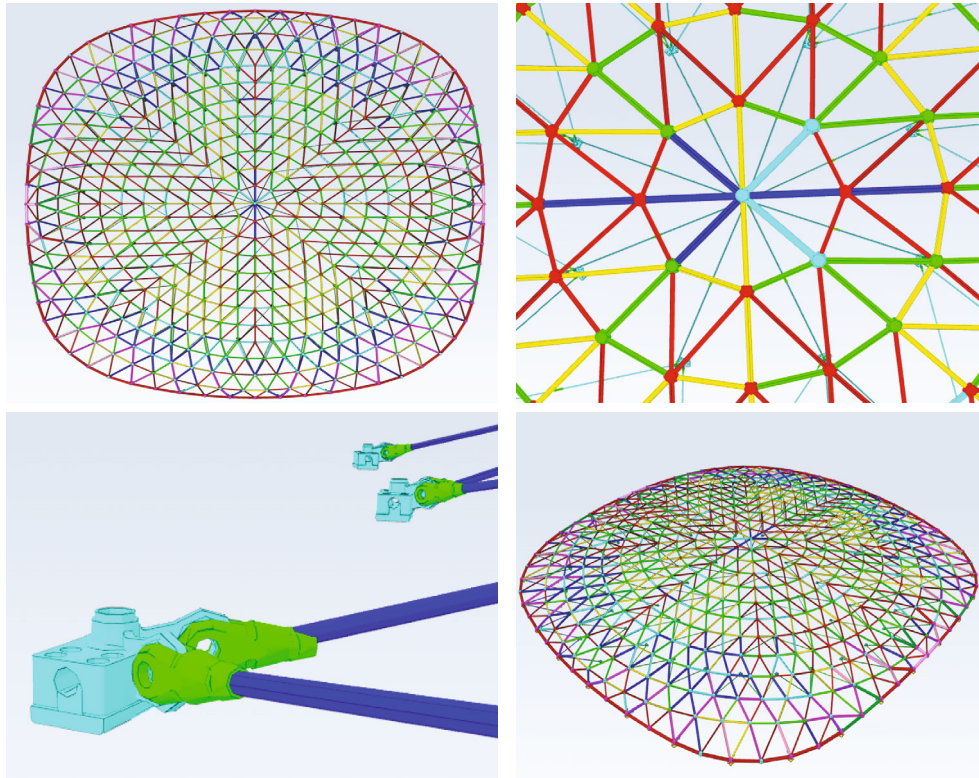
FIGURE 3: Application scene of digital twin of Hebei North University Gymnasium (the picture comes from the author's own drawing).

region. The gate area is preliminarily fixed by using a curing adhesive, and the bubbles that may be generated by the adhesive layer are extruded to ensure that the gate area and the surface of the structure are fully attached. Again, after the cured adhesive layer is air-dried (about 1 h), epoxy resin is applied to the fixed part of the gate area. Its purpose is to shield the crosstalk caused by external stress and, at the same time, protect the cured adhesive on the inside from the influence of the external corrosive environment. Finally, after all the adhesive layers are fully cured (about 24 h), follow-up tests are carried out. Since the strain transfer efficiency of the grating sensor is closely related to the properties of the adhesive layer, during the bonding process, the adhesive layer should be smeared evenly and the thickness is moderate to reduce the influence of the adhesive layer on the strain transfer efficiency of the sensor. Based on the above discussions on sensor network layout, sensor configuration, sensor bonding method, etc., the sensor system and structure integration are designed. For example, the digital twin application scenario of Hebei North University Gymnasium is shown in Figure 3.

3.7. Quality Control Measures in the Installation Stage of Embedded Sensors

(1) The on-site organization is as follows:

Because the sensor preembedding stage needs to follow the bridge construction progress, it has high construction requirements, which can neither delay the normal construction period nor affect the installation quality. The flow-type construction method is adopted, combined with the parallel construction

method to speed up the progress when necessary, that is, the work flow of forecasting installation in advance, compact installation process, and quick departure after installation. Since the sensor is installed in stages with the progress of the bridge construction, the bridge construction unit should be reported to the bridge construction unit 3 days before the installation is required, and the preparations before the installation should be done. The installation process should be compact and regular, and the installation should be carried out when the construction and installation team changes shifts as much as possible. After installation, only the engineer who recorded the installation data is left, and the rest can leave the site to ensure that the progress of the bridge construction is not affected.

(2) To control the installation quality, first of all, we can classify all the sensors that need to be embedded and installed according to the installation location according to the needs of the project. The area is divided according to the range of 500 meters, and a technical support person from a fiber grating sensor supplier company is arranged for each area to conduct real-time technical control. The main points of control are as follows:

(a) Recording the wavelength data of the fiber grating sensor in real time (monitor the initial value)

(b) Compiling record files of fiber grating sensor burial, including points, on-site pictures, sensor types, etc.

(c) Marking and recording the position of the optical fiber outgoing fiber, and report it to the construction unit, emphasizing that the optical cable should not be broken or buried in the later bridge construction process

(3) The main task of the construction team is to carry out the equipment according to the requirements of the technical personnel of the equipment supply company, which are classified into:

(a) Preparatory work before burying such as drilling and binding

(b) The sensor is buried

(c) Cable and traction of optical cable

The formula for covariance is as follows [19]:

$$X_F(X, Y) = E[(X - u_x)(X - u_y)], \tag{16}$$

where X and Y represent two random variables.

Data anomalies in bridge health monitoring belong to time series anomalies, that is, data anomalies are related to time. If the value of a subsequence in the time series deviates greatly from the values of other parts, and such deviation is not generated randomly, but in a way that is completely different from other subsequences, that is, this subsequence may be an abnormal subsequence. There are mainly three types of anomalies in bridge data: point anomaly, pattern anomaly, and sequence anomaly. A general point anomaly refers to a data point whose data value at a certain time point is significantly different from the threshold or abrupt change caused by the degradation of sensor performance or the mutation of external influence factors. The pattern anomaly refers to the existence of small continuous anomalies in the data sequence of a sensor. Such anomalies mostly occur when the sensor fails during continuous acquisition or the transmission line has faults, or it may be an anomaly displayed by obvious changes in the data caused by the gradual aging of the bridge, and there is a significant pattern difference with the continuous data in other time periods. Point exceptions can be thought of as pattern exceptions of length 1. Sequence anomaly is a time series that is significantly different from other time series and originates from different mechanisms. For eigenvalue decomposition,

$$A\eta = \lambda\eta, \tag{17}$$

$$A = Q \sum Q^{-1}. \tag{18}$$

The wave formula for light waves propagating in an optical fiber [20]:

$$\nabla^2 E + KNE + \nabla^2 \left(E \cdot \frac{\nabla\varepsilon}{\varepsilon} \right) = 0, \tag{19}$$

TABLE 1: Corresponding strain errors.

Actual strain ($\mu\varepsilon$)	Wavelength change (nm)	Sensitivity relative error (%)	Strain error ($\mu\varepsilon$)
100	0.12	0.008	0.08
1000	1.2	0.077	0.77
10000	12	0.774	7.74
20000	24	1.548	15.48

$$\nabla^2 h + KNh + \nabla^2 \left(h \cdot \frac{\nabla\varepsilon}{\varepsilon} \right) = 0, \tag{20}$$

where E, h are the electric field strength and the magnetic field strength.

4. Health Monitoring System Results

Taking the initial center wavelength of the fiber grating as 1550 nm, its strain sensitivity is 1.2 pm/$\mu\varepsilon$. Assuming that the actual strains generated are 100, 1000, and 10000, the corresponding strain errors are shown in Table 1. It can be seen from Table 1 that within the range of the fiber grating, the strain error is also within 15.48 $\mu\varepsilon$, that is, the influence of the center wavelength change of the fiber grating on the strain sensitivity coefficient is extremely small, which can be completely ignored in engineering applications.

According to the introduction of the sensitivity adjustment principle of the sensor, the sensitivity of the cable force sensor is affected by its main key parameters $K1$ and $K2$. The two parameters $K1$ and $K2$ have the same trend of influence on sensitivity and the same degree of influence [21, 22]. Among them, when the two parameters of $K1$ and $K2$ are in the range of 0-10, respectively, the sensitivity changes more sharply. After more than 10, the sensitivity change tends to be gentle with the increase of the parameters. Therefore, we are designing the variable diameter part of the sensor, considering that the two parameters of $K1$ and $K2$ are controlled within 10. The effect of sensor parameters on sensitivity is shown in Figure 4.

The analysis model is used to analyze the accident, find the cause of the accident, and predict and analyze the technical performance of the bridge project. Combining BIM technology with finite element technology, the bridge structure and the key parts of the bridge structure can be analyzed by finite element, and the safety of the structure can be monitored and evaluated. Combining BIM technology with finite element technology is shown in Figure 5.

When the monitoring result finds that the single pile load reaches 95% of the allowable value, the system will alarm, and the platform operator must stop the operation of the bridge and conduct an appropriate load shedding test on the area of the bridge until the alarm is cancelled and then gradually resume the bridge operation. The bridge column loads and alarm indicators are shown in Table 2.

According to various problems in the commissioning stage of the digital twin bridge health structure safety monitoring system, the site is investigated and probability statistics are
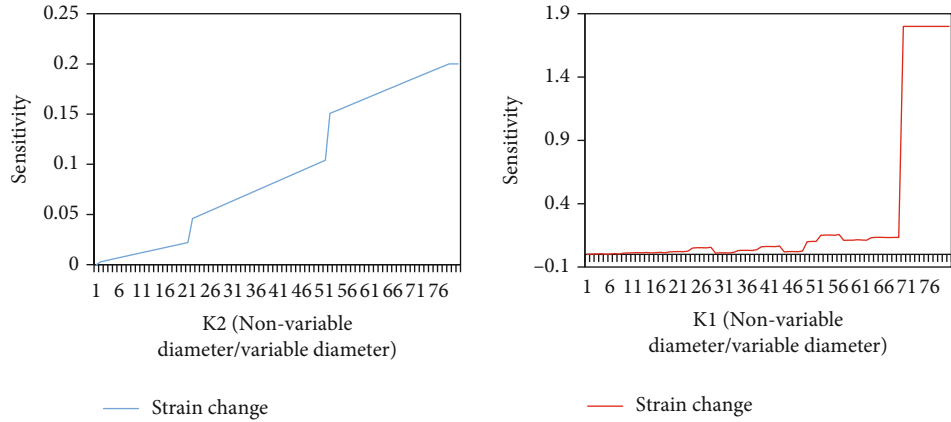
FIGURE 4: Effect of sensor parameters on sensitivity.
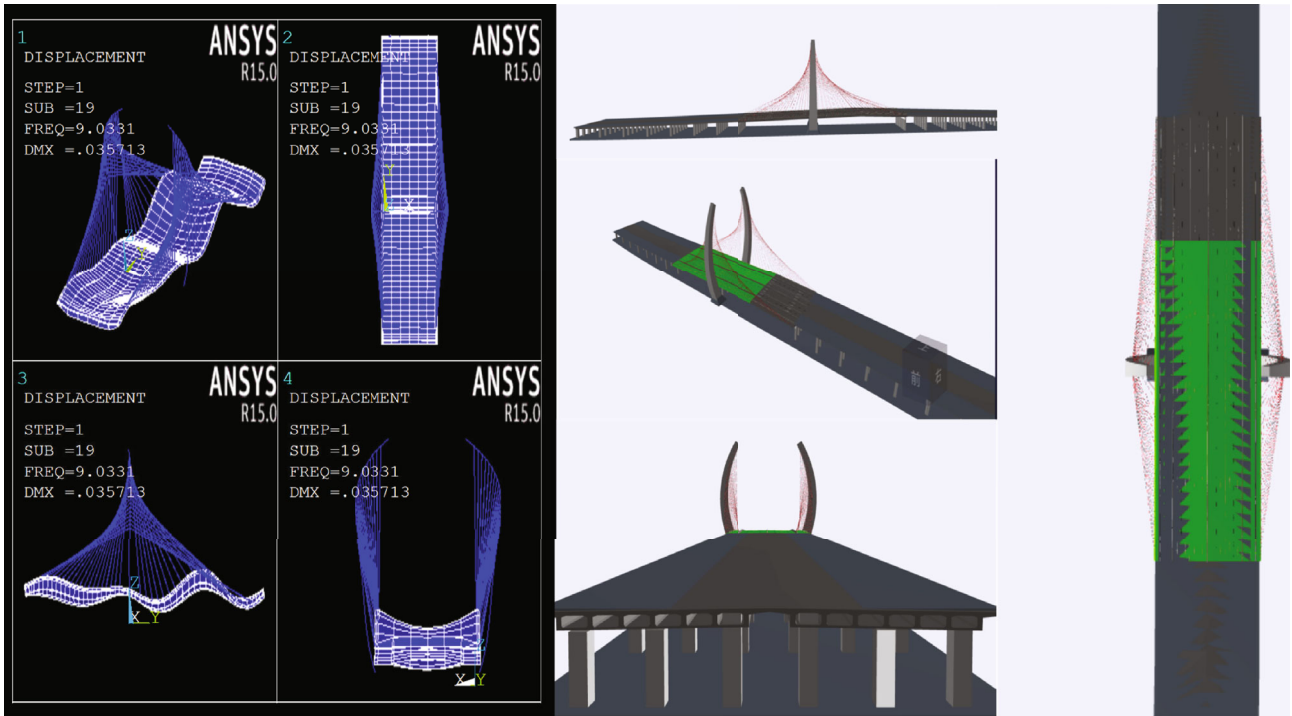
FIGURE 5: Combining BIM technology with finite element technology (the picture comes from the author's own drawing).

carried out, and the defects and frequencies are found in Table 3.

After adopting the standard data protocol, some manufacturers of niche products, such as fiber grating equipment suppliers, have difficulty in clear data protocol, difficult development, and problems in data debugging after development [23]. The problems of fiber grating equipment are shown in Table 4.

Under the two excitation methods, the accuracy rate of KNN varies with the K value. In the environmental excitation data set, the accuracy rate will gradually increase with the increase of the K value. When the K value is about 210, the accuracy rate reaches the highest 99.95%. When the K value continues to increase, the accuracy rate will slowly decrease

TABLE 2: Bridge column loads and alarm indicators.

Part of the bridge column serial number	Carrying capacity	Current stigma force (kN)	Residual stigma force (kN)
1	2059.07	1028.78	1030.88
2	2152.83	1171.35	981.67
3	2101.95	1435.43	666.45
4	2065.70	1046.76	1019.89

with the increase of the K value, and the overall change is not large. Therefore, on the environmental excitation data set, when the K value is set to 180, the accuracy rate is the

TABLE 3: Defects detected and frequency.

Project	Frequency	Cumulative frequency (%)
Sensor point data record error during installation	28	39.4
Repeated communication times of various data protocols	21	68
Repeatedly modify the system integration warning value settings	16	92.5
The data does not meet the standardization requirements	6	100

TABLE 4: Fiber Bragg grating equipment issues.

Project	Frequency	Cumulative frequency (%)
Manufacturer's data protocol development time is long	26	44.9
Data transmission is unstable after development and debugging	20	79.3
Industry differences are large, and it is difficult to connect	7	91.4
The manufacturer has other work arrangements and the new work content is not in place	5	100
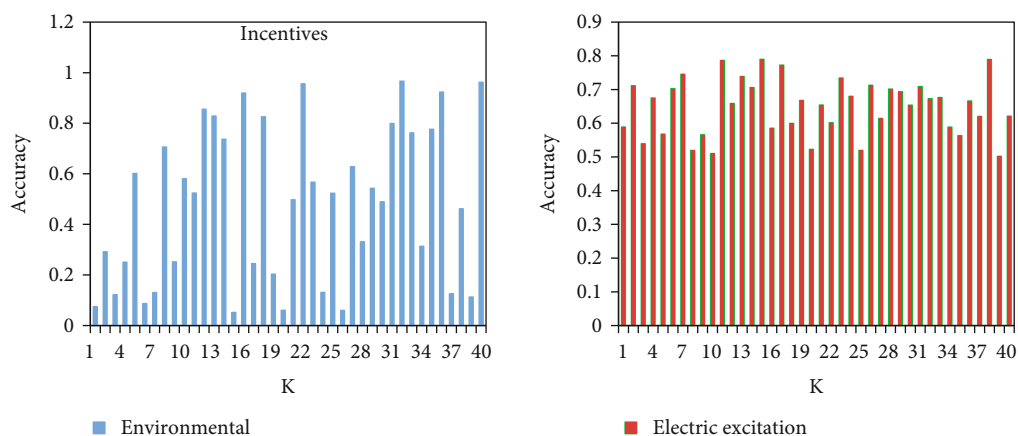
FIGURE 6: KNN parameter adjustment results in the environmental and electric excitation data sets.

highest and the evaluation result is the best. The parameter adjustment results of KNN in the environmental and electric excitation data sets are shown in Figure 6.

Acceleration sensor data were collected for a total of 12 days, and the sampling frequency of acceleration information was 100 Hz, which showed the process of bridge condition from healthy to damaged. The research center increased the number of accelerometers to monitor the acceleration information of the bridge structure again from 8.7 to 8.10. The acceleration sampling information on August 7 was 32 Hz, and the sampling information on 8.8-8.10 was 20 Hz. Some sampling dates and sampling frequencies are shown in Table 5.

In the experiment of single-variable pattern anomaly detection based on KNN distance, the compressed segmentation of the data sequence is first done. For the convenience of operation, the method uses the data in the form of text derived from the database. The selected data of each sensor is controlled at about 8000 data values.

First, taking deflection sensor data as an example, the fitting degree of the time series formed by the original data and the time series after segmentation is shown in Figure 7. When the segmentation error in the segmentation algorithm is set to 0.8 d, the number of original data is 8597, and the data

TABLE 5: Some sampling dates and sampling frequencies.

Date of data collection	Sampling frequency	Assessment of damage status
2018.1.1	100 Hz	Healthy
2018.5.5	100 Hz	Minor injury
2018.7.31	100 Hz	Severe injury

after compression is 1860, so the compression ratio is about 21.7%. At this time, the data before and after the segmentation can basically match, and the compression segmentation error can be adjusted reasonably according to the calculation requirements. The smaller the error, the closer to the original sequence, and the more data values.

The data set records the real-time linear acceleration response of the bridge at 4:20 p.m. local time on June 12, 2018 and the component changes of the gravitational acceleration in all directions. The acceleration time thread is shown in Figure 8.

The silhouette coefficients corresponding to different numbers of clusters, in general, with the increase of the number of clusters, the silhouette coefficient has a downward trend,
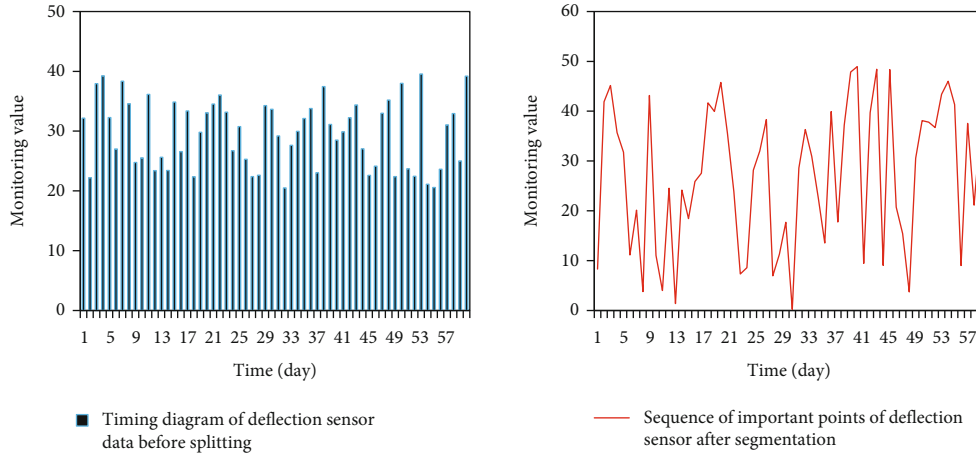
FIGURE 7: The fit of the time series formed from the original data and the time series after segmentation.
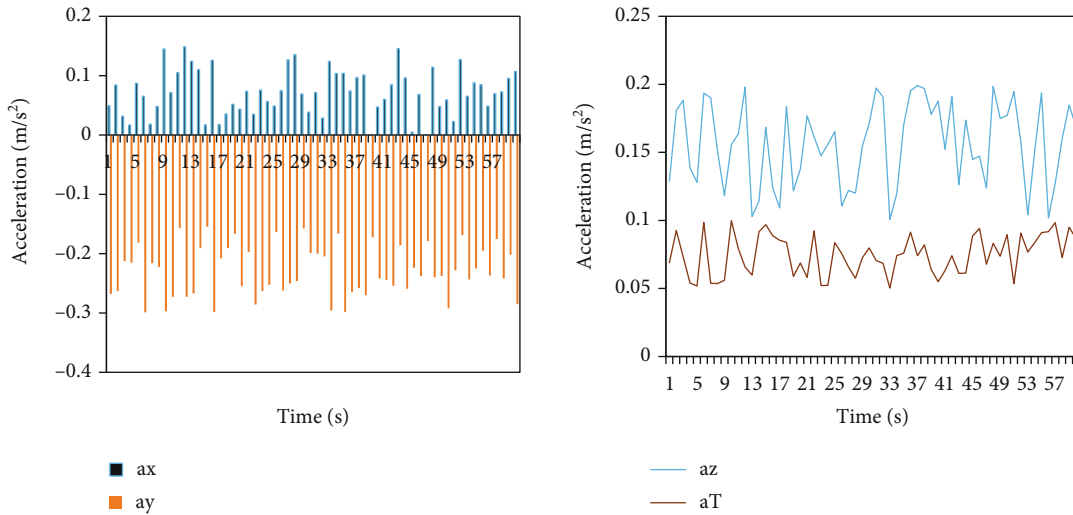
FIGURE 8: Acceleration time thread.

but this does not mean that the fewer the number of clusters, the better. Because with the increase of the number of clusters, the difficulty of model learning gradually increases, and the corresponding silhouette coefficient will decrease accordingly. The contour coefficients are set as shown in Table 6.

The initial value of K of the KNN model is set to 3, that is, the judgment of the new data point is based on the categories of the 3 "nearest neighbors" closest to it. When $K = 3$, the accuracy of the model on the training set is 95.31%, and the accuracy on the test set reaches 91.63%. Its ROC curve is shown in Figure 9, and the AUC area reaches 0.982.

5. Discussion

The main components of the bridge monitoring system are as follows: data acquisition module, data transmission module, data analysis and processing module, data management module, and user interface module. The data acquisition module is the bottom part of the whole monitoring system. According to the characteristics of different bridges, the

TABLE 6: Profile factor settings.

Number of clusters	Silhouette score (silhouette score)
2	0.1932
4	0.1712
5	0.1655

types and quantities of sensors used are different. The data transmission module uses a network constructed by a large number of hubs and routers to transmit the sensor signal data to the monitoring center. The data processing and analysis module preprocesses the data, eliminates data noise and data anomalies, and uses data analysis software to analyze and diagnose bridge health data for damage, the degree and location of damage, pay attention to and study the overall behavior and structural state changes of bridges, and the long-term development trend of bridge bearing capacity and durability. The data management module manages all related bridge structure information, health status monitoring information,
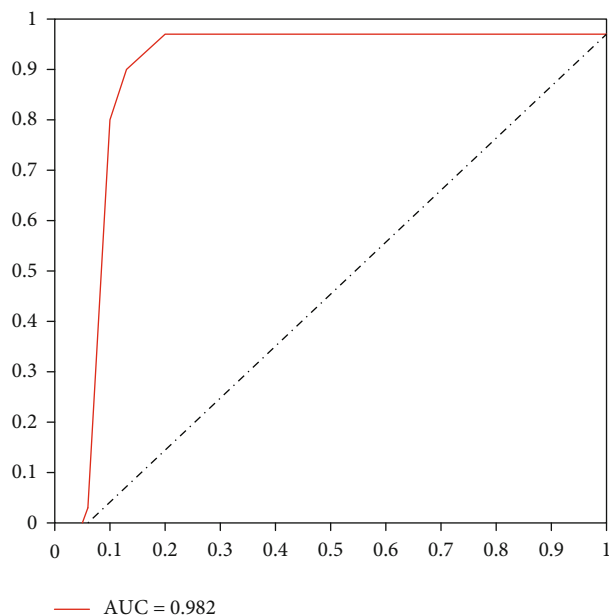
Figure 9: ROC curve.

data processing, and analysis results of the entire bridge. The user interface module presents the bridge-related information to the relevant staff through the visualization program.

The modern spatial structure is developing towards a large and complex direction. These large structures such as space shuttles, high-rise structures, new bridges, and long-span grid structures will be affected by design loads and various unexpected external factors (foreign object shock, vibration, earthquake, explosion, etc.) in complex service environments, and the severe vibration or shock can cause structural damage to varying degrees. The designed service life of large bridge structures can generally reach about one hundred years, and the working life of most bridges needs to last for decades or even hundreds of years. During the service period of bridges, different types of structural damages occur to bridges due to environmental factors, load states, human activity factors, performance variations of building materials, and natural disasters. When the damage accumulates to a certain extent, the accident of sudden structural damage will occur, and the safety of people's lives and properties will be greatly threatened, resulting in significant economic losses. There are many reasons for bridge accidents: engineering quality problems, insufficient postmaintenance of bridges, bridge damage, and functional degradation caused by natural causes, etc.

The traditional bridge monitoring technology generally conducts manual testing under the condition of interrupting bridge traffic. Through regular and nonregular onsite inspection and testing, the actual data is obtained and the test results are obtained by calculation and analysis. The traditional method is limited by time, manpower, measurement conditions, etc., cannot timely feedback evaluation results, is inefficient, has discontinuity, and needs to rely on engineers with rich experience. At the same time, the data collected by traditional methods are relatively not timely enough, are intermittent, and cannot fully and truly reflect the health status of bridges.

The application of BIM in the construction stage realizes the combination of personnel, machinery, materials, documents, etc. with the BIM model in construction, which makes the project schedule easy to control and adjust, improve project quality, control construction safety, and save construction costs. In the process of rotating construction, although the bridge is in a statically indeterminate cantilever state and the force is simple, the bridge is in a state of motion and force when it rotates, and it may be subject to unmeasurable and uncontrollable factors such as wind load, temperature, traction, and friction when it rotates. Therefore, it is necessary to carry out strict construction monitoring on the construction safety and quality of this stage, so as to avoid the phenomenon that the bridge cannot rotate normally or even the bridge overturns during the rotation.

Based on the application of the above BIM technology, more in-depth application research can be carried out on some information, such as regular inspection and rating, preventive screening technology, etc. For example, in the later operation and maintenance of bridges, the operation and maintenance information is transmitted to the BIM model information resource library to realize the transmission of model, coding, data, and file information from the construction period to the operation period, and carry out the whole process management of data monitoring, technical evaluation, comparison and tracking, and auxiliary decision-making.

BIM is widely used in construction, and it can simulate construction plans, carry out special construction, and make construction disclosures. Digital photogrammetry and panoramic technology are used to quickly obtain the original and real-time image data of the project, establish a panoramic system during the construction period, monitor the construction progress, facilitate onsite online management and project live query, and compare and analyze the planned and actual construction. Managing materials, construction data, responsible persons, etc., check the hidden dangers of construction quality and safety, and ensure construction quality and safety. Associating drawings with components, automatically nesting materials, using cloud technology for dimensional inspection, and combining 3D laser scanning to obtain 3D deviation values for the production and design of each component, assisting component quality control, and accurately controlling construction, etc.

Based on Web and digital twin technology, the research on monitoring and management of bridge swivel is carried out. The B/S architecture is used to build a bridge swivel monitoring platform, which integrates animation, BIM model, pictures, and monitoring data into the same interface. Digital twin technology is used to establish a five-dimensional model (physical bridge, virtual bridge model, connection, twin data, and application service) for monitoring and management of bridge swivel construction across high-speed railways and build a digital twin system architecture based on bridge swivel construction monitoring and management. Combined with the background engineering, the operation feasibility of the digital twin system is demonstrated, and the intelligent and automatic management of bridge rotation monitoring and control is realized.

The real swivel bridge and the virtual bridge exchange data through the twin data platform, and the twin data two-way drive the real swivel bridge object and the virtual swivel bridge. The twin data it contains include real-time monitoring data, computational simulation data, rotating body precontrol data, error analysis data, regulation rule data, feedback control data, and personnel construction management data. The monitoring data obtained by the monitoring sensors of the real bridge is transmitted to the virtual bridge through the digital twin platform to simulate the real bridge state and perform real-time monitoring and calculation simulation. The feedback control data generated in the virtual bridge is transmitted to the real bridge through the digital twin platform to control the construction of the bridge swivel. Judging from the operation of the current bridge health monitoring system, the difficulty is often not the collection of monitoring data, but how to process the massive monitoring data accumulated over time, extract the health status information of the bridge with effective data processing and analysis methods, and diagnose and evaluate the bridge. In various monitoring systems, the data processing module is usually the core component. Whether it is damage identification, safety assessment, or change prediction, only good data processing and analysis methods can ensure the meaning and value of the system [24].

6. Conclusion

Aiming at the inconsistency in the dimension of structural output response information and the time-consuming data analysis, this paper uses KNN to extract effective data features, thereby reducing the computational complexity of the algorithm and greatly reducing the learning difficulty of the damage assessment model, improving the accuracy and efficiency of evaluating models. Combined with the work content of swivel construction monitoring, a bridge swivel construction monitoring system is established, the composition and mutual relationship of the monitoring system are analyzed, and the partial composition of the system is reflected in combination with engineering examples. In this paper, design check calculation, monitoring prediction calculation, and key structural analysis are carried out for the background engineering, and the monitoring elements are analyzed for the calculation results of the swivel bridge. This paper proposes to establish a monitoring sensor family library and establish a representative monitoring sensor BIM model according to the monitoring requirements. In the field of engineering, the application of BIM technology should be further explored, such as digital twin reverse modeling technology and automatic identification technology of safety hazards.

Data Availability

Data sharing is not applicable to this article as no new data were created or analyzed in this study.

Conflicts of Interest

The authors state that this article has no conflict of interest.

References

[1] R. Min, Z. Liu, L. Pereira, C. Yang, Q. Sui, and C. Marques, "Optical fiber sensing for marine environment and marine structural health monitoring: a review," *Optics & Laser Technology*, vol. 140, no. 6903, article 107082, 2021.

[2] F. Xiaodan, "Design and implementation of remote health monitoring system for 3D visual bridge," *Procedia Engineering*, vol. 174, no. Complete, pp. 1330–1335, 2017.

[3] X. W. Ye, P. S. Xi, and Y. H. Su, "Analysis and probabilistic modeling of wind characteristics of an arch bridge using structural health monitoring data during typhoons," *Structural Engineering & Mechanics*, vol. 63, no. 6, pp. 809–824, 2017.

[4] H. Sarmadi, A. Entezami, M. Salar, and C. de Michele, "Bridge health monitoring in environmental variability by new clustering and threshold estimation methods," *Journal of Civil Structural Health Monitoring*, vol. 11, no. 3, pp. 629–644, 2021.

[5] T. D. Nguyen, T. Q. Nguyen, T. N. Nhat, H. Nguyen-Xuan, and N. K. Ngo, "A novel approach based on viscoelastic parameters for bridge health monitoring: a case study of Saigon bridge in Ho Chi Minh City – Vietnam," *Mechanical systems and signal processing*, vol. 141, p. 106728, 2020.

[6] B. Heitner, E. J. Obrien, and T. Yalamas, "Updating probabilities of bridge reinforcement corrosion using health monitoring data," *Engineering Structures*, vol. 190, no. JUL.1, pp. 41–51, 2019.

[7] M. M. Alamdari, N. Khoa, and Y. Wang, "A multi-way data analysis approach for structural health monitoring of a cable-stayed bridge," *Structural Health Monitoring*, vol. 18, no. 1, pp. 35–48, 2019.

[8] V. Subramaniyaswamy and R. Logesh, "Adaptive KNN based recommender system through mining of user preferences," *Wireless Personal Communications*, vol. 97, no. 2, pp. 2229–2247, 2017.

[9] J. Wannenburg and R. Malekian, "Physical activity recognition from smartphone accelerometer data for user context awareness sensing," *IEEE Transactions on Systems Man & Cybernetics Systems*, vol. 47, no. 12, pp. 3142–3149, 2017.

[10] V. Gupta, T. Priya, A. K. Yadav, R. B. Pachori, and U. Rajendra Acharya, "Automated detection of focal EEG signals using features extracted from flexible analytic wavelet transform," *Pattern Recognition Letters*, vol. 94, no. jul. 15, pp. 180–188, 2017.

[11] H. Sun, G. Qie, G. Wang et al., "increasing the accuracy of mapping urban forest carbon density by combining spatial modeling and spectral unmixing analysis," *Remote Sensing*, vol. 7, no. 11, pp. 15114–15139, 2015.

[12] F. Koopmans, L. N. Cornelisse, T. Heskes, and T. M. H. Dijkstra, "Empirical Bayesian random censoring threshold model improves detection of differentially abundant proteins," *Journal of Proteome Research*, vol. 13, no. 9, pp. 3871–3880, 2014.

[13] N. Arunkumar, K. Ramkumar, and V. Venkatraman, "Classification of focal and non focal EEG using entropies," *Pattern Recognition Letters*, vol. 94, no. jul. 15, pp. 112–117, 2017.

[14] S. A. Naghibi and M. M. Dashtpagerdi, "Evaluation of four supervised learning methods for groundwater spring potential mapping in Khalkhal region (Iran) using GIS-based features," *Hydrogeology Journal*, vol. 25, no. 1, pp. 1–21, 2017.

[15] B. Hou, H. Kou, and L. Jiao, "Classification of polarimetric SAR images using multilayer autoencoders and superpixels," *IEEE Journal of Selected Topics in Applied Earth Observations & Remote Sensing*, vol. 9, no. 7, pp. 3072–3081, 2016.

[16] N. Yala, B. Fergani, and A. Fleury, "Towards improving feature extraction and classification for activity recognition on streaming data," *Journal of Ambient Intelligence & Humanized Computing*, vol. 8, no. 2, pp. 177–189, 2017.

[17] Y. Song, J. Liang, J. Lu, and X. Zhao, "An efficient instance selection algorithm for k nearest neighbor regression," *Neurocomputing*, vol. 251, no. AUG.16, pp. 26–34, 2017.

[18] D. Guo, D. Zhang, and L. Zhang, "Sparse representation-based classification for breath sample identification," *Sensors and Actuators B: Chemical*, vol. 158, no. 1, pp. 43–53, 2011.

[19] A. Etminaniesfahani, A. Ghanbarzadeh, and Z. Marashi, "Fibonacci indicator algorithm: a novel tool for complex optimization problems," *Engineering Applications of Artificial Intelligence*, vol. 74, no. SEP., pp. 1–9, 2018.

[20] H. Lu, Y. Li, and C. Min, "Brain intelligence: go beyond artificial intelligence," *Mobile Networks and Applications*, vol. 23, no. 7553, pp. 368–375, 2017.

[21] D. Hassabis, D. Kumaran, C. Summerfield, and M. Botvinick, "Neuroscience-inspired artificial intelligence," *Neuron*, vol. 95, no. 2, pp. 245–258, 2017.

[22] O. I. Khalaf and B. M. Sabbar, "An overview on wireless sensor networks and finding optimal location of nodes," *Periodicals of Engineering and Natural Sciences*, vol. 7, no. 3, pp. 1096–1101, 2019.

[23] G. M. Abdulsahib and O. I. Khalaf, "An improved algorithm to fire detection in forest by using wireless sensor networks," *International Journal of Civil Engineering and Technology (IJCIET) - Scope Database Indexed*, vol. 9, no. 11, pp. 369–377, 2018.

[24] H. Song and M. Brandt-Pearce, "Range of influence and impact of physical impairments in long-haul DWDM systems," *Journal of Lightwave Technology*, vol. 31, no. 6, pp. 846–854, 2013.

Research Article

Health Promotion System for the Elderly's Daily Body Functions Based on Nanoprotective Technology

Ruixia Hu[1] **and Qi Hao** [iD] [2,3]

[1]*College of Physical Education, Shandong Sport University, Rizhao 276800, China*
[2]*School of Sports and Health, Linyi University, Linyi 276000, China*
[3]*Department of Leisure-Sports, Pai Chai University, Daejeon 35345, Republic of Korea*

Correspondence should be addressed to Qi Hao; haoqi@lyu.edu.cn

With the acceleration of China's aging trend, the physical health of the elderly needs more attention and research from us. In particular, many elderly people are prone to accidental injuries during exercise, so how to protect the health of the elderly through high-tech is worthy of more in-depth research. This measure can promote the establishment of a health system for the elderly. This article is mainly based on the research on the health promotion system of the elderly's daily body functions based on nanoprotective gear technology. It uses the literature method to read a lot of literature to understand the current research status of the elderly's daily body function and health and the application status of nanotechnology, through the questionnaire and survey method for testing the blood pressure, heart rate, pulse wave velocity, bone density, and other physical indicators of the surveyed elderly population, and organize and analyze the relevant data. In this survey, 28.8% of the elderly who regularly participate in physical exercise have high systolic blood pressure, 33.3% of the elderly who do not participate in exercise regularly have high systolic blood pressure, and most of them are in the low bone density stage. Therefore, nanocare technology can effectively protect the health of the elderly and provide protection during exercise. The research in this article is aimed at illustrating the establishment and improvement of the physical function and health promotion system of the elderly through the impact data on physical indicators and providing a factual basis for the elderly to better participate in physical exercise and improve the health quality of the elderly.

1. Introduction

The number of elderly people is increasing year by year, and the aging trend of the world population is becoming increasingly obvious. With the increase of age, the physical function of the elderly declines, the aging rate and incidence of internal organs also increase, and psychological problems gradually occur. The health problem of the elderly population is the most obvious problem in an aging society, so finding effective ways to improve the health of the elderly is the key. The World Health Organization's survey results also confirm the importance of improving healthy behaviors on the quality of life of the elderly, and it is essential to conduct surveys on improving the health of the elderly.

Universities and research institutions in various countries have increased their investment and research on nanotechnology. The development of nanotechnology has a certain socioeconomic and political background. The development of nanotechnology is inseparable from people's area of life. From physics to chemistry, from power to aviation, nanotechnology that integrates the strengths of multiple disciplines has been rapidly developed. Among them, nanoprotective technology is also under continuous research and development.

The intake of protein in the Isanejad M diet may be beneficial to the physical function (PF) of the elderly. They examined the cross-sectional and prospective associations of g/kg body weight (BW), fat mass (FM), and lean body mass (LM) with PF in 554 women aged 65.3–71.6 years

old. Research on osteoporosis risk factors and fracture prevention was carried out. Participants filled out questionnaires about lifestyle factors and 3 d food records in 2002. Body composition was measured by dual-energy X-ray absorption method, and PF was measured at baseline and 3-year follow-up. The definition of sarcopenia is based on the standards of the European Working Group on Elderly Sarcopenia. At baseline, women with higher protein intake (≥ 1.2 g/kg body weight) had grip strength/weight (GS/BM) ($P = 0.001$), knee extension/BM ($P = 0.003$), and single-leg posture ($P = 0.047$), when the chair rises ($P = 0.043$), squats ($P = 0.019$), squats on the ground ($P = 0.001$), and walks faster at 10 m ($P = 0.005$), the short-term physical performance battery score is better ($P = 0.004$). However, while recording the factors related to osteoporosis, this experiment does not account for the controllable variables [1]. Grimm B wearable sensors, especially the inertial measurement unit (IMU), can perform objective, effective, differentiated, and responsive physical function assessment during functional tests such as gait, climbing stairs, or sitting and standing. The most suitable method is to apply to each body part to accurately capture task completion time, spatiotemporal gait, and harshly testing or kinematic parameters specific to the affected limb. In activity monitoring (AM), the accelerometer is mainly used to derive energy consumption or parameters related to overall health (such as total steps). In older adults, it is most effective by studying specific events, such as stairs or high-intensity activities. By looking at qualitative parameters at the "micro" level of activity, such as rhythm or standing time, low cost and ease of use allow routine clinical applications, but there are many options for sensors, algorithms, tests, and parameter definitions. Selection and comparability are still difficult and require consensus or standardization [2]. Lin and Lin's existing health promotion system (HPS) has some shortcomings, such as lack of the ability to automatically plan exercise prescriptions (EP) for individuals, difficulty in obtaining physiological signals of users who are exercising, and lack of effective mechanisms for medical notification emergency situations for personnel users. To solve these shortcomings, in this research, they use wireless sensor network (WSN), mobile communication, and cloud computing technology to develop cloud-based HPS. HPS includes a health promotion cloud service platform that can build a user's physical health model and then generate appropriate EPs for users to perform various exercises. On the user side, in this study, they designed a motion-sensing device that can obtain the physiological signals and global positioning system (GPS) positioning information of users who exercise through WSN in time. Some sensors are designed in motion-sensing devices, such as GPS sensors. However, this technology can only provide location services and cannot provide more types of services related to healthy life [3].

The innovations of this article are as follows: (1) the combination of qualitative analysis and quantitative analysis is fully based on the analysis of data; (2) the combination of theoretical research and empirical research, and the in-depth study of nanotechnology and other theoretical foundations on the above, e is carried out in combination with the specific conditions of physical function and health of the elderly.

2. Promoting Research Methodology Based on Daily Physical Function in Healthy Elderly Nanotechnology Protective Gear

2.1. Nanoprotective Gear Technology. In the late 1980s, a new high-tech science and technology emerged in human society, which is nanotechnology [4]. The emergence of nanotechnology has played a leading role in the development of today's science and technology. This effect has changed the process of technological development to a certain extent and at the same time has changed the scope of research on the philosophy of technology [5]. The emergence of nanotechnology has opened up a brand-new research field, and the scope of its research and discussion is basically between nonmacro and nonmicro, which is what people have rarely paid attention to before [6]. In short, the development of nanotechnology has changed the traditional concept of human understanding and use of technology. It has not only changed the real life of human beings but also profoundly affected the ethics and morals of traditional human society. "Double-edged sword" is the proposition of the philosophy of technology [7, 8].

Through this understanding, we can feel that it is not easy to accurately define nanotechnology. On this basis, the foreign academic circles define nanotechnology as follows: "First, the research on the microcosm of 1-100 nm and the microcosm of molecules [9] can be used to conduct technical analysis and research on the molecules and atoms of materials. Second, research has the possibility of changing a certain characteristic of nanometers. [10]. Third, the ability to control and use the substance is within a personal range [11]."

Nanoprotective technology is a tool made of nanomaterials designed to provide protection for the elderly. By changing the size of nanobuilding units to design the properties and functions of materials [12], the internal and surface chemical properties and their combinations can be controlled. Nanotechnology is known as one of the three pillar industries in the 21st century [13]. Artificial nanomaterials are the foundation and core of nanotechnology [14, 15]. Due to the small size of the structure of artificial nanomaterials, it has special physical and chemical properties, such as small effects and complex structures, with large surface effects, very high reactivity, quantum results, etc. These characteristics bring unique characteristics to nanotechnology. Nanoresearch is highly unique, comprehensive, and social [16]. The disciplines it involves are a multidisciplinary synthesis, involving a number of research areas of emerging disciplines, and countries have also invested large funds in nanotechnology [17, 18].

The success of nanoprotective technology is a brand-new experience for the elderly, which not only provides comprehensive protection measures for the elderly but also reduces the burden on adult children. The development of the field of nanotechnology, on the one hand, can promote

the innovation of production methods. Nanotechnology can change the traditional production methods, guide human beings to produce necessary direct products on a personal level, and use existing materials to fully produce products needed for life [19]. The products produced in this way have improved performance, but the price has not increased much, so they have greater competitiveness. On the other hand, it can promote the improvement of cognitive style. Its appearance indicates that the level of human understanding of nature has reached a new level and has risen to a new height, allowing humans to understand the world from a new perspective, thereby improving human cognitive methods [20, 21]. The biggest problem with the development and application of nanoprotective gear technology at present is how protective its application is and the high cost, whether the elderly and their children can afford this price, and whether nanoprotective gear can be used.

2.2. Methods to Promote the Health of the Elderly's Daily Body Functions.

With the development of economy, the progress of science and technology, the improvement of living standards, and the improvement of medical and health conditions, the proportion of aging of the population in our country is increasing year by year [22]. We also found that while the overall level of public fitness exercise in my country is on the rise, the elderly's fitness exercise is still in the initial stage, and the overall poor health of the elderly is a general trend in the development of human life [23]. Regular exercise can resist the age effect of dysfunction and health disorders and can also reduce mortality and morbidity [24]. With the increase in the incidence of the elderly, through research and analysis, older people have the potential to improve both structure and function [25]. Moderate exercise, appropriate load, exercise time, exercise methods, etc. can promote blood circulation throughout the body, increase metabolism, improve bone, and improve adaptability to various organs and system functional loads. The elderly can also enrich their spare time through the above methods, satisfy people's spiritual needs, increase their sense of joy, establish good interpersonal relationships, improve people's body and mind, achieve their goals [26], delay aging, and improve health. The research results further confirmed that physical exercise has a good impact on the health of the elderly, and increasingly, people have clearly realized that physical exercise has a good effect on improving health and antiaging. The elderly are increasingly participating in physical exercise and at the same time enhance the national health. It provides a factual basis for people to better participate in physical exercise, to further promote the national fitness program and promote the active participation of the elderly in sports, and it provides a scientific and useful foundation. Improve people's and society's interest in older people's participation in sports and encourage them to actively participate in sports.

2.2.1. Physical Exercise.
Taking exercise as a means, using fitness, entertainment, health care, rehabilitation, and mental and intellectual training activities, according to the formation of growth and development and human skills, consciously and orderly promotes people's overall development, improves people's physical condition, improves physical strength, improves athletic ability, improves physical function, improves and maintains physical and mental health, improves lifestyle, and improves quality of life. Sport is not only a physical exercise but also a spiritual activity. Therefore, exercise not only affects physical health but also has a positive effect on mental health.

2.3. Health Promotion Model

2.3.1. Origin of Health Promotion Model.
In 1987, Pan De proposed a health promotion model, an action to improve health to achieve self-fulfillment and personal achievement. Everyone must maintain action to maintain and enhance peace and happiness. He believes that actions to improve health are for self-realization and personal achievement, and everyone will use actions to maintain and improve peace and happiness. This is a positive attitude. Through this healthy behavior, the individual can achieve the greatest potential to achieve the best state of health. The determinants of health promotion actions are divided into specific personal characteristics and experiences (the above actions, personal factors), specific action knowledge and feelings (action feelings, action disorders, self-efficacy, and action-related), and influences on actions (many have future action plans and urgent competition needs and preferences), three categories. The determinants of health promotion actions in the health promotion model can be used to evaluate patients' health awareness and enthusiasm for participating in health promotion activities. In action to improve health to achieve self-fulfillment and personal achievement, everyone must maintain action to maintain and enhance peace and happiness.

In 1987, American nursing expert Pan De first proposed the Health Promotion Lifestyle Scale, which was revised by Walker in 1996 and formulated HPLP-II. The scale contains six dimensions. Promoting a healthy lifestyle refers to all actions taken by individuals, families, communities, and society to improve peace, happiness, and the possibility of health. Based on the health promotion model, various forms have been developed to measure health status. Iran is using the scale of health-improving lifestyles to measure the health actions of Iranian elderly. It has good reliability and validity and good applicability.

2.3.2. Application of the Health Promotion Model in Nursing Practice.
Research on health promotion models has been applied to nursing practice in many countries. The health promotion model was first used in nursing practice abroad. The health promotion model can improve the dietary behavior of diabetic patients. In addition, it can also improve the loneliness symptoms of the elderly. Health education based on the health promotion model has a positive impact on improving social and mental health, delaying the aging process, improving the quality of life and physical health,

improving daily activities, and reducing the risk of disability. In this way, it can activate the essential motivation and beliefs of personal health, turn it into a healthy action, and promote the development of a healthy lifestyle at any level. To achieve a full recovery, reduce the recurrence rate and readmission rate. With the improvement of living standards, unhealthy behaviors, lifestyles, and living environments are more likely to increase the burden of disease.

3. Promote Research Experimental System Based on Daily Body Functions of Healthy Elderly Nanotechnology Protective Gear

3.1. The Establishment of a Model of Influencing Factors of the Physical Function and Health Promotion System of the Elderly

3.1.1. Build the Model Equation. The structural equation model consists of a measurement model and a structural model. In this study, the model equation can be represented by three matrix equations:

$$M = \Gamma_x \xi + \vartheta, \tag{1}$$

$$N = \Gamma_y \eta + \psi, \tag{2}$$

$$\eta = R\eta + \tau\xi + \omega. \tag{3}$$

Table 1 shows the meaning of the letters in the above formula. Equations (1) and (2) are the formulas of the measurement model, which, respectively, determine the position of the relationship between the external observation variable X and the external latent variable and the internal observation variable Y and the internal latent variable. Equation (3) is a structural model equation that determines the relationship between external latent variables and inherent latent variables.

3.1.2. Parameter Estimation Method. Establish an initial structural equation model, and verify the suitability of the model through data analysis. In the SEM analysis, 7 parameter estimation methods are provided, including ML, IV, TSLS, ULS, GLS, GWLS, and DWLS. In this paper, the maximum likelihood method (ML method) is used for parameter estimation.

3.1.3. Construction of the Theoretical Model of the Factors Affecting the Health of the Elderly. The theoretical construction of the structural equation model needs to be based on a certain theoretical foundation and practical experience. Previous literature studies have found that socioeconomic status affects the elderly's social support, family relationships, health status, and health-promoting lifestyle. For example, according to the research, high age, low education, and low income are important risk factors affecting the elderly. The main sources of living expenses, the existence of children, gender, and average monthly income are important factors that affect the level of social support for the empty-nest elderly. Family support also affects the elderly's social support, health status, and health-promoting lifestyle. Having

TABLE 1: The meaning of the letters in the above formula.

Letter	Meaning
M	Observed variables of exogenous latent variables
N	Observed variables of endogenous latent variables
η	Endogenous latent variables
Γ_x	X path coefficient of exogenous latent variables
Γ_y	Y path coefficient of endogenous latent variables
ξ	Exogenous latent variables
ϑ	Error of exogenous latent variable
ψ	Error of endogenous latent variable
ω	Staggered term

a spouse, children's filial piety, and living with children contributes to the mental health of the elderly, and the lack of timely care for spouses and children is easier for the elderly. Perceive loneliness and so on. The main factors affecting social support for the elderly in nursing facilities for the elderly are age, family status, number of visits, and the presence or absence of children.

Health status will also affect the social support of the elderly. In China, participation in social activities is causally related to the health of the elderly. If you are in good health, your chances of participating in cultural group activities and personal family activities will increase. At the same time, combined with the results of single factor analysis, on the basis of theoretical foundation and repeated verification, this study constructed a theoretical model of factors affecting the health and lifestyle of the elderly.

Construct a structural equation model based on the latent variables and observed variables extracted by exploratory factor analysis, and use the Amos22.0 software to fit the constructed model.

3.2. Monitoring System Model of Basic Health Parameters of the Elderly. The health parameter sensor is used to extract human physiological information. It is the basis of the monitoring system. The detection accuracy of the sensor is related to the effectiveness of the monitoring system, and its power consumption and wearing comfort are related to the actual application value of the monitoring system. This chapter considers the characteristics of the dynamic monitoring device, from the perspective of low power consumption, designing the detection circuit and signal processing algorithm of health parameters.

3.2.1. Design of ECG Signal Processing Algorithm. For systems used for long-term signal monitoring, due to limited resources and sensitive to power consumption, signal processing algorithms should have the characteristics of low computational complexity and high real-time performance. Smoothing filtering is a simple and practical filtering algorithm, which is widely used in medical monitoring systems and has a good filtering effect on power frequency interference.

The power frequency signal is a sine wave with a frequency of 50 Hz. We divide a period of the signal into N equal parts, and the sum of the signal values corresponding to each equal point is 0, namely

$$\sum_{i=1}^{n} \sin\left(i\frac{2\pi}{n} + \theta\right) = 0. \tag{4}$$

To achieve power frequency filtering, you only need to set the ECG signal sampling frequency to an integer multiple of 50 Hz. We assume that the ECG signal sampling frequency is 500 Hz, which is 10 times the power frequency. In other words, there are exactly 10 sampling points in a power frequency cycle, that is, $n = 10$, which is equivalent to dividing a power frequency signal cycle into 10 equal parts, and averaging 10 samples can theoretically eliminate the power frequency interference. Then, the difference equation is

$$t(n) = [x(n) + x(n-1) + x(n-2) + \cdots + x(n-9)]/10. \tag{5}$$

In the formula, $x(n), x(n-1) \cdots x(n-9)$ is the sampled signal, and $t(n)$ is the filtered ECG signal.

Performing the Z transformation on the above formula, we get

$$T(z) = \left[\left(X(z) + X(z) \cdot z^{-1} + X(z) \cdot z^{-2} \cdots + X(z) \cdot z^{-9}\right)/10\right]. \tag{6}$$

The transfer function is

$$Q(z) = \left(1 + z^{-1} + z^{-2} + \cdots + z^{-9}\right)/10. \tag{7}$$

3.2.2. Design of the Heart Rate Extraction Algorithm. Heart rate refers to the number of times the heart beats per minute, which is the reciprocal of the cardiac cycle. Every time the heart beats, a QRS complex is generated. Therefore, we can detect the heart rate by counting the number of times the R wave appears per unit time. The differential threshold method is the most widely used ECG signal R wave detection algorithm. It is a fast algorithm and is suitable for systems with high real-time requirements.

In the waveform electrocardiogram, the rise and fall of the edge of the R wave are the areas with the most dramatic changes in the trend. In this area, using the zero crossing point of the dominant number and the end point of the second derivative, the first or second derivative of the filtered ECC signal is performed to determine the position of the R wave that passes the threshold.

The first-order difference and the second-order difference of the electrocardiogram signal are obtained, and the total of the second-order differences is used as the detection standard of the R wave. The quadratic waveform uses the infinite order of the square of the center difference. Since the value of the center difference is an error, the first-order difference is as follows. The form is as follows.

$$h'(n) = \frac{(h(n+1) - h(n-1))}{2}. \tag{8}$$

The second-order difference form is

$$h''(n) = (2h(n+1) + h(n+2) - h(n-2) - 2h(n-1))/8. \tag{9}$$

In the formula, $h(n)$ is the filtered ECG signal sequence.

Then the first-order and second-order differences are squared and the square sum sequence $H(n)$ is obtained, which is equivalent to a nonlinear amplification of the signal, which significantly increases the proportion of high-frequency signals in the original signal. The calculation process is as follows:

$$H(n) = \left(h'(n)\right)^2 + \left(h''(n)\right)^2. \tag{10}$$

The square sum sequence $H(n)$ is combined with an appropriate threshold to detect the R wave and the signal difference calculation processing effect.

3.2.3. ECG Signal Detection Circuit. Only by improving the input impedance of the circuit and the common-mode interference suppression capability of the instrumentation amplifier itself, satisfactory results cannot be obtained. To further suppress the common-mode interference and improve the quality of ECG signal detection, a common-mode interference suppression circuit is designed on the basis of the above circuit. Its function is equivalent to inverting an amplifier, inverting and amplifying the detected common-mode signal before returning it to the human body to further eliminate common-mode signal interference.

We assume that the common-mode voltage of the human body is L_u, and the gain of the amplifiers U1A and U1B is 1, so the amplifier output voltage L_u can be regarded as equal to Lu. Among them are as follows:

$$L_u = i_{db} \times R6 + L_\circ, \tag{11}$$

$$L_u = i_{db} \times R6 - \frac{2R9}{R5} \times L_u'. \tag{12}$$

Thereby

$$L_u = \frac{i_{db} \times R6}{1 + 2R9/R5}. \tag{13}$$

If the right leg is directly grounded, then

$$L_u = i_{db} \times R6. \tag{14}$$

The gain of the circuit is

$$A_3 = R_{14}/(R_{12} + R_{13} + R_{14}). \tag{15}$$

TABLE 2: Elderly health promotion, lifestyle, and its score levels in various dimensions.

Dimension	Individual score	Total score	Behavior level	Sequence number
Self-actualization	2.65 ± 0.35	36.98 ± 0.28	Medium level	2
Health responsibility	2.22 ± 0.19	19.92 ± 0.12	Medium level	6
Movement	2.28 ± 0.06	6.83 ± 0.12	Medium level	5
Nutrition	2.86 ± 0.25	14.36 ± 0.05	Medium level	1
Interpersonal support	2.57 ± 0.29	12.89 ± 0.34	Medium level	3
Stress management	2.55 ± 0.37	15.35 ± 0.28	Medium level	4
Healthy lifestyle	2.53 ± 0.47	105.98 ± 19.61	Medium level	—
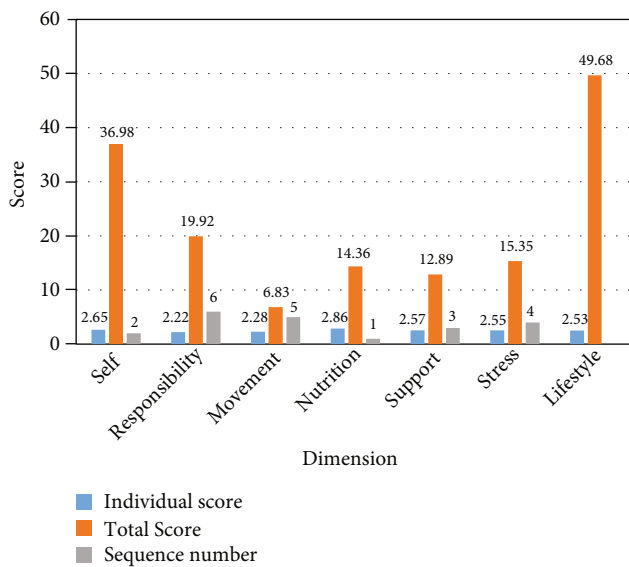
FIGURE 1: Elderly health promotion, lifestyle and its score levels in various dimensions.

4. A Health Promotion System for the Elderly's Daily Body Functions Based on Nanoprotective Technology

4.1. Elderly Health Promotion Lifestyle Physical Function and Its Analysis of the Scores.
It can be seen from Table 2 and Figure 1 that the total score for the health promotion lifestyle of the elderly in Province A in this survey is 105.98 ± 19.61 points, and the average score for each item is 2.53 ± 0.47 points. According to the evaluation criteria of the health-improving lifestyle scale, a healthy lifestyle and all aspects related to the promotion of the elderly are at a medium level. According to the average score of each dimension, the nutrition score (2.86 points) is the highest, and the rest are self-actualization (2.65 points), interpersonal support (2.55 points), stress management (2.53 points) and exercise (2.28 points), and health responsibility (2.22 points), among which the scores of nutrition, self-realization, interpersonal support, and stress management are higher than the total average score of health promotion lifestyle. The results suggest that the elderly have poor health responsibilities and exercise behaviors, and nutritional behaviors are the best.

4.2. Various Indicators of Physical Function of the Elderly.
BMI (body mass index) is an international standard used to measure body fat, weight, and health. It is mainly divided into the following: BMI < 18 is thin, 18.5-24.9 is normal (standard weight), 25-30.0 is overweight, 30.0-34.9 is grade I obesity, and 35.0-39.9 is grade II obesity.

According to the research data, as shown in Table 3 and Figure 2, the number of standard-weight elderly people who exercise regularly is 45, accounting for 50% of the total number, which is higher than the proportion of standard-weight elderly people who do not regularly participate in physical exercise. 41 obese elderly people regularly participate in sports, accounting for 45.5% of the total, far exceeding the proportion of obese people who do not regularly participate in sports. The proportion of elderly people who do not exercise regularly is higher than the proportion of elderly people who exercise regularly. Compared with men and women, the proportion of men who exercise regularly is higher than that of women, and the proportion of women who are too fat is 46.1% higher than that of women who hardly exercise. With the increase of age, body function gradually declines, and the elderly are prone to obesity. Through the body mass index test, people can judge their own health status, actively, participate in sports, control and prevent weight, and reduce the appearance of related diseases.

The blood pressure level is not only closely related to heart function, vascular resistance, and blood volume but also affected by factors such as nerves and body fluids. Blood pressure changes according to age, time, and climate. A happy mood and proper exercise can lower blood pressure, and large mood swings, high exercise intensity, and high work pressure can cause blood pressure to rise.

As shown in Table 4 and Figure 3, the blood pressure of most elderly people is in the normal range. The systolic blood pressure of the elderly who regularly participate in physical exercise reaches the normal range in 71.1%, and the diastolic blood pressure reaches the normal range in 85.5%. The systolic blood pressure of the elderly who did not regularly participate in physical exercise reached the normal range in 66.6%, and the diastolic blood pressure reached the normal range in 77.7%. 28.8% of the elderly who regularly participate in physical exercise are beyond the normal range of systolic blood pressure, and 12.2% of the elderly are higher than the maximum diastolic blood pressure. Health requires active participation in physical exercise to prevent disease and promote health. Compared

TABLE 3: BMI ratio analysis table for the elderly.

BMI classification	Participate in physical exercise regularly		Total	Participate in physical exercise infrequently		Total
	Male	Female		Male	Female	
<18, thin	1	1	2	—	—	—
18.5-24.9, normal	26	19	45	3	4	7
>25, overweight	25	16	41	1	6	7
30.0-34.9, first-degree obesity	1	1	2	1	3	4
35.0-39.9, second-degree obesity	—	—	—	—	—	—
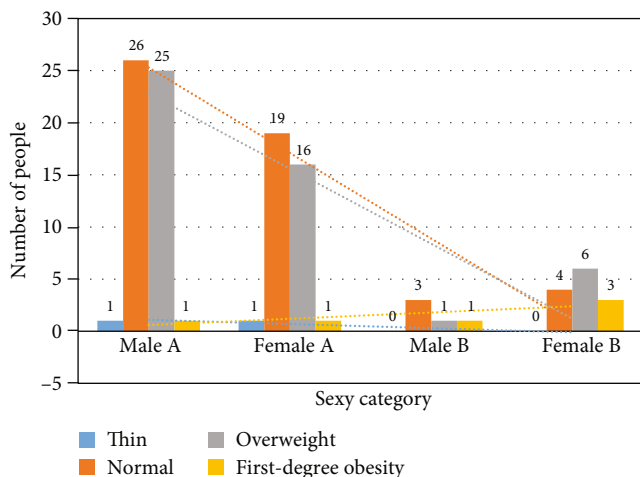
FIGURE 2: BMI ratio analysis for the elderly.

with the blood pressure of older men and women who regularly participate in physical exercise or infrequently participate in physical exercise, the proportion of men with high blood pressure is higher than that of women.

Blood pressure is an important indicator that reflects the state of cardiovascular function. With the increase of age, the physical function of the elderly decreases, the elasticity of the blood vessels decreases, and the blood pressure rises, which is prone to hypertension. Exercise can reduce high blood pressure, increase cholesterol levels, reduce harmful cholesterol levels, reduce weight, and prevent thrombosis. The elderly should choose appropriate exercise methods according to their health conditions, actively participate in exercise, maintain normal blood pressure, and effectively prevent the occurrence of cardiovascular diseases.

The size of the heart rate can reflect the functional state of the body and the changes of the cardiovascular system function to a certain extent, and it is a reference index for evaluating the cardiovascular function state and exercise effect. The heart rate of a normal person is 60-100 beats per minute. Less than 60 times is called slow heartbeat, and more than 100 times is called fast heartbeat (less than 160 times). The heart rate of women will be faster than the heart rate of men. The heart rate of the elderly increases between physical activity and mental excitement, and the heart rate decreases. Most patients with heart disease have a heartbeat rate of more than 160 beats per minute, or less than 40 beats per minute, and they have heartbeats, chest

pressure, and initial discomfort. People who regularly participate in sports and physical labor have a very low heart rate, less than 60 beats per minute. As long as there is no discomfort, this is normal.

As shown in Table 5 and Figure 4, 87.8% of the elderly who regularly participate in physical exercise maintain the normal heart rate range, 77.8% of the elderly who do not participate in physical exercise regularly reach the normal heart rate range, and 12.2% of the elderly who regularly participate in physical exercise are in the normal heart rate range. 50-60 times/min, which is also in the normal range, indicating that the health status of the elderly who regularly participate in physical exercise is higher than that of the elderly who do not regularly participate in physical exercise. Appropriate physical exercise can keep the heart rate stable. A small number of elderly people with low or high heart rates can improve their heart rate and promote their health by participating regularly. Elderly men and women who regularly take part in physical exercise have relatively good effects on participating in exercise, and there is not much difference in heart rate changes between the two. Appropriate exercise, maintaining a normal weight, and reasonable eating habits are all effective ways to improve heart rate.

As shown in Table 6 and Figure 5, nearly 70% of elderly men and women who regularly participate in physical exercise are in a normal state. Most elderly men and women who take part in physical exercise infrequently have abnormal phenomena, and the abnormality rate of men is much higher than that of women, which may be affected by daily life habits and eating habits.

Under normal circumstances, all blood vessels change with age, the elasticity of the large arteries decreases, the rigidity increases, the inner diameter of the blood vessels increases, the thickness of the internal medium increases, the blood vessels narrow, and the brain and physical strength decline. Arteriosclerosis refers to arterial wall hypertrophy, texture hardening, rough inner wall, and passage of grooves. The pathology is based on deep steatosis and cholesterol deposition in the arterial intestine to form a nonepithelial plate. These plaques stand out and cause blockage. Atherosclerosis is the general form of arteriosclerosis. That is the main cause of myocardial infarction and cerebral infarction. Arterial vascular disease will increase the damage to the heart, brain, kidney, and other organs, causing high mortality and high obstacles. Experts suggest that atherosclerosis-tonic thrombosis is a persistent overall disease and a systemic disease that needs to be prevented

TABLE 4: Analysis table of the influence of physical exercise on the blood pressure of the elderly.

Blood pressure test	Pressure classification, mmHg	Participate in physical exercise regularly		Participate in physical exercise infrequently	
		Male	Female	Male	Female
Systolic blood pressure	90-140	69.8	72.9	60.0	69.2
	>140	30.1	27.2	40.1	30.8
	<60	5.4	2.2	—	7.6
Diastolic blood pressure	60-90	84.9	86.5	60.2	84.7
	>90	15.2	8.3	40.3	7.7
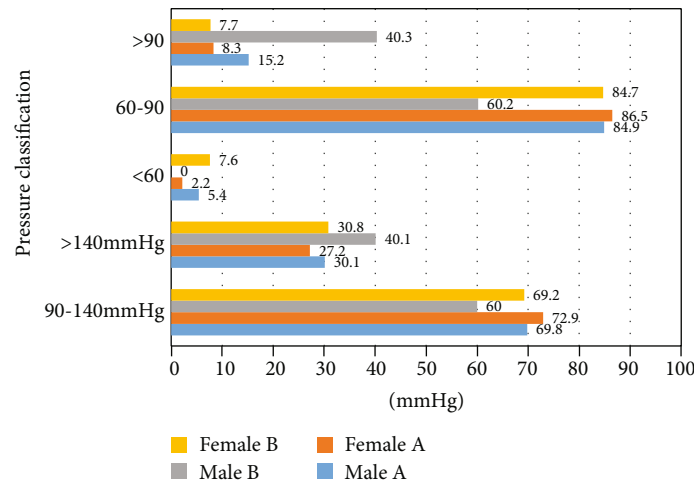
FIGURE 3: The influence of physical exercise on the blood pressure of the elderly.

TABLE 5: Analysis of the influence of physical exercise on the heart rate of the elderly.

Grouping	Participate in physical exercise regularly (%)		Participate in physical exercise infrequently (%)	
	50-60 (times/min)	60-100 (times/min)	50-60 (times/min)	60-100 (times/min)
Male	11.4	88.7	20.1	80.3
Female	13.6	86.5	23.6	75.8
Total	12.3	87.6	22.4	77.5
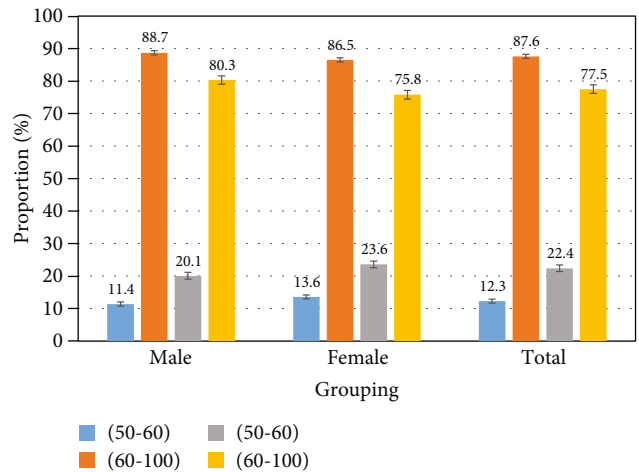
FIGURE 4: Analysis of the influence of physical exercise on the heart rate of the elderly.

in advance. At present, pulse wave velocity (PWV) (which refers to the speed at which the blood pumped from the heart reaches the hands and feet through the blood vessels) is used internationally. It is an index to predict the degree of atherosclerosis and the risk of coronary artery disease. The PWV of the aorta can also be used to predict the heart and an effective indicator of vascular disease to reflect the degree of arteriosclerosis. When blood vessel elasticity decreases, the blood vessel becomes hard, the speed of pulse conduction becomes faster, and PWV increases.

As shown in Table 7 and Figure 6, the average value of the pulse conduction velocity of men and women on the left and right sides of the elderly who regularly participate in physical exercise is less than 1700 m/s. Above 1800 m/s, the health status of the elderly who regularly participate in phys-

ical exercise is significantly better than that of the elderly who do not regularly participate in physical exercise. Through the T of the relevant data, there is a significant difference in pulse conduction velocity between male elderly who regularly participate in physical exercise and male elderly who do not regularly participate in physical exercise and female elderly who regularly participate in physical exercise and those who do not regularly participate in

TABLE 6: PWV statistical table of pulse wave velocity in the elderly.

Grouping	Category	Participate in physical exercise regularly		Participate in physical exercise infrequently	
		Abnormal	Normal	Abnormal	Normal
Male	Number of people	16	38	4	1
	Proportion	30.7	69.8	80.2	19.8
Female	Number of people	8	26	8	5
	Proportion	29.7	70.3	61.5	38.4
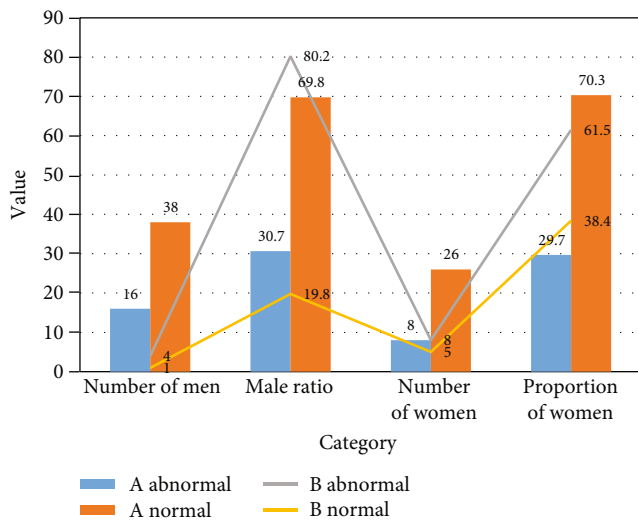
FIGURE 5: PWV statistical table of pulse wave velocity in the elderly.

FIGURE 6: Analysis of the influence of physical exercise on the pulse conduction velocity PWV of the elderly.

TABLE 7: Analysis of the influence of physical exercise on the pulse conduction velocity PWV of the elderly.

Gender	Group	Number of samples	Left	Right
Male	Test group B	55	1692.8	1649.3
	Control group B	6	1893.1	1932.9
Female	Test group G	47	1661.5	1668.7
	Control group G	15	1843.2	1854.5

physical exercise There is a significant difference in pulse conduction velocity among elderly women. Through regular physical exercise, blood supply to tissues and organs (heart, kidney, other important organs, etc.) is increased, tissue hypoxia is reduced, lipid metabolism is improve, plasma activity is increased, body weight is reduced, and blood coagulation is reduce, which helps increase the activity of the anticoagulant system in the blood and reduce the possibility of myocardial infarction. It helps to improve mood, divert patients' attention to the disease, mobilize patients' positive causes, and eliminate negative fears.

Bone density is an important indicator of bone quality, reflects the degree of osteoporosis, and is an important basis for predicting fracture risk. The bone content of minerals is closely related to the resistance of bone and the stability of the internal environment. This is not only an important indicator for evaluating human health but also an important indicator for evaluating and studying bone physiology,

human pathology and aging, and the diagnosis of various diseases of the body. The bone mineral density, in BND and normal youth and standard deviation (SD) high (+) or low (-) comparison T value, is the most important value in the diagnosis of osteoporosis.

As shown in Table 8 and Figure 7, the bone density of the elderly who regularly participate in physical exercise is 28.8% in the normal range, which is higher than that of the elderly who participate in physical exercise infrequently; -2.5 to -1 belong to the low bone density stage. And osteoporosis, the proportion of elderly people who regularly participate in physical exercise, is 48.9%, and the proportion of elderly people who hardly participate in sports is 55.6%. Compared with the proportion of elderly people who regularly participate in sports, the proportion of elderly people who hardly participate in sports is even higher. 16.7% of the elderly who exercise regularly suffer from osteoporosis, and 22.2% of the elderly who do not exercise suffer from osteoporosis. Combined with the above analysis, it can be seen that regular participation in physical exercise can strengthen bone. Muscles and bone are inseparable. Continuous, regular, and appropriate exercise can alleviate the degree of osteoporosis. In the elderly, muscle strength is weakened, mechanical stimulation is relatively reduced, and bone turnover tends to be negatively balanced, which will accelerate the development of osteoporosis. According to these data, the ratio of osteoporosis among elderly women

TABLE 8: Analysis table of the influence of physical exercise on bone mineral density of the elderly.

Grouping	Category	$T < -2.5$	$-2.5 < T < -1$	$-1 < T < 1$	$T > 1$
Test group	Male	3.8	56.7	32.1	7.3
	Female	35.2	37.8	24.4	2.9
	Total	16.8	48.9	28.9	5.6
Control group	Male	—	80.0	20.0	—
	Female	30.8	46.3	15.5	7.6
	Total	22.4	55.8	16.8	6.6
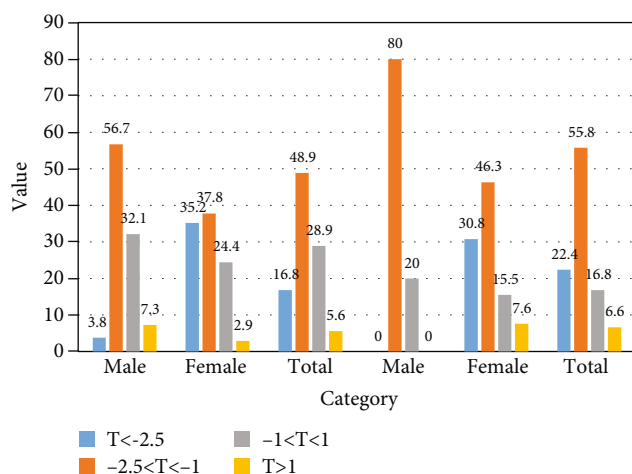
FIGURE 7: The influence of physical exercise on bone mineral density of the elderly.

who regularly participate in physical exercise and those who do not participate in physical exercise is much higher than that of men. The bone mineral content of normal people is closely related to gender and age, and there are differences between different genders in the same age group. Females are lower than males. The elderly women who often take part in physical exercise are also lower than men, which is related to the body structure of men and women.

Especially for the elderly with osteoporosis, the use of nanoprotective gear can better protect the bone health of the elderly. It can also avoid accidents while exercising and provide good protection for the elderly. The research of nanoprotective gear technology is exclusively customized for the elderly. Of course, it can also be applied to the sports of many young people. The purpose is to bring a better healthy lifestyle and improve the quality of healthy life.

5. Conclusion

This article is mainly based on the research of the elderly's daily body function and health promotion system based on nanoprotective technology. Using a variety of research methods, the model of the influence factors of the elderly body function and health promotion system was established, and the elderly body function and health status from the influencing factors was analyzed. And the role and effect of nanoprotective technology in the daily exercise of the elderly were highlighted.

The innovations of this article are as follows. First, qualitative analysis is combined with quantitative analysis, and qualitative analysis is fully based on the analysis of data; second, theoretical research is combined with empirical research and in-depth study of nanotechnology, etc. On the basis of the theory, empirical research is carried out in combination with the specific conditions of the physical function and health of the elderly.

There are still shortcomings in this article. Firstly, the amount of data in the questionnaire survey is not enough, the number of interviewers is not large enough, and the representativeness of the data is not strong enough; secondly, the nanoprotective technology is still immature, and more in-depth research and more extensive research are needed. In application experiment, in the future, the development of nanotechnology will bring increasingly convenient life to people, and at the same time, it will also bring better protection to the health of the elderly.

Data Availability

Data sharing not applicable to this article as no datasets were generated or analyzed during the current study.

Conflicts of Interest

The authors declare that they have no conflicts of interest.

References

[1] M. Isanejad, J. Mursu, J. Sirola et al., "Dietary protein intake is associated with better physical function and muscle strength among elderly women," *The British Journal of Nutrition*, vol. 115, no. 7, pp. 1281–1291, 2016.

[2] B. Grimm and S. Bolink, "Evaluating physical function and activity in the elderly patient using wearable motion sensors," *EFORT Open Reviews*, vol. 1, no. 5, pp. 112–120, 2016.

[3] S. S. Lin and J. J. Lin, "Development of a novel health promotion system based on wireless sensor network and cloud computing," *Sensors and Materials*, vol. 31, no. 3, pp. 939–952, 2019.

[4] P. Mellin, C. Jönsson, M. Åkermo et al., "Nano-sized by-products from metal 3D printing, composite manufacturing and fabric production," *Journal of Cleaner Production*, vol. 139, pp. 1224–1233, 2016.

[5] E. F. Kudina, E. Barkanov, and N. S. Vinidiktova, "Use of nanostructured modifiers to improve the operational characteristics of pipelines' protective coatings," *Glass Physics and Chemistry*, vol. 42, no. 5, pp. 512–517, 2016.

[6] V. R. Jokanovi, M. Zivkovic, and N. Zdravkovic, "A new approach to extraordinary efficient protection against COVID 19 based on nanotechnology," *Stomatoloski Glasnik Srbije*, vol. 67, no. 2, pp. 100–109, 2020.

[7] S. Stawarz, N. Witek, W. Kucharczyk, M. Bakar, and M. Stawarz, "Thermo-protective properties of polymer composites with nanotitanium dioxide," *International Journal of Mechanics and Materials Design*, vol. 15, no. 3, pp. 585–599, 2019.

[8] E. F. Kudina, E. Barkanov, and N. S. Vinidiktova, "Use of Nano-structured modifiers to improve the operational characteristics of pipelines' protective coatings," *Glass Physics and Chemistry*, vol. 42, no. 5, pp. 512–517, 2016.

[9] M. J. Koohsari, G. R. McCormack, T. Nakaya et al., "Walking-friendly built environments and objectively measured physical function in older adults," *Science*, vol. 9, no. 6, pp. 651–656, 2020.

[10] C. I. N. T. H. Y. A. Campos-Salazar, Y. A. M. I. L. E. T. Chacón-Araya, L. C. Solano-Mora, G. I. L. B. E. R. T. Brenes-Camacho, and J. A. Moncada-Jiménez, "Normative anthropometric and physical-function scores for Costa Rican older adults," *International Journal of Exercise Science: Conference Proceedings*, vol. 13, no. 1, pp. 12–12, 2017.

[11] J. A. Batsis, C. M. Germain, E. Vásquez, A. J. Zbehlik, and S. J. Bartels, "Physical activity predicts higher physical function in older adults: the osteoarthritis initiative," *Journal of Physical Activity & Health*, vol. 13, no. 1, pp. 6–16, 2016.

[12] Y. Sakamoto and Y. Ohashi, "The relationship between physical function in the elderly and judgment error in walking speed," *Journal of Physical Therapy Science*, vol. 29, no. 7, pp. 1176–1180, 2017.

[13] S. H. Paz, L. Jones, J. L. Calderón, and R. D. Hays, "Readability and comprehension of the geriatric depression scale and PROMIS physical function items in older African Americans and Latinos," *The Patient - Patient-Centered Outcomes Research*, vol. 10, no. 1, pp. 117–131, 2017.

[14] B. Gao, X. Ning, and P. Xing, "Shock wave induced nanocrystallization during the high current pulsed electron beam process and its effect on mechanical properties," *Materials Letters*, vol. 237, no. 15, pp. 180–184, 2019.

[15] T. Yunchao, C. Zheng, F. Wanhui, N. Yumei, L. Cong, and C. Jieming, "Combined effects of nano-silica and silica fume on the mechanical behavior of recycled aggregate concrete," *Nanotechnology Reviews*, vol. 10, no. 1, pp. 819–838, 2021.

[16] A. Kunihiko, M. Shin, I. Hiroaki et al., "Characteristics of the physical function of community-dwelling elderly suspected obstructive ventilatory impairment and restrictive ventilatory impairment," *Japanese Journal of Health Promotion & Physical Therapy*, vol. 6, no. 1, pp. 17–22, 2016.

[17] X. Q. Dong, S. M. Bergren, and M. A. Simon, "The decline of directly observed physical function performance among U.S. Chinese older adults," *The Journals of Gerontology Series A Biological Sciences and Medical Sciences*, vol. 72, suppl_1, pp. S11–S15, 2017.

[18] Y. Zhang, Y. Li, and C. Bai, "Microstructure and oxidation behavior of Si-MoSi$_2$ functionally graded coating on Mo substrate," *Ceramics International*, vol. 43, no. 8, pp. 6250–6256, 2017.

[19] K. Suzuki, S. Murata, K. Shiraiwa et al., "Association between falling and physical, cognitive, and mental functions in the elderly with exercise habits," *Japanese Journal of Health Promotion and Physical Therapy*, vol. 7, no. 4, pp. 171–175, 2018.

[20] K. Mori and Y. Akezaki, "Role of physical therapists in health care of the elderly," *Nippon Eiseigaku Zasshi (Japanese Journal of Hygiene)*, vol. 71, no. 2, pp. 126–132, 2016.

[21] S. Tanaka, K. Kamiya, N. Hamazaki et al., "Utility of SARC-F for assessing physical function in elderly patients with cardiovascular disease," *Journal of the American Medical Directors Association*, vol. 18, no. 2, pp. 176–181, 2017.

[22] K. Shiraiwa, S. Murata, T. Abiko, and J. Horie, "Difference in physical function due to differences in exercise frequency and duration of elderly people," *Japanese Journal of Health Promotion and Physical Therapy*, vol. 7, no. 3, pp. 121–126, 2017.

[23] L. D. Brown, A. H. Redelfs, T. J. Taylor, and R. L. Messer, "Comparing the functioning of youth and adult partnerships for health promotion," *American Journal of Community Psychology*, vol. 56, no. 1-2, pp. 25–35, 2015.

[24] Z. B. Khalesi, M. Simbar, S. A. Azin, and F. Zayeri, "Public sexual health promotion interventions and strategies: a qualitative study," *Electronic Physician*, vol. 8, no. 6, pp. 2489–2496, 2016.

[25] L. H. Sithole, "A situational analysis of ocular health promotion in the South African primary health-care system," *Clinical and Experimental Optometry*, vol. 100, no. 2, pp. 167–173, 2017.

[26] R. Loudoun and K. Townsend, "Implementing health promotion programs in the Australian construction industry," *Engineering Construction & Architectural Management*, vol. 24, no. 2, pp. 260–274, 2017.

Hindawi

Research Article

The Effect of Polymer Composite Materials on the Comfort of Sports and Fitness Facilities

Qingkun Feng[1] **and Lijun Wang** [2]

[1]*Institute of Physical Education and Health, Zhaoqing University, Zhaoqing, 526000 Guangdong, China*
[2]*Institute of Physical Education and Health, Yulin Normal University, Yulin, 537000 Guangxi, China*

Correspondence should be addressed to Lijun Wang; wanglj432@ylu.edu.cn

In a narrow sense, polymer composites refer to multiphase materials composed of polymers and other substances with different compositions, shapes, and properties. They can be divided into structural composites and functional composites. In a broad sense, polymer composite materials also include polymer blend systems, collectively referred to as "polymer alloys." The purpose of this paper is at studying how to study the impact of polymer composite materials on the adaptation and comfort of sports and fitness facilities. This paper puts forward the problem of comfort, which is based on the construction materials of sports equipment, and then elaborates on the polymer composite materials and makes a case design and analysis of the applicability of polymer composite materials in sports equipment being carried out. The experimental results show that 34.81% of the people are very satisfied and relatively satisfied with the quality identification of sports equipment and only 41.99% of the people are very satisfied and relatively satisfied with the feeling of sports equipment when exercising. Both are less than half of the total sample size, which shows that the current state of sports facilities is worrying.

1. Introduction

With the rapid development of the society, under the dual pressure of work and life, people pay more and more attention to healthy life. However, the current sports equipment and fitness facilities as a whole still cannot meet the people's fitness needs, which not only limits the public's participation in physical exercise but also exacerbates the contradiction between the public's growing fitness needs and the unbalanced and insufficient supply of fitness facilities. The wide application of polymer functional composite materials in sports equipment improves the comprehensive performance of sports equipment and fitness facilities and promotes the vigorous development of sports enterprises. In view of this, it is particularly important to discuss the design research of sports equipment and facilities in sports and fitness venues.

The improvement of the comfort of sports facilities will help alleviate the contradiction between the growing demand for sports activities and the lack of sports facilities, and it can help people improve people's comfort in sports activities. Convenient transportation, good sports environment, excellent sports equipment, and comfortable sports atmosphere can not only stimulate people's desire to engage in sports activities to a certain extent but also help them improve their physical condition and enjoy physical and mental health during exercise. Likewise, it helps extend the lifespan of sports facilities.

The innovation of this paper is that (1) this paper combines polymer composite materials with deep learning and introduces the theory and related methods of the neural network in detail and (2) in the face of the comfort of sports facilities, using questionnaires and analyzing the performance of polymer composite materials to analyze come in handy. Through the evaluation of the experimental results, in the selection of materials for sports equipment, materials and comfort should be given top priority and suitable materials will improve the comfort and experience of athletes.

2. Related Work

Since the 19th century, humans have used naturally modified polymer materials. After entering the 20th century, polymer materials entered a huge development stage. Atci E presented atomic models for the transport of single-component gases (CH_4, CO_2, H_2, and N_2) and binary gas mixtures (H_2/CO_2, H_2/N_2, and H_2/CH_4) in zeolitic imidazole framework (ZIF) membranes and ZIF/polymer composite membranes. The atomic model predictions are validated by comparison with available experimental data for ZIF-90 films. However, his experimental data was less [1]. Xin et al. reported a convenient and versatile strategy to prepare cesium lead bromide or organic lead halide methyl ammonium bromide polymer composites. They verified it by using methyl methacrylate, butyl methacrylate, and polystyrene and successfully built a prototype white light-emitting diode with viable color properties and narrow bandwidth. However, its application scope was limited [2]. Vaisanen et al. conducted a critical review of the impact of multiple types of waste, residues, or process by-products on NFPC and assessed their potential as NFPC components. However, his content was relatively brief [3]. Dang et al. investigated anisotropic aluminum nitride (AlN) whiskers and isotropic spheres as mixed fillers in the epoxy resin and polyvinylidene fluoride (PVDF) matrix to improve thermal conductivity of polymer composites. And polymer composites with mixed fillers of AlN whiskers and spheres with different volume ratios were prepared. However, his results were not comprehensive enough [4]. Moura et al. reported on the production and characterization of composites for wound healing applications, investigating bioactive glasses obtained by a sol-gel method and doped with two different metal ions. However, his performance was lower [5]. Khan A used chemical vapor deposition (CVD) technology to extract two different morphologies of carbon nanomaterials (CNM), namely carbon nanobeads (P1) and a mixture of carbon nanotubes and carbon nanobeads (P2). The morphology of the composites was analyzed by FESEM to study the interaction of fillers with the matrix to improve performance. However, his influence factors were more [6]. Zhang and Goekce summarized in situ and ex situ laser prototyping methods and downstream batch processing techniques for nanoparticle-polymer composites (LaNPCs) and discussed determining factors of polymer-solvent-laser parameterization on the target physical and chemical properties of composites. The advantageous features of this technique were demonstrated by highlighting representative works related to various promising applications. Finally, it described the challenges and prospects facing LaNPC, as well as perspectives on how recent research results are changing the direction of research in this field. However, their focus was not enough [7]. Li et al. investigated polymer composites reinforced by pristine and functionalized graphene to determine the improvement of the tribological properties of polymer composites. A molecular layer model with Fe atoms as the top nanolayer was established, and the tribological properties of the polymer composites were improved by sliding the top Fe nanolayer on the surface of the polymer matrix.
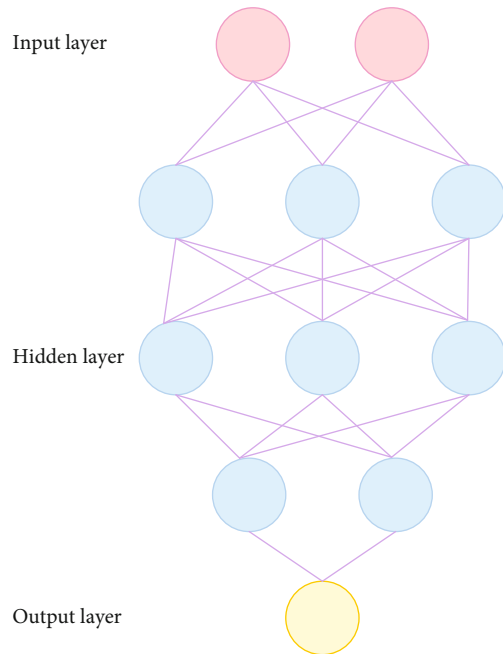
Figure 1: Architecture of an artificial neural network.

The simulation results show that the average friction coefficient and wear rate of the functionalized graphene/polymer composites are reduced by about 13% and 42.3%, respectively. However, their data were not accurate enough [8].

3. Classification Method of Polymer Composite Materials

3.1. Introduction to Deep Learning Based on Polymer Composite Material Classification. In recent years, deep learning technology has been successfully applied to speech recognition, handwriting recognition, and computer vision and achieved remarkable results in the fields of natural language self-processing [9]. The classification of polymer composites can also be carried out with the help of deep learning techniques.

The artificial neural network is an information processing system, which has some characteristics of ordinary BNN. In short, the artificial neural network can be regarded as an integrated system of the mathematical model of the human brain. The structure is shown in Figure 1. A large number of interconnected neurons constitute an ANN, and each neuron is interconnected with other neurons by having corresponding weights. In this, the knowledge to solve the problem can be represented by the weights. The structure of artificial neural network is composed of the feedforward network, feedback network, and mutual combination network. A neural network is an operational model that consists of interconnected connections between a large number of nodes (or neurons).

Deep learning is a very popular method in machine learning, covering theoretical viewpoints in many fields. It is to learn the inherent laws and representation levels of sample data. In order to realize more intelligent human-
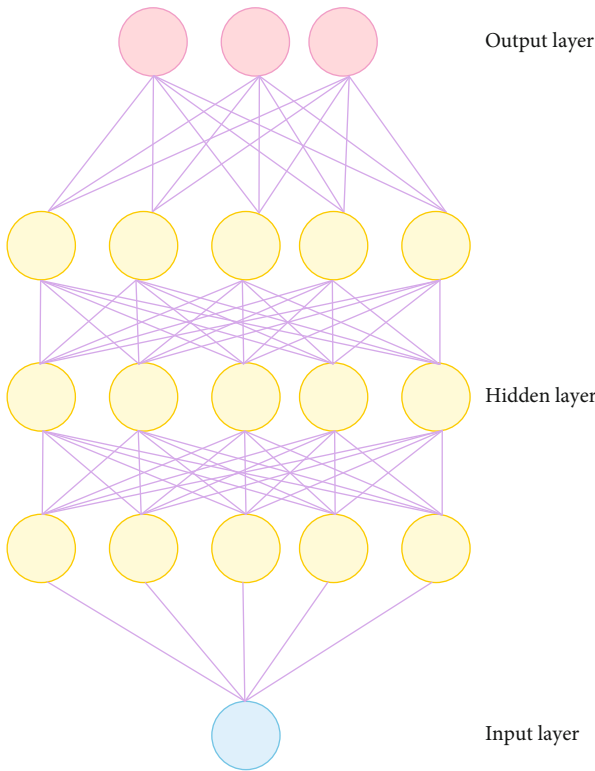
Figure 2: Deep neural network.

computer interaction, researchers imitate the human brain and thinking and establish various neural network models. Deep learning is one of them [10]. Deep learning is a multi-level representation learning method, learning data features by creating models, and finding a better data representation is the primary purpose of representation learning, as shown in Figure 2.

The convolutional neural network was first proposed in the 1980s. The idea of the CNN was inspired by human research on the cat visual system, but due to the limitations of computer resources at that time and other resource-limited problems, it could only stop there. The three major deep learning giants proposed a standard LeNet-5 network structure, using gradient descent for training, and achieved good experimental results, making it possible to train deep neural networks. The essence of the convolutional neural network is to construct multiple interconnected kernel convolution kernels, which can output data features and topological features. A structure is hidden between data by performing layer merging function on the data input side [11, 12], as shown in Figure 3.

As the number of layers continues to increase, the derived features become more and more abstract and these abstract features are finally merged through a fully connected hierarchy and classification problem. Feedback is resolved through Softmax or Sigmoid activation functions.

Before introducing Softmax regression, it is necessary to introduce logistic regression. Logistic regression is a simple binary classification algorithm that achieves classification by fitting the classification boundaries of the data and uses optimization methods such as gradient descent to determine
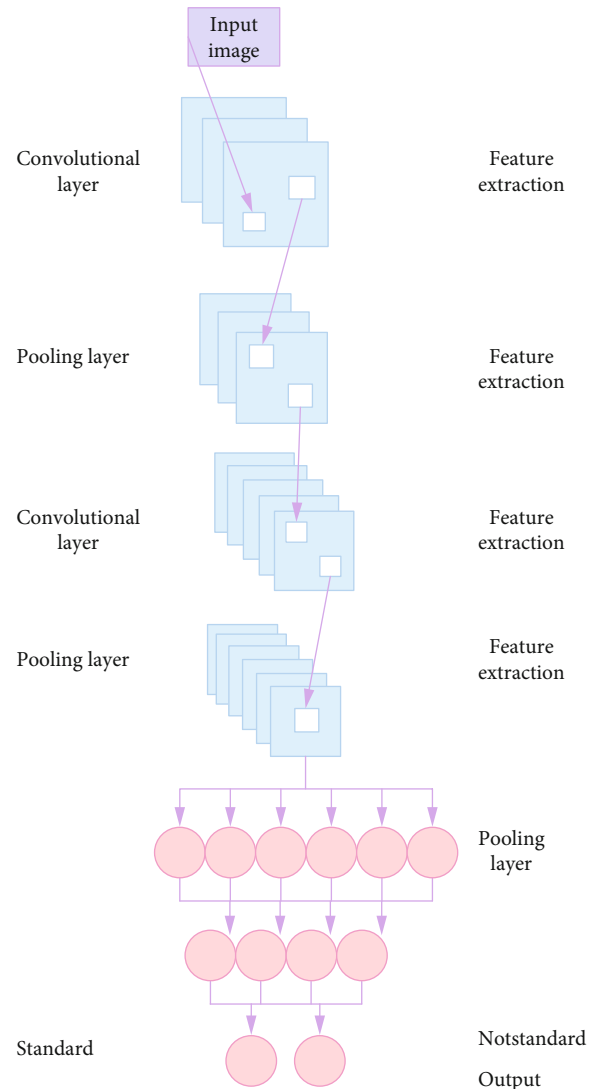
Figure 3: Convolutional network structure diagram.

the best regression coefficients [13]. One of the more important formulas in logistic regression is the step function:

$$Q(X) = \frac{1}{1 + E^{-\theta^Z X}}. \tag{1}$$

Its waveform is as follows; the value range is between [0,1]; Figure 4 is the logistic regression step function formula.

Its corresponding negative log-likelihood loss function is defined as

$$Q(\theta) = -\frac{1}{u} \left[\sum_{i=1}^{v} Y^i \log f_\theta(X^i) + (1 - Y^i) \log (1 - f_\theta(X^i)) \right]. \tag{2}$$

Based on linear regression, logistic regression applies a logistic function, but because of this logistic function, logistic regression has a favorable place in the field of machine learning [14].
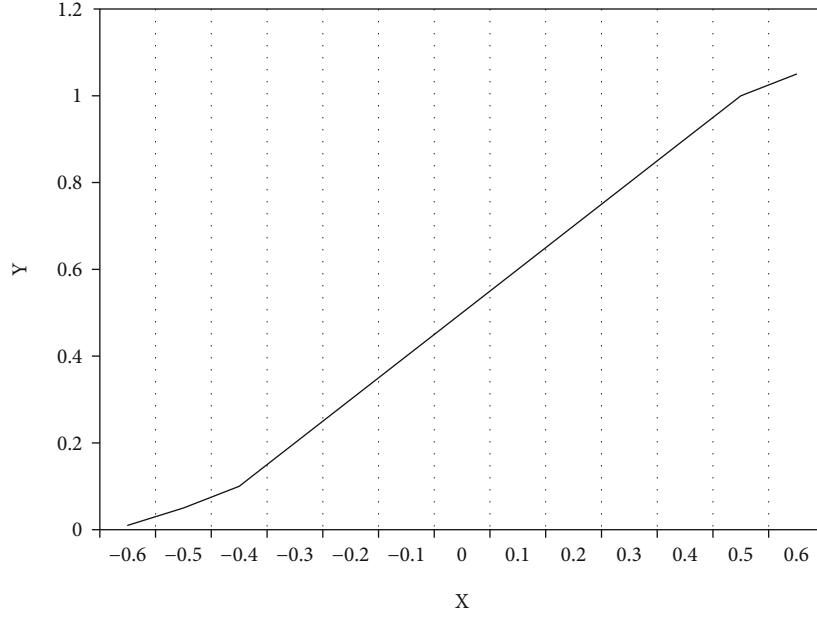
FIGURE 4: The logistic regression step function formula.

The assumption of the logistic regression model is as follows:

$$h_\varphi(t) = g(\varphi^Z t). \tag{3}$$

A commonly used logic function (and also the function mainly used in this paper) is the sigmoid function, and its expression is shown in formula (4):

$$g(x) = \frac{1}{1 + e^{-x}}. \tag{4}$$

The graph of this function is shown in Figure 5.

Therefore, the assumptions of the logistic regression model are as follows (5):

$$h_\varphi(t) = \frac{1}{1 + e^{-\varphi^Z x}}. \tag{5}$$

For the LR model, the classification is based on the following: for a given input variable t, calculate the probability that the output variable is 1 according to the selected parameters, that is,

$$h_\varphi(t) = P\left(\frac{y=1}{t;\varphi}\right). \tag{6}$$

The ReLu (rectified linear units) function is a popular activation function that has gradually replaced the sigmoid function. The function graph of ReLu is shown in Figure 6; it does not tend to saturate with the gradual increase of the input x.

Details of the Softmax classifier are as follows:

$$x(i|j) = \frac{\exp(V_i \cdot j)}{\sum_{w=1}^{W} \exp(V_w \cdot j)}. \tag{7}$$

Splitting the prediction function into two steps, taking the 1st row of V and multiplying that row with j,

$$V_{i \cdot j} = \sum_{a=1}^{d} Q_{iaxa} = f_j. \tag{8}$$

Calculating all f_w, $w = 1, \cdots, W$. Applying the Softmax function to obtain normalized probabilities,

$$x(i|j) = \frac{\exp(f_j)}{\sum_{w=1}^{W} \exp(f_w)} = soft\max(f)_j. \tag{9}$$

Softmax regression is an extension of logistic regression for solving multiple classification problems. Softmax regression is a supervised learning algorithm that can be combined with deep learning methods or unsupervised learning methods [15]. In logistic regression, the training sample set consists of samples labeled $\{(m^{(1)}, n^{(1)}), (m^{(2)}, n^{(2)}), \cdots, (m^{(x)}, n^{(x)})\}$ with the input feature $m^a \in \varphi^{y+1}$. The dimension of the feature vector m is $y + 1$, $m_0 = 1$. Supposing that the function is as follows,

$$h_\alpha(m) = \frac{1}{1 + \exp(-\alpha^T m)}. \tag{10}$$
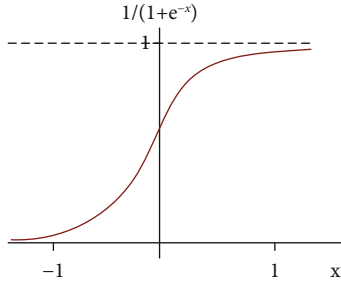
FIGURE 5: Sigmoid function diagram.
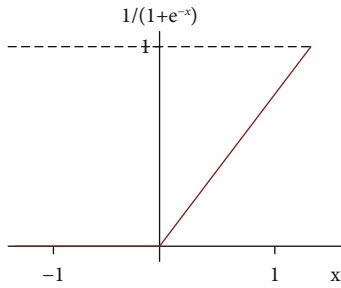
FIGURE 6: ReLu function diagram.

The model parameter α will be trained to minimize the cost function:

$$
S(\alpha) = -\frac{1}{x}\left[\sum_{i=1}^{x} n^{(a)} \log h_\alpha\left(m^{(a)}\right) \right.
$$
$$
\left. + \left(1 - n^{(a)}\right) \log\left(1 - h_\alpha\left(m^{(a)}\right)\right)\right]. \tag{11}
$$

In convolutional networks, the process of convolution includes two parameters: the first parameter is the input and the second parameter is the kernel function (i.e., the convolution kernel) [16]. The unit output by the convolution operation is called a feature map. Taking a two-dimensional image Q as input and the two-dimensional convolution kernel being P, the convolution of q and P is as follows:

$$
S(a, b) = (Q * P)(a, b) = \sum_{a}\sum_{b} Q(i, j) P(a - i, b - j). \tag{12}
$$

Mathematically, convolution is interactive because the convolution kernel is flipped relative to the input. However, most of the existing neural network libraries are based on a crosscorrelation function that does not flip the kernel and both methods are called convolution [17]. In this paper, the convolution is represented in this way. The convolution operations mentioned below are all convolution operations without flipping the convolution kernel. The crosscorrelation function is expressed as follows:

$$
S = (a, b) = (Q * P)(a, b) = \sum_{i}\sum_{j} Q(a + i, b + j) P(i, j). \tag{13}
$$

The convolutional neural network (CNN) is one of the structures of the deep learning network, which is characterized by a large number of convolution operations in the network structure. In addition, the activation function and pooling layer are also its basic structures. These three basic structures make it have better local perception characteristics and feature abstraction ability than multilayer perceptron (MLP) [18]. At present, the CNN has been widely used in many subfields of image processing and computer vision, such as image classification, image semantic segmentation, and visual object detection.

3.1.1. Calculation Output. For the l layer of the fully connected layer, the output result is as follows:

$$
A^x = g(C^x),
$$
$$
C^x = V^x A^{x-1} + Q, \tag{14}
$$
$$
E^z = \frac{1}{2}\sum_{k=1}^{l}(P_k^z - B_k^z)^2 = \frac{1}{2}\|P^z - B^z\|_2^2.
$$

In the formula, P^z is the expected output value of the zth sample and B^z represents the actual output value of the zth sample after the network operation.

3.1.2. Backpropagation. The data is calculated layer by layer through the network, and the error between the actual output and the expected output is obtained, which can be regarded as the sensitivity of the neuron base. The formula is as follows:

$$
\frac{\partial E}{\partial Q} = \frac{\partial E}{\partial C}\frac{\partial C}{\partial Q}. \tag{15}
$$

The formula for the sensitivity of layer x in the backpropagation stage is as follows:

$$
\delta^P = \left(V^{x+1}\right)^P \delta^{x+1} \bullet g'(C^p). \tag{16}
$$

The sensitivity of the output layer node is as follows:

$$
\delta = g'(C^x) \bullet (B^z - P^z). \tag{17}
$$

3.1.3. Weight Update. The derivation of the error for the x layer weight of the fully connected layer is the crossproduct of the x layer input and its sensitivity. The weight update formula is as follows:

$$
\frac{\partial E}{\partial V} = A^{x-1}(\delta^x)^P,
$$
$$
\Delta V^x = -\eta \frac{\partial E}{\partial V^x}. \tag{18}
$$

3.2. Polymer Composites. The biggest advantage of polymer composite materials is the advantages of various materials, such as high strength, light weight, temperature resistance, corrosion resistance, heat insulation, insulation, and other properties. According to the application purpose, select
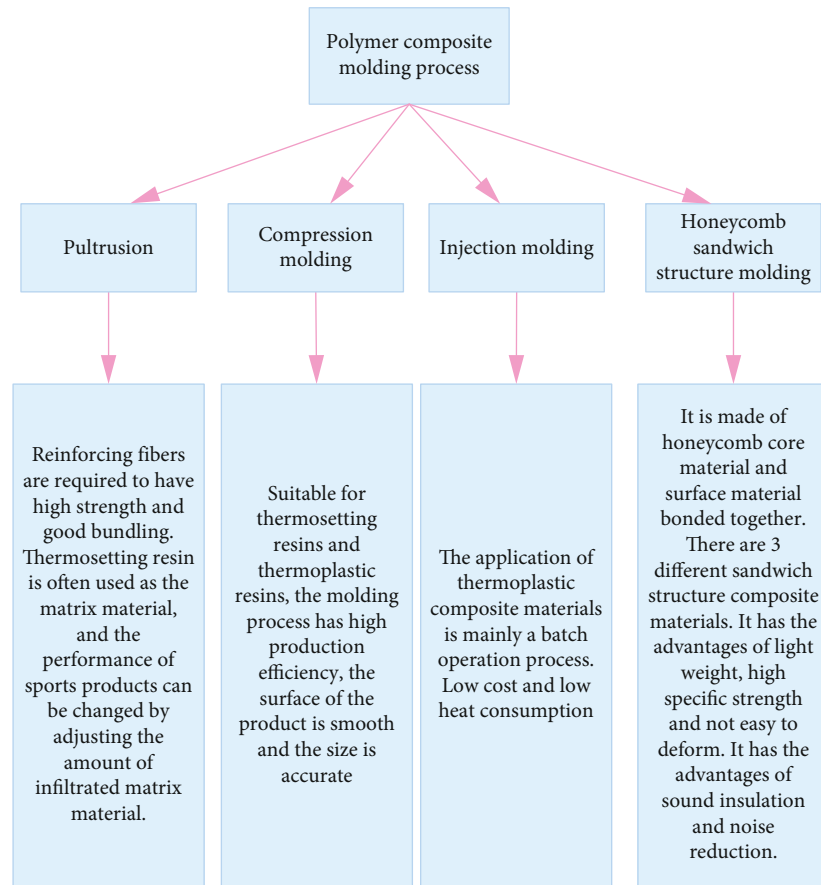
FIGURE 7: Polymer composite-type process.

polymer materials and other materials with special properties to make composite materials that meet the needs.

Polymer composite materials synthesized according to structural requirements are called polymer structural composite materials, and polymer structural composite materials synthesized according to different functional requirements are called polymer functional composite materials. Polymer functional composites are usually composed of the reinforcement phase and matrix phase. Generally, the commonly used reinforcing phases are fibrous materials, such as boron fibers, glass fibers, and carbon fibers. Dispersing them in a matrix phase enhances the overall strength, elasticity and impact resistance of the material. The function of the matrix phase is mainly to bond the dispersed material fibers into a group. The matrix phase materials generally have high special size and special strength, such as plastic epoxy resin, polypropylene, and polyimide. Due to its superior properties, it is used in the cutting-edge technology as well as defense and security. Due to the needs of sports, some sports equipment must have specific functions. Therefore, resin matrix materials are combined with materials with special functions, such as luminescence, antistatic, and magnetic properties, to form polymer functional composites [19, 20].

The molding process of polymer composite materials includes pultrusion molding, compression molding, injection molding, honeycomb structure molding, and other molding processes. The characteristics of some molding processes are shown in Figure 7.

4. Experiment and Analysis of the Comfort of Polymer Composites in Sports Facilities

4.1. Questionnaire Survey. A sample of 362 people was selected through the sampling survey, including 218 males and 144 females. It can be seen from the numbers that boys exercise more frequently than girls. The survey on the quality satisfaction of sports facilities is shown in Figure 8. The respondents showed a "∩" situation in the middle and two lows in terms of their recognition of the quality of sports equipment and their own proprioception during physical exercise. It can be seen in Figure 8(a) that among the quality recognition of sports equipment, 38 people chose to be more satisfied, accounting for 10.50%, 88 people chose to be more satisfied, accounting for 24.31%, the number of people who chose ordinary is 126, accounting for 34.81%, 78 people chose not satisfied, accounting for 21.55%, and 32 people chose very dissatisfied, accounting for 8.84%. As can be seen in Figure 8(b), among the feeling of sports equipment when exercising, 30 people choose very satisfied, accounting for 8.29%, 122 people choose relatively satisfied, accounting for 33.70%, 104 people choose in general, accounting for 28.73%, 74 people who are not satisfied, accounting for 20.44%, and 32 people who choose very dissatisfied,
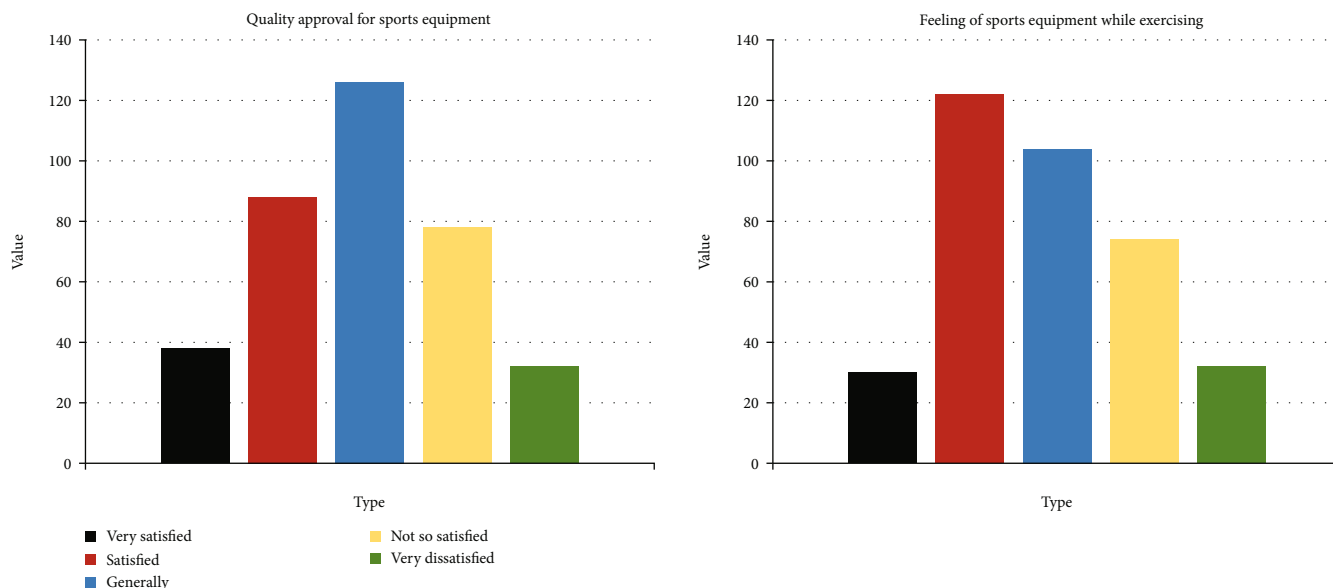
FIGURE 8: Respondents' satisfaction with the quality of sports equipment.

accounting for 8.84%. It shows that the respondents' recognition of the quality of sports facilities and equipment is generally at a medium level.

Figure 9(a) shows that sports facilities are occasionally damaged. As a sports facility, due to frequent use by people, 79.56% of occasional damage is normal. For this kind of normal damage, how the relevant departments should deal with it is a problem. The survey in Figure 9(b) shows that 80.66% of the respondents believe that these sports facilities have not been repaired and dealt with in time after the damage.

In addition, the survey on the maintenance and maintenance of sports facilities showed that 80% of the respondents believed that the relevant departments did not regularly maintain the sports facilities in a timely manner. More than 70% of the respondents believed that the relevant departments did not replace the damaged and irreparable equipment and facilities in time. Thirty percent of the respondents have a potential danger when engaging in physical exercise and feel that they may have potential safety hazards during the exercise process, and nearly 70% of the respondents will choose another kind of equipment for exercise.

To sum up, due to the needs of sports, some sports equipment must have specific functions. Resin-based matrix materials are combined with materials with special functions, such as glowing, antistatic, and magnetic, to form polymer functional composite materials. The following will analyze the experimental performance of polymer composite materials for sports equipment.

4.2. The Use of Common Polymer Composite Materials for Sports Equipment. Polymer engineering materials are used in the design and production of certain sports facilities and sports equipment to meet different sports needs, such as an equipment compact structure, heat resistance, corrosion resistance, and long service life. The available properties of some selected sports equipment materials are shown in Table 1.

Natural rubber and synthetic rubber are two types of rubber. In some sports, athletes will be subjected to a strong impact force and the rubber material can effectively reduce the impact force, thereby protecting the personal safety of the athletes, and can also effectively absorb shock and slip. Therefore, some rubber composite materials are often used in the design and production of sports equipment, such as high-elastic sports shoes for cushioning landing impact and protective equipment for cushioning impact. When the elastic material is subjected to external pressure, it does not break but causes reversible deformation; when the external force is removed, the rubber returns to its original shape. The main application aspects and properties of rubber materials in the sports field are shown in Table 2.

In the production and manufacture of sports facilities and equipment, rubber is one of the most widely used polymer materials, with excellent elastic properties, improving sports safety for athletes and providing athletes with a comfortable experience. Its rubber and composite materials are also widely used in ball equipment such as volleyball, basketball, and football, as well as dumbbells, shuttlecocks, racket outer layers, and racket handles. So, its rubber and composites are used for PVC. Its wide application can slow down the various impact forces received by the human body during use to exercise the body and significantly improve the safety and comfort of sports.

The sports industry is inseparable from the application of fiber polymer materials. Table 3 shows some related sports goods and materials, as well as some corresponding properties.

4.3. Impact of Polymer Composites on Comfort in Facilities. In the design and production of sports equipment, health and comfort should be the primary requirements for material selection. Coolmax fiber fabrics, cool plus fiber fabrics, or cotton fabrics are materials that perform well on this demand and can be used in the design and production of

(a) Respondents' perception of damage to sports facilities

(b) Respondents' views on the maintenance and handling of sports facilities
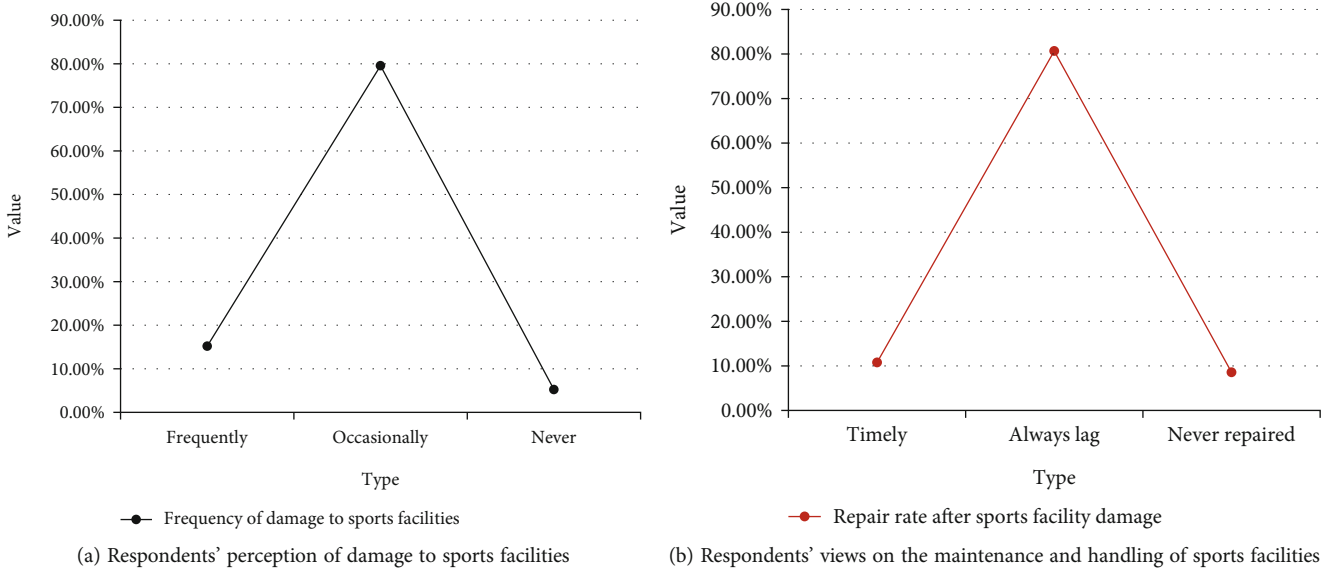
FIGURE 9: Respondents' survey on postmaintenance of sports equipment.

TABLE 1: Performance of polymer materials commonly used in sports equipment.

Sporting goods	Material	Effect
Sports bike	Polyetheretherketone, polycarbonate	Strong, heat resistance, impact resistance
Rubber track	Polyurethane rubber	Friction resistance, solvent resistance, oil resistance, aging resistance, high strength
Basketball	PVC	Antiaging and corrosion resistance
Table tennis	Polyester	High toughness and friction resistance

TABLE 2: Performance of polymer materials commonly used in sports equipment.

Sporting goods	Material	Chemical nature	Nature
Racing	Natural rubber cavity (NR)	Polyisoprene	For racing tires, with high elasticity
Sports shoes	Styrene butadiene rubber (SBR)	Polystyrene-butadiene	For shoe soles, antiwet and low rolling resistance
Protective equipment	Nitrile rubber (NBR)	Acrylonitrile-butadiene copolymerization	Strong oil resistance, aging resistance, friction resistance

sportswear. Swimsuits and wetsuits for water sports must be highly elastic, soft, and waterproof. Therefore, polyurethane can be treated by the combination of primer and final coating to reduce the resistance of water sports, can improve the comfort and freedom of athletes during water sports, and can effectively help athletes achieve better competition performance [21].

Today, most of the running tracks are built with plastic tracks, replacing the previous tracks with cement; the floors of sports fields and gyms also use plastic floors, which are very important to improve the comfort of athletes. Plastic runway and plastic floor have excellent recovery, sound absorption, shock absorption, abrasion resistance, and slip resistance. Compared with the traditional material track, the plastic track has significant elastic kinetic energy, strong force rotation, and vibration reduction ability, which can effectively reduce the impact force of the foot. The risk of injury to the athlete is reduced, and the athlete is more comfortable during training or competition without leg pain associated with prolonged exercise. The plastic track has a

certain breathability. At high temperatures, athletes are less likely to emit unpleasant odors. The composition of the plastic track is shown in Figure 10. The construction of the lower layer should ensure the stability of the foundation. The construction of the abovementioned fourth, fifth, and sixth layers is made of plastic materials. The outer layer of the main material is polyacrylic acid, which is closely related to the direct contact with athletes and has strong elasticity and comfort.

Materials commonly used in water sports facilities, such as rowing boats, jet skis, surfboards, and windsurfing boards, are both plastics and composites. These facilities must withstand the mass of athletes and resist the impact of water. Therefore, it must have strong hardness and rigidity. Therefore, composite fiber materials are usually added to plastic materials to improve the durability of the device and meet the needs of athletes. Most of these factories are made of thermoplastic and thermoset materials, which not only are lightweight but also allow athletes to control speed and direction, and have a good feel, thus improving the comfort

TABLE 3: Applications of fibrous polymer materials.

Sporting goods	Material	Nature
Sports clothing	Nylon, acrylic, polyester	Soft, antiwrinkle, comfortable, easy to wash, and quick dry
Rackets, pitch bars, bicycles, surfboards	Composite fiber material	High strength and elasticity
Golf clubs	Carbon fiber composite material	Increase the mass of the club head, provide greater power, and improve the initial speed and stability of the ball when flying
Ski board	Composite use of carbon fiber-reinforced plastics and other materials	Enhanced bearing capacity and increased stability
Sport bike	Carbon fiber-reinforced plastic	Reduce mass, improve rigidity, and increase driving comfort
Mountaineering equipment	Carbon fiber-reinforced plastic	Improve the strength of the climbing rope, enhance wear resistance, and ensure safety
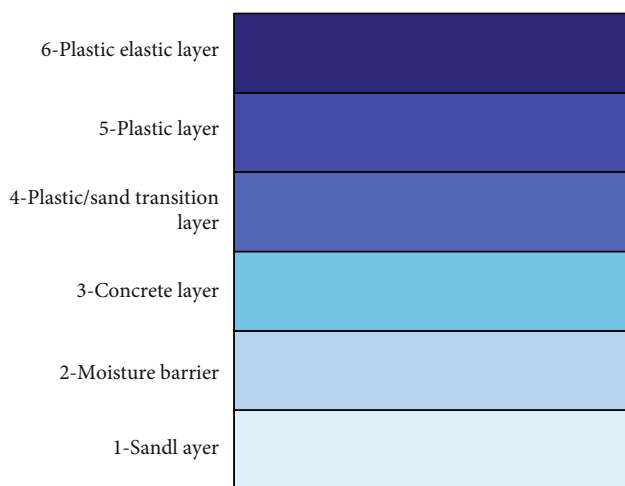
FIGURE 10: Plastic runway structure.

of sports. In addition to fiber-reinforced plastics, the outer layers of wakeboards, surfboards, and other aquatic facilities often use polyurethane foam composites with thermal insulation, which can reduce the energy consumption of athletes in the water to a certain extent [22]. Other functional materials are made with the motorboat saddle, which can significantly improve the comfort of use.

5. Discussion

First of all, through the study of relevant knowledge points of literature works, this paper initially masters the relevant basic knowledge and analyzes how to study the influence of polymer composite materials on the adaptability and comfort of sports and fitness facilities. The concept and deep learning algorithm of polymer composite materials are expounded, and the applicability of polymer composite materials in sports equipment is tested through experiments.

Comfort is the state of mind that a person is in a carefree, relaxed environment in an environment. It is the subjective feeling of people, including physical, psychological, environmental, and other aspects. There are clear physical and psychological differences between different age groups. So, comfort requires facilities in the public space environ-

ment to meet the needs of most people, while installing universal design facilities. For larger sports facilities, simple and varied designs can be installed to meet the needs of different age groups. When designing fitness facilities, factors such as different sizes and heights can be considered to meet the comfort of different groups of people [23]. The choice of material is very important, especially the parts that are in direct contact with people, which directly determines the comfort level of people.

Through the experimental analysis in this paper, it can be seen that polymer composite materials are widely used in the production and manufacture of sports equipment and facilities due to their wide range of sources. The casting process is simple and the cost is low. The use of composite materials has greatly improved the comfort and safety of sports equipment and facilities. With the continuous progress of science and technology, the production of sports facilities must go hand in hand with the development of science and technology in order to promote the development of national sports [24].

6. Conclusions

Since the reform and opening up, with the improvement of the quality of life, people have more free time and begin to gradually enjoy life and pursue health. This study mainly analyzes and discusses the factors that affect the comfort of sports facilities; the research focuses on the analysis of the design and construction of sports facilities and examines the comfort provided to residents during physical exercise. In the category of psychology, influencing factors vary by personal values, but also by personal emotions at different times. This is a relatively complex system. This study explores the factors that affect the comfort of sports facilities. This paper discusses the factors affecting the comfort of sports facilities and is aimed at further constructing the evaluation scale for the comfort of sports facilities, and establish a scientific, reasonable and flexible evaluation index system for the comfort of public sports facilities, and then continue to find and solve problems. For public sports facilities in the design, this scale can be used as a basis. Along with the overall planning of Khao Chung, the focus was on improving the comfort of public sports facilities. Therefore, this study will

conduct in-depth research on this issue in the future, construct a sports facility comfort assessment scale, and conduct a scientific assessment of the comfort of sports facilities.

Data Availability

No data were used to support this study.

Conflicts of Interest

There is no potential conflict of interest in this study.

Authors' Contributions

Qingkun Feng and Lijun Wang are co-first authors. Qingkun Feng is the first author; Lijun Wang is a co-first author. These two authors contributed equally to this work.

References

[1] E. Atci and S. Keskin, "Atomically detailed models for transport of gas mixtures in ZIF membranes and ZIF/polymer composite membranes," *Industrial & Engineering Chemistry Research*, vol. 51, no. 7, pp. 3091–3100, 2017.

[2] Y. Xin, H. Zhao, and J. Zhang, "Highly stable and luminescent perovskite-polymer composites from a convenient and universal strategy," *ACS Applied Materials & Interfaces*, vol. 10, no. 5, pp. 4971–4980, 2018.

[3] T. Vaisanen, O. Das, and L. Tomppo, "A review on new bio-based constituents for natural fiber-polymer composites," *Journal of Cleaner Production*, vol. 149, pp. 582–596, 2017.

[4] T. Dang, C. Y. Kim, Y. Zhang, J. F. Yang, T. Masaki, and D. H. Yoon, "Enhanced thermal conductivity of polymer composites via hybrid fillers of anisotropic aluminum nitride whiskers and isotropic spheres," *Composites Part B Engineering*, vol. 114, pp. 237–246, 2017.

[5] D. Moura, M. T. Souza, L. Liverani et al., "Development of a bioactive glass-polymer composite for wound healing applications," *Materials Science and Engineering: C*, vol. 76, pp. 224–232, 2017.

[6] A. Khan, P. Jagdale, M. Rovere, M. Nogués, C. Rosso, and A. Tagliaferro, "Carbon from waste source: an eco-friendly way for strengthening polymer composites," *Composites Part B Engineering*, vol. 132, pp. 87–96, 2018.

[7] D. Zhang and B. Goekce, "Perspective of laser-prototyping nanoparticle-polymer composites," *Applied Surface Science*, vol. 392, pp. 991–1003, 2017.

[8] Y. Li, S. Wang, and Q. Wang, "Enhancement of tribological properties of polymer composites reinforced by functionalized graphene," *Composites Part B Engineering*, vol. 120, pp. 83–91, 2017.

[9] V. A. Krasnyi and V. V. Maksarov, "Improving wear resistance of friction assemblies of oil-well pumps having seals from directionally reinforced polymer composites," *Chemical and Petroleum Engineering*, vol. 53, no. 1-2, pp. 121–125, 2017.

[10] W. Dominik, T. Krzysztof, M. Ireneusz, and D. Grzegorz, "Estimation of the perforation force for polymer composite conveyor belts taking into consideration the shape of the piercing punch," *International Journal of Advanced Manufacturing Technology*, vol. 98, no. 9-12, pp. 2539–2561, 2018.

[11] L. Zhang, N. De Greef, G. Kalinka et al., "Carbon nanotube-grafted carbon fiber polymer composites: damage characterization on the micro-scale," *Composites Part B Engineering*, vol. 126, pp. 202–210, 2017.

[12] Y. Kim, S. Jun, B. K. Ju, and J. W. Kim, "Heterogeneous configuration of a ag nanowire/polymer composite structure for selectively stretchable transparent electrodes," *ACS Applied Materials & Interfaces*, vol. 9, no. 8, pp. 7505–7514, 2017.

[13] S. Nallusamy and A. Karthikeyan, "Synthesis and wear characterization of reinforced glass fiber polymer composites with epoxy resin using granite powder," *Journal of Nano Research*, vol. 49, no. 1, pp. 1–09, 2017.

[14] A. Kumre, R. S. Rana, and R. Purohit, "A review on mechanical property of sisal glass fiber reinforced polymer composites," *Materials Today: Proceedings*, vol. 4, no. 2, pp. 3466–3476, 2017.

[15] S. Rat, M. Piedrahita-Bello, L. Salmon, G. Molnar, P. Demont, and A. Bousseksou, "Coupling mechanical and electrical properties in spin crossover polymer composites," *Advanced Materials*, vol. 30, no. 8, 2018.

[16] Y. Wu, K. Wang, S. Huang, C. Yang, and M. Wang, "Near-infrared light-responsive semiconductor polymer composite hydrogels: spatial/temporal-controlled release via a photothermal "sponge" effect," *ACS Applied Materials & Interfaces*, vol. 9, no. 15, pp. 13602–13610, 2017.

[17] C. Cheng, K. C. Ke, and S. Y. Yang, "Application of graphene-polymer composite heaters in gas-assisted micro hot embossing," *RSC Advances*, vol. 7, no. 11, pp. 6336–6344, 2017.

[18] I. Ngo, S. V. Prabhakar Vattikuti, and C. Byon, "A modified Hashin-Shtrikman model for predicting the thermal conductivity of polymer composites reinforced with randomly distributed hybrid fillers," *International Journal of Heat and Mass Transfer*, vol. 114, pp. 727–734, 2017.

[19] A. Gaffer, A. A. Kahlawy, and D. Aman, "Magnetic zeolite-natural polymer composite for adsorption of chromium (VI)," *Egyptian Journal of Petroleum*, vol. 26, no. 4, pp. 995–999, 2017.

[20] E. Solis-Ramos and M. Kumosa, "Synergistic effects in stress corrosion cracking of glass reinforced polymer composites," *Polymer Degradation & Stability*, vol. 136, pp. 146–157, 2017.

[21] Y. G. Luan, X. A. Zhang, S. L. Jiang, J. H. Chen, and Y. F. Lyu, "Self-healing supramolecular polymer composites by hydrogen bonding interactions between hyperbranched polymer and graphene oxide," *Chinese Journal of Polymer Science*, vol. 36, no. 5, pp. 584–591, 2018.

[22] E. Palesch, A. Knob, T. Plichta, and V. Cech, "Functional interlayers with controlled adhesion developed for polymer composites," *Thin Solid Films*, vol. 656, pp. 37–43, 2018.

[23] Y. Wang, Y. Hou, and Y. Deng, "Effects of interfaces between adjacent layers on breakdown strength and energy density in sandwich-structured polymer composites," *Composites Science and Technology*, vol. 145, pp. 71–77, 2017.

[24] J. Meng and S. Wang, "The construction of sports health management model based on deep learning," *Applied Bionics and Biomechanics*, vol. 2022, Article ID 5194665, 10 pages, 2022.

Research Article

RSM-Based Optimization of Fermentation Conditions and Kinetic Studies of Glutamic Acid and Lysine Production by *Corynebacterium glutamicum*

Saira Bashir,[1] Rashida Bashir,[2] Muhammad Pervaiz,[1] Ahmad Adnan ![ORCID],[1] Wahidah H. Al-Qahtani,[3] and Mika Sillanpaa ![ORCID][4,5]

[1]*Department of Chemistry, Government College University Lahore, Pakistan*
[2]*Division of Science and Technology, University of Education Lahore, Pakistan*
[3]*Department of Food Sciences &Nutrition, College of Food & Agriculture Science, King Saud University, Riyadh 11451, Saudi Arabia*
[4]*Department of Chemical Engineering, School of Mining, Metallurgy and Chemical Engineering, University of Johannesburg, P.O. Box 17011, South Africa*
[5]*Department of Biological and Chemical Engineering, Arhus University, Norrebrogade 44, 800 Aarhus, Denmark*

Correspondence should be addressed to Ahmad Adnan; ahmadadnan@gcu.edu.pk

Corynebacterium glutamicum is an authenticated microorganism that supports amino acid production consistent with dietary importance. Fermentation parameters like temperature, agitation speed, and carbon source concentration were optimized using response surface methodology. Surface response model suggested that optimal fermentation parameters including 30°C, 50 g/L glucose concentration, and shaking speed of 120 rpm furnished 14.2 g/L of glutamic acid and 5.1 g/L lysine, comparable with the predicted values. After optimizing fermentation parameters in shake flasks, the fermentation kinetics was studied in a stirred fermenter. The kinetic study revealed that the substrate consumption rate achieved a maximum level of 3.36 g/L/hour between 12 and 18 hours; afterwards, it decreased and fell to 1.9 g/L/hour. Average biomass yield over a period of 48 hours was 0.337 g/L; however, maximum biomass yield of 0.51 g/L was noted between 10 and 20 hours. Overall molar yield coefficient of CO_2 ($Y^C_{CO2/S}$) was found to be 0.234. The molar yield coefficient of biomass ($Y^C_{X/S}$) was 0.6 in exponential phase which decreased afterwards. This study indicates that the average biomass yield over a time of 48 hours was 0.337 g/L, with a maximum yield within 10 to 20 hours obtained under optimized conditions. The molar yield coefficient of CO_2 ($Y^C_{CO2/S}$) was found to be 0.234. The molar yield coefficient of biomass ($Y^C_{X/S}$) was 0.6 in exponential phase which decreased and fell to near zero at 48 hrs.

1. Introduction

Amino acids are the basic functional and structural units of proteins and play a major role in the regulation of vital metabolic pathways for the sustainable cultivation of microorganisms [1]. Amino acids are very helpful in promoting growth through several actions including efficient regulation of muscle protein, controlling growth and immunity of organisms, and optimizing the efficiency of food metabolism [2–4]. Since 1907, the production of monosodium glutamate

[5] has raised its demand in international market and gave a boost to amino acid production. A wide range of biochemical products have also multiplied as a result of their applications in industries particularly in the area of livestock as feed additive, as healthy ingredient in pharmaceuticals and cosmetics, and as seasoning in human nutrition [6]. Production of amino acids has been tremendously increased as these biomolecules have vast applications that include animal feed supplements, cosmetics, additives in food, chemicals in agriculture, and polymer materials.
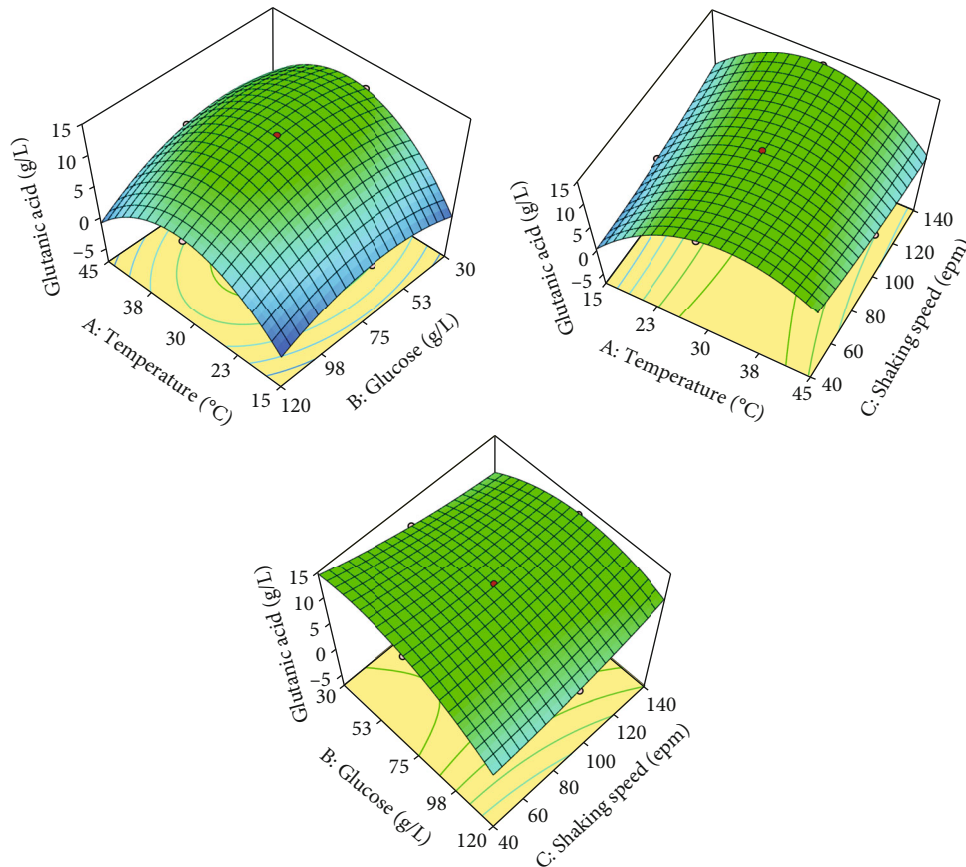
Figure 1: Synergism between parameters affecting glutamic acid production.

Fermentation is well thought-out as the most efficient, cost-effective, and beneficial technique in terms of amino acid synthesis. During fermentation, microorganisms use cheap raw materials as fermentation substrates. The process of fermentation is an advanced industrial method that uses several microorganisms to transform sugar substrates into a wide range of amino acids, both aerobically and anaerobically. A number of reasons contribute to the efficacy of amino acid synthesis by fermentation. First, as a result of fermentation, only the L-form stereoisomer of amino acids is produced which help escape any additional purification steps. Second, fermentation procedure is carried out at mild conditions which prevent any product degradation. Third, the maintenance costs are significantly less in comparison to the extraction processes [6, 7].

In recent years, varieties of technologies have been developed due to increased interest in amino acid production. Bacteria like *E. coli* and *C. glutamicum* are both useful for amino acid production through fermentation [7]. A variety of genetically engineered species have been applied under optimized conditions as amino acid producers. Lysine and glutamic acid are produced by genetically modified C. glutamicum with high yields up to 50% (*w/w*) [8, 9]. There are many strains of microorganisms that have been modified genetically and are used for amino acid production. *Corynebacterium glutamicum* is primarily aerobic, nonpathogenic, rod-shaped, Gram-positive bacterium, commonly recog-

nized as a safe (GRAS) creature for manufacturing bioelements like amino acids and nucleotides [10–12]. *C. glutamicum* was recognized in the biotechnology industry for amino acid production on a business scale containing L-lysine and L-glutamate as flavor enhancers since 1960 [13–15]. Since half a century after its discovery, this microorganism has participated in the amino acid production by fermentation and has an extensive and effective record in the biotechnological formation of L-lysine and L-glutamic acid [16, 17]. *C. glutamicum* is genetically modified for the production of glutamic acid with maximal yield (50% ww^{-1}), while aromatic amino acids are produced by genetically modified *Escherichia coli* [18].

2. Results and Discussion

2.1. RSM-Based Simultaneous Optimization of Temperature, Shaking Speed, and Carbon Source Concentration. Response surface methodology was followed for optimizing fermentation parameter including temperature, amount of glucose syrup (with 60% solids) in the fermentation medium, and rotational speed of an orbital shaking incubator. Many experiments were performed, and reaction conditions were carefully investigated to determine the optimum parameters for the production of glutamic acid (Figure 1) and lysine (Figure 2).
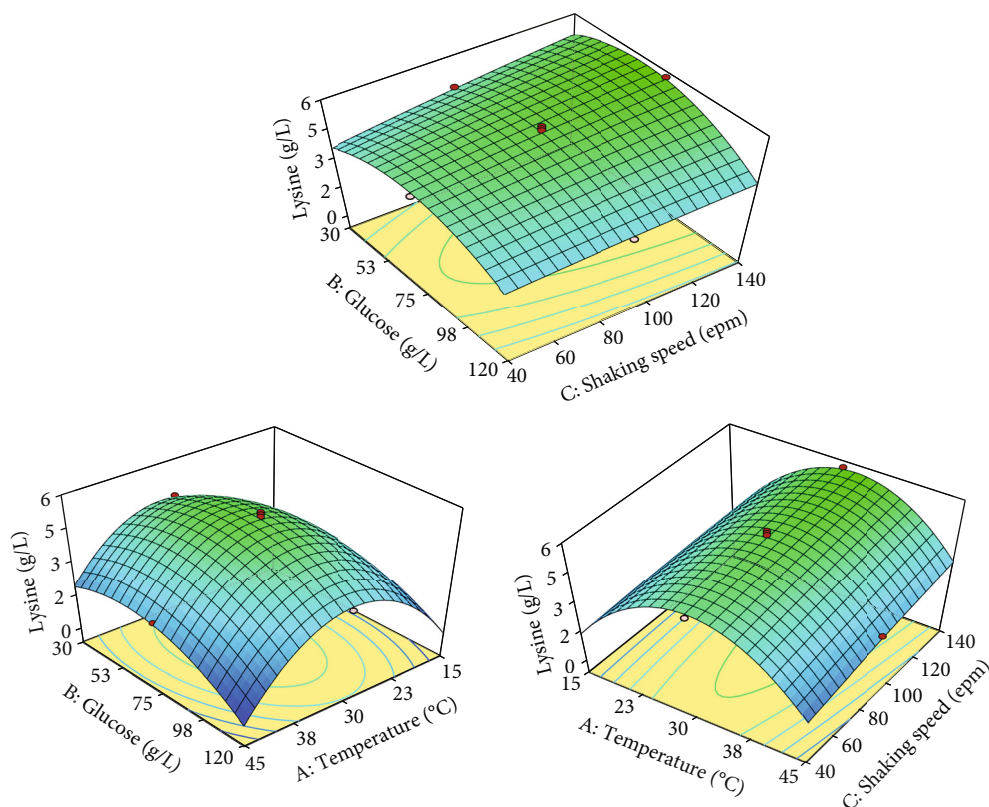
FIGURE 2: Synergism between parameters affecting lysine production.

The analysis of variance data indicated that the applied model has good fit over the selected range of fermentation conditions. Similarly, coefficient of variation range established that results produced are quite reliable and the experimental model can be effectively used to predict the responses. The high R^2 values of models for the optimization of glutamic acid and lysine production also affirm the validity of experimental models.

The analysis of variance data predicted that the temperature and glucose concentration significantly influence the production of glutamic acid as well as lysine while the effect of shaking speed was found to be nonsignificant for the production of amino acids with p values > 0.5.

Figures 1 shows that increasing the concentration of glucose up to 50 g/L, improved the production of glutamic acid up till it reached 65 g/L. Likewise, increasing the concentration of glucose up to 55 g/L improved the production of lysine to a level of 5.1 g/L and further increase in glucose concentration resulted in reduction in lysine yield.

Finally, validation experiments conducted under most desirable conditions revealed that the fermentation conditions embracing 30°C temperature, 50 g/L glucose concentration, and 120 rpm shaking speed furnished 14.2 g/L of glutamic acid and 5.1 g/L of lysine.

3. Fermentation Kinetics

3.1. Fermentation Pattern in a Stirred Fermenter. Figure 3 shows the conversion of the feather hydrolysate into micro-
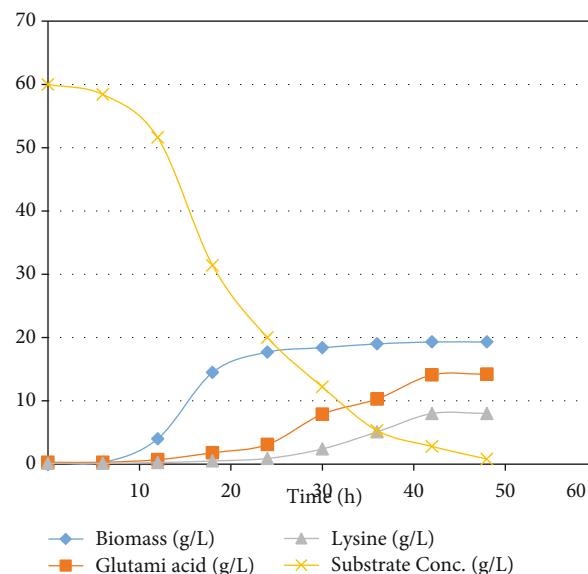
FIGURE 3: Fermentation profile of amino acid production in a stirred fermenter.

bial cell mass and amino acids as the function of fermentation period in the fermenter. The figure indicates that the rate of substrate consumption and biomass production was high for the first 30 hours of fermentation process. But amino acids were progressively released into the fermentation medium at
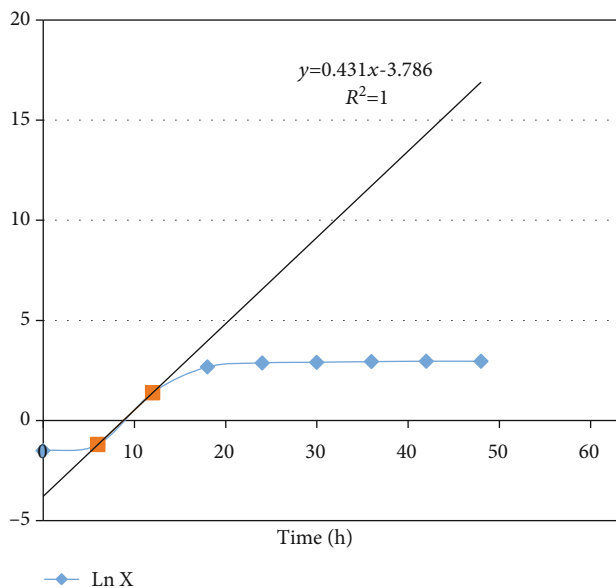
Figure 4: Growth curve showing specific growth rate.
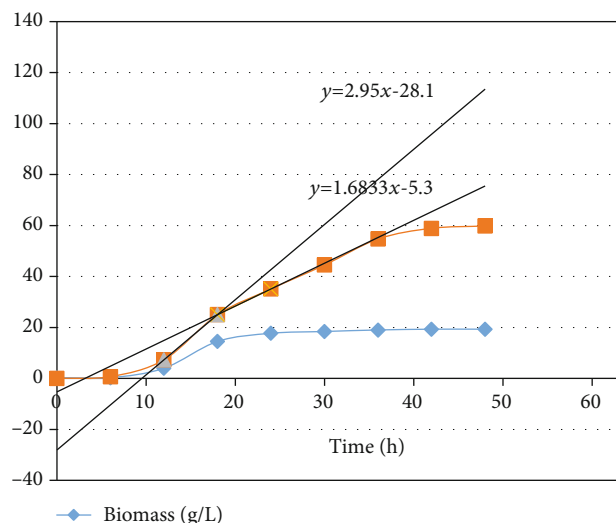
Figure 5: Concentration time graphs for substrate consumption rates.

an admirable level till 48 hours of submerged fermentation and beyond this, decline phase started.

3.1.1. Specific Growth Rates.
A graph (Figure 4) between natural log of biomass and fermentation time during the amino acid production revealed that there was a six-hour lag in growth in the stirred fermenter. Lag phase was followed by a brief logarithmic phase In the log phase, the specific growth rate was $0.43 \, h^{-1}$ which was gradually decreased. After 12-hour fermentation, the specific growth started to slow down, indicating the termination of true exponential phase. The generation time and the number of generations during the exponential growth phase were 1.6 h and 3.73, respectively.
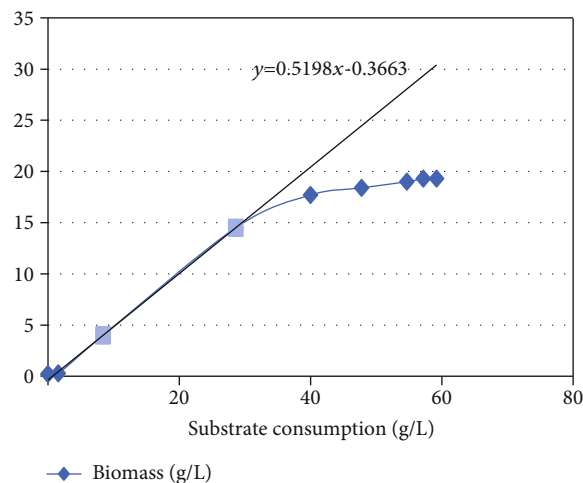
Figure 6: Biomass growth yield.
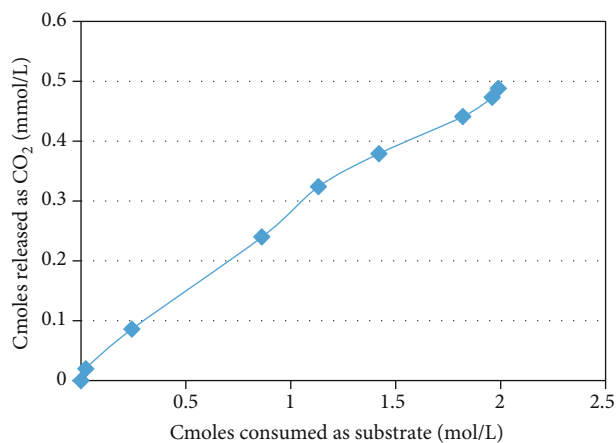
Figure 7: Molar yield coefficient of CO_2.

3.1.2. Substrate Consumption Rate and Specific Substrate Uptake Rate.
Concentration-time graph (Figure 5) for the substrate consumption shows substrate consumption rate at different levels. It is evident that initially, the rate of substrate consumption was very low and then, it increased with biomass as a function of time and achieved a maximum level of 3.36 g/L/hour between 12 and 18 hours; afterwards, it decreased and fell to 1.9 g/L/hour. This may be related to reduction in growth activity which in turn dropped the consumption rate. This may also be related to high value of Monod constant which does not allow complete utilization of the substrate. Average biomass yield over a period of 48 hours was 0.337 g/g; however, maximum biomass yield of 0.51 was noted between 10 and 20 hours as shown in Figure 6.

3.1.3. Growth Yield ($Y_{X/S}$) and Product Yield ($Y_{P/S}$).
It is pronounced from Figure 7 that biomass yield ($Y_{X/S}$) remained 0.52 during the log phase along with economic coefficient: 1.96 g substrate/g biomass. During the logarithmic phase, nearly 59.8% carbon of the consumed substrate was converted
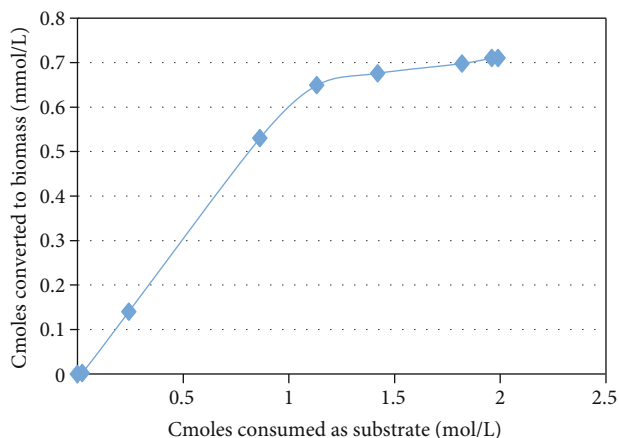
FIGURE 8: Molar biomass yield.

into biomass. However, after 24 hours, the metabolic activities slowed down and the substrate used participated mainly in providing the maintenance energy through oxidation resulting in a molar yield coefficient of CO_2 ($Y^C_{CO2/S}$) equal to 0.234.

Figure 8 shows that molar yield coefficient of biomass ($Y^C_{X/S}$) was 0.6 in the exponential phase which decreased afterwards. At the end of 48 hours, instantaneous conversion of substrate to microbial biomass fell to near zero.

4. Materials and Methods

4.1. Microorganism. *Corynebacterium* glutamicum was obtained from Biotechnology and Food Research Centre, PCSIR Lahore, and was maintained on preprepared nutrient agar slants. The cultured slants were refrigerated at 4°C.

4.2. Fermentation. The fermentation parameters were optimized in shake flasks using a shaking incubator (New Brunswick, USA) set at 120 rpm, whereas the fermentation kinetics was studied in a bioreactor of 7.5 L capacity (New Brunswick). Half liter of 18 h old vegetative inoculum was shifted to the bioreactor containing 4.5 L sterile fermentation medium. The medium already optimized in shake flasks consisted of (g/L), glucose syrup (60DS): 100; feather hydrolysate: 20; CaCl$_2$:2.0; NaCl:2.0; MgSO$_4$.7H$_2$O:0.5; yeast extract: 5.0; KH$_2$PO$_4$:v0.5; ammonium sulphate: 20; and K$_2$HPO$_4$: 1.0. The pH was set at 7.0 ± 0.2 which was maintained using 1 N phosphoric acid and 12.5% aqueous ammonia along with this temperature which was set at 30°C. During the period of fermentation, the rate of aeration was kept constant at 0.55/L/min and by controlling the speed of stirrer from 100 to 130 rpm, the dissolved oxygen (DO) was maintained at 20%.

4.3. Optimization of Fermentation Process. Response surface methodology was carried out for the optimization of fermentation process. The parameter selected for this purpose were as follows: temperature in the range of 15-45°C, amount of glucose syrup (with 60% solids) in the fermentation medium within the range of 30-120 g/L, and the rotational speed of the orbital shaking incubator between 40 and 140 rpm. Various experiments were carried out, and reaction conditions were cautiously monitored to find out the optimum conditions for the production of glutamic acid and lysine. The experimental data was checked against different statistical models, i.e., linear quadratic and factorial, and the model which best fitted on data was chosen for further optimization studies; the selection was made on the bases of different statistical parameters (i.e., sequential p value, lack of fit p value, R^2 value, and the normality as well as predicted vs. actual plots). The parameters and their interaction terms which could significantly affect the amino acid yield were determined by the help of ANOVA and response surface plots.

4.4. Biomass Estimation. Two methods were used to determine the microbial biomass that includes total dry cell mass and optical density measurements. Using a spectrophotometer, the optical density was set at 600 nm which helped in the determination of total cell concentration [19]. Culture tubes of 1 mL capacity were taken to measure dry cell weight in triplets. Tubes were centrifuged at room temperature for about 15 minutes with a speed of 13,000 rpm (ScanSpeed Mini, Denmark), and sterilized containers were used to collect the supernatant. Supernatant was built up for further analysis. 50 mM PB of pH 7.2 was taken in where stored pallets were resuspended and centrifuged in preweighed culture tubes and finally dried at 80°C until constant weight.

4.5. Amino Acid Analysis. The concentration of amino acids in the fermentation media was determined by the method of [20] using HPLC system with C-18 column and a photodiode array detector at 338 nm. Samples were eluted with a linear gradient of solvent A (40 mmol/L Na$_2$HPO$_4$, pH 6.8) and solvent b (10% H$_2$O, 45% methanol, 45% acetonitrile) at the flow rate of 2 mL/min.

4.6. Estimation of Protein Content. Total protein content was estimated according to the Lowry protocol. Bovine serum albumin was used as a standard in this method [21].

4.7. Estimation of Glucose Content. The glucose content was estimated by Miller reagent, which was based on the reduction of 3,5-dinitro-2-hydroxybenzoic acid to an orange-red complex, under alkaline conditions. The absorbance was taken at 540 nm.

4.8. Determination of CO_2. Evolution of carbon dioxide gas from the fermenter was determined by absorbing the gas in a known volume of 1.0 molar KOH solution [22]. The unused KOH was titrated against 0.1 M HCl. In this way, moles of carbon dioxide produced during a definite period of time were calculated. The rate of CO_2 evolution was determined as

$$\text{Rate of CO}_2 \text{ evolution} = \frac{\text{moles of CO}_2 \times 44}{\text{period of evolution(hours)}}. \quad (1)$$

Data Availability

The data used to support the findings of this study are included within the article.

Conflicts of Interest

The authors declare no conflict of interest.

Acknowledgments

References

[1] M. Cesari, G. P. Rossi, D. Sticchi, and A. C. Pessina, "Is homocysteine important as risk factor for coronary heart disease?," *Nutrition, Metabolism and Cardiovascular Diseases*, vol. 15, pp. 140–147, 2005.

[2] H. Yamane, S. Tomonaga, R. Suenaga, D. M. Denbow, and M. Furuse, "Intracerebroventricular injection of glutathione and its derivative induces sedative and hypnotic effects under an acute stress in neonatal chicks," *Neuroscience Letters*, vol. 418, no. 1, pp. 87–91, 2007.

[3] W. Guoyao, Y.-Z. Fang, S. Yang, J. R. Lupton, and N. D. Turner, "Glutathione metabolism and its implications for health," *The Journal of Nutrition*, vol. 134, no. 3, pp. 489–492, 2004.

[4] D. J. Weinert, "Nutrition and muscle protein synthesis: a descriptive review," *The Journal of the Canadian Chiropractic Association*, vol. 53, no. 3, pp. 186–193, 2009.

[5] C. Sano, "History of glutamate production," *The American Journal of Clinical Nutrition*, vol. 90, no. 3, pp. 728S–732S, 2009.

[6] M. D'Este, M. Alvarado-Morales, and I. Angelidaki, "Amino acids production focusing on fermentation technologies – a review," *Biotechnology Advances*, vol. 36, no. 1, pp. 14–25, 2018.

[7] M. Ikeda and S. Nakagawa, "The *Corynebacterium glutamicum* genome: features and impacts on biotechnological processes," *Appl MicrobiolBiotechnol*, vol. 62, no. 2-3, pp. 99–109, 2003.

[8] J. Becker, O. Zelder, S. Häfner, H. Schröder, and C. Wittmann, "From zero to hero—design-based systems metabolic engineering of Corynebacterium glutamicum for l-lysine production," *Metabolic Engineering*, vol. 13, no. 2, pp. 159–168, 2011.

[9] R. Aoki, M. Wada, K. T. NobuchikaTakesue, and A. Yokota, "Enhanced glutamic acid production by a H⁺-ATPase-defective mutant of Corynebacterium glutamicum," *Bioscience, Biotechnology, and Biochemistry*, vol. 69, no. 8, pp. 1466–1472, 2005.

[10] J. Becker and C. Wittmann, "Advanced biotechnology: metabolically engineered cells for the bio-based production of chemicals and fuels, materials, and health-care products," *Angewandte Chemie International Edition*, vol. 54, no. 11, pp. 3328–3350, 2015.

[11] E. Sgobba, L. Blöbaum, and V. F. Wendisch, "Production of food and feed additives from non-food-competing feedstocks: valorizing N-acetylmuramic acid for amino acid and carotenoid fermentation with Corynebacterium glutamicum," *Frontiers in Microbiology*, vol. 9, p. 2046, 2018.

[12] Y. Tsuge and H. Matsuzawa, "Recent progress in production of amino acid-derived chemicals using *Corynebacterium glutamicum*," *World Journal of Microbiology and Biotechnology*, vol. 37, no. 3, p. 49, 2021.

[13] T. Hermann, "Industrial production of amino acids by coryneform bacteria," *Journal of Biotechnology*, vol. 104, no. 1-3, pp. 155–172, 2003.

[14] I. Shiio, S. Otsuka, and M. Takahashi, "Effect of biotin on the bacterial formation of glutamic acid," *Journal of Biochemistry*, vol. 51, no. 1, pp. 56–62, 1962.

[15] N. A. Henke, D. Wiebe, F. Pérez-García, P. Peters-Wendisch, and V. F. Wendisch, "Coproduction of cell-bound and secreted value-added compounds: simultaneous production of carotenoids and amino acids by _Corynebacterium glutamicum_," *Bioresource Technology*, vol. 247, pp. 744–752, 2018.

[16] V. F. Wendisch, L. F. Brito, L. M. Gil et al., "The flexible feedstock concept in industrial biotechnology: metabolic engineering of *Escherichia coli*, *Corynebacterium glutamicum*, *Pseudomonas*, *Bacillus* and yeast strains for access to alternative carbon sources," *Journal of Biotechnology*, vol. 234, pp. 139–157, 2016.

[17] S. Kinoshita, S. Udaka, and M. Shimono, "Studies on the amino acid fermentation," *The Journal of General and Applied Microbiology*, vol. 3, no. 3, pp. 193–205, 1957.

[18] Q. Wang, S. Chen, J. Zhang, M. Sun, Z. Liu, and Z. Yu, "Co-producing lipopeptides and poly-γ-glutamic acid by solid-state fermentation of _Bacillus subtilis_ using soybean and sweet potato residues and its biocontrol and fertilizer synergistic effects," *Bioresource Technology*, vol. 99, no. 8, pp. 3318–3323, 2008.

[19] Y. Li, Z. K. Zhao, and F. Bai, "High-density cultivation of oleaginous yeast *Rhodosporidium toruloides* Y4 in fed-batch culture," *Enzyme and Microbial Technology*, vol. 41, no. 3, pp. 312–317, 2007.

[20] F. R. Antoine, C. I. Wei, R. C. Littell, and M. R. Marshall, "HPLC method for analysis of free amino acids in fish using o-phthaldialdehyde precolumn derivatization," *Journal of Agricultural and Food Chemistry*, vol. 47, no. 12, pp. 5100–5107, 1999.

[21] O. H. Lowry, N. J. Rosebrough, A. L. Farr, and R. J. Randall, "Protein measurement with the folin phenol reagent," *Journal of Biological Chemistry*, vol. 193, no. 1, pp. 265–275, 1951.

[22] D. W. Nelson and L. E. Sommers, "Total carbon, organic carbon, and organic matter," *Methods of Soil Analysis Part 3—Chemical Methods*, vol. 5, pp. 961–1010, 1996.

Research Article

Tissue Engineering Properties of Nanomaterials and Their Performance Evaluation for Repairing Athletic Ligament Injuries in Sports Dance

Manlan Niu[1] and Jingming Yan [iD] [2]

[1]*Department of General Education, Anhui Xinhua University, Hefei, 230088 Anhui, China*
[2]*School of Culture and Communication, Anhui Xinhua University, Hefei, 230088 Anhui, China*

Correspondence should be addressed to Jingming Yan; yanjingming@axhu.edu.cn

With the fast growth of nanotechnology, the usage of nuclear materials is becoming increasingly widespread, and the exposure of people, plants, and fauna to nanomaterials has become unavoidable. As scaffolds of biomaterials, nanomaterials are widely used in tissue engineering because of their good biocompatibility, noncytotoxicity, and noninflammatory reaction. In this paper, the tissue engineering properties of nanomaterials and their performance evaluation for repairing sports ligament injuries in dance sports were investigated. Sports ligament injury is a common sports disease, and ligament injury has a very serious impact on sports performance and sports life of athletes. In this paper, we takes football as an example, establishes a human body model of tendon-bone repair after anterior cruciate ligament reconstruction, evaluated the effect of injectable rhBMP-2 nanocontrolled release capsule on ligament bone tunnel interface repair, and evaluated from the scientific and biomechanical point of view. In addition, human ligament research and rabbit ligament supplementary experiment were carried out. In the study of human ligament, we selected 30 patients with unilateral polyarticular ligament injury caused by sports dance as the research subjects and randomly divided them into control group, experimental group, and blank group. The experimental group underwent the repair and reconstruction of rhBMP-2 nanocontrolled release capsule ligament. The results of human ligament study showed that the injectable rhBMP-2 nanocontrolled release capsules showed positive staining and uniform staining for ligament repair. The stiffness of the tender bony temple junction was 11.73%, 15.65%, and 50.59% greater in the test group than in the control group at 2, 4, and 8 weeks postoperatively, respectively.

1. Introduction

Ligaments connect bone to bone and are distinct fibrous tissues that either attach to the skin of the bone or fuse to the external shell of the articular bag to enhance the stabilization of the joint and prevent damage. Injury occurs when a ligament is stretched beyond its tolerance due to violence and nonphysiological activity. A partial injury to the ligament without causing a tendency to dislocate the joint is called a bruise. The ligament itself is completely ruptured, and the bone at its attachment site can also be avulsed, resulting in potential joint dislocation, subluxation, or even complete dislocation. Failure to treat ligament damage can lead to osteoarthritis. Therefore, its surgical repair and functional reconstruction are one of the most important research topics in the field of joint surgery. Although the development of modern surgery makes it possible for humans to replace damaged ligaments, there are still many problems. With the emergence of tissue engineering, a small number of tissue cells are used for in vitro culture and growth, adsorbed by highly biocompatible biological materials, degraded and absorbed in the body, and then inoculated into the body to form new vitality and related functions. Tissues are expected to achieve artificially activated toughness. The biological

characteristics of seed cells, scaffolds, and biologically active factors are the three main themes of tissue engineering.

In the research of tissue engineering ligament, suitable seed cells must be selected. The seed cells must have the ability to form new tissues. These cells can be exogenous, or they can be recruited from the local environment of the transplant recipient. The exogenous cells should be easy to obtain and have little damage to the donor site. The ability of proliferation and differentiation is strong when cultured in vitro, and it can be effectively repaired in the recipient area [1, 2]. At present, it is believed that fibroblasts are a kind of "pluripotent cells," which have different migration rates, adhesion, proliferation, and collagen synthesis capabilities in different tissues, but whether they can effectively repair in the environment of joint fluid is still controversial. Since the autologous patellar tendon graft still undergoes a process of necrosis and strength weakening after transplantation, let alone fibroblasts, therefore, it is not suitable as a seed cell [3, 4]. The purpose of this paper is to evaluate the tissue engineering properties of nanomaterials and their performance in the repair of ligament injury in sports dance sports, in order to make a certain contribution to the repair of ligament injury.

The innovations of this paper are as follows: (1) the tissue engineering properties of nanomaterials and the basic knowledge of repairing sports ligament injuries are introduced. (2) Follow up 30 patients to understand the basic situation, infection situation, and calculate the morbidity rate. In order to improve the research results, a supplementary experiment was also performed on 26 rabbits to verify the performance difference between the reconstructed ligament and the native ligament. (3) Through the local application of nanocontrolled release capsules, BMP-2 can reconstruct the tendon-bone tunnel interface of the anterior cruciate ligament, form a tendon-like structure at the bone anchor point, and reconstruct the intramedullary canal.

2. Related Work and This Paper's Work

With the development of science and technology, materials science and biomedicine are more and more closely integrated, and nanomaterials have made great achievements in biological applications. This paper focuses on the research status of nanomaterials in tissue-engineered ligament research and evaluates the performance of nanomaterials in repairing ligament injury. In order to improve the strength, flexibility, and biomechanical properties of the tested female basketball players, Kahn and Xu prepared a training plan for sports injury prevention and conducted a control experiment. Compared with the anterior and posterior training ligaments in the control group, Kahn' and Xu's damage reduction plan can dramatically alter the mobility, power, and biomechanical characteristics associated with ACL damage and reduce an athlete's exposure to damage. However, in the research process, Kahn and Xu did not consider the difference of individual factors; so, the experimental results are not very reliable [5]. In order to further understand the mechanism of ACL injury, Bertona et al. investigated the occurrence of ACL injury in a large number

of samples over the past 20 years and proved the relationship between the occurrence of ACL injury and dynamic knee alignment at the time of injury. Bertona' et al.'s research has not fundamentally solved the problem, and there is no data to show that the reliability is not high [6]. Malvasi et al. developed an online activity survey, which used a prospective method to record monthly participation in all major exercises related to the patient group. He conducted a reliability study by continuously enrolling 145 patients with ACL injury and retested the online activity survey two days after recording test answers. Malvasi et al.'s research methods are relatively new but lack of interpretable statistical analysis [7]. In order to explore the relationship between ACL-SRI score and strength and strength score after ACLR, Ithurburn et al. recruited 452 male athletes who underwent primary ACLR and conducted ACL-SRI questionnaire, isokinetic muscle strength test, and jumping test about 9 months after operation. In the research of Ithurburn et al., there is no objective view on the relationship between body strength and strength measurement; so, it needs further improvement [8].

3. Nanomaterials and Sports Ligament Injury

3.1. Nanomaterial Application. Nanomaterials include nanobiomaterials, which have the potential to become the core materials of biomaterials in the 21st century, which is due to the large number of fine nanostructures in their bodies. Nanomaterials can be divided into two levels: nano-ultrafine particle materials and nanosolid materials [9]. Nano-ultrafine particles refer to ultrafine particles with a particle size of 1-100 nm, and nanosolids refer to solid materials made of nano-ultrafine particles. And people are accustomed to control the composition or grain structure below 100 nanometers in length dimension called nanomaterials. In addition, nanobiomedical materials solve the urgent needs of high-performance tissue repair, organ replacement, disease diagnosis, and treatment [10, 11]. Nanostructure is a new system constructed or constructed according to certain rules on the basis of nanoscale material units [12]. It includes nanoarray system, mesoporous assembly system, and thin-film mosaic system.

Nanotechnology refers to the arrangement of atoms/molecules on the surface of nanoparticles through specific technical design to produce a special structure. And in the performance of specific technical properties or functions, such nanomaterials can be called nanotechnology [13]. Using nanotechnology to transform traditional tissue engineering materials, nanotissue engineering materials have unique biological characteristics, and the application research in the field of tissue engineering has attracted people's attention [14]. For example, nanoceramics, carbon nanowires, and nanometal materials are used for bone and cartilage tissue engineering; titanium nanomaterials, polylactic acid lactic acid nanomaterials, and nanofiber materials are used for artery tissue engineering; and peptide nanoskeleton and nanofiber are used for scaffold [15, 16]. At the same time, with the continuous advancement of science and technology, especially in the sunrise industry of the electronics industry,

nanotechnology has been greatly developed. It mainly focuses on electronic composite films, using ultrafine particles to improve the electrical, magnetic, and magneto-optical properties of the film, as well as magnetic recording, nanosensitive materials, etc.

3.2. Application of Nanomaterials in the Bone and Cartilage Tissue Engineering.

In nanophase ceramics, nanohydroxyapatite is a natural bone component; so, it can be used as a substitute for bone to achieve bone transplantation. They can promote the formation of mineralization. The composite material composed of hydroxyapatite nanocrystals and collagen is the tissue engineering material closest to the natural bone structure. The nanohydroxyapatite material is mixed with collagen at the ratio of $93:7$, $83:17$, and $81:19$ to form a composite material with a density of $2.8 \, g/cm^3$ [17, 18]. Through high-power electron microscopy, it can be observed that all composite materials and collagen structure are parallel, and their diameter and length are the same, 50-100 nm and $20 \, \mu m$, respectively [19, 20]. In addition, zinc oxide can react with titanium and aluminum, promote the formation of collagen and precipitation of calcification, and finally strengthen the activity of alkaline phosphatase.

Cartilage is composed of cartilage tissue and its surrounding perichondrium, and cartilage tissue is composed of chondrocytes, matrix, and fibers. According to the different fibrous components contained in cartilage tissue, cartilage can be divided into three types: hyaline cartilage, elastic cartilage, and fibrocartilage. Among them, hyaline cartilage has a wider distribution and a more typical structure. By studying the formation and development of human bones, we can discover how the human body regulates and assembles collagen and can also figure out the growth mechanism of calcium phosphate crystals and the human body's healing mechanism. On this basis, following the idea of bionics, a nanocrystalline calcium phosphate collagen bone repair material was invented to simulate the process of biomineralization and self-assembly. The porosity of the material is about 80%, and the void size is mainly distributed between 100 and $400 \, \mu m$ [21]. The hydroxyapatite crystals of the material have a particle size of about 30 nm and grow in the gaps between the collagen fibers. It can be found that they are axisymmetric with the collagen fiber structure, and they have an asynchronous structure before, which is similar to natural bone and nanosynthetic bones. The bone cells obtained through this harvesting technology are very similar to normal human bone cells, and they have excellent ductility and softness, as well as excellent plasticity [22, 23].

3.3. Repair of Sports Ligament Injury.

Ligaments connect bone to bone and are obvious fibrous tissues, either attached to the surface of the bone or fused with the outer layer of the joint capsule to strengthen the stability of the joint to avoid injury. Injury occurs when a ligament is stretched beyond its tolerance due to violence, resulting in nonphysiological activity. In the field of sports medicine, there is the most difficult problem; that is, in the network of relational ligaments, there are multiple ligaments injured, each ligament receives different degrees of damage, and the injury of multiple key ligaments destroys the stability of the knee [24]. When there is a nonphysiological movement in a certain direction, the ligaments that limit the movement of the knee joint to this direction must bear the brunt. The medial capsular ligament and medial collateral ligament are mainly damaged when the knee joint is externally rotated and abducted in the flexion position and is subjected to external violence. Severe cases can involve the anterior cruciate ligament and medial meniscus, which are the most common types of injury. Patients with multiple ligament injuries are very likely to suffer from medial and lateral meniscus injuries. Among them, the largest injury probability is the displacement of lateral and intra-articular ligaments, which will lead to dislocation and fracture of the joint. After ligament injury, there are usually small blood vessels rupture and hemorrhage, local pain, swelling, intraorganism hemorrhage, hematoma, joint swelling, movement disorder, and tenderness. On physical examination, the traction ligaments were found to be significantly painful, and if completely ruptured, the stability of the joint was reduced. Therefore, our goal in the future is to repair and reconstruct the ligament, which can fully help the establishment of bone and joint.

The knee joint is very unstable and usually has important nerve tissue (such as common peroneal nerve) and important blood vessels. One of the biggest difficulties is that it involves a variety of orthopedic disciplines, and a single doctor cannot effectively deal with orthopedic injuries in various disciplines, resulting in patients cannot achieve effective and timely treatment, which seriously hinders the athletes' sports career and subsequent normal life. At present, with the improvement of living standards, more and more young people like highly confrontational sports, such as football and basketball, which also increases the risk of joint ligament injury.

For the ligament damage that has occurred, if you do not intervene in time, it may lead to serious consequences. For example, it will cause knee instability. Secondly, it may accelerate the degradation of the patient's knee cartilage and eventually lead to the early appearance of osteoarthritis symptoms and will affect the quality of life of patients. Ligament injury should be treated early and fully repaired. If it is not treated in time, the joint will be repeatedly sprained, which will inevitably cause damage to articular cartilage, meniscus, and other important structures, resulting in premature aging of the joint and severe secondary traumatic arthritis. The key to its treatment lies in the repair of damaged ligaments. Partial tears can be directly sutured and repaired, while complete ruptures require surgery to transfer and reconstruct adjacent tendons, fascia, and other tissues. With the latest development of arthroscopic technology and the improvement of tissue library, arthroscopy is usually the next step in the reconstruction and repair of multiple knee ligament injuries. Excellent results have been achieved, and there is also a report of bilateral knee joint multiligament injury. One year after ligament reconstruction, the patient can return to leisure sports, but at the same time, there are still many issues that have not yet reached a consensus.

Due to the complex anatomical structure of the knee joint, it is usually difficult to reconstruct and repair multiple

ligament injuries, and these ligaments also have strict requirements for the repair sequence. If the reconstruction sequence is not correct, the repair effect is great, which meets the requirements, but the reliability and plasticity of transplantation can be ensured after the correct sequence and steps. In order to meet the requirements of reconstruction procedures, surgeons provide a series of suggestions: first, repair KD-I ligament injury and rupture and tendon reconstruction and repair, then KD-II: ACL + PCL injury, then KD-III type: ACL + PCL + MCL or (PMC/PLC) damage, and finally, repair type KD-IV ACL + PCL + MCL + (PLC)/ LCL) is damaged.

The ideal knee reconstruction implant should have the advantages of high toughness, high strength, convenient operation and microfixation, easy access to materials, and minimal postoperative complications. In the existing materials, there is still a lack of materials to meet these requirements, which can only be met by allogeneic transplantation and tendon transfer. Autogenous tendon transplantation is transplanted through the existing tendon and ligament in the body, usually taking PA bone or rope tendon two parts. Allogeneic transplantation is to rely on the implantation of artificial ligaments to meet the requirements. For multiple ligament injuries of the joint, it is generally necessary to reconstruct and repair multiple ligaments; so, it is not possible to use self-transplantation, but only rely on the means of allogeneic transplantation.

4. Experimental Materials and Methods

4.1. Experimental Materials and Experimental Methods and Equipment-Related Drugs.
In this experimental equipment, we used the following: antibacterial micro Qiao suture, electric drill, automatic dehydrator, basic surgical instruments, denture base tree, penicillin, pentobarbital sodium powder, and finally, denture base polymer and normal saline for injection.

4.2. Collection and Production of Patient Experimental Specimens.
A total of 30 patients with unilateral knee multi-ligament injury caused by sports dance were included in this study, including 6 cases of ACL, PCL, and MCL injury, 4 cases of ACL, PCL, and PLC injury, 8 cases of ACL and PCL injury, 6 cases of ACL and MCL injury, and 6 cases of PCL and MCL injury. These patients were all of grade III injury. There were 12 cases of left knee injury, 18 cases of right knee injury, 20 cases of male, and 10 cases of female. The average age of patients was 35.35 ± 2.31 years (18-55 years). There were 17 cases of traffic accident injury, 4 cases of falling injury, and 9 cases of acute sports injury. The main clinical manifestations were severe pain, swelling, and instability of knee joint. The time from injury to operation was 7.0-14.0 days, with an average of 10.12 ± 1.35 days.

This experiment is divided into three groups: the experimental group, the control group, and the blank group. The experimental group uses rhBMP-2 nanocontrolled release capsules to repair and reconstruct the ligaments, and the control group uses the current mainstream biological equipment to repair and reconstruct the ligaments. Repair and
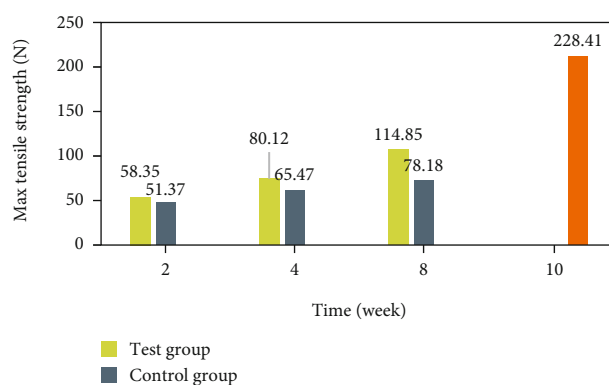
FIGURE 1: Maximum tensile strength histogram.

reconstruction were performed, and the ligament in the blank group was not damaged.

4.3. Collection and Production of Animal Experimental Specimens.
In this study, we also selected 24 adult rabbits with knee joint disease and 2 adult rabbits without joint disease to conduct supplementary experiment. These rabbits all met the requirements of cleanliness level, weighing 3.29 ± 0.26 kg, which could adapt to reproduction and environment. One week before the experiment, they were put into a new feeding environment for normal feeding activities. After that, the animals were treated according to the "guidelines for the treatment of experimental animals." Methods were as follows: 24 rabbits (48 knees in total) were operated on with the common specimen of bilateral knee tendon bone tunnel interface, and the experimental animals were divided into groups.

The experimental group used rhBMP-2 nanocontrolled release capsule to repair and reconstruct the ligament, the control group used the mainstream biological equipment to repair and reconstruct the ligament, and the blank group was that the ligament was not damaged.

According to the normal management, it was stored in the refrigerator at -80°C. The normal fixation, demineralization, slicing, and dyeing preparations were used as the normal indexes of the control. At the second, fourth, and eighth postoperative weeks, experimental animals in the test and control groups were executed under overanesthesia, and the knee joints were similarly extracted.

Before the test, thaw at room temperature and immerse the sample in saline, the resin is hardened to remove the bone, and the tendon thread is used as the braided part of the tendon. The sample is fixed on the Instron 8874 mechanical tester. First, the pretreatment is completed; that is, a tensile force of 5 N is applied to the test piece for 30 seconds, and then a tensile test is performed until the ligament yields and breaks. Set the traction speed to 3 mm/min, calculate the stiffness, and record the displacement distance and load strength. The stiffness value of the tendon-tunnel channel interface refers to the ability of the tendon-tunnel channel interface of the knee joint to resist elastic deformation under force, and its elastic deformation the degree is this value. Generally, the slope of the linear section is calculated from the linear section of the load-displacement curve.
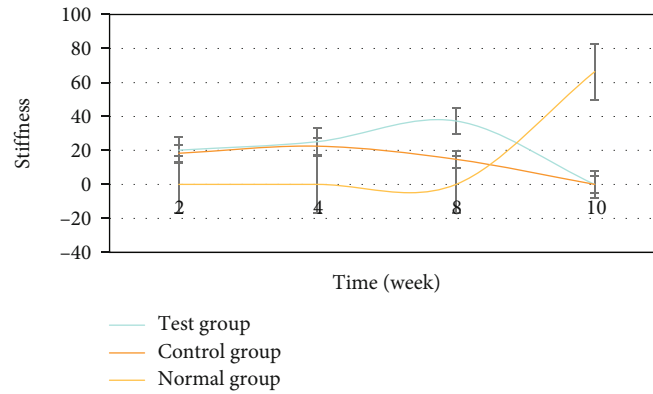
FIGURE 2: Stiffness histogram.

TABLE 1: Yamakado split type ($n = 8$, n).

Time		Tendon bone separation	Loose connective tissue link	Sharpey structure link	Direct link
	4 W	2	6	0	0
Test group	8 W	0	7	1	0
	16 W	0	1	7	0
	4 W	4	4	0	0
Control group	8 W	1	7	0	0
	16 W	0	2	6	0
	4 W	1	7	0	0
Blank group	8 W	0	4	4	0
	16 W	0	2	6	0

Tensile strength (N) is as follows: in a biomechanical tensile test, the maximum tensile strength at the tendon-bone tunnel interface of the knee joint sample can be a bearable value.

4.4. Experimental Analysis Method. Use IBM SPSS23.0 statistical software for statistical analysis. If the continuous variable presents a normal distribution, use the paired sample X^2 test.

$$X^2 = \sum \left(\frac{2(f0 - fc)}{fc} \right). \tag{1}$$

Among them, sending f_0 represents the actual number of times obtained, and f_c represents the theoretical number of times determined by the hypothesis.

If it does not conform to the normal distribution, please use the nonparametric test, the result is expressed as the median (interquartile range), and the difference is statistically significant, $P < 0.05$. Categorical variables are expressed in frequency (percentage) and tested using Fisher's exact probability method.

$$P = \frac{O_{1\bullet}!O_{2\bullet}!O_{\bullet 1}!O_{\bullet 2}!}{O_{11}!O_{12}!O_{21}!O_{22}!}, (N! = 1 \times 2 \times \cdots \times N). \tag{2}$$

The result shows that the variable matches the normal distribution, $P > 0.05$. Box plots are used to find outliers,
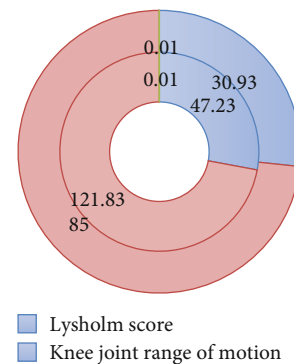
FIGURE 3: Lysholm score and range of motion of the knee joint before and after the last follow-up.

the categorical variable is Fisher's test, and $P < 0.05$ is considered statistically significant.

5. Experimental Results and Analysis

5.1. The Test Results of rhBMP-2 Nanocontrolled Release Capsule for Repairing Ligaments. The maximum tensile strength of tendon and bone tunnel interface in each group was as shown in Figure 1. The experimental group was repaired by rhBMP-2 nanocontrolled release capsule, the

TABLE 2: The results of the stability examination of the knee joint before and after the last follow-up.

Stability examination	Preoperative physical examination		Physical examination at the last follow-up		
	III degree positive	Negative	I degree positive	II degree positive	Negative
Front drawer test case (%)	24	0	3	3	18
Back drawer test case (%)	24	0	3	1	20
Lachman test case (%)	24	0	3	3	18
Flexion 30° eversion stress test example (%)	18	0	1	2	15
Flexion 30° varus stress test example (%)	4	0	1	0	3

control group was repaired according to the current main-stream surgical method, and the blank group was normal ligament without disease. The results showed that there was a significant difference between the experimental group and the control group at three time points after operation ($P < 0.005$).

As shown in Figure 1, the maximum tensile strength of the rhBMP-2 nanocontrolled release capsule for ligament repair is higher than that of the control group. Two weeks after the operation, there was no significant difference in the maximum tensile strength of the tendon-bone tunnel interface between the experimental group and the control group ($P > 0.005$). Eight weeks after surgery, there were significant differences in the maximum tensile strength of the tendon-bone tunnel interface among the three groups ($F = 219.32$, $P < 0.005$). The results show that the experimental group is better than the control group in terms of tensile strength, each group has been greatly improved, and the test values are very different.

The results of the postoperative study on the tendon tunnel interface stiffness are shown in Figure 2.

5.2. Composite Ligament Reconstruction ACL. According to Yamakado classification, the morphology was divided into tendon bone separation, loose connective tissue connection, Sharpey fiber structure connection, and direct connection. According to the Yamakado classification method, the morphological and histological observation was carried out at 4 W, 8 W, and 16 W. The results are shown in Table 1.

As can be seen from Table 1, in the use of rhBMP-2 nanocontrolled release capsules to reconstruct the joint ligaments (experimental group), after incising the skin, the implant was completely covered by the synovium, with bright luster, compact structure, superficial capillary growth, and joints light yellow glaze in the cavity. The interface between the ligament and the bone is wrapped in the new bone and becomes unified, and when the compression nail is removed, the ligament and the bone are firmly connected. In the current best-performing joint ligament reconstruction (control group), the surface of the implant is completely covered by synovium, the structure is compact, there are no blood vessels, and there are soft tissues around it. After removing the pin, the implant can be pulled out forcefully. In the unaffected normal joint ligaments (blank group), the surface is as smooth as normal tendons, and the ends are tightly connected to the bone tunnel.

All patients were followed up for 12-24 months (average 15.60 ± 2.65 months). All patients recovered well after operation. No knee instability and stiffness occurred. The postoperative follow-up results are shown in Figure 3.

It can be seen from Figure 3 that the active range of motion of the knee joint of 30 patients recovered significantly compared with that before the operation. At the last follow-up, the range of active motion of the knee joint increased to 121.83. Compared with 47.23 before operation, the difference was statistically significant ($P < 0.05$).

At the last follow-up, the positive rate of knee joint stability physical examination decreased significantly, and the difference was statistically significant ($P < 0.05$). The negative rate of anterior drawer test was 75%, and the positive rate was 25%. The positive rate of knee joint stability physical examination was shown in Table 2.

It can be seen from Table 2 that there are 3 cases of degree I positive and degree II positive; the negative rate of the back drawer test is 83.3%, and the positive rate is 16.7%, of which 3 cases are positive for degree I and 1 case is positive for degree II; the negative rate of Lachman test is 75%. The positive rate was 25%, of which 3 cases were positive for degree I and positive for degree II; 15 cases had no relaxation in the 30° flexion stress test, 2 cases of degree I relaxation, and 1 case of degree II relaxation, while the 30° buckling stress test was 0 cases. There were 3 cases of relaxation and 1 case of degree I relaxation. At the last follow-up, the Lysholm score of the knee joint reached 85.00 points, which was statistically different from 30.93 points before surgery ($P < 0.05$). IKDC rating at the last follow-up was as follows: 20 cases were normal (grade A), 8 cases were close to normal (grade B), and 2 cases were abnormal (grade C). The X-ray film and CT in the outpatient department after operation showed that the internal fixation and the bone canal were in good position, and the bone canal was not enlarged.

5.3. ACL Reconstruction in Animal Ligaments. Randomly select 3 groups (4 W, 8 W, 16 W) and divide them into the experimental group treated with rhBMP-2 nanocontrolled release capsules, the control group using the current mainstream surgery, and the normal diseased blank group, each with 4 mice The rabbit undergoes a CT examination. X-ray cross-sectional imaging of the rabbit femoral tunnel passes through the vertical axis. Each rabbit randomly selected 10 images and measured the CT value of the 1 mm² interface
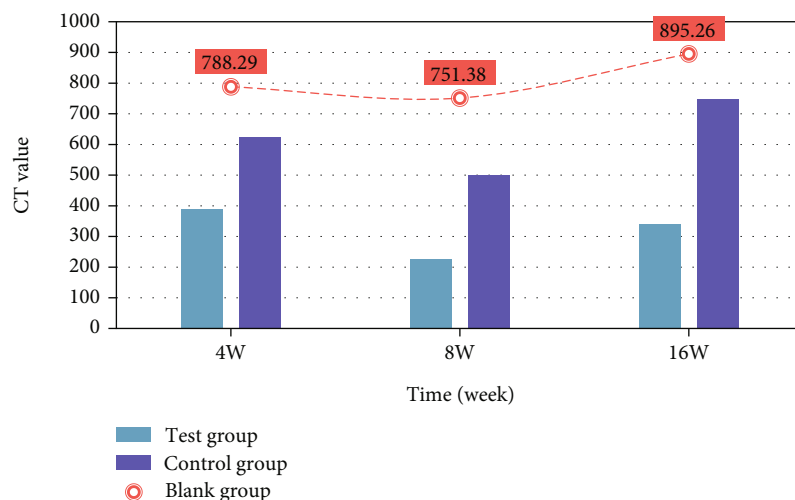
FIGURE 4: Detect CT value in different time periods.

between the screw and the bone. Measure the CT value of the $1\,mm^2$ area between the screw and the bone interface, use x and S to represent all the CT values measured in each group, and analyze the connection structure between the ligaments and the time of the bone in the day; after modification, the relative position of screw channel is shown in Figure 4.

It can be seen from Figure 4 that, similar to normal ACL, after the cruciate ligament is reconstructed, the nutrition needed by the implant is mainly provided by blood in the superficial synovial membrane, except for a small amount of synovial fluid in the joint cavity. Theoretically, this not only preserves the ligament stump and promotes the fusion of soft tissues and grafts but also an adequate blood supply also increases the nutrient supply of the graft, thereby allowing new synovial vascularization on the surface of the graft. Indicating that the reconstruction can be preserved, the survival rate of the ligament should be significantly higher than the unreserved stump group.

At the same time, the application of nanomaterials in tissue engineering is still in the early stage. Especially in biomedicine, most of the research is still in the stage of animal experiments, a large number of clinical trials are needed to confirm, and the biosafety of nanomaterials needs to be further improved. There are still many problems to be solved for clinical application: how to construct an ideal cell-nanomaterial interface, how to protect allogeneic biological tissues and cells cultured on nanoscaffold materials from being recognized and rejected by the recipient immune system, how to maintain the viability of cultured cells and maintain their function for a long time, and how to further improve the biocompatibility of nanomaterials.

6. Conclusions

The ligament is a bridge that maintains the close connection between bones. It is rich in elasticity and rich in collagen tissue. However, after the ligament is injured, it cannot be cured, and it is difficult to reach a healthy level. This also causes the joints to become extremely unhealthy: stable, but from causing serious damage to the relationship, the most causing deterioration and pain, the most typical cases of which are arthritis and meniscus injury. It is precisely because of this that we must reconstruct it, these reconstruction methods are mainly carried out through surgery, and most of them are through and means.

The experimental design of the ligament reconstruction model and the nanocontrolled release capsule manufacturing model is effective for basic research related to BMP-2 repairing the tendon-bone tunnel interface and can be used as a reference for experimental research models. In the early stage after injury and anterior cruciate ligament reconstruction, BMP-2 promotes the formation of a similar direct stagnant structure at the tendon-bone tunnel interface. Experiments show that rhBMP-2 can effectively promote and enhance the repair of the tendon and bone tunnel interface.

In this study, when the anterior cruciate ligament was reconstructed after knee injury, the injectable BMP-2 controlled release capsule was chosen when reconstructing the tendon-bone tunnel interface. The results showed that BMP-2 was performed after the reconstruction of the anterior cruciate ligament of the knee joint. After the reconstruction of the anterior cruciate ligament, the tendon tunnel interface helps to form a direct stop point, thereby improving the maximum tensile strength and stiffness of the tendon tunnel interface. This leads to improved pathophysiological properties and mechanical strength of the reconstructed ligament structure. In the next few years, nanoceramics in biomaterials will play a leading role in artificial bones, and inorganic and organic composite nanomaterials with various properties will also play a great role in interventional repair of ligament injuries. We will also conduct further in-depth research on this.

Data Availability

No data were used to support this study.

Conflicts of Interest

The authors declare that there are no conflicts of interest regarding the publication of this article.

Acknowledgments

References

[1] R. J. Bai, H. B. Zhang, H. L. Zhan et al., "Sports injury-related fingers and thumb deformity due to tendon or ligament rupture," *Chinese Medical Journal*, vol. 131, no. 9, pp. 1051–1058, 2018.

[2] I. Gans, J. S. Retzky, L. C. Jones, and M. J. Tanaka, "Epidemiology of recurrent anterior cruciate ligament injuries in National Collegiate Athletic Association Sports: the injury surveillance program, 2004-2014," *Orthopaedic Journal of Sports Medicine*, vol. 6, no. 6, p. 232596711877782, 2018.

[3] H. Qi and Y. Feng, "Analysis of clinical value of weight-bearing magnetic resonance diagnosis of ankle ligament sports injury," *IEEE Access*, vol. 8, pp. 62725–62737, 2020.

[4] J. Zaremski, J. McClelland, H. Vincent et al., "Sports-related elbow ulnar collateral ligament injury in the 21st century," *British Journal of Sports Medicine*, vol. 51, no. 4, pp. 412.1–41412, 2017.

[5] S. B. Kahn and R. Y. Xu, "Musculoskeletal sports and spine disorders," *Ulnar Collateral Ligament Injury*, vol. 30, pp. 139–143, 2017.

[6] A. Bertona, J. P. Zicaro, J. M. G. Viescas, N. Atala, C. Yacuzzi, and M. Costa-Paz, "Return to sports after acute simultaneous reconstruction of anterior cruciate ligament injury and grade III medial collateral ligament injury," *Orthopaedic Journal of Sports Medicine*, vol. 5, 1_suppl, p. 2325967117S0003, 2017.

[7] S. Malvasi, B. Gloyeske, M. Johnson, and T. Miller, "Multi-ligamentous knee injury in sports involving concomitant anterior cruciate ligament and patellar tendon disruption: a review of case reports," *International Journal of Athletic Therapy & Training*, vol. 21, no. 3, pp. 24–27, 2016.

[8] M. P. Ithurburn, M. V. Paterno, S. Thomas, T. E. Hewett, and L. C. Schmitt, "Knee function, strength, and maintenance of pre-injury sports participation after anterior cruciate ligament Reconstruction," *Medicine & Science in Sports & Exercise*, vol. 48, 5S Suppl 1, p. 445, 2016.

[9] X. Xu, D. Shahsavari, and B. Karami, "On the forced mechanics of doubly-curved nanoshell," *International Journal of Engineering Science*, vol. 168, p. 103538, 2021.

[10] A. Blasimann, I. Koenig, I. Baert, H. Baur, and D. Vissers, "218 Assessments for neuromuscular control after an anterior cruciate ligament injury to decide upon return to sports," *British Journal of Sports Medicine*, vol. 54, Suppl 1, p. A91, 2020.

[11] S. N. Parikh, "The Pediatric Anterior Cruciate Ligament || Pediatric and Adolescent ACL Injury and Sports Medicine," *The Early Years*, vol. 1, pp. 1–6, 2018.

[12] P. Wang, S. Wang, X. Zhang et al., "Rational construction of CoO/CoF2 coating on burnt-pot inspired 2D CNs as the battery-like electrode for supercapacitors," *Journal of Alloys and Compounds*, vol. 153374, 2019.

[13] B. Gao, N. Xu, and P. Xing, "Shock wave induced nanocrystallization during the high current pulsed electron beam process and its effect on mechanical properties," *Materials Letters*, vol. 237, no. 15, pp. 180–184, 2019.

[14] X. Cao, M. Liu, M. Zhao et al., "Synergetic PtNP@Co3O4 hollow nanopolyhedrals as peroxidase-like nanozymes for the dual-channel homogeneous biosensing of prostate-specific antigen," *Analytical and Bioanalytical Chemistry*, vol. 414, no. 5, pp. 1921–1932, 2022.

[15] A. Slagers and J. Zwerver, "222 Responsiveness of the anterior cruciate ligament – return to sports after injury (ACL-RSI) and injury – psychological readiness to return to sport (I-PRRS) scales," *British Journal of Sports Medicine*, vol. 54, Suppl 1, p. A22, 2020.

[16] D. C. Astur, M. Xerez, J. Rozas, P. V. Debieux, C. E. Franciozi, and M. Cohen, "Anterior cruciate ligament and meniscal injuries in sports: incidence, time of practice until injury, and limitations caused after trauma," *Revista Brasilra De Ortopedia*, vol. 51, no. 6, pp. 652–656, 2016.

[17] G. Harput, D. Tok, B. Ulusoy et al., "Translation and cross-cultural adaptation of the anterior cruciate ligament-return to sport after injury (ACL-RSI) scale into Turkish," *Knee Surgery, Sports Traumatology, Arthroscopy*, vol. 25, no. 1, pp. 159–164, 2017.

[18] M. Ahrend, A. Ateschrang, S. Döbele et al., "Rückkehr in den Sport nach operativer Versorgung einer hinteren Kreuzbandverletzung," *Orthopade*, vol. 45, no. 12, pp. 1027–1038, 2016.

[19] K. E. Webster and T. E. Hewett, "Is there value and validity for the use of return to sport test batteries after anterior cruciate ligament injury and reconstruction?," *Arthroscopy: The Journal of Arthroscopic & Related Surgery*, vol. 36, no. 6, pp. 1500-1501, 2020.

[20] K. E. Webster and J. A. Feller, "Clinical tests can be used to screen for second anterior cruciate ligament injury in younger patients who return to sport," *The Orthopaedic Journal of Sports Medicine*, vol. 7, no. 8, p. 232596711986300, 2019.

[21] J. K. Ha, J. G. Kim, K. H. Yoon et al., "Korean version of the anterior cruciate ligament-return to sport after injury scale: translation and cross-cultural adaptation," *Clinics in Orthopedic Surgery*, vol. 11, no. 2, pp. 164–169, 2019.

[22] S. Keays, P. Newcombe, and A. Keays, "Return to sport after anterior cruciate ligament (ACL) Injury: surgery versus no surgery. A long-term follow-up study," *Journal of ence and Medicine in Sport*, vol. 22, no. 2, p. S59, 2019.

[23] S. D. Peters, G. S. Bullock, A. P. Goode, G. E. Garrigues, D. S. Ruch, and M. P. Reiman, "The success of return to sport after ulnar collateral ligament injury in baseball: a systematic review and meta-analysis," *Journal of Shoulder and Elbow Surgery*, vol. 27, no. 3, pp. 561–571, 2018.

[24] S. Salatkait, L. Iupinskas, and R. Gudas, "Translation and cultural adaptation of Lithuanian version of the anterior cruciate ligament return to sport after injury (ACL-RSI) scale," *PLoS One*, vol. 14, no. 7, p. e0219593, 2019.

Retraction

Retracted: Application Value Analysis of Nanooptical Materials in Martial Art Single-Kick Protective Equipment

Journal of Nanomaterials

This article has been retracted by Hindawi following an investigation undertaken by the publisher [1]. This investigation has uncovered evidence of one or more of the following indicators of systematic manipulation of the publication process:

(1) Discrepancies in scope

(2) Discrepancies in the description of the research reported

(3) Discrepancies between the availability of data and the research described

(4) Inappropriate citations

(5) Incoherent, meaningless and/or irrelevant content included in the article

(6) Peer-review manipulation

The presence of these indicators undermines our confidence in the integrity of the article's content and we cannot, therefore, vouch for its reliability. Please note that this notice is intended solely to alert readers that the content of this article is unreliable. We have not investigated whether authors were aware of or involved in the systematic manipulation of the publication process.

In addition, our investigation has also shown that one or more of the following human-subject reporting requirements has not been met in this article: ethical approval by an Institutional Review Board (IRB) committee or equivalent, patient/ participant consent to participate, and/or agreement to publish patient/ participant details (where relevant).

Wiley and Hindawi regrets that the usual quality checks did not identify these issues before publication and have since put additional measures in place to safeguard research integrity.

We wish to credit our own Research Integrity and Research Publishing teams and anonymous and named external researchers and research integrity experts for contributing to this investigation.

The corresponding author, as the representative of all authors, has been given the opportunity to register their agreement or disagreement to this retraction. We have kept a record of any response received.

References

[1] S. Yu, "Application Value Analysis of Nanooptical Materials in Martial Art Single-Kick Protective Equipment," *Journal of Nanomaterials*, vol. 2022, Article ID 2714874, 8 pages, 2022.

Hindawi

Research Article

Application Value Analysis of Nanooptical Materials in Martial Art Single-Kick Protective Equipment

Shengwei Yu [ID]

Physical Education College of Zhengzhou University, Zhengzhou, 450000 Henan, China

Correspondence should be addressed to Shengwei Yu; yushengwei@peczzu.edu.cn

If there is no protective equipment in martial art single practice, it is very easy to be injured, so protective equipment in martial arts has been paid more and more attention. The protective effect of Wushu Sanda protective gear is related to the safety of every Wushu Sanda practitioner. The purpose of this paper is to study crystalline nanooptical materials and Wushu Sanda protective gear and propose the idea of using more crystalline nanooptical materials in the manufacture and use of Wushu Sanda protective gear. This paper mainly introduces the related content of crystalline nanooptical materials, martial art single-leg kick, and martial art single-leg protective gear and conducts experiments on crystalline nanooptical materials and martial art single-leg protective gear based on crystalline nanooptical materials. The experimental results show that the protective effect of protective equipment based on crystalline nanooptical materials can play a greater role than traditional protective equipment. In the experiments in this paper, the martial art single-leg kicking protective gear based on crystalline nanooptical materials has at least a 10% improvement in protective effect.

1. Introduction

With the improvement of people's living standards, more and more people who are interested in study and work will take time to participate in some activities, such as Wushu Sanda when they are in Wushu singles. However, there are often some factors that affect their own safety. Therefore, Wushu single protective equipment plays a pivotal role in the safety of martial art singles. Therefore, Wushu single-kick protective equipment plays an important role in protecting the safety of Wushu single kick. Due to its special microstructure, nanocrystalline materials have a series of excellent mechanical properties such as higher yield strength, hardness, and good wear resistance that conventional coarse-grained materials do not have and have attracted extensive attention from sports people.

In recent years, the safety of martial art single kick has become the focus of society and schools. How to effectively prevent and properly handle the safety accident of single kicking in martial arts is an important problem that all sectors of society need to think about and solve. The development of a reasonable use of martial art equipment is one of the ways to reduce safety accidents in martial arts. When practicing martial art movements, wearing martial art equipment reasonably can reduce self-injury caused by uncontrolled movements during practice.

With the development of society, nanocrystalline materials have attracted more and more attention. In one study, Shaat and Abdelkefi investigated the modeling and performance of mechanical resonators for biological cell mass detection, nanocrystalline material characterization, and human immunoviral disease diagnosis [1]. In their research, Ovid'ko and Sheinerman described the effect of free surfaces on grain boundary dislocation-mediated rotational deformation in nanocrystalline materials [2]. Likewise, other researchers have conducted extensive experimental studies on nanomaterials. Fang et al. experiments show that stress-driven grain growth will strongly affect the motion and distribution of dislocations in nanocrystalline materials. At the same time, their research also shows that nanotwins often originate from the generation and slip of partial dislocations, which are also affected by grain growth [3]. Tserpes et al. use finite element models to test and simulate tungsten-copper alloys with coarse and nanocrystalline microstructures. The effect of the sharpness of the

Berkovich indenter was also investigated. Experimental results show the superiority of nanocrystalline materials, with better convergence for the rounded tip of the indenter [4]. In terms of sports safety research, Hong et al. expand safe and healthy life sports activities in Korea by carrying out education, management, and best practices related to life sports safety in Germany and establish an accident prevention system in Korea [5]. At the same time, in order to examine the consistency of sports safety with school administration quality standards and teacher compliance practices, Jani et al. conducted an experiment using a questionnaire. The experimental results show that all schools have good quality standards for sports safety administration. There is a very close and important relationship between the quality standards of administration and the compliance of teachers' sports safety practices [6]. In the research of sports safety protective equipment, Park and Ko developed safety clothing, which is a must for young people to protect their bodies from accidental injuries and pursue activities and individuality [7]. These methods provide some references for our research, which have not been recognized by the public due to the short time and large scope of the relevant research. These researchers have outstanding performance in their respective research fields, but their research scope is often very large, which is not conducive to further in-depth experimental research.

The innovation of this paper lies in the research on crystalline nanooptical materials. Through the understanding of the properties of nanomaterials, especially the research on crystalline nanooptical materials, after fully understanding their unique mechanical properties, they are applied to the manufacture and use of martial art single-kick protective equipment. Through the use of crystalline nanooptical materials, not only can the role of nanomaterials be fully utilized but also the safety and reliability of martial art single-kick protective equipment can be improved. Nanomaterials and nanotechnology have provided new ideas and approaches for the research of modern equipment protection technology and laid the foundation for the breakthrough improvement of its performance.

2. Crystalline Nanooptical Materials and Motion

2.1. Crystalline Nanooptical Materials. Crystalline materials with a particle size of 1 to 250 nm are called nanocrystalline materials. Nanopowders can be used in thick-film technology to fabricate elongated conductive tunnels. The porous nanomaterial sintered body has strong activity and is suitable for catalysts and high-power capacitors. If the particle size of nanocrystalline material becomes smaller, its volume fraction will increase [8]. Generally speaking, the internal structure of nanocrystals consists of two different types of atoms. Atoms in a crystal are arranged in adjacent lattices, and there are different atomic spacings between grain boundary atoms. The proportion of atoms in the interface of nanocrystalline material is related to the tightness of the interface of nanocrystalline material. The following is a brief discussion on the related content of nanocrystalline materials [9].

2.1.1. Mechanical Properties of Nanocrystalline Materials

(1) Yield Strength. Yield strength is the stress that resists slight plastic deformation under external load, that is, the yield limit of metallic materials [10]. When the stress reaches a certain value and enters the yield stage, the deformation increases rapidly. At this stage, elastic deformation and local plastic deformation occur simultaneously. With increasing stress, the plastic strain changes greatly, but the stress and strain hardly change. This phenomenon is called yielding [11]. The maximum stress at this stage is called the upper yield point, and the minimum stress is called the lower yield point. Here, a relatively stable low yield point value is used as an indicator of material resistance, namely, yield strength or yield point [12]. The grain size has a great influence on the yield strength of the material. The most important factor affecting the yield strength is the size of the crystal force. Taking tensile strength as an example, under the same strain condition, for a sample with a small grain size, the smaller the uniformly distributed strain inside the grain, the smaller the dislocation density. Therefore, the yield strength is greater. The relationship between yield stress and grain size is based on the relationship between traditional coarse-grained materials, and its correlation formula conforms to the Hall-Petch relationship:

$$\partial_i = \partial_o + md^{1/2}. \tag{1}$$

(2) Scalability. Ductility refers to the property of a material stretching without breaking under an external load, and ductility refers to the property of a material rolling into a thin sheet without breaking under an external load. It is a mechanical property of a substance that expresses the ability of a material to deform plastically before fracture under force [13]. Under the action of shock and vibration loads, the material of the structure is required to be able to absorb a large amount of energy, and at the same time, it can produce a certain deformation without damage; that is, the structure or component is required to have good ductility. In conventional crystalline materials, the grain size decreases and the ductility of the material increases. The ductility of nanocrystalline materials is also affected by these deformation mechanisms. Zhang changed the grain size of the nanocrystalline material Zn by changing the processing times. The researchers found that the nanocrystalline material Zn can exhibit good strength and ductility at the same time after a period of treatment [14]. The processed material contains 30% larger grains. This optimal microstructure exhibits more strain hardening than other machined materials studied. It can be said that reasonable grain size distribution and strain hardening help to improve the ductility of the material [15].

(3) Anti-Hall-Petch Relationship. The general law of the Petch relationship is that the grain size decreases and the yield stress of the material increases. Figure 1 shows the HP relationship of the nanocrystalline material Cu.

From Figure 1, we can clearly find that as the particle size decreases below 25 nm, the HP relationship of
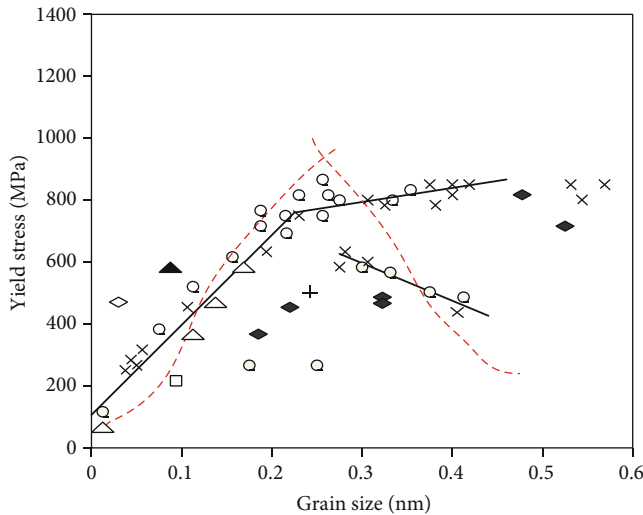
FIGURE 1: Variation of yield stress of Cu material with grain size from coarse to nanocrystalline.

nanocrystalline materials is not visible. The slope of the HP relationship for nanocrystalline materials decreases with decreasing grain size [16].

2.1.2. Fatigue Damage of Nanocrystalline Materials. Crack growth can be divided into two forms: unstable growth and subcritical crack growth. Unstable growth is a rapid crack growth process. An important condition for its occurrence is that the stress expansion coefficient of the crack tip inside the material reaches or exceeds the fracture toughness of the material [17]. Subcritical crack growth is a slow-growing process where microcracks develop inside the material before reaching critically fast and unstable growth conditions. For traditional fatigue testing, we get a very classic *SN* curve, the fracture curve between the cycles of the metal being fractured and the cyclic stress or alternating stress, where *S* and *N* represent the magnitude of the cyclic stress and fracture, respectively; pressure, respectively; and hours of the week [18]. The *SN* curve of the material can be divided into three parts: static strength stage, low cycle fatigue stage, and high cycle fatigue stage. Figure 2 shows the fatigue curve of the material.

The place where fatigue cracks are most likely to initiate is the place where it is most likely to slip, and the place that is most likely to slip is also the place where the local plastic deformation is the largest. Fatigue crack initiation, propagation, and fatigue strength are all affected by slip [19]. Grain refinement increases the barrier of grain boundaries, thereby slowing the initiation and propagation of fatigue cracks. The crack growth rate is a method for predicting crack growth rate and crack growth life of a mechanical structure, which belongs to the calculation method of the fatigue crack growth rate and crack growth length of mechanical structure. The main expression for the crack growth rate is

$$\frac{Da}{DW} = c(\Delta n)^t. \tag{2}$$
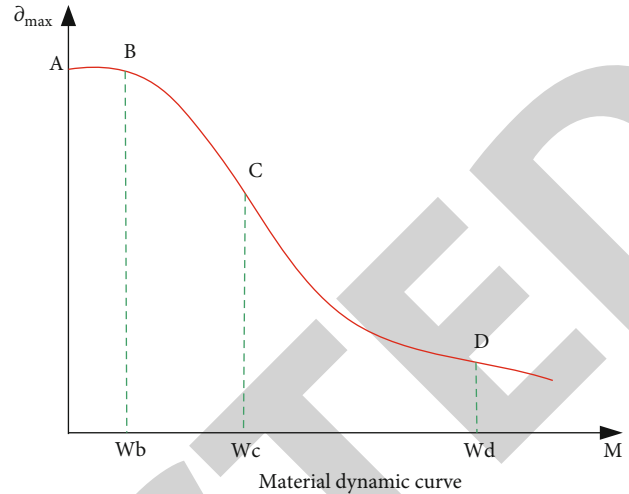
FIGURE 2: Fatigue curve of material.
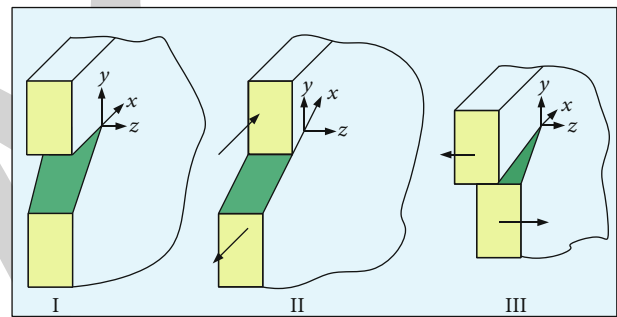
FIGURE 3: Three different forms of cracks.

With regard to cracks, cracks are mainly classified into Type I cracks, Type II cracks, and Type III cracks. As shown in Figure 3, there are three different forms of cracks.

(1) Mechanical Model. For the establishment of the mechanical model, the first consideration is the critical condition of crack initiation at the twin boundary. Numerous studies have found that cracks in nanotwinned materials usually originate from three places: grain boundaries, twin boundaries, and slip zones. In the fatigue cracking study of nanotwinned materials, it is found that under high-cycle fatigue loads, cracks generally originate from twin boundaries, and the initiation mechanism is due to the stress concentration generated by elastic anisotropy on both sides, dual interface [20]. Under low-cycle fatigue loads, the location of fatigue cracks becomes very complex.

(i) *Schmid Factor.* Zhang expresses the relationship between the shear stress α at the twin boundary and the resulting dislocation density β:

$$\alpha = \alpha_0 + MNc\sqrt{\beta}, \tag{3}$$

where M is a constant, N is the shear modulus, and c is the Burgers vector. Since the orientation of the twin boundary has an influence on the critical

condition of the twin boundary fracture, it can be known from Schmid's law that

$$\alpha = \varepsilon\lambda, \tag{4}$$

where ε represents the flow stress and λ represents the orientation factor. And due to the cumulative value of dislocations per unit length,

$$j = \sqrt{\beta}. \tag{5}$$

Derive from the above formula:

$$j = \sqrt{\beta} = \frac{m(\varepsilon - \varepsilon_0)}{MNc}. \tag{6}$$

If the average thickness of the twin boundary is set as E, the dislocation accumulation amount caused by different orientations is expressed as

$$j_m = \sqrt{\beta} = \frac{m(\varepsilon - \varepsilon_0)}{MNc}E. \tag{7}$$

(ii) *The Influence of Stacking Fault Energy.* The critical condition for considering the fracture of twin boundaries is only affected by the stacking fault energy. In face-centered cubic metals, in order to reduce the energy, a complete dislocation is decomposed into two incomplete dislocations, and the two incomplete dislocations are connected by a stacking fault band, that is, an extended dislocation [21]. When the extended dislocations are in equilibrium, the gravitational force θ per unit length produced by stacking faults and the repulsive force T produced by partial dislocations are balanced:

$$U = \frac{T}{\theta}, \tag{8}$$

where U represents the width of the stacking fault and is a constant. But when the dislocation moves and approaches the twin boundary, it will be repulsed by the twin boundary P. The equilibrium equation at this time is

$$P + \theta = \frac{T}{U}. \tag{9}$$

It can be seen from Wei Yujie's research that the expression of critical shear stress α during twinning deformation is

$$\alpha = \alpha_1 + \varepsilon\frac{8}{\pi}\frac{2 - w}{1 - w}\frac{E}{c}\delta k^i - \frac{2\theta_{th}}{Ek^i}. \tag{10}$$

As the shear rate α increases, the appearance of the extrudate shows unstable flow phenomena such as surface roughness, undulation, helical twist, and even melt fracture. Therefore, the shear stress during molding must be lower than α.

FIGURE 4: Martial art single kick.

2.2. Martial Art Singles and Their Protective Equipment. In a broad sense, martial art singles are also called sports. It refers to the basic means of consciously organizing social activities, improving people's physical strength, promoting all-round development, enriching social and cultural life, and promoting spiritual civilization [22]. Figure 4 shows martial art singles.

2.2.1. The Role of Single Kick in Martial Arts. Exercise promotes the growth of human bones and muscles, improves cardiopulmonary function, and improves the functional status of the blood circulatory system, respiratory system, and digestive system. In particular, it has a very important impact on the quality of people's mental health [23].

Mental health qualifications are formed by a combination of genetics and environment. They are intrinsic, basic, and relatively stable psychological qualities and characteristics. These psychological attributes and physiological characteristics determine whether to affect the individual's psychological, physiological, and social functions and then affect the individual's mental health [24]. Therefore, the quality of mental health is an important aspect of mental health that affects a person's level of mental health. Mental health quality and mental health are important signs of individual psychological phenomena. In a word, the quality of mental health is a stable psychological characteristic, and mental health is a state of psychological safety and happiness. The level of mental health quality is directly related to the level of mental health. Quality indicators of mental health often include many indicators of mental health.

(1) Evaluation Standard of Mental Health Quality. Scholars at home and abroad have a good understanding of the benchmark of mental health from different perspectives and social backgrounds. According to the college education and training goals and social development requirements of college students, the mental health standards of college students are determined by the following aspects: (1) normal cognitive ability [25], including sharp thinking, good memory, rich imagination, perception, and learning ability; (2)

Figure 5: Common sports protective gear.

healthy and stable interpersonal relationships: emotions, emotional stability, quick response, satisfaction, happiness and other positive emotions, as well as optimistic thoughts dominate, and can reasonably vent, adjust, and control negative emotions; (3) perfect personality, coordinated actions, excellent self-awareness, able to maintain the integrity and coordination of personality, and effectively control their own psychology and actions and keep the internal reflection of the action consistent with the external performance; and (4) harmonious interpersonal relationships: in study, life, and work, being good at communication and being able to objectively evaluate others, handle emergencies reasonably, accept the shortcomings of others, adapt to the environment, and establish harmonious interpersonal relationships.

(2) Mental Health Quality Measurement Tools. Mental health measurement tools are developed according to the development needs of various research fields, combined with definitions and evaluation criteria. At present, the commonly used mental health assessment tools mainly include the symptom self-rating scale and the Japanese revised personality question questionnaire. In addition, there are emotional state scales, depression self-assessment scales, mental health diagnostic tests, motor perception scales, existential personality scales, life events scales, and state characteristic anxiety scales. At the same time, the use of physiological indicators is mainly EMG, reaction time, heart rate and blood pressure, brain waves, and other evaluation methods.

2.2.2. Martial Art Single-Kick Protector. When people engage in martial art single kick, martial art single-kick protective equipment is essential. On the one hand, the protective equipment for martial art single-leg kicks needs to ensure that the personnel being used can be protected. On the other hand, the material of the protective equipment itself should not be harmful to the human body but provide high-quality protection for human activities. Due to the particularity of the composition and structure of nanocrystalline materials, its performance has been significantly improved compared with traditional materials, especially the particularity of super hardness, super modulus effect, etc., so it has become an important material for martial art single-kick protective equipment.

Table 1: Parameter comparison table.

Scope	Symbol	Value
Burgers vector size	C	0.266 nm
Taylor constant	Alpha	0.6
Lattice constant	Large	0.4 nm
Poisson's ratio	Phosphorus	0.49
Shear modulus	Meter	51 GPa

Table 2: Students' mental health scores.

	Know	Mood	Character	Adapt	Overall result
Actively participate in sports	68	79	64	78	289
Participate in sports occasionally	60	71	58	62	251

Table 3: Comparison of mental health quality in different age groups.

	Know	Mood	Character	Adapt
F value	10	5	3	4
Phosphorus	0.000	0.008	0.012	0.006

Table 4: Statistical table of protective effects of various types of protective gear.

	Ordinary protective gear	Nanomaterial protective equipment
Helmet	70%	91%
Goggles	69%	82%
Bracers	75%	93%
Waist protection	62%	80%
Knee pads	72%	86%

Safety protective equipment is a necessary preventive device to protect the safety and health of athletes during sports. Use specific shields, pendants, or floats to protect athletes through barriers, absorption, dispersion, and containment and protect part or the entire body of an athlete from external attack. The use of personal protective equipment is an important means to prevent or mitigate sports safety accidents. There are many classification methods for safety protection equipment, which can be classified according to the use, the protection part, and the nature of the raw materials used. According to different uses, it can be divided into cold-proof products, shock-proof products, antidrop products, mechanical trauma products, antifouling products, waterproof products, and life-saving products. According to the protective gear, there are 8 kinds of protective gears for the head, face, eyes, airway, ears, hands, feet, and body. The protective effect of various protective tools is limited. In order to prevent accidents, it is necessary to use protective tools correctly and choose protective equipment reasonably
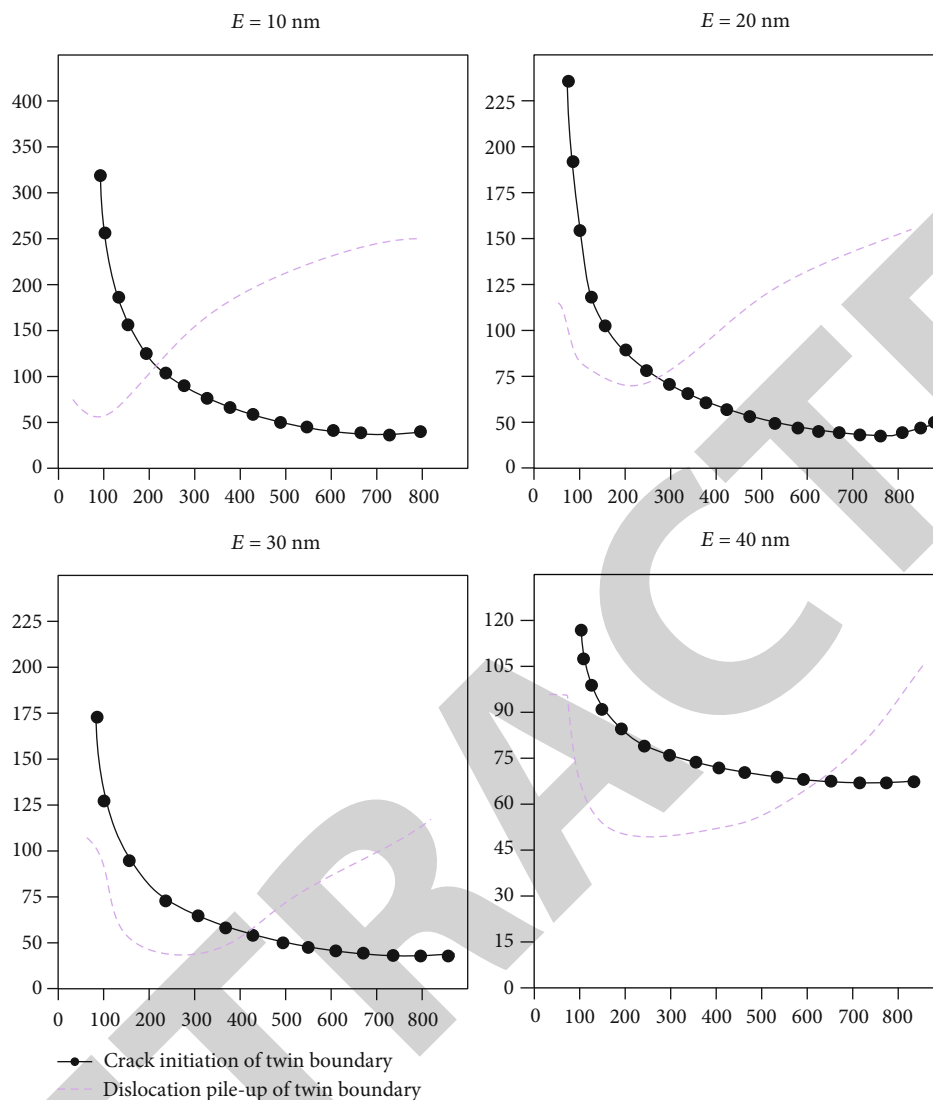
FIGURE 6: Relationship between crystal nanometer thickness and crack.

according to the type of exercise. Figure 5 is a common sports protective gear.

3. Experiments on Crystalline Nanooptical Materials and Martial Art Single-Kick Protective Equipment

3.1. Mechanical Experiments of Crystalline Nanooptical Materials. This experiment is based on the theoretical model of mechanics, taking crystalline nanooptical materials as the research object, to study the mechanical properties of crystalline nanooptical materials. In this experiment, pure copper samples with nanobimorph layers of different thicknesses were prepared, and tensile-tensile fatigue experiments under constant stress amplitude were carried out on these products. Pure copper has good electrical conductivity and is widely used in the manufacture of wires, cables, brushes, etc.; it has good thermal conductivity and is often used to manufacture magnetic instruments and meters that

must be protected from magnetic interference; it has excellent plasticity and is easy to be processed by hot pressing and cold pressing. Table 1 is a reference table of the parameters required in the calculation process of the mechanical model.

3.2. Wushu Single-Kick Research Experiment. This experiment investigates the form of physical exercise and the quality of mental health of students in a university. Good psychological quality is the foundation of a healthy life for college students, and having a healthy body and mind is an important guarantee for their adulthood, talent, and success. Tables 2 and 3 show the mental health quality scores of regular and infrequent physical exercisers, the mental health status of different age groups, respectively, and quality comparison.

As can be seen from Tables 2 and 3, students who actively participated in sports had higher mental health scores in every aspect than students who participated in

sports occasionally, indicating that students actively participated in sports.

3.3. Experimental Design of the Effect of Sports Protective Equipment Based on Crystalline Nanooptical Materials. For experiments on sports protective gear of nanooptical materials, first, an initial solution is provided; secondly, a metal compound is added to the initial solution and mixed under alkaline conditions to obtain an intermediate solution; finally, a quantum dot precursor is added to the intermediate solution to obtain nanomaterials, and then, the nanomaterials are added to the sports protective gear. During the experiment, a control experiment was also conducted on ordinary sports protective gear. In this experiment, data on the protective effects of different protective gears were collected. Table 4 is a statistical table of the protective effects of various protective gears in this experiment.

It can be seen from Table 4 that the performance of the protective gear with nanomaterial protective equipment is much higher than that of ordinary protective gear. It shows that nanomaterial protective equipment is better than ordinary protective equipment.

4. Experimental Analysis of Crystal-Based Nanooptical Materials and Sports Protective Equipment

4.1. Mechanical Experimental Results of Crystalline Nanooptical Materials. In this experiment, the mechanical properties of crystalline nanooptical materials were fully studied. During the experiment, the effect of the thickness of the crystalline nanomaterial bimorph on the crack suppression of the material was investigated. Combined with the experiments in this paper, a schematic diagram of the effect of the thickness of the crystalline nanooptical material wafer on the inhibition of crystal cracks is obtained, as shown in Figure 6:

It can be seen from Figure 6 that under the condition of constant applied load, when the thickness of the double crystal layer is $E = 10$ nm, the condition for the initiation of double grain boundary cracks is that the grain size $dG > 190$ nm; when the thickness of the double crystal layer $E = 30$ nm, the condition for the initiation of grain boundary cracks is that the grain size $dG > 420$ nm. From the data summarized in Figure 6, it can be seen that when the grain size cannot be refined, increasing the thickness of the twin layer can inhibit the initiation of twin boundary cracks, thereby improving the strength and hardness of the material.

4.2. Experimental Results of the Effect of Sports Protective Equipment Based on Crystalline Nanooptical Materials. According to Table 4, a comparison chart of the effects of sports protective equipment of different materials is obtained, as shown in Figure 7.

According to Figure 7, it can be concluded that it is a great improvement compared to conventional protection. It can be clearly seen from Figure 7 that the protective effect of sports protective equipment based on crystalline nanooptical materials has increased by an average of 12%.
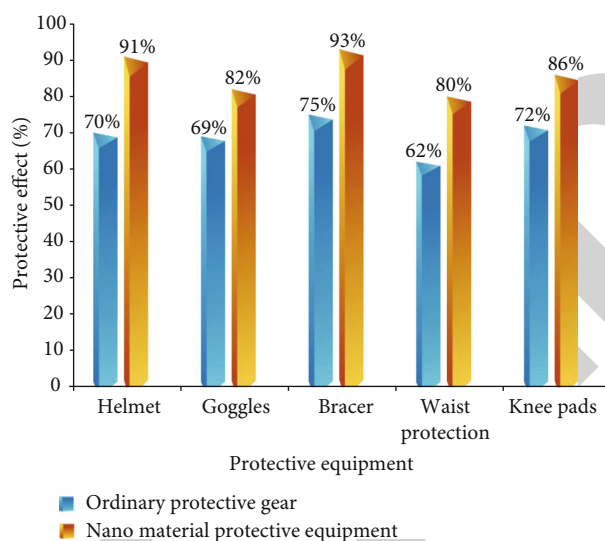
Figure 7: Comparison of different materials for sports protective equipment.

5. Conclusions

Nanooptical materials have high yield strength, hardness, and good wear resistance, making sports protective equipment based on crystalline nanooptical materials safe and reliable. Sex life is greatly improved. From the experiments in this paper, it can be concluded that the protective effect of sports protective gear based on crystalline nanooptical materials has been qualitatively improved, with a maximum increase of 21%.

Data Availability

No data were used to support this study.

Conflicts of Interest

The author declares that there are no conflicts of interest regarding the publication of this article.

References

[1] A. A. Saudi, "Modeling of mechanical resonators used for nanocrystalline materials characterization and disease diagnosis of HIVs," *Microsystem Technology*, vol. 22, no. 2, pp. 305–318, 2016.

[2] I. A. Ovid'ko and A. G. Sheinerman, "Free surface effects on rotational deformation in nanocrystalline materials," *Journal of Materials Science*, vol. 51, no. 13, pp. 6444–6451, 2016.

[3] F. Tan, Q. Fang, J. Li, and H. Feng, "Enhanced nanotwinning by special grain growth in nanocrystalline materials," *Journal of Materials Science*, vol. 55, no. 8, pp. 3618–3628, 2020.

[4] K. Tserpes, P. Bazios, S. Pantelakis, and N. Michailidis, "Nanoindentation testing and simulation of nanocrystalline materials," *Procedia Structural Integrity*, vol. 28, no. 6, pp. 1644–1649, 2020.

[5] D. S. Hong, J. H. Lee, and E. J. Kim, "A comparative study on the survey and recognition of life sports safety accidents in Korea and Germany," *Korean Journal of Sports Science*, vol. 27, no. 4, pp. 891–900, 2018.

Research Article

Innovative Artistic Design of Nanomaterial Products Based on Intelligent Algorithm

Wenji Yao[1] and Yue Ruan [2]

[1]*College of Art, Zhejiang Shuren University, Hangzhou, 310015 Zhejiang, China*
[2]*College of Information Science and Technology, Zhejiang Shuren University, Hangzhou, 310015 Zhejiang, China*

Correspondence should be addressed to Yue Ruan; 600971@zjsru.edu.cn

At present, algorithm technology has achieved very rapid development, and it is more and more widely penetrated and applied in people's production and life. Among them, product design based on intelligent algorithm has also been widely used. This technology plays an important role in promoting product innovation and design and contributes to the improvement and optimization of technology, showing very significant application benefits in the product design and development process of major enterprises. The application of intelligent algorithms in product design can not only make products more in line with customers' usage habits, but also products blessed with intelligent algorithms often have more commercial value. Therefore, in order to enhance the added value of commodities, innovative design of products has become a must. Nanomaterials must have unique properties that are unmatched by general building materials, such as high surface activity, strong oxidation, and superparamagnetic. This article mainly studies design strategies from two aspects, namely the innovation of material properties and application methods, and introduces the properties of nanomaterials, their application status, and the existing problems. And it starts from the application of intelligent technology in nanomaterial products, innovative design, and development prospects, combined with actual cases, to find a feasible way for the development of innovative design and research of nanomaterial products. On this basis, it is proposed that the idea of expanding the design should reunderstand and reposition the product design of nanomaterials and make the design more acceptable to more consumers. New design ideas and methods such as adjusting material properties through intelligent algorithms provide certain assistance and support for the application of intelligent algorithms in product design innovation practice. Some completed application practices are also presented to illustrate the rationality of the application of intelligent algorithms in nanomaterial products. The results show that the crowd search algorithm has the highest optimization degree and has good stability and optimization effect, and its standard deviation is the lowest close to 0.

1. Introduction

Materials are the material basis for human survival and development. In the 1980s, people regarded new materials, information technology, and biotechnology as important symbols of the new technology revolution, and it was considered to be one of the pillars of modern science and technology in the twenty-first century. As an indispensable element in product design, material innovation has formed a preliminary structure and system during the Bauhaus period in Germany. Common materials have many quality

defects, which lead to serious constraints in product design. And nanomaterials are completely different. With its excellent material quality, it can play an important and unique role in fields that ordinary materials cannot. Nanomaterials are one of the most important directions for the development of new materials in the twenty-first century. With the development of nanotechnology, the innovation of material properties can not only maintain the basic properties of nanomaterials, but also make up for the deficiencies and shortcomings of their properties to a large extent. In the process of product innovation and design, the initial stage
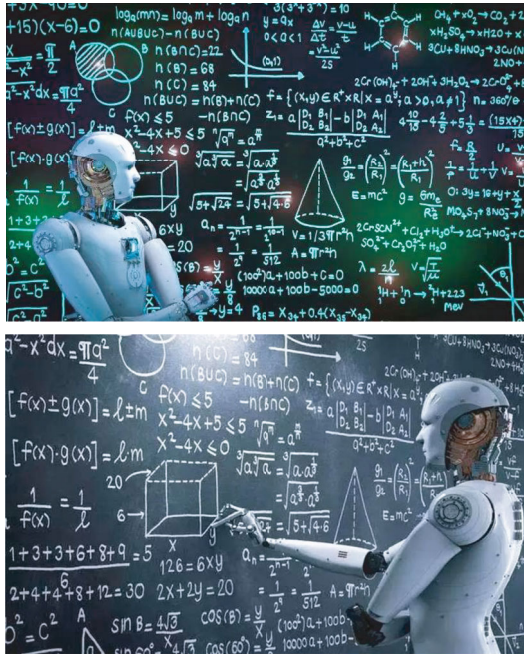
Figure 1: Artificial intelligence optimization algorithm diagram.

focused on divergent thinking and continued to expand outward with the design point as the center, seeking various possible design solutions.

Intelligent algorithm is based on intelligence and performs relatively fast global optimization, which can better simulate the initial design thinking in product innovation design. In the detailed design stage, the main focus is on convergent thinking, fully absorbing the design points of the excellent scheme and thinking in one direction. For the research and development and production of nanomaterial products, the innovation of product design and concept in the product development stage needs to meet people's objective requirements in a true sense, and at the same time, it must be implemented in the production process, so that it can be effectively realized. In this context, it is necessary to keep pace with the times and deeply study the design methods of nanomaterials. This paper makes full use of intelligent algorithm technology to lay a solid foundation for the research and development and innovation of new products, explore its new path for innovative practice, and effectively solve technical problems related to product design.

Based on the intelligent algorithm, the relationship between nanomaterial products and artistic design is discussed, the procedures and ways of applying intelligent algorithm to product innovation design are studied, and several algorithmic product innovation design models are proposed, and the development of an innovative design example system is one of the innovations of this paper.

2. Related Work

For the topic of "intelligent algorithm + nanomaterial products," some scholars have carried out research on it.

Yin got a highly ordered alumina obtained under ultrahigh vacuum (UHV) by NiAl(110) surface oxidation. He
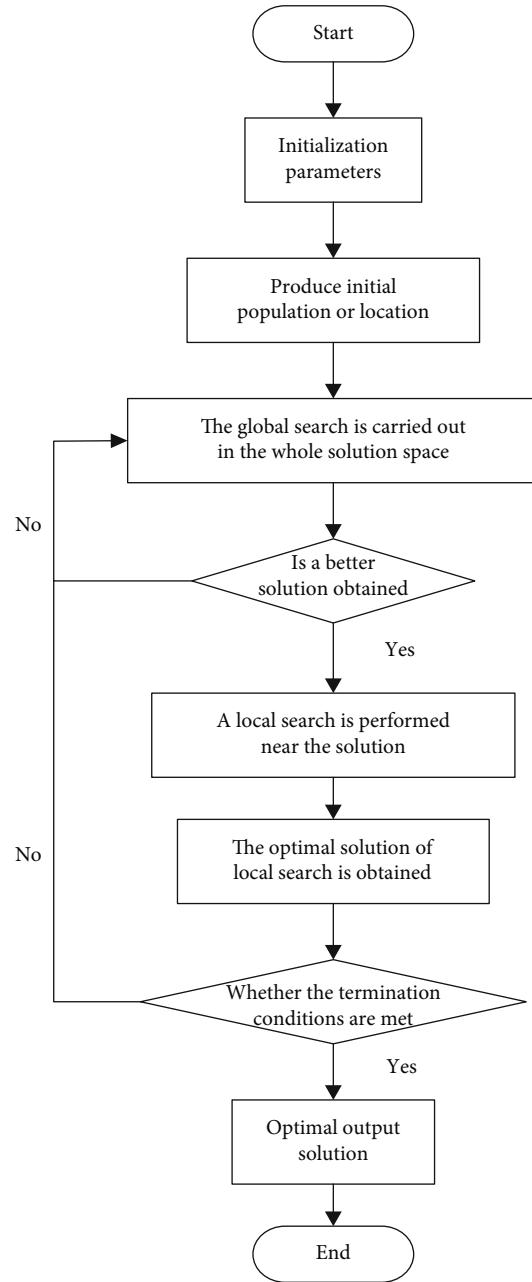
Figure 2: Basic flow chart of intelligent algorithm.

has coordinated UHV-type surface science and real-world experiments with amorphous aluminum oxide obtained by atomic layer deposition on silicon chips. He thoroughly characterized the Pt10 clusters through a combination of experimental techniques and theoretical analysis, showing the highest CO oxidation activity per platinum atom of CO oxidation catalysts. This catalytic system presents a coherent interdisciplinary picture [1].

Shivakumar investigated the 3-nm-thick boron layer in detail by preventing the interaction with the silicon substrate through a thin boron layer grown by chemical vapor deposition at 450°C. It forms the p-anode region of the PureB diode with zero metallurgical junction depth on the n-type silicon. Metals are deposited by electron beam-assisted
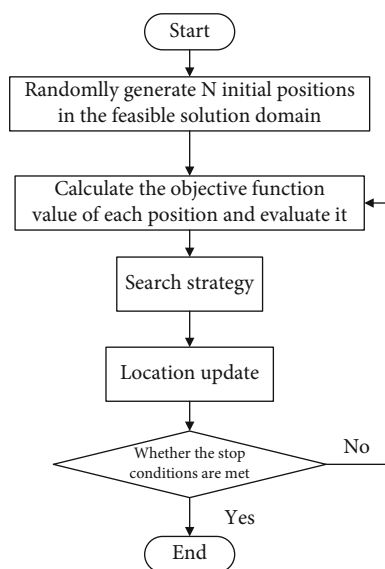
FIGURE 3: Solving steps of crowd search algorithm.

TABLE 1: The parameters of genetic algorithm.

Parameter factor	Physical description
Population size	N square grids
Neighbor structure	Moore
Update strategy	Linear scan
Selection operator	Select 2 adjacent positions of the individual
Crossover operator	Single point intersection
Crossover probability	P_c
Mutation operator	Nonuniform variation
Variation probability	P_m
Replacement strategy	Replace if the child is better than the parent
Genetic algebra	≤500
Termination conditions	User interaction experience

physical vapor deposition at room temperature and annealed at temperatures up to 500°C. It was verified by the nearly constant I–V characteristics of the PureB diodes and the microscopic examination of the deposited layers [2].

Agenor examined the interaction between access to finance, product innovation, and labor supply in a two-stage overlapping generational model of endogenous skill distribution and financial market imperfection. An ambitious policy aimed at alleviating the constraints on innovators' access to funding may allow a country to escape this trap by promoting idea generation and improving incentives for investment in skills [3].

Engelman aims to study the impact of intellectual capital on firm absorptive capacity and the impact of intellectual capital on product innovation. He believes that companies mobilize intellectual capital and other intangible assets through dynamic capabilities such as ACAP. He conducted a quantitative study, structural equation modeling, to verify the validity of structural and theoretical models. He found that intellectual capital does affect ACAP. His findings also show that ACAP affects product innovation, but each of its dimensions exhibits different effects [4].

Wang believes that product innovation not only enables organizations to introduce new products to the market, but also challenges organizations to update their technical capabilities. Through a longitudinal study of product introductions in the workstation industry, he found that capability extension reduces the chances of new product survival. In addition, he found that organizational boundaries moderate the negative relationship between capability extension and product survival. He derives the implications of the link between product innovation and capability development [5].

Hui studied the common domain name format of http://www.zol/, processed the data of consumer online reviews of three Huawei Mate phones, explored the correlation between online reviews and phone improvements, and made suggestions for future product improvements. This empirical study showed that changes in mobile phone functional satisfaction are strongly correlated with improvements in mobile phone performance. This research helps companies grasp market demand, understand consumer behavior, and improve the quality and efficiency of product innovation [6].

Bos examines the impact of access to imported intermediate inputs on firm-level product innovation in five developing countries, combining trade data with innovation survey data and developing a method to determine whether new inputs are critical for product innovation. He found evidence that the number of new imported varieties has a significant impact on product innovation that depends on new inputs and provides instructive evidence that this impact comes from access to better quality imported products [7].

3. Intelligent Algorithms, Nanomaterial Products, and Innovative Art Design

3.1. Intelligent Algorithm. Intelligent algorithms are new algorithms based on artificial intelligence. Like most computing, intelligent computing is a kind of natural computing inspired by nature. It first comes from biology; people imitate the evolution process of creatures in nature, thus abstracting such an algorithm [8]. In the process of continuous development, intelligent algorithms are slowly being applied to scientific problems, but these problems are also encountered by people in real life. Over time, people have summarized and summed up a special algorithm and named it intelligent algorithm. Figure 1 shows the AI optimization algorithm diagram.

In fact, the development of intelligent algorithms is far beyond imagination. With the development of time, new ideas of intelligent algorithms have sprung up, and various theories about intelligent algorithms have been proposed, and they have also been improved and updated. But despite this, the basic process of intelligent algorithm has not changed, and its basic process is generally shown in Figure 2. From the frame diagram of the algorithm, it was found that at the beginning of the algorithm operation, it must initialize
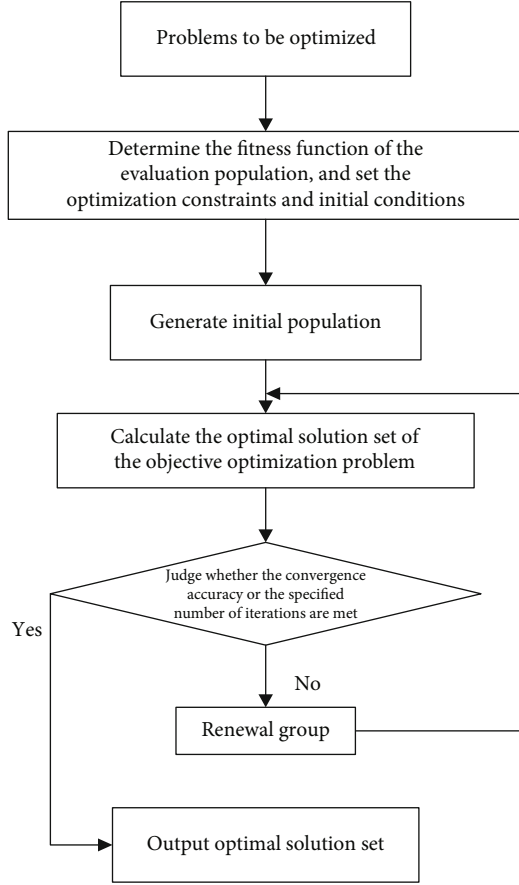
Figure 4: Multivariate optimization flow chart based on genetic algorithm.

Table 2: Convergence performance.

Algorithm	Evolutionary algebra reaching convergence	Number of times to reach convergence
PSO algorithm	68	912
GA algorithm	42	937
SOA algorithm	19	993

all the relevant parameters of the algorithm and then randomly generate a position, that is, the most initial solution [9]. Then, the solution space will generate a different solution according to certain rules; that is, a global search for the solution will be performed until a better solution is judged. According to the different conditions of the solution, the corresponding algorithm will be used to perform a local search near the more optimal solution, so as to further find the optimal solution, until the optimal solution satisfies the termination condition, and the output ends. Otherwise, the algorithm automatically loops and starts to research for the optimal solution [10].

3.1.1. Crowd Search Algorithm. Crowd search algorithm is a heuristic random search algorithm, which draws on human social experience, simulates human search behavior, and regards human self-interest behavior, altruistic behavior,

self-organization aggregation behavior, preaction behavior and uncertainty reasoning behavior as advanced intelligence. The body is analyzed and its model is established to calculate the search direction and step size. The crowd search algorithm is a relatively effective search method, and its main working principle is to use the local optimal method. In the search process, the algorithm first finds a continuous spatial position and then judges whether there is an optimal solution based on this position. If the optimal solution is not found at this position, the algorithm will redetermine a continuous space until the optimal solution is finally found. However, the optimal solution generated by the crowd search algorithm is often a local optimal solution, which is far from replacing the global optimal solution [11]. The operation flow of the SOA algorithm is shown in Figure 3.

In the process of searching the space, because the position and the search area are uncertain, the first thing that needs to be done is to determine the relative position of the search target and determine the area according to this position. Its specific function is described as follows:

$$y_i = y_{\max} - \frac{d - U_i}{d - U}(y_{\max} - y_{\min}), i = 1, 2, \cdots, d, \quad (1)$$

$$y_{ij} = \text{rand}(y_i, 1), j = 1, 2, \cdots, D. \quad (2)$$

In the above formula, y_i is a position parameter of the objective function value i; y_{ij} is the relative position of the objective function value i of the parameter j; U_i is the specific number of $x_i(t)$ after arranging the overall position in a certain order; D is the actual size of the search space.

According to some conditions about the position in formulas (1) and (2), we can now get the position parameter y_{ij}. According to the above two formulas, the step size formula can be obtained as

$$\beta_{ij} = \chi_{ij} - \sqrt{-\ln\left(y_{ij}\right)}. \quad (3)$$

Among them β_{ij} is a position space constant in j-dimensional space; χ_{ij} is a parameter of the basis function, and the formula for its value is

$$\chi_{ij} = \omega \cdot sab(x_{\min} - x_{\max}), \quad (4)$$

$$\omega = \frac{(R_{\max} - r)}{R_{\max}}. \quad (5)$$

In formula (5), $x_{\max}$ and $x_{\min}$ are the values of the relative position in the process of finding the optimal solution; ω is the weight transformation of the position; r and $R_{\max}$ are, respectively, the number of iterations the algorithm performs in the process of finding the optimal solution.

After the relative position information is obtained, the model is analyzed by estimating the target. In this process, the expected action direction $d_{i,\text{ego}}$, the actual movement direction $d_{i,\text{alt}}$, and the preparation action direction $d_{i,\text{pro}}$ of any i search targets can be obtained. Finally, through the

(a)

(b)
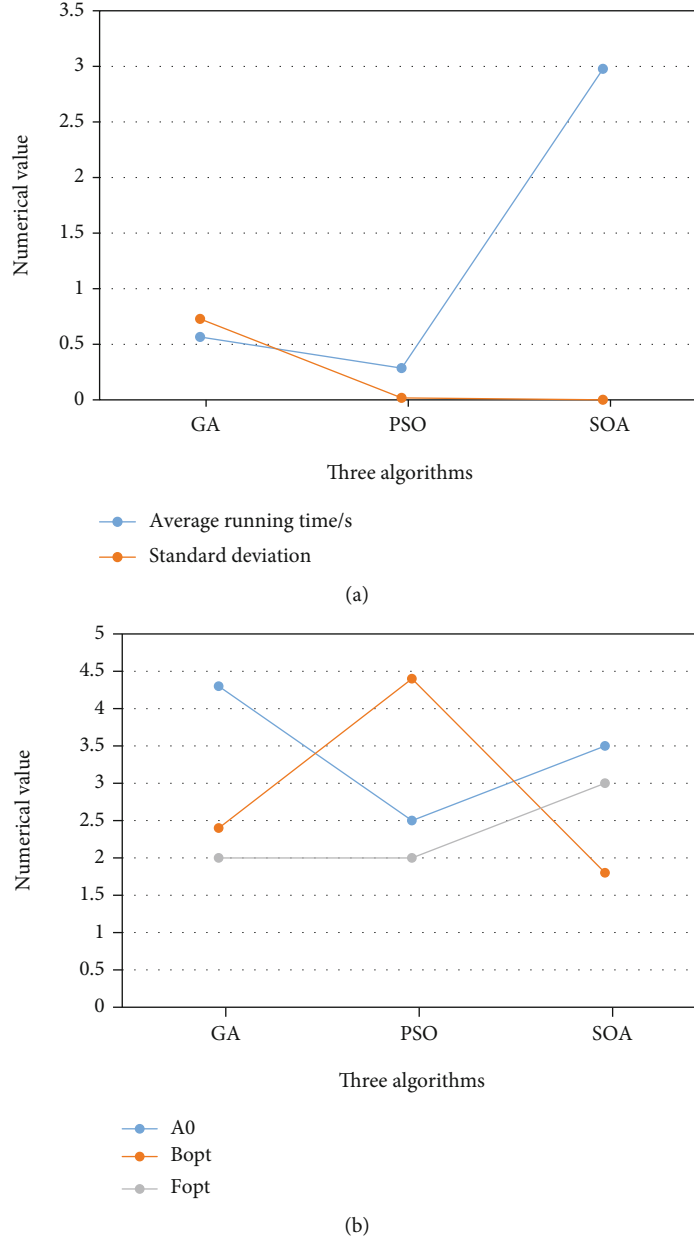
FIGURE 5: Statistical data and optimization results of three algorithms.

calculation of these three, we can get the final search direction.

$$d_{i,\text{ego}}(t) = p_{i,\text{best}} - y_i(t), \qquad (6)$$

$$d_{i,\text{alt}}(t) = g_{i,\text{best}} - y_i(t), \qquad (7)$$

$$d_{i,\text{pro}}(t) = y_i(t_1) - y_i(t_2), \qquad (8)$$

$$d_i(t) = \text{sign}\left(\chi_1 d_{i,\text{ego}} + \chi_2 d_{i,\text{alt}} + \omega d_{i,\text{pro}}\right). \qquad (9)$$

In the formula, $t_1, t_2 \in \{t, t-1, t-2\}$; $y_i(t_1)$; $y_i(t_2)$ are the initial positions of $\{y_i(t-2), y_i(t-1), y_i(t)\}$; $g_{i,\text{best}}$ is the relative optimal position in the space where the ith search target is located; $p_{i,\text{best}}$ is the possible target position

found by the ith search target; χ_1 and χ_2 are a real number randomly selected in the known interval $[0, 1]$.

The position transformation formula of the target to be searched is

$$\Delta y_{ij}(t+1) = \beta_{ij}(t)d_{ij}(t), \qquad (10)$$

$$y_{ij}(t+1) = y_{ij}(t) + \Delta y_{ij}(t+1). \qquad (11)$$

3.1.2. Genetic Algorithm. Genetic algorithm is a kind of random search algorithm that is widely used at present. Compared with other algorithms, it can operate directly on configuration parameters, so its operation is particularly simple. The algorithm is based on the typical principles of survival of the fittest. After the parameter configuration of

FIGURE 6: Nanoproducts.

the first-generation algorithm is generated, it can iterate and evolve continuously and finally produce more and more optimal approximate solutions [12]. The operations of crossover, mutation, and selection of genetic algorithm are carried out in a probabilistic way. The factors of the genetic algorithm are calculated by crossbreeding and mutation in biotechnology.

It is worth mentioning that the genetic algorithm can also realize the direct calculation of the product. In this process, the algorithm continuously evolves through the acquisition of product information. Genetic algorithms can also provide us with an analysis of different parts of the product when we need to do a corresponding analysis of that product. In the iterative process, the genetic algorithm has good convergence and high efficiency. By using the algorithm to simulate the components of the nanomaterial product, we can finally get the shape of the product [13].

But the genetic algorithm cannot solve the problems in dynamic simulation. In order to better demonstrate the dynamic process of product innovation, artistic design, and modeling, particle swarms were introduced to optimize the algorithm to a certain extent. The results show that the performance of the genetic algorithm optimized by particle swarm optimization is significantly better than that of the traditional genetic algorithm.

The reason why the genetic algorithm has such efficient performance is mainly because it uses an iterative calculation method in the process of numerical calculation. Compared with traditional algorithms, traditional iterative processes tend to fall into the loop of local optimization. The genetic-based iteration abandons the drawbacks of the traditional model, so that only the individual with the highest fitness in the global scope is kept as the optimal solution [14]. The relevant parameters of the genetic algorithm are set as shown in Table 1.

The optimization goal of this paper is to find the global optimal solution, so it is necessary for us to make certain improvements to the above algorithm to meet our design

of the innovative art of nanomaterial products. The optimization function is as follows:

$$g(x) = \min (T_E, H_e). \tag{12}$$

Similar to the objective function in most intelligent algorithms, we also introduce an objective function here called the fitness function. After considering the actual value of the fitness function, the fitness function is also adjusted as follows:

$$fit(f(x)) = \frac{1}{g(x)}. \tag{13}$$

The optimization model based on genetic algorithm is shown in Figure 4. Evolutionary rules are the main components of genetic algorithms, which can simulate natural phenomena such as birth, aging, illness, and death and determine the dynamic function of the state at the next moment according to the current state and its neighbors. At the same time, the central states will influence each other and promote the interaction between local populations. Its basic model is

$$If S^t = 1, S^{t+1} = \begin{cases} 1, A_i \le n \le B_i, \\ 0, n < A_j, n > B_j. \end{cases} \tag{14}$$

3.1.3. Particle Swarm Optimization Algorithm. Particle swarm optimization (PSO) is an emerging stochastic optimization algorithm that simulates the foraging behavior of birds, which can effectively optimize various functions. This algorithm relies on random processes and uses the concept of fitness value. On the basis of the previous intelligent algorithm, we introduce a new intelligent algorithm, namely particle swarm optimization algorithm. In an era of increasingly abundant data and information, particle swarm optimization algorithms are known for their multidata parallelism and simplicity. The algorithm has few control parameters, and the concept is particularly easy to understand. In actual operation, all particles are governed by two parameters, one determines the position of the particle, and the other determines the initial velocity of the particle. In terms of finding the optimal solution, the algorithm firstly seeks the individual optimal solution and then seeks the global optimal solution on this basis [15]. In the process of finding the solution, the particle needs to continuously change its position and velocity. The formula for its velocity and position is

$$b_{ij}(t+1) = q b_{ij}(t) + c_1 r_1 \left[p_{ij} - x_{ij}(t) \right] + c_2 r_2 \left[p_{jg} - x_{ij}(t) \right], \tag{15}$$

$$x_{ij}(t+1) = x_{ij}(t) + b_{ij}(t+1), (j = 1, 2, \cdots, n). \tag{16}$$

In the formula, q is the inertia weight, and its value is 1.49; c_1 and c_2 are positive learning factors, and its value is 0.5; r_1 and r_2 are random numbers, which are uniformly distributed between 0 and 1.

TABLE 3: IRTZ theory innovation method system.

Innovative thinking	Nine screen method	IFR method	Villain method	STC operator
Analytical tools	Contradiction analysis	Material field analysis	Function analysis	ARIZ algorithm
Problem solving tools	Invention principle	Separation principle	76 standard solution effect databases	
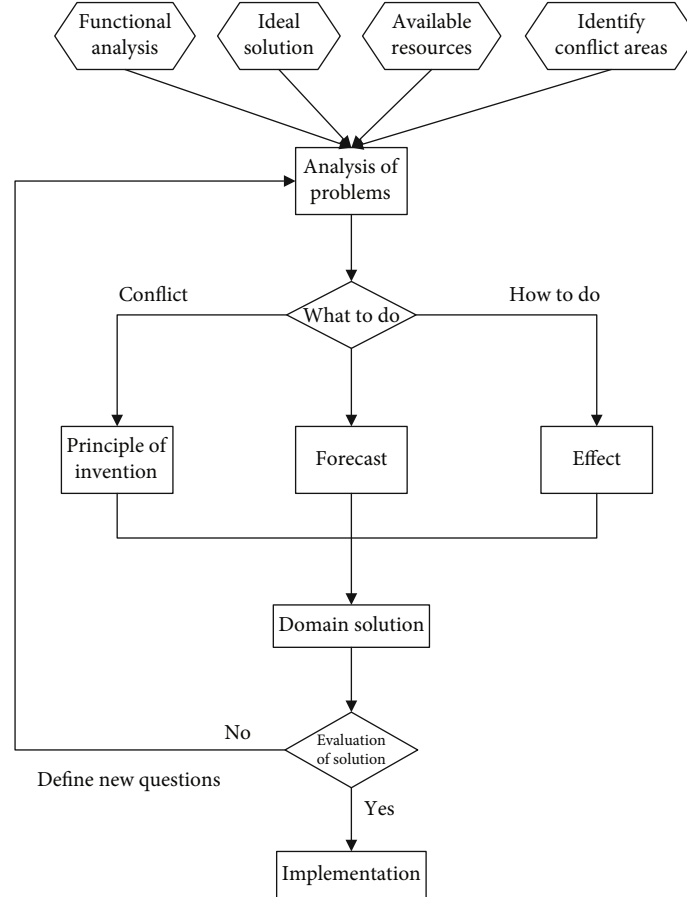
FIGURE 7: Flow chart of IRTZ.

TABLE 4: Test parameter setting.

Parameter	Set content
Yield strain	10.8
Breaking strength (GPa)	0.040
Fracture strain	17.4
Stretch feature	Stress-free platform
Yield strength (GPa)	0.453

The design objective function is

$$A_0 = \min \left\{ \max A(\beta_2, f) \right\}. \tag{17}$$

In addition, the speed update formula is

$$w_{id}^{k+1} + r_1 c_1 \left(p_{id} - z_{id}^{k} \right) = c_2 r_2 \left(p_{dg} - z_{id}^{k} \right) + v w_{id}^{k}. \tag{18}$$

Next, in order to test the stability and adaptability of the performance simulation algorithm, we selected three algorithms, respectively, and let them complete 1000 optimal solution searches alone to test their convergence. The final simulation statistical results are shown in Table 2.

Table 2 shows that in the process of finding the optimal solution for the three algorithms, the final test accuracy of each algorithm is above 90%, which shows that the three algorithms have relatively high efficiency in finding the optimal solution. In terms of convergence, the SOA algorithm has the lowest convergence, less than 2%, which fully demonstrates the superiority of the algorithm.

After calculating the standard deviation and search time of the above results, 15 optimized results were added, and all data were screened as a whole. Figure 5 is the final statistical result. The data analysis shows that the crowd search algorithm is the most optimized among the three algorithms, and the standard deviation is close to 0, which is 0.7 percentage points lower than the GA algorithm. Based on this, we

TABLE 5: Level 5 vocabulary difference subscale.

Modern	Natural	Plain	Light	Delicate	Soft	Refreshing	Safe	Individual
2	2	2	2	2	2	2	2	2
1	1	1	1	1	1	1	1	1
0	0	0	0	0	0	0	0	0
-1	-1	-1	-1	-1	-1	-1	-1	-1
-2	-2	-2	-2	-2	-2	-2	-2	-2
Traditional	Industrial	Gorgeous	Heavy	Rough	Rigid	Sloppy	Dangerous	Ordinary
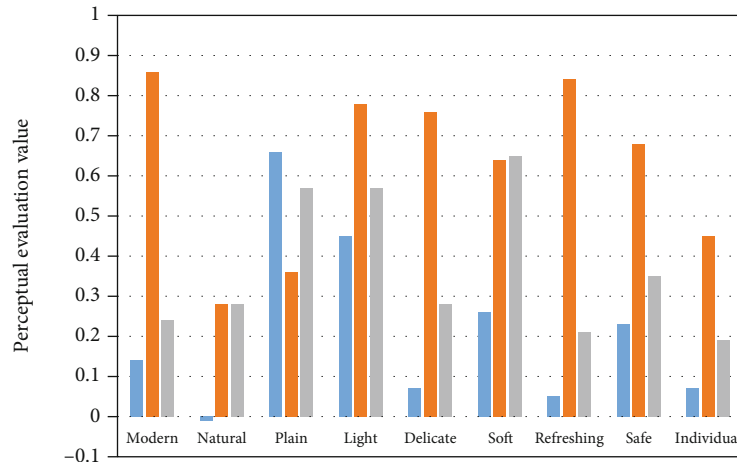
(a)
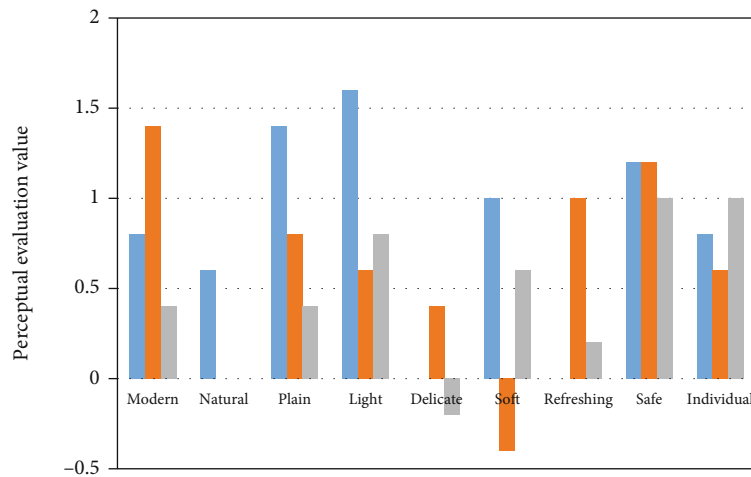
(b)

FIGURE 8: Online questionnaire and offline perceptual evaluation data statistics.

(a)
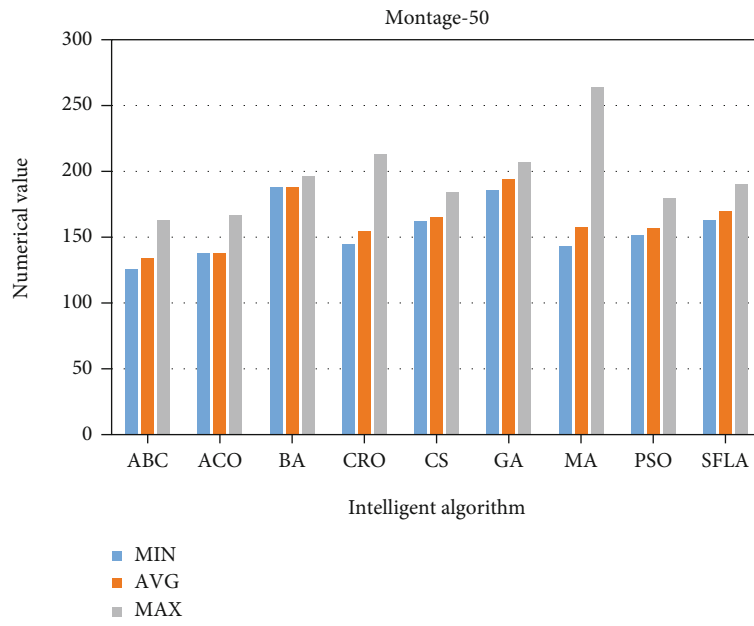
(b)

FIGURE 9: Continued.

(c)

FIGURE 9: Montage workflow completion time optimization results.

can draw relevant conclusions, that is, the innovative artistic design of nanomaterial products based on this algorithm has good stability and optimization effect.

3.2. Nanomaterial Products. Nanomaterials are ultrafine natural or man-made materials, mainly in the form of agglomerates or powders, and their grain size is nanometer. Its particle size is larger than atomic clusters but smaller than ordinary particles. The size is generally 100~102 nm, and the total number of elementary particles exceeds half. The surface activity of nanomaterials is relatively active, which makes nanomaterials have special electrical, mechanical, optical, magnetic, thermal, and other chemical properties. Nanomaterials mainly include nanoparticles, nanotubes, nanoblocks, nanofilms, and nanocomposites. Nanotechnology is a multidisciplinary science and technology that studies the properties and interactions of matter (including atoms and molecules) at the nanoscale (1~100 nm) and utilizes these properties. Nanotechnology is based on modern science and technology in many fields such as molecular biology, microelectronics, quantum mechanics, computer technology, and mesoscopic physics. It has been more than 20 years since the advent of nanomaterials and the technologies developed with them. The stage of material innovation and performance development has been roughly completed, and now it has entered the stage of technological improvement and comprehensive application [16].

3.2.1. Application of Nanomaterials and Key Products. As a new type of material, nanomaterials have been widely used in product design and have received extensive attention from the government and scientific researchers since its inception. The rapid development of nanotechnology is bound to trigger a new design revolution. In the 1980s, nanocalcium carbonate was developed. It is a new type of

ultrafine inorganic material with a particle size of usually 20~100 nm, but its technical content is relatively low. Due to its low price and high quality, it is widely used as an improved filling material. The data shows that nanocalcium carbonate materials have dominated the entire nanomarket and accounted for 29% of the overall size of the nano new material market. In addition to nanometer calcium carbonate, there are typical nanomaterials such as titanium dioxide and zinc oxide [17]. Figure 6 shows some common nanoproducts.

There are several nanomaterial technologies, devices, and products with excellent performance in the market, such as single electronic device, nanoblood glucose detector, immunochromatographic monitoring technology of nano-crystal bioprobe, nonpolluting nanowater-based paint, nanomodified high-power lithium ion battery, nanomodified solar cell, nano-self-cleaning cashmere sweater, nano-modified pigments, and nano-self-cleaning glass. Some typical application products of nanomaterials include nano-ceramic knife, nanozinc oxide coated refrigerator, and nano-titanium dioxide car paint [18].

3.2.2. User Needs of Nanomaterial Products

(1) Users pay attention to the functional satisfaction of products and hope that nanoproducts have many functions and can get feedback more quickly

For example, nanotoothpaste should not only clean teeth like normal toothpaste, but also diagnose oral diseases and reduce inflammation and pain. More importantly, the free nanohydroxyapatite component contained in the nano-toothpaste has the effect of protecting and repairing the gums. The most basic function of ordinary refrigerators is the function of refrigeration and preservation, but this is
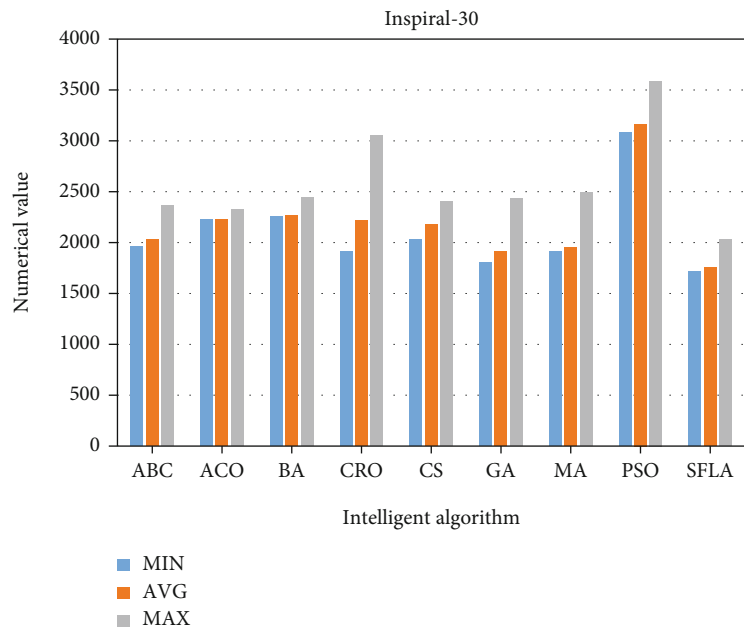
(a)
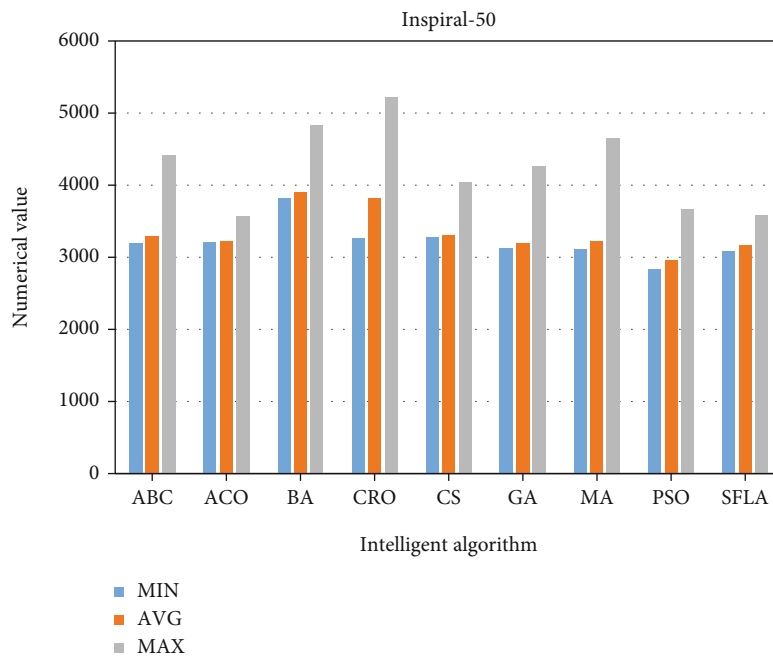
(b)

Figure 10: Continued.
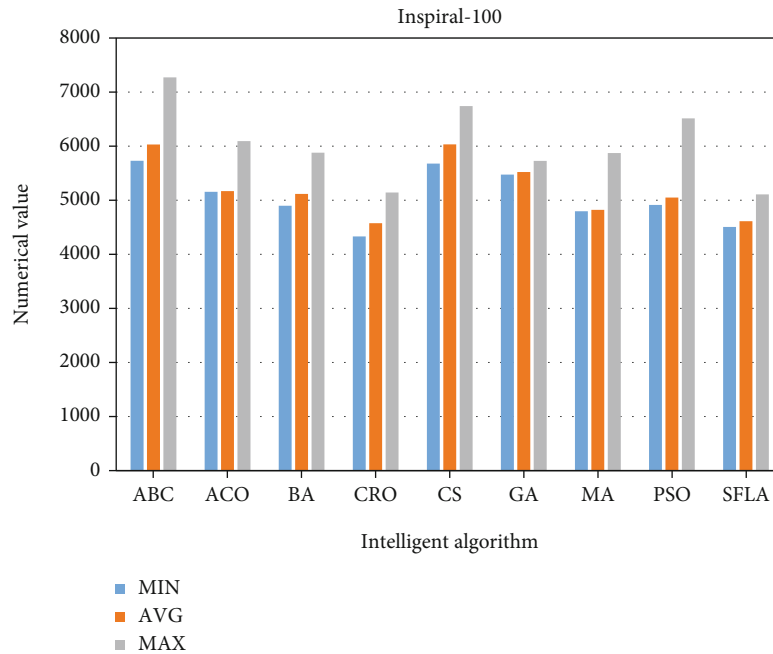
(c)

Figure 10: Inspiral workflow completion time optimization results.

not enough. People require that refrigerators coated with nanozinc dioxide can effectively help people to sterilize and inhibit bacteria, thereby reducing or even avoiding the unpleasant smell of food stored in the refrigerator due to spoilage or peculiar smell from food. Compared with ordinary skin care products, the cosmetic effect of nanoskin care products is faster and more efficient. In addition, people also require that nanoskin care products can quickly form resistance to the dermis of the skin so as to play a repair function on damaged cells and then instantly achieve the surprising effect of antiaging. The role of nanosilver clothing is radiation protection and can effectively treat skin diseases. People's demand for its physical therapy and as a health care product far exceeds the demand for its beauty, cold resistance, and frost resistance [19]. The car paint added with nanotitanium dioxide can increase the hardness and strength of the car surface and increase the wear resistance and impact resistance of the paint. Moreover, nanotitanium dioxide can change the angle of its visible light with the change of sunlight, thereby reducing light pollution and meeting people's requirements for environmental protection. Nanoceramic knives have greater hardness than diamond and can always maintain people's functional requirements for "sharpness" without grinding. Nanozirconia ceramics have strong chemical stability, acid and alkali resistance, and antifouling characteristics, so they are more clean and hygienic.

(2) The user attaches great importance to the reliability of nanoproducts and requires nanoproducts to be durable, safe, and reliable

As small as nanotoothpaste, skin care products, underwear, sunscreen in daily life, and as large as nanodrug deliv-

ery vehicles, these products are in direct contact with the internal cells of the human body or the external epidermis of the body. While they were astounding, people also demanded that they not be toxic, damage, or have other undesirable side effects to the cells inside the body. Another example is the products that are in direct contact with food, such as nanoknives, plastic wrap, and refrigerators that are common in the kitchen. It is required that it should not have a certain chemical effect with food, which will lead to food spoilage or residual or harmful substances on the surface of food [20].

(3) Nanoproducts meet the interactive needs of users, which is mainly reflected in the portability of nano products

Because of their small size, light weight, and strong plasticity, nanoproducts are loved by the public because of their portability. The thickness of nanosolar cells is only 2 nm~6 nm, which is very thin and small, so it is easy to carry. The nanoelectronic display has good flexibility, bending resistance, and light weight, which can be easily carried by users. It opens the door to the design of wearable electronic products, which can make the distance between electronic products and people even smaller.

3.3. Innovative Art Design. The poor definition of the initial state has become one of the main characteristics of product innovation design, which is a very creative problem-solving process. More specifically, at the beginning of the design, the designer has only an incomplete and vague mental representation of the upcoming design. This requires designers to understand how to implement the next steps in the

product innovation design process. Various loops in the process of innovative design have been studied and analyzed by a large number of scholars, such as iterative loops in problem space and pattern space, loops in problem definition, and loops in evaluation and generation stages [21]. IRTZ theory is a systematic, knowledge-based innovation method system, as shown in Table 3. It includes innovative thinking, analytical tools, and problem-solving tools, making it more operable and practical in application.

IRTZ is a problem-solving theory of invention, and the flow chart of IRTZ (shown in Figure 7) can be used as a description of IRTZ tools and methods.

The first step is to study and analyze the problems encountered. If contradictions and conflicts are found, the problems can be solved according to the principles. If the problem encountered is very clear but do not know how to solve it, then it needs to be used with some kind of effect to run a whole set of technological system evolution process that predicts innovation and then evaluate this process to achieve the final step. If a new problem is found during the implementation, the above process is repeated again until the problem is solved [22].

4. Nanomaterials and Models

4.1. Sensitivity of Nanomaterial Design Properties. In order to ensure the accuracy of the test, several nanomaterial simulation analysis methods are placed in the same test environment to test the accuracy ability. The settings of the test environment are mainly shown in Table 4.

In order to study the user's perceived intention needs, based on the online survey, the author distributed 100 questionnaires about the difference subscale of sensory vocabulary of nanomaterials. A total of 100 subjects' perception evaluations of nanomaterials were collected. According to the characteristics of materials, nine groups of perceptual adjectives, namely "clean and messy, natural and industrial, simple and gorgeous, light and heavy, safe and dangerous, modern and classical, individual and ordinary, delicate and rough, soft and hard," were selected. A 5-level lexical difference subscale was developed, as shown in Table 5. The nanomaterials involved in the questionnaire are all raw materials of the original color. According to the previous survey, the author also distributed 5 offline questionnaires with the same content as the online questionnaire. The results are shown in Figure 8. It can be seen from the survey that the respondents who filled out the offline questionnaire believed that the soft nano was the lightest and most comfortable to touch; the hard nano had the most modern features, and the wrinkled nano was softer than the hard nano. This clearly shows that there is a certain degree of deviation between the results of the online survey and the offline survey, with the maximum difference reaching 1.26. The reason why the perceptual evaluation of this material is so different is because there are also some differences in the visual and tactile effects [23].

According to Table 5, we can see that the softer nanomaterials give a more homely feel, while the harder nanomaterials give a modern freshness, and the wrinkled nanomaterials give a softer feeling. From the overall effect, good nanomaterials generally give people a simple and brisk feeling.

4.2. Montage Experimental Results. Under the Montage model, when the task volume is 25, 50, and 100, respectively, the maximum, average, and minimum values of the average completion time of each algorithm are shown in Figure 9. The formulas for calculating the mean and variance are

$$\bar{A}_i = \frac{\sum_{k=1}^{K} A_i^{\ k}}{K}, \tag{19}$$

$$\sigma = \left[\frac{\sum_{k=1}^{K} \left(\bar{A}_i - A_i^{\ k} \right)^2}{(K-1)} \right]. \tag{20}$$

σ and $\bar{A}_i$ represent the variance and mean of the ith evaluation value, where the range of i is $[1, 48]$.

According to Figure 9, the analysis is as follows: when the number of tasks is relatively small, the average completion time of algorithm ABC and algorithm ACO is lower than that of other algorithms, which are 74.13 and 76.17, respectively, while algorithm BA and algorithm GA are dwarfed. With the increase of the number of tasks, the average completion time of the algorithm ABO shows a significant upward trend, slowly surpassing all other algorithms, and also reduces its efficiency. In contrast, when the number of tasks is 25 and 50, the CRO completion time is relatively short. When the number of tasks is 100, the average completion time is the shortest among all algorithms. Compared to other algorithms, CRO is much more efficient in workflow completion time [24].

4.3. Inspiral Experiment Results. It can be analyzed from Figure 10 that when the amount of tasks is small, SFLA has the shortest average completion time, with a value of 2808.21, followed by ABC, and then GA. It is worth noting that the average completion time of algorithm MA is 0.7 times that of algorithm PSO. However, when the number of tasks is 100, among all algorithms, ABC has the longest average completion time, reaching 7287.47, followed by CS, reaching 6750.98. This comparative analysis reflects the extreme instability of the ABC algorithm in terms of average completion time. It can be concluded that as the number of tasks gradually increases, so does the time for each algorithm to run and complete. When the task volume is 100, the average completion time of CRO is the shortest, which is only three-quarters of the average completion time of CS.

5. Discussion

As a new type of material, nanomaterials have developed rapidly since entering the twenty-first century. They are receiving great attention and attention from the world, and researchers are also conducting in-depth research on them at a strategic height. The application of nanomaterials in product design is very exploratory, and this kind of exploration has special significance in the context of increasingly prominent environmental problems, so it has also attracted

great attention from relevant personnel. Nanomaterials have irreplaceable advantages in product design. Taking material properties and usage patterns as innovative strategies, they have played a positive role in people's reunderstanding and positioning of nanomaterial product design. At the same time, it also enables nanomaterial product design to play an important role in a broader commercial platform. The innovative artistic design of products based on various nanomaterials is a follow-up to the concept of environmental protection, because nanomaterials are multifunctional. At the same time, it is also suitable for various processing technologies, which makes it widely used in different product fields, so as to further explore and effectively analyze the product innovation design of nanomaterials. Crowd search algorithm is more stable than genetic algorithm and particle swarm algorithm. According to the actual problems and cases, the effectiveness of the optimization algorithm is verified, and it can be found that the designed optimization algorithm can achieve a good optimization effect in application.

6. Conclusion

Through the above research and analysis, we can clearly see that the innovative design technology assisted by intelligent algorithms has been widely used in the product design process. Better optimization results can be obtained, and the innovation and efficiency of product design can be effectively improved to a greater extent. According to different design ideas and concepts, it proposes a method of product innovation design based on genetic algorithm. The results show that this method is very practical because of its realization of innovation. In the future, in the process of product art design, the use of intelligent algorithms to assist product innovation technology will certainly achieve diversified development and make the methods and methods to effectively solve the problems in this process multidimensional. Through the use of advanced modern technical resources, designers can further improve their ability to control product design and their ability to innovate and create. Most importantly, these achievements can be given back to the society and users in a more diversified way. Combining the characteristics of product design practice, this paper promotes the construction of nanomaterial experience library, provides effective methods and approaches for design practice innovation, and gradually forms a new design mode of material perception experience, which is one of the important development directions in the future. This research lays a theoretical foundation for establishing a practical intelligent algorithm-assisted product innovation system. In the future, we will comprehensively consider adding relevant constraint mechanisms to combine them with relevant evolutionary mechanisms to establish a product innovation design system that meets the needs of different subjects.

Data Availability

No data were used to support this study.

Conflicts of Interest

There is no potential conflict of interest in this study.

References

[1] C. Yin, F. R. Negreiros, G. Barcaro et al., "Alumina-supported sub-nanometer Pt 10 clusters: amorphization and role of the support material in a highly active CO oxidation catalyst," *Journal of Materials Chemistry A*, vol. 5, no. 10, pp. 4923–4931, 2017.

[2] D. T. Shivakumar, T. Kneevi, and L. K. Nanver, "Nanometer-thin pure boron CVD layers as material barrier to Au or Cu metallization of Si," *Journal of Materials Science: Materials in Electronics*, vol. 32, no. 6, pp. 1–13, 2021.

[3] P. R. Agenor and O. Canuto, "Access to finance, product innovation and middle-income traps," *Research in Economics*, vol. 71, no. 2, pp. 337–355, 2017.

[4] R. M. Engelman, E. M. Fracasso, S. Schmidt, and A. C. Zen, "Intellectual capital, absorptive capacity and product innovation," *Management Decision*, vol. 55, no. 3, pp. 474–490, 2017.

[5] T. Wang and Y. Chen, "Capability stretching in product innovation," *Journal of Management*, vol. 44, no. 2, pp. 784–810, 2018.

[6] Z. Hui, H. Rao, and J. Feng, "Product innovation based on online review data mining: a case study of Huawei phones," *Electronic Commerce Research*, vol. 18, no. 1, pp. 3–22, 2018.

[7] M. J. D. Bos and G. Vannoorenberghe, "Imported input varieties and product innovation: evidence from five developing countries," *Review of International Economics*, vol. 27, no. 2, pp. 520–548, 2019.

[8] J. Vega-Jurado, S. Kask, and L. Manjarrés-Henriquez, "University industry links and product innovation: cooperate or contract?," *Journal of Technology Management & Innovation*, vol. 12, no. 3, pp. 1–8, 2017.

[9] L. Ardito and A. M. Petruzzelli, "Breadth of external knowledge sourcing and product innovation: the moderating role of strategic human resource practices," *European Management Journal*, vol. 35, no. 2, pp. 261–272, 2017.

[10] M. Olabisi, "The impact of exporting and foreign direct investment on product innovation: evidence from Chinese manufacturers," *Contemporary Economic Policy*, vol. 35, no. 4, pp. 735–750, 2017.

[11] S. Beugelsdijk and B. Jindra, "Product innovation and decision-making autonomy in subsidiaries of multinational companies," *Journal of World Business*, vol. 53, no. 4, pp. 529–539, 2018.

[12] R. Sanz-Valle and D. Jimenez-Jimenez, "HRM and product innovation: does innovative work behaviour mediate that relationship?," *Management Decision*, vol. 56, no. 6, pp. 1417–1429, 2018.

[13] T. R. Hannigan, V. P. Seidel, and B. Yakis-Douglas, "Product innovation rumors as forms of open innovation," *Research Policy*, vol. 47, no. 5, pp. 953–964, 2018.

[14] C. V. Ferreira, F. L. Biesek, and R. K. Scalice, "Product innovation management model based on manufacturing readiness level (MRL), design for manufacturing and assembly (DFMA) and technology readiness level (TRL)," *Journal of the Brazilian Society of Mechanical Sciences and Engineering*, vol. 43, no. 7, pp. 1–18, 2021.

[15] F. Schweitzer, E. Hende, and E. J. Hultink, "There's more than one perspective to take into account for successful customer integration into radical new product innovation: a framework and research agenda," *IEEE Transactions on Engineering Management*, vol. 67, no. 3, pp. 813–829, 2020.

[16] Y. Tang, X. Hu, and A. Montorosanchez, "University-industry interaction and product innovation performance of Guangdong manufacturing firms: the roles of regional proximity and research quality of universities," *The Journal of Technology Transfer*, vol. 45, no. 2, pp. 578–618, 2020.

[17] C. Liang, M. Cakanyildirim, and S. P. Sethi, "Can strategic customer behavior speed up product innovation?," *Production & Operations Management*, vol. 27, no. 8, pp. 1516–1533, 2018.

[18] I. B. Yang, S. G. Na, and H. Heo, "Intelligent algorithm based on support vector data description for automotive collision avoidance system," *International Journal of Automotive Technology*, vol. 18, no. 1, pp. 69–77, 2017.

[19] L. Sheng, B. Wang, and L. Zhang, "Intelligent adaptive filtering algorithm for electromagnetic-radiation field testing," *IEEE Transactions on Electromagnetic Compatibility*, vol. 59, no. 6, pp. 1765–1780, 2017.

[20] N. Mayadevi, V. P. Mini, and R. H. Kumar, "Fuzzy-based intelligent algorithm for diagnosis of drive faults in induction motor drive system," *Arabian Journal for Science and Engineering*, vol. 45, no. 3, pp. 1385–1395, 2020.

[21] H. Wang, L. Song, J. Liu, and T. Xiang, "An efficient intelligent data fusion algorithm for wireless sensor network," *Procedia Computer Science*, vol. 183, no. 3, pp. 418–424, 2021.

[22] P. Wang, S. Wang, X. Zhang et al., "Rational construction of CoO/CoF_2 coating on burnt-pot inspired 2D CNs as the battery-like electrode for supercapacitors," *Journal of Alloys and Compounds*, vol. 819, article 153374, 2019.

[23] X. Xu, D. Shahsavari, and B. Karami, "On the forced mechanics of doubly-curved nanoshell," *International Journal of Engineering Science*, vol. 168, article 103538, 2021.

[24] B. Zaarour and N. Mayhoub, "Effect of needle diameters on the diameter of electrospun PVDF nanofibers," *International Journal of BIM and Engineering Science*, vol. 4, no. 2, pp. 26–32, 2021.

Review Article

Effect of Various Factors on Plant Fibre-Reinforced Composites with Nanofillers and Its Industrial Applications: A Critical Review

M. Aravindh,[1] **S. Sathish,**[1] **L. Prabhu,**[1] **R. Ranga Raj** [ID],[2] **Murugesan Bharani** [ID],[3] **Pravin P. Patil,**[4] **Alagar Karthick,**[5,6] **and Rafael Luque**[6]

[1]*Centre for Machining and Material Testing, KPR Institute of Engineering and Technology, Coimbatore, 641407 Tamil Nadu, India*
[2]*Department of Aeronautical Engineering, Sri Ramakrishna Engineering College, Coimbatore, 641 022 Tamil Nadu, India*
[3]*School of Textile Leather and Fashion Technology Kombolcha 208, Kombolcha Institute of Technology, Wollo University, South Wollo, Ethiopia*
[4]*Department of Mechanical Engineering, Graphic Era Deemed to Be University, Bell Road, Clement Town, 248002 Dehradun, Uttarakhand, India*
[5]*Renewable Energy Lab, Department of Electrical and Electronics Engineering, KPR Institute of Engineering and Technology, Coimbatore, 641407 Tamil Nadu, India*
[6]*Departamento de Quimica Organica, Universidad de Cordoba, Edificio Marie Curie (C-3), Ctra Nnal IV-A, Km 396, E14014 Cordoba, Spain*

Correspondence should be addressed to Murugesan Bharani; bharani.murugesan@kiot.edu.et

The growing awareness of the environmental damage caused by petroleum-based fibres has led to an increase in renewable and biodegradable resources. The continually growing demand for eco-friendly and sustainable materials pushes automakers and material researchers to consider the ecological importance of their materials during fabricating, recovering, and disposal. Natural fibre-reinforced composites (NFRC) have been introduced into the automobile market substantially over the last ten years due to their renewability, eco-friendliness, recyclability, biodegradability, light weight, better specific strength, good resistance to impact and corrosion, abundantly available, ease of processing, and cost-effectiveness. Due to cost-effectiveness and weight reduction, NFRC is becoming a better replacement for petroleum/synthetic fibres like aramid, kevlar, carbon, and glass fibre-reinforced composites, and the transportation sector has instigated the use of these materials in many applications like car interiors and exteriors, dash boards, bumpers, spoilers, seat covers, and mirror casings. NFRC with nanofillers is gaining more attention in the field of engineering, particularly for automotive, defense, building, and construction applications due to better aspect ratio, larger surface area, and attractive properties. The mechanical, tribological, and thermal properties of plant fibre-reinforced composites can be improved through the incorporation of organic or inorganic nanofillers. The present review profoundly explores the effects of various factors influencing NFRC with nanofillers. This paper also summarises the effects of various chemical reagents, fabrication techniques, and industrial applications of NFRC.

1. Introduction

Increasing ecological threats and the diminution of petroleum-based products are dynamic forces that cause chemical industries to shift from petrochemicals to eco-friendly resources [1]. Material selection is crucial in the design and manufacture of a sustainable product [2]. Materials are investigated for their mechanical and thermal properties to improve the product efficiency and increase customer satisfaction [3]. Cellulosic fibres derived

from plants will play a vital role in this evolution as a significant renewable resource. NFRCs are one such material that offers flexibility during fabrication, desirable properties, and lower cost [4, 5]. Natural fibres act as reinforcing elements (discontinuous phase) in the composites used for various purposes. As a result, they have a more significant impact on a country's socioeconomic progress. Therefore, the exploitation of natural fibres to make sustainable and renewable products has engendered considerable attention. For example, NFRC has become increasingly important in the transportation segment where better strength characteristics and nondimensional change have to be combined amid less weight [6–8]. Biofibres are often derived from three sources: plants, animals, and minerals. Mineral-based fibres are underutilised in fibre-reinforced composite (FRC) research because they include asbestos, which is harmful to human health [9, 10]. On the other hand, plant-based fibres are endowed with hopeful distinctiveness, for example, cost effectiveness, biodegradability, ease of use, and excellent strength properties [11–15]. Figure 1 shows the classifications of natural fibres based on various categories. The performance of natural fibre is influenced by numerous factors such as plant seed quality, soil performance, fertiliser used, fibre maturity duration and age, fibre retting techniques, cultivation timing, retting degree, climatic change, fibre microfibrillar angle, fibre structure, fibre layer cell dimensions, fibre storage place, and fibre testing procedures [16–24]. Constituents such as cellulose, lignin, hemicellulose, pectin, waxes, oils, and moisture content make up natural fibres. The physical, mechanical, and thermal performance of NFRC can be influenced by many factors, including the selection of reinforcement and matrix, form of reinforcement, manufacturing methods adopted, volume/weight fraction of the reinforcement or matrix, the fibre aspect ratio, fibre matrix interaction, chemical reagents adopted for fibre treatment, stacking sequence, and orientation of the fibres, laminate curing temperature, and time [25–32]. Natural fibres are constructed as chemical constituents like cellulose, hemicellulose, lignin, wax, moisture, and ash content. The chemical constituents considerably vary between fibres to fibres and also affect the overall mechanical properties of the natural fibres. The diameters of the fibres varied considerably from the length of the individual filaments. The disadvantage of cellulosic fibres as reinforcement is that their hydrophilic nature makes them incompatible with thermoset or thermoplastic polymers, resulting in weak adhesion between the matrix and reinforcement because the polymer matrix is hydrophobic in nature [33–35]. However, adhesion between fibre and petroleum-based polymer should be enhanced with appropriate chemical treatment [36–38]. It is critical to building a better interphase for better composites in terms of performance; the external stress should be passed to fibres from polymeric resin. Chemical treatment is one method for natural fibres to maximise the adhesion at the interface. Since it minimises the amount of OH placed over the surface of the fibre and reduces the aspect ratio of the fibre, which improves the adhesion at the interface zone due to supe-

rior effective fibre surface area and aspect ratio. The outcome of fibre surface treatment depends on treatment time, type of reagent and its concentration, and temperature [39–44]. Different chemical reagents for various natural fibres include alkaline, benzoylation, acrylation, peroxide, silane, potassium permanganate, dewaxing, maleated coupling agent, stearic acid, graft copolymerization, acetylation, and isocyanate treatment [45–51].

Appropriate manufacturing techniques should be adopted to convert the raw materials into the final product without causing any defects. For the selection of proper manufacturing techniques to develop fibre reinforced composites, design and manufacturing experts would primarily consider a few factors. Such factors are size and shape of the end product, properties of reinforcement and matrix, processing characteristics of raw materials like processing temperature, pressure, curing time and curing temperature, production time, and manufacturing cost [52–57]. Conventionally, fibre-reinforced composites have been fabricated through various methods like autoclave, vacuum bag molding, compression molding, resin transfer molding, injection molding, filament winding, spray-up, and pultrusion [58–66]. The fibre/nanofiller-reinforced polymer composites are used in automobiles, aerospace, construction materials, packaging applications, and medical applications. Nanofillers could belong to organic and inorganic groups in nature. The particles like nanographeme, nanoclay, silica (SiO_2), nanomontmorillonite (MMT), titanium dioxide (TiO_2), carbon nanotube (CNT), calcium carbonate ($CaCO_3$), and n-SiC are inorganic fillers. However, the fillers, such as rice husk, coconut shell nanofiller, pinecone char, wood shaving char, and cellulosic nanofillers, are extracted from renewable sources and represent organic nanofillers [67–71]. For the nanocomposite preparation, nanofillers are mostly added using a weight fraction method in order to analyse the effect of filler loadings. Wagner et al. [72] revealed that the addition of just below 6 vol.% of polymer nanoparticles as reinforcements to make composite materials improved a wide array of properties like reduction in weight, dimensional stability, heat conductivity, and electrical conductivity. Saba et al. [73] in their research article showed that kenaf and jute fibres have a low density of 1.3 g/cm3 and bond well with thermosets (epoxy) and thermoplastic polymers. They also claimed that nanosized reinforcements develop better properties in the composite materials compared to their microsized counterparts. The review aims to summarise the effects of various factors influencing natural fibre-reinforced composites with nanofillers and various chemical reagents on different natural fibres. Furthermore, it summarises the effects of various manufacturing methods and industrial applications of NFRCs.

2. Effect of Various Factors on NFRC with Nanofillers

The influence of fibre length and weight fraction on the mechanical characteristics of agave/polypropylene composites was studied by Jayaraman [74]. He concluded that

FIGURE 1: Classification of plant fibres.

composite materials with a fibre length of more than 10 mm and a fibre weight fraction of between 15% and 35% revealed excellent mechanical performance. Stalin et al. [75] studied the mechanical properties of vetiver/banana/vinyl ester composites by varying the weight fraction of fibres. The mechanical properties of composites were improved by the hybridization of vetiver and banana fibre. Vinayaga-moorthy and Rajeswari [76] examined the mechanical properties of Vetiveria zizanioides/jute/glass composites by varying the weight fraction of fibres. Flexural, impact, compression, and hardness of hybrid composites were increased by 26.8%, 30.44%, 59.1%, and 28.65%, respectively. Sathishkumar et al. [77] analysed the mechanical characteristics of randomly oriented snake grass/banana/coir fibre hybrid composites. They revealed that the snake grass/banana and snake grass/coir fibre composites had better mechanical properties than banana/coir composites. Sanjay and Yogesha [78] studied the physical and mechanical properties of jute/kenaf/E-glass/epoxy hybrid composites. The mechanical properties of the laminates are influenced by the fibre arrangements and adhesion levels of the fabrics and the sequencing of high-strength fibre plies in the laminates. [79] examined the density and thermal stability of Furcraea foetida (FF) fibre-reinforced composites. The density of the Furcraea foetida fibre

(778 kg/m3) was relatively reduced in comparison with synthetic fibres, which are useful for making less dense products. FF fibres have a thermal stability of 320.5°C, which is much greater than thermoplastic polymerization temperatures. The effect of the volume fraction of snake grass fibre on tensile and flexural strength was analysed by Sathishkumar et al. [80]. They noticed that an increase in snake grass fibre of up to 25% exhibited the highest properties. Arpitha et al. [81] fabricated five different hybrid composites by using conventional manufacturing methods and varying fibre stacking sequences and studied the water absorption and tensile strength of sisal/glass/epoxy/filler composite laminates. They discovered that adding E-glass and SiC filler to composites can reduce voids and water absorption intake. Also, they revealed that the tensile strength of sisal/glass/epoxy/filler composites increased with an increase in glass fibre volume fraction. Sanjay and Yogesha [82] examined the effect of the fibre stacking sequence of jute, kenaf, and E-glass woven fabric composites on water absorption properties. The water absorption tests were performed on specimens immersed in three different water conditions: normal, distilled, and salt water. They observed that the hybridization of E-glass with jute and kenaf fibres decreases the maximum water absorption. Sanjay et al. [83] investigated the

TABLE 1: Effect of various factors on NFRC.

S. no	Fibres used	Factors influenced	Effects	Reference
1	Pineapple leaf	Fibre content	Tensile and flexural properties increase with fibre content.	[96]
2	Bamboo	Moisture absorption	An increase in moisture resulted in decreased interfacial shear strength.	[97]
3	Palmyra	Length and weight fraction	Better mechanical properties were obtained with a length of 55 mm and a weight of 55%.	[98]
4	Jute	Water absorption	An increase in water absorption resulted in poor flexural and compressive properties.	[99]
5	Banana/sisal	Length and weight	Up to 50% by weight, mechanical properties increased and water absorption decreased.	[100]
6	Banana/sisal	Weight fraction	The highest mechanical properties were obtained at 0.4%.	[101]
7	Chopped snake grass	Volume fraction	Improved mechanical properties when the volume fraction increases.	[80]
8	Abaca	Fibre loading	The mechanical properties showed an increasing tendency up to 40 wt.% of fibre loading.	[102]
9	Banana/sisal	Microfibrillar angle (MFA)	High tensile characteristics are seen in fibres with high cellulose content and a low MFA content.	[103]
10	Kenaf	Fibre content	Improved mechanical properties at 25% and 30% fibre content.	[104]
11	Luffa	Volume fraction of fibres	The mechanical characteristics of treated fibre composites were found to be optimal at 40% fibre volume fraction.	[105]
12	Snake grass	Volume fraction and fibre length	Improved mechanical properties of the short fibre isophthalic polyester composite were achieved at 25% V_f for the 30 mm fibre length.	[106]
13	Luffa cylindrica	Fibre content	Improved mechanical properties at 40% fibre content.	[107]
14	Oil palm	Aging and wear behavior	The wear test was carried out in dry conditions, and it was discovered that the composites immersed in engine oil and diesel performed better than the others.	[108]
15	Lantana camara	Load and fibre content	(1) The proportional wear loss increased in direct proportion to the increase in normal load (2) The optimum wear resistance property was obtained at a fibre content of 40%	[109]
16	Agave	Fibre length (3, 5, and 7 mm)	3 mm agave fibre reinforcement that has been alkali-treated had better mechanical properties.	[110]
17	Sansevieria cylindrica	Fibre length and weight	The mechanical characteristics of composites were optimal at 30 mm fibre length and then deteriorated beyond that.	[111]
18	Vakka	Volume fraction	Tensile characteristics improved as the percentage of vakka fibre in the composite increased.	[86]
19	Coir/silk	Fibre length	The mechanical characteristics of composites with 2 cm fibre length were the best.	[112]
20	Palm/coir fibre	Fibre weight fraction	The mechanical characteristics of composites with 30% fibre reinforcement were the best.	[113]
21	Sisal/nanoclay/polyester	Fibre and filler weight fraction	Improvement in tensile strength and water absorption when 25% sisal and 3% nanoclay.	[114]
22	Bagasse/nano-SiO$_2$/HDPE	Filler loading (2% to 5%)	Improvement in tensile strength by 71.46%.	[115]
23	Bagasse/nano-TiO$_2$/vinyl acetate	Filler loading (2%)	10% improvement in tensile strength.	[116]
24	Ramie/CNT/epoxy	Filler loading (0 to 0.6%)	Flexural strength and modulus were increased by 34% and 37%, respectively.	[117]
25	Bagasse/nanographene/PP	Filler loading	Improvement in mechanical properties such as tensile, flexural, and impact strength.	[118]
26	Jute/nanographeme/epoxy	Filler loading	Improvement in mechanical properties such as tensile, flexural, and impact strength.	[119]
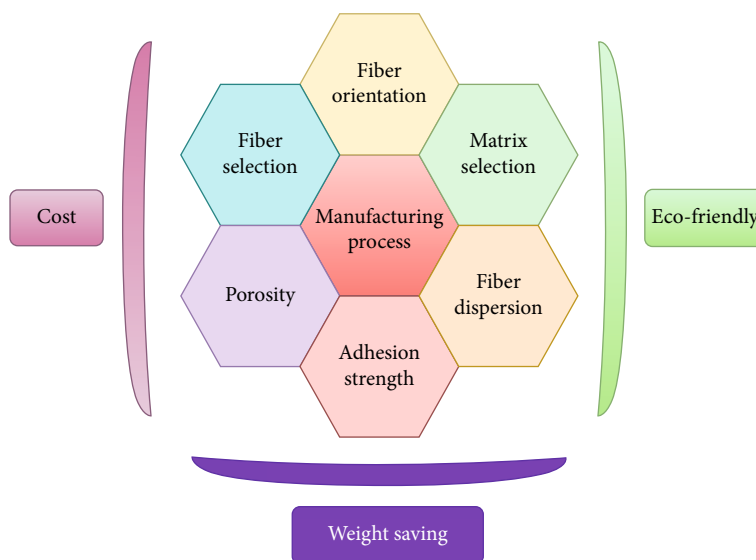
FIGURE 2: Various factors affecting NFRC.

hybridization effect of jute, kenaf, and E-glass fibres-reinforced hybrid composites on mechanical properties as a function of varying fibre layer sequences. They observed that incorporating glass fibre with jute and kenaf fibres enhanced the impact and interlaminar shear strength over pure NFRC. Compared to other laminates, the hybrid laminate with glass and kenaf fibre plies on the outside and jute fibre plies on the inside has improved characteristics. Vijay et al. [84] investigated the tensile strength, thermal stability, and surface properties of untreated and NaOH-treated Tridax procumbens fibres. They found that there was an increase in cellulose level after NaOH treatment and a decrease in hemicellulose, pectin, and wax, which improved thermal stability, tensile strength, and surface roughness. Sanjay et al. [85] assessed the tensile, flexural, and impact characteristics of hemp/glass fibre-reinforced hybrid composites as a function of fibre-layering sequences. They revealed that the incorporation of synthetic fibre with natural fibre decreased the water absorption and increased the mechanical properties of the composites. Murali Mohan Rao et al. [86] studied the tensile and flexural strength of composites made by strengthening vakka fibre into a polyester polymer as a function of the volume fraction of fibre. They revealed that vakka fibre composites had better tensile and flexural properties than banana and sisal fibre composites and were similar to bamboo-composite at the maximum volume fraction of fibre. Okubo et al. [87] analysed the flexural properties of bamboo/polypropylene composites. Due to enhanced bonding at the interface and fewer voids, the composite's flexural strength and flexural modulus increase by roughly 22% and 40%, respectively. Shanmugam and Thiruchitrambalam [88] studied the dynamic mechanical analysis of palmyra palm/jute/polyester hybrid composites. They observed that combining jute fibres with palmyra palm increased the impact and ILSS by 18% and 25%, respectively. Raghul et al. [89] present a detailed survey on the mechanical behavior of glass fibre reinforced epoxy composites with nanofillers. This composite is manufactured by the compression modelling method in the form of laminates. The weight fraction of the nanofiller in the matrix ranges from 1%wt to 7%wt. This nanocomposite consists of improved mechanical properties suitable for industrial manufacturing. Biswas [90] prepared an effect of silicon carbide (SiC) in bamboo/epoxy composites as a function of weight percentage of filler loadings. The optimum tensile and flexural strengths were observed at 10 wt.% SiC and 5 wt.% SiC, respectively. The highest hardness was found at 15 wt.% SiC. From the SEM analysis, it was concluded that poor adhesion is responsible for low mechanical strengths. Nguong et al. [91] studied the effect of n-SiC on polymer matrix composites with different weight loadings of fillers. They observed that the mechanical properties were increased when 1 wt.% of n-SiC was reinforced into the epoxy matrix. The tensile strength, flexural strength, and fracture toughness of the composites were significantly increased when fillers were added to the composites. The effect of the addition of silicon carbide to jute fibre-reinforced epoxy hybrid composite was studied by Ramadan et al. [92]. Jute fabric-reinforced epoxy composites with silicon carbide ranging from 2 to 8% were fabricated by the vacuum assisted resin infusion method. The jute fibre-reinforced composites with 4 vol.% SiC exhibited excellent tensile and flexural strength. The mechanical properties of the composite were decreased when the SiC content was exceeded by 4 vol.%. Finally, they observed that the addition of SiC to jute fibre reinforced epoxy composites significantly increased their tensile, flexural, and impact strength. Ali and Ahmad [93] have investigated the compressive strength, thermal stability, and morphology of the empty fruit bunch and nanoclay-reinforced hybrid polyurethane foam composites. The result reveals that the hybridization of empty fruit bunch and nanoclay enhances the mechanical and thermal

Stage	Factors effecting fiber quality

Plant growth
- Species of plant
- Crop cultivation
- Crop location
- Fiber location
- Local climate

Harvesting stage
- Cell wall thickness, coarseness of fiber
- Size and shape of lumen, porosity, microfibril angle
- Adherence between fibers and surrounding structure

Fiber extraction stage
- Decortication process
- Type of retting method

Degree of ripeness
- Hollow fiber
- Optimum strength
- Lignification

Supply stage
- Storage conditions
- Transportation conditions
- Age of fiber

Fiber processing
- Dry/mechanical
- Wet/steam explosion and ultrasound

Measurement conditions
- Tensile speed, gauge length
- Moisture temperature
- Different cross section of fibers at different points

Figure 3: Various factors affecting quality of natural fibres.

stabilities of the composites more than the empty fruit bunch alone filled composites. Olumuyiwa et al. [94] have studied the tensile, hardness, and impact strength of the coconut shell powder-reinforced polyethylene composite for different nanofiller loadings (5–25 wt.%). The hardness is found to be increased when the coconut shell filler loadings increase and the tensile strength, modulus of elasticity, impact energy, and ductility of the composite decrease with the increasing coconut shell filler loadings. They have also suggested that coconut shell powder-reinforced polyethylene composites are suitable for interior parts of automobiles. The thermal stability, electrical conductivity, water sorption, and mechanical properties of three different nanofillers (plastic waste char (PWC), wood shavings char (WSC), and pinecone char (PCC)) reinforced epoxy composites are analysed by Ahmetli et al. [95]. The result has revealed that the incorporation of nanochar particles enhances the mechanical and ther-

mal stability of the composites. Among three nanochar-filled composites, plastic waste char-filled composites have produced more thermal stability and decreased the moisture diffusivity of neat epoxy. Table 1 presents the effects of various factors influencing NFRC. Figure 2 shows various factors influencing NFRC. Figure 3 shows various factors influencing the quality of the natural fibre.

3. Effect of Chemical Treatments on NFRC with Nanofillers

Plant fibres generally consist of cellulose, hemicellulose, lignin, pectin, water-soluble, and waxy elements [120]. From the chemical point of view, the primary constituents of plant fibres are cellulose, in which Dglucopyranose units are linked together by b-(1-4)-glucosidic bonds; hemicelluloses consist mainly of D-pentose sugar units strongly bonded with cellulose fibrils through hydrogen
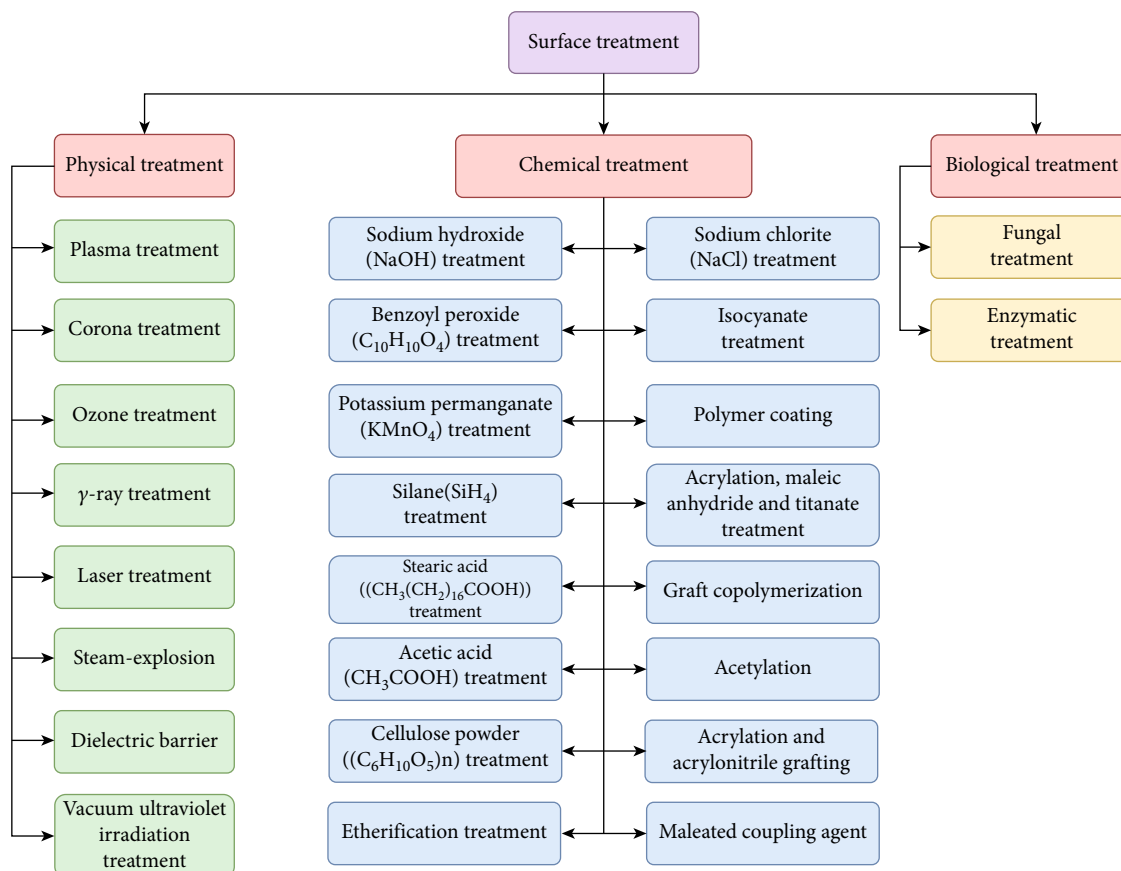
FIGURE 4: Types of chemical treatments.

bonding; and lignin, consisting of aromatic alcohol units such as coniferyl alcohol, sinapyl alcohol, and coumaryl alcohol [121, 122]. Pectin acts as an adhesive to hold fibres together in bundles and bundles to nonfibrous tissues. Hemicellulose, pectin, and lignin act like a matrix, whereas cellulose acts as reinforcement to the matrix, contributing to the strength of the fibre. Plant fibres are amenable to modifications as they bear hydroxyl groups (OH) from cellulose and lignin. The hydroxyl groups may be involved in hydrogen bonding within the cellulose molecules, thus reducing the matrix activity. Surface modifications can either stimulate OH groups or create new moieties that can interconnect with the polymer effectively [123]. Fibre surface characteristics such as adhesion, porosity, surface tension, and wetting can be enhanced upon chemical treatment. Surface modification of natural fibres can result in significant physical changes such as the removal of an oil or waxy layer, changes in fibre structure, density changes, and surface roughness changes [124, 125]. The interfacial adhesion of the composites can be enhanced by altering the fibre surface, altering the matrix, or altering both. Chemical treatment is necessary to improve the adhesion and wettability at the interface [126]. Figure 4 shows the types of various chemical treatments of natural fibres. Mwaikambo and Ansell [127] reported that alkalization improved the characteristics of kapok, sisal, jute, and hemp fibres, resulting in increased fibre–resin adhe-

sion and more incredible interfacial energy. Teli and Jadhav [128] studied the influence of NaOH reagent on the mechanical properties of Agave augustifolia fibres with changing reagent concentrations (i.e., 2, 5, 10, 15, and 20%) for 1 h and found the most extraordinary mechanical properties at 15%. Sawpan et al. [35] showed that the flexural properties of hemp fibre were enhanced by mercerization treatment with a NaOH concentration of 5%.

Dhanalakshmi et al. [129] assessed the alkali treatment effect on the flexural strength of areca fibre-reinforced epoxy composites and observed that flexural strength improved after treatment due to eliminating the hemicellulose, lignin, pectin, and waxes. After mercerization treatment, the characteristics of henequen fibres/high-density polyethylene composites improved owing to the elimination of a few lignin and hemicelluloses from the fibre surface, resulting in a larger contact surface area at the interface zone [130]. The 5% NaOH treatment increased the mechanical characteristics of Borassus fruit fibres by increasing their surface area and improving their interfacial properties [131]. Paul et al. [132] subjected banana fibre to permanganate treatment and investigated the influence of permanganate treatment on the tensile and flexural properties of banana-polypropylene composites. They found that the tensile and flexural properties increased by 5% and 10%, respectively. Lopez Manchado et al. [133] subjected flax fibre to acetylation treatment and analysed the influence of acetylation

TABLE 2: Effect of various chemical treatments on NFRC.

S. no	Fibres used	Type of chemical treatment	Effects	Reference
1	Sisal and roselle	Alkaline	Increased mechanical properties.	[141]
2	Alfa	Acetylation	Improved resistance to moisture absorption	[142]
3	Continuous henequen fibres	Silane (0.015 wt. %)	Improved mechanical properties.	[143]
4	Borassus fruit fibres	Alkaline	Thermal stability and tensile properties have been slightly improved.	[144]
5	Agave fourcroydes	Alkaline	Improved fibre matrix adhesion	[145]
6	Bagasse	Mercerization and acrylic acid	Superior tensile and flexural properties and reduced moisture absorption.	[145]
7	Unidirectional Roystonea regia	Alkaline	Improved tensile and flexural properties.	[146]
8	Sisal	Alkaline	Intracrystalline lignin and waxy, and resulted in improved mechanical interlocking.	[147]
9	Oil palm	Alkaline, acrylonitrile grafting, silane, acrylation, permanganate, acetylation, peroxide treatment	(1) Silane treatment-tensile strength reduced (2) Acrylation-enhanced tensile strength (3) Alkali and permanganate-tensile modulus increased (4) Silane and acrylate treatments showed optimum mechanical properties	[148]
10	Coir fibre	Alkaline	Interfacial adhesion between coir fibre and natural rubber was improved.	[149]
11	Sisal	Alkaline	The internal structure that resulted in a specific stiffness that was approximately the same as steel.	[150]
12	Kenaf	Alkaline	Improved mechanical properties	[151]
13	Ramie	Alkaline	Tensile strength of the ramie fibre improved from 4 to 18% compared to untreated fibre while Young's modulus decreased. Tensile strength increases as a result of a change in microfibrillar angle.	[152]
14	Bagasse	Alkaline	Improvement in tensile, flexural, and impact strength by 13%, 14%, and 16% compared to untreated fibres.	[153]
15	Sisal	Alkaline and benzoyl chloride treatment	Higher thermal stability.	[154]
16	Flax	Benzoyl chloride	Moisture absorption is reduced, and tensile properties are improved.	[155]
17	Jute	Alkaline	Improved dynamic mechanical properties.	[156]
18	Alfa	Styrene, acrylic acid, and maleic anhydride	These treatments resulted in reduced water uptake.	[157]
19	Kenaf	Alkaline	3% NaOH treatment led to ineffective removal of impurities. 9% NaOH cleaned the fibre surface.	[158]
20	Coir	Alkali and UV radiation	Higher shrinkage of the polymer grafted with fibre resulted in physicomechanical properties.	[159]
21	Sisal/5% nanomontmorillonite (MMT)/PP	Maleic anhydride grafted polypropylene	Improvement in tensile strength	[160]
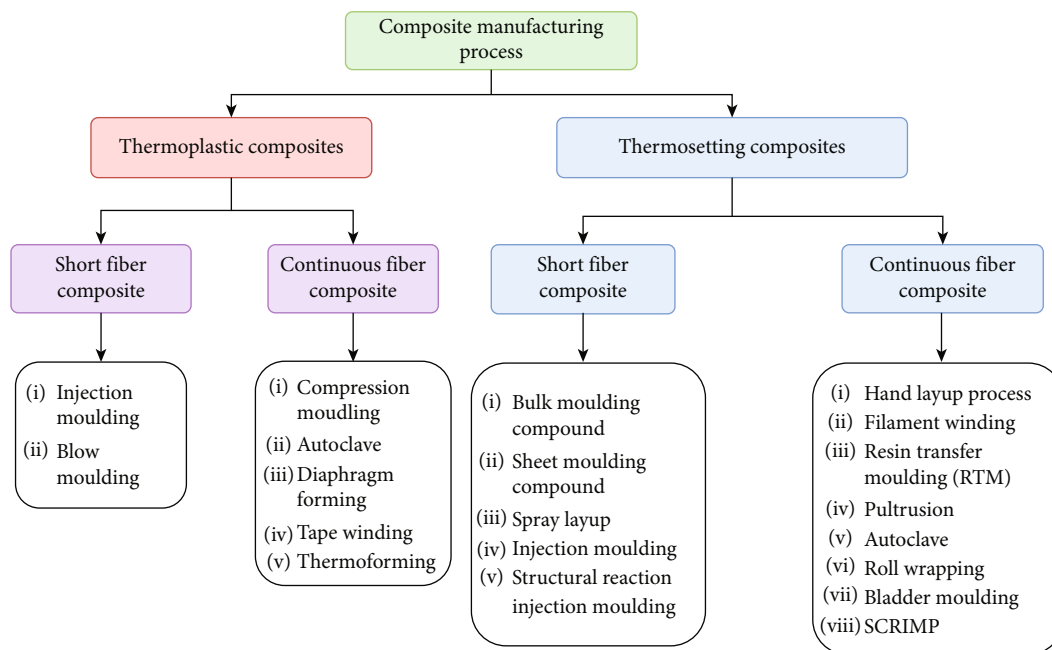
FIGURE 5: Classifications of manufacturing methods.

treatment on the thermal and mechanical properties of flax fibre-reinforced polypropylene composites. They found that the thermal and mechanical properties were enhanced by 50% and 25%, respectively. Singh et al. [134] discovered that an alkali-treated agave reinforced epoxy composite has better fracture strain and interfacial adhesion between fibre and matrix than an untreated fibre. Shanmugam and Thiruchitrambalam [88] revealed that the maleated anhydride-treated jute fibre-reinforced high-density polyethylene composite exhibits improved adhesion between fibre and matrix, which enhances the dynamic and static properties such as tensile, flexural, and impact strength. Singh et al. [134] investigated whether an alkali-treated agave-reinforced epoxy composite exhibits greater fracture strain and interfacial adhesion between the hydrophilic fibre and the hydrophobic matrix than an untreated fibre. Arbelaiz et al. [135] studied that 20 wt% of NaOH-treated flax fibre-reinforced polypropylene (PP) composites exhibited greater maximum interfacial shear strength (ILSS) than untreated flax fibre-reinforced composites. De Rosa et al. [136] observed that the composite containing 10% acetic acid-treated okra fibre has less tensile strength and Young's modulus than those containing untreated okra fibre-reinforced composites. Mwaikambo et al. [137] investigated the effect of alkaline treatment on the tensile and impact strength of hemp/euphorbia composites and reported that the tensile and impact strength increased by 30% each compared to untreated composites. Lopez Manchado et al. [133] examined the influence of alkaline treatment on the tensile and flexural properties of bamboo/polyester composites and found that the tensile and flexural strength increased by 10% and 2%, respectively, over untreated composites. [138] reported the result of alkali treatments on the mechanical properties of a jute/polyester composite. They observed

that 10% NaOH-treated fibre composites for 3 h provided an improvement in tensile strength, flexural strength, and impact strength. Shanmugam and Thiruchitrambalam [88] attempted to increase the mechanical properties of palmyra palm/jute/polyester hybrid composites by alkaline treatment with 5% NaOH for a duration of 30 min. They found that the mechanical properties such as tensile, flexural, and impact strength increased by 40%, 55%, and 4%, respectively. The new cane fibres were alkali treated for 24 hours at different concentrations of 2, 4, 6, and 8%, with the highest tensile and flexural strength being revealed at 6% [139]. The effect of mercerization on the flexural and impact strength of coir fibre-reinforced polyester composites was investigated by Prasad et al. [140]. The treated fibre composites outperformed the untreated ones due to stronger interfacial bonding between fibre and matrix after 72 hours of treatment with a 5% NaOH solution. Ragunathan et al. have fabricated rice husk powder-reinforced polypropylene/recycled acrylonitrile butadiene rubber composites by a melt mixing technique. The rice husk-filled composite is fabricated with silane and anhydride. The composites are characterised by mechanical, FTIR, and morphological properties. The composites influenced by anhydride exhibit better mechanical strength than the composites treated with silane. The coupling agent increases the bond between the rice husk filler and the matrix. Table 2 presents the effects of various chemical treatments on NFRC.

4. Effect of Various Manufacturing Methods on NFRC with Nanofillers

Shibata et al. [161] investigated the influence of the volume fraction of kenaf and bagasse fibres on reinforced corn starch composites manufactured by compression molding

TABLE 3: Effect of various manufacturing methods on NFRC.

S. no	Fibre/matrix	Manufacturing method used	Effects	Reference
1	Long discontinuous kenaf and jute-reinforced polypropylene	Hot-press	Maximum tensile strength and modulus were obtained at 40% fibre weight fraction.	[179]
2	Short bamboo fibre	Injection molding	Improved mechanical properties.	[180]
3	Chicken feather fibre/PLA	Injection molding	The SEM image indicated that an even distribution of CFF in the PLA matrix existed.	[181]
4	Sisal, banana, jute, and flax/propylene	Extrusion and compression molding	Enhanced the mechanical properties.	[182]
5	Silk/gelation	Compression molding	Mechanical properties were increased.	[183]
6	Agave/epoxy	Hand layup	Wear properties were improved.	[184]
7	Luffa/coir/PP	Injection molding	Mechanical properties were improved.	[185]
8	Luffa/thermoplastic starch	Compression molding	Mechanical properties were improved.	[107]
9	Luffa and groundnut/epoxy	Hand layup	Mechanical properties were improved.	[105]
10	Alfa/polyester	Hand layup	Mechanical properties increased up to 5% NaOH treatment.	[186]
11	Snake grass/polyester	Hand layup	Mechanical properties were improved.	[187]
12	Tea/epoxy	Compression molding	Mechanical properties were improved.	[188]
13	Cissus quadrangularis stem fibre/unsaturated polyester	Compression molding	Mechanical properties were improved.	[189]
14	Short Sansevieria cylindrica/polyester	Compression molding	Mechanical properties were improved.	[111]
15	Tapsi fibre	Hand layup	Mechanical properties were improved.	[190]
16	Prosopis juliflora/epoxy	Hand layup	Mechanical properties were improved.	[14]
17	Tea leaf fibre	Compression molding	Mechanical properties were improved.	[191]
18	Flax	Compression molding	Mechanical properties were improved.	[192]
19	Long jute fibre yarn	Injection molding	Mechanical properties were improved.	[173]
20	Short date palm leaves	Injection molding	Mechanical properties were improved.	[193]
21	Wood flour/6% MMT/PP	Injection molding	Tensile and flexural strength were improved by 20% and 13%, respectively.	[194]
22	Sisal/2-5% MMT/epoxy	Compression molding	Tensile strength and tensile modulus were improved by 27% and 47%, respectively.	[195]
23	Sisal/5% nanoclay/epoxy	Compression molding	Water absorption was reduced by 1/3 times.	[195]
24	Hemp/nanoclay/polyester	Compression molding	Water absorption and tensile strength were reduced by 8% and 20%, respectively.	[196]
25	Bamboo/MMT/HDPE	Melt compounding	Mechanical properties were decreased.	[197]
26	Bamboo/CNT/epoxy	Hand layup	Tensile strength and flexural strength were increased by 6.67% and 5.8%, respectively.	[198]

techniques and found that an increase in the volume fraction of kenaf and bagasse fibres led to an increase in the flexural modulus of composites by 60% and 66%, respectively. Barone [162] studied the influence of fibre length on the tensile, impact, and flexural strength of abaca fibre-reinforced phenolic composites manufactured by the compression molding technique and found that the fibre length of 30 mm was optimum for obtaining higher mechanical properties such as tensile, impact, and flexural strength. Kafi et al. [163] assessed the effect of styrene chemical treatment on the crack propagation of jute fibre-reinforced polyester composites manufactured by compression molding technique and reported that the resistance to crack propagation was enhanced when jute fibre was treated with styrene. Sharma and Kumar [164] investigated the effect of the weight frac-

tion of fibre on the flexural strength of banana fibre-reinforced polyurethane composites manufactured by a compression molding technique. They found that a fibre content of 15% by weight was optimum for achieving better flexural strength. Alamri and Low [165] reported that recycled cellulose fibre-reinforced epoxy composites manufactured by compression molding techniques with the weight content of fibre up to 46% had higher fracture toughness. Cao et al. [153] discovered that bagasse fibre-reinforced polyester composites manufactured by compression molding with 65% fibre content by weight had a 30% higher impact strength than other weight fractions of fibre. Jandas et al. [166] studied the effect of the volume fraction of banana fibres on the polylactic acid composite manufactured by the compression molding technique with 25% fibre
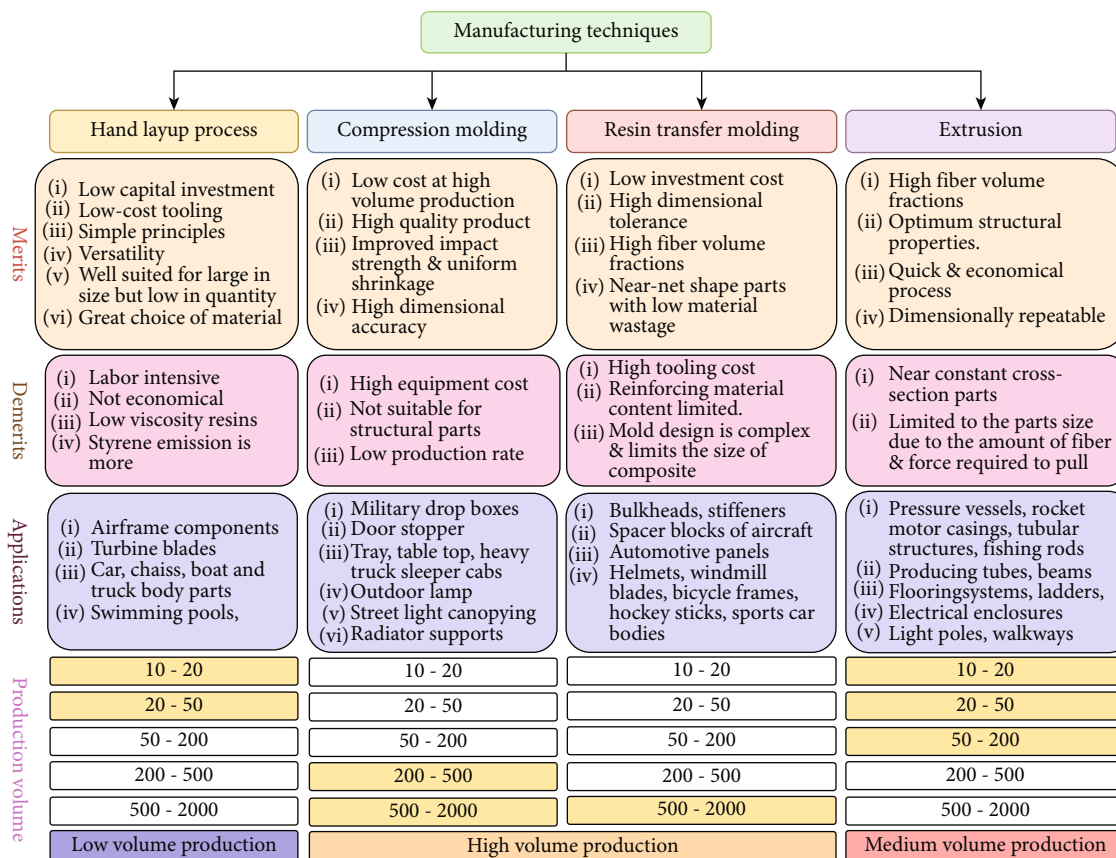
FIGURE 6: Merits, demerits, and applications of NFRC.

content by volume, resulting in higher impact strength compared to other volume fractions of fibres. Bledzki et al. [167] studied the influence of volume fraction on the impact strength of jute and flax fibre-reinforced epoxy hybrid composites manufactured by compression molding. They found that the impact strength of the hybrid composite was improved when there was an increase in the fibre content by volume and also reported that flax fibre-reinforced composites had greater maximum impact strength than jute reinforced composites. Yousif and El-Tayeb [168] studied the effect of fibre length and fibre diameter on the wear rate of oil palm fibre-reinforced polyester composites manufactured by hand layup technique and found that the fibre length of 1–1.5 mm and fibre diameter of 350 micro m ^{2}notably reduced the wear rate by about three to four times compared to pure polyester resin. El-Tayeb [169] investigated the influence of fibre length on the wear resistance of sugarcane fibre-reinforced polyester composites manufactured by hand layup technique and found that the composite with a fibre length greater than 5 mm has increased wear resistance due to less fibre pullout present at that length. Assarar et al. [170] studied the flax fibre-reinforced epoxy composite manufactured by hand layup technique and reported that water aging significantly increased the strain rate by 61% and decreased the Young's modulus by 40% of the composite compared to the manmade glass fibre. Venkateshwaran et al. [171] analysed the influence of NaOH

reagent on the mechanical properties of banana/epoxy composite manufactured by hand layup technique. They concluded that 1% alkaline-treated fibre increased the mechanical properties of untreated fibre composites. Ray et al. [172] analysed the influence of NaOH reagent on the ILSS of a jute/vinyl ester composite manufactured by hand layup technique and concluded that the fibre treated with 5% NaOH for 4 hrs gave 20% progress in the ILSS. Prasad et al. [140] studied the influence of NaOH reagent on the impact and flexural strength of coir/polyester composites manufactured by hand layup technique and noticed that the coir fibre bleached with 5% NaOH for 3 days gave a 40% enhancement in the impact and flexural strength. Gao and Mader [173] fabricated a jute fibre reinforced polypropylene composite using injection molding techniques and noticed that the fibre length was significantly influencing the tensile properties of the composite. Karmaker and Schneider [174] fabricated jute and kenaf fibre-reinforced polypropylene hybrid composites using injection molding techniques and reported that the hybrid composite had higher mechanical properties with maximum jute fibre than kenaf fibre. Bledzki et al. [175] analysed the influence of acetylation treatment on the mechanical characteristics of a flax fibre-reinforced polypropylene composite fabricated by injection molding technique. They concluded that the mechanical characteristics of the treated fibre composite increased by up to 35% compared to untreated fibre. Yang

Manufacturer	Model	Applications
Rover	2000 and others	Rear storage shelf/panel and insulations
Opel	Vectra, Astra, Zafira	Door panels, pillar cover panel and instrumental panel
Volkswagen	Passat, Golf, A4, Bora	Seat back, boot-lid finish panel and boot-liner
Audi	A2, A4, A6, A8, Roadstar, Coupe	Back door panel, spare tire lining, seat back and boot-liner
Daimle chrysler	A, C., E and S class, Evobus	Car dashboard/windshield, door panels and pillar cover panel
BMW	3,5,7 series and other pilot	Headliner panel, door panels noise insulations panels, seat back and moulded foot well things
Peugeot	406	Parcel shelf, seat backs and rear/front door panels
Fiat	Marea, punto, brava, alfa romeo 146, 156, 15	Door panel
General motors	Cadillac De Ville, Chevrolet Trail blazer	Corgo area floor mat and seat backs
Toyota	ES3	Interior parts and pillar garnish
Saturn	L300	Door panel and package trays
Volvo	V70, C70	Natural foams, seat padding and cargo floor tray
Ford	Mondeo CD 162, Focus	Door panels, boot-liner, B pillar, door inserts and food trays
Saab	9S	Door panels, roof cover, trunk panel
Renault	Clio, Twingo	Rear parcel shelf
Toyota	Brevis, Harrier, Celsior	Seat backs, floor mats, door panels and spare tire cover
Mitsubishi	-	Instrumental panel, door panels and cargo area floor
Mercedes benz	A, C., E and S classes	Glove box, door panels, Instrumental panel support insulation, Moulding rod/apertures, seat backrest panel, trunk panel, seat surface/backrest, internal engine cover, engine insulation, sun visor, bumper, interior insulation, wheel box and roof cover.

FIGURE 7: Automobile applications of NFRC [213–217].

et al. [176] investigated the influence of maleated anhydride treatment on the tensile strength of a rice husk fibre-reinforced polypropylene composite fabricated by injection molding technique and noticed that the tensile strength of the treated fibre composite was improved due to enhanced adhesion between the hydrophilic fibre and the hydrophobic matrix. Pickering et al. [177] analysed the influence of fungal and NaOH reagents on the mechanical characteristics of a hemp/polypropylene composite fabricated by injection molding technique. They noticed that the mechanical characteristics of fungal-treated and combined fungal/alkaline-treated composites were increased by 22% and 32%, respectively. Wielage et al. [178] fabricated flax and hemp fibre-reinforced polypropylene composites using injection molding techniques and noticed that maleated anhydride-grafted treatment significantly enhanced the dynamic
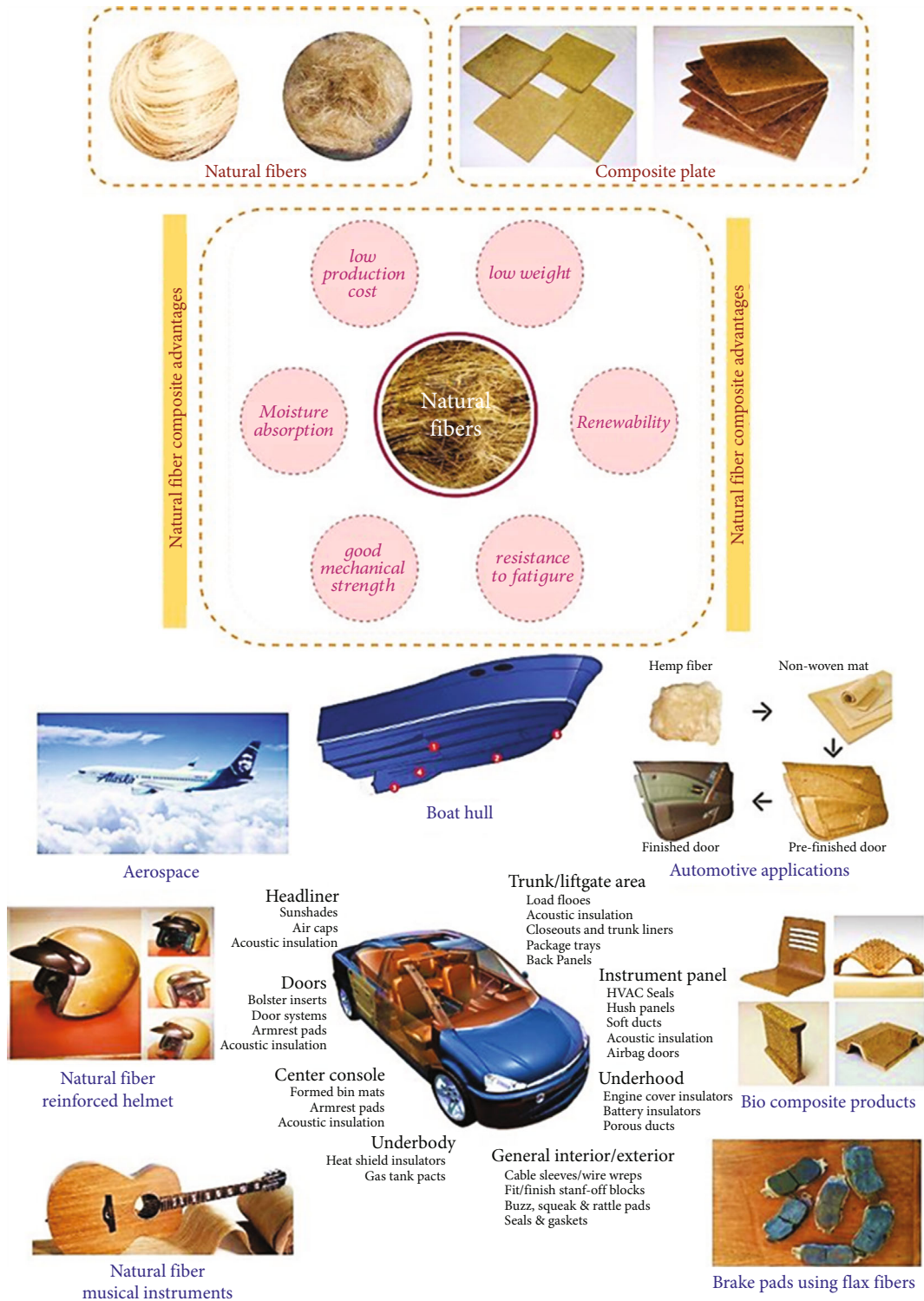
FIGURE 8: Industrial applications of NFRC [218–220].

mechanical properties of the composites compared to untreated fibre composites. Figure 5 shows the classifications of manufacturing methods for the NFRC. Table 3 presents the effect of various manufacturing methods on NFRC. Figure 6 presents the merits, demerits, and applications of NFRC.

5. Industrial Applications of NFRC

Composites reinforced with natural fibres are gaining more attention in the market right now, as demand for high strength-to-weight ratios for industrial applications grows. The NFRC material has a high strength-to-weight ratio,

TABLE 4: Applications of NFRC in various fields.

S. no	Fibre	Components	Reference
1	Flax/sisal	Door trim panels and cable linings	[221]
2	Kenaf	Automobile dashboards, carpet padding, and products as rope, twine, bagging, and rugs	[222]
3	Jute	Brake pad and car insulation	[223]
4	Sisal	Ropes, mats, carpets, and fancy articles	[15]
5	Soybean oil	High-quality paint enamel	[224]
6	Coconut	Interior trim and seat cushioning	[225]
7	Banana	Household telephone stand	[226]
8	Soy oil	Structural panels	[227]
9	Kenaf/glass	Car bumper	[228]
10	Coir	Liquid storage tanks	[229]
11	Sugar palm fibre	Brushes, ropes	[230]
12	Mature coconut	Textiles (mats and carpets), building (thermal insulation), and automobile (cushion and seat covers)	[231]
13	Ichu fibre	Construction material	[232]
14	Tapsi/karaya gum	Food and pharmaceutical industries	[233]
15	Date palm	Insulation material in buildings	[234]
16	Azadirachta indica	Car roofing, interior and exterior panels, home appliances, container boxes, particle boards, and parcel shelves.	[235]
17	Tridax procumbens	Ayurvedic medicines to treat liver disorders	[84]

moderate stiffness, impact resistance, durability, improved corrosion resistance, and excellent fatigue strength. Because of these numerous benefits, NFRC has found applications in construction, aircraft, defense, hockey sticks, homes, surgical equipment, leisure, ship hulls, and automobile parts [199–203]. Snake grass, bamboo, kenaf, flax, vetiver, areca, and ramie fibres are used in various applications like office furniture, textile products, ropes, home appliances, fishing nets, the paper industry, packing materials, and building materials [204]. Textiles, households, oil pipes, packing products, and structural panels were all made with hemp/epoxy composites. The roof cover, electronic panels, trunk panels, seatback covers, packing items, and support insulation are all made from kenaf. Fibre-reinforced composites in the bast and seed category were used in the glove box, back rest panels, filter cloths, wheel boxes, and household furnishings [205]. The pineapple and sisal fibre-reinforced hybrid composites were used in underfloor-body panels, partition panels, door cladding, parcel shelves, two-wheeler bumpers, crates, drainage pipe, table mats, fishing boats, and automobile body building [206]. The coir/epoxy composites were used in the seat cushions, mirror casings, storage tanks, postboxes, helmet casings, brushes, ropes, bags, brooms, door shutters, and building panels [207].

Daimler Chrysler used flax, cotton, sisal, and banana fibres for floor panels, dashboards, seat back rests, door panels, and pillar cover panels of A, C, and E class models. Lotus Peugeot used hemp and sisal fibre reinforced composites for packaging trays, door panels, interior mats, seat backs, and body panels of the eco-elsie 406 [208]. The coir/natural latex rubber-reinforced hybrid composites were used in seat belt lining, soundproofing

panels, particle boards, and parcel shelves. Flax, sisal, and coir fibres with thermoplastic matrix such as PP, PE, PS, and PVC were used in automobile components, containers for logistics, interior parts, and household products. Nippon Electric Company (NEC) used kenaf fibres to reinforce PLA biocomposite for mobile phone casings. Museeuw Bikes used flax and hemp fibres reinforced with epoxy composites for racing bicycle frames and casings for musical instruments [209]. Flax/sisal/epoxy composites were used in parcel shelves, curtains, seat backs, back cushions, floor mats, and interior panels for top-class vehicles [210]. Door bolsters, centre consoles, carriers for covered door panels, seat back panels, covered components for instrument panels, rear deck trays, pillars, covered inserts, seat backs, carriers for hard and soft armrests, door panels, headliners, side and backwalls, load floors, and trunk trim were all made from bast fibre-reinforced PP/polyester composites [211].The sisal/glass/filler/epoxy-reinforced composites were used in the frames, toys, and electronic panels [81]. The flax/epoxy composites were used in the aerospace-military aviation fuselage, rudder, slats, and wings [212]. Figure 7 presents various automobile applications of NFRC. Figure 8 shows industrial applications of NFRC. Table 4 presents applications of NFRC in various fields.

6. Conclusions

The exploitation of natural fibre-reinforced composites by using an emerging technology transforms the future of the coming days. The hydrophilic nature of natural fibres affects bonding to a hydrophobic polymer, which results in poor

mechanical properties. To overcome this issue, the natural fibre surface must be modified to promote better interaction between fibre and matrix. The innovative and commercial applications of natural fibre-reinforced composites can help develop new revolts to maintain our natural properties. Natural fibres such as flax, snake grass, ramie, vetiver, areca, kenaf, hemp, kenaf, pineapple, and bamboo are gifted to the transportation industry because of their renewability, sustainability, eco-friendliness, and biodegradability. Composites reinforced with natural fibres are gaining traction in the market as the market's demand for high strength-to-weight ratio for industrial applications grows. This extensive range of different benefits has led fibre-reinforced composites to find more applications in the automobile, aerospace, marine, biomedical, construction, household, and sports industries. Incorporating nanofillers to plant fibre-reinforced composites introduces a positive effect on physical and mechanical properties. Many investigations are revealed, reviewed, and presented in this article concerning the effects of various factors influencing different types of chemical treatment and manufacturing methods and industrial applications of natural fibres and reinforced composites.

Data Availability

The data used to support the findings of this study are included within the article.

Conflicts of Interest

The authors declare that there is no conflict of interest regarding the publication of this article.

Acknowledgments

References

[1] M. R. Sanjay and S. Suchart, "Lightweight natural fiber composites," *Journal of Applied Agricultural Science and Technology*, vol. 3, no. 2, p. 178, 2019.

[2] A. Lotfi, H. Li, D. V. Dao, and G. Prusty, "Natural fiber-reinforced composites: a review on material, manufacturing, and machinability," *Journal of Thermoplastic Composite Materials*, vol. 34, no. 2, pp. 238–284, 2021.

[3] H. Altenbach, J. Altenbach, W. Kissing, H. Altenbach, J. Altenbach, and W. Kissing, "Classification of composite materials," in *Mechanics of Composite Structural Elements*, pp. 1–14, Springer, Singapore, 2004.

[4] F. M. Al-Oqla and S. M. Sapuan, "Natural fiber reinforced polymer composites in industrial applications: feasibility of date palm fibers for sustainable automotive industry," *Journal of Cleaner Production*, vol. 66, pp. 347–354, 2014.

[5] M. Ramesh, C. Deepa, L. Rajesh Kumar, M. R. Sanjay, and S. Siengchin, "Life-cycle and environmental impact assessments on processing of plant fibres and its bio-composites: a critical review," *Journal of Industrial Textiles*, 2020.

[6] S. Sathish, T. Ganapathy, and T. Bhoopathy, "Experimental testing on hybrid composite materials," *Applied Mechanics and Materials*, vol. 592-594, pp. 339–343, 2014.

[7] M. Ramesh and L. Rajesh Kumar, "Bioadhesives," in *Green Adhesives*, R. B. Inamuddin, M. I. Ahamed, and A. M. Asiri, Eds., pp. 145–161, Wiley-Scrivener Publisher, 2020.

[8] A. Saravana Kumar, S. Maivizhi Selvi, and L. Rajeshkumar, "Delamination in drilling of sisal/banana reinforced composites produced by hand lay-up process," *Applied Mechanics and Materials*, vol. 867, pp. 29–33, 2017.

[9] R. Karnani, M. Krishnan, and R. Narayan, "Biofiber-reinforced polypropylene composites," *Polymer Engineering and Science*, vol. 37, no. 2, pp. 476–483, 1997.

[10] B. Singh, A. Verma, and M. Gupta, "Studies on adsorptive interaction between natural fiber and coupling agents," *Journal of Applied Polymer Science*, vol. 70, no. 9, pp. 1847–1858, 1998.

[11] S. Sathish, K. Kumaresan, L. Prabhu, and S. Gokulkumar, "Experimental investigation on mechanical and FTIR analysis of flax fiber/epoxy composites incorporating SiC, Al_2O_3 and graphite," *Romanian Journal of Materials*, vol. 48, pp. 476–482, 2018.

[12] S. Sathish, K. Kumaresan, L. Prabhu, and N. Vigneshkumar, "Experimental investigation on volume fraction of mechanical and physical properties of flax and bamboo fibers reinforced hybrid epoxy composites," *Polymers and Polymer Composites*, vol. 25, no. 3, pp. 229–236, 2017.

[13] D. G. Devadiga, K. Subrahmanya Bhat, and G. T. Mahesha, "Sugarcane bagasse fiber reinforced composites: recent advances and applications," *Cogent Engineering*, vol. 7, no. 1, article 1823159, 2020.

[14] P. Venkateshwar Reddy, R. V. Saikumar Reddy, J. Lakshmana Rao, D. Mohana Krishnudu, and P. Rajendra Prasad, "An overview on natural fiber reinforced composites for structural and non- structural applications," *Materials Today: Proceedings*, vol. 45, pp. 6210–6215, 2021.

[15] O. Akampumuza, P. M. Wambua, A. Ahmed, W. Li, and X. H. Qin, "Review of the applications of biocomposites in the automotive industry," *Polymer Composites*, vol. 38, no. 11, pp. 2553–2569, 2017.

[16] M. Ramesh, L. Rajeshkumar, A. Khan, and A. M. Asiri, "Self-healing polymer composites and its chemistry," in *Self-Healing Composite Materials, Woodhead Publishing*, pp. 415–427, Elsevier, 2020.

[17] S. Sathish, N. Karthi, L. Prabhu et al., "A review of natural fiber composites: extraction methods, chemical treatments and applications," *Materials Today: Proceedings*, vol. 45, pp. 8017–8023, 2021.

[18] N. Karthi, K. Kumaresan, G. Rajeshkumar, S. Gokulkumar, and S. Sathish, "Tribological and thermo-mechanical performance of chemically modified musa acuminata/corchorus capsularis reinforced hybrid composites," *Journal of Natural Fibers*, pp. 1–14, 2021.

[19] L. Prabhu, V. Krishnaraj, S. Sathish, S. Gokulkumar, M. R. Sanjay, and S. Siengchin, "Mechanical and acoustic properties of alkali-treated sansevieria ehrenbergii/camellia sinensis fiber–reinforced hybrid epoxy composites: incorporation of glass fiber hybridization," *Applied Composite Materials*, vol. 27, no. 6, pp. 915–933, 2020.

[20] S. Gokulkumar, P. R. Thyla, S. Sathish et al., "Acoustical and mechanical optimization of camellia sinensis/ananas comosus/

GFRP/epoxy composites by TOPSIS & weighted aggregates sum product assessment method," *Materials Today: Proceedings*, vol. 45, pp. 7980–7985, 2021.

[21] M. S. Sreekala, M. G. Kumaran, and S. Thomas, "Oil palm fibers: morphology, chemical composition, surface modification, and mechanical properties," *Journal of Applied Polymer Science*, vol. 66, no. 5, pp. 821–835, 1997.

[22] P. Herrera-Franco, A. Valadez-GonzaÂlez, and M. Cervantes-Uc, "Development and characterization of a HDPE-sand-natural fiber composite," *Composites Part B: Engineering*, vol. 28, no. 3, pp. 331–343, 1997.

[23] K. L. Pickering, A. Abdalla, C. Ji, A. G. McDonald, and R. A. Franich, "The effect of silane coupling agents on radiata pine fibre for use in thermoplastic matrix composites," *Composites: Part A*, vol. 34, no. 10, pp. 915–926, 2003.

[24] N. Karthi, K. Kumaresan, S. Sathish et al., "Effect of weight fraction on the mechanical properties of flax and jute fibers reinforced epoxy hybrid composites," *Materials Today: Proceedings*, vol. 45, pp. 8006–8010, 2021.

[25] M. Ramesh and L. Rajeshkumar, "Wood flour filled thermoset composites," *Thermoset Composites: Preparation, Properties and Applications, Materials Research Forum*, vol. 38, pp. 33–65, 2018.

[26] M. Kumaresan, S. Sathish, and N. Karthi, "Effect of fiber orientation on mechanical properties of sisal fiber reinforced epoxy composites," *Journal of Applied Science and Engineering*, vol. 18, pp. 289–294, 2015.

[27] M. Zwawi, "A review on natural fiber bio-composites, surface modifications and applications," *Molecules*, vol. 26, no. 2, p. 404, 2021.

[28] S. C. R. Furtado, A. L. Araújo, A. Silva, C. Alves, and A. M. R. Ribeiro, "Natural fibre-reinforced composite parts for automotive applications," *International Journal of Automotive Composites*, vol. 1, no. 1, pp. 18–38, 2014.

[29] L. Mohammed, M. N. M. Ansari, G. Pua, M. Jawaid, and M. S. Islam, "A review on natural fiber reinforced polymer composite and its applications," *International Journal of Polymer Science*, vol. 2015, 15 pages, 2015.

[30] S. Sathish, M. Kumaresan, N. Karthi, and T. D. Kumar, "Tensile and impact properties of natural fiber hybrid composite materials," *International Journal of Modern Engineering Research*, vol. 4, no. 9, pp. 9–12, 2014.

[31] L. Prabhu, V. Krishnaraj, S. Sathish, and V. Sathyamoorthy, "Experimental and finite element analysis of GFRP composite laminates with combined bolted and bonded joints," *Indian Journal of Science and Technology*, vol. 10, no. 14, pp. 1–7, 2017.

[32] N. Mohanta and S. K. Acharya, "Investigation of mechanical properties of luffa cylindrica fibre reinforced epoxy hybrid composite," *International Journal of Engineering, Science and Technology*, vol. 7, no. 1, pp. 1–10, 2016.

[33] L. G. Angelini and S. Tavarini, "Ramie [Boehmeria nivea (L.) gaud.] as a potential new fibre crop for the Mediterranean region: growth, crop yield and fibre quality in a long-term field experiment in Central Italy," *Industrial Crops and Products*, vol. 51, pp. 138–144, 2013.

[34] M. B. Hoque, M. Z. I. Mollah, M. R. I. Faruque, M. Abdul Hannan, and R. A. Khan, "Review on the mechanical properties of pineapple leaf fiber (PALF) reinforced epoxy resin based composites," *Research Journal of Engineering and Technology*, vol. 6, no. 4, pp. 855–860, 2021.

[35] M. A. Sawpan, K. L. Pickering, and A. Fernyhough, "Effect of various chemical treatments on the fibre structure and tensile properties of industrial hemp fibres," *Composites Part A: Applied Science and Manufacturing*, vol. 42, no. 8, pp. 888–895, 2011.

[36] N. M. Nurazzi, M. R. M. Asyraf, S. F. Athiyah et al., "A review on mechanical performance of hybrid natural fiber polymer composites for structural applications," *Polymers*, vol. 13, no. 13, 2021.

[37] A. Geremew and P. De Winne, "Treatment of natural fiber for application in concrete pavement," *Advances in Civil Engineering*, vol. 2021, Article ID 6667965, 13 pages, 2021.

[38] V. Mahesh, V. Mahesh, and D. Harursampath, "Influence of alkali treatment on physio-mechanical properties of jute–epoxy composite," *Advances in Materials and Processing Technologies*, pp. 1–12, 2021.

[39] S. Gokulkumar, P. R. Thyla, L. Prabhu, and S. Sathish, "Measuring methods of acoustic properties and Influence of physical parameters on natural fibers: a review," *Journal of Natural Fibers*, vol. 17, no. 12, pp. 1719–1738, 2020.

[40] L. Prabhu, V. Krishnaraj, S. Gokulkumar, S. Sathish, and M. Ramesh, "Mechanical, Chemical and Acoustical Behavior of Sisal - Tea Waste - Glass Fiber Reinforced Epoxy Based Hybrid Polymer Composites," *Materials Today: Proceedings*, vol. 16, pp. 653–660, 2019.

[41] A. Khenblouche, D. Bechki, M. Gouamid et al., "Extraction and characterization of cellulose microfibers from Retama raetam stems," *Polímeros*, vol. 29, no. 1, pp. 1–8, 2019.

[42] S. Das, "Mechanical properties of waste paper/jute fabric reinforced polyester resin matrix hybrid composites," *Carbohydrate Polymers*, vol. 172, pp. 60–67, 2017.

[43] M. S. Rahman, "Jute-a versatile natural fiber. Cultivation, extraction and processing," in *Industrial Applications of Natural Fibers Industrial Applications of Natural Fibers: Structure, Properties and Technical Applications*, J. Müssig, Ed., pp. 135–161, Wiley, 2010.

[44] H. Ku, N. Hao Wang, P. Koop, and M. Trada, "A review on the tensile properties of natural fiber reinforced polymer composites," *Composites Part B: Engineering*, vol. 42, no. 4, pp. 856–873, 2011.

[45] N. Karthi, K. Kumaresan, S. Sathish, S. Gokulkumar, L. Prabhu, and N. Vigneshkumar, "An overview: natural fiber reinforced hybrid composites, chemical treatments and application areas," *Materials Today: Proceedings*, vol. 27, no. 3, pp. 2828–2834, 2020.

[46] S. Sathish, L. Prabhu, S. Gokulkumar, N. Karthi, D. Balaji, and N. Vigneshkumar, "Extraction, treatment and applications of natural fibers for bio-composites–a critical review," *International Polymer Processing*, vol. 36, no. 2, pp. 114–130, 2021.

[47] A. Bartos, K. Nagy, J. Anggono et al., "Biobased PLA/sugarcane bagasse fiber composites: effect of fiber characteristics and interfacial adhesion on properties," *Composites Part A: Applied Science and Manufacturing*, vol. 143, article 106273, 2021.

[48] E. F. Rodriguesa, T. F. Maiaa, and D. R. Mulinaria, "Tensile strength of polyester resin reinforced sugarcane bagasse fibers modified by estherification," *Procedia Engineering*, vol. 10, pp. 2348–2352, 2011.

[49] A. Lavoratti, D. Romanzini, S. C. Amico, and A. J. Zattera, "Influence of fibre treatment on the characteristics of buriti

and ramie polyester composites," *Polymers & Polymer Composites*, vol. 25, no. 4, pp. 247–256, 2017.

[50] M. T. Zafar, S. N. Maiti, and A. K. Ghosh, "Effect of surface treatment of jute fibers on the interfacial adhesion in poly (lactic acid)/jute fiber biocomposites," *Fibers and Polymers*, vol. 17, no. 2, pp. 266–274, 2016.

[51] S. Sudha and G. Thilagavathi, "Effect of alkali treatment on mechanical properties of woven jute composites," *Journal of the Textile Institute*, vol. 107, no. 6, pp. 691–701, 2016.

[52] E.-R. Kenawy, A. A. Ghfar, S. Wabaidur et al., "Cetyltrimethylammonium bromide intercalated and branched polyhydroxystyrene functionalized montmorillonite clay to sequester cationic dyes," *Journal of Environmental Management*, vol. 219, pp. 285–293, 2018.

[53] S. M. Wabaidur, M. A. Khan, M. R. Siddiqui et al., "Oxygenated functionalities enriched MWCNTs decorated with silica coated spinel ferrite – a nanocomposite for potentially rapid and efficient de-colorization of aquatic environment," *Journal of Molecular Liquids*, vol. 317, p. 113916, 2020.

[54] M. Alok Mittal, G. S. Naushad, Z. A. ALothman, S. M. Wabaidur, and M. Alam, "Fabrication of MWCNTs/ThO2-nanocomposite and its adsorption behavior for the removal of Pb(II) metal from aqueous medium," *Desalination and Water Treatment*, vol. 57, no. 46, pp. 21863–21869, 2016.

[55] Z. A. Alothman, A. H. Bahkali, M. A. Khiyami et al., "Low cost biosorbents from fungi for heavy metals removal from wastewater," *Separation Science and Technology*, vol. 55, no. 10, pp. 1766–1775, 2020.

[56] M. Khan, A. A. Alqadami, S. M. Wabaidur et al., "Oil industry waste based non-magnetic and magnetic hydrochar to sequester potentially toxic post-transition metal ions from water," *Journal of Hazardous Materials*, vol. 400, article 123247, 2020.

[57] Z. ALOthman, "A review: fundamental aspects of silicate mesoporous materials," *Materials*, vol. 5, no. 12, pp. 2874–2902, 2012.

[58] L. Prabhu, V. Krishnaraj, S. Sathish et al., "A review on natural fiber reinforced hybrid composites: chemical treatments, manufacturing methods and potential applications," *Materials Today: Proceedings*, vol. 45, pp. 8080–8085, 2021.

[59] S. Sathish, K. Kumaresan, L. Prabhu, S. Gokulkumar, N. Karthi, and N. Vigneshkumar, "Experimental investigation of mechanical and morphological properties of flax fiber reinforced epoxy composites incorporating SiC and Al$_2$O$_3$," *Materials Today: Proceedings*, vol. 27, pp. 2249–2253, 2020.

[60] S. Gokulkumar, P. R. Thyla, L. Prabhu, S. Sathish, and N. Karthi, "A comparative study on epoxy based composites filled with pineapple/areca/ramie hybridized with industrial tea leaf wastes/GFRP," *Materials Today: Proceedings*, 2020.

[61] M. Y. Khalid, R. Imran, Z. U. Arif et al., "Developments in chemical treatments, manufacturing techniques and potential applications of natural-fibers based biodegradable composites," *Coatings*, vol. 11, no. 3, p. 293, 2021.

[62] M. J. Suriani, H. Z. Rapi, R. A. Ilyas, M. Petru, and S. M. Sapuan, "Delamination and manufacturing defects in natural fiber-reinforced hybrid composite: a review," *Polymers*, vol. 13, no. 8, p. 1323, 2021.

[63] T. T. Silva, P. H. P. M. Silveira, M. P. Ribeiro et al., "Thermal and chemical characterization of kenaf fiber (*Hibiscus cannabinus*) reinforced epoxy matrix composites," *Polymers*, vol. 13, no. 12, p. 2016, 2021.

[64] P. Sathiamurthi, K. S. Karthi Vinith, T. P. Sathishkumar, S. Arunkumar, and A. S. Anaamalaai, "Fiber extraction and mechanical properties of Agave Americana/kenaf fiber reinforced hybrid epoxy composite," *Materials Today: Proceedings*, vol. 46, pp. 8594–8601, 2021.

[65] H. Abdellaoui, H. Bensalah, J. Echaabi, R. Bouhfid, and A. Qaiss, "Fabrication, characterization and modelling of laminated composites based on woven jute fibres reinforced epoxy resin," *Materials and Design*, vol. 68, pp. 104–113, 2015.

[66] M. Maruf Billah, M. S. Rabbi, and A. Hasan, "A review on developments in manufacturing process and mechanical properties of natural fiber composites," *Journal of Engineering Advancements*, vol. 2, no. 1, pp. 13–23, 2021.

[67] M. Naushad, G. Sharma, and Z. A. Alothman, "Photodegradation of toxic dye using Gum Arabic-crosslinked- poly(-acrylamide)/Ni(OH)$_2$/FeOOH nanocomposites hydrogel," *Journal of Cleaner Production*, vol. 241, article 118263, 2019.

[68] A. Azhar, Y. Yamauchi, A. E. Allah et al., "Nanoporous iron oxide/carbon composites through in-situ deposition of prussian blue nanoparticles on graphene oxide nanosheets and subsequent thermal treatment for supercapacitor applications," *Nanomaterials*, vol. 9, no. 5, p. 776, 2019.

[69] A. Alqadami, M. A. Khan, M. R. Siddiqui, and Z. A. Alothman, "Development of citric anhydride anchored mesoporous MOF through post synthesis modification to sequester potentially toxic lead (II) from water," *Microporous and Mesoporous Materials*, vol. 261, pp. 198–206, 2018.

[70] I. Ali, O. M. L. Alharbi, Z. A. Alothman, and A. Alwarthan, "Facile and eco-friendly synthesis of functionalized iron nanoparticles for cyanazine removal in water," *Colloids and Surfaces B: Biointerfaces*, vol. 171, pp. 606–613, 2018.

[71] I. Ali, O. M. L. Alharbi, Z. A. ALOthman, A. M. al-Mohaimeed, and A. Alwarthan, "Modeling of fenuron pesticide adsorption on CNTs for mechanistic insight and removal in water," *Environmental Research*, vol. 170, pp. 389–397, 2019.

[72] S. Wagner, C. Collet, P. Madsen, T. Nakashizuka, R. D. Nyland, and K. Sagheb-Talebi, "Beech regeneration research: from ecological to silvicultural aspects," *Forest Ecology and Management*, vol. 259, no. 11, pp. 2172–2182, 2010.

[73] N. Saba, M. T. Paridah, K. Abdan, and N. A. Ibrahim, "Physical, structural and thermomechanical properties of oil palm nano filler/kenaf/epoxy hybrid nanocomposites," *Materials Chemistry and Physics*, vol. 184, pp. 64–71, 2016.

[74] K. Jayaraman, "Manufacturing sisal–polypropylene composites with minimum fibre degradation," *Composites Science and Technology*, vol. 63, no. 3-4, pp. 367–374, 2003.

[75] A. Stalin, S. Mothilal, V. Vignesh, M. Sanjay, and S. Siengchin, "Mechanical properties of hybrid vetiver/ banana fiber mat reinforced vinyl ester composites," *Journal of Industrial Textiles*, vol. 152808372093816, p. 152808372093816, 2020.

[76] R. Vinayagamoorthy and N. Rajeswari, "Mechanical performance studies onVetiveria zizanioides/jute/glass fiber-reinforced hybrid polymeric composites," *Journal of Reinforced Plastics and Composites*, vol. 33, no. 1, pp. 81–92, 2014.

[77] T. P. Sathishkumar, P. Navaneethakrishnan, S. Shankar, and J. Kumar, "Mechanical properties of randomly oriented snake grass fiber with banana and coir fiber-reinforced hybrid composites," *Journal of Composite Materials*, vol. 47, no. 18, pp. 2181–2191, 2013.

[78] M. R. Sanjay and B. Yogesha, "Studies on hybridization effect of jute/kenaf/E-glass woven fabric epoxy composites for potential applications: effect of laminate stacking sequences," *Journal of Industrial Textiles*, vol. 47, no. 7, pp. 1830–1848, 2018.

[79] P. Manimaran, P. Senthamaraikannan, M. R. Sanjay, M. K. Marichelvam, and M. Jawaid, "Study on characterization of Furcraea Foetida new natural fiber as composite reinforcement for lightweight applications," *Carbohydrate Polymers*, vol. 181, pp. 650–658, 2018.

[80] T. P. Sathishkumar, P. Navaneethakrishnan, and S. Shankar, "Tensile and flexural properties of snake grass natural fiber reinforced isophthallic polyester composites," *Composites Science and Technology*, vol. 72, no. 10, pp. 1183–1190, 2012.

[81] G. R. Arpitha, M. R. Sanjay, P. Senthamaraikannan, C. Barile, and B. Yogesha, "Hybridization effect of sisal/glass/epoxy/ filler based woven fabric reinforced composites," *Experimental Techniques*, vol. 41, no. 6, pp. 577–584, 2017.

[82] M. R. Sanjay and B. Yogesha, "Study on water absorption behavior of jute and kenaf fabric reinforced epoxy composites: hybridization effect of E-glass fabric," *International Journal of Composite Materials*, vol. 6, no. 2, pp. 55–62, 2016.

[83] M. R. Sanjay, G. R. Arpitha, P. Senthamaraikannan, M. Kathiresan, M. A. Saibalaji, and B. Yogesha, "The hybrid effect of jute/kenaf/E-glass woven fabric epoxy composites for medium load applications: impact, inter-laminar strength, and failure surface characterization," *Journal of Natural Fibers*, vol. 16, no. 4, pp. 600–612, 2019.

[84] R. Vijay, D. Lenin Singaravelu, A. Vinod et al., "Characterization of raw and alkali treated new natural cellulosic fibers from Tridax procumbens," *International Journal of Biological Macromolecules*, vol. 125, pp. 99–108, 2019.

[85] M. R. Sanjay, G. R. Arpitha, L. Laxmana Naik, K. Gopalakrishna, and B. Yogesha, "Experimental investigation on mechanical properties of hemp/E-glass fabric reinforced polyester hybrid composites," *Journal of Materials and Engineering Structures*, vol. 3, pp. 117–128, 2016.

[86] K. M. M. Rao, K. M. Rao, and A. V. R. Prasad, "Fabrication and testing of natural fibre composites: vakka, sisal, bamboo and banana," *Materials and Design*, vol. 31, no. 1, pp. 508–513, 2010.

[87] K. Okubo, T. Fujii, and Y. Yamamoto, "Development of bamboo-based polymer composites and their mechanical properties," *Composites Part A Applied Science and Manufacturing*, vol. 35, no. 3, pp. 377–383, 2004.

[88] D. Shanmugam and M. Thiruchitrambalam, "Static and dynamic mechanical properties of alkali treated unidirectional continuous palmyra palm leaf stalk fiber/jute fiber reinforced hybrid polyester composites," *Materials and Design*, vol. 50, pp. 533–542, 2013.

[89] K. S. Raghul, D. Nandakumar, and R. Jeyakumar, "Mechanical behaviour of glass fiber/epoxy modified with nano composites: a review," *International Journal of Innovative Research in Science, Engineering and Technology*, vol. 5, no. 7, pp. 76–81, 2016.

[90] S. Biswas, "Mechanical properties of bamboo-epoxy composites a structural application," *Advances in Materials Research*, vol. 1, no. 3, pp. 221–231, 2012.

[91] C. W. Nguong, S. N. B. Lee, and D. Sujan, "A review on natural fiber reinforced polymer composites," *International Journal of Materials and Metallurgical Engineering*, vol. 7, pp. 52–59, 2013.

[92] N. Ramadan, I. Taha, R. Hammouda, and M. H. Abdellatif, "Behaviour of hybrid SiC/jute epoxy composites manufactured by vacuum assisted resin infusion," *Polymers and Polymer Composites*, vol. 25, no. 5, pp. 333–344, 2017.

[93] E. S. Ali and S. Ahmad, "Bionano-composite hybrid polyurethane foam reinforced with empty fruit bunch and nanoclay," *Composites Part B: Engineering*, vol. 43, no. 7, pp. 2813–2816, 2012.

[94] T. I. Olumuyiwa and S. Samuel, "Study of mechanical behaviour of coconut shell reinforced polymer matrix composite," *Journal of Minerals and Materials Characterization and Engineering*, vol. 11, no. 8, pp. 774–779, 2012.

[95] G. Ahmetli, S. Kocaman, I. Ozaytekin, and P. Bozkurt, "Epoxy composites based on inexpensive char filler obtained from plastic waste and natural resources," *Polymer Composites*, vol. 34, no. 4, pp. 500–509, 2013.

[96] R. M. N. Arib, S. M. Sapuan, M. M. H. M. Ahmad, M. T. Paridah, and H. M. D. Khairul Zaman, "Mechanical properties of pineapple leaf fibre reinforced polypropylene composites," *Materials and Design*, vol. 27, no. 5, pp. 391–396, 2006.

[97] C. Honygan, M. Menghe, and D. Xin, "Influence of moisture absorption on the interfacial strength of bamboo/vinyl ester composites," *Composites: Part A*, vol. 40, no. 12, pp. 2013–2019, 2009.

[98] R. Velmurugan and V. Manikandan, "Mechanical properties of palmyra/glass fiber hybrid composites," *Composites Part A Applied Science and Manufacturing*, vol. 38, no. 10, pp. 2216–2226, 2007.

[99] M. D. Hazizan, L. Akil, C. Wei, Z. A. Mohd Ishak, A. Abu Bakar, and M. A. Abd Rahman, "Water absorption study on pultruded jute fibre reinforced unsaturated polyester composites," *Computer Science and Technology*, vol. 69, no. 11-12, pp. 1942–1948, 2009.

[100] N. Venkateshwaran, A. ElayaPerumal, A. Alavudeen, and M. Thiruchitrambalam, "Mechanical and water absorption behaviour of banana/sisal reinforced hybrid composites," *Materials & Design*, vol. 32, no. 7, pp. 4017–4021, 2011.

[101] M. Idicula, S. K. Malhotra, K. Joseph, and S. Thomas, "Dynamic mechanical analysis of randomly oriented intimately mixed short banana/sisal hybrid fibre reinforced polyester composites," *Composites Science and Technology*, vol. 65, no. 7-8, pp. 1077–1087, 2005.

[102] A. K. M. Bledzki, A. A. Mamun, and O. Faruk, "Abaca fibre reinforced PP composites and comparison with jute and flax fibre PP composites," *Journal of Express Polymer Letters*, vol. 1, no. 11, pp. 755–762, 2007.

[103] M. Idicula, P. A. Sreekumar, K. Joseph, and S. Thomas, "Natural fiber hybrid composites-a comparison between compression molding and resin transfer molding," *Polymer Composites*, vol. 30, no. 10, pp. 1417–1425, 2009.

[104] O. M. L. Asumani, R. G. Reid, and R. Paskaramoorthy, "The effects of alkali–silane treatment on the tensile and flexural properties of short fibre non-woven kenaf reinforced polypropylene composites," *Composites Part A: Applied Science and Manufacturing*, vol. 43, no. 9, pp. 1431–1440, 2012.

[105] R. Panneerdhass, A. Gnanavelbabu, and K. Rajkumar, "Mechanical properties of luffa fiber and ground nut reinforced epoxy polymer hybrid composites," *Procedia Engineering*, vol. 97, pp. 2042–2051, 2014.

[106] T. Sathishkumar, P. Navaneethakrishnan, S. Shankar, R. Rajasekar, and N. Rajini, "Characterization of natural fiber

and composites – a review," *Journal of Reinforced Plastics and Composites*, vol. 32, no. 19, pp. 1457–1476, 2013.

[107] K. Kaewtatip and J. Thongmee, "Studies on the structure and properties of thermoplastic starch/luffa fiber composites," *Materials and Design*, vol. 40, pp. 314–318, 2012.

[108] B. F. Yousif and N. S. M. EI-Tayeb, "Adhesive wear performance of T-OPRP and UT-OPRP composites," *Tribology Letters*, vol. 32, no. 3, pp. 199–208, 2008.

[109] C. Deo and S. K. Acharya, "Effect of moisture absorption on mechanical properties of chopped natural fiber reinforced epoxy composite," *Journal of Reinforced Plastics and Composites*, vol. 29, no. 16, pp. 2513–2521, 2010.

[110] K. Mylsamy and I. Rajendran, "Influence of fibre length on the wear behaviour of chopped Agave Americana fibre reinforced epoxy composites," *Tribology Letters*, vol. 44, no. 1, pp. 75–80, 2011.

[111] V. S. Sreenivasan, D. Ravindran, V. Manikandan, and R. Narayanasamy, "Influence of fibre treatments on mechanical properties of short Sansevieria cylindrica/polyester composites," *Materials and Design*, vol. 37, pp. 111–121, 2012.

[112] P. Noorunnisa Khanam, G. Ramachandra Reddy, K. Raghu, and S. Venkata Naidu, "Tensile, flexural, and compressive properties of coir/silk fiber-reinforced hybrid composites," *Journal of Reinforced Plastics and Composites*, vol. 29, no. 14, pp. 2124–2127, 2010.

[113] M. M. Haque, M. Hasan, M. S. Islam, and M. E. Ali, "Physico-mechanical properties of chemically treated palm and coir fiber reinforced polypropylene composites," *Bioresource Technology*, vol. 100, no. 20, pp. 4903–4906, 2009.

[114] B. Venkatram, C. Kailasanathan, P. Seenikannan, and S. Paramasamy, "Study on the evaluation of mechanical and thermal properties of natural sisal fiber/general polymer composites reinforced with nanoclay," *International Journal of Polymer Analysis and Characterization*, vol. 21, no. 7, pp. 647–656, 2016.

[115] S. B. Hosseini, S. Hedjazi, L. Jamalirad, and A. Sukhtesaraie, "Effect of nano-SiO2 on physical and mechanical properties of fiber reinforced composites (FRCs)," *Journal of the Indian Academy of Wood Science*, vol. 11, no. 2, pp. 116–121, 2014.

[116] G. D. Vilakati, A. K. Mishra, S. B. Mishra, B. B. Mamba, and J. M. Thwala, "Influence of TiO 2- modification on the mechanical and thermal properties of sugarcane bagasse-EVA composites," *Journal of Inorganic and Organometallic Polymers and Materials*, vol. 20, no. 4, pp. 802–808, 2010.

[117] X. Shen, J. Jia, C. Chen, Y. Li, and J. K. Kim, "Enhancement of mechanical properties of natural fiber composites via carbon nanotube addition," *Journal of Materials Science*, vol. 49, no. 8, pp. 3225–3233, 2014.

[118] M. Chaharmahali, Y. Hamzeh, G. Ebrahimi, A. Ashori, and I. Ghasemi, "Effects of nano-graphene on the physico-mechanical properties of bagasse/polypropylene composites," *Polymer Bulletin*, vol. 71, no. 2, pp. 337–349, 2014.

[119] V. Sridharan, T. Raja, and N. Muthukrishnan, "Study of the effect of matrix, fibre treatment and graphene on delamination by drilling jute/epoxy nanohybrid composite," *Arabian Journal for Science and Engineering*, vol. 41, no. 5, pp. 1883–1894, 2016.

[120] U. K. Komal, V. Verma, T. Ashwani, N. Verma, and I. Singh, "Effect of chemical treatment on thermal, mechanical and degradation behavior of banana fiber reinforced polymer composites," *Journal of Natural Fibers*, pp. 1–13, 2018.

[121] B. Sutradhar, M. Mesbah, and M. Hasan, "Effect of fiber ratio and chemical treatment on properties of banana and betel nut fiber reinforced hybrid polypropylene composites," *IOP Conference Series: Materials Science and Engineering*, vol. 438, 2018.

[122] A. Ashori, "Wood-plastic composites as promising green-composites for automotive industries!," *Bioresource Technology*, vol. 99, no. 11, pp. 4661–4667, 2008.

[123] H. Awais, Y. Nawab, A. Amjad, A. Anjang, H. M. Akil, and M. S. Abidin, "Environmental benign natural fibre reinforced thermoplastic composites: a review," *Composites Part C: Open Access*, vol. 4, article 100082, 2021.

[124] P. T. R. Swain and S. Biswas, "Influence of fiber surface treatments on physico-mechanical behaviour of jute/epoxy composites impregnated with aluminium oxide filler," *Journal of Composite Materials*, vol. 51, no. 28, pp. 3909–3922, 2017.

[125] A. Geremew, P. De Winne, T. A. Demissie, and H. De Backer, "An overview of the characterization of natural cellulosic fibers," *Key Engineering Materials*, vol. 881, pp. 107–116, 2021.

[126] A. R. Bunsell, Ed., "Introduction to the science of fibers," in *Handbook of Properties of Textile and Technical Fibers*, pp. 1–20, Woodhead Publishing, 2018.

[127] L. Y. Mwaikambo and M. P. Ansell, "Chemical modification of hemp, sisal, jute, and kapok fibers by alkalization," *Journal of Applied Polymer Science*, vol. 84, no. 12, pp. 2222–2234, 2002.

[128] M. Teli and A. Jadhav, "Effect of mercerization on the properties of pandanus odorifer lignocellulosic fibre," *IOSR Journal of Polymer and Textile Engineering*, vol. 4, no. 1, pp. 7–15, 2017.

[129] S. Dhanalakshmi, P. Ramadevi, and B. Basavaraju, "Effect of chemical treatments on tensile strength of areca fibre reinforced natural rubber composites," *IOSR Journal of Applied Chemistry*, vol. 8, pp. 43–52, 2015.

[130] A. Valadez Gonzalez, J. M. Cervantes Uc, and R. Olayo, "Chemical modification of henequen fibers with an organosilane coupling agent," *Composites Part B: Engineering*, vol. 30, no. 3, pp. 321–331, 1999.

[131] K. Obi Reddy, C. Uma Maheswari, J. I. Mukul Shukla, and A. Song, "Tensile and structural characterization of alkali treated borassus fruit fine fibers," *Composites Part B: Engineering*, vol. 44, no. 1, pp. 433–438, 2013.

[132] S. A. Paul, K. Joseph, G. G. Mathew, L. A. Pothen, and S. Thomas, "Influence of polarity parameters on the mechanical properties of composites from polypropylene fiber and short banana fiber," *Composites Part A: Applied Science and Manufacturing*, vol. 41, no. 10, pp. 1380–1387, 2010.

[133] M. A. Lopez Manchado, M. Arroyo, J. Biagiotti, and J. M. Kenny, "Enhancement of mechanical properties and interfacial adhesion of PP/EPDM/flax fiber composites using maleic anhydride as a compatibilizer," *Journal of Applied Polymer Science*, vol. 90, no. 8, pp. 2170–2178, 2003.

[134] J. I. Singh, V. Dhawan, S. Singh, and A. S. Pannu, "Effect of alkali treatment on mechanical properties of jute, sisal, banana, hemp and abaca fibres for polymer composite reinforcement," *International Journal of Mechanical Engineering and Technology*, vol. 8, pp. 1775–1784, 2017.

[135] A. Arbelaiz, G. Cantero, B. Fernández, I. Mondragon, P. Gañán, and J. M. Kenny, "Flax fiber surface modifications: effects on fiber physico mechanical and flax/ polypropylene

interface properties," *Polymer Composites*, vol. 26, no. 3, pp. 324–332, 2005.

[136] I. M. De Rosa, J. M. Kenny, D. Puglia, C. Santulli, and F. Sarasini, "Morphological, thermal and mechanical characterization of okra (*Abelmoschus esculentus*) fibres as potential reinforcement in polymer composites," *Composites Science and Technology*, vol. 70, no. 1, pp. 116–122, 2010.

[137] L. Y. Mwaikambo, N. Tucker, and A. J. Clark, "Mechanical properties of hemp-fibre-reinforced euphorbia composites," *Macromolecular Materials and Engineering*, vol. 292, no. 9, pp. 993–1000, 2007.

[138] A. C. de Albuquerque, K. Joseph, L. H. de Carvalho, and J. R. M. d'Almeida, "Effect of wettability and ageing conditions on the physical and mechanical properties of uniaxially oriented jute-roving-reinforced polyester composites," *Composites Science and Technology*, vol. 60, no. 6, pp. 833–844, 2000.

[139] M. D. Chikouche, A. Merrouche, A. Azizi, M. Rokbi, and S. Walter, "Influence of alkali treatment on the mechanical properties of new cane fibre/polyester composites," *Journal of Reinforced Plastics and Composites*, vol. 34, no. 16, pp. 1329–1339, 2015.

[140] S. V. Prasad, C. Pavithran, and P. K. Rohatgi, "Alkali treatment of coir fibres for coir-polyester composites," *Journal of Materials Science*, vol. 18, no. 5, pp. 1443–1454, 1983.

[141] A. Athijayamani, M. Thiruchitrambalam, U. Natarajan, and B. Pazhanivel, "Effect of moisture absorption on the mechanical properties of randomly oriented natural fibers/polyester hybrid composite," *Materials Science and Engineering: A*, vol. 517, no. 1-2, pp. 344–353, 2009.

[142] A. Bessadok, S. Marais, F. Gouanvé et al., "Effect of chemical treatments of alfa (Stipa tenacissima) fibres on water-sorption properties," *Composites Science and Technology*, vol. 67, no. 3-4, pp. 685–697, 2007.

[143] P. J. Herrera-Franco and A. Valadez-González, "Mechanical properties of continuous natural fibre-reinforced polymer composites," *Composites Part A: Applied Science and Manufacturing*, vol. 35, no. 3, pp. 339–345, 2004.

[144] K. Obi Reddy, C. Uma Maheswari, A. Varada Rajulu, and B. R. Guduri, "Thermal degradation parameters and tensile properties of borassus flabellifer fruit fiber reinforcement," *Journal of Reinforced Plastics and Composites*, vol. 28, no. 18, pp. 2297–2301, 2009.

[145] V. Vilay, M. Mariatti, R. Mat Taib, and M. Todo, "Effect of fiber surface treatment and fiber loading on the properties of bagasse fiber reinforced unsaturated polyester composites," *Composites Science and Technology*, vol. 68, no. 3-4, pp. 631–638, 2008.

[146] G. Govardhan and R. N. Rao, "Effect of fiber content and alkali treatment on mechanical properties of roystonea regia-reinforced epoxy partially biodegradable composites," *Bulletin of Materials Science*, vol. 34, no. 7, pp. 1575–1581, 2011.

[147] E. T. N. Bisanda, "The effect of alkali treatment on the adhesion characteristics of sisal fibers," *Applied Composite Materials*, vol. 7, no. 5/6, pp. 331–339, 2000.

[148] M. S. Sreekala, M. G. Kumaran, J. Seena, J. Maya, and S. Thomas, "Oil palm fiber reinforced phenol formaldehyde composites: influence of fiber surface modifications on the mechanical performance," *Applied Composite Materials*, vol. 7, no. 5/6, pp. 295–329, 2000.

[149] V. G. Geethamma, K. Thomas Mathew, R. Lakshminarayanan, and T. Sabu, "Composite of short coir fibres and natural rubber: effect of chemical modification, loading and orientation of fibre," *Polymer*, vol. 39, no. 6-7, pp. 1483–1491, 1998.

[150] L. Y. Mwaikambo and M. P. Ansell, "Mechanical properties of alkali treated plant fibres and their potential as reinforcement materials II. Sisal fibres," *Journal of Materials Science*, vol. 41, no. 8, pp. 2497–2508, 2006.

[151] A. M. Edeerozey, H. M. Akil, A. B. Azhar, and M. Z. Ariffin, "Chemical modification of kenaf fibers," *Materials Letters*, vol. 61, no. 10, pp. 2023–2025, 2007.

[152] K. Goda, M. S. Sreekala, A. Gomes, T. Kaji, and J. Ohgi, "Improvement of plant based natural fibers for toughening green composites– Effect of load application during mercerization of ramie fibers," *Composites Part A: Applied Science and Manufacturing*, vol. 37, no. 12, pp. 2213–2220, 2006.

[153] Y. Cao, S. Shibata, and I. Fukumoto, "Mechanical properties of biodegradable composites reinforced with bagasse fibre before and after alkali treatments," *Composites Part A: Applied Science and Manufacturing*, vol. 37, no. 3, pp. 423–429, 2006.

[154] K. Joseph, S. Thomas, and C. Pavithran, "Effect of chemical treatment on the tensile properties of short sisal fibre-reinforced polyethylene composites," *Polymer*, vol. 37, no. 23, pp. 5139–5149, 1996.

[155] B. Wang, S. Panigrahi, L. Tabil, and W. Crerar, "Pre-treatment of flax fibers for use in rotationally molded biocomposites," *Journal of Reinforced Plastics and Composites*, vol. 26, no. 5, pp. 447–463, 2007.

[156] D. Ray, B. K. Sarkar, S. Das, and A. K. Rana, "Dynamic mechanical and thermal analysis of vinylester-resin-matrix composites reinforced with untreated and alkali-treated jute fibres," *Composites Science and Technology*, vol. 62, no. 7-8, pp. 911–917, 2002.

[157] A. Bessadok, S. Roudesli, S. Marais, N. Follain, and L. Lebrun, "Alfa fibres for unsaturated polyester composites reinforcement: effects of chemical treatments on mechanical and permeation properties," *Composites Part A: Applied Science and Manufacturing*, vol. 40, no. 2, pp. 184–195, 2009.

[158] M. A. M. Edeerozey, M. A. Hazizan, A. B. Azhar, and M. I. Zainal Ariffin, "Chemical modification of kenaf fibers," *Materials Letters Journal*, vol. 61, no. 10, pp. 2023–2025, 2007.

[159] M. M. Rahman, A. K. Malik, and M. A. Khan, "Influence of various surface pre-treatment on the mechanical and degradable properties of photo grafted oil palm fibers," *Journal of Applied Polymer Science*, vol. 105, no. 5, pp. 3077–3086, 2007.

[160] I. D. Ibrahim, T. Jamiru, R. E. Sadiku, W. K. Kupolati, and S. C. Agwuncha, "Dependency of the mechanical properties of sisal fiber reinforced recycled polypropylene composites on fiber surface treatment, fiber content and nanoclay," *Journal of Polymers and the Environment*, vol. 25, no. 2, pp. 427–434, 2017.

[161] S. Shibata, Y. Cao, and I. Fukumoto, "Press forming of short natural fiber-reinforced biodegradable resin: effects of fiber volume and length on flexural properties," *Polymer Testing*, vol. 24, no. 8, pp. 1005–1011, 2005.

[162] J. R. Barone, "Polyethylene/keratin fiber composites with varying polyethylene crystallinity," *Composites. Part A, Applied Science and Manufacturing*, vol. 36, no. 11, pp. 1518–1524, 2005.

[163] A. A. Kafi, K. Magniez, and B. L. Fox, "Effect of manufacturing process on the flexural, fracture toughness, and thermomechanical properties of bio-composites," *Composites. Part A, Applied Science and Manufacturing*, vol. 42, no. 8, pp. 993–999, 2011.

[164] N. K. Sharma and V. Kumar, "Studies on properties of banana fiber reinforced green composite," *Journal of Reinforced Plastics and Composites*, vol. 32, no. 8, pp. 525–532, 2013.

[165] H. Alamri and I. M. Low, "Mechanical properties and water absorption behaviour of recycled cellulose fibre reinforced epoxy composites," *Polymer Testing*, vol. 31, no. 5, pp. 620–628, 2012.

[166] P. J. Jandas, S. Mohanty, and S. K. Nayak, "Mechanical properties of surface-treated banana fiber/polylactic acid biocomposites: a comparative study of theoretical and experimental values," *Journal of Applied Polymer Science*, vol. 127, no. 5, pp. 4027–4038, 2013.

[167] A. K. Bledzki, J. Gassan, and W. Zhang, "Impact properties of natural fiber-reinforced epoxy foams," *Journal of Cellular Plastics*, vol. 35, no. 6, pp. 550–562, 1999.

[168] B. F. Yousif and N. S. M. El-Tayeb, "The effect of oil palm fibers as reinforcement on tribological performance of polyester composite," *Surface Review and Letters*, vol. 14, no. 6, pp. 1095–1102, 2007.

[169] N. S. M. El-Tayeb, "A study on the potential of sugarcane fibers/polyester composite for tribological applications," *Wear*, vol. 265, no. 1–2, pp. 223–235, 2008.

[170] M. Assarar, D. Scida, A. El Mahi, C. Poilâne, and R. Ayad, "Influence of water ageing on mechanical properties and damage events of two reinforced composite materials: flax–fibres and glass–fibres," *Materials and Design*, vol. 32, no. 2, pp. 788–795, 2011.

[171] N. Venkateshwaran, A. E. Perumal, and D. Arunsundaranayagam, "Fiber surface treatment and its effect on mechanical and visco-elastic behaviour of banana/epoxy composite," *Materials and Design*, vol. 47, pp. 151–159, 2013.

[172] D. Ray, B. K. Sarkar, A. K. Rana, and N. R. Bose, "Effect of alkali treated jute fibres on composite properties," *Bulletin of Materials Science*, vol. 24, no. 2, pp. 129–135, 2001.

[173] T.-T.-L. Doan, S.-L. Gao, and E. Mäder, "Jute/polypropylene composites I. Effect of matrix modification," *Composites Science and Technology*, vol. 66, no. 7–8, pp. 952–963, 2006.

[174] A. C. Karmaker and J. P. Shneider, "Mechanical performance of short jute fibre reinforced polypropylene," *Journal of Materials Science Letters*, vol. 15, no. 3, pp. 201-202, 1996.

[175] A. K. Bledzki, A. A. Mamun, M. Lucka-Gabor, and V. S. Gutowski, "The effects of acetylation on properties of flax fibre and its polypropylene composites," *Express Polymer Letters*, vol. 2, no. 6, pp. 413–422, 2008.

[176] H.-S. Yang, H.-J. Kim, H.-J. Park, B.-J. Lee, and T.-S. Hwang, "Effect of compatibilizing agents on rice-husk flour reinforced polypropylene composites," *Composite Structures*, vol. 77, no. 1, pp. 45–55, 2007.

[177] K. L. Pickering, Y. Li, R. L. Farrell, and M. Lay, "Interfacial modification of hemp fiber reinforced composites using fungal and alkali treatment," *Journal of Biobased Materials and Bioenergy*, vol. 1, no. 1, pp. 109–117, 2007.

[178] B. Wielage, T. Lampke, H. Utschick, and F. Soergel, "Processing of natural-fibre reinforced polymers and the resulting dynamic—mechanical properties," *Journal of Materials Processing Technology*, vol. 139, no. 1-3, p. 140, 2003.

[179] S. Lee, S. Q. Shi, L. H. Groom, and Y. Xue, "Properties of unidirectional kenaf fiber-polyolefin laminates," *Polymer Composites*, vol. 31, no. 6, pp. 1067–1074, 2010.

[180] M. M. Thwe and K. Liao, "Durability of bamboo-glass fiber reinforced polymer matrix hybrid composites," *Composites Science and Technology*, vol. 63, no. 3-4, pp. 375–387, 2003.

[181] S. Cheng, K. Lau, T. Liu, Y. Zhao, P.-M. Lam, and Y. Yin, "Mechanical and thermal properties of chicken feather fiber/PLA green composites," *Composites Part B: Engineering*, vol. 40, no. 7, pp. 650–654, 2009.

[182] K. Oksman, A. P. Mathew, R. Långström, B. Nyström, and K. Joseph, "The influence of fibre microstructure on fibre breakage and mechanical properties of natural fibre reinforced polypropylene," *Composites Science and Technology*, vol. 69, no. 11-12, pp. 1847–1853, 2009.

[183] Q. T. H. Shubhra, A. K. M. M. Alam, and M. D. H. Beg, "Mechanical and degradation characteristics of natural silk fiber reinforced gelatin composites," *Materials Letters*, vol. 65, no. 2, pp. 333–336, 2011.

[184] K. Wong, U. Nirmal, and B. Lim, "Impact behavior of short and continuous fiber-reinforced polyester composites," *Journal of Reinforced Plastics and Composites*, vol. 29, no. 23, pp. 3463–3474, 2010.

[185] M. Sakthivel, S. Vijayakumar, and S. Ramesh, "Production and characterization of luffa/coir reinforced polypropylene composite," *Procedia Materials Science*, vol. 5, pp. 739–745, 2014.

[186] M. Rokbi, H. Osmani, A. Imad, and N. Benseddiq, "Effect of chemical treatment on flexure properties of natural fiber-reinforced polyester composite," *Procedia Engineering*, vol. 10, pp. 2092–2097, 2011.

[187] T. Sathishkumar, "Development of snake grass fiber-reinforced polymer composite chair," *Proceedings of the Institution of Mechanical Engineers, Part L: Journal of Materials: Design and Applications*, vol. 230, no. 1, pp. 273–281, 2016.

[188] S. Gokulkumar, P. R. Thyla, L. Prabhu, and S. Sathish, "Characterization and comparative analysis on mechanical and acoustical properties ofCamellia sinensis/ananas comosus/glass fiber hybrid polymer composites," *Journal of Natural Fibers*, vol. 18, no. 7, pp. 978–994, 2021.

[189] S. Indran and R. E. Raj, "Characterization of new natural cellulosic fiber from Cissus quadrangularis stem," *Carbohydrate Polymers*, vol. 117, pp. 392–399, 2015.

[190] K. H. Reddy, R. M. Reddy, M. Ramesh, D. Mohana Krishnudu, B. M. Reddy, and H. R. Rao, "Impact of alkali treatment on characterization of Tapsi (Sterculia Urens) natural bark fiber reinforced polymer composites," *Journal of Natural Fibers*, vol. 18, no. 3, pp. 378–389, 2021.

[191] L. Prabhu, V. Krishnaraj, S. Sathish, S. GokulKumar, and N. Karthi, "Study of mechanical and morphological properties of jute-tea leaf fiber reinforced hybrid composites: effect of glass fiber hybridization," *Materials Today: Proceedings*, vol. 27, pp. 2372–2375, 2020.

[192] M. Aly, M. S. J. Hashmi, A. G. Olabi et al., "Optimization of alkaline treatment conditions of flax fiber using Box–Behnken method," *Journal of Natural Fibers*, vol. 9, no. 4, pp. 256–276, 2012.

[193] R. Malkapuram, V. Kumar, and Y. S. Negi, "Recent development in natural fiber reinforced polypropylene composites,"

Journal of Reinforced Plastics and Composites, vol. 28, no. 10, pp. 1169–1189, 2009.

[194] A. Ashori and A. Nourbakhsh, "Preparation and characterization of polypropylene/wood flour/nanoclay composites," *European Journal of Wood and Wood Products*, vol. 69, no. 4, pp. 663–666, 2011.

[195] T. P. Mohan and K. Kanny, "Water barrier properties of nanoclay filled sisal fibre reinforced epoxy composites," *Composites. Part A, Applied Science and Manufacturing*, vol. 42, no. 4, pp. 385–393, 2011.

[196] M. Haq, R. Burgueño, A. K. Mohanty, and M. Misra, "Hybrid bio-based composites from blends of unsaturated polyester and soybean oil reinforced with nanoclay and natural fibers," *Composites Science and Technology*, vol. 68, no. 15-16, pp. 3344–3351, 2008.

[197] G. Han, Y. Lei, Q. Wu, Y. Kojima, and S. Suzuki, "Bamboo-fiber filled high density polyethylene composites: effect of coupling treatment and nanoclay," *Journal of Polymers and the Environment*, vol. 16, no. 2, pp. 123–130, 2008.

[198] P. K. Kushwaha, C. N. Pandey, and R. Kumar, "Study on the effect of carbon nanotubes on plastic composite reinforced with natural fiber," *Journal of the Indian Academy of Wood Science*, vol. 11, no. 1, pp. 82–86, 2014.

[199] D. Balaji, M. Ramesh, T. Kannan, S. Deepan, V. Bhuvaneswari, and L. Rajeshkumar, "Experimental investigation on mechanical properties of banana/snake grass fiber reinforced hybrid composites," *Materials Today: Proceedings*, vol. 42, pp. 350–355, 2021.

[200] M. Ramesh, C. Deepa, M. Tamil Selvan, L. Rajeshkumar, D. Balaji, and V. Bhuvaneswari, "Mechanical and water absorption properties of Calotropis gigantea plant fibers reinforced polymer composites," *Materials Today: Proceedings*, vol. 46, pp. 3367–3372, 2021.

[201] M. Ramesh, L. Rajeshkumar, C. Deepa et al., "Impact of Silane treatment on characterization of Ipomoea staphylina plant fiber reinforced epoxy composites," *Journal of Natural Fibers*, pp. 1–12, 2021.

[202] S. Sathish, K. Kumaresan, L. Prabhu, and S. Gokulkumar, "Experimental testing on mechanical properties of various natural fibers reinforced epoxy hybrid composite," *International Journal of Pure and Applied Mathematics*, vol. 11, no. 25, pp. 1–6, 2018.

[203] L. Prabhu, V. Krishnaraj, S. GokulKumar, S. Sathish, M. R. Sanjay, and S. Siengchin, "Mechanical, chemical and sound absorption properties of glass/kenaf/waste tea leaf fiber-reinforced hybrid epoxy composites," *Journal of Industrial Textiles*, vol. 51, no. 10, pp. 1674–1700, 2022.

[204] M. J. John and S. Thomas, "Biofibres and biocomposites," *Carbohydrate Polymers*, vol. 71, no. 3, pp. 343–364, 2008.

[205] T. Sen and H. N. Reddy, "Various industrial applications of hemp, kinaf, flax and ramie natural fibres," *International Journal of Innovation, Management and Technology*, vol. 2, pp. 192–198, 2011.

[206] S. M. A. Tawakkal, M. J. Cran, and S. W. Bigger, "Effect of kenaf fibre loading and thymol concentration on the mechanical and thermal properties of PLA/kenaf/thymol composites," *Industrial Crops and Products*, vol. 61, pp. 74–83, 2014.

[207] T. A. Ticoalu and F. Cardona, "A review of current development in natural fiber composites for structural and infrastructure applications," in *Proceedings of the Southern Region Engineering Conference (SREC '10)*, pp. 113–117, Toowoomba, Australia, November 2010.

[208] D. Verma and S. Sharma, "Green biocomposites: a prospective utilization in automobile industry," in *Green Biocomposites: Design and Applications*, M. Jawaid, M. S. Salit, and O. Y. Alothman, Eds., pp. 167–191, Springer, Cham, Switzerland, 2017.

[209] Lucintel, *Opportunities in Natural Fiber Composites*, Lucintel, Las Colinas, TX, USA, 2011.

[210] M. H. Norhidayah, A. A. Hambali, M. Y. bin Yaakob, M. Zolkarnain, and H. Y. S. Taufik, "A review of current development in natural fiber composites in automotive applications," *Applied Mechanics and Materials*, vol. 564, pp. 3–7, 2014.

[211] S. Witayakran, W. Smitthipong, R. Wangpradid, R. Chollakup, and P. L. Clouston, "Natural fiber composites: review of recent automotive trends," in *Reference Module in Materials Science and Materials Engineering*, pp. 166–174, Elsevier Publishing, Amherst, MA, USA, 2017.

[212] M. Ramesh, L. Rajeshkumar, and D. Balaji, "Influence of process parameters on the properties of additively manufactured fiber-reinforced polymer composite materials: a review," *Journal of Materials Engineering and Performance*, vol. 30, no. 7, pp. 4792–4807, 2021.

[213] O. Faruk, A. K. Bledzki, H. P. Fink, and M. Sain, "Biocomposites reinforced with natural fibers: 2000–2010," *Progress in Polymer Science*, vol. 37, no. 11, pp. 1552–1596, 2012.

[214] L. Yan, N. Chouw, and K. Jayaraman, "Flax fibre and its composites - a review," *Composites Part B Engineering*, vol. 56, pp. 296–317, 2014.

[215] T. Koizumi, N. Tsujiuchi, and A. Adachi, "The development of sound absorbing materials using natural bamboo fibers," *High-Performance Composite Structures*, vol. 4, no. 1, pp. 157–166, 2002.

[216] Y. Zou, S. Huda, and Y. Yang, "Lightweight composites from long wheat straw and polypropylene web," *Bioresource Technology*, vol. 101, no. 6, pp. 2026–2033, 2010.

[217] S. D. Dogan, U. Tayfun, and M. Dogan, "New route for modifying cellulosic fibres with fatty acids and its application to polyethylene/jute fibre composites," *Journal of Composite Materials*, vol. 50, no. 18, pp. 2477–2485, 2016.

[218] D. Zhao and Z. Zhou, "Applications of lightweight composites in automotive industries," in *Lightweight Materials from Biopolymers and Biofibers*, Y. Yang, H. Xu, and X. Yu, Eds., pp. 143–158, American Chemical Society, Washington, DC, USA, 2014.

[219] K. Roy, S. C. Debnath, A. Pongwisuthiruchte, and P. Potiyaraj, "Recent advances of natural fibers based green rubber composites: properties, current status, and future perspectives," *Journal of Applied Polymer Science*, vol. 138, no. 35, p. 50866, 2021.

[220] N. Ramli, N. Mazlan, Y. Ando et al., "Natural fiber for green technology in automotive industry: a brief review," in *The Wood and Biofiber International Conference (WOBIC 2017)*, pp. 1–7, Selangor, Malaysia, 2017.

[221] S. Kalia, B. S. Kaith, and I. Kaur, "Pretreatments of natural fibers and their application as reinforcing material in polymer composites-a review," *Polymer Engineering & Science*, vol. 49, no. 7, pp. 1253–1272, 2009.

[222] C. Xia, S. Q. Shi, L. Cai, and J. Hua, "Property enhancement of kenaf fiber composites by means of vacuum-assisted resin

transfer molding (VARTM)," *Holzforschung*, vol. 69, no. 3, pp. 307–312, 2015.

[223] N. Chand and U. K. Dwivedi, "Effect of coupling agent on abrasive wear behaviour of chopped jute fibre-reinforced polypropylene composites," *Wear*, vol. 261, no. 10, pp. 1057–1063, 2006.

[224] M. K. Gupta and R. K. Srivastava, "Mechanical properties of hybrid fibers-reinforced polymer composite: a review," *Polymer-Plastics Technology and Engineering*, vol. 55, no. 6, pp. 626–642, 2016.

[225] F. X. Espinach, "Advances in natural fibers and polymers," *Materials*, vol. 14, no. 10, p. 2607, 2021.

[226] R. D. Anandjiwala and S. Blouw, "Composites from bast fibres—prospects and potential in the changing market environment," *Journal of Natural Fibers*, vol. 4, no. 2, pp. 91–109, 2007.

[227] M. A. Dweib, B. Hu, H. W. Shenton, and R. P. Wool, "Bio-based composite roof structure: manufacturing and processing issues," *Composite Structures*, vol. 74, no. 4, pp. 379–388, 2006.

[228] M. M. Davoodi, S. M. Sapunan, D. Ahma, A. Aidy, A. Khalina, and M. Jonobi, "Mechanical properties of hybrid kenaf/glass reinforced epoxy composite for passenger car bumper beam," *Material Design*, vol. 31, no. 10, pp. 4927–4932, 2010.

[229] B. F. Yousif and H. Ku, "Suitability of using coir fiber/polymeric composite for the design of liquid storage tanks," *Materials and Design*, vol. 36, pp. 847–853, 2012.

[230] A. Atiqah, M. Jawaid, S. M. Sapuan, and M. R. Ishak, "Dynamic mechanical properties of sugar palm/glass fiber reinforced thermoplastic polyurethane hybrid composites," *Polymer Composites*, vol. 40, no. 4, pp. 1329–1334, 2019.

[231] G. C. Silva, D. A. Souza, J. C. Machado, and D. J. Hourston, "Mechanical and thermal characterization of native Brazilian coir fiber," *Journal of Applied Polymer Science*, vol. 76, no. 7, pp. 1197–1206, 2000.

[232] S. Mori, C. Tenazoa, S. Candiotti, E. Flores, and S. Charca, "Assessment of Ichu fibers extraction and their use as reinforcement in composite materials," *Journal of Natural Fibers*, 2020.

[233] D. L. Cerf, F. Irinei, and G. Muller, "Solution properties of gum exudates from *Sterculia urens* (Karaya gum)," *Carbohydrate Polymers*, vol. 13, no. 4, pp. 375–386, 1990.

[234] M. E. Ali and A. Alabdulkarem, "On thermal characteristics and microstructure of a new insulation material extracted from date palm trees surface fibers," *Construction and Building Materials*, vol. 138, pp. 276–284, 2017.

[235] P. Manimaran, P. Senthamaraikannan, K. Murugananthan, and M. R. Sanjay, "Physicochemical properties of new cellulosic fibers fromAzadirachta indicaPlant," *Journal of Natural Fibers*, vol. 15, no. 1, pp. 29–38, 2018.

Research Article

Investigation on Mechanical and Durability Performance of Reinforced Concrete Containing Red Soil as Alternate for M-Sand

S. Sebastin,[1] **M. Franchis David,**[1] **Alagar Karthick,**[2] **Ashita Singh,**[3] **J. Vanjinathan,**[4] **Sanjeev Kumar,**[5] **and Mahseena Akter Meem** (iD)[6]

[1]*Department of Civil Engineering, National Engineering College, K.R.Nagar, Kovilpatti, 628503 Tamil Nadu, India*
[2]*Department of Electrical and Electronics Engineering, KPR Institute of Engineering and Technology, Coimbatore, 641407 Tamil Nadu, India*
[3]*Department of Civil Engineering, University Institute of Technology, Rajiv Gandhi Proudyogiki Vishwavidyalay, Bhopal, 462033 Madhya Pradesh, India*
[4]*Department of Civil Engineering, Sathyabama Institute of Science and Technology, 600119, Chennai, Tamil Nadu, India*
[5]*Department of Civil Engineering, Graphic Era Deemed to Be University, Bell Road, Clement Town, 248002 Dehradun, Uttarakhand, India*
[6]*Department of Electrical and Electronic Engineering, Daffodil International University, Ashulia, Savar, Dhaka 1207, Bangladesh*

Correspondence should be addressed to Mahseena Akter Meem; mahseena33-919@diu.edu.bd

The river sand is a primary parameter in the concrete structure. This work replaces accessible locally accessible substitution materials like red soil and manufactured sand (M-Sand). In this paper, the mechanical properties and durability of concrete containing red soil and M-Sand have been studied. In this investigation, M30 grade concrete was used, and tests were conducted for two sets of combinations; i.e., red soil as a partial replacement for river sand seems to be 20%, 30%, 40%, 50%, and 60%, and red soil as a partial replacement for manufactured sand (M-Sand) seems to be 60%, 50%, 40%, 30%, and 20%. The compressive strength (7 days, 28 days, 90 days), split tensile strength (28 days), and flexural strength (28 days) have been determined. The combination S4-50% river sand + 50% red soil and S9-70% M-Sand + 30% red soil gives more compressive strength than other combinations. Similarly, the combination S3-60% river sand + 40% red soil and S6-40% M-Sand + 60% red soil gives more flexural and split tensile strength than other combinations. The scanning electron microscope (SEM) analysis, EDAX analysis, and durability tests like alkalinity, sulfate attack, and chloride attack have also been studied.

1. Introduction

Sand near the water's edge has long been prized for its suitability as a building material. The use of natural river sand is being expanded to increase its use. River sand may not be of adequate quality to be used for construction in any case. River sand (M-Sand) can be substituted for M-Sand to support solid growth. Smashing hard rock yields manufactured sand. Washing and inspecting the smashed sand are done to use it for development purposes. M-Sand has a diameter of less than 4.75 mm. The demand for waterway sand for construction has led to an increase in the use of M-Sand. The total development cost can be reduced by using M-Sand as an optional fine entire material. There are no natural and dissolvable compounds in cement and pollutions, such as residue, dirt, or dust, that can affect its quality. To achieve cubical M-Sand, new technology is used. Machines currently in use are being used to get the fundamental evaluation zone.

Indian states like Tamil Nadu, Kerala, and Karnataka, located in the southern part of the country, have some of

the best red soil. When compared to the other soil, the red one has more waste properties. Mud and limestone have molded it into its current form. When the limestone is raised, the earth on the land's periphery is mixed together and turned into red soil. Iron oxide builds up and turns the dirt red during this process, which generates heat and causes it to interact with one another. Because of the sun's heat, the color of the dirt is turning red in areas with little rainfall. Indian red soil contains less phosphorus, nitrogen, and lime than other soils in the world. Despite this, certain grains like wheat, rice, cotton, sugarcane, and heartbeats can grow on red soil if the manures are appropriate.

The concrete's compressive strength for 7 days, 14 days, and 28 days increases at a rate of up to 30% M-Sand, then decreases as the M-Sand rate increases. It was found that 30% M-Sand was the ideal percentage for compressive strength considerations. The concrete's split tensile and flexural quality decrease as the percentage of M-Sand increases for the first seven and 28 days, respectively. It was found that 30% M-Sand was the ideal percentage for compressive strength considerations. As a result, the compressive, tensile, and flexural strengths increased by up to 30 percent. M-Sand was the most crucial factor in each case [1].

Red mud can be used up to 15% of the weight of cement in concrete, based on the results of a study on concrete subjected to different rates of reddish mud. There was an increase in workability with an increase in the amount of red soil in concrete, while there was a decrease in workability with an increase in the red mud percentage. We can conclude that the increase in compressive quality is a result of the lengthy contemplation. At the same time, the rate of red mud has increased by up to 15%. After that, the percentage of ruddy mud in concrete as a cement replacement decreased significantly. The flexural strength of concrete increased up to 15% of the red mud substance, but its restraint also reduced as the red mud substance increased in concrete. The part's pliable strength increased as the red mud's extents grew to a specific limit. The ideal amount of red earth to substitute for cement was 15%. Quality deteriorated after that. The need for water maintenance decreased as the amount of red mud in concrete increased. It implies that red mud has pushed concrete's toughness to new heights. Elasticity decreased as red mud content in concrete increased [2].

The quality and invulnerability of red soil blended cement surpass those of plain cement. When it comes to porosity, red soil blended solid has a higher porosity than bare concrete. Penetrability is nonexistent in red soil that has been separated from a plain concrete. Small pores in fine soil allow it to hold water more firmly, making it more porous. It is a waste of liquid. On the off chance that you utilize this solid as part of RCC, there will be no steel utilization. It is possible to use red soil as a component of RCC and prestressed concrete. Inquire about shell structures, prestressed, and RCC, to confirm that red soil can be used as a parcel of multistory building after development is finished [3].

The earth soil is not a standalone aggregate material appropriate for construction work most particularly concrete generation. The production of the concrete requires the good amount of the M-Sand for better performance [4].

Appropriate measurement of self-curing gels will increment the quality and serviceability of concrete. M40 grade concrete is compared with the conventional concrete with the various proportions such as 0.1%, 0.2%, and 0.3% [5].

Replace natural coarse aggregates with E-plastic waste within the run of 0–16.5% and full substitution of fine aggregates with M-Sand for M30 mix. The flexural strength and tensile strength increased by 11% and 6%, respectively, due to the addition of the E-waste [6].

The red clay-concrete interface shows softening behavior beneath distinctive ordinary stress levels. The mobilized shear stress decreases decently with the number of cycles and, in this way, remains consistent after 500 cycles of loading. The reaction of interface subjected to cyclic loading appears clear aeolotropy due to shear directions in each cycle. Interface shear stiffness and damping ratio decrease with expanding cycle numbers. The red clay-concrete interface speaks to a generally contraction behavior in cyclic and postcyclic direct shear tests. The cyclic loading does not lead to degradation for postcyclic shear strength [7].

The expansion of red mud improved 7 days toughness due to the quickened hydration prepare, whereas decreased the workability and the mechanical properties of UHPC. The debased workability may influence the application within the building with complex shapes, but it can still be connected in common development. An ultrahigh strength of UHPC counting 40% red mud can be produced after high-temperature curing, in spite of the fact that the addition of red mud decreases the compressive strength [8].

The comprehensive utilization of red mud is primarily found in three areas: the development and chemical industry, the natural assurance and horticulture industry, and the profitable component extraction industry. A brief report is additionally made on the related research of ruddy mud within the areas of cement, concrete, glass, ceramics, adsorbents, geopolymers, catalysts, composite materials, sewage treatment, squander gas treatment, soil advancement, and profitable component recuperation [9].

The axial compressive behaviour of concrete column is improved significantly, by partial substitution of sand with 60% M-Sand for M30 grade concrete [10].

The exploratory work carried out by preparing five concrete mixtures changing 10% of M-Sand extending 60–100 percent by weight of fine aggregate, 15% by weight of cement, and 1% by volume of steel fiber; the fraction kept consistent based on past considers. Different extents of M30 grade concrete were inspected by conducting mechanical and flexural conduct tests. The results obtained are palatable for 80% of the M-Sand substitution. Extra M-Sand substitution tends to decrease concrete strength [11].

Manufactured fine total (M-Sand) was partly replaced by E-waste (E-sand) in several rates (0%, 10%, 20%, 30%, and 40%), with 0.45 water cement (W.C) proportion. With

reference of Indian standard (IS) 10262:2019 rules, M30 grade concrete was arranged. The flexural, compressive, split tensile strength, and chloride permeability tests were performed on concrete with different mix extents, and test results were related with the result of reference concrete. Partly replacing of 20% factory-made sand (M-Sand) by E-waste (E-sand) yields greatest strength and superior chloride permeability with progressed smaller scale structure than ordinary concrete [12].

The main objective is to move forward strength of concrete by utilizing pozzolanic materials such as silica rage, metakaolin, GGBS as partial substitution to weight of cement by changing percentages (5, 10, and 15), and M-Sand as complete substitution to river sand. In this article, the test work is primarily concentrated on analyzing the mechanical strength, split tensile strength conjointly nondestructive tests like rebound hammer, and ultrasonic pulse velocity tests was performed at an age of 7 days and 28 days [13].

The behavior of concrete utilizes M-Sand at M30 and M65 grades for which test work is carried out to know the compressive strength, flexural strength, and split tensile strength of concrete. The examples were tried at the ages of 7, 28, 56, and 91 days of curing. The test results have appeared that the need of water required to fulfill the workability condition and subsequently quality of cement is additionally marginally expanded. The results appear way better execution to replace with natural sand [14].

The GGBS is replaced for the manufactured sand by 30%, 35%, 40%, and 45%. At that point, the strength is gotten by carrying out compression, split tensile, and the flexural tests. At that point, the optimization value of the GGBS is found as 30%, and the impact of measure of coarse aggregate is found out with the optimized value of GGBS. Then, the durability tests are carried out for the corrosive activity due to sulfate, chloride, etc. At last, the results are examined, and the conclusions are obtained [15].

Slump decreases as GGBS content increases. When fine aggregate is replaced by 30% GGBS, the compressive strength increases by 8%. When 30% GGBS with fine aggregate is substituted for the fine total, the ductile strength increases by 17%. When 30% GGBS with fine aggregate is substituted for the fine total, the flexural strength increases by 44%. 30% GGBS for M-Sand is the ideal replacement for fine aggregate, as the quality improves when the fine aggregate is replaced with 30% GGBS. Compressive strength increases with the addition of each additional 20 mm of aggregate. The strength of an aggregate decreases as the size of the aggregate decreases.

There were issues related to the extended W/B proportion and decreased mechanical properties because the cement substance decreased and the water substance expanded compared to the planned blend. Because of this, compared to the substitution method, the expansion strategy utilizing liquefied red mud is recommended. Liquefied red mud was used to replace some cement because of concerns about changes in smoothness and mechanical properties of the concrete. The mechanical properties of the liquid red soil-included concrete were affected by the high alkaline environment created by the development of red mud on the hydration things of cement. Testing shows that slag

cement contains 20% LRM in addition to liquefied red mud (LRM) in the concrete mixture [16].

A superplasticizer can improve the workability of manufactured sand concrete, which is lower than regular concrete. Compressive strength, split tensile strength, and flexural strength of M-Sand have all increased in comparison to standard concrete as a result of its expansion. All grades of manufactured sand concrete have low water absorption and low penetration. Conventional concrete, on the other hand, appears to have lower corrosion and sulfate- and carbonation-resistance in all grades of concrete. In the interfacial move zone (ITZ), the unpleasant and prolonged structure of M-Sand helped reduce microcracks and, as a result, a strong bond between the cement network and the M-Sand at ITZ [17].

Using neutralized red mud as a partial replacement for cement, it can be said that 15% neutralized red mud is the perfect amount to use in blended cement tests (0% to 20% substitution of cement by neutralized red mud). When it comes to compressive strength, M 30 grade neutralized red mud concrete (i.e., 15% substitution) expands 21.712% within 28 days [18].

Compared to sweater curing in the development of fly ash class-C (20%), concrete's compressive strength decreases in the M20 and M30 grades when used in ordinary water curing. For seawater curing, compressive strength is 35.13 N/sq. mm, and for seawater curing without fly ash on the 84th day, compressive strength is 15.57 N/sq. mm. Due to a lack of consideration for seawater curing in red soil, the ultrasonic beat speed appears to have been created. In comparison to conventional water curing, the concrete's rebound pound resistance value is increased by 20% with fly ash class C to 38 in the 84th day using seawater mending for M30 concrete in red soil [19].

In the three-day and seven-day tests, the quality of the sand substituted for river sand was superior to that of regular concrete. When compared to regular concrete, the three-day strength of the 100 percent smash sand blend is about a seven-day improvement. There were no noticeable differences in the results when 30% fly ash was substituted for cement, and 0.3 M NaOH was used. The blend with stream sand replaced by 100% pulverised is stronger after 28 days than the regular mix [20].

When it comes to fine aggregate, manufactured sand could be a viable alternative. The close proximity of nanosilica makes significant progress in the strength of concrete with counterfeit sand at a much earlier age than in standard concrete. Nondestructive tests like rebound pound yielded values of compressive strength that met the requirements of IS codes for both mixes without and with 2% nanosilica development. The ultrasonic pulse velocity (UPV) test results show that both concrete blends for the M20 survey are excellent and palatable. Increasing the rate of substitution of characteristic sand with made sand increases the modulus of flexibility [21].

The main difference between stream sand and fabricated sand was the shape and conduct of the sand when it was incorporated into a concrete mixture. Aside from its roundness, the material's length-to-width ratio (L/W) was significantly larger than that of waterway sand, which had a lower L/W ratio than the manufactured sand. Concrete

conduct is less dependent on the sand's molecule size, shape, and surface. Making sand management solid requires a higher water-decreasing operator in order to achieve the comparative usefulness of stream sand containing concrete. High-quality concrete can be produced by using sand that has a higher roundness and length-to-width ratio.

The expansion of red soil as a stream sand alternative shows excellent results in terms of quality and impenetrability. When red soil was added to cement as a substitute, the material's mechanical properties were significantly improved. The quality and obscurity of the solid are greatly improved when red soil is used in place of stream sand. Contrasting stream sand and red soil, the effect quality property of red soil is usually quite good [22]. In place of stream sand, it is possible to use the powdered waste generated during the cleaning of fired tiles.

As solid properties improve in solidarity, engineered sand becomes a more important component in the production of superior cement. It is possible to reduce the environmental impact of solid concrete projects by using ultra-high-quality cement and fabricated sand instead of readily available waterway sand. When compared to regular, customary cement, the ultra-high quality cement made with made sand offers superior performance. The manufactured sand can be used in concrete as a partial or complete replacement for stream sand. When compared to typical regular cement, produced sand exhibits superior compressive quality when used in its place 100% [23].

Fractional substitution of metakaolin for cement and M-Sand for fine aggregate can significantly improve the compressive and flexural strength of concrete, allowing for new designs. M-Sand can be used as a limited substitute for conventional sand in specific applications. Using M-Sand in place of regular sand has a perfect substitution rate of 100%. Strength also rises as the rate at which metakaolin and M-Sand are produced and consumed increases [24].

Three grinding stages are recognized and shown for the red clay-concrete interface shear practices, to be specific coordinate adaptable stages, plastic softening stages, and remaining contact stages. Clay matrix furrowing developments on the interface are at the heart of each one of these examples. When the clay and concrete surfaces are in close contact, the shear quality on the interface is primarily influenced by an increased cohesion and grinding strength. The measured peak and remaining shear strength values in the smooth interface tests are remarkably close to each other with no shear development observed in the tests. It is clear that the shear failure plane lies on the clay–concrete smooth interface because the red clay's strength parameters are higher than those of the smooth interface [25].

Expansion of nanosilica leads to a noteworthiness increase within the characteristic strength and durability of concrete. Substitution of cement with 0.5% of nanosilica gives more strength than the M-Sand mix conjointly; the durability has been extended compared to the M-Sand mix. The self-weight of the nanoblend is lighter than the M-Sand and the conventional blend. The workability decreases with the addition of nanosilica compared to the routine blend and the M-Sand mix. The infiltration level of chlorides and acids is less in nanoconcrete compared to that of conventional and M-Sand blend [26]. Increment in

TABLE 1: Properties of fine aggregates.

Particular	River sand	M-Sand	Red soil
Specific gravity	2.633	2.623	2.537
Water absorption	1% by wt	2% by wt	4% by wt

red mud substance diminishes the compressive strength as well as tensile strength of concrete. Ideal rate of the substitution of cement by weight is found to be 25%. Concrete organized by utilizing red mud is sensible in enhancing works and gives beautifully brilliant appearance. Workability of concrete may get affected with increase of red mud but it can be made strides by counting superplastcizers. We utilize mix of red mud and cement for nonfundamental work [27].

The compressive strength and flexure strength of concrete can be moved forward by halfway substitution of silica fume for cement and M-Sand for fine aggregate. M-Sand can be utilized as halfway substitution for the normal sand, and the compressive and flexure strengths are expanded as the rate of M-Sand is extended up to perfect level. The ideal rate of substitution of normal sand by M-Sand is 50% [28, 29]. In this work, an endeavour is made to replace normally accessible waterway sand with locally accessible substitution materials. In this examination, the result of red soil as a replacement for sand and M-Sand for mechanical properties and durability of concrete has been researched. The mechanical properties for concrete specimens have been done for samples containing red soil and fabricated sand (M-Sand). In this examination, two arrangements of various mixes were considered.

2. Experimental Procedures

2.1. Materials Used. All blends use Ordinary Portland cement (OPC-53 grade). Cement has a specific gravity of 3.15. The river sand used in concrete has a specific gravity of 2.63. The specific gravity of M-Sand used in concrete is 2.623, which is an essential source of fine aggregate replacement.

Red soil has a specific gravity of 2.546, which is closer to that of river sand and M-Sand than other types of sand. To make up for the lack of stream and M-Sand, it is now used as a partial replacement in concrete. As a fine aggregate material in the concrete mix, red soil is sieved through a 420 micron strainer. Both strong and union fewer particles are present in it. A 20 mm sifter and a 12.5 mm filter are used to sieve the coarse total. All blends have a specific gravity of 2.78, which is the same for all.

2.2. Chemical Composition of Red Soil. The chemical composition of red soil are nonsoluble material (90.45%), iron (3.60%), aluminium (2.90%), organic matter (1%), magnesium (0.70%), lime (0.55%), carbon dioxide (0.30%), potash (0.23%), soda (0.10%), phosphorus (0.09%), and nitrogen (0.08%).

2.3. Material Testing

2.3.1. Fineness Modulus of Fine Aggregate. In order to control fine totals, sieve analysis is employed. They used
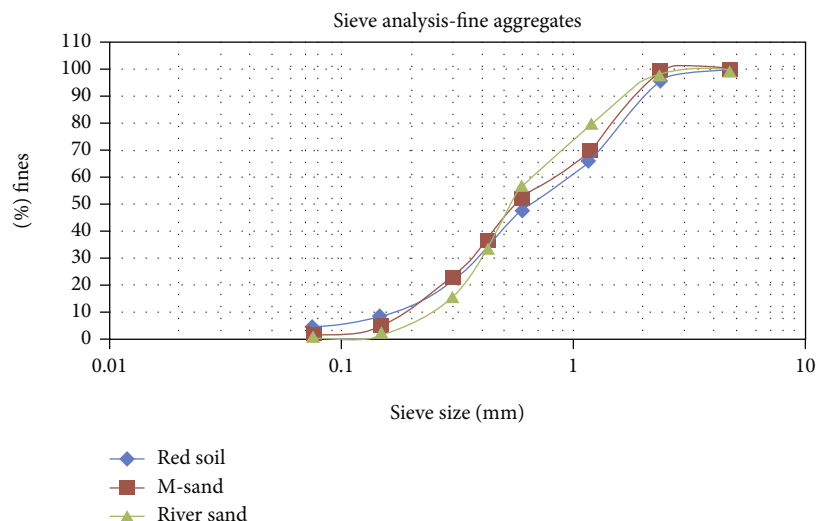
FIGURE 1: Sieve analysis graph for fine aggregates. Note: reviewing fine total materials was affirmed to zone II of table-9 of IS: 383-2016.

4.75 mm, 2.36 mm, and 1.18 m and 600 microns, 300 microns, and 150 microns and a container as filters for the study. Sifters were used to sieve the fine totals for a period of 10 minutes. The weight of the example was measured on each filter, and the total weight of the example was calculated. According to IS 383-2016, the strainer examination result for fine total materials and their prescribed range are shown in Table 1. In order to control fine totals, sieve analysis is employed. They used 4.75 mm, 2.36 mm, and 1.18 m and 600 microns, 300 microns, and 150 microns and a container as filters for the study. Sifters were used to sieve the fine totals for a period of 10 minutes. The weight of the example was measured on each filter, and the total weight of the example was calculated. The graphical portrayal of the sieve analysis result for fine total materials and their prescribed range as per IS 383-2016 is shown in Figure 1.

2.4. Properties of Fine Aggregate and Coarse Aggregate.
The properties of the fine total exposed to explicit gravity and water ingestion test as indicated by IS 2386 (part III) are shown in Table 1.

The properties of the coarse total exposed to explicit gravity, water ingestion, and fineness modulus test as indicated by IS 2386 (part III) are shown in Table 2.

2.5. Quality of Water.
As per IS456:2000, the water quality must be fulfilled. The accompanying boundaries are shown in Table 3.

The test results of the sample water are shown in Table 4.

2.6. Mix Proportions.
During this study, eleven different blends were analyzed in total. Fine natural river sand was used as the main ingredient in the control mix. Red soil is a partial replacement for a fine aggregate in the S1, S2, S3, S4, and S5 mixes, each of which has 20%, 30%, 40%, and 60%, respectively. S5, S6, S7, S8, and S10 are the mix of M-Sand and red soil that are traded for ordinary river sand.

TABLE 2: Properties of coarse aggregates.

S. no	Particulars	Values
1.	Specific gravity	2.78
2.	Water absorption	0.5% by weight
3.	Fineness modulus	2.175

TABLE 3: Water quality parameter as per IS456:2000.

Quality parameters	Minimum limit (ppm)
Chlorides	500
SO_3	1000
Alkali carbonates and bicarbonates	1000
Turbidity	2000

TABLE 4: Sample water quality parameter.

Quality parameters	Minimum limit (ppm)
Chlorides	99.28
SO_3	237
Alkali carbonates and bicarbonates	268
Turbidity	1.37

All the mix proportions have been listed in Table 5 with their corresponding mix extents.

2.7. Mix Ratios.
According to IS 10262:2009, the solid blend proportions utilized for each blend extents are determined and are shown in Table 6.

2.8. Mechanical Properties.
Compressive and flexural strengths of specimens have been described. The specimens' mechanical properties have been conveyed. At a time of 7 days, 28 days, and 90 days, the compressive strength, split tensile strength, and flexural strength of all cement were

TABLE 5: Mix proportions of various samples.

| Sample name | Cement (%) | Fine aggregate | | Red soil (%) | Coarse aggregate (%) |
		River sand (%)	M-Sand (%)		
CC	100	100	—	—	100
S1	100	80	—	20	100
S2	100	70	—	30	100
S3	100	60	—	40	100
S4	100	50	—	50	100
S5	100	40	—	60	100
S6	100	—	40	60	100
S7	100	—	50	50	100
S8	100	—	60	40	100
S9	100	—	70	30	100
S10	100	—	80	20	100

TABLE 6: Mix ratios.

Sample name	Cement	Fine aggregate	Coarse aggregate
CC	1	1.459	2.64
S1	1	1.441	2.64
S2	1	1.432	2.64
S3	1	1.422	2.64
S4	1	1.413	2.64
S5	1	1.404	2.64
S6	1	1.396	2.64
S7	1	1.403	2.64
S8	1	1.410	2.64
S9	1	1.417	2.64
S10	1	1.425	2.64

FIGURE 2: Concrete immersed 5% Na_2SO_4 and 5% $MgSO_4$ solution and surface change.

tested. There were 150 mm × 150 mm × 150 mm cube specimens and 150 mm diameter × 300 mm height cylindrical specimens used for the compressive strength and split tensile strength, respectively. Prisms of 100 mm × 100 mm × 500 mm have passed the flexural strength.

2.9. Durability Test. Red soil was used as a fractional substitute for river sand and M-Sand in concrete specimens that were tested for their strength. The cube specimens have been subjected to a durability test. Water curing has been applied

to the cast specimens. For a period of 28 days, the models were subjected to three different types of durability tests to determine the durability of concrete samples containing red soil and M-Sand. These tests examined the resistance to alkalinity, sulfate attack, and chloride attack.

2.9.1. Alkalinity Test. Alkaline attack on different concrete blends has been tested in accordance with IS 456 : 2000. Five percent sodium hydroxide (NaOH) water was used to immerse the concrete cubes. For this, three concrete

TABLE 7: Compressive strength of river sand and red soil combination.

Sample names	Compressive strength (N/mm^2)		
	Seven days	28 days	90 days
CC	28.31	42.96	43.70
S1	26.52	41.04	45.48
S2	27.71	39.55	46.81
S3	29.63	41.11	52.45
S4	30.32	42.22	53.48
S5	25.56	40.44	49.63
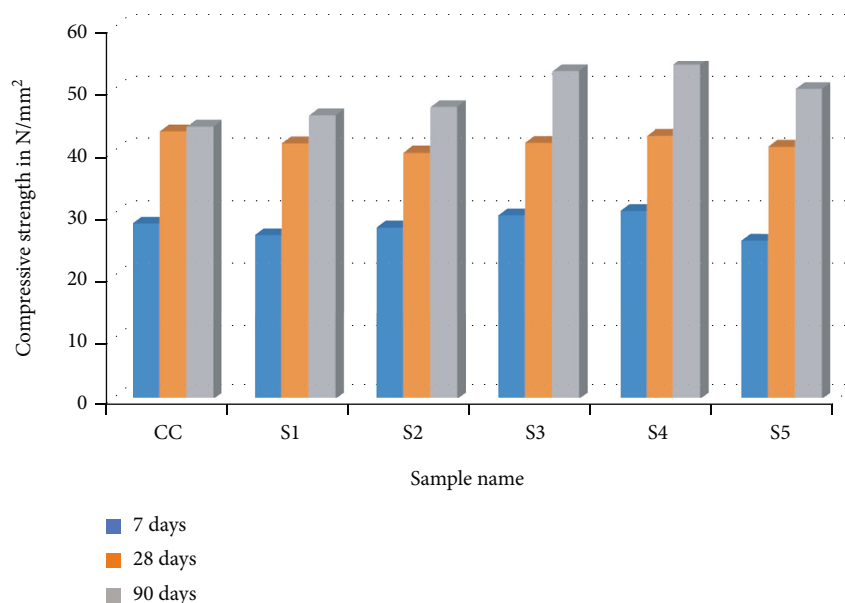
FIGURE 3: Compressive strength of red soil and river sand combination.

TABLE 8: Compressive strength of M-Sand and red soil combination.

Sample names	Compressive strength (N/mm^2)		
	Seven days	28 days	90 days
CC	28.31	42.96	43.70
S6	29.81	38.22	45.19
S7	32.80	35.85	45.33
S8	31.56	33.85	45.78
S9	27.40	38.67	46.00
S10	28.46	36.22	45.48

specimens were tested, one with red soil as a partial substitute for river sand and another with red soil as a partial substitute for M-Sand, immersed in a tub of soluble water containing 5% sodium hydroxide arrangement for aged 28 days. The results of tests conducted before and after treatment have been compared in terms of their weight. All examples show that the weight loss rate is the same. Percentage misfortune of significance of show and compressive strength was used to determine concrete's alkaline resistance [30–35].

2.9.2. Sulfate Attack Test. According to ASTM C1012:2004, the resistance of concrete to sulfate attacks has been considered. The concrete cubes were submerged in sulfate water, having 5% of sodium sulfate (Na_2SO_4) and 5% magnesium sulfate ($MgSO_4$) by volume of water. For these two arrangements of concrete specimens that were taken, one set of concrete models was made with red soil as a fractional swap for river sand and another set containing red soil as a partial substitution for M-Sand, for aged 28 days and permitted to dry for one day. At that point, specimens were dunked
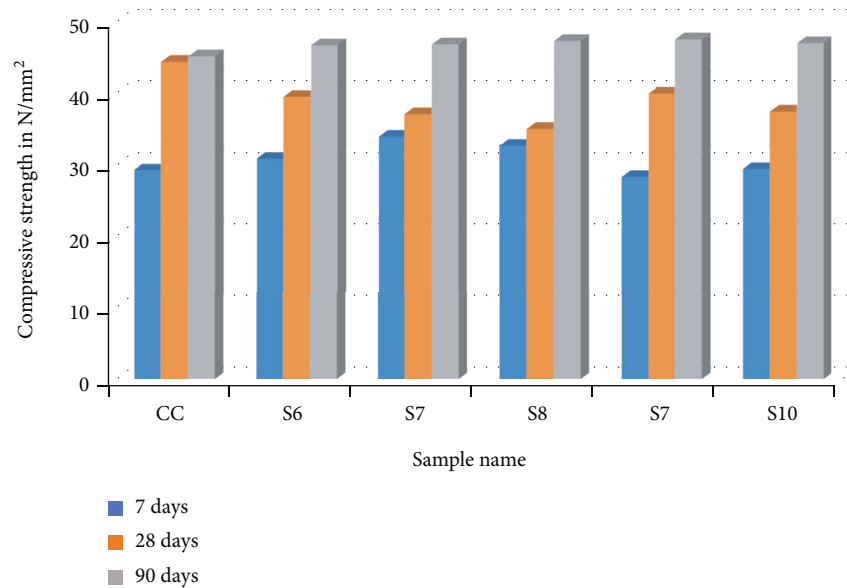
Figure 4: Compressive strength for M-Sand and red soil combination.

totally in a tub containing sulfate water having 5% of sodium sulfate (Na_2SO_4) and 5% magnesium sulfate ($MgSO_4$) for 28 days [36–40]. Following a time of 28 days, the specimens were taken and dried out. The weight of the models before treatment and after treatment is being looked at. The regular rate decrease in weight is found out for all the specimens as shown in Figure 2.

2.9.3. Chloride Attack Test. Two sets of concrete specimens were taken, one containing three concrete samples made with red soil as a partial substitution for sand and the other containing red soil as a partial substitution for M-Sand, for aged 28 days and allowed to dry for a day, according to BS 1881 standards. By completely immersing the models in a tub containing concentrated hydrochloric acid (HCL) with a normality of 1 N, the chloride attack test was carried out on concrete samples. It is necessary to add a certain volume of water to the water for 28 days [41–45]. These concrete samples were removed from the acid bath and dried out after a period of 28 days. There is a comparison of the specimens' weight before and after treatment. All samples' weight loss is averaged out to arrive at an overall weight loss percentage.

3. Results and Discussion

3.1. Compressive Strength. The compressive strength for concrete specimens containing red soil as a substitution of sand is shown in Table 7.

According to the above findings, the strength of the red soil and river sand-concrete samples was inferior to that of the standard mix after 28 days. However, after 28 days, the red soil in concrete begins to react with the cementitious materials in the concrete, resulting in a strong and durable product. In comparison to a standard mix, the strength of the concrete was increased by 1.5% [46–50]. The strength

Table 9: Split tensile strength for red soil and river sand combination.

Sample name	28-day strength (MPa)
CC	3.11
S1	2.46
S2	2.53
S3	2.56
S4	2.84
S5	2.85

for concrete samples containing red soil as partial substitution of sand is shown in Figure 3.

The compressive strength for concrete samples that have red soil as a replacement for M-Sand is shown in Table 8.

The compressive strength for concrete samples containing red soil as partial substitution of M-Sand is shown in Figure 4.

The results suggested that up to 70% of red soil as replacement material by weight of cement with M-Sand shows good compressive strength compared to conventional mix, but further addition of red soil results in the decrease of power. Similar to the previous results, the addition of red soil shows good strength in the later stage of concrete.

3.2. Split Tensile Strength. The tensile strength for samples containing red soil as a substitution for sand is shown in Table 9.

The split tensile strength for concrete samples containing red soil as a substitution for sand is shown in Figure 5.

The results suggest that up to 28 days, tensile strength for concrete samples containing both red soil and river sand was low compared to that of the standard mix. But after 28 days, the red soil present in concrete may react

28 days split tensile strength in N/mm^2
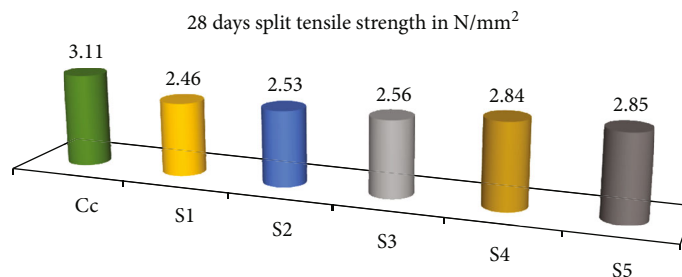
FIGURE 5: 28-day split tensile strength for red soil and river sand combination.

with the cementitious materials in concrete and show good tensile strength [50–54]. Tensile strength for concrete samples containing red soil as a replacement for M-Sand is shown in Table 10.

The split tensile strength for concrete samples containing red soil as substitution of M-Sand is shown in Figure 6.

The results suggested that up to 60% substitution for red soil by weight of cement with M-Sand shows good split tensile strength compared to conventional mix, but on further addition of red soil results in a decrease in strength. Similar to previous results, the addition of red soil shows good stability in the later concrete stage as shown in Figure 7.

3.3. Flexural Strength.

The flexural strength of samples containing red soil as a replacement for normal river sand is shown in Table 11. The flexural test specimen is presented in Figure 8.

The flexural strength for concrete samples containing red soil as substitution of sand is shown in Figure 9.

The flexural strength of the concrete samples containing red soil shows less power than that of the standard mix. The addition of red soil affects the flexural behaviour of the concrete to some extent. The flexural strength of the concrete samples containing red soil as a limited substitution for M-Sand is shown in Table 12.

The flexural strength for concrete samples containing red soil as a partial replacement for river sand is shown in Figure 10.

The flexural strength of the concrete samples containing 60% of red soil as a replacement along with M-Sand shows the same strength as that of the conventional mix, so this type of concrete can be used as a replacement in terms of flexural strength over the traditional concrete.

3.4. Durability Test.

The compressive strength for concrete samples containing red soil as a substitution for sand after the durability test is shown in Table 13.

For testing the durability of concrete samples, three different tests (i.e., alkalinity, sulfate, and chloride attack test) were conducted for concrete. In this investigation, the durability tests were conducted for 28 days. The 28-day durability test results for the concrete samples are shown in Table 14. The results indicate a slight reduction in the strength of concrete in the range of 4 to 7% as shown in Figure 11.

TABLE 10: Split tensile strength for M-Sand and red soil combination.

Sample name	28-day strength (MPa)
Cc	3.25
S6	3.34
S7	3.14
S8	3.11
S9	3.30
S10	3.23

The percentage reduction in weight of the concrete samples containing red soil as substitution of sand after the durability test is shown in Table 15.

The compressive test results of samples having red soil as a replacement for M-Sand after durability test are shown in Table 14.

The percentage reduction in weight of the concrete samples containing red soil as a sand replacement after durability test is shown in Table 16.

Similar to the river sand and red soil combinations, durability is also being conducted for samples containing M-Sand and red soil. But compared to the previous results, the reduction in strength was quite lofty in contrast to earlier combinations. So, these river and red soil combinations are light ahead in preference in terms of durability as shown in Figure 12.

When combining the test results of all the experiments, it can conclude that the S9 combination shows promising result in terms of both strength and durability perspectives. Moreover, for detailed understanding regarding the compositions and microstructure of red soil in both the combinations, the scanning electron microscope analysis was conducted for both the variety samples.

3.5. Scanning Electron Microscope (SEM) Analysis Test.

The microstructure of the concrete mixes was examined utilizing scanning electron microscope (SEM) which for all intents and purposes makes a difference to imagine the microstructure of the hydrated cement paste. The SEM analysis of S9 combinations is illustrated in Figure 13. The figure shows that the soil particles in the concrete samples show a sponge-like structure and have a wide variation of diameter in size. Due to the existence of minerals, CSH gel formation

28 days split tensile strength in N/mm^2
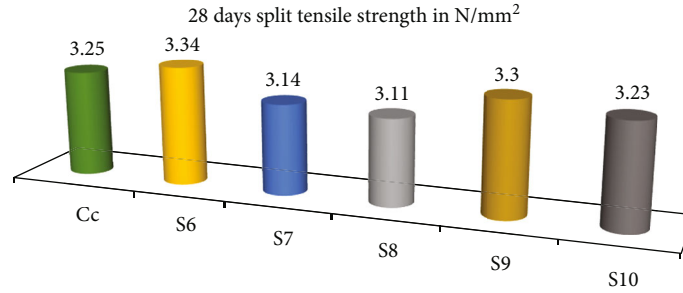
Figure 6: 28-day split tensile strength for M-Sand and red soil combination.

Figure 7: The split tensile test specimen.

Table 11: Flexural strength for river sand and red soil combination.

Sample name	28-day strength (MPa)
Cc	5.33
S1	4.54
S2	4.67
S3	4.40
S4	4.67
S5	5.07

28 days flexural strength in N/mm^2
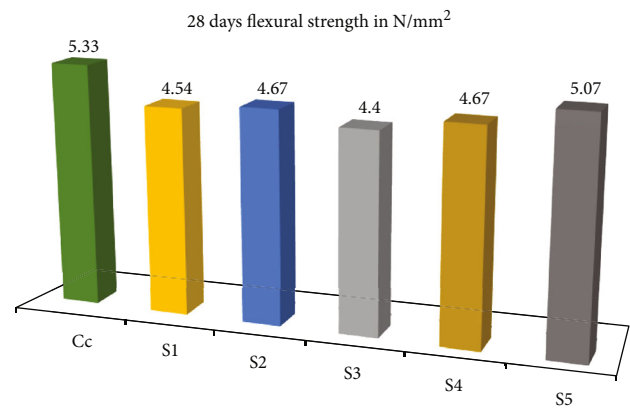
Figure 9: 28-day flexural strength for river sand and red soil combination.

Table 12: Flexural strength for M-Sand and red soil combination.

Sample name	28-day strength (MPa)
Cc	5.47
S6	5.47
S7	5.33
S8	5.20
S9	5.33
S10	5.20

Figure 8: Flexural test specimen.

is more for S9 combination (70% M-Sand +30% red soil) that leads to give better compressive strength.

3.6. EDAX Analysis. To determine the purity of the red soil particles, EDAX analysis was conducted on the concrete samples. The samples were placed on the copper grid coated with carbon, and the whole setup was placed inside an air evacuated chamber.

The EDAX results for S9 combination (70% M-Sand +30% red soil) show that the silica level has tremendously increased to 77.48% atom as shown in Figure 14.

28 days flexural strength in N/mm^2

Figure 10: 28-day flexural strength for M-Sand and red soil combination.

TABLE 13: Compressive strength of river sand and red soil combination after the durability test.

Test name	Compressive strength (MPa)	% reduction in strength
Control-mix (without any solution)	42.22 (S4)	—
Alkalinity test	39.11	7.37
Sulfate attack test	40.00	5.26
Chloride attack test	40.44	4.21

TABLE 14: Compressive test results for M-Sand and red soil combination in the durability test.

Test name	Compressive strength (MPa)	% reduction in strength
Control-mix (without any solution)	38.67 (S9)	—
Alkalinity test	36.00	6.90
Sulfate attack test	35.11	9.20
Chloride attack test	36.44	5.75
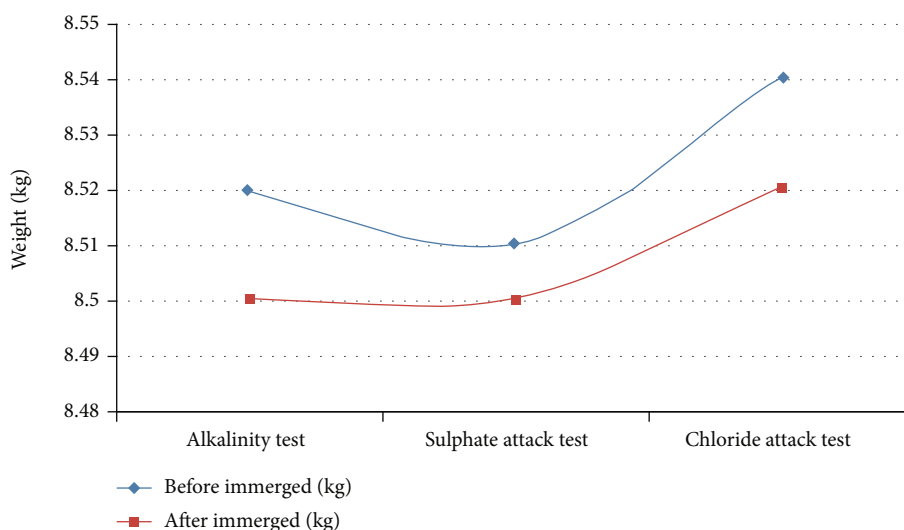
FIGURE 11: Before and after immersion weight for river sand and red soil combination.

TABLE 15: Weight loss for river sand and red soil combination after the durability test.

Test name	Before immersion Weight (kg)	After immersion Weight (kg)	% reduction in weight
Alkalinity test	8.52	8.50	2.35
Sulfate attack test	8.51	8.50	1.76
Chloride attack test	8.54	8.52	2.34

TABLE 16: Weight loss for M-Sand and red soil combination after the durability test.

Test name	Before immersion Weight (kg)	After immersion Weight (kg)	% reduction in weight
Alkalinity test	8.41	8.40	1.19
Sulfate attack test	8.57	8.54	3.50
Chloride attack test	8.42	8.39	3.56
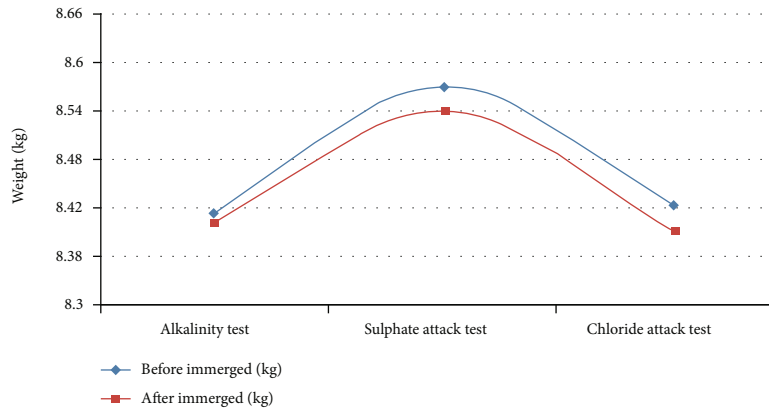
FIGURE 12: Before and after immersion weight for M-Sand and red soil combination.
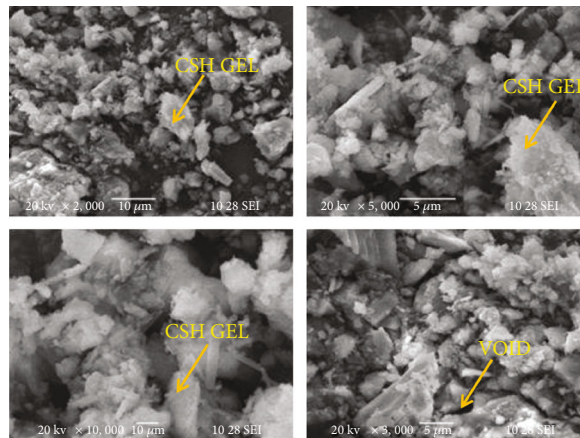
FIGURE 13: SEM analysis for S9 combination (70% M-Sand + 30% red soil).

Spectrum processing :
Peak possibly omitted : 9.799 keV

Processing option : All elements analyzed (Normalised)
Number of iterations = 6

Standard :
O   SiO2   1-Jun-1999 12:00 AM
Na   Albite   1-Jun-1999 12:00 AM
Mg   MgO   1-Jun-1999 12:00 AM
Al   Al2O3   1-Jun-1999 12:00 AM
Si   SiO2   1-Jun-1999 12:00 AM
S   FeS2   1-Jun-1999 12:00 AM
Ca   Wollastonite   1-Jun-1999 12:00 AM
Fe   Fe   1-Jun-1999 12:00 AM

Element	App Conc.	Intensity Corrn.	Weight%	Weight% Sigma	Atomic%
O K	31.23	0.6146	61.72	0.80	77.48
Na K	0.40	0.6745	0.73	0.23	0.63
Ng K	0.39	0.6531	0.72	0.18	0.60
Al K	2.04	0.7673	3.23	0.22	2.40
Si K	6.92	0.8322	10.10	0.33	7.22
S K	0.35	0.8701	0.49	0.18	0.30

FIGURE 14: EDAX analysis for S9 combination (70% M-Sand + 30% red soil).

4. Conclusion

In this paper, we have tried out two sets of combinations, one set of manufactured sand with red soil and another set of river sand with the red soil of 10 proportions, based on the following results.

4.1. The Combination of River Sand and Red Soil

(i) The sample name S4 (50% of red soil and 50% of river sand) gives the better compressive strength when compared to all other proportions of river sand with red soil

(ii) Likewise, sample name S5 (60% of river sand and 40% of red soil) gives better flexural strength and split tensile strength compared to all other proportions of river sand with red soil

4.2. The Combinations of Manufactured Sand (M-Sand) and Red Soil

(i) The sample name S9 (30% of red soil and 70% of manufactured sand) gives high compressive strength compared to all other proportions

(ii) Likewise, the sample name S6 (60% of red soil and 40% of manufactured sand) gives better flexural strength and tensile strength in contrast against various proportions

4.3. Durability Tests

(i) For the durability test, the S4 and S9 combination samples have been taken, which shows high 28-day compressive strength

4.4. Justification

(i) Red soil has high porosity and less permeability, and it can absorb a considerable quantity of water compared to ordinary river sand due to its minor pores. The concrete surface is low in permeability, increasing the durability of concrete where the steel corrosion can be prohibited. Compared to 100% river sand as a fine aggregate in concrete, the complete substitution of M-Sand and red soil concrete has shown better performance. Still, in the future, these are potential materials for replacing river sand

(ii) The manufactured sand has many fine particles, which is more than that of natural aggregate, so it may give a large contact area, which is the ultimate reason behind the increased strength of samples. But there will be a decrease in the workability of samples due to the fine particles present, which absorbs the large quantity of water. Thus, to keep the surface of the concrete in wet conditions, a large amount of mater has to be added. Therefore, strength is significantly high for the samples containing manufactured sand as sand replacement

(iii) Red soil is used as a best replacement material for sand to reduce the demand that developed on river sand. The concrete samples containing red soil and river sand show higher compressive strength than the mix containing M-Sand and red soil

Data Availability

The data used to support the findings of this study are included in the article.

Conflicts of Interest

The authors declare that there is no conflict of interest regarding the publication of this article.

References

[1] T. Mounika and G. L. Bhuvaneswari, "Strength characteristics of concrete by replacing natural sand by M-sand for M20 and M30 grade concrete," *International Journal Of Advance Scientific Research And Engineering Trends*, vol. 6, no. 2, 2021.

[2] T. Gupta, Y. Agrawal, and K. S. Kanyal, "Properties of sustainable concrete containing red mud: a review," *Journal of Scientific Research & Reports*, vol. 1, pp. 15–26, 2021.

[3] A. M. Arunmohan, S. Bharathi, L. Kokila, E. Ponrooban, L. Naveen, and R. Prasanth, "An experimental investigation on utilisation of red soil as replacement of fine aggregate in concrete," *Psychology And Education*, vol. 58, no. 2, pp. 8398–8403, 2021.

[4] B. F. Ogunbayo, O. C. Aigbavboa, K. E. Ogundipe, O. I. Akinradewo, L. M. Amusan, and A. O. Afolabi, "Experimental assessment of properties of earth soil used in concrete production," *Materials Science and Engineering*, vol. 1107, no. 1, article 012177, 2021.

[5] A. Karthick, K. K. Murugavel, A. Ghosh, K. Sudhakar, and P. Ramanan, "Investigation of a binary eutectic mixture of phase change material for building integrated photovoltaic (BIPV) system," *Solar Energy Materials and Solar Cells*, vol. 207, article 110360, 2020.

[6] S. Suleman and S. Needhidasan, "Utilization of manufactured sand as fine aggregates in electronic plastic waste concrete of M30 mix," *Materials Today: Proceedings*, vol. 33, pp. 1192–1197, 2020.

[7] X. Wang, H. Cheng, P. Yan, J. Zhang, and Y. Ding, "The influence of roughness on cyclic and post-cyclic shear behavior of red clay-concrete interface subjected to up to 1000 cycles," *Construction and Building Materials*, vol. 273, article 1211718, 2021.

[8] K. Yoganandam, V. Shanmugam, A. Vasudevan et al., "Investigation of dynamic, mechanical, and thermal properties of Calotropis procera particle-reinforced PLA biocomposites," *Advances in Materials Science and Engineering*, vol. 2021, Article ID 2491489, 7 pages, 2021.

[9] S. Wang, H. Jin, Y. Deng, and Y. Xiao, "Comprehensive utilization status of red mud in China: a critical review," *Journal of Cleaner Production*, vol. 289, article 125136, 2021.

[10] B. Vijaya, S. Senthil Selvan, and P. Vasanthi, "Experimental investigation on the behaviour of reinforced concrete column containing manufactured sand under axial compression," *Materials Today: Proceedings*, vol. 39, pp. 446–453, 2021.

[11] R. Abiraami, R. Anuradha, V. Johnpaul et al., "Mechanical and flexural behaviour study on fibrillated concrete as partial replacement of M-Sand and metakaolin," *Materials Today: Proceedings*, vol. 39, pp. 776–780, 2021.

[12] K. M. Mane, P. A. Nadgouda, and A. M. Joshi, "An experimental study on properties of concrete produced with M-sand and E-sand," *Materials Today: Proceedings*, vol. 38, pp. 2590–2595, 2021.

[13] G. N. Venkat, K. Chandramouli, and V. NagendraBabu, "Comparative study on mechanical properties and quality of concrete by part replacement of cement with silica fume, metakaolin and GGBS by using M–Sand as fine aggregate," *Materials Today: Proceedings*, vol. 43, pp. 1874–1878, 2021.

[14] A. Ayinampudi Kavya and V. Rao, "Experimental investigation on mechanical properties of concrete with M-sand," *Materials Today: Proceedings*, vol. 33, pp. 663–667, 2020.

[15] M. GS and K. T. Raja, "Experimental study on partial replacement of Msand with ground granulated blast slag," *International Research Journal on Advanced Science Hub (IRJASH)*, vol. 2, no. 7, pp. 60–66, 2020.

[16] G. Choe, S. Kang, and H. Kang, "Mechanical properties of concrete containing liquefied red mud subjected to uniaxial compression loads," *Materials*, vol. 13, no. 4, article 854, 2020.

[17] I. Mallum and K. Salihu, "Properties of concrete made with manufactured sand (M-Sand) as fine aggregate replacement: a review, Nigeria," *Journal of Engineering Science and Technology Research*, vol. 5, no. 2, pp. 40–54, 2019.

[18] A. B. Sawant, N. S. Parsekar, and N. S. Mane, "Experimental study on utilization of industry waste (red mud) in concrete," *International Research Journal of Engineering and Technology (IRJET)*, vol. 6, 2019.

[19] R. Sakthivel and V. Murugaiyan, "studies on the effect of normal water & sea water encorachment in red soil on concrete," *International Journal of Civil Engineering and Technology (IJCIET)*, vol. 10, no. 2, pp. 464–472, 2019.

[20] K. A. Gawade and M. R. Palaskar, "Mechanical properties of concrete with fly ash and manufactured sand," *A Multidisciplinary Peer Reviewed Journal*, vol. 313–315, 2018.

[21] G. P. Kumar, G. D. R. Naidu, P. Puspalatha, and P. M. Kumar, "An experimental study on non destructive tests and stress strain curves of M20 grade concrete with nano-silica using M-sand," *International Journal of Civil Engineering and Technology (IJCIET)*, vol. 8, no. 3, pp. 385–390, 2017.

[22] S. J. Alexander, A. Godwin, and S. Alexander, "Study on partial replacement of fine aggregate with red soil in concrete," *International Journal for Research in Applied Science & Engineering Technology (IJRASET)*, vol. 4, no. 5, pp. 138–145, 2016.

[23] C. Sudha, P. T. Ravichandran, K. Divyakrishnan, P. R. Kannanrajkumar, and A. Anand, "Study on mechanical properties of high performance concrete using M-sand," *Indian Journal of Science and Technology*, vol. 9, no. 5, 2016.

[24] D. Satyanarayana, D. Satesh, and E. V. Raghava Rao, "Optimization of partial replacement of natural sand by manufactured sand with metakaolin," *International Journal Of Research Publications In Engineering And Technology [IJRPET]*, vol. 2, no. 12, 2016.

[25] X. Chen, J. Zhang, Y. Xiao, and J. Li, "Effect of roughness on shear behavior of red clay – concrete interface in large-scale direct shear tests," *Canadian Geotechnical Journal*, vol. 52, no. 8, pp. 1122–1135, 2015.

[26] A. Jayaraman, M. Saravanan, and G. Anusha, "Comparative study on M-Sand concrete and (nano-silica with M-Sand concrete)," *International journal of Scientific Engineering and Technology Research*, vol. 3, no. 3, pp. 0444–0448, 2014.

[27] R. R. Rathod, N. T. Suryawanshi, and P. D. Memade, "Evaluation of the properties of red mud concrete," *Journal of Mechanical and Civil Engineering (IOSR-JMCE)*, vol. 1, pp. 31–34, 2014.

[28] A. B. Sawant, M. B. Kumthekar, and S. G. Sawant, "Utilization of neutralized red mud (industrial waste) in concrete, International," *Journal of Inventive Engineering and Sciences (IJIES)*, vol. 1, no. 2, 2013.

[29] T. Shanmugapriya and R. N. Uma, "Optimization of partial replacement of M-sand by natural sand in high performance concrete with silica fume," *International Journal of Engineering Sciences & Emerging Technologies [IJESET]*, vol. 2, no. 2, pp. 73–80, 2012.

[30] T. Aman Kumar, J. Saravanan, K. I. Kunal Bisht, and S. A. Kabeer, "A review on the utilization of red mud for the production of geopolymer and alkali activated concrete," *Construction and Building Materials*, vol. 302, article 124170, 2021.

[31] J. Shi, M. Li, W. Miao, and J. Ming, "Role of red mud in natural passivation and chloride-induced depassivation of reinforcing steels in alkaline concrete pore solutions," *Corrosion Science*, vol. 190, article 109669, 2021.

[32] X. Yuan, C. Liang, C. Ruan et al., "Low-cost synthesis of multi-walled carbon nanotubes using red soil as catalyst," *Diamond & Related Materials*, vol. 112, article 108241, 2021.

[33] A. Karthick, K. K. Murugavel, and P. Ramanan, "Performance enhancement of a building-integrated photovoltaic module using phase change material," *Energy*, vol. 142, pp. 803–812, 2018.

[34] J. V. M. Raman and V. Ramasamy, "Augmentation of dissimilar techniques for enhancing the concrete properties with recycled coarse aggregate and manufactured sand," *Journal Of Materials Research And Technology*, vol. 14, pp. 1180–1190, 2021.

[35] M. Ghalehnovi, E. A. Shamsabadi, A. Khodabakhshian, F. Sourmeh, and J. De Brito, "Self-compacting architectural concrete production using red mud," *Construction and Building Materials*, vol. 226, pp. 418–427, 2019.

[36] B. Ramesh, V. Gokulnath, and M. Ranjithkumar, "Review on the flexural properties of fiber reinforced self compacting concrete by the addition of M-sand," *Materials Today: Proceedings*, vol. 22, pp. 1155–1160, 2020.

[37] K. Alekseev, V. Mymrin, M. A. Avanci et al., "Environmentally clean construction materials from hazardous bauxite waste red mud and spent foundry sand," *Construction and Building Materials*, vol. 229, article 116860, 2019.

[38] W. C. Tang, Z. Wang, Y. Liu, and H. Z. Cui, "Influence of red mud on fresh and hardened properties of self-compacting concrete," *Construction and Building Materials*, vol. 178, pp. 288–300, 2018.

[39] I. M. Nikbin, M. Aliaghazadeh, S. H. Charkhtab, and A. Fathollahpour, "Environmental impacts and mechanical properties of lightweight concrete containing bauxite residue (red mud)," *Journal of Cleaner Production*, vol. 172, pp. 2683–2694, 2018.

[40] W. Shen, Z. Yang, L. Cao et al., "Characterization of manufactured sand: particle shape, surface texture and behavior in concrete," *Construction and Building Materials*, vol. 114, pp. 595–601, 2016.

[41] O. Paul Awoyera, O. Joseph Akinmusuru, and M. Ndambuki, "Green concrete production with ceramic wastes and laterite," *Construction and Building Materials*, vol. 117, pp. 29–36, 2016.

[42] B. Sawant, D. B. Kamble, and T. B. Shinde, "Utilization of industrial waste (red mud) in concrete construction," *International Journal of Innovative Research in Science and Engineering*, vol. 2, no. 3, pp. 112–121, 2016.

[43] V. Christina Mary and C. H. Kishore, "Experimental investigation on strength and durability characteristics of high performance concrete using GGBS and M-Sand," *ARPN Journal of Engineering and Applied Sciences*, vol. 10, no. 11, pp. 4852–4856, 2015.

[44] R. X. Liu and C. S. Poon, "Utilization of red mud derived from bauxite in self compacting concrete," *Journal of Cleaner Production*, vol. 112, pp. 384–391, 2015.

[45] M. N. Uddin, S. Velu, and P. Elumalai, "An experimental investigation of red soil based geopolymer mortar without Portland cement," *International Journal of Scientific & Engineering Research*, vol. 6, no. 5, pp. 1722–1732, 2015.

[46] B. Harish, "The properties of concrete in corporating red sand as fine aggregate," *International Journal of Research Sciences and Advanced Engineering*, vol. 2, no. 11, pp. 77–90, 2015.

[47] L. Reig, M. M. Tashima, M. V. Borrachero, J. Monzó, C. R. Cheeseman, and J. Payá, "Properties and microstructure of alkali-activated red clay brick waste," *Construction and Building Materials*, vol. 43, pp. 98–106, 2013.

[48] Y. Jani and W. Hogland, "Waste glass in the production of cement and concrete - a review," *Chemical Engineering*, vol. 2, no. 3, pp. 1767–1775, 2014.

[49] A. Pereira-de-Oliveira, J. P. Castro-Gomes, and P. M. S. Santos, "The potential pozzolanic activity of glass and red-clay ceramic waste as cement mortars components," *Construction and Building Materials*, vol. 31, pp. 197–203, 2012.

[50] P. E. Tsakiridis, S. Agatzini-Leonardou, and P. Oustadakis, "Red mud addition in the raw meal for the production of Portland cement clinker," *Journal of Hazardous Materials*, vol. 116, no. 1-2, pp. 103–110, 2004.

[51] M. S. Shetty and A. K. Jain, *Concrete Technology – Theory and Practice*, Chand Publishing, New Delhi, 2019.

[52] IS 10262, *Concrete Mix Proportioning - Guidelines*, Bureau of Indian standards, New Delhi, 2009.

[53] IS 383, *Specification for Coarse and Fine Aggregate from Natural Sources for Concrete*, Bureau of Indian standards, New Delhi, 1970.

[54] IS 516, *Methods of Test for Strength of Concrete*, Bureau of Indian standards, New Delhi, 1999.

Research Article

The Role of Nanomaterial Technology Industrialization Model in Promoting the Optimization of Financial Market Industrial Structure

Ning Han (ORCID)

Chengdu Jincheng College, Chengdu, 610000 Sichuan, China

Correspondence should be addressed to Ning Han; hanning020202@163.com

The material technology industrialization model is in promoting the adjustment of the financial market industrial economic structure. The experiment realized the adjustment of industrial economic structure by the adsorption of nano materials. TiO2-rGO was prepared firstly, and then Mn dioxide nanoparticles (HM NPs) were synthesized. The specific surface area and pore volume were determined by N2 adsorption BET method. The infrared spectrum was obtained by infrared spectrometer (MA). The sample was heated to 900°C at 10°C to determine TGA. In order to explore the surface composition and chemical element state of the material, X-ray photoelectron spectroscopy (XPS) was used with monochromatic al Ka ray. The structure and composition of the substance can be deduced by characterization. The Zr metal organic framework was applied to the adsorption of 2,4,6-trichlorophenol (2,4,6-TCP) in water. he experimental data show that the degradation efficiency of metronidazole is the best in the presence of visible light and hydrogen peroxide, which can reach about 80% in 60 minutes. The results show that nano materials and nanotechnology can promote the adjustment of economic structure of financial market industry, and have a great impetus to the entire financial industry.

1. Introduction

Nanotechnology, as one of the high-tech, has high value-added in the process of its development and application. It can not only bring great economic benefits, but also improve labor productivity and achieve better social effects. Science and technology is a double-edged sword. Nanotechnology brings great benefits and also has high risk characteristics. Nanotechnology is in the forefront of science and technology, and it is a new and high-level technology, with obvious characteristics of advanced research and many unpredictable factors. Therefore, to avoid harm and benefit, to reduce the negative effects of nanotechnology, we need the high guidance of philosophy. Among them, photothermal nanomaterials can convert the absorbed light energy into heat to increase the temperature of the surrounding environment, and have shown great application potential in tumor multi-mode imaging and optical therapy [1].

The development of financial technology will improve the efficiency of financial operations and bring a new environment for private enterprise financing and financial risk prevention, but it also brings new challenges to financial supervision [2]. According to the recent intensive signals released by the regulatory authorities, fintech will receive greater policy support, and fintech supervision will also be tightened simultaneously.

The application of nanomaterials is innovative for the development of financial industry. Song X uses fractal theory and thermal conduction theory to analyze the sensitivity of energetic materials, the correlation between thermal conduction and fractal dimension, and at the same time, he established a fractal heat conduction model for micron and nanometer energetic materials to verify the correctness of the model, Calculated the fractal dimension and surface fractal dimension of two nitramine explosives with different particle sizes. Although his research method is more detailed, but the consideration is not precise enough [3].

In this paper, nanomaterials are used as adsorbents to degrade organic matter in water, thereby greatly improving its photocatalytic efficiency. The adsorption efficiency of nano-adsorbents for heavy metal ions in water is better than other current adsorbents, and can be regenerated and reused. In the research of nanotechnology industrialization operation mechanism, transformation mechanism plays a connecting role. Universities and enterprises play an important role in the process of transformation. The State formulates relevant policies to encourage the transformation of nanotechnology achievements in universities and actively transform traditional industries. Health financial plays a role as a lubricant in the system of coordinated development of man and land, and the implementation of health financial plays an extremely important role in promoting the sustainable development of tourism [4, 5].

2. Financial Market and Nanomaterials

2.1. Financial Industry. Health financial industry should be based on people's needs for physical and mental health, with health as the goal, health therapy as the means, and recreation as the process to provide financial related services around the theme of health. The products provided by the health financial industry are the same as the general financial products, which are the specific products in the non physical form, but the production and operation modes are different. There are many production and service fields involved, and the industry boundary is fuzzy, so it has the characteristics of multi management; the differences of people's health and financial demand create the diversity of health financial products; only by optimizing the industrial structure, integrating management, management, technology and other means, and better coordinating the government and social resource elements, can we promote the scientific and healthy development of health financial industry [6, 7].

The most important thing of sustainable financial is to pay attention to the protection of ecological environment in the process of financial development, so as to avoid irreversible damage of financial resources in the process of development due to excessive development of natural resources and ecological environment damage [8]. Specifically speaking, sustainable financial means that in the process of developing tourism, we should also pay attention to the sustainability of development, and emphasize that the development of financial should be harmonious with local economy, society, culture and ecological environment. On the one hand, it means that the development of financial industry can not break through the local environmental carrying capacity; on the other hand, it means that the development of financial industry also needs to constantly innovate financial products and services according to the changes of economic and social forms, so as to continuously meet the market demand under different economic and social backgrounds [9, 10].

2.2. Nanomaterials Technology Industrialization Model. The dependence of nanotechnology industry on the development of nanomaterials technology can also be seen from the

dynamic development of high-tech industry. Without quantum theory, there will be no development of integrated circuits and computers; without the discovery of relativity and nuclear fission theory, there will be no widely used nuclear technology. Without the new achievements of molecular biology and genetics, there would be no biotechnology industry benefiting human beings [11]. This is mainly because the development of biotechnology is inseparable from the emergence of new research results. In the process of exploring this field, the theories and concepts formed will be widely used in our production and life. Human beings will establish new ideas which are quite different from the material world that can be observed by our naked eyes. It will greatly enrich our cognitive world and bring conceptual changes to human society. From the perspective of human development, nanotechnology promotes the miniaturization, high performance and environment friendliness of products, which will greatly save resources and energy, reduce excessive dependence on it, and promote the improvement of ecological environment [12]. In the input continuous image sequence, the gray value change of each independent pixel is subject to a single Gaussian probability function, then the Gaussian model of the nanoparticle is:

$$\mu_0(x, y) = \frac{1}{T} \sum_{i=0}^{T-1} f_i(x, y) \tag{1}$$

$$\sigma_0^2(x, y) = \frac{1}{T} \sum_{i=0}^{T-1} [f_i(x, y) - \mu_0(x, y)]^2 \tag{2}$$

In the formula, $f_i(x, y)$ represents the gray value of the i-th particle in the image.

As enterprises increase the demand for nanotechnology achievements, they are largely affected by the supply of nanotechnology achievements. Obviously, the more nanotechnology achievements enterprises have, the better position they can occupy in the competition. Different from traditional technological achievements, nanotechnology achievements are not completed by traditional experience or skills, but by the use of modern science and technology with high-tech content [13]. The research process is also a complex process, which requires a lot of human, material and financial resources. Therefore, there are two ways for enterprises to obtain nanotechnology achievements: one is to improve their independent research and development ability, improve their innovation ability, introduce talents to overcome difficulties, and obtain self-sufficiency of nanotechnology achievements. The second is to buy from scientific research institutes and universities for digestion and absorption. This scheme is more suitable for the development of enterprises, which not only saves the time of research and development, but also reduces the risk. At the same time, due to the competition of supply, the price drops, and reduces the purchase cost of enterprises [14, 15].

2.3. Industrial Economic Structure Adjustment. With the development of the economy and the improvement of production factors, industries are constantly growing and

changing, and adjustments and conversions between different industries often occur, thereby forming an industrial structure. Along with economic growth, the industrial structure is also undergoing transformation. Industrial structure adjustment refers to the mutual change and adjustment of production factors among various departments and regions. It includes two aspects: rationalization and advancedization of industrial institutions. The rationalization of industrial structure refers to the coordination of the quantity ratio of production factors between industries, the economic and technological linkage, in order to adapt to market demand and achieve the optimal industrial structure, the process of coordination and balance of all aspects of the industry and finally obtain the best benefits. The theory of sustainable development is closely related to the development of healthy tourism, and it is of great significance for the research and guidance of the development of healthy financial market [16, 17]. Only sustainable development can bring a healthy circular development result to finance.

Based on the perspective of spillover effects, the high-tech content of Internet products enables relevant practitioners to have higher quality and knowledge reserves. The flow of these high-quality employees promotes the overflow of manpower and can promote the improvement of the employment structure of the financial industry. It is of great significance for the financial industry that is positioned as a labor-intensive industry. On the other hand, Internet technology is applied to traditional industries to form a demonstration effect, through information sharing, knowledge and technology introduction, promote innovation, improve the production efficiency of financial industry and product added value, thereby improving the quality of financial industry development [18, 19]. Demonstration effect refers to the impact of changes in the consumption expenditure and income of some consumers or households on the consumption expenditure of other consumers and households, that is, consumers compare each other in space when they consume, and try to compare the consumption level. Above others or at least not below others of the same class. Therefore, consumers' consumption expenditure is not only affected by their own income, but also by other people's consumption expenditure and income.

3. Nanomaterials Adsorption Experiment on Scenic Wastewater

3.1. Experimental Equipment and Materials.
The main instruments used in the experiment are as follows: high performance liquid chromatography, ordinary optical microscope, laser confocal microscope, flow cytometer, enzyme-linked immunosorbent assay, laser, CO_2 constant temperature incubator, etc [20].

The main reagents used in the experiment are as follows: potassium permanganate, oleic acid, absolute ethanol, adriamycin hydrochloride, IR-780 iodide, sodium dihydrogen phosphate, disodium hydrogen phosphate, polyethylene glycol (PEG), dimethyl sulfoxide (DMSO), potassium bromide, MNP, etc [21].

3.2. Preparation of TiO2-rGO.
Firstly, 1.925 mg GO was dissolved in the mixed solution of 10 ml ethanol and 20 ml distilled water, and then 1.7 ml tetrabutyl titanate was slowly added into 10 ml ethanol to prepare mixed solution B. the mixed solution B was added dropwise into the high-speed stirring mixed solution A, and then transferred to a 50 ml reactor for 3 h and reacted at 200°C for 12 h. The product was centrifugally washed to neutral. The TiO2-rGO composite powder (rGO mass ratio of 0.5%) was obtained by washing once with alcohol and drying at 40°C for 24 h. Similarly, TiO2-rGO composite powders with 0-3% rGO mass ratio were obtained in a similar process [22, 23].

3.3. Synthesis of Manganese Dioxide Nanoparticles (HM NPs).
First use an electronic analytical balance to weigh 0.1 g of KMnO4 in a 100 ml flask, and then add 50 ml of ultrapure water. Stir the above solution on a magnetic stirrer at room temperature for 30 minutes, and the magnetic stirring speed is 600 r/min. After potassium permanganate is completely dispersed in ultrapure water, use a 2 mL syringe to take 1 ml of oleic acid (OA) and add it dropwise to the potassium permanganate solution at a very slow rate, and continue the reaction for 24 hours at room temperature. After the reaction, the original solution changed from purple-red to dark brown turbid liquid state. The post-processing is centrifugal treatment, the centrifugal speed is 10000 r/min, the centrifugation is three times, the centrifugation time is 8 min once, and the washing liquid is ethanol [24, 25].

3.4. Characterization of TiO2-rGO.
X-ray powder diffraction with cuka ray is used for the crystalline phase of the material. The scanning angle is 5° to 90° and the resolution is 0.02°. The specific surface area and pore volume were determined by N2 adsorption BET method. The infrared spectrum was obtained by NEXUS670 infrared spectrometer (MA) and KBr tablet pressing method [26]. The TGA (Q5000V3.15) was determined by heating the sample at 10°C to 900°C. In order to explore the surface composition and chemical element state of the material, X-ray photoelectron spectroscopy (XPS) was used with monochromatic Al Ka ray [27].

3.5. PTT Performance Evaluation.
Firstly, 0.3 mg/ml PDA-CE6 solution was prepared, and the heating conditions of laser wavelength of 808 nm and different energy powers of 2.0, 2.5, 3.0 and 3.5 W/cm2 were investigated; then 0.1, 0.2, 0.4 and 0.5 mg/ml PDA-CE6 solutions were diluted, respectively, as the experimental group, deionized water was used as the blank control group, and the laser irradiation power was 3 W/cm2 at the same wavelength. The temperature curves of different concentrations of pda-ce6 nanoparticles with different illumination time were plotted to evaluate the photothermal conversion ability of PDA-CE6 [28].

3.6. Adsorption Experiment.
Batch experiments were carried out in a 10 ml simulated wastewater system. In the experimental process, the concentration of adsorbent is controlled to 0.02 g/l, the pH of solution is adjusted by hydrochloric acid or sodium hydroxide, the ionic strength is mainly controlled by 1 m sodium chloride, and the pH affects the adsorption effect of TCP. We mainly control the pH range

from 3 to 10, and the kinetic experiment is carried out at the temperature of 30°C, and the concentration of TCP is 20 mg/L. In order to explore the thermodynamic characteristics of adsorption, the adsorption process was carried out in 10 ml of solution containing $0.5 \sim 20$ mg/L TCP at various temperatures of 303 K, 313 K and 323 K. Three parallel experiments were conducted in all experiments, and the average value of the three groups of experiments was taken as the experimental results.

4. Nano Materials in the Financial Market

4.1. Nanoparticles on Water Sources in Scenic Spots. Although the ecological benefits of financial industry cannot be accounted and counted independently, its characteristics and scale have been formed. At this stage, the state attaches importance to the ecological development of tourist attractions and financial products, and guides the financial industry to take the ecological road in policy. With the implementation of sustainable development strategy, the concept of ecological oriented financial industry is gradually introduced into China. Both the government and tourists have a profound understanding of the environmental impact of financial industry. The understanding of eco-financial and green financial is more and more in-depth. The ecological oriented financial mode is also getting more and more support from all walks of life. At this stage, although the financial industry is still mainly economic oriented, ecological orientation has begun to penetrate into all aspects of the development of financial industry. The degradation effect of nanoparticles on wastewater is shown in Table 1 and Figure 1. It can be found from the figure that the degradation efficiency of metronidazole by iron doped titanium dioxide in the presence of visible light and hydrogen peroxide is the best, which can reach about 80% in 60 minutes. Accordingly, the manganese doped titanium dioxide with the smallest band gap has poor degradation activity for metronidazole solution. This is because the structure of metronidazole is relatively stable and difficult to decompose, and the redox ability of holes or electrons generated by photocatalysts with too small band gap is also relatively weak. These two reasons lead to the poor degradation activity of manganese doped titanium dioxide. Therefore, iron doped titanium dioxide catalyst is the most suitable.

4.2. Nanomaterials on Tourism. The financial industry has entered the national strategic level. As a comprehensive strategic pillar industry, the development concept of ecological civilization of respecting nature, conforming to nature and protecting nature has been established. The financial industry has entered a new era of multi-dimensional, multi-dimensional and multi-dimensional development of economy, ecology and society. Under the guidance of the development concept of "innovation, coordination, green, openness and sharing" and the basic national policy of saving resources and protecting the environment, the financial industry has changed its concept and pursued more and more green development to promote the unity of environment and economy. Mesoporous silica is a new material developed in recent years. It has large specific surface area, regular pore structure, good thermal and chemical stability, so it has a wide application prospect in adsorption and separation, macromolecular catalysis and other fields. Silica is non-toxic, easy to obtain, exists in the form of aggregates, has good catalytic adsorption performance, and can provide enough pores and three-dimensional space for magnetic nanoparticles to be evenly dispersed in the interior. It can be used as a carrier to slow down the agglomeration of iron nanoparticles, and can be used to immobilize nanoparticles. The adsorption efficiency of silica for water sources of tourist attractions is shown in Table 2 and Figure 2. It can be seen from the figure that with the continuous reaction, the concentration of nitrate nitrogen continues to decrease. The removal rate reaches 98.3% in 30 min and almost 100% in 120 min. During the reaction process, 15.2% of nitrate nitrogen was reduced to nitrite nitrogen and remained in the solution in the form of intermediate by-products. With the reaction going on, it could be further converted into ammonia nitrogen, and 4.3% nitrite nitrogen remained in the final solution. The concentration of ammonia nitrogen has been increasing, and 79.4% of the final product is ammonia nitrogen. The total nitrogen decreased at first and then increased. Finally, the total nitrogen decreased by 15.5%.

Nanomaterials enterprises must rely on their own feasible business plans, excellent product functions and market prospects to attract venture capital, and obtain much-needed financial support and guidance in operation and management. This stage is also the key period for venture capital to consider entering and obtain certain equity, so as to lay the foundation for high return on investment in the future. In order to become a strategic partner or strategic shareholder of the enterprise. After the intervention of venture capital, due to the enhancement of financial strength and risk-taking ability of enterprises, some commercial banks familiar with the operation of two nano materials enterprises will moderately intervene and provide a certain degree of loan support. In addition, the entrepreneurial fund set up by the government to support high-tech enterprises also has a significant role in supporting enterprises at this stage. The main reason is that many companies today are the product of self-employment, and capital has become the most critical factor for these companies.

In the case of nano material adsorbent, the change of the number of tourists in recent five years is shown in Figure 3. As can be seen from the figure, the application of nano materials has greatly improved the health of tourist attractions. Especially in 2016, the number of tourists reached the peak in nearly five years, with 7.01 million. The change of the flow of people naturally affects the whole financial industry. Financial industry is a comprehensive industry, which is determined by the consumption characteristics of tourists. On the one hand, the consumption process of financial almost includes all the contents of life, that is, the multiple needs of food, housing, tourism, transportation, shopping, entertainment and so on during the period from leaving home to returning to the settlement. In order to meet the multiple needs of tourists, there must be a variety of different types of enterprises to provide tourists with goods and

TABLE 1: Degradation effect.

TiO2	1.666	1.288	3.951	3.967	3.770	4.177	1.509	4.510	3.831
Fe-TiO2	4.862	4.790	4.919	4.960	4.797	4.036	3.623	3.866	4.599
Mn-TiO2	6.517	2.044	3.173	4.452	6.232	4.814	3.207	2.086	5.232
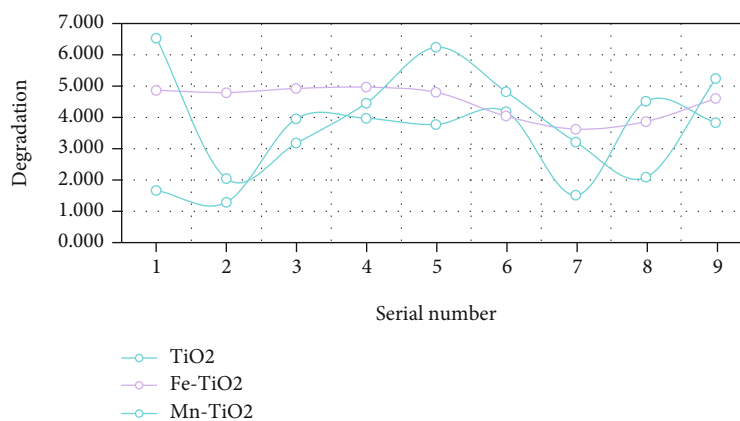
FIGURE 1: Degradation effect.

TABLE 2: The adsorption efficiency of silica for tourist attractions.

40 mg/L	0.43	0.36	0.32	0.52	0.52
100 mg/L	0.57	0.49	0.46	0.63	0.70
150 mgL	0.59	0.38	0.41	0.35	0.39
210mgy/L	0.37	0.58	0.82	0.93	0.68

services. On the other hand, financial consumption is diversified and tends to be personalized. Therefore, meeting the needs of financial consumers is not only reflected in the material aspects of tourist attractions, hotel facilities, transportation tools, but also in the cultural and spiritual aspects. This requires a higher level of cultural content and the quality of service personnel in tourist destinations. Therefore, as far as enterprises in different industries are concerned, the link of meeting the needs of consumers connects them together and makes them become a collection. The complexity and diversity of financial business constitute the comprehensive characteristics of tourism.

4.3. Changes in the Economic Structure of the Financial Market. To perfect the policy and regulation system of financial and cultural industry, we need to start from many aspects. First, break the status quo of coexistence of segmentation and industry barriers. Break through one of the management systems among industries such as the development and operation of financial and cultural attractions, financial accommodation and catering, financial and transportation, financial and entertainment, financial and commerce, and festivals and exhibitions, and establish and encourage various industries to compete with each other. A long-term policy and regulation system with multi-regulation and integration of cooperation and mutual promotion. Secondly, a sound and feasible safety policy and regulation system

should be improved. Formulate strict tourist attractions development and operation safety regulations, financial accommodation and catering safety standards, financial traffic safety laws and regulations, financial and entertainment business service quality standards, festivals and exhibitions safety guarantees and emergency response measures, and other financial and cultural industry guarantee policies and regulations system. Finally, improve the internal rules and regulations of various industries. Standardize the market order of various industries in the financial and cultural industry, and protect the rights and interests between the operators and consumers of the financial and cultural industry.

In the past, the environmental governance of financial industry is to control the end environmental pollution without changing the development mode, rather than the control of material flow and energy flow based on the source and the whole production cycle. In the past, the environmental governance was limited to the departments of resource management and environmental protection, rather than the cooperation of multiple departments and the joint governance of the whole society. In particular, with the implementation of the green awareness of financial industry by financial enterprises, the competition mode of financial enterprises has changed from the market competition mode to the dual competition mode of market competition and ecological competition. More and more financial enterprises adhere to the guidance of tourist satisfaction and gradually
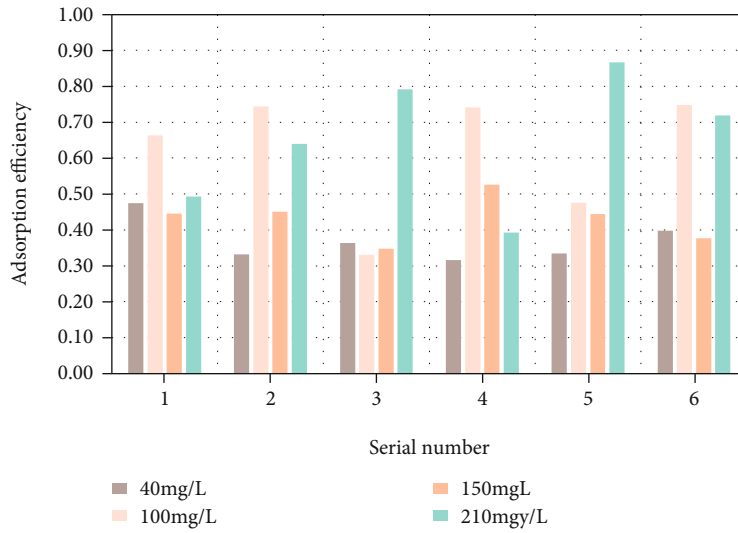
Figure 2: The adsorption efficiency of silica for water sources in tourist attractions.
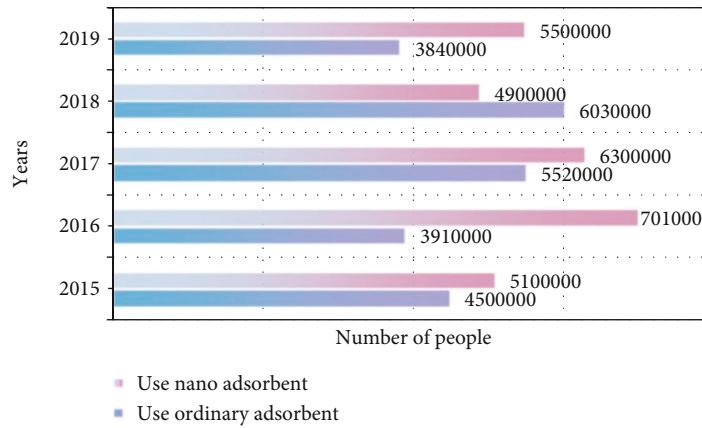
Figure 3: Changes in the number of tourists.
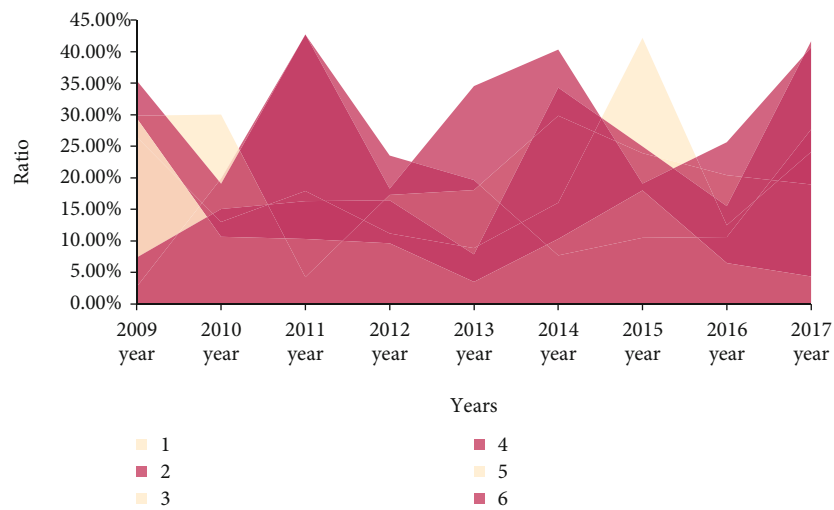
Figure 4: The proportion of China's financial industry's overall contribution to GDP.

improve the competitiveness of financial enterprises by providing more and more high-quality financial products and green financial products. And further strengthen the confidence of green development of financial enterprises. At the same time, with the improvement of tourists' education level and income level, the awareness of environmental protection and sustainable development of tourists is becoming stronger and stronger. The non environmental protection behaviors in financial cause less and less damage to the ecological environment of scenic spots, and the concept of green consumption is becoming more and more popular. The proportion of China's financial industry's comprehensive contribution to GDP is shown in Figure 4. In terms of economic benefits, the three major markets of domestic tourism, inbound financial and outbound financial in China's financial industry are booming in an all-round way. China has become the world's largest domestic financial market, the world's first largest international financial consumer, and the world's fourth largest financial destination country. China's financial industry has made more outstanding contributions to China's and the world's economic and social development, and has become an important member of the world's financial industry. Financial industry has become a new driving force to promote China's economic development. From the proportion index of financial industry's comprehensive contribution to GDP, we can see that the proportion of financial industry's comprehensive contribution to GDP showed an overall upward trend from 2009 to 2017. By 2017, the comprehensive contribution value of financial industry in China's GDP was as high as 913 billion yuan, accounting for 11.04% of the total, becoming an important industry in the tertiary industry.

5. Conclusions

At present, nanotechnology research in China has made some achievements, but the application of nanotechnology achievements is still in the primary stage, and the industrialization effect is not very ideal. Although nanotechnology has unique functions, it is not extravagant and needs practical implementation. Nanotechnology as the mainstream of high-tech industrialization, its progress is inseparable from the common development of computer technology, information technology and other fields. Only products and technologies recognized by the public can have a good market prospect. Nanotechnology, as a new technology, has a general cognition among researchers, but the general public's cognitive knowledge of nanotechnology remains on the surface, and some people are even misled by the words of some scheming people. They only see the negative side of nanotechnology and refuse or even reject nanotechnology and nanotechnology products. To a certain extent, it hinders the development of technology and social progress.

This paper defines the concepts related to the structure of financial culture industry, uses the Marxist theoretical basis related to the industrial structure of financial culture, and studies the innovation and development of the industrial structure of financial culture by using the methods of theoretical analysis, case comparison, literature research

and interdisciplinary research. The development of financial industry has been integrated into the global value chain and the world financial map; driven by innovation, China's financial industry has achieved remarkable improvement in quality and efficiency; the green development of financial industry has made considerable progress; the benign development of financial enterprises has become a strong support for the sustainable development of the industry. Of course, from these typical characteristics, we can find the problems of China's financial industry at present: the imbalance of supply and demand of financial industry, the difficulty of green transformation and upgrading; the lack of leading enterprises in the global value chain of financial enterprises, and the low competitiveness; the low value-added financial products have reduced the support for the sustainable growth of China's financial economy. The restriction of ecological environment on China's financial industry is increasingly apparent.

In this paper, a new type of photocatalyst TiO2-rGO was synthesized by the simultaneous high-temperature reduction of GO and high-temperature hydrolysis of titanium ester, which showed excellent photocatalytic activity under visible light. In this paper, the catalyst was characterized by XRD, DRS, TEM and other means, and its catalytic ability was tested by catalytic degradation of rhodamine B. The degradation results showed that TiO2-rGO under visible light showed excellent catalytic activity that TiO2 did not have in the past. In addition, through repeated degradation of Rhodamine B, TiO2-rGO showed excellent stability and reproducibility. Utilizing the advantages of nanomaterials can greatly reduce the degree of pollution of water bodies, ensure the cleanliness of water sources in scenic spots, and promote the economic development of tourism. The research is only for the financial industry, and the next research direction can be developed in other industries.

Data Availability

No data were used to support this study.

Conflicts of Interest

The authors declare that there are no conflicts of interest regarding the publication of this article.

Funding

References

[1] A. Justin, K. M. S. Sundararaj, A. A. Elngar, A. N. Subash, and B. C. Pillai, "Design, development and performance estimation of 110 kW kinetic heating simulation facilities for material studies–phase I," *Journal of Cybersecurity and Information Management*, vol. 5, no. 1, pp. 17–28, 2020.

[2] N. Metawa and S. Metawa, "Internet financial risk early warning based on big data analysis," *American Journal of Business and Operations Research*, vol. 3, no. 1, pp. 48–60, 2021.

[3] X. Song and Y. Wang, "An elementary fractal thermal conduction theory model for nanometer energetic materials," *Huozhayao Xuebao/chinese Journal of Explosives & Propellants*, vol. 41, no. 6, pp. 554–561, 2018.

[4] C. Yin, F. R. Negreiros, G. Barcaro et al., "Alumina-supported sub-nanometer Pt10clusters: Amorphization and role of the support material in a highly active CO oxidation catalyst," *Journal of Materials Chemistry A*, vol. 5, no. 10, pp. 4923–4931, 2017.

[5] E. Kaynak and E. E. Marandu, "Financial market potential analysis in Botswana: a Delphi study," *Journal of Travel Research*, vol. 45, no. 2, pp. 227–237, 2006.

[6] F. M. Díaz-Pérez and M. Bethencourt-Cejas, "CHAID algorithm as an appropriate analytical method for tourism market segmentation," *Journal of Destination Marketing & Management*, vol. 5, no. 3, pp. 275–282, 2016.

[7] K. Cielikowski and A. Brusokas, "Selected attractiveness factors of academic conferences as a product on the international Tourism market," *Tourism*, vol. 30, no. 1, pp. 13–20, 2020.

[8] M. Saracevic and N. Wang, "New Model of Sustainable Supply Chain Finance Based on Blockchain Technology," *American Journal of Business and Operations Research*, vol. 3, no. 2, pp. 61–76, 2021.

[9] H. I. Haponenko and A. V. Vasylenko, "The development tendencies of low-cost Airlines in Ukraine and their impact on the national Tourism Market," *Inform*, vol. 1, no. 504, pp. 189–196, 2020.

[10] C. Zhou, G. Qiao, and C. Ryan, "How might Chinese medium sized cities improve competitive advantage in the event Tourism market?," *Event Management*, vol. 21, no. 1, pp. 109–118, 2017.

[11] M. Vasileiou, P. Tsartas, and M. Stogiannidou, "Wellness tourism: integrating special interest tourism within the Greek financial market," *Tourismos*, vol. 11, no. 3, pp. 210–226, 2016.

[12] P. P. Hsu, "Examination of Taiwan's travel and tourism market cycle through a two-period Markov regime-switching model," *Tourism Management*, vol. 63, no. 12, pp. 201–208, 2017.

[13] X. Xu, D. Shahsavari, and B. Karami, "On the forced mechanics of doubly-curved nanoshell," *International Journal of Engineering Science*, vol. 168, article 103538, 2021.

[14] M. Sheresheva and J. Kopiski, "The main trends, challenges and success factors in the Russian hospitality and tourism market," *Worldwide Hospitality & Tourism Themes*, vol. 8, no. 3, pp. 260–272, 2016.

[15] Y. Liu, Y. Yao, and D. X. F. Fan, "Evaluating Tourism market regulation from Tourists' perspective: scale development and validation," *Journal of Travel Research*, vol. 59, no. 6, pp. 975–992, 2020.

[16] J. Kizielewicz, "Prospects of development of the cruise ship tourism market – the case study of the Baltic Sea region," *Prace Naukowe Uniwersytetu Ekonomicznego we Wrocawiu*, vol. 63, no. 7, pp. 244–255, 2019.

[17] K. Kammoun, A. Ghedira, and I. Ayoub, "Impacts of sky liberalization options on financial market dynamics: case study of Tunisia," *International Journal of Innovation and Applied Studies*, vol. 23, no. 2, pp. 192–203, 2018.

[18] D. Gračan, "The role of strategic management in the cruising Tourism market offer," *Journal of Maritime & Transportation Science*, vol. 51, no. 1, pp. 103–116, 2016.

[19] C. W. Chang, "Industrial structure and economic performance: the role of productive public expenditure," *Review of Development Economics*, vol. 23, no. 2, pp. 745–759, 2019.

[20] D. B. Audretsch, "Industrial organization and the Organization of Industries: linking industry structure to economic performance," *Review of Industrial Organization*, vol. 52, no. 1, pp. 1–18, 2000.

[21] X. Ni and P. Lin, "Grey relation analysis between industrila structure and economic growth based on panel data," *International Journal of Advanced Research*, vol. 6, no. 6, pp. 542–549, 2018.

[22] H. Zhang, Z. Zhang, and K. Sheng, "Influence of industrial structure optimization on economic growth in Shandong province," *Boletin Tecnico/technical Bulletin*, vol. 55, no. 20, pp. 230–237, 2017.

[23] A. Tomohara, "Relationships between international tourism and modes of foreign market access," *International Economics*, vol. 152, no. 12, pp. 21–25, 2017.

[24] J. H. G. Jeuring, "Discursive contradictions in regional tourism marketing strategies: The case of Fryslan, The Netherlands," *Journal of Destination Marketing & Management*, vol. 5, no. 2, pp. 65–75, 2016.

[25] S. C. Yoo and J. Y. Pan, "Financial marketing using VR 360 advertising: focusing on content format and type, novelty-seeking tendency, and viewing satisfaction," *Journal of Social ence*, vol. 59, no. 1, pp. 731–761, 2020.

[26] B. Foued and K. Sawsan, "The role of TOURISM marketing in enhancing tourism development: a comparative study between constantine and Amman cities," *Geojournal of Tourism and Geosites*, vol. 24, no. 1, pp. 146–160, 2019.

[27] J. Tham, S. M. F. Azam, and A. Sarwar, "Determinants of Tourist's satisfaction for effective financial marketing in Sabah, Malaysia: an empirical study," *European Academic Research*, vol. 6, no. 8, pp. 4153–4176, 2018.

[28] A. Nugroho, "ASEAN tourism marketing communication attribute : an exploratory research at Goaseantv," *European Research Studies Journal*, vol. 20, no. 3A, pp. 383–395, 2017.

Hindawi

Research Article

Nanocomposite Building Materials in Modern Architectural Design

XuHui Li [1] **and Yi Zhao** [2]

^{1}*Engineering Economics Department, Henan Finance University, Zhengzhou, 451464 Henan, China*
^{2}*Product Research and Development Department, Henan Guanghui Industrial Group Co. LTD., Zhengzhou, 450000 Henan, China*

Correspondence should be addressed to XuHui Li; lixuhui@hafu.edu.cn

Architecture is the precipitation of history, not only the embodiment of technical level but also the inheritance of history and culture. Excellent architecture contains high historical value and emotional factors, and it continues to deepen over time. Nanotechnology is a new technology that was born in the late 1980s and is emerging. It mainly refers to the study of the laws of motion and interactions of electrons, atoms, and molecules in the composition system of matter in the range of 0.1 to 100 nm. Nanomaterials have special properties and structures, and the composite materials made of them have the effect of strengthening and toughening the polymer by virtue of their high-quality strength and toughness. Therefore, the aim of this text is to explore the application of nanocomposite building materials in modern architectural design and analyze the advantages and development trends of new building materials. The method in this paper is to use the method of experimental comparison to analyze the performance improvement effect of nanocomposite building materials on the current main building materials of concrete. By establishing a model to study the impact on the shrinkage and mechanical properties of cement-based materials, it can also improve the environmental performance and comprehensive evaluation of building materials. Corresponding conclusions are drawn through data comparison. When the amount of nanocomposite building materials is 1.5%, the chemical shrinkage value of the cement paste will increase by 58.2%, and the shrinkage strain will increase by 15.3%. When the fly ash content is 20%, the chemical shrinkage value of cement paste is reduced by 30.5%, and the shrinkage strain of concrete is reduced by 8.8%. Therefore, adding nanocomposite building materials to cement-based materials can promote cement hydration, optimize pore structure, and to a certain extent can make up for the shortcomings of mineral admixtures and achieve better improvement effects.

1. Introduction

Nanotechnology is a new technology emerging in the late 1980s. The emerging nanomaterial technology has been applied in many fields, especially in new building materials. Materials are the basic elements of architecture. As an important material carrier for the inheritance and development of modern civilization and cultural spirit, architecture carries decisive significance. Therefore, it is very important to construct elegant, beautiful, and practical buildings. The performance of materials is to integrate all buildings. Nanocomposite building materials have brought an unprecedented revolution to modern architectural design with

their unique properties and unique characteristics of light, electricity, heat, and magnetism. Making an appropriate material design strategy has become an important part of modern architectural design.

The traditional building materials are mainly cement concrete, and the current consumption is about 2 billion cubic meters, which is an indispensable building material at present [1]. However, as people's requirements for building design become higher and higher, some problems in concrete itself have gradually expanded. After years of exposure to the air, cracks and damage will inevitably occur, and the rigidity of ordinary cement concrete is too high, and the flexibility is insufficient. The environmental protection is

poor in the production process, which restricts the development of concrete in the future architectural design [2, 3]. As an indispensable part of building materials, the amount is considerable, and the requirements for stability and durability are very strict. The future development trend of modern architectural design is bound to be in line with the development of nanomaterials. Development is linked together [4]. Many scholars have done a lot of research on nanocomposites, and they all believe that nanomaterials are very important in new building materials, and they can get better development space in future special constructions [5]. In the research of foreign scholars, nano-conforming building materials are regarded as an unprecedented revolution. Combined with nanotechnology, many new materials can be developed, which are in line with today's architectural design concepts. The use of nanomaterials to shield ultraviolet rays can improve the antiaging yellowing performance of the wall, greatly improve the strength of plastic pipes, and increase the service life [6, 7]. Domestic research has also begun to explore the development and application of nanomaterials and nanotechnology in building materials and found that nano-conforming building materials also have a good self-cleaning function, which is useful for antibacterial and antimildew coatings in buildings and some conductive materials. Functionally developed conductive coatings have a positive guiding role [8]. Therefore, nano-building materials have great economic and social benefits in the field of building materials.

This article starts with the meaning and relationship between nanocomposite building materials and modern architectural design and explores the influence of different building materials on modern buildings. Through the experiment of improving the performance of concrete with nanomaterials, future solutions are proposed, so as to more accurately grasp the direction of modern architectural design and propose more optimized treatment plans. This will help promote the innovation and development of building materials. By comparing and analyzing specific experimental results, we can find out the balance between quality assurance and environmental friendliness and organically combine the two. Provide technical experience with reference value for future architectural design, obtain the similarities and differences of research directions through comparative advantage analysis, learn advanced experience, make suggestions for improvement in the selection of future building materials and in-depth understanding of more properties of nanocomposite building materials, strengthen the specialization and accuracy of architectural design, and provide theoretical basis for the field of materials science.

2. Theoretical Basis and Method

2.1. Core Concepts

2.1.1. Nanocomposite Materials. Nanocomposites are based on resins, rubbers, ceramics, and metals as the continuous phase and nanosized metals, semiconductors, rigid particles and other inorganic particles, fibers, carbon nanotubes, and other modifiers as the dispersed phase. The method uniformly disperses the modifier in the matrix material to form a composite system containing nanometer-sized materials in one phase, and the system material is called nanocomposite material. Since its inception, nanotechnology has gained the attention of the world. After more than 20 years of theoretical research, it has become one of the most promising technology industries [9, 10]. The use of nanotechnology can be applied to many industries, can greatly promote the development of productivity, and has achieved good results in medical, construction, military, and other aspects [11]. In the field of architecture, nanocomposite coating is the nanopowder used in the coating to get a kind of aging resistance, radiation resistance, high peel strength, or some special functions of the coating, in building materials which has been applied and has shown its unique charm. The same nanoparticle in different sizes will have different effects; different kinds of nanoparticles can also play the same role in the coating [12, 13]. Through this unique structure and excellent performance, it will be used in a wider range of fields, such as aerospace, transportation, culture, and sports. The development of new materials can determine the level of a country's industry, and all countries in the world have put nanocomposite materials in a priority development position and can be in a leading position in future international competition. There are many kinds of nanocomposites, including nanopolymer matrix composites, carbon nanotube functional composites, and nano-tungsten-copper composites [14].

2.1.2. Architectural Design. The so-called architectural design is the application of "virtual reality" technology in urban planning, architectural design, and other fields. Architectural design refers to a series of ideas and ideas about the building proposed by the designer according to the construction task before the building is built and then displayed through drawings or documents [15]. Excellent architectural design will consider various problems that occur during the entire building construction process and propose preparatory plans and emergency measures. Therefore, building construction is more of a holistic project. Architectural design must not only consider the construction requirements but also calculate the material preparation, construction organization work, and the conditions that various types of work rely on in production and construction [16, 17]. Only in this way can we coordinate and cooperate with each other, so that the entire project can be successfully completed within the predetermined investment limit and in accordance with the predetermined plan carefully considered. Architectural design in a narrow sense refers to the use of technology to turn virtual reality into reality, and design tools are becoming more and more advanced. It bids farewell to traditional drawing operations and uses human-computer interaction, real architectural space, and large-area 3D terrain simulation technology to make it more realistic. Accurately express the architectural design concept [18, 19]. Use dynamic interaction to meet the various requirements and uses expected by users and society, and conduct comprehensive and multiangle judgments and inspections of future buildings. At the same time, it can also achieve real-time switching and comparison of multiple environmental effects.

Observe the scene from any angle, distance, and degree of precision; accept customer experience feedback; and make timely adjustments, saving unnecessary cost and waste. With the development of society and the advancement of science and technology, the content of architecture and the problems to be solved are becoming more and more complex, and more and more related disciplines are involved.

2.2. Application of Nanomaterials in Building Materials

2.2.1. Application of Nanomaterials in Concrete Materials. Cement concrete is a general term for engineering composite materials that are mixed with water such as cement, sand, and stone to form a whole. Cement concrete has always played a pivotal role in the construction industry. As a traditional building material, it has made important contributions to the social industrialization and infrastructure construction of various countries. Its output and consumption are constantly increasing, but at the same time, the loss has always been high. [20]. Therefore, the use of nanomaterials to develop cement-based composite materials has become the focus of the material field. Under the new architectural design requirements, people's expectations for building materials are getting higher and higher, such as sound absorption, antifreeze, high strength, and high toughness. Nanomaterials have excellent characteristics such as small size effect, quantum effect, and surface and interface effects and combined with concrete can form very effective composite materials [21]. Use nanotechnology to develop new types of concrete, and use the excellent properties of nanomaterials to improve the strength, construction performance, and durability of concrete. In construction engineering, it can not only fill cement voids and increase concrete fluidity, but it can also improve the interface structure between cement stone and aggregate in concrete, improving the strength, impermeability, and durability of the concrete.

2.2.2. Application of Nanomaterials in Architectural Coatings. The core of the building is reinforced concrete, and the coating as the exterior of the building cannot be separated from the addition of nanomaterials. Traditional coatings always have various problems, such as poor scrub resistance, poor finish, and aging resistance. Nanocomposite coatings can be divided into nanomodified coatings and nanostructured coatings. Using some functions of nanoparticles to modify existing coatings to improve the performance of coatings, such coatings are called nanomodified coatings; for coatings prepared by some special processes, in which the fineness of a special component is in the nanometer range grade, such coatings are called nanostructured coatings [22]. The use of nanocomposite coatings can effectively improve the performance of concrete. When used in coatings, it will have antiaging, antiradiation, high peel strength, or some special functions, which greatly improves the use effect of coatings. Due to the particularity of its surface and structure, nanomaterials have excellent properties that are difficult to obtain with general materials. By combining with reinforced concrete materials, there is a great opportunity to obtain composite materials with excellent performance, so that the traditional coating function is modified, and macromaterials have many special and unprecedented excellent properties. Nanocomposite building materials can be used as composite materials for exterior decoration through nanocoating materials composed of nanoparticles, and traditional coatings can be modified by adding nanoparticles. The advantage of this method is that the cost is less and the preparation process is relatively simple. The actual use process is feasible and does not require a complete application of nanomaterials, which can improve the comprehensive performance of concrete. This is also the method of most current building material selection, and due to technical and cost issues, it is also in modern architectural design, one aspect to focus on.

2.2.3. The Application of Nanotechnology in Ceramic Materials. Due to the mechanical properties of the second phase, oxide nanomaterials have an artistic process that is different from ordinary ceramics. Relatively, the cost and consumption are naturally rising. Cermets containing 20% nano-cobalt powder are high-temperature-resistant materials for rocket jet nozzles. In this respect, they are superior to homogeneous traditional ceramic materials. In the field of building materials, ceramics have always been loved by people, so ceramic materials are added Nanomaterials are the development direction in modern architectural design. In recent years, the development and application of nanocomposite ceramics have been relatively mature. The introduction of nanodispersed phases into the micron-level matrix for compounding can greatly increase the fracture strength and fracture toughness of the material by 2 to 4 times and increase the maximum use temperature by 400°C~600°C; it can also improve the hardness, elastic modulus, creep resistance, and fatigue damage resistance of the material. Nanotechnology's porous ceramic (ceramic microporous material) material may filter and separate industrial waste gas. Porous ceramics provide strong heat resistance and chemical corrosion resistance, as well as being long lasting and low maintenance.

3. Experiment on the Influence of Nanomaterials on Concrete Materials

3.1. Experimental Materials. The main raw materials used in this article are cement, mineral admixtures, and nanocomposite silica. Cement is an ordinary Portland cement used in construction and meets the national safety and health standards. Since its inception, cement concrete has been the most important structural material in construction engineering and has been widely used. For cement-based materials, in order to better compare the effects, mineral powder and fly ash are also used to restrict the concrete by using its compressive strength and elastic modulus. Table 1 shows the performance of the cement used this time.

The performance data of the experimental materials are shown in Table 2. Among them, the average particle size of fly ash is 4.10 μm, the median diameter is 3.08 μm, and its specific surface area is 600 square meters per kilogram;

TABLE 1: Properties of cement.

Setting time		Stability	Compressive strength (MPa)		Flexural strength (MPa)	
Initial setting	Final coagulation	Qualified	3 d	28 d	3 d	28 d
2 h 30 min	3 h 42 min		22.3	50.1	5.4	8.9

TABLE 2: Physical properties of mineral blends.

Nature	Fine aggregate	Coarse aggregate
Specific weight (t/m^2)	2.62	2.6
Bulk density (t/m^2)	1.50	1.58
Void ratio (%)	42	38
Water absorption (%)	2.2	0.6
Crushing value (%)	1.2	0.35
Silt content (%)	2.9	1.1
Fineness modulus	2.5	1.3

FIGURE 1: Chemical shrinkage of cement paste with different silica content at various ages.

the average particle size of mineral powder is 12.34 μm, the median diameter is 9.89 μm, and the specific surface area is 360 square meters per kilogram. At the same time, the nanocomposite building material silica was used as the experimental material, and the fumed nanosilica hydrophilic-300 (hydrophilic type) produced by Shanghai Aladdin Biochemical Technology Company was selected. The purity is about 99%. The specific surface area is 300 square meters per gram, and the particle size is in the range of 7-40 nm. Nano-silicon dioxide (English name nano-silicon dioxide) is an inorganic chemical material, commonly known as silica. Because it is ultrafine and nano-scale, with a size range of 1~100 nm, it has many unique properties, such as optical properties against ultraviolet rays, which can improve the aging resistance, strength, and chemical resistance of other materials. Finally, in order to ensure a scientific experimental environment, the admixtures that are often used in the preparation of cement-based materials, including water-reducing agents and expansion agents, are also added. The water-reducing agent used in this test is Wanshan brand naphthalene water-reducing agent, which has a relatively stable chemical structure, with a solid content of 92% or more and a water-reducing rate of 18%-28%. The expansion agent used in this test is UEA-type expansion agent produced by Shandong Yantai Hongxiang Building Materials, with an alkali content of 0.3%, and the recommended dosage is 0.3%-0.5%.

3.2. Experimental Process. First, the density test and the specific surface area test are carried out. The density of mineral blends is measured by liquid displacement method. After high-temperature drying, it is cooled in a dry environment and then wiped clean with filter paper, and 80 g sample is taken out. Put it in a pycnometer, use ultrasonic vibration to completely eliminate air bubbles, and use formula to calculate density. After calculating the mass of the material in
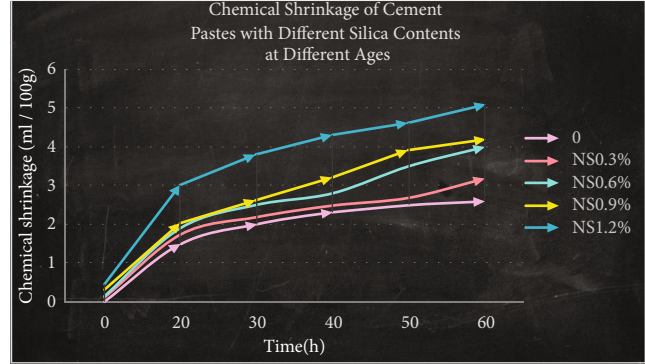
the same way, put it into the FBT-9 full-automatic specific surface area tester for repeated calculations.

$$\rho = \frac{p}{v_2 - v_1},$$
$$W = \rho V (1 - \varepsilon). \tag{1}$$

Subsequently, add nanocomposite materials and concrete for mixing; first, add water and disperse in ultrasonic for 6 minutes; then, add cement, mineral admixtures, and additives; stir for 2 minutes at different mixing speeds; and place them in the curing room for curing after vibrating. You can get the bulk density and porosity of the sand. As we all know, the comprehensive performance of concrete can be reflected by slump, so the test of concrete slump is also essential. According to the "Standard for Test Methods of Mechanical Properties of Ordinary Concrete" (GB/T50081-2002), the pressure resistance test is carried out. The sample is placed directly under the testing machine until the sample structure is broken, and the average value is obtained after repeated testing. In the process of testing the chemical shrinkage test of cement, test pieces are made with the help of molds. After the test pieces are formed, they are cured in a standard curing room and then, the molds are removed. The shrinkage test pieces are placed in a constant temperature and humidity room for curing, and then put the test piece into it. Read the dial indicator value after the specimen rack.

Finally, the results can be obtained by analyzing various data. The added nanocomposite silica itself also has stronger pozzolanic properties. During the production process, it speeds up the setting time of concrete and increases the

toughness of the surface. The induction period of cement hydration exotherm can also be shortened by using nanosilica. In contrast, other mineral blends have not achieved this effect. Although the shrinkage time is accelerated to a certain extent, the compactness and uniformity need to be improved.

3.3. Experimental Significance. Through the above experiments, it can be known that the use of nanocomposite building materials can promote the process of cement hydration, increase the shrinkage of cement-based materials, and promote the hydration reaction of cement at the same time. Cement-based composite materials refer to Portland cement as the matrix and alkali-resistant glass fibers, general-purpose synthetic fibers, various ceramic fibers, high-performance fibers such as carbon and aramid, metal wires, and natural plant fibers and mineral fibers as reinforcements, a composite material formed by adding fillers, chemical additives, and water through a composite process [23, 24]. This shows that the current concrete-based architectural design ideas can be improved, and environmentally friendly, novel solutions can be added to match the nanocomposite materials that meet the quality requirements. As a basic issue of architecture, materials have always been the core of architectural design research. The selection of building materials is not only the use of different construction requirements and material characteristics but also the embodiment of architectural design and cultural skills. The architectural design displayed by different building materials is also very different. Therefore, in modern architectural design, the natural properties of the material and the emotional cognition of the material itself are equally important. Only in this way can we be comfortable in architectural design. Only when the professional skill attributes of architectural design and emotional belonging are integrated it is possible to make progress in the inheritance of traditional culture, science and technology, and concepts in architectural manufacturing. Therefore, the use of new materials, including nanocomposite building materials, is an innovation in life concepts and design concepts, which is particularly important for designers to grasp the relationship between architecture, space, and materials. At the cultural level, the continuous adjustment of architectural design is the development of design ideas and the enrichment of the practical process. The perfect combination of material materials and structural construction, as well as the natural environment, achieves practical, cognitive, and aesthetic social functions.

4. Data Analysis

As shown in Figure 1, the degree of shrinkage of cement is different according to different degrees of nanocomposite materials. With the increase of time, the change gradually increases. The chemical shrinkage without addition is a normal change, and the degrees of shrinkage are, respectively, 0 ml/g, 1.5 ml/g, 2 ml/g, 2.3 ml/g, 2.5 ml/g, and 2.6 ml/g. When the blending amount is 0.3%, the degree of shrinkage is 0.1 ml/g, 1.75 ml/g, 2.2 ml/g, 2.5 ml/g, 2.7 ml/g, and 3.2 ml/g, respectively. It can be seen that with
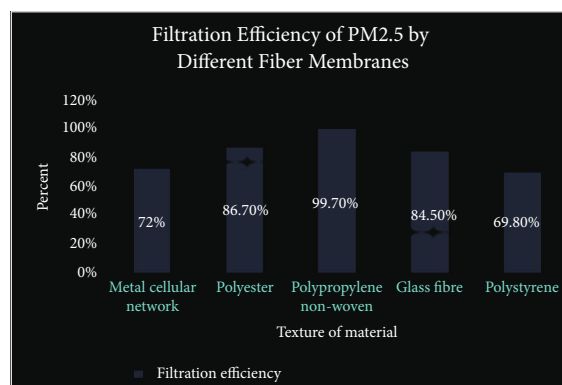
FIGURE 2: Filtration efficiency of different material fiber membranes for PM2.5.
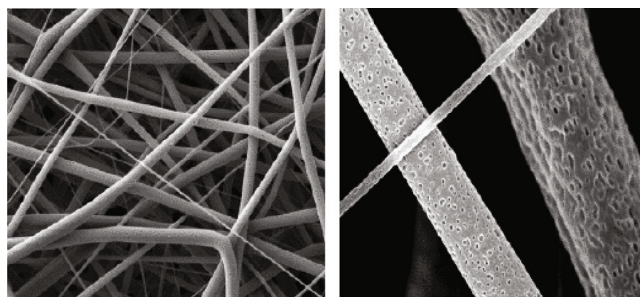
FIGURE 3: Nanocomposite fiber membrane under an electron microscope.

the increase of time, the small amount of addition does not change much at the beginning, but after 50 hours, the gap begins to widen. When the blending amount is 0.6%, the degree of shrinkage is 0.15 ml/g, 1.9 ml/g, 2.5 ml/g, 2.8 ml/g, 3.5 ml/g, and 4.0 ml/g, respectively. When the blending amount is 0.9%, the degree of shrinkage is 0.3 ml/g, 2 ml/g, 2.6 ml/g, 3.2 ml/g, 3.9 ml/g, and 4.2 ml/g, respectively. These two compare at 40 hours. There have been different changes in growth rate. When the blending amount is 1.2%, the degree of shrinkage is 0.45 ml/g, 3 ml/g, 3.8 ml/g, 4.3 ml/g, 4.6 ml/g, and 5.1 ml/g, respectively.

The use of nanocomposite building materials can prepare excellent fiber membranes, which can effectively purify indoor air while adsorbing harmful components. As shown in Figure 2, the fiber membrane made of metal honeycomb mesh has a filtration efficiency of only 72% for PM2.5. The polypropylene nonwoven fabric made of nanoparticles can intercept 99.7% of particulate matter when filtering PM2.5 and more embodies the environmental protection characteristics of architectural design. The fiber membrane made of polyester fiber material can achieve 86.7% of filtration effect, which is far inferior to nanomaterials. In addition, the use of glass fiber materials can intercept 84.5% of particulate matter, while polystyrene can achieve a filtering effect of 69.8%. The comparison shows that in the future, under the
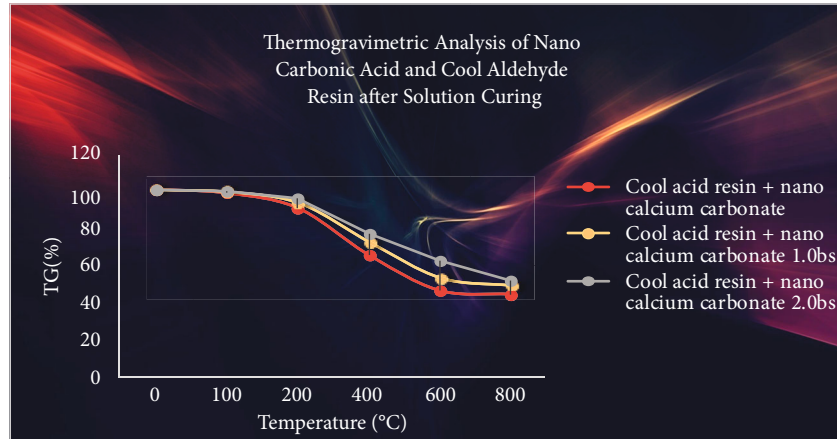
FIGURE 4: Thermogravimetric analysis diagram of nano-carbonic acid and phenolic resin after fusion and curing.

environmental protection and green architectural design concept, nanocomposite building materials will definitely access to a broad market.

As shown in Figure 3, the observation and research using an electron microscope can find that when the sampling speed is controlled to 1.0 ml/h, the particulate filtering polylactic acid material has extremely strong stability. Due to the low boiling point of chloroform, it is volatile and therefore, it will cause holes on the fiber surface. This creates a resultant force with balance properties during use. Under the same conditions of temperature, humidity, and spinning speed, the increase in voltage has a small effect on the diameter, but it will affect the depth of the hole. With the increase in voltage, the more obvious the hole formation, the deeper the hole depth and the hole and the clearer the interface. Under the same temperature, humidity, and voltage conditions, the injection speed has a small effect on the hole size and depth but has a greater effect on the fiber diameter. The fiber diameter increases as the injection speed increases. The high-quality properties of nanocomposite materials can resolve external influences and ensure the stability of the overall structure.

As shown in Figure 4 (figure from http://www.baidu.com/), by exploring the thermogravimetric analysis after the fusion and curing of nano-carbonic acid and phenolic resin, it can be seen that the thermal stability of nanocomposite materials is enhanced when making building materials, and the heat loss is low. On the whole, in the experimental environment, the three curves are in a state of weight loss as the temperature increases. At the starting temperature, the initial weight loss temperature is not much different, all of which are 100%. The first curve changes. It is 98%, 90%, 65%, 46%, and 44%. The second curve has a heat loss mass percentage of 49% at 800 degrees, and the third curve has a heat loss mass percentage of 44% at 800 degrees. In comparison, the slope of the first curve is small, indicating that the thermal reaction rate of the modified sol system becomes smaller, so that it is sufficient to obtain the thermal stability of the nano-carbonate and acid resin system after the modifier is added. There is increased performance and less heat loss.

5. Conclusion

With the continuous growth of the economic level and the improvement of the construction level, people's requirements for buildings are also constantly updated, which affects the development of architectural concepts, architectural design, building materials, and construction. Infrastructure construction is also an important industry for the development of a country's national economy, so the demand is very broad. In the current construction industry in most countries, the consumption of building materials accounts for more than half of the total consumption. 52% of the huge demand and consumption is concentrated in steel and cement. Therefore, the improvement of building materials will not only change the style of building design; it will promote the safety, applicability, and durability of engineering buildings. As an important branch of ecological environmental materials, according to its meaning, ecological building materials should refer to the coordination with the ecological environment in the process of material production, use, disposal, and recycling, to meet the minimum resource and energy consumption, minimum or no environmental pollution, and the best use performance; the highest recycling rate requires the design and production of building materials [25, 26].

Inferred from the current development speed, the problem of building energy consumption has gradually become an urgent problem that needs to be solved. It will not only cause a certain degree of waste but also cause considerable pollution to the environment. Therefore, under the influence of various conditions, new building materials occupy an increasingly important position. Many countries in the world have listed nanotechnology as an important national basic project. Although nanotechnology has not yet been widely applied to the market, a large amount of basic research has been completed at the technical and theoretical level, and some cutting-edge technologies have gradually been applied to cutting-edge fields. However, there are still some technical problems that have not been well perfected, such as how to control the structure and performance of nanomaterials. The cost of nanocomposite

building materials in modified concrete and architectural coatings is very high, and it will take time to fully apply. As a new discipline, nanotechnology will inevitably affect all areas of society, and it will inevitably have an inestimable effect on the performance improvement and use of traditional building materials. Nanocomposite building materials conform to the development trend of economy, environmental protection, green, and energy saving and have become the top priority of current architectural design considerations in the future and represent the future development prospects of the construction industry. At present, the nanocomposite building material system that has been timed is complete and diverse, and its share in the market continues to expand. With the promotion of China's sustainable development strategy and the development of the construction field, new building materials will surely have their unique advantages in the construction industry, shine brilliantly, and promote human development and progress.

Architecture, as a special expression of culture and history, integrates the national and ethnic styles and the customs of various regions in the early design stage. In the architectural design process, we must fully consider the cultural connotation and the future direction of architectural manufacturing. The performance of architecture should reflect the humanistic spirit of different times. Material is the material carrier of the building and through it reflects the spiritual temperament that the building should have. With the development and development of new technologies, architectural design has made great breakthroughs in the way of expression, giving designers more imagination. On this basis, the current materials should be used optimally, their shortcomings should be reasonably compensated, strengths should be used to avoid weaknesses, and the synchronization of the times should be emphasized.

Data Availability

No data were used to support this study.

Conflicts of Interest

There is no potential conflict of interest in this study.

References

[1] N. Lukuttsova, A. Pykin, Y. Kleymenicheva, A. Suglobov, and R. Efremochkin, "Nano-additives for composite building materials and their environmental safety," *International Journal of Applied Engineering Research*, vol. 11, no. 11, pp. 7561–7565, 2016.

[2] M. Sumesh, U. J. Alengaram, M. Z. Jumaat, K. H. Mo, and M. F. Alnahhal, "Incorporation of nano-materials in cement composite and geopolymer based paste and mortar - A review," *Construction & Building Materials*, vol. 148, pp. 62–84, 2017.

[3] K. Jankovic, S. Stankovic, D. Bojovic, M. Stojanovic, and L. Antic, "The influence of nano-silica and barite aggregate on properties of ultra high performance concrete," *Construction & Building Materials*, vol. 126, pp. 147–156, 2016.

[4] T. D. Ngo, Q. T. Nguyen, T. P. Nguyen, and P. Tran, "Effect of nanoclay on thermomechanical properties of epoxy/glass fibre composites," *Arabian Journal for ence & Engineering*, vol. 41, no. 4, pp. 1251–1261, 2016.

[5] Y. Chi, J. Chu, M. Chen et al., "Directly deposited graphene nanowalls on carbon fiber for improving the interface strength in composites," *Applied Physics Letters*, vol. 108, no. 21, article 211601, 2016.

[6] Y. C. Chen, K. P. Yu, W. C. Shao, C. H. Tseng, and W. C. Pan, "Novel mold-resistant building materials impregnated with thermally reduced nano-silver," *Indoor Air*, vol. 28, no. 2, pp. 276–286, 2018.

[7] J. Ying, B. Zhou, and J. Xiao, "Pore structure and chloride diffusivity of recycled aggregate concrete with nano-SiO$_2$ and nano-TiO$_2$," *Construction and Building Materials*, vol. 150, pp. 49–55, 2017.

[8] L. Xue, B. Sanz, A. Luo et al., "Hybrid surface patterns mimicking the design of the adhesive toe pad of tree frog," *ACS Nano*, vol. 11, no. 10, pp. 9711–9719, 2017.

[9] T. I. Panina, J. N. Tolchkov, A. G. Tkachev, Z. A. Mikhaleva, and A. I. Popov, "Efficiency of application of complex nano-modifying additives based on zeolites in building materials," *Nanotechnologies in Construction*, vol. 8, no. 5, pp. 116–132, 2016.

[10] M. Eftekhari, S. Mohammadi, and M. Khanmohammadi, "A hierarchical nano to macro multiscale analysis of monotonic behavior of concrete columns made of CNT-reinforced cement composite," *Construction and Building Materials*, vol. 175, pp. 134–143, 2018.

[11] Y.-Y. Wang, J.-F. Su, E. Schlangen, N.-X. Han, S. Han, and W. Li, "Fabrication and characterization of self-healing microcapsules containing bituminous rejuvenator by a nano-inorganic/organic hybrid method," *Construction and Building Materials*, vol. 121, pp. 471–482, 2016.

[12] V. D. C. Correia, S. F. Santos, R. S. Teixeira, and H. Savastano Junior, "Nanofibrillated cellulose and cellulosic pulp for reinforcement of the extruded cement based materials," *Construction and Building Materials*, vol. 160, pp. 376–384, 2018.

[13] J. Wang, P. Du, Z. Zhou, D. Xu, N. Xie, and X. Cheng, "Effect of nano-silica on hydration, microstructure of alkali-activated slag," *Construction and Building Materials*, vol. 220, pp. 110–118, 2019.

[14] H. Hasan, B. Huang, M. Saafi et al., "Novel engineered high performance sugar beetroot 2d nanoplatelet-cementitious composites," *Construction and Building Materials*, vol. 202, pp. 546–562, 2019.

[15] B. Shu, L. Zhang, S. Wu, L. Dong, Q. Liu, and Q. Wang, "Synthesis and characterization of compartmented Ca-alginate/silica self- healing fibers containing bituminous rejuvenator," *Construction and Building Materials*, vol. 190, pp. 623–631, 2018.

[16] H. Maile, "Architectural design as an expression of religious tolerance:," *Journal of the Society of Architectural Historians*, vol. 76, no. 3, pp. 281–301, 2017.

[17] J. Rosenkrantz and J. Louis-Rosenberg, "Dress/code democratising design through computation and digital fabrication," *Architectural Design*, vol. 87, no. 6, pp. 48–57, 2017.

[18] D. L. C. Hennebury, "Review:Michigan modern: design that shaped America, by Amy l. Arnold and Brian d. Conway andMid-Michigan modern: Frank Lloyd Wright to Googie,

by Susan j. Bandes," *Journal of the Society of Architectural Historians*, vol. 76, no. 4, pp. 565–568, 2017.

[19] A. Narath, "Review: A house in the sun: modern architecture and solar energy in the cold war, by Daniel A. Barber," *Journal of the Society of Architectural Historians*, vol. 77, no. 2, pp. 232-233, 2018.

[20] Y. Mclane and J. Pable, "Architectural design characteristics, uses, and perceptions of community spaces in permanent supportive housing," *Journal of Interior Design*, vol. 45, no. 1, pp. 33–52, 2020.

[21] B. Yurtsever and C. Polatoğlu, "A secret component in architectural design studio: the "filtering" concept," *Open House International*, vol. 43, no. 2, pp. 60–68, 2018.

[22] Y. Tang, "Combined effects of nano-silica and silica fume on the mechanical behavior of recycled aggregate concrete," *Nanotechnology Reviews*, vol. 10, no. 1, pp. 819–838, 2021.

[23] X. Xu, D. Shahsavari, and B. Karami, "On the forced mechanics of doubly-curved nanoshell," *International Journal of Engineering Science*, vol. 168, p. 103538, 2021.

[24] X. Xu, B. Karami, and D. Shahsavari, "Time-dependent behavior of porous curved nanobeam," *International Journal of Engineering Science*, vol. 160, p. 103455, 2021.

[25] B. Gao, N. Xu, and P. Xing, "Shock wave induced nanocrystallization during the high current pulsed electron beam process and its effect on mechanical properties," *Materials Letters*, vol. 237, no. 15, pp. 180–184, 2019.

[26] G. Bo, L. Chang, H. Chenglong et al., "Effect of Mg and RE on the surface properties of hot dipped Zn–23Al–0.3Si coatings," *Science of Advanced Materials*, vol. 11, no. 4, pp. 580–587, 2019.

Research Article

The Application of Nanoparticle Ceramic Materials in the Design of Modern Handicrafts

Zhimin Gao ⬤,[1] **Seungjin Lee,**[2] **and Jiaxi Huang**[1]

[1]*College of Fine Arts and Design, Huaihua University, Huaihua, 418000 Hunan, China*
[2]*Graduate School of Education, Sehan University, Jeollanam-do 58447, Republic of Korea*

Correspondence should be addressed to Zhimin Gao; gzm@hhtc.edu.cn

With the development of society, people's purchasing power is gradually increasing, and more and more people choose to buy handicrafts. The popularity of handicrafts has also promoted the development of production technology and production materials, and high-quality handicrafts are most favored by consumers. As an enduring material, ceramics are also under continuous development. This article is aimed at studying nanoceramic materials and gaining a detailed understanding of the classification, structure, and manufacturing process of nanoceramic materials. In the experimental stage of this article, through the analysis of whether nanoceramic materials and technology are used in modern crafts, it is verified whether nanoceramic materials contribute to the advancement of modern craft design and the growth of product sales. This article shows through experimental research that the application of nanoceramic materials to handicrafts can not only increase its sales by more than 30% but also increase its sales unit price by 36%.

1. Introduction

People need materials in order to make products. In product design, material is the most basic thing to ensure the function and shape of the product. Regarding the definition of matter, it generally refers to the raw materials used by human beings as objects, which are the basis for the existence of all natural and artificial objects. Since the beginning of the Neolithic age, humans made stone tools consciously, so the design and materials were closely integrated. Design is an engraving activity with dual functions of material and spirit, physiology, and psychology. Material is the basic condition for realizing design. More than a century later, the development classics of product design reflect strong nationalization and various languages and cultural contents, with rich spiritual and cultural connotations. There are many types and quantities of materials suitable for modern product design. People have used ceramics as raw materials for a long time. Silicon has long been one of the most basic raw materials for making ceramic materials. With the continuous innovation of society, most of the new ceramic materials and ceramic products are mainly composed of pure oxides, carbides, and nitrides. In the era of modern industrial production, ceramics still bear an important role and mission in modern product design by virtue of its unique color, texture, and inherent quality. Handicraft refers to the art of handicraft with a unique style. It is different from the arts and crafts that mass produce standardized daily use handicrafts by means of large-scale industrial mechanization. Handicrafts refer to products made purely by hand or with the help of tools.

Decorative art is a bridge connecting human spiritual civilization and material civilization. Ceramic art is a formal feature. It not only embodies the value of beauty in appearance but also embodies the craftsmanship and production technology of people to create beauty. At the same time, the combination of craftsmanship and decoration needs to be manipulated through artistic techniques to get its exquisite artistic effect. More and more people are pursuing ceramic art. Our ideal lies in its changes. We use the beauty created by ceramic art to embellish people's daily life environment, improve people's lives, and further

enhance people's artistic vision. Ceramic art is designed to meet the material and spiritual requirements of the people in their work and life. Indeed, as a product of traditional Chinese culture, ceramics have undergone continuous development, change, and innovation of decorative patterns in the early lacquered pottery era. The materials and technology of ceramics and the continuous update and progress of craftsmen reflect the diligence and wisdom of the Chinese people. It has become China's far-reaching cultural heritage. Of course, we should look at the mainstream of Chinese traditional culture and the fundamental source of national culture. The continuation of this traditional culture and the continuity of the evolution of totems depend on the study of decorative images that are close to the reliability of human life and art. All in all, the application of ceramics in the design of modern industrial products shows its unparalleled charm and appeal. Modern ceramic decoration design is inseparable from the trend of the times, modern craft materials, technology, and aesthetic preferences. We must keep pace with the times, grasp the requirements of the times, grasp the market and technical information of modern ceramic art and crafts, and strive to create more and more updated ceramic products. The design of modern art and crafts needs to combine the completion of ceramic art with art and then make new features of pottery.

With the continuous development of society, ceramic materials and their production technology are also constantly evolving. Simonenko et al. stated that nanocrystalline (19 nm) silicon carbide powder is made by combining the sol-gel treatment of the finely dispersed and chemically reactive SiO_2-C system with the carbothermic synthesis under vacuum medium temperature (1400°C). Porous ceramic materials can be produced by hot pressing methods [1]. In addition to porous ceramic materials, Scribot et al. have shown through experiments that using red mud and broken glass soda as raw materials, heat treatment at 600-800°C for 1 hour can also successfully synthesize new foamed geopolymer materials [2]. In the research on the production of ceramic materials, Kairakbaev et al. used the Mossbauer effect to establish the distribution of iron ions during the firing of acid-resistant ceramic materials using production waste as raw materials. Studies have shown that by calculating the area of the double peaks of the spectrum, the iron compounds on the surface of the studied sample are mainly represented by hematite. In this case, the acid resistance of the sample is reduced [3]. At the same time, in the further development of ceramic materials, Baranova and Valiakhmetov have shown through continuous practice results that through the minimum preparation of raw materials used, a corundum material with high thermal stability can be obtained. The corundum material can be used to produce the parts of the molybdenum heater insulator in the voltage stabilizer furnace for the stabilizer casting blade made of high-temperature alloy [4]. Through the continuous advancement of ceramic manufacturing technology, the development of nanoceramic materials is getting faster and faster. Yin et al. prepared Al_2O_3-based micro-nano-composite ceramic tool materials by hot pressing. The tribological behavior and wear mechanism on metals (stainless steel, chromium

steel) and cemented carbide (Si3N4) were studied. Yin et al.'s research shows that when it rubs with stainless steel, the friction coefficient is the smallest and the wear rate is the largest [5]. With the continuous development of nanoceramic production technology, the use of nanoceramics in various fields is also becoming wider and wider. In medicine, Liu et al. said that the nanoceramic coating on the surface of titanium-based metal implants is a potential clinical choice in orthopedic surgery. Stem cells have been found to have osteogenic ability, and it is necessary to study the effect of functionalized nanoceramic coatings on stem cell differentiation and proliferation in vivo [6]. In the application and research of ceramic crafts, Ivkovi et al. studied Belgrade ceramic craftsmanship and craftsman's archaeology through ceramic petrography and chemical analysis, as well as the production technology of these porcelains, including ceramic bodies, slips, and glazes. And use the chaîne opératoire conceptual framework to explain the results [7]. Although ceramic manufacturing technology and manufacturing processes are beginning to be used in more and more fields, the cost of production and use of ceramic materials is much higher than that of other materials, and ceramic materials require high technical levels of production, especially nanoceramics. It needs to use the latest production equipment for production, the production cycle is long, and the cost is high.

The innovation of this article is to incorporate modern nanoparticle ceramic technology into the design of modern handicrafts and to apply advanced nanoceramics to the design of contemporary handicrafts, so that contemporary handicrafts can fully demonstrate the beauty of the fusion of modern technology and modern design. I mainly researched the characteristics and production technology of nanoparticle ceramics to find the most suitable ceramic materials for contemporary handicraft design, so as to better promote the design and promotion of modern industrial products. Because of its high strength, high hardness, corrosion resistance, high temperature resistance, and other characteristics, ceramic materials have become the development center of new materials and received extensive attention, and the application field is also expanding.

2. The Application of Nanoparticle Ceramic Materials in the Design of Modern Handicrafts

2.1. Ceramic Materials. Ceramic materials are one of the most common materials in daily life and play an important role that most materials cannot replace in people's daily work and life. Because of its fragile surface, the ceramics that people produce early have the shortcomings of fragility and low flexibility. With the large-scale application of nanoceramic technology in ceramic production, we hope to produce ceramic materials with higher strength, better flexibility, and wider applicability, such as ceramics that can be used for metal preparation [8, 9]. Nanoceramics are a new type of ceramic material that appeared around 1970. The development of nanotechnology means that the microstructure, grain boundaries, and particles of ceramic materials have

changed. All of these are to improve the compression resistance, foldability, and plasticity of the material. Ceramic engineering has overcome many shortcomings, which have important effects on electrical, thermal, magnetic, optical, and other mechanical properties. Nanoceramic materials have gradually become engineering materials that can replace traditional industries [10].

2.1.1. Preparation of Nanoceramics.

Different from traditional ceramic sintering, in the process of nanoceramic sintering, cutting countermeasures must be studied in order to control particles [11]. The special sintering method of nanoceramics can control the size of nanoceramic particles, so as not to have a serious impact on the inherent characteristics of nanoceramics after growth [12]. As shown in Figure 1, there are mainly four methods.

2.1.2. The Structural Foundation and Basic Performance of Ceramics

(1) Ceramic Material Bonding Bond. Chemical bonding is divided into strong bonding and weak bonding. Among them, strong bond refers to metal bond, covalent bond, and ionic bond, and weak bond generally refers to hydrogen bond and van der Waals bond [13]. Most people think that covalent bonds and ionic bonds are the most important structural combination of ceramic materials. However, after detailed investigation and research, they will find that the bonding properties of ceramic materials vary widely, and there are usually many intermediate types of ceramics. Usually people can judge the degree of ion binding by using electronegativity [14]. The ratio of ion bonding in the ceramic structure composed of two elements a and b can be calculated from the formula given in

$$M = 1 - \exp\left[-\frac{(X_a - X_b)}{4}\right].$$ (1)

In the formula, M is the ratio of ion binding components and X_a and X_b are the electronegativity of element a and element b, respectively. In the formula, if the difference between X_a and X_b is greater, M is greater. That is, the ratio of ion binding becomes larger. Conversely, the smaller the difference between X_a and X_b, the smaller M is. In other words, the proportion of covalent bonds becomes larger [15]. When $X_a = X_b$, the measured ceramic materials are all covalent bonds, and there are no ionic bonds. In general, the ion bonding ratio of oxides is higher than the ion bonding ratio of carbides, and the ion bonding ratio of nitrides is higher.

(2) Pauling's Rule. The most basic characteristic of Pauling's rule is to use positive ion coordination polyhedrons as the basic structural unit instead of the common lattice structure as the basic structural unit. Therefore, when studying its complex structure, the unit presented by it has its own uniqueness [16]. This rule plays a very important role in understanding the structure of ionic crystals, and it also plays a great reference for crystals with covalent bonds and ions. However, this rule is not suitable for crystals with a single structure [17]. There are 5 rules in total, which are imported as described in Figure 2.

The first rule: the positive ion is in the center, surrounded by many negative ions to form a polyhedron. The algebra of the radius of the positive and negative ions determines the distance between the positive and negative ions. In actual practice, most of the time ions are described as spheres with a fixed volume. A^+ and A^- represent the radius of positive and negative ions, respectively, and the coordination number of positive ions can be represented by the value of A^+/A^-. Put positive ions into a gap smaller than its volume to form a stable structure. In particular when the size of the positive ion is consistent with the size of the gap, the formed structure is very stable. Conversely, if the size of the gap is larger than the size of the cation, the structure formed will become unstable [18]. Table 1 shows the relationship between A^+/A^- and the coordination number.

The second rule: electricity tariff rules. This rule firstly plays a decisive role in the distribution of the number of vertices and polyhedrons and secondly determines whether the result of studying a certain crystal is stable. This rule shows that there is also a certain algebraic relationship in the crystal structure; specifically, there is a certain relationship between the values of positive and negative ions [19]. In other words, the algebraic sum of the electrostatic bonding strength of the positive ions in the vicinity of the negative ions to the negative ions is equal to the value of the negative ions, and the deviation is less than 1/4. The formula for electricity tariff rules is as follows:

$$E^- = \sum_n S_n = \sum_n \frac{E^+}{W}.$$ (2)

The third rule: the rule of cotop, face, and edge of polyhedron. The rule is to measure the structural stability of the crystal from the connection mode of the polyhedron. Pauling's law proposes that whether the ionic crystal structure is stable is subject to the collection of polyhedrons. In other words, the structural stability of coplanar crystals is weaker than that of different polyhedral crystals connected at the edge of a common edge [20]. This is due to the presence of high valence positive ions in gaps with low coordination numbers. The intensity of electrostatic coupling can be allocated to adjacent coordinated negative ions, but it cannot completely shield the electric field emitted by positive ions. If the number of common edges between anion polyhedrons increases, the distance between cations becomes shorter. At this time, the repulsive force that is not completely shielded between the cations becomes larger [21]. In particular, when a plurality of such polyhedrons is coplanarly connected, the stability of the crystal structure may decrease. Therefore, the polyhedrons of a crystal with a stable structure are not the same edge or the same plane but are formed at the same angle.
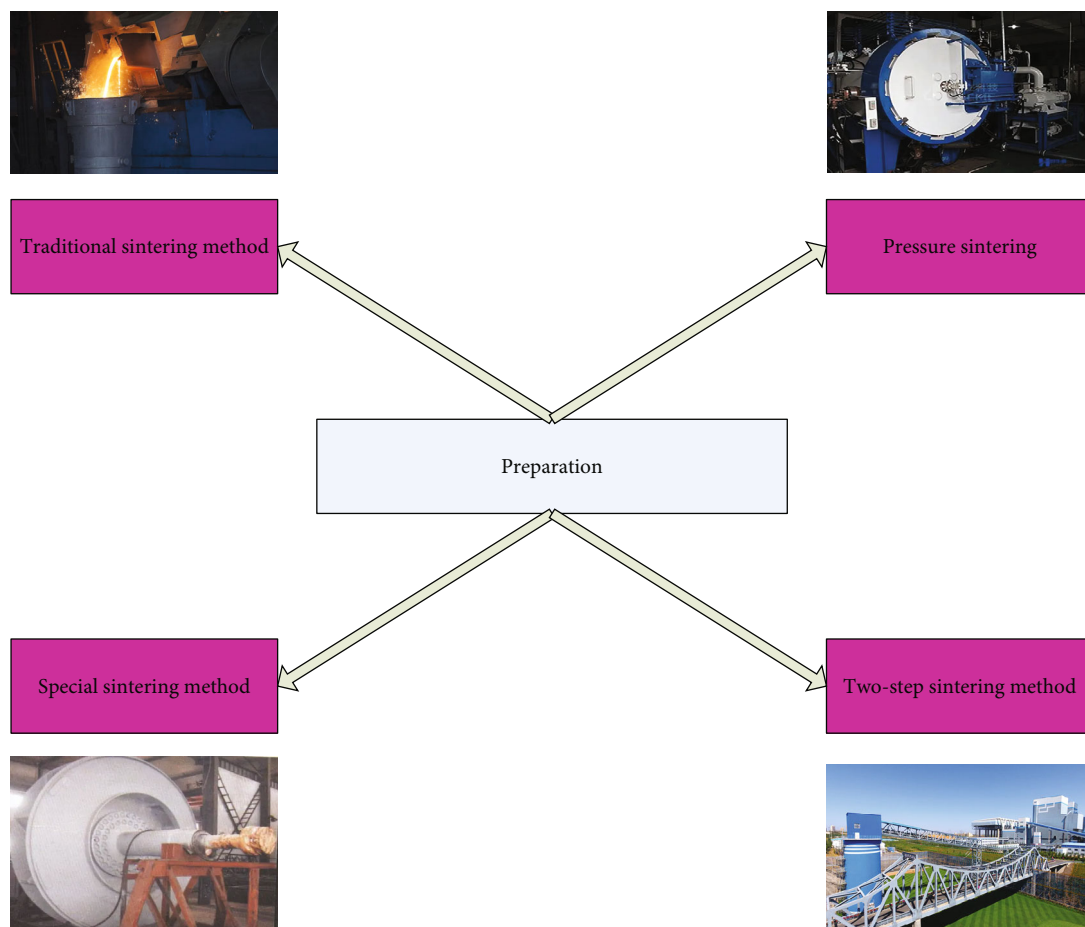
FIGURE 1: Four manufacturing methods of nanoparticle ceramic materials.
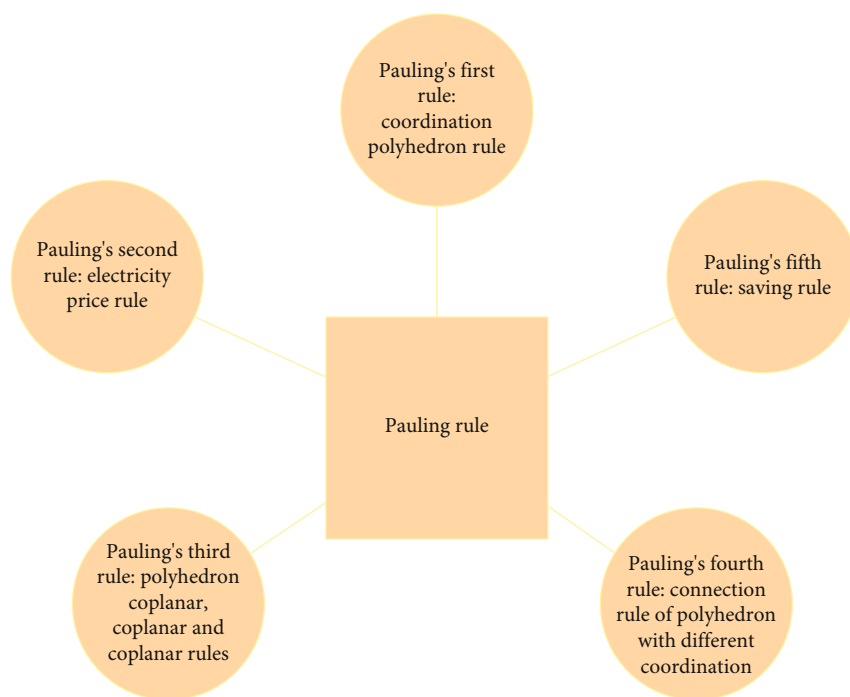
FIGURE 2: Pauling rule.

TABLE 1: Relationship between A^+/A^- and the coordination number.

A^+ to A^- radius ratio	Coordination number	Coordination polyhedron
0.000~0.155	2	Dumbbell shape
0.155~0.255	3	Plane triangle
0.255~0.414	4	Tetrahedron
0.414~0.732	6	Octahedron
0.732~1.000	8	Cube
1.000	12	Tetrahedron

The fourth rule: this rule shows that if there are multiple different cations in the same ionic crystal structure, polyhedrons with high atomic valence and low coordination are likely to fail to connect to each other [22]. For example, in $BaTiO_3$, the titanium oxide octahedrons are not connected on the same plane or common edge but connected only at the upper corners. Fortsulight is divided into tetrahedron (SiO_4) and octahedron (MgO6) two coordination polyhedrons, but the Si^{4+} coordination number is low and the electricity cost is high, so it is connected by tetrahedron (SiO_4) and separated by octahedron (MgO_6) [23].

The fifth rule: saving rules. This rule shows that in the same ionic crystal, there is a tendency to minimize the number of different structural units. In other words, cations of the same type must be in the same coordination environment [24]. The basis of this rule is the symmetry and periodicity of the crystal structure. The basic units that make up the crystal are of different types and large numbers, and when each basic unit forms its own regularity and periodicity, they will interfere. As a result, a stable crystal structure cannot be formed.

(3) Typical Crystal Structure. Ceramic structures are generally more complex, but generally speaking, the following typical structures are inseparable. This can be considered the most densely filled voids in which positive ions are filled into negative ions [25–27]. The following briefly introduces several typical ceramic structures. The first introduction is the perovskite-type structure, and its structure is shown in Figure 3.

The perovskite-type composite compound has the general formula WTY3, and the coordination number is $W : T : Y = 12 : 6 : 6$. The radii Q_W, Q_T, and Q_Y of W, T, and Y ions have the following relationship:

$$Q_W + Q_Y = \sqrt{2}(Q_Y + Q_T). \tag{3}$$

The above equation is the condition for the spheres of radii Q_W, Q_T, and Q_Y to contact. But in fact, there is a certain radius difference between the W-site ions and the oxygen ions, and the T-site ions may not contact the oxygen ions constituting the octahedron [28]. Therefore, the
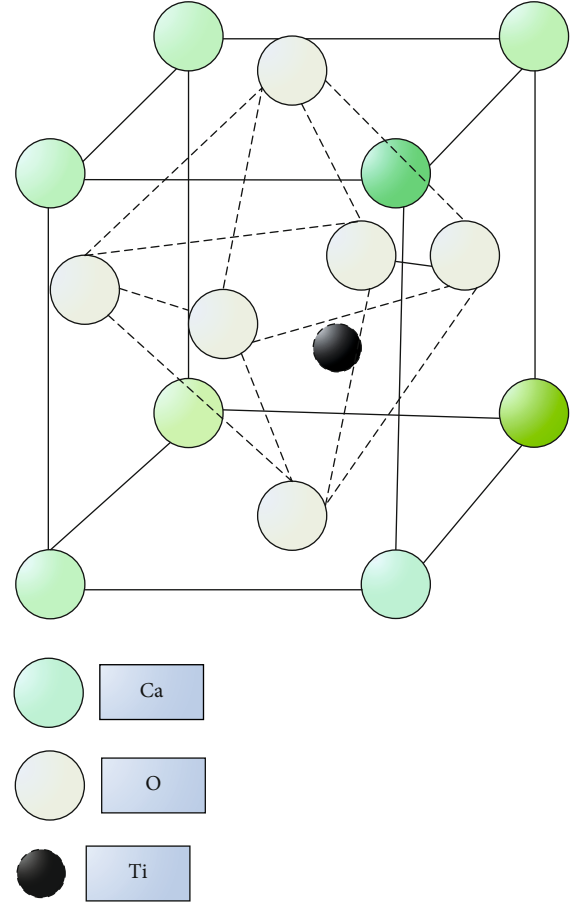
FIGURE 3: Perovskite crystal structure.

tolerance of the radius can be expressed by the tolerance coefficient e, which can be expressed by the following relational formula:

$$Q_W + Q_Y = \sqrt{2}e(Q_T + Q_Y). \tag{4}$$

The value of e ranges from 0.77 to 1.10. In the case of $e = 0.77$ to 1.10, the structure of the WTY3 compound is a perovskite type. When the value of e is not within this range, it will change to another crystal structure. In the case of $e < 0.77$, it is a ferro-titanium-type structure. In the case of $e > 1.10$, there is a calcite or calcite structure.

(4) Basic Properties of Ceramic Materials. Dielectric constant is the main parameter reflecting the dielectric properties or polarization properties of piezoelectric smart materials under the action of electrostatic field ε. Piezoelectric components for different purposes have different requirements for the dielectric constant of piezoelectric smart materials. When the shape and size of piezoelectric smart materials are certain, the dielectric constant ε is determined by measuring the inherent capacitance (CP) of piezoelectric smart materials. In many materials, the specific permittivity is an indispensable characteristic parameter, reflecting the ability of the charge storage material. This is closely related to the

polarization of the material. The relationship between the polarization parameter and the specific permittivity R can be obtained from cloud computing and Mossotti's equation:

$$\frac{R_I - 1}{R_I + 1} = \frac{1}{3R_0} \sum j N_j \propto_j. \tag{5}$$

The above formula reflects the relationship between the polarizability and the specific permittivity, combining the macroscopic quantity and the microscopic quantity.

The quality factor is a parameter for measuring the electric field, especially the internal dielectric loss of the medium in the AC electric field. The quality coefficient Qu is generally expressed as follows:

$$\frac{1}{\tan \delta} = Qu = \frac{\omega_r^2}{2\pi FY}. \tag{6}$$

It can be concluded from formula (6) that the Qu $*$ F value is a physical quantity reflecting material loss and an important parameter to explain the quality of ceramic microwave dielectric properties. The Qu $*$ F value of ceramic materials can be increased by selecting suitable raw materials and improving the preparation and sintering process. Only an excellent preparation method can ensure that the dielectric loss of the ceramic is small.

(5) Performance Requirements of Ceramic Packaging Materials. This package mainly plays the role of transporting and supporting chips and electronic components, connecting electronic circuits, sending signals, and protecting heat dissipation. Therefore, as shown in Table 2, ceramic packaging materials mainly have electrical and mechanical requirements.

For packaging materials, the most important requirements for electrical properties are dielectric loss and insulation resistance. The dielectric loss can be expressed by the tangent value of the phase angle of the polarization current of the delayed material voltage, which is the following relational formula:

$$\tan A = Wcr. \tag{7}$$

In the formula, A is the loss angle, W is the signal frequency, and c and r are the circuit distribution parameters. Over time, the signal sent to the material will disappear in the form of heat, so especially in high-frequency applications, it is necessary to reduce the dielectric loss. The signal transmission speed v can be expressed by equation (8):

$$v = \frac{s}{\sqrt{\varepsilon e}}. \tag{8}$$

2.2. Alumina Composite Ceramic Materials

2.2.1. The Structure, Performance, and Application of Al_2O_3 Ceramics. At present, Al_2O_3 ceramics are one of the largest

TABLE 2: Properties of ceramic packaging materials.

Nature	Specific requirements
Electrical properties	Low dielectric loss High insulation voltage
Mechanical properties	High mechanical strength Easy to achieve multiple layers Flat and smooth surface
Other properties	Easy to metallize Resistant to oil and chemical corrosion

production and widely used ceramic materials in the world. Not only is it widely used in the most cutting-edge technical fields such as national defense and aerospace but also due to its heat resistance, corrosion resistance, wear resistance, and other characteristics, part of the material made of it can completely replace part of the metal material. Through effective dispersion and recombination, nanoceramic composites make heterogeneous nanoparticles uniformly dispersed and retained in the ceramic matrix structure, which greatly improves the toughness and wear resistance and high-temperature mechanical properties. Nanoceramic materials can not only bend freely without cracks like metal materials at low temperature but also carry out mechanical cutting like metal materials and even make ceramic springs. These excellent mechanical properties of nanoceramic materials make them widely used in cutting tools, bearings, automobile engine parts, and so on. Figure 4 shows the schematic diagram of the microstructure of the Al_2O_3 ceramic-sintered body.

Al_2O_3 ceramic materials have excellent physical properties and chemical stability (high mechanical strength, wear resistance, high temperature resistance, corrosion resistance, high hardness, excellent insulation properties, low dielectric loss, etc.). At the same time, Al_2O_3 ceramics are widely used in machinery, aerospace, electronic instruments, electric power, and chemical industries.

2.3. Nanoceramic Materials. At present, the preparation of nanoceramics is still relatively small, but through the efforts of a large number of researchers, a variety of oxide nanoceramics have been successfully prepared, and a perfect sintering theory has been formed, which provides theoretical and experimental support for the preparation of $BiFeO_3$ nanoceramics. Compared with the traditional solid-phase reaction method and rapid liquid-phase sintering method, it has the advantages of high product particle purity, convenient operation, simple synthesis conditions, and easy control. The sintering theory and research progress of nanoceramics are introduced as follows.

2.3.1. Introduction to the Sintering Theory of Nanoceramics. At the microstructure level, sintering refers to the process of powder solid phase material transfer, accompanied by particle growth and densification. Sintering generally includes volatilization-condensation, surface diffusion, grain boundary diffusion, bulk diffusion, plastic deformation, and
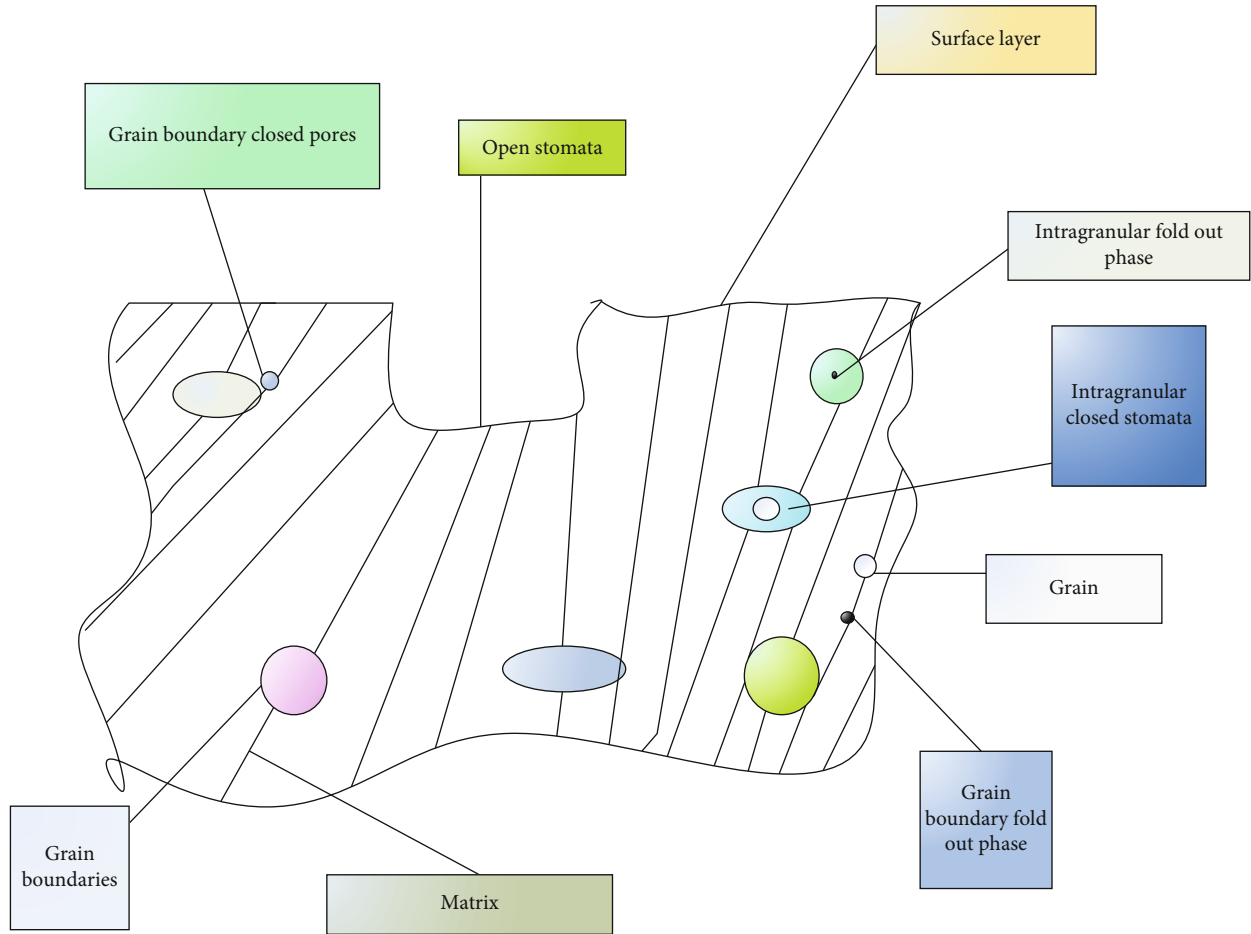
FIGURE 4: Schematic diagram of the microstructure of the Al_2O_3 ceramic-sintered body.

other processes. In the process of densification, only particle diffusion, volume diffusion, and plastic deformation play a role. In the process of sintering without external stress and in the densification of ceramics, only particle diffusion and volume diffusion play a role. Taking the effect of particle diffusion as an example, the rate of change of all particle diffusion can be expressed as follows:

$$\frac{Ac}{Ax}\bigg| WQ = B_{WQ} \frac{\alpha_{WQ}}{(2\pi m * r * t)^{1/2}} * \frac{\Omega N_{\text{flat}} E_{WQ}}{KY} * \sum B. \quad (9)$$

Among them, m is the gas constant, t is the absolute temperature, and Ω is the volume of the unit powder. The absolute shrinkage is expressed as the sum of grain boundary diffusion and bulk diffusion, which can be expressed as

$$\frac{DV}{VDt}\bigg| D = B \frac{DV}{VDt}\bigg| WQ + \frac{DV}{VDt} V = M * R * \sum b. \quad (10)$$

In the formula, C is a constant related to temperature and A is the area of grain boundaries. The change of grain

TABLE 3: The main raw materials used in the experiment.

Drug name	Chemical formula	Molecular weight	Specification
Ferric nitrate	$Fe(NO_3)_3$	404	500 g
Bismuth nitrate	$Bi(NO_3)_3$	485.07	500 g
Tetrabutyl titanate	$C_{16}H_{36}O_4Ti$	223	500 ml
Ethylene glycol	$(CH^2OH)_2$	123.22	100 g
Absolute ethanol	C_2H_6O	46.07	500 ml
Nitric acid	HNO_3	60.05	500 ml

size in the process of grain growth can be expressed by the following formula:

$$\frac{E_R}{E_T} = \left(L_{B-A} * I_{B-A} + L_W * I_W + L_Q * I_Q \right) B. \quad (11)$$

2.3.2. Preparation Principle of BiFeO$_3$-Based Nanoceramics
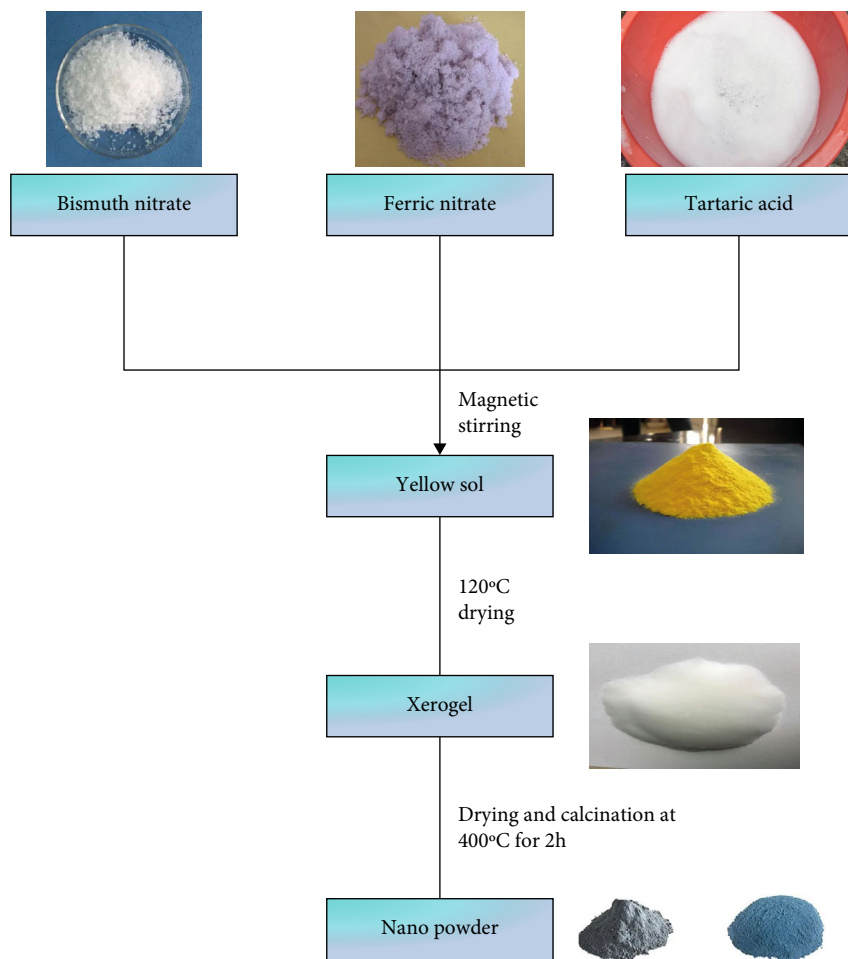
Figure 5: Preparation flowchart of BiFeO$_3$ nanopowder.
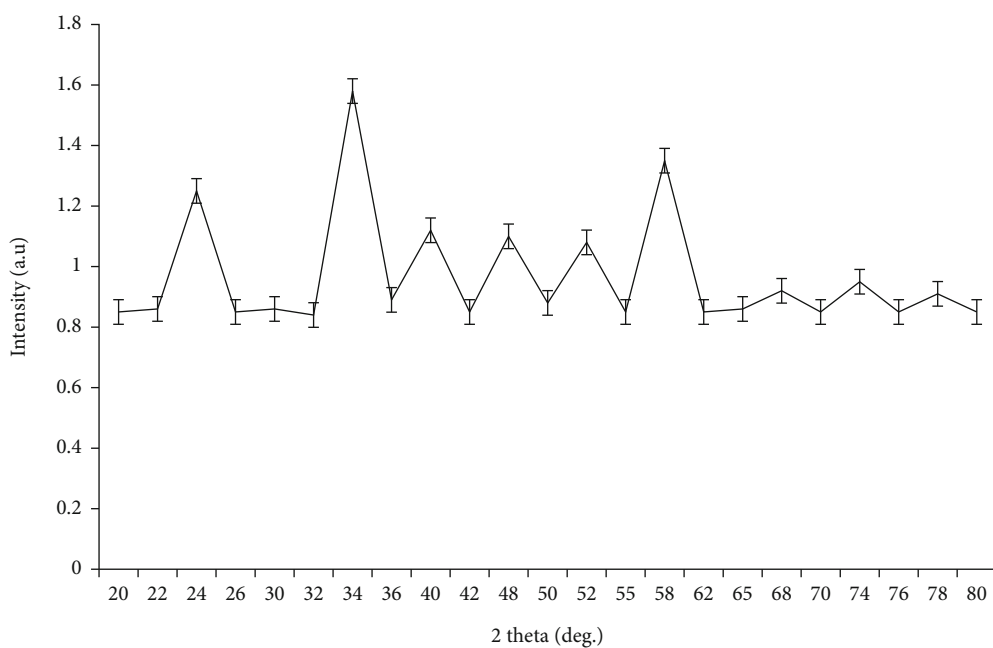
Figure 6: XRD pattern of BiFeO$_3$ nanopowder.

(1) Experimental materials and experimental equipment, as shown in Table 3

(2) Performance characterization

First, the resistance analysis of the ceramics is carried out, and the surface of the ceramic samples is ground and polished and electrodes are covered. Among them, the relationship between the imaginary part of the impedance and the corresponding frequency is

$$X'' = r \left[\frac{\omega rc}{1 + (\omega rc)^2} \right]. \tag{12}$$

The relationship between the imaginary part of the electric modulus and the frequency is

$$T'' = \frac{\varepsilon_0}{c} \left[\frac{\omega rc}{1 + (\omega rc)^2} \right]. \tag{13}$$

Among them, ω is the angular frequency $= 2\pi F$ and $\varepsilon_o = 8.854 * 10^{-14}\,\text{F}\cdot\text{cm}^{-1}$ is the dielectric constant in vacuum. The maximum value of the semicircle is the peak value of the Debye peak, and the frequency corresponding to the peak value is

$$\omega_{\text{MAX}} = 2\pi F = (rc)^{-1}. \tag{14}$$

The maximum resistance value r and the minimum capacitance value c are extracted by the relaxation peaks of $X'' - F$ and $T'' - F$. From formula (12), the following can be obtained:

$$X'^{'}{}_{\text{MAX}} = \frac{r}{2},$$
$$T'^{'}{}_{\text{MAX}} = \frac{\varepsilon_0}{2c}. \tag{15}$$

When extracting the contribution of defects to Debye relaxation, the extracted system grain boundary and grain conductance can be fitted by fitting, and the relationship between conductance and temperature obeys the Arrhenius formula:

$$\alpha = \alpha_0 \exp\left(-\frac{\text{Wa}}{Ki}\right), \tag{16}$$

where α is the conductivity, K is the Boltzmann constant, i is the absolute temperature, and Wa is the activation energy.

$$\text{In}(\alpha) = \text{In}(\alpha) - \frac{\text{Wa}}{Ki}. \tag{17}$$

The activation energy obtained by fitting can distinguish the dominant defect types of the system. When

TABLE 4: Experimental raw material manufacturers and purity.

Raw material	Material formula	Production address	Purity
Alumina (a1)	Al_2O_3	Imported from Japan	>99.90%
Alumina (a2)	Al_2O_3	Imported from Japan	>99.90%
Alumina (a3)	Al_2O_3	Imported from Japan	>99.90%
Alumina (a4)	Al_2O_3	Imported from Japan	>99.90%
Alumina (a5)	Al_2O_3	Imported from Japan	>99.90%
Alumina (a6)	Al_2O_3	Domestic	>99.90%
Alumina (a7)	Al_2O_3	Domestic	>99.90%
Alumina (a8)	Al_2O_3	Domestic	>99.90%
Alumina (a9)	Al_2O_3	Domestic	>99.90%
Lanthanum oxide	La_2O	Domestic	>99.90%
Yttrium oxide	Y_2O_3	Domestic	>99.90%

extracting the contribution of the defect type to the dielectric relaxation, by fitting the relationship between the relaxation time T and the reciprocal of the absolute temperature:

$$T = T_0 \exp\left(-\frac{\text{We}}{Ki}\right), \tag{18}$$

the relaxation time can be calculated from the frequency corresponding to the peak in the $X'' - F$ spectrum:

$$T = \frac{1}{2\pi F_{\text{max}}}. \tag{19}$$

(3) Ceramic preparation process

$BiFeO_3$ and a series of materials derived from it belong to single-phase perovskite oxide-type multiferroic materials, with ferroelectric, piezoelectric, dielectric, electrooptical, ferromagnetic, photovoltaic, and magnetoelectric coupling, photocatalysis, etc. at the same time above room temperature effect. It has important application prospects in many new smart devices. The mixed nitrate solution is prepared according to the stoichiometric ratio of 1 : 1 of $Fe(NO_3)$ 3.9h2o and Bi (NO3) 3.5h2o or Fe_2O_3 and Bi_2O_3. Glycine is added as fuel, 5~10 ml of oxalic acid is added for dehydration, and the resulting solution is put into a microwave oven and heated with 800 W power. After evaporating the water, it is heated for 10~20 seconds. The mixture undergoes a rapid combustion reaction to obtain loose nanoparticle powder products. The obtained granular

TABLE 5: Name, model, and manufacturer of experimental equipment.

Experimental equipment name	Device model	Equipment manufacturer
Density tester	DE-120 M	Hongtuo Instrument Co., Ltd.
Microwave network analyzer	4284A	Agilent Corporation
X-ray diffraction analyzer	X'pert Pro MPD	Netherlands PANalytical
Electronic Vernier caliper	0-150	Chengdu Chuanliang Tools Co., Ltd.
Hydraulic jack machine	QYL-32	Shanghai Hunan Jack Manufacturing Factory
Precision electronic balance	JA-5003	Shanghai Sunny Scientific Instrument Co., Ltd.
Flowing powder production line and continuous ball mill		
Flow-type frit production line and continuous frit kiln		
Rotary hydraulic brick press and dry glazing process		
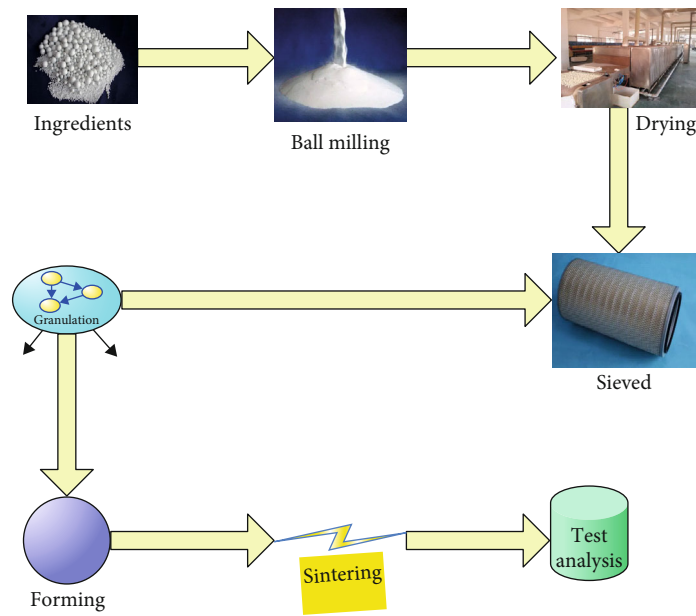
FIGURE 7: Flowchart of ceramic preparation.

powder is pressed into small pieces by a tablet press to obtain a block sample. Then, the bulk sample was sintered in a microwave oven and quenched to room temperature to obtain the product with uniform-size $BiFeO_3$ prepared by this method having high purity, uniform particle size, and adjustable particle size. $BiFeO_3$ adopts a sol-gel method to prepare nanopowder, and the preparation process is shown in Figure 5.

After the dry gel is ground and sieved, it is placed in a muffle furnace and calcined at 400°C for 2 hours to completely drain the organic matter and nitrate in the dry gel and at the same time obtain pure $BiFeO_3$ nanopowder. The XRD of the nanopowder is shown in Figure 6.

The preparation process of nanoceramics mainly includes the preparation, molding, and sintering of nanopowder. The methods are as follows: (1) settlement method, (2) in situ solidification method, and (3) sintering or hot pressing method.

It can be seen from Figure 6 that there is no obvious second phase in the nanopowder. According to the Scherer formula,

$$Q = \frac{wy}{E \cos \vartheta}, \tag{20}$$

where Q is the grain size, w is the Scherrer constant with a value of 0.89, E is the half-height width of the diffraction peak of the measured sample, θ is the diffraction angle, y is the X-ray wavelength, and its value is 0.154056 nm for the known nanopowder. The grain size is 15.95 nm.

3. Experimental Design and Result Analysis

3.1. Preparation of Nanoceramics in the Application of Handicrafts. The preparation methods of nanomaterials can be divided into physical method, chemical method,

(a) Sintering temperature

(b) Sintering temperature
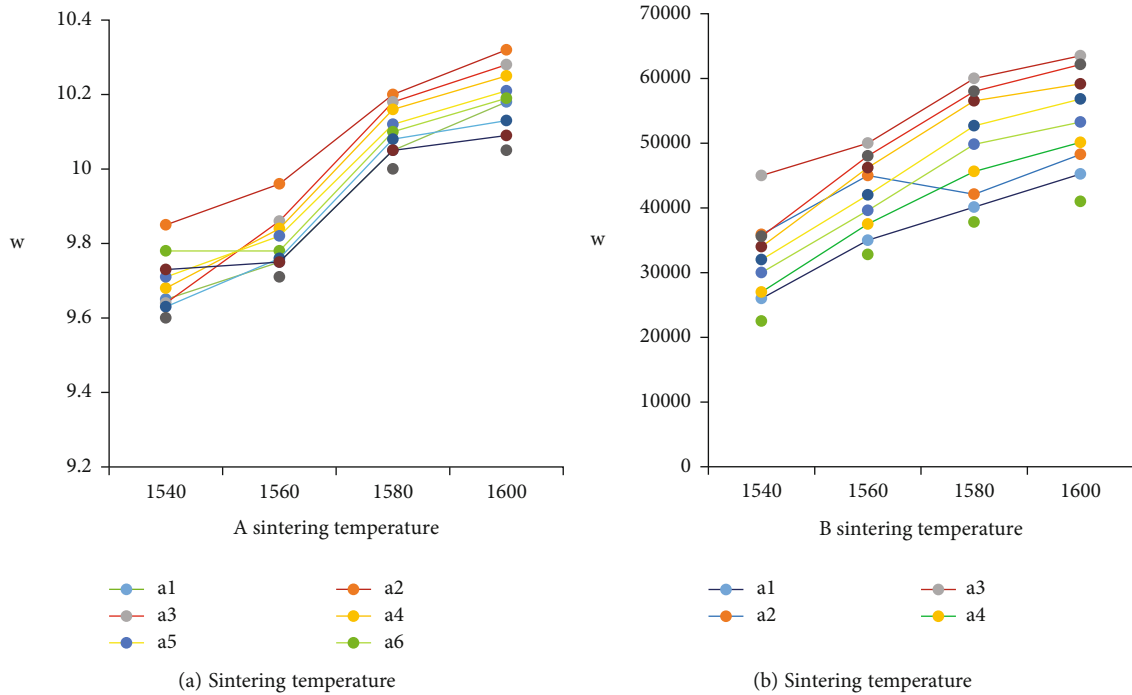
FIGURE 8: Al_2O_3 ceramic dielectric performance test results.

(a) Sintering temperature

(b) Sintering temperature
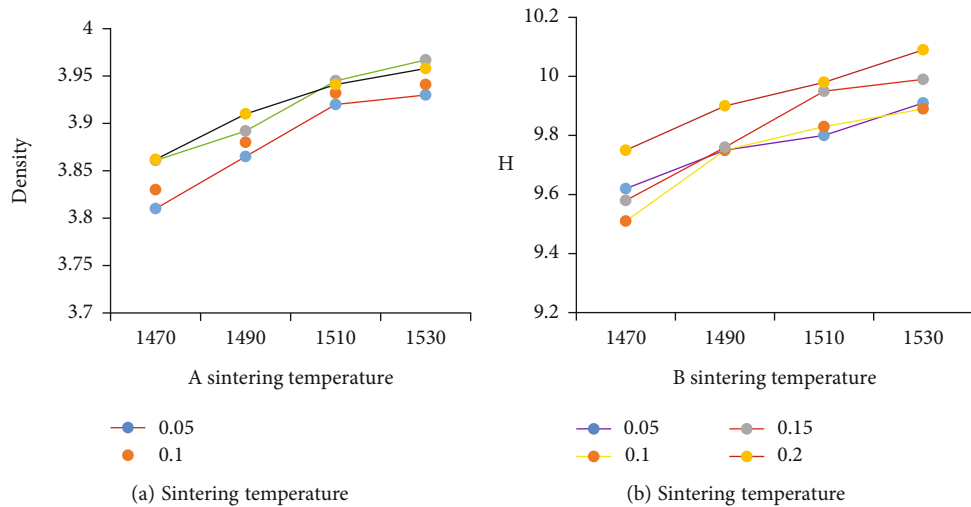
FIGURE 9: The density and dielectric constant of Al_2O_3 ceramics change with the sintering temperature.

and other methods. Physical methods include crushing method, deposition method, sputtering method, etc. Chemical methods include sol-gel method, precipitation method, evaporation solvent pyrolysis method, oxidation-reduction method, solvothermal method, etc.

LAO$_3$ and Y_2O_3 have better performance on the absorption and emission peaks of transparent ceramics, while $BiFeO_3$ is not suitable for application in this field. The main raw materials used in this experiment are high-purity Al_2O_3, La_2O_3, and Y_2O_3 with different particle sizes from different manufacturers. The name, molecular formula, manufacturer, and purity are shown in Table 4.

After calculating and weighing the raw materials, use the solid-phase sintering method to prepare Al_2O_3 ceramics, test the sintered samples, and perform performance analysis. Table 5 shows the main equipment and test equipment used in the entire preparation and testing process.

This article uses the most commonly used solid-phase sintering method in industrial production to prepare 99 alumina ceramics. The ceramic preparation process is shown in Figure 7.

The advantages of the solid-phase reaction sintering method for preparing ceramic samples are as follows: the experimental conditions are easy to control, the preparation process is relatively simple, the cost is relatively low, and the
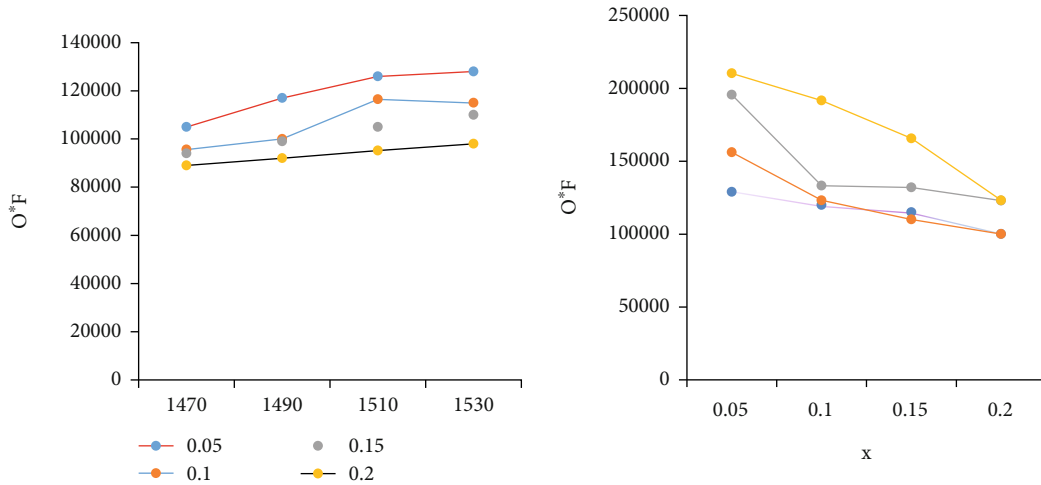
FIGURE 10: Variation curve of the ceramic $O * F$ constant value with sintering temperature.
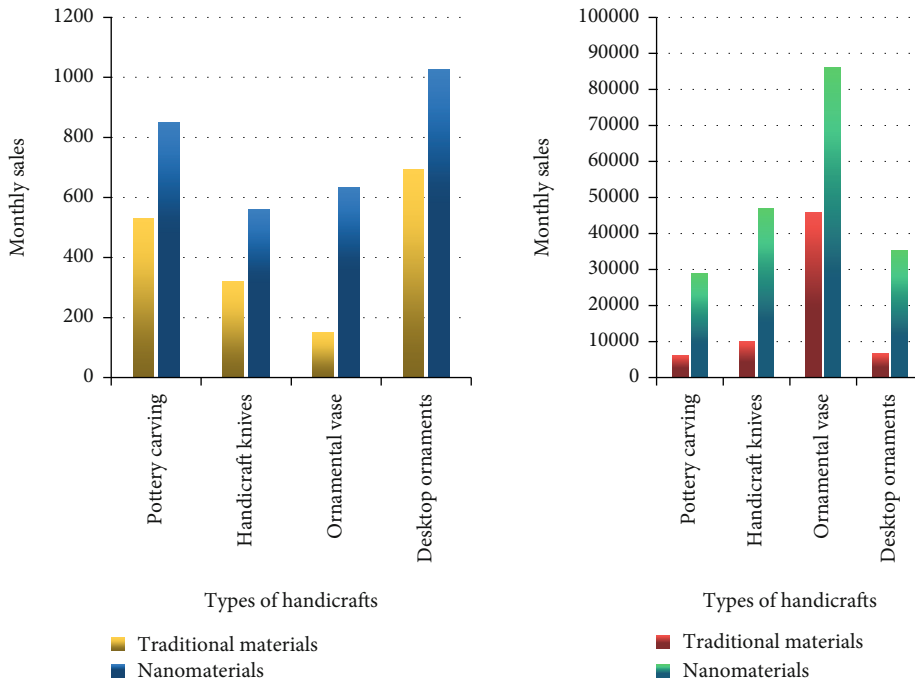
FIGURE 11: Sales volume and sales comparison chart of handicrafts with different materials.

chemical composition of the raw materials of this method is uniform, easy to popularize, and suitable for large-scale industrial production; the disadvantage is that the calcination temperature is high and energy consumption is high. It is easy to introduce impurities during the grinding process, and the process parameters are more complicated.

3.2. Preparation Results of Nanoceramics in the Application of Handicrafts. In this section, the solid-phase reaction sintering method commonly used in industrial production is used to prepare pure Al_2O_3 ceramics. The raw materials involved are nine kinds of high-purity Al_2O_3 powders with different particle sizes from different manufacturers, num-

bered a1~a9. Using a vector network analyzer, the microwave dielectric properties of the sintered ceramic samples were tested. The test result is shown in Figure 8.

It can be seen from Figure 8 that as the sintering temperature increases, the relative permittivity and $Q \times f$ value of Al_2O_3 ceramics numbered a1 to a9 increase. This shows that as the sintering temperature increases, the pores in the ceramic are gradually discharged, the grain size becomes larger, the ceramic compactness becomes better, and the relative permittivity and $Q \times f$ value are closely related to the density and grain size of the ceramic material. It can be seen from Figure 8(b) that the $Q \times f$ value of a3 Al_2O_3 ceramics is much higher than that of the other 8 Al_2O_3

ceramics. Compared with other Al_2O_3 ceramics, it exhibits extremely excellent microwave dielectric properties.

The density test was performed on the ceramic samples after sintering. Figure 9 shows a graph of the density and dielectric constant of Al_2O_3 ceramics as the sintering temperature changes.

As shown in Figure 9, it can be seen that the ceramic becomes dense with the increase in the sintering temperature, and its density increases with the increase in temperature. At the same time, with the increase in MgO doping amount, the density of ceramic samples increased first and then decreased. At 1530°C, when doped with 0.15% MgO, the density of Al_2O_3 ceramics reached the maximum 3.961 g/cm^3.

Then, use the vector network analyzer to test the microwave performance of the sintered ceramic samples. As shown in Figure 10, the ceramic $O * F$ constant value changes with the sintering temperature:

It can be seen from Figure 10 that as the sintering temperature increases, the ceramic density gradually increases, the relative dielectric constant also increases, and the $Q \times f$ value of MgO-doped Al_2O_3 ceramics increases. Since the relative permittivity of MgO is 9.7, the relative permittivity of pure Al_2O_3 ceramics is relatively close, and the amount of MgO doped is small, it has little effect on the relative permittivity of MgO-doped Al_2O_3 ceramics.

3.3. The Application of Nanoparticle Ceramic Materials in the Design of Modern Handicrafts.

3.3. The Application of Nanoparticle Ceramic Materials in the Design of Modern Handicrafts. Through the investigation and analysis of the sales volume of some modern handicrafts made with nanoceramic materials and the sales volume of traditional handicrafts, Figure 11 is obtained.

From the data in Figure 11, it can be concluded that not only has the sales volume of handicrafts using nanoceramic materials increased greatly but also the average sales volume is more than 35% higher than that of handicrafts made of ordinary materials, and the selling price is due to the use of new materials. The new production process has also increased the price of a single product. According to a comprehensive analysis, the average selling price of crafts using nanoceramic materials is at least 40% higher than that of traditional crafts.

4. Discussion

This article is devoted to the research of nanoceramic materials and applies them to modern handicrafts. This article discusses the production process, manufacturing technique, and manufacturing materials of nanoceramic materials. While discussing, we will also apply it to our modern handicrafts in the experimental stage and then conduct research and analysis on the sales volume and sales of modern handicrafts, so as to better explore the use of nanoparticle ceramics in modern handicrafts. In addition, this article mainly conducts sufficient research on the different forging methods of nanoceramics and conducts experiments on nanoceramics in terms of dielectric loss and temperature resistance. The experimental results in this article also show that nanoceramic materials have a wear resistance, high temperature resistance, corrosion resistance, hardness, insula-

tion performance, dielectric loss rate, and other aspects superior to ordinary ceramic materials.

The analysis of the experimental cases in this article shows that the performance of nanoceramic materials is much better than that of other materials, and its use in modern handicrafts has also been favored by most consumers. Modern handicraft design and production manufacturers can make full use of the existing nanoceramic technology and integrate it into the design of handicrafts. Of course, enterprises can also choose good production materials and production techniques according to their own conditions to help them develop better.

In this paper, the production of nanoceramics is firstly studied, and the raw materials that are more suitable for the production of nanoceramics are obtained through experiments, and then, the nanoceramic materials after the improvement of production are studied, and the nanoceramic materials that are more suitable for use in daily life are selected. Finally, through the research on the sales and price of handicrafts using nanoceramic materials in daily life, the survey results show that not only can modern handicrafts using nanoceramic materials occupy a 30% advantage in sales but also it is better than traditional crafts.

5. Conclusions

Through the analysis of this case, the following conclusions can be drawn: modern handicrafts designed and manufactured using nanoceramic materials can not only increase the sales and selling prices of modern handicrafts by more than 30% but also increase the use value and ornamental value of the products. There has also been a qualitative leap in collection value. As one of the three main materials, ceramic materials are world-renowned as unique craft buildings. Modern handicraft design is an important carrier reflecting its culture. Excellent handicraft design should not only reflect the uniqueness and superiority of product information but also use cultural connotation to highlight the taste, grade, and value of the design. While modern handicraft design reflects contemporary culture, it is also the demand for modern design innovation in terms of the expression strategy of design creativity, the shaping of the brand image, and the ecological design concept of materials. For example, in this case, the merchants who use nanoceramic materials to design and produce modern handicrafts, because of the use of nanoceramic technology, make their product sales, and sales prices have a great leap. It can be seen that the average selling price of handicrafts using nanoceramic materials is at least 40% higher than that of traditional handicrafts.

Data Availability

Data sharing is not applicable to this article as no new data were created or analyzed in this study.

Conflicts of Interest

The authors state that this article has no conflict of interest.

Acknowledgments

References

[1] E. P. Simonenko, A. V. Derbenev, N. P. Simonenko et al., "Production of porous ceramic materials using nanodisperse SiC powder," *Russian Journal of Inorganic Chemistry*, vol. 62, no. 7, pp. 863–869, 2017.

[2] C. Scribot, W. Maherzi, M. Benzerzour, Y. Mamindy-Pajany, and N. E. Abriak, "A laboratory-scale experimental investigation on the reuse of a modified red mud in ceramic materials production," *Construction and Building Materials*, vol. 163, no. FEB.28, pp. 21–31, 2018.

[3] A. K. Kairakbaev, V. Z. Abdrakhimov, and E. S. Abdrakhimova, "Study by Mössbauer-spectroscopy of iron oxides in acid-resistant ceramic materials based on production waste," *Refractories and Industrial Ceramics*, vol. 61, no. 2, pp. 183–187, 2020.

[4] T. F. Baranova and S. A. Valiakhmetov, "Ceramic material for making heat-resistant products," *Refractories and Industrial Ceramics*, vol. 57, no. 1, pp. 46–49, 2016.

[5] Z. Yin, J. Yuan, C. Huang, Z. Wang, L. Huang, and Y. Cheng, "Friction and wear behaviors of Al_2O_3/TiC micro-nano-composite ceramic sliding against metals and hard materials," *Ceramics International*, vol. 42, no. 1, pp. 1982–1989, 2016.

[6] X. Liu, M. Li, Y. Zhu, K. W. K. Yeung, P. K. Chu, and S. Wu, "The modulation of stem cell behaviors by functionalized nanoceramic coatings on Ti-based implants," *Bioactive Materials*, vol. 1, no. 1, pp. 65–76, 2016.

[7] J. Živković, V. Bikić, M. Georgakopoulou, and J. C. Carvajal López, "Archaeology of craft and artisans in the Ottoman Empire: a case of ceramic production in Belgrade during the sixteenth and seventeenth centuries," *Archaeological and Anthropological Sciences*, vol. 13, no. 4, pp. 1–21, 2021.

[8] F. A. Al-Harbi, N. M. Ayad, A. S. ArRejaie, H. A. Bahgat, and N. Z. Baba, "Effect of aging regimens on resin nanoceramic chairside CAD/CAM material," *Journal of Prosthodontics*, vol. 26, no. 5, pp. 432–439, 2017.

[9] A. Bhutani, B. Goettel, A. Lipp, and T. Zwick, "Packaging solution based on low-temperature cofired ceramic technology for frequencies beyond 100 GHz," *Components, Packaging and Manufacturing Technology, IEEE Transactions on*, vol. 9, no. 5, pp. 945–954, 2019.

[10] Y. Tang, M. Yu, Z. Zhang et al., "A novel tungstate $Li_3Nd_3W_2O_{12}$ with garnet structure for low-temperature cofired ceramic technology," *Journal of the European Ceramic Society*, vol. 40, no. 4, pp. 1386–1389, 2020.

[11] E. Gliozzo, "Ceramic technology. How to reconstruct the firing process," *Archaeological and Anthropological Sciences*, vol. 12, no. 11, pp. 1–35, 2020.

[12] E. Aloupi-Siotis, "Ceramic technology: how to characterise black Fe-based glass-ceramic coatings," *Archaeological and Anthropological Sciences*, vol. 12, no. 8, pp. 1–15, 2020.

[13] H. Chen, W. Che, X. Wang, and W. Feng, "Size-reduced planar and nonplanar SIW Gysel power divider based on low temper-

ature co-fired ceramic technology," *Microwave and Wireless Components Letters, IEEE*, vol. 27, no. 12, pp. 1065–1067, 2017.

[14] H. Ren, Y. H. Lee, E. A. Wu et al., "Nano-ceramic cathodes via co-sputtering of Gd–Ce alloy and lanthanum strontium cobaltite for low-temperature thin-film solid oxide fuel cells," *ACS Applied Energy Materials*, vol. 3, no. 9, pp. 8135–8142, 2020.

[15] K. A. Mishra, "Sol-gel-based nanoceramic materials: preparation, properties and applications," Springer International Publishing, 2017.

[16] V. Kumar, S. Pandey, A. Kumar et al., "Investigation of dielectric, magnetic and impedance spectroscopic properties of $CaCu_{3-X}Mn_XTi_{4-X}Mn_XO_{12}$ (X = 0.10) nano-ceramic synthesized through semi-wet route," *Journal of Materials Research and Technology*, vol. 9, no. 6, pp. 12936–12945, 2020.

[17] W. Hu, J. Xu, X. Lu et al., "Corrosion and wear behaviours of a reactive-sputter-deposited Ta_2O_5 nanoceramic coating," *Applied Surface Science*, vol. 368, pp. 177–190, 2016.

[18] J. Zou, H. B. Ma, J. J. Liu, W. M. Wang, G. J. Zhang, and Z. Y. Fu, "Nanoceramic composites with duplex microstructure break the strength-toughness tradeoff," *Journal of Materials Science and Technology*, vol. 58, no. 23, pp. 1–9, 2020.

[19] K. Heck, H. Paterno, A. Lederer, F. Litzenburger, R. Hickel, and K. H. Kunzelmann, "Fatigue resistance of ultrathin CAD/CAM ceramic and nanoceramic composite occlusal veneers," *Dental Materials*, vol. 35, no. 10, pp. 1370–1377, 2019.

[20] N. A. Makarov, D. Y. Zhukov, M. A. Vartanyan, D. O. Lemeshev, and E. E. Nazarov, "Thermodynamic analysis as a method of picking modifiers in silicon carbide ceramic technology," *Glass and Ceramics*, vol. 73, no. 11-12, pp. 450–453, 2017.

[21] F. Domenico, "Ceramic technology: the air bubble defect in sanitaryware production," *Ceramic World Review*, vol. 26, no. -TN.118, p. 182, 2016.

[22] D. Atley and P. Suzanne, "Radiocarbon dating of ceramic materials: progress and prospects," *Radiocarbon*, vol. 22, no. 3, pp. 987–993, 1980.

[23] B. Zhong, Z. Chai, L. Xia, G. Wen, S. Cheng, and Y. Huang, "A novel polymeric precursor for boron nitride ceramics: synthesis, characterization, and ceramic conversion," *International Journal of Applied Ceramic Technology*, vol. 13, no. 5, pp. 929–936, 2016.

[24] R. S. De Lange, J. H. Hekkink, K. Keizer, and A. J. Burggraaf, "Formation and characterization of supported microporous ceramic membranes prepared by sol-gel modification techniques," *Journal of Membrane Science*, vol. 99, no. 1, pp. 57–75, 1995.

[25] N. K. Vail, B. Balasubramanian, J. W. Barlow, and H. L. Marcus, "A thermal model of polymer degradation during selective laser sintering of polymer coated ceramic powders," *Rapid Prototyping Journal*, vol. 2, no. 3, pp. 24–40, 1996.

[26] G. Bo, L. Chang, H. Chenglong et al., "Effect of Mg and RE on the surface properties of hot dipped Zn–23Al–0.3Si coatings," *Science of Advanced Materials*, vol. 11, no. 4, pp. 580–587, 2019.

[27] L. Zeng, J. Shi, J. Luo, and H. Chen, "Silver sulfide anchored on reduced graphene oxide as a high-performance catalyst for CO_2 electroreduction," *Journal of Power Sources*, vol. 398, pp. 83–90, 2018.

[28] L. Zeng, X. P. Guo, G. A. Zhang, and H. X. Chen, "Semiconductivities of passive films formed on stainless steel bend under erosion-corrosion conditions," *Corrosion Science*, vol. 144, no. 1, pp. 258–265, 2018.

Research Article

Nanoselenium on Aerobic Endurance Exercise Adaptation

Guiping He[1] and Long Liu ⓘ [2]

[1]*Anyang Vocational and Technical College, Anyang, 455000 Henan, China*
[2]*Collage of Physical Education, Beibu Gulf University, Qinzhou 535011, Guangxi, China*

Correspondence should be addressed to Long Liu; liulong@aynu.edu.cn

If the load exercise exceeds a certain degree, it will lead to sports injury. The main reason for this phenomenon is that the human body produces a lot of free radicals after sports training. Free radicals can attack human cells and cause lipid peroxidation to damage cell membrane. The human body can improve the antioxidant capacity of the body by supplementing some trace elements. Selenium, iodine, zinc, iron, and calcium are all trace elements that contribute to antioxidants in the body. Nanoselenium is of great interest among many immune modulators because of its high antioxidant properties and remarkable immune protective function. In this paper, grey rabbits were used as the research object to carry out aerobic endurance training. Nanoselenium and placebo were supplemented in each group. The evaluation model of nanoselenium on aerobic endurance exercise was established by system control method, exhaustion compensation method, and analytic hierarchy process. The adaptive changes of nanoselenium on aerobic endurance exercise of grey rabbits were studied in detail, and the effects of exercise and antioxidant on the body were observed. Compared with the previous research methods, the difference is that the decentralized control theory is introduced as the guiding ideology of the research. According to the experimental results, the accuracy of the overall experimental results is improved by about 20%, and the accuracy is higher, which has certain practical value.

1. Introduction

Selenium is one of the essential trace elements for human body, which is crucial for human survival and development. As an emerging bionanotechnology, research on the preparation of selenium nanoparticles is gaining more and more attention and has a broad application prospect. After exercise training, the human body will produce a lot of free radicals, such as oxygen free radicals and hydroxyl radicals, which have high oxidation activity. They are very unstable and highly active. They attack cell membrane and mitochondrial membrane and react with unsaturated fatty acids in membrane, resulting in enhanced lipid peroxidation and changes in membrane fluidity and permeability. This destroys the integrity of cell membrane structure. Lipid peroxidation injury of cell membrane is an important mechanism of exercise-induced fatigue and injury. In order to eliminate sports fatigue and quickly reduce sports injury and improve the body's sports ability, we must try to reduce

the production of excessive free radicals in the body or increase the body's ability to remove free radicals.

The production of reactive oxygen species (ROS) can cause serious oxidative damage to proteins, lipids, and genomic structures. Shirvani et al.'s study showed that the production of reactive oxygen species increased during high-intensity exercise training. The purpose of Shirvani et al.'s study was to investigate the effects of high-intensity intermittent training on the levels of 8-oxoguanidine DNA glycosidase (OGG1) and 8-hydroxy-2'-deoxyguanosine (8-OHdG) in brain and liver tissues [1]. In Shubhangi et al.'s study, Shubhangi et al. reported (a) the biosynthesis of selenium nanoparticles (SE NPs) and (b) the protective effect of selenium nanoparticles on broilers [2]. An effective bacterial strain isolated from farmland soil has been identified as pantoea aggregate (GenBank: KU500622). It can tolerate high concentration of selenium dioxide (9 mm) and produce selenium nanoparticles under aerobic conditions. The results show that the selenium nanoparticles are amorphous and

spherical, and the particle size is less than 100 nm. Shubhangi et al. studied that selenium NP supplementation could significantly restore these values in the control group, even higher than that in the control group. Efruxifermin (EFX) is an Fc-FGF21 fusion protein. The adverse effects of EFX were prevented by simultaneous exposure to selenium nanoparticles (0.6 mg per kg feed) in poultry feed. Maynar et al. studied the changes of serum copper, chromium, manganese, nickel, and selenium contents of high-level athletes [3]. Before the training, 80 professional athletes with different metabolic patterns were recruited. The control group consisted of 31 sedentary participants from the same geographical area. Copper, chromium, manganese, nickel, and selenium were analyzed by inductively coupled plasma mass spectrometry (ICP-MS). Selenium ecotoxicology is one of the most famous examples of the effects of biotransformation and food chain transfer of toxic elements on the environment. However, it has been gradually recognized that biotransformation of selenium by microorganisms and plants may also be the key to in situ bioremediation of selenium pollution in large-scale situations (such as agricultural drainage systems). A kind of euryhaline algae (Chlorella vulgaris) was isolated from the wastewater containing selenium. The aerobic biotransformation activity of Chlorella vulgaris to seleno anion was studied by GCMS and multinuclear magnetic resonance (NMR). Fan et al. found that the algae were active in the volatilization of alkyl selenides, the production of hypothetical selenide precursors of alkyl selenides, and the precipitation of selenium, while exhibiting a very low accumulation of toxic selenomethionine in free form. Therefore, this kind of microalgae is of great significance for in situ bioremediation and biogeochemical cycle of selenium in contaminated saline alkali soil [4].

So far, different bacteria have linked selenite resistance with the production of metal selenium nanoparticles (senps). Although senps have many biotechnological applications in different fields, the molecular mechanism of their microbial genesis has not been fully understood. Alpaca is a physiologically multifunctional β-protein associated bacterial group [5]. Here, Tan et al. reveal another physiological characteristic of CIB strain, which is related to its resistance to seleno anion and the formation of senps. Selenium oxygen anion reduction is an effective detoxification or assimilation process in organisms, but its mechanism is poorly understood [6]. Se (VI)/SE (IV) was reduced to selenium nanoparticles (senps) with less toxicity. For se (VI) reduction, sulfate reduction and Se (VI) reduction showed a competitive relationship. When the required sulfate-reducing genes were destroyed, Se (VI) did not reduce to red senps. Therefore, the reduction of Se (VI) is catalyzed by enzymes in the sulfate reduction pathway. In the aspect of Se (IV) reduction, SERT, a potential molybdenum oxidoreductase, was screened and further applied to the analysis of Se (IV) reduction. Selenite is the main form of selenium in aerobic soil, but different from selenite, the mechanism of plant absorbing selenite is not clear. Ming et al. studied the effects of different concentrations of selenite and selenite on the absorption, transport, and selenium forms of wheat through hydroponic experiment. Nanoselenium (100-500 nm) has

high bioavailability and relatively low toxicity [7]. Gulyás et al. studied the effects of selenium-free control diet and nanoselenium diet supplemented with 4.25 mg/kg DM on liver proteome of broilers. Two-dimensional gel electrophoresis (2D-PAGE) and trypsin digestion (LC-MS) were used for differential proteomic analysis. A total of 788 protein spots were detected in the two groups, and the intensity of 18 protein spots was significantly different ($P < 0.05$). Compared with the control group, the expression of 8 kinds of proteins was increased, and the expression of 5 kinds of proteins was decreased. The function of the differentially expressed proteins indicated that dietary stress was caused by high-dose selenium supplementation. Selenium supplementation can affect the metabolism and antioxidant system of fatty acids and carbohydrates and increase the content of actin in cytoskeleton and the expression of actin regulatory protein [8]. Nanoselenium avoids the side effects of selenium, but little research has been done on the adaptation of aerobic endurance exercise.

In this paper, the effects of different selenium sources and selenium supplement time on growth performance, plasma antioxidant capacity, and tissue selenium deposition of gray rabbits were studied.

2. Research Methods

2.1. Decentralized System Control Method. In this paper, in the evaluation model of the effect of nanoselenium on aerobic endurance exercise, the transfer function of the controlled object is $g(s) = y(s) - U(s) = n(s) - D(s)$, and the control system is $K(s) = P(s) - Q(s)$. Where $n(s)$ and $D(s)$ are the zero polynomials and pole polynomials of $G(s)$, and the degree of $D(s)$ is not less than the degree of $n(s)$, where $p(s)$ and $Q(s)$ are the zero and pole polynomials of $K(s)$, and the degree of $Q(s)$ is not less than that of $P(s)$. The expression is as follows:

$$y_{re\int}^{-1} = \frac{1}{A_{re\int}(s)} y_{re\int}(0), \omega(s) = \frac{1}{A_\omega(s)} \omega(0). \tag{1}$$

Let the zeros of $A(s)$ and $A(J)$ lie in the right semiclosed plane of the complex plane. The least common multiple of these two polynomials is $A(s)$, as shown in Figure 1.

The connections in Figure 1 are as follows:

$$
\begin{aligned}
e &= \frac{D(s)Q(s)}{N(s)P(s) + D(s)Q(s)} y_{re\int} - \frac{Q(s)}{N(s)P(s) + D(s)Q(s)} \omega \\
&= \frac{D(s)Q(s)}{N(s)P(s) + D(s)Q(s)} \cdot \frac{1}{A_{re\int}(s)} y_{re\int}(0) \\
&\quad - \frac{Q(s)}{N(s)P(s) = D(s)Q(s)} \cdot \frac{1}{A_\omega(s)} \omega(0).
\end{aligned}
\tag{2}
$$

In the evaluation model of the effect of nanoselenium on aerobic endurance exercise, the objective is to make the system composed of data of each group form a closed loop, and the internal stability makes the steady value of output value y
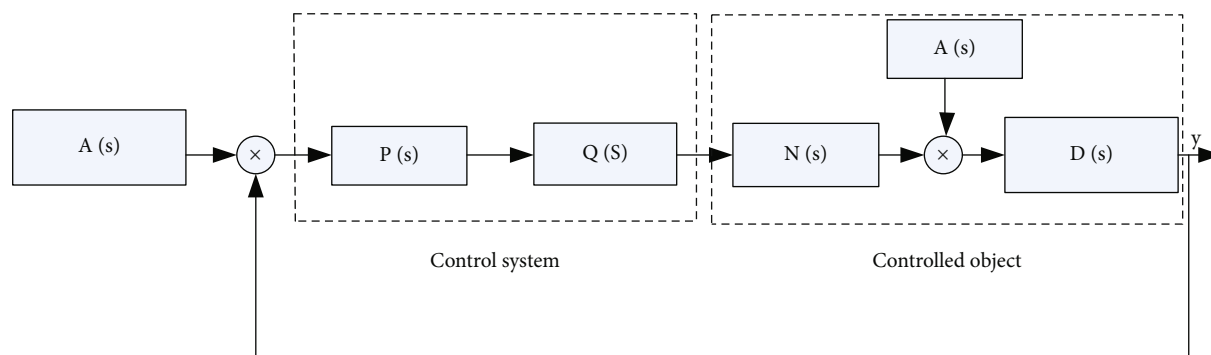
F<small>IGURE</small> 1: Relationship diagram of experimental coefficients.

independent of the interference factor ω, and track the reference output value y, which is expressed as follows:

$$\lim e(t) = \lim s \cdot e = 0, \forall \overline{y_{re}}\int(0), \bar{\omega}(0). \tag{3}$$

The condition for the establishment of formula (3) is that $Q(s)$ is divided by both sums. This means that the control system contains a model of external instability. This calculation method can make the experimental data more accurate [9, 10].

2.2. Preparation Method of Nanoselenium.

Nanoselenium has higher biological activity than selenium and is the safest of known selenium products.

Selenium is an essential trace element with a small gap between effective and toxic doses. Red monomeric selenium has the same antioxidant, immunomodulatory, and antiaging functions of selenium, but its toxicity is lower than that of general inorganic and organic selenium. In order to ensure the stability and reliability of the prepared cross immunochromatographic strip, the qualified nanomarker must be stable, economical, and sensitive.

The preparation of nanoselenium requires the purity and grade of water and reagents. In the process of experiment, it was found that the size of nanoselenium particles prepared by ordinary deionized water was not uniform, and the suspension stability was poor. Only by using ultrapure water of $18.2 \, m\Omega$ can the selenium nanoparticles with uniform size and dispersion be prepared. In addition, the beaker and centrifuge tube used in the experiment must be clean and free of strong ions. Otherwise, the prepared nanoselenium solution will become turbid and cannot be used in subsequent experiments. In addition, all reagents must be analytically pure, and the purity must be greater than 99.7%. The results show that the nanoselenium prepared by low-grade chemical reagent has irregular morphology and uneven size, the color development effect of the test paper is poor, and the sensitivity is low [11].

Nanoselenium has many stabilizers. In this study, BSA, glucose, gelatin, gum Arabic powder, SDS, PEG, and PVP were used as stabilizers to prepare nanoselenium. Only glucose, Arabian gum powder, SDS, and SDS + peg can be used as markers for cross immunochromatography. However, the performance of the test strips prepared from glucose and SDS was not stable, and the difference between batches was large. The preparation of LFICS with Arabic gum powder as stabilizer requires high protein labeling concentration and high preparation cost of test paper. When SDS and peg are used as templates, they are considered to be the chemical reagents commonly used in the preparation of LFICS. SDS is an anionic surfactant, which can reduce the background interference of LFICS and reduce the false-positive results. Nail is a kind of polymer compound, which can increase the stability of sol [12, 13].

2.3. Exhaustion Compensation Method.

In order to evaluate the relative biological efficiency of nutrients, depletion compensation method is usually used. The model of nutrient deficiency was established. Usually, animals are fed on a nutrient-deficient diet for a period of time and then supplemented with different forms of nutrition. According to the influence of nutrients on the relevant indicators of animals, determine whether the nutrients are deficient and the effects of supplements on experimental animals [2, 14].

At present, there are several methods to study the biological potency of selenium: (1) isotope tracer method is used to evaluate the absorption, retention, and excretion of selenium, but the test cycle is relatively short, but the cost is high. (2) Slope ratio method is a commonly used method to evaluate the relative biological potency of nutrients, that is, to select a nutrient form, define its biological potency as 100% and establish a regression curve with nutrients as reference. According to the reference index, the slope of nutrient of $20000 \, m^3$ was calculated, and the relative bioavailability of nutrient to be tested was obtained. At present, the slope ratio method is the main method to evaluate the relative biological potency of selenium, that is, taking sodium selenite as the standard reference material, the biological potency of sodium selenite is defined as 100%. The loss compensation method is used to feed animals with selenium deficiency diet to achieve the effect of selenium deficiency and then add different selenium sources at different levels or at the same time and at different times Source. By comparing the relative indexes of selenium, such as the deposition of selenium in tissues and the activity of GPX in tissues and plasma, the regression equations of these indexes with selenium level or selenium supplement time

were established, and then the slope of sodium selenite and selenium source was compared to determine the relative value [15, 16]. In this study, we established a model of selenium deficiency in grey rabbits and then added three selenium sources: sodium selenite, yeast selenium, and biological nanoelement selenium. The effects of three selenium sources on growth performance, antioxidant capacity, and tissue selenium deposition of grey rabbits were analyzed to evaluate the relative biological efficacy of biological nanoelement selenium.

2.4. Analytic Hierarchy Process. Analytic hierarchy process (AHP) is a multicriteria decision-making method. This method can combine qualitative analysis with quantitative analysis. Its basic idea is to decompose complex decision-making problems in order to obtain an ordered hierarchical structure. Then, the relative importance of each index is compared in the hierarchical model, and several judgment matrices are constructed. Then, the relative importance weight of each level element is calculated; finally, according to the total ranking of each level, the relative weight of all indicators in the whole hierarchical model is calculated, and the research problems are comprehensively evaluated. In China, AHP has been successfully used to solve many problems. To study the data asset evaluation model, AHP method can be used to determine the index weight and calculate the complete evaluation model. The local variables of a function are independent and do not affect each other, and recursion must be approximated to the condition of exit from recursion, otherwise, it is infinite recursion. On the basis of strict mathematical theory, AHP can not only carry out qualitative analysis but also ensure the effectiveness of quantitative analysis, so the evaluation results are more convincing [17]. Hierarchical analysis is not only suitable for situations where there is uncertainty and subjective information but also allows the use of experience, insight, and intuition in a logical manner.

According to the related theory of AHP, the basic idea of AHP depends on the nature of the problem and the overall objective to be achieved, to decompose complex decision-making problems and get several lower-level indicators. Then, the hierarchical structure model is established, and then, the judgment matrix is constructed according to the structure model. Finally, the weight coefficient of each index is calculated to sort the total hierarchy.

(1) *Establish Hierarchical Model.* In the process of analyzing the hierarchical structure, the most important step is to establish the hierarchical structure model of indicators and construct the judgment matrix according to the structure model. Only after the judgment matrix has passed the consistency test can it be analyzed and calculated. The structural model can be divided into three levels. The highest level is the target level, which is the purpose and problem of decision-making. The middle layer is the factor to be considered in decision-making, which is the standard of decision-making, and the lowest level is the alternative scheme of decision-making. In this paper, the hierarchical model refers

to the hierarchical model constructed by the factors that affect the value of data assets. In the construction process, we need to consider the value factors. Experts, references, and other methods can be consulted to consider [18]. Hierarchical model is the basis of data asset evaluation model

(2) *Establish Judgment Matrix.* After the construction of the hierarchy model, the judgment matrix is established according to the indicators in the hierarchy model. The judgment matrix represents the relative importance of all factors in this layer to a certain factor in the upper layer [19]. Judgment matrix has an important impact on the follow-up results and is also the embodiment of the quantitative nature of AHP. The construction of judgment matrix can refer to the opinions of experts, and the elements of judgment matrix can be assigned by relevant professionals. When assigning values to the elements of the judgment matrix, the nine level scaling method can be used (i.e., the relative importance between indicators is represented by the number 1 to 9 and its reciprocal), which is also the most commonly used method in AHP. The specific scaling method is shown in the table

Hierarchical analysis treats the research object as a system and makes decisions according to the way of thinking of decomposition, comparative judgment, and synthesis, which has become an important tool of system analysis developed after mechanistic analysis and statistical analysis. Based on the number of specific experimental data, the accuracy of the data was qualitatively analyzed to verify the validity of the analysis model. The specific analysis model is shown in Figure 2.

3. Experimental Design

There were 80 adult male grey rabbits, all of them were in normal condition. According to the different sampling time, they were divided into a nonexercise selenium supplement group, B exercise supplement selenium group, C exercise group, and D no exercise no selenium supplement group. According to the time, the test cycle of each exercise group was controlled. Each exercise group was divided into control group and Nan Kuang se group, as shown in Table 1.

After adaptive training, the training lasted for 30 minutes, and the running speed was 25 meters per minute. Exercise six days a week. The temperature is controlled at 20-25 °C. The humidity is 60-80%.

In addition to normal feeding, the rats in the supplement group were given intragastric administration of 200 UG/kg body weight from 6:00 to 8:00 every night. The control group was given placebo at the same time and dose.

According to different sampling requirements, the specific sampling procedures are as follows: after the grey rabbits were killed, the stomach of quadriceps femoris was taken, the liver was washed with normal saline ~ dried and weighed with filter paper, homogenized with 0.2 mol/
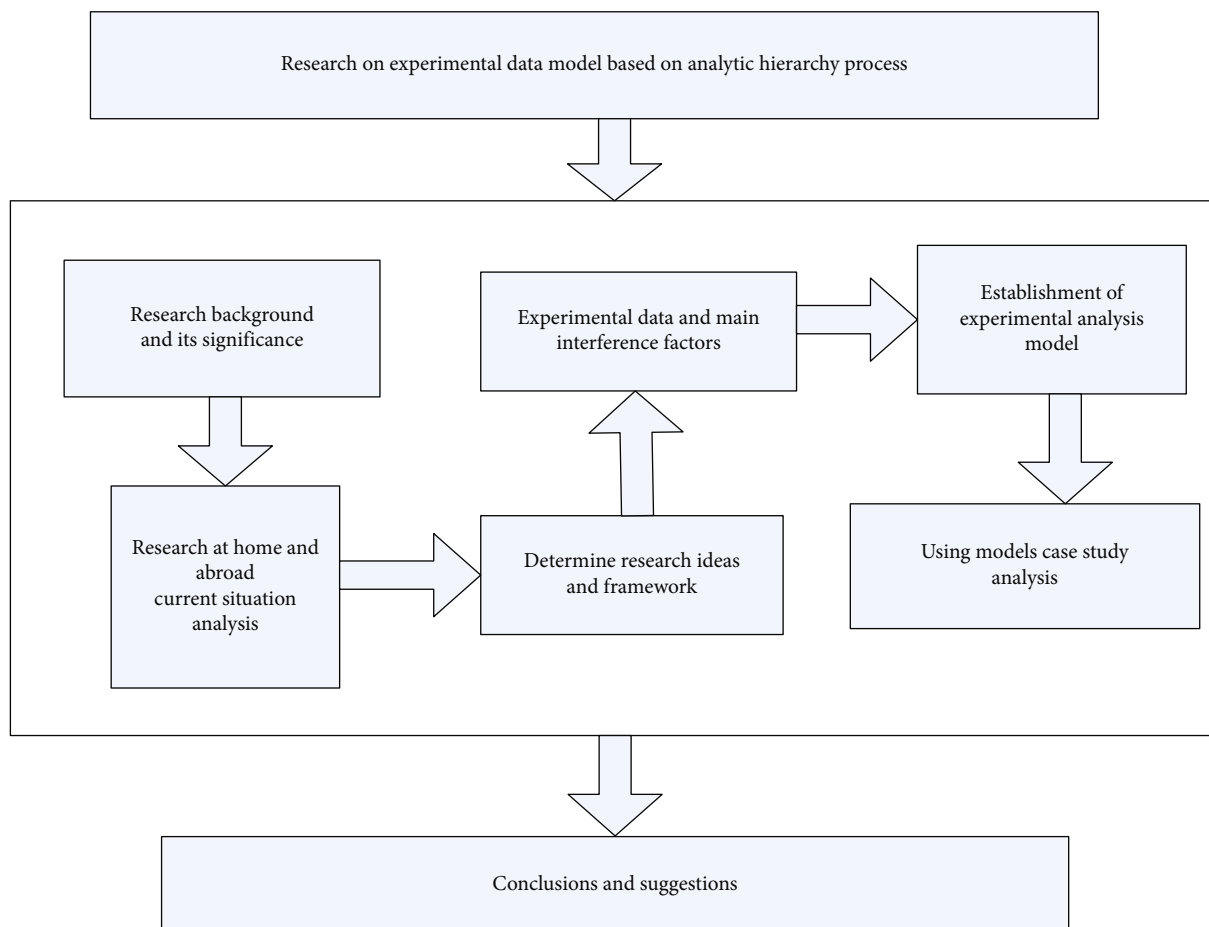
Figure 2: Analysis model establishment diagram.

Table 1: Experimental control group.

Grouping	Group 1	Group 2	Group 3	Group 4
No movement (A)	5	5	5	5
It is moving (B)	5	5	5	5
Selenium supplement before exercise (C)	5	5	5	5
Supplement selenium after exercise (D)	5	5	5	5

1 sucrose (pH = 7.5), and centrifuged with (0.005 mol/1 trishcl, 0.0001 mol/1 EDTA) at 2000 rpm for 20 minutes, and the concentrations of SOD, MDA, and GSH PX in the supernatant were measured.

Preparation of 10% liver homogenate: take about 0.1 g liver, put it into 2mlep tube with steel ball, add 1 ml PBS ice, put it into homogenizer, and homogenize the prepared homogenate at 4°C. The determination methods of selenium content in liver homogenate were as follows:

(1) *Standard Curve.* Take the enzyme plate, add protein standard solution o, turn 1 and 8 wells into 2, 4, 6, 8, 12, 16, and 20 UL in turn, and add deionized water in each well to make up the total volume of each well is 20″L, and the corresponding protein content is 0, 0.5, 1. 0, 2.0, 4.0, 6.0, 8.0, and 10. The BCA working

solution was prepared according to the standard curve and sample quantitative preparation method, in which the ratio of reagent A to reagent B was 50 : 1 and fully mixed

(2) Add 200 ml BCA working solution to each well

(3) Shake the enzyme plate for 30s, place it at 37°C for 30 min, measure the absorbance at 562 nm, add 20 μl sample, and then add 200 plbca working solution. After addition, the mixture was fully mixed, diluted at 37°C for 30 min, and the absorbance was determined at 562 nm

(4) After moderately diluting the sample, add 20 L sample, then add 200 plbca working solution, fully mix, incubate at 37°C for 30 min, and measure the

TABLE 2: Indexes of grey rabbits.

Grouping	SOD	GSH-PX	MDA
A	133.311 ± 16.251	125.311 ± 15.452	133.271 ± 17.223
B	135.311 ± 16.752	113.311 ± 167.163	112.321 ± 17.184
C	140.311 ± 17.833	125.331 ± 17.854	125.361 ± 17.455
D	151.261 ± 17.644	132.211 ± 13.355	121.671 ± 17.366

TABLE 3: Indexes of grey rabbits.

Grouping	SOD	GSH-PX	MDA
A	133.311 ± 16.251	125.311 ± 15.452	133.271 ± 17.223
B	135.311 ± 16.752	113.311 ± 167.163	112.321 ± 17.184
C	140.311 ± 17.833	125.331 ± 17.854	125.361 ± 17.455
D	151.261 ± 17.644	132.211 ± 13.355	121.671 ± 17.366

absorbance at 562 nm; according to the absorbance value of the sample, calculate the selenium content in the sample through the standard curve

4. The Effect of Nanoselenium on Aerobic Endurance Exercise of Grey Rabbits

As shown in Table 2, SOD of quadriceps femoris in group C was higher at rest before exercise, decreased immediately after exercise, and slightly increased at 2 hours after exercise, while GSH PX decreased immediately after exercise and significantly decreased at 2 hours after exercise, with significant difference compared with that before exercise; MDA increased immediately after exercise. 2 hours after exercise, the value decreased slightly, but still higher than that at rest.

After a week of training, the sod value of preexercise group was significantly higher than that of quiet group ($P < 0.05$), and there were significant differences between the two groups immediately after exercise and 3 hours after exercise ($P < 0.05$); the value of GSH-Px decreased immediately after exercise, but did not recover 3 hours after exercise, which was still lower than that before exercise; MDA value before exercise was higher than that before quiet, immediately after exercise was higher than that before exercise, and decreased at 2 hours after exercise.

As shown in Table 3, the content of selenium in liver of grey rabbits after selenium supplement was higher than that in normal control group ($1.32 \pm 0.065 \, \mu g/g$) ($P < 0.05$). The content of selenium in liver of group C ($1.8 \pm 16.251 \, \mu g/g$) and group D ($1.6 \pm 16.752 \, \mu g/g$) was significantly higher than that in group A ($1.67 \pm 0.31 \, \mu g/g$) ($P < 0.05$).

After a week of training, the sod value of preexercise group was significantly higher than that of quiet group ($P < 0.05$), and there were significant differences between the two groups immediately after exercise and 3 hours after exercise ($P < 0.05$); the value of GSH-Px decreased immediately after exercise, but did not recover 3 hours after exercise, which was still lower than that before exercise; MDA value before exercise was higher than that before quiet, immedi-

ately after exercise was higher than that before exercise, and decreased at 2 hours after exercise.

As shown in Figure 3, the content of selenium in liver of grey rabbits after selenium supplement was higher than that in normal control group ($1.32 \pm 0.065 \, \mu g/g$) ($P < 0.05$). The content of selenium in liver of group C ($1.8 \pm 16.251 \, \mu g/g$) and group D ($1.6 \pm 16.752 \, \mu g/g$) was significantly higher than that in group A ($1.67 \pm 0.31 \, \mu g/g$) ($P < 0.05$).

Selenium content in liver cells of grey rabbits was detected in vitro. 926 cells were treated with H2O2 as an inducer of oxidative stress. The effects of low concentration (0.5 and $1 \, \mu m$) of nanoselenium on endothelial cell oxidative damage were studied by detecting the related markers of cell viability and oxidative stress. The results of MTT assay and LDH activity assay showed that H2O2 induced vascular endothelial cell viability decreased and LDH leakage increased, while nanoselenium pretreatment for 24 hours could significantly inhibit H2O2 induced vascular endothelial cell injury. It was found that hydrogen peroxide could increase the content of malondialdehyde, decrease the activities of SOD and GPX, and decrease the content of glutathione, which indicated that hydrogen peroxide-induced oxidative stress, and nanoselenium pretreatment could significantly reduce the oxidative stress induced by hydrogen peroxide. These results indicate that low concentration of nanoselenium can protect vascular endothelial cells from H2O2-induced injury through antioxidant effect.

As shown in Figures 4 and 5, before exercise, SOD index decreased (1 week), increased (2-4 weeks), and exceeded. The results show that the GSH PX index is relatively unstable, with an increase in volatility (1.3 weeks) and a decrease in volatility (2.4 weeks), but there is no significant difference between them. MDA increased (1 week) and decreased (2-4 weeks), close to the level of 0 weeks, and decreased with continuous exercise.

At 3 hours after liver exercise, SOD index increased with continuous exercise, and there was significant difference between 2-4 weeks and 0 weeks. On the one hand, free radicals have a great influence on the activity of SOD in the liver during 0-week transportation; on the other hand, it also
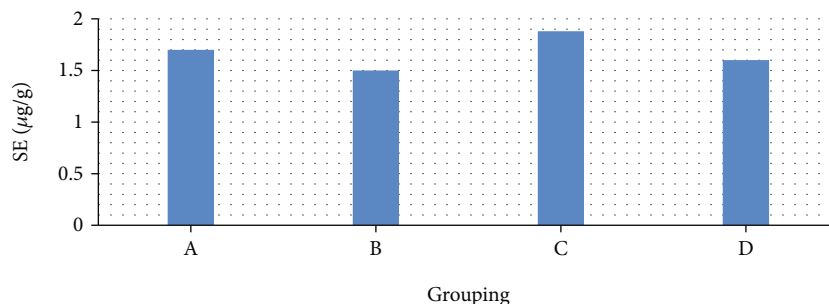
FIGURE 3: Selenium concentration in animal liver cells.
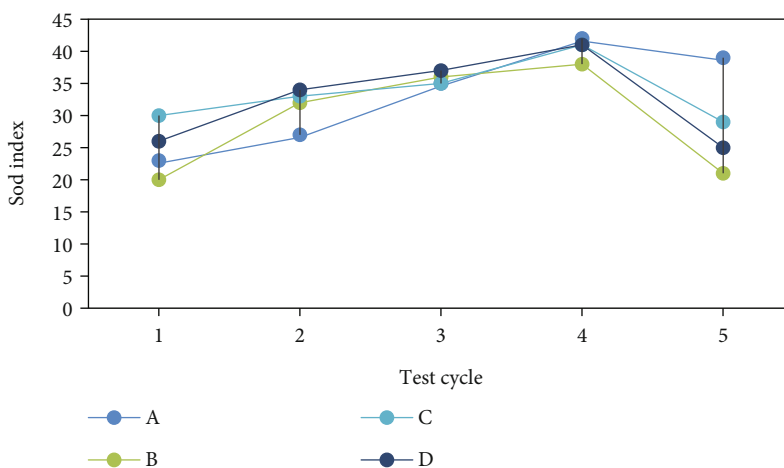
FIGURE 4: Sod index chart.

FIGURE 5: GSH PX index chart.

reflects the strong adaptability and recovery ability of visceral organ liver to exercise. As the exercise continued, GSH PX index also showed an overall upward trend, and there were significant differences between the values at week 1 and week 4 and those at week 0. Combined with the activity levels of GSH PX in the second and third weeks of exercise and before exercise, the difference may be due to the lower operating value in the first week, rather than caused by exercise factors; MDA first increased and then decreased in the first week, and the value of the third and fourth week was close to the level of 0 week. The preexercise value is the recovery value 24 hours after the last training of each week. The results showed that the activities of SOD and GSH PX did not fully recover after 0 week of training, but the values of 3 hours in the first week after exercise were very close to those before exercise, while the results of 2-4 weeks showed that the recovery of antioxidant enzyme activity was basically completed 3 hours after exercise. Compared with the
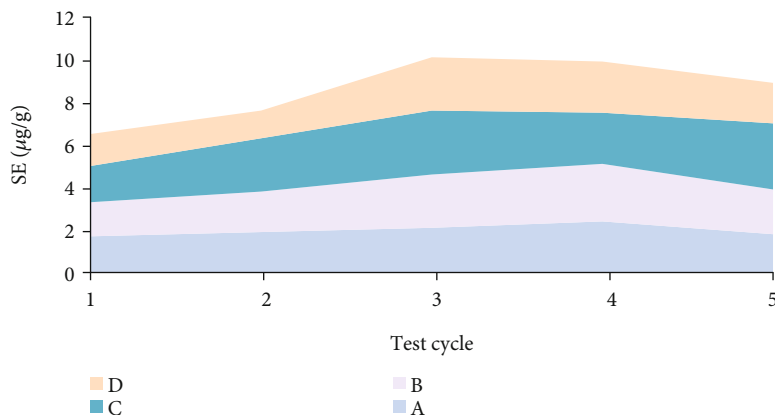
FIGURE 6: Selenium content cycle chart.

changes of antioxidant enzymes in quadriceps femoris, it was found that the recovery efficiency of liver was higher 3 hours after the first week of exercise, and the enzyme activity was close to the level before exercise.

There was no significant difference in SOD and GSH PX at 4 weeks after liver exercise, but increased continuously from 0 to 4 weeks. MDA first increased (week 1), then decreased (week 2-4), close to the level of week 0. The mobile trend is downward. The increase of antioxidant enzyme activity indicated that the stress ability of liver to stimulation was enhanced on the basis of adaptive exercise.

As shown in Figure 6, after a week of intensive training, the accumulation of free radicals in quadriceps femoris increased, and the consumption of SOD and GSH PX increased, resulting in the decrease of SOD and GSH PX activity after exercise, and the change of SOD was significant, which still affected the recovery period. 3 hours after exercise, the changes of antioxidant enzymes in liver were different from those in quadriceps femoris. The recovery rate of SOD was higher than that of resting state. The level of GSH PX also changed significantly. Although nanoselenium products were supplemented at the same time, the emergency capacity of antioxidant enzymes was still very poor in the first week. However, the changes of liver and quadriceps femoris were different 3 hours after exercise. We think it may be related to liver function. However, due to the lack of comparison between the selenium supplement group and the control group, the effect of nanoselenium in the first week needs further analysis. After the second week of exercise, the activities of SOD and GSH PX increased immediately, and the body under the pressure of exercise increased.

GSH PX is an important enzyme that catalyzes the decomposition of hydrogen peroxide. Its active center is selenocysteine, and selenium is an important component of GSH px. After two weeks of supplementation of nanoselenium, we believe that the activity of GSH PX is increased, the ability of scavenging tian0 is enhanced, and the stress capacity is increased due to the increase of selenium content in vivo. However, H0 is not only an inhibitor of SOD but also an inhibitor of superoxide anion.

The activity of SOD will also destroy the structure of SOD and make it lose its activity irreversibly. After adding nanoselenium, the ability of GSH PX and the activity of SOD were improved. Based on hydroxyl radical quenching, rhodamine B fluorescence method can be used to detect the free radical scavenging effect and antioxidant effect of antioxidants. The free radical scavenging effects of selenium nanoparticles (senp), ascorbic acid (VC), and sodium selenite (Na2SeO3) were determined by fluorescence method. With the increase of antioxidant concentration, their ability to scavenge hydroxyl radicals also increased. When the concentration reached a certain level, the scavenging rate decreased. Within a certain concentration range, there was a linear relationship between antioxidant concentration and elimination rate.

These results indicate that selenium nanoparticles are not only stronger than ascorbic acid but also stronger than inorganic salts of selenium, especially in the dose. It is an antioxidant with strong antioxidant activity, which may be the reason why the biological activity of selenium nanoparticles is higher than that of traditional inorganic salts.

5. Discussion

In order to eliminate sports fatigue and reduce sports injury, it is necessary to reduce excessive free radicals in the body. The body relies on certain enzymes and antioxidants to remove free radicals. Proper selenium supplementation can improve the activity of glutathione peroxidase (GSH PX) and enhance the antioxidant capacity of human body. In this study, selenium nanoparticles were prepared, and their scavenging effects on free radicals were studied.

In this paper, through the establishment of nanoselenium on aerobic endurance exercise evaluation model, the effect of nanoselenium on biological aerobic exercise was studied by detecting the related markers of cell viability and oxidative stress. The results of MTT assay and LDH activity assay showed that H2O2 induced vascular endothelial cell viability decreased and LDH leakage increased, while nanoselenium pretreatment for 24 hours could significantly inhibit H2O2 induced vascular endothelial cell injury. It was found that hydrogen peroxide could increase the content of malondialdehyde, decrease the activities of SOD and GPX, and decrease the content of glutathione, which

indicated that hydrogen peroxide-induced oxidative stress, and nanoselenium pretreatment could significantly reduce the oxidative stress induced by hydrogen peroxide. These results indicate that low concentration of nanoselenium can protect vascular endothelial cells from H2O2-induced injury through antioxidant effect.

Due to the limited experience of the author, the research scope is small, but nanoselenium has many functions, such as antibacterial, anticancer, anti-inflammatory, and antioxidant. However, there are still many problems when nanoselenium is used as a disease treatment drug, antibacterial material, or nutritional supplement. Therefore, it is necessary to develop some analytical and detection methods, especially fluorescent labeling technology, to trace nanoselenium in vivo. In order to further expand the application and product development of nanoselenium in biomedical field, it is necessary to continue to explore and research.

Data Availability

No data were used to support this study.

Conflicts of Interest

The authors declare that there are no conflicts of interest regarding the publication of this article.

Acknowledgments

References

[1] H. Shirvani, H. TaheriChadorneshin, and F. Kimiagar, "The effect of intense endurance exercise training and consumption of cinnamon powder on sex hormones in trained male cyclists," *Journal of Military Medicine*, vol. 19, no. 3, pp. 245–252, 2017.

[2] S. Shirsat, A. Kadam, R. S. Mane et al., "Protective role of biogenic selenium nanoparticles in immunological and oxidative stress generated by enrofloxacin in broiler chicken," *Dalton Transactions*, vol. 45, no. 21, pp. 8845–8853, 2016.

[3] M. Maynar, F. Llerena, I. Bartolomé et al., "Seric concentrations of copper, chromium, manganesum, nickel and selenium in aerobic, anaerobic and mixed professional sportsmen," *Journal of the International Society of Sports Nutrition*, vol. 15, no. 1, 2018.

[4] W. M. Fan, A. N. Lane, and R. M. Higashi, "Selenium biotransformations by a euryhaline microalga isolated from a saline evaporation pond," *Environmental Science & Technology*, vol. 31, no. 2, pp. 569–576, 1997.

[5] H. Fernández-Llamosas, L. Castro, M. L. Blázquez, E. Díaz, and M. Carmona, "Biosynthesis of selenium nanoparticles by Azoarcus sp," *Microbial Cell Factories*, vol. 15, no. 1, 2016.

[6] Y. Tan, Y. Wang, Y. Wang et al., "Novel mechanisms of selenate and selenite reduction in the obligate aerobic bacterium Comamonas test osteroni S44," *Journal of Hazardous Materials*, vol. 359, pp. 129–138, 2018.

[7] C. M. Zhang, F. Lai, A. X. Gao, and X. B. Zhou, "Absorption, translocation and redistribution of selenium supplied at different growth stages of rice," *International Journal of Agriculture and Biology*, vol. 19, no. 6, pp. 1601–1607, 2017.

[8] G. Gulyás, E. Csosz, J. Prokisch et al., "Effect of nano-sized, elemental selenium supplement on theproteome of chicken liver," *Journal of Animal Physiology & Animal Nutrition*, vol. 101, no. 3, pp. 502–510, 2017.

[9] M. Iwasaki, N. Miki, Y. Tsuchiya, K. Nakajima, and Y. Nishihara, "Synthesis of benzoisoselenazolone derivatives by nickel-catalyzed dehydrogenative direct selenation of C(sp2)–H bonds with elemental selenium in air," *Organic Letters*, vol. 19, no. 5, pp. 1092–1095, 2017.

[10] G. E. Schwartz, J. C. Hower, A. L. Phillips, N. Rivera, A. Vengosh, and H. Hsu-Kim, "Ranking coal ash materials for their potential to leach arsenic and selenium: relative importance of ash chemistry and site biogeochemistry," *Environmental Engineering Science*, vol. 35, no. 7, pp. 728–738, 2018.

[11] S. Javed, A. Sarwar, M. Tassawar, and M. Faisal, "Conversion of selenite to elemental selenium by indigenous bacteria isolated from polluted areas," *Chemical Speciation & Bioavailability*, vol. 27, no. 4, pp. 162–168, 2015.

[12] E. Zonaro, E. Piacenza, A. Presentato et al., "Ochrobactrum sp. MPV1 from a dump of roasted pyrites can be exploited as bacterial catalyst for the biogenesis of selenium and tellurium nanoparticles," *Microbial Cell Factories*, vol. 16, no. 1, 2017.

[13] D. Song, X. Li, Y. Cheng et al., "Aerobic biogenesis of selenium nanoparticles by _Enterobacter cloacae_ Z0206 as a consequence of fumarate reductase mediated selenite reduction," *Scientific Reports*, vol. 7, no. 1, p. 3239, 2017.

[14] S. Chekachak, M. M. Shamsi, and S. Soudi, "Assessment of aerobic training with selenium nanoparticles supplementation effects on cytokines levels of liver tissue in 4T1 breast cancer mice," *Iranian Journal of Endocrinology & Metabolism*, vol. 19, no. 2, pp. 116–125, 2017.

[15] Q. Li, J. Zhang, R. Yang, Z. Gao, J. Shan, and P. Liang, "Evaluation and exploration of se-enriching effects of microbial nano-selenium on several kinds of vegetable," *Agricultural Biotechnology*, vol. 7, no. 5, pp. 31–33, 2018.

[16] L. Wang, J. Yin, B. Yang et al., "Serious selenium deficiency in the serum of patients with Kashin-Beck disease and the effect of nano-selenium on their chondrocytes," *Biological Trace Element Research*, vol. 194, no. 1, pp. 96–104, 2020.

[17] L. N. Borovikova, A. V. Titova, A. I. Kipper, and O. A. Pisarev, "Effect of the temperature of synthesis on the spectral and dimensional characteristics of selenium-chymotrypsin nanocomplexes," *Russian Journal of Physical Chemistry A*, vol. 89, no. 3, pp. 469–471, 2015.

[18] M. A. Al Kahtani, "Effect of both selenium and biosynthesized nanoselenium particles on cadmium-induced neurotoxicity in albino rats," *Human & Experimental Toxicology*, vol. 39, no. 2, pp. 159–172, 2019.

[19] S. J. Bunglavan, A. K. Garg, R. S. Dass, and S. Shrivastava, "Effect of varied levels of selenium supplementation in nano form on growth, nutrient intake and digestibility in Wistar albino rats," *Indian Journal of Animal Research*, vol. 52, no. 2, pp. 248–253, 2018.

Research Article

Nanoligament Combined with Athlete's Rehabilitation Training on the Therapeutic Effect of Sports Ligament Injury

Xing Tian[1] **and Xianliang Wu** [2]

[1]*Institute of Physical Culture, Zhangjiakou University, Zhangjiakou, 075000 Hebei, China*
[2]*School of Road Bridge and Architecture, Chongqing Vocational College of Transportation, Jiangjin, 402247 Chongqing, China*

Correspondence should be addressed to Xianliang Wu; wuxianliang@cqjy.edu.cn

Ligament injury is a ligament injury caused by excessive or improper exercise. The purpose of this paper is to analyze the optimal recovery time of patients after anterior cruciate ligament reconstruction and to provide some reference guidance for clinical rehabilitation after ACL reconstruction. Ligament injury not only directly affects the stability of joints but also causes motor dysfunction, thus directly affecting the normal life of patients. A ligament injury occurs when the ligament site is cut or subjected to violent or prolonged stress, and the ligament is stretched beyond its capacity. At present, the treatment cycle of motor ligament injury is relatively long, and the treatment effect needs to be further improved. Rehabilitation training is a kind of functional exercise, also known as functional exercise. For the damaged ankle joint, progressive functional rehabilitation training is one of the irreplaceable treatment and rehabilitation methods in the rehabilitation process, which can effectively improve the sports performance of athletes. Therefore, it is of great significance to explore scientific and efficient treatment methods for motor ligament injury. The purpose of this study is to explore the application value of nanoligaments combined with rehabilitation training of athletes in the treatment of patients with ligament injuries. In this paper, 82 patients with motor ligament injuries treated in our hospital from January 2019 to January 2020 were selected as the final study subjects and randomly divided into control group and observation group, with 41 patients in each group. The control group received a single treatment with nanoligament implantation, while the observation group received a comprehensive treatment with nanoligament implantation combined with rehabilitation training of athletes. Changes in HSS, Lysholm, Lkss, daily life ability, and complications of the two groups of patients before and after treatment were compared. It was found that HSS (The HSS knee scoring criteria involves pain, function, range of motion, muscle strength, flexion deformity, stability, and deduction items.), Lysholm, Lkss, and daily life ability scores of patients in the two groups were increased after treatment compared with before treatment, but the increase was larger in the observation group. All experiments and subjects in the article were conducted under the condition of knowing and signing the agreement. In addition, the probability of complications and ligament injury recurrence in the observation group was 3.12% and 0.97%, respectively, far lower than that in the control group. In order to make the patient recover as soon as possible and return to work as soon as possible, it is necessary to carry out rehabilitation treatment as soon as possible after the operation of the patient, instead of continuously delaying the timing of rehabilitation treatment. *Conclusion.* Nanoligaments combined with rehabilitation training of athletes can improve the therapeutic effect of sports ligament injuries and effectively improve the knee joint function and daily life ability of patients. The timing of rehabilitation intervention is not the sooner the better. Within one to two weeks, such rehabilitation intervention will produce better therapeutic effects.

1. Introduction

Ligament injuries are ligament injuries caused by excessive or improper exercise. Ligament injuries not only directly affect the stability of joints but also cause motor dysfunction, thus directly affecting the normal life of patients [1]. At present, anterior cruciate ligament reconstruction is very effective in the treatment of ligament injury, so it is fully

applied in the treatment of ACL injury. After ligament damage, its recovery ability is low, which is widely used in clinical autograft, allograft, and artificial ligament grafts in the way of treatment, but in the overall exercise ligament damage with a long cycle of treatment, treatment effect also needs to be further promoted; exploring scientific and efficient way of treating sports ligament injury is of great significance [2, 3]. The ankle lateral ligament injury is the most common ankle injury. Whether it is the general population or high-level athletes in the process of work, life, and sports, they are prone to ankle injury due to the influence of the external environment or their own factors. The most common and most frequent joint injury is the lateral ankle ligament injury. However, the final curative effect of anterior ligament reconstruction does not only depend on precise and successful surgery. The complete cure of the patient cannot be guaranteed after surgery. Reasonable postoperative rehabilitation training is also a link that cannot be ignored in rehabilitation treatment.

For the evaluation of knee joint function, proprioceptive indicators are often selected, such as joint position sense, kinematic sense, vibration sense, and balance function, among which the measurement of joint position sense is the most used. There is a problem in competitive sports that we cannot avoid and urgently need to solve, that is, sports injuries that are hard to avoid in training and competition [4]. Because sports injury is an objective phenomenon, no matter what kind of competitive events, only in accordance with the scientific law of gradual training, can methodically improve the level of sports and competition results. On the contrary, not following the scientific law of the growth of motor skills and the scientific law of athletes' physical and mental development will easily lead to the occurrence of injury. For athletes, the occurrence of sports injury is inevitable, but it is necessary to understand the relevant knowledge of injury, which can take effective rehabilitation training after injury, to minimize or avoid the occurrence of injury to athletes training and competitive level caused by the adverse impact. The application of artificial ligaments in the treatment of ligament damage has a history of over 100 years. As early as 1903, foreign scholars proposed the use of silk thread substitutes for ligament repair and carried out relevant case studies, which finally proved that silk ligament implantation could stabilize the joint structure to some extent [5]. The scholar believed that although the growth process of connective tissue was hindered to some extent under silk fibers, once the silk connective tissue was finally formed, the tissue would have good function and emergency [6]. In 1906, other scholars confirmed the conclusion that silk thread was a good material for artificial ligament through experimental progress. In the 1970s and 1980s, artificial ligaments began to be used in the clinical treatment of ligament injuries [7]. In 1973, the FDA approved the treatment of inhibition of artificial ligaments. Jenkins demonstrated in 1978 that carbon fiber could be used in the manufacture of artificial ligaments and that carbon fiber only stayed in human tissues for a short time. The main purpose of the existence of carbon fiber artificial ligaments is to promote the formation of new tissue fibers [8, 9]. In view of

this argument, many scholars have put forward different views. In 1980, Kennedy et al. used synthetic fibrous ligaments in clinical treatment. Such ligaments are less active in the human body and have good biocompatibility, which can share the weight of ligaments sutured and avoid premature absorption of ligaments for transplantation. Some scholars have used cruciate ligaments in postpartum reconstruction of acl and achieved good short-term therapeutic effects [10]. However, a large amount of clinical time indicates that there is a great friction between the artificial ligament of the above materials and the bone, which has a great impact on the service life of the artificial ligament. The emergence of nanomaterials solves this problem well. Currently, nanomaterials are widely used in biomedicine [11, 12]. The role of the knee joint should not be underestimated, but it is prone to injury during the process of functioning. The degree of injury and the treatment effect and rehabilitation effect after the injury all need to adopt certain evaluation standards.

The specific method for measuring the range of motion of the knee joint is as follows: the center of the angle ruler is placed on the lateral epicondyle of the femur, the fixation arm is placed at the midline of the femur, aligned with the greater trochanter, and the moving arm is placed on the midline of the fibula, aligned with the direction of the midline of the lateral malleolus, and placed well. After positioning, fix the knee angle ruler on the affected limb, and let the patient do the maximum flexion and extension of the knee joint without weight-bearing. Rehabilitation training is a related physical activity to promote the improvement and recovery of the function of the injured part as soon as possible [13]. With the continuous updating of medical concepts, people pay more and more attention to postoperative rehabilitation training [14]. Rehabilitation training makes up for the deficiency of traditional treatment, can realize the rapid healing of injury, and plays an important role in the recovery of the function of the injured part. At present, the application of rehabilitation training in clinical follow-up treatment is more and more extensive, and it also plays an important role in clinical treatment. In this paper, a comprehensive treatment method of nanoligaments combined with rehabilitation training of athletes was proposed, and the changes of HSS, Lysholm, Lkss, daily life ability, and complications of the two groups of patients before and after treatment were compared by means of clinical analysis of cases. The effectiveness of this treatment method has been proved, indicating that this method is worthy of extensive promotion in clinical treatment. The study in this paper not only promoted the renewal of the treatment mode and the improvement of the treatment effect of the injury of the motor ligament but also laid a theoretical foundation for the later development of related studies.

2. Theoretical Elaboration

2.1. Ligament Injury.
Ligaments are connections between bones and are relatively obvious microscopic structures. Some ligaments are attached to the surface of bones, while others are fused to the outer layer of the joint capsule.

Ligaments can improve joint stability and reduce and avoid joint injury. Under the condition of external violence, the body will form nonphysiological activities, which will cause excessive stretching of the ligaments, so that its ability to withstand the stretching is far beyond the tolerance of the ligaments, and the ligaments will suffer permanent injuries. The local injury to the ligament that does not involve the joint is called a transitional injury. Complete ligament fracture and avulsion of the bone at the ligamentum attachment site may lead to potential joint dislocation, supracrustal dislocation, or even complete dislocation. The main causes of ligament injury are external factors, such as impingement. Injuries of ligaments caused by sports are called sports ligament injuries. Ligament injuries are usually accompanied by bleeding caused by rupture of small blood vessels, pain and swelling in local areas, and a series of pain and swelling in the ligament tissues, as well as movement disorders in joint parts. Moreover, once the ligament is pulled, there will be significant pain. If the ligament is completely broken, the stability of the human joint will be greatly reduced. The examination to determine ligament injury mainly includes X-ray examination, magnetic resonance examination, arthroscopy, and other special examinations [15]. When ligament damage occurs, first aid treatment must be given to reduce the deep injury caused by ligament damage. First aid treatment for ligament damage includes elevation of the affected limb, cold compress, and compression. After the ligament is injured, it must be treated and comprehensively repaired quickly. If the ligament injury is not treated in time, the joint will be repeatedly injured, and a series of important structures such as the meniscus and articular cartilage will be damaged over time, resulting in joint lordosis, and even further development of secondary traumatic arthritis in severe cases. Repair of damaged ligaments is the focus and core of the treatment of ligament injuries. Partial rupture of ligaments can be repaired by direct suture, and complete ligament exercise can be reconstructed by artificial ligaments and tissue metastasis.

2.2. *Rehabilitation Training.* After the injury occurs, the related physical activities to promote the functional improvement and recovery of the injured part as soon as possible are called rehabilitation training. In addition to some serious injuries that require bed rest, some general injuries may require appropriate exercise. Scientific and reasonable physical activity training can realize the rapid healing of injury and play an important role in the recovery of the function of the injured part. The purpose of rehabilitation training mainly includes four aspects: first, keep good physical condition. The use of rehabilitation training can effectively avoid the occurrence of muscular atrophy, so that the limb can maintain normal motor ability and cardiopulmonary function. Second is to prevent the occurrence of comprehensive symptoms of suspension. The human body will establish various types of conditioned reflex in the long time of activities. If the body activity and movement stop suddenly, the movement balance of the body will be destroyed, and in severe cases, the functional disorder of the severity of the nerd will occur. Thirdly, scientific rehabil-

itation training after physical injury can improve joint stability and promote metabolism of injury location and speed of injury recovery. Fourthly, the use of rehabilitation training can gradually balance the normal metabolism of the body, avoid weight gain caused by rest, and improve the recovery time of injury. The principles of rehabilitation training include the following aspects: first, diagnostic correctness. Correct and comprehensive diagnosis is an important basis for the development of scientific rehabilitation training plan. Second is the principle of individual treatment. The development of rehabilitation training plan should be individualized, and relevant strategies should be developed according to the actual situation of patients such as age and function, so as to promote the continuous improvement of patients' muscle strength and joint activity. Thirdly, the premise of rehabilitation training is not to aggravate the injury and affect the recovery of the injured part. Therefore, the local and systemic movements of patients should not be stopped immediately, and the muscle training should be carried out as soon as possible. Fourthly, the rehabilitation training plan should be comprehensive, insist on gradual progress, and attach importance to the appropriateness of the amount of exercise. In rehabilitation training, it cannot be accomplished overnight. The scope, time, and frequency of training activities should be improved from small to large and slowly. Be guided by the principle of moderation. Too much rapid training can aggravate the injury.

2.3. *Nanotechnology and Nanoligaments.* At present, nanotechnology is widely used in the medical field, which is mainly reflected in stomatology, drug delivery, gene therapy, cardiovascular disease treatment, and orthopedic medicine. First is the application in the oral cavity. In recent years, nanotechnology has been widely used in dental composites and tooth reconstruction. The two most common nanomaterials are filler materials and nanohybrids. Second is nanotechnology load drug function. With the continuous maturity of nanotechnology, the concept of "magic bullet" gradually appeared in the medical field and gradually developed into a systematic nanoloaded drug and delivery system. The formation of this system marks that the research on pharmaceutical preparations has gradually stepped to a higher stage. Third is nanotechnology and gene therapy. At present, low delivery efficiency and unknown direction are the difficulties of gene therapy, but there are great risks in using viral vectors for gene therapy. In order to realize the scientific design of targeted vector, some scholars have tried to introduce nanotechnology into gene therapy. At present, the use of nonviral nanoparticles has been able to successfully realize the transmission of DNA, and the application prospect of gene therapy has been further expanded. Fourth, nanotechnology treats cardiovascular disease. Fifthly, the application of nanotechnology in orthopedics is mainly used as the construction of new bone components. The nanometer size, the number of interfaces and the number of free surfaces, and the interaction between nanometer units are the three common characteristics of nanomaterials. The most commonly used nanomaterials in clinical practice in the new stage include inorganic, organic, and loaded nanomaterials.

Different nanomaterials have different application scope in the medical field, and the use of each nanomaterial should be considered according to its characteristics.

Nanometer ligaments are artificial ligaments mainly composed of nanomaterials. These artificial ligaments overcome the deficiencies of traditional artificial ligaments, have good biological characterization, have the advantages of nontoxicity and low infectivity, and do not hinder the normal growth of tissues around the human body. The most important thing is that the friction between the artificial ligament and the bone is relatively small, so the life of the artificial ligament is relatively long, and it has a long-term effect on ligament injury. Generally speaking, nanoligaments, as artificial ligaments, are suitable for wide application in the field of medicine due to their unique advantages. After the implantation of nanoligaments into human body, as a scaffold material, human microcells can be successfully implanted and attached on the nanoligaments and have a good growth state. This indicates that the three-dimensional structure and biocompatible characteristics of the nanoligament should be good, and it is a brand new scaffold material capable of effectively repairing ligament damage, which can be further studied and used. At present, the key to the preparation of nanoligaments is to produce intelligent nanobiomimetic materials with special functions to effectively regulate the specific properties of cells, so as to further improve the biological activity and compatibility of nanoligaments. For a long time to come, the preparation of nanoligaments still has great room for improvement.

3. Case Analysis Experiment

3.1. Experimental Subjects.
In this study, 82 patients with motor ligament injuries treated in our hospital from January 2019 to January 2020 were selected as the final research subjects. The inclusion criteria of the experimental subjects were as follows: first, after imaging detection, it was determined to be motor ligament injury; second, the subjects were all over 18 years old. Thirdly, sports ligament surgery and related treatment were selected. The time period from ligament injury to operation was 3 weeks to 17 months. Fourthly, the patient has relatively clear consciousness and understanding ability and can independently complete the questionnaire survey and relevant scoring test. Fifthly, the patients and their families all volunteered to participate in this experiment and signed a consent form. The exclusion criteria for subjects were as follows: first, patients with an abnormal mental state or some degree of drug dependence; second, patients with other types of severe disease; and third, patients with low compliance and compliance. The 82 patients were randomly divided into two groups (41 patients in each group), the control group and the observation group. The control group included 14 female patients and 27 male patients, with an average age of 29.6 years. The observation group included 13 female patients and 28 male patients, with an average age of 29.4 years old. There was no significant statistical difference in the basic data of the two groups of patients, which could be used for the experimental comparison in this paper.

3.2. Experimental Methods.
Patients in the control group were implanted with nanoligaments during the surgical treatment. During the implantation of nanoligaments, attention was paid to the rejection response of the body to avoid infection. After the operation, only the traditional way of rehabilitation was used, mainly repose. Observation group of patients with intraoperative implantation of nanoligament, postoperative use of athlete way of rehabilitation training for recovery, and specific rehabilitation training method is as follows: after the surgery using pressurized elastic band to bind up the limb, external use fixed support, to practice straight a ligament out slowly, the side of the operation in training of muscle and ligament surrounding tissues; one day after the surgery, quadriceps femoris muscles were trained for contraction, and the joints were autonomously pressed or lifted, 15 times in a group, 10 times a day. 2 d after the operation, the range of motion of the ligaments on the surgical side was trained. The ligaments on the surgical side were elevated with a pillow in the sitting position, and the ligaments were relaxed after stretching for 10 s. The training duration was 5 min each time, 3 times a day. After the operation, the ligament function was trained in 3D. The ligament flexion and extension angle was between 0° and 30°. The ligament was trained once every half an hour and twice a day. Then, according to the doctor's advice, walk with the help of tools and try to carry out weight training. The weight of the weight-bearing object should increase gradually. 2 to 4 weeks after the operation, proprioception was reconstructed, and balance strength was trained, activity strength of one side of the injured ligament was further improved, and rehabilitation training time was reasonably prolonged. From April to June after the surgery, the ligament resistance training should be carried out, and some training such as swimming should be arranged reasonably to help the further recovery of ligament function.

3.3. Evaluation Index.
With reference to the existing research materials, the writer will determine the final evaluation index for the following several aspects: first, the ligament function evaluation, before and after treatment for 6 months, is ligament score (HSS), and by using the Lysholm ligament function (LKSS) to assess the patient ligament function, HSS score includes pain, activity level, function, muscle strength, acute and buckling stability a few main dimension, such as the final income comes higher scores on behalf of the ligament functional recovery, the better. LKSS scores mainly include swelling, pain, squatting, and other aspects. 100 is normal, more than 80 is excellent, 70 to 79 is good, 60 to 69 is qualified, and less than 60 is poor. Second is self-efficacy evaluation. The GSES table was used to evaluate patients' self-efficacy before and after treatment, including their ability to solve and deal with things. The higher the final score, the higher the patient's sense of self-efficacy. Third is daily life evaluation. The BI table was used to evaluate the patient's daily life ability. The evaluation content included multiple aspects of the patient's daily life, and the final score was in direct proportion to the patient's daily life ability. Fourth is statistical observation of complications

TABLE 1: HSS score data table.

Group	Time	Pain	Function	Activity	Muscle strength	Flexion deformity	Stability
Observation group	Before treatment	15.26	12.65	11.76	6.21	5.63	6.22
	After treatment	25.56	18.41	16.23	9.05	9.24	9.32
Control group	Before treatment	15.31	12.68	11.83	6.32	5.64	6.23
	After treatment	21.16	15.61	14.02	7.86	7.96	7.98

*Data came from the experimental analysis.
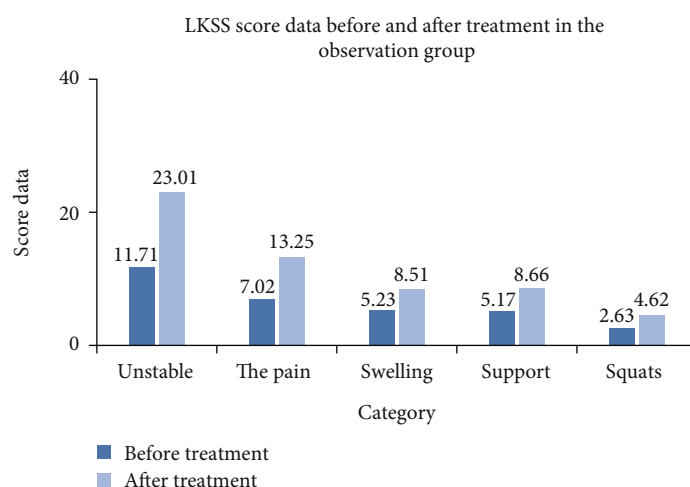
FIGURE 1: LKSS score data of the observation group before and after treatment.
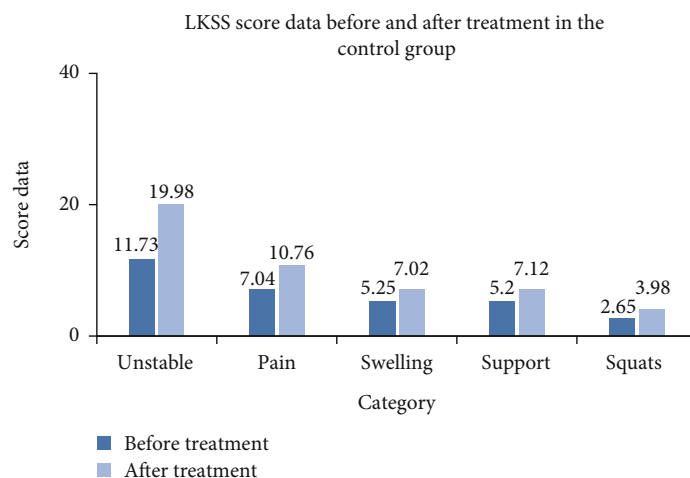
FIGURE 2: LKSS score data of the control group before and after treatment.

and recurrence rate. Postoperative complications and recurrence were counted in the two groups.

3.4. Experimental Data Statistics. SPSS statistical software was used to conduct statistical collation of experimental data. After the completion of data statistics, computer graphics software was used to draw data charts and draw relevant experimental conclusions based on the analysis of data charts. In the process of data recording, the accuracy and comprehensiveness of experimental data must be guaranteed to avoid conclusion errors due to experimental data errors.

4. Experimental Results and Discussion

4.1. Experimental Results

4.1.1. HSS Data Comparison. Table 1 is the HSS score data table. It can be seen from the data in the table that after treatment, the HSS score of patients in the control group

GSES table data comparison
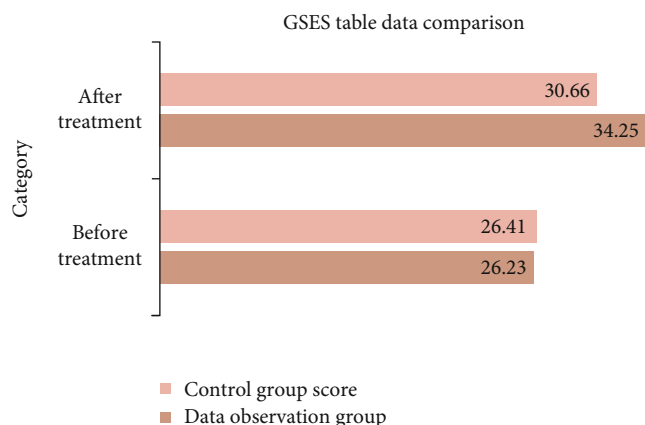
Figure 3: Comparison of GSES table data.

and the observation group increased as well as before treatment. However, compared with the control group, patients in the observation group were significantly higher in pain, muscle strength, activity, function, and stability after the treatment with the nanotube combined with athlete rehabilitation training.

4.1.2. Comparison of LKSS Scores. Figures 1 and 2, respectively, show the LKSS scores of patients with motor ligament injury in the observation group and the control group before and after treatment. As can be seen from the data in the figure, the LKSS scores of patients in both groups before and after treatment presented an increasing trend. But on the whole, the scores of exercise patients in the observation group improved more in all dimensions before and after treatment. Therefore, the combination of nanoligaments and rehabilitation training for athletes can effectively improve the function of ligaments in patients.

4.1.3. Comparison between CSES Table and BI Index Score. Figures 3 and 4, respectively, show the GSES table data in contrast with BI index score data, the data we can see from the picture; after treatment, the observation group and control group in the GSES table and BI experienced score rise, but the whole observation group of patients with GSES table and BI index score was significantly higher than the control group patients. This indicates that the use of nanoligaments combined with rehabilitation training for athletes can promote the continuous improvement of patients' self-efficacy and daily life ability.

4.1.4. Comparison of Complications and Recurrence Rates. Table 2 shows the data of complications and recurrence after treatment in the two groups. It can be seen from the data in the table that the probability of complications and recurrence of ligament injury in the control group is 17.21% and 16.54%, respectively, while the probability of complications and recurrence of ligament injury in the observation group is 3.12% and 0.97%, respectively. This indicates that the combined treatment of nanoligaments combined with rehabilitation training for athletes has a stronger safety compared with the single treatment, which can greatly reduce the

possibility of recurrence of ligament injuries, and has a good therapeutic effect.

4.2. Discussion of Experimental Results. Ligament injury is a condition of ligament injury caused by sports. Ligament injury will have a direct impact on the overall stability of human joints, promote the continuous acceleration of joint degradation, and thus have a very adverse impact on ligament, joint function, and the quality of life of patients. At present, the treatment of ligament injury is still dominated by arthroscopic revascularization. However, due to the complex overall structure of ligaments and joints, the recovery of fitness, function and exercise ability is also relatively complex. If the patient performs joint immobilization unscientifically or rests in bed for a long time after surgery, it will directly affect the dynamic balance of the joints and ligaments, and even lead to muscle atrophy, which is not conducive to the recovery of the patient's motor function. Therefore, attention must be paid to rehabilitation training after treatment, which can not only promote the improvement of nursing efficiency but also greatly improve the final treatment effect.

At present, studies of nanometer materials applied in tissue engineering is still at the primary stage, especially in the biomedical field; a lot of research is still in the stage of animal experiments, according to a lot of clinical experiments which verified the conclusion; in addition, the application of nanometer materials in the process of biological safety needs further improvement. Due to the continuous steps of nanotechnology, subdisciplines related to nanotechnology have been established and improved, such as nanoelectronics, biology, medicine, and materials science. The fusion between nanomaterials and the above disciplines is getting closer and closer. Some experts predict that nanoceramics will play an important role in the manufacture of artificial bones for a long period of time in the future, and organic and inorganic composite nanomaterials with various properties will certainly play an important role in the interventional repair of ligament injuries. Existing research data show that human ligaments are composed of many fibers, and these fibers have a stopping point at both the tibia and femur. When the knee joint is at different positions, some of the fibers are tensioned and play a role in stabilizing the knee joint. Therefore, when the motor ligament is completely broken, it is extremely important to use the nanoligament to reconstruct the human ligament. For the patients with partial injury of the motor ligament, they can make corresponding choices according to their specific conditions. Animal experiments confirmed that the toughness and elasticity of the healed ligaments were almost the same as that of the injured anterior ligaments. The experiment in this paper confirmed that the overall function and stability of ligamentum knee joints of patients with ligament injuries were significantly improved after rehabilitation training of athletes. The muscles near the knee joint can compensate for the instability of the knee joint under slow motion. If the muscles around the joint are weak, effective control of the joint cannot be achieved. Whether ligaments can realize the effective play of motor function is also closely related
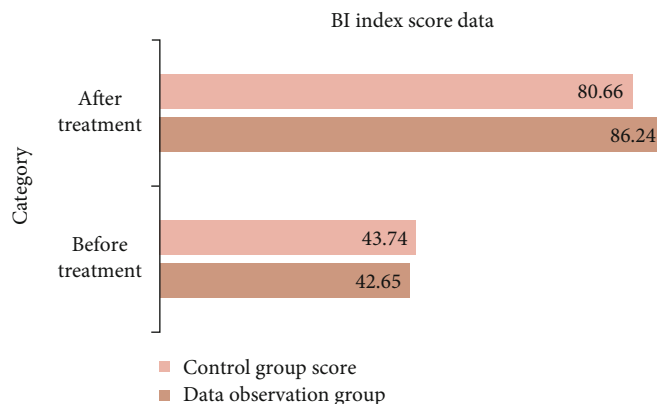
BI index score data

FIGURE 4: BI index scoring data.

TABLE 2: Data of complications and recurrence in the two groups.

Group	Complications	Recurrence rate
Control group	17.21%	16.54%
Observation group	3.12%	0.97%

*Data came from the experimental analysis.

to the recovery of proprioception of human body. Therefore, after the completion of the corresponding surgical treatment, patients with sports injuries should also strengthen the muscle strength and proprioceptive training in the early stage to avoid muscular atrophy and other conditions, so as to effectively prevent secondary knee injuries caused by sports ligament injuries.

In this study, the control group was treated only by nanoligament implantation, while the observation group was given rehabilitation training for athletes after the completion of nanoligament implantation, so as to highlight the patients' initiative in rehabilitation training and develop reasonable rehabilitation training strategies according to their own deficiencies. On the basis of stabilizing the injury condition, the recovery of life ability and overall motor function of the patients was promoted. The results showed that the HSS and LKSS functional scores of the patients in the observation group were significantly higher than those in the control group after 6 months of treatment, and the improvement of daily life ability of the patients in the observation group was much better than that of the control group. In addition, the author has also made after treatment for patients with complications and recurrence monitoring; monitoring results show that the observation group of patients with postoperative complications and recurrence of ligament damage probability is significantly lower than the control group, two groups of results and no statistical difference; however, this may be caused by experimental sample number less, which later still needs thorough expansion of research samples.

To sum up, the use of nano-combined athlete rehabilitation therapy can promote the overall treatment effect of patients with ligament injury, and promote the effective improvement of joint ligament function in patients, and is also beneficial to patients' self-efficacy and further improvement of daily living ability. It has good clinical application value and is worthy of further promotion in clinical experiments.

5. Conclusion

Sports injury and rehabilitation training are closely linked and affect each other. It is very necessary to carry out active and effective rehabilitation training after the occurrence of injury, which can promote the rapid recovery of the injured part of the athletes. There are many types of sports injuries, and rehabilitation training programs for different injuries are different. It is necessary to study targeted rehabilitation training for the common injury parts in sports, such as knee joint and ankle joint. In this paper, a comprehensive treatment method of nanoligaments combined with rehabilitation training of athletes was proposed, and the changes of HSS, Lysholm, Lkss, daily life ability, and complications of the two groups of patients before and after treatment were compared by means of clinical analysis of cases. To sum up, the rehabilitation treatment of articular ligament in athletes can promote the overall treatment effect of patients with ligament injury, and promote the effective improvement of ligament function of patients, and is also beneficial to the patient's self-efficacy and further improving the ability of daily life. It has a good curative effect and is worthy of further promotion in clinical trials. However, the exact clinical application of this treatment method needs further research and exploration.

Data Availability

No data were used to support this study.

Conflicts of Interest

The authors declare that there are no conflicts of interest regarding the publication of this article.

References

[1] J. Midum, W. S. Jong, and L. H. Il, "Anatomical relationships between muscles overlying distal transverse carpal ligament and thenar motor branch of the median nerve," *Clinics in Orthopedic Surgery*, vol. 10, no. 1, pp. 89–93, 2018.

[2] A. M. Samuel, P. J. Diaz-Collado, L. K. Szolomayer et al., "Incidence of and risk factors for knee collateral ligament injuries with proximal tibia fractures: a study of 32,441 patients," *Orthopedics*, vol. 41, no. 2, pp. e268–e276, 2018.

[3] D. Kalirathinam, H. A. Hashim, and M. S. B. Ismail, "Muscle strength and balance training in subjects with lateral ankle ligament injury of athletes," *Research Journal of Pharmacy and Technology*, vol. 11, no. 9, pp. 3841–3847, 2018.

[4] G. H. Choi, H. Ko, W. Pedrycz, A. K. Singh, and S. B. Pan, "Recognition system using fusion normalization based on morphological features of post-exercise ECG for intelligent biometrics," *Sensors*, vol. 20, no. 24, p. 7130, 2020.

[5] R. Ravikanth, M. Abraham, A. Pilar, and A. Alapati, "MRI diagnosis in multiligamentous injuries of knee with associated dislocations and neurovasacular sequelae: a retrospective analysis of injury patterns," *Egyptian Rheumatology and Rehabilitation*, vol. 46, no. 4, pp. 278–284, 2019.

[6] M. Xu, Q. Zhang, S. Dai, X. Teng, Y. Liu, and Z. Ma, "Double bundle versus single bundle reconstruction in the treatment of posterior cruciate ligament injury: a prospective comparative study," *Indian Journal of Orthopaedics*, vol. 53, no. 2, pp. 297–303, 2019.

[7] A. Uzunkulaoğlu and N. Çetin, "Hypermobility syndrome and proprioception in patients with knee ligament injury," *Eastern Journal of Medicine*, vol. 24, no. 1, pp. 38–41, 2019.

[8] T. Li and Z. J. Sun, "Treatment of ankle fracture with deltoid ligament injury," *Zhonghua Yi Xue Za Zhi*, vol. 99, no. 21, pp. 1601–1603, 2019.

[9] M. G. Siegel, "Editorial commentary: variations of national health systems: time from injury to surgery can affect anterior cruciate ligament-medial collateral ligament treatment outcomes," *Arthroscopy The Journal of Arthroscopic and Related Surgery*, vol. 36, no. 1, pp. 212-213, 2020.

[10] M. Mangone, A. Bernetti, M. Paoloni et al., "Motor imagery and rehabilitation of a professional soccer player after anterior cruciate ligament injury: a case report," *Medicina Dello Sport Rivista Di Fisiopatologia Dello Sport*, vol. 70, no. 1, pp. 109–115, 2017.

[11] M. M. Al-Qattan and K. Al-Zahrani, "An unusual pre-ligamentous thenar motor branch of the median nerve," *European Journal of Plastic Surgery*, vol. 40, no. 3, pp. 259–262, 2017.

[12] J. K. Andersson, "Treatment of scapholunate ligament injury," *Efort Open Reviews*, vol. 2, no. 9, pp. 382–393, 2017.

[13] S. Alazzawi, M. Sukeik, M. Ibrahim, and F. S. Haddad, "Management of anterior cruciate ligament injury: pathophysiology and treatment," *British Journal of Hospital Medicine*, vol. 77, no. 4, pp. 222–225, 2016.

[14] T. Y. Kim, S. H. Kim, and H. Ko, "Design and implementation of BCI-based intelligent upper limb rehabilitation robot system," *ACM Transactions On Internet Technology*, vol. 21, no. 3, pp. 1–17, 2021.

[15] F. Q. Kareem and A. M. Abdulazeez, "Ultrasound medical images classification based on deep learning algorithms: a review, Fusion: Practice and Applications," *Fusion: Practice and Applications*, vol. 3, no. 1, pp. 29–42, 2021.

Research Article

A New Type of ECG Signal Acquisition and Storage Nonvolatile Chip Embedded in Mobile Devices for Sports Monitoring

Dading Zhang [1,2]

^{1}*Department of Physical Education, Science and Technology College Gannan Normal University, Ganzhou, 341000 Jiangxi, China*
^{2}*Department of Leisure Sports, Jungwon University, Chungbuk 28024, Republic of Korea*

Correspondence should be addressed to Dading Zhang; 2013003@gnnu.edu.cn

In the fast-paced development of life in today's society, the use of ECG signals is not only used in the medical direction to scan patients; portable ECG signal acquisition tools can collect and analyze the corresponding ECG signals in time and respond to the wearer in time, so that the user can make timely adjustments or seek medical treatment in time to avoid a malignant situation that occurs. For people in sports, the collection of ECG signals is more helpful to the arrangement and estimation of training conditions. Based on nonvolatile memory technology, data will not be lost when the computer is turned off or suddenly or unexpectedly shut down. This research puts forward the design of an antiexercise ECG monitoring system that collects ECG signals for a group that is in the process of exercise. Use mathematical calculation system to classify, and conduct in-depth analysis of the reasons for poor anti-interference ability, and use the original denoising algorithm calculation as the basis to adapt to the dynamic situation in the opposite situation to the normal ECG signal acquisition in the static state. The collection is modified from the original basis. This research proposes an improved scheme for multichannel acquisition. Chips of semiconductor memory devices based on nonvolatile memory are embedded in mobile devices for use. The experimental results in this paper show that the comparison experiment ratio of collecting ECG signals from the sixth, third, fourth, and fifth directions can effectively reduce the mean square error (MSE), and the error of channel 6 is directly from 0.1598. It is down to 0.00143. Several other items showed a significant decrease. It shows that the anti-interference ability of the ECG monitoring system can be further enhanced by increasing the number of collection terminals.

1. Introduction

1.1. Background. In today's society where speed is the main development, the fast-paced life and work have produced huge pressures, and people's physical conditions are basically in a subhealthy physiological state, which is one of the cases where there are no serious illnesses and many minor problems. Today's smart Internet is undergoing rapid development. With the widespread popularity of its applications, research in the direction of the medical industry has also begun to reform itself. This should be due to the pressure brought by digital networking. The worries about medical resources have now initially become an important influence plaguing its development. The masses now have the burden of "difficult and expensive" medical treatment for the medical industry. In addition, society has entered a

serious aging trend. The continued development of the medical industry is the focus of global attention. For patients with heart disease, there is a medical gap that is difficult to bridge. According to medical statistics, more than 71% of heart disease cases occur outside the hospital, and three-fifths of them immediately die at home. Therefore, the existence of an ECG signal collector that can detect the time of a heart attack by a system with monitoring performance has an inevitable effect. When a disease occurs, it can feedback information in time, and the wearer who receives the prompt information in time can respond to it in the first time and make corresponding treatment in time. Therefore, the best treatment time will not be missed. So most patients can get timely diagnosis and treatment when they are sick and can be treated with the help of medical advice and can avoid death. Therefore, if they can wear portable health

appliances to monitor heart function and real-time monitoring and diagnosis, it will play an important role in alleviating diseases and implementing aid. For athletes, the ECG monitoring system can allow trainers to better understand the physical information of the athlete and avoid physical injury; it can also enable the athlete to maintain the exercise intensity and make the exercise effect better.

1.2. Significance. As far as the ECG signal acquisition and monitoring system is concerned, most of the current ECG monitors on the market require a static environment to collect ECG information, and the overall appearance is not too small. Even if there are portable ECG monitors on the market today, most of them are inefficient and relatively expensive. The test results are somewhat unreliable. Therefore, further research on the portable ECG monitoring system is also the focus of the development of the medical industry. The portable ECG signal monitoring system is in urgent need of further research and is also an important measure in the medical industry.

1.3. Related Work. Based on the current social population's emphasis on health, the ECG signal that can monitor the physical condition to a certain extent has been deeply researched. In the current research on the collection and storage of ECG signals, Son et al. first reported on their observations of these writing characteristics in the article: (1) log writing dominates storage writing. (2) Overwriting is frequently in mobile storage. And most importantly, (3) these overlays only change a small part of the data. Based on these observations, they recommend using a nonvolatile write buffer backed by small capacitors and using it to store small writes persistently without logging. This allows them to completely avoid those lowercase log writes, which helps to significantly reduce log-induced writes while still providing the same level of data consistency and durability [1]. The traditional PoP structure using FC-BGA (Flip Chip-BGA) has some problems in package warpage and thickness. To solve these problems, Tanaka et al. developed an embedded device package called MCeP (Molded Core Embedded Package) for the bottom package of the PoP structure. MCeP consists of a top substrate, a bottom substrate, and an embedded layer, and the IC device is encapsulated in the embedded layer by molding resin. This kind of package has the beneficial characteristics of reducing package warpage. The package warpage can be controlled by optimizing the thickness and material of each layer (top substrate, bottom substrate, and embedded layer) [2]. Lai and Shynk propose a two-stage continuous cancellation (SC) algorithm that sequentially separates the fetal and maternal heartbeats from the intrauterine electrocardiogram (IuECG) signal containing the fetal and maternal QRS complex. The ECG signal is modeled as a series of fetal, maternal, and noise events. Peak detection is first used to locate potential fetal and maternal QRS complexes, called candidate events. Each stage automatically generates source templates from candidate events in the initialization stage and then classifies the remaining candidate events according to template matching technology. Before the weaker signals are initialized and

classified, the detected stronger signal events are subtracted from the composite ECG signal. Once the fetal and maternal complex is successfully detected and separated, the counting mechanism will be used to derive the corresponding heart rate [3]. Prove the capacitive effect and nonvolatile storage capability. A low-power passive filter is designed, which can be used in the design of reprogrammable analog circuits, paving the way for future multifunctional nanodevices [4]. As an active material for supercapacitor electrodes, biomass-derived carbon has attracted much attention due to its environmental friendliness, richness, and porosity. In this case, in Keppetipola et al., activated carbon prepared from coconut shell through a simple activation process (water or steam as the activator) is used as the active material in the electrode of the environmentally friendly supercapacitor. Studies have shown that the activated carbon produced by this method exhibits a graphite phase, high surface area, and large pore volume [5]. Xu et al. proposed a method for denoising and baseline drift correction of electrocardiogram (ECG) signals based on a complete set of adaptive noise into empirical mode decomposition (CEEM-DAN) and wavelet threshold. Although CEEMDAN is based on empirical mode decomposition (EMD), it represents a significant improvement over the original EMD by overcoming the problem of mode mixing [6]. Abdullah et al. proposed a robust method for extracting fetal maternal heart rate from noninvasive composite abdominal electrocardiogram (aECG) signals. The proposed method is based on the fully integrated empirical mode decomposition (CEEM-DAN) method with adaptive noise, in which the composite aECG signal is decomposed into its constituent frequency components, called intrinsic mode function (IMF) or simply "mode." The separated IMF is then manually selected according to the possible maternal-fetal heart rate information and further processed to quantify maternal-fetal heart rate and variability analysis [7]. The research expertise of the above scholars is extremely high and requires a deeper understanding of it and experience. During the verification process, the experimental samples are difficult to collect, and the operation technology requirements are high, and it is difficult to operate.

1.4. Innovation. Most ECG signal monitoring systems on the market today have a common defect; that is, only when the test subject with testing needs is in a certain static situation, a qualified ECG signal sample can be extracted. That is to say, the ECG signal receiving system of the existing portable ECG monitoring system on the market has poor antiexercise interference ability [8], because the human body will have a larger breathing pattern after exercise, which is more intense. The respiration of the ECG signal will cause the collected ECG signal to be mixed with larger amplitude noise, which will distort the sample recorded in the ECG signal, and excessive noise will cause the waveform of the ECG signal to be distorted. Therefore, in this case, it is very necessary to study and explore the experimental design of antiexercise portable ECG monitor to improve the performance of ECG anti-interference.

2. Collect Nonvolatile Memory Based on ECG Signal

2.1. The Basic Principle of Nonvolatile Storage Based on ECG Signal Acquisition. Nonvolatile memory is a computer memory whose stored data does not disappear when the current is turned off. The main classification of current nonvolatile memory is shown in Figure 1. The storage is divided according to the different ways of data processing, and the nonvolatile semiconductor memory is divided into two types [9]. Random access memory allows reading and writing of stored data, but when the power is turned off and power is lost, it will cause the stored data source to lose its storage content [10]; read-only memory operates normally without external interference. In the case that only the data content in the storage unit is allowed to be read, the stored data content cannot be modified [11]. Its advantage lies in the stored data even when the power is lost. The samples can also be kept intact [12].

The modern system chip design of the IP core based on the nonvolatile storage circuit allows system designers to explore different system architectures. The application of the IP core makes the system architecture unnecessary to study each module in-depth [13]. This method effectively reduces the complexity of the problems encountered in the design process [14]. This can shorten the design cycle and speed up the product speed. You can use existing process solutions more effectively and reduce costs [15]. Embedded nonvolatile memory is used as part of many current system solutions. Not only can it provide the ability to change the execution data on each software production line or on-site software. Communication applications include mobile phones, mobile phone communication devices and smart cards, and in-vehicle electronic devices. This design can extend the life of the entire system, reduce the chip area [16], and save costs.

2.2. Nonvolatile Memory Programming Mechanism Based on ECG Signal. Nonvolatile storage [17] can be freely written and modified by the user, such as programmable, erasable programmable, electrically erasable, flash memory, and storage. Among them, the programmable ROM is manufactured with fuses, and the interconnection between memory cells is realized by blowing the fuses [18]. ROM is an abbreviation for read-only memory that can only read and cannot write information. Erasable programmable ROM uses ultraviolet rays to inject and remove hot electrons from the floating gate of the memory cell to achieve memory programming and erasing operations [19]. Both electrically erasable PROM and flash memory belong to electrically erasable nonvolatile memory; PROM is short for programmable read-only memory. Their working mechanism is to inject electrons into floating gate devices through electrical means [20]. Below, we mainly discuss the two types of programming and erasing. The main methods are FN tunnel effect and channel hot electron injection.

The threshold voltage VT of the floating gate transistor can be changed by programming. A high voltage is connected to the source grounding gate terminal and the drain

terminal. The high potential difference will generate a strong electric field, and then, the strong electric field will cause electron avalanche injection. When the electrons get enough energy, they will pass through the first insulating oxide layer and be trapped by the floating gate. Therefore, floating gate transistors are also called floating gate avalanche injection.

(1) FN tunneling effect: for nonvolatile memory, the tunneling effect is an important injection method [21]. Macroscopic quantum tunneling is one of the fundamental quantum phenomena; that is, when the total energy of a microscopic particle is less than the height of the potential barrier, the particle can still pass through the potential barrier [22]. Electrically programmable read-only memory (EPROM) uses channel hot electron injection for programming, but hot electron injection cannot be used for erasing. EPROM erasing is achieved by irradiating ultraviolet rays (UV) onto the unit through a closed transparent window. When EPROM is programmed and read, it is addressed in the unit of byte, and each byte can be addressed separately [23]. However, when erasing with ultraviolet light, the entire memory area will be affected. At the same time, UV erasing has problems such as time-consuming, poor durability, and low reliability. EPROM uses UV erasing, so a quartz window needs to be provided in the package, which leads to higher costs for EPROM packaging. On the other hand, EPROM has a simple structure and high density, so it can produce large-capacity memory at a lower cost, so there is still a certain market in some applications that do not require frequent erasure and reprogramming [24]. But due to price and reliability reasons, EPROM was replaced by flash memory. The electron passes through the tunnel, and its current density is expressed as

$$G = \delta V_{\text{ing}}^2 \exp\left\{-\frac{\beta}{V\text{ing}}\right\}, \tag{1}$$

$$\delta = \frac{Q^3}{8\pi H \Phi r} \frac{n}{n^*}, \tag{2}$$

$$\beta = 4\sqrt{2n^*} \frac{\varphi_n^{3/2}}{3HQ}. \tag{3}$$

In the equation, H represents the Planck constant, Φr is the barrier height when injected at the interface, Q represents the charge of a single electron, and n represents the free electron. Among them, $H = h/2\pi$

(2) Thermal injection of carriers: the process of electron injection is to inject electrons into the floating gate through the discharge of the memory cell area [25]. The electric field receives the electric field from it. If there is a positive voltage and when the electrons pass through the substrate and the gate, the barrier
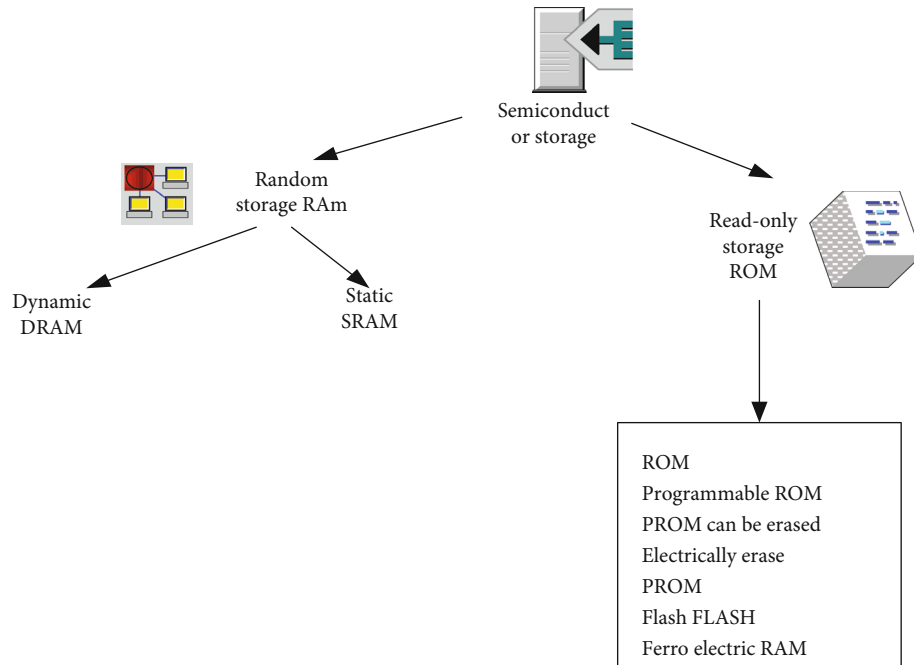
Figure 1: Storage classification.

between the oxides rises 3.3 eV with the negative voltage of VDS. The control gate VCG absorbs electric heat to the floating gate. Since the floating gate is surrounded by silicon dioxide and has no contact with other things, and silicon dioxide is an excellent insulator, the negative charges captured by the floating gate are not easily lost and can stay in the floating gate for a long time. For a long time, even if there is no power supply voltage, it will not be affected at all. This is the reason why the memory with floating gate transistor as the core component is called nonvolatile memory [26]

In fact, almost all current nonvolatile memories are based on floating gate transistors [27], and the different types of nonvolatile memories are mainly due to their different erasing mechanisms. This EPROM cell structure is shown in Figure 2. Figure 2(a) is a diagram of the corresponding basic structure of the storage unit; Figure 2(b) is a cross-sectional view from the perspective of the installation direction of the structural diagram on the left, and Figure 2(c) shows the schematic diagram of the circuit structure of its operation. But the improvement of EEPROM function comes at the expense of area. Because EEPROM performs various operations in bytes, its memory cell is composed of two transistors, one is a memory transistor [28], and the other is a selection transistor. Compared with a tube of EPROM, EEPROM has two transistors.

Table 1 shows the voltage value of each port of the EEPROM cell under different operating conditions.

Flash memory (FLASH) is combined with electronic processing and removal to realize your EPROM tube. It can be deleted completely, or the function can be deleted in one operation.

Currently, there are two types of flash memory systems: NOR-based flash memory (FLASH) memory used for program and data storage and NAND-based flash memory (FLASH) storage tools required for large-capacity data storage, such as memory cards and state disk devices. Flash, Flash EEPROM, was proposed in 1984 and soon developed into the most widely used nonvolatile memory structure. Flash memory is equivalent to a technical combination of EPROM and EEPROM. It is based on a floating gate structure and uses avalanche hot electron injection programming and electrical signal erasing. However, unlike EEPROM, the erasing of Flash is not done in bytes. Block erase is performed on a subpart of the memory. Although it is not as flexible as EEPROM in this respect, its advantages are also obvious. The cell structure eliminates the access transistor, so that the cell area is significantly reduced, the density is higher, the integration level is improved, and the production cost is reduced.

2.3. ECG Signal Noise. The ECG signal not only contains a variety of noise interference, but its own waveform also has unpredictable volatility, which is an unstable nonlinear signal. When analyzing and detecting ECG signals, it is often necessary to decompose and analyze the local information. Therefore, the classic Fourier transform technology obviously cannot be satisfied. The short-time Fourier transform developed on the basis of the Fourier transform to some extent made up for the shortcomings of the former localization analysis. The phase of the Fourier transform is very sensitive to noise. Even if a small segment of the data is wrong, the phase obtained by the Fourier transform will be much different from the real phase [29]. But because it still uses a continuous periodic sine function as the transform base function, it leads to its time domain. Analyzing ability and
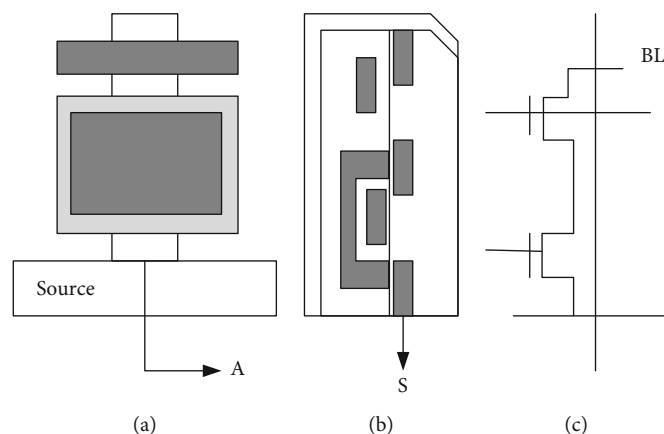
FIGURE 2: Schematic diagram of structure, storage unit, and cross-section.

TABLE 1: Port voltage under different operations.

Port	EEPROM		
	Erase	Program	Read
VCG	15.5	GND	2.4
VSG	15.5	15.5	3.3
VD	GND	15.5	1.5
VS	GND	FLOAT	GND
VB	GND	GND	GND

frequency domain analysis ability often constrain each other and cannot adapt to signals with changeable time-frequency characteristics at the same time. In recent years, wavelet transform has developed rapidly, and the technical level has become more mature. Because of its excellent time-frequency analysis and localized analysis characteristics, wavelet transform has been applied to many fields such as earthquake prediction, petroleum exploration, image processing, and speech recognition.

The ECG signal is the physiological signal of the human body, and it is a weak signal. In the process of collection and transmission, it will be interfered with by the electrical characteristics, the environment, and the activities of the human body itself, and it will be doped with many noises and interferences.

(1) Power frequency noise: power frequency interference comes from the electromagnetic field emitted by the power frequency power supply and the transmission line near the equipment. Line frequency noise is generally related to the measurement and use environment. However, the source of interference in the environment still exists, so further processing is still needed in the monitoring center

(2) Baseline drift noise: the basic noise comes from the human body. The body and tissues in the thoracic cavity will change to different degrees when a person breathes. The small change in the electrode's skin interface impedance becomes the influence of the amplitude. In addition, the amplitude of the ECG waveform is recorded on the body surface, affecting the image. This type of noise rarely has signal interference, and the frequency is usually less than 1 Hz. When such a curve is superimposed on the ECG waveform, the waveform changes, making it difficult to analyze and analyze the ECG waveform, especially the segments that affect the ECG waveform

(3) EMG noise: EMG noise interference is a very large interference, which can change up to 30 mV inside and outside the human epidermis. The ECG signal is input through the electrodes on the body surface, causing noise interference

(4) Motion artifact noise: since the ECG monitoring terminal is movable, the movement of the user in daily life will inevitably cause slight movement or jitter in the contact part of the electrode, which will cause the difference between the electrode and the skin. The impedance changes, causing contact noise. This interference generally lasts for a long time, and the amplitude can exceed the amplitude of the ECG signal and even lead to the full output of the amplifier, resulting in jump interference

3. System Design of Multichannel ECG Monitoring against Exercise Interference

The frequency response curve of the filter is not a perfect step curve, but a straight line with a slope. Therefore, even after the filter is used to denoise, the noise near the ECG signal frequency still exists. Noise seems to affect the ECG signal, so improve the signal to get a good ECG signal.

3.1. ECG Signal Measurement Based on Exercise Monitoring. The electrocardiogram is an important indicator to measure the bioelectricity produced by the human body. The reason for the electrocardiogram is that the energy cycle of the heart involves changes in its volume. Since the human body can be regarded as a very valuable conductor, the exchange capacity of the heart can be quickly transferred to the surface of the human body. Therefore, by attaching electrodes to the surface of the body, the capacitance during the heartbeat can

TABLE 2: Main noise of ECG signal.

Noise	Power frequency interference	EMG interference	Baseline drift
Frequency	50 Hz and high frequency harmonics	0-1000 Hz	0.05-2 Hz
Amplitude	Less than 50% of the ECG signal wave value	5 mV	ECG signal peak 15%
Manifestations	There are regular small ripples	Irregular small ripples	Up and down shift of heart waves

be separated, and the heartbeat can completely collect electrical signals to obtain the corresponding electrocardiogram [30].

First, determine the item of the original item listed. Key indicators include ECG signal and noise. These usually include the influence of power frequency, route drift, and EMG interference, as shown in Table 2. Power frequency interference is generally 50 Hz power line interference and a small amount of interference resolution. Due to the distribution of the human body surface, the human body has an antenna effect. In addition, under normal circumstances, whenever the ECG receives a signal, a long time reading occurs, which affects the frequency response. The skin volume of the outer and inner layers of the human body is 30 millivolts. If the skin stretches slightly, it will drop to 25 mV. Therefore, a skin capacitance of up to 5 mV should be superimposed on the ECG signal. This is the noise that people see due to myoelectric contraction. When users are stressed and affected by certain diseases, EMG frequencies may occur. Briefly summarize the main noises into a table:

3.2. Improvement Direction of Acquisition Circuit Based on Motion Monitoring. Simply put, the amplifier circuit is to amplify the weak signal provided by the signal source to drive the load to work normally. The failure of the amplifier operating circuit is random, and this random error causes the initial phase of the multisignal receiving system to be different, and the phase difference is not constant. In this experiment, the six purchased terminals passed a signal processing circuit. Each signal processing circuit has two operational amplifiers on the chip, but each amplifier in the amplifying circuit and filter circuit corresponds to the operational amplifier chip. In fact, only one of them is used, and the other op amps in the chip are in idle state. The advantage of this design is that it is easy to debug the circuit at each stage. There are two disadvantages. One is the high cost, and the other is the increase in errors caused by subtle differences in the circuit. Between each amplifier is not neutral. Therefore, if allowed, high-performance machines should be purchased. The difference between twins is not limited to cousins, because the difference between two amplifiers packaged on the same chip is much smaller than the difference in appearance and appearance of the amplifiers packaged on two chips. Therefore, you can choose a chip with greater internal noise to reduce errors. The best scenario for this test is to buy a chip with internal noise and send the signal to the amplifier on the chip. Reduce the random error reported by the amplifier circuit parameters. The loop created in this experiment has no obvious effect on efficiency, so you do not have to spend time rebuilding the loop based on the above improvements, but as the number of

receiving channels increases, the error will be random. There is no doubt that the circuit will affect the experiment, so if you encounter this problem in future experiments, please install electrical equipment according to the above procedures.

3.3. Hybrid Algorithm Design. Based on the sum of wavelet coefficients of wavelet transform, the collected ECG signals are classified. The analysis method of wavelet transform inherits and develops the idea of localization of short-time Fourier transform and at the same time overcomes the shortcomings of window size that does not change with frequency. It is an ideal tool for signal time-frequency analysis and processing. After classifying the interference factors, analyze them one by one and divide them into 6 branches.

As shown in Figure 3, even if the original signal is processed by the filter circuit, there is still residual noise, resulting in distortion of the ECG signal.

4. Hybrid Algorithm Denoising Algorithm and Experimental Results

4.1. Wavelet and Independent Component Analysis. The ECG signal is located in the low frequency region of 0.03-45 Hz, which is relatively stable, and the noise signal usually appears as a high signal. Therefore, as shown in Figure 4, it is best to use the wavelet transform method to decompose the noisy original signal. Noise is usually in high-frequency wavelet coefficients, which is characterized by large amplitude and small size in the ECG signal. When the wavelet coefficient is similar to the noise, it is characterized by small amplitude and large value. Based on the above characteristics, an initialization method can be used to process the wavelet coefficients. The algorithm block diagram is shown as in Figure 5.

As shown in Figure 6, it can be seen that the baseline drift of the six ECG signals caused by respiration has been basically eliminated, and other interference components have also been greatly weakened.

However, the ECG signal in Figure 6 still contains residual power frequency interference and other intermediate frequency noise components. The reason for this is that the frequency of the noise is similar or even the same as the frequency of the ECG signal. Therefore, the threshold method cannot separate the ECG signal and noise. In order to finely filter the noise, independent component analysis methods must be used. The independent component analysis method is based on the mutual statistical independence between the sources. Compared with traditional filtering methods and accumulative averaging methods, independent component analysis does not destroy the details of other signals while
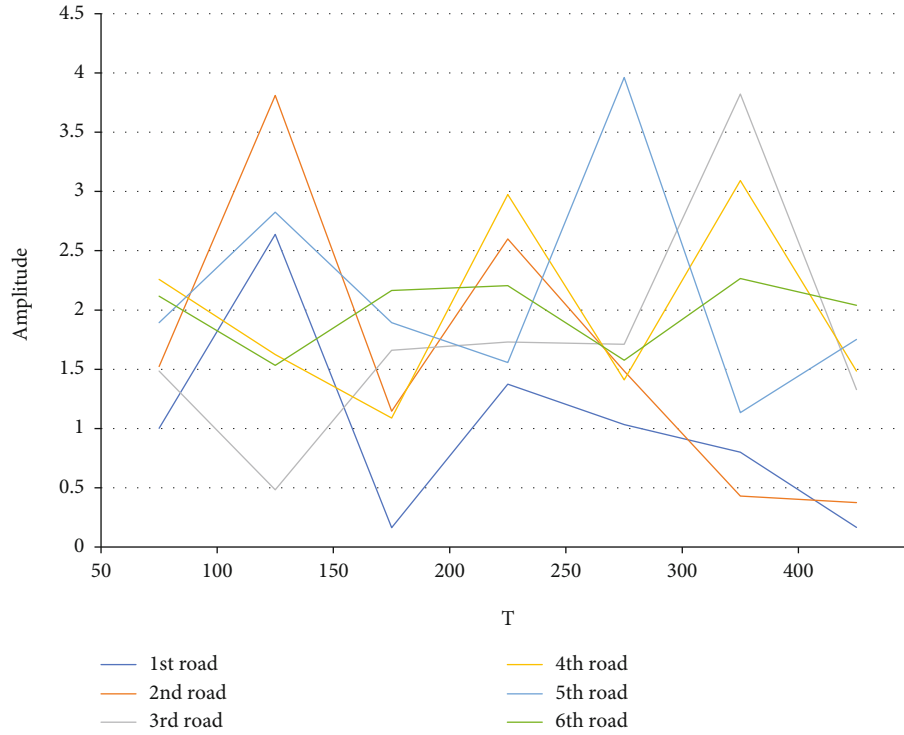
FIGURE 3: Timing diagram of the original electrical signal.
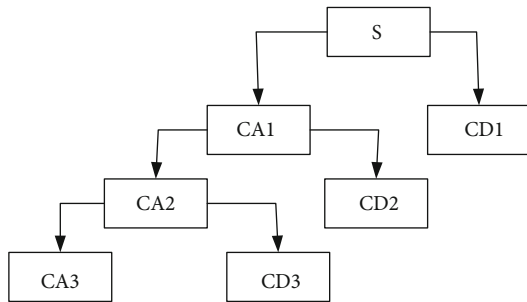
FIGURE 4: Schematic diagram of the decomposition process.

eliminating noise, and the denoising performance is often much better than traditional filtering methods. This experiment has 6 signal acquisition channels, which are sufficient to estimate the residual power frequency interference and EMG interference. The six signal channels are analyzed independently to obtain separated ECG signal and noise, as shown in Figure 7.

It can be seen that the residual noise of the ECG signal is suppressed, and the waveform is closer to the standard ECG signal.

If you compare the advantages and disadvantages of the four methods, it is far from enough to make qualitative statements based on observation methods. However, when conditions permit, mathematical evaluation indicators should be used to make quantitative statements. For quantitative analysis, two indicators, signal-to-noise ratio (SNr) and root mean square error (MSe), are used. The signal-to-noise ratio refers to the ratio of the power of the propagated signal to

the power of the noise involved in the process of signal propagation. That is to say, the larger the signal-to-noise ratio, the stronger the noise suppression capability. Root mean square error (MSe) is the arithmetic square root of variance, which is used to measure the degree of dispersion of a set of numbers itself, which can better reflect the actual situation of the predicted value error, as shown in Equations (4) and (5). Among them, Y_i represents the amplitude corresponding to time i, while X_i represents the estimated amplitude after processing.

$$\text{SNr} = 10 \times \log 10 \left[\sum_{I=1}^{t} \frac{X_i^2}{\left(X_i^2 - Y_i^2\right)} \right], \quad (4)$$

$$\text{MSe} = \frac{1}{t} \sum_{I=1}^{t} (Yi - Xi)^2. \quad (5)$$

The experimental results are shown in Figure 8. It can be seen that when compared with each other, the line graph does not show monotonous characteristics, and it seems that the results are contrary to expectations.

4.2. Problems Encountered Based on Motion Signal Acquisition. The results of this experiment do show that the quality of the six-channel acquisition and the five-, four-, and three-channel acquisition signal quality is not regular at all. If you do not carefully analyze it, it is too sloppy to conclude from the results. This section will focus on the analysis process and point out the difference between the actual
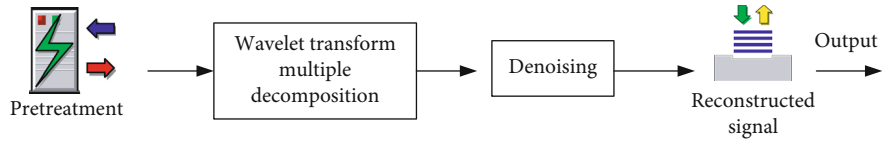
FIGURE 5: Schematic diagram of denoising process.
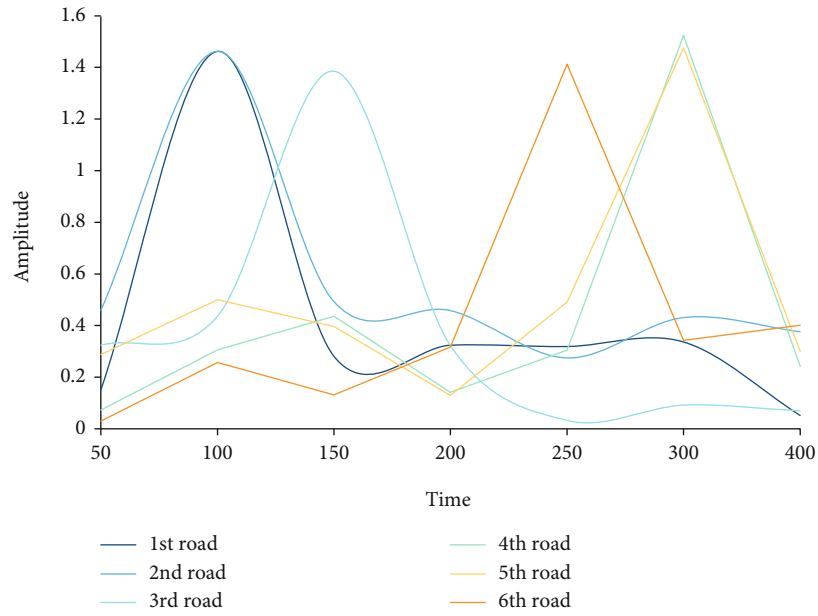
FIGURE 6: ECG with baseline drift removed.
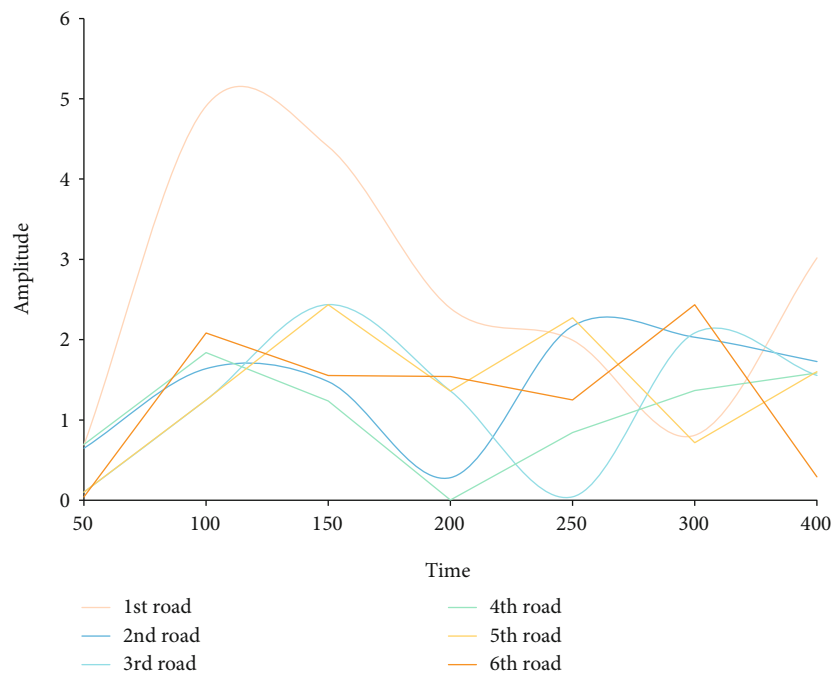
FIGURE 7: Acquisition signal after unmixing.
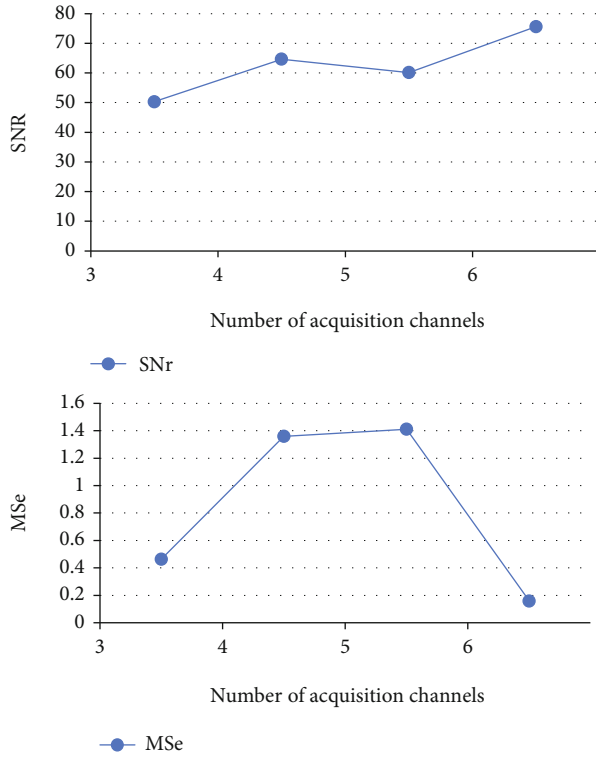
FIGURE 8: Line chart after comparison experiment.

situation and the ideal situation described in theory. Review the expression of independent component analysis again:

$$\begin{bmatrix} x1 \\ x2 \\ \vdots \\ xn \end{bmatrix} = \begin{bmatrix} a11, a12 \cdots a1n \\ a12, a22 \cdots a2m \\ \vdots \\ an1, an2 \cdots anm \end{bmatrix} \begin{bmatrix} s1 \\ s2 \\ \vdots \\ sm \end{bmatrix}, \quad (6)$$

which is

$$X = Bh. \quad (7)$$

Using evaluation indicators, three, four, five, and six of the six acquisition signals are registered, and then, independent component analysis is performed in turn to investigate whether the acquisition signal registration will affect the quality of the estimated source signal, and it is also semiqualitative. Analyze the influence of signal synchronization on the quality of the estimated source signal. The comparison between the evaluation SNr and MSe after registration and the comparison before registration is shown in Figure 9:

It can be seen that the synchronization of the signal has a great influence on the results of the independent component analysis.

4.3. Improvement of ECG Signal Registration Method Based on Exercise Monitoring. The meaning of the convex peak of the function $M(x)$ is as follows:

$$\begin{cases} M'(x) = 0, \\ M''(x) < 0. \end{cases} \quad (8)$$

Or

$$\begin{cases} M'(x + \Delta x) < 0, \\ M'(x - \Delta x) > 0, \\ M'(x) = 0. \end{cases} \quad (9)$$

Based on the second derivative of the signal, Equation (8) and Equation (9) are two ways of expressing the logical relationship.

Since the ECG signal needs to be converted by A/D, the ECG signal changes from a continuous signal to a discrete signal, and a differential operation is required:

$$\mathrm{diff}\, M(xn) = \frac{M(xn) - M(xn - 1)}{n - (n - 1)} = M(xn + 1) - M(xn). \quad (10)$$

Among them, $M(xn)$ represents the standard amplitude change time n, and $M(xn)$ represents the previous standard value. The advantage of determining the ECG signal is that you can see the highest point xn of the value point, which shows the uniqueness of this point:

$$\begin{cases} M(xn) - M(xn - 1) > 0, \\ M(xn + 1) - M(xn) < 0. \end{cases} \quad (11)$$

Based on improving the efficiency of the code, the symbolic function is used in combination with the maximum value. The meaning of the symbolic function is

$$\mathrm{sign}\,(x) = \begin{cases} 1, x \le 0, \\ -1, x > 0. \end{cases} \quad (12)$$

Therefore, the maximum candidate points satisfy

$$\mathrm{diff}\,\{\mathrm{sign}\,[\mathrm{diff}\, M(xn)]\} = -2. \quad (13)$$

By extracting the sample points that meet the conditions in the ECG signal, the maximum preselection $x1 \cdots xn$ can be obtained:

Since there are many sample points in the ECG signal that meet the conditions of maximum value discrimination, it is necessary to judge by the amplitude relationship of the maximum value belonging to the wave crest. Therefore, the conditions that need to be filtered by the threshold are

$$M(xn) \ge \mathrm{thresh}. \quad (14)$$

Filter the remaining extreme points based on nonpeak
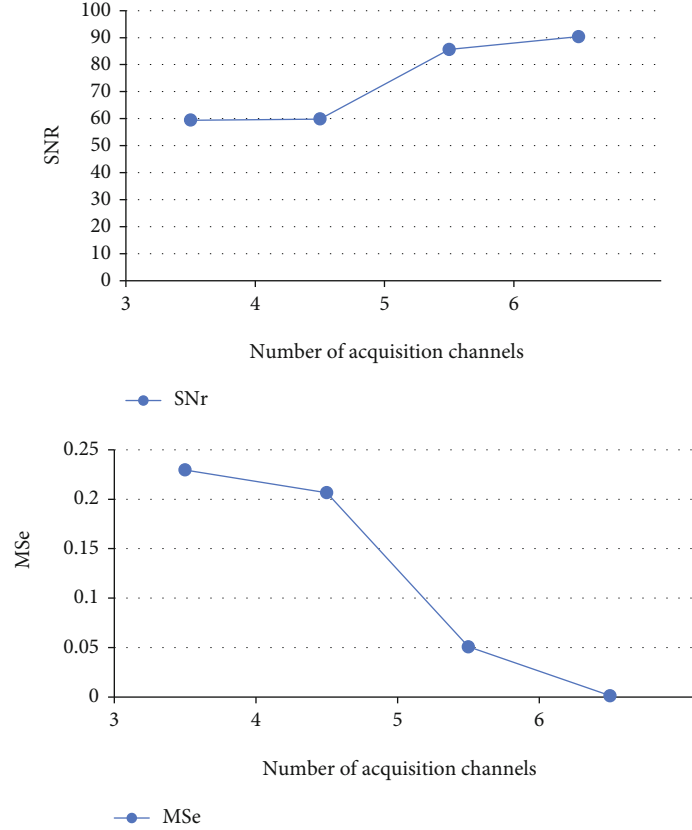
FIGURE 9: Polyline comparison after matching.

extreme points. Use time relationship to separate major and minor peaks. The selection conditions based on the ECG cycle are

$$Mn + 1\text{-}M \leq \frac{t}{2}. \tag{15}$$

Among them, T is the period of an ECG waveform, and the main peak and the secondary peak belonging to an ECG cycle can be separated by this filtering condition.

$$\bar{x} = \sum_{I=1}^{6} xi. \tag{16}$$

Then, pass the time compensation amount of the signal:

$$\Delta xi = xi - \bar{x}. \tag{17}$$

Generally, the advantage of using the average value as the registration position instead of taking a signal as the reference is that it reduces the influence of circuit delay on the signal and can compensate for the delay caused by each processing circuit. The principle is similar to that of multiple experiments. The average value improves the accuracy of the collected signal in terms of time.

5. Conclusions

In this article, we use wavelet transform to decompose the original signal in multiple layers, and each layer will get an approximate signal. The more decomposed layers, the stronger the integrity of the approximated signal, but it will also increase the amount of calculation. We use wavelet transform and independent component analysis algorithms to process the collected ECG signals and analyze the unrecorded signal processing results in detail. It can be seen that the transient ICA model and the signal quality evaluation parameters are sensitive to the signal. Synchronize this feature to make the results meet expectations. In addition, by comparing the 6-channel acquisition method after signal registration with 5-channel, 4-channel, and 3-channel, it is proved for the first time that the quality of the ECG signal collected by the system can be improved by increasing the number. When the experiment is running stably, the ECG monitoring system increases the number of collection terminals by collecting ECG signals in 6 directions, 5 directions, 4 directions, and 3 directions. In addition, this paper refines the registration method, so that the registration algorithm has the effect of suppressing spikes. In terms of time accuracy, the average registration method is used to create the reconstructed ECG signal after registration, which makes it better than the original signal.

Data Availability

The data that support the findings of this study are available from the corresponding author upon reasonable request.

Conflicts of Interest

The author declares no conflicts of interest.

References

[1] M. Son, J. Ahn, and S. Yoo, "Nonvolatile write buffer-based journaling bypass for storage write reduction in mobile devices," *Computer Aided Design of Integrated Circuits & Systems*, vol. 37, no. 9, pp. 1747–1759, 2018.

[2] K. Tanaka, Y. Machida, A. Nakamura, M. Umehara, and T. Koyama, "Development of embedded device package, MCeP (molded core embedded package)," *Journal of Japan Institute of Electronics Packaging*, vol. 20, no. 6, pp. 418–424, 2017.

[3] K. C. Lai and J. J. Shynk, "A successive cancellation algorithm for fetal heart-rate estimation using an intrauterine ECG signal," *IEEE Transactions on Biomedical Engineering*, vol. 49, no. 9, pp. 943–954, 2002.

[4] S. Ranjan, B. Sun, G. Zhou, Y. A. Wu, L. Wei, and Y. N. Zhou, "Passive filters for nonvolatile storage based on capacitive-coupled memristive effects in nanolayered organic-inorganic heterojunction devices," *ACS Applied Nano Materials*, vol. 3, no. 6, pp. 5045–5052, 2020.

[5] N. M. Keppetipola, M. Dissanayake, P. Dissanayake et al., "Graphite-type activated carbon from coconut shell: a natural source for eco-friendly non-volatile storage devices," *RSC Advances*, vol. 11, no. 5, pp. 2854–2865, 2021.

[6] Y. Xu, M. Luo, T. Li, and G. Song, "ECG signal de-noising and baseline wander correction based on CEEMDAN and wavelet threshold," *Sensors*, vol. 17, no. 12, article 2754, 2017.

[7] B. Q. Abdullah, K. P. Sharvan, and S. Dilbag, "Quantification of feto-maternal heart rate from abdominal ECG signal using empirical mode decomposition for heart rate variability analysis," *Technologies*, vol. 5, no. 4, pp. 68–68, 2017.

[8] K. Tabassum, H. Shaiba, N. A. Essa, and H. A. Elbadie, "An efficient emergency patient monitoring based on mobile ad hoc networks," *Journal of Organizational and End User Computing*, vol. 34, no. 4, pp. 1–12, 2022.

[9] B. Khaddoumi, H. Rix, O. Meste, M. Fereniec, and R. Maniewski, "Body surface ECG signal shape dispersion," *IEEE transactions on Bio-Medical Engineering*, vol. 53, no. 12, pp. 2491–2500, 2006.

[10] C. Kyrkou, C. S. Bouganis, T. Theocharides, and M. M. Polycarpou, "Embedded hardware-efficient real-time classification with cascade support vector machines," *IEEE Transactions on Neural Networks& Learning Systems*, vol. 27, no. 1, pp. 99–112, 2017.

[11] W. Ying, H. Li, and X. Li, "A case of on-chip memory sub-system design for low-power CNN accelerators," *IEEE Transactions on Computer-Aided Design of Integrated Circuits and Systems*, vol. 37, no. 10, pp. 1971–1984, 2017.

[12] R. Garibotti, L. Ost, A. Butko, R. Reis, A. Gamatié, and G. Sassatelli, "Exploiting memory allocations in clusterised many-core architectures," *IET Computers& Digital Techniques*, vol. 13, no. 4, pp. 302–311, 2019.

[13] D. Zhu, Y. Li, W. Shen, Z. Zhou, L. Liu, and X. Zhang, "Resistive random access memory and its applications in storage and nonvolatile logic," *Journal of Semiconductors*, vol. 38, no. 7, article 071002, 2017.

[14] K. Huang, Z. Rong, and L. Yong, "Racetrack memory-based nonvolatile storage elements for multicontext FPGAs," *IEEE Transactions on Very Large Scale Integration Systems*, vol. 24, no. 5, pp. 1885–1894, 2016.

[15] R. Micheloni, "Solid-state drive (SSD): a nonvolatile storage system," *Proceedings of the IEEE*, vol. 105, no. 4, pp. 583–588, 2017.

[16] I. Hwang, W. Wang, S. K. Hwang et al., "Multilevel non-volatile data storage utilizing common current hysteresis of networked single walled carbon nanotubes," *Nanoscale*, vol. 8, no. 19, pp. 10273–10281, 2016.

[17] M. Schmidt, J. W. Krug, and G. Rose, "Reducing of gradient induced artifacts on the ECG signal during MRI examinations using Wilcoxon filter," *Current Directions in Biomedical Engineering*, vol. 2, no. 1, pp. 175–178, 2016.

[18] O. Singh and R. K. Sunkaria, "ECG signal denoising via empirical wavelet transform," *Australasian Physical& Engineering Sciences in Medicine*, vol. 40, no. 1, pp. 219–229, 2016.

[19] S. Goel, P. Tomar, and G. Kaur, "A fuzzy based approach for denoising of ECG signal using wavelet transform," *International Journal of, Bio-Science and Bio-Technology*, vol. 8, no. 2, pp. 143–156, 2016.

[20] I. Kaur, R. Rajni, and A. Marwaha, "ECG signal analysis and arrhythmia detection using wavelet transform," *Journal of the Institution of Engineers*, vol. 97, no. 4, pp. 499–507, 2016.

[21] A. A. Ahmad, A. I. Kuta, and A. Z. Loko, "Analysis of abdominal ECG signal for fetal heart rate estimation using adaptive filtering technique," *International Journal of Image, Graphics and Signal Processing*, vol. 9, no. 2, pp. 19–26, 2017.

[22] G. Nishanthi, A. Yuvashree, J. Joseph, and R. Supraja, "Personnel monitoring system using mobile application during the COVID 19," *Journal of Cognitive Human-Computer Interaction*, vol. 2, no. 2, pp. 40–49, 2022.

[23] D. Panigrahy and P. K. Sahu, "Extended Kalman smoother with differential evolution technique for denoising of ECG signal," *Australasian Physical& Engineering Sciences in Medicine*, vol. 39, no. 3, pp. 783–795, 2016.

[24] D. Panigrahy and P. K. Sahu, "Extraction of fetal ECG signal by an improved method using extended Kalman smoother framework from single channel abdominal ECG signal," *Australasian Physical& Engineering Sciences in Medicine*, vol. 40, no. 1, pp. 191–207, 2017.

[25] H. Rakshit and M. A. Ullah, "A new efficient approach for designing FIR low-pass filter and its application on ECG signal for removal of AWGN noise," *IAENG Internaitonal Journal of Computer Science*, vol. 43, no. 2, pp. 176–183, 2016.

[26] P. Xiong, H. Wang, M. Liu, F. Lin, Z. Hou, and X. Liu, "A stacked contractive denoising auto-encoder for ECG signal denoising," *Physiological Measurement*, vol. 37, no. 12, pp. 2214–2230, 2016.

[27] N. Polat and S. K. Kayhan, "FPGA implementation of LSD-OMP for real-time ECG signal reconstruction," *Turkish Journal of Electrical Engineering and Computer Sciences*, vol. 29, no. 4, pp. 1887–1907, 2021.

[28] W. Li, B. Li, H. Guo, Y. Fang, F. Qiao, and S. Zhou, "The ECG signal classification based on ensemble learning of PSO-ELM algorithm," *Neural Network World*, vol. 30, no. 4, pp. 265–279, 2020.

[29] R. Muthusivagami, "A survey on ECG signal denoising using S-transform and SG filtering," *International Journal of Advanced Research*, vol. 8, no. 8, pp. 332–336, 2020.

[30] Y. A. Altay, A. S. Kremlev, and K. A. Zimenko, "Evaluation of low-frequency noise relationship in multichannel registration of ECG signal," *Izvestiâvysših Učebnyh Zavedenij Priborostroenie*, vol. 63, no. 7, pp. 626–633, 2020.

Research Article

Photocatalytic Activity of Green Construction TiO$_2$ Nanoparticles from *Phyllanthus niruri* Leaf Extract

Annin K. Shimi,[1] **Saikh Mohammad Wabaidur,**[2] **Masoom Raza Siddiqui,**[2] **Md Ataul Islam,**[3] **Kantilal Pitamber Rane,**[4] **and T. S. Arul Jeevan** [iD][5]

[1]*Department of Physics, Manonmaniam Sundaranar University, Tirunelveli, Tamil Nadu 627012, India*
[2]*Department of Chemistry, College of Science, King Saud University, Riyadh 11451, Saudi Arabia*
[3]*Division of Pharmacy and Optometry, School of Health Sciences, Faculty of Biology, Medicine and Health, University of Manchester, Manchester, UK*
[4]*KCE College of Engineering and Management, Jalgaon, Maharashtra 425001, India*
[5]*Department of Chemistry College of Natural and Computational Sciences, Mizan Tepi University, Tepi, Ethiopia*

Correspondence should be addressed to T. S. Arul Jeevan; jejeevan@mtu.edu.et

The present research work reports the facile and green synthesis of TiO$_2$ nanoparticles from *Phyllanthus niruri* leaf extract using the coprecipitation method. The plant biomolecules were responsible for the nanoproduction and exhibited reduction and stabilization activity. The green synthesized TiO$_2$ nanoparticles were analyzed in various characterization methods. The crystalline size (23 nm) and anatase phase of TiO$_2$ nanoparticles were analyzed from X-ray diffraction study. The reduction and stabilization response functional group of TiO$_2$ nanoparticles was studied from FTIR analysis. The optical properties of TiO$_2$ nanoparticles were constructed from the UV-DRS technique, and their calculated bandgap is 3.16 eV. The spherical morphology and their existing materials were identified using FESEM with EDX. The catalytic activity of TiO$_2$ nanoparticles was examined against methylene blue dye under ultraviolet and visible light irradiation. It was detected that ultraviolet irradiation showed higher photocatalytic activity than visible light irradiation. In addition, visible light irradiation provides the above 90 percentage degradation of methylene blue dye. Hence, TiO$_2$ nanoparticles were proposed as a potential catalyst of photocatalytic dye degradation application and water remediation activities.

1. Introduction

Nanoscience is one of the most widely used and effective fields of research in scientific discovery. Nanotechnology has recently become a highly advanced technology with intra- and interstudy spanning chemistry, physics, biology, material science, and medicine. The production of nanometer-sized materials of various morphologies and sizes, as well as monodispersion, is an important field of research in nanoscience [1, 2]. Nanoparticles of varying sizes, shapes, and controlled disparity are synthesized by many researchers. Catalysis, optical, electric, and magnetic aspects; diagnostics; biological probes; and display devices are among the applications for metal nanoparticles [3].

The synthesis of metal and metal oxide nanoparticles is an existing field of material chemistry that has piqued interest due to applications in a wide range of fields, including air and water purification, medicine, antimicrobials, information technology, photocatalytic, antimicrobial, energy reservoirs, and biosensors [4]. Nanomaterial synthesis methods are divided into physical and chemical processes due to their enormous surface area. These procedures, however, are not ideal for medical and biological applications due to their environmental hazards. As a consequence, researchers are opting for a green synthesis method to synthesize nanomaterials although it is efficient, environmentally friendly, and cost effective [5, 6]. Green synthesis is an exciting material science approach [7–9]. Plants provide a better platform

for nanoparticle manufacturing since they do not contain hazardous compounds and provide natural capping agents [10]. Numerous organic substances are widespread in nature extracts including amino acids, proteins, polysaccharides, alkaloids, flavonoids, and phenolic compounds [11–13]. TiO$_2$ has become extremely prevalent in a broad spectrum of applications [14–24]. TiO$_2$ is an excellent material for photocatalysis and biomaterial creation [25]. Titania's biocompatibility makes it suitable for use in bone tissue engineering for bone regeneration and healing [26]. TiO$_2$ is a powerful catalyst that may be used to remove a variety of contaminants from the environment and has been shown to clean water and surfaces [26–34]. The Phyllanthus genus is one of the most prominent groupings of plants traded in India as a raw herbal medication [35]. The Phyllanthus genus, which belongs to the *Euphorbiaceae* family, contains over 1000 species that are found on tropical and subtropical continents like America, Africa, Australia, and Asia. The Phyllanthus genus is widely applicable in the human medical system [35–39]. *Phyllanthus niruri* has been used in traditional medicine to treat lung and skin-related diseases. The presence of various biologically active substances serves an impeccable role in the reduction, capping, and stabilization processes. These plant compounds reduced the toxicity level during the production of nanophase materials. Moreover, the plant derivatives obtained various bioactive elements that can be used in antibacterial, antifungal, and diabetic-related applications [39–47]. The bioreduction compounds of lignin, saponins, and flavonoids give the chemical-free zero-valent atom and provoke the stabilization process. In addition, these biocompounds increased microbial resistivity and are highly appreciable in liver-related diseases. The present work investigates the nanoproduction of TiO$_2$ nanoparticles using *Phyllanthus niruri* leaf extract. The structural, optical, and morphological entities of the synthesized nanoparticles were investigated. In addition, the photocatalytic activity of the synthesized nanoparticles was observed from ultraviolet and visible light irradiation.

2. Experimental

2.1. Materials. The titanium tetra isopropoxide (TTIP) (Sigma-Aldrich, AR grade, purity > 99 percent) was used to synthesize the TiO$_2$ nanoparticles. Fresh leaves of *Phyllanthus niruri* were collected from Tirunelveli, and their extract was used as a bioreductant. The methylene blue dye was purchased from HiMedia. There are no extra chemicals were used for the purification and synthesis process.

2.2. Green Synthesis of TiO$_2$ NPs. The *Phyllanthus niruri* leaf extract and 0.1 M TTIP solutions were used in the green synthesis of TiO$_2$ nanoparticles. 0.1 M TTIP solution was poured into 90 mL leaf extract under magnetic stirring. The stirring and biomolecules of the leaf extract have modified the color into white and produced precipitation. The white precipitation was centrifuged for 12000 rpm for 15 minutes two times. The obtained pellets were filtered with Whatman no. 1 filter paper and kept in an oven for 200°C at 3 hrs. Finally, the white TiO$_2$ nanoparticles are character-

ized by various analyses. The formation of TiO$_2$ is depicted in Scheme 1.

2.3. Characterization. The synthesized TiO$_2$ nanoparticles were evaluated by structural, optical, and morphological analyses. The crystalline property of TiO$_2$ nanoparticles was observed from the X-ray diffractometer (XRD) (PANalytical X-ray diffractometer, Cu-Kα radiation = 0.154 nm, angle 10°–80° and 40 kV/15 mA). The optical property of TiO$_2$ nanoparticles was captured from the UV Shimadzu 2700 UV-DRS spectrophotometer. The functional group and formed TiO$_2$ nanoparticles were recorded from the FT-IR (PerkinElmer, 400–4000 cm^{-1}, USA). The morphological entity was observed from scanning electron microscopy (HRSEM-SEM, Carl Zeiss, Germany) coupled with material identification energy-dispersive X-ray spectroscopy (EDX).

2.4. Photocatalytic Activity. The photocatalyst of TiO$_2$ nanoparticles was performed against visible and UV light irradiation to determine the photocatalytic MB dye degradation. The light source is an important key factor to modify the rate of degradation to degrade the organic pollutants. The 10 ppm MB (100 mL) dye solution was inoculated with a 10 mg photocatalyst. After that, the combined solution was kept in dark condition to attain the adsorption-desorption equilibrium level. Finally, the mixed solution was placed in UV and visible light circumstances. The irradiated samples were withdrawn (5 mL) in a regular interval (30 minutes) to measure the degradation efficacy of TiO$_2$ nanoparticles. The photocatalytic dye degradation efficacy was observed from the following equation: dye degradation efficiency $= C - C_1/C$, where C is the initial dye absorbance at time $= 0$, C_1 is the dye absorbance with light at time $= 30$ min, and t is the time.

3. Results and Discussion

3.1. X-Ray Diffraction (XRD). The X-ray diffraction pattern of the green synthesized TiO$_2$ nanoparticles is shown in Figure 1. The structural, crystallite size and material phases were identified from X-ray diffraction. The obtained peaks are 25.27° (1 0 1), 37.86° (0 0 4), 48.23° (2 0 0), 54.31° (1 0 5), 55.09° (2 1 1), 62.62° (1 1 8), and 75.21° (2 1 5) compared with those of the standard JCPDS card no. 78-2486 [48, 49]. The anatase phase of TiO$_2$ nanoparticles exhibits enhanced catalytic activity than the rutile and brookite phases. The photocatalyst TiO$_2$ nanoparticle crystallite size was calculated from the Debye Scherrer formula, and their calculated value is 23 nm in (1 0 1) plane at a high-intensity peak. The lowest crystallite size demonstrates the large surface area and outstanding photocatalytic activity of the synthesized materials.

3.2. FTIR Analysis. The plant active functional groups of the TiO$_2$ nanoparticles were analyzed by FTIR spectrum and displayed in Figure 2. The broad peak at 4000–3500 cm^{-1} specifically at 3420 cm^{-1} belongs to hydroxyl groups of O–H stretching vibration [50]. The band at 2923 cm^{-1} is attributed to C-H vibrations. The C-H vibrations are restricting
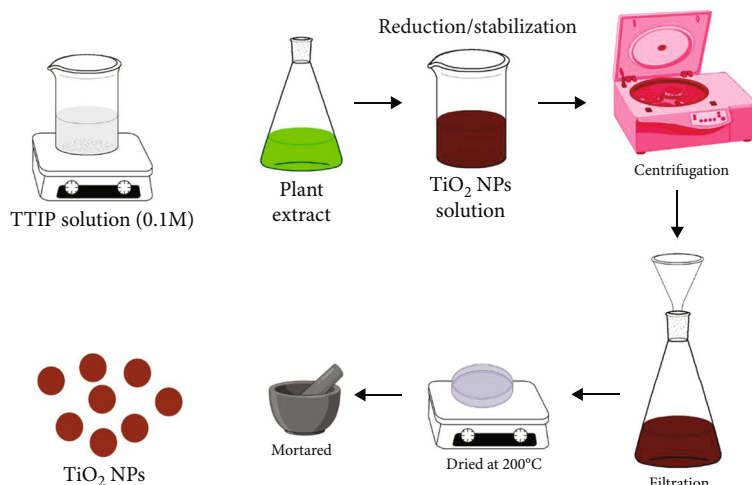
SCHEME 1: Synthesis formation of TiO$_2$ nanoparticles.
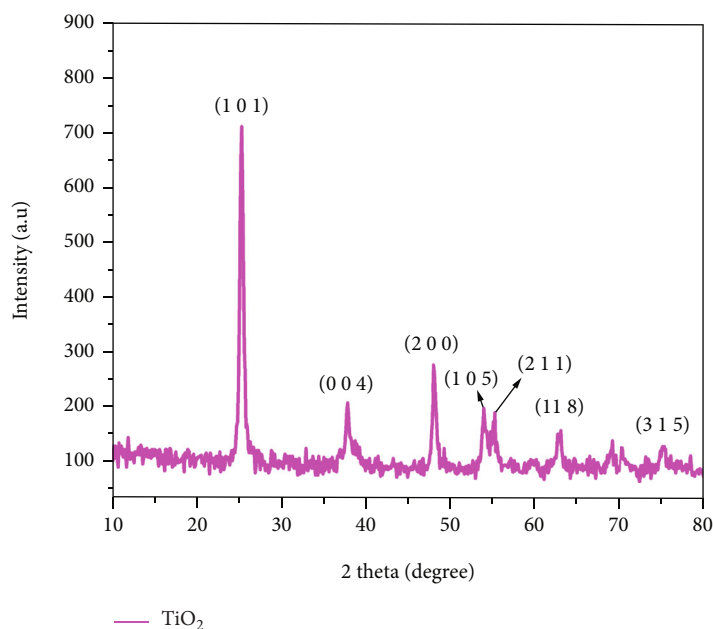
FIGURE 1: XRD diffraction pattern of green synthesized TiO$_2$ NPs.

the phase changes and promote the organic precipitation in synthesis time. Another prominent peak of TiO$_2$ nanoparticles is located at 1627 cm^{-1}, which can be ascribed to C=C which came from plant carbon molecules. The carbon molecules are associated with hydrogen and oxygen from the source materials. The carbon association produces the −C-O stretching and −C-H bending to the source precursors [50–53]. These compounds come from the plant extract biomolecules which can control the growth of the particles and reduction/stabilization activity. The peak at 720 cm^{-1} is attributed to the Ti-O stretching bands. The stretching modes of Ti-O-Ti all are observed at 500–700 cm^{-1} [54]. The plant bioderivatives produce the nonvalent atoms through the flavonoids, saponins, and lignin. These plant derivatives are responsible for metal and oxygen bond for-

mation. The formed metal and oxygen elements were stabilized from plant derivatives.

3.3. UV-DRS Analysis.

The optical properties of the TiO$_2$ nanoparticles were performed from the UV-DRS technique. The DRS spectrum is shown in Figure 3(a) which can indicate the optical reliability of the TiO$_2$ nanoparticles in the UV region at 390 nm. The optical transformations and their defects were determined the bandgap of the materials. There is no adsorption edge involved in the visible region which can denote the highest photonic energy. The optical bandgap values are calculated from Tauc eqn. The calculated bandgap value shows the relationship between the incident photon energy of semiconductors and absorption coefficient: $\alpha h\upsilon = A(h\upsilon - \text{Eg})^n$, where α is the absorption coefficient, υ is
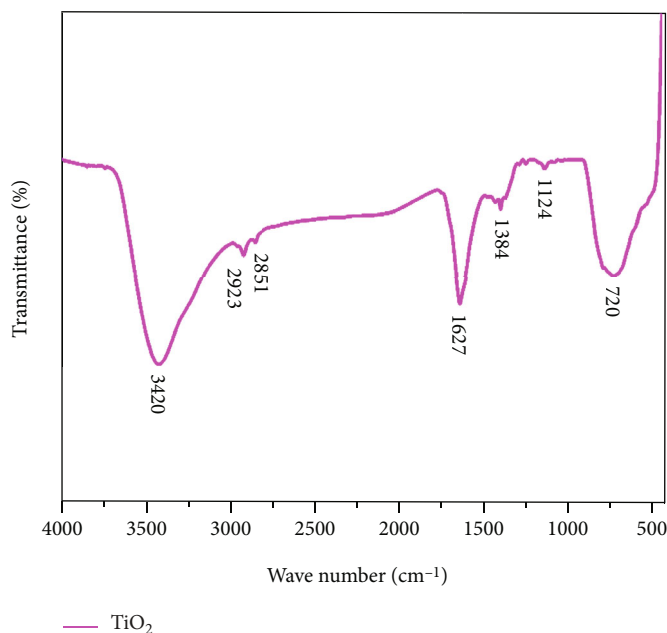
FIGURE 2: FTIR spectrum of green synthesized TiO_2 NPs.

(a)

(b)
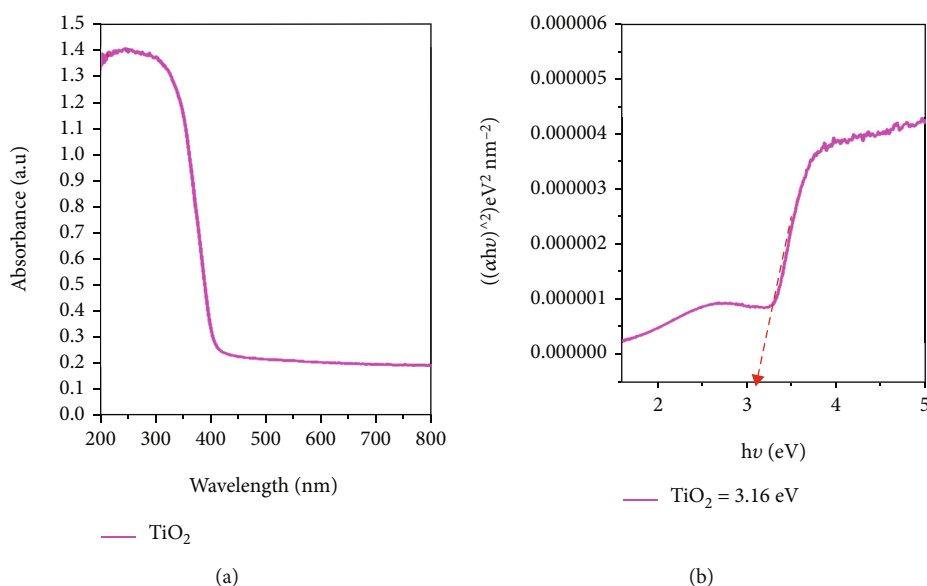
FIGURE 3: (a) UV-DRS absorption spectrum and (b) bandgap energy spectrum of green synthesized TiO_2 nanoparticles.

the frequency, Eg is the Bandgap, and n is the 1/2 direct bandgap semiconductor. The obtained band gap is 3.16 eV. The wide bandgap of TiO_2 nanoparticles exhibited the charge carrier formation and liberation in the photocatalytic activity [55, 56].

3.4. FESEM with EDX. Figure 4 shows the surface morphological and elemental analysis of green synthesized TiO_2 nanoparticles. FESEM images represent the spherical morphology with even distribution on the surface. The formed spherical shape and their smaller size particles accelerate the free radical formation. The existing plant biomolecules occupied the surface which gives the agglomerations and large grain size particles. The existing plant molecules derived the irregular distribution of the TiO_2 nanoparticles. The spherical shape is a more benefit able shape in catalytic activity than other shapes due to their large surface area [57–60]. The EDX spectrum displays the Ti and O element existence over the surface. The remaining small peaks exhibit the plant molecules which was well explained in FTIR analysis. The elemental percentages were displayed in Figure 4(d). The Ti elements occupied the major places in synthesized TiO_2 nanoparticles. The FE-SEM morphology images showed the spherical and semispherical shapes of the TiO_2 nanoparticles. The spherical shape occupied the major area of the TiO_2 nanoparticles which are attached to
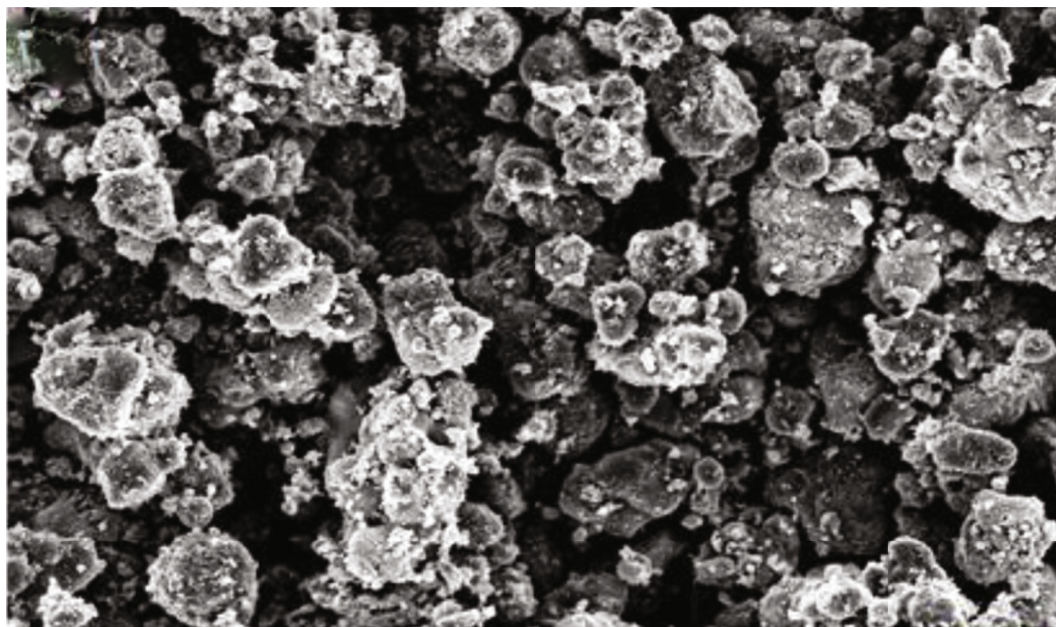
1 μm EHT = 5.00 KV Signal A = Inlens
    WD = 5.6 mm Mag = 10.00 KX

(a)
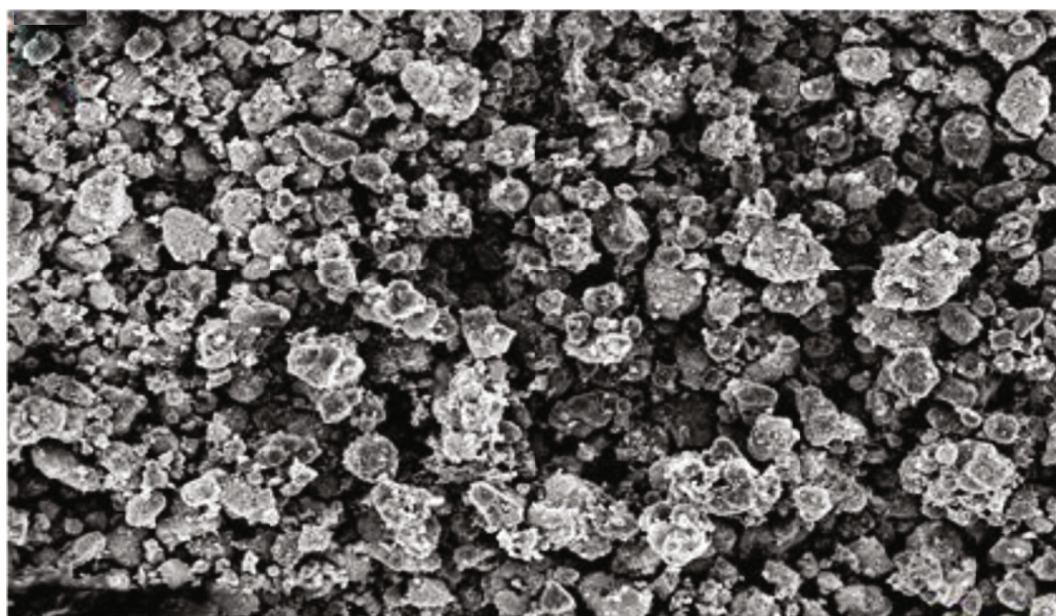
2 μm EHT = 5.00 KV Signal A = Inlens
    WD = 5.6 mm Mag = 5.00 KX

(b)

Figure 4: Continued.

cps/eV

Element	Atomic %	Weight %
Ti	59.94	81.75
O	40.06	18.25
Total	100	100

(c)

(d)
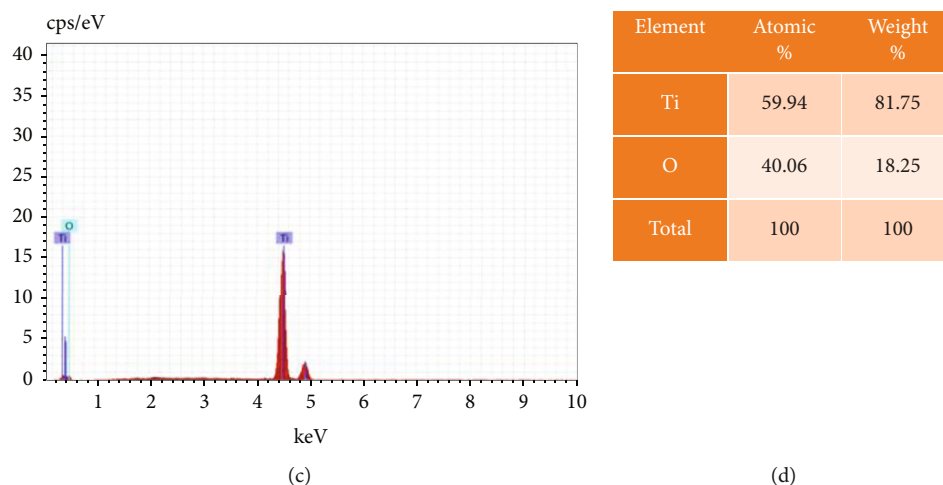
FIGURE 4: (a, b) FESEM images, (c) EDX spectrum, and (d) EDX table of green synthesized TiO$_2$ nanoparticles.

TiO$_2$ = 30 nm
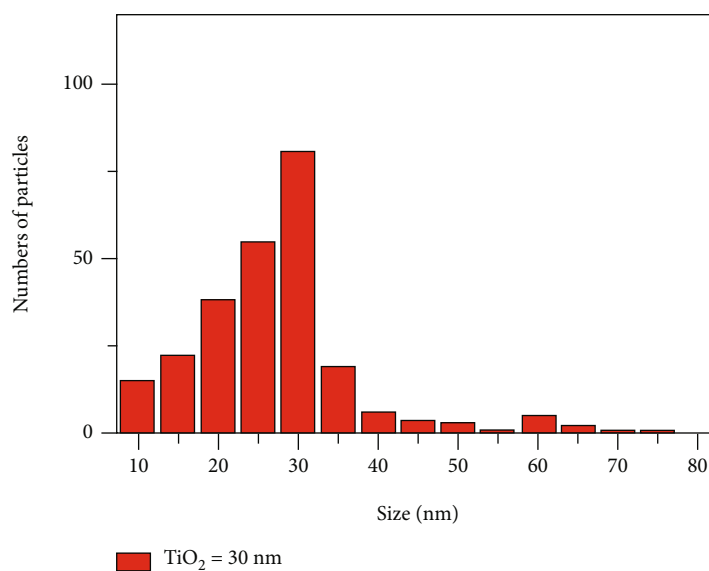
FIGURE 5: Histogram of green synthesized TiO$_2$ nanoparticles.

it shown as larger grain size particles due to their plant derivatives. The excessive plant compounds construct the layer over the TiO$_2$ surface and merged the two particles. Therefore, it shows semispherical and spherical shapes. The distribution of the TiO$_2$ nanoparticles was calculated from ImageJ software, and their values are displayed in Figure 5.

3.5. Photocatalytic Activity. The green synthesized TiO$_2$ nanoparticles against methylene blue dye under different light sources are shown in Figures 6(a) and 6(b). The visible light irradiation slowly increased the degradation rate due to the reactive sites of the catalyst. Above 60 minutes of visible light irradiation exhibits the higher degradation because of their OH radicals which provokes the oxidation of the dye molecules [61, 62]. The plant biomolecules sustained the electron-hole pair recombination which derived strong oxi-

dation and reduction of dye molecules over the catalyst. This process takes 60 minutes to 90 minutes with the migration of electrons and holes of the concern bands. The ultraviolet irradiation exhibits the vigorous degradation than visible light irradiation due to their OH radicals [16–23]. The ultraviolet light provokes the electron mobilization and evoked the electron-hole pair which promotes better degradation efficiency. The 30-minute ultraviolet light irradiation of TiO$_2$ nanoparticles exhibited above 80% degradation. The ultraviolet irradiation (98.2%) of TiO$_2$ nanoparticles showed enhanced degradation efficiency than visible light irradiation (94.42%) (Figure 7(a)). The photocatalyst efficiency was calculated from the C/C_0 spectrum (Figure 7(b)) The degradation efficiency is dependent on a light source, catalyst dosage, pH, and dye concentration [63]. TiO$_2$ nanoparticles are extensively used in photocatalytic activity due to their wide bandgap and e-h pair restriction property. The anatase
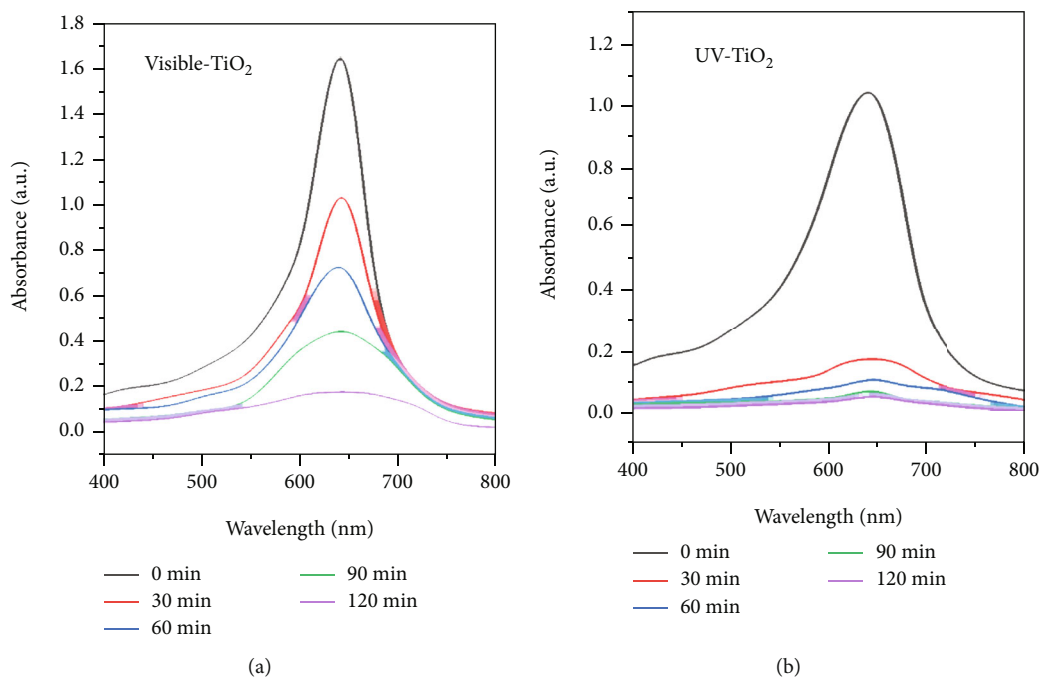
FIGURE 6: Photocatalytic degradation spectrum of the green synthesized TiO_2 nanoparticles.
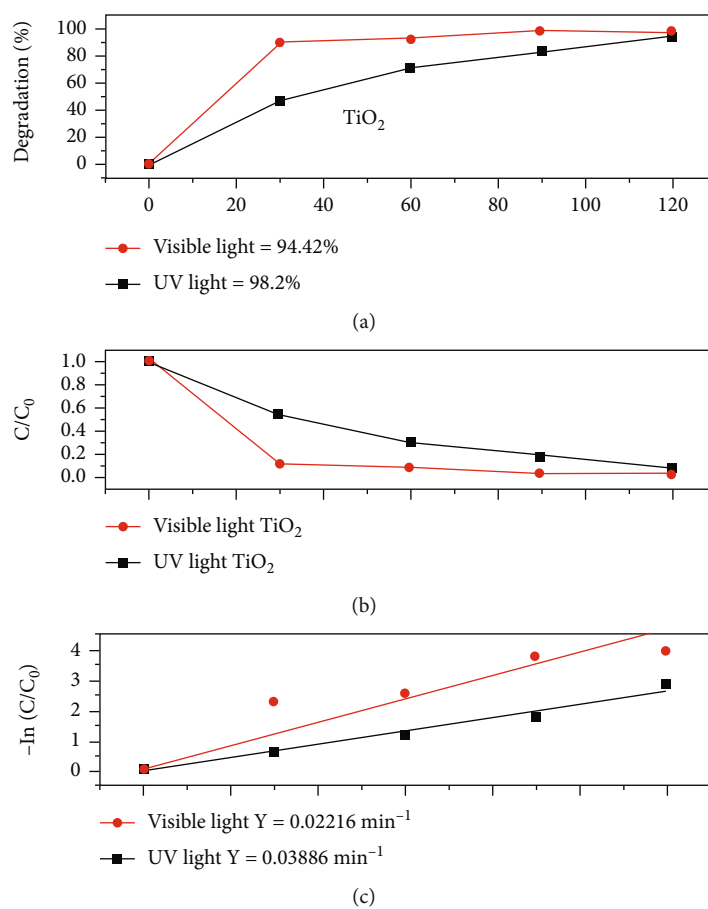
FIGURE 7: (a) Degradation efficacy, (b) C/C_0 absorption rate, and (c) photocatalytic degradation kinetics study of the green synthesized TiO_2 nanoparticles.

TABLE 1: Photocatalytic MB degradation of TiO_2 nanoparticles.

S. no	Nanomaterial	Time (min)	Source	Degradation percentage	References
1	TiO_2	120	UV-Vis	89	[70]
2	TiO_2	240	UV-Vis	70	[71]
3	TiO_2	60	UV-Vis	76	[72]
4	TiO_2	90	Solar light	90	[73]
5	Co/TiO_2	150	UV-irradiation	80	[64]
6	$Mn-TiO_2$	240	Visible light	88	[65]
7	TiO_2	60	UV	72.4	[66]
8	TiO_2	60	UV-Vis	90.4	[67]
9	TiO_2/PET	10	UV-vis	88	[74]
10	TiO_2	**120**	UV	**98.2**	Present work
11	TiO_2	**120**	Visible light	**94.4**	Present work
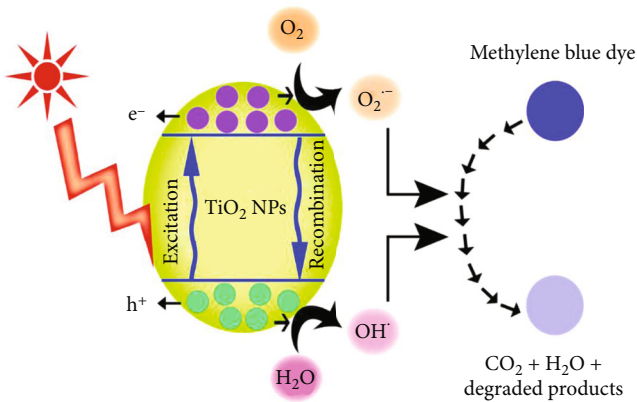
FIGURE 8: Photocatalytic degradation mechanism of green synthesized TiO_2 nanoparticles.

TiO_2 nanoparticles exhibited a wide bandgap (3.16 eV) and lower crystallite size and large surface area which was ensured by DRS, XRD, and FESEM analyses, respectively. The degradation rate of the catalyst was constructed from pseudo-first-order kinetics (Figure 7(c)). The kinetic equation is as follows: $-\ln(C_t/C_0) = -Kt$, where C_t is the light irradiated dye absorbance at time t, C_0 is the initial dye absorbance at time $t = 0$, and t is the activity time of degradation. The obtained pseudo-first-order kinetics delivered the ultraviolet irradiation potential which is more effective than visible light irradiation. The present work is compared with earlier published work of TiO_2 nanoparticles. The comparison of TiO_2 nanoparticle photocatalytic activity is tabulated in Table 1. The pure and doped TiO_2 photocatalytic degradation work is reported. The degradation is based on the light source, size, dopants, and surface area. The table denotes the catalytic activity of TiO_2 nanoparticles in various doping, light sources, and time. The visible light irradiation degradation is low compared to ultraviolet irradiation but the addition of metal compounds increased the catalytic efficiency. Free radicals production increased the oxidation ability of dye molecules. The radical formations are evoked in visible light irradiation [64–67]. The present visible light irradiation catalytic activity produced the superoxides and radicals which exhibited a better photocatalytic dye degrada-

tion activity than previously reported works. Therefore, the present work focused on visible and ultraviolet light irradiation and demonstrates that biogenic TiO_2 nanoparticles prove heightened degradation ability against the MB dye.

The photocatalyst mechanism of the TiO_2 nanoparticles is shown in Figure 8. The mechanism of TiO_2 nanoparticle-excited electrons traveled from the valence band to the conduction band during the illumination. The modified electrons and holes get a reduction and oxidation property. The generated charge carriers produce free radicals and superoxides. These compounds dissociated the dye molecules to noxious compounds [61, 62, 68, 69]. The UV light irradiation inhibits the e-h pair very strappingly and produces an enormous amount of free radicals than visible light irradiation. The detailed mechanism is as follows:

$$
\begin{aligned}
TiO_2 + h\nu &\longrightarrow e^-(C.B) + h^+(V.B)., \\
(H_2O \longrightarrow H^+ + OH^-) + h^+(V.B) &\longrightarrow H^+ + \cdot OH, \\
O_2 + e^-(C.B) \longrightarrow O_2^- + H^+ + OH^- &\longrightarrow HO_2^\cdot + {}^-OH, \\
HO_2^\cdot + {}^-OH + h^+(V.B) &\longrightarrow \cdot OH.
\end{aligned}
$$
(1)
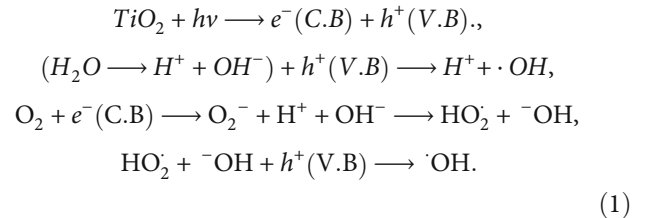
Based on the results, specify that the green synthesized TiO_2 nanoparticles have upgraded catalytic activity and enhanced dye adsorption behavior in ultraviolet light irradiation. Hence, the green synthesized TiO_2 nanoparticles detached the dye molecules from the aquatic surface and more powerful degradation in the ultraviolet region.

4. Conclusion

The current work reported the green production of nanoparticles from *Phyllanthus niruri* leaf extract. The plant extract using nanoparticles is an eco-friendly and noxious-free reduction to synthesize the nanophase materials. The photocatalyst of the TiO_2 structural tetragonal pattern was confirmed by XRD, and their size 23 nm was calculated using the Debye Scherrer equation. The plant derivatives and their reduction/stabilization involved biomolecules, and their functional groups were identified from FTIR spectroscopy.

The optical measurement and their wide bandgap values were evident by DRS analysis. The spherical surface and elemental investigation were obtained from FESEM with EDX. The photocatalyst of TiO_2 nanoparticles was performed in ultraviolet and visible light irradiation against MB dye. The results exposed that ultraviolet irradiation of TiO_2 nanoparticles exhibited better catalytic activity than visible light photocatalytic activity. Therefore, constructed on the results of the current study, we recommended that the green synthesized TiO_2 nanoparticles are a more active and high possible catalyst in wastewater removal treatment.

Data Availability

All research data used to assist the findings of this work are included within the manuscript.

Conflicts of Interest

The authors have no conflict of interests.

Acknowledgments

References

[1] D. Mandal, M. E. Bolander, D. Mukhopadhyay, G. Sarkar, and P. Mukherjee, "The use of microorganisms for the formation of metal nanoparticles and their application," *Applied Microbiology and Biotechnology*, vol. 69, no. 5, pp. 485–492, 2006.

[2] S. M. Yedurkar, C. B. Maurya, and P. A. Mahanwar, "Synthesis of nanoparticles by green chemistry process and their application in surface coatings: a review," *Archives of Applied Science Research*, vol. 8, no. 5, pp. 55–69, 2016.

[3] R. Subbaiya, R. S. Lavanya, K. Selvapriya, and M. Masilamani Selvam, "Green synthesis of silver nanoparticles from Phyllanthus Amarus and their antibacterial and antioxidant properties," *International Journal of Current Microbiology and Applied Sciences*, vol. 3, no. 1, pp. 600–606, 2014.

[4] E. T. Bekele, B. A. Gonfa, O. A. Zelekew, H. H. Belay, and F. K. Sabir, "Synthesis of titanium oxide nanoparticles using root extract of kniphofia foliosa as a template, characterization, and its application on drug resistance bacteria," *Journal of Nanomaterials*, vol. 2020, Article ID 2817037, 10 pages, 2020.

[5] V. Helan, J. J. Prince, N. A. Al-Dhabi et al., "Neem leaves mediated preparation of NiO nanoparticles and its magnetization, coercivity and antibacterial analysis," *Results in Physics*, vol. 6, pp. 712–718, 2016.

[6] I. Hussain, N. B. Singh, A. Singh, H. Singh, and S. C. Singh, "Green synthesis of nanoparticles and its potential application," *Biotechnology Letters*, vol. 38, no. 4, pp. 545–560, 2016.

[7] B. E. Azar, A. Ramazani, S. T. Fardood, and A. Morsali, "Green synthesis and characterization of $ZnAl_2O_4$@ZnO nanocomposite and its environmental applications in rapid dye degradation," *Optik*, vol. 208, article 164129, 2020.

[8] S. TaghaviFardood, A. Ramazani, F. Moradnia, Z. Afshari, S. Ganjkhanlu, and F. YekkeZare, "Green synthesis of ZnO nanoparticles via sol-gel method and investigation of its appli-

[9] S. TaghaviFardood, F. Moradnia, S. Moradi, R. Forootan, F. YekkeZare, and M. Heidari, "Eco-friendly synthesis and characterization of α-Fe2O3 nanoparticles and study of their photocatalytic activity for degradation of Congo red dye," *Nanochemistry Research*, vol. 4, no. 2, pp. 140–147, 2019.

cation in solvent-free synthesis of 12-aryl-tetrahydrobenzo[α]xanthene-11-one derivatives under microwave irradiation," *Chemical Methodologies*, vol. 3, no. 6, pp. 696–706, 2019.

[10] C. R. Resmi, P. Sreejamol, and P. Pillai, "Green synthesis of silver nanoparticles using Azadirachta indica leaves extract and evaluation of antibacterial activities," *International Journal of Advanced Biotechnology and Research*, vol. 4, pp. 300–303, 2014.

[11] A. Thirumurugan, P. Aswitha, C. Kiruthika, S. Nagarajan, and A. N. Christy, "Green synthesis of platinum nanoparticles using *Azadirachta indica*-an eco- friendly approach," *Materials Letters*, vol. 170, pp. 175–178, 2016.

[12] S. Dewanjee, M. Kundu, A. Maiti, R. Majumdar, A. Majumdar, and S. C. Mandal, "In vitro evaluation of antimicrobial activity of crude extract from plants Diospyros peregrina, Coccinia grandis and Swietenia macrophylla trop," *Journal of Pharmacy Research*, vol. 6, p. 773, 2007.

[13] A. K. Bhattacharjee and A. K. Das, "Phytochemical survey of few Mysore plants," *Economic Botany*, vol. 23, no. 3, pp. 274–276, 1969.

[14] K. S. Landage, G. K. Arbade, P. Khanna, and C. J. Bhongale, "Biological approach to synthesize TiO2 nanoparticles using Staphylococcus aureus for antibacterial and anti-biofilm applications," *Journal of Microbiology & Experimentation*, vol. 8, no. 1, pp. 36–43, 2020.

[15] I. Halomoan, Y. Yulizar, R. M. Surya, and D. O. B. Apriandanu, "Facile preparation of CuO- $Gd_2Ti_2O_7$ using *Acmella uliginosa* leaf extract for photocatalytic degradation of malachite green," *Materials Research Bulletin*, vol. 150, article 111726, 2022.

[16] Y. Yulizar, D. O. B. Apriandanu, and R. M. Surya, "Fabrication of novel SnWO4/ZnO using Muntingia calabura L. leaf extract with enhanced photocatalytic methylene blue degradation under visible light irradiation," *Ceramics International*, vol. 48, no. 3, pp. 3564–3577, 2022.

[17] A. Indriyani, Y. Yulizar, R. T. Yunarti, D. O. B. Apriandanu, and R. M. Surya, "One-pot green fabrication of $BiFeO_3$ nanoparticles via *Abelmoschus esculentus L* leaves extracts for photocatalytic dye degradation," *Applied Surface Science*, vol. 563, article 150113, 2021.

[18] Y. Yulizar, J. Gunlazuardi, D. O. B. Apriandanu, and T. W. W. Syahfitri, "CuO-modified $CoTiO_3$ via *Catharanthus roseus* extract: A novel nanocomposite with high photocatalytic activity," *Materials Letters*, vol. 277, article 128349, 2020.

[19] Y. Yulizar, D. O. B. Apriandanu, and F. L. Hakim, "Two-phase synthesis in n-hexane–water, characterization, and photocatalytic activity of ZnO/Bi2Sn2O7 nanocomposite," *JOM*, vol. 73, no. 1, pp. 441–449, 2021.

[20] Y. Yulizar, A. Eprasatya, D. O. B. Apriandanu, and R. T. Yunarti, "Facile synthesis of ZnO/GdCoO$_3$ nanocomposites, characterization and their photocatalytic activity under visible light illumination," *Vacuum*, vol. 183, article 109821, 2021.

[21] Y. Yulizar, D. O. B. Apriandanu, and A. P. Wibowo, "Plant extract mediated synthesis of Au/TiO_2 nanocomposite and its photocatalytic activity under sodium light irradiation," *Composites Communications*, vol. 16, pp. 50–56, 2019.

[22] Y. Yulizar, D. O. B. Apriandanu, and R. I. Ashna, "La$_2$CuO$_4$-decorated ZnO nanoparticles with improved photocatalytic activity for malachite green degradation," *Chemical Physics Letters*, vol. 755, article 137749, 2020.

[23] Y. Yulizar, E. Kusrini, D. O. B. Apriandanu, and N. Nurdini, "Datura metel L. leaves extract mediated CeO2 nanoparticles: synthesis, characterizations, and degradation activity of DPPH radical," *Surfaces and Interfaces*, vol. 19, article 100437, 2020.

[24] J. Abdul, S. Salman, K. H. Ibrahem, and F. A. Ali, "Effect of culture media on biosynthesis of titanium dioxide nanoparticles using Lactobacillus crispatus material and methods: results and discusion," *International Journal of Advanced Research*, vol. 2, no. 5, pp. 1014–1021, 2014.

[25] C. Jayaseelan, A. A. Rahuman, S. M. Roopan et al., "Biological approach to synthesize TiO$_2$ nanoparticles using *Aeromonas hydrophila* and its antibacterial activity," *Spectrochimica Acta Part A: Molecular and Biomolecular Spectroscopy*, vol. 107, pp. 82–89, 2013.

[26] R. Joerger, T. Klaus, and C. G. Granqvist, "Biologically produced silver-carbon composite materials for optically functional thin-film coatings," *Advanced Materials*, vol. 12, no. 6, pp. 407–409, 2000.

[27] W. M. Tolles and B. B. Rath, "Nanotechnology, a stimulus for innovation," *Current Science*, vol. 85, no. 12, pp. 1746–1759, 2003.

[28] A. Vishnu Kirthi, A. Abdul Rahuman, G. Rajakumar et al., "Biosynthesis of titanium dioxide nanoparticles using bacterium *Bacillus subtilis*," *Materials Letters*, vol. 65, no. 17–18, pp. 2745–2747, 2011.

[29] C. Gélis, S. Girard, A. Mavon, M. Delverdier, N. Paillous, and P. Vicendo, "Assessment of the skin photoprotective capacities of an organo-mineral broad-spectrum sunblock on two ex vivo skin models," *Photodermatology, Photoimmunology & Photomedicine*, vol. 19, no. 5, pp. 242–253, 2003.

[30] S. Hussain, X. Yang, M. K. Aslam et al., "Robust TiN nanoparticles polysulfide anchor for Li-S storage and diffusion pathways using first principle calculations," *Chemical Engineering Journal*, vol. 391, article 123595, 2020.

[31] S. Hussain, A. J. Khan, M. Arshad et al., "Charge storage in binder-free 2D-hexagonal CoMoO$_4$ nanosheets as a redox active material for pseudocapacitors," *Ceramics International*, vol. 47, no. 6, pp. 8659–8667, 2021.

[32] S. Hussain, M. Hassan, M. S. Javed et al., "Distinctive flower-like CoNi$_2$S$_4$ nanoneedle arrays (CNS-NAs) for superior supercapacitor electrode performances," *Ceramics International*, vol. 46, no. 16, pp. 25942–25948, 2020.

[33] S. Hussain, N. Ullah, Y. Zhang et al., "One-step synthesis of unique catalyst Ni$_9$S$_8$@C for excellent MOR performances," *International Journal of Hydrogen Energy*, vol. 44, no. 45, pp. 24525–24533, 2019.

[34] S. Hussain, M. S. Javed, S. Asim et al., "Novel gravel-like NiMoO$_4$ nanoparticles on carbon cloth for outstanding supercapacitor applications," *Ceramics International*, vol. 46, no. 5, pp. 6406–6412, 2020.

[35] D. K. Ved and G. S. Goraya, *A Text Book of Demand and Supply of Medicinal Plants in India*, NMPB, New Delhi and FRLHT,, Bangalore, India, 2008.

[36] D. W. Unander, G. L. Webster, and B. S. Blumberg, "Usage and bioassays in *Phyllanthus* (Euphorbiaceae). IV. Clustering of antiviral uses and other effects," *Journal of Ethno-Pharmacology*, vol. 45, no. 1, pp. 1–18, 1995.

[37] G. L. Webster, "Classification of the Euphorbiaceae," *Annals of the Missouri Botanical Garden*, vol. 81, no. 1, pp. 3–32, 1994.

[38] B. Joseph and S. J. Raj, "An overview: pharmacognostic Properties of Phyllanthus amarus Linn," *International Journal of Pharmacology*, vol. 7, no. 1, pp. 40–45, 2010.

[39] G. Ravikant, R. Srirama, U. Senthilkumar, K. N. Ganeshaiah, and R. Umashaanker, "Genetic Resources of Phyllanthus in Southern India: Identification of Geographic and Genetic Hot Spots and Its Implication for Conservation," in *Phyllanthus Species*, Scientific Evaluation and Medicinal Applications, pp. 97–118, CRC Press, 2011.

[40] A. K. Khanna, F. Rizvi, and R. Chander, "Lipid lowering activity of *Phyllanthus niruri* in hyperlipemic rats," *Journal of Ethnopharmacology*, vol. 82, no. 1, pp. 19–22, 2002.

[41] J. Meena, R. A. Sharma, and R. Rolania, "A review on phytochemical and pharmacological properties of Phyllanthus amarus Schum. and Thonn," *International Journal of Pharmaceutical Sciences and Research*, vol. 9, no. 4, pp. 1377–1386, 2018.

[42] K. Narendra, J. Swathi, K. M. Sowjanya, and A. Krishna Satya, "Phyllanthus niruri: a review on its ethno botanical, phytochemical and pharmacological profile," *Journal of Pharmacy Research*, vol. 5, no. 9, pp. 4681–4691, 2012.

[43] S. Shanavas, A. Priyadharsan, S. Karthikeyan et al., "Green synthesis of titanium dioxide nanoparticles using *Phyllanthus niruri* leaf extract and study on its structural, optical and morphological properties," *Materials Today: Proceedings*, vol. 26, pp. 3531–3534, 2020.

[44] A. Panneerselvam, J. Velayutham, and S. Ramasamy, "Green synthesis of TiO2 nanoparticles prepared from Phyllanthus niruri leaf extract for dye adsorption and their isotherm and kinetic studies," *IET Nanobiotechnology*, vol. 15, no. 2, pp. 164–172, 2021.

[45] M. Sathish Kumar, M. Saroja, and M. Venkatachalam, "Characterization and antimicrobial activity of green synthesized zinc sulphide nanoparticles using plant extracts of Phyllanthus niruri," *International Journal of Chemical Sciences*, vol. 15, no. 2, pp. 123–130, 2017.

[46] K. Singh, M. Panghal, S. Kadyan, U. Chaudhary, and J. P. Yadav, "Green silver nanoparticles of Phyllanthus amarus: as an antibacterial agent against multi drug resistant clinical isolates of Pseudomonas aeruginosa," *Journal of Nanobiotechnology*, vol. 12, no. 1, p. 40, 2014.

[47] W. W. Andualem, F. K. Sabir, E. T. Mohammed, H. H. Belay, and B. A. Gonfa, "Synthesis of copper oxide nanoparticles using plant leaf extract of Catha edulis and its antibacterial activity," *Journal of Nanotechnology*, vol. 2020, Article ID 2932434, 10 pages, 2020.

[48] M. D. Purkayastha, T. P. Majumder, M. Sarkar, and S. Ghosh, "Carrier Transport and Shielding Properties of Rod-Like Mesoporous TiO2–SiO2 Nanocomposite," *Radiation Physics and Chemistry*, vol. 192, article 109898, 2021.

[49] Y. Huang, J. Liang, M. Xu et al., "Stereotaxically constructed graphene modification of CuO-Cu2O/TiO2 microspheres for boosted lithium and sodium storage performance," *Journal of Electronic Materials*, vol. 51, no. 1, pp. 47–56, 2021.

[50] A. Chinnathambi, S. Vasantharaj, M. Saravanan et al., "Biosynthesis of TiO 2 nanoparticles by Acalypha indica; photocatalytic degradation of methylene blue," *Applied Nanoscience*, vol. 11, pp. 1–8, 2021.

[51] S. S. Bahri, Z. Harun, S. K. Hubadillah et al., "Review on recent advance biosynthesis of TiO2nanoparticles from plant-mediated materials: characterization, mechanism and application," *IOP Conference Series: Materials Science and Engineering*, vol. 1142, no. 1, article 012005, 2021.

[52] M. Saleem, M. Y. Naz, S. Shukrullah, S. Ali, and S. T. A. Hamdani, "Ultrasonic biosynthesis of TiO2 nanoparticles for improved self-cleaning and wettability coating of DBD plasma pre-treated cotton fabric," *Applied Physics A*, vol. 127, no. 8, 2021.

[53] R. Aswini, S. Murugesan, and K. Kannan, "Bio-engineered TiO2nanoparticles usingLedebouria revolutaextract: larvicidal, histopathological, antibacterial and anticancer activity," *International Journal of Environmental Analytical Chemistry*, vol. 101, no. 15, pp. 2926–2936, 2021.

[54] A. Fall, I. Ngom, M. Bakayoko et al., "Biosynthesis of TiO2 nanoparticles by using natural extract of Citrus sinensis," *Materials Today: Proceedings*, vol. 36, pp. 349–356, 2021.

[55] K. Lingaraju, R. B. Basavaraj, K. Jayanna et al., "Biocompatible fabrication of TiO2 nanoparticles: antimicrobial, anticoagulant, antiplatelet, direct hemolytic and cytotoxicity properties," *Inorganic Chemistry Communications*, vol. 127, article 108505, 2021.

[56] M. K. Singh and M. S. Mehata, "Temperature-dependent photoluminescence and decay times of different phases of grown TiO2 nanoparticles: carrier dynamics and trap states," *Ceramics International*, vol. 47, no. 23, pp. 32534–32544, 2021.

[57] L. Zhou, Z. Shen, S. Wang et al., "Construction of quantum-scale catalytic regions on anatase TiO$_2$ nanoparticles by loading TiO$_2$ quantum dots for the photocatalytic degradation of VOCs," *Ceramics International*, vol. 47, no. 15, pp. 21090–21098, 2021.

[58] G. Nabi, A. Majid, A. Riaz, T. Alharbi, M. A. Kamran, and M. Al-Habardi, "Green synthesis of spherical TiO2 nanoparticles using Citrus limetta extract: excellent photocatalytic water decontamination agent for RhB dye," *Inorganic Chemistry Communications*, vol. 129, article 108618, 2021.

[59] K. S. Khashan, G. M. Sulaiman, F. A. Abdulameer et al., "Antibacterial activity of TiO2 nanoparticles prepared by one-step laser ablation in liquid," *Applied Sciences*, vol. 11, no. 10, p. 4623, 2021.

[60] K. Mallikarjuna, S. V. P. Vattikuti, R. Manne et al., "Sono-chemical synthesis of silver quantum dots immobilized on exfoliated graphitic carbon nitride nanostructures using ginseng extract for photocatalytic hydrogen evolution, dye degradation, and antimicrobial studies," *Nanomaterials*, vol. 11, no. 11, p. 2918, 2021.

[61] K. N. Pandiyaraj, D. Vasu, R. Ghobeira et al., "Dye wastewater degradation by the synergetic effect of an atmospheric pressure plasma treatment and the photocatalytic activity of plasma-functionalized Cu–TiO$_2$ nanoparticles," *Journal of Hazardous Materials*, vol. 405, article 124264, 2021.

[62] J. Singh, S. Juneja, R. K. Soni, and J. Bhattacharya, "Sunlight mediated enhanced photocatalytic activity of TiO$_2$ nanoparticles functionalized CuO- Cu$_2$O nanorods for removal of methylene blue and oxytetracycline hydrochloride," *Journal of Colloid and Interface Science*, vol. 590, pp. 60–71, 2021.

[63] S. Sagadevan, J. A. Lett, G. K. Weldegebrieal et al., "Enhanced gas sensing and photocatalytic activity of reduced graphene oxide loaded TiO$_2$ nanoparticles," *Chemical Physics Letters*, vol. 780, article 138897, 2021.

[64] P. Monazzam and B. F. Kisomi, "Co/TiO2 Nanoparticles: Preparation, Characterization and Its Application for Photocatalytic Degradation of Methylene Blue," *Desalination and Water Treatment*, vol. 63, pp. 283–292, 2017.

[65] R. Chauhan, A. Kumar, and R. P. Chaudhary, "Structural and photocatalytic studies of Mn doped TiO$_2$ nanoparticles," *Spectrochimica Acta Part A: Molecular and Biomolecular Spectroscopy*, vol. 98, pp. 256–264, 2012.

[66] L. Gnanasekaran, R. Hemamalini, R. Saravanan, K. Ravichandran, F. Gracia, and V. K. Gupta, "Intermediate state created by dopant ions (Mn, Co and Zr) into TiO$_2$ nanoparticles for degradation of dyes under visible light," *Journal of Molecular Liquids*, vol. 223, pp. 652–659, 2016.

[67] P. Karuppasamy, N. R. N. Nisha, A. Pugazhendhi, S. Kandasamy, and S. Pitchaimuthu, "An investigation of transition metal doped TiO$_2$ photocatalysts for the enhanced photocatalytic decoloration of methylene blue dye under visible light irradiation," *Journal of Environmental Chemical Engineering*, vol. 9, no. 4, article 105254, 2021.

[68] M. R. Bindhu, T. D. Willington, M. R. Hatshan, S. M. Chen, and T. W. Chen, "Environmental photochemistry with Sn/F simultaneously doped TiO2 nanoparticles: UV and visible light induced degradation of thiazine dye," *Environmental Research*, vol. 207, article 112108, 2021.

[69] E. T. Helmy, E. M. Abouellef, U. A. Soliman, and J. H. Pan, "Novel green synthesis of S-doped TiO$_2$ nanoparticles using *Malva parviflora* plant extract and their photocatalytic, antimicrobial and antioxidant activities under sunlight illumination," *Chemosphere*, vol. 271, article 129524, 2021.

[70] M. Aravind, M. Amalanathan, and M. Mary, "Synthesis of TiO2 nanoparticles by chemical and green synthesis methods and their multifaceted properties," *SN Applied Sciences*, vol. 3, no. 4, pp. 1–10, 2021.

[71] D. Achudhan, S. Vijayakumar, B. Malaikozhundan et al., "The antibacterial, antibiofilm, antifogging and mosquitocidal activities of titanium dioxide (TiO$_2$) nanoparticles green-synthesized using multiple plants extracts," *Journal of Environmental Chemical Engineering*, vol. 8, no. 6, article 104521, 2020.

[72] R. J. Barnes, R. Molina, J. Xu, P. J. Dobson, and I. P. Thompson, "Comparison of TiO2 and ZnO nanoparticles for photocatalytic degradation of methylene blue and the correlated inactivation of gram-positive and gram-negative bacteria," *Journal of Nanoparticle Research*, vol. 15, no. 2, 2013.

[73] K. S. Saranya, V. V. T. Padil, C. Senan et al., "Green synthesis of high temperature stable anatase titanium dioxide nanoparticles using gum kondagogu: characterization and solar driven photocatalytic degradation of organic dye," *Nanomaterials*, vol. 8, no. 12, p. 1002, 2018.

[74] S. A. Yasin, J. A. Abbas, M. M. Ali, I. A. Saeed, and I. H. Ahmed, "Methylene blue photocatalytic degradation by TiO2 nanoparticles supported on PET nanofibres," *Materials Today: Proceedings*, vol. 20, pp. 482–487, 2020.

Hindawi

Retraction

Retracted: Application and Optimization of Wing Structure Design of DF-2 Light Sports Aircraft Based on Composite Material Characteristics

Journal of Nanomaterials

This article has been retracted by Hindawi following an investigation undertaken by the publisher [1]. This investigation has uncovered evidence of one or more of the following indicators of systematic manipulation of the publication process:

(1) Discrepancies in scope

(2) Discrepancies in the description of the research reported

(3) Discrepancies between the availability of data and the research described

(4) Inappropriate citations

(5) Incoherent, meaningless and/or irrelevant content included in the article

(6) Peer-review manipulation

The presence of these indicators undermines our confidence in the integrity of the article's content and we cannot, therefore, vouch for its reliability. Please note that this notice is intended solely to alert readers that the content of this article is unreliable. We have not investigated whether authors were aware of or involved in the systematic manipulation of the publication process.

Wiley and Hindawi regrets that the usual quality checks did not identify these issues before publication and have since put additional measures in place to safeguard research integrity.

We wish to credit our own Research Integrity and Research Publishing teams and anonymous and named external researchers and research integrity experts for contributing to this investigation.

The corresponding author, as the representative of all authors, has been given the opportunity to register their agreement or disagreement to this retraction. We have kept a record of any response received.

References

[1] F. Li, S. Zhang, and W. Cheng, "Application and Optimization of Wing Structure Design of DF-2 Light Sports Aircraft Based on Composite Material Characteristics," *Journal of Nanomaterials*, vol. 2022, Article ID 6967016, 10 pages, 2022.

Research Article

Application and Optimization of Wing Structure Design of DF-2 Light Sports Aircraft Based on Composite Material Characteristics

Fenglei Li,[1,2] Shengnian Zhang [ID],[1] and Wanxiang Cheng[1]

[1]*School of Physical Education and Sport Training, Shanghai University of Sport, Shanghai 200438, China*
[2]*School of Physical Education, East China University of Technology, Nanchang, 330013 Jiangxi, China*

Correspondence should be addressed to Shengnian Zhang; 18403037@masu.edu.cn

Compared with ordinary metal structures, advanced composite materials have the characteristics of high strength, high rigidity, and light weight. The use of composite materials in aircraft structures is currently a hot research topic. This research mainly discusses the optimization design of the composite wing structure of the DF-2 light sports aircraft. This article takes the DF-2 light sports aircraft planned to be produced by the company as the source. Based on its overall design basis, aerodynamic requirements, and the original wing structure design, according to the composite material aircraft structure design theory and method, the aircraft wing structure is carried out. Composite materials are materials with new properties that are composed of two or more materials with different properties at the macroscale by physical and chemical methods. Composite materials can be divided into functional composite materials and structural composite materials according to the nature of the application. Functional composites are materials with special functions, such as conductive composites, ablative materials, and frictional composites. At present, the main research is on structural composite materials, which are composed of two components: matrix material and reinforcing material. The new structural scheme design and structural strength analysis are designed to meet the structural strength requirements of the wing and the lightest weight. In this paper, according to the force transmission characteristics of different structural types of the wing, the characteristics of the load transmission are analyzed, and the shape parameters and load parameters of the wing structure design are used as initial conditions, and the quantitative analysis model of the wing structure is constructed according to the requirements of strength, stiffness, and stability. Through rapid mathematical modeling and analysis of the wing structure, the weight and efficiency of different configurations can be evaluated. Through the quantitative analysis model of the wing, the wing structure type can be quickly determined according to the wing parameters in the preliminary design, which makes the basis for the selection of the wing structure type. After optimization, the weight of the wing structure decreased from 0.966 kg to 0.803 kg, a decrease of 16.87%. The designability of composite materials is one of its major characteristics. By optimizing the layup angle, layup sequence, and dropout area, the performance indicators of the structure are finally improved. This research will promote the further development of the aerospace field.

1. Introduction

Compared with the conventional mechanical structure design, aviation structural design requires very strict control of its structural weight. Because composite materials have superior performance in this respect, they are favored by aviation

manufacturers and are more and more widely used in the design of aircraft structures.

Excessive cost is still the main obstacle restricting the large-scale application of composite materials in aircraft structures. If manufacturing and assembly problems are considered at the design stage, the aircraft can have an

adjustable lift-to-drag ratio, shorter take-off and landing distance, less fuel consumption, wider range, higher ceiling, and higher mobility and stealth performance. And stealth performance is another important trend in the development of composite materials.

Composite structures have different structural properties due to the different percentage and sequence of layering at different angles. Yuan et al.'s loading of Au nanoparticles (AuNPs) onto environmentally sensitive polymer microgels is increasingly used to regulate their optical properties and catalytic activity. Here, they synthesized a composite polymer microgel composed of poly (n-isopropylacrylamide-co-3-methylpropyltrimethoxysilane)/poly (acrylic acid) with a core-shell structure and used nanoparticles to load AuNPs onto the network chain of the polymer microgel in a controlled manner. The prepared AuNP composite has good pH sensitivity. Therefore, the electromagnetic coupling between AuNPs can be regulated by the swelling/deswelling of polymer microgels under various acidic/alkaline conditions. More importantly, the coordination interaction between carboxyl groups and Cu ions in the PAA chain is altered by changing the content of Cu ions at different pH conditions, thus modulating the local surface plasmon resonance of AuNPs. These structural characteristics of the prepared composite microgel can adjust the optical properties of AuNPs in the following ways [1]. Chesterman et al. believe that resin-based composites (RBC) are increasingly used in posterior tooth restoration. The growing demand for aesthetically pleasing, tooth color restorations, coupled with patient concerns about using mercury-containing restorations, has driven the explosion in RBC material use. With the minamata convention of 2013 calling for the phasing out of dental amalgam and dental schools increasingly teaching RBC repair techniques for posterior teeth, the dental industry's reliance on RBC repair for posterior teeth is likely only to grow. To simplify and speed the placement of large rear RBCs, manufacturers produce a range of materials that can be placed in single or deeper increments, called bulk RBCs. In a relatively short period of time, many bulk RBCs have become available, with incremental depths of between 4 and 10 mm. The placement of these large incremental RBCs may reduce the time required to repair after placement, thus reducing technical sensitivity [2]. Palumbo et al. believe that thermoelastic signal phases associated with inherent dissipation processes occurring in materials have been used to locate and assess damage areas in a quantitative manner. In addition, thermoelastic phase analysis leads to the evaluation of the durability limits of composites. In fact, by comparing the results with those provided by standard test methods, the potential of the proposed procedure is shown first as a nondestructive technique for continuous monitoring of damage to composite structures subjected to fatigue loads and secondly as a fatigue limit index [3]. Boumhaout et al.'s work deals with the thermomechanical properties of composites made from mortar and date fiber mesh (DPF). The objective is to evaluate the thermal and mechanical properties of this material for building insulation. The volume percentage of date FibreNet in tested samples ranged from 0% to 51%. The thermal characteristics of the sample are experimentally determined in terms of conductivity, diffusivity,

Table 1: Main performance parameters of composite materials used in wing structure.

Material	T700/epoxy	Fabric_T700	NOMEX
Axial modulus (GPa)	120	56	0.3
Transverse modulus (GPa)	9	56	0.3
Z-direction modulus (GPa)	9	8	91
Shear modulus (XY/GPa)	4.8	4.6	0.06
Shear modulus (YZ/GPa)	4.8	4.6	20
Shear modulus (XZ/GPa)	4.8	4.6	30
Poisson's ratio (XY)	0.3	0.15	0.33
Poisson's ratio (YZ)	0.3	0.15	0.01
Poisson's ratio (XZ)	0.3	0.15	0.01

capacity, and flow rate. In addition, the bending and compression strengths of the samples were systematically evaluated. DPF grid has a positive effect on the thermomechanical properties of composites. In fact, it significantly improves the insulation ability of mortar, increases the thermal diffusion damping rate, and makes mortar lighter. DPF mesh also improves the ductility of mortar and meets the mechanical requirements of building materials [4]. Based on plant waste corn cob and nitrogen source melamine, Li et al. adopted an innovative method to controllable synthesis of multistage nanotube @ mesoporous carbon composites through heat treatment. Corn cobs provide a carbon source and a small amount of Fe as a catalyst, while melamine provides a nitrogen source. The corn cob is pretreated with concentrated sulfuric acid and then mixed with melamine. After calcination at 800°C for 2 hours, a large number of thin walled nitrogen-doped carbon nanotubes (MWNTS) grew vertically on mesoporous carbon skeleton with unique structure. The diameter of the nanotubes is about 50 nm, and their length varies between 0.1 and 20 μm, which can be controlled by adjusting the ratio of the pretreated corn cob to melamine. At the same time, the composite material has stable interconnect pores and channels with a surface area up to 1100 m^2/g, which significantly accelerates the ion and electron transport rates [5]. In the assembly of composite components, the fastener holes need to be processed not only in large quantity and high quality requirements but also difficult, which is one of the most difficult processing procedures in composite processing. It is easy to produce delamination, tearing, splitting, and other phenomena when making holes in composite materials, so the hole making connection is an important link that affects the assembly quality of composite components. Composite layup optimization is to optimize the design in the combination of these types of layup angles, while considering the laying position of each layer of composite materials, so as to maximize the excellent properties of composite materials [6].

The honeycomb sandwich structure has been widely used in aircraft structural parts due to its excellent bending stiffness characteristics. The full-height sandwich structure is used on the control surface, which achieves a significant weight

reduction effect on the premise of ensuring strength and rigidity [7]. Combining the design theories and methods of composite laminates and sandwich panels, as well as the introduction of bioengineering structural design concepts and topological structure design concepts, this article will maximize the use of composite materials to design the wing in detail. According to the requirements of the initial design, after designing and analyzing the initial structure, tests were carried out to prove the feasibility of the design. From the test, it can be seen that the initial design is relatively conservative, and the strength of the material and the rigidity of the structure are still too high. Based on this situation, a lightweight design of the wing was implemented. Regarding the feasibility and operability of the molding scheme of various structural components, the explanation is based on the analysis of factors such as the existing technical level and manufacturing cost, manufacturing cycle, and technical level of personnel.

2. Optimized Plan for Composite Wing

2.1. Optimizing the Thickness of Composite Material Structure Ply

2.1.1. Establishment of Optimization Model. The honeycomb structure has high deformation and supporting force and is suitable as a candidate for a deformed structure. However, the general honeycomb cannot be actively deformed, and the active deformation honeycomb based on shape memory materials has a slow deformation speed and cannot meet the requirements of an adaptive structure [8].

If the material structure and shape of the honeycomb core layer are determined, the core layer structure can be treated as a laminate when designing the honeycomb core layer composite structure. The core layer is just another layer, and the thickness is the same as the height of the core layer. The core material of the skin's honeycomb is NOMEX honeycomb [9]. The closed wing box structure is composed of the skin and the beams and ribs of the wing. The skin of the wing box is mainly used for torsion, improving the torsional rigidity of the skin and making the skin with high damage and peeling resistance. It is covered by carbon fiber cloth. Fabric is the outermost layer of the T700 wing, and the carbon fiber cloth is composed of longitudinal fibers and transverse fibers. The main performance parameters of the composite materials used in the wing structure are shown in Table 1.

2.1.2. Stiffness Performance of Composite Laminates. The physical equations of laminates can be derived from the classical laminate theory of composite materials [10, 11]:

$$\begin{pmatrix} V \\ M \end{pmatrix} = \begin{pmatrix} A & B \\ C & D \end{pmatrix} \begin{Bmatrix} \chi \\ \gamma \end{Bmatrix}. \tag{1}$$

N is the resultant force array in the middle of the laminate; M is the resultant moment array in the middle of the laminate [12].

Since the lower wing panel mainly bears the tensile load, the tensile load-bearing capacity of the initial model of the

TABLE 2: Test protocol and results.

Test number	$W1$ /mm	$W2$ /mm	Wing tip deformation/mm	Maximum stress/MPa
1	320	190	19.551	184.11
2	280	190	11.836	126.1
3	360	190	11.92	122.07
4	320	223	23.011	173.84
5	280	223	15.327	121.21
6	360	223	16.614	101.76
7	320	256	22.55	183.54
8	280	256	13.633	76.959
9	360	256	15.613	91.109

open area can be calculated first. In order to explore other properties of the open-ended laminate, the stability load-bearing capacity and postbuckling load-bearing capacity of the structure are also calculated. Analyze the calculation result and use it as the design basis for the reinforcement scheme of the opening area. Tensile stiffness array of laminate A is as follows[13]:

$$A = \sum_{k=1}^{n} Q(Z_K - Z_{K-1}) = \sum_{k=1}^{n} Qh_K. \tag{2}$$

Laminated plate tension and bending coupling stiffness matrix B are as follows [14]:

$$B = \frac{1}{2} \sum_{K=1} Q\left(Z_K^2 - Z_{K-1}^2\right) = \sum_{K=1} QZHK + 1. \tag{3}$$

Among them, Z represents the distance between the middle surface and the middle surface of the k-th layer [15, 16].

The plies involved in this article are symmetrical and balanced pavement designs, and a reasonable pavement structure design that meets the requirements of structural rigidity, strength, and stability has been found.

2.2. Kriging Model.
In this paper, the response surface method of Kriging model is applied to the optimization of the wing spar position, thereby improving the prediction accuracy of its response surface. In the Kriging model, the original unknown function can be expressed as follows [17]:

$$y(x) = f(x) + Z(x), \tag{4}$$

where $f(x)$ is an unknown function of x.

The predicted estimated value $y(x)$ of the response value $y(x)$ at the unknown vector x is given by the following formula [18, 19]:

$$\widehat{y}(x) = \widehat{\beta} + r^T(x)R^{-1}\left(y(x) - f\widehat{\beta}\right). \tag{5}$$
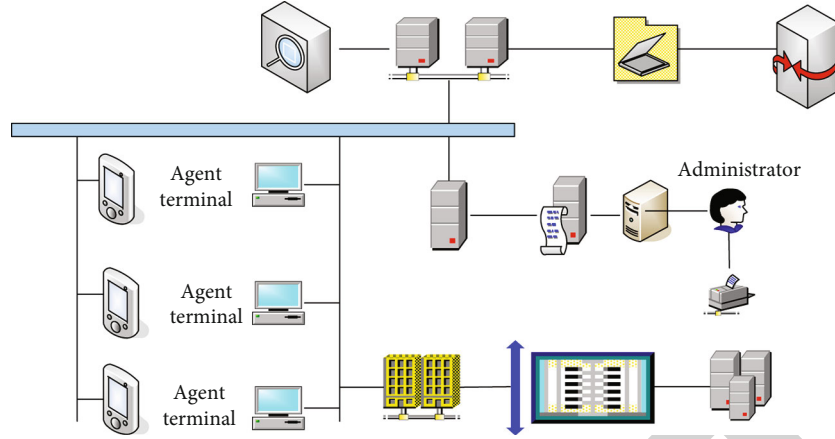
FIGURE 1: The integration process of genetic evolution.
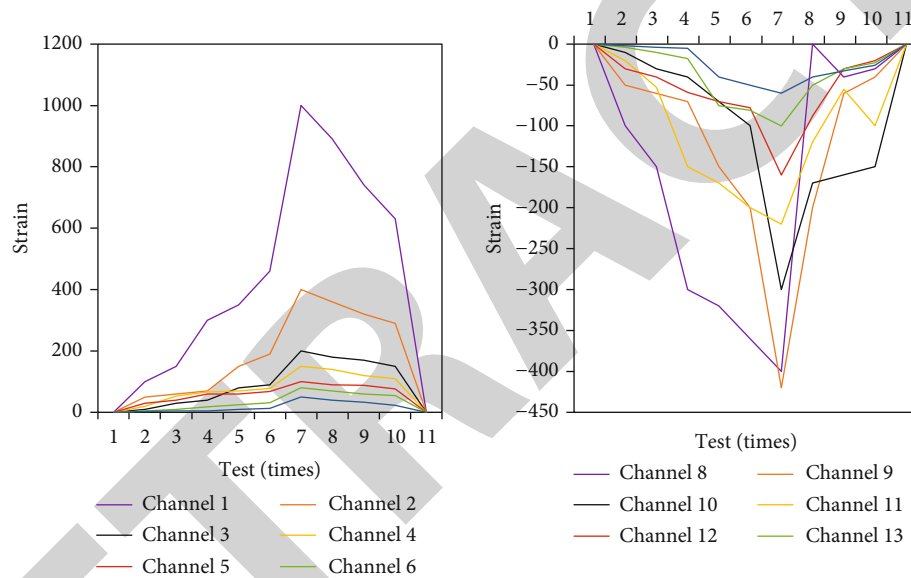
FIGURE 2: Strain of each test point.

Among them, $r^T(x)$ is the correlation vector between the unknown vector x of length n and the sample data [20].

$$r^T(x) = [R(x, x_1), R(x, x_2), R(x, x_3), \cdots, R(x, x_n)]^T. \quad (6)$$

From the narrative about the Kriging model, we can know that having a certain amount of sample data is the premise of establishing the Kriging model. When selecting samples in the entire design space, a limited number of samples should be used. It is possible to fully reflect the characteristics of the design space, which requires experimental design. There are many methods of experimental design, such as full factorial design and central composite design. This paper uses the central composite design method to arrange the response surface test, which is designed on three levels, and a total of 9 sets of parameter variables $W1$ and $W2$ are designed. The test plan and results are shown in Table 2.

2.3. Optimal Mathematical Model. Since changing the position of the spar has little effect on the quality of the wing, it is not considered here. Under the condition of meeting the strength requirements, the stiffness of the structure is selected as the objective function, which is measured by the deformation of the wing tip [21].

According to the constraints of the wing geometry size, the variation ranges of the parameter variables $W1$ and $W2$ are, respectively, taken as $280\,\text{mm} \leq W1 \leq 360\,\text{mm}$ and $190\,\text{mm} \leq W2 \leq 256\,\text{mm}$, and the optimized mathematical model can be described as follows [22, 23]:

$$\begin{cases} \min S(X) \\ |F|_{\max}(x) - 1 < 0 \\ X_i \leq X_n \leq X_k. \end{cases} \quad (7)$$
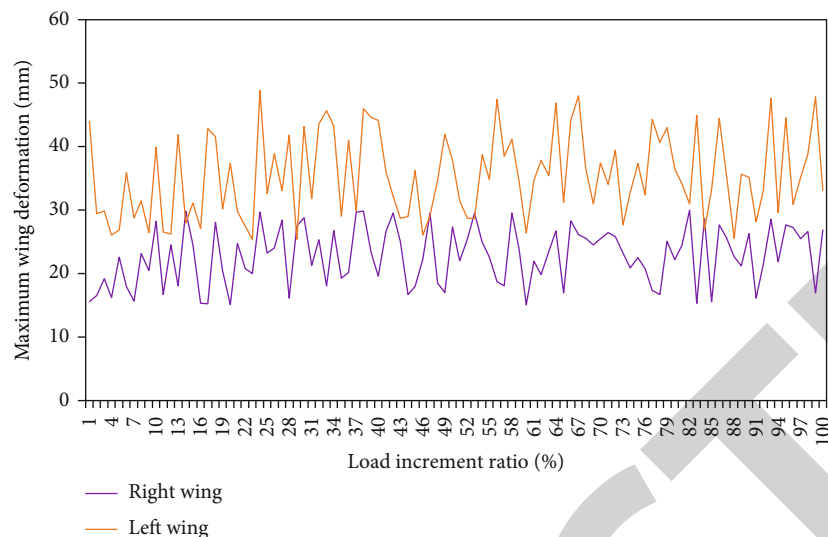
Figure 3: Left and right wing stiffness test.

Among them, S is the stiffness index. This paper selects the maximum deformation of the wing tip to characterize it; X_n is the position parameter of the spar; F is the failure factor of the wing structure [24].

2.4. Optimized Structure. ISIGHT can integrate various types of simulation software into a unified framework. The setting of input files and output files; the writing of the call commands of the process simulation software; the drawing, reading, and writing of parameters; the selection of design variables; and other comprehensive optimization algorithms create the entire design process to achieve generalization, automation, parameterization, and visualization, eliminating the limitations of conventional settings in the accounting process. ISIGHT has powerful postprocessing functions. Users can draw optimization process curves, output data tables, and generate analysis reports.

The ISIGHT software has the data interface of many mainstream engineering software, so it can fully realize the data transmission between various software. Using the ISIGHT software to integrate MATLAB and ABAQUS, a multi-island genetic algorithm for optimizing stack thickness is realized. First, use MATLAB to generate the layup information of the front and rear wing beams, and send the layup information. The results were imported into the ABAQUS software, and a finite element model was established for the calculation. The calculated structural quality, TSui-Wu damage coefficient, and maximum deformation displacement information are introduced by MATLAB, and selection and transfer operations are performed to generate the next generation of hierarchical information and then generate the next generation of genetic evolution. The integration process is shown in Figure 1.

2.5. Load Test. The design load test is a test to evaluate the ability of the test piece to bear the design load. In all major design cases, the load usually must be 100% of the design load. However, in the main structure, under the premise of ensuring the structural strength, a certain proportion of the initial design load can be load tested on a part of the design case. For each main design case, when the test load exceeds the use load test, the load needs to be adjusted in stages according to an increment of less than 5% of the design load at each stage, as well as strain, displacement, and damage. The test parts must be measured and recorded periodically. The test piece can bear 100% of the design load, and the structure will not be damaged for at least 3 seconds under 100% of the design load.

3. Optimization Results of Composite Wing Structure of DF-2 Light Sports Aircraft

It can be seen from the curve shape of Figure 2 that when the titanium alloy joint is subjected to the maximum load, the strain at each test point will not change, but will change linearly. After the load is completely removed, the strain will all return to zero. Observe all the distortion curves and obtain the maximum distortion curve of the curve corresponding to each 10 channels; the maximum value is 1019 $\mu\varepsilon$. The position of the tenth strain gauge is the connection structure between the wing and the fuselage at the wing beam. According to calculations, the stress value at this point is 1088 MPa. Therefore, the maximum stress is all less than 42.73 MPa. Because the tensile strength of the titanium alloy is 900 MPa, it can be seen that all the measurement points meet the strength requirements of the titanium alloy. Moreover, the finite element simulation data, the contrast test data, and the finite element simulation of the stress value of 10~131 MPa are much larger than the actual test data. This is the result of finite element simulation analysis and contact. The use of components to establish bolted connections has stress concentration, and the finite element simulation error is very large. Therefore, in the connection of the titanium alloy, the maximum stress value of the composite material and the titanium alloy that reaches 1079 MPa is a big error. Combined with the previous engineering design experience, the structural design here will
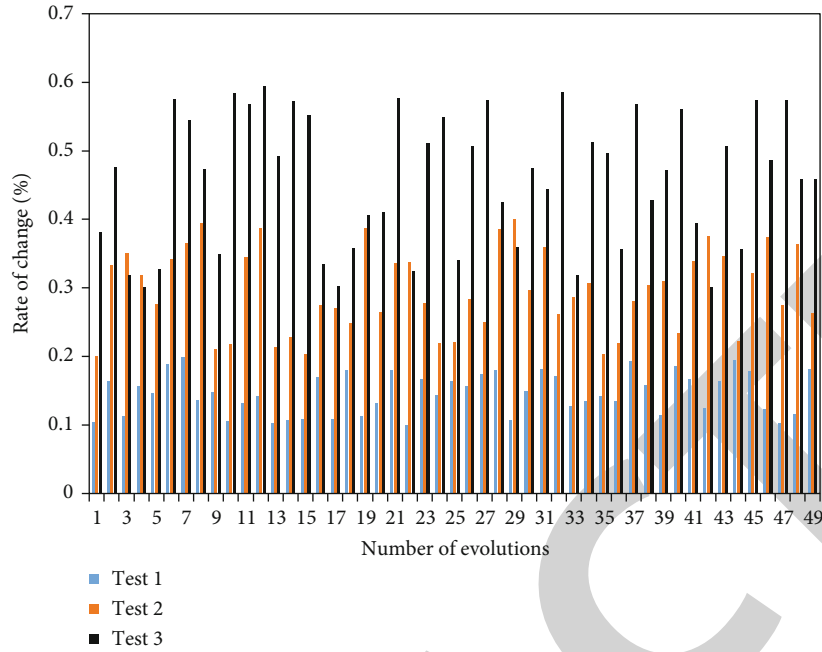
Figure 4: Evolutionary process.
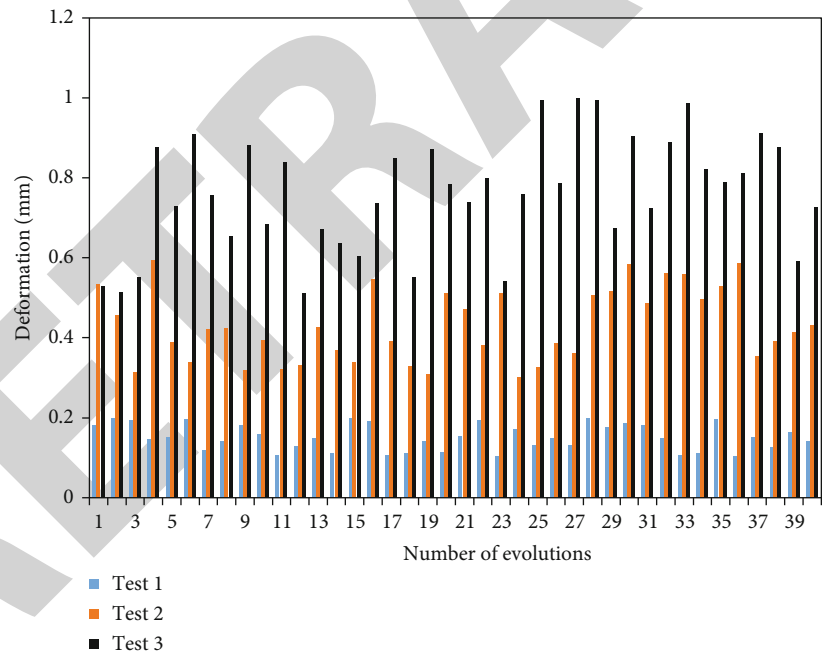
Figure 5: The evolution process of laminate ply angle optimization.

not fail but can meet the strength requirements. The strain of each test point is shown in Figure 2.

It can be seen from Figure 3 that the deformation curves of the left and right wing ends are quite different. When the test load is applied in stages, the left and right wing ends often have a deviation of about 20 mm. This is mainly due to the error of the measurement position selected by the test operator during the measurement process and the unstable initial configuration. The maximum deformation of the blade

obtained by finite element simulation is 96.519 mm. The maximum deformation error and simulation data of the left and right wings are 16.81% and 8.39%, respectively. Since the test data and simulation data are both above 180 mm, the rigidity of the wing structure is very high, which meets the conditions. The left and right wing stiffness test is shown in Figure 3.

After 10 generations of genetic evolution, the 753th evolutionary individual in the eighth generation was found

Table 3: Hierarchical optimization results of wing structure.

	Parameters before optimization	Parameters after optimization
Beam ratio 1	0.3	0.32
Beam ratio 2	0.75	0.78
Beam ratio 3	0.3	0.27
Beam ratio 4	0.75	0.86
Beam 1 width (mm)	15	15.21
Beam 2 width (mm)	15	14.23
Rib 1 (mm)	300	267.21
Rib 2 (mm)	600	576.34

Table 4: The height record of the root and tip of the wing at both ends of the wing during the test.

Load	Left wing tip height	Left root height	Left wing difference	Right wing tip height
10% load	253.98	214.46	39.52	241.8
20% load	267.9	216.88	51.02	245.28
30% load	273.6	218.54	55.06	254.22
40% load	275.5	211.56	63.94	256.2
50% load	284.68	212.8	71.88	258.42
60% load	291.62	214.58	77.04	265.00
70% load	294.00	208.46	85.54	268.38
80% load	299.02	208.28	90.74	272.82

to meet the design requirements and the lowest quality individual. The layer thickness information expressed is as follows: the variable cross-section area of the front beam 1-7 is 6/4/2/2/2/2/2, and the variable cross-section area of the rear beam 1-7 is 8/4/4/2. The weight of the wing structure decreased from 0.966 kg to 0.803 kg, a decrease of 16.87%. The evolution process is shown in Figure 4.

The angle optimization of the laminate ply adopts the same method as the thickness optimization, and the evolution process is shown in Figure 5.

Through the first-level optimization of the beam and rib layout and the second-level optimization of the composite material ply, the structural mass is reduced from 1.173 kg to 0.803 kg, and the mass is reduced by 31.54%. The maximum deformation displacement of the structure changed from 34.49 mm to 40.95 mm, an increase of 18.7%. The failure factor of Tsai-Wu changed from 0.512 to 0.472, a decrease of 7.8%. Through the grading optimization study of the wing structure, a good weight reduction effect has been achieved under the premise of meeting various design indicators. The hierarchical optimization results of the wing structure are shown in Table 3. The Tsai-Wu criterion will be applied to determine the safety factor for composite orthotropic shells. This criterion considers the total strain energy (including distortion energy and expansion energy) for predicting failure.

During the test, the record of the height of the wing root and wing tip at both ends of the wing during the test is shown in Table 4. The data in the table is plotted against the aforementioned analysis data. Since this test is a load test, the design load (150% use load), 87.2 mm of the analysis result is converted into the use load result, and the resulting deformation is 58.1 mm. Therefore, the error of the test and analysis results is 3%, which is considered acceptable within the scope of the project, and neither of them exceeds the overall required value.

Quantitative analysis method is a method for analyzing the quantitative characteristics, quantitative relationships, and quantitative changes of social phenomena. The quantitative analysis model method is used to model and analyze the two structural types of beam configuration and monolithic configuration. With the shape parameters as the initial conditions, the mathematical analysis model is constructed, and the weight of the wing structure under different loads is obtained by changing the value of the load. The relationship curve with load is shown in Figure 6. The load density at the root of the wing is 1357 N/mm. It can be seen from Figure 6 that the monolithic configuration is selected at this load level, and the weight of the wing structure is lighter.

4. Discussion

After the outer panel and the number of positions of the composite wing are fixed, the components need to be assembled. However, most of the initial researches on the manufacturing process of composite wings mainly focus on the design, molding, and performance testing of composite parts. There is almost no research on the assembly process of composite parts, especially the assembly of composite parts. The structural optimization technology of composite materials refers to engineering application technologies that improve the rigidity, strength, and stability of fiber-reinforced resin matrix composites by optimizing layer shape, ply angle, and other layer information. As the proportion of aircraft structural composite materials increases, the assembly of aircraft composite structures will account for an increasing proportion of aircraft assembly. New assembly tools must fully consider the structural characteristics of composite materials, combined with new technologies such as flexibility and reconstruction, and improve the quality and efficiency of assembly during the design process. Different load-bearing levels will affect the choice of wing structure and the internal configuration of the wing structure. Before explaining the influence of different load levels on the wing structure layout, the single wing load level range must be defined. The typical stress modes of various wing structures are beam type, monolithic type, and multiwall type. Based on the above analysis, the choice of wing structure mainly affects the rigidity and stability
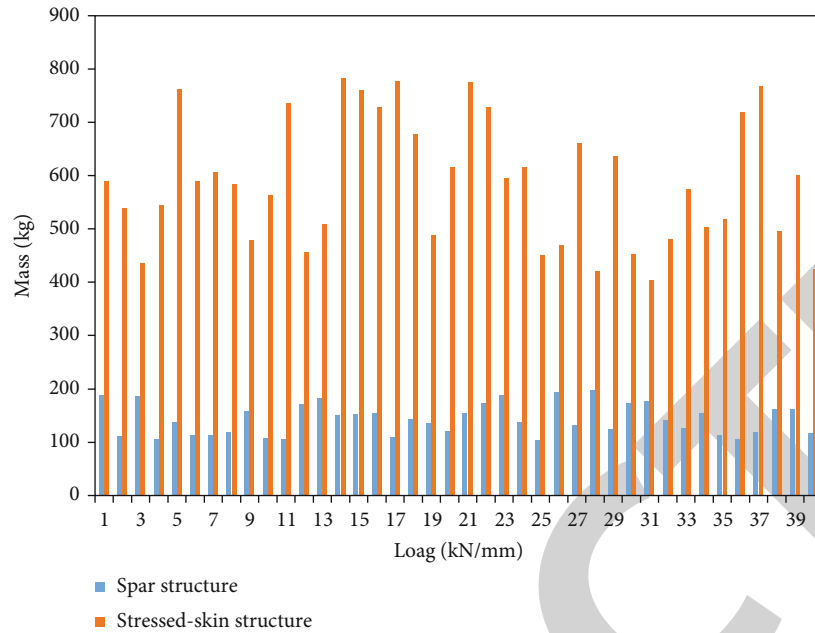
Figure 6: The relationship between the weight of the wing structure and the load under different loads.

of the wing structure. In the assembly process, it is necessary to repeatedly optimize the assembly sequence to find a suitable assembly process to ensure the adjusted assembly of the chassis. In addition, due to the limitations of natural material forming processes and methods, compared with metal components, the manufacturing geometric accuracy of composite components is not easy to control and can be assembled due to large rigidity, brittle matrix, and weak interlayer strength. The deformation is very small, and it is generally not allowed to drop, and it is difficult to correct the assembly gap. These all show the high components of composite components [25, 26].

The connection design and strength analysis of composite structures are different from those of metal structures. The influencing factors of composite material structure are much more complicated than the influencing factors of metal structure, and the damage mechanism is essentially different from the influencing factors of metal structure. Regarding the metal connection, according to the plasticity of the metal material, the load can be redistributed to the multinail connection, and the force of each nail element becomes uniform. After confirming the connection strength of the nail elements, each nail element is loaded. However, composite materials are brittle materials with small plastic deformation, multiple nail connections, and large difference in load distribution of nail elements. In addition, the nail holes in the connecting parts of the composite material cut off the reinforcing fibers, resulting in a complicated stress distribution and a more serious stress concentration problem at the end of the hole. There are various types of combinations of wing separation surfaces. Therefore, it is necessary to comprehensively consider the overall structural characteristics and determine the appropriate power transmission path according to the link components such as the beam edge between the wing segments and the long truss configuration. There is a unified design of the connection

method of the wing separation surface, which largely depends on the designer's design experience [27].

Composite materials are widely used in aerospace and completely replaced metals in some fields such as wind power blades. Carbon fiber reinforced composite material (CFRP) has the advantages of high specific strength, high specific rigidity, and high heat resistance, so it is widely used in ultra-high-speed aircraft. Due to corrosion resistance, fatigue resistance, and design, composite materials can be used in complex environments such as plains, plateaus, and the sea. The working hours and maintenance intervals become longer, and they can play an irreplaceable role in some areas such as forwards. Compared with the traditional optimization method, the optimization method adopted in this paper has a series of optimization characteristics, including generalization, automation, parameterization, and visualization. For complex design variables such as panel and number of bits, the platform can be optimized at the same time. The optimization results show that the structural quality is reduced, the strength and rigidity are improved, and the optimization efficiency of the composite material is improved. This research includes finite element theoretical research on laminated plate structure and honeycomb sandwich structure. The typical structure of the composite wing, such as the main beam, will be analyzed and optimized according to the general requirements of the engineering field [28, 29].

The extensive use of composite materials in the aviation field actually brings many possibilities to the structural design of aircraft. This is because, compared with metal materials, composite materials have higher strength and higher designability. The wing layer has orthotropic anisotropy, and the structural characteristics are determined by the angle and order of the layers. In the past, the aircraft manufacturing and assembly process, the number of tools,

the size, and the diversity all have the disadvantages of high cost and a lot of labor costs for disassembly and assembly. To cooperate with automated robotic mining systems, reconfigurable, low-cost design, and manufacturing technologies are required. The positioning configuration adopts a modular design, which can complete the positioning of the dynamic module and modify the mode of the dynamic module by moving various dynamic modules. This technology is very important for reducing costs and achieving flexible assembly.

According to the anisotropy and unevenness of the lamination of the composite material, the longitudinal and transverse characteristics are completely different, and the tensile characteristics and compression characteristics are also different. According to the anisotropy, the direction of each layer of the composite material can be adjusted at will, personalized design according to various structures and uses, and the elastic properties and strength properties of the material can be adjusted according to various needs to obtain the best structural effect. The deformable aircraft can change its shape according to different flight conditions, so it can obtain the best performance in the entire flight process. The outer panel of a deformable aircraft can not only deform with the structure but also needs to withstand the air load. Foaming material is a new type of composite material using fuel gas filler. There are many types of foam materials, but they generally have the following characteristics: light weight, material saving, low thermal conductivity, excellent heat insulation performance, excellent sound insulation effect, impact load absorption, excellent cushioning performance, and high strength.

With the intensification of market competition, the aviation industry has undergone fundamental changes in the performance and cost of aircraft design concepts. Aircraft designers and manufacturers have begun to focus on ways to reduce aircraft costs to obtain higher performance, and as a result, they have carried out aircraft design. In addition to considering the aerodynamic shape and structural weight, manufacturing possibilities, manufacturing costs, and other factors must also be considered. The final decision of the design plan not only considers the mechanical point of view (aerodynamic characteristics and structural characteristics) but also considers whether the structure is easy to manufacture and whether it can accept manufacturing costs and other factors. According to the final design plan, factors such as aerodynamics, structure, manufacturing possibilities, and manufacturing costs are comprehensively balanced. The use of smart materials and structures can realize the configuration and reorganization of the aircraft during flight and obtain the best air performance. In the future, airplanes can fly like birds, and intelligently deformed airplanes are an important direction for future development of airplanes. The deformable aircraft can be adapted to various flight conditions by changing its configuration to achieve the best overall performance. Deformable technology, high energy density drive technology, and adaptive construction technology are still the main technologies for realizing deformable aircraft [30].

5. Conclusion

This article first introduces the main types of wing structures and the design characteristics of composite materials and then summarizes the main methods of modern wing structure selection and design and proposes a quantitative analysis model method that combines force transmission analysis with finite element. According to the force transmission characteristics of different components, a specific construction method that is different from the construction standard of the quantitative analysis model is provided. Next, a quantitative analysis model of the beam configuration and the monolithic configuration is constructed, and the load-weight characteristic curve of the structure is displayed. The box section simulation process restores the actual stress distribution of the wing structure through multiple modeling analyses. The calculation formula for important elements of the stability of the box segment has been optimized to ensure the accuracy of the calculation results. On this basis, through the strength analysis of the wing structure, the classification method, the optimized size layout of the wing structure, and the optimization process analysis and comparison of the structural efficiency of the design schemes, the best design of the wing can be completed quickly and accurately structure. This article did not study the ply sequence and ply optimization of composite laminate structure or sandwich structure. In the future, it should be combined with related theories and algorithms to make the structure design more perfect.

Data Availability

The data that support the findings of this study are available from the corresponding author upon reasonable request.

Conflicts of Interest

The authors declare that they have no conflicts of interest.

References

[1] Y. Zuo, J. Zhao, Y. Gao, and Y. Zhang, "Controllable synthesis of P(NIPAM-co-MPTMS)/PAA–Au composite materials with tunable LSPR performance," *Journal of Materials Science*, vol. 52, no. 10, pp. 9584–9601, 2017.

[2] J. Chesterman, A. Jowett, A. Gallacher, and P. Nixon, "Bulk-fill resin-based composite restorative materials: a review," *British Dental Journal*, vol. 222, no. 5, pp. 337–344, 2017.

[3] D. Palumbo, R. D. Finis, G. P. Demelio, and U. Galietti, "Study of damage evolution in composite materials based on the thermoelastic phase analysis (TPA) method," *Composites Part B Engineering*, vol. 117, pp. 49–60, 2017.

[4] M. Boumhaout, L. Boukhattem, H. Hamdi, B. Benhamou, and F. Ait Nouh, "Thermomechanical characterization of a biocomposite building material: mortar reinforced with date palm fibers mesh," *Construction & Building Materials*, vol. 135, pp. 241–250, 2017.

[5] H. Li, Y. Gong, C. Fu et al., "A novel method to prepare a nanotubes@mesoporous carbon composite material based on

Retraction

Retracted: Realization of a Noncontact IC Chip with Embedded Ferroelectric Memory in an Auxiliary Timing Device for Sports Games

Journal of Nanomaterials

This article has been retracted by Hindawi following an investigation undertaken by the publisher [1]. This investigation has uncovered evidence of one or more of the following indicators of systematic manipulation of the publication process:

(1) Discrepancies in scope

(2) Discrepancies in the description of the research reported

(3) Discrepancies between the availability of data and the research described

(4) Inappropriate citations

(5) Incoherent, meaningless and/or irrelevant content included in the article

(6) Peer-review manipulation

The presence of these indicators undermines our confidence in the integrity of the article's content and we cannot, therefore, vouch for its reliability. Please note that this notice is intended solely to alert readers that the content of this article is unreliable. We have not investigated whether authors were aware of or involved in the systematic manipulation of the publication process.

Wiley and Hindawi regrets that the usual quality checks did not identify these issues before publication and have since put additional measures in place to safeguard research integrity.

We wish to credit our own Research Integrity and Research Publishing teams and anonymous and named external researchers and research integrity experts for contributing to this investigation.

The corresponding author, as the representative of all authors, has been given the opportunity to register their agreement or disagreement to this retraction. We have kept a record of any response received.

References

[1] J. Chen, "Realization of a Noncontact IC Chip with Embedded Ferroelectric Memory in an Auxiliary Timing Device for Sports Games," *Journal of Nanomaterials*, vol. 2022, Article ID 9933084, 12 pages, 2022.

Hindawi

Research Article

Realization of a Noncontact IC Chip with Embedded Ferroelectric Memory in an Auxiliary Timing Device for Sports Games

Jian Chen [ID]

Department of Physical Education, College of Engineering and Technology, Chengdu University of Technology, Leshan, 614000 Sichuan, China

Correspondence should be addressed to Jian Chen; 18402422@masu.edu.cn

The research direction of the new generation of embedded memory can be summarized into two types of embedded nonvolatile memory and embedded volatile memory; the research on online testing of embedded memory started in the past ten years, and there are few research results. This article analyzes the feasibility of the noncontact IC chip in the embedded ferroelectric memory of the sports game auxiliary timing device and is aimed at obtaining an optimized embedded ferroelectric memory by analyzing the relevant data to achieve the update and update of the sports game timing device system. Early sports event timing methods generally use manual timing (stopwatch) or camera shooting timing; this method is inefficient, poor real-time, huge workload, and prone to errors. This research mainly focuses on the analysis and discussion of the material structure and performance of the embedded ferroelectric memory and the process of noncontact IC chip. This article uses custom welding circuit technology to prepare the best ferroelectric filter in the test part and verifies the influence of temperature on the material; in order to understand the properties of ferroelectric materials at the electronic and atomic level, a first-order statistical method is obtained. The numerical calculation results of the experiment verify that the evaluation value of the serial port synchronization module as a whole exceeds the pulse synchronization; the network synchronization as a whole exceeds the code synchronization, and the result of the network time service module is the opposite, but as a whole, each module of the noncontact IC chip has strong performance adaptability; in the application of auxiliary timing, the maintainability of noncontact IC chip is quite outstanding, and the maximum value is 7.97; a large number of complex simulation system tasks can be completed by simple and direct tasks.

1. Introduction

Competitive sports highlights a new development culture, and promoting sports development has become one of the important strategies for the development of sports in many countries [1]. The continuous improvement of athletes' competitive sports level will make the education system gradually become another important foundation for the cultivation of competitive sports reserve talents after the competitive sports system [2]. The development of competitive sports is not only an expectation to cultivate high-level athletes with all-round development of morality, intelligence, and physical fitness but also a useful supplement to the competitive sports system and a useful reference to foreign competitive sports [3]. This is the fundamental reason why competitive sports has attracted the attention of the Chinese people, continues to develop, and has a bright future. The development of competitive sports urgently needs to strengthen the research of competitive sports events, but most of the existing researches are partial and unilateral status quo investigations or macrotheoretical analysis on the organization, management, construction, and training guarantee of competitive sports teams [4].

With the rapid development of VLSI technology and the rapid promotion of the concept of Internet of Things, the importance of information storage has become more and more obvious [5]. Embedded memory originally refers to the memory integrated on the embedded microprocessor chip, used for code or other long-term data storage. Now

in a broad sense, the storage circuit uses the same process as other working circuits and is integrated into a chip to work. The main purpose of this is to greatly reduce the delay of the data interface and to greatly accelerate the speed of the memory and reduce the application [6]. The research direction of the new generation of embedded memory can be summarized into two types of embedded nonvolatile memory and embedded volatile memory. Embedded non-volatile memory is divided into high-speed and low-power applications. These types of memories are aimed at different applications, and all have strong application prospects [7].

New embedded nonvolatile memory (eNVM) for large-scale technology nodes such as ferroelectric field effect transistors (FeFET) has been studied in depth and is very promising. Sasaki et al. describe a magnetic resonance wireless power transmission system with auxiliary coils. The system was proposed to supply power from the bed to an "implantable cardioverter defibrillator" (ICD) device. ICDs are the most effective treatment for preventing sudden cardiac death (SCD), with supportive pacing and antitachycardia pacing, low-energy cardioversion, and high-energy defibrillation [8]. In this study, a 1/2 scale model was used to study the power efficiency of a magnetic resonance wireless power transmission system with auxiliary coils. When the transmission distance is 100 mm and the main resistance is $20\,\Omega$, the maximum transmission efficiency of using the auxiliary coil is about 70% higher than that when the auxiliary coil is not used [9]. For the first time, Popov et al. observed direct bonding on Si or C-sapphire substrates and hydrogen transfer from the silicon layer in the silicon on sapphire (SOS) structure through HREM for the first time. The conclusion is that the OII phase is mainly stabilized by high compressive stress [10]. Kobayashi et al. designed and manufactured a nonvolatile SRAM by integrating with ferroelectric HfO_2 capacitors and proved its storage/recall operation before/after power failure through experiments. The sub-10 nm thick ferroelectric HfO_2 capacitor has obtained excellent ferroelectricity and memory characteristics. NVSRAM with ferroelectric HfO_2 capacitors can be a candidate for cost-effective, normally off, and ultralow power embedded memory solutions for IoT power management [11]. Inference and on-chip learning can be facilitated by further eNVM technology options, such as multibit operations and linear switching. Lederer et al. introduced the advantages of FeFETs based on hafnium oxide for such applications because they have a basic three-terminal structure that can selectively activate or deactivate selected devices and adjust linearity and dynamic range for certain applications. In addition, the effects of the material properties of the ferroelectric layer, the thickness of the interface layer, and the scaling on the device performance are discussed [12]. Chien et al. recommend embedding 256 kb resistive random access (ReRAM) in the microcontroller unit as a data buffer for communication with independent flash memory. It is manufactured using a combination of TSMC0.18 μm process and Industrial Technology Research Institute ReRAM back-end process. Simulations show that compared with other nonvolatile memory (such as ferroelectric RAM), ReRAM buffers run at least 51% faster [13]. Khan et al. studied the potential of ferroelectric field effect transistor technology in current embedded nonvolatile mem-

ory applications and future memory, bionic, and alternative computing models. The material and device-level challenges involved in high-volume manufacturing of advanced technology nodes ($\leq$10 nm) are emphasized, which is reminiscent of the challenges encountered in the early development of high-K metal gate transistors [14]. Ferroelectric field effect transistors (FeFETs) based on ferroelectric hafnium oxide (HfO_2) films show great potential for future embedded nonvolatile memory applications. Yurchuk et al. verified the possibility of charge trapping in HfO_2-based FeFET memory during standard operation. The single-pulse ID-VG technique (MOS tube Id-Vg curve data) was used to analyze in detail the kinetics of charge trapping and its interaction with ferroelectric polarization switching. In addition, the impact of charge trapping on important storage characteristics (such as retention and durability) has also been studied [15]. These studies have carried out detailed research through experiments. They have carried out data acquisition on related objects such as embedded memories of ferroelectric materials. However, it can be found that their research angles are relatively single and belong to the study of physical properties. The demonstration of the practical application of the experimental results is still lacking.

Ferroelectric film is the basis of ferroelectric memory. According to the requirements of embedded ferroelectric memory for ferroelectric materials, the microstructure and electrical properties of different parts of thin ferroelectric film are discussed, and a good integrated capacitor is provided through customized integration technology. The analysis of the etch degradation process of ferroelectric films during aggregation shows that the magnitude of the reheat treatment does not completely correct the cause of etch degradation. In the high-speed memory, we used a conventional bandgap reference voltage-controlled oscillator charge pump scheme [16]. As for the design of low power consumption, we implement the reference current reference and reference voltage reference with circuits, respectively. The program makes full use of the high-speed and precise calculations in data processing to design some of the best automated business automation and continuous and efficient operation of the business. On the basis of in-depth research on data mining technology, we eliminate general data miningalgorithms and develop intermediate class libraries as technical tools and process analysis for sports events. For the specific development process of a noncontact IC card chip, methods such as gated clocks and optimized layout structures are used to reduce chip area and reduce chip power consumption.

2. Embodiment of the Auxiliary Function of Ferroelectric Memory

2.1. The Combination of Sports Events and Computer Technology. People have gradually realized the original concentrated advantage. After all, the high-intensity stand-alone training program is a highly developed model based on high investment, high elimination rate, and low throughput. It is a systematic cultural study at the expense of young people's cost of improving the level of competition [17]. With the rapid development of computer technology and network technology, people have ushered in a new era of network

characterized by information and knowledge. The information that people are exposed to, especially digital information, is increasing exponentially. As the most powerful tool for modern human development, computer technology will inevitably play an inescapable responsibility in the development of sports competition. Through information management, the problems of large number of participants in previous competitions and sports competitions, complex project settings, tight timeliness, and difficulty in scheduling have been solved [18]. Computer technology uses relevant information to automatically generate graphics, tables, etc. to provide users with high-level information services to meet the requirements of statistical analysis and decision support proposed by users. The information can also provide relevant information to coaches and athletes participating in the competition in a timely and accurate manner. With the rapid development of science and technology, the use of high-tech technology to assist referees in judgment has become a reality, the accuracy of judgments has also been improved, and the pressure on referees has also been reduced. The use of high technology plays an important role in the accuracy and speed of task execution. And it has been widely used in the judicial procedures of many sports events. In order to improve the level of sports competition, more and more countries continue to apply new technologies to sports competitions [19]. The clear 3D animation display, the rapid response within a few seconds, and the pressure line or out-of-bounds gap accurate to the millimeter are all showing the world the convenience and precision that high-tech brings us.

Data mining is the process of searching for information hidden in a large amount of data through algorithms. Data mining brings data technology to the next level. It not only needs and transfers past data but also discovers multiple connections between data, thereby promoting the generation of useful information [20]. The system can not only express the business logic flow in reality but also store and process the business in reality and persist the corresponding data according to the data model. When there is an error in the data that needs to be modified, in the face of a less rigorous system, you only need to provide a corresponding means to repair the error, not the information that cannot be modified [21]. The communication and low coupling between the modules are fully considered, and more user loads can be quickly met, and it can be expanded downward when the system utilization is not high, saving costs.

2.2. Embedded Ferroelectric Memory and Noncontact IC Chip. Driven by fast-paced memory products, a number of successful memory technologies have emerged in the memory field in the past ten years, eliminating traditional technologies in the industry and expanding the application space of memory technologies [22]. As the concept of the Internet of Things and consumer applications have grown substantially, embedded storage applications have begun to flourish. Embedded memory has also encountered bottlenecks in its further development. At present, the process and manufacturing of memory cells are also at a relatively advanced level in the world, but at the same time, it also

encounters general problems in new memory research, such as process volatility and instability. It poses challenges to process research and circuit design. More and more new memory technologies pursuing different product segments are introduced one by one [23]. For the new generation of nonvolatile embedded memory, low power consumption, low cost, high speed, and other characteristics are required. The market for modern processors and embedded applications is extremely competitive, and only those competitors with high production characteristics and performance can win. Due to the importance of standard transmission interfaces and standard procedures for interoperability, middleware has become an integral part of many measurement tasks. For application software development, middleware is more important than system and network services [24].

With the substantial increase in chip integration, circuit design and application pose new challenges to discrete memories. Limited by the frequency of incoming and outgoing signals, the high-speed clock cannot be transmitted to the chip, providing a clock signal for the overall operation of the chip [25]. If the peak value is too high, the power supply voltage will drop too much, which may cause the chip to reset or fail to work normally, showing that the working distance of the card becomes shorter. The charge pump used in a good memory needs to meet the driving voltage and driving current and has the smallest possible area and power consumption. The specific design depends on different types of memory [26]. New devices combining ferroelectric materials and semiconductor devices have gradually been applied. Ferroelectric memory is a nonvolatile memory produced by a combination of thin ferroelectric film and CMOS technology. Bonded film is a key component of embedded ferroelectric memory; it is the specific application of spontaneous polarization of integrated ferroelectric film and its inversion retention characteristics under the action of electric field [27]. The field of embedded ferroelectric storage devices is a major breakthrough in microelectronics technology and information storage and manufacturing technology. It has opened up many new ways for the fame and development of microelectronics technology, information storage, and manufacturing technology and greatly stimulated the research and development of various universities. In order to understand the properties of ferroelectric materials at the electronic and atomic level, humans have developed a first-order calculation method, in which electrons are the main calculation object for the interaction of intermediate ions [28, 29]. The relationship between the strength of the ferroelectric capacitor and the electric field is

$$
\bar{R}_a = \bar{R}_i - \left(\bar{R}_o + \bar{R}_{\sin}\right)\left\{\frac{1}{\pi} \sin\left[a\chi_a\left(\bar{R}_i + \bar{R}\right)\right] + \frac{1}{2}\right\},
$$
$$
O = i \bullet \frac{l\bar{R}}{L} = i * \frac{l}{L\bar{R}}\left(\delta_i \frac{\bar{L}}{m} + p\right). \tag{1}
$$

Among them, $\bar{L}$ is the voltage, m is the thickness, and i is the area. Calculating the polarization intensity of the capacitor. It is different during the voltage rise $\bar{R}$ and fall

phases. The corresponding expression is automatically selected according to the change of the input voltage during the simulation, that is

$$\chi = f_i - \frac{\left(\|f_i + f_{i-1}\|\right) \otimes 1}{\left(1 + \alpha^{(f+f_i)}\right) + m},$$

$$i : f_i = L\alpha^{-\chi(a+a_i)^2} + l(l-1), \tag{2}$$

$$\alpha : \delta = O\left[\cos l\sqrt{\phi(i + i_{m-1})}\right] \otimes l(f_i).$$

In the design and simulation of large-scale integrated circuits, it will take more time and reduce the simulation efficiency f_i. δ is the residual polarization in the positive and negative directions, and the maximum value that can be reached in the other direction is calculated by the formula:

$$i = \int_{\forall i \in \delta} (m-1)\left(\bar{R}(i-1)\right) l\bar{R}\left(\bar{R} + \chi_{i-1}\right),$$

$$f' = \sqrt{\delta_{i-1}}\left(\cos^2(\alpha_{i=1}l) - \delta_{i-1} \bullet \frac{\alpha}{\alpha_{-1}}\right). \tag{3}$$

The phase f' of the detection signal represents the sign of the charge, and the amplitude δ_{i-1} of the electrostatic force signal reflects the density of the polarized charge or the magnitude of the electric potential.

3. Ferroelectric Memory and Noncontact IC Chip Auxiliary Timing Experiment

3.1. Properties of the Embedded Ferroelectric Memory. In the mid-1990s, ferroelectric memory products were already on the market. Ferroelectric memory has become one of the most promising new members in the memory family. Since the ferroelectric device does not require an external or current power supply to maintain the two states, it can be used to make a storage device to store digital data, and the storage device can maintain its internal storage information without a power supply. The composite film storage unit has an excellent editing function, which can temporarily maintain its intelligent state. Ferroelectric random access memory is a nuclear mode of operation. After this kind of destructive reading, the data needs to be rewritten, so a large number of erasing and rewriting tasks will be accompanied in the information reading process. The concept of memory is very wide and has multiple levels and types, but in the process of information storage, data must be converted into binary data. With a large number of reads and writes, reliability problems such as fatigue failure will occur. In the case that the continuous reduction of the size of the memory cell will cause various problems, many researchers have realized that breaking the limitations of binary storage will greatly increase the storage density of the memory. When the memory cell is read, the state of the memory cell will change due to the read operation. After each read, the original position is damaged, and a voltage must be applied to restore the original polarization. The schematic diagram of the structure of the ferroelectric memory storage unit is shown in Figure 1.

The development of material science research, material preparation technology, and microelectronic integration technology has made great progress in the application of ferroelectric thin films in nonvolatile memory. Initially, researchers focused on the use of ferroelectric thin film polarization. Ferroelectric memory inserts can be written at bus speed; there is no write delay during data transmission, there are no restrictions on the amount of data transmission and write delay, and the system can complete the writing of the entire chip. Compared with other memories, the writing speed of ferroelectric memories is more than 10,000 times faster. The reading speed is also very fast, and there is no obvious speed difference from the writing process. The performance comparison of embedded ferroelectric memory, EEPROM, and FLASH is shown in Table 1.

Studying the morphology and microstructure of ferroelectric thin films is very important for analyzing the performance of ferroelectric thin films and mechanical devices. The electrical properties and customization content of thin ferroelectric thin films are the same as those of general ferroelectric materials, but there are special considerations in the application of thin film materials, and the research methods and technologies are different. Ferroelectric thin film is a key component of ferroelectric memory. High-quality thin ferroelectric thin film is the foundation and stability of ferroelectric memory, and the quality of ferroelectric thin film is reflected by specific performance parameters. The memory-related parameters of different storage unit power consumption are shown in Table 2.

Embedded ferroelectric memory is essentially a combination of the functions of a semiconducting CMOS circuit and an integrated ferroelectric capacitor. Therefore, from a process point of view, the two can form different device structures during the process of mutual integration. Although many experiments have been done to improve the retention of ferroelectric storage and improve it, the visual problem between ferroelectrics and semiconductors has not been well resolved. The analysis of the crystalline and electrical properties of ferroelectric films with different structures shows that the electrical properties of ferroelectric films are closely related to the crystalline properties of the films. The experimental setup is shown in Figure 2.

The grain boundaries between the surface grains and the internal grain boundaries will not affect the overall electrical environment of the film. Ferroelectric memory uses the different orientations of polarized electric domains and the reversal movement of electric domains to store and read information. The preparation and processing of the ferroelectric film will affect the performance of the coupling circuit. At the same time, the processing of the thin ferroelectric film and the back-end coupling circuit will also cause certain damage to the thin ferroelectric film, resulting in the degradation of the ferroelectric capacitor.

The development of microelectronics, optoelectronics, sensors, and other related technologies has also put forward further demands for the miniaturization, thin-film, and high-density applications of ferroelectrics. From the perspective of the device structure, the integrated ferroelectric capacitor is mainly used to replace the ordinary dielectric
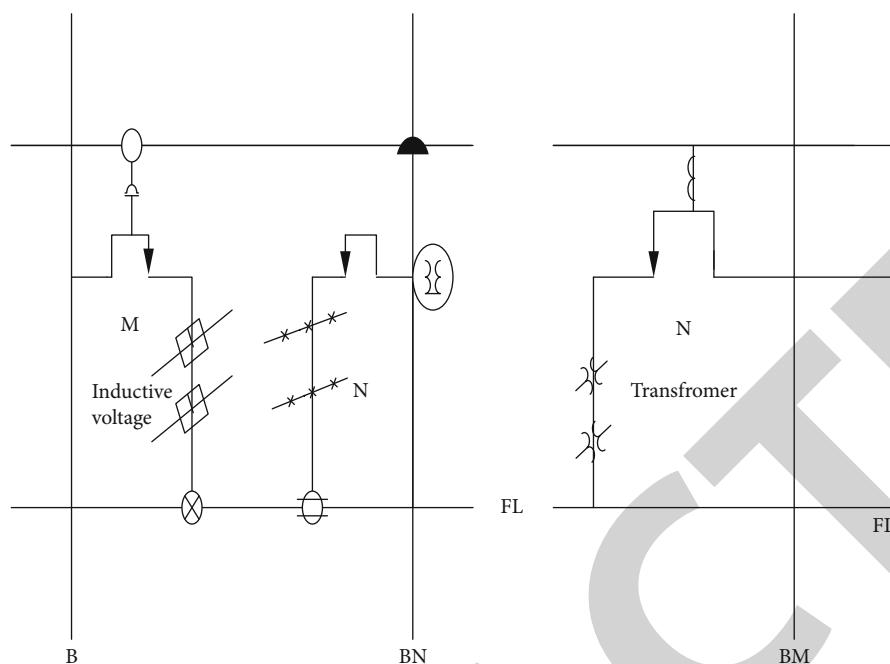
FIGURE 1: Storage unit structure.

TABLE 1: Three kinds of memory performance parameters.

Parameter	FLASH	EEPROM	Ferroelectric memory
Unit structure	1A	2A	2A2R
Write time	12	2	150
Read time (ns)	125	205	115
Write voltage (V)	21	12	4/2.7
Number of reads and writes	2A10	2A10	4A20
Quiescent current (μA)	17	3	25
Maximum write operation current (mA)	37	10	6
Maximum read operation current (mA)	16	9	8

TABLE 2: Storage unit power consumption.

Memory	Maximum power consumption	Minimum power consumption	Average power consumption
RF8* 502	573.27	2.11	2.07
RF6* 287	888.01	0.874	19.4
POS5G* 6	2.69	1.75	47.3
PISK*7 (6021)	572.41	3.96	8.76
PISK*7	28.96	3.96	6.08

capacitor in the semiconductor memory. There are many types of ferroelectric memory storage cells. After the amplifier outputs the signal, the ferroelectric capacitor should be rewritten to restore the destroyed polarization state. After the amplifier generates a signal, the ferroelectric capacitor

should be rebuilt to restore the damaged polarization state. In terms of electrodes, the existing ferroelectric materials do not have the negative crystalline properties of traditional Pt electrodes, which affect the performance of the materials. Although pulsed laser technology can effectively control the composition of the film, the problem of small particles on the surface of the film and the preparation of large-area film coatings is a problem that needs to be solved. The content of molecules at different temperatures is shown in Figure 3.

It can be seen that the ferroelectric properties of the samples with different holding time are different. This is mainly due to the influence of the holding time on the grain size and film structure, resulting in different ferroelectric properties. The lower electrode material controls the structure and electrical properties of the ferroelectric thin film, and the interaction between the electrode material and the substrate directly determines the function and life of the ferroelectric memory. The development of the information age requires large-capacity and small-sized memory, which means that
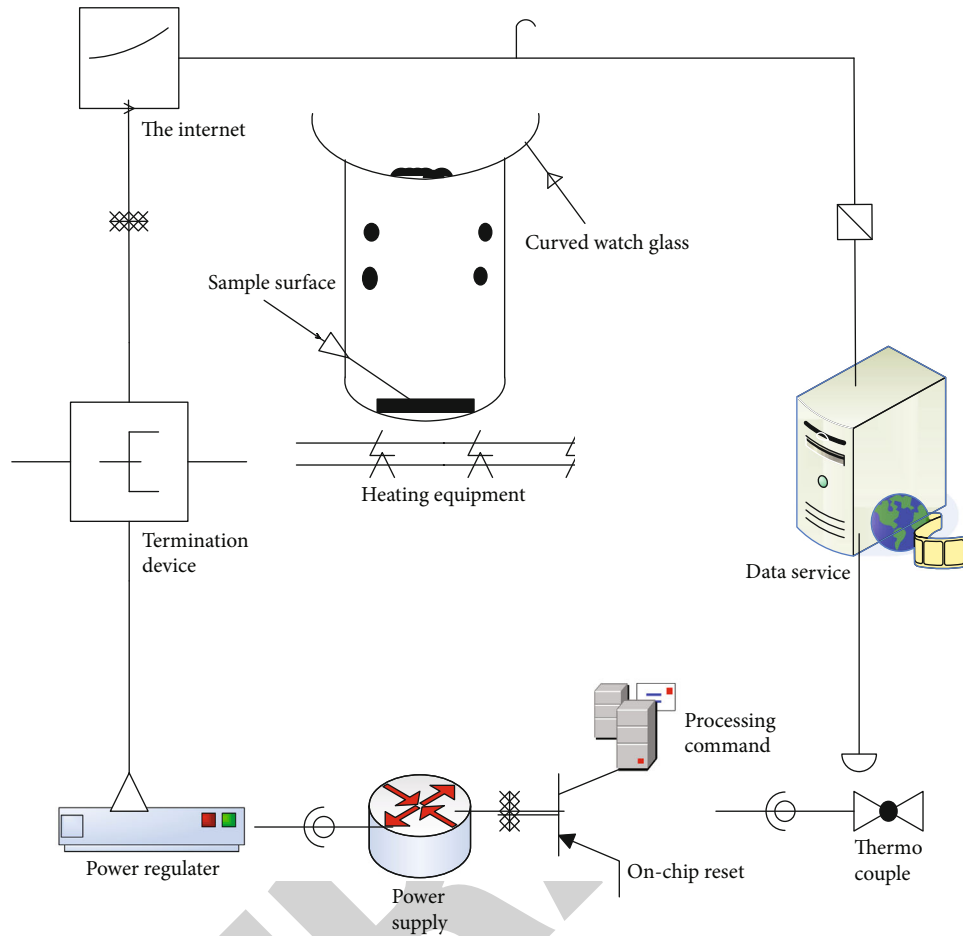
FIGURE 2: Experimental setup test.

the density of the storage unit needs to be increased, and the volume of the storage unit needs to be reduced. The size of the ferroelectric film as a storage medium is also reduced. The residual polarization capacity of the material should be as large as possible, so that the small ferroelectric capacitor area can accept a large polarization current change, which is beneficial to reduce the cell area of the ferroelectric memory. The dielectric frequency should be small because high-frequency dielectric materials will produce a large linear conversion rate, which obscures the availability of the polarization conversion curve. Under the action of an external electric field, the ferroelectric observes the turning polarization through the destruction and development process of the data and the movement of the surrounding particles. The corresponding relationship between the drive capability of the ferroelectric memory and the area, capacitance, and power consumption is shown in Table 3.

3.2. Application of Noncontact IC Chip in Time Monitoring. Even for two-state storage based on epitaxial ultrathin film, the writing of the storage state is very unstable. By applying a current-limited writing method, the storage device can realize multilogic state storage. Ferroelectric reversible diodes cannot maintain a high switching ratio storage state

after power failure. In order to promote the application of such electronic storage devices, the problem of maintaining high switching ratio storage after power failure must be solved. Because the interface barrier is affected by the internal defects of the electrode and the ferroelectric material, although the ferroelectric memory based on the ferroelectric capacitor is a relatively new operating system, its characteristics and mechanical properties are still unclear and require in-depth study. With the development and progress of society, smart cards have been widely used in many fields, especially noncontact IC cards, work permits, and identity certificates. The characteristic coefficient of noncontact IC chip is shown in Figure 4.

In fact, although the same preparation parameters are used when different substrates are used, the quality of the prepared films is not the same. Therefore, the design of low-power circuits has developed innovative and scientific methods. With the gradual improvement of integrated circuit design technology, there will be fewer and fewer ways to reduce chip power consumption, and the share of power consumption will also become smaller and smaller. Reducing the area of the chip can avoid large parasitic resistance and capacitance and can reduce the power consumption of the chip. Use it to establish a connection with the internal
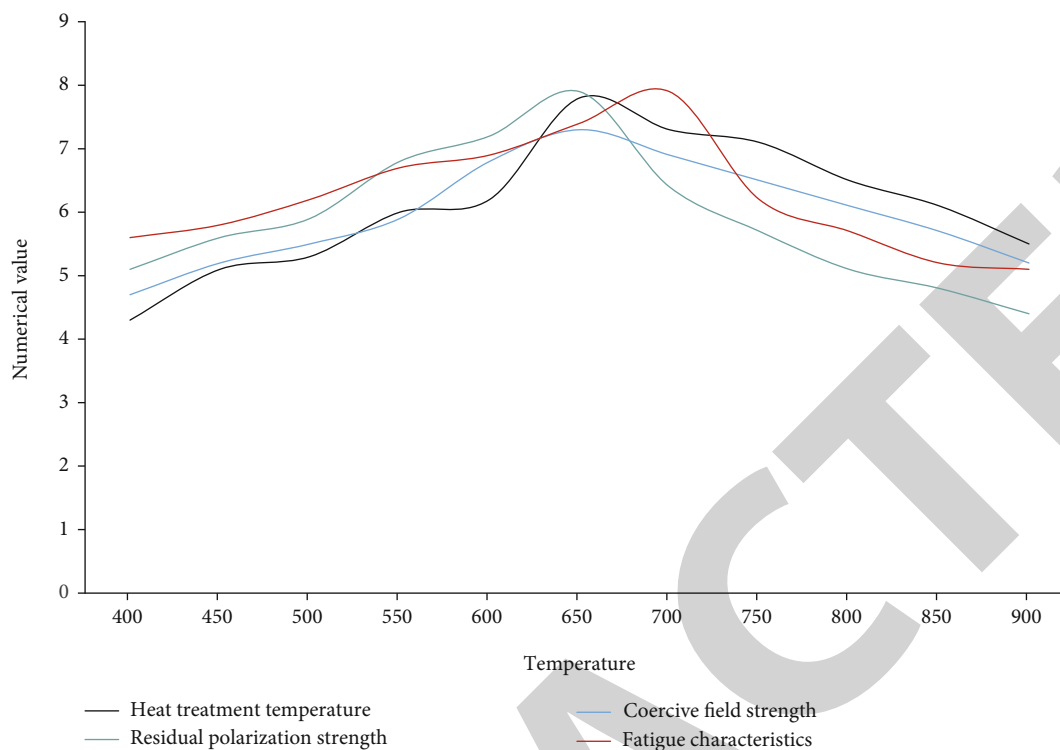
Figure 3: Temperature affects volatilization parameters.

Table 3: Related correspondence index.

Drive capability	Area	Capacitance	Power consumption
CL	4.98*1.89	0.0078	0.0021
C1	4.98*2.19	0.0127	0.0013
C2	4.98*3.71	0.0328	0.0117
C3	4.98*5.01	0.0691	0.0248
C4	4.98*7.82	0.219	0.0569

circuit. It can not only make test points but also can be used for imaging and repairing. Analyzing the application of IC chip is shown in Figure 5.

The biggest feature of the noncontact IC card system is the use of RFID technology for noncontact identification. The antenna of the IC card contact is not integrated on the chip. On the one hand, this increases the cost of card manufacturing, and on the other hand, it also limits the flexibility of applications, thereby limiting the application range of noncontact IC cards. The chip card IC is mounted on the label using flip chip technology. This type of label is usually attached to the horizontal surface of the paper and covered with adhesive on the back. In this way, the antenna has a winding on the back of the ferrite core, and a film mark is made as a sticker mark, and a round shape is provided. Digital correction uses a group of different living body signal worlds to reflect the distributed digital information and only needs to locate and judge the change of the living body signal during the demodulation process. In order to maximize the antinoise capability of the system, channel coding technology is needed to manage possible or existing errors.

Channel coding is to change the original digital signal with no equivalent or equivalent to a digital signal with normal or equivalent enhancement. Data intrusion is achieved by controlling the access status of storage areas and redundant storage. Controlling the access status of the storage area can prevent the destruction of the stored data when an error occurs. Simulating different synchronized data for evaluation in different modules is shown in Figure 6.

Obviously, the evaluation value of the serial port synchronization module as a whole exceeds the pulse synchronization; the network synchronization as a whole exceeds the code synchronization, and the result is the opposite in the network time service module, but the overall performance of each module of the noncontact IC chip is adaptable. If the external time reference source is a wired source, the program is also used for correction to obtain a more accurate second pulse. The time synchronization device sends out a pulse signal at regular intervals. After receiving this pulse, the timing equipment uses the rising or falling edge of the pulse to calibrate the local clock. Comparison of function consumption before and after optimization is shown in Figure 7.

When performing functional simulation of the chip, record the real-time flip information of each device of the chip, combine the parasitic parameter information of the power supply network and the signal network, and analyze the power consumption, IRDrop, and electromigration problems caused by all the flips in the chip at the same time. The first clock of the first standby synchronization system receives the wireless time service, and the time service is sent by the other party. We can set the view to receive the time
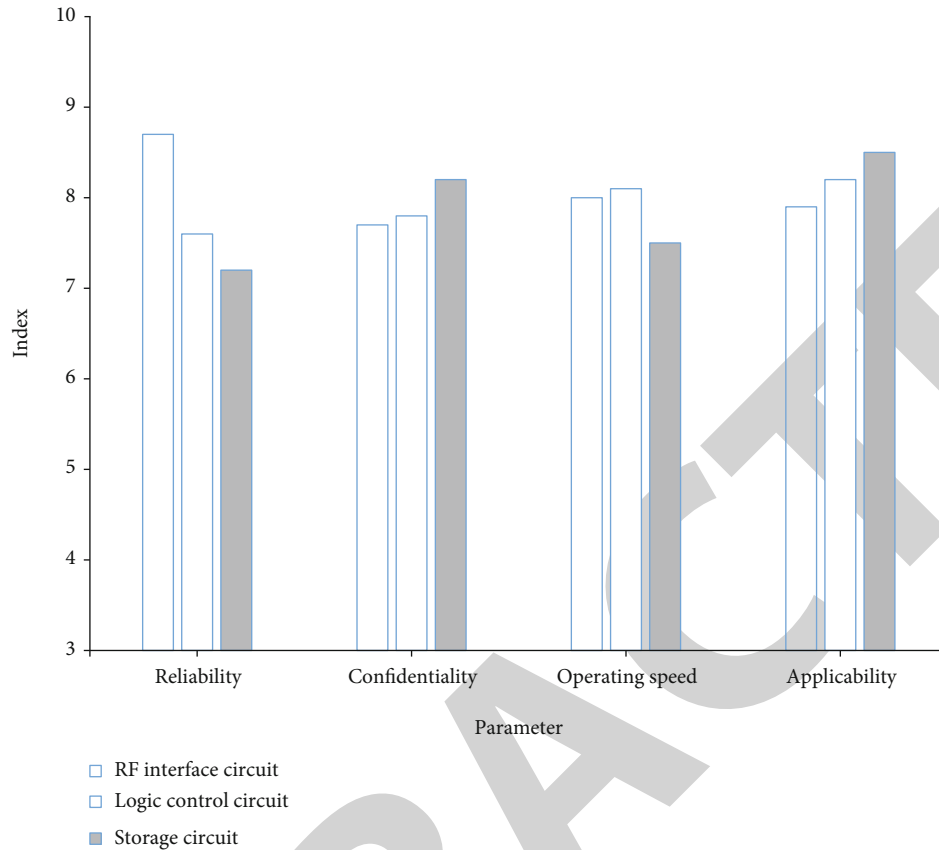
FIGURE 4: Noncontact IC chip.

service sent by the top-level synchronization. Analyze the feasibility of simulating auxiliary timing for this operating design, and the result is shown in Figure 8.

Judging from the 9 test results of noncontact IC chips, the feature of maintainability is quite prominent in the application of auxiliary timing, with a maximum value of 7.97. According to the requirements of traditional gymnasium design and sports competition rules, it provides a fair competition environment for athletes, the gymnasium prohibits the use of natural lighting during the game, and artificial lighting is used without skylights. The consequence of this design is that the use of the stadium requires the help of artificial equipment. The introduction of skylight lighting has greatly reduced the energy consumption of gymnasiums, and the enthusiasm of university gymnasiums to open to the outside world is also increasing day by day. The noncontact IC of embedded ferroelectric material can realize a large number of complex simulation system tasks through simple and easy operations in time, which greatly reduces the labor of competitors, improves performance, and ensures the accuracy and reliability of data, the probability of technology and economy, and the feasibility of management.

4. Discussion

As the parts in the form of circular circuits become smaller and smaller, the coupling degree is higher and higher, and

the speed is getting faster and faster; people in the manufacturing chain have found many problems that cause it and gradually focus their work on the design and research of energy efficiency optimization. The process size of the coupling circuit is getting smaller and smaller, the number of transistors that can be accommodated in a single area increases, and the area of the cut leads to an increasing power density, which is prone to overheating. Adjust the loading process and design constraints according to the characteristics of the chip module, and plan the additional loading plan of the chip according to the average flip position of the display during normal operation; complete all stored back-end programs, save time, usage, and other parameters according to the previous storage characteristics to ensure the continuity of the design. Then, complete various verifications of the chip to ensure the correctness of the chip design. The weak ferroelectricity of ultrathin films needs to be detected by special instruments. Piezoelectric atomic force microscope is a commonly used tool for detecting ferroelectric properties. Although it has been very advanced, it still needs development in the detection of weak ferroelectricity. With the continuous progress of integrated circuit design and manufacturing technology, the proportion of embedded memory in the chip is getting higher and higher. Due to the increase of transistor density in embedded memory, it is easy to find internal defects, and people have conducted in-depth research on the test of embedded
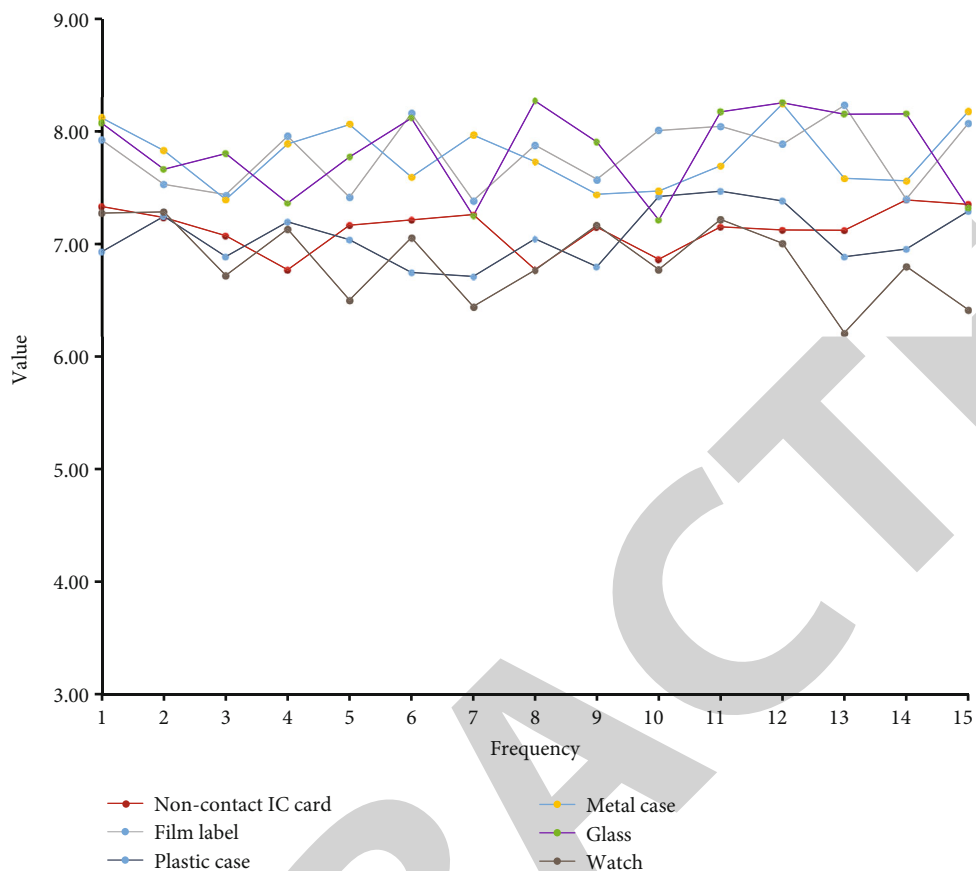
Figure 5: Application of noncontact IC chip.
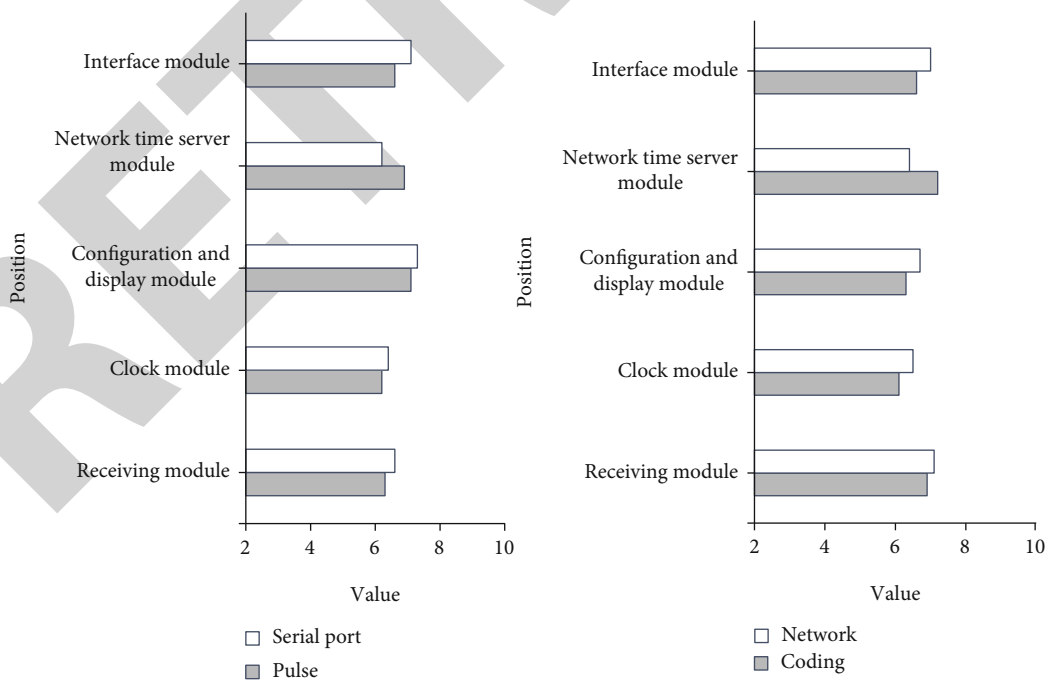
Figure 6: Synchronized formal parameters under different module positions.
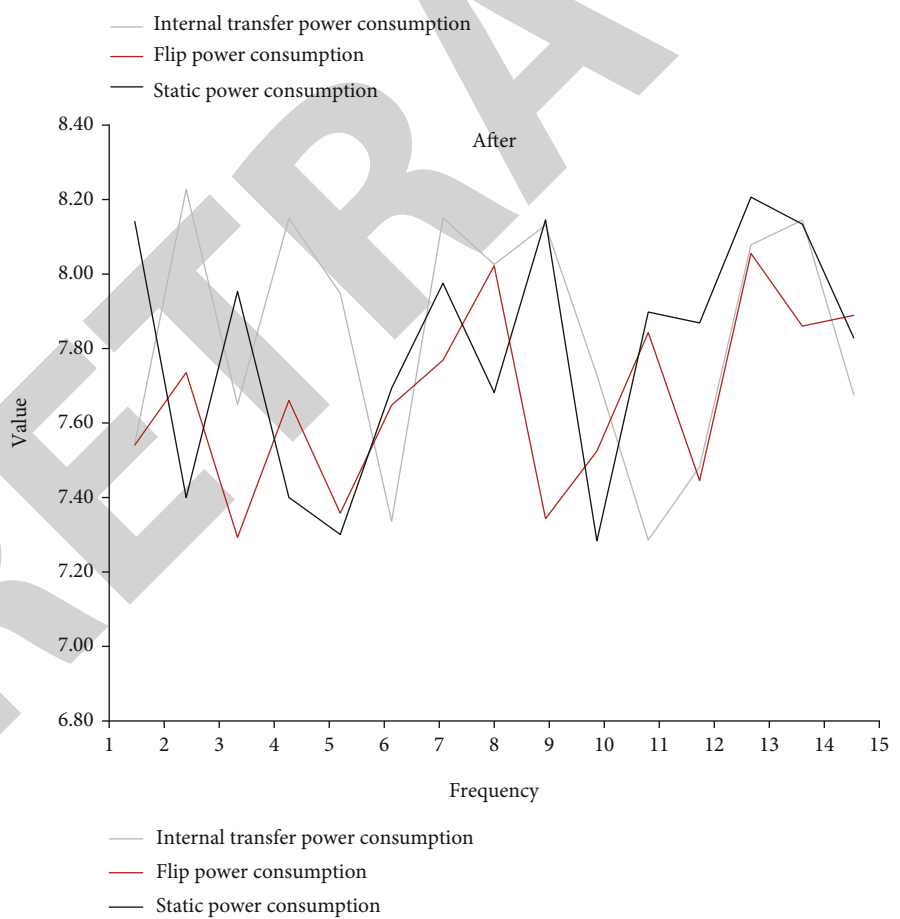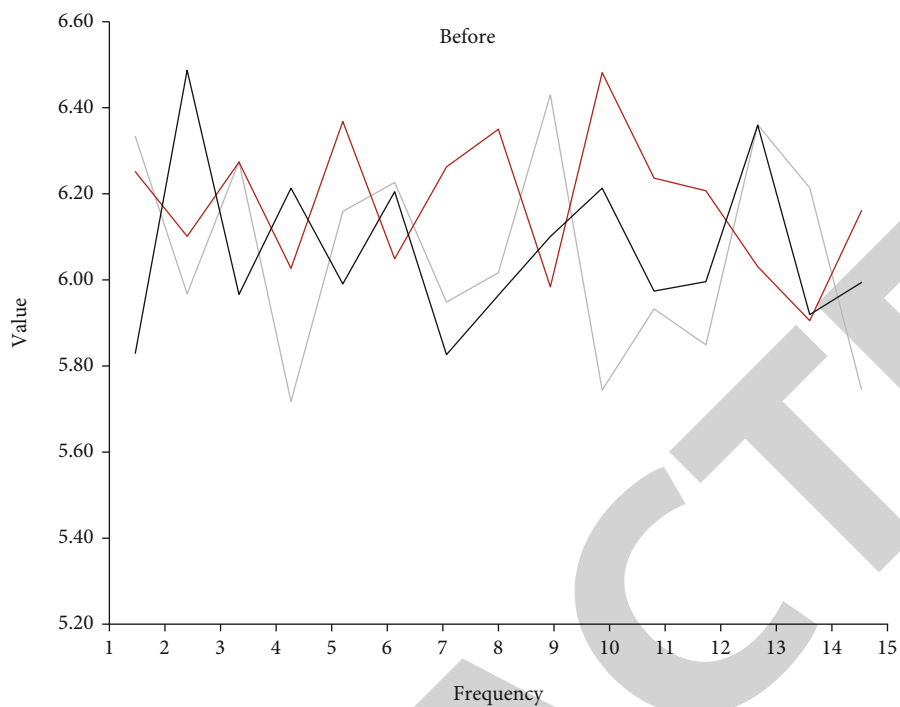
Figure 7: Comparison before and after function consumption optimization.
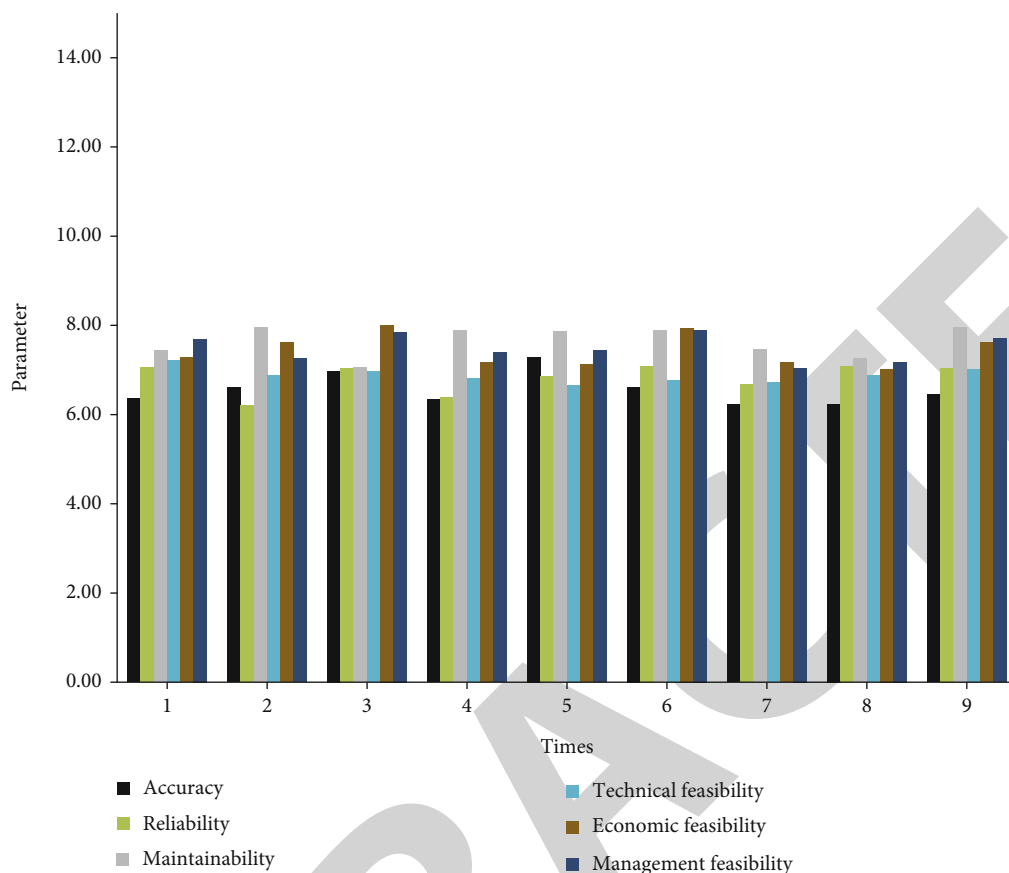
FIGURE 8: Auxiliary timing test results.

memory. With the further improvement of film preparation technology, the preparation technology of epitaxial film has been mastered by many scientific workers.

5. Conclusion

At present, the system only recognizes the functions of game score statistics, and there are many shortcomings in providing humanized services and drills throughout the game. In terms of practice, it analyzes and sorts out general college gymnasiums, college gymnasiums that take into account urban competitions, and urban gymnasium space design data models and provides suggestions for optimization of the space design of the competition hall and activates the space design thinking of the competition hall, gets rid of some misunderstandings in the current design, and broaden the vision of the current space design. Out of the consideration of both urban events and the use of competitive sports, the choice of technology should be based on the needs of both aspects, respect the principle of rationality of technology, and must not blindly use it to cause unnecessary waste. The key to solving this problem lies in two aspects. On the one hand, it is necessary to further study the process of resistive random access memory to reduce the current of the write operation as much as possible. On the other hand, it is to optimize the high-voltage module plan and try to use a smaller capacitor to achieve the appropriate operating current, which is also the next step in the work of resistive random access memory. Since many future research and development environments are currently undergoing research and development, ferroelectric memory has unique advantages compared to other types of memory; ferroelectric memory is very likely to become a new product that replaces existing traditional memory and flash memory. In recent years, noncontact IC cards have integrated data protection and cryptography, electronic computing technology, manufacturing technology, and many other professional application technologies, forming an independent technical field. The combination of the two overcomes the main technical obstacles to the integration of ferroelectrics and semiconductor devices, making it possible to integrate ferroelectric devices compatible with semiconductor technology, and has greatly promoted the development of ferroelectric thin film preparation and material research.

Data Availability

No data were used to support this study.

Conflicts of Interest

The authors declare no conflicts of interest.

Research Article

Application of Multiple Random Forest Algorithm in Image Segmentation of Nanoparticles

Zhongyuan Ji [iD] [1,2,3] **and Yuchen Wang** [2,3]

[1]*College of Electronic and Information Engineering, Nanjing University of Aeronautics and Astronautics, Nanjing,
211106 Jiangsu, China*
[2]*College of Criminal Justice, Shandong University of Political Science and Law, Jinan, 250014 Shandong, China*
[3]*Key Laboratory of Evidence-Identifying in Universities of Shandong, Shandong University of Political Science and Law, Jinan,
250014 Shandong, China*

Correspondence should be addressed to Zhongyuan Ji; 000929@sdupsl.edu.cn

Because of its large specific surface area, small particle size, high surface energy, and unique nanoeffect, the morphological characteristics of nanoparticles are the key factors affecting the properties of materials. How to detect and evaluate the morphological characteristics of nanoparticles is the first problem to be solved in the preparation and application of nanomaterials. The main purpose of this paper is to use TEM to recognize the image features of nanoparticles and introduce the transmission electron microscope and image edge segmentation method and random forest algorithm. A method integrating the in situ characterization of modern electron microscopy and the measurement of the electrical properties of nanomonomers was developed. In this paper, a multielectrode TEM in situ electrical measurement platform is prepared, which improves the contact during the integration of nanomaterials and improves the electrical measurement accuracy of the TEM in situ electrical method. In this paper, based on the random forest algorithm, a multirandom forest algorithm is proposed. Due to the different gray levels of images referenced by the multirandom forest algorithm, the segmentation results are processed by FCM clustering algorithm. Experimental results show that in terms of image segmentation accuracy, the minimum Jaccard coefficient obtained by multiple random forest algorithm is 89% and 95%, respectively, which is obviously better than watershed segmentation method and maximum entropy threshold segmentation. In the aspect of automatic image segmentation of nanoparticles, the image segmentation accuracy is the highest when the sample block size and the number of sample blocks selected in the multiple random forest algorithm are $5 * 5$, 7500, and 35, respectively. Therefore, the multirandom forest algorithm has achieved high accuracy in image segmentation of nanoparticles, which provides valuable information for the preparation and application of nanomaterials. A new type of TEM dark-field imaging diaphragm was prepared, which greatly improved the imaging quality of weak-phase bulk materials represented by graphene and nonspiral biological samples represented by intracellular polyvesicles.

1. Introduction

At present, the traditional CMOS process is close to the limit of development, and the traditional means of improving the performance of nanoelectronic devices by reducing the device size will become less and less feasible in the foreseeable future. Application requirements such as high-performance computing and big data have put forward higher requirements

on the computing speed and reliability of electronic devices. In recent years, with the continuous research of image processing technology in the field of computer, the emergence of electron microscope provides the possibility for people to explore the mystery of the micro world. After years of development, it has become an indispensable tool in modern science and technology. For nanomaterials, the size and distribution of nanoparticles determine the physical and chemical properties of

nanomaterials. Therefore, the measurement and characterization of nanoparticle size are an important aspect of nanomaterial structure research, especially the measurement of nanoparticle distribution has important practical significance. Nanoparticle recognition refers to the extraction and analysis of particle features in nanoparticle images. Transmission electron microscopy (TEM) is an important tool for characterizing nanomaterials [1]. It can observe the submicroscopic or ultramicrostructure which cannot be seen under the optical microscope below 0.2 μm.

Strzeciwilk et al. describe the results of TEM training at TiC Crystal and Co. Teak crystals are prepared using high temperature superconductivity (HTS) technology using cobalt as high temperature oil. The physical structure of the crystal is investigated by natural metal. X-ray phase analysis of the samples was performed. Li et al. focused on the study of twins in bulk metals FCC and BCC and their effects on the mechanical properties of all metals. It is possible that these unique defects are directly related to the properties of the macro machine that uses the flexible mounting tool to simultaneously degrade the nanomachine and the nanoimage [2, 3]. Mayer et al. combine double-angle shear geometry and flat-bore compression at nanointerter to determine the mechanical properties of these films under shear stress. In order to further explain the voltage attenuation failure device, TEM-mounted tests were performed on TEM sheets with dual markers. Aluminum layer thicknesses of 50 nm and 100 nm were used to indicate the effect of the restriction on deformation. Compared to the 100 nm sample (423 ± 28.7 MPa), the tensile strength of the 50 nm sample is higher (690 ± 54 MPa) [4]. Shen and Sun introduce external fields such as electronics, thermal energy, light field, and electricity to TEM, which can create a nanolaboratory at TEM and compare real-world environments. Therefore, in addition to static structural design, the indoor TEM can also recognize the capabilities of the two-dimensional material structure and the evolution of performance. This extension is expected to handle and create two-dimensional materials in individual size, providing the necessary features and properties for future applications [5].

Lyon et al. reduced Au to water-soluble gold-plated iron magnetic oxide nanoparticles with a diameter of 60 nm on the surface 2-Fe2O3 or Fe3O4 oxidized particles partially from recycled hydroxylamine. The morphology and optical properties of the core/shell particles depend on the amount of gold deposited, while the magnetic properties are very independent of the amount of gold added [6]. Wei et al. solve this problem by synchronizing 30 nm nanoprecipitation via Ostwald maturation. When the prefrontal cortex has a large swelling of the membrane, 2 hours of boiling or 10 days of ambient aging allow the gelatinous material to grow into a nonuniform nanoparticle [7]. Nayral et al. prepared core-core nanocomposites consisting of a sn0 core and a thin-layer tin oxide with thermal decomposition of [{Sn (Nm2) 2} 2] containing a small amount of water control in anisole. The particles are exposed by electron microscopy (TEM, HRTEM, and SEM), X-ray diffraction (XRD), photoelectron spectroscopy (XPS), and Mossbauer (Mssbauer) spectroscopy. TEM micrographs show the magnitude of a

particle's rotation, and their distribution depends on the initial test conditions, such as temperature, time, water concentration, and pretin concentration [8]. Copolymers of ε-caprolactone and L-lactide (pCLLA) with different monomer fractions were synthesized at the rate of GEH polymerization and the drug accumulated in large amounts of PCL, PLLA, and their copolymers were prepared by precipitation. Large particles are indicated by XRD, TEM, and attenuation luminescence. The size of LiYF4 molecules can be adjusted by converting the F ratio to lanthanide ions. After passivation with oleic acid ligands, LiYF4 nanoparticles can be readily dispersed in various nonpolar liquids, such as hexane, cyclohexane, dichloromethane, and toluene [9, 10].

This paper mainly introduces the transmission electron microscope, image edge segmentation method, and random forest algorithm. In this paper, based on the random forest algorithm, a multirandom forest algorithm is proposed. Due to the different gray levels of images referenced by the multirandom forest algorithm, the segmentation results are processed by FCM clustering algorithm. The experimental results show that the multirandom forest algorithm achieves high accuracy in the segmentation of nanoparticles. The electrodes prepared by this technique can be easily improved into excellent ohmic contacts when integrated with nanomaterials, which can reduce the influence of contact resistance on the measurement of electrical properties. In addition, the technology realizes the adjustable number, size, and spacing of electrodes, and it is easy to obtain contact resistance information by multiterminal electrical measurement, so as to obtain more reliable electrical properties.

2. TEM and Nanoparticles

2.1. Transmission Electron Microscope. Since the advent of the world's first transistor in 1947, integrated circuits based on microelectronics technology have greatly changed human production and lifestyle. During this period, the development of integrated circuits has always followed Moore's law, that is, the number of integrated transistors per unit area doubles every 18 months, and the critical size of transistors shrinks by a factor of 0.7 every 18 months. By 2009, the feature size of the marketed microprocessors in integrated circuits has reached 45 nm, the 32 nm size is brewing into mass production, and the industry and academia have aimed at 22 nm.

Transmission electron microscope (TEM) is one of the important tools to detect the micromorphology, crystal structure, and chemical composition of materials. It uses a short wavelength high-energy electron beam as the incident light source [11]. Under a certain accelerating voltage, the electron beam converges through the electromagnetic lens and passes through the sample, thus obtaining the subangstrom spatial resolution.

TEM is generally composed of three parts: electronic optical part (lighting system, imaging system, observation, and recording system), vacuum part (vacuum system and vacuum display instrument), and electronic part (various power supply, safety system, and control system). Electron optics is the core part of electron microscope. According to

the different types of electron gun in lighting system, TEM can be divided into thermal emission transmission electron microscope and field emission transmission electron microscope. In TEM, an incident electron beam is generated by heating the filament with lanthanum hexaborate (LaB6). Tungsten wire is used as electron emission source of field emission TEM. Under the strong electric field, the internal electrons will be emitted from the filament surface above the barrier due to the tunneling effect. Compared with thermal emission, field emission can produce electron beam with higher brightness, better coherence, and single wavelength. Combined with the TEM-SPM technique, the structure-dependent in situ electrical measurement experiments were carried out on a variety of nanomaterials. First press the gold tip of the STM with the gold electrode inside the sample holder. It was then slowly separated under TEM observation until atomically sized gold nanowires were obtained. Since the entire stretching process can be imaged in TEM, the width of the nanowires is controlled to be only a single atom wide.

(1) Lighting system

The electrical system is essentially an electrical circuit breaker, a condenser, an electronic pistol, and a printer. Your job is to provide a light source with high brightness, low beam angle, good contrast, and stable beam. In order to meet the requirements of the dark field image, the light beam can be adjusted to 2-3 degrees.

(1) Electron gun

The electron gun is the light source that emits electrons. It is actually an electrostatic lens composed of cathode, grid, and anode. The cathode is the source of free electrons. There are usually direct heating and close contact heating as well as cathode separation, each of which remains independent. In electron microscopy, the cathode is usually made of heated filament and tungsten metal, which has the characteristics of low cost, low brightness, and short life. The cathode is the source of free electrons. Once the cathode is heated, it can produce free electrons, anode, and cathode electric field. The anode can attract the cathode that emits free electrons and change its motion state from chaos to orderly orientation. After the cathode grid is biased, it can produce the convergence effect of the electron beam, that is, to gather to the central axis, so that the electron beam is in the center of the axis the movement can be carried out through anode and injection gun to form the required light source to irradiate the sample.

Within a certain limit, the amount of free electrons emitted by the filament is proportional to the heating current intensity, but after this limit is exceeded, the current continues to increase, which can only reduce the service life of the filament, but cannot increase the amount of free electrons emitted. We call this critical point the filament saturation point, which means that the emission of free electrons has reached "full capacity" and can no longer be added. In normal use, the heating current of the filament is often adjusted and set at a position close to saturation, which is called "undersaturation point." In this way, the service life of the filament can be extended to the maximum extent under the condition that a large amount of free electron emission can be obtained.

The grid is located between the cathode and anode, near the end of the filament. It is a cap-shaped metal object with a small hole in the center for the electron beam to pass through. Apply a negative voltage of 0-1000 v (cathode) to the grid. This negative voltage is called gate bias, its height is different, and users can adjust it according to their needs. The grid bias voltage can make the electron beam converge to the central axis and control and restrain the electron emission on the filament to a certain extent.

The working principle of the electron gun: under the action of the filament power supply, the current flows through the cathode of the filament and heats it to above 2500°C. Free electrons are generated and escape from the surface of the filament. When the power is turned on, an accelerating voltage is generated. The positive charge generated on the anode surface forms a positive electric field, and the free electrons on the cathode surface escape after being affected by the electric field and are emitted by the electron gun to form a power supply. In the process of electron microscope, the filament can be adjusted to the low saturation point, and the beam current can be controlled by adjusting the gate bias voltage.

In the electron microscope, the acceleration voltage is also adjustable, so as long as the acceleration voltage is increased, the penetration can be enhanced, because the acceleration of voltage will reduce the wavelength, and the smaller the wavelength, the stronger the penetration. Although this can improve the resolution, but also brings the corresponding disadvantages, that is, the reduction of imaging contrast. Therefore, when the application of high-resolution observation is not pursued, a lower acceleration voltage can be selected to obtain a larger imaging contrast, especially for biological samples with low contrast, it is sometimes advantageous to choose a lower acceleration voltage.

(2) Condenser

The capacitor is under the gun. The condenser is composed of a first condenser and a second condenser. The purpose of setting a condenser in the electron microscope is to gather the electron beam emitted by the electron gun into a spot with uniform brightness and adjustable irradiation range and project it on the sample below. After the electron beam passes through the capacitor, a uniform spot with adjustable irradiation range is formed and projected onto the sample. The first condenser is a strong magnetic field lens, and the second one is a weak magnetic field lens. All levels of capacitors are used together to adjust the diameter of the light beam spot, so as to change the intensity of illumination brightness. The corresponding adjustment knob is generally set on the control panel of the electron microscope. The first concentrator and the second concentrator have different magnetic pole shape and working current, so the first concentrator has stronger magnetic field strength, while the

second concentrator has lower magnetic field strength. The method of changing the brightness by adjusting the capacitance current is actually an indirect method. The maximum brightness is limited by the electron beam. In order to change the brightness of the light to a greater extent, the size of the electron beam can be fundamentally changed by adjusting the gate bias voltage in the electron gun mentioned above. The main requirements for magnifying imaging lenses such as intermediate mirrors and projection mirrors are to obtain the highest magnification required for high resolution and the lowest magnification required to find a suitable field of view under the condition of shortening the height of the lens barrel as much as possible. It is also hoped that their aberrations, distortions, and axial astigmatism are as small as possible when conducting electron diffraction image analysis, doing special observations such as selected-area diffraction and small-angle diffraction.

The condenser is located below the electron gun and is generally composed of one stage, which are called the first and second condensers in order from top to bottom. The purpose of setting the condenser in the electron microscope is to condense the electron beam emitted by the electron gun into a light spot with uniform brightness and adjustable illumination range and project it on the sample below. The structures of the first condenser and the second condenser are similar, but the shape of the pole piece and the working current are different, so the strength and use of the magnetic field formed are also different. The first condenser is a strong magnetic field lens, and the second condenser is a weak magnetic field lens. The condensers of all levels are used together to adjust the diameter of the illumination beam spot, thereby changing the intensity of the illumination brightness. Generally, it is set on the electron microscope control panel. There are corresponding adjustment knobs.

(2) Imaging system

(1) Sample room

The sample chamber is under the condenser, and there is a sample stage for loading the sample. The sample stage must be able to move on the horizontal plane and direction to select and move the observation field. Correspondingly, it is equipped with a joystick or a rotating handwheel, which is a precise adjustment mechanism to move left and right in a certain direction. Modern high-end electron microscopes can be equipped with a computer-controlled motor-driven sample stage, which strives to be accurate when moving, stable when fixed, and can make label-type positioning marks on the sample by the computer, so that users can rely on it when they need to do retrospective comparison. Computer positioning search is difficult to achieve in manual selection operations.

Because of the short electron wavelength and weak penetration, it is necessary to make very thin samples. At this time, ultrathin slicing machine is needed for cutting. In order to achieve better cutting effect, diamond cutter or special glass cutter is required for ultrathin slicer. The sample is first installed on the copper wire and then fixed on the sample table. The sample table and the sample holding rod are integrated, which is a very fine part. There is an O-shaped rubber sealing ring in the middle of the sample bar, and the surface of the sealing ring is coated with vacuum grease to isolate the vacuum between the sample chamber and the outside of the mirror body.

(2) Objective

The objective lens is the most important part of electron microscope. Its function is to keep the phase of the elastic scattering beam converging on the focusing plane from the difference direction of the sample. A scattering pattern containing the sample structure or diffraction pattern will converge the elastic scattering beam of the same sample point on the image plane to form the sample group corresponding to the microscopic image. The quality of TEM depends on the quality of objective lens to a great extent.

The objective lens is a strong magnetic lens with a very short focal length, which requires extremely high working conditions such as material purity, processing accuracy, and pollution conditions during use. The core problem of improving the resolution index of an electron microscope is the comprehensive assessment of the performance design and process manufacturing of the objective lens. The focal length is as short as possible, the aberration is small, and the space is expected to be large, which is convenient for sample manipulation, but there are many contradictory links in the middle.

The function of the objective lens is to enlarge the main image, change the working current of the objective lens, and adjust the focal length. An electron microscope is used to change the operating current of the objective. After passing through the sample, the electron beam is projected onto the objective lens to form the first image, which usually determines the imaging accuracy. If there is an error in this kind of imaging, even if the error is very small, it will be displayed at a higher magnification once it is amplified.

(3) Intermediate mirror and projection mirror

An intermediate mirror, a first projection mirror, and a second projection mirror are arranged below the objective to complete the further magnification of the objective lens imaging. The total magnification of electron microscope is the product of objective lens, intermediate lens, and projection lens. The intermediate lens is mainly used for secondary magnification or reduction of objective lens imaging. By changing the position of the intermediate lens, the imaging operation or electron diffraction operation is controlled. The imaging operation is to enlarge the image of the objective lens and display it on the fluorescent screen. In order to obtain the imaging operation, the objective plane of the central lens and the image plane of the objective lens should overlap. The operation of electron diffraction is to reduce the object image and display it on the fluorescent screen. Through the imaging operation mode, we can obtain the morphology, structure, and other information of the sample, while the phase analysis of the sample requires the diffraction operation mode.

In the TEM-SPM method, the Schottky contact between the sample and the electrode is easy to form, which affects the measurement of the electrical properties of nanomaterials. Currently, TEM-SPM optimizes the contact between nanomaterials and electrodes by applying Joule heat generated by a suitable current. The contact Schottky resistance obtained in this way is large, the resistance difference between different contacts is obvious, and the TEM-SPM method is difficult to improve to the ohmic contact.

2.2. Medical Ultrasound Imaging Based on Edge Segmentation Method.

Edge is the important visual information contained in the image, and it contains most of the information of the image [12]. Edge detection is a key step in image processing and machine vision. The effect of edge detection is very important for image analysis and understanding. Images contain a lot of information, but not all of it [13–15]. By edge detection, not only the structural attributes of the image are preserved but also the information irrelevant to the image processing target is eliminated, greatly reducing the amount of data contained in the image, and finally, the edge information we need is obtained [16–18]. The edge-based segmentation method is used to detect the gray change of the discontinuous position image in terms of texture, gray level, and color and reflect the gray level gradient, represented by $\nabla f(a, b) = \partial f / \partial f i + \partial f / \partial f j$ [19]. The edge detection operator $e(a, b) = \sqrt{f_a^2(a, b) + f_b^2(a, b)}$ is defined, which is the amplitude of $\nabla f(a, b)$. To simplify the calculation, it can also be defined as the sum of the absolute values of the partial derivatives f_a, f_b:

$$e(a, b) = |f_a(a + b)| + |f_b(a + b)|. \tag{1}$$

(1) Sobel operator

Sobel operator image a point is as the center, in the neighborhood of $3 * 3$D direction and the partial derivative of the direction [20, 21]. The formula of Sobel operator is as follows:

In the vertical direction:

$$\begin{aligned} S_1(x, y) = |&f(x - 1, y - 1) + 2f(x, y - 1) + f(x + 1, y - 1) \\ &- (f(x - 1, y + 1) + 2f(x, y + 1) + f(x + 1, y + 1))|. \end{aligned} \tag{2}$$

In the horizontal direction:

$$\begin{aligned} S_2(x, y) = |&f(x - 1, y - 1) + 2f(x - 1, y) + f(x - 1, y + 1) \\ &- (f(x + 1, y - 1) + 2f(x + 1, y) + f(x + 1, y + 1))|. \end{aligned} \tag{3}$$

Select a threshold T, if $S_1(x, y) > T$, it means there is edge passing in the vertical direction of (x, y), and (x, y) is edge point. In the same way, if $S(x, y) > T$, also means edge point in (x, y) [22].

(2) Roberts operator

The gradient in the Roberts algorithm can be seen as the difference between two pixels in any vertical direction. The Roberts operator, on the other hand, takes the difference between two adjacent pixels in the diagonal direction:

$$\Delta_i f = f(x, y) - f(x + 1, y + 1), \tag{4}$$

$$\Delta_j f = f(x, y + 1) - f(x + 1, y). \tag{5}$$

Its gradient amplitude value is

$$R(x, y) = |\Delta_i f| + |\Delta_j f|, \tag{6}$$

or

$$R(x, y) = \sqrt{\Delta_i^2 f + \Delta_j^2 f}. \tag{7}$$

The convolution operator is expressed as

$$\Delta_i f = \begin{vmatrix} 1 & 0 \\ 0 & -1 \end{vmatrix}, \Delta_j f = \begin{vmatrix} 0 & 1 \\ -1 & 0 \end{vmatrix}. \tag{8}$$

Select the close value T appropriately, if $R(x, y) > T$, then, (x, y) is the edge point.

(3) Laplace operator

Laplace operator is a second derivative operator, whose center of function is zero in the frequency domain is symmetric, so it has rotation invariance. This graph is processed by Laplace operator, and the pixel has the feature of zero gray mean. The Laplace transform of a two-dimensional graph function is the isotropic second derivative. The formula is as follows:

$$\nabla^2 f(a, b) = \frac{\partial^2 f(a, b)}{\partial a^2} + \frac{\partial^2 f(a, b)}{\partial b^2}. \tag{9}$$

Let us write it as a difference:

$$\begin{aligned} \nabla^2 f(x, y) = &f(x - 1, y) + f(x, y + 1) + f(x + 1, y) \\ &+ f(x, y - 1) - 4f(x, y). \end{aligned} \tag{10}$$

2.3. Random Forest Algorithm

2.3.1. Bagging Algorithm.
The principle of bagging algorithm is to determine the training set, get the number of training samples, and determine the number of weak classifiers. Then, the samples are randomly put back from the training set until the samples are equal to the training samples. If the number of existing weak classifiers reaches the standard, stop sampling and construct a strong classifier by voting strategy as the final classification result. If the number of weak classifiers is not enough, the samples are randomly put back from the training set.

2.3.2. Random Forest Algorithm. The principle of a random forest algorithm is the development of many independent decision trees, and each decision tree can be trained independently with training samples [23]. Each decision tree is according to the training plan. In order to create decision trees, it is necessary to create a corresponding number of training programs. Creation of N training units is from an original training base with a statistical modeling process. The test samples are categorized according to randomly assigned subtrees, and the results of each background are summarized. As a powerful classifier, the random forest algorithm has a strong power.

Random forest algorithm has many excellent characteristics. Random forest algorithm can be applied in many fields and has achieved excellent performance. It has the following advantages: (1) the algorithm is simple and easy to understand and easy to implement; (2) it can detect the interaction between features in the training process; (3) it has good antinoise ability and good ability to deal with a certain amount of data loss; (4) it can be processed in parallel.

3. Experimental Design

3.1. Experimental Design. These data include 800 transmission electron microscope (TEM) images of nanoparticles with an acceleration voltage of 70 kV and a magnification of 6000.

When the nearest neighbor field is initialized, a 5×5 window is used to sample the reference image set a uniformly and independently, and a set of 8000 effective blocks is obtained.

In the process of image block matching, the matching block of the block to be searched is searched step by step. Table 1 shows the experimental results of one query block under three different search steps and calculates the best five matching blocks. Di represents the distance between the query block and the 6-neighborhood block.

The weights of the corresponding tag matching blocks are extracted and optimized. Six query blocks are selected, and the similarity weights between the optimal matching of each query and the five blocks are calculated according to the formula.

From Tables 1 and 2, we can get the d_i and w_i values of each query block, search out the optimal image matching block of the query block, and finally extract the optimal matching block for weighting to reconstruct the initial segmentation results of nanoparticles.

3.2. Experimental Steps. In this experiment, n reference images with different gray levels are extracted from database X and y for decision tree algorithm processing: (1) generate n-ary tree through training set; (2) analyze the path generation rules of n-tree generated; (3) predict or classify new data according to the generated rule set. After processing, n decision trees are generated, and a single random forest is collected to form multiple random forests. Input the image a to be segmented and output the segmentation result of image a of each random forest classifier. In the experiment, n different random forest classifiers are used to get the segmentation results of N graphs a. After getting n different

TABLE 1: Experimental results of three different search steps.

Search step size	The distance value Di between query block and 6 domain block					
	D1	D2	D3	D4	D5	D6
4	38	65	295	85	125	315
2	59	315	65	326	106	178
1	79	48	71	35	105	299

TABLE 2: Similarity weight between query block and optimal block.

Image block number	Similarity weight W1 between the query block and the best matching block				
	W1	W2	W3	W4	W5
1	0.2235	0.2156	0.2030	0.1985	0.1923
2	0.2185	0.2015	0.1985	0.1867	0.1815
3	0.2376	0.2278	0.2056	0.1975	0.1862
4	0.2163	0.2085	0.1989	0.1875	0.1832
5	0.2623	0.2073	0.1975	0.1865	0.1812
6	0.2185	0.2015	0.1956	0.1929	0.1918

segmentation results, FCM clustering algorithm is used for processing. The steps of FCM clustering algorithm are as follows:

(1) The gray values of N pixels with the same coordinates in the segmentation results are extracted, and the $X * y$ samples with sample size n are finally obtained

(2) According to the obtained $x * y$ samples of N, the probability of the points expressed as nanoparticles in each sample s is calculated. Let $n(a, b)$ be the number of points labeled as nanoparticles in row a and column B of N segmentation results, and $P(a, b)$ is the probability of points labeled as nanoparticles in column A and column B in n segmentation results

(3) By calculating the probability p of nanoparticles for all the sample data, we can construct the probability map of the base film obtained by N results

(4) FCM clustering is performed on the calculated probability graph

(5) Through the above four steps, after completing the classification of $X * y$ samples, the postprocessing of N segmentation results is completed. After constructing the probability map of nanoparticles, the structure of nanoparticles was extracted by FCM clustering, and the segmentation results with high accuracy were obtained after optimization

4. Analysis of Experimental Results

4.1. Evaluation of Image Segmentation Accuracy. In this paper, the segmentation results are compared with the

TABLE 3: Jaccard similarity coefficient of three different methods.

Method	Image 1	Image 2	Image 3	Image 4	Image 5
Multiple random forest algorithm	0.92	0.93	0.89	0.95	0.91
Watershed segmentation method	0.88	0.86	0.92	0.92	0.89
Weighted median filter	0.58	0.45	0.58	0.64	0.55
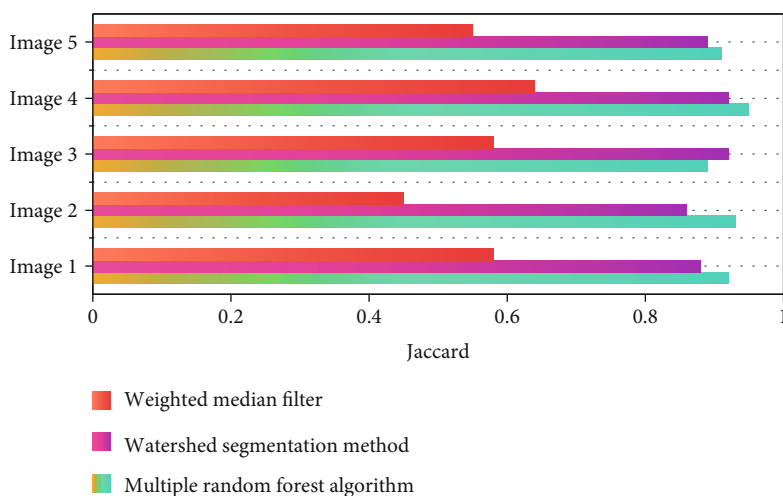
FIGURE 1: Jaccard similarity coefficient of three different methods.
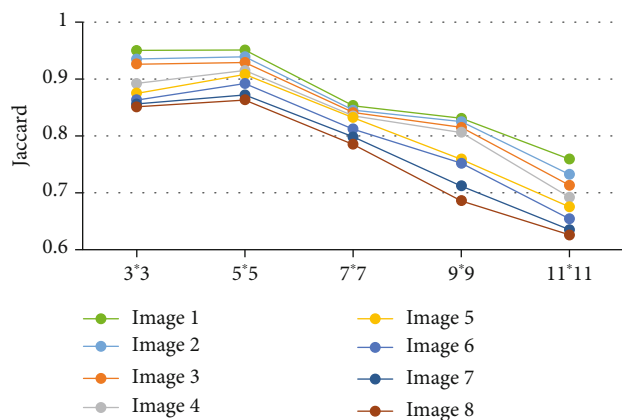
FIGURE 2: Effect of sample size on segmentation accuracy.
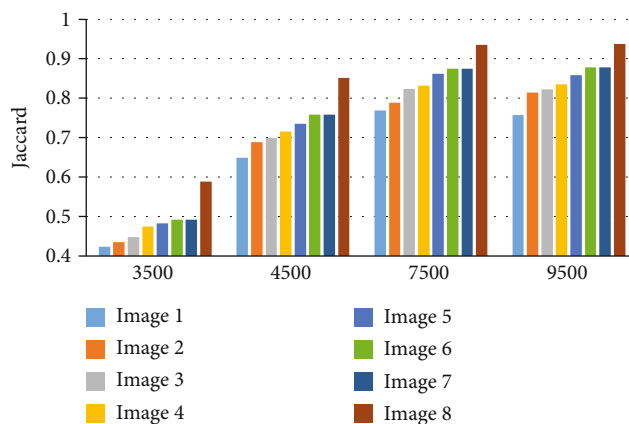
FIGURE 3: The influence of sample number on segmentation results.

manual segmentation golden standard image, and the Jaccard index is used to evaluate the segmentation results. Jaccard index is a geometric similarity measure function. The larger the Jaccard value, the better the segmentation performance. The formula is as follows:

$$\text{Jaccard}(X, Y) = |X \cap Y| / |X \cup Y|. \tag{11}$$

In the formula, a and B are the results of manual segmentation and automatic segmentation, respectively, and the overlap rate of nanoparticle regions between the two results is calculated. The similarity coefficient is between [0,1]. The Jaccard value is 1 when the manually segmented nanoparticle region completely overlaps with the auto segmented basement

membrane region, and 0 when there is no overlap term. The closer to 1, the higher the similarity, the better the segmentation effect.

In this paper, we use multiple random forest algorithm, watershed segmentation method, and maximum entropy threshold segmentation to detect TEM images of 800 groups of nanoparticles. Jaccard similarity coefficient of three different methods is shown in Table 3.

As can be seen from Figure 1, the minimum Jaccard coefficient obtained by the multiple random forest algorithm is 89%, and the highest is 95%. The lowest and highest Jaccard coefficients are 86% and 92%, respectively. The lowest and highest Jaccard coefficients are 45% and 58%, respectively. For the same group of images, from left to right is
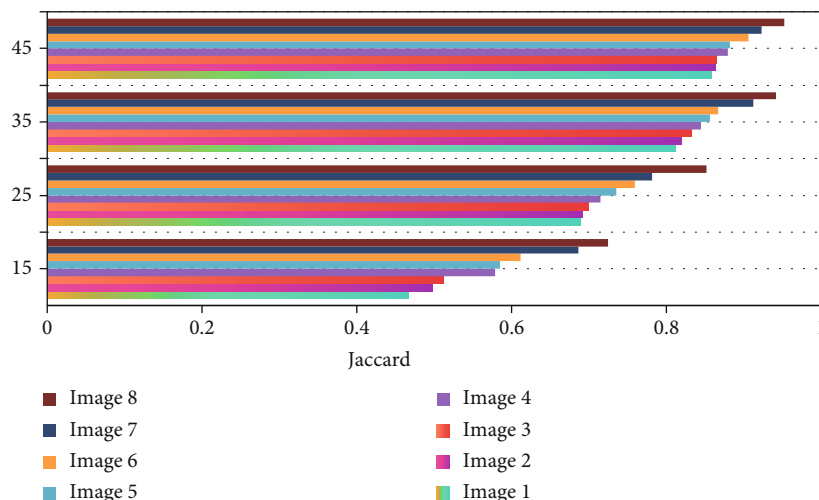
FIGURE 4: The influence of the number of random forests on segmentation results.

corresponding to the multirandom forest algorithm, watershed segmentation method, and maximum entropy threshold segmentation Jaccard coefficient.

4.2. The Size of Sample Block Affects the Segmentation Result.
In the initialization process, the size of sample block directly affects the accuracy of segmentation results. In this experiment, eight groups of images are selected to calculate the influence of sample block size on the segmentation results of each group, as shown in Figure 2.

As can be seen from Figure 2, when the size of the sample block is less than $5 * 5$, the segmentation accuracy does not change much; when the size of the sample block is greater than $5 * 5$, the segmentation accuracy begins to decline. Considering the segmentation results and computational complexity, the computational complexity of $5 * 5$ size is less than $3 * 3$ size in the case of low image accuracy. Therefore, the size of the sample block is suggested to be $5 * 5$.

4.3. The Influence of the Number of Evenly Distributed Samples on Segmentation Results.
In the process of image block matching, the number of evenly distributed samples directly affects the result of image segmentation. In this experiment, we selected 8 groups of images to calculate the effect of sample size on the segmentation effect of each group of images, as shown in Figure 3.

The smaller the number of samples, the worse the segmentation effect. This is mainly because the sample block contains too little information, resulting in poor matching effect and resulting in poor segmentation effect. When the number of samples is more than 7500, the accuracy of segmentation has little change. Considering the segmentation results and computational complexity, this paper suggests that 7500 is the most suitable sample size.

4.4. The Influence of the Number of Random Forests on Segmentation Results.
In the process of multirandom forest algorithm segmentation, the number of constructed forests has a direct impact on the image segmentation results. In

this experiment, eight groups of images are selected, and the influence of the number of forests on the segmentation effect is calculated.

It can be seen from Figure 4 that the segmentation effect is gradually enhanced with the increase of the number of selected forests ($n \leq 35$). This is mainly because the information of gray distribution is too little, which will lead to poor matching effect and poor segmentation effect. When the number of random forests is 15, the segmentation accuracy of 8 groups of images is very different. The main reason is that when building multiple random forests, some images will choose the training images with similar gray levels, so the segmentation accuracy is higher than other images. With the increase of the number of random forests, the segmentation accuracy of 8 groups of images is gradually improved. When the number of trees is more than 35, the segmentation accuracy changes little. Considering the segmentation results and computational complexity, the number of forests should be set to 35.

The experimental results show that in terms of image segmentation accuracy, the Jaccard coefficient obtained by the multiple random forest algorithm is significantly better than watershed segmentation method and maximum entropy threshold segmentation and is more suitable for the segmentation of nanoparticles. Multiforest algorithm uses multiple random forest classification. When the number of forests is large enough, there will always be one or more training images whose gray value is close to the gray value of the segmented image. It overcomes the problem of low image accuracy caused by gray difference between different images and improves the segmentation accuracy of nanoparticles. When the size of the sample block is less than $5 * 5$, the segmentation accuracy does not change much when the size of the sample block is less than $5 * 5$; when the size of the sample block is greater than $5 * 5$, the segmentation accuracy begins to decline. It is suggested that the size of the sample block should be $5 * 5$. When the number of samples is more than 7500, the accuracy of segmentation does not change much. With the increase of the number of selected forests ($n \leq 35$), the segmentation effect is

gradually enhanced. When the number of trees is more than 35, the segmentation accuracy changes little. When the multiple random forest algorithm is used, the best result is when the number of forests is set to 35.

5. Conclusion

With the development of materials science, nanoparticles have large specific surface area, small particle size, high surface energy, and unique nanoeffect. The morphology of nanoparticles is a key factor affecting the properties of materials.

In this paper, we mainly study the image recognition of TEM nanoparticles. We mainly introduce transmission electron microscopy, image edge segmentation, and random forest algorithm. In this paper, based on the random forest algorithm, a multirandom forest algorithm is proposed. Due to the different gray levels of images referenced by the multirandom forest algorithm, the segmentation results are processed by FCM clustering algorithm. This paper improves the imaging quality of TEM for weak phase bulk materials and biological samples, builds a multielectrode TEM in situ electrical platform based on microchips, realizes pollution-free etching with atomic precision, prepares nanodots, and observes coulombs. The blocking phenomenon was observed, the nanowire-induced fracture process was observed, and the nanowire fracture mechanism was studied. The minimum and maximum Jaccard coefficients obtained by multiple random forest algorithm are 89% and 95%, respectively. The lowest and highest Jaccard coefficients are 86% and 92%, respectively. The lowest and highest Jaccard coefficients are 45% and 58%, respectively. The Jaccard coefficient of the proposed algorithm is higher than that of watershed segmentation and maximum entropy threshold segmentation. In the aspect of automatic image segmentation of nanoparticles, the image segmentation accuracy is the highest when the sample block size and the number of sample blocks selected in the multiple random forest algorithm are $5 * 5$, 7500, and 35, respectively. As the feature size of CMOS shrinks to the nanometer scale, the electromigration of metal interconnects seriously affects the reliability of microelectronic devices. After the metal nanowires are prepared on the microchip, the microscopic dynamic changes in the metal electromigration can be directly observed by using the TEM in situ electrical technology, and the metal electromigration mechanism can be further studied, thereby providing a guarantee for increasing the reliability of electronic devices. Using TEM in situ electrical technology to study the working mechanism of new memory devices, new memory devices such as resistive memory and phase change memory have attracted much attention because of their fast speed and high storage density. Uniformity is an urgent problem to be solved in the large-scale application of these new memory devices. After the new memory device is fabricated on the microchip, the working process of the device is directly observed by TEM in situ electrical technology, and the working mechanism of the device is analyzed, thereby reducing the uniformity problem of the new memory device.

In this paper, the multirandom forest algorithm is proposed because of the randomness of the automatic segmentation method of nanoparticle image. The next step is how to improve the speed of automatic segmentation of nanoparticle image and ensure the accuracy of image segmentation.

Data Availability

No data were used to support this study.

Conflicts of Interest

The authors declare that there are no conflicts of interest regarding the publication of this article.

Acknowledgments

References

[1] T. Nandhini and M. Vigneshwaran, "On neutrosophic nano αg# ψ-closed sets in neutrosophic nano topological spaces," *International Journal of Neutrosophic Science*, vol. 5, no. 2, pp. 67–71, 2020.

[2] D. Strzeciwilk, P. Tkacz, and Z. Wokulski, "Transmission electron microscope studies of TiC crystals," *Crystal Research and Technology*, vol. 35, no. 11-12, pp. 1295–1303, 2015.

[3] N. Li, J. Wang, S. Mao, and H. Wang, "In situnanomechanical testing of twinned metals in a transmission electron microscope," *MRS Bulletin*, vol. 41, no. 4, pp. 305–313, 2016.

[4] C. Mayer, N. Li, N. Mara, and N. Chawla, "Micromechanical and _in situ_ shear testing of Al -SiC nanolaminate composites in a transmission electron microscope (TEM)," *Materials Science & Engineering A*, vol. 621, pp. 229–235, 2015.

[5] Y. Shen and L. Sun, "Setting up a nanolab inside a transmission electron microscope for two-dimensional materials research," *Journal of Materials Research*, vol. 30, no. 21, pp. 3153–3176, 2015.

[6] J. L. Lyon, D. A. Fleming, M. B. Stone, P. Schiffer, and M. E. Williams, "Synthesis of Fe oxide core/Au shell nanoparticles by iterative hydroxylamine seeding," *Nano Letters*, vol. 4, no. 4, pp. 719–723, 2004.

[7] M. Wei, A. J. Ruys, B. K. Milthorpe, and C. C. Sorrell, "Solution ripening of hydroxyapatite nanoparticles: effects on electrophoretic deposition," *Journal of Biomedical Materials Research*, vol. 45, no. 1, pp. 11–19, 1999.

[8] C. Nayral, E. Viala, P. Fau et al., "Synthesis of tin and tin oxide nanoparticles of low size dispersity for application in gas sensing," *Chemistry*, vol. 6, no. 22, pp. 4082–4090, 2000.

[9] H. Ge, Y. Hu, S. Yang, X. Jiang, and C. Yang, "Preparation, characterization, and drug release behaviors of drug-loaded ?-caprolactone/L-lactide copolymer nanoparticles," *Journal of Polymer Science*, vol. 75, no. 7, pp. 874–882, 2000.

[10] J. Wang, F. Wang, J. Xu et al., "Lanthanide-doped LiYF4 nanoparticles: synthesis and multicolor upconversion tuning," *Comptes Rendus Chimie*, vol. 13, no. 6, pp. 731–736, 2016.

[11] J. Zhao, J. Huang, R. Wang, H. R. Peng, and S. Ji, "Investigation of the optimal parameters for the surface finish of k9 optical

glass using a soft abrasive rotary flow polishing process," *Journal of Manufacturing Processes*, vol. 49, pp. 26–34, 2020.

[12] P. Muneesawang, C. Sirisathitkul, and Y. Sirisathitkul, "Multi-level segmentation procedure for measuring the size distribution of nanoparticles in transmission electron microscope images," *Advanced Materials*, vol. 7, no. 4, pp. 769–783, 2015.

[13] S. Mcvitie, S. Hughes, K. Fallon et al., "A transmission electron microscope study of Neel skyrmion magnetic textures in multilayer thin film systems with large interfacial chiral interaction," *Scientific Reports*, vol. 8, no. 1, p. 5703, 2018.

[14] B. M. Morrow, E. K. Cerreta, R. J. Mccabe, and C. N. Tomé, "Transmission electron microscope in situ straining technique to directly observe defects and interfaces during deformation in magnesium," *JOM*, vol. 67, no. 8, pp. 1721–1728, 2015.

[15] T. Xu, S. Lu, and H. Zhang, "Transmission electron microscope evidence of telocytes in canine dura mater," *Journal of Cellular and Molecular Medicine*, vol. 20, no. 1, pp. 188–192, 2016.

[16] S. Dong, S. Zhao, Y. Wang, T. Pang, and Y. Ru, "Analysis of blood cell autophagy distribution in hematologic diseases by transmission electron microscope," *Zhonghua Xueyexue Zazhi*, vol. 36, no. 2, pp. 144–147, 2015.

[17] K. Adachi, N. Moteki, Y. Kondo, and Y. Igarashi, "Mixing states of light-absorbing particles measured using a transmission electron microscope and a single-particle soot photometer in Tokyo, Japan," *Journal of Geophysical Research-Atmospheres*, vol. 121, no. 15, pp. 9153–9164, 2016.

[18] M. Krysztof, T. Grzebyk, A. Górecka-Drzazga, K. Adamski, and J. Dziuban, "Electron optics column for a new MEMS-type transmission electron microscope," *Bulletin of the Polish Academy of Sciences, Technical Sciences*, vol. 66, no. 2, pp. 133–137, 2018.

[19] C. Wang, Q. N. Chan, R. Zhang et al., "Automated determination of size and morphology information from soot transmission electron microscope (TEM)-generated images," *Journal of Nanoparticle Research*, vol. 18, no. 5, pp. 1–15, 2016.

[20] E. J. Kim, Y. H. Jeong, B. A. Kang, and H. C. Choe, "Nanotubular structure on the Ti–29Nb–5Zr alloy by scanning transmission electron microscope," *Journal of Nanoscience and Nanotechnology*, vol. 15, no. 1, pp. 595–599, 2015.

[21] X. Li, Z. Chen, A. Taflove, and V. Backman, "Optical analysis of nanoparticles via enhanced backscattering facilitated by 3-D photonic nanojets," *Optics Express*, vol. 13, no. 2, pp. 526–533, 2005.

[22] O. Lee, S. H. Lee, S. H. Jeong et al., "A quantitative study of nanoparticle skin penetration with interactive segmentation," *Medical & Biological Engineering & Computing*, vol. 54, pp. 1469–1479, 2016.

[23] Y. Chen, W. Zheng, W. Li, and Y. Huang, "Large group activity security risk assessment and risk early warning based on random forest algorithm," *Pattern Recognition Letters*, vol. 144, pp. 1–5, 2021.

Research Article

Nanoligament Combined with Tennis Exercise on Rehabilitation Training for Treatment of Ligament Injury Patients

Jun Chen [1] **and Yiting Chen** [2]

[1]*PE Institute, Southwest Petroleum University, Chengdu, 610500 Sichuan, China*
[2]*Art Institute, Southwest Petroleum University, Chengdu, 610500 Sichuan, China*

Correspondence should be addressed to Jun Chen; 201799010024@swpu.edu.cn

This article mainly studies the effect of nanoligament combined with tennis on the rehabilitation of ligament injury patients. This article first uses nanoligaments made by ACL reconstruction technology to give targeted rehabilitation treatment to patients with ligament injuries, analyzes the internal structure of the knee joint cavity ligaments, and clarifies the rehabilitation of ACL injuries and other combined injuries. The construction method of nanoligament composite fiber composite ligament is mainly introduced. Secondly, the nanoligament damage mechanism can be used to prevent excessive knee deformation and internal rotation. Finally, the nanoligament is combined with the fiber composite ligament, and the silk fibroin filament yarn is used as the axis to form a composite structure on the fiber composite ligament structure to strengthen the rehabilitation effect for patients with ligament injury. In this study, combined with the data analysis of patients with nanoligament injury, it was found that after 50 patients have undergone corresponding tennis training and knee flexion angle observation, the recovery speed is 5 times faster than that of ordinary patients. The experimental results show that the combination of nanoligaments and tennis has a positive effect on rehabilitation training for patients with ligament injury.

1. Introduction

1.1. Background and Significance. Anterior cruciate ligament (ACL) injury is a common serious sports injury. The anterior cruciate ligament has the important function of restricting the excessive advancement of the hard bone and controlling the rotation. Knee joint instability occurs after the anterior cruciate ligament is damaged. Since then, meniscus cartilage injury, articular cartilage injury, and knee arthritis symptoms are treated. Treatment is a hot spot in the field of sports medicine. About 3.5 million anterior cruciate ligaments are damaged in the United States each year, and the annual medical cost is $6.5 billion. With the development of China's national strength and sports competition, the incidence of anterior cruciate ligament injury has increased significantly, but there are also studies showing that the incidence of anterior cruciate ligament injury in Chinese athletes is 0.39%. The main cause of anterior cruciate ligament rupture is sports injuries, accounting for more

than 70%, and the most affected people are basketball and football. For the treatment of patients with ligament injuries, people have developed nanoartificial ligaments to reconstruct anterior cruciate ligaments and use the exercise effect of tennis to strengthen the repair of sports injuries.

The material of the nanoartificial ligament is polyethylene terephthalate (PET), which is the same as the material of surgical sutures and artificial blood vessels and has good biocompatibility. It can effectively share the gravity and be absorbed by the human body. It is safe to use and will not cause rejection. The nanoartificial ligament adopts the bionic structure design, and the two end structures are densely woven in the middle; there is loose free fiber in the middle, and the mechanical properties are good. In addition, the tennis exercise accelerates the repair of the patient's physical function, and the effect is more excellent [1, 2]. The safety and functional evaluation of the knee joint is an important part of the evaluation of the efficacy after ACL reconstruction. Currently, Lachman is used to evaluate the

front and back stability of the knee joint, and the axial movement test is used to evaluate the rotation stability of the knee joint. Flexible stability is required in activities [3]. Modern three-dimensional walking analysis technology provides a new method for objectively, accurately, and quantitatively evaluating the stability and function of sports knee joints and is widely used to evaluate the efficacy after ACL reconstruction [4, 5].

1.2. Related Work. Seijas mentioned in his paper that an anterior cruciate ligament (ACL) injury is a highly injured accident in the working area of young athletes. The use of bone grafts, despite being a treatment option, can still cause postoperative problems, such as pain in the anterior knee, which limits its use and leads people to prefer alternative grafts. Their purpose was to evaluate whether the application of PRGF can reduce the pain of the anterior knee at the donor site reconstructed by BTB-ACL. The materials and methods they used are as follows: 55 patients participated in double-blind and randomized clinical trials, compared two groups of patients who used ACL transplantation for ACL reconstruction, and whether they used PRGF at the donor site after harvesting the graft. Knee pain results compared with the control group: the pain in the donor site of the PRGF group was reduced, and there was a significant difference in the first two months of follow-up [6]. Kim's research believes that various knee joint injuries caused by anterior cruciate ligament have been identified as important risk factors for the development of knee osteoarthritis (OA). However, no studies have been conducted using large sample studies to examine the relationship between ACL and OA. His research goal was to use the National Health Insurance Service Cohort data to study the impact of ACL injuries and other related knee joint structures on the development of OA. It also designed a retrospective cohort study of epidemiology and set up a database of epidemiological research service groups from the active adult population of the National Health Insurance [7]. Gomes' study believes that knee osteoarthritis (KOA) lacks sufficient treatment response outcome indicators. The role of ultrasound in the treatment of inflammatory joints and periarticular diseases has been well established, but its application in OA is less. The purpose is to develop a new high-resolution US protocol to assess the structure and inflammation of primary knee osteoarthritis. The scanning protocol was jointly developed by three high-level rheumatologists with similar experience in the United States. The proposed scheme has been shown to be reliable for patients with KOA and is therefore a promising tool that can be used for clinical practice and research purposes [8].

1.3. Innovation in This Article. The main innovative work of this paper includes the following aspects: (1) use modern three-dimensional gait analysis technology to evaluate the dynamic knee rotation stability and lower extremity function after ACL reconstruction with nanoartificial ligament and compare it with patients after autologous tendon transplantation. (2) The expression of PDGF and BMP-2 in the tendon-bone interface was measured by immunohistochem-

istry, which laid a certain foundation for further clarification of the vascularization of the tendon-bone interface and the specific bone formation mechanism. The research in this paper can provide a perfect and improved development suggestion for the rehabilitation training of patients with ligament injury and can also provide new ideas for the research in the field of medical rehabilitation.

2. Nanoligament Combined with Tennis Training Method for Rehabilitation Training

2.1. Nanoligament Based on ACL Reconstruction Technology. ACL reconstruction was performed in a supine position. Bone and joint endoscopy was performed after bleeding, and the knee joint cavity was regularly checked to confirm ACL injuries and other beds. At this time, first consider using nanoligaments to help patients deal with ligament injuries; first deal with combined injuries: the extent of half-moon cartilage injury, shaping, subtotal resection, total resection, or suture [9, 10]. According to the principles of isometric reconstruction surgery described in the literature, reassemble the ACL and regularly maintain the ACL gap. First, use special locators to create tunnels for the hard bones and thigh bones. The external connector of the cervical bone is approached through the inside of the front, the center of the opening of the Qinggu tunnel joint is 7 mm in front of the PCL, and the blind needle forms a cervical bone tunnel with a diameter of 6.5 mm through the ACL stump [11, 12]. Then, arrange the thigh bone external device through the hard bone tunnel. The center of the inner mouth of the thigh bone tunnel is located in the hepatology of the right knee. The liver and the lower edge of the posterior wall fall 6 mm. The position of the femur is generally determined by medical instruments. Drill the guide pin through the femur in reverse, penetrate the skin in front of and on the side of the thigh, make a 4 cm skin incision at the point of the femoral needle, use a series of cannulas to protect the soft tissue of the thigh, and drill from the lateral femur with a guide needle Through the femoral tunnel reaching the knee joint, the specific scheme is shown in Figure 1 [13, 14].

Once the bone tunnel is established, the nanoligaments will be installed and fixed. Select 150 bundles of fibrous LARS artificial nanoligaments (AC 120 2B) from the left or right knee [15]. Electric wires are introduced from the external opening of the thigh tunnel through the knee joint and connected through the hard bone tunnel. Place the LARS artificial ligament on the steel wire, and after the external port of the bony tunnel passes through the knee joint, the LARS artificial nanoligament will pass the ACL stump from bottom to top. The free fiber enters the thigh tunnel 1 mm, and the external ligament rotates slightly outward. Along the external opening of the thigh tunnel, connect the 8 mm diameter interface to squeeze the screw to fix the ligament. Attach a loop of artificial nanoligament at the end of the bone, bend or unfold the knee joint 30 times, adjust the ligament tension, confirm the knee joint mobility, spine angle projection, and confirm whether the LARS artificial nanoligament will affect the impact between the head and the posterior cruciate ligament (PCL) [16, 17]. In a 30- to 40-degree
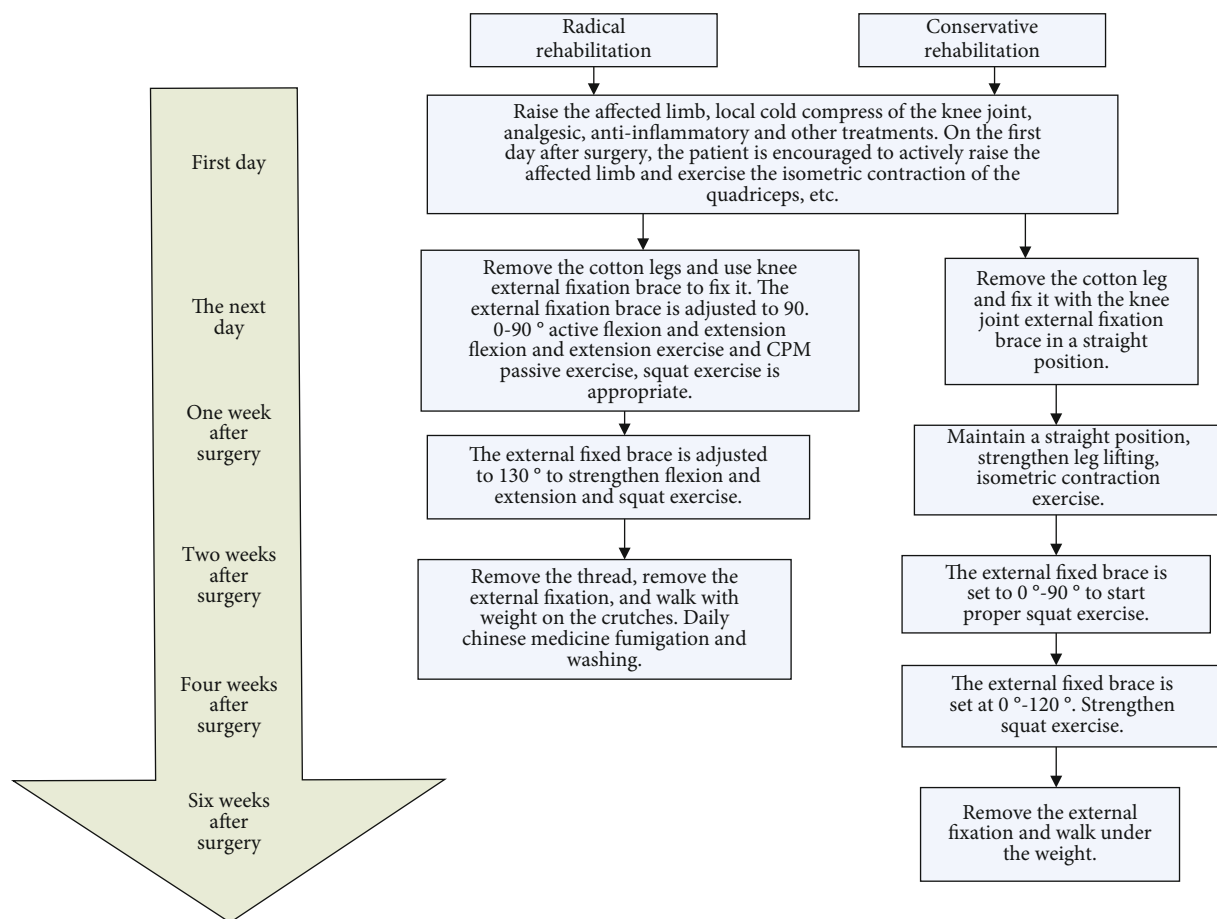
Figure 1: ACL reconstruction technique treatment plan.

bend of the knee, push the hard bone backwards and use three 15 mm diameter interfaces to braid the screw to fix the hard bone end of the ligament. Cut the extra ligament outside the femoral tunnel and the hard bone tunnel, and suture the incision [18, 19].

Use the same rehabilitation program in the four centers. No bracing is required after surgery. From the first day after the operation, the quadriceps muscle function training was started. Subsequent training programs and training volumes are determined according to the degree of recovery. The next day, the ground was partially weight-bearing. The knee ROM reached 0°-90° 1 week after the operation. Partial weight-bearing of abduction was 1-2 weeks after operation, and it gradually transitioned to complete weight-bearing at 4 weeks after operation. Daily activities resumed 6 weeks to 3 months after surgery, started jogging 4 months after surgery, and gradually resumed unrestricted exercise 3 to 6 months after surgery [20, 21].

After the operation, apply pressure to all patients, wrap the bandage in a correct position and fix it, raise the affected arms and legs, apply a local cold compress to the knee joints, relieve pain, and implement anti-inflammatory treatment. On the first day after surgery, it is best for patients to straighten the affected limbs and take active measures such as the sand head muscles [22, 23]. The cotton legs were removed the next day after rehabilitation removal surgery.

The knee joints were fixed with external support frames. The external fixed struts had a range of motion of 0°-90° (0° full expansion). They adjusted the position and encouraged patients to go out [24]. Within the setting range of the fixed bracket, nonsupporting bearings activate bending and extend knee joints and continuous manual mechanical movement. Partial weight support can be used for squat exercise after one week of surgery. At this time, the patient's physical function has gradually recovered. Continue to observe for another week. At this time, the patient's physical function has gradually recovered. Continue to observe for another week, and the external fixed bracket is removed two weeks after surgery. Knee joint active flexion and renal motion indicate the supporting part of weight walking [25].

2.2. Structure of Knee Ligaments and Damage Mechanism. The medial structure of the knee ligament is divided into three layers from the surface layer to the myocardium. The medial ligament (MCL) and the medial joint capsule and their thick parts have the function of preventing excessive dryness of the knee joint. The lateral structure is divided into 3 layers, the first layer is the urethral tube branch and the posterior expansion of the arm, and the second layer is the anterior knee muscle membrane and the posterior part of the quadriceps and the two knee bands. The third layer is the half-moon ligament, lateral half-moon ligament, arcuate

ligament, and joint capsule. The posterior structure is reinforced by the posterior structure formed by the wrist tendon and the forearm thigh and its accessory structure. It is separated from the joint capsule by the synovial capsule; the posterior part is healed with the joint capsule and the medial meniscus. The side structure mainly prevents excessive knee reversal, and the second role is to prevent excessive knee deformation and internal rotation. The anterior cruciate ligament and posterior cruciate ligament of the joint. The anterior cruciate ligament can be divided into the anterior medial, posterior and external junctions, and the anterior internal junction. In knee extension, the long axis of the attachment surface is nearly vertical. The cross section of the attachment end of the tibia is approximately triangular, with the base facing forward and the tip facing backward. The important function of this angle is to prevent forelimb bones, medial rotation, knees, and hyperextension. The posterior cruciate ligament can be divided into anterior posterior and posterior and posterior interior. The anterior and external are tense, the posterior and internal are slack, the posterior and internal are stretched when the knee is stretched, and the anterior and external are slack.

The most common electromechanical damage to the medial ligament is the direct violence on the side of the knee joint, which leads to knee trauma and damage to the medial ligament. Because the lower dead point of the medial ligament is wider, it is generally stopped at the thigh or joint space where the injury occurs near the ligament. If the violence is severe or the knee joint rotates and hurts in parallel, ligament rupture and joint dislocation may occur simultaneously. Lateral ligament injuries are mostly caused by direct violence against the medial knee, and the incidence is significantly lower than that of the medial ligament ligaments, and the posterior tendon is damaged by the hard bone mutation and lateral ligament injury. There are damaged ligaments and arcuate ligaments in the lateral structure. If the violence is large, the posterior structure of the knee joint will be damaged, and the cruciate ligaments can be merged. When walking or exercising, it will cause pain above the fibular head on the posterolateral side of the knee. In addition, the patient will also cause pain on the outside of the knee joint when the patient bends his legs or crosses his legs. The damaged mechanism of the anterior cruciate ligament often bends, and the lateral turn is injured, causing the medial ligament to be injured. There are also few trauma injuries, partial or complete fracture of the anterior cruciate ligament. Damage to the posterior cruciate ligament often occurs when the forearm is hardened; that is, the posterior cruciate ligament ruptures in front of the muscle bone. The posterior cruciate ligament is affected by femoral osteoporosis and the posterior cervical bone platform. The ligament may be injured when bending occurs. Excessive knee injury may cause posterior cruciate ligament injury.

2.3. Construction Method of Nanoligament Combined Fiber Composite Ligament.
Since the mechanical properties of ligament materials made of regenerated silk fibroin materials cannot meet the requirements, the dense structure of liga-

FIGURE 2: Schematic diagram of nanoligament fabric formation.

ment materials composed of natural silk fibroin fibers affects the adhesion and growth of cells. The above silk fibroin materials have their own performance defects, and we combine three methods to form artificial nanoligaments to form a regenerated silk fibroin nanoligament composed of silk fibroin fibers, silk fibrils, and natural silk fibrils. The main structural design of the regenerated silk fibroin fiber composite nanoligament still uses YTS2-24 vertical rotary polishing machine and core brake. It can demonstrate well the original basic structure of the regenerated silk fibroin nanoligament. The schematic diagram of fabric formation is shown in Figure 2 (picture from http://www.pixabay.com). During the construction process, silk fibers were first woven with cashmere, which greatly improved the shortcomings of the easily deformable tubular fabric. Second, the outer gauze is used to dye the fabric layer between natural silk fibrin fibers and cotton, and the outer gauze is used to make the fabric layer. After being controlled with an angle of $45 + 2°$, the outer layer of the electrospun nanofiber membrane with a thickness of 3 mm is packaged. This fibrous membrane is one of the main ways to prepare nanofibrous materials, which can be effectively applied to the immobilization of enzyme catalysts. As a result, the broad fabric layer is woven with natural silk fibroin fibers from the packaging raw yarn. Finally, the composite structure of regenerated silk fibroin fiber composite nanoligaments is composed of electrospun nanofiber membranes and natural silk fibrous fiber fabrics.

According to the conclusion of the mechanical properties of the ligament material formed by different layers of natural silk fibroin fibers, if weaving 8 layers, the mechanical properties of the material are close to the human ACL, so during the formation of composite nanoligaments, the individual layer fiber weaving method is matched with two different silk fibroin fiber materials. In the hybrid project, the ratio of electrospun nanofiber membranes to natural silk fibroin is 1 : 1; that is, the number of fabric layers formed by natural silk fibroin fibers is 8 layers, while the electrospun nanofiber membranes have 7 layers. The silk fibroin filaments are woven into the middle of the nanoligament material as a shaft yarn. This ratio is mainly to unify the applicability and functionality of the nanoligaments.

3. Nanoligament Rehabilitation Training Experiment

3.1. Experimental Sample. The subjects of this experiment were 100 patients with different degrees of ligament injury. According to their prevalence, 50 patients underwent corresponding nanoligament surgery. In the subsequent rehabilitation training, data collection was carried out. First, tennis was added to 100 rehabilitation patients to assist in knee flexion. The experiment recorded the knee flexion test results of 50 nanoligament treatment and nontreatment patients. Later, different tennis techniques were used to record the recovery of patients with nanoligaments. Finally, do another set of comparative tests. Patients treated with nanoligaments were divided into three groups to test the knee flexion angle. The LARS group, the HT group, and the control group were 2.7 ± 1.3 degrees, 2.8 ± 2.5 degrees, and 2.1 ± 2.7 degrees, respectively. These different knee flexion angles represent different degrees of injury in rehabilitation patients, which are used as experimental variable data in this paper.

3.2. Experimental Environment Classification Setting. The degree of knee nanoligament damage can be divided into 3 degrees: first degree: ligament fiber rupture, local pain, no change in joint stability; second degree: most ligament fiber rupture, severe local reaction, function is obviously limited, but almost does not affect the stability of the joint; third degree: the ligament is completely damaged. According to the pressure test after ligament injury, the degree of the edge of the joint surface can be divided into mild (6 mm), intermediate (6-15 mm), and severe (greater than 15 mm). The treatment of first-degree and second-degree injuries requires conservative treatment. Patients with mildly injured ligament rupture and minor restlessness can also be treated conservatively. Conservative treatment is largely aimed at the patient population without severe impairment of joint stability. Four to 7 weeks of fixed plaster to strengthen the quadriceps movement can obtain satisfactory results. If the lateral ligament and surrounding tissue are severely damaged, unstable, or the cruciate ligament or meniscus is damaged, it should be repaired in time.

3.3. Experimental Procedure

(1) Experimental preparation: exclude patients with carotid artery injury and related fractures. The patient was placed in a supine position and underwent spinal canal anesthesia. In many cases of ligament injury, epidural block anesthesia is used. The inflatable tourniquet near the thigh was pressurized. Reconfirm the stability of the front, back, inside, outside, and rotation of the knee

(2) Experimental examination: arthroscopy device (arthroscopy equipment belongs to medical imaging equipment, mainly including American Stryker brand monitors, cold light sources, cameras, and image systems) and knee arthroscopy, standard surgical method for knee arthroscopy, anterior cruciate ligament reconstruction device. After stopping the blood, pressurize the tourniquet and check the blood in the joints. First, check the joint cavity, repair the damaged meniscus, perform suture, formation or resection, check the end and continuity of ACL and PCL, regularly clean, and explore under the microscope to maintain the stability of ACL and PCL. This is for the late replacement of blood circulation and blood circulation reconstruction of ligaments and the rapid recovery of inherent tolerance. Observe the medial and lateral articular walls of the hematoma under a microscope, observe the structural damage signals of the medial and lateral sides, and perform knee cartilage injury and classification

(3) Reconstruction of the posterior cruciate ligament: insert the PCL tibial catheter into the posterior tibia from the anterior medial aspect. In addition, it can also be placed under the observation of the posterior medial approach, and its front end is embedded in the exit of the tibial tunnel. Select the guide pin through the anterior cortex of the tibia (45- to 50-degree direction), select the appropriate diameter of the drill according to the size of the graft, to avoid nerve and blood vessel damage at the roost, and please pay attention to the tibia. The bones and soft tissues remaining in the tunnel are cleaned to avoid sharp parts. Similarly, a rocket tunnel of the same diameter was excavated using a femoral locator. After the tunnel is completed, the needle is inserted into the tibial tunnel from front to back, and the front end of the needle is slightly curved to facilitate the clamping of the intercondylar notch. Similarly, the femoral wire or microbridge stays ahead and follows the tibial tunnel to a single figure. The traction line of the head button is close to the traction line of the femur to connect the femur. The lead is pulled to rotate the built-in button, and the graft is retracted by 6 mm. The button is pressed parallel to the cortex of the femur at the external opening of the bone tract, and the tibial end of the graft is tightened, and the distal bone tract is fixed with absorbable nails larger than the same diameter

(4) Anterior cruciate ligament reconstruction: connect the tibial tunnel guide, position the top of the guide at the midpoint of the line between the anterior angle of the lateral meniscus and the medial condyle (a more accurate positioning method), and follow the locator drill into the guide pin and observe whether the position of the needle point is accurate under the microscope. Then, use the tibial drill bit to drill the tibial tunnel of the same diameter along the guide pin to clean the excess tissue of the tunnel. Then, use the femoral end guide to locate the ACL. At the top dead center, after the positioning is accurate, drill the guide pin along the positioner, use a 4.5 mm diameter hollow drill and the same implant diameter drill bit to drill the rocket-shaped tunnel, and the guide pin is pulled to place the pull wire.

Connect the graft traction line with the indwelling traction line in the knee flexion position, pull it out along the tibial tunnel, joint cavity, and femoral tunnel, flip the button so that the button is parallel to the femoral cortex embedded in the external opening of the bone tract, and tighten the end of the tibia. Fix the distal bone tract with absorbable nails larger than the same diameter. After the reconstruction is completed, the position relationship of the reconstructed ligament can be checked under the microscope again, and there is no intercondylar impact when the joint is moving

4. Analysis of Postoperative Rehabilitation of Patients Treated with Nanoligaments

4.1. Effect of Different Tennis Stretching Exercises on Patients after Nanoligament Surgery. In tennis, the functional traction of the body's flexibility mainly reflects the lateral flexion and expansion of the entire spine, so the lateral flexion and expansion of the body are indicators of testing the body's flexibility. Ligaments are distributed throughout the body, preventing bones from bending and expanding. The entire range of motion of the ligaments is very large and can be used for bending and elongation movements around the front axis. Nanoligaments treat patients with lateral flexion motions around the rotation axis and orbital motions and circular motions around the vertical axis. Generally, ligament activity is large, and rib activity is low. Ligaments are the key to maintaining joint movements of the body. The trunk is the core that connects the limbs and the head. The brain communicates commands to all parts of the body and controls the core connection of body movement. According to the biomechanics principles of tennis technical action, the center of gravity of the body should be kept stable during the strike, the body should not be shaken during the strike, and the quality of the strike should not be affected. The range of motion of the ligament should be maintained on a relatively fixed vertical axis.

As can be seen from Figure 3, after 8 weeks of training, the performance of each experimental group has been improved in the bending test of the side of the body of patients treated with nanoligaments, which is accelerated by nearly 5 times faster than that of general treated patients through static stretching exercises The sport effect is the most ideal. The static stretching exercise is to continuously and stably stimulate the stability of the ligament of the subject, thereby improving the structural function of skeletal muscles. With the deepening of the training phase, the static stretching exercise is more beneficial to the training effect of nanotreatment patients. Subjects can improve the level of flexible quality training in system management and increase the degree of lateral ligament curvature. In the process of stretching, the human lumbar spine does not have many muscle protection functions. It is necessary to pay attention to the muscles of the spine muscles in the lumbar spine, square muscles in the lumbar spine, and part of the erector spinae. The main function of the human waist and abdomen is not to simply improve the mobility of the joints, but to
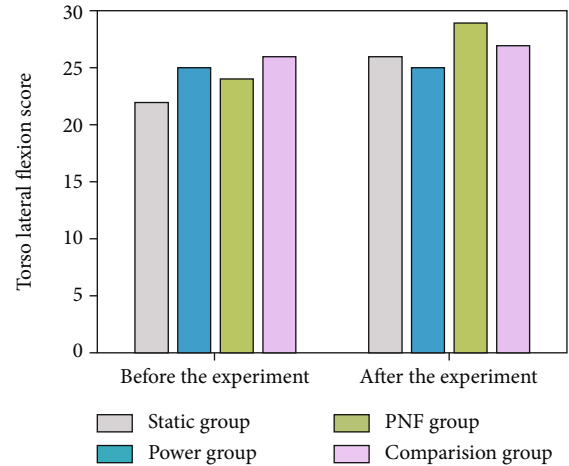
FIGURE 3: Comparison of the results of each group's lateral flexion test.
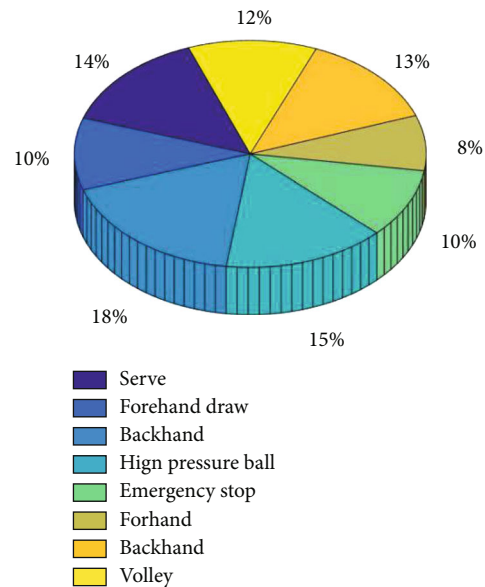
FIGURE 4: Table of the types of technical actions that affect the occurrence of knee ligament injury.

TABLE 1: Technical action factors affecting the occurrence of knee injury.

Serial number	Relevant factors	Load factor
1	Unfamiliar technical action	0.75
2	Technical moves are difficult	0.73
3	Technical action is very standard	0.24
4	Wrong technical action	0.78

emphasize painless activities within the normal range of human motion, so pay attention not to damage the lumbar spine during the stretching exercise. No matter what kind of stretching method is used, you must avoid sneak attacks and oppressions. Pay attention to it in sections, increase

TABLE 2: Knee flexion and extension and rotation angle.

Knee flexion and extension angle during standing	LARS group	HT group	Compare group	p value group
Heel	2.7 ± 1.3	2.8 ± 2.5	2.1 ± 2.7	0.457
Knee bending angle	31.2 ± 8.6	6.9 ± 3.5	31.5 ± 8.8	0.354
Knee flexion angle	7.1 ± 3.5	30.8 ± 4.7	6.8 ± 3.2	0.452
Maximum internal rotation	5.3 ± 1.4	5.2 ± 1.0	4.8 ± 1.5	0.321
Minimum internal rotation	7.2 ± 0.9	7.8 ± 1.3	5.2 ± 1.6	<0.002

the range of ligament movement in a slow and powerful way, and improve the body's ability to stretch the body of the tennis ligament patient while ensuring safety. And the breathing adjustment mentioned in the previous specific experimental program can make the stretching exercise get better results.

4.2. Analysis of Tennis Movement Technical Movements on Patients after Nanoligament Operation.

As the key reason that affects whether a person's ligament is vulnerable to damage, technical action should be divided into various factors for analysis and research. Patients with different ages of nanoligament treatment should show their own type of technical action. The difference is very limited, and the analysis and research on the types and factors of technical actions should not be divided into different age groups.

The data in Figure 4 shows that the technical actions that caused the injury of the nanoligaments to treat patients were ranked as follows: 14% serve, 10% backhand ball, 18% forehand ball, 100% backhand ball fifteenth, 10% for emergency stop change, 8% for high pressure ball, 13% for forehand, and 12% for interception. For tennis players, every incorrect technical action may lead to damage to the knee ligaments. Among them, serving, backhand drawing, forehand drawing, and backhand cutting cause a high probability of knee injury. But at the same time, every standard action can avoid a knee injury. Therefore, the treatment of patients with nanoligaments can use standardized actions to accelerate the speed of recovery.

According to the sociological statistical methods and statistical principles, using SPSS 15.0 data analysis software, the load factor range of 16 causative factors is $0 < K < 1$; that is, the larger the K value, the more likely to have knee ligament injury, and the more Xiaoyue is conducive to the protection of the knee joint. Because the influence of each factor on the knee ligament injury is not absolute, it is impossible to have $K = 0$ or $K = 1$. The specific load factor is shown in Table 1.

Analysis of the data in Table 1 shows that the technical action factors greatly affect whether the rehabilitation of patients with ligament injury can be accelerated. This requires that the technical movements mastered by the patients in training must conform to the characteristics of tennis and at the same time meet the requirements of physiological anatomy or try to comply with the principles of biomechanics. Effective and correct technical actions are conducive to the full play of athletes' physiology and psychology and help nanoligament treatment patients to achieve good rehabilitation results.
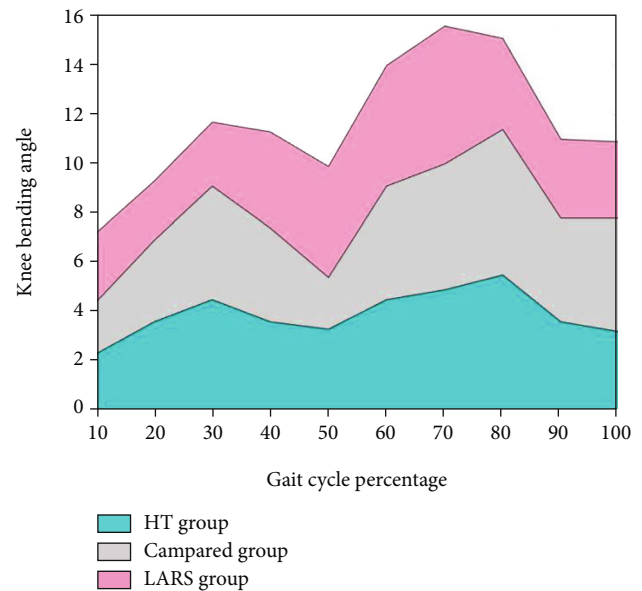
FIGURE 5: Knee flexion and extension angle when walking.

4.3. Analysis of Knee Flexion Angle after Nanoligament Treatment.

Using one-way analysis of variance (ANONA), the time-distance parameters, knee internal rotation, external rotation angle, knee flexion, knee extension angle, and sagittal plane vertical reaction of the LARS group and the HT group affected lower limbs and normal control force comparison. SPSS 12.0 software was used for all statistical analysis. The significance level is $a < 0.04$. Sagittal knee angle during stance: the knee flexion angle when the heel is on the ground is 2.7 ± 1.3 degrees, 2.8 ± 2.5 degrees, and 2.1 ± 2.7 degrees in the LARS group, the HT group, and the control group, respectively. There was no difference between the three groups (statistical significance $p > 0.04$). The maximum knee flexion angle and the minimum knee flexion angle in the standing period are 31.2 ± 8.6 degrees and 6.9 ± 3.5 degrees, 31.5 ± 8.8 degrees and 7.1 ± 3.5 degrees, and 30.8 ± 4.7 degrees and 6.8 ± 3.2 degrees in the LARS group, the HT group, and the control group, respectively. Compared with the three groups, the difference was not statistically significant ($p > 0.05$), as shown in Table 2 and Figure 5.

The knee rotation angle of patients with nanoligaments during walking is shown in Table 2 and Figure 6. The maximum internal rotation angle was 5.3 ± 1.4 degrees, 5.2 ± 1.0 degrees, and 4.8 ± 1.5 in the LARS group, the HT group, and
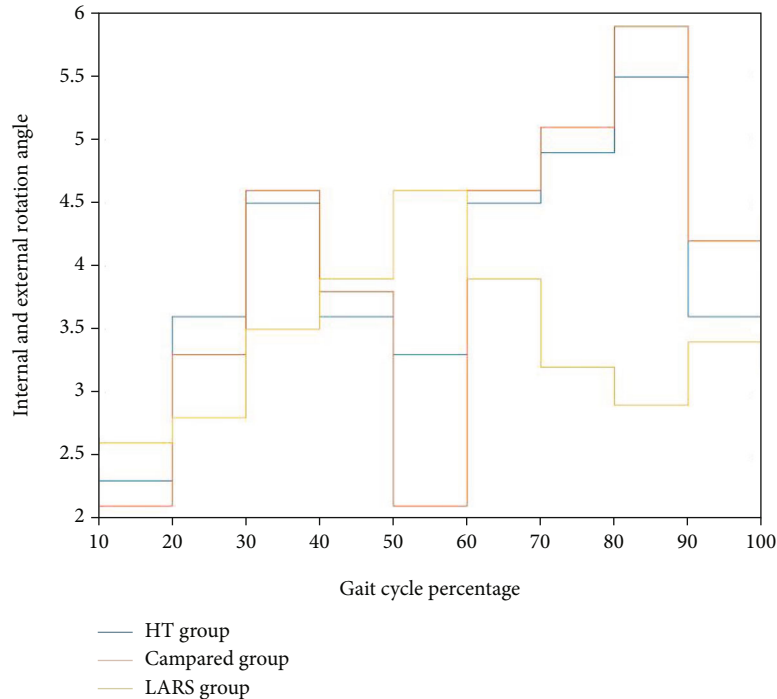
FIGURE 6: Knee rotation angle when walking.

the control group, respectively. There was no statistically significant difference between the three groups ($p > 0.04$). The maximum external rotation angle of the knee joint was 7.8 ± 1.1 degrees, 8.2 ± 1.4 degrees, and 5.6 ± 1.9 degrees in the LARS group, the HT group, and the control group, respectively. The HT group and the LARS group were significantly larger than the control group ($p < 0.002$). There was no significant difference between the HT group and the LARS group ($p > 0.04$). Based on the above data and image analysis, nanoligament injury patients undergo tennis training and technical movement analysis after surgery, and a certain knee bending angle will also affect the rehabilitation effect of nanoligament treatment patients. Within a reasonable range, the corresponding rehabilitation training will speed up.

5. Conclusions

This research is aimed at the current clinical application of nanoligaments and the research of tennis sports on rehabilitation patients with sports injuries and the surface modification of nanoligament materials to improve their biocompatibility. And because of their small size, nanomaterials are very different from traditional materials in terms of optical properties, electrical properties, and chemical activity. The special properties of nanomaterials make it have full play in ECL sensing; in particular, some emerging nanomaterials are paid attention by researchers due to their superior performance and are widely used in ECL. Some inspirations can be obtained from this, which helps to clarify the future research direction of artificial ligaments.

This study further confirmed that from the biomechanical point of view, the combination of nanoligaments and

tennis can promote the healing of the tendon and bone boundary surface after surgery. In order to avoid reconstruction failure caused by ACL slack, theoretical support is provided. The results of this experiment also show that the synthesized nanomaterials can act as a scaffold in the body, allowing PRP to slowly and fully release growth factors, gradually absorbed by new bone growth, and finally replaced by new bone, which is a more suitable scaffold.

In this study, at the early stage after surgery, the interface with a strength similar to the rest point is directly reduced. For the buffering of the stop stress, the mechanical characteristics of this rest point structure are better than the indirect rest point, and the bonding force of the tendon-bone interface is improved. This provides us with a new way of thinking, that is, after ACL transplantation, early recovery of work and exercise ability, to avoid failure of reconstruction caused by ACL relaxation and to promote functional rehabilitation in clinical practice. This experiment has only been studied in morphology, and the more direct evidence is that it needs the support of biomechanical experiments. Although this paper has carried out a profound study on the rehabilitation training of patients with ligament injury by using nanoligament combined with tennis exercise therapy, there are still many deficiencies. We will study appropriate treatment methods and means from more perspectives based on the existing technology and level and continuously improve the quality of rehabilitation treatment.

Data Availability

No data were used to support this study.

Conflicts of Interest

The authors declare that there are no conflicts of interest regarding the publication of this article.

Acknowledgments

References

[1] I. Singh and R. Narasimhan, "Notch sensitivity in nanoscale metallic glass specimens: insights from continuum simulations," *Journal of the Mechanics and Physics of Solids*, vol. 86, pp. 53–69, 2016.

[2] R. M. A. Domingues, S. Chiera, P. Gershovich, A. Motta, R. L. Reis, and M. E. Gomes, "Enhancing the biomechanical performance of anisotropic nanofibrous scaffolds in tendon tissue engineering: reinforcement with cellulose nanocrystals," *Advanced Healthcare Materials*, vol. 5, no. 11, pp. 1364–1375, 2016.

[3] S. E. Smith, R. A. White, D. A. Grant, and S. A. Grant, "Gold and hydroxyapatite nano-composite scaffolds for anterior cruciate ligament reconstruction: in vitro characterization," *Journal of Nanoscience & Nanotechnology*, vol. 16, no. 1, pp. 1160–1169, 2016.

[4] H. Yang, Z. Wang, C. Li, and C. Xu, "Nanoporous PdCu alloy as an excellent electrochemical sensor for H_2O_2 and glucose detection," *Journal of Colloid & Interface Science*, vol. 491, pp. 321–328, 2017.

[5] Y. Yang and W. Tang, "Elastic modulus determination at different levels of periodontal ligament in nanoindentation," *Journal of Southeast University*, vol. 33, no. 1, pp. 33–38, 2017.

[6] R. Seijas, X. Cuscó, A. Sallent, I. Serra, O. Ares, and R. Cugat, "Pain in donor site after BTB-ACL reconstruction with PRGF: a randomized trial," *Archives of Orthopaedic & Trauma Surgery*, vol. 136, no. 6, pp. 829–835, 2016.

[7] S. G. Kim, S. Y. Lee, Y. H. Lee, and S. Y. Lee, "The epidemiological study of post-traumatic knee osteoarthritis after knee ligament or meniscus injuries using national health insurance service (nhis) 514, 866 cohort data: retrospective cohort study," *British Journal of Sports Medicine*, vol. 51, no. 4, pp. 342.2–34342, 2017.

[8] J. L. Gomes, A. Sepriano, S. Falcao et al., "AB0954?A new ultrasonography protocol for the assessment of primary knee osteoarthritis," *Annals of the Rheumatic Diseases*, vol. 75, Supplement 2, pp. 1227.3–121228, 2016.

[9] N.-Y. Han, J.-Y. Hong, J.-M. Park et al., "Label-free quantitative proteomic analysis of human periodontal ligament stem cells by high-resolution mass spectrometry," *Journal of Periodontal Research*, vol. 54, no. 1, pp. 53–62, 2019.

[10] B. Alonso, F. B. Sobrón, C. Vidal, and J. Vaquero, "Pretibial pseudocyst after anterior cruciate ligament reconstruction with a biocomposite screw," *Acta Ortopédica Mexicana*, vol. 30, no. 3, pp. 150–153, 2016.

[11] M. Papandreou, E. Billis, G. Georgoudis, G. Papathanasiou, and J. Gliatis, "Ultrasonography study: supraspinatus muscle thickness evaluation on dominant versus non dominant shoulder on tennis players," *Journal of Exercise, Sports & Orthopedics*, vol. 3, no. 1, pp. 1–5, 2016.

[12] E. Bolach, B. Bolach, and K. Seniuk, "Analysis of training loads in the introductory micro-cycle during the phase of specific preparation of wheelchair tennis players," *Nephron Clinical Practice*, vol. 21, no. 3, pp. 36–49, 2013.

[13] G. D. Shifflett, D. W. Green, R. F. Widmann, and R. G. Marx, "Growth arrest following ACL reconstruction with hamstring autograft in skeletally immature patients: a review of 4 cases," *Journal of Pediatric Orthopaedics*, vol. 36, no. 4, pp. 355–361, 2016.

[14] A. Grassi, C. L. Ardern, G. M. Marcheggiani Muccioli, M. P. Neri, M. Marcacci, and S. Zaffagnini, "Does revision ACL reconstruction measure up to primary surgery? A meta-analysis comparing patient-reported and clinician-reported outcomes, and radiographic results," *British Journal of Sports Medicine*, vol. 50, no. 12, pp. 716–724, 2016.

[15] B. T. Samuelsen, K. E. Webster, N. R. Johnson, T. E. Hewett, and A. J. Krych, "Hamstring autograft versus patellar tendon autograft for ACL reconstruction: is there a difference in graft failure rate? A meta-analysis of 47, 613 patients," *Clinical Orthopaedics & Related Research*, vol. 475, no. 10, pp. 2459–2468, 2017.

[16] I. D. Smith, A. Irfan, J. S. Huntley, and S. J. Spencer, "What is the best treatment for a child with an acute tear of the anterior cruciate ligament?," *Journal of Paediatrics and Child Health*, vol. 54, no. 9, pp. 1037–1041, 2018.

[17] P. B. Kumar and D. R. Parhi, "Vibrational characterization of a human femur bone and its significance in the designing of artificial implants," *Military Operations Research*, vol. 14, no. 3, pp. 222–226, 2017.

[18] R. Mannem, M. Dubois, M. Koeberl, D. Kosempa, and S. Erickson, "Glenoid avulsion of the glenohumeral ligament (GAGL): a case report and review of the anatomy," *Skeletal Radiology*, vol. 45, no. 10, pp. 1443–1448, 2016.

[19] E. Santana and A. Portela, "Dual boundary element analysis of fatigue crack growth, interaction and linkup," *Engineering Analysis with Boundary Elements*, vol. 64, pp. 176–195, 2016.

[20] R. M. Palmieri-Smith, K. L. Cameron, L. J. DiStefano et al., "The role of athletic trainers in preventing and managing post-traumatic osteoarthritis in physically active populations: a consensus statement of the Athletic Trainers' Osteoarthritis Consortiuma," *Journal of Athletic Training*, vol. 52, no. 6, pp. 610–623, 2017.

[21] L. L. Laslett, J. P. Pelletier, F. M. Cicuttini, G. Jones, and J. Martel-Pelletier, "Measuring disease progression in osteoarthritis," *Current Treatment Options in Rheumatology*, vol. 2, no. 2, pp. 97–110, 2016.

[22] N. Fischer, N. M. Mathonia, G. Hoellerich et al., "Surviving murine experimental sepsis affects the function and morphology of the inner ear," *Biology Open*, vol. 6, no. 6, pp. 732–740, 2017.

[23] P. S. Thayer, S. S. Verbridge, L. A. Dahlgren, S. Kakar, S. A. Guelcher, and A. S. Goldstein, "Fiber/collagen composites for ligament tissue engineering: influence of elastic moduli of sparse aligned fibers on mesenchymal stem cells," *Journal of Biomedical Materials Research Part A*, vol. 104, no. 8, pp. 1894–1901, 2016.

[24] C. Gonzalez-Lluch, P. J. Rodriguez-Cervantes, L. Forner, and A. Barjau, "Inclusion of the periodontal ligament in studies on the biomechanical behavior of fiber post-retained restorations: an in vitro study and three-dimensional finite element analysis," *Proceedings of the Institution of Mechanical Engineers, Part H: Journal of Engineering in Medicine*, vol. 230, no. 3, pp. 230–238, 2016.

[25] A. Houben, J. Van Hoorick, J. Van Erps, H. Thienpont, S. Van Vlierberghe, and P. Dubruel, "Indirect rapid prototyping: opening up unprecedented opportunities in scaffold design and applications," *Annals of Biomedical Engineering*, vol. 45, no. 1, pp. 58–83, 2017.

Research Article

Application of Metal Oxides Prepared Based on Ferroelectric-Based Photoelectric Conversion Materials in the Thermal Degradation of Polybrominated Diphenyl Ethers

Lan Gao [1,2] **Min Li,**[3] **Lijing Huo,**[1] **and Pengfei Zhang**[1]

[1]*College of Biochemistry & Environmental Engineering, Baoding University, Baoding, 071000 Hebei, China*
[2]*Hebei Technology Innovation Center for Green Management of Soil-Borne Diseases, Baoding University, Baoding, 071000 Hebei, China*
[3]*Xingtai University, Xingtai, 054001 Hebei, China*

Correspondence should be addressed to Lan Gao; gaolan@bdu.edu.cn

In today's environment where the society attaches great importance to environmental pollution, there has been a certain amount of research at home and abroad to explore the solutions to pollution of the large amount of polluting and persistent harmful substances that remain in nature. And most people think that it is necessary to solve the problem of pollution in two ways. (1) Energy: without discussing other energy sources, we will only discuss the main oil of today's energy. The treatment and use of this energy will cause pollution to a certain degree, and it has been overexploited. The exploration of new energy sources and increasing the use of natural energy such as wind and solar energy are the main research directions today. (2) Degradation of existing pollutants: nowadays, due to the rapid development of various industries, attention to environmental pollution has reached a point that cannot be ignored. As a kind of brominated flame retardant, polybrominated diphenyl ethers are widely used because of their low price and stable chemical properties, mostly in electronic appliances, building materials, textiles, furniture, and other products. But the substance is extremely harmful. This article focuses on the degradation treatment of tetrabromodiphenyl ether, which is one of the polybrominated diphenyl ethers that are long-lasting and difficult to be degraded in the environment. It has become an emerging persistent organic pollutant due to its toxicity, persistence, and bioaccumulation. Based on the reduction and debromination of zero-valent iron, the effect of debromination of tetrabromodiphenyl ether is explored under the coupling effect of the nanosized iron powder with the smaller particles of zero-valent iron and vitamin B_{12}. The experimental results in this paper show that when the dosage of nanoiron powder is between $0.0\,g/L$ and $0.15\,g/L$, according to the degradation diagram, the reaction rate is continuously strengthened with the increase of nanoiron powder. When the dosage of nanoiron powder is $0.15\,g/L$-$1.0\,g/L$, the effect will be weakened with the increase of the concentration. Therefore, an increase in the concentration of nanoiron powder will promote the progress of the debromination reaction. But when it reaches a certain level, the reaction rate will gradually decrease until it stops.

1. Introduction

The current state of environmental pollution cannot be underestimated. Through the diffusion of the food chain in nature, the atmosphere, and the air, pollutants are permeated around people, which have affected people's daily life, and even the weather has undergone abnormal changes due to its influence. The intensification of the greenhouse effect will have serious consequences. Now, the era is devel-

oping rapidly. With the advancement of related scientific research results of computer network portable technology, the process of electrical appliance industrialization has accelerated and expanded. Nowadays, a large number of electronic devices are updated every year, resulting in a large amount of electronic waste. Polybrominated diphenyl ethers (PBDEs) are widely used as flame retardants in industrial production and they are widely used in plastic flame-retardant parts in electronic appliances. By analyzing the

physical and chemical properties, exposure pathways, and pollution levels of PBDEs, this article summarizes the main pathways of photodegradation and aerobic and anaerobic microbial degradation. This article makes a corresponding risk assessment for its carcinogenic properties and compares the risk of impact in various environments. Through the risk comparison between adults and children, this article explores the catalytic debromination effect of metal oxides under sunlight. Metals and vitamin B_{12} have catalytic reduction effects and are highly efficient in the field of degrading organic matter. Therefore, this article proposes the debromination reaction of tetrabromodiphenyl by metal combined with vitamin B_{12} and conducts corresponding experiments on the effects of various metals.

Polybrominated diphenyl ethers are a type of global organic pollutants that are widespread in the environment. Because of its good flame retardancy, it is often used as an additive flame retardant and widely used in various products. In the process of production and use, it can be released from the product and enter the ecosystem through various channels. But it has high bioaccumulation effect and high carcinogenicity. It has a great impact on the environment, and children are more affected by its toxicity than adults. It can be seen that the research on the degradation direction of polybrominated diphenyl ethers is of inevitable significance. Now, a large amount of electronic waste is generated every year. The flame-retardant plastics of electronic waste release highly toxic by-products during their disposal, and related research has attracted the attention of many scholars. The original treatment of e-waste may release a large amount of organic pollutants into the environment, but its scale and mechanism still need to be fully resolved. Li et al. have carried out heat treatment and open burning of typical electronic waste, namely, plastics and printed circuit boards. The emission factor of the sum of 39 polybrominated diphenyl ethers ($\sum_{-}(39)$PBDE) in the heat treatment is $817 - 1.60 \times 10 \sim (5)$ng g $\sim (-1)$ and undetected $-9.14 \times 10 \sim (4)$ ng g $\sim (-1)$. In open burning, airborne particulate matter (87%) is the main carrier of PBDEs, followed by residual ash (13%) and gaseous components (0.3%). In the open fire heat treatment, they were 30%, 43%, and 27%, respectively. Evaporation and reabsorption may be the main emission mechanism of slightly brominated BDE, but severely brominated BDE is often related to particles produced by heating or combustion. The different size distributions of PBDEs in the emission source and nearby air indicate a remarkable reprocessing process in the atmospheric diffusion process [1]. The triglyceride of ricinoleic acid and the acid residue contain both hydroxyl and double bonds, which can be easily functionalized. Hydroxyl groups can be converted into phosphorous esters of different structures, and unsaturated groups can easily be added to bromine. Using spectroscopy and thermal methods, Howell and Ostrander fully characterize castor oil derivatives that contain phosphorus, bromine, or phosphorus and bromine. The thermal stability and degradation modes of these compounds have been evaluated by thermogravimetric analysis and infrared spectroscopy [2]. In terms of phosphorus-based flame retardants, Daniel and Howell use four phosphorus esters derived from industrially

obtained glucose derivative isosorbide as starting materials. After thermal degradation, the four esters showed different degradation curves. Phosphate esters provide better coke yields than phosphonates and phosphinates, the latter being more thermally stable. Fourier transform infrared spectroscopy and thermogravimetric analysis were used to monitor the thermal stability of the compound under constant temperature and variable time. Studies have shown that degradation is accompanied by the release of corresponding phosphoric acid [3]. By rationally manufacturing metal nanostructures to excite plasmon resonance, the efficiency of hot carrier excitation can be significantly improved. Ishii et al. have conducted in-depth research on these plasma-enhanced photoelectric and photothermal conversion from a basic and application-oriented perspective. Among them, it exclusively uses gold and silver. In contrast, this progress report covers nonmetallic materials that can be used for plasma-enhanced photoelectric and photothermal conversion [4]. After exploring and researching many modified anodic oxides, Chen et al. tried to summarize the latest developments in the rational design and modification of these oxides before, during, and after anodization. Each part completely solves the reasonable design strategy, aiming to improve the overall PEC performance [5]. Park et al. proposed and researched a transparent light-emitting diode (LED) panel with a 16×16 multicolor LED array for signage applications. As a transparent electrode, it can use established simulation models to manufacture and characterize three layers of oxide/metal/oxide (OMO) with various Al interlayer thicknesses. Using commercial ray tracing optics and SPICE simulation tools, Park et al. designed the LED panel and studied its optical and electrical characteristics. In addition, in order to solve the waveguide effect and voltage drop problems of the entire panel, they integrated additional optical structures and various OMO widths in the design. The results show that the OMO electrode interconnection and the proposed design consider the key aspects of implementing transparent LED digital signage applications [6]. Guo et al.'s research results show that low temperature is an important way to improve the stability of high-concentration precursor solutions in the sol-gel process. In addition, a stable precursor solution is used, followed by spin coating and sequential layer annealing. Then, a thick BLFO film is prepared on an indium tin oxide/glass substrate, which has a perovskite structure without impurity phases. In particular, it can obtain a high remanent polarization (P r) of 42.85 $\mu C/cm^2$. This may be related to lanthanum doping, preferred (110) orientation and relatively dense microstructure [7]. The scholars' research discussed above has certain auxiliary guidance for the research of this paper, but most of the abovementioned research processes require special professional techniques and a deep understanding of experimental supplies in order to further avoid the process harm. Its content is too complicated, and the experiment process is accompanied by certain dangers and the harmfulness of gases, so more attention should be paid to the experiment.

The innovations of this article are as follows: (1) It is proposed to use nanoscale iron powder for debromination
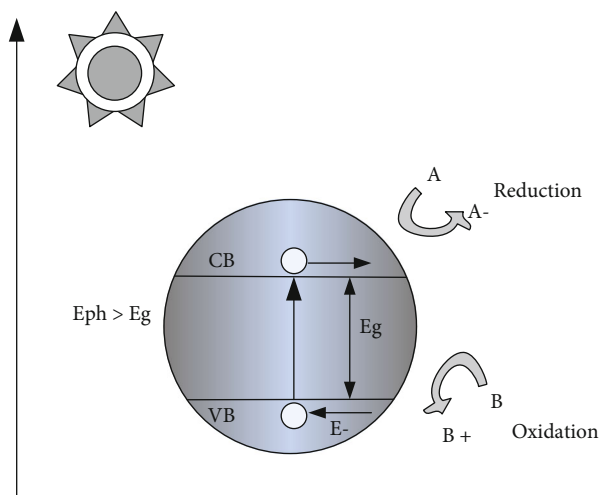
FIGURE 1: The basic principle of photocatalysis of metal oxide materials.

reaction; (2) after coupling vitamin B$_{12}$ and iron powder, the tetrabromodiphenyl ether is debrominated, and the Good results; and (3) the degradation ability of various metals such as Al, Zn, Fe, and Sn on the reduction and debromination of tetrabromodiphenyl ether was discussed. And this article analyzes the effect of debromination with the addition of vitamin B$_{12}$.

2. Polybrominated Diphenyl Ethers Based on Metal Oxides

2.1. Application of Metal Oxides in the Catalytic Degradation of Pollutants Under Sunlight. Now, the world is facing the same dilemma, that is, the shortage of available energy and the increasingly serious environmental pollution. It has caused extreme weather in the global climate [8]. And the emission of greenhouse gases has caused global warming. People attach great importance to sustainable and pollution-free new energy sources in nature [9]. The first thing that comes to our mind is solar energy. As a daily visible and very important existence in nature, solar energy has naturally attracted people's attention. Solar cells, photocatalytic hydrogen production, and photocatalytic degradation of organic pollutants are all intuitive manifestations of people's utilization of solar energy [10]. Metal oxide semiconductor materials are used for photovoltaic power generation, hydrogen production, and catalytic decomposition [11]. Due to the different properties of metal elements, the oxides formed by them exhibit different properties and application characteristics, such as in a wide range of environmental pollution control, metal oxide materials can be used as catalysts and adsorbents to treat industrial toxic waste gas and environmental organic pollutants [12]. In semiconductor materials, when the energy is greater than the band gap, the surface can be irradiated with light energy to absorb the light energy. Electrons are excited from the valence band to the conduction band and become holes. Figure 1 shows its catalytic texture, which can improve catalytic efficiency.

For the research of metal semioxide semiconductor materials, there have been research directions for related content as early as before. It was discovered that titanium dioxide can catalyze the start of hydrogen production under the action of sunlight [13]. The photocatalysis of metal oxide semiconductor materials has been rapidly developed. Through the study of the photocatalytic reaction of a variety of metal oxide materials, it is found that the hyperactive metal oxides have a certain degree of restrictive conditions in the reaction effect of photocatalytic hydrogen production. From all researches on catalytic hydrogen production, it is found that not all metal oxide semiconductor materials can be used for catalytic hydrogen production. However, the application of this material in environmental protection has only begun to develop and prevail in the past ten years. Studies have found that titanium dioxide can catalyze the degradation of organic pollutants polychlorinated biphenols under ultraviolet light in the sun [14]. In the research of metal oxide materials in the past few years, it can be said that this material has become an important research object in the chemical field for the treatment of pollutants due to its high efficiency, less secondary pollution, low cost, and easy preparation [15].

2.2. Polybrominated Diphenyl Ethers Based on Metal Oxides. Polybrominated diphenyl ethers are abbreviated as PBDEs, which are brominated flame retardants [16]. PBDEs are aromatic compounds based on bromine-substituted hydrogen atoms in biphenyls. According to the position and number of bromine substitutions, there are 209 kinds of homologues. It has good flame retardant properties and stable performance. It is also widely used in electronics, electrical appliances, fabrics, building materials, petroleum, and other industries because of its low price and low impact on materials [17]. PBDEs have the characteristics of low vapor pressure and strong lipophilicity at room temperature, high boiling point, and low solubility in water. It has a fairly stable chemical structure [18], and its chemical structure is shown in Figure 2. It is difficult to degrade through physical, chemical, or biological means.

The flame retardant properties of PBDEs are gas phase flame retardant, and the specific mechanism is as follows. PBDEs are decomposed by heat to generate HBr, which can capture active free radicals that transfer combustion chain reactions [19]. It can produce bromine free radicals with lower activity, which can slow down or stop the combustion reaction. In addition, HBr is a high-density, low-flammability gas [20]. It can not only dilute the oxygen in the air but also cover the surface of the material. It can be isolated from the air to slow down combustion and spontaneous combustion [21]. However, if it is in a high temperature environment, it can release bromine atoms and burn it under certain conditions, which will generate more toxic PBDD/DFs.

Studies have shown that PBDEs are a variety of pollutants found in the environment and have been detected in a variety of environmental media such as water, air, soil, organisms, and humans [22]. Highly brominated diphenyl ether is soluble in water or volatilized in the air and

Oxygen atom

Br, m

Br, n

M + n = 1 – 10
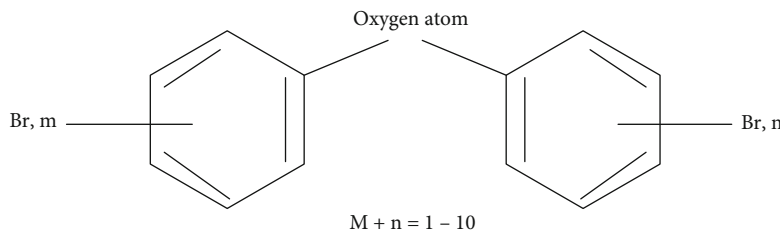
FIGURE 2: The chemical structure of polybrominated diphenyl ethers.

deposited on organisms. It is debrominated in the natural environment, decomposed into low-brominated diphenyl ether, and then passed through water, air, bioaccumulation, etc. The path propagates in the environment and finally constitutes the path [23]. The environmental behavior of PBDEs mainly includes the movement between pollution sources, environmental media, and the transformation and final fate during the movement [24]. Its impact on the environment is shown in Figure 3.

Because PBDEs are persistent in the environment, their increasing exposure routes bring great risks to human health [25].

3. Health Risks of Polybrominated Diphenyl Ether PBDEs Based on Optoelectronic Materials

Nowadays, people have a certain degree of awareness about the pollution of polybrominated diphenyl ethers, and the amount of exposure in the environment is increasing day by day, and the substance has a certain degree of carcinogenic risk. This ingredient is a serious hazard to human health, especially for children who are underdeveloped. This chapter evaluates the health risks posed by polybrominated diphenyl ethers and discusses the carcinogenic risks posed by them. Exposure refers to the exposure of the human body to one or more physical, chemical, or biological factors in time and space. There are two ways to expose. External exposure refers to the level of external environmental pollutants that the human body directly contacts; internal exposure refers to the actual exposure level of these pollutants in the body after being absorbed by the human body through various interfaces and other biological material samples to obtain the concentration of pollutants [26, 27].

3.1. Evaluation of PBDEs Exposure in Smoke. Respiratory inhalation is an important way to be affected by smoke pollution. Compared with other methods, breathing and inhalation of PBDEs is the main way of human exposure [28]. For the inhalation method, the risk assessment method affected by pollutants is adopted this time. The evaluation method calculates the concentration of pollutants contained in the flue gas in a specific scenario, and the calculation equation is as follows:

$$HRsingle = \frac{Rair \times inhC \times HEInh \times HF \times HD}{QHF \times BL}, \quad (1)$$

$$HRtotal = HRsingle \sum_{1-i}^{i=10} BDEs. \quad (2)$$

Among them, InhC represents the volume of air breathed by adults every day, and the related parameter value is $1.6E + 0.1$. HEInh represents the absorption conversion factor of the lungs, and the value of this parameter is $7.5E + 0.5$. HF represents the frequency of exposure, and the value is $2.5E + 0.2$. HD represents the exposure period of an adult, and the parameter is $2.5E + 0.1$. The value of the life cycle BL is $2.6E + 0.4$. The concentration factor QHF of PM10 is $1.4E + 1.2$. These values are combined with Equations (1) and (2), plus the required measurement values in the area, namely, the particle concentration Rair in the flue gas, the average monomer exposure concentration Rair, and the total concentration HRtotal of lifetime exposure. The calculation results are shown in Table 1.

It can be seen from Table 1 that under different regeneration temperatures, the lifetime exposure concentration of PBDEs in the flue gas to adults is different [29, 30]. The general trend is that as the temperature increases, the exposure concentration continues to increase.

3.2. Risk Assessment Method. Health risk assessment includes noncarcinogenic risk assessment and carcinogenic risk assessment. The classification is based on whether the pollutants have carcinogenic properties. The formula for calculating the carcinogenic risk (CHF) of toxic compounds is

$$CHF = HC \times RUN. \quad (3)$$

In Equation (3), CHF represents the carcinogenic risk index of respiratory inhalation, and HC is the concentration of compound exposure and the carcinogenic risk RUN per unit of respiratory inhalation [31]. After referring to the toxicity of PCBs and the intake factors, the RUN value is calculated, and the following is calculated:

The carcinogenic risk of smoke also increases with the increase in temperature, which is consistent with the exposure level. The higher the level of exposure, the higher the risk of cancer. In the temperature range of 180-210°C, compared with the US EPA health risk standards, the carcinogenic risk of tribromo and nonabromodiphenyl ether is between 1.0E-03 and 1.0E-01. Its carcinogenic risk level is in a high position, and the carcinogenic risk values of other homologues are all higher than 1.0E-01, and its carcinogenic risk level is very high [32].
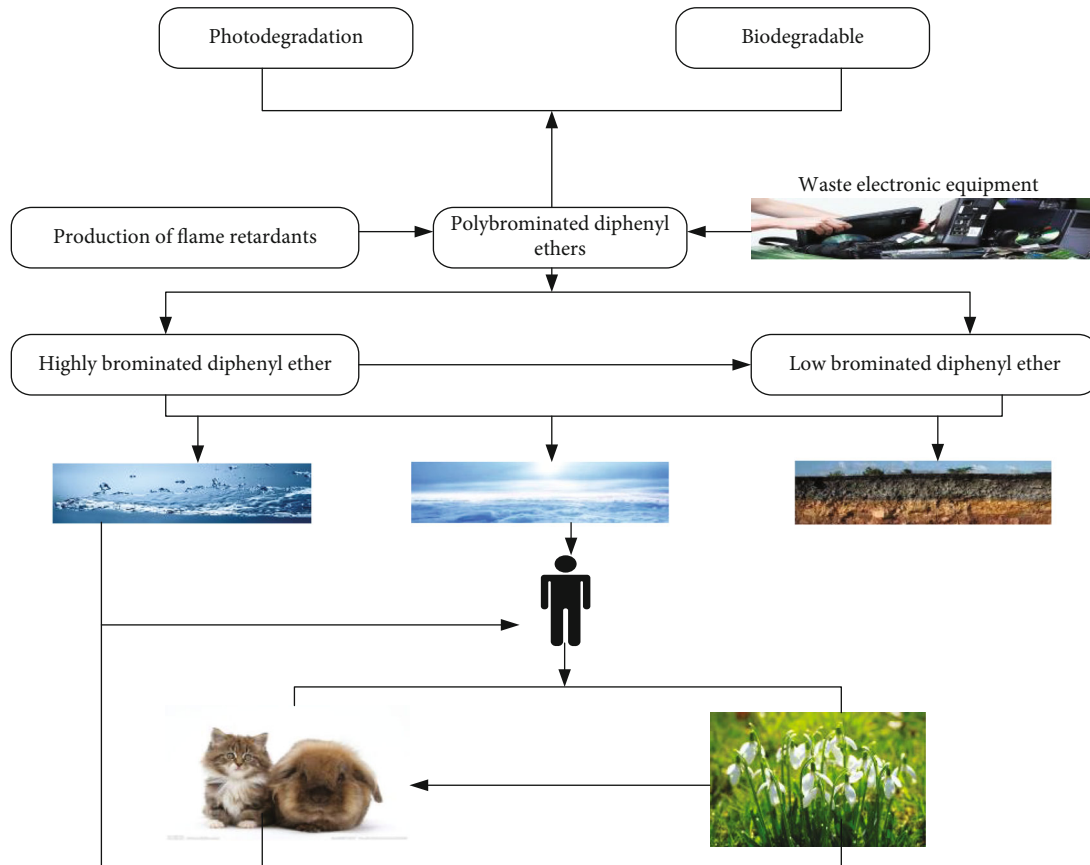
FIGURE 3: Environmental behavior characteristics of polybrominated diphenyl ethers.

TABLE 1: Respiratory exposure of PBDEs in flue gas at different temperatures.

Exposure level of each series	180-190°C	190-200°C	200-210°C
Tri	0.26	0.12	0.13
Tetra	0.26	0.18	0.2
Penta	0.34	0.32	0.25
Hexa	0.77	1.46	1.2
Hepta	1.65	2.17	3.16
Oeta	0.1	0.28	0.33
Nona	0.06	0.18	0.18
Deca	8.17	11.12	12.06
PBDEs	11.7	15.9	17.5

3.3. Exposure Risk Assessment Model. Exposure mainly refers to the process by which the human body is exposed to chemicals through different environments. It is closely related to the exposure time, way, and intensity. The selection of parameters is the basis for risk evaluation [33]. With reference to relevant literature, this section selects three models of breathing inhalation, skin contact, and hand-oral ingestion to analyze PBDE exposure. Among them, the hand-oral intake route is unique to children, and the details are as follows:

Model of breathing and inhalation method:

$$\text{Hinh} = \frac{R \times \text{IC} \times L}{\text{BW}}, \quad (4)$$

$$R = \frac{\text{MC} \times \text{BS}}{U \times Q}. \quad (5)$$

In Equations (4) and (5), Hinh represents the way of breathing and inhalation, R represents the release of PBDEs in the air, IC represents the inhalation rate, L represents the daily exposure time, and BW represents the quality of the inhaled population. The indoor volume U and the ventilation rate Q are related to each other. BS is the contact area. MC represents the daily release of indoor PBDEs.

Exposure model by skin contact:

$$\text{Hderm} = \frac{\text{MC}' \times \text{RA} \times L}{\text{BW}}. \quad (6)$$

Hderm is the amount of exposure by skin contact, and B is the probability of PBDEs migrating to the hands. RA represents the contact area of the skin.

Hand-oral intake model:

$$\text{Horal} = \frac{M \times \text{LH} \times \text{BS} \times \text{HF}}{\text{BW}}. \quad (7)$$

TABLE 2: Experimental reagents and material list.

Reagent materials	Chemical formula	Purity
Vitamin B_{12}	$C_{63}H_{88}O_{14}N_{14}PCO$	98%
Tetrabromodiphenyl ether	$C_{12}H_6C_{12}H_6Br_4O$	95%
Nano iron powder	Fe	99%
Methanol	CH_3OH	Chromatogram pure
Tetrahydrofuran	C_4H_8O	Analytically pure
Hydrochloric acid	HCl	Analytically pure
Sodium hydroxide	NaOH	Analytically pure
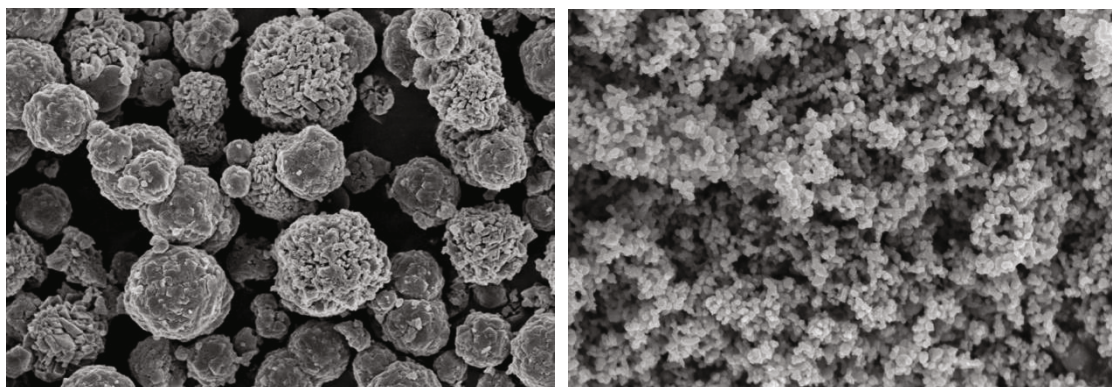
FIGURE 4: Scanning electron microscope image of reduced iron powder and nanoiron powder.
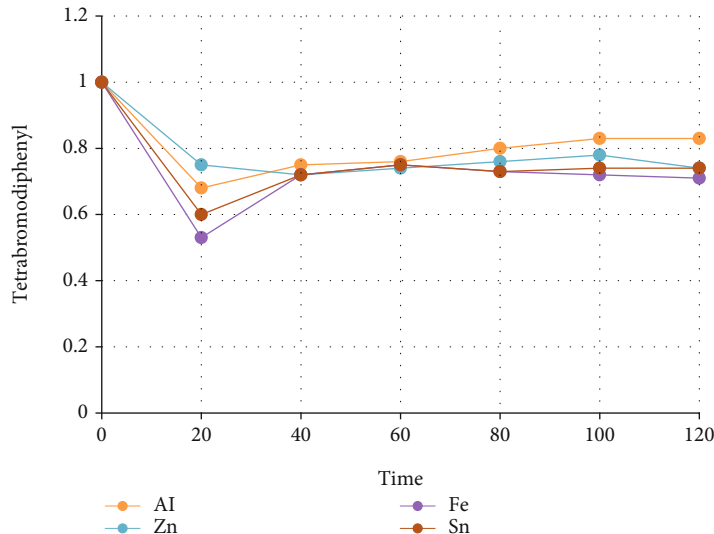
FIGURE 5: Degradation effects of different metals.

Horal represents the exposure by hand-oral ingestion, and LH is the transfer probability of PBDEs per exposure. HF represents the probability of contact.

As polybrominated diphenyl ethers are widely used as flame retardants in a variety of consumer products, the per capita annual exposure continues to rise. Moreover, bioaccumulation and environmental persistence may increase the risk of human carcinogenesis. Therefore, the following models can be used to assess its potential nonchemical carcinogenic risk:

$$EP = \frac{Hinh + Hderm + Horal}{CfD}. \tag{8}$$

Among them, the risk of nonchemical carcinogenesis is represented by EP, and the noncarcinogenic reference dose of pollutants is CfD.
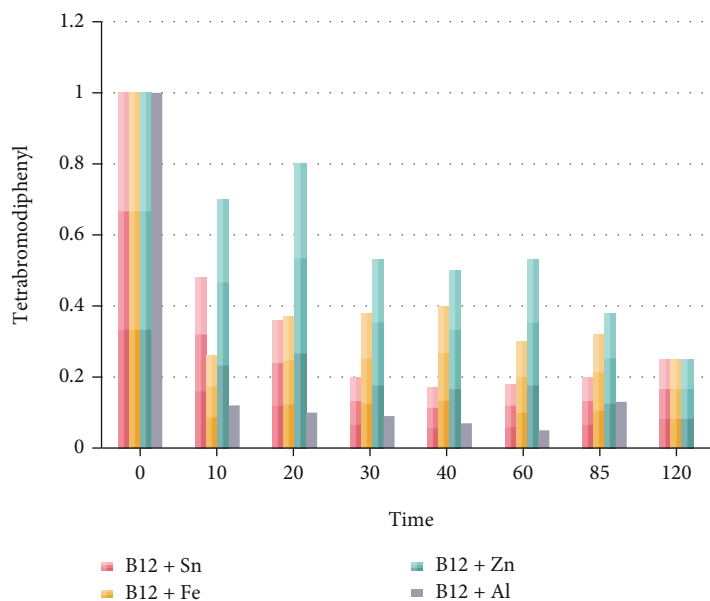
Figure 6: Different metals coordinate the debromination effect of B_{12}.
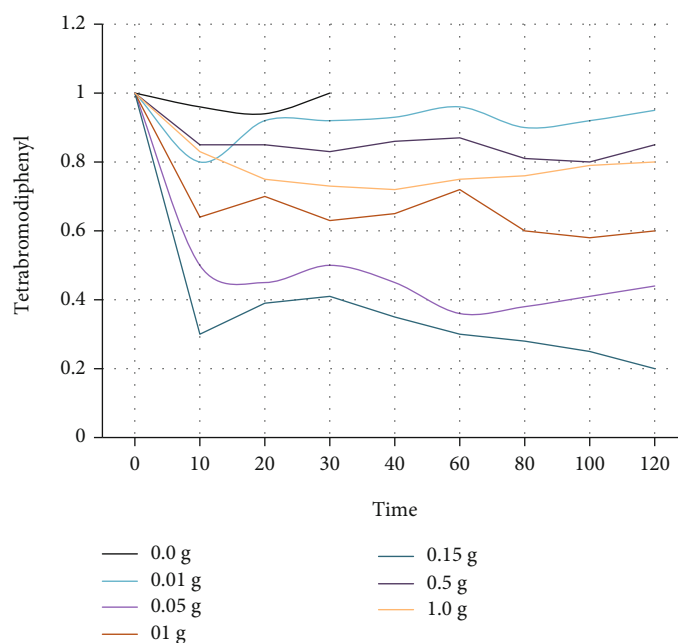
Figure 7: The effect of increasing nanometer iron powder on debromination.

3.4. Degradation of PBDEs.

Biodegradation: it refers to the reduction of harmful substances by microorganisms in the natural environment [34]. Microbial degradation can be divided into two types: (1) aerobic degradation, which is mainly through the isolation and cultivation of a certain strain that has high degradability for PBDEs, and (2) anaerobic degradation, which refers to the use of the extracted anaerobic bacterial populations to debromine and degrade PBDEs through the cultivated bacterial species, because PBDEs will undergo debromination and degradation reactions to varying degrees in an anaerobic environment.

Photodegradation Method: it refers to the photolysis reaction of most harmful substances in the natural environment under the action of absorbed sunlight [35]. As an important way to transform PBDEs, PBDEs are degraded by absorbing the ultraviolet band in sunlight.

Zero-valent Iron Degradation: it is a relatively popular degradation method in recent years. It is mainly a degradation method of debromination of PBDEs through zero-valent metals [36].

Hydrothermal Reaction Treatment: it is a common treatment method in daily life. For example, tetrabromobisphenol
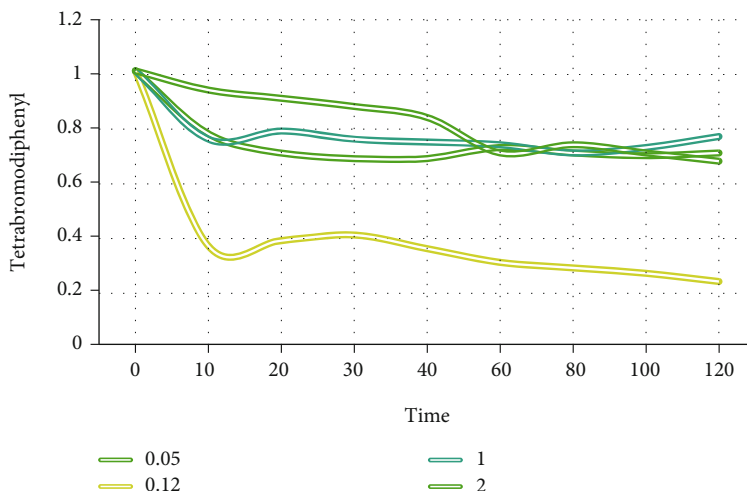
FIGURE 8: The effect of increasing B_{12} on debromination under the same quality of iron powder.
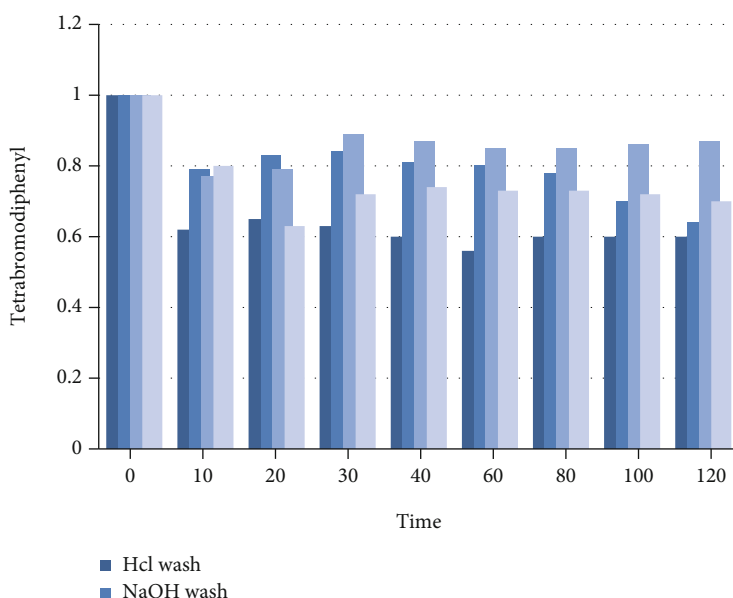
FIGURE 9: The effect of pretreatment on debromination.

reacts in high temperature subcritical water for a period of time, and the debromination reaction occurs [37] .

Composite Degradation Technology: based on the stable and long-lasting characteristics of PBDEs, a single degradation method cannot completely produce a good degradation effect on PBDEs. Therefore, the fusion application of multiple degradation methods can achieve a relatively good effect on its degradation [38].

3.5. Metal-Based Oxide Debromination Experiment. This experiment uses vitamins and zero-valent metal particles to decompose low-concentration halogenated organic matter in the soil and other systems to achieve actual therapeutic effects. The zero-valent iron reduction/debromination method has been developed in recent years. Because iron is a very active metal, and its chemical properties are also

very active, it is more and more popular. Facts have proved that it has greater electronegativity and redox characteristics. It can reduce a variety of pollutants. There are several other advantages of zero-valent iron in the treatment of pollutants. Due to its electrochemical properties, it has a certain role, such as in microelectrolysis. In addition, due to its porous material properties, it has the effect of adsorbing organic pollutants in a specific pH range. Compared with zero-valent iron powder, nanoiron powder has finer particles. This experiment uses metal materials, which decompose tetrabromodiphenyl ether under the combined action of vitamin B_{12}. Then, by observing the effect of each addition of zero-valent iron on the experimental effect, the experiment discussed the decomposition effect of various metals and the possibility of decomposition in the scene of fusion with vitamin B_{12}.
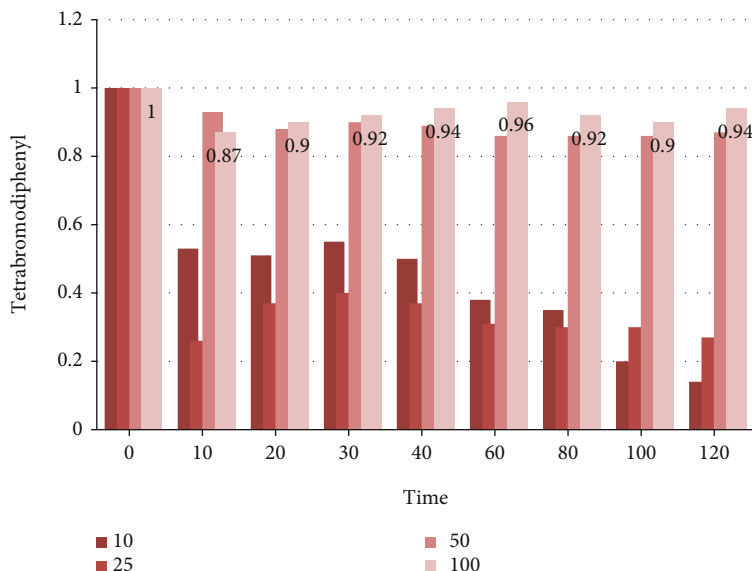
FIGURE 10: The effect of initial concentration on the debromination effect of tetrabromodiphenyl ether.

3.6. Reagents Needed for Experiment.
The main experimental materials are shown in Table 2.

3.7. Sample Analysis Method for Degradation Experiment.
The total amount of the reaction solution for the decomposition and debromination experiment is 30 mL. The experiment was carried out in a 50 mL three-necked flask, adding 500 mg/L of tetrabromodiphenyl ether stock solution and an initial concentration of 10 mg/L of tetrabromodiphenyl ether. Brominated diphenyl ether reaction liquid is a mixed solution of methanol and water. It is added with different amounts of vitamin B_{12} and nanoiron powder. It uses sodium hydroxide or hydrochloric acid to adjust the pH. The rotation speed is controlled to 220 rpm under protective gas and light-proof conditions. All reactions are completed under normal temperature and pressure.

3.8. Scanning Electron Microscopy (Sem) Analysis of Nanometer Iron Powder.
The scanning electron micrographs of iron powder and nanoiron powder are shown in Figure 4, respectively.

As shown in Figure 4(a), the particles of reduced iron powder are relatively coarse. The scanning electron micrograph of the nanoiron powder is shown in Figure 4(b). In contrast, the nanoiron powder has a much smaller particle size and the diameter is in the nanometer range. The study found that nanoiron powder is more reactive than ordinary iron powder and iron filings, and it has a larger specific surface area due to the nanosize effect. With strong reactivity and excellent adsorption performance, it has been widely studied and applied.

4. Result Analysis

4.1. The Influence of Different Metals on the Debromination Effect of Tetrabromodiphenyl Ether.
The results of degradation effect of different metals Al, Zn, Fe, and Sn are shown in Figure 5.

The decomposition rates of metals Al, Zn, Fe, and Sn are 16.64%, 24.20%, 29.04%, and 27.44%, respectively. Its low decomposition efficiency is mainly due to the high reduction of active metals, which can reduce many pollutants. It also has specific electrochemical and adsorption characteristics, electrolysis, and adsorption of pollutants. Therefore, the main catalytic reaction without a catalyst leads to less decomposition of pollutants. Secondly, in the larger metal particles and partial oxidation of their surface, etc., tetrabromodiphenyl ether is likely to deteriorate. The results show that the decomposition effect is Fe>Sn>Zn>Al. This may be related to the nature of the metal itself. The slow decomposition rate of aluminum is mainly due to the formation of a dense oxide film in the environment, which hinders the reaction.

4.2. The Effect of Different Metals and Vitamin B_{12} on the Debromination Effect of Tetrabromodiphenyl Ether.
Coupling Al, Zn, Fe, and Sn with B_{12} to degrade, the experiment takes a certain quality of metal B_{12}. The experimental results are shown in Figure 6.

As shown in Figure 6, the decomposition rates of metals and vitamins after coupling are 84.57%, 82.41%, 82.81%, and 98.89%. From the point of view of the increase of time, the decomposition rate shows an obvious decreasing trend with the passage of time, but the decomposition rate of several metals maintains a stable state at the end, respectively. The results show that the coupling of the ball-milled aluminum powder with B_{12} can efficiently and quickly decompose tetrabromodiphenyl ether. The reason for the impact may be that the ball mill restored the aluminum reduction ability. It destroys the oxide layer on the surface and makes the reaction more thorough.

4.3. 4.2 The Influence of the Dosage of Main Reactants on Debromination.
The dosage of nanometer iron powder affects the debromination effect. For the reaction system, when the dosage of B_{12} is 0.1 mM, the degradation diagram
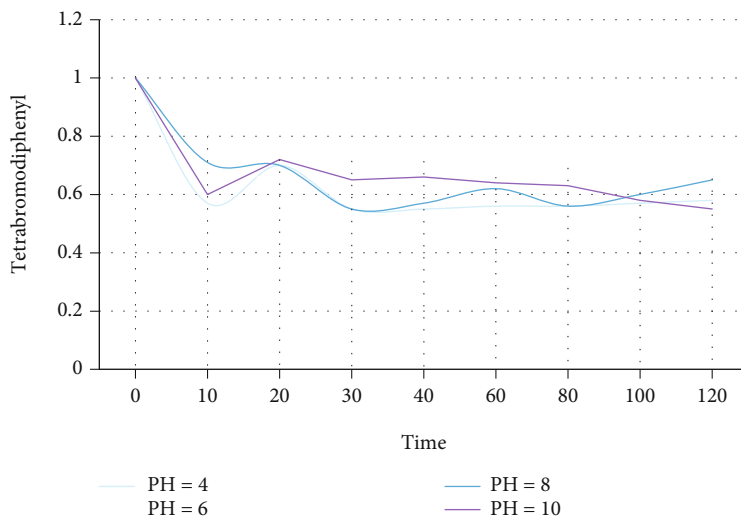
FIGURE 11: The effect of pH on the debromination effect.
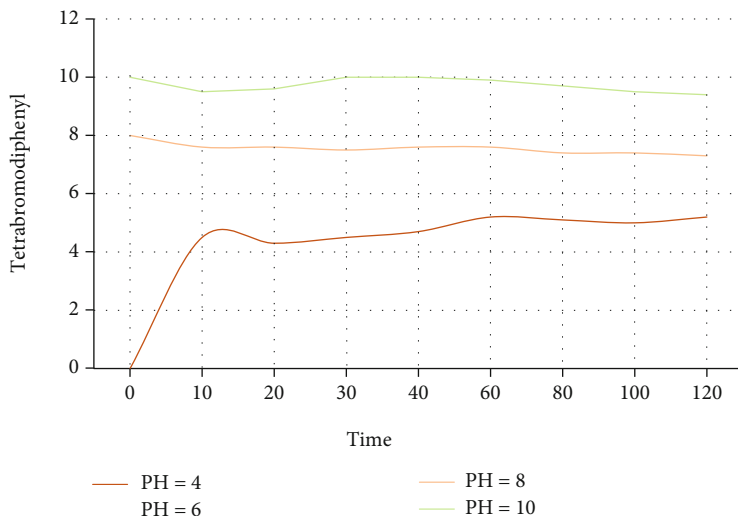
FIGURE 12: pH changes during the process.

of the dosage of nanometer iron powder on the debromination effect is shown in Figure 7.

As shown in Figure 7, the amount of nanoiron powder ranges from 0.0 g/L to 0.15 g/L. With the increase in the amount of nanoiron powder, the decomposition rate of tetrabromodiphenyl ether has a slope change. When the dosage of nanoiron powder is from 0.15 g/L to 1.0 g/L, the effect decreases as the concentration increases. This may be due to the increase in the concentration of nanoiron powder that can provide more reaction sites. If the concentration is too high, the hydrogen concentration generated by iron corrosion that covers the iron surface and interferes with the reaction will be too high. Therefore, increasing the concentration of nanoiron powder will accelerate the dehydrogenation reaction, but when it reaches a certain level, the reaction rate gradually decreases and stops.

The influence of the dosage of B_{12} on the debromination effect of tetrabromodiphenyl ether is shown in Figure 8. Under the dosage of 0.15 g/L nanoiron powder, this article

discusses the effect of vitamin B_{12} dosage on the degradation of tetrabromodiphenyl ether. In the range of 0.0 mM-0.1 mM, increasing the dose of vitamin B_{12} will accelerate the degradation efficiency. At concentrations between 0.1 and 2.0 mM, the degradation rate decreases as the concentration increases. When the amount of vitamin B_{12} is gradually increased to a certain amount, tetrabromodiphenyl ether is rapidly degraded within 120 minutes. This shows that increasing the vitamin B_{12} level within a certain range will significantly increase the rate of reaction degradation. Too high levels of vitamin B_{12} can interfere with electron transfer.

4.4. The Influence of Pretreatment Process on the Debromination Effect of Tetrabromodiphenyl Ether. When the reduced iron powder is subjected to various pretreatments and combined with B_{12}, the decomposition effect of the nanoiron powder is significantly higher than that of acid washing, alkaline washing, and methanol washing, as shown

in Figure 9. Alkaline washing refers to a high-strength lye solution prepared with sodium hydroxide and sodium carbonate or trisodium phosphate to soften, loosen, emulsify, and disperse deposits; pickling refers to the use of acid solution to remove oxide scale and rust on the surface of steel method. According to the degradation rate, the pretreatment methods are sorted into acid washing, alkaline washing, nanoiron powder, and methanol treatment processes. This is due to the large specific surface area and fine particles of the nanoiron powder, which can provide more reaction sites, which in turn can better provide electrons for the reaction. The results show that the effect of pickling is better than alkaline washing and methanol washing. Acid can remove the oxide film on the metal surface, clean the surface, and improve the debromination effect.

The initial concentration range of tetrabromodiphenyl ether is 10-100 mg/L. After 120 minutes of reaction, the result of measuring the effect on the dehydrogenation effect is shown in Figure 10. The degradation efficiency of tetrabromodiphenyl ether continued to decrease as the initial concentration increased. The removal rates after the reaction were 91.62%, 82.44%, 13.63%, and 5.39%, respectively. This is mainly because when the reaction concentration of tetrabromodiphenyl ether is low, nanoiron can provide a large effective surface area. So increasing the contact area ratio of the reaction will result in more active sites. So its dismantling is relatively complete. Therefore, if the pollutant concentration increases before the reaction, the tetrabromodiphenyl ether will eventually contact the nanoiron surface only after fierce competition. It can cover the surface when it is fully occupied, and only when it comes into contact with other molecules can it cause interference. Therefore, its debromination effect has been reduced.

4.5. The Influence of pH on the Debromination Effect of Tetrabromodiphenyl Ether. The initial pH of the system is 4.0 to 10.0, and the reaction is carried out under alkaline conditions. Figure 11 shows the effect of the initial pH of the system on the removal rate of tetrabromodiphenyl ether. The weakly acidic system environment is conducive to the dehydrogenation reaction. If the pH value changes during the reaction, the initial pH value of the system will become acidic, and the concentration of tetrabromodiphenyl ether will drop rapidly. The results show that the reaction is easier to proceed under acidic conditions, while the reaction is slower under alkaline conditions. The main reason is that the high hydrogen ion concentration enhances the cleaning ability of the metal, increases the corrosion rate, and at the same time promotes the production of reducing substances, thereby promoting the reaction, and vice versa. As the H+ concentration in the system increases, iron corrosion occurs rapidly, and its surface is blocked. This is not conducive to the progress of the reaction.

The change in pH value in Figure 12 shows a trend of small fluctuations during the reaction time, which is basically stable thereafter. With the initial increase of pH, the final degradation of tetrabromodiphenyl ether was 5.36, 7.08, 7.25, and 9.45. Under acidic conditions, the increase in pH may be due to the consumption of H+ or the production of OH-. As the pH increases, the slowing down of degradation may be due to the fact that the reaction is basically stable. Iron dissolves in the aqueous medium and emits electrons to produce H2. These reactions increase the pH. Under acidic and neutral conditions, as an electron acceptor, H+ can compete with tetrabromodiphenyl ether for electrons.

5. Conclusions

This paper discusses that the environmental behavior of PBDEs is the basis for their pollution prevention and control, due to their far-reaching impact on social and economic development and human health. Therefore, it is urgent to develop a fast, efficient, and thorough polybrominated diphenyl ether degradation technology. In the experiment, we studied the catalytic reduction effect of tetrabromodiphenyl ether and influencing factors with nanoiron powder and vitamin B_{12}. The experiment investigated the effects of vitamin B_{12} dosage, iron dosage, pH value, pretreatment conditions, reaction concentration, pH change value, etc. on the decomposition rate of tetrabromodiphenyl ether. The optimal reaction conditions for the catalytic reduction of tetrabromodiphenyl ether with nanoiron powder and vitamin B_{12} are as follows: the amount of nanoiron powder is 0.15 g/L, the amount of vitamin B_{12} is 0.1 mM, and the initial pH value is 6.0 under pickling. It is the best reaction condition under all the listed conditions. The removal rate of 10 mg/L tetrabromodiphenyl ether after 120 minutes of reaction is as high as 91.62%. Compared with traditional zero-valent iron powder, nanoiron powder has stronger reducing power and higher surface activity. This means that it can provide more active centers for the reaction.

Data Availability

No data were used to support this study.

Conflicts of Interest

The authors declare that there are no conflicts of interest regarding the publication of this article.

Acknowledgments

References

[1] T. Y. Li, J. F. Zhou, C. C. Wu, L. J. Bao, L. Shi, and E. Y. Zeng, "Characteristics of polybrominated diphenyl ethers released from thermal treatment and open burning of E-waste," *Environmental Science & Technology*, vol. 52, no. 8, pp. 4650–4657, 2018.

[2] B. A. Howell and E. A. Ostrander, "Thermal degradation of flame-retardant compounds derived from castor oil," *Journal*

of Thermal Analysis and Calorimetry, vol. 138, no. 6, pp. 3961–3975, 2019.

[3] Y. G. Daniel and B. A. Howell, "Thermal degradation of bisphosphorus esters of isosorbide," *Journal of Thermal Analysis and Calorimetry*, vol. 131, no. 1, pp. 1–7, 2018.

[4] S. Ishii, S. L. Shinde, and T. Nagao, "Nonmetallic materials for plasmonic hot carrier excitation," *Optical Materials*, vol. 7, no. 1, article 1800603, 2019.

[5] Y. Z. Chen, D. J. Jiang, Z. Q. Gong, J. Y. Li, and L. N. Wang, "Anodized metal oxide nanostructures for photoelectrochemical water splitting," *International Journal of Minerals Metallurgy and Materials*, vol. 27, no. 5, pp. 584–601, 2020.

[6] J. Y. Park, H. Jeon, N. Park et al., "Design of Transparent Multicolor LED Signage with an Oxide-Metal-Oxide Interconnect Electrode," *Journal of the Korean Physical Society*, vol. 77, no. 1, pp. 82–86, 2020.

[7] S. J. Guo, C. H. Yang, X. M. Jiang, P. P. Lv, and G. D. Hu, "High ferroelectric performance of Bi0.9La0.1FeO3 thick film by optimizing preparation precursor solution," *Journal of Sol-Gel Science and Technology*, vol. 80, no. 1, pp. 174–179, 2016.

[8] X. Zhao, M. Liu, Y. Liu, Y. Li, S. Zhang, and K. du, "Aerobic degradation of 4-monobrominated diphenyl ether: identifying and characterizing three strains isolated from Populus tomentosa phyllosphere," *Journal of Environmental Studies*, vol. 26, no. 3, pp. 1385–1392, 2017.

[9] Q. Li, F. Yang, G. Su et al., "Thermal degradation of polybrominated diphenyl ethers over as-prepared Fe_3O_4 micro/nano-material and hypothesized mechanism," *Environmental Science and Pollution Research*, vol. 23, no. 2, pp. 1540–1551, 2016.

[10] M. Al-Harahsheh, M. Altarawneh, M. Aljarrah, F. Rummanah, and K. Abdel-Latif, "Bromine fixing ability of electric arc furnace dust during thermal degradation of tetrabromobisphenol: experimental and thermodynamic analysis study," *Journal of Analytical and Applied Pyrolysis*, vol. 134, pp. 503–509, 2018.

[11] L. Xiang, H. Sheng, M. Xu et al., "Reducing plant uptake of a brominated contaminant (2,2′,4,4′-tetrabrominated diphenyl ether) by incorporation of maize straw into horticultural soil," *Science of the Total Environment*, vol. 663, p. 29, 2019.

[12] Y. Zhang, W. Ni, and Y. Li, "Effect of siliconizing temperature on microstructure and phase constitution of Mo-MoSi$_2$ functionally graded materials," *Ceramics International*, vol. 44, no. 10, pp. 11166–11171, 2018.

[13] L. Xiong, H. Liyue, Z. Fancai et al., "Effect of decabrominated diphenyl ether exposure on spatial learning and memory, the expression and phosphorylation of hippocampal glutamate receptor subunits in adult Sprague-Dawley rats," *Journal of Toxicological Sciences*, vol. 43, no. 11, pp. 645–657, 2018.

[14] A. O. Souza, M. J. Tasso, A. M. Oliveira et al., "Evaluation of polybrominated diphenyl ether toxicity on HepG2 cells-hexabrominated congener (BDE-154) is less toxic than tetrabrominated congener(BDE-47)," *Basic & Clinical Pharmacology&Toxicology*, vol. 119, no. 5, pp. 485–497, 2016.

[15] M. Zhang, J. Lu, Y. He, and P. C. Wilson, "Photocatalytic degradation of polybrominated diphenyl ethers in pure water system," *Frontiers of Environmental Science & Engineering*, vol. 10, no. 2, pp. 229–235, 2016.

[16] C. P. Tso and Y. H. Shih, "The influence of carboxymethylcellulose (CMC) on the reactivity of Fe NPs toward decabrominated diphenyl ether: the Ni doping, temperature, pH, and anion effects," *Journal of Hazardous Materials*, vol. 322, pp. 145–151, 2017.

[17] R. Liu, D. O. Nelson, S. Hurley et al., "Association between serum polybrominated diphenyl ether levels and residential proximity to solid-waste facilities," *Environmental Science&Technology*, vol. 50, no. 7, pp. 3945–3953, 2016.

[18] A. Khaled, C. Richard, L. Redin et al., "Characterization and photodegradation of polybrominated diphenyl ethers in car seat fabrics from end-of-life vehicles," *Environmental Science & Technology*, vol. 52, no. 3, pp. 1216–1224, 2018.

[19] Q. Cong, M. Ren, T. Zhang, F. Cheng, and J. Qu, "Graphene/β-cyclodextrin Membrane: Synthesis and Photoelectrocatalytic Degradation of Brominated Flame Retardants," *ChemistrySelect*, vol. 6, no. 32, pp. 8435–8445, 2021.

[20] M. Xie, P. Wang, R. Zhang, X. Yu, and Y. Zhao, "Direct-band-gap electroluminescence from germanium with subband engineering utilizing a metal-oxide-semiconductor structure," *IEEE Transactions on Electron Devices*, vol. 67, no. 5, pp. 2016–2021, 2020.

[21] N. Tao, "Challenges and promises of metal oxide nanosensors," *Acs Sensors*, vol. 4, no. 4, pp. 780–780, 2019.

[22] W. Sakamoto, "Improvement of photoinduced properties of narrow bandgap ferroelectric thin film utilizing localized surface Plasmon resonance of silver nanoparticles," *Journal of the Society of Powder Technology Japan*, vol. 54, no. 12, pp. 809–816, 2017.

[23] L. Yong, X. Zhi-Jun, F. Li-Qun et al., "Preparation and properties of multi-effect potassium sodium niobate based transparent ferroelectric ceramics," *Acta Physica Sinica*, vol. 69, no. 24, pp. 247702–247702, 2020.

[24] B. D. Mai, H. T. Nguyen, and D. Q. Hoang, "A novel composite from Nanodispersed silica and an organic ferroelectric of diisopropylammonium bromide: preparation, characterization and dielectric properties," *Materials Transactions*, vol. 60, no. 10, pp. 2132–2136, 2019.

[25] P. Chen, K. Yi, J. Liu, Y. Hou, and B. Chu, "Effects of density inhomogeneity in green body on the structure and properties of ferroelectric ceramics," *Journal of Materials Science:Materials in Electronics*, vol. 32, no. 12, pp. 16554–16564, 2021.

[26] B. Gao, X. Ning, and P. Xing, "Shock wave induced nanocrystallization during the high current pulsed electron beam process and its effect on mechanical properties," *Materials Letters*, vol. 237, no. 15, pp. 180–184, 2019.

[27] G. Bo, L. Chang, H. Chenglong et al., "Effect of mg and RE on the surface properties of hot dipped Zn–23Al–0.3Si coatings," *Science of Advanced Materials*, vol. 11, no. 4, pp. 580–587, 2019.

[28] V. P. Panchenko, N. Y. Tabachkova, A. A. Ivanov, B. R. Senatulin, and E. A. Andreev, "Preparation and properties of Zn4Sb3-based thermoelectric material," *Semiconductors*, vol. 51, no. 6, pp. 714–717, 2017.

[29] P. Wang, T. Yao, Z. Li et al., "A superhydrophobic/electrothermal synergistically anti-icing strategy based on graphene composite," *Composites Science and Technology*, vol. 198, article 108307, 2020.

[30] J. Zhao, J. Huang, R. Wang, H. R. Peng, and S. Ji, "Investigation of the optimal parameters for the surface finish of k9 optical glass using a soft abrasive rotary flow polishing process," *Journal of Manufacturing Processes*, vol. 49, pp. 26–34, 2020.

[31] X. Zhang, Z. Li, X. Wang, and J. Yu, "The fractional kelvin-voigt model for circumferential guided waves in a viscoelastic fgm hollow cylinder," *Applied Mathematical Modelling*, vol. 89, pp. 299–313, 2021.

[32] L. Zeng, J. Shi, J. Luo, and H. Chen, "Silver sulfide anchored on reduced graphene oxide as a high -performance catalyst for CO_2 electroreduction," *Journal of Power Sources*, vol. 398, pp. 83–90, 2018.

[33] X. Cao, M. Min Liu, J. L. Zhao, J. Xia, T. Zou, and Z. Wang, "Synergetic PtNP@Co3O4 hollow nanopolyhedrals as peroxidase-like nanozymes for the dual-channel homogeneous biosensing of prostate-specific antigen," *Analytical and Bioanalytical Chemistry*, vol. 414, no. 5, pp. 1921–1932, 2022.

[34] A. Borrelli, D. Grandi, M. Fabrizio, and M. C. Patria, "A non-isothermal phase-field model for piezo–ferroelectric materials," *Continuum Mechanics and Thermodynamics*, vol. 31, no. 3, pp. 741–750, 2019.

[35] Y. Wang, Y. Fu, J. Li, W. Li, and Y. He, "Preparation and properties of Ba0.8Sr0.2TiO3/CoFe$_2$O$_4$ heterostructure layered multiferroelectric composite film," *Gongneng Cailiao/Journal of Functional Materials*, vol. 48, no. 9, pp. 09105–09109, 2017.

[36] R. Barabas, N. Muntean, G. Szabo, K. Maurer, and L. Bizo, "Preparation and characterizations of new biomaterials by anthocyanins adsorption on hydroxyapatite-based materials," *Studia Universitatis Babes-Bolyai Chemia*, vol. 62, no. 4, pp. 253–268, 2017.

[37] K. Hoffman, M. Mendez, A. M. Siega-Riz, A. H. Herring, A. Sjödin, and J. L. Daniels, "Lactational exposure to polybrominated diphenyl ethers and its relation to early childhood anthropometric measurements," *Environmental Health Perspectives*, vol. 124, no. 10, pp. 1656–1661, 2016.

[38] T. M. Brown, P. S. Ross, and K. J. Reimer, "Transplacental transfer of polychlorinated biphenyls, polybrominated diphenylethers, and organochlorine pesticides in ringed seals (Pusa hispida)," *Archives of Environmental Contamination&Toxicology*, vol. 70, no. 1, pp. 20–27, 2016.

Hindawi

Research Article

Feasibility of the Development of New PVC/Fine Sand Imitation Stone Composite Materials to Promote Rural Urbanization

Yi Wei [ORCID]

College of Art, Shandong Management University, Jinan, 250357 Shandong, China

Correspondence should be addressed to Yi Wei; 14438120050210@sdmu.edu.cn

At present, with the acceleration of rural urbanization, people's market demand for new building materials is also increasing, and the research and development of new PVC/fine sand imitation stone composite materials are also in continuous progress and development. The purpose of this article is to analyze the feasibility of developing new PVC/fine sand imitation stone composite materials to promote rural urbanization and propose the application of more new PVC/fine sand imitation stone composite materials to our urbanization construction. In, we first conducted research on the new PVC/fine sand imitation stone composite material and rural urbanization, and then, we conducted research on the various properties of the new PVC/fine sand imitation stone composite material and the development of rural urbanization. The research results show that the new PVC/fine sand imitation stone composite material has at least 400% improvement in compressive performance compared with the traditional PVC material, and it is also better than the traditional PVC material in terms of the material expansion and contraction performance, which is more conducive to the application our rural urbanization is under construction.

1. Introduction

Urbanization is a natural historical process in which nonagricultural industries agglomerate in cities and towns and rural populations are concentrated in cities and towns along with the development of industrialization. It is an objective trend in the development of human society. Traditional urbanization has led to a series of problems in my country, such as uneven regional development, low resource carrying capacity, excessive reliance on land support, and environmental pollution. Therefore, a new type of urbanization has emerged. Polyvinyl chloride, as one of the world's earliest industrialized plastics, is one of the five general purpose resins. It has been widely used in national life and social economy because of its excellent performance and economic price. Polyvinyl chloride has excellent physical properties and has outstanding performance in corrosion resistance, chemical stability, and flame resistance. Compared with other materials, it has the advantage of low price. Therefore, PVC is widely used, and its use is in thermoplastic resin. It is second only to polyethylene, accounting for one-third of the total global synthetic resin

consumption. In the social environment with the rapid development of science and technology and the gradual expansion of the application scope of polymer materials, the requirements for various materials in urbanization construction are getting higher and higher, and plastic products are required to meet the more and more precise division of labor, and the needs of the industry are increasing.

Architecture is a symbol of human civilization, and the regional and nationality of architecture are expressed by building materials. Although many people have conducted research on PVC composite materials, the research focuses on the application of PVC composite materials in traditional buildings, and there is no systematic detailed classification of contemporary applications of PVC composite materials. In the construction of a new type of urbanization, in today's urgent need for regional feelings, we take the application of PVC composite materials as the core part of in-depth research, apply its divergent thinking to all aspects of urbanization, and actively explore the use of bamboo and wood. The ideological expression, aesthetic expression, and technical expression of the local materials

represented by brick and stone in the new urbanization construction have summarized a set of guiding principles, which will be implemented in the future new urbanization construction and promote regional culture. With the rapid development of contemporary construction technology and new materials, the expression methods of PVC composite materials are no longer limited to traditional techniques. Under the guidance of new concepts and new processes, many innovative expression methods have been formed. The artistic appeal and spiritual symbolism of bamboo, wood, brick, and stone improve the aesthetic quality and cultural connotation of the building and give people the enjoyment of beauty [1]. The buildings in the new urbanization construction should strive to achieve equal emphasis on traditional PVC composite materials and modern technology and try to find a new way of innovation in the continuation. This is not only a respect for the local natural environment and national culture, but also a warning for modern people to lose themselves and blindly seek development.

With the continuous progress of society, the process of rural urbanization is also accelerating. Goodall SK based the research on the migration of nomads from rural to urban areas in the western Ladakh Himalayas and stated that the case study is consistent with the rapid urbanization currently underway in Leh related to [2]. Arouri M's survey on rural urbanization found that urbanization has stimulated the transition from agricultural activities to nonagricultural activities in rural areas. Rural households have experienced a decrease in agricultural income and an increase in wages and nonagricultural income. And urbanization helps rural families reduce the poverty rate of expenditure [3]. The development of the government governance system is also a major factor in promoting rural urbanization. In a study, Oke D analyzed some related factors of Lagos urbanization caused by rural to urban migration. The research results show that the education and modern transportation provided by the Lagos government are crucial to the country's urbanization drive [4]. In the process of rural urbanization, some problems inevitably arise. Guo Y's in-depth case study of the South China Sea in the Pearl River Delta revealed the unexpected seriousness between local villagers and migrant workers in villages undergoing effective urbanization, social inequality, and isolation [5]. Although some problems will inevitably arise in the process of rural urbanization, they cannot stop the development of urbanization. As a commonly used PVC composite material in rural construction, it is also undergoing continuous innovation and development. Dan-Asabe B pointed out that Dum Palm particle-reinforced polyvinyl chloride (PVC) composites were developed with relatively low-cost materials, providing overall light weight and good mechanical properties, which can be used as potential applications for pipeline materials [6]. Sacramento AS described a new method of producing antibody-like bionic materials in the study of composite materials. It includes the preparation of composite imprinting materials that have never appeared before, with highly conductive supporting nanostructures, and the assembly of highly conductive polymer layers at low temperatures [7].

In the research on the production of composite materials, people are also making continuous progress. In a research conducted by Lyubimova ON, a mathematical model and simulation method for calculating the temperature field and material property distribution in the production process of composite materials were provided to better study composite materials [8]. Although the continuous development of PVC composite materials has improved its own usability, PVC composite materials have also made some people not consider using them as building materials for houses and their decorations due to their low heat resistance [9].

The innovation of this article lies in the full research and analysis of new PVC composite materials and rural urbanization. The new PVC/fine sand imitation stone composite materials are used in rural urbanization construction, and new composite materials with more wear resistance, corrosion resistance, high flame resistance, and lower prices are introduced into rural urbanization construction. This is to help rural people build their homes by using more cost-effective materials.

2. Development of New PVC/Fine Sand Imitation Stone Composite Materials and Methods to Promote Rural Urbanization

2.1. PVC Material. Polyvinyl chloride, called PVC, is a white powder with an amorphous structure. In 1835, the Von Liebig Institute in Houston, Germany, synthesized vinyl chloride, and in 1872, Barman synthesized polyvinyl chloride [10, 11]. However, actual PVC products were not produced in the USA until the 1920s, and a large-scale production in Europe will begin in the next 20 years. Because of its abundant raw materials, the manufacturing process is very mature, the price is very low, and the uses are very wide. It is still second only to polyethylene resin in the world [12]. The two main general purpose resins account for 29% of the world's total synthetic resin production. There are many processing methods for PVC processing, such as molding, lamination, injection molding, extrusion molding, calendar ring, and brooch molding. PVC can manufacture software products and hardware products. Among them, software products mainly include artificial leather, films, steel wire sheaths, and soft boards, and hardware products mainly include boards, doors, windows, pipes, valves and other configuration materials [13]. Chlorinated polyethylene has excellent flame retardancy and high chemical resistance [14].

Polyvinyl chloride is a noncrystalline polymer, and its main feature is that it is amorphous, nonbranched, and regularly arranged with lock-like links. The polymerization degree n of polyvinyl chloride is generally 500~2000. This material is a material with high mechanical strength, and its chemical properties are very stable [15]. Due to the large amount of chlorine molecules in the molecular structure, it has high polarity and excellent flame retardancy. Plastic products made of polyvinyl chloride have excellent advantages such as abrasion resistance, acid resistance, alkali resistance, and insulation [16]. However, the optical

and thermal stability of the device is relatively low, and if no thermal stabilizer is added, it starts to decompose at 100 degrees Celsius. Experiments show that the higher the temperature, the faster the decomposition [17]. At present, the PVC industry is developing rapidly all over the world and has broad prospects. All countries are optimistic about the possibilities of PVC and the benefits of the ecological environment. With its outstanding and unique performance, PVC has proved its role to the world. Yes, social development needs it, and environmental protection needs it. This is an inevitable trend of the progress of our human social civilization [18].

2.1.1. Preparation of PVC Composite Materials. According to the formula, the uniformly mixed materials are supplied to the extruder barrel through the hopper. Under the action of the rotating movement of the screw, the material mixture moves along the rotation until it is pressed in front of the barrel, and then is cooled and formed, and the pushed product is completed. Figure 1 shows part of the production machine required for the preparation of PVC composite materials [19]. These machines have their own preparation process, in different forms.

Figure 2 shows the production flow chart of the new PVC/fine sand imitation stone composite material.

A composite material is a combination of one material as the matrix and another as the reinforcement [20]. Various materials complement each other in terms of performance, resulting in a synergistic effect, so that the comprehensive performance of the composite material is better than that of the original material to meet various requirements. With PVC as the matrix, it is divided according to different types of reinforcements. There are currently 4 categories. PVC composite materials: one is fiber, the other is powder, and the third is granular, such as PVDC and polyurethane.

After the preparation of the PVC composite material, the thermal conductivity and flame retardant performance should be tested separately. In the production process, since PVC is a heat-sensitive material, even adding a heat stabilizer can only increase the decomposition temperature and prolong the stabilization time without decomposition [21]. This requires that the molding processing temperature of PVC should be strictly controlled. In particular, rigid PVC, because its processing temperature is very close to the decomposition temperature, often decomposes due to improper temperature control. The quality of extrusion granulation is closely related to the characteristics of the extruder, the structure of the head, the temperature, the feeding speed, the rotation speed of the main engine, the traction speed, and other factors. In the thermal conductivity test, the composite material sample is made into a circular sample with a diameter of 6 mm, and the upper temperature of the instrument is set to 36°C, and the lower temperature is set to 15°C, when the indicator does not change more than 0.1 within one minute. Put the sample on the thermal conductivity tester at °C, start the test after the thermal conductivity is stable, test once a minute, start counting, and measure three times within the range of the value difference

not exceeding 5% [22]. The calculation formula of thermal conductivity:

$$\frac{\Delta W}{\Delta T} = \lambda * Q \frac{\theta_1 - \theta_2}{H}. \tag{1}$$

When testing the flame retardancy of PVC composite materials, the sample size is as follows: length × width × height = $(100 \, \text{mm}) \times (6.5 \pm 0.5 \, \text{mm}) \times (3 \pm 0.5 \, \text{mm})$. During the test, first consult the literature to estimate the range of the oxygen index of the sample, adjust the oxygen and nitrogen proportionally to this value, clamp the sample vertically on the iron clamp, and then use an igniter to ignite [23]. Adjust the ratio of oxygen and nitrogen, and observe the burning distance of the sample after 3 minutes until the burning of the sample starts timing. If it exceeds 60 mm, it means that the oxygen concentration is high and adjusts it downward; if it is less than 60 mm, it means that the oxygen concentration is low and adjusts it upward. When it reaches 60 mm in 3 minutes, the oxygen content is the oxygen index of the composite material. The calculation formula of oxygen index is as follows:

$$\text{OT} = \frac{\text{WO}_2}{\text{WO}_2 + \text{WM}_2} * 100\%, \tag{2}$$

where OT represents the oxygen index, WO_2 represents the oxygen flow rate, and WM_2 represents the nitrogen flow rate.

2.1.2. Composite Material Processing Performance Test. The polymer melt can exhibit viscous flow and elastic deformation under the influence of external force, so the processing and molding of PVC are manifested in viscous flow [24]. The most basic manifestation of its processing performance is its rheological properties, and rheological properties refer to the viscous flow of materials. For a long time, scholars have established the relationship between the speed and torque in the torque rheometer for the first time, to the research on the theoretical model of the processing conditions, rheological parameters and geometric dimensions of the torque rheometer, and then to Bousmina. Based on the power law fluid equation, a series of theoretical derivations are carried out, and the following relational expressions are obtained. When the fluid flows in the pipeline, the distance it flows in a certain period of time is the flow velocity. The flow velocity generally refers to the average flow velocity of the fluid, and the unit is m/s.

$$\Gamma = 2^{2N+1} \pi^{N+1} \text{WLR}^2{}_B M^N \frac{1 + q^{N+1}}{\left[N \left(\beta^{2/N} - 1 \right) \right]^N}, \tag{3}$$

$$R_n = 2^{n+1} \pi^{n+1} \text{LR}_B^2 \frac{1 + q^{n+1}}{\left[n \left(\beta^{2/n} - 1 \right) \right]^n}, \tag{4}$$

$$\beta = \frac{R_B}{R_I}, \tag{5}$$
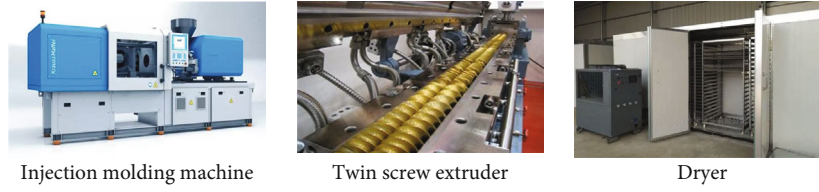
FIGURE 1: Part of the machine diagram for preparing PVC composite materials.
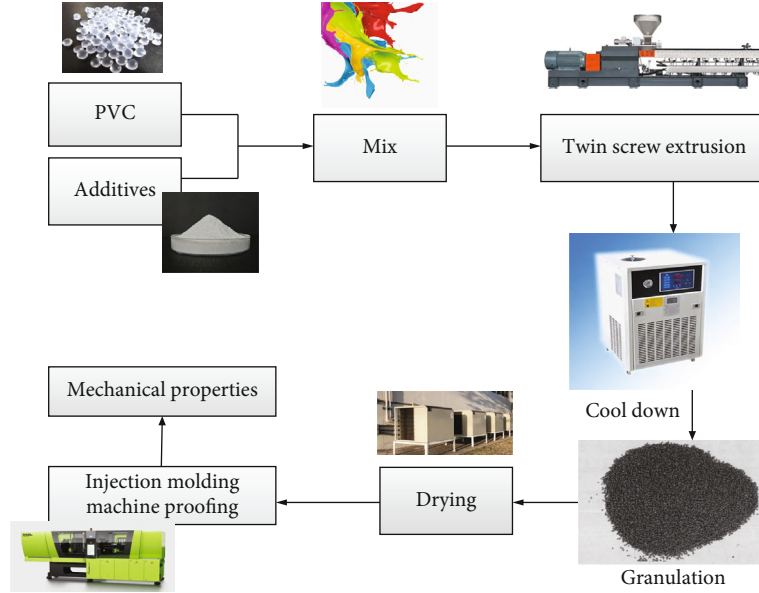
FIGURE 2: The production flowchart of the new PVC/fine sand imitation stone composite material.

where R_B is the equivalent radius; R_I is the radius of the mixer; L is the length of the rotor; q is the speed ratio of the two rotors; Γ is the balance torque, $N \cdot m$; W is the consistency coefficient; n is the power law index; and WL is the indicator. The above formula can be transformed to obtain the rotor equivalent radius R_I formula, as shown in

$$R_I = \frac{R_B}{\left[1 + (4\pi N/n)(2\pi WLR_B^c(1 + q^{N+1}/\Gamma))^{1/n}\right]^{n/2}}. \quad (6)$$

Bousmina also gave the calculation formula of the shear rate and shear viscosity of the polymer melt in the torque rheometer, as shown in

$$\chi = \chi_{1/2} = \frac{2^{2(1+(1/N))}\pi n}{N} \frac{\beta^{2/N}}{(1 + \beta)^{2/N}\left(\beta^{2/N} - 1\right)}, \quad (7)$$

$$\eta(\chi) = \frac{\Gamma}{\pi L(R_B + R_I)(1 + q^{N+1})\chi}. \quad (8)$$

However, when Bousmina calculates the melt viscosity and equivalent radius, it is calculated according to the set temperature of torque rheology. It does not take into account the actual temperature of the material in the cavity, so some scholars have carried out temperature correction.

The relationship between viscosity and temperature is as follows:

$$\eta = A \exp(\Delta Q/RE). \quad (9)$$

From the above formula:

$$\frac{\eta(E)}{\eta(E)'} = \frac{\Gamma(E)}{\Gamma(E)'} = \exp\left[\frac{\Delta Q}{R}\left(\frac{1}{E} - \frac{1}{E'}\right)\right]. \quad (10)$$

2.2. Rural Urbanization. "Urbanization" has a very rich connotation. It was in the twentieth century that urbanization gradually became popular and accepted by the masses. With the development of society and economy, the concept and connotation of urbanization are constantly enriched and improved [25]. Scholars in various fields have given meaning to urbanization from various angles. Sociologists believe that urbanization is a process by which rural residents enjoy the material and spiritual enrichment brought about by urban development and urban production and lifestyle changes. Many scholars have studied this transformation through the illiteracy rate, mass communication penetration rate, and language uniformity rate. Demographers believe that urbanization is a process in which local populations continue to gather in cities and cities. This process will inevitably lead to an increase in the number of cities and cities. The essence of urbanization is the

urbanization of the population. Many scholars' research on the level of urbanization is also based on the ratio of urban permanent residents to the total population [26].

2.2.1. Development History of Urbanization.

The urbanization process since the founding of New China is roughly divided into three stages. The first stage: 1949~1957. Soon after the founding of the People's Republic of China, it entered a period of large-scale industrialization and urban construction under the "First Five-Year Plan." The second stage: from 1958 to 1978. The urban population accounts for 30%~70% of the total population. Urbanization has entered a period of rapid development, and the urban population can exceed 50% in a relatively short period of time and then rise to about 70%. The third stage: Since 1978, since the reform and opening up, China has entered a stage of steadily advancing urbanization. The implementation of a series of reform and opening policies has greatly promoted the development of urbanization. In the 42 years from 1978 to 2020, the level of urbanization in China has increased from 17.9% to 63.89%. Figure 3 shows the development map of China's urbanization process.

2.2.2. Measurement of Urbanization Level.

The level of urbanization is an important indicator of the social and economic development of countries and regions. It has always been the focus of scholars to determine the level of urbanization in line with reality through scientific and objective methods [27]. There are many methods to measure the level of urbanization, which can generally be divided into four categories: entropy method, population index method, other main index method, and compound index method.

The first introduction is the entropy method. "Entropy" is the measure of uncertainty. Experiments show that the more elements, the more comprehensive the index, the smaller the uncertainty, and the smaller the entropy. Experiments show that the fewer the elements, the higher the unilateralist of the index, and the greater the uncertainty [28]. Therefore, the degree of dispersion of the index can be judged from the result of the entropy value. Experiments show that the smaller the entropy value, the greater the weight and the greater the degree of dispersion. Experiments show the greater impact of indicators on the results and vice versa. The calculation steps of the entropy method are as follows:

(1) Matrix construction and standardization: Assuming a comprehensive evaluation of the y indicators of w objects, a matrix of 18 $w \times y$ can be established, where Amn represents the value of the nth indicator in the m area, $m = 1, 2, \cdots, W, n = 1, 2, \cdots, y$; w is the number of regions, and y is the number of indicators

(2) Data standardization: The unit, positive and negative directions, and the size of various indicators are different, and the original data must be standardized. The formula for calculating the positive index is as follows:

$$A'_{mn} = (A_{mn} - \min \{A_n\})/(\max \{A_n\} - \min \{A_n\}). \quad (11)$$

The calculation formula of the negative index is

$$A'_{mn} = (\max \{A_n\} - A_{mn})/(\max \{A_n\} - \min \{A_n\}). \quad (12)$$

(3) Calculate the proportion of the j-th index value in the i-th year:

$$T_{mn} = \frac{A'_{mn}}{\sum_{m=1}^{w} A'_{mn}}. \quad (13)$$

(4) Calculation of index entropy:

$$O_n = -K \sum_{m=1}^{w} (T_{mn} * \ln T_{mn}). \quad (14)$$

(5) Calculation of entropy redundancy:

$$D_m = 1 - O_n. \quad (15)$$

(6) The weight of the indicator:

$$q_m = \frac{D_m}{\sum_{n=1}^{w} D_m}. \quad (16)$$

(7) Evaluation scores for individual indicators:

$$E_{mn} = q_m * A'_{mn}. \quad (17)$$

(8) Comprehensive level score of the i-th year:

$$E_m = \sum_{n=1}^{y} E_{mn}. \quad (18)$$

The second introduction is the population index method, which indicates that the level of urbanization is
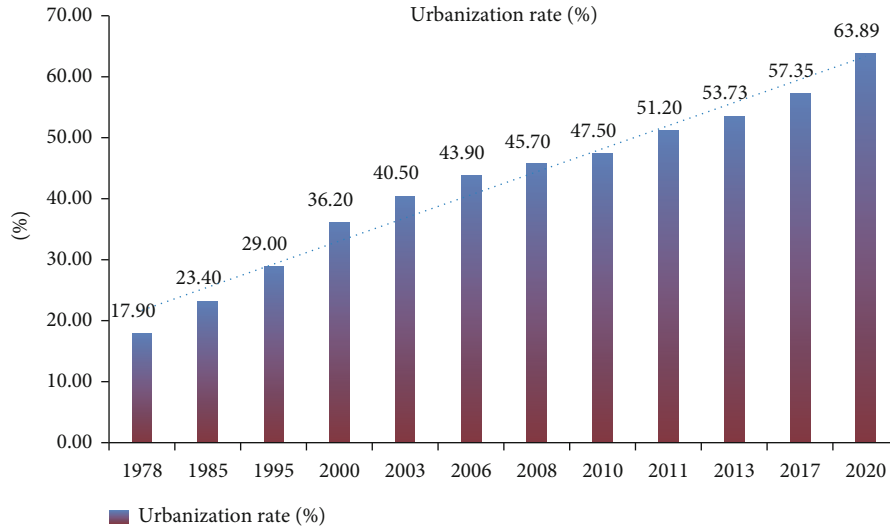
Figure 3: Development of China's urbanization process.

the ratio of the urban population (or urban nonagricultural population) to the total population. The formula is as follows:

$$CU = \frac{U}{C} * 100\%, \tag{19}$$

where CU represents the level of urbanization, C represents the total population, and U represents the urban population. Towns and villages are the two basic forms of human settlements, and their essence is the agglomeration of population in space. From the perspective of population aggregation, the difference between towns and villages lies in the fact that towns have large populations, large scales, and high densities, and the opposite is true in rural areas [29]. Population urbanization is the process of population transfer and agglomeration from rural to urban areas. It is the result of the combined effect of the "pull force" of cities and towns and the "push force" of rural areas. It is the essence of urbanization.

Finally, the compound index method is introduced, which refers to selecting several or more indicators that reflect the various characteristics of urbanization, and by calculating the weights of each indicator and summing them, the total score representing the comprehensive level of urbanization in a country or region is obtained. The mathematical expression of this method is as follows:

$$P = \sum F_i G_i, \tag{20}$$

where P refers to the comprehensive level of urbanization, F_i refers to the value of various indicators in urbanization, and G_i refers to the weight corresponding to each indicator. The compound index method is to overcome the shortcomings and limitations of the single index method, trying to measure the comprehensive level of urbanization from multiple perspectives of the connotation of urbanization [30]. Although the compound index method can fully reflect the

connotation of urbanization, its biggest disadvantage lies in its strong pertinence and weak versatility.

2.2.3. The Development and Content of New Rural Urbanization. With the continuous development of society, the process of urbanization in rural areas has been accelerating. With the continuous development of urbanization, rural infrastructure has been improved, basic housing conditions have been improved, and the presence of large industrial and commercial enterprises has provided a large number of employment opportunities for people in rural areas. However, with the development of urbanization, farmland resources in rural areas are continuously lost, environmental pollution has increased, and large numbers of rural people have migrated to cities. Figure 4 shows the problems caused by the process of rural urbanization in some areas.

In the process of rural urbanization development, five requirements must be followed, namely, integrating urban civilization on the basis of protecting rural culture, integrating urban-rural integration with local characteristics, new-type urbanization must focus on environmental protection, and new-type urbanization. When the "elements" are pushed forward neatly, the reform of the land management system must be followed up. Figure 5 is a schematic diagram of the five requirements for the development of rural urbanization.

2.2.4. Characteristics of Urbanization. First, people are the core of development. The core of the scientific concept of development is people-oriented. The new type of towns urges cities to provide complete basic public services; solve the problems of difficult medical treatment, expensive medical treatment, and difficulty in schooling; and realize the equalization of rural residents in pension insurance, medical treatment, salary level, children's education, housing, and comprehensive coverage. The permanent population of the city enables the vast number of migrant workers entering the city to also enjoy the public services that urban

Land pollution   Air pollution   Migration

FIGURE 4: Part of the problems caused by the process of rural urbanization.

The integration of rural culture and urban culture   Local specialties   Environmental protection

Rural urbanization

Land management   Overall advance
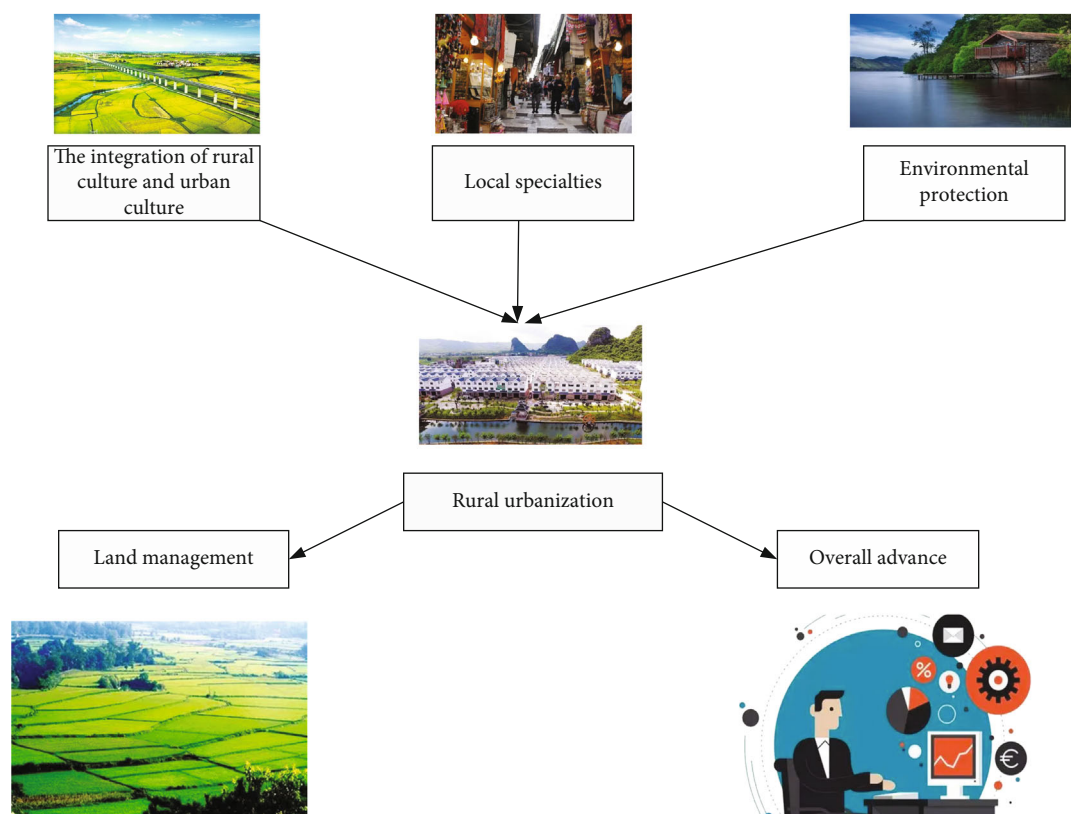
FIGURE 5: Five requirements for the development of rural urbanization.

Before cleaning   After cleaning
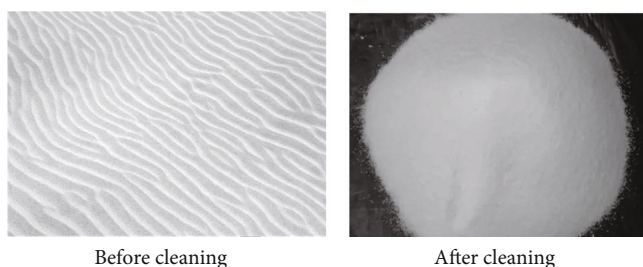
FIGURE 6: Comparison of fine sand before and after treatment.

residents should have and then live and work in peace and contentment.

The second point is the intensification of development models. Intensive development refers to improving labor productivity by improving technology and improving man-agement methods, continuously reducing energy consumption and production costs, and improving the quality and efficiency of production factors to achieve economic growth.

The third point is to coordinate urban and rural development. Traditional urbanization refers to the transfer of rural

TABLE 1: World demand for several commonly used plastics.

Plastic type	1990/ 10,000 tons	2010/ 10,000 tons	2016/ 10,000 tons	26-year growth rate
HDPE	1200	3590	4690	4.6
PVC	1870	3610	5470	6.0
EPS	280	620	750	5.2
PA	200	360	400	5.3
PET	270	1650	2130	5.1
LDPE	1980	4020	4970	4.1
PP	1390	5190	6890	5.2
ABS, ASA	380	830	960	4.1
PC	150	440	510	3.8
PU	560	1290	1560	5.4
Total	9180	22770	30210	

population to cities, and the indicator to measure the level of urbanization is also the proportion of urban permanent residents to the total population of the city. The urbanization model that sends samples can be said to be a "population transfer" urbanization path. However, urbanization is also a comprehensive indicator that reflects the level of economic development of a region. The new urbanization believes that as the speed of urbanization continues to accelerate, the urban industrial structure is continuously adjusted and further optimized, and the economic links between cities and regions become closer. The flow of resources between urban and rural areas is more convenient and effective, the income gap between urban residents and rural residents will continue to shrink, basic social welfare will be equalized, development barriers between urban and rural areas will be eliminated, and the integrated development of urban and rural areas will be truly realized. The coordinated development of urban and rural areas is to maintain equal emphasis on urban and rural areas and narrow the gap. The two forms of social and economic spatial organization of urban and rural areas cannot be homogenized. The construction of new rural areas must maintain the local characteristics and original features of rural areas. Persisting in the coordinated development of urban and rural areas and urban radiation and driving rural development and rural promotion and support for the rise of cities are an effective way to enhance the overall economic and social development of a country and region, and it is also the only way to long-term development.

The fourth point is the sustainability of development. The new urbanization adheres to the premise of "ecological protection" and achieves simultaneous urbanization in the four aspects of population, society, economy, and land. With the advancement of new urbanization, the protection and construction of urban ecology should be equally emphasized, industrial upgrading should be accelerated, the development of modern service industries and modern agriculture should be accelerated, the gap between urban and rural areas should be continuously narrowed, and the

fruits of social development can be shared by all, and the rational development and utilization of energy should be achieved by controlling the rate of economic growth. Coordinating the relationship between man and nature with resources effectively curbs the "urban diseases" caused by traditional urbanization, such as traffic congestion, environmental degradation, and polarization between the rich and the poor, so as to achieve an orderly, healthy, and sustainable development of towns.

2.3. New PVC/Fine Sand Imitation Stone Composite Material. The new PVC/fine sand imitation stone composite material is a new composite material made by combining PVC material and fine sand. This material is superior to traditional composite materials in terms of heat resistance, scalability, and impact resistance. This article mainly introduces the production of the composite material.

2.3.1. Preliminary Treatment of Fine Sand. The fine sand we see is basically free of impurities, and the sand grains are relatively regular, but it cannot be denied that some sand grains are attached to the surface of yellow-brown. In the pretreatment of fine sand, it is first necessary to rinse with water to remove the mud and attachments on the surface of the fine sand and to increase the twisting force between the surface of the fine sand and the PVC molecular chain before use. In order to make the surface of the fine sand look rough and concave, alkali immersion cleaning is performed. After these cleaning steps are completed, polar chemical bonds will be formed on the surface of the fine sand. Figure 6 is a comparison diagram of fine sand before and after cleaning:

2.3.2. Pretreatment of PVC/Fine Sand Imitation Stone Composite Material. The first step is to modify the surface of the fine sand and use a coupling to correct the surface of the pretreated fine sand. Increase the friction force indicated by the fine sand, make the reinforced material (fine sand) compatible with the matrix (PVC), and improve the performance effect of promoting various characteristics of the composite material after forming. Secondly, the required components of the composite material are proportioned, and the dyeing treatment is carried out. According to the performance requirements of composite materials, the matrix can be divided into one or more types using polymer compounds. As a reinforcing material, the fine sand and the addition amount can also be adjusted in a wider range according to different usage requirements. The general purpose is to add to the quality of PVC and fine sand at a ratio of 1 : 3 and use other additives such as composite heat stabilizers. A variety of color series using organic pigments is to dye the modified sand and the dyeing of the mixture of PVC and sand (or pure PVC) to have a better effect and also make the color of the composite material uniform and bright. The third step is to use an internal mixer to mix the modified and dyed sand and PVC and add plasticizers for mixing and preplasticization and thermal stability to compress them. It can also be molded by extrusion molding, injection molding, and other methods. Finally, there is the surface treatment part. The surface treatment uses
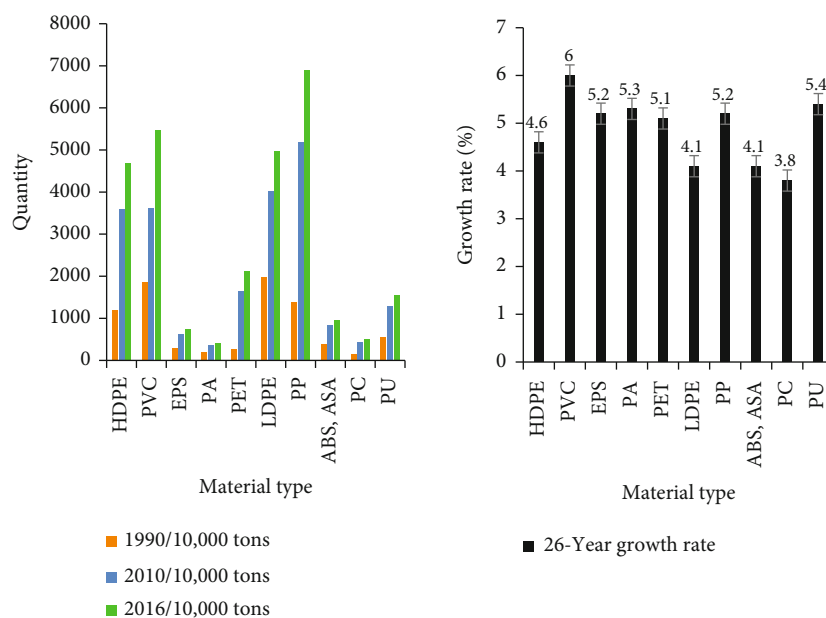
FIGURE 7: Changes in world demand for several common plastics.

PVC/fine sand composite material to evenly disperse the fine sand particles on the substrate. The color of the fine sand particles and the accumulation state of the particles will be changed by the corresponding process. The surface of the composite material can show the texture of various sandstones. Its appearance can be made into a smooth surface with limited molding once, or it can be formed only once.

3. Experimental Design and Result Analysis of New PVC/Fine Sand Imitation Stone Composite Materials and Promotion of Rural Urbanization Construction

3.1. Investigation and Result Analysis of Changes in the Consumption Demand of PVC Materials. The demand for plastics is increasing worldwide. According to the relevant data of the world plastics industry, from 1990 to 2016, all kinds of plastics in the world have been growing steadily. Table 1 shows the global demand for some commonly used plastics.

According to the latest data report from an agency in the USA, the global demand for plastic pipes has steadily increased at an annual rate of 8.5% from 2013 to 2017. Among them, chlorinated polyethylene is a resin suitable for manufacturing pipes. PVC is an organic polymer compound polymerized by vinyl chloride under the condition of a starting agent. It is one of the world's five main general purpose plastics and is supported in all fields. It is now a plastic variety second only to polyvinyl chloride and polypropylene.

According to Table 1, we can get the world demand change diagram of several commonly used plastics around the world, as shown in Figure 7.

TABLE 2: Vicat softening temperature table of common plastics.

	Minimum softening temperature	Maximum softening temperature
Polyvinyl acetate	35	85
Polyoxymeth	165	185
Polystyrene	70	115
Polypropylene	160	170
Polyvinyl chloride	60	85
Nylon12	170	180
Compound PVC	90	110

From Figure 7, we can see that the main market shares are polyethylene plastic (PE), polypropylene plastic (PP), polyvinyl chloride plastic (PVC), and polystyrene plastic (PS), and the future of plastics in the market Demand will also continue to expand. Among them, PVC has the fastest growth rate, reaching a growth rate of 7%.

3.2. Test and Analysis of the Heat Resistance Performance of the New PVC/Fine Sand Imitation Stone Composite Material. Vicat softening temperature is an important index for evaluating the heat resistance of materials and reflecting the physical and mechanical properties of products under heating conditions. The higher the Vicat softening temperature of the material, the higher the dimensional stability of the material when heated, the lower the possibility of thermal deformation, and the higher the heat resistance of the material. Table 2 is the Vicat softening temperature table of some common plastics.
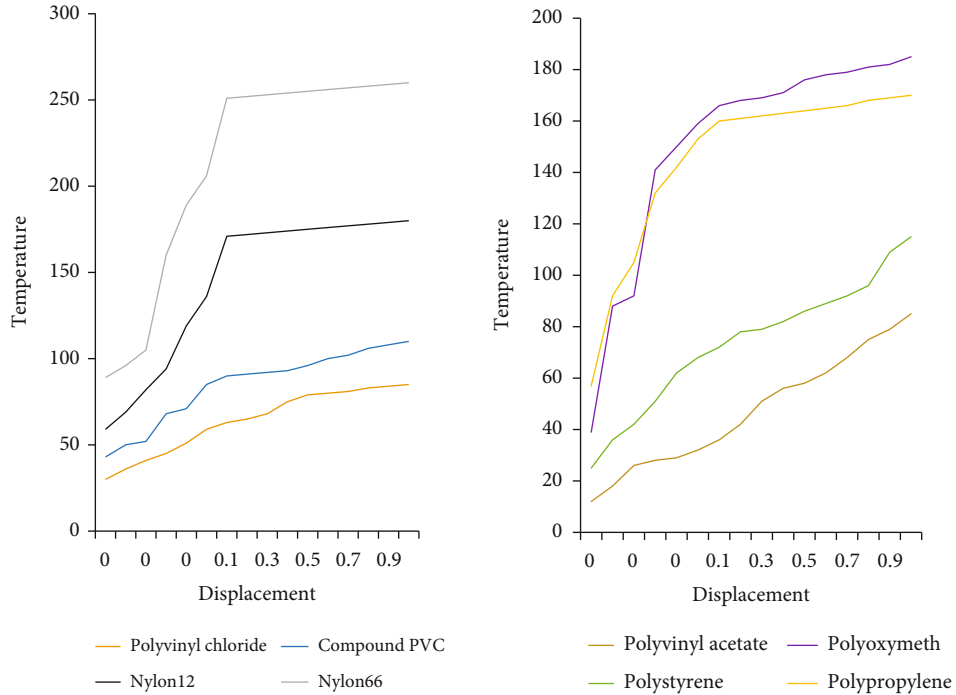
FIGURE 8: Comparison of Vicat softening temperature of some materials.

According to Table 2 and related literature data, we can get the Vicat softening temperature comparison chart of some plastics, as shown in Figure 8:

According to Figure 8, we can conclude that the Vicat softening temperature of some materials such as polyoxymethylene, polypropylene, and nylon 12 exceeds 160°C, while the Vicat softening temperature of ordinary PVC materials is 63°C. The average Vicat softening point of the sand imitation stone composite material is 103°C. Although materials such as polyoxymethylene and polypropylene have higher heat resistance than PVC materials, these materials are not suitable for ordinary construction. Although the heat resistance of traditional PVC materials is not high, it also meets the requirements of modern and ordinary construction. With the development of new PVC composite materials, its heat resistance is higher than that of ordinary PVC materials, so it has a wider range of applications and is more popular than traditional PVC materials. Due to its high chemical stability, it can be used to make anticorrosion pipelines, pipe fittings, oil pipelines, centrifugal pumps, and blowers. The rigid board of PVC is widely used in the chemical industry to make the lining of various storage tanks, corrugated boards of buildings, door and window structures, wall decorations, and other building materials. Due to its excellent electrical insulation properties, it can be used in the manufacture of plugs, sockets, switches, and cables in the electrical and electronic industries.

3.3. Comprehensive Performance Test and Result Analysis of the New PVC/Fine Sand Imitation Stone Composite Material.

In order to better test the various properties of the new PVC/fine sand imitation stone composite material, we conducted related experiments on the composite mate-

TABLE 3: Compressive strength performance test table.

	Test result 1	Test result 2	Average value
1	9.2	9.6	9.4
2	8.6	9.0	8.8
3	10.8	10.4	10.6
4	16.4	15.2	15.8
5	18.6	19.6	19.1
6	12.9	13.1	13.0

TABLE 4: Scale performance test table.

	Test result 1	Test result 2	Average value
1	98	112	105
2	152	156	154
3	182	184	183
4	194	206	200

rial's compression resistance, abrasion resistance, and scalability. Table 3 and Table 4 are the compressive strength performance test table and the expansion performance test table of the new PVC/fine sand imitation stone composite material, respectively.

According to the experimental results in Table 3 and Table 4, it can be concluded that the average compressive strength of the new PVC composite material is higher than $9KJ/m^2$, and the average value of its expansion performance is greater than 100 MPa. The reason for the large difference
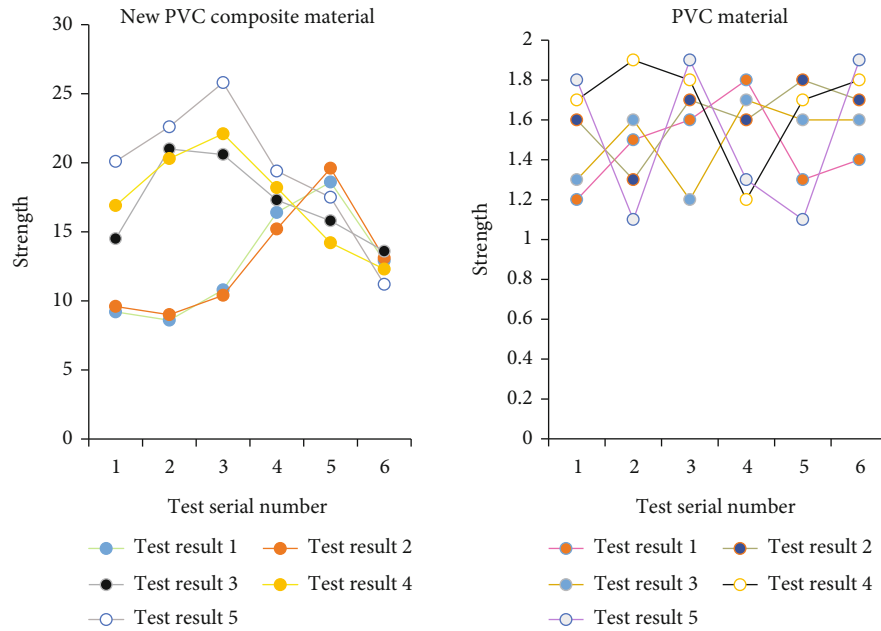
FIGURE 9: Comparison of the compressive strength of the new and old PVC materials.

between the experimental data of the same material is that the given pressure is quite different. According to some other experimental data, we get a comparison chart of the compressive strength of the new PVC composite material and the compressive strength of ordinary PVC, as shown in Figure 9:

According to Figure 9, we can find that the compressive strength of the new PVC composite material is more than 400% higher than that of the ordinary PVC material. Therefore, the application range of the new PVC fine sand imitation stone composite material in the construction of rural urbanization will be much larger than that of ordinary PVC materials. The two properties of pressure resistance and elasticity can be regarded as outstanding features of the new PVC/fine sand imitation stone composites.

3.4. Rural Urbanization Survey and Result Analysis. This survey is aimed at a certain province in central China. We have investigated the changes in population and urban size in the development of rural urbanization in this province. We analyze from three perspectives: population, number of towns, and number of companies. The specific survey results are shown in Table 5:

According to Table 5, we can see that with the development of rural urbanization in this province, the number of rural urban population has increased, and the number of industrial enterprises in rural urban areas is also increasing. According to some data we have, we have obtained the changes in China's urban population over a period of time, as shown in Figure 10:

According to Figure 10, we can see that between 2008 and 2015, the proportion of urban population has increased by 10%, and the number of people absorbed by the eastern region far exceeds that of other regions, accounting for more than 70% of the total population. With the acceleration of

TABLE 5: Changes in various factors in rural urbanization.

	Population	Number of towns	Number of companies
2014	2501000	3	15
2015	2543000	4	21
2016	3620100	5	29
2017	3692001	7	35
2018	3764100	9	41
2019	3859000	12	48
2020	3964001	15	55
2021	4042100	17	64

the urbanization process, the vigorous construction of various infrastructures, the development of houses, and the development of industry, people's demand for new PVC materials will gradually increase.

4. Discussion

This article is devoted to the research of the new PVC/fine sand imitation stone composite material, and the development of the new PVC/fine sand imitation stone composite material is applied to the feasibility study of our rural urbanization. We not only discussed the new PVC/fine sand imitation stone composite material, but also studied the preparation material and preparation process of the new PVC/fine sand imitation stone composite material. At the same time, we also conducted research and analysis on our urbanization development process and other aspects. In this article, we have analyzed the demand for PVC materials. Through the study of the new and old PVC materials, the results show that the new PVC/fine sand imitation stone
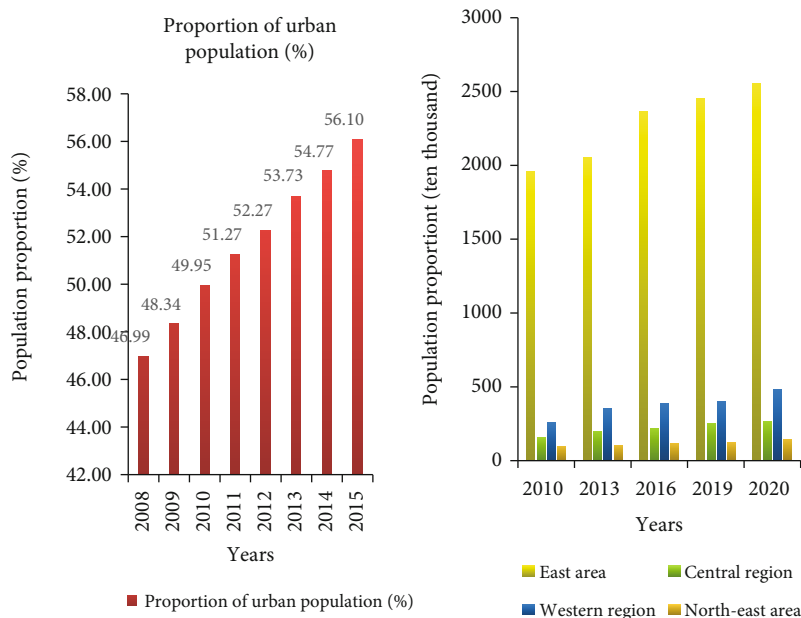
Figure 10: Urban population change map.

composite material is more in line with the product's compressive strength and expansion performance.

Through the analysis of the case in this article, we can conclude that the development and application of the new PVC/fine sand imitation stone composite material are more conducive to rural urbanization. In the process of urban construction, people can apply the new PVC/fine sand imitation stone composite material to our house construction, house decoration, parks, bridges, and guardrails. By using the new PVC/fine sand imitation stone composite material, not only can it improve its compression resistance, abrasion resistance, and heat resistance, but the appearance of the new PVC/fine sand imitation stone composite material is more tactile and cost-effective. It is cheaper than other materials.

This article starts with the global demand for PVC materials. Through the changes in demand for PVC, the performance test, and analysis of the new PVC/fine sand imitation stone composite material, the advantages of the new PVC/fine sand imitation stone composite material in the rural urbanization construction are studied. Research and analysis show that the new PVC/fine sand imitation stone composite material has more advantages in terms of comprehensive performance, use, cost, and appearance and has more application markets in rural urbanization.

5. Conclusions

Through the research and analysis of the results of the experiments and cases in this article, we have come to an important conclusion: With the continuous development of society, the process of rural urbanization is also developing rapidly, and China's urbanization rate increased during 2008-2015 alone, by 10%. The development of urbanization is indispensable to the construction of various infrastruc-

tures in cities and towns, and the new PVC/fine sand imitation stone composite materials have also played an indispensable role in these constructions. Our research shows that the compressive performance of the new PVC/fine sand imitation stone composite material is 400% higher than that of the traditional PVC material, and there has been a lot of improvement in the elasticity of the material. In the construction of urbanization, more use of new PVC/fine sand imitation stone composite materials can not only improve the reliability of the building, but also reduce the construction cost of the building. While the above conclusions are obtained in this paper, due to the limitation of time, energy, and processing conditions, there are still some imperfections in the experiment, which need to be further improved.

Data Availability

No data were used to support this study.

Conflicts of Interest

The authors declare that there are no conflicts of interest regarding the publication of this article.

References

[1] P. Wang, T. Yao, Z. Li et al., "A superhydrophobic/electrothermal synergistically anti-icing strategy based on graphene composite," *Composites Science and Technology*, vol. 198, article 108307, 2020.

[2] S. K. Goodall, "Rural-to-urban migration and urbanization in Leh, Ladakh," *Ladakh. Mountain Research & Development*, vol. 24, no. 3, pp. 220–227, 2004.

[3] M. Arouri, A. B. Youssef, and C. Nguyen, "Does urbanization reduce rural poverty? Evidence from Vietnam," *Economic Modelling*, vol. 60, pp. 253–270, 2017.

[4] D. Oke, K. G. Bokana, and O. A. Shobande, "Some correlates of rural-urban led urbanization in Lagos, Nigeria," *Review of Urban & Regional Development Studies*, vol. 29, no. 3, pp. 185–195, 2017.

[5] Y. Guo, J. Zhu, and X. Liu, "Implication of rural urbanization with place-based entitlement for social inequality in China," *Cities*, vol. 82, pp. 77–85, 2018.

[6] B. Dan-Asabe, S. A. Yaro, and D. S. Yawas, "Micro-structural and mechanical characterization of doum-palm leaves particulate reinforced PVC composite as piping materials," *AEJ-Alexandria Engineering Journal*, vol. 57, no. 4, pp. 2929–2937, 2018.

[7] A. S. Sacramento, F. Moreira, J. L. Guerreiro, A. P. Tavares, and M. G. F. Sales, "Novel biomimetic composite material for potentiometric screening of acetylcholine, a neurotransmitter in Alzheimer's disease," *Materials Science and Engineering*, vol. 79, no. oct., pp. 541–549, 2017.

[8] O. N. Lyubimova and M. A. Barbotko, "Modeling of heat transfer due to induction heating of laminated glass-metal materials," *Thermophysics and Aeromechanics*, vol. 28, no. 1, pp. 87–102, 2021.

[9] N.'. A. Yusof, S. S. M. Ishak, and R. Doheim, "An exploratory study of building information modelling maturity in the construction industry," *International Journal of BIM and Engineering Science*, vol. 1, no. 1, pp. 6–19, 2018.

[10] S. Han, ""Hollow Village" evolution and policy control from the perspective of rural urbanization: a case study of Jiangsu Province," *Asian Agricultural Research*, vol. 3, no. 264, pp. 26–30, 2016.

[11] H. E. Unal, U. Birben, and F. Bolat, "Rural population mobility, deforestation, and urbanization: case of Turkey," *Environmental Monitoring and Assessment*, vol. 191, no. 1, pp. 1–12, 2019.

[12] L. Christiaensen and M. Gindelsky, "Demography, urbanization and development: rural push, urban pull and urban push?," *Journal of Urban Economics*, vol. 98, no. Mar., pp. 6–16, 2017.

[13] T. Isobe, T. Seike, Y. Kim, A. Ito, and Y. Harada, "Analyzing the material flow of PVC scrap in East Asia," *Journal of Life Cycle Assessment Japan*, vol. 12, no. 3, pp. 196–207, 2016.

[14] A. Banawi, O. Aljobaly, and C. Ahiable, "A comparative review of building information modeling frameworks," *International Journal of BIM and Engineering Science*, vol. 2, no. 2, pp. 23–48, 2019.

[15] A. Uherkova, Z. Adamec, J. Kadavý, M. Kneifl, and R. Knott, "Coppice-with-standards between urbanization and rural development of forestry," *Pub Recreat Lands C*, vol. 2018, pp. 85–89, 2018.

[16] X. Cui, J. Xiao, Y. Wu et al., "A graphene composite material with single cobalt active sites: a highly efficient counter electrode for dye-sensitized solar cells," *Angewandte Chemie*, vol. 128, no. 23, pp. 6820–6824, 2016.

[17] X. Cui, J. Xiao, Y. Wu et al., "A graphene composite material with single cobalt active sites: a highly efficient counter electrode for dye sensitized solar cells," *Angewandte Chemie International Edition*, vol. 55, no. 23, pp. 6708–6712, 2016.

[18] H. Chen, Y. Xu, J. Yang, and Y. Liu, "A novel discrete computational tool for microstructure-sensitive mechanical analysis of composite materials," *Materials Science & Engineering A*, vol. 659, pp. 234–241, 2016.

[19] D. Oliveira, L. A. Calixto, I. M. Fukuda et al., "Compatibility of polyvinyl chloride (PVC) medical devices and other polymeric materials with reactive ion etching (RIE) and inductively couple plasma (ICP) sterilization using a quality by design (QbD) approach," *Journal of Pharmaceutical Innovation*, vol. 13, no. 2, pp. 110–120, 2018.

[20] P. Wang, S. Wang, X. Zhang et al., "Rational construction of CoO/CoF2 coating on burnt-pot inspired 2D CNs as the battery-like electrode for supercapacitors," *Journal of Alloys and Compounds*, vol. 819, p. 153374, 2019.

[21] Y. Zhang, W. Ni, and Y. Li, "Effect of siliconizing temperature on microstructure and phase constitution of Mo–Mosi2 functionally graded materials," *Ceramics International*, vol. 44, no. 10, pp. 11166–11171, 2018.

[22] K. Oesterreichische and G. Zeitschrift, "Die Starken der Natur nutzen Endlosfaser-PVC-Composites sorgen fur uberragende Materialeigenschaften," *Oesterreichische kunststoff zeitschrift*, vol. 47, no. 3/4, pp. 56-57, 2016.

[23] A. Y. Tzivadze, A. Y. Fridman, E. M. Morozova et al., "Materials based on carbon-filled porous layers of PVC cyclam derivatives cross-linked with the surfaces of asbestos fabric fibers," *Russian Journal of Physical Chemistry A*, vol. 90, no. 8, pp. 1644–1649, 2016.

[24] D. Trichet, E. Chauveau, and J. Fouladgar, "Asymptotic calculation of equivalent electromagnetic and thermal properties for composite materials," *IEEE Transactions On Magnetics*, vol. 36, no. 4, pp. 1193–1196, 2000.

[25] J. Huang, "Empirical study on effects of different types of urbanization on consumption structure of rural residents in China," *Asian Agricultural Research*, vol. 6, pp. 30–34, 2017.

[26] D. Palumbo, R. D. Finis, G. P. Demelio, and U. Galietti, "Study of damage evolution in composite materials based on the thermoelastic phase analysis (TPA) method," *Composites Part B Engineering*, vol. 117, pp. 49–60, 2017.

[27] A. R. Ghasemi and M. Moradi, "Low thermal cycling effects on mechanical properties of laminated composite materials," *Mechanics of Materials*, vol. 96, pp. 126–137, 2016.

[28] I. Zlotnikov, E. Zolotoyabko, and P. Fratzl, "Nano-scale modulus mapping of biological composite materials: theory and practice," *Progress in Materials Science*, vol. 87, no. JUN., pp. 292–320, 2017.

[29] H. Li, Y. Gong, C. Fu et al., "A novel method to prepare a nanotubes@mesoporous carbon composite material based on waste biomass and its electrochemical performance," *Journal of Materials Chemistry A*, vol. 5, no. 8, pp. 3875–3887, 2017.

[30] B. Salvadori, E. Cantisani, M. P. Colombini, and C. G. R. Tognon, "Painted fiberglass-reinforced contemporary sculpture: investigating composite materials, techniques and conservation using a multi-analytical approach," *Applied Spectroscopy*, vol. 70, no. 1, pp. 174–185, 2016.

Hindawi

Research Article
Optimal Design of Sports Event Timer Structure Based on Ferroelectric Memory

Jiannan Liu [1] and Cailie Chen [2]

[1]Sport Department, Chongqing Jiaotong University, Chongqing 400074, China
[2]College of Mechanical and Vehicle Engineering, Chongqing University, Chongqing 400000, China

Correspondence should be addressed to Cailie Chen; chencailie@cqu.edu.cn

Sports events are an indispensable part of popularization and strong entertainment and can promote the physical and mental health of the people and the construction of cultural and spiritual civilization. Therefore, it is necessary to use a timer to record and analyze data during the game. In the traditional sense, the game timer is a fixed system. And now we can design sports event timer operations through mobile phones, computers, and other equipment to assist in the calculation of game time and competition. Ferroelectric memory is a kind of random access memory, which combines the fast read and write access of dynamic random access memory with the ability to retain data. Based on this, the ferroelectric memory timer proposed in this paper is intended to improve the accuracy and fairness of sports events. Therefore, this article has tested the function of the timer designed in this article by studying the ferroelectric memory and experimental construction and testing methods and finally concluded that the design is reasonable, but there is still a problem of data susceptibility. The experimental results show that there is a certain gap between the time interval measurement level of the timer and SR, the difference is 47 ps, the pulse width difference is controlled at 0.004, and the measurement uncertainty of timer interval is better than 60 ps. This shows that the timer can be applied, but it needs further improvement.

1. Introduction

Ferroelectric memory has the characteristics of small size and low power consumption. It has a wide frequency range used in sports competitions, mainly used for timing sports events, and can also be used as other equipment such as stylus pens and other physical sports counting tools. Its internal structure is relatively simple, the volume is relatively small, the performance is stable, and the anti-interference ability is very good. Large storage space, small size, and light weight are one of the main characteristics of ferromagnetic materials. This feature is also closely related to the application value: when used in sports timers, it can not only realize the data storage function but also effectively improve the efficiency of the game.

The sports event timer is a device that can record the time of the event. It consists of a display screen, buttons, and a timer. Count according to the time of the sporting event and display it on the display screen, so that you can visually see all the data recorded on the display. This not only improves work efficiency but also avoids erroneous actions. Specifically, it releases the clock information in real-time and accurately through the front-end multiseed clock equipment, so that the time of each intelligent system is centralized and synchronized. After the game is over, the statistics and analysis of the data in the game timer are also a technical method [1]. In order to achieve the structural optimization design of the sports game timer, it is necessary to implement its technical indicators on the software.

When the traditional timer is used for sports competitions, the data to be displayed is usually first input to the display and then displayed on the display. Although this has the advantages of intuitiveness and convenient operation. But to a certain extent, it will give people a feeling of cumbersome, inconvenient, and error-prone. So there are many researches on sports timers and ferroelectric memory. Memory allows

designers to write data to nonvolatile memory faster and more frequently at a lower price [2]. Among them, Li et al. took the FM28V100 ferroelectric memory model as the research object, conducted electron radiation experiments, and studied the damage law of the total radiation dose of the ferroelectric memory under different working methods and different radiation sources [3]. An'an et al. conducted an experimental study on the single-event effects of medium and high energy protons on two commercial ferroelectric memories and found that one of the devices exhibited single-event reversal and functional interruption under proton irradiation [4]. Feizhuan et al.'s traditional basketball game uses manual scoring or flops and uses a timer to complete the game timing. This timing and scoring involve many human factors, which affect the fairness of the game and the fairness of performance to a certain extent [5]. Pengcheng combined the NBA game rules and put forward a 24-second countdown overall plan for basketball games based on the AHDL language [6]. In order to overcome the shortcomings of existing microcontroller timer applications that cannot be paused or restarted, Kang describes a timer that uses external interrupts to pause or restart [7]. Xiaocheng et al. proposed the design requirements of basketball timers according to FIBA's requirements for the DE10_Lite timer and functions of Uniview Technology [8]. In sports events, the accuracy of the timer is a symbol of fairness in the arena. The ferroelectric memory has the characteristics of less interference, so it is a way of choice to apply it to the timer.

The innovation of this paper is to compare the advantages between them by studying the types of ferroelectric memory, ferroelectric film capacitors, ferroelectric storage technology, and structure and functional principles, then propose a sports timer based on ferroelectric memory, and carry out this system structure design and analysis. Through analysis and design and further experimental verification, the designed timers are compared in terms of pulse width and time accuracy. Thereby, the experimental data results and conclusions can be drawn.

2. The Structure Timer of Sports Event Timer Based on Ferroelectric Memory

2.1. Ferroelectric Memory

2.1.1. Classification of Ferroelectrics. Ferroelectric crystals include gallium arsenide, lamination, multijunction, and perovskite. Among all ferroelectric crystals, the perovskite structure is the most typical and common structure. Although it was later discovered that CaTiO3 is actually a twisted perovskite structure, the name still exists [9, 10].

2.1.2. Ferroelectric Film Capacitor. Ferroelectric film capacitors are a type of flat capacitors. Using the knowledge of dielectric physics, we know that the charge H stored in a capacitor can be expressed as

$$H = S \cdot C. \tag{1}$$

Among them, S is the area of the capacitor plate, and C is

the electric displacement vector in the ferroelectric film. The definition of electric displacement vector is

$$C = M(F) + \theta_0 F, \tag{2}$$

where F is the electric field strength (physical quantity indicating the strength and direction of electric field), and the θ_0 is dielectric constant. M is the polarization intensity, which is a nonlinear function of F. The electric field strength F can be expressed as

$$F = \frac{v}{t}, \tag{3}$$

where v is the voltage and t is the thickness of the ferroelectric film. The polarization intensity M can be expressed as

$$M(F) = \theta_0 \left(\theta_q(F) - 1 \right) \cdot F. \tag{4}$$

θ_q is the relative permittivity, which is also a function of the electric field F. Substituting formula (1) into formula (2) and taking into account that the relative permittivity of ferroelectrics is usually much greater than that, we can get

$$C(F) = \theta_0 \cdot \theta_q(F) \cdot F \approx \theta_0 \cdot \left(\theta_q(F) - 1 \right) \cdot F = M. \tag{5}$$

Substituting this approximate expression into equation (1), we can get

$$P = G_{\text{dip}} + G_F + G_g. \tag{6}$$

Formula (6) relates the microscopic physical quantity in the ferroelectric film to the macroscopic measurable charge quantity. Iron sheet structure film is composed of several grains with different sizes. The total free energy P of the polycrystalline film is composed of three parts. The surface depolarization field does work G_F, the domain wall pinning field does work G_g, and the dipole flips work G_{dip}, namely,

$$P = G_{\text{dip}} + G_F + G_g. \tag{7}$$

If the film is very thin and can only accommodate one layer of electrical domains, the polarization direction of the ferroelectric domains is perpendicular to the electrode and the orientation is the same, then:

$$F = -\frac{1}{\theta_0} M. \tag{8}$$

If the situation is a little more complicated, the polarization direction of the domains perpendicular to the interface will periodically change, and this distribution makes G_{dip} reach the minimum value. At this time, there are

$$G_F = \frac{\theta^* \cdot k \cdot M_0 \cdot v}{t}. \tag{9}$$

Among them, t is the thickness of the film, k is the width of the electric domain, M_0 is the polarization intensity in each electric domain, v is the volume of the entire film, and θ^* is a factor related to the dielectric constant. If the rolling work μ_{wall} is determined per unit area of the domain wall, the total work G_g done by the domain wall is

$$G_g = \frac{\mu_{wall}}{k} \cdot v. \qquad (10)$$

Combining formulas (9) and (10), there are

$$G_F + G_g = \frac{\theta^* \cdot k \cdot M_0 \cdot v}{t} + \frac{\mu_{wall}}{k} \cdot v. \qquad (11)$$

When formula (11) takes the minimum value, there are

$$k = \sqrt{\frac{\mu_{wall} \cdot t}{\theta^* \cdot M_0^2}}. \qquad (12)$$

From formula (12), the following conclusion can be drawn: as long as the polarization of the ferroelectric thin film is not zero, the ferroelectric domain width is a finite domain wall. Neither work nor domain width k will be 0 [11, 12].

2.1.3. The Structure and Function Principle of Ferroelectric Memory.
The function of storing data in ferroelectric memory is mainly completed by ferroelectric capacitors with thin-film ferroelectric materials as the carrier [13]. Generally speaking, ferroelectric materials do not contain "iron," but refer to ferroelectric crystals. Compared with traditional nonvolatile memory such as EEPROM and FLASH, ferroelectric memory has lower leakage current, because the data storage of ferroelectric memory is not carried out by free electrons, but by atomic polarization [14, 15]. When an electric field is applied to a ferroelectric crystal, the central atom inside the ferroelectric crystal will move and change with the distribution of the electric field. When the atom gains a certain amount of energy, the violent movement of free carriers in the crystal expands rapidly, causing the charge to collapse [16]. In this case, the polarization of the ferroelectric material is a certain function of the applied electric field. When the applied electric field disappears, the polarization of the ferroelectric material becomes stable, and the corresponding data information is stored in the ferroelectric crystal [17, 18].

Figure 1 shows the hysteresis loop block diagram of the ferroelectric capacitor and the block diagram of the ferroelectric memory. In (1), the abscissa represents the applied electric field, and the ordinate represents the polarization intensity. Figure (a) is a schematic diagram of 1T1C ferroelectric memory. Among them, the word line is connected to the gate of the transistor to control the turn-on and turn-off of the transistor. The bit line is connected to the source of the transistor. Figure (b) is a block diagram of 1T2C ferroelectric memory, the structure is similar to 1T1C ferroelectric memory [19, 20].

The manufacturing technology of ferroelectric memory integrates ferroelectric thin film process and traditional CMOS process. Ferroelectric memory not only includes a ferroelectric memory array that stores data but also includes CMOS peripheral circuits that amplify and read signals, control timing signals, and data latch functions [21, 22].

FRAM has many advantages and is suitable for embedded systems. It is a new type of memory with relatively mature industrialization technology. It can work in extreme environments and may replace Si-based devices that currently require heat preservation devices to be used in spacecraft or aerospace probes. In order to reduce launch costs or increase satellite functions, it is considered to have great potential for space applications. Compared with SRAM, although ferroelectric memory is not advantageous in terms of speed and price, from the perspective of the overall design, ferroelectric memory still has certain advantages. Ferroelectric memory is very resistant to electromagnetic radiation, elementary particle radiation, and nuclear radiation. They generally will not interfere with the stored information due to the radiation of a single charged particle, and they can withstand high dose rates of X-rays and neutrons and large total doses of radiation [23].

2.2. Sports Event Timer Based on Ferroelectric Memory.
The sports event timer based on ferroelectric memory is mainly composed of two parts: hardware circuit and software program. A simple circuit diagram is designed in the hardware part. First use a multimeter to measure whether the connection between each device and the microcontroller is correct. Then through the analysis of the data, the corresponding parameter values are obtained and displayed. At the same time, these variables can be converted into voltage signals and input to the PC terminal.

The sports event timer based on ferroelectric memory uses the digital pulse waveform to convert the data into the required signal through the analog circuit and then process it by the single-chip microcomputer. The output of the analog circuit is a sine wave, variance, time interval, and other parameter information; and in actual use, due to some uncertain factors that affect the final result, it will lead to large errors or inaccurate realization of moving objects within the measurement value range. And so on, digital integrated circuits can be used to complete data acquisition and control.

The working principle of ferroelectric memory is first, in the display, there is a sliding rheostat and two data drive boards. When a certain number appears on the display screen (red LED red light). Then connect the data line to the intermediate relay control module for data recording and storage; finally, the corresponding time, location, and other information will be displayed on the display screen for people's reference (including the time unit of sports events). The structure design of the ferroelectric memory mainly utilizes a sliding rheostat and two light-emitting diodes. The specific design is shown in Figure 2.

The game timer based on ferroelectric memory does not need to be modified in the program. First, it is simulated by software, and then, its function and implementation method
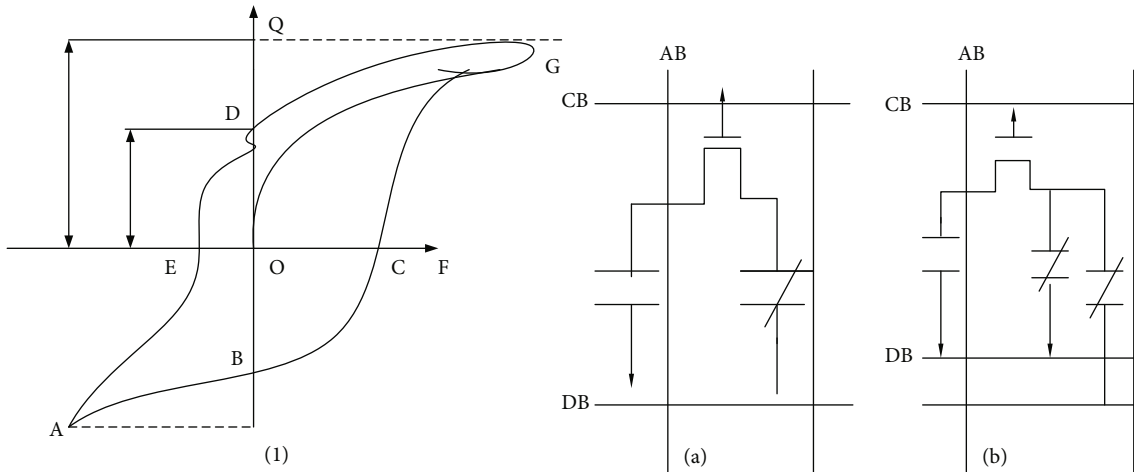
FIGURE 1: Electric circuit of ferrocapacitance and ferroelectric memory circuit structure.
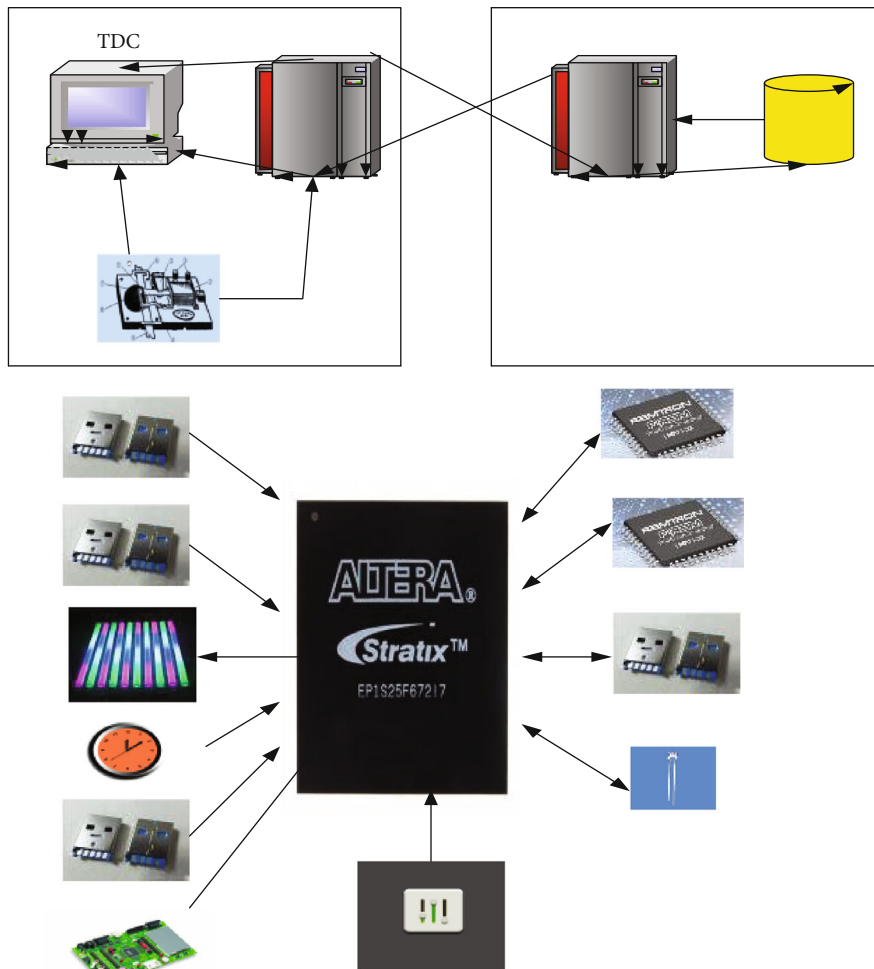
FIGURE 2: Functional block diagram of Stratix FPGA development board.

are improved. When used, the display was found to be the same as the previous design. However, because there are many interference factors in the hardware circuit that affect the display effect of the display screen and cannot save the

data content information well; second, the software part does not add the corresponding module so that it can better utilize the functions of the PC to complete the accuracy index required by timer (for example: time and speed).

2.3. *Design of Two-Step Timer.* The two-step TDC is actually not a fixed circuit structure, but a TDC design idea that combines two TDC basic structures. Usually, two structures with complementary advantages are selected for design in the basic implementation structure of TDC. In order to take into account the time resolution accuracy and dynamic range of this subject, while completing the layout design in the smallest possible area, a combination of pulse counting TDC and delay line-based TDC was selected. The two-step TDC combines the advantages of the basic clock cycle counting method and the delay line-based TDC two timing methods and can achieve both dynamic range and time resolution accuracy. The "two-step" of two-step TDC has a dual meaning. The first meaning is expressed in the structure of the TDC. The start signal and the stop signal, respectively, represent the timing start signal and timing end signal of the TDC. The two-step TDC has a two-stage structure, namely, the fine interpolator and the coarse timer. These two modules are also the two most critical modules of the two-step TDC. They have their own division of labor when measuring the time interval to be measured.

Choosing a suitable delay unit is very critical for realizing the ideal time resolution accuracy of TDC. The structures of delay units that are often used include inverters, buffers, differential inverters, and switching inverters. The inverter has the greatest advantages in terms of structure, time resolution accuracy, and area. Regarding the delay line structure, the design challenge is to ensure the linearity of the circuit. The inverter structure is single-ended input and single-ended output, which is more sensitive to noise. Using an inverter as a delay unit is bound to introduce fine interpolator greater nonideal factors. Therefore, considering the structure, time resolution accuracy, area, and antinoise ability, a differential inverter is used as the delay unit.

Based on the Cadence platform, the simulation of the fine timer is carried out. A rising edge signal is input to the fine timer during simulation, and the rising edge signal passes through the delay unit on the delay line. The position of the rising edge will lag equidistantly on the time axis, and the simulation results are consistent with the theoretical analysis. At the same time, it can be seen that after the input rising edge signal passes through the delay line, there is a delay, and the delay of each delay unit is about 186 ps. Therefore, the designed two-step TDC fine interpolator has a time resolution accuracy of 186 ps and a dynamic range of 2 ns.

The coarse adjustment timer is a circuit that can record the number of clock cycles of the reference clock, that is, the pulse timer. A binary timer can be used in the specific circuit design. The basic unit of a binary timer is an edge-type flip-flop. Among them, if you want to realize the function of clearing the output state of the coarse adjustment timer, the trigger needs to be improved.

The two-step TDC uses a coarse adjustment timer to process the time to be measured that is an integer multiple of the reference clock period, while the residual time uses a 16-bit fine interpolator for processing. Its timing error sources are the timer and the interpolator.

The work of the two key circuit modules of the two-step TDC-the fine interpolator and the coarse timer is controlled by the edge signal. The signal propagates in the circuit and will inevitably be interfered by noise, parasitics, and other factors, which will cause the signal to be distorted. One of the most straightforward ways to optimize single-shot accuracy is to increase the frequency of the reference clock. Another way to improve the single input accuracy of TDC is to interpolate the residual time, where the residual time refers to the time less than one reference clock cycle, that is, the part of the time processed by the fine interpolator in the two-step TDC.

The overall block diagram and workflow of the hardware design are shown in Figure 3. The hardware of this system includes single-chip microcomputer MSP430F149 and its peripheral circuit parts (reset circuit and clock crystal oscillator), relay part, independent button part, display part, and drive circuit part. The whole circuit is controlled by the single-chip MSP430F149; the key control mode, time, and step are driven by ULN2803; and the corresponding data is displayed on the LCD12864 display.

Driven by the clock circuit, the single-chip microcomputer can run normally and stably, mainly because of the operation of the clock circuit, which helps each component of the single-chip microcomputer to perform its own work well. This kind of operation among them is automatic. The clock circuit uses pulse signals to satisfy the operation of the hardware part. In order to proceed with the work progress of the circuit from the initial state, it is necessary to make the core parts of the system in the initial state.

For the clock circuit, from the point of view of the microcontroller, the significance of the clock circuit is to provide a signal that the circuit system can perform stably, and this signal is timed. In order to achieve such a state, two parts are required, one part is that the other part of the crystal oscillator is a matching peripheral circuit, and the so-called timing time is the timing clock of the system. Time is the timing clock of the system. The clock circuit is an oscillator, which provides a beat to the single-chip microcomputer. The single-chip microcomputer must perform various operations under the control of this beat. Therefore, the single-chip microcomputer will not work normally without a clock circuit. The clock circuit itself does not control anything. The clock circuit helps the microcontroller to work in a stable state. The subsystem clock, auxiliary clock signal, and main clock signal provide signals for the MSP430F149 microcontroller. The subsystem clock provides services for some peripheral high-speed operating circuit modules, the auxiliary clock signal provides services for some peripheral low-speed operating circuits, and the main clock signal is a normal circuit module operating in a stable state.

3. System Testing and Analysis

After the system design is completed, it is necessary to build an experimental platform to evaluate the performance of the system. First, it introduces the experimental testing methods and evaluation indicators used in this article. Then select the
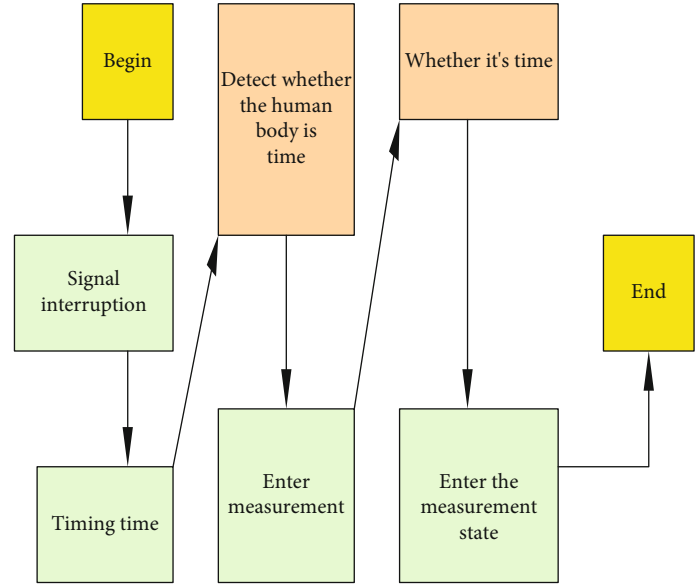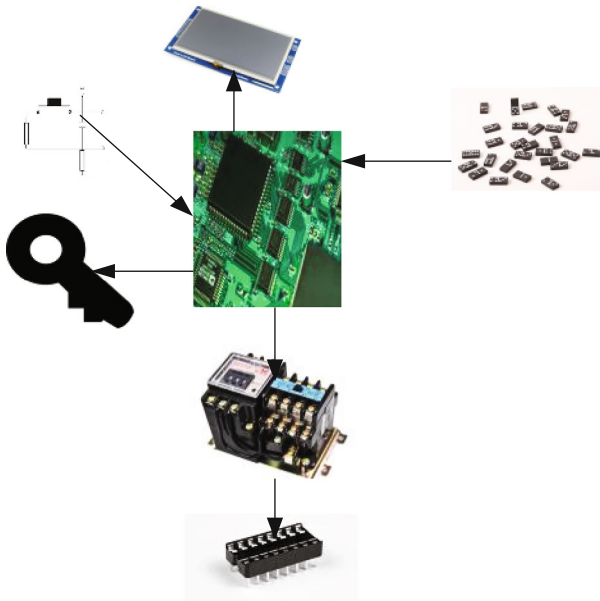
Figure 3: Overall block diagram and workflow of hardware design.

Table 1: Timer comparison with SR540 data results.

Time	Calculagraph	SR540	Time interval	Standard deviations
0	506.67	506.42	57.6/10.2	0.0562
1800	506.73	506.43	57.5/9.9	0.0573
3600	506.75	506.45	57.3/10.3	0.0596
5400	506.81	506.46	56.6/9.8	0.0654
7200	506.79	506.44	57.2/9.4	0.0725
9000	506.75	506.43	56.6/9.3	0.0849

signal source to test the accuracy of the timer's measurement. Finally, test the timer's time interval and pulse width measurement functions separately, use the test data to evaluate the performance indicators of the timer, and analyze the problems in the timer.

3.1. Test Method. The test platform with design specifications can make the test results more credible and provide a better reference for practical applications. In the field of time interval measurement, comparison method and fixed time interval measurement method are two commonly used test methods.

The comparison method is to use different measuring instruments to test the same signal source at the same time under the same external environment. The signal to be measured and the reference time are both generated by the same clock source and then transmitted to the measuring instrument through the same path, and the measurement is performed at the same time. This series of operations emphasizes the "same source." Then compare the measured results. In order to measure the performance of the developed measuring instrument, another instrument with very excellent performance is usually required. In this test platform, the measurement result of the SR540 time interval

timer with the best performance in the field of time measurement is selected as a reference for comparison.

The fixed time interval test method is to use the time interval measurement timer to measure the signal source to produce a fixed time interval without considering the cable and device delay. This method is simple to operate, and the result is more intuitive, but the signal quality of the signal source is very high. However, the accuracy of the time-to-digital conversion circuit is getting higher and higher, and the requirements for the signal source are getting higher and higher. At present, it is difficult to find a suitable signal source for testing in many cases. For this reason, this test platform does not design the realization of the fixed time interval test method separately but adopts the combination of the above two methods.

This platform uses the SR540-Timer universal time interval measurement device to compare with a channel of the timer, uses the 10 MHz signal generated by the National Time Service Center Clock Tower as the reference signal of the timer and the time base SR540, and then compares the time base of the 1 pps signal. The pulse distribution amplifier generates two signals to be measured, and each signal is sent through three channels and then sent from the other output terminal of the SR540 and the timer; the timer is connected to send the measurement results to the upper computer for processing. Different cable lengths can set different time intervals.

3.2. Evaluation Index. To design a measurement system, it is usually necessary to give the actual performance of the system, and scientific evaluation indicators are needed to evaluate the performance. In the field of time-frequency measurement, it is generally necessary to give the two indicators of system measurement deviation and measurement accuracy. Measurement deviation is usually affected by the stability of the time base, internal noise, trigger noise, and
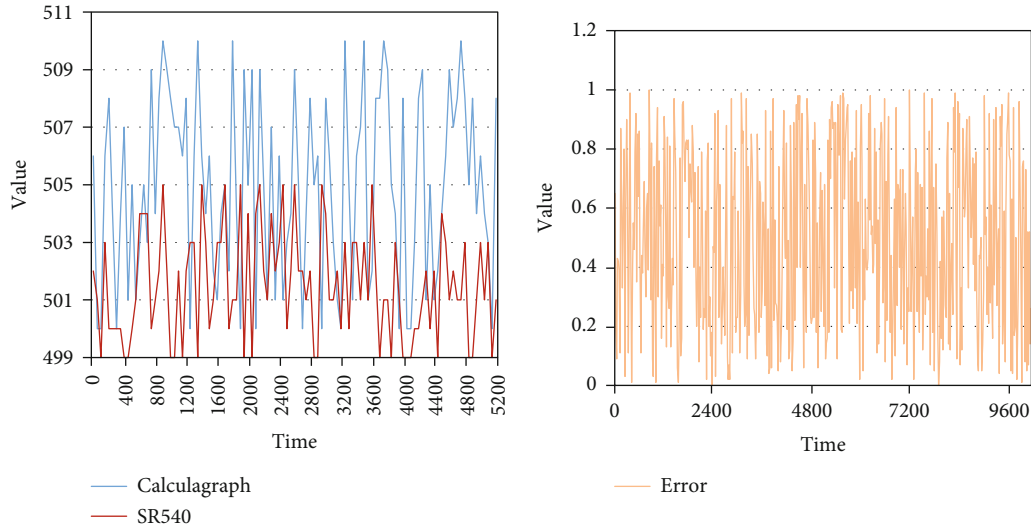
FIGURE 4: Alignment of timer and SR540 measurements and error plots.

TABLE 2: Timer and SR540 pulse width measurement contrast and error value.

Time	Calculagraph	SR540	Error
0	204.859	204.857	0.41
1000	204.857	204.856	0.45
2000	204.856	204.852	0.44
3000	204.86	204.854	0.56
4000	204.856	204.855	0.47
5000	204.854	204.853	0.45
6000	204.852	204.854	0.53
7000	204.853	204.856	0.46
8000	204.854	204.856	0.55
9000	204.855	204.857	0.5

uncertainty within the system. This concept is considered more when the "absolute" value of the measurement is more important. This paper uses the standard deviation of the experimental data to characterize the measurement accuracy of the system. This is because the designed test platform mainly uses the delay line test method, that is, two delay lines of different lengths and different delays are used to send the signal to be measured into the measurement. The channel is tested. Two different delay lines produce a fixed time interval, but the exact true value of this interval cannot be determined, so it is more appropriate to use the standard deviation as an evaluation index of measurement accuracy. The standard deviation is usually a statistic used to characterize the degree of dispersion of the system measurement value relative to the mean value.

3.3. System Test. First, analyze and evaluate the accuracy of the system measurement. Test the time interval measurement function of the timer. When measuring, the reference clock uses the 10 MHz frequency signal of the clock room of the National Time Service Center. The signal to be mea-

sured is 1 pps. The signal is delayed by a length of 100 m extension cable. The timer generally has 2-4 measurement channels, which will trigger sr540, so as to adjust the level to be consistent with the trigger level of this system.

Evaluate the accuracy of the system measurement. In the actual test, the measurement value of the SR540 can be regarded as the true value based on the test method of the comparison method, and the timer and the SR540 can be measured synchronously. Subtract the value of to get the difference between the two, which can be regarded as the accuracy of the system.

When measuring the pulse width, first, when configuring the chip, set the function to pulse width measurement, that is, configure the value of configuration register 1 to 2 f. In actual measurement, TDC-GPX2 internally connects measurement pins 1 and 3 (or 2 and 4) to an input pin (STOP1 or STOP2). The rising edge is measured by channel 1 (or 2), and the falling edge is measured by channel 3 (or 4). Then make the difference of the measurement result to get the value of pulse width.

4. Analysis of Test Results

4.1. Time Interval Measurement Performance Test. Calculate the measurement results and summarize the results with Table 1. The experimental value takes 2.5 hours of synchronized measurement results and then statistics on this measurement result. From the standard deviation statistical results, it can be seen that the timer measurement interval accuracy is 56.3 ps, and the SR540 measurement interval accuracy is 9.3 ps. It can be shown that the time interval timer can achieve a single measurement accuracy better than 60 ps, which has reached a relatively good level, but there is still a certain gap with SR540.

As shown in Figure 4, to evaluate the accuracy of the system measurement, in the actual test, the measurement value of the SR540 can be regarded as the true value based on the test method of the comparison method, and the value
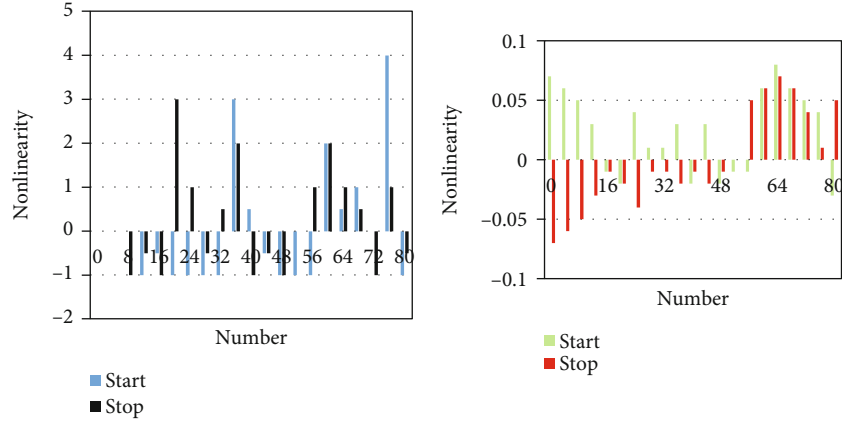
Figure 5: Start and stop differential integral nonlinear error results comparison.

Table 3: Simulation of the adjustment range of the oscillator.

VCTRL	26°C, 3 V		-50°C, 3 V	
	F	K	F	K
1	423		409	
1.2	463		432	
1.4	694		676	
1.6	789	649	767	752
1.8	892		865	
2	1100		1005	
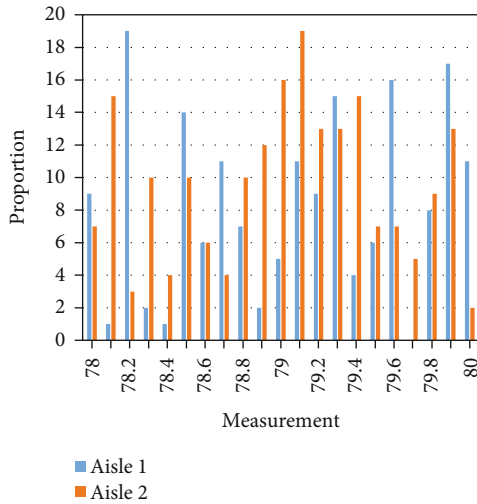
Figure 6: Probability distribution of measurement results.

measured by the timer and the SR540 synchronized measurement is subtracted. The difference between the two can be regarded as the accuracy of the system. It can be seen from the data that the accuracy test in two ways can ensure that the deviation of the system measurement is less than 495 ps.

4.2. Pulse Width Measurement Performance Test.
In terms of measurement accuracy, the measurement result of this function is still compared with the pulse width measurement result of SR620. The pulse width to be measured is the 1 pps signal of the clock room of the National Time Service Center, and the reference clock is the 10 MHz signal of the clock room. This paper randomly selects 10 data for analysis, as shown in Table 2.

In Table 2, the error is controlled below 0.6, and the pulse width measurement range is around 204.85. Among them, the timer is not much different from the SR540, and the performance basically meets the standard requirements.

4.3. Differential and Integral Nonlinear Error Test.
As shown in Figure 5, we can see the result of the differential nonlinearity error of a delay line (start), where the maximum value is 4 LSB and the minimum value is -1 LSB, where 1 LSB = 189.4 ps. It is the differential nonlinearity error of another delay line (stop), the maximum value is 3 LSB, the minimum value is -1 LSB, and 1 LSB = 173.6 ps. Start delay line's integral nonlinear error, the maximum value is 0.08 LSB, the minimum value is -0.03 LSB, and the average value of integral nonlinear error is 0.014 LSB, of which 1 LSB = 189.4 ps. The integral nonlinear error of the stop delay line, the maximum value is 0.07 LSB, the minimum value is -0.07 LSB, and the average value of integral nonlinear error is -0.03 LSB, where 1 LSB = 173.6 ps.

4.4. Oscillator Distribution Requirements.
Changes in temperature and process will affect the frequency range of the output clock signal of the circuit. In order to ensure that the frequency of the output clock signal of the circuit can reach the design value, it is usually desirable to have the oscillator tuning range within the system frequency requirement range. The details are shown in Table 3.

When the temperature changes from low to high, the threshold voltage becomes smaller and Kvco decreases. The output frequency of the oscillator increases with the increase of its control voltage, which meets the theoretical requirements.

4.5. System Multichannel Measurement Conformance Test.
This timer can measure multiple channels at the same time, so test the consistency of the measurement of different
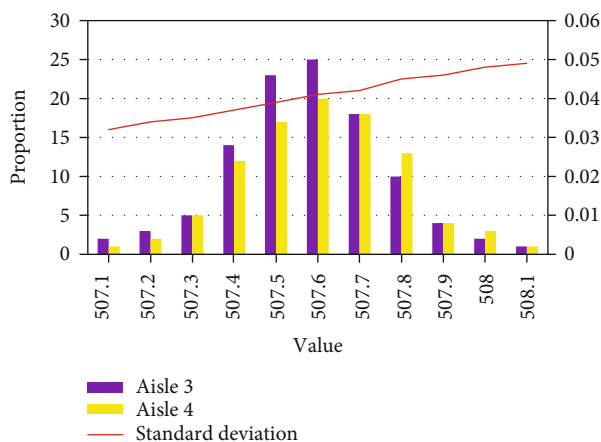
Figure 7: Multichannel measurement result distribution.

channels of the system. In this test, the second, third, and fourth channels are used to test the 100 m extension cable. Channel 2 is connected to the 1 pps signal output by the pulse distribution amplifier. Analyzing the multichannel calculation data, we get Figures 6 and 7.

It can be seen from Figure 6 that in a set of data, the fine measurement value and the final measurement result are normally distributed, indicating that the source of error in this measurement is mainly random error, but the single-channel fine measurement value is not very standardized. The normal distribution indicates that the measurement results are affected by errors other than random errors. But the final measured value still shows a more standardized normal distribution.

As shown in Figure 7, it can be seen from the statistical results of the standard deviation that the 3-channel measurement accuracy is 46.7 ps, and the 4-channel measurement accuracy is 33.2 ps. The measurement consistency of each channel is better, and the measurement accuracy is better than 50 ps. The results show a normal distribution, which further shows that the main source of noise that causes system measurement errors is random noise.

5. Conclusion

The ferroelectric memory is mainly composed of a data register, two counting units, and four output modules. The core of the device is a block circuit for timing, which includes a display, buttons, buzzer alarm indicator, and other components. During sports games, ferroelectric memory chips are used as carriers to transmit the sports event time information to the processor and save it. Then according to the program control the LED light to turn on or off the required sports data register to display the current time and start date, the end of the game, the results after the game, and the summary number after the game. Determine the size of each part and the connection relationship between each component according to the parameter values such as the movement time label and time as a reference basis. This article mainly uses the time interval measurement method and the experimental comparison method to study the equipment accu-

racy of the ferroelectric memory in the system in the sports timer. Through various experimental investigation results, it is concluded that the measurement uncertainty of the timer interval designed in this paper is better than 60 ps, the measurement data is accurate and reliable, and the signal pulse width measurement performance can be consistent with the international leading measurement equipment SR540. The timer in this article has certain fluctuations in the measurement result of the frequency signal, and its performance is not ideal. It needs to be processed by a suitable filtering algorithm to improve the frequency measurement accuracy of the timer.

Data Availability

No data were used to support this study.

Conflicts of Interest

The authors declare that there are no conflicts of interest regarding the publication of this article.

References

[1] V. Jain, M. Swami, and R. Bansal, "Exploratory data analysis on username-password dataset," *Fusion: Practice and Applications*, vol. 4, no. 1, pp. 5–14, 2021.

[2] M. Ismail, N. El-Rashidy, and N. Moustafa, "*Mobile cloud database security: problems and solutions*," *Fusion: Practice and Applications*, vol. 7, no. 1, pp. 15–29, 2021.

[3] Q. Li, J. An'an, G. Hongxia et al., "Research on 60Co gamma rays and total electron dose effects of ferroelectric memory," *Acta Physica Sinica*, vol. 67, no. 16, pp. 272–279, 2018.

[4] J. An'an, G. Hongxia, Z. Fengqi, G. Weixin, and O. Y. Xiaoping, "Experimental study on the single-event functional interruption effect induced by high-energy protons in ferroelectric memory," *Acta Physica Sinica*, vol. 67, no. 23, pp. 248–254, 2018.

[5] F. Feizhuan, D. Jing, and L. Shuai, "Design of basketball match timing and coring device based on single chip computer," *Digital World*, vol. 169, no. 11, pp. 109–109, 2019.

[6] Z. Pengcheng, "Design of 24-second countdown timer for basketball game based on AHDL language," *Electronic technology and software Engineering*, vol. 150, no. 4, pp. 81-82, 2019.

[7] F. Kang, "The application of single-chip timer in timer design," *Fujian Computer*, vol. 35, no. 5, pp. 103–105, 2019.

[8] F. Xiaocheng, L. Ping, and Z. Dehua, "Basketball timer experiment based on DE10_lite," *Journal of Electrical & Electronic Education*, vol. 42, no. 3, pp. 125–128, 2020.

[9] W. Zhiming, "Elementary school science based on concept transformation strategy exploration-record of the demonstration lesson of "making a one-minute timer"," *Teaching Management and Education Research*, vol. 3, no. 10, pp. 72–77, 2018.

[10] J. Wei, "The production of countdown timer based on action script," *Computer Knowledge and Technology*, vol. 13, no. 16, pp. 185-186, 2017.

[11] T. Zerong, "Analysis of MCS-51 single-chip stopwatch design," *Success: Education*, no. 16, pp. 35–37, 2017.

[12] Z. Chao, W. Miao, and Z. Hongxin, "Design and simulation analysis of digital circuit "stopwatch" based on Proteus," *Electronic Design Engineering*, vol. 28, no. 10, pp. 46–50, 2020.

[13] V. K. Rishu and S. A. Sinha, "Advancements in encryption techniques for enhanced data security over cloud," *Journal of Cybersecurity and Information Management*, vol. 8, no. 2, pp. 51–59, 2021.

[14] D. Shihua and S. Zubin, "Design and implementation of high-precision electronic stopwatch based on EDA technology," *Science and Technology Innovation and Application*, vol. 275, no. 19, pp. 98-99, 2019.

[15] Q. Believes, C. Yiguang, T. Enling, and H. Yafei, "Damage effect and thermal evolution induced by femtosecond pulsed laser irradiation FRAM," *Acta Luminescence*, vol. 40, no. 6, pp. 815–825, 2019.

[16] T. Pengfei, L. Bo, W. Jinbin, Z. Xiangli, G. Hongxia, and W. Fang, "Simulation of the effect of ionizing radiation on the domain structure of ferroelectric thin films," *Natural Science Journal of Xiangtan University*, vol. 41, no. 4, pp. 30–39, 2019.

[17] C. Linggang, C. Hongyue, D. Zhihong, and Z. Ximan, "Application research of ferroelectric memory in strapdown inertial navigation system," *China Equipment Engineering*, no. 11, pp. 184-185, 2019.

[18] L. Shuang, Z. Yinlian, T. Yunlong, Z. Sirui, M. Jinyuan, and M. Xiuliang, "Evolution of ferroelectric vortex structure in superlattice," *Chinese Journal of Chinese Electron Microscopy Society*, vol. 37, no. 4, pp. 14–18, 2018.

[19] W. Pengbo, "Fault model of ferroelectric memory and march C-1T1C test," *Henan Science and Technology*, vol. 39, no. 28, pp. 9–12, 2020.

[20] Y. Dina, "The MSP430 family adds an intelligent analog combination to make the MCU flexible and configurable," *Microcontrollers and Embedded System Applications*, vol. 18, no. 7, pp. 99–99, 2018.

[21] S. Shiyu, S. Hongjia, Z. Xiangli, Z. Yi, and W. Jinbin, "Research on the storage characteristics and reliability of metal-ferroelectric layer (BNT)-insulating layer (YSZ)-semiconductor (Si) diodes," *Modern Applied Physics*, vol. 8, no. 2, pp. 62–66, 2017.

[22] W. Peng, W. Shansheng, W. Min, S. Zhimin, and H. Rui, "Research on water temperature measurement device for intelligent drilling wells," *Electronics World*, vol. 15, pp. 40–42, 2019.

[23] Y. Qiao, L. Xiaochi, and C. Mingchao, "Research progress in preparation technology of barium strontium titanate nanopowders," *Chinese Ceramics*, vol. 53, no. 1, pp. 9–14, 2017.

Hindawi

Research Article

Effect of Graphene Fillers on the Water Absorption and Mechanical Properties of NaOH-Treated Kenaf Fiber-Reinforced Epoxy Composites

R. Ranga Raj [iD],[1] **S. Sathish,**[2] **T. L. D. Mansadevi,**[1] **R. Supriya,**[1] **S. Sekar,**[3] **Pravin P. Patil,**[4] **and Mahtab Mashuq Tonmoy** [iD][5]

[1]*Department of Aeronautical Engineering, Sri Ramakrishna Engineering College, Coimbatore, 641 022 Tamil Nadu, India*
[2]*Centre for Machining and Material Testing, KPR Institute of Engineering and Technology, Coimbatore, 641407 Tamil Nadu, India*
[3]*Department of Mechanical Engineering, Rajalakshmi Engineering College, Rajalakshmi Nagar Thandalam, Chennai, 602 105 Tamil Nadu, India*
[4]*Department of Mechanical Engineering, Graphic Era Deemed to Be University, Bell Road, Clement Town, 248002 Dehradun, Uttarakhand, India*
[5]*Department of Computer Science and Engineering, Daffodil International University, Dhaka 1207, Bangladesh*

Correspondence should be addressed to R. Ranga Raj; rrr.aero@gmail.com
and Mahtab Mashuq Tonmoy; mahtab15-2079@diu.edu.bd

This paper is focused on developing composites using kenaf fibers, epoxy polymer, and incorporation of graphene fillers. The kenaf fibers are treated with 5% NaOH to remove the hydrophilic nature and reinforced it with the hydrophobic matrix. The composites are fabricated using the compression moulding technique by keeping 60 wt.% epoxy as constant, and the graphene and kenaf fiber weights are changed accordingly. The samples for tensile, flexural, impact, hardness, and water absorption tests are prepared as per the ASTM D3039, D790, D256, D2240, and D572 standards, respectively. The effect of graphene fillers in the 5% NaOH-treated kenaf fibers reinforced with the epoxy matrix is tested. Among the various samples, sample 4 which has 6% graphene addition in the epoxy matrix reinforced with 5% treated kenaf fiber displayed the highest tensile strength of 63 MPa, flexural strength of 97 MPa, impact strength of 9.56 kJ/m^2, hardness value of 97, and lower water absorption of 5.13%. This is due to the proper dispersion of graphene fillers in the matrix which caused better interfacial adhesion between the fiber and matrix. The water absorption test showed the lowest value in sample S5 as the graphene fillers obstruct water penetration in the fibers. SEM analysis is done on the prepared samples to study the surface flaws and structural changes.

1. Introduction

The usage of synthetic fibers has created many threads to the environment which prompted the researchers to search for an alternative material. Natural fibers diminish ecological risks, and they can be used as a composite by reinforcing it with the polymer matrix [1]. Researchers have worked on natural fibers to identify their expanded applications and benefits. Natural fibers can be obtained from plants, animals, and a mineral base. Plant fibers as reinforcement material play a prominent role in developing natural fiber composites [2–4]. Among the plant fibers, bast and leaf fibers provide good mechanical properties because of their stiffness and hard structure. Generally, plant fibers can be divided into the primary cell wall and secondary cell wall. The primary cell wall comprises disordered cellulose, hemicellulose, lignin, pectin, etc. The secondary cell wall has crystalline cellulose in which S2 cell is responsible for mechanical properties. Hemicellulose acts as a matrix material that surrounds the cellulose structure, and lignin provides extra strength by protecting the fiber from external damage. This makes the cellulose have strength and stiffness. As the cell divides, the

cellulose and lignin amount rise, but the polyose content remains the same throughout [5–7]. The properties of natural fibers when reinforced with polymer matrix includes fiber content, orientation, microfibrillar angle, the interfacial bond between the fiber and matrix, and high water content [8]. However, when plant fibers get reinforced with the hydrophobic matrix, it results in poor bonding leading to less mechanical properties. This is because hemicellulose absorbs more water content from the atmosphere and forms new hydrogen bonds on the surface which makes the fiber to be hydrophilic. This hydrogen bond formation can be reduced by treating the fibers chemically with different processes. In addition to this, the components such as lignin, pectin, wax, and oily substances will be removed to a better extent, and it will result in enhanced stability of the fiber [9–11]. The properties that impact the influence between the fiber and matrix are expressed as follows: (i) proper mating of two unique materials, (ii) dispersion of fiber content in the matrix, (iii) orientation of fiber, and (iv) better surface interaction. Upon treating the fibers with different treatment processes, the mechanical properties of composites get enhanced by reduced water intake and better interfacial adhesion [12–14]. Sreenivasan et al. [15] reported that potassium permanganate-treated short Sansevieria cylindrica-reinforced polyester composites showed minimum water intake when compared to other treated fibers. Mylsamy and Rajendran [16] studied the effect of alkali treatment and optimum treatment percentage on agave Americana fibers. The optimum treatment is found to be 5%, and the treated fiber reduced the noncellulosic components and thereby enhanced the tensile property of the fiber. This is in line with the author. The mechanical and tribological properties can further be enhanced by incorporating fillers with the polymer matrix [17]. Fillers are additive materials that are used to enhance wear resistance, thermal stability, and flame resistance. The property of filler depends on its size, aspect ratio, and chemical composition. Ganesan et al. [18] assessed the effect of nanoclay filler and eggshell powder on the mechanical properties of jute fiber/polyester composite. The author concluded that the incorporation of filler enhanced the mechanical properties of the composite even if it is not chemically treated. The NaOH-treated jute fiber reinforced with eggshell powder (1.5%)+nanoclay (1.5%)/polyester matrix showed the highest flexural strength of 39.52 MPa than the untreated fiber. The increment is due to filler addition which hindered the formation of crack. Venkateshwar et al. [19] investigated the effect of different fillers (Al_2O_3, $CaCO_3$, and TiO_2) on the influence of mechanical properties of Prosopis juliflora epoxy-reinforced composites. The author reported that Al_2O_3 filler mixed uniformly in the matrix which resulted in enhanced bond strength. Benin et al. [20] concluded that Prosopis juliflora/epoxy composites with 12% barium sulfate filler provided superior mechanical properties. This is because the fillers and matrix remain bonded properly. Banyan fiber reinforced with 4% graphene incorporation in the epoxy matrix showed a higher tensile strength of 40.6 MPa and flexural strength of 163.23 MPa. This increment is due to the proper dispersion of graphene fillers in the matrix [21].

Nanofillers for instance graphene and carbon nanotubes have been proven to enhance the mechanical properties and reduced the water absorption content in the composites [22, 23]. For this experimental work, kenaf fiber (*Hibiscus cannabinus*) has been preferred because of its ability to produce in various environmental circumstances [24]. A study demonstrated that kenaf fiber can be used to create panels for furniture, seats, and armrests. It was also suggested that kenaf-reinforced composite materials might be used as noise obstacles and sound dampers [25]. This experiment work highlights the significance of incorporating graphene as a filler material in 5% alkali-treated kenaf fiber-reinforced epoxy composites. The above combination has not been reported in any literature data. The major purposes of the paper are expressed in the following ways: (1) effect of 5% NaOH treatment on kenaf fibers, (2) addition of graphene fillers with various proportions (0%, 2%, 4%, 6%, and 8%) in the matrix, (3) examining the mechanical and water absorption properties in the prepared composites, and (4) analyze the surface morphology of the prepared samples using SEM.

2. Materials

Kenaf fibers were purchased from KCT, Tifac core, Coimbatore, India. Epoxy resin (LY 556) and hardener (HY 951) are chosen as matrix material, and it has been collected from Covai Seenu & Company Coimbatore, Tamil Nadu. As per the manufacturer's suggestions, it is mixed in the ratio of 10 : 1. The resin and hardener are combined to generate a chemical effect that turns the liquid stage into a solid [26, 27]. Graphene as a filler material is added to the matrix material with various proportions (0%, 2%, 4%, 6%, and 8%).

2.1. Treatment of Kenaf Fibers. Kenaf fibers are immersed in 12 litres of distilled water for 1day to eliminate the unwanted particles residing on them. Later, the fibers are left to dry in the air for 24 hours. Dried kenaf fibers are soaked in 5% NaOH to remove the hydrophilic nature to a better extent. This 5% NaOH composition is 60 ml of NaOH in 12 litres of water. Treated kenaf fibers are washed thoroughly in distilled water to remove the additional NaOH present in them. Then, the fibers are left to dry in the air for 1day.

2.2. Fabrication of Graphene-Filled Composites. The treated kenaf fibers were cut into 30 cm length with the help of a cutter based on the moulding constraints. Graphene filler and epoxy resin cannot be mixed thoroughly as the resin chosen is highly viscous. To avoid this constraint, the graphene powder was scattered into the epoxy resin and then whisked for a prolonged period of 40 min at 80°C. Then, the hardener was added to the graphene/epoxy mixture in the ratio of 10 : 1. Aluminium plates of dimension 300 ∗ 300 ∗ 5 mm are chosen for the compression moulding process (Supplier: Modern Plastics Pvt Ltd., Coimbatore, India). To obstruct heating of the plates, white grease is applied to them. For sample 1, the epoxy resin along with the hardener was poured on the surface of the aluminium plate, and then,

the 5% NaOH-treated kenaf fibers are placed above the resin mixture in a unidirectional way. Then, the epoxy resin along with the hardener was poured above the fiber. For other samples, it was prepared by the addition of graphene fillers (2%, 4%, 6%, and 8%) into the epoxy resin, and the same process is repeated as mentioned above. The prepared laminates are processed in the compression moulding machine, and they are kept at a temperature of 130°C, with a pressure of 35 bar for 45 minutes. Later, the laminates are left for the curing process for 50 minutes. With the help of a diamond cutter, the final laminate of dimensions (300 ∗ 300 ∗ 5 mm) is removed from the mould. The prepared laminated can be tested mechanically as per the ASTM standard. Table 1 shows the composition of the prepared sample.

2.3. Physical and Mechanical Tests

2.3.1. Tensile Test. It is one of the mechanical tests to determine the material behaviour under applied load. The samples are prepared as per the ASTM D3039 requirement with a dimension of 250 ∗ 25 ∗ 5 mm and a crosshead speed of 2 mm/min [28]. It was tested in a computerized universal testing machine (Supplier: Aimil Ltd., India). Before the testing process, the samples are mounted onto the machine, and utilizing a hydraulic system, they are gripped to avoid dislocation. The value of each sample tested is noted. A total of three samples were tested in each composition, and the average value is taken for the analysis.

2.3.2. Flexural Test. This test determines how much a material will bend under the applied load. The samples for this test are prepared as per the ASTM D790 requirement with a dimension of 125 ∗ 12.7 ∗ 5 mm and a crosshead speed of 2 mm/min [10]. It was tested in a computerized universal testing machine, and the values for each sample are recorded. A total of three samples were tested in each composition, and the average value is taken for the analysis.

2.3.3. Impact Test. This test determines how much a material can absorb toughness during the applied load. The samples for this test are prepared as per the ASTM D256 requirement with dimensions of 65 ∗ 12.7 ∗ 5 mm [10]. It was tested using digitalized Izod impact test, and the values for each sample are taken. A total of three samples were tested in each composition, and the average value is taken for the analysis.

2.3.4. Hardness Test. This test determines how much a material will experience localized deformation under mechanical indentation or scratching. The samples for this test are prepared as per the ASTM D2240 requirements with dimensions of 20 ∗ 20 ∗ 5 mm [10]. Shore D durometer is used to test the samples. At 6 different locations, the indentations were made, and the mean values are noted.

2.3.5. Water Absorption Test. The resistance to absorbing water is tested using this test. The samples are prepared as per the ASTM D572 requirements with dimensions 64 ∗ 12.7 ∗ 5 mm [29]. The samples are immersed in distilled water for 5 days at room temperature, and the changes are

TABLE 1: Composition of the prepared samples.

Sample number	Kenaf fiber (wt.%)	Epoxy resin (wt.%)	Graphene (wt.%)
S1	40	60	0
S2	38	60	2
S3	36	60	4
S4	34	60	6
S5	32	60	8

noted accordingly. After a certain interval of time, the samples are taken out and wiped with a cloth, and then, the weight of the sample is measured. The amount of water absorbed in a sample is determined using the below-mentioned formula, where W_b represents the final weight after immersion, W_a indicates the initial weight of a sample, and W shows the percentage of water absorbed.

$$W = \frac{W_b - W_a}{W_a} * 100. \tag{1}$$

2.4. SEM Analysis. A scanning electron microscope was used to analyze the surface flaws and structural changes of the prepared samples using SEM JEOL JSM-6510LA. For this technique, the operating voltage is 25 kV.

3. Result and Discussion

3.1. Tensile Strength. Tensile values of each composite under various loads are presented in Figure 1. 6 wt.% Gr fillers reinforced in treated kenaf/epoxy composite showed a maximum value of 63 MPa, and 0 wt.% Gr fillers showed the minimum value of 36 MPa. With the addition of Gr fillers, the tensile strength increased, and beyond a certain limit, it begins to decline. Sample S4 which have 6 wt.% Gr fillers proved to have maximum tensile strength and optimum content. This value is obtained because of the nature of graphene incorporated as a filler material. Graphene fillers obstruct the water molecules to penetrate the fiber, thereby creating proper bonding between the fiber and matrix. Graphene filler has a strong C-C bond which makes it difficult to rearrange its positions resulting in brittle nature [30]. Furthermore, the 6 wt.% Gr reinforced in treated kenaf/epoxy composite bonded properly, and graphene particles are dispersed uniformly in the matrix, thereby enhancing tensile strength than other Gr variations. 6 wt.% Gr fillers provided better interlocking with the fiber-matrix adhesion, and when stresses are applied, it is distributed evenly in the composite [31]. In sample S5, 8 wt.% Gr fillers reinforced in treated kenaf/epoxy composite showed a tensile strength of 58 MPa which is greater than 0 wt.% Gr, 2 wt.% Gr, and 4 wt.% Gr fillers samples and less than 6 wt.% Gr filler sample. With an increase in Gr fillers, the agglomeration of particles tends to take place, and crack propagation will not occur which indicated that the addition of graphene fillers makes the composite resulting in enhanced brittleness instead of higher tensile strength [21]. 8 wt.% Gr fillers will undergo a necking process within a short duration, and the
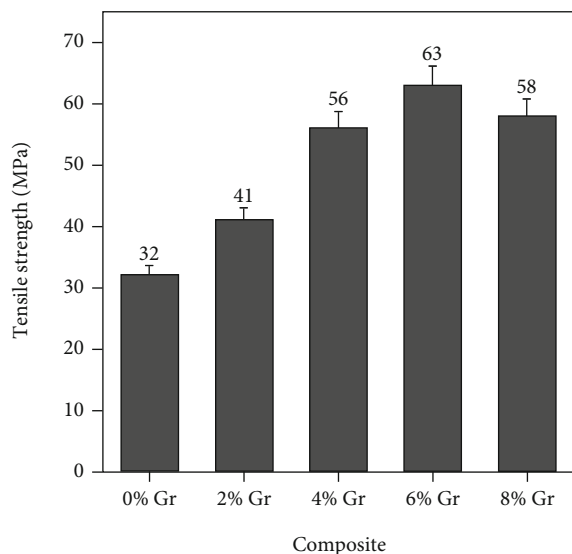
FIGURE 1: Tensile strength of graphene-filled kenaf/epoxy composites.

FIGURE 2: Flexural strength of graphene-filled kenaf/epoxy composites.

material breaks rapidly because of the brittle nature of graphene. 4 wt.% Gr fillers showed a value of 56 MPa which is greater than 0 wt.% Gr and 2 wt.% Gr and lower than 6 wt.% Gr and 8 wt.% samples. This decrement is because this concentration is not sufficient to hinder void formation in the matrix when compared to the 6 wt.% Gr filler sample [32]. 2 wt.% Gr filler sample showed a tensile strength of 41 MPa which is greater than 0 wt.% Gr and lesser than other graphene samples. This concentration reduced void content comparatively less than other Gr samples. In sample S1, the kenaf fibers are treated with 5% NaOH, and it is reinforced with epoxy resin to remove the noncellulosic contents to a good extent. The tensile strength of 32 MPa is attained due to the removal of impurities. 5% NaOH effectively removes this, but some constituents tend to degrade and created a void in it resulting in ease of water penetration also decrease in tensile strength.

3.2. Flexural Strength. The values of each sample for the flexural test are presented in Figure 2. Sample S4 displays the highest flexural strength of 97 MPa followed by sample S5 (94 MPa), sample S3 (89 MPa), sample S2 (73 MPa), and sample S1 (67 MPa). Sample S4 showed the highest flexural strength because the 6 wt.% Gr fillers with the matrix enhanced the bonding in the interface, thereby promoting better load sharing capability. Also, 6 wt.% graphene addition proved to be an optimum concentration because the fillers are dispersed uniformly in the matrix, thereby reducing holes and enhancing the flexural properties. 8 wt.% Gr fillers in sample S5 showed flexural strength of 94 MPa which is lower than sample S4 and higher than all other samples. This is due to the reason that 8 wt.% Gr fillers caused agglomeration in the matrix; also when reinforced with treated kenaf fiber, it resulted in improper interfacial bonding between the fiber/matrix. With 8 wt.% Gr addition, the flexural property of the composite starts to decline because of delamination between the layers. Also, 8 wt.% Gr fillers did not disperse throughout which caused some
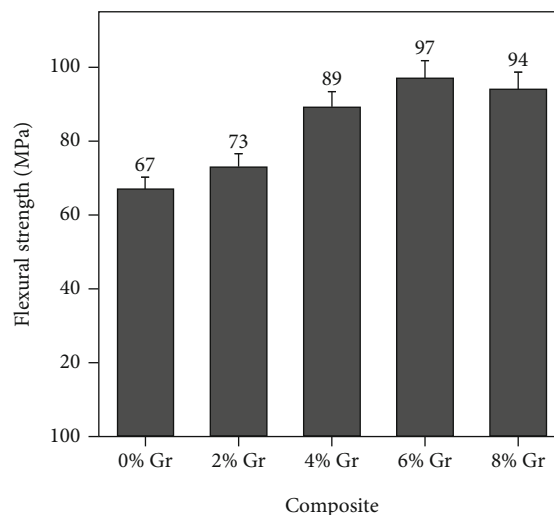
debris in that region, and when the load is applied, the sample showed lower flexural properties and enhanced brittleness of the composite [21]. 4 wt.% Gr and 2 wt.% Gr fillers in samples 3 and 2 are insufficient to hinder void formation causing fiber pull-out in the surface and resulting in lower flexural strength of value 89 MPa and 73 MPa when compared to 6 wt.% Gr and 8 wt.% Gr filler samples, respectively. In sample S1, treated kenaf fibers removed the hydrophilic nature in the fiber and have been well bonded with the matrix. But the load distribution did not occur evenly in the composite because of the microgaps present in it leading to a decrease in flexural strength of a value 67 MPa when compared to other varying Gr filler samples.

3.3. Impact Strength. It determines how much a material can absorb energy under applied load. The values of each sample for this test are displayed in Figure 3. Sample S4 showed maximum impact strength of $9.56 \, \text{kJ/m}^2$ and minimum impact strength of $4.85 \, \text{kJ/m}^2$. 6 wt.% Gr fillers in sample S4 showed the highest impact strength ($9.56 \, \text{kJ/m}^2$) as 6 wt.% graphene addition absorbed more energy before the inception of brittle behaviour. This is because the optimum concentration of graphene into the matrix resulted in better interlocking between the fiber and the matrix. The increase in impact strength depends on factors like the toughness of the composite, compatibility between the fiber and matrix, and proper dispersion of filler material into the matrix [21]. 4 wt.% Gr fillers in sample S3 showed an impact strength of $7.32 \, \text{kJ/m}^2$ which is higher than 8 wt.% Gr filler samples. 4 wt.% Gr fillers absorbed more energy than 8 wt.% Gr fillers, and this is due to the fact that 4 wt.% Gr fillers did not make the composite crack easily, whereas the addition of Gr fillers beyond 6 wt.% made the composite embrittle. 8 wt.% Gr filler in sample S5 showed an impact strength of $7.18 \, \text{kJ/m}^2$ which is greater than 0 wt.% Gr and 2 wt.% Gr and less than 6 wt.% Gr and 4 wt.% Gr filler samples. This is due to the agglomeration of graphene particles in the matrix region which caused the composite to lose its
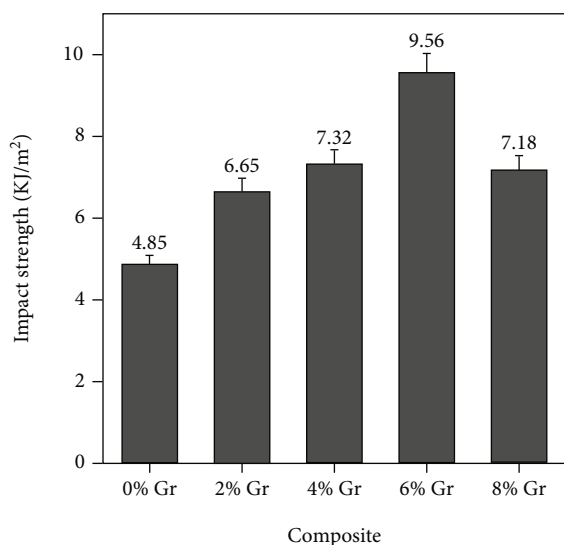
FIGURE 3: Impact strength of graphene-filled kenaf/epoxy composites.

FIGURE 4: Hardness values of graphene-filled kenaf/epoxy composites.

ductile nature and hence resulted in a reduction in impact strength. 2 wt.% Gr filler in sample S2 showed an impact strength of 6.65 kJ/m^2 which is lower than 6 wt.% Gr, 4 wt.% Gr, and 8 wt.% Gr fillers and greater than 0 wt.% Gr filler sample. This is due to the reason that 2 wt.% Gr did not hinder the void formation as compared to 6 wt.% Gr, 4 wt.% Gr, and 8 wt.% Gr filler samples. Sample S1 which has 0 wt.% Gr filler showed the lowest impact strength of 4.85 kJ/m^2 when compared to all other Gr fillers with varying samples. This is because when it is treated, the fibers are split into smaller ones making it withstand load, but the microgaps which are present in the composite led to a reduction in lower impact strength.

3.4. Hardness. It will determine how much a material can withstand penetration depth when the load is applied to it. If the material is brittle, then the hardness will be more [21]. The hardness value of each sample is displayed in Figure 4. 8 wt.% Gr filler in sample S5 showed a maximum hardness value of 97, and 0 wt.% Gr in sample S1 showed a lower hardness value of 56. 8 wt.% Gr filler in sample S5 showed a higher hardness value because the brittle nature of graphene particles also resisted penetration when the load is applied on it when compared to all other samples. 6 wt.% Gr filler in sample S4 showed a hardness value of 89, and this is greater than 0 wt.% Gr, 2 wt.% Gr, and 4 wt.% Gr fillers and also lesser than 8 wt.% Gr filler samples. 6 wt.% Gr filler showed uniformed dispersion of graphene in the matrix and enhanced the interfacial bonding between the fiber/matrix, but the addition of more graphene fillers showed resistance to penetration. 4 wt.% Gr filler in sample 3 showed a hardness value of 81 which is greater than 0 wt.% Gr and 2 wt.% Gr and lower than 8 wt.% Gr and 6 wt.% Gr filler samples. 4 wt.% Gr filler did not lock the void formation resulting in fiber pull-out from the surface which resulted in lowering of hardness value. In the sample S2, 2 wt.% Gr filler in the matrix is not sufficient to increase the hardness
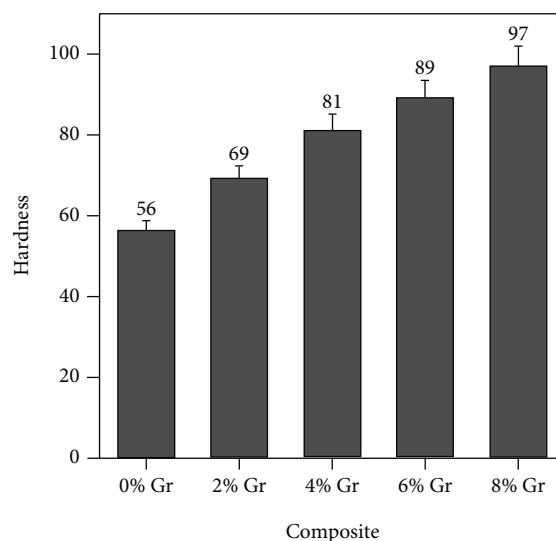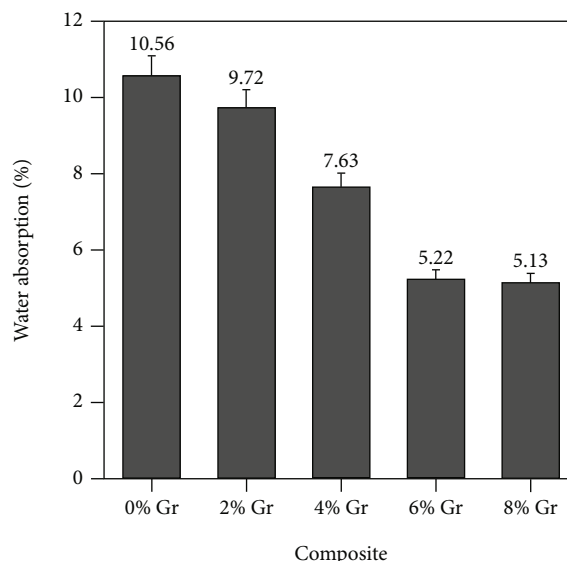
FIGURE 5: Water absorption of graphene-filled kenaf/epoxy composites.

value, so this composite displayed a hardness value of 69 which is higher than 0 wt.% Gr filler but higher than other Gr filler samples. The treated kenaf fibers reinforced with epoxy matrix in sample S1 showed a hardness value of 56 which is lower than all other Gr filler samples. 5% NaOH-treated kenaf fibers provided a rough surface, so the sample resisted penetration initially, but after a certain period, it failed because of some hydrophilic nature in the fiber.

3.5. Water Absorption Tests. This test is used to determine the hydrophilic nature of the fibers. The values of water absorption tests for all samples are displayed in Figure 5. Sample S5 which have 8 wt.% Gr filler reinforced in treated kenaf/epoxy composite showed more resistance to water absorption than other samples. Graphene plays an obstacle

(a)

(b)

(c)

(d)
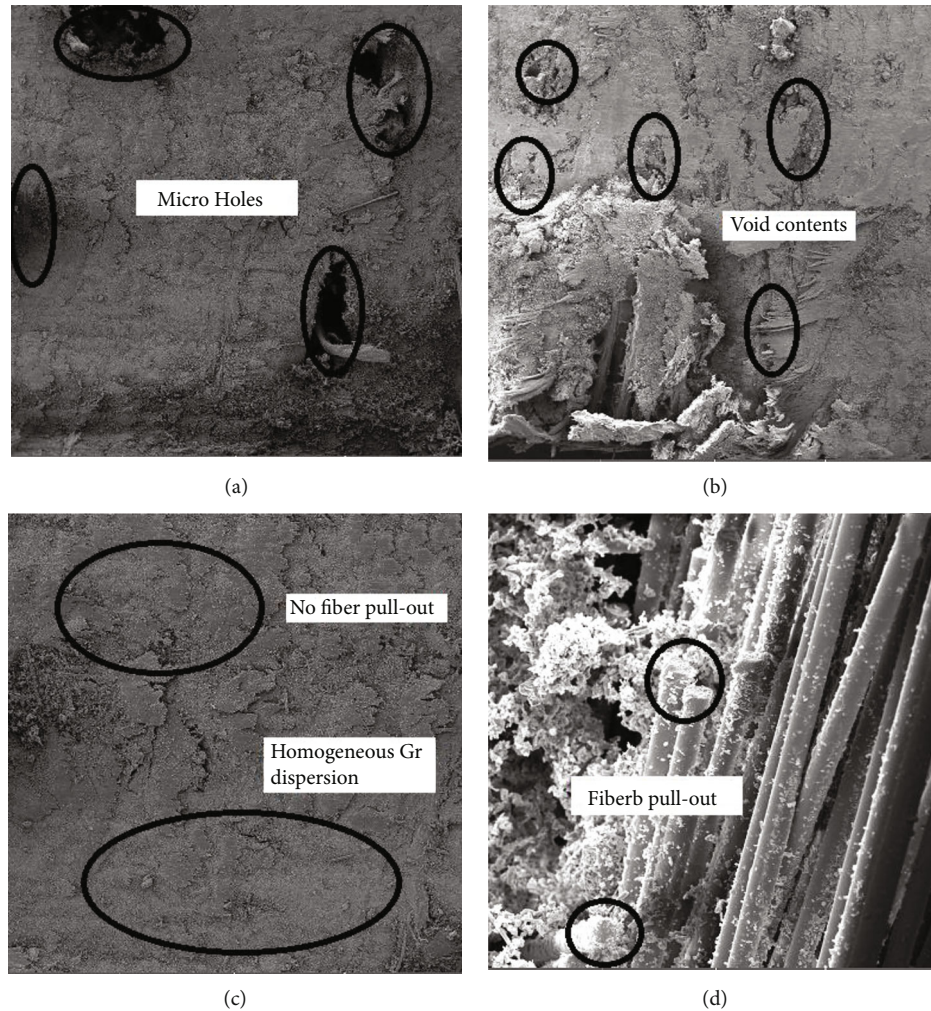
Figure 6: (a–d) represents SEM images for various concentration of graphene filler reinforced in treated kenaf/epoxy composite.

in transporting water to the composites [22]. With the addition of graphene fillers, the void content is minimized, thereby locking it with the matrix and leading to better interfacial adhesion between the fiber and matrix. Due to this reason, the water absorption test displayed lower valves. Sample S1 showed high water absorption of 10.56% when compared to all other Gr filler samples. The kenaf fibers are treated with 5% NaOH to remove the impurities and noncellulosic content like hemicellulose and pectin, and then, it is reinforced with epoxy resin. Even after treating the kenaf fiber, it possesses some hydrophilic nature and void content. With 2 wt.% Gr addition in sample S2, the gaps present in the matrix are removed partially, and some holes allowed the fibers to interact with water molecules, thereby absorbing water content. Sample S2 showed a water absorption value of 9.72 than sample S1 but higher than all other Gr filler samples. The addition of graphene fillers resisted water penetration by locking the void formation. In sample S4, 6 wt.% Gr addition resisted water absorption as the concentration of filler addition locks the void from interacting with the water molecules. 6 wt.% Gr filler showed a value of 5.22 which is lower than sample S5.

3.6. SEM Analysis. Figure 6(a) represents the SEM image of sample S1 which consists of 5% NaOH-treated 40 wt.% kenaf fiber reinforced with epoxy resin. This sample showed a rough surface due to the removal of noncellulosic components in it, but there are a few microholes that are present in the matrix after the treatment. These microholes may create stress concentration leading to the deterioration of mechanical properties of the composites [33]. In sample S2, the 2 wt.% Gr addition disperses well with the matrix by hindering void formation to some extent, so the water absorption is reduced, and the interfacial bond will be better than 0 wt.% Gr filler sample. This change can be seen in Figure 6(b). In sample S3, 4 wt.% Gr filler reinforced in treated kenaf/epoxy composites showed proper bonding and minimal void content in the matrix. Figure 6(c) represents the SEM image of sample S3 which showed well dispersion of graphene with the matrix, no fiber pull-out, and proper interfacial adhesion between the fiber and matrix. Above 6 wt.% Gr incorporation with the matrix leads to fiber pull-out. According to Zhang et al. [33], after 5% NaOH treatment, the interfacial adhesion between the kenaf fibers and the matrix was greatly improved with 6 wt.% Gr. Treated kenaf fibers with 6 wt.% Gr had extremely greater tensile strength than other

composition, and the fracture of treated kenaf fibers could greatly enhance the mechanical strength of composites. In Figure 6(d), the SEM image of sample S5 has 8 wt.% Gr incorporation with the matrix which displayed agglomeration in the matrix region causing weak interfacial adhesion between the fiber and matrix. The poor fiber/matrix interface could not provide sufficient stress transport; thus, the mechanical properties of the composites decreased significantly. Severe fiber/matrix debonding with nanofillers could be witnessed due to the poor interfacial adhesion between fibers and the matrix, as shown in Figure 6(d). The unnecessary voids and microholes in the composites (S1 and S2) were witnessed at lower/higher weight fraction of graphene, which may reduce the reinforcing effect of the nanofillers resulting in the reduction of mechanical properties [21].

4. Conclusion

The mechanical and water absorption test is carried out for the various concentrations of reinforcement graphene filler with kenaf. Increment in mechanical properties strongly depends on the uniform dispersion of graphene in the matrix. The major findings of incorporating graphene in the treated kenaf/epoxy composites are discussed as follows. Graphene plays a major role in obstructing water penetration in the composite, thereby minimizing void concentration in it. The investigation proved that the addition of graphene improved the performance of the composite thermal stability. With more than 6 wt.% Gr filler reinforced in treated kenaf/epoxy composites, the properties like tensile, flexural, and impact strength start to decline, but maximum hardness value of 97 is achieved at 8 wt.% Gr filler sample. Beyond 6 wt.% graphene addition, the composite becomes embrittle causing agglomeration in the matrix and reduction in mechanical properties. SEM analysis is done to study the morphological surface of various graphene concentrations reinforced in treated kenaf/epoxy composites. 6 wt.% Gr filler sample is found to optimum, and this displayed no fiber pull-out, better bonding in the SEM analysis.

Data Availability

The data used to support the findings of this study are included in the article.

Conflicts of Interest

The authors declare that there is no conflict of interest regarding the publication of this article.

Acknowledgments

References

[1] J. Rout, M. Misra, S. Tripathy, S. K. Nayak, and A. K. Mohanty, "The influence of fibre treatment on the performance of coir-polyester composites," *Composites Science and Technology*, vol. 61, no. 9, pp. 1303–1310, 2001.

[2] K. L. Pickering, M. G. Aruan Efendy, and T. M. Le, "A review of recent developments in natural fibre composites and their mechanical performance," *Composites: Part A*, vol. 83, pp. 98–112, 2016.

[3] S. Sathish, K. Kumaresan, L. Prabhu, and N. Vigneshkumar, "Experimental investigation on volume fraction of mechanical and physical properties of flax and bamboo fibers reinforced hybrid epoxy composites," *Polymers and Polymer Composites*, vol. 25, no. 3, pp. 229–236, 2017.

[4] M. Zwawi, "A review on natural fiber bio-composites, surface modifications and applications," *Molecules*, vol. 26, no. 2, article 404, 2021.

[5] K. Yoganandam, V. Shanmugam, A. Vasudevan et al., "Investigation of dynamic, mechanical, and thermal properties of Calotropis procera particle-reinforced PLA biocomposites," *Advances in Materials Science and Engineering*, vol. 2021, Article ID 2491489, 7 pages, 2021.

[6] X. Wang, L. Chang, X. Shi, and L. Wang, "Effect of hot-alkali treatment on the structure composition of jute fabrics and mechanical properties of laminated composites," *Composites*, vol. 12, no. 9, p. 1386, 2019.

[7] K. S. Ali, V. Mohanavel, M. Ravichandran, S. Arungalai Vendan, T. Sathish, and A. Karthick, "Microstructure and mechanical properties of friction stir welded SiC/TiB2 reinforced aluminum hybrid composites," *Silicon*, vol. 14, no. 7, pp. 3571–3581, 2022.

[8] K.-t. Laua, P.-y. Hunga, M.-H. Zhu, and D. Hui, "Properties of natural fiber composites for structural engineering applications," *Composites Part B Engineering*, vol. 136, pp. 222-223, 2018.

[9] R. Latif, S. Wakeel, N. Zaman Khan, A. Noor Siddiquee, S. Lal Verma, and Z. Akhtar Khan, "surface treatments of plant fibers and their effects on mechanical properties of fiber-reinforced composites: a review," *Journal of Reinforced Plastics and Composites*, vol. 38, no. 1, pp. 15–30, 2019.

[10] M. J. John and S. Thomas, "Biofibres and biocomposites," *Carbohydrate Polymers*, vol. 71, no. 3, pp. 343–364, 2008.

[11] B. S. Susheel Kalia and I. K. Kaith, "Pretreatments of natural fibers and their application as reinforcing material in polymer composites—a review," *Polymer Engineering and Science*, vol. 49, no. 7, pp. 1253–1272, 2009.

[12] M. Ramesh, "Kenaf (Hibiscus cannabinus L) fibre based biomaterials: a review on processing and properties," *Progress in Materials Science*, vol. 78-79, pp. 1–92, 2016.

[13] M. Ramesh, L. Rajeshkumar, and V. Bhuvaneswari, "Leaf fibres as reinforcements in green composites: a review on processing, properties and applications," *Emergent Materials*, pp. 1–25, 2021.

[14] M. Ramesh, "Flax (Linum usitatissimum L) fibre reinforced polymer composite materials: A review on preparation, properties and prospects," *Progress in Materials Science*, vol. 102, pp. 109–166, 2019.

[15] V. S. Sreenivasan, D. Ravindran, V. Manikandan, and R. Narayanasamy, "Influence of fibre treatments on mechanical properties of short Sansevieria cylindrica /polyester composites," *Materials & Design*, vol. 37, pp. 111–121, 2012.

[16] K. Mylsamy and I. Rajendran, "Investigation on physio-chemical and mechanical properties of raw and alkali-treated Agave americana fiber," *Journal of Reinforced Plastics and Composites*, vol. 29, no. 19, pp. 2925–2935, 2010.

[17] O. T. Adesina, T. Jamiru, E. R. Sadiku, O. F. Ogunbiyi, and L. W. Beneke, "Mechanical evaluation of hybrid natural fibre–reinforced polymeric composites for automotive bumper beam: a review," *International Journal of Advanced Manufacturing Technology*, vol. 103, no. 5-8, pp. 1781–1797, 2019.

[18] K. Ganesan, C. Kailasanathan, M. R. Sanjay, P. Senthamaraikannan, and S. S. Saravanakumar, "A new assessment on mechanical properties of jute fiber mat with eggshell powder/nano clay-reinforced polyester matrix composites," *Journal of Natural Fibers*, vol. 17, pp. 482–490, 2018.

[19] P. V. Reddy, P. R. Prasad, D. M. Krishnudu, and P. Hussain, "Influence of fillers on mechanical properties of prosopis juliflora fiber reinforced hybrid composites," *Materials Today: Proceedings*, vol. 19, pp. 384–387, 2019.

[20] S. R. Benin, S. Kannan, A. J. Moses, and R. J. Bright, "Mechanical Characterization of Proposis Juliflora Reinforced Polymer Matrix Composites with Filler Material," *Materials Today: Proceedings*, vol. 33, pp. 1110–1115, 2020.

[21] T. Ganapathy, R. Sathiskumar, M. R. Sanjay et al., "Effect of graphene powder on banyan aerial root fibers reinforced epoxy composites," *Journal of Natural Fibers*, vol. 18, no. 7, pp. 1029–1036, 2021.

[22] S. G. Prolongo, A. Jiménez-Suárez, R. Moriche, and A. Ureña, "Influence of thickness and lateral size of graphene nanoplatelets on water uptake in epoxy/graphene nanocomposites," *Applied Science*, vol. 8, no. 9, article 1550, 2018.

[23] N. H. Mohammad Zulfli, A. Abu Bakar, and W. S. Chow, "Mechanical and water absorption behaviors of carbon nanotube reinforced epoxy/glass fiber laminates," *Journal of Reinforced Plastics*, vol. 32, no. 22, pp. 1715–1721, 2013.

[24] N. Sgriccia, M. C. Hawley, and M. Misra, "Characterization of natural fiber surfaces and natural fiber composites," *Composites Part A: Applied Science and Manufacturing*, vol. 39, no. 10, pp. 1632–1637, 2008.

[25] A. A. M. Mazuki, *Fabrication, Characterization, and Properties of Pultruded Kenaf Reinforced Unsaturated Polyester Composites*, University of Sains, George Town, Malaysia, 2010.

[26] H. James and D. Houston, "Natural-fiber-reinforced polymer composites in automotive applications," *Journal of Management*, vol. 58, no. 11, pp. 80–86, 2006.

[27] R. Ranga Raj, J. Yoganandh, M. S. Senthil Saravanan, and S. Sathiesh Kumar, "Effect of graphene addition on the mechanical characteristics of AA7075 aluminum nanocomposites," *Carbon Letters*, vol. 31, no. 1, pp. 125–136, 2021.

[28] R. Rangaraj, S. Sathish, T. L. D. Mansadevi et al., "Investigation of weight fraction and alkaline treatment on catechu Linnaeus/Hibiscus cannabinus/Sansevieria ehrenbergii plant fibers-reinforced epoxy hybrid composites," *Advances in Materials Science and Engineering*, vol. 2022, Article ID 4940531, 9 pages, 2022.

[29] M. Kamaraj, E. A. Dodson, and S. Datta, "Effect of graphene on the properties of flax fabric reinforced epoxy composites," *Advanced Composite Materials*, vol. 29, no. 5, pp. 443–458, 2020.

[30] R. Zheng, X. Hao, Y. Yuan, Z. Wang, K. Ameyama, and C. Ma, "Effect of high volume fraction of B_4C particles on the micro-structure and mechanical properties of aluminum alloy based composites," *Journal of Alloys and Compounds*, vol. 576, pp. 291–298, 2013.

[31] J. R. Potts, D. R. Dreyer, C. W. Bielawski, and R. S. Ruoff, "Graphene-based polymer nanocomposites," *Polymer*, vol. 52, no. 1, pp. 5–25, 2011.

[32] W. Nuthong, P. Uawongsuwan, W. Pivsa-Art, and H. Hamada, "Impact property of flexible epoxy treated natural fiber reinforced PLA composites," *Compos Energy Procedia*, vol. 34, pp. 839–847, 2013.

[33] K. Zhang, W. Liang, F. Wang, and Z. Wang, "Effect of water absorption on the mechanical properties of bamboo/glass-reinforced polybenzoxazine hybrid composite," *Polymers and Polymer Composites*, vol. 29, no. 1, pp. 3–14, 2020.

Hindawi

Research Article

Amorphous Alloys and Ferroelectric Nanomaterials and the Repair of Athletic Ligament Injuries in Soccer

Chao Ma [ID]

Physical Education College, Inner Mongolia Minzu University, Tongliao, 028000 Inner Mongolia, China

Correspondence should be addressed to Chao Ma; machao@imun.edu.cn

Amorphous alloy refers to the orderly arrangement of the internal structure of various substances in nature. Amorphous solid materials include amorphous inorganic materials, amorphous polymers, and amorphous alloys. Amorphous alloys, also known as glassy alloys or metallic glasses, are atomically condensed, long-range disordered, and short-range ordered alloy materials that have the distinctive properties of both metals and glasses. Ligament injury is damage caused by different degrees of damage to the ligaments of a certain part of the body. The purpose of this paper is to investigate amorphous alloys and ferroelectric nanomaterials and the repair of athletic ligament injuries in the soccer game, using the excellent properties of amorphous alloys and ferroelectric nanomaterials to solve the problem of athletic injuries. Knee and ankle injuries and muscle strains account for a large percentage of soccer injuries. In this paper, researches and explorations have been conducted on the preparation of new composite magnetic nanomaterials, the construction of immunosensor interfaces, and the development of new signal amplification and renewable immunosensors. The rehabilitation effect of the medial collateral ligament of the athlete's knee joint is used as the research object, and various methods are used. In-depth investigation and research and statistical analysis of the data obtained one by one were carried out. The experimental results in this article show that from the age of ligament injury, the number of people between 18 and 20 is relatively small, and the number of people aged 20–40 is relatively large. The number of people who have been trained for three years and above is 5, and the proportion of ligament injuries is 0.8%; the number of training for two years is 33, and the proportion of ligament injuries is 13.7%, the number of training for one year is 98, and the proportion of ligament injuries is 40.7%, and the number of training for six months is 105, and the proportion of ligaments is 44.8%.

1. Introduction

1.1. Background. In line that scientific and artistic fields are constantly evolving, sports in China have also been flourishing. More and more sports, as well as sporting events, are getting more and more attention, especially soccer. It is a good thing for the whole society that soccer is being taken seriously, but along with the focus on performance, we should also be concerned about the physical injuries of the athletes. Soccer consists of many high-intensity and decisive action confrontations, and its fast and variable nature, high level of confrontation, and tight schedule contribute to the high incidence of sports injuries. Basically all athletes have different degrees of physical injuries, maybe a back injury or a leg injury, which are closely related to the sports injuries

we are discussing. Sports injuries are not like the bumps and bruises of our lives, especially ligament strains, which take a long time to recover from and are difficult to resist medication. Random ligament injuries have a significant impact on the life of the operator. However, until now, there has been no direct and effective way to treat sports ligament injuries and only some degree of pain relief. This type of injury is mostly characterized by localized pain in the knee joint along with swelling, flexion, and extension difficulties, and often walking difficulties, which in the long run can cause fear in daily training and affect the performance of technical movements. Currently, widely used amorphous alloy materials can be deformed according to their magnetic characteristics and are highly sensitive to external stresses. Compared with the traditional is metal magnetic material, non-alloy

material atomic arrangement disorder, high resistivity, has high permeability, low loss, can improve transformer efficiency, reduce mention, and reduce weight. In addition, nanomaterials are very small in size and can present acoustic, optical, electrical, magnetic, and thermal properties [1]. With the new characteristics, if nanomaterials can be combined with amorphous alloy materials, they may produce unexpected results when applied to the repair of ligament injuries.

1.2. Significance. The combination of nanomaterials and amorphous alloy materials in the repair of ligament injuries can fill the current lack of effective treatment of ligament injuries and promote the progress of medical care; curb the adverse effects of ligament injury on athletes, so that they can continue to struggle in their careers and improve China's sports performance; expand the use of nanomaterials and explore their functions; nanomaterials have the advantages of large specific surface area and conductivity, nanomaterials have the advantages of large specific surface area and conductivity, and their application in the construction of immunosensors can effectively improve the above shortcomings of immunosensors.

1.3. Related Work. With the development of the national economy, sports continue to receive attention, and sports performance has become the focus of national attention. But in following sporting events, it is found that the physical ailments of athletes are otherwise ignored, especially ligament injuries have caused fatal injuries to athletes. We must find an effective way to contain it. Based on basic sciences, Pearce obtained the unanimous opinion of the members of the ESSKA-AFAS Ankle Instability Team to propose a best evidence method. Before the experiment, base scientific and proclinical data on bone cell recovery after ligament rebuilding, as well as the reconstruction of sensorimotor control, were reviewed, and then members of the ESSKA-AFAS ankle instability team obtained information about the ankle based on this evidence. Rehabilitation recommendations were proposed for the early postoperative period, early recovery phase, and goal-oriented late rehabilitation and recovery exercise phases, and practical and evidence-based guidelines were adopted for the rehabilitation and recovery activities after the surgery of the lateral ankle ligament [2]. In order to obtain amorphous alloys with high plasticity, Shan SF designed a series of 100xTMx alloys to investigate the effect of Nb and Y additions on plasticity. 100xTMx alloy means $Ti_{40} Zr_{25} Cu_9 Ni_8 Be_{18}$, where $x = 0$, 1, 2, 3, and 4 and TM = Nb. The plasticity of different bulk amorphous alloys was investigated by measuring the plastic deformation energy (PDE) during loading. The obtained results indicate that the inclusion of Nb decreases the PDE level, contributes to the creation of more than one fracture zone, and obviously increases the breaking force and complexity, but the inclusion of element Y decreases the breaking force and plastic strain of the alloy [3]. Kuji systematically prepared different microstructures by annealing B-rich Fe-Si-B-Cr amorphous plates to obtain the best mechanical and processing properties of the alloy. Anneal-

ing is a metal heat treatment process that involves slowly heating the metal to a certain temperature, holding it for a sufficient amount of time, and then cooling it at a suitable rate. The purpose is to reduce hardness and improve machinability, reduce residual stress, stabilize dimensions, and reduce deformation and cracking tendencies. Thermal, structural, and mechanical analyses show that the early reaction sequence of the amorphous alloy after annealing is characterized by structural relaxation, heterogeneous nucleation of the surface α-Fe (Si) phase, and homogeneous nucleation of the metastable Fe3B nuclei, which is influenced by the α-encircled Fe shell [4]. Danylyak analyzed the thermal stability and crystallization kinetic parameters of $Fe_{82}Nb_2B_{14}REM_2$ (REM = Y, Gd, Tb, or Dy) amorphous metal alloys by differential scanning calorimetry. Iron-based alloys were crystallized in two stages; we calculated the activation energy of the two stages of crystallization of amorphous alloys according to the Kissinger, Ozawa, and Augis-Bennett models. The process of doping $Fe_{84}Nb_2B_{14}$ alloy with rare earth metals leads to an increase in temperature, crystallization activation energy, and frequency factor. The doping of rare earth metals leads to a decrease in the crystallization rate constant of alloys revealing their resistance to temperature treatment [5]. Fangping conducts the experiment by preprocessing the Zr-based amorphous alloy with ultrasonic-assisted vibration microcompression at different amplitudes and frequencies and then compresses the sample until it breaks. The process is simulated by the finite element analysis software ABAQUS. By comparing the results of simulation and experiment, the reliability of the finite element model is verified. At 0, 19, 27, 36, and 43 μm ultrasonic amplitudes and 20, 25, 30 and 35 kHz frequencies, the effect of energy flux density on the room temperature deformation behavior of Zr-based amorphous alloys was studied. The results show that as the ultrasonic amplitude and frequency increase, the elastic modulus decreases, the equivalent stress distribution becomes more uniform, and the formability improves. This is due to the increase in temperature caused by ultrasonic vibration and the increase in the free volume concentration of the compressed sample. However, studies have found that when the ultrasonic energy flow density increases, the formability of amorphous alloys decreases [6]. Ding summarizes studies that provide information on releases of ENM in occupational settings, in different industrial activities, and during the use of various nanomaterials. It also assesses background information—like the amount of material processed, protective measures, and measurement strategies—to understand which release scenarios may lead to exposure. High-energy processes, such as synthesis, spraying, and processing, are associated with the release of large numbers of primarily small-sized particles. The current analysis suggests that process-based release potential can be ranked to help prioritize release assessments, which can be useful in stratifying exposure assessment methods and guiding the implementation of workplace safety strategies [7]. Huang suggested that nanomaterials could be used in the field of sports therapy. Nanoscale materials have been widely used as reagents for therapeutic and diagnostic (i.e., therapeutic diagnostics)

purposes. He discusses some general design considerations for advanced therapeutic diagnostic materials from a diagnostic and therapeutic perspective, as well as the challenges of their use. Common classes of nanoscale biomaterials have been shown to have diagnostic and therapeutic potential, with size variations such as control and surface modifications that can modulate biocompatibility and interaction with target tissues [8]. These theories have discussed tropical damage, amorphous alloys, and ferroelectric nanomaterials to a certain extent. Because of the limitations in the research, the actual operation is not very rational and not practical.

1.4. Innovation. It is the first time that amorphous alloys and ferroelectric nanomaterials are used in the rehabilitation of ligament injuries. This is a new attempt for the entire medical field. If this method can be promoted, it will achieve a new breakthrough in sports ligament injuries. A porous nanogold film was modified on the surface of the glassy carbon electrode of the large specific surface area and strong adsorption capacity of nanogold.

2. Amorphous Alloys and Ferroelectric Nanomaterials and Repair Methods for Sports Ligament Injuries

2.1. Ferroelectric Nanomaterials. Nanomaterials are materials in which at least one dimension in three-dimensional space is at the nanometer size (1-100 nm) or consists of them as the basic unit, which is approximately equivalent to the scale of 10 to 1000 atoms closely aligned together [9, 10]. At the beginning of the twentieth century, related researchers discovered the dielectric properties of substances, combining organic matter with ferroelectric phenomena for the first time. Because of its low density, easy processing, and low price, it has been widely used. After research, it has been found that there are four kinds of crystals in ferroelectric nanomaterials, and the four kinds of substrates can be converted to each other [11]. The specific conversion is shown in Figure 1:

In the middle of the last century, the emergence of new materials is the rapid development of nanomaterials. In the subsequent gradual development, as researchers continue to explore theories, the scope of application of nanomaterials has become wider and wider. Nanoceramics have small grain size, and the grains can easily move on other grains; therefore, nanoceramic materials have very high strength and high toughness as well as good ductility; these characteristics make nanoceramic materials can be cold processed at room temperature or sub-high temperature, making them ductile and high-performance ceramics [12]. In recent years, the continuous improvement of science and technology has forced the upgrading of traditional materials. Due to the limitations of various functions, traditional scientific and technological materials can no longer meet the requirements of modern technology. New nanomaterials have a lot of room for development. From the offline situation, the entire nanomaterials are still in their infancy, and the subsequent development is still very violent. At this stage, although researchers choose different nanomaterials for experiments,
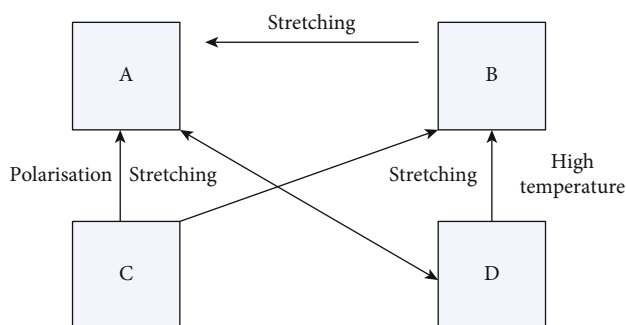
Figure 1: Four crystalline transformation relationships.
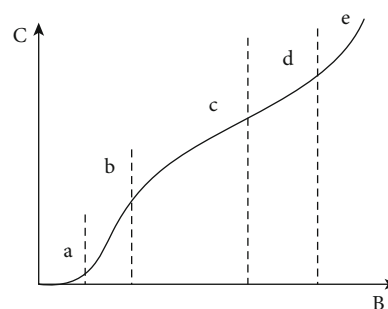
Figure 2: Magnetization of amorphous alloy materials.

but so far there have been no more satisfactory results. In short, nanomaterials are very important functional materials, and the research and application of their characteristics still need continuous research and exploration [13, 14]. The ratio of the number of surface atoms to the total number of atoms in a nanocrystal particle increases dramatically as the particle diameter becomes smaller. For example, at a particle diameter of 10 nm, the particle contains 4000 atoms, and the surface atoms account for 40%; at a particle diameter of 1 nm, the particle contains 30 atoms, and the surface atoms account for 99%.

2.2. Amorphous Alloy. Amorphous alloys refer to alloyed materials that are condensed by atoms and have an orderly structure [15]. According to the form of amorphous alloys, they can be divided into ribbons, fibers, filaments, and powders. Amorphous alloys have low elasticity, high toughness, high resistivity, high chemical activity, resistance to radiation damage, and high corrosion resistance. Amorphous alloys have their own microstructures, so it causes the lack of many functions of amorphous alloys, but amorphous alloys also have unique properties [16]. In terms of chemical functionality, compared with ordinary alloy materials, the corrosion resistance of amorphous alloys is very good. This unique advantage provides convenience for its wide application in various fields. After research by researchers, the quality of corrosion resistance is determined by the structure and composition of the substance, and the structure and formation of amorphous alloys are relatively uniform, so it has good corrosion resistance. Structural uniformity refers to a substance without structural defects such as grain boundaries and lattice defects. Composition uniformity refers to
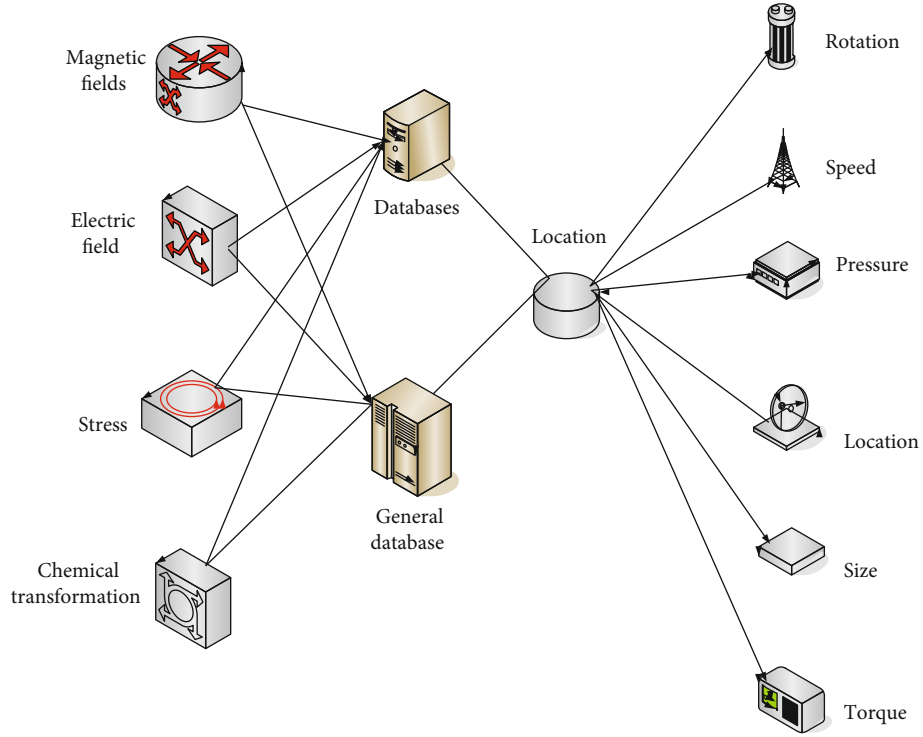
FIGURE 3: Magnetic sensor and magnetic relationship diagram.

the absence of static inclusions and heterogeneous components in the substance. The homogeneity of the composition is due to the fact that it is a fast-hardening material and the various atoms are "localized" before they can diffuse, so there are no fluctuations in composition like segregation, inclusions, and heterogeneity in the crystalline state. Since amorphous alloy materials are satisfied, the corrosion resistance is high [17].

Amorphous alloy itself has magnetic characteristics, but because the level of development is not enough, it is difficult to directly obtain its specific quantity; usually we use the saturation magnetic induction to reflect; function expression is as follows:

$$S = \phi_0(G + K) * (G + K). \tag{1}$$

Among them, S represents the magnetic induction intensity, K represents the magnetization intensity, and ϕ_0 represents the constant.

In the technical magnetization diagram, the amorphous alloy material is basically the same as the ordinary alloy material, as shown in Figure 2:

According to Figure 2, the main influencing factor in the magnetization process is the reversible domain wall displacement or reversible domain rotation in zone a. The magnetization degree is weak in zone b, the initial magnetization rate is large in zone c, the domain rotation plays a major role in zone d, and the wall movement and domain rotation of the internal domains in zone e are all completed.

When the magnetization of amorphous alloy materials is relatively weak, the function expression is as follows:

$$Q = \alpha_1 T + \beta T^2,$$
$$W = \varphi_1 T + 4\pi\beta T^2. \tag{2}$$

Among them, Q represents the magnetization intensity, α_1 represents the magnetic susceptibility, T represents the magnetic field intensity, β represents the constant, W represents the magnetic induction intensity, and φ_1 represents the initial permeability. Figure 3 is a schematic diagram of the relationship between magnetic sensors and magnetism:

When it comes to the magnetism of amorphous alloy materials, the stretching effect is involved, which essentially refers to the energy exchange of the material. The specific function expression is as follows:

$$\begin{cases} \iota = \iota(T, \chi), \\ W = W(T, \chi), \end{cases}$$
$$\begin{cases} \chi = \chi(W, \iota), \\ T = T(W, \iota), \end{cases} \tag{3}$$

where W represents the magnetic induction intensity, T represents the magnetic field intensity, ι represents the stress, and χ represents the strain.

The electromechanical coupling coefficient has a certain relationship with the permeability and elastic modulus

FIGURE 4: Common ligament injuries.

of amorphous alloy materials, which can be expressed as follows:

$$d^2 = \frac{\lambda_a - \lambda_b}{\lambda_z} = \frac{S_Q - S_K}{S_O}, \tag{4}$$

where λ_1, λ_2 represents the reversible permeability of the amorphous alloy material under steady stress and constant strain and S_Q, S_K represents the elastic modulus of the amorphous alloy material under steady magnetic induction and steady magnetic field strength, where

$$d^2 = \omega \left(\frac{\varphi \delta}{\varphi N} \right)^2 + \frac{\lambda_1 - \lambda_2}{\lambda_Z},$$
$$S = \frac{9}{4} \frac{S\gamma_c^2}{\pi N_c^2} v_i \left(\frac{N}{N_c} \right)^2, \tag{5}$$

where ω represents the magnetic susceptibility, δ represents the expansion ratio, δ_c represents the saturation magnetostriction coefficient, N represents the magnetization, N_c represents the saturation magnetization, v_i represents the reversible permeability, and S represents the elastic modulus.

In operation, stress sensitivity can be used to evaluate the magnetostrictive effect and inverse magnetostrictive effect of amorphous alloy materials. The specific function expression is as follows:

$$T = \frac{3\gamma_c N_C}{2L_i} \sin^2 \rho_0 \cos \rho_0, \tag{6}$$

where γ_c represents the saturation magnetostriction coefficient, N_c represents the saturation magnetization, L_i represents the uniaxial magnetic anisotropy, and ρ_0 represents the angle between the magnetization vector and the magnetic field.

The electromagnetic induction effect refers to the mutual induction phenomenon of electricity and magnetism. For a

TABLE 1: Patient status table.

Group	Male	Female	18-20	20-30	30-40
1	15	7	2	7	5
2	13	5	3	9	12
3	10	9	4	8	8
4	12	3	1	11	13

TABLE 2: Clinical efficacy comparison experiment.

Group	Excellent	Good	Generally	Difference
1				
Forward	0	0	3	15
Rear	0	5	8	6
2				
Forward	0	0	5	10
Rear	7	12	13	3
3				
Forward	0	7	3	13
Rear	0	10	11	2
4				
Forward	0	3	6	12
Rear	3	7	9	5

closed loop coil with a magnetic core, the function expression can be as follows:

$$L_j = -F \frac{d\mu}{di} = -FS \frac{dU}{di} = -FS \frac{d(\iota G)}{di}, \tag{7}$$

where L_j represents the induced voltage, μ represents the magnetic flux, F represents the number of coils, S represents the cross-sectional area of the magnetic core, U represents the magnetic induction intensity of the magnetic core, ι represents the magnetic permeability of the magnetic core, and G represents the magnetic field intensity.

TABLE 3: Validation of validity.

Group	Total people	Percentage (%)	Effective number of people in the structure	Percentage (%)	Number of people valid for content	Percentage (%)
Invalid	0	0	0	0	0	0
Poor results	1	9	3	27	1	9
General	0	0	2	18	0	0
Good	2	18	3	27	3	27
Excellent	5	45	4	36	1	9

If the permeability does not change with time, it means that it can be used to detect the change of the magnetic field. The specific detection is as follows:

$$L_j = -\iota F S \frac{dG}{di}. \tag{8}$$

It has been demonstrated by experimental studies that the Hall effect of ferromagnetic materials can be expressed as

$$\kappa_g = H_0 Q + \phi_0 N(H_1 - SH_0) = H_0 Q + \phi_0 H_c N, \tag{9}$$

where B represents the magnetic induction intensity of the applied magnetic field, N represents the intrinsic magnetization strength, S represents the demagnetization factor, H_0 represents the normal hall coefficient, H_1 represents the abnormal hall coefficient, and H_c represents the spontaneous hall coefficient.

In a low field, the induction intensity of amorphous alloy materials is very small, dominated by anomalous effects, which can be expressed as follows:

$$P_f = \left| \frac{\beta \mu_f}{\beta_W} \right|_{W \longrightarrow 0} = P_c,$$
$$P_{df} = \left| \frac{\beta \mu_f}{\beta_W} \right|_{W \geq N_c} = P_0. \tag{10}$$

When the external field changes the magnetic field, the amorphous alloy material will have an induced voltage phenomenon, and its function expression is as follows:

$$u_N = -\chi_a J_a \frac{dQ_a}{di} \infty - \frac{N_c{}^2 J_a}{g_a} \frac{dQ_a}{di}, \tag{11}$$

where χ_a represents the circumferential differential permeability, J_a represents the cross-sectional area of the axial magnetic circuit, Q_a represents the circumferential magnetic field strength, N_c represents the saturation magnetization, and g_a represents the circumferential magnetic anisotropy.

2.3. Sports Ligament Injury. With the continuous development of economy, people pay more and more attention to the all-round development of people [18]. The country is also advocating the all-round development of people's "ethics, intelligence, physique, beauty, and labor." Therefore, China's sports industry has also taken off. However, injury

TABLE 4: Length of ligament injury training survey.

Group	Number of people	Proportion (%)
More than three years	5	0.8
Two years	33	13.7
One year	98	40.7
Half a year	105	44.8%

in sports training is an inevitable problem. Once an injury occurs, it will not only cause great harm to the body, but also affect the performance of the game and reduce the performance of the game [19]. According to statistics, in addition to common abrasions in sports, the most common injury is ligament. Ligaments are the most critical and complex joints of the human body. Ligaments connect bone to bone and are distinct fibrous tissues that either attach to the surface of the bone or fuse with the outer layer of the joint capsule to enhance the stability of the joint and prevent injury. Injury occurs when the ligament is stretched beyond its tolerance by violence that produces nonphysiological activity. No matter what training is being performed, the flexible cooperation of ligaments is required. Because of excessive use, the probability of injury is also greatly increased. Usually we divide ligaments into medial collateral ligament, lateral collateral ligament, anterior cruciate ligament, and posterior cruciate ligament. Both sides of the medial collateral ligament, including longitudinal and oblique fibers, are used to prevent knee rotation instability. The medial side is the main structure that maintains the stability of the medial knee joint. It is related to all parts of the body. The main function is to prevent outward movement; when the knee joint is flexed, the calf is suddenly adducted and internally rotated, and the lateral collateral ligament may be injured [20, 21]. The posterior cruciate ligament starts after the spine of the embryonic bone. The posterior cruciate ligament is also an important structure to maintain the knee joint. Its injury can cause the instability of the knee joint and damage other structures in the joint. Figure 4 is a picture of common ligament injuries:

3. Amorphous Alloy and Ferroelectric Nanomaterials and the Repair Experiment of Sports Ligament Injury

3.1. Case Selection and Grouping. The experimental subjects were all patients with ligament injury, aged between 18 and
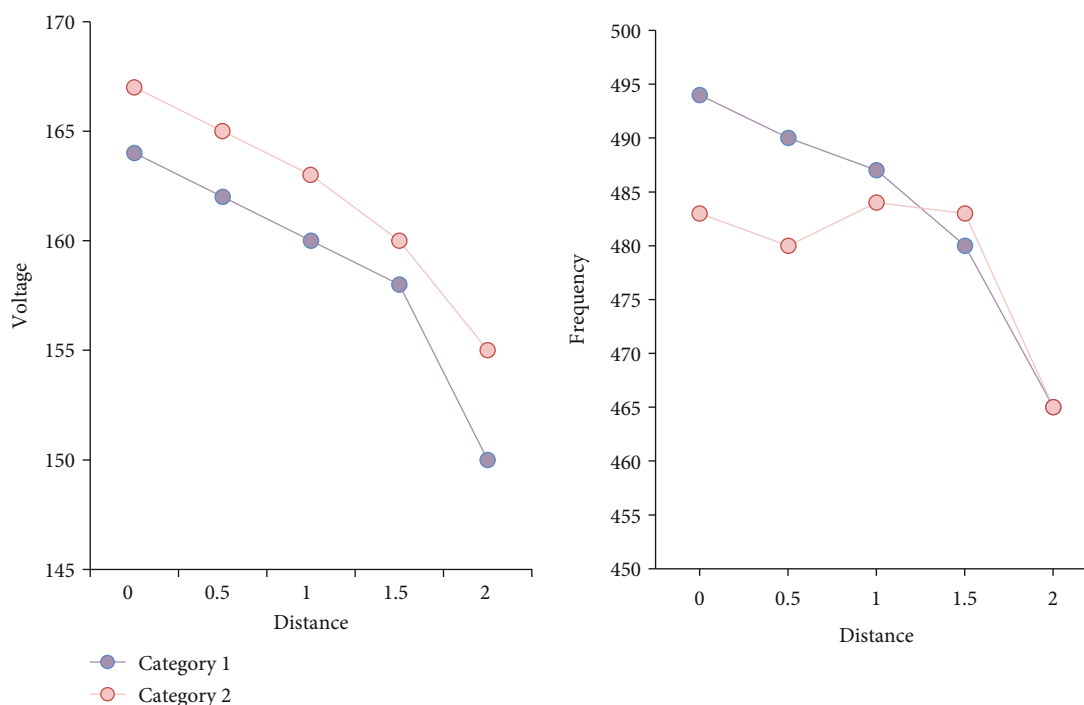
Figure 5: Schematic diagram of the forces applied.

40 years old, and were divided into 4 groups for separate experiments, and statistics were made according to the characteristics of the patients' age, symptoms, and gender [22]. The specific data is as follows:

According to the data in Table 1, in the four groups, the probability of male ligament injury is greater than that of females. Although there may be population base reasons, this situation is not obvious from the experimental data. From the perspective of the age of ligament injury, the number of people between 18 and 20 is relatively small, and the number of people with ligament injuries between 20 and 40 years old is relatively large. This reflects the flexibility of the ligament to a certain extent. Once injured, the possibility of a complete cure is very small [23].

3.2. Comparison before and after Treatment. There is no difference between the four groups of patients with ligament injury before treatment, and they are not comparable. Once different treatments are passed, we can explore the differences in treatments from the treatment results [24].

According to the data in Table 2, it can be seen that the results of treatments arranged by different groups are not the same. In the first group, the good before treatment is 0, the good after treatment is 0, the good before treatment is 0, the good after treatment is 5, the normal before treatment is 3, and the normal after treatment is 8, and the difference before treatment is 15, and the difference after treatment is 6. In the second group, the good before treatment is 0, the good after treatment is 7, the good before treatment is 0, and the good after treatment is 12. Before treatment is generally 5, after treatment is generally 13, the difference before treatment is 10, and the difference after treatment is 3; in the third group, the good before treatment is 0, and the good after

treatment is 0. It is 7 for good before treatment, 10 for good after treatment, 3 for normal before treatment, 11 for normal after treatment, 13 for poor before treatment, and 3 for poor after treatment; in the fourth group, the good is 0 before treatment, the good is 3 after the treatment, the good is 3 before the treatment, the good is 7 after the treatment, the general is 6 before the treatment, the general is 9 after the treatment, the difference before treatment was 12, and the difference after treatment was 5. According to the overall treatment effect, the treatment effect of the second group is better, and the treatment effect of the third group is relatively poor [25].

3.3. Treatment Effect Test. In order to explore the effectiveness of the treatment effect, it is not only necessary to look at the operation, but also the probability of recurrence. In order to ensure the validity of the data and scientifically and reasonably reflect the content of the research and discussion, we have analyzed the collected data in various ways. In order to increase the authority of the conclusions, we have invited relevant researchers to conduct research based on the survey questions rationality assessment. The details are as follows:

According to the data in Table 3, in the total number of questionnaires, 0% of people think it is invalid, 9% think that the effect is not good, 0% think that the average person thinks the effect is good, and 18% think that the effect is very good. In the structural effectiveness survey, 0% of people think that the effect is invalid, 27% think that the effect is not good, 18% think that the average person thinks the effect is good, 27% think that the effect is good, and the proportion thinks that the effect is very good 36%; in the content validity survey, 0% of people think it is invalid, 9% think the effect
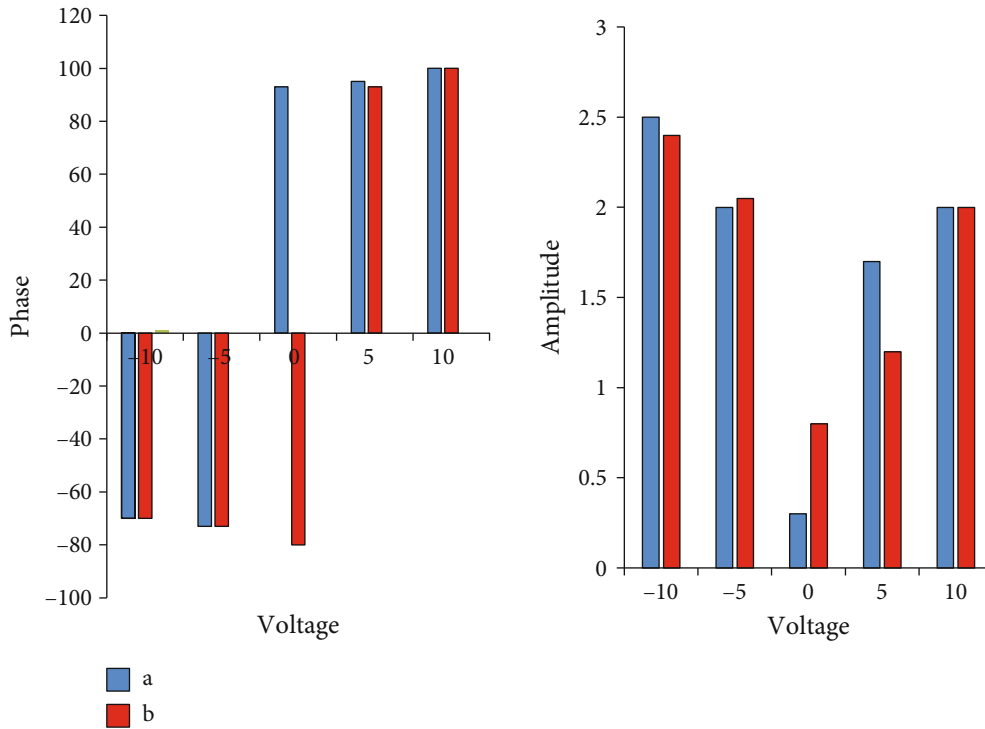
Figure 6: Nanoferroelectric material properties.
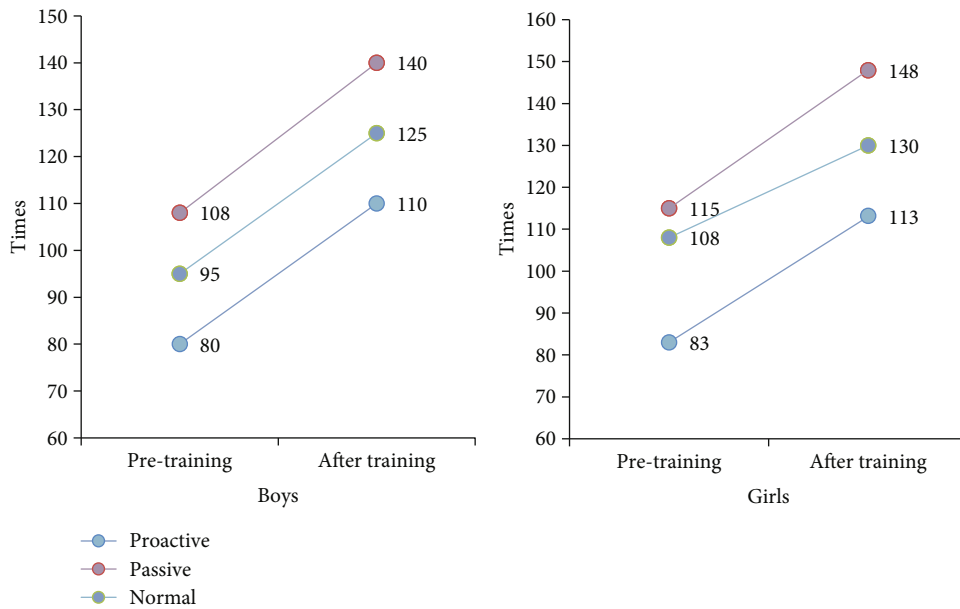
Figure 7: Ligament rehabilitation training values.

is not good, 0% think the effect is good, 27% think the effect is very good, and 9% think the effect is very good. According to the survey results, although the overall treatment effect is not good, the data obtained is still valid. The side proves that the validity survey method is correct and can continue to be implemented.

According to the data in Table 4, it can be seen that ligament injury training is prone to occur. In the survey data, the number of people who trained for three years or more was 5, the percentage of ligament injuries was 0.8%, the number of people who trained for two years was 33, the percentage of ligament injuries was 13.7%, and the number of people who trained for one year was 98. The proportion was 40.7%, the number of training for half a year was 105, and the proportion of ligament injuries was 44.8%. According to ten sentences, ligament injuries often occur at the beginning of training, which is closely related to the training method and self-protection consciousness. The more training

time, the less chance of ligament injury, so to a certain extent the protection of ligaments. In addition to medical treatment, it is more important to increase the awareness of self-protection, find the correct training method, and reduce the probability of injury. In this way, the ligaments can be maintained in a good state without frequent injuries.

4. Amorphous Alloys and Ferroelectric Nanomaterials and the Repair Analysis of Sports Ligament Injuries

4.1. Amorphous Alloy Material Design. According to Figure 5, the distance change during the whole experiment is within 2 mm, but the voltage change is within 20 V. Although there is a linear downward trend in the performance of the entire image, the actual value is very small and difficult to measure; this phenomenon also occurs in the frequency; the distance change is only 2 mm, and the frequency is only 30 kHz floating, which will cause great difficulty to the subsequent data capture.

4.2. Ferroelectric Properties of Nanomaterials. According to the data in Figure 6, the performance of the amorphous alloy material changes greatly by changing the voltage during the experiment. When the voltage is negative, the value obtained is also negative. When the voltage is positive, the obtained value is also a positive value. When the voltage is zero, one of the obtained values is a positive value, and the other is a negative value, which indicates that the material has strong ferroelectricity. When the voltage is -10 V, the amplitude difference between the two is very small. When the voltage is -5 V, the two substances are almost the same. When the voltage is 0 V, the two substances begin to have a gap. When the voltage is 5 V, the difference between the two substances in the gap began to narrow. When the voltage was 10 V, the two substances were almost the same.

4.3. Ligament Rehabilitation Training. According to the data in Figure 7, before rehabilitation training, the gap between male and female active knee flexion angles is very small. Passive knee flexion angle is 95 degrees for boys and 115 degrees for girls. From this data, it can be shown that girls' ligaments are more flexible and injured during training. The probability is lower. After a period of training, the active knee bending angle of boys is 125 degrees, the active knee bending angle of girls is 130 degrees, and the knee bending angle of women is still greater than that of men. This proves the previous point of view. In passive knee bending training, the angle of boys after training has reached 140 degrees, and the angle of girls has reached 148 degrees. Although the overall situation has not changed, it has changed significantly from before training, indicating that this training is effective.

5. Conclusions

With the continuous advancement of science and technology, sports and sports performance have received unprecedented attention, but we must pay attention to the physical condition of the athletes while focusing on honor. The topic of this paper is the repair of amorphous alloys and ferroelectric nanomaterials and the repair of sports ligament injuries in soccer. It is expected that the excellent properties of amorphous alloys and ferroelectric nanomaterials will play a role in the treatment of ligaments. In the experiment, this paper mainly completed the following tasks: (1) Research and exploration were carried out from the preparation of new composite magnetic nanomaterials, the construction of immunosensor interface, and the development of new signal amplification and renewable immunosensors. (2) Various methods have been used to conduct in-depth investigations and studies and statistical analysis of the data obtained one by one, to formulate the corresponding rehabilitation training plan. (3) The excellent characteristics and sensitivity of amorphous alloys and ferroelectric nanomaterials are higher than those of conventional methods, with a wide linear range, and are expected to be applied in the field of clinical testing. However, there are still many shortcomings in the experimental work: (1) The experimental subjects are not large enough, and they are only searched in a limited range, which cannot represent the ligament training situation of various sports, so the data obtained is not universally representative. (2) The strength and flexibility of vulnerable parts should be strengthened during the training process. Due to the complexity of sports and different characteristics, it is impossible to provide accurate training methods.

Data Availability

No data were used to support this study.

Conflicts of Interest

The author declares that there are no conflicts of interest regarding the publication of this article.

References

[1] B. Gao, N. Xu, and P. Xing, "Shock wave induced nanocrystallization during the high current pulsed electron beam process and its effect on mechanical properties," *Materials Letters*, vol. 237, no. 15, pp. 180–184, 2019.

[2] C. J. Pearce, Y. Tourné, J. Zellers, R. Terrier, P. Toschi, and K. G. Silbernagel, "Rehabilitation after anatomical ankle ligament repair or reconstruction," *Knee Surgery Sports Traumatology Arthroscopy Official Journal of the Esska*, vol. 24, no. 4, pp. 1130–1139, 2016.

[3] S. F. Shan, H. Wang, B. Zhang, Y. Z. Jia, and M. Z. Ma, "Influence of niobium and yttrium on plastic deformation energy and plasticity of Ti-based amorphous alloys," *China Foundry*, vol. 18, no. 1, pp. 60–67, 2021.

[4] C. Kuji, K. Takenaka, M. Mizutani, K. Shimada, T. Kuriyagawa, and T. J. Konno, "Crystallization behavior and machining properties of annealed Fe–Si–B–Cr amorphous alloys," *Journal of Materials Science*, vol. 56, no. 29, pp. 16697–16711, 2021.

[5] M.-O. M. Danylyak and L. M. Boichyshyn, "Thermal stability of Fe82Nb2B14REM2 amorphous alloys," *Materials Science*, vol. 55, no. 6, pp. 921–929, 2020.

[6] F. Liu, X. Liu, and Y. Lou, "Simulation study of the influence of ultrasonic energy flow density on the properties of zirconium-based amorphous alloys at room temperature," *IOP Conference Series: Materials Science and Engineering*, vol. 490, no. 5, pp. 52017–52017, 2019.

[7] Y. Ding, T. A. J. Kuhlbusch, M. van Tongeren et al., "Airborne engineered nanomaterials in the workplace–a review of release and worker exposure during nanomaterial production and handling processes," *Journal of Hazardous Materials*, vol. 322, no. Part A, pp. 17–28, 2017.

[8] H. Huang and J. F. Lovell, "Advanced Functional Nanomaterials for Theranostics," *Advanced Functional Materials*, vol. 27, no. 2, p. 1603524, 2017.

[9] P. Wang, S. Wang, X. Zhang et al., "Rational construction of CoO/CoF_2 coating on burnt-pot inspired 2D CNs as the battery-like electrode for supercapacitors," *Journal of Alloys and Compounds*, vol. 819, p. 153374, 2020.

[10] X. Xu, D. Shahsavari, and B. Karami, "On the forced mechanics of doubly-curved nanoshell," *International Journal of Engineering Science*, vol. 168, p. 103538, 2021.

[11] S. Karpman, P. Reid, L. Phillips, Z. Qin, and D. P. Gross, "Combative sports injuries: an Edmonton retrospective," *Clinical Journal of Sport Medicine*, vol. 26, no. 4, pp. 332–334, 2016.

[12] Y. Zhang, Y. Li, and C. Bai, "Microstructure and oxidation behavior of $Si-MoSi_2$ functionally graded coating on Mo substrate," *Ceramics International*, vol. 43, no. 8, pp. 6250–6256, 2017.

[13] B. Coufalová and J. Pinkava, "Some aspects of criminal liability for sports injuries," *International and Comparative Law Review*, vol. 14, no. 2, pp. 59–69, 2014.

[14] C. Herdy, R. Vale, J. D. Silva et al., "Occurrence and type of sports injuries in elite young Brazilian soccer players," *Archivos de Medicina del Deporte*, vol. 34, no. 3, pp. 66–70, 2017.

[15] C. Cui, H. Deng, C. Deng, X. Wang, Y. Shan, and Z. Song, "Study on the effect of low molecular hydrocarbon compounds on coal spontaneous combustion," *Fuel*, vol. 318, p. 123193, 2022.

[16] N. Skulkina, O. A. Ivanov, A. K. Mazeeva et al., "Magnetization processes in ribbons of soft magnetic amorphous alloys," *The Physics of Metals and Metallography*, vol. 119, no. 2, pp. 127–133, 2018.

[17] T. Geng, Z. Zhu, W. Li, and H. Zhang, "Preparation and mechanical properties of ZrCu-based amorphous alloy," *Jinshu Rechuli/Heat Treatment of Metals*, vol. 43, no. 8, pp. 13–17, 2018.

[18] X. Li, J. Zheng, G. Lu, Y. Liu, D. Yu, and S. Li, "Preparation of Fe-Pd based nanoporous amorphous alloys and their electrocatalytic properties during decomposition of formic acid," *Materiali in Tehnologije*, vol. 54, no. 5, pp. 661–667, 2020.

[19] H. Chen, D. Yang, Z. Li et al., "The importance of the deep deltoid ligament repair in treating supination- external rotation stage IV ankle fracture: a comparative retrospective cohort study," *BioMed Research International*, vol. 2020, Article ID 2043015, 8 pages, 2020.

[20] S. K. Jin, K. W. Young, H. K. Cho, and S. M. Lim, "Arthroscopic anterior talofibular ligament repair for chronic ankle instability with concomitant lesions of the ankle," *Arthroscopy and Orthopedic Sports Medicine*, vol. 7, no. 1, pp. 1–7, 2020.

[21] N. Matsumura, Y. Kawano, R. Furuhata, H. Kimura, T. Suzuki, and T. Iwamoto, "Comparison between trans-articular and subacromial stabilization with ligament repair for acute acromioclavicular dislocation," *The Open Orthopaedics Journal*, vol. 14, no. 1, pp. 8–14, 2020.

[22] F. Figueroa, D. Figueroa, and J. Espregueira-Mendes, "Hamstring autograft size importance in anterior cruciate ligament repair surgery," *EFORT Open Reviews*, vol. 3, no. 3, pp. 93–97, 2018.

[23] C. Heusdens, G. P. Hopper, L. Dossche, and G. M. Mackay, "Anterior cruciate ligament repair using independent suture tape reinforcement," *Arthroscopy Techniques*, vol. 7, no. 7, pp. e747–e753, 2018.

[24] J. List and G. S. Difelice, "Preoperative magnetic resonance imaging predicts eligibility for arthroscopic primary anterior cruciate ligament repair," *Knee Surgery, Sports Traumatology, Arthroscopy*, vol. 26, no. 2, pp. 1–12, 2017.

[25] J. T. Mehl, C. Kia, M. Murphy et al., "Posteromedial ligament repair of the knee with suture tape augmentation: a biomechanical study," *The American Journal of Sports Medicine*, vol. 47, no. 12, pp. 2952–2959, 2019.

Research Article

Mathematical Model and Simulation Calculation Method Based on the Exfoliation of Single-Layer Graphene from Dispersed Carbon Nanotubes

Xudong Sha and Li Zhao [iD]

Department of Mathematics and Physics, Zibo Normal College, Zibo, 255100 Shandong, China

Correspondence should be addressed to Li Zhao; 9029001017@zbnc.edu.cn

Graphene is a two-dimensional material with excellent performance and unique structure. Since its successful manufacturing in 2004, it has quickly become a research hotspot in the fields of materials, chemistry, physics, and engineering. This article focuses on the study of exfoliated single-layer graphene based on dispersed carbon nanotubes and understands the related theories of carbon nanotubes and exfoliated single-layer graphene on the basis of literature data. The mathematical model and simulation calculation method are analyzed, and then, the effect of the single-layer graphene peeling based on the dispersed carbon nanotubes is tested, mainly to the experimental verification of the peeling process parameters and the influence of the dispersant on the peeling effect, and then, the peeled graphite quality of the graphene was tested, and the test results showed that the thickness of single-layer pure graphene is 0.6-0.9 nm, and the experimental statistics show that the graphene of single-layer and double-layer occupies 81% of the experimental sample; most of the single-layer graphene exfoliated based on dispersed carbon nanotubes in this paper is single-layer, two-layer graphene, and a relatively small amount of multilayer graphene.

1. Introduction

In recent years, due to the widespread application of computer technology and the mature development of computing technology, a new round of scientific and technological revolution has been produced for computer simulation methods [1, 2]. In addition to theoretical research and empirical analysis, computer molecular simulation has also become another important scientific investigation method for people to understand the microcosm. At the same time, it is the main tool and method for new material design research [3, 4]. The computer extracts numerical values related to atomic diffusion coefficient, electron diffusion orbital through dynamic simulation, and numerical values that cannot be reflected in theoretical research or experiments [5, 6].

As a major type of petrochemical raw material, carbon nanotubes are widely used in the separation, refining, and processing of products in the chemical industry such as petrochemical, gasoline, and natural gas [7]. The special physical properties of various aspects, such as electricity, have attracted the attention of foreign scientists [8, 9].

The natural absorption isotherms of hydrogen atoms in pore size carbon nanotubes at different working temperatures have been found that under high and low temperature conditions, a moderate increase in the diameter of the carbon tube can also help hydrogen storage [10]. Therefore, some researchers have developed almost equivalent models to analyze the mechanical properties of carbon tubes used as reinforcement materials. The research results show that when the total integral number of carbon nanotubes is fixed, the measured value of sidewall/resin carbon nanotubes

increases as the diameter of carbon nanotubes increases and continues to remain constant after exceeding the specified value. When the diameter of carbon nanotubes reaches sixty to eighty nanometers, the strength of the single-wall carbon/composite is maximized. When the volume fraction of carbon nanotubes changes, it can be found that as the volume fraction of carbon nanotubes increases, the measured value of Young's axis also increases accordingly. In other words, when the volume fraction of carbon tubes reaches 25%, the axial elastic modulus of the composite resin with the same orientation of carbon nanotubes can reach 330 GPa. At the same time, in the case of composite resins in which carbon nanotubes are randomly distributed in the range of 0 to 7%, as the volume fraction of carbon nanotubes increases, the measured value also increases [11]. Some researchers studied the exfoliated graphene and chose N,N-dimethyl-propylamine, N-(3-dimethylaminopropyl)methacrylamide, and 2-(tert-butylamino)methacetonitrile. As a solvent, it participates in the production of graphene, but because the content of the graphene diffuser produced by it varies greatly and, at the same time, due to the continuous expansion of raw materials and the continuous peeling of the precipitate, the content of graphene in the solution reaches 15 mg/mL^{-1}. This is due to the strong interaction between the substance in the solution and the graphene. Therefore, the interaction between the solvent and graphene is the key reason for determining the content of graphene in the solution, and it is also the main reason to consider when choosing the solvent [12]. Some researchers used three different molecular ratios. The preparation of graphene solution was studied through the three-proportion system method. The above three parts of the mixed solution must be mixed at a high speed of 120 revolutions per minute for ten minutes before use, and the solution and the coloring solvent must be thoroughly mixed. When the molar ratio of BA reached 1 : 3, the dispersed content of graphene was as high as 6.5 mg/mL. When the NBA molar ratio reaches 1 : 4, the graphene content is only 0.09 mg/mL, and when the molar ratio reaches 1 : 3, it is only one-72nd, and it also shows that this ratio will make the n-butanol molecule internal self-bonding generated, so that the individual DMF solution can be stripped to obtain graphene, but different mixed solutions can neither guarantee the dispersion stability of graphene nor the stability of the graphene diffusion liquid, so different mixed solutions can affect graphene. The diffusion concentration produced a great difference [13]. This type of research lacks data support, and the conclusions drawn are still open to question. In summary, the research on the preparation of graphene has attracted much attention, but the preparation process is affected by many factors, so it is necessary to investigate these factors in depth.

This paper studies the exfoliation of single-layer graphene based on dispersed carbon nanotubes and analyzes the structure of carbon nanotubes, the preparation method of exfoliated single-layer graphene, and the factors affecting the stripping effect on the basis of literature data. Research is carried out based on the mathematical model and simulation calculation method of the single-layer graphene exfoliated by dispersed carbon nanotubes, and then, the graphene exfoliated by this method is tested, and relevant conclusions are drawn from the test results.

2. Carbon Nanotubes and Exfoliated Single-Layer Graphene

2.1. The Structure of Carbon Nanotubes.
The basic structure of the carbon tube can be obtained using graphene sheet mapping [14]. The grid of the graphite sheet is represented by the vector $C = na_1 + ma2$ (n and m are integers, and a_1 and a_2 are the unit vectors of the graphite layer) [15]. The basic process of using flat grid points in the graphite layer to make carbon nanotubes is shown in the figure: starting from grid point zero, first use grid point A to establish grid vector C, and then, establish a line perpendicular to vector C, and then use points O and B to indicate. This point is a threaded grid point in the two-dimensional layer of the graphite layer, and the vector OB is a convertible vector, represented by T (see Figure 1). The straight line OD is a line parallel to the unit vector A, and the angle between the carbon-carbon bond of the hexagonal lattice perpendicular to the vector ODC and the sawtooth axis along the sawtooth axis of the hexagonal graphite lattice and the OD is θ. A line C passing through the spiral vector perpendicular to point A and a line perpendicular to point OB intersect at point B at point B'. The atomic weight contained in the rectangular OAB'B is the atomic weight contained in the single-walled carbon nanotube unit cell. On the axis OB, roll the powder sheet and align OB and A with the axis AB$'$ or align the axis OB with the axis AB$'$ to form the circumference of the main body of single-walled carbon nanotubes, and form the single-walled carbon tube of the main body at OB; the OA is formed around the single-walled carbon tube. Throughout the development process, it has been found that two parameters (n and m) can be used to describe single-walled carbon tubes. Regardless of the attribute, the structure of single-walled carbon nanotubes is completely determined by two quantities (n and m) (diameter and helix angle or both showing the graphite sheet structure index or helix vector C and translation vector T). Therefore, only selecting the spiral vector C of the graphite mesh determines the basic structure of the carbon tube and various technical parameters [16].

2.2. Preparation Method of Exfoliated Single-Layer Graphene

2.2.1. Mechanical Peeling Method.
The mechanical peeling method, as the name implies, is to use external physical and mechanical forces to resist the van der Waals force between the toner layers to peel the toner [17]. The raw material often used here is highly oriented pyrolytic graphite. The process of manufacturing graphene involves gradually grinding centimeter-sized graphite blocks into smaller graphite flakes, and then grinding them into nanoscale graphite flakes. Graphite flakes continue to decompose and become thinner and thinner.

2.2.2. Liquid Phase Exfoliation Method.
The liquid phase exfoliation method is a solution that can be produced
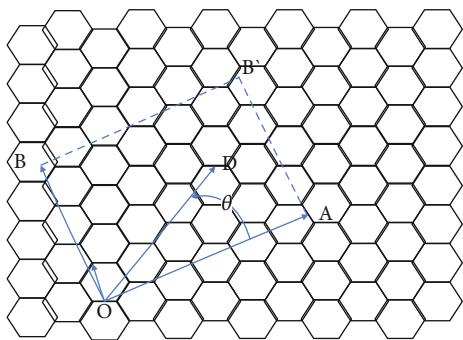
Figure 1: Schematic diagram of graphene sheet mapping to carbon nanotubes.

industrially, and it is also suitable for the manufacture of graphene composite materials [18]. The exfoliation method must overcome the van der Waals force between graphite layers, and the diffusion of graphite in liquid is the most direct and effective way to reduce the van der Waals force. Therefore, the liquid phase exfoliation method generally includes the following three stages: (1) the diffusion process of graphite in the solvent; (2) the auxiliary exfoliation by means of ultrasound, microwave, shear, heating, and electrochemistry; and (3) graphite obtained by centrifugation. The exfoliation preparation of graphene solution can include two types of substances: direct liquid phase exfoliation and auxiliary liquid phase exfoliation [19]. Figure 2 is a schematic diagram of the principle that the solvent disperses graphene in the solution smoothly.

2.2.3. Chemical Vapor Deposition Method. After decomposing some carbon-containing compounds, other forms of carbon can be converted to graphitic carbon. In subsequent catalysis experiments, the researchers found that the contact of hydrocarbons or carbon vapor with nickel or single crystal platinum can also form a graphite layer [20]. Subsequent studies have shown that the filled *d* orbitals of transition metals can absorb some carbon atoms. This provides a basis for the preparation of graphene by CVD [21]. When the carbon material is decomposed at a high temperature, the carbon atoms combine with the metal to form a carbon source. Due to the limited amount of molten metal carbon, sp2 hybrid carbon is deposited to form graphene. The type, concentration, and duration of the carbon source introduced during the deposition process have a significant impact on the size and number of graphene layers obtained. Figure 3 shows the preparation process of the CVD method.

2.2.4. Granulator Method. When the granulator rotates at a high speed, the water tank on the granulator rotates around the main shaft of the turntable and rotates around its own main shaft, thereby realizing planetary motion. Under the influence of high-speed centrifugal force, the crushing ball and the material in the tank rotate together at high speed, and a higher kinetic energy is formed in the relative movement between the crushing ball and the material. The shear stress and compressive stress between them cause the material to be stripped and crushed. The use of granulation in

graphene production roughly includes wet granulation and dry granulation. The main medium of granulation is organic solvent (such as DMF, NMP, and cyclobutane) [22].

2.3. Factors Affecting Peeling Effect. Because the surface energy of graphene is high, the surface energy of the solution selected in the production process must be consistent with the surface energy of graphene, and it can diffuse into the solution stably. But at the same time, solutions suitable for exfoliating graphene are usually expensive and toxic. Water is the most commonly used solution, which is relatively safe and has the highest biocompatibility. However, the surface tension of water is far from that of graphene. Regarding this issue, R&D personnel have done a lot of research and added surfactants to adjust the H tendency so that the graphene is exfoliated from the water phase [23].

2.4. Simulation Calculation Method. Molecular simulation is usually a classic engineering-based research method, including molecular engineering, Monte Carlo, and molecular dynamic simulation [24]. This method regards the molecular model or system as a classical engineering model and calculates the molecular energy by repeatedly sampling the constitutive space of the molecular system to obtain the molecular orbital and structural properties. Molecular dynamic (MD) simulation is a type of molecular simulation that not only studies the structural properties of molecular systems but also analyzes the thermodynamics, migration, and chemical properties of the system. Therefore, it is widely used in materials, biopharmaceuticals, chemistry, and other fields.

(1) The molecular dynamic simulation process is mainly composed of the following three parts. (1) Calculate the total kinetic energy of the entire system. (2) Calculate the internal force of each molecule (atom) from the relationship between kinetic energy and force. Then, according to Newton's classical mechanics, the position of the atom can be inferred. (3) Solve physical quantities such as dynamics and thermodynamic properties according to the structural properties of the system [25]

(2) Some important issues in molecular dynamic simulation

2.4.1. Potential manipulation and energy optimization. Dynamic function is a form of function that controls the interaction force between atoms, which directly determines the dynamic energy of a system composed of different atoms, and is the most important parameter to control dynamic simulation [26]. For each atom, various potential characteristics must be selected to explain the interaction between them. A typical potential function is usually formed by superimposing various forms of interaction between individuals, such as the following equation:

$$U = \sum U_{bonds} + \sum U_{angles} + \sum U_{dihedral} + \sum U_{improper} \\ + \sum U_{inverison} + \sum U_{cross} + \sum U_{\text{int } er}. \tag{1}$$
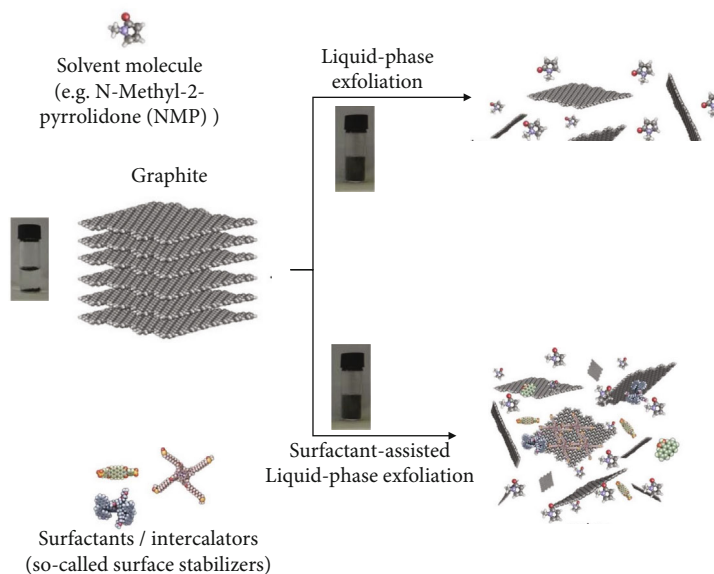
FIGURE 2: Liquid phase exfoliation (LPE) process.
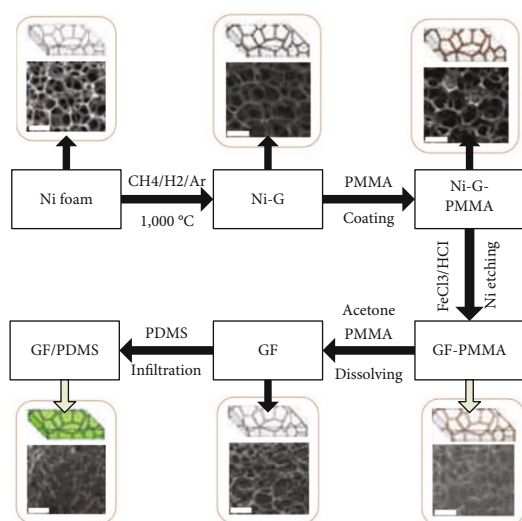
FIGURE 3: Schematic illustration of the preparation of grapheme by CVD method.

In the formula, the following are shown: (1) the potential energy caused by the expansion and contraction of the bond; (2) potential energy caused by the bending of the bond angle; (3) the potential energy when the dihedral angle deviates from the equilibrium position; (4) potential energy caused by pseudo-distortion; (5) potential energy caused by face flip; (6) interaction, potential energy caused by coupling; and (7) intramolecular nonbond interaction.

2.4.2. Conditions. In order to generate relatively accurate regular statistical data and accurately predict the macroscopic properties of materials and structures, it is necessary to perform MD simulations on systems with a large number of microscopic particles. However, due to the limitations of existing calculation conditions, up to 108 particles can be simulated, which is different from the macroscopic size,

which is not enough at present. Periodic restrictions are usually introduced in the dynamic simulation to eliminate the restrictions as much as possible. In other words, the creation of a central unit gives a period limit that allows the system to recur in space and expands the system to infinity [27].

2.4.3. Overall and temperature and pressure control. MD simulates the motion of the system on the atomic scale, and the molecules perform a large amount of thermal motion. Therefore, statistics must be performed on the system containing a large number of particles to represent the statistical sample. In addition, the system for studying thermodynamics cannot be infinite, it must be finite. In quantum mechanics, the sum of the quantum states of each small particle in a thermodynamic system is its microscopic state. As a statistical engineering concept, the collection represents a collection of thermodynamic systems with the same macroscopic state but not necessarily the same microscopic state. The macroscopic state of the thermodynamic system mainly includes temperature (T), pressure (P), volume (V), and energy (E). Therefore, in the case of the same chemical composition of the system, the set can be divided into volume and energy harvesting NVE ensemble, pressure and temperature NPT set, same volume and temperature NVT set, etc.

When different holistic therapies are used in the system, the molecules in the system are in different states. Therefore, for different structures and molecules, different sets must be selected accordingly to control macroscopic conditions such as temperature and pressure.

The dynamic simulation in this paper mainly adopts the Berenson constant temperature variable method and proportional coefficient constant pressure method to control.

(1) Berenson variable scale thermal bath method. This method performs temperature control by connecting the analog system to a thermostatic bath with a temperature of

T. This means that the heat exchange rate is proportional to the temperature difference between the two.

$$\frac{dT(t)}{dt} = \frac{T_0 - T(t)}{\tau}.\tag{2}$$

1 is called the relaxation time, and the smaller the equilibrium time, the shorter (usually choose c~0. lps). As mentioned earlier, the dynamic simulation uses the difference formula to approach the differential equation step by step. Here, Taylor's expansion and Fourier's law are used to expand in 2 places to solve the problem:

$$T(t) = T_0 + (T(0) - T_0)e^{-t/\tau},\tag{3}$$

$$\frac{T(t + \Delta t/2)}{T(t - \Delta t/2)} = \lambda^2,\tag{4}$$

where 3 is the acceleration factor.

2.5. Principles of Simulation Calculation. The basic principle of molecular dynamics is to first reflect all kinds of particles to its original position and momentum and then adjust the motion rules of these particles to completely obey the Newtonian equation of motion [28]. The data can be used to solve the equations to obtain displacement, velocity, and acceleration. The principles of statistical physics calculate system mechanics, thermodynamics, kinetics, and their properties.

Imagine a system composed of N particles; the sum of the total kinetic energy and kinetic energy of the particles is the total kinetic energy of the entire system. According to Newton's second law, the acceleration of particle i is

$$a = \frac{F}{m}.\tag{5}$$

According to classical mechanics, force 1 received by each particle i is the negative gradient of the potential energy function U:

$$F_i = -\nabla_i U.\tag{6}$$

It can be seen from the above that the basic principle of molecular dynamic modeling is to first obtain the dynamic ability of the particles from the relative position of the moving particles and then calculate the force acting on the particles and the acceleration of motion by Newton's second law. After that, through the original velocity and initial displacement, the velocity and displacement after time t can be obtained, and then, through repeated cycles, the velocity and displacement of new particles can be obtained every day. The basic principle of solving the Newtonian equation of motion above is to resolve a normal quadratic differential equation step by step through the finite difference method in a very short time step. Some classic calculations are summarized below.

(1) The Verlet algorithm is usually the simplest and is loved by many researchers. Its generation is the result of Taylor's expansion of particle coordinates at time t:

$$r(t + \Delta t) = r(t) + V(t)\Delta t + \frac{1}{2!}a(t)(\Delta t)^2 + \cdots,\tag{7}$$

$$r(t + \Delta t) = r(t) - V(t)\Delta t + \frac{1}{2!}a(t)(\Delta t)^2 + ..\cdots\tag{8}$$

Add the two equations together to get

$$r(t - \Delta t) = -r(t - \Delta t) + 2r(t) + a(t)(\Delta t)^2\tag{9}$$

3. Mathematical Model and Simulation Calculation Method Based on the Exfoliation of Single-Layer Graphene from Dispersed Carbon Nanotubes

3.1. The Idea of Exfoliating Single-Layer Graphene with Dispersed Carbon Nanotubes

(1) Establish a mathematical model based on the high-speed centrifugal motion of the crushing sphere in the crushing cavity and the motion trajectories of the collision sphere and the shear sphere

(2) The centrifugal shear strength is calculated according to the model

(3) Calculate the scattering limit length of the blind zone between the spheres based on the model, that is, the boundary scattering zone

3.2. Preparation Process. Take 0.8 kg of carbon nanotube powder, 3 kg of dispersant, and 20 m of solvent, and the solvent is NMP. After the above materials are stirred and dispersed in the dispersion tank, they are continuously transported to the 30-liter crusher through a constant-speed diaphragm pump and a 30-liter crusher. The inner cavity is straight 244 mm. In the crusher, the material is continuously supplied to the crusher in a continuous crushing mode. The crusher continuously crushes and outputs the crushed materials at the same time and be crushed and dispersed at a high speed of 11 m/s for 10 hours to form a viscous dispersion of carbon nanotubes.

3.3. Establishment of Carbon Nanotube Model. The carbon tube has a hexagonal crystal structure. Each carbon atom in the carbon nanotube is connected by three other connected carbon atoms, among which the sp two-hybridization is the most important. Single-walled carbon nanotubes can also produce graphene-level mapping, so that the regular hexagonal lattice of carbon nanotubes forms a certain angle with the axis. In other words, the carbon nanotubes now appear to be spiral and have chiral characteristics.

It can be divided into three types: sawfish type, armchair type, and spiral type.

In this article, the Materials Studio modeling software is used to create carbon nanotube models and hybrid carbon nanotubes with different structural parameters. The diameter of the carbon nanotube structure is 8.14 A and the length is 120.52 A.

3.4. Centrifugal Friction Shear Strength.

The simulation calculation method provided in this article is based on the rapid centrifugal movement of the crushing balls in the crushing chamber. The balls collide with each other and shear, peel off the single-wall graphene, and disperse the carbon nanotubes. The mathematical model of collision and friction between spheres calculates the shear strength 1 between spheres as follows.

$$P_d = \frac{F_c}{(1/2)S_q} = \frac{4\rho v^2 r^2}{3R^2}, \tag{10}$$

$$n_i = \frac{V_1}{V_2} = \frac{3m}{4\rho\pi r^3}, \tag{11}$$

$$\sum P = n_i P_d = \frac{mv^2}{\pi R^2 r}, \tag{12}$$

where 1 is the linear velocity of the centrifugal movement of the sphere, R is the radius of the grinding cavity, r is the radius of the sphere, 2 is the shear friction between the two spheres, and S sphere is the surface sphere of the grinding cavity. V is the volume of a single sphere, 5 is the density of the sphere, 3 is the shear strength of the friction between the spheres, 6 is the number of spheres, m is the total mass of the sphere, and 4 is the shear force and the shear strength between the total friction.

3.5. The Dispersion Limit Length of the Dispersion Limit Zone.

Table 1 takes a 30 L grinder with a direct inner cavity of 244 mm and a linear velocity of 11 m/s as an example to calculate the selection of balls and the limit dispersion table:

From the data in Table 1, we can see that when the diameter of the sphere is less than $1.2\mu m$, the dispersion limit length of the limit dispersion zone is less than $1\mu m$. In other words, the dispersion is performed at the nanometer level. The diameter r of the sphere is less than $0.38\mu m$, and the shear strength reaches the limit value of 650.12 GPa, which is the peeling of graphite flakes. The toner flakes are peeled to form a single layer of graphene dispersed in the liquid.

3.6. Stripping Parameters.

The grinding process contains a variety of process parameters that need to be balanced and controlled, such as graphene exfoliation and carbon nanotube diffusion. Through the peeling and diffusion effects after the test, the main parameters of the entire processing flow are determined. After the process parameters are selected, the process parameters need to be strictly controlled to achieve graphene exfoliation and carbon nanotube diffusion. Due to the change of process parameters, the results of delamination and diffusion will be quite different.

3.7. Graphene Detection Method

(1) At present, graphene characterization mainly includes graphene morphology characterization and thickness characterization. The UV spectrophotometer mainly measures the absorbance and concentration of the graphene dispersion obtained by the liquid phase separation method. XRD is used as a tool for measuring crystallinity and interplanar spacing. The 2θ angle of the crystal can be combined with the Bragg equation to calculate the interplanar spacing of the crystal, and the change in the crystal structure can be inferred from the change in 2θ. Graphite is a stable structure formed by stacking graphene sheets, $2\theta = 26.6°$, and the corresponding interplanar spacing is 0.335 nm. When graphite is exfoliated into graphene, the structure of graphite is destroyed, and the peak intensity of graphite at 26.6° is significantly reduced, the peak shape becomes wider, and the intensity and peak can be reduced. The Raman spectrum of graphene contains different D and G peaks. The degree of graphene defects can be judged by the ratio of the D peak to the G peak. The greater the ratio of the two, the greater the defect. XPS can measure the carbon and oxygen content of graphene. Generally speaking, the higher the oxygen content of graphene, the higher the degree of substitution of the original structure of graphene, and the larger the defects in graphene. The Raman and XPS characterization results are complementary to each other. Both SEM and HR-TEM can characterize the external shape of graphene nanosheets. Among them, SEM can measure the internal shape and area of graphene nanosheets and characterize the external shape of multiple graphene sheets, but because of the low resolution, the detailed internal structure of each graphene sheet cannot be clearly seen. HR-TEM's ultrahigh resolution technology can overcome this problem. In the HR-TEM graph, the shape and thickness of the graphene sheet can be clearly seen, and the number of internal grid patterns can be known by magnifying the edge of the graphene sheet and determining the number of graphene layers. At the same time, HR-TEM's selected area electron diffraction (SAED) technology can also make people distinguish single-layer, double-sided, and multilayer graphene. AFM can measure the internal thickness of graphene nanosheets. This function also makes it a powerful tool to characterize the number of graphene layers. By combining the thickness of single-layer graphene, the number of multilayer graphene sheets can be measured, and the distribution of the thickness and number of layers of the prepared graphene nanosheets can be calculated through mathematical statistics of specific numbers

TABLE 1: Select ball and limit dispersion table.

Ball diameter (μm)	Friction shear strength (GPa)	Dispersion limit length l (um)	Remark
1.41	184.98	1.10	Micron dispersion
1.22	215.73	0.95	
1.12	258.98	0.79	Nanodispersion (dispersion of carbon nanotubes)
0.61	431.55	0.49	
0.42	647.23	0.32	Nanodispersion, there will be flattening and tearing phenomenon (exfoliation of single-layer graphene)
0.39	650.12	0.31	
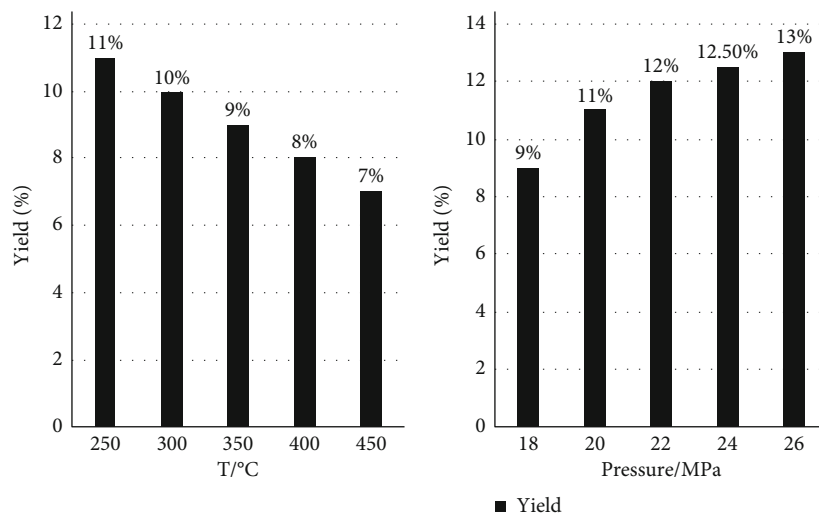
FIGURE 4: Influence of preparation conditions on the effect of exfoliating single-layer graphene.

TABLE 2: Effect of speed on graphene production during centrifugation.

Entry	Rotating speed (rpm)	Time (min)	Yield (%)
1	500		15
2	1000	35	11
3	1500		7

(2) UV-Vis is one of the most commonly used methods to characterize the concentration of graphene. According to Lambert's law, the absorbance of a dilute solution is directly proportional to the thickness of the liquid layer and the concentration of the substance. The reason for being limited to dilute solutions is that the average distance between substances increases at high concentrations, and individual graphene particles are affected by neighboring particles and their charges, changing their ability to absorb specific radiation

4. Based on the Effect of Stripping Single-Layer Graphene from Dispersed Carbon Nanotubes

4.1. The Influence of Preparation Conditions on the Effect of Exfoliating Single-Layer Graphene

(1) The influence of various temperature and pressure variables on the performance of graphene is studied, and the experimental results are shown in Figure 4

As shown in Figure 4, at a high temperature of 250°C, the rate of graphene formation is about ten percent. When the high temperature rises to 450°C, the rate of graphene formation is reduced from 10% to 7%. When the high temperature exceeds 450°C, the solvent decomposes in a large amount. But facts have also proved that high temperature is not conducive to graphene peeling. Due to the increase in pressure, the utilization rate of graphene has increased. When the pressure rises by 26 MPa (the maximum operating pressure allowed by the reactor), the utilization rate of graphene will reach 12%. High pressure may also be thought to help exfoliate graphene.

(2) A brief study of the influence of speed on graphene output during centrifugation is shown in Table 2

It can be seen from Table 2 that under the same reaction conditions and the same separation time, the yield of graphene samples is 15% when the speed is 500 rpm, the yield of graphene samples is 11% when the speed is 1000 rpm, and the yield of graphene samples is 1500 rpm when the speed is 1500 rpm. The rate is 7%. The yield of graphene samples decreases as the rotation speed increases.
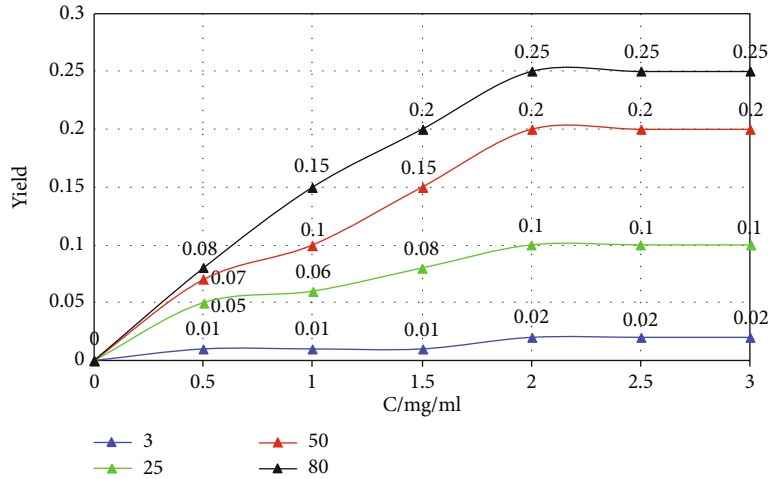
Figure 5: Influence of the amount of dispersing aids on the effect of exfoliating single-layer graphene.

Table 3: Calculated value of excess molar volume.

Water volume fraction (Vw)	Density	Excess molar volume
1.0	0.997	0.00
0.9	0.999	-0.10
0.8	1.002	-0.25
0.7	1.005	-0.44
0.6	1.008	-0.67
0.5	1.010	-0.96
0.4	1.011	-1.22
0.3	1.001	-1.61
0.2	0.998	-154
0.1	0.982	-1.23

4.2. The Influence of the Amount of Dispersing Aids on the Peeling Effect of Single-Layer Graphene.

The system was prepared with different concentrations of dispersing aids and peeled at 3500 rpm for 15 minutes and then centrifuged at 1100 rpm for 35 minutes to obtain a graphene dispersion. The law of concentration is shown in Figure 5.

It can be seen from Figure 5 that, as the concentration of the dispersant increases, the concentration begins to decrease and eventually stabilizes and no longer changes. The initial increase in the concentration of the dispersion aid is due to the fact that it provides more stabilizers for the adsorption of the graphene surface, resulting in an increase in the stability of the dispersed graphene. However, when the polymer concentration exceeds the critical value (2 mg/mL), the dispersed graphene concentration does not increase but decreases. This phenomenon is because the excess dispersant molecules entangle with each other to form supramolecular structures such as micelles. The supramolecules are too large to enter the outer layer of the space graphene sheet, and as a result, the amount of graphene dispersed does not increase. In short, the optimal dispersion concentration of 2 mg/mL is selected and then determined as a constant process parameter.

4.3. Stability of Graphene Dispersion.

Under normal circumstances, the stability of solute molecules (hereinafter referred to as graphene) in solution mainly depends on three kinds of interactions: the interaction between the solvent and the solute, the interaction between the solvent and the solvent, and the interaction between the solute. In the mixed solvent system, the solvent-cosolvent interaction also has a significant impact on the solvent-solute interaction and solute stability. Excess molar volume, as a kind of excess thermodynamic force, and excess molecular volume may reflect the interaction between molecules in the mixture. For a mixed system of water and TMU, the excess molecular weight can be calculated by the following formula. Table 3 shows the calculated value of excess molar volume.

$$V^E = [xM_1 + (1-x)M_2]\rho - xM_1\rho_1 - (1-x)M_2\rho_2. \quad (13)$$

In the formula, 1 and 2 represent the density of water, TMU and water-TMU and mixed solvent, respectively, and 3 and 4 represent the density of water and TMU, respectively.

It can be seen from Table 3 that when the volume fraction of water is 0.3, the excess molecular volume of the mixed solvent is the minimum, and the dispersion concentration of graphene is the maximum.

The concentration of the dispersion aid is selected as 2 mg/mL, and the relationship between the eccentricity of the graphene concentration (left) and the sedimentation time (right) is obtained. The initial graphite concentration is 80 mg/mL, the shear removal time is 15 minutes, and the solution is left for 6 hours. Remove the supernatant and centrifuge at different speeds for 35 minutes. Take the supernatant and measure the absorbance. After calculating the concentration, take the supernatant and observe the concentration of the graphene dispersion after different precipitation times. The results are shown in Figure 6.

It can be seen from Figure 6 that the graphene concentration is inversely proportional to the eccentricity. If the centrifugation speed is slow, a high-concentration graphene
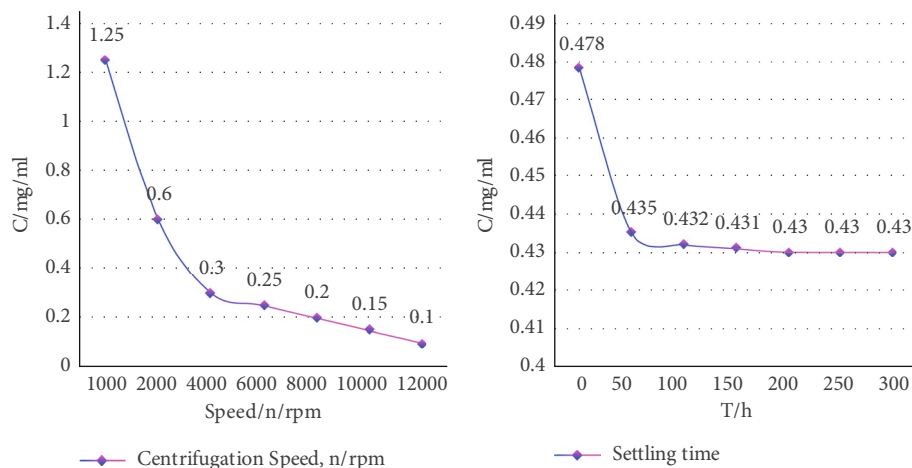
Figure 6: Stability of graphene dispersion.
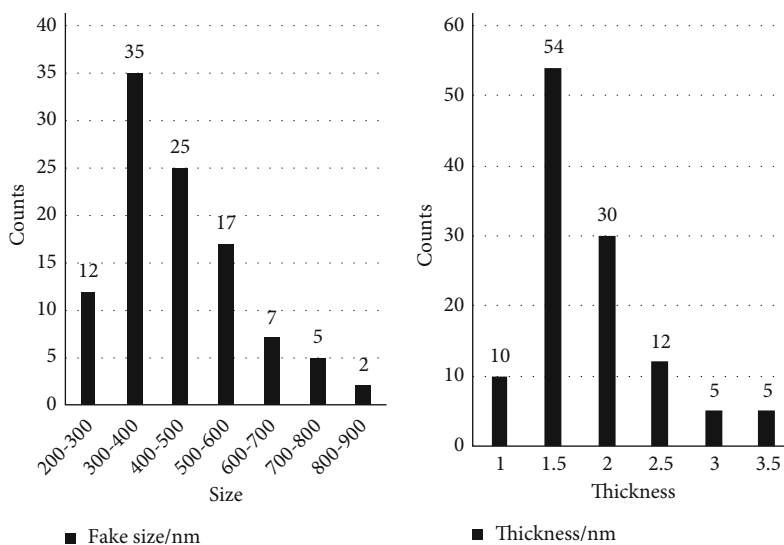
Figure 7: Evaluation results of graphene peeling state.

dispersion can be obtained. On the contrary, the obtained graphene concentration is low. In the actual preparation process, the concentration and stability of the graphene dispersion are the most significant factors. At high eccentricity, the graphene dispersion is very stable, but the concentration is low. The obtained graphene has a high concentration, but the dispersibility is unstable. Precipitation experiments show that after 2 days at room temperature, about 96% of graphene is still stably dispersed in the system. This indicates that the entire system is in a stable state.

4.4. Evaluation of the Exfoliation State of Graphene. The AFM and TEM testing methods were used to characterize the exfoliation state of graphene, and the resulting sheet size distribution and thickness distribution are shown in Figure 7.

It can be seen from Figure 7 that more than half of the graphene sheets are 300-500 nanometers in size, and more than 80% of the graphene sheets are about 1.5 nanometers

in size. The thickness of a single layer of pure graphene is 0.6-0.9 nm, and the thickness of each layer is slightly larger than that of pure graphene, because the graphene sheet here adsorbs a dispersion aid. Thickness statistics show that most of the graphene obtained in the experiment is single-layer, double-layer, and a very small part of graphene with few layers.

5. Conclusions

This article focuses on the exfoliation of single-layer graphene based on dispersed carbon nanotubes. This paper establishes a mathematical model based on the high-speed centrifugal motion of the crushing ball in the crushing cavity and the motion trajectories of the collision ball and the shearing ball. According to the model, the centrifugal shear strength and the scattering limit length of the blind zone between the spheres are calculated, that is, the boundary scattering region. After understanding the relevant theories,

the exfoliated single-layer graphene based on dispersed carbon nanotubes is analyzed, and then, the exfoliated single-layer graphene based on this method is examined. The test results show that the thickness of each layer of the graphene stripped in this paper is slightly larger than that of pure graphene, because the graphene sheet here adsorbs the dispersion aid, and most of the graphene stripped in the experiment is in a single-layer and double-layer layers; very few of them are multilayered. Most of the data in this study are from data sources, but a small part of the data does not have sufficient evidence to prove that it is true and effective.

Data Availability

No data were used to support this study.

Conflicts of Interest

The authors declare that there are no conflicts of interest regarding the publication of this article.

References

[1] D. Voiry, J. Yang, J. Kupferberg et al., "High-quality graphene via microwave reduction of solution-exfoliated graphene oxide," *Science*, vol. 353, no. 6306, pp. 1413–1416, 2016.

[2] Z. M. Markovic, "Semi-transparent, conductive thin films of electrochemical exfoliated graphene," *RSC Advances*, vol. 6, no. 45, pp. 39275–39283, 2016.

[3] M. P. Weir, D. W. Johnson, S. C. Boothroyd et al., "Extrinsic wrinkling and single exfoliated sheets of graphene oxide in polymer composites," *Chemistry of Materials*, vol. 28, no. 6, pp. 1698–1704, 2016.

[4] T. Tomašević-Ilić, J. Pešić, I. Milošević et al., "Transparent and conductive films from liquid phase exfoliated graphene," *Optical and Quantum Electronics*, vol. 48, no. 6, 2016.

[5] Z. S. Metaxa, "Exfoliated graphene nanoplatelet cement-based nanocomposites as piezoresistive sensors: influence of nanoreinforcement lateral size on monitoring capability," *Ciência & Tecnologia dos Materiais*, vol. 28, no. 1, pp. 73–79, 2016.

[6] T. Zhan, X. Wang, X. Li, Y. Song, and W. Hou, "Hemoglobin immobilized in exfoliated Co$_2$Al LDH-graphene nanocomposite film: Direct electrochemistry and electrocatalysis toward trichloroacetic acid," *Sensors and Actuators B Chemical*, vol. 228, pp. 101–108, 2016.

[7] X. Xu, B. Karami, and D. Shahsavari, "Time-dependent behavior of porous curved nanobeam," *International Journal of Engineering Science*, vol. 160, article 103455, 2021.

[8] T. Kavinkumar and S. Manivannan, "Uniform decoration of silver nanoparticle on exfoliated graphene oxide sheets and its ammonia gas detection," *Ceramics International*, vol. 42, no. 1, pp. 1769–1776, 2016.

[9] A. Radocea, T. Sun, T. H. Vo, A. Sinitskii, N. R. Aluru, and J. W. Lyding, "Solution-synthesized chevron graphene nanoribbons exfoliated onto H:Si(100)," *Nano Letters*, vol. 17, no. 1, pp. 170–178, 2017.

[10] Y. Ma, D. Bai, X. Hu et al., "Robust and antibacterial polymer/mechanically exfoliated graphene nanocomposite fibers for biomedical applications," *ACS Applied Materials & Interfaces*, vol. 10, no. 3, pp. 3002–3010, 2018.

[11] A. Sham and S. M. Notley, "Adsorption of organic dyes from aqueous solutions using surfactant exfoliated graphene," *Journal of Environmental Chemical Engineering*, vol. 6, no. 1, pp. 495–504, 2018.

[12] C. I. Idumah, A. Hassan, and S. Bourbigot, "Influence of exfoliated graphene nanoplatelets on flame retardancy of kenaf flour polypropylene hybrid nanocomposites," *Journal of Analytical and Applied Pyrolysis*, vol. 123, pp. 65–72, 2017.

[13] G. T. Usca, J. Hernandez-Ambato, C. Pace, L. S. Caputi, and A. Tavolaro, "Liquid-phase exfoliated graphene self-assembled films: low-frequency noise and thermal-electric characterization," *Applied Surface Science*, vol. 380, pp. 268–273, 2016.

[14] L. Zeng, J. Shi, J. Luo, and H. Chen, "Silver sulfide anchored on reduced graphene oxide as a high-performance catalyst for CO$_2$ electroreduction," *Journal of Power Sources*, vol. 398, pp. 83–90, 2018.

[15] Z. Ji, M. Perez-Page, J. Chen, and S. Holmes, "Nitrogen doped reduced electrochemically exfoliated graphene oxide inserted carbon black as novel catalyst support for the hydrogen fuel cell," *ECS Meeting Abstracts*, vol. MA2020-02, no. 36, pp. 2323–2323, 2020.

[16] S. Mypati, A. Sellathurai, M. Kontopoulou, A. Docoslis, and D. P. J. Barz, "Synthesis and performance evaluation of exfoliated graphene nanoplatelet hydrogels as electrodes for supercapacitors," *ECS Meeting Abstracts*, vol. MA2020-01, no. 10, pp. 863–863, 2020.

[17] Á. Gallardo-López, J. Castillo-Seoane, C. Muñoz-Ferreiro, C. López-Pernía, A. Morales-Rodríguez, and R. Poyato, "Flexure strength and fracture propagation in zirconia ceramic composites with exfoliated graphene nanoplatelets," *Ceramics*, vol. 3, no. 1, pp. 78–91, 2020.

[18] M. D. Nurhafizah, A. A. Aziz, A. B. Suriani, A. Mohamed, and T. Soga, "Low-temperature exfoliated graphene oxide incorporated with different types of natural rubber latex: electrical and morphological properties and its capacitance performance," *Ceramics International*, vol. 46, no. 5, pp. 5610–5622, 2020.

[19] P. Wang, T. Yao, Z. Li et al., "A superhydrophobic/electrothermal synergistically anti-icing strategy based on graphene composite," *Composites Science and Technology*, vol. 198, article 108307, 2020.

[20] J. You, B. Oh, Y. S. Yun, and H.-J. Jin, "Improvement in barrier properties using a large lateral size of exfoliated graphene oxide," *Macromolecular Research*, vol. 28, no. 8, pp. 709–713, 2020.

[21] A. Islam, B. Mukherjee, K. K. Pandey, and A. K. Keshri, "Ultrafast, chemical-free, mass production of high quality exfoliated graphene," *ACS Nano*, vol. 15, no. 1, pp. 1775–1784, 2021.

[22] Q. Cui, P. Thakur, C. Rablau, I. Avrutsky, and M. M. C. Cheng, "Miniature optical fiber pressure sensor with exfoliated graphene diaphragm," *IEEE Sensors Journal*, vol. 19, no. 14, pp. 5621–5631, 2019.

[23] A. Kaur and R. C. Singh, "Temperature sensor based on exfoliated graphene sheets produced by microwave assisted freezing induced volumetric expansion of carbonated water," *Journal of Materials Science: Materials in Electronics*, vol. 30, no. 6, pp. 5791–5807, 2019.

[24] J. Gnidakouong, X. Gao, A. Kafy, J. Kim, and J. H. Kim, "Fabrication and electrical properties of regenerated cellulose-loaded exfoliated graphene nanoplatelet composites," *Carbon Letters*, vol. 29, no. 2, pp. 115–122, 2019.

[25] M. Ahmed and T. Imae, "Effect of external magnetic field on cyclic voltammetry of exfoliated graphene-based magnetic composites with conductive polymer and carbon dots," *Journal of Magnetism and Magnetic Materials*, vol. 491, article 165604, 2019.

[26] V. Vasanthi, T. Logu, V. Ramakrishnan, K. Anitha, and K. Sethuraman, "Study of electrical conductivity and photo-electric response of liquid phase exfoliated graphene thin film prepared via spray pyrolysis route," *Carbon Letters*, vol. 30, no. 4, pp. 1–7, 2019.

[27] X. Xu and Y.-L. Hsieh, "Aqueous exfoliated graphene by amphiphilic nanocellulose and its application in moisture-responsive foldable actuators," *Nanoscale*, vol. 11, no. 24, pp. 11719–11729, 2019.

[28] C. Deng, X. Wang, Y. Shan, and Z. Song, "Study on the effect of low molecular hydrocarbon compounds on coal spontaneous combustion," *Fuel*, vol. 318, article 123193, 2022.

Research Article

IoT-Based Intelligent System for Internal Crack Detection in Building Blocks

J. Chinna Babu,[1] **M. Sandeep Kumar,**[2] **Prabhu Jayagopal** (ID)**,**[2] **V. E. Sathishkumar** (ID)**,**[3] **Sukumar Rajendran,**[2] **Sanjeev Kumar,**[4] **Alagar Karthick** (ID)**,**[5] **and Akter Meem Mahseena** (ID)[6]

[1]*Department of Electronics and Communications Engineering, Annamacharya Institute of Technology and Sciences, Rajampet, 516126 Andhra Pradesh, India*

[2]*School of Information Technology and Engineering, Vellore Institute of Technology, Vellore, Tamil Nadu 632014, India*

[3]*Department of Industrial Engineering, Hanyang University, Seoul, Republic of Korea*

[4]*Department of Civil Engineering, Graphic Era (Deemed to Be University), Bell Road, Clement Town, 248002 Dehradun, Uttarakhand, India*

[5]*Renewable Energy Lab, Department of Electrical and Electronics Engineering, KPR Institute of Engineering and Technology, Coimbatore, 641407 Tamil Nadu, India*

[6]*Department of Electrical and Electronic Engineering, Daffodil International University, Ashulia, Savar, Dhaka 1207, Bangladesh*

Correspondence should be addressed to V. E. Sathishkumar; srisathishkumarve@gmail.com
and Akter Meem Mahseena; aktermeem.m@yahoo.com

Cracks that are detected in concrete structures represent significant damage, and they can lead to a detrimental effect on the structure's durability. Their identification in a timely manner can help ensure structural safety and guide in-depth maintenance operation. Automatic detection of such cracks has been proposed using internal crack detection utilizing ultrasonic sensors in concrete. Cracks within the concrete can be detected using ultrasonic sensors. In this investigation, we introduced an intelligent method that is aimed at developing a crack detection scheme using ultrasonic sensors. These ultrasonic sensors are used for the detection of cracks in buildings which cannot be seen with our naked eyes; they are capable of alerting authorities via SMS message and providing the cracks' location via GSM and GPS modules. To monitor internal cracks in the concrete cubes and cylinders, the ultrasonic sensors can be fixed at the centre of the cube which will be used for interval crack monitoring based on crack detection technology. The grade of concrete used for testing is M_{25}, and it is well mixed with the ingredients of cement, fine aggregate, coarse aggregate, and water. The concrete is placed in the cube moulds having the dimensions $150\,\text{mm} \times 150\,\text{mm} \times 150\,\text{mm}$. The cylinders used in the case of the experimental analysis are of the dimensions of $150\,\text{mm}$ diameter and $300\,\text{mm}$ height. These specimens are cast and kept in the curing tank for 28 days to attain the maximum strength. After completion of the curing period, the specimens were taken out from the tank and weighed. After this weighing process, the cubes and cylinders are about $8.884\,\text{kg}$ and $13.399\,\text{kg}$, respectively. The information about the cracks can be displayed on the LCD, and also, the transmitted short message about the cracks can be exchanged between the devices using IoT.

1. Introduction

Concrete is the most often utilized material in the world for numerous civil infrastructure projects such as bridges and buildings. They are safely constructed by superimposing the various loads to the foundation, but their structural integrity is compromised by a variety of operating environmental factors. As a result, their strength is critical in nature, maintaining a high level of safety structures and durability, and their efficiency factors are critical because civil

infrastructure accounts for a significant portion of the national economy. The adopted ultrasonic sensor system can be classified into two major modules, namely, the hardware module and the software module. An ultrasonic sensor has two main parts, (a) the transmitter and (b) the receiver; the transmitter sends out a signal after it has been reflected off the surface or cracks [1, 2]. The principle of the ultrasonic sensor emits short bursts of high-frequency sound at regular intervals. Background interference is effectively suppressed by using ultrasonic sensors. Almost all materials which reflect the sound can be detected regardless of hue. Microultrasonic sensors are ideal for target distances ranging from 20 mm to 10 m, and they will record the time, pinpoint precision, etc. Some of the sensors can even resolve the signal to 0.025 precision [3, 4].

In this, the ultrasonic sensors play a major role in spotting the crack inside the concrete cube. Through ultrasonic ways, the cracks in the surface can be detected and the depth can be displayed. The GSM (Global System for Mobile Communication), GPS (Global Positioning System), and microcontroller-based broken bridge track detection are, when implemented, an efficient method for the detection of cracks which are present in the tracks. If a stretch is detected, then this sensor will send a signal to the Arduino UNO board which will activate the GPS receiver to exchange the information using IoT [5, 6].

In this paper, we proposed a low-cost, low-power IoT-based embedded technology to help and improve the safety standards for cylindrical concrete by preventing the cracks and impediments in the buildings. The testing crack prototype can identify fractures and impediments on buildings and cracks quickly. The findings indicate that this proposed technology will improve the dependability of safety systems [7–9]. By incorporating these characteristics into real-time applications, it can reduce the accidents by up to 70%. The major objectives of the paper are given below.

(1) The proposed IoT-based GPS and GSM for the internal crack detection system is an assisting unit that uses ultrasonic sensors to identify the cracks in cylindrical concrete available in buildings and bridges, etc.

(2) These sensors will check for the presence of a crack and displays the message on the LCD display if it exists. If the crack is detected, the data can be communicated using IoT

(3) As a result, the proposed method reduces automobile accidents and saves lives and also reduces the economic losses. This method is highly effective in reducing the need of human assistance in detecting cracks

2. Existing Method and Review of Literature

Crack detection is a telltale sign that a building is deteriorating. Crack detection is frequently required during the maintenance stage of a civil structure. In addition, inspection of the structural integrity based on crack analysis becomes substantial for the service life perdition of the structure. The process of determining the cracks using manual processes for large-scale structures is tedious and time-consuming, and many researchers are proposing their models based on image-processing concepts, which allows for a more rapid and efficient measurement of cracks in concrete [8, 9]. The general framework of these models is shown in Figure 1.

Figure 1 depicts an image-processing methodology based on an automated methodology for concrete detection. This model numerically expresses the crack defects, and this method can also be used to detect the internal cracks [10–12].

Figure 1 depicts an image-processing methodology based on an automated methodology for concrete detection. This model numerically expresses the crack defects, and this method can also be used to detect the internal cracks [11, 13].

For identifying and analyzing concrete surface cracks, Hsieh et al. [8] developed an automated technique-based image-processing system. Crack detection is performed based on the crack analysis which is performed on a picture of a concrete surface, and the crack width, length, and area are calculated. A numerical model for crack flaws was created by Bao et al. [3], and the suggested technique is used to identify and quantify the cracks. Mak and Picken suggested an image-based automated crack identification model for postdisaster building evaluation; the authors show that the suggested method may provide considerable benefits in postdisaster building element analysis based on numerical tests [14].

Chidambaram and colleagues [15] offer a hybrid detection method that incorporates both digital picture correlation and acoustic emission. The Otsu method and Sobel's filtering in Talan et al.'s work made use of image-processing techniques to identify cracking flaws in digital pictures. A multifractal analysis of crack patterns was carried out by Gonzalez et al. [16] with applications in reinforced concrete shear walls. In [17], Otsu suggested the identification of surface cracks in tunnel linings based on infrared pictures, and it is an effective crack identification method. Low contrast, uneven light, and severe noise pollution are all prevalent problems in tunnel lining photos, and the proposed solution is capable of addressing them.

Furthermore, one of the most important tasks of pavement surveys is to detect cracks that occur on the pavement surface. It is because if cracks are found early and properly repaired, the cost of road reconstruction can be reduced by up to 80% [18]. As a result, numerous image-processing methods for detecting asphalt pavement cracks where fissures have been formed. Image thresholding algorithm-based road crack identification models by Subramanian et al. [19], Alam et al. [20], and Kogilavani et al. [21] have all provided solutions.

Furthermore, many scholars [22–24] have established models based on edge detection algorithms. Nonetheless, the above-mentioned crack detection models' performance is frequently hampered by the complex texture of asphalt pavement and the shading conditions of digital images [25]. As a result, more sophisticated methods such as to
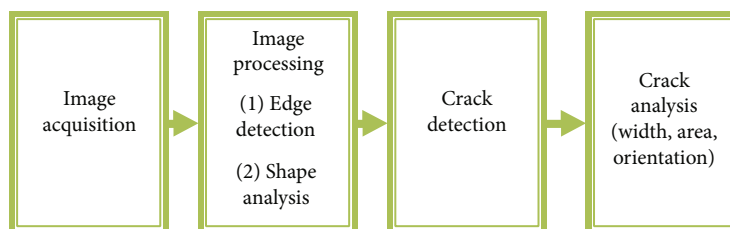
FIGURE 1: Image-processing-based crack detection model.

boost fracture detection performance, beam let transform [21], and shadow reductions [22] have been applied. According to a survey of the literature, applying intelligent image-processing models for automatic crack identification and analysis is becoming more popular.

The mode input is the original image captured by the digital camera. The suggested enhanced Otsu technique is then used to apply the image-thresholding procedure on the original picture. The M2GLD algorithms, as well as the classic Otsu algorithm, were discussed in the previous section, which make up the suggested improved Otsu technique. Following the picture penalization procedure, the picture concentrated effort procedure is used to remove noisy pixels and the noncrack objects mentioned in Figure 2. The research work is considered an image-based automatic crack identification model for postdisaster building evolution; the authors show that the suggested method can provide significant benefits in postdisaster building element analysis based on a numerical experiment [26, 27]. Furthermore, one of the most important tasks of concrete surveys is to detect cracks that occur on the pavement surface. If the cracks are found at early stages and they can be properly repaired, the cost of road reconstruction can be reduced by as much as 80%. As a result, numerous image-processing methods for detecting asphalt pavement cracks have been developed. The image-processing procedure is divided into two steps: firstly, the area with less than a particular number of pixels (Np) are removed, and then, an axis is added to the image length of an object, where

$$ARI = \frac{L_M}{L_N}. \tag{1}$$

The major axis and minor axis lengths are measured using an object-circumscribed ellipse [11–15]. The major axis and minor axis lengths are L_M and L_N, respectively.

The limitations of the existing methods are as follows. This is the research gap identified in existing methods. The limitations are as follows:

(1) The existing method does not have an IoT-based GPS and GSM for internal crack detection system which is an assisting unit that uses ultrasonic sensors to identify the cracks in cylindrical concrete available in buildings and bridges, etc.

(2) The sensors used in the existing method are unable to detect the presence of a crack

(3) Due to these limitations, the existing method cannot reduce the automobile accidents and cannot reduce the economic losses. That is why the existing methods are not effective in reducing the need of human assistance in detecting cracks

3. Materials and Method

3.1. Proposed Method. The "GPS and GSM for internal crack detection" is an assisting unit that uses ultrasonic sensors to identify cracks in cylindrical concrete. The sensors are used to detect the presence of cracks and display the message on an LCD display if the cracks are detected [16–18]. As a result, this proposed method reduces the automobile accidents and saves lives and also reduces the economic losses [19]. The block diagram of the proposed method is shown in Figure 3. The objectives of the proposed method are given below.

(1) The proposed IoT-based GPS and GSM for internal crack detection is an assisting unit that uses ultrasonic sensors to identify the cracks in cylindrical concrete available in buildings and bridges, etc.

(2) Detect impediments trying to access the concrete structures (e.g., buildings, bridges, and dams)

(3) The sensors will check for the presence of a crack and displays the message on the LCD display if it exists. If the crack is detected, the data can be communicated using an IoT device

(4) As a result, the proposed method reduces automobile accidents and saves lives and also reduces the economic losses. This method is highly effective in reducing the need of human assistance in detecting cracks

3.2. Block Diagram for Proposed Method

3.2.1. Arduino UNO. Arduino is a user-friendly hardware and software platform which is freely available, and it is an open source software. The Arduino board can detect input like light from a sensor, a button like in Figure 3, or a twitter tweet and convert them to outputs such as turning a motor, lighting and LED, or turning on a computer. Anything may be posted on the internet. The Arduino IDE (Integrated Development Environment) is a piece of software developed by Arduino that is used to write, compile, and upload code to Arduino devices. This is an open source programme, which is simple to install and use to start compiling code
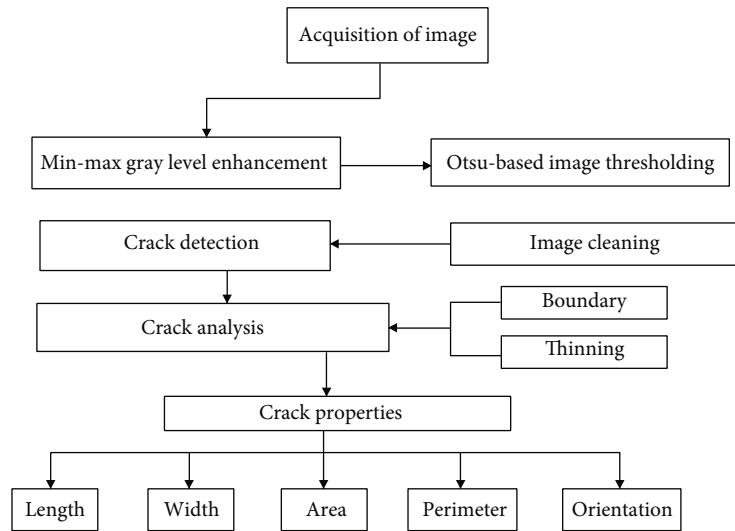
FIGURE 2: Image enhancements with the proposed method.
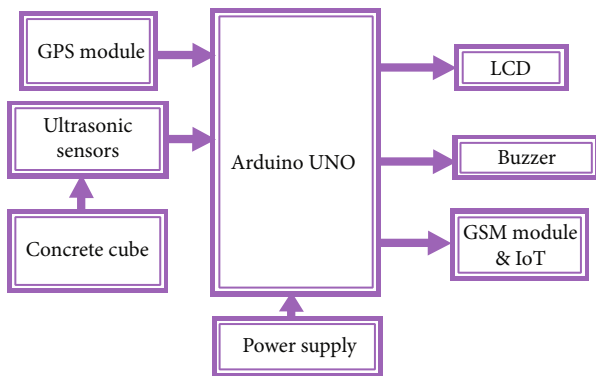
FIGURE 3: Block diagram of the proposed method.

FIGURE 4: Ultrasonic wave travel in air.

on the fly, and is compatible with almost all Arduino modules. The Arduino IDE is an open source software that is used to write and build code for the Arduino module. It is easily accessible for operating systems such as Mac, Windows, and Linux, and it is based on the Java Platform. This environment includes built-in methods and instructions for debugging, modifying, and compiling code.

3.2.2. GSM Module. A GSM modem is also known as a GSM module, and it is a hardware device which uses GSM technology used to connect remote networks. From the standpoint of the mobile phone network, they are substantially identical to a regular phone, including the requirement for a SIM card to identify themselves to the network.

3.2.3. Ultrasonic Sensor. Ultrasonic waves travel at a faster rate than normal sound waves (i.e., the sound that humans can hear). Ultrasonic sensors send ultrasonic pulses into the air and detect reflected waves from objects. Ultrasonic sensors contain a wide range of features such as intrusion alarm systems, automated door openers, and backup sensors for vehicles.

New application industries such as industrial automation equipment and automotive electronic industries are growing and will continue to rise in parallel with the rapid expansion of information processing technology. The research work [14] developed a unique piezoelectric ceramics manufacturing method to create several types of ultrasonic sensors which are small and have very high performance. The below-mentioned catalog's information will assist in making the best use of ultrasonic sensors.

3.3. HC-SR04 Sensor Features

(i) The operating voltage is +5 V

(ii) 2 cm to 450 cm theoretical measuring distance

(iii) 2 cm to 80 cm practical measuring distance

(iv) 3 mm precision

(v) Covered measuring angle: 15°

(vi) 15 mA is the operating current

(vii) 40 Hz is the operating frequency

3.4. HC-SR04 Ultrasonic Sensor: Working. This sensor is frequently used in a variety of applications including distance measurement or object detection. The ultrasonic transmitter and receiver are housed in two eye-like projections on the module's front. The sensor is based on the elementary concept

$$\text{Distance} = \text{Speed} \times \text{Time}. \qquad (2)$$

(a)   (b)
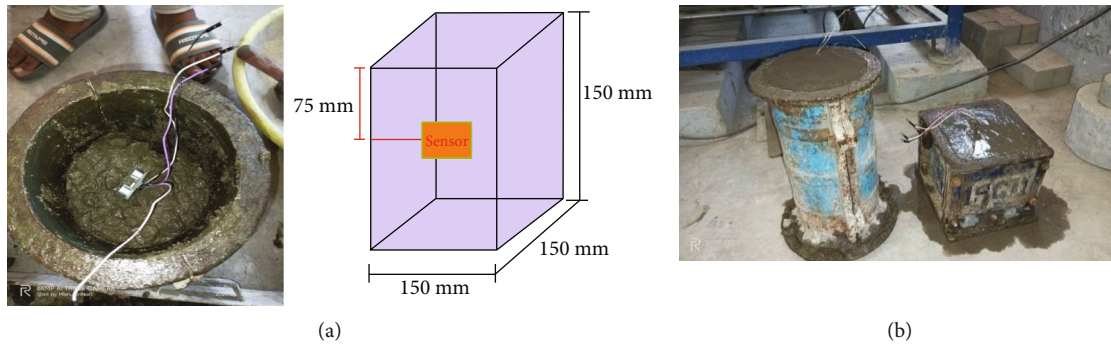
FIGURE 5: (a) Ultrasonic sensors are placed inside the concrete cube and its depth. (b) Wired connections after placing ultrasonic sensors in the concrete cube and cylinder.

The ultrasonic transmitter emits an ultrasonic wave that passes through the air and is reflected back toward the sensor if it comes into contact with any substance. The ultrasonic receiver module detects the reflected wave as depicted in Figure 4.

3.4.1. LCD Display (16 ∗ 2). A liquid crystal display (LCD) screen is a type of electronic display that can be used for a variety of purposes. A 16 ∗ 2 LCD display module is a low-cost module that can be found in a wide range of devices and circuits. A 16 ∗ 2 LCD has two lines and can display 16 characters per line.

3.4.2. Buzzer. A buzzer is also known as a beeper, and it is an auditory signaling device which is mechanical, electromechanical, or piezoelectric. Buzzer and beepers are commonly used in alarm clocks and timers and to validate human input such a mouse click or keyboard keystroke.

4. Result and Discussions

The ultrasonic sensors are placed in a concrete cube as shown in Figure 4, and after 24 hours, these cube specimens are taken out from the moulds and kept in a water tank for curing as shown in Figures 5(a) and 5(b). After 28 days, the curing process can be done, and the specimens are tested for compression under a compressive testing machine (CTM) as per IS 516:1959. If the cracks are not found in the specimen, then it shows no crack detected on the LCD as shown in Figure 6.

If the cracks are found in the concrete cube, the sensors detect the location and width of the crack present, and if the crack is not detected, this means that it does not send any message to the mobiles as shown in Figure 5. If the crack is detected, this means it sends via SMS to the mobile as shown in Figures 7–9. After detecting the crack, the message is displayed on the LCD. For reference, the sensors were named as left and right, where the depth is 11 for one concrete cube, and the data is communicated to the mobile along with the latitude and longitude. Figures 8(a) and 8(b) represent the depth of the cracks available in the right and left sides of the cube. The sensors are placed at the right and left sides of the cube. If the crack is detected by the sen-

FIGURE 6: Specimens kept under curing for 28 days.

FIGURE 7: Displayed message on LCD, when no crack is detected.

sors, then the message is displayed on the LCD connected to the system.

The left sensor is housed within a rectangular cube. As the pressure increases, fractures emerge inside the concrete, which are detected by the sensor and sent through SMS to a smart phone as shown in Figure 10. By not receiving the track's echo, the ultrasonic sensors can detect cracks in buildings and bridges. If the track's echo is received, then that gives the information that no crack is detected in the track. The output of the ultrasonic sensor is rounded and sent to a microcontroller that is linked to GPS and GSM.

To monitor internal cracks in the concrete cubes and cylinders, the ultrasonic sensors were fixed at the centre of the cube which will be used for interval crack monitoring based on crack detection technology. The grade of concrete used is M_{25} and well mixed with the ingredients of cement,

(a)
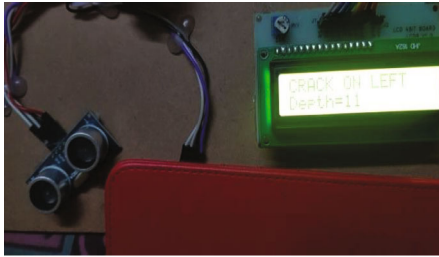
(b)

Figure 8: (a) Detection of internal cracks through LCD display (right). (b) Detection of internal cracks through LCD display (left).
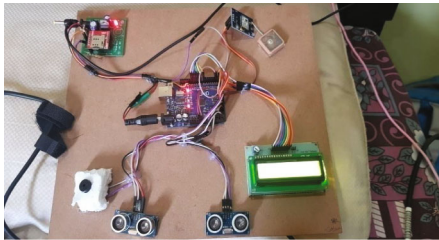
Figure 9: Experimental sensors in the cube setup before placing the cylinder.
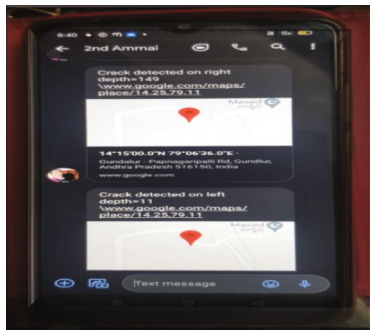
Figure 10: Received message in mobile, when crack is detected.

Table 1: Cube strength for 7 days and detected crack sizes.

S. no.	Load in N	7-day cube compressive strength in N/mm^2	Cracks in mm
1.	50	2.22	0.00
2.	75	3.33	0.00
3.	100	4.44	0.15
4.	125	5.56	0.20
5.	150	6.67	0.30
6.	175	7.78	0.30
7.	200	8.89	0.75
8.	250	11.11	0.75
9.	275	12.22	1.00
10.	300	13.33	1.00
11.	325	14.44	1.75
12.	358	15.91	2.50

Table 2: Cube strength for 14 days and detected crack sizes.

S. no.	Load in N	14-day cube compressive strength in N/mm^2	Cracks in mm
1.	50	2.22	0
2.	100	4.44	0.20
3.	150	6.67	0.50
4.	200	8.89	0.50
5.	250	11.11	0.70
6.	300	13.33	0.70
7.	350	15.56	0.90
8.	400	17.78	1.26
9.	450	20.00	1.55
10.	515	22.88	1.95
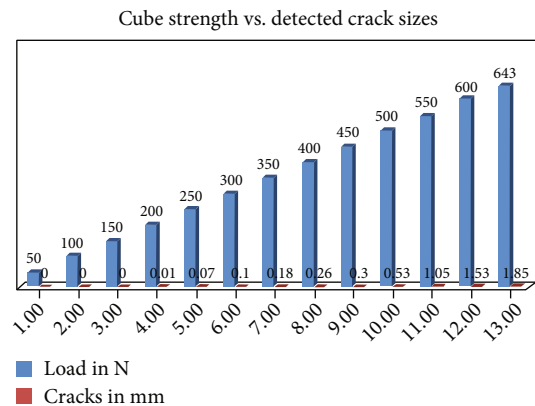
Figure 11: Cube strength vs. detected crack sizes.

a compressive testing machine, and connections were given as shown in Figures 2, 3, and 4. The load is applied gradually with an intensity of 1.4 kN/s. And the results were taken for every 50 N which are shown in Table. 1. The cube and cylinder calculations mentioned in Tables 1 and 2 are given below.

fine aggregate, coarse aggregate, and water. The concrete is placed in the cube moulds having the dimensions 150 mm × 150 mm × 150 mm and the cylinders of dimensions of 150 mm in diameter and 300 mm in height. These specimens were casted and kept in a curing tank for 28 days to attain the maximum strength. After completion of the curing period, the specimens were taken out from the tank and weighed. Cubes and cylinders are about 8.884 kg and 13.399 kg, respectively. Now, the specimens were kept under

Figure 12: Cylinder strength and detected crack sizes.

	28-days splitting tensile strength in N/mm²									
	0.35	0.71	1.06	1.41	1.77	2.12	2.48	2.83	3.18	3.59
Cracks in mm	0	0	0.05	0.1	0.3	0.5	1.15	2.65	3.15	3.5

Table 3: 28-day cube strength and detected crack sizes.

S. no.	Load in N	28-day cube compressive strength in N/mm²	Cracks in mm
1.	50	2.22	0.00
2.	100	4.42	0.00
3.	150	6.67	0.05
4.	200	8.89	0.10
5.	250	11.11	0.10
6.	300	13.33	0.15
7.	350	15.56	0.18
8.	400	17.78	0.26
9.	450	20.00	0.30
10.	500	22.22	0.53
11.	550	24.44	1.05
12.	600	26.67	1.53
13.	643	28.58	1.85

Table 4: Cylinder strength for 7 days and detected crack sizes.

S. no.	Load in N	7-day splitting tensile strength in N/mm²	Cracks in mm
1.	25	0.71	0.00
2.	50	1.06	0.10
3.	75	1.41	0.50
4.	100	1.77	1.30
5.	125	2.12	1.90
6.	179	2.53	2.50

From Figures 11 and 12 and Tables 1, 2, 3, 4, 5, and 6, it is found that the cracks that are detected by the sensors are good enough, and these can be used in monitoring the health of structures. These sensors can be utilized such that a structure which is in a seismic zone can detect and monitor the vibrations that are coming from the earth, and these will be displayed on the screen. The cracks and the vibration sensors can be used for the structures which are under construction and which are already constructed. The sensors are placed in concrete structures for the detection of vibration alerts and cracks, and the information can also be exchanged

Table 5: Cylinder strength for 14 days and detected crack sizes.

S. no.	Load in N	14-day splitting tensile strength in N/mm²	Cracks in mm
1.	25	0.35	0.00
2.	50	0.71	0.00
3.	75	1.06	0.05
4.	100	1.41	0.10
5.	125	1.77	0.30
6.	150	2.12	0.50
7.	175	2.48	1.15
8.	193	2.73	2.65

Table 6: Cylinder strength for 28 days and detected crack sizes.

S. no.	Load in N	28-day splitting tensile strength in N/mm²	Cracks in mm
1.	25	0.35	0.00
2.	50	0.71	0.00
3.	75	1.06	0.05
4.	100	1.41	0.10
5.	125	1.77	0.30
6.	150	2.12	0.50
7.	175	2.48	1.15
8.	200	2.83	2.65
9.	225	3.18	3.15
10.	254	3.59	3.50

between the devices using IoT, so that this proposed method can save the lives of the people living in the buildings.

5. Conclusion

This paper describes the intelligent method for detecting the cracks and impediments in pillars of buildings. This method is cost effective, the reliability of safety measures in collapsing older structures can be improved as a result of this new creative technology, and also, this method is used to identify faults in tracks of the bridges. This helps to detect the cracks in buildings which are not visible to our necked eyes. It is capable of alerting authorities via SMS message and providing the cracks' locations via GSM and GPS modules. This method cannot cause any damage to nearby structures. The design is extremely efficient and user-friendly. The detection of fractures in a surface is very simple using this method. It is simple to use, and power consumption is also very low. Reduction of accidents can be effectively minimized by using this method. Therefore, it is concluded that this intelligent system is very effective and can minimize the accidents that can be caused during disasters by providing the information through mobiles and buzzer sounds.

Data Availability

The data used to support the findings of this study are included in the article.

Conflicts of Interest

The authors declare that there is no conflict of interest regarding the publication of this article.

References

[1] C. Gentile and A. Saisi, "OMA-based structural health monitoring of historic structures," in *8th international operational modal analysis conference, IOMAC 2019*, pp. 671–688, Copengahen; Denmark, 2019.

[2] A. C. Altunışık, F. Y. Okur, S. Karaca, and V. Kahya, "Vibration-based damage detection in beam structures with multiple cracks: modal curvature vs. modal flexibility methods," *Nondestructive Testing and Evaluation*, vol. 34, no. 1, pp. 33–53, 2019.

[3] Y. Bao, Z. Chen, S. Wei, Y. Xu, Z. Tang, and H. Li, "The state of the art of data science and engineering in structural health monitoring," *Engineering*, vol. 5, no. 2, pp. 234–242, 2019.

[4] I. Dikmen, M. T. Birgonul, and S. Han, "Using fuzzy risk assessment to rate cost overrun risk in international construction projects," *International Journal of Project Management*, vol. 25, no. 5, pp. 494–505, 2007.

[5] Y. Frimpong, J. Oluwoye, and L. Crawford, "Causes of delay and cost overruns in construction of groundwater projects in a developing countries; Ghana as a case study," *International Journal of Project Management*, vol. 21, no. 5, pp. 321–326, 2003.

[6] Y. Fujino, D. M. Siringoringo, Y. Ikeda, T. Nagayama, and T. Mizutani, "Research and implementations of structural monitoring for bridges and buildings in Japan," *Engineering*, vol. 5, no. 6, pp. 1093–1119, 2019.

[7] D. Hester and A. González, "A wavelet-based damage detection algorithm based on bridge acceleration response to a vehicle," *Mechanical Systems and Signal Processing*, vol. 28, pp. 145–166, 2012.

[8] T. Y. Hsieh, S. T. Lu, and C. H. Wu, "Statistical analysis of causes for change orders in metropolitan public works," *International Journal of Project Management*, vol. 22, no. 8, pp. 679–686, 2004.

[9] A. Idrus, M. F. Nuruddin, and M. A. Rohman, "Development of project cost contingency estimation model using risk analysis and fuzzy expert system," *Expert Systems with Applications*, vol. 38, no. 3, pp. 1501–1508, 2011.

[10] J. H. Jung and H. K. Lee, "Identification analysis of cost overrun risk through cause analysis of contract change of public construction project," *Journal of the Regional Association of Architectural Institute of Korea*, vol. 14, no. 3, pp. 277–286, 2012.

[11] J. H. Jung, D. Y. Kim, and H. K. Lee, "The computer-based contingency estimation through analysis cost overrun risk of public construction project," *KSCE Journal of Civil Engineering*, vol. 20, no. 4, pp. 1119–1130, 2016.

[12] C. H. Kim, B. H. Lee, and L. S. Kang, "Contingency estimating through risk analysis of construction projects," *KSCE journal of civil and environmental engineering research*, vol. 19, pp. 813–813, 1999.

[13] A. R. Prasad, R. Shankar, C. K. Patil, A. Karthick, A. Kumar, and R. Rahim, "Performance enhancement of solar photovoltaic system for roof top garden," *Environmental Science and Pollution Research*, vol. 28, no. 36, pp. 50017–50027, 2021.

[14] S. Mak and D. Picken, "Using risk analysis to determine construction project contingencies," *Journal of Construction Engineering and Management*, vol. 126, no. 2, pp. 130–136, 2000.

[15] S. Chidambaram, S. S. Ganesh, A. Karthick, P. Jayagopal, B. Balachander, and S. Manoharan, "Diagnosing breast cancer based on the adaptive neuro-fuzzy inference system," *Computational and Mathematical Methods in Medicine*, vol. 2022, Article ID 9166873, 2022.

[16] R. C. Gonzalez, R. E. Woods, and S. L. U. Eddins, *Digital Image Processing Using MATLAB*, earson Prentice Hall, Upper Saddle River, New Jersey, 2004.

[17] N. Otsu, "A threshold selection method from gray-level histograms," *IEEE Transactions on Systems, Man, and Cybernetics*, vol. 9, no. 1, pp. 62–66, 1979.

[18] A. Rimkus, A. Podviezko, and V. Gribniak, "Processing digital images for crack localization in reinforced concrete members," *Procedia Engineering*, vol. 122, pp. 239–243, 2015.

[19] M. Subramanian, M. S. Kumar, V. E. Sathishkumar et al., "Diagnosis of retinal diseases based on Bayesian optimization deep learning network using optical coherence tomography images," *Computational Intelligence and Neuroscience*, vol. 2022, 15 pages, 2022.

[20] S. Y. Alam, A. Loukili, F. Grondin, and E. Rozière, "Use of the digital image correlation and acoustic emission technique to study the effect of structural size on cracking of reinforced concrete," *Engineering Fracture Mechanics*, vol. 143, pp. 17–31, 2015.

[21] S. V. Kogilavani, J. Prabhu, R. Sandhiya et al., "COVID-19 detection based on lung CT scan using deep learning techniques," *Computational and Mathematical Methods in Medicine*, vol. 2022, Article ID 7672196, 2022.

[22] Y. O. Ouma and M. Hahn, "Wavelet-morphology based detection of incipient linear cracks in asphalt pavements from RGB camera imagery and classification using circular Radon transform," *Advanced Engineering Informatics*, vol. 30, no. 3, pp. 481–499, 2016.

[23] A. Ebrahimkhanlou, A. Farhidzadeh, and S. Salamone, "Multifractal analysis of crack patterns in reinforced concrete shear walls," *Structural Health Monitoring*, vol. 15, no. 1, pp. 81–92, 2016.

[24] J. C. Babu, N. M. Rao, K. Ramana, and V. Bhaskar, "A dynamic hybrid decoder apprroach using EG-LDPC codes for signal processing applications," *Wireless Personal Communications*, vol. 122, no. 2, pp. 1435–1454, 2022.

[25] Y. Li and C. Wang, "Research advances in long-life of worldwide bridges and corresponding reflections," *Bridge Construction*, vol. 49, no. 2, pp. 17–23, 2019.

[26] L. Peng, S. Zheng, P. Li, Y. Wang, and Q. Zhong, "A comprehensive detection system for track geometry using fused vision and inertia," *IEEE Transactions on Instrumentation and Measurement*, vol. 70, pp. 1–15, 2020.

[27] R. Dharmaraj, S. S. Bhadauria, K. Mayilsamy et al., "Investigation of Reinforced Concrete Column Containing Metakaolin and Fly Ash Cementitious Materials," *Advances in Civil Engineering*, vol. 2022, 13 pages, 2022.

Research Article

The Latest Technology of Polycrystalline Ferroelectric Composite Materials in the Design of the Shovel Frame Structure of the Vibratory Excavating Shovel of the Harvester

Lei Hao [ID] **and Yanliang Jie**

College of Mechanical and Electrical Engineering, Xi'an Traffic Engineering Institute, Xi'an, 710300 Shaanxi, China

Correspondence should be addressed to Lei Hao; haolei@xjy.edu.cn

China is a large agricultural country. With the development of industrial production, mechanized harvesting has become an inevitable development trend of agricultural material harvesting. In this paper, based on the latest technology of polycrystalline ferroelectric composite materials in the design of the shovel frame of the harvester's vibrating excavating shovel, the relevant theories of the polycrystalline ferroelectric composite material and the shovel frame of the harvester's vibrating excavating shovel are based on the literature. After understanding, the shovel frame structure of the vibrating excavating shovel of the harvester was designed, and the latest technology of polycrystalline ferroelectric composite material was introduced in the design of the shovel frame of the vibrating excavating shovel of the harvester to make the vibration system have better performance. The designed shovel frame structure is tested, and the test results show that the horizontal output force received by the shovel designed in this paper increases with the increase of speed and is minimized at 0.26 m/s. The vertical output force decreases first and then increases with the increase of speed. It is the smallest when the running speed is 0.39 m/s. The horizontal working resistance is always greater than the vertical working resistance, and it can be seen that the design of the shovel frame structure can be realized in actual work.

1. Inductions

Nowadays, because China's grain crop harvesting work is still labor-based and the level of mechanization of crop production is relatively low, a large amount of labor intensity, labor, and time plus huge costs have significantly reduced agricultural output. Production has had a great negative impact [1, 2]. At present, although some places have adopted mechanical harvesting of crops, they are only used for trenching, and engineers are required to participate in excavation, harvesting, and installation at the same time. Therefore, the degree of mechanization is relatively low. So, harvesting must be mechanized to increase labor efficiency and reduce labor intensity [3, 4].

In the harvester, the vibration function of the harvester is also the main part of the harvester's work. The vibration equipment is also the basic equipment for harvesting. Its

structure and motion parameters have a significant impact on the crop damage rate and the labor intensity of manual drilling [5, 6]. Therefore, optimizing and improving the performance of the shock absorber are very important for improving the working efficiency of the harvester.

Aiming at the research on the vibrating shovel of the harvester, some researchers have developed a cassava harvester with a drilling excavator with a built-in main knife structure. The principle is that the main knife penetrates the bottom of the tuber to completely separate the potato soil during harvest. The combine harvester includes harvesting tools, tuber cleaning/traction device, and collector/combiner. In addition to the lifting/loading device, it also has a device to loosen the soil around the cassava tubers, pull the tubers smoothly off the ground, and then use the device to load them onto the truck. Compared with previous harvesters, an advanced feature of this type of machine is the

integration of conveyor and harvester from separation to loading. However, the research on excavation parts and vibrating screens is still in the preliminary test stage, and the relevant research theories are not yet mature. Most cassava harvesters cannot carry out fully mechanized harvesting operations, and more research work is required to use the machines, especially the subsequent finishing operations. In addition, due to different geography and planting conditions, these machines are not completely suitable for cassava harvesting in our country. For this reason, it is necessary to develop a cassava harvester suitable for China's production conditions in accordance with the actual development of cassava in China [7]. Some researchers also pointed out that among the various combined harvesters produced at home and abroad, the excavator screen excavator is particularly suitable for peanut harvesting and film waste collection operations in China. It has the advantages of a low fruit drop rate, the recovery of residual film, the whole film, and the above-ground/underground broken film that can be recovered at the same time, and the recovery rate of residual film is high. However, the traditional single-screen excavator has problems such as large vibration and low soil cleaning effect. In recent years, China has invested a lot of manpower, material, and financial resources in the research and development of film waste-recycling machines, but the current film waste-recycling machines on the market have a single function and low economic performance and commercial value. These are all factors restricting the development of agricultural mechanization in China [8]. Some scholars believe that the excavation and harvesting of most agricultural products have gone through three main stages: shoveling, farming, and mechanical harvesting. Nowadays, the most developed countries have achieved almost mechanized harvesting, but in economically underdeveloped areas, manual harvesting is still the main harvesting method. Digging harvesters generally include digging, soil separation, placement (or collection), and other processes. Among them, excavation equipment and separation and transportation equipment are important components that determine the quality of excavation and harvesting [9]. In the study of polycrystalline ferroelectric composite materials, relevant researchers pointed out the characteristics of polycrystalline ferroelectric composite materials [10]: ferroelectric materials have strong spontaneous polarization, and the iron-based material of the bismuth layer has a high Curie working temperature. In the inspection of the entire bismuth ferroelectric layer material, it does not involve the extraction of the bismuth oxide layer produced by the B-based iron material, the lanthanide A site, and the relaxation type, and the high Curie of most bismuth layer iron materials' working temperature is above 500. At the same time, the ferroelectric material with the bismuth layer has good temperature stability in terms of high dielectric and piezoelectric properties, and the ferroelectric material with the bismuth layer also has an ultrahigh mechanical quality coefficient that reduces the dielectric constant and dielectric loss (2000-7200). Because of the high nonpolarization and low insulation effect of the bismuth oxide layer, the iron-bonded bismuth layer material also has an ultrahigh temperature coefficient of resistivity. This is due to the role of the bismuth peroxide layer in the defect, which

makes the perovskite layer more stable, so the contour structure of the bismuth layer ferroelectric material has better fatigue resistance [11]. Other researchers pointed out that multi-iron composites are materials that combine two or more custom-made iron materials in different ways. Among them, composite magnetic electrical materials are a hot research topic. Compared with single-phase magnetic materials, composite magnetic materials have a higher magnetic coupling coefficient, and the temperature of the Curie ferroelectrics and ferromagnets is much higher than at room temperature. Because of these advantages, composite magnetoelectric materials have been extensively studied [12]. In summary, with the development of mechanized production, more and more people begin to pay attention to the design of harvesters, but most of them stay in the theoretical part, and the mechanical applications of the design are not extensive.

This paper studies the shovel frame structure of the vibrating excavating shovel of the harvester, which is the latest technology of polycrystalline ferroelectric composite materials, and analyzes the characteristics of the polycrystalline ferroelectric composite material and the shovel frame structure of the vibrating excavating shovel of the harvester on the basis of literature data. We prepare the theoretical foundation for the following structural design, then design the shovel frame of the harvester's vibrating excavating shovel on the basis of these theories, test the designed structure, and draw relevant conclusions through the test results.

2. Shovel Frame Structure of the Polycrystalline Ferroelectric Composite Material and the Vibrating Shovel of the Harvester

2.1. Characteristics of Polycrystalline Ferroelectric Composite Materials. In addition to the macroscopic characteristics of the electrical group, iron materials have two important characteristics: the structure of the electrical domain and the Curie temperature.

(1) Electric domains refer to small regions with the same spontaneous polarization direction of ferroelectric materials. The boundaries between electrical regions are called domain walls [13]. If the angle between the polarization directions of adjacent electrical regions is 180°, then this region is called a field 180°. If the angle between the polarization directions of adjacent electrical regions is 90°, it is called a field of 90°, as shown in Figure 1. The electric field can be reversed under the action of external force and electric field. This is called electric field change. Applying an electric field opposite to the direction of spontaneous polarization to a ferroelectric substance can reverse the sector by up to 180°, but applying a compressed voltage or a voltage parallel to the direction of spontaneous polarization can reverse the sector by 90°

(2) The spontaneous polarization phenomenon of ferroelectrics only exists in a specific temperature range,
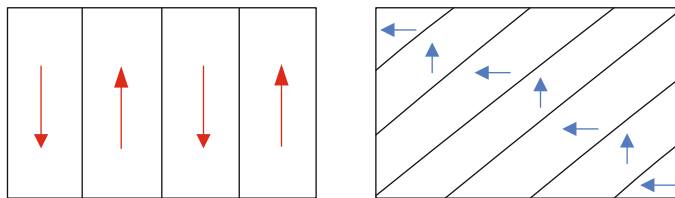
FIGURE 1: Schematic diagram of domain structure.

and the spontaneous polarization disappears if the temperature exceeds a certain temperature. The ferroelectric has undergone a phase change process from the ferroelectric phase to the normal dielectric phase [14]. That is, the temperature of the corresponding ferroelectric phase transition is called the Curie Tc temperature. Near the Curie temperature, ferroelectrics have many properties, such as dielectric response, piezoelectric response, and pyroelectric effect. Therefore, the Curie temperature change is one of the important means to adjust the physical properties of ferroelectrics

2.2. Application of Polycrystalline Ferroelectric Composite Materials

(1) Research on iron scale effect: due to the development of the thin iron film and ultrafine iron powder technology, the phenomenon of iron size has become a practical problem, so it must be studied in depth in time. Humans first theoretically predicted the changes of spontaneous polarization, phase transition temperature, and dielectric sensitivity of materials with time scales and measured the critical electric strength of typical ferroelectrics [15]. The above results have not only led to the design of a large number of integrated steel electrical components and thin composite materials but also promoted the development of modern polycrystalline ferroelectric composite material theory under limited time scale conditions

(2) Basic research and application research on ferroelectric liquid crystals and ferroelectric polymers: studies have confirmed that the liquid crystals in the inclined laminar flow phase composed of iron chiral atoms have ferroelectricity. In terms of performance, ferroelectric liquid crystals are very advantageous in electrooptical display and nonlinear optical applications. The electrooptical display is mainly through the reversal of polarized light, and its speed is several orders of magnitude higher than that of ordinary filamentary liquid crystal [16]. For nonlinear optics, the effect of second or high-frequency harmonic output exceeds the usual inorganic constitutive nonlinear optics application crystals. Ferropolymers were only recognized more than ten years ago and have a long history with thermoelectrics and piezoelectrics [17]. However, some new types of ferroelectric

polymers did not appear until ten years ago. After research, the iron polymer discovered has a wider range of compositions and different structures, so more ferroelectrics appeared later, which expanded the research field of ferroelectric physics and developed new applications

(3) Research on integrated ferroelectrics: the combination of the thin iron film and semiconductor is called integrated ferroelectric, and the research on this material is very extensive [18]. The basic form of ferroelectric memory is random access ferroelectric memory. It was initially considered to be the main purpose of research, and it was not commercialized until 2000 [19]. Compared with the 1950s and 1960s, modern materials and technologies have solved some important problems. First, the use of thin films helps to reduce the depolarization voltage and integrate with standard silicon or circuits, and the fatigue performance is significantly improved, resulting in multiple inverted iron films, which have gradually realized important uses in memory. At the same time, the application of ferroelectric thin films is not limited to the storage field but also includes ferroelectric effect transistors and ferroelectric random access memories. In addition to memory, the built-in ferroelectrics can also be used in infrared detection and imaging equipment, ultrasonic and surface acoustic equipment, and optoelectronic equipment. It can be seen that the built-in thin film devices have huge application prospects

2.3. The Shovel Frame Structure of the Vibratory Excavating Shovel of the Harvester

2.3.1. Working Principle of Harvester. As shown in Figure 2, the excavator operation process has typical cyclic characteristics, whether it is a front excavator or a reverse excavator drilling method. The cycle process mainly includes five stages: drilling, emptying the bucket, rotating, unloading, and drilling. The important stage of drilling design energy consumption is also the stage when the working device is subjected to drastic random load changes. During the entire drilling phase, very complex physical and mechanical phenomena occur between the bucket and the soil, that is, the soil is destroyed. The bucket is the first tangent to the ground at a specific initial speed and cutting force. If it is a forward drilling method, the main purpose is to destroy the integrity of the accumulated soil. After being completely destroyed, gravity causes the soil to roll into the shovel. At
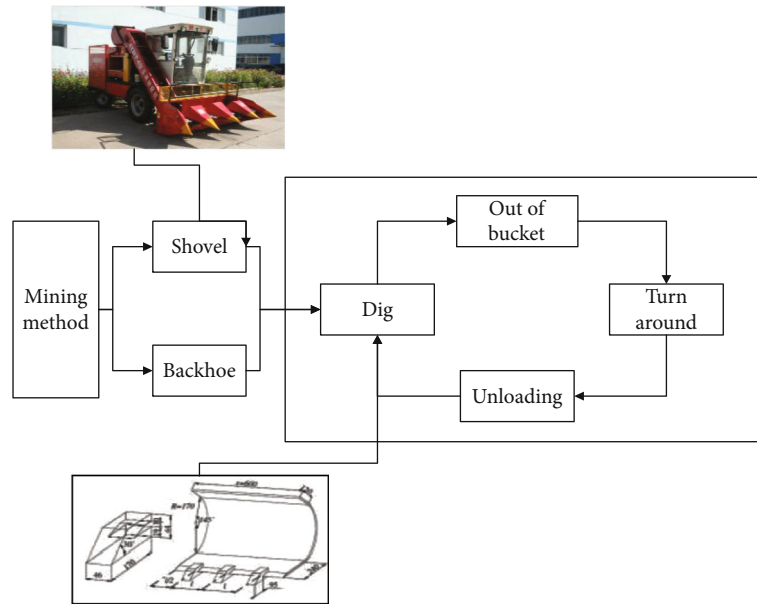
FIGURE 2: Working principle of the harvester.

the same time, the bucket continues to cut deeply until the bucket is full. This mode of operation mainly occurs in open-pit mining and mineral blasting. The main purpose of excavator drilling is to destroy the soil structure.

2.3.2. The Relevant Parameters of the Shovel Frame of the Vibratory Excavating Shovel of the Harvester

(1) The Surface Inclination of the Vibrating Shovel of the Harvester. The vibrating shovel is also one of the main parts of the digging harvester, which directly affects the efficiency of the whole machine, and the shovel surface angle a is the main reason that affects the quality of the excavator [20]. Inappropriate viewing angles can cause soil retention and increase operating power. The design principle of angle a is to make the excavated material rise to a certain height along the surface of the bucket machine to prevent the excavated material from falling in the middle direction. At the same time, the excavation object should also do the following: the excavation is smooth, and it is transferred to the rear vibrating screen to gradually eliminate soil dirt.

According to design experience, if the angle a is larger, the crop soil mixture will be scattered on both sides and trapped in the digging shovel. In fact, the angle a is determined by many factors, such as the ability to loosen the soil, the height of the drilling material lifted by the excavator, and the characteristics of the soil. The larger the angle a, the weaker the ground, but it also increases the digging resistance and tends to maintain the ground. The smaller the angle a, the smaller the digging resistance of the excavator, the better the ground, and the higher the penetration efficiency, but the crushing effect of the shovel on the ground is reduced. At $a = 25°$, the moderately hard sandy loam is obviously blocked. So, in summary, the inclination value of the shovel surface is initially set in the range of 18°-26°.

2.3.3. Vibration Drive Device.
The drive unit is mainly used to drive vibration. The drive unit is mainly composed of a drive shaft, a front-drive joint, a rear-drive joint, a cam-drive arm, and a cam block. The transmission structure transmits power from the power output shaft of the tractor to the drive shaft. The drive shaft drives the cam to reciprocate. The front-drive connector and the rear-drive connector move forward and backward at the same time under the influence of the eccentric drive arm during driving [21].

The design of the drive camshaft arm is mainly used for the reverse movement of the two vibrating rods. The mass of the eccentric transmission vibrating arm is 2.67 kg, the eccentricity is 9 mm analyzed by the 3D software center of gravity analysis unit, and the calculated moment of inertia is 0.024 kg m. When the eccentric drive arm rotates, the inertial force will be generated, which will cause the whole machine to vibrate and affect the stability and service life of the machine tool. Therefore, it is necessary to balance the vibration. Therefore, it is necessary to install an eccentric mass with the moment of inertia such as an eccentric drive arm on the drive shaft. The mass is 1.78 kg, and the eccentricity (the distance from the center of the camshaft to the drive shaft) is 13.5 nm. The eccentric block of the eccentric transmission arm and the camshaft are symmetrical about the axis of the transmission shaft and are both located on the transmission shaft to neutralize the moment of inertia generated during operation.

2.4. Related Calculation Model.
The discrete element method (DEM) is a numerical simulation method for calculating complex discrete systems, mainly used to calculate the mechanical and kinematic properties of granular materials [22]. When analyzing mechanical problems, many mechanical or motion systems are usually involved. The laws and states of each system can be expressed and calculated through the interaction of mathematical analysis functions.

For the more complicated problems when using this mathematical analytical function method, new arithmetic methods have emerged, such as the finite element method (FEM) and the discrete element method. The finite element method divides the system to be analyzed into microscopic units, approximates each unit with a simple mathematical analysis function with limited degrees of freedom, and calculates the increase of the entire system through each microscopic unit. Similar to the idea of the finite element method, the discrete element method treats the entire system as a collection of interacting discrete units, analyzes the interaction between the discrete units, and then combines the mechanical action and exchange of energy between the units to obtain the analysis results of the entire discrete system and the mechanical influence on the external structure [23].

In summary, this paper uses the Hertz-Mindlin model to carry out discrete element numerical simulation experiments [24]. Suppose there are two spheres with radii of R_1 and R_2, and δ_n is the amount of normal overlap:

$$\delta_n = R_1 + R_2 - \left| \vec{r}_1 - \vec{r}_2 \right|, \tag{1}$$

where $\vec{r}_1$ and $\vec{r}_2$ are the vector positions of the centroids of the two particles.

Then the size of the contact radius a is equal to

$$a = \sqrt{\delta_n R^*}. \tag{2}$$

In the formula, R^* is the equivalent radius of the particle, and the derivation formula is as follows:

$$\frac{1}{R^*} = \frac{1}{R_1} + \frac{1}{R_2}. \tag{3}$$

The normal phase force between particles F_n is

$$F_n = \frac{4}{3} E^* (R)^{1/2} \delta_n^{3/2}, \tag{4}$$

$$\frac{1}{E^*} = \frac{1 - \lambda_1^2}{E_1} + \frac{1 - \lambda_2^2}{E_2}, \tag{5}$$

where E^* is the equivalent elastic modulus between particles, E_1 and E_2 are the elastic modulus of two spherical particles, respectively, and λ_1 and λ_2 are the Poisson's ratio.

The normal damping force calculation formula is

$$F_n^d = -2\sqrt{\frac{5}{6}}\beta\sqrt{S_n m^*} v_n^{rel}, \tag{6}$$

$$m^* = \frac{m_1 m_2}{m_1 + m_2}, \tag{7}$$

$$v_n^{rel} = \left(\vec{v}_1 + \vec{v}_2 \right) \times \vec{n}. \tag{8}$$

Among them, m^* is the mass equivalent, m_1, m_2 is the mass of the two particles, and v_n^{rel} is the relative velocity of the normal phase between the two particles.

The calculation formula of the tangential force between particles is

$$F_t = -S_t d_t, \tag{9}$$

$$S_t = 8G^* \sqrt{R^* \alpha}, \tag{10}$$

$$G^* = \frac{2 - \nu_1^2}{G_1} + \frac{2 - \nu_2^2}{G_2}, \tag{11}$$

where G^* is the gravitational velocity.

The calculation formula of tangential damping force is

$$F_t^d = -2\sqrt{\frac{5}{6}}\beta\sqrt{S_t m^*} v_t^{rel}. \tag{12}$$

In the formula, v_t^{rel} is the tangential relative velocity between the two particles.

3. The Shovel Frame Structure Design of the Vibratory Excavating Shovel of the Harvester

3.1. Application of the Latest Technology of Polycrystalline Ferroelectric Composite Materials.
The shovel frame structure of the excavating shovel of the harvester should be applied to the ferroelectricity of the polycrystalline ferroelectric composite material to realize good control of the shovel frame structure. This article expands the application of the polycrystalline ferroelectric composite material in the vibration system.

3.1.1. Principle of Vibration System.
The excavator designed in this research adopts the principle of vibration. When the vibrating excavator is working, the control unit adopts a pulse generator (motor, rotary valve). The structure of the oil circuit of the vibrating cylinder retracts the piston rod of the vibrating cylinder, and the shovel mounted on the piston rod vibrates and destroys the soil. Since the shovel returns through the return spring, it can drive the shovel to vibrate back and forth in a balanced position [24].

3.1.2. Vibration Structure.
The vibrating shovel is driven by a ZL50G loader and provides a hydraulic drive. The hydraulic system of the vibrating excavator is powered by a gear pump connected in series with the main pump of the loader ZL50G. The gear pump drives four parallel vibrating oil cylinders to move, and the excavating shovel moves under each vibrating oil cylinder. The vibrating cylinder periodically provides active vibration, and the return spring provides a specific pressure to reset the shovel [25]. The excavating shovel is made of a 65Mn steel plate and is fixed on the component with bolts, which can be easily replaced after wear.

Based on the above analysis, the control during the vibration process is very critical. Therefore, in order to have a better control capability of the vibration system, an integrated ferroelectric is used to design the system circuit.

3.2. Design of the Opening Angle of the Shovel Surface of the Shovel.
The design of the opening angle of the drilling shovel directly affects the resistance of the drilling. If the opening
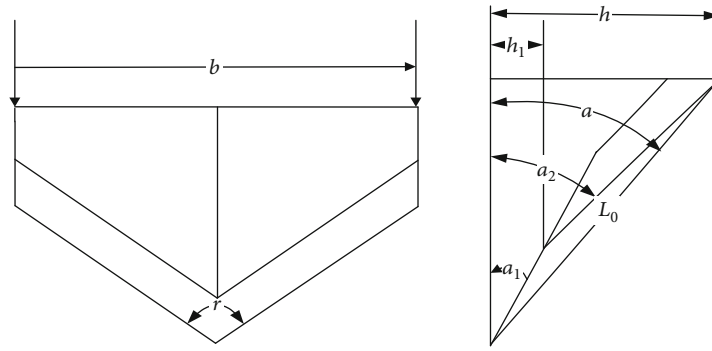
FIGURE 3: Geometry diagram of the blade edge.

angle of the digging shovel surface is too large, the stems, leaves, and weeds are not easy to be cut during the operation of the digging shovel, and the movement resistance is large, which will increase the power consumption of the machine and increase the manufacturing cost [26]. Therefore, it is necessary to adjust the opening angle r of the digging shovel blade so that the stems, leaves, and weeds can slide smoothly along the edge of the shovel blade to reduce the digging resistance.

In the structural design of the second-order curved shovel, the opening angle of the shovel surface directly affects the digging resistance of the shovel surface during excavation. If the opening angle of the shovel surface is too large, the shovel blade will be difficult to cut stems, leaves, and weeds and will be easily tangled, resulting in a sharp increase in drilling resistance and increased energy consumption. Therefore, it is necessary to effectively control the opening angle of the shovel surface. To achieve the purpose of cutting stems, leaves, and weeds, reduce the resistance to drilling. According to the geometric relationship shown in Figure 3, the total resistance p of the stem, weeds, and soil at the end of the leaf is decomposed along the direction of the leaf and perpendicular to the direction of the leaf. The geometric relationship is as follows:

3.2.1. Design of Inclination Angle of Shovel. In order to study the change law of convex curved shovel resistance with the inclination of the shovel face and the length of the shovel body, the virtual shovel face inclination is introduced into the resistance calculation formula to realize the approximate calculation of the curved shovel. When the virtual shovel surface inclination and the length of the shovel body are unknown quantities, the calculation results are shown in Figure 4.

The comprehensive analysis in Figure 4 shows that under various combinations of the virtual shovel surface length and the subsurface inclination angle, the drilling resistance increases with the increase of the drilling depth. In addition, the length of the virtual surface of the shovel also has a certain influence on the resistance of the shovel. Under the same combination of digging shovel surface inclination angle, as the virtual length of digging shovel surface increases, the digging resistance tends to decrease, but the effect is not significant. In the actual design, the surface

length of the excavating shovel should not be too long; otherwise, the soil-blocking phenomenon will be more serious when harvesting crops. On the other hand, it is unfavorable for the soil separation of the next vibrating device, and the load capacity of the tool alone is increased to increase the power consumption.

In order to study the variation of convex curved shovel resistance with the height of the shovel surface, the virtual shovel surface height is introduced into the resistance calculation formula to realize the approximate calculation of the curved shovel. When the virtual shovel surface height is an unknown quantity, the calculation results are shown in Figure 5.

The analysis of the change curve of top resistance with the height of the primary shovel (Figure 5) shows that the resistance of the shovel decreases with the increase of the height of the primary shovel. It can be seen that the height of the stepped excavating shovel has a great influence on the excavation resistance. Therefore, when designing the excavating shovel, the height of the stepping excavating shovel must be appropriately selected so that the digging resistance will not become too high. The resistance of the shovel is also closely related to the combination of shovel inclination. Analyzing Figure 5, it can be seen that even if the slope of the main shovel changes, the slope of the auxiliary shovel will not change. When the shovel resistance changes and the inclination of the front surface of the main shovel is determined, if the inclination of the auxiliary shovel surface increases, the resistance of the shovel surface increases sharply. Therefore, the change of the inclination angle of the secondary excavator has a great influence on the resistance, and it is more obvious. The difference in the inclination angle of the two steps can be used to measure the crushing ability of the surface of the secondary excavating shovel. The greater the difference, the higher the crushing capacity, but the greater the surface resistance of the shovel.

After analyzing and studying the relationship between the inclination angle of the secondary surface curve and the drilling resistance, it may be found that the inclination angle of the main excavator surface must be smaller than the secondary inclination angle, and the difference between the two inclination angles cannot be too large or too small. If the value is too high, if the surface soil compressibility of
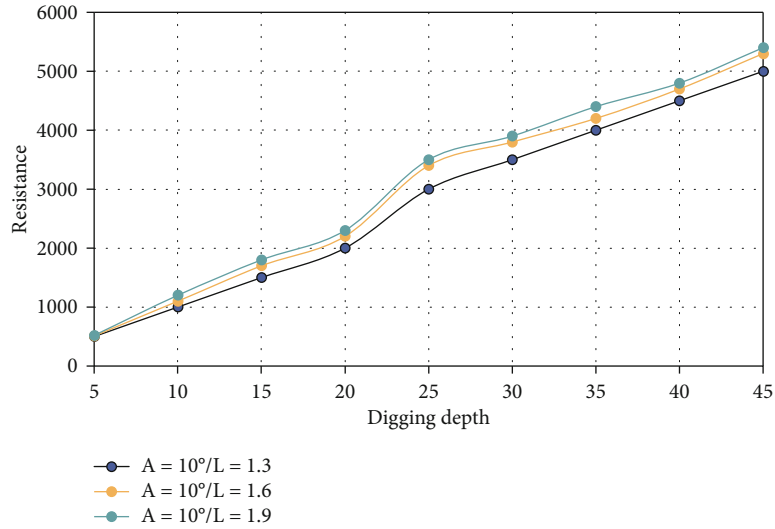
FIGURE 4: The relationship curve between digging depth and resistance when combined with different inclination angles.
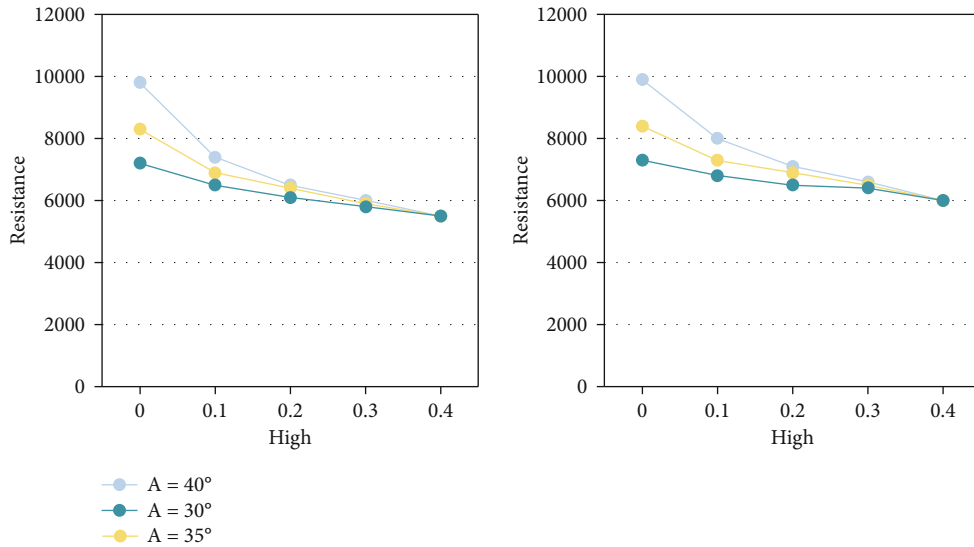
FIGURE 5: Change curve with the height of the primary excavating shovel.

the digging shovel is low, the surface resistance of the digging shovel will increase sharply. If the value is too low, the soil will not have enough compressibility, but the resistance will be relatively low. Based on the above situation, the combined inclination angle of the convex surface of the excavating shovel pair is 15° and 30°.

3.3. Shovel Body Length Design. The length design of the shovel body should follow this principle. The length of the shovel body cannot be too long or too small. The length of the shovel body of the digging shovel is so long that the resistance between the soil body and the shovel surface is very small. However, when harvesting, the rear edge of the digging shovel surface is seriously blocked, which makes the crop fragile and affects the harvesting effect. The length of the shovel body is too small to cause the crops to be brought to the vibration chain of the conveyor before break-
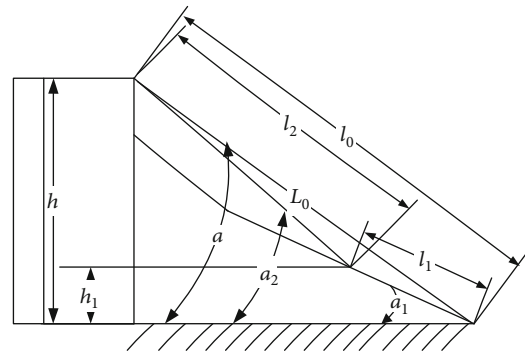
FIGURE 6: Schematic diagram of the length of the shovel body.

ing, it is also difficult to break due to vibration, and the energy consumption of the vibration chain of the conveyor increases sharply. Therefore, the length design of the shovel
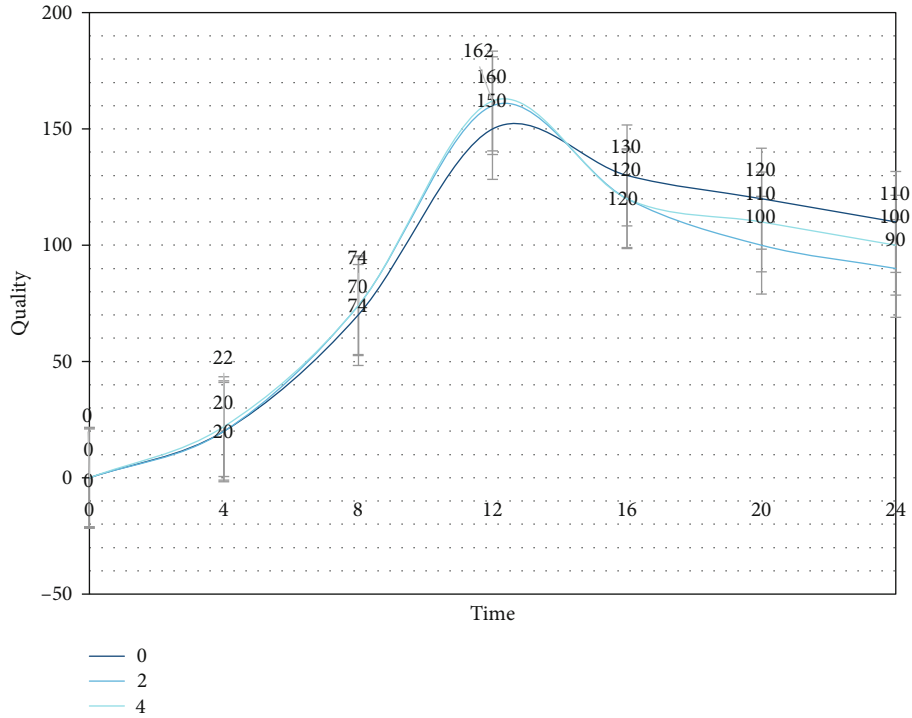
FIGURE 7: The bucket material quality change curve with time.

body should comprehensively consider the above factors and carry out a reasonable design.

The length of the shovel body is determined as shown in Figure 6, l_0 is the virtual shovel face length, l_1 is the first shovel face length, l_2 is the second shovel face length, a is the virtual shovel face inclination, a_1 is the first shovel face inclination, a_2 is the inclination angle of the second-stage shovel surface, h is the height of the rear end of the shovel body, and h_1 is the height of the first-stage shovel surface.

The actual design of the shovel body length should ensure that the speed is not zero when moving to the rear end of the first section; otherwise, the soil cannot be transported in time, causing a blockage.

3.4. Design of the Number of Teeth. For the bucket model for three different numbers of teeth (the number of teeth is 0, 2, and 4), a three-dimensional numerical model of the natural accumulation of noncohesive minerals during bucket drilling was established, the bucket manipulation process was visualized, and the bucket load during the entire drilling period was extracted. Compared with the previous model test and overall test method, the numerical simulation method guarantees the consistency of the test to a large extent, avoids the reproducibility and reproducibility of the model test, improves the reliability of the results, and reduces the influencing factors. The test cost and test cycle are reduced [27]. The experimental results are processed, and three types of hopper material quality curves that change with time (Figure 7) are extracted to explain the filling information and flow of the hopper material.

Through the processing of the test results, as shown in Figure 7, three types of bucket material quality changes that

TABLE 1: Discrete element simulation parameters.

Parameter	Numerical value
Soil particle radius (m)	0.001~0.003
Number of simulated soil particles	400000
Soil density (kg/m^2)	1540
Soil Poisson's ratio	0.3
Soil shear modulus (Pa)	$1.01e + 06$
Digging shovel density (kg/m$'$)	7890
Poisson's ratio of digging shovel	0.269
Shear modulus of shovel (Pa)	$8.2e + 10$
Time step (s)	$2.65e - 05$
Total simulation time (s)	52~53

change over time are extracted, and the filling information and flow of the materials in the bucket are described. The figure shows that the quality curves of the three buckets tend to be the same but have different widths and different final constant values. From 0 to 15 seconds, the quality of the three buckets will be significantly improved. Within 0-4 seconds, the gradient becomes smaller, indicating that the integrity of the material has been destroyed by the bucket teeth, and it begins to flow into the bucket. Starting from 4 seconds, the slope of the curve increases sharply. Large means that the material starts to enter the bucket quickly in large quantities. The slopes of the three curves are similar, but due to the difference in the number of bucket teeth, the quality of the bucket begins to vary. This difference is maximized in 6 seconds. The mass of the four-tooth bucket is

Table 2: Discrete element simulation results 1.

Working speed (m/s)	Horizontal force of the shovel (N)	Vertical force of the shovel (N)
0.26 m/s	55.91	55.65
0.37 m/s	62.21	47.89
0.48 m/s	66.12	52.34

Table 3: Discrete element simulation results 2.

Working speed (m/s)	Horizontal force of the shovel (N)	Vertical force of the shovel (N)
0.26 m/s	55.91	55.65
0.39 m/s	66.99	44.21
0.52 m/s	89.43	59.76

Table 4: Discrete element simulation results 3.

Working speed (m/s)	Horizontal force of the shovel (N)	Vertical force of the shovel (N)
0.35 m/s	55.81	55.52
0.37 m/s	66.99	44.89
0.39 m/s	89.43	59.76

43.40 tons. Compared with the teeth in bucket 0, the mass of the 2,964-ton bucket is almost 46.4% higher.

Observe the change of each curve from the maximum mass of the entire bucket to the final speed. The less the number of bucket teeth, the more stable the quality of the bucket and full bucket, that is, the more stable the maximum mass and final speed. The fewer the number of teeth, the lower the quality of the spilled material when the material quality in the bucket is maximized. Therefore, from the test results, it may be a reasonable choice to place less or no teeth on the nonsticky drilling material.

4. The Shovel Frame Structure Test of the Vibrating Excavating Shovel of the Harvester

In this chapter, using the EDEM discrete element modeling software, according to the physical and mechanical parameters of the soil, a soil particle model was established, combined with field test conditions, and a 3D model of the harvester for simulation adjustment was created. A particle factory will be built to simulate the work of the harvester. The movement of the ground and the power of the shovel were observed in the process. The harvester uses discrete data methods to simulate working resistance at six different operating speeds (0.26 m/s, 0.35 m/s, 0.37 m/s, 0.39 m/s, 0.48 m/s, and 0.52 m/s). A discrete data method is used to study the feasibility of harvester, and a new digital design research method is provided for this.

4.1. Establishment of Discrete Element Model. Use the EDEM software to simulate and analyze the working resistance of the harvester. In addition to obtaining the physical and material parameters of the soil and harvester in advance, it is also necessary to select the correct contact model and create a soil particle model. Create geometry for the shovel model, set limits for the simulation area, create a particle factory, and run the simulation.

4.2. Selection of Discrete Element Simulation Parameters. The closeness of the discrete simulation results to the actual field test results mainly depends on the choice of discrete simulation parameters. The selection of parameters is to consult relevant documents and make adjustments according to the simulation process. The specific simulation parameter values are shown in Table 1.

4.3. Discrete Element Simulation Results and Analysis. The simulation test adopts a single-factor test, which only changes the forward speed of the excavating shovel along the negative direction of the X-axis. The forward speed of the excavating shovel is adjusted in the six simulation tests. The negative direction along the X-axis is 0.26 m/s, 0.35 m/s, 0.37 m/s, 0.39 m/s, 0.48 m/s, and 0.52 m/s, respectively. The simulation results are divided into three groups. The specific data results are shown in Tables 2–4.

Analyzing the above simulation test data table, if other simulation parameters are consistent, changing the forward speed of the excavating shovel in the negative direction of the X-axis increases with the increase of the horizontal force of the excavating shovel. The increase first decreases and then increases. The working speed is 0.39 m/s, and the horizontal working resistance is always greater than the vertical working resistance.

5. Conclusions

This paper studies the shovel frame structure of the vibratory excavating shovel of the harvester with the latest technology of polycrystalline ferroelectric composite materials. After understanding the relevant theories, the shovel frame structure of the vibrating excavating shovel of the harvester is designed. In the shovel frame structure, the latest technology of polycrystalline ferroelectric composite material is introduced to make the vibration system have better performance, and the designed shovel frame structure is tested through actual tests. The test result shows that when the minimum speed is 0.26, the vertical resultant force first decreases and then increases with the increase of speed. The operating speed is 0.39 m/s, and the horizontal operating resistance is always greater than the vertical operating resistance. Therefore, the shovel frame structure designed in this paper is feasible in actual work. However, there are still some shortcomings in the research process of this article, which are mainly manifested in the absence of an actual field experiment.

Data Availability

No data were used to support this study.

Conflicts of Interest

The authors declare that there are no conflicts of interest regarding the publication of this article.

References

[1] Y. Dong, M. J. Hossain, and J. Cheng, "Performance of wireless powered amplify and forward relaying over Nakagami- fading channels with nonlinear energy harvester," *IEEE Communications Letters*, vol. 20, no. 4, pp. 672–675, 2016.

[2] G. Litak, M. I. Friswell, and S. Adhikari, "Regular and chaotic vibration in a piezoelectric energy harvester," *Meccanica*, vol. 51, no. 5, pp. 1017–1025, 2016.

[3] P. S. Mederski, M. Bembenek, Z. Karaszewski, A. Łacka, A. Szczepańska-Álvarez, and M. Rosińska, "Estimating and modelling harvester productivity in pine stands of different ages, densities and thinning intensities," *Croatian Journal of Forest Engineering*, vol. 37, no. 1, pp. 27–36, 2016.

[4] Y. Wang, W. Liang, T. Cheng, Z. Song, and F. Qin, "Sealed piezoelectric energy harvester driven by hyperbaric air load," *Applied Physics Letters*, vol. 108, no. 3, p. 33902, 2016.

[5] S. P. S. Guerra, G. Oguri, and R. Spinelli, "Harvesting eucalyptus energy plantations in Brazil with a modified New Holland forage harvester," *Biomass & Bioenergy*, vol. 86, no. Mar., pp. 21–27, 2016.

[6] Z. Hameed and K. Moez, "A 3.2 V –15 dBm adaptive threshold-voltage compensated RF energy harvester in 130 nm CMOS," *IEEE Transactions on Circuits & Systems I Regular Papers*, vol. 62, no. 4, pp. 948–956, 2015.

[7] R. Hosseini and M. Hamedi, "An investigation into resonant frequency of trapezoidal V-shaped cantilever piezoelectric energy harvester," *Microsystem Technologies*, vol. 22, no. 5, pp. 1127–1134, 2016.

[8] L. Q. Chen, W. A. Jiang, M. Panyam, and M. F. Daqaq, "A broadband internally-resonant vibratory energy harvester," *Journal of Vibration & Acoustics*, vol. 138, no. 6, 2016.

[9] Y. Zhang, T. Wang, A. Luo, Y. Hu, X. Li, and F. Wang, "Micro electrostatic energy harvester with both broad bandwidth and high normalized power density," *Applied Energy*, vol. 212, pp. 362–371, 2018.

[10] Y. Zhang, W. Ni, and Y. Li, "Effect of siliconizing temperature on microstructure and phase constitution of Mo-MoSi$_2$ functionally graded materials," *Ceramics International*, vol. 44, no. 10, pp. 11166–11171, 2018.

[11] X. Liu, L. Huang, K. Ravichandran, and E. Sanchez-Sinencio, "A highly efficient reconfigurable charge pump energy harvester with wide harvesting range and two-dimensional MPPT for internet of things," *IEEE Journal of Solid-State Circuits*, vol. 51, no. 5, pp. 1302–1312, 2016.

[12] H. Xiao, X. Wang, and S. John, "A multi-degree of freedom piezoelectric vibration energy harvester with piezoelectric elements inserted between two nearby oscillators," *Mechanical Systems & Signal Processing*, vol. 68, pp. 138–154, 2016.

[13] S. Lemey, S. Agn Ee Ssens, P. V. Torre, K. Baes, J. Vanfleteren, and H. Rogier, "Wearable flexible lightweight modular RFID tag with integrated energy harvester," *IEEE Transactions on Microwave Theory and Techniques*, vol. 64, no. 7, pp. 2304–2314, 2016.

[14] C. K. Jeong, S. B. Cho, J. H. Han et al., "Flexible highly-effective energy harvester via crystallographic and computational con-trol of nanointerfacial morphotropic piezoelectric thin film," *Nano Research*, vol. 10, no. 2, pp. 437–455, 2017.

[15] D. Pan, Y. Li, and F. Dai, "The influence of lay-up design on the performance of bi-stable piezoelectric energy harvester," *Composite Structures*, vol. 161, pp. 227–236, 2017.

[16] P. Li, S. Gao, H. Cai, and L. Wu, "Theoretical analysis and experimental study for nonlinear hybrid piezoelectric and electromagnetic energy harvester," *Microsystem Technologies*, vol. 22, no. 4, pp. 727–739, 2016.

[17] P. Wang, T. Yao, Z. Li et al., "A superhydrophobic/electrothermal synergistically anti-icing strategy based on graphene composite," *Composites Science and Technology*, vol. 198, article 108307, 2020.

[18] G. Bo, L. Chang, H. Chenglong et al., "Effect of mg and RE on the surface properties of hot dipped Zn–23Al–0.3Si coatings," *Science of Advanced Materials*, vol. 11, no. 4, pp. 580–587, 2019.

[19] X. Wang, C. Chen, N. Wang et al., "A frequency and bandwidth tunable piezoelectric vibration energy harvester using multiple nonlinear techniques," *Applied Energy*, vol. 190, pp. 368–375, 2017.

[20] H. C. Song, P. Kumar, D. Maurya et al., "Ultra-low resonant piezoelectric MEMS energy harvester with high power density," *Journal of Microelectromechanical Systems*, vol. 26, no. 6, pp. 1226–1234, 2017.

[21] M. Gao, W. Ping, C. Yong, R. Chen, and D. Cai, "Design and verification of a rail-borne energy harvester for powering wireless sensor networks in the railway industry," *IEEE Transactions on Intelligent Transportation Systems*, vol. 18, no. 99, pp. 1596–1609, 2017.

[22] N. Sharpes, A. Abdelkefi, H. Abdelmoula, P. Kumar, J. Adler, and S. Priya, "Mode shape combination in a two-dimensional vibration energy harvester through mass loading structural modification," *Applied Physics Letters*, vol. 109, no. 3, p. 033901, 2016.

[23] C. Tao, Y. Xia, W. Liu, H. Liu, L. Sun, and C. Lee, "A hybrid flapping-blade wind energy harvester based on vortex shedding effect," *Journal of Microelectromechanical Systems*, vol. 25, no. 5, pp. 845–847, 2016.

[24] J. H. Kim, J. S. Kim, S. H. Han, H. W. Kang, H. G. Lee, and C. I. Cheon, "(K,Na)NbO$_3$-based ceramics with excess alkali oxide for piezoelectric energy harvester," *Ceramics International*, vol. 42, no. 4, pp. 5226–5230, 2016.

[25] Q. Lu, L. Liu, F. Scarpa, J. Leng, and Y. Liu, "A novel composite multi-layer piezoelectric energy harvester," *Composite Structures*, vol. 201, no. OCT., pp. 121–130, 2018.

[26] K. Adamski, J. Adamski, J. A. Dziuban, and R. Walczak, "Inkjet 3D printed miniature water turbine energy harvester-flow meter for distributed measurement systems," *In Multidisciplinary Digital Publishing Institute Proceedings*, vol. 1, no. 4, pp. 578–578, 2017.

[27] Y. Tan, D. Ying, and X. Wang, "Review of MEMS electromagnetic vibration energy harvester," *Journal of Microelectromechanical Systems*, vol. 26, no. 1, pp. 1–16, 2017.

Research Article

Research on Airflow Cooling Characteristics of Titanium Alloy Engine Blade Surface Machining

Lei Qiu [iD],[1] **Shaoyong Zheng,**[2] **Lanlan Liu,**[3] **Shuli Hong,**[1] **and Jun Chi**[1]

[1]*School of Mechanical Engineering, Ningbo University of Technology, Ningbo Zhejiang, China*
[2]*Zhejiang People Industry Facilities Co., Ltd, Hangzhou Zhejiang, China*
[3]*Department of Mechanical Engineering, JiangXi Technical College of Manufacturing, Nanchang, Jiangxi, China*

Correspondence should be addressed to Lei Qiu; qiulei@nbut.edu.cn

This paper studied the airflow cooling during blade surface processing and explained the applicable occasions of airflow cooling. The flat heat transfer model was used to study the characteristics of the cooling airflow during blade surface processing. The study of the model showed that the cooling coefficient of the airflow was affected by speed and pressure. Furthermore, the generation and strength of the autogenous cooling airflow were closely related to the physical properties of the grinding tool. In terms of processing heat generation, this paper used the Johnson-Cook material constitutive model to calculate the residual heat on the surface of the processed blade, and the surface temperature rise was within a controllable range. For the airflow intensity generated by the high-speed rotation of the tool, the airflow preset method was used to verify whether it meets the processing conditions.

1. Introduction

Due to the difficult processing of materials [1], the complexity of the shape, the diversity of materials, the diversity of various blade, etc., the difficulty of blade processing has been heavy. The key technologies of blade processing are thorny problems that the aviation industry urgently needs to overcome. Taking compressor blades as an example, they need to be forged or cast billet, milling, surface grinding, and other processes (such as manual polishing of the blade surface and dynamic balance adjustment of the blade) [2, 3] before they can be assembled to the shaft system; Figures 1 and 2 show a milled blade and its surface grinding technology. The machining accuracy of the blade has a great influence on the high-speed rotation accuracy of the shaft system and the performance of the whole machine [4–6]. In recent years, the development of blades with small aspect ratios and curved blades has put forward new requirements for blade processing accuracy and processing methods [7, 8]; the reason for this difficulty is that the geometry of the small aspect ratio blade is more complex than that of the general blade, which is difficult to complete with the existing processing technology. Such blades often need to undergo more complex surface grinding and surface coating layer process treatment. In summary, blade surface processing technology is the core technology of blade production.

Cooling during blade processing is a long-term concern. Due to the heat dissipation of titanium alloys, the surface of the blades will be ablated during the processing, and the local high temperature during the processing of nickel-based alloy blades will change the properties of the blade materials. The form of cooling and the control of cooling conditions are factors that cannot be ignored in blade processing technology.

2. Application of Airflow Cooling and Mathematical Model

There are many cooling methods for surface grinding [9–11]. In the grinding machine processing that uses a high-speed rotating hard grinding wheel as a grinding tool, coolant is usually used for cooling. This cooling method can not only take away the high temperature generated by

FIGURE 1: Blades formed by CNC milling.

FIGURE 2: Blade surface grinding technology.

FIGURE 3: Flat plate heat transfer model.

state of the workpiece will not be changed; third, the air flow launching device can be far away from the workpiece, thereby preventing interference in space; fourth, under the same power, the speed of the gas flow is higher than that of the liquid, which helps to increase the circulation frequency of the cooling gas. Obviously, the shortcomings of airflow cooling must be paid attention to and overcome. Due to the Brownian motion of gas molecules, the cooling airflow spreads quickly; therefore, a cooling airflow recovery device must be installed during the grinding process of the blade surface using airflow cooling. Since the recycled airflow is mixed with chips falling off the surface of the blade, abrasive particles dropped due to abrasive belt wear and various metal dusts, the processing environment must be ventilated, smoke and fire are prohibited, and employees must be equipped with breathing system protective masks.

The cooling air flow passes through the surface of the blade being processed and takes away the heat generated by the processing. This physical process can be illustrated by a flat plate heat transfer model. In the model shown in Figure 3, a certain microelement on the surface of the blade is taken as the research object. Since the selected microelement is small enough, its surface can be regarded as a plane approximately. The surface of the microelement is parallel, and the influence of the difference in the direction of the air movement can be corrected on this model. It is worth noting that according to the definition of fluid mechanics, the airflow velocity near the blade is distributed in a gradient, the airflow velocity closer to the blade is slower, and the airflow velocity farther away from the blade is faster. However, in this model, whether the blade or the airflow microelements are small enough that the airflow gradient distribution is very weak, which is ignored for the convenience of calculation.

The temperature distribution under this condition can be analyzed by the method of combining the N-S equation and the energy equation. When the cooling airflow and the processing speed reach a steady state, the governing equations of air flow heat transfer near the blade element should satisfy the following conditions.

Mass conservation equation:

$$\frac{\partial \rho}{\partial t} + \frac{\partial (\rho u_i)}{\partial x_i} = 0. \tag{1}$$

the processing heat, but it also can wash the surface of the workpiece and the surface of the grinding wheel at the same time and then take away the chips. In the abrasive belt grinding process, since the base material of the abrasive belt is a flexible material, it is not suitable to use a liquid cooling medium, and airflow is often used as a cooling medium. Compared with liquid, airflow cooling does not have particularly high cooling efficiency, but it has several obvious advantages.

First of all, the airflow cooling will not change the properties of the abrasive belt base material, the airflow cannot be attached between the abrasive belt base material and the contact wheel, and the movement form of the abrasive belt will not be changed; secondly, the airflow will not form residues on the surface of the workpiece and will not spread to the gap between the workpiece and the fixture, and the movement

Figure 4: Temperature distribution of the abrasive grain group passing through the highest peak of the blade.
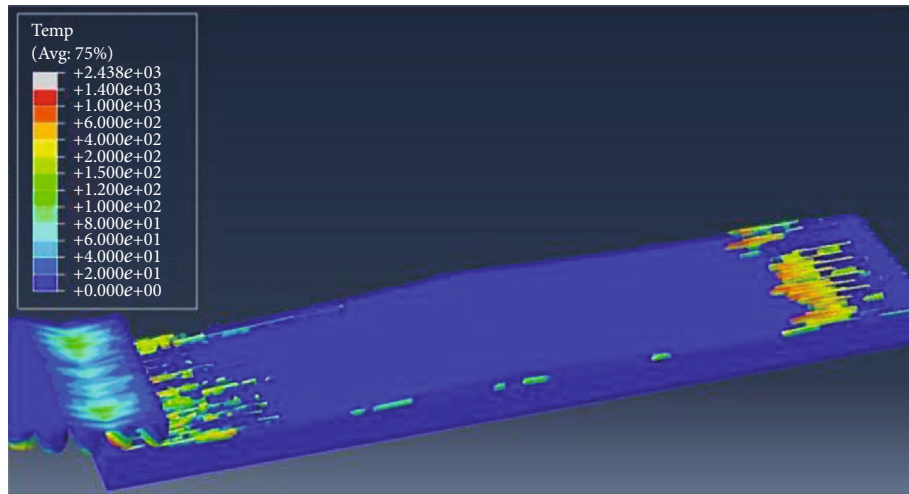
Figure 5: Temperature distribution of the abrasive grain group leaving the blade.

Momentum conservation equation:

$$\frac{\partial(\rho u_i)}{\partial t} + \frac{\partial(\rho u_i u_j)}{\partial x_i} + \frac{\partial p}{\partial x_i} - \frac{\partial \tau_{ij}}{\partial x_j} + \rho g_i + S_i = 0. \qquad (2)$$

In the above two formulas, t is the cooling airflow density, p is the airflow pressure, u is the airflow velocity, τ is the viscous stress tensor, and S is the source term of the momentum equation.

The energy conservation equation in the cooling airflow region is

$$\frac{\partial(\rho c_p T)}{\partial t} + \frac{\partial(\rho u_i c_p T)}{\partial(x_i)} - \frac{\partial}{\partial x_i}\left(k_e \frac{\partial T}{\partial x_i}\right) - S_T = 0. \qquad (3)$$

The energy conservation equation in the microelement region of the processed blade is

$$\frac{\partial(\rho c_p T)}{\partial t} - \frac{\partial}{\partial x_i}\left(k \frac{\partial T}{\partial x_i}\right) - Q_T = 0. \qquad (4)$$

In the above two formulas, c_p is the specific heat capacity, Q_T is the heat source, k_e is the effective thermal conductivity, k is the molecular thermal conductivity, S_T is the source term of the energy equation, and k and k_e satisfy the following relationship:

$$k = k_e - k_r. \qquad (5)$$

The definition of k_r is

$$k_r = \frac{c_p \mu_r}{P_r}. \qquad (6)$$
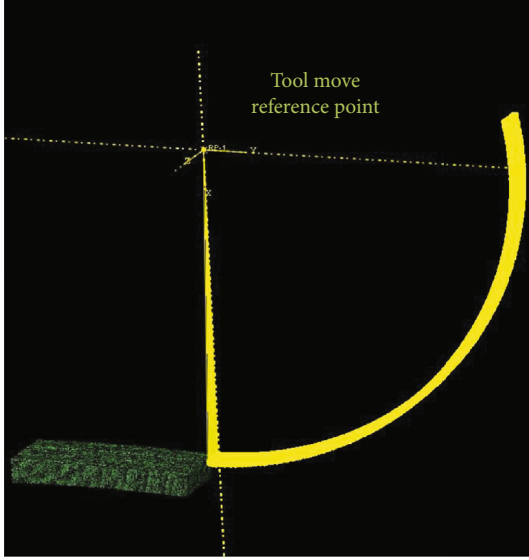
Figure 6: Motion constraint of the stationary state of the blade.
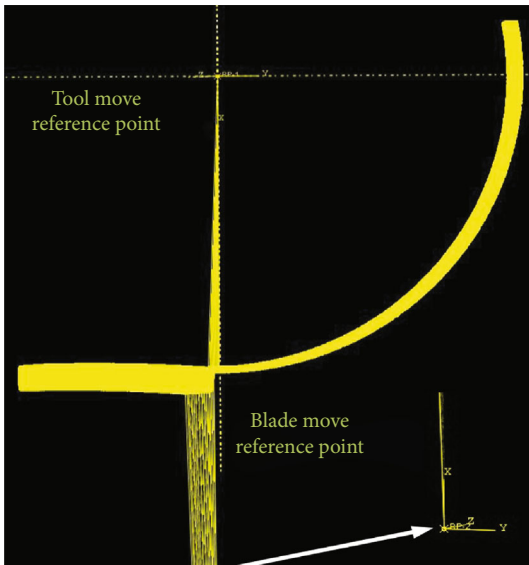
Figure 7: Motion constraints in the case of both blade and abrasive belt movement.

In the above formula, μ_r is the turbulent viscosity coefficient, and P_r is the turbulent Prandtl number.

For the model in Figure 3, the following empirical formula can be used to calculate the heat transfer coefficient:

$$Nu = \frac{\alpha l}{\lambda} = 0.664 R_e^{1/2} P_r^{1/3}. \tag{7}$$

It can be seen from the above formula that the change of the turbulent Prandtl number of the cooling airflow is caused by the change of the turbulent viscosity coefficient, and the change of the Prandtl number causes the change of the plate heat transfer coefficient. However, the heat

transfer coefficient is not only affected by the Prandtl number, but also by the airflow Reynolds number. The definition of the turbulent Reynolds number shows that when the speed and pressure of the cooling airflow change, its Reynolds number will change, which will make the blades microelement's heat transfer coefficient changes.

3. Numerical Calculation Model for Processing Temperature

In this paper, the heat generated during the surface grinding of the blade microelement is simulated. The blade material is a new titanium alloy Ti6Al4V. The Johnson-Cook material constitutive model is a thermo-viscoplastic constitutive model suitable for this blade material. The reason for choosing the Johnson-Cook constitutive model is that this constitutive model can not only adapt to the thin-wall shape characteristics of the blade, but also is commonly used in titanium alloys. Research on the dynamic constitutive relationship of metals and mature numerical calculation programs can often achieve better results in grinding mechanism simulation. The mathematical expression of Johnson-Cook material constitutive model is

$$\sigma = (A + B\varepsilon^n) \left[1 + C \left(\ln \frac{\varepsilon}{\varepsilon_0} \right)^m \right] \left[1 - D \left(\frac{T - T_0}{T_0} \right)^k \right]. \tag{8}$$

In the above formula, A, B, n, C, and m are material constants, respectively, representing the yield stress intensity, strain strengthening coefficient, strain strengthening index, strain rate strengthening parameter, and temperature strain rate sensitivity under quasi-static conditions; σ is the flow stress; T_m is the melting point temperature; T is the temperature of the blade material, T_r is the reference temperature, usually designated as the ambient temperature of the simulation experiment; ε is effective plastic strain, and ε_0 is the reference strain rate. The Johnson-Cook material constitutive model parameters of Ti6al4v are shown in Table 1.

In addition to the constitutive model, the simulation of such problems must also define failure criteria. During the grinding process of the blade surface by abrasive particles, the blade material undergoes deformation similar to shear failure under the plowing action of the abrasive particles. Therefore, the failure parameters of the blade material can be defined as follows:

$$\omega = \sum \left(\frac{\Delta \varepsilon^{\mathrm{pl}}}{\varepsilon_{\mathrm{f}}^{\mathrm{pl}}} \right). \tag{9}$$

In the above formula, $\Delta \varepsilon^{\mathrm{pl}}$ is the increase in plastic strain, and $\Delta \varepsilon_{\mathrm{f}}^{\mathrm{pl}}$ is the amount of failure strain.

The failure strain $\Delta \varepsilon_{\mathrm{f}}^{\mathrm{pl}}$ is a function related to the strain rate, compressive stress deviator stress ratio, temperature,
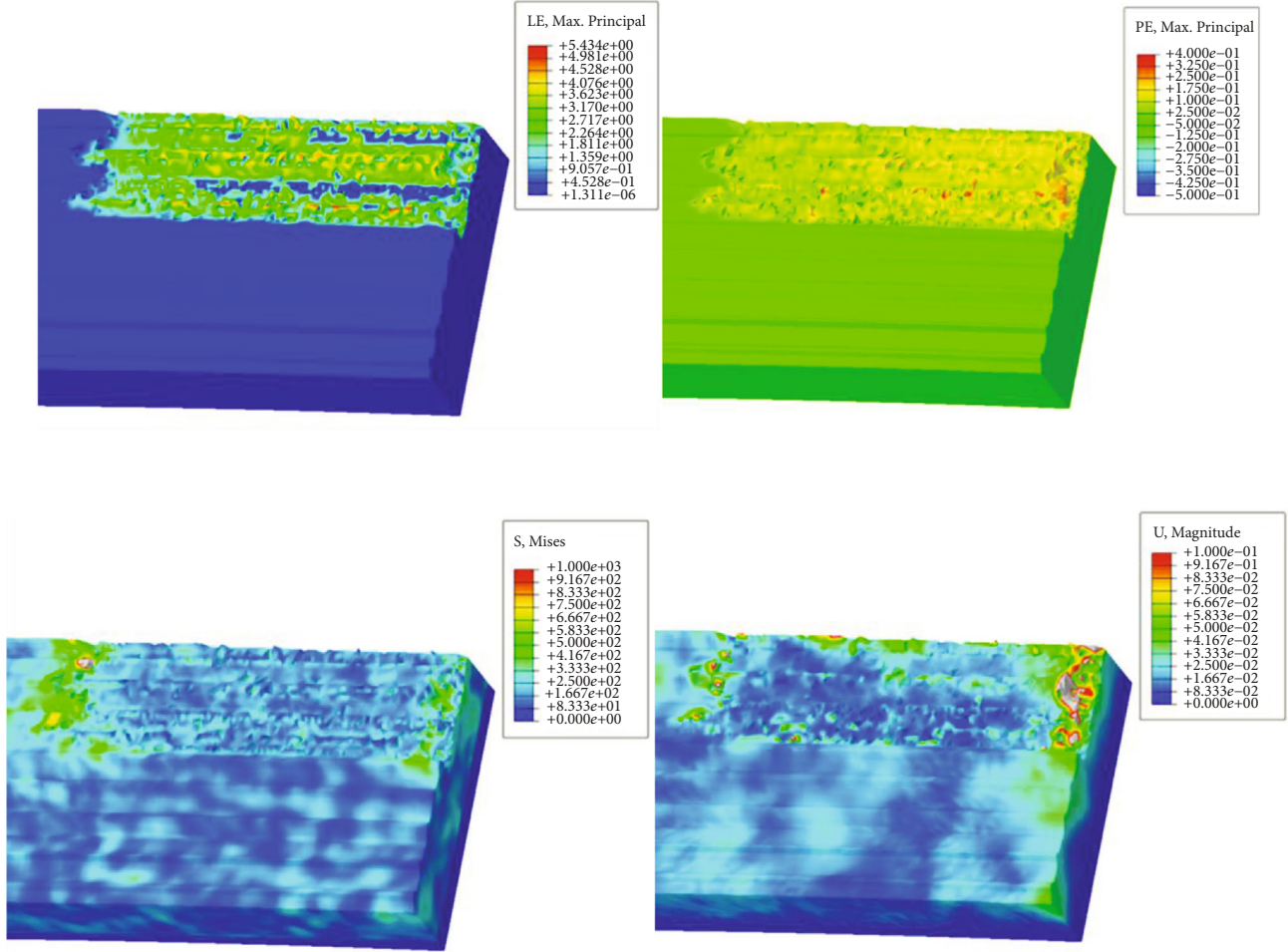
FIGURE 8: Simulated calculated blade surface with blade feed motion when the abrasive belt is in the initial wear stage.

and other parameters, and its expression is

$$\varepsilon_{\mathrm{f}}^{\mathrm{pl}} = \left[\mathrm{d}_1 + \mathrm{d}_2 e^{(\mathrm{d}_3 (p/q))} \right] \left[1 + \mathrm{d}_4 \left(\frac{\dot{\varepsilon}^{\mathrm{pl}}}{\dot{\varepsilon}_0} \right) \right] (1 + \mathrm{d}_3 \theta). \quad (10)$$

The dimensionless strain rate in the above formula is denoted as $\varepsilon^{\mathrm{pl}\bullet}/\varepsilon_0{}^\bullet$, and the compressive stress deviatoric stress ratio is denoted as p/q, where p is the compressive stress and q is the Mises stress. For material Ti6al4v, d1, d2, d3, and d4 are invalid parameters, and their values are shown in Table 2.

4. Analysis of the Results of Numerical Calculations

The temperature change of the material during processing can be obtained after analysis using the finite element software ABAQUS. In this paper, The temperature cloud diagram of the processing process is used to analyze the temperature change during this process. The results are shown in Figures 4 and 5. It can be clearly seen from these two figures that the area where the temperature rises sharply is the area where the chips remain, that is, the valley area of

the milling texture. In the peak area of the milling texture, the temperature of the blade surface element does not rise sharply. The reason for this phenomenon is as follows: on the one hand, because the simulation analysis is a single grinding, the microelements on the blade surface are not constantly rubbed, which causes the temperature of the system to rise and accumulate. On the other hand, the large amount of heat generated during grinding is mostly attached to the chip body. The grinding simulation setting defaults that the cut chips are completely separated from the workpiece, so there is a significant temperature increase in the area where the chips remain. The areas where there are no residual chips, that is, those areas where the chips have been evacuated, will not cause a sharp rise in the surface temperature of the blade. The heat generated by mechanical friction during processing is removed with the removal of chips. It can be seen that it is very necessary to remove chips in time.

This paper distinguishes two different simulations and experiments in which the blade is at rest and the blade is in motion, in order to maximize the accuracy of the calculation. Figures 6 and 7, respectively, show the constraints of these two simulations; due to the different constraint conditions, the former cannot be simply defined as the state where the speed of the latter is zero. The simulation calculation amount of the blade and the belt at the same time is several

FIGURE 9: Cooling air flow velocity in the contact area during blade machining.

FIGURE 10: Cooling air flow velocity in the space near the processing area.

times that of the static and fixed state of the blade. In addition, the geometric characteristics of the original shape of the blade surface in the collection and distribution model should be as close as possible to the real blade blank surface.

Except that the setting of abrasive material parameter G_m is controlled by empirical value, other detailed parameters setting can be carried out as described below:

The hardness parameter H of the abrasive particle group is controlled by changing the parameters of the material. Change the speed of the reference point rotation (load-boundary condition) by setting the speed values of the six degrees of freedom in the boundary conditions, thereby controlling the movement frequency f of the abrasive particle group. On this basis, the linear velocity vs. of the abrasive particle group is controlled by changing the radius of gyration of the abrasive particle group movement (that is, the distance between the reference point and the abrasive particle group). Similarly, this control method is also adopted for the motion parameter v_w of the blade surface model,

We can control the normal force Fn between the blade and the abrasive particle group by changing the MPC contact option parameter (interaction-MPC constraint) in the constraint options. The definition of MPC is multipoint constraints; that is, the constraint point is not a single contact

form. The tangential force Ft between the blade and the group of abrasive particles is controlled by setting the interaction property-tangential behavior in the interaction property, and the number of revolutions N of the abrasive particle group in a period of time is controlled by setting the time step (step-time period). The cooling condition constant adopts the default preset value, that is, the reduced air flow rate (Kg/min) produced by the high-speed rotation of the grinding tool, so that the workpiece can be effectively cooled during processing.

Figure 8 shows a set of simulation results that meet the above settings. The results show that the machining results achieve the expected results under the cooling conditions of the air flow generated by the grinding tool. The cooling condition constant changes due to changes in various parameters of the tool, and the cooling effect brought about by this change is in line with the processing requirements.

5. Experiment and Analysis

According to the above calculation results, the airflow generated by the high-speed rotating grinding tool can meet the requirements of velocity and flow rate; meanwhile, the heat carried by the chips will not cause the local temperature of the blade surface to rise too high. This paper uses an air flow meter to measure the cooling air flow conditions in the actual process. Figures 9 and 10 show that when the machine rotates at a certain speed, the air velocity in the contact area of the blades and the contact wheel and the air velocity in the space near the processing area are, respectively, 7.413 m/s and 5.903 m/s, and the airflow temperature is about 15 degrees Celsius.

In an open situation, the total pressure ratio of the cooling airflow can be set to 1.1, the airflow temperature is 288 k, the atmospheric pressure is 0.101 Mpa, and the air density is 1.2 Kg/m3. At this time, the cooling airflow mass flow on the processing surface can be used as follows The formula shown approximates:

$$q_m = V\rho_0\Pi. \tag{11}$$

In the above formula, q_m is the mass flow rate of the cooling gas, ρ_0 is the air density, and Π is the total pressure ratio of the airflow.

If the area of the air flow around the processing area is 0.01m^2, then the air flow rates of the two are 5.75Kg/min and 4.57Kg/min, respectively. In the simulation calculation, it can be considered that the cooling airflow generated by the rotation of the grinding tool is equivalent to the flow rate of 5kg/min. More powerful ventilation air flow and cooling effect need to be achieved by generating cooling airflow through an air compressor. Obviously, the cooling effect of the airflow is closely related to the geometry of the tool. The research in this article can give such a processing idea: it is possible to design a processing tool that can not only conform to the blade surface grinding, but also generate high-speed cooling airflow due to the movement of the tool itself. This tool will change the shape of the contact wheel of the belt machine. These work will be carried out in further research.

6. Summary and Outlook

On the basis of the plate heat transfer model, the characteristics of the cooling airflow during the blade surface processing are studied. The cooling coefficient of the airflow is affected by the speed and pressure. The generation and strength of the self-generating cooling airflow are closely related to the physical properties of the grinding tool. In terms of processing heat generation, this paper uses the Johnson-Cook material constitutive model to calculate the residual heat on the surface of the processed blade, and the surface temperature rise is within a controllable range.

For the airflow intensity generated by the high-speed rotation of the tool, the airflow preset method is used to verify whether it meets the processing conditions. In the subsequent research, in addition to the plate heat transfer model, the conical capillary model can also be used as the cooling airflow model. It is necessary to improve the shape of the processing tool so that it can not only meet the requirements of blade surface processing, but also generate high-speed cooling airflow. Future research can be combined with cooling and lubrication, air flow types, etc. to increase the breadth and depth of research.

Data Availability

The data that support the findings of this study are available from the corresponding author upon reasonable request.

Conflicts of Interest

The authors declared no potential conflicts of interest with respect to the research, authorship, and/or publication of this article.

Acknowledgments

References

[1] F. Klocke, S. L. Soo, B. Karpuschewski et al., "Abrasive machining of advanced aerospace alloys and composites," *Cirp Annals-manufacturing technology*, vol. 64, no. 2, pp. 581–604, 2015.

[2] G. A. Oosthuizen, *Innovative Cutting Materials For Finish Shoulder Milling Ti-6A1-4V Aero-Engine Alloys*, Stellenbosch University of Stellenbosch, Western Cape, 2009.

[3] Z. Chen, Y. Shi, X. Lin et al., "A profile-adaptive compliant polishing tool for aero-engine blade finishing process," *The International Journal of Advanced Manufacturing Technology*, vol. 102, no. 9-12, pp. 3825–3838, 2019.

[4] B. Denkena, V. Boess, D. Nespor, F. Floeter, and F. Rust, "Engine blade regeneration: a literature review on common technologies in terms of machining," *The International Journal of Advanced Manufacturing Technology*, vol. 81, no. 5-8, pp. 917–924, 2015.

[5] S. B. T. Raj, "Advanced material for front fan blade manufacturing," *Imperial Journal of Interdisciplinary Research*, vol. 3, no. 5, pp. 80–88, 2017.

[6] R. K. Vimal and G. Dhanjayan, "Improving fatigue life of gas turbine fan blade using advanced composite materials," *IOP Conference Series: Materials Science and Engineering*, vol. 455, no. 1, article 012035, 2018.

[7] N. S. Babu and K. J. Rao, "Strength assessment of fan blade with different materials," *Science and Technology*, vol. 6, no. 1, pp. 266–283, 2019.

[8] X. U. Xiaohu, Z. H. Dahu, H. Zhang, Y. A. Sijie, and D. I. Han, "Application of novel force control strategies to enhance robotic abrasive belt grinding quality of aero-engine blades," *ChineseJournal of Aeronautics*, vol. 32, no. 10, pp. 2368–2382, 2019.

[9] S. C. Xiu, Y. D. Gong, and G. Q. Cai, "Study on effect of grinding fluid supply parameters on surface integrity in quick-point grinding for green manufacturing," *Advanced Materials Research*, vol. 53-54, pp. 209–214, 2008.

[10] C. Mao, H. Zou, Y. Huang, Y. Li, and Z. Zhou, "Analysis of heat transfer coefficient on workpiece surface during minimum quantity lubricant grinding," *International Journal of Advanced Manufacturing Technology*, vol. 66, no. 1-4, pp. 363–370, 2013.

[11] H. Singh, V. S. Sharma, S. Singh, and M. Dogra, "Nanofluids assisted environmental friendly lubricating strategies for the surface grinding of titanium alloy: Ti6Al4V-ELI," *Journal of Manufacturing Processes*, vol. 39, no. MAR., pp. 241–249, 2019.

Hindawi

Research Article

An Experimental Study on the Repair of Spinal Cord Injury after Exercise Based on Multifunctional Material-Like Particles

Zhaoshu Ouyang,[1,2] **Guang Tang,**[3] **Shibin Tang,**[2] **and Linyan Peng** [3]

[1]*Department of Spinal Surgery, Affiliated Hospital(Clinical College) of Xiangnan University, Chenzhou, 423000 Hunan, China*
[2]*Hunan Chenzhou Orthopaedic Hospital, Chenzhou, 423000 Hunan, China*
[3]*Affiliated Hospital of Xiangnan College, Chenzhou, 423000 Hunan, China*

Correspondence should be addressed to Linyan Peng; 1490540114@xs.hnit.edu.cn

Spinal cord injury is a serious neurological injury disease. With the improvement of living standards in China in recent years, we began to develop sports hobbies, so the cases of sports spinal cord injury also increased. The main cause of spinal cord injury is the microenvironment after spinal cord injury, which prevents nerve regeneration. With the support of the state and the efforts of regenerative medical scientists in China, remarkable progress has been made in the reconstruction of microenvironment after spinal cord injury in recent years. The scaffold was combined with multifunctional nanoparticle repair technology to reconstruct the microenvironment of nerve regeneration by transplantation. The purpose of this paper is to carry out an experimental analysis on the repair of spinal cord injury after exercise based on multifunctional nanomaterial particles, and this paper takes badminton as an example to explore. The microenvironment of spinal cord injury was improved by implantation of multifunctional nanomaterial particles and nerve regeneration collagen scaffold. We found 48 patients with spinal cord injury after badminton and divided them into two groups. The pilot group was treated with a multifunctional nanomaterial granular nerve scaffold, whereas the treatment in the control group was with ordinary drugs. The experimental group was followed up for nine months, starting one month after the surgery. After nine months of experimental investigation, we found that the treatment of multifunctional nanoparticle nerve scaffold can not only reduce the injury area and scar formation but also promote the regeneration of nerve microenvironment and the recovery of body function and motor function of patients and reduce the inflammatory reaction caused by injury and pain.

1. Introduction

Spinal cord injury is the most serious complication of the spinal cord, which has the characteristics of high disability rate, high morbidity rate, high mortality rate, and many complications [1]. Spinal cord injury belongs to the central nervous system injury, and its repair after injury has always been a major problem in the international medical community [2]. At present, with the rapid development of high-altitude work, modern transportation industry, and the endless variety of difficult sports injuries, the incidence of this disease is increasing year by year. What follows is the highly degraded physical health and quality of life of the patients, as well as the heavy mental and economic burden to the patient's family and even the whole society, which greatly hinders the development of society [3].

Following spinal cord injury, some conduction tracts in the medulla spinalis, such as the corticospinal tract [4], can regenerate and grow into the medulla spinalis distal to the injury, but this does not significantly improve motor function after playing badminton in spinal cord injury patients. This is mainly due to the fact that after spinal cord injury, although some nerve fibers in the corticospinal tract can sprout and grow, they cannot form the correct neural

circuit with the motor center of the nerve loop originally dominated by the lower part of the injury. It affects the recovery of original nerve function.

With the continuous development of modern biomedical diagnosis and treatment technology, the original traditional disease diagnosis mode and treatment mode can no longer meet the needs of precision medicine and personalized medicine [5]. Multifunctional diagnosis and treatment mode, with its own accuracy, reliability, and the function of multiple examinations at the same time, has been highly praised by patients and medical workers. Multifunctional nanoparticle [6] technology, that is to integrate multiple components with different properties into one nanoparticle, can conduct real-time tracking and adjuvant treatment of disease diagnosis and treatment through its own physical and chemical properties at the same time of diagnosis and treatment. Therefore, in this paper, we applied the multifunctional nanoparticle technology to the treatment of spinal cord injury, combined the multifunctional nanoparticles with collagen nerve scaffold [7], and improved the wound site of patients with spinal cord injury due to badminton sports, as far as possible to reduce the pain of patients, shorten the recovery cycle, and reduce the burden of patients.

Multifunctional composite nanostructures are usually composed of two parts: the core and the outer shell [8]. Compared with the common simple nanostructures, core-shell nanostructures play a good role in protecting the core components, especially the easily oxidized or unstable components, and significantly improve the physical and chemical stability of multifunctional particles. In addition, the biocompatible shell outside the core can effectively reduce the biological toxicity of nanoparticles, improving the biological dispersion ability and phagocytosis efficiency of nanoparticles [9]. Core shell structure [10] can also effectively improve the connectivity of multifunctional nanoparticles with other biomolecules by changing the shell composition, so that the nanoparticles have better targeting and drug-loading capacity. In addition, the composition of the core and the shell can be selectively changed according to the specific application requirements, so that the multifunctional nanoparticles have the characteristics of both at the same time, so as to achieve a variety of biomedical diagnosis and treatment purposes. At present, core-shell nanomaterials with different functions have been widely used in electronic instruments, biomedicine, optics, and catalysis.

In this paper, we will analyze the pathological mechanisms of marrow injury from all aspects, starting from the physiological structure of the marrow, from chronic spinal cord injury to acute spinal cord injury. From the theme of this paper, the application of multifunctional nanomaterial particles in the treatment of spinal cord injury is described. The objectives are to analyze the research status and prospect of multifunctional nanomaterial particles in the treatment of spinal cord injury and combine the multifunctional nanomaterial particles with collagen nerve scaffold to maximize the efficacy of both in spinal cord injury.

2. Mechanism of Spinal Cord Injury

2.1. Physiology of the Spinal Cord. The medulla spinalis not only connects the brain to the peripheral nerves but also produces spinal reflexes [11]. The spinal cord begins in the medulla oblongata at the base of the brain, passing across the greater foramen and through the vertebral canal. In humans, the spinal cord ends at the level of the first lumbar spine, while in rats the spinal cord ends at the level of the third lumbar spine. In the process of growth, the growth rate of the lumbar spine is faster than that of the spinal cord, so the spinal nerve under the cervical spine passes through the intervertebral foramen under the corresponding vertebral body. From the inside to the outside, the spinal cord is covered by the leptomeningeal, arachnoid, and dural H-layer fibrous tissue. There is a subarachnoid space filled with cerebrospinal fluid [12] between the pia mater and arachnoid. There are fibrous connective tissue and adipose tissue between the dura mater and spinal plate. These structures, along with the spine, protect the spinal cord. The gray matter of the spinal cord is located in the center and surrounded by white matter. The gray matter is composed of interneurons, neuronal cell [13], dendrites, afferent nerve fibers, and glial cells. The peripheral white matter is mainly composed of multiple groups of myelinated axons. These axons with different functions are called fiber bundles or fiber pathways, which run longitudinally along the spinal cord. Some axons send information down from the brain to the peripheral nerves, while others transmit information from the peripheral nerves to the brain.

At present, spinal cord injury can be divided into three stages.

(1) Acute stage: in the first few days after injury, the main necrosis cells and then hematoma appear in the gray matter of the spinal cord, compressing the surrounding tissues, causing edema and microcirculation disorders, and aggravating the spinal cord injury

(2) Secondary reaction stage: injury after several minutes to a few weeks, including continuous ischemia and necrosis of cells, inducing or promoting apoptosis and necrosis of nerve cells, injured sites and surrounding areas

(3) Chronic stage: it can last for several days or even years, the range of apoptosis continues to grow, and scar formation, cystic regional expansion, and changes in nerve impulse transmission pathway were observed; some patients even have chronic central pain such as hyperalgesia and allergy

2.2. Primary Injury and Secondary Injury. When the spinal cord is severely injured, or the most common sudden impact, compression or vascular blockage, nerve injury has begun. We call it "primary injury." The primary injury is the mechanical injury of spinal cord caused by the injury itself, which results in necrosis of intramedullary cells and interruption of axons. It can be divided into spinal cord

concussion, spinal cord contusion and hemorrhage, spinal cord compression, cauda equina injury, etc. It can lead to permanent irreversible dysfunction of the spinal cord. The prognosis and rehabilitation were in direct proportion to the degree of injury at that time. At present, the local treatment of primary spinal cord injury is not effective. This is mainly because the local treatment of primary spinal cord injury is not suitable for primary spinal cord injury.

A series of harmful biological reactions caused by mechanical spinal cord injury are called "secondary injury." Secondary injury occurs after primary injury, sometimes more severe than primary spinal cord injury, leading to central hemorrhage and necrosis to edema and apoptosis area 2-3 cm long near the spinal cord, which is often replaced by glial scar tissue in the late stage. The mechanisms include microcirculation, free radical and lipid peroxidation, excitatory amino acid theory, calcium overload, electrolyte disturbance, and inflammatory reaction. It is one-sided to discuss one or more pathological injury mechanisms. Secondary injury is the result of multiple mechanisms. The interaction of various mechanisms affects the development of spinal cord injury. Secondary injury can occur within minutes to weeks after primary injury and last for several years. It can develop to both ends of the spinal cord, leading to more severe nerve damage, and eventually into a chronic phase.

It is very necessary to understand the biochemical and cytological mechanisms of primary and secondary spinal cord injury [14]. Therefore, we can study the treatment methods of these two periods to reduce the area of secondary injury and promote nerve regeneration. In 1911, Allen removed the inflammatory fluid from the spinal cord injury area in dogs and found that the motor function of dogs was significantly improved. Therefore, he proposed the concept of secondary spinal cord injury. With the development of research, Dr. Allen proposed that local hemorrhage at the injury site could lead to more severe spinal cord injury.

2.3. Apoptosis. Apoptosis [15] is a kind of programmed cell death that occurs under physiological or pathological conditions. Trauma can also lead to apoptosis. There is clear morphological and histological evidence that spinal cord injury can induce apoptosis. Apoptosis occurs in neurons, oligodendrocytes, microglia, and astrocytes. After spinal cord injury, oligodendrocytes in white matter die within weeks due to demyelination. Apoptotic cells were found in dentate and monkey and human spinal cord injury, which indicated that the active cell death aggravated the injury degree of central nervous system. The mechanism of apoptosis after spinal cord injury has not been fully studied, but the apoptosis of microglia and oligodendrocytes is closely related, suggesting that the activity of microglia may be related to apoptosis.

2.4. Inflammatory Response Theory. Inflammatory response theory: immune inflammatory response is the mechanism of self-defense and repair when the body is injured. Studies have shown that in spinal cord injury, the main inflammatory cells involved are neutrophils, monocytes, lymphocytes, and microglia in nerve cells. After spinal cord injury, resident microglia are activated, leukocytes rapidly infiltrate into the injured area and release unfavorable cytokines and reactive oxygen species, which leads to more leukocyte aggregation and more serious tissue damage. Secondary inflammatory reaction often plays a negative role in injuring spinal cord tissue, destroying and repairing, and promoting apoptosis and excessive hyperplasia of scar. A scholar believes that human intervention can control the development of secondary inflammatory response in favor of spinal cord repair; otherwise, inflammatory reaction will promote cell apoptosis and expand the scope of injury. Some studies suggest that inflammatory reaction is not completely harmful, it may play a beneficial role in the process of nerve tissue repair.

2.5. Chronic Stage of Spinal Cord Injury. The chronic stage of spinal cord injury includes slight demyelination of white matter, dissolution of gray matter, deposition of connective tissue [16], proliferation of reactive glial cells, and eventually formation of therapeutic scars. Glial scar [17] is mainly composed of reactive astrocytes, microglia (macrosatellite cells), extracellular matrix, and chondroitin sulfate polysaccharide. It acts as a barrier to prevent axons from passing through. About 25% of patients with spinal cord injury will form cystic cavity around glial scar [18]. Syringomyelia is usually caused by syringomyelia, which usually causes neuropathic pain. As a result, many patients develop pain syndrome, which eventually leads to depression. The mechanisms of pain and depression following spinal cord damage have not been clearly studied, but animal experiments have found that neurons from the back corners of the spinal cord are hyperexcitable for several weeks after injury, which could be associated with pain. In addition, studies have shown that chronic pain is related to the activation of the hypothalamic pituitary adrenal axis, and chronic pain is an inevitable stressor. The activation of HPA axis can also cause the release of glucocorticoid, which is closely related to depression.

3. Research on the Repair of Spinal Cord Injury with Nanomaterials

3.1. Research Background of Spinal Cord Injury. Spinal cord injury leads to partial or total loss of function below the wound. It not only brings great changes to patients and their families but also brings economic losses far beyond our expectation. The quality of life of patients with spinal cord injury is the lowest compared with other healthy people or disabled people. The average quality of life of patients with spinal cord injury is low, and their ability of self-care is low. They are eager to recover and to be able to take care of themselves. In this paper, we studied the changes of physical function of patients with spinal cord injury for nine months under two different treatment methods: multifunctional nanoparticle nerve scaffold and drug treatment, hoping to change the life status of patients with spinal cord injury.

3.2. Research Status. In view of the current high incidence rate and high disability rate of spinal cord injury, treatment

after onset has been a hot and difficult point in clinical research. At present, medical researchers divide the mechanism of spinal cord injury into two kinds: mechanical primary mechanism and biochemical secondary injury mechanism. We should choose appropriate treatment methods to block the two different injury mechanisms. At present, animal experiments and some clinical studies have confirmed the neuroprotective effects of surgery, drug therapy, and genetic engineering therapy on spinal cord injury. However, the specific surgical treatment and drug protection mechanism are not mature and controversial. It is expected that more research results will be translated into clinical practice to benefit patients with spinal cord injury.

3.3. Research Prospects.
As one of the world's medical problems, the research on the treatment of spinal cord injury has attracted the attention of researchers and clinical scholars. The number of clinical studies on spinal cord injury is increasing. However, there are still some key problems to be solved.

(1) Analysis of microenvironment of nerve regeneration: after spinal cord injury, injury will lead to local ischemia, hypoxia, edema, stem cell activation and other reactions, and then axon demyelination, glial cell proliferation, nerve cell necrosis, and other problems, and finally form a cavity or scar injury is not conducive to nerve regeneration microenvironment. The process of continuous dynamic change is accompanied by the dynamic changes of various signal molecules and cells in the microenvironment

(2) Regeneration and repair mechanism of complete spinal cord injury: spinal cord injury can be divided into complete injury and incomplete injury. After incomplete spinal cord injury, some axons with intact nerves can regenerate and recover their functions by means of springing. However, complete spinal cord injury can completely cut off the nerve, and its regeneration and repair mechanism were a key issue to be studied

(3) Clinical research path of spinal cord injury: although relevant clinical studies have been carried out, there are still some problems to be solved in the clinical research of spinal cord injury. For example, due to the existence of spinal cord shock, the current commonly used Asian classification is not suitable for judging the severity of acute spinal cord injury. How to judge a patient as a complete injury? The scars of old spinal cord injury in patients will inhibit nerve regeneration. It is difficult to distinguish the scar tissue of old spinal cord injury from normal nerve tissue in operation and to remove the scar

The repair of spinal cord injury is a complex process, which involves not only spinal cord injury but also peripheral nerve and muscle degeneration, as well as different psychological changes of patients. Therefore, it is necessary to establish a complete psychological rehabilitation plan for spinal cord injury, which is combined with the continuous development of regenerative medicine technology, and repair the spinal cord tissue and reconstruct the injured spinal cord through the combination of multifunctional nanoparticles and nerve regeneration scaffold. In the near future, nerve regeneration and motor function recovery of patients with spinal cord injury will be realized.

3.4. Research Methods.
First of all, we need to determine the purpose of the study and the content of the study and select the research object reasonably for the experiment. We selected 48 eligible patients with spinal cord injury after badminton. Under the condition of ensuring the patients' knowledge, we randomly divided the patients into two groups, 24 people in each group. From the patients' choice of treatment, the influence of nanoparticle nerve scaffold on body weight recovery, the promotion of motor function recovery by nanoparticle nerve scaffold, and the alleviation effect of nanoparticle nerve scaffold on inflammatory reaction were explored. Finally, the data were collected and sorted out to study the effect of multifunctional nanomaterials on the repair of spinal cord injury after badminton.

3.5. Experimental Process.
The microenvironment is not conducive to nerve regeneration after spinal cord injury, which mainly includes the following: (1) primary injury and secondary injury lead to nerve cell death; (2) lack of nutritional factors to promote nerve regeneration; and (3) cell proliferation forms scar tissue and some chemical molecules in scar, such as chondroitin sulfate proteoglycans (CSPGs), which act as physical and chemical barriers to nerve regeneration. On the one hand, they inhibit the growth of axons; on the other hand, they inhibit the differentiation of neural stem cells into neurons. With the deepening of research, scientists gradually realize that due to the complex microenvironment formed after spinal cord injury, single strategy is difficult to effectively promote the repair of spinal cord injury, and the combination of multiple strategies is the focus of spinal cord injury repair. It is the most suitable and effective method to reconstruct the microenvironment of spinal cord regeneration by using multifunctional nanoparticles.

At present, multifunctional nanomaterial particle collagen scaffold for nerve regeneration is used. It is a kind of polymer material. We prepared the nerve regeneration scaffold by coating the multifunctional nanoparticles on the collagen nerve scaffold and then implanted the scaffold into the spinal cord injury site of the experimental group. Due to the characteristics of the growth of spinal cord nerve cells, the ideal spinal cord injury repair material structure should be cell oriented, that is, it can guide the orderly growth of cell axons. According to the characteristics of longitudinal and orderly growth of spinal cord neurons, nerve fibers were guided to extend orderly. The results showed that compared with the control group, the function of the patients was significantly improved, and the basic movement of the patients showed coordination and mobility. Histological and immunocytochemical analysis showed that the recovery may be due to the decrease of tissue loss and glial scar. After 9

TABLE 1: General information of patients.

Project		Experimental group (N = 24)	Control group (N = 24)
Age	15-25	5	7
	26-35	12	11
	35-45	7	6
Place of residence	Countryside	9	12
	Town	15	12
Marital status	Married/cohabitation	19	15
	Divorced/unmarried	5	9
Fitness	Frequently	4	5
	Occasionally	8	8
	Rarely	6	4
	Never	6	7

months of follow-up, the patient had no obvious adverse reactions, which initially proved that nerve regeneration collagen scaffold transplantation was safe.

For the control group, we were on medication. Only two drugs, methylprednisolone and sialic acid tetrasaccharide ganglioside, were found to have significant effects on recovery from spinal cord injuries and have obvious effects on the rehabilitation of spinal cord injury. The dose and course of treatment determined by NASCIS should be strictly followed. There are many similarities between GM-1 and MP in pharmacological mechanism, such as reducing tissue edema, reducing lipid peroxidation, reducing the production of free radicals, and stabilizing membrane structure. GM-1 can also promote axon growth, stimulate synaptic formation, and improve nerve conduction function. GM-1 was given 48 hours after injury and lasted for several months. At the same time, they received medical observation together with the experimental group.

4. Results and Discussion

4.1. General Information Survey. As shown in Table 1, in order to improve the biological experimental study on the repair of spinal cord injury after badminton with multifunctional nanomaterial particles, we collated the general data of patients in the experimental group and the control group. From the above data, we can see that the age of patients with spinal cord injury due to badminton is mainly between 26 and 35 years old. However, no matter when the experimental group is still in the control group, the patients who often exercise are relatively few. From this, we know that as long as the 26-35 age groups are office workers, it is precisely because they usually lack exercise, so they are more likely to be injured in sports.

4.2. Selection of Treatment Methods for Spinal Cord Injury. At present, the common spinal cord treatment methods in China include multifunctional nanoparticle nerve scaffold, drug therapy, and stem cell therapy. We investigated the patients with spinal cord injury after badminton in a certain
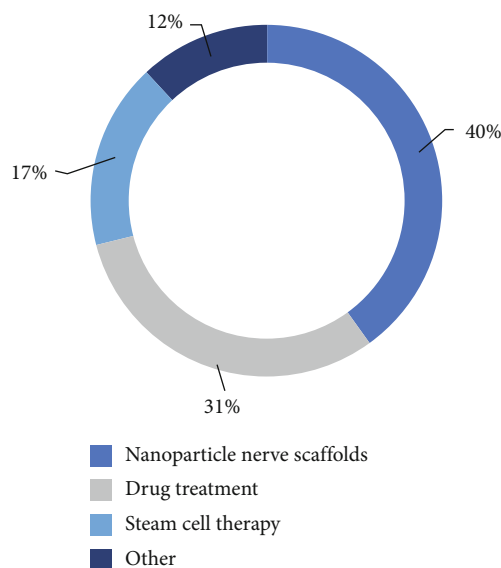
FIGURE 1: Selection of current methods of spinal cord injury quality.

place from 2017 to 2019 and calculated the treatment method when treating spinal cord injury.

As shown in Figure 1, the current common clinical treatment of spinal cord injury is focused on nanoparticle nerve scaffold treatment, which accounts for 40% of the clinical treatment of spinal cord injury. The second is drug therapy. Compared with the surgical treatment of nanoparticle nerve scaffold, the clinical selection rate of drug treatment is less, but still accounts for 31%. And stem cell therapy accounts for 12%. In addition, other methods also accounted for 17%, which shows that some of these methods still have certain development prospects.

4.3. Weight Recovery of Patients after the Operation of Nanomaterial Nerve Scaffold. After some medical research, we know that the recovery of patients' body weight is closely related to the recovery of patients' body function.
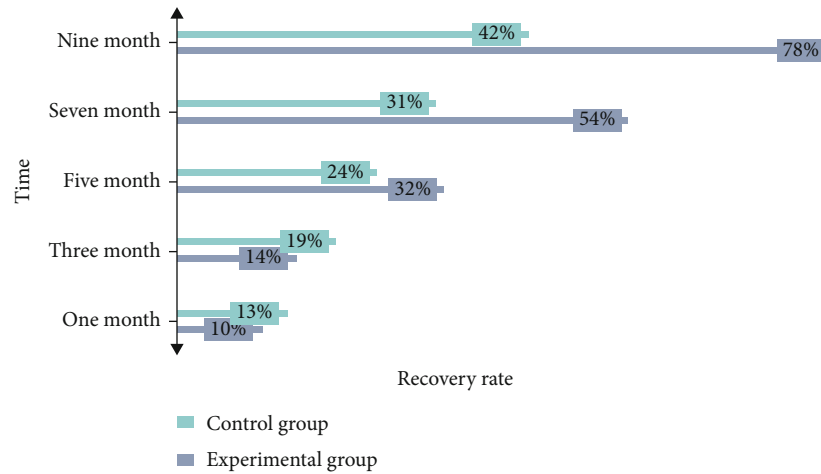
Figure 2: Weight gain of patients after nerve stenting with nanomaterials.
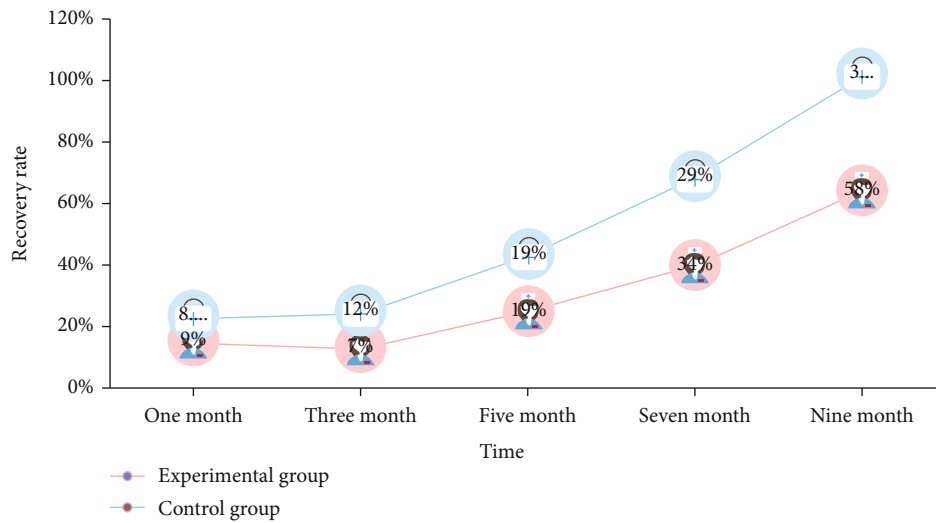
Figure 3: Recovery rate of motor function promoted by nanoparticle nerve scaffolds.

Postoperative weight recovery of patients is conducive to speeding up the recovery of bodily functions.

As shown in Figure 2, we recorded and compared the weight of patients in the experimental group and the control group one month after operation. According to the research, the weight recovery of patients after surgery represents the recovery of patients' body function to a certain extent. From the comparison of our data, we can see that the weight of the experimental group and the control group in the observation period is rising, but relatively speaking, from the first to the third month, the body weight of the experimental group and the control group was almost the same, but from the fifth month, the body weight of the experimental group rapidly recovered, and the recovery speed was much faster than that of the control group.

4.4. Nanomaterial Nerve Scaffold Promotes the Recovery of Motor Function. During the 9-month follow-up treatment, we recorded not only the weight data of the two groups but also the recovery level of motor function. Motor func-

tion is very important for everyone, especially for patients with spinal cord injury due to badminton.

As shown in Figure 3, we started recording from the first month after surgery. In the first month, the motor functions of the experimental group and the control group were at the same level. In the third month, the motor function of patients in the experimental group decreased slightly due to some reasons after operation, but in the follow-up treatment, the motor function quickly caught up with the control group, and in the fifth month, the motor function of the experimental group recovered rapidly, while the recovery of the control group was relatively slow. It can be seen that nanoparticle nerve scaffold can promote the recovery rate of motor function.

4.5. Nanoparticle Nerve Scaffold Reduces Inflammatory Response. In the recovery process of the disease, no matter whether it is surgical treatment or delayed treatment, as long as there is a wound, there is the possibility of inflammation, so we also recorded the experimental group of patients in the
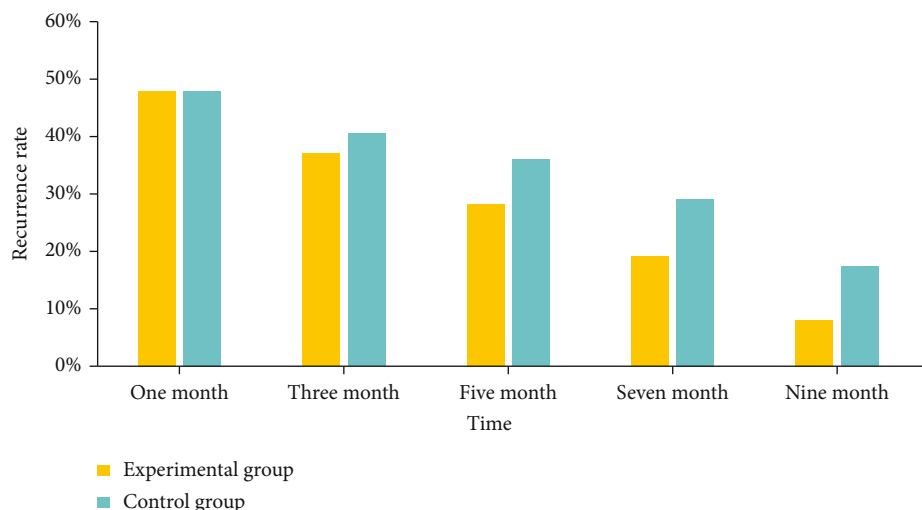
Figure 4: Inflammatory changes after nerve stenting of nanoparticles.

control group during the experimental period of inflammatory reaction.

As shown in Figure 4, we monitored the inflammatory response of the pilot and controlled patients from the first month after surgery. In the first month, the inflammatory response rates in the test and control arms were very similar. In the following eight months, the rate of inflammatory response in both groups decreased. But with the passage of time, the inflammatory response rate of the experimental group decreased much faster than that of the control group. After nine months, the inflammatory response rate of the experimental group decreased from 45% at the beginning to 8% at the ninth month. The control group was treated with drugs, from 47.85% at the beginning to 17% at the ninth month.

5. Conclusions

This paper mainly explores the repair of spinal cord injury after badminton sports with multifunctional nanomaterial particles. After spinal cord injury, patients will have a certain degree of movement disorders, and at the same time, various functions of the body will also have different degrees of problems, for example, urinary system infection, hydronephrosis, and dysuria. The follow-up treatment of spinal cord injury is not only a challenge to the patient's bearing capacity but also a heavy burden for the patient's family. Based on this point, we began to explore the use of multifunctional nanomaterial particle nerve scaffold for the treatment of patients. We found 48 patients with spinal cord injury after badminton exercise and divided them into two groups. The experimental group was treated with multifunctional nanoparticle nerve scaffold surgery, and the control group was treated with drug therapy. After nine months of treatment data recording, we compared the data and found the following three points: first, although the weight of the control group and the experimental group increased after operation,

the overall recovery rate and recovery rate of the experimental group were much higher than those of the control group. The weight recovery after the operation represents the recovery of body function to a certain extent. It can be seen that the surgical treatment of multifunctional nanoparticle nerve scaffold has great help for the recovery of body function of patients with spinal cord injury after badminton exercise. Second, we focus on the recovery of motor function of patients with nanoparticle nerve scaffold. From one month after the operation, we recorded nine months. Although motor function was recovering in both control and laboratory patients, it recovered quite quickly and increased in magnitude over time in the laboratory group versus the control group. Third, we observed the inflammatory response after the nanoparticle nerve scaffold surgery. In the first month, because of the surgical wound, the inflammatory reaction of the experimental group was slightly stronger than that of the control group. But in the follow-up treatment, the inflammatory reaction of the experimental group of patients quickly went down. Through the above three points, we found that the multifunctional nanoparticle nerve scaffold treatment can make the body function and motor function of patients recover quickly, shorten the treatment cycle, and greatly reduce the pain of patients and the burden of patients' families. At the same time, it can greatly and rapidly reduce the postoperative inflammatory reaction of patients. In addition, we also investigated the treatment options of spinal cord injury patients with badminton sports in a hospital from 2017 to 2019. Among them, 40% of the patients chose nanoparticle nerve stent surgery. To sum up, it is meaningful and promising to study the experiment of repairing spinal cord injury after badminton with multifunctional nanomaterial particles.

Data Availability

No data were used to support this study.

Conflicts of Interest

The authors declare that there are no conflicts of interest regarding the publication of this article.

Acknowledgments

References

[1] C. Schuld, S. Franz, K. Brüggemann, L. Heutehaus, and R. Rupp, "International standards for neurological classification of spinal cord injury: impact of the revised worksheet (revision 02/13) on classification performance," *Journal of the American Paraplegia Society*, vol. 39, no. 5, pp. 504–512, 2016.

[2] V. Arora and I. Verma, "Aicardi's diseases of the nervous system in childhood: Alexis Arzimanoglou, University Hospitals of Lyon, France with Anne O'Hare, Michael V Johnston, Robert Ouvrier (eds)," *The Indian Journal of Pediatrics*, vol. 86, no. 10, pp. 972–972, 2019.

[3] S. Abd-Elsalam, F. El-Kalla, L. A. Ali et al., "Pilot study of orphenadrine as a novel treatment for muscle cramps in patients with liver cirrhosis," *United European Gastroenterology Journal*, vol. 6, no. 3, pp. 422–427, 2018.

[4] A. Swayne, C. O'Gorman, N. Sheikh et al., "059 Teratoma with glycine, NMDA & VGKC antibodies presenting with severe weakness, respiratory failure & corticospinal tract dysfunction," *Journal of Neurology Neurosurgery & Psychiatry*, vol. 89, no. 6, pp. A24.2–A2A25, 2018.

[5] M. Elhoseny, G. Ramírez-González, O. M. Abu-Elnasr, S. A. Shawkat, N. Arunkumar, and A. Farouk, "Secure medical data transmission model for IoT-based healthcare systems," *Ieee Access*, vol. 6, pp. 20596–20608, 2018.

[6] S. Thakur, S. Sharma, S. Thakur, and R. Rai, "Green synthesis of copper nano-particles using Asparagus adscendens roxb. Root and leaf extract and their antimicrobial activities," *International Journal of Current Microbiology and Applied ences*, vol. 7, no. 4, pp. 683–694, 2018.

[7] K. J. Li, S. J. Yang, K. Li, Y. T. Wei, and J. Ge, "Research on the effect of biological glue on augmenting the viscosity of tissue engineering retinal nerve scaffolds," *Zhonghua yan ke za zhi Chinese journal of ophthalmology*, vol. 54, no. 4, pp. 277–282, 2018.

[8] B. Zaarour and N. Mayhoub, "Effect of needle diameters on the diameter of electrospun PVDF nanofibers," *International Journal of BIM and Engineering Science*, vol. 4, no. 2, pp. 26–32, 2021.

[9] X. Xu, D. Shahsavari, and B. Karami, "On the forced mechanics of doubly-curved nanoshell," *International Journal of Engineering Science*, vol. 168, p. 103538, 2021.

[10] J. P. Ahn, S. Y. Han, N. S. Lee, Y. G. Jeong, and M. Y. Kim, "Highly luminescent and anti-photobleaching core-shell structure of mesoporous silica and phosphatidylcholine modified superparamagnetic iron oxide nanoparticles," *Nanomaterials*, vol. 10, no. 1312, pp. 1–14, 2020.

[11] A. Matsugi, "Do changes in spinal reflex excitability elicited by transcranial magnetic stimulation differ based on the site of cerebellar stimulation," *Somatosensory and Motor Research*, vol. 35, no. 2, pp. 80–85, 2018.

[12] Y. Liu, X. He, Y. Li, and T. Wang, "Cerebrospinal fluid cd4+ t lymphocyte-derived mirna-let-7b can enhances the diagnostic performance of Alzheimer's disease biomarkers," *Biochemical and Biophysical Research Communications*, vol. 495, no. 1, pp. 1144–1150, 2018.

[13] A. J. Hayes and M. James, "Glycans and glycosaminoglycans in neurobiology: key regulators of neuronal cell function and fate," *Biochemical Journal*, vol. 475, no. 15, pp. 2511–2545, 2018.

[14] X. Lian, C. C. Shen, H. J. Sun, and Y. J. Zeng, "Cytological mechanism of astragaloside IV in promoting repair of bone defects," *Journal of Biological Regulators and Homeostatic Agents*, vol. 33, no. 2, pp. 511–516, 2019.

[15] X. Li, Q. Lu, W. Xie, Y. Wang, and G. Wang, "Anti-tumor effects of triptolide on angiogenesis and cell apoptosis in osteosarcoma cells by inducing autophagy via repressing wnt/β-catenin signaling," *Biochemical and Biophysical Research Communications*, vol. 496, no. 2, pp. 443–449, 2018.

[16] B. Karabulut, N. Dönmez, C. C. Göret, C. Ataş, and Ö. Kuzu, "Reactions of subcutaneous connective tissue to mineral trioxide aggregate, Biodentine®, and a newly developed BioACTIVE Base/Liner," *Scanning*, vol. 2020, no. 1, Article ID 6570159, 10 pages, 2020.

[17] Y. Liu, D. X. Ban, C. Ma et al., "Photodynamic therapy mediated by upconversion nanoparticles to reduce glial scar formation and promote hindlimb functional recovery after spinal cord injury in rats," *Journal of Biomedical Nanotechnology*, vol. 12, no. 11, pp. 2063–2075, 2016.

[18] P. Ferial, A. A. Resmije, A. Yll et al., "Evaluation of spontaneous bone healing after enucleation of large residual cyst in maxilla without graft material utilization: case report," *Acta Stomatologica Croatica*, vol. 52, no. 1, pp. 53–60, 2018.

Retraction

Retracted: Meta-Analysis of the Main Components of Nanophotodynamics Combined with Traditional Chinese Medicine in the Treatment of Tumors

Journal of Nanomaterials

This article has been retracted by Hindawi following an investigation undertaken by the publisher [1]. This investigation has uncovered evidence of one or more of the following indicators of systematic manipulation of the publication process:

(1) Discrepancies in scope

(2) Discrepancies in the description of the research reported

(3) Discrepancies between the availability of data and the research described

(4) Inappropriate citations

(5) Incoherent, meaningless and/or irrelevant content included in the article

(6) Peer-review manipulation

The presence of these indicators undermines our confidence in the integrity of the article's content and we cannot, therefore, vouch for its reliability. Please note that this notice is intended solely to alert readers that the content of this article is unreliable. We have not investigated whether authors were aware of or involved in the systematic manipulation of the publication process.

Wiley and Hindawi regrets that the usual quality checks did not identify these issues before publication and have since put additional measures in place to safeguard research integrity.

We wish to credit our own Research Integrity and Research Publishing teams and anonymous and named external researchers and research integrity experts for contributing to this investigation.

The corresponding author, as the representative of all authors, has been given the opportunity to register their agreement or disagreement to this retraction. We have kept a record of any response received.

References

[1] Y. Liu, Y. Li, and Y. Wen, "Meta-Analysis of the Main Components of Nanophotodynamics Combined with Traditional Chinese Medicine in the Treatment of Tumors," *Journal of Nanomaterials*, vol. 2022, Article ID 4552356, 14 pages, 2022.

Hindawi

Research Article

Meta-Analysis of the Main Components of Nanophotodynamics Combined with Traditional Chinese Medicine in the Treatment of Tumors

Ying Liu,[1] **Yanwei Li,**[1] **and Yulong Wen** [2]

[1]*Clinical Medical College/Affiliated Hospital, Chengdu University of Traditional Chinese Medicine, Chengdu,*
610032 Sichuan, China
[2]*School of Basic Medical Sciences, Chengdu University of Traditional Chinese Medicine, Chengdu, 611137 Sichuan, China*

Correspondence should be addressed to Yulong Wen; wenyulong@cdutcm.edu.cn

At present, cancer has become one of the main reasons that affect people's life and health. With the development of nanomaterials and nanotechnology, tumor phototherapy such as photodynamic therapy, photothermal therapy, and combination therapy has been developed rapidly. Based on this, this paper proposes to take gastric cancer, esophageal cancer, liver cancer, intestinal cancer, and pancreatic cancer as the starting point and apply the methods of network meta-analysis to comprehensively carry out the horizontal comprehensive evaluation of the efficacy and safety of traditional Chinese medicine injections. It is hoped that this article can provide high-quality evidence-based medicine for clinical decision-making and promote clinical rational drug use. The purpose of this paper is to study the meta-analysis of the main components of tumor treatment with nanophotodynamics combined with traditional Chinese medicine. The experimental results in this paper show that non-small-cell lung cancer has the largest number of evaluations, with 77 evaluations, accounting for 38.5% of the total frequency of tumor types. This may be related to the fact that lung cancer ranks first in the morbidity and mortality of malignant tumors. It is followed by the evaluation times of liver cancer and gastric cancer, which were 29 times and 25 times, respectively, accounting for 14.5% and 12.5% of the total frequency of tumor types. The therapeutic effect of SM-NP light therapy group on tumor was significantly higher than that of free Ce6 light therapy group, and its destruction and killing effect on tumor tissue was greater.

1. Introduction

The high recurrence rate, easy spread, and poor prognosis of tumors are the main challenges of clinical treatment. Currently, surgery, chemotherapy, and radiotherapy are the three main methods of clinical treatment of cancer. It has been widely used in tumor therapy, but it is difficult to inhibit it. It is effective in the treatment of malignant tumors. An ideal therapeutic strategy can not only effectively and safely remove tumors in situ but also prevent tumor metastasis by activating the body's immune system to recognize and remove tumor cells.

Chemotherapy is one of the important methods for the treatment of malignant tumors. However, traditional chemotherapeutic drugs lack tumor selectivity and have serious side effects. Photodynamic therapy is a new cancer treatment method developed in recent years. Photosensitive drugs enter the body and accumulate under the concentration and generate singlet active oxygen under the action of laser light of absorption wavelength, thereby producing cytotoxic effect. As a safe and efficient cancer treatment, photodynamic therapy can not only directly kill tumor cells but also potentially improve the immunogenicity of tumor cells. It induces an antitumor immune effect and meets the clinical demand for combined tumor therapy.

The innovation of this paper is to explore new research methods to comprehensively evaluate the efficacy and safety of different types of traditional Chinese medicine injections in the treatment of digestive system tumors, which has important academic significance and clinical value. This

paper evaluates the antitumor efficacy and biosafety of photodynamic nanodrugs by analyzing the data, which is the basis for clinical tumor treatment application method and data reference.

2. Related Work

In recent years, photodynamic therapy (PDT) has become a research hotspot in the field of tumor therapy due to its noninvasive and spatiotemporal controllable advantages. Synergistic therapy and precise drug delivery at the tumor site have emerged as a promising strategy to achieve tumor eradication. Here, Li et al. prepare smart near-infrared fluorescence imaging-guided nanoliposomes L@CY@DOX by encapsulating a chemotherapeutic drug (doxorubicin), liposome (L), and a near-infrared (NIR) photosensitizer (CY). It can enhance the therapeutic effect of chemotherapeutic PDT in cancer treatment [1]. Lack of selectivity of tumor cells and overproduction of glutathione (GSH) are two major challenges for efficient and safe cancer PDT, because they cause damage to normal tissues and scavenge ROS in cancer cells. Herein, Pan et al. report a GSH-responsive nanophotosensitizer based on CoOOH nanosheets for PDT of cancer. The current nanophotosensitizers represent a promising smart platform to synergistically improve the therapeutic index and safety of PDT [2]. Recently developed photodynamic therapy has received much attention for achieving effective root canal disinfection. It uses an optimized nontoxic photosensitizer (PS) such as indocyanine green (ICG). It is an integral part of this technology. Therefore, the aim of Akbari et al.'s study was to improve the photodynamic properties of ICG by incorporating ICG into nanographene oxide (NGO). It prepared NGO-ICG as a new PS and evaluated the antibacterial effect of NGO-ICG on Enterococcus faecalis after photodynamic therapy [3]. The application of traditional photodynamic therapy (PDT) is often limited by insufficient oxygen supply, and it is difficult to achieve high PDT efficacy. Herein, Qin et al. combine liposomes with photosensitizers indocyanine green (ICG) and perfluorooctyl bromide (PFOB) to develop a novel oxygen-enriched photodynamic nanospray for postoperative cancer therapy. This oxygen-enriched photodynamic nanospray strategy may open new avenues for clinically effective postoperative cancer therapy [4]. Photoimmunotherapy is a new treatment approach that is minimally invasive for malignant tumors. Here, Zhang et al. designed a targeted multifunctional black phosphorus (BP) nanoparticle, modified with PEGylated hyaluronic acid (HA) for photothermal/photodynamic/ photoimmunotherapy. In vitro and in vivo experiments demonstrated that HA-BP nanoparticles have good biocompatibility, stability, and sufficient efficacy in the combined photothermal therapy (PTT) and photodynamic therapy (PDT) treatment of cancer. Zhang et al.'s research expands the biomedical applications of BP nanoparticles, demonstrating the potential of modified BP as a multifunctional therapeutic platform for future cancer treatment [5]. Wang et al. design a versatile and powerful nanoplatform. They have cleverly integrated multiple molecules with therapeutic and diagnostic properties to stimulate the delivery of responsive drugs to lesions. This is still a huge challenge. Here, Wang et al. report a facile and ingenious cross-linked nanogel based on medicinal chemical cross-linking as a straightforward strategy to overcome assembly instability. This work provides a unique strategy for designing a series of prodrug nanogels as a universal drug delivery platform for precise disease therapy and diagnosis [6]. Deng et al. developed the mitochondria-targeted biodegradable polymer polylactic acid. The data suggest that X-PDT treatment has cytoreductive, antiproliferative, and profibrotic effects. The nanocarriers effectively enhance the radiosensitization effect, which makes it possible to enhance the radiation effect [7]. Lack of selectivity of tumor cells and overproduction of glutathione (GSH) are two major challenges for efficient and safe cancer PDT because they cause damage to normal tissues and scavenge ROS in cancer cells. Herein, Wei et al. reported a GSH-responsive nanophotosensitizer based on CoOOH nanosheets for PDT of cancer [2]. However, the shortcomings of these studies are that the model construction is not scientific enough and the data is limited to adapt to more complex situations.

3. Nanophotodynamic Therapy-Related Methods of Tumor

3.1. Advantages and Development Status of Photodynamic Therapy for Cancer

3.1.1. Photodynamic Therapy. Over the past few decades, photodynamic therapy (PDT) has undergone tremendous progress as a treatment modality. It includes age-related macular degeneration, psoriasis, atherosclerosis, and various malignancies. It mainly activates the photosensitizer (PS) accumulated at the tumor site by light with a specific wavelength. The activated PS transfers energy to surrounding oxygen molecules, resulting in the reduction of oxygen and the generation of reactive oxygen species (ROS) (Figure 1). Oxidation of biomacromolecules results in tumor reduction, vascular damage, local acute inflammation, and immune responses [8].

Compared with traditional treatment methods, PDT is due to its weak invasiveness, ideal convenience and flexibility, effective curative effect, and high patient acceptance. It has laid a solid foundation for the clinical application of PDT. Since the advent of the first approved PDT prodrug procarbazine in 1970, three photosensitizers, protoporphyrin, verteporfin, and 5-aminolevulinic acid, have been approved by the FDA. More than 16 drugs have subsequently entered clinical trials or are on the market. Compared with traditional treatments, PDT still has many limitations as a first-line clinical treatment due to the lack of effective photosensitizers, appropriate light doses, and effective photosensitizer delivery [9].

In drug delivery systems, light is a common external stimulus used to trigger drug release. Compared with complex and uncontrollable internal stimuli, light can control drug release in a more controllable time and space. Based on the process of PDT oxygen consumption and ROS generation, PDT can be combined with nanomedicines sensitive
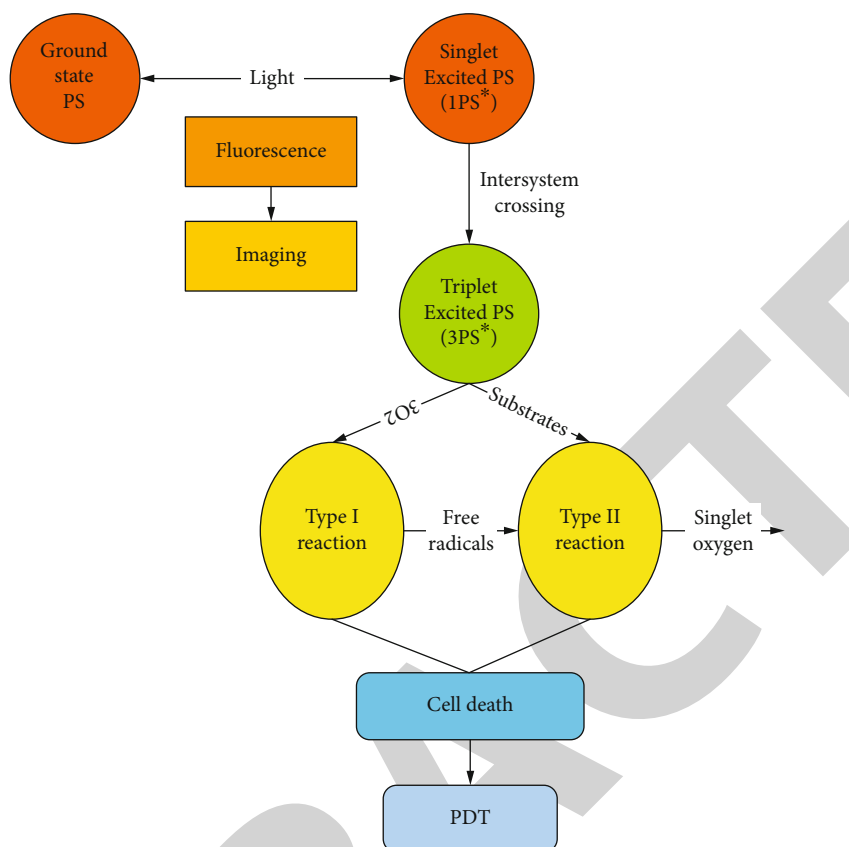
FIGURE 1: Schematic diagram of a typical photodynamic reaction.

to the tumor microenvironment (such as ROS, hypoxia), and finally, it achieves a positive feedback and synergistic treatment effect [10].

3.1.2. Advantages of Photodynamic Therapy for Cancer. Photosensitizers, excitation light, and oxygen molecules are three important elements for PDT. The mechanism of action of photodynamic therapy is to utilize the selective enrichment of photosensitizers in tumor tissue. It converts oxygen into reactive oxygen species (ROS) that can kill cells through a laser-triggered photosensitizer with strong tissue penetration. It can oxidatively damage surrounding organelles and biomolecules, eventually inducing tumor cell necrosis and apoptosis, sealing tumor blood vessels, and causing vascular damage [11]. In addition, photodynamic therapy is often accompanied by the production of acute inflammation. Through the recruitment and activation of immune cells such as neutrophils and dendritic cells at the tumor site, acute inflammation in the local tumor is triggered, and an immune response is generated to further kill the tumor.

3.1.3. Tumor Phototherapy. In recent years, cancer, namely, malignant tumor, has become one of the important diseases threatening human health worldwide, although human beings have deeply researched on the mechanism and treatment of cancer for decades. However, the increasing number of new cases of cancer and the high mortality rate still pose a huge challenge to the current clinical cancer treatment

methods. Existing mainstream cancer treatments include surgical resection, chemotherapy, or radiation therapy, but these treatments have their own limitations. Although surgical resection has a good therapeutic effect on early-stage solid tumors, its therapeutic effect on metastatic tumors is limited. In addition, in order to ensure the curative effect during the operation, a large amount of normal tissue adjacent to the tumor is often removed, thereby causing significant damage to the patient's body. Chemotherapy is a commonly used clinical treatment method to control tumor growth through systemic administration. While killing cancer cells, it also kills a large number of normal cells, and it is easy to induce cancer cells to develop resistance to chemotherapeutic drugs, which often leads to the failure of treatment [12].

Radiation therapy is a common clinical cancer treatment method that induces cancer cell death by irradiating cancer cells with radionuclides or ionizing radiation. Due to the controllability of radiation, that is, the irradiation range, the systemic toxicity caused by radiotherapy is significantly lower than that of chemotherapy by systemic administration. However, radiotherapy still irradiates the normal tissues around the tumor to different degrees, causing obvious side effects. In view of this, on the basis of existing cancer treatment methods, combined with the advantages of multiple disciplines such as tumor biology, material science, and instrument manufacturing, new cancer treatments are developed. It has received more and more attention and research to meet the needs of current clinical cancer patients.
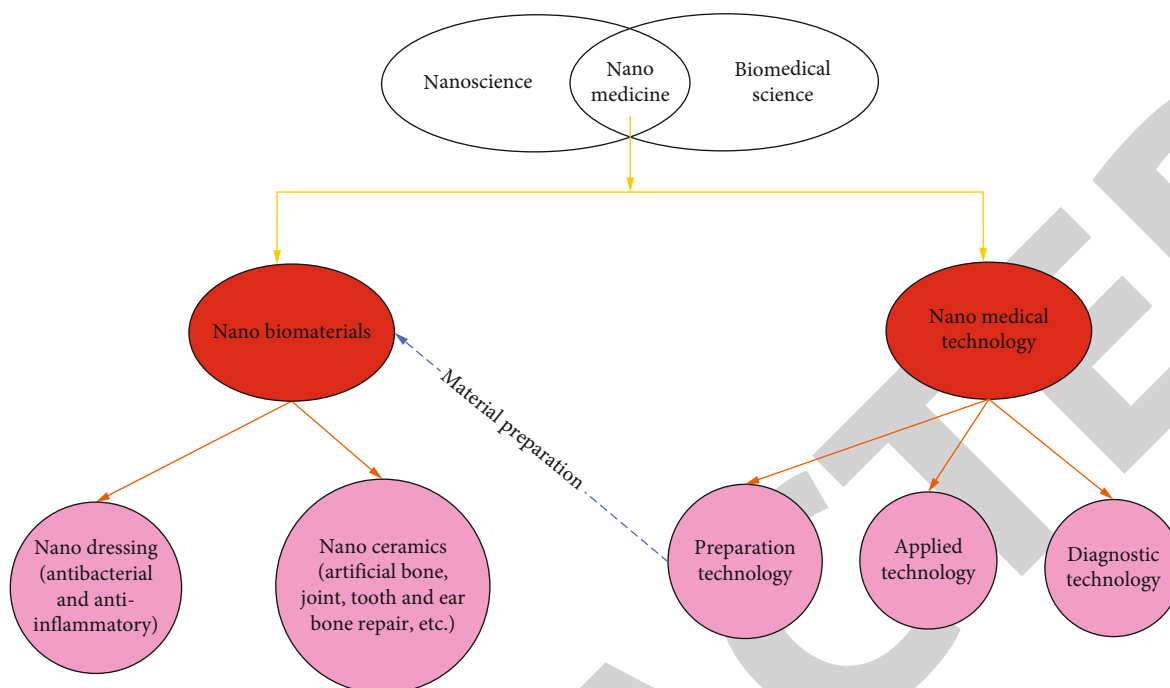
Figure 2: Overview of nanomedicine.

At present, a large number of studies have shown that many new cancer treatment methods (such as tumor immunotherapy, phototherapy, and gene therapy) and tumor treatment strategies under image navigation have good application prospects. At the same time, by combining with the commonly used clinical treatment methods, it also endows these traditional cancer treatment methods with new vitality and development opportunities and provides new options for the safe and efficient treatment of tumors [13].

3.2. Application of Nanomaterials. In the past few decades, nanomaterials have been extensively researched and developed and have been successfully applied in the fields of catalysis, medicine, sensors, and biology. In particular, it has also received extensive attention in water treatment and wastewater treatment. Moreover, the flow properties of nanomaterials in solution are very high. Nanomaterials have a relatively large specific surface area due to their small size, so they have strong adsorption capacity and reactivity. It has been reported that heavy metals, organic pollutants, inorganic anions, and bacteria can be successfully removed by many kinds of nanomaterials [14].

Due to the unique size-dependent properties of nanomaterials, they have a profound impact on various application fields such as the construction industry, products of daily life, and medical and healthcare. Figure 2 is an overview of nanomedicine.

Nano-antibacterial materials have attracted much attention due to their stable performance, good antibacterial effect, and low price. For example, nanotitanium oxide material has photocatalytic effect, which can decompose toxic gases such as formaldehyde and benzene and kill bacteria on its surface. Nanometer self-cleaning materials have great development

space. Nanomaterials also have many applications in catalysis. Catalysts play an important role in the field of chemistry. Catalysts can increase the reaction rate and shorten the reaction time. Most of the traditional catalysts have low catalytic efficiency and difficult preparation, resulting in waste of raw materials, reducing economic benefits, and polluting the environment. Nanomaterials have many active sites. It can greatly improve the reaction rate and control the progress of the reaction. It can even make chemical reactions that were previously inoperable go smoothly.

Nanoparticles used as catalysts are as follows:

(1) Metal nanoparticles

(2) Nanoparticles are supported on porous supports, which can further increase the selectivity of catalysts

(3) Compound nanoparticles

Nanomaterials are used in lithium electrical energy to improve cycle life. It can undergo some reactions that cannot occur in other materials, increasing the charge-discharge rate [15]. At present, nanomaterials can be well used as contrast agents in medical imaging. The mechanism by which nanobiomaterials promote the repair of damaged tissue is shown in Figure 3. Nanoparticles are widely used in biomedicine and can be used as biochips, bioprobes, etc. New medicines require new means of drug delivery so that side effects can be reduced and better efficacy can be achieved. Nanotechnology drug delivery can deliver drugs directly to cells and to targeted tissues.

3.3. Unsupervised Learning. The difference between unsupervised learning and supervised learning is that data does
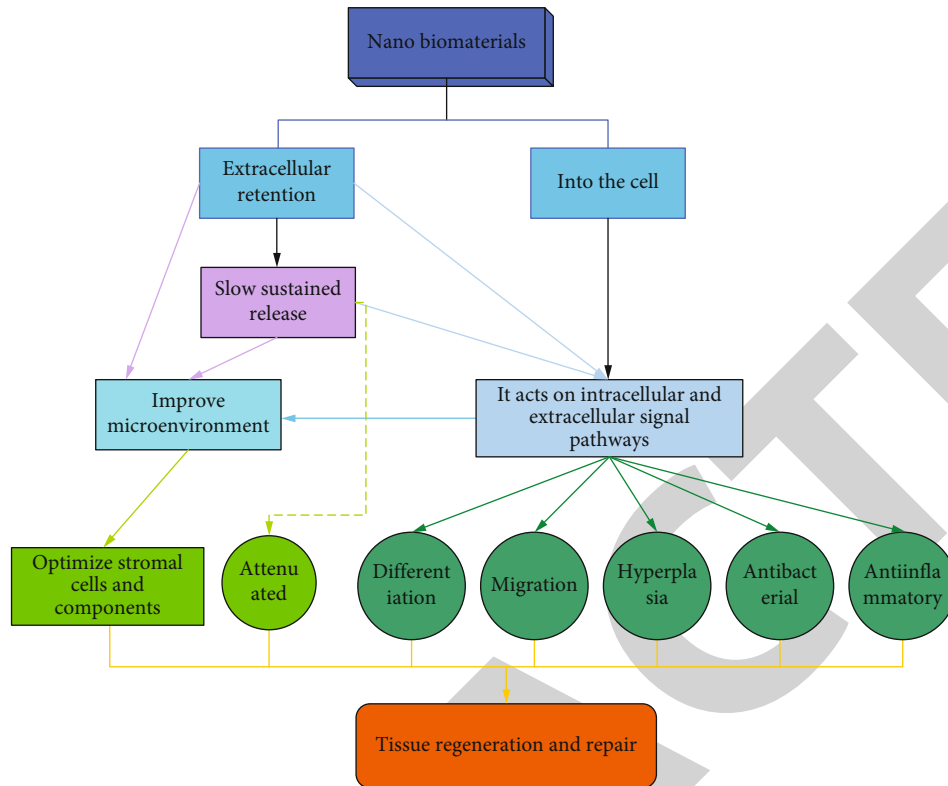
FIGURE 3: Mechanism of nanobiomaterials to promote repair of damaged tissue.

not need to be identified in advance. According to different learning method rules and the clustering characteristics of the data itself, this paper finds the corresponding internal rules and finds useful hidden information in the complex and disordered data [16].

3.3.1. Clustering Algorithm. Clustering algorithm is a kind of classification and grouping of things with the same attributes. It classifies cluttered sets of data into meaningful clusters. The essence of a clustering problem is an optimization problem, but this optimization must satisfy certain clustering conditions or clustering rules. The advantage of clustering is that the processing time is fast, the operation is simple, and it is easy to explain; the disadvantage is that the parameters need to be set when using, and sometimes, the result may be locally optimal. The classification of clustering algorithms is shown in Figure 4 [17, 18].

(1) Data Standardization. In order to eliminate the influence of different dimensions of the original data, this paper adopts the cluster analysis method in the data preprocessing, and the original data needs to be standardized. The normalized formula is

$$A_{mn} = \frac{B_{mn} - \overline{B_n}}{\sqrt{\operatorname{var}\left(B_n\right)}} \quad (m = 1, 2, \cdots, j), \tag{1}$$

$$\overline{B_n} = \frac{1}{j} = \sum_{m=1}^{j} B_{mn}, \tag{2}$$

$$\sqrt{\operatorname{var}\left(B_n\right)} = \sqrt{\frac{1}{j} \sum_{m=1}^{j} \left(B_{mn} - B_n\right)^2}, \tag{3}$$

(2) Define the Distance. Assuming that there are j sample data in a b-dimensional space, the formula for calculating the distance between sample m and sample n is as follows:

$$D_{mn} = \sum_{k-1}^{b} |A_{mk} - A_{nk}|. \tag{4}$$

The formula calculates the absolute value distance.

$$D_{mn} = \sqrt{\sum_{k=1}^{b} \left(A_{nk} - A_{mk}\right)^2}. \tag{5}$$

The formula calculates the Euclidean distance.

$$D_{mn} = \operatorname{MAX}_{1 \le k \le b} |A_{mk} - A_{nk}|. \tag{6}$$

The formula calculates the Chebyshev distance.

Usually, the smaller the distance is, the closer the similarity of the sample objects of the study is.

(3) Similarity Coefficient. The similarity coefficient of any two b-dimensional vectors can be used to measure the similarity of these two vectors in the b-dimensional space. The
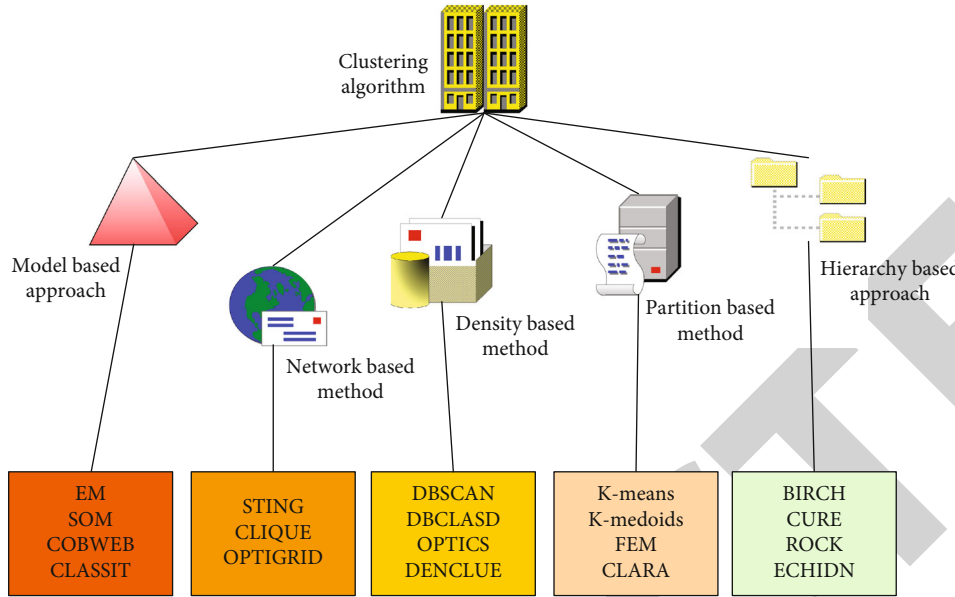
FIGURE 4: Classification of clustering algorithms.

similarity coefficient C_{mn} is used to represent, where m and n are the two vectors to be compared. C_{mn} satisfies symmetry; that is, the two vectors to be compared satisfy $C_{mn} = C_{nm}$. In general, the cosine of the angle between two vectors is a common similarity coefficient:

$$\text{COS}(\theta_{mn}) = \frac{\sum_{k=1}^{b} A_{mk} A_{nk}}{\sqrt{\sum_{k=1}^{b} A_{mn}^2 A_{nk}^2}}. \tag{7}$$

3.3.2. K-Means Clustering

(1) K-Means Algorithm. The K-means algorithm is an unsupervised algorithm. As a classical clustering method, it is widely used to solve various partitioning and clustering problems, and it is still one of the most widely used clustering algorithms. At the same time, the K-means algorithm is also the basis for many more complex clustering techniques. While there have been many improvements to clustering methods today, the K-means algorithm is not outdated or obsolete and, in fact, may be more popular now than ever. The central idea of K-means clustering is to divide n data objects according to the number of categories K given in advance, so as to minimize the difference within each class and maximize the difference between classes. The flowchart of the K-means algorithm is shown in Figure 5 [19, 20].

The K-means algorithm is also known as the k-means algorithm. The algorithm idea is roughly as follows: it randomly selects k samples from the sample set as cluster centers and calculates the distances between all samples and the k "cluster centers." For each sample, it is divided into the cluster where the closest "cluster center" is located, and the new "cluster center" of each cluster is calculated for the new cluster.

According to the description, we can roughly guess the three main points for implementing the K-means algorithm: selection of the number of clusters k, the distance from each sample point to the "cluster center", and according to the newly divided cluster, updating the "cluster center."

(2) Key Points of K-Means Algorithm.

(1) Selection of k value

The choice of k is generally determined according to actual needs, or the value of k is directly given when the algorithm is implemented.

(2) The measure of distance

A sample is given:

$$M^i = \left\{ M_1^i, M_2^i, \cdots, M_p^i \right\}, \tag{8}$$

$$M^j = \left\{ M_1^j, M_2^j, \cdots, M_p^j \right\}, \tag{9}$$

where $i, j = 1, 2, \cdots, t$ represents the number of samples and p represents the number of features.

(a) Ordinal attribute distance measures (discrete attributes {1, 2, 3} or continuous attributes)

Minkowski distance

$$D_{\text{mk}}\left(M^{(i)}, M^{(j)} \right) = \left(\sum_{u=1}^{p} \left| M_u^i - M_u^j \right|^h \right)^{1/h}. \tag{10}$$
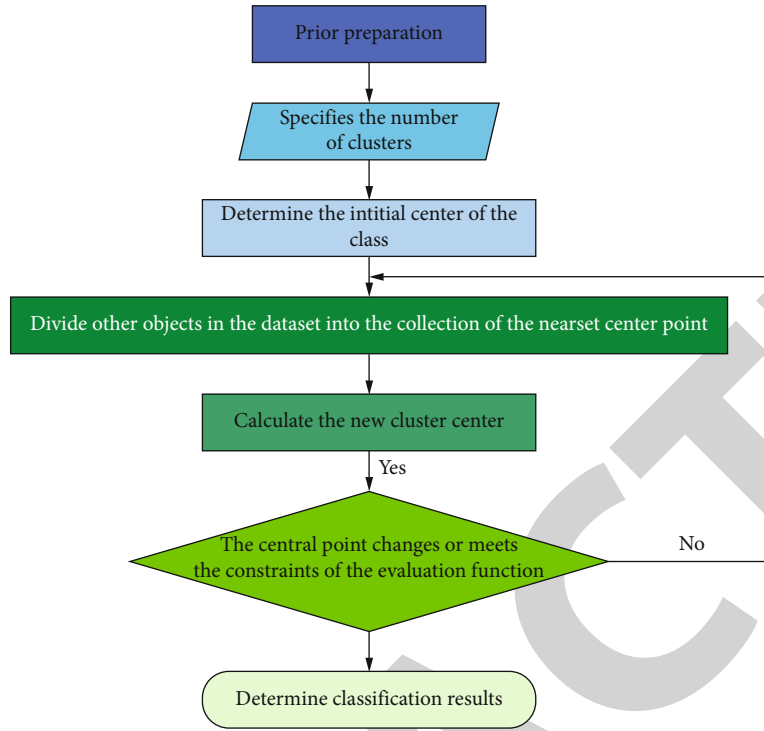
Figure 5: Flowchart of the classic K-means algorithm.

Euclidean distance refers to the Minkowski distance when $h = 2$:

$$D_{\text{ed}}\left(M^{(i)}, M^{(j)}\right) = \left\| M^{(i)} - M^{(j)} \right\|_2 = \sqrt{\sum_{u=1}^{p} \left| M_u^i - M_u^j \right|^2}.$$

$$(11)$$

Manhattan distance refers to the Minkowski distance when $h = 1$:

$$D_{\text{man}}\left(M^{(i)}, M^{(j)}\right) = \left\| M^{(i)} - M^{(j)} \right\|_1 = \sum_{u=1}^{p} \left| M_u^i - M_u^j \right|. \quad (12)$$

(b) Disordered attribute distance metrics (such as {airplane, train, ship})

VDM (Value Difference Metric)

$$\text{VDM}_h\left(M_u^i, M_u^j\right) = \sum_g^k \left| \frac{y_u, M_u^i, g}{y_u, M_u^i} - \frac{y_u, M_u^j, g}{y_u, M_u^j} \right|^h. \quad (13)$$

Among them, y_u, M_u^i represents the number of samples whose value is M_u^i on attribute u, and y_u, M_u^i, g represents the number of samples whose value is M_u^i on attribute u in the g th sample cluster. $\text{VDM}_h(M_u^i, M_u^j)$ represents the VDM distance between two discrete values M_u^i and M_u^j on attribute u.

(c) Mixed attribute distance metric, which is a combination of ordered and disordered:

$$\text{MinkovDM}_h\left(M^i, M^j\right)$$
$$= \left(\sum_{u=1}^{p_s} \left| M_u^i - M_u^j \right|^h - \sum_{u=p_s+1}^{p} \text{VDM}_h\left(M_u^i, M_u^j\right) \right)^{1/h} \quad (14)$$

Among them, p_s contains ordered attributes and $p - p_s$ unordered attributes.

The data set in this article is a continuous attribute, so the Euclidean distance is mainly used in the code to measure the distance.

(3) Update "cluster center"

For each divided cluster, calculate the mean value of the sample points in each cluster, and it uses the mean value as the new cluster center.

3.4. Genetic Algorithms

3.4.1. Overview. Genetic algorithm (GA) is a new global optimization algorithm developed in recent years. It is based on evolution theory and adopts design methods such as genetic combinatorial optimization technology, genetic variation, and natural selection.

Genetic algorithm is an optimization search algorithm based on biological evolution theory and molecular genetics. It first encodes possible solutions to a particular problem,

called chromosome-encoded solutions. This paper randomly selects N chromosomes as the initial group and then calculates the fitness of each chromosome according to the value of the evaluation function. It is predetermined that the best performance value of a chromosome is the highest fitness value, the chromosome with the highest fitness value is selected for replication, and a new set of chromosomes is created. These chromosomes are more customized to the environment through genetic operators. People will eventually adapt to the new environment, and forming a better group becomes the best solution to the problem [21, 22].

3.4.2. Basic Algorithm. The execution of the genetic algorithm involves many random operations, first considering the result of the selection. In standard genetic algorithms, selection criteria are based on the principle of proportionality. Therefore, through the action of the ith selector, the expected value of the number of people who will continue to exist in the next generation is $n(g_i / \sum g)$; then, there is

$$\bar{g}(P, t) = \frac{1}{n(P, t)} \sum g_i. \tag{15}$$

Then,

$$n(P, t + 1) = n(P, t) \cdot \frac{\bar{g}(P, t)}{g(t)}. \tag{16}$$

The equation shows that the effect of the selection operator will increase (decrease) the ability of a pattern above (below) the average to be applied across generations, improving quality.

Then, it analyzes the role of the crossover operator. This plan can obviously be maintained in the next generation if there is no intersection or if the intersection point is beyond the character positions specified on the left and right ends of the figure. Therefore, the probability R_s that the P mode will continue to exist in the next generation should satisfy

$$R_s \geq 1 - R_c \cdot \frac{\varphi(P)}{(L - 1)}. \tag{17}$$

Taking into account the effects of selection and crossover, there are

$$n(P, t + 1) \geq n(P, t) \cdot \bar{f}(P, t) \cdot \left[\frac{1 - R_c \cdot \varphi(P)}{(L - 1)/\bar{g}(t)} \right]. \tag{18}$$

Finally, because R_m represents the probability of the mutation operator acting, the constant probability is $1 - R_m$. If all the specified characters remain unchanged, the P pattern can naturally continue to exist in the next generation, the probability $(1 - R_m)^{O(P)}$; R_m is usually not large; then, under the action of the mutation operator, the probability of P continuing to exist is

$$(1 - R_m)^{O(P)} \approx 1 - R_m \cdot O(P). \tag{19}$$
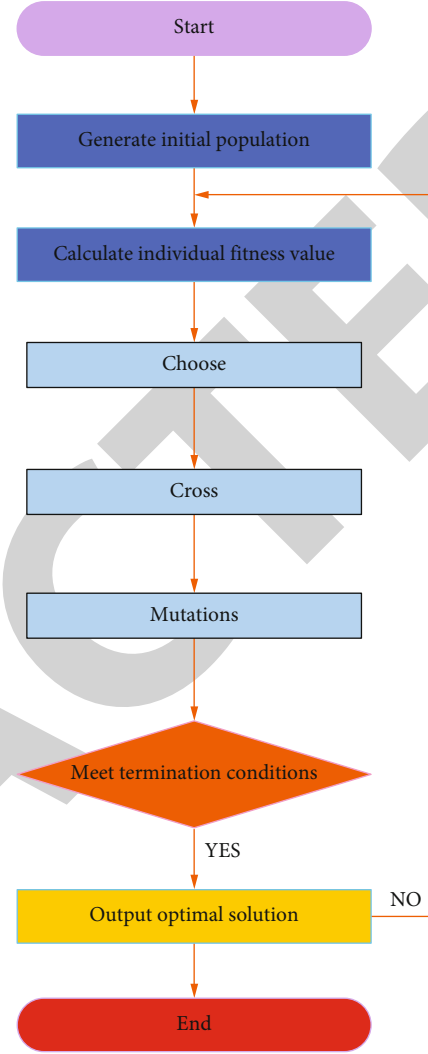
FIGURE 6: Genetic algorithm flowchart.

The probability of unreserved is about $O(P) \cdot R_m$. So, taking into account the functions of selection, crossover, and mutation operators, we end up with

$$n(P, t + 1) \geq n(P, t) \cdot \bar{g}(P, t) \cdot \frac{\left[1 - R_c \cdot (\varphi(P)/(L - 1)) \cdot R_m \right]}{\bar{g}(t)}. \tag{20}$$

Specifically, if $\bar{g}(P, t) = g(t)(1 + c)$, $c > 0$ is a constant, then

$$n(P, t) = n(P, t - 1)(1 + c) = n(P, O)(1 + c)^t. \tag{21}$$

The flowchart of the standard genetic algorithm is shown in Figure 6.

$y = 3.272x$
$R^2 = 0.855$

Number of published articles
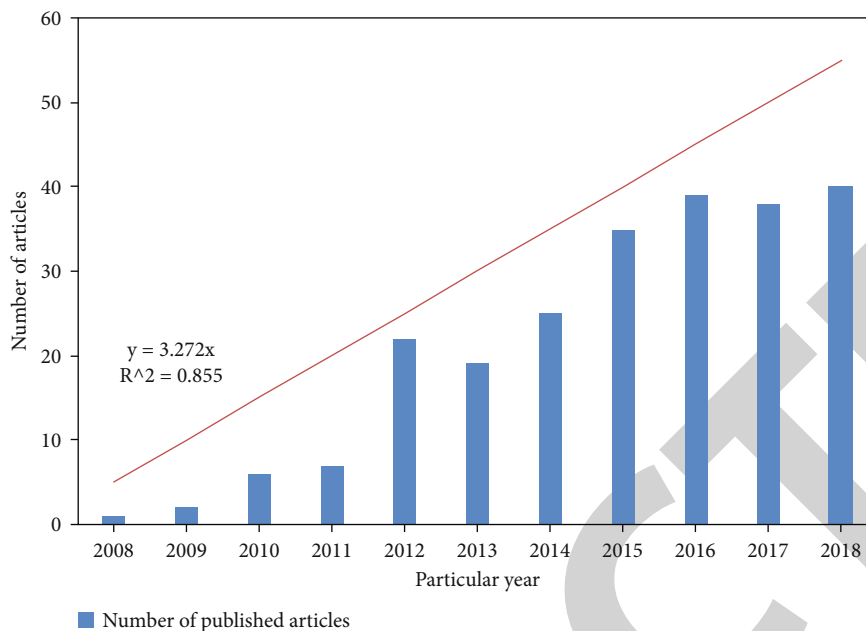
FIGURE 7: 2008-2018 published status of systematic review and meta-analysis of traditional Chinese medicine injections in the treatment of tumor diseases at home and abroad.

4. Network Meta-Analysis Experiment of Traditional Chinese Medicine Injections in the Treatment of Digestive System Tumors

4.1. Current Status of Systematic Review/Meta-Analysis of Traditional Chinese Medicine Injections in the Treatment of Tumor Diseases. Since the publication of the first systematic review of TCM injections for oncology in 2008, with the increase of years, the number of publications of related systematic reviews/meta-analyses has also increased ($y = 3.272x$, $R^2 = 0.855$). As shown in Figure 7 3 papers were published before 2009, 35 papers were published from 2010 to 2012, 156 papers were published from 2013 to 2017, and 40 papers were published in 2018 [23].

4.2. Tumor Types Involved. Among the 198 systematic reviews/meta-analyses retrieved, 2 classic meta-analyses are aimed at the treatment of multiple tumors with a single variety of traditional Chinese medicine injections. In addition, the other 196 such systematic reviews/meta-analyses were all single-species or multispecies TCM injections for the treatment of a single type of tumor. The total frequency of occurrence of different types of tumors was 200. Among them, non-small-cell lung cancer has the most evaluation times, with 77 evaluation times, accounting for 38.5% of the total frequency of tumor types. This may be related to the fact that lung cancer ranks first in the morbidity and mortality of malignant tumors. The second was the evaluation times of liver cancer and gastric cancer, which were 29 and 25, respectively, accounting for 14.5% and 12.5% of the total frequency of tumor types. In addition, 17 studies only mentioned evaluating the disease as "tumor." It does not describe the type of tumor in detail. The types of tumors involved are shown in Table 1. The number of cases for different types of tumors is shown in Figure 8.

4.3. Involving Varieties of Traditional Chinese Medicine Injections. Among the 198 systematic reviews/meta-analyses included in this study, 14 network meta-analyses and 4 classic meta-analyses, respectively, evaluated multiple varieties of traditional Chinese medicine injections. The rest of the literature is only for a single variety of traditional Chinese medicine injections. A total of 14 TCM injection varieties were involved in the included systematic review/meta-analysis. The total occurrence frequency of different varieties of traditional Chinese medicine injections is 352 times. It accounted for 15.6% of the total frequency of Chinese medicine injections, followed by Shenqi Fuzheng injection and Aidi injection; the frequency of occurrence was 50 times and 45 times, accounting for 14.2% and 12.8%, respectively. For traditional Chinese medicine injections, there is a frequency of 10 or more occurrences, as shown in Table 2, for the varieties involved in the evaluation. It includes Fufang Kushen injection, Shenqi Fuzheng injection, Aidi injection, Kangai injection, Cinobufasu injection, Kanglaite injection, Brucea oil emulsion injection, Xiaoaiping injection, and Delisheng injection.

At the same time, this study summarizes the following 14 varieties of traditional Chinese medicine injection components and functional indications. It further analyzes the relationship between its components, efficacy and indications, and the treatment of tumors.

A summary of the dominant varieties of traditional Chinese medicine injections based on cluster analysis is shown in Table 3.

(1) To carry out the evaluation of clinical efficacy of traditional Chinese medicine injections in the treatment of gastric cancer, esophageal cancer, liver cancer, bowel cancer, and pancreatic cancer using network meta-analysis and the ranking of the

TABLE 1: Statistics of tumor types involved.

Serial number	Disease	Frequency of occurrence	Percentage
1	Non-small-cell lung cancer	77	38.5%
2	Liver cancer	29	14.5%
3	Gastric cancer	25	12.5%
4	Tumor	17	8.5%
5	Malignant pleural and peritoneal effusion	12	6%
6	Colorectal cancer	9	4.5%
7	Lung cancer	8	4%
8	Mammary cancer	8	4%
9	Esophageal cancer	8	4%
10	Cancer pain	4	2%
11	Lymphoma	3	1.5%

therapeutic effects. The ranking of different outcome indicators suggests that traditional Chinese medicine injections are the best drugs for the treatment of different digestive system tumors. The cluster analysis results show that (1) for the treatment of gastric cancer with traditional Chinese medicine injection combined with FOLFOX chemotherapy, in terms of improving the total clinical efficiency and improving the quality of life, astragalus polysaccharide combined with FOLFOX chemotherapy and Kangai injection combined with FOLFOX chemotherapy have more advantages than other traditional Chinese medicine injections. In terms of alleviating adverse reactions, astragalus polysaccharide combined with FOLFOX chemotherapy, sodium cantharidate, and vitamin B and FOLFOX chemotherapy have advantages over other traditional Chinese medicine injections. In addition, in the treatment of gastric cancer with traditional Chinese medicine injection combined with XELOX chemotherapy, Brucea chinensis oil emulsion and compound Sophora flavescens have more advantages than other traditional Chinese medicine injections in improving the total clinical effective rate and improving the quality of life indicators. Mushroom polysaccharide has more advantages than other traditional Chinese medicine injections in terms of alleviating adverse reaction indicators. (2) In improving the survival rate of patients with esophageal cancer, cinobufacini and Kangai injections combined with radiotherapy are dominant in the comprehensive ranking. Compound Sophora flavescens injection combined with radiotherapy has an advantage in the comprehensive ranking of the clinical total effective rate and the improvement of quality of life. (3) In the study of traditional Chinese medicine injection combined with

hepatic artery embolization in the treatment of liver cancer, compared with the cluster analysis results of other traditional Chinese medicine injections, Brucea oil emulsion and cinobufagin combined with TACE were dominant in the comprehensive ranking of survival rate. Kanglaite and astragalus polysaccharide combined with TACE are dominant in the comprehensive ranking of clinical total effective rate and quality of life improvement. Shenmai combined with TACE is dominant in the comprehensive ranking of adverse reactions. (4) Compared with the cluster analysis results of other traditional Chinese medicine injections, Xiaoaiping injection assisted by FOLFOX chemotherapy regimen in the treatment of colorectal cancer has the advantage in the comprehensive ranking of clinical efficacy and quality of life improvement

(2) In terms of safety, traditional Chinese medicine injections combined with radiotherapy or chemotherapy can alleviate the occurrence of adverse reactions. However, few adverse reactions caused by TCM injections have been reported in RCTs, so no definite conclusion can be drawn

4.4. Establishment of Animal Tumor Model. The experimental animals were BALB\c mice, 4.4-6.5 weeks old, weighing 11-16 g, female. In large-scale culturing of murine breast cancer cells 4T1, collecting 4T1 cells in the logarithmic growth phase, and counting them in a cytometer, the medium was used to prepare a cell suspension of 1×10^7 /mL. The $50 \mu L$ cell suspension was subcutaneously injected into the right back of BALB\c mice. After one week of culture, the tumor size was measured with a vernier caliper regularly. When the tumor volume was about $58 - 110 \text{mm}^3$, it could be used as a tumor model for in vivo research. Tumor volume was calculated according to the following formula:

$$V_{\text{Tumor volume}} = L_{\text{Tumor length diameter}} \cdot \frac{M^2_{\text{The widest diameter of a tumor perpendicular to the longest diameter}}}{2} . \tag{22}$$

(a)

(b)
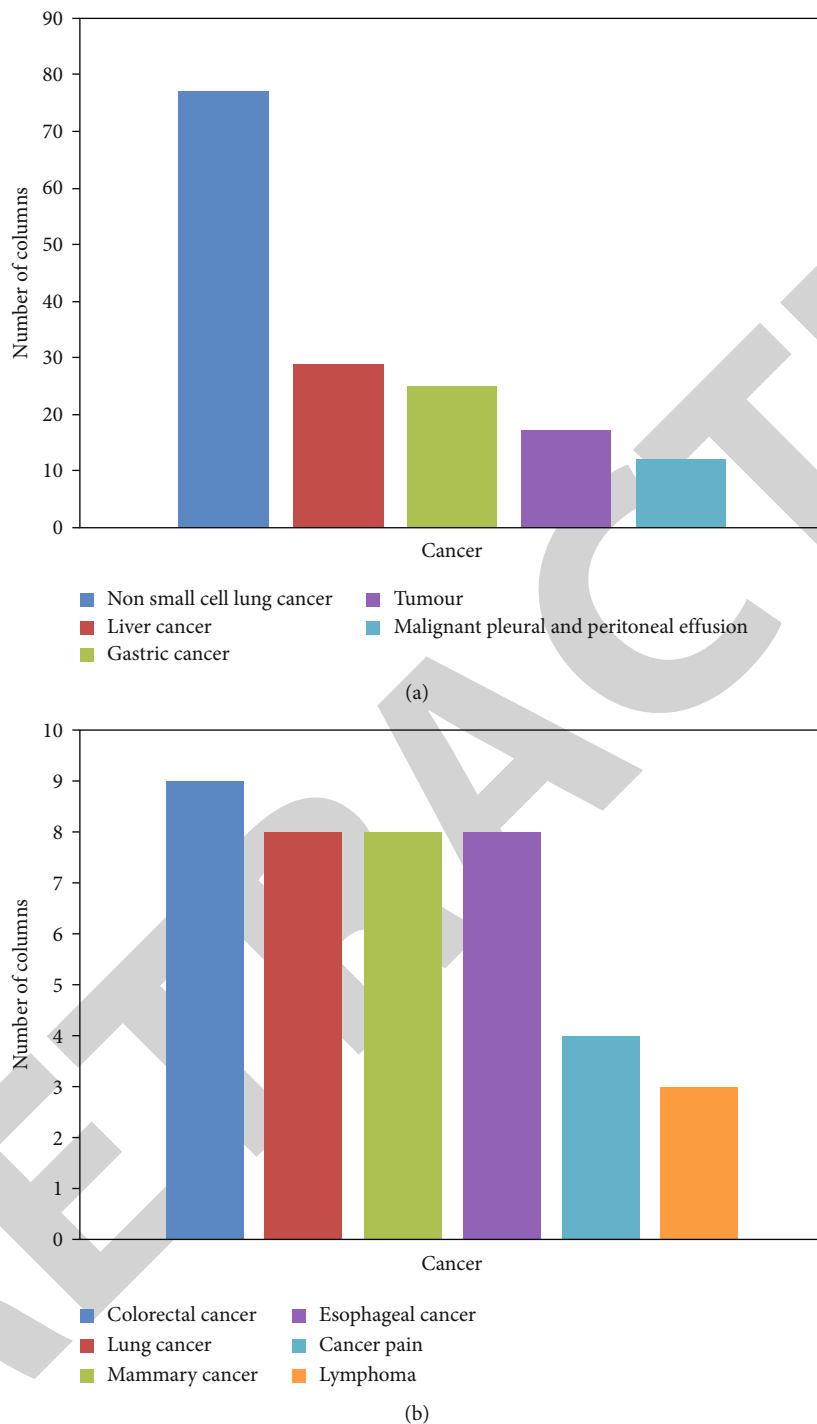
FIGURE 8: Plot of the number of cases for different types of tumors.

In order to observe the histopathological changes of SM-NPs in photothermal/photodynamic synergistic treatment of tumors, a single dose of PBS, free Ce6, and SM-NPs was injected into tumor-bearing mouse via tail vein. The tumor tissue was irradiated with laser 24 hours after administration, and a nonirradiated control group was set, respectively. Six hours after laser irradiation, the tumor-bearing mice were sacrificed and the heart, liver, spleen, lung, kidney, and tumor tissues were taken out for H&E staining. It can be seen from Table 4 that sporadic areas of cell necrosis and infiltration of inflammatory cells can be observed in the tumor tissue of the free Ce6 light treatment group. In the SM-NP tumor tissue, obvious necrosis area and a large number of inflammatory cell infiltration can be seen. The results showed that the therapeutic effect of the SM-NP light therapy group on tumor was significantly higher than that of

Table 2: Statistics of traditional Chinese medicine injection varieties involved in the systematic review/meta-analysis of tumor diseases.

Serial number	Disease	Frequency of occurrence	Percentage
1	Compound Sophora flavescens injection	55	15.6%
2	Shenqi Fuzheng injection	50	14.2%
3	Aidi injection	45	12.8%
4	Kangai injection	35	9.9%
5	Cinobufacini injection	29	8.2%
6	Kanglaite injection	27	7.7%
7	Javanica oil emulsion injection	25	7.1%
8	Xiaoaiping injection	18	5.1%
9	Delisheng injection	14	4.0%
10	Elemene injection	13	3.7%
11	Lentinan injection	12	3.4%
12	Ginseng polysaccharide injection	10	2.8%
13	Shenfu injection	10	2.8%
14	Astragalus polysaccharide injection	9	2.6%

Table 3: Summary table of dominant varieties of traditional Chinese medicine injection based on cluster analysis.

Name of digestive system tumor	Intervention measures of the control group	Outcome indicators	The dominant varieties of traditional Chinese medicine injection obtained by cluster analysis
Gastric cancer	FOLFOX chemotherapy regimen	Total clinical effective rate, quality of life, and adverse reactions	Astragalus polysaccharide injection, Kangai injection, sodium pincer, and vitamin B injection
Gastric cancer	XELOX chemotherapy regimen	Total clinical effective rate, quality of life, and adverse reactions	Brucea javanica oil emulsion injection, compound Sophora flavescens injection, Lentinan injection
Esophageal cancer	Radiotherapy	Clinical total effective rate, quality of life, adverse reactions, survival rate	Compound Sophora flavescens injection, Shenqi Fuzheng injection, compound Sophora flavescens injection, Cinobufagin injection, Kangai injection
Esophageal cancer	Chemotherapy	Total clinical effective rate, quality of life, and adverse reactions	Compound Sophora flavescens injection
Liver cancer	TACE	Clinical total effective rate, quality of life, adverse reactions, survival rate	Brucea javanica oil emulsion injection, cinobufagin injection, Kanglaite injection, astragalus polysaccharide injection, Shenmai injection
Colon cancer	FOLFOX chemotherapy regimen	Total clinical efficiency and quality of life	Xiaoaiping injection
Pancreatic cancer	Chemotherapy	Total clinical effective rate, quality of life, and adverse reactions	Javanica oil emulsion injection, Kanglaite injection, Aidi injection

the free Ce6 light therapy group, and its destruction and killing effect on the tumor tissue was greater. Table 4 shows that the histopathology of the heart, liver, spleen, lung, and kidney tissue in each treatment group has no obvious changes. The results showed that although SM-NPs had a strong killing effect on tumor tissue, it was safe for the heart, liver, spleen, lung, kidney, and other tissues and had no obvious toxic and side effects.

5. Discussion

At present, malignant tumor has become one of the most serious diseases threatening human health. The World Health Organization's report on cancer in the world says there are 14 million new cancer cases and 8.2 million deaths worldwide each year. When malignant tumors occur, it increases the difficulty of treatment and the risk of life. Therefore, how to effectively prevent and treat cancer, especially to prevent tumor metastasis or recurrence, is an urgent problem to be solved in current scientific research.

There are three main methods of treating cancer: surgery, chemotherapy, and radiation. However, traditional treatment methods have disadvantages such as large trauma, large toxic and side effects, prone to multidrug resistance, damage to the immune system, and difficulty in avoiding tumor recurrence. In recent years, tumor immunotherapy has become one of the important research fields, an important breakthrough, and an important development direction of tumor therapy.

TABLE 4: The ratio of tumor volume to the volume before treatment in each group after 12 days of treatment and the comparison results between each group (t test).

Project	SM-NPs/IR	SM-NPs/Vc/IR	Ce6/IR	PBS/IR	SM-NPs	Ce6
$\frac{V_{\text{After treatment}}}{V_{\text{Before treatment}}}$ $(\bar{X} \pm S)$	0.42 ± 0.29	1.88 ± 0.34	3.08 ± 0.44	3.90 ± 0.29	3.43 ± 0.36	4.13 ± 0.29
SM-NPs/IR	—	0.000	0.000	0.000	0.000	0.000
SM-NPs/Vc/IR	—	—	0.052	0.007	0.007	0.002
Ce6/IR	—	—	—	0.289	0.272	0.103
PBS/IR	—	—	—	—	0.829	0.688
SM-NPs	—	—	—	—	—	0.529
Ce6	—	—	—	—	—	—

Phototherapy is a new way of thinking in current cancer treatment research. It is also one of the hottest research areas in biomedical applications, which is fundamentally due to the advantages of phototherapy with high treatment accuracy, minimal tissue damage, and no drug resistance. At present, the common phototherapy reagents mainly have shortcomings such as low absorbance, poor water solubility, easy aggregation, easy quenching of fluorescence, and poor dark toxicity. In this paper, combining the performance advantages of organic semiconductor nanoparticles and photosensitizers, a series of high-performance organic nano-phototherapy agents were designed, and their applications in tumor phototherapy were initially explored.

6. Conclusion

Organic semiconductor nanomaterials are nanostructured materials. Due to its strong light absorption, stable light, high brightness, and good biocompatibility, it has been widely used in bioimaging, antibacterial, antitumor, gene therapy, and drug release in the past decade. In this study, a network meta-analysis of traditional Chinese medicine injections in the treatment of digestive system tumors was carried out, and the clinical efficacy and safety of different varieties of traditional Chinese medicine injections were systematically, scientifically, and comprehensively evaluated. At the same time, Bayesian theory was used to identify the dominant varieties of traditional Chinese medicine injections and to optimize the program of adjuvant radiotherapy and chemotherapy for the treatment of digestive system tumors. It provides high-quality evidence-based medical evidence for clinical use.

Data Availability

No data were used to support this study.

Conflicts of Interest

The authors declare that there is no conflict of interest with any financial organizations regarding the material reported in this manuscript.

Authors' Contributions

Ying Liu and Yanwei Li contributed equally to this work and should be considered co-first authors.

References

[1] M. Li, H. Ma, C. Shi et al., "A cyanine-based liposomal nanophotosensitizer for enhanced cancer chemo-photodynamic therapy," *Chemical Research in Chinese Universities*, vol. 37, no. 4, pp. 925–933, 2021.

[2] W. Pan, M. Shi, Y. Li, N. Li, and B. Tang, "A GSH-responsive nanophotosensitizer for efficient photodynamic therapy," *RSC Advances*, vol. 8, no. 74, pp. 42374–42379, 2018.

[3] T. Akbari, M. Pourhajibagher, F. Hosseini et al., "The effect of indocyanine green loaded on a novel nano-graphene oxide for high performance of photodynamic therapy against _Enterococcus faecalis_," *Photodiagnosis & Photodynamic Therapy*, vol. 20, pp. 148–153, 2017.

[4] Y. Qin, B. Cao, J. Li, S. Liao, and X. Yu, "An oxygen-enriched photodynamic nanospray for postsurgical tumor regression," *ACS Biomaterials Science and Engineering*, vol. 6, no. 11, pp. 6415–6423, 2020.

[5] X. Zhang, J. Tang, C. Li, Y. Lu, and J. A. Liu, "A targeting black phosphorus nanoparticle based immune cells nano-regulator for photodynamic/photothermal and photo-immunotherapy," *Bioactive Materials*, vol. 6, no. 2, pp. 472–489, 2021.

[6] Y. Wang, M. Zu, X. Ma, D. Jia, and Z. Xu, "Glutathione-responsive multifunctional "Trojan Horse" nanogel as a nanotheranostic for combined chemotherapy and photodynamic anticancer therapy," *ACS Applied Materials & Interfaces*, vol. 12, no. 45, pp. 50896–50908, 2020.

[7] W. Deng, K. J. Mckelvey, A. Guller, A. Fayzullin, and E. M. Goldys, "Application of mitochondrially targeted nanoconstructs to neoadjuvant X-ray-induced photodynamic therapy for rectal cancer," *ACS Central Science*, vol. 6, no. 5, pp. 715–726, 2020.

Research Article

Health-Care Technology of Badminton Sports Based on Nanotechnology

Qiuning Wen [1,2]

[1]*Department of Physical Education, Science and Technology College Gannan Normal University, Ganzhou, 341000 Jiangxi, China*
[2]*Department of Leisure Sports, Jungwon University, Chungbuk 28024, Republic of Korea*

Correspondence should be addressed to Qiuning Wen; 2013015@gnnu.edu.cn

Nanotechnology has become an important technology that cannot be ignored in high and new technology, and the application of nanomaterials is to design all aspects of life. With the more popularization of badminton, the blending of the two is also increasing. The purpose of this paper is to discuss the combination of sports health care and nanotechnology in badminton. This paper starts with the application of nanotechnology in badminton racket materials, hoping to explore the impact of nanotechnology on badminton sports health care. In this paper, 130 testers of different ages from different schools were selected for 17 weeks of badminton training. By comparing the physical fitness indicators before and after, this paper finds the impact of badminton on physical health. The experimental results show that badminton exercise training has an impact on human health and has a significant impact on human height, weight, and lung capacity.

1. Introduction

Badminton is a traditional Chinese sport. In recent years, the excellent performance of the national badminton team in international competitions has gradually brought the fitness function of badminton into the public's field of vision. It integrates social, entertainment, fitness, stress relief, and other attributes into one and improves the body's physical health and physical self-esteem. It makes badminton the best choice for contemporary teenagers to carry out extracurricular sports training activities. In addition, the continuous increase of badminton extracurricular training activities, the gradual rise of badminton club training, and the expansion of badminton teachers and referees and other professionals have not only laid a foundation for the extracurricular badminton sports training for senior primary school students. It also provides a guarantee for their physical health and the development of physical self-esteem.

The global science and technology and economy are in a stage of rapid development, and information technology, biomedical technology, and nanotechnology have become three important technologies side by side. And nanotechnology is a key basic technology. It lays a solid foundation for the development of information technology and biotechnology. Nanotechnology has also increasingly become the focus of competition in the world's high-tech fields. Nanotechnology is more and more deeply affecting and changing people's production, life, and thinking. Its impact on economy, politics, and society is more reflected in the fierce competition between countries for nanotechnology research and application.

This paper mainly has the following two innovations: (1) This paper is based on the research of value proposition generation in the process of nanotechnology commercialization from a layered perspective. This paper mainly analyzes the generation of value propositions in the process of nanotechnology commercialization from the industry level, company level, and specific business level. (2) About the research on the connection of value proposition generation in the process of nanotechnology commercialization, this paper mainly analyzes the influencing factors, typical obstacles, and targeted strategies in the process of value proposition generation in nanotechnology commercialization.

2. Related Work

The emergence of nanomaterials has greatly changed people's lives, and nanotechnology has penetrated into all aspects of life, and there are many studies on it. Mihail C examined progress in nanotechnology development since 2000, achievements over the past decade, and opportunities for research, education, innovation, and social outcomes worldwide by 2020 [1]. Duhan J S believed that nanotechnology is an interdisciplinary field of study. He discussed the potential uses and benefits of nanotechnology in precision agriculture. Tools and techniques based on modern nanotechnology have the potential to solve various problems of traditional agriculture [2]. Lee CH conducted research on the science and engineering of water purification, especially oil-water separation. His research goals are to provide a comprehensive review on oil-water separation by nanotechnology and organic chemistry and to improve understanding of the environmental issues of water purification using nanotechnology [3]. Reis CP believed that nanotechnology has developed alternative routes of administration, namely, those based on nanotechnology. Nanoparticles made of synthetic or natural materials have been shown to successfully overcome the inherent barriers to insulin stability, degradation, and absorption across the gastrointestinal tract and other mucosal membranes [4]. Mirkin CA discussed emerging nanotechnology-based tools. These tools have the potential to dramatically impact cancer research, diagnosis, and treatment. His research explains how nanotechnology exploits the size, shape, and composition-dependent properties of nanomaterials. It provides new tools for precision cancer medicine [5]. Weng Y highlighted the latest progress in nanotechnology-based system development. The system can deliver ocular drugs and genes to the eye through corneal absorption, periocular injection, and intravitreal injection for the treatment and diagnosis of ocular diseases. Then, he discussed and prospected the applications and challenges of nanosystems in ophthalmology [6]. Falagan-Lotsch P saw it as a nanoactivation method currently on the market or in development, such as antimicrobial food contact surfaces/packaging, nanoactivated sensors for rapid detection of pathogens/contaminants, and nanodelivery biocidal methods. It showed great potential in the food industry [7]. Michal reviewed the research progress of nanoantibacterial drugs in the past two years and introduced their unique properties, mode of action, and activity against multidrug-resistant bacteria and biofilms [8]. Since the launch of the US National Nano Initiative (NNI) in 2000, nanotechnology research has become the focus of global attention. Various countries have formulated nanotechnology plans relative to their national conditions. It strives to seize the commanding heights of science and technology strategy in the twenty-first century and to seize the initiative of future economic development [9].

3. Nanotechnology Algorithms and Applications

3.1. Nanotechnology. Nanoscience and technology is one of the foundations of the new era of science and technology in this century. A nanometer is a unit of length and is one billionth of a meter. Studying the properties of materials and their applications in the range of 0.1 to 100 nm structure scale is what we call nanotechnology, and sometimes nanoscience and technology are also collectively referred to as nanotechnology. Nanotechnology is a technology to manufacture new materials, new devices, and research new processes based on nanoscience through new methods. The concept of nanoscience and technology is expressed differently in different literatures. But it will continue to improve as the discipline develops, and more detailed concepts will be drawn. Nanotechnology is based on advanced science and technology at the nanoscale and is the product of the combination of modern science and modern technology. Nanoscience and technology is the product of the interlaced and compatible theory and high technology, not just the expansion of a single discipline. Nanoscience and technology holds enticing prospects in terms of basic research. As a technology, nanotechnology will provide human beings with novel products and devices with specific functions. Nanoscience and technology are full of opportunities and challenges [10, 11].

Due to its unique properties, nanotechnology is widely used in military, medical, environmental energy, biological research, and other fields. It has brought great positive significance to national security and people's life, changed people's original production methods, improved production efficiency, and reduced energy consumption. And in the field of the environment, it is not far behind. The catalyst developed by it can effectively solve the problem of sewage and air quality [12, 13]. The huge positive significance of nanotechnology and some undiscovered potential values have made the world carry out crazy research on it, forming a "nanostorm" [14]. Among them, nanomaterials include four common forms of nanopowder, nanofiber, nanofilm, and nanoblock [15], as shown in Figure 1:

Nanotechnology contributes to the utilization of new energy sources. Hydrogen is abundant in nature. After burning, it will not pollute the environment, so it is regarded as a new type of energy in today's society. However, some previous technologies cannot achieve the best effect of hydrogen transportation and storage. The researchers discovered that carbon nanotubes are a material that can store hydrogen. The surface area of 1G carbon nanotubes can reach hundreds of square meters, and a large amount of absorbed hydrogen can be released by slight heating at room temperature. And this technology is expected to be included in the application stage in the future, when human beings can use hydrogen on a large scale to replace scarce fossil energy. Yet, the air we breathe will also change dramatically, as shown in Figure 2:

It is not difficult to see that the definitions of nanotechnology have different focuses on nanotechnology. The UNESCO definition highlights the convergence of nanoscale research at both theoretical and applied levels. The National Nanotechnology Innovation Organization's definition highlights the novel properties of materials and systems at the nanoscale. The NSF definition emphasizes convergent fusion at the nanoscale. The EU's seventh framework plan lists
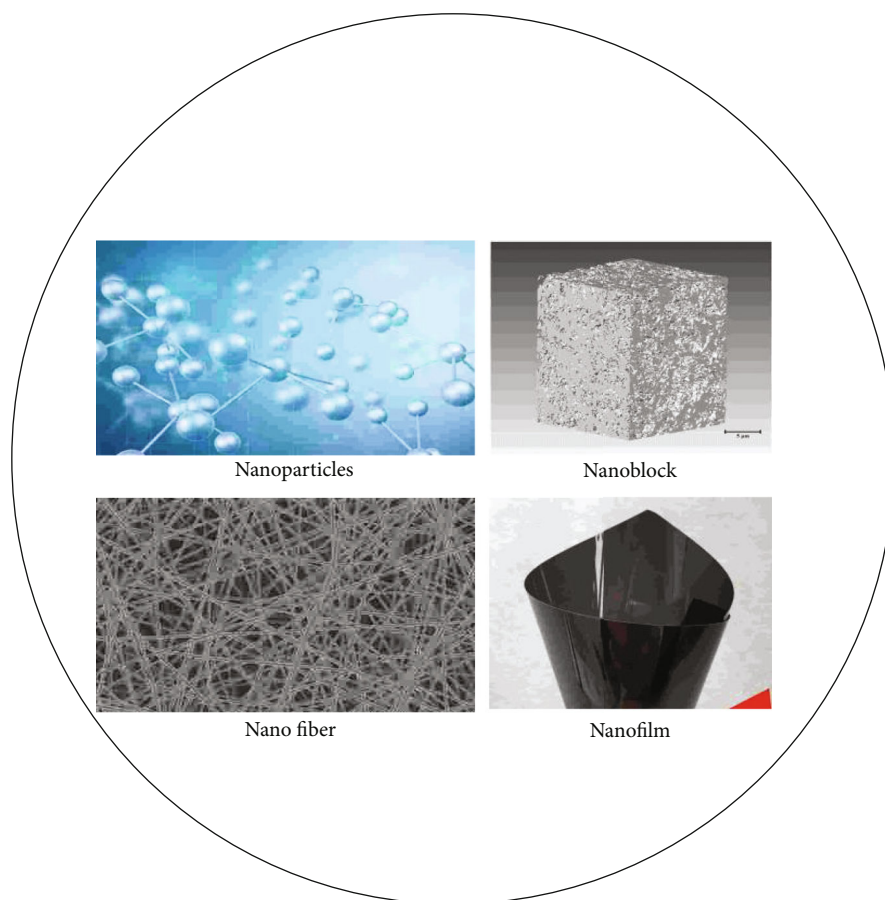
Figure 1: Four forms of nanomaterials.
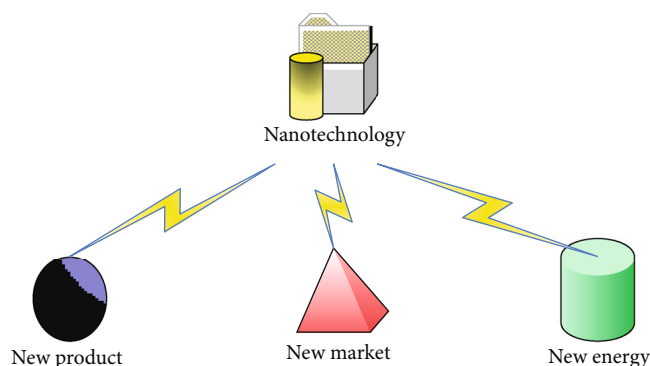
Figure 2: The economic impact of nanotechnology.

many areas related to nanotechnology. At the same time, these definitions have in common: First, they all reflect the scope of research at the nanoscale. Second, they all focus on the novel properties exhibited by matter at the nanoscale [16, 17], as shown in Figure 3:

3.2. Applications of Nanotechnology. Nanotechnology, like previous new technologies, was first used in the military field to prove its huge military value. When this technology emerged, people had glimpsed its broad prospects in the military field. The US Department of Defense clearly recognized the importance of nanotechnology a decade ago and has

played an important role in supporting this field. The US Department of Defense website reported in February 2001 that the US Department of Defense announced that in 2001, it awarded \$8.75 million to 16 nanometer research projects. It has also awarded 14 research institutions of \$15 million annually since 2002 to carry out nanotechnology research in 15 basic disciplines and engineering fields. Nanotechnology has brought global medical care to another level, and it has opened up new windows for biopharmaceuticals and chemical pharmaceuticals with its unique structure and properties. Because there is still a lot of work in the basic theory and application development, it is still in the research and development stage. Therefore, although a lot of research on the preparation, structure, and properties of nanobiomedical materials has been carried out, it is still in its infancy. Therefore, we look forward to people's further exploration. Experts pointed out that due to the introduction of nanotechnology in the future, the production of medicines and the delivery of medicines will undergo fundamental changes [18–19], as shown in Figure 4:

3.3. Application of Nanotechnology in Badminton Health Care. The application of nanomaterials has been very extensive and can be seen everywhere in our daily life. It has a lot of applications in light industry, chemical industry, machine manufacturing, electronic product manufacturing, and other fields. Nanomaterials will play a major role in future life, and
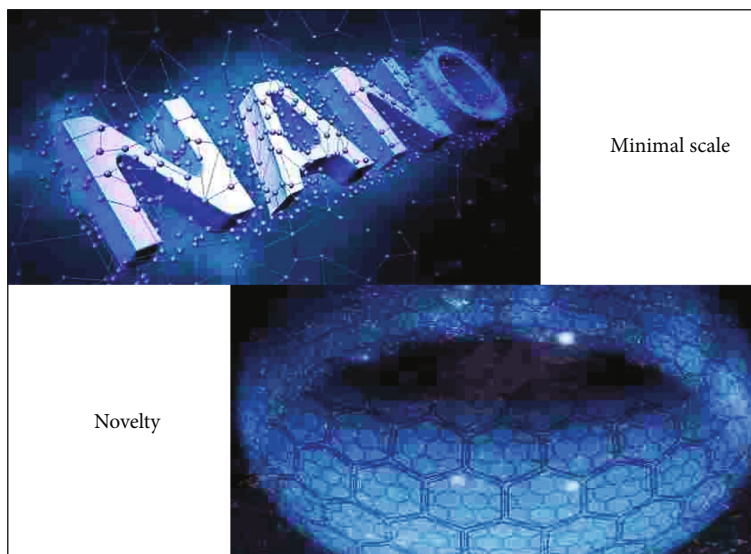
FIGURE 3: Nanotechnology.
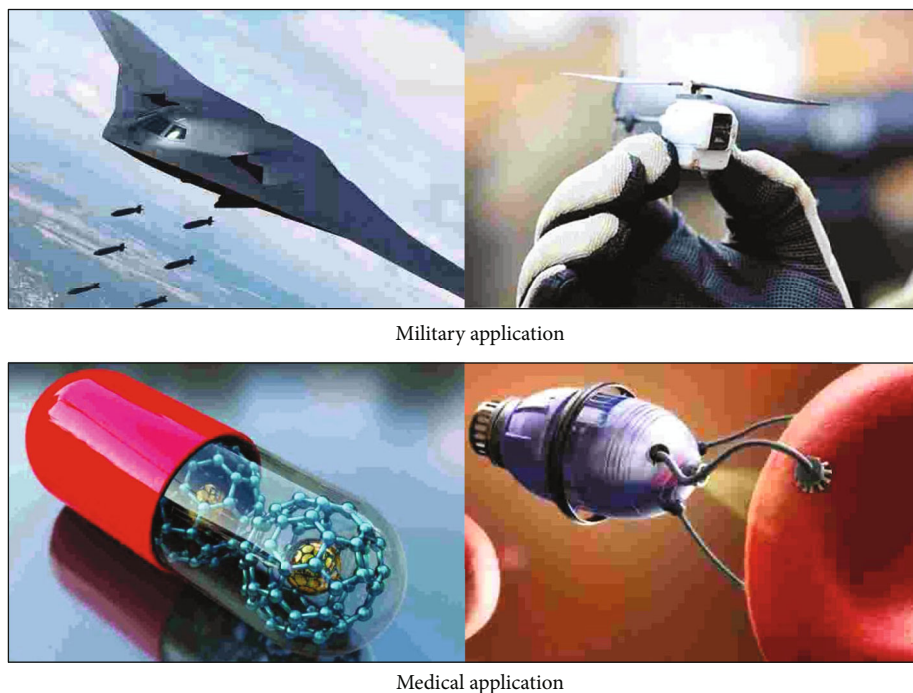
FIGURE 4: Nanotechnology applications.

nanotechnology will bring more variety to our lives. The dominance of nanotechnology demonstrates its social value that cannot be ignored. It is widely and strongly applied to all fields of society with its unique properties, promoting the stable and orderly development of society [20–21].

In the field of badminton, with the excellent properties of nanomaterials, nanomaterials have in-depth applications in badminton rackets, protective gear, and others, as shown in Figure 5:

In this century, the nano industry must be one of the main industries leading the development of the science and technology industry. Nanotechnology and nanomaterials

have penetrated into various industries of the national economy, such as medical industry, environmental energy, computer industry, biological research, national security, and aerospace. It promotes the rapid growth of the national economy, and its economic impact will certainly exceed that of the information industry [22, 23].

3.4. Nanotechnology Hidden Markov Models. Hidden Markov model (hidden Markov model, HMM for short) is a statistical model, which is used to describe a Markov process with hidden unknown parameters. The difficulty is to determine the implicit parameters of the process from the

Nanotechnology racket   Nanotechnology ball net   Nanotechnology protective gear
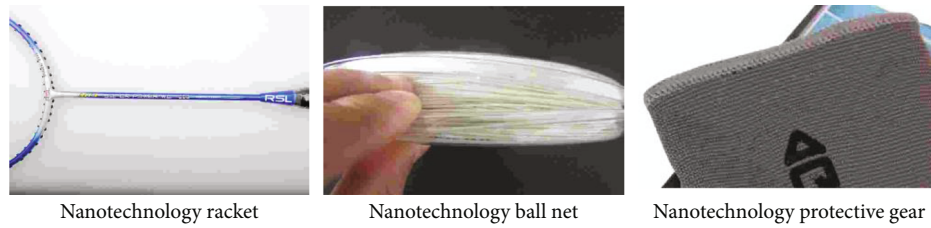
FIGURE 5: Nanotechnology racket.

observable parameters. These parameters are then used for further analysis, such as pattern recognition.

Many properties of hidden Markov models are used to solve real-world practical problems. According to the different types of data processed, hidden Markov models can be divided into discrete hidden Markov models and continuous hidden Markov models. Discrete hidden Markov models are the basis of continuous hidden Markov models and are easier to understand. The remainder of this chapter will give a detailed introduction to discrete hidden Markov models and continuous hidden Markov models.

3.4.1. Elements of Hidden Markov Model. A hidden Markov model (HMM) can be described by five elements, including 2 state sets and 3 probability matrices:

The number of hidden states N is the number of unobserved states. The hidden states satisfy the Markov property, which is the actual hidden state in the Markov model. Implicit states are usually not available through direct observation.

The number of observable states M is the number of states that can be clearly observed. Its observable state is associated with the hidden state in the model. It can be obtained by direct observation. The number of observable states does not have to be the same as the number of hidden states (the number of different colored sticks thrown in the above example).

The implicit state transition probability matrix A describes the transition probability between states in the HMM (the probability of transitioning the person who throws a small stick in the example). It can be expressed as $a_{ij} \in A$. a_{ij} represents the probability of transitioning from state i to state j at time t, where $1 \le i$; $j \le N$.

The observation state radiation probability matrix B (the probability that the specified person throws the specified color stick in the example) can be expressed as $b_j(k) \in B$. $b_j(k)$ represents the probability of selecting the observation feature as x_k from the state j at time t, where $1 \le j \le N$; $1 \le k \le M$.

The initial state probability matrix π represents the probability matrix of the hidden state at the initial time $t = 1$. It can be expressed as $\pi_i \in \pi$; π_i represents the probability of selecting state i at time $t = 1$, where $1 \le i \le N$.

3.4.2. Training of Hidden Markov Models. When training an HMM for a given problem or specified dataset, consider the joint probability of the hidden state (S_i) and the observable state (O_i) and simplify it with the intrinsic properties of Markov chains for continuous data. The resulting joint probability:

$$\Pr(S, O) = \Pr(S_1) \prod_{t=2}^{T} \Pr(S_t|S_{t-1}) \prod_{t=1}^{T} \Pr(O_t|S_t). \quad (1)$$

3.4.3. Probability Calculation of Observable Sequences. To calculate the probability of observing the sequence $O = O_1, O_2, \cdots, O_T$, it is assumed that the model parameters λ are known, namely, the parameter values A, B, and π are all known. For a given λ, the computation is done by considering every possible sequence of states that can produce an observation sequence O. The sum of the obtained probabilities is the probability of producing the observation sequence O through the model parameters λ.

Supposing the implicit state sequence that may produce the observation state sequence O is

$$S = S_1, S_2, \cdots, S_T, \quad (2)$$

$$\Pr(O|S, \lambda) = \prod_{i=1}^{T} \Pr(O_i|S_i, \lambda), \quad (3)$$

$$\Pr(O|S, \lambda) = b_{S1}(O_1)b_{S2}(O_2), \cdots, b_{ST}(O_T). \quad (4)$$

Under the condition that the model parameter is λ, the probability that the hidden state sequence is S is calculated as follows:

$$\Pr(S|\lambda) = \pi_{S_1} a_{S_1 S_2} a_{S_2 S_3}, \cdots, a_{S_{T-1} S_T}. \quad (5)$$

Substituting formula (5) into formula (1), we get

$$\Pr(S, O) = \Pr(S|\lambda)\Pr(O|S, \lambda), \quad (6)$$

$$\Pr(O|S, \lambda) = \Pr(O|S, \lambda)\Pr(S|\lambda). \quad (7)$$

By considering every possibility that can produce an implicit state of the observation sequence O, the probability of obtaining the observation state sequence O from the model parameters λ can be obtained. The following formula is obtained

$$\Pr(O|\lambda) = \sum_{all\ S} \Pr(O|S, \lambda)\Pr(S|\lambda), \quad (8)$$

$$\pi = \begin{bmatrix} \Pr(Person\ 1) \\ \Pr(Person\ 2) \\ \Pr(Person\ 3) \end{bmatrix} = \begin{bmatrix} 0 \\ 1 \\ 0 \end{bmatrix}$$

Prior probability matrix

	Person 1	Person 2	Person 3
red	0.09	0.6	0.01
Yellow	0.1	0.05	0.4
Blue	0.03	0.03	0.3
Green	0.07	0.02	0.2
Black	0.6	0.17	0.01
White	0.01	0.08	0.02
Orange	0.1	0.05	0.06

Observation emission probability matrix

	Person 1	Person 2	Person 3
Person 1	0.2	0.4	0.3
Person 2	0.1	0.5	0.4
Person 3	0.4	1.5	0.1

State transition probability matri

Figure 6: Parameter matrix.

$$\Pr(O|\lambda) = \sum_{S_1, S_2, \cdots, S_T} \pi_{S_1} a_{S_1 S_2} a_{S_2 S_3}, \cdots, a_{S_{T-1} S_T} b_{S_1}(O_1) b_{S_2}(O_2), \\ \cdots, b_{S_T}(O_T). \tag{9}$$

In order to better explain the calculation method derived from formula (8) and formula (9), let us start from the beginning again with the example of a person throwing a small stick. With the parameter values given in Figure 6, the expression is used to calculate the probability of observing the sequence {red, green}.

Here, the sequence $O = \{red, green\}$ is observed. For all hidden state sequences S, the probability of finding the observation sequence O is

$$\Pr(O|\{person2, person1\}) = 0.6 \times 0.1 \times 0.07, \tag{10}$$

$$\Pr(O|\{person2, person3\}) = 0.6 \times 0.4 \times 0.2, \tag{11}$$

$$\Pr(O|\{person2, person2\}) = 0.6 \times 0.1 \times 0.02. \tag{12}$$

The total probabilities obtained are

$$\Pr(O|\lambda) = 0.0546. \tag{13}$$

In all possible states, the probability of observing the sequence O is calculated, and in formula (13), these calculated probabilities are summed, so that the probability of observing the sequence O of the HMM, the parameter λ, is obtained. The computational complexity of using formulas (2) to (9) to calculate the probability is quite high. For example, for an HMM with N hidden states, the time complexity of the exhaustive search is $2TN^T$, where T is the length of the observation sequence. Therefore, it is necessary to find some other alternative ways to calculate the probability of observation sequence.

3.4.4. Forward-Backward Algorithm. Forward-backward algorithm is a relatively less computationally intensive method that can calculate the probability of an observation sequence. The forward variable $\alpha_t(i)$ is defined as

$$\alpha_t(i) = \Pr(O_1, O_2, \cdots, O_t, S_{t=i}|\lambda), \tag{14}$$

where $\alpha_t(i)$ is the local observation sequence probability, which represents the probability that, for a given λ, the observation sequence is state i at time t. The specific steps of the forward-backward algorithm are as follows:

Initialization: For all states i, $\alpha_1(i) = \pi_i b_i(O_1)$, where $i \in \{1 \text{ to } N\}$.

Induction: For each time point t, a value of the forward variable $\alpha_t(i)$ can be obtained, and for each time point $t = 2, \cdots, T$ and all states j ($j \in \{1 \text{ to } N\}$) recursively calculate the forward variable $\alpha_t(j)$:

$$\alpha_t(j) = \left[\sum_i \alpha_{t-1}(i) a_{ij}\right] b_j(O_t). \tag{15}$$

Termination: For a given HMM, the probability of observing sequence O can be calculated by the following formula:

$$\Pr(O|\lambda) = \sum_i \alpha_T(i). \tag{16}$$

In this method, each state at time $t - 1$ is fully computed before considering the state at time t. Therefore, for a given HMM model λ, the last state in the operation constitutes the final probability of producing the observation sequence O. It can be found that the time complexity of the forward algorithm is $N^2 T$, where N refers to the number of hidden states and T refers to the length of the observation sequence.

The backward algorithm is similar to the forward algorithm and is used to calculate the probability of the observation sequence for a given λ. The backward variable $\beta_t(i)$ is defined as follows:

$$\beta_t(i) = \Pr(O_{t+1}, O_{t+2}, \cdots, O_T|S_{t=i}, \lambda). \tag{17}$$

As in formula (17), $\beta_t(i)$ represents the backward variable, which refers to S_i at time t, where λ is known and S_i is the hidden state. The final probability is as in

$$\Pr(O|\lambda) = \sum_i \pi_i b_i(O_1) \beta_1(i). \tag{18}$$

As described above, both forward and backward
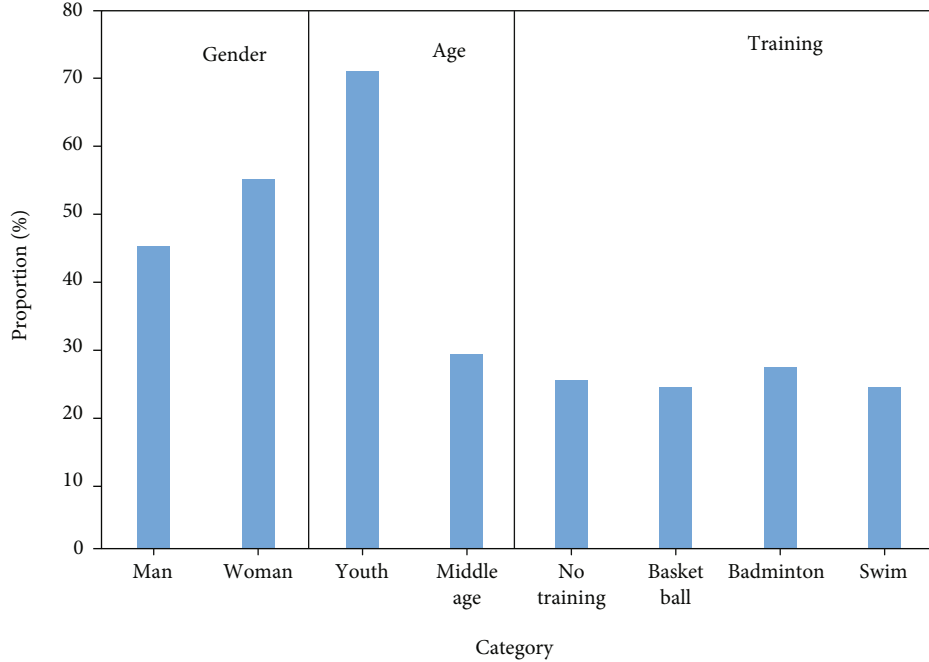
FIGURE 7: Basic information of research objects.

algorithms can be used to compute $\Pr(O|\lambda)$ to evaluate problems. Forward and backward algorithms can also be used together to solve the problem of model parameter estimation.

4. Badminton Health Care

4.1. Objects and Methods. Constitution refers to the quality of human life. It is a comprehensive and relatively stable feature of the human body on the basis of heredity and acquisition in terms of human body shape structure, physiological function, physical quality, psychological quality, and adaptability. A healthy physique is the basis for ensuring people's normal life, study, and work. Among them, a healthy physique is characterized by normal development and symmetry in the human body morphological structure. In terms of physiological function, it shows that the physiological functions of various organ systems in the human body are normal. In terms of physical fitness, it is mainly reflected in strength, speed, and endurance to meet the physical needs of general labor and sports. On the level of psychological quality, it is manifested in having psychological characteristics suitable for its age and gender and being able to withstand corresponding psychological pressure. Adaptability is reflected in the body's natural adaptability and social adaptability to resist common pathogens and enable the body to integrate into society and interact with others normally.

In order to explore the different effects of students participating in badminton extracurricular training on physical health and physical self-esteem, three primary schools (JE Primary School, QS Primary School, and CT Primary School) were randomly selected. This article is based on the grouping criteria of only participating in extracurricular

TABLE 1: List of questionnaires.

Questionnaire type	Questionnaires	Effective questionnaire	With good efficiency
Network questionnaire	100	96	96%
Paper questionnaire	30	30	100%
Add up to	130	126	96.92%

TABLE 2: Physical fitness measuring instruments and testing method.

Physical index	Measuring instrument
Height	Height meter
Weight	Weight meter
Vital capacity	Pneumatometer
50-meter run	Stopwatch
One-minute sit-ups	Count
One-minute jump rope	Stopwatch, starting whistle, and skipping rope
50×8 round trip	Stopwatch

training in badminton, basketball, and swimming, and not participating in any extracurricular sports training. Participation in various sports in the standard is in the range of six months to one year, and the level of sports ability is equal. Before the investigation, this article will visit and check the physical health status of all participants in the experiment. This article confirms that the participants are in good physical and mental health and explains the procedures for this experiment to the subjects. The data collectors introduced the purpose and precautions of this questionnaire
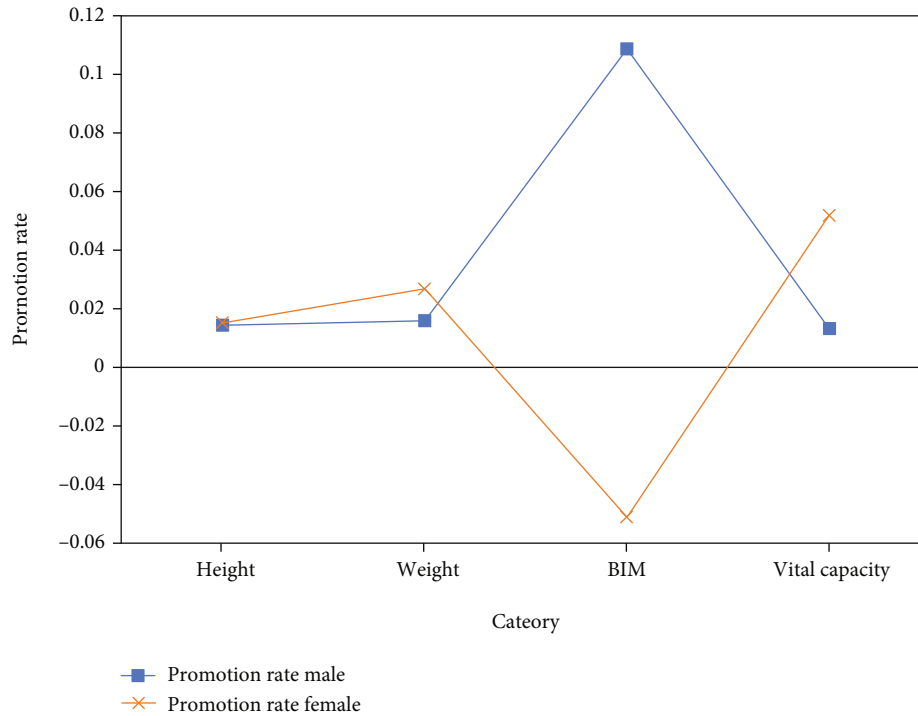
FIGURE 8: The improvement rate of badminton on physical function.

TABLE 3: Effects of badminton on body function and form.

	Training former male	Training former female	After training male	After training female
Height (cm)	169.99	162	172.45	164.46
Weight (kg)	56.99	47.72	57.9	49
BIM	20.8	18.4	23.06	17.46
Vital capacity (ml)	3739.79	2906.15	3789.6	3057.07

to the school physical education teachers and training team coaches in detail. It is convenient to answer the feedback information that is not understood during the questionnaire and data collection process in a timely manner. Physical education teachers and coaches in each school assist in distributing questionnaires, read out instructions, and explain filling requirements. It promises to keep the information filled in confidential and to fill in truthfully by the participants. In this paper, the fifth and sixth grade students of three primary schools are divided into four groups: no training, badminton, basketball, and swimming, and a total of 130 students in four groups are selected from each school. Later, due to the physical discomfort of 1 student and the failure of the assessment questionnaire for 3 students, 4 special subjects were excluded, and 126 students were retained as the research subjects of this experiment. The 126 study subjects were in good health and had no disease or other factors that would make them unfit to participate in the experiment. Among them, the number of students who participated in extracurricular training in badminton, basketball, and swimming and those who did not participate in the training were 34, 32, 30, and 34, respectively. In terms of gender distribution, there are 70 boys and 60 girls, and the proportions of each group are shown in Figure 7:

In order to explore the impact of badminton on the development of physical self-esteem among Chinese senior primary school students, this study uses the physical self-esteem scale to investigate the research subjects. The physical self-esteem scale for children is based on the PSDQ and PSPP and combines the characteristics of Chinese development and growth. It is divided into 12 different dimensions of health, appearance, strength, speed, flexibility, endurance, coordination, physical attractiveness, motor skills, physical activity, physical worth, and overall self-esteem. They collectively reflect the physical self-esteem of adolescents. The scale has a total of 78 items, and items 1, 13, 25, 37, 49, 61, 73, and 76 reflect the health subscale. 2, 14, 26, 38, 50, and 62 items reflect the physical attractiveness subscale. 3, 15, 27*, 39, 51*, 63, 74, and 77 items reflect the motor skills subscale. 4*, 16*, 28, 40, 52, and 64 reflect physical activity subscales and more. It takes about 20–25 minutes to fill in the answer, using a five-level scoring method; each subscale is scored separately and not included in the total score of the scale.
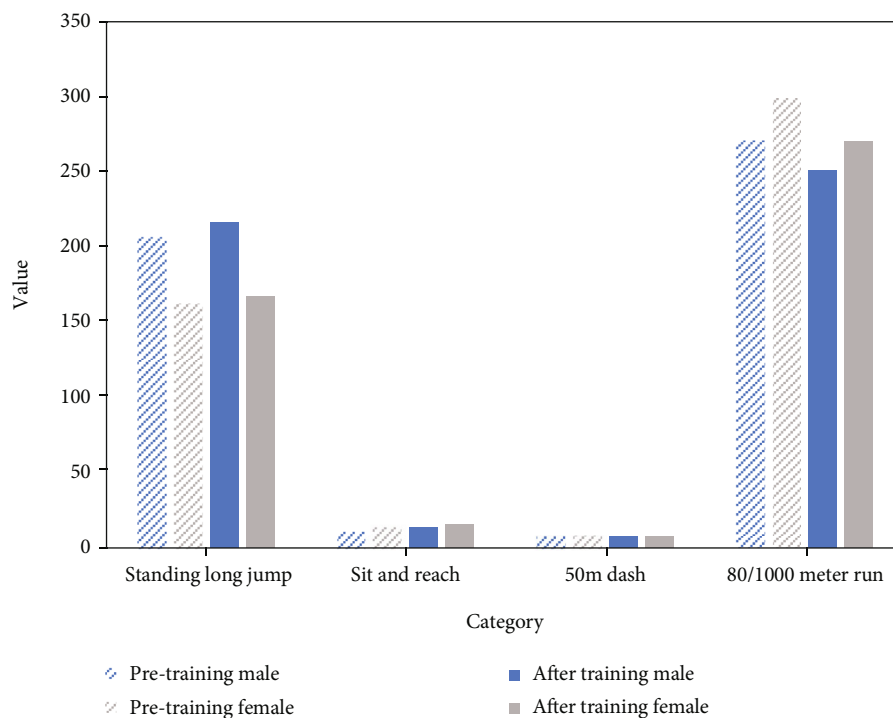
FIGURE 9: Analysis of the impact of badminton on physical fitness.

In view of the need to fill in the physical self-esteem scale questionnaire for the grouped students, the author conducted a physical fitness index test on 130 students participating in the experiment in three primary schools, and then, the paper distributed, filled in, and collected the questionnaire. After informing the students to fill in the requirements, they supervise the students to fill in the questionnaires according to their own specific conditions and subjective feelings within half an hour. Correlation analysis was performed on all questionnaires. A total of 130 questionnaires were distributed this time, 130 questionnaires were recovered, and the recovery rate was 100%. Among them, 126 are valid questionnaires, and the effective rate is 97.67%, as shown in Table 1:

The physique measuring instruments and test methods are shown in Table 2.

4.2. Physical Fitness Results. At the beginning of the design of the experiment, the body shape of the experimental subjects was changed. As the first indicator of the impact of badminton on the physique of middle school students, the reason is that height represents the growth and physical condition of human bones. Height is greatly affected by external and internal factors, including eating habits, age, and gender. Weight is a horizontal standard for judging health or not and determines a person's physical function. On this basis, the ratio of height to weight (i.e., BMI) is a long-standing internationally recognized standard for measuring body mass index. According to Chinese management, the standard is (18.5–23.9) kg/m², and the ideal body mass index is 22 kg/m². Through the experiments of the first stage, we observe the experimental results. As can be seen from Figure 8 and Table 3, through 15 weeks of badminton exer-

cise, the experimental data of the experimental group and the control group show that in terms of body shape, the boys have $P > 0.05$ in terms of body weight and BMI value, and there is no significant effect. The height is significant at $P < 0.05$ and has an effect. However, because the height growth rate of boys and girls is about 1.5%, this is normal growth, because middle school students are in the stage of physical growth and development. For girls, $P > 0.05$ for height and weight, and $P < 0.05$ for BMI, which has a significant effect. Therefore, it can be concluded that badminton has an impact on the height of boys' and girls' BMI in terms of body shape of high school students.

In this paper, strength quality, speed quality, endurance quality, and flexibility quality are used as the indicators of this experiment. The experiments corresponded to standing long jump, 50-meter sprint, 800/1000-meter run, and forward bending while sitting. It can be seen from Figure 9 that before and after training, regardless of gender and category, there is a certain improvement. Therefore, it can be concluded that badminton can improve the aerobic endurance of high school students.

4.3. Comparative Analysis of Different Exercise Modes. It can be seen from Figure 10 that there are differences in the physical health indicators of students participating in badminton extracurricular training and other groups. (1) The sit-up scores of the students who participated in the extracurricular badminton training were higher than those of other groups, and there was an extremely significant difference with the nontraining and basketball groups ($P < 0.01$). (2) The 50-meter running scores of the students who participated in the extracurricular badminton training were higher than those of the nontraining group, and there was a significant
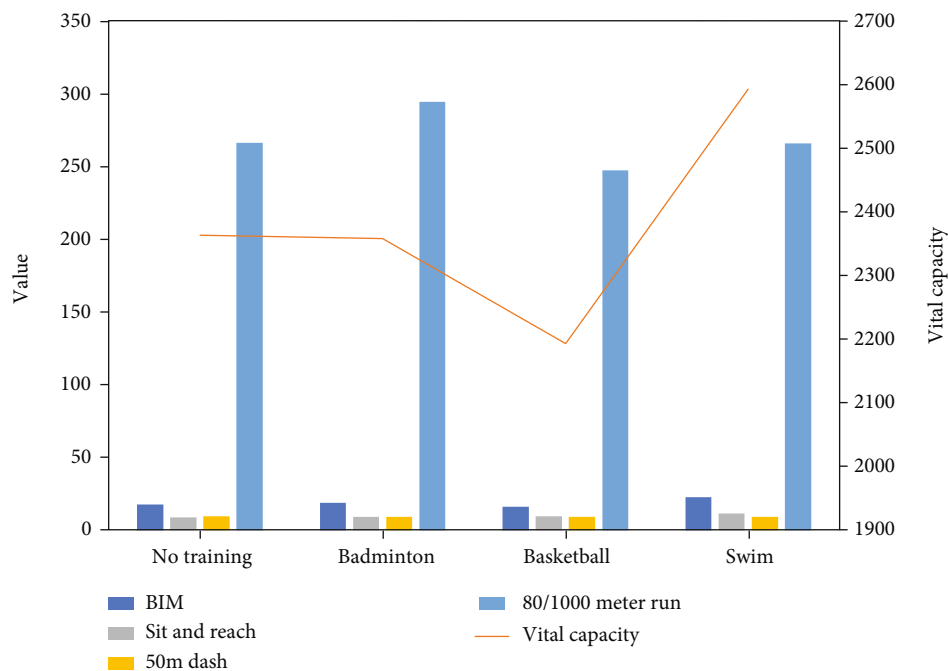
FIGURE 10: Comparison of health care by different sports.

difference ($P < 0.05$). (3) The vital capacity scores of students participating in swimming training were higher than those of other groups, and there was a significant difference ($P < 0.05$). (4) There was no significant difference between the scores of students participating in extracurricular badminton training and the scores of other groups in terms of BMI, one-minute rope skipping, 50∗8 round-trip running, and sitting forward bending ($P > 0.05$). In addition, it can be seen from the average situation that the average scores of students participating in badminton extracurricular training in the 50-meter run and sit-ups are higher than those of other groups. It shows that the speed quality and muscle strength quality of students participating in badminton extracurricular training are better than those of other groups.

5. Conclusion

Through one-way statistical analysis on the physical self-esteem index and overall self-esteem of the fifth and sixth grade students participating in badminton extracurricular training and the scores of students in the no-training group, basketball group, and swimming group, we can see that students who participated in badminton training had extremely significant differences with other groups in the six scales of physical attractiveness, motor skills, appearance, flexibility, coordination, and physical self-esteem ($P < 0.01$). In addition, the multiple comparisons of the scores of the senior primary school students participating in badminton training and the students in the no training group, the basketball group, and the badminton group in these six dimensions can be clearly seen: In the multiple comparison of appearance subscale scores, the appearance scores of the senior primary school students in the badminton group (3.72 points)

were higher than those of the basketball group students (3.22 points). And there was a significant difference in the scores between the two groups ($P < 0.05$). In the multiple comparison of the scores of the flexibility subscale, the flexibility score of the senior primary school students in the badminton group (3.93 points) is much higher than that of the swimming group students (3.39 points) and the basketball group students' scores (3.08 points). There was an extremely significant difference in flexibility scores between the badminton group and the basketball group ($P < 0.01$), and there was a significant difference between the badminton group and the swimming group ($P < 0.05$).

Data Availability

No data were used to support this study.

Conflicts of Interest

The authors declare that they have no conflicts of interest.

References

[1] M. C. Roco, C. A. Mirkin, M. C. Hersam, and C. S. Alrokayan, "Nanotechnology research directions for societal needs in 2020: summary of international study," *Journal of Nanoparticle Research*, vol. 13, no. 3, pp. 897–919, 2011.

[2] J. S. Duhan, R. Kumar, N. Kumar, P. Kaur, K. Nehra, and S. Duhan, "Nanotechnology: the new perspective in precision agriculture," *Biotechnology Reports*, vol. 15, no. 15, pp. 11–23, 2017.

[3] C. H. Lee, B. Tiwari, D. Zhang, and Y. K. Yap, "Water purification: oil–water separation by nanotechnology and environmental concerns," *Nano*, vol. 4, no. 3, pp. 514–525, 2017.

[4] C. P. Reis and C. Damgé, "Nanotechnology as a promising strategy for alternative routes of insulin delivery," *Methods in Enzymology*, vol. 508, no. 508, pp. 271–294, 2012.

[5] C. A. Mirkin, T. J. Meade, and S. H. Petrosko, "Nanotechnology-based precision tools for the detection and treatment of cancer," *Anticancer Research*, vol. 35, no. 10, pp. 481–501, 2017.

[6] Y. Weng, J. Liu, S. Jin, W. Guo, X. Liang, and Z. Hu, "Nanotechnology-based strategies for treatment of ocular disease," *Acta Pharmaceutica Sinica B*, vol. 7, no. 3, pp. 281–291, 2017.

[7] P. Falagan-Lotsch, E. M. Grzincic, and C. J. Murphy, "New advances in nanotechnology-based diagnosis and therapeutics for breast cancer: an assessment of active-targeting inorganic nanoplatforms," *Bioconjugate Chemistry*, vol. 28, no. 1, pp. 135–152, 2017.

[8] M. Natan and E. Banin, "From nano to micro: using nanotechnology to combat microorganisms and their multidrug resistance," *FEMS Microbiology Reviews*, vol. 41, no. 3, pp. 302–322, 2017.

[9] J. Song, Y. Li, X. Guo, K. N. Shen, and X. Ju, "Making mobile health information advice persuasive: an elaboration likelihood model perspective," *Journal of Organizational and End User*, vol. 34, no. 4, pp. 1–22, 2022, Computing(forthcoming).

[10] H. Song and M. Brandt-Pearce, "A 2-D discrete-time model of physical impairments in wavelength-division multiplexing systems," *Journal of Lightwave Technology*, vol. 30, no. 5, pp. 713–726, 2012.

[11] Y. Hong, M. Wan, and Z. Li, "Understanding the health information sharing behavior of social media users," *Journal of Organizational and End User Computing (JOEUC)*, vol. 33, no. 5, pp. 180–203, 2021.

[12] G. Song, L. Cheng, Y. Chao, K. Yang, and Z. Liu, "Emerging nanotechnology and advanced materials for cancer radiation therapy," *Advanced Materials*, vol. 29, no. 32, 2017.

[13] L. B. Naves, C. Dhand, J. R. Venugopal, L. Rajamani, S. Ramakrishna, and L. Almeida, "Nanotechnology for the treatment of melanoma skin cancer," *Progress in Biomaterials*, vol. 6, no. 1-2, pp. 13–26, 2017.

[14] D. Jasinski, F. Haque, D. W. Binzel, and P. Guo, "The advancement of the emerging field of RNA nanotechnology," *ACS Nano*, vol. 11, no. 2, pp. 1142–1164, 2017.

[15] D. Lin, Y. Liu, and Y. Cui, "Reviving the lithium metal anode for high-energy batteries," *Nature Nanotechnology*, vol. 12, no. 3, pp. 194–206, 2017.

[16] P. Senellart, G. Solomon, and A. White, "High-performance semiconductor quantum-dot single-photon sources," *Nature Nanotechnology*, vol. 12, no. 11, pp. 1026–1039, 2017.

[17] E. C. Yusko, B. R. Bruhn, O. M. Eggenberger et al., "Real-time shape approximation and fingerprinting of single proteins using a nanopore," *Nature Nanotechnology*, vol. 12, no. 4, pp. 360–367, 2017.

[18] C. Y. Chen, C. M. Wang, H. H. Li, H. H. Chan, and W. S. Liao, "Wafer-scale bioactive substrate patterning by chemical lift-off lithography," *Beilstein Journal of Nanotechnology*, vol. 9, no. 1, pp. 311–320, 2018.

[19] L. Wang, M. Boutilier, P. R. Kidambi, D. Jang, N. G. Hadjiconstantinou, and R. Karnik, "Fundamental transport mechanisms, fabrication and potential applications of nanoporous atomically thin membranes," *Nature Nanotechnology*, vol. 12, no. 6, pp. 509–522, 2017.

[20] C. A. Otey, F. M. Pavalko, and K. Burridge, "An interaction between alpha-actinin and the beta 1 integrin subunit in vitro," *Journal of Cell Biology*, vol. 111, no. 2, pp. 721–729, 1990.

[21] M. Hadjidemetriou and K. Kostarelos, "Evolution of the nanoparticle corona," *Nature Nanotechnology*, vol. 12, no. 4, pp. 288–290, 2017.

[22] S. Howorka, "Building membrane nanopores," *Nature Nanotechnology*, vol. 12, no. 7, pp. 619–630, 2017.

[23] F. Pi, Z. Hui, and L. Hui, "RNA nanoparticles harboring annexin A2 aptamer can target ovarian cancer for tumor-specific doxorubicin delivery," *Nanomedicine: Nanotechnology, Biology, and Medicine*, vol. 13, no. 3, pp. 1183–1193, 2017.

Hindawi

Research Article

Design Analysis and Test Verification of Double-Layer Gradient Coating Reinforced Concrete Flexural Strength

Qiang Pei [ID],[1] **Yihan Xiang,**[1] **Shuncai Hu,**[1] **Yiwang Bao,**[2] **and Weihong Li** [ID][1]

[1]*Dalian University, College of Architectural Engineering, Dalian 116622, China*
[2]*China Academy of Building Materials Science, Beijing 100024, China*

Correspondence should be addressed to Weihong Li; liweihong@dlu.edu.cn

The residual compressive stress of concrete members can offset the tensile stress caused by some external load and hinder the generation and expansion of surface cracks to enhance the flexural strength of concrete. In order to carry out this strengthening method, the single-layer and double-layer gradient coatings mixed by sulphate aluminium cement with different amounts of expansion agent on the surface of concrete specimens were discussed, and the theoretical calculation formula of surface compressive stress caused by this was deduced. Combined with experimental data, the influence of surface compressive stress on flexural strength of concrete was studied. The results demonstrate that the greater the surface compressive stress generated in the coating, the better the effect of improving the flexural strength of concrete. To obtain sufficient surface compressive stress, it is recommended that the cross-sectional product ratio of the substrate to the coating is more than 80; the higher the elastic modulus of the coating, the greater the surface compressive stress; the smaller the shrinkage rate of the coating, the greater the surface compressive stress. The improvement effect of double-layer gradient coating on the flexural strength of concrete is better than that of single-layer coating. Compared with the reference specimen without coating, the improvement rates of double-layer gradient coating on the early and late flexural strength of concrete are 57.7% and 45.7%, respectively.

1. Introduction

Concrete has become the most widely used civil engineering materials in practical construction projects due to its high compressive strength, low cost, easy access to raw materials, and convenient construction. It plays a key role in promoting the development of social economy. With the development of science and technology, concrete buildings will gradually develop in the direction of large scale, high layers and large span in the future. However, the low flexural strength of most concrete used nowadays can lead to surface cracking of large concrete structures (such as foundation slab, wall slab, floor slab and underground structure, etc.), and even affect the safety performance and service life of concrete structures. [1–3]. Improving the flexural strength of concrete through diverse ways has become one of the

urgent problems to be solved, so it has gradually become a research hotspot of experts and scholars.

The incorporation of reinforcement with high tensile strength in concrete is one of the first measures to enhance the flexural strength of concrete structures, and the premature cracking of concrete in the tensile area limited the use of reinforced concrete components in large span or bearing power load structures. The emergence of prestressed concrete solves this problem. It uses the high compressive strength of concrete to make up for its low flexural strength and utilizes the precompression method to indirectly improve the flexural strength of concrete. In essence, it changes the crack-prone characteristics of concrete, which is very effective for saving steel, reducing the size of the structural section, reducing the weight of the structure, preventing cracking, and reducing deflection. In addition, with

the further development of research and development work, various mineral admixtures, fibers, additives, and nanophase materials, polymer has been applied by scholars to improve the flexural strength of concrete and has achieved good results. The research status is as follows:

Tolmachov et al. [4] added water reducer, mineral admixture, and fiber into concrete to increase its flexural strength by 25.7%. Singh et al. [5] found that the flexural strength of RAP concrete could be increased by 10% by adding 10% (mass fraction) silica fume. Zhang et al. [6] found that when the fly ash content was 20% (mass fraction, the same below), the flexural strength of recycled concrete could be increased by 29.9%. On this basis, the flexural strength could be further increased by 11.4% by adding 1% water reducer, while the flexural strength of concrete could be increased by 30.7% by adding 10% silica fume. Somasekharaiah [7] showed that when 10% silica fume was added to the concrete, and 1% steel fiber and 0.25% polypropylene fiber were mixed in the concrete, the strength improvement rate reached 71.5%. Mahadik et al. [8] found that different dosages (volume fraction of 0.25%~1%) of steel fiber had different degrees of improvement effect on the flexural strength of concrete, and when the dosage was 0.75%, it was the best, and the improvement rate reached 43.3%. Bhat and Alam [9] found through a large number of tests in the concrete mixed with 0.5% to 2% (volume fraction) of steel fibers can improve its flexural strength, the flexural strength of concrete at the early age became the highest when the steel fiber content was 2%. Bi et al. [10] found that the flexural strength of polypropylene fiber with a length of 18 mm and a dosage of $0.6 \, kg/m^3$ was increased by 32.3% when it was mixed with concrete.

Turlapati and Chintapalli [11] suggested that the flexural strength of polypropylene fiber with a volume fraction of 1% could be increased by 35%. Wyrzykowski et al. [12] combined expansion agent, super absorbent polymer, and shrinkage-reducing agent to make the prestress of central concrete reach about 2.5 MPa~3.0 MPa. Yang et al. [13] found that when the content of expansive agent was 6% (mass fraction), the early and late flexural strength of concrete could be enhanced by 6.2% and 4.1%, respectively. Li et al. [14] found that when the content of nanosilica was 5% (mass fraction), the flexural strength of lightweight concrete could be enhanced by 17.5%. Saafi et al. [15] incorporated 0.35% reduced graphite oxide into cement-based composites, resulting in an increase of 134% in flexural strength. Wang et al. [16] found that the flexural strength of concrete could be increased by 12% by adding 0.5% carbon nanotubes and 1.0% polyvinyl alcohol nanosecond emulsion. Liu et al. [17] added 7% acrylic acid (AA) and 1-acrylamido-2-methylpropanesulfonic acid (AMPS) polymer into concrete to increase its flexural strength by 61.2%.

However, all of the above technical ways to improve the flexural strength of concrete have limitations. The production process of prestressed concrete members is complex, the technical requirements are high, and special tension equipment and professional technical operators are needed. At the same time, the construction cost of prestressed concrete structures is large, and the engineering cost of fewer components is high. The application of mineral admixtures in concrete provides a driving force for the sustainable development of resources, and its beneficial effect on the performance of concrete is no doubt. However, industrial waste residue used as mineral admixtures is after all an industrial byproduct, so there are also some problems. For example, silica fume will aggravate the shrinkage of concrete, and fly ash and slag will reduce the initial mechanical properties of concrete. At the same time, the measures taken to stimulate the activity of mineral admixtures may lead to hidden dangers such as alkali aggregate reaction, weak resistance to sulfate attack, and poor compatibility of admixtures [18–22]. The incorporation of fiber into concrete can significantly enhance the flexural strength of concrete, while studies have shown that the incorporation of steel fiber has no obvious enhancement effect on the compressive strength of concrete, and there are also problems such as high unilateral cost and construction difficulties. Basalt fiber production process energy consumption is enormous, and process control is not easy. Ordinary glass fiber is brittle and easy to break, easy to be damaged in the mixing process, and plant fibers have problems such as elevated water absorption, poor alkali resistance, and difficult processing [23, 24]. Nanomaterials are not only expensive but also need to consider the dispersion problem in the use process, and their application in concrete needs to be further studied [25, 26]. There continue to be some deficiencies in the overall performance of polymer concrete when it is modified by a single polymer. The incorporation of chemical admixtures will lead to changes in the structural quality of polymer membranes, which will have a negative impact on concrete [27, 28].

In addition to the abovementioned prestressed concrete, another successful application of prestressed reinforcement technology is the tempered glass. The tempered glass can improve the strength of the glass by 2~5 times by forming a layer of preloading stress on the surface of the ordinary glass, and at the same time, it can improve its thermal stability and safety performance, and it has been comprehensively promoted and popularized worldwide since the beginning of the 20th century [29–31]. Both in the field of concrete and glass, prestressed reinforcement design of macroscopic structure is adopted. The compressive stress is introduced into the material or component in advance to offset the external tensile stress, so as to increase the strain of the matrix cracking due to tension, and improve the fracture strength, reliability, and durability of the material. In recent years, a prestress design of high strength and high damage tolerance composite ceramics comparable to the prestress distribution of tempered glass has produced good results [32, 33]. In fact, as long as it can be realized, this method can be applied to any brittle material, and concrete is one of the typical brittle materials, with the property of compressive and tensile resistance. Therefore, this study introduces the idea of surface prestress design into concrete. By double-layer gradient coating of sulphate aluminium cement with different expansion agents, Because of the difference shrinkage rate between Coating 1 and Coating 2, Coating 1 and concrete, the surface residual compressive stress is formed on concrete surface to offset the flexural stress

caused by external load, so as to prevent or reduce the formation and expansion of surface cracks, thereby improving the flexural strength of concrete and extending its service life. The method is simple to operate, not limited by the component size and shape, and more economical, while the substrate does not need to consider the compatibility with the new material, which has good application prospects.

2. Theoretical Analysis

The principle of prestressed concrete to enhance the flexural strength of structural members is to produce precompression stress in concrete and pretension stress in steel through the reinforcement in the tensile zone. The precompression stress can reduce or offset the tensile stress caused by the external load, so that the tensile stress of structural members is not large or even in the compression state, so as to improve the flexural strength of concrete structural members. In turn, coating the surface of the tensile zone of concrete with coating shrinkage rate less than the shrinkage rate of the substrate will produce precompression stress on the surface of the concrete and produce a balanced pretension stress inside the concrete, which is the same as the principle of improving the flexural strength of prestressed concrete. Only one of the precompression stresses is generated inside the concrete, and one is generated on the surface of the concrete. If a double-layer gradient coating with different shrinkage rates is applied on the concrete surface, the second coating (coating 2) shrinkage rate < the first coating (coating 1) shrinkage rate, the surface residual compressive stress in both coating 1 and coating 2, the double-layer gradient coating, which can further enhance the flexural strength of the concrete. The residual stress distribution diagram of prestressed concrete, single-layer coated concrete, and double-layer gradient-coated concrete is shown in Figure 1.

To determine the feasibility of this idea, this paper first derived the theoretical calculation formula of the surface compressive stress generated by applying double-layer gradient coating, assuming the contraction ratio of coating 1 and coating 2 is α_{c1} with α_{c2}, and the shrinkage rate of concrete substrate is α_s, the cross-sectional diagram of the length direction of the test piece before and after the coating is shown in Figure 2. Assuming that no constraint exists in the ideal free shrinkage case, the shrinkage of coating and substrate is shown in the dashed line section of Figure 2, and the shrinkage rate of coating 1, coating 2, and substrate can be indicated by formula (1), (2) and (3).

$$\alpha_{c1} = \frac{\delta_{11}}{L}, \tag{1}$$

$$\alpha_{c2} = \frac{\delta_{12}}{L}, \tag{2}$$

$$\alpha_s = \frac{\delta_2}{L}. \tag{3}$$

In the formula, the amount of free contraction of the coating 1 and the coating 2 is δ_{11} and δ_{12}, δ_2 is the length direction of the substrate, and L is the initial length of the sample. In fact, because the tight binding of the interface has deformed the coating identical to the substrate, assuming that the overall amount of cooperative deformation of the composite sample is δ, and the overall shrinkage rate is $\bar{\alpha}$:

$$\bar{\alpha} = \frac{\delta}{L}. \tag{4}$$

The residual stress in the coating and the substrate is balanced, assuming the surface compressive stress in the coating 1 and the coating 2 are σ_{c1} and σ_{c2}, the tensile stress in the substrate to balance the surface compressive stress is σ_s, under the action of stress, the linear deformations of coating 1 and coating 2 are d_{11} and d_{12}, the linear deformation of the substrate is d_2. According to the relationship between stress and strain, formulas (5), (6), and (7) can be obtained:

$$d_{11} = \frac{\sigma_{c1}}{E_{c1}} \times L. \tag{5}$$

$$d_{12} = \frac{\sigma_{c2}}{E_{c2}} \times L. \tag{6}$$

$$d_2 = \frac{\sigma_s}{E_s} \times L. \tag{7}$$

The elastic modulus of the coating 1 and the coating 2 is E_{c1} and E_{c2}, respectively, E_s is the elastic modulus of the substrate, which is known or tested. To facilitate derivation and analysis, assuming the cross-section area of the coating 1 and the coating 2 is equal, known from the substrate tensile stress and the coating compressive stress in the cross section:

$$\sigma_{c1} S_c + \sigma_{c2} S_c = -\sigma_s S_s. \tag{8}$$

From Figure 2, d_{11}, d_{12}, δ_{11}, δ_{12}, and δ_2 has the following geometric relationship:

$$d_{11} = \delta - \delta_{11}, \tag{9}$$

$$d_{12} = \delta - \delta_{12}, \tag{10}$$

$$d_2 = \delta_2 - \delta. \tag{11}$$

Combined with formula (3), (4), (7), (8) and (11) can get formula (12):

$$\sigma_{c1} + \sigma_{c2} = \left(\frac{S_s}{S_c}\right) \cdot E_s \cdot (\alpha_s - \bar{\alpha}). \tag{12}$$

It can be seen by formula (12) that the surface compressive stress is not a material constant, and it is related to the cross-sectional product ratio of the coating to the substrate. In order to more intuitively evaluate the surface compressive stress of various shapes and dimensions, it is best to use the material constant instead of the unknown quantity, and the extraordinary parameters can be expressed in combination with the

(a)

(b)

(c)
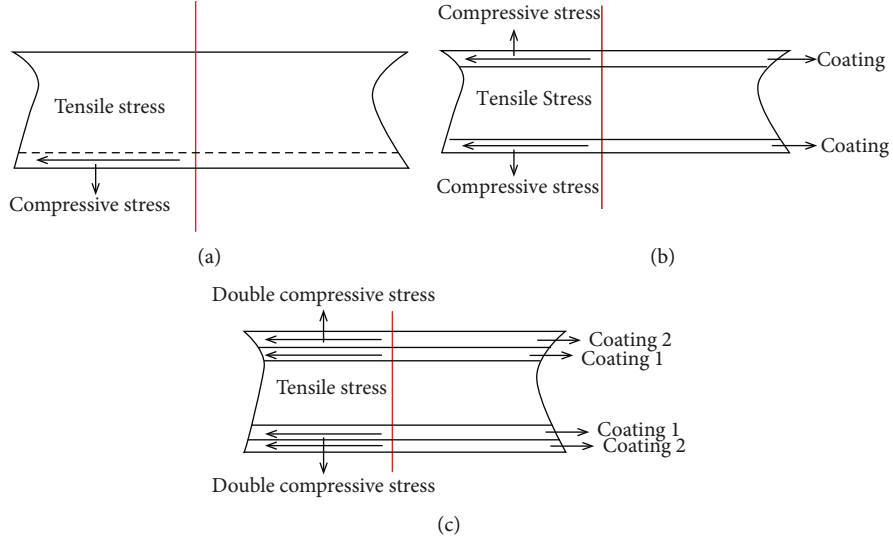
FIGURE 1: Residual stress distribution diagram of prestressed concrete (a), single-layer coating concrete (b), and double-layer gradient coating concrete (c).
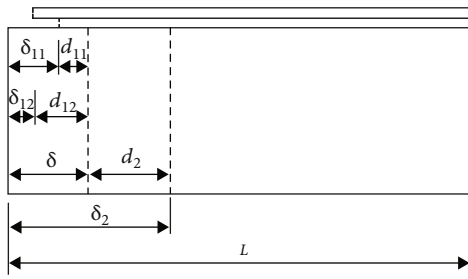
FIGURE 2: Cross-sectional diagram of coating specimen.

FIGURE 4: Theoretical relationship between surface compressive stress and cross-sectional area ratio under four shrinkage ratios.

TABLE 1: Chemical composition of cement and expansion.

Material	CaO	SiO$_2$	Al$_2$O$_3$	SO$_3$	Fe$_2$O$_3$	MgO
P·O42.5R	56.78	22.61	7.01	1.94	2.89	3.73
SAC42.5	49.50	8.51	20.17	14.91	1.97	0.77
HME®-IV	52.56	1.03	13.61	28.33	0.66	1.81

FIGURE 3: Theoretical relationship between surface compressive stress and cross-sectional area ratio under four modulus ratios.

above formula:

$$\bar{\alpha} = \frac{[E_{c1}\alpha_{c1} + E_{c2}\alpha_{c2} + E_s \cdot \alpha_s \cdot (S_s/S_c)]}{[E_{c1} + E_{c2} + E_s \cdot (S_s/S_c)]}. \tag{13}$$

Combining equation (12) and equation (13), the calculation formula of surface compressive stress caused by double-

TABLE 2: Performance indicators of the expansion agent.

| Inspection item | Fineness | | Limited expansion Rate (%) | | Compressive strength (MPa) | |
	Sieve residue (1.18 mm) (%)	Specific surface area (m²·kg⁻¹)	In water (7d)	In air (21d)	7d	28d
Performance indicator	0	390	0.102	0.034	40.0	53.4

TABLE 3: Mixture ratio of coating and substrate.

| Sample no. | Mixture ratio of substrate (kg·m⁻³) | | | | Mixture ratio of coating (%) | |
	C	W	S	G	SAC42.5	HME®-IV
Control	350	190	648	1177	/	/
SC -0%	350	190	648	1177	100%	0%
SC -6%	350	190	648	1177	94%	6%
SC -10%	350	190	648	1177	90%	10%
DC-0%-10%	350	190	648	1177	Coating 1: 100% Coating 2: 90%	Coating 1: 0% Coating 2 : 10%

layer gradient coating can be obtained:

$$\sigma_{c1} + \sigma_{c2} = \left(\frac{S_s}{S_c}\right) \cdot E_s \cdot \alpha_s \left\{ 1 - \left[\frac{E_{c1}\alpha_{c1}}{E_s\alpha_s} + \frac{E_{c2}\alpha_{c2}}{E_s\alpha_s} + \frac{S_s}{S_c}\right] / \left[\frac{E_{c1}}{E_s} + \frac{E_{c2}}{E_s} + \frac{S_s}{S_c}\right] \right\}.$$

(14)

Similarly, the formula for the surface compressive stress generated by a single-layer coating can be deduced as described above:

$$\sigma_c = \left(\frac{S_s}{S_c}\right) \cdot \left\{ 1 - \left[\frac{E_s S_s}{E_c S_c} + \frac{\alpha_c}{\alpha_s}\right] / \left[1 + \frac{E_s S_s}{E_c S_c}\right] \right\} E_s \cdot \alpha_s.$$

(15)

In the formula, σ_s is the tensile stress generated in the substrate and balanced with the surface compressive stress, S_c and S_s are the cross-sectional areas of coating and substrate, respectively. E_c and E_s are the elastic modulus of coating and substrate, respectively, α_c and α_s are the shrinkage of coating and substrate, respectively.

It can be seen from formula (14) that the magnitude of the surface compressive stress in the double-layer gradient coating is closely related to the cross-sectional area ratio, elastic modulus ratio and shrinkage ratio between the coating and the substrate. Therefore, the magnitude of surface compressive stress can be adjusted by these parameters to achieve the effect of optimal design. In this paper, the cross-sectional product of the concrete substrate has been determined, and its shrinkage rate and elastic modulus are also a fixed value (Obtained $\alpha_s = 330 \times 10 - 6$, $E_s = 28.1$ GPa through test), allowing qualitative analysis of surface compressive stress generated in double-layer gradient coating based on formula (14).

First, the elastic modulus value and contraction rate value of coating 1 are taken as the invariants, and when the shrinkage and elastic modulus of coating 2 are variables,
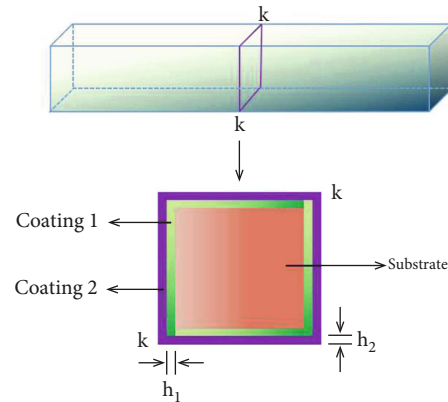
FIGURE 5: Schematic of the double-coated specimen.

the variation trend of the surface compressive stress generated in the double-layer gradient coating with the ratio of the cross-sectional area of the substrate to the coating is analyzed. It is assumed that the shrinkage ratios of coating 1 and coating 2 to substrate ($\alpha_{c1}/\alpha_s = 0.6$, $\alpha_{c2}/\alpha_s = 0.3$) are both fixed values. When the elastic modulus ratio of coating 1 to substrate is $E_{c1}/E_s = 0.6$, and the elastic modulus ratio of coating 2 to substrate is $E_{c2}/E_s = 0.6⊠ 0.9⊠ 1.2⊠ 1.5$, respectively, the variation trend of surface compressive stress in the double-layer gradient coating with the cross-sectional area ratio of substrate to coating is shown in Figure 3. It is assumed that the elastic modulus ratio of coating 1 and coating 2 to substrate ($E_{c1}/E_s = 0.8$, $E_{c2}/E_s = 0.5$) is a fixed value. When the shrinkage ratio of coating 1 to substrate is $\alpha_{c1}/\alpha_s = 0.6$, and the shrinkage ratio of coating 2 to substrate is $\alpha_{c2}/\alpha_s = 0.2, 0.3, 0.4, 0.5$, respectively, the variation trend of the surface compressive stress generated in the double-layer gradient coating with the cross-sectional area ratio of the substrate to the coating is shown in Figure 4.

Preparation of substrate ⟶ Preparation completed demoulding after 24h ⟶ Preparation of coating

Spraying coatings ⟶ Spraying completed ⟶ Smoothing completed
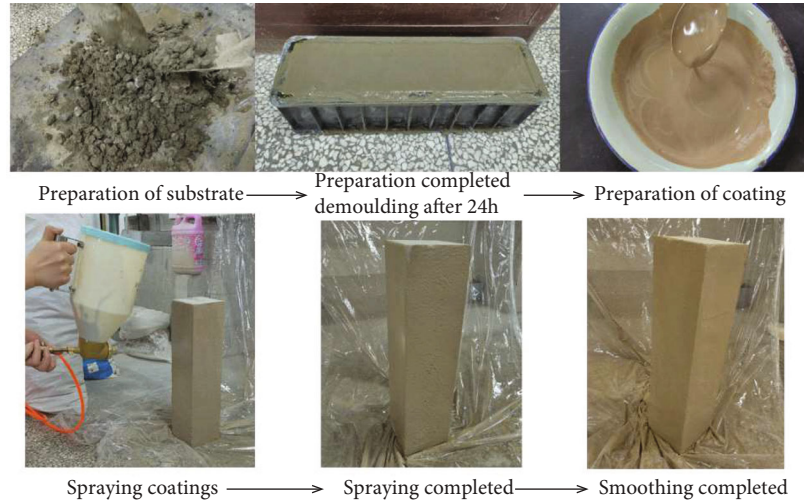
FIGURE 6: Preparation process of coated concrete specimen.

As shown from Figure 3, when the elastic modulus of the coating 2 is a single variable, the surface compressive stress $(\sigma_{c1} + \sigma_{c2})$ increases with the increase of E_{c2}/E_s; according to Figure 4, when the shrinkage rate of the coating 2 is a single variable, the surface compressive stress $(\sigma_{c1} + \sigma_{c2})$ decreases with the increase of α_{c2}/α_s; Figures 3 and 4 show that the surface compressive stress $(\sigma_{c1} + \sigma_{c2})$ increases first with the increase of S_s/S_c, and plateaus after $S_s/S_c > 80$. Similarly, when the elastic modulus value of the coating 2 is taken as invariants, and the shrinkage rate value and the elastic modulus value of the coating 1 are the variables, the trend of surface compressive stress changes with the cross-sectional area ratio value of the substrate and the coating, which is completely consistent with the above.

Considering the above analysis: (1) on the premise of coating 2 shrinkage < coating 1 shrinkage < substrate shrinkage, the smaller the shrinkage of coating 1 and coating 2, the greater the surface compressive stress. (2) The higher the elastic modulus of coating 1 and coating 2, the greater the surface compressive stress. (3) In order to obtain enough surface compressive stress, it is suggested that $S_s/S_c > 80$.

3. Experiment

3.1. Materials. According to the above theoretical analysis, it can be seen that the shrinkage rate of coating 2 < that of coating 1 < that of substrate is the prerequisite for the generation of surface compressive stress, and the concrete will contract during the hardening process. Therefore, in this study, the slightly expanded sulphoaluminate cement was selected as the main component of the coating material, and the shrinkage rate of the coating material was adjusted by adding different amounts of concrete efficient expansion agent, so as to ensure the smooth generation of surface compressive stress.

Ordinary Portland cement (P·O42.5R) and sulphate aluminate cement (SAC42.5) were selected as cement in the concrete substrate and coating, respectively. Fine aggregate in substrate was medium sand with fineness modulus M_x

FIGURE 7: Flexural strength test.

FIGURE 8: Elastic modulus test of coating.
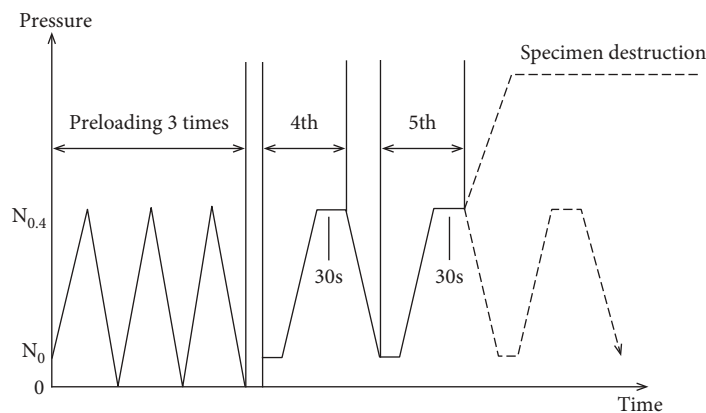
FIGURE 9: Schematic diagram of the loading method of the coating elastic modulus.

= 2.82, and the coarse aggregate was stone with continuous gradation of 5~30 mm in particle size. Calcium oxide-calcium thialuminite compound expansion agent (HME®-IV) was used for the expansion agent, and water was laboratory tap water. The chemical composition of the cement and the expansion agent is shown in Table 1, and the performance indicators of the expansion agent are shown in Table 2.

3.2. Design of Coating and Substrate. In order to facilitate the test of the shrinkage rate and elastic modulus of the coating material, the low content of expansion agent and sulphate aluminate cement was selected as the coating in this experiment, and five groups of test schemes were designed. Among them, the blank test group without coating had a total of one group; the single-layer coating consisted of three groups, which were composed of sulphate aluminate cement and 0%, 6%, and 10% expansion agent, respectively. There was a group of double-layer gradient coating, the first layer and the second layer were the substrate of sulphate aluminate cement and expansion agent with the contents of 0% and 10%, respectively, so that the shrinkage difference between the two layers reaches the maximum. The water-cement ratio of the coating is 0.5, and the mixture ratio of the reference specimen without the coating and the substrate with the coating were consistent. The mixture ratio of the coating and the substrate is given in Table 3.

3.3. Methods

3.3.1. Preparation of Coated Concrete Test Specimens. After the concrete substrate was poured, solid, and flattened, it shall be covered with plastic film and placed in the room with an ambient temperature of $(20 \pm 1)°C$. After 24 h, the concrete surface shall be cleaned and moistened with a wet rag. The prepared coating was evenly sprayed on the concrete surface (four faces in the length direction) and smoothed with a scraper. Double-layer gradient coating sprays the second coating immediately after spraying the first coating and smoothing with a scraper, and the test schematic diagram is shown in Figure 5, where k is a cross-section, h_1 for the thickness of the first coating, and h_2 for the

FIGURE 10: Elastic modulus test of substrate.

thickness of the second coating. The specific preparation process of coated concrete specimen is shown in Figure 6.

3.3.2. Flexural Strength Test. The prepared specimens were cured to 7d and 28d at $(60 \pm 5)%$ relative humidity and $(20 \pm 1)°C$, and then, according to GB/T 50081-2019 guidelines, the specimens of size $100\,mm \times 100\,mm \times 400\,mm$ were tested for measuring flexural strength by universal testing machine (Figure 7), and the controlled loading rate was 0.05 MPa/s. Take the average value of the flexural strength test results of a group of 3 specimens as the test result.

3.3.3. Coating and Substrate Shrinkage Rate Test. According to JC/T 313-2009 guidelines, the specimen size of 25 mm × 25 mm × 280 mm was tested for measuring shrinkage rate of the coating by JH-320 alkali aggregate specific length meter. Specimen size of $100\,mm \times 100\,mm \times 515\,mm$ was tested for measuring shrinkage rate of the concrete by HSP-540 shrinkage apparatus as per GB/T 50082-2009 guidelines. After the molding of the specimen, the initial length was measured after the curing condition of 1d under the above discount strength test, the specimen length changes after curing to 28d to calculate the shrinkage rate of 28d age, and the shrinkage rate of the coating and
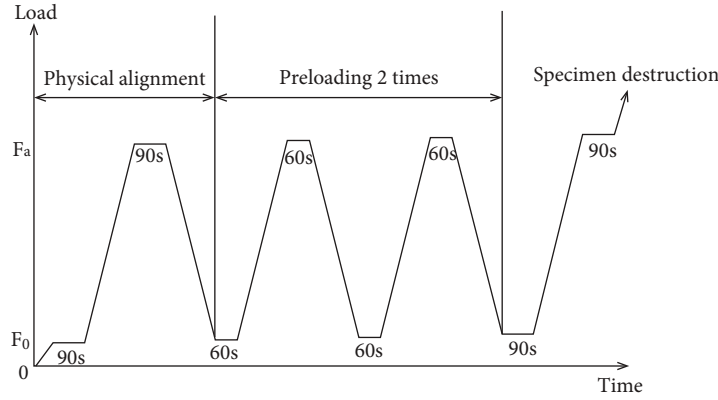
FIGURE 11: Schematic diagram of the loading method of the substrate elastic modulus.

TABLE 4: Test results of shrinkage rate and elastic modulus of coating and concrete.

Sample no.	S_s/mm^2	S_c/mm^2	$\alpha_s/\%$	$\alpha_c/\%$	E_s/MPa	E_c/MPa
SC-0%	10000	100	-0.330	0.020	2.81×10^4	1.80×10^4
SC-6%	10000	100	-0.330	0.056	2.81×10^4	2.00×10^4
SC-10%	10000	100	-0.330	0.081	2.81×10^4	1.75×10^4
Sample no.	S_s/mm^2	S_c/mm^2	$\alpha_s/\%$	$\alpha_{c1}|\alpha_{c2}/\%$	E_s/MPa	$E_{c1}|E_{c2}/MPa$
DC-0%-10%	10000	100	-0.330	0.020|0.081	2.83×10^4	18000|17500

substrate was calculated as the formula:

$$S_{28} = \frac{(L_{28} - L_1)}{L_0} \times 100\%. \tag{16}$$

In formula, S_{28} indicates the shrinkage rate of 28d (positive expansion and negative contraction); L_{28} is the length of 28d, mm; L_1 is the initial length of the specimen, mm; L_0 is the effective length of the specimen (coating specimen 250, substrate specimen 485), mm. Take the average value of the shrinkage rate test results of a group of 3 specimens as the test result.

3.3.4. Coating and Substrate Elastic Modulus Test. In order to calculate the theoretical value of surface residual compressive stress generated in the coating, the elastic modulus of the coating and the concrete substrate at the age of 28d were tested by the dial indicator method. Specimen size of 70.7 mm × 70.7 mm × 220 mm was tested for measuring elastic modulus of the coating by TM-3 mortar elastic modulus tester as per JGJ/T70-2009 guidelines (Figure 8), and the loading speed was set to 0.5 kN/s. The schematic diagram of the loading method is shown in Figure 9, N_0 is the initial load at a stress of 0.3 MPa and $N_{0.4}$ is the pressure at 40% of the axial compressive strength.

Specimen size of 150 mm × 150 mm × 300 mm was tested for measuring elastic modulus of the concrete substrate by TM-2 concrete elastic modulus tester as per GB/T 50081-2019 guidelines (Figure 10), and the loading speed was set to 0.3 MPa/s. The schematic diagram of the loading method is shown in Figure 11, F_0 is the initial load with a stress of 0.5 MPa, and F_a is the load at 1/3 axial compressive strength. Take the average value of the elastic modulus test results of a group of 3 specimens as the test result.

3.3.5. Microscopic Test. The interface morphology and microstructure between coating and substrate were observed by JSM-6360LV scanning electron microscope. The sample preparation steps were as follows: after the flexural strength test of the specimen, a small sample was cut at the section of the specimen to be tested and then immersed in anhydrous ethanol solution for 24 h to stop the hydration reaction; finally, the test sample was placed in a 100°C oven for drying for 12 h. The surface of the sample to be tested needs to be sprayed with gold for 30 min before using scanning electron microscope to observe the sample, so as to increase the conductivity of the sample and make the observation of the interface microstructure clearer.

4. Results and Discussion

4.1. Theoretical Value Calculation of Surface Compressive Stress. According to the qualitative analysis in Section 2, the thickness of the coating should be less than 1.25 mm. Therefore, the thickness h of the single-layer coating and the thickness h_1 and h_2 of the double-layer gradient coating were both set to 1 mm in the test of this study, that was, the cross-sectional area ratio of coating to substrate remained unchanged. In order to verify that the surface compressive stress of the gradient coating is greater than that of the change of coating shrinkage rate and elastic modulus, the shrinkage rate and elastic modulus were tested (Table 4), and the theoretical values of the surface compressive stress

TABLE 5: Theoretical values of the surface compressive stress in the coating.

Sample no.	S_s/S_c	E_s/E_c	α_c/α_s	E_s/MPa	$|\alpha_s|$/%	σ_c/MPa
SC-0%	100	1.56	-0.61	2.81×10^4	0.330	9.48
SC-6%	100	1.41	-1.70	2.81×10^4	0.330	17.67
SC-10%	100	1.61	-2.45	2.81×10^4	0.330	19.83
Sample no.	S_s/S_c	$E_{c1}/E_s|E_{c2}/E_s$	$\alpha_{c1}/\alpha_s|\alpha_{c2}/\alpha_s$	E_s/MPa	$|\alpha_s|$/%	$\sigma_{c1}+\sigma_{c2}$ /MPa
DC-0%-10%	100	0.64|0.62	-0.61|-2.45	2.83×10^4	0.330	29.02

Note: When the surface compressive stress is calculated, the shrinkage of the substrate is absolute value.
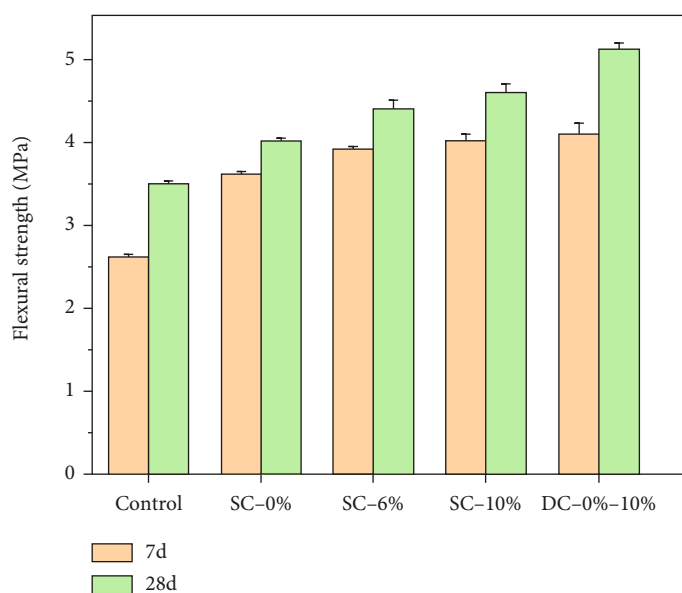
FIGURE 12: Flexural strength of uncoated specimens and coated specimens.

were calculated based on Equations (14) and (15), respectively. The calculation results are shown in Table 5.

According to Table 4, the shrinkage rate of all coating materials is positive and still expanding at 28d, while the concrete substrate is shrinking, and the shrinkage rate is coating 2 < coating 1 shrinkage rate, which shows that the coatings used in the test meet the prerequisite conditions for generating surface compressive stress.

The SC-0% group is the single-layer coating group without expansion agent in the coating, and the DC-0%-10% group is the double-layer gradient coating group with 10% expansion agent content on the basis of SC-0% group. It can be seen from Table 5, the surface compressive stress in the coating of DC-0%-10% group is 29.02 MPa, the surface compressive stress is increased by 206.1% compared with the SC-0% group. The coating of SC-10% in the single-layer coating group was the same as that of coating 2 in the double-layer gradient coating group, and the surface compressive stress in the coating of DC-0%-10% group was still higher than that of SC-10% group by 9.19 MPa. In the three single-layer coating groups, with the increase of the content of expansion agent in the coating from 0% to 10%, the shrinkage rate of the coating showed a downward
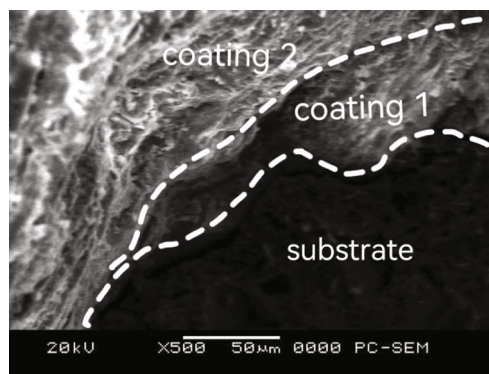
FIGURE 13: Interface morphology between coating and substrate.

trend, while the elastic modulus of the coating changed little, and the surface compressive stress in the coating increased.

The above analysis shows the following. (1) The surface compressive stress generated by the double-layer gradient coating group is significantly higher than that generated by the single-layer coating group, which also verifies the conclusion of the theoretical derivation of the double surface

(a)

(b)
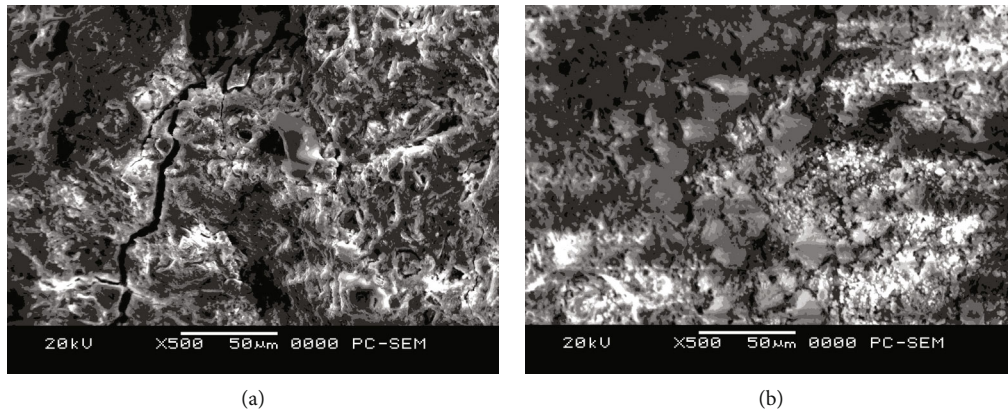
Figure 14: Internal morphology of substrate at interface between uncoated specimen (a) and coated specimen (b).

compressive stress in Section 2. (2) When the cross-sectional area ratio of the coating to the substrate is a fixed value and the elastic modulus ratio changes little, with the decrease of the coating shrinkage, the surface compressive stress in the coating increases, which is consistent with the conclusion obtained in the qualitative analysis.

4.2. Experimental Verification of Improving Flexural Strength of Concrete. To further verify the improvement effect of the double-layer gradient coating on the flexural strength of concrete than the single-layer coating and to study the influence of the surface compressive stress on the flexural strength of concrete, the 7d and 28d flexural strength of uncoated and coated specimens were tested. The test results are shown in Figure 12.

It can be seen from Figure 12 that compared with the reference specimen without coating, whether single-layer coating or double-layer gradient coating can improve the 7d and 28d flexural strength of concrete, even the lowest group of 7d flexural strength in the coated specimen (SC-0%) also reached the 28d flexural strength of the reference specimen without coating (Control).

The effect of surface compressive stress on the early flexural strength of concrete was better than that on the later flexural strength. In the single-layer coating group, 7d and 28d flexural strength of concrete specimens increases with the increase of expansion agent content in the coating. The 7d and 28d flexural strength improvement rates of SC-0% group were 38.5% and 14.3%, respectively, the improvement rates of 7d and 28d flexural strength in SC-6% group were 50.0% and 25.7%, respectively, and the 7d and 28d flexural strength improvement rates of SC-10% group were 53.8% and 31.4%, respectively. The flexural strength of double-layer gradient coating group (DC-0%-10%) was better than that of the other three single-layer coating groups. The early and late flexural strength was 4.1 MPa and 5.1 MPa, respectively, and the strength improvement rate was 57.7% and 45.7%. This shows that the method proposed in this study to produce double surface compressive stress by coating double-layer gradient coating on the surface of concrete is feasible and effective for improving the flexural strength at early and late stages.

Combined with the theoretical values of surface compressive stress in Section 4.1 and the test results of flexural strength in this section, it can be found that the compressive stress on the surface of concrete and the improvement effect on the flexural strength of concrete with coated double-layer gradient coating are greater than those with coated single-layer coating. In the single-layer coating group, under the premise of small changes in the elastic modulus of the coating, with the increase of the content of expansion agent in the coating, the shrinkage rate of the coating decreases, and the surface compressive stress generated in the coating increases. The improvement effect on the flexural strength of concrete is also becoming more and more obvious. It can be seen that the greater the surface compressive stress generated in the coating, the better the effect of improving the flexural strength of concrete.

4.3. SEM Microanalysis. Good adhesion between the coating and the concrete substrate is the premise of the surface residual compressive stress, and it is also the key to the overall and common stress of the concrete components after coating. Figure 13 shows the micromorphology of the interface between the double-layer coating and the concrete substrate at the age of 28d. It can be observed from the figure that the boundary between the coating and the substrate is obvious and closely integrated, indicating that the cement slurry with expansion agent as the coating can better bond with the concrete substrate and further generate surface residual compressive stress.

Figure 14 shows the SEM comparison results of the concrete substrate at the interface between the double-layer gradient coating and the uncoated specimen at the age of 28d. Figure 14(a) shows that there are obvious cracks in the substrate of uncoated concrete, and the overall structure is uneven and irregular; compared with the uncoated specimen, the overall structure of the double-layer coated concrete substrate in Figure 14(b) is dense, and the internal cracks are significantly reduced.

This phenomenon may be due to the coating increases the wettability of the substrate surface and improves the water-cement ratio between the coating and the substrate, which promotes the hydration of the interface cement. At

the same time, the expansion agent reacts to generate a large number of AFt crystals that are interwoven to fill and cut off the capillary pores, so that the large pores are reduced and the total porosity is reduced, thereby improving the compactness of the microstructure at the interface [34]. The improvement of the pore structure at the interface by the coating reduces the overall moisture loss of the specimen, thereby reducing the shrinkage stress caused by the moisture loss of the pores, which is conducive to reducing the shrinkage cracking of concrete. In addition, the in-plane compressive stress of the surface itself is compressed and densified, which hinders the expansion of surface microcracks, and can improve the flexural strength of concrete [2].

The above microscopic analysis results show that the improvement effect of low shrinkage coating on the flexural strength of concrete is due to the fact that the generated surface compressive stress reduces the tensile stress caused by the external load and inhibits the generation and propagation of surface cracks. On the other hand, it is due to the improvement effect of coating on the structure of the interfacial transition zone.

5. Conclusions

(1) The theoretical analysis of double-layer gradient coating enhancing concrete flexural strength shows that the size of the surface compressive stress is related to the cross-section product ratio, elastic modulus ratio, and shrinkage rate ratio of the substrate and the coating, so through these parameters, the size of the surface compressive stress can be adjusted to achieve the optimal design effect. When the parameters of the substrate are unchanged, the higher the elastic modulus of the coating, the greater the surface compressive stress; the smaller the shrinkage of the coating, the greater the surface compressive stress; when the cross-sectional area ratio of substrate to coating is more than 80, the surface compressive stress is larger

(2) Coated on the concrete surface by double-layer gradient coating, the first layer is pure sulfate cement mixed with 10% expansion agent, Because the shrinkage rate of Coating 1 is between that of concrete and Coating 2, surface compressive stresses are formed between Coating 1 and Coating 2, and between Coating 1 and concrete, respectively, during the curing process. which effectively improves the early and later fracture strength by 77.7% and 45.7%, respectively, compared with the uncoated reference test

(3) By combining the theoretical value of surface compressive stress of the coating test and the flexural strength test results, it was found that the double-layer gradient coating test produces more surface compressive stress and higher flexural strength than the single-layer coating test; the smaller the shrinkage rate of the coating, the greater the surface com-

pressive stress, the higher the flexural strength. It can be shown that the greater the surface compressive stress generated in the coating, the better the improvement effect of the concrete flexural strength

(4) SEM test results show that the coating mixed with expansion agent and cement can be safely and stably attached to the concrete substrate. The coating can improve the density of the interface with the substrate and hinder the formation and propagation of surface cracks

The strengthening method adopted in this study can provide a new idea for improving the flexural strength of cement-based materials, but there are still some problems that need further study, mainly including the following:

(1) The more specific relationship between the ratio of different cross-sectional area, elastic modulus ratio and shrinkage ratio, and the flexural strength of specimens is taken as the focus of future research

(2) In the future research, various types of coatings can be selected for further study to further increase the effect of surface residual compressive stress on the flexural strength of concrete

(3) In the future research, the coating can be coated by machine, which can reduce the deviation of the test results caused by manual operation

Data Availability

Data sharing is not applicable to this article as no new data were created or analyzed in this study.

Conflicts of Interest

The authors declare that they have no conflicts of interest.

Acknowledgments

References

[1] L. H. Zhang, M. H. Tan, Y. P. Ma, and K. R. Wu, "Study on properties of bonding and shrinkage cracking of PP fiber cement [J]," *Building Materials Journal*, vol. 1, pp. 17–21, 2001.

[2] J. S. Qian, D. Qiao, L. Shi, Y. D. Dang, and Z. Wang, "Influence of external coating on concrete properties and mechanism of action [J]," *Journal of the Chinese Ceramic Society*, vol. 37, no. 12, pp. 2090–2096, 2009.

[3] C. J. Shi, A. Jiménez, A. F. Palomo, and A. Palomo, "New cements for the 21st century: the pursuit of an alternative to

Portland cement [J]," *Cement and Concrete Research*, vol. 41, no. 7, pp. 750–763, 2011.

[4] S. Tolmachov, O. Belichenko, D. Zakharov, G. Vatulia, A. Plugin⊠, and O. Darenskyi, "Influence of additives on flexural strength of concrete," *MATEC Web of Conferences*, vol. 116, article 01019, 2017.

[5] S. Singh, G. D. Ransinchung, and P. Kumar, "Effect of mineral admixtures on fresh, mechanical and durability properties of RAP inclusive concrete," *Construction and Building Materials*, vol. 156, pp. 19–27, 2017.

[6] M. M. Zhang, S. L. Wang, S. M. Zhang, and B. Zhang, "Effect of mineral admixtures on mechanical properties of recycled concrete [J]," *Bulletin of the Chinese Ceramic Society*, vol. 36, no. 5, pp. 1505–1511, 2017.

[7] S. H. M. Adanagouda and H. M. Somasekharaiah, "Strength and durability studies on hybrid fiber reinforced high-performance concrete for silica fume based mineral admixture," *IOP Conference Series: Earth and Environmental Science*, vol. 822, no. 1, article 012041, p. 012041, 2021.

[8] S. A. Mahadik, S. K. Kamane, and A. C. Lande, "Effect of steel fibers on compressive and flexural strength of concrete [J]," *International Journal of Advanced Structures and Geotechnical Engineering*, vol. 3, no. 4, pp. 388–392, 2014.

[9] A. A. Bhat and S. Alam, "Impact of steel fiber on the mechanical property of concrete containing mineral admixture," *IOP Conference Series: Earth and Environmental Science*, vol. 889, no. 1, article 012004, 2021(8pp).

[10] J. Bi, Y. C. Zhang, W. W. Chen, W. Liu, and L. Y. Xiong, "Study on the effect of polypropylene fiber on mechanical performance of concrete [J]," *Bulletin of the Chinese Ceramic Society*, vol. 34, no. 6, pp. 1694–1699, 2015.

[11] V. Turlapati and V. Chintapalli, "A comparative study on performance of synthetic and natural fibers on compressive and flexural strength of concrete," *Advanced Engineering Forum*, vol. 36, pp. 97–113, 2020.

[12] M. Wyrzykowski, G. Terrasi, and P. Lura, "Expansive high-performance concrete for chemical-prestress applications," *Cement and Concrete Research*, vol. 107, pp. 275–283, 2018.

[13] Y. L. Yang, Q. Y. Ma, H. Q. Fei, Y. Y. Zhang, and J. S. Zhang, "Test and analysis of the influence of moisture content and expansion agent on the fold resistance of ready-mixed compensation shrinkage concrete [J]," *Concrete*, vol. 2, pp. 128–131, 2015.

[14] R. Li, D. Z. Wang, and Y. F. Meng, "Study on mechanical properties of fly ash ceramsite concrete reinforced by mineral admixtures [J]," *Bulletin of Science and Technology*, vol. 32, no. 2, pp. 92–95+99, 2016.

[15] M. Saafi, L. Tang, J. Fung, M. Rahman, and J. Liggat, "Enhanced properties of graphene/fly ash geopolymeric composite cement," *Cement and Concrete Research*, vol. 67, pp. 292–299, 2015.

[16] Z. K. Wang, J. Fan, and G. Y. Li, "Effect of carbon nanotubes/polyvinyl alcohol on mechanical properties and drying shrinkage of concrete [J]," *Journal of the Chinese Ceramic Society*, vol. 48, no. 10, pp. 1653–1658, 2020.

[17] Q. Liu, Z. Lu, X. Liang, R. Liang, Z. Li, and G. Sun, "High flexural strength and durability of concrete reinforced by _in situ_ polymerization of acrylic acid and 1-acrylanmido-2-methyl-propanesulfonic acid," *Construction and Building Materials*, vol. 292, p. 123428, 2021.

[18] Y. M. Chen, X. Y. He, Y. X. Li, and Y. Su, "Research progress and existing problems of mineral admixtures [J]," *Materials Reports*, vol. 8, pp. 28–31, 2006.

[19] G. A. Rao, "Long-term drying shrinkage of mortar – influence of silica fume and size of fine aggregate," *Cement and Concrete Research*, vol. 31, no. 2, pp. 171–175, 2001.

[20] M. S. Meddah, M. A. Ismail, S. El-Gamal, and H. Fitriani, "Performances evaluation of binary concrete designed with silica fume and metakaolin," *Construction and Building Materials*, vol. 166, pp. 400–412, 2018.

[21] S. A. Kagadgar, S. Saha, and C. Rajasekaran, "Mechanical and durability properties of fly ash based concrete exposed to marine environment," *Selected Scientific Papers—Journal of Civil Engineering*, vol. 12, no. 1, pp. 7–18, 2017.

[22] Y. Shi, J. H. Zhu, D. L. He, X. D. Luo, and T. Wu, "Effect of mineral admixtures on mechanical properties and cracking trend of concrete [J]," *Journal of the Chinese Ceramic Society*, vol. 47, no. 11, pp. 1605–1610, 2019.

[23] M. Bai, D. T. Niu, L. Jiang, and Y. Y. Miao, "Study on improving mechanical properties and microstructure of concrete with steel fiber [J]," *Bulletin of the Chinese Ceramic Society*, vol. 32, no. 10, pp. 2084–2089, 2013.

[24] F. Yi, "Research progress of plant fiber concrete [J]," *Construction Materials & Decoration*, vol. 34, pp. 125-126, 2017.

[25] J. X. Wang and L. J. Wang, "Research progress on the application of nanomaterials in concrete [J]," *Concrete*, vol. 11, pp. 18–21, 2004.

[26] Z. Y. Xie, H. Zhou, Q. C. Li, and D. X. Li, "Research progress in preparation of nano-silica sol and its application in cement-based materials [J]," *Materials Reports*, vol. 34, no. S2, pp. 1160–1163, 2020.

[27] P. M. Wang, G. R. Zhao, and G. F. Zhang, "Mechanism of redispersable emulsion powder in cement mortar [J]," *Journal of the Chinese Ceramic Society*, vol. 46, no. 2, pp. 256–262, 2018.

[28] K. Li, Z. Q. Wei, H. X. Qiao, C. G. Lu, and J. Guo, "Research progress on the effect of four kinds of admixtures on the properties of polymer modified cement-based materials [J]," *Materials Reports*, vol. 35, no. S1, pp. 654–661, 2021.

[29] D. J. Green, R. Tandon, and V. M. Sglavo, "Crack arrest and multiple cracking in glass through the use of designed residual stress profiles," *Science*, vol. 283, no. 5406, pp. 1295–1297, 1999.

[30] L. Wondraczek, J. C. Mauro, J. Eckert et al., "Towards ultra-strong glasses," *Advanced Materials*, vol. 23, no. 39, pp. 4578–4586, 2011.

[31] J. C. Mauro, C. S. Philip, D. J. Vaughn, and M. S. Pambianchi, "Glass science in the United States: current status and future directions," *International Journal of Applied Glass Science*, vol. 5, no. 1, pp. 2–15, 2014.

[32] Y. W. Bao, F. H. Kuang, Y. Sun et al., "A simple way to make pre-stressed ceramics with high strength," *Journal of Materiomics*, vol. 5, no. 4, pp. 657–662, 2019.

[33] Y. W. Bao, Y. Sun, F. H. Kuang, F. H. Li, and D. T. Wan, "The development and exploration of high-strength prestressed ceramics [J]," *Journal of Inorganic Materials*, vol. 35, no. 4, pp. 399–406, 2020.

[34] L. Huang, W. D. Zhuo, Y. Gu, G. P. Shang, and X. Y. Huang, "Experimental study on influence of interface agent on interface bonding performance of new and old concrete [J]," *Journal of Fuzhou University (Natural Science Edition)*, vol. 46, no. 3, pp. 396–402, 2018.

Hindawi

Research Article

Influence of Nanomodified Waterproofing Agent on the Performance of Rigid Waterproof Concrete in Underground Engineering

Jianxiang Sun,[1,2] **Chuqi Shi** ![ORCID],[3] **Pengping Li,**[1,2] **and An Li**[1,2]

[1]*CCCC Fourth Harbor Engineering Institute Co., Ltd., Guangzhou, 510230 Guangdong, China*
[2]*Southern Marine Science and Engineering Guangdong Laboratory, Zhuhai, 519082 Guangdong, China*
[3]*Guangzhou Research Institute of Construction Industry Co., Ltd., Guangzhou, 510663 Guangdong, China*

Correspondence should be addressed to Chuqi Shi; 201610102881@mail.scut.edu.cn

Waterproof and impermeable problems seriously affect the safe use, normal structure, and working life of concrete projects. The waterproof performance of concrete can be improved by mixing with a proper amount of waterproofing agent; nevertheless, the early strength of concrete will be seriously affected. With the development of complex structures such as large spans in soil and water engineering and the increasingly complex engineering environment, people have put forward higher requirements for the working performance, strength, impermeability, durability, and intelligence of cement-based materials required. This article compares the changes in compressive strength, fluidity, and water permeability of mixed concrete by controlling the two variables of waterproofing agent and nanosilica. Combining the results of XRD microstructure analysis, the influence of nanosilica and waterproofing agent on the performance of concrete is explored. Moreover, it is hoped that other excellent properties of concrete can be improved, and a waterproof material with good opacity can be found. The test results show that after adding waterproofing agent alone, the 3 d compressive strength of concrete is decreased by 14.81%, the water permeability is reduced by 71.6%, and the depth of carbonic acid molecules at 28 d is also decreased by 37.3%. On the other hand, compared with concrete using waterproof coating alone, after adding in nanosilica, the 3 d compressive strength is increased by about 30%, and the water immersion height is decreased. The results show that the addition of polymer has a great influence on the compressive strength and carbonic acid resistance of concrete.

1. Introduction

Nanowaterproofing agent is a high-quality waterproofing agent that can maintain water resistance for a long time, with the functions of antimigration, water reduction, and performance improvement; this is a new generation of high-energy environmentally friendly products. Concrete can play a certain waterproof role in building structures, so it is widely used in waterproof buildings. However, in many engineering projects, concrete has not achieved the expected waterproof effect, resulting in serious water leakage in many building structures, which brings great inconvenience to production and life.

Because of the special properties of nanoparticles, some properties of the material can be changed after the addition of the nanoparticles, which can endow the material with special property required by the user, or make the special performance of the material more excellent [1]. At the same time, it can also help to open up the research road of material modification theory. Manufacturers and users of nanomodified materials put forward new requirements for material properties, such as stronger waterproof performance [2]. Frequent maintenance and leak repairs increase the economic expenditure and may not receive good results. With the development of modern society, the utilization of underground space has become popular, and the

requirements for waterproof technology are getting higher and higher.

Regarding the performance of concrete, relevant scientists have done a lot of research. Tanaka et al. had challenged the development of innovative asphalt mixtures, in view of the fact that the water stranded on the concrete deck of the highway bridge would significantly deteriorate and aggravate its damage. This asphalt mixture could ensure sufficient water resistance even during the limited time for concrete bridge repairs. After years of basic laboratory tests, a specially designed modified asphalt was developed, the performance of the mixture was specified, and its durability was checked using APT equipment, thereby obtaining a prototype mixture. Through the staged field test, the best construction method was finally obtained [3].

Sanytsky et al. were committed to the development of nanomodified cement-based composite materials in the field of self-cleaning building materials. The particle size distribution of the main components of multicomponent cement such as ultrafine zeolite and limestone, titanium dioxide, and kaolin additives was given. The interface degree of active surface in Portland cement and auxiliary cementing material was calculated. Studies had shown that due to the synergistic effect, anatase and rutile mixtures could be added to cement-based composite materials to improve the performance of self-cleaning gypsum. The mathematical programming method was used to study the effect of titanium dioxide and kaolin additives on the mechanical properties of nano-modified multicomponent cement. The results obtained by XRD and SEM methods showed that the addition of TiO_2 nanoparticles with a high specific surface area to the cement paste would result in the formation of a denser microstructure in the cemented matrix [4].

The purpose of Pacheco-Torres et al. is to evaluate the effect of surface roughness and bond strength between steel and concrete surfaces in two different ways. In this study, push-out tests were performed to evaluate the interface behavior between steel and concrete bonded using epoxy resin. Roughness is obtained by forming grooves on the surface of the specimen. From this study, it can be concluded that the epoxy resin used in the study can be safely used as an adhesive between steel sections and concrete bridge decks with a compressive strength of less than 50 MPa [5].

Regarding nanomodified materials, related scientists have done a lot of research. Li et al. studied the influence of nanosilica and silicone oil paraffin emulsion mixed with flue gas desulfurization gypsum on its water resistance. They mixed nanosilica with desulfurized gypsum, explored how the waterproof and mechanical properties of desulfurized gypsum were affected by the particle size and content of nanosilica, and analyzed its waterproof mechanism. They combined with the microscopic morphology analysis of the gypsum sample, the appropriate size of nanosilica filled the crystal pores and reduced the porosity, and this changed the structure and morphology of the gypsum crystals to a certain extent. The dense oil-hydrophobic film and nanosilica produced a compact gypsum structure, which prevented water molecules from entering the gyp-

sum, thereby improving the performance of FGD gypsum [6]. Xu et al. incorporated nano-ZrO_2 concentrate into phenolic epoxy resin to prepare a nanomodified coating system. They used a combination of electrochemical methods and surface characterization methods and evaluated the corrosion performance of the coating in a hot mixed acid solution, focused on the extent to which the corrosion performance of the coating was affected by the content of nano-ZrO_2. The results showed that the addition of 1% and 3% of nano-ZrO_2 could effectively improve the corrosion resistance of the coating, while the addition of 5% of nano-ZrO_2 reduced the corrosion resistance of the coating. The coating containing 3% nanometer ZrO_2 showed the smallest species diffusion, the lowest average roughness (5.94 nm), and the highest C/O ratio (4.55) and coating resistance and showed the best corrosion performance in the coating samples [7]. Liao et al. prepared aliphatic amine-modified layered silicate clay by n-octadecylamine intercalation method. It was an organically modified clay, which was a new type of phase change material. Through the ion exchange reaction, when the equivalent ratio of ODA-HCl to Na+-MMT was 1, and measured by X-ray diffraction (XRD) analysis, the interlayer corridor of the silicate-layered structure extended from 12 Å to 28 Å. The obtained organoclay could be used as a good heat storage and phase change material [8]. Irshidat and Al-Saleh studied the thermal and fire resistance properties of nanoclay-modified cement mortar. To prepare the modified mortar mixture, they replaced part of the cement with montmorillonite nanoclay (0-2% of the cement weight). The fire resistance was evaluated by comparing the residual mechanical strength of the heated sample and the control sample. Through XRD and SEM tests, the effects of nanoclay on the chemical composition and microstructure of the thermally damaged samples were evaluated, respectively. The experimental results showed that the nanoclay-modified cement mortar had higher compressive, tensile, and flexural strength than the control sample, especially at higher temperatures. Due to high-temperature exposure, the addition of nanoclay significantly reduced the degradation of the tensile and flexural strength of the cement mortar. SEM images showed that due to high-temperature exposure, the presence of nanoclay reduced the density and width of fine-line cracks that appeared along the cement matrix [9]. These methods provide some references for our research.

This article sets up a control group experiment, by controlling one variable unchanged and changing another variable; a comparative analysis study is carried out; and comparisons are made between groups. The changes in the cement-related properties after mixing various materials are studied, and the changes in the microanalysis of the cement are observed. By analyzing the crystal structure and chemical composition of concrete, the principles and laws of concrete performance affected by different components are summarized. The novelty of this experiment lies in the addition of new research content and research methods, while verifying the existing experimental results.

2. Methods for the Performance of Rigid Waterproof Concrete

2.1. Concrete Waterproofing Agent. Among the many chemical admixtures, there is a concrete waterproofing agent that can fill the capillary channels inside the concrete. And it has the ability to reduce the material's ability to attract water and the ability of water to penetrate concrete under hydrostatic pressure [10, 11]. Waterproofing agent can significantly improve the ability of concrete to repel water, so as to achieve the purpose of improving the durability of concrete [12].

Water-repellent active materials have a waterproof effect, reduce plasticity and surface tension, and reduce harmful holes that concrete can easily allow water to penetrate [13]. In the presence of colloids or other ingredients, use waterproof media to block and fill the pores, and the cement concrete will remain in the pores after hardening. Because the road blocking the pores is blocked, the way for water to penetrate into the concrete is reduced, so as to achieve the purpose of waterproofing [14]. Cutting the pores promotes the airflow in the waterproofing medium to be evenly distributed in the concrete, generating closed small bubbles, blocking the capillary channels, and increasing the density of the concrete. This makes the concrete from hydrophilic to hydrophobic [15]. There are active hydrophobic ingredients in the watertight area. After adding concrete, a hydrophobic layer can be formed on the capillary wall. This weakens the capillary adsorption and reduces the water absorption rate of concrete. This hydrophobic effect can effectively prevent water vapor and nonpressurized water from entering the concrete. From the research results of hydration products, after adding waterproof materials, almost no new hydration products are formed, and some new products formed by water-resistant active substances that may be colloids are formed [16].

The functions of concrete waterproofing agent include effectively enhancing the waterproof function and antiseepage function of concrete. Incorporating a watertight medium into the concrete promotes changes in the pore structure of the concrete and releases gel at the same time. The gel fills the internal pores of concrete, and the density is 6-9 times that of unimpregnated concrete [17]. It significantly improved the performance of mortar and reduced bleeding rate. It can replace limestone to a certain extent, overcome hollowing and scaling, reduce soil ash, save work, and improve efficiency; it can delay the heat release rate of cement and effectively prevent the fracture of concrete; it is also possible to store cement while maintaining the same strength and decline as the reference concrete [18–19].

The use of waterproofing agent has certain functions of water reduction, plasticization, and surface tension reduction, which can reduce the harmful pores in the concrete that easily seep water and at the same time make the concrete uniform and dense, thereby improving the ability of concrete to resist pressure water.

In the waterproofing agent, there are components that form colloid or other blocking and filling capillary pores. After the cement concrete hardens, it stays in the capillary pores, cuts off the capillary pores, and makes it difficult for water to enter, so as to achieve the purpose of waterproofing.

The air-entraining component in the waterproof profile produces some small and uniform closed air bubbles in the concrete, which blocks the capillary passage and improves the impermeability of the concrete.

Make concrete from hydrophilic to hydrophobic. There are active hydrophobic components in the waterproof profile. After adding concrete, a hydrophobic layer can be formed on the wall of the capillary, which weakens the adsorption of the capillary, thereby reducing the water absorption of the concrete. This hydrophobic effect is effective in preventing water vapor and unpressurized water from entering the concrete but has little effect on preventing the penetration of pressurized water.

2.2. The Impact of Nanomaterials on Concrete. Because of the special properties of nanomaterials, the mixing of nanomaterials into concrete will change some of the properties of the concrete. The specific performance is in the following important aspects:

(1) Cement stone is mainly composed of three parts: cement that has not reacted with water, the reaction product after the reaction between cement and water, and pores. Pores are the spaces that can be filled by the other two parts in the cement stone [20]. The strength of cement stone is inversely proportional to the number of pores and directly proportional to the density of cement stone. Adding nanomaterials to concrete can fill the remaining pores in the cement, making the overall structure of the concrete denser and stronger [21]

(2) Nanomaterials have the characteristics of small size, large surface, and high chemical activity. The addition of nanomaterials to the cement matrix not only directly involves the hydration process of the cement but also promotes the hydration process of the cement through the secondary hydration reaction with the hydration product. Especially, it improves the strength of concrete [22, 23]

(3) Nanomaterials accelerate the hydration reaction of cement and act as a catalyst, and the faster hydration of cement is beneficial to increase the initial strength of concrete. There are many chemical bonds on the surface of nanomaterials, and these chemical bonds are also very active, so there is no need to form a stable C-S-H phase during the hydration process [24]. The C-S-H phase is formed directly on the surface of the nanomaterial, and the loose hydrated cinnamic acid gel is transformed into a lattice structure centered on the nanoparticle. Thus, a general, uniform, and dense secondary interface can be formed in a good state [25, 26]

(4) Nanomaterials can significantly reduce the dense distribution and directional arrangement of calcium hydroxide at the interface between concrete cement

slurry and aggregate, which helps to improve the comprehensive performance of the interface, thereby improving the strength and durability of cement-based materials

Due to its special physical and chemical characteristics, nanomaterials have the following important roles in concrete: cement stone is composed of unhydrated cement particles, hydration products, and capillary pores. Capillary pores are the spaces in the cement stone that are not filled by cement particles and hydration products. The fewer the capillary pores, the denser the cement stone and the higher the strength. Nanomaterials can fill the capillary pores inside cement-based materials, making the internal structure of concrete more compact. Cement particles are equivalent to coarse aggregates, and nanomaterials play a good role in filling, which can reduce the total porosity in cement-based materials, effectively refine pores, and reduce critical pore size, thereby improving the compactness and durability of cement-based materials.. Nanomaterials are smaller in size, are larger in surface energy, and have great chemical activity. The addition of nanomaterials to cement-based materials can not only directly participate in the cement hydration process but also promote the process of cement hydration through secondary hydration reactions with hydration products, thereby improving the strength of concrete, especially cement-based materials' early strength.

2.3. Concrete Performance. Concrete has the following basic properties:

(1) Impermeability: the ability and performance of concrete materials to resist pressure penetration by water and oil not only reflect the ability of concrete to resist water flow. It also affects concrete performance, carbonization, and chloride ion penetration [27]

(2) Frost resistance: under the conditions of water adsorption and continuous low temperature, the concrete material has experienced multifrozen soil cycle, retaining its original properties or not significantly reducing the original properties

(3) Corrosion resistance: the ability to resist the corrosive and destructive effects of the surrounding environment is called corrosion resistance

(4) Fluidity: the concrete mixture flows under its own weight or mechanical vibration, and the mechanical vibration can flow evenly and densely on the formwork. It reflects the dilution consistency of the concrete mixture and the ability to fill the form [28]

(5) Compressive strength: when concrete is subjected to continuous and slowly increasing external pressure, the limit of pressure that the concrete can withstand per unit area at the critical point of destruction

From the research results of hydration products, few new hydration products formed crystals after the incorporation

of water repellent. The new products formed by some water repellents are likely to be colloids.

3. Experiments on the Performance of Rigid Waterproof Concrete

3.1. Preparation before the Experiment. Some raw materials that need to be prepared before starting the experiment:

(1) Cement. Use the data in Table 1 as a technical standard to ensure that the cement used in the experiment meets the standard

(2) Water repellent. For example, Table 2 is used as the performance standard of waterproofing agent, and the materials used in the study are all waterproofing agents with a cement content of 2%

(3) Nanomaterials. For example, Table 3 is used as the technical standard for nanomaterials

Trial mixing is carried out in the laboratory, and the mixed ingredients, proportions, and test mixing are obtained, such as the concrete materials shown in Table 4.

In order to better mix the concrete, the mixing process shown in Figure 1 is used in the lubrication process: first, wet the mixing drum of the concrete mixer, pour all the coarse aggregates during the mixing process, then pour the half sand, and then pour the cement (according to the test requirements, add different amounts of anticorrosion and hydrophobic substances). After the mixing is completed, reduce the amount of water and water pouring, and mix horizontally. Turn off the machine after the mixing is complete. If you find that the fluidity of the concrete is obviously low, add an appropriate amount of water-reducing agent and mix horizontally until the flow rate meets the requirements. Then, determine the amount of water-reducing agent, quickly load the mixed concrete into the test shell, and swing it firmly.

3.2. Experimental Process

3.2.1. Liquidity Test Experiment. To quantitatively analyze the fluidity of concrete, it is necessary to use the index of slump. According to the "Standard for Test Methods of Performance of Ordinary Concrete Mixtures," the experimental procedures and precautions for concrete test experiments are formulated. Before the test, take a clean water source and use a brush to moisten the inner wall of the slump cylinder and the tamping rod, and put a funnel of appropriate size on the top of the cylinder. Put it on the iron plate, step on the pedal with your feet, and slowly adjust and fix it. The mixed concrete is taken out and divided equally into three parts, and the three layers of space in the cylinder are filled with concrete, respectively. The height of each layer is set to 1/3 of the cylinder height, and the plug is inserted about

TABLE 1: GB175-2007 quality standard for ordinary Portland cement.

Insoluble matter (%)		≤0.75
Insoluble matter (%)		≤5.0
Sulfur trioxide (%)		≤3.5
Loss on ignition (%)		≤5.0
Chloride ion (%)		≤0.06
Fineness (%)		≤10.0
Setting time	Initial setting (h:min)	≥0:45
	Final coagulation (h:min)	≤10:00
Flexural strength	Three days (MPa)	≥3.5
	Twenty-eight days (MPa)	≥6.5
Compressive strength	Three days (MPa)	≥16
	Twenty-eight days (MPa)	≥42.5
Stability		Qualified

TABLE 2: KIM waterproof agent technical form.

Physical property		
Inspection items	Measured results	
Appearance	Light gray powder	
Particle size (μm)	40-150	
Bulk density (g/cm^3)	~1.4	
Proportion	~2.8	
Curing properties		
Curing properties	Test method	Detection result
Permeability	Taywood/Valenta	-70%
Shrinkage cracking	BS 1881-5	-25%
Freeze thaw resistance	BS 5075-2	-87%
Compressive strength	BS EN12390-3	+8%
Flexural strength	BS EN12390-5	+7%
Elastic modulus	BS 1881-122	+16%

TABLE 3: Test report of nanocinnamon dioxide.

Inspection items	Quality standard	Measured results
Appearance	White powder	Compliant
Average particle size (nm)	50 ± 5	50
Specific surface area (m^2/g)	200 ± 30	200
Content (%)	≥90.5	99.7
pH value	5-7	6.8
Surface treatment section	Nothing	Nothing
Loss on ignition (%) 950 × 2 h	≤6.0	0.5
Arsenic	1.0	Qualified
Lead	1.0	Qualified

25 times in each layer. The stopper is injected into a spiral shape from the outside, and each penetration detection point is distributed as evenly as possible on the surface. Especially when printing the bottom, the tip of the knife must pene-trate the entire depth. When lightly impacting the second layer and the previous layer, the tip of the knife must penetrate the surface of the next layer. When inserting and punching the upper layer, make sure that the concrete of the upper layer is poured and lift it higher or with the top layer of the caving drum. After completion of cementing, the concrete is wiped with a knife. After removing the concrete on the floor by the side of the drum, the foldable pipe rises vertically and firmly. At this time, check the difference between the upper body point and the height of the cylinder, which is the slump.

3.2.2. Compressive Strength Test. When determining the compressive strength of concrete, strictly refer to the "Standard for Test Methods for Mechanical Properties of Ordinary Concrete." The main equipment includes the pressure tester, ruler, and brush as shown in Figure 2.

The specific steps of the experiment are as follows:

(1) Dry the test piece taken out from the curing site and the water on the upper and lower bearing plates, and start the experiment immediately

(2) The sample should be placed under the pressure plate or backing plate of the testing machine. If a sample is formed, the upper surface should be perpendicular to the storage area of the sample. The center of the sample should correspond to the center of the pressure plate under the testing machine. In the test mode or worksheet, adjust the ball position and adjust the contact balance

(3) When the specimen begins to deform, pay attention to it. When the specimen deforms sharply and reaches the critical point of being destroyed, stop adjusting the throttle, and record the load value when the specimen is broken

(4) Use the following formula to calculate the compressive strength of the test piece:

$$X_{CC} = \frac{M}{N}, \tag{1}$$

where X_{CC} is the compressive strength of test piece (MPa), M the destroy load of specimen (N), and N the pressure-bearing area of the test piece (mm^2).

3.2.3. Water Penetration Test. Based on the Standard for Test Methods of Long-term Performance and Durability of Ordinary Concrete, the water penetration test is carried out after preparing the materials required for the experiment. To quantify the water penetration resistance of concrete, the water penetration resistance of concrete is expressed by measuring the average water penetration height under constant water pressure. The water penetration testing machine used is shown in Figure 3.

The specific method of the test is as follows:

TABLE 4: Composition and proportion of each sample of concrete.

Group	Composition and proportion of admixture
P1	Ordinary concrete
P2	Ordinary concrete + 2%waterproof agent
P3	Ordinary concrete + 2%waterproof agent + 1%nanosilica
P4	Ordinary concrete + 2%waterproof agent + 1.5%nanosilica
P5	Ordinary concrete + 2%waterproof agent + 2%nanosilica
P6	Ordinary concrete + 2%waterproof agent + 1%nanosilica + 0.01%PowderA
P7	Ordinary concrete + 1.5%nanosilica + 0.01%PowderA
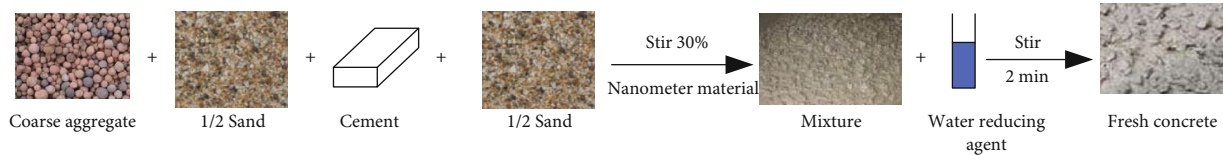
FIGURE 1: Schematic diagram of concrete pulling and mixing sequence.

FIGURE 2: Pressure testing machine.

(1) Take out the test piece one day before the curing time of the test piece is reached, and wipe it with a clean damp cloth. Air-dry the test piece or use other methods to dry it, and seal it after the surface of the test piece is completely dry

(2) Coat the side of the sample with a layer of molten paraffin containing a small amount of resin, and then, preheat the sample with a spiral pressure heating furnace or an electric furnace. In order to fix the sample on the bottom of the test model, release the pressure after the test model is completely cooled, and touch the test model with paraffin on the side of the test piece. When the paraffin slowly melts but does not flow, it indicates that the preheating temperature of the test model has reached the standard

(3) When the test piece meets the test standard, start the water penetration tester. Open the valve at the test position to make all the water seeping from the hole flow into the test pit. After the test pit is filled with water, close the gate and install the sealed test piece on the impermeability instrument

(4) After the test piece is installed, immediately open the valve under the test position to constantly control the water pressure in each time period, and control the pressurization time to no more than five minutes. When a stable pressure is reached, record this time as the start time of the experiment. Before the pressure reaches a stable level, always pay attention to the penetration of water on the end surface of the test piece. When water immersion occurs on the end face of the test block, the test block stops the test, the time is recorded as the end of the experiment, and the height of the test block is taken as the water penetration height of the test block. If the end surface of the test piece is not immersed in water, the test is terminated after the test is completed, and the test piece is taken out. During the test, when water is found to seep out from around the test piece, it must be sealed again

(5) Place the test piece taken out of the impermeable meter on the pressure plate. Diameter steel buffer sheets are arranged in the center of the upper and lower end surfaces of the test piece in the diameter direction, and check whether they are in the same vertical plane. Then, start pressing and divide the specimen into two halves along the longitudinal area. After dividing the test block, use the waterproof mark to trace the watermark

(6) The trapezoid plate is placed on the dividing surface of the test piece, and the water inlet height of each measuring point is measured at equal intervals along the water bottle with a steel ruler for accurate reading. When reading, if the measurement point is blocked with aggregate, the water penetration height near the two ends of the aggregate is measured and the average value is taken. The average value can be

Figure 3: Water penetration resistance testing machine.
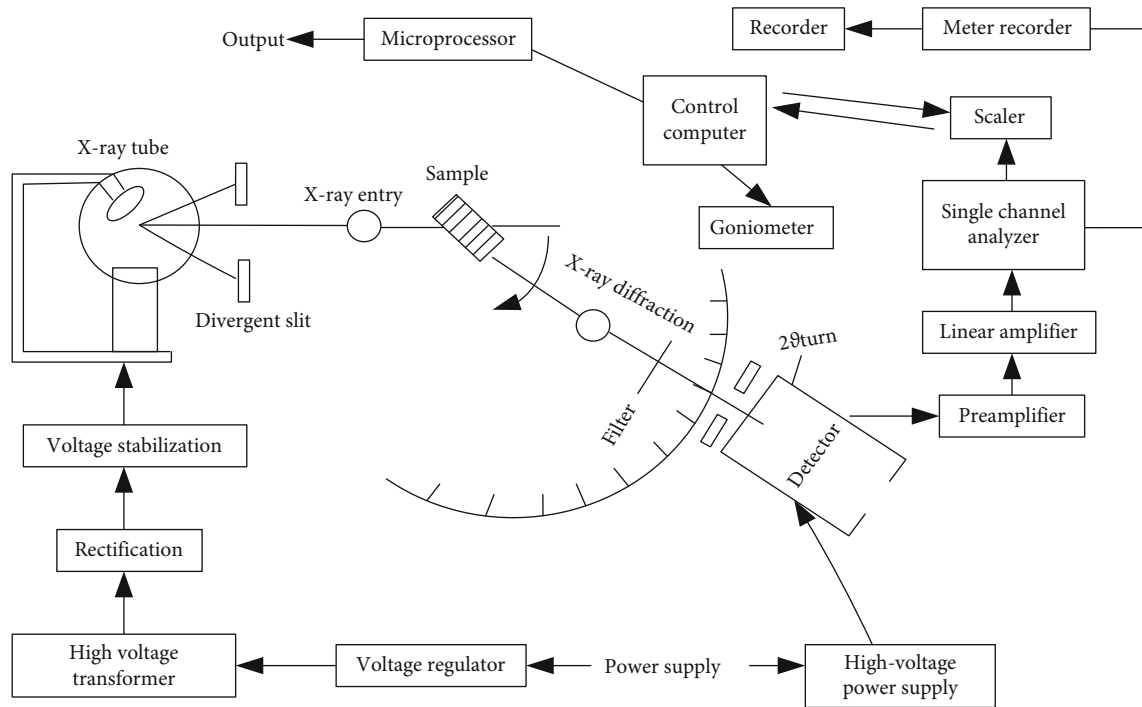
Figure 4: Block diagram of diffractometer composition.

used as the water immersion height of the measurement point

3.2.4. Phase Analysis-X-Ray Diffraction Analysis.

XRD is the abbreviation of X-ray diffraction. The material is diffracted by light to cause the transformation of atoms in the atomic layer and obtain a diffraction pattern. X-rays are a type of short-wavelength electromagnetic waves that can penetrate quite thick objects. Light crystals formed by electron transfer in the inner layer of X-ray molecules under the irradiation of high-speed moving electrons can act as photons. The coherent scattering formed by multiple atoms or ionic molecules causes an impact on the light, which in turn affects the intensity of the scattered rays. The maximum intensity of light formed by the overlapping of divergent waves from several molecules is called diffracted light of light. It can be obtained by the following formula:

$$2M \sin \theta = \alpha, \tag{2}$$

where M is the plane distance and α is the wavelength.

The measurement angle is based on rays of known wavelengths, and then, the crystal plane distance is calculated, which is mainly used for X-ray structure analysis. Another way to determine the angle is to use a known metal crystal to calculate the wavelength of the characteristic X-ray. The calculated characteristic X-ray wavelength can also be used to find the elements contained in the sample from existing data. Figure 4 is a block diagram of the diffractometer.

Prepare the test sample: after testing the compressive strength, take a specific test block, dismantle it, and put it in absolute ethanol to stop the final water. Before the test, use the mortar to mash the powder. After passing through the 80 square-hole sieve, it is double-sealed with a sealed bag and stored for later use.

3.2.5. Pore Structure Analysis.

In this test, a pressure system test is used to test the hole structure. The pump will not penetrate most pressure materials. The pump can be forced into the pores of the porous solid under the action of only external force. Generally speaking, the pressurized pressure is
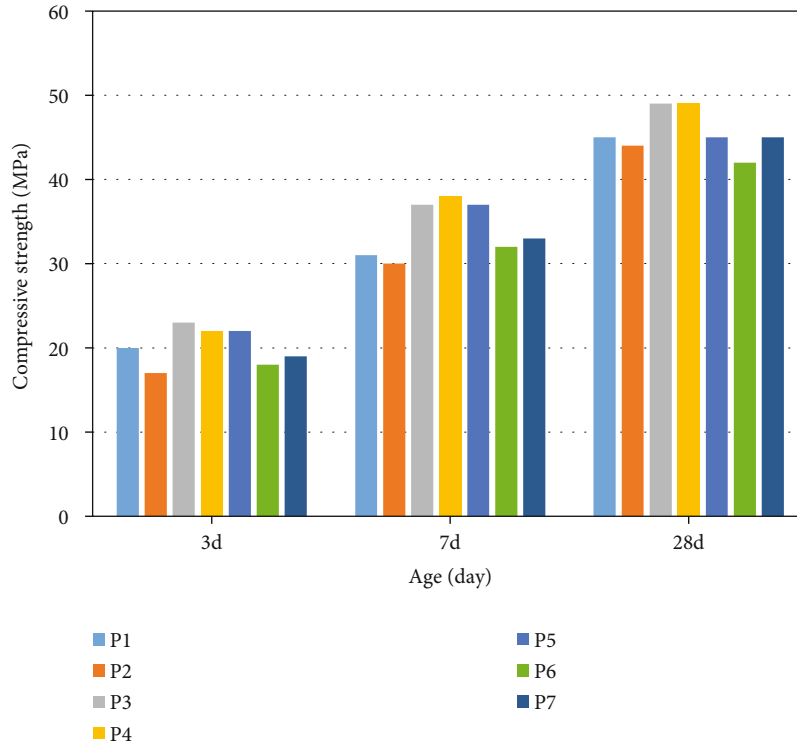
FIGURE 5: Comparison diagram of compressive strength and concrete compressive strength.
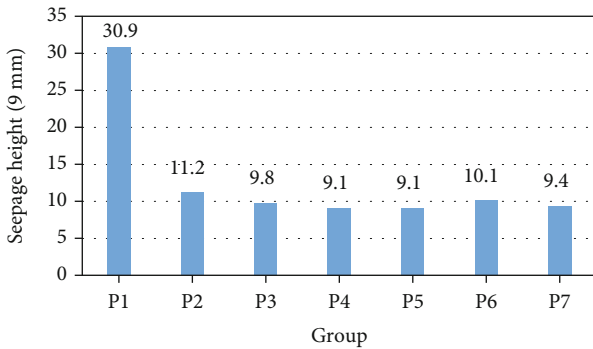
FIGURE 6: Comparison diagram of water penetration height of each sample.

equal to the surface tension of the capillary orifice pump. The relationship between hole radius and external pressure is as follows:

$$M = -\frac{2m \cos \alpha}{N}, \tag{3}$$

where M is the capillary pore radius, N is the pressure applied to the pump, α is the wetting angle of the pump to the solid, and m is the surface tension of the pump.

4. Experimental Analysis of Waterproof Concrete Performance

4.1. Concrete Fluidity. In this test, different amounts of water-reducing agent are added to control the slump to

remain basically the same. During the mixing process, it can be clearly observed that after adding nanometers, the fluidity of the concrete is obviously affected, and the content of the required water-reducing agent increases. Finally, the slump of each test group is basically maintained at between, which meets the specification requirements.

4.2. Compressive Strength of Concrete. The compressive strength of each sample concrete is shown in Figure 5.

Through the analysis of the above data, it can be seen that the mixing of water-repellent agent seriously affects the early strength of concrete. This is because the fluidity of concrete is improved by the addition of organic water-repellent agent and has a retarding effect. The incorporation of nanomaterials solves the problem of low strength in the early stage, and the compressive strength in the later stage is also greater than that of the benchmark group. The incorporation of PowderA has an effect on the strength of concrete, and the early decrease is obvious. This is also because PowderA is an organic material, which is not good for the early strength.

In the compressive strength test, the 3 d strength of the P7 group concrete after adding KIM waterproofing agent decreased by 14.81%, and by 28 d, it only decreased by 3.94% with the P1 group. The strength of P3, P4, and P5 added with nanosilica increases significantly, especially the 3 d strength which increases by about 30%. However, the strength of the specimens doped with different amounts of nanosilica differed by less than 3%. Because nanosilica fills and refines a large number of pores in the concrete, it makes the apparent structure of the concrete denser, thereby

TABLE 5: Comparison of concrete impermeability test results.

Group	P2	P3	P4	P5	P6	P7
Reduction rate of each group relative to P1 group	71.6%	75.1%	76.9%	76.9%	74.4%	76.1%

TABLE 6: Peak value of main substances.

Sample	Crystal plane/crystal								
	(001)/CH			(101)/CH			C_3S		
	3 d	7 d	28 d	3 d	7 d	28 d	3 d	7 d	28 d
P1	946	1199	1099	692	870	812	490	490	332
P2	988	978	1140	756	886	869	460	328	571
P3	1116	1150	640	700	717	645	480	339	307
P4	804	546	993	714	652	650	521	541	416
P5	753	822	862	677	708	578	578	348	340
P6	474	427	967	606	682	620	377	302	453
P7	586	604	736	649	653	749	541	374	683

promoting the development of concrete strength. The specimens with PowderA have lower early strength, reaching the level of P1 group by 28 d.

The incorporation of nanosilica will cause the loss of concrete slump. With the increase of nanosilica content, the slump drops sharply, and the fluidity of the concrete mixture will gradually decrease. In order to make up for the slump loss, the required water-reducing agent content increases. The specific surface area of nanomaterials is very large. Although their incorporation reduces part of the filling water, it greatly increases the surface adsorption water, which greatly increases the water consumption of standard cement consistency.

4.3. Concrete Anti-Water Penetration Test. The water penetration test was carried out after 28 days of curing of the specimen. The test result is shown in Figure 6.

By calculating the reduction rate of the permeable height in each group of samples relative to the P1 group, the effects of various composite waterproofing agents on the water permeation resistance of concrete were analyzed. The results are shown in Table 5.

From the above test data analysis, it can be seen that after adding KIM waterproofing agent, the ability of concrete to resist water penetration is greatly improved. On this basis, the density of concrete added with nanosilica is improved, and the water penetration resistance is further strengthened. In PowderA, a small amount of air will be introduced, so the impermeability of concrete will be slightly reduced. The combination of nanosilica and KIM waterproofing agent and the combination of nanosilica and PowderA have roughly the same waterproof penetration effect, but the combined effect of the three has a certain degree of impermeability.

4.4. X-Ray Diffraction Analysis. By analyzing the results of X-ray diffraction, it can be seen that the XRD diffraction spectra of each group are basically the same. Among them, 29.4° is selected, and 18.1° and 39.4° are selected as the characteristic peaks of calcium hydroxide. By comparing the

characteristic peaks, a semiquantitative method is used to determine the amount of the corresponding substance. The main substance peaks obtained by ray diffraction analysis are shown in Table 6.

First, analyze the content of C_3S, which can be seen from Table 6:

(1) Compare the P7 group with the P1 group; the content of C_3S in the sample was similar at 3 d; the content of P1 group was more than that of P7 at 7 d, and the content of the P7 group was more than that of the P1 group at 28 d

(2) Compare the P3, P4, and P5 groups; the content of c in the samples showed a decreasing trend at 3 d, 7 d, and 28 d, and the cement hydration continued to be uniform

(3) Compare the P6 group with the P4 group; the P6 group showed fluctuations similar to that of the P7 group. The content increased significantly at 28 d, even exceeding the content at 3 d, and it was quite low at 7 d

5. Conclusion

The effect of nanomodified waterproofing agent on the performance of underground rigid waterproof concrete was studied by designing the impermeability durability test of concrete with different proportions. Comparing with the case of adding the waterproofing agent only, the early strength of concrete was significantly improved by adding nanomodified waterproofing agent. The concrete modified by nano-SiO_2 showed good improvement in water resistance, seepage resistance, and chloride ion penetration resistance, nearly double the water resistance and seepage resistance of ordinary concrete; in addition, the chloride ion penetration resistance was better than that of single water repellent. There are still many deficiencies in this paper, such as the lack of analysis of the reasons for the influence of nanomodified materials on concrete and the incomplete perspective on the influence of nanomodified materials on concrete. Nanomaterials are the new materials of the century. They exhibit unique properties in physics, chemistry, structure, etc., which lead to their research and applications in various fields. In the field of construction engineering, researchers add nanomaterials to traditional building materials to improve the performance of traditional building materials and give new application value. More comprehensive research should be done on the specific influence and mechanism of nanomaterials on concrete properties, and all research results should be combined to classify the types of nanomaterials and the influence of nanomaterial dosage on concrete and formulate

corresponding standards, so as to provide a theoretical basis for the target concrete to select the corresponding nanomaterials and dosage according to the required performance index.

Data Availability

The data used to support the findings of this study are available from the corresponding author upon request.

Conflicts of Interest

The authors declare that there are no conflicts of interest regarding the publication of this article.

Acknowledgments

References

[1] B. Gao, N. Xu, and P. Xing, "Shock wave induced nanocrystallization during the high current pulsed electron beam process and its effect on mechanical properties," *Materials Letters*, vol. 237, no. 15, pp. 180–184, 2019.

[2] X. Xu, B. Karami, and D. Shahsavari, "Time-dependent behavior of porous curved nanobeam," *International Journal of Engineering Science*, vol. 160, p. 103455, 2021.

[3] T. Tanaka, O. Kamada, and A. Maruyama, "Development of asphalt pavement with waterproof performance on concrete slab bridge," *Journal of Japan Society of Civil Engineers, Ser. E1 (Pavement Engineering)*, vol. 72, no. 3, 2016.

[4] M. Sanytsky, T. Kropyvnytska, M. Hohol, and R. Kotiv, "Nano-modified cementing composites for self-cleaning building materials," *Budownictwo o Zoptymalizowanym Potencjale Energetycznym*, vol. 9, pp. 7–14, 2020.

[5] R. Pacheco-Torres, E. Cerro-Prada, F. Escolano, and F. Varela, "Fatigue performance of waste rubber concrete for rigid road pavements. Construction and Building," *Construction and Building Materials*, vol. 176, pp. 539–548, 2018.

[6] J. Li, J. Cao, Q. Ren et al., "Effect of nano-silica and silicone oil paraffin emulsion composite waterproofing agent on the water resistance of flue gas desulfurization gypsum," *Construction and Building Materials*, vol. 287, no. 8, pp. 123055–123055, 2021.

[7] W. Xu, Z. Wang, E. H. Han, S. Wang, and Q. Liu, "Corrosion performance of nano-ZrO_2 modified coatings in hot mixed acid solutions," *Materials*, vol. 11, no. 6, pp. 934–934, 2018.

[8] C. Y. Liao, J. Y. Chiou, and J. J. Lin, "Phase change materials of fatty amine-modified silicate clays of nano layered structures," *RSC Advances*, vol. 7, no. 38, pp. 23530–23534, 2017.

[9] M. R. Irshidat and M. H. Al-Saleh, "Thermal performance and fire resistance of nanoclay modified cementitious materials," *Construction and Building Materials*, vol. 159, pp. 213–219, 2018.

[10] X. Tian, W. Wang, N. Tian, C. Zhou, C. Yang, and S. Komarneni, "Cr (VI) reduction and immobilization by novel carbonaceous modified magnetic Fe_3O_4/halloysite nanohybrid," *Journal of Hazardous Materials*, vol. 309, pp. 151–156, 2016.

[11] D. Gao, Z. Sheng, Y. Liu et al., "Protein-modified CuS nanotriangles: a potential multimodal nanoplatform for in vivo tumor photoacoustic/magnetic resonance dual-modal imaging," *Advanced Healthcare Materials*, vol. 6, no. 1, p. 1601094, 2017.

[12] H. L. Zhang, M. M. Su, S. F. Zhao, Y. P. Zhang, and Z. P. Zhang, "High and low temperature properties of nano-particles/polymer modified asphalt," *Construction & Building Materials*, vol. 114, pp. 323–332, 2016.

[13] Y. Tang, Z. Chen, W. Feng, Y. Nong, C. Li, and J. Chen, "Combined effects of nano-silica and silica fume on the mechanical behavior of recycled aggregate concrete," *Nanotechnology Reviews*, vol. 10, no. 1, pp. 819–838, 2021.

[14] A. Benvidi, M. T. Nafar, S. Jahanbani, M. D. Tezerjani, M. Rezaeinasab, and S. Dalirnasab, "Developing an electrochemical sensor based on a carbon paste electrode modified with nano-composite of reduced graphene oxide and $CuFe_2O_4$ nanoparticles for determination of hydrogen peroxide," *Materials Science & Engineering C Materials for Biological Applications*, vol. 75, pp. 1435-1436, 2017.

[15] E. Marwa, H. Hassan, and H. Aly, "Immobilization of magnetic nanoparticles onto amine-modified nano-silica gel for copper ions remediation," *Materials*, vol. 9, no. 6, pp. 460–460, 2016.

[16] M. Li, X. Liu, T. Xu, Y. Nie, H. Li, and C. Zhang, "Synthesis and characterization of nanosized MnZn ferrites via a modified hydrothermal method," *Journal of Magnetism & Magnetic Materials*, vol. 439, pp. 228–235, 2017.

[17] Q. Chen, H. Liu, M. Chi, Y. Wang, and X. Wei, "Experimental study on influence of trap parameters on dielectric characteristics of nano-modified insulation pressboard," *Materials*, vol. 10, no. 1, pp. 90–90, 2017.

[18] C. Yoshikawa, J. Qiu, Y. Shimizu, C. F. Huang, O. J. Gelling, and E. van den Bosch, "Concentrated polymer brush-modified silica particle coating confers biofouling-resistance on modified materials," *Materials Science & Engineering C Materials for Biological Applications*, vol. 70, pp. 272–277, 2017.

[19] K. L. Koh, X. Ji, A. Dasari, X. Lu, S. K. Lau, and Z. Chen, "Fracture toughness and elastic modulus of epoxy-based nanocomposites with dopamine-modified nano-fillers," *Materials*, vol. 10, no. 7, p. 776, 2017.

[20] M. Roushani, S. J. Hoseini, M. Azadpour, V. Heidari, M. Bahrami, and M. Maddahfar, "Electrocatalytic oxidation behavior of NADH at Pt/Fe_3O_4/reduced-graphene oxide nanohybrids modified glassy carbon electrode and its determination," *Materials Science & Engineering C*, vol. 67, pp. 237–246, 2016.

[21] M. S. Konsta-Gdoutos, G. Batis, P. A. Danoglidis et al., "Effect of CNT and CNF loading and count on the corrosion resistance, conductivity and mechanical properties of nanomodified OPC mortars," *Construction and Building Materials*, vol. 147, pp. 48–57, 2017.

[22] R. Roychand, S. De Silva, D. Law, and S. Setunge, "High volume fly ash cement composite modified with nano silica, hydrated lime and set accelerator," *Materials & Structures*, vol. 49, no. 5, pp. 1997–2008, 2016.

[23] C. M. Subramaniyam, M. M. Islam, T. Akhter et al., "A chemically modified graphene oxide wrapped porous hematite nano-architecture as a high rate lithium-ion battery anode material," *RSC Advances*, vol. 6, no. 86, pp. 82698–82706, 2016.

[24] S. Xu, N. Xie, X. Cheng et al., "Environmental resistance of cement concrete modified with low dosage nano particles," *Construction and Building Materials*, vol. 164, pp. 535–553, 2018.

[25] G. Leila and J. Hassan, "Morphological characterization of tungsten trioxide nanopowders synthesized by sol-gel modified Pechini's method," *Materials Research*, vol. 20, no. 6, pp. 1713–1721, 2017.

[26] C. Fang, X. Yu, R. Yu, P. Liu, and X. Qiao, "Preparation and properties of isocyanate and nano particles composite modified asphalt," *Construction and Building Materials*, vol. 119, pp. 113–118, 2016.

[27] X. L. Xing, Y. F. Zhou, S. Y. Gao, J. B. Wang, Y. L. Yang, and Q. X. Yang, "Nano-twin in surface modified bainite induced by laser surface modification," *Materials Letters*, vol. 165, pp. 79–82, 2016.

[28] A. M. Al-Sabaeei, M. Napiah, M. Sutanto et al., "Physicochemical, rheological and microstructural properties of nano-silica modified bio-asphalt," *Construction and Building Materials*, vol. 297, no. 2, p. 123772, 2021.

Hindawi

Research Article

Rehabilitation Treatment and Monitoring of Ankle Achilles Tendon Ligament Injury in Athletes Repaired by Nanomaterials

Fanghui Li, Ping Liu ⬛, Yijun Lou, and Shumei Yi

College of Physical Education, Pingxiang University, Pingxiang, 337055 Jiangxi, China

Correspondence should be addressed to Ping Liu; 22010029@pxu.edu.cn

During sports, athletes' incorrect technical movements and direct physical confrontation can easily cause ankle injuries. Joint ligament injury is a common injury in sports. A ligament injury is an injury to the ligaments in a part of the body caused by varying degrees of injury. Clinical manifestations include localized swelling, pressure pain or joint instability, and pain that increases when pulled in the direction of violence. In order to further investigate the rehabilitation methods of nanomaterials for repairing the ankle Achilles tendon ligament injury in athletes, nanomaterials are materials in which at least one dimension in three-dimensional space is at the nanometer size (1-100 nm) or consists of them as the basic unit, which is approximately equivalent to the scale of 10 to 1000 atoms closely aligned together. In this paper, we found that the healing rate of patients was over 90% by the dynamic balance system combined with surface electromyography, surgical treatment, and extracorporeal shock wave. It can be seen that the dynamic balance system combined with surface electromyography (SEMG), surgical treatment, rehabilitation therapy of Taijiquan exercise, and extracorporeal shock wave therapy have significant effects on the rehabilitation of athletes' ankle and Achilles tendon ligament injuries and can effectively alleviate and resolve athletes' ankle Achilles tendon ligament injury.

1. Introduction

With the vigorous development of sports in China, people are more interested in participating in physical exercise. Not only professional athletes but also people who participate in physical exercise will inevitably suffer from ankle injury. Ankle sprain is a relatively common injury in sports, and injuries cause great pain to athletes. The saddle joint of the talus is wide in front and narrow in back, with the wider part entering the ankle point in dorsal extension and the narrower part entering the ankle point in plantarflexion. The anatomical and physiological characteristics of the ankle joint make it more prone to inversion and valgus sprains during plantarflexion. The ankle joint is composed of the articular surface of the lower end of the tibia and fibula and the talar pulley, so it is also called the talar calf joint. It is one of the important joints of the human body. It mainly depends on the ankle joint extension and plantar flexion.

The instability caused by ankle sprain is divided into lateral instability and medial instability. Clinical manifesta- tions of ankle sprains include pain and swelling at the site of the sprain immediately after the injury, followed by skin bruising and, in severe cases, immobility of the affected foot due to pain and swelling. The incidence of lateral instability combined with articular cartilage injury is 55%. It is mainly talar cartilage injury, most of which are located on the medial talar articular surface. The rate also increased signif- icantly, with a median instability associated with cartilage damage of 98%. Lateral collateral ligament injuries are common in the exercise population, and a comprehensive rehabilitation plan is a crucial outcome. Most literature on nonsurgical and postoperative rehabilitation includes observation reports and case studies, and primary studies comparing rehabilitation programs have not been published. The goal of an injured athlete is not only to return to the game without functional restrictions but also to address risk factors and prevent future injuries [1, 2].

Kyo Chul and others believe that nearly a century ago, a serious ankle sprain was considered to be an ankle ligament injury. With the advancement of imaging and surgical

techniques and the development of tools, the treatment of ankle sprains (including subtalar injuries) has greatly improved. The ankle ligament repair or reconstruction has been improved anatomically and has less trauma than before. Here, the term "'reconstruction" refers to nonanatomic reconstruction, which is a replacement reconstruction with a short fibular tendon, such as the Evans procedure, which significantly alters the biomechanical mechanisms of the ankle and subtalar joint under weight bearing. Rather, tendon transplantation to reconstruct ligaments has become the standard for treating severely injured ligaments, but it does not reproduce the original ultrastructure of the ankle ligaments [3]. The anatomical structure of the ligament includes a ligament with a distal end at both ends, and the structure should also have proprioceptive functions. To date, it is still impossible to reconstruct a fully functional anatomical ligament. The cooperation between regenerative medicine and surgical technology is expected to improve the reconstruction of ankle ligaments. However, we need more time to develop a technology to reconstruct the ideal ligament complex. Lee and Hogan believe that ligament sprain refers to the tearing of fibrous tissue in the ligament and is the main cause of foot and ankle complex injuries during field sports; external rotation of the foot is considered to be the main injury mechanism with ankle sprains. There are specific types of ligament damage; however, the effect of the magnitude and direction of the load vector on the in situ stress state of the ankle ligament has not been quantified in the literature. Finding the maximum injury tolerance of a human foot with an acceptable single ligament subfracture distribution, using a previously developed and fully validated foot and ankle joint model to reproduce a series of joint foot rotations experienced during high-risk athletic activities.

In view of the susceptibility of sprained ankle joints, on the basis of traditional treatment, special attention should be paid to prevention and rehabilitation during rehabilitation. This article analyzes and summarizes the causes, diagnostic methods, treatment measures, and prevention methods of athletes' ankle joint injuries, with a view to helping athletes train scientifically and actively cooperate with medical staff to effectively avoid and reduce the occurrence of ankle joint injuries and its adverse effects. Repairing ankle ligament injuries can relieve the patient's pain and for the athlete can lead to timely training and good performance.

2. Proposed Method

2.1. Reasons for Ankle Injury. Ankle sprains usually occur when our body loses its center of gravity, causing damage to the soft tissues on the outside or inside of the foot, such as ligaments and joint capsules, during sports such as walking or running and jumping.

(1) More common in sports related to jumping

Sports events such as figure skating, alpine skiing, freestyle skiing, and basketball and gymnastics often require athletes to make jumping movements, and as the difficulty of the movement continues to increase, athletes engaged in these events have the possibility of ankle injury much higher than other athletes. The function of the ankle joint is mainly completed within a range of 70°-140° extension and flexion. When the ankle joint has excessive valgus and external rotation, varus and internal rotation, or the talus backwards, it violently impacts forward. When the tibial articular surface, the ankle joint is easily damaged, most of which are strains of the medial and lateral ligaments of the ankle joint [4]. The ankle joint is often subjected to excessive amplitude movements, so that the ankle points do not match the talar articular surface, which will cause ankle joint misalignment, which mainly refers to the medial and lateral or anterior and posterior displacement of the talus. Of these, the talar outward and forward are more common. When the ankle joint is sprained, the muscle ligaments are weak, and the joints are loose and unstable. During the activity, the lower end of the tibia and the inner and outer sides of the talus impact each other on the joints, which can also damage soft eyes, affect joint activities, and hinder normal activities.

(2) Insufficient preparation activities

The mechanism of ankle joint injury caused by insufficient preparation activities. In general sports, before doing exercises or competitions, do some activities that make the body heat and nervous system such as running and jumping, and then do some stretching of the limbs and joints. For amplitude activities, these activities can adjust the body parts to a state suitable for high-intensity exercise as soon as possible before normal sports training or competition. If the previous preparation activities are insufficient, the nervous system, the blood circulation system, and related muscle tissues are not fully mobilized, and the body lacks the necessary coordination, flexibility, and stretchability, and the ankle joint muscle ligament stretch may not be sufficient. Improved, the excitability of the nervous system is relatively low, the antagonist muscles cannot be fully relaxed in a timely manner, coupled with rushing into these exercises or competitions, sudden jump movements or landing instability; it is easy to cause ankle injury [5]. During training or competition breaks, sometimes due to venue, number of people, or other factors, the interval between two activities is longer, and athletes often ignore the proper preparation activities before entering the next exercise. The stretchability of the muscle has been reduced to a certain degree, but the physical strength has been restored to a certain degree. In the second exercise, the range and strength of the movement are relatively large and the speed is relatively fast. This has hidden the sprains of the ligaments of the joints or muscle tension. There is a high possibility of injury. In addition, a considerable part of the athletes only focused on improving the extensibility of large muscle groups and the amplitude of large joints in the preparation activities, while neglecting to improve the functional conditions of other small joints (such as the ankle joint) [6].

(3) Other factors

There are also other factors, such as training with injuries, excessive local load, paralysis of the mind, wrong technical movements, poor venues, excessive excitement, and

lack of protection, which can also cause ankle injuries. For example, the investigation center for the most common injuries in alpine skiing found that ankle ligament injuries were more caused by incorrect technical movements of athletes [7–9]. During training, if the venue is not good, it is easy to make the action fail. Poor weather conditions can also lead to injury accidents. In the summer, the temperature is too high, the athletes have difficulty concentrating, and their physiological adaptability is poor, which is prone to accidental injuries. In the cold winter, the muscles are stiff, the coordination of movements is not good, and it is easy to cause damage to the ankle muscle ligaments.

2.2. Rehabilitation Treatment of Ankle Achilles Tendon Ligament Injury. Rehabilitation gymnastics is a specially choreographed unarmed, or with the help of equipment, limb movement, and functional exercise gymnastics to enable the sick and injured to achieve the purpose of prevention, treatment, and rehabilitation.

(1) Rehabilitation gymnastic therapy

Action 1: take a sitting position and land on the edge of the calcaneus. Use the toe of the affected ankle to write 1 English letter at a time, and write 26 English letters once. Action 2: "Car windshield wiper" training. Take the seat with your feet flat on the ground, with your toes facing forward, and rotate the affected ankle to simulate the movement of the car's windshield wiper. Come out to touch the ground. Action 3: take a seated position to train the lower leg. In the sitting position, the ankle-limb limb is used for hoisting training. It is required to raise the calf as high as possible, and at the same time, keep the toes away from the ground. Then, put the heel back to its original position [10]. Action 4: stand on one leg (partially load-bearing). When standing, place one hand on the table, transfer part of the body weight to the side of the affected ankle, and hold it for 15 s. Increase the time for 15 s each time until you can use the ankle support for 45 s. Then, gradually increase the amount of body mass that can be supported until it can support all of its own body mass. Action five: training of varus and eversion of the affected ankle. Inversion training uses the outside of the affected ankle to rest on a fixed object, such as the edge of a table leg or door frame. Use the ankle to apply force for 2 s. Eversion training is to use the inside of the ankle's foot against a fixed object to push it inward for 3 seconds. Action six: use the training belt to train the ankle inside and out. Take a seated position, straighten your knees, use a training strap to fix one end to a heavy object (such as a table foot), and wrap one end around the inside of the ankle or the outside of the small toe. The ankle varus training is to rotate the foot away from the table foot with the foot, and then return to the initial position, count one training, be careful not to perform calf movements, external rotation training is to train the belt around the outside foot of the toe to turn out actions. Action seven: stand on one leg to support the whole, lifting training. Take the ankle-footed standing position, flex the knee on the healthy side, keep your feet away from the ground, and maintain a full body support for about 30s. Action eight: use a large towel to fold into a rectangle, the size is consistent with the size of the patient's feet. At the beginning of training, use both hands to support the support to ensure safety, gradually squat, and then stand up. With the progress of rehabilitation, gradually give up the help of supports, use their own muscle and nervous system to adjust the balance, and perform squat training. At a higher stage, the affected foot stands alone on the towel, and the rehabilitation teacher throws it to his body. Ball (you can change the direction and quality of the ball to increase the difficulty of training). For those athletes who are engaged in sports, conditions can be used for spa treatments, stepping, jumping, or kicking in various directions in waist-deep water [11].

(2) Traditional Chinese medicine therapy

(1) Mild ligament damage

Immediately after the injury, apply cold compresses to reduce the formation of hematomas. Local swelling can obviously be infused with cold water or externally applied with ice cubes. Replace once every 3 minutes for 30 minutes to constrict blood vessels and relieve local congestion. After 24 hours of sprain, switch to hot compress therapy, soak the towel with warm water or hot vinegar, hot wine, etc., and put it on the wound for 30 minutes. It can improve blood and lymph fluid circulation 1-2 times a day, which is conducive to blood stasis on the wound. And exudative absorption, in addition to self-reinforcing muscles and tendons, first slowly pull out and stretch the ankle joint, after a short time to do varus and eversion movements, do not use local manual rubbing in the early stage of injury, you can use Chinese medicine external application The rice dumplings are crushed into fine powder and mixed with frankincense into milk powder, which is adjusted to a paste with wine or egg white and applied to the wound, and the dressing is changed once a day [12].

(2) Severe ligament injury

Closed sticky plaster fixation method: the local drug is closed with a 2% lidocaine needle 1.5 ml and prednisolone acetate 0.5 ml. The ankle joint is placed in a mild valgus position with viscous fixation. If there is damage to the anterior fibula ligament and then slightly extended, the viscous paste passes from the inside of the foot through the plantar and lateral malleolus to the mid-anterolateral midsection of the calf. -4 strips, then use bandages to strengthen the fixation, usually 3 weeks can be fixed. Can be used 2% procaine 2 ml, plus acetic acid and acetaminophen 2 ml, for pain point closure, once a week, 3 times a course of treatment. Massage and acupuncture combined with fixed methods: acupuncture points such as Fengshi, Zusanli, Taixi, Kunlun, Qiuxu, Jueju, Jiexi, Taichong, and Ashi can be selected. Acupuncture (retaining needle for 15-30 min), once a day, to clear the qi of the meridians [13]. Restriction of ankle motion can be fixed with adhesive tape (rubber plaster) or bandages for 1-2 weeks. Those with medial collateral ligament injury should be inverted and fixed, those with lateral collateral ligament injury should be inverted and fixed to reduce the

tension of the injured ligament and accelerate the injury of the ligament. Repair. If the lateral collateral ligament of the ankle is damaged, take 3 pieces of 2.5-3 cm wide tape to valgus the affected foot. The first piece of tape starts from the inside of the foot and passes through the front of the lateral malleolus to the front of the calf and then behind the tape. Adhere the second and third tapes in parallel, and then apply bandages outside. It can also be treated with proprietary Chinese medicines. Sanqi injury pills, betta pills, Yunnan Baiyao, Qilisan, and conventional administration are used. It usually recovers in about 15 days [14].

(3) Tai Chi exercise

Patients are organized to participate in the study and exercise of prescribed Taijiquan movements. During exercise, attention is required to focus on activities that hurt the ankle. In the early treatment stage, surgical therapy is the main part, and some rehabilitation exercises are performed at the same time as surgical therapy. The focus of rehabilitation treatment during this stage is to prevent symptoms such as ankle instability or recurrent dislocation. After 3 weeks, patients with ankle ligament injuries were trained in Taijiquan, ranging from small to large. When the ankle was active, the two strengths penetrated each other, embracing each other, and running in parallel. During this period of training, it is required to increase the body's center of gravity. The body's center of gravity projection should be as close to or around the injured ankle as possible to prevent the injury from getting worse. It is not required to do the complete movement of Taijiquan. After 5-6 weeks, with the gradual recovery of the ankle injury, the body's center of gravity should gradually decrease when performing Taijiquan exercises, so that the distance of muscle work will increase accordingly. When playing Taijiquan, there is no need to focus on mental concentration. Under the control of consciousness, the mind of the practitioner always focuses on the injured ankle and the whole set of movements, eliminates the interference of other thoughts, and focuses on directing the functions of all organ systems throughout the body to cooperate with the injured ankle. Movement effectively prevents repeated ankle ligament injuries [15]. In the later stage of rehabilitation, in order to increase the left and right ankle ligament activity, perform "left cloud hand" or "right cloud hand" and other movements. Such movements can be moved laterally. Through training, the left and right ankle ligament activities can be guaranteed. In order to increase the full range of motion, "Left and Right Knee Staggers" is used. This move includes back and forth movements, left and right movements, outward abduction, inner buckle, lifting, and other movements to fully move the ankle ligaments; in order to make the ankle ligaments, the increase in the range of activity should be practiced in spiral-type arc movements, such as "left and right mustang split mane." The angle of body rotation is large, and the center of gravity gradually transitions to one foot. Because the center of gravity of the entire body moves smoothly, a certain height moves at a constant speed or constant speed, so that the ankle ligaments can be safely and fully exercised [11]. Regular exercise of this kind can not only promote the healing of ligaments

and shorten the recovery time but also enhance the flexibility and flexibility of the ankle ligaments.

(4) Extracorporeal shock wave therapy

Extracorporeal shock wave is a mechanical pulsed pressure wave transmitted through the medium of physics mechanism, which can produce good therapeutic effect on a wider range of human tissues where pain occurs through the positioning and movement of the treatment probe. Cavitation is the basis of ESW's effect on soft tissues. In the process, shock wave bubbles will be generated. Such bubbles will rapidly expand within a few microseconds and then burst after $100\,\mu$s, resulting in secondary, spherical shock waves, shearing. Tissue, release free radicals, target soft tissues that impinge on the lesion, resulting in axial damage, local bleeding, ecchymosis, hematoma, etc. When the energy of ESW is lower than $0.12\,$mJ/mm^2, the permeability of the cell membrane can be triggered, while when the energy of ESW is $0.5\,$mJ/mm^2, the changes of cytoplasm and mitochondria are mainly caused. Although the role of ESW in the treatment of soft tissue injuries is relatively clear, its mechanism of action is uncertain. Studies have found that ESW can promote the formation of new blood vessels, improve microcirculation, and promote the recovery of neural tissues by directly activating the healing process of soft tissues. Hausdorf et al. called the application of different ESW to the rabbit femoral end 10 days later and observed a decrease in local blood flow and bone metabolism. They believed that the process of ESW stimulation and promotion of tendon healing may be through local microfracture and damage to promote local growth factors and NO release to achieve tissue repair [12].

2.3. Nanomaterials. Nanomaterials are materials with nanoscale structures, which can be divided into zero-dimensional nanomaterials and one-dimensional nanomaterials according to their specific dimensions, and it has been asserted that when one can arrange and combine substances on very small dimensions, various materials of novelty will be obtained. The ratio of the number of surface atoms to the total number of atoms in a nanocrystal particle increases dramatically as the particle diameter becomes smaller. For example, at a particle diameter of 10 nm, the particle contains 4000 atoms and the surface atoms account for 40%; at a particle diameter of 1 nm, the particle contains 30 atoms and the surface atoms account for 99%. It was not until the end of the last century when the first International Conference on Nanoscience and Technology was held in the United States that theoretical research and contemporary science and technology were formally combined, which marked the official birth of nanotechnology. When the size of a material is at the nanometer level, the number of atoms on the surface of the material will increase dramatically, and this number will far exceed the number of ordinary materials, when the chemical activity of the material will be greatly increased. At the same time, nanomaterials are comparable to or smaller than the wavelength of light waves, the wavelength of de Broglie and the coherence length of superconducting

states, and the periodic boundaries of the materials are destroyed, resulting in "novel" optical, electrical, magnetic, acoustic, and thermodynamic properties; in addition, nanomaterials have quantum size effect and macroscopic quantum tunneling effect. These unique characteristics provide the conditions for the wide range of applications of nanomaterials. With the continuous in-depth development of theory and practice, nanostructures not called systems have been established at present. Along with the maturity of application, the uniqueness of nanomaterials plays a pivotal role in the field of biotechnology and advanced manufacturing.

3. Experiments

3.1. Dynamic Balance System Combined with Surface Electromyography (SEMG) Experimental Monitoring

(1) Wu, the research subject, suffered severe strain on the right ankle Achilles tendon, and developed strained periarthritis, which was manifested as local thickening, tenderness, and a feeling of induration. The right Achilles tendon still had a thickening of 5 cm in length. According to the degree of soft tissue damage, it was II degree, and some ligaments were lacerated. Zhang, the Achilles tendon side collateral ligament excessive pull, acute sprain, I degree injury, slight swelling, physical examination and early isokinetic strength test, neither of them suffered severe pain in the ankle, joint effusion and other phenomena. Wu's wound suture is located in the posterior midline incision. The tendon sheath has been separated and the degenerative tissue has been removed. The scar has a slight swelling. The pain arc is located at the fibula long and short muscle stops. Wu's pain point is located at the tibialis anterior muscle stop. The symptoms of the two patients were similar. Both suffered from weakness of the posterior ankle muscles, the range of motion of the joints and dorsiflexion was small, and there was a large difference in the muscle strength of the left and right ankle joints. Myasthenia gravis is mainly characterized by partial or generalized skeletal muscle weakness, easy fatigue, aggravation of symptoms after activity, and reduction of symptoms after rest and is generally serious, long-lasting, and difficult to treat

(2) Research method: the Biodexpro3 isokinetic force measurement system (according to the test standards specified by the Chinese Medical Association) was used to orient the heart slowly 60%/s X5 times, mainly to test the ankle joint dorsiflexor maximal muscle strength index; 180% fast/s X25 times, the main test of muscle endurance indicators, a total of 4 tests before and after rehabilitation treatment, and the comparative analysis of the measurement indicators. In the test, the two people stood with the affected leg in turn, flexed their knees about 90° on the healthy leg, and stood continuously for 30 seconds. According to the stability program set by

the system, they performed "8-1" levels in order from easy to difficult, with the soles of the feet as much as possible. It moves close to the center of the display screen and moves in the same part. It can perform various actions such as front collar back and back, inversion, and eversion as the platform rotates. Tested 2 times before and after treatment

3.2. Surgical Treatment Monitoring

(1) General information: 16 cases of ankle fractures with triangular ligament rupture were surgically treated, including 10 males and 6 females. X-ray examination of the ankle joint laterally and ankle points was performed routinely before operation. After the internal fixation of the lateral malleolus fracture is completed during the operation (if the posterior malleolus fracture needs to be fixed as well), if the ankle perspective shows that the ankle joint is in good position, the external rotation stress test of the ankle joint should also be performed, and those with negative tests do not need surgery. Triangular ligament. If it is positive, it needs to be explored to repair the triangular ligament. This group accounts for 14 cases; if the intraoperative perspective shows that the medial malleolus talar space has not recovered, it is considered that the insertion of the gap after the rupture of the triangular ligament results in poor reduction. Triangle ligament, this group accounted for 2 cases

(2) Surgical methods: after the ligament was exposed in 16 patients in this group, the fracture sites were as follows: 5 cases at the medial malleolus rupture, 6 cases at the middle rupture, and 5 cases at the talar rupture. The person who broke at the medial malleolus was screwed in two 2.8 mm absorbable anchors or metal anchors at the center of the malleolus for repair; the middle fracture was sutured directly with l-0 absorbable suture; screw in two 2.8 mm absorbable anchors or metal anchors at the dead center for repair. When knotting sutures, you should pay attention to shortening the length of the original ligament slightly. Observe under direct vision to maintain the appropriate medial space of the ankle joint. Do not overtighten the ligament to shorten too much and affect the later function recovery. For type AO type C fractures, the preoperative judgment may be associated with lower liver fat combined injury, and the lower liver fat combined should be fixed. In this group, 4 patients with type C fractures were still positive after the deep repair of the triangular ligament was completed. Therefore, the liver fat joint is fixed under the liver fat hook. Finally, the superficial layer of the fractured triangular ligament was sutured with 2-0 absorbable sutures, and the incision was closed layer by layer

3.3. Rehabilitation Monitoring of Taijiquan Exercise

(1) Research subjects: the research objects came from different groups such as teachers, students, and

workers in a university, and 76 patients with ankle ligament injuries were selected (average age: 30.47 ± 9.05 years). And randomly selected 41 cases (average age 31.42 ± 8.35 years old) as the experimental group, mainly Taijiquan exercise. The remaining 35 patients (mean age 29.35 ± 9.45 years) were used as the control group for routine rehabilitation training

(2) Research methods: the subjects were randomly divided into the control group and the experimental group and organized to participate in the study and exercise of the prescribed Taijiquan movements. During the exercise, the rehabilitants were required to focus on the activities of injured ankles. In the early treatment stage, both groups are mainly surgical treatment, and medical staff assists in some rehabilitation exercises at the same time of surgical treatment. At this stage, the focus of rehabilitation treatment is to prevent symptoms such as ankle instability or recurrent dislocation. After 3 weeks, 41 patients with ankle ligament injuries in the experimental group performed Taijiquan exercise, with a small amount of exercise. During the early training, the patient exercised under the guidance of an expert. With the help of Tai Chi during the ankle movement, the two strengths penetrated each other, embracing each other, and running in parallel. During this period of training, it is required to increase the body's center of gravity. The body's center of gravity projection should be as close to or around the injured ankle as possible to prevent the injury from getting worse. It is not required to do the complete movement of Taijiquan. During this period, the control group mainly carried out some conventional rehabilitation training, began to perform standing posture exercises, and then carried out partial weight-bearing exercises. After 5-6 weeks, with the gradual recovery of ankle injuries, the body's center of gravity during the Taijiquan exercise in the experimental group should gradually decrease, so that the distance of muscle work will increase accordingly, and the physiological pressure on the ankle ligaments will gradually increase. The control group began to carry weight-bearing walking training; and gradually extended the training time (maximum 45 minutes) and performed exercises such as running, jumping, and stepping up and down in the later stage of rehabilitation

3.4. Extracorporeal Shock Wave Therapy Monitoring

(1) Research subjects: 40 athletes with ankle ligament injuries were selected, including 22 males and 18 females; the course of disease was 3 months and 1 year. They were randomly divided into an external shock wave (ESW) treatment group of 25 cases (14 men and 11 women) and a closed control group of 15 cases (8 men and 7 women). Both groups were diagnosed by physical examination and ankle MRI before treatment. Inclusion criteria are as follows:

(1) aged 16 years or older, (2) no history of surgery and cardiovascular and cerebrovascular diseases, (3) the contralateral ankle is normal, (4) the range of motion of the ankle joint is the same on both sides before the injury, (5) preoperative X-ray examination confirmed no history of fractures, (6) local skin was free of infection, necrosis, allergies and other symptoms, and (7) all athletes had no midfoot and forefoot ligament injuries

(2) Treatment method

(1) ESW group: DolorClast radiation shock wave therapeutic apparatus produced by Swiss EMS company is used for treatment. The patient was placed in supine position, and the pain points at the ankle ligament injury were identified by palpation, and the blood vessels and nerve distribution areas were avoided. Then, the coupling agent was locally applied, and the ESW treatment head was vertically aligned with the tenderness site, and the pressure was set to 2.0-4.0 bar, impact frequency 6 Hz, impact pulses 2000 times at each part, handle pressure is medium. The impact energy is adjusted according to the patient's tolerance, and the impact treatment is performed with a larger pressure tolerated by the patient. 3 to 4 times is a course of treatment, with a maximum of no more than 2 courses, and the interval between the two treatments is 7 days

(2) Closed group: the same position as above, after the pain point of the ankle ligament was determined, the pain point was injected with triamcinolone 1 ml and 2% lidocaine 1 ml suspension, closed once every 5-7 days, 3 times as 1. The course of treatment should not exceed 2 courses at most, in order to prevent the accumulation of medicinal fluid in the local tissue and damage to the local tissue

4. Discussion

4.1. Dynamic Balance System Combined with Surface Electromyography (SEMG) Experiment Monitoring and Analysis

(1) Comparison of healthy and affected calf circumference and joint activity before and after treatment

Comparison of calf circumference and joint mobility between the two before and after rehabilitation is shown in Table 1:

It can be seen from Table 1 that the ankle and calf circumference of the two people increased rapidly in more than one month, while the range of joint activity increased significantly, almost doubled. Over time, it can withstand the normal amount of training, no adverse reactions, swelling at the Achilles tendon subsided, and pain has been significantly reduced. Comparative examination found no significant difference in calf circumference, and the sides tended to balance.

TABLE 1: A comparative study of leg circumference and joint mobility between the two before and after rehabilitation.

	Calf girth	Range of joint activity
Before treatment	-1.6 ± 0.5	$46.8° \pm 1.2$
After treatment	0.8 ± 1.0	$85.3° \pm 1.6$

Note: the positive sign indicates that the affected side is thicker than the healthy side, and the negative sign is opposite.

(2) Changes in muscle function before and after rehabilitation training

Due to the influence of individual differences, the maximum strength index mainly takes the ratio of peak torque to weight, also known as relative peak torque (PT/BW), which represents the relative muscle strength of muscle contraction; strength endurance is mainly through work fatigue (ER, unit (%)) to reflect its ability. It specifically represents the fatigue resistance of muscles during repeated contractions. The lower the endurance index, the stronger the muscle's resistance to fatigue, indicating that the endurance is better. Then, observe the two people's long-term muscle work to maintain muscle tension and stress. The maximum strength and strength endurance indicators are shown in Table 2 and Figures 1 and 2. Muscular endurance is the ability of the body to perform sustained muscular work for long periods of time, i.e., the ability to fight fatigue. Endurance includes two aspects, namely, muscular endurance and cardiovascular endurance.

From Table 2 and Figures 1 and 2, it can be seen that with the passage of time, the relative peak torque values of the right ankle plantar flexor muscle groups continued to increase, the dorsiflexor muscles were basically flat, and the work fatigue index decreased gradually, indicating that the strength level of the right ankle was significantly improved, and the antifatigue ability was improved. The right ankle even surpassed the uninjured left ankle in some strength levels.

In summary, after the rehabilitation treatment cycle, the calf muscle fibers of the two people increased, and the corresponding strength and muscle fatigue resistance were significantly improved, indicating that better results were achieved through rehabilitation treatment.

4.2. Surgical Treatment Monitoring Analysis

(1) All fractures have healed. The average healing time of fractures is l2.8 weeks (10 to 14 weeks). There were no cases of delayed fracture healing and fracture nonunion, and no wound complications occurred

AOFAS ankle-hindock function score: excellent in 8 cases, good in 8 cases, excellent and good rate was 100%, with an average of 93 points (85-100 points). The VAS pain score was 0.94 points (0-2 points). Specific patient information is shown in Table 3.

(2) Anatomy of the triangular ligament: the triangular ligament is a fan-shaped complex structure composed of multiple ligaments. The deltoid ligament is the main ligamentous structure that stabilizes the medial

aspect of the ankle joint and functions to maintain the normal anatomical position of the talus and prevent its exostosis and dislocation. The anatomy of the triangular ligament is still controversial. It is generally believed that the triangular ligament is composed of shallow and deep layers. Milner et al. believe that the main basis for distinguishing deep and shallow layers is the number of joints they cross. A joint, but sometimes it is not absolute

4.3. Monitoring and Analysis of Rehabilitation Treatment of Taijiquan Exercise

(1) Rehabilitation assessment results

After 76 patients with ankle ligament injury were subjected to follow-up, investigation, and statistics for 12-15 months (average of 12.5 months in the experimental group and 13.8 months in the control group), the following criteria were used to evaluate the effect of rehabilitation treatment shown.

As can be seen from Figure 3, the rehabilitation assessment results are as follows: excellent: no reinjury, no pain during walking, ankle dorsiflexion angle of 20°-30°, plantar flexion of 40°-50°, no lameness, easy squatting, and normal joint function; good: no reinjury, good function of the joint cavity and tendon sheath, back extension of 10°-20°, plantar flexion of 25°-40°, mild swelling and pain after walking a long distance, slightly lameness, more convenient to squat, and can maintain normal work; poor: there is reinjury, the injury recovers slowly, pain and lameness are obvious during walking, the ankle is swollen and unstable, back extension is 0°-5°, plantar flexion is 5°-15°, and it is inconvenient or difficult to squat.

(2) Comparison of rehabilitation effects

Compare the curative effect of the experimental group with the curative effect of the control group. The evaluation results are tested by x2, as shown in Figure 4.

As can be seen from Figure 4, the healing effect of the experimental group was significantly better than that of the control group ($P < 0.05$) (see Table 4). Tested by x2: $P < 0.05$.

The results show that the exercise of Taijiquan allows the ankle ligament to be exercised, which effectively prevents the occurrence of contracture, ankle instability, and recurrent dislocation. When playing Taijiquan, there is no need for mental attention. Under the control of consciousness, the mind of the practitioner always focuses on the injured ankle and the whole set of movements, eliminating the interference of other thoughts, and focusing on directing the functions of all organ systems throughout the body to cooperate with the injured ankle. Performing activities effectively prevents repeated ankle ligament injuries.

4.4. Monitoring and Analysis of Extracorporeal Shock Wave Therapy

(1) Comparison of VAS scores

The comparison of VAS scores is shown in Table 5.

TABLE 2: Comparison of four tests of right muscle strength (affected side) before and after two persons.

Test target	Flexor plantaris at 60°/s				Flexor dorsal at 60°/s			
	Right 1	Right 2	Right 3	Right 4	Right 1	Right 2	Right 3	Right 4
Peak moment (Newton A kind of rice)	75.7	97.9	111.1	116.3	52.1	41.9	49.0	56.8
Peak torque/weight (%)	94.6	122.4	138.9	145.4	65.1	52.4	61.3	71.0
Total work (joules)	136.5	224.5	260.9	270.9	157.1	140.6	181.7	218.0
Average power (Watts)	49.9	74.4	86.9	75.8	55.3	45.8	54.5	60.4
Work fatigue (%) (180°/s)	56.2	29.8	28.0	13.7	26.5	16.3	19.3	21.2
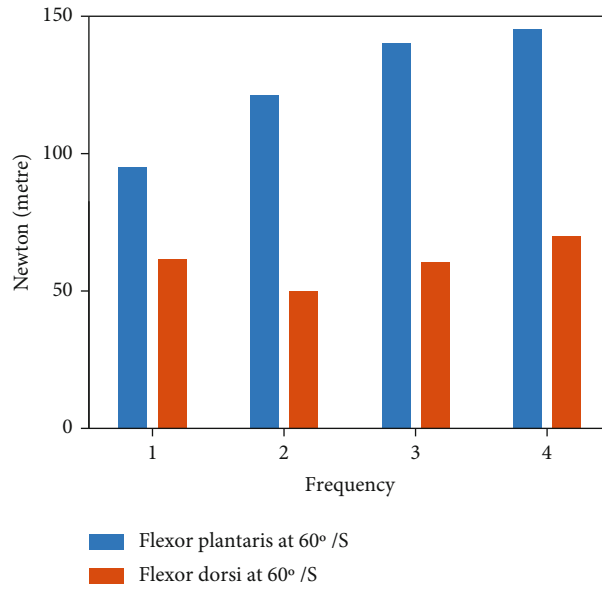
FIGURE 1: 4 relative peak moment changes before and after.
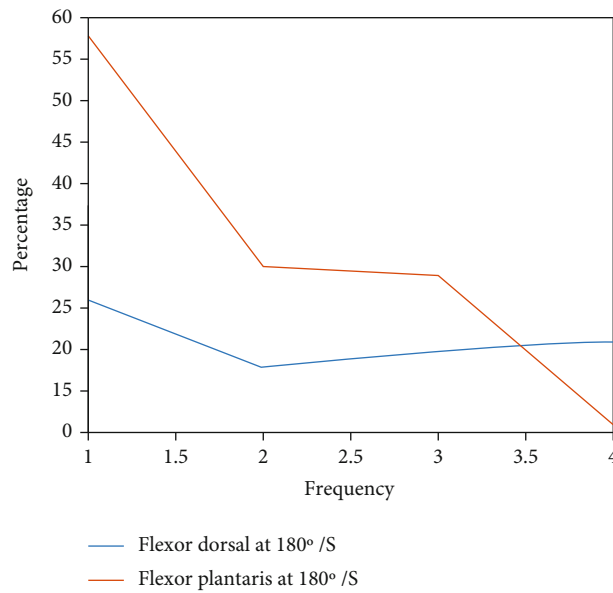
FIGURE 2: Change of fatigue degree before and after 4 times of work.

TABLE 3: Materials of 16 patients.

Case	Age (years)	Involved side	AOFAS score (pre/post)	VAS score (pre/post)	Follow-up Time/months
1	22	Left	100/100	0/0	30
2	35	Left	100/97	0/1	38
3	42	Left	90/90	0/1	48
4	48	Left	100/87	0/2	84
5	52	Left	100/97	0/0	32
6	68	Right	90/85	0/2	72
7	38	Right	100/97	0/1	64
8	52	Right	100/90	0/1	42
9	40	Left	100/97	0/0	34
10	40	Left	100/90	0/2	40
11	31	Right	100/97	0/1	65
12	64	Right	90/87	0/2	32
13	40	Right	100/90	0/1	36
14	41	Left	100/90	0/1	41
15	38	Left	100/97	0/0	40
16	30	Right	100/97	0/0	52
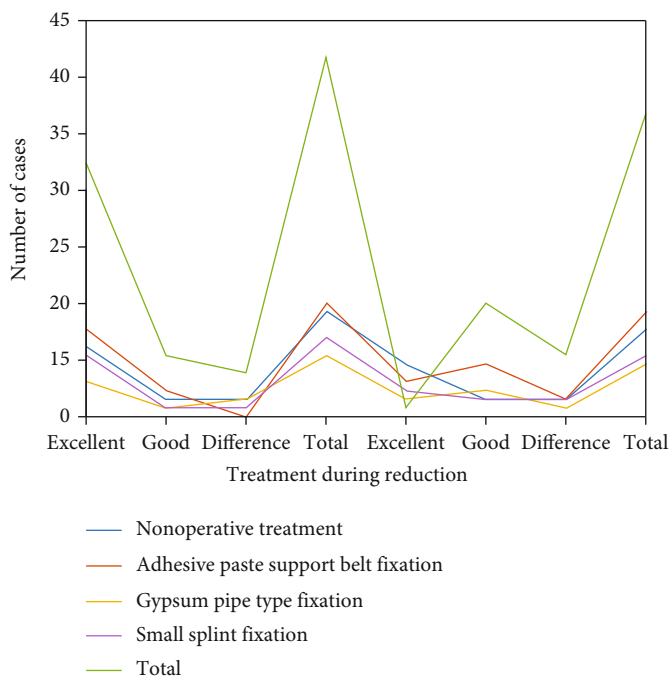
FIGURE 3: Rehabilitation evaluation results of the experimental group and control group.

As can be seen from Table 5, there was no significant difference in VAS scores between the two groups before treatment, at the end of treatment, and 4 weeks after treatment ($P > 0.05$), and there was a significant difference in VAS scores at 8 weeks after treatment ($P < 0.05$). At the same time, the VAS scores of the two groups before treatment were significantly different from those at the end of treatment, 4 weeks, and 8 weeks after treatment ($P < 0.05$).

(2) Kofoed score comparison

Kofoed score comparison is shown in Table 4.

It can be seen from Table 4 that there was no significant difference in the scores of the Kofoed observation indexes before treatment between the two groups ($P > 0.05$); the scores of pain, function, and activity of the ESW treatment group after treatment were significantly higher than those of the closed treatment group, with significant differences.
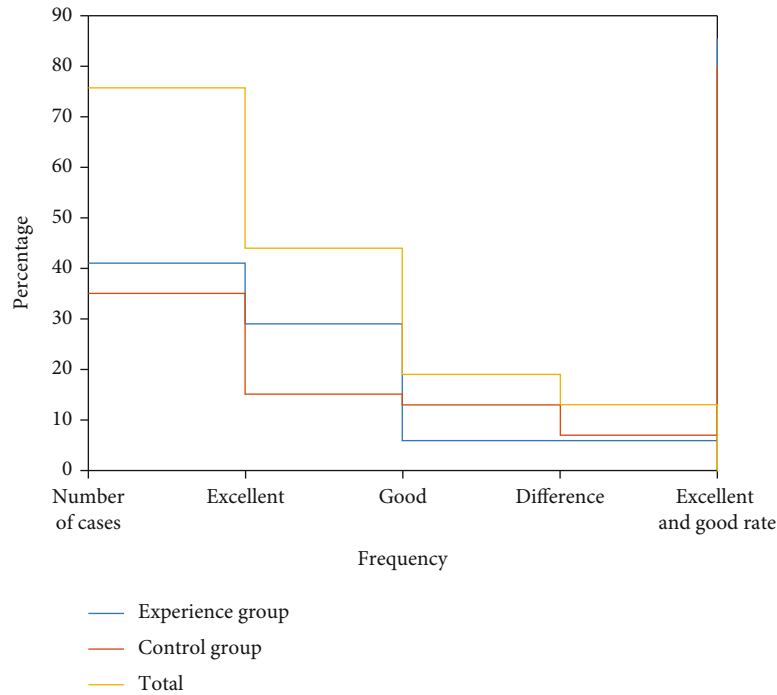
Figure 4: Comparison of rehabilitation effect between experimental group (41 cases) and control group (35 cases).

Table 4: Comparison of Kofoed scores between the two groups before and after treatment.

Kofoed observation index	Group ESW		Closed group	
	Preoperative	Postoperative	Preoperative	Postoperative
Pain	12.00 ± 8.66	40.60 ± 8.46	14.00 ± 10.56	26.67 ± 11.29
Function	7.08 ± 4.14	23.52 ± 3.64	8.40 ± 4.84	17.00 ± 4.63
Activity degree	4.52 ± 1.90	16.60 ± 2.47	5.07 ± 2.34	13.13 ± 3.00
Total	23.60 ± 14.70	80.72 ± 14.57	27.47 ± 17.74	56.80 ± 18.92

Table 5: VAS scores of patients in both groups before and after treatment.

Group	Number of cases	Before treatment	At the end of treatment	4 weeks after treatment	8 weeks after treatment
Group ESW	25	8.40 ± 1.19	3.72 ± 1.40	2.72 ± 1.37	2.40 ± 1.44
Closed group	15	8.53 ± 1.12	3.40 ± 1.12	3.33 ± 1.11	4.73 ± 1.98

Sexual significance ($P < 0.05$). The shortest recovery time for recovery training after treatment in the two groups: The shortest recovery time ($5.52 ± 1.36$ weeks) for athletes after training in the ESW treatment group was significantly shorter than that in the closed treatment group ($6.60 ± 1.76$ weeks) ($P < 0.05$).

5. Conclusions

For a long time, many sports workers and athletes have believed that "sports injuries are inevitable" and that "without sports injuries, high-level sports performance cannot be achieved," which has no scientific basis. The fundamental way to reduce exercise operations is to adhere to the principle of prevention. We must carefully analyze and study the various factors that are likely to cause injuries, summarize our experience, and gradually form the concept of injury prevention in ideology. With sufficient attention, the illness must not be delayed, and the acute injury gradually evolves into a chronic injury. To this end, this paper presents a study on rehabilitation and monitoring of Achilles tendon ligament injuries in athletes based on nanomaterial repair.

In this paper, we found that the dynamic balance system combined with surface electromyography (SEMG) experimental monitoring, surgical treatment monitoring, rehabilitation therapy monitoring of Taijiquan exercise, and monitoring of extracorporeal shock wave therapy. The dynamic balance system combined with surface electromyography (SEMG) treatment can increase the calf muscle fibers, increase the corresponding strength and muscle

fatigue resistance, and achieve good curative effects. Surgical treatment can accelerate fracture healing, with a cure rate of 93%. It has a significant effect on the rehabilitation of ankle ligament sprains; Taijiquan exercises can exercise the ankle ligaments and effectively prevent the occurrence of contractures, ankle instability, and recurrent dislocations; the analgesic effect of extracorporeal shock wave treatment on patients with ankle ligament injuries Compared with the traditional closed treatment, the effect is more durable and effective.

The results of this study indicate that ESW also has a strong analgesic effect on pain after soft tissue injury. In this article, immediately after treatment and 4 weeks after treatment, the VAS scores of the ESW group and the closed group were significantly lower than before the treatment, indicating that the two treatment groups had better analgesic effects in the early stage and there was no difference. The VAS score of the ESW group at 8 weeks after treatment was significantly lower than that of the closed group, indicating that the effect of closed treatment was less than 8 weeks after treatment, and the analgesic effect of ESW lasted longer. In addition, the total effective rate in the ESW group was also significantly higher than that in the closed group after treatment. Therefore, we believe that the analgesic effect of ESW on patients with ankle ligament injury is more durable and effective than traditional closed treatment.

Data Availability

The data that support the findings of this study are available from the corresponding author upon reasonable request.

Conflicts of Interest

The authors declared no potential conflicts of interest with respect to the research, authorship, and/or publication of this article.

Acknowledgments

References

[1] X. Yang, Y. Zhu, and X. Xiang-yang, "Ankle joint distraction arthroplasty for severe ankle arthritis," *BMC Musculoskeletal Disorders*, vol. 18, no. 1, p. 96, 2017.

[2] T.-Y. Kim, S.-H. Kim, and H. Ko, "Design and implementation of BCI-based intelligent upper limb rehabilitation robot system," *ACM Transactions on Internet Technology*, vol. 21, no. 3, pp. 1–17, 2021.

[3] K. C. Seo, S. H. Park, and K. Y. Park, "Impact of wearing a functional foot orthotic on the ankle joint angle of frontal surface of young adults with flatfoot," *Journal of Physical Therapy Science*, vol. 29, no. 5, pp. 819–821, 2017.

[4] H. Lee and N. Hogan, "Energetic passivity of the human ankle joint," *IEEE Transactions on Neural Systems & Rehabilitation Engineering A Publication of the IEEE Engineering in Medicine & Biology Society*, vol. 24, no. 12, pp. 1416–1425, 2016.

[5] A. Elbaz, I. Magram-Flohr, G. Segal, A. Mor, and L. Kalichman, "Association between knee osteoarthritis and functional changes in ankle joint and Achilles tendon," *The Journal of Foot and Ankle Surgery*, vol. 56, no. 2, pp. A327–A327, 2017.

[6] H. Wang and S. R. Brown, "The effects of total ankle replacement on ankle joint mechanics during walking," *Journal of Sport and Health Science*, vol. 6, no. 3, pp. 340–345, 2017.

[7] C. Vanden Berg, E. A. Crawford, E. S. Enselman, C. B. Robbins, and A. Bedi, "Restricted Hip Rotation Is Correlated With an Increased Risk for Anterior Cruciate Ligament Injury," *Arthroscopy: The Journal of Arthroscopic and Related Surgery*, vol. 33, no. 2, pp. 317–325, 2017.

[8] G. H. Choi, H. Ko, W. Pedrycz, A. K. Singh, and S. B. Pan, "Recognition system using fusion normalization based on morphological features of post-exercise ECG for intelligent biometrics," *Sensors*, vol. 20, no. 24, p. 7130, 2020.

[9] H. Zhu, H. Wei, B. Li, X. Yuan, and N. Kehtarnavaz, "Real-time moving object detection in high-resolution video sensing," *Sensors*, vol. 20, no. 12, p. 3591, 2020.

[10] N. Özada, "The effect of collateral ligament injury on cartilage contact in knee joints modeled with six degrees of freedom," *Journal of Mechanics in Medicine & Biology*, vol. 16, no. 3, p. 1650080, 2016.

[11] M. P. Cote, "Editorial Commentary: ,narrow knee intercondylar Notch width is a risk factor for anterior cruciate ligament injury, and hetrogeneous methods are a risk factor for "between study" error in meta-analyses," *Arthroscopy: The Journal of Arthroscopic and Related Surgery*, vol. 34, no. 3, pp. 901-902, 2018.

[12] T. Rezapour, E. E. Devito, M. Sofuoglu, and H. Ekhtiari, "Perspectives on neurocognitive rehabilitation as an adjunct treatment for addictive disorders: from cognitive improvement to relapse prevention," *Progress in Brain Research*, vol. 224, no. 3, pp. 345–369, 2016.

[13] H. Hu, "Common types and countermeasures of ankle ligament injury caused by intense basketball movement," *Nigerian Journal of Clinical Practice*, vol. 20, no. 8, pp. 1036–1039, 2017.

[14] L. E. Simons, C. B. Sieberg, C. Conroy, E. T. Randall, and D. E. Logan, "Children With Chronic Pain: Response Trajectories After Intensive Pain Rehabilitation Treatment," *Journal of Pain Official Journal of the American Pain Society*, vol. 19, no. 2, pp. 207–218, 2018.

[15] G. F. Unger, "Early medical rehabilitation after neurosurgical treatment of malignant brain tumours in Slovenia," *Radiology and Oncology*, vol. 50, no. 2, pp. 139–144, 2016.

Research Article

Nanotube Combined Rehabilitation Therapy in the Treatment of Knee Arthritis in Basketball Players

Yi Zheng [ID]

College of Physical Education, Xuchang University, Xuchang, 461000 Henan, China

Correspondence should be addressed to Yi Zheng; 12003043@xcu.edu.cn

With the improvement of people's attention to health, basketball is a sport that can strengthen the body and deeply loved by people. However, basketball involves a lot of physical activity and a quick stop technique, which increases the risk of arthritis. The reason for this paper is to concentrate on the utilization of nanotube joined restoration treatment in the treatment of knee joint pain in basketball players. This paper first introduces the structure and properties of carbon nanotubes, analyzes the pathology of knee arthritis and the causes of knee arthritis in basketball players, and discussed the knee arthritis rehabilitation treatment method. According to the diagnostic criteria of osteoarthritis and the significant incorporation and rejection measures, a sum of 50 patients with knee osteoarthritis were chosen as the review subjects and separated into test gathering and control bunch. The benchmark group was treated with conventional electroacupuncture, and the exploratory gathering was treated with nanotubes as repair materials for knee arthritis. The experimental results show that the application of nanotube combined rehabilitation therapy in the treatment of knee arthritis in basketball players is practical to a certain extent. The total score of WOMAC in the two groups after treatment decreased to a certain extent compared with that before treatment, but the difference in the experimental group was more obvious, and the difference was significant after statistical analysis ($P < 0.05$).

1. Introduction

Influenced by international high-level games, such as the NBA, basketball is gaining popularity among the general public. However, basketball players may suffer some sports injuries due to the influence of factors such as fierce confrontation, fierce competition, frequent physical contact, and playing environment. On the one hand, sports injury will not only bring physical inconvenience and pain to basketball participants but also affect their normal work and study. Serious injury will also make people physically disabled and even lose their lives. On the other hand, sports injuries have a negative impact on the smooth development of basketball.

As a normal one-layered nanomaterial, carbon nanotubes stand out because of their one of a kind construction and physical and synthetic properties. Carbon nanotubes have strong mechanical properties, stable chemical properties, special electronic structure, and optical properties and have a wide range of applications in material variation and environmental science, especially in the field of biomedicine. The discovery and development of special properties of carbon nanotubes is a very active research, which has laid a foundation for the treatment of knee arthritis patients.

Acrisio et al. reported theoretical studies on the structure and phonon properties of single-walled and double-walled carbon nanotubes under hydrostatic pressure. Their results confirmed a dramatic change in the volume of the single-walled carbon nanotubes at high pressures [1]. Their report did not address the real problem. Loredo-perez et al. aimed to quantitatively study the injurious spontaneity, knee edema, proinflammatory cytokines, bone mineral density, and microstructure of unilateral knee arthritis mice fed a high-fat diet. Their method was to give standard diets (SD) and HFD to male ICR mice starting at 3 weeks of age. The serum levels of il-1 and il-6 were first injected by CFA and then analyzed by ELISA for RANKL and microcomputed tomography [2]. Although they conducted quantitative

studies on mice fed with HFD, they still need to conduct qualitative studies. Straker et al. team found that arthritis of the hip and knee afflicts those who continue to pursue exercise as they age. They discussed mechanical measures to reduce joint load, including support, footwear, and foot orthotics/insoles. Biomechanical considerations of applying gait retraining and joint unloading techniques are proposed [3]. The method they proposed has no practical application value.

This paper first introduces the structure and properties of carbon nanotubes, analyzes the pathology of knee arthritis and the causes of knee arthritis in basketball players, and discussed the knee arthritis rehabilitation treatment method. According to the diagnostic criteria of osteoarthritis and the relevant inclusion and exclusion criteria, a total of 50 patients with knee osteoarthritis were selected as the study subjects. The control group was treated with ordinary electroacupuncture, and the experimental group was treated with nanotubes as repair materials for knee arthritis. The experimental results show that the application of nanotube combined rehabilitation therapy in the treatment of knee arthritis in basketball players is practical to a certain extent. Nanotube can withstand high temperature and is harder than steel, so it has a higher repair effect than traditional repair methods [4].

2. Treatment of Knee Arthritis with Nanotube and Rehabilitation Therapy

2.1. Nanotubes.
As typical one-dimensional nanomaterials, carbon nanotubes (CNTs) have unique physical, chemical, and electronic properties [5, 6]. Carbon nanotubes are one-dimensional hollow tubular nanomaterials formed by curling graphite sheet layers. Single-walled carbon nanotubes are framed by twisting a solitary layer of graphite, and multi-walled carbon nanotubes are shaped by twisting different layers of graphite [7, 8]. The specific structure formed by carbon nanotubes is related to the Angle and curvature when the graphite sheet is curled into a tube, so it may have different chirality, which are zigzag, armchair, and chiral.

Because of the unique and stable special topological structure of CNTs, CNTs will not break when subjected to bending but can achieve elasticity according to volume changes, with high strength and toughness [9]. It has excellent performance in physical mechanics, electricity, heat, and so on. When CNTs or their functionalized products are added to polymer or composite materials, their physical and mechanical properties, thermal properties, and electrical properties can be improved to a certain extent.

2.2. Basketball Players and Knee Arthritis

2.2.1. Knee Arthritis.
Osteoarthritis (OA) is a chronic osteoarthritis with prominent pathological features. OA is a kind of degenerative change of articular cartilage and secondary bone hyperplasia [10, 11]. Clinically, chronic joint pain, stiffness, swelling, and joint dysfunction are the main manifestations. As the knee joint is the most complex joint in the whole body with the highest load and the heaviest shear force, osteoarthritis (KOA) is most likely to occur at this joint [12, 13]. The symptoms of KOA are mainly manifested as knee swelling and pain when walking up and down stairs, sitting and standing up, knee pain and discomfort, etc. There will also be swelling, popping, and fluid accumulation in patients [14]. The clinical manifestations are degeneration of local cartilage tissue of knee joint, formation of osteophyte at knee joint edge, and changes of subchondral bone reactivity [15].

The entire course of disease development affects not only the articular cartilage but also the entire knee joint, including the subchondral bone, joint capsule, ligament, synovium, and the surrounding muscles of the knee joint [16, 17]. The onset of the disease is characterized by abnormal biochemical metabolism of the knee cartilage, and then damage to the structure of the knee joint, resulting in fibrosis, gap, ulcer, and damage to the entire knee joint surface, leading to knee joint pain and abnormal function [18].

2.2.2. Causes of Knee Joint in Basketball Players.
Basketball sports have a lot of physical activities and technical movements such as quick stop. When basketball players use these technical movements to play games, they are likely to cause great sports injuries to themselves. During the movement of the knee, the knee needs to bounce and squat continuously. This instantaneous explosive action keeps the knee in a bent state for a long time, which will cause the knee joint to bear a lot of extra load, thus causing sports injuries. The knee is the most vulnerable part during exercise. Once this part is damaged, the level of the athlete will be greatly affected, and this effect is not short-term, it will cause great harm to the athlete.

2.3. Knee Arthritis Rehabilitation Therapy

2.3.1. General Treatment.
If KOA patients' symptom is lighter, function is normal, should be given priority to with preventive measures and daily care, to related education and help the patients study, also should have the health-related behavior in daily life, to be able to slow the progress of the disease, and make the patient's quality of life improved, make the medical expenses of patients with lower [19, 20]. The contents of KOA education include posture, joint function, joint protection, disease, psychology, and so on. Patients should be allowed to understand the basic knowledge of the disease, to avoid catching cold or staying in a certain position for a long time, as well as excessive joint load. For obese patients, they should adopt such methods as diet control, weight loss, restriction of climbing activities, insistence on driving instead of walking, and reduction of activities when joints swell and should pay attention to the combination of work and rest, thereby gradually enhancing their physique. A systematic review of evidence-based medicine shows that therapeutic interventions based on patient education, exercise therapy, and weight control measures are not only cost-effective but also have good long-term efficacy and should be used as the core clinical treatment. Core treatments include self-management, health education, weight and information control, and psychological

intervention. Health education can significantly improve the short-term and long-term efficacy of KOA therapy.

2.3.2. Drug Therapy. Acetaminophen, nonsteroidal anti-inflammatory and analgesic drugs, traditional Chinese medicine, blood-activating and collateral-activating drugs or dialectical drugs, and external drugs can be used. Tramadol and other drugs can be used for severe pain [21, 22]. The use of acetaminophen (Max. 4 g/d, OTC single dose <650 mg) as the preferred therapeutic agent has been recommended in several guidelines. If full-dose acetaminophen is not effective in patients, ACR recommends oral or local administration of nonsteroidal anti-inflammatory or intra-articular injection of corticosteroids. Now, clinical also commonly used chondroitin sulfate, glucosamine, double reactine and vitamins, and other drug treatment. It has been reported that intra-articular injection of corticosteroids, sodium hyaluronate, deer and melon polypeptides, ozone, and joint cavity irrigation has been widely used and achieved good results. At present, there is still no strong evidence to prove that glucosamine, chondroitin, and other nutritional treatments can be used as the routine treatment of OA. Corticosteroids can relieve joint pain in the short term, but long-term repeated use can cause joint damage. Therefore, the authoritative guidelines are recommended to be used under certain conditions. Although there are many research methods for restoring articular cartilage, such as changing joint load and periosteum, perichondrium transplantation, chondrocyte and mesenchymal stem cell transplantation, artificial matrix, and growth factors, there is no method that can completely restore normal articular cartilage. Against glucosamine or chondroitin drugs, intra-articular injection of hyaluronic acid, duloxetine, and opioid painkillers is not recommended.

2.3.3. TCM Treatment. There are many methods such as internal administration of traditional Chinese medicine, external treatment, acupuncture and moxibustion, massage, acupotomy, and new treatment combining traditional techniques with modern science and technology. In the theory of the meridians, the meridians have the functions of articulation of limbs, restraint of bones, viro-body, and locomotion. Based on the theory of tendons, the special features and rules of tendons diseases were studied, and the tendon disease has carried on the thorough exploration, and it was concluded that pathological tendons were the pathogenic factors of tendons diseases, and a simple and feasible diagnostic method was put forward, which laid a solid theoretical foundation for the treatment. Silver needle therapy is beneficial to the communication and combination between the theory of biomechanic dynamic balance and the etiology and pathology of chronic soft tissue injury in the overall concept of traditional Chinese medicine and western medicine surgical treatment and has achieved good results. Acupuncture points in traditional Chinese medicine are closely related to vascular nerves. Under the stimulation of acupuncture points, blood supply of knee joint is improved and blood stasis is improved. Acupuncture can also directly stimulate the nerve tissue or pain source area conducting pain sensation, block the pain conduction in the nerve fiber, and inhibit the response of spinal dorsal horn cells to injurious stimuli. It may also effectively strengthen the function of muscle groups in various parts of the knee joint, consolidate the normal physiological function of the knee joint, and maintain the stability. The short-term and long-term effects of early knee arthritis were observed, and the results were more satisfactory than that of drug therapy. In the aspect of antiexercise fatigue, acupuncture therapy has advantages that other therapies do not have. The action mechanism of traditional Chinese medicine therapy is complex, and the study on the action principle is yet to be further studied. The traditional Chinese medicine therapy and the emerging Chinese medicine therapy have different standards in terms of treatment norms, which also need to be further developed.

2.3.4. Physical Therapy. Physical therapy was aimed at alleviating or eliminating the symptoms of KOA through the rational use of various physical factors. Such methods can improve local blood circulation, relieve muscle spasm, promote the absorption and dissipation of joint inflammation, and reduce bone pressure and pain. Compared with internal medicine and surgery, physical factor therapy is more economical in cost and can reduce medical costs. At the same time, it is additionally of incredible importance to work on patients' personal satisfaction and lessen family and social weight. Physical therapy generally uses physical properties such as sound, optics, electricity, or mechanics as well as cold and heat conduction to carry out corresponding treatment without sequelae [23]. The application of low-intensity pulsed ultrasound to promote cartilage repair in osteoarthritis has been found to have a good effect. The application of modulated medium frequency electrotherapy has a continuous and significant effect on relieving knee joint pain and is of great significance. The results of low-frequency thermal vibration magnetic therapy showed that the pain intensity score of the patients was significantly reduced after treatment. Low-intensity laser intravascular irradiation for elderly osteoarthritis can reduce the dosage of NSAIDS. Some scholars have summarized the physiotherapy scheme of KOA. If the acute knee joint swelling is obvious, the main method should be analgesia and detumescence. At the same time, cold therapy can be used to shrink the local blood vessels so as to reduce exudation and increase the pain area. In the chronic phase, ultrasound therapy and warm or micro heat ultrashort wave and microwave therapy should be used to enhance the local blood circulation. For example, if ligament and soft tissue are involved, medium frequency or low frequency electrotherapy should be used to release adhesion. If necessary, two physical factors can be combined to improve the therapeutic effect.

2.3.5. Exercise Therapy. Maintain normal composition and structure and mechanical properties of articular cartilage must make the joints have a certain weight, while maintaining the normal articular cartilage type, intensity, and frequency of the load there is a wide range, but when the intensity or frequency of the load above or below this range,

destroy the balance of the synthesis of articular cartilage degradation mechanism, composition, and ultrastructural changes of cartilage. Proper exercise is necessary to maintain the normal use of articular cartilage. Sports training has the advantages of noninvasive, efficient, and lasting and is favored by more and more doctors at home and abroad.

Through exercise training, the muscle strength around the knee joint is enhanced, and the symptoms of muscle atrophy are alleviated, so as to ensure the normal transmission of joint mechanics. At the same time, the stability of joints has been improved, so that the joints in a good state of protection can prevent the development of OA. Quadriceps strength training can steadily improve knee joint function and increase walking distance. Clinicians often use this training method to improve knee joint function. Routine quadriceps muscle strength training can relieve symptoms and slow down the progression of joint degeneration to a certain extent. Meanwhile, it can also increase the mobility and stability of the knee joint and inhibit or slow down the vicious cycle of joint instability in KOA. Although many scholars believe that training quadriceps muscle strength can relieve the symptoms of joint pain, strengthening quadriceps muscle strength training cannot improve the joint movement of the knee joint. Although quadriceps exercise improved muscle weakness, it did not achieve the desired effect of improving the symptoms of KOA. However, the researchers still agree that quadriceps rehabilitation exercise can be performed according to patients' different conditions and individual differences.

With the exception of the quadriceps, the stability of knee activity is determined by the ratio of muscle strength between the quadriceps and the hamstring. In patients with KOA, the extensor knee and the flexor knee muscles have the same loss of strength. Therefore, attention should be paid to both the knee extensor muscle strength training and the flexor knee muscle strength training. The results can improve the muscle strength, further coordinate the flexor and extensor muscle strength ratio, and increase the stability of the knee joint, thus effectively controlling or slowing down the development of KOA's disease. Constant speed muscle strength training requires the assistance of exercise equipment, through the equipment to adjust the resistance at a constant speed, and in the process of movement, the muscle in all angles can occur to maximum contraction and maximum tension, so as to achieve the best training effect. Isokinetic muscle strength training can effectively improve the muscle strength of quadriceps femoris and other muscle groups around the knee joint, significantly improve the stability of the joints of patients with KOA, and effectively improve the joint function of patients. However, isokinetic muscle training equipment has the characteristics of expensive, complicated operation, and high treatment cost, so it is still difficult to popularize at present. Chain of lower limb muscle training can effectively improve the limb motor function, muscle chain training emphasized to joint training of muscles, rather than a single muscle training, confirmed in the muscle chain theory emphasizes the balance between muscle in the chain and the importance of coordination, and lower limb muscle chain have positive

effects on KOA rehabilitation training. However, there is a difference between isokinetic muscle strength training and quadriceps muscle strength enhancement between male and female patients. Through isokinetic muscle strength training, the quadriceps muscle strength can be effectively enhanced in male KOA patients. However, this concept is not suitable for female KOA patients.

Insisting on isometric length, isometric tensioning exercise can make joint ache alleviate effectively, make joint stability increase, and make joint function improve, and its long-term effect is better than sodium hyaluronate. Because range of motion is positively correlated with the risk of injury and falls, increasing range of motion can help reduce pain. For KOA patients, emphasis should be placed on stretching the quadriceps, hamstrings, and triceps of the calf to increase the range of motion of the joint. Static stretch training had a significant therapeutic effect on KOA patients. Six weeks of static stretch training resulted in a significant decrease in WOMAC osteoarthritis index score. For the KOA patients treated with joint slackening, a medical procedure, the strolling velocity and step length of the patients altogether worked after therapy contrasted and before therapy, and the aggravation was essentially diminished. The effect was significantly better than that of the low-frequency pulse electric group, but the difference was not significant compared with the electric stimulation group 4 weeks after the end of treatment. Acupuncture combined with proprioceptive sensation training is conducive to the improvement of patients' proprioceptive sensation, which has a positive effect on the stability, flexibility, and self-control of the affected knee joints, and at the same time improves and consolidates the efficacy of acupuncture. In overweight patients, weight loss combined with exercise or even weight loss alone can achieve better results in alleviating pain, improving function, muscle strength, and quality of life. Therefore, weight control is strongly recommended as a necessary treatment. In addition to weight loss, joint stress reduction exercises can be performed by water movement or suspension. Patients with KOA must be trained with aerobic exercises due to lower limb dysfunction and decreased body capacity. Aerobic exercise can enhance heart and lung function. For the elderly, moderate and low-intensity aerobic exercise such as walking, gymnastics, tai chi, and swimming can be used in the remission period of KOA patients. After aerobic exercise, KOA patients not only effectively relieved their joint pain but also improved their body function, increasing their walking speed and walking distance and maintaining their body function for about 18 months. Therefore, to lower the intensity of the exercise, adhering to long-term training is able to obtain better results. Numerous studies have shown that exercise is not only a cure for KOA but also a way to prevent it. Should, therefore, on the basis of KOA patients to evaluate their physiological characteristics, the condition of monitoring of autologous, develop sustainable personalized safe, effective, strong adaptability of exercise prescription, make movement dysfunction in patients with improved, pain relief and disease development delay, delay or avoid surgery time and improve the quality of life.

TABLE 1: Comparison of distribution of gender, age, and disease course of patients.

Group	Number of cases	Male	Female	Age	Course of disease (month)
Experience group	25	14	11	26	6
Control group	25	13	12	25	5.8

TABLE 2: Comparison of WOMAC scores between the two groups before and after treatment.

Symptoms	Group	Integral	
		Experimental group	Control group
The pain	Before	11.21	10.78
	After	3.32	3.96
Stiff joints	Before	32.07	31.15
	After	46.61	45.89
Physiological function	Before	3.79	4.85
	After	2.14	2.93
The total score	Before	21.21	25.63
	After	27.14	33.41

3. Experiments of Nanotube Combined Rehabilitation Therapy

3.1. Subjects. In this paper, patients with KOA basketball players who were qualified for primary screening from January 2019 to June 2019 for diagnosis and treatment were selected for the observation of cases, and they were allocated to two groups by random number table in chronological order. The experimental group used nanotubes and electroacupuncture combined with rehabilitation therapy. Electroacupuncture is based on traditional acupuncture and moxibustion by adding low-frequency pulsed electrical stimulation, and through acupuncture and moxibustion to regulate qi, the human body's biological microcurrent is combined with acupuncture. The patients in the control group were treated with cupping. A total of 50 patients conforming to this study were included. The specific data are shown in Table 1.

3.2. Diagnostic Criteria. The analytic models of this study were intermittent knee torment in the knee over the most recent multi month; X-beam pictures (standing or weight-bearing) showed restricting of joint space, subchondral osteosclerosis or potentially cystic degeneration, and osteophyte arrangement at joint edges.

3.3. Experimental Methods. Each subject was given a two-week course of treatment as follows:

Hamstring training: In the prone position, perform the following movements: (1) straight knee and hip extension training; (2) bend the knee and bend the calf; (3) internal

and external rotation of the calves; and (4) internal and external rotation of lower limbs.

Acupuncture point selection is as follows: yinmen point, weizhong point, weiyang point, yingu point, heyang point, and chengshan point; the method of acupoint selection was in accordance with the national standards of acupuncture and moxibustion points. The depth and angle of acupuncture were also in accordance with the standards. After obtaining qi, the acupuncture was replenished and deflated, and the acupuncture was retained for 30 min.

Yk-2000a modulated if frequency therapeutic instrument was used, and the electrodes were placed in popliteal fossis-side juxtaposition. The osteoarthropathy prescription in the multistep treatment procedure was selected, and the treatment lasted for 20 min. The intensity of current output should be adjusted according to the patient's tolerance and comfort level.

3.4. Statistical Methods. Results statistical analysis was processed by statistical product and service solutions 20.0 statistical software. The comparison of measurement data met the t-test of normal distribution with homogenous selection of variance, while the t' test of nonhomogenous selection of variance did not meet the rank-sum test of normal distribution. The comparison of counting data was conducted by X^2 test, and the rank-sum test was conducted by rank data. All measurement data are represented by XSD. $P < 0.05$ indicated that the difference was statistically significant. The statistical analysis methods of measurement data can be divided into parametric test method and nonparametric test method.

4. Discussion of Nanotube Combined Rehabilitation Therapy

4.1. Comparison of WOMAC and VAS Scores between the Two Groups

4.1.1. Comparison of WOMAC Scores between the Two Groups before and after Treatment. Toward the finish of the one courses of treatment, the two gatherings acquired specific impacts on the WOMAC manifestation all out score. It was speculated that both the electroacupuncture group and the normal acupuncture group had treatable KOA, while the treatment group had better efficacy than the control group. WOMAC single symptom score, pain, joint stiffness, and physiological function under the two treatment methods have obtained a certain effect. Comparison of WOMAC scores before and after treatment is shown in Table 2 and Figure 1.

As should be visible from Table 2 and Figure 1, the all out WOMAC score of the test bunch changed essentially with the treatment, that is to say, $P < 0.05$, which was measurably critical. The complete score of WOMAC in the benchmark group changed essentially with the treatment, and the combined t-test showed $P < 0.05$, which was genuinely huge. In this way, it tends to be estimated that the improvement of absolute indications in the exploratory gathering and control bunch after treatment is superior to
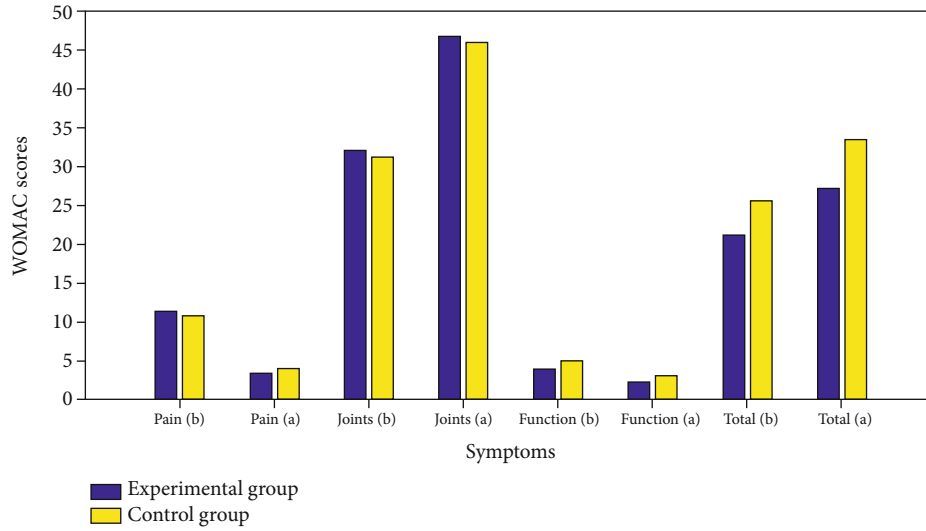
Figure 1: Comparison of WOMAC scores between the two groups before and after treatment.
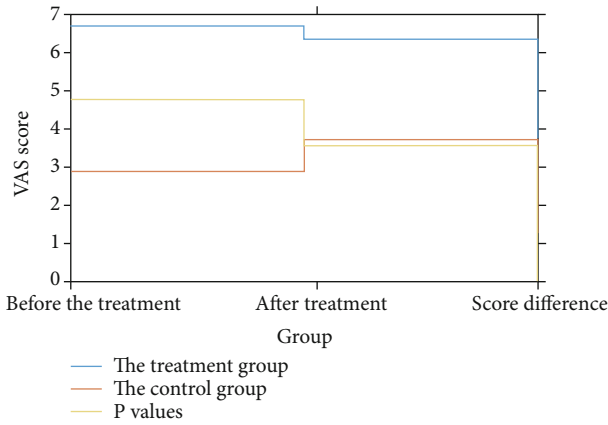
Figure 2: Comparison of VAS scores.
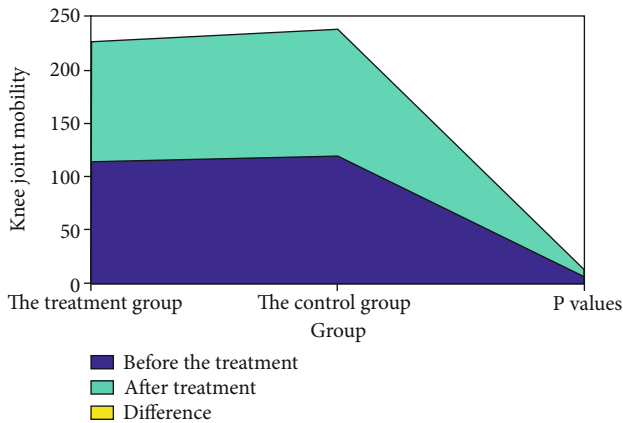
Figure 3: Comparison of knee joint mobility between the two groups.

that before treatment. The distinction in the absolute score between the two gatherings was huge ($P < 0.05$), so it very well may be viewed as that the test bunch was superior to

the benchmark group in working on the complete side effects. You can see the comparison between the control group and the experimental group, and the experimental group is significantly better than the control group.

According to the single symptom score, the pain score of the experimental group was significantly different before and after treatment, with statistical significance ($P < 0.05$). The changes of joint stiffness before and after treatment were significant ($P < 0.05$). There were significant differences in the scores of physiological function before and after treatment ($P < 0.05$). Therefore, it could be considered that the improvement of each single symptom in the treatment group was better than that before treatment. In the control group before and after treatment, the pain single score difference is obvious, with statistical significance ($P < 0.05$), joint stiffness score changes before and after the treatment, with statistical significance ($P < 0.05$), and physiological function score before and after the treatment, with statistical significance ($P < 0.05$), can be thought of as controlled in improving individual symptoms after treatment and was better than before treatment.

4.1.2. Comparison of VAS Scores. The VAS is a pain scale that gives pain a score of 10, with a score of 2 showing no aggravation, a score of 10 demonstrating serious agony, and a center score demonstrating changing levels of torment. Patients were approached to check the degree of agony on a size of 2 to 4 for gentle pain, 5 to 7 for moderate torment, and 8 to 9 for serious torment. Correlation aftereffects of VAS scores between the two gatherings are displayed in Figure 2.

As can be seen from Figure 2, there was a huge distinction in VAS score between the treatment bunch and the treatment bunch ($P < 0.05$). The VAS score of the benchmark group changed fundamentally with the treatment ($P < 0.05$). Along these lines, it tends to be presumed that the improvement of all out side effects in the treatment bunch and the benchmark group is superior to that before
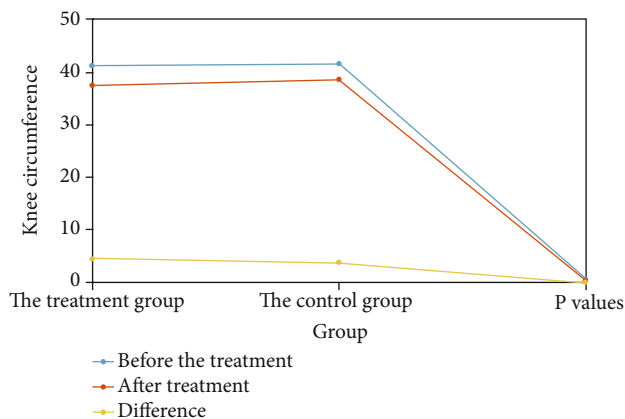
FIGURE 4: Comparison of knee circumference between the two groups.

treatment. There was no critical distinction in VAS score between the two gatherings before treatment ($P > 0.05$). VAS scores of the two gatherings were viewed as equivalent before treatment, and the distinction in VAS scores between the two gatherings was critical after treatment ($P < 0.05$). It very well may be viewed as that the corrective impact of the treatment bunch is superior to that of the benchmark group. So you could argue that the treatment group was better at improving pain symptoms than the control group.

4.2. Comparison of Knee Joint Mobility and Circumference Diameter between the Two Groups

4.2.1. Comparison of Knee Joint Mobility between the Two Groups.
With the treatment, the scope of movement and the circuit breadth of the knee joint in the two gatherings was improved, and the thing that matters was genuinely huge. The impact of working on the scope of movement in the test bunch was superior to that in the control needle therapy bunch. Electroacupuncture has a solid pain relieving impact, and this study accepts that the scope of movement of the joint is generally impacted by torment, which makes it comprehended that the adequacy of the nanotube in working on the scope of movement of the joint is superior to that of the control group. The examination consequences of knee joint portability between the two gatherings are displayed in Figure 3.

As should be visible from Figure 3, the scope of movement of the joints when treatment was fundamentally divergent in the treatment bunch, with factual importance ($P < 0.05$). The scope of movement of the joints in the benchmark group was essentially different with the treatment ($P < 0.05$). Along these lines, it very well may be theorized that the improvement of absolute indications in the test gathering and control bunch after treatment is superior to that before treatment. There was no critical contrast in scope of movement between the two gatherings before treatment ($P > 0.05$), demonstrating that the scope of movement of the knee joint before treatment was equivalent between the two gatherings, and there was no huge distinction in scope of movement between the two gatherings after treat-

ment ($P > 0.05$). Along these lines, it tends to be theorized that the improvement of scope of movement in the test bunch is like that in the benchmark group.

4.2.2. Comparison of Periknee Diameter between the Two Groups.
With the treatment, the two gatherings of joint versatility and knee around the improvement, measurably critically contrast. The distinction between the two gatherings of changes around the knee joint was not measurably huge, showing that there was no distinction in the capacity of the two gatherings to switch up the knee joint. In other words, the experimental group has the same effect of reducing knee swelling as the control group. The comparison of the two groups of data is shown in Figure 4.

The data in Figure 4 represent the pathogenic causes of external causes to the knee joint. As should be visible from Figure 4, there was a critical contrast in the periwidth of the knee joint in the treatment bunch with the treatment ($P < 0.05$). The fringe distance across of the knee joint was altogether unique with treatment in the benchmark group ($P < 0.05$). Subsequently, it very well may be viewed as that the periknee breadth of the test bunch and the benchmark group is more modest than that before the treatment. There was no critical distinction in the peribreadth of the knee joint between the two gatherings before treatment ($P > 0.05$), showing that the periwidth of the knee joint before treatment was practically identical between the two gatherings, while there was no huge contrast in the perimeasurement of the knee joint between the two gatherings after treatment ($P > 0.05$). The outcomes showed that there was no distinction in the peribreadth of knee joint between the two gatherings after treatment, and the degree of progress in the periwidth of knee joint was something similar between the two gatherings.

5. Conclusions

In this review, the utilization of nanotube joined with recovery treatment in the treatment of knee joint pain was considered by noticing WOMAC and VAS scores with the treatment in the trial bunch and the benchmark group and looking at the scope of movement and periphery of knee joint in the two gatherings. The outcomes showed that the utilization of carbon nanotubes in the restoration treatment of knee joint pain was more powerful than the recovery treatment alone.

Albeit the pathogenesis of KOA cannot be completely explained in this review, biomechanical factors assume a significant part in the pathogenesis and treatment of KOA. Clinicians should lead a thorough and comprehensive evaluation and make treatment arrangements for joint security and personal satisfaction improvement in patients with KOA. In the treatment of KOA, consideration ought to be paid to the general insurance and thorough treatment of the knee joint.

The treatment time in this study was only 2 weeks, and knee osteoarthritis, as a chronic disease, requires a longer treatment time to improve its condition. Compared with its long treatment time, the treatment time of only 2 weeks

in this study is relatively short, and due to the different curative effects, the follow-up results of this study also have certain differences. There are still some deficiencies in the study of knee arthritis in this paper, which is expected to be made up for in future research.

Data Availability

No data were used to support this study.

Conflicts of Interest

The author declares that they have no conflicts of interest.

References

[1] L. A. Acrisio, R. B. Capaz, and A. G. Souza Filho, "Structural and phonon properties of bundled single- and double-wall carbon nanotubes under pressure," *The Journal of Physical Chemistry C*, vol. 116, no. 42, pp. 22637–22645, 2012.

[2] A. A. Loredo-Pérez, C. E. Montalvo-Blanco, L. I. Hernández-González et al., "High-fat diet exacerbates pain-like behaviors and periarticular bone loss in mice with CFA-induced knee arthritis," *Obesity*, vol. 24, no. 5, pp. 1106–1115, 2016.

[3] J. S. Straker, C. N. Vannatta, and K. Waldron, "Treatment strategies for the master athlete with known arthritis of the hip and knee," *Topics in Geriatric Rehabilitation*, vol. 32, no. 1, pp. 39–54, 2016.

[4] G. Bo, L. Chang, H. Chenglong et al., "Effect of Mg and RE on the surface properties of hot dipped Zn–23Al–0.3 Si coatings," *Science of Advanced Materials*, vol. 11, no. 4, pp. 580–587, 2019.

[5] I. Jeon, Y. Matsuo, and S. Maruyama, "Single-walled carbon nanotubes in solar cells," *Topics in Current Chemistry*, vol. 376, no. 1, p. 4, 2018.

[6] J. Yang, H. Sun, H. Liang et al., "A highly efficient metal-free oxygen reduction electrocatalyst assembled from carbon nanotubes and graphene," *Advanced Materials*, vol. 28, no. 23, pp. 4606–4613, 2016.

[7] E. Secchi, S. Marbach, A. Niguès, D. Stein, A. Siria, and L. Bocquet, "Massive radius-dependent flow slippage in carbon nanotubes," *Nature*, vol. 537, no. 7619, pp. 210–213, 2016.

[8] S. Zhang, L. Kang, X. Wang et al., "Arrays of horizontal carbon nanotubes of controlled chirality grown using designed catalysts," *Nature*, vol. 543, no. 7644, pp. 234–238, 2017.

[9] R. Avriller, S. Latil, and F. Triozon, "Chemical disorder strength in carbon nanotubes: magnetic tuning of quantum transport regimes," *Physical Review B*, vol. 74, no. 12, p. 1406, 2017.

[10] J. H. Lee, S. Lee, S. J. Choi, Y. H. Choi, and K. Lee, "The effects of extracorporeal shock wave therapy on the pain and function of patients with degenerative knee arthritis," *Journal of Physical Therapy Science*, vol. 29, no. 3, pp. 536–538, 2017.

[11] D. Y. Ponzio, U. A. M. Syed, K. Purcell et al., "Low prevalence of hip and knee arthritis in active marathon runners," *Journal of Bone & Joint Surgery American*, vol. 100, no. 2, pp. 131–137, 2018.

[12] H. Zheng, B. Tulu, W. Choi, and P. Franklin, "Using mHealth app to support treatment decision-making for knee arthritis: patient perspective," *Egems*, vol. 5, no. 2, p. 7, 2017.

[13] E. Rowbotham and A. Grainger, "Magnetic resonance imaging of arthritis of the knee," *Seminars in Musculoskeletal Radiology*, vol. 21, no. 2, pp. 113–121, 2017.

[14] T. Yunchao, C. Zheng, F. Wanhui, N. Yumei, L. Cong, and C. Jieming, "Combined effects of nano-silica and silica fume on the mechanical behavior of recycled aggregate concrete," *Nanotechnology Reviews*, vol. 10, no. 1, pp. 819–838, 2021.

[15] K. H. Lee, H. Kang, T. Kim, and S. Choi, "A case of unusual septic knee arthritis with Brucella abortus after arthroscopic meniscus surgery," *Acta Orthopaedica et Traumatologica Turcica*, vol. 50, no. 3, pp. 385–387, 2016.

[16] J. J. Cho, S. Totterman, R. K. Elmallah, T. W. Kim, B. Lee, and M. A. Mont, "An MRI evaluation of patients who underwent treatment with a cell-mediated gene therapy for degenerative knee arthritis: a phase IIa clinical trial," *Journal of Knee Surgery*, vol. 30, no. 7, pp. 694–703, 2017.

[17] M. F. Hasan, M. A. Mandal, M. A. Rahman et al., "Effect of ultrasound therapy on patients with osteoarthritis of the knee joint," *Kyamc Journal*, vol. 7, no. 2, pp. 750–757, 2017.

[18] M. A. Elbadawy, "Effectiveness of periosteal stimulation therapy and home exercise program in the rehabilitation of patients with advanced knee osteoarthritis," *Clinical Journal of Pain*, vol. 33, no. 3, p. 1, 2016.

[19] V. S. Schäfer, W. A. Schmidt, M. Backhaus, and W. Hartung, "Arthritis of the knee joint in rheumatoid arthritis-evaluation of treatment response by ultrasound in daily clinical practice," *Open Rheumatology Journal*, vol. 10, no. 1, pp. 81–87, 2016.

[20] C. F. Roques and P. Queneau, "SPA therapy for pain of patients with chronic low back pain, knee osteo- arthritis and fibromyalgia," *Bulletin de l'Académie Nationale de Médecine*, vol. 200, no. 3, pp. 575–587, 2016.

[21] J. Lee, J. H. Kim, E. J. Chung, and B. H. Lee, "Functional state of knee arthritis patients and related factors," *Journal of Physical Therapy Science*, vol. 29, no. 2, pp. 323–327, 2017.

[22] J. W. Han, D. K. Lee, and C. B. Park, "The immediate effects of taping therapy on knee pain and depression in patients with degenerative arthritis," *Journal of Physical Therapy Science*, vol. 30, no. 5, pp. 704–706, 2018.

[23] O. C. Ann, F. S. Tee, and V. Y. Nen, "A study on satisfaction level among amateur web application developers towards pigeon-table as nano web development framework," *Journal of Organizational and End User Computing (JOEUC)*, vol. 31, no. 3, pp. 97–112, 2019.

Hindawi

Research Article

Application of Nanostent Materials Combined with Sports Rehabilitation Therapy in the Treatment of Hip Injury in Outdoor Sports Athletes

Dan Li [ORCID]

College of Physical Education, Xuchang University, Xuchang, 461000 Henan, China

Correspondence should be addressed to Dan Li; 12003040@xcu.edu.cn

With the rapid development of outdoor sports in our country, the condition of hip joint injury of athletes appears constantly. With the continuous progress of modern biotechnology and iatrotechnique, nanomaterials are also gradually used in the treatment of biological medicine. The purpose of this study is to use nanoscaffold materials in combination with athletics rehabilitation therapy to treat and analyze hip injuries in athletes. In this study, 290 patients with hip injuries in our hospital from June to October 2019 were studied. The hip joint injury patients were divided into the control group and the experimental group according to sex and age. The recovery of the hip joint injury in normal condition, the recovery in the pharmacotherapy, and the recovery in the combined therapy with the nanoscaffold material were compared. The function of nanoscaffold materials in experiments can be determined by detecting changes in related indicators in vivo. The results showed that there were 48 cases of ligament injury, accounting for 67.7% of hip joint injury. 22 cases had muscle and tendon injury, and 12 cases had articular cartilage injury and bursa injury. There was no significant difference in red blood cells, lymphocytes, and white blood cells after nanoscaffold material drug delivery therapy, while parathyroid hormone and osteocalcin changed greatly, which indicated that nanoscaffold material carrier therapy could promote the absorption and treatment of drugs in hip joint. Therefore, the research conclusions of this paper is that nanoscaffold material combined with rehabilitation therapy can effectively treat athletes with hip joint injury. It will contribute to the research and practical application of nanomaterials in modern medicine.

1. Introduction

1.1. Background Significance. Hip joint is the most important joint to support body weight in walking. It is very important for the standing position and movement of the body. However, the pain of hip joint activities will have a serious impact on the movement and function of the lower limbs of patients, especially the quality of life of patients including normal work and research. The incidence of hip joint deformation arthropathy, avascular necrosis of thigh head, hip heteromorphic syndrome, and hip joint pain caused by hip infection are high. In outdoor sports, the hip joint is more prone to injury.

The construction of titanium dioxide nanoscaffold materials not only is similar to the natural roughness of the artificial bone material of the artificial titanium but also has excellent hydrophilicity and greatly improves the cell adhesion and proliferation on the surface. Osteoblast-related cells can promote differentiation, proliferation, and induction. Titanium dioxide nanoscaffold materials have excellent adaptability to current biological fixation and embedding technology. Scanning electron microscopy (SEM) showed that osteoblasts have grown into tubular structures of titanium dioxide nanoscaffold materials that can immobilize bone cells. Microporous structures of specific size titanium dioxide nanopowders effectively reduce adhesion of bacteria

and promote growth and formation of bone tissue. Titanium dioxide nanoscaffold material coating is considered to be an excellent drug carrier because of its high surface area ratio. These excellent characteristics are widely used in biomedical fields.

1.2. Related Work. In the study of rehabilitation treatment of hip joint injury, Jana believes that the musculoskeletal model must adapt to the patient's unique geometry to predict the patient's specific hip load. His study compared the accuracy of anisotropic and isotropic scaled musculoskeletal models and hip force prediction from standard patient-specific skeletal geometry standards. His method is to analyze 356 hips of 250 adult pelvic radiographs. He applied three scaling methods: hip spacing anisotropic scale, iliac height, iliac width, lateral and inferior trochanter, isotropic scaling of pelvic width, and isotropic scaling of hip spacing. At the same time, he used the inverse static model to estimate the hip joint force when standing on one leg. The accuracy of his method is not high [1]. The Lopes et al.'s study compared the ROM of the hip joint between male patients with contact ACL injury and noncontact ACL injury. Their method was to compare the ROM of ipsilateral hip joint between 35 male patients with contact ACL injury (contact group) and 45 patients with non-contact ACL injury (noncontact group). In addition, imaging evaluation of the hip joint is also used to assess the presence of cam and clamp deformities. His method is unstable [2]. Morimoto et al.'s study measured the electromyographic activity of piriformis muscle in seven hip joint movements with a filament electrode. His method was to first select 11 healthy men without severe low back pain or lower limb injury. A filament electrode was inserted into piriformis muscle, and the surface electrode was attached to the hip muscle and the dominant brachial trunk muscle. Then, the EMG signal amplitudes of 7 kinds of hip joint movements were measured: hip neutral lateral supine abduction, hip neutral lateral supine abduction, hip joint internal rotation lateral supine abduction, hip joint external rotation prone extension, hip joint external rotation prone external rotation, hip joint pronation prone external rotation, and hip joint supine extension. They used repeated measurements of one-way ANOVA to examine the EMG of each of the seven hip movements. Their method is not practical [3].

1.3. Work of This Paper. In this paper, the structure of carbon nanoscaffold materials and the classification by layer number, chirality, and morphology are introduced. Then, the mechanical, electrical, and thermal properties of carbon nanoscaffold materials are described in detail. This study also describes hip injury and BASRI-hip score and gives examples of common sports injuries and events. This study describes the characteristics of hip joint movement of sports athletes. In this study, 298 patients in our hospital were divided into different groups according to age and gender. The experimental group was given drug therapy and nanoscaffold material combined rehabilitation therapy, respectively, and the control group was compared with the normal treatment. Observe the changes of blood indexes in the injured part of hip joint and the change of self-state to judge the therapeutic effect. According to the results, the therapeutic effects of hip patients of different genders are different. From the analysis of the treatment of hip joint injury with nanoscaffold material drug loading, the hip joint injury and the type and frequency of injury tissue structure are different in different age groups. The nanoscaffold material combination therapy in this study is very effective in the treatment of hip joint injury.

2. Carbon Nanoscaffold Materials and Hip Joint Injury of Sports Athletes

2.1. Structure of Carbon Nanoscaffold Materials. Carbon nanoscaffold materials (CNTs) are seamless tubular structures formed by single or multilayer graphite sheets wound around the same axis. The tube wall is a cylindrical surface composed of carbon atoms produced by SP2 hybridization and a hexagonal grid formed by three carbon atoms around it. The two ends are hemispherical rich rings composed of five rings and seven rings. This is formed by the coverage of lean molecules [4, 5]. It can be seen that the structure of carbon nanoscaffold material is a slightly complex one-axis multilayer structure. Carbon nanoscaffold materials (CNTs) are standard one-dimensional carbon nanomaterials because of their nanosized radial size and microscale axial size, showing a very large aspect ratio. In order to better understand the structure of carbon nanoscaffold materials, the academic community mainly uses the following three methods to classify carbon nanoscaffold materials.

2.1.1. Classification by Layers. Depending on the number of layers, the carbon nanoscaffold materials are divided into single and multilayer. The smaller the diameter of multi-walled carbon nanoscaffold materials, the larger the spacing between layers. The smaller the diameter, the larger the radius of curvature, the greater the spacing between layers, and the van der Waals force between layers [6, 7].

2.1.2. Classification by Chirality. The single-layer carbon nanoscaffold materials can be considered to be formed by curling the graphite sheet with hexagonal network structure [8, 9]. The graphite sheet structure is shown in Figure 1. Among them, a_1 and a_2 are the unit vectors of the 6-ring lattice with an included angle of 60°. In the figure, select point O as the origin and point OA as toward point A. This vector is the chiral vector of carbon nanoscaffold materials as shown below. Through point O, create the vertical vector ob of vector OA. This vector is the translation vector of carbon nanoscaffold materials as t. Through point B, the vector BB' is parallel to the vector OA. Secondly, OABB is the original unit of carbon nanoscaffold materials. The angle between vector OA and vector OD is the rotation angle, and the range is $0° \le |\theta| \le 30°$. The structure of SWCNTs can be expressed by chiral vector C_h

$$C_h = na_1 + ma_2 = (n, m). \tag{1}$$

n, m is an integer and $0 \le |m| \le n$. The rotation angle θ can be expressed by C_h and a_1
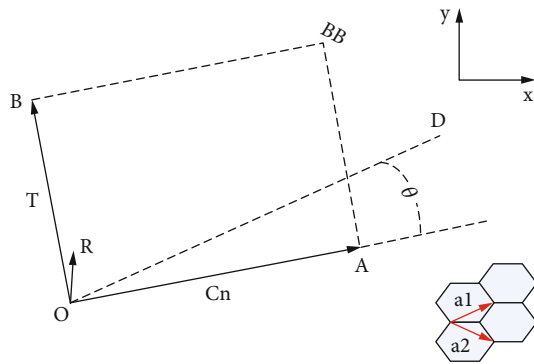
Figure 1: Schematic diagram of carbon nanoscaffold materials formed by graphene sheet.

$$\cos\theta = \frac{C_h a_1}{|C_h||a_1|} = \frac{2n+m}{2\sqrt{n^2+m^2+mn}}. \tag{2}$$

The rotation angle θ varies with n, m. When $\theta = 0°$ and $\theta = 30°$, the CNTs are not helical but chiral. Specific types are divided into armchair type and zigzag type. When $0° \leq |\theta| \leq 30°$ carbon nanoscaffold materials helix, they show chiral structure [10].

2.1.3. Classification by Morphology.

According to the various shapes of carbon nanoscaffold materials, in addition to the standard cylindrical shape, carbon nanoscaffold materials can also be divided into L-type, Y-type, or T-type and other different types. These different morphologies of carbon nanoscaffold materials are based on unique topologies. Moreover, there are uncertainties in the preparation process. Now, according to their morphology, carbon nanoscaffold materials can be classified into three types: blocking type, onion type, sea urchin type, variable diameter type, bamboo type, rosary type, spiral type, spindle type, and other abnormal types [11, 12].

2.2. Properties of Carbon Nanoscaffold Materials

2.2.1. Mechanical Properties.

The SP^2 hybridization of carbon atoms in carbon nanoscaffold materials makes the strength of carbon nanoscaffold materials very high. In ideal condition, the tensile strength of CNTs is about 800 GPa, and the shear strength is about 500 MPa. In addition, the strength of carbon nanoscaffold materials is about 100 times of steel, about 20 times of carbon fiber, the density of carbon nanoscaffold materials is one sixth of steel, and the weight is half of carbon fiber. The elastic modulus and hardness of carbon nanoscaffold materials are the same as those of diamond, and the CNTs have excellent softness and can keep the original shape after twisting, bending, and stretching. Due to the excellent mechanical properties of carbon nanoscaffold materials, it is called "super fiber" in the field of nanomaterials and has a very wide prospect [13, 14].

2.2.2. Thermal Properties.

Because CNT is large in aspect, heat is transmitted in the axial direction, and the thermal conductivity in the radial direction is average. In this study,

3000 K CNT extends only in the radial direction, and six ring structures remain on the wall of the tube. When the axial size of carbon nanoscaffold materials exceeds 10 nm, the thermal conductivity may reach 6000 W/m·k at room temperature and 280 W/m·k at low temperatures. In certain size ranges, carbon nanoscaffold material length and thermal conductivity are linear functions. Carbon nanoscaffold materials can be used as additives for composite materials and can help improve the thermal conductivity of composite materials [15, 16].

2.2.3. Electrical Performance.

The electrical properties of carbon nanoscaffold materials are very unique, which may show various conductive properties such as semiconductors and metals. The chiral classification of carbon nanoscaffold materials shows that the rotation angle of carbon nanoscaffold materials is determined by the integers n and M. the conductivity of carbon nanoscaffold materials is closely related to the rotation angle. In some studies, armchair carbon nanoscaffold materials exhibit excellent electrical conductivity when $n = M$. In the case of zigzag and chiral carbon nanoscaffold materials, $N - M = 3Q$ (q is an integer) denotes metallicity. When $nm = 3Q$ is not satisfied, the semiconductor property is indicated. The conductivity of carbon nanoscaffold materials is not only related to the size and rotation angle but also vulnerable to the influence of electric and magnetic fields. If the electric and magnetic fields are applied, carbon nanoscaffold materials will change from metal to semiconductor. The good conductivity and curvature radius of carbon nanoscaffold materials are very small, the open electric field is very low, and the field emission characteristics of carbon nanoscaffold materials are very good [17, 18].

2.3. Hip Joint Injury.

According to the BASRI hip scoring system for ankylosing spondylitis, >12 points were defined as radiation-induced femoral joint lesions. On the images, there are subchondral bone marrow edema, synovial fluid, abnormal synovial enhancement, or arthritis, which are considered to be signs of active inflammatory changes. Moreover, subchondral erosive destruction, articular cavity stenosis, sclerosis, and stiffness are considered to be the results of chronic inflammatory changes. Body fluid was defined as sufficient fluid around the neck of the leg or the inflated femoral joint capsule on T2 or stir images. Symptomatic femoral joint disease is defined as present or past pain or limitation of femoral joint motion [19, 20].

The hip joint with an abnormal X-ray was given a score of 1. The score of 0 indicates that the hip joint is normal; the score of 1 indicates that the hip joint may be abnormal; the score of 2 indicates that the hip joint is mildly abnormal and the joint space is narrowed significantly; the score of 3 indicates moderate abnormalities in the hip joint, and the joint space is >2 mm; the score of 4 indicates severe abnormalities in the hip joint, the bones have been deformed, and the contact range between the articular surfaces of the bilateral bones is >2 cm.

2.4. Common Sports Injuries and Events.

The following are the common sports injuries and events:

(1) Femoral head fracture: most of the complications of hip joint dislocation and easy injury items are white driving and car racing [21].

(2) Femoral neck fracture: the fracture of adduction or abduction is caused by osteoporosis and falling down, which is easy to be injured in the elderly who participate in sports.

(3) Femoral neck Palau fracture: race class periodic heavy load and easy to hurt events are long-distance runners and recruits.

(4) Hip joint sprain and synovium imbedding: sprained hind leg has "lengthening" phenomenon; you can easily get hurt in gymnastics [22].

(5) Dislocation of hip joint: anterior, posterior, and central dislocation and easy injury items are bicycle and car race [23].

(6) Femur tip slip: Sports injuries due to gymnastics and wrestling can easily lead to disorders of blood supply to the epiphysis.

(7) Osteoarthritis of the femoral head: excessive training in adolescence causes the bone supply disorder of the femoral epiphyseal; fragile events are gymnastics or long distance running.

(8) Hip joint disease: dancing too much can also cause hip injuries.

(9) Contracture and elastic effects of tibial tract: these may be associated with hip injections, and simple injury events are jumping [24].

(10) Iliopsoas key bounce and psoas muscle sliding: it is related to the slight over Zhong or "side leg" exercise, and the vulnerable items are gymnastics and dance.

(11) Bursitis: Gymnastics can also easily lead to iliac hematomas and femoral nerve palsy, hip hyperextension injuries or muscle strains when the buttocks hits the ground.

(12) Intertrochanteric fracture of femur and tendon strain and operation end disease: sprain or hip injury during hurdle and easy injury items are hurdle, gymnastics, and dance.

(13) Trochanteric bursitis of femur: the greater trochanter rubs against the iliotibial tract during running. The vulnerable event is middle and long distance running [25].

2.5. Hip Joint Movement Characteristics of Sports Athletes. The special physical characteristics of sports refers to the main physical characteristics shown in mechanics and biology for the purpose of maximizing sports efficiency under the permission of competition rules. In the new gymnastics, mastering the characteristics and training rules of sports is the precondition of physical training. Cognitive characteristic is an important link to improve the level of physical training. Understanding and mastering specific training rules is to improve training efficiency. Maintain the basic conditions of high-quality training for a long time. In the case of new sports, the flexibility of the hip joint can be improved more scientifically by correctly understanding the characteristics of the athletes' hip joint, correctly grasping the strength of the hip joint and understanding the characteristics of the hip joint. The wide movable area of the hip joint is one of the important sports characteristics of the player's hip joint [26, 27].

3. Nanoscaffold Material Preparation and Hip Joint Injury Treatment Experiment

3.1. Data of Experimental Objects. This data group collected 290 joint fractures and dislocation of sciatic nerve damage in my hospital from June to October 2019. They were 7-59 years old (average 32.83 ± 10.12 years). All patients have complete blood circulation, liver function, renal function, coagulation function, erythrocyte sedimentation rate (ESR), C-reactive protein (CRP) and HLA-B27 gene determination, parathyroid hormone (PTH), osteocalcin, 25 hydroxyvitamin D3, end elongation peptide of N type I bone collagen, and B bone, as a result of reren's special placement determination test, Dr or joint CT examination of the pelvis, and iliac MRI results of the joint.

3.2. Preparation of TiO_2 Nanoscaffold Material Cladding Structure. Pure titanium is used for preheating, after removing the oxide film on the surface, grinding, cleaning, and drying. Electrochemical anodizing establishes an electrochemical anodizing system in which the titanium side is the anode and the platinum side is the anode. In the mixed solution system of the cathode, ammonium fluoride, and ammonium hydrogen phosphate, the oxidation voltage is controlled by a constant 15 V for 60 minutes. Scanning electron microscopy (SEM) confirmed that the coating structure of nanosized TiO_2 nanoscaffold material is TiO_2 nanoscaffold material. According to the various specifications required in the subsequent experiments, cylindrical titanium dioxide nanoscaffold material-coated titanium rods with a length of 30 mm and a diameter of 3 mm and a thin titanium dioxide nanoplate with a length of 10 mm and a width of 10 mm were fabricated. Put the sample into a steam pressure cooker at 120°C, kill the bacteria for 30 minutes, and then use it after ultrasonic cleaning and drying. Moreover, pure Ti metal samples are cut into the same size for use.

3.3. Preparation of TiO2 Nanoscaffold Material Coating Loaded with Gentamicin. A pipette was used to determine the concentration of 1 mg of the prepared intercontinental mycin solution (100 mg/mL), which was added to the prepared 10 mm × 10 mm TiO_2 nanoscaffold material-coated film and then removed. When the negative pressure device is opened in the dark, the suction value of negative pressure gradually rises, and the air pressure in the plastic pipe slowly drops to 0.01 KPa. After about 2 hours, the TiO_2 nanoscaffold material sheet was removed, and the surface of the TiO_2 nanoscaffold material sheet was cleaned with 20 mL

TABLE 1: Types of hip joint injury in sports.

Damage form	Male		Female	
	Number of injured	Proportion	Number of injured	Proportion
Muscle and muscle leg injury	22	20.3	30	48.5
Ligament injury	48	44.5	42	67.7
Bursa injury	12	11.2	28	45.1
Bone marrow injury	2	1.8	24	38.8
Articular cartilage injury	12	11.2	4	6.6
Nerve injury	2	1.8	30	48.5
Fracture	2	1.8	8	12.8
Others	18	16.8	0	0

of 0.01 M phosphoric acid buffer, and the liquid used to detect ultraviolet light was recovered. The drug loading efficiency and mass of TiO_2 nanoscaffold materials with negative allergen were calculated according to the change of concentration of kanamycin in the solution. In the above experiments, the concentration of L-arginine solution was increased to 200 mg/mL and 300 mg/mL, and the experiment was continued under the same conditions. In the above experiments, the drug loading rates of TiO_2 nanoscaffold materials at various concentrations of rhizomycin were measured and compared.

3.4. In the Determination of Gentamicin Standard Curve, the Specific Steps Are as Follows:

(1) Weigh the allergen powder with a precision balance of 10 μ g, 25 μ g, 50 μ g, 100 μ g, 200 μ g, 500 μ g, and 1000 μ g, respectively, and dissolve them in 10 mL 0.01 M PBS buffer solution. Mix well, and use as standard solution for future use

(2) PBS buffer solution was prepared as blank control

(3) The UV absorption values of different concentrations of gentamycin standard solution were determined by UV spectrophotometer at 320 nm wavelength. The standard curve (UV absorption value and the concentration of gentamycin in the solution) was drawn between the two wavelengths, and the regression equation was established

(4) In the above experiments, 2 mL of intercontinental mycin solution measured in each round was completely vibrated. The ultraviolet absorbance value at 320 nm was measured, and the value was restored to the standard curve and regression equation to obtain the concentration of rhizomycin

4. Nanoscaffold Materials Combined with Rehabilitation Therapy for the Treatment of Hip Joint Injuries

4.1. Type and Frequency of Hip Joint Injury. According to the second standard of sports medicine, the types of injury are divided into muscle leg injury, joint injury, synovial fluid bag injury, bone injury, bone injury, and nerve injury. The types of hip joint injury tissue structure in sports are shown in Table 1.

According to the classification in Table 1 of the patients with femoral joint injury in our hospital, the histological types of hip joint injury of Chinese sports athletes were analyzed. The investigation shows that 48 of 290 sports athletes suffer from ligament injury, accounting for 67.7% of hip joint injury. 22 cases had muscle and tendon injury, and 12 cases had articular cartilage injury and capsule injury. Ligament injury ranks first in the type of tissue structure of hip joint injury. The main tissue structures of Chinese sports athletes are hip joint injury, ligament injury, muscle and tendon injury, articular cartilage injury, synovial fluid bag injury, and bone end injury. Some athletes were injured on the hip joint at the same time, which was very serious. The season of hip joint injury of athletes is shown in Figure 2.

According to Figure 2, 108 athletes who were injured in the femoral joint of the athletes were classified, and the injury season often occurred in winter and then continued in summer. And the spring and autumn players were injured. The main reasons are low temperature in winter, high muscle viscosity of athletes, poor preparation, and so on. In hot summer, athletes consume a lot of energy and can not supplement energy in time, and concentration force decreases.

4.2. Therapeutic Effect of Different Gender Hip Joint Patients Based on Nanoscaffold Material Combination Therapy. To exclude the impact of gender factors on the test results, we compared the differences between the two case groups. The distribution of hemoglobin, red blood cell, and red blood cell and the sedimentation rate of red blood cells were different statistically between men and women. In addition, the special arrangement of Austin starch ($t = 2.06$, $P = 0.041$), β-bone collagen ($t = 2.073$, $P = 0.040$), and t-pinp ($t = 2.070$, $P = 0.008$) also showed that these bone metabolism indexes were found to be statistically different between the two female groups There are no statistical differences. The experimental test results are shown in Table 2.

As can be seen from Table 2, although the number of cases in this survey is less than that of men, the possibility of hip joint injury is much higher than that of men.
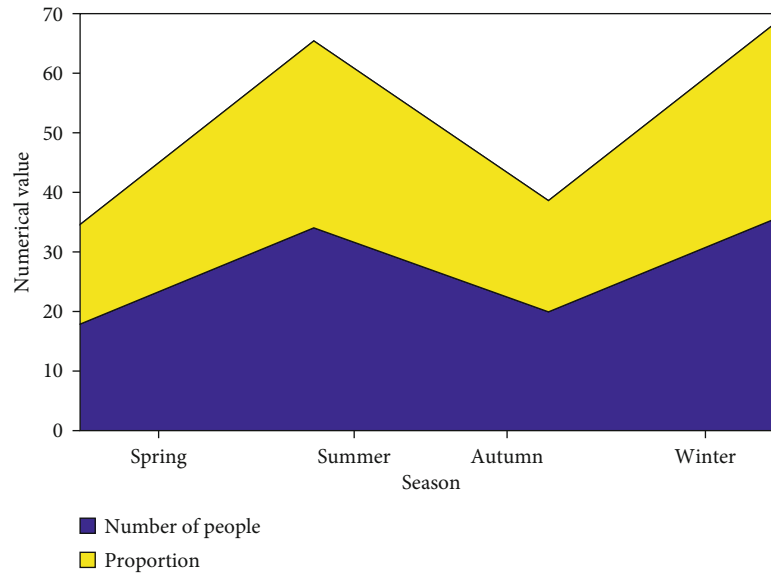
Figure 2: Season of hip joint injury.

Table 2: Experimental results.

Project	Male		Female	
	Experience group	Control group	Experience group	Control group
Number of cases	67	108	34	24
WBC (10^9/L)	7.14 ± 3.29	8.43 ± 8.64	8.28 ± 6.52	7.36 ± 3.05
LYM (10^9/L)	1.86 ± 0.66	1.95 ± 0.63	1.88 ± 0.67	1.93 ± 0.77
RBC (10^9/L)	4.30 ± 0.62	4.52 ± 0.60	3.91 ± 0.75	4.05 ± 0.41
Hb (g/L)	116.36 ± 19.22	128.37 ± 22.14	104.76 ± 15.12	113.18 ± 13.31
PTH (pg/mL)	27.63 ± 12.47	30.76 ± 17.77	33.64 ± 11.85	37.67 ± 25.33
t-PINP (ng/mL)	84.57 ± 68.48	59.98 ± 52.73	56.74 ± 74.32	42.11 ± 30.07
Osteocalcin (ng/mL)	29.77 ± 19.25	22.54 ± 24.47	20.21 ± 15.35	20.21 ± 8.61

WBC: white blood cell; LYM: lymphocyte; RBC: red blood cell; Hb: hemoglobin; PTH: parathyroid hormone; t-PINP: amino extension end of total type I collagen; osteocalcin: osteocalcin.

The clinical symptoms of hip joint injury are typical groin pain and pain accompanied by dyskinesia of femoral joint. The pain may be caused by acute inflammation and changes of hip joint capsule and synovial nerve. In this study, hip symptoms and image observations were completely inconsistent. This may be related to the following reasons: hip pain and exercise restriction can affect personal subjectivity. The experimental results are shown in Figure 3.

In Figure 3, the number of red blood cells, hemoglobin, and distribution range of red blood cells have a great relationship with femoral joint injury, which can be seen that this is related to hip joint score. The red blood cell distribution width (RDW) and the component of red blood cell routine width reflect the variability of red blood cells in circulation. Traditionally, RDW is a reference index to determine anemia. In many studies, RDW is associated with many diseases, such as polycystic ovary syndrome, coronary artery disease, and heart failure. Inflammation may be the main reason for the

relationship between these diseases and RDW, and RDW can be used as an indicator of chronic inflammation.

4.3. Analysis of Hip Joint Injury in Different Age Groups. Through the investigation of the injury age of athletes, reflect the characteristics of injury age of athletes. As shown in Figures 4, 290 sports athletes were investigated. In the survey, the main age is 12-17 years and over 50 years, accounting for 34.8% and 37.6% of the players' questionnaire survey, a total of 72.4%. The age distribution of hip joint injury athletes is shown in Figure 4.

As can be seen from Figure 4, women aged 9 to 14 are more injured, while men aged 10 to 16 are more injured. This may be related to the athlete's puberty and joint flexibility. Adolescent athletes are prone to hip injuries due to long-term exercise because their bones are still growing. Over the age of 35, the number of patients with the disease continues to increase with age; both men and women are the same. This is because the physical strength of middle-aged and
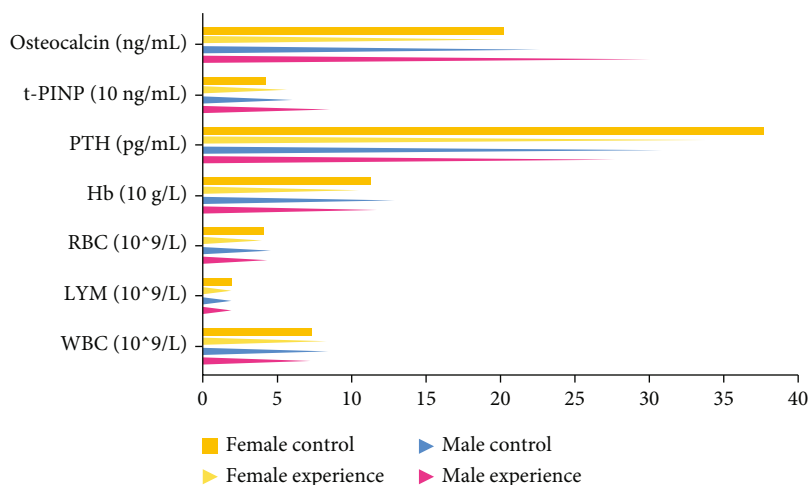
FIGURE 3: Experimental results.
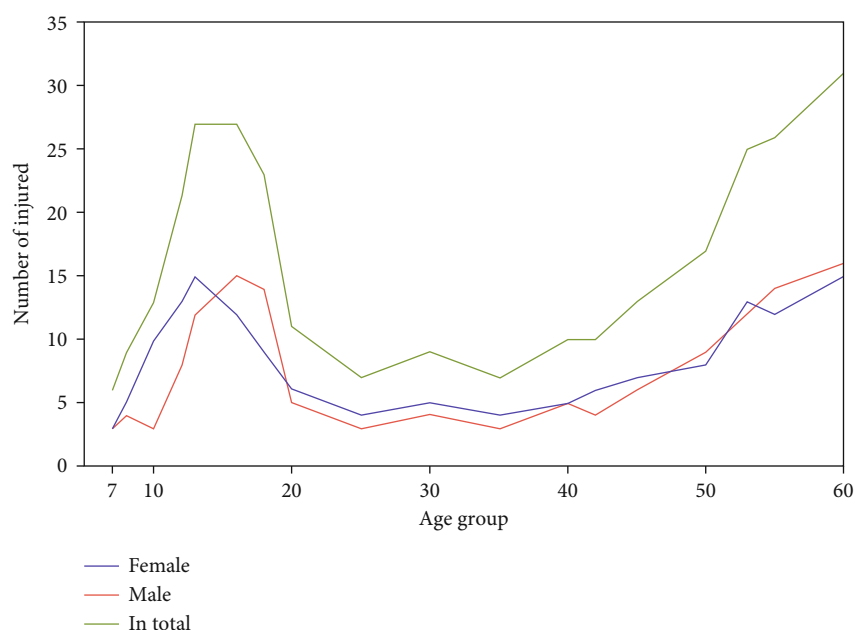
FIGURE 4: Age distribution of hip injury athletes.

elderly people decreases, the bones gradually relaxed, and a lot of problems are accumulated between joints.

4.4. Treatment of Hip Joint Injury with Nanoscaffold Material Drug Loading. Staphylococcus aureus was cultured for 4 hours, and Staphylococcus aureus was observed by a laser scanning confocal microscope on three different materials (pure Ti metal, titanium dioxide nanoscaffold material coating structure material without rhizomycin, and titanium dioxide nanoscaffold material coating structure material containing rhizomycin) on the surface. The colony number and density of Staphylococcus aureus on the surface of pure Ti metal and titanium dioxide nanoscaffold material coating structure material without sulfur group mildew increased significantly. The number of Staphylococcus aureus on the surface of titanium dioxide nanoscaffold material coating

structure material was less than that on pure Ti metal surface, but there were still a large number of Staphylococcus aureus appeared throughout the field of vision, but not more, which is obviously concentrated. There was no significant change in the number of Staphylococcus aureus on the surface of titanium dioxide nanoscaffold material coating with rhizomycin compared with that observed in 1 hour. The therapeutic effect of different materials of nanoscaffold material is shown in Figure 5.

It can be seen from Figure 5 that the colonies of Staphylococcus aureus on the surfaces of three different materials (pure Ti free, titanium dioxide nanoscaffold material coating structure material containing past mycin, and titanium dioxide nanoscaffold material coating structure material containing past mycin) after incubation for 1 hour and 4 hours were compared by using image Pro software under a laser
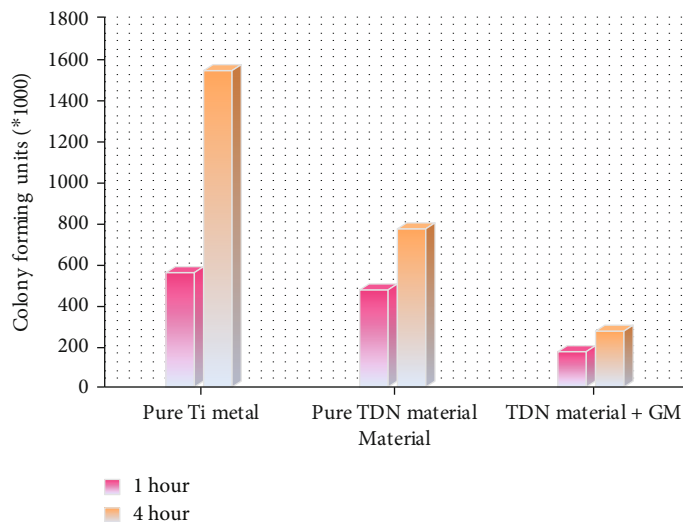
FIGURE 5: Therapeutic effect of different materials of nanoscaffold materials.

scanning confocal microscope. Regardless of the incubation time of 1 hour or 4 hours, the count of Staphylococcus aureus on the surface of titanium dioxide nanoscaffold materials coated with gentamicin was significantly lower than that of the information group, and the difference was statistically significant ($P < 0.5$). After 1 hour, the amount of S. aureus and S. aureus in the titanium dioxide nanoscaffold material coating material group was less than those on the pure Ti metal surface, but the difference was not statistically significant. After 4 hours of culture, the number of Staphylococcus aureus in the titanium dioxide nanoscaffold material coating structure material group was much lower than that of pure Ti metal surface, and the difference was significant.

5. Conclusion

The initial "explosive" release characteristics of TiO2 nanoscaffold material coating with rhizomycin can not play a long-term antibacterial effect in vivo. In animal experiments, Staphylococcus aureus is a common clinical bacterium, which has no obvious effect on the rare fungal infection after artificial joint replacement. In addition, the team has a small number of experimental animals, and the results may be biased. The clinics also have individual differences. Animal experiments alone cannot be extended to clinics. Through the company's internal experiments, it has been confirmed that the titanium dioxide nanoscaffold material coating structure material filled with rhizomycin can effectively inhibit the initial occurrence of infection around the artificial joint after artificial joint replacement, and it has a new therapeutic scheme significance for clinical prevention of infection around artificial joint after artificial joint replacement.

In this study, although there is no significant difference in age and disease course between patients with hip joint injury and those with normal hip joint, according to the Spearman correlation analysis, the degree of hip joint injury is negatively related to the age of onset; that is, the lower the age of onset, the more hip joint occurs. The possibility of damage will increase. There were fewer cases in women than

in men in this study, but the probability of hip injury was much higher than in men. The clinical symptoms of hip joint injury are typical inguinal pain and pain accompanied by hip joint dyskinesia. The pain may be caused by acute inflammation or changes in the hip capsule and synovial nerves. This conclusion has great reference significance for promoting the treatment of hip joint injury.

The injury rate of hip joint is 47%, which is the main injury site of Chinese sports athletes. There is a positive correlation between the training years of Chinese sports athletes and the incidence of hip joint injury. Training, talent selection, rules and technology development, nutrition, and other factors are the main causes of hip joint injury of sports athletes. Due to the coach's improper guidance on psychology, cultural quality, flexible sports, clothing, and venue equipment and other factors, it will also have different degrees of impact on sports athletes' hip joint injury. The main effective countermeasures to prevent hip joint injury are to pay attention to scientific and reasonable training methods, strengthen the muscle strength training around the hip joint of athletes, strengthen the standardization of technical sports, do a good job in proper preparatory activities, and establish a scientific Hip protection selection mechanism, improve the public's attention to hip protection, and promote the safety of outdoor sports.

Data Availability

No data were used to support this study.

Conflicts of Interest

The authors declare no conflicts of interest.

References

[1] J. Hornova, V. Kralj-Iglič, D. R. Pedersen, and M. Daniel, "Effect of patient-specific model scaling on hip joint reaction force in one-legged stance – study of 356 hips," *Acta of*

bioengineering and biomechanics/Wroclaw University of Technology, vol. 19, no. 4, pp. 103–108, 2017.

[2] O. V. Lopes, J. L. E. Gomes, and D. F. S. Leandro, "Range of motion and radiographic analysis of the hip in patients with contact and non-contact anterior cruciate ligament injury," *Knee Surgery Sports Traumatology Arthroscopy*, vol. 24, no. 9, pp. 2868–2873, 2016.

[3] Y. Morimoto, T. Oshikawa, A. Imai, Y. Okubo, and K. Kaneoka, "Piriformis electromyography activity during prone and side-lying hip joint movement," *Journal of Physical Therapy Science*, vol. 30, no. 1, pp. 154–158, 2018.

[4] S. J. Park, Y. M. Kim, and H. R. Kim, "The effect of hip joint muscle exercise on muscle strength and balance in the knee joint after meniscal injury," *Journal of Physical Therapy ence*, vol. 28, no. 4, pp. 1245–1249, 2016.

[5] D. Rudin, M. Manestar, O. Ullrich, J. Erhardt, and K. Grob, "The anatomical course of the lateral femoral cutaneous nerve with special attention to the anterior approach to the hip joint," *Journal of Bone & Joint Surgery*, vol. 98, no. 7, pp. 561–567, 2016.

[6] M. F. Çatma, S. Ünlü, Ö. Ersan, and A. Öztürk, "Treatment of the bullet, traversing femoral neck, lodged in hip joint: initial arthroscopic removal and subsequent cartilage repair," *Journal of Orthopaedic Case Reports*, vol. 6, no. 4, pp. 13–16, 2016.

[7] M. F. Çatma, A. Öztürk, and M. A. E. Aksekili, "Clinical and functional outcomes of bullet removal from hip joint: five year follow-up of 3 cases," *Duzce Medical Journal*, vol. 6, no. 3, pp. 60–64, 2016.

[8] D. Zhao and H. Xie, "Strategy and discussion of hip joint preserving surgery treatments for adult osteonecrosis of the femoral head," *Chinese Journal of Reparative and Reconstructive Surgery*, vol. 32, no. 7, pp. 792–797, 2018.

[9] Q. Naziri, R. Abraham, J. P. Scollan et al., "Primary total hip arthroplasty for gunshot injury-induced secondary arthritis of the hip: what are the outcomes?," *Journal of Hip Surgery*, vol. 1, no. 4, pp. 200–204, 2018.

[10] T. Yasuda, Y. Yokoi, K. Oyanagi, and K. Hamamoto, "Hip rotation as a risk factor of anterior cruciate ligament injury in female athletes," *Journal of Physical Fitness & Sports Medicine*, vol. 5, no. 1, pp. 105–113, 2016.

[11] Z. Budinski, S. Budinski, M. Vranjes, M. Obradovic, M. Mikic, and M. Milankov, "The relationship between the range of moton of the hip joint with ruptured anterior cruciate ligament," *Medicinski Pregled*, vol. 69, no. 5-6, pp. 160–166, 2016.

[12] H. B. Kak, S. J. Park, and B. J. Park, "The effect of hip abductor exercise on muscle strength and trunk stability after an injury of the lower extremities," *Journal of Physical Therapy ence*, vol. 28, no. 3, pp. 932–935, 2016.

[13] S. Ziying and C. Ping, "Efficacy of bisphosphonates combined with recombinant human parathyroid hormone 1-34 in elderly patients with lumbar or hip joint injury caused by osteoporosis," *Latin American Journal of Pharmacy*, vol. 38, no. 1, pp. 51–56, 2019.

[14] S. Wan, L. Qi, X. Xu, C. Tong, and Z. Gu, "Deep learning models for real-time human activity recognition with smartphones," *Mobile Networks and Applications*, vol. 25, pp. 743–755, 2020.

[15] H. Zhang, C. Song, W. Zhao, A. Yin, J. Zhu, and G. Ren, "Influence of different abduction angles of hip joint on stress distribution of femoral neck," *Shengwu yixue gongchengxue zazhi*, vol. 33, no. 2, pp. 274–278, 2016.

[16] P. Lertwanich, A. Plakseychuk, S. Kramer et al., "Biomechanical evaluation contribution of the acetabular labrum to hip stability," *Knee Surgery, Sports Traumatology, Arthroscopy*, vol. 24, no. 7, pp. 2338–2345, 2016.

[17] A. Babu, A. Gupta, P. Sharma, P. Ranjan, and A. Kumar, "Blunt traumatic superior gluteal artery pseudoaneurysm presenting as gluteal hematoma without bony injury: a rare case report," *Chinese Journal of Traumatology*, vol. 19, no. 4, pp. 244–246, 2016.

[18] M. Yasuhiro, "Gender-related differences in lower limb alignment, range of joint motion, and the incidence of sports injuries in Japanese university athletes," *Journal of Physical Therapy ence*, vol. 29, no. 1, pp. 12–15, 2017.

[19] L. N. Solomin, M. V. Andrianov, M. Takata, and H. Tsuchiya, "Reference positions for transosseous elements in femur: a cadaveric study," *Injury-international Journal of the Care of the Injured*, vol. 47, no. 6, pp. 1196–1201, 2016.

[20] D. V. Kosynkin, A. L. Higginbotham, A. Sinitskii et al., "Longitudinal unzipping of carbon nanotubes to form graphene nanoribbons," *Nature*, vol. 458, no. 7240, pp. 872–876, 2009.

[21] H. Cheng, Y. Zhao, Y. Fan, X. Xie, L. Qu, and G. Shi, "Graphene-quantum-dot assembled Nanotubes: a new platform for efficient Raman enhancement," *ACS Nano*, vol. 6, no. 3, pp. 2237–2244, 2012.

[22] Y. Zhang, Y. Li, and C. Bai, "Microstructure and oxidation behavior of Si-MoSi$_2$ functionally graded coating on Mo substrate," *Ceramics International*, vol. 43, no. 8, pp. 6250–6256, 2017.

[23] B. K. Vijayan, N. M. Dimitrijevic, J. Wu, and K. A. Gray, "The effects of Pt doping on the structure and visible light photoactivity of titania Nanotubes," *Journal of Physical Chemistry C*, vol. 114, no. 49, pp. 21262–21269, 2010.

[24] Y. Zhu, A. Marianov, H. Xu, C. Lang, and Y. Jiang, "Bimetallic Ag-Cu supported on graphitic carbon nitride nano-scaffold materials for improved visible-light photocatalytic hydrogen production," *ACS Applied Materials & Interfaces*, vol. 47, no. 11, pp. 311–318, 2018.

[25] N. Wang, Z. Bai, Y. Qian, and J. Yang, "Double-walled Sb@TiO$_2$−xnanotubes as a superior high-rate and ultralong-lifespan anode material for Na-ion and Li-ion batteries," *Advanced Materials*, vol. 28, no. 21, pp. 4126–4133, 2016.

[26] S. Konduri, H. M. Tong, S. Chempath, and S. Nair, "Water in single-walled aluminosilicate nano-scaffold materials: diffusion and adsorption properties," *The Journal of Physical Chemistry C*, vol. 112, no. 39, pp. 15367–15374, 2008.

[27] R. Leghrib, T. Dufour, F. Demoisson, N. Claessens, F. Reniers, and E. Llobet, "Gas sensing properties of multiwall carbon nanotubes decorated with rhodium nanoparticles," *Sensors & Actuators B Chemical*, vol. 160, no. 1, pp. 974–980, 2011.

Research Article

High-Efficiency Power Generation Device of Magnetic Declination Thermoelectric Material and Multisource Coordination Optimization of Distribution Network

Lifeng Zhang and Xiaofang Wu [ID]

Ordos Vocational College, Ordos, 017000 Ordos, China

Correspondence should be addressed to Xiaofang Wu; zlf1115@imut.edu.cn

The first-order phase transition compounds have attracted widespread attention from refrigeration enterprises and scientists due to their giant magnetocaloric effect and refrigeration temperature region spanning room temperature. Magnetic substances are crystal structures composed of magnetic ions or atoms with a certain thermal motion or vibration. This research mainly discusses the multisource coordination optimization of magnetic declination thermoelectric material efficient power generation device and distribution network. In this study, large doses of MnFe(P,Si) compounds with different ratios were prepared. The reason for choosing a large dose is that the properties and structures of the samples prepared in a large amount and a small amount will be more or less the same for the samples fired in the same proportion and in the same process. At the same time, mass production also prepares for future mass production. Thermomagnetic power generation described in this study is a form of power generation that converts thermal energy directly into electrical energy. The conversion of thermal energy to electric energy is realized by the change of magnetization in the closed coil by the thermomagnetic material in the magnetic field environment, and then, the change of the magnetic flux in the closed coil is realized. The distribution network refers to the power network that receives electrical energy from the transmission network or regional power plants and distributes it locally through distribution facilities or distributes it to various users step by step according to the voltage. It is composed of overhead lines, cables, towers, distribution transformers, isolating switches, reactive power compensators, and some ancillary facilities. A network that plays an important role in distributing electrical energy in the power grid. This research starts with the active distribution network scheduling priority and the distribution network scheduling coordination control framework. Combined with the scheduling and operation characteristics of each component in the distribution network, the coordinated optimization scheme of the distribution network and the source-network load-storage coordinated control framework are investigated and analyzed. The scheduling resources of the model include the power of the substation flowing into the distribution network, the output of the adjustable distributed power source, the output value of the energy storage element, the closing status of the tie switch, and the section switch. In the study, it was found that when the Fe content was 0.63, the Curie temperature of the compound could reach 273 K at the highest. Scientifically designing a thermomagnetic power generation demonstration device is an important part of the realization of thermomagnetic power generation. The magnetic declination thermoelectric materials designed in this study will help to improve the power generation efficiency.

1. Introduction

The rapid development of nanotechnology and advanced material synthesis technology provides convenience for the continuous improvement of the dimensionless thermoelectric figure of merit of thermoelectric materials. This in turn promotes thermoelectric power generation technology to play an active role in civil fields, such as automobiles and ships. Thermoelectric power generation technology has both social and economic benefits in the recycling and reuse of industrial waste energy.

Although the power generation efficiency of the energy system is reduced when the scale is reduced, its consequent reduction in transmission losses makes people see the feasibility of studying such systems. As a new microminiature energy source, the microthermoelectric power generation system has no moving parts, reliable operation, no noise, and low pollution. It can be an ideal solution as a miniature power supply for electronic systems. Compared with traditional energy, new energy has many advantages, but due to various technical defects, there is no new energy that can replace the dominant position of fossil energy in the energy structure.

It gives the temperature distribution function in the magnetic declination thermoelectric system structure according to the energy relation. It also uses the existing thermoelectric module parameters to establish continuous mathematical models for the one-dimensional symmetric and two-dimensional symmetric thermoelectric system structures. It also gives a discrete mathematical model for the distribution law of thermocouple pairs. On this basis, necessary parameter corrections were made to the model in combination with factors such as heat conduction process, structural gap, energy dissipation, and the adoption of porous structure. Thermocouples are temperature measuring elements commonly used in temperature measuring instruments. It is based on making full use of the continuity of the temperature distribution function of the system and discretizing the thermocouple pair. It performs multivariate optimization on the parameters of the thermoelectric system structure model. Based on the design goals, this paper proposes design indicators such as system efficiency function and volume energy density function and obtains the optimal value range of the system structure size and main model parameters.

2. Related Work

As a new microminiature energy source, the magnetic declination thermoelectric power generation system has no moving parts, no noise, reliable operation, and low pollution. It can be used as an ideal solution for the micropower supply of electronic systems. Magnetic declination refers to the angle between the magnetic meridian at any point on the earth's surface and the geographic meridian. Because compass and magnetic compass are the simplest devices to measure magnetic declination, the history of discovery and measurement of magnetic declination is also very early. Takahashi et al. believed that the power package dispatch system is expected to become one of the advanced distribution systems for controlling power, providing energy on demand, and reducing energy consumption. They designed and experimentally verified a power packet router to implement a networked power packet distribution system. Previously developed routers forwarded power packets directly to the load. And the new router forwards the packet to the other router with an information tag reattached to the power payload. In addition, new routers can adjust the start time of forwarding received power packets to other sites, thereby taking advantage of the router's integrated storage capacity

[1]. Wang and Lin studied the Minimum Distribution Cost Problem (MDCP) for a flow model of specialized manufacturing networks in order to simulate the distillation or decomposition of products in some manufacturing processes [2]. Ravadanegh et al. developed an integrated approach to the problem consisting of power distribution system reconfiguration, capacitor allocation, and simultaneous sizing and siting of renewable energy sources. It also improves the accountability and system performance parameters of the power system. They looked for solutions that are closer to the characteristics of reality. Load forecasts, market price errors, and uncertainties associated with variable output power of wind-distributed generators were all taken into account. They adopted NSGA-II combined with fuzzy set theory to solve the above multiobjective problem. The scheme they proposed ultimately resulted in a solution with minimum voltage deviation, maximum voltage stability, less contamination, and lower cost. Costs include new equipment installation cost, reconfiguration cost, power loss cost, reliability cost, cost of purchasing energy from the electricity market, line upgrade cost, and operation and maintenance cost of distributed generation [3]. Mehmood et al. believed that the life of a battery in a battery energy storage system (BESS) is affected by various factors such as the battery's operating temperature, depth of discharge, and the amount of charge/discharge current supplied to or drawn from the battery. They found the optimal location and size of the BESS for voltage regulation in power distribution systems [4]. Kulmala et al. believed that congestion management is one of the core drivers of smart power distribution systems. Distributed energy sources were used for network control for cost-effective network interconnection of distributed generation (DG) and better utilization of network assets. The main purpose of congestion management was to prevent voltage violations and overload the network. Congestion management algorithms can also be used to optimize network status. They proposed hierarchical and distributed congestion management concepts for future distribution networks with large-scale DG and other controllable resources in medium- and low-voltage networks. The control concept aims to run the network at the lowest cost while maintaining an acceptable network state. The hierarchy consists of three levels: the primary controller operates based on local measurements, the secondary control optimizes the set point of the primary controller in real-time, and the tertiary control utilizes load and production forecasts as its inputs. It implements network reconstruction algorithms and connections to the market. The primary controller is at the connection point of the controllable resource. The secondary controller is located in the primary and secondary substations, and the tertiary control is located in the control center. Therefore, the control is spatially distributed and operates on different time scales [5]. Mohtashami et al. proposed a multiyear distribution network planning optimization model. This was used to manage the operations and capacity of distribution systems with significant penetration of distributed generation (DG). Models take into account investments in traditional network and smart grid technologies. It includes dynamic line ratings, quadrature boosters, and

active network management. It also optimizes the settings of network control devices and takes into account their network cut DG output access arrangements (corporate or non-corporate) when necessary. They had carried out a series of studies on the UK 33 kV actual distribution network to test the model. The main purpose of the research was to evaluate and compare the performance of different investment methods, namely, incremental investment and strategic investment. The study also demonstrated the ability of the model to determine the optimal DG connection point to reduce the overall system cost [6]. Chen et al. through Matlab modeling and simulation proved that the algorithm was suitable for distributed generation (DG) distribution network fault location, which has a certain rapidity and fault tolerance [7]. The introduction of new energy will bring new problems and inconveniences in energy conversion, management, operation, etc., which requires the study of new supporting technologies for coordination. With the development of society, the depletion of fossil energy and the indiscriminate exploitation of resources has led to environmental deterioration, and the situation faced by human beings has become more and more severe. Under the current situation, many countries are vigorously developing green energy and have made considerable achievements. The introduction of new energy will bring new problems and inconveniences in energy conversion, management, operation, etc., which require the study of new supporting technologies for coordination. Therefore, how to comprehensively utilize new energy and traditional energy and realize the complementary advantages between the two is an important issue we are currently facing. As a developing country, China is developing rapidly, and energy consumption and heat emission are topics that cannot be underestimated. A large amount of heat energy emissions will not only bring environmental problems but also aggravate natural disasters such as the greenhouse effect and acid rain.

3. Methods for High-Efficiency Power Generation of Magnetic Declination Thermoelectric Materials

3.1. Thermoelectric Materials for Power Generation. Assuming that the internal load of a thermoelectric material module is R_L, a heat source q can also be added to provide heat so that the temperature difference between the two ends of the conductor is maintained by $T_1 - T_2$. The potential difference generated across the conductor is $(S_2 - S_1) * (S_1 - S_2)$, and the power generated is [8]

$$W = \left[\frac{(\beta_P - \beta_N)(T_1 - T_2)}{R_L - R} \right]^2 R_L. \quad (1)$$

Considering the heat flow provided by the heat source, most of the heat passes through the conductors by means of heat conduction. But there are parts of the heat flow that need to be balanced against the Peltier effect and Joule heating in general. The Peltier effect means that when a current passes through a loop composed of different conductors, in

addition to irreversible Joule heat, the junctions of different conductors will endothermic and exothermic phenomena with different current directions.

$$Q = k(T_1 - T_2) + (\beta_1 - \beta_2)IT_1 - \frac{I^2R}{2}. \quad (2)$$

The current density I is

$$I = \frac{(\beta_1 - \beta_2)(T_1 - T_2)}{(R_1 + R_2)}. \quad (3)$$

Therefore, the choice of load is generally to achieve maximum efficiency [9]

$$M = (1 + ZT)^{1/2}. \quad (4)$$

It gets the efficiency formula:

$$\eta = \frac{T_1 - T_2}{T_1} \cdot \frac{M - 1}{M + \chi T_1/T_2}. \quad (5)$$

It can be seen that the larger the M, the higher the efficiency. However, the size of M is mainly related to Z and temperature, so the value of ZT has a great influence on the efficiency of TEG materials.

For the design of thermoelectric sheets and the modeling of microminiature thermal structures, this paper is aimed at designing a microminiature thermoelectric conversion system as efficient as possible. Thermoelectric conversion systems are usually composed of thermal structures and thermoelectric conversion modules. Therefore, a thermoelectric unit model that comprehensively considers the thermal model and the electrical model is established. After that, it will build a complete thermoelectric conversion system model on this basis. The materials used to manufacture thermoelectric generators or thermoelectric coolers are called thermoelectric materials, which are materials that can realize the interactive transformation of electrical energy and thermal energy.

3.2. Principle of Thermomagnetic Power Generation Device. When the thermomagnetic power generation material (Mn, Fe)2(P, Si) is in a strong magnetic field, when the hot water passes through, when the temperature is higher than the Curie temperature of the thermomagnetic power generation material, the thermal motion of the atoms intensifies. The kinetic energy possessed by the thermal motion of atoms is sufficient to overcome the exchange between spin-magnetic moments. The spin moment of the magnetic atoms inside the material changes from parallel arrangement to disorder, and the magnetization becomes zero instantaneously. The thermomagnetic power generation material is transformed from a ferromagnetic state to a paramagnetic state, and the magnetic field becomes smaller. When the magnetic flux passing through the induction coil decreases, an induced current is generated in the induction coil. Conversely, when cold water passes through, the temperature of the thermomagnetic power generation material is lower than the Curie

temperature, and the atomic thermal motion weakens when the temperature decreases. The exchange action between the spin magnetic moments makes the magnetic atom spin magnetic moments return to the parallel arrangement from the disorderly arrangement. The magnetization changes from zero to a certain value instantaneously, and the thermomagnetic power generation material changes from a paramagnetic state to a ferromagnetic state. When the magnetic field increases, the magnetic flux passing through the induction coil increases, which will also generate a reverse induced current in the induction coil. Hot water and cold water alternately pass through the induction coil plastic tube thermomagnetic power generation material, and the ferromagnetic state and paramagnetic state of the thermomagnetic power generation material periodically transform each other near the Curie temperature. This will generate a periodic alternating induced current and realize the direct conversion of thermal energy into electrical energy. The principle of thermomagnetic power generation device is shown in Figure 1. For the design of thermoelectric power generation sheet, it is generally required that the larger the output power per unit volume, the better, that is, the larger the volume-specific power, the better. In the actual design process, when the area and other parameters of the thermoelectric power generation sheet are determined, and the length of the galvanic coupler arm is short to a certain extent; the output power of the power generation sheet will reach the maximum. If it continues to shorten, its power will show a downward trend [10].

For the energy storage devices connected in the network, the property rights are set to be owned by the distribution network operation and maintenance company, and they can participate in the operation and scheduling of the distribution network. Its scheduling cost C_t^E:

$$C_t^E = \sum \lambda P_t^E \Delta T \qquad (6)$$

For any distribution network node i, the power balance formula in polar coordinate form can be listed as follows [11]

$$P_i = U \sum U (G \cos \beta + B \sin \beta) \qquad (7)$$

$$Q_i = U \sum U (G \cos \beta - B \sin \beta) \qquad (8)$$

Among them: P_i and Q_i are the injected active and reactive power of node i, respectively [12].

When using Newton-Raphson's method to solve a nonlinear system of equations, it is necessary to write out its modified equations [13]

$$\Delta P_i = P - U_i \sum U (G \cos \beta + B \sin \beta), \qquad (9)$$

$$\Delta Q_i = P - U_i \sum U (G \cos \beta - B \sin \beta). \qquad (10)$$

3.3. $Mn_{1.23}FexP_{0.3}Si_{0.3}$ Compound Structure and Magnetic Test

3.3.1. Material Preparation.
The Mn flakes, Fe powder, P powder, and single-crystal Si block used in the experiment are calculated in a ratio of $Mn_{1.23}FexP_{0.3}Si_{0.3}$ ($x = 0.6$, 0.63, 0.63, 0.67, 0.7, and 0.73). It is weighed with an electronic balance. It was ball milled with a high-energy planetary ball mill (pulverisette-3) for 10 h under argon protection. It then precompresses the sample into a block under the pressure of 8 T and then puts it into a quartz tube for vacuuming (vacuum degree < 10-3 Pa), fills it with argon gas to 2×10^3 Pa, and seals the quartz tube. The sealed samples were placed in a vertical annealing furnace for sintering at 11009°C for 2 h and then lowered to 830°C for 20 h and then quenched.

3.3.2. Sample Characterization and Performance Measurement.
The X-ray diffraction (XRD) spectrum of the sample was measured with a Philips PW-1830 X-ray diffractometer (Cu-Kα, $h = 0.134184$ nm) at room temperature (293 K), the measurement step was 0.01°, and the collection point time was 4 s. It measures the magnetic properties of compounds with a LakeShore 7407 vibrating sample magnetometer [14].

Voltage constraints:

$$V_{K,\min} < V_K < V_{K,\max}, \qquad (11)$$

where V_k is the voltage at node k [15].
Line current constraints:

$$I \leq I_{l,\max}, \quad l \in n_l. \qquad (12)$$

In the formula, I_l is the number of branches in the power supply island network after the power supply is restored. $I_{l,\max}$ is the maximum current value allowed for line I.

Microgrid output constraints [16]

$$P_{j,\min} \leq P \leq P_{j,\max}. \qquad (13)$$

$P_{j,\max}$ and $P_{j,\min}$ are the upper and lower limits of the active power sent by the microgrid j, respectively [17].

Charge load available capacity constraints [18]

$$EV \leq EV_{k,\max}. \qquad (14)$$

$EV_{k,\max}$ is the upper limit of the available capacity of the charging power [19].

The dispatch model takes the total operating cost of the distribution network in a single dispatch period as the objective function.

$$\min F = \sum \left(C_t^g + C_t^{DG} + C_t^{ESS} + C_D^t \right). \qquad (15)$$

In the formula, time t represents the current time period [20].

The cost of purchasing electricity from the grid:

$$C_b = \sum_g^{NG} CP \Delta T. \qquad (16)$$
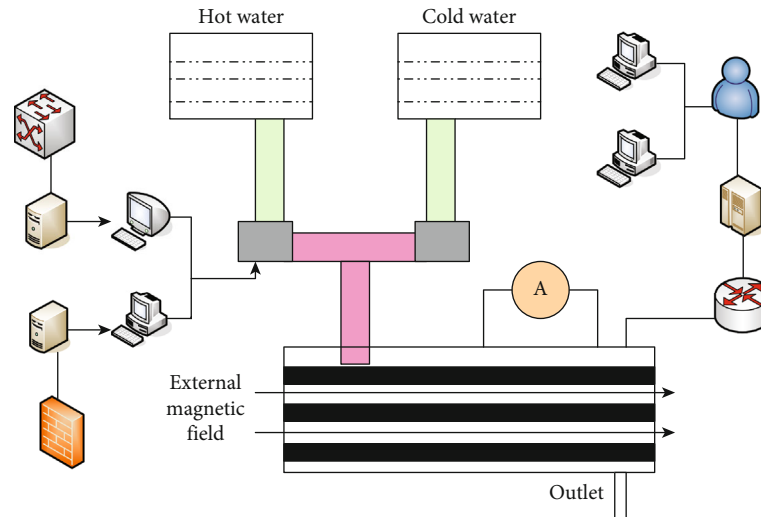
Figure 1: Principle of thermomagnetic power generation device.

Among them, g represents the feeder at the exit of the b substation, and NG represents the total number of substation feeders connected to the distribution network.

3.4. Design of Thermomagnetic Power Generation Device.
The thermomagnetic power generation device is composed of six parts: magnetic field system, cold and heat source system, automatic control electronic switch, induction coil, sensitive ammeter, and thermomagnetic power generation material.

(1) Magnetic field system: the strong magnetic material NdFeB is used to make a cylindrical strong permanent magnet as the driving magnetic field. The length is 20 cm, the inner diameter is 9 cm, the outer diameter is 20 cm, and the maximum magnetic induction intensity is $B = 0.8$ T. The direction of the magnetic field is radial. The plastic tube with the magnetic material placed in the outer coil is placed in the inner magnetic field area of the cylindrical strong magnet, and its function is to make the thermomagnetic power generation material reach saturation magnetization

(2) Cold and heat source system: the heat source is a domestic water heater, the maximum temperature can reach 100°C; the cold source is tap water

(3) Automatic electronic switch: the two electronic switches are, respectively, connected with the heat source and the cold source water inlet pipe. The electronic switch is controlled by a single-chip microcomputer. The hot and cold water passes through the thermomagnetic power generation material in the plastic pipe alternately, and different times can be set according to needs. The thermomagnetic power generation material periodically changes in cold and heat

(4) Induction coil: the induction coil is wound on a plastic tube by a hand-winding machine, and the wound coil is painted with insulating paint to protect the coil. After the thermal-magnetic power generation material is installed inside the plastic pipe, the two ends are cut with nylon rods and the outside is sealed with a rubber sheet

(5) Microammeter: measure the thermal-magnetic power generation current, and use wires to connect the induction coil and the microammeter [21]

(6) Thermomagnetic power generation material: the annealed thermomagnetic power generation material is cut into 1.3 mm thin slices with a wire cutting machine. The thin copper wires are used to connect them, leaving a gap in the middle to facilitate the passage of water and improve the heat exchange capacity between the material and water. The cut thermomagnetic power generation material can also be turned into small particles. The thermomagnetic power generation device designed in this study is shown in Figure 2

3.5. Multisource Optimization Model for Microgrid Power Supply Recovery.
After the distribution network fails, the real-time monitoring of the DMS is used to obtain the sum of the power available for all microgrids in the outage area $\sum L_i$ and the total power $\sum MG_j$ of the load in the outage area, and the microgrid power supply recovery scheme is selected [22].

$$\sum L_i \le \sum MG_j. \tag{17}$$

After the power distribution network fails, the real-time monitoring of DMS is used to obtain the sum of the external power of all microgrids in the nonfault outage area $\sum MG$
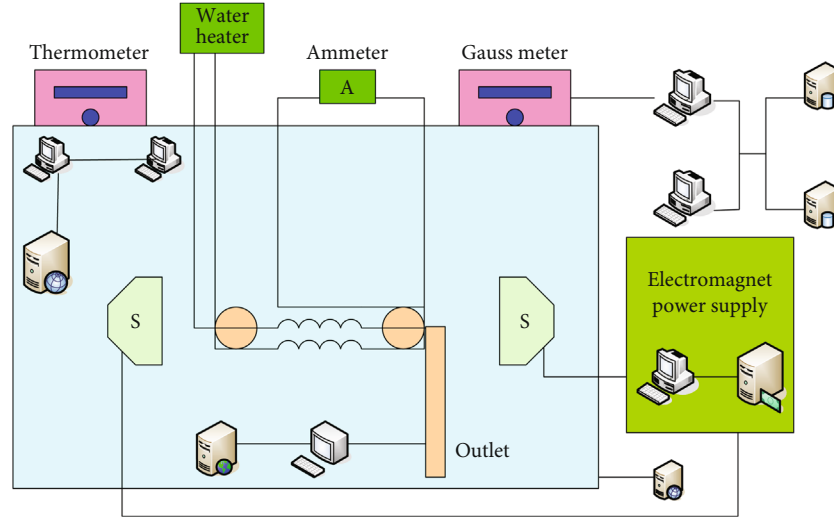
FIGURE 2: The thermomagnetic power generation device designed in this paper.

and the total power of the load in the outage area $\sum L_i$.

$$\sum L - \sum EV \leq \sum MG \leq \sum L_i. \qquad (18)$$

The multilevel rapid power supply restoration scheme proposed in this study considers the economics of network operation after the power supply of the distribution network is restored. Therefore, in the optimal power flow mathematical model, the optimization objective is to minimize the active network loss of the power supply island after the power supply is restored [23]

$$\min M = \min \sum I^2 R, \qquad (19)$$

where I is the line transmission current; R is the line resistance.

The theoretical output power of a single thermocouple pair tends to increase with the increase of the temperature difference between its two sides in a large range and also tends to increase with the increase of the current. In comparison, the effect of temperature difference on the thermocouple's power generation efficiency is more obvious. Tide constraints:

$$U \sum_{J=1} YU = P + Q, \qquad (20)$$

where P and Q are the values of active power and reactive power injected by node i, respectively.

4. Multisource Coordination Optimization Results of Thermoelectric Material Efficient Power Generation Device and Distribution Network

Figure 3 shows the XRD spectrum of the $Mn_{1.23}Fe_xP_{0.3}Si_{0.3}$ series compounds. It can be seen from the XRD spectrum that when the Fe content is 0.63, it is a single Fe_2P-type hex-agonal structure. The impurity phase of this series of compounds is one of $(Mn, Fe)_3Si$ or $(Mn, Fe)_3Si_3$. With the increase of Fe content, the first impurity phase is $(Mn, Fe)_3Si_3$. Then, the peak intensity decreased gradually until the Fe content was 0.67, the $(Mn, Fe)_3Si$ impurity phase appeared, and then the peak intensity gradually increased.

It can be seen from Table 1 that when x is between 0.6 and 0.63, the unit cell volume V and the lattice constant a gradually increase. When x is between 0.63 and 0.73, the change rule of the unit cell volume V is not obvious. The lattice constants and unit cell volumes of the $Mn_{1.23}Fe_xP_{0.3}Si_{0.3}$ series compounds are shown in Table 1.

The change of magnetization with temperature of $Mn_{1.23}Fe_xP_{0.3}Si_{0.3}$ ($x = 0.6, 0.63, 0.63, 0.67, 0.7,$ and 0.73) series compounds is shown in Figure 4. The cooling and heating curves do not overlap, indicating that there is thermal hysteresis. When the Fe content is 0.63, the thermal hysteresis of the compound is at least 1 K. When the Fe content is 0.6, the maximum thermal hysteresis of the compound is 21 K. The Curie temperature (Tc) of a compound can be determined by taking the partial derivative of the M-T heating curve. It can be seen that when the Fe content is 0.63, the maximum Curie temperature of the compound is 273 K. When the Fe content is 0.6, the minimum Curie temperature of the compound is 207 K.

$Mn_{1.23}Fe_xP_{0.3}Si_{0.3}$ samples were prepared and cut into 1.3 mm thin slices by a wire cutting machine. The samples were taken with masses of 30 g, 100 g, 130 g, and 200 g, respectively, and put into a thermomagnetic power generation device with $N = 1030, 2000, 2700,$ and 3300 coil turns, and the hot water temperature was about 80°C. Through the analysis of the measurement data, whether it is a flake sample or a particle sample, the induced current increases with the increase of the sample mass. The reason is that the mass increases, the total number of magnetic atoms increases, the total magnetic moment increases, and the change rate of the total magnetic flux of the sample around the Curie temperature increases. For samples of the same mass, the induced current produced by the granular sample
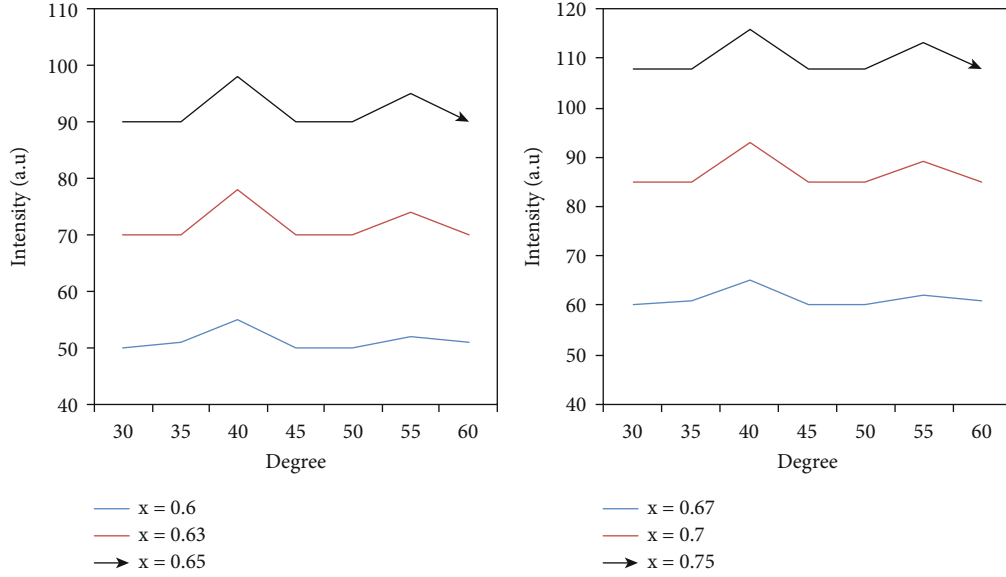
Figure 3: XRD spectra of $Mn_{1.23}FexP_{0.3}Si_{0.3}$ series compounds.

Table 1: Lattice constant and unit cell volume of $Mn_{1.23}FexP_{0.3}Si_{0.3}$ series compounds.

x	a (nm)	c (nm)	V (nm^3)
0.6	0.6030	0.3414	0.1082
0.63	0.6064	0.3399	0.1083
0.63	0.6063	0.3404	0.1083
0.67	0.6060	0.3407	0.1084
0.7	0.6048	0.3407	0.1079
0.73	0.6012	0.3480	0.1089

is greater than that produced by the flake sample. The variation of the induced current is shown in Figure 5.

When a sample of the same mass is placed in the coil, the induced current I increases with the increase of the number of turns N of the coil. According to Faraday's law of electromagnetic induction, the induced electromotive force is proportional to the number of turns of the coil. The relationship between the induced current and the number of coil turns is shown in Figure 6.

Figure 7 shows the XRD diffraction of Sn-bonded M $n_{1.23}Fe_{0.63}P_{0.3} - xSi_{0.3} + x$ series composite compounds. Through qualitative analysis of XRD patterns, it can be known that the compound and the main phase are still Fe_2P-type structure of MnFe(P,Si).

This shows that the main phase structure of the bonded compound has not changed (A ($Mn_{1.23}Fe_{0.63}P_{0.48}Si_{0.32}$), B ($Mn_{1.23}Fe_{0.63}P_{0.46}Si_{0.34}$), C ($Mn_{1.23}Fe_{0.63}P_{0.44}Si_{0.36}$), and D ($Mn_{1.23}Fe_{0.63}P_{0.42}Si_{0.38}$)). There is an impurity peak around 43° which is Fe_3Si_3. After data comparison, it is found that the peaks at 31.7° and 32.3° belong to metal Sn. Both metallic Sn and impurity peaks have negative effects on the magnetocaloric properties of the compounds themselves.

The lattice constants and unit cell volumes of the M $n_{1.23}Fe_{0.63}P_{0.3} - xSi_{0.3} + x$ series bonding compounds are

shown in Table 2. From Table 2, we can see that the lattice constants a and b and the unit cell volume V have no significant changes. It can only be seen that the lattice constant a slowly decreases, b increases slowly, and the unit cell volume V gradually increases. The lattice constants and unit cell volumes of the $Mn_{1.23}Fe_{0.63}P_{0.3} - xSi_{0.3} + x$ series bonding compounds are shown in Table 2.

The output results of the nonlinear active distribution network multisource collaborative optimization scheduling model are shown in Table 3.

Because this model is linear, the linear programming solver CPLEX is used to solve it. The calculation time is 2.9 s, and the total running cost is 27728.922 yuan. It can be seen that the fast calculation method can greatly improve the solution speed while maintaining high accuracy. The improvement of computational efficiency brought by the linear algorithm is more obvious in solving large-scale systems with multiple nodes and multiple times. The planned output power of the substation within 24 hours is shown in Figure 8.

Based on the multisource collaborative optimization nonlinear scheduling model of network reconfiguration, the SBB mixed integer nonlinear programming solver is called in GAMS, and the optimal collaborative scheduling scheme of active distribution network energy storage, flexible load, and tie switch position control is obtained. Compared with the operation results obtained by the dispatching model without considering dynamic reconfiguration, it can verify the effective application of dynamic reconfiguration in the coordinated optimal operation of the distribution network system. The planned output of the substation is shown in Table 4.

Strategy 2 considers energy storage factors more than strategy 1. The total operating cost of the active distribution network is reduced by 3383.42 yuan, and the electricity sales revenue from the distribution network to the main network
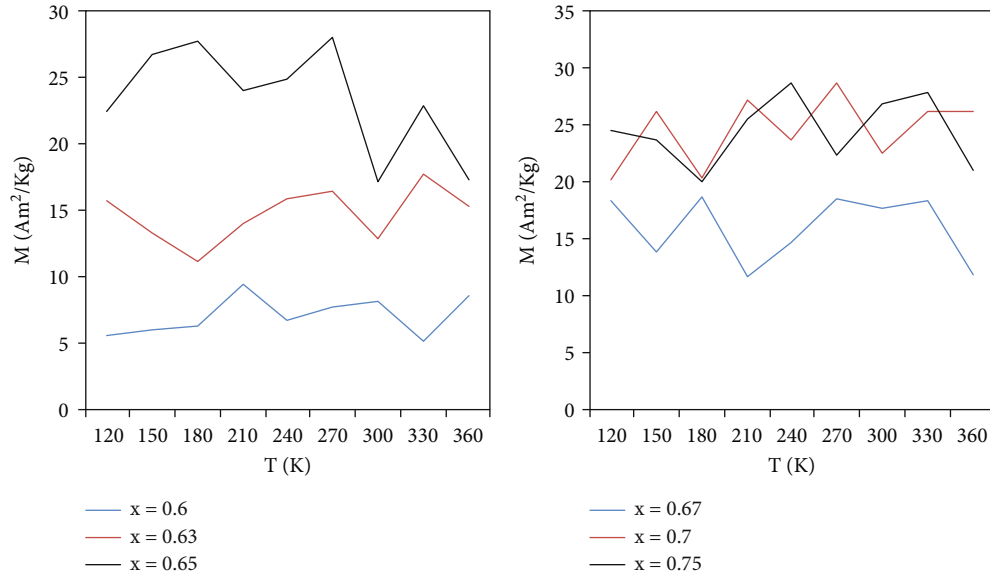
FIGURE 4: Magnetization of $Mn_{1.23}FexP_{0.3}Si_{0.3}$ ($x = 0.6, 0.63, 0.63, 0.67, 0.7$, and 0.73) series compounds as a function of temperature.
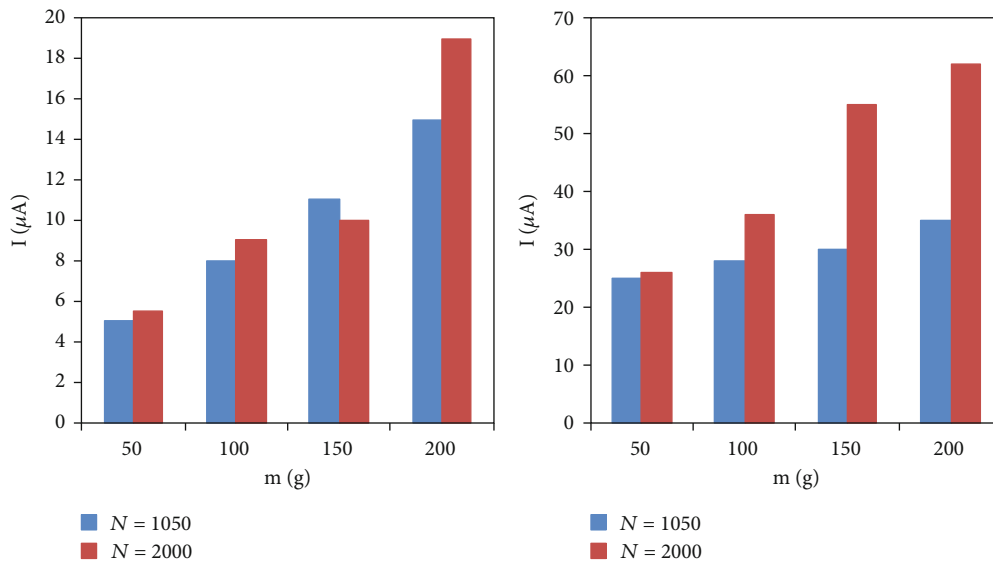
FIGURE 5: Variation of induced current.

is 996.03 yuan, an increase of 734.13 yuan compared with strategy 1. The operating costs of the distribution network under different dispatching strategies are shown in Table 5.

The operator's distributed power parameters are shown in Table 6.

The matching and optimization process of each parameter inside the thermoelectric power generation device is an extremely comprehensive problem. It is not only related to material technology but also related to factors such as structure selection and layout. Therefore, another important research direction to improve the system thermoelectric power generation efficiency is to balance the influence of various parameters on the output power and thermoelectric conversion efficiency to seek the optimal matching. The load state of the active distribution network is shown in Figure 9.

5. Discussion

In the past few hundred years, with the rapid development of industrialization and urbanization all over the world, the demand for energy has also increased rapidly. The excavation and utilization of large-scale fossil energy have resulted in a sharp decrease in energy reserves, and at the same time, the harmful substances produced during energy consumption also directly lead to the deterioration of the environment. At this stage, adjusting the energy structure transformation is an effective way to solve the current global energy and environmental problems.

The access of distributed power sources changes the power flow direction and network structure of the distribution network. When its penetration rate is too high, it may
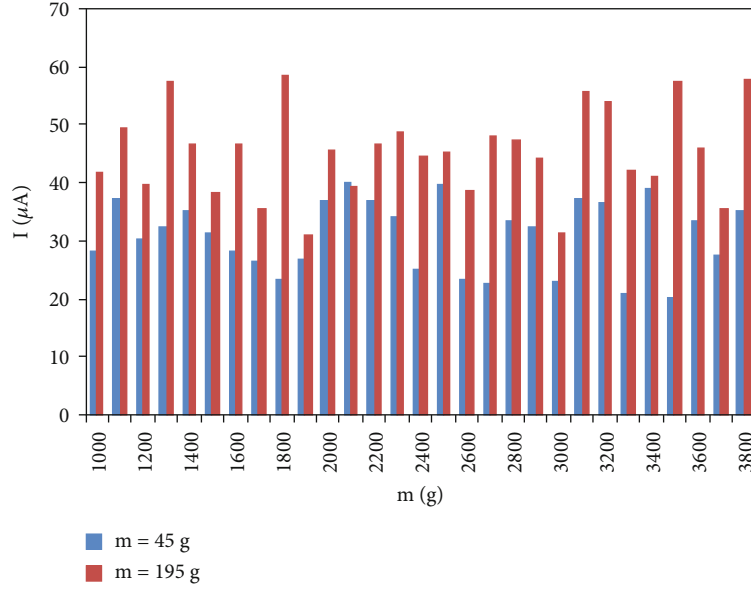
FIGURE 6: Induced current vs. coil turns.
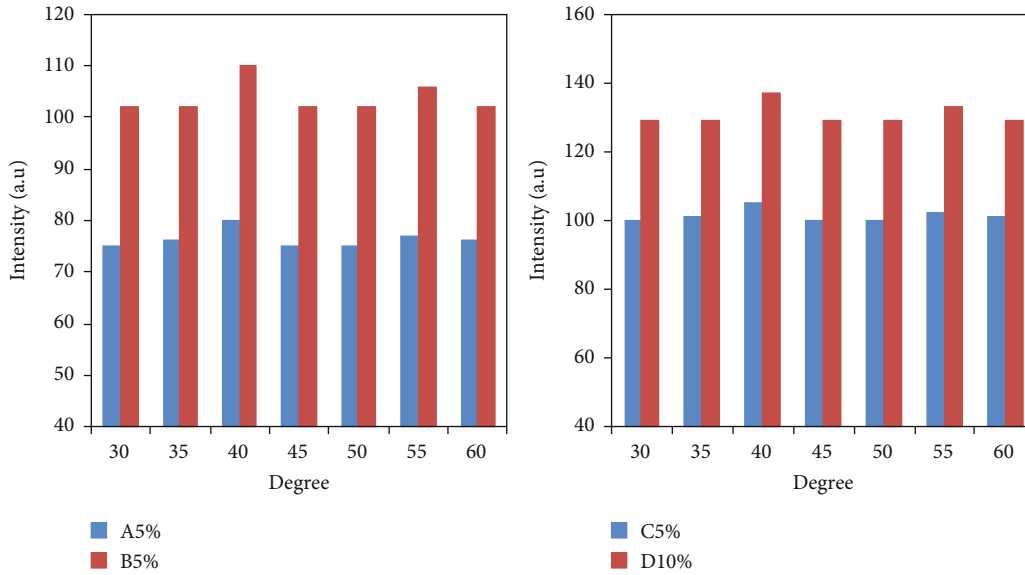
FIGURE 7: XRD diffraction of Sn-bonded $Mn_{1.23}Fe_{0.63}P_{0.3} - xSi_{0.3} + x$ series composite compounds.

TABLE 2: Lattice constant and unit cell volume of $Mn_{1.23}Fe_{0.63}P_{0.3} - xSi_{0.3} + x$ series bonding compounds.

Serial number	a (nm)	c (nm)	V (nm^3)
3%A&B	2.6272	2.3313	2.1281
10%A&B	2.6263	2.3399	2.1283
3%C&D	2.6267	2.3323	2.1287
10%C&D	2.6262	2.3327	2.1 283

TABLE 3: Output results of multisource collaborative optimization scheduling model using nonlinear active distribution network.

Active P (MW)	Period
T1	2.6307
T2	2.7338
T3	2.1798
T4	2.2633
T5	2.6834

cause the voltage limit of multiple distribution network nodes mainly access nodes to be exceeded, and the power flow will be sent back to the upper-level power grid. In addition, the randomness and intermittency of the distributed power supply itself will also cause problems such as voltage

fluctuations in the distribution network. In the military, the use of a microthermoelectric power generation system can greatly improve the combat effectiveness of the army. Microthermoelectric power generation systems can provide
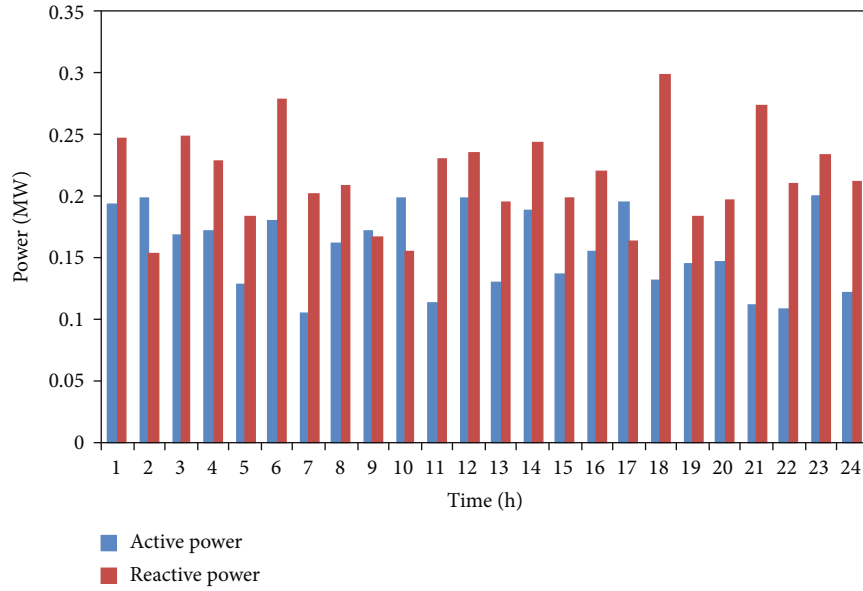
Figure 8: Substation planned output power within 24 h.

Table 4: Substation planned output.

Time	Substation (MW)	
	First	Second
T1	4.2	0.8
T2	3.3	1.7
T3	3.1	2.3
T5	2.6	3.4
T6	2.1	4.2

Table 5: Distribution network operating costs under different dispatch strategies.

Strategy	Power generation cost (yuan)	Equivalent operating cost of energy storage (yuan)
Strategy 1	24747.7	4272
Strategy 2	16949.2	4272.4
Strategy 3	17476.4	4272
Strategy 4	22742.3	4212.4
Strategy 5	14421.2	2177.4

Table 6: Distributed power parameters for operators.

Distributed power	Installed capacity (kW)	Number of installed units (units)
Photovoltaic	350	10
Diesel generators	350	6
Micro gas turbine	520	2
Energy storage device	610	2

the biggest weakness of the existing technology, storage battery, fuel cell, etc., is that the time that can provide electric energy is short. The microthermoelectric power generation system can provide a relatively long power supply in a small volume.

Distributed power generation is an important way to utilize new energy. With the advancement of energy transformation and the increase of energy demand, the penetration rate of distributed power generation in the distribution network is gradually increasing. The large-scale access of DG has changed the structure of the original distribution network. Coupled with the uncertainty of DG's own output, when it is connected to different capacities and different locations, it will have different effects on the operating characteristics of the distribution network such as voltage distribution. Combined with the distribution law of the temperature field and its potential field, comprehensively considering the output characteristics and structural reliability of thermoelectric power generation, the parameters of the thermoelectric power generation device are optimized and matched, and a reasonable structural layout scheme is designed. It improves the thermoelectric conversion efficiency while reducing reliability problems caused by mechanical stress and environmental factors.

power drives for military robots or military electronic equipment. When military robots are used for reconnaissance, their volume is generally relatively small due to the need for concealment. In field operations, the conventional power system has been unable to ensure the smooth flow of military communications, which requires the miniaturization of the power system. In these cases, energy supply is very important. In addition to the characteristics of large volume,

FIGURE 9: Load status of active distribution network.

In addition to increasing the temperature of the heat source, improving the heat dissipation conditions of the cold source and rationally arranging the cooling system are also effective ways to improve the thermoelectric conversion efficiency of the system and improve the performance of the system. First of all, choosing a reasonable heat exchange method and heat exchange medium, such as oil cooling, air cooling, water cooling, or phase change heat, can improve the performance of the system to a certain extent. Secondly, optimizing the shape and structure of the radiator components and increasing the heat dissipation area of the radiator components are important measures to improve and maintain the system temperature difference.

The characteristics of thermoelectric power generation devices make such devices play a more important role in plateau weather stations, outposts, and other places where electricity is difficult to use. When natural gas or oil pipelines pass through desolate areas, the combustion heat of natural gas or oil can be used to provide them with a temperature difference working environment. The performance of magnetic declination thermoelectric materials is also related to temperature difference. This means that both the thermal conductivity and the electrical conductivity of the material will affect the thermoelectric conversion efficiency of the material.

6. Conclusion

The thermal conductivity and electrical conductivity of magnetic declination thermoelectric materials are realized by the movement of internal carriers. Metal Sn and metal Zn are light metals with low melting point and good electrical conductivity. The powder compound of metal Zn or metal Sn and MnFe(P, Si) material is mixed uniformly, sealed in a quartz tube under the protection of high-purity argon gas, and sintered near the melting point of metal Zn or metal Sn. This makes the metal Sn or the metal Zn dissolve rapidly

to function as a metal bond. The efficiency of the thermoelectric power generation device also depends on the heat dissipation and heat conduction device matched with it, as well as the thermoelectric coupling effect inside the thermoelectric power generation device. Therefore, the efficiency of thermoelectric conversion device is also related to parameters such as temperature difference, load resistance, loop current, and internal resistance of power generation devices. Therefore, the optimal matching between the load and the internal structural parameters of the thermoelectric power generation device is also an important issue to improve the thermoelectric conversion efficiency of the system.

Data Availability

No data were used to support this study.

Conflicts of Interest

There are no potential competing interests in our paper.

Authors' Contributions

All authors have seen the manuscript and approved to submit it to your journal.

Acknowledgments

References

[1] R. Takahashi, K. Tashiro, and T. Hikihara, "Router for power packet distribution network: design and experimental verification," *IEEE Transactions on Smart Grid*, vol. 6, no. 2, pp. 618–626, 2015.

[2] I. L. Wang and S. J. Lin, "A network simplex algorithm for solving the minimum distribution cost problem," *Journal of Industrial & Management Optimization*, vol. 3, no. 4, pp. 929-930, 2017.

[3] S. N. Ravadanegh, M. Oskuee, and M. Karimi, "Multi-objective planning model for simultaneous reconfiguration of power distribution network and allocation of renewable energy resources and capacitors with considering uncertainties," *Journal of Central South University*, vol. 24, no. 8, pp. 1837–1849, 2017.

[4] K. K. Mehmood, S. U. Khan, and S. J. Lee, "Optimal sizing and allocation of battery energy storage systems with wind and solar power DGs in a distribution network for voltage regulation considering the lifespan of batteries," *IET Renewable Power Generation*, vol. 11, no. 10, pp. 1303–1313, 2017.

[5] A. Kulmala, M. Alonso, S. Repo et al., "Hierarchical and distributed control concept for distribution network congestion management," *IET Generation, Transmission & Distribution*, vol. 11, no. 3, pp. 663–673, 2017.

[6] S. Mohtashami, D. Pudjianto, and G. Strbac, "Strategic distribution network planning with smart grid technologies," *IEEE Transactions on Smart Grid*, vol. 8, no. 6, pp. 2656–2664, 2017.

[7] K. Chen, Y. Zhang, and H. Wang, "Fault-section location of distribution network containing distributed generation based on immune algorithm," *Dianli Xitong Baohu yu Kongzhi/Power System Protection and Control*, vol. 43, no. 24, pp. 37–62, 2017.

[8] A. A. S. Emhemed and G. M. Burt, "An advanced protection scheme for enabling an LVDC last mile distribution network," *IEEE Transactions on Smart Grid*, vol. 3, no. 3, pp. 2602–2609, 2017.

[9] J. Zhao, J. Wang, Z. Xu, C. Wang, C. Wan, and C. Chen, "Distribution network electric vehicle hosting capacity maximization: a chargeable region optimization model," *IEEE Transactions on Power Systems*, vol. 32, no. 3, pp. 4119–4130, 2017.

[10] G. Xu, Z. Wang, J. Zhou et al., "Rotor loss and thermal analysis of synchronous condenser under single-phase short-circuit fault in the transmission line," in *JIEEE Transactions on Energy Conversion*, 2022.

[11] M. Abdelaziz, "Distribution network reconfiguration using a genetic algorithm with varying population size," *Electric Power Systems Research*, vol. 142, no. JAN., pp. 9–11, 2017.

[12] D. Shelar and S. Amin, "Security assessment of electricity distribution networks under DER node compromises," *IEEE Transactions on Control of Network Systems*, vol. 4, no. 1, pp. 23–36, 2017.

[13] L. Kai, S. Zhong, and F. Zhu, "A NDN IoT content distribution model with network coding enhanced forwarding strategy for 3G," *IEEE Transactions on Industrial Informatics*, vol. 14, no. 99, pp. 2723–2733, 2018.

[14] Z. Ma, Y. Shang, H. Yuan et al., "Holistic performance evaluation framework: power distribution network health index," *Iet Generation Transmission & Distribution*, vol. 11, no. 9, pp. 2184–2193, 2017.

[15] S. Han, D. Kodaira, and S. Han, "An automated impedance estimation method in low-voltage distribution network for coordinated voltage regulation," *IEEE Transactions on Smart Grid*, vol. 7, no. 2, pp. 1012–1020, 2017.

[16] L. Wang, S. Sharkh, and A. Chipperfield, "Optimal decentralized coordination of electric vehicles and renewable genera-tors in a distribution network using A^* search," *International Journal of Electrical Power & Energy Systems*, vol. 98, no. JUN., pp. 474–487, 2018.

[17] S. Mishra, D. Das, and S. Paul, "A comprehensive review on power distribution network reconfiguration," *Energy Systems*, vol. 8, no. 2, pp. 227–284, 2017.

[18] W. U. Lizhen, L. Jiang, and X. Hao, "Reactive power optimization of active distribution network based on optimal scenario generation algorithm," *Power System Protection & Control*, vol. 43, no. 13, pp. 132–139, 2017.

[19] D. Zeng, G. Wang, and J. Guo, "Adaptive current protection scheme for distribution network with inverter-interfaced distributed generators," *Automation of Electric Power Systems*, vol. 41, no. 12, pp. 86–92, 2017.

[20] Q. Qi, J. Wu, and C. Long, "Multi-objective operation optimization of an electrical distribution network with soft open point," *Applied Energy*, vol. 208, no. dec. 13, pp. 734–744, 2017.

[21] L. Thurner, A. Scheidler, A. Probst, and M. Braun, "Heuristic optimisation for network restoration and expansion in compliance with the single-contingency policy," *Iet Generation Transmission & Distribution*, vol. 11, no. 17, pp. 4264–4273, 2017.

[22] F. U. Yang, J. Liao, and L. I. Zhenkun, "Day-ahead optimal scheduling and operating of active distribution network considering violation risk," *Proceedings of the CSEE*, vol. 37, no. 21, pp. 6328–6338, 2017.

[23] M. Mikolajkova, C. Haikarainen, and H. Saxen, "Optimization of a natural gas distribution network with potential future extensions," *Energy*, vol. 125, pp. 839–848, 2017.

Research Article

Application of Supramolecular Polymer Nanoparticles in Controlled Release System of Anticancer Drugs

Zhichao Ma[1] **and Jie Qi** [ID] [2]

[1]*School of Physical Education, Wuhan Business University, Wuhan, 430056 Hubei, China*
[2]*Physical Education College, Shanghai Normal University, Shanghai 200234, Shanghai, China*

Correspondence should be addressed to Jie Qi; qijieyzh@shnu.edu.cn

Nanoscience is a comprehensive, interdisciplinary course based on many advanced sciences and technologies that has developed rapidly in recent decades. Nanotechnology has been widely used in biomedicine, materials science, chemistry, physics, information and electronic engineering, and other fields. Nanomaterials have been widely used in various research fields because of their many excellent properties, such as quantum size phenomenon, small size phenomenon, and quantum mechanics. Surface effects and tunneling phenomena have now become the focus of scientific research. Controlled release means that the drug is released quantitatively and uniformly through the controlled release coating film, so that the concentration of the drug in the blood remains unchanged. This paper is aimed at studying the application and performance of nanoparticles in the controlled release system of anticancer drugs. This paper addresses the issue of the controlled release of anticancer drugs. This question is based on nanoparticles. Therefore, it was elaborated around supramolecular polymer nanoparticles, and a case design and analysis of its use in the controlled release system of anticancer drugs was carried out. The experimental results showed that when laser irradiation and GSH coexisted, the dissolution rate and cumulative dissolution rate of DOX were the highest, and the total release within 3 h was close to 53%. This result indicates that the release of DOX from DOX@HMPB@PEI-SS-HA is both photosensitivity and redox responsive, and the photosensitivity predominates.

1. Introduction

Chemotherapy plays an important role in various cancer treatments, but traditional chemotherapy cannot achieve key goals such as stable drug delivery, targeting, stabilization point, and timely release. We hope these issues will be resolved. In recent years, the controlled stimulated release of nanomedicines has been a research hot spot. Since artificial intelligence and production planning were proposed, genetic algorithm, as a global optimization algorithm, has been widely used. It has comprehensive applications in image processing, machine learning, computer-aided design, and other fields.

Cancer is one of the main culprits that endanger human health and threaten human life, which has always been the focus of doctors. By controlling drug release, it can be achieved through membrane control systems and in vivo diffusion systems. Targeted drug release functions can be achieved through biorecognition mechanisms, permeation mechanisms, and in vitro control. This series of means ensures that the blood drug concentration remains stable, and the patient can get the best effect by taking the drug.

The innovation of this paper is the following: (1) This paper combines drug controlled release with a decision tree algorithm and genetic algorithm and introduces the theories and related methods of the two algorithms in detail. (2) In the face of drug controlled release, this paper divides the experimental samples into four groups. Through the evaluation of the experimental results, this paper compares the performance of nanoparticles in it. It is concluded that nanoparticles play a positive role in the controlled release of anticancer drugs.

2. Related Work

At the end of 1959, the concept of the nanometer was first proposed by a Nobel Prize winner. But really effective nanoscale research began in the 1960s. In the past decade, scientists have begun to shift their focus to the study of related nanomaterials. And it has achieved fruitful research results in the preparation process. Kumar et al. discuss the structure, morphology, and optical properties of the prepared samples. Its refinement revealed a single-phase hexagonal wurtzite structure without any impurity phase. It enhances the understanding of the structural and optical properties of Co/Mn codoped nanocrystals. However, their data is less [1]. Chevigny et al. investigated the dispersion mechanism of nanocomposites composed of polymer-grafted nanoparticles mixed with free chains of the same polymer. Through the analysis of the interparticle structure factor, they extracted the thickness of the spherical crown of the grafted brush and correlated it with the degree of dispersion: the aggregation of the particles was associated with a significant collapse of the grafted chains. However, their conclusions are not comprehensive enough [2]. Ammari et al. work on the mathematical modeling of plasmonic nanoparticles. They analyze how plasmonic resonances change and broaden as nanoparticles change in size and shape. By analyzing the imaginary part of Green's function, it was shown that super-resolution and superfocusing can be achieved using plasmonic nanoparticles. However, their analysis process is relatively simple [3]. Son et al. report on the nonvolatile memory characteristics of bistable organic memory (BOM) devices. Transmission electron microscopy (TEM) images show an isotropic distribution of gold nanoparticles around the PVK colloidal surface. However, their content is not novel enough [4]. Cabezón et al. conducted a series of experiments to explore the potential of anti-transferrin receptor 8D3 monoclonal antibodies (mAbs) to transport neurotherapeutics in the BBB. They also discuss the trade-offs of using this technique in their application and draw conclusions. Along with other volume electron microscopy imaging techniques, SBF-SEM is a powerful method worth considering for studying drug transport across the BBB. However, the influencing factors of their experiment are not single [5]. Examination of surface morphology by Han et al. revealed rod-like PANI nanoparticles encapsulated with ATP clay particles, confirming their Pickering emulsion stabilizer properties. They examined the ER performance of PANI@ATP nanoparticles dispersed in silicone oil under different electric field strengths. ER fluid flowing in particles PANI@ATP exhibits typical electrorheological behavior, and its shear stress curve is in good agreement with the Cho-Choi-Jhon model of the rheological formula of state. However, their data are not accurate enough [6]. Ke et al. reported the photothermal energy transfer efficiency of gold nanoparticles of different sizes by evaluating the temperature distribution of laser-activated particle suspensions in water. The results show that the photothermal properties of gold nanoparticles are size-tunable. However, they did not proceed from reality [7]. Sheikholeslami and Bhatti investigated the forced fusion heat transfer of nanoparticles in a porous half-ring under the action of a uniform magnetic field. Ultimately, they concluded that the velocity of nanoparticles increases with Darcy and Reynolds numbers and that the heat transfer rate is highest for flaky particles. The Nusselt number increases with increasing nanoparticle volume fraction, Darcy number, and Reynolds number and decreases with increasing Lorentz force [8, 9]. However, their process is more complicated.

3. Methods for Drug Controlled Release

3.1. Application of Nanomaterials in Drug Controlled Release Systems. The rise of nanotechnology in the 1980s was a very horizontal and rapidly growing field of research. The fusion of nanotechnology with biology, materials science, and medicine has created a new branch of nanomedicine. The specific application of "nanomedicine" in disease diagnosis, treatment, and monitoring has revolutionized the treatment methods of traditional medicine, which can alleviate the suffering of patients and improve people's health [10]. Due to their unique chemical and physical properties, nanomaterials have many advantages in drug management and have been extensively evaluated and studied by scientists and clinicians.

The drug release behavior of traditional chemotherapy methods is uncontrollable. After the drug molecule enters the blood, it is distributed throughout the body through the diffusion mechanism. The drug molecule usually needs to undergo protein binding, metabolism, excretion, and other steps, and the drug concentration decreases rapidly. Only a small amount of the anticancer drug eventually reaches the tumor site. The use of nanomaterials as drug carriers in this paper can effectively transfer drugs to the site of injury. It achieves targeted release and controls the drug release rate.

Most polymeric nanomaterials are biodegradable and biocompatible. It can control the metabolic kinetics of drugs through surface chemical modification [11]. Therefore, they are very suitable as drug carriers: they are commonly used to make nanocarrier polymers, both natural and synthetic polymers. Natural polymers include chitosan, albumin, heparin, dextran, gelatin, sodium alginate, and collagen. Synthetic polymers include polyethylene glycol (PEG), polyglutamic acid (PGA), polylactic acid (PLA), polycaprolactone (PCL), polylactide-co-glycolide (PLGA), and N-(2-hydroxypropyl)-methacrylamide copolymer (PHPMA) [12].

3.2. Decision Tree Algorithm

3.2.1. Overview. Decision tree learning algorithms are inductive learning algorithms based on a set of sample data sets (data samples can also be referred to as examples), focusing on conclusions drawn from disturbed and irregularly sampled data sets (concepts). It represents the classification rules, where the data samples should be able to be embodied in the form of "attribute inference."

A decision tree is a tree structure that automatically sorts data. It is a tree-structured knowledge representation that can be directly transformed into classification rules. It can

be thought of as a tree-based predictive model. Among them, the root node of the tree is the entire space of the data set, and each child node corresponds to a separation problem. It is a test on a single variable that splits a spatial data set into two or more parts; each worksheet node is a data separator with sorted results. Decision trees can also be interpreted as a special form of rule sets, which are characterized by a hierarchical organization of rules. The decision tree algorithm is mainly aimed at the learning method of "classifying discrete variables into feature types," and for continuous variables, they must be discrete in order to learn and classify [13, 14].

The learning decision tree adopts the object detection method. It compares the eigenvalues of the internal nodes of the decision tree and judges that the branch conclusion of the next node is in the leaves of the node decision tree according to different eigenvalues. Figure 1 briefly describes the process of creating a decision tree.

3.2.2. Basic Algorithm.
The internal nodes of the decision tree are features or feature sets, the leaf nodes are the categories or conclusions of learning differentiation, and the features of internal nodes are test attributes or separation attributes.

After a decision tree is created by learning from a sample data set, a new set of unknown data can be sorted. When using decision trees to sort data, top-down backtracking is used. It judges and compares the eigenvalues of the internal nodes of the decision tree and decides which branch will be switched according to the different attribute values obtained from the leaf nodes.

According to the description, it can be seen that the path from the root node to the drawing node corresponds to the connection rules, and the entire decision tree corresponds to the combination selection of the rules. For example, Figure 2 represents a decision tree; A, B, C in the figure are attribute names; and $a_1, a_2, b_1, b_2, c_1, c_2$ are the values of attributes A, B, C, respectively. When the value of attribute A is a_1 and the value of attribute B is b_2, it belongs to the second category.

According to various attributes of the internal nodes of the decision tree, decision trees can be divided into the following types.

When each internal node of a decision tree contains only one attribute, it is called a univariate decision tree. But when the inner nodes of a decision tree contain many variables, it is called a multivariate decision tree. Each internal node can have two or more branches, depending on the number of different feature values for the tested feature.

(1) ID3 Algorithm.
On the basis of the CLS learning algorithm, later generations have proposed a variety of decision tree learning algorithms, the most important of which is the ID3 algorithm proposed in 1979. The ID3 algorithm is a decision tree learning algorithm based on information inheritance, which is the representative of the decision tree algorithm. Most of the algorithms have been improved and applied on top of them. The information theory is introduced into the decision tree algorithm, and the divide and

conquer strategy is adopted [15]. When selecting features at all levels of a decision tree, all features are identified, and the feature with the largest information gain is selected as the decision tree node, which is determined by the different values of the feature [16, 17]. Finally, this paper adopts a decision tree to classify the new samples.

In this paper, the sample data set is set as S, and the purpose is to divide the sample data set into m categories. Assuming that the number of sample data belonging to class a is X_a and the total number of sample data in S is $|S|$, then the probability that a sample data belongs to class a is $p(X_a) \approx X_a/|S|$. At this time, the uncertainty degree of the decision tree for dividing X (that is, the information descendant) is

$$H(S, X) = H(S) = -\sum_{a=1}^{m} p(X_a) \log_2 p(X_a). \tag{1}$$

If attribute c is chosen for control (assuming attribute i has n distinct values), the uncertainty (conditional continuity) is

$$H\left(\frac{S}{X}\right) = -\sum_{a=1}^{m}\sum_{b=1}^{n} p(X_a, c = c_b) \log_2\left(\frac{X_a}{c} = c_b\right). \tag{2}$$

Then, the amount of information provided by attribute c for classification is

$$I(S, c) = H(S) - H\left(\frac{S}{c}\right). \tag{3}$$

In the formula, $I(S, c)$ represents the reduction degree of information entropy after selecting feature c as the classification feature. Therefore, it should choose to maximize feature $i(S, c)$. As a categorical feature, decision trees that do this have the greatest certainty.

It can be seen that the ID3 algorithm chooses to retain the CLS algorithm, a sentence of information theory, and it is recommended to select the attribute maximizing $I(S, c)$ as the criterion for selecting the classification attribute test feature. Figure 3 shows the specific process of the ID3 algorithm.

When the ID3 algorithm is used as the discriminant model, the number of samples in the experiment, that is, the discriminant results, is shown in Table 1.

(2) C4.5 Algorithm.
The C4.5 algorithm was proposed in 1993. It evolved from the ID3 algorithm, inherits the advantages of the ID3 algorithm, and adds new methods and functions [18]. The main body of the algorithm consists of three parts: C4.5 tree, pruning algorithm C4.5 pruning, and rule generation algorithm C4.5 rules.

The C4.5 tree algorithm selects the feature with the highest information gain rate in the current sample set as the test feature. It is based on the theory of information genetics and finally builds a complete decision tree. For continuous

Input training set

Classification algorithm learning

Input test set
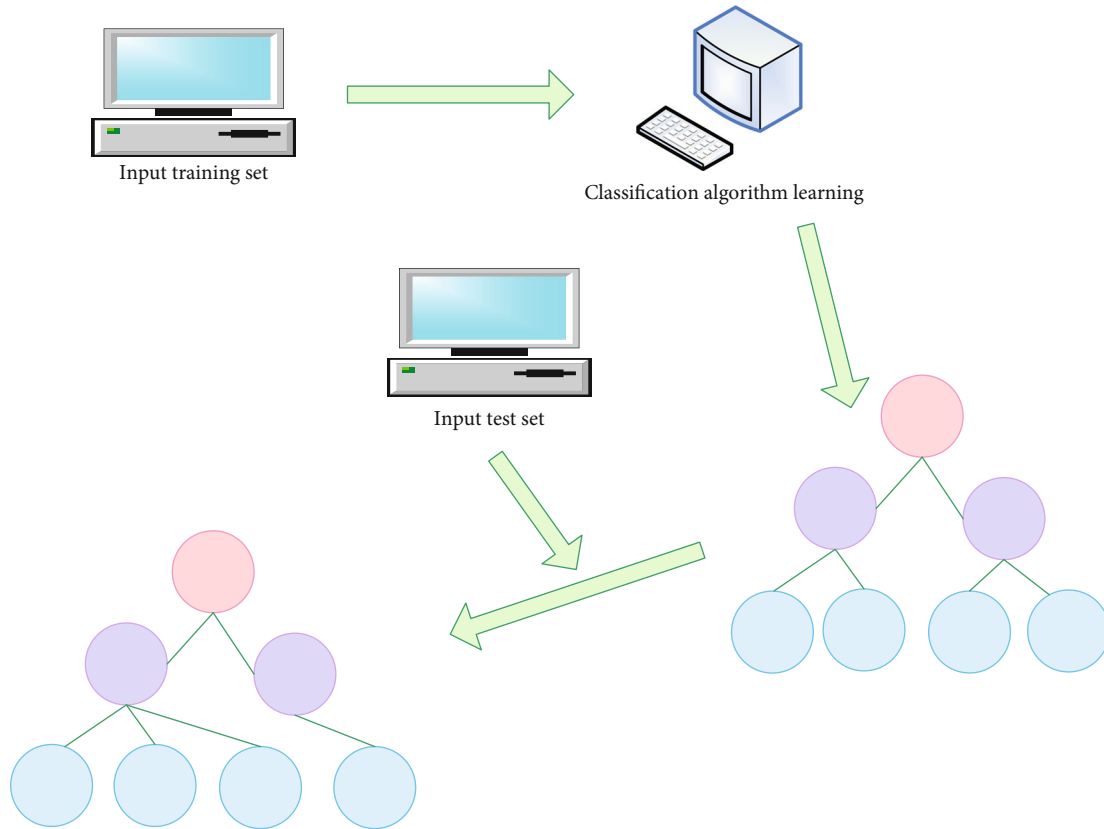
FIGURE 1: Decision number generation process.
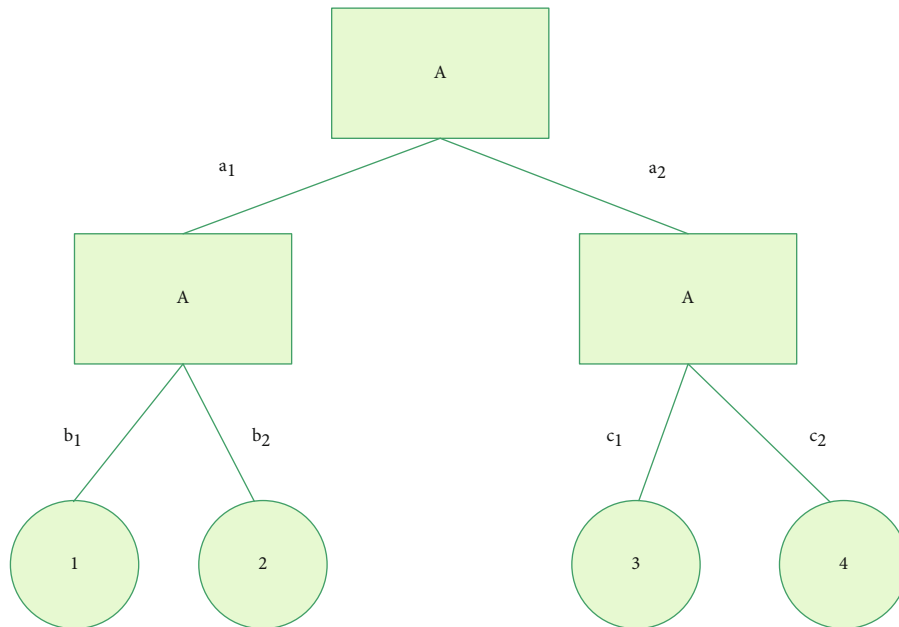
FIGURE 2: Simple decision tree.

features, separate first, that is, divide the values of continuous features into different intervals, which is convenient for processing. C4.5 pruning uses an error-based pruning method to prune the entire decision tree to obtain a simplified decision tree. C4.5 rules converts a complete decision tree into a set of if.then rules and then simplifies them. Both simplified decision trees and rule sets resulting from pruning or rule creation processes can be used for classification.
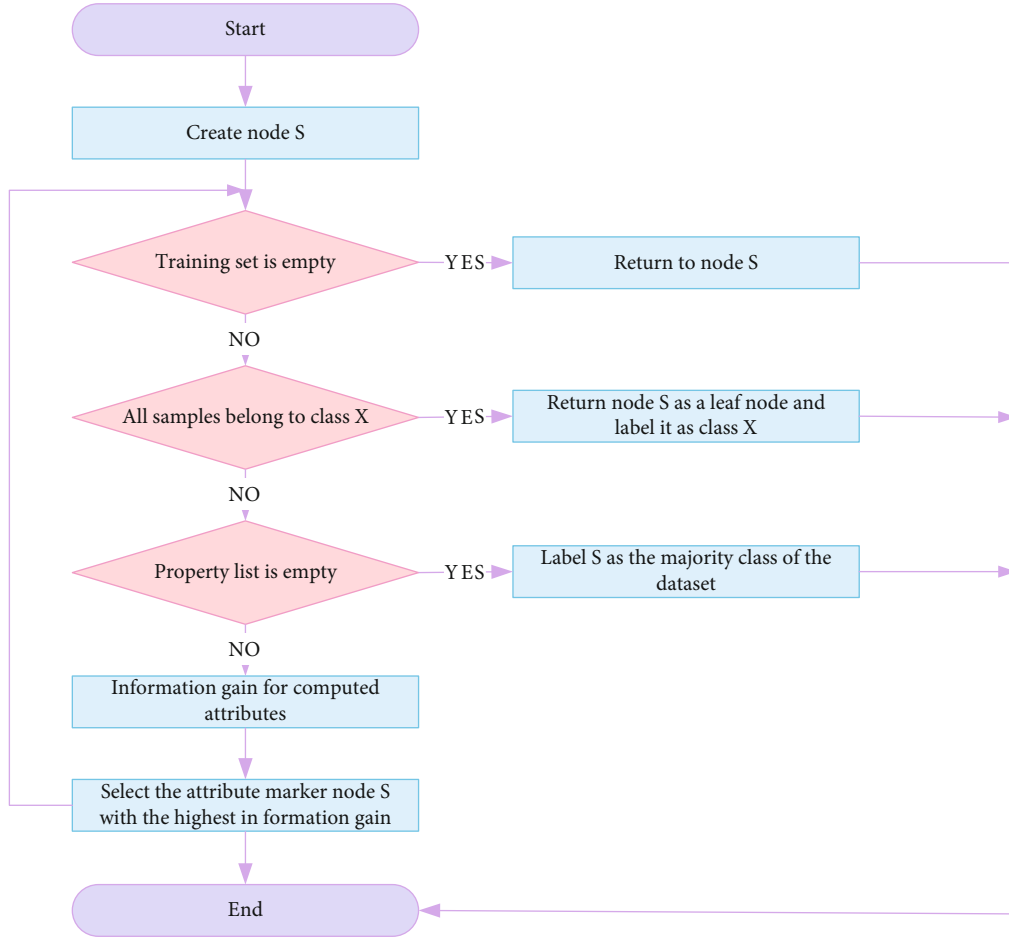
FIGURE 3: ID3 algorithm flowchart.

TABLE 1: ID3 algorithm discrimination accuracy when data sources are different.

The amount of data	Legacy ID3
500	0.539
1000	0.616
1500	0.672
2000	0.728
2500	0.715
3000	0.694

Its basic idea is the following: for the sample set W, it is assumed that the variable i has m features, that is, the eigenvalues i_1, i_2, ... The number of samples i_1 in which i_k corresponds to the value of i is m_1, respectively. $m_1 + m_2 + \cdots + m_k = m$ should be present if m is the total number of samples. The entropy value $H(S, i)$ of the feature i is used to determine the cost of obtaining the information of the sample feature i, namely,

$$H\left(\frac{S}{i}\right) = -\sum_{a=1}^{k} p(i_a) \log_2 p(i_a) \approx -\sum_{a=1}^{k} \frac{m_a}{m} \log_2 \frac{m_a}{m}. \quad (4)$$

The information acquisition rate is defined as the ratio of the average mutual information to the cost of acquiring information, namely,

$$E(S, i) = \frac{I(S, i)}{H(S, i)}. \quad (5)$$

That is, the information acquisition rate refers to the amount of information acquired from the unit cost, which is a measure of the relative uncertainty of the amount of information. Taking the information gain rate as the criterion for selecting the experimental characteristics, the characteristic i with the largest $E(S, i)$ should be selected as the experimental characteristic [19].

The pruning strategy adopted by the C4.5 algorithm is pessimistic error correction, and the misclassification rate is estimated as

$$W(j) = \frac{q(j)}{P(j)}. \quad (6)$$

The continuity corrected error rate is

$$W'(j) = \frac{q(j) + 1/2}{P(j)}.$$ (7)

Accordingly, the misclassification rate of subtree J_j is

$$W(J_j) = \frac{\sum q(a)}{\sum P(a)},$$ (8)

where i takes the leaves of the subtree, so the corrected misclassification rate is

$$W'(J_j) = \frac{\sum (q(a) + 1/2)}{\sum P(a)}.$$ (9)

Then,

$$W'(J_j) = \frac{\sum \left(q(a) + P_{J_j}/2\right)}{\sum P(a)},$$ (10)

where P_T is the number of leaves on the node.

Using the training data, child nodes always produce fewer errors than their respective nodes, but when the correct numbers are used, this does not happen, because they depend on the number of cards, not just the number of errors [20].

The standard deviation is calculated as follows:

$$SE\left[u'(J_a)\right] = \sqrt{\frac{u'(J_j) * \left(P(a) - u'(J_a)\right)}{P(a)}}.$$ (11)

Among them, for nodes, there are

$$u'(a) = q(a) + \frac{1}{2}.$$ (12)

And for the subtree, there are

$$u'(J_j) = \sum q(a) + \frac{P_{J_j}}{2}.$$ (13)

The flowchart of the C4.5 algorithm is shown in Figure 4.

When the C4.5 algorithm is used as the discriminant model, the number of samples in the experiment, that is, the discriminant results, is shown in Table 2.

3.3. Genetic Algorithms

3.3.1. Overview. The genetic algorithm (GA) is a new global optimization algorithm developed in recent years. Based on the viewpoint of biological genetics, the self-adaptive optimization of individuals is realized through natural selection, inheritance, mutation, and other mechanisms. This reflects the evolutionary process of "natural selection and survival of the fittest" in nature. It is based on the theory of evolution

and adopts design methods such as genetic combinatorial optimization technology, genetic variation, and natural selection.

The genetic algorithm is an optimization search algorithm based on biological evolution theory and molecular genetics. It first encodes possible solutions to a particular problem, called chromosome-encoded solutions. It randomly selects N chromosomes as the initial group and then calculates the fitness of each chromosome based on the value of the evaluation function. It is predetermined that the best performance value of the chromosome is the highest fitness value, and the chromosome with the highest fitness value is selected for replication. It creates a new set of chromosomes. These chromosomes are more tailored to the environment through genetic operators, and people will eventually adapt to the new environment. Forming a better group becomes the best solution to the problem [21, 22].

3.3.2. Basic Algorithm. The execution of the genetic algorithm involves many random operations, first considering the result of the selection. In standard genetic algorithms, selection criteria are based on the principle of proportionality. Therefore, through the action of the ith selector, the expected value of the number of people who will continue to exist in the next generation is $n(f_i/\sum f)$; then, there is

$$\bar{f}(P, t) = \frac{1}{n(P, t)} \sum f_i.$$ (14)

Then,

$$n(P, t + 1) = n(P, t) \cdot \frac{\bar{f}(P, t)}{\bar{f}(t)}.$$ (15)

The formula shows that the effect of the selection operator will increase (decrease) the ability of a pattern above (below) the average to be applied across generations, improving quality.

Then, it analyzes the role of the crossover operator. This plan can obviously be maintained in the next generation if there is no intersection or if the intersection point is beyond the character positions specified on the left and right ends of the figure. Therefore, the probability R_s that the P mode will continue to exist in the next generation should satisfy

$$R_s \geq 1 - R_c \cdot \frac{\varphi(P)}{L - 1}.$$ (16)

Taking into account the effects of selection and crossover, there are

$$n(P, t + 1) \geq n(P, t) \cdot \bar{f}(P, t) \cdot 1 - R_c \cdot \frac{\varphi(P)/(L - 1)}{\bar{f}(t)}.$$ (17)

Finally, because R_m represents the probability of the mutation operator acting, the constant probability is $1 - R_m$. If all the specified characters remain unchanged, the P pattern can naturally continue to exist in the next
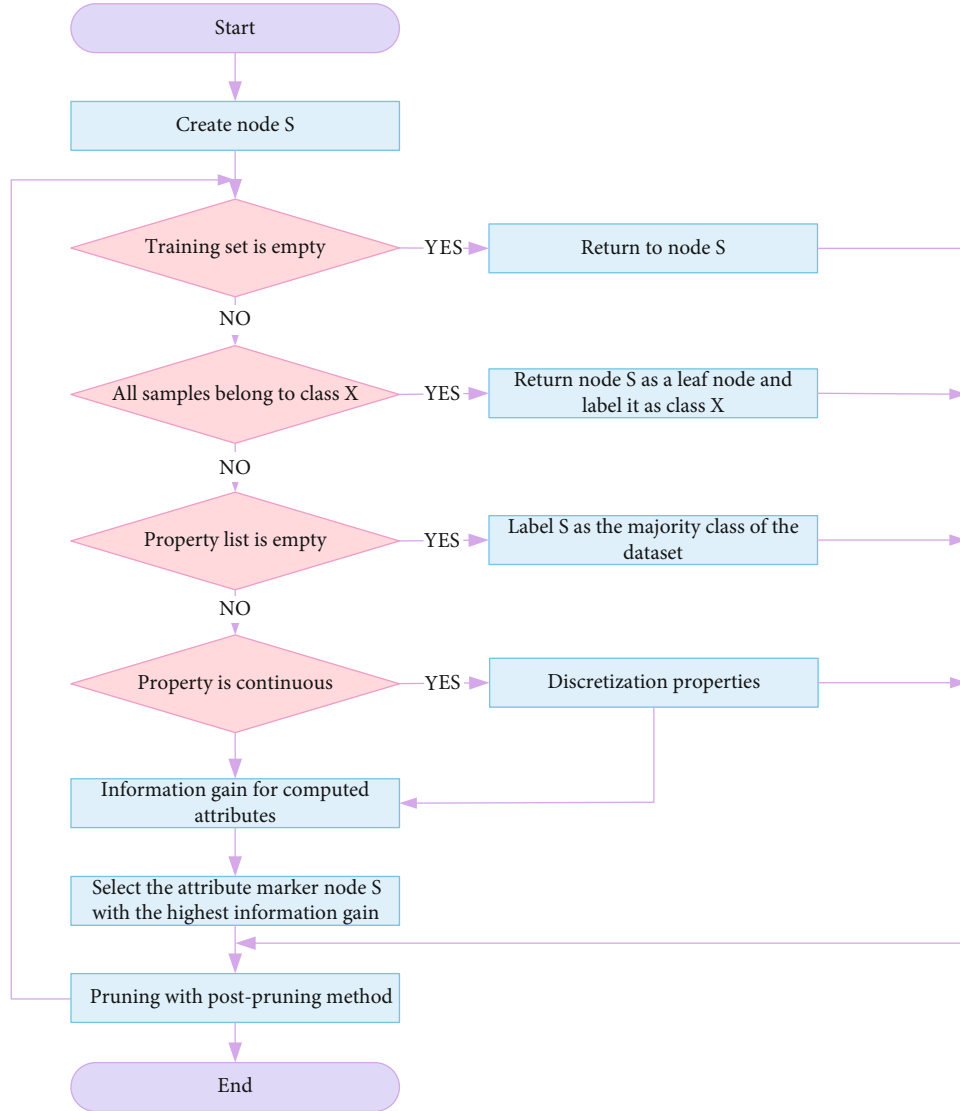
FIGURE 4: C4.5 algorithm flowchart.

TABLE 2: Discrimination accuracy of C4.5 algorithm when data sources are different.

The amount of data	Legacy C4.5
500	0.757
1000	0.732
1500	0.680
2000	0.629
2500	0.652
3000	0.705

generation, the probability $(1 - R_m)^{O(P)}$, R_m is usually not large, and then under the action of the mutation operator, the probability of P continuing to exist is

$$(1 - R_m)^{O(P)} \approx 1 - R_m \cdot O(P). \quad (18)$$

The probability of unreserved is about $O(P) \cdot R_m$. So, taking into account the functions of selection, crossover, and mutation operators, we end up with

$$n(P, t + 1) \geq n(P, t) \cdot \bar{f}(P, t) \cdot \frac{1 - R_c \cdot \varphi(P)/L - 1 \cdot R_m}{\bar{f}(t)}. \quad (19)$$

Specifically, if $\bar{f}(P, t) = f(t)(1 + c)$, $c > 0$ is a constant, then

$$n(P, t) = n(P, t - 1)(1 + c) = n(P, O)(1 + c)^t. \quad (20)$$

The flowchart of the standard genetic algorithm is shown in Figure 5.

Coding and initial population: since the algorithm itself cannot directly deal with the number of solutions, it is necessary to pass the coding form of the genotype string structure.
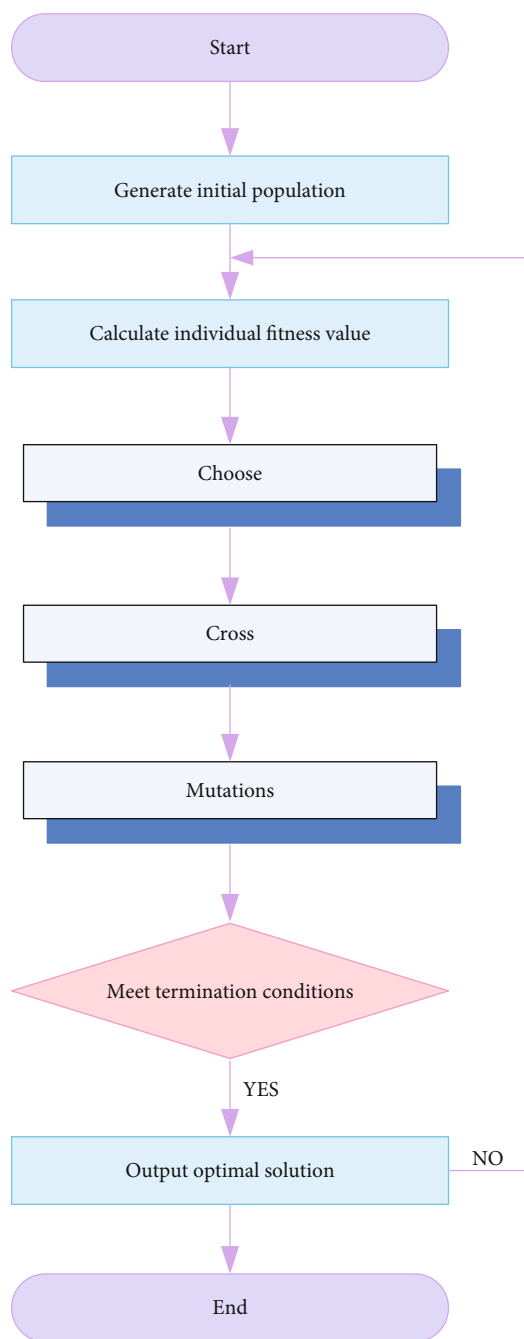
FIGURE 5: Genetic algorithm flowchart.

It can be represented by binary and other forms, such as 11001. And it generates n initial groups according to the encoding form, and n is usually set according to the actual situation.

Fitness calculation: fitness calculation is to evaluate the individual's pros and cons through an evaluation function. It is the main basis for the next round of operation of the genetic algorithm, so the design of the fitness algorithm is very important.

Choosing an action.

Crossover: crossover is to exchange some information with each other for two individuals that are successfully paired randomly to form a new individual and then calculate the fitness. If the fitness data of the new individual improves, it means that the individual is optimizing in the desired direction.

Variation: in order to make the individuals in the population diverse, it prevents the problem of generating local solutions. In this paper, some parts of the individual are manipulated and changed, so that the group can survive and develop better.

4. Experiment and Analysis of Polymer Nanoparticles in Drug Controlled Release

4.1. Experiment Preparation. At present, nanodrug carriers have been widely used in cancer therapy, oral drugs, gene carriers, intracellular targeted drug delivery, quantitative drug delivery, immune-enhancing vaccines, and the prevention and treatment of vascular retention [23]. Figures 6(a) and 6(b) belong to the type of polymer nanomaterials.

Anticancer drug release experiments were divided into four groups: (1) pH 7.4, (2) pH 7.4+GSH, (3) pH 7.4+NIR laser irradiation, and (4) pH 7.4+GSH+NIR laser irradiation. The dissolution medium of the corresponding two groups (1) and (3) was PBS at pH 7.4. The dissolution medium of both groups (2) and (4) was pH 7.4 PBS containing 20 mM GSH.

First, 1 mg of DOX@HMPB@PEI-SS-HA was uniformly dispersed in 1 mL of the corresponding dissolution medium and transferred to a dialysis bag (MWCO = 3500 Da). Then, the dialysis bags were put into 5 mL of the corresponding dissolution medium, respectively, and the culture was continued in a constant temperature environment of 37°C. For groups (1) and (2), the system needs to be placed in a dark environment with a constant temperature of 37°C; for groups (3) and (4), the system must be irradiated with an 808 nm laser (power density is 1.5 W/cm^2). It is illuminated 10 min before each sampling. When the preset time points are reached, 2 mL of the samples to be tested are removed and 2 mL of the same dissolution medium is quickly replenished. According to the absorbance curve of the tested sample, the absorbance of the tested sample was calculated, and the cumulative DOX dissolution rate corresponding to different time points was determined.

The in vitro dissolution experiment of each system needs to be repeated three times, and the average value of the three times is the release amount of DOX.

In this experiment, two methods of CLSM and FCM were used for detection, and two methods of MTT and Live-Dead were used for analysis. In this paper, the cytotoxicity of HMPB@PEI-SS-HA and DOX@HMPB@PEI-SS-HA was evaluated, respectively.

4.2. Experimental Results. The PVP-coated solid PB NPs were etched by HCl to form HMPB NPs. We then combined electrostatic layer-by-layer self-assembly and chemical cross-linking to selectively adsorb PEI-SH and HA-SH onto the surface of HMPB NPs. PEI-SH and HA-SH can react to generate disulfide bonds, and HMPB@PEI-SS-HA can be obtained (as shown in Figure 7).

(a) Polymeric micelles

(b) High polymer
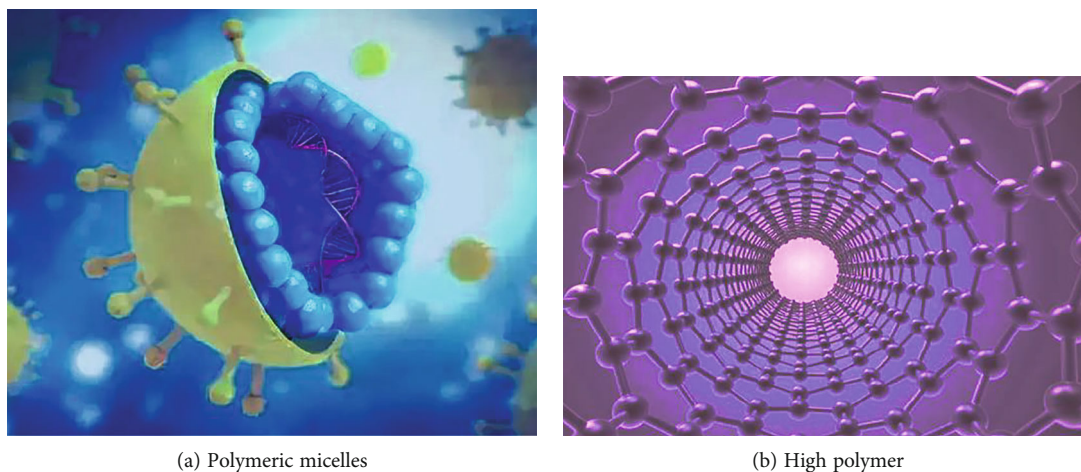
Figure 6: Polymer nanomaterials.

(a)

(b)
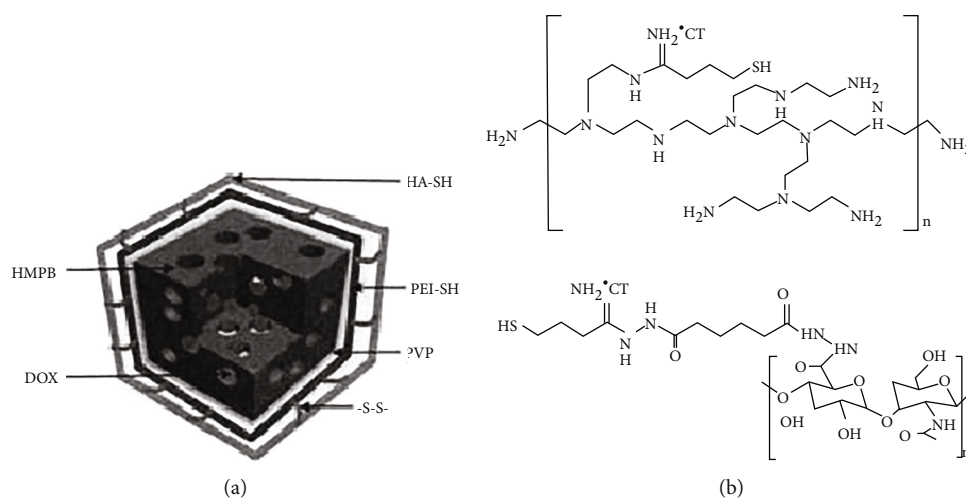
Figure 7: Schematic diagram of HMPB@PEI-SS-HA.

Table 3: Particle size of products at different stages of preparation.

Name	Hydrodynamic diameter (nm)
PB	103.52
HMPB	111.60
HMPB@PEL-SH·	125.49
HMPB@PEI-SS-HA	142.83

Zeta potential and particle size of products at different preparation stages were detected by DLS. With the progress of the assembly process, the particle size of the NPs also gradually increased, and the results are shown in Table 3.

HMPB is a hollow mesoporous structure with a huge specific surface area and pore volume. It becomes an ideal carrier for loading anticancer drugs. When DOX was loaded into HMPB@PEI-SS-HA, when the mass ratio of the two was 1/1.2, the drug loading reached 46%, and the encapsulation efficiency was close to 94%. In addition to the structural characteristics, the reasons for the high loading capacity, the electrostatic interaction between the positively charged DOX and the negatively charged HMPB@PEI-SS-HA, and the formation of coordination bonds between Fe(II) and DOX in HMPB play a positive role in the drug loading capacity.

Next, we investigated the release rule of DOX from DOX@HMPB@PEI-SS-HA. The results in Figure 8 show that the release of DOX has both redox and light responsiveness. Figure 8(a) is the dissolution curve of the control group at 24 h in Figure 8(b). In the environment with neither NIR laser irradiation nor GSH, the release rate of DOX from DOX@HMPB@PEI-SS-HA was very slow, the dissolution basically reached equilibrium within 24 h, and the total release amount was around 20%. This result can be attributed to the particularly low exchange efficiency of the inner charge and the outer dissolution medium through the pores of the HMPB. This is beneficial for minimizing toxicity and side effects in healthy tissue. At the same time, it also shows that DOX@HMPB@PEI-SS-HA is very stable and will not burst suddenly during the blood circulation process, resulting in the sudden release of anticancer drugs.

As shown in Figure 8(b), when there was only GSH, the dissolution rate of DOX was faster than that of the control

(a) Dissolution curve of control group at 24 h

(b) Comparison of dissolution rates of four groups
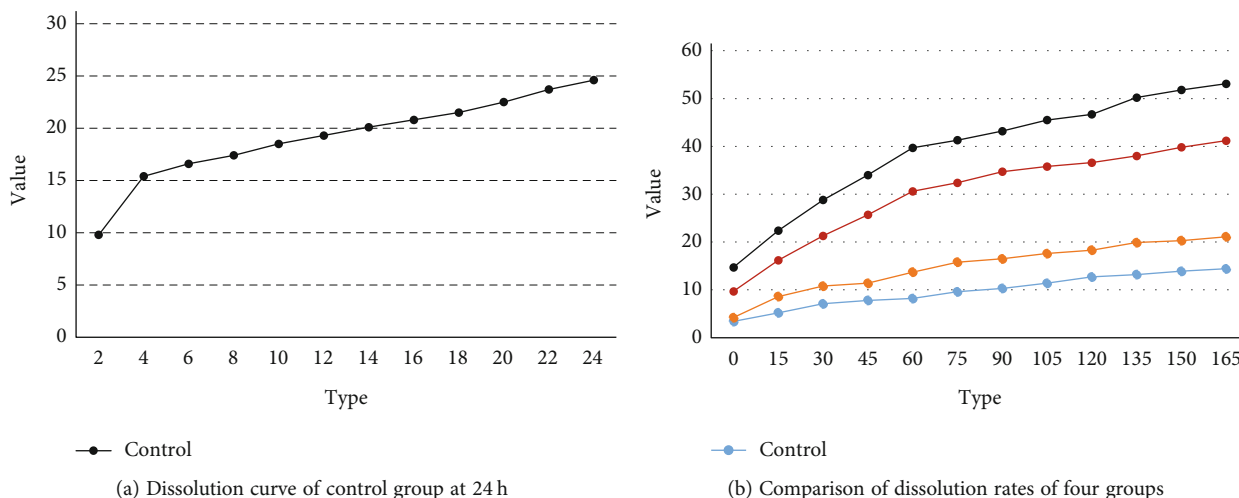
FIGURE 8: In vitro drug release behavior of DOX@HMPB@PEI-SS-HA.

group, and the cumulative dissolution rate was about 22% at 3 h. It shows that the disulfide bond in the carrier is broken under reducing conditions, destroying the PEI-SS-HA part in its structure. It makes the internal DOX and the water phase medium in closer contact, and the exchange efficiency is improved. In the environment with only NIR laser irradiation, compared with the control group, the dissolution rate of DOX was significantly accelerated, and the cumulative release at 3 h exceeded 40%. It is mainly because of the strong photothermal properties of HMPB itself.

On the one hand, the laser irradiation significantly increased the temperature of the system, which increased the solubility of DOX in the dissolution medium. It simultaneously accelerates the DOX exchange efficiency between the inner space of the nanocapsule and the outer environment. On the other hand, because HMPB is inside the carrier, NIR irradiation directly destroys the structure of HMPB. Therefore, the overall structure of the carrier will collapse, resulting in a significant increase in the DOX release rate. When laser irradiation and GSH coexisted, the dissolution rate and cumulative dissolution rate of DOX were the highest, and the total release within 3 h was close to 53%. This result indicates that the release of DOX from DOX@HMPB@PEI-SS-HA is both photosensitivity and redox responsive, and the photosensitivity predominates.

4.3. Experimental Analysis. In the experiments, a NDDS with both NIR and redox responsiveness, DOX@HMPB@PEI-SS-HA, was designed and synthesized. Due to the hollow mesoporous structure of HMPB, the DOX drug loading reached 46%. Anticancer drug release experiments showed that the strong photothermal properties of HMPB accelerated the release rate of DOX from DOX@HMPB@PEI-SS-HA when irradiated with an NIR laser. In addition, DOX dissolution also has redox responsiveness, but photosensitivity dominates. Cell uptake experiments also confirmed that DOX@HMPB@PEI-SS-HA could target and bind to the CD44 receptor. The results of the cytotoxicity evaluation further confirmed the positive effect of the photothermal properties of HMPB on accelerating the release of anticancer

drugs and killing cells. HMPB@PEI-SS-HA can not only load DOX but also deliver other anticancer drugs. Due to its high drug loading capacity, low toxicity, and excellent photothermal properties, it has broad application prospects in the field of photochemical combination therapy.

5. Discussion

First of all, through the study of the relevant knowledge points of the literature works, this paper has initially mastered the relevant basic knowledge. This paper analyzes how to study the application of nanomedicine in the controlled release of anticancer drugs based on the decision tree algorithm and genetic algorithm. This paper expounds the concepts and related technical algorithms of the two algorithms and explores the application of polymer nanomedicines. In this paper, the applicability of nanomedicines in the controlled release of anticancer drugs is analyzed by experiments.

Nanoscience is a comprehensive, multidisciplinary discipline based on many advanced scientific technologies that have developed rapidly in recent decades. Nanotechnology has been widely used in biomedicine, materials science, chemistry, physics, information and electronic engineering, and other fields. Nanomaterials have been widely used in various research fields because of their many excellent properties, such as quantum size phenomenon, small size phenomenon, and quantum mechanics. Surface effects and tunneling phenomena have now become the hot spots of scientific research. However, scientific researchers still face great challenges in the preparation of nanomaterials with different shapes and properties and their applications. Researchers hope to better understand the microstructure of nanomaterials and control their shape, structure, composition, and others [24, 25].

In this paper, the experimental analysis shows that the organic-inorganic composite nanocapsules are prepared by polymer nanoparticles, and the DOX drug loading reaches 46%. The in vitro release rate and total nanoparticle release rate were significantly improved. Cellular uptake and

cytotoxicity experiments further confirmed the positive role of supramolecular polymer nanoparticles in controlling the release of anticancer drugs and cell death.

6. Conclusion

Today, functional nanodrug carriers have become a necessary and important means for cancer diagnosis and treatment. Therefore, the preparation and application of functional nanocarriers have become the focus of chemical and biomedical workers. The key to producing functional nanocarriers is the functionality of their materials. Supramolecular polymers with multiple stimuli-responsive properties are compared to conventional covalent polymers. Because of its nonhomogeneity, it is harmonized and repairable. The superior performance and time-synchronized and seeded copolymers have unique advantages in functional modification and self-assembly due to more side chains. There are many reports on the self-assembly of supramolecular polymers and graft copolymers, but their application in the fabrication of functional nanodrug carriers remains to be further developed. In addition, it is necessary to change the manufacturing method of polymers to find polymers through simple modification or reversibility to improve the function of preparation and performance of drug carriers.

Data Availability

The data that support the findings of this study are available from the corresponding author upon reasonable request.

Conflicts of Interest

The authors declare that they have no conflicts of interest.

Acknowledgments

References

[1] A. Kumar, R. Jose, K. Fujihara, J. Wang, and S. Ramakrishna, "Structural and optical properties of electrospun TiO$_2$ nanofibers," *Journal of Alloys and Compounds*, vol. 698, no. 26, pp. 532–538, 2017.

[2] C. Chevigny, F. Dalmas, E. D. Cola, D. Gigmes, and J. J. Jestin, "Polymer-grafted-nanoparticles nanocomposites: dispersion, grafted chain conformation, and rheological behavior," *Macromolecules*, vol. 44, no. 1, pp. 122–133, 2011.

[3] H. Ammari, P. Millien, M. Ruiz, and H. Zhang, "Mathematical analysis of plasmonic nanoparticles: the scalar case," *Archive for Rational Mechanics and Analysis*, vol. 224, no. 2, pp. 597–658, 2017.

[4] D. I. Son, D. H. Park, J. B. Kim et al., "Bistable organic memory device with gold nanoparticles embedded in a conducting poly (N-vinylcarbazole) colloids hybrid," *The Journal of Physical Chemistry C*, vol. 115, no. 5, pp. 2341–2348, 2011.

[5] I. Cabezón, E. Augé, M. Bosch et al., "Serial block-face scanning electron microscopy applied to study the trafficking of 8D3-coated gold nanoparticles at the blood–brain barrier," *Histochemistry & Cell Biology*, vol. 148, no. 1, pp. 3–12, 2017.

[6] W. J. Han, S. H. Piao, and H. J. Choi, "Synthesis and electrorheological characteristics of nanoparticles via Pickering emulsion polymerization," *Materials Letters*, vol. 204, no. oct. 1, pp. 42–44, 2017.

[7] J. Ke, D. A. Smith, and A. Pinchuk, "Size-dependent photothermal conversion efficiencies of plasmonically heated gold nanoparticles," *Journal of Physical Chemistry C*, vol. 117, no. 51, pp. 27073–27080, 2017.

[8] M. Sheikholeslami and M. M. Bhatti, "Forced convection of nanofluid in presence of constant magnetic field considering shape effects of nanoparticles," *International Journal of Heat & Mass Transfer*, vol. 111, no. aug., pp. 1039–1049, 2017.

[9] S. Zhou and B. Tan, "Electrocardiogram soft computing using hybrid deep learning CNN-ELM," *Applied Soft Computing Journal*, vol. 86, article 105778, 2020.

[10] M. Gericke, P. Schulze, and T. Heinze, "Nanoparticles based on hydrophobic polysaccharide derivatives—formation principles, characterization techniques, and biomedical applications," *Macromolecular Bioscience*, vol. 20, no. 4, pp. 3853–3859, 2020.

[11] M. Wei, N. Chen, J. Li et al., "Polyvalent immunostimulatory nanoagents with self-assembled cpg oligonucleotide-conjugated gold nanoparticles," *Angewandte Chemie International Edition*, vol. 51, no. 5, pp. 1202–1206, 2012.

[12] Y. Zhao, H. Li, S. Wan et al., "Knowledge-aided convolutional neural network for small organ segmentation," *IEEE Journal of Biomedical and Health Informatics*, vol. 23, no. 4, pp. 1363–1373, 2019.

[13] Y. S. Shon, W. P. Wuelfing, and R. W. Murray, "Water-soluble, sulfonic acid-functionalized, monolayer-protected nanoparticles and an ionically conductive molten salt containing them," *Langmuir*, vol. 17, no. 4, pp. 1255–1261, 2001.

[14] J. G. Parvani, M. D. Gujrati, M. A. Mack, W. P. Schiemann, and Z. R. Lu, "Abstract B45: silencing ß3 integrin by targeted ECO/si RNA nanoparticles inhibits EMT and metastasis of triple-negative breast cancer," *Cancer Research*, vol. 77, 2 Supplement, pp. B45–B45, 2017.

[15] S. Sengan, O. I. Khalaf, P. Vidya Sagar, D. K. Sharma, L. Arokia Jesu Prabhu, and A. A. Hamad, "Secured and privacy-based IDS for healthcare systems on E-medical data using machine learning approach," *International Journal of Reliable and Quality E-Healthcare (IJRQEH)*, vol. 11, no. 3, pp. 1–11, 2022.

[16] W. Yan, M. Ramos, B. E. Koel, and W. X. Zhang, "As (III) sequestration by iron nanoparticles: study of solid-phase redox transformations with X-ray photoelectron spectroscopy," *Journal of Physical Chemistry C*, vol. 116, no. 9, pp. 5303–5311, 2012.

[17] E. McGillicuddy, I. Murray, S. Kavanagh et al., "Silver nanoparticles in the environment: sources, detection and ecotoxicology," *Science of the Total Environment*, vol. 575, no. jan. 1, pp. 231–246, 2017.

[18] M. José-Yacamán, H. Terrones, L. Rendón, L. Rendón, and J. M. Domínguez, "Carbon structures grown from decomposition of a phenylacetylene and thiophene mixture on Ni nanoparticles," *Carbon*, vol. 33, no. 5, pp. 669–678, 1995.

[19] D. J. C. Ji-Yang, V. V. Kumar, J. F. Li, and Z. Q. Tian, "Probing electrochemical interfaces using shell-isolated nanoparticles-

enhanced Raman spectroscopy," *Current Opinion in Electro-chemistry*, vol. 1, no. 1, pp. 16–21, 2017.

[20] J. Liang, H. Yan, P. Puligundla, X. Gao, Y. Zhou, and X. Wan, "Applications of chitosan nanoparticles to enhance absorption and bioavailability of tea polyphenols: a review," *Food Hydro-colloids*, vol. 69, no. AUG., pp. 286–292, 2017.

[21] M. Mollick, D. Rana, S. K. Dash et al., "Studies on green synthesized silver nanoparticles using _Abelmoschus esculentus_ (L.) pulp extract having anticancer (_in vitro_) and antimicrobial applications," *Arabian Journal of Chemistry*, vol. 12, no. 8, p. 2572, 2019.

[22] W. Qian, M. Murakami, Y. Ichikawa, and Y. Che, "Highly efficient and controllable PEGylation of gold nanoparticles prepared by femtosecond laser ablation in water," *Journal of Physical Chemistry C*, vol. 115, no. 47, pp. 2271–2277, 2017.

[23] E. Vaculikova, V. Grunwaldova, V. Kral, J. Dohnal, and J. Jampilek, "preparation of candesartan and atorvastatin nanoparticles by solvent evaporation," *Molecules*, vol. 17, no. 11, pp. 13221–13234, 2012.

[24] M. Faustini, A. Capobianchi, G. Varvaro, and D. Grosso, "Highly controlled dip-coating deposition of fct FePt nanoparticles from layered salt precursor into nanostructured thin films: an easy way to tune magnetic and optical properties," *Chemistry of Materials*, vol. 24, no. 6, pp. 1677–1688, 2017.

[25] Y. Li, T. Qin, T. Ingle, W. He, J. J. Yin, and T. Chen, "Differential genotoxicity mechanisms of silver nanoparticles and silver ions," *Archives of Toxicology*, vol. 91, no. 1, pp. 509–519, 2017.

Research Article

A Design Optimization Method with Sparse Scattered Data and Evolutionary Computation

Yuxiang Liu ⬤,[1] **Shipei He,**[2] **Wei Liu,**[2] **and Xihong Chen**[1]

[1]*Air and Missile Defense College, Air Force Engineering University, Xi'an 710051, China*
[2]*Jiangnan Institute of Electromechanical System Design, Guizhou 590009, China*

Correspondence should be addressed to Yuxiang Liu; 2018210798@mail.chzu.edu.cn

Engineering design can be regarded as an iterative optimization process. This process is difficult because of two main problems: the first is that computer-aided engineering (CAE) is time-consuming in terms of evaluating design solutions, while the second is the high dimensionality of design solutions. In the research community, a surrogate model is proposed to deal with the first problem while an evolutionary algorithm is adopted for the second. In this work, we develop a new method with only sparse scattered data, which is very common in many practical scenarios. The surrogate model can also assign a penalty factor for the predicted value, and this penalty factor can be used as one of the targets of the evolutionary algorithm to balance global exploration and local exploit. We also adopt a new evolutionary strategy, which can search high-dimensional space. Three groups of experiments are conducted to validate the proposed methods. The experimental results show that the surrogate model can predict performance and the corresponding penalty factor, the evolutionary strategy is better in terms of searching high-dimensional space compared with other evolutionary strategies, and the whole method can generate new design solutions that are near to the known design solutions. The experimental results show that this method can be used in practical scenarios, especially where they only have sparse scattered data.

1. Introduction

Engineering design is a complex process involving different design activities, and it can be generally regarded as the iteration of design and validation. Currently, with the help of well-developed computer-aided design (CAD) and computer-aided engineering (CAE) systems, the design model can be parameterized and the validation process can be simulated computationally. Therefore, engineering design can be regarded as an optimization problem [1], and different aspects of product can be optimized, such as shape optimization [2] and reliability optimization [3].

$$\hat{x} = \arg \max \ f(\mathbf{x}), \tag{1}$$

$$\mathbf{x} \in \Omega, \tag{2}$$

where $\mathbf{x} = [x_1, x_2, \cdots, x_n]$ is a parameter vector representing a design solution, Ω is the feasible solution space of $\mathbf{x}$, $\hat{x}$ is the optimal solution, and $f(\mathbf{x})$ is the evaluation function of design solutions. CAE has played the role of $f(\mathbf{x})$ successfully in engineering design for many years. However, two characters of such function make the optimization extremely complex and difficult. The first is derivative unavailable, which means the gradient-descent methods are invalid [4]; the second is time-consuming [5], which means the evaluation of the function requires extensive computational resources. In addition to above difficulties, the high dimensionality of the design space is another problem making the optimization difficult.

A response surface model (RSM) [6] is a method adopted to deal with the first two difficulties, and it is a statistical method that explores the relationships between design variables $\mathbf{x}$ and one or more response variables $f(\mathbf{x})$ [7]. The RSM method is also called as a surrogate model, metamodels, or emulators in different scenarios [8], and the underlying idea is to replace the computationally expensive model with a computationally cheaper one [8, 9]. In this

work, we use the terminology of "surrogate model" referring to the latter one.

Many technical methods can be used to build a surrogate model, such as linear or nonlinear interpolation, Kriging [10], neural network, radial basis function [11], and Gaussian process [12]. Although these methods have been successfully applied in solving many engineering problems, some remaining problems are hindering the applications of the surrogate model in engineering design. In many scenarios of applying the surrogate model successfully, either the available data is sufficient or the method of data collection is deliberately designed, such as "grid" data or "orthogonal" data. However, there are many different scenarios where the data is "sparse," which means the amount of available data is small, and "scattered," which means the data is located randomly in the feasible design space.

The main contribution of this paper is to propose a surrogate model method and a high-dimensional design space exploration method, respectively. We first attempt to build a surrogate model based on "sparse scattered" data and then use a new evolutionary strategy to explore and exploit the high-dimensional space. The combination of the two can realize the rapid generation from sparse scattered point data to a design scheme. The rest of the paper is structured as follows. Section 2 provides some related works for this study. Section 3 explains the technical details of both building a surrogate model and the evolutionary strategy. Section 4 conducts several groups of experiments to validate the proposed method. Section 5 summarizes this research and identifies some possible future works.

2. Related Works

In this section, some existing key techniques related to this work will be explained, including the surrogate model and evolutionary strategies.

2.1. Surrogate Model. There are many methods for building a surrogate model, and these methods can be categorized based on different criteria. From the perspective of data characteristics, there are methods for both grid data and scattered data. If the data is collected through Design of Experiment (DOE) [13], we can get regular grid data, and the surrogate model is easy to build. For low-dimensional problem, the Delaunay triangulation [14], natural neighbor interpolation [15], spline interpolation [16], and so on can be used to build the surrogate model, while for high-dimensional problems, the simple nearest-neighbor interpolation [17], Kriging [10], and so on can be used to build the surrogate model. Zhou et al. presented the nearest-neighbor value (NNV) interpolation algorithm for the improved novel enhanced quantum representation of digital images (INEQR). Experiments show that the proposed interpolation method has higher performance in high-resolution image recognition [18]. Qian et al. proposed a general sequential constraint updating approach based on the confidence intervals from the Kriging surrogate model (SCU-CI). Results illustrate that the proposed SCU-CI approach can generally ensure the feasibility of the optimal solution under a reason-

able computational cost [19]. If the data is collected randomly, we can only get irregular grid data, which are also called scattered data. In this situation, the surrogate model becomes difficult to be constructed. There are already some methods to deal with this problem, such as triangulated irregular network, radial basis function [20, 21], and Kriging [10]. de Oliveira et al. proposed a new approach for occlusion detection—the surface-gradient-based method (SGBM) applied to a triangulated irregular network (TIN) representation. Experimental results demonstrated the feasibility of the SGBM for occlusion detection in the true orthophoto generation [22]. She et al. present a novel battery aging assessment method based on the incremental capacity analysis (ICA) and radial basis function neural network (RBFNN) model [23].

From the perspective of key techniques, the methods can also be categorized as interpolation and fitting. The former attempts to build a hypersurface that exactly passes the existing data, while the latter treats existing data as noise-contained data and attempts to find a hypersurface that minimizes the errors, and the hypersurface is unnecessary passing existing data. From the perspective of complexity, the methods can be categorized as a linear model or nonlinear model.

Although the surrogate models have been used widely in many domains, the successful applications always rely on either grid data or sufficient data. However, in many practical scenarios, the existing data is neither grid data nor sufficient. The data is sparse and scattered, and methods that fit for such situations should be developed.

2.2. Evolutionary Computation. Evolutionary computation is a commonly used method to search optimal solutions from design space. Most of the evolutionary computation methods follow the same framework, but they improve the algorithm by developing different evolutionary strategies, including crossover, mutant, and selection.

Many evolutionary strategies are developed to improve the algorithm from two perspectives. The first perspective is developing a new crossover and mutant method to generate new offspring, such as differential evolution- (DE-) based method [24, 25], immune-based method [26], particle swarm optimization- (PSO-) based method [27], and probabilistic model-based method [28]. The second perspective is developing a new selection method, such as decomposition-based method [29], preference-based method [30], indicator-based method [31], and hybrid method [32]. Although the above improvements contribute to solving many design problems, there is also requirement for developing evolutionary strategies for optimizing a high-dimensional problem.

3. Methodology

In this section, we will explain the proposed method in detail. Generally, the method has two main parts, including surrogate model construction and design solution searching. In the first part, a surrogate model, which receives design solutions as input and return performances as output, will be constructed based on a two-stage interpolation process. In the second part, we adopt a new

mutant strategy, to search the high-dimensional space. The two parts will be detailed in the following two sections, respectively.

3.1. Surrogate Model Construction.

We first define the data structure used to build a surrogate model and then explain the underlying ideas of the two-stage interpolation process, and finally, we explain the technical detail of this method. The mathematical symbols used in this work are summarized in Table 1.

3.1.1. Data Structure.

Typically, there are two kinds of data in many engineering design problems, and they are design solution and the corresponding performance. A design solution can be represented by a vector $\mathbf{x} = [x_1, x_2, \cdots, x_d]$, in which $x_1, x_2, \cdots, x_d$ are parameters that determine the design solution, and d is the dimensionality of the design solution $\mathbf{x}$. A performance is a measurement of design solution $\mathbf{x}$, and design solution $\mathbf{x}$ commonly has several performances for evaluation. Besides, the performance can be different under different working conditions $\mathbf{c} = [c_1, c_2, \cdots, c_l]$, in which $c_1, c_2, \cdots, c_l$ are parameters that determine the working conditions, such as temperature and velocity which can jointly define a two-dimensional $l = 2$ working condition. Therefore, the performance can be represented by a $k \times m$ matrix where k is the kinds of performances and m is the total number of working conditions.

$$\mathbf{p} = \begin{bmatrix} p_{11} & p_{12} & \cdots & p_{1m} \\ p_{21} & p_{22} & \cdots & p_{2m} \\ \vdots & \vdots & \vdots & \vdots \\ p_{k1} & p_{k2} & \cdots & p_{km} \end{bmatrix}. \tag{3}$$

Generally, we have a $n \times k \times m$ matrix as database D for building the surrogate model, where n is the number of known design solutions. As shown in Figure 1, we know the k kinds of performance under m different working conditions of n known design solutions. It is noteworthy to say that the n known design solutions are scattered in the high-dimensional space.

3.1.2. Underlying Considerations and Assumptions.

Based on the above data, the goal is to construct a surrogate model that receives a design solution $\mathbf{x}'$ and a group of working conditions $\mathbf{c}'$ as input and outputs the corresponding performances of the design solution $\mathbf{x}'$ under working conditions $\mathbf{c}'$. It is noteworthy that the design solutions $\mathbf{x}'$ and working conditions $\mathbf{c}'$ are generally not contained in the database D.

We can regard the surrogate model as a function $\mathbf{p} = f(\mathbf{x}, \mathbf{c})$. This function maps value from $d + l$ dimensional space R^{d+l} to k dimensional space R^k, and this high-dimensional mapping requires more data to train. Since we only have sparse scattered data, two critical assumptions are drawn before learning the surrogate model.

TABLE 1: The mathematical symbols used in this work.

#	Symbols	Explanation
1	$\mathbf{x}$	A design solution
2	x	A parameter of the design solution $\mathbf{x}$
3	d	The dimensionality of the design solution $\mathbf{x}$
4	$\mathbf{c}$	A working condition
5	c	A parameter of the working condition $\mathbf{c}$
6	l	The dimensionality of the working condition $\mathbf{c}$
7	$\mathbf{p}$	The performance of a design solution
8	k	The total kinds of performance
9	m	The total number of working conditions
10	n	The total number of known design solutions
11	D	The training database
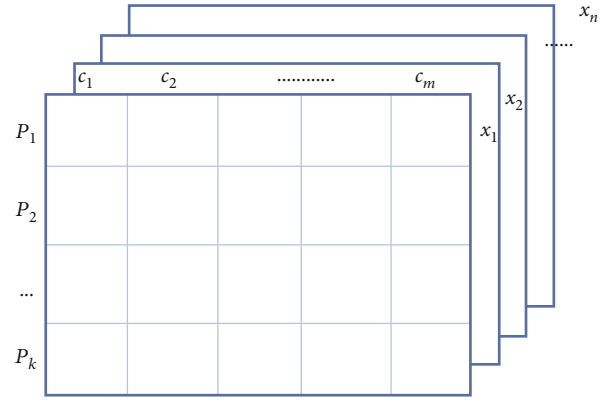
FIGURE 1: The data structure of the existing training data.

Assumption 1. For different design solutions, the mappings from working condition to performance are identical.

Based on Assumption 1, we do not need to learn a dedicated mapping (maps from working condition to performance) for different design solutions, which is necessary if the surrogate model is built, like $\mathbf{p} = f(\mathbf{x}, \mathbf{c})$. Therefore, we can divide the surrogate model into two stages, of which the first stage maps design solution $\mathbf{x}'$ to performances $\mathbf{p_c}$ under existing working conditions $\mathbf{c}$ by $\mathbf{p_c} = g(\mathbf{x}')$, while the second stage maps $\mathbf{c}'$ to performance under unknown working condition by $\mathbf{p} = h(\mathbf{c}')$. By this assumption, some dependences among design solutions, working conditions, and performance are ignored, and this loses the data requirement for training the surrogate model.

Assumption 2. The design solutions that are like existing design solutions are more feasible.

Based on Assumption 2, we make the surrogate model to assign a penalty factor for the predicted performance. If the new design solution $\mathbf{x}'$ is far from the known design

solutions, the penalty factor should be high and vice versa. This penalty factor will be used during the design optimization process, and it helps to shrink the searching space and keeps the design solution close to the regions where some design solutions are known.

3.1.3. Two-Stage Interpolation. The surrogate model can be implemented by two-stage interpolation. In both two stages, the inverse distance weighting (IDW) [33] is adopted to implement the interpolation, which computes an unknown value based on the following equation:

$$\widehat{y} = \frac{\sum_{i=1}^{Q} w_i \times y_i}{\sum_{i=1}^{Q} w_i}, \tag{4}$$

where Q is the total number of data points used to predict new value $\widehat{y}$ and w_i is the weight of the ith data point. In the IDW method, the weight is calculated by

$$w_i = \frac{1}{\left\| x / - x_{\mathbf{i}} \right\|^{P/2}}, \tag{5}$$

where $\mathbf{x}'$ is the data point that the performance is unknown; $\mathbf{x}_i$ is the ith data point; $\| \ \|$ is to calculate the distance between two data points in the high-dimensional space R^n; P is the order the distance, and this is a metaparameter to control the weights.

Based on this, given an unknown design solution $\mathbf{x}'$ and unknown working condition $\mathbf{c}'$, we can first interpolate to get the performances of the design solution $\mathbf{x}'$ under known working conditions $\mathbf{c}$ and then further interpolate to get the performances of the design solution $\mathbf{x}'$ under unknown working conditions $\mathbf{c}'$. We also need to assign penalty factors to the predicted performances of unknown design solutions and working conditions. In this work, we simply use the Euclidean distance as a measurement of penalty factors, and the value can be calculated by

$$\text{PF} = \text{PF}_1 + \text{PF}_2, \tag{6}$$

where PF_1 is the penalty factor of the first stage and it can be obtained by (7), while PF_2 is the penalty factor of the second stage and it can be obtained by (8).

$$\text{PF}_1 = \frac{1}{Q} \sum_{i=1}^{Q} \left\| x' - x_i \right\|^{P/2} \tag{7}$$

where Q is the total number of design solution used to predict the performance; $\mathbf{x}'$ is the data point that the performance is unknown; $\mathbf{x}_i$ is the ith data point used to predict the performance; $\| \ \|$ is to calculate the distance between two data points in the high n dimensional space R^n; P is the order of the distance, and this is a metaparameter to control the weights.
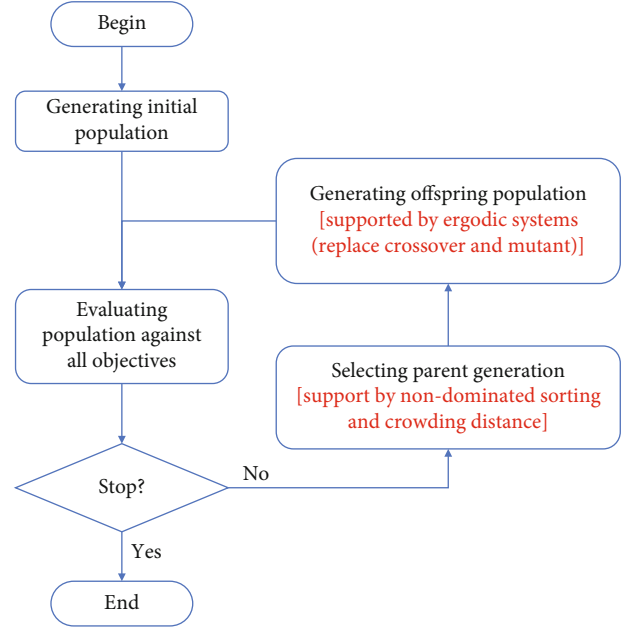
FIGURE 2: The main framework of ergodic evolution.

$$\text{PF}_2 = \frac{1}{R} x \sum_{j=1}^{R} \left\| c' - c_j \right\|^{P/2} \tag{8}$$

where R is the total number of known working conditions used to predict the performance of unknown working conditions, $\mathbf{c}'$ is the working condition that the performance is unknown, and $\mathbf{c}_j$ is the jth working condition used to predict the performance.

3.2. Design Solution Searching. Based on the method of surrogate model construction in Section 3, a surrogate model can be obtained, which receives design solution and working conditions as input and predicts performances and its corresponding penalty factor as output. Based on this surrogate model, we will adopt an evolutionary algorithm to explore the design space. The penalty factor will be taken as one of the fitness functions during the evolutionary process.

Basically, most evolutionary algorithms follow the same framework. As shown in Figure 2, the critical difference is the operation of "generating offspring population," which is marked by a bold rectangle. The traditional crossover and mutant operations are replaced by a simple ergodic system. The detail can be found in Algorithm 1. As shown in the algorithm, the ergodic system adopted in this work is a logistic map, and it is used to generate a random number for generating new offspring. The ergodic evolution method has the advantages of ergodicity and regularity and performs better in dealing with high-dimensional design space.

4. Experiment

In this section, we conduct three groups of experiments to validate the proposed method. The first group is to test whether the surrogate model can predict the performance;

Generate an initial population. Evaluate the fitness for each individual.
/* D and EP **initialization***/ **for** i =1 to PS **do**
for j =1 to Dim **do**
/* DR **as a random value***/ **if** $rand$ [0, 1) < DR **then**
$D_{i,j} = -1$
else
$D_{i,j} = +1$
end if
$EP_{i,j} = rand(0,1)$
end for end for
Evaluate the fitness for each offspring individual
Select n individuals as target individuals
/***Ergodic Search***/**for** G =1 to $maxIter$ **do**
for i =1 to PS **do**
k=rand(1,Dim)
for j =1 to Dim **do**
if $rand[0, 1)$ < Cr **or** $j == k$ **then** $mutant_{i,j} = target_{i,j} * (1 + D_{i,j} * EP_{i,j})$ $ergodic_{i,j} = mutant_{i,j}$
else
$ergodic_{i,j} = target_{i,j}$
end if end for
/***Selection***/
Nondominant sort target vectors of G_{th} and $G -1_{th}$ generations Apply crowding distance
Select n individuals as target individual
end for
/* D and EP **update***/ **for** i =1 to PS **do**
for j =1 to Dim **do**
$EP_{i,j} = logistic\ map(EP_{i,j})$
if $rand[0, 1)$ < DR **then**
$D_{i,j} = -1$
else
$D_{i,j} = +1$
end if end for
end for end for
return the optimum

ALGORITHM 1:Nondominant sorting- and crowding distance selection-based ergodic evolution algorithm. PS: population size; Dim: dimension; D: direction factor; DR: direction factor rate; EP: ergodic parameter; G: generation; maxIter: maximum generation; i: index of individual; j: index of dimension; Cr: mutant rate; targeti,j: individual to generate offspring.
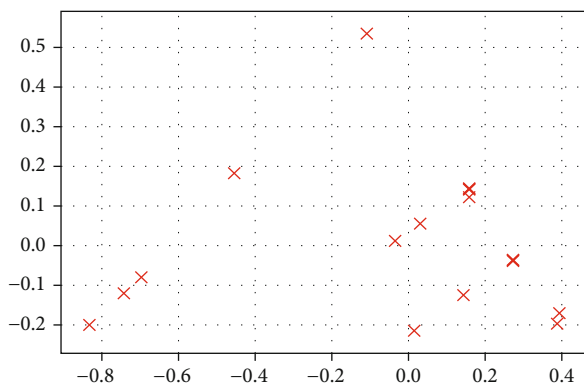
FIGURE 3: The 2-dimensional representation of the 20 known design solutions.

TABLE 2: Experiment result of this surrogate model (first stage).

P	Q	15	10	5	3	2
1		0.01440	0.01371	0.01310	0.01340	0.01344
2		0.01488	0.01443	0.01362	0.01398	0.01359
3		0.01511	0.01462	0.01397	0.01398	0.01365
4		0.01518	0.01471	0.01406	0.01440	0.01369
5		0.01522	0.01476	0.01412	0.01445	0.01371

TABLE 3: Experiment result of the surrogate model (second stage).

P	R	10	5	3	2	1
1		0.02360	0.01690	0.01533	0.01289	0.01879
2		0.02619	0.01766	0.01533	0.01289	0.01879
3		0.02717	0.01781	0.01533	0.01289	0.01879
4		0.02761	0.01787	0.01533	0.01289	0.01879
5		0.02775	0.01790	0.01533	0.01289	0.01879

the second group is to test whether the ergodic evolution can search the high-dimensional space; the last group is to test the method as a whole and to validate the feasibility of applying it in practice.

CE

NSGA-11

RE
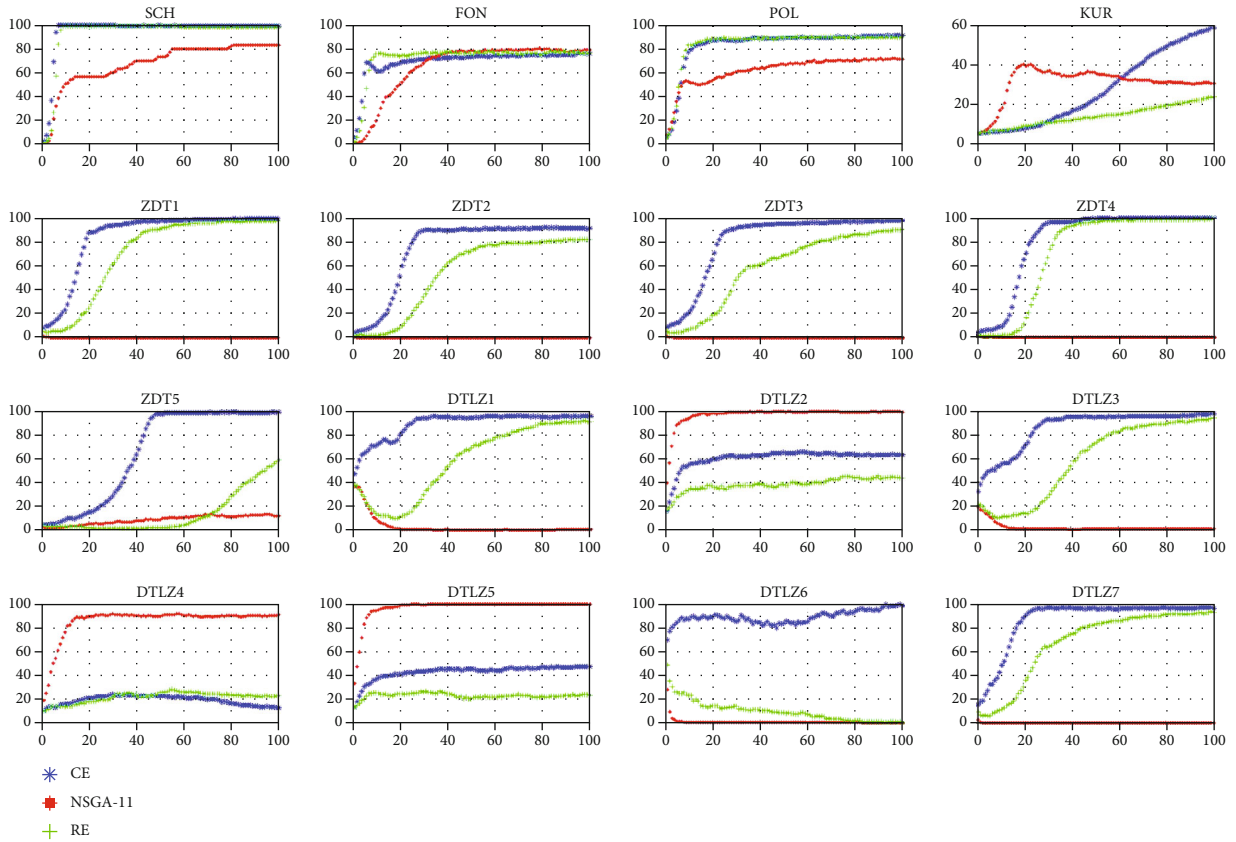
Figure 4: The average number of individuals in the nondominant frontier of the three algorithms. The blue star is CE, the green plus sign is RE, and the red dot is NSGA-II.
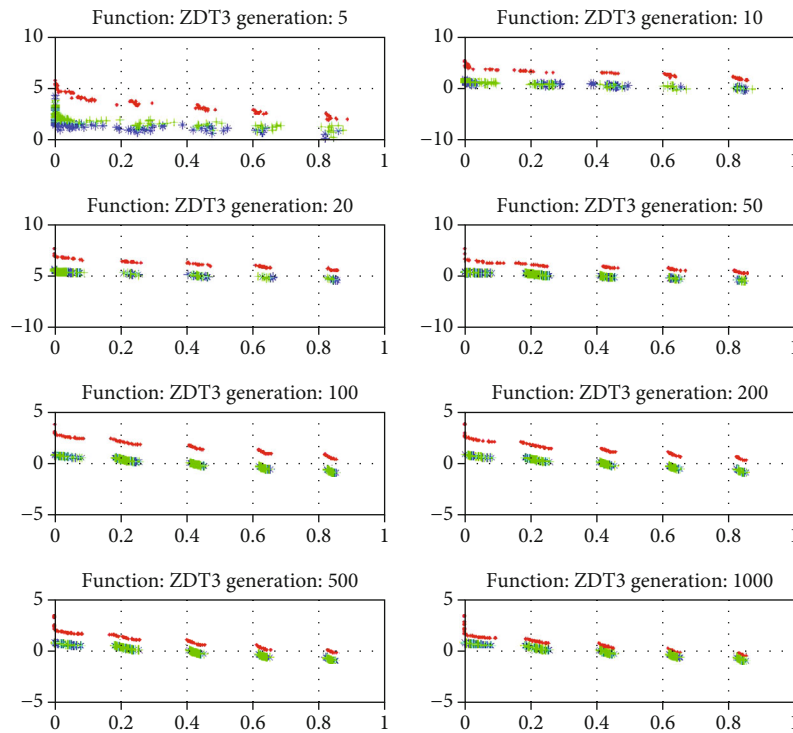
Figure 5: The Pareto frontier of the three algorithms in different generations (ZDT3). The blue star is CE, the green plus sign is RE, and the red dot is NSGA-II.
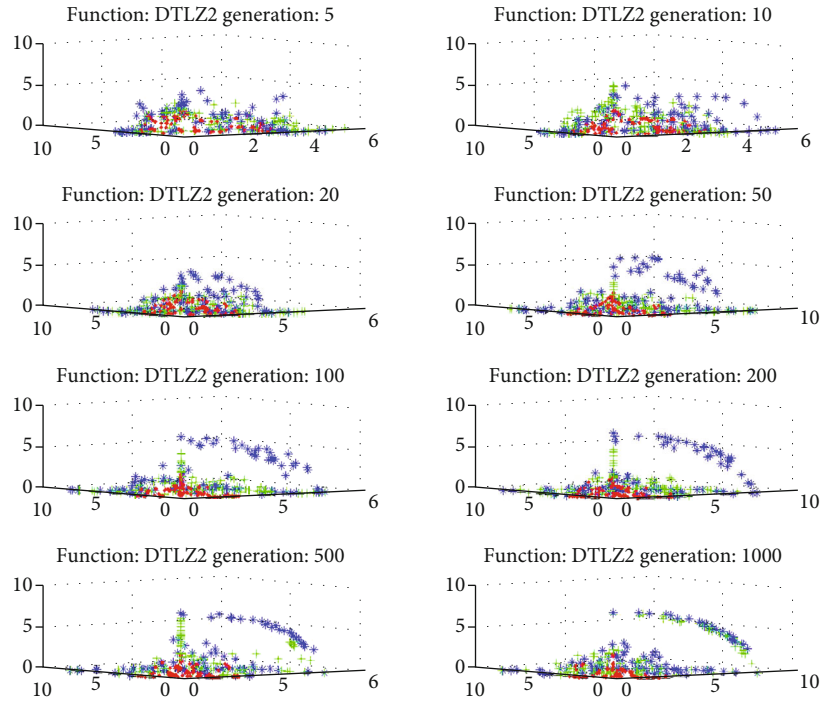
FIGURE 6: The Pareto frontier of the three algorithms in different generations (DTLZ2). The blue star is CE, the green plus sign is RE, and the red dot is NSGA-II.
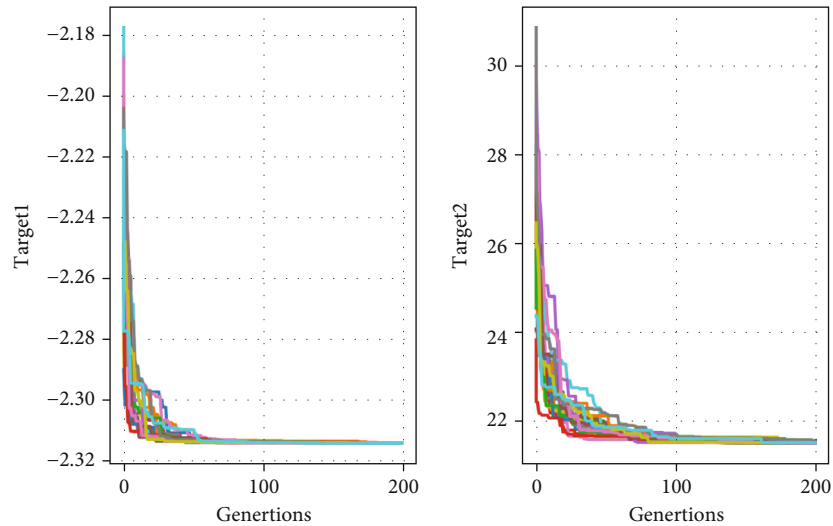
FIGURE 7: The evolutionary process of the two targets of 20 runs.

During the experiments, we use a small dataset provided by a research institute of aerodynamic. This dataset includes 20 known design solutions with 4 design parameters in each design solution and 4 kinds of performance under 28 working conditions. Since the 4-dimension design solutions cannot be shown in a figure, we process the 20 design solutions by Principal Component Analysis (PCA) and plot the first two components in a figure. From Figure 3, we can find that the data is sparely scattered in the design space. We regard the data with less training data and sparse distribution of the main parameter data points in the problem as sparse scattered data.

4.1. Experiment on the Surrogate Model. Based on the method illustrated in surrogate model construction of Section 3, a surrogate model based on sparse scattered data can be constructed. This section conducts several experiments to test the model and find the optimal metaparameters of the surrogate model, such as Q in (4) and P in (5).

Since the proposed method involves two stages, we test the two stages, respectively. For the first stage, we conduct experiment based on the 10-fold crossvalidation method. This method splits all 20 data into 10 groups and uses 9 groups as training data and uses the last group as test data in each experiment. In each experiment, we calculate an

TABLE 4: The design solutions in nondominated Pareto front of 4 runs.

Run #	Run 1				Run 2			
1	12	0	13	3.3	12	0	13	3.2
2	12	0	13	3.4	12	0	13	3.3
3	12	0.4	7	3.5	12	0	13	3.4
4	12.8	0.4	7	3.5	12	0	7	3.5
5	12.8	0.8	7	3.5	12	0.4	7	3.5
6	13.6	0.8	7	3.5	12.8	0.4	7	3.5
7	13	0.5	7.1	3.5	12.8	0.5	7	3.5
8	12.8	0.9	7.1	3.5	13	0.6	7	3.5
9	13	0.9	7.1	3.5	12.9	0.8	7	3.5
10	12.8	0.4	7.3	3.5	13	0.6	7.1	3.5
11	12.8	0.4	7.7	3.5	12	0	13	3.5
12	12	0	13	3.5	13.2	0.8	7	3.6
13	12.8	0.4	7	3.7	12.9	0.7	7	3.8
14	12.8	0.8	7	3.9	12.9	0.8	7	3.8
15	12	0.7	13	4.6	12.9	0.8	7.1	3.8
16	12	0.7	13	4.7	12	0.7	13.1	4.7
17	12	0.7	13	4.8	12	0.5	13.1	4.8
18	12	0.7	13.1	4.9	12	0.6	13.1	4.8
19	12	0.9	13.1	4.9	12	0.6	13.1	4.9
20	12	0.9	13.7	4.9	12	0.8	13.1	4.9
Run #	Run 3				Run 4			
1	12	0	13	3.2	12	0	13	3.3
2	12	0	13	3.3	12	0	13	3.4
3	12	0	13	3.4	12	0	7	3.5
4	12	0	7	3.5	12.8	0.4	7	3.5
5	12.8	0.4	7	3.5	12.8	0.5	7	3.5
6	13.2	0.5	7	3.5	12.8	0.9	7	3.5
7	12.8	0.8	7	3.5	12.8	1.1	7	3.5
8	13.2	1.2	7	3.5	12	0	13	3.5
9	12.8	0.6	7.2	3.5	12.8	0.6	7	3.6
10	13	0.6	7.4	3.5	12.8	0.7	7	3.6
11	12	0	13	3.5	13	0.7	7	3.6
12	12.8	0.9	7	3.6	12.9	1	7	3.7
13	12.8	0.4	7	3.8	12.8	0.5	7	3.8
14	12.8	0.6	7	4.1	12.8	0.5	7	4
15	12	0.4	13	4.8	12	0.4	13	4.5
16	12	0.7	13	4.8	12	0.4	13	4.6
17	12	0.7	13.1	4.8	12	1.4	13	4.7
18	12	0.9	13.1	4.8	12	0.2	13	4.8
19	12	0.4	13	4.9	12	0.4	13	4.8
20	12	1.2	13.1	4.9	12	0.4	13	4.9

averaged error by (9), and after 10 times of experiment, the error of the first stage is averaged again.

$$e = \frac{1}{2} \times \sum_{i=1}^{2} \sqrt{\frac{1}{28} \times \sum_{j=1}^{28} \left(\widehat{p}_{ij} - p_{ij} \right)^2}, \qquad (9)$$

where P_{ij} is the value of the ith predicted performance under the jth working condition, while the P_{ij} is the real value of the ith performance under the jth working condition. Table 2 shows the results of different configurations of Q and P, and we can find that the surrogate model has the smallest error when $P = 1$ and $Q = 5$.
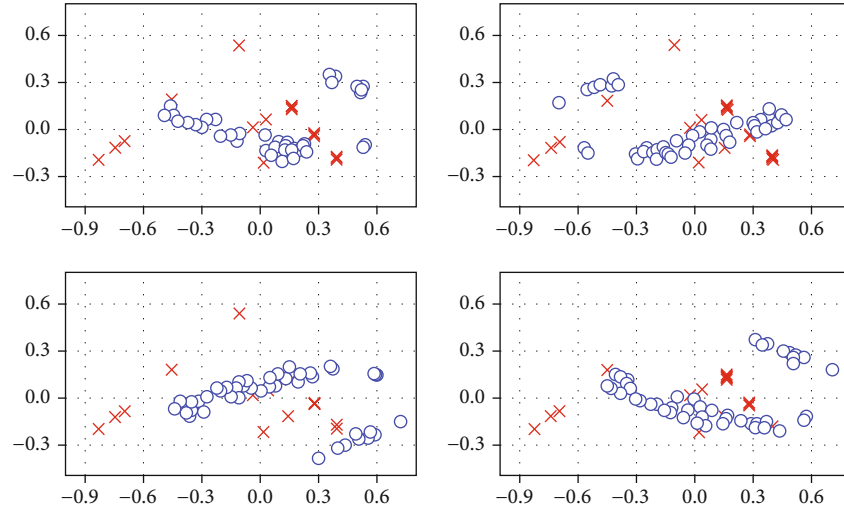
FIGURE 8: The 2-dimensional representation of the 20 known design solutions.

For the second stage, we also conduct experiment based on the 10-fold crossvalidation method. In each experiment, we calculate an averaged error by (9), and after 10 times of experiment, the error of the second stage is averaged again. Table 3 shows the results of different configurations of R and P, and we can find that the surrogate model has the smallest error when $P = 1$ and $R = 2$.

4.2. Experiment on Ergodic Evolution. In this section, we validate the ergodic evolution algorithm in terms of the capability of searching high-dimensional space. In this experiment, 16 benchmark functions are adopted as the test problems, including SCH, FON, POL, KUR, ZDT1, ZDT2, ZDT3, ZDT4, ZDT6, DTLZ1, DTLZ2, DTLZ3, DTLZ4, DTLZ5, DTLZ6, and DTLZ7. These benchmark functions are well known, and the detail can be found in [34].

We compare the performance of ergodic evolution with NSGA-II, which is a well-known evolutionary algorithm proposed in [35], and random evolution (RE), which is the same as Algorithm 1 except that the ergodic system is replaced by a general random generator. The crossover rate and mutation rate of NSGA-II are set to 0.9 and 0.1, respectively.

For each benchmark function, we run the three algorithms 30 times. For each run, the algorithms run 1000 generations with 100 individuals in each generation. After all experimental results are obtained, we conduct nondominant analysis. First, all individuals in the same generation of the three algorithms are combined, and then, count the number of individuals in the nondominant frontier after nondominant analysis. Figure 4 shows the averaged result (30 runs) of the top 100 generations. From the figure, we can clearly see that the proposed method is superior to NSGA-II and RE for most of the benchmark functions except DTLZ2, DTLZ4, and DTLZ5.

In addition, we plotted the Pareto frontiers of 5th, 10th, 20th, 50th, 100th, 200th, 500th, and 1000th generation of the three algorithms. Considering the length limitation, we only

show the figures of ZDT3 (Figure 5) and DTLZ2 (Figure 6) in this paper.

4.3. Experiment on the Whole Method. In this section, we validate the proposed method. For the ergodic evolution, two targets are adopted. The first is a function of the 4 performances provided by the aerodynamic institute, while the second is calculated by equation (5). The surrogate model is constructed with $P = 1$, $Q = 5$, and $R = 2$.

We run the whole algorithm 20 times, and Figure 7 shows the evolutionary process of the two targets. For each run, the algorithm evolves 200 generations, and there are 100 individuals in each generation. The figures include 20 lines indicating the evolutionary process of the 20 runs, and each point in the line indicates the minimum value of targets in one generation. As we can see, the algorithm converges to minimum targets almost within 100 generations.

We randomly select 4 runs and list 20 design solutions in the nondominated Pareto front in Table 4. We plot the generated design solutions and known design solutions in a single figure, and both are proceeded by PCA. From Figure 8, we can find that most of the generated design solutions are near to known design solutions, which prove that the proposed method can achieve rapid exploration of high-dimensional space. This result is reasonable since the second target of the CE restricts the algorithm to exploit new design solutions in the space near to the known design solutions.

From the extensive experiment results above, we find that (1) the adoption of some basic assumptions or prior knowledge can relax the requirement of data for training the surrogate model. The prior knowledge here represents views of designers on design problems. In this work, we simply adopt two basic assumptions, and the whole model is divided into two parts, and some unimportant relationships are ignored by the surrogate model. Therefore, we think transferring basic assumption or prior knowledge into a computational manner and integrating it with the surrogate model are feasible ways to build a surrogate model with only

sparse and scattered data. (2) The simple IDW method can train the surrogate model. However, in different scenarios, IDW may not always be feasible, and some advanced methods like Kriging and RBF network should be adopted and validated. (3) One of the merits of the proposed method is that the searching space can be expanded with the addition of more known design solutions. This means that this method is fit for both sparse and scattered data and relatively bigger data.

5. Conclusion

To train a surrogate model with only sparse and scattered data and find new design solutions based on this surrogate model, this work proposed a two-stage interpolation-based method for the surrogate model and adopts CE to explore the high-dimensional space. This paper uses PCA to reduce the dimension of data and prove the characteristics of sparse and scattered data. Then, combining the two-stage interpolation and ergodic evolution method, the sparse scattered point data is generated into the design method. Three groups of experiments show that the surrogate model can predict performances, and the CE is efficient in terms of exploring high-dimensional space.

Although this work proposes a feasible method to deal with the problems, some remaining problems require extensive research works. In the future, we will enhance the method from the following aspects.

(i) This work only adopts basic assumptions to relax the data requirement, and the data requirement can be further relaxed by incorporating prior knowledge, such as experts' experience and physical law. The main problem will be the technique of embedding prior knowledge into surrogate models

(ii) In this work, the penalty factor is important and the simple Euclidean distance is used. In the future, some nonlinear function of the Euclidean distance can be used to measure the penalty factor. The difficulty will be how to predefine or learn a nonlinear function for the penalty factor

Data Availability

No data were used to support this study.

Conflicts of Interest

The authors declare that there are no conflicts of interest regarding the publication of this article.

References

[1] W. Yi, Y. Zhou, L. Gao, X. Li, and C. Zhang, "Engineering design optimization using an improved local search based epsilon differential evolution algorithm," *Journal of Intelligent Manufacturing*, vol. 29, no. 7, pp. 1559–1580, 2018.

[2] A. R. Yıldız, "A new design optimization framework based on immune algorithm and Taguchi's method," *Computers in Industry*, vol. 60, no. 8, pp. 613–620, 2009.

[3] P. Zhu, Y. Zhang, and G. Chen, "Metamodeling development for reliability-based design optimization of automotive body structure," *Computers in Industry*, vol. 62, no. 7, pp. 729–741, 2011.

[4] A. R. Conn and S. L. Digabel, "Use of quadratic models with mesh-adaptive direct search for constrained black box optimization," *Optimization Methods and Software*, vol. 28, no. 1, pp. 139–158, 2013.

[5] S. Shan and G. G. Wang, "Survey of modeling and optimization strategies to solve high-dimensional design problems with computationally-expensive black-box functions," *Structural and Multidisciplinary Optimization*, vol. 41, no. 2, pp. 219–241, 2010.

[6] I. Karen, N. E. C. M. E. T. T. İ. N. Kaya, and F. Öztürk, "Intelligent die design optimization using enhanced differential evolution and response surface methodology," *Journal of Intelligent Manufacturing*, vol. 26, no. 5, pp. 1027–1038, 2015.

[7] Wikipedia, "Response surface methodology," 2017, https://en.wikipedia.org/wiki/Response_surface_methodology/.

[8] R. Mallipeddi and M. Lee, "An evolving surrogate model-based differential evolution algorithm," *Applied Soft Computing*, vol. 34, pp. 770–787, 2015.

[9] W. Gong, A. Zhou, and Z. Cai, "A multioperator search strategy based on cheap surrogate models for evolutionary optimization," *IEEE Transactions on Evolutionary Computation*, vol. 19, no. 5, pp. 746–758, 2015.

[10] T. W. Simpson, T. M. Mauery, J. J. Korte, and F. Mistree, "Kriging models for global approximation in simulation-based multidisciplinary design optimization," *AIAA Journal*, vol. 39, no. 12, pp. 2233–2241, 2001.

[11] R. G. Regis and C. A. Shoemaker, "Combining radial basis function surrogates and dynamic coordinate search in high-dimensional expensive black-box optimization," *Engineering Optimization*, vol. 45, no. 5, pp. 529–555, 2013.

[12] Z. Qian, C. C. Seepersad, V. R. Joseph, J. K. Allen, and C. F. J. Wu, "Building surrogate models based on detailed and approximate simulations," *Journal of Mechanical Design*, vol. 128, no. 4, pp. 668–677, 2006.

[13] C. Tang, K. Gee, and S. Lawrence, "Generation of aerodynamic data using a design of experiment and data fusion approach," in *In: Aiaa Aerospace Sciences Meeting and Exhibit*, Reno, Nevada, January 2005.

[14] M. De Berg, O. Cheong, M. Van Kreveld, and M. Overmars, *Computational Geometry: Introduction*, Springer, 2008.

[15] Q. Li, S. Chen, and X. Luo, "Using meshless local natural neighbor interpolation method to solve two-dimensional nonlinear problems," *International Journal of Applied Mechanics*, vol. 8, no. 5, p. 1650069, 2016.

[16] S. H. Hong, L. Wang, T. K. Truong, T. C. Lin, and L. J. Wang, "Novel approaches to the parametric cubic-spline interpolation," *IEEE Transactions on Image Processing*, vol. 22, no. 3, pp. 1233–1241, 2013.

[17] L. M. Surhone, M. T. Tennoe, and S. F. Henssonow, *Nearest-Neighbor Interpolation*, Betascript Publishing, 2013.

[18] R. G. Zhou, W. W. Hu, G. F. Luo, X. A. Liu, and P. Fan, "Quantum realization of the nearest neighbor value interpolation method for INEQR," *Quantum Information Processing*, vol. 17, no. 7, pp. 1–37, 2018.

[19] J. Qian, J. Yi, Y. Cheng, J. Liu, and Q. Zhou, "A sequential constraints updating approach for Kriging surrogate model-assisted engineering optimization design problem," *Engineering with Computers*, vol. 36, no. 3, pp. 993–1009, 2020.

[20] R. G. Regis, "Constrained optimization by radial basis function interpolation for high-dimensional expensive black-box problems with infeasible initial points," *Engineering Optimization*, vol. 46, no. 2, pp. 218–243, 2014.

[21] R. G. Regis and C. A. Shoemaker, "Constrained global optimization of expensive black box functions using radial basis functions," *Journal of Global Optimization*, vol. 31, no. 1, pp. 153–171, 2005.

[22] H. C. de Oliveira, A. P. Dal Poz, M. Galo, and A. F. Habib, "Surface gradient approach for occlusion detection based on triangulated irregular network for true orthophoto generation," *IEEE Journal of Selected Topics in Applied Earth Observations and Remote Sensing*, vol. 11, no. 2, pp. 443–457, 2018.

[23] C. She, Z. Wang, F. Sun, P. Liu, and L. Zhang, "Battery aging assessment for real-world electric buses based on incremental capacity analysis and radial basis function neural network," *IEEE Transactions on Industrial Informatics*, vol. 16, no. 5, pp. 3345–3354, 2020.

[24] X. Qiu, J. X. Xu, K. C. Tan, and H. A. Abbass, "Adaptive cross-generation differential evolution operators for multiobjective optimization," *IEEE Transactions on Evolutionary Computation*, vol. 20, no. 2, pp. 232–244, 2016.

[25] K. Sethanan and R. Pitakaso, "Improved differential evolution algorithms for solving generalized assignment problem," *Expert Systems with Applications*, vol. 45, pp. 450–459, 2016.

[26] Z. Zhang, "Multiobjective optimization immune algorithm in dynamic environments and its application to greenhouse control," *Applied Soft Computing*, vol. 8, no. 2, pp. 959–971, 2008.

[27] A. Rahimi-Vahed, S. Mirghorbani, and M. Rabbani, "A new particle swarm algorithm for a multi-objective mixed-model assembly line sequencing problem," *Soft Computing*, vol. 11, no. 10, pp. 997–1012, 2007.

[28] W. Dong and X. Yao, "Unified eigen analysis on multivariate Gaussian based estimation of distribution algorithms," *Information Sciences*, vol. 178, no. 15, pp. 3000–3023, 2008.

[29] R. Carvalho, R. R. Saldanha, B. Gomes, A. C. Lisboa, and A. Martins, "A multi-objective evolutionary algorithm based on decomposition for optimal design of Yagi-Uda antennas," *IEEE Transactions on Magnetics*, vol. 48, no. 2, pp. 803–806, 2012.

[30] L. Rachmawati and D. Srinivasan, "Multiobjective evolutionary algorithm with controllable focus on the knees of the Pareto front," *IEEE Transactions on Evolutionary Computation*, vol. 13, no. 4, pp. 810–824, 2009.

[31] J. Bader and E. Zitzler, "Robustness in hypervolume-based multiobjective search," *Computer Engineering and Networks Laboratory*, vol. 317, 2010.

[32] A. Zhou, B. Y. Qu, H. Li, S. Z. Zhao, P. N. Suganthan, and Q. Zhang, "Multiobjective evolutionary algorithms: a survey of the state of the art," *Swarm and Evolutionary Computation*, vol. 1, no. 1, pp. 32–49, 2011.

[33] G. Y. Lu and D. W. Wong, "An Adaptive Inverse-Distance Weighting Spatial Interpolation Technique," *Computers & Geosciences*, vol. 34, no. 9, pp. 1044–1055, 2008.

[34] S. Huband, P. Hingston, L. Barone, and L. While, "A review of multiobjective test problems and a scalable test problem toolkit," *IEEE Transactions on Evolutionary Computation*, vol. 10, no. 5, pp. 477–506, 2006.

[35] K. Deb, S. Agrawal, A. Pratap, and T. Meyarivan, *A Fast Elitist Nondominated Sorting Genetic Algorithm for Multi-Objective Optimization: NSGA-II*, Springer, Berlin Heidelberg, 2000.

Research Article

Preparation and Performance Study of Carbon Fiber Composite Electroplated Carbon Badminton Racket

Ziying Sheng and Kai Wen 🆔

School of Physical Education, Wuhan Business University, Wuhan, 435600 Hubei, China

Correspondence should be addressed to Kai Wen; 20150740@wbu.edu.cn

Driven by the slogan of "Fitness for All", more and more people are participating in sports, which also promotes the popularity of the sports equipment market, of which badminton rackets are an important part. With the improvement of people's economic level, there are higher requirements for the materials of various sports equipment. It is expected that badminton rackets will not only be light, but also bearable, and the electroplated carbon in carbon fiber composites has such properties. Therefore, the purpose of this paper is to study the preparation of badminton rackets by electroplating carbon with carbon fiber composite materials and to study its performance. In this paper, the properties of carbon fiber composites are tested and analyzed, and the relevant chemical formulas are used to explain them. The experimental results of this paper show that after using the same pressure to conduct experiments on wooden, iron, steel, steel-aluminum, carbon-aluminum, and carbon bats, it is found that the bearing capacity of wooden bats is only 28%, the damage degree of badminton racket is 54%, while the bearing capacity of carbon racket is 89%, and the damage degree of badminton racket is 12%. This fully shows that the badminton racket made of electroplated carbon material not only has a much higher bearing capacity than badminton rackets of other materials, but also has a much lower damage degree than badminton rackets of other materials. Therefore, badminton rackets made of electroplated carbon are more durable and more popular.

1. Introduction

The demand for high-performance composite materials, especially in the fields of defense, military, and aerospace, has contributed to the rapid development of science and technology. Carbon fiber composite material is one of the most widely used composite materials, and the properties of carbon fiber directly determine the properties of the composite material. Scientific researchers in various countries have conducted many studies on the composition and structure of carbon fibers and their properties. Since the beginning of the twenty-first century, the properties of carbon fibers have been continuously optimized and improved, and the research on the manufacturing process of composite materials has also deepened, striving to make composite materials more efficient and simpler to manufacture.

A further study of carbon fiber materials is the study of their composite materials. In the molding process of carbon fiber composite materials, including hand molding and stretching. The resin conveying molding process is to perform the reinforcement material into a closed shape and solidify it under vacuum and pressure conditions. This process is simple and convenient and is widely used. In the aerospace field, in addition to the excellent properties of the composite material itself, it is also found that the carbon fiber composite material containing some shape memory effect maintains the shape memory ability.

The innovations of this paper are as follows: (1) This paper introduces the theoretical knowledge of carbon fiber composite materials and electroplated carbon and uses carbon fiber composite material and electroplated carbon to analyze how carbon fiber composite material and electroplated carbon play a role in the preparation and performance research of badminton racket. (2) This paper expounds the properties of carbon fiber materials and electroplated carbon. It is found through experiments that the

badminton rackets made of carbon fiber materials and electroplated carbon are of better quality and more popular.

2. Related Work

With the increasing emphasis on sports in China, the number of people participating in sports is also increasing rapidly. Mizuno found that people developed fully automatic badminton robots that could catch and serve in the same environment as a human badminton player. In the system he invented, the robot could automatically move to where the shuttlecock would fall and hit it back with a normal badminton racket. Mizuno gave a general introduction to a fully automatic badminton robot, but did not describe it with a practical example [1]. Park believes that shoulder and elbow injuries account for a considerable proportion of injuries in badminton. Because badminton requires repetitive, high-velocity overhead movements that place high loads on the upper body joints, badminton players often experience shoulder and elbow pain and decreased function. His research is mainly to evaluate the abnormality of the shoulder and elbow tendon in badminton players and to explore its correlation with clinical symptoms. Forty-nine badminton players participating in the leisure badminton club were invited to the sports training center for experiments. Park only introduced the object of the experiment, and did not explain the process of the whole experiment, resulting in no corresponding conclusions [2]. Duncan's study examines the impact of changes in physical and psychological arousal on badminton short serve performance in competitive and practice environments. He experimented with 20 badminton players (10 males and 10 females), with short serve measured at rest, midway, and end of a badminton-specific training program. The results showed that the performance of the short serve in practice was significantly better compared to the game, while the performance of the short serve in the real game was not very good. This is because in the real game, the athlete will have anxiety and tension, which will affect the performance. Although he conducted experiments on 20 athletes and analyzed the results of the experiments, there was no solution to the experimental results [3]. Minkai found that despite the well-known importance of badminton in sports, badminton is poorly defined and lacks research. In contrast to general training typically used to improve a badminton player's on-court agility, Reactive Initiation Training (RIT) challenges perceived speed, requiring only quick steps in the direction of the shuttlecock. His research explores comparing the speed of body reflexes to reaction initiation exercises to determine whether these exercises are effective in improving on-court agility. 20 badminton novices were divided into two halves and received physical reaction speed and reaction initiation training on the court. Before and after training, they took on-court agility tests with pre-judgment and without pre-judgment. The results showed that both training methods reduced the average running time, but only the reaction initiation training additionally reduced initiation time

and its proportion in those time-consuming positions. He designed and practiced the process of the whole experiment, but there is no specific experimental data to prove the authenticity of the experiment [4]. Yuan found that the loading of gold nanoparticles (AuNPs) onto environmentally sensitive polymer microgels is increasingly used to tune their optical properties and catalytic activities. Here, he synthesized composite polymer microgels with a core-shell structure and controllably loaded AuNPs onto the network chains of the polymer microgels. The results show that the prepared AuNPs composites have good pH sensitivity; thus, the electromagnetic coupling between AuNPs can be regulated by polymer microgels under various acidic conditions. But he did not explain in detail why this study was done [5]. Akhtar discovered that cellulose, a natural biopolymer commonly used as a support agent, has enhanced applicability and properties. The cellulose he isolated from the waste was used for silver nanoparticle (Ag-NPs) impregnation by a simple and reproducible method. Cellulose (Ag-Cel) prepared from Ag-NPs was characterized by powder X-ray diffraction, Fortier transform infrared spectroscopy, and scanning electron microscopy. Its thermal stability was investigated by thermogravimetric analysis. Although the scholar has carried out detailed experiments, no corresponding conclusions have been drawn [6].

3. Test Method of Carbon Fiber Composite Material Electroplating Carbon Performance

3.1. Application of Carbon Fiber Composite Materials. In carbon fiber composites, if the carbon fibers in the matrix are stretched along the fibers, the strain capacity of all fibers is the same, and some fibers will not affect the effect of other fibers after failure [7]. The broken fibers did not play a role, but the other fibers played their part as usual. According to this characteristic, if the material is damaged, especially in the use of sports equipment, it will not cause serious performance degradation. According to this characteristic, the personal safety of the athlete can be ensured [8].

Badminton is a sport suitable for all ages. In sports, the hardness and durability of badminton rackets have a great influence on the sports performance [9]. For example, some sub-rackets are prone to breakage, which can affect an athlete's level. The structure diagram of the badminton racket made of electroplated carbon material is shown in Figure 1.

As shown in Figure 1, with the development of science and technology, electroplated carbon badminton rackets have appeared in the sporting goods market. Carbon fiber has the characteristics of high hardness and toughness. In specific applications, carbon fiber and other substances are usually combined to form carbon fiber composite materials [10]. At the same time, the electroplated carbon should have excellent mechanical properties after curing, and in addition, it should have good fluidity, which is convenient for curing and molding. The application fields of carbon fiber composite materials are shown in Figure 2.

As shown in Figure 2, in the structure of carbon fiber composites, fiber reinforcement takes on the heavy
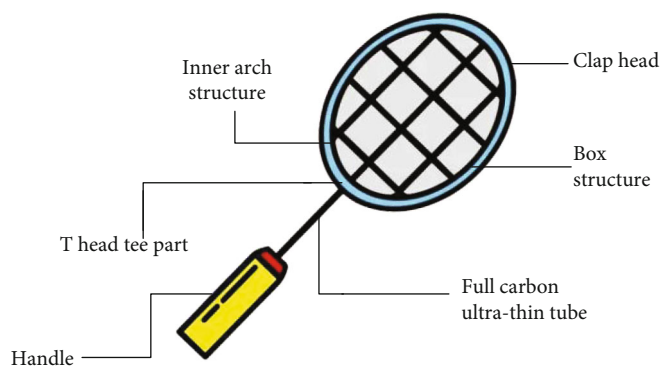
FIGURE 1: Electroplated carbon badminton racket.
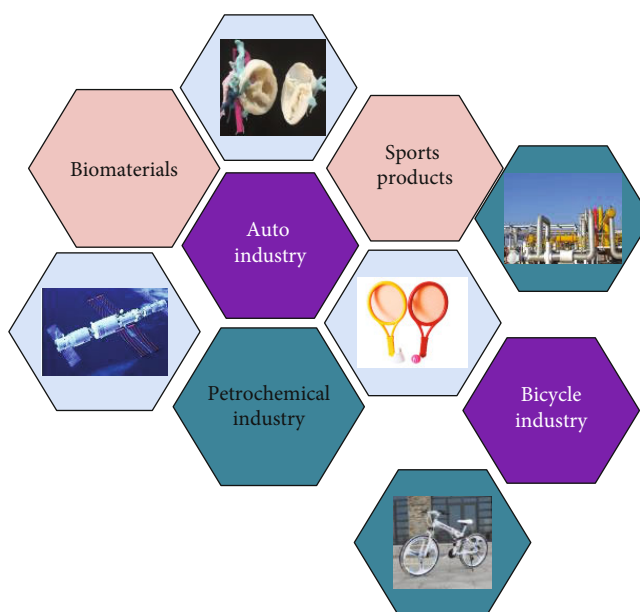
FIGURE 2: Application areas of carbon fiber composites.

responsibility of the mechanical properties of the composites. The electroplated carbon is responsible for the task of fixing and strengthening and protects the carbon fiber from damage from the external environment. Therefore, the electroplated carbon and carbon fiber reinforcement of composite materials need to have excellent wettability and adhesion [11]. The good performance of carbon fiber self-recovery after deformation is shown in Figure 3.

As shown in Figure 3, the performance of the composite material depends on the ratio of reinforcement to matrix and the performance of the individual components. The general reinforcing materials are carbon fibers, glass fibers, plastic fibers, etc. In addition to metals, ceramics, and other materials, the matrix is mainly a resin material. Reinforcing materials can increase material strength and improve mechanical properties [12].

3.2. Characteristic Analysis of Electroplated Carbon in Carbon Fiber Composites. In the process of glass transition of electroplated carbon, the mechanical properties of the

resin will be quite different before and after. As the ambient temperature gradually increased, the free volume of the electroplated carbon molecules began to expand. When the temperature reaches the glass transition temperature, the free volume of the electroplated carbon molecules is sufficient, so the configuration of the electroplated carbon molecules is fully changed and adjusted, and the movement of the molecular chain is very active [13]. The analysis of electroplated carbon with different formulations is shown in Figure 4.

As shown in Figure 4, because the #20 formula has too little electroplating carbon, the performance in the DMA test is not ideal. Therefore, in the DSC test, it is no longer necessary to test the #20 type electroplated carbon, and only the DSC test of the #40, #60, and #80 samples is required. The three proportioned samples were scanned at different constant heating rates, and the apparent activation energy E_a was calculated according to the Kissinger formula; apparent activation energy can give a clearer physical meaning to elementary reactions, that is, the difference between the average
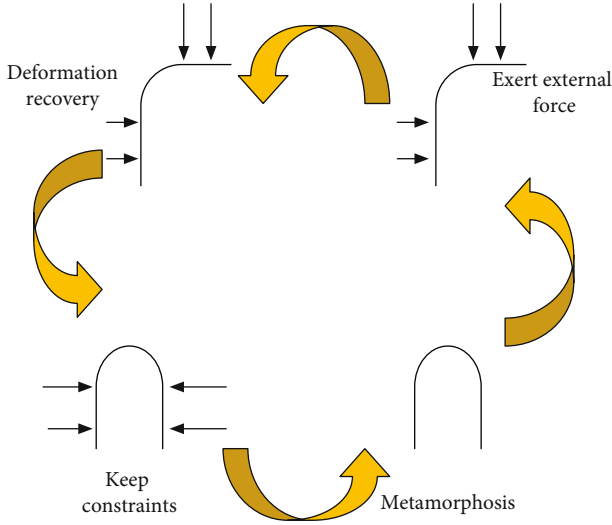
FIGURE 3: Good performance of carbon fiber self-recovery after deformation.

energy of the activated molecule and the average energy of all molecules [14], as shown as follows:

$$-\frac{E_a}{R} = \frac{dIn\left(\Phi/T_P^2\right)}{d(1/T_P)}, \tag{1}$$

where Φ represents the temperature rise rate, T_P represents the peak temperature, E_a represents the activation energy, and R represents the molar gas constant. According to the Kissinger method, when using the Kissinger method to determine the activation energy of crystallization of amorphous materials, it should be ensured that the crystallization fractions corresponding to the selected temperature are not very different; otherwise, large errors will be introduced, and the kinetic formula can be approximated as

$$H = A \cdot \exp\left(-E_a/RT\right) \tag{2}$$

Among them, the pre-entropy factor A is

$$A = \frac{\Phi E_a \exp\left(E_a/RT_P\right)}{RT_P^2} \tag{3}$$

The corresponding peaks of the three exothermic peaks in the DSC scan at different heating rates are shown in Table 1.

As shown in Table 1, the second exothermic peak disappeared when the temperature increased. Because the reaction rate was too fast, the reaction was not sensitive enough to temperature, so it was incorporated into the third peak, which was used to test the viscosity of electroplated carbon as a function of temperature using the temperature ramp mode of rotational rheology. The time-sweep mode was used to test the relationship between the viscosity and time of electroplated carbon at a constant temperature [15]. The kinetic parameters of the curing reaction are shown in Table 2.

It can be seen from Table 2 that solidification is a Chinese word, which chemically refers to the process of transforming substances from low molecules to high molecules, and also refers to the process of forming certain fixed views and viewpoints on things [16]. When the specific gravity of electroplating carbon increases, both E_a and A of the curing reaction of the system will increase. This is because the energy required for the electroplating carbon homopolymerization reaction is larger than the other two curing reactions [17]. With the increase of carbon content in electroplating, the difference between #60 and #80 is an order of magnitude from #40, while the difference between #60 and #80 is not obvious, indicating that the addition of electroplating carbon can prolong the service life of the mixed resin [18]. Electroplating carbon under different vision is shown in Figure 5.

As shown in Figure 5, the ability of a metallic material to resist permanent deformation or fracture under static load, and it can also be defined as proportional limit, yield strength, breaking strength, or ultimate strength. In order to ensure the full progress of the curing reaction, the curing temperature needs to be higher than the glass transition temperature, which can ensure good mechanical properties and curing degree of the electroplated carbon after curing [19].

3.3. Density Test. In this paper, the method of electroplating is used to electroplate the carbon fiber with nickel, and the metallization modification is carried out. The effect of nickel on the wettability of the carbon fiber interface was investigated by observing the high temperature spheroidization of the copper plating layer during the heat treatment process. By testing the thermal shock resistance of the carbon fiber composite wire, the bonding force between the carbon fiber and the copper coating was studied [20].

Archimedes' principle generally refers to Archimedes' law. An important principle of hydrostatics, which states that an object immersed in a stationary fluid, experiences a buoyant force equal to the weight of the fluid displaced by the object, directed vertically upward and through the centroid of the displaced fluid [21]. The actual density of carbon fiber copper composites is measured using Archimedes' principle:

$$F = pgv \tag{4}$$

p represents the density of distilled water and g represents the volume of distilled water displaced by immersion of the composite in distilled water. The volume V of the composite material at this time is

$$V = \frac{m_1 - m_2}{p} \tag{5}$$

Then, the density p of the composite material is

$$p = \frac{m_1 p}{m_1 - m_2} \tag{6}$$

(a) Storage modulus

(b) Loss modulus
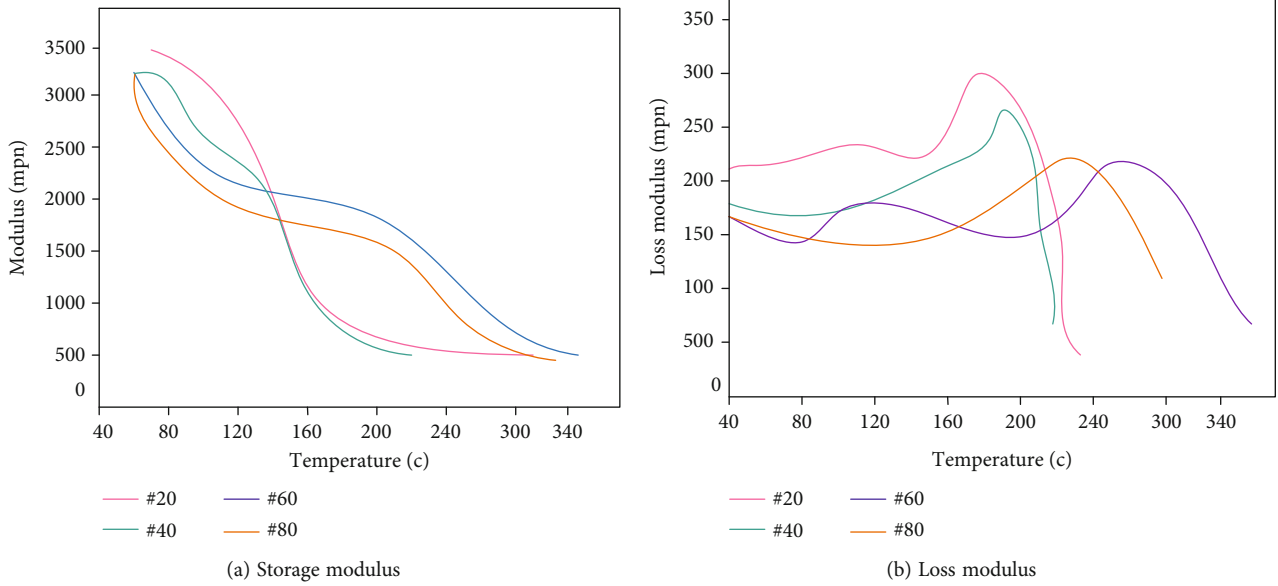
FIGURE 4: Electroplated carbon with different formulations.

TABLE 1: Corresponding peak temperature (Tp) of exothermic peak of electroplated carbon curing system at different heating rates.

System	Heating rate (K/min)	$T_{P1}(K)$	$T_{P2}(K)$	$T_{P3}(K)$	$T_{P4}(K)$
#40	6	420.4	457.0	470.3	486.9
	12	453.0	462.1	483.2	489.0
#60	6	431.7	460.9	498.5	505.6
	12	458.9	465.6	480.3	489.3
#80	6	439.6	462.5	492.4	499.5
	12	460.8	470.1	498.8	505.8

TABLE 2: Curing reaction kinetic parameters.

System	E_a(kJ/Mol)	A(min-1)	H_{25}(min-1)
#40	62.5	3.43×10^7	4.75×10^{-6}
#60	73.2	4.65×10^8	5.46×10^{-7}
#80	81.6	1.96×10^9	1.63×10^{-7}

Then, the density p_r of the composite material is

$$p_r = \frac{p_1}{p_2} \tag{7}$$

Among them, p_1 is the actual density of the composite material, and p_2 is the theoretical density of the composite material.

3.4. Test of Thermal Conductivity.
Raman spectroscopy is a type of scattering spectroscopy. Raman spectroscopy is an analysis method of Raman scattering effect, which analyzes the scattering spectrum with different frequencies from the incident light to obtain information on molecular vibration and rotation, and is applied to the study of molecular structure. Raman spectroscopy is an important means to study the structure of carbon materials, which reflects the changes in the structure of carbon materials from the perspective of chemical structure [22]. The thermal conductivity K is measured by a laser thermal conductivity meter, and the thermal conductivity calculation formula is

$$K = \alpha \cdot \rho \cdot C_\rho \tag{8}$$

where K is the thermal conductivity, α is the thermal diffusivity, ρ is the density, and C_ρ is the specific heat capacity.

In recent decades, many outstanding research results have emerged in China in the field of materials, among which carbon fiber composite materials have been widely used in modules ranging from module shells and cabinets to aircraft fuselages [23]. However, how to objectively and quantitatively evaluate the electromagnetic pulse protection performance of this new type of composite material, such as the radio frequency impedance characteristics of the composite material, the electrical conductivity of the composite material under the action of a magnetic field, and the impedance characteristic of the composite material under the action of lightning pulse, it involves multidisciplinary knowledge such as mechanical structure, electromagnetic field propagation, instrument measurement, and materials. At present, there are not many people engaged in research in this field in China, which restricts the development and improvement of new materials [24].

3.5. Nickel Electroplating and Electroplating Carbon on Carbon Fiber Surface.
The pretreated carbon fibers are electroplated with nickel. The carbon fiber content in the plating solution was kept at about 0.2 g/L, and the short carbon fibers were put into the nickel plating solution for ultrasonic

Normal multiples of
electroplated carbon

500 times of
electroplated carbon
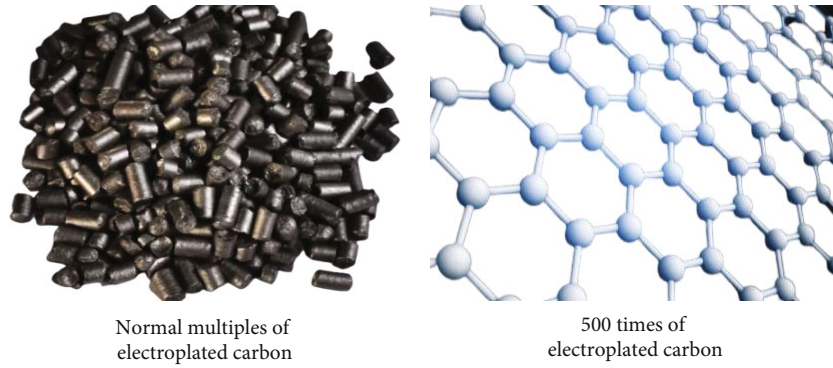
FIGURE 5: Electroplated carbon under different vision.

stirring. When the short carbon fibers are all settled on the bottom cathode copper plate, the power is turned on, and the thickness of the nickel layer is controlled by the electroplating time. The reaction that occurs at cathode Ni during nickel plating is

$$Ni^{2+} + 2e = Ni \tag{9}$$

The main reaction that occurs at anode Ni^{2+} is

$$Ni\text{-}2e = Ni^{2+} \tag{10}$$

If the anode current density is too large, anode passivation is likely to occur, accompanied by the progress of the side reaction $O_2\uparrow$ as

$$2H_2O - 4e = O_2\uparrow + 4H^+ \tag{11}$$

Therefore, in the process of electroplating, the current density is strictly controlled to ensure the quality of the coating.

The nickel-plated carbon fibers were repeatedly ultrasonically cleaned with distilled water, and then copper-plated. The carbon fiber content in the plating solution was maintained at about 0.4 g/L. When the nickel-plated carbon fibers were ultrasonically stirred in the solution, the power was turned on. The temperature of the plating solution was 40 °C and the current density was 2.5 A/dm. The reaction that occurs at cathode Cu during copper plating is

$$Cu^{2+} + 2e = Cu \tag{12}$$

The main reaction that occurs at anode Cu^{2+} is

$$Cu\text{-}2e = Cu^{2+} \tag{13}$$

In the process of copper plating, it is still necessary to control the current density. Excessive current density will also be accompanied by side reactions.

The electroplated copper-plated and nickel-plated copper carbon fibers were taken out, repeatedly washed with distilled water for 3 times, then filtered and cleaned with anhydrous alcohol on a suction filter, and finally placed in a vacuum drying box for drying.

Since metal is easily oxidized in the air, it is inevitable that some coatings will be oxidized to form oxides during the cleaning and drying process of carbon fibers. The coating of the oxide is relatively poor, which will affect the subsequent experiments, so the copper oxide must be reduced. The carbon fiber is put into a vacuum tube furnace for reduction, and the reaction that occurs is

$$H_2 + CuO \longrightarrow H_2O \tag{14}$$
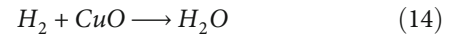
Electroplating time is an important factor to control the thickness of the coating, and the method of determining the thickness of the carbon fiber surface layer by metallographic method is difficult to implement. Therefore, this paper uses the weighing method to estimate the average thickness of the coating. The weighing method is the method recommended by the International Organization for Standardization. It is only suitable for gases that do not react between components, components and the inner wall of the cylinder, and condensable components that are completely gaseous under experimental conditions. The calculation formula of the average thickness of the coating is

$$\Delta r = \left(\sqrt{1 + \frac{\rho_c \Delta G}{\rho_c N_i G}} - 1 \right) d \tag{15}$$

In the formula, ΔG is the weight gain rate of carbon fiber before and after nickel electroplating; ρ_c and $\rho_c N_i$ are the density of carbon fiber and nickel, respectively; and d is the diameter of carbon fiber.

Many studies have shown that there are two main factors that affect the thermal shock resistance of coatings. The first is the difference between the thermal expansion coefficient of the coating and the base material. The thermal expansion coefficient of the metal copper coating is larger, while the thermal expansion coefficient of the matrix carbon fiber is smaller. Due to the difference in thermal expansion coefficient, thermal stress will be generated between carbon fiber and copper during the cooling and heating cycle. The calculation formula of thermal stress is

$$\sigma th = \frac{E_f}{1 - \nu} \cdot (\alpha_r - \alpha_s) \cdot (T_s - T_r) \tag{16}$$

FIGURE 6: Application of carbon fiber composites in sports equipment.

In the formula, α_r and α_s are the thermal expansion coefficients of the substrate and the coating, respectively, and T_s and T_r are the temperatures of the coating and the substrate, respectively. It can be seen from the formula that the smaller the thermal expansion coefficient between materials, the smaller the thermal stress will be. The greater the interfacial bonding strength, the better the thermal shock resistance of the coating.

Since carbon fiber is a carbon material, it has a lower theoretical specific capacity ae^-. In general, researchers improve the actual cycle Li_aC of carbon fibers through surface modification, biological preparation of carbon fibers, etc., so that it can approach the theoretical capacity to the greatest extent:

$$aLi^+ + C(carbon fiber) + ae^- \leftrightarrow Li_aC \qquad (17)$$
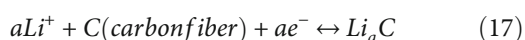
4. Experiment and Analysis of Carbon Fiber Composite Material Electroplating Carbon

4.1. Experiment and Analysis of the Properties of Carbon Fiber Composites. In many sports, athletes hope that the equipment can meet the characteristics of light weight and high strength at the same time, while the density of carbon fiber composite materials is only 1.76 to 1.80 g/cm^3, and the density of metal materials is several times that of carbon materials. For example, steel has a density of 7.87 g/cm^3 and aluminum has a density of 2.7 g/cm^3. These materials do not meet certain special sports needs. The application of carbon fiber composite materials in sports equipment is shown in Figure 6.

As shown in Figure 6, therefore, the carbon material is lightweight and high in strength and is very suitable for

TABLE 3: Physical properties of different reinforcement materials.

Reinforcing material	Density/ g·cm-3	Tensile strength/ GPa	Elastic modulus/ GPa	Elongation/ %
Carbon fiber	1.69	3.47	232	1.48
Glass fiber	2.58	3.47	69	2.56
Boron fiber	2.39	1.38	378	0.37
Alumina fiber	3.87	1.38	408	0.87

TABLE 4: Comparison of badminton rackets made of different materials.

Club type	Racket quality/g	Handshake quality/g	Shock absorption
Standard metal	768	47.8	5.7
Light metal	589	47.8	4.9
Carbon fiber	342	47.8	7.8
Lightweight carbon fiber	309	47.8	8.9

use in sports equipment. Carbon materials are widely used in some sports such as bicycles, sailboats, poles, golf, and rackets. The physical properties of different reinforcing materials and the comparison of badminton rackets made of different materials are shown in Table 3 and Table 4.

As shown in Table 3, carbon materials have high fatigue resistance compared with metals and are very suitable for the manufacture of large rackets. As the competition in

(a) Effect of sintering temperature on density

(b) Effect of sintering temperature on thermal conductivity of composites
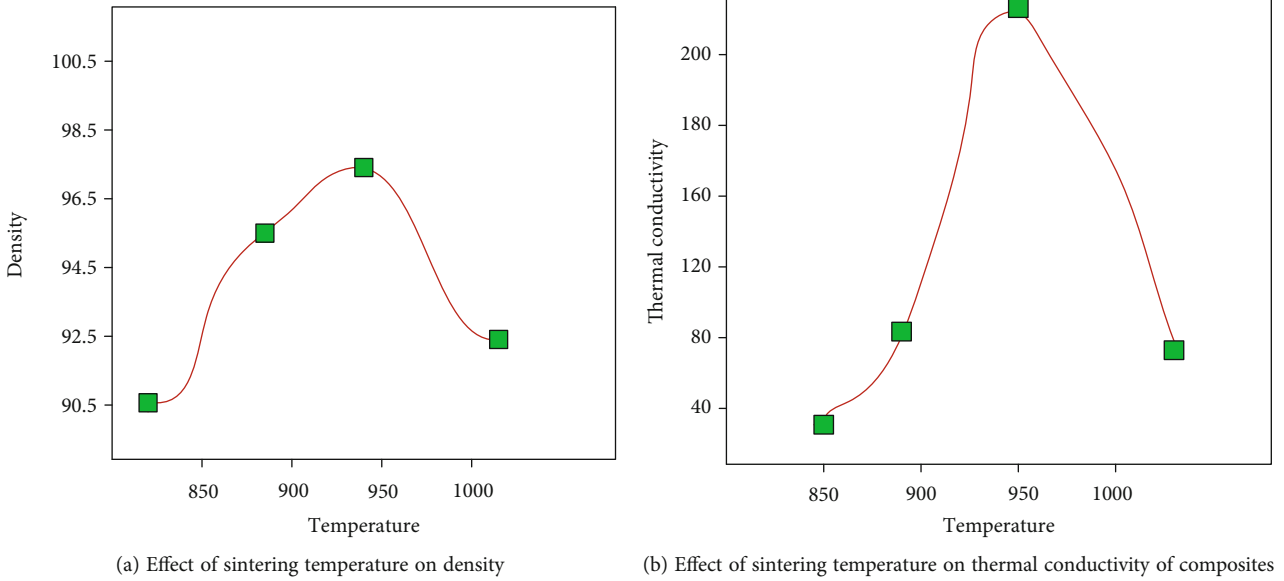
FIGURE 7: Effect of sintering temperature on composites.
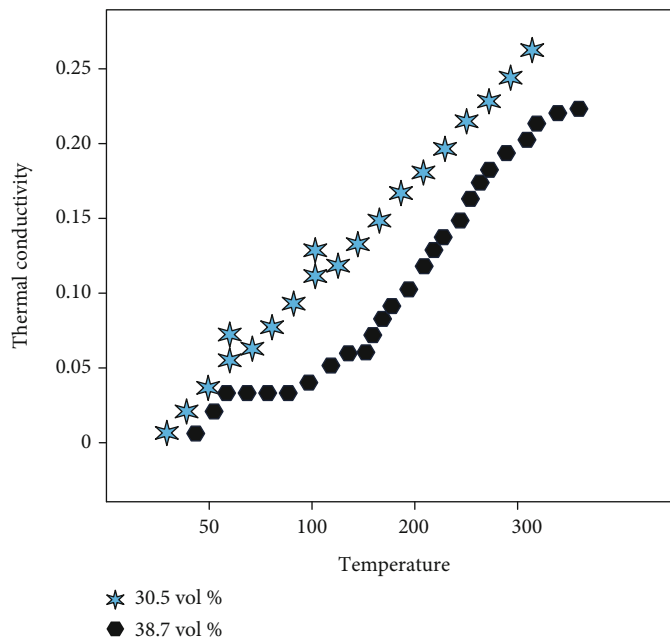
FIGURE 8: The expansion ratio of composites with different carbon fiber volume fractions as a function of temperature.

sports becomes more and more intense, the requirements in the field of rackets are also increasing.

As shown in Table 4, the interface problem of metal matrix composites has always been a hot and difficult problem in research, and the bonding state between the interfaces has an important impact on the performance of the composites. The interface between carbon fiber and copper has high interfacial energy, which will lead to poor wettability between carbon fiber and copper. This poor wettability

results in the simple mechanical bonding of the interface between carbon fiber and copper, and it is difficult to prepare carbon fiber composites with good interfacial bonding, which limits its performance.

The sintering temperature also has a great influence on the thermal conductivity of the composites, and the thermal conductivity changes with the increase of the sintering temperature, and the density is the same. With the increase of sintering temperature, the thermal conductivity first

(a)

(b)
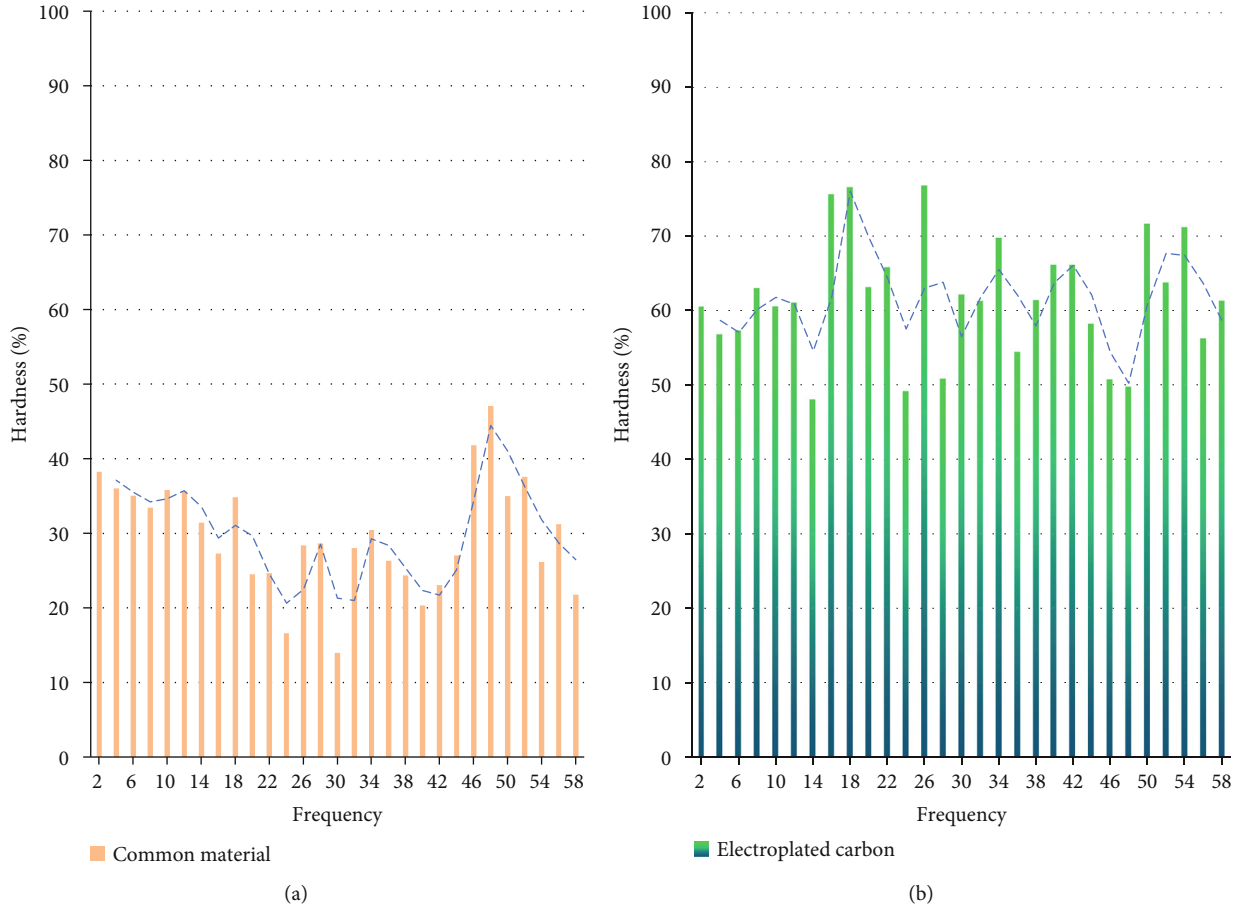
FIGURE 9: Bearing capacity of badminton rackets of different materials under the same force. (a) Bearing capacity of badminton racket made of ordinary material. (b) Bearing capacity of badminton racket made of electroplated carbon material.

increases and then decreases and reaches the maximum value at 950°C. The effect of sintering temperature on the composites is shown in Figure 7.

It can be seen from Figure 7 that when the test temperature is relatively low, the thermal expansion difference between the composite materials formed by different sintering temperatures is very small, and as the test temperature increases, the difference becomes larger and larger. The average thermal expansion of the samples sintered at 950°C is the largest, and the average thermal expansion of the samples sintered at 850°C is the smallest.

It can be seen from Figure 7 that the density has an important influence on the thermal conductivity of the composite material; the higher the density p, the higher the thermal conductivity of the material. The effect of porosity λ on composites is

$$\lambda = \lambda_s (1 - p) \tag{18}$$

The relationship between the expansion ratio and temperature of the composites with different carbon fiber volume fractions is shown in Figure 8.

It can be seen from Figure 8 that with the increase of the volume fraction of carbon fibers, the expansion rate of the composite material shows a decreasing trend. Objects

TABLE 5: Comparison of the bearing capacity of badminton rackets of different materials.

	Pressure	Affordability	Level of damage
Wooden racket	30	28%	54%
Iron beat	30	32%	58%
Steel and aluminum	30	40%	43%
Carbon aluminum racket	30	65%	28%
Carbon racket	30	89%	12%

expand and contract due to changes in temperature. The change in length magnitude caused by a unit temperature change is expressed by the thermal expansion coefficient. When the volume fraction of carbon fiber volume fraction increases, the thermal expansion coefficient of the composite becomes smaller. On the other hand, the addition of carbon fiber to the matrix will form the interface and internal stress, which will affect the thermal expansion of the composite. With the increase of carbon fiber content, the interface and internal stress will increase, and the influence on thermal

expansion will be greater, so the thermal expansion coefficient will also decrease.

Direct electroplating-hot pressing is a good method for preparing short carbon fiber composites. Carbon fibers overlap each other in the process of electroplating and maintain uniform dispersion in the subsequent cleaning, drying, and hot pressing processes and can prepare composite materials with uniform distribution of carbon fibers.

4.2. Experiment and Analysis of Electroplated Carbon Badminton Racket. After the electroplated carbon badminton racket is produced, its durability needs to be tested through actual use. Hardness, bearing capacity, etc. all need to be verified. In order to enhance the scientificity of the test, this paper conducted an experiment on a badminton coach to let him use badminton rackets of different materials and test the endurance of badminton rackets under the same force, so as to compare their hardness and draw conclusions. The bearing capacity of badminton rackets of different materials under the same force is shown in Figure 9.

As shown in Figure 9, when testing the flexibility, mechanical bending equipment can be used to apply pressure to badminton rackets of different materials and compare their ability to withstand the same pressure. In this paper, experiments were carried out on wooden, iron, steel, steel-aluminum, carbon-aluminum, and carbon bats, as shown in Table 5.

As shown in Table 5, the bearing capacity of wooden, iron, steel, steel-aluminum, carbon-aluminum, and carbon beats under the same pressure was analyzed. It is found that only the carbon racket has a relatively high bearing capacity and a relatively low degree of damage, so now the mainstream material of the racket is mainly carbon racket. The racket made of this material is of good quality and light weight, which can make athletes swing faster and use less effort. Due to the influence of other factors, such as users, use environment, and frequency of use, the results of this experiment are not completely reliable, and there are certain differences.

5. Conclusions

With the development of science and technology, people's quality requirements for various things are getting higher and higher. The development of China's aviation industry is inseparable from the contribution of carbon fiber composite materials. Carbon fiber composites have been widely used in many fields because of their good properties. This article first gives a general introduction to carbon fiber composite materials and electroplated carbon so that people can understand the properties and principles of the two and then use the relevant chemical formulas to analyze their properties. Finally, it is found that both have super-strength properties. In the experimental part, this paper compares the physical properties of electroplated carbon and different reinforcing materials and draws the conclusion that the fatigue strength of carbon fiber composites is much higher than that of metal materials. Then, the hardness and bearing capacity of electroplated carbon badminton rackets were compared. Under

the same force and pressure, the electroplated carbon badminton racket is not only more durable, but also harder than other badminton rackets. Therefore, it is very necessary to study the preparation and performance of electroplated carbon badminton rackets.

Data Availability

The data that support the findings of this study are available from the corresponding author upon reasonable request.

Conflicts of Interest

The authors declare that they have no conflicts of interest.

References

[1] N. Mizuno, T. Makishima, K. Tsuge, S. Kondo, and S. Yamakawa, "Development of automatic badminton playing robot with distance image sensor," *IFAC-PapersOnLine*, vol. 52, no. 8, pp. 67–72, 2019.

[2] J. Park, Y. H. Lee, I. D. Kong, J. S. Chang, T. Kim, and H. C. Lee, "Ultrasonographic changes of upper extremity tendons in recreational badminton players: the effect of hand dominance and comparison with clinical findings," *British Journal of Sports Medicine*, vol. 51, no. 4, pp. 370.1–37370, 2017.

[3] M. J. Duncan, C. Chan, N. D. Clarke, M. Cox, and M. Smith, "The effect of badminton-specific exercise on badminton short-serve performance in competition and practice climates," *European Journal of Sport Science*, vol. 17, no. 2, pp. 119–126, 2017.

[4] M. Dong, J. Lyu, T. Hart, and Q. Zhu, "Should agility training for novice badminton players be physically or perceptually challenging?," *The Journal of Sports Medicine and Physical Fitness*, vol. 59, no. 12, pp. 2015–2021, 2019.

[5] Z. Yuan, Z. Jia, Y. Gao, and Z. Ying, "Controllable synthesis of P(NIPAM-co-MPTMS)/PAA–Au composite materials with tunable LSPR performance," *Journal of Materials Science*, vol. 52, no. 16, pp. 9584–9601, 2017.

[6] J. Akhtar, A. Ali, I. Haq, J. Akhtar, and M. Zia, "Synthesis of ag-NPs impregnated cellulose composite material: its possible role in wound healing and photocatalysis," *IET Nanobiotechnology*, vol. 11, no. 4, pp. 477–484, 2017.

[7] N. Lewis and D. Nocera, "Powering the planet: chemical challenges in solar energy utilization," *Proceedings of the National Academy of Sciences of the United States of America*, vol. 103, no. 43, pp. 15729–15735, 2006.

[8] B. M. Dobratz, "Properties of chemical explosives and explosive simulants," *Llnl Explosive Handbook*, vol. 51, no. 3-4, pp. 339-340, 2018.

[9] W. A. Rutala and D. J. Weber, "Infection control and hospital epidemiology disinfection of endoscopes: review of new chemical sterilants used for high-level disinfection," *Infection Control and Hospital Epidemiology*, vol. 20, no. 1, pp. 282–288, 2017.

[10] Y. Zhang, X. Zhao, X. Zhang, and J. Sun, "The influence of chemically enhanced backwash by-products (CEBBPs) on water quality in the coagulation–ultrafiltration process," *Environmental Science and Pollution Research*, vol. 23, no. 2, pp. 1805–1819, 2016.

[11] T. Murata and J. Batkhuu, "Biological activity evaluations of chemical constituents derived from Mongolian medicinal forage plants and their applications in combating infectious diseases and addressing health problems in humans and livestock," *Journal of Natural Medicines*, vol. 75, no. 4, pp. 729–740, 2021.

[12] S. Baeckens, K. Huyghe, R. Palme, and R. V. Damme, "Chemical communication in the lacertid lizardPodarcis muralis: the functional significance of testosterone," *Acta Zoologica*, vol. 98, no. 1, pp. 94–103, 2017.

[13] J. Brunink, J. R. Haak, J. G. Bomer, D. N. Reinhoudt, M. A. Mckervey, and S. J. Harris, "Chemically modified field-effect transistors; a sodium ion selective sensor based on calix[4]arene receptor molecules," *Analytica Chimica Acta*, vol. 254, no. 1-2, pp. 75–80, 1991.

[14] Y. Zhang, Y. Li, and C. Bai, "Microstructure and oxidation behavior of Si-MoSi$_2$ functionally graded coating on Mo substrate," *Ceramics International*, vol. 43, no. 8, pp. 6250–6256, 2017.

[15] M. Hayyan, M. A. Hashim, and I. M. Alnashef, "Superoxide ion: generation and chemical implications," *Chemical Reviews*, vol. 116, no. 5, pp. 3029–3085, 2016.

[16] L. Zeng, J. Shi, J. Luo, and H. Chen, "Silver sulfide anchored on reduced graphene oxide as a high -performance catalyst for CO$_2$ electroreduction," *Journal of Power Sources*, vol. 398, pp. 83–90, 2018.

[17] T. P. Guinee and P. F. Fox, "Salt in cheese: physical," *Chemical and Biological Aspects. Cheese*, vol. 1, no. 4, pp. 317–375, 2017.

[18] M. N. Bhuiyan, J. U. Chowdhury, and J. Begum, "Chemical investigation of the leaf and rhizome essential oils of Zingiber zerumbet (L.) Smith from Bangladesh," *Bangladesh Journal of Pharmacology*, vol. 4, no. 1, pp. 9–12, 2017.

[19] S. Szopa, B. Aumont, and S. Madronich, "Assessment of the reduction methods used to develop chemical schemes: building of a new chemical scheme for VOC oxidation suited to three-dimensional multiscale HOx-NOx-VOC chemistry simulations," *Atmospheric Chemistry and Physics Discussions*, vol. 5, no. 1, pp. 2519–2538, 2017.

[20] T. Ruedas and D. Breuer, "On the relative importance of thermal and chemical buoyancy in regular and impact-induced melting in a Mars-like planet," *Acta Materialia*, vol. 51, no. 16, pp. 4679–4691, 2017.

[21] L. Zeng, X. P. Guo, G. A. Zhang, and H. X. Chen, "Semiconductivities of passive films formed on stainless steel bend under erosion-corrosion conditions," *Corrosion Science*, vol. 144, no. 1, pp. 258–265, 2018.

[22] M. Romaniello, F. Primas, M. Mottini, M. Groenewegen, G. Bono, and P. Francois, "The influence of chemical composition on the properties of Cepheid stars," *Astronomy & Astrophysics*, vol. 488, no. 2, pp. 731–747, 2008.

[23] T. Hueckel, M. Ciantia, B. Mielniczuk, M. S. El Youssoufi, and L. B. Hu, "Modeling physico-chemical degradation of mechanical properties to assess resilience of geomaterials," *Journal of Non-Crystalline Solids*, vol. 27, no. 2, pp. 273–283, 2017.

[24] J.-H. Lee and E.-J. Jae-Moon, "A study on the recognition of badminton brand using big data analysis," *Korean Journal of Sport Science*, vol. 26, no. 3, pp. 125–137, 2017.

Hindawi

Research Article

Application and Microstructure Properties of Nanomaterials in New Concrete Materials

Jialu Zhang [1,2] Cheng Shen,[3] and Guangfen Diao[1,4]

[1]*Nanjing Forestry University, Nanjing, 210000 Jiangsu, China*
[2]*Nanjing Jiangbei New Area Railway Construction Investment Co., Ltd, Nanjing, 210000 Jiangsu, China*
[3]*Jiangsu Testing Center for Quality of Construction Engineering Co., Ltd, Nanjing, 210000 Jiangsu, China*
[4]*Nantong Jiarun Holding Group Co., Ltd, Nantong, 226311 Jiangsu, China*

Correspondence should be addressed to Jialu Zhang; gracezhang@njfu.edu.cn

This article takes the application of nanomaterials in new concrete materials as the research object and explores the defects of nanomaterials in improving the toughness and tensile capacity of traditional concrete by analyzing the effects of nanomaterials on the structure and properties of new concrete. This article takes the application of nano-SiO_2 in new concrete materials as an example. Firstly, the experiment of preparing nanoconcrete was carried out, and then, aiming at the experimental results, a detailed analysis and discussion on the effects of nano-SiO_2 on the shrinkage, mechanical properties, and microstructure of the new concrete materials were carried out. The research results show that the cement paste with nano-SiO_2 is much better in chemical shrinkage than the cement paste without admixture, and the chemical shrinkage value of the cement paste with nano-SiO_2 increases significantly in the early setting stage. The chemical shrinkage values are 11.4%, 26.7%, 53.9%, and 94.2%, respectively, according to the amount of nano-SiO_2 added. With the extension of the setting period, the growth rate of the shrinkage value of cement paste slows down; nano-SiO_2 can improve the compressive capacity and strength of concrete, and with the increase of the amount of compressive strength, the value of compressive strength is also increasing. In the early stage of coagulation, when the nano-SiO_2 dosage is 1.6%, the compressive strength of the coagulation for 3 days is 39.02%. With the prolongation of the setting period, the increase in compressive strength continues to increase, but the growth rate slows down; the addition of nano-SiO_2 has changed the microstructure of concrete. Nano-SiO_2 has high pozzolanic activity, which can promote the hydration process of cement, and because of the small particles, it can fill the voids of concrete, thereby improving its compactness and mechanical strength.

1. Introduction

1.1. Background and Significance. In recent years, with the rapid development of the social econoour, the process of industrialization and urbanization has also been accelerating, which is manifested in the construction and improvement of various infrastructures. Concrete, as the most widely used construction material in the construction industry, has also been used in the largest amount. In recent years, its demand has also increased exponentially. However, due to the problems of insufficient toughness and tensile resistance caused by the components of concrete materials, many projects have collapsed and damaged, which has a major impact on casualties and property losses. Seeking new building materials and improving the quality of building materials are the demands of many parties.

Nanomaterials were born in the 1960s and have been widely used since the 21st century. For example, it has played a huge application value in medical, chemical, electronic industry, and biochemical fields. It is a new type of material with excellent physical and chemical properties, which is different from the atomic and molecular characteristics of microscopic particles and different from macroscopic objects. Nanomaterials are mesoscopic structural materials with singular characteristics [1]. Because of their small size, they exhibit strange properties that neither

microscopic particles nor macroscopic objects possess. The development of nanomaterial technology is a revolution in the history of materials science and construction engineering [2]. Its unique properties of light, electricity, heat, and magnetism have had a huge impact on the development of the construction industry and civil engineering. Adding nanomaterial into traditional concrete and other building materials to change the composition structure of traditional concrete can greatly improve the mechanical properties and durability of new concrete, thereby improving its toughness and tensile capacity [3].

1.2. Related Work. Since the advent of nanomaterials in the 1960s, more and more experts and scholars have paid attention to it due to its special properties. Huang and Lovell pointed out that nanomaterials have been widely used as reagents for therapeutic and diagnostic (therapeutic) applications. They note that research efforts in nanomaterials have changed beyond the in vitro investigation of emerging substances to the conception of substances that work on more contextually relevant patterns of animal disorders, thus multiplying the opportunity for therapeutic clinical conversion. Common categories of nanoscale biomaterials, consisting of magneto nanoparticles as well as volume particles, upswitched granules, dielectric silica granules, charcoal-based granules, and organochromatic dye-based granules, exhibit the diagnostic and therapy applications of biomaterials. Changes like dimensional manipulation and process surface modification allow for regulation of ecological compatibility and interaction from the intended organization. Demands for better treatment for testing disorders and intensified chemical therapies, as well as practical thoughts on the need for climatologically scalable nanomaterials, are set to be crucial drivers [4]. Xiangzhen et al. have also stated that temporary structural failures frequently occur in dynamic tension (e.g., spalling) when reinforced structures are loaded by detonating and impact velocity charges. The precise forecast of structural failure due to static forces is known to be a competitive issue. In their study, they suggest a nonlocal damage-dependent modelling to forecast temporary elastic failure of specific concrete material building on the relatively recently developed localized porous square product model. In this nonlocal pattern, the interference fields diminish as the extent of insolation grows, and this results in an ideal characterization of the total damage area and the free surface localization, i.e., the lack of localization disappears in such areas. The statistical illustrations of one-dimensional peel tests and two-dimensional dynamic tension tests on concrete slabs show that a less damage-dependent nonlocal model can address the full range of restrictions of the primal nonlocal market. A general model predicated on nonlocal injuries was then validated on the basis of two experiments, the divided Hopkinson extension lever test and the adapted divided Hopkinson lever (scattered) trial. Mathematical demonstrations indicate that the suggested nonlocal induction model can provide a sensible estimate of the location of mechanical dynamic tension failure. However, the topographic example does not properly forecast dynamic tension failure, while the primitive nonto-

pographic model does not forecast several cracks at high load rates [5]. The advantages of nanomaterials in construction have only emerged in recent years. Therefore, there is not much research on nanomaterials in the construction industry. Based on this, it is very meaningful to study the application of nanomaterials in new concrete materials.

1.3. Innovation in This Article. The innovations in this article are mainly reflected in the following aspects: (1) It is proposed to apply nanomaterials to new types of concrete. The excellent properties of nanomaterials can effectively improve the defects of traditional concrete toughness, tensile strength, compression, and insufficient durability. (2) Take nano-SiO_2 as an example through experiments to specifically explore the influence of nanomaterials on the performance and structure of concrete, turn abstraction into concrete, and make the article easy to understand. The article provides a suggestion for optimization and improvement of concrete materials in the construction industry and can also provide new ideas for the research of nanomaterials.

2. Nanomaterial and Their Application in New Concrete Materials

2.1. Nanomaterials. Nanomaterials are a new and hot new material science in the past two years and have received extensive attention and research from all walks of life since its inception. It refers to a material that is at least one-dimensional in the three-dimensional space at the nanometer level. Because of its small size, it exhibits singular characteristics that are very different from the atoms and molecules of microscopic particles and macroscopic objects. The form of particles between microscopic atoms and macroscopic individuals. The size of nanomaterials is in the range of 1-100 nm, which is equivalent to the scale of 10-1000 atoms closely packed together [6, 7].

2.1.1. Characteristics and Effects of Nanomaterials. Nanomaterial particles are small and larger than the surface volume. When the diameter of the nanoparticle is 10 nanometers, the body of the nanoparticle contains more than 4000 atoms, and the atoms on the surface account for 40%; when the diameter of the particle drops to 1 nanometer, the particle body contains 30 atoms, and the body surface atoms will account for 99%, which means that almost all the atoms are concentrated on the surface of the particle [8, 9]. The number of atoms on the surface of the nanoparticles and the total number of atoms increase dramatically with the reduction of the diameter of the nanoparticles. This strange characteristic has led to the nanomaterials having many special properties that are not available in general materials, manifested in various effects, as follows:

First: surface and interface effects. The so-called surface and interface effects are manifested in the phenomenon that the number and total number of surface atoms of nanomaterial particles will increase sharply and violently as the diameter of nanoparticles becomes smaller. When the diameter of the nanoparticle is 10 nanometers, the number of atoms on the surface of the particle will occupy 40%, and as the

diameter of the particle continues to decrease, the percentage of its surface atoms will increase significantly; when the diameter of the nanoparticle continues to decrease to about 1 nanometer, the percentage of atoms on the surface will increase to more than 90%, and then, all the atoms contained in the particles will be concentrated on the surface. Due to the violent increase in the number of surface atoms, particles will have extremely high surface energy, easily combine with other atoms, and will have high stability and chemical activity [10].

Second: small size effect. The external morphology of nanomaterials is a tiny crystalline particle. In terms of individual particle morphology, nanomaterials are similar to atoms and molecules in the microscopic world, but from the surface of the entire nanomaterial, it has the ability to be compared with macroscopic objects. It has a huge body surface area. Therefore, nanomaterial is a kind of special material body which is different from microscopic particles and macroscopic individuals. For ultrafine particles such as nanomaterials, the size becomes smaller and the body surface area increases, which produces various peculiar properties and also significantly improves its strength, toughness, and hardness, showing greater than other materials. The advantages are reflected in its acoustic, optical, electrical, thermal, and magnetic properties. For example, the combination of nanomaterials and metal materials makes the nanometals much harder than normal normal metals; the combination of calcium fluoride and nanomaterials can bend flexibly at room temperature without breaking, etc. [11, 12].

Third: quantum size effect. When a nanomaterial with a large specific surface area is split into discrete energy levels from the continuous energy band, the spacing between energy levels will increase as the particle size decreases. When the spacing between energy levels is greater than thermal energy, electrical energy, or magnetic field energy, nanomaterial particles will produce a series of anomalous properties that are different from macroscopic and microscopic particles, that is, the quantum size effect of nanomaterials [13].

Fourth: macro quantum tunnel effect. The ability of microscopic particles to penetrate the barrier is called tunneling. And for ultrafine particles such as nanomaterials, due to their special magnetization, it also has this kind of tunneling effect. The ability of nanomaterials to penetrate the barriers of the macroscopic system but change their own special properties is called the macroscopic quantum tunneling effect of nanoparticles [14].

Fifth: volume effect. The volume of nanomaterial particles is very small, and the number of atoms contained in the body is very small. Therefore, it is impossible to describe many phenomena with the mass of infinite atoms. This is the volume effect of nanomaterials [15].

2.1.2. Classification of Nanomaterials. With the deepening of research, nanomaterials are now mainly divided into the following categories:

First: nanoceramics. Nanoceramics use nanotechnology to incorporate nanopowder into ordinary engineering ceramics to change the properties of ordinary ceramic materials, so that the finished ceramic products have higher flexibility, hardness, and strength and overcome the problems of traditional ceramics that are brittle and fragile [16, 17].

Second: nanopowder. Nanopowder refers to powder or particles with a diameter of less than 100 nm and is a solid particulate material between microscopic particles and macroscopic objects.

Third: nanofibers. Nanofiber is a linear material with a diameter between 1 and 100 nm and a long length. It is mainly used for the manufacture of components of quantum computers and photonic computers in the future.

Fourth: nanofilm. Nanofilm is divided into granular film and dense film. A particle film is a thin film that sticks to nanoparticles with a small gap in the middle; a dense film refers to a film with a tight film layer and a particle size of nanometers.

Fifth: nanoblock. Nanoblocks are nanocrystalline materials that are shaped by nanopowder by high pressure or crystallized by metal liquid. It is mainly used for ultrahigh strength materials and smart metal materials [18, 19].

2.2. New Concrete Materials. It is the most widely used and most used building material in the construction industry. The traditional concrete is mainly made of cement, with the addition of aggregates such as water, stones, and sand. If necessary, chemical admixtures and mineral admixtures (such as fly ash and mineral powder) are added, and they are evenly distributed according to the appropriate ratio. The condensed artificial stone made of agitation is a basic building material. For a long time in the past, concrete has been used for the construction of housing infrastructure projects due to its fire resistance, compression resistance, and extremely convenient characteristics in production and use. It has also been used to this day. However, with the development of social technology and the continuous improvement of people's requirements for the quality of building materials, some problems of traditional concrete, such as poor toughness and weak tensile capacity, have gradually been exposed. Traditional concrete can no longer meet the needs of the current society. Looking for new energy materials or new technologies to improve the performance of traditional concrete has become an important research direction in the construction industry and civil engineering and other fields [20, 21].

New concrete is based on traditional concrete materials using modern technological means or adding new material energy, so that the structural composition and performance of traditional concrete can be changed, and its aspects such as toughness, tensile strength, mechanical properties, and durability are improved. Performance of an improved building material [22]: compared with traditional concrete, the new type of concrete shows more powerful performance advantages. At present, new concrete is mainly made of nanotechnology and nanomaterials to improve traditional concrete [23].

2.3. Application of Nanomaterials in New Concrete Materials. Due to its small particle size and large body

surface area, nanomaterials can show strong hardness, strength, and toughness when combined with other atoms. The combination of concrete and nanomaterials can well solve its lack of toughness and tensile strength problem. As mentioned earlier, there are different classifications of nanomaterials, and nanomaterials used in concrete materials are also diverse. The main applications are mainly the following:

First: *the application of nanometer ore powder in new concrete materials.* Nanomaterials have special properties such as surface and interface effects, small size effects, quantum size effects, macroscopic quantum tunneling effects, and volume effects. Therefore, when combined with other materials, they can give the combined materials different properties from traditional materials. The nanometer ore powder added to the new concrete mainly includes nanometer SiO_2, nanometer CaCO3, and nanometer silicon powder. Using nanotechnology to add nanometer ore powder to the concrete makes its atomic structure into nanometer level, which can greatly improve the strength and hardness of the concrete, toughness, and durability [24].

Second: *the application of nanometal powder in new concrete.* Nanometal powder has the characteristics of high strength, high hardness, and good plasticity. At the same time, because of its surface effect and good activity, it can be added to concrete to produce functional electromagnetic shielding concrete. However, since there are many types of nanometal powders, to make the best electromagnetic shielding concrete, the appropriate nanometal nonpowder must be selected [25, 26].

Third: *the application of nanometal oxides in new concrete materials.* The use of nanometal oxides can make smart cement concrete, such as self-alarm devices. The addition of nanometal oxides can make the concrete have a strong conductive function. If a sensor made of nanometal oxides is inserted into the concrete, then the concrete will be able to realize the alarm and monitoring functions of the outside world [27, 28].

Fourth: *the application of nanocomposites in new concrete materials.* Nanocomposite is a new type of material developed based on the combination of basic nanomaterials and other materials. Adding nanocomposites to concrete can not only improve the compressive strength, tensile strength, and ductility of concrete but also improve durability of concrete [29, 30].

3. Preparation Experiment of Nanoconcrete

Nanomaterials are widely used in new concrete materials. Based on the different types of nanomaterials, the nanoadditives mixed in concrete materials are also different, and different nanoadditives have shown to improve the performance of concrete materials. In order to specifically analyze the improved performance of nanomaterials on concrete properties, this paper selected nano-SiO_2 as a nanoadditive added to new concrete materials for experimental research.

3.1. Experimental Object and Purpose. In this experiment, the application of nano-SiO_2 in new concrete materials was taken as the research object and theme of the experiment, and the purpose was to explore the effects of nano-SiO_2 on the shrinkage performance, mechanical properties, internal structure, durability, and other aspects of the new concrete materials.

3.2. Raw Materials Used in the Experiment

3.2.1. Cement. Cement is the basic material of concrete, accounting for the largest proportion. The cement used in this experiment is ordinary Portland cement, and its main components and properties are shown in Tables 1 and 2.

3.2.2. Aggregate. The aggregate of concrete is composed of coarse aggregate and fine aggregate. The coarse aggregate used in this experiment is broken limestone, and the fine aggregate is siliceous natural river sand.

3.2.3. Chemical Admixture. The chemical admixture is added to improve the performance of the concrete and make it more suitable for the external service environment. Commonly used chemical admixtures are water reducing agents, which are divided into fatty acid salt series, naphthalene sulfonate series, melamine resin series, sulfamate series, and polycarboxylate series. The naphthalene sulfonic acid is used in this experiment. Water reducer, swelling agent, and UEA swelling agent are also used in this experiment.

3.2.4. Mineral Admixture. Whether the concrete has good tensile strength, durability and corrosion resistance has a decisive relationship with its mineral admixture. The performance of the mineral admixture can directly affect the performance of the concrete, so the mineral admixture added to the concrete is selected. Mixing is very important. The mineral admixtures used in this experiment are ore powder and fly ash, and their chemical composition is shown in Table 3.

3.2.5. Nanomaterial. The nanomaterial used in this experiment is nano-SiO_2 in nanoore powder. Its example diameter is between 6 and 50 nm, the specific surface area is 250⊠/g, and the purity is greater than 99%.

3.2.6. Water. It is general civilian tap water.

3.3. Experimental Steps and Methods

3.3.1. Measuring the Density and Specific Surface Area of Cement, Mineral Powder, and Fly Ash. *Step 1.* Place the cement, ore powder, and fly ash samples in an oven to dry, and then, put them in a desiccator to cool to room temperature.

Step 2. Pour appropriate amount of anhydrous kerosene into the pycnometer, the volume is between 0 and 1 ml, then close the lid tightly and place it in a constant temperature water bath, and take out the recorded reading V_1 after 20 minutes.

Step 3. Wipe the upper part of the pycnometer not in contact with kerosene, then pour 60 g of cement, mineral powder, and fly ash samples, and use ultrasonic vibration until there are no more air bubbles in the bottle.

TABLE 1: Chemical composition of cement.

Chemical composition (%)	SiO$_2$	CaO$_3$	Al$_2$O$_3$	MgO3	Fe$_2$O$_3$	SO$_3$
Content	21.3	52.14	6.52	3.18	3.77	4.98

TABLE 2: Properties of cement.

Setting time		Stability	Compressive strength (MPa)		Flexural strength (MPa)	
Initial setting	Final setting	Qualified	4D	27D	4D	27D
2.5 h	3.5 h		25.7	50.0	5.5	8.7

TABLE 3: Chemical composition of mineral powder and fly ash.

Chemical composition (%)	SiO$_2$	CaO$_3$	Al$_2$O$_3$	MgO3	Fe$_2$O$_3$	SO$_3$
Mineral powder	31.12	34.45	14.23	11.45	0.31	2.47
Fly ash	61.34	2.13	28.12	0.82	5.04	0.36

Step 4. Put the pycnometer in the constant temperature water bath again, read V2 after 20 minutes, and then use formula (1) to calculate the density of cement, mineral powder, and fly ash.

$$\rho = \frac{P}{V_2 - V_1}, \tag{1}$$

where ρ stands for density, P stands for mass, V_1 stands for the first reading, and V_2 stands for the second reading.

Step 5. Use the density of cement, mineral powder, and fly ash calculated in the above steps and formula (2) to calculate the quality of the sample, and then, place the sample in the automatic specific surface area measuring instrument to measure the specific surface area, a total of three measurements. Then, go to the average.

$$W = \rho V (1 - \varepsilon), \tag{2}$$

where W represents the sample mass of cement, mineral powder, and fly ash, ρ represents the sample density, V represents the volume of the particle film layer, and ε represents the porosity of the film layer.

3.3.2. Measuring the Packing Density and Porosity of Sand and Gravel. Step 1. Take a 3 L sample of sand and stone in an oven and dry it; then, cool to room temperature.

Step 2. Remove the excessively large sand and gravel, and then, divide the rest into two parts of the same quality.

Step 3. Take one of them and put it into the volume cylinder twice before and after. Each time it is installed, a cylindrical steel pipe with a diameter of 10 mm is put into the cylinder to hit the ground. The steel pipe is perpendicular to the ground during the impact, about 20-25 hits.

Step 4. After the impact is completed, load another sample into the cylinder until it exceeds the mouth of the cylinder, and smooth the cylinder mouth with a ruler.

Step 5. Weigh the total weight of the sample and the volumetric cylinder to calculate the packing density and porosity of the gravel.

3.3.3. Mixing Cement. Step 1. Nano-SiO$_2$ is placed in water and dispersed with ultrasound for 5 minutes.

Step 2. Put cement, mineral powder, fly ash, and chemical admixture weighed according to a certain proportion into the pure paste mixing pot and stir slowly for 3 minutes.

Step 3. Put the ultrasonically treated nano-SiO$_2$ into the stirring pot, stir slowly for 1 minute and a half, then let it stand for 10 s, and then stir quickly for 1 minute.

Step 4. Put the well-mixed clean mud into the mold, and let it stand after setting.

Step 5. To prepare concrete, first, put nano-SiO$_2$ into water and disperse it with ultrasonic wave for 5 minutes.

Step 6. Put cement, mineral powder, fly ash, chemical admixture, and coarse and fine aggregate weighed according to a certain proportion into the concrete mixing pot and mix slowly for 6 minutes.

Step 7. Pour in nano-SiO$_2$ treated with ultrasonic wave and stir for 5 minutes.

Step 8. Pour the mixed concrete into the mold and set it under high pressure and then let it stand for curing.

4. Analysis of the Influence of Nanomaterials on the Performance of New Concrete Materials

In the third part of the article, we used nano-SiO$_2$ as a specific example to conduct the preparation experiment of nanoconcrete. The experimental results show that the addition of nano-SiO$_2$ changed the chemical composition of the original traditional concrete, greatly improved its chemical and physical properties, and showed the excellent performance that traditional concrete does not have. In this chapter, we will make a specific analysis and discussion on
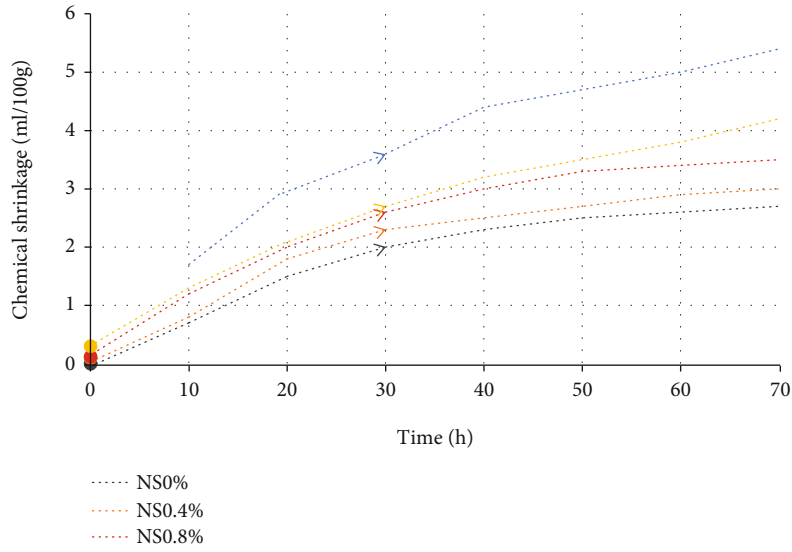
FIGURE 1: Chemical shrinkage of cement paste after 4 days of setting.
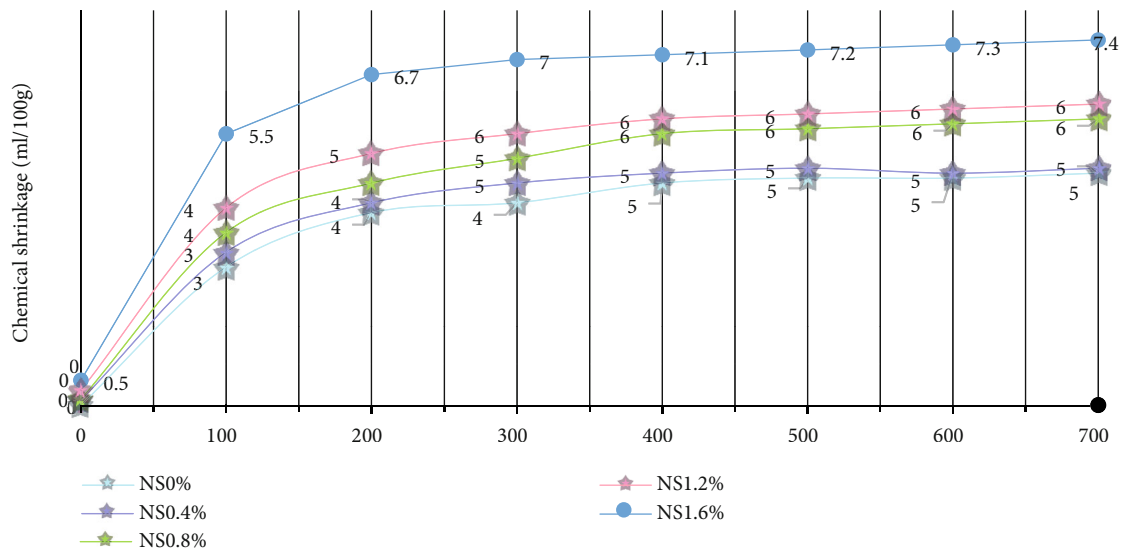
FIGURE 2: Chemical shrinkage of cement paste after 27 days of condensation.

TABLE 4: Concrete mix ratio.

NS content	Water	Cement	Gravel	Water reducer and swelling agent	Mineral powder and fly ash
NS0%	165	623	650	12.65	114
NS0.4%	165	621.7	650	12.65	114
NS0.8%	165	617.8	650	12.65	114
NS1.2%	165	624	650	12.65	114
NS1.6%	165	619.55	650	12.65	114

the improvement of nano-SiO$_2$ on the performance of new concrete materials.

4.1. Effect of Nano-SiO$_2$ on Chemical Shrinkage of Cement Paste.

Nano-SiO$_2$ has high pozzolanic activity. Adding it to cement paste can shorten the setting time of cement paste and reduce its fluidity, which is very helpful for improving the strength of cement. In order to deeply analyze the effect of nano-SiO$_2$ on the chemical shrinkage of cement paste, we mixed four different amounts of nano-SiO$_2$ (0.4%, 0.8%, 1.2%, and 1.6%) into the preparation of cement paste and record the chemical shrinkage value of each setting period and compare it with the cement paste without nano-SiO$_2$. The results are shown in Figures 1 and 2.

From Figure 1, we can see that the cement paste added with nano-SiO$_2$ has a much faster chemical shrinkage value than the cement paste without nano-SiO$_2$, and the chemical shrinkage effect is significant. The chemical shrinkage value of cement paste of SiO$_2$ increases rapidly, and the chemical shrinkage value gradually increases with the increase of the amount of nano-SiO$_2$ added. When the cement paste was set for 3 days, the amount of nano-SiO$_2$ added was 0.4%, 0.8%, 1.2%, and 1.6%. The corresponding chemical shrinkage values increased by 11.4%, 26.7%, 53.9%, and 94.2%, respectively. From Figure 2, we can see that the chemical shrinkage value of the cement paste doped with nano-SiO$_2$ increased significantly in the early stage, but with the increase of the setting time, the growth rate of the chemical shrinkage value slowed down, but it was still increasing. At 27 days of coagulation, the chemical shrinkage values of the cement pastes with nano-SiO$_2$ dosages of 0.4%, 0.8%, 1.2%, and 1.6% increased by 3.5%, 17.6%, 31.2%, and 58.9%, respectively. The cement paste doped with nano-SiO$_2$ has a significantly increased chemical shrinkage value than the undoped cement paste, and its chemical shrinkage value continues to increase with the increase of the added amount. This shows that nano-SiO$_2$ can affect the chemical shrinkage effect of cement paste and reduce its setting time, and because of its high pozzolanic activity, it is also conducive to improving the compactness and uniformity of cement paste.

4.2. Effect of Nano-SiO$_2$ on the Compressive Capacity of New Concrete.

In order to study the effect of nano-SiO$_2$ on the compressive capacity and strength of new concrete, after keeping the water, aggregate, chemical admixture, and mineral admixture constantly, we make four kinds of nano-SiO$_2$ (0.4%, 0.8%, 1.2%, and 1.6%) instead of cement to add to concrete, the compressive strength of the setting time on the 3rd, 7th, 28th, and 60th days was tested, and at the same time, it is compared with the compressive strength of concrete without nano-SiO$_2$. The combination of concrete with different amounts is shown in Table 4, and the compressive strength of concrete in each setting period is shown in Table 5 and Figure 3.

It can be seen from Table 5 and Figure 3 that the addition of nano-SiO$_2$ can significantly improve the compressive strength of concrete in the early setting stage, and as the amount of admixture increases, the compressive strength

TABLE 5: Increased value of nano-SiO$_2$ content in concrete compressive strength.

NS content	3D	7D	28D	60D
NS0.4%	9.67	5.67	5.75	5.60
NS0.8%	18.25	11.25	12.13	12.11
NS1.2%	37.88	18.04	12.5	12.34
NS1.6%	39.02	20.19	13.01	12.86

increase value also continues to increase. When nano-SiO$_2$ is added, the amount is 1.6%, the compressive strength of the coagulation period is 3 days and 7 days, respectively, increased by 39.02% and 20.19%, but with the extension of the coagulation period, the increase in compressive strength is not large, and when the coagulation period is on the 60th day, its compressive strength increased by only 12.86%. This shows that nano-SiO$_2$ can improve the early resistance of concrete, but with the extension of time, its compressive performance becomes less obvious. The reason is that the nano-SiO$_2$ particles have a small volume and a large specific surface area, have high pozzolanic activity, and can react with calcium hydroxide produced by the hydration of cement in concrete to promote the hydration process of cement, thereby improving its coagulation. Because of its small volume, nano-SiO$_2$ can fill the voids in the concrete, improve the density of rice concrete, and thus improve the early compressive capacity and strength of concrete. However, as the amount of nano-SiO$_2$ added increases, its chemical shrinkage value will also increase, which slows the cement water process of the concrete, resulting in a decrease in the growth rate of the compressive strength of the concrete in the later period.

4.3. Effect of Nano-SiO$_2$ on the Microstructure of New Concrete.

Nano-SiO$_2$ has a variety of specific properties, and it can change the internal structure and composition of concrete materials when combined with new concrete materials. In order to explore the microstructure changes of concrete doped with nano-SiO$_2$, we have drawn the XRD pattern of the concrete before and after nano-SiO$_2$ is added, as shown in Figure 4.

Figure 4 is the XRD pattern of the concrete before and after the nano-SiO$_2$ is added. From the figure, it can be seen that the diffraction peak of the internal structural components of the concrete changes greatly, which shows that after the nano-SiO$_2$ is added, the microstructure of the concrete has changed a lot. It promotes the hydration process of concrete cement, narrows the pores between concrete systems, makes the concrete components more closely connected, and is conducive to improving its mechanical strength.

5. Conclusions

In recent years, econooour has developed rapidly. Various real estate industries and infrastructure construction units have developed rapidly. Concrete, as the largest and most extensive building material, has become a very promising project. However, in today's modernized society, the
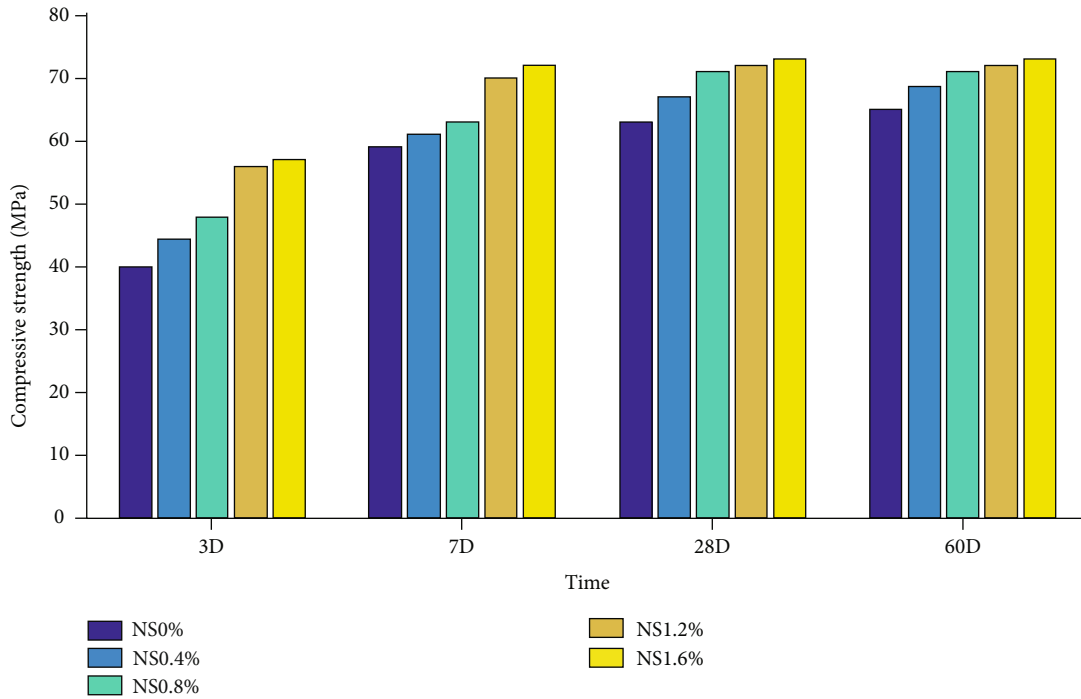
FIGURE 3: Compressive strength of concrete with different nano-SiO$_2$ content at each setting time.
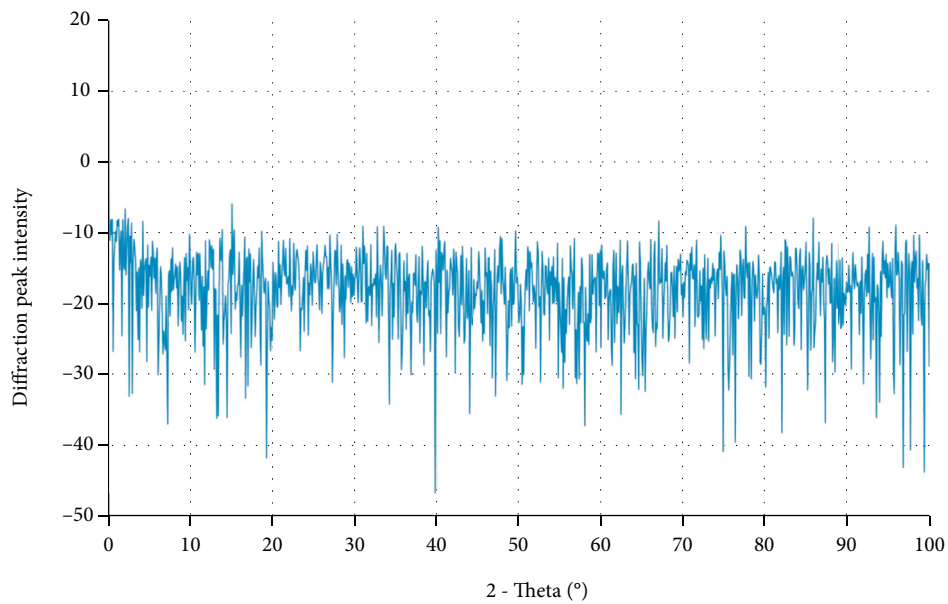
FIGURE 4: XRD pattern of concrete before and after incorporation of nano-SiO$_2$.

application requirements of concrete are getting higher and higher. Due to its structural composition, traditional concrete often shows poor toughness, insufficient compression and tensile capacity, and poor endurance in engineering construction. Unable to adapt to more severe service environment and other issues, it is particularly important to strengthen the improvement of the traditional concrete performance structure.

Nanomaterials are a new type of high-tech materials. Because of their small particle size and large specific surface area, they have special properties that many other materials do not have. The combination of nanomaterial and new concrete materials on the market can produce concrete materials with better performance effects, which have a great influence and help to improve the mechanical, chemical, and physical properties of concrete.

This study obtained through experimental analysis that nano-SiO$_2$ can significantly improve the chemical shrinkage value and compressive strength of concrete. Due to its high pozzolanic activity and small particle volume, it can fill the pores of concrete, improve its interface structure, and promote the compactness and compressive capacity of the concrete system. In short, the addition of nano-SiO$_2$ has greatly improved the performance of concrete and obviously improved its previous defects. Although the optimization of traditional concrete materials has been deeply studied in this paper by using nanomaterials, there are still many deficiencies. The depth and breadth of the research in this paper are not enough. In the process of this research, the selection and acquisition of experimental data are absolutely ideal. The completeness and effectiveness are not enough. Some interference factors involved in the experimental process are not considered. My academic level research is also limited. The research on the application of nanomaterials is still in the preliminary stage. In the future, in our work, we will study appropriate methods and means from more perspectives based on the existing technology and level and continuously improve the research content.

Data Availability

No data were used to support this study.

Conflicts of Interest

The authors declare that there are no conflicts of interest regarding the publication of this article.

References

[1] P. Wang, S. Wang, X. Zhang et al., "Rational construction of CoO/CoF2 coating on burnt-pot inspired 2D CNs as the battery-like electrode for supercapacitors," *Journal of Alloys and Compounds*, vol. 819, article 153374, 2019.

[2] J. Zhao, J. Huang, Y. Xiang et al., "Effect of a protective coating on the surface integrity of a microchannel produced by micro-ultrasonic machining," *Journal of Manufacturing Processes*, vol. 61, pp. 280–295, 2021.

[3] Y. Tang, Z. Chen, W. Feng, Y. Nong, C. Li, and J. Chen, "Combined effects of nano-silica and silica fume on the mechanical behavior of recycled aggregate concrete," *Nanotechnology Reviews*, vol. 10, no. 1, pp. 819–838, 2021.

[4] H. Huang and J. F. Lovell, "Advanced functional nano-materials for heranostics," *Advanced Functional Materials*, vol. 27, no. 2, p. 1603524, 2017.

[5] K. Xiangzhen, F. Qin, and H. Jian, "A new damage-based non-local model for dynamic tensile failure of concrete material," *International Journal of Impact Engineering*, vol. 132, no. -OCT., article 103336, 2019.

[6] Y. Shi and B. Zhang, "Correction: recent advances in transition metal phosphide nano-materials: synthesis and applications in hydrogen evolution reaction," *Chemical Society Reviews*, vol. 45, no. 6, pp. 1781–1781, 2016.

[7] L. Canesi and I. Corsi, "Effects of nano-materials on marine invertebrates. ence of the Total," *Environment*, vol. 565, no. -sep. 15, pp. 933–940, 2016.

[8] D. Bozyigit, N. Yazdani, M. Yarema et al., "Soft surfaces of nano-materials enable strong phonon interactions," *Nature*, vol. 531, no. 7596, pp. 618–622, 2016.

[9] T. Sun, N. A. Bornhöft, K. Hungerbühler, and B. Nowack, "Dynamic probabilistic Modeling of environmental emissions of engineered Nanomaterials," *Environmental Science & Technology*, vol. 50, no. 9, pp. 4701–4711, 2016.

[10] G. M. Deloid, J. M. Cohen, G. Pyrgiotakis, and P. Demokritou, "Preparation, characterization, and *in vitro* dosimetry of dispersed, engineered nanomaterials," *Nature Protocols*, vol. 12, no. 2, pp. 355–371, 2017.

[11] S. Choi, H. Lee, R. Ghaffari, T. Hyeon, and D. H. Kim, "Recent advances in flexible and stretchable bio-electronic devices integrated with nano-materials," *Advanced Materials*, vol. 28, no. 22, pp. 4203–4218, 2016.

[12] L. Jiang, Y. Liu, S. Liu et al., "Adsorption of estrogen contaminants by graphene nano-materials under NOM preloading: comparison with carbon nanotube, biochar, and activated carbon," *Environmental ence & Technology*, vol. 51, no. 11, pp. 6352–6359, 2017.

[13] K. Zheng, M. I. Setyawati, D. T. Leong, and J. Xie, "Antimicrobial silver nano-materials," *Coordination Chemistry Reviews*, vol. 357, no. FEB., pp. 1–17, 2018.

[14] P. Liu, R. Qin, G. Fu, and N. Zheng, "Surface coordination chemistry of metal nano-materials," *Journal of the American Chemical Society*, vol. 139, no. 6, pp. 2122–2131, 2017.

[15] A. H. Khan, S. Ghosh, B. Pradhan et al., "Two-dimensional (2D) nano-materials towards electrochemical nanoarchitectonics in energy-related applications," *Bulletin of the Chemical Society of Japan*, vol. 90, no. 6, pp. 627–648, 2017.

[16] G. Bo, L. Chang, H. Chenglong et al., "Effect of Mg and RE on the surface properties of hot dipped Zn–23Al–0.3 Si coatings," *Science of Advanced Materials*, vol. 11, no. 4, pp. 580–587, 2019.

[17] E. J. Hong, D. G. Choi, and M. S. Shim, "Targeted and effective photodynamic therapy for cancer using functionalized nano-materials," *Acta Pharmaceutica Sinica B*, vol. 6, no. 4, pp. 297–307, 2016.

[18] X. Cao, C. Tan, X. Zhang, W. Zhao, and H. Zhang, "Solution-processed two-dimensional metal dichalcogenide-based nano-materials for energy storage and conversion," *Advanced Materials*, vol. 28, no. 29, pp. 6167–6196, 2016.

[19] R. J. Moon, G. T. Schueneman, and J. Simonsen, "Overview of cellulose nano-materials, their capabilities and applications," *JOM*, vol. 68, no. 9, pp. 2383–2394, 2016.

[20] D. Elieh-Ali-Komi and M. R. Hamblin, "Chitin and chitosan: production and application of versatile biomedical nano-materials," *International journal of Advanced Research*, vol. 4, no. 3, p. 411, 2016.

[21] H. Ying, G. Xiang, and Y. Xinshun, "Defect repairs by new materials and new technology of marine wharf concrete," *Building Materials World*, vol. 38, no. 3, pp. 13–15, 2017.

[22] B. Gutarowska, R. Kotynia, D. Bielinski et al., "New sulfur organic polymer-concrete composites containing waste materials: mechanical characteristics and resistance to biocorrosion," *Materials*, vol. 12, no. 16, p. 2602, 2019.

[23] B. Körber, D. Stephan, and W. U. WiTraBau, "New materials developments for concrete pipes: opportunities and obstacles for industrial application," *Betonwerk + Fertigteil Technik*, vol. 83, no. 2, pp. 36–36, 2017.

[24] S. Fei, "The discussion on a new type of ultra high strength concrete materials to improve the bearing capacity of the

groove-shaped beam," *Shanxi Transportation Science & Technology*, no. 6, pp. 48–51, 2016.

[25] N. Beuntner and K. C. Thienel, "Calcined clays as alternative supplementary cementitious materials: new aspects of concrete technology pertaining to their use," *Betonwerk + Fertigteil Technik*, vol. 83, no. 2, pp. 50–50, 2017.

[26] Y. Ju, L. Wang, H. Xie et al., "Visualization of the three-dimensional structure and stress field of aggregated concrete materials through 3D printing and frozen-stress techniques," *Construction & Building Materials*, vol. 143, no. JUL.15, pp. 121–137, 2017.

[27] T. Xu, Q. Chen, Z. Zhang, X. Gao, and G. Huang, "Investigation on the properties of a new type of concrete blocks incorporated with PEG/SiO$_2$ composite phase change material," *Building and Environment*, vol. 104, no. aug., pp. 172–177, 2016.

[28] L. Kaiqing, X. Duotian, Y. Shijue, Z. Qiuhong, Z. Qingfeng, and Y. Xing, "Experimental study on the mix ratio of new ceramsite concrete materials," *Concrete*, no. 4, pp. 147–150, 2017.

[29] M. A. A. Aldandooh, N. M. Bunnori, M. A. M. Johari, A. Jamrah, and A. Alnuaimi, "Retrofitting of damaged reinforced concrete beams with a new green cementitious composites material," *Composite Structures*, vol. 142, no. May, pp. 27–34, 2016.

[30] X. Kong, Q. Fang, L. Chen, and H. Wu, "A new material model for concrete subjected to intense dynamic loadings," *International Journal of Impact Engineering*, vol. 120, no. OCT., pp. 60–78, 2018.

Research Article

Application of Spectroscopy Technology in Nanomaterials in Identification of Chinese Paintings

Lili Bai [ID],[1] **Heung Kou** [ID],[2] **and Zi Kong**[3]

[1]*College of Fine Arts and Design, Nanning Normal University, Nanning, 530100 Guangxi, China*
[2]*Faculty of Arts and Education, Sehan University, Jeollanam-Do, 57447 Mokpo, Republic of Korea*
[3]*Chinese Women Painters Association, China National Academy of Painting, Beijing, 100048 Beijing, China*

Correspondence should be addressed to Heung Kou; sehan668nn@163.com

The authenticity of calligraphy and painting is an important knowledge in the collection and research of Chinese painting and calligraphy. The identification of folk painting and calligraphy is usually conducted by experts and scholars engaged in cultural relics, archaeology, painting and calligraphy, and ancient buildings. Relying only on the identification of experience and literature and history, there are certain limitations, and it is difficult to form convincing. Spectroscopic technology mainly uses the characteristic spectral lines of molecules or atoms to judge the chemical composition and relative content of substances, so that different molecular structures of substances can be determined and distinguished; thus, it becomes an effective tool for exploring the molecular structure of substances; therefore, it has been widely used in nanomaterials, biomedicine, cultural relic identification, and other fields. Raman spectroscopy is the most common spectroscopic technique in scattering spectroscopy. When light passes through a material surface, in addition to light transmission and light absorption, light scattering can also be observed. In addition to the original incident light frequencies (Rayleigh scattering and Tyndall scattering), the scattered light also includes some new frequencies, which are called Raman scattering, and its spectrum is Raman spectrum. In this paper, Raman spectroscopy is used to study nanomaterials and calligraphy and painting, and the Raman spectra of real and fake calligraphy and painting, as well as the light absorption rate and degradation rate of nanomaterials at different temperatures, are analyzed experimentally. The results show that the Raman spectrum of the authentic calligraphy reaches the maximum when the wave number is 1000; the peak of the Raman spectrum of the authentic fresco reaches the maximum when the wave number is 1400. The average light absorption rate of nanomaterials in was 47.2%, and the average catalytic degradation rate was 53.6%; the average light absorption rate of nanomaterials was 68.9%, and the average catalytic degradation rate was 62.4%. There are obvious differences in peak shape, peak intensity, peak frequency, etc. between genuine and fake calligraphy and painting. The spectrum of genuine works has good consistency, so the authenticity of calligraphy and painting can be distinguished according to the difference between the spectrums.

1. Introduction

Indian scientists discovered the Raman scattering effect in 1928 [1]. In the following decades, due to the weak intensity of Raman scattered light and the low energy of the excitation light source mercury arc lamp, it has not been widely used in practice. Until the emergence of laser Raman spectrometer and Fourier transform technology, people can use laser as a light source to study the vibrational state of molecules more comprehensively and provide more information on molecular

structure, which greatly improves the detection sensitivity of Raman spectroscopy. Subsequently, the application fields of Raman spectroscopy have become increasingly extensive, and special seminars on Raman spectroscopy in various disciplines (medicine, geology, biology, etc.) will be held at the biennial International Raman Spectroscopy Conference. The application range of Raman spectroscopy covers optics, quantum mechanics, electromagnetism, group theory, molecular spectroscopy, and other disciplines and has been widely used in materials, chemical industry, petroleum, polymer, biology,

environmental protection, geology, and other fields. This paper mainly focuses on the application of Raman spectroscopy in the identification of calligraphy and painting and nanomaterials.

The art of Chinese painting and calligraphy is the crystallization of five thousand years of Chinese civilization and a historical treasure in the process of Chinese social development. It reflects the real life of ancient Chinese people from many fields, embodies the unique philosophical concepts and aesthetic concepts of the Chinese nation, and is a material for studying the history of human society. Through the analysis of calligraphy and painting works, we can understand the background information of the era of calligraphy and painting creation, brush and ink skills and drawing methods, as well as the subjective emotions that the author wants to convey, thereby inferring the era of painting and calligraphy, the development of painting technology, and the identification and restoration of painting and calligraphy. When analyzing calligraphy and painting works, the first task is to protect the integrity of the calligraphy and painting. The structure of some works is very complex, and the old ones have even been worn and faded, which makes it difficult to identify calligraphy and painting works. Raman spectroscopy reflects the molecular properties of substances, which will not cause any damage to the object, and requires a small amount of samples. It has the characteristics of fingerprint rapidity, sensitivity, and simplicity. Therefore, Raman spectroscopy has been widely used in the identification and research of calligraphy and painting. In this paper, Raman spectroscopy was used to identify Chinese paintings and calligraphy and to study the light absorption properties and catalytic activity of nanomaterials. Combining traditional Chinese painting and calligraphy with modern advanced technology, new concepts and ideas are used in the current calligraphy and painting appraisal, so that calligraphy and painting can be appraised and appreciated more accurately and objectively, and the authenticity of calligraphy and painting can be identified, to make a reasonable value judgment on the artistry of calligraphy and painting and improve the overall level of the appraisal and appreciation of calligraphy and painting. It provides some feasible references for calligraphy and painting researchers and has certain positive significance for the collection, protection, and research of calligraphy and painting.

2. Related Work

In terms of theoretical research, experts and scholars at home and abroad have discussed the application and development prospects of spectroscopy technology in various fields and have done related research in the application of nanomaterials. Gallas et al. investigated five silica samples by infrared spectroscopy and a homemade thermogravimetric infrared spectroscopy (TG-IR) apparatus to quantify and compare the affinity of these five silicas for water. TG-IR measurements allow precise determination of the molar absorption coefficient, which is independent of the source of the sample and the concentration of silanol groups on the silicon. Experiments showed that the accessibility decreased with the increase of alcohol content, and the silica samples changed linearly with the concentration of adsorbed water [2]. Gibson et al. analyzed

NICMOS transmission spectra using a residual permutation algorithm and found that previously published transmission spectra could be restored when the same model was used for system effects, and that the transmission spectra changed considerably when the instrument model was changed slightly. They concluded that NICMOS transmission spectroscopy is highly influenced by the system model and cannot be used as a robust detection of molecules [3]. Bunker et al. studied the long K-band spectrum to measure the star formation rate in the system, searching for eight damped absorber emission values for $z > 2$. Under two different simplifying assumptions, (1) assuming a large disk, the spatial density of DLA at $z = 2.3$ is equal to the spatial density of present-day spiral galaxies. (2) In the layering hypothesis, the DLA size at $z = 2.3$ is the same as the gas size of the current spiral galaxy. They search for compact emission sources within a solid angle of 11×2.5 arcsec2 for each system. Compared to the previous most sensitive spectral searches, the studied samples were twice as large, the limit was twice as deep, and the measured solid angles were three times larger [4]. Crowther et al. studied the ISO-SWS spectrum of the Wolf-Rayet galaxy NGC 5253 to provide estimates of its stellar population. They used photoionization models and the latest theoretical O star flux distributions to derive the effective stellar temperature and ionization parameters. They assessed the distribution of highly ionized nebula lines in Wolf-Rayet galaxies in an evolutionary synthesis model, distinguishing regions where different infrared fine structure lines are formed [5]. Sasaki et al. used scanning electron microscopy and Fourier transform infrared spectroscopy to analyze the morphological features and chemical composition (Er) of the bone surface after YAG and CO_2 laser ablation. The experimental group was irradiated with continuous YAG and CO_2 lasers, and the position of the conventional micromotor drilling was used as the control group. Fourier transform infrared spectroscopy showed that the chemical composition of the bone surface after YAG laser ablation was basically the same as that after motor drilling. And after laser irradiation, no toxic substances were detected [6]. Yamada et al. investigated the kinetics of room temperature ionic liquid 1-butyl-3-methylimidazolium bis (trifluoromethylsulfonyl) imide (BmimNTf2) using two-dimensional infrared vibrational echo spectroscopy and polarization-selective pump probe. They observed the long-time-scale structural spectral diffusion components at 600 ps, as well as short- and intermediate-time scales for selenocyanate anion (SeCN–) measurements. Experiments have shown that 2-SeCN-Bmim+ is sensitive to local motions in the ionic region, which affect the spectral diffusion and redirection of small, anionic, and neutral molecules [7]. Yan et al. studied solid-phase redox transitions with X-ray spectroscopy and he used high-resolution X-ray spectroscopy (HR-XPS) to observe multivalent arsenic reacting nZVI particles with aqueous As(III). They believe that the morphology of arsenic in the nanoparticles depends largely on the loading of nZVI. Most of the arsenic is found in the reduced state in the nZVI environment, resulting in rapid depletion of Fe(0) cores and arsenic sequestration in oxide formation. Encapsulation of arsenic in most of the solid phase suggests that nZVI is a more powerful arsenic scavenger [8].

3. Spectroscopy and Nanomaterials

3.1. Raman Spectroscopy. Raman scattering effect is an inelastic scattering phenomenon caused by crystal structure, symmetry, charge, and other factors [9]. Raman spectra are significantly different in different substances, so Raman spectra are also called "fingerprints." Based on the Raman effect, qualitative, quantitative, and structural analysis can be performed on the Raman peak position, peak value, line type, line width, and number of spectral lines of the sample. When light enters the surface of an object, most of the light will be transmitted or absorbed, and only 0.1% of the photons will be scattered [10, 11]. During scattering, after the molecule absorbs energy, it will transition from the ground state to the virtual energy level and then drop from the virtual energy level to a lower energy level and release the scattered light. Raman spectroscopy includes optics, quantum mechanics, electromagnetism, molecular structure, molecular spectroscopy, and other disciplines and its applications in chemistry, physics, biology, medicine, environmental science, and other fields. These applications vary in nature, from purely qualitative to highly quantitative.

Light scattering is another natural phenomenon besides light absorption, light reflection, light transmission, and light emission, and it is an interaction between light and matter. Light scattering is caused by the collision of incident photons with objects in a certain direction, and the incident photons are shifted from the original incident direction [12]. Scattered light generally contains information about the structure of matter and is accompanied by changes in energy. It can be divided into elastic scattering and inelastic scattering according to the size of its fall back to the lower energy layer. The so-called elastic scattering, also known as Rayleigh scattering, means that when the excited molecule is deexcited, its energy level returns to the initial energy level, and the scattering energy is equal to the excitation energy. On the other hand, inelastic scattering is Raman scattering. When the excited molecule is deexcited, its energy level returns to the noninitial energy level, and the scattering energy is not the same as the excitation energy. There are two types of Raman scattering: Stokes scattering and anti-Stokes scattering. The energy of Stokes scattering is less than the energy of excitation, and the molecule is deexcited and falls back to an energy level higher than the initial energy level. On the other hand, the energy of anti-Stokes scattering is greater than the energy of excitation, and the molecule falls back to an energy level lower than the initial energy level. Generally, the Stokes scattering intensity is larger than the anti-Stokes intensity [13], and this process is shown in Figure 1.

It can be seen from the transition diagram of the energy level that both Raman scattering and Rayleigh scattering are caused by the transition of the ground state electrons to the virtual state under the excitation of the incident light and then to the ground state and emitting scattered light [14]. In Rayleigh scattering, since the electron does not interact with the phonon, its energy does not change, that is, its scattering frequency does not change with the frequency of the incident light. In Raman scattering, when electrons enter the virtual state, they will interact with phonons, which will cause the loss of phonon energy, resulting in the scattered light energy being smaller or greater than the incident light energy. That is, the frequency of scattered light decreases or increases by $\Delta \nu$ compared with the frequency of incident light, which corresponds to the Stokes or anti-Stokes Raman scattering process, respectively.

Raman scattering spectrum is a form of reflecting Raman shift, that is, the wavenumber difference between excitation light and scattered light. Raman scattering, unlike Rayleigh scattering, is a type of inelastic scattering, and in this case, Stokes light as the wavelength increases, and when the wavelength is reduced, it is anti-Stokes light. The principle of Raman scattering is shown in Figure 2. By detecting the scattered photons, Raman spectra can be obtained. Different bands correspond to the vibrational frequencies of different functional groups. Each molecule has a unique spectrum, called a "fingerprint," based on its chemical bonds and its specific vibrational frequency.

Raman spectroscopy is a type of molecular vibrational spectroscopy. It corresponds to the change of intramolecular vibrational energy level, carries information, such as the composition and structure of the substance itself, and has high specificity. It is a good spectral detection method [15]. One of the advantages of Raman spectroscopy is that the excitation light source can be selected at will. From the principle of Raman scattering, it can be seen that the frequency shift of the Raman spectrum has nothing to do with the frequency of the light source, and different light sources can be selected according to different samples. Secondly, Raman scattering is generated by the laser, which has strong directivity and can measure tiny samples in a very small area, thereby realizing long-distance noncontact detection. Since the laser has good monochromatic properties, good orientation ability, and high energy density, using it as an excitation light source can greatly improve the excitation efficiency. Raman spectroscopy does not need to prepare samples and can directly measure the measured objects, such as ancient painting pigments and traces left at crime scenes, so that they can be preserved intact [16]. Third, Raman spectroscopy can identify the chemical composition of cells. This method does not require labeling and staining and allows semiquantitative analysis of proteins, lipids, and DNA through vibrational spectroscopy, which can visually display their intracellular distribution. Fourth, Raman spectroscopy has a wide detection range. Since both polar molecules and nonpolar molecules can form Raman spectra, the detection objects of Raman spectra are very wide, including inorganic substances, organic substances, polymers, minerals, animal and plant tissues, and catalysts.

In spectroscopy, the grating resolution is usually defined as

$$R = \frac{\lambda}{\Delta\lambda} = m \times N. \tag{1}$$

Among them, $\Delta\lambda$ refers to the minimum wavelength difference that the wavelength λ can resolve. m refers to the spectral order, and N is the total number of grating scales. Here, $\Delta\lambda$ depends not only on the resolving power of the dispersing element but also on the construction parameters
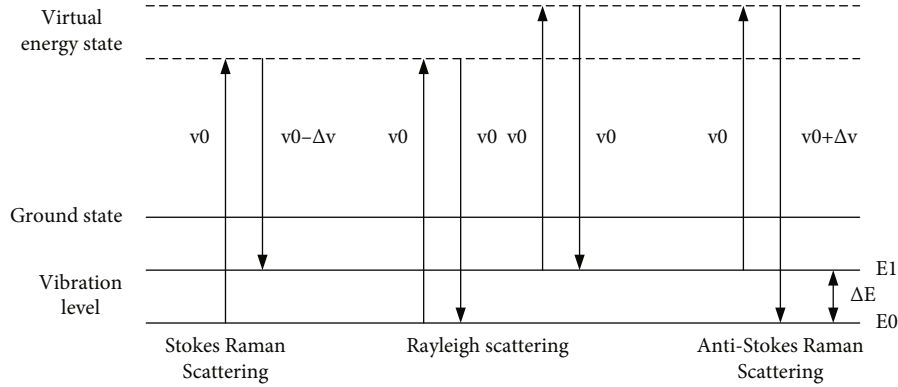
Figure 1: Energy level diagram for scattering process.
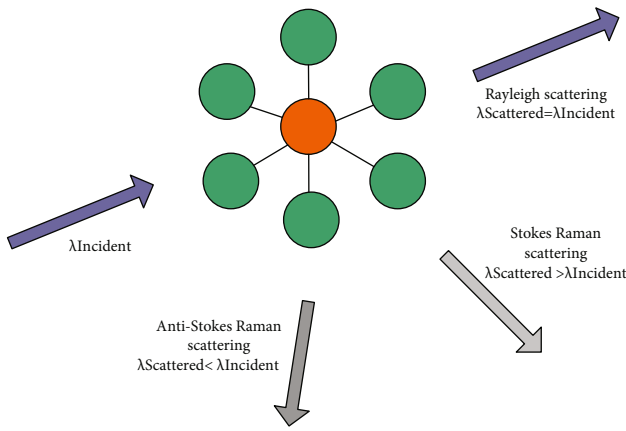
Figure 2: Principles of Raman scattering.
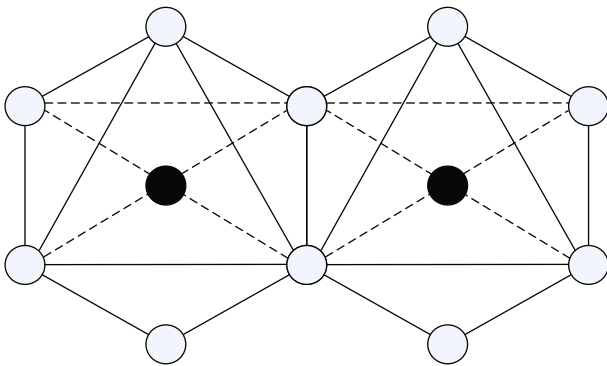
Figure 3: Crystal structure of rutile.

and diffraction angle, respectively. Clearly, when the incident angle and the diffraction angle are equal, the increase of the incident angle makes the spectral order increase.

At present, to evaluate the quality of Raman spectra, there are mainly methods for estimating the standard deviation of noise, which are discussed below. The random noise in the Raman spectrum is formed by the superposition of many random noise sources, which can be considered to satisfy the Gaussian distribution and belong to the Gaussian noise. Assuming that the Gaussian noise in the original signal is N, its standard deviation is σN, the signal filtered by a high-pass filter G is N', the standard deviation is $\sigma N'$, and the unit impulse response sequence of the high-pass filter is $g(n)$. Then, the power spectral density of N and the spectrum of the high-pass filter are the following formulas, respectively:

$$P(w) = \sigma_N^2, \tag{3}$$

$$G(w) = \sum_{n=-\infty}^{+\infty} g(n) e^{-jnw}, \tag{4}$$

where w represents the digital angular frequency, $w \in [-\pi, \pi]$.

N' is N obtained after being filtered by high-pass filter G, which should satisfy

$$N' = N * G, \tag{5}$$

where a represents a convolution, and its spectrum satisfies

$$F'(w) = F(w) \cdot G(w). \tag{6}$$

Among them, $F(\omega')$ and $F(\omega)$ represent the spectrum of N' and N, respectively. For the power-limited signals N' and N, they are limited in the range of $[-T/2, T/2]$, and their spectrums are $F_T'(\omega)$ and $F_T(\omega)$, respectively, which satisfy

$$F_T'(w) = F_T(w) \cdot G(w). \tag{7}$$

When T tends to infinity, the following formula is obtained:

such as the slit size, the focal length of the spectrometer, and the optical quality of the optical components. Increasing the total number of grating lines or increasing the spectral order can improve the spectral resolution. The optical properties of a grating can be described by the following formula:

$$m\lambda = d(\sin i + \sin r). \tag{2}$$

Here, λ refers to the diffraction wavelength, d refers to the grating constant, and i and r refer to the incident angle

FIGURE 4: Crystal structure of anatase.

TABLE 1: Crystal structure parameters of rutile and anatase.

Property	Rutile	Anatase
Crystal system	Tetragonal system	Tetragonal system
Lattice constant	$a = 4.5936$	$a = 3.784$
	$c = 2.9587$	$c = 9.515$
Space group	P42/mnm	I41amd
Molecule number	2	2
Ti-O bond length	1.949 (4)	1.939 (4)
	1.980 (2)	1.965 (2)
O-Ti-O bond angle	81.2°	77.7°
	90.0°	92.6°
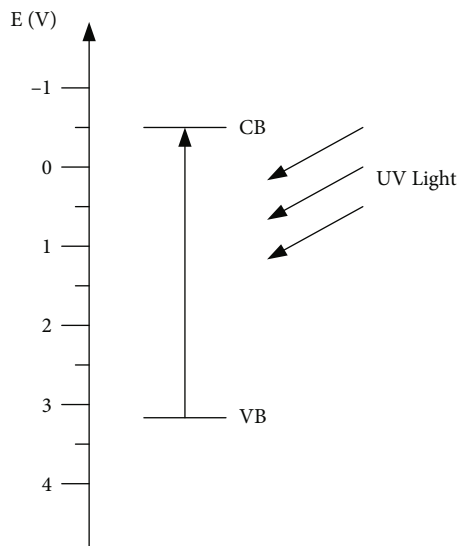
FIGURE 5: Light reaction mechanism.

$$\lim_{T \to \infty} F_T'(w) = G(w) \cdot \lim_{T \to \infty} F_T(w). \tag{8}$$

The power spectral density of N' is shown in

$$P'(w) = |G(w)|^2 \cdot \lim_{T \to \infty} \frac{1}{T} |F_T(w)|^2. \tag{9}$$
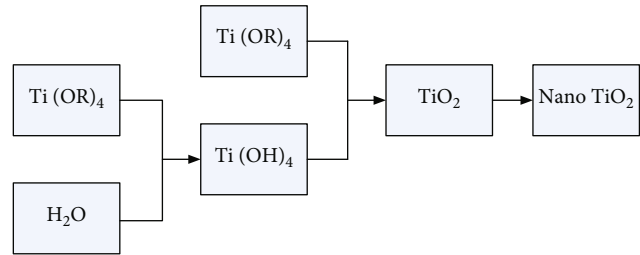
FIGURE 6: Process flow chart for preparing.

It can get

$$P'(w) = |G(w)|^2 \cdot P(w). \tag{10}$$

Since the autocorrelation function and the power spectrum function are mutual Fourier transforms, the autocorrelation function $R(\tau')$ of the filtered signal N' is shown in

$$R'(\tau) = \frac{1}{2\pi} \int_{-\infty}^{+\infty} P'(w) e^{-jw\tau} dw. \tag{11}$$

Moreover, defined by the power-limited signal autocorrelation function, the following formula is obtained:

$$R'(\tau) = \lim_{T \to \infty} \frac{1}{T} \int_{-T/2}^{T/2} N'(t) N'(t + \tau) dt. \tag{12}$$

Let $\tau = 0$, and formula (12) can be transformed into

$$R'(0) = \lim_{T \to \infty} \frac{1}{T} \int_{-T/2}^{T/2} |N'(t)|^2 dt. \tag{13}$$

Since the mean value of the high-pass filtered signal N' is zero, the following formula can be derived.

$$R'(0) = \sigma_N'^2. \tag{14}$$

Combining formulas (3), (4), (9), (10), (14), it can be deduced that

$$R'(0) = \sigma_N^2 \sum_{n=-\infty}^{+\infty} g^2(n) = \sigma_N^2 \|g\|^2. \tag{15}$$

It can be concluded from the above derivation that the noise variance filtered by a high-pass filter is equal to the noise variance in the original signal multiplied by the square of the modulus of the filter's response vector.

The core idea of the noise standard deviation estimation method is to use the high-pass filtered noise standard deviation to estimate the noise standard deviation in the original signal. Gaussian noise is mainly concentrated in the high-frequency domain. After the original signal is high-pass filtered, the low-frequency signal is filtered out. The high-frequency signal that passes through is mainly noise, and the interference of the signal is very small. At this time, it is more

TABLE 2: The relationship between hydrolysis reaction temperature and gel time.

Hydrolysis temperature	Gel time
20°C	48~72 h
30°C	30~35 h
40°C	18~20 h
50°C	<8 h

TABLE 3: Relationship between calcination temperature and average particle size of TiO.

Calcination temperature	Particle size
400°C	48~72 h
500°C	30~35 h
600°C	18~20 h
700°C	<8 h

accurate to calculate the standard deviation of the filtered noise, and then, the standard deviation of the noise in the original signal can be estimated by formula (15).

The specific operation is as follows: set the wavelet coefficients on two adjacent small scales to be $wc_1(n)$、$wc_2(n)$, respectively, and their correlation coefficient to be $Cor_1(n)$, $n = 1, 2, \cdots L$, where L represents the length of the discrete signal. The correlation coefficient $Cor_1(n)$ satisfies the

$$Cor_1(n) = wc_1(n) \cdot wc_2(n). \tag{16}$$

Normalizing the energy of $Cor_1(n)$ so that the energy of the new correlation coefficient $Cor_2(n)$ is equal to the energy of $wc_1(n)$. Let the energies of $Cor_1(n)$ and $wc_1(n)$ be E_{Cor_1} and E_{wc_1}, respectively, and formulas (17) and (18) are as follows:

$$E_{cor1} = \sum_{n=1}^{L} |Cor_1(n)|^2, \tag{17}$$

$$E_{wc1} = \sum_{n=1}^{L} |wc_1(n)|^2. \tag{18}$$

The new correlation coefficient $Cor_2(n)$ can be expressed as

$$Cor_2(n) = Cor_1(n) \cdot \sqrt{E_{wc1}/E_{cor1}}. \tag{19}$$

Comparing $Cor_2(n)$ with $wc_1(n)$, if the position n_0 satisfies the formula (20), the wavelet coefficient $wc_1(n_0)$ at n_0 is considered to be caused by the signal, and it is set to zero, thus obtaining the small-scale wavelet coefficient $wc'_1(n)$ with the signal interference removed, using formula (15) again, the noise standard deviation of the original signal can be estimated.

$$Cor_2(n_0) \geq |wc_1(n_0)|. \tag{20}$$

3.2. Nanomaterials. Nanomaterials are an emerging material that appeared in the 1980s, usually referring to the particle structure with nanometer size. Because nanoparticles have special properties that are significantly different from individual materials and single molecules, such as size effect, surface effect, volume effect, quantum effect, and macroscopic quantum tunneling effect; therefore, it has a wide range of applications in the fields of electronics, optics, chemical industry, ceramics, biology, and medicine [17, 18]. The preparation, structure, properties, and photocatalytic mechanism of TIOZ materials has been an important topic in the field of photocatalysis since it was discovered in the early 1970s that TIOZ electrodes have the function of splitting water under sunlight. After entering the 1990s, with the rapid development of nanotechnology, nanophotocatalysis technology has been widely used, and its particle size, surface area, and other technologies have also been further developed, and to a certain extent, the improvement of its quantum efficiency is achieved through the design of materials.

Photocatalysis technology is through photocatalysis, and the electrons in the valence band of the semiconductor are excited to transition to the conduction band to form a pair of electrons and holes and react with O_2 and H_2O/OH^- on the surface of the catalyst to generate free radicals, so that the organic compounds are gradually decomposed into small molecular substances such as CO_2 and H_2O. Since the research of semiconductor photocatalytic oxidation technology, many semiconductor catalysts with catalytic effect have been discovered, such as TiO_2, ZnO, SnO_2, Fe_2O_3, $BiVO_4$, Cu_2O, CdS, and C_3N_4 [19]. Among them, TiO_2 is in a leading position among many semiconductor catalysts due to its nontoxic and harmless, strong stability and strong redox ability.

It is a white powder in nature, TiO_2 mainly rutile, anatase, brookite, and $TiO_2(B)$ phase. Generally speaking, the crystalline titanium dioxide prepared at low temperature is anatase and brookite phases, while the rutile phase is stable at high temperature. Among them, the rutile and anatase forms TiO_2 are the most widely used in the field of photocatalysis, and the two crystal forms TiO_2 exhibit different properties due to structural differences. Both rutile type and anatase type TiO_2 are composed of octahedrons with Ti as the center and O as the corner, TiO_6 as the basic unit, and both phases belong to the tetragonal crystal system. The main difference lies in the connection mode between the octahedrons and the degree of lattice distortion [20]. The crystal structure is shown in Figures 3 and 4. The connection between octahedrons is mainly connected by common edges and common corners. In the anatase type TiO_2, each octahedron is connected with the surrounding eight octahedrons (four common edges and four common corners), whereas in the rutile type TiO2, each octahedron is connected to ten surrounding octahedra (two common edges and eight common corners). Because the crystal connection method is different, the degree of crystal distortion of the anatase type is also stronger, so the symmetry and stability of the rutile type TiO_2 lattice are higher than those of the anatase type TiO_2, and in the crystal coordination structure, the more the number of common edges, the worse the stability of the crystal structure. Therefore, the most stable crystal phase of titanium dioxide is the rutile phase, both
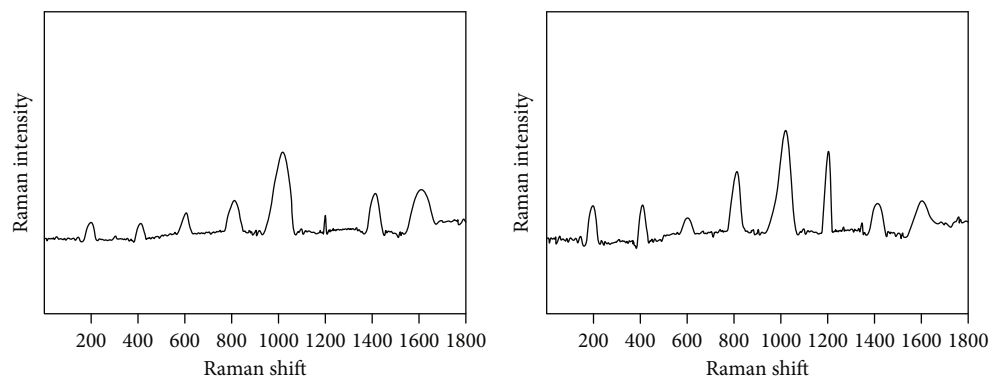
FIGURE 7: Raman spectra of authentic and fake calligraphy. (a) shows the Raman spectrum of the authentic calligraphy, and (b) shows the Raman spectrum of the calligraphy fake.
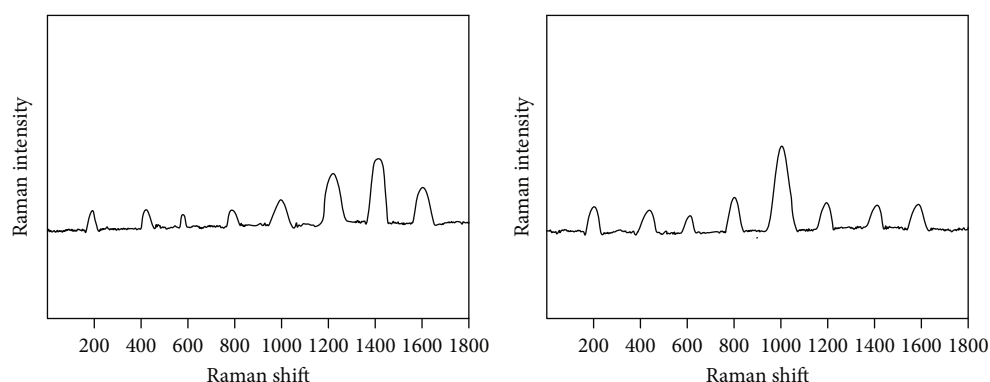
FIGURE 8: Raman spectra of authentic and fake murals. (a) shows the Raman spectrum of the authentic mural, and (b) shows the Raman spectrum of the fresco fake.
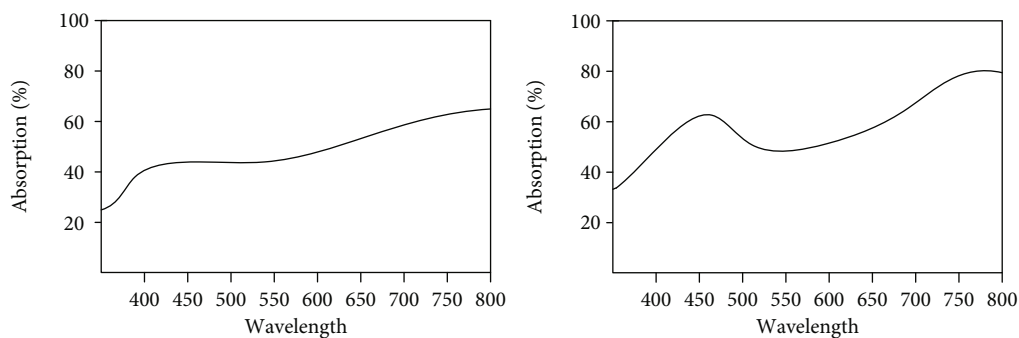
FIGURE 9: Optical absorptivity of nanomaterials at different temperatures. (a) is the light absorption rate of nanomaterials, and (b) shows the light absorption rate of nanomaterials.

anatase phase and brookite phase can be transformed into rutile phase during high temperature treatment, and this process is generally irreversible at a phase transition temperature of 500-600°C.

Table 1 presents crystallographic data for rutile and anatase types, The Ti-Ti bond distance (3.57 Å) in the rutile phase structure is larger than that in the anatase phase structure (3.79 Å). The Ti-O bond distance (1.949 Å) in the rutile phase structure is shorter than that in the anatase phase structure (1.939 Å). The density of rutile phase TiO_2 material

(4.25) is greater than that of anatase phase TiO_2 material (3.89).

Titanium dioxide is a wide-band semiconductor material. The forbidden band width of the anatase phase grain is 3.2 eV, the forbidden bandwidth of the rutile phase grain is 3.02 eV, and the forbidden band width of the brookite phase grain is 2.96 eV. The valence band of TiO_2 includes the 3d orbital of Ti and the 2p orbital of O, while the conduction band only includes the 3d orbital of Ti [21]. When TiO_2 is irradiated with a light beam with a wavelength below
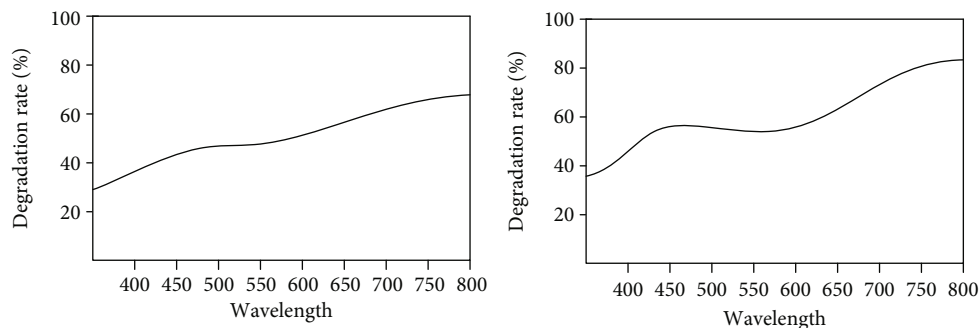
Figure 10: Photocatalytic activity of nanomaterials at different temperatures. (a) shows the photocatalytic degradation rate of nanomaterials, and (b) shows the photocatalytic degradation rate of nanomaterials.

Table 4: Photocatalytic reaction rates at different voltages.

TiO_2	Voltage	2 h	4 h	6 h	8 h	10 h
	25 V	1.12	1.46	1.71	2.27	2.70
Reaction speed	35 V	1.29	2.05	2.11	2.65	2.34
	45 V	1.69	2.23	2.50	2.23	2.06

387 nm, the electrons in its valence band are excited into the conduction band, thereby forming an energy-efficient electron e^- with a negative charge, and form a hole h^+ with a punctual point in the valence band. The reaction principle is shown in Figure 5.

The sol-gel method uses titanium alkoxides or inorganic salts as precursors to form sols through the hydrolysis reaction of the precursors, and the hydrolyzed precursors are further condensed to form gels, and finally, the desired materials are prepared by drying and heat treatment. The process is shown in Figure 6. Tetrabutyl titanate is hydrolyzed in water or alcohols to form oligomers, and the oligomers interact and polymerize to form a three-dimensional network structure with Ti-O-Ti as the polymer unit. At the beginning of the chemical reaction, a large number of small molecules are formed by hydrolysis and polymerization. They form long molecular chains through polymerization, and cross-linking and branching occur between the long molecular chains and small molecules, forming two-dimensional, three-dimensional, and even multidimensional networks and then forming gels. Among them, the morphology, size, crystallinity, and surface properties of the gel particles are affected by the components of the solution, pH, reaction temperature, and other factors. The size, morphology, crystallinity, and surface properties of nano-TiO_2 particles can be regulated by controlling the experimental conditions. The relationship between the hydrolysis reaction temperature and the gelation time is shown in Table 2.

Finally, the organic components of the gel are removed through heat treatment processes such as drying and calcination to obtain nano-TiO_2. The relationship between the calcination temperature and the average particle size of TiO_2 is shown in Table 3. Generally speaking, when the polymer chain has obvious branching and cross-linking, there are a lot of holes in the colloid, and it has good structural stability. However, when the branching and cross-linking of the colloid chain is not obvious, the pores in the colloid are not large, the structure will be relatively fragile, and it is easy to break during the calcination process.

4. Experiment of Spectroscopic Technique in Chinese Painting Identification

Using Raman spectroscopy technology, two authentic calligraphy and mural paintings and their fakes during the Song Dynasty were analyzed, and their respective Raman spectra were obtained, as shown in Figures 7 and 8. Figure 7 shows the Raman spectra of genuine calligraphy and fakes. Figure 8 shows the Raman spectra of the original and fake murals.

Through the analysis of Figure 7, it can be seen that the Raman spectra of genuine and fake calligraphy are significantly different. The calligraphic authentic Raman spectrum has peaks at 200, 400, 600, 800, 1000, 1200, 1400, and 1600 in the 0-1800 cm^{-1} wavenumber range. And when the wave number is 1000 cm^{-1}, the peak is the largest, followed by the peaks at 1400 and 1600 cm^{-1}. The Raman spectrum of the calligraphic fake also has peaks at 200, 400, 600, 800, 1000, 1200, 1400, and 1600 in the wavenumber range of 0-1800 cm^{-1}. Different from the real one, the fake Raman spectral peaks are concentrated between 800 and 1200 cm^{-1}.

By analyzing Figure 8, it can be seen that the Raman spectra of the authentic and fake murals are significantly different. The authentic Raman spectrum of the fresco has peaks at 200, 400, 600, 800, 1000, 1200, 1400, and 1600 in the 0-1800 cm^{-1} wavenumber range. When the wave number is 1400 cm^{-1}, the peak value is the largest, followed by the peak value at 1200 and 1600. The Raman spectrum of the fresco fake also has peaks at 200, 400, 600, 800, 1000, 1200, 1400, and 1600 cm^{-1} in the wavenumber range of 0-1800 cm^{-1}. Unlike the real one, the fake Raman spectrum peaks around 1000 cm^{-1}.

By selecting Rhodamine B as a typical photocatalytic degradation research object, the test of the degradation ability of the nanomaterial TiO_2 sample is characterized. The test results are shown in Figures 9 and 10. Figure 9 shows the light absorptivity of nanomaterials at different temperatures. Figure 10 shows the photocatalytic degradation rates of nanomaterials at different temperatures.

Through the analysis of Figure 9, it can be known that the absorption rate of TiO_2 with light is different at different temperatures. When the temperature is 400°C, the light absorption rate of TiO_2 with a wavelength of 800 nm is the highest, reaching 64.9%. The light absorption rate for the wavelength of 400~600 nm is basically the same, which is maintained at about 42.1%; the light absorption rate for the wavelength of 600~800 nm increases steadily. When the temperature is 600°C, TiO_2 has the highest absorption rate of light with a wavelength of 780 nm, reaching 80.4%. The absorption rate of light with a wavelength of 400 nm is 48.7%, and the absorption rate of light with a wavelength of 450 nm is 61.2%; the absorption rate of light with a wavelength of 550~750 nm increases from the initial 53.2% to 79.5%.

From the analysis of Figure 10, it can be seen that the catalytic degradation rate of TiO_2 to light varies greatly at different temperatures. When the temperature is 400°C the catalytic degradation rate of light with a wavelength of 450 nm is 41.7%, and the catalytic degradation rate of light with a wavelength of 650 nm is 58.3%. When the temperature is 600°C the catalytic degradation rate of light with a wavelength of 450 nm was 54.6%, and the catalytic degradation rate of light with a wavelength of 650 nm was 64.3%.

Exploring the photocatalytic activity of nanomaterials involves two parameters: photocatalytic degradation rate and reaction rate. In addition to the photocatalytic degradation rate, the reaction rate should also be studied. Table 4 shows the photocatalytic reaction rates of nanomaterials at different voltages.

It can be seen from Table 4 that when the voltage is 25 V, the best photocatalytic activity appears in the TiO_2 nanomaterials prepared under the condition of 10 h, and its reaction rate constant is 2.70×10^{-3} min^{-1}. When the voltage is 35 V, the best photocatalytic activity appears in the TiO_2 nanomaterials prepared under the condition of 8 h, and the reaction rate constant is 2.65×10^{-3} min^{-1}. When the voltage is 45 V, the best photocatalytic activity appears in the TiO_2 nanomaterials prepared under the condition of 6 h, and its reaction rate constant is 2.50×10^{-3} min^{-1}. At the same voltage, the reaction rate constant first increases and then decreases with time.

5. Conclusion

An important part of the identification of calligraphy and painting is to identify the authenticity, and the identification of the authenticity of calligraphy and painting has always been a major subject of Chinese painting and calligraphy collection and research. In the identification of calligraphy and painting, Raman spectroscopy is used increasingly. Using Raman spectroscopy to assist in the identification of cultural relics can not only speed up the identification but also reduce the artificiality and subjectivity in the identification process, improve the accuracy and objectivity of identification, reduce the probability of errors in identification, and shorten the identification time. After spectral analysis, the spectra of genuine and fake calligraphy and painting have great differences in peak shape, intensity, and frequency, and the spectrum of genuine works shows good consistency, so that the authenticity can be distinguished from the difference in the spectra. The use of spectral technology can not only ensure the accuracy of identification but also prevent damage to calligraphy and painting. Therefore, Raman spectroscopy is a nondestructive and accurate in situ analysis method, which is suitable for the precise analysis of antiques, calligraphy, and painting. The application of Raman spectroscopy technology in cultural relics, calligraphy, and painting has enriched the identification methods of cultural relics, calligraphy, and painting and improved its scientificity and credibility. With the advancement of science and technology, spectroscopic technology will be an important method of calligraphy and painting identification. However, in-depth study of calligraphy and painting identification requires research on this paper. By observing the scanning electron microscope image of the rice paper, we can analyze the general proportion of leather and grass in the paper from the structure of the surface of the rice paper or the number of long and short fibers in the paper and further use this method to identify the year and type of the rice paper.

Data Availability

The data underlying the results presented in the study are available within the manuscript.

Conflicts of Interest

The authors declare that they have no conflicts of interest.

References

[1] L. Ping, J. A. Rodriguez, and T. Asakura, "Desulfurization reactions on Ni2P(001) and alpha-Mo2C (001) surfaces: complex role of P and C sites," *The Journal of Physical Chemistry B*, vol. 109, no. 10, pp. 4575–4583, 2017.

[2] J. P. Gallas, J. M. Goupil, A. Vimont et al., "Quantification of water and silanol species on various silicas by coupling IR spectroscopy and in-situ thermogravimetry," *Langmuir*, vol. 25, no. 10, pp. 5825–5834, 2009.

[3] N. P. Gibson, F. Pont, and S. Aigrain, "A new look at NICMOS transmission spectroscopy: no conclusive evidence for molecular features," *Monthly Notices of the Royal Astronomical Society*, vol. 6, no. S276, pp. 478-479, 2010.

[4] A. J. Bunker, S. J. Warren, D. L. Clements, G. M. Williger, and P. C. Hewett, "Limits on the star formation rates of z>2 damped Lyα systems from Hα spectroscopy," *Monthly Notices of the Royal Astronomical Society*, vol. 309, no. 4, pp. 875–884, 1999.

[5] P. A. Crowther, S. C. Beck, A. J. Willis, P. S. Conti, P. W. Morris, and R. S. Sutherland, "Properties of hot stars in the Wolf-Rayet galaxy NGC 5253 from ISO-SWS spectroscopy," *Monthly Notices of the Royal Astronomical Society*, vol. 304, no. 3, pp. 654–668, 1999.

[6] K. M. Sasaki, A. Aoki, S. Ichinose, T. Yoshino, S. Yamada, and I. Ishikawa, "Scanning electron microscopy and Fourier transformed infrared spectroscopy analysis of bone removal using Er: YAG and CO_2 lasers," *Journal of Periodontology*, vol. 73, no. 6, pp. 643–652, 2002.

[7] S. A. Yamada, H. E. Bailey, A. Tamimi, C. Li, and M. D. Fayer, "Dynamics in a room-temperature ionic liquid from the cation perspective: 2D IR vibrational echo spectroscopy," *Journal of*

the American Chemical Society, vol. 139, no. 6, pp. 2408–2420, 2017.

 [8] W. Yan, M. Ramos, B. E. Koel, and W. X. Zhang, "As(III) sequestration by iron nanoparticles: study of solid-phase redox transformations with X-ray photoelectron spectroscopy," *Journal of Physical Chemistry C*, vol. 116, no. 9, pp. 5303–5311, 2012.

 [9] S. Bell and S. Dick, "Quantitative surface-enhanced Raman spectroscopy of single bases in oligodeoxynucleotides," *Faraday Discussions*, vol. 205, no. 5, pp. 517–536, 2017.

[10] R. G. Janssen, J. Duynhoven, and W. Verboom, "Studies on the dynamics of Phosphorylatedp-tert-Butylcalix[6]arenes by using 2D NMR spectroscopy," *Journal of the American Chemical Society*, vol. 118, no. 15, pp. 3666–3675, 1996.

[11] T. B. And and M. Bieri, "Time-resolved in situ ATR spectroscopy of 2-propanol oxidation over Pd/Al 2 O 3: evidence for 2-Propoxide intermediate," *Journal of Physical Chemistry B*, vol. 108, no. 35, pp. 13364–13369, 2017.

[12] G. Poppe, C. Wijers, and A. V. Silfhout, "Ir spectroscopy of CO physisorbed on NaCl (100): microscopic treatment," *Physical Review B: Condensed Matter*, vol. 251, no. 7, pp. 7917–7929, 2017.

[13] C. Li, P. Liu, C. Zou, F. Sun, J. M. Cioffi, and L. Yang, "Spectral-efficient cellular communications with coexistent One- and two-hop transmissions," *IEEE Transactions on Vehicular Technology*, vol. 65, no. 8, pp. 6765–6772, 2016.

[14] M. Puech, H. Flores, F. Hammer, and M. D. Lehnert, "3D spectroscopy with VLT/GIRAFFE," *Astronomy & Astrophysics*, vol. 455, no. 1, pp. 131–134, 2006.

[15] T. H. Prettyman, N. Yamashita, M. J. Toplis et al., "Extensive water ice within Ceres' aqueously altered regolith: evidence from nuclear spectroscopy," *Science*, vol. 355, no. 6320, pp. 55–59, 2017.

[16] D. J. C. Ji-Yang and V. V. Kumar, "Probing electrochemical interfaces using shell-isolated nanoparticles-enhanced Raman spectroscopy," *Electrochemistry*, vol. 1, no. 1, pp. 16–21, 2017.

[17] B. Gao, X. Ning, and P. Xing, "Shock wave induced nanocrystallization during the high current pulsed electron beam process and its effect on mechanical properties," *Materials Letters*, vol. 237, no. 15, pp. 180–184, 2019.

[18] J. J. Peterson and T. D. Krauss, "Fluorescence spectroscopy of single lead sulfide quantum dots," *Nano Letters*, vol. 6, no. 3, pp. 510–514, 2017.

[19] L. Zeng, J. Shi, J. Luo, and H. Chen, "Silver sulfide anchored on reduced graphene oxide as a high -performance catalyst for CO_2 electroreduction," *Journal of Power Sources*, vol. 398, pp. 83–90, 2018.

[20] N. Bastian, E. Emsellem, M. Kissler-Patig, and C. Maraston, "Young star cluster complexes in NGC 4038/39," *Une chaire de médecine au XVe siècle; un professeur à l'Université de Pavie de 1432 à 1472*, vol. 445, no. 2, pp. 471–483, 2006.

[21] L. S. Rothman, I. E. Gordon, and Y. Babikov, "The HITRAN2016 molecular spectroscopic database," *Journal of Quantitative Spectroscopy & Radiative Transfer*, vol. 130, no. 11, pp. 4–50, 2017.

Hindawi

Research Article

Application Preparation of High-Performance Iron-Based Powder Metallurgy Sintered Materials in Sports Industry

Baifang Yang [iD]

Training Center of Teacher Teaching Development, Harbin Normal University, Harbin, 150025 Heilongjiang, China

Correspondence should be addressed to Baifang Yang; yangbaifang@hrbnu.edu.cn

Nowadays, the rapid development of sports science and technology has brought about the vigorous development of the sports industry, which is worth studying for a long time in the future. This article aims to use metallurgical sintering technology to prepare high-performance iron-based powder materials and apply them in the traditional sports industry to produce new sports equipment. This article proposes a metallurgical sintering method, that is, the use of a process of powdered iron-containing materials through a series of operations to finally obtain a new agglomerate and to obtain the required new physical and mechanical properties of materials or products. A new type of material is made and used in the traditional sports industry to meet the high-quality needs of sports equipment in the current era. According to survey statistics, my country's sports industry has been developing rapidly in the past five years. It has increased from 1,901.13 billion yuan in 2016 to 2,869.35 billion yuan in 2020. Sports investment and financing events have also dropped from 313 to 105, but the entire sports industry's investment is getting bigger and bigger. The number of employees in the national sports industry has also exceeded the 2 million mark. In the future, the sports industry is also an industry with great potential for development.

1. Introduction

At present, traditional sports equipment mostly uses wood or metal materials. The physical properties of these materials limit the strength of sports equipment to a large extent. With the development of science and technology, new materials are widely used in various sports equipment and even become a key factor in determining the outcome of competitive sports. Based on the excellent characteristics of various new materials, such as high strength, specific modulus, light weight, wear resistance, good damping performance, and strong design ability, the performance of sports equipment has been significantly improved, and it has been widely used. Traditional exercise equipment has a short life span, low safety, and significant limitations. In this paper, sintering technology is used to prepare high-performance iron-based powder metallurgy materials, which are used in the traditional sports industry to manufacture fitness, rehabilitation, sports, and other sports equipment. In our country, science and technology have always been the primary productive forces, but in the sports industry, the rapid development

and progress of sports science and technology are the primary productivity of the sports industry. Since 1992, my country has vigorously developed sports science and technology, and with the continuous development of the times, sports science and other related sciences have gradually merged, which has led to the continuous production of new interdisciplinary subjects and the development of new science and technology and materials. In this context, the technology of this paper may be widely used in daily life in the future.

Through the preparation of high-performance iron-based powder metallurgy sintered materials, the traditional sintering technology is used to produce new high-performance iron-based powder materials, which are used in the sports industry to realize high-performance iron-based materials and the theory of sports fields. At the same time, the preliminary integration of the levels also preliminarily promotes the application research of high-performance iron-based materials and sintering technology in the field of sports equipment. In the follow-up, corresponding products can be produced and put into daily life

applications. Sports goods produced by applying advanced sports science and technology and materials are also very important in our daily lives. Not only is that, in competitive sports, sports equipment is also the top priority, which can completely affect a person's strength. Nowadays, with the rapid development of sports science and technology, the current sports industry is increasingly dependent on sports science and technology. As an emerging field of science and technology, high-performance iron-based powder metallurgy materials will be used in sports and even other fields in the future. Therefore, this article is based on this, with the topic of the application of high-performance iron-based powder metallurgy materials in the sports industry, theoretically studying the feasibility of this technology, and laying the groundwork for possible future development.

Shui et al. introduced a method of preparing iron-based friction materials directly from vanadium-containing titanium magnetite concentrates using in situ carbothermal reaction and sintering. The influence of Ni content (1-4%, mass fraction, the same below) on the microstructure and the mechanical properties and wear properties of iron-based friction materials were studied. The results show that the sintered sample is composed of iron matrix, graphite lubricating phase, and hard particles (mainly TiC). The former is mainly in the form of reflected electromagnetic wave energy to attenuate electromagnetic radiation, so that the transmitted electromagnetic wave energy is reduced; the latter is mainly in the form of absorption of electromagnetic wave energy to attenuate electromagnetic radiation, so that the electromagnetic wave return reflection energy is reduced. The matrix is mainly composed of layered pearlite with higher strength and higher hardness than ferrite. Compared with the sintered samples without Ni, the structure and performance of iron-based friction materials with different Ni content are improved to different degrees. The low Ni content (1%-2%) promotes the sintering process, exhibiting reduced pores and uniform distribution of lubricating graphite phase and hard particles. In addition, the hardness and wear performance are significantly improved. As the Ni content increases, when the Ni content exceeds 2%, not only the number of pores increases but also the graphite phase and hard particles segregate in the microstructure, resulting in a decrease in material hardness and wear resistance. In summary, when the Ni content is 2%, the structure and performance are the best. But he did not experiment with detailed data on other metals, compared the structure and properties of several different metals, and finally reached a conclusion [1]. Due to low cost, high availability, and high strength, iron-based composite materials have been widely used in many industrial applications such as bearings, camshafts, connecting rods, pulleys, various valves, and oil pump gears in automobiles and other industries. Mahdi and Mahmood aim to prepare Fe-10 vol. % Cu-(0–5) wt. % nano-Y2O3 composite materials through powder metallurgy technology and study its physical and mechanical properties. The powder was mixed in a ball mill for 30 minutes and then uniaxial compacted at a 700 MPa room temperature for 3 minutes. The green sample was sintered at 1000°C for 1 hour. Not only is the absorption intensity greater

(-16.9 dB) but the absorption bandwidth is also wider (4.2 GHz). The results of Mahdi and Mahmood's research show that nanoyttrium oxide has a significant effect on the physical and mechanical properties of Fe-10%Cu composites. As the content of nanooxides increased from 0% to 3%, the bulk density increased by 0.92%, and the true porosity decreased by 6.4%. Mahdi and Mahmood increased Y2O3 to 1%, the Vickers microhardness increased by 5.9% and then gradually decreased when it further increased by more than 1%. As the content of nanooxides increases from 0% to 3%, the wear rate is reduced by 21%. On the other hand, increasing Y2O3 to 5% reduces the compressive strength by 47%. However, his research results do not have specific examples of combining with other industries to support his theoretical research results [2]. Over the years, technological development has had a huge impact on sports performance and has promoted the development of specific materials and manufacturing processes for sports-related products. In this context, Ribeiro et al. used the internal coupling effect of fiber-reinforced plastic (FRP) to design and develop a new snowboard technology using anisotropic layer design. This work involves the technical, economic, and environmental assessment of skis made of three alternative materials, namely, carbon, glass, and flax fiber-reinforced plastics. It shows how life cycle analysis can support product design and development by using innovative technologies to apply life cycle engineering methods to the ski design process. In this case, the material selection and fiber placement angle will have a significant impact on the stiffness of the resulting FRP, so in the three dimensions of the analysis, namely, cost, environment, and technology. Natural fiber is the most environmentally friendly choice, glass fiber is the best economically, and carbon fiber is the best in terms of technical performance. Therefore, Ribeiro et al. consider and weigh the importance attributed to each analysis dimension to allow aggregate analysis of alternatives and make informed decisions. His research is to use plastics for the manufacture of sports equipment and does not use metal to make a comparison to prove the diversity of experimental results [3, 4].

In this paper, metallurgical sintering technology is used to prepare high-performance iron-based powder materials and apply them in the traditional sports industry to produce new sports equipment. The sintering method refers to adding various iron-containing powdery substances to a certain amount of solvent, fuel and water, after stirring, fusion and granulation, it is put into the sintering equipment, so that the material undergoes a series of physical and chemical changes, and finally presents a dense combination.. It can be seen that the impedance matching and attenuation characteristics of absorbing materials are mainly determined by the values of dielectric constant and magnetic permeability of the materials. In addition, the material matrix ratio, material thickness, geometric effect, and other factors also affect the absorbing effect of the absorbing material. In the traditional sports industry, most of the metal and wood materials are used for the production of sports equipment. Such products are not only bulky but also have certain disadvantages in other properties. And the sports equipment made of the

new high-performance iron-based powder material we use has the characteristics of light weight, good quality, and good torsion resistance and can even be used in professional competitions. Through the rapid development of the sports industry in recent years, coupled with the continuous innovation of sports science and technology, various disciplines, industries, and sports are blended with each other, and newer technologies are used in the sports industry.

2. Preparation Method of High-Performance Iron-Based Powder Metallurgy Sintered Material

2.1. Sintering Method. The sintering method is a traditional handicraft process, that is, a traditional firing process that converts the original powdery raw material into a dense combination. In the early days, people have begun to use the sintering process to produce many things, such as porcelain, powder metallurgy, refractory materials, and high-temperature materials. These products are widely used in our daily lives. Under the general production situation, after the powdery object is formed, a polycrystalline material can be obtained after a sintering method, which is a dense combination. It can increase the loss of electromagnetic waves inside the material and thus improve the wave absorption performance of the material, which provides a guiding direction for designing the composition and structure of wave-absorbing composites. Under microscope observation, it can be seen that its structure includes pores and crystals. [5]. The sintering process may affect the properties of the original material, because it will affect the size of the pores of the object, the size of the crystalline particles, and the distribution and shape of the grain boundaries. The specific process of the sintering method is shown in Figure 1.

Since the particle size is related to the sintering temperature and the holding time of the peak temperature, SEM is used to observe the microstructure of sintered silver under different process conditions, and the particle size is counted according to the linear interpolation method [6]. With the increase of sintering current or energization time, the size of silver particles after sintering increases significantly. The effect of different cladding layer thicknesses on the magnetic properties was investigated by varying the experimental cladding silicon oxide process with the help of a silane coupling agent for the activation of iron-nickel alloys of micron size. It was found that the saturation magnetization strength of the material decreased with increasing the cladding layer thickness, while the effect on the coercivity was not significant. Since grain growth is caused by grain boundary migration, the grain boundary migration rate can be expressed by the following formula:

$$V_a = M_a \times F_a. \tag{1}$$

Among them, M_a represents the mobility of the grain boundary; F_a represents the driving force. And the relationship between M_a and temperature can be expressed by the

following formula:

$$M_a = \frac{(D_a * \omega)}{(K * T * W_a)}. \tag{2}$$

Among them, D_a is the diffusivity of the grain boundary; W_a is the boundary width; ω is the atomic volume; K is the Boltzmann constant; T is the absolute temperature [7]. The driving force F_a can be expressed as follows:

$$F_a = A \times \frac{\sigma_a}{D_g}. \tag{3}$$

Among them, σ_a is the surface energy; D_g is the average particle size. Grain boundary diffusion can lead to grain growth, as described in the above formula. Therefore, the grain boundary migration rate is proportional to the grain growth rate, that is, dD_g/dt.

$$\frac{dD_g}{dt} = \frac{A \times \sigma_a \times D_a \times \omega}{(K \times T \times W_a \times D_g)}. \tag{4}$$

After formula integration, you can get

$$D_g{}^2 - D_{g0}{}^2 = k \times t. \tag{5}$$

Among them, D_{g0} is the grain size when t is equal to zero? Therefore, we can conclude that when the energization time is extended or the sintering current is increased, the migration rate of the grain boundary will increase, resulting in an increase in the grain size. Especially when the electrification time is 180 s, it can be found that the silver particles have obvious coarsening [8].

Although the current sintering peak temperature is high, the very short sintering time inhibits the growth of sintered silver particles. Formulated by haulage:

$$\sigma = \sigma_0 + kd^{-a}. \tag{6}$$

Among them, σ is the shear strength; σ_0 and k are constants independent of size; d is usually between 0.5 and 1.

The Heywang-Jonker model proposes that the barrier height (ϕ) and acceptor state density (N_s) of the sample can be estimated from the resistance temperature $R - t$ curve. According to semiconductor theory, the relationship between barrier height (ϕ) and grain boundary resistance:

$$\rho = \rho_0 \exp\left(\frac{e\varphi}{kT}\right). \tag{7}$$

Among them, ρ_0 is a constant, e refers to the basic charge, T is the Kelvin temperature, and k is the Boltzmann constant [9]. When the sample temperature is lower than the Curie temperature T_C, the potential barrier is offset by the spontaneously polarized electrons of the ferroelectric phase. When the temperature rises above the
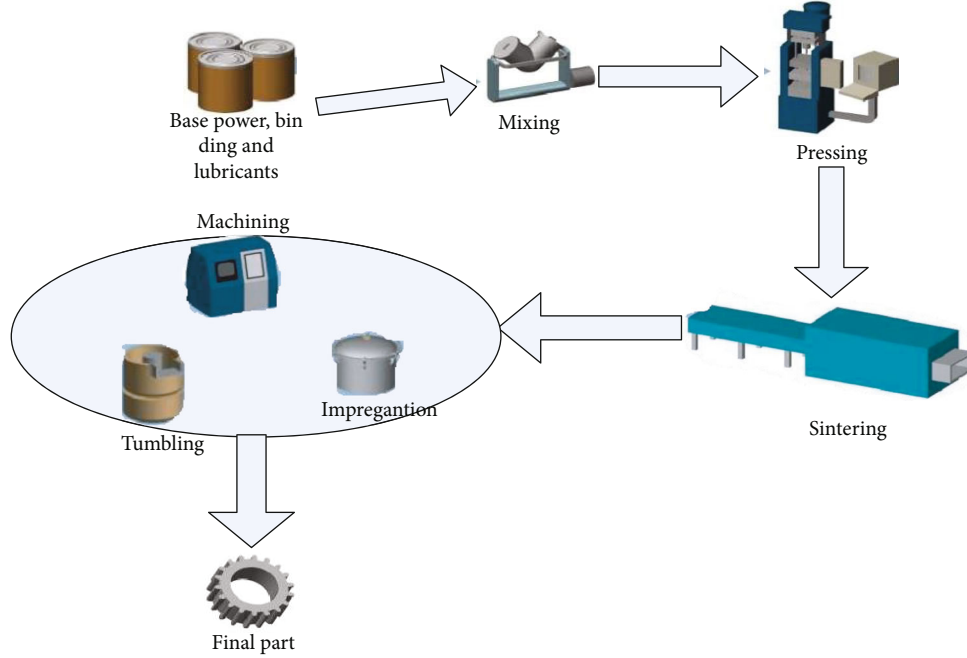
FIGURE 1: Preparation process of sintering method.

Curie temperature T_C,

$$\varphi = \frac{eN_S^2}{8\varepsilon_0\varepsilon_r N_d}. \tag{8}$$

N_S is the acceptor state density, Nd is the donor doping concentration, ε_r is the relative permittivity, and ε_0 is the vacuum permittivity. By (7) and (8), the resistance ρ can be expressed as

$$\rho = \rho_0 \exp\left(\frac{eN_S^2}{8\varepsilon_0\varepsilon_r N_d kT}\right). \tag{9}$$

2.2. Powder Metallurgy Methods. Powder metallurgy is a traditional process that uses metal powder or a mixture of metal powder and nonmetal powder as raw materials for smelting and uses technical means such as sintering and forming to finally produce metal materials, composite materials, and various other types of products. Mean is as shown in Figure 2. Powder metallurgy is a kind of powder sintering technology; ceramic firing in daily life also belongs to this technology, so most of the powder metallurgy methods or techniques can also be applied to the production of ceramic materials. The powder metallurgy method has many advantages and benefits. However, in high-frequency field applications, on the one hand, due to the skinning effect of soft magnetic alloy materials, the electric field is mainly concentrated on the surface of the material, which can create uncontrollable hazards. It can solve the problem of the urgent need to develop new materials to replace the original materials. Soft magnetic metal nanoparticles have gained wide interest in applications such as catalysts, biosensors, clinical medicine, super-

capacitors, water treatment, and microwave absorbing materials due to their potential properties. It will play a very important role in future life [10].

The Archimedes drainage method is used to detect the density ρ of each sample, and the surface is treated with wax to improve the accuracy of the test. Use BSM-200.4 electronic analytical balance to measure the quality [11]. Calculate the sample density according to formula ((10), where m_1 is the mass of the sample in air (g), m_2 is the mass (g) after sealing wax, m_3 is the suspended mass in water (g), and ρ_w is the density of water (g/cm^3). ρ_{wax}Is the density of paraffin wax (g/cm^3).

$$\rho = \frac{m_1}{m_2 - m_3/\rho_w - m_2 - m_1/\rho_{\text{wax}}}. \tag{10}$$

The porosity of the sintered matrix is the key parameter of the infiltration amount in the subsequent copper infiltration process. After the density of the sintered matrix is measured, the matrix porosity ε can be calculated according to formula (11) [12]. ρ_0 is the theoretical density of the sintered matrix (g/cm^3), and ρ is the measured density of the sintered matrix (g/cm^3).

$$\varepsilon = \left(1 - \frac{\rho}{\rho_0}\right) \times 100\%. \tag{11}$$

The material composition of the working layer and the nonworking layer of the bimetal valve seat ring is different, and the thermal expansion coefficient is different. Therefore, the radial shrinkage rate k of the two layers of materials needs to be tested before and after copper infiltration [13]. A screw micrometer (accuracy: 0.01 mm) is used to measure
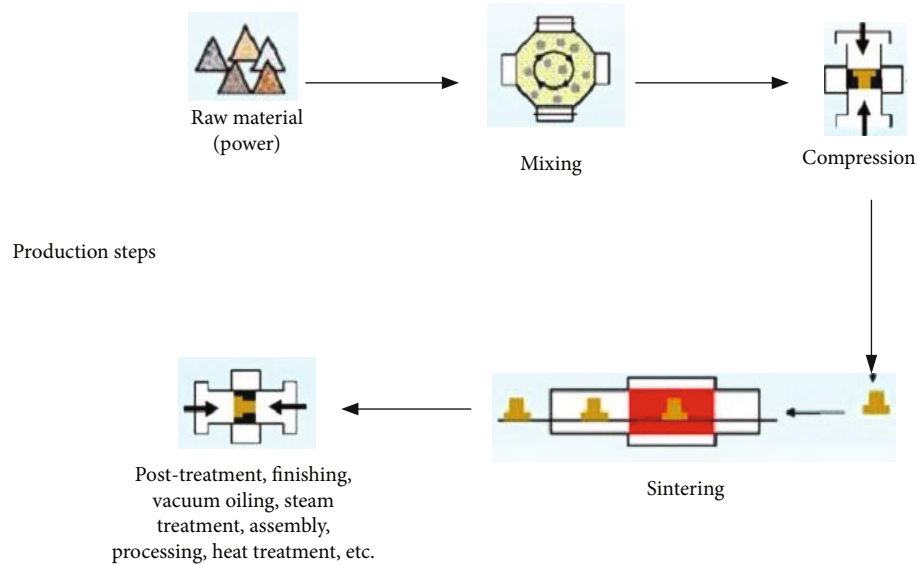
FIGURE 2: Detailed production steps of powder metallurgy method.

the size of the sample before and after the copper infiltration and calculated according to formula (12), d_1 is the diameter before copper infiltration (mm), and d_2 is the diameter after copper infiltration (mm).

$$k = \left(\frac{d_2 - d_1}{d_1}\right) \times 100\%. \tag{12}$$

The strength of ring-shaped powder metallurgy parts is often tested by crushing test. The ring-shaped sample is subjected to radial load until it is crushed to obtain the maximum load F, and the crushing strength is calculated by formula (13). Among them, F is the maximum load (N), D_1 is the outer diameter of the ring (cm), h is the height of the ring (cm), and e is the thickness of the ring (cm).

$$K = \frac{F(D_1 - \mathrm{h})}{eh^2}. \tag{13}$$

In order to detect the interface bonding strength of the two layers of the bimetal seat ring, a tensile strength test is required [14]. Calculate the tensile strength according to formula (14). F_b is the maximum load (N) that the sample bears when it is broken, and S_0 is the original cross-sectional area of the sample (mm).

$$\sigma = \frac{F_b}{S_0}. \tag{14}$$

Collision theory collision-contact reaction is a necessary condition for the reaction between molecules. The higher the concentration of the substance participating in the chemical reaction is the greater the probability of collision, and the faster the chemical reaction. Therefore,

there are

$$v = kC_A C_B. \tag{15}$$

Pulverization and products are two items included in powder metallurgy technology. Pulverizing is mainly a metallurgical process, that is, its literal meaning; while products are through metallurgical processes, and finally, products are obtained [15]. The powder products in our daily life are often beyond the scope of ordinary metallurgy and materials. Usually, they are combined with multiple disciplines of technology, which may include machinery, mechanics, materials, and environment, and are multiple disciplines. Especially in this era, 3D printing technology is very developed, and current metallurgical technology often includes CAD, mechanical engineering, control engineering, materials science, and computer technology, which makes metallurgical technology a very demanding and professional knowledge. Powder metallurgy technology is now very common and widely used in factories, as shown in Figure 3 for the powder metallurgy process.

2.3. Sports Industry. The sports industry is a whole industry that integrates the provision of sports products for the society, the organization of sports activities, and the economic sector that includes sports. The sports industry is a very important sector in our country and an indispensable part of the national economy. Like other industries, the sports industry focuses on market performance and economic benefits. But at the same time, it also has its own unique characteristics different from other industries [16]. For example, the important function of their products is to enhance the physical quality of the people, promote the development of social production, promote the national spirit, and ultimately realize the overall development of individuals and the overall progress of social culture. In a broad sense, the
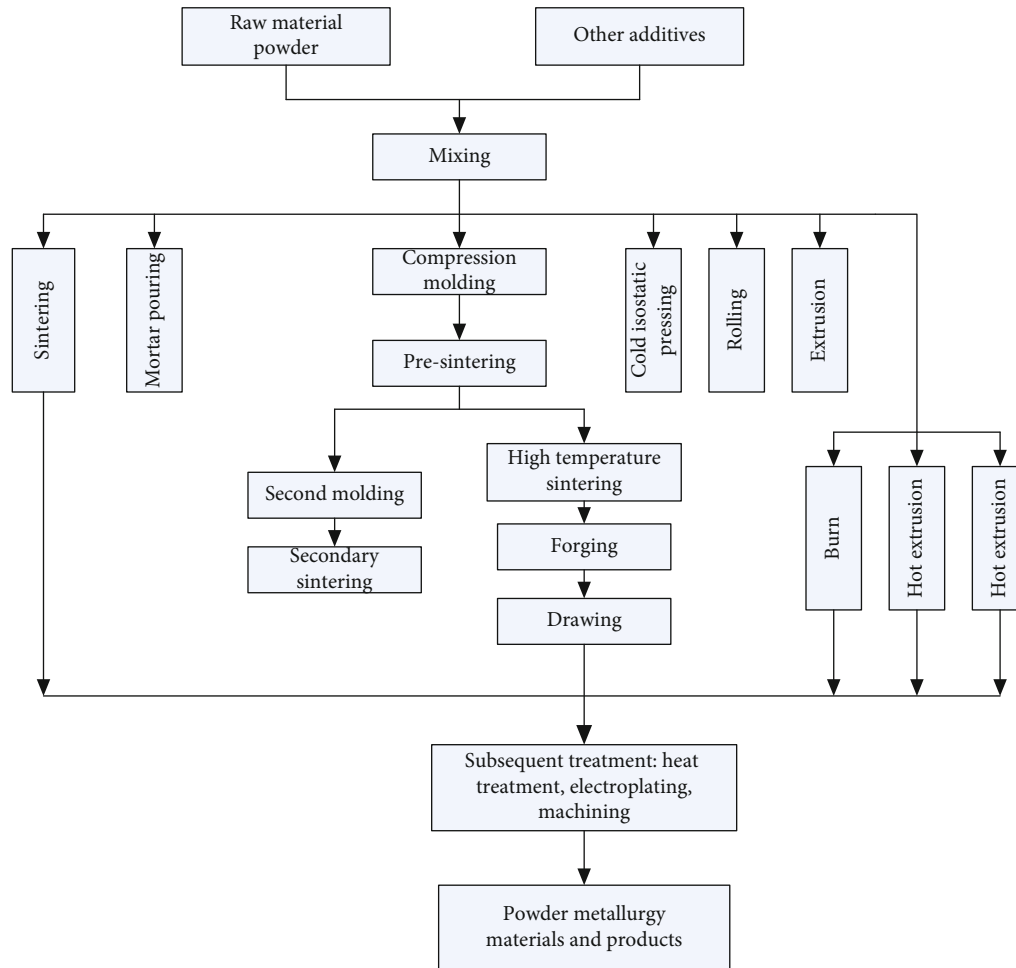
FIGURE 3: Brief introduction diagram of powder metallurgy process.

sports industry includes all business activities related to sports, including the production and management of sports equipment products and sports service products; in a narrow sense, sports products refer to the "sports service industry" or "energy Some sports companies that enter the market but are also profitable" [17]. The industrial chain of the sports industry is the lifeblood of it. It is the general idea of all sports and its derivative industries. All sports industries are developed around it. The sports industry chain is shown in Figure 4.

3. Experiments of Metallurgical Materials in the Sports Industry

3.1. Hardware Design. This experiment is to apply high-performance iron-based powder through sintering technology and finally successfully prepare the material for application in the sports industry. In the experiment, the current sintering technology was used to realize the connection process between the IGBT chip and the silver-plated copper substrate and the DBC substrate [18]. Therefore, 99.95% of the copper purchased in this paper is cut into a substrate with a size of 22 mm ×15 mm ×1.5 mm according to the size of the matching chip. In order to avoid the oxidation problem of the bare cop-

per substrate during the sintering process, the cut copper is electroplated, and 5 μm silver is plated in each direction [19]. As shown in Figures 2 and 3, the processed silver-plated copper and DBC substrate and the IGBT chip are used in the experiment, the IGBT chip size is 6.5 mm × 4.87 mm × 0.12 mm. The IGBT chip and the DBC substrate are quickly sintered and connected by an integrated device to realize the connection between the IGBT chip and the substrate. Among them, the power supply adopts AC-DC-AC-DC conversion technology (IGBT inverter technology), microcomputer control technology, and modern power electronic technology; the time control can reach millisecond precision; and the control response and control accuracy are greatly improved. Due to the use of DC output, its manufacturability is significantly improved [20]. Sintering is one of the most critical parts. The process flow chart of the sintering system is shown in Figure 5. It can process powdered metal or nonmetal materials through specific methods such as firing and finally successfully obtain a dense combination and successfully applied to sports equipment [21].

3.2. Software Design. This experiment also carried out corresponding data collection, data analysis, data processing, and summary work on the computer system, combined with
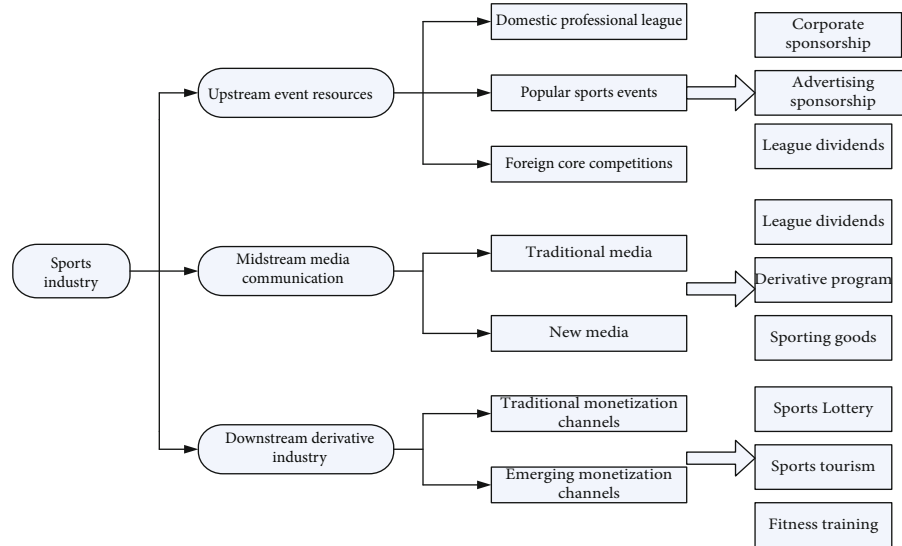
FIGURE 4: Overall block diagram of the sports industry chain.
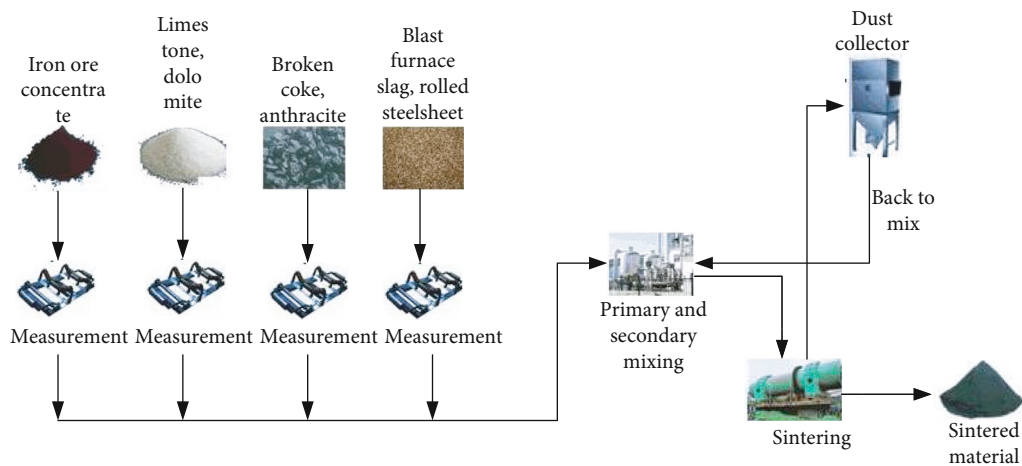
FIGURE 5: Schematic diagram of the process flow of the sintering system.

computer technology, communication technology, network technology, etc., and finally successfully prepared a high-performance iron-based metallurgy that meets the requirements [22, 23]. The transient thermal resistance value of the connection sample between the IGBT chip and the substrate is used to characterize the thermal performance of the sintered silver joint. Transient thermal resistance is characterized by a transient thermal resistance test system independently developed by our laboratory. This system includes a test circuit board that drives and controls IGBT chips, an oscilloscope (TektronixDPO4104B) for real-time monitoring of IGBT output waveforms, and a test circuit for IGBT chips. Collector-emitter programmable DC power supply (RIGOLDP1116A) with heating current, high-efficiency water-cooled heat sink, PVC still air box to avoid the influence of air disturbance on the test results, integrated test control, data acquisition, and data processing software pack-

age and computer carrier [twenty three]. In order to verify the feasibility of the nanosilver connection sample between the IGBT chip and the substrate obtained by the current-assisted sintering method, this paper uses a double-pulse test device for electrical switching characteristics to characterize the electrical switching performance of the IGBT postwelded sample connected with the nanosilver solder paste, as shown in Figure 6 below.

3.3. Overall Design. This article is in the traditional sports industry, in the field of sports equipment and sports equipment, the use of high-performance iron-based powder metallurgy materials through traditional sintering technology, and finally a composite polymer material [24]. Up to now, most of the sports, fitness, and entertainment equipment we use in our daily life are designed and manufactured by metal materials or wood, but the physical characteristics of
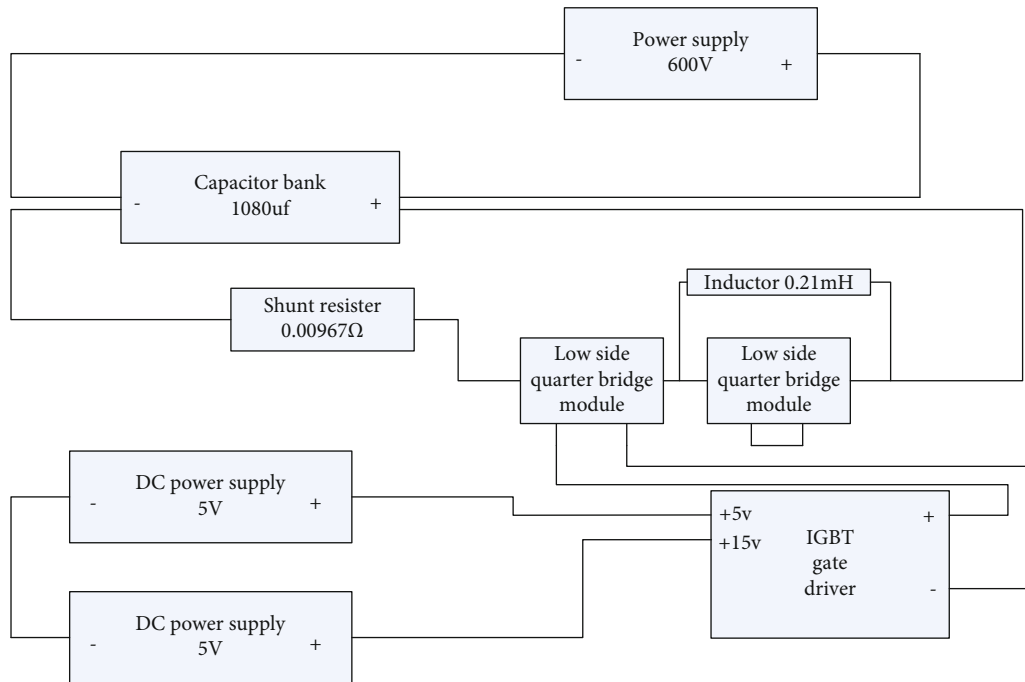
FIGURE 6: Circuit diagram of the double pulse test device.

these materials themselves have led to the strength of the manufactured appliances. With the continuous advancement of science and technology and the continuous successful research and development of various new materials, various new materials have also been widely used in the production of various sports equipment, even in some sports competitions [25]. According to the excellent properties of various new materials, such as high strength, special measurement, light weight, good wear resistance, strong damping performance, and strong design, various materials are widely used in the production of sports equipment.

4. Data Analysis and Discussion Based on Experiments

4.1. Data Analysis Based on Sintering Technology. With the progress of the times and the continuous discovery and utilization of various new materials, and the continuous development of various manmade materials in daily life, the scope of cemented carbide continues to develop and expand. And the performance requirements of cemented carbide are constantly improving. In the 1990s, the research and preparation of cemented carbide with extremely small nanostructured carbides became a huge hot spot. After many inspections, people found that without changing the binder phase content, when the grain size of tungsten carbide is less than $1\,\mu m$, the hardness and strength of the cemented carbide can be significantly improved. And the growth rate has also declined. This leads to a significant reduction in grain size, especially the carboxyl groups of nanocrystalline cement. Hardness and durability will evolve a lot. The German Dust Metallurgical Company has established a grading standard for cemented carbide according to the particle size, as shown in Table 1.

The specific production stages of sintering technology: (1) low-temperature presintering stage. At this stage, it is necessary to produce metal or nonmetal recovery and absorb gas and volatilize water and then carry out the exclusion and decomposition of the embossing; (2) at this stage, there will be a chemical phenomenon called recrystallization. The deformed crystals in the particles will recover and produce a new type of crystal. At the same time, oxides on the surface will be reduced and sintering will be formed at the interface is the completion stage of high-temperature insulation. At this stage, a large number of closed pores will be formed, and at the same time, the full flow and diffusion of the gas will be completed, so that the size and number of small pores will decrease, but the density of the entire sintered body will be greatly increased. The specific situation is shown in Figure 7.

The stacking fault energies of some metals and alloys are shown in Table 2. Through detailed data, it is found that iron is a typical face-centered cubic crystal structure with low stacking fault energy. During the fusion process, the nanoiron grains follow the grain boundary moves and develop, so the nanoiron paste has the matching conditions during the fusion process. Many twins were found in the joint made of silver nanoiron alloy. The nanoiron glue was continuously irradiated with an electron beam at about 200°C. According to TEM observation, a large number of twins were formed at the edges of the iron particles. However, the number of twins will decrease over time until they disappear completely.

The conversion rate between different metals is different. In this experiment, we used several metals and alloys, such

TABLE 1: Cemented carbide grain size classification standards of the society of powder metallurgy.

Alloy grain size	Nanocrystalline	Ultrafine crystal	Submicrocrystalline	Fine grain	Medium crystal	Coarse crystal	Extra coarse crystal
WC grain size (μm)	<0.2	0.2 ~ 0.5	0.5 ~ 0.8	0.8 ~ 1.3	1.3 ~ 2.5	2.5 ~ 6.0	>6.0
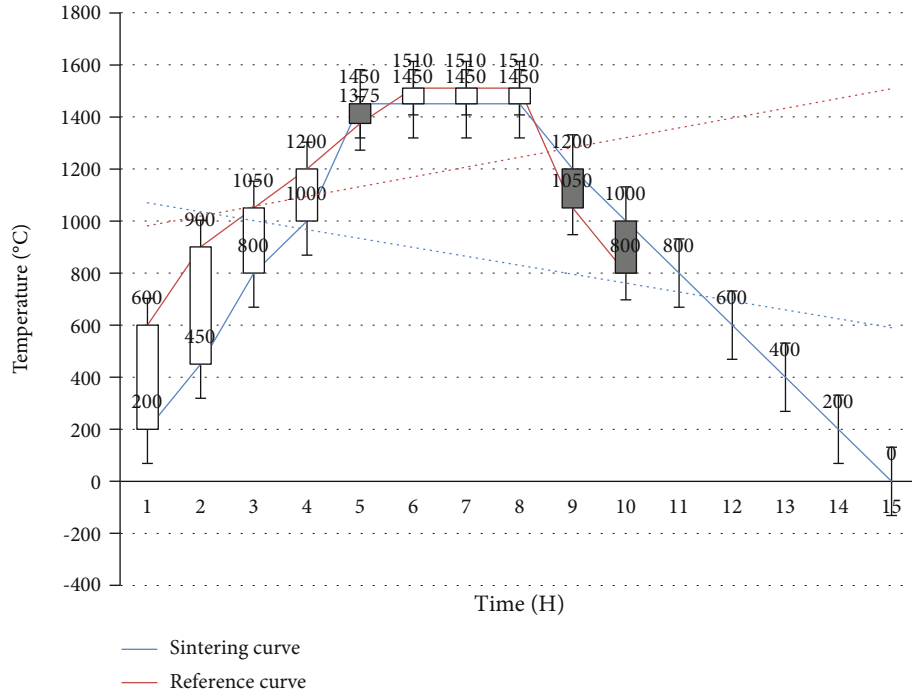
FIGURE 7: Reference curve of sintering process.

TABLE 2: Stacking fault energy values of some metals and alloys.

Material	Ni	Al	Fe	Cu	Au	Ag	Stainless steel
Stacking fault energy (mj)	400	200	18	70	60	20	15
Stacking fault energy (mj)	400	200	18	70	60	20	15

as gold, silver, copper, iron, and stainless steel. The conversion rates between them are high and low. In the experiment, we are studying high-performance iron-based metallurgical materials, so we value the conversion rate of iron or the conversion rate of iron-containing alloys. The conversion rates of different metals at different temperatures are shown in Figure 8.

Preliminary study on the preheating time of fusion pressure the preheating temperature, sintering current, and excitation time basically determine the range of parameters to be discussed in the fusion process. On this basis, the mechanical and thermal properties of the interface between the IGBT chip and the substrate are mainly investigated. The microstructure of the gold-plated copper

rods with different fusion current activation time preheating temperature and different preheating time is shown in Table 3 to ensure the reliability of the experimental data. At least 5 samples are repeated for each group of experiments, and finally, the average value of each group of experimental data is taken as the final result.

In the traditional sports industry, most of the materials used are heavy, wear-resistant, and cheap, such as iron, aluminum, wood, and other materials. The sports equipment made in this way is very heavy, and resistant to torsion, the performance such as hitting feedback is not very good, but the price is cheap, so many people may discard it after using it once, which also causes a certain degree of pollution. However, in this research, we used the new technology to produce high-performance iron-based metallurgical materials. This material is used in the production of sports equipment, making the new sports equipment light in weight, wear-resistant, and resistant to torsion. And many other features, and when damaged, we can also recycle the secondary production. After in-depth research on the application scenarios of high-performance iron-based materials, I calculated the expected improvement (p) of this material in the field of sports equipment for other projects, as shown in Table 4, that is, under
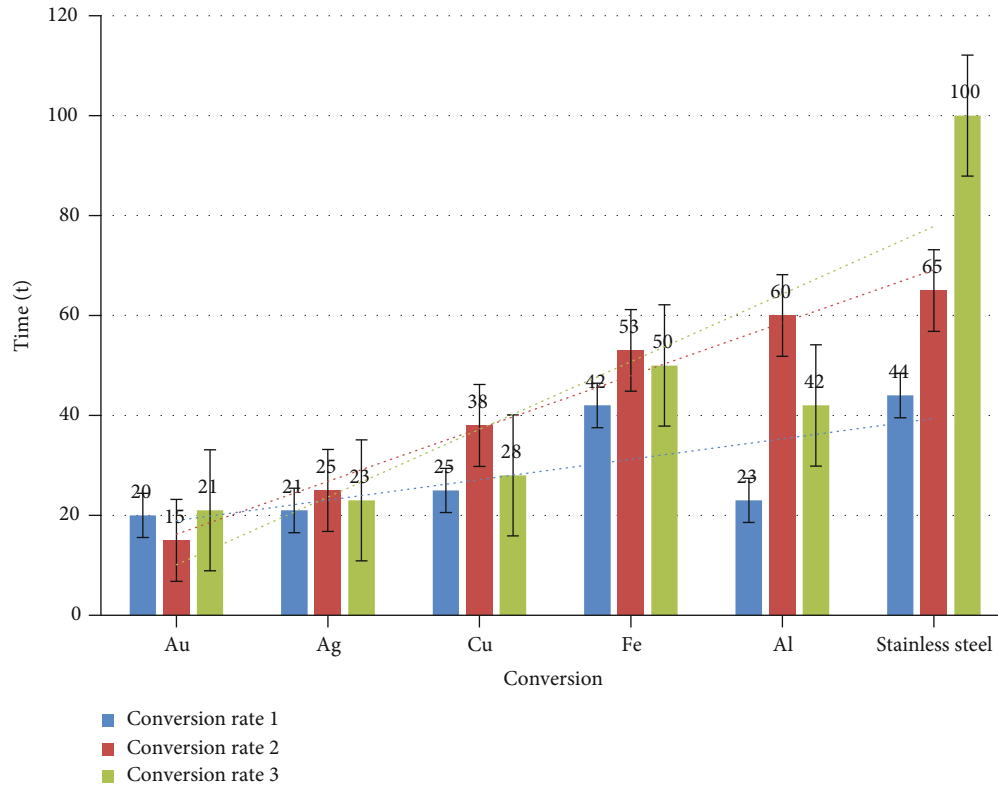
FIGURE 8: Comparison of conversion rates of different metals.

TABLE 3: Summary table of sintering process experiment.

Condition no.	Current (kA)	Current-on time (s)	Predrying temperature (°C)	Predrying time (min)
1	1.2	150	90	20
2	1.6	150	90	20
3	2.0	150	90	20
4	2.4	150	90	20
5	2.0	90	90	20
6	2.0	120	90	20
7	2.0	180	90	20
8	2.0	150	60	20
9	2.0	150	120	0
10	2.0	150	150	10

theoretical conditions, calculate the sports performance of using high-performance iron-based materials in the direction of improving the performance of a certain aspect based on previous data, and compare them with the sports performance of sports equipment using existing composite materials, expressed as a percentage. A theoretical expected value is called the expected lift.

The sports industry is a very important sector in our country and an indispensable part of the national economy. Like other industries, the sports industry focuses on market performance and economic benefits. But at the same time, it also has its own unique characteristics different from other industries. For example, the important function of their products is to enhance the physical quality of the people, promote the development of social production, promote the national spirit, and ultimately realize the overall development of individuals and the overall progress of social culture. With the daily needs of people for sports, sports are not only for physical health. With the rapid development and improvement of sports and related industries, sports have also become a consumer product for people's daily leisure and entertainment. Sports investment and financing have become more and more frequent with the improvement of the sports industry. Figure 9 shows the actual situation of my country's sports industry investment and financing in the past five years.

The sports industry is a very promising industry, and damage to sports and fitness equipment in our daily lives is also a very important aspect. As shown in Table 5, according to estimates, in 2019 alone, the total output value of the national sports industry was 2,948.3 billion yuan, a very significant increase compared to 2018. The construction of daily sports facilities reached more than 20 billion yuan, and the current price increased by 41.7%, accounting for 1.9% of the added value. According to data, from 2016 to 2020, the output value and added value of my country's sports industry are increasing year by year, and many new brands and emerging sports are produced in my country every year. The specific data is shown in Figure 10.

TABLE 4: Comparison of high-performance iron-based materials and traditional alloys.

Sports	Sports equipment	Expected lift
Single parallel bars	High-performance iron-based materials	52.3%
Single parallel bars	Traditional alloy	51.3
Dumbbells	High-performance iron-based materials	17.7%
Dumbbells	Traditional alloy	17.3%
Shot put	High-performance iron-based materials	28.0%
Shot put	Traditional alloy	27.4%
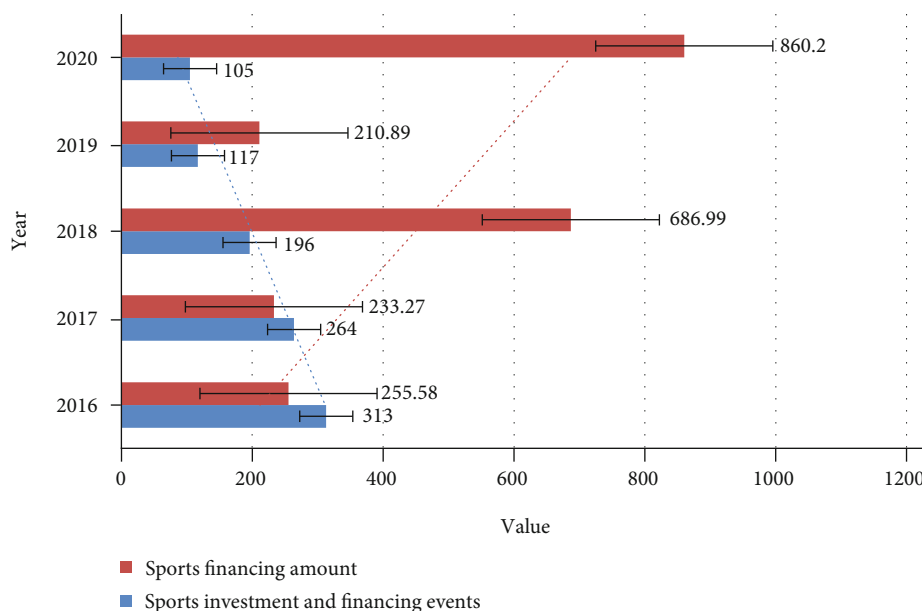
FIGURE 9: China's sports investment and financing events and financing amount from 2016 to 2020.

TABLE 5: 2019 national sports industry status.

Category name	Total (100 million yuan)		Structure (%)	
	Total output	Value added	Total output	Value added
Sports industry	29483.4	11248.1	100.0	100.0
Sports service industry	14929.5	7615.1	50.6	67.7
Sports goods and related products manufacturing	13614.1	3421.0	46.2	30.4
Sports facilities construction	939.8	211.9	3.2	1.9

4.2. Discussion. Sintering technology is a traditional handicraft process, that is, a traditional firing process that converts the original powdery raw material into a dense combination. This article uses sintering metallurgy to produce high-performance iron-based powder materials and then applies them to the sports industry. Its ferrite grains are very small and can only be embedded in amorphous carbon, which makes the ferrite not play the role of lower coercivity. These are two unrelated industries, but through the rapid development of the sports industry in recent years, coupled with the continuous innovation of sports science and technology the integration of various disciplines, industries, and sports make this topic very meaningful for research. For different applications, it is necessary to choose different substances to be compounded with FeNi alloy to meet the application requirements. In the early days, people have already begun to use the sintering process to produce many things, such as porcelain, powder metallurgy, refractory materials, and high-temperature materials. These products are widely used in our daily lives and widely used in our daily lives. In this experiment, we applied this method to produce a new type of material for sports equipment, which can enable the industry to produce new sports equipment with good quality and strong functionality for use in our daily lives, and
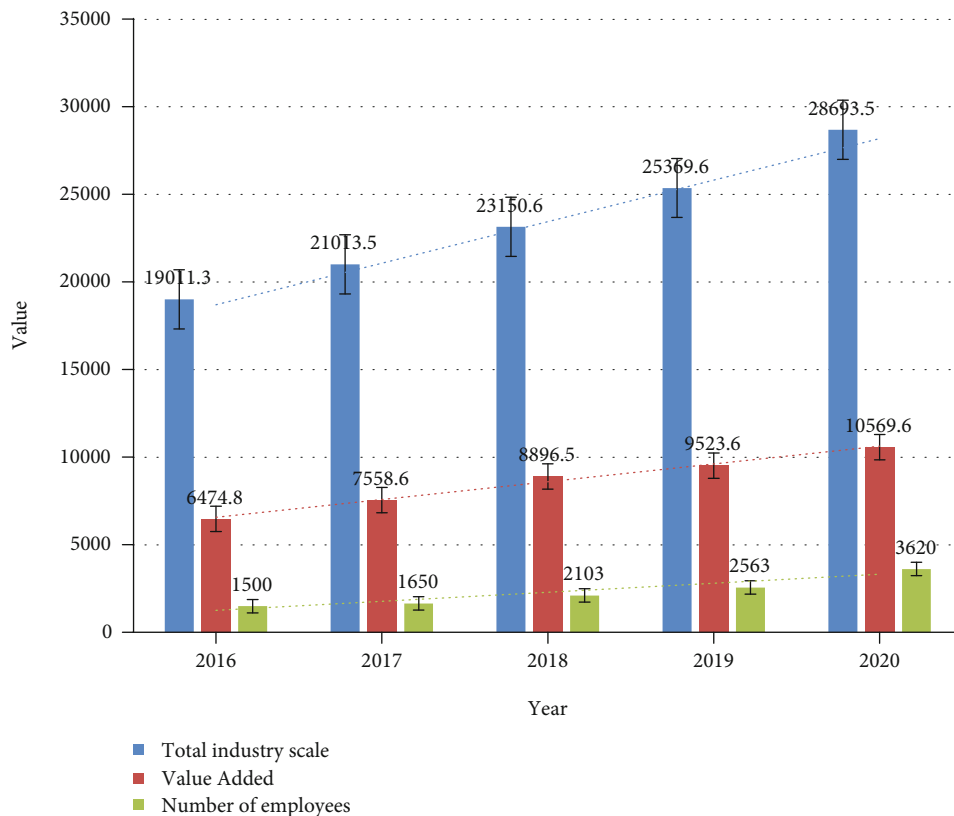
FIGURE 10: Statistics on the scale and increase of China's sports industry from 2016 to 2020.

possibly used in sports equipment. In professional competitions, according to recent trends, this situation is very possible.

5. Conclusions

This article is based on the traditional sports industry, using the sintering method to produce high-performance iron-based powder metallurgy materials, which are used in the development of related sports equipment in the current sports industry. The sintering metallurgical method is a very traditional method, which has been widely used in daily life by our working people since ancient times. Since the beginning of the 21st century, various emerging industries have developed vigorously. As one of the pillars of our country, the sports industry has also begun to develop rapidly. At this stage, it continues to integrate with all walks of life to develop new sports science and technology. Traditional sports equipment basically uses materials such as metal or wood, which are not only cumbersome but also of low quality. In this era of rapid development, they are on the verge of being eliminated. Based on this, we want to design and develop a new type of material for the production of sports equipment, using traditional technology and the current rapid development of the industry. Although our research is still in the theoretical stage, as long as we develop it and realize it, it is believed that it will be widely used in the sports industry for a long time in the future.

Data Availability

No data were used to support this study.

Conflicts of Interest

There are no potential competing interests in our paper.

Authors' Contributions

The author has seen the manuscript and approved to submit to your journal.

References

[1] Y. Shui, K. Q. Feng, H. F. Yue, Y. Y. Zhang, and Z. D. Yan, "Effect of Ni content on iron-based friction material prepared by in-situ synthesized from vanadium-bearing titanomagnetite concentrates," *Cailiao Gongcheng/Journal of Materials Engineering*, vol. 46, no. 9, pp. 73–79, 2018.

[2] F. Mahdi and O. Mahmood, "Effect of yttrium oxide on mechanical and physical properties of Fe–10%Cu composite," *Tikrit Journal of Engineering Sciences*, vol. 27, no. 3, pp. 67–72, 2020.

[3] I. Ribeiro, J. Kaufmann, U. Goetze, P. Peças, and E. Henriques, "Fibre reinforced polymers in the sports industry - life cycle engineering methodology applied to a snowboard using anisotropic layer design," *International Journal of Sustainable Engineering*, vol. 12, no. 3, pp. 201–211, 2019.

[4] D. Tang, Z. Shuliang, and Y. Liang, "Research on the preparation and shielding properties of W–Ni–Fe alloy material by liquid phase sintering," *Powder Metallurgy*, vol. 61, no. 1, pp. 28–35, 2017.

[5] I. A. Stenina, P. V. Minakova, T. L. Kulova, A. V. Desyatov, and A. B. Yaroslavtsev, "LiFePO4/carbon nanomaterial composites for cathodes of high-power lithium ion batteries," *Inorganic Materials*, vol. 57, no. 6, pp. 620–628, 2021.

[6] G. T. Tigineh, G. Sitotaw, A. Workie, and A. Abebe, "Synthesis, characterization and in vitro antibacterial studies on mixed ligand complexes of iron (III) based on 1,10-phenanthroline," *Journal of the Korean Chemical Society*, vol. 65, no. 3, pp. 203–208, 2021.

[7] M. A. Haddad and N. Sedighi, "Elemental analysis of air-full dust in world heritage city of Yazd by laser induced breakdown spectroscopy," *Journal of the Earth and Space Physics*, vol. 47, no. 1, pp. 127–144, 2021.

[8] S. Wu, Z. Li, T. C. Sun, J. Kou, and C. Xu, "The mechanism of CaCO3 in the gas-based direct reduction of a high-phosphorus oolitic iron ore," *Physicochemical Problems of Mineral Processing*, vol. 57, no. 4, pp. 117–124, 2021.

[9] K. Liu, C. Le, F. Zhao, M. Tang, and C. Wu, "Preparation of iron-based pre-alloyed powders by water-gas atomization and its application in diamond tools," *Jingangshi yu Moliao Moju Gongcheng/Diamond and Abrasives Engineering*, vol. 38, no. 2, pp. 32–36, 2018.

[10] A. G. Meilakh, "The influence of iron powder cladding with nickel on properties of sintered materials," *Inorganic Materials: Applied Research*, vol. 8, no. 3, pp. 469–472, 2017.

[11] X. M. Yang, J. Y. Li, G. M. Chai, D. P. Duan, and J. Zhang, "Critical assessment of P2O5 activity coefficients in CaO-based slags during dephosphorization process of iron-based melts," *Metallurgical & Materials Transactions B*, vol. 47, no. 4, pp. 2330–2346, 2016.

[12] X. Tian, J. Zhao, X. Wang, H. Yang, and Z. Wang, "Performance of Si_3N_4/(W, Ti)C graded ceramic tool in high-speed turning iron-based superalloys," *Ceramics International*, vol. 44, no. 13, pp. 15579–15587, 2018.

[13] R. Setiadi and F. Franky, "The analysis of factors affecting preparation level for the industry 4.0 era in the COVID-19 pandemic on employees in DKI Jakarta," *Society*, vol. 9, no. 1, pp. 115–123, 2021.

[14] G. Feng, Y. Ma, L. Hu, M. Zhang, and Y. Zhou, "Preparation and application of high performance bio-based polyvinyl chloride plasticizer. Gaofenzi Cailiao Kexue Yu Gongcheng/polymeric," *Materials Science and Engineering*, vol. 34, no. 6, pp. 16–21, 2018.

[15] Y. A. Fan, Z. A. He, A. Yjs, H. Song, S. Liao, and J. Ren, "Formic acid as additive for the preparation of high-performance $FePO_4$ materials by spray drying method," *Ceramics International*, vol. 43, no. 18, pp. 16652–16658, 2017.

[16] Y. H. Cheng, F. Huang, R. Liu, J. L. Hou, and G. L. Li, "Test research on effects of waste ceramic polishing powder on the permeability resistance of concrete," *Materials and Structures*, vol. 49, no. 3, pp. 729–738, 2016.

[17] H. P. Zhang, P. K. Bai, J. H. Wang, and Y. L. Dong, "Preparation of rapid-hardening, early-strengthening, high-density composite cement based on Dinger–Funk equation," *Arabian Journal for Science and Engineering*, vol. 45, no. 5, pp. 3719–3730, 2020.

[18] C. Wang, G. Zhao, Y. Zheng, K. Zhang, P. Ye, and X. Cui, "Study on the preparation of high performance concrete using steel slag and iron ore tail-ings," *Journal of New Materials for Electrochemical Systems*, vol. 22, no. 4, pp. 217–223, 2019.

[19] W. Zhao, B. Y. Wang, C. S. Zhou, G. C. Zhang, and X. Han, "Research on preparation of light-weight and high-intensity ceramsites with shangluo vanadium tailings," *Rengong Jingti Xuebao/Journal of Synthetic Crystals*, vol. 46, no. 9, pp. 1858–1863, 2017.

[20] T. Hayduk and M. Walker, "Do applicants care? Assessing the influence of socially responsible communication on job seekers in the sport industry," *International Journal of Sport Communication*, vol. 11, no. 1, pp. 18–40, 2018.

[21] M. Kim, "How Phil knight made Nike a leader in the sport industry: examining the success factors," *Sport in Society*, vol. 23, no. 9, pp. 1512–1523, 2020.

[22] H. Weller, A. Streller, and E. F. Purinton, "Brand equity and partnership fit: strategic alliance considerations for the professional sports industry," *International management review*, vol. 15, no. 1, pp. 19–35, 2019.

[23] W. Hao and J. Sun, "Quantitative analysis of data mining application and sports industry financing mechanism based on cloud computing," *International Journal of Grid and Distributed Computing*, vol. 9, no. 12, pp. 233–244, 2016.

[24] A. A. Murtazin, "An algorithm for implementing public-private partnership tools in the sports industry management system," *Economics and Management*, vol. 26, no. 7, pp. 793–799, 2020.

[25] J. Ma and H. Feng, "Review and practice logic of "internet +sports industry" under major epidemic situation," *Science*, vol. 2, no. 2, pp. 101–115, 2020.

Research Article

Application of Nanofiber Material Based on Electrospinning Technology in Sports Rehabilitation of Basketball Player's Wrist Joint

Guang Yang,[1] Haitao Yang [ID],[2] Meng Wang,[2] Yangjie Sun [ID],[2] and Miao Wang[3]

[1]*College of Physical Education, Taiyuan University of Technology, Taiyuan, 030002 Shanxi, China*
[2]*Physical Education Department, Beijing University of Technology, Beijing 100124, China*
[3]*College of Physical Education and Training, Harbin Sport University, Harbin, 150008 Heilongjiang, China*

Correspondence should be addressed to Yangjie Sun; sunyangjie@bjut.edu.cn

Wrist joint plays an indispensable role in our daily life. The injury of wrist joint has a great influence on the fine movement of the hand and upper limb. For example, you cannot do joint movements, you cannot carry things, and life is very inconvenient. It is necessary to distinguish the types of wrist disorders and take effective rehabilitation methods in time. Wrist joint has a great impact on people's life and work, and the rehabilitation of wrist joint has become a research hotspot in rehabilitation medicine and medical engineering. Carpal tunnel syndrome is the most common peripheral nerve entrapment disease in clinical practice, with a very high incidence. According to data, the incidence of carpal tunnel syndrome in the general population abroad is 1%-5%, while that in special populations is as high as 14.5% above. In order to solve the problem of rehabilitation of wrist joint, using electrospinning technology, the polymer solution is prepared into nanofiber materials with strong adsorption and good filterability under the action of high-voltage electric field. And using some small-sized nanofibers that are similar to organs in shape and structure, as well as their excellent degradability and biocompatibility, this material is used in the research of wrist joint movement rehabilitation. In this paper, sports rehabilitation training is carried out on the wrist joint of basketball players, and the nanofiber material is effectively combined with sports rehabilitation training. By comparing the rehabilitation of athletes who did not use nanofiber materials, the role of nanofiber materials in sports rehabilitation was studied. This article analyzes the three parts of the radial joint, the wrist joint, and the ulnar joint before and after the sports rehabilitation training for basketball players with functional impairments and compares the sports rehabilitation of the basketball players without nanofiber materials. This article analyzes the three parts of the radial joint, the wrist joint, and the ulnar joint before and after the sports rehabilitation training for basketball players with functional impairments and compares the sports rehabilitation of the basketball players without nanofiber materials.

1. Introduction

1.1. Background Meaning. Wrist joint is the most flexible joint in human upper limb, which can complete various complex and accurate movements. It is not only used frequently in life but also bears the largest load in the process of supporting, pushing, and pulling. The wrist joint is a complex joint composed of multiple joints, including the radiocarpal joint, the intercarpal joint, and the carpal metacarpal joint. In a narrow sense, the wrist joint refers

to the joint between the lower end of the radius and the first row of carpal bones (except the pisiform bone), that is, the radiocarpal joint; but from a functional point of view, the wrist joint should actually include the radiocarpal joint, the intercarpal joint, and the radioulnar joint. The lateral joints, which are unified in motion, the wrist joint is located deep in the carpal tunnel. The wrist joint is the main part to complete the function of the upper limb, and it is easy to cause injury in daily life. It plays an indispensable role in our daily life. Once the wrist joint is damaged, people's life and work

will be greatly affected. Especially for basketball players who need to use it frequently, if their wrist joint is injured, and the untreated and unreported injury will continue to reduce their ability and lead to poor team performance [1]. In the rehabilitation of wrist joint injury, early and correct functional exercise is very important for the recovery of wrist joint function. It can promote blood circulation, accelerate metabolism, prevent muscle atrophy, and enhance muscle strength through muscle movement. Rehabilitation medicine of wrist joint involves many aspects, and there are many methods of wrist rehabilitation training, such as electrocardiography signal control method, AR method, thermotherapy, occupational therapy, mechanical movement, and exercise therapy. However, due to the complexity of wrist joint, the rehabilitation treatment of wrist joint has always been one of the difficult problems in rehabilitation medicine and medical engineering, and it is also a hot research topic in medical field. In recent years, with the emergence of electrospinning technology and nanofiber materials, researchers have seen a new research idea of wrist rehabilitation training.

Electrospinning is a special form of electrostatic atomization of polymer fluids. At this time, the atomized and split substances are not tiny droplets, but tiny polymer jets, which can run for a long distance and eventually solidify into fibers. Electrospinning is a special fiber manufacturing process in which a polymer solution or melt is jet-spun in a strong electric field. Under the action of the electric field, the droplet at the needle changes from a spherical shape to a conical shape (that is, a "Taylor cone") and extends from the tip of the cone to obtain fiber filaments. In this way, polymer filaments with nanometer diameters can be produced.

Some nanofiber materials are very useful in biomedicine. They are similar to human organs in morphology and structure and have excellent degradation and biocompatibility. The smaller the size of the nanofiber particles, the larger the surface area. Because the surface particles lack the coordination of adjacent atoms, the surface energy is extremely unstable, and it is easy to combine with other atoms, showing strong activity. Human organs are similar. These nanofibers can replace biological organs for organ transplantation, repair, and treatment. Because of its small grain size, the size of internal pores or defects is greatly reduced, and it is not easy to break through the crystal and has unique super plasticity. It is mainly used in artificial bone and artificial joint. Carbon nanofibers have good biocompatibility and strong adsorption. They play an important role in the strength and toughness of artificial organs and can be used in the blood purification system. The application of nanopolymer materials has been involved in immunology, drug-controlled release carrier, and interventionism diagnosis and treatment. Due to the various characteristics of these nanomaterials, researchers will make great breakthroughs in biomedical research.

1.2. Related Work. The rehabilitation training of wrist joint and the application of electrospinning technology and nanofiber materials have always been the research hot spot in the academic field. Erben prepared nanofibers and microfiber mats through a new combination of alternating current (AC) electrospinning and bubble electrospinning, Nanofiber refers to a wire-like material with a diameter of nanometer scale and a large length with a certain aspect ratio. In addition, the fibers that are modified by filling nanoparticles into ordinary fibers are also called nanofibers. In a narrow sense, the diameter of nanofibers is between 1 nm and 100 nm, but in a broad sense, fibers with a fiber diameter below 1000 nm are called nanofibers. Microfiber mat refers to nonwoven sheet scrap functional fibers with a fiber diameter of less than 5 μm [2]; however, the practicability of this method is not as good as that of this paper. Warzoha et al. studied the effect of randomly oriented grapheme nanofibers on the overall thermal properties of organic paraffin PCM [3], but the amount of data that this method needs to collect is too large. Iida et al. studied the stability of the distal radioulnar joint (DRUJ) at different wrist joint positions and examined the relative contribution of each ligament component of the triangular fibrocartilage complex (TFCC) to the stability of DRUJ [4], but the research object of this method is too one-sided. Wu et al. studied the effects of processing parameters such as rotation speed, working pressure, carbonation, and SPS temperature on the diameter of nanofibers [5], but the data needed to be calculated by this method is too complicated. Yan et al. prepared a beaded nanocomposite Li3V2(PO4)3(LVP) grown on carbon nanofibers (CNF) through electrospinning and heat treatment. The preparation method is more precise and simple [6]; however, the operation steps of this method are too many and the operation is too complicated [7], but the cost of this method is too high. Pujari et al. studied the potential benefits of vibration stimulation as a motor intervention and its application in exercise rehabilitation [8], but this method is not suitable for all patients. Han's research is aimed at investigating the current sports rehabilitation industry and finding out the possibility of improving rehabilitation policies [9]; however, the experimental results of this study are not accurate, and there are some errors. Although the relevant research of the above scholars has achieved some results to some extent, most of them are theoretical exploration, with few practical applications, and there is no conflict for the research content of this paper, so the research of this paper is of great significance.

1.3. Innovation of This Article. This article uses nanofiber materials produced by electrospinning technology to improve the sports rehabilitation training of athletes' wrist joints and combines nanofiber materials with sports rehabilitation to make the effect of sports rehabilitation better. The innovations of this article are mainly reflected in the following: (1) using the method of comparative analysis, according to whether nanofiber materials are used in sports rehabilitation training and observe the rehabilitation of the two athletes within five weeks; (2) this article links nanofiber materials with sports rehabilitation and obtains further innovations in sports rehabilitation programs, while expanding the application fields of nanofibers; and (3) this article conducts a comparative analysis from various aspects of

the athlete's wrist joints to ensure the comprehensiveness of the data and the accuracy of the experimental results, including the ruler and wrist angle, the first moon angle, and the ship moon angle, and other aspects of the related indicators for analysis.

2. Proposed Method

2.1. Electrospinning Technology. Electrospinning technology is a technology that overcomes surface tension and viscosity force in a non-Newtonian polymer solution under the action of a high-voltage electric field to obtain nano- to submicron fibers by stretching and bending. Fluids that satisfy a linear relationship between shear stress and shear strain rate are called Newtonian fluids, and those that do not satisfy the linear relationship are called non-Newtonian fluids. Electrospinning technology has changed people's understanding of materials and their properties by manufacturing optimized one-dimensional nanostructures, that is, nanofibers [10]. In recent years, electrospinning has become a promising method to obtain long and continuous fibers with nanometer diameter from a variety of polymers [11]. As a perfect combination of high voltage and nanotechnology, it has injected fresh blood into traditional high-voltage technology. The current background of international research has identified the electrospinning process as one of the key technologies for obtaining nanofibers [12]. Electrospun fibers have attracted attention in many fields, such as tissue engineering, coaxial cables, and drug release due to their huge specific surface area and high porosity. The experimental device of electrospinning technology consists of a high-voltage DC power supply, a sample tube with capillary tube, and a collection plate. The positive pole of the power source output by the DC power supply is connected to the metal electrode inserted into the sample tube, and the negative pole is connected to the receiving plate. With the in-depth research on electrospinning technology in recent years, the laboratory has designed a variety of electrospinning devices that can control the behavior of fiber properties, geometry, and arrangement.

Electrospinning is a modern and effective method that uses an electric field to produce fine fibers whose diameter can be reduced to nanometers [13]. The experimental process of electrospinning technology is as follows: Firstly, the polymer solution is loaded into the sample tube, and the tilt angle of the spinneret is adjusted to make the droplets hang on the spinneret. Turn on the power, and a gradient electric field is formed between the nozzle and the receiving plate. At this time, the electric field force experienced by the nozzle droplets will counteract the surface tension of the liquid. When the two are equal, a "Taylor cone" is formed at the spinneret. Further increase the voltage and the electric field can overcome the surface tension of the liquid. A Taylor cone is formed by the illusion of a liquid under an electric field (or a gravitational field or a pressure field). The Taylor cone is sharp and unusual, and no weapon in the world can match it. And from the tip of the cone is a jet of liquid as thin as a hair. The cone is named after a generation of fluid mechanics guru Taylor, because he used the theory to calcu-

late the angle of the cone. At this time, the tiny stream of dotted liquid is ejected from the spinneret in the form of fiber bundles and moves toward the negative electrode. In this process, the fiber bundle undergoes a series of bending instability processes and electric field stretching processes. The fiber bundles gradually split, and the diameter continuously decreases. At the same time, the solvent gradually evaporates from the fiber surface, and the dried nanofiber falls on the collecting plate. The positive charge of the fiber is partially neutralized by the negative charge accumulated on the negative electrode, forming multiple layers of positively charged nanofibers. The applied voltage, the flow rate, and the distance from the injector to the collector have a moderate effect on the fiber diameter, while the needle gauge has a small effect on the fiber diameter [14].

Electrospinning technology can be regarded as a special case of electrospray technology. Its principle and related formulas are as follows. The droplet at the top of the spinning tube is convex hemispherical under the action of surface tension. When a voltage of a certain potential is applied in the liquid, the curvature of the droplet surface will gradually change. When the potential reaches the critical value of V_c, the droplet is gradually elongated by a Taylor cone with an angle of 49.3 degrees. The small droplets split by the jet at the tip of the Taylor cone have high monodispersity, and the drug is integrated into the droplets. After the droplets are dried, highly monodisperse nanodrug particles can be obtained, and the obtained nanodrug particles can reach ERP. The effect of targeted drug delivery effectively enhances the efficacy of the drug. The data here comes from actual tests by relevant scientists. The value V_c of the critical potential can be determined by the following formula:

$$V_c = \left(\frac{2H}{L}\right)^2 \left[\ln\left(\frac{2L}{R}\right) - 1.5\right](0.117\pi\gamma R). \tag{1}$$

In the formula, H represents the distance between the capillary and the earth pole, L represents the length of the capillary, radius R represents the radius of the capillary, and γ represents the surface tension of the liquid.

For the hemispherical droplet suspended on the end of the capillary, the solution electrospray/electrospun voltage V is similar to the formula of V_c in formula (1), and its value can be expressed as

$$V = 300(20\pi\gamma r)^{0.5}. \tag{2}$$

The r in the formula represents the radius of the droplet suspended at the end of the capillary. The premise of satisfying formula (2) is that the droplet is surrounded by air. and the fluid in the droplet is a simple molecule. The strength and conductivity of the liquid play a vital role in the dynamics of electrospinning.

2.2. Nanofibers. Nanofibers are linear materials with a nanometer scale diameter and a large length with a certain aspect ratio. Its diameter is between 1 nm and 10 nm. The smaller the diameter of the nanofiber, the higher the tensile strength

[15]. Nanofibers are classified into two categories according to their types: fibers having a nanometer diameter and fibers modified by filling conventional fibers with Na-no particles. So far, there are many methods for preparing nanofibers, such as stretching method, template synthesis method, self-assembly method, electrostatic spinning method, and solution jet spinning method. Pass nanofibers have larger surface area and smaller pore size than other materials and have stronger adsorption, good filterability, and barrier ability and excellent adhesion and heat preservation.

The advantages of nanofibers are as follows: First, due to their small diameter, they have a very large size effect, including excellent electrical, magnetic, optical, and thermal aspects. Secondly, the regular arrangement of molecules allows self-organization, thus exhibiting a unified function. Third, in biomedicine, it can be combined with cells to make nanofibers with specific structures. Due to these advantages of nanomaterials, in recent years, nanofibers have found markets in the fields of healthcare, energy, and defense [16]. At the same time, the improvement of the practical value of nanofibers has also promoted the rapid development of its preparation technology.

Based on the unique characteristics of nanofibers, researchers have conducted corresponding research in the following areas: First, in biomedicine, small-sized nanofibers are similar to organs in morphology and structure. Some fibers have excellent degradability and biocompatibility, so cell scaffolds can be cultured. It can be used for tissue and organ repair, as a carrier for drug-controlled release systems and wound coverings [17]. Secondly, about the environment, due to the fiber membrane, the diameter of the fiber is small, the porosity is high, and the uniformity is good. These characteristics of electrospun nanofibers can be used to prepare adsorption materials and filter materials, which can be effectively combined with submicron filtration, and can be applied in atomic industry, aseptic room, precision industry, finishing and other industries, and greatly improve its filtering effect. When nanofibers are used as barrier materials, they can be used as separators between positive and negative electrodes of batteries, because they can prevent the movement of particles and specific ions. For example, the fiber network made of vinyl chloride acrylonitrile copolymer resin by air injection method has high density and high blocking efficiency. As a special battery separator, it can also work in acid and alkaline medium for a long time. In the field of sensor, nanofiber membrane has high specific surface area and excellent structure controllability, which makes it an ideal material for improving sensor performance and preparing high-performance sensor. Nanofiber mats usually exhibit high particle capture efficiency, but due to their more compact structure, they may also lead to higher air flow resistance than macrofiber materials [18]. Due to its hydrophilicity, nontoxicity, and biocompatibility, electrospun nanofiber mats can be used in tissue scaffolds and wound dressings [19]. In addition, researchers have also used nanofibers in protective clothing, aerospace, energy, and magnetic fields and have made significant progress.

2.3. Wrist Joints.

The wrist joint is an important joint of the human arm. It can make up for the lack of freedom of the shoulder and elbow joint. It is a typical elliptical joint. The wrist joint connects the hand and the forearm, is an important part of the upper limb support and thrust, and can withstand heavy loads. Wrist joints, including radiowrist joint, interwrist joint, and ulnar joint, are the most complex joints in the human body. This complex mechanism is conducive to the functioning of the hand. The radiowrist joint is an elliptical deformed ball-and-socket joint, which is a hinge-like motion system with the wrist bone. The radiocarpal joint transfers the load from the forearm to the hand and promotes the fine work of the hands and fingers by providing a considerable degree of stability [20]. Due to different hand movements, the carpal bone is divided into three kinematic chains according to the articular surface of the distal radial carpal. The central chain contains the moon bone, skull, and radius. The side chain is mainly boat-shaped, which can stabilize the wrist bone. The internal measurement chain controls the rotation of the hand, including the triangular fibrocartilage disc, the triangular bone, and the hook bone. Damage to any of the anatomical structures, or even fractures, will affect the function of the entire wrist joint.

In a narrow sense, the wrist joint refers to the joint formed between the lower end of the radius and the proximal row of the wrist bone (not including the pea bone). However, from a functional point of view, wrist joints include the following: (1) the proximal articular surface of the scaphoid, lunate and triangle bones are used as the joint head, and the wrist joint surface of the articular disk below the radius and ulna is used as the joint; (2) distal radioulnar joint; and (3) wrist joints: construct adjacent carpal bones in stages. The bones are intertwined and in contact with each other, connected to each other by complex ligaments and tendons, and have varying degrees of mobility. Due to the complex structure, many joints, and ligaments, the wrist joint is highly flexible. The anatomical properties of the wrist joint allow the wrist joint to move in two planes, frontal uplift offset (abduction and adduction) and surface flexion/extension (palm flexion and extension). The stability of the wrist joint is mainly caused by the wrapping of the joint capsule and the traction of the intercarpal ligaments.

Most of the wrist joint movement is done by the radiowrist joint. In biomechanics, the ulna may be regarded as the pillar of radius activity [21]. It has three degrees of freedom for flexion, extension, contraction, and a certain limit of circular motion. Among them, turning the palm toward the center of the hand is called wrist flexion, also called palm bending; turning to the back of the hand is called wrist extension, also called palm extension; movement in the direction of the thumb is called radial bending. Movement in the direction of the little finger is called ulnar flexion; movement to the outside of the body is called outward rotation; movement to the inside of the body is called internal rotation. There are many kinds of wrist motion theory: the traditional two-row theory, Taleisnik wrist column theory, Gilford's hinge theory, etc.

2.4. Sports Rehabilitation.

Sports rehabilitation is a noninvasive and effective treatment method for sports injuries [22]. In recent years, due to social leisure behaviors, sports rehabilitation after joint or other parts of the body has been injured

and has become more and more important [23]. The purpose of sports rehabilitation training is to improve the patient's physical function and athletic ability. Patients can be assisted by rehabilitation therapists or train their own muscle strength. Sports rehabilitation originated in the sports world and is used for rehabilitation exercises for athletes injured. Sports rehabilitation is a new "trinity" cross-discipline where sports and health medicine overlap, and it is an important part of modern rehabilitation [24]. With the development of medicine, exercise rehabilitation is also suitable for certain diseases, such as stroke, Parkinson's disease, high blood pressure, heart disease, diabetes, and lung diseases.

For sports players, it is important to determine strategies to prevent injuries, optimize rehabilitation, and improve performance [25]. In a sense, the key to the success or failure of sports rehabilitation also depends on the implementation of personal prescriptions and exercise prescriptions. Its content mainly includes form, intensity, time, frequency, and matters. The most important forms of exercise are appropriate resistance exercises and conditioning exercises, as well as aerobic exercises. They can also perform some powerful physical tasks, such as housework and indoor fitness exercises. Exercise intensity is mainly divided into low intensity, medium intensity, and high intensity. It is necessary to comprehensively evaluate the patient's general condition and medical condition according to the patient's risk category and select and exercise the appropriate exercise intensity. It should be noted that the exercise intensity, duration, and exercise frequency of different patients are not exactly the same. Exercise intensity setting methods mainly include age prediction method, heart rate reserve method, resting heart rate+20 method, peak oxygen uptake method, and anaerobic threshold method. When planning an exercise, the main requirement is to ensure patient safety first. Based on this, the intensity and time will gradually increase, and the time of each exercise depends on the situation, ranging from 30 minutes to 1 hour.

Sports rehabilitation training mainly focuses on joint mobility, muscle strength, and functional sports exercises. Rehabilitation treatment requires the participation of the therapist and his family. The therapist will teach the patient's family how to recover and what to pay attention to during the training process. This allows the family to perform simple rehabilitation after returning home to maintain the patient's athletic performance. Family rehabilitation can not only improve the rehabilitation effect but also reduce the economic pressure of the family and form a joint rehabilitation model of hospital and family. During the exercise, the principles of science, applicability, long term, and regularity must be followed, and the frequency should be at least three times a week. Therefore, in order to consider the exercise rehabilitation process to better perform rehabilitation exercises, according to the consensus of the medical profession, exercise rehabilitation is divided into three stages, the first stage is the hospitalization period, and the second stage is the initial discharge period and outpatient rehabilitation. The third stage is the maintenance stage of outpatient rehabilitation. Standardized exercise rehabilitation can not only alleviate the pain and discomfort of patients but also improve exercise endurance, improve mental state, improve overall quality of life, and reduce patients' medical expenses.

3. Experiments

3.1. Test Subject. This article selects two basketball players' sports rehabilitation data before and after wrist joint damage in different periods for experiments. The athlete who uses nanomaterials in wrist exercise rehabilitation is called Athlete A, and the other is called Athlete B. Rehabilitation training was carried out for two athletes, and the specific conditions of the radial joints, wrist joints and ulnar joints, were observed before and after the training, so as to analyze the role of nanomaterials in wrist joint sports rehabilitation.

3.2. Experimental Data. For the statistics on the degree of wrist joint damage of two basketball players before rehabilitation, the collected wrist-related data include the flexion and extension angles of the radius palm inclination angle, radius ulnar deflection angle, ulna carpal angle, radial moon angle, head moon angle, boat moon angle, carpal angle, radial head angle, and radial boat angle. Table 1 shows the degree of damage to the wrist of the two athletes.

The wrist joint damage data of the two athletes in Table 1 were collected in different periods. In the existing medical data, we can know that the normal angle of each carpal joint is shown in the rightmost column of Table 1. In addition, the medical data shows that the angle change of the palmar inclination angle of the radius indicates the fracture of the distal radius; the change of the ulnar deflection angle of the radius indicates the dislocation of the wrist joint or the fracture of the distal radius; the change of the ulnar angle indicates the fracture of the wrist or the dislocation of the wrist joint; radial-lunar flexion > 15° indicates unstable palm flexion, and dorsal extension > 10° indicates unstable back extension; head-lunar angle > 20° indicates wrist instability; boat moon angle > 70° indicates unstable wrist dorsal extension, and <30° indicates instability of wrist flexion; radial head angle > 26° indicates instability of the wrist joint; radial boat angle > 75° indicates instability of the wrist joint.

4. Discussion

4.1. Rehabilitation of the Radial Joint. We analyze the rehabilitation of the wrist joints of two basketball players and compare the rehabilitation of the radial joints of the two athletes with and without nanomaterials for sports rehabilitation training. In order to analyze the effect of nanomaterials on the exercise rehabilitation of the radial joint. With 7 days as a check cycle, we check the extension and flexion angles of the athlete's radius and ulnar angle, radial moon angle, radial head angle, and radial boat angle within 35 days. The final result is shown in Figure 1.

The broken line in Figure 1 represents the recovery of the radial ulnar angle and the radial moon angle of the radial joint within five weeks of athlete A and athlete B. The bar graph shows the recovery of the radial head angle and radial boat angle of the radial joints for athlete A and athlete B in five weeks. The data of radius ulnar angle and radial moon angle are subject to the data of the left main axis, and the data of radial head angle and radial boat angle are subject

TABLE 1: Wrist damage data table.

	Athlete A	Athlete B	Normal
Radial pal-mar angle	Normal	Normal	10-15°
Radius and ulnar deflection angle	15°	15°	21-25°
Ulnar angle	18°	18°	21-51°
Radial moon angle	Buckling15° Back stretch10°	Buckling13° Back stretch10°	0°
Head moon angle	25°	25°	0-15°
Boat moon angle	Buckling20° Back stretch75°	Buckling20° Back stretch75°	30-60°
Carpal angle	Normal	Normal	130°
Radial head angle	30°	30°	6-26°
Radial boat angle	80°	80°	55-75°
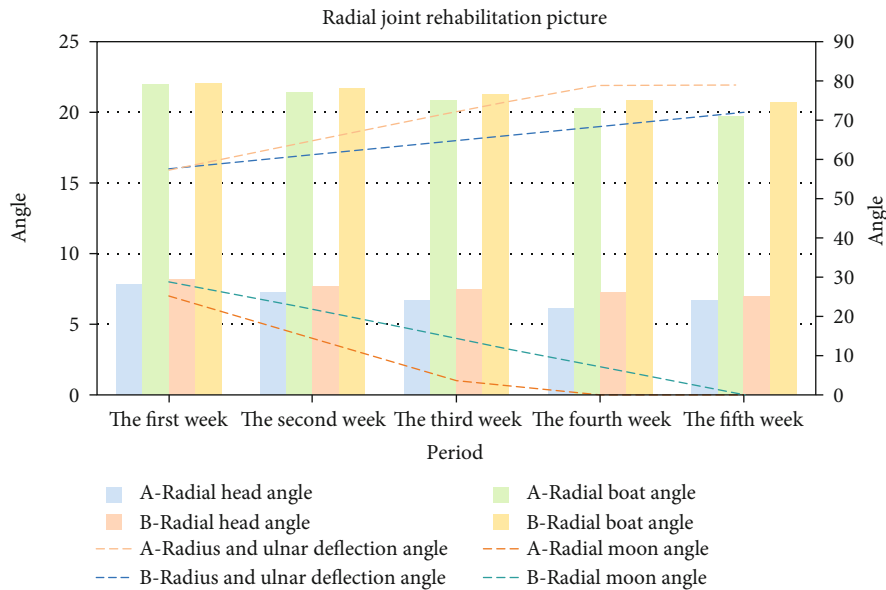
FIGURE 1: Comparison of the rehabilitation of the radius joint.

to the data of the right secondary axis. According to the data in Figure 1, it can be seen that athlete A's radial joint recovered faster than athlete B's in the same cycle. Therefore, the rehabilitation effect of sports rehabilitation training using nanofibers is better than that of sports rehabilitation training without nanofibers, and the recovery ability is stronger.

4.2. Rehabilitation of Other Parts of the Wrist. With 7 days as an inspection cycle, we check the recovery of the ulnar wrist angle, head moon angle, and boat moon angle of the two athletes within 35 days after sports rehabilitation training. The final result is shown in Figure 2.

According to Figure 2, the wrist joint recovery of the two athletes in five weeks can be seen, athlete A who uses nanofibers for sports rehabilitation has a faster recovery speed, and the time required for rehabilitation training is shorter. Athlete B who does not use nanofibers requires a longer period of time for sports rehabilitation and a slower recovery speed.

4.3. Comparison of Rehabilitation Effects between the Two. After five weeks of sports rehabilitation training for two athletes and observation, we can understand that nanofiber materials have a certain influence on the rehabilitation effect of wrist joint sports rehabilitation training. By comparing the degree of wrist joint recovery of the two athletes in five weeks, the final result is shown in Figure 3.

According to the data in Figure 3, it can be seen that the rehabilitation effect of athlete A who uses nanofiber materials for sports rehabilitation training is better than that without nanofiber materials. And before the end of the rehabilitation, the average degree of rehabilitation per week was 0.3 faster than that of athletes who did not use nanofiber materials. Ordinary sports rehabilitation training is about 2 times faster than wrist joints without rehabilitation training, and sports rehabilitation training using nanofiber materials is about 3 times faster than wrist joints without rehabilitation training.

Rehabilitation picture
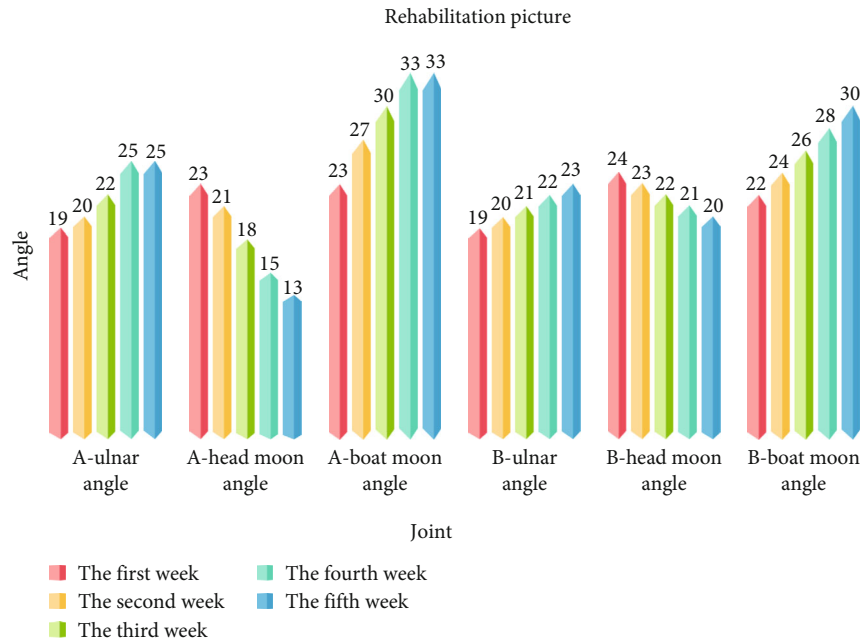
Figure 2: Rehabilitation of other parts of the wrist joint.

Rehabilitation degree comparsion chart
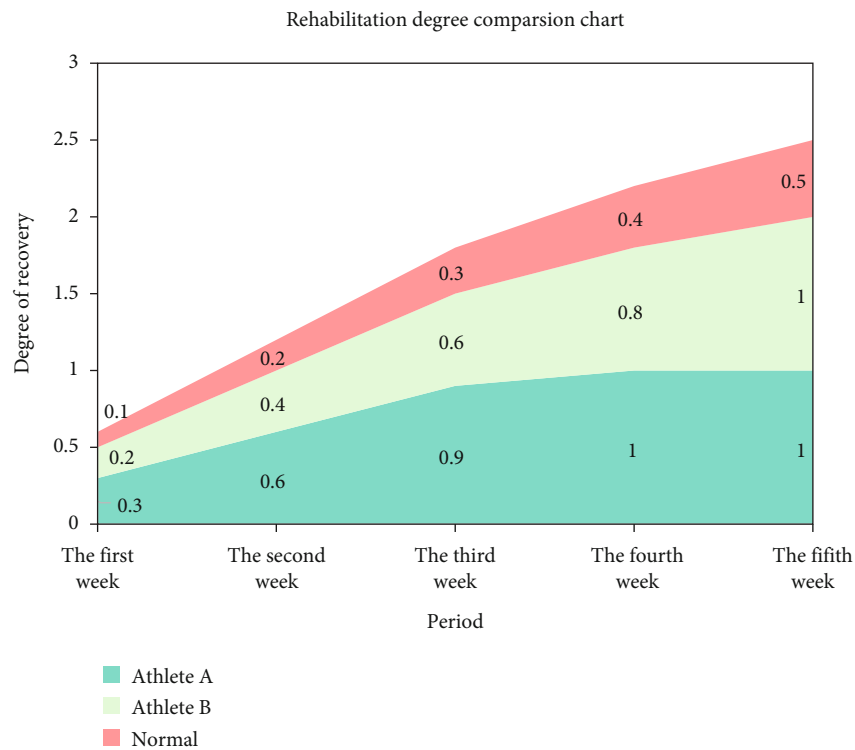
Figure 3: Comparison chart of rehabilitation degree.

4.4. The Application of Nanofibers in Sports Rehabilitation.
By collecting data on sports rehabilitation in the past 5 years, we can understand the use of nanofiber materials in sports rehabilitation in recent years and analyze the proportion of nanofiber materials used in sports rehabilitation. The final result is shown in Figure 4.

It can be known from the data in Figure 4 that in the early years, the application of nanofiber materials in sports rehabilitation was relatively small, and it was in a state of research and development. Later, with the progress of science and technology and the mass production of nanofiber materials, as well as scholars' research on nanofiber materials. Nanofiber materials
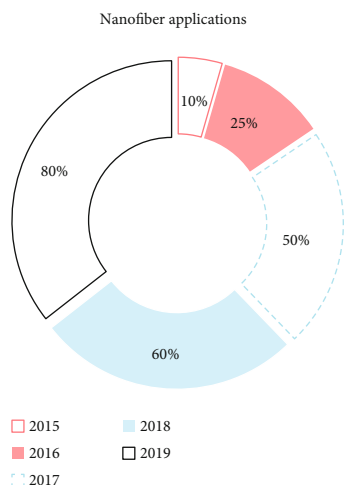
Figure 4: The use of nanofibers in sports rehabilitation.

have become more and more widely used in various fields. As many experiments have proved that nanofiber materials have good rehabilitation effects in sports rehabilitation, the application of nanofiber materials in sports rehabilitation is also increasing year by year.

This article has made corresponding research results on the application of nanofiber materials based on electrospinning technology in the rehabilitation of basketball athletes' wrist joints. However, due to the limited time, the experiment still has many areas to be improved and perfected. This experiment is based on the wrist joint as the research object. In the follow-up experiments, other parts can be combined with nanofiber materials for sports rehabilitation training, so as to understand the role of nanofibers in sports rehabilitation more comprehensively and concretely. Since this study only studied the inclination angle of each part of the wrist joint and did not consider other causes of damage to the wrist joint, the different degrees of damage to the wrist joint can be studied in future studies to ensure the integrity of the experiment.

5. Conclusions

The wrist joint is one of the more important joints on the human body. It connects the two parts of the arm and the palm and plays a vital role in the movement of the human hand. If the wrist joint is damaged; then, people's daily life will also be greatly affected, causing great inconvenience to people. Since the internal structure of the wrist joint in the human body is relatively complex, effective and rapid exercise rehabilitation is the focus of medical researchers.

This article conducts sports rehabilitation training on the wrist joints of basketball players and effectively combines nanofiber materials with sports rehabilitation training. By comparing the rehabilitation of athletes who did not use nanofiber materials, the role of nanofiber materials in sports rehabilitation was studied. Finally, the five-week experimental data of two athletes proved that the combination of nanofiber materials and sports rehabilitation can make the athlete's wrist joint rehabilitation faster and has a better rehabilitation effect than ordinary sports rehabilitation training.

Data Availability

No data were used to support this study.

Conflicts of Interest

The authors declare that they have no competing interests.

References

[1] R. A. Karasch, F. A. Brown, E. A. Smith, and W. C. Paske, "Objective screening parameters for training-rehabilitation of sports teams," *Journal of Clinical Engineering*, vol. 40, no. 4, pp. 210–219, 2015.

[2] J. Erben, T. Kalous, and J. Chvojka, "Ac bubble electrospinning technology for preparation of nanofibrous mats," *ACS Omega*, vol. 5, no. 14, pp. 8268–8271, 2020.

[3] R. J. Warzoha, R. M. Weigand, and A. S. Fleischer, "Temperature-dependent thermal properties of a paraffin phase change material embedded with herringbone style graphite nanofibers," *Applied Energy*, vol. 137, pp. 716–725, 2015.

[4] A. Iida, S. Omokawa, H. Moritomo et al., "Effect of wrist position on distal radioulnar joint stability: a biomechanical study," *Journal of Orthopaedic Research*, vol. 32, no. 10, pp. 1247–1251, 2014.

[5] X. Wu, S. Mahalingam, A. Amir et al., "Novel preparation, microstructure, and properties of polyacrylonitrile-based carbon nanofiber–graphene nanoplatelet materials," *ACS Omega*, vol. 1, no. 2, pp. 202–211, 2016.

[6] B. Yan, L. Chen, T. Wang, J. Xu, H. Wang, and G. Yang, "Preparation and characterization of $Li_3V_2(PO_4)_3$ grown on carbon nanofiber as cathode material for lithium-ion batteries," *Electrochimica Acta*, vol. 176, pp. 1358–1363, 2015.

[7] H. Ba, "Medical sports rehabilitation deep learning system of sports injury based on MRI image analysis," *Journal of Medical Imaging and Health Informatics*, vol. 10, no. 5, pp. 1091–1097, 2020.

[8] A. N. Pujari, R. D. Neilson, S. S. Aphale, and M. Cardinale, "Upper limb vibration prototype with sports and rehabilitation applications: development, evaluation and preliminary study," *Healthcare Technology Letters*, vol. 4, no. 1, pp. 44–49, 2017.

[9] S.-Y. Han, "Status and improvement direction of sports rehabilitation," *Korean Journal of Sports Science*, vol. 26, no. 1, pp. 197–208, 2017.

[10] S. Chavan and S. M. Shendokar, "Analysis of variance—electrospinning of nylon 6 nanofibers with optimum diameter," *Advanced ence Letters*, vol. 22, no. 4, pp. 808–814, 2016.

[11] L. R. Manea, R. Scarlet, N. Amariei, E. Nechita, and I. G. Sandu, "Study on behaviour of polymer solutions in electrospinning technology," *Revista de Chimie -Bucharest- Original Edition-*, vol. 66, no. 4, pp. 542–546, 2015.

[12] L. R. Manea, B. Cramariuc, V. Caunii, and I. Sandu, "Equipment for obtaining polimeric na-no fibers by electrospinning technology I. constructive and functional elements of the computerized electrospinning equipment," *Materiale Plastice*, vol. 52, no. 1, pp. 82–86, 2015.

[13] M. Mirjalili and S. Zohoori, "Review for application of electrospinning and electrospun na-no fibers technology in textile industry," *Journal of Nanostructure in Chemistry*, vol. 6, no. 3, pp. 1–7, 2016.

[14] F. C. Chang, K. K. Chan, and C. Y. Chang, "The effect of processing parameters on formation of lignosulfonate fibers produced using electrospinning technology," *BioResources*, vol. 11, no. 2, pp. 4705–4717, 2016.

[15] E. Fallahiarezoudar, M. Ahmadipourroudposht, N. M. Yusof, and A. Idris, "Influence of process factors on diameter of core (γ-Fe2O3)/shell (polyvinyl alcohol) structure magnetic nanofibers during co-axial electrospinning," *International Journal of Polymeric Materials*, vol. 64, no. 1, pp. 15–24, 2015.

[16] R. Ramakrishnan, J. Gimbun, F. Samsuri et al., "Needleless electrospinning technology – an entrepreneurial perspective," *Indian Journal of ence & Technology*, vol. 9, no. 15, pp. 1–11, 2016.

[17] Y. Liu, A. Nguyen, A. Allen, J. Zoldan, Y. Huang, and J. Y. Chen, "Regenerated cellulose micro-nano fiber matrices for transdermal drug release," *Materials ence and Engineering C*, vol. 74, pp. 485–492, 2017.

[18] R. Al-Attabi, Y. Morsi, J. A. Schutz, and L. F. Dumée, "One-pot synthesis of catalytic molybdenum based nanocomposite nano-fiber membranes for aerosol air remediation," *Environment*, vol. 647, pp. 725–733, 2019.

[19] D. Lei, L. Zhu, and L. O. Papermaking, "Cellulose na-no fibers reinforced electrospun nano-fiber mats containing poly(vinyl alcohol) and waterborne polyurethane," *Journal of Functional Materials*, vol. 46, no. 3, pp. 03110–03114, 2015.

[20] K. Kobayashi, K. Kazama, and M. Sakamoto, "In vivo assessment of articular contact at radiocarpal joint during dorsal/palmar flexion and ulnar/radial deviation," *Experimental Mechanics*, vol. 3, no. 1, pp. 215–220, 2018.

[21] A. H. Törnvall, F. A. Ekenstam, C. G. Hagert, and L. Irstam, "Radiologic examination and measurement of the wrist and distal radio-ulnar joint: new aspects," *Acta Radiologica Diagnosis*, vol. 27, no. 5, pp. 581–588, 1986.

[22] Q. Huasheng, P. Weimin, L. Ran, and L. Xintong, "Sports rehabilitation of chronic ankle instability: research status and characteristics," *Chinese Journal of Tissue Engineering Research*, vol. 36, no. 1, pp. 7-8, 2018.

[23] M. Schmitt-Sody and C. Valle, "Rehabilitation after sports injuries : current concepts and data," *Der Unfallchirurg*, vol. 118, no. 2, pp. 122–129, 2015.

[24] W. Daan, "Dilemma and countermeasure on talent training and teaching of "trinity" sports rehabilitation," *Contemporary Sports Technology*, vol. 18, no. 7, pp. 7–10, 2017.

[25] T. Dn, "Hybridized hierarchical deep convolutional neural network for sports rehabilitation exercises," *IEEE Access*, vol. 8, no. 1, pp. 118969–118977, 2020.

Research Article

Development and Research of Health Examination and Nursing Technology Based on Nanotechnology

Shuai Li [ORCID]

College of Physical Education, Anyang Normal University, Anyang, 455000 Henan, China

Correspondence should be addressed to Shuai Li; lishuai@aynu.edu.cn

With the improvement of the socio-economic level and the continuous popularization of health concepts, more and more people have increased their attention to physical health and often go to physical examinations to protect their health. Nanotechnology, also known as nanotechnology, is a technology for studying the properties and applications of materials with structural dimensions in the range of 1 nm to 100 nm. The rapid development of nanotechnology has provided an important guarantee for healthy physical examination and nursing methods. Therefore, it is necessary to conduct research on the development of health examination and nursing technology based on nanotechnology. Nursing safety means that nursing staff should strictly follow the nursing system and operation procedures in carrying out nursing work, execute medical orders accurately, and implement nursing plans to ensure that patients are physically and mentally safe during treatment and rehabilitation. Based on the development and research of health examination nursing technology under nanotechnology, 220 physical examinees in our hospital were selected and divided into experimental group and control group according to whether nanotechnology-based physical examination nursing method was applied, and then, the physical examination time, physical examination efficiency, and the coincidence degree of physical examination results were compared. The results showed that the physical examination time of the experimental group was 58.94 ± 31.40 min, while that of the control group was 73.74 ± 38.95 min; the difference between the two groups was 14.8 ± 7.55 min, with statistical significance ($P < 0.05$). Therefore, it can be seen that the development and research of health examination nursing technology based on nanotechnology can effectively improve the level of medical care service and the satisfaction of physical examinees.

1. Introduction

With the development and progress of human society, people pay more and more attention to health. People no longer feel satisfied with pure material life but pay more attention to how to improve their quality of life. Early treatment of disease and disease-free prevention has become the life philosophy that people pursue. Regular health checkups can help detect early signs of disease and prevent or delay the onset of disease. Therefore, annual inspections have become a health choice for more and more people.

Physical examination refers to the process of examining subjects through medical means and methods to understand the health status of subjects, early detection of diseases or health damage, and a comprehensive assessment of the health status [1]. The physical examination includes clinical items such as internal medicine, surgery, ophthalmology, otorhinolaryngology, anorectology, and gynecology routine. The purpose of the health check is to assess the health of people, screen for diseases and risk factors, and provide one-way preventive consultation and intervention measures to prevent the onset of diseases or aggravate existing diseases to achieve the purpose of prevention [2]. In other words, medical examinations are aimed at most subjects in society who have no subjective symptoms [3]. Compared with others, this emphasizes the initiative of the subjects and replaces mandatory physical examination with active physical examination. Health is one's own, health is dynamic, health is social, and health is proactive. Regular comprehensive health checkups are required to understand one's health

status, to adopt the best approach and intensity, to improve immunity and resistance to disease, and to detect health risk factors early.

Wider uses the cations released by the cation exchange reaction of nanocrystals to induce fluorescent dyes and detect trace amounts of biomolecules, with good results. This shows the great potential of using portable point-of-care testing equipment to detect biomarkers [4]. Harrison uses polyethylene glycol glucose gold nanoparticles (PEG-Glu-GNP) as the imaging probe for CT and PET scans. Mice injected with gold nanoparticles can be examined by high-resolution micro-CT, and the gray density and CT can be determined [5]. PET-CT is a perfect integration of the functions of the highest-grade PET scanner and advanced spiral CT equipment, which is mainly used clinically for the early detection and diagnosis of major diseases in the fields of tumor, brain, and heart. Farrar used reverse microemulsion technology to further prepare core-shell quantum dot fluorescent nanoparticles with amino and phosphate groups, thereby successfully identifying liver parenchymal cells [6]. van Houwelingen et al. pointed out that the specific distribution of superparamagnetic iron oxide magnetic nanoparticles in biological tissues can help improve the MRI contrast between tumors and normal tissues at that site. MRI, also known as magnetic resonance imaging, uses the magnetic resonance phenomenon to obtain electromagnetic signals from the human body and reconstruct information about the body. It can be applied to MRI to diagnose tumors and other diseases [7]. Murphy uses magnetic iron oxide particles as a carrier to immobilize protease A and uses its ability to specifically bind hepatitis B virus surface antigen antibodies to achieve the purpose of measuring hepatitis B virus [8]. The microfluidic biochip based on nickel oxide nanorods prepared by Ridley et al. can determine the total cholesterol concentration in human blood through electrochemical detection method [9]. Cholesterol is actually an important substance indispensable to human tissue cells. High-density cholesterol has a protective effect on blood vessels; if low-density cholesterol is high, the risk factor for coronary heart disease will increase.

Compared with the previous research on health examination and nursing technology literature, the innovative content of this article is roughly divided into the following points: The first point is the application of nanotechnology as the main aspect. The previous literature mostly introduces human factors such as physical examination and nursing. The second point is to clarify the huge effect of nanotechnology on health examination and nursing technology, because the literature has paid less attention to this in the past.

2. Theory of Health Checkup

Health checkups include medical examinations using medical methods and methods to understand people's health status and find clues to diseases and health risks early. Health checkup is a health-centered physical examination, which refers to the medical examination of the subject through medical means and methods to understand the health status of the subject and to detect disease clues and hidden health problems at an early stage. This includes special medical examinations required by the state, such as occupational medical examinations, medical examinations for practitioners, enrollment, enlistment, marriage registration, medical examinations provided by basic public health services, and new types of local cooperation examinations [10]. But it does not include people who use union medical funds or participate in new rural joint medical care.

Health check is a diagnosis and treatment measure [11]. Secondly, the quality of diagnosis and treatment is the core element of quality control in health examinations. Therefore, the core of medical examination quality control is the quality of supervision and treatment. The central determinant of the quality of diagnosis and treatment is the skill level of medical staff and the composition of related medical devices [12]. In general, the survival and development of a hospital depends on quality, which in turn depends on talents and management. Therefore, there is no doubt that the quality of diagnosis and treatment is an eternal topic in the quality control of health examinations.

There are still some misunderstandings about the health check in some areas, such as Japan, so the local people take the health check late [13]. In pursuit of economic benefits, they sacrificed the quality of diagnosis and treatment and ignored the quality of management. Health checks are becoming more and more important, but they have not attracted enough attention from managers. For example, some excellent managers do not want to go to the health check center for management work, and some do not want to go to the health check center of the health check center [14]. All these hinder the transition from medical experience management to scientific management. Health checks require internal, external, female, eyes, ears, nose, throat, oral cavity, ultrasound, radiology, and laboratory department checks. It can be said that the physical examination center is the epitome of outpatient clinics [15]. Its quality is closely related to people's health and life. Without a sound management system as a guarantee, the quality of the test is also questionable. Health management is a process of holistic management of health risk factors of an individual or a population. Its purpose is to mobilize individual and collective initiatives to effectively use limited resources to achieve maximum health outcomes. Good management quality can not only mobilize the enthusiasm, initiative, and creativity of medical staff but also promote healthy external competition among medical laboratories. At the same time, by continuously attracting outstanding medical staff to engage in health examination work, the professional development of health examination can be promoted.

Physical examination and medical services have some things in common and have their own characteristics. Health check is an action to pursue health and a process of obtaining comprehensive health information [16]. Candidates are usually healthy or unhealthy people who have higher requirements for service quality. Therefore, the quality control of a health examination organization is not only the professional level of medical personnel inspection and the performance of the equipment used in the diagnosis and treatment process but also the evaluation of the health

examination management system of the organization and the implementation of the processing technology platform. The level of service is reflected in the workflow. Due to the lack of advanced science and technology and effective management methods in the past, medical staff had to spend a lot of manpower and material resources to process various inspections and inspection reports, and their work efficiency was very low. Today, the rapid development of science and technology provides technical support for the computerization of medical examinations. The health check has realized the computerization of the health check by establishing the foundation of network technology and introducing information management software [17]. Many application results show that the introduction of information management software for physical examination work can not only improve work efficiency, reduce errors and accidents, and reduce the waiting time of subjects but also make the stored information an ideal for scientific research and optimization of decision-making management select. As shown in Figure 1, to do a good job of health examination and nursing should start from the following points.

Make good training and work arrangements for nursing staff. Reasonably arrange the working hours of nursing staff, conduct batch retraining, improve the quality and ability of nursing staff, and continuously improve their work ability. They are trained on emergency handling capabilities every month, and emergency plan training is conducted on emergency situations to improve the actual combat capabilities of nursing staff [9]. The head nurse organizes the work reasonably according to the nurse's skills and position and improves the reward system according to the level of completion of the nurses to encourage work. The chief nurse will arrange the positions of the nurses reasonably and ensure that there is a staff member for each position, depending on the number of daily inspections. In daily work, in order to ensure the smooth progress of the physical examination, two nurses are required at the front desk, and the nurses will carefully answer the questions of each enquirer with the patient to improve their satisfaction.

Make preparations for each link of the physical examination. Nursing staff should strengthen contact with the health department to avoid having multiple auditors in the long-term testing department, thereby extending the testing time. In one link, the nursing staff brings the medical examiner to the place and procedure of the examination to avoid delays caused by unfamiliar situations [18]. When telling the doctor to complete each examination, the corresponding doctor must sign on it to prevent leakage. In order to improve the efficiency of nursing work, improve compliance, and shorten the inspection time, the examination room of the medical center needs clear signs to guide the examinee to conduct various examinations. Not only that, but various physical examination procedures need to be improved to avoid emergencies such as blood fainting, needle fainting, and low blood sugar.

Improve service methods to ensure a quiet and comfortable environment in the examination room, and separate the examiners from patients with other diseases. Establish a reasonable and convenient path for medical examiners, install
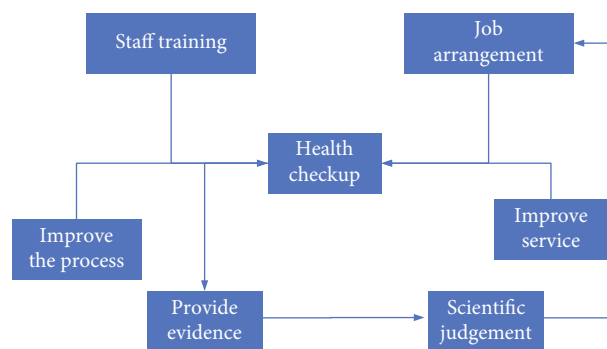
FIGURE 1: Important criteria for health checkup.

all medical examination items on the same floor, and provide one-stop service for the entire medical examination to shorten the time for medical examiners to go up and down the stairs [19]. Paste the relevant knowledge flow chart of the interview on the stairs and walls to ensure that the inspected personnel complete all the exams in the shortest time. After the physical examination, assess the health of the examiner. If there is any problem, we will promptly notify the medical examiner and make appropriate arrangements for the medical examiner's follow-up visit or entry.

3. Application of Nanotechnology in Medicine

Nanotechnology is a high technology with a wide range of disciplines and interdisciplinary development developed in 1980 [20]. When the material reaches the nanometer size, its characteristics will change, thus showing special characteristics, such as small size effect, surface effect, quantum size effect, and macroscopic quantum tunneling. In recent years, bio-related nanobiotechnology has developed rapidly and has become a frontier and hot spot in the international biotechnology field. When nanobiology develops to a certain technology, nanobiological cells with recognition ability can be made from nanomaterials, and biomedicine that can absorb cancer cells can be injected into human body and can be used for targeted killing of cancer cells. It has broad application prospects and clear industrialization prospects in the field of medicine and health. Technologies such as nanomedical carriers, nanomedical materials, nanobiosensors and imaging technologies, and microsmart medical devices will lead to new developments in diagnosis and treatment methods.

Nanodiagnostic technology is the application of nanobiotechnology in molecular diagnosis, which is very important for the development of personalized therapy. At present, research on nanobiotechnology in clinical diagnosis mainly focuses on nanobiosensors and imaging technologies, manufacturing nanorobots at the cellular level for repair, biomarker extraction and measurement, and applications in other fields [21]. Nanodiagnostic technology aims at early diagnosis of diseases and improvement of treatment effects. The application of nanotechnology in health examinations is shown in Figure 2.

Nanotechnology is used in in vitro molecular detection projects. Nanobiomolecule detection methods can be used
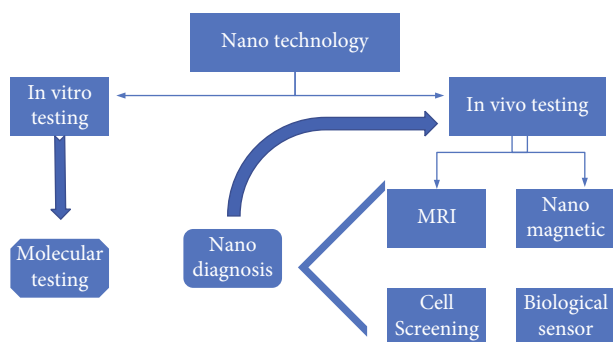
Figure 2: Application of nanotechnology in physical examination.

for clinical diagnosis. Due to the very low content of the detected molecules, the detection sensitivity of this method is very high [22]. The unique properties of nanomaterials greatly improve the sensitivity and convenience of molecular detection. Various signal amplification methods for detecting ultrasmall biomolecules have been studied. A change in the properties of a particle caused by a sharp increase in the ratio of the number of surface atoms to the total number of atoms as the particle diameter becomes smaller. For example, at a particle diameter of 10 nm, the particle contains 4000 atoms and 40% of the surface atoms; at a particle diameter of 1 nm, the particle contains 30 atoms and 99% of the surface atoms. For example, the detection performance of cation exchange amplifiers based on ZnS nanoclusters is better than enzyme-linked immunosorbent assay (ELISA), with a detection limit of 1/1000.

Nanotechnology is also used in in vivo molecular detection projects. Gold nanoparticles are nontoxic and biocompatible nanomaterials. The synthesis method is simple, the particle size is controllable, the surface is chemically active, it is easy to modify or adsorb other substances, and it has unique photoelectric properties [23]. There are many researches on the application of gold nanoparticles in the field of biology. After the injection of gold nanoparticles, the mice were examined by high-resolution micro-CT to determine the gray density, and the attenuation value of particle excretion over time was determined by CT [24]. After injection of PEG-Glu-GNP, the outline of the tumor is easily distinguished from the surrounding tissues. This complex probe can diagnose diseases in the body early and help detect cancer or cancer metastasis early. In addition, the development of neurotransmitters in the body and participation in brain chemistry monitoring help us better understand the pathological and physiological effects of biomolecules. In this study, a new type of glass capillary encapsulated in gold nanoparticles is reported, which can sense dopamine in the brain. The results showed that Au/GCNE modified by perfluorosulfonic acid can be successfully used to monitor striatal dopamine in anesthetized rats. The high quantum dot is a core-shell nanobody with Cd Se as the core and Cd S or Zn S as the shell and has excellent spectral characteristics. Water-soluble quantum dots provide a very broad application prospect in research fields such as biochemistry. It has low cytotoxicity and can be used for ultrasensitive detection of living cells and nonisotopically

labeled biomolecules in vivo. The unique labeling characteristics of quantum dot technology will undoubtedly make it a leading technology for DNA detection (DNA chip), protein detection (protein chip), and the detection of biomolecules in protein-protein interactions. This provides a new method for the preparation of antigen and antibody and the principle of body-receptor (enzyme-substrate) reaction. At the same time, it will greatly promote the rapid development of bioimaging and biopharmaceutical technology, which will bring huge progress in the diagnosis and treatment of diseases.

The emergence of nanomaterials has completely changed the medical detection technology, making it one of the frontier areas of public concern. Nanodiagnosis is the use of the extremely high sensitivity of nanotechnology for early diagnosis of diseases [25]. The tools needed for nanodiagnostics include quantum dots, gold nanoparticles, and cantilevers, where quantum dots have high photostability. This requires the molecules being detected to interact with the nanoparticles to generate a strong signal to detect the sample. (1) Nanomaterials exhibit many excellent physical properties in biomedical imaging applications. In the field of nanoimaging, small superparamagnetic iron oxide nanoparticles coated with biomolecules provide anatomical details and help achieve real-time monitoring of treatment. Magnetic resonance imaging (MRI) to detect cancer is widely used as a contrast agent. Compared with traditional diagnostic methods, certain cancer cells can be detected earlier (months or years). Nanoimaging technology can also be used to detect residual or metastatic cancer cells after chemotherapy. (2) Since magnetic nanoparticles have the advantages of easy handling and large specific surface area, the application of functionalized magnetic nanoparticles is very attractive. Current magnetic separation research involves many aspects of the biological field, such as the removal of metal ions from the blood, the concentration of proteins and nucleic acids, and the recovery and repetition of immobilized enzymes. (3) When there is a small amount of cancer cells in the tissue or blood, they can be accurately detected by specific techniques, which can provide early diagnosis and treatment of patients and indeed provide patients with valuable treatment time and improve the cure rate [26]. Therefore, cell screening is very important. The immunomagnetic bead cell screening method can separate high-purity cells from complex cell mixtures within minutes. Nanotechnology can improve accuracy by enhancing or even completely transforming the screening of biomarkers in tissues and body fluids. (4) Nanobiosensors in the field of cancer research and sensors based on nanotechnology are expected to achieve early diagnosis of various cancers. The sensitivity of the nanosensor is very high. During blood testing, when a specific cancer cell antibody preset in the sensor encounters the corresponding antigen, the sensor current will change, and the change in the current can identify cancer cells in the blood, type, and concentration. At present, more and more venture capital invested in this field, but this technology still has technical problems that need to be solved in practical applications. In the future, various nanosensors will be integrated and placed in the human body to allow early detection of various diseases.

4. Experiments on Health Examination and Nursing

4.1. Experiment Preparation

4.1.1. Subject.
There was a selection of 220 medical examiners in our hospital from March 2018 to March 2019, of which 116 were males and 104 were females. The age ranged from 18 to 65 years old, with an average of 33.67 ± 5.73 years old. A total of 60 medical staff, 18 doctors, 4 chief nurses (senior nurses), 11 intermediate, 10 junior, and 17 nurses participated in the medical examination center. For inclusion criteria, all subjects underwent physical examinations and signed all informed consent forms. For exclusion criteria, there are serious communication problems. The conditions of the experimental subjects are shown in Table 1.

4.1.2. Experimental Group.
Magnetic nanoparticles with a particle size of less than 20 nm usually exhibit superparamagnetic and can be widely used in clinical diagnosis. At present, the more mature and rapidly developing application in clinical diagnosis is mainly magnetic resonance imaging. Therefore, magnetic resonance imaging of nanomaterials was used as the standard to distinguish the experimental group from the control group. The experimental group will use MRI technology applied with magnetic nanoparticles, and the control group will use traditional imaging technology for physical examination. 110 people per group, the ratio of male to female in each group is 58 : 52.

The porous $Fe_3O_4@SiO_2$ nanoparticles have uniform morphology, ordered pore size distribution, and good acid response. At the same time, the nanocarrier has excellent biocompatibility, strong antipain drug loading capacity, and excellent nutrition-guided fan orientation. In addition, the relaxation rate of $Fe_3O_4@SiO_2$ nanoparticles in an acidic environment is significantly improved, which provides a more direct method for detecting cancer tissues by magnetic resonance imaging. Therefore, $Fe_3O_4@SiO_2$ nanoparticles can target and deliver therapeutic agents loaded into tissues in the body and monitor the therapeutic changes in the tissues in real time through magnetic resonance imaging.

4.1.3. Preparation of $Fe_3O_4@SiO_2$ Core-Shell Nanoparticles.
According to the classic hydrolysis method, the core-shell structured silica-coated Fe_3O_4 nanospheres were synthesized. A specific method is to uniformly disperse 0.1 g of synthetic Fe3O4 nanospheres in a mixed solution of 140 ml of ethanol and 20 ml of distilled water to form a colloidal solution and then add 2 ml of concentrated ammonia to the solution. Stir mechanically for 10 minutes. Then, a mixed solution of 1.5 ml TEOS and 10 ml ethanol was gradually added to the colloidal solution, stirred at room temperature for 30 hours, collected with a magnet, washed several times with ethanol and distilled water, and dried in vacuum.

Disperse 0.1 g of the synthesized core-shell $Fe_3O_4@SiO_2$ nanoparticles uniformly in distilled water, add 10 g 8 g/L NaBH4 ice water solution, and pour the mixed solution into the PTFE hydrothermal reaction solution and heat it at 80°C. The reaction was kept at °C for 12 hours. Finally, the product

was collected on a magnet; washed 3 times with propanol, ethanol, and water; and dried in a vacuum drying oven at 30°C overnight. Add $Fe_3O_4@SiO_2$ as a contrast agent to the magnetic resonance device.

4.1.4. Experimental Instruments and Reagents.
The experimental instruments and reagents are as follows: automatic blood analyzer, EDTA-K2 vacuum anticoagulation tube, automatic urine analyzer, magnetic resonance meter, electrocardiograph, and CT detector.

4.2. Experiment Content.
Before the experiment, fully understand the needs of examinees, solicit opinions from relevant experts, and strive to meet the needs of medical examiners at all levels, and refer to literature. It is necessary to combine the characteristics of the physical examination center and the characteristics of the examinee to establish a physical examination path diagram to learn and understand the meaning and standards of the clinical nursing path.

Use the nursing service satisfaction questionnaire and various nursing quality work questionnaires compiled by our hospital to collect statistics on the health examination and nursing work quality scores. Develop complete rules and regulations based on different scores. Health check contents are as follows: internal medicine, surgery, otolaryngology, oral cavity, 5 items of hepatitis B, blood test, urine test, electrocardiogram, chest X-ray, thyroid B ultrasound, prostate B ultrasound (male), uterus, and appendix B if necessary. Endoscopy will be performed, such as ultrasound (for women), B-ultrasound of the liver and pancreas, and CT. Coordinate the reasonable examination sequence and scientific physical examination process of each group of medical examiners, and ensure that every link in the physical examination path can operate normally. Each physical checkpoint has one or two full-time staff to provide nursing services.

4.2.1. Routine Blood Test.
Both groups of patients were collected at 9 o'clock in the morning. The experiment used venous blood collection. The patient's cubital vein was selected as the venous blood collection site. After cleaning and disinfecting the skin, the disposable blood collection needle was connected to a vacuum anticoagulant. Collect the blood in a test tube with a blood volume of 5-8 ml. After the blood is collected, add a diluent to the anticoagulation tube to dilute the sample, and shake it gently to mix well. The control group adopted the peripheral blood sampling method. The left hand of the patient was selected, the skin of the index finger was cleaned and disinfected, and then, the blood was collected with a disposable lancet and placed in an anticoagulation tube. After the blood samples of the two groups were shaken well, the blood analyzer was used for routine blood tests. All samples are tested within 2 hours after blood collection. Strictly follow the operating

TABLE 1: Basic situation of experimental subjects.

Number	Age	Sex ratio	Number of medical staff
220	33.67 ± 5.73	116 : 104	60

TABLE 2: Health physical examination and nursing service level.

Group	Knowledge propaganda	Care etiquette	Communication skills
Control group	8.46 ± 0.87	9.56 ± 0.69	8.02 ± 0.35
Trial group	8.51 ± 0.76	9.64 ± 0.74	7.97 ± 0.28

procedures of the automatic blood analyzer, and perform regular maintenance and quality control on the instrument before use. Strictly follow the instructions of the kit to keep the equipment stable and check and maintain blood cells to ensure stable operation of the equipment. Under the condition of continuous operation for 24 hours, the instrument is automatically cleaned and calibrated according to the program, and the values of various parameters are controlled within the normal measurement range.

4.2.2. Urine Routine. All women need to clean their vulva and collect specimens. After the specimens are sent to the laboratory, they are inoculated with fully mixed urine in a 35°C incubator using a 1 μL loop and cultured for 18-24 days to colonize colonies. Liquid forming element analysis can quantitatively calculate white blood cells and bacteria. After mixing the urine sample, use an automatic urine forming element analyzer to detect the number of bacteria and white blood cells in the urine, and report it in "units/μL."

4.2.3. Evaluation Criteria. After the physical examination is completed, a statistical score will be made on the length of the physical examination, the efficiency of the physical examination, the reliability of the physical examination, the satisfaction of the medical examiner, and the degree of interest in statistical treatment. Use t-test and $\chi 2$ test, and use the SPSS 10.0 software package to process and analyze all data. The inspection level is $\alpha = 0.05$.

5. Results of Health Checkup Care

5.1. The Development and Research Effect Comparison of Health Examination and Nursing Technology Based on Nanotechnology. The core of high-quality services is to provide customers with safe, high-quality, efficient, and satisfactory nursing services and to integrate the "patient-centered" nursing service concept into physical examination. High-quality service is an inevitable product of the development of the times and social progress. Innovating the physical examination path model and creating a standardized physical examination path are specific signs of improving quality services. With the implementation of the physical examination certificate, the nursing staff of the physical examination center must be enthusiastic about their work, have a good service attitude to the candidates, and have good nursing skills. "From passive service to active service, from active service" service concept "to touching service" provides all nursing staff with beautiful, more common problems, more information, and more detailed services. As shown in Table 2, there is basically no difference in the level of health examination and nursing service of different groups.

As shown in Table 2, the health knowledge preaching score of the nursing staff in the control group was 8.46 ± 0.87 points, and the nursing etiquette and communication skills were 9.56 ± 0.69 and 8.02 ± 0.35 points, respectively. The scores of health knowledge presentation, nursing etiquette, and communication ability of the experimental group were 8.51 ± 0.76, 9.64 ± 0.74, and 7.97 ± 0.28 points, respectively. In general, the two sets of data are not statistically significant.

Nanobiotechnology has great development potential. It can be used as a more sensitive and rapid response clinical diagnostic reagent, providing a valuable basis for the advancement of disease prevention and treatment. Taking into account the heterogeneity between patients, personalized medicine combining nanoclinical medicine and molecular biomarkers can ensure excellent efficacy and safety. Therefore, health checkup and nursing technology based on nanotechnology can effectively reduce checkup time and improve checkup efficiency.

As shown in Figure 3, after applying the health checkup and nursing technology under nanotechnology, the time of the physical examination of the experimental group was significantly reduced. The time of the physical examination of the experimental group was 58.94 ± 31.40 min, and that of the control group was 73.74 ± 38.95 min; the difference between the two is 14.8 ± 7.55 min, and the two groups of data are statistically significant ($P < 0.05$). The physical examination efficiency score of the experimental group physical examination subjects was 8.72 ± 0.68 points, and the physical examination time of the control group physical examination subjects was 7.29 ± 1.23 points. It is obvious that the health examination and nursing technology based on nanotechnology are more mature, saving a lot of time in the physical examination.

The detection accuracy of physical examination items is also an important criterion for measuring health examination and nursing technology. Therefore, the credibility scores on the physical examination items are compared to determine which group has the higher accuracy of the physical examination. Comparing the experimental group using nanotechnology health examination and nursing technology with the control group, the data is statistically significant, $P < 0.05$.

As shown in Figure 4, the reliability scores on the physical examination items of the experimental group using nanotechnology health examination and nursing technology are distributed in the range of 6.57-8.69. In contrast to the control group, the reliability scores on the physical examination items are distributed at 5.28—within the 6.85 interval. This also shows that due to the application of nanotechnology, the experimental group has significantly improved the health examination and nursing technology and can have a very clear judgment on the health of the examinee. At this point, the health examination and nursing technology of nanotechnology have been applied. The experimental group has a very big advantage.

5.2. Analysis on the Satisfaction of Medical Examiners Based on the Health Examination and Nursing Technology Based on Nanotechnology. During the physical examination, the
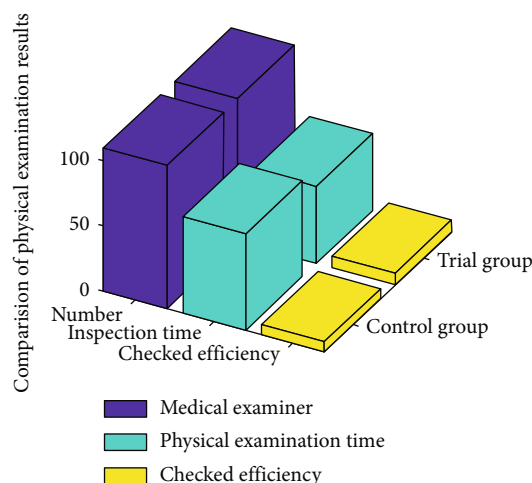
FIGURE 3: Comparison of physical examination results between the two groups.

FIGURE 5: Comparison of satisfaction values between the two groups.
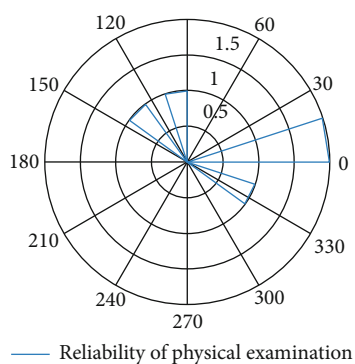
FIGURE 4: Comparison of physical examination reliability scores.
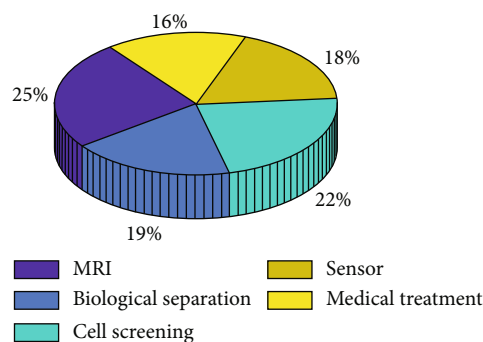
FIGURE 6: Classification of nanotechnology in health checkup.

nursing staff will actively communicate with the patient and their family members according to the patient's psychological endurance and understanding ability and explain the current medical technology used to treat and treat the disease. Nursing staff should conduct some tests on patients who may have depression and then provide counseling and psychological counseling to them to reduce the psychological pressure of patients and seek to win their trust in order to establish a good nurse-patient relationship. While carrying out necessary communication, compare the medical examination satisfaction of the two groups of examinees to observe whether the application of nanotechnology can be favored by the examinees.

As shown in Figure 5, the satisfaction value of the experimental group continues to rise with the increase in the number of people undergoing physical examinations, from the initial 87.67% to the final 88.97%. In the control group, the satisfaction value fluctuates greatly. This shows that the experimental group based on nanotechnology-based health examination and nursing technology has achieved more satisfaction with the examinees by virtue of less examination time and accurate examination results. In contrast, the control group experienced fluctuations in satisfaction, and the high probability was related to its poor physical examination experience.

Nanotechnology-based physical examination and nursing technology not only provide advanced clinical diagnostic methods, such as magnetic resonance imaging during physical examination, bioisolation, and cell screening, but also provide the convenience provided by nanorelease drugs and nanobiosensors. Therefore, the position of nanotechnology in health examination and nursing is very important. In order to see the specific application of nanotechnology in health examination and nursing more intuitively, it is expressed as a percentage.

As shown in Figure 6, the main application of nanotechnology in health checkup care is magnetic resonance imaging (MRI), which accounts for 22%. The special properties of nanoparticles make them an excellent contrast agent, which can make the imaging clearer and more intuitive, so as to understand the internal structure of the examinee more clearly, and achieve the purpose of protecting health.

6. Conclusions

(1) The research background of this article is that with the improvement of socio-economic level and the continuous popularization of health concepts, more and more people have increased their attention to physical health and often participate in physical

examinations to protect their health. The rapid development of nanotechnology has provided an important guarantee for healthy physical examination and nursing. Nanotechnology plays an important role in health examination and nursing. Therefore, it is necessary to conduct research on the development of health examination and nursing technology based on nanotechnology

(2) The purpose of this article is to start with the development and research of health examination and nursing technology under nanotechnology. 220 physical examination patients in our hospital are selected and divided into experimental group and control group according to whether the physical examination and nursing method under nanotechnology is applied. The experimental group prepares Fe3O4@SiO2 core-shell nanoparticles as the MRI contrast agent for detection. The control group does not use it by default. Data statistics are made on the physical examination time, physical examination efficiency, and physical examination results, and then, the physical examination time, physical examination efficiency, and physical examination results coincide with each other

(3) The experimental data shows that after applying the health checkup nursing technology under nanotechnology, the checkup time of the experimental group's checkups is significantly reduced, the checkup time of the checkups in the experimental group is 58.94 ± 31.40 min, and the checkup time of the checkups in the control group is 73.74 ± 38.95 min; the difference between the two is 14.8 ± 7.55 min, and the two groups of data are statistically significant ($P < 0.05$). The physical examination efficiency score of the experimental group was 8.72 ± 0.68 points, and the physical examination time of the control group was 7.29 ± 1.23 points. This clearly shows that the health examination and nursing technology based on nanotechnology are more mature, saving a lot of time in the physical examination

Data Availability

No data were used to support this study.

Conflicts of Interest

The author declares that there are no conflicts of interest regarding the publication of this article.

Acknowledgments

References

[1] T. Okura, T. Tsuji, K. Tsunoda et al., "Study protocol and overview of the Kasama Study: creating a comprehensive, community-based system for preventive nursing care and supporting successful aging," *Journal of Physical Fitness & Sports Medicine*, vol. 6, no. 1, pp. 49–57, 2017.

[2] S. F. Paparella, "What's in your kit? A safety checkup may be in order," *Journal of Emergency Nursing Jen Official Publication of the Emergency Department Nurses Association*, vol. 41, no. 6, pp. 513–515, 2015.

[3] K. Szczerbińska, E. Topinková, P. Brzyski et al., "Delivery of care to nursing home residents with diabetes: results from the SHELTER study," *Journal of the American Medical Directors Association*, vol. 17, no. 9, pp. 807–813, 2016.

[4] J. Wider, "Tips for giving your organization a telehealth checkup," *Health Management Technology*, vol. 38, no. 4, pp. 6–9, 2017.

[5] P. Harrison, "A birthday checkup for the NHS at 70," *Gastrointestinal Nursing*, vol. 16, no. 7, pp. 51–51, 2018.

[6] C. F. Farrar, "Transforming home health nursing with telehealth technology," *Nursing Clinics of North America*, vol. 50, no. 2, pp. 269–281, 2015.

[7] C. T. M. Van Houwelingen, R. G. A. Ettema, H. S. M. Kort, and O. Ten Cate, "Internet-generation nursing students\view of technology-based health care," *Journal of Nursing Education*, vol. 56, no. 12, pp. 717–724, 2017.

[8] K. Murphy, "Is technology affecting our health?," *Nursing Made Incredibly Easy*, vol. 14, no. 4, pp. 44–52, 2016.

[9] J. Ridley, A. Ischayek, V. Dubey, and K. Iglar, "Adult health checkup: update on the Preventive Care Checklist Form©," *Canadian Family Physician Médecin De Famille Canadien*, vol. 62, no. 4, pp. 307–313, 2016.

[10] N. R. Yancey and N. R. Yancey, "Ubiquitous technology in healthcare and teaching-learning: scourge or blessing?," *Nursing Science Quarterly*, vol. 30, no. 3, pp. 207-208, 2017.

[11] R. M. Brown, "Thinking of serving nursing abroad: how technology assists nurses on mission trips," *Nursing Clinics of North America*, vol. 50, no. 2, pp. 399–410, 2015.

[12] H. G. Buck, "Does health care technology work for or against older adults?," *Journal of Gerontological Nursing*, vol. 43, no. 8, pp. 3-4, 2017.

[13] P. V. E. Mcclintock, "Size really does matter: the nanotechnology revolution," *Contemporary Physics*, vol. 60, no. 2, pp. 204-205, 2019.

[14] V. Subramanian, E. Semenzin, D. Hristozov et al., "Sustainable nanotechnology decision support system: bridging risk management, sustainable innovation and risk governance," *Journal of Nanoparticle Research*, vol. 18, no. 4, pp. 1–13, 2016.

[15] C. M. Castro, H. Im, C. Le, H. Lee, R. Weissleder, and M. J. Birrer, "Exploring alternative ovarian cancer biomarkers using innovative nanotechnology strategies," *Cancer and Metastasis Reviews*, vol. 34, no. 1, pp. 75–82, 2015.

[16] J. L. Rivera and J. W. Sutherland, "A design of experiments (DOE) approach to data uncertainty in LCA: application to nanotechnology evaluation," *Clean Technologies and Environmental Policy*, vol. 17, no. 6, pp. 1585–1595, 2015.

[17] T. Mori, "Utilizing nanotechnology and novel materials and concepts for advanced thermoelectric and thermal management technology development," *Semiconductors*, vol. 51, no. 7, pp. 965–967, 2017.

[18] A. D. Maynard and D. Y. H. Pui, "Nanotechnology and occupational health: new technologies - new challenges," *Journal of Nanoparticle Research*, vol. 9, no. 1, pp. 1–3, 2016.

[19] A. D. Maynard, "Nanotechnology: assessing the risks," *Nano Today*, vol. 1, no. 2, pp. 22–33, 2006.

[20] A. Csáki, G. Maubach, D. Born, J. Reichert, and W. Fritzsche, "DNA-based molecular nanotechnology," *Single Molecules*, vol. 3, no. 5-6, pp. 275–280, 2002.

[21] M. C. Hersam, N. P. Guisinger, and J. W. Lyding, "Silicon-based molecular nanotechnology," *Nanotechnology*, vol. 11, no. 2, pp. 70–76, 2000.

[22] P. B. da Silva, E. S. de Freitas, J. Bernegossi et al., "Nanotechnology-based drug delivery systems for treatment of tuberculosis—a review," *Journal of Biomedical Nanotechnology*, vol. 12, no. 2, pp. 241–260, 2016.

[23] B. Fonseca-Santos, M. P. D. Gremião, and M. Chorilli, "Nanotechnology-based drug delivery systems for the treatment of Alzheimer's disease," *International Journal of Nanomedicine*, vol. 10, no. 10, pp. 4981–5003, 2015.

[24] L. Gao and X. Yan, "Nanozymes: an emerging field bridging nanotechnology and biology," *Science China Life Sciences*, vol. 59, no. 4, pp. 400–402, 2016.

[25] W. Tingting, "Study on the effect of applying health examination route nursing method in physical examination nursing work," *Contemporary Medical Essays*, vol. 15, no. 18, pp. 219-220, 2017.

[26] A. Abudujilili, "An Observation of acute myocardial infarction complicated with syndrome of elderly patients with emergency resuscitation effect[j]," *Smart Health*, vol. 3, no. 5, pp. 101-102, 2017.

Research Article

Binder-Loaded Amorphous Nanometer Calcium Phosphate in Preventing Enamel Demineralization in Orthodontic Patients

Juan Gao [ID],[1] **Ni Dang,**[2] **Qian Zhang,**[3] **Ying Liang,**[1] **Xue Wei,**[1] **and Anxiu Xu**[1]

[1]*Department of Orthodontics, Guiyang Hospital of Stomatology, Guiyang, 550002 Guizhou, China*
[2]*Department of Stomatology, Xi'an Hospital of Traditional Chinese Medicine, Xi'an, 710000 Shaanxi, China*
[3]*Temporomandibular Joint Expert Clinic, Guiyang Hospital of Stomatology, Guiyang, 550002 Guizhou, China*

Correspondence should be addressed to Juan Gao; 1253848776@qq.com

With the popularization of oral health knowledge, people have gradually realized the importance of orthodontic treatment in oral health, so the number of patients undergoing orthodontic treatment has increased significantly. To improve the effect of orthodontic treatment, this article mainly studied the application of adhesives loaded with amorphous nanocalcium phosphate in the prevention of enamel demineralization in orthodontic patients. In the experiment, we used spray-drying technology to synthesize NACP. The collected dry particles were dispersed with absolute ethanol, sonicated for 10 minutes, dropped on a 200 ordinary carbon support film, and then dried and observed with a transmission electron microscope (TEM). Prevention of enamel demineralization in orthodontic patients was by adhesive-loaded amorphous nanocalcium phosphate. In this experiment, the membrane dialysis method was used to release the drug-loaded nanoparticles. The MH-5 microhardness tester was used to randomly select 3 positions on the buccal area of the enamel surface to measure the microhardness. After measuring the microhardness of each point, take the average of the readings of the 3 positions. Before and after the experiment, the difference of the enamel surface microhardness before and after the experiment was statistically analyzed. Before the scanning electron microscope observation, to avoid contamination of the window area of the enamel surface, which will cause interference with the scanning electron microscope observation, we use acetone to remove the acid-resistant nail polish coated on the enamel surface. Clean the attachments on the surface of the teeth first, then fix, dehydrate, and dry. When the release time reaches 52 h, the cumulative release rates of Cur in pH 5.4 and pH 7.4 buffers are 85.84 and 64.68%, respectively. The results show that by adjusting the concentration of PAA, it is possible to configure a mineralized liquid that can not only use the fluidity of NACP to penetrate into the collagen fibers but also transform into HAP within a suitable time, to achieve the purpose of repairing demineralized dentin.

1. Introduction

In recent years, inorganic nanoparticles have attracted much attention due to their unique materials and size dependence. In addition to its good stability, easy control of morphology, and size, it also has optical, magnetic, and other physical properties and has a wide range of applications in drug delivery and tumor imaging. The chemotherapeutic drugs are loaded on the surface and pore structure of inorganic nanoparticles through physical, chemical action, or surface functional groups, and the drugs are transported into the organism through the cell membrane to achieve the therapeutic effect. Calcium phos-

phate is a typical inorganic nanoparticle, which has good biocompatibility and will not cause rejection in the organism, so it has obvious advantages in drug delivery, bioceramics, and bone repair. In organisms, ACP has better osteoconductivity and biodegradability than HAP and TCP, and some of its properties can be adjusted by changing its components. Amorphous calcium phosphate (ACP) is a general term for short-range ordered and long-range disordered calcium phosphates. ACP can be classified as having a variable chemical composition (the Ca/P ratio can vary from 1.0 to 2.0), a class of calcium phosphate salts with similar chemical properties to glass. ACP is an amorphous intermediate phase of calcium

phosphate found during the synthesis of hydroxyapatite (HAP) under neutral or acidic conditions, so X-ray diffraction analysis shows amorphous features.

Among calcium phosphate materials, ACP exhibits better osteoconductivity and biodegradability and has been widely used in the demineralization and remineralization of tooth enamel, bone defect treatment, and drug carriers. However, ACP is a metastable phase, it is very easy to transform into a crystal form, and it has poor dispersion in solution and is easy to agglomerate, which seriously affects the application of ACP in organisms. CPP-ACR (casein phosphopolypeptide-amorphous calcium phosphate) can effectively prevent enamel demineralization and promote the remineralization of enamel demineralization that has occurred.

Jiang et al. prepared stable nanoamorphous calcium phosphate (NACP) with polyethylene glycol as a stabilizer to obtain nanosized amorphous adsorbents [1]. Feng et al. explored the effect of a novel bioabsorbable stent composed of PLLA and ACP nanoparticles on inflammation and calcification of surrounding tissue after stent implantation in porcine coronary arteries [2]. Zhang et al. performed 20 cycles of hypophosphite adsorption-desorption on the polymer-supported ferric iron nanocomposite HFO@201 [3].

When fluoride is used alone, remineralization mainly occurs on the surface of tooth enamel caries. Once fluoride ions contact calcium and phosphorus ions, fluorapatite will quickly form on the surface of the tooth, preventing mineral ions from continuing to enter the caries. The deep layer hinders the remineralization of the deep layer. When CPP and fluoride ions exist at the same time, the entire layer of enamel caries can be remineralized. CPP can prevent the rapid transformation of calcium phosphate stage, and the mineral components can diffuse in the form of ions. Below the surface of the carious lesion, an active gradient is formed, which promotes remineralization throughout the entire layer of enamel carious lesions. This in vitro remineralization model after enamel acid etching strongly illustrates that lysozyme can stabilize a higher concentration of calcium and phosphorus ions into an amorphous state. Under the degradation of sodium hypochlorite and the induction of glycine, it can promote the remineralization of early enamel caries.

2. Method and Experiment

2.1. Experimental Equipment and Materials.

The main instruments are incubator, microhardness tester, laboratory PH meter, bt25s electronic scale, anaerobic culture tank, 61MXW-80A vortex oscillator, GSP-9050MBE constant temperature water-proof incubator, complete automatic biochemical analyzer, scanning electron microscope, energy spectrum analyzer, etc. [4].

The main materials used in the experiment are dipotassium hydrogen phosphate, calcium chloride dihydrate, 4-hydroxyethylpiperazine, ethanesulfonic acid, 1% sodium hypochlorite rinse, 37% phosphoric acid gel, etc. [5].

2.2. Subjects.

100 patients were randomly selected from the fixed orthodontic patients, 50 males and 50 males, aged between 12 and 16 years old, with permanent teeth. All patients were treated with the standard square wire arch technique, and the average treatment period was 20 months, which was set as the observation group. The control group consisted of a random selection of 200 normal people aged 12-16 years without fixed correction, 100 men and women each.

Inclusion criteria. The experimental group had normal tooth morphology, well-developed enamel, and no hard tissue diseases such as enamel demineralization, fluorosis, and tetracycline. The control group was those with normal tooth morphology, no enamel development defects, and no enamel demineralization.

Exclusion criteria. The experimental group was unable to follow up on time and adhere to treatment, and the control group were tetracycline teeth, fluorosis teeth, and other enamel development defects [6].

2.3. Synthesis of Nanometer Amorphous Calcium Phosphate (NACP).

Spray-drying technology was used to synthesize NACP. 1.5125 g anhydrous acetic acid was added to 500 mL distilled water to prepare a spray solution. Then, 0.8 g calcium carbonate ($CaCO_3$) and 5.094 g anhydrous calcium hydrogen phosphate ($CaHPO_4$) were dissolved in acetic acid solution. Add distilled water to the solution until the total volume of the solution reaches 1 L. The concentration of acetic acid is 25 mmol/L. The solution is sprayed by a nozzle located in a spray chamber with hot air flow at 10 mL/min feed rate. The collected dry particles were dispersed with absolute ethanol, vibrated with ultrasonic for 10 minutes, dropped on a 200 ordinary carbon support films, and observed by transmission electron microscope (TEM) after drying. The powder specific bet (Brunauer-Emmet-Teller) specific surface area was analyzed using a physical/chemical adsorption analyzer [7]. The preparation of NACP nanoparticles is shown in Figure 1.

Amorphous calcium phosphate (ACP) is generally considered a transition phase in the formation of calcium phosphate in aqueous environments. Generally speaking, ACP may be the first phase in the precipitation and crystallization process of calcium phosphate solution, which can be obtained by the rapid mixing of calcium and phosphorus solutions. The chemical composition of ACP is not fixed and is often related to the calcium and phosphorus concentrations and pH values in the reaction solution. As for the structure of the ACP, there is no clear conclusion so far. The IR spectrum of ACP shows a broad absorption peak for phosphate radicals. XRD results show that the compound is amorphous Through electron microscopy, it can be observed that ACPs are generally round spheres with diameters between 20 and 200 nm. ACP appears to have the short-range structure of apatite, but due to the very small size of the crystals, it shows an amorphous phase on the XRD pattern. This conclusion has been confirmed by X-ray absorption spectroscopy.

Sodium cyclopentadienyl is a colorless solid, but the sample will appear pink due to oxidation. Solutions of sodium cyclopentadienyl in THF are commercially available. It can be prepared by treating cyclopentadiene with sodium. The reaction is usually carried out by heating sodium to a molten state in dicyclopentadiene. Previously common practice was to use "sodium wire" or "sodium sand," which was obtained
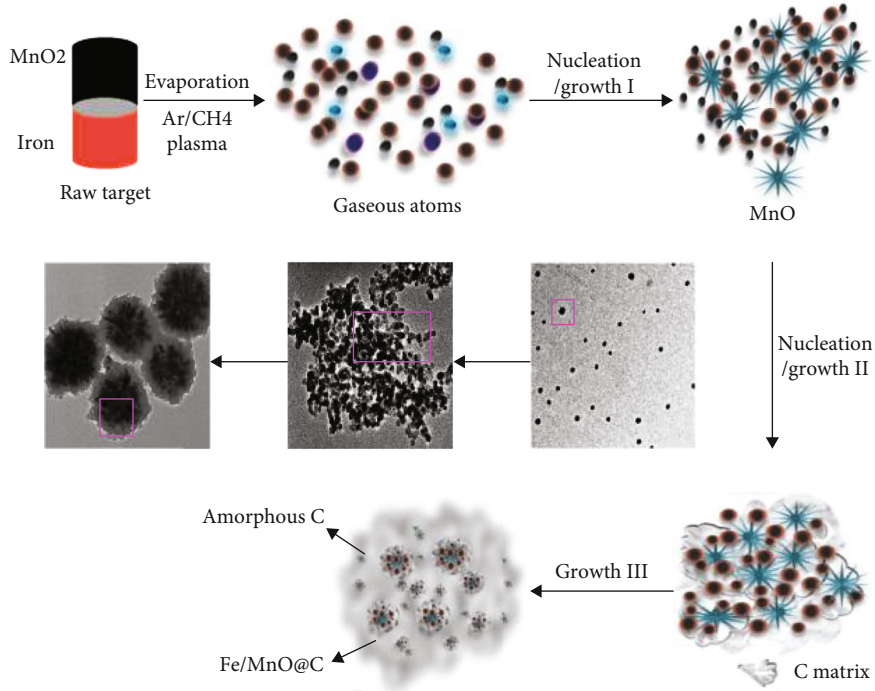
FIGURE 1: Preparation of NACP nanoparticles.

in the form of fine dispersion by melting and refluxing sodium in xylene with rapid stirring.

Define a binary comparison criterion [8]:

$$\tau(p\,;x,y) = \begin{cases} 1, & p(x) < p(y), \\ 0, & p(x) \geq p(y). \end{cases} \quad (1)$$

The formula is as follows [9]:

$$Z = \iint_w g(X)g^T(X)dX,$$

$$G(i,j) = \sqrt{G_x^2(i,j) + G_y^2(i,j)}, \quad (2)$$

$$\theta(i,j) = \text{arc}\left(\frac{G_x(i,j)}{G_y(i,j)}\right).$$

When the image is blurred and the noise is small, the working state of the gradient operator is a satisfactory continuous image $f(x,y)$, and the position gradient (x,y) can be expressed as a carrier [10]. If G_x and G_y are used to represent the gradient change of $f(x,y)$ along the X and Y directions, the gradient vector can be expressed as follows [11]:

$$f(x,y) = \begin{bmatrix} \dfrac{\partial f(x,y)}{\partial x} \\[2mm] \dfrac{\partial f(x,y)}{\partial y} \end{bmatrix}. \quad (3)$$

A transformation method based on the tangent function is as follows [12]:

$$D_o = \frac{D_M}{2}\left[1 + \frac{\tan\left(\alpha\pi(x/D_M - 1/2)\right)}{\tan\left(\alpha\pi/2\right)}\right]. \quad (4)$$

The specific steps of the BP neural network algorithm are as follows: each connection has a weight. If the j-node is in the exit layer or the hidden layer [12], the net input to the j-node E_j is as follows:

$$E_j = \sum_i w_{ij}S_i + \theta_j. \quad (5)$$

Given the net input E_j of node j, the output of S_j of node j is as follows [13]:

$$S_j = \frac{1}{\left(1 + e^{-I_j}\right)}. \quad (6)$$

As the burden and bias representing the prediction error of the network are continuously updated, the error propagates backwards [14]. For the node of the output layer j, the error Err_j calculation formula is as follows:

$$\text{Err}_j = S_j\left(1 - S_j\right)\left(G_j - S_j\right). \quad (7)$$

Computing the error of j nodes on the hidden layer requires a weighted sum of j-related node errors on the next layer [15]. The error of the hidden layer of the j node is as follows:

$$\text{Err}_j = S_j\left(1 - S_j\right)\sum_k \text{Err}_k w_{kj}. \quad (8)$$

w_{jk} is the connection weight from node k to node j in the next higher layer [16], and Err_k then is the error of node k.

The propagated errors are reflected by updating the weights and biases [17, 18]. The formula for weight update is as follows, where Δw_{ij} is w_{ij} the weight change amount.

$$\Delta w_{ij} = (1)\mathrm{Err}_j S_i,$$
$$w_{ij} = w_{ij} + \Delta w_{ij}. \tag{9}$$

The offset is updated by the following equation, where $\Delta \theta_j$ is θ_j the offset change.

$$\Delta \theta_j = (1)\mathrm{Err}_j,$$
$$\theta_j = \theta_j + \Delta \theta_j. \tag{10}$$

2.4. In Vitro Drug Release. In this experiment, membrane dialysis was used to release the drug-loaded nanoparticles. First, put 5 mL Cur-ACP nanoparticles (2 mg/mL) in a pretreated dialysis bag with a molecular weight cut-off of 34 kDa, immerse the dialysis bag in a 100 mL beaker (protect from light), and place the beaker in a shaker (37°C, 70 rpm) [19, 20]. The in vitro drug release process is shown in Figure 2.

2.5. Antioxidant In Vitro. In this determination, 1 mL of samples with various concentrations (2, 4, 6, 8, and 10 μg/mL) was mixed with 2 mL of 0.1 mM DPPH solution [21]. After that, the mixed solution was kept at room temperature and protected from light for 30 minutes [22].

$$\mathrm{Inhibition}(\%) = \frac{A_0 - A_1}{A_0} \times 100\%. \tag{11}$$

Among them, A_0 is the absorbance of the control group, and A_1 is the absorbance of the sample.

2.6. Preparation of New Antibacterial Remineralization Functional Orthodontic Adhesive. As shown in Table 1, the first new type of orthodontic adhesive was prepared by adding 5% by mass of MAE-DB to PEHB resin. MAE-DB and NACP with mass ratios of 5% and 40% were added to PEHB to prepare the second new type of orthodontic adhesive, referred to as PND. Adding more than 40% of NACP to the resin will affect the adhesive properties and mechanical properties of the resin, so the addition concentration of 40% is selected. The whole preparation process is carried out in a dark room, and the resin mixture is mixed evenly with a mixing knife, and the air bubbles are removed by vacuum. The adhesive is prepared within 0.5 h before each use, and the unused ones are discarded after the test and no longer used [23, 24].

Take 0.5 g of mussel shell powder in a 100 mL beaker, add 40 mL of propionic acid with a concentration of 5% to make it fully react, take the supernatant after centrifugation, dilute the obtained solution to 50 mL, and then dilute the concentration to 0.06 M 50 mL of phosphoric acid solution was added dropwise to the beaker. After the dropping was

completed, 0.6 mmol of sodium tripolyphosphate was added to the beaker. After 30 min of reaction, 6 g of urea was added. After stirring to fully dissolve the urea, the beaker was placed at 90°C. In a water bath, it was stirred for 3 min and then allowed to stand until precipitation appeared. The precipitate was centrifuged, washed twice with deionized water and twice with ethanol, and dried at 70°C for 24 h to obtain ACP white powder.

2.7. Testing of Mechanical Properties of New Orthodontic Adhesives. Transbond XT paste (TB), a commonly used orthodontic adhesive in clinical practice, was selected as a commercial control, and three adhesives (TB, PD, and PND) were used to make test pieces with a size of 25 mm × 2 mm × 2 mm. The surface was cured with LED light curing lamp (output light intensity is 1200 mW/cm^2) for 60 s. After fully curing, the specimen was placed in a constant temperature water bath at 37°C for 24 h. Each group has 5 test pieces. A three-point bending test was carried out on a computer-controlled universal testing machine with a span of 20 mm and a pressing speed of 1 mm/min, to test the flexural strength and elastic modulus of the material. The flexural strength is calculated by the following formula [25]:

$$S = 3P_{\max} \frac{L}{(2bh^2)}. \tag{12}$$

Among them, $P_{\max}$ is the breaking load, L is the span, b is the width of the specimen, and h is the height of the specimen.

The modulus of elasticity is calculated by the following formula:

$$E = \left(\frac{P}{d}\right)\left[\frac{L^3}{(4bh^3)}\right]. \tag{13}$$

The load P divided by the displacement d is the slope of the load-displacement curve in the linear elastic region [26].

2.8. Microhardness Measurement. In this experiment, the MH-5 microhardness instrument was used to randomly select 3 positions on the buccal test area of the enamel surface to measure the microhardness. After measuring the microhardness of each point, the average of the readings of the 3 positions was taken. Use this method to calculate the final surface microhardness value of the tooth enamel. Nanohardness and elastic modulus are measured by a nanoindenter. The test uses a continuous hardness measurement method. The depth of pressure is 600 nm. The calculation formula of hardness and elastic modulus is as follows:

$$S = \beta\sqrt{\lambda} E_r h,$$
$$\frac{1}{E_r} = \frac{(1 - v_i^2)}{E_i} + \frac{(1 - v_s^2)}{E_s}. \tag{14}$$

In the formula, S represents the contact hardness, h represents the depth of pressure measurement, E_r is the reduced
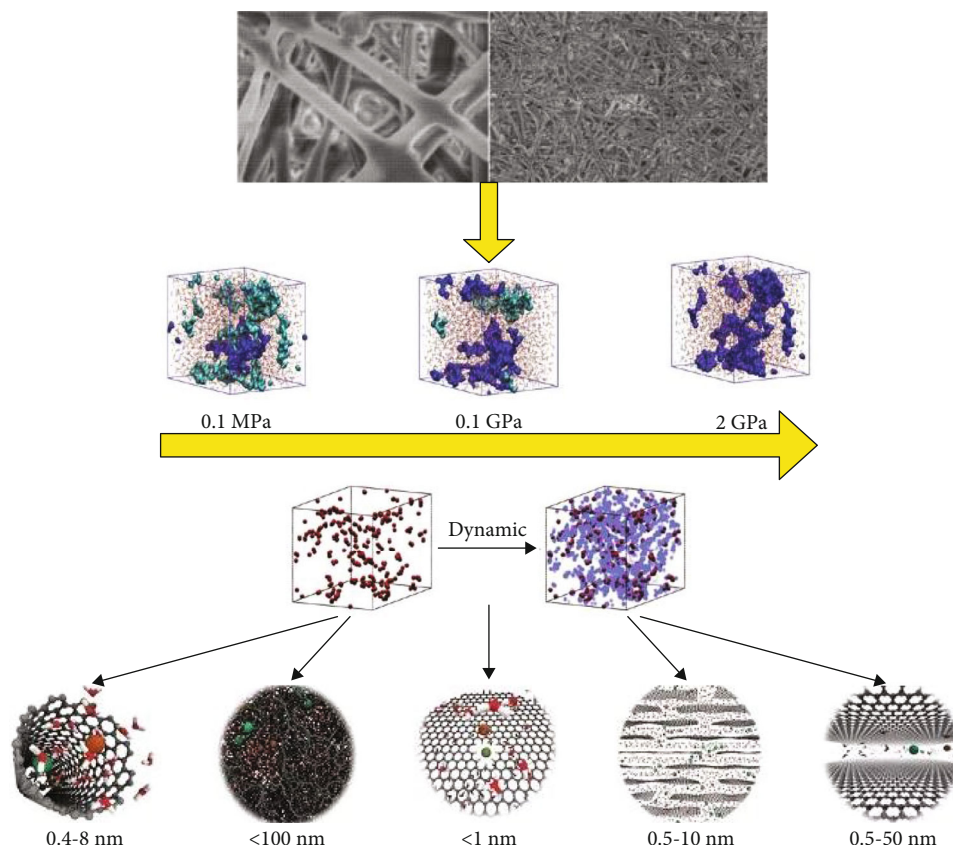
FIGURE 2: In vitro drug release process.

TABLE 1: Composition and mass fraction of two experimental adhesives.

Glue	PEHB	MAE-DB	NACP
PD	95	5	0
PND	55	5	40

Young's modulus, and E_i and E_s are determined by the Young's modulus of the probe and the sample.

2.9. Scanning Electron Microscope Surface Observation. In this experiment, two samples were drawn from each group according to the random number table for scanning electron microscopy (JEOLJSM-6390LV) observation in the window area of the tongue and palate. Before the scanning electron microscope observation, to avoid contamination of the window area of the enamel surface, which will cause interference with the scanning electron microscope observation, we use acetone to remove the acid-resistant nail polish coated on the enamel surface. Clean the attachments on the surface of the teeth first, then fix, dehydrate, and dry. Because the surface of the tooth is not charged, its electrical conductivity is also relatively poor, so the charging effect and discharge effect will be caused when observing with a scanning electron microscope, which will affect the observation of the image of the enamel surface. Therefore, it is necessary to check

the sample before observing the sample. The surface of the sample is sprayed with gold to increase the conductivity of the test surface of the sample. Finally, the samples are placed to the sample stage according to the original grouping order. When observing the image for collection, each experimental group can be distinguished according to the quadrant.

2.10. Statistical Analysis. All data were entered into the computer through EXCEL, and single-factor analysis was used to compare whether the enamel surface roughness values and microhardness values of each group were statistically different. The test standard was $P = 0.05$. The statistical results are completed by the SPSS13.0 statistical software.

3. Results

The comparative analysis of the labial surface pH of the upper and lower anterior teeth is shown in Figure 3. The results showed that no matter which group of patients, the pH was lower than that of the mandibular teeth, and the difference was statistically significant ($P < 0.05$).

Table 2 shows the comparison of the teeth between the anterior teeth of the same name. Table 3 shows the comparison of the labial pH of the teeth between the anterior teeth of the same name. It can be seen from the results that no matter the upper and lower jaws, there is no statistically significant difference in pH ($P > 0.05$).
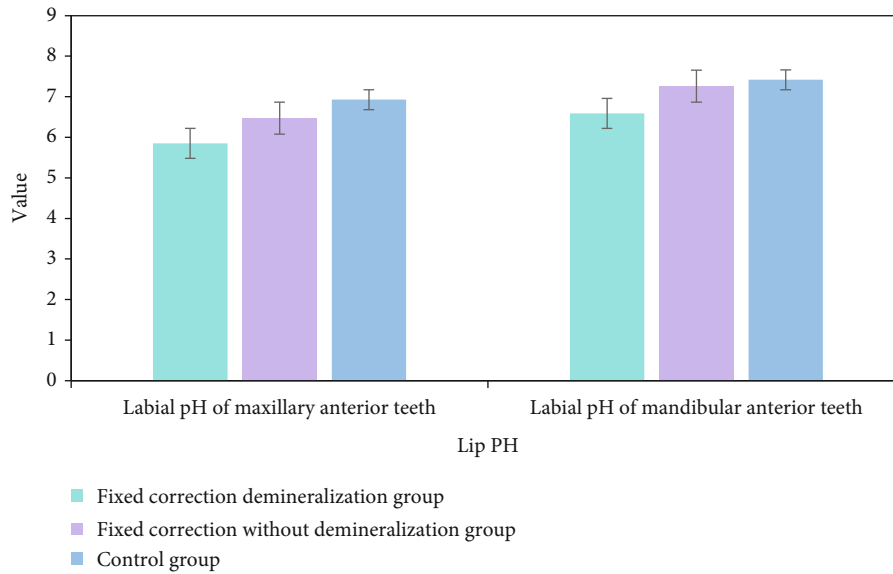
FIGURE 3: Comparative analysis of the labial pH of the upper and lower anterior teeth.

TABLE 2: Comparison of the labial pH between the left and right sides of the upper jaw with the same name anterior teeth.

Tooth	Left	Right	t	P
I1	6.64 ± 0.22	6.71 ± 0.15	1.92	>0.05
I2	6.40 ± 0.12	6.46 ± 0.20	1.37	>0.05
C	6.89 ± 0.18	6.91 ± 0.17	0.94	>0.05

TABLE 3: Comparison of pH between the anterior teeth of the same name on the left and right sides of the mandible.

Tooth	Left	Right	t	P
I1	7.29 ± 0.28	7.34 ± 0.21	1.29	>0.05
I2	7.33 ± 0.23	7.30 ± 0.14	0.87	>0.05
C	7.07 ± 0.16	7.10 ± 0.26	0.73	>0.05

Calcium phosphate remineralization method contributes to the prevention of enamel leukoplakia lesions and promotes remineralization of demineralized enamel. Dental resin materials containing calcium phosphate can release calcium and phosphorus ions, which become calcium and phosphorus ion reservoirs for plaque neutralization and tooth surface, preventing enamel demineralization and promoting remineralization.

The N_2 adsorption-desorption isotherm and BJH pore size distribution of NACP nanoparticles are shown in Figure 4. The sample shows an IV-type isotherm of H1 hysteresis loop, which is a typical mesoporous structure. From the measured data, it can be seen that the BET surface area of NACP nanoparticles is $41.414 \, m^2/g$, and the total pore volume and average pore diameter are about $0.165 \, 6cm^3/g$ and 10.5 nm, respectively.

Figure 5 shows the slow release process of NACP nanoparticles in vitro at 37°C and different pH. There was no sig-

nificant difference in the cumulative release of drugs in different pH buffers 5 h before release. However, as time increases, the drug release rate of Cur-ACP nanoparticles in pH 5.4 is faster than the release rate in pH 7.4. This is because NACP will gradually decompose in an acidic environment, thereby causing the loaded drug will be released slowly. When the release time reaches 52 h, the cumulative release rates of Cur in pH 5.4 and pH 7.4 buffers are 85.84 and 64.68%, respectively.

The quartiles of the proportion of Actinomycetes at different stages of treatment are shown in Figure 6. After wearing the fixed appliance, the proportion of some bacteria in the total flora also changed. Three kinds of bacteria (Streptococcus mutans, Lactobacillus, and Actinomycetes) accounted for the proportion of total bacteria. Kruskal-Wallis H rank-sum test analysis of multiple independent sample comparisons found that the proportions of Streptococcus mutans and Lactobacillus exist between group differences ($P < 0.05$). For the proportion of Actinomycetes in the total flora, there was no significant change among the groups ($P > 0.05$). Further use of pairwise comparison found that, compared with individuals who did not receive orthodontic treatment, the fixed appliance worn for less than 1 year, 1-2 years, and more than 2 years showed Streptococcus mutans and mutant in the local plaque of the tooth surface. The proportion of Lactobacillus in the total flora was significantly increased ($P < 0.05$), but the Kruskal-Wallis H rank-sum test analysis of multiple independent sample comparisons found that the proportion of Streptococcus mutans and Lactobacillus in the flora increases but does not occur continuously with the extension of the treatment time (the proportion of Streptococcus mutans and Lactobacillus in the partial plaque with the tooth surface after the fixed appliance is worn for less than 1 year, 1-2 years, and more than 2 years. The difference in proportion is not significant, $P > 0.05$).

The surface roughness of the seven different samples is shown in Figure 7. In the first month of the experiment, the
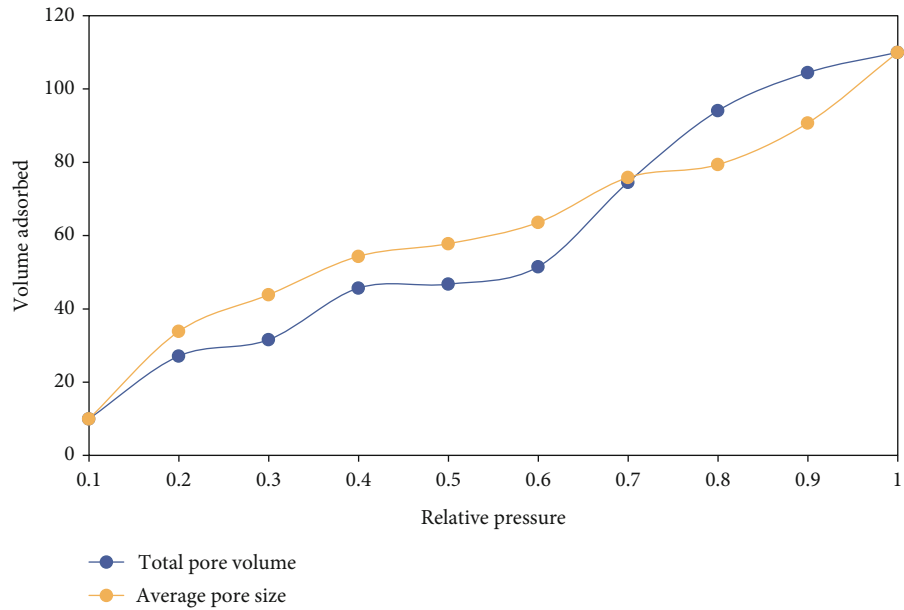
FIGURE 4: N^2 adsorption-desorption isotherm and BJH pore size distribution of NACP nanoparticles.
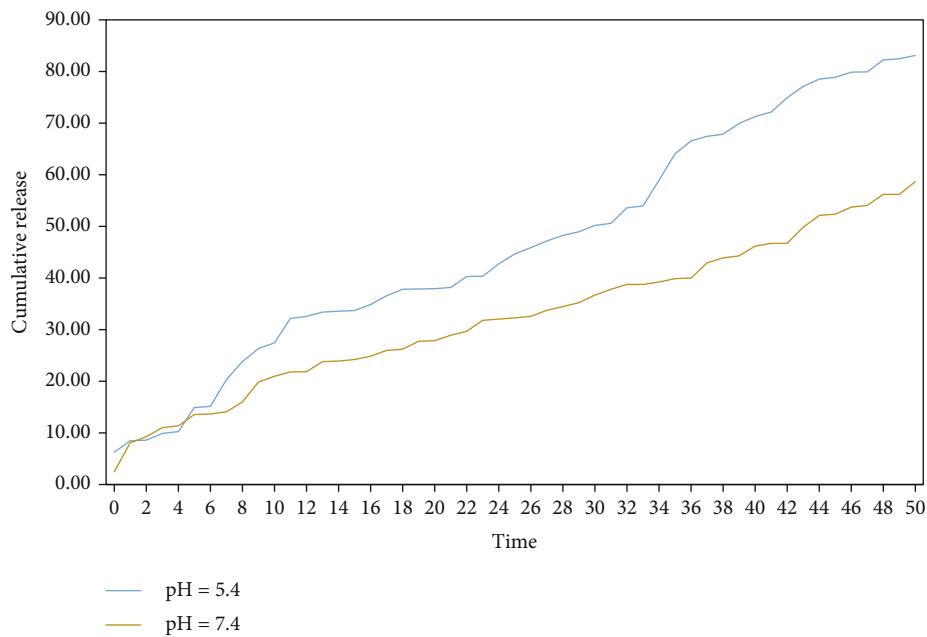
FIGURE 5: The slow drug release process of NACP nanoparticles in vitro at 37°C and different pH.

enamel surface roughness of the D group was significantly lower; two and three months of the experiment, the enamel surface roughness of each treatment group was significantly reduced. Compared with group G, the difference was significant ($P < 0.05$), the enamel surface roughness of group B was significantly lower than that of other groups ($P < 0.05$), and group C was significant compared with group D, group E, and group F difference. It can be seen that different influencing factors will have various effects on the surface roughness of different samples.

The scanning electron microscope situation is shown in Figure 8. In a dry environment, after the treatment of 37% phosphoric acid and GC treatment agent, the enamel cracks or enamel peeling of the GC adhesive group after two unloadings all showed different degrees of enamel cracking or enamel peeling, especially the second unloading was more prominent. In the area covered by the enamel adhesive, there are residual resin protrusions embedded in the micropores of the enamel after removing the brackets, and the bonding is tight, and the bonding surface has no obvious cracks.
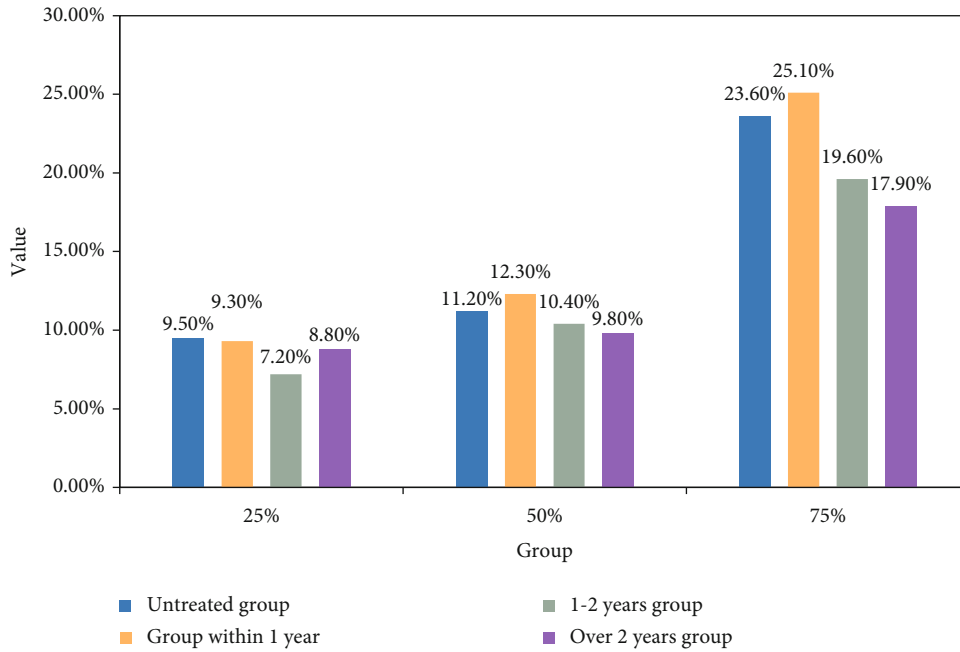
FIGURE 6: Quartiles of the proportion of Actinomycetes at different stages of correction.
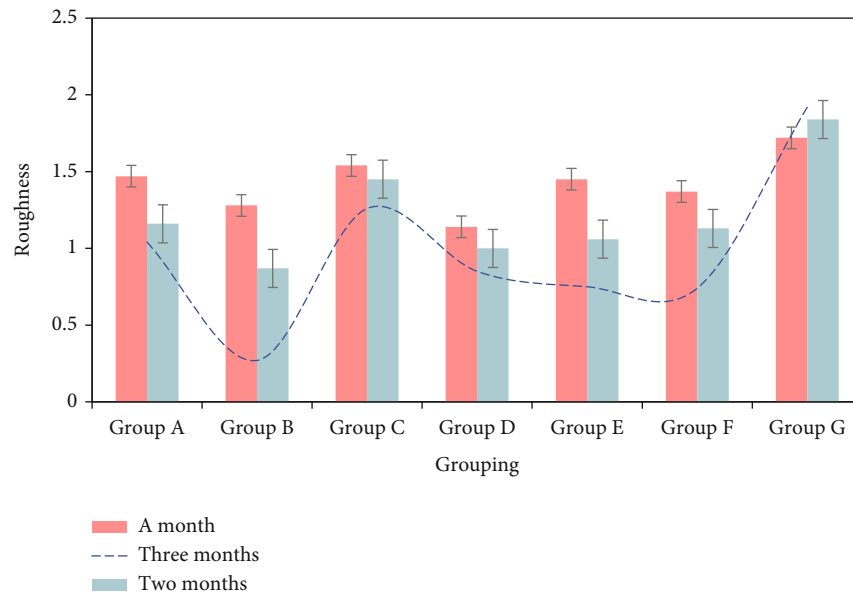
FIGURE 7: The surface roughness of seven different samples.

According to the analysis of the bonding process, these protrusions are mainly caused by no fillers. The liquid component of the enamel adhesive with good penetration and physical bonding properties is formed. This protrusion is considered beneficial to tooth health and still has an anticaries effect and does not need to be removed. Moreover, its anticaries effect compensates for the side effects caused by the improved bonding method to expand the acid etched area.

The comparison of the demineralization rates is shown in Table 4. Comparison of enamel demineralization rates between groups A, B, and C is as follows: group B and group A are different in demineralization rate, group A is higher than group B ($\chi^2 = 19.227$, $P \leq 0.01$); group C is demineralized compared with group A. The rate is different in group A than in group C ($\chi^2 = 21.892$, $P \leq 0.01$); there is no difference in demineralization rate between group B and group C ($\chi^2 = 0.053$, $P = 0.818$). The new composite material based on the binder-loaded amorphous nanocalcium phosphate can effectively seal the open dentinal tubules, and its effect has a certain resistance to abrasion and acid, which provides
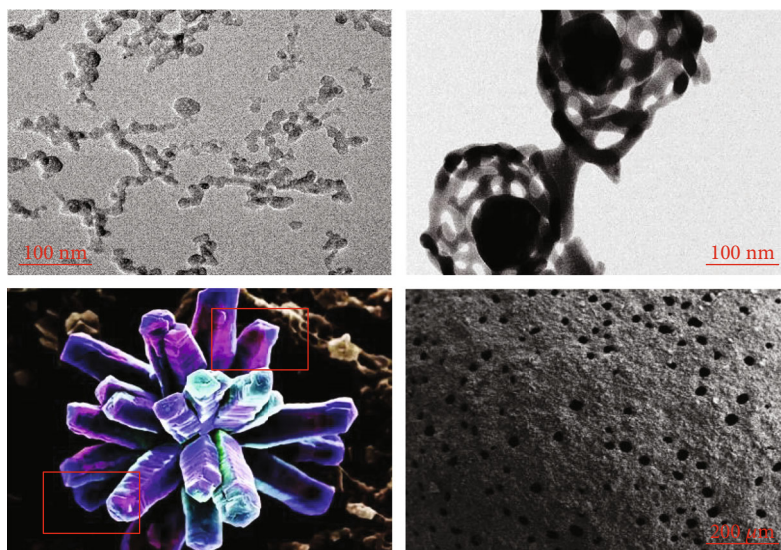
FIGURE 8: Scanning electron microscope situation.

TABLE 4: Comparison of the demineralization rate of the three groups A, B, and C.

	Demineralization rate	χ^2 value	P value
Group A and group B			
Group A	26.41	19.227	≤0.01
Group B	14.35		
Group A and group C			
Group A	26.41	21.892	≤0.01
Group C	13.82		
Group B and group C			
Group B	14.35	0.053	0.818
Group C	13.82		

a new experimental basis for the clinical treatment of dentin hypersensitivity.

The averages of the three groups of EDI indexes A, B, and C are shown in Figure 9. It can be seen from the figure that the average of the EDI index of the group A is the highest. Comparison between group B and group A is as follows: $t = 2.929$, $P = 0.008$, group A is higher than group B, which is statistically significant; comparison between group C and group A is as follows: $t = 2.911$, $P = 0.008$, group A is higher than group C, and there is statistical significance; comparison between group B and group C is as follows: $t = 0.340$, $P = 0.737$, and there is no statistical significance.

The comparison of the numbers and proportions of the two groups of Streptococcus mutans and Actinomycetes is shown in Table 5. The number of Streptococcus mutans in the demineralization group was significantly increased compared with the nondemineralization group.

4. Discussion

The crystalline phase transition of ACP is an autocatalytic process, and its crystallization curve is s-shaped. Phase transition is the process in which a substance changes from one phase to another, so the crystallization process is a phase transition process. There are many factors that affect the phase transition of ACP, mainly including the pH value of the solution, the temperature of the system, and the addition of foreign ions or molecules. Under alkaline conditions, ACP finally phases into hydroxyapatite in aqueous solution, and the phase transition rate is very slow (pH = 9.00). The increase in acidity increases the speed of amorphous intersecting. At pH = 3.4, the amorphous phase only exists for a few minutes, but the phase becomes calcium-deficient hydroxyapatite (DCPD) instead of apatite, and ACP evolves to calcium-deficient under physiological pH conditions. And phosphate hydrolyzed apatite. Temperature has a great influence on the phase change of ACP. It takes about three days for the phase change at 10°C, two hours at 25°C, and complete phase change within 30 minutes when it rises to 37°C. The influence of foreign ions and molecules on the phase transition of ACP is also essential. In fact, organisms use the interaction of biological macromolecules with calcium ions and phosphate ions to control the amorphous as the precursor of biomineralization.

The change in the gloss of the tooth surface is one of the manifestations of demineralization. It will become caries if it develops further without treatment. Generally, tooth enamel demineralization can be divided into two forms, namely, surface demineralization and subsurface demineralization. After the remineralization of early enamel caries, mineral salts can stay in part of the enamel that has been demineralized in a certain form, resulting in an increase in the microhardness of the caries area and a decrease in porosity. The histomorphology shows that the surface layer and dark zone are widened, the area of caries is reduced, and the negative birefringence of the glazed surface is enhanced under the polarized light microscope. In the caries lesion area, the positive birefringence tends to the negative birefringence, and the microscopic X-ray shows an increase in density. In addition, remineralization not only refers to the deposition of
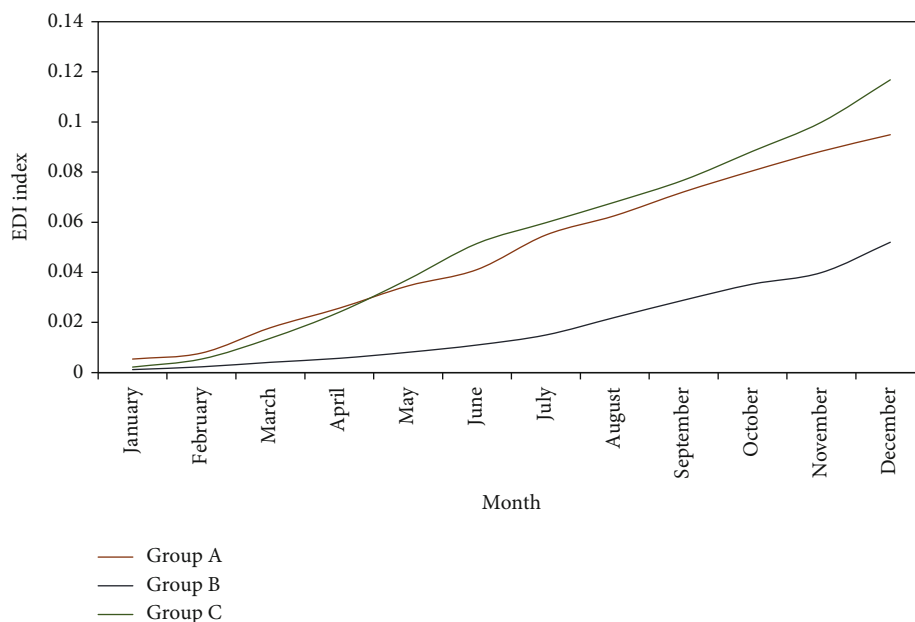
FIGURE 9: The average of the three groups of EDI indexes A, B, and C.

TABLE 5: Comparison of the numbers and proportions of the two groups of Streptococcus mutans and Actinomycetes.

Bacteria	Number		The proportion	
	Demineralization group	Undemineralized group	Demineralization group	Undemineralized group
Streptococcus mutans	11.13 ± 0.72	10.63 ± 0.91	1.20 ± 1.07	0.44 ± 0.48
Actinomycetes	12.08 ± 0.24	12.11 ± 0.57	6.50 ± 4.57	8.59 ± 10.51

minerals in the oral cavity on the surface of the tooth and the diseased part under normal conditions but also can occur during the formation of dental caries.

The anterior teeth of the same name are similar in shape, and the contact surfaces and methods of the left and right anterior teeth of the same name and the toothbrush are similar when individuals perform daily oral cleaning such as brushing their teeth. This may also be one of the reasons. In the same dental arch, there is a statistical difference in the pH of the labial surface of the teeth without the same name. In the maxillary arch, the pH of the labial surface of the canine teeth is higher than that of the central incisor ($P < 0.05$), and both are significantly higher than that of the lateral incisor ($P < 0.05$); this may be related to the position of the teeth in the oral cavity and the distance of the salivary gland opening. For example, the pH of the labial surface of the maxillary lateral incisor is lower than that of the canine. Plaque is easy to accumulate, especially after bonding and fixing the appliance, it affects its cleaning and makes the pH of the lip surface lower than the central incisor. There is no significant difference in pH between mandibular lateral incisors and central incisors. Therefore, the central incisors and lateral incisors of the mandibular incisors receive the washing and buffering effect of saliva resemblance. This is similar to the difference in enamel demineralization in fixed orthodontics.

Due to the low compliance of patients, topical fluoride regimens are usually difficult to work. Calcium and phosphate ions released from calcium phosphate biomaterials form ion reservoirs in dental plaques. The supersaturated calcium and phosphorus ion pool helps prevent demineralization and promote enamel remineralization. In traditional calcium phosphate materials, the diameter of calcium phosphate fillers is mostly about 55 microns, which leads to restrictions on the filler addition ratio and the release of calcium and phosphorus ions. The new type of amorphous calcium phosphate nanoparticles (NACP) has a diameter of about 110 nm. Because of its small particle size and large specific surface area, it has a high level of Ca and P ion release ability and the ability to promote tooth enamel remineralization. In addition, resin composites containing this type of NACP filler can "smartly" release high concentrations of calcium and phosphorus ions in an environment with a pH value close to 4 (cariogenic environment and enamel demineralization environment), and increase the local pH to above 5.5. Reduce the enamel demineralization rate, and after the pH rises above 5, the release of ions will be significantly reduced, preserving the effectiveness of the internal filler of the material.

The copolymer has a large difference in solubility between the hydrophilic and hydrophobic segments and can self-assemble into nanomicelles with a fairly narrow size

distribution and typical core-shell structure in water. Polyethylene glycol (PEG) is often used as the hydrophilic segment of polymer micelles, and the hydrophobic segment is polylactic acid (PLA), chitosan (CS), polycaprolactone (PLC), etc. The inner core can be loaded with poorly water-soluble drugs to increase the solubility of the drugs in aqueous solutions, while the hydrophilic outer shell can maintain the steric stability of the micelles. Polymer micelles can escape the nonspecific uptake of the reticuloendothelial system (RES) due to their small size distribution; the preparation methods of micelles are simple and diverse, and the conditions are mild; targeting molecules can be coupled on the surface of the micelles to enable the drug to achieve the target to deliver, thereby improving the efficacy of drugs. These advantages make polymer micelles have broad application prospects in the delivery of poorly soluble drugs.

5. Conclusions

Enamel demineralization of orthodontic teeth is a very serious problem, especially for patients with poor oral hygiene, and it is necessary to take active preventive measures as soon as possible. The self-etching bonding technology breaks through the traditional phosphoric acid etching and combines a variety of research results to reduce enamel damage and demineralization. It has special advantages in preventing enamel demineralization and is worthy of further research. The surface of the enamel after acid etching demineralization is rougher, and the porosity is greater, which is conducive to the penetration and fitting of the adhesive. The nanoactive filler contained in the adhesive is easier to combine with the demineralized enamel, thereby enhancing the hardness. Over time, the loss or increase of minerals ultimately determines whether WSL or even dental caries will advance, stabilize, or degenerate. Therefore, improving the ability of tooth enamel to resist demineralization and promoting its remineralization is an effective method to inhibit WSL and dental caries. In the experiment, the synthetic peptide at the C-terminus of enamel protein improved the directional connection of the nanoparticles and promoted the orderly transformation of the nanoparticles into enamel-like HAP crystals. Ordered particle arrangement may be a preparatory step before crystal formation and growth, which is in line with the concept of particle-attached crystallization (CPA) in the nonclassical mineralization theory. In this study, CMC and PA are used to simulate proteins related to biomineralization, and ACP is stabilized and arranged by forming CMC/ACP nanocomposites, and then, small particles are arranged in a queue and specifically bound to the enamel surface.

Data Availability

Data sharing is not applicable to this article as no datasets were generated or analyzed during the current study.

Conflicts of Interest

The authors declare that they have no conflicts of interest.

References

[1] L. Jiang, Y. Li, Y. Shao et al., "Enhanced removal of humic acid from aqueous solution by novel stabilized nano-amorphous calcium phosphate: behaviors and mechanisms," *Applied Surface Science*, vol. 427, pp. 965–975, 2018.

[2] G. Feng, C. Qin, F. Sha, Y. Lyu, and X. Jiang, "Evaluation of inflammatory and calcification after implantation of bioabsorbable poly-L-lactic acid/amorphous calcium phosphate scaffolds in porcine coronary arteries," *Journal of Nanomaterials*, vol. 2021, Article ID 6652648, 8 pages, 2021.

[3] Y. Zhang, X. She, X. Gao, C. Shan, and B. Pan, "Unexpected favorable role of Ca~(2+) in phosphate removal by using nanosized ferric oxides confined in porous polystyrene beads," *Environmental Science & Technology*, vol. 53, no. 1, pp. 365–372, 2019.

[4] M. Mohamed, W. Refaat, and S. Morcos, "Effect of different fluoride releasing bonding agents in preventing of enamel demineralization around orthodontic brackets," *Egyptian Orthodontic Journal*, vol. 50, no. 12, pp. 13–34, 2020.

[5] S. Chakraborty, H. Kidiyoor, and A. K. Patil, "Effect of light-curable fluoride varnish and conventional topical fluoride varnish on prevention of enamel demineralization adjacent to orthodontic brackets: a comparative study," *The Journal of Indian Orthodontic Society*, vol. 54, no. 1, pp. 14–23, 2020.

[6] R. Reddy, R. Manne, G. C. Sekhar, S. Gupta, N. Shivaram, and K. R. Nandalur, "Evaluation of the efficacy of various topical fluorides on enamel demineralization adjacent to orthodontic brackets: an in vitro study," *The Journal of Contemporary Dental Practice*, vol. 20, no. 1, pp. 89–93, 2019.

[7] N. B. Ulusoy, A. A. Oba, and Z. C. Cehreli, "Effect of Er, Cr: YSGG laser on the prevention of primary and permanent teeth enamel demineralization: SEM and EDS evaluation," *Photomedicine and Laser Surgery*, vol. 38, no. 5, pp. 308–315, 2020.

[8] B. Panariello, A. Azabi, L. Mokeem et al., "The effects of charcoal dentifrices on Streptococcus mutans biofilm development and enamel demineralization," *American Journal of Dentistry*, vol. 33, no. 1, pp. 12–16, 2020.

[9] D. A. Krivtsova and E. E. Maslak, "Monitoring the results of enamel demineralization treatment with the caries infiltration method (according to laser fluorescence value)," *Pediatric Dentistry And Dental Profilaxis*, vol. 20, no. 1, pp. 37–41, 2020.

[10] D. H. Shivananda, W. Ansar, A. R. Dinsha et al., "Effectiveness of various dental varnishes in prevention of enamel demineralization around orthodontic brackets: an in vitro study," *The Journal of Contemporary Dental Practice*, vol. 21, no. 6, pp. 621–625, 2020.

[11] T. I. Vieira, A. K. Alexandria, J. Menezes et al., "Characterization and effect of nanocomplexed fluoride solutions on the inhibition of enamel demineralization created by a multispecies cariogenic biofilm model," *Clinical Oral Investigations*, vol. 24, no. 11, pp. 3947–3959, 2020.

[12] H. Mo, J. Kim, and S. Oh, "Comparison of prevention methods against enamel demineralization adjacent to orthodontic bracket using fluoride," *The Journal of the Korean Academy of Pedtatric Dentistry*, vol. 46, no. 3, pp. 293–300, 2019.

[13] M. L. Torres-Garcia, L. D. Llavore, A. Bungay, J. D. Sarol Jr., R. R. Pineda, and K. . Peñas, "Benzalkonium chloride in an orthodontic adhesive: its effect on rat enamel demineralization using color-based image analysis," *American Journal of Orthodontics & Dentofacial Orthopedics*, vol. 155, no. 1, pp. 88–97, 2019.

[14] L. T. Trevelin, J. Villanueva, C. A. Zamperini, M. T. Mathew, A. B. Matos, and A. K. Bedran-Russo, "Investigation of five α-hydroxy acids for enamel and dentin etching: demineralization depth, resin adhesion and dentin enzymatic activity," *Dental Materials*, vol. 35, no. 6, pp. 900–908, 2019.

[15] R. Swetha, S. Manipal, M. Rajmohan et al., "Demineralization of tooth enamel surface at different immersion times of sport drink and buffering effect of casein derivative against enamel erosion," *International Journal of Advanced Research*, vol. 8, no. 10, pp. 926–935, 2020.

[16] Y. Tang, Z. Chen, W. Feng, Y. Nong, C. Li, and J. Chen, "Combined effects of nano-silica and silica fume on the mechanical behavior of recycled aggregate concrete," *Nanotechnology Reviews*, vol. 10, no. 1, pp. 819–838, 2021.

[17] C. Xiyue, L. Min, Z. Mu et al., "Synergetic PtNP@Co3O4 hollow nanopolyhedrals as peroxidase-like nanozymes for the dual-channel homogeneous biosensing of prostate-specific antigen," *Analytical and Bioanalytical Chemistry*, vol. 414, no. 5, pp. 1921–1932, 2022.

[18] H. Jasim, D. Al-Dabagh, and M. Mahmood, "Effect of different bracket types on Streptococcus mutans count in orthodontic patients using fluoridated toothpaste," *Journal of Baghdad College of Dentistry*, vol. 32, no. 2, pp. 1–4, 2020.

[19] G. Bo, X. Ning, and X. Pengfei, "Shock wave induced Nano crystallization and its effect on mechanical properties," *Materials Letters*, vol. 237, no. 15, pp. 180–184, 2019.

[20] C. Puyén-Goicochea, J. Armas-Pérez, and M. Ortiz-Pizarro, "Effect of an educational intervention via WhatsApp on the oral hygiene orthodontic patients," *International Journal of Odontostomatology*, vol. 14, no. 4, pp. 575–580, 2020.

[21] M. F. N. Feres, O. Eissa, M. G. Roscoe, and T. El-Bialy, "Comparison of the condyle sagittal position of class I and class II division 2 in orthodontic patients," *The Journal of Contemporary Dental Practice*, vol. 21, no. 9, pp. 977–981, 2020.

[22] A. Kolemen, H. S. Hasan, and A. Azzawi, "Medline diastema of orthodontic patients - prevalence and etiology in Erbil population - a cross-sectional study," *International Journal of Research in Pharmaceutical Sciences*, vol. 11, no. 4, pp. 5997–6003, 2020.

[23] T. Finkelstein, Y. Shapira, A. M. Pavlidi et al., "Canine transposition–prevalence, distribution and treatment considerations among orthodontic patients," *The Journal of Clinical Pediatric Dentistry*, vol. 44, no. 4, pp. 268–273, 2020.

[24] O. Svystun, L. Schropp, A. Wenzel, J. M. D. C. Silva, M. H. Pedersen, and R. Spin-Neto, "Prevalence and severity of image-stitching artifacts in charge-coupled device–based cephalograms of orthodontic patients," *Oral Surgery, Oral Medicine, Oral Pathology and Oral Radiology*, vol. 129, no. 2, pp. 158–164, 2020.

[25] J. V. Ashley, R. S. Ireland, and D. J. Plunkett, "Does the All Wales Universal Orthodontic Referral Form enable accurate triage of new NHS orthodontic patients? A service evaluation," *British Dental Journal*, vol. 228, no. 5, pp. 355–360, 2020.

[26] B. S. B. Bahar, S. R. Alkhalidy, E. G. Kaklamanos, and A. E. Athanasiou, "Do orthodontic patients develop more gingival recession in anterior teeth compared to untreated individuals? A systematic review of controlled studies-ScienceDirect," *International Orthodontics*, vol. 18, no. 1, pp. 1–9, 2020.

Hindawi

Research Article

Local Dimming Algorithm of Automotive LCD Instrument Based on Otsu and Maximum Entropy

Tianfu Liu [iD] and Chunqiu Tang

School of Mechanical and Electrical Engineering, Wuhan University of Technology, Wuhan, 430070 Hubei, China

Correspondence should be addressed to Tianfu Liu; ltf999@whut.edu.cn

In order to reasonably reduce the energy consumption of automotive LCD instrument and improve the display quality, a new local dimming algorithm is proposed in this paper. Firstly, the gray image of the input image is obtained by using the maximum principle, and then, the LED backlight brightness value is obtained by using Otsu method and maximum entropy method. The BMA backlight smoothing algorithm is improved by combining bilinear interpolation algorithm, and the dimming image is obtained by using pixel compensation algorithm based on logarithm. Then, for low brightness images, high brightness images, low contrast images, and high contrast images, typical algorithms are used to simulate and compare, and the image processing effects of various local dimming algorithms are analyzed. Finally, the entropy weight method is used to objectively evaluate the local dimming algorithm. The results show that the new local dimming algorithm reduces the energy consumption and improves the display quality, which verifies the effectiveness of the proposed algorithm.

1. Introduction

LCD in automobile liquid crystal instrument is different from OLED. It is a nonautonomous light-emitting display device, which needs to rely on backlight module to provide backlight [1]. Because LED has the characteristics of energy saving, environmental protection, and long service life, the straight down LED backlight module is widely used as its backlight in automotive LCD instruments. However, the output brightness of the traditional backlight is constant, resulting in high energy consumption, poor contrast, and light leakage of the display. In order to solve this series of problems, researchers proposed a local dimming algorithm. The local dimming algorithm divides the image into several partitions, and the backlight source changes accordingly according to the pixel content of the corresponding partition. More basic local dimming algorithms include max method, average method, sqrt method, and standard deviation method [2]. Max method takes the maximum gray value of the corresponding partition as the backlight brightness value, which will not cause obvious loss of details, but the energy-saving effect is poor. The average method takes

the average gray value of the corresponding partition as the backlight brightness value. Compared with the max method, the average method has better energy-saving effect, but it is prone to gray truncation. Sqrt method and standard deviation method obtain the backlight brightness value of the corresponding partition on the basis of average method. Compared with average method, sqrt method retains more image details and reduces energy consumption to a certain extent compared with max method, but it is also prone to gray truncation. At the same time, there are typical local dimming algorithms such as error correction method, CDF threshold method, and IMF method [3, 4]. In the error correction method, the weighting coefficient before the correction value is fixed, resulting in some images cannot get the ideal LED backlight brightness value, and the scope of application is limited. Both CDF threshold method and IMF method are suitable for high brightness images and can enhance the contrast of images, but for images with a large proportion of dark scenes, the LED backlight brightness obtained by the two algorithms is low, which is easy to cause excessive pixel compensation and is easy to lose details. In recent years, some scholars have proposed better local

dimming algorithms. Wu [5] proposed a new local dimming algorithm that uses the improved hybrid leapfrog algorithm to extract the backlight brightness, which improves the image contrast. Song et al. [6] proposed a local dimming algorithm based on deep learning that directly generates a compensation image from the input image without any backlight dimming level information. Zhang et al. [7] proposed a new adaptive local dimming method to change the backlight brightness value in combination with human visual characteristics. Zhao [8] proposed a local dimming algorithm based on image local brightness. Although some scholars at home and abroad have proposed some local dimming algorithms, there is still much room for improvement in energy saving and improving display quality. This paper presents a local dimming algorithm for automotive LCD instrument, which improves the display quality and reduces the energy consumption.

2. A New Local Dimming Algorithm

Otsu method has good processing effect for bimodal image and image edge region in gray histogram. It has the characteristics of simple calculation, high real-time performance, and relatively good processing effect. It is often used to obtain the initial threshold in the field of threshold segmentation. However, because Otsu method only considers the maximization of target and background segmentation when doing threshold segmentation, it is often difficult for Otsu method to obtain a better segmentation threshold for some images whose gray value of target and background is close. Otsu method has a good processing effect for the image with obvious distinction between the background layer and the target layer, that is, the image with double peaks in the gray histogram, and also in the edge area of the gray value of the image. The maximum entropy method and Otsu method have a good complementary effect. They have a good recognition and segmentation effect in the region with low discrimination between the background and the target boundary, while the processing effect in the edge region of gray image is poor [9]. By comprehensively analyzing the advantages and disadvantages of existing local dimming algorithms, this paper proposes a local dimming algorithm based on OTSU and maximum entropy, including local dynamic backlight extraction algorithm, backlight smoothing algorithm, and pixel compensation algorithm.

2.1. Backlight Extraction. The specific steps of the new backlight region extraction algorithm are as follows:

(1) Convert the input image into a gray image by using the maximum principle

Firstly, this paper uses the maximum principle to gray the input image to obtain the gray image; that is, the maximum value of the red, green, and blue primary colors of each pixel is taken as the gray value of the pixel. By using the maximum principle to obtain the gray value, it can ensure that the brightness value of LED backlight calculated in the subsequent backlight extraction algorithm will not be too
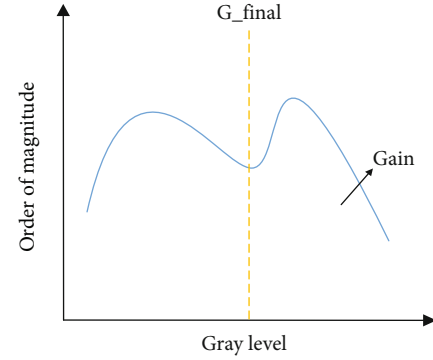
Figure 1: Schematic diagram of gain region.

Figure 2: Block effect simulation diagram.

low, so as to avoid the impact on the image display effect due to excessive pixel compensation to a great extent. At this time, the three primary colors of red, green, and blue are represented by eight channels, which is 256 levels; the quantization range of the gray value is 0-255, as shown in

$$\text{gray}(x, y) = \max\left(R(x, y), G(x, y), B(x, y)\right). \quad (1)$$

In the formula, $R(x, y)$, $G(x, y)$, and $B(x, y)$ are the three primary color components of red, green, and blue at the pixel.

(2) Obtain the first level target value by using Otsu method

After obtaining the gray image of the input image, the Otsu method (maximum inter class variance method) is used to adaptively select the first level target value according to the gray image of each image partition. The specific steps are as follows:

For an image with a resolution of $A \times B$, it contains M gray levels $\{0, 1, 2, \cdots, M - 1\}$, and N_i is the number of pixels with gray level i, as shown in

$$P_{Oi} = \frac{N_i}{AB}. \quad (2)$$

In the formula, P_{Oi} is the gray probability corresponding to the gray level i, where $\sum_0^{M-1} P_{Oi} = 1$ and $P_{Oi} \geq 0$.

If the segmentation threshold is f, the gray image pixels are divided into $[0, f]$ and $[f + 1, M - 1]$, that is, corresponding to background Back1 and target Back2. $P_1(f)$ and $P_2(f)$ are the total pixel probabilities of background Back1 and
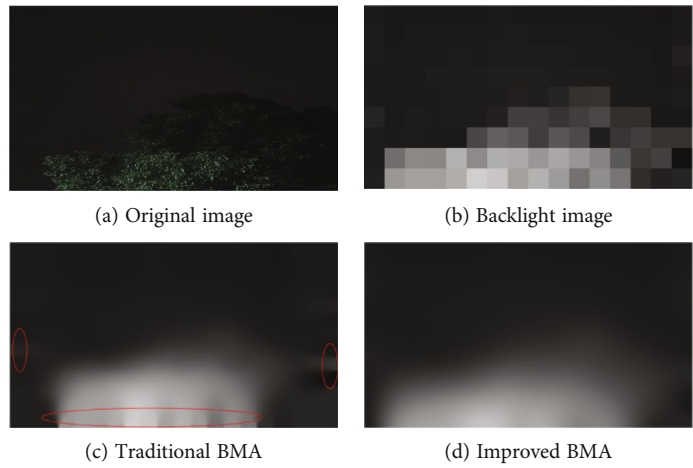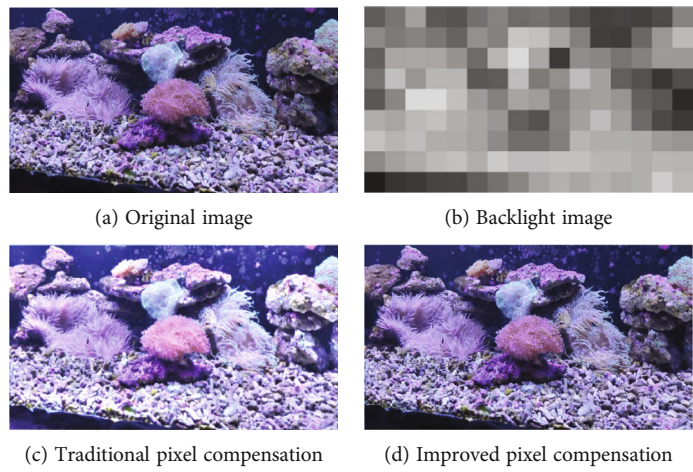
(a) Original image

(b) Backlight image

(c) Traditional BMA

(d) Improved BMA

Figure 3: Effect comparison of backlight smoothing algorithm.

(a) Original image

(b) Backlight image

(c) Traditional pixel compensation

(d) Improved pixel compensation

Figure 4: Effect comparison of pixel compensation algorithm.

(a) Low brightness

(b) High brightness

(c) Low contrast

(d) High contrast

Figure 5: Sample image.

(a) Max

(b) Average

(c) Sqrt

(d) SD

(e) ECM

(f) CDF

(g) IMF

(h) New
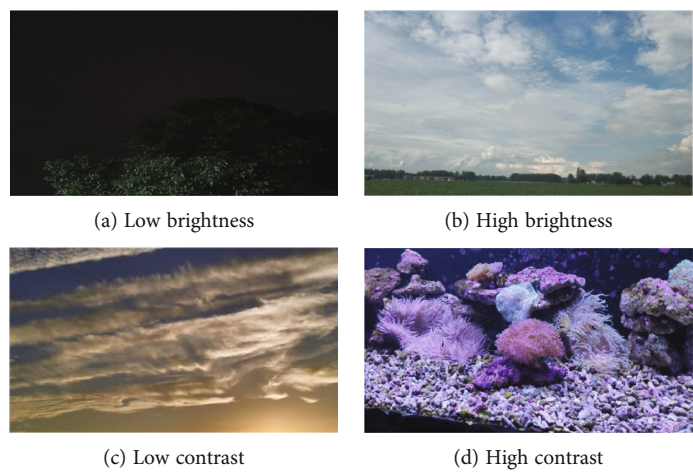
FIGURE 6: Low brightness image simulation diagram.

target Back2, respectively, and $\mu_1(f)$ and $\mu_2(f)$ are the average gray values of background Back1 and target Back2, respectively, as shown in

$$\mu_1(f) = \sum_{i=0}^{f} i \frac{P_{Oi}}{P_1(f)},$$
$$\mu_2(f) = \sum_{i=f+1}^{M-1} i \frac{P_{Oi}}{P_2(f)}, \tag{3}$$

where μ_0 is the average gray value of the input image and C is the inter class variance, as shown in

$$C(f) = P_1(f)(\mu_1(f) - \mu_0)^2 + P_2(f)(\mu_2(f)\text{-}\mu_0)^2$$
$$= P_1(f)P_2(f)(\mu_1(f) - \mu_2(f))^2, \tag{4}$$
$$C(G1) = \max_{1 \leq f \leq M-1} C(f).$$

In the formula, $C(G1)$ is the maximum interclass variance and $G1$ is the target threshold.

(3) Obtain the secondary target value by using the maximum entropy method On the basis of Otsu method

Within the range of [90%, 110%] of the primary target value obtained by Otsu method, the secondary target value is obtained by maximum entropy method. The specific steps are as follows:

Taking the segmentation threshold f_2 as the boundary, it is divided into two parts: Back3 and Back4, which correspond to gray areas $[0, f_2]$ and $[f_2 + 1, M - 1]$, respectively. $P_{e1}(f_2)$ and $P_{e2}(f_2)$ are the probability sum of gray levels in two gray areas, respectively.

The sum of information entropy th_{total} of Back3 and Back4 is

$$\text{th}_{\text{total}}(f_2) = \text{th}(\text{Back3}) + \text{th}(\text{Back4})$$
$$= -\sum_{i=0}^{f_2} \frac{P_{Oi}}{P_{e1}} \ln \frac{P_{Oi}}{P_{e1}} - \sum_{i=f_2+1}^{M-1} \frac{P_{Oi}}{P_{e2}} \ln \frac{P_{Oi}}{P_{e2}}. \tag{5}$$

For the flat part of the curve in the gray histogram of the input image, the information entropy is large; the steep region with less gray level information is the region with low complexity and low information entropy. By traversing f_2 in the gray range of $[0.9G1, 1.1G1]$, the gray level $G2$ corresponding to the maximum value of $\text{th}_{\text{total}}(f_2)$ is the secondary target value.

(a) Max

(b) Average

(c) Sqrt

(d) SD

(e) ECM

(f) CDF

(g) IMF

(h) New

FIGURE 7: High brightness image simulation diagram.

(4) Calculate the target segmentation threshold

The target segmentation threshold G_final is obtained by comprehensively considering the primary target value and secondary target value in steps (2) and (3).

$$G\_\text{final} = \frac{G1 + G2}{2}. \tag{6}$$

(5) Calculate the backlight brightness value

The area where the gray value is greater than G_final is regarded as the gain area gain, as shown in Figure 1.

After obtaining the gain region, the relevant idea of error correction method is used, as shown in

$$\begin{aligned} \text{BL}_\text{gain} &= \text{mean}(\text{gain}), \\ K &= \frac{\text{BL}_\text{gain} - G\_\text{final}}{\text{BL}_\text{max}}, \\ \text{BL}_\text{new} &= \text{BL}_\text{avg} + K \times \frac{\left(\text{BL}_\text{max} - \text{BL}_\text{avg}\right)^2}{255}. \end{aligned} \tag{7}$$

In the formula, BL_gain is the average gray value of the gray image gain area; K is the gain coefficient. Cor is the correction amount obtained by introducing the error correction method, and BL_new is the backlight brightness value of LED lamp obtained by applying the new local dynamic backlight extraction algorithm.

2.2. Backlight Smoothing. Due to the light diffusion of LED lights in adjacent zones, it will affect adjacent zones. If the pixel is compensated directly, there will be obvious "block effect" in the image. Therefore, before pixel compensation, backlight smoothing is needed to eliminate the "block effect." The simulation effect of block effect is shown in Figure 2. At present, LSF algorithm and BMA algorithm are widely used for backlight smoothing. Compared with LSF algorithm, BMA algorithm has the advantages of simple operation, less hardware resources, and better backlight smoothing effect. However, because the traditional BMA algorithm uses a simple surrounding image processing when expanding the matrix for smoothing filtering, it will cause some loss to the final backlight smoothing effect. The algorithm adopts bilinear interpolation expansion method when expanding the matrix. This method effectively considers the image information of the original matrix, and the performance of the algorithm is improved.

(a) Max

(b) Average

(c) Sqrt

(d) SD

(e) ECM

(f) CDF

(g) IMF

(h) New
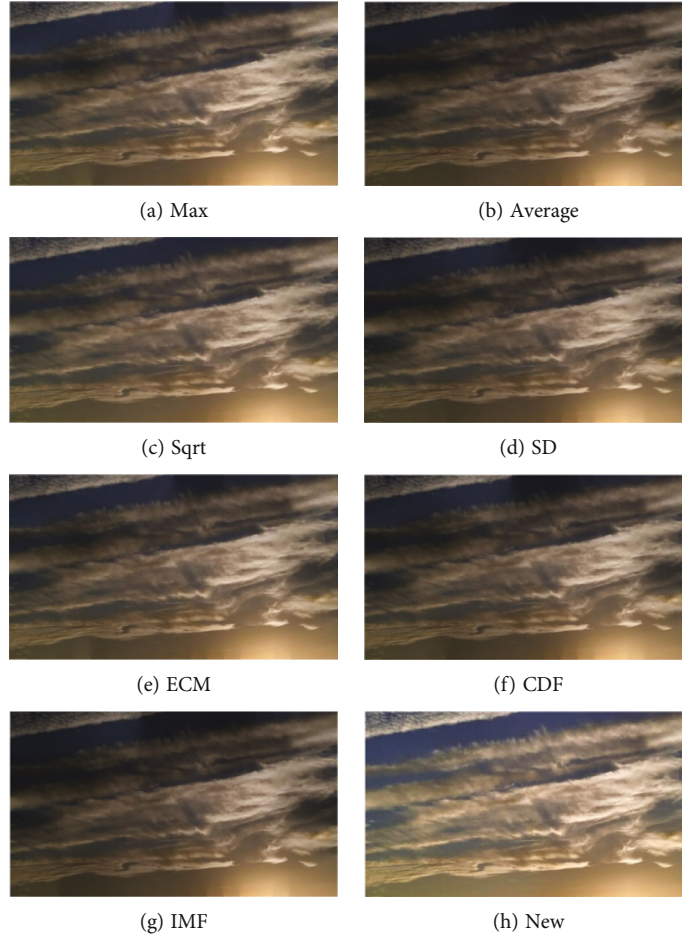
FIGURE 8: Low contrast image simulation diagram.

The core idea of the improved BMA algorithm is as follows:

(1) The surrounding mirror image is only a simple copy of the boundary, resulting in a large error. The bilinear interpolation algorithm is used to expand the matrix, which fully considers the nearest four vertices around the pixel to be calculated. In the initial matrix expansion, the bilinear interpolation algorithm is used to replace the traditional method of surrounding mirror image to expand the matrix to obtain the expansion matrix BL_{exp}, as shown

$$
BL_{exp} = \begin{bmatrix}
BL_{bil_{1,1}} & BL_{bil_{1,2}} & BL_{bil_{1,3}} & L & BL_{bil_{1,c}} & BL_{bil_{1,c+1}} & BL_{bil_{1,c+2}} \\
BL_{bil_{2,1}} & BL_{bil_{2,2}} & BL_{bil_{2,3}} & L & BL_{bil_{2,c}} & BL_{bil_{2,c+1}} & BL_{bil_{2,c+2}} \\
BL_{bil_{3,1}} & BL_{bil_{3,2}} & BL_{bil_{3,3}} & L & BL_{bil_{3,c}} & BL_{bil_{3,c+1}} & BL_{bil_{3,c+2}} \\
M & M & M & M & M & M & M \\
BL_{bil_{r,1}} & BL_{bil_{r,2}} & BL_{bil_{r,3}} & L & BL_{bil_{r,c}} & BL_{bil_{r,c+1}} & BL_{bil_{r,c+2}} \\
BL_{bil_{r+1,1}} & BL_{bil_{r+1,2}} & BL_{bil_{r+1,3}} & L & BL_{bil_{r+1,c}} & BL_{bil_{r+1,c+1}} & BL_{bil_{r+1,c+2}} \\
BL_{bil_{r+2,1}} & BL_{bil_{r+2,2}} & BL_{bil_{r+2,3}} & L & BL_{bil_{r+2,c}} & BL_{bil_{r+2,c+1}} & BL_{bil_{r+2,c+2}}
\end{bmatrix}. \tag{8}
$$

(a) Max

(b) Average

(c) Sqrt

(d) SD

(e) ECM

(f) CDF

(g) IMF

(h) New
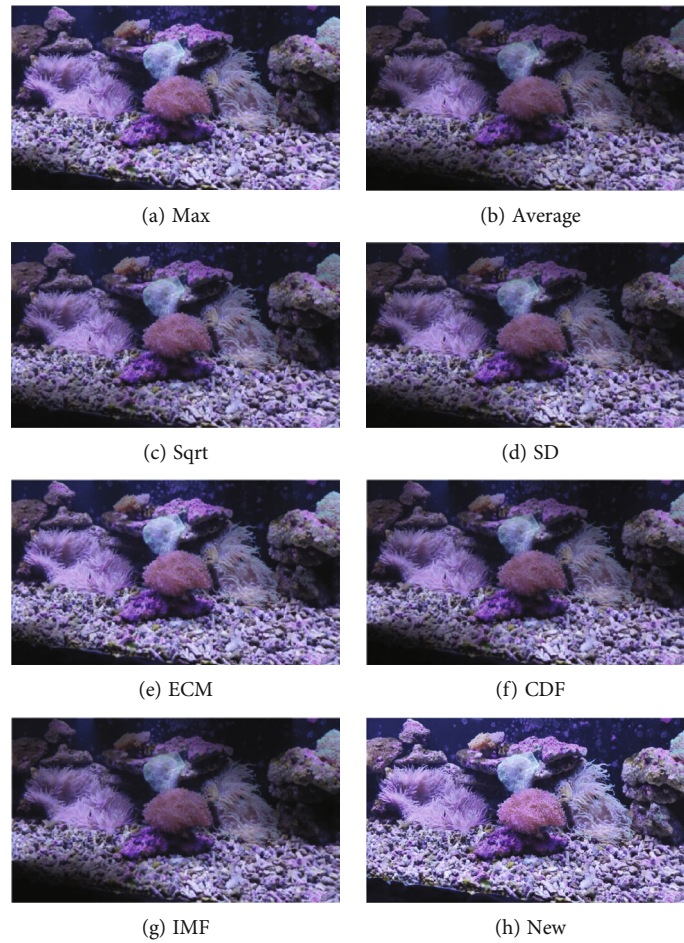
FIGURE 9: High contrast image simulation diagram.

(2) The backlight smoothing initial expansion matrix BL_{exp} is smoothed by equation (9) to obtain the initial smoothing filter matrix BL_{filt}

$$
\begin{aligned}
\mathrm{BL}_{\mathrm{filt}_{i,j}} = {} & 0.32 \times \mathrm{BL}_{\mathrm{bil}_{i,j}} + 0.1 \times \left(\mathrm{BL}_{\mathrm{bil}_{i,j\text{-}1}} + \mathrm{BL}_{\mathrm{bil}_{i,j+1}} \right) \\
& + 0.1 \times \left(\mathrm{BL}_{\mathrm{bil}_{i\text{-}1,j}} + \mathrm{BL}_{\mathrm{bil}_{i+1,j}} \right) + 0.07 \\
& \times \left(\mathrm{BL}_{\mathrm{bil}_{i\text{-}1,j\text{-}1}} + \mathrm{BL}_{\mathrm{bil}_{i\text{-}1,j+1}} + \mathrm{BL}_{\mathrm{bil}_{i+1,j\text{-}1}} + \mathrm{BL}_{\mathrm{bil}_{i+1,j+1}} \right).
\end{aligned}
\tag{9}
$$

(3) After smoothing the matrix, the nearest neighbor interpolation algorithm is replaced by bilinear interpolation algorithm to double the size of the matrix

(4) Repeat steps (1)~(3) twice. Finally, the bilinear interpolation algorithm is used to expand the smoothing filter matrix to the size of the original image. The comparison of algorithms is shown in Figure 3

2.3. Pixel Compensation. If the brightness value of LED backlight obtained by the local dynamic backlight extraction algorithm is too small, the traditional pixel compensation algorithm will lead to overcompensation of image pixels,

which will lead to gray truncation and poor reliability of the algorithm. This paper proposes a pixel compensation algorithm based on logarithm, which can stretch the low brightness region and enhance the high brightness region, which reduces the distortion of the image to a great extent, as shown in

$$
V(x, y) = \ln \left(\left(\frac{\mathrm{gray}_{\max}}{g(x, y)} \right)^{0.2} \times e \right),
$$
$$
\begin{cases}
R'(x, y) = V(x, y) * R(x, y), \\
G'(x, y) = V(x, y) * G(x, y), \\
B'(x, y) = V(x, y) * B(x, y).
\end{cases}
\tag{10}
$$

In the formula, $\mathrm{gray}_{\max}$ is the maximum gray value of each image partition gray image; $g(x, y)$ is the backlight smoothing value at pixel (x, y) obtained by backlight smoothing of LED backlight brightness matrix; $V(x, y)$ is the pixel adjustment coefficient.

The comparison between traditional pixel compensation algorithm and logarithm-based pixel compensation algorithm is shown in Figure 4.

Table 1: Subjective evaluation effect.

	Max	Average	Sqrt	SD	ECM	CDF	IMF	New
Low brightness	Substandard	Substandard	Substandard	Substandard	Substandard	Substandard	Substandard	Good
High brightness	Substandard	Good	General	General	General	General	General	Good
Low contrast	Good	Substandard	General	General	General	General	Substandard	Good
High contrast	Good	Good	Good	Good	Good	Good	Good	Good

Table 2: Objective evaluation index of local dimming algorithm.

Index	Calculation formula	Evaluation significance
SER	$SER = (1-(BL\_AVG/255)) \times 100\%$	Energy-saving effect
OFR	$OFR = OF_{sum}/A \times B$	Image retention effect
CR	$CR = MAX(BL)/MIN(BL)$	Image display enhancement effect

Table 3: Objective evaluation results.

Algorithm	Low brightness				High brightness				Low contrast				High contrast			
	SER	OFR	CR	SUM	SER	OFR	CR	SUM	SER	OFR	CR	SUM	SER	OFR	CR	SUM
Max	65	80	60	70.71	70	80	68	68.73	70	80	80	77.20	75	80	80	78.33
Average	85	50	70	63.38	80	80	85	83.16	80	62	80	69.17	80	80	85	81.92
Sqrt	65	65	50	60.34	70	80	72	71.26	70	74	70	72.40	75	85	80	79.74
SD	80	60	60	64.09	70	80	80	76.33	70	70	80	71.19	75	85	85	81.66
ECM	70	70	60	66.89	70	80	75	73.16	70	74	80	73.60	75	85	80	79.74
CDF	80	70	60	68.94	70	80	80	76.33	70	71	80	71.80	75	85	80	79.74
IMF	85	55	80	68.91	70	80	85	79.50	80	62	80	69.17	75	85	85	81.66
New	85	85	70	80.34	80	80	85	83.16	80	82	80	81.20	80	85	85	83.33

3. Effect Verification of Local Dimming Algorithm

On the MATLAB platform, different local dimming algorithms are used to simulate low brightness image, high brightness image, low contrast image, and high contrast image. The resolution of the test image is 1920×1080, and image partition is 16×9. The sample image is shown in Figure 5, and the simulation results are shown in Figures 6–9.

According to the simulation results, six testers are invited to subjectively evaluate the simulation images according to the five grades of excellent, good, general, substandard, and inferior in the closed dark light environment. The results are shown in Table 1.

4. Algorithm Evaluation

4.1. Evaluation Index. Based on the comprehensive analysis of the classical objective evaluation methods, this paper proposes to take the energy-saving rate (SER), overflow rate (OFR), and contrast (CR) as the objective evaluation indexes for the regional dimming algorithm, as shown in Table 2.

In the formula, BL_AVG is the average brightness of all LED backlights corresponding to an input image, and the value range is $[0 - 255]$; OF_{sum} is the total number of pixel overflow after pixel compensation; MAX(BL) and MIN(BL) are the maximum and minimum brightness of LED back-

light obtained by using the regional dynamic backlight extraction algorithm.

4.2. Result Analysis. Three objective evaluation indexes of energy saving rate, overflow rate, and contrast are extracted from the backlight brightness value and backlight compensation pixel value. In this paper, the entropy weight method based on objective indexes is used to evaluate and score the algorithm, eliminate the interference of subjective factors, give weights to each objective evaluation index, and then convert it into the quantification of the quality evaluation of regional dimming algorithm.

The evaluation results obtained by entropy weight method are shown in Table 3.

Table 1 evaluates the image from the subjective visual perception of the tester, and Table 3 analyzes the processing effect of the algorithm from the objective indicators. The consistency between Tables 1 and 3 is good, which verifies the excellent processing effect of the algorithm proposed in this paper on reducing energy consumption and improving display quality.

5. Discussion

(1) A new local dimming algorithm for automotive LCD instrument is proposed, which can reduce energy consumption and improve display quality. It mainly

includes the comprehensive use of Otsu method and maximum entropy method to determine the brightness value of LED backlight, the improvement of BMA backlight smoothing algorithm by bilinear interpolation, and the pixel compensation algorithm based on logarithm

(2) The new local dimming algorithm and other local dimming algorithms proposed in this paper are simulated and analyzed on four typical images. It is found that the local dimming algorithm proposed in this paper can effectively improve the display quality, which shows that this algorithm has wide applicability

(3) The entropy weight method is used to objectively evaluate the quality of the algorithm, which proves that the local dimming algorithm proposed in this paper can effectively reduce energy consumption and improve the display quality

Data Availability

No data were used to support this study.

Conflicts of Interest

There is no potential conflict of interest in this study.

References

[1] H. Jia, "Who will win the future of display technologies?," *National Science Review*, vol. 5, no. 3, pp. 427–431, 2018.

[2] F. W. Li, W. Q. Jin, X. B. Shao, X. Wang, L. L. Zhang, and K. L. Zhang, "Progress of high dynamic range liquid crystal display technology based on LED backlight with area control technology," *Optical Technique*, vol. 35, no. 6, pp. 835–839, 2009.

[3] Y. Z. Liu, X. R. Zheng, and J. B. Chen, "Dynamic backlight signal extraction algorithm based on threshold of image CDF for LCD-TV and its hardware implementation," *Chinese Journal of Liquid Crystals and Displays*, vol. 25, no. 3, pp. 449–453, 2010.

[4] F.-C. Lin, Y.-P. Huang, L.-Y. Liao et al., "Dynamic backlight gamma on high dynamic range LCD TVs," *Journal of Display Technology*, vol. 4, no. 2, pp. 139–146, 2008.

[5] H. Y. Wu, *Research on Local Dimming Algorithm Based on HDR Display*, Tianjin University, 2018.

[6] S.-J. Song, Y. In Kim, J. Bae, and H. Nam, "Deep-learning-based pixel compensation algorithm for local dimming liquid crystal displays of quantum-dot backlights," *Optics Express*, vol. 27, no. 11, pp. 15907–15917, 2019.

[7] S. J. Song, Y. I. Kim, J. Bae, and H. Nam, "Adjustable adaptive local dimming method," *Laser & Optoelectronics Progress*, vol. 57, no. 12, pp. 221–229, 2020.

[8] C. Zhao, G. Q. Lyu, L. Wu, L. M. Zhu, and Q. B. Feng, "Dynamic dimming algorithm for liquid crystal display based on local brightness of image," *Chinese Journal of Liquid Crystals and Displays*, vol. 35, no. 3, pp. 234–241, 2020.

[9] S. Yi, G. Zhang, J. He, and S. Li, "Maximum entropy image segmentation based on maximum interclass variance," *Computer Engineering & Science*, vol. 40, no. 10, pp. 1874–1881, 2018.

Research Article

Mixed Interlaminar Fracture Toughness and Durability of Composites under Humid and Hot Conditions

Mingyong Li [ID],[1] Xia Meng,[2] and Qingyi Zhang[3]

[1]*Department of Architectural Engineering, Shaoxing University Yuanpei College, Shaoxing 312000, China*
[2]*Gansu Institute of Earthquake and Seismic Engineering, Gansu Provincial Seismological Bureau, Lanzhou, 730000 Gansu, China*
[3]*Chengdu Branch of China Railway Scientific Research Institute Co., Ltd., Chengdu, 610000 Sichuan, China*

Correspondence should be addressed to Mingyong Li; 18767583669@usx.edu.cn

Composite material is a new material prepared by several raw materials with different forms or properties through new processing methods. The composite not only maintains the advantages of the properties of each component but also can obtain the comprehensive properties that cannot be achieved by a single component through the complementarity and correlation of the properties of each component. The purpose of this paper is to study the effect of wet and hot conditions on the interlaminar fracture toughness and durability of composites. In this paper, the interlaminar fracture toughness and durability are studied, and the prediction and analysis method under wet and hot conditions is carried out. The effects of hot and humid conditions on interlaminar fracture toughness and durability were analyzed. The experimental results show that the longitudinal compressive strength of the unidirectional composite at 120°C and 1.00% moisture absorption is 29.53% lower than that at 20°C and 0.50% moisture absorption. Due to the high moisture absorption of aramid fiber, the longitudinal compressive strength of unidirectional aramid composite fiber will be significantly reduced in the humid and warm environment.

1. Introduction

Due to the special properties of nanomaterials, they are regarded as new materials in the 21st century. Advanced composites have been more and more used in aerospace and cycle fields because of their excellent properties, such as high special strength. The vulnerability and nonuniformity of the composite material itself make the failure of the hinge part of the composite material more complex, and the failure characteristics of the damage are also more complex. Its fracture performance is very different from that of metal materials. In addition, the connecting parts of composites are also very different. However, due to the complexity of composites and the continuous emergence of various new fibers and matrix materials, the influence of the humid and hot environment on the mechanical and fatigue properties of composites is not obvious. At present, there is no complete and accurate evaluation system.

Advanced composites are increasingly used in the main structures of aircraft and automobiles. Due to the low inter-laminar strength, delamination is one of the most serious failure modes in composites and their structures. It is widely used in the cohesion model and virtual crack closure technology to predict the delamination of composites and their structures under tensile, compressive, or impact loads [1, 2]. Therefore, the interlaminar fracture toughness of composites is very important for the design and analysis of composites and their structures. Interlaminar fracture toughness is generally considered an inherent property of composites, which needs to be obtained by a delamination test. Therefore, it is very important to develop a simple and accurate test method to determine the interlaminar fracture toughness.

The innovations of this paper are as follows. (1) This paper combines damp-heat conditions with composites and introduces the relevant methods of interlaminar fracture toughness considering damp-heat conditions in detail. (2) In the face of hot and humid conditions, the fracture toughness and durability of composites are studied in this paper. By evaluating the experimental results and comparing the data

changes, it is concluded that the longitudinal compressive strength of unidirectional aramid composite fiber will be significantly reduced in the humid and hot environment.

2. Related Work

The influence of the environment is complex. For example, high temperature and moisture absorption will increase the plasticity of the matrix and increase the delamination toughness. On the other hand, it will cause microcracks in the matrix, will affect the bonding strength between the fiber matrix, may reduce the toughness, and will have different effects on different types of resins. Zhang et al. studied the effects of lime content, slag content, and moisture content on the thermal and wet properties of lime slag/soil composites by the response surface method and lime preparation process. The results showed that the lime content, slag content, and moisture content will affect the overall thermal and wet properties. Under the action of alkaline excitation and micro aggregate, the optimized lime slag/soil composite has the advantages of compact structure, reasonable mechanical properties, and comprehensive properties of heat and moisture. However, their data is less [3]. Zong et al. adopted the uniform experimental design and multiple nonlinear regression formula. They studied the Ce-La dose results (Ce-La molecular ratio and tetrabutyl titanate). The effects of the volume ratio of tetrabutyl titanium to tetraethyl orthosilicate on the hygroscopicity and photocatalytic properties of Ce-La/TiO_2 hollow microspheres were studied. The results show that these four factors have an effect on hygroscopicity. However, their research is not comprehensive enough [4]. Kasaragadda et al. applied superhydrophobic coatings to the surfaces of carbon, Kevlar, and glass fiber composites to eliminate the absorption of water by the composite structure. The test results show that when the composite surface is coated with a superhydrophobic coating, the moisture absorption is much smaller than that of the uncoated composite sample. However, their influencing factors are not single [5]. Yu et al. used the strong van der Waals force between superaligned carbon nanotubes (SACNT) to design a self-supporting 3D CNT/$CaCl_2$ radiator, which has better heat dissipation performance than aluminum fins. This high-efficiency refrigerator provides another heat management method for electronic products. However, their content is not novel enough [6]. Tanaka et al.'s study measured the specific volume and softening point of the resin by a single fiber drawing test at room temperature, 40°C, and 80°C. It was used to evaluate the fiber/matrix interface characteristics of the CF/PA9T composite model, and the results were compared with those of the CF/PA6 and CF/PA12 composite models. The resin expansion and interfacial shear strength of CF/PA9T model composites decreased with the increase in temperature, and the decreased range of interfacial shear strength of CF/PA9T model composites was less than that of CF/PA6 and CF/PA12 model composites. The reduction of high-temperature residual stress below 80°C does not cause chemical modification and softening of the resin but reduces the interfacial shear strength of the fiber matrix.

However, their process is more complicated [7]. Liu et al. expanded its application in the electronics and membrane industry. It is aimed at developing radiation with heat resistance, conductivity, and moisture resistance by using PCT as the reactive reinforcement and applying the solid-state interface reaction (SSIR) between PCT and PA6. According to the results, SSIR occurred between PA6 and PCT. However, their research is not specific enough [8]. Chen et al. mixed natural corn starch with galactomannan (NS-GM) to produce the starch-galactomannan complex after wet heat treatment (HMT). They studied the in vitro digestibility and physicochemical properties of starch and starch-galactomannan complex. Their study found that the resistant starch content of HMT NS-GM composite granules was related to the galactose/mannose residue ratio of galactomannan. However, their conclusion is not comprehensive [9]. Han et al. synthesized a unique amino-functionalized metal-organic skeleton (sN-MIL) with a small pore size and low specific surface and developed a new heat-resistant and moisture-resistant bismaleimide (BD) resin with ultralow dielectric loss and high toughness. They discussed in depth the reasons behind these attractive properties of sN-MIL/BD composites. However, their content is not detailed enough [10].

3. Interlaminar Fracture Toughness Method considering Wet and Hot Conditions

3.1. Composites in Hot and Humid Conditions

3.1.1. Composite Material. Composite material is a new material prepared by several raw materials with different forms or properties through new processing methods. The new material processed and prepared by composite means has a clear interface between the organizational components in the material, which not only maintains some excellent characteristics of the original material components but also has superior characteristics that the original material components do not have. Composite materials include the matrix and reinforcement. Among them, the reinforcement plays an important role in bearing the external load in the composite, and the static properties of the composite are mainly determined by the characteristics of the reinforcement [11, 12].

The matrix of another main part of the composite mainly plays the role of coordination with the added solid. The solid added plays the role of supporting and fastening the solid added, and the load transfer between the solid added and the solid added protection. Matrix materials can also improve some properties of composites. In this paper, resin is selected as the base material because of its low density and ceramic as the die material because of its high-temperature resistance, and metal as the die material must obtain higher hardness and shear properties. As we all know, polymer matrix composites have another name in engineering applications, also known as resin matrix composites. In practical engineering applications, we use more thermoplastic resins and thermosetting resins. Among thermosetting resins, epoxy resin has the advantages of strong adhesion

and good corrosion resistance. It has been widely used in engineering applications, with good fiber surface permeability and convenient processing, preparation, hardening, and casting. Thermoplastic resin has good processability [13, 14]. Therefore, when the heating temperature reaches the transition temperature, they will soften again. Based on this excellent performance, it is easier to manufacture cast composites, and this resin has very good fracture resistance and high hardness. The drawback is that the coefficient of this resin is not high and the heat resistance is not very good.

3.1.2. Influence of the Damp and Hot Environment on Composites.

During the use of composite materials, they will encounter the changing atmospheric environment. They will be used in nature with changing temperature T and relative humidity RH for a long time. When the natural environment's temperature and humidity are relatively high, water molecules may enter the polymer components and further diffuse. In view of the tiny cracks and gaps in the composite structure and the defects contained in the internal interface of the composite, the penetration rate and saturated moisture absorption rate of water in the material will be improved. The mechanical properties and electromagnetic properties of composites are bound to be greatly affected by them. In the end, the utilization efficiency of composites will be reduced and even the products will be damaged [15]. Water molecules penetrate into the tissue between the fiber and the matrix, causing the glue of these parts to lose viscosity and be transmitted to the fiber through the interface, resulting in fiber damage.

It is generally believed that glass fiber and carbon fiber do not absorb moisture, while aramid fiber has greater moisture absorption. It can be seen from Table 1 that the hygroscopicity of the glass fiber- and carbon fiber-reinforced composites is significantly lower than that of the resin matrix. The hygroscopicity of the aramid fiber-reinforced composites is four times that of the resin matrix. The phenomenon of water corrosion of glass fiber is found.

The influence of the liquid and warm environment on fiber-reinforced resin matrix composites is the synergistic effect of humidity and temperature, which is mainly due to the different degrees of damage to the resin matrix and the connection interface between reinforced fiber and resin/fiber. Heating can accelerate the moisture absorption rate, increase the moisture absorption balance of the material, and reduce the equilibrium time.

3.2. Fracture Mechanics Solution of Composite DCB.

Due to the low interlaminar strength of laminates, delamination is the most common and main failure form.

From the point of view of mechanical fracture, separation belongs to the propagation behavior of the interlayer crack. According to the classification of cracks in fracture mechanics, their separation is mainly divided into three ways: I, II, and II, which depend on the stress at the edge of the crack. Type I separation, with the edge stress perpendicular to the crack surface, belongs to the open type. Type II

TABLE 1: Water absorption of the material after immersion in water for 7 days (10^{-2} g/cm^3).

Material temperature	22°C	60°C	100°C
Epoxy resin	0.24	0.39	1.12
Glass fiber-reinforced composites	0.13	0.24	0.68
Carbon fiber-reinforced composites	0.24	0.33	0.82
Aramid fiber-reinforced composites	0.48	0.68	4.78

separation, with the edge stress parallel to the crack surface, belongs to the shear type. Type III peeling, with the peak voltage on the crack surface perpendicular to the crack, tears in the propagation direction. In engineering practice, the stress state at the crack tip is often a complex stress state, which is the composite of the three basic types [16, 17].

3.2.1. Griffith's Energy Release Rate.

According to Griffith's law, the energy release rate refers to the energy consumed per unit of the newly generated surface area during fracture, as shown in Figure 1.

The mathematical form of the energy release rate can be expressed as follows:

$$G = \frac{\delta \prod}{\delta M} = \frac{\delta(W - U)}{\delta M} = \frac{1}{N} \cdot \frac{\delta(W - U)}{\delta m}, \quad (1)$$

where u represents the total strain energy, w represents the external force work, M represents the surface area of the newly generated crack surface, n represents the specimen width, and DM is the crack growth increment. Using the following relationship: $C = \varepsilon/P$, $W = P\varepsilon$, and $U = 1/2P\varepsilon$, formula (1) can be transformed into the following form:

$$G = \frac{1}{2N} P^2 \frac{\delta C}{\delta m}, \quad (2)$$

where P and ε are the applied load and opening displacement, respectively. C represents the flexibility of the DCB specimen.

3.2.2. Fracture Mechanics Solution Based on the Beam Theory.

The energy release rate of the DCB sample shown in Figure 2 can be analyzed by the basic beam theory.

According to Euler's beam theory, the opening displacement of DCB sample δ and the force P applied at both ends have the following relationship:

$$\varepsilon = \frac{2Pm^3}{3E_{xx}A}, \quad (3)$$

where E_{xx} represents the elastic modulus of the sample along the fiber direction, M represents the crack length, h is the thickness of the single cantilever beam, a represents the section moment of inertia of the single cantilever beam, and $A = 1/12Nh^3$.
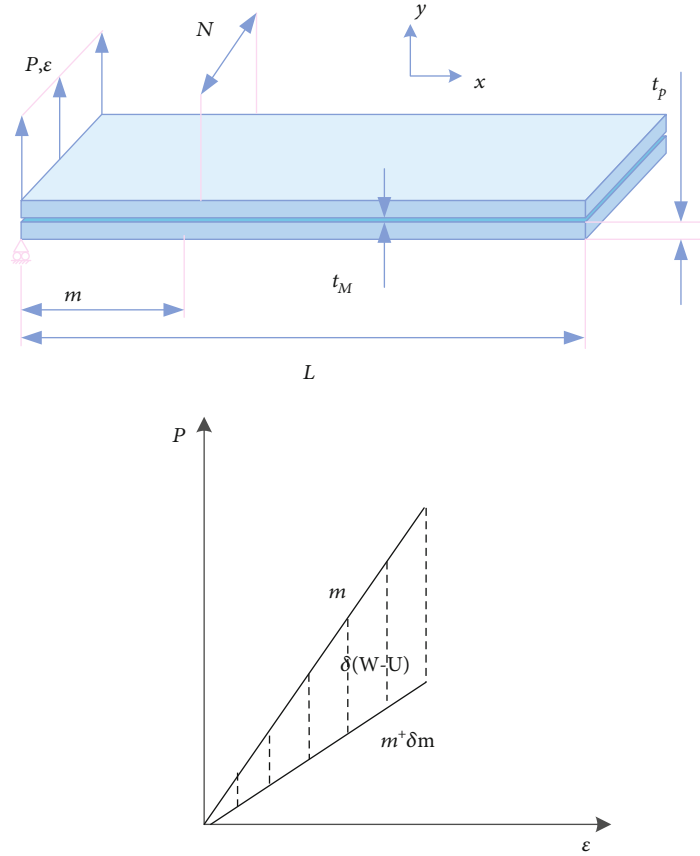
FIGURE 1: Schematic diagram of Griffith's energy release rate.
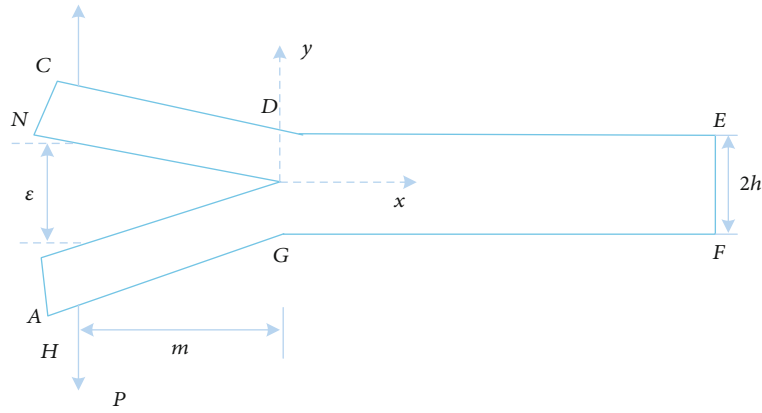
FIGURE 2: DCB sample.

By introducing formula (3) into formula (2), the expression of the energy release rate based on Euler's beam theory can be obtained:

$$G = \frac{1}{N} \cdot \frac{P^2 m^3}{3E_{xx}A}. \tag{4}$$

Using formula (3) and its transformation form, the energy release rate G in formula (4) can be rewritten as follows:

$$G = \frac{9E_{xx}A \cdot \varepsilon^2}{4Nm^4}, \tag{5}$$

$$G = \frac{3P\varepsilon}{2Nm}, \tag{6}$$

$$G = \frac{1}{N} \cdot \sqrt{\frac{9P^4 \cdot \varepsilon^2}{4E_{xx}A}}. \tag{7}$$

Theoretically, the energy release rate calculated by formulas (4)–(7) should be the same. However, if the load and displacement obtained from the finite element are used and the energy release rate is calculated by the four formulas, the accuracy of their results is different. The reason is that the load-displacement relationship of the DCB sample given in formula (3) is an approximate solution.

3.2.3. Two-Dimensional Elastic Solution. Formula (3) introduces some simplified assumptions when calculating the load-displacement relationship of the DCB sample: the energy in the DCB sample is only stored in arms ABCD and AIHG. As shown in Figure 2, strain energy is also stored in the noncracked region DEFG, but this is not considered in formula (3). In addition, the uncracked region is deformed and not completely rigid as required by the simple cantilever theory. Therefore, formula (3) used to calculate the load-displacement relationship of the DCB sample is inaccurate [18]. In order to overcome the shortcomings of the simple beam model, the researchers used the orthogonal scaling method and finite element analysis (FEA) to give the solution of the energy release rate of the two-dimensional orthotropic DCB:

$$G = \frac{P^2 m^2}{N \cdot E_{xx}A} \left(1 + 2\alpha \frac{h}{m} + \alpha^2 \frac{h^2}{m^2}\right), \tag{8}$$

where

$$\alpha = \left[0.677 + 0.146(\beta\text{-}1) - 0.0178(\beta\text{-}1)^2 \right. \\ \left. + 0.00242(\beta\text{-}1)^3\right] \cdot \left(\frac{E_{yy}}{E_{xx}}\right)^{-1/4}, \tag{9}$$

$$\left(\frac{E_{yy}}{E_{xx}}\right)^{-1/4} \beta = \frac{\sqrt{E_{xx}E_{yy}}}{2G_{xy}} - \sqrt{v_{xy}E_{yx}}. \tag{10}$$

E_{xx}, E_{yy} and G_{xy} are Young's modulus and the shear modulus, respectively; v_{xy} and v_{yx} are Poisson's ratios. For isotropic materials, $\beta = 1$ and $\alpha == 0.677$, which is consistent with the two-dimensional elastic solution of isotropic DCB. For the case of $M/H \gg 1$, the energy release rate given by formula (8) is very close to that obtained by formula (4) based on the simple beam theory.

3.2.4. Finite Element and Verification. A two-dimensional finite element model is established to verify the accuracy of formulas (4)–(8) in calculating the energy release rate of orthotropic DCB. The boundary conditions of the finite element model are shown in Figure 3, in which the lower left hinge point is fixed ($u_x = u_y = 0$), and the concentrated force P is applied at the upper left point. The mechanical proper-
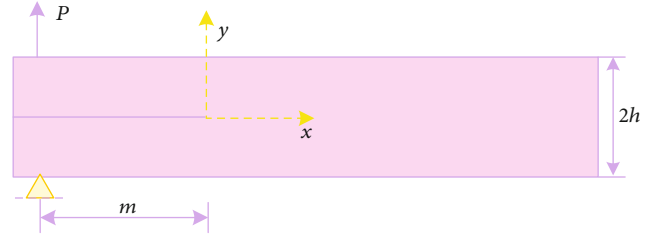
FIGURE 3: Finite element model network planning and boundary conditions.

ties of the composites used in the finite element model are as follows: $E_{xx} = 110$ GPa, $E_{xx} = E_{yy} = 8.07$ GPa, $G_{xy} = G_{xz} = 3.79$ GPa, $G_{yz} = 3.28$ GPa, $v_{xy} = v_{xz} = 0.32$, and $v_{yz} = 0.45$. Through the linear elastic finite element analysis, the opening displacement required to calculate the energy release rate in formulas (5)–(7) is obtained. It is difficult to obtain the solution of $x = -2$ at the point of $y = -H$, because it is difficult to obtain the singularity of the displacement at the point of $y = -M$.

3.3. Double Flexibility Method for Determining Interlaminar Fracture Toughness

3.3.1. Method Overview. It can be seen from Figure 3 that most solutions of Euler's beam theory (except formula (7)) are not accurate enough when actually calculating the energy release rate of the DCB sample. Therefore, these formulas need to be modified before they can be used. The researchers studied the complex deformation of the crack edge and proposed the concept of equivalent crack length $m_{\text{eff}} = m + \Delta$, i.e., modified beam theory (MBT), whose compliance type can be expressed as follows:

$$C = \frac{8(m + \Delta)^3}{E_{xx}Nh^3}. \tag{11}$$

E_{xx} is Young's modulus, and H is the thickness of the single cantilever beam.

According to the ASTM standard, the Δ can be assured. The linear regression method is used to linearly adjust the compliance cube root $C^{1/3}$ related to the crack length M. The intersection of the straight line and the M axis is m, as shown in Figure 4.

By replacing formula (11) with formula (2) and through appropriate transformation, the formula of the critical energy release rate is as follows:

$$C_{\text{AC}} = \frac{3P\varepsilon}{2N(m + |\Delta|)}. \tag{12}$$

Similarly, the flexibility calibration method (CC) and the modified flexibility calibration method (MCC) can also correct the flexibility. The flexibility expressions are formulas (13) and (14), respectively:

$$C = Mm^r, \tag{13}$$
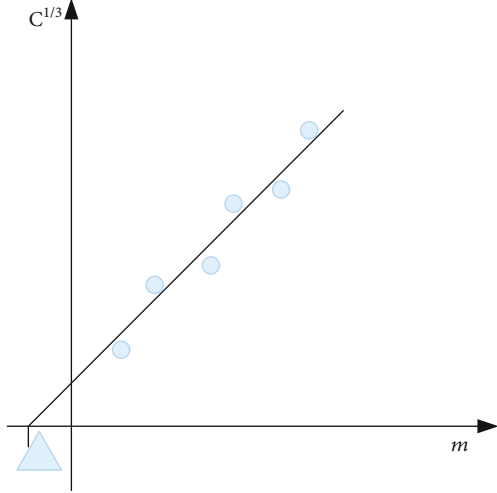
Figure 4: Modified beam theory.

$$C = \frac{1}{M_1^3}\left(\frac{m}{h} - M_2\right)^3. \tag{14}$$

Among them, R and M_1 are also obtained by the linear regression adjustment method similar to Δ. By introducing formulas (13) and (14) into formula (2), respectively, the corresponding expression of the critical energy release rate can be obtained:

$$G_{AC} = \frac{rP\varepsilon}{2Nm}, \tag{15}$$

$$C_{AC} = \frac{3P^2 C^{2/3}}{2M_1 Nh}. \tag{16}$$

According to formulas (12), (15), and (16), the three methods proposed by ASTM must record the crack propagation length and the corresponding force and displacement and determine the correction coefficients a, R, and M_1 in real time. This process is troublesome, and if tested in the high- and low-temperature environment, the method of the ASTM standard will be very difficult to achieve. Based on the contents, we propose a double flexibility method for the fracture resistance of composite DCB specimens without real-time recording of the crack length.

3.3.2. Theory of the Double Flexibility Method. In fact, if there is a highly accurate relationship between the applied load P, the crack length m, and the opening displacement ε, it is not necessary to measure the crack length, the applied load, and its corresponding displacement at the same time. In this paper, a high-precision relationship between force-displacement-crack length is established by using the solution of the high-precision energy release rate given by predecessors [19]. In this paper, the energy release rate solution formula (8) obtained from the two-dimensional elastic analysis is adopted, and formula (8) is brought into formula (2) for indefinite integration. The relationship between the

applied load P and the displacement ε of orthotropic DCB can be obtained as follows:

$$C = \frac{\varepsilon}{P} = \frac{24}{NE_{xx}}\left(\frac{m^3}{3h^3} + \alpha\frac{m^2}{h^2} + \alpha^2\frac{m}{h}\right). \tag{17}$$

In this paper, the finite element model is used to verify the accuracy of formulas (3) and (17) in calculating DCB flexibility. When m/h is not used, the relative difference between formulas (3) and (17) and the finite element results are shown in Figure 5. It can be seen that formula (3) obtained from Euler's beam theory is too simple to calculate the flexibility of DCB, but the flexibility formula (17) obtained by integration is quite accurate.

For isotropic DCB, α is a constant value, equal to 0.677. Therefore, Young's modulus E_{xx} required in formula (7) can be obtained by the following method: the DCB test is conducted to obtain the force-displacement curve of the linear elastic loading section so as to obtain the DCB flexibility under the initial crack, which is brought into formula (17) to finally determine Young's modulus E_{xx}. After E_{xx} is determined, the fracture toughness of isotropic DCB can be calculated directly from formula (7) without measuring the crack length.

For anisotropic DCB, E_{xx} and α are unknowns. In order to determine these two parameters, a double flexibility method is proposed in this paper; that is, the flexibility C_0 loaded in the DCB test curve and the flexibility C_1 unloaded are used. The crack lengths corresponding to flexibility C_0 and C_1 are m_0 and m_1, respectively, which can be easily obtained by ultrasonic M-scan. It brings the two groups of crack lengths and corresponding flexibility into formula (17) to obtain the following:

$$C_0 N = \frac{24}{E_{xx}}\left(\frac{m_0^3}{3h^3} + \alpha\frac{m_0^2}{h^2} + \alpha^2\frac{m_0}{h}\right), \tag{18}$$

$$C_1 N = \frac{24}{E_{xx}}\left(\frac{m_1^3}{3h^3} + \alpha\frac{m_1^2}{h^2} + \alpha^2\frac{m_1}{h}\right). \tag{19}$$

It takes into account α as a positive number, where α and E_{xx} are as follows:

$$\alpha = \frac{-Y - \sqrt{Y^2 - 4XZ}}{2X}, \tag{20}$$

$$E_{xx} = \frac{24}{NC_1}\left(\frac{m_1^3}{3h^3} + \alpha\frac{m_1^2}{h^2} + \alpha^2\frac{m_1}{h}\right), \tag{21}$$

where

$$X = \frac{m_1}{h}C_0 - \frac{m_1}{h}C_1,$$

$$Y = \frac{m_1^2}{h^2}C_0 - \frac{m_0^2}{h^2}C_1, \tag{22}$$

$$Z = \frac{m_1^3}{3h^3}C_0 - \frac{m_0^3}{3h^3}C_1.$$
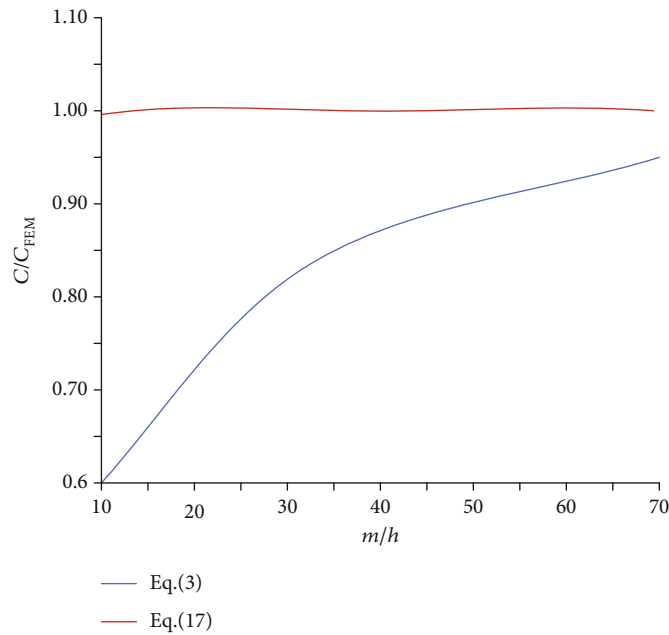
FIGURE 5: Formulas (3) and (17) calculate the relative difference between the botulinum toxin and finite element results.

TABLE 2: Composite material performance.

Material			Compound material				
Stretch	Strength (MPa)	84.76				Glass transition temperature T_g (°C)	218
	Modulus (GPa)	3.29	Impact strength (kgcm/cm^2)	14.0			
	Elongation at break (%)	3.34				Heat distortion temperature (°C)	198
Compression	Strength (MPa)	167.18				Density ρ (g/cm^2)	1.256
Bending	Strength (MPa)	134.47	Fracture toughness GIC (J/m^2)	95			
	Modulus (GPa)	3.66				Saturated moisture absorption in boiling water (%)	3.3

After determining α and E_{xx}, determine the relationship between flexibility C and crack length M. Using formula (17), the crack length m can be expressed as follows:

$$m = \sqrt[3]{\alpha^3 + \frac{\varepsilon N E_{xx}}{8P}} \cdot h - \alpha h. \tag{23}$$

That is, when the P force and ε displacement are known, the crack length can be calculated without additional measurement.

By introducing formula (23) into formula (8), the expression of the energy release rate without the crack length can be obtained:

$$G = \frac{P^2 h^2 \left(\alpha^3 + (\varepsilon N E_{xx}/8P)\right)^{2/3}}{N E_{xx} A}. \tag{24}$$

The significance of the formula is that the crack propagation length and fracture strength can only determine the duration of the test procedure from the force and displacement information during the test. It avoids measuring the crack propagation length during the test and makes it

suitable for the hardness test environmental conditions of the type I interlayer under test conditions, such as low temperature [20, 21].

4. Experiment and Analysis of Interlaminar Fracture Toughness and Durability in the Humid and Hot Environment

4.1. Interlaminar Fracture Toughness Test

4.1.1. Materials. In this study, the hardness and heat resistance of the composite used are relatively good, and some of its main properties are shown in Table 2.

All the 24 ply unidirectional plates used in the test are about 4 mm thick. The cut specimen is 165 mm long and 30 mm wide. In one section of the test piece, a layer of Teflon film with a length of about 35 mm is prepaved in the middle layer as a prefabricated layer. The shape and geometric dimensions of the test piece are shown in Figure 6. After cutting, the test piece shall be dried and hygroscopic.

4.1.2. Load-Displacement Curve. Under normal temperature and dry conditions, the typical load-displacement curve of
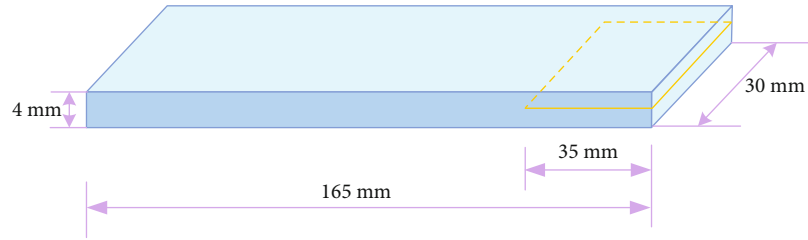
FIGURE 6: Shape and size of the test piece.

(a) Load-displacement curve of the MMF test under the normal temperature and dry state

(b) Test load-displacement curve with moisture absorption of 1.15% at 120°C
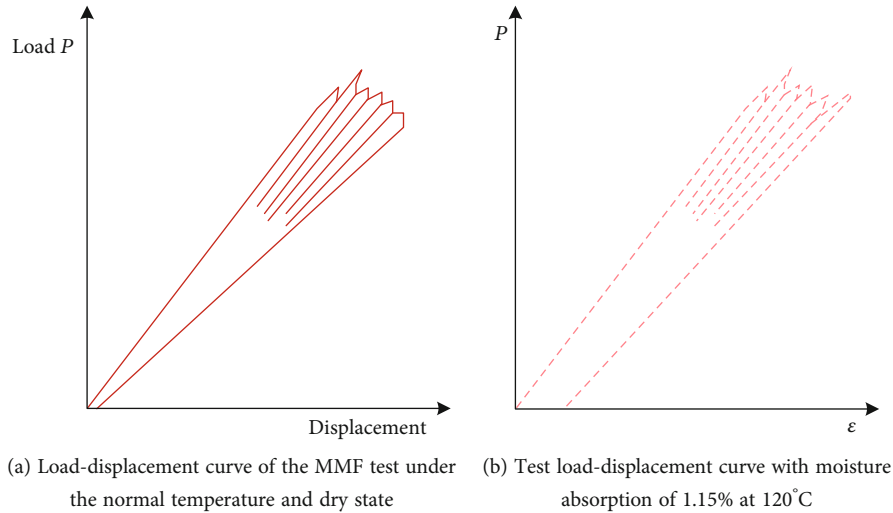
FIGURE 7: Comparison diagram of the load-displacement curve of the MMF specimen test.

the hybrid test is shown in Figure 7(a). Before crack propagation, the load-displacement curve is linear. When the crack propagates, it enters the nonlinear section. This is because the crack propagates, the crack length m increases, the stiffness of the beam decreases, the load-displacement curve of the crack propagation thickness is different from that before the crack propagation, and the slope of the straight-line section of the unloading curve decreases. In this environment, the unloading line is always straight and points to the origin. It can be seen that the linear relationship is established and there is no permanent deformation. It can be inferred that there is no plastic deformation problem [22]. In fact, from the shape of the unloaded specimen, there is no residual deformation.

In the high-temperature and high-humidity environment, the load-displacement curve of the MMF specimen has entered the nonlinear response section before crack propagation. This is most prominent in the test at 120°C and 1.15%, as shown in Figure 7(b). It is inferred that there is a certain plastic deformation at the tip of the crack before the crack propagation, and the crack propagates only after the plastic deformation. In terms of mechanism, the glass transition temperature of the interlayer resin decreases at high temperature after moisture absorption. The ambient temperature is very close to the glass transition temperature of the material after moisture absorption [23]. With the increase of material fluidity and high stress at the crack tip, plastic flow and plastic deformation easily occur. From the

test piece after the test, there is indeed permanent deformation.

In addition, the unstable propagation of cracks can be observed during the test.

It can be seen from the load-displacement curve that in the initial stage of crack propagation, when the crack is small, the load increases with the increase of crack length, and the crack propagation is steady; in the later stage of crack propagation, the crack is long. Under the displacement loading mode, the load decreases and the propagation belongs to an unsteady state.

4.1.3. Fracture Failure Criterion. According to the test results, the type I and type II component values of pure type I and type II interlaminar fracture toughness and mixed type interlaminar fracture toughness are calculated by using the previous calculation formula. The criterion of crack (delamination) propagation under the complex load can be traced, and the scatter diagram of G_I-G_{II} can be made. The pure type I action state is regarded as the special state of G_{IIa}, and the pure type II action state is regarded as the state of $G_{IIa} = 0$ and $G_{IIa} = G_{IIc}$. The layered G_I-G_{II} scatter diagram of specimens with different moisture contents under different temperature conditions is shown in Figure 8.

By comparing these figures, it can be found that in the dry state, whether at room temperature of 30°C or high temperature of 120°C, the dispersion of measured data is very small, and the envelope characteristics of delamination
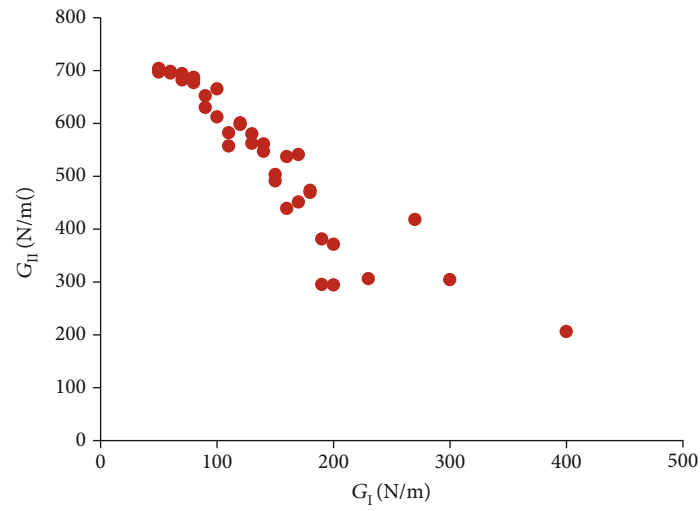
(a) G_I-G_{II} diagram of the dry specimen at 30°C
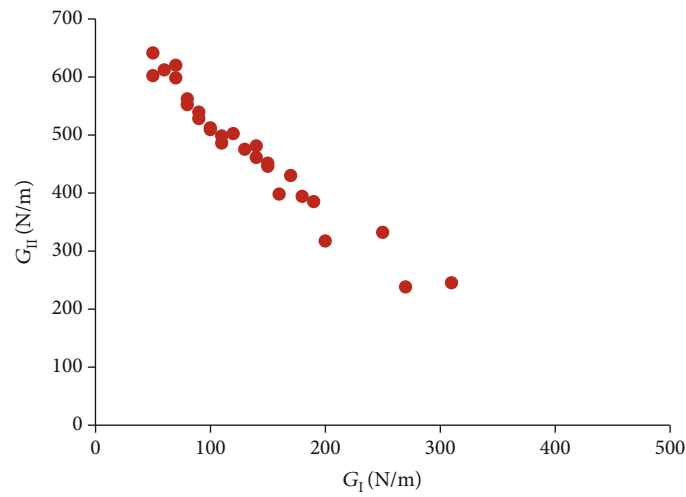
(b) G_I-G_{II} diagram of the dry specimen at 120°C
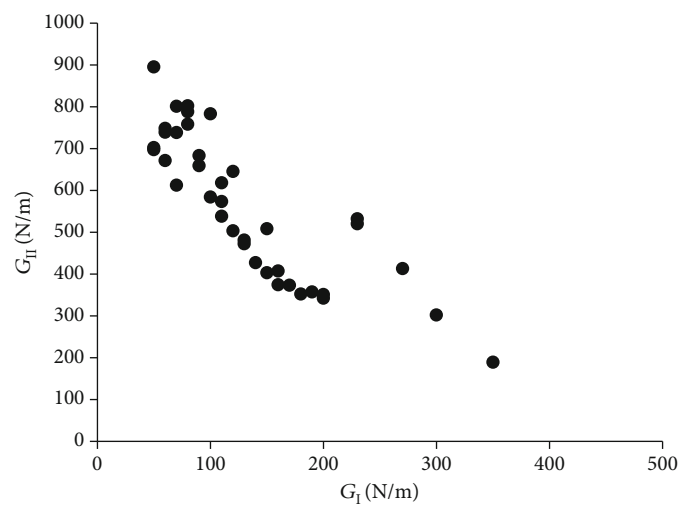
(c) G_I-G_{II} diagram of the high-moisture absorption specimen at 30°C

FIGURE 8: Continued.
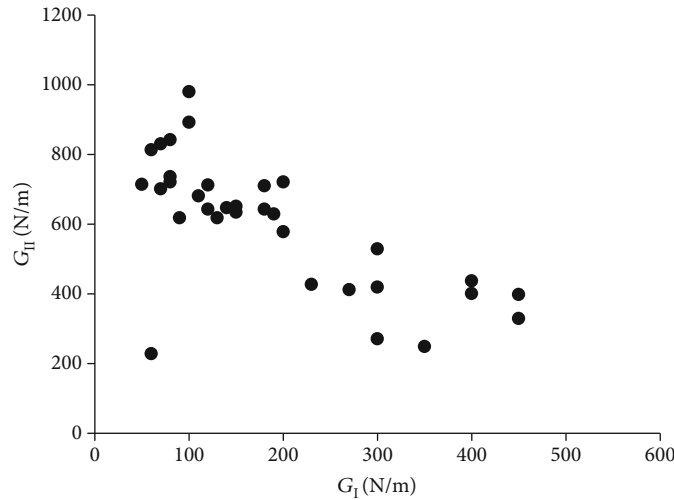
(d) G_I-G_{II} diagram of the high-moisture absorption specimen at 120°C

FIGURE 8: G_I-G_{II} scatter diagram under different conditions.

failure are obvious. Except G_{Ic}, other points are basically in a straight line. Therefore, it can be determined that the delamination criteria of composite unidirectional plates in the dry state are straight lines. However, G_{Ic} is not on this straight line, which shows that there are inconsistencies between the calculation formula of pure type I and that of type I stratification in mixed stratification. In particular, the value of G_{Im} is larger than that of G_{Ic}. This is difficult to explain from the perspective of energy.

4.2. Durability Test. The relative strength of the composites after aging at 95°C and heat was 88%. However, the humid and hot environment will have a great impact on the resin matrix and interface. The change of the resin matrix or interface properties will change its failure mechanism and failure mode and affect the longitudinal tensile strength. For brittle resin or carbon fiber composites with a strong interface, the mild liquid and thermal environment can increase their longitudinal tensile strength. For the flexible resin or weak interface, the liquid and thermal environment will reduce the strength. It can be seen from Table 3 that liquid heat has little effect on the longitudinal strength and measurement of unidirectional composite carbon fiber. For unidirectional glass fiber composites, the tensile strength decreases significantly because the glass fiber is corroded by the liquid and thermal environment. The surface treatment of glass fiber and its combination with resin directly affect the effect of protecting glass fiber from water corrosion, which has a great impact on the tensile strength of glass fiber composites.

Because the warm and humid environment will lead to the softening of the resin matrix, when the resin matrix softens, its coefficient will be significantly reduced. This will significantly reduce the longitudinal compressive strength of unidirectional composites, and the performance will degenerate into nonlinearity. Under high temperature and humid-

ity, the compressive strength decreases, but the compressive strength under room temperature and humidity is basically unchanged. With the increase in temperature, the hygroscopicity increases, and the strength and coefficient decrease significantly. It can be seen from Table 3 that the longitudinal compressive strength of unidirectional composites at 120°C and 1.00% moisture absorption is 29.53% lower than that at 20°C and 0.50% moisture absorption. Due to the high moisture absorption of aramid fiber, the longitudinal compressive strength of unidirectional aramid composite fiber will be significantly reduced in the humid and warm environment [24, 25].

4.3. Accumulation of Mechanical Property Degradation. The hygroscopic environment of composites is constantly changing. When the hygroscopic environment conditions change, the hygroscopic characteristics of composites also change. The mechanical properties will further change on the basis of the influence of the previous wet and hot environment, and the changes in properties will accumulate. In this process, the mechanical properties of the material may be reduced or partially recovered under wet and hot conditions. As shown in Figure 9(a), the performance of the composite decreases after time Δt_1 in humid and hot environment 1. In the process of time Δt_2, the mechanical properties of the composites recovered due to the decrease in moisture absorption or the change in temperature.

As the hygroscopic characteristics of the materials will change after the change in the humid and hot environment, the change law of the mechanical properties of the composites will also change. Therefore, this paper adopts the equivalent of the performance degradation amount. As shown in Figure 9(b), it is assumed that the performance degradation amount of composite material after time Δt_1 is equal to the performance degradation amount after time t_{21} under humid and hot environment 1.

TABLE 3: Effect of damp-heat conditions on the resistance of composites.

Moisture absorption (%)	Temperature (%°C)	E_x (GPa)	E_y (GPa)	X' (MPa)	X (MPa)	Y (MPa)	Y' (MPa)	S (MPa)
0.50	-30	183	10.60	1510	1507	42	261	71
0.50	20	180	10.10	1490	1490	38	244	66
1.00	120	168	7.60	1402	1050	26	167	45

(a) Accumulation of degradation of damp-heat aging performance

(b) Equivalent relationship of performance degradation
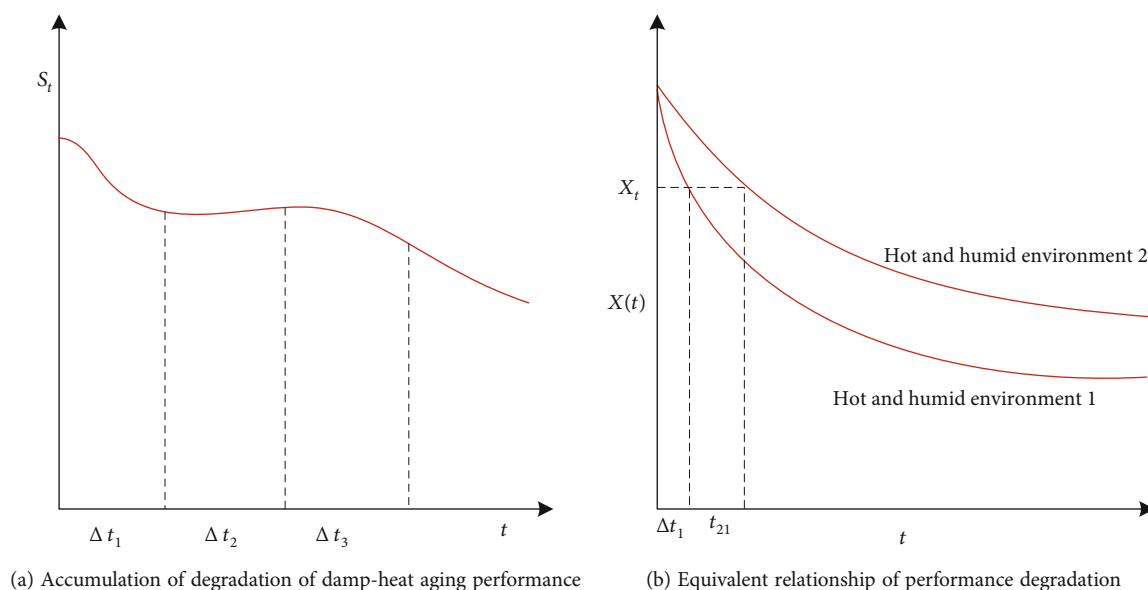
FIGURE 9: Mechanical property degradation data.

5. Discussion

Firstly, through the study of relevant knowledge points of literature works, this paper has preliminarily mastered the relevant basic knowledge. This paper analyzes how to study the interlaminar fracture toughness and durability of composites in the humid and hot environment. This paper expounds on the concept and related methods of interlaminar fracture toughness, explores the composites in the humid and hot environment, and analyzes the interlaminar fracture toughness and durability through experiments.

After absorbing water, the mechanical properties of polymer matrix composites will change. The mechanical properties of liquid will also change due to the change in moisture absorption. Generally speaking, the axial properties of unidirectional composites are not greatly affected by moisture absorption, while the transverse and shear properties of materials are reduced due to the influence of the liquid and thermal environment on the matrix and interface [26]. When the moisture absorption reaches saturation, the hydrodynamic properties of the composites also tend to have a constant value.

The experimental analysis shows that moisture absorption has no obvious effect on the breaking resistance of the material at room temperature. At high temperatures, moisture absorption will increase the dimensional hardness of the composites. The temperature has the least effect on the mixed dimension fracture hardness of the dry sample, and

the moisture absorption of the sample is relatively high. When the temperature is lower than 60°C, the hardness changes slightly. When the temperature is higher than 60°C, the hardness increases with the increase in temperature. Through the microfracture analysis, it is found that the single action of moisture absorption or high temperature makes the matrix toughness enhanced, and the fracture presents a ductile fracture morphology. The two work together to enhance the viscosity of the resin matrix.

6. Conclusion

Because polymers will age under the influence of external environmental factors, moisture and heat are the most important factors leading to the aging of composites. Therefore, the design and use departments in this paper pay special attention to the possible damage and mechanical properties of such composites in the humid and warm environment, which is an important guarantee and premise to promote their reasonable and effective implementation. The research on wet aging of composites is a research topic with theoretical and practical significance. Although some progress has been made, its important role in guiding practical engineering applications still needs to be further studied. The work of this paper is only a preliminary exploration, and there are still many topics that need further research.

Data Availability

No data were used to support this study.

Conflicts of Interest

The authors declare that there is no conflict of interest with any financial organizations regarding the material reported in this manuscript.

References

[1] B. Gao, X. Ning, and P. Xing, "Shock wave induced nanocrystallization during the high current pulsed electron beam process and its effect on mechanical properties," *Materials Letters*, vol. 237, no. 15, pp. 180–184, 2019.

[2] X. Zhang, Z. Li, X. Wang, and J. Yu, "The fractional Kelvin-Voigt model for circumferential guided waves in a viscoelastic FGM hollow cylinder," *Applied Mathematical Modelling*, vol. 89, pp. 299–313, 2021.

[3] L. Zhang, Y. Liu, G. Sang, and Y. Zhai, "Heat & moisture comprehensive property for lime-slag/soil composites based on response surface methodology," *Acta Materiae Compositae Sinica*, vol. 34, no. 5, pp. 1095–1102, 2017.

[4] Z. Zong, L. Yang, H. Zhang, and L. Xiong, "Preparation of environment coordination Ce-La/TiO$_2$ composites and photocatalytic-moisture-heat properties," *Cailiao Gongcheng/Journal of Materials Engineering*, vol. 46, no. 5, pp. 145–150, 2018.

[5] S. Kasaragadda, I. M. Alarifi, M. Rahimi-Gorji, and R. Asmatulu, "Investigating the effects of surface superhydrophobicity on moisture ingression of nanofiber-reinforced bio-composite structures," *Microsystem Technologies*, vol. 26, no. 2, pp. 447–459, 2020.

[6] W. Yu, G. Zhang, C. Liu, and S. Fan, "Hard carbon nanotube sponges for highly efficient cooling *via* moisture absorption–desorption process," *ACS Nano*, vol. 14, no. 10, pp. 14091–14099, 2020.

[7] K. Tanaka, N. Hosoo, and T. Katayama, "Effects of temperature on the fiber matrix interfacial properties of carbon fiber reinforced highly heat resistant polyamide resin," *Journal of the Society of Materials Science Japan*, vol. 66, no. 10, pp. 746–751, 2017.

[8] Y. Liu, S. Jiang, W. Yan, J. Qin, and J. Yu, "Enhanced thermal property and anti-moisture absorption of PA6/P (*N*-(4-carboxyphenyl)maleimide-alt-triallyl isocyanurate) composites based on solid-state interfacial reaction," *Journal of Materials Research and Technology*, vol. 9, no. 5, pp. 11291–11302, 2020.

[9] Y. Chen, X. Xiong, and Q. Gao, "Digestibility and physico-chemical properties of starch-galactomannan complexes by heat-moisture treatment," *Food Hydrocolloids*, vol. 77, pp. 853–862, 2018.

[10] X. Han, L. Yuan, A. Gu, and G. Liang, "Development and mechanism of ultralow dielectric loss and toughened bismaleimide resins with high heat and moisture resistance based on unique amino-functionalized metal-organic frameworks," *Composites Part B Engineering*, vol. 132, pp. 28–34, 2018.

[11] Y. Su, J. Li, and X. Zhang, "A coupled model for heat and moisture transport simulation in porous materials exposed to thermal radiation," *Transport in Porous Media*, vol. 131, no. 2, pp. 381–397, 2020.

[12] W. Peng, Y. Tao, L. Ziqiang et al., "A superhydrophobic/electrothermal synergistically anti-icing strategy based on graphene composite," *Composites Science and Technology*, vol. 198, article 108307, 2020.

[13] A. A. Dalinkevich, T. A. Nenasheva, and I. G. Kalinina, "The role of interfacial effects in hydrothermal aging of aramid composites," *Protection of Metals and Physical Chemistry of Surfaces*, vol. 57, no. 2, pp. 352–360, 2021.

[14] L. Calabrese, L. Bonaccorsi, P. Bruzzaniti, E. Proverbio, and A. Freni, "SAPO-34 based zeolite coatings for adsorption heat pumps," *Energy*, vol. 187, article 115981, 2019.

[15] A. Purohit and A. Satapathy, "Dry sliding wear characteristics of epoxy composites filled with steel industry slag and sludge particles: a comparative study," *Materials Today Proceedings*, vol. 5, no. 5, pp. 11906–11913, 2018.

[16] I. Ahmadi, "Evaluation of effective thermal diffusivity and conductivity of fibrous materials through computational micromechanics," *Heat & Mass Transfer*, vol. 53, no. 1, pp. 277–290, 2017.

[17] D. Aydin, S. P. Casey, X. Chen, and S. Riffat, "Numerical and experimental analysis of a novel heat pump driven sorption storage heater," *Applied Energy*, vol. 211, pp. 954–974, 2018.

[18] R. Panduro and J. L. Mantari, "Hygro-thermo-mechanical behavior of classical composites," *Ocean Engineering*, vol. 137, pp. 224–240, 2017.

[19] T. R. Rigolin, M. C. Takahashi, D. L. Kondo, and S. H. P. Bettini, "Compatibilizer acidity in coir-reinforced PLA composites: matrix degradation and composite properties," *Journal of Polymers and the Environment*, vol. 27, no. 5, pp. 1096–1104, 2019.

[20] Y. Chen, D. Li, X. Q. Xie, Y. Gao, and Y. L. He, "Theoretical modeling and experimental validation for the effective thermal conductivity of moist silica aerogel," *International Journal of Heat and Mass Transfer*, vol. 147, article 118842, 2020.

[21] W. Liu, W. Xi, R. Hu et al., "Preparation and characterization of sodium silicate/epoxy resin composite bonded Nd-Fe-B magnets with high performance," *Journal of Rare Earths*, vol. 37, no. 10, pp. 1083–1087, 2019.

[22] N. Banik, V. Dey, and G. Sastry, "An overview of lignin & hemicellulose effect upon biodegradable bamboo fiber composites due to moisture," *Materials Today Proceedings*, vol. 4, no. 2, pp. 3222–3232, 2017.

[23] F. Zhang, Z. F. Shi, Z. Z. Ma et al., "Silica coating enhances the stability of inorganic perovskite nanocrystals for efficient and stable down-conversion in white light-emitting devices," *Nanoscale*, vol. 10, no. 43, pp. 20131–20139, 2018.

[24] J. B. Alvey, J. Patel, and L. D. Stephenson, "Experimental study on the effects of humidity and temperature on aerogel composite and foam insulations," *Energy and Buildings*, vol. 144, pp. 358–371, 2017.

[25] Z. Candan, S. M. Shaler, J. P. Heller, and R. Edgar, "Enhancing dimensional stability of oriented strand composites within biorefinery," *Maderas Ciencia Y Tecnología*, vol. 19, no. 3, pp. 387–398, 2017.

[26] A. Y. Shaulov, R. A. Sakovich, E. M. Nechvolodova et al., "The modification of poly (metal phosphates) by pentaerythritol," *Polymer Science, Series B*, vol. 62, no. 5, pp. 534–539, 2020.

Research Article

Repair Effect of Nanomaterials on Meniscus Injury Induced by Calisthenics Exercise

Wensuo Lian[1] **and Jinling Wang**[2]

[1]*Department of Leisure Sports, Jungwon University, Chungbuk 28024, Republic of Korea*
[2]*Graduate Department, Capital University of Physical Education and Sports, Beijing 100191, China*

Correspondence should be addressed to Jinling Wang; 20008001109@cupes.edu.cn

With the development of aerobics, more and more college students participate in this sport, but more and more sports injuries of students. Sports injuries directly or indirectly affect the normal study and life of college students. Therefore, it is very important to study the sports injuries of college students and their causes for improving the sports level of college students and promoting their healthy growth. And it provides proper precautions. This paper presents the investigation of nanomaterials, deep learning, and MRI images of meniscal injuries and concludes that the injury rate of high-level competitive aerobics athletes is 100%, and the top 4 injured parts are the wrist, ankle, waist, and knee. It can be seen that the meniscus injury occurs more frequently.

1. Introduction

Physical exercise is the best way to enhance physical fitness and improve the quality of life. In particular, sports such as aerobics, which are full of passion and vitality, are more and more sought after by more and more people. Aerobics is a sport that integrates gymnastics, dance, and music; is based on aerobic exercise; and is characterized by health, strength, and beauty. It is not only a popular fitness method for body building and cultivating sentiment but also an item of competitive sports. However, the problem of sports injury caused by high-level aerobic exercise has become an important problem affecting the normal training of athletes. Therefore, it is very urgent to study the injury causes and preventive measures of high-level athletes.

With the improvement of the competitive level of competitive aerobics athletes, the functions and coordination of various organs and body systems have not only reached a high level but also approached the physiological limit. Although competitive aerobics is a non-Olympic event, the state's support is relatively weak and there is no dedicated team of doctors. Therefore, improving the injury prevention and control ability of high-level aerobics teams has important guiding significance.

The innovation of this paper lies in the application of nanomaterials to study the repairing effect of aerobics-induced meniscus injury, which has a certain clinical trial and innovation.

2. Related Work

The 21st century is an era of rapid progress in biological and medical research. Nanotechnology has a particularly obvious interdisciplinary nature. Many scholars have conducted research on nanotechnology. Yin et al. thoroughly characterized the Pt10 clusters through a combination of experimental techniques and theoretical analysis, showing the highest CO oxidation activity per platinum atom of CO oxidation catalysts, and this catalytic system presents a coherent interdisciplinary picture [1]. Shivakumar et al. verified by nearly unchanged PureB diode I–V characteristics and microscopic examination of the deposited layers. In order to obtain this result, it is required that the silicon surface must be cleaned before B deposition [2]. Here, Hu et al. introduced a new method based on two-dimensional electron resonance and thermal displacement measurements to measure the two-dimensional energy loss temperature of a sample by combining these measurements

with first-principle modeling [3]. Zhao et al. used a new model to analyze the hydrogenation kinetics of Mg-Ce-Ni nanocomposites during the synthesis process and established a hydrogenation reaction rate control mechanism in the range of 300-680 k [4]. Ross and Yamaguchi described the effect of mechanical properties and polishing tool structure on tool-target surface contact during polishing. In addition to abrasive type and size, this also affects polishing characteristics, especially material removal at grain boundaries, grain enhancement, grain displacement, and nanoscale geometry of the polished surface [5]. Nanoimprint lithography (NIL) is an emerging high-resolution parallel patterning method that targets areas where e-beam and high-end lithography are expensive and cannot provide sufficient resolution at reasonable throughput. Currently, structures with feature sizes smaller than 5 nm have been achieved, and the resolution is limited by the ability to make reliefs. For historical reasons, the term nanoimprint lithography refers to a thermal imprint process. In ultraviolet (UV) NIL, photopolymerizable resins are used with UV clear stamps. In both of these processes, film squeeze flow and capillary action play a central role in understanding the NIL process. Kam and Torres provided an overview of NIL, focusing on general principles and concepts rather than specific process issues and state-of-the-art tools and processes. They also discussed the material aspects of printing and resists. Kam and Torres gave some specific applications where the imprint method had significant advantages over other construction methods. Finally, areas where further development in this field is needed are discussed [6]. Recently, large plastic deformations have been observed in compressive tests of biotemplated, anisotropic, and hierarchically structured silica monoliths. Based on the nanoscale structure of the material, Opdenbosch and Zollfrank fabricated a dynamic model in which parallel silica struts are compressed and sheared longitudinally. The resulting interfacial shear forces lead to continuous plastic deformation during cyclic loading with a gradual increase in force, matching the observations from mechanical tests. Opdenbosch and Zollfrank report physical parameter values obtained by fitting model curves to measured curves, their relationship to previous structural observations, and their utility in tailoring the complex mechanical behavior of this novel material [7]. However, the shortcomings of these studies are that the model construction is not scientific enough and the conditions are limited to adapt to more complex situations.

3. Nanomaterials and Related Methods

3.1. Nanomaterials

3.1.1. Definition of Nanomaterials. Generally speaking, nanomaterials refer to materials whose size is between 1 and 100 nm. Because nanomaterials have nanoscale dimensions, their properties, such as physical, electrical, optical, and magnetic properties, are significantly different from conventional materials. Many nanomaterials are catalytic, adsorptive, and highly reactive [8].

3.1.2. Application of Nanomaterials. In the past few decades, nanomaterials have been extensively researched and developed, and have been successfully applied in the fields of catalysis, medicine, sensors, and biology. In particular, it has also received extensive attention in water treatment and wastewater treatment. Due to their small size, nanomaterials have a relatively large specific surface area, so they have strong adsorption capacity and reactivity, and the flow properties of nanomaterials in solutions are very high. It has been reported that heavy metals, organic pollutants, inorganic anions, and bacteria can be successfully removed by many kinds of nanomaterials [9]. Due to the unique size-dependent properties of nanomaterials, they have a profound impact on various application fields such as the construction industry, products of daily life, and medical and healthcare. Figure 1 is an overview of nanomedicine.

Nano antibacterial materials have attracted much attention due to their stable performance, good antibacterial effect, and low price. For example, nanotitanium oxide material has photocatalytic effect, which can decompose toxic gases such as formaldehyde and benzene, and kill bacteria on its surface. Nanoscale self-cleaning materials have great development space [10]. Nanomaterials also have many applications in catalysis. Catalysts play an important role in chemistry because they can increase reaction rates and shorten reaction times. Most of the traditional catalysts have low catalytic efficiency and difficult preparation, resulting in waste of raw materials, reducing economic benefits, and polluting the environment. Nanomaterials have many active sites, which can greatly improve the reaction rate, control the progress of the reaction, and even make the chemical reaction that could not be carried out smoothly [11].

Nanoparticles used as catalysts are as follows: (1) metal nanoparticles; (2) nanoparticles are supported on porous supports, which can further increase the selectivity of catalysts; and (3) compound nanoparticles. Due to its small size, high voltage, and low self-discharge rate, lithium batteries are widely used in portable electronic devices such as mobile phones, notebook computers, power tools, and electric vehicles

Nanomaterials are used in lithium electric energy to improve cycle life and can take place in some reactions that cannot occur in other materials and increase the rate of charge and discharge. At present, nanomaterials can be well used as contrast agents in medical imaging. The mechanism of nanobiomaterials to promote the repair of damaged tissue is shown in Figure 2 [12]. Nanoparticles are widely used in biomedicine and can be used as biochips, bioprobes, etc. New medicines require new means of drug delivery so that side effects can be reduced and better efficacy can be achieved. Nanotechnology drug delivery can deliver drugs directly to cells and to targeted tissues [13].

3.1.3. Synthesis of Nanomaterials. The preparation methods of nanomaterials can be roughly divided into physical methods, chemical methods, and other methods. Among
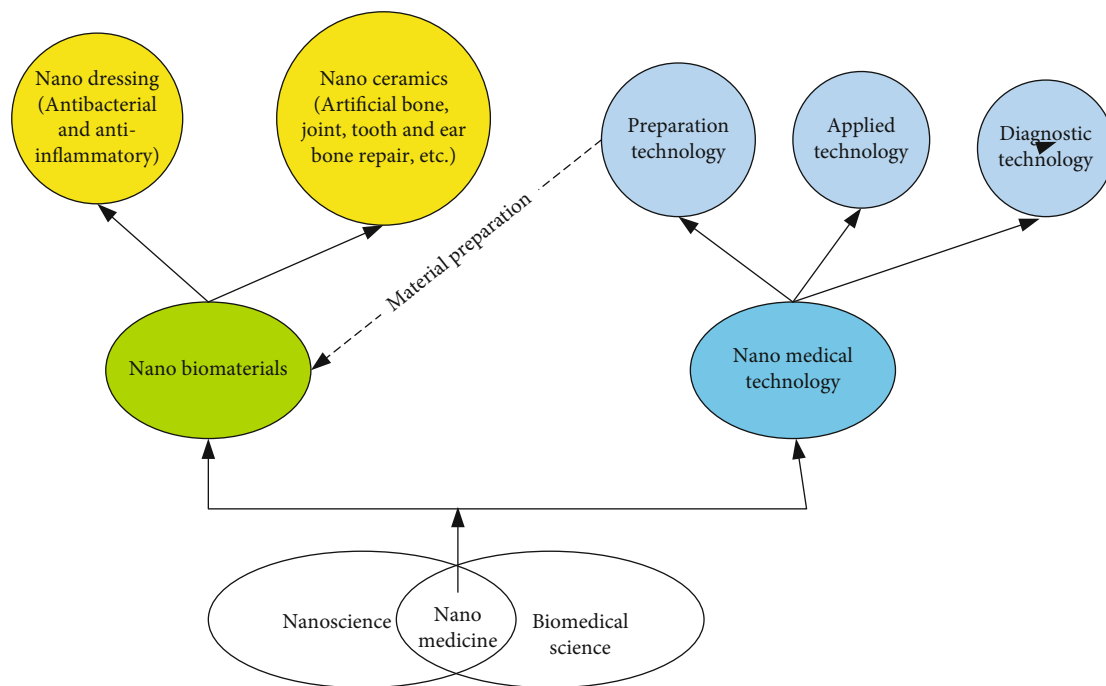
FIGURE 1: Overview of nanomedicine.
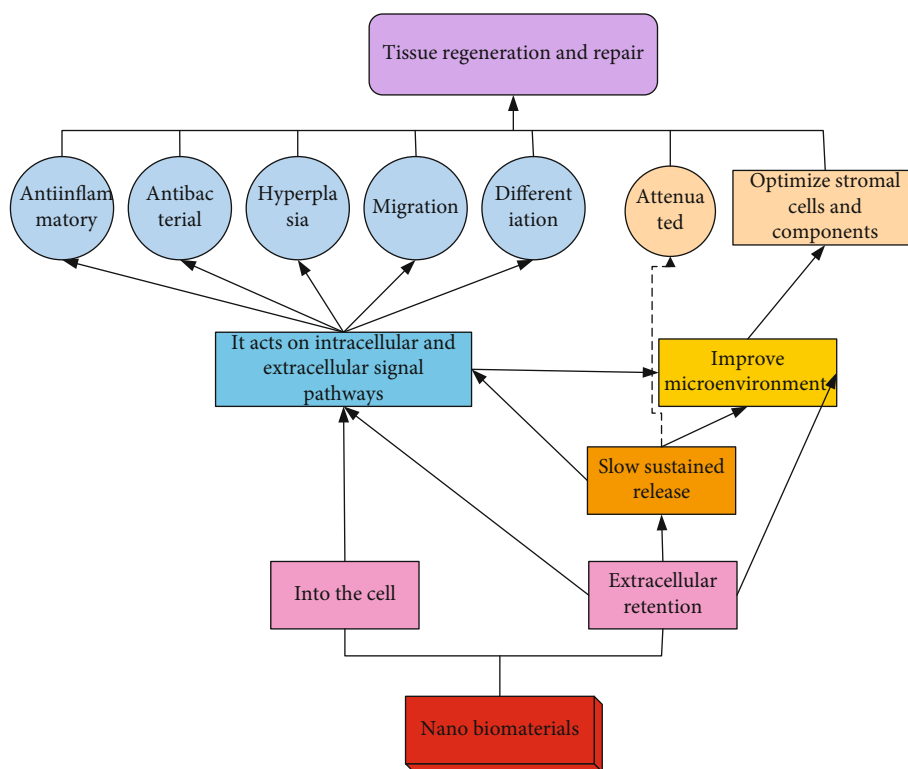
FIGURE 2: Mechanism of nanobiomaterials to promote the repair of damaged tissue.
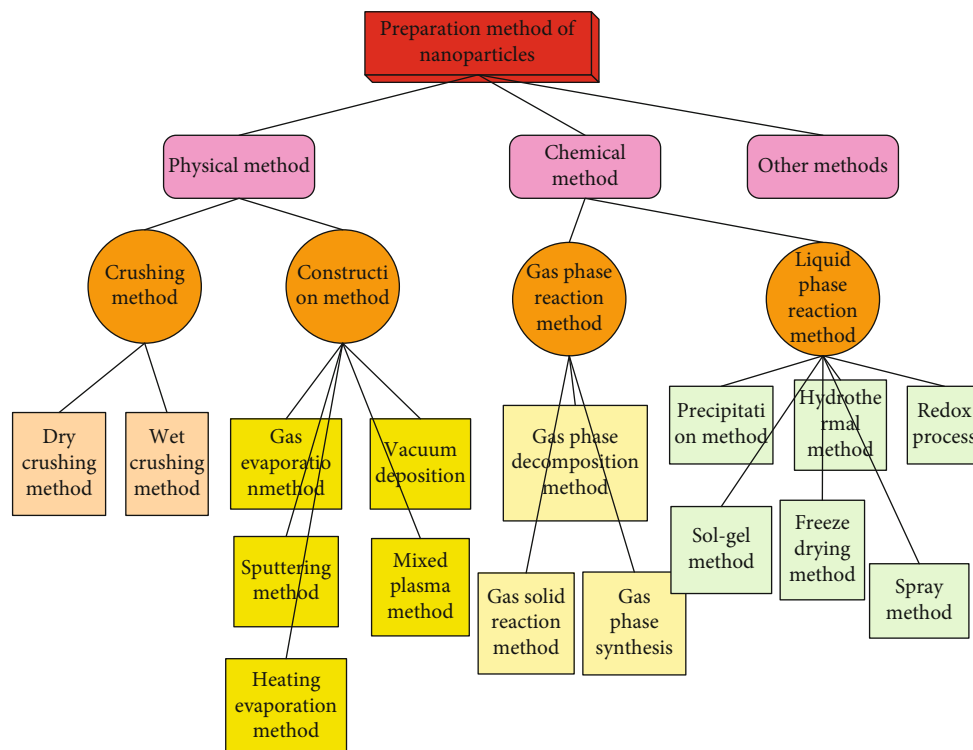
FIGURE 3: Nanoparticle preparation method.

them, physical methods include the pulverization method, deposition method, and sputtering method. Chemical methods include the sol-gel method, precipitation method, evaporative solvent pyrolysis method, redox method, and solvothermal method. Figure 3 shows the nanoparticle preparation method [14].

3.1.4. Characterization of Nanomaterials. In order to explore the mysteries of the nanoworld, the structure and properties of nanoparticles must be characterized. The characterization of nanomaterials is the modern analysis and detection technology and related theoretical knowledge about particle composition, structure, morphology, etc. Usually, we obtain the composition, particle size, morphology, structure, and interface of nanoparticles by inductively coupled plasma emission spectroscopy, scanning electron microscopy, transmission electron microscopy, atomic force microscopy, X-ray diffraction, and X-ray photoelectron spectroscopy. The average particle size, particle size distribution, composition, and interface of nanomaterials all affect their physicochemical properties. Figure 4 shows the commonly used characterization methods for nanomaterials [15].

3.2. Overview of the Development of Finite Element Analysis Based on MRI

3.2.1. Medical Imaging Technology. With computer assistance, in order to complete the construction of accurate physical and geometric models of anatomical organs, how to accurately extract the information contained in images (CT, MRI) is the key to current computer-assisted surgical guidance and treatment [16].

3.2.2. MRI Nuclear Magnetic Resonance Imaging Technology. With the development of imaging and the continuous improvement of surgical methods, the choice of surgical treatment of breast cancer has also changed. The range of surgical indications has also expanded, but it is limited to accurate diagnosis and surgery. It has a better therapeutic effect and therefore has a more prominent clinical significance in MRI examinations [17]. Figure 5 is a meniscus segmentation device based on a magnetic resonance image, and Figure 6 is a process of obtaining a meniscus segmentation result from an MRI image.

3.3. Introduction of Deep Learning Based on the Repairing Effect of Meniscus Damage. Deep learning is a very popular method in machine learning, covering a wide range of theoretical perspectives. In order to achieve more intelligent human-computer interaction, researchers imitate the human brain and thinking and establish various neural network models; deep learning is one of them. Deep learning is a multilevel representation learning method, learning data features by creating models, and finding a better data representation is the primary purpose of representation learning, as shown in Figure 7 [18].

The processing method of deep learning is nonlinear, and the processed data can be speech, images, text, etc., which can be learned from low-level to high-level abstract features [19].

3.4. Supervised Deep Learning Algorithms. In regression analysis, it is subdivided into various types according to the number of independent variables, dependent variables,
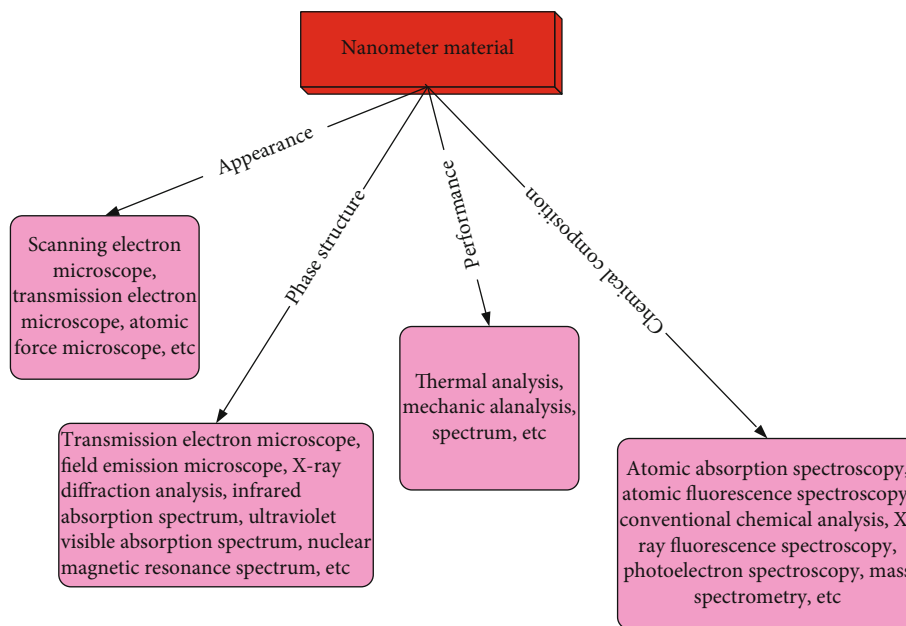
Figure 4: Nanomaterial characterization techniques.
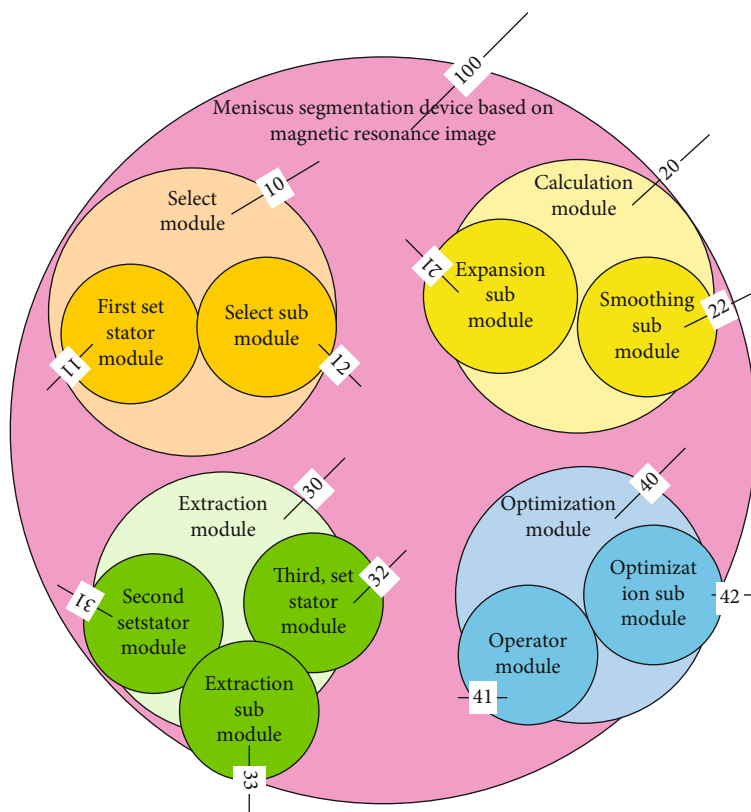
Figure 5: Meniscus segmentation device based on magnetic resonance images.
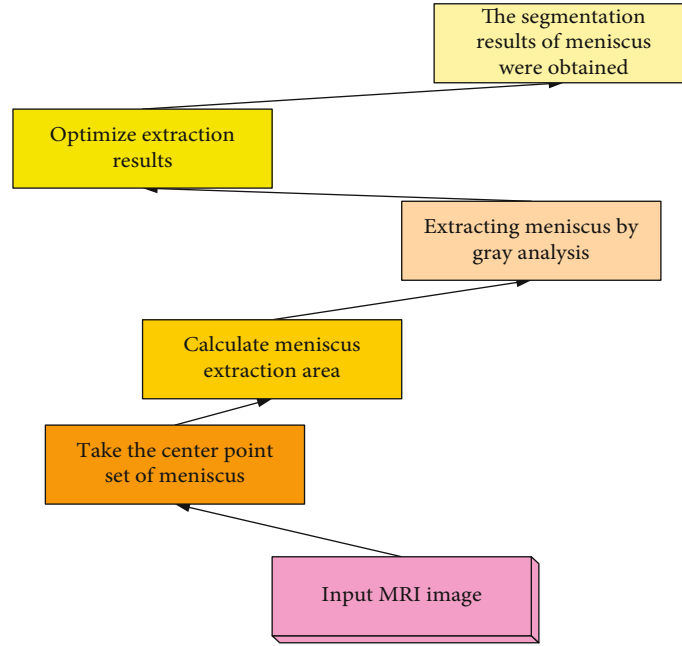
FIGURE 6: The process of obtaining meniscus segmentation results from MRI images.
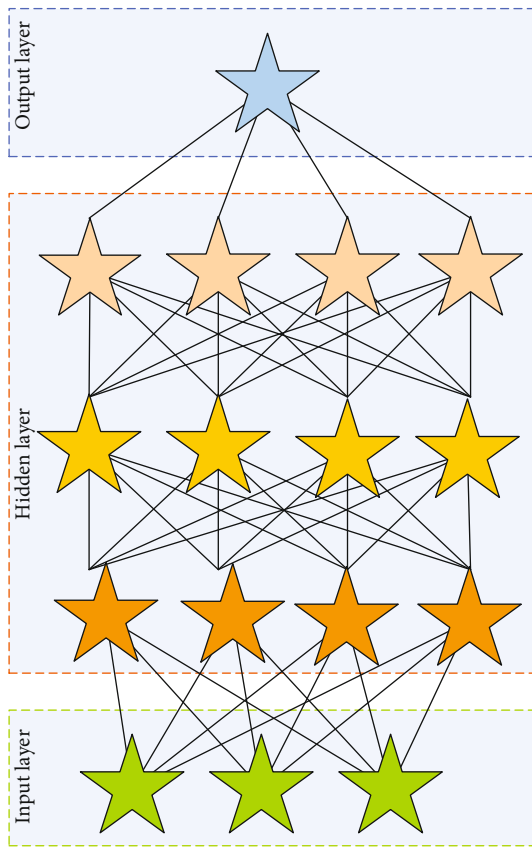
FIGURE 7: Deep neural network.

and the relationship between them. Regression methods in classification include logistic regression (LR), Softmax as an LR model is generalized on multiclassification problems, and Softmax regression is often used as the final classifier

layer in supervised deep learning. The following is a detailed introduction from Softmax to convolutional neural networks [20].

3.4.1. Softmax Classifier. Before introducing Softmax regression, it is necessary to introduce logistic regression. Logistic regression is a simple binary classification algorithm that implements classification by fitting the classification boundaries of the data and uses optimization methods such as gradient descent to determine the best regression coefficients. One of the more important formulas in logistic regression is the step function: $Q(X) = 1/(1 + E^{-\theta^Z X})$; its waveform is as follows, the value range is $[0, 1]$ [21].

Its corresponding negative log-likelihood loss function is defined as

$$Q(\theta) = -\frac{1}{u}\left[\sum_{m=1}^{u} Y^m \log f_\theta(X^m) + (1 - Y^m) \log (1 - f_\theta(X^m))\right]. \tag{1}$$

LR is a special case of Softmax when dealing with binary problems. Two probabilities need to be solved in LR: $T(Y = 1|X; \theta)$ and $T(Y = 0|X; \theta)$. In Softmax regression, there are J probabilities, and its general function representation

$$T(i) = \frac{\exp\left(\theta_m^Z X\right)}{\sum_J^{J=1} \exp\left(\theta_m^Z X\right)}. \tag{2}$$

The negative log-likelihood loss function at this time is

$$Q(\theta) = -\frac{1}{u} \left[\sum_{m=1}^{u} \sum_{n=1}^{J} M\{Y^m = n\} \log \frac{E^{\theta_n^Z X^m}}{\sum_{l=1}^{J} E^{\theta_l^Z X^m}} \right], \quad (3)$$

where $M\{\bullet\}$ indicates that when its value is true and the result of the function is 1; otherwise, it is 0; then, the objective function is optimized by gradient descent [22].

3.4.2. Convolutional Neural Network. The convolutional neural network (CNN) is a kind of deep learning network structure, which is characterized by a large number of convolution operations in the network structure. In addition, activation functions and pooling layers are also its basic structures. These three basic structures make it have better local perception characteristics and feature abstraction ability than multilayer perceptron (MLP). At present, CNN has been widely used in many subdivisions of image processing and computer vision, such as image classification, image semantic segmentation, and visual object detection [23].

(1) Calculate the Output. For the l layer of the fully connected layer, the output is

$$\begin{cases} A^x = g(C^x), \\ C^x = T^x A^{x-1} + P. \end{cases} \quad (4)$$

Among them, T^x and P are the weights and biases, and $g(\bullet)$ is the sigmoid activation function, and the output range of this function is in $[0, 1]$. Assuming that d is the current sample number, the dth sample error is E^d:

$$E^d = \frac{1}{2} \sum_{k=1}^{l} \left(S_k^d - B_k^d \right)^2 = \frac{1}{2} \left\| S^d - B^d \right\|_2^2. \quad (5)$$

In the formula, S^d is the expected output value of the dth sample, and B^d is the actual output value of the dth sample after the network operation.

(2) Backpropagation. The data is calculated layer by layer through the network, and the error between the actual output and the expected output is obtained, which can be regarded as the sensitivity of the neuron base. The formula is

$$\frac{\partial E}{\partial P} = \frac{\partial E}{\partial C} \frac{\partial C}{\partial P}. \quad (6)$$

The formula for the sensitivity of layer x in the backpropagation stage is

$$\delta^s = \left(T^{x+1} \right)^S \delta^{x+1} \bullet g'(C^s). \quad (7)$$

The sensitivity of the output layer node is

$$\delta = g'(C^x) \bullet \left(B^d - S^d \right). \quad (8)$$

(3) Weight Update. The derivation of the error for the x layer weight of the fully connected layer is the cross product of the x layer input and its sensitivity. The weight update formula is

$$\frac{\partial E}{\partial T} = A^{x-1} (\delta^x)^S, \quad (9)$$

$$\Delta T^x = -\eta \frac{\partial E}{\partial T^x}. \quad (10)$$

The specific training process of the convolutional layer is as follows:

We input the data to the convolution layer for convolution calculation and get

$$A_n^x = g \left(\sum_{m \in W_n} A_m^{x-1} \bullet T_{mn}^x + P_n^x \right), \quad (11)$$

where T is the weight, P is the bias, and 1 is the set of input feature maps [24].

As shown in formula (17), it is shown that the computation is the gradient of the convolutional layer:

$$\delta_n^x = \beta_n^{x+1} \left(g'(C_n^x) \bullet \text{up}(\delta_n^{x+1}) \right), \quad (12)$$

where up($\bullet$) is the upsampling calculation.

Through the above calculation, the gradient of the given feature map was gotten. The following equation shows the gradient of the bias basis obtained by summing the sensitivity of the feature map nodes in the x layer:

$$\frac{\partial E}{\partial P_n} = \sum_{i,j} (\delta_n^s)_{ij}. \quad (13)$$

The gradient of the convolution kernel weights is calculated as follows:

$$\frac{\partial E}{\partial K_{mn}^x} = \text{rot180} \left(\text{conv2} \left(A_m^{x-1}, \text{rot180}(\delta_n^x), '\text{valid}' \right) \right). \quad (14)$$

The same is true when updating the weights and biases with the above formula.

The pooling sampling layer training process is as follows:

$$A_n^x = g \left(\beta_n^x \text{down} \left(A_n^{x-1} \right) + P_n^x \right). \quad (15)$$

Among them, down($\bullet$) is the pooling function and β and P represent the weight and bias, respectively.

The difficulty of the pooled sampling layer is also the calculation of the gradient. If the pooled sampling layer is followed by a fully connected layer, its sensitivity can be calculated by the BP algorithm; if the pooled sampling layer is

followed by a convolutional layer, the sensitivity meter calculation formula is

$$\delta_n^x = g'(C_n^x) \bullet \text{conv2}\left(\delta_n^{x+1}, \text{rot180}(K_n^{x+1}), 'full'\right). \quad (16)$$

The calculation process of the bias in the pooled sampling layer is the same as that in the convolutional layer, but the calculation formula of the weight β is as follows:

$$\frac{\partial E}{\partial P_n} = \sum_{i,j} (\delta_n^x \bullet f_n^x)_{ij}. \quad (17)$$

In the formula,

$$f_n^x = \text{down}(A_n^{x-1}). \quad (18)$$

Finally, the weights are updated by formulas (17) and (18).

3.5. Knee MRI and Meniscus Characteristics. In recent years, deep learning has made breakthroughs, and its application in the field of data analysis has grown rapidly. At present, deep learning has become the main application tool of machine learning in the field of image recognition and computer vision. In the biomedical field, deep learning is rapidly becoming the state-of-the-art in computer-aided diagnosis, resulting in increasing diagnostic accuracy. In the field of medical images, deep learning methods are applied everywhere from lesion detection, image segmentation, image registration to classification.

The meniscus is an important part of the knee joint and is a soft tissue structure, as shown in Figure 8. It consists of two crescent-shaped structures, which are located between the femur and the tibia and play a role in joint cushioning. The one near the inside of the knee joint in the leg is called the medial meniscus and has a larger opening that resembles a crescent; closer to the outside is the lateral meniscus, which has a smaller opening and is a crescent close to the full moon, which is wrapped in the middle by the medial meniscus. The sharp corners on the front side are called front corners, and the rear corners are called rear corners. At the knee joint, the femur, tibia, and meniscus are surrounded by peripheral ligament connections, one part is connected at the angle of the meniscus, and one end is on the leg bone. Its structure is relatively complex. If it is not presented in the form of a section, the meniscus is wrapped in it, making it difficult to observe.

4. Repair Experiment and Analysis of Nanomaterials on Meniscus Injury Caused by Calisthenics Exercise

4.1. Information on Meniscal Injury

4.1.1. Cause

(1) Traumatic injury: when the knee is in flexion, the medial and lateral menisci can move forward and backward with the femur due to rotation. When this paradoxical movement is outside the normal range, a tear of the meniscus can occur [25]

(2) Degenerative injury: due to age and exercise factors, such as excessive walking, it may cause frequent stimulation of the meniscus and frictional loads beyond the normal physiological range. As a result, the pathological changes such as tissue degeneration and minor damage of the meniscus are gradually aggravated to the degree of tearing

4.1.2. Clinical Manifestations

(1) Pain

Severe pain occurs immediately after trauma. The pain is worse with activity, but not as severe as before.

(2) Swelling

At the time of the injury or a few hours after the injury, the knee joint may swell and sometimes bruise under the skin.

(3) Sound

There is a sound in the knee joint during activities, which is mostly caused by the abnormal friction and bounce of the ruptured meniscus with the tibia and femur when the knee joint is active.

(4) Interlock phenomenon

During the extension and flexion activities of the knee joint, there is often a phenomenon of sudden "stuck" resulting in the inability to extend and flex the knee joint, which is called interlocking phenomenon.

4.1.3. Check

(1) MRI

MRI, the imaging method of choice for detection of meniscal injuries, also observes the condition of the collateral and cruciate ligaments. The nature of the pain can be

(a) Front view of the knee joint

(b) Top view of the meniscus
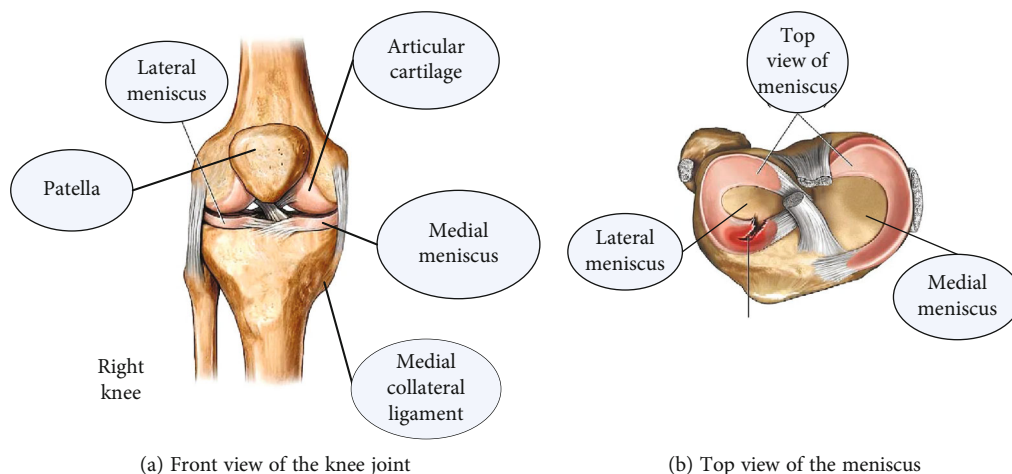
FIGURE 8: Schematic diagram of the structure of the knee joint and meniscus.

tugging, tearing, or colic-like persistent pain, and the pain range occurs on the side of the injury. Over time, the pain will gradually reduce and focus on the local area.

(2) McFarland's sign test

It has a high reference value for diagnosis. Subcutaneous congestion is the result of bleeding due to ligament damage.

(3) Extrusion test

When the knee is nearly straight, passively abduct or adduct the calf to squeeze the torn meniscus and cause pain.

(4) Arthroscopy

This is the basis for the final diagnosis. When the knee joint is actively or passively moved, this phenomenon can be relieved by itself, and the activity returns to normal. There are also cases where the interlock does not recover and the joint is permanently unable to straighten and flex.

4.2. Characteristics and Analysis of Injury Rate of High-Level Competitive Aerobics Athletes. In this survey, "a specific time" is the moment of filling out the survey form as the end of time and 12 months from this. In this paper, according to the research needs, the statistical number of sports injuries is limited to the frequency of injuries in the last year after the athlete achieved the corresponding level. Considering that the time continuity and cumulative effect of chronic injury will have a great impact on the statistical effect, therefore, the chronic injury is only counted once for the injury nature column in the questionnaire, and the sum of the actual numbers for acute injury is calculated. Statistics show that the injury rate of high-level competitive aerobics athletes is 100%. This shows that the investigators have suffered from sports injuries in the past year. Table 1 was prepared based on the frequency distribution data of the incidence frequency obtained by the questionnaire.

It can be seen from Table 1 that with the improvement of the level and the length of training years, the number of inju-

ries will gradually increase. In the early stage of high level, there may be about 3 injuries, but in the later stage of high level, the number of injuries is mainly 6 or more. It can be seen that injuries are a common occurrence for high-level athletes and must be experienced all the time. Injuries seem to be an unavoidable problem associated with high-intensity training and daily high-intensity training as skill levels improve and develop.

It can be seen from Figure 9 that the most frequently treated parts of the national team are the waist, knee, and wrist, followed by the shoulder, hip, ankle, elbow, and back. Among them, most of the waist is lumbar muscle strain, and microwave or thermal magnetic therapy is often used for physiotherapy. Most of the back is fatigued after training. All athletes who perform back treatment use low-frequency electrical stimulation and relaxation instruments, which are equivalent to electrotherapy massage. Both the knee and the wrist belong to joints, and their injury prevention measures are very similar, so the knee joint is used as the representative to discuss. Actions of competitive aerobics jumps, body jumps, flexion and split jumps, twists, high kicks, Ilyushin, Kossack jumps, side split jumps, exchange jumps, scissor kicks, scissor jumps, etc. have a strong impact on the knees. This can easily cause knee pain, swelling, flexion and extension disorders, etc., and then atrophy of the quadriceps femoris and imbalance of the thigh and calf muscles. To prevent the disease from worsening in the case of uninterrupted training, it can be strengthened to prevent from the following aspects:

(1) The use of sports protective support belt can effectively prevent the aggravation of injury

(2) They should perform functional exercises, including strength, flexibility, motor sensory, and proprioceptive training. Flexibility has high requirements in competitive aerobics. Special functional exercises can not only prevent injuries but also improve sports performance, killing two birds with one stone. The common way is PNF exercises, specifically participating in primary prevention. The exercise of

TABLE 1: Incidence frequency of high-level competitive aerobics athletes in China in the past year.

Sport level frequency	1-2 times	3-5 times	≥6 times
National level	40%	37%	23%
National master	20%	38%	42%
International master	10%	12%	78%

TABLE 2: Comparison of age, height, and weight between healthy group and patients.

Group	Health group	Patient group	Inspection value	P value
Number of cases	20	20		
Age	30.52 ± 5.33	32.52 ± 5.02	-1.592	0.110
Weight	74.38 ± 14.08	73.18 ± 11.69	0.422	0.680
Height	176.02 ± 5.84	174.89 ± 3.88	1.240	0.226
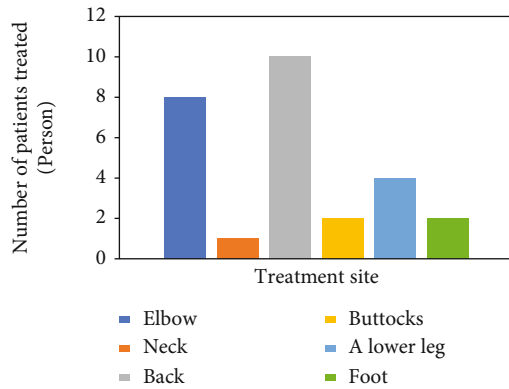
FIGURE 9: Distribution map of treatment sites for aerobics national training team during 2020\11-2021\11. Note: the statistics take one month as a small unit. If someone has performed multiple treatments on the same part within a month, it will be counted only once. However, the same parts of the same object in different months of the 12-month period are accumulated on the basis of the above. Such statistics not only reduce the interference of the injury healing process on the overall injury characteristics but also reduce the interference of the individual injury characteristics of the same subject with multiple treatments on the overall injury characteristics.

balance ability can greatly improve the neuromuscular control ability of the body and promote the coordination and stability of the body. The recovery of the athlete's balance ability and proprioceptive control ability is the key to reducing the risk of reinjury. Balance pads, active boards, and other balance exercise equipment can be used to enhance limb stability. The trampoline exercise used by the national aerobics training team is actually a functional exercise to enhance the sense of movement and proprioceptive training

(3) Physiotherapy. Any injury has the ability to repair itself, but research shows that the biochemical composition of tissue repaired by itself is different from that of uninjured tissue. Therefore, active stimulation by external means is helpful for the recovery of structure and function and also helps to improve the ability to respond to exercise and prevent the occurrence of injury. The commonly used physiotherapy methods for chronic knee injuries include microwave therapy, thermomagnetic therapy, ultrashort wave therapy, and ultrasonic therapy. Among them, ultrasound is mainly used for the removal of

scar tissue and adhesions. The efficacy of microwave, thermomagnetic, and ultrashort mainly lies in the deep penetration of thermal effect, which can focus on promoting blood circulation in the affected area and promoting damage repair. During the treatment of the national team members, a total of 9 people have used the above methods, of which 7 people showed significant improvement, and continued to maintain a large amount of exercise training without any suspension of training. To sum up, the overall tertiary prevention of injuries for high-level athletes can enable athletes to fully and actively deal with sports injuries that accompany the improvement of competition, which is conducive to improving the body's ability to withstand high-intensity training, resulting in a good training adaptation

4.3. Comparison of Gender, Age, and Weight of Patients. Table 2 shows that the age comparison between the healthy group and the patient group was not statistically significant ($T = -1592$, $P = 0.110 > 0.05$); there was no statistical significance in height ($T = 1.240$, $P = 0.226 > 0.05$) and no statistical significance in weight ($T = 0.4226$, $P = 0.680 > 0.05$).

Table 3 shows the comprehensive score comparison made by the back-end algorithm layer of the Internet cloud of the foot space posture evaluation and analysis system based on all the gait data of the testee's feet within one minute. It is mainly assessed from four aspects: gait stability, bipedal symmetry, initiation ability, and deceleration ability. The results show that

(1) In patients with unilateral meniscus injury, the stability, symmetry, and starting ability of gait before surgery were significantly lower than those of the healthy group and the gait data obtained after surgery, which indicates that meniscus injury has a significant impact on gait stability, symmetry, and startup ability. Factors such as uneven force on both lower extremities and the patient's own fear caused by factors such as knee instability, knee flexor muscle weakness, and pain in the affected limb after meniscus injury were considered

(2) There was no statistical difference in the stability, symmetry, and starting ability of the gait after surgery and the healthy group, indicating that the comprehensive evaluation of the gait after meniscus

TABLE 3: Comparison of gait comprehensive score between the healthy group and patient group.

Group	Health group	Patients before operation	Postoperative patients	F value	P value
Stability	98.67 ± 0.68	95.01 ± 1.56	98.70 ± 0.69	145.99	<0.01
Symmetry	95.60 ± 2.78	91.29 ± 3.61	95.29 ± 2.89	19.91	<0.01
Starting ability	89.05 ± 5.66	76.61 ± 4.41	88.11 ± 3.21	66.55	<0.01
Deceleration capacity	88.77 ± 5.78	84.99 ± 5.88	86.55 ± 5.01	1.24	0.28

surgery was close to the normal gait, the kinematic data was generally normal, and the surgical effect was more reliable

(3) There was no statistical difference in the deceleration ability between the patients before and after surgery and the healthy group, which may be related to the lower requirements of knee joint stability and muscle strength for gait deceleration exercise. It cannot be ruled out that the result error is caused by the small number of times of reentry and the large error of deceleration movement data collection in this experiment

5. Discussion

The research on sports injuries in advanced aerobics is a step that cannot be ignored in the scientific development of aerobics. At present, with the rapid development of science and technology, people are no longer satisfied with using "sports performance" as an index to evaluate the effect of training but pay more attention to evaluating the effect of training, that is, the relationship between the input and output of training.

Nanomedicine is also a promising drug, as it is not easily absorbed by the human body when prepared in nanopowder or suspension. Nanomedicine is pasted on the affected area and can be absorbed directly through the skin without injection. But in aerobics, strength quality is a very critical link, so it is necessary to have excellent strength quality.

During training, athletes continue to work hard to achieve better results and keep crossing borders. To break themselves, they cause multiple sports injuries. How to improve the effective prevention of aerobic injury has become a major problem faced by coaches and athletes. At present, the clinically preferred treatment for meniscal injury is arthroscopic surgery, which can well complete the trimming and shaping of the damaged meniscus. It can eliminate the pain, noose, joint instability, and other symptoms caused by meniscus injury and significantly improve the function of the knee joint.

6. Conclusions

This study found that the loss of postoperative muscle strength of the affected limb had a significant impact on postoperative gait. Postoperative muscle strength of the affected limb, especially the decrease of knee flexor muscle strength and postoperative pain are the two main causes of

postoperative gait abnormalities in patients with meniscus injury. Another study has shown that muscle tension can be improved by exercising the muscle strength around the knee joint. The release of fascial adhesions has great benefits and is helpful for improving joint stability and internal circulation. Combined with the above data, patients with meniscus injury should be given appropriate lower extremity functional exercises after surgery to improve the muscle strength around the joints. It should be an equally important measure to eliminate postoperative pain, edema and other conventional treatments.

Data Availability

The data that support the findings of this study are available from the corresponding author upon reasonable request.

Conflicts of Interest

The authors declare that they have no conflicts of interest.

References

[1] C. Yin, F. R. Negreiros, G. Barcaro et al., "Alumina-supported sub-nanometer Pt10clusters: amorphization and role of the support material in a highly active CO oxidation catalyst," *Journal of Materials Chemistry A*, vol. 5, no. 10, pp. 4923–4931, 2017.

[2] D. T. Shivakumar, T. Kneevi, and L. K. Nanver, "Nanometer-thin pure boron CVD layers as material barrier to Au or cu metallization of Si," *Journal of Materials Science: Materials in Electronics*, vol. 32, no. 6, pp. 1–13, 2021.

[3] X. Hu, P. Yasaei, J. Jokisaari, S. Öğüt, A. Salehi-Khojin, and R. F. Klie, "Mapping thermal expansion coefficients in free-standing 2D materials at the nanometer scale," *Physical Review Letters*, vol. 120, no. 5, pp. 55902.1–55902. 6, 2018.

[4] Q. Zhao, F. Yang, H. Li, and J. Liu, "Study on hydrogenation kinetics of Mg-Ce-Ni heterogeneous nanometer level material," *Chinese Rare Earths*, vol. 39, no. 6, pp. 77–85, 2018.

[5] D. Ross and H. Yamaguchi, "Nanometer-scale characteristics of polycrystalline YAG ceramic polishing," *CIRP Annals*, vol. 67, no. 1, pp. 349–352, 2018.

[6] A. Kam and C. Torres, "Nanoimprint lithography," *Journal of Vacuum Science & Technology B Microelectronics & Nanometer Structures*, vol. 14, no. 6, pp. 4129–4133, 2017.

[7] D. V. Opdenbosch and C. Zollfrank, "Modeling the compressive behavior of anisotropic, nanometer-scale structured silica," *Advanced Engineering Materials*, vol. 21, no. 6, pp. 1801097–1801097, 2019.

[8] L. Hasanah, A. B. D. Nandiyanto, B. Mulyanti et al., "Effect of crystal orientation on tunneling currents in an anisotropic Si/Si0.5Ge0.5/Si heterostructure with a nanometer-thick barrier-Science Direct," *Materials Today Proceedings*, vol. 5, no. 5, pp. 13711–13717., 2018.

[9] M. N. Norizan, Y. Miyazaki, Y. Ohishi, H. Muta, and S. Yamanaka, "The nanometer-sized eutectic structure of Si/CrSi 2 thermoelectric materials fabricated by rapid solidification," *Journal of Electronic Materials*, vol. 47, no. 4, pp. 2330–2336, 2018.

[10] M. Bonifazi, V. Mazzone, N. Li, Y. Tian, and A. Fratalocchi, "Free-electron transparent metasurfaces with controllable losses for broadband light manipulation with nanometer resolution," *Advanced Optical Materials*, vol. 8, no. 1, pp. 1900849.1–1900849. 8, 2020.

[11] H. Song and M. Brandt-Pearce, "Range of influence and impact of physical impairments in long-haul DWDM systems," *In Journal of Lightwave Technology*, vol. 31, no. 6, pp. 846–854, 2013.

[12] Y. Wang, M. Nakano, Y. Kashiwabara, H. Matsuoka, and Y. Iwasa, "Transport properties of a few nanometer-thick TiSe_2 films grown by molecular-beam epitaxy," *Applied Physics Letters*, vol. 113, no. 7, pp. 73101.1–73101.4, 2018.

[13] B. Gao, N. Xu, and P. Xing, "Shock wave induced nanocrystallization during the high current pulsed electron beam process and its effect on mechanical properties," *Materials Letters*, vol. 237, no. 15, pp. 180–184, 2019.

[14] A. Ottomaniello, J. Keeley, P. Rubino, L. H. Li, and A. Tredicucci, "Optomechanical response with nanometer resolution in the self-mixing signal of a terahertz quantum cascade laser," *Optics Letters*, vol. 44, no. 23, pp. 5663–5666, 2019.

[15] D. P. Adams, M. J. Abere, C. Sobczak, and M. A. Rodriguez, "Stabilizing effects of oxidation on propagating formation reactions occurring in nanometer-scale metal multilayers," *Thin Solid Films*, vol. 688, pp. 137349.1–137349.11, 2019.

[16] Y. L. Ge, Y. F. Zhang, Y. Yang et al., "Enhanced adsorption and catalytic degradation of organic dyes by nanometer iron oxide anchored to single-wall carbon nanotubes," *Applied Surface Science*, vol. 488, pp. 813–826, 2019.

[17] S. Surya, R. Thangamuthu, S. Kumar, and G. Murugadoss, "Synthesis and study of photovoltaic performance on various photoelectrode materials for DSSCs: optimization of compact layer on nanometer thickness," *Superlattices and Microstructures*, vol. 102, pp. 424–441, 2017.

[18] S. Y. Chen and Y. Qin, "Nanometer pore structure and geological controlsof shale samples in northern Hebei Province," *China Natural Gas Geoscience*, vol. 28, no. 6, pp. 873–881, 2017.

[19] X. Zhi, L. P. Zhong, Z. C. Guo, F. J. Zhao, J. Liang, and L. University, "Study on performance and preparation of anti-ultraviolet nano composite material CeO_2-SiO_2 co precipitation kernel coated with SiO_2 by carbonization method," *Chinese Rare Earths*, vol. 38, no. 3, pp. 68–75, 2017.

[20] J. H. Lee, "Nonvolatile balanced ternary memory based on the multiferroelectric material GeSnTe2," *The Journal of Physical Chemistry Letters*, vol. 10, no. 23, pp. 7470–7474, 2019.

[21] Z. Song and H. Zhao, "Preparation and characterization of mullite-silica aerogel composite material," *Open Journal of Organic Polymer Materials*, vol. 8, no. 4, pp. 43–52, 2018.

[22] V. Polischuk, V. Y. Karaseva, E. S. Dzlievaa, A. P. Gorbenkoa, and I. I. Mironova, "Modification of the texture of a polymer material surface in dust plasma," *Technical Physics*, vol. 62, no. 3, pp. 496–498, 2017.

[23] A. T. Shora and F. A. Khanday, "Three-dimensional analytical modeling and performance analysis of triple material trigate silicon-on-insulator MOSFET," *International Journal of Numerical Modelling*, vol. 32, no. 3, pp. e2571–e2571.14, 2019.

[24] S. Kamal, K. P. Bera, M. Usman et al., "Phosphor-free electrically driven white light emission from nanometer-thick barium–organic framework films," *ACS Applied Nano Materials*, vol. 4, no. 3, pp. 2395–2403, 2021.

[25] H. Zhu, H. Wei, B. Li, X. Yuan, and N. Kehtarnavaz, "Real-time moving object detection in high-resolution video sensing," *Sensors*, vol. 20, no. 12, p. 3591, 2020.

Hindawi

Research Article

Force-Electric Coupling of Nanoscale Ferroelectric Domains Based on Piezoelectric Force Microscopy (PFM)

Xusheng Wang [ID] **and Chenchen Feng**

Xi'an University of Technology, Xi'an, 710048 Shaanxi, China

Correspondence should be addressed to Xusheng Wang; xswang@xaut.edu.cn

Piezoelectric and ferroelectric materials are widely used in various types of microelectronics due to their excellent mechanical and electrical coupling characteristics. In recent years, piezoelectric force microscopy has developed into a powerful tool for analyzing nanoscale ferroelectric materials. However, quantitative analysis based on PFM is difficult to properly study it. This article studies the related issues of PFM quantitative analysis. First, the relationship between the effective piezoelectric coefficient and piezoelectric coefficient of different materials is analyzed from the PFM nanometer scale to analyze the force-electric coupling effect. The study found that the effective piezoelectric coefficient is closely related to the intrinsic electroelastic constant of the material. Secondly, the analysis of the nanoscale piezoelectric deformation of ferroelectric materials shows that under the conductive SPM probe, as the clustering with the probe increases, the in-plane displacement first increases and then decreases, and the out-of-plane displacement gradually decreases. Finally, the half-width region of the nanoscale ferroelectric response domain was analyzed by PFM. Taking the in-plane and out-of-plane domains of 180° and 90° domains as examples, the relationship between the response boundary domain and the tip radius was analyzed, and the results showed that whether the PFM can effectively solve the problem of detection and analysis depends on the half-width of the response boundary domain, and the resolution of the vertical PFM is higher than that of the lateral PFM.

1. Introduction

Because PFM has the ability to be highly sensitive to the local detection of piezoelectric sensors, PFM has been widely used to study the microstructure and properties of new ferroelectric materials. By using PFM nanoscale detectors to perform image scanning on ferroelectric materials, not only can the domain structure signal be grasped more efficiently, but also special iron structure domains can be established, and the changes related to the performance of the brake can be studied. In some materials containing more iron elements, because ferroelectric domains and ferromagnetic domains are closely connected, it is important to process iron and manipulate the iron domains through PFM. However, due to the unbalanced characteristics of the electric field, the high-load electric field caused by the PFM conductive probe, and the complex and long-term electromechanical interaction between the test materials, the quantitative

analysis of the PFM test is still very difficult. Nanoscale electromagnetic coupling hinders the research of ferroelectric materials and delays the development of electronic components produced by nanoscale electromagnetic coupling.

Many scholars at home and abroad have studied the analysis of the electromechanical coupling of nanoscale ferroelectric domains based on piezoelectric force microscopy (PFM) and have achieved certain research results. For example, Chen et al. proposed functional materials, which refer to the continuous or gradual change of single or multiple superimposed properties of materials in a certain direction, which are used to adapt to different environments and develop distinctive functional materials. As the material parameters of functional materials gradually change, the thermal and stress mismatch in the material structure is greatly alleviated. The size and spatial distribution of all constituent materials are optimized, so that the advantages of all constituent materials can be effectively used, and the most advanced materials'

needs for multifunctional technology can be met [1]. But the complex structure of ferroelectric materials can affect the PFM technique to analyze the electromechanical coupling effect. After comparing and analyzing several separate models, Kuerban et al. finally decided to adopt a combined forecasting model. Combined forecasting is the weighted average of forecasts obtained by different forecasting methods to reach the final forecast result. The forecast result is generally better than that the prediction results of each single model are an effective way to improve the prediction accuracy of the model, and the results are more reliable [2]. Xing and other scholars combined the comprehensive load statistics of the formatting module and the overall module load of the module to carry out applied research on the power load and carried out the composite model characteristics, influencing factors and evaluation indicators of the power load indicators of the subindustry of my country's power system. According to the time-sharing principle, a load composition model for different industries is proposed. According to the characteristics of short-term load forecasting and combined with domestic and foreign engineering experience, various solutions to the load forecasting problem are comprehensively analyzed [3]. In the 1940s, a scientific researcher discovered a piezoelectric ceramic material with excellent performance and easy to make and store. This material can change the chemical composition and polarization phenomenon in a targeted manner. According to its advantages in piezoelectric coefficient, electrical coupling coefficient, and stable performance, the application of piezoelectric ceramics has been rapidly expanded [4]. Capeli et al. conducted a tip crack fracture experiment on single crystal niobium. This experiment observes and examines the morphological characteristics of interface cracks and further measures the fracture hardness and atomic separation requirements. This experiment finally showed that although niobium is a flexible material and has many variants, the cracks at the interface of the two materials remain as sharp atomic cracks, and no extreme cracks will appear [5]. Although researchers have carried out a lot of related work in this area, quantitative analysis based on PFM will encounter many difficulties, that is, the complex structure of ferroelectric materials will affect the PFM technology to analyze the effect of force-electric coupling.

This article introduces the characteristics of piezoelectric and ferroelectric materials and analyzes the relationship between the effective piezoelectric coefficient and the piezoelectric coefficient of different piezoelectric materials under the decoupling and full coupling methods based on the working principle of PFM; comparing the effective piezoelectric coefficients of different materials under decoupling and full coupling, comparing the time-induced in-plane and out-of-plane displacement responses of single-domain ferroelectrics with PFM detection. Then, take PZT-4 as an example according to the genetic algorithm optimization; the piezoelectric coefficient is inversely optimized to obtain the optimal piezoelectric coefficient; then, the single-domain and complex ferroelectric domain nanoscale piezoelectric deformation are analyzed, and finally, the $BaTiO_3$ ceramic piezoelectric ceramic material is used as an example

to analyze the half-width of the domain boundary response of the in-plane and out-of-plane domains of 180 degrees and 90 degrees varies with the radius of the tip. Through these experiments, it can be known that PFM technology is an important nanoscale ferroelectric material analysis tool in the study of ferroelectric domains.

2. Introduction of Piezoelectric Force Microscopy and Performance Analysis of Ferroelectric Domain Materials

2.1. PFM Working Principle. When a ferroelectric crystal exerts a mechanical force in a certain direction, confinement charges are formed on the corresponding crystal surface. The amount of charge is related to the amount of mechanical stress applied. This phenomenon is called the positive piezoelectric effect. On the other hand, if an external electric field is applied to the ferroelectric crystal, the ferroelectric crystal will also deform, which is called the piezoelectric inverse effect. PFM is a novel scanning probe microscope (SPM) based on the inverse piezoelectric effect of ferroelectric samples. Its working principle diagram is shown in Figure 1.

As shown in Figure 1, during PFM operation, an alternating voltage was applied to the SPM conductive probe to generate an electric field between the conductive probe and the bottom electrode. According to the inverse piezoelectric effect, the detection sample changes its shape under the action of an electric field, causing the material surface to displace, thereby pushing the cantilever beam to twist. The twist signal is reflected from the laser to the spectral detector and then sent to the amplifier lock. Computer-generated PFM signals include signal amplitude and phase signals. The amplitude depends on the local mechanical and electrical coupling of the sample, and the phase is related to the internal polarization direction. In the multisample power tracking detection experiment, regions with different polarization directions have different degrees of electric field, which triggers the conduction effect of the probe, so that the piezoelectric images show different response resolutions. On the other hand, the feedback signal determines the distance between the probe and the specimen, so the interaction force between the probe and the model remains constant. At this time, special specimens can be developed according to the size of the specimens [6, 7].

2.2. Characteristics and Applications of Piezoelectric and Ferroelectric Materials. Piezoelectric material is a special type of intermediate electrical material. Due to its piezoelectric properties, it can identify the conversion between electricity and electricity. This conversion will produce changes under external loads such as mechanical force, electric field, temperature field, and light, thereby having piezoelectric, ferroelectric, pyroelectric, and nonlinear optical characteristics. When the electric domain changes the electric structure under the action of the medium thermal field, the electric heat generated by the ferroelectric material can provide the ferroelectric material for the infrared detector; when the applied stress field changes, the electric domain structure will also change, and the ferroelectric material will produce
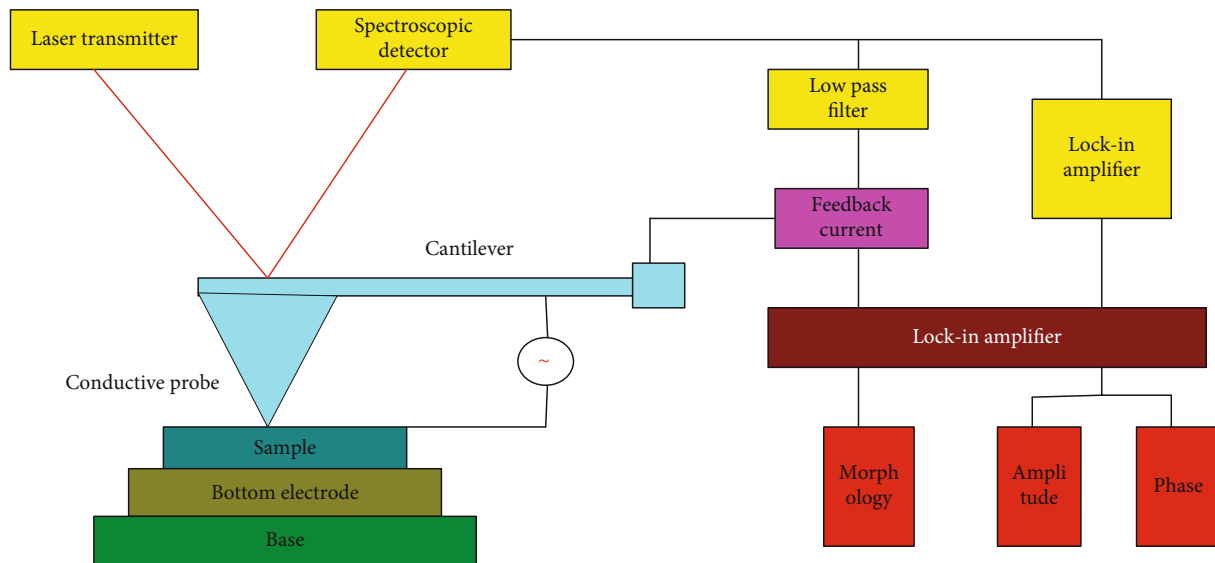
FIGURE 1: Working principle diagram of piezoelectric force microscope.

the piezoelectric effect which makes the application of ferroelectric materials in sensors and energy maps have a variety of research types. The polarization and conversion of the ferroelectric crystal produce a typical hysteresis model with the change of the applied electric field, which has the characteristics of the reverse polarization electric field and can be applied to the ferroelectric memory. The discovery of these properties has led to the production of ferroelectric materials in various microelectronic components, such as thermal elements and electrical transducers [8].

The positive piezoelectricity of piezoelectric materials is simply the ability to convert force into electricity. Specifically, it refers to the internal polarization when the external force is increased in a certain direction by the special structure of the dielectric material, which causes the material structure to deform. At this time, positive and negative charges are generated on the two opposite surfaces. The other is the inverted piezoelectric effect, in layman's terms, it converts electricity into a force that causes deformation. When the electric field is removed, the deformation of the dielectric will return to its original shape [9]. Therefore, the polarization direction of piezoelectric materials is also a very important research part.

Since the polarization phenomenon can occur in the ferroelectric material itself, and the ferroelectric material usually exists in multiple regions, each region has the same polarization direction. The regions with uniform polarization directions are called electrical domains, and the boundaries between domains are called wall domains. Generally speaking, each domain has an "end-to-end" polarity, so that there is no constrained charge at the boundary between domains, and the electrostatic energy in the boundary area is not reduced. The introduction of domains reduces the energy and electrostatic energy of the system, but introduces the energy of the wall domains, making the ferroelectric structure correspond to the minimum static energy in the

system [10, 11]. Since the center of the positive and negative charges does not enter the ferroelectric material, the relative arrangement of the positive and negative charges changes under the change of the external thermal field, causing spontaneous changes in polarization. The charge filtered by the surface of the ferroelectric material cannot maintain complete free movement on the road surface and the accumulated material, thereby generating a potential difference between the surface of the ferroelectric material and the surface of the material. This phenomenon is called the thermoelectric effect. Since all four sides of the material are heated at the same time, the positive and negative center displacements of the corresponding symmetry are the same, which is different from the piezoelectric effect. It shows that pyroelectric materials must have a greater range and spontaneous polarity, so pyroelectric materials have piezoelectricity. Driven by an electric field with a strong optical frequency or a DC electric field, ferroelectric materials will produce photoelectric effects and nonlinear optical effects. The refractive index of the ferroelectric material changes with the change of the additional charge, and the secondary fiber effect is generated with the regular change of the electric field. The secondary electro-optic effect refers to the birefringence of the isotropic material under the action of an external electric field, resulting in a change in the refractive index, and the change in the refractive index is proportional to the square of the electric field intensity. The material with central symmetry has no primary electrostatic effect, and the secondary fiber effect is very common in any dielectric material. The refractive index change is not only related to the external electric field but also the refractive index of the ferroelectric material can be changed by increasing the mechanical force. High-energy light is the source point light that radiates ferroelectric materials, generating bipolar electric pulses that can be driven by electromagnetic waves of a certain frequency.

2.3. Point Charge and Its Electric Field. In the PFM test, the SPM conductive probe is similar to a moving electrode [12]. By adding a certain voltage to the SPM conductive probe, a nonuniform electric field is induced in the virtual electric field space. Compared with the test sample, the SPM probe is very small, and the tip size can reach the nanometer level. By comparing the different shapes and thicknesses of the SPM probe and the test sample, people can regard the electric field caused by the SPM probe as an electric field caused by a point charge or a series of mirror charges, where the equivalent charge can also be used the equivalent capacitance between the SPM probe, and the sample is judged [13, 14]. The SPM conductive probes used in the experiment have different shapes, but mainly include conical, spherical, and disc shapes.

During the working process of PFM, a quantitative voltage is applied to the SPM probe, and an electric field probe is introduced. Compared with the SPM probe, the test material can be considered as a semi-infinite body. Therefore, the spatial electric field shaped by the conductive probe can be equal to the electric field induced by a point charge. According to the charge imaging method, it can be assumed that there is a mirror charge Q above the test sample from the sample surface. It can be seen from the singularity theorem of the mirror image method that the introduced image charge is outside the required field, and its introduction does not change the boundary conditions of the required field. Therefore, we can use the electric field generated by the charge Q to balance the space electric field shaped by the SPM probe, thereby simulating the distribution of the space electric field [15].

During PFM operation, a quantitative voltage is applied to the SPM probe, and an electric field probe is introduced. Compared to the SPM probe, the test material can be regarded as a semi-infinite body. Therefore, the space electric field created by the conductive probe can be equal to the electric field induced by the point charge. According to the charge imaging method, the charge imaging technique refers to the method of monitoring the calcium ion concentration in the tissue using a calcium ion indicator. In nervous system research, calcium ion imaging technol-ogy is commonly used to monitor the changes of calcium ions in neurons, indicating neuronal activity. With calcium imaging technology, the originally silent electrophysiological activity has become a vivid, colorful, and flickering spectacular image. It can be assumed that, viewed from the sample surface, there is an image charge Q above the test sample. It can be seen from the singularity theorem of the mirror image method that the introduced image charge is outside the required field, and its introduction does not change the boundary conditions of the required field. Therefore, we can use the electric field generated by the charge Q to balance the space electric field formed by the SPM probe, thereby simulating the distribution of the space electric field [15].

2.4. The Electroelastic Field Method between the Conductive Tip and the Sample

(1) Decoupling method

The essential idea of the force electrolytic coupling method is to separate the electrostatic field and the elastic electric field and evaluate them separately. The specific ideas are as follows: first, the finite electrostatic field model is used to calculate the internal piezoelectric electric field distribution of piezoelectric materials without considering the influence of the force-electric coupling; second, the internal pressure is considered to be the pressure generated by the electric field, so elasticity and stress can be solved by the rebound relationship; finally, the Green's function of the decoupling of the ferroelectric surface is used to obtain the piezoelectric displacement on the surface of the ferroelectric material. For the balanced distribution of ferroelectric materials detected by the SPM conductive probe, assuming that its polarization direction is perpendicular to the horizontal direction, the SPM conductive probe can be treated as a loading point for loading Q, where h is the height from the sample surface [8]. Using the loading image method, the potential $\varphi(\rho, z)$ distribution of the entire space can be obtained.

$$\varphi(\rho, x_3) = \begin{cases} \dfrac{Q}{2\pi\lambda_0(k+1)\sqrt{\rho^2 + (x_3 + h)^2}}, & x_3 \geq 0, \\[4mm] \dfrac{Q}{4\pi\lambda_0}\left[\dfrac{1}{\sqrt{\rho^2 + (x_3 + h)^2}} - \dfrac{k-1}{k+1}\dfrac{1}{\sqrt{\rho^2 + (x_3 - h)^2}}\right], & x_3 < 0. \end{cases} \tag{1}$$

Among them, $\rho = \sqrt{x_1^2 + x_2^2}$ and λ_0 are the vacuum permittivity, $k = \sqrt{\lambda_{11}\lambda_{33}}$ is the effective pressure permittivity, $\gamma = \sqrt{\lambda_{33}/\lambda_{11}}$ is the dielectric anisotropy factor, which reflects the difference between in-plane and out-of-plane dielectric properties, and x_1 represents the horizontal direction in the three-dimensional coordinate axis. In the right direction, x_3 represents the vertical downward direction, and x_2 is perpendicular to x_1 and x_3, respectively. The electric field is the gradient of the electric potential, namely,

$$E_i = \frac{-\partial \varphi}{\partial x_i}. \tag{2}$$

Assuming that the voltage applied to the needle tip is φ_o and the radius of curvature of the needle tip is R_o, the effective point charge model shows:

$$Q = \frac{2\pi \lambda_o R_o \varphi_o (k+1)}{k}, \tag{3}$$

$$d = \frac{R_o}{k}. \tag{4}$$

The charged probe causes an electric field to form inside the piezoelectric material, and the piezoelectric material produces strain under the action of the electric field due to the inverse piezoelectric effect. This piezoelectric accessory can be seen as an internal filter, namely,

$$s_{mn}^T = d_{mnk} E_k. \tag{5}$$

Among them, d_{mnk} is the piezoelectric tensor component on the three-dimensional image, and the repetition index k ($k = 1, 2, 3$) satisfies the weighted summation. Because piezoelectric tension destroys the dynamic equilibrium state of the system, internal stress e_{mn} and stress σ_{jl} are generated:

$$e_{mn} = s_{mn} - s_{mn}^T, \tag{6}$$

$$\sigma_{jl} = C_{jlmn} \left(s_{mn} - s_{mn}^T \right). \tag{7}$$

Among them, C_{jlmn} is the stiffness sensor component of the elastic component. By comparing the displacements of piezoelectric and elastic structures and introducing half-space elastic Green's function $G_{ij}(x, x')$, the surface displacement of the material can be obtained as:

$$u_i(x) = \int_0^\infty dx_3' \int_{-\infty}^\infty dx_2' \int_{-\infty}^\infty dx_1' C_{jlmn} d_{mnk} E_k\left(x'\right) \frac{\partial G_{ij}\left(x, x'\right)}{\partial x_l'}. \tag{8}$$

For a uniform ferroelectric material and the polarization orientation are perpendicular to the surface of the material, the Fourier transform can be used to solve the surface displacement to obtain the analytical form of the surface in-plane and out-of-plane displacement:

$$u_1(\rho, 0) = \frac{Q}{2\pi \lambda_o (k+1)} x_1 \frac{[d_1 g_1(\gamma) + d_2 g_2(\gamma) + d_3 g_3(\gamma)]}{\sqrt{\rho^2 + h^2} \left(\sqrt{\rho^2 + h^2} + h \right)}, \tag{9}$$

$$u_2(\rho, 0) = \frac{Q}{2\pi \lambda_o (k+1)} x_2 \frac{[d_1 g_1(\gamma) + d_2 g_2(\gamma) + d_3 g_3(\gamma)]}{\sqrt{\rho^2 + h^2} \left(\sqrt{\rho^2 + h^2} + h \right)}, \tag{10}$$

$$u_3(\rho, 0) = \frac{Q}{2\pi \lambda_o (k+1)} \frac{[d_1 g_1(\gamma) + d_2 g_2(\gamma) + d_3 g_3(\gamma)]}{\sqrt{\rho^2 + h^2}}. \tag{11}$$

Among them, d_1, d_2, and d_3 are voltage coefficients, $g_1(\gamma) = 2 + \gamma + 2(1 + \gamma)v/(1 + \gamma)^2$, $g_2(\gamma) = -\gamma/(1 + \gamma)^2$, $g_3(\gamma) = \gamma/(1 + \gamma)^2$, and v is Poisson's ratio.

(2) Fully coupled method

Since the force-electric coupling between the needle tip and the sample is axisymmetric, it can be solved by the Hankel integral transformation method [16, 17]. The Hankel integral transformation pair defined for any function $F(r, z)$ is:

$$\tilde{F}(\xi, z) = \int_0^\infty F(r, z) r J_p(\xi r) dr, \tag{12}$$

$$F(r, z) = \int_0^\infty \tilde{F}(\xi, z) \xi J_p(\xi r) d\xi. \tag{13}$$

Among them, in the three-dimensional coordinate axis, r represents the horizontal axis to the right, z represents the vertical axis downward, $J_p(\xi r)$ is the first-type Bessel function of order p, and ξ is the polar axis in the Fourier space.

3. Analysis and Research on the Electromechanical Coupling of Nanoscale Ferroelectric Domains Based on Piezoelectric Force Microscopy (PFM)

3.1. Research Content. There are three main research contents in this article. First, when using the PFM technology to quantitatively analyze the nanoscale piezoelectric coefficients, it is discussed whether the effective voltage coefficient under the decoupling method and the fully coupled method is compared with the actual voltage coefficient, and whether the two methods will overestimate or underestimate the conductive SPM probe [18] surface displacement caused by the needle. The second is to analyze PFM to detect nanoscale piezoelectric deformation of single-domain ferroelectric materials and complex ferroelectric domains. The third is to analyze the half-width of the domain boundary response half-width of the in-plane domain and the out-of-plane domain of the vertical angle and the lateral angle and discuss the effect of the PFM vertical resolution and the lateral resolution [19].

3.2. Research Methods. This article mainly uses the literature data method and the comparison method to obtain the relevant properties and research directions of ferroelectric materials by searching literature, compare the effective piezoelectric coefficients of different materials under decoupling and full coupling, and compare PFM to detect single-domain ferroelectric samples the in-plane and out-of-plane displacement response caused by the time, and

TABLE 1: Piezoelectric, dielectric, and elastic constants used in the calculation.

Material	d_1 (pm/V)	d_2 (pm/V)	d_3 (pm/V)	ν	F
$BaTiO_3$	-77	265	187	0.35	0.78
$PbTiO_3$	-6.5	62	48	0.26	0.81
PZT (Zr/Ti = 48/52)	42	158	107	0.31	1.24
PZT-8	-100	320	304	0.30	0.72
PMN-42%PT	-27.9	1418.6	101.2	0.25	2.65
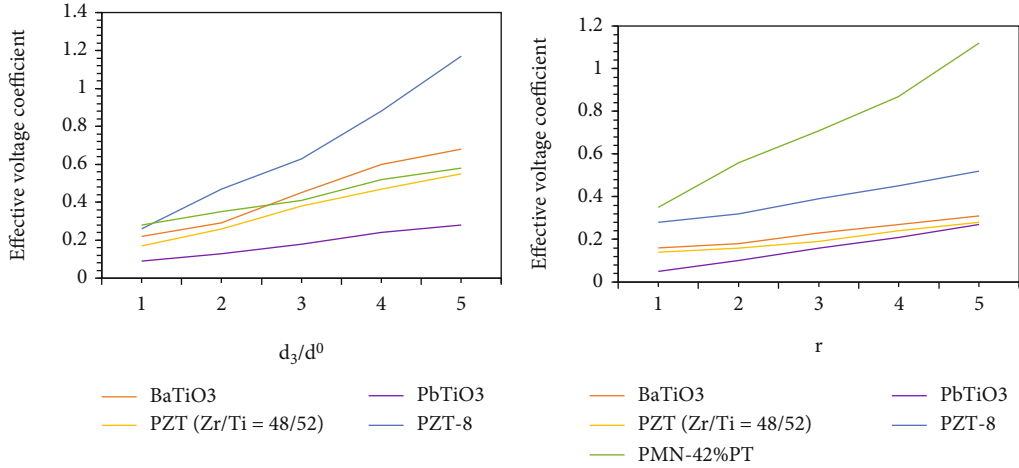
FIGURE 2: The relationship between effective piezoelectric coefficient and piezoelectric coefficient and dielectric anisotropy factor of different materials.

the half-width of the domain boundary response of the in-plane and out-of-plane domains of the $BaTiO_3$ ceramic piezoelectric ceramic material with 180 degrees and 90 degrees domains change with the radius of the tip [20].

4. Based on Piezoelectric Force Microscopy (Pfm) Nanoscale Ferroelectric Domain Force-Electric Coupling Analysis

4.1. Quantitative Analysis of Nanoscale Piezoelectric Coefficients Based on PFM

(1) Effective piezoelectric coefficient based on decoupling method

In order to quantitatively analyze the relationship between the effective piezoelectric coefficient and the inherent parameters of the material, select $BaTiO_3$, $PbTiO_3$, PZT (Zr/Ti = 48/52), PZT-8, and PMN-42%PT as examples, and the corresponding inherent material parameters are shown in Table 1. In order to clearly see the difference between the effective piezoelectric coefficient and the inherent piezoelectric coefficient, the correction factor f of the material is defined. The results show that the correction factor of PZT-8 is the smallest with a value of 0.72, while the correction factor of PMN-42%PT is the largest at 2.65. There is no obvious trend in the correction factor between different materials. In addition, for different materials, the correction

factor may be greater than 1 or less than 1, which indicates that the piezoelectric coefficient of the PFM test may be overestimated or underestimated, which makes the quantitative analysis of the piezoelectric coefficient of the PFM technology more difficult.

Figure 2 shows the relationship between the effective piezoelectric coefficient of different materials and the piezoelectric coefficient and dielectric anisotropy factor. Fixing all other material parameters and changing only the piezoelectric coefficient d_3, then the linear relationship between the effective piezoelectric coefficient $d*_3$ and the piezoelectric coefficient d_3 can be obtained. Although there is a linear relationship between $d*_3$ and d_3, the slopes of $d*_3$ and d_3 are different for different materials, which means that the piezoelectric coefficients of other materials cannot be accurately obtained by calibrating with reference to the material. The effective piezoelectric coefficient of different materials and the dielectric anisotropy factor r are obviously nonlinear, especially for PMN-42%PT, the corresponding effective piezoelectric coefficient increases sharply as r increases. The obvious nonlinear characteristics of $d*_3$ and r in PMN-42%PT are mainly due to its large d_2. It is worth noting that although the piezoelectric coefficient is fixed, the effective piezoelectric coefficient still changes with the elastic constant and the dielectric constant. This shows that the quantitative analysis of the piezoelectric coefficient for the PFM technology requires all other material parameters to be known.

TABLE 2: Properties of piezoelectric ceramics.

Material	Elastic constant (GPa)	Piezoelectric coefficient (C/m^2)	Dielectric constant (10^{-9} F/m)
PZT-4	138.67	12.8	6.521
PZT-5A	124.00	12.6	8.127
BaTiO$_3$	150.14	11.5	9.842
(Ba$_a$Ca$_b$)TiO$_3$	158.33	10.8	8.786
PZT (Zr/Ti = 48/52)	124.74	5.92	4.812
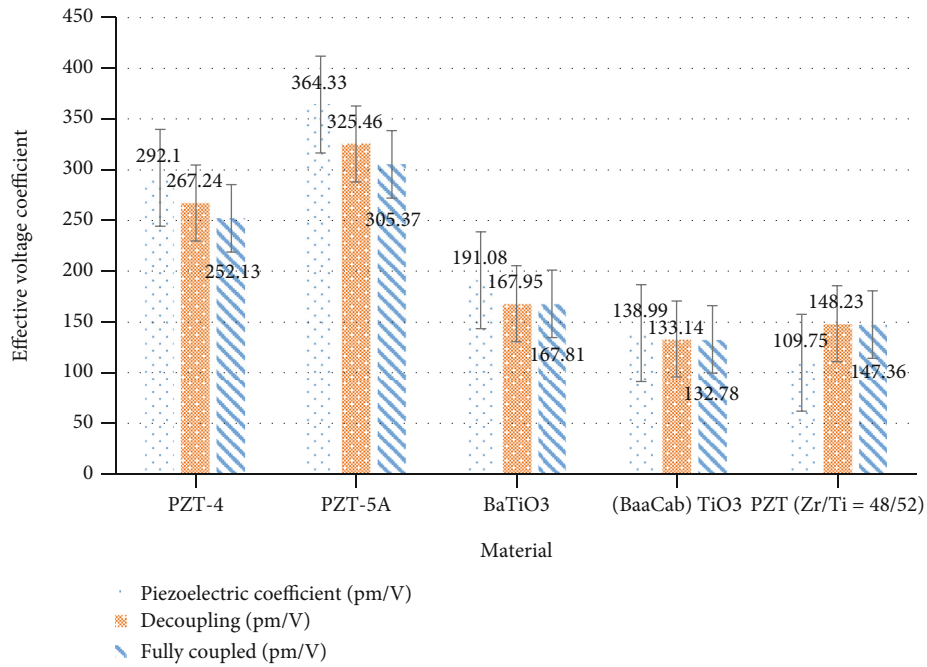
FIGURE 3: Effective piezoelectric coefficients of different materials.

(2) Effective piezoelectric coefficient based on the full coupling method

This paper selects five different piezoelectric materials, namely, PZT-4, PZT-5A, BaTiO$_3$, (BaaCab)TiO$_3$, and PZT (Zr/Ti = 48/52), and the comparative analysis is based on the full coupling method and the decoupling method. The difference of effective piezoelectric coefficient, further analyze the relationship between effective piezoelectric coefficient and material inherent parameters. The actual material parameters corresponding to the selected materials are shown in Table 2. The elastic constant of PZT-4 material is 138.67 GPa, the piezoelectric coefficient is 12.8 C/m^2, and the dielectric constant is 6.521×10^{-9} F/m; PZT-5A material the elastic constant is 124.00 GPa, the piezoelectric coefficient is 12.6 C/m^2, and the dielectric constant is 8.127×10^{-9} F/m; the elastic constant of BaTiO$_3$ material is 150.14 GPa, the piezoelectric coefficient is 11.5 C/m^2, and the dielectric constant is 9.842×10^{-9} F/m; the elastic constant of (BaaCab)TiO$_3$ material is 158.33 GPa, the piezoelectric coefficient is 10.8 C/m^2, and the dielectric constant is 8.786×10^{-9} F/m; PZT (Zr/Ti = 48/52); the elastic constant of the material is 124.74 GPa, the piezoelectric coefficient is 5.92 C/m^2, and the dielectric constant is 4.812×10^{-9} F/m.
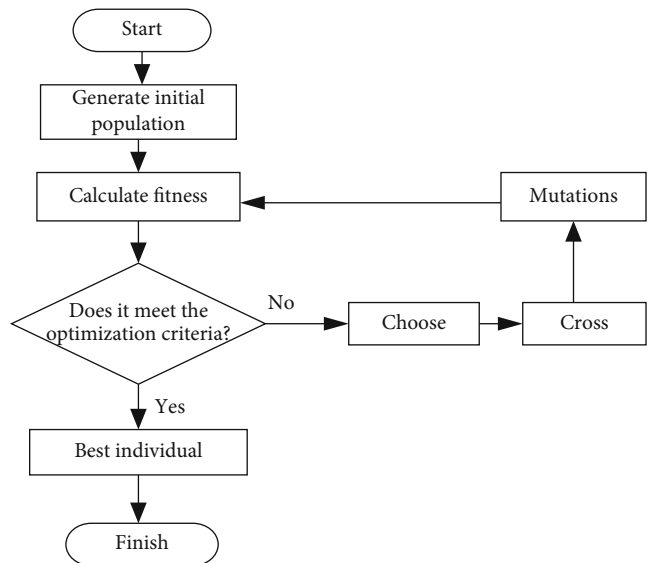
FIGURE 4: Basic flow chart of genetic algorithm.
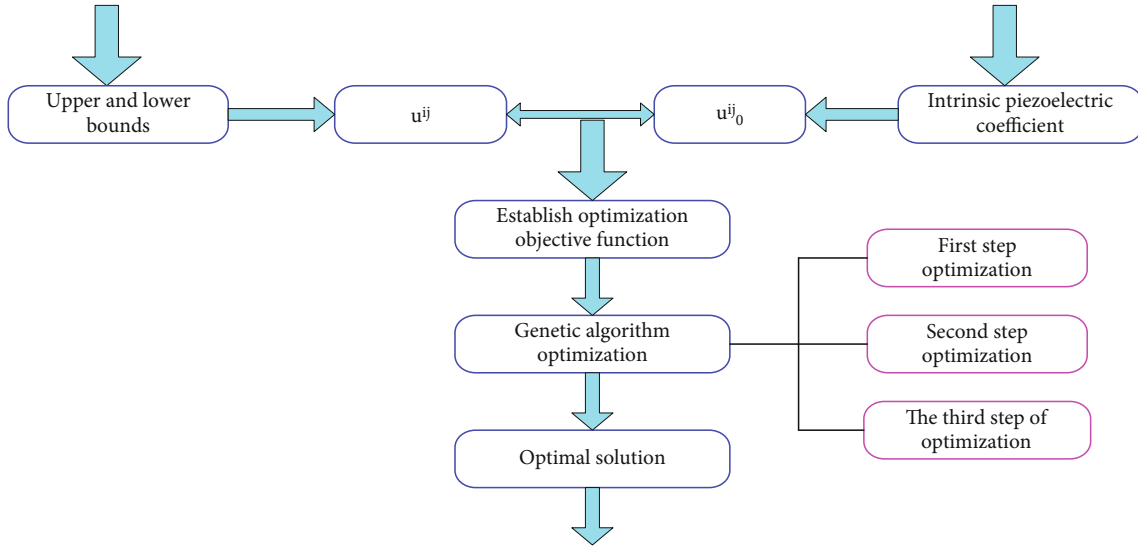
FIGURE 5: Piezoelectric coefficient optimization process.

Analyzing the difference of the effective piezoelectric coefficients of the two theories, the effective piezoelectric coefficients obtained by the two theories for different materials are summarized as shown in Figure 3. The effective piezoelectric coefficient of PZT-4 material in decoupling mode is 267.24 (pm/V), and the effective piezoelectric coefficient in full coupling mode is 252.13 (pm/V); PZT-5A material is effective in decoupling mode the piezoelectric coefficient is 325.46 (pm/V), the effective piezoelectric coefficient in the fully coupled mode is 305.37 (pm/V); the effective piezoelectric coefficient of the $BaTiO_3$ material in the decoupling mode is 167.95 (pm/V), fully coupled the effective piezoelectric coefficient in the mode is 167.81 (pm/V); the effective piezoelectric coefficient of $(Ba_aCa_b)TiO_3$ material in the decoupling mode is 133.14 (pm/V), and the effective piezoelectric coefficient in the fully coupled mode is 132.78 (pm/V); the effective piezoelectric coefficient of PZT (Zr/Ti = 48/52) material in decoupling mode is 148.23 (pm/V), and the effective piezoelectric coefficient in full coupling mode is 147.36 (pm/V). It can be seen from these data that compared with the actual piezoelectric coefficient, whether it is a decoupling method or a fully coupled method, the corresponding effective piezoelectric coefficient may be overestimated or underestimated. Moreover, compared with the fully coupled method, decoupling analysis tends to underestimate the surface displacement caused by the conductive SPM probe.

(3) Inversion of piezoelectric coefficient

There is an obvious nonlinear relationship between the effective piezoelectric coefficient and the intrinsic material constant. Therefore, we propose a method to inversely optimize the electroelastic constant of the material under different test conditions. It is based on this idea, focusing on the inversion of piezoelectric coefficients based on genetic algorithm (GA). The idea of genetic algorithm originates from the most suitable survival process in biological evolution, and its basic process is shown in Figure 4. They first randomly generate

populations and evaluate the suitability of the main population; then, select parent individuals based on suitability, such as roulette selection method, traversal sampling, and competitive bidding; secondly, transfer or reorganize the selected parent individuals; transfer or after reorganization, in order to prevent the optimization result from appearing a local minimum, the population will change with a small probability; finally, if the newly generated population reaches the optimization of the termination condition, the optimization result is output; otherwise, the second step is returned.

The inversion optimization of piezoelectric coefficients uses PZT-4 material as an example, and the three piezoelectric coefficients are optimized through multistep optimization. The optimization process is shown in Figure 5. The first step is to consider the three piezoelectric coefficients e_1, e_2, and e_3, and perform simultaneous optimization. The three piezoelectric coefficients obtained by the first optimization are recorded as e^1_1, e^1_2, e^1_3, and $e_1 = e^1_1$ in the second optimization. Only optimize the other two piezoelectric coefficients e_2, e_3, and then, you can get e^2_2, e^2_3. In the third step of optimization, $e_3 = e^2_3$, and $e_1 = e^1_1$, and only e_3 is optimized separately.

The piezoelectric coefficient results obtained by the three-step optimization are shown in Table 3. The intrinsic piezoelectric coefficients e^0_1, e^0_2, and e^0_3 of the three steps are 11.5, -5.4, and 14.7. After the first step of optimization, the optimized voltage coefficients e_1, e_2, and e_3 are 11.486, -5.346, and 14.822, respectively; after the second step of optimization, the optimized voltage coefficients e_1, e_2, and e_3 are 11.487, -5.428, and 14.604, respectively; after three-step optimization, the optimized voltage coefficients e_1, e_2, and e_3 are 11.532, -5.398, and 14.676, respectively.

4.2. Analysis of Nanoscale Piezoelectric Deformation of Ferroelectric Materials

(1) Nanoscale piezoelectric deformation of single-domain ferroelectric materials

TABLE 3: Optimal piezoelectric coefficient and intrinsic piezoelectric coefficient of PZT-4.

	Intrinsic piezoelectric coefficient (C/m^2)			Optimized piezoelectric coefficient (C/m^2)		
	e^0_1	e^0_2	e^0_3	e_1	e_2	e_3
1	11.5	-5.4	14.7	11.486	-5.346	14.822
2	11.5	-5.4	14.7	11.487	-5.428	14.604
3	11.5	-5.4	14.7	11.532	-5.398	14.676

(a)

(b)
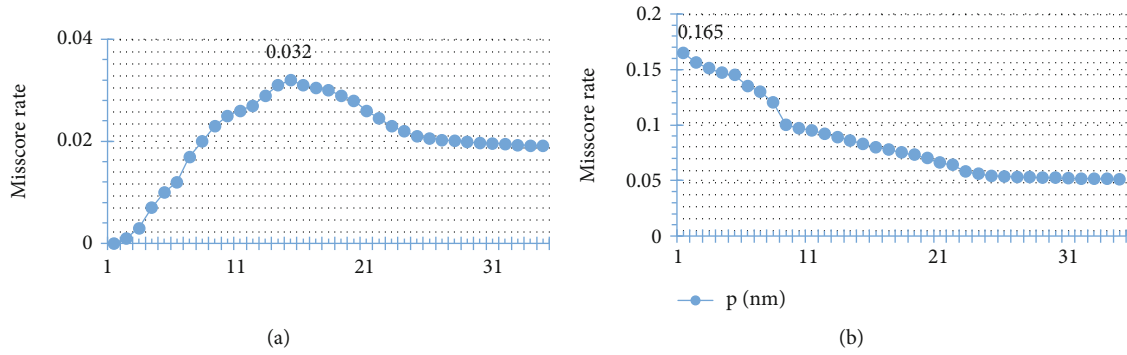
FIGURE 6: Spatial distribution of surface displacement caused by PFM detecting single-domain ferroelectric samples: (a) and (b) are the in-plane and out-of-plane displacement responses, respectively.

- 180 degree in-plane domain
- 180 degree out-of-plane domain
- 90 degree in-plane domain
- 90 degree out-of-plane domain
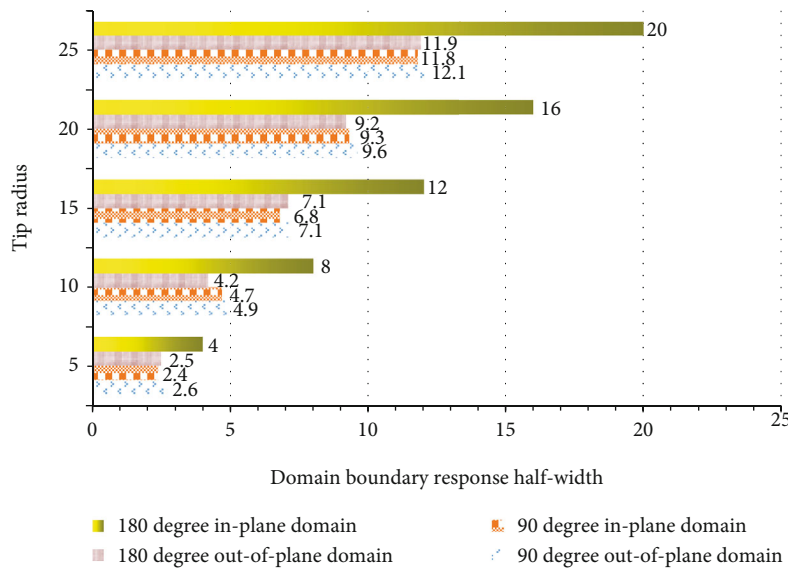
FIGURE 7: Comparison of the half-width of the domain boundary response of the 90-degree and 180-degree in-plane and out-of-plane domains of BaTiO$_3$ ceramics as a function of the tip radius.

The surface displacement of a single-domain ferroelectric sample is calculated by the nanoscale piezoelectric response displacement equation. Figure 6 shows the spatial distribution of the surface displacement caused by PFM detecting a single-domain ferroelectric sample. (a) shows the in-plane displacement response. (b) The figure shows the out-of-plane displacement response. From the results shown in the figure, it can be seen that the deformation displacement is highly concentrated and uneven. The out-of-plane displacement under the conductive SPM probe has a maximum value of 0.165 nm. As the distance from the conductive SPM probe is

farther, the out-of-plane displacement under the conductive SPM probe gradually decreases; while the in-plane displacement is farther away from the conductive SPM. In the process of the probe, it increases first and then decreases, with a maximum value of 0.032 nm at 16 nm away from the probe. The nanoscale piezoelectric deformation of single-domain ferroelectric samples will lay the foundation for the analysis of complex ferroelectric domain structures.

(2) Nanoscale piezoelectric deformation of complex ferroelectric domains

Ferroelectric materials usually contain complex microdomain structures, such as 180-degree electrical domains and 90-degree electrical structures. Due to this unbalanced microdomain structure, it is difficult to quantitatively analyze the piezoelectric response of nonferrous metal materials, which brings great difficulty to the PFM test and analysis work. Compared with a single nonferrous metal material, the polarization vector of a ferroelectric material is not uniformly distributed in the multiple fusion structure, but three nonuniform distribution dimensions are known, which determines the inherent piezoelectric coefficient of its tensor coefficient and also leads to the local intrinsic piezoelectric coefficient tensor which also presents a complex distribution. However, there is a uniformly distributed intrinsic piezoelectric coefficient tensor in a single electric domain region, and independent and uniform piezoelectric coefficient sensors are internally distributed in individual regions. This can be obtained by the spatial coordinates of the piezoelectric coefficient tensor in a single coordinate domain.

4.3. Domain Boundary Response Half-Width Analysis. In this experiment, the $BaTiO_3$ ceramic material was used as an example to compare the change of the half-width of the domain boundary response of 90-degree and 180-degree in-plane domains and out-of-plane domains with the tip radius. An angle of 90 degrees represents PFM vertical detection, and an angle of 180 degrees represents PFM lateral detection. It can be seen from Figure 7 that whether it is a 180-degree domain or a 90-degree domain, whether it is an in-plane or out-of-plane domain, the domain boundary broadening increases with the increase of the tip radius. It shows that the linear curves corresponding to the 180-degree domain and the 90-degree domain are very close, and the anisotropy of the in-plane polarization has little effect on the results of the PFM measurement of the domain boundary thickness. Under the same tip radius, the domain boundary response half-width of a 180-degree in-plane domain is larger. For example, when the tip radius is 25 nm, the corresponding domain boundary response half-width of a 180-degree out-of-plane domain is 11.9 nm, but 180 degrees the domain boundary response half-width corresponding to the in-plane domain is 20 nm, which means that the lateral PFM has a worse resolution than the vertical PFM.

5. Conclusion

The continuous improvement of the requirements of multifunctional materials has promoted the continuous development of functional composite materials and multifield coupling materials, making more and more materials have multifield coupling characteristics. The continuous development of nanotechnology has led to the emergence of various new SPM technologies, which have prompted everyone to study the multifield coupling behavior caused by various SPM probes. The quantitative analysis of experimental data is very important for the study of nanoscale ferroelectric materials. To this end, this paper established a nanoscale piezoelectric deformation method for analyzing complex ferroelectric domain structure, explained a series of PFM test results of nanoscale deformation of complex ferroelectric domain structure, and analyzed the nanoscale pressure of ferroelectric materials for PFM quantitative test. The electrical response provides a good guide plan and provides a reference for the experimental preparation of ferroelectric materials with strong electrical coupling performance, thereby promoting the application of nanoscale ferroelectric materials.

Data Availability

No data were used to support this study.

Conflicts of Interest

The authors declare that there is no conflict of interest with any financial organizations regarding the material reported in this manuscript.

Acknowledgments

References

[1] Z. Chen, J. Luo, I. Doudevski, S. Erten, and S. H. Kim, "Atomic force microscopy (AFM) analysis of an object larger and sharper than the AFM tip," *Microscopy and Microanalysis*, vol. 25, no. 5, pp. 1106–1111, 2019.

[2] Z. Kuerban, Z. Maiming, and A. Tusiyiti, "Analysis of land use change and driving force of Bole city based on remote sensing image," *Agricultural Biotechnology*, vol. 7, no. 4, pp. 233–239, 2018.

[3] C. Xing, L. Liu, Y. Cui, and D. Ding, "Analysis of base bitumen chemical composition and aging behaviors via atomic force microscopy-based infrared spectroscopy," *Fuel*, vol. 264, p. 116845, 2020.

[4] H. Al-Khalid, "Nano-scale properties of warm-modified bituminous binders determined with atomic force microscopy," *Road materials and pavement design: an international journal*, vol. 18, no. sup2, pp. 189–202, 2017.

[5] R. A. Capeli, F. M. Pontes, D. S. L. Pontes et al., "Nanoscale investigation of ferroelectric and piezoelectric properties in (Pb,Ca)TiO 3 thin films grown on LaNiO 3 /LaAlO 3 (100) and Pt/Si(111) using piezoresponse force microscopy," *Materials Letters*, vol. 196, pp. 64–68, 2017.

[6] F. Tao, "Nano-scale energy harvester of piezoelectric/piezomagnetic structures with torsional mode," *Mechanical Systems and Signal Processing*, vol. 112, no. 11, pp. 147–153, 2018.

[7] M. Jahanshahi, H. Ahmadi, and A. R. Khoei, "A hierarchical hyperelastic-based approach for multi-scale analysis of defective nano-materials," *Mechanics of Materials*, vol. 140, p. 103206, 2020.

[8] Y. Yang and K. Kim, "Size dependency of a ZnO nanorod-based piezoelectric nanogenerator evaluated by conductive atomic force microscopy. Taehan-Kŭmsok-Hakhoe-chi,"

Journal of the Korean Institute of Metals and Materials, vol. 58, no. 1, pp. 67–75, 2020.

[9] A. Quintero, P. Gergaud, J. M. Hartmann et al., "Analysis of Sn behavior during Ni/GeSn solid-state reaction by correlated X-ray diffraction, atomic force microscopy, and ex-situ/in-situ transmission electron microscopy," *ECS Transactions*, vol. 98, no. 5, pp. 365–375, 2020.

[10] H. Kobayashi, "Improvement of the SGS model by using a scale-similarity model based on the analysis of SGS force and SGS energy transfer," *International Journal of Heat and Fluid Flow*, vol. 72, no. 8, pp. 329–336, 2018.

[11] W. Jie and L. Yuehua, "Analysis on influencing factors of force-deformation of bridge pile foundation based on rock slope," *Boletin Tecnico/Technical Bulletin*, vol. 55, no. 9, pp. 722–727, 2017.

[12] S. Chen and J. Wang, "Analysis of interpolating element-free galerkin scaled boundary method for piezoelectric cracks," *Mechanical Engineering*, vol. 53, no. 6, pp. 53–59, 2017.

[13] T. Yang, S. L. Wang, and W. Liu, "Restoring-force model of modified RAC columns with silica fume and hybrid fiber," *Journal of Central South University*, vol. 24, no. 11, pp. 2674–2684, 2017.

[14] D. Seol, B. Kim, and Y. Kim, "Non-piezoelectric effects in piezoresponse force microscopy," *Current Applied Physics*, vol. 17, no. 5, pp. 661–674, 2017.

[15] J. Kwon and H. Cho, "Piezoelectric heterogeneity in collagen type I fibrils quantitatively characterized by piezoresponse force microscopy," *Engineering*, vol. 6, no. 12, pp. 6680–6689, 2020.

[16] M. H. Korayem, A. Alipour, and D. Younesian, "Vibration suppression of atomic-force microscopy cantilevers covered by a piezoelectric layer with tensile force," *Journal of Mechanical Science & Technology*, vol. 32, no. 9, pp. 4135–4144, 2018.

[17] Y. Wang, L. M. Vu, T. Lu et al., "Piezoelectric responses of mechanically exfoliated two-dimensional SnS2 nanosheets," *ACS Applied Materials & Interfaces*, vol. 12, no. 46, pp. 51662–51668, 2020.

[18] M. G. Ruppert, A. G. Fowler, M. Maroufi, and S. O. R. Moheimani, "On-chip dynamic mode atomic force microscopy: a silicon-on-insulator MEMS approach," *Journal of Microelectromechanical Systems*, vol. 26, no. 1, pp. 215–225, 2017.

[19] L. O. Otieno, T. T. Nguyen, S. J. Park, Y. J. Lee, and B. O. Alunda, "Feedforward compensation for hysteresis and dynamic behaviors of a high-speed atomic force microscope scanner," *Journal of the Korean Physical Society*, vol. 80, no. 4, pp. 325–336, 2022.

[20] S. C. Obilikpa, U. P. Onochie, C. S. Nweze, B. O. Kalu, and K. B. I. Anazodo, "Design and numerical simulation of a novel high-speed multi-degrees of freedom piezoelectric positioner," *Tamkang Journal of Science and Engineering*, vol. 24, no. 3, pp. 407–414, 2021.

Retraction

Retracted: Application of Nanoscaffold Material Combined with Exercise Rehabilitation Therapy in the Treatment of Athletes with Hip Injuries

Journal of Nanomaterials

This article has been retracted by Hindawi following an investigation undertaken by the publisher [1]. This investigation has uncovered evidence of one or more of the following indicators of systematic manipulation of the publication process:

(1) Discrepancies in scope
(2) Discrepancies in the description of the research reported
(3) Discrepancies between the availability of data and the research described
(4) Inappropriate citations
(5) Incoherent, meaningless and/or irrelevant content included in the article
(6) Peer-review manipulation

The presence of these indicators undermines our confidence in the integrity of the article's content and we cannot, therefore, vouch for its reliability. Please note that this notice is intended solely to alert readers that the content of this article is unreliable. We have not investigated whether authors were aware of or involved in the systematic manipulation of the publication process.

In addition, our investigation has also shown that one or more of the following human-subject reporting requirements has not been met in this article: ethical approval by an Institutional Review Board (IRB) committee or equivalent, patient/participant consent to participate, and/or agreement to publish patient/participant details (where relevant).

Wiley and Hindawi regrets that the usual quality checks did not identify these issues before publication and have since put additional measures in place to safeguard research integrity.

We wish to credit our own Research Integrity and Research Publishing teams and anonymous and named external researchers and research integrity experts for contributing to this investigation.

The corresponding author, as the representative of all authors, has been given the opportunity to register their agreement or disagreement to this retraction. We have kept a record of any response received.

References

[1] M. Xiang, F. Cao, J. Peng, and G. Bai, "Application of Nanoscaffold Material Combined with Exercise Rehabilitation Therapy in the Treatment of Athletes with Hip Injuries," *Journal of Nanomaterials*, vol. 2022, Article ID 6582511, 12 pages, 2022.

Research Article

Application of Nanoscaffold Material Combined with Exercise Rehabilitation Therapy in the Treatment of Athletes with Hip Injuries

Maojuan Xiang,[1] **Feng Cao,**[1] **Jiangui Peng,**[2] **and Guangbin Bai**[1]

[1]*Department of Physical Education, Xidian University, Xi'an, 710126 Shaanxi, China*
[2]*Physical Education and Teaching Department, Fujian Agricultural University, Fuzhou, 350002 Fujian, China*

Correspondence should be addressed to Guangbin Bai; baigb@xidian.edu.cn

A nanoscaffold is a porous scaffold. It injects antibiotics, cells, and polymer particles into damaged cavities in the form of injectables and forms hydrogels after the molecules self-assemble at the injection site. Sports rehabilitation is a new frontier field integrating sports, health, and medicine, also known as physical therapy. It is the use of various sports methods for the injured or disabled, so that they can fully recover their physical functions and spirits, and can make them reintegrate into society. It mainly studies the relationship between sports and health. Among the tissue engineering scaffolds used as seed cell carriers, nanomaterials are playing an increasingly important role in the study of joint injury and repair due to their unique effects such as cell adhesion and proliferation. The purpose of this paper is to study a reliable nanoscaffold material for the treatment of patients with hip injuries in athletes and to observe its actual effect in combination with sports rehabilitation therapy. In this paper, an electrospinning method was proposed to prepare nanoscaffold materials, and the nanoscaffold materials were applied to the exercise rehabilitation process of two groups of hip patients, and the data of the patients' rehabilitation were calculated. The results showed that the OD value of the cells in the exercise rehabilitation therapy using nanofiber scaffolds increased significantly, and the average daily growth rate of the OD value was 0.112. And the rehabilitation after 5 months was 19.8 points higher in hip range of motion score, 11.3 points higher in overall function score, and 6.2% lower in complication rate compared with ordinary exercise rehabilitation therapy. Therefore, it can be concluded that the therapy of the nanofiber scaffold material combined with exercise rehabilitation can more efficiently help patients with hip joint injury to recover, and the probability of complications is lower compared with the traditional exercise rehabilitation therapy.

1. Introduction

With the development of science and technology, nanomaterials have become important materials used in many fields, including the production of materials for medical equipment. Because athletes are too intense in the process of exercise, they often cause joint damage, especially for the hip joint. The hip joint is the most critical part of the movement of the lower limbs of the human body, and the treatment of the hip joint is particularly important. Although traditional

exercise rehabilitation therapy can help patients recover to a certain extent, its efficiency is not high, and it is more dependent on the exercise method of physician medical treatment, so it is necessary to propose a more efficient exercise rehabilitation therapy. In this way, hip patients can relieve hip pain and restore normal movement of the hip joint as soon as possible. With the advancement of the pathological research of hip joint injury, some progress has been made in the mechanism of treatment of hip joint injury. Many factors combined with exercise rehabilitation therapy

can promote the effect of treatment. However, these are only some single substances that promote treatment. How to integrate these accelerators to better improve the expression of nutritional factors, and whether there will be countermeasures, need to be explored and studied. In addition to expressing neurotrophic factors to repair hip joint injury, the treatment of hip joint injury can also regulate the expression of genes, which can play a role in repairing damaged tissue.

The innovation of this paper is that (1) an electrospinning method was proposed to prepare nanoscaffold materials, and the nanoscaffold materials were applied to the exercise rehabilitation process of two groups of hip patients, and the data of the patients' rehabilitation were calculated. (2) Using the control method, the OD value of the cells and the postoperative rehabilitation effect of the two groups of patients were compared. (3) Conduct in-depth theoretical research on the subject content, and analyze the research status of the subject-related content of this paper.

2. Related Work

Regarding the research on exercise rehabilitation therapy, many scholars in China have carried out related research. Among them, Buckthorpe et al. described how the properties of water support the functional recovery process after ACLR (anterior cruciate ligament reconstruction). Buckthorpe et al. recommended that if the main properties of hydrotherapy (density, hydrostatic pressure, buoyancy, and viscosity) are properly applied to rehabilitation practice, then it can be used to achieve the six main goals after ACLR, namely, (1) help reduce pain and swelling, (2) support gait recovery, (3) support the maintenance and/or development of cardiovascular health, (4) help accelerate and optimize movement pattern retraining, (5) allow earlier introduction of plyometric and strength training, and (6) support the relationship between session recovery and optimal load management [1]. Li et al.'s study employed an effective motion measurement method based on inertial sensor networks to measure children's motor abilities to verify the effectiveness of systemic CP rehabilitation. Li et al. proposed a new skeletal vector-based dynamic model to reconstruct the posture of children during exercise training to evaluate the effect of exercise rehabilitation. An Extended Kalman Filter (EKF) is used to fuse sensor signals to measure the motion of body parts, the accuracy of which is verified by the OptiTrack optical system. Li et al. used statistical analysis methods to analyze the motor function rehabilitation of SD children. The results are reassuring, and the lower extremity motor function of some children has been improved after rehabilitation training [2]. Flaherty provided research-based evidence to support the use of these modalities in pain management and to reduce the use of pain medications, including opioids. Mechanisms of action, applications, contraindications, and adverse effects of cryotherapy, pulsed electromagnetic field therapy, transcutaneous electrical nerve stimulation, and laser therapy are reviewed. It has been shown that adding one or more of these therapies to an anaesthetic pain management regimen can improve outcomes and reduce potential drug side effects [3]. Temkin-Greener et al. conducted data surveys based on methods such as minimal data set assessments, vital statistics, nursing home comparison websites, LTCFocus, and district health resource files. Findings suggest that facilities with for-profit missions and more therapists may be more motivated to maximize treatment utilization, even among the sickest residents [4]. They evaluated the therapeutic techniques and rehabilitation used by physical therapists in the treatment of patients with plantar fasciitis. Based on a retrospective review, Fraser et al. concluded that although plantar fasciitis is a common musculoskeletal disorder, a small proportion of patients with plantar fasciitis are treated by a physical therapist. Most patients evaluated by a physical therapist received manual therapy and supervised rehabilitation sessions as part of their care plan [5]. Murray et al.'s study systematically assessed the evidence supporting the efficacy, prescribing, and progression patterns of vestibular rehabilitation therapy (VRT) in concussion patients. Nine of the studies reported improved outcomes. However, level I evidence from only 1 study showed that when VRT (in combination with cervical treatment) was compared with usual care, heterogeneity in study type and outcome precluded meta-analysis. Eight studies used habituation and adaptation exercises, 9 studies used balance exercises, and there was a lack of standardization in prescribing and progression patterns. It was then concluded that there is currently limited evidence on the optimal prescribing and efficacy of VRT in patients with mTBI/concussion. The available evidence, though weak, shows promise in this population. This requires further high-level studies to evaluate the effect of VRT in patients with mTBI/concussion with vestibular and/or balance dysfunction [6]. The research of the above scholars has promoted the application of sports rehabilitation therapy to a certain extent and, at the same time, has done some practical tests, but most of them are based on theoretical research. And the joint nanoscaffold material for sports rehabilitation treatment of patients with hip joint injury is also less involved, so the research in this paper is of pioneering significance.

3. Exercise Therapy Based on Hip Joint Nanoscaffold Materials

3.1. Nanoscaffold Materials. Nanomaterials are materials that have at least one dimension in three-dimensional space on the nanometer scale (1-100 nm) or are the basic units built around them. This corresponds to a dense scale of about 10 to 1000 atoms. Nanomaterials are an important part of nanotechnology. Nanotechnology refers to the general term for manufacturing technologies whose processing precision reaches the limit value of one order of processing size, and its crystal lattice spacing is about 1 to 100 nanometers [7, 8].

Since the advent of nanoparticle materials in the 1970s, the development process can be divided into three stages in terms of research connotation and characteristics. The first stage (before 1990) mainly explored the preparation of nanoparticle powders or synthetic blocks of various materials by various methods in the laboratory, studied the methods for evaluating and characterization, and explored the special properties of nanomaterials that are different

from ordinary materials. The research objects are generally limited to single materials and single-phase materials, which are usually referred to as nanocrystalline or nanophase materials internationally. The second stage (1990~1994). The focus of attention is how to use the physical and chemical properties of nanomaterials to design nanocomposite materials. The synthesis and physical property exploration of composite materials once became the dominant direction of nanomaterial research. The third stage (1994-present). Nanoassembly systems and artificially assembled nanostructured material systems are becoming a new hotspot in nanomaterial research. Internationally, such materials are called nanoassembled material systems or nanoscale patterned materials. Its basic connotation is that nanoparticles and their nanowires and tubes are the basic units assembled in one-dimensional, two-dimensional, and three-dimensional spaces to form a system with nanostructures.

Nanomaterials can be divided into nanofilms, nanopowders, nanofibers, nanoblocks, and nanoceramics according to their material properties, as shown in Figure 1.

Nanostructure is a new system constructed or constructed according to certain rules on the basis of nanoscale material units. It includes a nanoarray system, mesoporous assembly system, and thin-film mosaic system. Research on nanoarray systems has focused on binary systems formed by the alignment of metal nanoparticles or semiconductor nanoparticles on an insulating substrate. The nanoparticle and mesoporous solid assembly system has some new effects due to the characteristics of the particle itself and the coupling with the matrix at the interface.

Nanomaterials can be divided into nanocomputers, nanosensors, nanobiomaterials, nanosemiconductor materials, and other fields according to their application scope, as shown in Figure 2.

Nanobiomaterials can also be divided into two categories, one is the nanomaterials that are suitable for the interior of the organism, such as various nanosensors, which are suitable for disease monitoring, early diagnosis, and later treatment. These nanoscale mechanical systems can quickly identify the location of the disease and can accurately guide the drug into the diseased location without damaging other normal body parts or clearing the deposits in fat and removing the thrombus in the cardiovascular and cerebrovascular. At the same time, they can also be used to kill viruses and eliminate cancer cells [9, 10].

The preparation methods of nanomaterials include (1) the evaporation condensation method under inert gas. It is usually formed by high pressure forming of particles with a particle size of 1-100 nm with a clean surface, and nanoceramics also need to be sintered. A variety of nanosolid materials has been successfully developed abroad by the above-mentioned inert gas evaporation and vacuum in situ pressurization methods, including metals and alloys, ceramics, ionic crystals, amorphous, and semiconductor nanosolid materials. This method has also been successfully used in China to make nanomaterials such as metals, semiconductors, and ceramics. (2) Chemical method: (i) hydrothermal methods, including hydrothermal precipitation, synthesis, decomposition, and crystallization, are suitable for the prep-

aration of nanooxides; (ii) hydrolysis methods include sol-gel method, solvent volatilization decomposition method, latex method, and evaporation separation method. (3) Comprehensive method. A preparation method is formed by combining the physical vapor method and chemical deposition method. Other methods generally include ball milling and jet processing.

A nanoscaffold is a porous scaffold. It injects antibiotics, cells, and polymer particles into damaged cavities in the form of injectables and forms hydrogels after the molecules self-assemble at the injection site. Figure 3 shows the use process of the nanoscaffold material. It is now believed that this type of fine particle can be assembled by combining traditional controlled release systems with surface engineering and self-organization via growth factors and other signaling molecules. Superior biomimetic scaffolds, especially biopolymer self-assembled hydrogels, are formed for this purpose. Nanoscaffolds have great prospects for drug control and regenerative medicine [11, 12].

Nanotechnology basic theoretical research and new material development and other applied research have developed rapidly and have been widely used in traditional materials, medical equipment, electronic equipment, coatings, and other industries. With the increasing investment in nanotechnology application research in various countries, the process of industrialization of new nanomaterials will be greatly accelerated, and the market size will increase in volume. Several products such as nanocalcium carbonate, nanozinc oxide, and nanosilicon oxide in nanopowder materials have formed a certain market scale. Nanopowder widely used nanoceramic materials, nanotextile materials, nanomodified coatings, and other materials have also been successfully developed, and industrial production has been initially realized. The application of nanopowder particles in medical diagnostic preparations and microelectronics is shifting from experimental research results to industrialized production of products.

3.2. Exercise Rehabilitation Therapy. Sports rehabilitation is a new frontier field integrating sports, health, and medicine, and it mainly studies the relationship between sports and health. Particularly for some adult hip bones, the damage is mostly caused by high-energy violence. This kind of high-energy violence also often causes damage to the distal articular surface of the hip bone and the surrounding tissues, ligaments, skin and soft tissues, nerves, blood vessels, and other injuries. Fractures are prone to redisplacement after manual reduction, and it is difficult to restore the integrity of the articular surface. External fixation of the elbow joint is required in the early stage after manual reduction, which may easily lead to the loss of elbow joint function. Strong internal fixation provides a prerequisite for the early postoperative functional rehabilitation training of patients [13, 14]. Immobilization of the affected limb for too long can easily lead to obstruction of lymphatic and venous return, fibrin deposition, and serous fibrous exudation in the tissues around the joint. This can cause fibrous adhesions, edema of the joint capsule and surrounding muscles, fibrosis, and
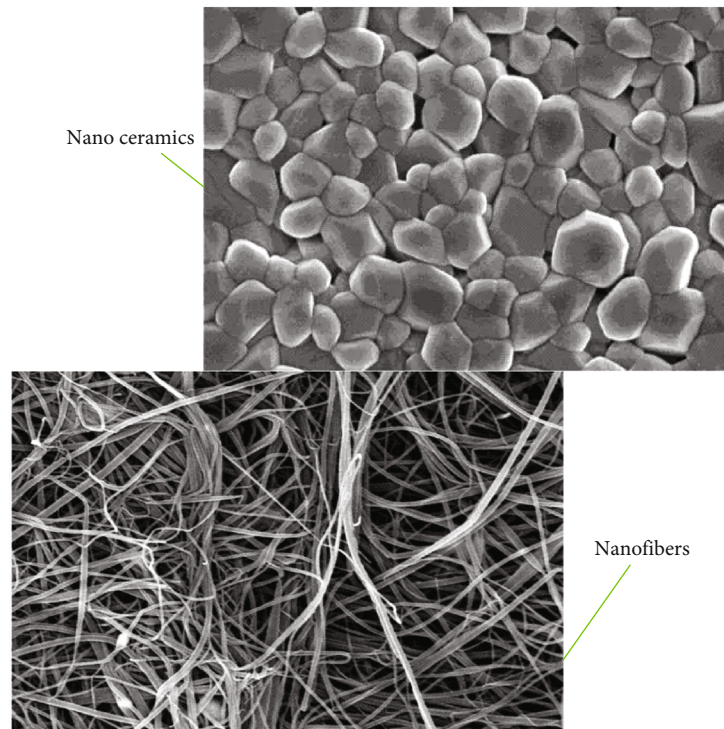
Figure 1: Nanomaterials.
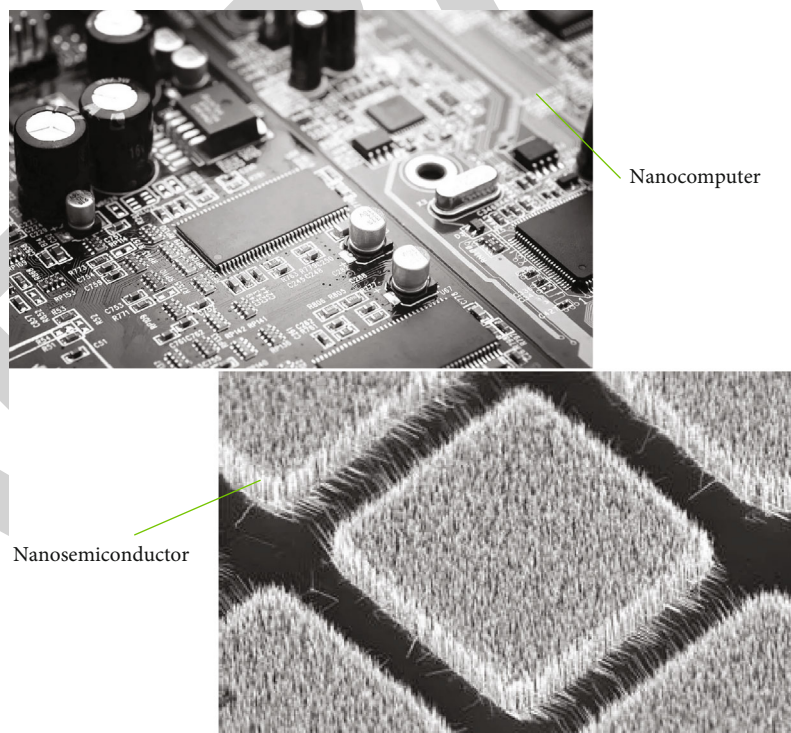
Figure 2: Applications of nanomaterials.

contractures, resulting in impaired elbow mobility, resulting in elbow stiffness.

The soft tissues around the hip joint, such as fascia, muscle bonds, and muscles, determine the high lateral stability of the hip joint. However, the sagittal flexion and extension range of motion is also larger, and while improving its flexion and extension range of motion, it is also necessary to pay attention to strengthening its lateral stability.
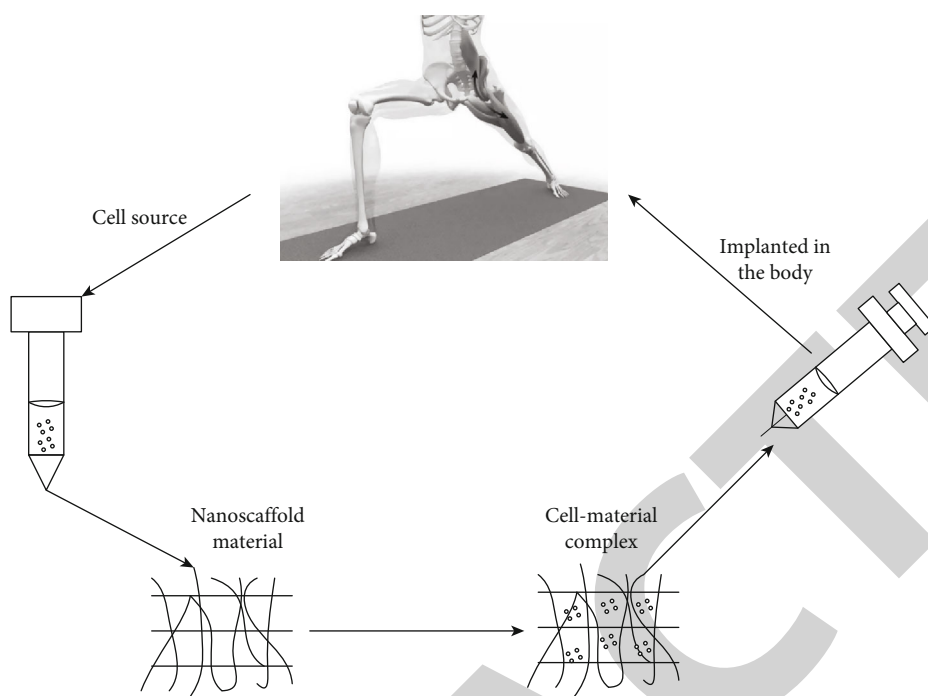
Figure 3: Application process of nanoscaffold materials.

Sports rehabilitation therapy: 3-5 days after surgery, perform leg movement, lift, and leg contraction training. After 2-4 weeks, begin to perform hip flexion and extension exercises. After 6-8 weeks, traditional functional rehabilitation training with muscle strength training for the affected limb is the main method.

Commonly used traditional sports rehabilitation equipment includes training beds, stationary bicycles, and suspension frames, as shown in Figure 4.

Table 1 shows the safety assessment scale of sports rehabilitation for fracture patients. Evaluate the patient's rehabilitation exercise score, and formulate a personalized rehabilitation prescription based on the score. The table has a total score of 100. Rehabilitation exercise is safer for more than 60 points; 40-60 minutes of rehabilitation exercise should be cautious and closely observed; 0-40 points are mainly muscle isometric contractions, and early isotonic contractions are not suitable.

3.3. Patients with Hip Injury. With the aging of the population, the incidence of hip diseases in the elderly will also increase significantly, such as femoral head necrosis, fractures, and femoral arthritis. The pain and joint dysfunction caused by it have become an important factor affecting the quality of life in the elderly. At the same time, due to trauma and improper lifestyle, the incidence of hip disease among young people has increased. Particularly for athletes who have been doing leg exercises for a long time, the use of the hip joint is more frequent, and various injuries of the hip joint are more likely to occur [15, 16]. The emergence

of these hip diseases makes more and more patients have to accept hip treatment. The specific parts of the hip joint are shown in Figure 5.

The main causes of hip injury are trauma; vascular plunger, deformity, and tumor of the hip; hip compression; hip inflammation; and others such as deformity, demyelinating degenerative diseases. The pathological process mainly includes primary injury and secondary injury. The final result will have a large negative impact on the physiological function of the hip joint due to neuronal and glial cell death, axonal degeneration and formation of myelin sheaths, cystic cavities, etc. The specific situation is shown in Figure 6.

Common treatments for hip injuries include decompression therapy with surgery or prevent the use of large doses of drugs. This method has a neuroprotective effect on acute hip injury. Expression of factors that inhibit axon regeneration can be blocked. There is rehabilitation through exercise, or injection of neurotrophic factors to repair damaged myelin. At present, the use of nanoscaffold materials combined with exercise rehabilitation therapy to treat hip joint injury is a new hot research direction [17, 18]. Table 2 shows the evaluation method of functional rehabilitation after hip injury.

At present, the mechanism of bone marrow mesenchymal exercise rehabilitation therapy in the treatment of hip injury is not very clear. It is known that the characteristics of bone marrow mesenchymal cells are as follows: self-replication ability, asymmetric division ability to differentiate into other cells, surface markers with primitive cells, and homing. With these characteristics, the treatment of hip joint injury can have better results by selecting the appropriate exercise rehabilitation therapy approach and

(a) Training bed

(b) Stationary bike

(c) Suspension frame

FIGURE 4: Commonly used sports rehabilitation equipment.

TABLE 1: Exercise rehabilitation safety evaluation form.

Score	Fixed reliability	Integrity of soft tissue
60 to 80	Strong immobilization for immediate weight bearing	——————
40 to 60	Postoperatively with the help of	Reasonable surgical approach (less trauma)
20 to 40	Brace function active movement	The ligament solution is fixed and repaired firmly
1 to 20	Can resist body gravity but not resistance	The ligament of the joint is sutured, and the tension is partially resisted during the operation
0 marks	To maintain alignment, external fixation, traction, etc.	The ligaments of the joint are sutured, and the tension cannot be resisted during the operation

the appropriate time. The pathological mechanism of hip joint injury is mainly the damage of the hip joint barrier caused by the hip joint injury, which leads to the entry of some bacteria into the hip joint injury site. And because of cytotoxicity, ischemia and hypoxia-induced apoptosis are initiated.

The biggest problem with sports rehabilitation therapy for hip injury lock is that the details of its operation are not fully understood. According to the current research, it may be derived from the following aspects: exercise rehabilitation therapy can migrate to the injured site autonomously and differentiate into nerve cells; the mediating role of exercise rehabilitation therapy; exercise rehabilitation therapy can inhibit the activation of certain apoptosis factors. However, the specific causal mechanism remains to be studied.

The research trend of exercise rehabilitation therapy in the treatment of hip injuries will develop towards the synergistic effect of multiple factors. That is to say, the effect of simple exercise rehabilitation therapy is not ideal, and various promoting factors need to be integrated, and the target gene that can promote axonal repair should be transfected into the hip joint. Although there are still many problems to be solved, with the deepening of research, the details of sports rehabilitation therapy for hip injuries will eventually be fully understood. At that time, more treatment methods will also be applied in the clinic, and by combining various methods and taking advantage of their advantages, a convenient, stable, and less traumatic treatment method will surely be found, so as to overcome the problem of repairing hip joint injury [19, 20].

(a)

(b)
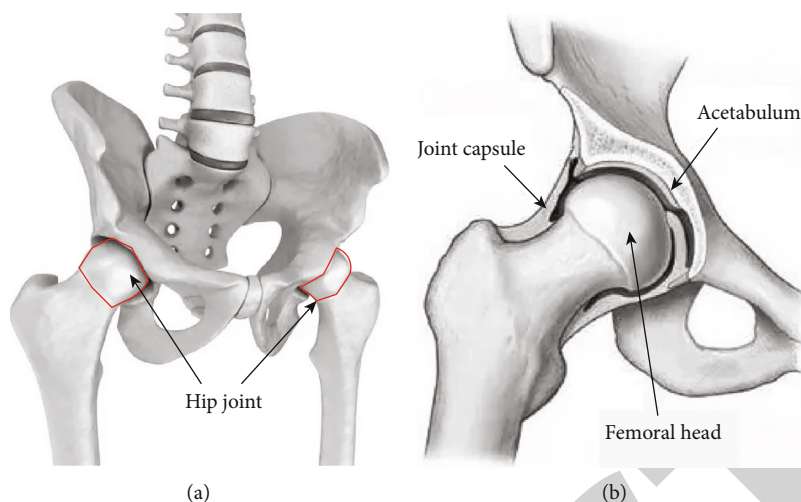
Figure 5: Hip joint.
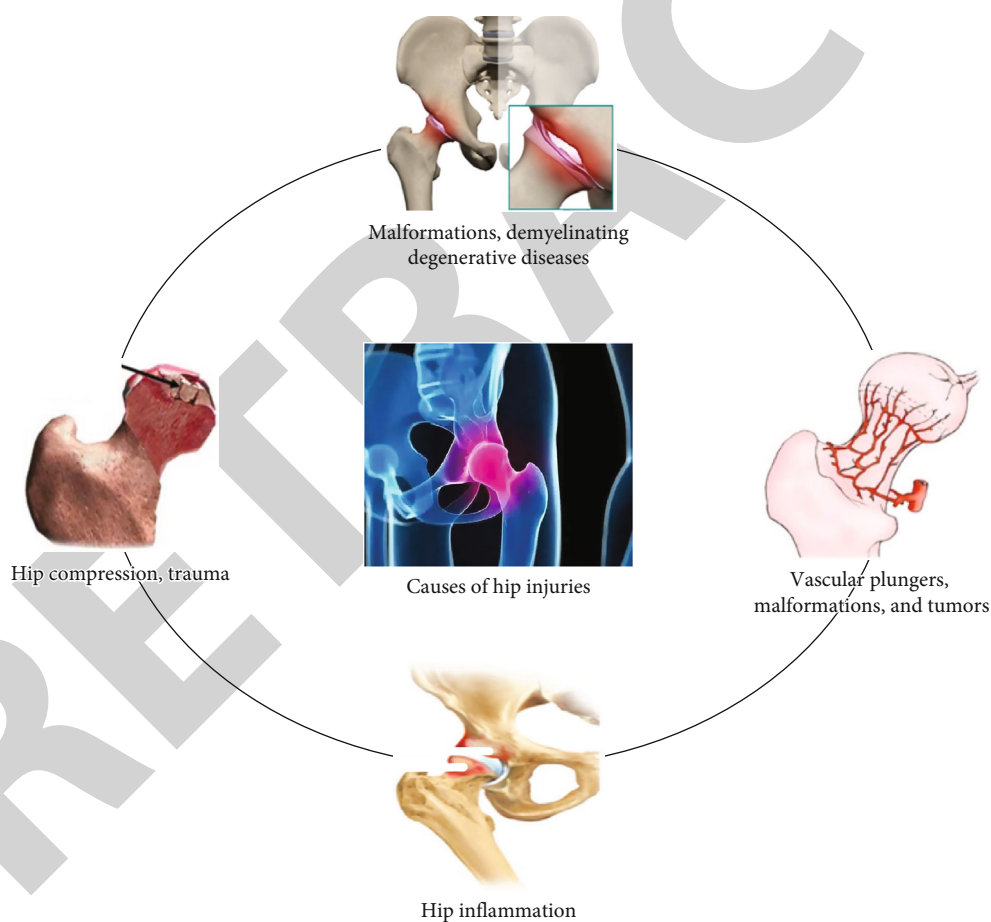
Figure 6: Causes of hip injuries.

4. Test of the Assisted Rehabilitation Effect of Nanoscaffolds

4.1. Exercise Rehabilitation Efficacy Algorithm. In order to facilitate the calculation of the movement process, this paper establishes the coordinate system of the lower limbs of the human body as shown in Figure 7. The hip joint is the key driving part of the movement of the entire lower limb, which is the origin of the coordinate system, and the hip joint and the knee joint are regarded as articulations.

For the motion process of the thigh system, set the angle in the horizontal direction and its corresponding angular

TABLE 2: Hip joint function evaluation table.

Flexion	Pain and dysfunction	Score
Loss of extension < 15°, flexion > 130°	No pain and functional impairment	Excellent
Loss of extension < 30°, flexion > 120°	Mild functional impairment	Good
Loss of extension < 40°, flexion > 90°	Pain with activity, moderate functional impairment	Generally
Loss of extension < 40°, flexion > 90°	Frequent pain, severe functional impairment	Not good
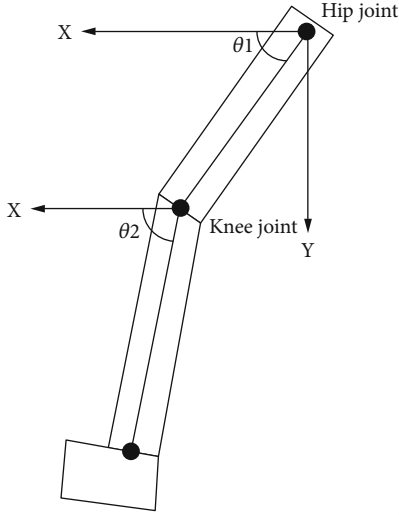
FIGURE 7: Human lower limb coordinate system.

velocity and angular acceleration to x_{1i}, x_{2i}, and x_{3i}; then, the motion equation is

$$
\begin{aligned}
x_{1i}(k) &= \theta_1, \\
x_{2i}(k) &= \dot{\theta}_1 = w_1, \\
x_{3i}(k) &= \ddot{\theta}_1 = \dot{w}_1 = \beta_1.
\end{aligned}
\tag{1}
$$

Among it, k represents the kth motion situation.

$$
\begin{cases}
\theta_1(k+1) = \theta_1(k) + w_1(k)t_s, \\
w_1(k+1) = w_1(k) + \beta_1(k)t_s, \\
\beta_1(k+1) = \beta_1(k).
\end{cases}
\tag{2}
$$

The equation of state can be obtained:

$$
\begin{cases}
x_{1i}(k+1) = x_{1i}(k) + x_{2i}(k)t_s, \\
x_{2i}(k+1) = x_{2i}(k) + x_{3i}(k)t_s, \\
x_{3i}(k+1) = x_{3i}(k).
\end{cases}
\tag{3}
$$

Output equation:

$$
\begin{cases}
y_{1i}(k) = g \cos x_{1i}(k) + x_{3i}(k)d_1, \\
y_{2i}(k) = -g \sin x_{1i}(k) - x_{2i}{}^2(k)d_1.
\end{cases}
\tag{4}
$$

In the equation, g is the acceleration of gravity.

Similarly, for the movement process of the calf system, let its variable be x_{12}, x_{22}, and x_{32}.

$$
\begin{aligned}
x_{12}(k) &= \theta_2, \\
x_{22}(k) &= \dot{\theta}_2 = w_2, \\
x_{32}(k) &= \ddot{\theta}_2 = \dot{w}_2 = \beta_2.
\end{aligned}
\tag{5}
$$

The equation of state is

$$
\begin{cases}
x_{12}(k+1) = x_{12}(k) + x_{22}(k)t_s, \\
x_{22}(k+1) = x_{22}(k) + x_{32}(k)t_s, \\
x_{32}(k+1) = x_{32}(k).
\end{cases}
\tag{6}
$$

Output equation:

$$
\begin{cases}
y_3(k) = g \cos x_{1i}(k) + x_{3i}(k)(l + d_2), \\
y_4(k) = -g \sin x_{1i}(k) - x_{2i}{}^2(k)(l + d_2).
\end{cases}
\tag{7}
$$

According to the Kalman filter principle, the Kalman filter is a linear minimum variance filtering algorithm. By making certain assumptions about the statistical characteristics of the input signal and noise, the state space method is used to describe the system. According to the current measured value and the estimated value of the previous moment, the signal can be processed in real time through recursive calculation. It can not only process stationary random signals but also process multidimensional and nonstationary random signals. It is an important method for solving state estimation and filtering problems in various dynamic systems. The nonlinear state-space model is obtained:

$$
\begin{aligned}
X_k &= f(X_{k-1}, k-1) + W_{k-1}, \\
Z_k &= h(X_k, k) + V_k.
\end{aligned}
\tag{8}
$$

Among them, X_k is the multidimensional state set, Z_k is the multidimensional observation set, and W_k and V_k are the noise state set and observation set. h represents a nonlinear function.

Expand h by Taylor series, leaving only the first-order term, then:

$$
Z_k = h(\widehat{X}_{k,k-1}, k) + \left.\frac{\partial h}{\partial X_k}\right|_{\widehat{X}_{k,k-1}} (X_k - \widehat{X}_{k,k-1}) + V_k.
\tag{9}
$$
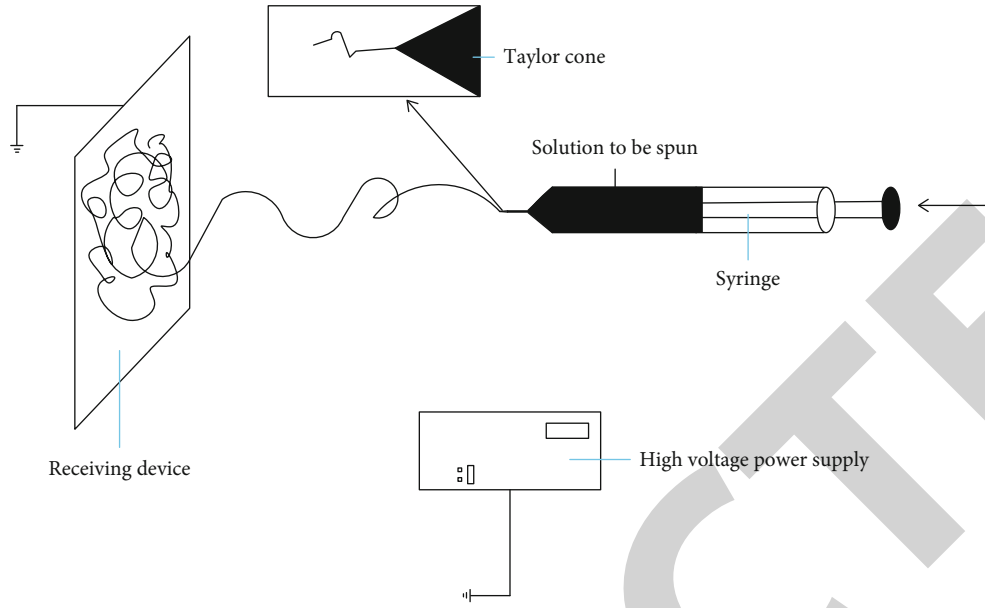
Figure 8: Electrospinning method.

Assume:

$$\left.\frac{\partial h}{\partial X_k}\right|_{\widehat{X}_{k,k-1}} = H_k,$$

$$y_k = h\left(\widehat{X}_{k,k-1}, k\right) - \left.\frac{\partial h}{\partial X_k}\right|_{\widehat{X}_{k,k-1}} \widehat{X}_{k,k-1}. \tag{10}$$

Then, the equation can be observed as

$$Z_k = H_k X_k + y_k + V_k. \tag{11}$$

The status update method is

$$\widehat{X}_{k,k-1} = f\left(\widehat{X}_{k,k-1}, k-1\right). \tag{12}$$

Observe the update method:

$$K_k = P_{k,k-1} H_k^T \left[H_k P_{k,k-1}\right]^{-1},$$

$$P_{k,k} = \left[I - K_k H_k\right] P_{k,k-1}. \tag{13}$$

In the equation, P represents the variance and $\widehat{X}_{k,k-1}$ represents the filtered mean.

A signal is the carrier of information, a function of time or space that transmits information. In the process of signal detection and transmission, it is inevitable to be disturbed by external environment and internal noise. In order to obtain the desired signal, it is necessary to filter the signal and suppress other signals to obtain the desired signal. Filtering refers to a method or technique of extracting a specific desired signal from an interfering signal. Different filtering methods and means are selected according to the nature of the signal, the criterion of estimation, and the way of observing the information.

Table 3: Main experimental instruments.

Laboratory apparatus	Type
SEM	Zeiss AURIGA FIB, DE
TEM	Zeiss, DE
FTIR	Perkin-Elmer, USA
Universal tensile testing machine	Instron USA

4.2. Preparation of Nanoscaffold Materials. The research and development of nanoscaffold materials have been practical for a period of time, and its preparation methods have also begun to diversify. Among them, the typical preparation method of nanoscaffold materials is electrospinning. Electrospinning is a special form of electrostatic atomization of polymer fluids. At this time, the atomized and split substances are not tiny droplets, but tiny jets of polymer, which can travel a considerable distance and eventually solidify into fibers. Electrospinning is a special fiber manufacturing process in which a polymer solution or melt is jet-spun in a strong electric field. Under the action of the electric field, the droplet at the needle will change from spherical to conical (namely "Taylor cone"), and fiber filaments are obtained by extending from the tip of the cone. In this way, polymer filaments with nanometer diameters can be produced. The method is specifically shown in Figure 8.

Electrospinning nanofibrous materials can effectively control the fine structure of fibers. Combining substances with low surface energy, materials with superhydrophobic properties can be obtained. It has high specific surface area and porosity, which can increase the action area between the sensing material and the detected object and can greatly improve the performance of the sensor.

The main process of electrospinning is dispersed and continuous phases that can be prepared separately. In order to
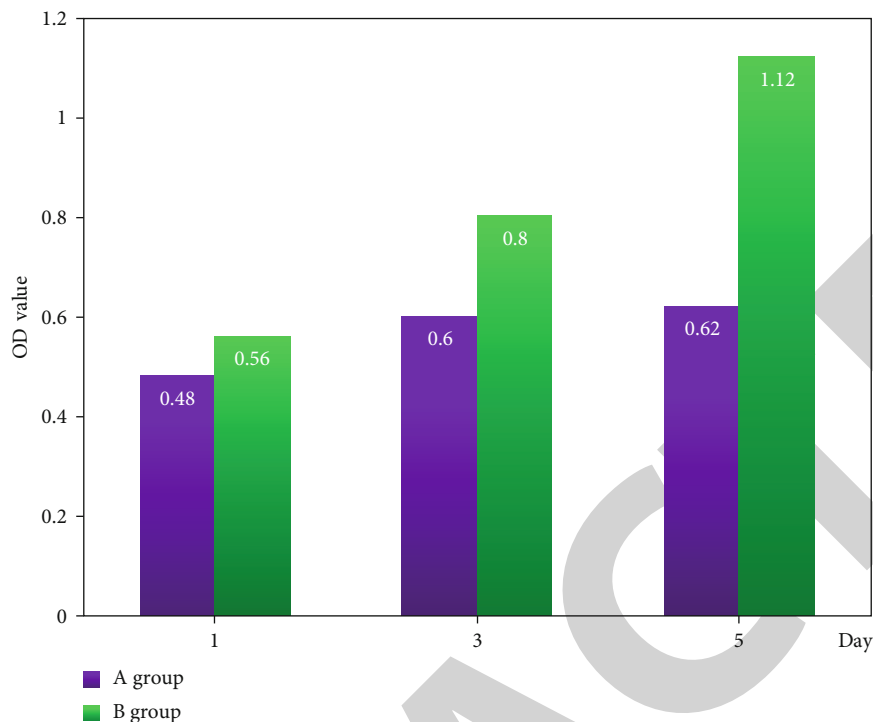
Figure 9: Hip joint cell proliferation.

form the desired solution state, the solution can be configured. The resulting solution is subjected to an electrospinning process under specific conditions, obtaining functional nanofibrous scaffolds.

Cell growth is affected by the surrounding environment and responds differently to different substrate environments. The ultrasmall size of the nanoscaffolds promoted cell adhesion but limited cell infiltration. In this experiment, microfibers were introduced into nanofibers to prepare micronanofiber scaffolds, combining the advantages of microfibers and nanofibers [21].

4.3. Testing through Experiments. In this experiment, 50 patients with hip joint injury from two groups A and B were selected for exercise rehabilitation therapy after surgery. Among them, group A was ordinary exercise rehabilitation therapy, and group B was nanofiber scaffold combined with exercise rehabilitation therapy. Other parameters are as follows: the voltage is 17 kV, the drum speed is 300 r/min, and the selected experimental instruments are shown in Table 3.

4.4. Experimental Analysis and Results. According to the observation of the SEM microscope, the proliferation of hip joint cells in the two groups of patients was obtained, as shown in Figure 9.

As can be seen from Figure 9, the OD value of group A was 0.48 on the first day, the OD value of group B was 0.56, the OD value of group A on the second day was 0.6, and the OD value of group B was 0.8. On the third day, the OD value of group A was 0.62, and the OD value

Table 4: Hip joint function recovery.

Item	A group	B group
Knee range of motion	73.8	93.6
General hip function	85	96.3
Knee complication ratio	16.1%	9.9%

of group B was 1.12. The average growth rate of OD value in group B was 0.112 per day, while that in group A was only 0.028. Therefore, it can be seen that the cell proliferation ability of group B was significantly higher than that of group A.

According to the observation, the hip function recovery of the two groups of patients after 5 months is shown in Table 4.

As can be seen from Table 4, compared with the exercise rehabilitation of the two groups of hip patients after 5 months, the hip mobility score of group A was 73.8. Group B was 93.6, and group B was 19.8 points higher than group A. Group A's overall hip function score was 85, group B was 96.3 points, and group B was 11.3 points higher than group A. The complication probability in group A was 16.1%, while group B was only 9.9%, and group B was 6.2% lower than group A. Therefore, it can be concluded that the therapy of the nanofiber scaffold material combined with exercise rehabilitation can more efficiently help patients with hip joint injury to recover, and the probability of complications is lower compared with the traditional exercise rehabilitation therapy.

5. Discussion

In the experimental process of this study, although many valuable data have been obtained, there are still some problems that need to be further explored. Therefore, we can also explore from the following aspects:

(1) In the process of preparing nanoscaffold materials by electrospinning, we can try to optimize the process parameters to prepare bimodal fiber scaffolds with shell-core structure

(2) In the process of electrospinning, try to mix electrospinning PCL with good mechanical properties and biological macromolecular proteins (such as silk fibroin) and growth factors (such as MGF) with biological functions. One-step methods can then be utilized in order to prepare excellent biomaterials with special functions

(3) In the comparison of the two groups of experiments, the amount of data detection is relatively small, and the frequency of data collection should be increased to make the data more reliable

6. Conclusions

In the abstract, this paper firstly summarizes the overall content of the full text, then introduces the background of exercise rehabilitation therapy in the introduction, introduces the role of nanomaterials, and summarizes the innovations of this paper. In the related work section, some related studies are listed to understand the current situation of the related content studied in this paper. Then, in the theoretical research part, the definition, characteristics, classification, and application fields of nanomaterials are firstly introduced, and then, the related content of sports rehabilitation therapy is introduced, including its concept, specific therapy, training equipment, and evaluation method. Then, the related content of hip joint injury is introduced. Finally, an electrospinning method was proposed to prepare nanoscaffold materials, and the nanoscaffold materials were applied to the exercise rehabilitation process of two groups of hip joint patients, and the data of the patients' rehabilitation were calculated. It is concluded that the therapy of the nanofiber scaffold material combined with exercise rehabilitation can more efficiently help patients with hip joint injury to recover, and the probability of complications is lower compared with the traditional exercise rehabilitation therapy.

Data Availability

No data were used to support this study.

Disclosure

We confirm that the content of the manuscript has not been published or submitted for publication elsewhere.

Conflicts of Interest

There are no potential competing interests in our paper.

Authors' Contributions

All authors have seen the manuscript and approved to submit to your journal.

Acknowledgments

References

[1] B. Matthew, "Benefits and use of aquatic therapy during rehabilitation after ACL reconstruction -a clinical commentary," *International Journal of Sports Physical Therapy*, vol. 14, no. 6, pp. 978–993, 2019.

[2] J. Li, Z. Wang, S. Qiu, X. Shi, and B. Liang, "Using body sensor network to measure the effect of rehabilitation therapy on improvement of lower limb motor function in children with spastic diplegia," *IEEE Transactions on Instrumentation and Measurement*, vol. 69, no. 11, pp. 9215–9227, 2020.

[3] M. J. Flaherty, "Rehabilitation therapy in perioperative pain management," *Veterinary Clinics of North America: Small Animal Practice*, vol. 49, no. 6, pp. 1143–1156, 2019.

[4] A. Tg, A. Tl, B. Tc, and A. Sc, "Rehabilitation therapy for nursing home residents at the end-of-life," *Journal of the American Medical Directors Association*, vol. 20, no. 4, pp. 476–480.e1, 2019.

[5] J. J. Fraser, N. R. Glaviano, and J. Hertel, "Utilization of physical therapy intervention among patients with plantar fasciitis in the United States," *The Journal of Orthopaedic and Sports Physical Therapy*, vol. 47, no. 2, pp. 49–55, 2017.

[6] D. A. Murray, D. Meldrum, and O. Lennon, "Can vestibular rehabilitation exercises help patients with concussion? A systematic review of efficacy, prescription and progression patterns," *British Journal of Sports Medicine*, vol. 51, no. 5, pp. 442–451, 2017.

[7] A. V. Vasiliadis, A. Maris, A. Tsoupli, and A. Saridis, "Rehabilitation exercise program after surgical treatment of quadriceps tendon rupture: a case report," *Physical Therapy in Sport*, vol. 39, no. 5, pp. 82–89, 2019.

[8] E. H. Senorski, K. Samuelsson, and C. Thomeé, "Return to knee-strenuous sport after anterior cruciate ligament reconstruction: a report from a rehabilitation outcome registry of patient characteristics," *Arthroscopy*, vol. 25, no. 5, pp. 1364–1374, 2017.

[9] W. Y. Wong, Y. L. Ng, P. W. Fung, K. M. Mok, P. S. H. Yung, and K. M. Chan, "Comparison of treatment effects on lateral epicondylitis between acupuncture and extracorporeal shockwave therapy," *Asia-Pacific Journal of Sports Medicine, Arthroscopy, Rehabilitation and Technology*, vol. 7, no. C, pp. 21–26, 2017.

[10] A. M. Briggs and K. E. Dreinhfer, "Rehabilitation 2030: a call to action relevant to improving musculoskeletal health care

Hindawi

Research Article

Heterogeneous Deformation and Microstructure of TWIP Steel under Damage and Fracture

Fuyuan Dong,[1,2] **Mingxu Zhang,**[1] **and Junfeng Hou** [1,2]

[1]*School of Materials Science and Engineering, North Minzu University, Yinchuan, 750021 Ningxia, China*
[2]*Key Laboratory of Powders & Advanced Ceramics, North Minzu University, Yinchuan 750021, Ningxia, China*

Correspondence should be addressed to Junfeng Hou; 2015030@nmu.edu.cn

Materials have always been a research hotspot in the chemical industry. With the continuous development of technology, the iteration of materials research has become faster and faster. Steel has strong toughness and tensile strength, and it is widely used in construction and other fields. However, one problem that cannot be avoided is the fracture of steel. The purpose of this paper is to analyze the damage and fracture of TWIP steel. In this paper, a microstructure characterization calculation method based on TWIP is proposed, which can effectively analyze the fracture surface, and for the performance of TWIP steel, this paper uses two different TWIP steels for comparative analysis. The results of this paper show that the HDI hardening rate of 22Mn0.6C TWIP steel is higher than that of 22Mn0.6C3Al TWIP steel.

1. Introduction

Twin-induced plasticity steel, also known as TWIP, is a new second-generation high-strength transportation steel developed in China. TWIP steel has attracted extensive attention in the automotive and other industries due to its comprehensive mechanical properties such as high strength, high plasticity, and high strain hardening ability. TWIP steel is usually a relatively stable single-phase austenite structure under the condition of no external load at room temperature. When plastic deformation occurs under the applied load, due to the formation of deformation twins, it will extend without necking, resulting in relatively excellent mechanical properties.

As one of the high-strength steels for automobiles, TWIP steel enjoys high strength, high plasticity, and high strain hardenability, as well as high energy absorption and excellent formability. The good comprehensive mechanical properties of TWIP steel show considerable development potential in the exploration of a new generation of automotive lightweight technology, which has attracted extensive attention in the steel and automotive industries. However, TWIP steel is prone to hydrogen-induced cracking, which is intergranular brittle fracture behavior under low stress.

The occurrence of this dangerous brittle fracture makes the service safety of TWIP steel face an unprecedented challenge, which not only restricts its development but also becomes a bottleneck for its wide application. Therefore, it is necessary to conduct microscopic research on TWIP steel.

The innovations of this paper are as follows: this paper takes 22Mn0.6C and 22Mn0.6C3Al TWIP steels as the research objects; based on the stress distribution relationship, through the loading-unloading-reloading tensile test, the evolution of the stress induced by heterogeneous deformation in the material is quantitatively investigated. The study found that the heterogeneous deformation-induced stress of the two steels increased with the increase of strain, and the contribution of deformation twins to the heterogeneous deformation-induced stress in TWIP steel was limited. Further microstructural analysis also confirmed that deformation twins hinder the geometrically necessary dislocation density more weakly than grain boundaries, so the heterogeneous deformation around the deformation twins is smaller.

2. Related Work

At present, universities and enterprises at home and abroad have developed various TWIP steels with different

compositions and have conducted in-depth research on their processing technology, microstructure, and mechanical properties. The plastic deformation of TWIP steel involves a variety of deformation mechanisms (dislocation slip, deformation twinning, and martensitic transformation), and there are complex coupling effects between different mechanisms, so the source of its excellent mechanical properties has been controversial. Peng et al. believe that stacking fault dynamics is rarely covered by scholars. So they investigated new physical insights into the dynamics of stacking faults in TWIP steels [1]. In order to overcome the relative sheet formability problem of TWIP steel, Kim et al. used TWIP core three-layer construction steel plate to produce a mild steel sheath cladding. In order to optimize the design of layer structure materials, they theoretically and experimentally studied the strain hardening exponent n and strain rate sensitivity m of the laminate [2]. Mohammadzadeh studied the nanocrystals of TWIP steel. He conducted experiments on the structure of microscopic molecules. He believes that the current technology is sufficient to analyze the atomic level, so it is necessary to conduct microscopic steel fracture surface analysis. This is confirmed by the experimental results of TWIP microcrystals with a stress dependence [3]. Hu et al.'s research is more microscopic. They aim to use SEM to analyze the microstructure changes of TWIP steel. Their experimental results prove this, but their experiments lack the necessary data support; there are not many types of steel studied without self-preparation [4]. According to Peng and Zhang's study, by controlling the volume fraction of the TWIP core area, the TWIP core steel sheet covers a wide range of yield and tensile strength and ductility levels required for automotive steel sheets, thus providing a new application for multifunctional automotive steel sheets [5]. Wang et al.'s experiments found that nanotwins were also observed in single-pass and double-pass samples as a result of secondary twinning [6]. Unfortunately, there is still no clear conclusion on the evaluation and method research of hydrogen-induced cracking of TWIP steel and on how to effectively improve the resistance to hydrogen-induced cracking and the fracture mechanism at home and abroad.

3. TWIP Steel and Fracture Nonuniform Deformation

3.1. Deformation Mechanism of TWIP Steel

3.1.1. The Stacking Fault Energy of TWIP Steel. The calculation of stacking fault energy (SFE) is very important for the research of TWIP steel, and it can provide many references for the composition design, alloying element control, and service conditions (such as temperature) of TWIP steel [7, 8]. The calculation of stacking fault energy is mainly based on dislocation theory, and the slip plane and twin plane of austenitic steel with face-centered cubic structure are {1,1,1}. The total dislocation can be decomposed into two incomplete dislocations, the region between the two incomplete dislocations is called stacking fault, and the energy change caused by dislocation is called stacking fault energy.

Stacking faults are formed by the expansion of incomplete dislocations under the action of shear stress, and the stacking fault energy is the work done to overcome the elastic interaction of dislocations. The stacking fault energy is an important factor affecting the deformation mechanism of austenitic steel, but there is no perfect and unified method for the calculation of stacking fault energy. The stacking fault energy results obtained by different methods may vary greatly. There are three commonly used calculation methods for stacking fault energy in TWIP steel alloy systems: based on the method of measuring incomplete dislocation distances by transmission electron microscopy (TEM), the method of measuring stacking fault probability based on X-ray diffraction (XRD), and the calculation of stacking fault energy based on thermodynamic models [9, 10].

Mn is the most important alloying element in TWIP steel. Mn has two functions: (1) Mn expands the austenite phase region and increases the austenite stability. (2) Mn affects the stacking fault energy of alloy elements, but the relationship between Mn content and stacking fault energy is nonlinear, as shown in Table 1. Thermodynamic models also confirmed this nonlinear relationship.

3.2. Interface of Metal Materials. The interface of metal structural materials has a great influence on its performance, and the interface characteristics of materials usually play a dual role. For the improvement of material mechanical properties (such as fine grain strengthening), the interface generally plays a more positive role; however, from the perspective of material failure, the interface often becomes the initiation site of failure damage, but this cannot be generalized. For austenite-based metal materials, there are usually grain boundaries inside the material, and the types of grain boundaries are different. If a phase transformation occurs, there are also phase boundaries. In addition, from the perspective of material failure, the fracture surface (fracture) of the material is also an extremely important interface, which can be used as the direct evidence of failure [11–13].

3.2.1. Fracture Surface (Fracture). The fracture surface, which is often referred to as the fracture, is the matching surface formed after the material breaks during the test or service process and is one of the most important evidences for the failure analysis of engineering materials. The fracture records the irreversible deformation of the material before fracture under the coupling action of the applied load and the service environment and the whole process of crack initiation and propagation until the final fracture. At the same time, the fracture morphology is affected by factors such as stress state, environmental medium, and material properties [14–16]. Usually, the typical hydrogen embrittlement fracture is characterized by the intergranular fracture morphology, and the degree of convexity and concave of the fracture varies greatly with different hydrogen embrittlement susceptibilities. Therefore, to deeply understand the failure and fracture behavior of materials, it is necessary to quantitatively characterize the fracture. Through quantitative characterization, the correlation between the mechanical

Table 1: Effects of different Mn contents on stacking fault energy of austenitic steels.

Component part	Layer fault energy (mJ/m^2)
Fe-16Mn	26 ± 3.1
Fe-18Mn	22 ± 2.6
Fe-20Mn	18 ± 2.2
Fe-22Mn	15 ± 1
Fe-22Mn-3Al-3Si	15 ± 3
Fe-25Mn-3Al-3Si	21 ± 3
Fe-28Mn-3Al-3Si	38.8 ± 5

properties of materials and the failure mechanism can be directly established.

3.2.2. Phase Interface. Usually, the interface existing between two solid phases with different crystal structures is called a phase boundary, such as the phase interface in duplex stainless steel. After the phase transformation, the interface between the new phase and the parent phase can also be formed; for example, the ε/γ phase interface is formed after the ε martensitic transformation occurs in TWIP steel. The so-called different structures include materials with different qualities, either in the symmetry of the crystal structure or in the lattice parameters (such as the phase interface between α martensite and ferrite) or in the type of bonding, which will make the phase boundary have very complex structural characteristics [17]. If the two-phase interface is completely ordered and perfectly matched, the interface is called a coherent phase interface. If there are local dislocations at the interface through the relaxation process, the interface with relatively small elastic distortion in the local area is called a semicoherent phase interface. If the interface is completely disordered, it is an incoherent phase boundary.

In general, phase interfaces with very strict coherent relationships are particularly rare. A typical coherent phase boundary is the interface between the face-centered cubic (FCC) phase and the dense hexagonal (HCP) phase after the cobalt phase transition. Since the two phases have the same close-packed properties, but have different stacking orders on both sides of the interface, it is a phase interface with lower energy. In the process of martensitic transformation or in the early stage of precipitation, some phase boundaries can also be regarded as coherent phase interfaces. At this time, the phase boundaries are phase interfaces with a certain orientation relationship, that is, a habitual relationship. Figure 1 shows the geometry of a coherent interface.

A semicoherent phase boundary is a particularly common type of phase boundary. Taking the interface formed by misfit dislocations in epitaxial growth as an example, for example, the two crystal structures have the same lattice, and the slight difference is only manifested in lattice parameters or the angle between lattices (<10%). If a coherent phase interface is to be formed, a large amount of distortion must be generated in the crystal, then by introducing misfit dislocations along the interface, the changes in lattice parameters or included angles can be coordinated, as shown in Figure 2. This concentrates the distortion in the vicinity of the dislocation line, thereby relaxing the coherent elastic distortion of the crystal, which is consistent with the principle of minimum energy.

3.2.3. Grain Boundary. Metal structural materials are usually polycrystalline, and the boundaries between different grains are grain boundaries. Compared with the coherent and incoherent phase interfaces, the lattice distortion of the grain interface is larger, so it has a greater impact on the mechanical behavior (fracture behavior, creep behavior, and corrosion behavior) of the material. Therefore, grain boundaries occupy a high enough position in the study of crystal defects [18, 19]. Generally, grain boundaries can be divided into small-angle grain boundaries and high-angle grain boundaries. The grain boundaries in materials such as TWIP steel are mainly composed of high-angle grain boundaries.

The widely accepted model of high-angle grain boundary structure is the coincident position lattice model. If the two grains separated by the grain boundary are regarded as interpenetrating, some of their lattice points will be coincident, and these coincident lattice points will constitute a new lattice, that is, the coincidence position lattice (CSL). The coincident lattice has nothing to do with the crystal interface, but the orientation relationship of the crystal interface relative to the coincident lattice has a great influence on the interface structure. When the interface is the most densely packed surface of the coincident lattice, the interface has a relatively complete lattice matching degree, the mismatch is small, and the interface energy is also the lowest. Of course, it does not mean that any interface with an orientation relationship has a high density of coincident lattice points. Then if the reciprocal $\sum$ of the coincidence lattice point density is used to represent the coincidence degree, for the face-centered cubic crystal, among the grain boundaries with the [110] direction as the rotation axis, the ones with higher coincidence degree have $\sum 3$, $\sum 9$, and $\sum 11$ grain boundaries. These correspond to rotations of 70.5°, 39°, and 129.5° around the [110] axis, respectively. Figure 3 shows the geometry of the $\sum 3$ grain boundary.

3.3. Microstructure Characterization Calculation Method. The phase content in the annealed samples was measured by XRD (Ultima IV), the target was a copper rake, the wavelength was 1.5406 A, the scanning speed was 20°/min, and the scanning range was 40°~100°. The normal tensile test is carried out at room temperature, and the gauge length of the sample is $20 \times 5 \times 1.3 \, mm^3$. The size of the dynamic hydrogen charging slow strain rate tensile test specimen is the same as that of the normal tensile test specimen, and the tensile rates are $1 \times 10^{-5} \, S^{-1}$, $5 \times 10^{-6} \, S^{-1}$, and $1 \times 10^{-6} \, S^{-1}$, respectively. Using in situ electrochemical hydrogen charging, the hydrogen charging solution is 3%NaCl + 3 g/LNH$_4$SCN, the hydrogen charging current density is 5 A/m^2, and platinum wire is used as the counter electrode for electrochemical hydrogen charging. The test device is shown in Figure 4. All tensile tests were carried out on a microcomputer-controlled stress corrosion slow tensile testing machine model QB/LC-JL-159-2010. After dynamic

Distortion-free coherent phase boundary   Distorted coherent phase boundary
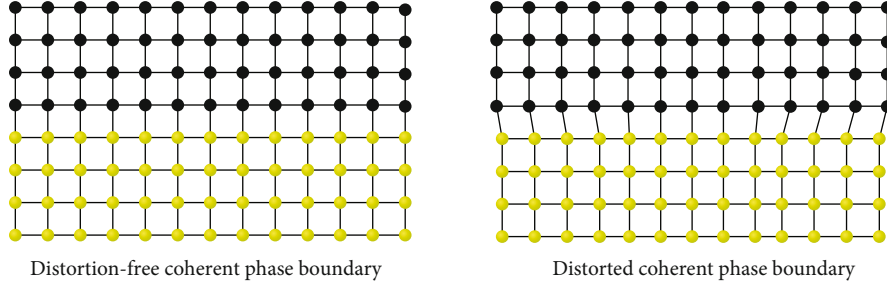
Figure 1: Geometry of the coherent interface.

Semi-coherent phase boundary   Incoherent phase boundary
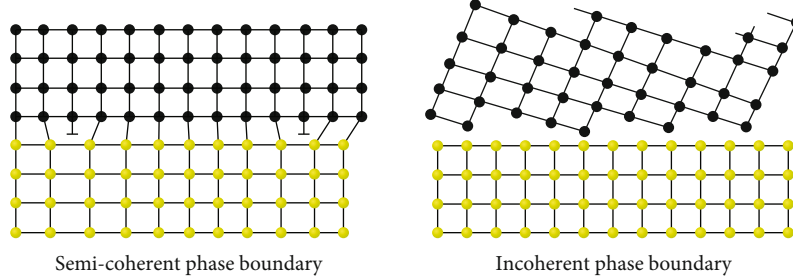
Figure 2: Geometry of a semicoherent interface.

hydrogen charging and stretching at a slow strain rate, the fracture morphology of the fractured specimens was observed with a field emission scanning electron microscope (electron microscope model) with a working voltage of 20 kV and a working distance of 12-13 mm. In this work, the loss of elongation is used to characterize the hydrogen embrittlement susceptibility; usually, the hydrogen embrittlement susceptibility (E_{lose}) is calculated by the following formula:

$$E_{lose} = \frac{E_{h(air)} - E_{h(H)}}{E_{h(air)}} \times 100\%. \tag{1}$$

Among them, $E_{h(air)}$ is the uniform elongation of stretching in air, and $E_{h(H)}$ is the uniform elongation of stretching under in-situ hydrogen charging.

The fracture morphology under scanning electron microscope (SEM) usually enjoys a certain degree of undulating fracture surface, with obvious height difference (elevation) at μm scale. Obtaining accurate elevation data is extremely challenging using traditional surveying methods. SEM images are two-dimensional grayscale images, but the differences in different grayscales throughout the image provide an effective indirect method. White indicates the raised area, which represents the highest position (its value is 255). Gray indicates the position between them. Therefore, the gray value can be expressed by the following formula:

$$A(x, y, G) \sim A(x, y, H). \tag{2}$$

Calculate the box counting dimension method and projection covering method, and preprocess and cut each original SEM image. The original SEM image is rectangular (768×1624 pixels), and six areas (upper left, upper middle,

upper right, lower left, lower middle, and lower right) are cropped in such an image. For example, Figure 5 shows the upper right and lower left positions.

Based on the projection coverage algorithm, as shown in Figure 6, it is proposed to calculate the fractal dimension D_s of a single surface area. The rough surface area A_k enclosed by the projected grids $a, b, c,$ and d can be approximately expressed as

$$A_k = S_1 + S_2 = \sqrt{p_1(p_1 - ab)(p_1 - ad)(p_1 - bd)}$$
$$+ \sqrt{p_2(p_2 - bc)(p_2 - cd)(p_2 - bd)},$$

$$p_1 = \frac{(ab + ad + bd)}{2},$$

$$p_2 = \frac{(bc + cd + bd)}{2},$$

$$ad = \sqrt{(x_1 - x_2)^2 + (y_1 - y_2)^2 + (H_1 - H_2)^2},$$

$$A_T(\delta) = \sum_{}^{N(\delta)} A_k(\delta). \tag{3}$$

After the above formula, it can be shown that the grid overlay projection algorithm is effective and can determine the fixed pixel value in the image, where $N(\delta)$ is the total number of boxes. In this paper, the images are distributed in boxes of different sizes, which can be defined as a power law, and the formula is expressed as

$$A_T(\delta) = \sum_{}^{N(\delta)} A_k(\delta) \sim \delta^{2-D}. \tag{4}$$
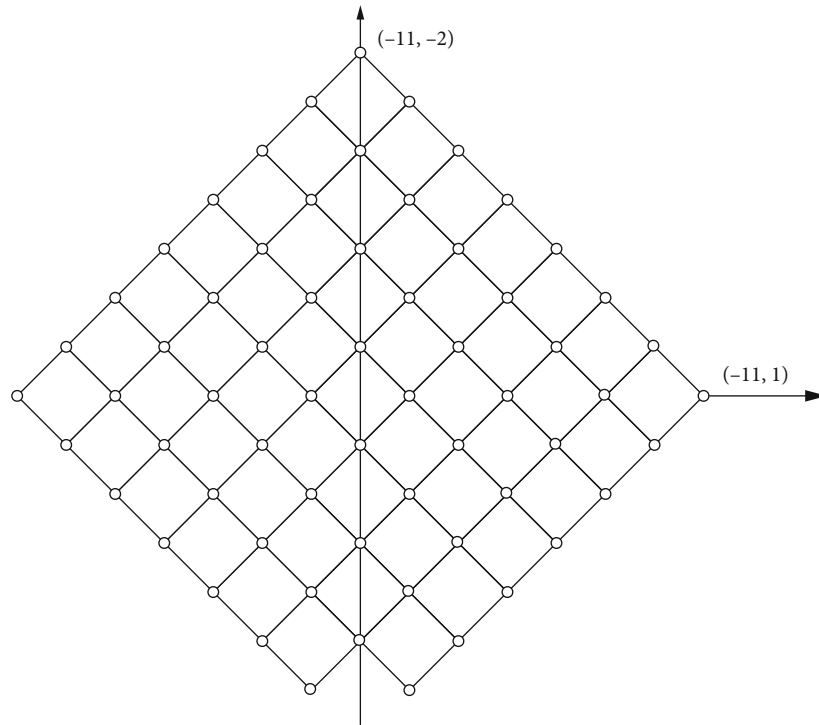
FIGURE 3: Geometric structure of the grain boundary of lattice $\sum 3$ at the coincident position.
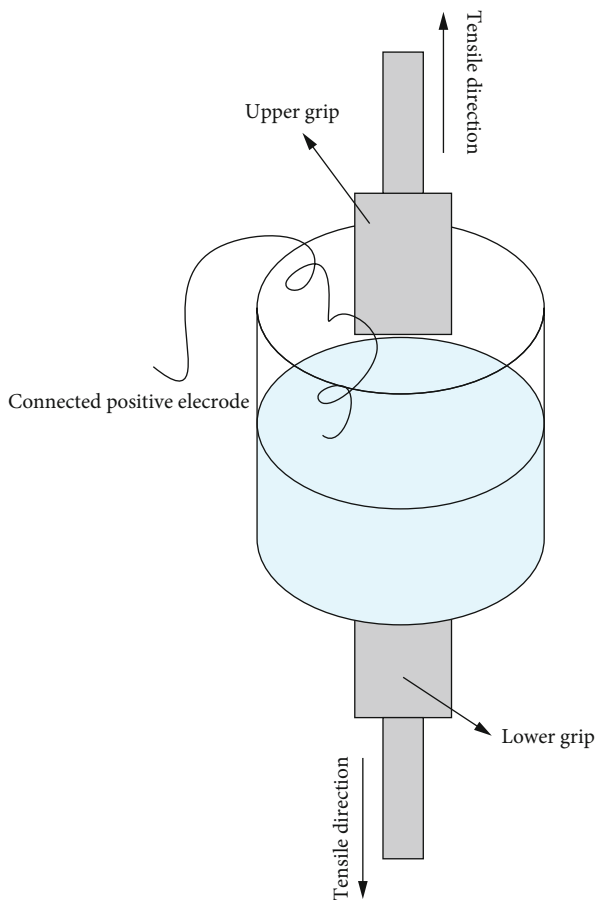
FIGURE 4: Schematic diagram of the in situ electrochemical hydrogen charging slow strain rate stretching device.

A_T is the total rough area, and when $\delta \longrightarrow 0$, A_T is close to the actual surface area.

Generalized entropy $H_q(\delta)$ and generalized dimension D_q are defined as

$$H_q(\delta) = \frac{\ln \sum_{i=1}^N h_i^q}{1-q},$$

$$D_q = -\lim_{\delta \longrightarrow 0} \frac{H_q(\delta)}{\ln \delta} = \frac{\tau(q)}{q-1} \quad \left(q=1, D_1 = \frac{h_i \ln h_i}{\ln \delta} \right).$$

(5)

After calculation, we can find that there are many definitions that are not perfect, but as shown in Figure 6, the multifractal spectrum can be expressed by the following formulas:

$$f(\alpha) = -\lim_{\delta \longrightarrow 0} \frac{\ln (N(\alpha))}{\ln (\delta)},$$

$$\alpha(q) = \lim_{\delta \longrightarrow 0} \frac{\ln (h_i)}{\ln (\delta)},$$

(6)

where $\alpha(q)$ is the singularity exponent and $f(\alpha)$ is the multifractal spectral function. $N(\alpha)$ represents the α integral value in $[\alpha, \alpha + d\alpha]$. Through the legend transformation, $f(\alpha)$ and $\alpha(q)$ can be given as follows:

$$\alpha(q) = \frac{\partial_\tau(q)}{\partial q},$$

(7)

(a)

(b)

(c)
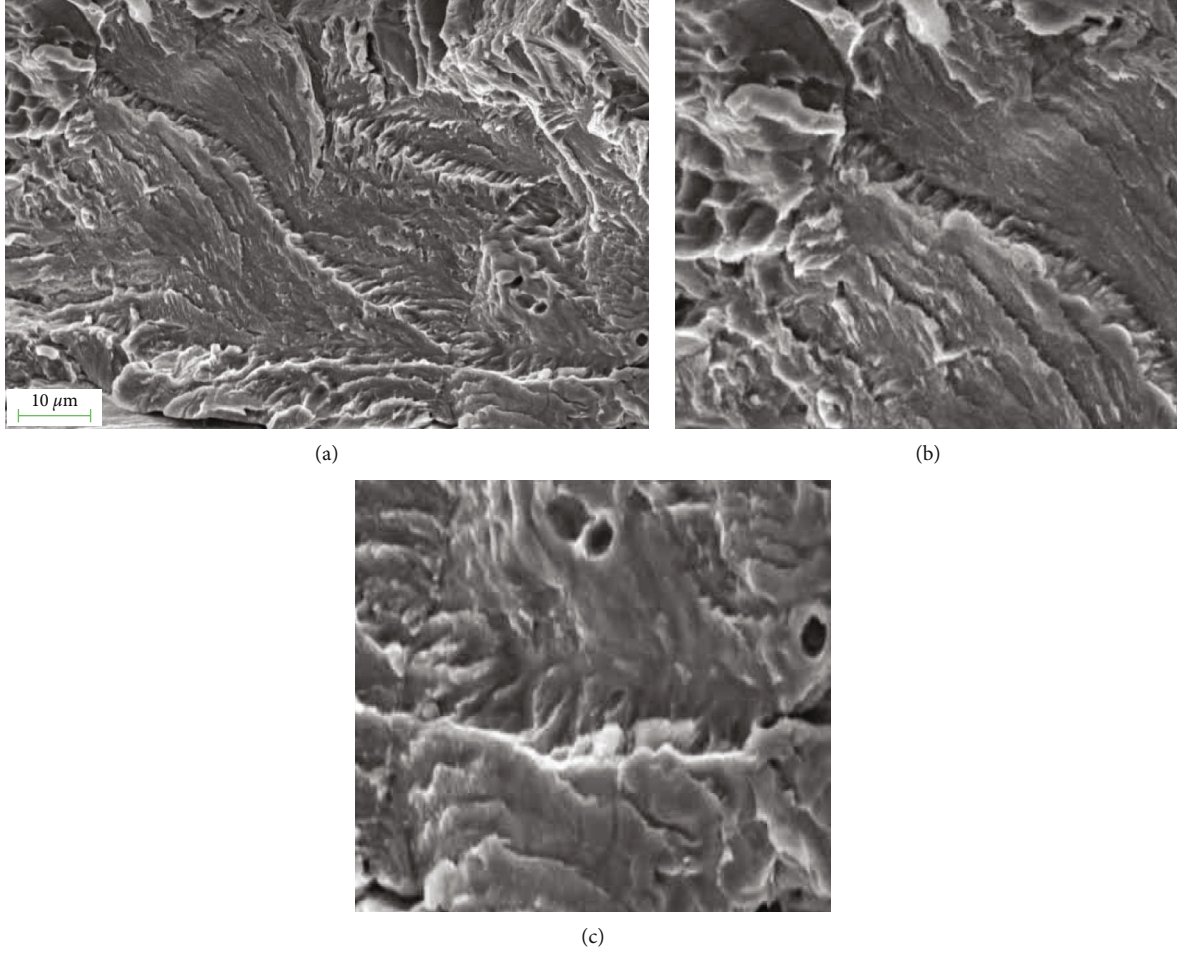
FIGURE 5: Fracture diagram of digital image recognition technology processing.

$$f(\alpha) = \alpha(q)q - \tau(q). \tag{8}$$

According to the definition of function $\tau(q)$, formulas (7) and (8) can be rewritten as

$$\alpha(q) = \lim_{\delta \longrightarrow 0} \frac{1}{\ln \delta} \sum_i \mu_i \ln (h_i),$$

$$f(\alpha) = \lim_{\delta \longrightarrow 0} \frac{1}{\ln \delta} \sum_i \mu_i(\mu_i). \tag{9}$$

Among them,

$$\mu_i = \frac{h_i^q}{\sum_i h_i^q}. \tag{10}$$

4. Deformation and Microscopic Analysis of TWIP Steel under Damage Fracture

4.1. Thermomechanical Treatment Process. The 22Mn0.6C and 22Mn0.6C3Al TWIP steels used in the experiment were cast into ingots by vacuum smelting, and the weight of the ingots was 75 kg. Subsequently, the ingots were cut with

risers, and samples were taken on the ingots, and the chemical composition of the steel was measured by emission spectroscopy as shown in Table 2.

The chemical compositions of the TWIP steels used in this chapter are shown in Table 2. For convenience, Fe-22Mn-0.6C and Fe-22Mn-0.6C-3Al are abbreviated as 22Mn0.6C and 22Mn0.6C3Al, respectively, in the remainder of this chapter. Figure 7 shows the schematic diagram of the thermodynamic processing of the two TWIP steels: first, the ingots of the two steels were homogenized and heat-treated in an argon atmosphere at 1423 K for 2 h. Subsequently, it is hot rolled to 3 mm thick plate in the temperature range of 1373 K to 1223 K. Then, using a twin-roll mill, the hot-rolled sheet was cold-rolled in multiple passes into a 1.5 mm sheet. Finally, the 22Mn0.6C and 22Mn0.6C3Al steels were recrystallized and annealed at 1123 k and 1173 k for 0.5 h, respectively, and then quickly quenched in water after being taken out to obtain initial materials with uniform equiaxed grains. Tensile specimens were taken from the initial sheet by wire cutting, with the long axis of the specimen parallel to the rolling direction of the sheet.

In this paper, the loading-unloading-reloading method is used to measure HDI stress, and its principle is shown in Figure 8. In the measurement method, first, the hysteresis
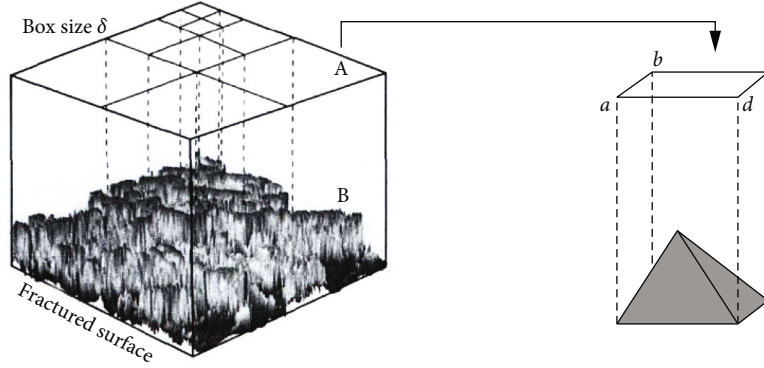
FIGURE 6: The schematic diagram of the projection coverage algorithm to calculate the fractal dimension of the fracture.

TABLE 2: Element content (wt.%).

Steel	22Mn0.6C	22Mn0.6C3Al
Mn	21.26	21.45
C	0.55	0.58
Al	0.003	2.86
Si	0.11	0.13
S	0.006	0.005
P	0.008	0.010
Fe	Margin	Margin
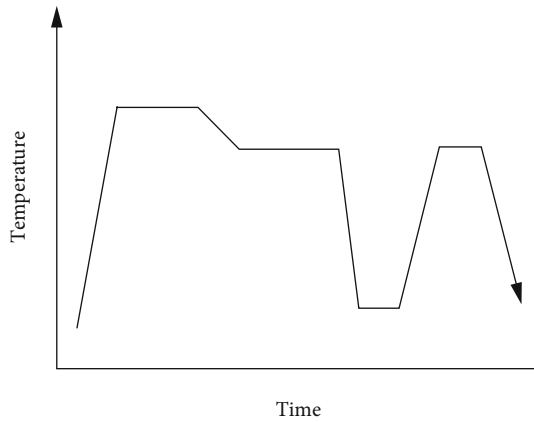
FIGURE 7: Schematic diagram of thermodynamic processing of TWIP steel.

loop is obtained through the loading-unloading-reloading process. Then, the unloading yield stress (σ_u) and the reloading yield stress (σ_r) are measured on the unloading and reloading curves, respectively, and finally the HDI stress (σ_{HDI}) is obtained:

$$\sigma_{HDI} = \frac{\sigma_u + \sigma_r}{2}. \tag{11}$$

In addition, the effective stress (σ_{eff}) can also be obtained by subtracting the HDI stress from the total flow stress.

4.2. Initial Microstructure. Figure 9 shows the frequency distribution of grain sizes of two TWIP steels and their log-normal distribution fitting curves. The average grain sizes obtained by statistics are 4.9 μm and 4.3 μm, respectively. The approximately equal grain size helps to elucidate the role of deformation twinning in heterogeneous deformation-induced strengthening.

4.3. Variation of HDI Stress. Figure 10 shows the variation of HDI stress with true strain in both steels. Repeated load-unload-reload tensile tests were performed on two steels at strain levels of 0.01, 0.02, 0.03, 0.04, 0.06, 0.09, 0.11, 0.14, 0.17, 0.19, 0.21, 0.26, 0.31, and 0.34, as shown in Figure 10 (a). Figure 10(b) shows the load-unload-reload curve at 0.14 true strain, and it can be seen that both steels have significant hysteresis loops. Figure 10(c) shows that the HDI stress increases with increasing strain, and the HDI stress of the two steels is approximately equal until 0.11 true strain. Thereafter, as the strain increases, the gap between HDI stresses becomes larger, and at 0.34 true strain, the HDI stress of 22Mn0.6C steel is 104 MPa larger than that of 22Mn0.6C3Al steel. Error bars for HDI stress values were obtained from three replicate experiments. The HDI stress values of the two steels were fitted using the power exponential relationship $\sigma_b = \sigma_{b0} + K\varepsilon^n$, as shown in Figure 10(c). In the fitted curve, σ_{b0}, K, ε, and n represent the intrinsic strength, material strengthening coefficient, true strain, and strain hardening exponent, respectively. It can be seen that the empirical formula can fit the change of HDI stress value well, but its hidden physical meaning still needs to be further explored in the future. In 22Mn0.6C TWIP steel, σ_{b0}, K, and n are 149.8 MPa, 1250.2 MPa, and 0.875, respectively; in 22Mn0.6C3A1 TWIP steel, σ_{b0}, K, and n are 165.7 MPa, 877.0 MPa, and 0.733, respectively.

It can be seen from the stress-strain curve that the plastic loss of the three samples at a strain rate of $1 * 10^{-6} \, S^{-1}$ is greater than that at a strain rate greater than $1 * 10^{-5} \, S^{-1}$. This indicates that the plastic loss increases with decreasing strain rate. At the strain rate of $1 * 10^{-5} \, S^{-1}$, the plastic loss of the three specimens ($T0 \longrightarrow T10 \longrightarrow T30$) gradually increased. However, at the strain rate of $1 * 10^{-6} \, S^{-1}$, the hydrogen embrittlement susceptibility of T0 specimen is greater than that of T10 and T30. The calculated results of
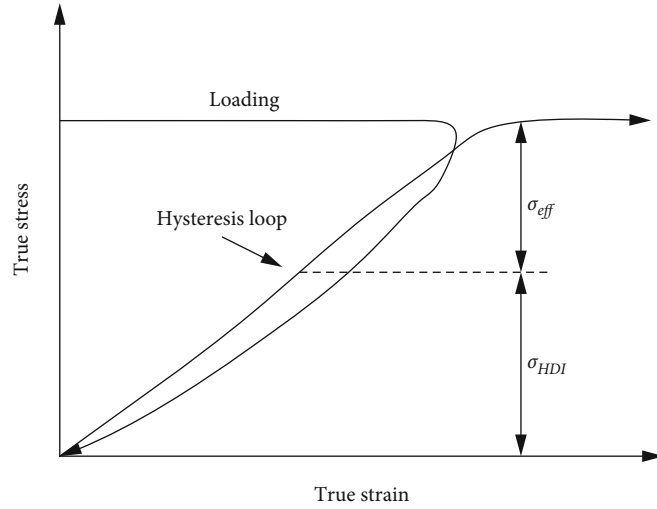
FIGURE 8: Load-unload-reload schematic.
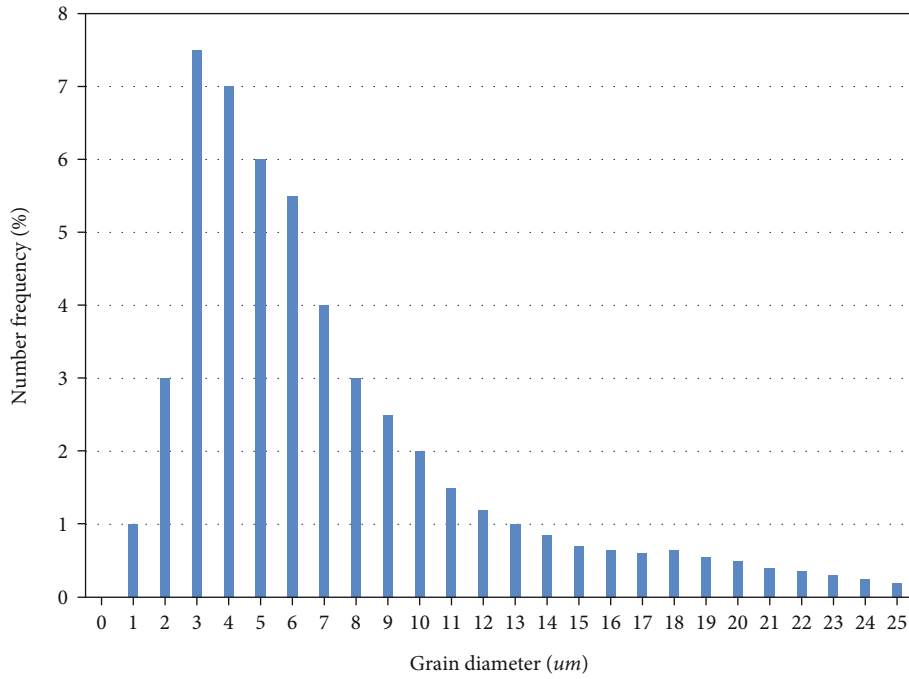
FIGURE 9: Grain size distribution.

(a)

(b)

(c)
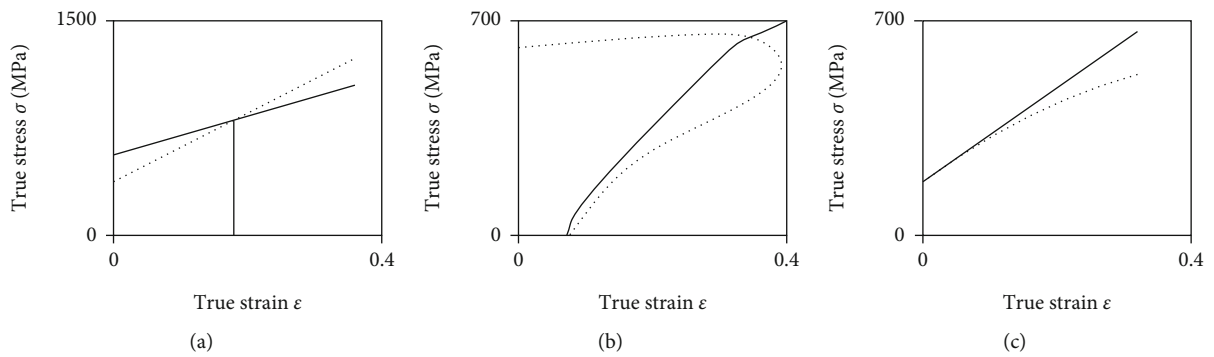
FIGURE 10: HDI stress of TWIP steel specimen. Among them: (a) loading-unloading-reloading tensile curve; (b) is an enlarged view of the area marked by the dotted box in (a); (c) the relationship between HDI stress and strain.

TABLE 3: Brittleness sensitivity (E_{loss}).

Sample	$1*10^{-5}$ S^{-1}	$1*10^{-6}$ S^{-1}
T0	64 ± 1.52	94 ± 0.32
T10	74 ± 0.67	83 ± 0.72
T30	78 ± 0.74	93 ± 1.38

the brittle sensitivity are shown in Table 3. The fitting results show that the HDI hardening rate of 22Mn0.6C TWIP steel is higher than that of 22Mn0.6C3Al TWIP steel.

5. Conclusions

Gradient substructure 22Mn0.6C TWIP steel was prepared by a simple pretorsion method, which combines high yield strength, tensile strength, and plasticity. Gradient substructure samples were found to have greater heterogeneous plastic deformation at the grain scale and at the specimen scale, which resulted in higher heterogeneous deformation-induced strengthening and hardening, compared to the homogeneous coarse-grained structure. More dislocations and deformation twins are formed inside the gradient substructure samples, which hinder the short-range motion of mobile dislocations, resulting in higher effective stress strengthening and hardening. Therefore, the excellent mechanical properties of the graded substructure TWIP steel originate from the synergistic contribution of its higher heterogeneous deformation-induced stress and short-range effective stress. The gradient substructure design strategy is a reasonable method to prepare high strength and high plasticity TWIP steel.

Data Availability

No data were used to support this study.

Conflicts of Interest

The authors declare that there is no conflict of interest with any financial organizations regarding the material reported in this manuscript.

Acknowledgments

References

[1] W. Peng, S. Xu, and L. Jl, "Atomistic simulation for deforming complex alloys with application toward TWIP steel and associated physical insights," *Journal of the Mechanics & Physics of Solids*, vol. 98, no. jan., pp. 290–308, 2017.

[2] J. G. Kim, S. M. Baek, W. T. Cho et al., "On the rule-of-mixtures of the hardening parameters in TWIP-cored three-layer steel sheet," *Metals and Materials International*, vol. 23, no. 3, pp. 459–464, 2017.

[3] R. Mohammadzadeh, "Reversible deformation in nanocrystalline TWIP steel during cyclic loading by partial slip reversal and detwinning," *Materials Science and Engineering*, vol. 782, no. Apr.24, pp. 139251.1–139251.8, 2020.

[4] Y. Hu, Y. Su, and F. Xiaoxiao, "Microstructure and texture evolution of Fe-33Mn-3Si-3Al TWIP steel on strain," *Journal of Wuhan University of Technology (Materials Science)*, vol. 34, no. 1, pp. 176–182, 2019.

[5] L. Peng and J. Zhang, "Tensile property and microstructure of Fe-22Mn-0.5C TWIP steel," *Materials Science and Engineering A*, vol. 707, no. nov.7, pp. 373–382, 2017.

[6] L. Wang, A. J. Benito, J. Calvo, and M. J. Cabrera, "Equal channel angular pressing of a TWIP steel: microstructure and mechanical response," *Journal of Materials Science*, vol. 52, no. 11, pp. 6291–6309, 2017.

[7] L. Peng and J. Zhang, "Twinning and dynamic strain aging behavior during tensile deformation of Fe- Mn-C TWIP steel," *Materials ence & Engineering A*, vol. 700, no. jul.17, pp. 250–258, 2017.

[8] J. Park, M. Kang, and S. S. Sohn, "Tensile properties of cold-rolled TWIP-cored three-layer steel sheets," *Materials Science & Engineering A*, vol. 686, no. FEB.16, pp. 160–167, 2017.

[9] V. García-García, I. Mejía, F. Reyes-Calderón, and H. Hernández-Belmontes, "Thermo-mechanical-microstructural simulation of double-pass welding process in a TWIP steel by FE formulation and probabilistic model," *The International Journal of Advanced Manufacturing Technology*, vol. 111, no. 3-4, pp. 1115–1134, 2020.

[10] G. Li, P. Lan, J. Zhang, and G. Wu, "Refinement of the solidification structure of austenitic Fe-Mn-C-Al TWIP steel," *Metallurgical and Materials Transactions B*, vol. 51, no. 2, pp. 452–466, 2020.

[11] L. Zeng, X. P. Guo, G. A. Zhang, and H. X. Chen, "Semiconductivities of passive films formed on stainless steel bend under erosion-corrosion conditions," *Corrosion Science*, vol. 144, no. 1, pp. 258–265, 2018.

[12] A. Bb, C. Beb, and A. Fcb, "Effect of hydrogen on fracture locus of Fe–16Mn–0.6C–2.15Al TWIP steel," *International Journal of Hydrogen Energy*, vol. 45, no. 58, pp. 34227–34240, 2020.

[13] F. Zen and S. Aslanlar, "Mechanical and microstructural evaluation of resistance spot welded dissimilar TWIP/martensitic steel joints," *The International Journal of Advanced Manufacturing Technology*, vol. 113, no. 11-12, pp. 1–17, 2021.

[14] R. Kalsar, P. Khandal, and S. Suwas, "Effects of stacking fault energy on deformation mechanisms in Al-added medium Mn TWIP steel," *Metallurgical and Materials Transactions A*, vol. 50, no. 8, pp. 3683–3696, 2019.

[15] M. Madivala and W. Bleck, "Strain rate dependent mechanical properties of TWIP steel," *JOM Journal of the Minerals, Metals and Materials Society*, vol. 71, no. 4, pp. 1291–1302, 2019.

[16] H. Kamali, H. Xie, H. Bi et al., "Effects of strain rate on the microstructure and texture evolution of a TRIP-TWIP metastable austenitic stainless steel during bending," *Journal of Materials Science*, vol. 57, no. 5, pp. 3727–3745, 2022.

[17] V. Torganchuk, I. Vysotskiy, S. Malopheyev, S. Mironov, and R. Kaibyshev, "Microstructure evolution and strengthening mechanisms in friction-stir welded TWIP steel," *Materials Science and Engineering*, vol. 746, no. FEB.11, pp. 248–258, 2019.

[18] J. Zhao, J. Huang, R. Wang, H. R. Peng, and S. Ji, "Investigation of the optimal parameters for the surface finish of k9 optical glass using a soft abrasive rotary flow polishing process," *Journal of Manufacturing Processes*, vol. 49, pp. 26–34, 2020.

[19] V. Braga, R. H. M. Siqueira, S. M. Carvalho, R. A. F. Mansur, D. Chen, and M. S. F. Lima, "Mechanical behavior and microstructure of a fiber laser–welded TWIP steel," *International Journal of Advanced Manufacturing Technology*, vol. 104, no. 1-4, pp. 1245–1250, 2019.

Research Article

Micro Nanoengraving Technology and Aesthetic Practice of Architectural Sculpture Art

Weili Zhu[1] **and Dong Wei** [2]

[1]*Arts and Humanities Education Center, North China University of Water Resources and Electric Power, Zhengzhou, 450046 Henan, China*
[2]*School of Art and Design, North China University of Water Resources and Electric Power, Zhengzhou, 450046 Henan, China*

Correspondence should be addressed to Dong Wei; weidong2021@ncwu.edu.cn

Micro nanotechnology refers to the emerging technology of material production using a single atomic or molecular structure. The structure and size of materials range from one to 100 microns or nanometers. In this paper, micro nanotechnology is used to study the aesthetic practice of sculpture technology and architectural sculpture art. This paper aims to combine traditional art ideas with science and technology to promote common development. This paper first introduces the micro nanoengraving technology and architectural sculpture art, it includes the definition of works, classification of works, and research on artistic commonalities and differences, and then summarizes the characteristics of micro nanoengraving materials. Finally, this paper will carry out aesthetic practice of sculpture works based on micro nanocreation. Finally, this paper compares with the works created by traditional technology. The results show that the recognition and creativity evaluation of sculpture works based on micro nanocreation have reached more than 8 points. It verifies the effectiveness of the technology.

1. Introduction

As an important part of art career, sculpture technology and architectural sculpture art have a development history of thousands of years. For buildings in the traditional sense, it generally refers to the safe and reliable living space built with hard materials, with various styles. Famous traditional buildings include ancient Roman architecture, Gothic architecture, and classical garden architecture. It is not only a work of art but also an important medium for transmitting and preserving culture. However, the architectural sculpture discussed in this paper refers to a kind of microangle. In fact, microcarving art also has a very long history of development. This kind of microcarving cannot be clearly recognized by the naked eye and can be viewed with the help of a microscope. Since the advent of microscope in the mid-20th century, the microcarving technology has made unprecedented progress. It has a strict innovation in size. In the past, most microcarving works were in millimeters.

Now it has entered the micro nanoera, so it is also called micro nanocarving technology and micro nanoarchitectural sculpture art.

With the progress of the times and the innovation of science and technology, micro nanoscience and technology has become one of the focuses of market development. The main forms of its development include micro nanoprocessing, micro nanomanufacturing, micro nanomaterial application, and micro nanoengraving. At present, researchers have developed more new micro nanocarving methods that can perfectly combine the traditional carving art in the process of technological renewal, such as laser method, chemical vapor deposition method, and computer-aided design method. As one of the construction parts of micro nanoscience and technology, micro nanocarving technology and micro nanoarchitectural sculpture art have developed at a higher level in the microworld. Its journey of exploring micro nanocarving technology and the artistic charm of micro nanoarchitectural sculpture is also ongoing.

At present, there is little research on the aesthetic practice of sculpture technology and architectural sculpture art. This paper puts forward a novel art research direction based on micro nanotechnology. It can provide a perfect and improved development suggestion for the engraving industry under micro nanotechnology, and it can also provide new ideas for the research of artistic aesthetics practice.

2. Related Work

In recent years, many scholars have studied micro nanotechnology. Shi J described the nanopore detection mechanism based on translocation. He gave specific examples of nucleic acid analysis and sequencing based on nanopores. This method identifies strategies that can improve the resolution of nanopores. Finally, he discussed the future research direction of promoting nanopore technology to practical application [1]. Tian X has successfully prepared SnO2 micro and nanostructured biscuits by ovalbumin assisted sol-gel method. His experimental results showed that with the increase of calcination temperature, the photoluminescence efficiency of micro and nano will increase [2]. Shah P explored many emerging nanotechnologies. He studied a silver nanocluster nanotechnology based on DNA encapsulation with attractive optical properties [3]. Rohini R believed that the protective characteristics of surge arresters help to reduce the cost of insulation design of electrical systems. He applied this method to micro and nanosamples to verify its effectiveness [4]. Ho C proposed an auxiliary method to overcome the difficulty of drilling sapphire. He studied the effect of adding micro and nanobubbles to the original electrolyte and confirmed that micro and nanobubbles can assist ECDM [5]. Taheri A A considered a two-dimensional transient model with tumor biological tissue. He embedded micro nanosuperparamagnetic materials in the tumor area. The results show that the use of micro nanomaterials will significantly reduce the temperature of healthy tissues around cancer cells, so as to achieve a more favorable therapeutic effect [6]. To sum up, after the exploration in recent years, the application of micro nanotechnology has been deeply studied by many scholars, but there is not much research on the aesthetic practice of architectural sculpture art. Therefore, in order to further promote the development of sculpture art industry, it is urgent to study the aesthetic practice of micro nanosculpture technology and architectural sculpture art.

3. Architectural Sculpture Art and Micro Nanotechnology

3.1. Overview of Micro Nanocarving Technology and Architectural Sculpture Art. Before studying micro nanocarving technology and architectural sculpture art, we need to understand the concept of micro nanoart. In previous studies, many scholars believe that micro nanoart is an art work with micro nanosize characteristics created based on micro nanotechnology [7].

3.1.1. Definition of Micro Nanoengraving Technology and Architectural Sculpture Art. Based on the concept of micro nanoart, we can understand that a work should be called micro nanocarving technology and architectural sculpture art works. It needs to meet two conditions: one is that the work is small in size, and the other is that the work has certain ornamental and artistic value [8].

3.1.2. Classification of Micro Nanocarving Technology and Architectural Sculpture Works of Art. Micro nanocarving technology and architectural sculpture art works can be classified from four levels, as shown in Table 1:

(1) Angle

Based on the different perspectives of micro nanoengraving technology and architectural sculpture art works, we can divide them into two-dimensional works and three-dimensional works. The two-dimensional works are mainly patterns, which are carved on the surface of special materials. This kind of work carves symbolic patterns according to the thoughts and ideas that the creator wants to convey. It can only be viewed through microscopic observation instruments (such as atomic force microscope). The three-dimensional carving works are very three-dimensional, and the length, width, and height of the works are generally in microns or nanometers. It uses electron microscope imaging, and its works using three-dimensional engraving technology are often more lifelike than two-dimensional works. And the carving is more difficult than two-dimensional.

(2) Creative craft

Based on the difference of micro nanoengraving technology and the creation process of architectural sculpture art works, we can be divided into traditional works and processed works [9]. Traditional works generally follow the ancient microcarving technology, as shown in Figure 1. These two works are carved on jade and needles. It is difficult to observe the specific content only with the naked eye. It needs the help of a general microscope, and the processed works have higher eyeballs than traditional works. It is not only unrecognizable by the naked eye but also cannot be clearly viewed by even a general microscope. It needs an electron microscope with high resolution. It also has high requirements for carving tools [10].

(3) Size

Based on the different creation processes of micro nanocarving technology and architectural sculpture works, we can divide the works into different levels, as shown in Table 2:

The traditional carving works that follow the ancient carving technology we mentioned are usually 100 micrometers or 100 nanometers. Although the size of some traditional works exceeds the hundred micro and nanolevel, and even reaches the millimeter level, if the engraving of the nuances of the whole work conforms to the hundred micro and nanolevel, we also call it the hundred micro and

TABLE 1: Classification of works of art.

Scope	Sequence	Level
	1	Angle
Work classification	2	Production process
	3	Size
	4	Creative inevitability
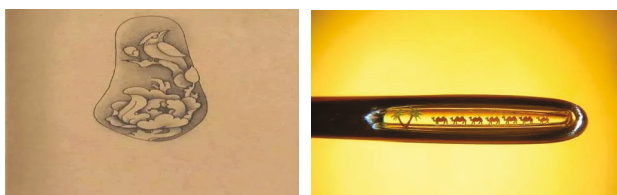
FIGURE 1: Ancient miniature sculptures.

TABLE 2: Different levels of classification of the size of engravings.

Classification level	Ordinal value	Rank
	1	Micron level
Size of work	2	Nanometer level
	3	100 micrometer level
	4	100 nanometer level

nanolevel engraving works. The processing works based on micro and nanotechnology include [11].

(4) Inevitability of creation

Based on the different inevitability of micro nanocarving technology and architectural sculpture art works, we can divide them into intentional works and unintentional works. As the name suggests, intentional works refer to works produced under the guidance of purpose [12]. The creation of many microcarving masters is just the microcarving creation under the premise of purpose, while the unintentional creation refers to the accidental discovery or exploration in research and work. This kind of creation often appears in laboratories that need micro observation. And its creation is in the form of works, as shown in Figure 2. These two pictures are wonderful patterns found on the tested object.

3.1.3. Commonalities between Carving Technology and Architectural Sculpture Art. The emergence and development of carving technology and architectural sculpture art stem from human production activities. And it was directly influenced by religion, philosophy, and other social ideologies in various periods. These two-dimensional and three-dimensional art works are not only the crystallization of the times, thoughts, feelings, and aesthetic concepts but also an important record of the materialization of social development. To understand the relationship between the two, we

must first explore the basis of their symbiotic relationship. We can elaborate from the following four aspects:

(1) Premise of functional requirements

When it comes to architecture or sculpture, we naturally classify them into the category of art and rarely notice that they are directly related to human survival. This starts with the essence of architecture and sculpture. In a narrow sense, the subject considered by architecture is centered on houses or buildings. Greek philosophers called architecture a shelter against wind and rain. French scholars summarized the essence and origin of architecture as the primitive man's search for shelter, and called it the basic house.

In fact, for human beings, architecture and sculpture are more important as necessities than luxury goods [13]. In other words, their emergence is inevitable. The first thing that human beings solve at birth is the problem of survival. When this problem is properly solved, they will care about spiritual things. Therefore, architecture and sculpture should not only meet human physiological needs but also meet human psychological needs [14]. First, we can produce and live as a tool, and then we can care about the beauty of the tool. The requirement from quantitative change to qualitative change is the development process of carving. Similarly, buildings first appeared in order to protect people from the wind and rain and against the dangerous nature. The first thing to solve is whether there are problems. When these basic requirements are met, people will care about the comfort and beauty of buildings, and then start to pursue things at the spiritual level [15]. People began to build spiritual dwellings and public buildings for God. It is a strange phenomenon that residential buildings have not changed much for thousands of years. The greatest contributor to the development of buildings is public buildings. It can be seen that after the basic survival requirements of mankind are met, more attention will be paid to ideology. Therefore, the basic value requirements of architecture and sculpture should be the same.

(2) Aesthetic proposal

The understanding of geometric beauty of architectural form was described as early as the century BC. Later, influenced by the aesthetic thoughts of scholars, architects began to be particularly keen to reveal the mystery of Architectural Formal Beauty from the relationship between geometry and numbers. They use the superposition and change of geometric prototypes such as square, regular triangle, golden section ratio, and circle to shape a beautiful architectural form. The harmonious proportion of the human body is also the focus of the Greeks. Therefore, a large number of sculptures in ancient Greece are based on the beautiful human body to carve (Figure 1) of gods. At the same time, they believe that the human body can be used as the measure of all things. Therefore, in their concept, in order to obtain the beauty of buildings, they must make the buildings have the proportional relationship and harmonious order in line with the beauty of human body.
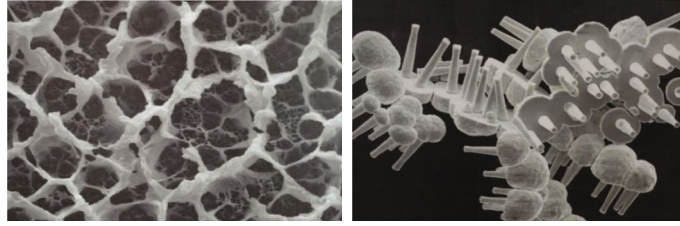
FIGURE 2: Unintentional micro-engraving works.

(3) Asylum in spiritual places

Through the ages, people's interest in nonpractical aspects and the labor paid for them have greatly exceeded the practical aspects. With the progress of human civilization and the improvement of material acquisition ability, sculpture and architecture show less and less demand for material functions. The expression of ideology, culture, and spiritual consciousness has become an important content. While sculpture and architecture have become the carrier of cultural expression, they have also become the sustenance of spiritual appeal. On the one hand, they show the materialization of human spiritual sustenance; on the other hand, they show the spiritual demand for beauty. As an important medium that leads the material world of architecture to the spiritual world of art, sculpture art with a long history has been changing people's environment. It edifies people's sentiment and stands there for a long time with buildings, witnessing the evolution of human material world and spiritual world.

(4) Subordinate relationship between sculpture and architecture

First, sculptures are attached to buildings. In this case, sculpture can be regarded as a part of architecture, which cannot exist independently. Most of the time, it plays the role of decorative structure. Secondly, sculpture works can enter the architectural space environment. Sculptures in this situation can exist as independent works of art and show their own modeling beauty in the general environment of architecture.

Most of the time, sculpture is the relationship between cooperation and obedience to architecture. From the perspective of practical needs, a large number of sculptures do belong to this category. However, if we only define these two majors as such a subordinate relationship, we underestimate the role of sculpture itself. It ignores the function of carving and weakens the subject consciousness of carving. In fact, the space effect that sculpture can convey is as important as architecture. Sculpture is not only the decoration and appendage of architecture but also the prototype of building space framework together with architecture. The two should have indivisible integrity. Putting aside the limitation of sculpture to talk about an architectural work is not in line with the consciousness of integration in the builder's psychology. Architecture without carving aura is like a body without soul, which is also a kind of blasphemy to the architecture itself.

In the classical period, sculpture was attached to architecture. However, in the modern landscape, it is difficult to say that some structures belong to sculpture or architecture. In the modern environment, the relationship between sculpture and architecture is complementary, interactive, and complementary. They have undoubtedly greatly enriched the form of place space. The combination of sculpture and architecture makes their design no longer isolated, and the integration of design techniques is closer. At the same time, it is of positive significance to the shaping of the whole environment.

3.1.4. Differences between Carving Technology and Architectural Sculpture Art. As two similar disciplines, architecture and sculpture have many similarities in characteristic forms and many differences in essential characteristics. It is these differences that lead to the independence of the two disciplines. In short, architecture is often restricted by function, science, technology, and other factors. Sculpture works can express space more freely. Their differences can be summarized as follows:

(1) Functional differences

Architecture is a high unity of material and spirit, which is in the critical state of pragmatic beauty and artistic beauty. The consideration of function, beauty, and meaning of architecture covers a wide range. In architectural design, the layout of space streamline is very important. The layout of architectural functions has a great impact on the shape of buildings and even the internal space form. Therefore, the design of buildings must first comply with the functions they should have. This consideration is reflected in all stages of the design process. Whether it is the coordination with the base environment, the relationship between space or the organization of streamline, it directly affects the final form of expression of the building. Sculpture seems to be the opposite. The sculptor's pursuit of higher cultural purity and beauty is a kind of sculptural work. It has a strong expressive force, highlighting the artist's self-awareness and emotional expression. It is an effective supplement to the spatial framework on the premise of ensuring that its own has the most basic aesthetic effect. Its attention to beauty greatly exceeds its practicability.

(2) Spatial performance difference

Sculpted space refers to the sculpted shape, while architectural space mainly refers to the internal use space of the

building. It is closely related to the use function of the building. Although the form language of architecture seems more abstract and geometric, it aims to separate or contain the practicability of space. The spatial form of architecture must first meet the functional needs, in addition to meeting people's aesthetic requirements. Engineering structure, technology, and materials will also more or less affect the form of architectural space.

(3) Differences in internal structure

Due to the different sizes of sculptures and buildings, their internal structures are very different. The small scale and no internal space of the sculpture determine its flexibility. Most of the artist's energy is spent on how to mount and carve the outside, and it can build the internal construction of carving at will. As long as it can support the work, it is enough. But buildings are much more complex. Although small-scale building models can also be simulated in the scheme deliberation and creation stage, due to mechanical and engineering factors, we cannot treat real buildings in the way of building models. For example, when building a model, the overhang of a cantilever beam may only depend on the strength of the model material itself, but its equal overhang in a real project needs much more complex calculation and node support.

3.2. Characteristics of Engraving Materials Based on Micro Nanotechnology. Micro nanotechnology has a wide range of applications. At present, it has given full play to its application value in many valuable fields, especially its optical properties have always been paid attention to by the research community. This paper mainly studies the optical properties of engraving materials for nanotechnology according to the principle of optical properties.

Previous studies have shown that there are [16] in a wide range of light intensity:

$$-dI = \alpha I dx. \tag{1}$$

The definitions of parameters in Formula (1) are shown in Table 3:

By integrating with this formula, the light intensity after passing through the medium with thickness is obtained [17]:

$$I = I_0 e^{-ad}. \tag{2}$$

I_0 is the initial light intensity, which is called Lambert's law.

As an electromagnetic wave, the energy flux density of light is expressed by Poynting vector. Light intensity is the time average of energy flow density. For the convenience of calculation, the electric field and magnetic field are expressed as [18]:

$$\begin{aligned}
\vec{E} &= \frac{1}{2}\vec{E}_m e^{-i\omega t} + \frac{1}{2}\vec{E}_m^* e^{i\omega t}, \\
\vec{H} &= \frac{1}{2}\vec{H}_m e^{-i\omega t} + \frac{1}{2}\vec{H}_m^* e^{i\omega t}.
\end{aligned} \tag{3}$$

TABLE 3: Interpretation of each parameter in the formula.

Sequence	Formula parameters	Paraphrase
1	dI	Increment of light intensity
2	dx	Thickness of light passing vertically
3	α	The absorption coefficient of a substance
4	d	Thickness of light passing through

Plane simple harmonic wave [19]:

$$\frac{\left|\vec{H}_m\right|}{\left|\vec{E}_m\right|} = c\varepsilon_0\sqrt{\varepsilon}. \tag{4}$$

If it is taken, then [20]:

$$I = \frac{1}{T}\int_0^T \left(\vec{E} \times \vec{H}\right)dt = \frac{1}{4}c\varepsilon_0\left[\sqrt{\varepsilon^*} - \sqrt{\varepsilon}\right]\left|\vec{E}\right|^2. \tag{5}$$

It can also be expressed as [21]:

$$I = \frac{1}{2}c\varepsilon_0 n\vec{E}_m\vec{E}_m^* = \frac{1}{2}c\varepsilon_0 n\left|\vec{E}_m\right|^2. \tag{6}$$

If the wave vector direction is along the x axis, then [22]:

$$\left|\vec{E}_m\right|^2 = \left|\vec{E}_0\right|^2 e^{-2\omega Kx/c} = \left|\vec{E}_0\right|^2 e^{-\alpha x}. \tag{7}$$

So,

$$I = \frac{1}{2}c\varepsilon_0 n\left|\vec{E}_0\right|^2 e^{-\alpha x} = I_0 e^{-\alpha x}. \tag{8}$$

This is the law of solid light absorption, visible absorption coefficient [23]:

$$\alpha = \frac{2\omega K}{c} = \frac{4\pi K}{\lambda}. \tag{9}$$

Formula (9) shows that the free light coefficient also represents the absorption of light by a solid.

After the semiconductor absorbs photons, it causes the planter excitation and increases the conductivity. The increased conductivity is called photoconductivity. This additional photoconductivity comes from the inter band transition of carriers or the excitation of impurities. The work done by light to photocurrent in unit time and unit volume is called optical power density, which is equal to:

$$W = \left\langle \vec{J} \times \vec{E} \right\rangle. \tag{10}$$

< > means averaging the time. Using the complex forms of and above, we can get [24]:
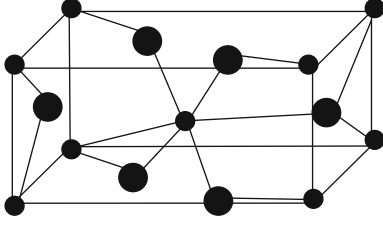
FIGURE 3: Carbon dioxide crystal structure.
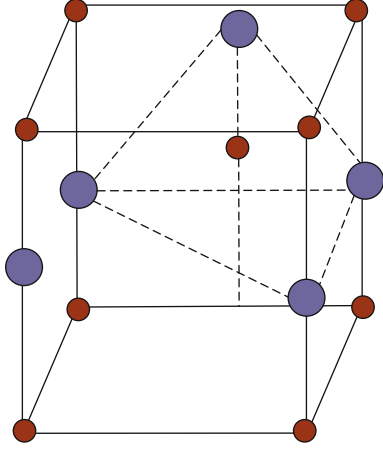
FIGURE 4: Zinc oxide crystal structure.
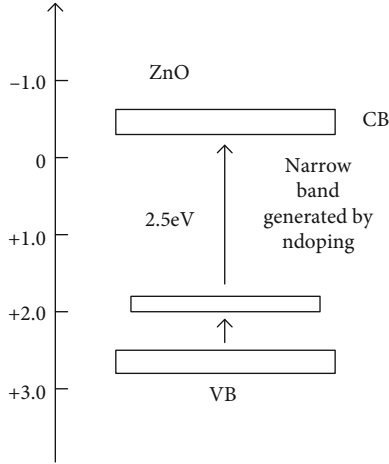
FIGURE 5: Visible light absorption of doped zinc oxide.

$$W = \frac{1}{2}\varepsilon_0 \omega \varepsilon_i \left| \vec{E}_m \right|^2 = \frac{1}{2}\varepsilon_0 \omega x \left| \vec{E}_m \right|^2. \tag{11}$$

It can be seen here that the imaginary part of the dielectric constant or the imaginary part of the polarizability is related to the free current.

The absorptivity is defined as the ratio of absorbed energy to incident energy. When the light is vertically incident on a solid surface, the incident light intensity (i.e., aver-
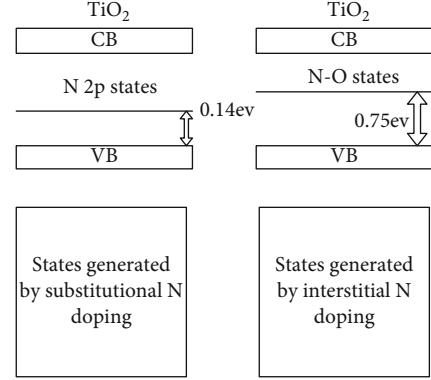
FIGURE 6: Visible light absorption of doped titanium dioxide.

age energy flow density) is, and the absorbed energy flow density is equal to the optical power density multiplied by the thickness, then [25]:

$$A = \frac{\varepsilon_0 \omega \varepsilon_i d}{\varepsilon_0 cn} \frac{\left| \vec{E}_m \right|^2}{\left| \vec{E}_0 \right|^2} = \frac{\omega \varepsilon_i d}{cn} e^{-\alpha d}. \tag{12}$$

In air, when the film thickness is very small, ignoring the attenuation of amplitude after light flux, we get:

$$A \approx \frac{\omega \varepsilon_i}{cn} d = \alpha d. \tag{13}$$

The optical power and optical absorptivity can also be expressed as:

$$W = \frac{1}{2}\sigma_r \left| \vec{E}_m \right|^2.$$
$$A \approx \frac{\sigma_r d}{\varepsilon_0 cn}. \tag{14}$$
$$\alpha \approx \frac{\sigma_r}{\varepsilon_0 cn}.$$

When light shines on a solid, according to the conservation of energy, the relationship between absorptivity, reflectivity, and transmittance is:

$$A + R + T = 1. \tag{15}$$

From Michaelis formula:

$$\vec{H} = \frac{\bar{n}\sqrt{\varepsilon_0/\mu_0} \left(\vec{s}_0 \times \vec{E} \right)}{\mu}. \tag{16}$$

$\vec{s}_0$ is the unit vector of the wave vector. It defines the optical admittance of the medium as:

TABLE 4: Artist personal information.

Sequence	Age	Working time
artist 1	21	5 years
artist 2	33	12 years
artist 3	45	21 years
artist 4	38	18 years
artist 5	27	10 years

$$Y = \frac{\vec{H}}{\vec{s}_0 \times \vec{E}} = \bar{n}\sqrt{\frac{\varepsilon_0/\mu_0}{\mu}}. \tag{17}$$

For medium, its optical admittance is:

$$Y = \frac{\vec{H}}{\vec{s}_0 \times \vec{E}} = \bar{n}. \tag{18}$$

The unit of optical admittance in formula (18) adopts free space admittance.

The more common carving materials are zinc oxide and titanium dioxide, which are often used by carving artists because of their unique comprehensive properties, such as good chemical stability, low cost, nontoxic, high quantum efficiency, and redox ability. Titanium dioxide exists in many forms in nature. Its crystal structure is shown in Figure 3:

Zinc oxide also has a variety of morphologies, such as nanocomb, nanorod, nanohelix, nanobelt, nanowire, and nanocrystal. Its crystal structure is shown in Figure 4:

The visible light absorption after doping two materials is shown in Figures 5 and 6:

4. Artistic Aesthetic Practice

This paper uses micro nanotechnology to create a sculpture sample and test its aesthetic practice. The general evaluation of works of art comes from two aspects: the general evaluation of works of art. That is the external evaluation and internal evaluation of the work. External evaluation includes whether the structural proportion of the work is uniform and whether the appearance is aesthetic. This is the most intuitive and basic evaluation index in aesthetic practice. In addition, it also includes the richness and unity of works. The external evaluation of works includes whether the works realize the unity of identification and creativity, practicability, and artistry. As the evaluation of aesthetic practice is affected by many factors, the evaluation method of this paper adopts the subjective evaluation method. Five sculpture artists were invited to evaluate the works of this article. The personal information of the five artists is shown in Table 4. Then, this paper compares the evaluation results with the evaluation results of traditional sculpture works. The evaluation system is bit score system. The full score of each evaluation index is 10. The higher the score, the better

the evaluation of the work. The evaluation results are shown in Figures 7–10.

(1) Proportion and aesthetic evaluation of works

As can be seen from Figure 7, the average overall score of the proportion of sculpture works created based on micro nanotechnology in the evaluation of six artists is about 8.46 points, and the average overall score of aesthetic feeling of works is 8.25 points. The average score of the proportion of works created in traditional crafts in the evaluation of six artists is about 8.20 points, and the average score of the overall aesthetic feeling of works is 8.11 points.

(2) Evaluation of richness and unity of works

It can be seen from Figure 8 that the average overall score of the richness of the sculpture works created based on micro nanotechnology in the evaluation of six artists is about 7.79 points, and the average overall score of the unity of the works is 8.05 points. The average overall score of the richness of works created in traditional crafts in the evaluation of six artists is about 7.87 points, and the average overall score of the unity of works is 8.04 points.

(3) Work identification and creative evaluation

As can be seen from Figure 9, the average overall score of work identification of sculpture works created based on micro nanotechnology in the evaluation of six artists is about 8.44 points, and the average overall score of work creativity is 8.48 points. The average overall score of works created in traditional crafts in the evaluation of six artists is about 8.45 points, and the average overall score of works' creativity is 8.30 points.

(4) Practical and artistic evaluation of works

As can be seen from Figure 10, the sculpture works created based on micro nanotechnology in this paper have an average overall score of about 7.57 points for practicability and 8.25 points for artistry in the evaluation of six artists. The average value of the overall practical score of the works created in the traditional craft in the evaluation of the six artists is about 7.56 points, and the average value of the overall artistic score of the works is 8.17 points.

5. Discussion

By comparing the scores of micro nanosculpture works with traditional craft sculpture works, the following conclusions can be drawn:

(1) In terms of the proportion and aesthetic feeling of works, the overall average score of the proportion of sculpture works created based on micro nanotechnology is 0.26 points higher than that of sculpture works created under traditional technology. The overall average aesthetic score of the works in this paper is 0.14 points higher than that of the sculpture

(a)

(b)
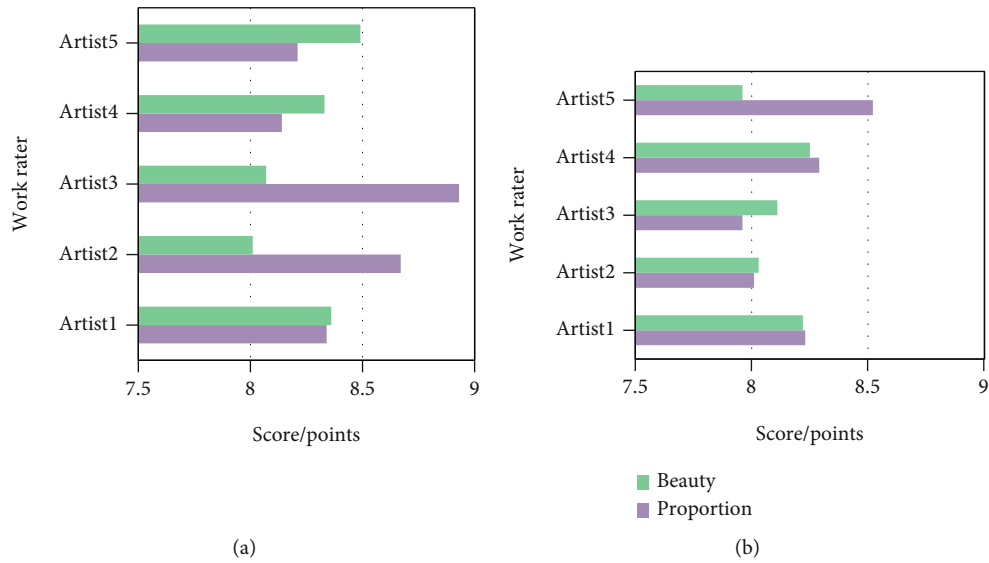
FIGURE 7: Proportion and aesthetic evaluation of works. (a) Proportion and aesthetic evaluation of the work in this article. (b) Proportion and aesthetic evaluation of traditional works.

(a)

(b)
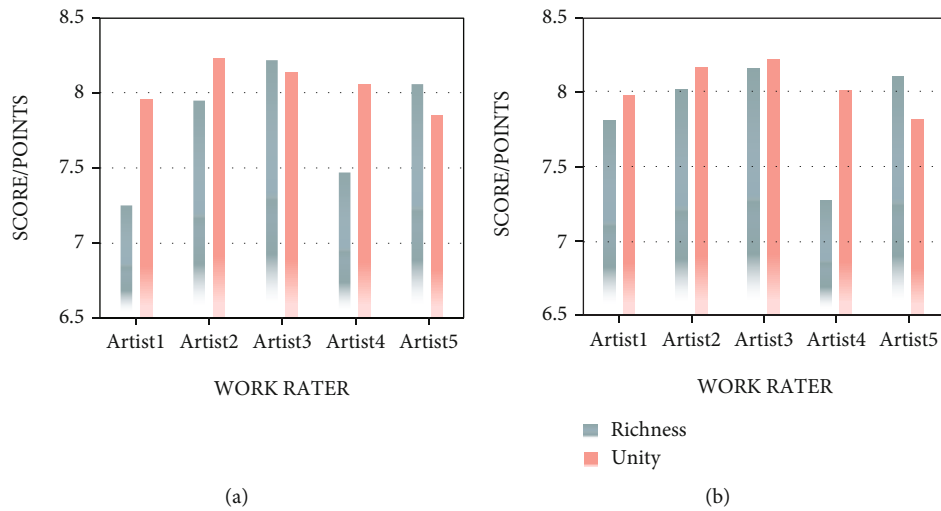
FIGURE 8: Evaluation of the richness and unity of work. (a) The evaluation of the richness and unity of this work. (b) The evaluation of the richness and unity of traditional works.

works created under the traditional technology. It shows that the sculpture works created in this paper are symmetrical in structure, uniform in proportion, and in line with public aesthetics

(2) At the level of richness and unity of works, the overall mean value of the richness score of sculpture works created based on micro nanotechnology is 0.08 points lower than that of sculpture works created under traditional technology. The overall average score of the unity of works in this paper is 0.01 higher than that of sculpture works created under traditional technology. It shows that the richness of the works created in this paper is weaker than the traditional craft works, but it has advantages in the overall unity of the works

(3) At the level of work identification and creativity, the difference between the overall average of the identification score of sculpture works created based on micro nanotechnology and the overall average of the identification score of sculpture works created under traditional technology is 0.01. The overall average score of the creativity of the works in this paper is 0.18 points higher than that of the sculpture works created under the traditional technology, which shows that the works created in this paper are generally recognizable. But it has high creativity

(4) At the level of practicability and artistry, the overall average score of the practicability of sculpture works created based on micro nanotechnology in this paper is 0.01 points higher than that of sculpture works

(a)

(b)

Recognition
Creativity
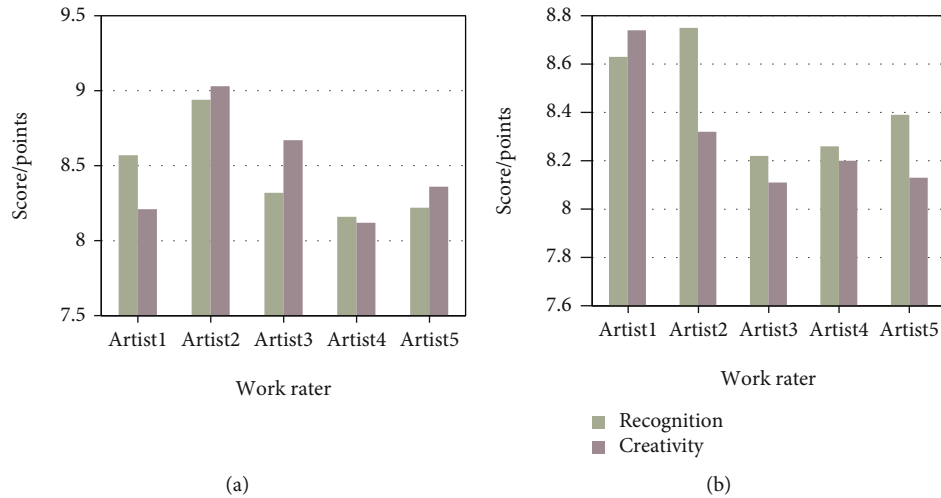
FIGURE 9: Work recognition and creativity evaluation. (a) The identification and creativity evaluation of this work. (b) The identification and creativity evaluation of traditional works.

(a)

(b)

Practicality
Artistry
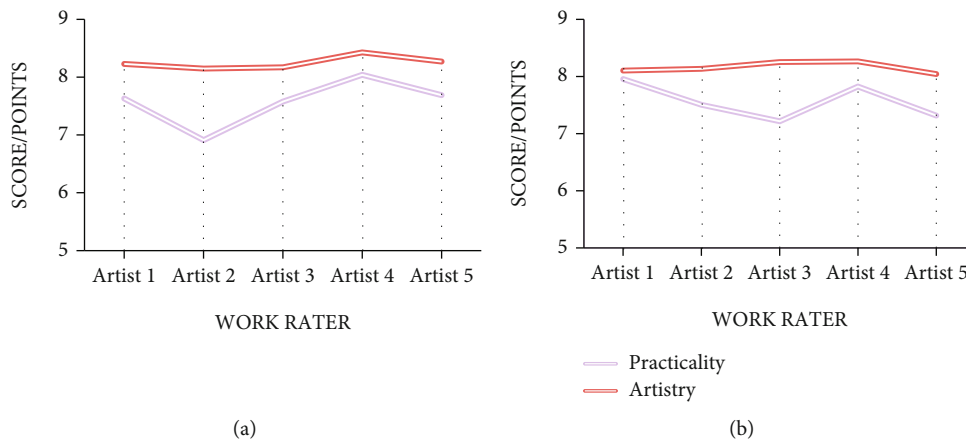
FIGURE 10: Practicality and artistic evaluation of works. (a) The practical and artistic evaluation of this work. (b) The practical and artistic evaluation of traditional works.

created under traditional technology. The average score of traditional sculpture works is 0.08. It shows that the works created in this paper have high practicability and artistry

The whole comparative aesthetic practice data show that under the same conditions of other experiments, through the evaluation and test of different projects, the sculpture works created based on micro nanotechnology are superior in terms of proportion, beauty, unity, creativity, practicability, and artistry. And in terms of the richness and identification of the works, there is little gap between them and the works created based on traditional technology. It shows that the carving technology and architectural sculpture art based on micro nanotechnology have good application value and artistic value, which can promote the diversified development of the art market.

6. Conclusion

Since ancient times, sculpture technology and architectural sculpture art have been an indispensable part of art and culture in the process of human history. In order to make it sustainable, it needs to meet the characteristics of the times and innovate. Micro nanocarving technology and architectural sculpture art are the products of traditional art in the development of the times. Micro nanoengraving technology and architectural sculpture art are a composite creation process. It not only involves the subjective art field and art concept but also includes objective scientific theoretical knowledge, although the current stage of micro nanoart is not yet mature, and there are many inherent defects. With the diversified development of the art field and the continuous renewal of science and technology, especially under the background of the improvement and progress of

nanoscience and technology, micro nanocarving technology and architectural sculpture art are bound to usher in a considerable future.

Although this paper uses micro nanotechnology to deeply study the carving technology and the aesthetic practice of architectural sculpture, there are still many deficiencies. In the process of this study, the acquisition of aesthetic practice evaluation data is carried out under absolutely ideal conditions, and the integrity and effectiveness are not enough. It does not take into account some interference factors involved in the evaluation process. The depth and breadth of this research are not enough, the author's academic level research is also limited, and the research on micro and nanotechnology is still in the preliminary stage. In the future work, it will study appropriate research translation methods and means from more angles according to the existing technology and level for the purpose of improving the research quality.

Data Availability

This article does not cover data research. No data were used to support this study.

Conflicts of Interest

The authors declare that they have no conflicts of interest.

References

[1] J. Shi, J. Hou, and Y. Fang, "Recent advances in nanopore-based nucleic acid analysis and sequencing," *Microchimica Acta*, vol. 183, no. 3, pp. 925–939, 2016.

[2] X. Tian, S. Lian, and W. Jin, "Egg albumin-assisted sol–gel synthesis and photo-catalytic activity of SnO2 micro/nano-structured biscuits," *Journal of Sol-Gel Science and Technology*, vol. 85, no. 2, pp. 402–412, 2018.

[3] P. Shah, S. K. Cho, P. W. Thulstrup et al., "MicroRNA biomarkers in neurodegenerative diseases and emerging nanosensors technology," *Journal of Movement Disorders*, vol. 10, no. 1, pp. 18–28, 2017.

[4] R. Rohini and C. P. Sugumaran, "Enhancement of electrothermal characteristics of micro/nano ZnO based surge arrester," *Journal of Electrical Engineering & Technology*, vol. 16, no. 1, pp. 469–481, 2021.

[5] C. C. Ho, B. H. Huang, and P. C. Chu, "A study based on electrochemical discharge assisted by hollow electrode and micro-nano bubble to process transparent non-conductive brittle materials," *The International Journal of Advanced Manufacturing Technology*, vol. 115, no. 1-2, pp. 367–382, 2021.

[6] A. A. Taheri and F. Talati, "FDM-based 2D numerical study of hyperthermia cancer treatment by micro/nano-phase-change materials," *Iranian Journal of Science and Technology, Transactions of Mechanical Engineering*, vol. 44, no. 4, pp. 1077–1089, 2020.

[7] J. Sun, X. Shi, and Y. Du, "A robust, flexible superhydrophobic sheet fabricated by in situ growth of micro-nano-SiO2 particles from cured silicone rubber," *Journal of Sol-Gel Science and Technology*, vol. 91, no. 1, pp. 208–215, 2019.

[8] Y. Lian, H. Chen, C. Mu, J. Deng, and S. Lei, "Experimental investigation and mechanism analysis of tungsten disulfide soft coated micro-nano textured self-lubricating dry cutting tools," *International Journal of Precision Engineering and Manufacturing-Green Technology*, vol. 5, no. 2, pp. 219–230, 2018.

[9] W. Bian, T. Yao, M. Chen, C. Zhang, T. Shao, and Y. Yang, "The synergistic effects of the micro-BN and nano-Al2O3 in micro-nano composites on enhancing the thermal conductivity for insulating epoxy resin," *Composites Science and Technology*, vol. 168, pp. 420–428, 2018.

[10] Y. Lian, J. Deng, and B. Yao, "Influence of different cemented carbides on fabricating periodic micro-nano textures by femtosecond laser processing," *Surface and Coatings Technology*, vol. 317, pp. 166–171, 2017.

[11] Q. Hu, W. Jiang, Y. Li et al., "The effects of morphology on physicochemical properties, bioactivity and biocompatibility of micro-/nano-bioactive glasses," *Advanced Powder Technology*, vol. 29, no. 8, pp. 1812–1819, 2018.

[12] R. Gholami, A. Darvizeh, and R. Ansari, "Analytical treatment of the size-dependent nonlinear postbuckling of functionally graded circular cylindrical micro-/nano-shells," *Iranian Journal of Science and Technology: Transactions of Mechanical Engineering*, vol. 42, no. 2, pp. 1–13, 2017.

[13] H. Liu, X. Jin, and D. Zhou, "Potential application of functional micro-nano structures in petroleum," *Petroleum Exploration and Development*, vol. 45, no. 4, pp. 745–753, 2018.

[14] S. Huang, X. Wang, Q. Zhu, X. Li, J. G. Li, and X. Sun, "Systematic synthesis of REVO4 micro/nano crystals with selective exposure of high energy 001 facets and luminescence (RE lanthanide and Y0.95Eu0.05)," *Journal of Materials Research and Technology*, vol. 9, no. 6, pp. 12547–12558, 2020.

[15] A. Reyes, G. A. Guerrero, and G. R. Ortiz, "Microstructural, microscratch and nanohardness mechanical characterization of secondary commercial HPDC AlSi9Cu3-type alloy," *Journal of Materials Research and Technology*, vol. 9, no. 4, pp. 8266–8282, 2020.

[16] M. Lojka, F. Antoník, and D. Sedmidubsk, "Phase-stable segmentation of BSCCO high-temperature superconductor into micro-, meso-, and nano-size fractions," *Journal of Materials Research and Technology*, vol. 9, no. 6, pp. 12071–12079, 2020.

[17] M. Kim, S. M. Lee, S. J. Lee, Y. W. Kim, Liang-Li, and D. W. Lee, "Effect on friction reduction of micro/nano hierarchical patterns on sapphire wafers," *International Journal of Precision Engineering and Manufacturing-Green Technology*, vol. 4, no. 1, pp. 27–35, 2017.

[18] A. Vkp, B. Rk, and A. Ac, "Performance characterization of Bi2O3/Al nanoenergetics blasted micro-forming system," *Defence Technology*, vol. 15, no. 1, pp. 98–105, 2019.

[19] Z. Y. Hu, Y. L. Sun, J. G. Hua, Y. H. Yu, Q. D. Chen, and H. B. Sun, "Femtosecond laser nano-fabrication with extended processing range," *IEEE Photonics Technology Letters*, vol. 31, no. 2, pp. 133–136, 2019.

[20] Y. Mamunya, L. Matzui, L. Vovchenko et al., "Influence of conductive nano- and microfiller distribution on electrical conductivity and EMI shielding properties of polymer/carbon composites," *Composites Science and Technology*, vol. 170, pp. 51–59, 2019.

[21] Z. Ding and K. Xu, "Recent progress in imaging technology combined with nanomaterials for medical applications," *Micro & Nano Letters*, vol. 14, no. 12, pp. 1263–1267, 2019.

[22] S. Michael, "Dancing in the streets: known for merging perfor-
     mance and sculpture, Liz Glynn re-creates a Gilded Age ball-
     room for a must-see public art installation," *Architectural
     digest*, vol. 74, no. 3, pp. 62–64, 2017.

[23] R. Blurton, "The Great Plateorm at Vijayanagara. Architecture
     and Sculpture," *Journal of the Royal Asiatic Society*, vol. 28,
     no. 2, pp. 392–395, 2018.

[24] H. Martin, "Shape shifter," *Architectural Digest*, vol. 75, no. 4,
     pp. 46–49, 2018.

[25] R. Sefcu, V. Pitthard, and H. Danova, "An analytical investiga-
     tion of a unique medieval wood sculpture and its monochrome
     surface layer," *Wood Science and Technology*, vol. 52, no. 2,
     pp. 541–554, 2018.

Research Article

Biomimetic Design and Biocompatibility of Biomimetic Calcium Carbonate Nanocomposites for Skeletal Muscle Injury Repair

Yan Han (ID)

College of Physical Education, Xuchang University, Xuchang, 461000 Henan, China

Correspondence should be addressed to Yan Han; 22014015@xcu.edu.cn

As an important part of the human body, skeletal muscle is easily damaged in the process of exercise. The purpose of this study is to investigate the controllable construction and biocompatibility of biomimetic calcium carbonate nanocomposites in exercise skeletal muscle repair. In this study, adult healthy mice were selected as the research objects. First, the mice were anesthetized with 2.5% pentobarbital sodium. Then, the mice were fixed and hit with steel balls on the middle part of the gastrocnemius muscle abdomen to establish a skeletal muscle contusion model. The mice were killed by cervical dislocation under anesthesia. The injured gastrocnemius muscles were quickly removed to prepare the cell suspension. 0.8600 g chitosan was weighed and dissolved in 200 ml deionized water. Then, 0.0660 g of calcium chloride dihydrate was added and stirred to dissolve to prepare chitosan calcium carbonate composite. The calcium carbonate composite material with a length of 8.0 cm is cut into a square sheet of stainless steel. The stainless steel plate was sterilized and then placed in a 12 culture plate to dilute the full cells in the culture bottle. The cells were seeded in 12 well culture plates, and $100\,\mu L$ cells and $600\,\mu L$ medium were added to each well. The samples were cultured in the incubator (there were three control holes in each group for SEM test, three control holes for fluorescence measurement, and six control holes for MTT measurement). The plates were taken out and placed in a new 24 plate. $1000\,\mu L$ medium was added. Then. $100\,\mu L$ MTT solution was added into each well. The biocompatibility test was conducted for 4 h. The GSH PX level in the chitosan calcium carbonate composite group was lower than that in the natural recovery group ($P < 0.01$). The results showed that chitosan calcium carbonate composite could promote the growth of skeletal muscle cells.

1. Introduction

The research on biomimetic materials has long been a hotspot in materials research. In recent years, biomimetic calcium carbonate nanocomposites have attracted more and more attention because of their special structure and good properties. On the basis of optimizing the material structure, the main purpose is to obtain a kind of composite bionic material with strong combination of organic and inorganic energy. On the other hand, through the biomimetic process, the ultimate goal is to make the mechanical properties of the composite materials obtained through formula adjustment controllable. The preparation methods include self-assembly, spin coating, chemical deposition, and compression molding. Bionic film and molding materials were obtained. In recent years, some people have obtained linear long materials with simulated structures using graphene as raw materials. Although the injured skeletal muscle has a strong regenerative capacity, severe trauma, such as loss of muscle tissue, exceeds the natural and complete recovery capacity of skeletal muscle, the clinical treatment has limited effect, and there is no satisfactory bone grafting program at present. Autologous bone is regarded as the "gold standard" of bone defect replacement material because of its excellent osteogenic properties, osteogenic induction, bone electrical conductivity, complete biocompatibility, nontoxicity, and no immune problems. Generally, with a history of trauma or overwork and fatigue, symptoms show localized muscle pain and tenderness.

Many reasons such as trauma and skull tumors can cause skull defects. Skull defects endanger the health of patients, so the repair of the defects is essential. At present,

repair materials include autologous bone, allogeneic bone, and artificial materials. Autogenous bone repair is the best, but its supply is insufficient and its application is limited. Allogeneic bone has severe rejection, which hinders its application. There are many kinds of artificial materials, such as hydroxyapatite and bioceramics, but they have serious side effects and are gradually eliminated. Currently, titanium alloy materials are the most widely used, with good biocompatibility, stable physical and chemical properties, and easy shaping. Carbon fiber has good mechanical properties and biocompatibility, which can improve the mechanical strength of other materials. Bioinert ceramics mainly refer to ceramic materials with stable chemical properties and good biocompatibility, such as alumina, zirconia, and medical carbon materials. The structure of these ceramic materials is relatively stable, the bonding force in the molecule is strong, and they all have high strength, wear resistance, and chemical stability.

Calcium carbonate (CaCO3) nanoparticles have barrier properties and biodegradability effects on polylactic acid (PLA). Aframehr et al. prepare nanocomposite membranes with various CaCO3 nanoparticle contents (0, 3, 5, 10, and 15 wt%) by solution casting method. He uses constant volume and variable pressure equipment to evaluate the permeability of nitrogen (N2), oxygen (O2), and carbon dioxide (CO2) at different pressures and temperatures. In addition, he also observed that the gas permeability of the sample decreased by increasing the feed pressure and increased by increasing the temperature. There are too few experimental data in his research [1]. Acar et al. compared the effect of coffee dyeing on the color of 3 different CAD/CAM restoration materials and nanocomposite resins. He evaluated the color change ($n = 5$) of samples mixed with dental ceramics (VITA Enamic) and nanocomposite resins (Filtek Supreme Ultra Universal) due to thermal cycling. He thermally cycled samples with thicknesses of 0.5 to 0.7 mm and 1 to 1.2 mm for 5000 cycles. The color coordinates obtained from the spectroradiometer are used to calculate the CIEDE2000 color difference ($\Delta E00$) due to thermal cycling in the coffee. Use ANCOVA to analyze the color difference between the thicknesses as covariates between materials. He used the Tukey-Kramer test to analyze the significant difference in average thickness. His research lacks comparative experiments [2]. Nguyen et al. completed the preparation and characterization of modified and unmodified polypropylene- (PP-) wood powder (WP) composites under fixed processing conditions. He used different techniques to study the influence of the size and content of wettable powders and the content of compatibilizers on the properties of composite materials. Scanning electron microscope micrographs show that the distribution of WP in the PP matrix is relatively uniform. His research sample is too small [3]. De France et al. believe that although injectable hydrogels have multiple advantages in biomedical applications, their generally weak mechanical properties often limit their applications. He described that in situ gelling nanocomposite hydrogels based on poly(oligoethylene glycol methyl methacrylate) (POEGMA) and rigid rod-shaped cellulose nanocrystals (CNC) can overcome this challenge. By physically incorporating CNCs into the cross-linked POEGMA hydrogel, he can easily customize the macroscopic properties, including gelation rate, swelling kinetics, mechanical properties, and hydrogel stability. The strong adsorption of the aldehyde and hydrazide modified POEGMA precursor polymer on the surface of CNCs can promote the uniform dispersion of CNCs in the hydrogel and give physical cross-linking in the entire network. His research is not novel enough [4].

In this study, adult healthy mice were selected. First, the mice were anesthetized with 2.5% sodium pentobarbital, and the mice were fixed and then hit the midsections of the bilateral gastrocnemius muscles with steel balls to create skeletal muscle blunt contusion models. The mice were killed by cervical dislocation under anesthesia, and the injured gastrocnemius muscles of both sides were quickly taken to prepare the cell suspension. Weigh 0.8600 g of chitosan and dissolve it in 200 mL of deionized water. Then add 0.0660 g calcium chloride dihydrate, stir to dissolve, and prepare chitosan calcium carbonate composite material. The chitosan-calcium carbonate composite material prepared by using a stainless steel sheet as a base is cut into a square with a side length of 0.8 cm. Sterilize the stainless steel sheet and place it in a 12-well culture plate to dilute the overgrown cells in the culture flask. The cells were seeded in a 12-well culture plate, and 100 μL of cells and 600 μL of culture medium were added to each well. Incubate in an incubator (including three control holes for each group of samples when doing SEM test, three control holes for each group of samples when measuring fluorescence, and six control holes for each group of samples when measuring MTT). Ceramic artificial bone is the use of bioceramics as a repair material for bone tissue defects or deletions and uses it to form a mesh scaffold structure to promote and guide bone tissue.

2. Skeletal Muscle Injury Repair Experiment

2.1. Bionic Materials. Inspired by biological materials, we use the principles of bionics to study the formation mechanism of biological materials and apply them to the synthesis of new materials in the future, to be able to design and synthesize organic materials, inorganic materials, organic-inorganic composite materials, functional, and even smart materials; it is a research hotspot that has developed rapidly in recent years and has developed into a popular research in multiple disciplines and fields such as chemistry, materials, and life sciences [5, 6]. Calcium carbonate material is loaded with rare earth metals or other functional components, which can realize the functions of comprehensive diagnosis, treatment or diagnosis and treatment, and is used for imaging diagnosis and treatment [7, 8]. The minimum energy parameter is expressed as follows:

$$E_{\text{snake}} = \int_0^1 EV(s)ds = \int_0^1 \left\{ E_{\text{int}} V(s) + E_{\text{image}} V(s) + E_{\text{cins}} V(s) \right\} ds. \tag{1}$$

Among them, it can represent the internal energy of a

substance [9, 10]. The constituent materials of natural bio-composites range from organic natural sugars to various proteins and inorganic minerals [11, 12]. The research, design, and synthesis of new materials have brought new methods and routes [13, 14]. Based on the advantages of calcium carbonate material and its wide range of existing applications, its application in the medical field will be more complete, the technology will be more mature, and it will definitely contribute to solving the problems in the human medical field. Reducing the cost of products is the biggest advantage of calcium carbonate, because the price of calcium carbonate is the lowest price among all fillers, and the plastic products compounded with it are of course the lowest price [15, 16].

2.2. Nanomaterials.

With the continuous progress and development of science and technology, nanotechnology is also constantly improving. Nowadays, nanotechnology can be seen everywhere in people's daily life and is applied to all aspects of life. Many nanotherapeutic drugs in clinical and preclinical stages are polymer nanoparticles, which have been widely studied as therapeutic carriers. The design of polymer nanoparticles is based on their biocompatibility and biodegradability [17]. Most of these nanoparticles are formed by the self-assembly process of block copolymers, which are composed of two or more polymer chains with different hydrophilic properties [18, 19]. The resulting structure is very suitable for drug delivery. The hydrophobic core can carry a large number of therapeutic drugs, and the hydrophilic shell provides three-dimensional protection for the nanoparticles [20]. Used to express the compressive resistance of polymer nanomaterials, including

$$\eta(X, \mu) = \frac{1}{2\pi^{n/2}|m|} e^{-1/2(X-\mu)\sum(X+\mu)} + \mu K. \qquad (2)$$

Among them, the larger the molecule, the stronger its cohesion [21, 22]. Other widely studied nanodrug delivery systems include metal nanoparticles. Metal-containing nanoshells are usually composed of inert metals (such as gold or titanium) and are used to control the release of chemotherapeutic drugs. These systems have unique characteristics [23]. Although these metal ions are inert and biocompatible, they will remain in the body in large quantities after administration, and the accumulation of metal particles formed by repeated administration may cause toxicity [24, 25]. For nanomedicine, its therapeutic effect is better, and the toxicity is lower [26]. In fact, the progress of nanomedicine is rapidly applied to clinical practice [27, 28].

2.3. Nanomaterial Preparation Experiment.

PBT is milky white translucent to opaque, semicrystalline thermoplastic polyester, with high heat resistance, toughness, fatigue resistance, self-lubricating, low friction coefficient, not resistant to strong acid and alkali, resistant to organic solvents, flammable, and decomposed at high temperature [29]. Dilute the prepared nano-CaCO3 suspension with deionized water, and observe the particle dispersion in the solution with a transmission electron microscope. Take a part of the nano-

CaCO3 suspension after multiple washing and drying, and then grind to obtain CaCO3 particles, which are combined with the initial nano-CaCO3 particles, and cellulose ether dispersant was analyzed by infrared spectroscopy together. The extruded strip was brittle under liquid nitrogen conditions, and the section was vacuum-plated. The morphology of the section was observed with a scanning electron microscope (SEM), and the accelerating voltage was 20 kV. For PCΠnano2CaCO3 samples with the same thermal history. The pure PC sample is analyzed by gel permeation chromatography, the column PLgel is 5 μm, tetrahydrofuran is selected as the solvent, the test temperature is $T = 35°C$, and PS is used as the standard sample. The sample is injected, the tensile performance is in accordance with the GBΠT104021992 standard, and the bending performance is in accordance with the GBΠT934121988 standard. The impact performance is tested according to the GB/T183421996 standard.

After the resin matrix is filled with nano-CaCO3, the tensile strength and flexural strength have been improved to different degrees. The impact strength of PP composites has increased, and the impact strength of PBT and PC composites has decreased slightly. Combined with the GPC results, it can be considered soft, method does not cause mechanical and thermal degradation of the system matrix when preparing polymer Π nanoparticle composites, and is a new method for preparing nanocomposites of polar and nonpolar polymers. Especially for PP systems, the processing method can only rely on the addition of nanoparticles, which can simultaneously play a role in strengthening and toughening. Scanning electron microscopy photos of nanoporous silicon: a side view and by top view, as shown in Figure 1.

2.4. Main Equipment.

Corotating twin-screw extruder, SHJ220, Nanjing Jiente Mechanical & Electrical Co., Ltd.; Ultrasonic Disperser, VCF21500, Sonic & Materials Inc., USA; Scanning Electron Microscope, JSM25900LV, Japan JEOL Co., Ltd.; Transmission Electron Microscope, HITACHTH2600, Japan Hitachi Co., Ltd.; infrared spectroscopy; Nicolet20SXB Fourier transform infrared spectrometer, American Thermoelectric Nicolas; gel permeation chromatography: Agilent1100Series gel permeation chromatograph, American Agilent company; injection machine, PS40E5ASE type, Nissei Resin Industry Co., Ltd.; Shimadzu universal material testing machine, type AG210TA, Shimadzu Corporation; cantilever beam impact testing machine, type UJ240, material testing machine factory in Chengde City, Hebei Province.

2.5. Selection of Experimental Subjects.

The animals used in this experiment are adult healthy mice, a total of 96 mice, weighing 2.6-3.0 kg, and are half male and female. The food and activities of the experimental animals were good, the skin and mucous membranes were intact, and the epiphyses were closed. The experimental equipment is shown in Table 1.

2.6. Skeletal Muscle Blunt Injury Model.

Skeletal muscle injuries are an important component of trauma in sports
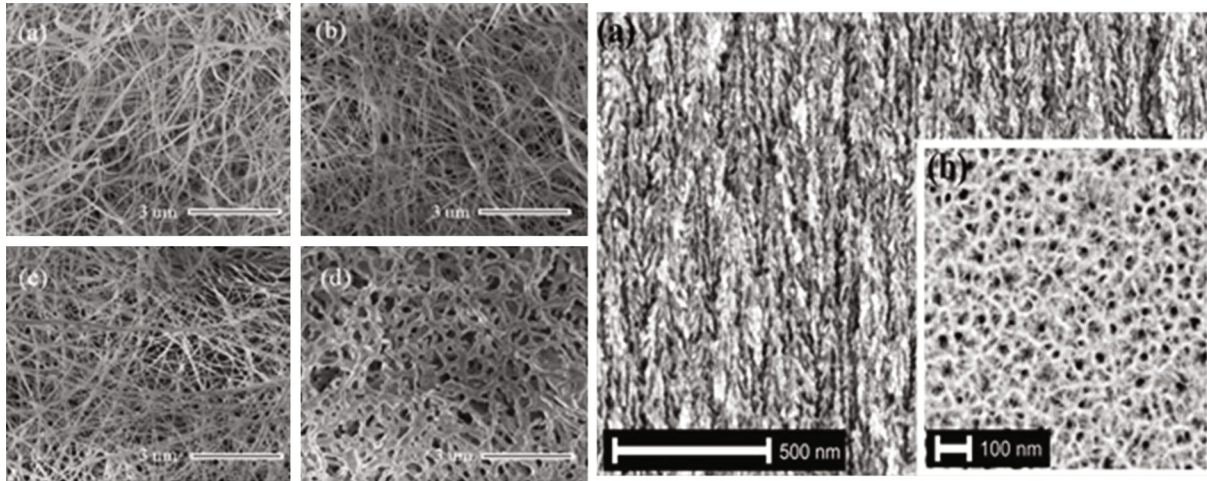
Figure 1: Scanning electron micrograph of nanoporous silicon.

Table 1: Experimental equipment.

Equipment name	Model	Manufacturer
Vacuum multitarget magnetron sputtering instrument	KCCK-III	Shenyang Kecheng
Field emission scanning electron microscope	S-4800	Hitachi
X-ray diffractometer	D8 discover	Bruker
Transmission electron microscope	JEM-2100	JEOL
Inverted fluorescence microscope	IX71-Olympus	Olympus

medicine, with injury rates ranging from 10% to 55%. Because treatment failure can delay an athlete's return to play, which can be weeks or months, and lead to recurrence, the management of musculoskeletal injuries requires extreme measures. A simple and reproducible blunt skeletal muscle modelling method is adopted. After the mice were anesthetized by intraperitoneal injection of 2.5% sodium pentobarbital, they were fixed at the knee joint extension at 0° and the ankle joint extension at 90°. A solid stainless steel ball with a mass of 16.8 g and a diameter of 15.9 mm was placed on the top of a transparent tube. (Height 100 cm, inner diameter 16.0 mm) after free fall, it hits the striking device vertically. The bottom of the striking device hits the middle of the abdominal muscles of the mouse bilateral gastrocnemius muscles. The striking position is fixed (the striking area is 20 mm^2), the skin is intact after injury, there is no tibiofibular fracture, and the anatomy confirmed that the damage rate was 100%.

2.7. Animal Selection and Weighing. The genes of mice are very similar to those of humans. The mice are mammals, and their genomes are very similar to those of humans. The effect of using them in genetic experiments is very good, and the cause can be found through experiments on mice, to study the regularity of disease and treatment methods. Strictly according to the time point of the experimental grouping, the mice were killed by cervical dislocation under anesthesia. The injured gastrocnemius on both sides was quickly taken. The gastrocnemius muscle of the same part was taken in the control group, and the material was fixed. The excess connective tissue was carefully removed and

rinsed with 4°C physiological saline. The filter paper was soaked and weighed, and the muscle weight/body weight was used to reflect the relative change of muscle wet weight. Among them, the right gastrocnemius of each group was made into paraffin specimens for histomorphological examination, part of the left gastrocnemius was tested immediately by flow cytometry, and the other was placed in liquid nitrogen for western blotting.

2.8. Flow Cytometric Detection of Skeletal Muscle Tissue. The fresh gastrocnemius tissue ($n = 6$/group) of 1 d and 3 d after blunt skeletal muscle injury was rinsed with PBS and cut into small pieces of about 1-2 mm^3, and 30 times the amount of tissue protease solution (0.1% trypsin mixed with 0.02% EDTA + 0.1 μg/mL collagenase), transfer the pipette to the erlenmeyer flask, place it in a 37°C incubator for 2 h, shake once every 5-10 min, and pass the digestion solution through 300 mesh filter through a strainer, centrifuge at 300 g for 5 minutes, and discard the supernatant. Wash with PBS solution containing 0.1% BSA by centrifugation for 1-2 times; adjust the cell concentration to 1×10/mL with PBS solution containing 0.1% BSA. Add 3 μL CD11b antibody (PE labeled), 10 μL F4/80 antibody (FITC labeled), incubated for 30 minutes at room temperature in the dark, rinse with sterile PBS solution for 1-2 times, add 200 μL 0.5% sterile paraformaldehyde (PFA) solution for fixation, and flow cytometry detects the number of macrophages.

2.9. Preparation of Chitosan Calcium Carbonate Composite. Ethanol is an important organic solvent and is widely used

in medicine, paint, sanitary products, cosmetics, oils, and fats, accounting for about 50% of the total consumption of ethanol. Ethanol is an important basic chemical material. The cut stainless steel sheet was sonicated in absolute ethanol and ultrapure water for 5 minutes to remove oil stains and impurities on the surface and then dried naturally in a nitrogen atmosphere for later use. Weigh 0.8600 g of chitosan and dissolve it in 200 mL of deionized water, adjust the pH to 5.0 with a molar concentration of 2 M HCl solution, and then adjust the pH to 5.0 after stirring for 12 hours. Then take 50 mL of the above solution in a beaker, then add 0.0660 g calcium chloride dihydrate (that is, the final concentration is 9 mM), and stir to make it dissolved. Then add 0.0711 g of ammonium bicarbonate (that is, the final concentration is 18 mM), stir to dissolve. Then use the above solution as the mother solution for electrochemical deposition in a three-electrode system (reference electrode: Ag-AgCl electrode; counter electrode: Pt wire electrode; working electrode: stainless steel sheet). The stainless steel sheet obtained after the electrodeposition process is gently washed in distilled water and air-dried naturally in a clean and dry environment.

2.10. Cell Culture

(1) Cell culture refers to a method that simulates the in vivo environment (sterility, suitable temperature, pH, certain nutrient conditions, etc.) in vitro to make it survive, grow, reproduce, and maintain its main structure and function. Cut the bare stainless steel sheet and the chitosan-calcium carbonate composite material prepared with the stainless steel sheet as a base into a square with a side length of 0.8 cm

(2) Sterilize the front and back sides of the cut film with alcohol and UV, then place it in a 12-well culture plate, digest the overgrown cells in the culture flask, and then dilute. The cells were seeded in a 12-well culture plate, and $100 \mu L$ of cells and $600 \mu L$ of culture medium were added to each well. Incubate in an incubator with a content of 5% CO2 at 37°C (wherein, each group of samples is set with three control holes when doing SEM test, and each group of samples is set with three control holes when measuring fluorescence, and when measuring MTT, each group of samples is set 6 control wells)

2.11. Cytotoxicity Test.

The CCK-8 method was used to study the toxicity of chitosan calcium carbonate composite materials on cells. The skeletal muscle cells in the logarithmic growth phase were seeded in a 96-well plate at a density of 8×10^3/well, grown adherently for 4 h, then added a medium mixture containing different concentrations of chitosan calcium carbonate composite material (final concentration 5, 25, 50, 150, and $300 \mu g$/mL), set a medium without nanoparticles as a control group, and continue to culture for 48 h. After removing the nanoparticle medium and mixing the treatment solution, add $10 \mu L$ CCK-8 solution to each well. A microplate reader (Thermo, USA) was used to detect the absorbance at a wavelength of 450 nm,

and the reference wavelength was 630 nm. Finally, the cell viability (%) was calculated according to the experimental data. Repeat the experiment three times.

2.12. Cell Fluorescence Microscopy Characterization.

First, take out the composite material for cell culture from the culture plate on the first 1, 3, 5, 7, and 9 days, and wash it with 0.1 mol/L PBS buffer three times, each washing for 2 s. Then fixed with 1% paraformaldehyde, and then add $1000 \mu l$ PBS and $50 \mu L$, 0.1 mg/mL DAPI dye to each well for staining. Then continue to incubate in an incubator for 2 hours and rinse with PBS 3 times for a few seconds each time, and finally observe with a fluorescence microscope.

2.13. Biocompatibility Test of Composite Materials.

First, take out the composite material for cell culture from the culture plate on days 1, 3, 5, 7, and 9. Then take out the slides, place them in a new 24-well culture plate, add $1000 \mu L$ of culture medium, then add $100 \mu L$ of MTT solution to each well, continue to incubate for 4 h, wait until the culture solution is aspirated, and then add DMSO solution ($1000 \mu L$/well). Finally, $150 \mu L$ of solution is extracted from each well in the 96-well plate, the wavelength of 490 nm is selected, and the a value of each well is detected on the microplate reader.

2.14. Data Statistics.

Statistical analysis method: in all experimental data, the measured data is represented by $X \pm S$, and the comparison between and within groups is analyzed by single factor variance. Paired comparisons between groups were carried out by LSD test, and there were statistical differences when $P \leq 0.05$.

3. Skeletal Muscle Injury Repair

3.1. Cell Detection and Analysis.

Chemiluminescence method for cell viability test: ATP adenosine triphosphate combines adenine, ribose, and 3 phosphate groups. It releases more energy when hydrolyzed and is the most direct source of energy in the body. The ATP luminescence method analyzes cell activity and proliferation by detecting the content of ATP in the cell. The common ATP luminescence method uses exogenous firefly luciferin/luciferase to oxidize with intracellular ATP to generate photons and monitor the luminosity to detect ATP content to analyze cell activity and proliferation.

The vitality value of the normal control group (A) was 55.5429, and it increased significantly on the 3rd day after injury (B); after the intervention of chitosan, calcium carbonate composite material, on the 5th day after injury, the chitosan calcium carbonate composite material group (C). The level of GSH-Px was significantly lower than that of the natural recovery group (D) ($P < 0.01$); on the 10th day after injury, the GSHPx expression level of the chitosan calcium carbonate composite group (E) was also significantly lower than that of the natural recovery group (E). Group (F) ($P < 0.05$), suggesting that the chitosan calcium carbonate composite material promotes the repair of injury. The cell detection results are shown in Table 2. It can be observed from Table 2 that the GSH-Px of normal rats is at a low level, and it rises rapidly after injury, significantly increases on the

TABLE 2: Cell test results.

Substance time	GSH-Px	MPO
Normal group (A)	55.5429 ± 14.6182	195.1150 ± 34.4581
Day 3 after injury (B)	136.1833 ± 18.9154	360.2419 ± 26.0723
Day 5 after injury (C)	93.9429 ± 22.4785	$265.4867 \pm 15\ 4892$
Day 5 after injury (D)	$11\ 7.9429 \pm 18.7348$	$33\ 18584 \pm 20.1084$
Day 10 after injury (E)	68.5714 ± 20.2318	$21\ 9.4896 \pm 25.9215$
Day 10 after injury (F)	94.4857 ± 15.7812	294.9852 ± 17.0487

3rd day after injury, and then begins to decline, and after the intervention of chitosan, calcium carbonate composite material, after injury on the 5th day, the GSH-Px level of the chitosan calcium carbonate composite group was lower than that of the natural recovery group ($P < 0.01$); during the decline process, the chitosan calcium carbonate composite group decreased faster than the natural recovery group. The difference was statistically significant ($P < 0.01$). The vitality value of the normal control group (A) was 195.1150, and it increased significantly on the 3rd day after injury (B); after the intervention of chitosan, calcium carbonate composite material, on the 5th day after injury, the chitosan calcium carbonate composite material group (C), the expression level of MPO was significantly lower than that of the natural recovery group (D) ($P < 0.01$); on the 10th day after injury, the MPO level of the chitosan calcium carbonate composite group (E) was significantly lower than that of the natural recovery group (F) ($P < 0.01$). The MPO of normal mice was at a low level, and it increased rapidly after injury. It increased significantly on the 3rd day after injury and then began to decrease. After the intervention of chitosan, calcium carbonate composite material, on the 5th day after injury, the chitosan calcium carbonate MPO level of the composite material group was lower than that of the natural recovery group ($P < 0.01$); during the decline process, the chitosan calcium carbonate composite material group decreased faster than the natural recovery group, and the difference was statistically significant ($P < 0.01$). Compared with the normal control group, the chitosan calcium carbonate composite material group and the natural recovery group had significant expression of skeletal muscle cell mRNA ($P < 0.05$); after the intervention of the chitosan calcium carbonate composite material, the skeletal muscle cell mRNA expression level of the natural recovery group (D) was 1.45 times that of the chitosan calcium carbonate composite material group (C), and the difference was significant ($P < 0.01$); on the 10th day after injury, the mRNA expression level of skeletal muscle cells was natural. The recovery group (E) was 1.32 times that of the chitosan calcium carbonate composite material group (F), and the difference was significant ($P < 0.05$).

3.2. MTT Test Analysis of Skeletal Muscle Cells. The density of cells on the surface of the Chi-CaCO3NWs/SS composite material during different culture times is significantly smaller than that of the cells on the surface of the Chi-CaCO3NFs/SS composite material, indicating that ChiCaCO3NFs/SS can provide a good environment for cell growth and spreading, and is also conducive to further proliferation and differentiation of cells. The MTT test analysis result is shown in Figure 1. To further illustrate the good biocompatibility of the ChiCaCO3NFs/SS composite material, we conducted a comparative test of cell culture on a blank stainless steel plate. The density of the cells on the surface of the stainless steel plate is significantly higher than that of the Chi_CaCO3NWs/SS and Chi-CaCO3NFs/SS composite materials. It is much smaller, that is, the growth of cells on the surface of the chitosan-calcium carbonate composite material is clearly more vigorous than that on the blank stainless steel sheet, and this advantage becomes more obvious with the extension of the culture time. It shows that the composite material has a good promotion effect on cell growth. In addition, to further clarify the effect of the composite material on cell growth and understand the growth of MC3T3 cells on the surface of the composite material, we also performed the MTT test to quantitatively observe the difference between the two. The MTT test can indirectly but quantitatively reflect the number of cells.

It can be seen from Figure 2 that the activities of the three groups of cells are increasing with the extension of the culture time, but the Chi-CaCO3NWs/SS composite material and Chi-CaCO3NFs/SS cell activity increase of the chitosan-calcium carbonate nanocomposite is very obvious, indicating that the chitosan-calcium carbonate nanocomposite can promote the growth and proliferation of cells. Among them, the cell growth on the Chi-CaCO3NFs/SS (blue) composite material is the fastest, and it is on the ninth day. The cell activity is close to twice the cell activity on the blank stainless steel plate. It shows that the Chi-CaCO3NFs/SS composite material has a good promotion effect on cell growth.

3.3. Performance Analysis of Composite Materials. To determine the composition of the ChiCaCO3 composite material, we did an XRD test on it. As can be seen, there is a strong peak at $2\theta = 43.8$, which is a characteristic peak inherent in the stainless steel sheet substrate. The strong peaks at $2\theta = 23.2, 29.6, 36.0, 39.6, 47.6,$ and 48.80 coincide with the standard peaks of calcium carbonate on the standard card, corresponding to the 12, 104, 110, 113, 018, and 116 crystal faces of calcite, respectively. The peaks obtained at $2\theta = 24.0, 36.4$ coincided with the peak positions of the standard peaks of chitosan and were identified as the characteristic peaks of chitosan. It shows that the Chi-CaCO3
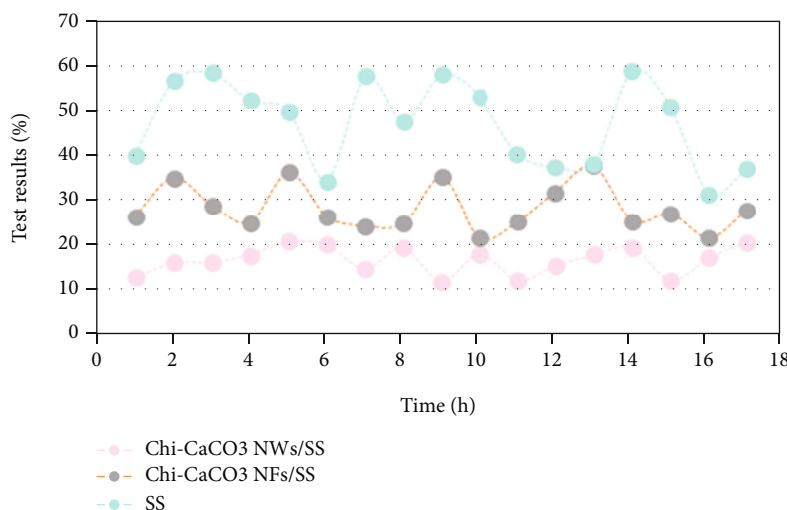
FIGURE 2: MTT test analysis results.

composite material is composed of chitosan and calcite-type calcium carbonate. At the same time, it can be found that the peak of chitosan is relatively weak, mainly because chitosan is organic, and it is difficult to form stable crystals under this condition. To prove that the CaCO3-ChiNFs/SS composite material has certain mechanical properties, we compared the tensile strength of the smooth stainless steel sheet and the stainless steel sheet as the substrate for electrochemical power deposition to obtain the CaCO3-ChiNFs/SS composite material. From the experimental results, it shows that the tensile strength of the smooth stainless steel sheet cut to a certain shape is $727.1 \pm 14.66MP$, the tensile strength of the CaCO3-ChiNFs/SS composite material under the corresponding conditions has been significantly improved, and its strength reached $1317.2 \pm 3.651MP$. First of all, it shows that the uniform and compact structure of CaCO3-ChiNFs itself has strong integrity, which is the result of the interweaving and close integration of the fiber network that combines the advantages of organic and inorganic materials. This is also similar to the structure of "cement mortar" composed of alternate organic-inorganic shells. At the same time, it also shows that the use of stainless steel sheet as a base not only facilitates the on-demand tailoring of materials but also increases the mechanical properties of the body as a bone tissue material. For biological materials, the properties of the surface of the material can determine part of its biological activity. When the material has proper wettability, it can promote the spread and growth of cells, because the water-soluble surface can provide a humid environment for healthy cell growth. The wettability of the smooth stainless steel sheet, CaCO3-chiNWs/SS, and CaCO3-chiNFs/SS surfaces was tested. The contact angle of the smooth stainless steel sheet is $93 \pm 7.0°$, the contact angle of CaCO3-chiNWs/contact angle of SS is $64.3 \pm 7.0°$, and the minimum contact angle of CaCO3-chiNFs/SS is $32.4 \pm 4.6°$.

This result shows that CaCO3-chiNFs/SS has good water wettability, and its surface state can be cell adhesion and spreading. Provide a good environment, which is more hopeful as a skeletal muscle repair and replacement material
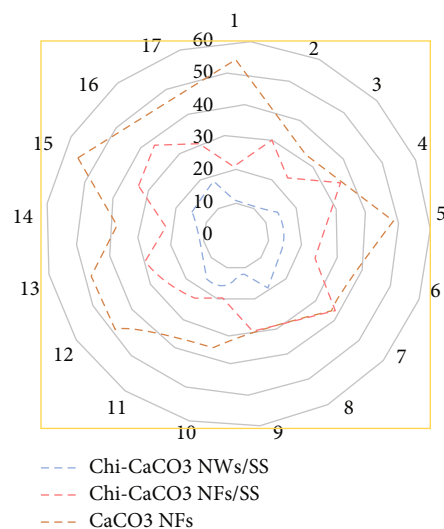
FIGURE 3: Wetting test results.

to provide cells with a more suitable platform for their growth, proliferation, and differentiation, as shown in Figure 3.

3.4. Biocompatibility Analysis of Composite Materials. The skeletal muscle cells were cultured on the surface of ChiCaCO3NFs/SS that had been sterilized beforehand. After the cells had grown for 3 days, they were pretreated, and then the morphology of the cells was characterized by a scanning electron microscope. Skeletal muscle cells are laid flat on the surface of the three-dimensional network fibers. They are larger in size, and the cell bodies and network fibers are firmly combined. And it can be seen that the cells protrude many pseudopods, which have penetrated into the network fibers. It shows that Chi-CaCO3NFs/SS can provide a good environment for cell growth and spread, and it is also conducive to the further proliferation and differentiation of cells. As we all know, the surface properties and nanostructures of
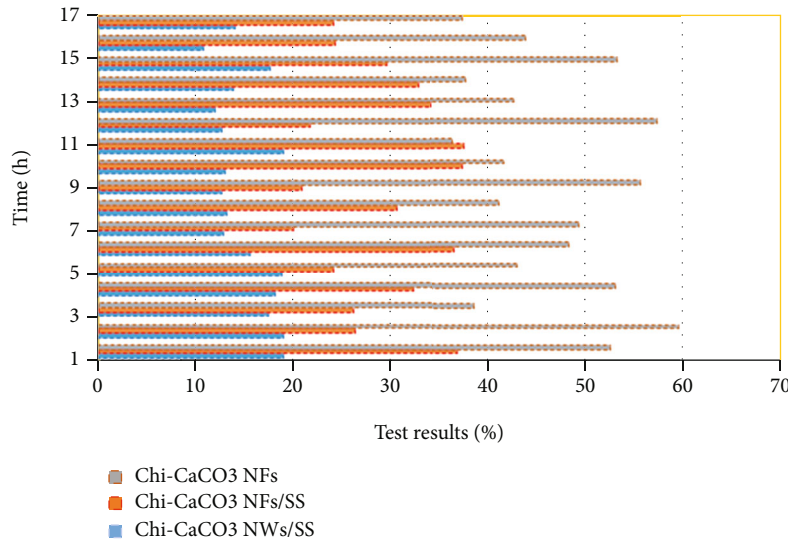
FIGURE 4: Biocompatibility analysis results of composite materials.

biological materials can significantly affect cell growth and viability. Therefore, we did a comparative experiment, cultured skeletal muscle cells on the surface of Chi-CaCO3NWs/SS composite material and under the same experimental conditions, and then performed SEM characterization. The cells appear round and become thicker, that is, the cells are not spread well, but exist in the form of clumps. The results show that the surface of the Chi-CaCO3NWs/SS composite material cannot provide for the spread, growth, and differentiation of the cells. Surface environment very well. The above results show that the three-dimensional network fiber of Chi-CaCO3NFs/SS has good biocompatibility, making it a potential material for repairing damaged bone in tissue engineering.

Hemolysis test was used to evaluate whether Chi-CaCO3NFs/SS has a damaging effect on red blood cells. The red blood cells were exposed to 5 different gradient concentrations of Chi-CaCO3NWs/SS solution, and normal saline and double distilled water were set as negative and positive controls, respectively. After incubating for 1 h, 2 h, and 3 h, they were observed under a microscope. It can be seen that compared with the negative control group, even with the highest concentration (300ug/mL) of nanoparticles incubated for 3 h, the number and morphology of red blood cells did not change significantly. On the contrary, due to the lysis of red blood cells, the double-distilled water treatment group has almost no intact red blood cells remaining under the 1 h microscope. After the red blood cells are lysed, hemoglobin will be released, and the supernatant after centrifugation will show red. Clearly, this phenomenon is more obvious in the double-distilled water treatment group. At the same time, the hemoglobin content in the supernatant is directly proportional to its OD value. The t-test analysis of the OD value of the supernatant in each EP tube found that, compared with the negative control group, the red blood cells incubated with the gradient concentration of Chi-CaCO3NWs/SS solution; there was no statistical difference in the OD value of the serum ($P > 0.05$); on the con-

trary, there was a significant statistical difference compared with the positive control group ($P < 0.01$). The biocompatibility analysis result of the composite material is shown in Figure 4.

3.5. Cytotoxicity Analysis. To confirm the biocompatibility of the Chi-CaCO3NWs/SS composite material, the CCK-8 method was used to detect its effect on cell viability. After the mouse skeletal muscle cells were treated with Chi-CaCO3NWs/SS composite for 48 hours, the cell activity showed a downward trend with the increase of nanoparticle concentration. When the concentration is lower than 50ug/mL, compared with the control group, the activity of the two cells is only slightly reduced, but there is no statistical difference ($P > 0.05$). When the concentration was increased to $50 \mu g/mL$, the difference in toxic effects was statistically significant ($P < 0.05$). The activities of the two cell types were 83.6% and 87.5%, which were still above 80%. The results of the cytotoxicity analysis are shown in Figure 5. Based on the concentration required for cytotoxicity detection and cell imaging of Chi-CaCO3NWs/SS, in other experimental projects, we set the maximum concentration to $50 \mu g/mL$. The blood test results showed that the skeletal muscle toxicity sensitive indicators ALP and ALT had no abnormal changes compared with normal rats, and the HE staining results did not find obvious pathological changes; the nephrotoxicity sensitive indicators urea nitrogen and creatinine levels were also within the normal range. The sections show that the glomerulus and renal tubules are structurally intact; cardiotoxicity is often used as an important indicator of drug toxic side effects. The STAINED picture shows that myocardial cells are tightly arranged and orderly, and the structure of each part is complete; there are no other organ tissue sections. Appears noticeable pathological changes. It can be seen from the cell proliferation experiment that skeletal muscle cells can grow, divide, and proliferate well after inoculation. The cell activity of the experimental group and the negative control group increased significantly with time, and there was no significant
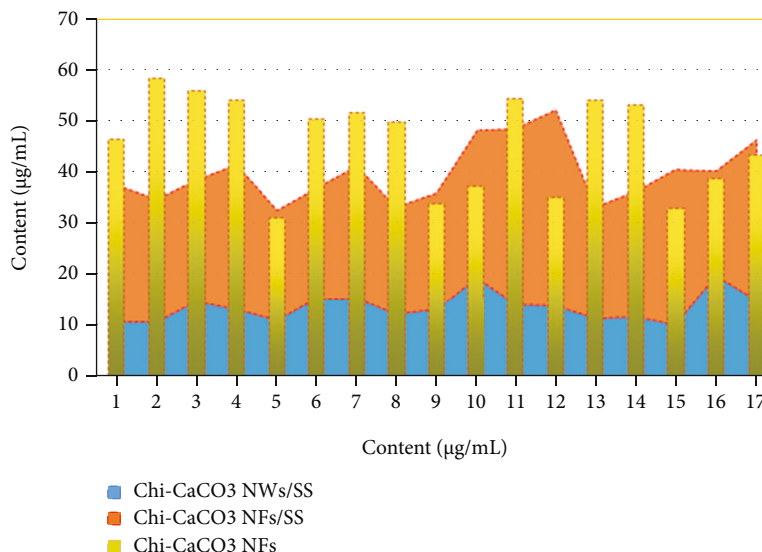
Figure 5: Cytotoxicity analysis results.

difference between the two groups in the statistical analysis. And the RGR of the experimental group and the negative control group was ≥100%, and the cytotoxicity was 0; while the positive control group had RGR < 30%, the cytotoxicity was 4, and the cell growth status was poor. After 24 hours of culture, the growth rate of cell viability of L929 in the experimental group was significantly higher than that in the normal culture group. It can be seen that C2C12 has higher cell activity and proliferation rate than Lg29.

4. Conclusion

The power of exercise comes from skeletal muscle contraction, which is a high energy consumption process. As a result, the body's normal energy balance relationship develops in the direction of imbalance. To prevent the influence of energy imbalance on the body, the mechanisms that reverse this change trend are activated. At present, the research on skeletal muscle injury and repair is no longer limited to muscle satellite cells themselves. The role of immune cells in the repair of skeletal muscle damage is gradually being recognized, and its role and mechanisms are in the preliminary stage of exploration and become a new research focus. Skeletal muscle during strenuous exercise or acute injury can produce a large number of free radicals and neutrophil infiltration in the damaged muscles, followed by a series of inflammatory reactions caused by macrophage invasion. Biomimetic nanomaterials can solve this problem well.

In this study, adult healthy mice were selected. First, the mice were anesthetized with sodium pentobarbital, and the mice were fixed with steel balls to strike the midsections of the bilateral gastrocnemius muscles to create skeletal muscle blunt injury models. The mice were killed by cervical dislocation under anesthesia, and the injured gastrocnemius muscles of both sides were quickly taken to prepare the cell suspension. Weigh and dissolve chitosan in deionized water. Then add calcium chloride dihydrate, stir to dissolve, and prepare chitosan calcium carbonate composite material.

The chitosan-calcium carbonate composite material prepared by using a stainless steel sheet as a base is cut into a square with a side length. Sterilize the stainless steel sheet and place it in a culture plate to dilute the overgrown cells in the culture flask and cultivate them in an incubator.

The skeletal muscle cells were cultured on the surface of ChiCaCO3NFs/SS which had been sterilized beforehand, and then, the cell morphology was characterized by scanning electron microscope. Skeletal muscle cells are laid flat on the surface of the three-dimensional network fibers. They are larger in size, and the cell bodies and network fibers are firmly combined. And it can be seen that the cells protrude many pseudopods, which have penetrated into the network fibers. It shows that Chi-CaCO3NFs/SS can provide a good environment for cell growth and spread, and it is also conducive to the further proliferation and differentiation of cells. In summary, there are many types of calcium carbonate medical materials, which combine the inherent good biocompatibility, osteoconductivity, and good hardness of calcium carbonate materials, as well as the advantages of polymers, collagen, biomolecules, metals, and other materials to make up for the shortcomings of calcium carbonate material are high brittleness. The successful application of calcium carbonate medical composite materials expands the application and development space of calcium carbonate materials in the field of biomedicine. The above results indicate that the material has no inhibitory effect on cell growth and is a qualified noncytotoxic material. It can be seen that the mice can tolerate the experimental concentration of Chi-CaCO3NWs/SS. This new type of nanomedicine carrier will not negatively affect its growth and development, nor will it cause histopathological changes in major organs. Normal skeletal muscle injury often occurs in high-intensity exercise training, more than habitual activities or physical labor. The repair of skeletal muscle injury has always been a basic issue of long-term attention and research in the sports medicine community. Many researchers have carried out research from different angles. Many aspects of research have been carried out, but many mechanistic problems have not been completely solved.

Data Availability

No data were used to support this study.

Conflicts of Interest

The authors declare that they have no conflicts of interest.

References

[1] W. M. Aframehr, B. Molki, P. Heidarian, T. Behzad, M. Sadeghi, and R. Bagheri, "Effect of calcium carbonate nanoparticles on barrier properties and biodegradability of polylactic acid," *Fibers & Polymers*, vol. 18, no. 11, pp. 2041–2048, 2017.

[2] O. Acar, B. Yilmaz, S. H. Altintas, I. Chandrasekaran, and W. M. Johnston, "Color stainability of CAD/CAM and nanocomposite resin materials," *Journal of Prosthetic Dentistry*, vol. 115, no. 1, pp. 71–75, 2016.

[3] C. Q. Nguyen, T. Y. O. Doan, and P. D. L. Nguyen, "Effect of nanoclay on thermal, mechanical and liquid absorption properties of epoxy-clay nanocomposite," *Journal of Applied Polymer Science*, vol. 100, no. 5, pp. 4173–4180, 2016.

[4] F. K. J. De, K. J. Chan, and E. D. Cranston, "Enhanced mechanical properties in cellulose nanocrystal–poly(oligoethylene glycol methacrylate) injectable nanocomposite hydrogels through control of physical and chemical cross-linking," *Biomacromolecules*, vol. 17, no. 2, pp. 649–660, 2016.

[5] A. Raffaella, R. V. V. Petrescu, and S. Roberto, "Hybrid ceramo-polymeric nanocomposite for biomimetic scaffolds design and preparation," *American Journal of Engineering & Applied Sciences*, vol. 9, no. 4, pp. 1096–1105, 2016.

[6] T. C. Merkel, B. D. Freeman, R. J. Spontak et al., "Sorption, transport, and structural evidence for enhanced free volume in poly(4-methyl-2-pentyne)/fumed silica nanocomposite membranes," *Chemistry of Materials*, vol. 15, no. 1, pp. 109–123, 2003.

[7] G. Wang, S. Wang, W. Sun, Z. Sun, and S. Zheng, "Synthesis of a novel illite@ carbon nanocomposite adsorbent for removal of Cr (VI) from wastewater," *Journal of Environmental Sciences*, vol. 57, no. 7, pp. 62–71, 2017.

[8] L. Xing and Z. Ma, "A glassy carbon electrode modified with a nanocomposite consisting of MoS_2 and reduced graphene oxide for electrochemical simultaneous determination of ascorbic acid, dopamine, and uric acid," *Microchimica Acta*, vol. 183, no. 1, pp. 257–263, 2016.

[9] M. Farrokhi-Rad, T. Shahrabi, S. Mahmoodi, and S. Khanmohammadi, "Electrophoretic deposition of hydroxyapatite-chitosan-CNTs nanocomposite coatings," *Ceramics International*, vol. 43, no. 5, pp. 4663–4669, 2017.

[10] J. Choi and M. Tsapatsis, "MCM-22/silica selective flake nanocomposite membranes for hydrogen separations," *Journal of the American Chemical Society*, vol. 132, no. 2, pp. 448-449, 2010.

[11] Z. Li, J. A. Larsson, P. Larsson et al., "Copper/molybdenum nanocomposite particles as catalysts for the growth of bamboo-structured carbon nanotubes," *The Journal of Physical Chemistry C*, vol. 112, no. 32, pp. 12201–12206, 2008.

[12] J. Singh, M. Srivastava, A. Roychoudhury, D. W. Lee, S. H. Lee, and B. D. Malhotra, "Bienzyme-functionalized monodispersed biocompatible cuprous oxide/chitosan nanocomposite platform for biomedical application," *The Journal of Physical Chemistry B*, vol. 117, no. 1, pp. 141–152, 2013.

[13] S. Moradi, P. Aberoomand-Azar, S. Raeis-Farshid, S. Abedini-Khorrami, and M. H. Givianrad, "The effect of different molar ratios of ZnO on characterization and photocatalytic activity of TiO_2/ZnO nanocomposite," *Journal of Saudi Chemical Society*, vol. 20, no. 4, pp. 373–378, 2016.

[14] L. Mei, P. Zhang, J. Chen et al., "Non-enzymatic sensing of glucose and hydrogen peroxide using a glassy carbon electrode modified with a nanocomposite consisting of nanoporous copper, carbon black and nafion," *Microchimica Acta*, vol. 183, no. 4, pp. 1359–1365, 2016.

[15] B. Gao, X. Ning, and P. Xing, "Shock wave induced nanocrystallization during the high current pulsed electron beam process and its effect on mechanical properties," *Materials Letters*, vol. 237, no. 15, pp. 180–184, 2019.

[16] H. Song and M. Brandt-Pearce, "Range of influence and impact of physical impairments in long-haul DWDM systems," *Journal of Lightwave Technology*, vol. 31, no. 6, pp. 846–854, 2013.

[17] H. Wei, Q. Zhang, Y. Yao, L. Liu, Y. Liu, and J. Leng, "Direct-write fabrication of 4D active shape-changing structures based on a shape memory polymer and its nanocomposite," *ACS Applied Materials & Interfaces*, vol. 9, no. 1, pp. 876–883, 2017.

[18] S. Mortazavinik and M. Yousefi, "Preparation, magnetic properties and microwave absorption of Zr–Zn–Co substituted strontium hexaferrite and its nanocomposite with polyaniline," *Russian Journal of Applied Chemistry*, vol. 90, no. 2, pp. 298–303, 2017.

[19] S. Pandey, "Highly sensitive and selective chemiresistor gas/vapor sensors based on polyaniline nanocomposite: a comprehensive review," *Journal of Science: Advanced Materials and Devices*, vol. 1, no. 4, pp. 431–453, 2016.

[20] D. Zhang, H. Chang, P. Li, and R. Liu, "Characterization of nickel oxide decorated-reduced graphene oxide nanocomposite and its sensing properties toward methane gas detection," *Journal of Materials Science: Materials in Electronics*, vol. 27, no. 4, pp. 3723–3730, 2016.

[21] A. A. Alqadami, M. Naushad, M. A. Abdalla, M. R. Khan, and Z. A. Alothman, "Adsorptive removal of toxic dye using Fe_3O_4–TSC nanocomposite: equilibrium, kinetic, and thermodynamic studies," *Journal of Chemical & Engineering Data*, vol. 61, no. 11, pp. 3806–3813, 2016.

[22] J. Kim, H. Kim, and W. J. Kim, "Single-layered MoS_2–PEI–PEG nanocomposite-mediated gene delivery controlled by photo and redox stimuli," *Small*, vol. 12, no. 9, pp. 1184–1192, 2016.

[23] M. Gholami, M. T. Vardini, and G. R. Mahdavinia, "Investigation of the effect of magnetic particles on the crystal violet adsorption onto a novel nanocomposite based on κ-carrageenan-g- poly methacrylic acid," *Carbohydrate Polymers*, vol. 136, no. 12, pp. 772–781, 2016.

[24] D. Ma, S. B. Peh, G. Han, and S. B. Chen, "Thin-film nanocomposite (TFN) membranes incorporated with super-hydrophilic metal-organic framework (MOF) UiO-66: toward enhancement of water flux and salt rejection," *ACS Applied Materials & Interfaces*, vol. 9, no. 8, pp. 7523–7534, 2017.

[25] Y. Lin, X. Liu, T. Ye, H. Yang, F. Wang, and C. Liu, "Preparation and microwave absorption property of graphene-supported $CoFe_2O_4$/$Y_3Fe_5O_{12}$ nanocomposite," *Journal of Materials ence: Materials in Electronics*, vol. 27, no. 8, pp. 8177–8182, 2016.

[26] M. Dinari, M. M. Momeni, and M. Goudarzirad, "Dye-sensitized solar cells based on nanocomposite of polyaniline/graphene quantum dots," *Journal of Materials ence*, vol. 51, no. 6, pp. 2964–2971, 2016.

[27] M. Miculescu, V. K. Thakur, F. Miculescu, and S. I. Voicu, "Graphene-based polymer nanocomposite membranes: a review," *Polymers for Advanced Technologies*, vol. 27, no. 7, pp. 844–859, 2016.

[28] A. Alfadhel and J. Kosel, "Magnetic nanocomposite cilia tactile sensor," *Advanced Materials*, vol. 27, no. 47, pp. 7888–7892, 2015.

[29] H. Zhu, H. Wei, B. Li, X. Yuan, and N. Kehtarnavaz, "Real-time moving object detection in high-resolution video sensing," *Sensors*, vol. 20, no. 12, p. 3591, 2020.

Research Article

Photothermal Effect Based on Bionic Nanomaterials in the Treatment of Football Sports Injuries

Jiarui Xing[1] **and Huilin Li** [2]

[1]*Graduate School, Jose Rizal University, Mandaluyong, 10048 Manila, Philippines*
[2]*College of Physical Education, Xuchang University, Xuchang, 461000 Henan, China*

Correspondence should be addressed to Huilin Li; xcxingahongyou@xcu.edu.cn

As more and more people love football and participate in more and more football matches, the physical injuries in the confrontation are getting more and more serious. In recent years, bionic photothermal nanomaterials have shown great application potential in disease treatment. Biomimetic photothermal nanomaterials are functional and intelligent materials with special excellent performance that are designed and synthesized by using natural biomimetic principles. Photothermal therapy (PTT) technology is a new treatment technology in recent years. On the one hand, photothermal therapy technology can convert light energy into heat energy through photothermal conversion factor (PTCA). Molecular water-soluble drugs penetrate into the skin to replace the existing injection administration methods with higher risk and low patient compliance and oral administration methods that generally cause first-pass effects, improve the utilization and efficiency of drugs, and can give provide patients with better treatment. The purpose of this article is to explore the application of the photothermal effect of bionic nanomaterials in the treatment of football sports injuries. The method adopted in this paper is to synthesize different bionic photothermal nanomaterials and synthesize bionic photothermal nanomaterials that are fused with cell membranes, thereby promoting the application of photothermal therapy technology in the treatment of sports injuries; further, by synthesizing bionics wrapped by fusion membranes, photothermal nanomaterials introduce collaborative photothermal therapy technology. The experimental results show that the photothermal effect of nanobiomimetic materials is used to treat common injuries caused by football sports. Compared with traditional treatment methods, HA-CuS gel and near-infrared treatment are applied to the skin with the injured tissue of the experimental group. It dropped to 85.7% in 2 h then gradually dropped to 84.2%, and the recovery speed was significantly accelerated.

1. Introduction

Football injuries refer to various physical injuries caused by athletes in football matches. Because football is more intense, and the physical quality and sports skills of athletes are high requirements, and football injuries often occur. In addition to common bruises and contusions, the most common injuries are ankle sprains, muscle tightness, and contusions on the front and back of the thigh, and knee injuries are the second most common [1]. Among them, meniscus inhabitation, knee ligament tears, bone fractures, and osteochondrosis are relatively rare, but once they occur, treatment is more difficult. It needs to rely on some advanced medical technology to treat football sports injuries.

The key to photothermal treatment technology is photothermal conversion factor. At present, there are many types of photothermal conversion nanomaterials that have been studied most. The list is mainly divided into the following categories: high-cost photothermal conversion nanomaterials composed of precious metals and rare metals, new synthetic carbon based on light-to-heat conversion nanomaterials, old-fashioned organic compounds, light-to-heat conversion nanomaterials, and semiconductors composed of light and heat conversion nanomaterials [2, 3]. It has been shown that the abovementioned heat has poor biocompatibility to thermal nanomaterials and cannot escape from the human immune system, and no precise damage has been observed [4, 5].

Years of research and analysis on football sports injuries have shown that the incidence of sports injuries in regular college football teams is 211.9%, among which athletes' injuries are mainly concentrated in the ankle joints of the feet, knee joints, thighs, calf muscles, and feet of the legs. Toes, hip joints, etc. and ankle sports injuries have the highest incidence; the results of sports injuries mainly include contusions, sprains, bruises, residual limbs, residual limbs, etc. The main reason for sports injuries is insufficient mastery of their skills. Even the lack of training level is mostly caused by human factors, including lack of scientific training and other objective factors. At the same time, it puts forward targeted suggestions to promote the improvement of skills and tactics in football team training in mainstream colleges and universities, prevents sports injuries, and provides useful help [6–8]. Studies have shown that football players' injuries are mainly concentrated in the lower limbs, especially in the ankle. The main causes of injuries are improper technical exercises, protection errors, insufficient preparations, and other factors, as well as increased frequency of sports injuries, which should attract people's attention. We propose appropriate preventive measures to further prevent and reduce sports injuries in future training and competitions [9]. In the past ten years, photothermal hyperthermia has become a new treatment technique. It uses the largest external energy to heat cells or tissues, degenerate and necrosis of cells or tissues, and then plays a role in repairing cells [10]. This method is usually a more moderate method, which is less harmful to the human body. The main sources of external energy for heating cells or tissues are radio frequency, microwave oven, focused ultrasound, and laser [11]. The normal cells or tissues of the human body emit heat when the temperature of the human body rises, accelerate blood flow, and expand blood vessels. Therefore, even if the temperature of the normal tissues or cells of the human body rises to 43°C, it will not cause great damage and can self-dissipate [12–14]. In necrosis, the new intercellular blood vessels are malformed and develop abnormally, their shape is abnormal, and the endothelial cells of the internal vascular endothelial cells are very fragile and easy to destroy. Therefore, the cells or tissues cannot dissipate heat normally and rise and cannot be adjusted and repaired. The cells are killed at high temperatures.

This article starts with the meaning of bionic nanomaterials and sports injuries and explores the relationship between the treatment effects of bionic materials based on the degree of injury. By establishing injury models, using biomimetic nanomaterials to observe different changes in cell, tissue and bone activity and conduct comparative studies, we can more accurately grasp the disease process and explore the impact of biomimetic nanomaterials on treatment. This is conducive to the promotion of medical research problems, innovative methods to solve problems, and a good theoretical basis for the treatment of football injuries and other diseases caused by them. By comparing the changes and analyzing the specific experimental results, we can find the basic point of balance between the body's response and drug efficacy, and organically combine the two, provide valuable technical experience for future experiments, draw out the similarities and differences in research directions through comparative advantage analysis, and learn advanced experience at the same time, and make suggestions for improvements in future medical technology advancements, in-depth understanding of the body's pathological conditions, and strengthening of medical expertise. Specialization and accuracy provide theoretical basis for the medical field.

2. Theoretical Basis and Method

2.1. Core Concepts

2.1.1. The Concept of Football Damage. According to foreign records, football is one of the sports with the highest injury rate [15]. Minor injuries are wear and tear, fractures, and dislocations, and ruptures of internal organs can be severe. According to the Guangdong Provincial Sports Commission Medical Bureau (classified by training effect), minor injuries accounted for 47.8%, moderate injuries accounted for 19%, and severe injuries accounted for only 3.2%. Approximately, 86% of injuries are limbs [16, 17]. In addition to common bruises and contusions, the most common injury is an ankle sprain. The muscles of the front and back of the thigh are tight and bruised. Knee injuries ranked second. Among them, meniscus inhabitation, knee ligament tears, bone fractures, and osteochondrosis are relatively rare, but if they occur, it is a bad news for athletes. The treatment methods are currently immature, and the effects of drug treatment are mediocre and difficult to cure, seriously affecting the sports career of football players and cause them great difficulties. For many professional football players, the meniscus or bone has been removed in some medically developed countries. Since goalkeepers often drop the ball and fall, they are vulnerable to wrist (scaphoid fracture) and elbow injuries (bursitis and hematoma). Therefore, the average goalkeeper must wear a sweater, elbow pads, and gloves [18, 19].

2.1.2. Photothermal Treatment. Photothermal therapy is a medical technique for minimally invasive treatment using photoheat developed in recent years. This technology uses photothermal modified materials to directly increase the local temperature by directly irradiating the site with light, thereby killing cells and significantly reducing the body's systemic toxicity. Therefore, photothermal therapy is one of the therapeutic techniques that have the potential to replace surgical therapy. The light-to-heat conversion material can convert the energy of the laser into heat, thereby generating high temperature in the cell area of the human body. The high temperature will heat the cell structure and cause the cell to die quickly. Near-infrared lasers, whose main wavelength range is from 700 to 1100 nm, have a very strong ability to penetrate biological tissues for human or animal tissues and have very little residue in the body after passing through the human body. It can be widely used in the treatment of sports injuries and has become one of the important light sources widely used in the medical field [20, 21]. In order to promote the application of photothermal therapy technology, the development of photothermal

conversion nanomaterials with good biocompatibility and high conversion efficiency is the current focus of photothermal therapy. Nanomaterials with a particle size in the range of 10-200 nm can avoid the body kidney and cam clearly and selectively penetrate into the tissue. The use of nano-photothermal rice materials for photothermal therapy is an effective method [22].

2.2. Light-to-Heat Conversion Nanomaterials

2.2.1. Introduction to Nanomaterials. Currently, the most studied photothermal conversion nanomaterials include noble metal photothermal conversion nanomaterials, carbon-based photothermal conversion nanomaterials, organic compounds photothermal conversion nanomaterials, and semiconductor photothermal conversion nanomaterials. The carbide nanomaterials that convert from heat to heat mainly include gold nanostructures and palladium nanostructures [23]. The photothermal conversion characteristics of precious metals are produced by the plasmon resonance effect of nanoparticles on the surface, which is directly related to the morphology of precious metal nanostructures: gold nanorods, gold nanometer dials, gold nanoparticles, etc. However, as the temperature increases, the photothermal conversion nanomaterials of precious metals will undergo morphological changes, resulting in unstable light and thermal conversion properties, which limits the widespread use of precious metals as photothermal conversion materials in disease treatment [24].

2.2.2. Specific Realization Form. Carbon-based nanomaterials for light and heat conversion mainly include graphene structures and carbon nanotubes. In principle, it does not affect the photothermal conversion characteristics of carbon-based photothermal conversion nanomaterials after long-term laser irradiation, but the preparation and functionalization of carbon-based photothermal conversion nanomaterials are complex, and their light absorption coefficient is relatively low. The photothermal conversion nanomaterials mainly include organic infrared dyes, porphyrin liposomes, and high molecular polymers [25]. Compared with other types of light and heat conversion nanomaterials, this type of tube property conversion nanomaterials can be biodegraded, but they are easily directly degraded by light under long-term laser irradiation. As a research hotspot of nanomedicine, copper sulfide (CuS) nanoparticles in semiconductor photothermal conversion nanomaterials have the advantages of simple preparation process, stable photothermal conversion performance, excellent biocompatibility, and low production cost [26].

2.2.3. Application of Photothermal Nanomaterials. The key points in treatment are issues such as immune system escape and precise targeting to reach the site. Under normal circumstances, our tissues have permeation and retention effects (EPR), and humans use these two effects to design photothermal nanomaterials and guide them to the passive targeting of markers. One of the most important issues is how to extend the residence time of nano-biomimetic materials in organisms. In order to extend the residence time of photothermal materials in organisms, polyethylene glycol is often used to modify the materials, and this method can be used to a certain extent, increase the hydrophilicity of the surface of nanomaterials, reduce the elimination of imitation biomass by the immune system when inside the body, and reduce the interaction between nanomaterials and components in the blood, thereby avoiding attack and elimination by the body's immune system [27, 28]. In order to improve the targeting ability of nanomaterials, active molecules, such as aptamers and penetrating peptides, can be modified on the surface of nanomaterials. Recent studies have shown that there is an antipolyethylene glycol immune response in animals and humans. Polyethylene glycol can cause blood clotting and cell coagulation. To a certain extent, it cannot completely prevent nanomaterials from being processed by the machine. In efficacy, while a single targeted modified nanomaterial is difficult to adapt to the microenvironment in the body, it is difficult to achieve its theoretical targeting effect after entering the body. In recent years, effective methods have used cell membranes to camouflage the upper layer of nanomaterials and modify the nanomaterials to obtain bionic nanomaterials that have the ability to escape the immune system. Biomimetic nanomaterials have good development prospects in drug transportation, imaging, detoxification, vaccine design, and photothermal therapy. The cell membrane wrapped nanomaterial mainly includes two parts: a synthetic nanomaterial core and an outer cell membrane. The core synthesized in the biomimetic nanomaterial can be organic or inorganic nanomaterials with different biological and therapeutic functions. The outer cell membrane used to camouflage the nanomaterial nucleus can be red blood cell membrane, white blood cell membrane, cancer cell membrane, platelet membrane, macrophage membrane, and fusion membrane.

3. Experimental Verification

3.1. Experimental Materials. Through the application, 60 people with sports injuries in the affiliated hospital of the medical university where the author is located were selected, including 30 men and 30 women. In order to create research variables, all patients were randomly divided into 6 groups with 10 people in each group to ensure that the weight of the patients was normal. In the early stage of the experiment, in a well-ventilated environment, ensure that the room temperature is about 22 degrees, the relative humidity is maintained at about 55%, and the light time is maintained at more than 10 hours. Keep adequate food and drinking water. Conventional catering is provided by the medical center, and the MCT required for the establishment of the entire model is selected from sigma. When each group is treated to the appropriate age, the injured tissue should be selected for observation of related indicators. The main reagents include ECL chemiluminescence fluid (Genview company in the United States), and the main instruments include color Doppler ultrasound diagnostic apparatus, optical microscope (Germany LEICA, DM3000).

TABLE 1: Laser light scattering detector detects the molecular weight distribution of HA before and after heating.

Time	Before heating(mV)	After heating(mV)
5 min	12	12
10 min	12	12
15 min	12	12
20 min	15	16
25 min	35	36
30 min	20	21
35 min	11	11
40 min	10	10
45 min	8	9
50 min	7	6

TABLE 2: GPC curve of molecular position distribution before and after HA heating detected by differential detector.

Time	Before heating(mV)	After heating(mV)
5 min	0.69	0.68
10 min	0.69	0.68
15 min	0.69	0.68
20 min	0.69	0.67
25 min	0.73	0.73
30 min	0.70	0.70
35 min	0.6	0.59
40 min	0.69	0.7
45 min	0.69	0.68
50 min	0.69	0.68

3.2. Experimental Process. First, complete the preparation of HA-CuS nanoparticles. 150 mg of HA was added to 20 mL of 4 mL CuCb solution, after stirring for 30 min at room temperature, and 1.6 mL of 50 mM Na2S solution and 36 mg of trisodium citrate were added to the system. After stirring quickly, let it stand and heat in a water bath at 80°C for 30 minutes. Centrifuge at 12000 rpm for 30 minutes, discard the supernatant, add deionized water to the sedimentation towel, and resuspend at 12000 rpm for 30 minutes, repeat twice to obtain HA-CuS nanoparticles. The synthesis process of the blank CuS nanoparticles is the same as the above steps, but HA is not added. HA is an acidic mucopolysaccharide. During the synthesis of HA-CuS nanoparticles, it needs to be heated in a water bath at 80°C for 30 minutes. In order to explore whether the treatment will affect the structure of HA, gel permeation chromatography (GPC) is used in this chapter. The molecular weight distribution of HA is tested. Use two detectors: laser light scattering detector and differential detector to detect the HA solution and the unheated HA solution after heating in a water bath at 80°C for 30 min. The HA retention time detected by the two detectors did not change before and after the HA solution was heated. That is, before and after heating, the molecular weight distribution of HA is basically the same. Experimental results show that during the synthesis of HA-CuS nanoparticles,
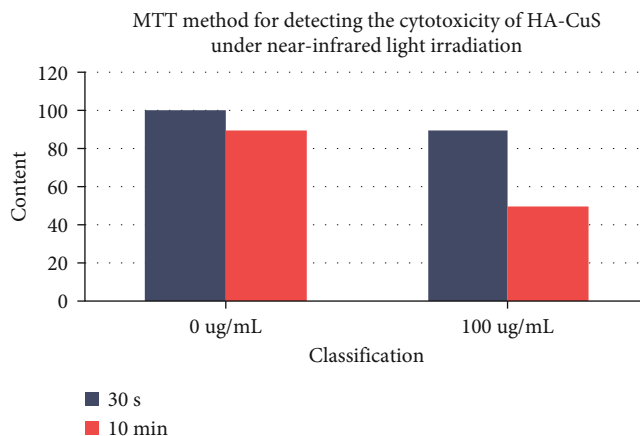
FIGURE 1: MTT method to detect the cytotoxicity of HA-CuS under near-infrared light irradiation.
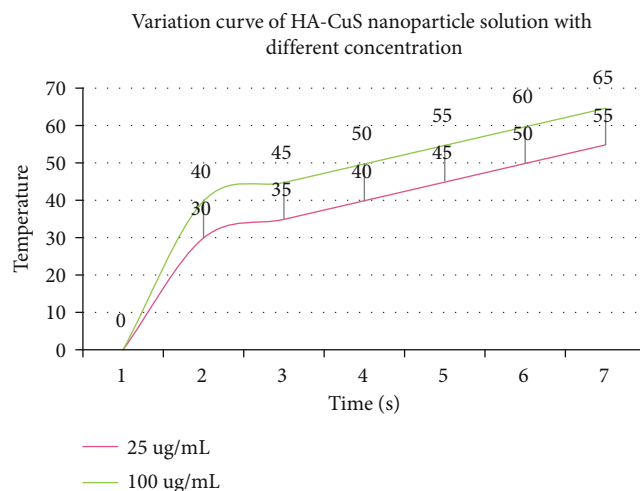
FIGURE 2: Variation curves of HA-CuS nanoparticle solutions with different concentrations.

the molecular weight of HA will not be affected by the heating during the synthesis process and remains stable, which provides conditions for the successful synthesis of HA-CuS. The laser light scattering detector detects the molecular weight distribution of HA before and after heating as shown in Table 1. The GPC curve of molecular position distribution before and after HA heating detected by the differential detector is shown in Table 2.

Stain the RBC membrane with DIL staining solution, and stain the B16F10 cell membrane with DIO staining solution. According to the ratio of B16F10 cell membrane to RBC membrane mass ratio of 1 : 1, mix the B16F10 cell membrane with the RBC membrane uniformly and ultrasound at 39°C for 10 minutes to complete the cell membrane fusion. 0.5 mL of 0.3 mg/mL B16F10 membrane solution was added to 0.5 mL of 0.2 mg/mL CuS nanoparticle solution, and the membrane was wrapped by ultrasound for 10 min at room temperature. The reaction system was centrifuged at 10,000 rpm for 5 minutes at 4°C to remove excess membrane. The precipitate is CuS@B16F10 nanoparticles and

Thermal cycle curve of 1000 jg/mL HA-CuS nano-solution
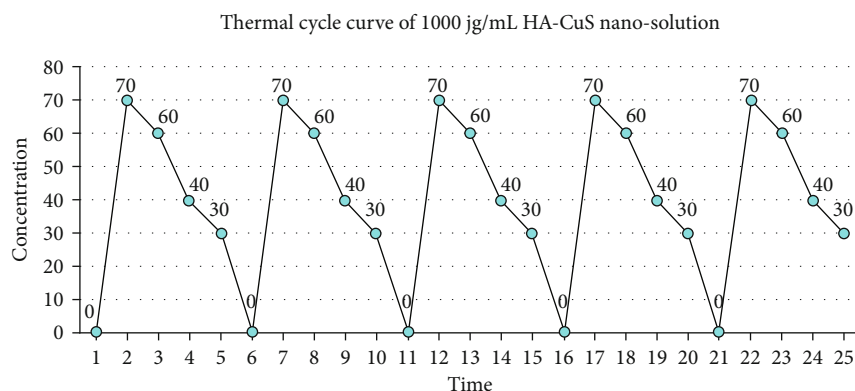
Figure 3: Cooling and heating cycle curve of 1000 jg/mL HA-CuS nanosolution.
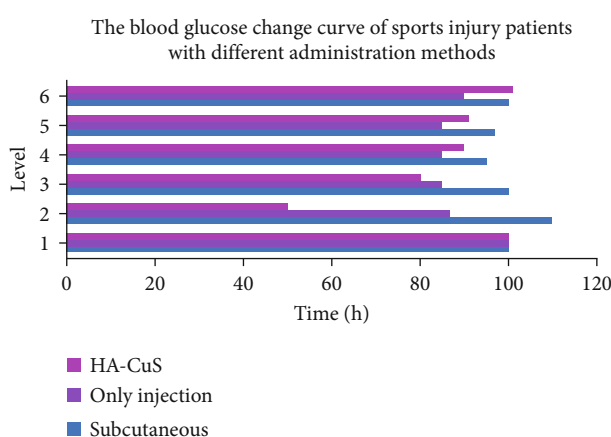
Figure 4: Blood glucose changes in sports injury patients with different administration methods.

resuspended in FJ deionized water. Similarly, complete the RBC film alone package and B16F10 film alone package. Thus, CuS@RBC nanoparticles and CuS@R16 nanoparticles were obtained.

3.3. Experimental Results. HA is a very promising mucopolysaccharide that mediates transdermal administration and has excellent biocompatibility. The modification of CuS nanoparticles with HA has an important effect on improving its biological toxicity. Before using HA-CuS nanoparticles for biological applications or disease treatment, it is necessary to detect their cytotoxicity. In this chapter, the MTT method is used to detect the cytotoxicity of HA-CuS nanoparticles using NHDF cells. Transfect NHDF cells with a series of sample solutions of different concentrations (200 pg/mL, 100 pg/mL, 50 pg/mL, 25 ig/mL, and 10Hg/mL), and use MTT to detect cell viability even at a high concentration of 200 ng/mL under the condition of sample treatment, the survival rate of cells is also above 90%, indicating that HA-CuS nanoparticles have no direct cytotoxicity.

4. Data Analysis

HA-CuS gel-mediated transdermal drug delivery is realized under the irradiation of near-infrared light. Before the bio-

logical application of HA-CuS gel-mediated transdermal drug delivery in animal experiments, near-infrared light must be performed in stimulated HA-CuS cellularity test. A high-power 980 nm near-infrared laser ($0.58\ \mathrm{W/cm^2}$) was used to irradiate the HA-CuS-intaken NHDF cells and normal NHDF cells for 30 s and 10 min. The results are shown in Figure 1. Normal NHDF cells had a cell survival rate of 91.1% after 10 minutes of near-infrared laser irradiation, while NHDF cells that had taken HA-CuS had a cell# viability rate of 89.1% after 30 s of near-infrared light irradiation, and the time was extended to 10 minutes. The cell survival rate is only 57.6%. The experimental results show that HA-CuS has lower cytotoxicity when the near-infrared light is stimulated for a short time, and when the near-infrared light stimulation time is increased to 10 min, HA-CuS has a higher photothermal conversion property. Therefore, when HA-CuS gel-mediated transdermal administration is performed, the irradiation time of near-infrared light must be controlled.

The concentration of HA-CuS nanoparticle solution is an important factor affecting its photothermal conversion. We have prepared a series of HA-CuS nanoparticle solutions with different concentrations (1000 pg/mL, 500 pg/mL, 100 jg/mL, 50 fig/mL, and 25 ng/mL) to examine its light-to-heat conversion capability. We use a 980 nm near-infrared light source, adjust the intensity to $0.7\ \mathrm{W/cm2}$, irradiate the solution for 600 s, and record the temperature every 2 s, so as to obtain the temperature change curve of HA-CuS nanoparticle solutions with different concentrations as shown in Figure 2.

First, we conducted a temperature increase test on deionized water for damaged tissue cells. Within 600 s, the temperature of deionized water only increased by 13°C, while the h-rise temperature of the HA-CuS nanoparticle solution without concentration was 18.4°C, (25 pg/mL), 26.3°C (500 ng/mL), 32.7°C (100 pg/mL), 39.7°C (500 pg/mL), and 43.4°C400pg/mL). This result shows that HA-CuS nanoparticle solution has strong light-to-heat conversion capability. In addition, with the increase of time, the heating efficiency of the HA-CuS nanoparticle solution continues to weaken. This is because as the temperature increases, the heat loss of the solution increases, and the material can quickly convert the near-infrared light energy

into heat energy, and five is released into the aqueous solution and the surrounding environment, which also shows from the side that HA-CuS nanoparticles have good light-to-heat conversion ability. As the concentration of the HA-CuS nanoparticle solution increased, the material did not undergo coagulation. This is because the HA-CuS nanoparticle played a protective role and made the CuS nanoparticle uniform and stable at a higher concentration. At the same time, we further tested the stability of the photothermal conversion of HA-CuS nanoparticles. We took the highest concentration of HA-CuS nanoparticles solution (1000 pg/mL) in the above series of solutions for 5 times of excitation for 600 s. Cooling hot and cold cycle. The results are shown in Figure 3. The highest peaks of the solution temperature are 69.4°C, 69.3°C, 69.1°C, 69.3°C, and 69.2°C. The slight temperature peak changes indicate that HA-CuS nanoparticles have stable and repeatable light thermal conversion capability.

We use exercise-impaired patients as disease models to study the feasibility of the biological application of HA-CuS gel-mediated transdermal drug delivery. After applying HA-CuS gel on the back of the patients in the experimental group, they were blown dry with a hair dryer, then the gel-treated skin was irradiated with near-infrared light, the gel was wiped off, and the insulin-containing patch was applied to the treated skin with continuous absorption of the drug. The patients in the control group directly attached patches with insulin, directly injected insulin subcutaneously and did not undergo any treatment. Use a blood glucose meter to monitor blood glucose changes every 2 hours until 10 hours. The experimental results of each group are compared as shown in Figure 4. The blood sugar of the control group patients without any treatment and the control group patients who directly applied the patch without skin treatment has been at a high level; the skin is treated with HA-CuS gel and near infrared and then the insulin patch is applied. The blood glucose of the experimental group of patients dropped to 85.7% at the 2nd hour, then gradually dropped to 84.2%, and finally rose to 99.6% at the 10th hour; the blood glucose level of the control group who received direct subcutaneous insulin injection dropped rapidly to 52.7% at the 2nd hour. After that, it rose rapidly, and the blood glucose levels at 6 h, 8 h, and 10 h were 93.1%, 97.1%, and 105.7%. The above experimental results show that the transdermal insulin infusion mediated by HA-CuS gel can stabilize the blood glucose level at a lower level for a longer period of time than the conventional subcutaneous insulin injection, providing a stable and effective treatment for the treatment of sports injuries.

5. Conclusion

The photothermal effect of HA-CuS nanoparticles is used to thermally ablate the skin, mediating a new way of transdermal drug delivery. HA-CuS nanoparticles have good biocompatibility and light-to-heat conversion properties. Under low-intensity near-infrared light irradiation, HA-CuS gel is sufficient to cause damage to the stratum corneum without damaging the deeper skin and can effectively make

BSA penetrate into the skin. Taking type 1 injury as the disease model and insulin as the water-soluble macromolecular drug model, the transdermal drug delivery method mediated by HA-CuS gel can keep the patient's blood sugar at a stable low level for a long time. The transdermal drug delivery method based on the photothermal effect of HA-CuS nanoparticles has great prospects in future clinical applications because of its superior biocompatibility and controllable and stable therapeutic effect.

Use HPDA@[OMV-CC] nanoparticles to perform photothermal therapy and immunotherapy on the injured site. HPDA@[OMV-CC] nanoparticles have good biocompatibility; HPDA@[OMV-CC] nanoparticles have good light-to-heat conversion properties at 1064 nm; HPDA@[OMV-CC] nanoparticles have the same targeting properties. The ability to source damaged tissues can effectively restore damaged cells under near-infrared light; HPDA@[OMV-CC] nanoparticles can increase the amount of dendritic cells entering the lymph nodes and promote the maturation of dendritic cells. In future research, the ability of HPDA@[OMV-CC] nanoparticles' photothermal therapy and immunotherapy for sports injuries can be studied in vivo and further biosafety studies. On the basis of existing research, the ability to increase immunotherapy by fusing bacterial outer membrane vesicles provides a new direction for the application of biomimetic photothermal nanomaterials in the treatment of sports injuries.

Data Availability

The data that support the findings of this study are available from the corresponding author upon reasonable request.

Conflicts of Interest

The authors declare that they have no conflicts of interest.

References

[1] D. Forsdyke, A. Smith, M. Jones, and A. Gledhill, "Infographic: psychosocial factors associated with outcomes of sports injury rehabilitation in competitive athletes," *British Journal of Sports Medicine*, vol. 51, no. 7, pp. 561–561, 2017.

[2] A. M. K. De, C. M. S. P. De, B. C. Kelly, Z. J. L. Amin, and C. C. N. Moreira, "Arthroscopic treatment of osteochondral lesions of the talus," *Annals of the Academy of Medicine, Singapore*, vol. 24, no. 1, pp. 32–34, 2016.

[3] S. M. Allan and N. J. Rothwell, "Inflammation in central nervous system injury," *Philosophical Transactions of the Royal Society of London*, vol. 358, no. 1438, pp. 1669–1677, 2003.

[4] L. Leocani, G. Magnani, T. Locatelli et al., "People with mild cognitive impairment are at increased risk," *Serious Injury*, vol. 12, 6 Supplement, pp. 1–13, 2018.

[5] J. A. Haagsma, N. Graetz, I. Bolliger, M. Naghavi, and T. Vos, "The global burden of injury: incidence, mortality, disability-adjusted life years and time trends from the global," *Burden of Disease Study*, vol. 22, no. 1, pp. 3–18, 2016.

[6] J. I. Bisson, J. P. Shepherd, D. Joy, R. Probert, and R. G. Newcombe, "Early cognitive-Behavioural therapy for post-

traumatic stress symptoms after physical injury," *British Journal of Psychiatry*, vol. 184, no. 1, pp. 63–69, 2004.

[7] Y. Haiyan, J. Liu, X. Fan, W. Yan, and Z. Liu, "Bionic micro-Nano-bump-structures with a good self-cleaning property: the growth of Zno nanoarrays modified by polystyrene spheres," *Materials Chemistry and Physics*, vol. 170, no. 1, pp. 52–61, 2016.

[8] K. Hallsworth, L. Jopson, D. E. Jones, and M. I. Trenell, "Exercise therapy in primary biliary cirrhosis: the importance of moving while sitting on a surgical waiting list—a case study," *Frontline Gastroenterology*, vol. 7, no. 3, pp. 167–169, 2016.

[9] N. Pauli, P. Andréll, M. Johansson, B. Fagerberg-Mohlin, and C. Finizia, "Treating trismus: a prospective study on effect and compliance to jaw exercise therapy in head and neck cancer," *Head & Neck*, vol. 37, no. 12, pp. 1738–1744, 2015.

[10] Y. Hiraizumi, T. Nakajima, Y. Sato, and T. Imanishi, "Kaatsu training as a new effective exercise therapy in a case of femoral medial condyle osteonecrosis," *International Journal of Kaatsu Training Research*, vol. 12, no. 1, pp. 1–4, 2016.

[11] S. Pouwels, D. Hageman, L. N. M. Gommans et al., "Preoperative exercise therapy in surgical care: a scoping review," *Journal of Clinical Anesthesia*, vol. 33, no. 1, pp. 476–490, 2016.

[12] J. Jielile, A. Badalihan, B. Qianman et al., "Clinical outcome of exercise therapy and early post-operative rehabilitation for treatment of neglected Achilles tendon rupture: a randomized study," *Knee Surgery, Sports Traumatology, Arthroscopy*, vol. 24, no. 7, pp. 2148–2155, 2016.

[13] M. Porte, K. Patte, A. Dupeyron, and J. Cottalorda, "Exercise therapy in the treatment of idiopathic adolescent scoliosis: is it useful?," *Archives de Pédiatrie*, vol. 23, no. 6, pp. 624–628, 2016.

[14] T. Ikeda, J. Aizawa, H. Nagasawa et al., "Effects and feasibility of exercise therapy combined with branched-chain amino acid supplementation on muscle strengthening in frail and pre-frail elderly people requiring long-term care: a crossover trial," *Applied Physiology, Nutrition, and Metabolism*, vol. 41, no. 4, pp. 438–445, 2016.

[15] F. S. Koopman, E. L. Voorn, A. Beelen, G. Bleijenberg, and F. Nollet, "No reduction of severe fatigue in patients with post-polio syndrome by exercise therapy or cognitive behavioral therapy," *Neurorehabilitation and Neural Repair*, vol. 30, no. 5, pp. 402–410, 2016.

[16] U. Dalgas, "Exercise therapy in multiple sclerosis and its effects on function and the brain," *Neurodegener Dis Manag*, vol. 7, no. 6s, pp. 35–40, 2017.

[17] G. Bo, L. Chang, H. Chenglong et al., "Effect of mg and RE on the surface properties of hot dipped Zn–23Al–0.3Si coatings," *Science of Advanced Materials*, vol. 11, no. 4, pp. 580–587, 2019.

[18] J. R. Dahlqvist and J. Vissing, "Exercise therapy in spinobulbar muscular atrophy and other neuromuscular disorders," *Journal of Molecular Neuroence*, vol. 58, no. 3, pp. 388–393, 2016.

[19] O. C. Ann, F. S. Tee, and V. Y. Nen, "A study on satisfaction level among amateur web application developers towards pigeon-table as nano web development framework," *Journal of Organizational and End User Computing (JOEUC)*, vol. 31, no. 3, pp. 97–112, 2019.

[20] J. M. Scott, T. S. Nilsen, D. Gupta, and L. W. Jones, "Exercise therapy and cardiovascular toxicity in cancer," *Circulation*, vol. 137, no. 11, pp. 1176–1191, 2018.

[21] H. Song and M. Brandt-Pearce, "Range of influence and impact of physical impairments in long-haul DWDM systems," *Journal of Lightwave Technology*, vol. 31, no. 6, pp. 846–854, 2013.

[22] Y. Chigira, T. Oda, M. Izumi, and T. Yoshimura, "Effects of exercise therapy during dialysis for elderly patients undergoing maintenance dialysis," *Journal of Physical Therapy Ence*, vol. 29, no. 1, pp. 20–23, 2017.

[23] R. M. Miller, A. Popchak, D. Vyas, S. Tashman, and R. E. Debski, "Effects of exercise therapy for the treatment of symptomatic full-thickness supraspinatus tears on in vivo glenohumeral kinematics," *Journal of Shoulder and Elbow Surgery*, vol. 25, no. 4, pp. 641–649, 2016.

[24] S. S. Tan, C. H. Teirlinck, J. Dekker, L. M. Goossens, and M. A. Koopmanschap, "Cost-utility of exercise therapy in patients with hip osteoarthritis in primary care," *Osteoarthritis and Cartilage*, vol. 24, no. 4, pp. 581–588, 2016.

[25] B. Dejaco, B. Habets, C. Van Loon, S. van Grinsven, and R. van Cingel, "Eccentric versus conventional exercise therapy in patients with rotator cuff tendinopathy: a randomized, single blinded, clinical trial," *Knee Surgery, Sports Traumatology, Arthroscopy*, vol. 25, no. 7, pp. 1–9, 2016.

[26] H. Hamasaki, "Interval exercise therapy for type 2 diabetes," *Current Diabetes Reviews*, vol. 14, no. 2, pp. 129–137, 2018.

[27] F. Desmeules, J. Boudreault, C. E. Dionne et al., "Efficacy of exercise therapy in workers with rotator cuff tendinopathy: a systematic review," *Journal of Occupational Health*, vol. 58, no. 5, pp. 389–403, 2016.

[28] P. E. Mintken, A. W. Mcdevitt, J. A. Cleland et al., "Cervicothoracic manual therapy plus exercise therapy versus exercise therapy alone in the management of Individuals with shoulder pain: a multicenter randomized controlled trial," *The Journal of Orthopaedic and Sports Physical Therapy*, vol. 46, no. 8, pp. 617–628, 2016.

Hindawi

Research Article

The Immunological Properties of Nanomaterials for Repairing Knee Ligament Sports Injuries

Xueliang Li [ID]

College of Physical Education, Xuchang University, Xuchang, 461000 Henan, China

Correspondence should be addressed to Xueliang Li; 12014114@xcu.edu.cn

With the development of science and the advancement of medicine, there are more and more treatment methods for repairing knee ligament sports injuries. At present, the common method of ligament repair is to implant artificial synthetic materials or natural biological materials into the body to form artificial ligaments to repair and reconstruct damaged ligaments. Existing ligament repair techniques are often accompanied by sequelae, and the implants are not well adapted. The purpose of this article is to compare the degree of repair of damaged ligaments after implantation of artificial ligaments made of different nanomaterials and to study the mechanical properties, biomechanical properties, and immunological properties of artificial ligaments implanted in the body, in order to explore the role of different artificial ligaments on knee ligament repair. According to the different synthetic materials of artificial ligaments, the experimental subjects were divided into three groups: silk fibroin polycaprolactone nanofiber membrane group (SF/PCL), polycaprolactone nanofiber membrane group (PCL), and control group. By comparing the biocompatibility, cell adhesion, cell proliferation rate, and repair ability of collagen fiber formation of the experimental scaffold after implantation in the body, as well as its immunological performance, the results of the study showed that compared with PCL, SF/PCL increased its biocompatibility by 25%, increased its cell proliferation by 57%, increased its somatic cell adhesion by 35%, and increased its collagen fiber formation by 12%, the porosity is about 60%, and the load is as high as $907 \pm 132 \, \mathrm{N}$. The data shows that the silk fibroin polycaprolactone nanofiber membrane scaffold has good biocompatibility, degradability, and mechanical properties.

1. Introduction

Ligament injury is one of the common sports system injuries in clinical practice, which usually leads to a decline in work and sports ability. After ligament injury, there are usually small blood vessels rupture and hemorrhage, local pain, swelling, intraorganism hemorrhage, hematoma, joint swelling, movement disorder, and tenderness. On physical examination, the traction ligaments were found to be significantly painful, and if completely ruptured, the stability of the joint was reduced. With the increase in sports activities and the aging of the population, this number is still rising. Traditional treatment methods include conservative treatment, sutures, autologous and allogeneic transplants, and artificial prostheses. As a result, the tissue structure cannot be restored to its mechanical strength and movement angle before injury. Therefore, exploring methods that can effectively promote lig-

ament regeneration and repair has extremely important clinical significance and application value.

With the development of science and technology, materials science and biomedicine are more and more closely integrated, and nanomaterials have made great achievements in biological applications. The knee ligament is the main static and stable structure for knee flexion and rotation activities, and it plays an extremely important role in maintaining the stability of the knee joint [1]. Knee ligament injury is a high-energy injury, often accompanied by serious injury to other parts [2]. For damaged ligament tissues, we need scaffold materials to promote the regeneration of damaged tissues in the body, the application of surface modification and separation, and culture of cytokines, and seed cells are specific methods for constructing and selecting scaffold materials; a large number of scholars have done a lot of research in this direction [3]. By modifying the surface of

artificial ligaments with biologically active materials, the surface biological properties of the graft are improved, and the formation of the new bone at the interface is promoted. Therefore, in order to achieve compactness, therefore, nanomaterials with surface modification through nanotechnology are widely used. It is very necessary to apply nanomaterials in the repair of artificial ligaments to bring good news to human health.

This article discusses the immunological performance of nanomaterials for repairing knee ligament sports injuries and sets high standards for the selection of tissue engineering scaffolds. The mechanism of the stent in the process of repairing damaged ligaments and the problems discovered and resolved during the research process are also studied. Read et al. first proposed the application of engineered histology in the medical field and proposed a feasible treatment plan for repairing ligaments using nanomaterial scaffolds [4, 5]. Zult et al. first proposed the use of electrospinning technology to fuse silk fibroin and polycaprolactone nanofibers to improve the compatibility of materials and further improve the repair ability of damaged ligaments [6]. Kim et al. used to change the voltage value to explore the relationship between material and fiber diameter and find the best value between voltage and fiber diameter [7]. Evangelopoulos et al. first discovered the effect of SF concentration on fiber diameter during the experiment. When the optimal concentration is reached, the fiber diameter is uniform and neatly arranged, and the compatibility is best at this time [8]. Although their research has introduced various applications of nanomaterials, there is not much research on the repair of artificial ligaments. Therefore, this study is necessary.

This article summarizes and analyzes the research experience and results of many predecessors. In addition, this article has made some innovations in research content and research methods. The specific innovations are as follows: first, this paper constructs the SF/PCL composite nanomaterial for the first time and studies its formation mechanism. The effect of SF content on the repair properties of artificial ligaments in SF/PCL blends is proposed. Secondly, this article uses electrospinning technology to construct a SF and PCL hybrid scaffold for the first time and studied the interaction mechanism of PCL and SF/PCL. Third, this article is the first to use scanning electron microscope observation, infrared spectroscopy, and thermal analysis to study the compatibility of silk fibroin and gelatin in hybrid nanofibers. The combination method is used to analyze statistical data, and the normal analysis of variance and multivariate analysis is used for formal combination verification. The use of electron microscope observation not only effectively increases the observation multiple and improves the clarity of the electron microscope but also can analyze the degree of healing of the artificial ligament.

2. Pathological Study on the Indexes of Off-Pump Transplantation

2.1. The Role of Knee Ligaments and the Impact on the Body after Injury. Ligament injury should be treated early and

fully repaired. If it is not treated in time, the joint will be repeatedly sprained, which will inevitably cause damage to articular cartilage, meniscus, and other important structures, resulting in premature aging of the joint and severe secondary traumatic arthritis. The key to its treatment lies in the repair of damaged ligaments. Partial tears can be directly sutured and repaired, while complete ruptures require surgery to transfer and reconstruct adjacent tendons, fascia, and other tissues. Ligaments are dense connective tissue, mainly composed of collagen fibers. The main ligaments of the knee joint are the anterior cruciate ligament, the posterior cruciate ligament, the medial collateral ligament, and the lateral main ligament. They cross each other and are covered by the synovial membrane, located outside the synovial cavity, and are considered to be the central movement hub of the knee joint [9]. The role of the anterior cruciate ligament is as follows: during the extension and bending of the knee joint, the two bundles cross and twist, thereby increasing the stability of the knee joint. It has the functions of preventing forward displacement of the tibia, over extension of the knee, over bending of the knee, and prevention of knee virus and valgus [10]. The role of the posterior cruciate ligament is as follows: in order to limit the posterior movement of the tibia, ensure the stability of the posterior knee joint and limit the hyperextension of the tibia, and to a certain extent, limit the internal rotation, adduction, and abduction of the tibia tendon [11]. Each bremsstrahlung cooperates with other major belts and organizations to perform certain functions. Each major ligament of the knee joint contributes to the spontaneous tension interlocking inside and outside the joint, which not only becomes a powerful stabilizing device but also completes the function of the knee joint together [12]. Ligament injury has the ability to repair itself, but after the injury, the overall stability of the knee joint will change, and the load stress shared by different structures will also change from the normal situation [13]. After the injury of the posterior cruciate ligament, the function of the posterior cruciate ligament is good in the short and medium-term injuries, but in the later stage, it will lead to poor knee function, joint disease, and advanced osteoarthritis [14]. Anterior cruciate ligament injury can lead to knee osteoarthritis. The degeneration of articular cartilage in the later stage of the posterior cruciate ligament injury is related to the long-term abnormal mechanical environment after the posterior cruciate ligament injury, which makes the anterior cruciate ligament degeneration. Further exacerbated the instability of the knee joint [15, 16]. However, the rupture of the posterior cruciate ligament will also affect the function and structure of the anterior cruciate belt. The mechanical environment is responsible for the development of ligament tissue, and changes in the stress on the tissue will cause changes in the structure and function of tissues and organs. This process is called organizational remodeling [17]. The mechanical properties of the front crossbelt are changed under reduced tensile stress, and the tensile strength is reduced. When the ligament structure is exposed to a reduced stress environment, the longer the time, the greater the damage to the mechanical properties of the ligament and tissue structure. Even for short-term stress relief, it takes a

long time to restore the mechanical properties of the ligament [18]. When the stress on the ligament decreases, we also find that the strength and stiffness of the ligament decrease. Ligament rupture can damage the stability of the knee joint and cause abnormal knee joint mechanics, which may be caused by damage to other tissues inside and outside the joint. Without timely treatment and intervention, knee pain and dysfunction will eventually occur [19]. After the back-crossbelt is injured, cartilage degeneration will occur, leading to osteoarthritis. In general, ligament injuries are accompanied by some complications. The complications of different ligament injuries are not necessarily the same, but all of them will cause inconvenience to the movement of the human body, and even lead to disability in severe cases.

2.2. Mechanism of Repairing Damaged Ligaments by Implanting Artificial Ligaments of Nanomaterials into the Body.

The material of the artificial ligament is a nondegradable fiber with good chemical stability, but its hydrophobicity is strong, and the cell compatibility is poor. In order to improve the hydrophilicity and biocompatibility of materials used for surface treatment and modification, the development of nanotechnology and nanomaterials provides new methods to improve the biocompatibility of materials [20]. The surface area of nanomaterials increases, and the hydrophilicity increases, which can absorb more cells and extracellular matrix proteins. The nanostructures and patterns on the material surface can significantly improve the biocompatibility of orthopedic implants [21]. Researchers believe that the formation of nanopatterns and structures on the surface of the implant can promote the erection and proliferation of osteoblasts in vitro and promote bone formation and bone remodeling on the surface of endophytic bacteria in the body. In the torsion test, the internal fracture of the mineralized bone tissue and the interface between the bone tissue and the implant were intact [22]. Nanocomposites are commonly used as surface modification materials for prosthetic implants, which can greatly improve the affinity between the implant and the surrounding bone tissue. Nanocomposites overcome the shortcomings of common materials in performance. The surface of the artificial ligament implant is coated. Nano and nanocomposite materials have better advantages and excellent functions. Nano enhances the proliferation of osteoblasts and the synthesis of cell proteins and improves alkaline phosphatase (activity and mass deposition), thereby enhancing the tight integration of bones and internal plants and thereby increasing the use rate of prostheses [23]. Like cells adhere and grow better on the nanocomposite coating group, and the cell density will increase over time [24]. The thermal method after spraying is used to apply a nanocrystalline coating on the surface of the implant, which can maintain the structural integrity of the coating, increase the crystallinity, and improve the long-term stability of the implant coating in the body [25]. The nanocoating layer has good cell compatibility, and the nanocoating has excellent biocompatibility and biological activity, increasing the biological activity of the graft and increasing the adhesion of osteoblasts [26]. The composite material is composed of synthetic materials.

In the normal coating group, the experimental group showed higher cell growth and proliferation rates and better effects, thereby improving the hydrophilicity of the implant. In vitro cell tests showed that the coating group greatly promoted the adhesion of osteoblasts and enhanced cell proliferation. Relevant studies have shown that, compared with the uncoated group, the cell expression level was higher, and as the expression amount increased, the expression became more active [27, 28]. Nanocomposite coatings have been successfully used in ligament tissue engineering implant materials. Nanostructure is a new system constructed or constructed according to certain rules on the basis of nanoscale material units. Applying the nanostructured artificial ligament to ligament injury will greatly improve its structural strength.

As the content of nanofibers increases, the microstructure of the formed scaffold changes from a layered structure to a porous structure, indicating that its formability has been significantly improved [3]. More importantly, the content of nanofibers in the silk fibroin solution also affects the mechanical properties and stability of the scaffold in water. Without any posttreatment, a porous scaffold that can maintain the original overall structure and porous microstructure in water can be obtained, and its retention rate in water exceeds 85% [29]. Compared with traditional silk fibroin scaffold materials, the scaffold material has lower crystallinity and faster degradation performance; so, it shows good hydrophilicity and better biocompatibility. The application in the tissue field provides a richer matrix material [1]. The relationship between cell proliferation rate and nanofiber content is shown in formulas (1) and (2).

$$T(s) = \sum_{j=1}^{v} \frac{M_f}{D} * \log 2(d) + J^V, \tag{1}$$

$$V = L * \text{snb} \left[\sum_{i=1}^{nl} (y_i^n - f y_i y_l + y_l^n) + \sum_{im+1}^{n_l+n_R} (y_i^n - f y_i y_R + y_R^n) \right], \tag{2}$$

where V is the cell proliferation rate, and $T(S)$ is the content of nanofibers.

3. Experimental Detection of the Experimental Group and Normal Group

3.1. Experimental Sample Preparation and Experimental Methods.

First weigh the silk fibroin powder of the corresponding mass, add it to the mixed solvent, seal it with plastic wrap, then sonicate it for 1 h until the silk fibroin powder is evenly dispersed in the mixed solvent, and then add 4.0 g PCL. The membrane is sealed and heated in an oil bath at 40°C for 24 h until the PCL is completely dissolved, and the spinning solution is uniform and stable. SF/PCL spinning parameters are different, used for electrospinning: receiving distance 10 cm, bolus speed 2 mL/h, receiving speed 140 r/min, and voltage 15 kV. SF/PCL spinning parameters under the same composition were as follows:

receiving distance 10 cm, bolus injection speed 2 mL/h, receiving speed 140 r/min, and voltage 12-25 kV. The blended fiber membrane obtained by electrospinning is vacuum dried and stored. A certain amount of collagen is dissolved in an acetic acid solution to prepare a collagen solution with a concentration of 10%. After mixing, centrifuge to remove air bubbles, then remove the wire mesh holder, cut it to the width of the hole, and start making. Spread a layer of collagen and freeze at 20 degrees for about half an hour. Spread the thread and stretch it under certain tension. Then, spread a denser layer of collagen and freeze it at 15 degrees. Wrap them in tin foil, freeze them at 10°C for 4 hours, drain them in a vacuum dryer, and cut them into various lengths for in vivo repair. Divide 20 white rabbits into three groups and implant SF/on the PCL of the injury group. The PCL implantation injury group and control group were as follows. Chloral hydrate was injected intraperitoneally, the ear vein was anesthetized with a catheter, fixed in the supine position, the upper and lower legs in front of the left and right knee joints were shaved, and the left or right knee was randomly selected as the experimental group or the control group and disinfected with compound iodine. Put a sterile small hole towel on the skin and make an incision on the inside of the knee joint. The upper end starts from the upper part of the femur, and the lower end reaches the inside of the tibia, approximately the length. Cut the skin and fascia in turn to expose the medial collateral ligament of the knee joint, separate it, and then remove the ligament from it. The knee joint moved several times, and the tension of the reconstructed ligament was satisfactory. The wound was closed layer by layer, and the ear vein was placed with sterile gauze. After the operation, the medial collateral ligament specimen was fixed with formalin for several hours, and the ligament was cut. Embed the fractured tissue and scar in paraffin, slice, stain, and observe the arrangement and density of scar collagen under light. Use a microscope to understand its healing.

3.2. Experimental Results. In the first week after implantation, the number of human-derived cells in the injured area gradually decreased over time. Two weeks after implantation, these genes were detected in the damaged part of the ligament. The secretory ligament matrix promotes ligament repair. SF/PCL scaffold can only help ligament repair and secrete ligament extracellular matrix and can also secrete growth factors to affect ligament regeneration. Most growth factors accelerate cell proliferation, and FS/PCL may also synthesize various factors that can induce musculoskeletal tissue. The expression of chemokines and growth factors is involved in tissue repair and regeneration before and after stent implantation. The cells express chemokines one week after implantation and still express two weeks after implantation, indicating that SF/PCL can secrete chemokines to attract host cells to participate in the formation of new ligaments. The overall observation results four weeks after implantation showed that all the damaged areas of the abdominal cavity window were repaired by connective tissue, and the muscle and spinal cord tissue was significantly proliferated. There was no significant difference between the two groups. There was no significant difference in the muscle health collagen content of each group every week. Thirty days after implantation, a dense tissue was formed, which was mainly composed of spindle-shaped lyocells and collagen fiber bundles. After being implanted in the body, the engineered ligament will undergo a maturation process. Although collagen fibers are still relatively scarce and small and uniform in diameter, collaborative mechanical stimulation can still promote the maturation of collagen fibers. The diameter of collagen fibers increased by about 25%, and the expression of ligament-specific transcription genes and extracellular matrix genes increased during ligament repair. At 12 weeks, the maximum tensile force of the experimental group was significantly higher than that of the control group.

3.3. Material Selection and Physiological Characteristics of Tissue Engineering Scaffold for Knee Ligament Repair. The repair of damaged ligaments is completed by the tissue engineering scaffold implanted in the body; so, the selection of the scaffold is more demanding. The extracellular matrix (ECM) is not only the supporting structure of cells but also functional. It creates a dynamic three-dimensional microenvironment for cells, realizes the signal transmission between the cell nucleus and the extracellular matrix, and promotes cell adhesion, proliferation, migration, and differentiation. Therefore, it is particularly important to imitate the composition and structure of ECM in tissue engineering. It has been found that cell-collagen interaction affects cell growth and differentiation. The biggest advantage of electrospun nanofibers as a tissue engineering scaffold is that it can simulate the composition and structure of the extracellular matrix (ECM). The ideal tissue engineering material should have the following characteristics: nontoxic; that is, the material itself and its degradation products will not produce inflammation and toxic reactions; it has good biocompatibility, biodegradability, and degradation adaptability and will not cause inflammatory and toxic reactions. In short, as a matrix material for different seed cells, the inoculated cells can be positioned, attached, and positioned to grow and proliferate. At the same time, the material can arrange cells orderly in the scaffold space, differentiate with specific functions, and synthesize appropriate extracellular matrix (ECM). In addition, when transplanting functional tissue engineering into the body, the scaffold material should also have mechanical support functions, blood pressure resistance, blood compatibility, thermal stability, and dimensional stability. This material was selected as the primary problem medical treatment for electrospun nanofiber biomaterials. Anterior cruciate ligament (ACL) cells and NIH3T3 cells can adhere, proliferate, and secrete the extracellular matrix on the scaffold material. The scaffold material has excellent biocompatibility and certain mechanical properties, and the maximum tensile force of the experimental group is significantly higher than that of the control group. The grafts coated with SF can greatly induce new bone formation, and the average width of the graft bone interface is significantly lower than the control group. In addition, the surface of the ligament graft also stimulates the high

expression of bone morphogenetic protein and vascular endothelial growth factor at the local interface. SF/PCL infiltrated many megakaryocytes, the inflammatory response was mild, and there were many fibroblasts and new blood vessels around. The absorbable material placed in the anterior cruciate ligament (ACL) reconstruction graft gradually degrades and absorbs with the growth of new tissue after surgery and is finally completely replaced by collagen fibrous tissue. Histological examination confirmed that there was no obvious lymphocyte infiltration, the cells were spindle-shaped, the fibrous tissue was arranged neatly and evenly, and capillary hyperplasia was visible. And the discovery of nonself-tissue alleles indicates that the implanted cells remain viable. The mixed form of nanofibers can promote the proliferation of ACL fibroblasts. Cell morphology analysis shows that the mixed nanofiber material scaffold has better biocompatibility than PCL nanofiber. SF/PCL nanofibers are biomaterials with application potential, suitable for ligament tissue engineering repair. Fibroblasts have been successfully planted on the scaffold material and adhere to and grow well on the material. The results show that the constructed scaffold material has good three-dimensional configuration and biocompatibility, and it is expected to provide a new type of scaffold material for repairing anterior cruciate ligament injury. The data analysis showing the influence of fiber diameter on tensile strength and elongation is shown in Table 1.

It can be seen from the above chart 1 that when the concentration of SF/PCL is 45%, the fiber diameter is the largest, the arrangement is uniform, and the stability is good. Its tensile strength increases by 30%, and the elongation rate increases to 62.5%. Affected by the SF concentration, it increases with the increase of the concentration at the initial stage, and when it is 45% higher, it decreases with the increase of the concentration. The material concentration directly affects the performance of the material.

3.4. Factors Affecting the Repair Performance of Nanomaterial Scaffolds and Immunological Performance. When silk fibroin material is added to PCL, the diameter of the fiber is relatively small, about 290 nanometers, and a bead-shaped fiber is formed. This is because the spinning solution is relatively thin, the surface tension is small, and the electric field force is large to obtain traction. The lower surface tension is not conducive to the complete volatilization of water. Beads appear very easily; after adding silk powder, fine particles will adhere to the PCL fiber. With the addition of silk powder, the composition continues to increase, from 4.8% to 45%. The diameter of the composite fiber also increased from 320 nm to 440 nm. After adding silk fibroin powder, the bead fiber gradually disappeared, and the diameter of the composite fiber increased without being fully extended. When the SF/PCL concentration is 45%, the composite fiber has the largest diameter, and the fiber distribution is more uniform. At this time, the compatibility between silk fibroin powder and polycaprolactone is the best. If the content of silk fibroin powder continues to increase, if the viscosity of the solution is too high, the silk fibroin

TABLE 1: The effect of fiber diameter on tensile strength and elongation.

Group	Fiber diameter	Tensile strength (MP)	Elongation (%)
The first	292	3.55	38.9
Second	438	4.5	62.8
Third	250	4.2	50.4

powder seems to agglomerate obviously, and the diameter of the composite fiber is reduced to 350 nm. The compatibility of silk fibroin powder with polycaprolactone deteriorates, the spinnability of the spinning solution decreases, and the fiber thickness is uneven. The gaps between the fibers are large, and the fibers are bent and deformed. Because the concentration is too large, the electric field force is not enough to overcome the surface tension of the liquid and reduce the relative amount of solvent. The volatilization of the solvent causes the fiber to coagulate and deform the fiber. When the SF/PCL concentration is 45%, the silk fibroin powder in the composite fiber does not appear lumpy, indicating that the concentration at this time is moderate. During the experiment, when the voltage was increased from 15 kV to 25 kV, the fiber diameter increased from 440 nm to 465 nm, and the fiber diameter did not change significantly, but at 20 kV, the fiber diameter was uniform, and the gap between the fibers was large. At 25 kV, the fiber diameter changes again. The size is different, because the applied voltage is too large, the large amount of charge in the solution will make the spinneret spin faster and faster, and the traction will pull out a large amount of solution, resulting in uneven fiber thickness. When the concentration is 45%, the voltage difference affects the uniformity of the fiber diameter. When the voltage is 18 kV and 21 kV, the fiber diameter is 480 nm and 524 nm, the fiber diameter is the same thickness, and the fiber arrangement is uniform and compact. The electric field force overcomes the surface tension of the solution during the stretching process, so that after the fibers are completely solidified, the arrangement is more uniform. The graft has varying degrees of inflammation in the early postoperative period, and there is inflammatory cell infiltration around the artificial ligament. Considering that inflammation affects the regeneration of tissue collagen, leading to the formation of fibrous blisters, controlling inflammation can help improve the transplanted ligament. Hyaluronic acid can be greatly reduced, and hyaluronic acid has been shown to have the ability to inhibit the activity of inflammatory cytokines.

4. Analysis and Discussion of Influencing Factors in Repairing Injured Ligaments with Stents

4.1. Analysis of the Results of Repairing Damaged Ligaments with Nanomaterial Scaffolds. The test results show that the crystallinity of polycaprolactone is not the main factor affecting the difference in mechanical properties, but the

increase in the crystallinity of the stent through heat treatment should further enhance the mechanical properties of the stent. PCL provides space to repair cell adhesion and growth, while SF/PCL provides sufficient mechanical strength. The research results show that, compared with PCL scaffold, SF/PC scaffold has more collagen deposition and rougher collagen production, and its mechanical properties are closer to normal tissues. After adding silk fibroin, the morphology of nanofibers is improved, the diameter of nanofibers is reduced, and the hydrophilicity of the material is increased. The mixed form of nanofibers can promote the proliferation of ACL fibroblasts. Cell morphology analysis shows that the mixed nanofiber material scaffold has better biocompatibility than PCL nanofiber. This proves that SF/PCL nanofibers are biomaterials with application potential and are suitable for ligament tissue engineering repair. At the same time, protein drugs embedded in silk fibroin can maintain its activity for a long time.

The maximum load of SF/PCL artificial ligament is 2.73 times that of human ACL, and it is resistant to repetition. The strength of twisting and bending can prevent damage caused by excessive traction; SF/PCL ligament fibers line up the normal physiological structure of people, and the gap between the fibers is moderate, which is conducive to the normal growth of human tissues, increases the viscoelasticity of ligaments, and avoids wear and tear. Peeling is as follows: LARS ligament has stable performance and is not affected by the human body's biological reaction process; 6 months after surgery, it was found that there are collagen fibers and vascular endothelial cells in the artificial ligament. The patient does not have acute synovitis and feels good; the patient who reconstructed ACL with SF/PCL ligament has no synovial inflammation and serious complications. The biomechanical test data of different experimental groups are shown in Table 2.

The results of the study showed that the biomechanics of the body was changed. Compared with the PCL group, the maximum load of SF/PCL increased by 28%, the stiffness decreased by 10%, and the energy increased by 75%, indicating that the addition of SF material affects the biomechanics and improves the ligament.

The SF/PCL artificial ligament is made of high-strength polyester fiber: its design combines the principles of bionics, the internal structure is similar to normal human ligaments, and the longitudinal fibers in the joints are elastic but not elongated and the external mesh of the joint. The fibrous fibers provide strength without being stretched, and there is no transverse fiber structure inside. The fiber structure promotes the growth of tissue cells and achieves the purpose of repair and reconstruction. It can prevent the friction between the fibers from generating debris particles, thereby avoiding the occurrence of synovitis. In addition, the material has good plasticity and can mimic the movement of normal human ligaments according to the rotation of the ligaments, and the fatigue strength depends on the number of fibers, as shown in Figure 1.

TABLE 2: Experimental group biomechanics test data.

Group	Maximum load	Stiffness	Energy	Displacement
The first	36.1 ± 22.7	21.8 ± 8.5	40.6 ± 35.4	2.3 ± 0.5
Second	47.0 ± 7.4	24.3 ± 3.1	78.1 ± 32.9	3.3 ± 1.0
Three	88.2 ± 18.3	46.21 ± 1.8	171.2 ± 90.5	3.3 ± 1.1
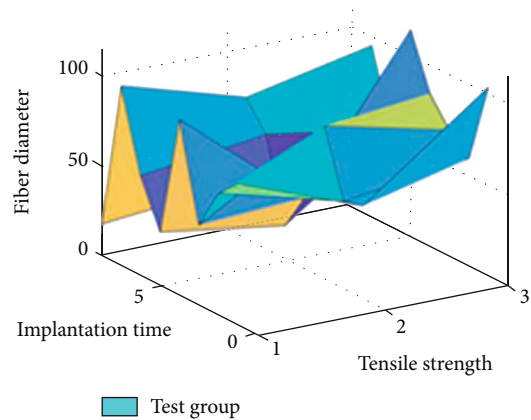
FIGURE 1: The effect of stent implantation time on fiber diameter and tensile strength.

The data analysis results shown in Figure 1 clearly show that the extensibility of bone marrow stromal stem cells increased by 38% after SF treatment, and the ability to adhere to cells was greatly enhanced, which was twice that of the PCL group, and the morphology was significantly better than that of the untreated group. The proliferation rate of artificial ligament cells after SF treatment increased significantly. The quantitative phosphatase activity was 12% higher than that of the untreated group.

The SF/PCL scaffold has similar compressive modulus and mechanical strength to human trabecular bone. By culturing human osteoblasts, it was found that the cells can maintain the phenotype and show higher levels of alkaline phosphatase and mineral deposits. SF and PCL are raw materials, and SF/PCL stents are made by free surface electrospinning. The scaffold can improve the osteogenic differentiation of bone marrow mesenchymal stem cells derived from human cord blood, promote alkaline phosphatase activity and the expression of bone cell-specific transcription factors, osteocalcin, and type I collagen, and is an ideal bone tissue engineering supporting materials, as shown in Figure 2.

From the data in Figure 2, it can be seen that the artificial ligament scaffold increased the cell proliferation rate, the number of cells increased with time, the extracellular genes of the control group decreased, and a large number of cells adhered to the SF/PCL patch, which was higher than the control 67% of the group and was 30% higher than that of the PCL group, inflammation-related genes were 40% lower than the blank group, and adhesion-related genes were 25% higher than the blank group.
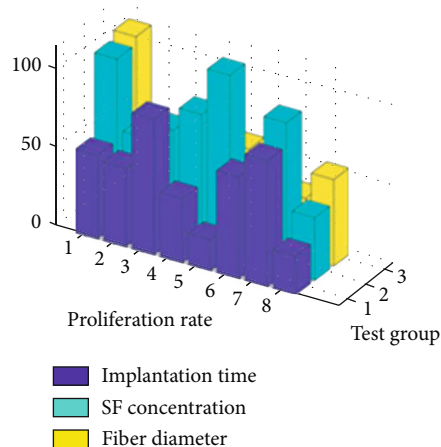
FIGURE 2: The relationship between SF concentration and fiber diameter and elongation.

4.2. Analysis of Biological Characteristics of Silk Fibroin Polycaprolactone Nanofibers. In the spinning process, the fiber diameter distribution is uneven, the dispersion is large, the mass fraction is 15%, and the effect on the spinning solution is more obvious. When the mass fraction of the spinning solution is 13%, the obtained nanofibers have a regular morphology, a small diameter, and a relatively uniform diameter distribution. When the mass fraction is 11%, the diameter of the fiber is the smallest, the average diameter is close to 100 nm, the diameter distribution is relatively concentrated, and the dispersion is small. Therefore, the mass fraction of the spinning solution can be 11% and 13%, as shown in Figure 3.

It can be seen from the data in Figure 3 that the voltage also has a certain effect on the engineering tissue scaffold. When the voltage reaches 20 kV, the fiber diameter is uniform, and the gap between the fibers is larger. At this time, the diameter increases by 8%. When the voltage continues to increase, the concentration slowly increases, the fiber diameter varies, and the gap becomes smaller, which affects the infiltration of cells. Such a scaffold will hinder the repair of the damaged ligament.

Polycaprolactone (PCL) and SF are used to manufacture three-dimensional porous scaffolds through electrospinning technology. The addition of sericin enhances the adhesion and proliferation of human skin fibroblasts on the material. The hybrid nanofiber scaffold prepared by this technology is more conducive to the proliferation of ligament keratinocytes and fibroblasts. The scaffold material with SF as the matrix can well promote the growth of fibroblasts and can help wound healing and reconstruct the function of damaged ligaments, as shown in Figure 4.

It can be seen from Figure 4 that the stent implantation time affects the repair of various ligament functions. After one week of implantation, the human source in the injured area is reduced by 30%, and the stromal cells increase by 13% at the second week. After 30 days of implantation, the collagen fiber diameter increases by 25%, 12 weeks, and the maximum pulling force is higher than the control group.
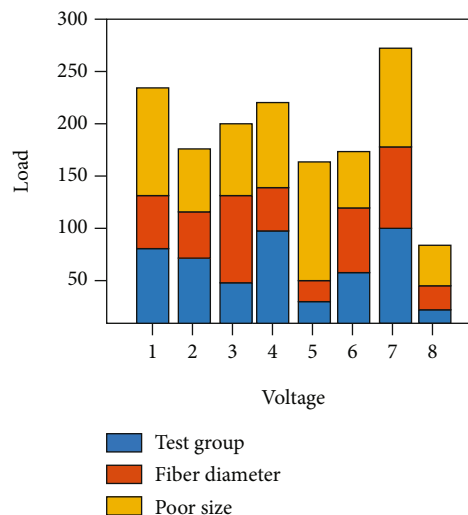
FIGURE 3: The fiber diameter changes with the voltage affect the artificial ligament load.
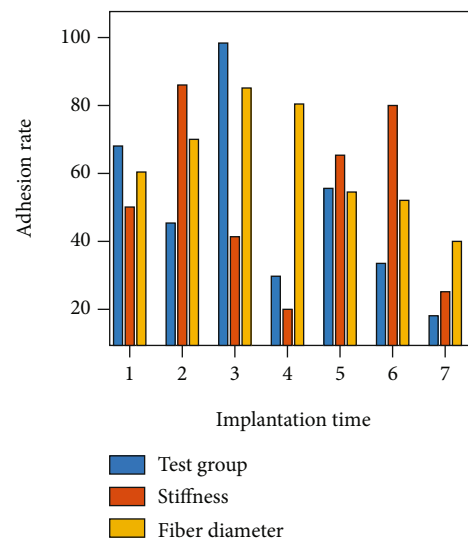
FIGURE 4: The effect of stent implantation time on adhesion rate.

5. Conclusions

(1) In the process of tissue engineering scaffold repairing damaged ligaments, the concentration of SF increases, the fiber diameter increases, the traction force increases, the tensile strength increases by 30%, the stretching rate increases to 62.5%, and the maximum load ratio of SF/PCL is as follows. The PCL group increased by 28%, stiffness decreased by 10%, and energy increased by 75%. When increased to a certain extent, the fiber diameter is uniform, the pores are large, and the arrangement is neat, which is conducive to cell infiltration, generating new cells, and rebuilding damaged ligaments

(2) The research in this paper shows that the SF/PCL scaffold can make more use of damaged ligaments

to recover, increase biocompatibility by 25%, increase cell proliferation rate by 57%, increase somatic cell adhesion rate by 35%, and increase collagen fiber formation by 12%, the porosity is about 60%, and the load is as high as $907 \pm 132\,N$. However, a large number of cells adhere to the SF/PCL membrane, which is higher than 67% in the control group and 30% higher than in the PCL group. Inflammation-related genes are lower than 40% in the blank group, and adhesion-related genes are 25% higher than those in the blank group. The data shows that the performance of the artificial ligament has been greatly changed by adding SF

(3) The study found that when the mass ratio of nanofibers to ordinary silk fibroin is $1:7$, the mechanical properties of the scaffold are the best. The crystallinity of the scaffold material is reduced by 23%, the degradation performance is increased by 31%, and the hydrophilicity is increased by 60%. The compatibility is improved by 58%. These factors meet the conditions of the ideal scaffold required by tissue engineering and become the first choice for repairing knee ligament injuries. This result has given scientists a new understanding of the selection of scaffolds and laid a new foundation for the development of medicine

Data Availability

The data that support the findings of this study are available from the corresponding author upon reasonable request.

Conflicts of Interest

The author declares that he/she has no conflicts of interest.

References

[1] A. Pinsino and V. Matranga, "Sea urchin immune cells as sentinels of environmental stress," *Developmental & Comparative Immunology*, vol. 49, no. 1, pp. 198–205, 2015.

[2] W. S. Tin-Tin, K. T. T. Chaw, and M. Yadanar, "Nano-sized secondary organic aerosol of diesel engine exhaust origin impairs olfactory-based spatial learning performance in pre-weaning mice," *Nanomaterials*, vol. 5, no. 3, pp. 1147–1162, 2015.

[3] A. Shah and M. A. Dobrovolskaia, "Immunological effects of iron oxide nanoparticles and iron-based complex drug formulations: therapeutic benefits, toxicity, mechanistic insights, and translational considerations," *Nanomedicine*, vol. 14, no. 3, pp. 977–990, 2018.

[4] P. J. Read, J. L. Oliver, and S. C. M. B. De, "Neuromuscular risk factors for knee and ankle ligament injuries in male youth soccer players," *Sports Medicine*, vol. 46, no. 8, pp. 1059–1066, 2016.

[5] O. C. Ann, F. S. Tee, and V. Y. Nen, "A study on satisfaction level among amateur web application developers towards pigeon-table as nano web development framework," *Journal of Organizational and End User Computing (JOEUC)*, vol. 31, no. 3, pp. 97–112, 2019.

[6] T. Zult, A. Gokeler, J. J. A. M. van Raay, R. W. Brouwer, I. Zijdewind, and T. Hortobágyi, "An anterior cruciate ligament injury does not affect the neuromuscular function of the non-injured leg except for dynamic balance and voluntary quadriceps activation," *Knee Surgery, Sports Traumatology, Arthroscopy*, vol. 25, no. 1, pp. 1–12, 2016.

[7] D. G. Kim, H. J. Kwon, Y. H. Jeong et al., "Mechanical properties of bone tissues surrounding dental implant systems with different treatments and healing periods," *Clinical Oral Investigations*, vol. 20, no. 8, pp. 2211–2220, 2016.

[8] D. S. Evangelopoulos, S. Kohl, S. Schwienbacher, B. Gantenbein, A. Exadaktylos, and S. S. Ahmad, "Collagen application reduces complication rates of mid-substance ACL tears treated with dynamic intraligamentary stabilization," *Knee Surgery Sports Traumatology Arthroscopy*, vol. 25, no. 8, pp. 2414–2419, 2017.

[9] A. Benjaminse, B. Otten, and A. Gokeler, "Motor learning strategies in basketball players and its implications for ACL injury prevention: a randomized controlled trial," *Knee Surgery Sports Traumatology Arthroscopy Official Journal of the Esska*, vol. 25, no. 8, pp. 1–12, 2015.

[10] C. Mouton, D. Theisen, T. Meyer et al., "Noninjured knees of patients with noncontact ACL injuries display higher average anterior and internal rotational knee laxity compared with healthy knees of a noninjured population," *American Journal of Sports Medicine*, vol. 43, no. 8, pp. 1918–1923, 2015.

[11] K. H. Frosch, R. Akoto, T. Drenck, M. Heitmann, C. Pahl, and A. Preiss, "Arthroscopic popliteus bypass graft for posterolateral instabilities of the knee," *Operative Orthopdie Und Traumatologie*, vol. 28, no. 3, pp. 193–203, 2016.

[12] T. West, L. Ng, and A. Campbell, "The effect of ankle bracing on knee kinetics and kinematics during volleyball-specific tasks," *Scandinavian Journal of Medicine and ence in Sports*, vol. 24, no. 6, pp. 958–963, 2014.

[13] C. Domnick, M. Herbort, M. J. Raschke et al., "Converting round tendons to flat tendon constructs: does the preparation process have an influence on the structural properties?," *Knee Surgery, Sports Traumatology, Arthroscopy*, vol. 25, no. 5, pp. 1561–1567, 2017.

[14] D. Wang, K. T. Yamaguchi, M. H. Jones, and A. Miniaci, "KOOS and IKDC scales may be inadequate in evaluating patients with multiple ligament knee injuries: a systematic review," *Journal of ISAKOS: Joint Disorders & Orthopaedic Sports Medicine*, vol. 1, no. 2, pp. 82–86, 2016.

[15] M. Neagu, Z. Piperigkou, K. Karamanou et al., "Protein biocorona: critical issue in immune nanotoxicology," *Archives of Toxicology*, vol. 91, no. 3, pp. 1031–1048, 2017.

[16] H. Song and M. Brandt-Pearce, "Range of influence and impact of physical impairments in long-haul DWDM systems," *Journal of Lightwave Technology*, vol. 31, no. 6, pp. 846–854, 2013.

[17] R. Augustine, P. Dan, A. Sosnik et al., "Electrospun poly(vinylidene fluoride-trifluoroethylene)/zinc oxide nanocomposite tissue engineering scaffolds with enhanced cell adhesion and blood vessel formation," *Nano Research*, vol. 10, no. 10, pp. 3358–3376, 2017.

[18] K. Jagiello, B. Chomicz, A. Avramopoulos et al., "Size-dependent electronic properties of nanomaterials: how this novel class of nanodescriptors supposed to be calculated?," *Structural Chemistry*, vol. 28, no. 3, pp. 635–643, 2017.

[19] T. Hasan, "Mechanical properties of nanomaterials: a review," *Nanotechnology Reviews*, vol. 9, no. 1, pp. 259–273, 2020.

[20] M. Nahavandi and S. M. Monirvaghefi, "The effect of electroless bath pH on the surface properties of one-dimensional Ni-P nanomaterials," *Ceramics International*, vol. 46, no. 2, pp. 1916–1923, 2020.

[21] A. A. Pathan, K. R. Desai, and C. P. B. P. Bhasin, "Improved photocatalytic properties of NiS nanocomposites prepared by displacement method for removal of rose bengal dye," *Current Nanomaterials*, vol. 2, no. 3, pp. 169–176, 2018.

[22] G. K. Tripathi and R. Kurchania, "Effect of doping on structural, optical and photocatalytic properties of bismuth oxychloride nanomaterials," *Journal of Materials ence Materials in Electronics*, vol. 27, no. 5, pp. 5079–5088, 2016.

[23] Y. Guo, K. Xu, C. Wu, J. Zhao, and Y. Xie, "Surface chemical-modification for engineering the intrinsic physical properties of inorganic two-dimensional nanomaterials," *Chemical Society Reviews*, vol. 44, no. 3, pp. 637–646, 2015.

[24] M. Y. Shahid, A. Anwar, and F. Malik, "Effect of Sr-doping on ferroelectric and dielectric properties of sol-gel synthesized BaTiO3 thin films," *Digest Journal of Nanomaterials and Biostructures*, vol. 12, no. 3, pp. 669–677, 2017.

[25] F. Huang, A. H. Yan, Z. H. Liao et al., "Self-assembled synthesis of hollow Nb3O7F nanomaterials based on Kirkendall effect and its photocatalytic properties," *Materials & Processing Report*, vol. 30, no. 3, pp. 144–150, 2015.

[26] L. Xu, J. Xiang, R. Peng, and Z. Liu, "Recent advances in the development of nanomaterials for DC-based immunotherapy," *Science Bulletin*, vol. 61, no. 7, pp. 514–523, 2016.

[27] Q. H. Quach and J. C. Y. Kah, "Non-specific adsorption of complement proteins affects complement activation pathways of gold nanomaterials," *Nanotoxicology*, vol. 11, no. 3, pp. 1–39, 2017.

[28] Y. Zhang, W. Ni, and Y. Li, "Effect of siliconizing temperature on microstructure and phase constitution of Mo-MoSi$_2$ functionally graded materials," *Ceramics International*, vol. 44, no. 10, pp. 11166–11171, 2018.

[29] Q. V. Le, J. Suh, and Y. K. Oh, "Nanomaterial-based modulation of tumor microenvironments for enhancing chemo/immunotherapy," *The AAPS Journal*, vol. 21, no. 4, pp. 1–19, 2019.

Hindawi

Research Article

Clothing Nanometer Antimite and Antibacterial Based on Deep Learning Technology

Hai Liu [1,2]

[1]*Department of Big Data, Jiangxi Institute of Fashion Technology, Nanchang, 330201 Jiangxi, China*
[2]*Clothing Big Data Research Center, Jiangxi Institute of Fashion Technology, Nanchang, 330201 Jiangxi, China*

Correspondence should be addressed to Hai Liu; liuhai@jift.edu.cn

With the improvement of people's living standards, the living conditions and environment of residents have changed, and there are also more and more electrical appliances such as air conditioners, air purifiers, and humidifiers. People's living environment and office environment are increasingly closed, which makes it easy for mites to breed and multiply. The changes in the living environment have made many people more and more aware of health and safety issues. Under these conditions, it is mainly used in the field of biomedicine. In the high-tech field, nanomaterials with antimite and antibacterial properties have entered the field of clothing and home textiles. With the advancement and development of science and technology, nanomaterial technology tends to mature and becomes a major player in the field of clothing. However, nanosilver alone has some defects, such as large nanoparticles, poor antimite and antibacterial effect, high cost, easy oxidation, and strong toxicity. Therefore, the preparation of new nanocomposite materials is of great significance for the application of nanotechnology to the field of clothing. In this paper, the antimite and antibacterial properties of different nanomaterials on clothing were explored through deep learning technology combined with experimental methods. According to the experiments in this paper, the $Ag/TiO_2(ATA)$ nanocomposites have obvious antibacterial and acarid effects, and the antibacterial and acarid rates are close to 100% under the conditions of visible light and dark light.

1. Introduction

Bacterial mites are ubiquitous organisms in human life. It has strong vitality, rapid reproduction, and strong ability to adapt to the environment. Some pathogenic microorganisms invade the human body through direct contact or the surrounding environment, which seriously threatens human health and interferes with human normal life. As a necessities of human life, textiles are very easy to breed bacteria and be contaminated with microorganisms such as mites that endanger human health due to their own structural problems. Coupled with the surface temperature, humidity, oil, and sweat of the human body, natural conditions are created for the reproduction of microorganisms. With the development of society and the advancement of science and technology, people's demand for the comfort and functionality of textiles is increasing, so some textiles with special functions are favored by consumers. With the introduction

and rapid development of the concept of deep learning, people use some of its algorithms and features to apply deep learning technology to antibacterial and antimite nanoclothing. Through these algorithms, the antibacterial and antimite properties of nanocomposites are more deeply recognized.

Because nanocomposite materials have the characteristics of antibacterial, antimite, nontoxic, tasteless, and strong stability, clothing fabrics have also begun to use this special material. This has made a significant contribution to the promotion of the textile industry. The use of deep learning, a multilayer neural network learning algorithm, to explore the antibacterial and antimite effect of clothing nanometers better demonstrates the benefits of nanocomposite materials used in clothing fabrics.

The following related researches on deep learning and antibacterial and antimite composite nanomaterials were found through sorting out. Dong Y has summarized recent advances in deep learning-based acoustic models under his

research and investigated the motivations and insights behind the techniques. Models such as recurrent neural networks U+0028 RNNs U+0029 and convolutional neural networks U+0028 CNNs U+0029, which can effectively utilize variable-length contextual information, were discussed, as well as their various combinations with other models. Then, the end-to-end optimized model was described, focusing on feature representations learned jointly with the rest of the system, connectionist temporal classification U+0028 CTC U+0029 standard, and attention-based sequence-to-sequence translation models. Robustness issues in speech recognition systems were further elaborated, and acoustic model adaptation, speech enhancement, and separation, and robustness training strategies were discussed [1]. Oshea T proposed and discussed several new applications of deep learning at the physical layer. A fundamentally new approach was developed by interpreting the communication system as an autoencoder. It shows how to extend this idea to networks of multiple transmitters and receivers and presents the concept of radio transformer networks as a means of incorporating expert domain knowledge into machine learning models. Finally, the application of convolutional neural networks on raw IQ samples for modulation classification is shown. Its accuracy is competitive compared to traditional schemes relying on expert features [2]. Kermany D S has built a deep learning framework-based diagnostic tool for screening patients with common treatable blinding retinal diseases. It used transfer learning to train neural networks with a fraction of the data of traditional methods. This approach can be applied to a data set of optical coherence tomography images, demonstrating comparable performance to human experts in classifying age-related macular degeneration and diabetic macular edema. By highlighting the regions identified by the neural network, a more transparent and interpretable diagnosis can be provided. This further demonstrated the general applicability of the artificial intelligence system in diagnosing pediatric pneumonia using chest X-ray images. This tool may ultimately help to expedite the diagnosis and referral of these treatable diseases, thereby facilitating early treatment and thus improving clinical outcomes [3]. Ravi D provided a comprehensive up-to-date review of research employing deep learning in health informatics. A critical analysis of the technology's relative merits, potential pitfalls, and future prospects is presented. They mainly focused on key applications of deep learning in translational bioinformatics, medical imaging, pervasive sensing, medical informatics, and public health [4]. Wang D L summarized the recent research progress of deep learning-based supervised speech separation. First, the background of speech separation and the concept of supervised separation are introduced. Then, it discusses the three main components of supervised separation: learning machine, training target, and acoustic features. Most of the overview is about separation algorithms and reviewing monophonic approaches, including speech enhancement (speech-nonspeech separation), speaker separation (multispeaker separation), and speech deredundancy, as well as multimicrophone techniques. Generalization problems specific to supervised learning are discussed. They provided a historical perspective on how progress was made [5]. Cheng C showed that functional graphene nanomaterials (FGNs) are

an emerging material. It has extremely unique physical and chemical properties and physiological capabilities to interfere with and/or interact with biological organisms. Therefore, FGN offers multiple possibilities for various biological applications. In addition to their use in drug/gene delivery, phototherapy, and bioimaging, recent studies have shown that FGNs can significantly facilitate interfacial biological interactions, especially with proteins, mammalian cells/stem cells, and microbes. FGNs can adsorb and concentrate nutritional factors including proteins in physiological media. In addition, FGNs can also interact with cocultured cells through physical or chemical stimulation, thereby significantly modulating their cell signaling and biological properties [6]. Shivakumar D T demonstrated that metallization layers of aluminum, gold, or copper can be prevented from interacting with silicon substrates by thin boron layers grown by chemical vapor deposition (CVD) at 450°C. A 3-nm-thick boron layer was investigated in detail. It forms the p-anode region of the PureB diode with zero metallurgical junction depth on the n-type silicon. Metals were deposited by electron beam-assisted physical vapor deposition (EBPVD) at room temperature. It is annealed at temperatures up to 500°C. In all cases, the B layer is an effective material barrier between metal and silicon. The almost unchanged I–V characteristics of the PureB diodes and the microscopy of the deposited layers were examined and verified. In order to obtain this result, it is required that the silicon surface must be cleaned before B deposition. Otherwise, any silicon surface contamination will prevent complete B coverage, resulting in increased current flow, sometimes Schottky-like. For Au, the room temperature interaction with Si is excessive through such pinholes in the B layer after annealing at 500°C [7]. These documents are very detailed for the introduction of deep learning and nanomaterials and have great reference value for the writing of this article.

In this paper, the antibacterial and antimite properties of nanocomposites under different conditions were explored through deep learning methods. And during the experiment, it was found that the ATA nanocomposite is the most suitable for clothing fabrics. Under the same conditions, compared with elemental Ag nanomaterials, ATA has stronger stability and antimite and antibacterial properties, and the cost of using materials is lower.

2. Method of Nanometer Antimite and Antibacterial for Clothing Based on Deep Learning

Research on deep learning has a long history. Deep learning originated from artificial neural networks and is also classified as machine learning. Deep learning conveys image categories and features through a multilayer information network [8–10]. It is mainly used in the field of artificial intelligence and studies multiple interdisciplinary subjects, such as neural networks, image feature modeling, image recognition, and target detection. In 1943, the deep neural network based on deep learning was first proposed, and it was found that the neural network had a strong ability to learn self-features; in 1957, the perceptron model came out to deal

(a)

(b)
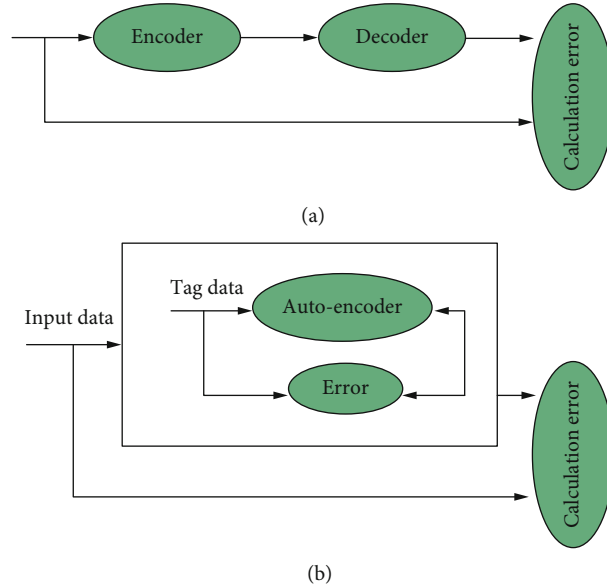
FIGURE 1: Unsupervised learning and supervised learning modes.

with the two-class problem; in 1986, the BP neural network based on neural network was proposed; in 2006, the concept of deep learning was first proposed; since 2014, the extensive application of deep learning in deep learning in image recognition has improved the accuracy of image recognition. With the continuous development and maturity of deep learning technology, the application of deep learning is becoming more and more extensive, and this technology is used in more and more fields.

2.1. Autoencoder. Autoencoder is an unsupervised learning algorithm that connects encoder and decoder across layers [11]. The input layer, hidden layer, and output layer constitute the autoencoder. By compressing the input data into another low-dimensional data to output the data set, it is divided into two parts: the encoder and the decoder [12]. In general, determining the expression of input data is mainly to see whether the output data is consistent with the input data. If they are inconsistent, the parameters should be adjusted so that the resulting data has the smallest error and is close to the output data and the input data [13]. The results are shown in Figure 1. The entire encoder contains two convolutional layers and one pooling layer. The convolutional layers work together to extract feature maps. The pooling layer performs downsampling and finally outputs the feature map. The decoder is the final network output. The connection layer between the encoder and the decoder mainly connects the corresponding feature maps and then becomes the data input of the next convolutional layer.

When the decoder activation function is followed by identity, the squared error function is obtained. The identity condition needs to satisfy the normal distribution:

$$Q(t, x) = t - x^2. \tag{1}$$

When the decoder activation function is a sigmoid function, the cross entropy function is obtained:

$$Q(t, x) = -\sum_{o=1}^{n} [t_o \log(x_o) + (1 - t_o) \log(1 - x_o)]. \tag{2}$$

Finally, the overall loss function is obtained:

$$K_{(AF)}(\varepsilon) = \sum_{c \in s} Q(t, g(f(t))). \tag{3}$$

2.2. Restricted Boltzmann Machine. Restricted Boltzmann machine neurons are relatively simple. It consists of two groups of neurons in the input layer and the hidden layer and is a stochastic network model [14]. Here, it is assumed that the input layer is b and the hidden layer is a. As can be seen from Figure 2, each neuron in the input layer and the hidden layer is related to each other. But if the neurons in each network model are independent, the neurons in each layer are not connected to each other [15]. Restricted Boltzmann machine has been applied in dimension reduction, classification, collaborative filtering, feature learning, and topic modeling.

The basic structure of RBM is not limited by orientation. Assuming that the values of neurons in these two layers are between 0 and 1, $k_i \in \{0, 1\}$, $m_x \in \{0, 1\}$, w and e represent the number of neurons in the input layer and hidden layer, respectively. If the specific values of the input neurons have been given, p_i is not equal to 0. The formula that will result in the combined model is

$$E(k, m, \alpha) = -\sum_{i=1}^{w} \sum_{x=1}^{e} g_{ix} k_i m_x - \sum_{i=1}^{w} p_i k_i - \sum_{x=1}^{e} q_x m_x, \tag{4}$$

where g_{ix} represents the weight coefficients of the input layer and the hidden layer; p_i represents the bias term of each neuron in the input layer; q_x represents the bias term of each neuron in the hidden layer; and α represents the grid parameter of the RBM.
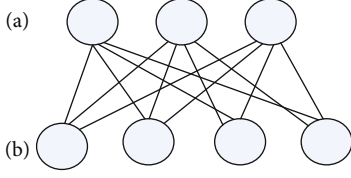
FIGURE 2: Restricted Boltzmann machine model.

Using the Boltzmann algorithm to determine the proportional distribution function $Z(\varepsilon)$, the formula can be obtained. Boltzmann machine is used to combine the advantages of multilayer feedforward neural network and discrete Hopfield network in network structure, learning algorithm, and dynamic operation mechanism. It is based on discrete Hopfield network and has learning ability. It can find the optimal solution through a simulated annealing process.

$$f(y, x) = \frac{1}{z(\varepsilon)} \exp\left(-E(y, x; \varepsilon)\right) = \frac{1}{z(\varepsilon)} \prod_{ij} e^{w_r y_i x_j} \prod_i e^{a_i y_i} \prod_j e^{b_j x_j}, \tag{5}$$

$$Z(\varepsilon) = \sum_y \sum_x \exp(-E(y, x; \varepsilon)). \tag{6}$$

A proportional distribution function $Z(\varepsilon)$ of t is input to the data. According to the marginal distribution of the combined probability distribution $f(y, x)$, the problems encountered in real life can be solved, and the following formula can be obtained:

$$f(t) = \frac{1}{Z(\varepsilon)} \sum_x \exp(-E(t, x; \varepsilon)). \tag{7}$$

The grid parameter ε is calculated using the RBM feature extraction method. The subsequent input data is obtained through the calculated grid parameters. It refers to the boundary of grid parameter domain calculated according to the characteristics of 3D grid (while the fixed boundary method is artificially specified). Assuming that the number of samples is W, then, the measurement method of the grid parameters is the likelihood function, and the formula is as follows:

$$\varepsilon = \arg \ \max_\varepsilon \sum_{w=1}^{W} \log\left(p\left(t^{(w)}\right)\right). \tag{8}$$

The optimal parameter ε of the network with the maximum value of the $L(\varepsilon) = \arg \ \max_\varepsilon \sum_{w=1}^{W} \log\left(p(t^{(w)})\right)$ function is measured by the method of stochastic gradient ascent (SGA). The partial derivative value of each network parameter is a $\log\left(p(t^{(w)})\right)$ function, which can be obtained by the following formula:

$$\frac{\chi l}{\chi \varepsilon} = \sum_{w}^{W} \left(\left\langle \frac{\chi\left(-E\left(t^{(q)}, x\right)\right)}{\chi \varepsilon} \right\rangle_{p(\varepsilon)} - \left\langle \frac{\chi\left(-E(t, x)\right)}{\chi \varepsilon} \right\rangle_{p(t, x)} \right). \tag{9}$$

When the partial derivatives of the specific parameters g_{ix}, p_i, and q_i of the likelihood function have only one simple parameter facing the training grid, the following formula can be obtained:

$$\frac{\chi p(t)}{\chi g_{ij}} = \left\langle t_i x_j \right\rangle_{p(x)} - \left\langle t_i x_j \right\rangle_{p(t, x)}, \tag{10}$$

$$\frac{\chi p(t)}{\chi(p_i)} = \left\langle t_i \right\rangle_{p(x)} - \left\langle t_i \right\rangle_{p(t, x)}, \tag{11}$$

$$\frac{\chi p(t)}{\chi(q_i)} = \left\langle t_i \right\rangle_{p(x)} - \left\langle t_i \right\rangle_{p(t, x)}. \tag{12}$$

Assuming that t_0 represents the input layer data, according to the obtained data visualization, the activation value of each hidden layer w_0 is calculated by the method of the sigmoid network activation function, and the following formula is obtained:

$$p(t_0 = 1 | w_o) = 1 / \left(1 + \exp\left(-\sum_i v_i g_{ij} + q_i \right) \right). \tag{13}$$

According to the characteristics of the symmetry of the RBM grid structure, when the hidden layer is in the active state, the activation value of the input layer can be obtained according to the following formula:

$$p(t_i = 1 | t_0) = 1 / \left(1 + \exp\left(-\sum_j t_i w_{ij} + a_j \right) \right). \tag{14}$$

2.3. Deep Belief Network. A deep belief network is a type of machine learning that consists of multiple RBM networks. It is a probabilistic generative model built between data and labels, which can be applied to both unsupervised learning and supervised learning [16–18]. RBM network consists of visible layer and hidden layer. By definition, unsupervised learning is used to deal with the sample set not marked by classification when designing the classifier. Supervised learning refers to the process of using a group of samples of known categories to adjust the parameters of the classifier to achieve the required performance, which is also called supervised training or teacher learning. The difference is that supervised learning means that a set of data is given manually and the attribute value of each data is also given. For each sample in the data set, we want the algorithm to predict and give the correct answer: regression problem and classification problem. In unsupervised learning, data is not labeled or has the same label. Its network structure is shown in Figure 3.

As can be seen from Figure 3, the deep belief network is composed of RBM structures [19]. Deep belief networks
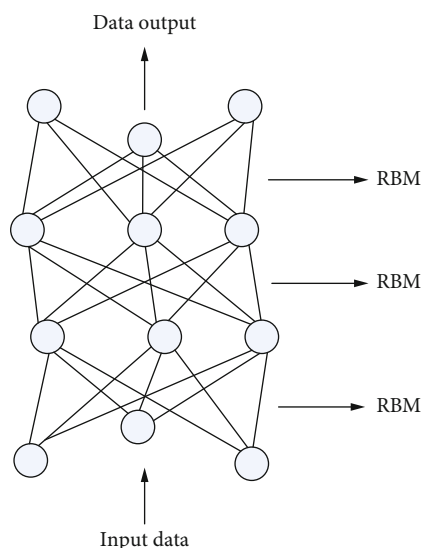
Figure 3: DBN deep learning model.

solve the difficult problem of training multilayer neural networks. It achieves data features by training the weights between each constituent neuron. The deep belief network training process is carried out step by step. In the training process of each layer of neurons, the feature image of the hidden layer is inferred through the data, and the previously obtained hidden layer is used as the data vector of the next layer to progress layer by layer, and so on. Finally, the entire deep belief network is fine-tuned through supervised learning [20]. After the above actions, a basic supervised learning algorithm is completed by concatenating the final results [21].

3. Deep Neural Network

Since the deep neural network is extended from the traditional neural network, the research of the deep neural network has not been effectively developed for a long time, and it has been in the research stage of one or two hidden layers [22]. It does not perform well in forward propagation, back propagation, and gradient descent, and is not even as good as a single hidden layer neural network. In this regard, many scholars have been exploring what causes the deep neural network to have poor ability to deal with problems [23]. At present, the methods of training neural networks are based on the idea of back propagation; that is, according to the error calculated by the loss function, the weight of the depth network is updated and optimized by gradient back propagation.

According to the answers given by most scholars, two main reasons are summarized: First, the value of the initial parameters affects the neural network, which is also the drawback of the gradient descent method. Second, the increase of grid parameters leads to an increase in the number of neural network layers. The neural network is originally a fitter, which aggravates the overfitting of the deep neural network, and the final result is not good [24]. At first, each object is regarded as a cluster, and then, these clusters are merged step by step according to some criteria. The distance between the two clusters can be determined by the similarity of the nearest data points in the two different clusters. The clustering process is repeated until all clusters meet the number of clusters.

It has been proven by practice that the weight matrix can be shifted by training the initial weights of the deep neural network step by step, which makes the in-depth study of the deep neural network go a step further. Some experts proposed to train a DBN in the forward direction based on the RBM network and then expand the DBN in the reverse direction. Finally, the whole network is regarded as a complete AE using the traditional BP algorithm for repeated training [25]. BP network can learn and store a large number of input-output mode mapping relationships without revealing the mathematical equations describing this mapping relationship in advance. In this way, AE actually becomes the first successfully trained deep autoencoder on the intelligent algorithm. The initial training process of the deep neural network is shown in Figure 4.

3.1. Convolutional Neural Network. Convolutional neural network is divided from artificial neural network, which is a multilayer neural network structure with the ability of deep learning [26]. Convolutional neural networks rely on convolutional and downsampling layers to extract data. The weight of some neurons in the same layer is the same, and it is not completely connected with neurons, but each layer has multiple neurons connected to each other [27]. The convolutional neural network is extended into two parts: The first part is the convolutional layer and the pooling layer (downsampling layer). The second part is the fully connected layer and the output layer. The input layer is where the algorithm begins to affect the entire network output value. The convolutional layer mainly plays the function of extracting features and is an important part of the entire neural network. The pooling layer samples the output data and obtains the feature map after the convolutional layer. Each neuron of the fully connected layer is connected to the neurons of the output layer to achieve the function of a classifier.

The concept of weight sharing means that the value of the local receptive field in the convolutional neural network is the same in the process of feature image generation. Neurons have the same features but recognize staggered two-dimensional planes. The weight sharing feature allows the neural elements of the neural network in a two-dimensional plane to be translated but not deformed. It also shows the same feature data during the weight sharing process.

The downsampling operation is a nonlinear dimensionality reduction operation. It can make difficult-to-recognize special images easier to identify through dimensionality reduction methods. It simplifies the entire neural network and reduces the number of neural elements in the neural network, but does not affect the final output. As shown in Figure 5, it is the basic structure of convolutional neural network.

Convolutional neural networks are more widely used in object detection. A new breakthrough has been found for improving the accuracy of target detection through the convolutional neural network method.
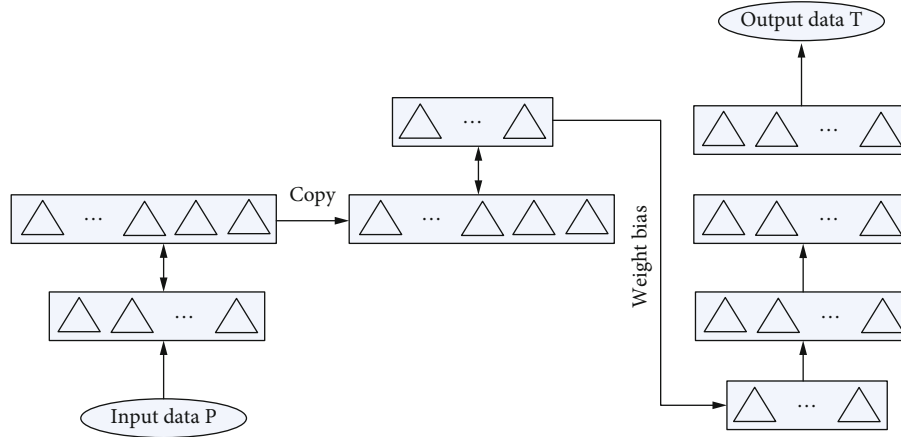
Figure 4: Pre-training process of deep neural network.
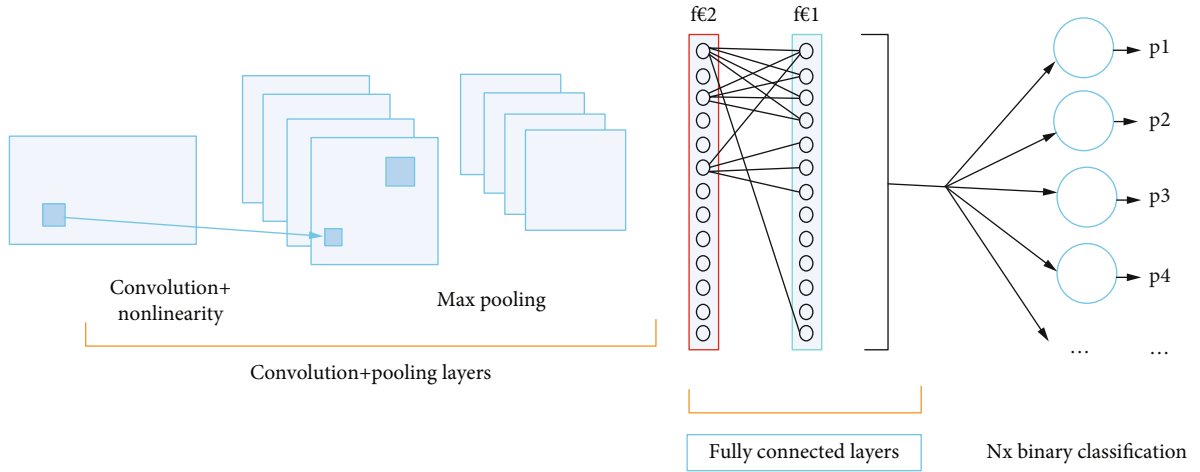
Figure 5: The structure of the convolutional neural network.

A feature map on a convolutional layer in a convolutional neural network is connected to the corresponding convolution kernel. By introducing an activation function after calculation, and then calculating the feature with the activation function, each input data can be accurately obtained [28]. The data of each output is formed by combining multiple feature maps, and the formula is obtained:

$$v_i^w = f(x_i^w), \tag{15}$$

$$x_i^w = \sum_{k \in M_i} v_i^{w-1} \cdot a_{ki}^w + r_i^w, \tag{16}$$

where v_i^w is the i-th output data of each convolutional layer w in the convolutional network; x_i^w is the activation value of the i-th layer of the w-th convolutional layer of the convolutional network; M_i is the feature data set for calculating the activation value x_i^w; $f(\bullet)$ is the activation function in the convolutional neural network; a_{ki}^w is the convolution kernel vector set in the convolutional network; and r_i^w is the final bias function of the convolutional network.

The activation function set by the pooling layer in each convolutional network is denoted by down($\bullet$). In each pooling layer, the output feature map convolved by each convolutional network can be obtained by the following formula:

$$x_i^w = \int_i^w \text{down}(v_i^{w-1}) + r_i^w. \tag{17}$$

In a convolutional network where each convolutional layer is connected to each other, the input of all connected convolutional layers is the combination of all 2D feature images. All input influence degree coefficients are summed by convolution. Finally, the feature output of each connected convolutional layer can be obtained by using the preset activation function, which can be obtained

$$x_i^w = m_i^w v^{w-1} + r_i^w. \tag{18}$$

According to each weight, the final output is the convolutional layer sensitivity. The object can be classified, identified, predicted, or decided according to its characteristics. In
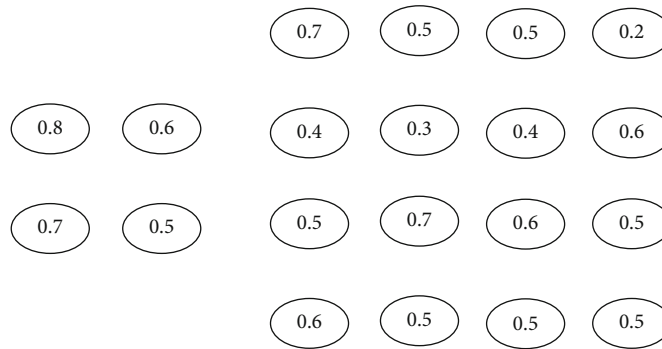
Figure 6: Upsampling operation diagram.
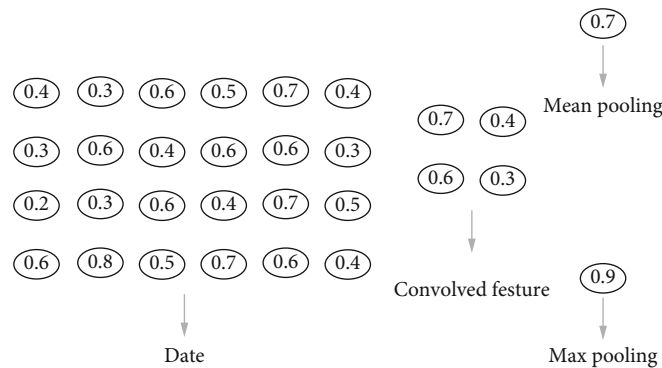
Figure 7: Schematic diagram of the operation of convolution and pooling.

this process, the most important step is feature extraction, that is, how to extract the features that can distinguish things to the greatest extent:

$$\phi_x^l = \int_x^{l+1} \left(\lambda' \left(u_x^l \right) \circ \mathrm{up} \left(\phi_x^{l+1} \right) \right). \tag{19}$$

By implementing the convolutional layer using the Kroneckers product, the function can be obtained:

$$\mathrm{up}(z) = z \otimes 1_{n \times n}. \tag{20}$$

According to the maximum pooling used above, put 4 in the model ×4 region is regarded as the set of some characteristics, that is, the set of activation values of a certain layer in the neural network. A large number means that some specific features may be detected. The features in the upper left quadrant may be a vertical edge, an eye, or cap features that people are afraid to encounter. The upsampling operation shown in Figure 6 can be obtained.

After the input image is extracted by the convolution layer image, additional image features are obtained by pooling. Figure 7 is a process diagram of image convolution and pooling.

The fully connected layer inputs a multidimensional vector. Each vector is converted into a bunch of vectors, and the sensitivity can be used to calculate the weight of each neuron. The formula for calculating the sensitivity of the fully connected layer is

$$\phi_x^l = \left(w^{l+1} \right)^R \phi^{l+1} \circ f' \left(v^l \right). \tag{21}$$

The actual training of the convolutional neural network has nothing to do with the previous input variables; it only reacts to the input variables. Because the bacteriostatic rate of ATA composites within 24 hours is constantly changing, in a day, if the time data of a certain hour of the day is randomly selected to analyze the results, the fluctuation of the data of the previous hour or the next hour will be ignored. Therefore, the change data of one day must be sampled.

4. The Research Experiment and Analysis of Nanometer Antimite and Antibacterial of Clothing Based on Deep Learning Technology

The application of nanomaterials in clothing is mainly to integrate nanomaterials into fabric fibers. For the antimite and antibacterial properties of clothing nanometers, the main method is to add substances with antibacterial properties into nanofibers. With the deepening of research, substances with antibacterial properties are mainly divided into the following two categories according to the properties of the substances: (1) Metals and metal oxides. Metal oxide antibacterial materials mainly include ZnO, TiO_2, and Fe_3O_4. (2). The surface chemical structure of house dust mite before and after ATA nanomaterial treatment showed that the structure of lipid, protein, and polysaccharide of

TABLE 1: Effect of load time on fabric load.

Load time	Load fabric number	Weight of fabric before load/g	Weight of fabric after load/g	Load/g	Load per 0.75 g fabric/g
	1-1	17.42	18.34	0.91	0.04
3 min	1-2	17.85	18.78	0.93	0.04
	1-3	17.22	18.12	0.91	0.04
	2-1	17.72	18.88	1.16	0.05
5 min	2-2	17.24	18.41	1.17	0.05
	2-3	17.26	18.18	1.20	0.05
	3-1	17.51	18.71	1.20	0.05
7 min	3-2	18.24	19.41	1.18	0.05
	3-3	18.42	18.42	1.18	0.05

TABLE 2: Antibacterial effect of *Escherichia coli* fabrics under load time.

		Under visible light				Under dark conditions	
Load time	Parallel plate number	Number of colonies/piece	Viable bacteria concentration/cfu/ml	Bacteriostatic rate/%	Number of colonies/piece	Iable bacteria concentration/cfu/ml	Bacteriostatic rate/%
3 min	1	2×10	0.020×106	99.60	5×10	0.04×106	98.88
	2	3×10	0.03×106		7×10	0.07×106	
5 min	1	0	0	100	0	0	100
	2	0	0		0	0	

TABLE 3: Bacteriostatic rate of *Staphylococcus aureus* at 3 min loading.

	Under visible light		Under dark conditions		
Plate number	Average number of colonies/piece	Bacteriostatic rate/%	Average number of colonies/piece	Viable bacteria concentration/cfu/ml	Bacteriostatic rate/%
1	48×10	99.96	48×10	4.80×106	99.95
2	170×10		205×10	0.021×106	

mite body wall changed; TiO2 is a typical photocatalytic antibacterial material, which has the characteristics of low toxicity, low price, acid and alkali resistance, and strong antibacterial ability under UV irradiation; and Ag ion is the most efficient metal ion antibacterial agent known at present. It has the advantages of good antibacterial effect, low antibacterial concentration, killing many kinds of bacteria, and strong drug resistance. Taking Ag, TiO_2, and ATA as research objects, their antibacterial properties were analyzed. Ag ion is a metal ion antibacterial agent that can kill many kinds of bacteria and has strong drug resistance; TiO_2 is a good photocatalyst; ATA has strong stability. The absorbance values of different materials are detected using deep learning techniques. Bacterial growth kinetics were analyzed according to the degree of change in absorbance value. The absorption coefficient is related to the wavelength of the incident light and the material passed by the light. As long as the wavelength of the light is fixed, the absorption coefficient of the same material will remain unchanged. When a beam of light passes through a light absorbing substance (usually a solution), the solute absorbs light energy and the intensity of light decreases. Absorbance is a physical quantity used to measure the degree of light absorption.

4.1. *Preparation of ATA Antibacterial Fabric.* 9 pieces of treated fabrics (20 cm × 20 cm) were immersed in ATA nano-solution at different times. Each corresponds to a different parallel sample. They were taken out at different times, squeezed out excess liquid, and passed through an oven drying process at 125°C for 15 minutes. Then, the change of the fabric before and after loading and the loading of the antibacterial agent of the fabric in different time periods were measured. The longer the load time, the worse the fabric load.

It can be seen from Tables 1 and 2 that in the presence of light, the antibacterial activity of ATA against *Escherichia coli* reaches 99.60% and 100% in two time periods; in the absence of light, the antibacterial activity of ATA against *Escherichia coli* reaches 99.60% and 100%. The bacteriostatic rate of the two cases is basically close to 100%, and the antibacterial effect is excellent.

According to Table 3, the antibacterial performance of *Staphylococcus aureus* is very good in the presence of light
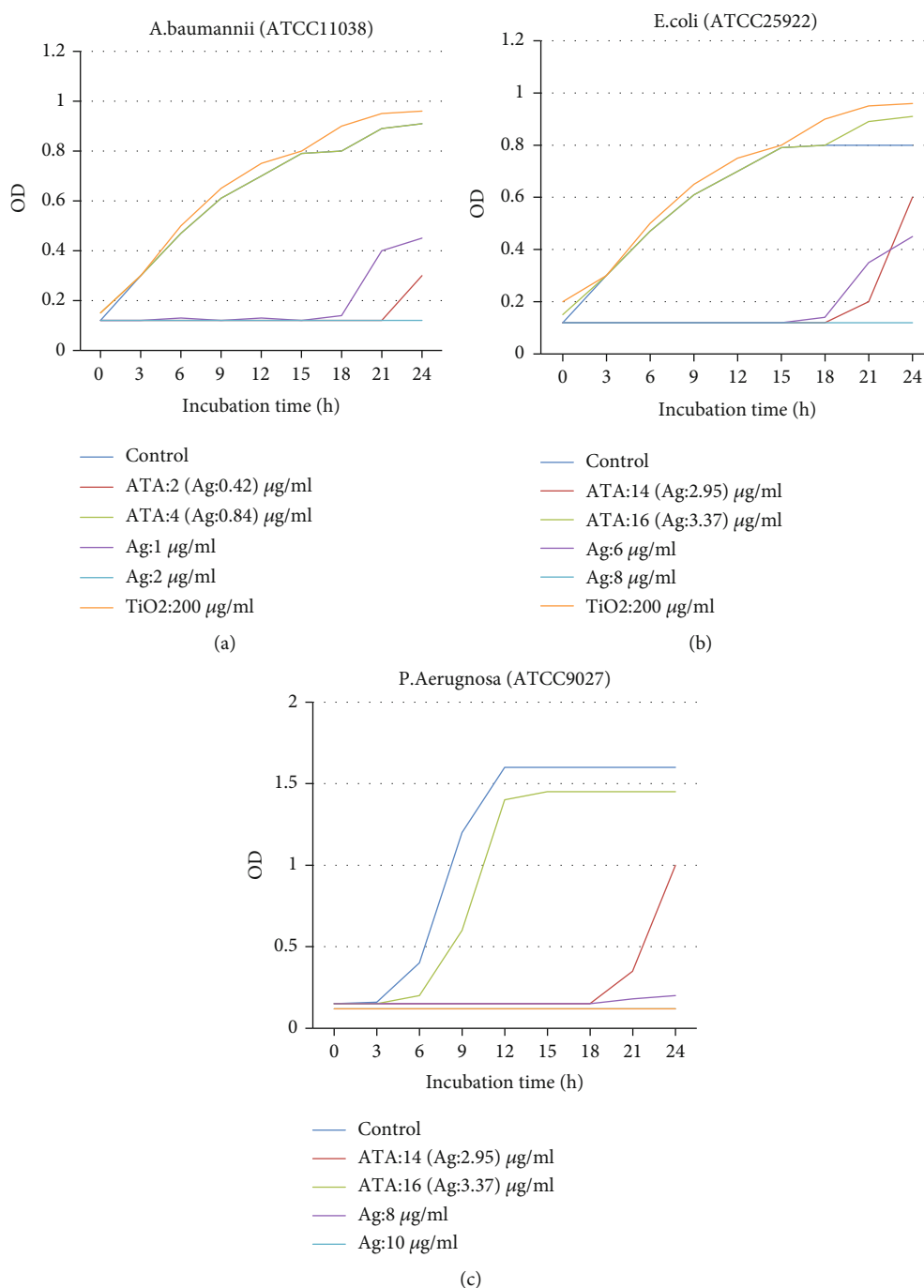
Figure 8: The analysis of the activity of ATA against Gram-negative bacteria.

or in the dark, and the bacteriostatic rate is basically close to 100%.

4.2. ATA against Gram-Negative Bacteria.

The experimental objects were *Acinetobacter baumannii*, *Escherichia coli*, and *Pseudomonas aeruginosa*.

As shown in Figure 8, the minimum inhibitory concentration values of ATA against Gram-negative bacteria are: *Acinetobacter baumannii* was 10 μg/ml. *Escherichia coli* was 16 μg/ml. *Pseudomonas aeruginosa* is 16 μg/ml. Ag concentrations in ATA were 2.11, 3.37, and 3.37 μg/ml. The mini-

mum inhibitory concentrations corresponding to elemental Ag were 4, 8, and 10 μg/ml. And 200 μg/ml still has only weak antibacterial effect. The results of the minimum inhibitory concentration test showed that ATA has strong antibacterial ability against all the tested strains. With the increase of ATA and Ag concentrations, its antibacterial activity was enhanced, and the reproduction and growth rate of all bacteria slowed down rapidly.

4.3. ATA against Gram-Positive Bacteria.

The experimental subjects were *Streptococcus pneumoniae*, *Staphylococcus*
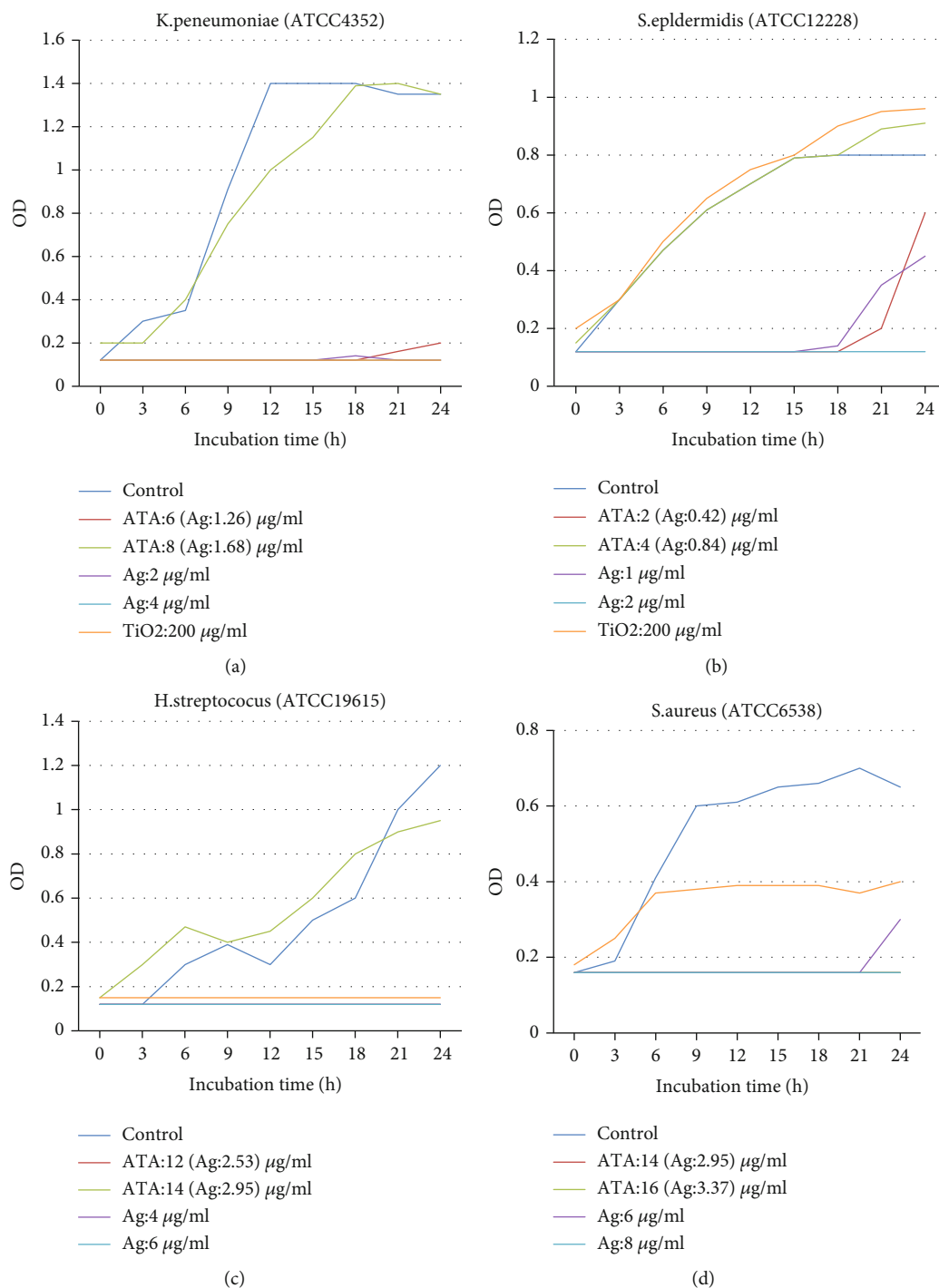
Figure 9: The analysis of ATA against Gram-positive bacteria.

epidermidis, *Streptococcus hemolyticus*, and *Staphylococcus aureus*.

Figure 9 shows that the minimum inhibitory concentrations of ATA against Gram-positive bacteria were 4 μg/ml for *Streptococcus pneumoniae*, 8 μg/ml for *Staphylococcus epidermidis*, 14 μg/ml for *Streptococcus hemolyticus*, and 16 μg/ml for *Staphylococcus aureus*. ml. The Ag concentrations in ATA were 0.84, 1.68, 2.95, and 3.37 μg/ml, respectively; the minimum inhibitory concentrations corresponding to elemental

Ag were 2, 4, 6, and 8 μg/ml. 200 μg/ml TiO$_2$ has only weak antibacterial effect on all the above bacteria. At the minimum inhibitory concentration, the content of Ag in ATA was about 1/2 to 1/3 of that of elemental Ag. That is to say, ATA not only has powerful broad-spectrum antibacterial properties, but also greatly reduces the use of Ag and achieves the purpose of saving precious metal Ag. Even if the concentration of pure TiO$_2$ reaches 200 μg/ml, there is only a weak antibacterial effect. These results imply the occurrence of synergistic antibacterial

TABLE 4: Comparison of minimum inhibitory concentrations of TiO_2, Ag and Ag/TiO_2.

Bacterial species and number	Gram species (negative-; positive +)	TiO_2 minimum inhibitory concentration ($\mu g/ml$)	Ag minimum inhibitory concentration ($\mu g/ml$)	ATA minimum inhibitory concentration ($\mu g/ml$)
A. baumannii	—	More than 200	4	10 (Ag:2.11; TiO2:7.89)
E. coli	—	More than 200	8	16 (Ag:3.37; TiO2:12.63)
P. aeruginosa	—	More than 200	10	16 (Ag:3.37; TiO2:12.63)
S. pneumoniae	+	More than 200	2	4 (Ag:0.84; TiO2:3.16)
S. epidermidis	+	More than 200	4	8 (Ag:.68; TiO2:6.32)
S. hemolyticus	+	More than 200	6	14 (Ag:2.95; TiO2:11.05)
S. aureus	+	More than 200	8	16 (Ag:3.37, TiO2:12.63)

(a)

(b)
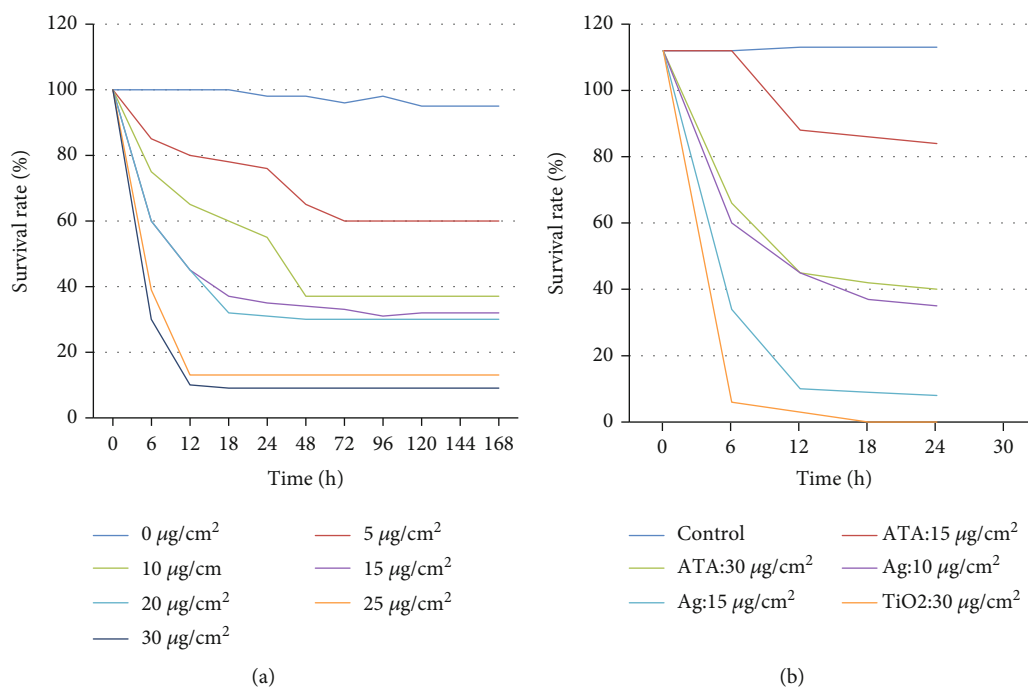
FIGURE 10: The relationship between the antihouse dust mite activity and time of the samples at different concentrations.

properties of ATA, possibly because Ag and TiO_2 have different antibacterial action mechanisms. In addition, the minimum inhibitory concentration of ATA was lower than that of other inorganic antibacterial materials. Table 4 is the comparative data of minimum inhibitory concentration of TiO_2, Ag, and Ag/TiO_2.

Through experiments, it was found that adding different amounts of TiO_2 to the nanomaterials can effectively inhibit the activity and survival rate of bacteria. Its main antibacterial mechanism is that TiO_2 kills bacteria by destroying their cell walls. Compared with Ag nanomaterials, ATA nanometers have small particle size and strong stability. Under the same dosage, the Ag concentration in ATA is about 1/2-1/3 of that of elemental Ag, which saves the cost of Ag to a great extent.

4.4. Antimite Activity Analysis of ag/TiO_2. The antimite activity of ATA against house dust mites was evaluated by the method of deep learning technology. It can be seen from Figure 10 that ATA has a strong ability to remove mites. According to the treatment of house dust mites with differ-

ent doses of ATA, the survival rates of house dust mites after 24 hours were 76%, 46%, 33%, 27%, 5%, and 2%, respectively. When the time was extended to seven days (168 h), the survival rate of house dust mites did not change significantly, but only slightly decreased. As can be seen from Figure 10, ATA, Ag, and TiO_2 have obvious antimite effects within 24 hours, and the effect is not so obvious after 24 hours, and ATA has a synergistic antimite effect.

5. Discussion

This paper mainly discusses and studies the antimite and antibacterial effect of clothing nanometers based on deep learning technology. In this paper, the antibacterial and antimite effects of Ag, TiO_2 and Ag/TiO_2 (ATA) nanocomposites were experimentally studied by using deep learning algorithm. It compares the antibacterial and antimite properties of different composite nanomaterials under different conditions. According to the experiments, the nanomaterials with the strongest antibacterial properties and the most suitable for integration into clothing fabrics are obtained. The

experimental results show that the deep learning technology can be used in the research on the antibacterial and antimite of clothing nanometers. And under this technology, the antimite and antibacterial experiments of nanomaterials have obtained satisfactory results.

6. Conclusions

Ag, TiO$_2$, and Ag/TiO$_2$ (ATA) nanocomposites have certain antimite and antibacterial effects and are widely used. However, the Ag/TiO$_2$ (ATA) nanocomposites prepared by Ag and TiO$_2$ have stronger stability and better antibacterial properties. With the advancement of social technology, Ag/TiO$_2$ (ATA) nanocomposites are used more and more widely as a bacteriostatic agent, and the development prospect is getting better and better. The synergistic antimite effect of ATA was obtained by evaluating the antimite activity of ATA against house dust mites by using deep learning technology. Within 24 hours, TA, Ag, and TiO$_2$ had obvious antimite effects during this period.

Data Availability

The data that support the findings of this study are available from the corresponding author upon reasonable request.

Conflicts of Interest

The authors declared no potential conflicts of interest with respect to the research, author-ship, and/or publication of this article.

References

[1] Y. Dong and J. Li, "Recent progresses in deep learning based acoustic models," *IEEE/CAA Journal of Automatica Sinica*, vol. 4, no. 3, pp. 396–409, 2017.

[2] T. Oshea and J. Hoydis, "An introduction to deep learning for the physical layer," *IEEE Transactions on Cognitive Communications & Networking*, vol. 3, no. 4, pp. 563–575, 2017.

[3] D. S. Kermany, M. Goldbaum, and I. W. Ca, "Identifying medical diagnoses and treatable diseases by image-based deep learning," *Cell*, vol. 172, no. 5, pp. 1122–1131.e9, 2018.

[4] D. Ravi, C. Wong, F. Deligianni et al., "Deep learning for health informatics," *IEEE Journal of Biomedical & Health Informatics*, vol. 21, no. 1, pp. 4–21, 2017.

[5] D. L. Wang and J. Chen, "Supervised speech separation based on deep learning: an overview," *IEEE/ACM Transactions on Audio, Speech, and Language Processing*, vol. 1, no. 99, pp. 1–1, 2017.

[6] C. Cheng, S. Li, A. Thomas, N. A. Kotov, and R. Haag, "Functional graphene nanomaterials based architectures: biointeractions, fabrications, and emerging biological applications," *Chemical Reviews*, vol. 117, no. 3, pp. 1826–1914, 2017.

[7] D. T. Shivakumar, T. Kneevi, and L. K. Nanver, "Nanometer-thin pure boron CVD layers as material barrier to Au or Cu metallization of Si," *Journal of Materials Science: Materials in Electronics*, vol. 32, no. 6, pp. 1–13, 2021.

[8] R. Surendran, O. I. Khalaf, and C. Andres, "Deep learning based intelligent industrial fault diagnosis model," *CMC-Computers, Materials & Continua*, vol. 70, no. 3, pp. 6323–6338, 2022.

[9] H. Lu, Q. Liu, X. Liu, and Y. Zhang, "A survey of semantic construction and application of satellite remote sensing images and data," *Journal of Organizational and End User Computing (JOEUC)*, vol. 33, no. 6, pp. 1–20, 2021.

[10] G. Suryanarayana, K. Chandran, O. I. Khalaf, Y. Alotaibi, A. Alsufyani, and S. A. Alghamdi, "Accurate magnetic resonance image super-resolution using deep networks and Gaussian filtering in the stationary wavelet domain," *IEEE Access*, vol. 9, pp. 71406–71417, 2021.

[11] B. A. Palmer, D. Gur, S. Weiner, L. Addadi, and D. Oron, "The organic crystalline materials of vision: structure–function considerations from the nanometer to the millimeter scale," *Advanced Materials*, vol. 30, no. 41, p. 1800006.1-1800006. 10, 2018.

[12] N. Akhtar and A. Mian, "Threat of adversarial attacks on deep learning in computer vision: a survey," *IEEE Access*, vol. 6, pp. 14410–14430, 2018.

[13] T. Kooi, G. Litjens, and B. V. Ginneken, "Large scale deep learning for computer aided detection of mammographic lesions," *Medical Image Analysis*, vol. 35, pp. 303–312, 2017.

[14] S. Dörner, S. Cammerer, J. Hoydis, and S. Ten Brink, "Deep learning-based communication over the air," *IEEE Journal of Selected Topics in Signal Processing*, vol. 1, no. 1, pp. 132–143, 2017.

[15] X. Wang, L. Gao, and S. Mao, "CSI phase fingerprinting for indoor localization with a deep learning approach," *IEEE Internet of Things Journal*, vol. 3, no. 6, pp. 1113–1123, 2016.

[16] G. B. Goh, N. O. Hodas, and A. Vishnu, "Deep learning for computational chemistry," *Journal of Computational Chemistry*, vol. 38, no. 16, pp. 1291–1307, 2017.

[17] S. N. Alsubari, S. N. Deshmukh, A. A. Alqarni et al., "Data analytics for the identification of fake reviews using supervised learning," *CMC-Computers, Materials & Continua*, vol. 70, no. 2, pp. 3189–3204, 2022.

[18] M. Fanqi, C. Wenying, and W. Jingdong, "Semi-supervised software defect prediction model based on tri-training," *KSII Transactions on Internet and Information Systems*, vol. 15, no. 11, pp. 4028–4042, 2021.

[19] N. Kussul, M. Lavreniuk, S. Skakun, and A. Shelestov, "Deep learning classification of land cover and crop types using remote sensing data," *IEEE Geoscience and Remote Sensing Letters*, vol. 14, no. 5, pp. 778–782, 2017.

[20] A. K. Gorshenin, V. Y. Korolev, and A. M. Tursunbaev, "Median modifications of the EM-algorithm for separation of mixtures of probability distributions and their applications to the decomposition of volatility of financial indexes," *Journal of Mathematical Sciences*, vol. 227, no. 2, pp. 176–195, 2017.

[21] F. Gu, H. Zhang, W. Wang, and S. Wang, "An expectation-maximization algorithm for blind separation of Noisy mixtures using Gaussian mixture model," *Circuits, Systems, and Signal Processing*, vol. 36, no. 7, pp. 2697–2726, 2017.

[22] W. Fu, J. Chen, and Y. Bo, "Source recovery of underdetermined blind source separation based on SCMP algorithm," *IET Signal Processing*, vol. 11, no. 7, pp. 877–883, 2017.

[23] T. Zeng and C. Liu, "A two-stage separation algorithm for weak correlation source signals," *Wireless Personal Communications*, vol. 117, no. 3, pp. 2441–2452, 2021.

[24] C. Chen and W. K. Kim, "The application of micro-CT in egg-laying hen bone analysis: introducing an automated bone

separation algorithm," *Poultry Science*, vol. 99, no. 11, pp. 5175–5183, 2020.

[25] H. Elfaig, W. Elsayed, and H. Ahmed, "Preparation and characterization of chitosan/silver nano-composite and its application on Nile water as antibacterial materials," *MRS Advances*, vol. 5, no. 26, pp. 1331–1338, 2020.

[26] F. Karabudak, R. Yesildal, and E. E. Sukuroglu, "An investigation of corrosion resistance and antibacterial sensitivity properties of nano-Ag-doped TiO_2 coating and TiO_2 coating grown on NiTi alloy with the micro-arc oxidation process," *Arabian Journal for Science and Engineering*, vol. 42, no. 6, pp. 2329–2339, 2017.

[27] Y. Choi, J. Jang, H. J. Koo, M. Tanaka, K. H. Lee, and J. Choi, "Alginate-chitosan hydrogel patch with beta-glucan nanoemulsion for antibacterial applications," *Biotechnology and Bioprocess Engineering*, vol. 26, no. 1, pp. 71–77, 2021.

[28] Y. Liu, Q. Q. Li, H. Zhang, S. P. Yu, L. Zhang, and Y. Z. Yang, "Research progress on the use of micro/nano carbon materials for antibacterial dressings," *New Carbon Materials*, vol. 35, no. 4, pp. 323–335, 2020.

Research Article

Application of Nanotubes Combined with Ethnic Sports Rehabilitation Therapy in the Treatment of Patients with Knee Arthritis

Juan Li (ID)

College of Physical Education, Xuchang University, Xuchang, 461000 Henan, China

Correspondence should be addressed to Juan Li; 12008080@xcu.edu.cn

National sports are traditional sports of ethnic minorities and sports with strong national characteristics. Sports performances generally include weightlifting, boxing or martial arts, gymnastics, skating, high jump, sprint, and hurdles. Such as knee joints that are particularly vulnerable to injury. Therefore, ordinary ethnic sports athletes are particularly vulnerable to injury. Ethnic sports rehabilitation therapy uses some exercises to enable patients to obtain full or partial exercise functions. Training methods for sensory function recovery were used. Ethnic sports rehabilitation therapy is a common rehabilitation therapy for ethnic sports athletes to resume sports training, such as table tennis, tennis, cycling, fishing, climbing, skating, weightlifting, and wrestling. However, with economic development and social progress, the treatment of knee arthritis is closely integrated with nanotubes combined with national sports rehabilitation therapy, and it has been increasingly used in competitive sports and national fitness. From 2003 to 2020, the medical research literature on nanotechnology increased from 20 to more than 20,000. This article presents a way for treating knee arthritis sufferers by combining nanotubes with ethnic sports rehabilitation therapy and discusses the clinical therapeutic effect of nanotubes combined with ethnic sports rehabilitation therapy in the treatment of knee arthritis patients. It provides a certain basis for the treatment of patients with knee arthritis. This article selected 100 knee patients, who, as research subjects, visited our facility for medical treatment between June 2016 and June 2020, and divided 100 patients into two groups, 50 patients in the experimental group and 50 patients in the control group. For patients, the experimental group used nanotubes combined with ethnic sports rehabilitation therapy to treat patients, and the control group used ethnic sports rehabilitation therapy to treat patients. The experimental results show that nanotubes combined with ethnic sports rehabilitation therapy can speed up the treatment process of patients with knee arthritis. When the experiment lasted only 5 days, patients in the control group scored an average of 3 points, and on the last day, they scored an average of 6.9 points. In the experimental group, the average score of patients on the fifth day of the experiment was 5 points, and the average score of patients on the last day was 9.7 points. The knee joint patients in the experimental group have higher walking ability, up-and-down ability, knee flexion, and knee swelling. In the control group, among them, the first to recover from knee arthritis is the ability to walk, and the slowest recovery is the flexion of the knee joint.

1. Introduction

National sports refer to the traditional sports activities of all nationalities in the world, such as Chinese martial arts, qigong health preservation, etc. National sports refer to the sports events and activities of ethnic minorities in a country [1]. As an important part of human sports culture, national sports reflect the horizontal inheritance relationship of national culture from its own characteristics, which can be said to be a means of national education. Along the direction of inheritance and innovation, the national movement has explored the combination of popularization and improvement, the combination of mass and professionalism, the combination of traditional sports and modern sports and has made gratifying progress [2]. Therefore, it can be popularized in the future national sports activities.

Generally speaking, sports rehabilitation refers not only to the rehabilitation after injury but also to actively improve

the ability to prevent sports injury. Preventive rehabilitation is an important part of sports rehabilitation, reasonable exercise training is the basic guarantee of preventing sports injury, and the stability of spine, bone, ligament and muscle plays an important role in prevention and rehabilitation [3]. In the traditional modern rehabilitation system, including physical therapy, speech therapy, psychotherapy, and occupational therapy. Among them, athlete therapy, physical therapy, and stress therapy are the most common [4]. Compression therapy is the application of positive or negative pressure to treat dysfunction. For example, the positive pressure of muscles is used to relieve muscle spasm, and the negative pressure of limbs is used to treat limb vasodilation and improve tissue metabolism. The purpose of exercise rehabilitation is to treat sports injury and chronic diseases. Exercise therapy and physical therapy are two ways of thinking of exercise rehabilitation. Among them, exercise therapy is to slow the patients back to normal through a certain amount of exercise; physical therapy is a widely used treatment concept; it promotes the rehabilitation of patients through sound, light, electromagnetic heat and other means; homework therapy is a kind of treatment concept aimed at helping patients recover normal life function [5]. For example, when a patient exercises, one hand accidentally falls to the ground, resulting in a broken wrist. In the process of rehabilitation, occupational therapists are responsible for the recovery of normal writing and eating of injured limbs, which involves the recovery of some good tactile and proprioception training, which is different from the first two treatments. With the increasing popularity of mass sports, sports injuries, nutrition matching in the process of sports, self-protection, and so on have become the knowledge that the public urgently needs to know. Exercise therapy is to treat through a certain amount of exercise, physical therapy is to promote the recovery of patients by means of sound, light, electromagnetic heat, etc., and pressure therapy is to apply positive or negative pressure therapy [6]. In the past, the major of sports rehabilitation and health was mainly for professional athletes, and there were few talents with systematic knowledge of the combination of medical treatment and sports. Therefore, relevant talents have always been a hot demand for training bases and fitness clubs [7].

Knee arthritis is a chronic arthritis disease, mostly in the middle-aged and the elderly and sports people [8]. Joint diseases are common on these aspects. If knee pain recurred within a month, from mild to severe, accompanied by the sound of joint friction movement, temporary stiffness in the morning, X-ray shows narrowing of joint space, subchondral bone sclerosis or cystic change, osteophyte formation, or joint edge bone hyperplasia, it can be considered osteoarthritis [9]. Early knee pain should pay attention to joint protection measures: appropriate rest, weight loss, prevent excessive joint movement, and weight-bearing, to avoid mechanical injury. Physical therapy is more suitable for chronic knee osteoarthritis and has a good effect on relieving subacute inflammation. A variety of physical therapy forms, including hot compress, electric therapy, magnetic therapy, infrared ray, spa, mineral spring bath, mud therapy, wax therapy, ion and penetration method, to strengthen the functional exercise of the affected limb can be chosen: increase the range of joint activity and strengthen the exercise of muscles. Nanotubes are 10000 times thinner than human hair, 100 times harder than steel, and have good thermal conductivity at 3593°C [10]. Nanotubes can be used not only as metal conductors but also as semiconductors for computer chips and superconduct at very low temperatures. Nanotube technology is mainly reflected in nanotechnology. Nanotechnology is the use of atoms and molecules to manufacture new materials. It is a technology to study the composition of materials with a size range of less than 100 nanometers. At this level, the research and processing of materials and material technology are called nanotechnology. This small space is the size range of atoms and molecules and the space in which they interact. In such a scale space, due to quantum effects, localization, and large surface and interface effects, many properties of matter have undergone qualitative changes. Nanotechnology is the study of nanophenomenon and material control, especially the extension of existing science and technology in nanoresearch.

Traditional knee arthritis patients have to rely on ethnic sports rehabilitation therapy to treat the knee joint, but for some elderly people, the effect of sports rehabilitation therapy is not obvious. Nanotechnology has increasingly infiltrated all facets of our lives as biological information technology continues to advance. Matthew explains how the characteristics of water aid functional recovery following ACLR. Matthew believes that if the major properties of hydrotherapy (density, hydrostatic pressure, buoyancy, and viscosity) are effectively applied to rehabilitation practice, specific protocols and supplemental videos for the use of hydrotherapy following ACLR can be developed to help implementation [11]. The continuous improvement of nanotherapy technology systems, especially the continuous improvement of nanodrug delivery systems, has enabled nanotherapeutics to achieve significant development in the medical field. When nanomedicine enters the human body, it will passively or actively target the nanocarrier, and then, it can be selectively delivered to the injured site. Nanotherapy reduces the harm of drug treatment to the human body to a minimum. On the other hand, the nanocarrier packaged with the therapeutic drug will protect the drug from biodegradation, allow the sustained release of the drug, and prolong the duration of the drug. In general, the targeted nanodrug delivery system has better therapeutic effects and fewer side effects. It is the best choice for knee arthritis treatment. Nanocarriers are widely used in the delivery of anti-knee arthritis drugs, plastids and dendrimers, micelles, nanocapsules, nanomaterials, and many other nanoparticles. These nanodelivery drug systems have achieved remarkable results in the treatment of knee arthritis. Combining nanotubes with traditional ethnic sports rehabilitation therapy to treat patients is the main research focus of this article.

The innovation of this paper is to propose a method combining nanotubes and national sports rehabilitation therapy to treat patients with knee arthritis and to discuss the clinical efficacy of combining nanotubes and national sports rehabilitation therapy for patients with knee arthritis [12].

2. Theoretical Basis and Core Concepts

2.1. Onset Factors of Knee Arthritis. The onset causes of knee arthritis mainly include four aspects: environmental factors, weight factors, age factors, and diet factors. Among them, environmental factors and diet are the main reasons. People who live in humid and cold environment all year round are most likely to suffer from knee arthritis, which is mainly due to low temperature and blood supply disturbance. Secondly, obesity and strong body incidence rate is high, overweight, and knee joint pressure increased. The incidence rate of arthritis is also higher with age. The accumulated strain of joints for many years is an important reason for the knee arthritis in the elderly. Finally, malnutrition is also one of the pathogenic factors of knee arthritis. There is no blood vessel in the articular cartilage, and the nutrition it needs depends on absorbing from the synovial fluid. The repair of cartilage is accomplished by the division and reproduction of outer chondrocytes and the secretion of matrix by chondrocytes. Due to the lack of nutrition and oxygen supply, the proliferation of chondrocytes will be affected, resulting in the reduction of cartilage matrix, insufficient cartilage regeneration, weakening of cartilage, and easy wear of load-bearing area [13]. The repair of cartilage is accomplished by the division and reproduction of the outer chondrocytes and the secretion of matrix by the chondrocytes.

2.2. Clinical Manifestations of Knee Arthritis. Whether suffering from knee arthritis can observe whether the knee joint trauma visible. After the occurrence of knee arthritis, often in the knee joint long bone spur, early bone hyperplasia does not affect the surrounding tissue, with the continuous growth of bone spur; it will gradually affect the surrounding tissue, the formation of inflammatory reaction. The symptoms of knee arthritis mainly include swelling of knee joint, pain of going up and down stairs, pain and discomfort of knee joint when sitting, swelling, tinnitus, and effusion will appear in patients. If not treated in time, it will cause joint deformity and disability, knee synovitis, ligament damage, meniscus injury, knee joint free body, popliteal cyst, chondromalacia of patella, palmar bursitis, knee varus, etc. The diagnosis method of early knee arthritis can be analyzed according to the joint swelling. The joint swelling comes from synovial hyperplasia and intra-articular effusion. In the early stage, it often occurs due to sprain and cold, and it will become persistent swelling later. There is a rubbing sensation or a popping sound when the joint moves.

The main symptoms of knee arthritis are knee swelling and pain, pain when walking up and down stairs, and knee pain when sitting. Patients with swelling, ringing, and effusion, if not treated in time, patients will cause joint deformity and disability. Knee synovitis, ligament injury, meniscus injury, free body of knee joint, popliteal cyst, chondromalacia of patella, goose foot bursitis, knee varus, and other knee diseases often occur [14]. If you stand up when the knee pain discomfort, activity after a period of time symptoms has been reduced, knee arthritis symptoms are obvious, and it should take timely treatment measures to reduce the symptoms of knee arthritis. Oral glucosamine drugs, including glucosamine sulfate and other raw materials to synthesize cartilage, can improve the cartilage state of the knee joint, or lie down, straighten the lower limb, and platform the affected limb to 45 degrees for 3-5 seconds. 20 times, this will increase the strength of the quadriceps muscles to achieve the purpose of protecting the knee joint [15].

2.3. Knee Joint Is Not Aligned with the Lower Limb. The mechanical axis or alignment of the lower limbs is determined by a line from the center of the tibial joint to the center of the femur, which runs from the center of the tibial joint to the center of the femur. The uneven distribution of knee joint load is consistent with the high incidence of medial knee osteoarthritis. Varus deformity and right knee joint deformity are the most common lower limb deformity. Knees aligned with the varus are described as arched legs, while knees aligned with the valgus are described as touching knees. Valgus alignment affects the load distribution on the articular surface and reduces the bearing area. The whole lower limb is a complete exercise chain. Therefore, the arrangement of bones can affect the load pattern at one level and have a profound impact on other levels [16].

2.4. Biomechanical Load and Lower Extremity Osteoarthritis. Some studies have shown that the mechanical mechanism and biomechanical changes of the stressed joint play an important role in promoting the occurrence and development of knee arthritis. The experimental results showed that the total effective rate of nanotubes combined with ethnic exercise rehabilitation therapy in the experimental group was 100%, while the control group believed that only ethnic exercise rehabilitation therapy accounted for 60%. Nanotubes combined with national sports can speed up the treatment of knee arthritis patients and improve the quality of life of knee arthritis patients. A theory that repeated mechanical loading accelerates "wear" of joints has been supported by studies by obese people and professionals who often bend their knees or load. The incidence rate of knee arthritis was monitored for 11 years through a discharge registry in a Swedish hospital. The body mass index (BMI), waist circumference, waist-hip ratio, body weight, and body fat percentage of 1126 men and 16934 women were measured. This study provides strong evidence for the association between obesity and the incidence rate of osteoarthritis in the knee and hip joints. All overweight indicators are associated with the incidence of osteoarthritis of the knee, and BMI is the most dangerous. The incidence rate of hip osteoarthritis is normal, but significant. This study confirms the close association between obesity, mechanical loading and increased risk of knee joint and hip arthritis [17].

The theory of "wear and tear" has been supported by some people engaged in sports related undertakings and related researchers in the industry. The team conducted a longitudinal assessment of the relationship between lacquer joint use and knee arthritis in a multi occupational population. The occupational status and knee osteoarthritis were evaluated by weight-bearing arthrography over 40 years old. The working characteristics of the subjects were their

physiological needs and their relationship with knee flexion. 43.4% : 26.8% of men who engaged in flexion and had at least moderate physiological needs a higher risk of knee osteoarthritis than those who did not participate in both activities. These results suggest that for men, the combination of knee flexion and physiological needs may be the main cause of knee arthritis [18].

2.5. Exercise Rehabilitation for Knee Arthritis.
Exercise therapy to prevent and treat knee arthritis is mainly to increase the muscle training around the knee joint. By exercising the muscle strength of the affected limb joint, it can prevent and control muscle weakness and muscle atrophy. Strengthening muscle strength can increase the stability of the joint, protect the joint, and prevent the development of osteoarthritis. The commonly used muscle strength training methods include isometric and isokinetic training [19]. The main exercise of this paper is hip flexion.

The main methods of exercise rehabilitation in the treatment of knee arthritis are hip four position exercise, clam type exercise, and sitting hip joint flexion exercise. Hip joint four exercises are mainly to exercise the flexors, extensors, adductors, and abductors of the hip joint. Clamshell exercise, the project for the gluteal muscle, thigh lateral muscle, tensor fascia lata, and knee joint muscle exercise. Although hip flexion exercise in sitting position is named after hip flexion and extension, strengthening hip flexor muscle is very important for knee joint strength. When these muscles are strong and work properly, the knees also become strong.

2.6. Nanotube Combined with Exercise Rehabilitation in the Treatment of Knee Arthritis.
Nanotube combined with exercise rehabilitation therapy refers to the treatment of nanodrug at the same time of exercise rehabilitation treatment for knee joint patients. The nanotube drugs selected in this paper are polypeptide nanoselenium and functionalized nanoruthenium drugs. Nano drugs have unique properties, such as active or passive targeting at the injured site, improving the high efficiency of drug loading, intelligent drug release, and long-term kinetics. Secondly, peptide nanoselenium can improve the growth and reproductive performance of animals, improve the metabolic capacity of the body, and has a very good effect on the treatment of knee arthritis. Generally speaking, the greater the surface lipophilicity of nanoparticles, the stronger the binding force with regulatory proteins. Therefore, it is necessary to increase the hydrophilicity of nanoparticles in vivo. This is an important purpose to select the surface modification materials of nanoparticles. At the same time, the physical properties of nanoparticles can be modified to obtain new functions. Exercise rehabilitation therapy has a good effect in the treatment of knee arthritis. The combination of nanodrug therapy and national sports rehabilitation treatment, taking internal and external exercise, will have better treatment effect in patients with knee joint.

2.7. Prevention and Treatment of Knee Arthritis.
Prevention and treatment of knee arthritis should pay attention to keep warm, avoid wearing high-heeled shoes for a long time, pay attention to body posture when walking, and often participate in outdoor activities. When the temperature drops in winter, the knee joint is cold, the blood vessels contract, and the blood circulation is not smooth, which often makes the joint stiff and painful. Therefore, keep warm in cold weather, and if necessary, wear knee protection to prevent the knee from being cold. High heeled shoes change the curve of lower limb strength. In order to reduce the impact on the knee joint and avoid the impact and wear of knee joint cartilage, the elderly should choose thick shoes with soft and elastic soles in their daily activities. Pay attention to your posture when you walk. Do not bend down when you work. Do not bend your legs when you walk. Avoid squatting for a long time. Do not keep an action for a long time. Always change your posture. For example, after a period of practice, you can develop a good habit, for example, after standing every day, stretch your legs, tie horse steps, and develop a good habit of protecting your legs. Finally, we should often participate in outdoor activities. Before doing Yanko dance and Taijiquan, we should make full preparations. We should gently extend the knee to increase the flexibility and flexibility of the lower limbs. After the activity, exercise the knee. When practicing Taijiquan, the range of action should not be too large, and the squatting posture should not be too low, so as to avoid damage to the knee joint caused by weight-bearing.

3. Experimental Analysis and Methods

3.1. Experimental Objects and Standards.
The study time selected in this article is from June 2016 to June 2020. The relevant data of 100 patients with knee arthritis admitted to this hospital during this period were analyzed. All patients were divided into two groups according to the difference in treatment plan: the experimental group and the control group. The patients in the experimental group were treated with nanotubes combined with ethnic sports rehabilitation therapy, and the patients in the control group only received ethnic sports rehabilitation therapy. There is a total of 50 patients in the experimental group and 50 patients in the control group. The experiment lasted for one month. After the experiment, the rehabilitation of knee joint patients was compared according to the results of the experiment.

3.2. Rehabilitation Treatment of National Sports.
Before treatment, X-ray was used to make detailed diagnosis on the pain site of patients and to understand the tissue around the knee joint. The control group was treated with national sports rehabilitation during the period of knee arthritis. The rehabilitation treatment of national sports included three kinds of movements, and the patients in the control group did it twice a day. The three groups of movements include four hip exercises, clamshell exercises, and hip flexion exercises in sitting position. After the three movements, Taijiquan exercise is conducted for 30 minutes every day.

Hip four exercises include abduction, adduction, flexion, and extension. When doing abduction exercise, the upper body should be straight, the right leg should be lifted outward, and then, the left leg should be changed to do 4
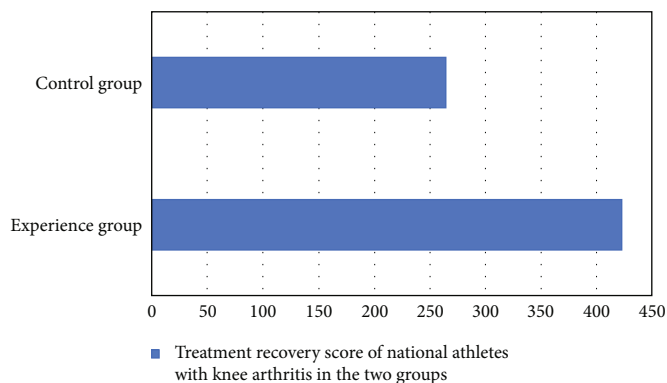
FIGURE 1: Treatment recovery score of national athletes with knee arthritis in the two groups.

groups, 8 in each group. In each group, do the right leg extension in 8 directions. When doing the forward bending training, the right leg should be extended forward, and then, the left leg should be changed. There are 4 groups of 8 in each group. When doing the back-extension training, the right leg should be extended backward, and then, the left leg should be changed to do 4 groups with 8 in each group. When doing this exercise, it is required to find a chair as an aid to avoid falling down accidentally; keep the upper body upright during the whole process; do not follow the lower limb to tilt the upper body; the whole process of ankle joint extension as far as possible, that is, bend to the knee joint direction (hook foot) as far as possible.

Clamshell exercise: lie on the ground on one side with the head rest on one arm. The pelvis should always be vertical to the ground. When the legs are opened, the pelvis should not fall back at the same time. During the movement, pay attention to the leg, keep the shoulder, hip, and ankle joints in a straight line. Bend the hip 45 degrees and bend the knee about 90 degrees. Put the left foot directly on the right foot and exert force on the left leg to make the knee slowly away from the body. Then, slowly return to the starting action, once done on both sides; do two groups, you can also use the cello belt to increase the intensity of exercise.

Hip flexion exercise in sitting position: patients are required to sit on a chair and lift their knees vertically. During the exercise, the upper body of the seat is required to keep straight. Each group has 8 legs and 4 groups.

Taijiquan training: two times a day to practice all the movements of Taijiquan, estimated to take 30 minutes.

In the process of exercise, it is appropriate to feel pain. With the improvement of the condition, the angle of flexion of knee joint should be gradually expanded. But do not excessively pursue the angle, causing the secondary damage.

3.3. Nanotube Combined with Sports Rehabilitation Therapy.
The experimental group was treated with nanotubes combined with sports rehabilitation therapy. The method was as follows: Before treatment, X-rays were used to make detailed diagnosis of the painful part of the patient and to understand the tissues around the knee joint of the patient. On the basis of ethnic sports rehabilitation therapy in the control group, the research group took a 30 mm × 40 mm
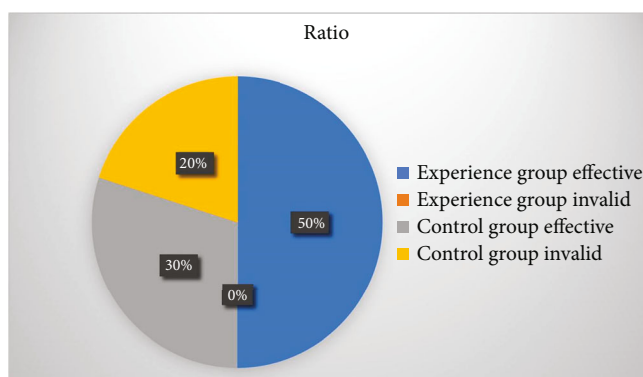
FIGURE 2: The rate of effective treatment in both groups.

square cloth to make a traditional Chinese medicine package. There are manual methods and automatic machine methods for the production methods of traditional Chinese medicine bags, including weighing and wrapping. The traditional Chinese medicine package contained peptide nanoselenium and functionalized nanoruthenium drugs, Heding, Liangqiu, massage the acupoints of Zusanli, Dubi, Yanglingquan, and Yinlingquan before applying plaster. Polypeptide nanoselenium and functionalized nanoruthenium drugs can deliver drugs to the inflammation of the knee joint. Chinese herbal medicines such as Heding, Liangqiu, and Blood Sea have very good effects on the treatment of knee arthritis. Then, apply the Chinese medicine pack to the knee joint. This step is implemented for three consecutive treatment courses, each treatment course includes 10 days, and this step is once every two days. At the same time, the patient's health exercise was strengthened during the treatment, and the exercise content was the same as the control group.

3.4. Observation Indicators for Treatment of Knee Arthritis.
To observe the clinical efficacy of patients suffering from knee arthritis in the experimental group and the control group, the effect of knee arthritis recovery is mainly carried out from the following three aspects. First, the degree of pain: The visual analogue scoring system is used to assess pain severity on a scale of 0-10 points, with 7-10 points indicating no discomfort, 4-6 points indicating mild pain, 1-3 points indicating moderate pain, and 0 indicating severe
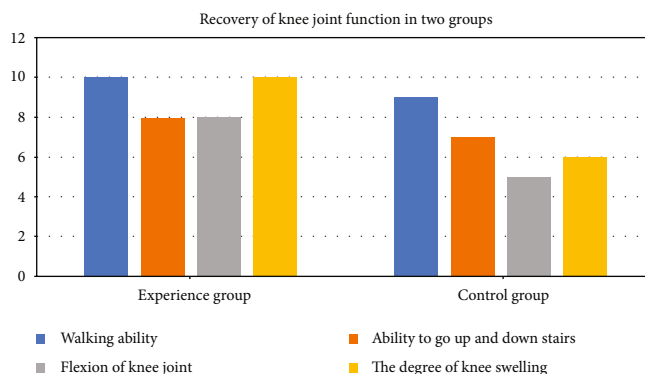
Figure 3: Recovery of knee joint function in two groups.

pain. After that, the average score of the two groups was statistically evaluated, and the average score of the effect of knee arthritis recovery of the two patient groups was calculated. Second, the efficacy evaluation criteria are as follows: effective: After treatment, the patient's clinical symptoms have improved; ineffective: after treatment, the patient's clinical symptoms did not improve; and (3) the patient's knee joint function recovery. The knee joint function score scale was used to evaluate the knee joint function of patients. The evaluation items of the score sheet include walking ability, ability to go up and down, knee flexion, knee swelling, etc. The total score for each evaluation is 10 points.

The clinical curative effect is based on the relevant diagnosis and treatment standards for osteoarthritis: knee joint stiffness and pain disappear, no friction sound during joint movement, and the effect is obvious after the movement function returns to normal; knee joint pain is reduced during movement, effectively improving the friction performance.

3.5. Statistical Methods. SPSS22.0 statistical software was used to examine the experimental data. Taking the sum of the scores of the treatment effects of knee arthritis as the standard, calculate the recovery scores of patients suffering from knee arthritis in the experimental group and the control group and the percentage of knee arthritis patients considered to be effective or ineffective in this group, which constitutes. The ratio is expressed as a percentage, and the effect of patient treatment is compared according to the number. The number of patients is counted as n, and the average count is expressed as x.

4. Experimental Results and Analysis

The data for this study comes from 100 individuals with knee arthritis who were examined at our institution between June 2016 and June 2020. Among them, there are 50 patients in each group. First of all, the effect of the recovery of knee arthritis patients. The pain scores and observe the scores of the two groups were compared.

It can be observed from the statistics in Figure 1 that the 50 patients with knee arthritis in the experimental group received a score of 467 in the treatment of nanotube combined with ethnic sports rehabilitation, and the 50 patients in the control group with arthritis The patient's score in

the rehabilitation of ethnic sports is 265 points. Among the 50 people in the experimental group, 50 of them all had a painless range for the treatment of nanotube combined with ethnic sports rehabilitation. Two of them scored 7 points, 9 people scored 8 points, and 9 individuals scored 9 points and 30 people scored 10 points for a total of 467 points. The 50 patients in the control group scored 265 points, of which 8 people scored 2 points, 12 people scored 5 points, 25 people scored 6 points, 3 people scored 7 points, and 2 people scored 9 points. In the control group, 5 people felt no pain, 37 people felt some pain, and 8 people felt severe pain. The data in this section shows that the treatment of nanotubes combined with Chinese medicine packs has a very good effect on the treatment of knee arthritis. This is because nanomedicine can deliver the medicine to the inflamed part of the knee joint, which can more effectively treat knee arthritis.

Figure 2 shows the data from the control group on the left, and the primary sentence from the experimental group on the right. The experimental group, which accounts for 100% of the total number of participants in this group, feels that the combination of nanomedicine and ethnic sports rehabilitation treatment is successful, as shown by the statistics in Figure 2. Thirty respondents in the control group felt ethnic sports therapy was successful, accounting for 60%, and 20 people thought that ethnic sports therapy was ineffective, accounting for 40%.

The total scores of the knee joint patients in the experimental group who received nanomedicine therapy in combination with national sports rehabilitation were better than those in the control group, as shown in Figure 3. In the experimental group, 50 people were judged on walking ability. The average score given is 10 points, the average score given for the ability to go up and down is 8 points, the average score given by 50 people is 8 points for knee flexion, and 50 for knee swelling. The average score given by a person is 10 points. It shows that after a month of treatment, the recovery ability of knee arthritis patients is the best in terms of walking and knee swelling. This also shows that the pressure on the knee joint during walking is relatively small. At the same time, the ability to go up and down and the flexion of the knee joint is not particularly good in most people. The main reason is that the flexion of the up and down, and the knee joint requires higher knee joints. On the contrary, in

FIGURE 4: Scores in both groups during the experiment.

the control group, among the 50 people who only received ethnic sports rehabilitation, the average walking ability score was 9 points, the knee flexion degree was 50, and the average walking ability score was 7 points. People's average score is 5 points. In terms of knee swelling, 50 people's average score is 6 points. The data in the control group also showed that the ability of knee arthritis patients to recover is the ability to walk first, and the most difficult thing to recover is the flexion of the knee joint.

It can be seen from the data in Figure 4 that with the increase of the experimental time, the two schemes are effective, but the patients in the experimental group using nanotubes combined with ethnic sports rehabilitation therapy are significantly better than those in the ethnic sports therapy alone. The patients in the control group gave a higher average score, and the highest score for this stage was ten. When the experiment only lasted for 5 days, the patients in the control group scored an average of 3 points, and on the last day, they scored an average of 6.9 points. In the experimental group, on the fifth day of the experiment, the patients scored an average score of 5 points, and the patients scored an average score of 9.7 points on the last day. This experiment shows that nanotubes combined with national sports can speed up the treatment of patients with knee arthritis and improve the quality of life of patients with knee arthritis.

5. Conclusions

The incidence of knee arthritis in our country has been increasing among middle-aged and elderly people, especially our country is now entering the stage of aging population, so the treatment of knee arthritis is a matter of great importance. Knee arthritis refers to an inflammatory disease that occurs in the knee joint and surrounding tissues. This article mainly uses ethnic sports rehabilitation therapy combined with nanomedicine to have a better therapeutic effect on knee osteoarthritis. The experimental results show that the total effective rate of nanotubes combined with ethnic sports rehabilitation therapy in the experimental group is 100%, and the control group believes that only ethnic sports rehabilitation therapy accounts for 60%. The experimental group is significantly higher than the control group. After treatment, the walking ability, knee flexion score, and knee swell-

ing scores of the experimental group were higher than those of the control group. During the experiment, the scores of the experimental group were also higher than those of the control group, indicating that nanotubes combined with national sports rehabilitation Treatment can speed up the treatment time of patients with knee arthritis and improve the quality of life of patients with knee arthritis. In summary, the combination of nanotubes and ethnic sports rehabilitation therapy has a significant effect on knee osteoarthritis. This method can be used for reference in clinical applications.

Data Availability

The data that support the findings of this study are available from the corresponding author upon reasonable request.

Conflicts of Interest

The author declares that he/she have no conflicts of interest.

References

[1] L. Hongling, "Analysis of the application of acupuncture combined with rehabilitation therapy in the treatment of stroke patients with hemiplegia," *Chinese Community Doctors*, vol. 31, no. 12, pp. 100-101, 2015.

[2] W. A. N. G. Lei and J. I. A. N. G. Shangrun, "Clinical effect of oryzanol combined with sports therapy in the treatment in patients with neurasthenia," *Harbin Medical Journal*, vol. 163, no. 74, pp. 783–785, 2016.

[3] W. Wang, "Clinical efifcacy of benazepril therapy combined with spironolactone in the treatment of primary aldosteronism in patients with essential hypertension," *Chinese Community Doctors*, no. 7, pp. 711-712,714, 2015.

[4] A. R. A. I. Katsumitsu, "The effectiveness of combined treatment with medication and rehabilitation in patients with early rheumatoid arthritis," *Japanese Journal of Joint Diseases*, vol. 54, no. 57, pp. 75–77, 2018.

[5] V. D. Sidorov and S. B. Pershin, "Rehabilitation of the patients with osteoarthritis," *Voprosy Kurortologii Fizioterapii I Lechebnoi Fizicheskoi Kultury*, vol. 92, no. 5, pp. 28–34, 2015.

[6] T. Y. Kim, S. H. Kim, and H. Ko, "Design and implementation of BCI-based intelligent upper limb rehabilitation robot system," *ACM TRANSACTIONS ON INTERNET TECHNOLOGY*, vol. 21, no. 3, pp. 1–17, 2021.

[7] Department of Physical Medicine and Rehabilitation, Istanbul Medical Faculty, Istanbul University et al., "The effect of visco supplementation on neuromuscular control of the knee in patients with osteoarthritis," *Journal of Back and Musculoskeletal Rehabilitation*, vol. 245, no. 107, pp. 872–879, 2016.

[8] H. Wang, C. Zhang, C. Gao et al., "Effects of short-wave therapy in patients with knee osteoarthritis: a systematic review and meta-analysis," *Clinical Rehabilitation*, vol. 65, no. 72, pp. 477–480, 2017.

[9] K. D. Quervain, "Evaluation and treatment strategies in the rehabilitation of patients with musculoskeletal disorders," *Arthritis + Rheuma*, vol. 28, no. 2, pp. 108–111, 2015.

[10] R. K. Elnaggar and M. A. Elshafey, "Effects of combined resistive underwater exercises and interferential current therapy in patients with juvenile idiopathic arthritis: a randomized

controlled trial," *American Journal of Physical Medicine & Rehabilitation*, vol. 95, no. 2, pp. 96–102, 2016.

[11] B. Matthew, "Benefits and use of aquatic therapy during rehabilitation after ACL reconstruction -a clinical commentary," *International Journal of Sports Physical Therapy*, vol. 14, no. 6, pp. 978–993, 2019.

[12] J. Choi, C. Choi, S. Kim, and H. Ko, "Medical information protection frameworks for smart healthcare based on IoT," in *PROCEEDINGS OF THE 9TH INTERNATIONAL CONFERENCE ON WEB INTELLIGENCE, MINING AND SEMANTICS (WIMS 2019)*, 2019.

[13] Y. El Miedany, E. G. M. Maha, S. Youssef, and D. Palmer, "FRI0114 Development of the patient motivation questionnaire: conceptualizing and measuring motivation in patients with inflammatory arthritis," *Annals of the Rheumatic Diseases*, vol. 75, Supplement 2, pp. 469.3–46469, 2016.

[14] S. N. Baydogan, E. Tarakci, and O. Kasapcopur, "Effect of strengthening versus balance-proprioceptive exercises on lower extremity function in patients with juvenile idiopathic arthritis: a randomized, single-blind clinical trial," *American journal of physical medicine & rehabilitation / Association of Academic Physiatrists*, vol. 94, no. 6, pp. 417–428, 2015.

[15] Y. Zhang, L. Sun, H. Song, and X. Cao, "Ubiquitous WSN for healthcare: recent advances and future prospects," *IEEE Internet of Things Journal*, vol. 1, no. 4, pp. 311–318, 2014.

[16] G. Xiao-Ning, "Effect of aerobic rehabilitation combined with psychological rehabilitation therapy in perioperative patients with breast cancer," *China Modern Medicine*, vol. 48, no. 54, pp. 54–56, 2018.

[17] L. I. Caiyun, X. Liu, Y. Hou, and M.O. Lixin, "Clinical efficacy of Chinese medicine rehabilitation therapy combined with cervical vertebra exercise in the treatment of cervical spondylosis," *Clinical Laboratory Journal (Electronic Edition)*, vol. 235, no. 56, pp. 656–659, 2017.

[18] X. Fang, "Clinical effect of Yangxin Anshen decoction combined with scraping therapy in the treatment of patients with neurasthenia insomnia," *Chinese Community Doctors*, vol. 753, no. 46, pp. 218–220, 2016.

[19] X. U. Wei, S. Dan, and C. Na, "Effect of press-needle acupuncture analgesia combined with rehabilitation training on knee pain and dysfunction of patients with knee osteoarthritis," *Chinese Journal of General Practice*, vol. 25, no. 207, pp. 72–79, 2017.

Retraction

Retracted: Electrospinning of Nanofiber-Based Materials and Application of the Technology to Lower Extremity Joint Exercise Rehabilitation

Journal of Nanomaterials

This article has been retracted by Hindawi following an investigation undertaken by the publisher [1]. This investigation has uncovered evidence of one or more of the following indicators of systematic manipulation of the publication process:

(1) Discrepancies in scope

(2) Discrepancies in the description of the research reported

(3) Discrepancies between the availability of data and the research described

(4) Inappropriate citations

(5) Incoherent, meaningless and/or irrelevant content included in the article

(6) Peer-review manipulation

The presence of these indicators undermines our confidence in the integrity of the article's content and we cannot, therefore, vouch for its reliability. Please note that this notice is intended solely to alert readers that the content of this article is unreliable. We have not investigated whether authors were aware of or involved in the systematic manipulation of the publication process.

In addition, our investigation has also shown that one or more of the following human-subject reporting requirements has not been met in this article: ethical approval by an Institutional Review Board (IRB) committee or equivalent, patient/participant consent to participate, and/or agreement to publish patient/participant details (where relevant).

Wiley and Hindawi regrets that the usual quality checks did not identify these issues before publication and have since put additional measures in place to safeguard research integrity.

We wish to credit our own Research Integrity and Research Publishing teams and anonymous and named external researchers and research integrity experts for contributing to this investigation.

The corresponding author, as the representative of all authors, has been given the opportunity to register their agreement or disagreement to this retraction. We have kept a record of any response received.

References

[1] J. Ma and S. Baek, "Electrospinning of Nanofiber-Based Materials and Application of the Technology to Lower Extremity Joint Exercise Rehabilitation," *Journal of Nanomaterials*, vol. 2022, Article ID 6437728, 8 pages, 2022.

Research Article

Electrospinning of Nanofiber-Based Materials and Application of the Technology to Lower Extremity Joint Exercise Rehabilitation

Jingmiao Ma[1] and Seung-Soo Baek [2]

[1]*Department of Physical Education, Sang Myung University, Jongnogu, 03016 Seoul, Republic of Korea*
[2]*Exercise Rehabilitation Research Institute, Sang Myung University, Jongnogu, 03016 Seoul, Republic of Korea*

Correspondence should be addressed to Seung-Soo Baek; 18409472@masu.edu.cn

This study mainly explores the electrospinning of nanofiber-based materials and the application of the technology to lower extremity joint exercise rehabilitation. In response to people's concerns, this study mainly discusses electrospinning technology from the aspects of the safety of nanomaterials prepared by electrospinning technology and the application of nanomaterials prepared by electrospinning technology in lower limb joints. In the safety study of nanomaterials, six groups of experiments were set up to measure the joints of nanomaterials prepared by electrospinning technology under pressures of 500 N, 510 N, 520 N, 530 N, 540 N, and 550 N. For compression resistance, when the pressure is 540 N, the compressive performance of the nanomaterial is preferably 96%. In terms of the application of nanomaterials, 100 patients with lower extremity sprains in the Affiliated Hospital of Sun Yat-sen University were divided into 5 groups and then divided into 6 groups. Patient recovery rate when the device is applied to the patient's lower extremity joint. Patients had the best recovery rate of 92% when the immobilization device was used for 6 days. The use of arthrodesis did not affect the patient's other factors. The experimental results show that when the pressure is 540 N and the fixation device is used for 6 days, the nanofiber material prepared by electrospinning technology has the best rehabilitation effect on lower limb joint movement.

1. Introduction

1.1. Background and Significance. Traditional nanofibrous materials are seriously impractical due to their increasing pressure and corrosion resistance. Whether in the field of biology or construction, people are eager to find a technology to improve nanomaterials, so that the safety performance and corrosion resistance of nanomaterials can be improved to a higher level. With the continuous research of relevant experts, the preparation of nanofiber materials based on electrospinning technology is proposed.

Electrospinning technology is widely used in many fields, and the application of nanomaterials can improve various properties of nanomaterials. Nanomaterials are highly concerned by the medical community as an auxiliary rehabilitation material. The application of electrospinning tech-

nology to the preparation of nanomaterials can not only increase the yield of nanomaterials but also improve various properties of nanomaterials. Improvements in equipment have helped a lot [1].

1.2. Related Work. In Trejo et al.'s research, nylon 6 nm Monburon cloth and silk yarn and stylish fabrics of Eugansa were combined to construct a complete flying object. This work is the first demonstration that laser cutting and ultrasonic technology are used to process electrospun nanofabrics. The morphology and mechanical properties of the composite cloth are analyzed [2]. Although this study did an experimental comparison, it did not divide in terms of detailed parameters. Cianci et al. believe that epoxy resin (LX) A 4 is a metabolite of aladinic acid (arachidonic acid) produced by epoxy kinase. Its therapeutic effect is fully

standardized on various models of cells, preclinical and clinical. Among them, LXA 4 promotes tissue repair of periodontal disease and can also regulate the function of human periodontal ligament stem cells (hPDLSC) [3]. The clinical treatment effect of LXA 4 is obvious, but the study did not discuss it in depth. Jiang et al. believe that nanofibers, as the main component of one-dimensional nanomaterials, have many uses. Electrospinning is a convenient and effective method for constructing nanofibers. However, in the conventional preparation method, since only unoriented nanofibers can be obtained, its applicability is greatly hindered. In recent decades, a lot of effort has been devoted to optimizing preparation methods. By improving the spinning structure, extraction, and separation of nanofibers, successfully aligned nanofibers (ANF) have been successfully obtained. Due to insufficient system evaluation of ANF, their research will outline the application of ANF in electronic spinning-based preparation, tissue engineering regeneration, sensors, reinforcement materials, sensors, and energy machines. ANF's extensive application in tissue engineering regeneration provides a detailed explanation on this point. In the energy sector, ANF will focus on PEM fuel cells. Finally, we summarize the issues and prospects of ANF development [4]. The research only raised many conceptual questions, and specific experiments need to be further explored. Su et al. prepared multilayered TiO2 nanofibers (TiO2-NF) and nanoparticles (TiO2-NP) by template support method and single solvothermal method, respectively. The decomposition of methylene blue (MB) was used as a reaction model to evaluate the photocatalytic properties of these prepared materials. It is important that TiO2-NF prepared by template-assisted solvent heating has a multilayer structure [5]. The study confirmed that TiO2-NF can improve the photocatalytic rate but did not specifically determine the catalytic effect.

1.3. Innovation and Related Content. The main purpose of this study is to discuss the safety of the nanofiber material prepared by electrospinning technology and the application of the nanomaterial prepared by electrospinning technology in the joints of lower extremities. The joint fixation device uses the recovery of the patient's lower extremity joint to evaluate the nanofiber material prepared by electrospinning technology. The main contents are as follows:

(1) Discuss the development of electrospinning technology from the perspective of domestic and foreign research. In-depth analysis of the preparation of nanomaterials by electrospinning technology was used to find out the beneficial inspiration for this research

(2) Conduct an in-depth discussion on electrospinning technology to find out the best method for preparing nanomaterials and related formulas that may be used. The preliminary discussion on the preparation method of nanomaterials is helpful for further research of the experiment

(3) Control the variables related to the experiment when conducting the experiment. The experiment of elec-trospinning technology actually involves the experiment of the solidity of the nanomaterials and deeply grasps the experimental concept to discuss the characteristics and applications of the nanomaterials in the experimental process

(4) The analysis of data after the experiment is based on tables and figures. Through the relevant software, the experiment is processed to draw the best solution and the most practical nanotechnology

2. Electrospinning Technology

2.1. Optimization of Electrospinning Technology. The structure of the mixed nanofiber membrane prepared by electrospinning technology is not outstanding in quality. In water, the reacted nanofiber membrane will partially dissolve and shrink significantly. Moreover, the mechanical properties of the fiber membrane are insufficient and need to be further strengthened, so it is necessary to link the polyvinyl alcohol/chitosan electrospun nanofiber membrane. The fiber membrane is treated with alcohol solution or alcohol vapor. The degree of expansion and shrinkage of the fiber membrane treated with alcohol is reduced, the strength characteristics, quality characteristics, covalent bond expansion, and shrinkage of the nanofiber membrane are improved, and the toughness of the sample is greatly improved, thereby achieving the purpose of cross-linking [6, 7]. At the same time, it is necessary to pay attention to the different conditions of patients in the application of nanomaterials in lower limb joints, so it is necessary to conduct a careful examination of patients before using nanomaterials for rehabilitation treatment [8].

In the field of nanobatteries, due to its excellent conductive properties, it is a widely used carbon material in the research of lithium-sulfur batteries, which can greatly improve the conductivity of battery anode materials. The carbon-silicon composite material can not only improve the conductivity of the active sulfur of the positive electrode but also effectively inhibit the diffusion of polyurethane to the negative electrode through physical adsorption and ease the volume expansion of the positive electrode. It is an electrode material in the working process of the battery. And sometimes, there is research in the field of machinery. This can improve battery performance, but the capacity is small and the decay is fast. Then, sulfur is coated with a carbon material, and the carbon material is used as a conductive skeleton to realize electron transmission. After the porous carbon fiber is prepared by the electrospinning method, the pores of the carbon fiber are filled with sulfur by the liquid-phase deposition method, which is the best preparation method for the battery. When the current density is $6^\circ C$, the initial specific capacity of the battery increases by 800 milliamperes per gram [1, 9, 10]. Liquid-phase deposition belongs to liquid-phase epitaxy technology of the semiconductor growth process.

2.2. Application of Electrospinning Technology in Nanofiber Materials. In the field of nanocatalyst materials, nanometals are an excellent catalyst, combining nanomaterial carriers with

nanocopper and composite catalysts, substitutes for precious metal catalysts such as platinum and gold, many organic reactions have better catalyst characteristics, and high capacitor electrodes. The material and copper oxide have good electrochemical properties. To this end, researchers have been developing nanocomposites with various morphologies, sizes, and characteristics to meet the various applications and needs of today's society. Nanometal is an excellent high-temperature material. The traditional preparation method is mainly based on wet spinning, and the fibers can be obtained in the micron level. At present, there is little research on the preparation of nanometal nanofibers by electrospinning technology. Nanometal can be prepared by electrospinning technology. Nanofibers have good metal tensile properties, so the performance of nanometallic materials can be optimized [11]. By changing the environment of the textile fluid with electric current, the nanoparticles can adapt to the environment in the textile fluid.

The angle of the PAN nanofiber test sample and the droplet formation is one hundred degrees, the material surface has almost no hydrophilic groups, and the hydrophilicity is poor. The average static contact angle of AOPAN nanofibers was reduced to 80 degrees after treatment of PAN nanofibers with amino modification technology. Therefore, a certain number of hydrophilic groups are added to the surface of AOPAN nanofibers modified by amino acids to improve the hydrophilicity. With the further change of ATRP technology of AOPEN nanofibers, the average static contact angle of polymerized nanofibers is reduced to 50 degrees, which can further improve the hydrophilicity of nanofibers. This is because a large number of groups are introduced on the surface of the transplanted nanofibers. In promoting the improvement of hydrophilicity, the carboxyl group plays a very good role, and the hydrophilicity is greatly improved [12]. Electrospinning technology is used to prepare nanometal materials in water, and the manufacturing process of nanometal materials is clearly displayed.

2.3. Research Methods of Nanomaterials by Electrospinning Technology

(1) Polymer research method. During the preparation of the textile solution, the nanomaterials are introduced into the fiber-forming polymer matrix, and then, spinning is performed. This method has a certain influence on the process of electronic spinning; nanoparticles become very easy to aggregate. Therefore, the difficulty of this technology is how to improve the adaptability between nanoparticles and textile liquor. The surface of the nanoparticles can be modified, and the ligand can be rotated in the liquid phase. However, the application of nanosurface modification technology is limited due to its complicated process, and may not be suitable for most nanoparticles and textile solutions [13, 14]. Controlled release of drugs can not only be used in the field of biomedicine, wound repair, biological tissue engineering, and other aspects of the fiber filter material in the gas filtration liquid filtration and personal protection and other fields but also can be applied to the shell of ships, the inner wall of oil pipelines, high-rise glass, automobile glass, and so on [15]

(2) Medical research method. Nanomaterials in medical research, first of all, the comparison of the lower limb pretreatment of sEMG and the wavelet transform-based filtering method in the traditional filtering method, are more effective than the wavelet transform method for noise removal processing of signal filtering. Next, using the three types of time-domain feature value changes, the action at the start of sEMG is determined. Next, the eigenvectors of the lower limb sEMG are studied, and finally, the eigenvalues of the time domain and the frequency domain are extracted. The neural network is trained by using the characteristic values of the time domain and frequency domain features and their joint features as the input of the neural network, where the BP neural network classifier classifies the two operation modes of lower limb bending and design will expand the application range [16, 17]

(3) Carbonization treatment method. During the carbonization process, since the graphite ring structure is formed after dehydrogenation, the PAN will not collapse during the carbonization process. The fiber membrane shrinks during the preoxidation process. Therefore, in order to ensure the specific structure of the fiber, during the preoxidation process, a specific mass object can be used to extend the film in the vertical direction to maintain the fiber state. Clamping the nanofiber bundles at both ends of the jar and placing them in a tubular furnace can produce a fixing material with its own high temperature resistance. In order to prepare the aluminum foil for direct oxidation, the orientation structure of the fiber can be maintained during the preliminary oxidation according to the adsorption force between the fiber film and the aluminum foil. In the preoxidation process, the fiber bundle is covered with glass, and the binding force of glass gravity on the fiber bundle maintains the structure of the fiber bundle [18–20]

(4) Electrostatic treatment method. Generally speaking, it includes the following steps. First, the precursor containing the target material and the organic polymer are mixed, and an organic solvent is added to form a viscous yarn solution. Then, the solution is injected into the high-voltage electrospinning yarn with a specific voltage for spinning and collection. The general electronic spinning system is mainly composed of three parts: high-voltage electrostatic electric field power supply, spinning port discharged from nanofibers, and ground plate. The high-voltage power supply is generally a DC power supply, and the voltage range of the AC power supply is generally sixty volts. The output end is connected to the spinning port, and the other end is grounded. The spinning port is usually a metal needle with a specific

diameter, and the diameter of the spinning port affects the diameter of the nanofiber. The solution is usually discharged directly into the cylinder by gravity, and there is also a peristaltic pump connection for controlling the uniform flow of droplets. The power receiving plate for the metal plate usually uses a ground wire to make the potential of the power receiving plate zero. Therefore, the electrospinning of the output voltage of the high-voltage power supply is the spindle voltage. Another type of device, connecting the attraction device to the receiving board, can not only expand the electric field strength but also reduce the output voltage of the high-voltage power supply [21]

(5) Sprinkler method based on nanomaterials. Three hundred times higher than single nozzle electrospinning efficiency. Multinozzle devices can improve production efficiency but can also cause other problems. For example, during the electrospinning process, since the sprinkler heads are charged, if multiple sprinkler heads are used, an electrostatic repulsive force will be generated between different sprinkler heads, affecting the formation of the jet. Therefore, multiple sprinkler devices of different layouts are designed to reduce mutual repulsion between sprinkler heads. The six needle ring configuration device can not only obtain a stable jet aircraft but also avoid the interference of environmental factors such as air flow. Under the premise of ensuring fiber quality, we improve the production efficiency of fibers and contribute to promoting the mass production and practical application of electric field spinning fibers

2.4. Formulas Used in the Preparation of Nanofiber Materials. In the preparation of nanomaterials by electrospinning technology, it is necessary to conduct a comprehensive study of nanomaterials through performance and actual application. At this time, relevant formulas will be used to explain them.

(1) In the signal recognition of human body, the information transmission function of nanomaterials plays a huge role. The relevant formula is as follows:

$$m_k(t) = \sum_{i=1}^{N} u_k(t) \times \delta(t - \tau_1) \times p_k(t) \times g_{ki}(t) \times M \tag{1}$$

In information transmission, usually the signal transmission requires a certain process, and the transmission time will also be affected by related factors. When using nanomaterials for human body information collection, the time factor and the temperature factor of the nanomaterials need to be considered. The longer the time, the more sensitive the reaction of the nanomaterials, because the nanomaterials

need time to continuously activate during the information transmission.

(2) When processing the collected information with special equipment, the information needs to be processed first. The relevant formula is as follows:

$$u_p(t) = \sum_{k=1}^{M} [u_k(t) \times l_k(t)] = \sum_{k=1}^{M} \left[\sum_{i=1}^{M} \delta(t_k - t_{ki}) \right] (t_k + t_i) \tag{2}$$

The processing of information is carried out in segments, each segment needs to be refined, and then, the image description of the information. The entire process is carried out in a complete processor, which can be directly filtered from the table when data extraction is performed.

(3) In the conduction information of nanomaterials, the conduction distance and the average power of conduction are very important. The relevant formula is as follows:

$$vS_{1(\omega)} = S_y(w)(1 - \cos \omega\Delta) = 4S_y(w) \sin^2\left(\frac{\omega\Delta}{2}\right) \tag{3}$$

When the conducted power is constant, the larger the cosine value of the conduction process, the lower the conduction rate of the nanomaterial. The greater the sinusoidal value during conduction, the greater the rate of conduction. In most medical devices, the rate of change in the rate of nanomaterial conduction will be focused on. For the nanomaterials with larger conduction rate, they will be used first.

(4) The stress performance of nanomaterials reflects the bearing capacity of nanomaterials to a certain extent, and the related formula is expressed as follows:

$$\sigma_m^2 = \frac{1}{2\pi} \int_{-\infty}^{+\infty} S_m(\omega) d_\omega = \frac{1}{2\pi} \int_{-\infty}^{+\infty} |H(\omega)|^2 S_m(\omega) d_\omega \tag{4}$$

$$\sigma_y^2(t) = \frac{1}{2\pi} \int_{-\infty}^{+\infty} S_y(t, \omega) d_\omega = \sigma_m^2 c^2(t) \tag{5}$$

The value of the stress change can directly reflect the quality of the nanomaterial. In general, the stress value of nanomaterials with large specific surface area will also increase; of course, this is to exclude the specific surface area under the environment not affected by temperature. Nanomaterials are highly durable materials, and their corresponding stress coefficients will directly determine the lifetime of nanomaterials.

TABLE 1: Related equipment used before the experiment.

Equipment name	Specification	Manufacturer
Constant temperature oil bath device	Temperature-controlled magnetic stirring	Germany
Infrared spectrometer	NiN10	American Asia Pacific
High temperature power supply	DMP303	Hefei Power Supply Company
Precision grouting machine	LPS-5A	Changhe Electric Appliance Company
Electron microscope	PM-80	Sino-American
Pressure sensor	MQ-50	Kunshan Instrument Company
Data analyzer	AM3240C	Electronic Technology Research Institute
Spectrum analyzer	TNC-20	China to Federal Group
Assembly machine	1313	Japan

3. Electrospinning Technology Experiment

3.1. Experimental Equipment. The relevant experimental data needs to be measured before the experiment. The relevant equipment used before the experiment is shown in Table 1. The function of the assembling machine is to systematically assemble the joint fixing device of nanomaterial synthesis during the experiment, which avoids certain errors caused by the experiment in the process of manual assembly. The function of the frequency analyzer is to control the transmission rate and transmission time of the signal during the experiment. The data analyzer is designed to comprehensively collect the data that appears during information processing to prevent the omission of information during the experiment. In addition to controlling the external environment, we also need to control the internal environment reasonably in order to get more accurate results [22]. The data analyzer is controlled by the computer throughout the use. The role of the pressure sensor is equivalent to further data mining of the experiment through the data returned by the pressure sensor when applying pressure to the fixture. The function of the optical instrument is to observe the rehabilitation state of the patient at any time without changing the fixed instrument during the experiment.

3.2. Control of Experiment-Related Factors. We pay attention to controlling related factors during the experiment. When conducting safety experiments, the measurement of the joint fixture must be performed in a safe environment. Each time a measurement is taken, relevant data records are required. The value of pressure is within a reasonable range. During the experiment of the application of the joint fixation device, the joint fixation device needs to be polished to prevent the patient from being scratched during the experiment. During the experiment, the patients had the same degree of sprains, and the patients had the same sprained parts.

3.3. Experimental Process. In the study of the safety of nanomaterials, six groups of experiments were set up to measure the joints of nanomaterials prepared by electrospinning technology under the pressure of 500 N, 510 N, 520 N, 530 N, 540 N, and 550 N and compression resistance.

In terms of application of nanomaterials, 100 patients with sprains of lower extremities who were admitted to the

TABLE 2: Study the compressive performance of nanomaterial joint fixtures at different pressures.

	Pressure (N)					
Number of groups	Compression rate (%)					
	500	510	520	530	540	550
Group 1	50	60	71	80	96	67
Group 2	40	50	61	73	90	62
Group 3	36	43	52	60	85	57
Group 4	28	38	45	55	70	52
Group 5	21	30	41	48	65	47
Group 6	17	25	38	44	49	36

TABLE 3: Rehabilitation status of patients with sprained lower extremities at different days.

	Heaven number (d)					
Number of groups	Recovery rate (%)					
	1	2	3	4	5	6
Group 1	47	60	70	80	87	92
Group 2	40	51	62	72	78	83
Group 3	33	40	50	68	66	76
Group 4	21	31	40	53	57	62
Group 5	24	33	40	46	47	55
Group 6	18	25	28	40	38	48

Affiliated Hospital of Sun Yat-sen University were divided into 5 groups, and each group of experimenters was divided into 20 people. A total of 6 groups of days at 1 d, 2 d, 3 d, 4 d, 5 d, and 6 d were used to observe the recovery rate of the patients when the nanomaterial fixation device prepared by electrospinning technology was applied to the patients' lower limb joints.

4. Analysis of Electrospinning Technology

4.1. Summary of Experimental Data. The compressive performance of the nanomaterial joint fixation device when studying different pressures is shown in Table 2.

The performance of nanomaterials is usually determined by the molecular structure of nanomaterials. In general, the
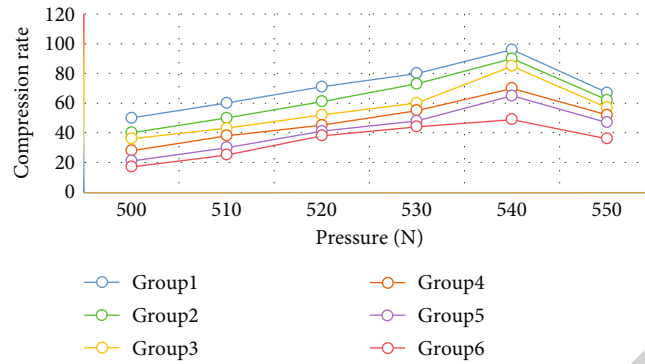
FIGURE 1: Safety performance of lower limb joint fixation device under different pressures.

structural stability of carbon is higher than other similar elements. In the field of nanomaterials, carbon element is the dominant factor. It can be seen from the data in the table that, to a certain extent, the compression performance of the nanomaterial joint fixation device gradually changes with the change of the pressure value. When the pressure value reaches a point, the compression rate of the nanomaterial reaches the highest. Then, it showed a downward trend.

In terms of the application of nanomaterials, the rehabilitation situation of patients with sprained lower extremities at different days is shown in Table 3.

In the process of sports rehabilitation, as the number of days continues to change, the patient's recovery gradually improves, and one of the inevitable factors is the patient's own self-healing. However, because the recovery situation of the patients in the table improved more quickly and was significantly higher than normal, the lower limb joint fixation device played an important role in this. And as time goes by, the recovery rate of patients gradually rises and tends to a stable state.

4.2. Experimental Data Analysis. The safety performance of the lower limb joint fixation device under different pressures is shown in Figure 1. In the figure, when the pressure is 500 N, the safety performance of the 6 sets of data is at the lowest state. The measurement time during the experiment was carried out on the same day to avoid different measurement results caused by different time. Through comparison, it is found that the safety performance also increases when the pressure value gradually increases, but when the pressure value reaches a certain range, it will reach a critical value. As the pressure continues to increase, the entire fixing device is in a state of being easily broken. If this limit is exceeded, the safety performance will be affected. The nanomaterials after applying pressure are no longer suitable for the fixation of the patient's lower limbs.

As the pressure changes, the safety rate of the lower limb joint fixation device is shown in Figure 2. The concept of pressure change is quoted in the figure. The value 1 represents 500 and the value 2 represents 510. When the pressure is 540 N, the compressive performance of the nanomaterials is preferably 96%. When the pressure is 500 N, the maximum value of the measured safety performance is 50%.
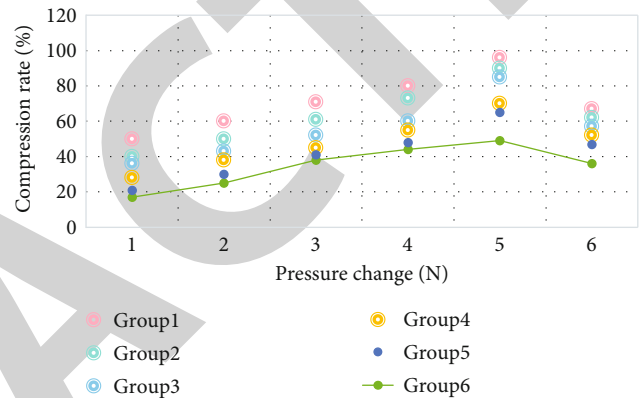
FIGURE 2: With changes in pressure, the safety rate of the lower extremity joint fixation device.

The safety performance of the nanomaterial itself has not changed, and the value measured during the experiment represents the actual safety rate under a certain pressure. With the constant change of the pressure value, the highest position is reached when the pressure is 540 N, that is, the safety of the lower limb joint fixing device at this time is the best. Within a certain range, the force sustained by nanomaterials is directly related to safety performance.

With the gradual change of the number of days, the patient's recovery is shown in Figure 3. At a certain number of days, the overall recovery of group 6 is relatively low. Most of the reasons for this situation are due to the different circumstances of the patients, but the overall recovery shows an upward trend with time. Therefore, the specimens collected during the experiment meet the experimental requirements. The recovery effect of the patients in group 4 was lower than that in group 1 on the first day, but after the use of the lower extremity joint fixation device, the patients showed that the recovery situation surpassed that of group 1. It shows that the joint fixation device with nanomaterial as the main power shows a good trend in the use of patients.

The corresponding change of the patient's recovery rate with time is shown in Figure 4. When the fixed device was used for 6 days, the recovery rate of the patient was the best, at 92%. Among them, the fixing device is equivalent to auxiliary treatment to prevent the patient from being injured
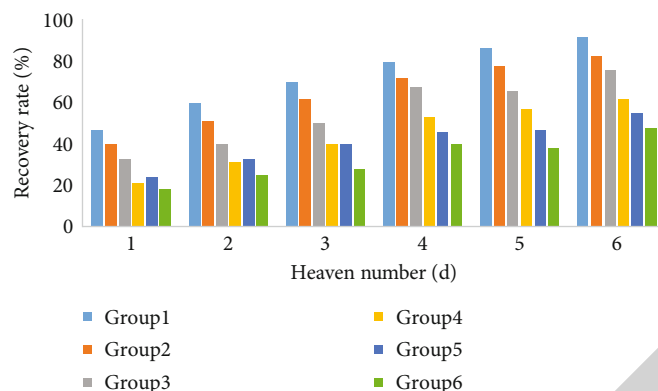
FIGURE 3: As the number of days gradually changes, the patient's recovery.
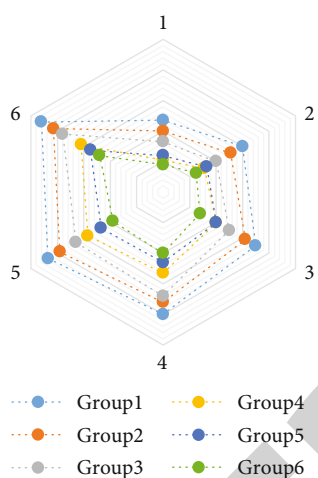
FIGURE 4: Corresponding changes in the recovery rate of patients over time.

again. The recovery rate of the patients in group 1 is generally low, but when the time changes, the recovery rate shows a rising state. The recovery rate of the patients in group 6 is higher at a certain number of days. In this case, it is more suitable for the rehabilitation of patients. The data in the figure also tends to the sixth group. The recovery level of the patients in group 2, group 2, and group 3 is lower than the recovery rate of normal patients, indicating that the patients in these three situations have poor recovery treatment effects.

5. Conclusion

Starting from the background at home and abroad, this research deeply explores the preparation of electrospun nanofiber materials and its application in the rehabilitation of lower extremity joints, and a series of experiments have made breakthroughs, confirming the safety and reliability of nanomaterials. Rehabilitation treatment effect is good. Open up new ideas for further research on nanomaterials.

As a high-strength material with broad development prospects, nanomaterials have made outstanding contributions in the fields of construction, medicine, aviation, and so on. Especially in recent years, the country has paid attention to and supported high-tech and high-information materials, and nanomaterials have become more and more widely used as a landmark application for many polymer materials.

This study explores the strength of nanomaterials from the safety performance of nanomaterials and explores the effect of nanomaterials on the recovery rate of nanomaterials in medicine from the application of nanomaterials. We analyze the practical properties of nanomaterials from different angles. In a certain pressure range and a certain time, the use of nanomaterials is the best. This study has a very important value for the discussion of nanomaterials.

Data Availability

No data were used to support this study.

Conflicts of Interest

The authors declare that they have no conflicts of interest.

Acknowledgments

References

[1] R. Ramakrishnan, J. Gimbun, F. Samsuri et al., "Needleless Electrospinning Technology – An Entrepreneurial Perspective," *Indian Journal of ence and Technology*, vol. 9, no. 15, pp. 1–11, 2016.

[2] N. K. Trejo, C. G. Reyes, V. Sanchez, D. Zhang, and M. W. Frey, "Developing composite nanofibre fabrics using electrospinning, ultrasonic sewing, and laser cutting technologies," *International Journal of Fashion Design Technology & Education*, vol. 9, no. 3, pp. 192–200, 2016.

[3] E. Cianci, O. Trubiani, F. Diomede et al., "Immobilization and delivery of biologically active Lipoxin A4 using electrospinning technology," *International Journal of Pharmaceutics*, vol. 515, no. 1-2, pp. 254–261, 2016.

[4] M. Jiang, M. Wang, S. Wei, and Z. Chen, "Aligned electrospun nanofibers based on electrospinning technology," *Progress in Chemistry Beijing*, vol. 28, no. 5, pp. 711–726, 2016.

Research Article

Rehabilitation Training and Prevention of Athlete's Hind Thigh Muscle Injury Based on IoT Intelligent Data

Peng Sun [ORCID]

Institute of Physical Education and Health, Yulin Normal University, Yulin, 537000 Guangxi, China

Correspondence should be addressed to Peng Sun; mrsunpeng@ylu.edu.cn

With the rapid development of information science today, the Internet of Things technology is gradually being applied to all walks of life, and the multifunction and intelligentization of instruments have gradually become the focus of people's attention. In recent years, domestic track and field sports have developed to a certain extent, but at the same time, it must also be noted that there are still some difficulties and problems in the development of domestic track and field sports. This article was aimed at studying the application of the rehabilitation training and prevention of athletes' hind thigh muscle group injury based on the intelligent data of the Internet of Things and puts forward the idea of using the intelligent data of the Internet of Things to better use in sports rehabilitation and prevention. This article describes in detail track and field training, athletes' hindquarters muscle injury, and so on. The application experiment of rehabilitation training and prevention of athlete's hind thigh muscle group injury based on the intelligent data of the Internet of Things has been made. The experimental results show that the rehabilitation training and prevention program of athletes' hind thigh muscle injury based on the intelligent data of the Internet of Things can effectively reduce the athlete's muscle injury during training, and it is more than 10% higher than the traditional prevention program. It can effectively improve the bad and wrong movement patterns of athletes, improve their own stability, flexibility, and balance, optimize the transmission of the body's power chain, and improve the athletes' ability to perform competitively.

1. Introduction

Track and field training in physical education institutions is an important part of track and field training in China [1]. Sports school track and field training has provided a large number of excellent talents for the national track and field team, and some athletes have achieved excellent results in the world competition [2]. But for a long time, sports injury has been one of the important factors restricting the health and sustainable development of competitive sports. It not only affects the normal training of athletes but also ends the sports career of athletes prematurely, which is not only a personal regret for athletes but is also a major loss and waste of resources in competitive sports, which is one of the problems to be solved urgently in competitive sports.

The basic skills of athletes should be improved and corrected in time. In addition, the learning and mastering of new technology should be arranged in the period when ath-letes are in good physical and mental state, so as to avoid learning technology under physical and mental fatigue and bad state [3]. Preparatory activities have made full physical and mental preparation for formal training, which must be paid attention to in training. In winter preparation, athletes should also pay attention to clothing and preparation time. Different special events have fixed action patterns and specific muscle groups [4].

The main reasons that affect the prevention and rehabilitation of sports injuries of college athletes are as follows: the increasing number of sports competitions makes athletes do not have enough time for systematic and complete rehabilitation training, and sports injuries are accumulated and repeated. The existing rehabilitation training is difficult to meet the training requirements of athletes, and it is difficult to achieve effective recovery after high-intensity training. [5]. The subject consciousness of athletes refers to their cognition and consciousness of sports injury in training [6].

Track and field athletes are in the process of physical and mental development. In terms of time, sports injury can be divided into early, middle, and late [7]. In the early stage of sports injury, the manifestations of sports injury in this period are local tissue ischemia, obvious pain in the injured part of athletes, a large amount of tissue fluid exudation, and swelling in the injured part [8].

In this paper, the method of experimental research is used to understand the influence of the injury of the posterior femoral muscle group of track and field athletes and to find out the way of sports injury of track and field athletes through theoretical analysis and experimental research; through data recording, sorting, calculation, drawing, and analysis, the data are processed. Through the simulation of the statistical data set of the later rehabilitation training and prevention of the injury of the posterior femoral muscle group of track and field athletes, combined with the data, the role of the posterior femoral muscle group in the track and field sports is empirically analyzed and combined with the effective data. The article further summarizes and sorts out the specific methods of the athlete's posterior thigh muscle injury, the specific requirements of the exercise movements, the advanced movements, and the training load characteristics, enriches and improves the training methods and contents of the sports injury in the physical function training system of college athletes, provides theoretical and practical guidance for coaches, athletes, and other researchers of college long jump training teams and other training teams, and further improves the scientific, systematic, informatization, and rationalization level of the training system of college training teams.

2. Injury of Posterior Femoral Muscles of Track and Field Athletes

2.1. Track and Field Training. The development of track and field athletes needs years of training. Athletes mainly rely on the functions of the ATP-CP system. The absolute speed level of the track and field athlete determines the performance. The speed of the athlete mainly depends on the elongation-contraction ability of the knee and ankle extensor muscles and the ability of the hip joint to contract concentrically. The coordination of speed and explosiveness is the key to determining track and field performance. However, due to the influence of the basic training conditions of track and field and the professional level of coaches, some athletes have different degrees of sports injury, which affects the quality and systematization of the basic training stage. In track and field training, some coaches still rely on experience training, lack of deep understanding of scientific training, and pay too much attention to competition results, which is not conducive to the development of athletes. This situation leads to different degrees and types of sports injuries. The training of high level athletes in track and field is a systematic project. In the system training, the training is carried out in stages. Different training stages complement each other to form a system [9, 10]. If there are more and more serious sports injuries in training, it will not only affect the quality of training but also break the training system. With the increase of modern sports events, the intensity of training is increasing day by day, and even competition is used instead of training. This increases the risk of injury to athletes. With its unique charm, sports attract people to participate in it and enjoy the tension, excitement, excitement, and joy after winning the whole process. It has multiple functions of promoting social development. More and more modern sports training load trend content orientation, load measurement specialization, many years of training process, and training team composition diversification, which means that the complexity of modern sports training organization and implementation and the requirements of comprehensive training are higher, and the requirements of human body in psychology are more and more in-depth, so the actual needs of social activities are higher and higher [11, 12]. Sports have higher requirements and standards for athletes participating in sports competitions. After a long period of practice, sports have become a practical social activity to realize the individual social value of athletes. This is the essential characteristic and internal requirement of sports training. The performance of sports mainly depends on the existing level of athletes [13]. The ultimate goal of competition and training is to achieve excellent results. Psychological ability plays an important role in the ability constitution of track and field athletes. The process of athletes' long-term training until the highest achievement is closely related to individual psychological development [14]. In the early stage of scientific development, people's understanding of sports is relatively low, and they pay attention to the physiological response of body function. Although they have a corresponding understanding of psychology, the research still needs to be strengthened. At the same time, some social factors that are expected by the outside world, lack of psychological coordination and cooperation, often lead to the situation is not ideal, lack of psychological adjustment and maintenance, resulting in their own regret, anger, and other psychological differences. Psychological ability is the key to achieve the level of athletes and achieve ideal sports results. For athletes engaged in sports, the level of motivation to a certain extent affects the performance of individuals or the quality and effect of daily sports training. The realization of social value and self-worth of athletes needs long-term motivation. The quality of incentive determines the realization of incentive demand and the degree of target acquisition. Therefore, athletes have formed professional representatives for a long time. In other words, professional competition and long-term guidance and training are the long-term mechanism of athletes' long-term work. Will quality is the basic guarantee for athletes to overcome the tough training competition [15].

2.2. Posterior Femoral Muscle Damage. "Injury" has a broader and richer meaning and scope than "sports injury," and the meaning and scope of "sports injury" is more specific and detailed, especially referring to various acute and chronic injuries that occur during sports. Therefore, the word "injury" includes "sports injury," and "sports injury" is more professional, scientific, normative, and rational than "injury" in sports application. Patients with severe injuries

need to be hospitalized for a long time and lose their ability to exercise completely, especially the pull injury of posterior femoral muscle group. The main reason of lower extremity injury is the theory of muscle involvement. If the lower extremity hemorrhage cannot be absorbed, it will form fibrous tissue and new bone. For example, too much treading and retreating will make flexor and squat muscles, flexor digitorum, and posterior tibial muscles contract repeatedly, causing a series of pathological changes of periosteum of legs. No matter what the cause of periostitis, if the local load can be in the early stage, timely adjustment of running, jumping, and support can reduce exercise, appropriate treatment can be taken to reduce inflammation and tissue repair process, and adaptive changes will also occur, which will improve the load capacity of bone tissue. Therefore, coaches and athletes should fully consider the mechanism of sports injury and reasonably adjust the training plan when making the training plan. The main reason why the waist and back are easy to be damaged is that the gravity exceeds the endurance of the trunk for a period of time. The proximal end of the rowing bone is relatively narrow and long, and the longitudinal span between the two rows of carpal bones is the most likely to be fractured in the carpal bone. However, due to the track and field without using the wrist, only the wrist closely related to the throwing event and the injured wrist of track and field athletes are relatively low.

Injury of the thigh muscles is common in track and field, football, etc. Although most injuries do not require surgical treatment, athletes need to rest for 2-8 weeks before returning to the level before injury. After athletes resume normal training and competition, repeated posterior femoral muscle strains can lead to longer recovery time, chronic pain, and dysfunction and can even end of their sports careers. Due to the serious consequences of tension, a lot of manpower, material, and financial resources are invested to prevent the tension of the posterior femoral muscles and improve the rehabilitation effect of tension. Strains mainly occur when the muscles are stretched. Strains are related to muscle strains, not to muscle contraction force and speed. Muscle strain is defined as the ratio of muscle relative resting length increment to muscle resting length. In a given human movement, when the muscle length increments are similar, the optimal length of the muscle is shorter, the strain of the muscle is larger, and the risk of injury increases. On the other hand, when the optimal muscle length is similar, the greater the muscle length increment, the greater the muscle strain and the greater the risk of strain. Sprinting is the most important form of movement that leads to the pulling of the posterior femoral muscles. The huge load of the posterior femoral muscles is the cause of the traction. Therefore, we believe that the early stage of the support stage is a high-risk stage of tug-of-war. The tug-of-war for muscles is caused by excessive strain, and huge muscle contraction is not a necessary condition. On the one hand, it affects the size of the muscle strain by affecting the optimal length of the muscle; on the other hand, it may also affect the biomechanical characteristics of the lower limbs during sprinting, thereby affecting the length increase of the posterior femoral muscle group and ultimately affecting the size of the strain

and changing the risk of contingency. Insufficiency of the hamstrings is considered to be the main cause of hamstring injuries. Deficiencies in the hamstrings can result in insufficient hamstrings against the quadriceps during knee extension during the swing phase. Assuming that this is the mechanism of hamstring injury, it is a further inference that the imbalance of muscle strength at the thigh is the cause of hamstring injury.

The hamstring is mainly composed of type II fibers of fast twitch fibers. This muscle group is a typical biarticular muscle, consisting of the biceps femoris located on the back of the thigh, the long and short biceps, and the semitendinosus located on the back of the thigh muscle and semimembranosus muscle. In running movements (especially fast movements), the biceps femoris and semimembranosus are powerful extensors of the hip joint, while semimembranosus is the agonist for knee flexion and calf flexion in addition to coextending the hip. However, the current training methods cannot train this muscle group well, so in high-speed exercise, the injury and recurrence of the posterior femoral muscle group are very common. Severe strain of the proximal part of the posterior femoral muscle group may also affect the lower limb function of the patient. Incomplete recovery after injury will lead to repeated or aggravation of the disease, resulting in difficult recovery, and the second injury is often more serious than the previous one. Repeated injury of the posterior group of extensor muscles may lead to lumbar deformation and reduce the deformation and range of motion of the knee joint, the adhesion of the common peroneal nerve, the reduction of the strength of the quadriceps femoris, and so on. At the same time, it will increase the risk of other parts of the lower limb, such as the anterior cruciate ligament. Serious pull injury of posterior femoral muscle group not only brings great pain to athletes but also brings great economic loss to clubs or sports teams. More than half of the injuries were related to the biceps femoris, and most of them occurred in the long head of biceps femoris. Because the long head and the short head of biceps femoris are controlled by different nerves, this unique dual innervation makes asynchronous nerve stimulation lead to asynchronous contraction of muscles, thus weakening the ability of muscles to produce effective tension control strong load, and at the same time, the relatively short length of muscle fibers also makes pulling. In a given human action, the shorter the optimal muscle length, the greater the muscle tension, and the higher the risk of injury. Serious traction injury of posterior femoral muscle group may be caused by exceeding the physiological limit in a certain exercise process, or it may be the result of long-term microinjury accumulation. It is also possible that the two mechanisms together lead to the final result of the strain. Although jumping, slow overstretching, and so on will cause the strain of the posterior thigh muscles, sprint is still the most important form of exercise.

2.3. *Preventive Measures.* The main problem of the injury mechanism of the posterior femoral muscles during sprinting is the injury time. In addition to the large knee flexion, the hip extension supports the early stage. In order to resist

the acceleration of the forward swing of the leg, the strong contraction of the posterior femoral muscles produces greater knee flexion in the final stage of the swing. The early support period and the later swing period are both high-risk periods of sprained posterior femoral muscles. In daily walking and squatting positions, the knee and hip joints have completed the bending movement, and these two joints have opposite effects on the extension of the thigh muscles. This unique dual innervation causes asynchronous nerve stimulation to cause muscles to contract asynchronously. All three muscles of the posterior femoral muscle come from the ischial tuberosity behind the pelvis. Therefore, when the forward angle of the pelvis increases, the posterior thigh muscles will be in a longer state, which may increase the risk of injury. In certain human activities, the greater the muscle tension, the greater the risk of injury. The optimal length of the posterior femoral muscle group with a history of strain may be shorter, and the risk of restrain may increase. Therefore, the knee flexion angle at the moment of maximum knee flexion can be used to reflect the strain risk of the posterior femoral muscles. Is the change in the optimal length the cause of the previous strain or the result of the previous strain? The ability of tired muscles to resist stretching decreases. In the case of absorbing the same energy, fatigued muscles will stretch longer than nonfatigue muscles, so it is easier to reach a stretched tension state, and the risk of fatigued muscles is higher. Power imbalance is a potential risk factor for posterior femoral muscle stretch injury. The imbalance of strength mainly includes the weakness of the posterior femoral muscle, the imbalance of the strength of the posterior femoral muscles on both sides, and the low strength ratio of the posterior femoral muscle to the quadriceps muscle. The strength of the posterior femoral muscles and quadriceps is relatively weak. In the late stage of the sprint, the eccentric contraction of the posterior femoral muscles is not enough to prevent the swing of the front legs, which may lead to excessive stretching of the posterior femoral muscles, resulting in tension. Because the deformation of the posterior femoral muscle group mainly occurs in the process of strong eccentric contraction, the centripetal muscle force ratio is said to not reflect the actual function of the posterior femoral muscle group. The ratio of centrifugal force to centripetal quadriceps is widely used. During sprinting, the maximum muscle tension of the thigh muscle group is much greater than the maximum muscle tension at the maximum muscle stretching speed, and the maximum muscle stretching speed is much greater than the maximum muscle tension at the maximum muscle tension. Although the occurrence of muscle strain is not directly related to the speed of muscle contraction, once the strain occurs, the speed of muscle stretching may affect the degree of muscle strain and tear. The most important thing in functional recovery is not to force it. We should step up the practice step by step. Pain means overload and delayed recovery.

Functional recovery takes pain as an important indicator, and it is gradually performed in the order of flexibility, muscle strength, speed, coordination ability, and overall endurance, and functional recovery is achieved in the shortest time. Acupuncture, massage, and other treatments called physiotherapy must also be performed under the guidance of a doctor. The purpose of functional recovery is to restore the normal state before the injury. It can perform normal activities as before, with the previous strength and explosive power, restore the active area of the joints, and obtain the maximum muscle strength. If you return to the state before the injury, you can return to the court. The first step of the functional recovery plan is emergency treatment, the second step is to restore the range of motion of the joint, and the third step is to restore strength. The next step is to restore muscle strength. The most difficult part of functional recovery training is the recovery of muscle strength. The recovery of muscle strength is very important, especially for athletes who need muscle strength and explosiveness. Equipment is also essential in the training of muscle function recovery. When an athlete is injured, the countermeasures should be from the initial prevention to the subsequent treatment and rehabilitation. The general prevention method is daily physical exercise and storage, so as to improve their own quality. Before the training, we should also be able to reasonably restore our relaxed nature and work hard in medical work. When there is a treatment problem, it cannot be delayed from on-site first aid to late delivery. After receiving treatment, athletes should be able to maintain their confidence in recovery and recover in time. The excessive damage of the skeletal muscle system is mainly caused by the long-term fatigue effect that exceeds the capacity of the lower limbs to bear the structure. It is related to the overload and repetitive stress of the musculoskeletal system. Although in many structures of the skeletal muscle system, repeated stress may lead to overuse injury, this does not mean that in order to avoid injury, the stress of the skeletal muscle system should be reduced to a very small extent.

Positive adaptation occurs when the applied repeated stress is below the mechanical limit of the structure and there is sufficient time interval between the stresses. On the other hand, negative adaptation is that the applied stress exceeds the mechanical limit at a certain moment. As for the location of the injury, the results are different due to different athletics. Usually, when many athletes have a poor grasp of the landing angle when taking off, or have problems in technical movements, they will make the speed too fast and then make the body fall unreasonably. Normally, strains on large muscle groups are caused by excessive force during take-off. When you land and move the center of gravity downward, your legs are more prone to problems. All joints and ankles are prone to pain and swelling. In ankle joints, severe cases often have varus or valgus, blood stasis on the instep or ankle joint, local tenderness is obvious, and the tenderness is more serious when the ankle joint is active. In the throwing event, the most likely injury is muscle strain. Different sports levels or genders have different injuries due to different bodies. In this way, if the technical action is correct, the problem can be alleviated. In many cases, insufficient preparation and lack of specific strength and flexibility of the elbow joint will exacerbate the problem. Usually, when an athlete is just injured, the body will respond to stress, namely, pain and swelling. When these problems arise, emergency response is the most important.
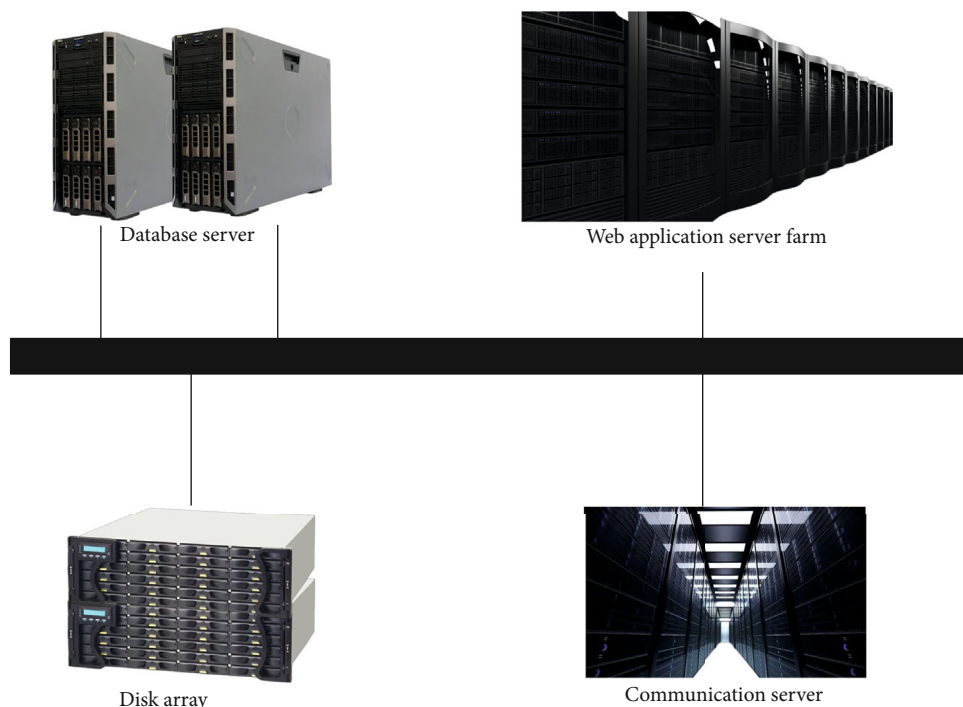
Figure 1: Data acquisition server deployment diagram.

Table 1: Athlete's sport type situation table.

	Walking race	Running	Thrown	Jumping class	Omnipotent
Male	5	7	8	3	7
Female	6	5	9	2	8

The usual first aid methods are braking, cold compress, compression, and supine. Braking means stopping motion. When the movement stops, swelling can be further controlled. When bleeding problems occur, they can also be minimized. In case of bleeding, if you cannot get ice in time, you can choose pressure bandaging. Pressure bandages allow blood to enter the tissue and absorb it well. There are many ways to bandage. In order to reduce inflammation, swelling, and pain after injury, the methods used are braking, cold compress, compression, elevation. and fixation. Then, surgery is performed. In order to promote blood circulation, warm treatment should be performed from the site with less pain and more damage, and it is also the beginning of the process of functional recovery.

2.4. IoT Smart Data. The Internet of Things technology is a comprehensive technology that connects objects to the Internet according to a certain communication protocol through communication equipment, sensors, data acquisition and processing systems, positioning systems, and other equipment. Through the Internet of Things, operations such as intelligent monitoring, positioning, and management of objects can be realized. In recent years, due to a large amount of investment in human and material resources, the application system based on the Internet of Things technology has also been continuously developed and improved. However, in the process of continuous improvement of information technology, some unstable factors have also appeared. A large amount of spam has caused great troubles to data collection. Based on this, the research on intelligent data collection systems based on the Internet of Things technology is also particularly important.

Data acquisition is one of the cores of data management system. Data acquisition is the process of using sensors and other measuring devices to collect and input information from outside the system to the inside of the system. Generally, the collected information is converted into electrical signals and transmitted to the system for identification. In the rehabilitation training and prevention of track and field athletes' hindfemoral muscle injury, the role of IoT intelligent data is more prominent. Intelligent data collection based on the Internet of Things technology can accurately record the rehabilitation training performed by track and field athletes after muscle injury in the past, can be stored for a long time, and can be accessed at any time. At the same time, the intelligent technology of the Internet of Things can identify and record some sports actions that may cause muscle damage in track and field sports, which greatly reduces the risk of athletes causing muscle damage in track and field sports. Figure 1 is a deployment diagram of an intelligent data collection server based on the Internet of Things technology.

3. Research Objects and Methods

3.1. Experimental Subjects. In this paper, 60 athletes in Hebei Province were selected randomly, including 30 men and 30 women. Then, a series of training and recovery were carried out. The 60 athletes were observed, and the status quo of the
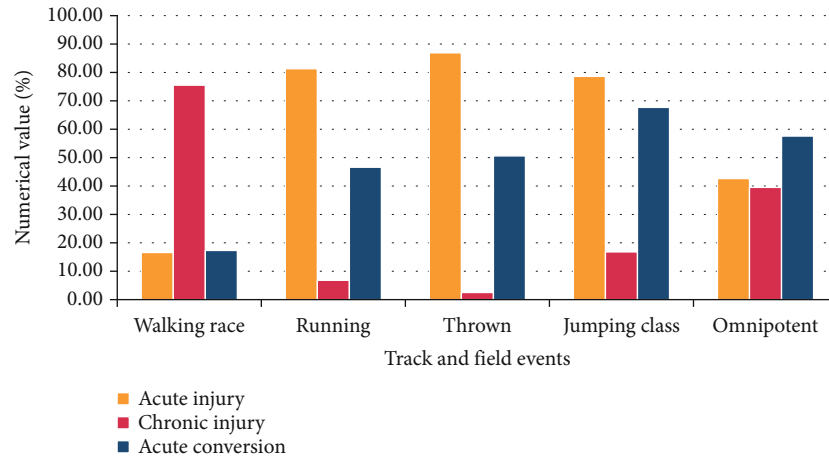
FIGURE 2: Analysis of the nature of sports injury.

TABLE 2: Analysis of the nature of sports injury.

Track and field events	Acute injury	Chronic injury	Acute conversion
Walking race	16.60%	75.50%	17.30%
Running	81.30%	6.80%	46.60%
Thrown	86.90%	2.50%	50.60%
Jumping class	78.60%	16.80%	67.70%
Omnipotent	42.60%	39.50%	57.60%

injury of the posterior thigh muscle group and its prevention and recovery were analyzed. Table 1 is a table of the sports types of 60 athletes.

3.2. Experimental Method

(1) Flexibility training: before the formal training, the subjects complete 5-10 minutes of warm-up by jogging and then complete a series of training after that. The subjects lie on a horizontal pad. The trainer uses one hand to raise the lower limbs of the subjects, while the other hand is placed on the anterior superior iliac spine of the opposite side to prevent pelvis rotation. The trainer shall ensure that the knee joint of the subject is in the straight position during the whole process. When the trainer feels that there is a great resistance or finds that the pelvis of the subject begins to tilt, he shall stop raising the measured leg. At this time, the hip joint bending angle is the maximum hip joint bending angle for flexibility training. Flexibility training intervention to further verify whether the flexibility of the posterior femoral muscle group will affect the risk of strain. As for the 16 week flexibility intervention training of runners, the flexibility training did not significantly reduce the strain rate of the posterior femoral muscle group

(2) Sprint training: the subjects wore tight clothes and trousers, pasted reflective markers on their bodies, and determined the placement of electrodes for biceps femoris, semitendinosus and semimembranosus muscles on both sides according to the anatomical markers on the body surface and the freehand examination. Shave the hair on the skin surface of the preset electrode and wipe it with 75% alcohol. Two recording electrodes were attached to the highest part of the muscle ventral eminence during each muscle contraction to be measured, which was consistent with the direction of the muscle fiber. The distance between the centers of the two electrodes was 2 cm, and a reference electrode, a signal transmitter, was placed close to the recording electrode. The running distance is about 35 meters. The subjects stand at a straight distance of about 20 meters from the force measuring platform to prepare for the starting position. After hearing the command, they run through the training area as fast as possible. It is considered as an effective training for the subjects with normal gait, no step adjustment and training foot on the force measuring platform. The subjects completed three effective exercises on each side of the leg and rested for 60 seconds between each exercise. The three-dimensional coordinates, surface electromyography, and ground reaction force signals of the subject's body surface were collected during each training

(3) Isokinetic strength training: after the sprint training, the subjects keep the original body surface marker points unchanged, first complete the static standing calibration to collect the three-dimensional coordinates of all marker points, because the seat will block the waist points during isokinetic strength training, so remove the waist points after the calibration. The subjects sit on the isokinetic training instrument and keep the hip flexion about 90°. The thigh and calf of the training leg are fixed on the seat and the mechanical arm, respectively, to prevent compensatory action so as to ensure that only the flexion and extension of the knee can be completed. The flexion and extension axis of the knee is aligned with the
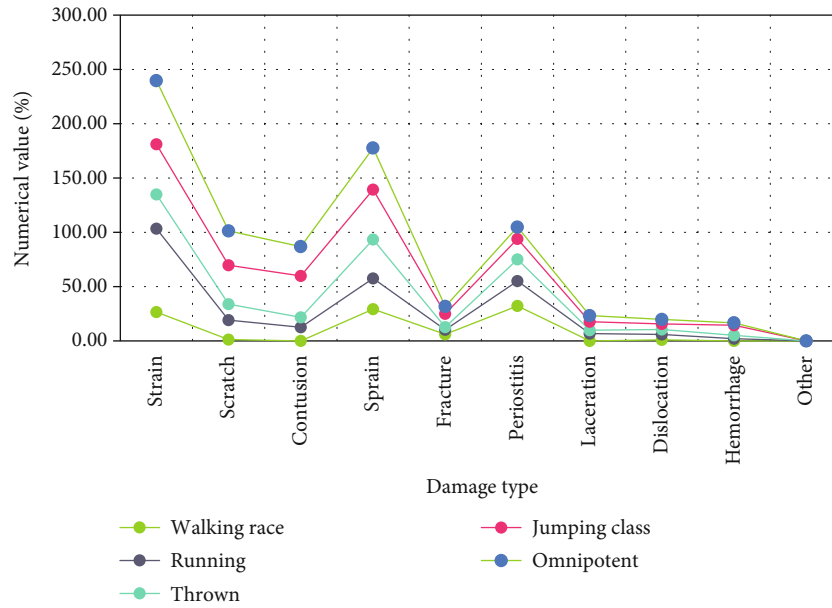
FIGURE 3: Analysis of sports injury types.

TABLE 3: Analysis of sports injury types.

Damage type	Walking race	Running	Thrown	Jumping class	Omnipotent
Strain	26.60%	76.80%	31.50%	46.20%	58.60%
Scratch	1.30%	17.90%	14.60%	35.90%	31.60%
Contusion	0	12.50%	9.20%	38.20%	26.90%
Sprain	29.20%	28.30%	35.90%	45.90%	38.30%
Fracture	6.10%	4.20%	2.40%	12.20%	6.80%
Periostitis	32.20%	22.90%	19.90%	18.90%	10.90%
Laceration	0	6.70%	3.10%	7.90%	5.60%
Dislocation	1%	4.90%	4.60%	5.10%	4.20%
Hemorrhage	0	2.10%	3.10%	9.20%	2.20%
Other	0	0	0	0	0

rotation axis of the mechanical arm. The range of motion of the arm is 110° and the position of the arm is 0° when the knee is fully extended. The subjects did their best to complete three equal speed knee bending movements with an angular velocity of 10/s for 90 seconds between each time. The three-dimensional coordinates and isokinetic moment data of the body surface mark points were collected during each training

(4) Strength training: during the formal training, the athletes stand on the pedal with their feet fully in contact with the pedal. The knees should not be bent as much as possible. They should stand up straight and back and hold the handrail with both hands, and the legs should be retracted horizontally or vertically. Stretch until the athlete feels the back of the thigh muscles are sore and can retract by himself. According to the focus of strength training, that is, maximum strength, relative strength, strength

endurance, and speed strength, different load intensity is used for training

Literature analysis method: through consulting related books, such as sports therapeutics, sports psychology, sports injury, track and field kinematics, sports science, and sports statistics, to provide a preliminary basis for this study, and then collect relevant literature at home and abroad from CNKI, and analyze the relevant literature. Mathematical analysis: SPSS22.0 statistical software was used to process the relevant data of long jumpers, the results were expressed as mean and variance (M ± SD), two-sided t-test was used, and the P value less than 0.05 indicated statistical significance, providing data support and authoritative basis for the analysis of training methods for sports injury prevention. Logic analysis method: by using the method of judgment and reasoning, this paper analyzes the injury of the posterior femoral muscle group of track and field athletes, explains its causes, provides the corresponding scientific basis for training and competition, summarizes, sorts out, analyzes all the
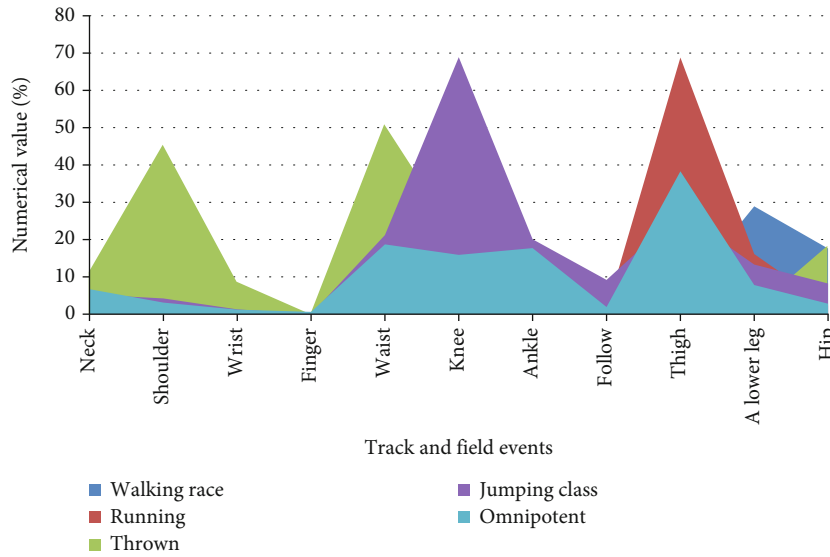
FIGURE 4: Analysis of damaged parts.

TABLE 4: Analysis of damaged parts.

Track and field events	Walking race	Running	Thrown	Jumping class	Omnipotent
Neck	0%	1.30%	11.30%	5.30%	6.70%
Shoulder	0%	1.80%	45.40%	4.20%	3.10%
Wrist	0%	3.10%	8.70%	1.30%	1.20%
Finger	0%	0%	0%	0%	0.60%
Waist	26.30%	18.80%	50.90%	21.20%	18.70%
Knee	34.50%	38.70%	20.30%	68.90%	15.90%
Ankle	6.90%	17.90%	6.20%	20.10%	17.70%
Follow	3.10%	1.10%	0.20%	9.20%	1.90%
Thigh	4.60%	68.80%	16.20%	27.20%	38.30%
A lower leg	28.90%	16.10%	1.30%	13.30%	7.80%
Hip	17.60%	2.30%	18.30%	8.20%	2.80%

TABLE 5: Prevention and attention in various aspects.

	Special training	Adjustment recovery	Physical training	Mental training	Skill training	Nutrition
Walking race	9	8	8	5	6	4
Running	8	7	6	5	6	2
Thrown	7	8	9	6	5	7
Jumping class	8	6	7	6	7	4
Omnipotent	9	8	8	6	5	7

documents, sorts out and processes all the data, synthesizes the results of logical analysis, and draws relevant conclusions. Field investigation method: This article uses the opportunity of internship in the training team of the academy to observe the process of physical function training of athletes and observes and records the training methods used by athletes to prevent sports injury and the arrangement of training load, which provides a solid foundation for the writing of this article practical basis.

Strength is the power source of human sports, strength training is the key factor to improve the performance of competitive sports, and it is the most concerned problem of modern competitive sports training. A comprehensive and systematic understanding of the theory and methods of sprint strength training, the advantages and disadvantages of various strength training methods, as well as the diagnosis and evaluation methods of strength training effect are the basis of competitive sports training, the guarantee of effectiveness and pertinence of strength training, and the premise of sports training innovation and breakthrough. In the training, the strength of the mobilized posterior thigh muscles is different. In the strength training, the effect of the flexible
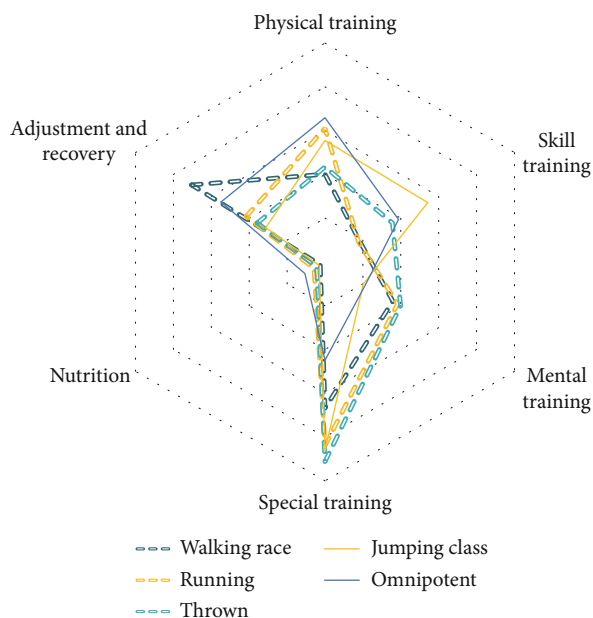
FIGURE 5: Preventive analysis.

TABLE 6: Muscle injury data sheet.

	Walking race	Running	Thrown	Jumping class	Omnipotent
Strain	8.2%	5.8%	9.5%	6.5%	8.1%
Sprain	6.8%	8.2%	6.3%	8.9%	9.2%
Periostitis	2.5%	9.2%	5.1%	3.8%	4.6%
Scratch	3.1%	5.0%	2.1%	3.2%	2.9%
Fracture	2.0%	5.4%	3.6%	4.0%	2.9%

strength training device on the posterior thigh muscles is better than the traditional method. The training effect of the comprehensive training device of flexibility and strength on the longitudinal flexibility is more obvious than that of the traditional method. The flexibility training of the posterior thigh muscle group needs persistence, and long-term persistence can get better results. Flexible strength training device has a positive effect on the strength and flexibility of the posterior thigh muscles. It can effectively prevent the injury of the posterior femoral muscle group of athletes in special sports.

4. Discussion and Analysis of Experimental Results

4.1. Analysis of Track and Field Injuries

4.1.1. Analysis of the Nature of Sports Injury. According to statistical analysis of data, as shown in Figure 2 and Table 2, the nature of sports injuries includes acute injuries, chronic injuries, and acute to chronic injuries. Acute injury is caused by one-time violence; chronic injury is caused by long-term local overload, which exceeds the capacity of the tissue. Chronic to acute injury is caused by early acute injury without timely and reasonable treatment. In track and field

sports, walking injury is the main form of injury, accounting for 75.5% of the total injury. The main nature of sports injuries in running events is acute injuries and chronic injuries, accounting for 81.3% and 46.6%, respectively. The sports injuries of throwing events are mainly acute injuries and chronic injuries, accounting for 86.9% and 50.6%, respectively. Long jump sports injuries are mainly acute injuries and chronic injuries, accounting for 78.6% and 67.7%, respectively. Acute, chronic and acute to chronic events accounted for 42.6%, 39.5%, and 57.6%, respectively.

4.1.2. Analysis of Sports Injury Types. According to the statistical analysis of data, as shown in Figure 3 and Table 3, due to the different characteristics, movements, speed, strength, and other performance of different items, the types of sports injuries are also different. Sprains and periostitis were the main sports injuries, accounting for 26.6%, 29.2%, and 32.2% of the total injuries, respectively. Muscle strain is the main injury in running events, accounting for 76.8% of the total. Sprains, periostitis, and abrasions accounted for 28.3%, 22.9%, and 17.9%, respectively. The main sports injuries in throwing events were 31.5% of strain injuries, 35.9% of sprain injuries, and 19.9% of periosteal inflammation injuries. The types of sports injuries in long jump are sprains, contusions, sprains, abrasions, and periostitis, accounting for 46.2%, 38.2%, 45.9%, and 35.9%, respectively.

4.2. Track and Field Prevention Analysis

4.2.1. Analysis of Damaged Parts. According to the statistical analysis of the data, as shown in Figure 4 and Table 4, different sports show obvious characteristics at the location of sports injuries. The main injuries are the waist, knees, calves, and buttocks. The main parts of running injuries are waist, knee, ankle, and thigh. The main parts of sports injuries are waist, knee, and hip, which account for the largest proportion. As there are more all-around sports, there are also more injured parts, especially the waist, ankles, and thighs. Due to the characteristics of different sports forms, speed, duration, and muscle names, the occurrence of sports injuries also has its own characteristics. In the training, the coach should fully consider the muscle strength and weight-bearing parts of different items and arrange the general quality training and special training, training and recovery, and the intersection of different training parts and content. During the training, the coaches of different projects should pay attention to the uncomfortable reactions in the first half of the different projects and actively communicate with the athletes. If there is fatigue, discomfort, and minor injury, it should be adjusted and handled in time to prevent serious sports injuries.

4.2.2. Prevention Analysis. Table 5 shows the athletes' attention to prevention in various aspects to prevent muscle damage during exercise (1-10 points, the higher the score, the higher the attention).

According to the statistical analysis of data, as shown in Figure 5, the first three key points of running sports injury prevention are special training, adjustment recovery, and physical fitness training; the first three points of throwing
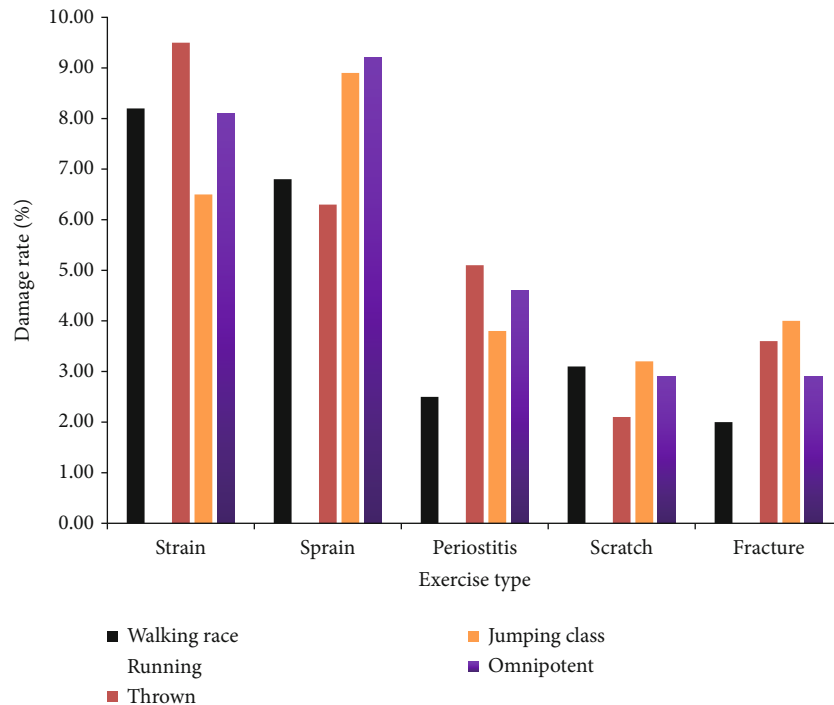
FIGURE 6: Diagram of the prevention of muscle injury based on the intelligent data of the Internet of Things.

sports injury prevention are special training, physical training, and psychological training. The first three points of the long jump are special training, physical training, and technical training; the top three all-rounders are physical training, adjustment and recovery, and special training. On the whole, sports training is increasingly valued by coaches. In addition, most track and field coaches attach great importance to recovery after training. To some extent, rehabilitation is the continuation of training. If the recovery work is not done well, it will affect the next training. It is worth noting that modern sports training pays more and more attention to psychological factors and nutritional supplements. In particular, nutritional supplements have special significance for the prevention of sports injuries and should attract the attention of coaches.

4.3. Prevention Analysis of Muscle Injury in Track and Field Sports Based on Intelligent Data of the Internet of Things. In this experiment, an experiment was conducted on the prevention of athletes' muscle injury based on the intelligent data of the Internet of Things, and the athlete's muscle injury was recorded in the experiment. Table 6 is a table of experimental results of preventing muscle damage based on the intelligent data of the Internet of Things.

According to Table 6, a diagram of the prevention of muscle damage based on the intelligent data of the Internet of Things can be drawn, as shown in Figure 6.

According to Figure 6, it can be seen that the program of preventing sports muscle injury based on the intelligent data of the Internet of Things has achieved great results, greatly reducing the probability of athletes causing muscle injury in sports. In this experiment, the highest rate of muscle dam-

age was only 9.2%, which was 18.6% higher than the effective rate of the traditional prevention program. Through the comparison of peak muscle torque on the subject's knee flexor muscle strength and knee extensor muscle strength, it is found that the subject's flexor and extensor muscle strength match is ideal, and the flexion of the left and right knee joints is ideal. The extensor muscle strength is more balanced. However, there is a significant difference in the explosive force level of the knee flexor muscle group compared with the knee extensor muscle group during high-speed exercise through the explosive force parameters (using the rapid strength index and the force rate), which may be one of the factors that affect sports performance and lead to the injury of the posterior femoral muscle group potential factors.

5. Conclusions

(1) In the stance phase, the main torques that control the movement of the lower limbs are the muscle torque and the external torque generated by the ground reaction force; the main torques that control the movement of the lower limbs in the swing phase are the muscle torque and the inertial moment generated by the link movement. The moment of inertia has a significant effect on the motion at the end of support and swing

(2) At the initial stage of support and the end of swing, the stress state of the hamstrings is similar, that is, the external torque pulls the hamstrings in the opposite direction at the same time, making it under huge

stress and strain, so both the initial stage of support and the end of swing are similar high-risk period for hamstring injury

(3) The main parts of running sports injuries are waist, knee, ankle, and thigh. Injury sites also showed diversity, with waist, ankle, and thigh injuries being the most obvious. The main measures to eliminate sports fatigue are jogging and relaxing, sleeping, and massage

(4) Most track and field athletes have experienced torture of posterior femoral muscle damage during training, and the degree of injury is higher. The degree of injury is mostly mild to moderate, but it still seriously affects the training and life of athletes

(5) The degree of occurrence of sports injuries of track and field athletes is as follows: does not affect training, suspends training, and treats sports injuries. The main parts of the walking project are the waist, knees, calves, and hips

(6) The muscle injury prevention program based on the intelligent data of the Internet of Things can greatly reduce the probability of athletes causing muscle injury during exercise, and its effective rate is increased by 18%

It is suggested that the prevention of physical function injury should be promoted and integrated into the daily training of the long jump training team and other training teams, so as to achieve the effect of injury prevention and treatment on the basis of improving the athletes' special performance ability. The concept and method of physical function training has not been introduced for a long time, and its theoretical and practical experience is relatively immature. Therefore, it is necessary to fully study and understand its theoretical knowledge and connotation when applying it and to constantly explore and summarize in specific practice.

Data Availability

The data that support the findings of this study are available from the corresponding author upon reasonable request.

Conflicts of Interest

The author declared no potential conflicts of interest with respect to the research, author-ship, and/or publication of this article.

Acknowledgments

References

[1] A. Saxena and C. Eakin, "Articular talar Injuries in Athletes," *American Journal of Sports Medicine*, vol. 35, no. 10, pp. 1680–1687, 2007.

[2] B. Hainline, J. A. Drezner, A. Baggish, K. G. Harmon, and P. D. Thompson, "Interassociation consensus statement on cardiovascular care of college student-athletes," *Journal of the American College of Cardiology*, vol. 67, no. 25, pp. 2981–2995, 2016.

[3] G. Korobeynikov, L. Korobeynikova, S. Iermakov, and M. Nosko, "Original article reaction of heart rate regulation to extreme sport activity in elite athletes," *Journal of Physical Education and Sport*, vol. 16, no. 154, pp. 976–981, 2016.

[4] D. J. MacDonald, J. Côté, M. A. Eys, and J. Deakin, "The role of enjoyment and motivational climate in relation to the personal development of team sport athletes," *Sport Psychologist*, vol. 25, no. 1, pp. 32–46, 2016.

[5] M. R. Abdullah, A. B. H. M. Maliki, R. M. Musa, N. A. Kosni, and M. Haque, "Multi-hierarchical pattern recognition of athlete's relative performance as a criterion for predicting potential athletes," *Journal of Young Pharmacists*, vol. 8, no. 4, pp. 463–470, 2016.

[6] C. Mockdeceneves, J. F. Filgueirasmeireles, P. H. B. Decarvalho, S. Sousaalmeida, and M. E. Caputoferreira, "Body dissatisfaction among artistic gymnastics adolescent athletes and non-athletes," *Revista Brasilra de Cineantropometria e Desempenho Humano*, vol. 18, no. 1, pp. 82–92, 2016.

[7] S. Nepocatych, G. Balilionis, and E. K. O'Neal, "Analysis of dietary intake and body composition of female athletes over a competitive season," *Montenegrin Journal of Sports Science & Medicine*, vol. 6, no. 2, pp. 57–65, 2017.

[8] A. Ströhle, "Sports psychiatry: mental health and mental disorders in athletes and exercise treatment of mental disorders," *European Archives of Psychiatry & Clinical Neuroscience*, vol. 269, no. 2, pp. 1–14, 2018.

[9] S. P. Cumming, R. S. Lloyd, J. L. Oliver, J. C. Eisenmann, and R. M. Malina, "Bio-banding in sport: applications to competition, talent identification, and strength and conditioning of youth athletes," *Strength & Conditioning Journal*, vol. 39, no. 2, pp. 34–47, 2017.

[10] H. Zhu, H. Wei, B. Li, X. Yuan, and N. Kehtarnavaz, "Real-time moving object detection in high-resolution video sensing," *Sensors*, vol. 20, no. 12, article 3591, 2020.

[11] W. J. Morgan and L. S. Slowman, "Acute hand and wrist injuries in athletes: evaluation and management," *Journal of the American Academy of Orthopaedic Surgeons*, vol. 9, no. 6, p. 389, 2016.

[12] M. Fanqi, W. Cheng, and J. Wang, "Semi-supervised software defect prediction model based on tri-training," *KSII Transactions on Internet and Information Systems*, vol. 15, no. 11, pp. 4028–4042, 2021.

[13] A. A. Flatt and M. R. Esco, "Heart rate variability stabilization in athletes: towards more convenient data acquisition," *Clinical Physiology and Functional Imaging*, vol. 36, no. 5, pp. 331–336, 2016.

[14] E. Joy, A. Kussman, and A. Nattiv, "2016 update on eating disorders in athletes: a comprehensive narrative review with a focus on clinical assessment and management," *British Journal of Sports Medicine*, vol. 50, no. 3, pp. 154–162, 2016.

[15] T. Clifford, D. M. Allerton, M. A. Brown et al., "Minimal muscle damage after a marathon and no influence of beetroot juice on inflammation and recovery," *Applied Physiology Nutrition & Metabolism*, vol. 42, no. 3, pp. 263–270, 2017.

Hindawi

Research Article

Application of Carbon Nanocomposite Sensing and Functional Magnetic Nanomaterial in the Sports Industry and Its Biosecurity Research

Zhenpeng Li,[1] Zhigan Li,[2] and Zecheng Zhang [ID][3]

[1]*Sports Group, Zhongshan Yangxianyi Middle School, Zhongshan, 528403 Guangdong, China*
[2]*Department of Sports Medicine, Guangzhou Sport University, Guangzhou, 510075 Guangdong, China*
[3]*Sports College, Hainan University, Haikou, 570228 Hainan, China*

Correspondence should be addressed to Zecheng Zhang; 991913@hainanu.edu.cn

Nanomaterial science is a particularly important research field in modern science and technology, which has attracted wide attention and research from all walks of life since its inception and has formed a relatively perfect category of science and technology. The purpose of this paper is to explore the application of carbon nanocomposite sensing and functional magnetic nanomaterial in the sports industry and their biosecurity research. This paper first discusses the research progress of nanocomposite in biosecurity and concludes that chemical modification can reduce the negative biological effects of nanomaterial, then puts forward the research methods on nanocomposite in the sports industry, and then selects nanosilver composites to explore and study the effects of different particle sizes and concentrations on the antibacterial properties of Aspergillus and test and characterize the properties of nanocomposite. The stability of nanocomposite modification electrodes is also explored. The results show that nanosilver has excellent bactericidal effects on both AF293 and Gra04. In particular, 8.08×10^{-5} mol/L and 4.03×10^{-5} mol/L nanosilver has a bacteriological rate of 100%, indicating that the growth of all fungal spores can be completely inhibited, and when the content of 10 wt% is found, the thermal conductivity of PHBE-MWNT pressure-sensitive composite materials is achieved 0.6975 W/(m-K), 1.8 times the MWNT pressure-sensitive glue, higher than the pure pressure-sensitive glue about 255%.

1. Introduction

Microorganisms are beneficial and harmful to human survival. The secondary metabolites of many bacterial species are antibiotics that are very useful for human diseases, and because of the short growth cycle and rapid reproduction of microorganisms, they are used in genetic breeding, which is of great significance. At the same time, microorganisms can also lead to the prevalence of infectious diseases, and 50% of human diseases are caused by viruses. Some microorganisms are spoilage, that is, cause undesirable changes in food odor and tissue structure. The evolutionary history of human society is the history of giving full play to the advan-

tages of favorable bacteria to improve one's own life and to improve the quality of life by solving harmful bacteria. When the size of the material is reduced to a nanoscale, there will be some unique and interesting phenomena that cannot be observed in macromaterials, but these phenomena have not been found in the macrorange. Material scientists have discovered many materials with this phenomenon, such as quantum stimulation limits (quantum dots) for inorganic semiconductor nanomaterial, ultra-submagnetic (SPIONS) for iron oxide nanoparticles and localized surface plasma resonance (LSPR), for precious metal nanoparticles. It is an exciting task to solve practical problems by using the special properties of nanomaterial. The characteristics

of nanomaterials mainly include surface and interface effects, small size effects, quantum size effects, and macroscopic quantum tunneling effects.

To explore all aspects of nanocomposites, because of their smallness, they are not conducive to experimental exploration, but also because of their smallness, so nanocomposites are explored, so that it can provide reliable help not only in microbial research but also for clinical medicine and disease early warning of biomolecule detection methods which provide an important reference.

According to the research progress at home and abroad, different scholars have also made corresponding investigations in the research of carbon nanocomposite material sensing and functionalized magnetic nanomaterial: Zhao et al. conducted laboratory research on the performance of nanocarbon/copolymer SBS/rubber powder composite modified asphalt and chose nanocarbon particles modified by titanate coupling agent as the modifier. The morphology, microstructure, and surface properties of the prepared nanocomposite adsorbent were measured and analyzed by FESEM, TGA, XRD, FT-IR, and zeta potential. Batch experiments on the adsorption of Cr (VI) were carried out to determine the adsorption performance of the composites [1]. Wang et al.'s chemically synthesized conductive nanocomposites consisting of poly (PPy) are compared to components such as Cdots or PPy. It shows higher conductivity. The conductive film of this composite material is used for high sensitivity and selective detection of bitter acids in water and soil. This is the first report on conductivity-based sensing applications for Cdot nanocomposite, as opposed to traditional fluorescence-based sensing methods [2]. Pal et al. studied the composite modified asphalt prepared by Cdots and the high-speed shearing method for nanocarbon/copolymer SBS/rubber powder, used in extended tests, softening point tests, permeability tests, dynamic shear rheometer (DSR) tests, and curved beam rheometer (BBR) tests to evaluate physical performance [3]. Jiang et al. have produced a diamond-like carbon (G/a-C:H) nanocomposite film mixed with graphene by liquid phase electrochemical method. The growth mechanism of the nanocomposite membrane is proposed and discussed. The deposited coating material was measured using scanning electron microscopy (SEM), Raman spectroscopy, spread electron microscopy (TEM), and Fourier transform infrared (FTIR) spectra. The results show that graphene sheets are evenly dispersed in the hydrogenated amorphous carbon (a-C:H) matrix [4]. Xu and Zhang have developed an easy preparation method for nanocomposite consisting of graphene oxide and manganese dioxide nanowires (GO/MnO2NWs). The basic form, structure, and composition of the resulting substance are characterized by a transmission electron microscope, X-ray diffraction, and N2 adsorption and desorption [5]. Hien et al. have successfully developed an effective electrochemical method for the production of poly phenylamine/multiwall carbon nanotube nanocomposite on the fork-finger platinum microelectrics to improve biosensor performance. The shape and properties of nanocomposite were studied through field emission scanning electron microscopes and ultraviolet visible spectra

[6]. Amir et al.'s study discusses the effects of effective functionalization on signal sensitivity observed on 6-TG electrooxidation on CA-Fe3O4 NPs, with the use of bare and niacin (NA) functional Fe3O4 NP modified glass carbon electrode compared. The experimental results provide sufficient evidence to support the importance of favorable functions for achieving higher signal sensitivity of 6-TG electrooxidation [7]. Cao et al. studied the prepared ZnONR sensors, MWCNT sensors, and ZnONR/MWCNT ethanol gas sensitivity of nanocomposite gas sensors. ZnONR/MWCNT nanocomposite sensors exhibit higher response, faster response recovery, and better ethanol selectivity than ZnONR and MWCNT sensors [8]. However, these studies have not combined the application of sports industry and its biological safety to make some progress.

The innovative focus of this paper is mainly reflected in the following: (1) the paper introduces the research on biosecurity of nanocomposite and concludes that chemical modification can reduce the negative biological effects of nanomaterials and puts forward research methods based on nanocomposite in the sports industry. (2) The performance of nanocomposite is analyzed from a biological point of view, and the properties of nanocomposite are tested and characterized, and the stability of nanocomposite modified electrodes is explored.

2. Methods in Biosecurity and Sports for Nanocomposite

2.1. Biosecurity in Nanocomposite. Due to the industrialization of nanotechnology, people's daily life and occupation with nanomaterial contact are increasingly frequent, so the use of nanomaterial on the body and the environment may also cause more attention. Some of the nanoparticles newly created by engineering science may be cancer-causing. Researchers found that fish developed brain cancer after ingesting small amounts of carbon nanomaterials. Laboratory mice developed symptoms of lung disease after inhaling carbon nanotubes, as if they had inhaled asbestos particles. So far, the study of the biological effects of nanomaterial is still in its infancy, and scientists have only made preliminary studies on the biological effects of carbon-based nanomaterial and metals and their oxide nanomaterial [9]. When a biological material exceeds the nanosize (1-100 nm), it has a very good surface area due to its size close to the biological atomic scale, allowing it to interact directly with individual biological atoms [10]. Nanomaterials show the good electronic, optical, magnetic, mechanical, and other properties inherent in nanoscale, making it more sensitive to the surrounding environment and the target molecules in the sample, which is conducive to detection. Nanoelectrochemical sensors made from these nanomaterials have achieved some results in simplifying the detection process, improving sensitivity, reducing detection limits, and reducing costs, as shown in Figure 1.

The biological effects of nanomaterial are closely related to their physical and chemical properties, biological cells are at micron scale, and nanomaterials extremely easily enter into biological cells and interact with them, thus affecting
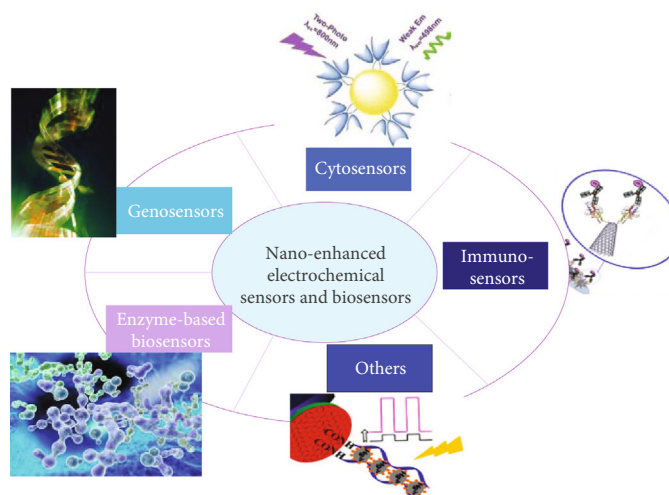
Figure 1: Schematic diagram of electrochemical sensors and biosensors based on nanomaterial and nanostructures.
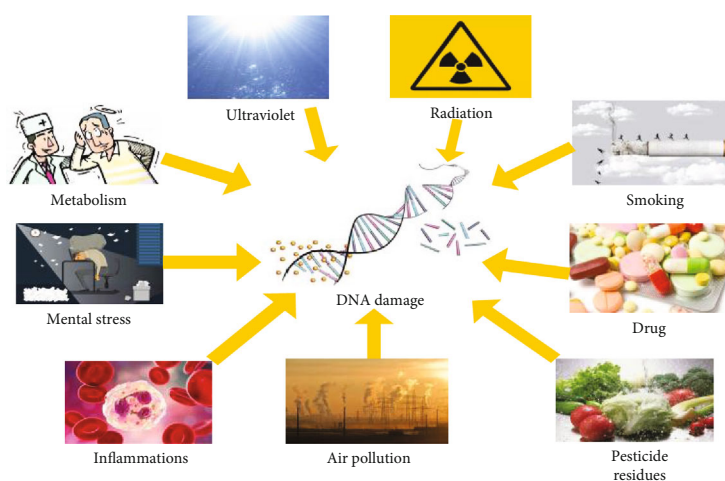
Figure 2: Factors affecting biological damage.

biological functions [11]. Figure 2 represents the factors that affect biological damage. Because of their small size, these tiny factors are difficult to detect, and they are quietly hidden around us, which will slowly erode our bodies. Scientific studies have confirmed that some micron-scale compounds that appear in the form of stable clusters are nontoxic, but when they are heated into smaller-scale nano- or ultra-microlevel particles, they can also show some toxicity, such as having rats contain 20 nm of PFC (PTEF). Nanoparticles breathe 15 min in the air, and most rats die within the next 4 hours, instead containing 130 nm PTEF. Rats breathing in the air did not see discomfort [12].

The biological effects of nanomaterial are not only influenced by particle size but are also closely related to their structure. With the quantitative change of particle size, the qualitative change of particle properties will be caused under certain conditions. The change in macroscopic physical properties due to particle size reduction is called the small size effect. For ultrafine particles, the size becomes smaller and the specific surface area increases significantly, resulting in a series of novel properties as follows. The study found

that tubular structure carbon nanomaterials (MWCNTs) and onion-like carbon nanomaterial (MWCNO) in the same dose and in the same size range showed different toxic effects and mechanisms on human fibroblasts. MWCNTs cause a strong immune and inflammatory response from fibroblasts in the human skin, while MWCNO is a genetically induced response of fibroblasts to external stimuli [13]. The cytotoxicity of single-walled carbon nanotubes (SWNTS), multiwall carbon nanotubes (MWNT10), and fullerene (C60) to alveolar macrophages was then compared; its cytotoxicity from strong to weak isSWNTS > MWNT10 > C60; for SWNTS concentration of $11.30 \, \mu g/cm^2$ at a concentration of $22.6 \, \mu g/cm^2$, there was significant cytotoxicity, while for C at a concentration of $226 \, \mu g/cm^2$, there is still no significant cytotoxicity [14]. It has also been reported that surface-derived treatment of C60 reduces nanotoxicity to human epidermal cells (HDFs) by 100,000 times, showing that chemical modification can reduce the negative biological effects of nanomaterial.

At present, there is no unified international evaluation criterion on the biological stability of nanomaterial [15].

Nanomaterial can interfere with endogenous metabolism or signal transduction pathways in a very weak way, thus disrupting the biochemical function of cells, and the results are difficult to show in short-term toxicity analysis. Therefore, when evaluating the biological efficacy of nanomaterial using short-term or subchronic experiments, a representative in vivo or in vitro environment should be used, a negative and positive control group should be set up, and the entire experimental process should be calibrated [16].

2.2. Methods on Nanocomposite Materials in the Sports Industry

(1) Factor analysis and spatial effects

Factor analysis is an analytical method that uses the idea of "low dimension" to extract a few representative factors from many original variables [17]. The KMO test statistic is an indicator used to compare simple and partial correlation coefficients between variables. It is mainly used in factor analysis of multivariate statistics, which can also be used to study the similarity between variables in multifactor analysis. The mathematical concept of KMO test statistics is as follows:

$$\text{KMO} = \frac{\sum\sum_{m \neq n} t_{mn}^2}{\sum\sum_{m \neq n} t_{mn}^2 + \sum\sum_{m \neq n} u_{mn}^2}, \quad (1)$$

where t_{mn} is a simple correlation coefficient between a variable a_m and a_n other variables, u_{mn}, and a partial correlation coefficient between a variable and a variable that a_m controls the a_n remaining variables. As can be seen from the formula (1), KMO statistics range from 0 to 1. The closer the KMO value is to 1, the stronger the correlation between the variables, and the more suitable the original variable is for factor analysis [18]. The closer the KMO value is to 0, the weaker the correlation between the original variables, and the less suitable the original variable is for factor analysis [19].

Once the KMO test has passed, factor analysis is possible. The mathematical model of factor analysis is as follows.

With the original g variables, $L_1, L_2, L_3, \cdots, L_g$, and all of which have been standardized, each variable can be $i(i < g)$ represented by a linear combination of $D_1, D_2, D_3, \cdots, D_i$ factors, as follows:

$$\begin{cases} L_1 = k_{11}D_1 + k_{12}D_2 + \cdots + k_{1i}D_i + \omega_1, \\ L_2 = k_{21}D_1 + k_{22}D_2 + \cdots + k_{2i}D_i + \omega_2, \\ \cdots \\ L_g = k_{g1}D_1 + k_{g2}D_2 + \cdots + k_{gi}D_i + \omega_g. \end{cases} \quad (2)$$

Formula (2) can also be expressed as a matrix, $L = KD + \omega$, where D is a common factor; K is a load matrix of factors and is a factor load, $k_{mn}(m = 1, 2, \cdots, g; n = 1, 2, \cdots, i$ representing the first m load of the original variable on the nth common factor; ω is a special factor, which is the part of the

original variable that cannot be interpreted by the public factor, with an average value of 0.

Then, construct the weight function, mainly by using the variance contribution rate of each common, and then, get the comprehensive evaluation function; the formula is as follows:

$$D = \sum_{m=1}^{e} \sigma_m D_m, \quad (3)$$

where $\sigma_m = \varphi_m / \sum_{m=1}^{e} \varphi_s$ indicates the weight of the ith measurement factor.

Spatial relevance is when a region's behavior or phenomenon affects an adjacent region; i.e., features with similar behavior or phenomena are spatially brought together [20]. Therefore, there is a functional relationship d between the observation variable of the ith w_{tm} space observation unit and the observation variable of its adjacent region. Its general expression is

$$w_m = d(w_1, \cdots, w_{m-1}, w_{m+1}, \cdots, w_t) + \omega_m, \quad m = 1, \cdots, t, \quad (4)$$

in the formula, representing ω_m random interference items.

Spatial structure heterogeneity, also known as spatial structure inconsistency and spatial structure differences, is determined by the spatial structure measurement mode of the second main source of spatial structure efficiency [21]. Spatial heterogeneity shows the characteristics of events or phenomena in different regions of the space environment [22]. Spatial heterogeneity can be expressed as

$$q_a = g_a(p_a, \varphi_a, \sigma_a). \quad (5)$$

a represents the space observation unit, $a = 1, \cdots, i$. g_a is the function relationship between q_a-dependent variables and p_a arguments, parameter variables, φ_a and random interference items σ_a.

Typically, a linear relationship is described as follows:

$$q_a = P_a \varphi_a + \sigma_a \quad (6)$$

in formula represents the P_a vector used to interpret the variable, represents the parameter vector that the φ_a explanatory variable has an effect q_a, is the q_a explanatory variable that represents the observation of a region, and is a random σ_a interference term.

Global spatial self-correlation can measure the self-correlation between regions in the overall research space. Common domain-wide spatial self-correlation metrics are Global Moran's I statistics, assuming a vector, described as follows:

$$I = \frac{\sum_{a=1}^{m}\sum_{b=1}^{m} u_{ab}(t_a - \bar{t})(t_b - \bar{t})}{\sum_{a=1}^{m}\sum_{b=1}^{m} u_{ab}\sum_{a=1}^{m}(t_a - \bar{t})^2} = \frac{\sum_{a=1}^{m}\sum_{b=1}^{m} u_{ab}(t_a - \bar{t})(t_b - \bar{t})}{D^2\sum_{a=1}^{m}\sum_{b=1}^{m} u_{ab}}. \quad (7)$$

m is the total number of regions in the study area, the u_{ab} spatial weight; t_a and t_b are the properties of regions a and b,

respectively; $\bar{t} = (1/m)\sum_{a=1}^{m} T_a$ is the average of the property; $D^2 = (1/m)\sum_{a=1}^{m}(t_a - \bar{t})^2$ is the variance of the property.

When the Global Moran I index is measured, it is also tested, usually using the X test the formula as follows:

$$X = \frac{M - F(M)}{\sqrt{U(M)}}. \tag{8}$$

Among them, $F(M)$ is the theoretical mean and $U(M)$ is the theoretical standard deviation.

Essentially, the Local Moran I index is a decomposition of Global Moran's I, a global spatial autocorrelation statistic. For the ith region, it takes the form of

$$I_a = \frac{m^2}{\sum_a \sum_b u_{ab}} \times \frac{(t_a - \bar{t})\sum_b u_{ab}(t_b - \bar{t})}{\sum_b (t_b - \bar{t})^2}. \tag{9}$$

The Local Moran I index is tested similar to the global index.

(2) Linear regression model in sport

In practice, there are often many factors that influence a phenomenon, so multiple regression analysis methods are often used to study the interaction between a variable and many variables [23]. In practical problems, the establishment of a multiple regression model can analyze complex problems in a diversified manner, making them easier to understand, so as to solve the problem. A multilinear regression model can be formed when there is a linear association between the resolved variable and the resolved variable. The usual form of a multilinear regression model is

$$y = \varphi_0 + \varphi_1 x_1 + \varphi_2 x_2 + \cdots + \varphi_n x_n + \delta, \tag{10}$$

where it is called a dependent variable and is called an $x_1, x_2, \cdots, x_n$ argument; $\varphi_1, \varphi_2, \cdots, \varphi_n$ is n plus 1 argument to be evaluated, is a constant, is φ_0 a regression parameter, and is a random $\varphi_1, \varphi_2, \cdots, \varphi_n \delta$ error.

The GWR model can be represented as

$$f_a = \partial_0(s_a, t_b) + \sum_{b=1}^{h} \partial_b(s_a, t_b)x_{ab} + \varphi_a, \quad a = 1, 2, \cdots, m. \tag{11}$$

(s_a, t_b) is the spatial coordinate of the first sample point, $\partial_b(s_a, t_b)$, and the bth regression factor of the a sample point is a random error φ_a term. For ease of expression, you can shorthand the above as

$$f_a = \partial_0 + \sum_{b=1}^{j} \partial_{ab} x_{ab} + \varphi_a, \quad a = 1, 2, \cdots, m. \tag{12}$$

If $\partial_{1b} = \partial_{2b} = \cdots = \partial_{mb}$, the GWR model then becomes a normal linear regression model.

Further, based on "data that is farther away from the observation data closer to position i has a greater impact on the estimate," the GWR model parameters can be estimated using weighted least squares:

$$\widehat{\partial}(s_a, t_b) = \left(C^E U(s_a, t_b) C \right)^{-1} C^E U(s_a, t_b) F, \tag{13}$$

where $\widehat{\partial}$ is the estimate of ∂, m is the number of spatial sample points, b is the number of arguments, U_{am}, and the position; a depiction model is given to the data point, the weight of m, which is the corresponding spatial $U(s_a, t_b)$ weight matrix.

How to select the appropriate threshold L is the key to the distance threshold method. The distance between data point b and regression point a is recorded as l_{ab} comparing the l_{ab} value to L; if l_{ab} is greater than L, the weight is 0, otherwise 1; the formula is as follows:

$$U_{ab} = \begin{cases} 1 & l_{ab} \le L, \\ 0 & l_{ab} > L, \end{cases} \tag{14}$$

where spatial relationships are measured by distance:

$$U_{ab} = \frac{1}{l_{ab}^{\alpha}}. \tag{15}$$

In the upper class, α is the appropriate constant, generally with a value of 1 or 2, which corresponds to the square of the distance countdown and the distance countdown, respectively.

The continuous monotony decreasing function is used to reveal the correlation between distance and weight, in which Gauss function method is a more common function; the specific formula is as follows:

$$U_{ab} = \exp\left(-\left(\frac{l_{ab}^{\alpha}}{k} \right)^2 \right). \tag{16}$$

k is a nonnegative attenuation parameter that illustrates the correlation between weights and distance coefficients and is also called bandwidth. It can be found by the formula sub (16); the larger the broadband k, the lower the rate of weight decay with the increase of distance. If the broadband k is smaller, the rate of weight decay increases as the distance increases, as does Figure 3 for the Gauss spatial right function.

In practice, data points that have little effect on regression parameters are usually cut off and do not participate in the calculation [24]. In this case, the Gauss function is replaced by a finite Gaussian function, which is the most commonly used method.

$$U_{ab} = \begin{cases} \left[1 - \left(\frac{l_{ab}}{k} \right)^2 \right]^2 & l_{ab} \le k, \\ 0 & l_{ab} > k. \end{cases} \tag{17}$$
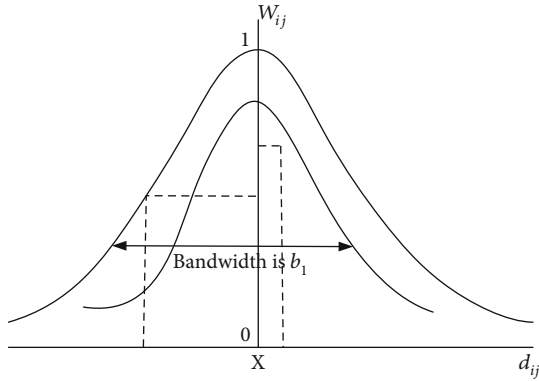
Figure 3: Gauss space weight function.

Akaike also made improvements to the parameter estimation method of the greatly similar principle, and on this basis, a more general mode l selection criterion, namely, Akaike information criteria, is given. The AIC guidelines are defined as

$$AIC = -2lnH\left(\widehat{\delta}_H, x\right) + 2r. \tag{18}$$

Among them, $\widehat{\delta}_H$ is for a very similar estimate and r is the number of unknown parameters.

AIC guidelines are widely used in practice. In the early days, the AIC criterion was applied to nonparametric regression analysis to select smooth parameters, the formula being

$$AICc = 2mln\left(\widehat{\theta}\right) + mln(2\pi) + m\frac{m + tr(T)}{m - tr(T)}. \tag{19}$$

Here, AICc represents the "modified" AIC estimate and m is the size of the sample point, represents the standard distance between the random error term and the estimate, represents the trace of the GWRT matrix, and is a function of bandwidth. The value of the AIC can also be used to judge whether GWR modeling is better than OLS modeling.

To find out how to choose the best bandwidth method, cross-validation is recommended, which is based on local regression analysis, the formula of which is represented as follows:

$$CV = \sum_{a=1}^{m}\left[f_a - \widehat{f}_{\neq a}(m)\right]^2, \tag{20}$$

where $\widehat{f}_{\neq a}(b)$ is the sum value of f_a; i.e., the observation of point a itself is deleted when fitting. This way, when bandwidth m becomes very small, the model only fits near regression point a, included in bandwidth m. Sample points in the range do not include a itself [25]. The smaller the CV value, the better the model fits. In the actual calculation, in order to select the optimal bandwidth m and its CV value, you can select multiple bandwidths b at the calculation and measure their CVs separately value to find the best result. The application of carbon nanocomposite sensing and functional

magnetic nanomaterial in the sports industry is studied in Figure 4 [26–28].

3. Experimental Results of Carbon Nanocomposite Sensing and Functional Magnetic Nanomaterial in Biosecurity Research

3.1. Exploration of Nanosilver Composites of Different Particle Sizes and Concentrations in the Biological Field. In order to analyze the performance of nanocomposites from a biological point of view, this paper selects nanosilver composites to explore and study the effects of their different particle sizes and concentrations on the antibacterial properties of aspergillosis [29].

(1) Effects of different particle sizes on the antibacterial properties of Aspergillus AF289

Table 1 shows the results of the experiment showing the same concentration (12.12×10^{-5} mol/L) of nanosilver solution; at 10 nm to 40 nm, the antibacterial effect in the particle size range is very significant, especially 10 to 25 nm. Nanosilver antibacterial rate reached 80%, so the antibacterial effect on fungal spores under this particle size is most obvious.

(2) Effects of different particle sizes on the resistance of the drug-resistant bacteria Gra04 to aspergillation

In Table 2, experimental results show the same concentration (12.12×10^{-5} mol/L) of nanosilver solution; at 10 nm to 40 nm, the antibacterial effect in the particle size range is very significant, especially the nanosilver antibacterial rate of 10 to 25 nm that reached 80%, so the antibacterial effect on fungal spores is most obvious under this particle size.

(3) Effects of different concentrations on the antibacterial properties of aspergillosis AF293

As can be seen from Table 3, different concentrations of nanosilver have different antibacterial activities against AF293 of pentomycin. In experiments with the same particle size, nanosilver series dilution concentration, in the range of 2.02×10^{-5} mol/L to 16.16×10^{-5} mol/L nano-silver has a significant antibacterial effect, especially 8.08×10^{-5} mol/L and 4.03×10^{-5} mol/L. The bacteriostatic rate reached 100%, indicating that the growth of all fungal spores could be completely inhibited [30].

(4) Effects of different concentrations on the resistance of Gra04, a drug-resistant bacteria of aspergillation

In Table 4, the experimental results show that different concentrations of nanosilver have different antibacterial activities against the drug-resistant bacteria Gra04 of penicillin. In experiments with the same particle size nanosilver series dilution concentration, in the range of 2.02×10^{-5} mol/L to 16.16×10^{-5} mol/L, nanosilver has a significant
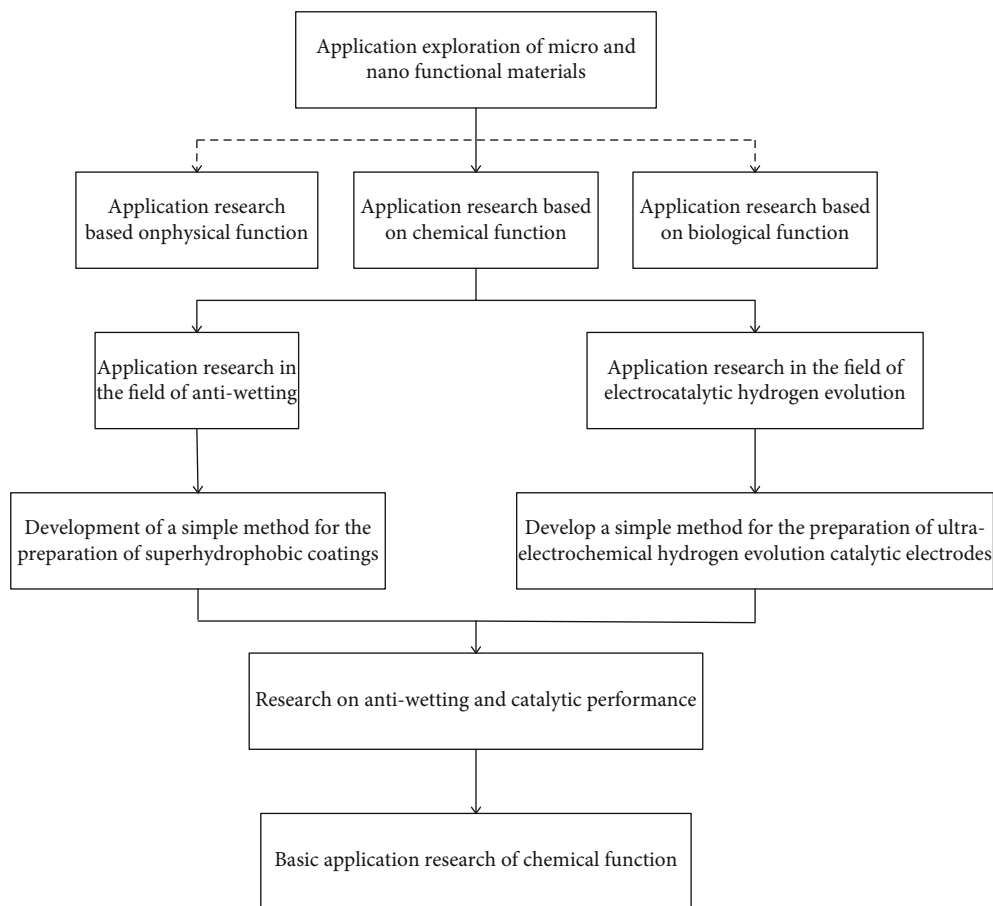
FIGURE 4: Main technical route.

TABLE 1: Determination of the antibacterial rate of Aspergillus fumigatus AF289 with different particle diameters of nanosilver.

AgNPs (10^{-5} mol/L)	Examples of experiments		Total colonies (cfu/mL)	Antibacterial rate (%)
	1	2		
10~15 nm	11	8	19	79
20~25 nm	9	9	18	78
30~40 nm	13	5	18	68
Control	39	51	90	

TABLE 2: Determination of the antibacterial rate of nanosilver with different particle diameters on the resistant bacteria Gra04 of Aspergillus fumigatus.

AgNPs (10^{-5} mol/L)	Examples of experiments				Total colonies (cfu/mL)	Antibacterial rate (%)
	1	2	3	4		
10~15 nm	61	62	21	20	151	80
20~25 nm	59	69	11	9	149	81
30~40 nm	19	6	81	67	166	76
Control	159	168	158	169	669	

TABLE 3: Determination of the antibacterial rate of Aspergillus fumigatus AF293 with different concentrations of nanosilver.

AgNPs (10^{-5} mol/L)	Examples of experiments		Total colonies (cfu/mL)	Antibacterial rate (%)
	1	2		
15.15	31	26	57	39
11.11	9	8	17	80
7.07	0	0	0	100
3.03	0	0	0	100
1.01	9	6	15	79
Control	39	45	84	

TABLE 4: Determination of the antibacterial rate of different concentrations of nanosilver to the resistant strain Gra04 of Aspergillus fumigatus.

AgNPs (10^{-5} mol/L)	Examples of experiments				Total colonies (cfu/mL)	Antibacterial rate (%)
	1	2	3	4		
15.15	160	168	109	131	566	18
11.11	49	61	21	20	151	80
7.07	0	0	0	0	0	100
3.03	0	0	0	0	0	100
1.01	26	19	0	0	45	92
Control	159	169	158	168	654	

antibacterial effect, especially 8.08×10^{-5} mol/L and 4.03×10^{-5} mol/L. The bacteriostatic rate reached 100%, indicating that the growth of all fungal spores could be completely inhibited.

3.2. Performance Testing and Characterization of Nanocomposites. The tensile strength and thermal conductivity of PSA, MWNT/PSA, and DABP-MWNT/PSA composites are tested with electronic pullers and thermal coefficients, as shown in Figure 5.

As can be seen from Figure 5, the stretch strength of the decompression carbon nanotubes of DABP liquid crystal is more significant than that of the undefined carbon nanotubes. The maximum tensile strength of pure pressure-sensitive adhesive is 0.5048 MPa, and the pressure-sensitive adhesive nanocomposite is produced with MWNT and DAP-MWNT technology, respectively, and the maximum tensile strength of pressure-sensitive adhesive composites will be significantly increased due to the increase of nanoparticle concentration, and for DABP-MWNTs/under different nanoparticle contents, the tensile strength of the pressure-sensitive composite is greater than that of the MWNT/pressure-sensitive composite. When the MWNT content is 2 wt%, the DABP-MWNT/pressure-sensitive composites have a tensile strength of 14.19 MPa, which is greater than MWNTs. The 1.914 MPa of pressure-sensitive composites is approximately 641% higher than pure pressure-sensitive composites, approximately 27 times higher than pure pressure-sensitive adhesives. In the description of carbon nanotubes due to defects such as easy reunion and poor compatibility with pressure-sensitive adhesives, its excellent mechanics have been unachievable,

and the effect of improving the properties of pressure-sensitive adhesives is not obvious, and the carbon nanotubes have been functionalized by DABP liquid crystals because DABP and MWNTs combine to π-π interactions, the reunion of carbon nanotubes inhibited the dispersion, and compatibility of carbon nanotubes in pressure-sensitive adhesives is improved, which makes the dynamics of pressure-sensitive adhesive composites significantly improved [26]. In addition, if the concentration of nanoparticles is further increased, the pressure-sensitive adhesive complex required in the mold will not be formed, so the maximum concentration of nanoparticles in the pressure-sensitive adhesive complex that detects the dynamic properties is 2.0 wt%.

It can be found from the figure that the thermal conductivity of pure pressure-sensitive adhesives is only 0.1965 W/(m-K), which has been modified by MWNTs and DABP-MWNTs, and due to the increase in the concentration of nanoparticles, the thermal conductivity of pressure-sensitive adhesive complexes is further improved. Compared with carbon nanotubes that have not been functionalized by liquid crystals, DABP-MWNTs have a particularly strong effect on the thermal conductivity of pressure-sensitive adhesives. At various nanoparticle concentrations, the thermal conductivity of DABP-MWNT/pressure-sensitive adhesive composites is larger than that of MWNT/pressure-sensitive adhesive composites. This is due to defects such as the ease of reuniting of the carbon nanotubes themselves and poor compatibility with pressure-sensitive adhesives, which make their excellent thermal conductivity impossible, thus improving the thermal conductivity of pressure-sensitive adhesives without significant effect, but through
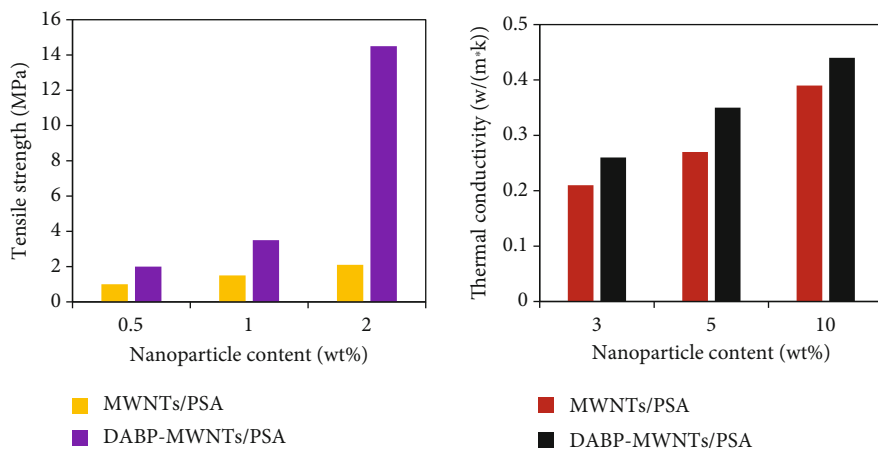
FIGURE 5: The influence of nanocomposite tensile strength and thermal conductivity.

FIGURE 6: The relationship between storage modulus and scanning frequency.

FIGURE 7: The relationship between mechanical properties and filler content.

FIGURE 8: Chronoamperometry graph.

FIGURE 9: Differential pulse voltammograms.

tent of MWCNTs increases; as a result, the energy storage capacity of PDLA/PHA/MWCNT nanocomposites increases as well. When a platform appears in the low-frequency area of the energy storage module G' curve, it usually indicates the formation of a overseepage network. The energy storage modulus G' of PDLA/PHA mixture increases monotonically as the frequency of scanning increases, showing the end flow behavior of the viscous polymer melt. When the MWCNT content in PDLA/PHA/MWCNT nanocomposites is 0.6 wt%, the material appears in the low-frequency zone with energy storage modulus platform which indicates that the critical content of MWCNTs forming a network structure is 0.6 wt%. PDLA/PHA/MWCNT-g-PLLA nanocomposites show similar patterns of change. However, its rheological percolation content is lower, 0.4 wt%. The above results indicate that the rheological percolation network structure is the conductive percolation network structure.

Composite PHA in the material improves the brittleness of the PDLA while significantly reducing the tensile strength of the PDLA. It can be seen from Figure 7 that the tensile strength of PDLA/PHA blends increases with the increase of MWCNT content. When the content of MWCNTs increased from 0 wt% to 1.2 wt%, the tensile strength of PDLA/PHA/MWCNT and PDLA/PHA/MWCNT-g-PLLA nanocomposites increased from 32.1 MPa to 45.1 MPa and 50.2 MPa, respectively. However, there was no significant change in the fracture elongation of the two composites. It is worth noting that PDLA/PHA/MWCNT-g-PLLA nanocomposites are always more tensile than PDLA/PHA/MWCNT nanocomposites at the same filler content. This is because MWCNTs-g-PLLA is selectively dispersed in the substrate PDLA and has a large adhesion to the substrate's interface (building composites). The enhancement effect on the substrate is more significant. Based on the above discussion, the formation of MWCNT and MWCNT-g-PLLA networks can significantly enhance PDLA/PHA mixes, resulting in weak to strong transitions. In addition, this transition can be achieved by adding a small amount of MWCNTs-g-PLLA compared to MWCNTs. Once the nanofiller network is formed, the strength of the two nanocomposites will stabilize with the increase of nanofillers.

3.3. Stability of the Nanocomposite Modified Electrode.

The stability of nanocomposites as electrodes is one of the important parameters to measure the quality of sensors. Timing current method is a kind of electrochemical method related to the function between the measurement of voltage response and current duration. When time tends to be infinite, the voltage will also be closer to zero as the content of surface active substances in the high-voltage electrode decreases gradually with electrolytic time. In this paper, the stability of modified electrodes is studied by the timing current method, as shown in Figure 8.

In this paper, the stability of modified electrodes is studied by timing current in different concentrations of TNP solutions. As the concentration of the TNP solution increases, the response current page for the modified electrode increases, and the current gradually stabilizes after approximately 50 seconds of timing, indicating that the

DABP, the carbon nanotubes after the functionalization of liquid crystal have better dispersion and compatibility in the pressure-sensitive glue, which makes the thermal conductivity of the pressure-sensitive adhesive composite material improve greatly. When the content is 10 wt%, the thermal conductivity of the DABP-MWNT/pressure-sensitive composites reaches 0.4208 W/(m-K), which is MWNTs/1.1 times the pressure-sensitive glue, which is about 114% higher than the pure pressure-sensitive glue.

Rheological parameters such as storage modulus (G') are very useful in detecting the dispersion state of fillers, especially when forming the percolation network structure of anisotropic fillers. For PDLA/PHA/MWCNT and PDLA/PHA/MWCNT-g-PLLA nanocomposites at 180 degrees C in energy storage module G' and filler content, the graph of scan frequencies is shown in Figure 6. As can be seen from the figure, in the low-frequency region, MWCNTs tend to form a network structure in the PDLA substrate as the con-

FIGURE 10: Hydrogen evolution catalytic performance graph.

prepared nanocomposite modified electrode pair TNP has good stability and electrocatalytic activity.

In addition, we use DPV as shown in Figure 9.

We immersed NQS/GO GCE in a 1.0 mM potassium iron cyanide solution and then added creatine to the solution continuously and examined the electrochemical behavior of different concentrations of creatinine on the electrodes. It can be seen from the figure that with the increase of creatinine concentration in the solution, the peak current decreases gradually. This is mainly due to the ability of creatinine to react with NQS on the electrode surface, causing the electrode surface to change, resulting in a gradual decrease in peak current.

The electrodeposition parameters, especially the sedimentary current density, have a significant effect on the hydrogenic catalytic properties of Co/CoP-NF catalysts. The catalysts produced were named Co/CoP-NF-2, Co/CoP-NF-5, and Co/CoP-NF-8. Figure 10 describes the hydrogenic catalytic properties of Co/CoP-NF-2, Co/CoP-NF-5, and Co/CoP-NF-8 catalysts. Obviously, the Co/CoP-NF-5 catalyst showed the highest hydrogenic catalytic activity, the hydrogen-based catalysis of Co/CoP-NF-8 was moderate, and the hydrogen-analysis catalysis of Co/CoP-NF-2 was the worst. The values of switching current density and hydrogen analysis performance are shown in Table 5, from which the Co/CoP-NF-5 catalyst has the highest exchange current density, further demonstrating that it has the highest hydrolytic catalytic activity.

4. Discussion

It is well known that nanosilver has a good killing property, against bacteria, fungi, mold, and other pathogens. Therefore, we have studied the nanosilver experiment to kill smoke and mold. Experimental results show that at concentrations of 4.04×10^{-5} mol/L, nanosilver-to-smoke mold with a particle size of 10 to 15 nm (drug-resistant and wild strains) is better killed. Therefore, nanosilver has a great prospect in the killing treatment of drug-resistant strains. In addition, nanosilver sterilization is likely caused by nano-

TABLE 5: Co/CoP-NF catalyst HER performance parameters under different deposition current densities.

Deposition current	n_{10} (mV)	n_{100} (mV)	b (mV)	j_0 (mV)
0.3	81	209	101	1.69
0.6	38	129	69	2.99
0.9	39	171	102	2.79

silver damage to the integrity of the cell wall and cell membrane, resulting in the outflow of material from the cell. However, the most critical issue for nanosilver particles is biosecurity. It is now known that nanosilver is indeed toxic, so it is urgent to find the right dose and concentration of sterilization that are harmless to humans. At the same time, based on the mechanism of a pronuclear replacement reaction between organic matter NQS and creatine, a new method of creatine coloric testing based on NQS/GO nanocomposites is established. The sensing mechanism is proved by UV-vis and electrochemical techniques. Experimental results show that NQS can be combined with GO through π-π and can effectively improve the effectiveness of color detection. The absorbance of solvents and the added creatinine content has a good linear relationship within the specified content range. Direct visual sensing methods are simple, fast, sensitive, economical, and selective, so we do not need some sophisticated analytical instruments to achieve rapid detection. It provides an important reference for the detection of biomolecules in clinical medicine and disease early warning and a new method for exploring the principle of visual sensors.

5. Conclusions

Using the thermal conductivity factor instrument, the thermal conductivity of PSA, MWNT/PSA, and PHBE-MWNT/PSA composites was detected, and the results showed that after the transformation of MWNTs and PHBE-MWNTs, the thermal conductivity was increased,

and the thermal conductivity of pressure-sensitive adhesive composites was significantly improved due to the increase of nanoparticle concentration. Compared with nanotubes that have not been functionalized by liquid crystals, PHBE-MWNTs have improved their thermal conductivity in pressure-sensitive adhesives. This is due to the fact that PHBE and MWNTs can be combined with π-π interactions, inhibiting the unification of carbon nanotubes and improving their dispersion and compatibility in pressure-sensitive glues, which makes the thermal conductivity of pressure-sensitive composite materials significantly improved. When the content is 10 wt%, the thermal conductivity of the PHBE-MWNT pressure-sensitive composite material is 0.6975 W/(m·K), which is MWNTs 1.8 times the pressure-sensitive glue, which is about 255% higher than the pure pressure-sensitive glue. At the same time, the effects and antibacterial mechanisms of nanosilver on the antibacterial effects of the drug-resistant bacteria Gra04 of aspergillosis AF293 and aspergillosis were studied. The nanosilver produced in this paper has excellent sterilization effects on both AF293 and Gra04. In particular, 8.08×10^{-5} mol/L and 4.03×10^{-5} mol/L nanosilver has a 100% bacteriological rate of both, indicating that the growth of all fungal spores can be completely inhibited. Through DIC microscope observation, nanosilver causes protein denaturation by destroying the proteins in spores, further causing the rupture of cell walls and cell membranes.

Data Availability

Data sharing is not applicable to this article as no new data were created or analyzed in this study.

Conflicts of Interest

The authors state that this article has no conflict of interest.

References

[1] W. Zhao, X. Xie, G. Li, J. Geng, M. Bao, and M. Wang, "Research on the influence of nanocarbon/copolymer SBS/rubber powder composite modification on the properties of asphalt and mixtures," *Advances in Materials Science and Engineering*, vol. 2020, 16 pages, 2020.

[2] G. Wang, W. Shan, S. Wen, Z. Sun, and S. Zheng, "Synthesis of a novel nanocomposite adsorbent for removal of Cr(VI) from wastewater," *Journal of Environmental Sciences*, vol. 57, no. 7, pp. 62–71, 2017.

[3] A. Pal, M. P. Sk, and A. Chattopadhyay, "Conducting carbon dot-polypyrrole nanocomposite for sensitive detection of picric acid," *ACS Applied Materials & Interfaces*, vol. 8, no. 9, pp. 5758–5762, 2016.

[4] J. L. Jiang, X. Zhang, J. F. Du, Q. Wang, J.-F. Dai, and Z.-Q. Wei, "Electrochemical deposition and field emission properties of graphene/diamond-like carbon nanocomposite films," *Acta Physico-Chimica Sinica*, vol. 32, no. 7, pp. 1839–1843, 2016.

[5] H. L. Xu and W. D. Zhang, "Graphene oxide–MnO$_2$ nanocomposite-modified glassy carbon electrode as an effi-cient sensor for H$_2$O$_2$," *Chinese Chemical Letters*, vol. 28, no. 1, pp. 143–148, 2017.

[6] H. T. Hien, H. T. Giang, T. Trung, and C. Van Tuan, "Enhancement of biosensing performance using a polyaniline/multiwalled carbon nanotubes nanocomposite," *Journal of Materials Science*, vol. 52, no. 3, pp. 1694–1703, 2017.

[7] M. Amir, M. M. Tunesi, R. A. Soomro, A. Baykal, and N. H. Kalwar, "Sensitive determination of 6-thioguanine using caffeic acid-functionalized Fe3O4 nanoparticles as an electrochemical sensor," *Journal of Electronic Materials*, vol. 47, no. 4, pp. 2198–2208, 2018.

[8] F. Cao, C. Li, M. Li, H. Li, and B. Yang, "ZnO nanorod/multi-walled carbon nanotube nanocomposite for ethanol vapour detection," *Micro & Nano Letters*, vol. 13, no. 6, pp. 779–783, 2018.

[9] W. Thomas, C. Sarsons, C. M. Platnich et al., "Maltol-functionalized Fe$_3$O$_4$ nanoparticles as T2 magnetic resonance imaging contrast agents," *ChemistrySelect*, vol. 1, no. 8, pp. 1602–1606, 2016.

[10] J. Nelis, D. Migliorelli, S. Jafari et al., "The benefits of carbon black, gold and magnetic nanomaterials for point-of-harvest electrochemical quantification of domoic acid," *Microchimica Acta*, vol. 187, no. 3, pp. 1–11, 2020.

[11] L. Ma, Y. Liu, L. Liu et al., "Simultaneous activation of short-wave infrared (SWIR) light and paramagnetism by a functionalized shell for high penetration and spatial resolution theranostics," *Advanced Functional Materials*, vol. 28, no. 6, pp. 1705057–1705194, 2018.

[12] J. N. B. W. B. Liu and J. L. Shi, "Chemical design and synthesis of functionalized probes for imaging and treating tumor hypoxia," *Chemical Reviews*, vol. 117, no. 9, pp. 6160–6224, 2017.

[13] X. Zou, Z. Wei, J. Du, X. Wang, and G. Zhang, "Preparation and properties of magnetic-fluorescent microporous polymer microspheres," *Chemical Research in Chinese Universities*, vol. 34, no. 4, pp. 684–690, 2018.

[14] Y. Li, J. Liu, Y. Fu, Q. Xie, and Y. Li, "Correction to: Magnetic-core@dual-functional-shell nanocomposites with peroxidase mimicking properties for use in colorimetric and electrochemical sensing of hydrogen peroxide," *Microchimica Acta*, vol. 186, no. 7, pp. 1–9, 2019.

[15] A. Modi, S. Singh, and N. Verma, "Improved performance of a single chamber microbial fuel cell using nitrogen- doped polymer-metal-carbon nanocomposite-based air-cathode," *International Journal of Hydrogen Energy*, vol. 42, no. 5, pp. 3271–3280, 2017.

[16] A. Murray, K. Skene, and K. Haynes, "The circular economy: an interdisciplinary exploration of the concept and application in a global context," *Journal of Business Ethics*, vol. 140, no. 3, pp. 369–380, 2017.

[17] F. M. Shimizu, A. M. Pasqualeti, F. R. Todo et al., "Monitoring the surface chemistry of functionalized nanomaterials with a microfluidic electronic tongue," *ACS Sensors*, vol. 3, no. 3, pp. 716–726, 2018.

[18] G. Wu, A. Santandreu, W. Kellogg et al., "Carbon nanocomposite catalysts for oxygen reduction and evolution reactions: from nitrogen doping to transition-metal addition," *Nano Energy*, vol. 29, no. 1202, pp. 83–110, 2016.

[19] G. Tian, W. Wang, Z. Li, Y. Kang, and A. Wang, "From spent dye-loaded palygorskite to a multifunctional palygorskite/carbon/Ag nanocomposite," *RSC Advances*, vol. 6, no. 48, pp. 41696–41706, 2016.

[20] J. C. Lin, "Radio-frequency radiation safety and health: a research program on the human impact of the wireless telecommunications and other electromagnetic-field-emitting systems," *Ursi Radio Science Bulletin*, vol. 77, no. 4, pp. 107-108, 2017.

[21] S. A. Qasmi, S. Pirzada, A. Ghani, and S. Mohsin, "Survey on proper and safe use of biological safety cabinets (BSCs) in research, bio-medical and animal laboratories in Karachi, Pakistan a cross sectional study," *Journal of Biosafety and Biosecurity*, vol. 2, no. 2, pp. 77–80, 2020.

[22] I. Rai, R. K. Bachheti, C. K. Saini, A. Joshi, and R. S. Satyan, "A review on phytochemical, biological screening and importance of wild apricot (Prunus armeniaca L)," *Oriental Pharmacy & Experimental Medicine*, vol. 16, no. 1, pp. 1–15, 2016.

[23] Y. Zheng, K. Wang, J. Zhang et al., "Simultaneous quantitative detection of helicobacter pylori based on a rapid and sensitive testing platform using quantum dots-labeled Iimunochromatiographic test strips," *Nanoscale Research Letters*, vol. 11, no. 1, p. 62, 2016.

[24] Q. P. Yang, M. Ouyang, G. Y. Yang et al., "Research on ecological stoichiometry in bamboos: from biological basis to applications in silviculture of bamboo forests," *Chinese Journal of Plant Ecology*, vol. 40, no. 3, pp. 264–278, 2016.

[25] S. Duan and C. Juan, "Research on the relationship between sports media and the healthy development of football industry: a case study in Spain football club Real Madrid," *Journal of Computational and Theoretical Nanoscience*, vol. 13, no. 3, pp. 2187–2192, 2016.

[26] B. Gao, X. Ning, and P. Xing, "Shock wave induced nanocrystallization during the high current pulsed electron beam process and its effect on mechanical properties," *Materials Letters*, vol. 237, no. 15, pp. 180–184, 2019.

[27] P. Wang, S. Wang, X. Zhang et al., "Rational construction of CoO/CoF_2 coating on burnt-pot inspired 2D CNs as the battery-like electrode for supercapacitors," *Journal of Alloys and Compounds*, vol. 819, p. 153374, 2019.

[28] Y. Tang, Z. Chen, W. Feng, Y. Nong, C. Li, and J. Chen, "Combined effects of nano-silica and silica fume on the mechanical behavior of recycled aggregate concrete," *Nanotechnology Reviews*, vol. 10, no. 1, pp. 819–838, 2021.

[29] P. Wang, T. Yao, Z. Li et al., "A superhydrophobic/electrothermal synergistically anti-icing strategy based on graphene composite," *Composites Science and Technology*, vol. 198, article 108307, 2020.

[30] L. Zeng, J. Shi, J. Luo, and H. Chen, "Silver sulfide anchored on reduced graphene oxide as a high -performance catalyst for CO_2 electroreduction," *Journal of Power Sources*, vol. 398, pp. 83–90, 2018.

Research Article

Individual and Catalytic Co-Pyrolysis of Agricultural Outcomes and Polymeric Materials over Nano-HZSM-5 Zeolite: Synergistic Effects and Yield Analysis for Heating Applications

C. Sowmya Dhanalakshmi [ID],[1] **N. Ahalya,**[2] **P. Vidhyalakshmi** [ID],[3] **C. Krishnaraj** [ID],[4] **N. Selvam,**[5] **Pravin P. Patil,**[6] **S. Kalippan,**[7] **and S. Prabhakar** [ID][8]

[1]Department of Mechanical Engineering, SNS College of Technology, Coimbatore, Tamil Nadu, 641035, India
[2]Department of Biotechnology, MS Ramaiah Institute Technology, Bengaluru, Karnataka, 560054, India
[3]Department of Electronics and Instrumentation Engineering, Kongu Engineering College, Perundurai, Erode, Tamil Nadu, 638060, India
[4]Department of Mechanical Engineering, Karpagam College of Engineering, Coimbatore, Tamil Nadu, 641032, India
[5]Department of Electrical and Electronics Engineering, M.Kumarasamy College of Engineering, Karur, Tamil Nadu, 639113, India
[6]Department of Mechanical Engineering, Graphic Era Deemed to be University, Bell Road, Clement Town, Dehradun, Uttarakhand, 248002, India
[7]Department of Mechanical Engineering, Velammal Institute of Technology, Chennai, Tamil Nadu, 601204, India
[8]Department of Mechanical Engineering, Automotive Engineering Stream, Wollo University-KIOT, Ethiopia 208

Correspondence should be addressed to S. Prabhakar; prabhakar@kiot.edu.et

The catalytic effect of nano-HZSM-5 zeolite on co-pyrolysis of cotton shell (CS) and municipal plastic wastes (MPW) was studied. The influence of reaction temperature during individual pyrolysis, blending ratio, and catalytic effects was studied by applying constant heating rate. The experiments were conducted in a fixed bed batch type reactor. The hindering effect during catalytic decomposition of MPW was carried out and its positive synergistic effect on liquid oil yield was analysed. The reaction temperature for all the experiments are fixed based on the decomposition rate obtained from thermogravimetric study. The experimental outcomes revealed that during co-pyrolysis, the formation of char was reduced to 7.2 wt% with increased liquid oil yield of 66.5 wt%. Furthermore, adding catalyst for co-pyrolysis process improved the reaction by decreasing char formation. During catalytic process, the maximum liquid oil output was 69.3 wt% at 500°C temperature, CS/MPW ratio of 1 : 2. When compared to co-pyrolysis process, the catalytic co-pyrolysis showed 4.21 wt% higher liquid oil yield. The physical analysis of the oil shows maximum hating value of 34.6 MJ/kg. The FTIR study on catalytic co-pyrolysis oil shows the presence of aliphatic and aromatic hydrocarbons.

1. Introduction

The increased energy demand and rapid industrialisation due to the population and modern lifestyle force researchers to find alternative sources for conventional fuels. According to the survey conducted in the middle of 2020, the need for global energy is expected to increase by 30% over the next two decades in order to sustain rapid urbanisation [1]. Every

living being requires a healthy atmosphere in order to thrive and develop. One of the biggest issues is the degradation of ecosystems caused by the discharge of inorganic and organic pollutants from various industries and automotive engines [2, 3]. There has been considerable demand around the world to investigate the production and use of biofuels for heat and power applications [4]. Fossil fuels have played a major part in satisfying current energy demands, but their

widespread usage has aggravated serious environmental challenges, including global warming. Utilising biofuels for power production has increased nowadays due to flexible conversion methods and increased fuel properties. It is an alternative energy source that can replace fossil fuels by up to 30% to 40% in the near future [5]. The augmented solid waste output by the growing population provides carbon-rich energy resources and gives a widespread option for the production of energy. This could also help with the waste disposal problems.

Biomass is generally classified as virgin biomass, waste biomass, or agricultural residues. It can be converted into energy-rich fuels through various conversion processes. Lignocellulosic biomass obtained from agricultural wastes is a carbon-free renewable energy source and is an excellent resource for biofuels and chemicals [6]. The basic elements of biomass are categorised as cellulose, hemicelluloses, and lignin (20–30%). Cellulose comprises the major part of the total components (about 40 to 45%). Apart from this, some amounts of extractives, hydrocarbons, and inorganic components are also present. Matured agricultural wastes, commonly called as agro-wastes, are the end product of any agricultural process. The safe disposal of these residues is a challengeable one without affecting environmental sustainability. Due to agricultural activities, the quality of land waster and water bodies is being affected much. Pesticides used to meet global agricultural demand are the primary source of water and soil pollution [7]. These pesticides contaminate water through rain and irrigation systems [8]. In order to remove these contaminants from the body of water, Wabaidur et al. [9] and Alothman et al. [10] utilised absorption techniques through multiwalled nanocomposite and biosorbents. These wastes are typically burned in the open field after harvesting, and this practice is becoming more common, resulting in increased air pollution [11, 12]. The burning of agro-residues on farms is currently a substantial contributor to global warming [13]. As a result, policymakers are now tasked with identifying the best solution to address the aforementioned issues by effectively utilising agricultural wastes to generate clean energy. Converting solid waste into value-added products is a step towards a sustainable world [14]. Pyrolysis has become a popular technology due to its faster reaction time, low energy consumption, and generation of solid carbon-rich fuel as well as value-added liquid products. Khan et al. [15] developed a hydrochar by utilising sesame oil cake through hydrothermal carbonisation conducted at a temperature of 150–250°C. The produced hydrochar was utilised for the adsorption of metal ions from water. Alqadami et al. [16] developed citric anhydride anchored mesoporous metal organic framework to absorb nonessential lead (Pb) trace elements from water. Cotton shell (*Gossypium arboretum*) often known as tree cotton. It is one of the most important crops that plays a significant role in India's economic development. It is cultivated on a wide range of soils, such as black clayey, red soil, and black and mixed black soil. Cotton seeds are extracted and used to make high-viscous oil. The pressed oil is used for burning and biofuel production. Nabi et al. [17] produced cotton seed oil methyl ester and utilised for

IC engine operation. This study showed lower exhaust gas emissions, except for NOx.

Plastics are the materials produced from fossil fuels that have become an integral element of modern life. They are more durable, weigh less, and have a lower cost. Many plastics are made from polyethylene (PE), polypropylene (PP), polystyrene (PS), polyvinyl chloride (PVC), and polyethylene-terephthalate (PET) [18]. They are nonbiodegradable and can endure for more than a hundred years. The global rate of waste plastics has been increasing rapidly for the past two decades. In India, over 3.4 million tonnes of plastic waste were generated in the financial year 2020, an increase of more than 1.0 million tonnes compared to 2018. In Tamil Nadu, plastic waste generation is around 0.43 million tonnes per annum, of which 0.4 million tonnes are collected and segregated by the local urban bodies. Used plastics are generally recycled to produce new and useful products. When recycling is done properly, it can reduce the dependence on landfills and conserve resources. But at present, only 15–20% of total plastic waste can be recycled using traditional sorting and grinding [19]. The process of energy recovery from used plastics is an alternative way and is gaining more attention nowadays. There are many innovative and promising methods available today that can convert waste plastics into fuels and other valuable resources.

Incineration and pyrolysis are the two main processes that are being utilised for energy recovery from plastics in many studies [20, 21]. Incineration is a simple energy recovery process that converts hydrocarbons to combustion products. Incinerating plastic waste creates environmental pollution. Burning in an open field or in a controlled environment emits poisonous gases which is very dangerous to all living organisms [22]. Pyrolysis is an effective technique that converts plastic waste into energy-rich liquid oil. It is a thermal decomposition method that is performed without supplying air. Pyrolysis is a temperature-dependent process that is generally performed at a low, medium, or high temperature to break the structure [23]. Co-pyrolysis is another technique that produces synthetic liquid fuel with improved properties. It is also a very effective method of utilising two or more dissimilar feedstocks. Many reports have reported the maximum liquid oil yield through the co-pyrolysis process. Co-pyrolysis of plastics with agricultural waste is directed towards synergistic effects that possibly improve the favourable properties of the products [24]. Burra and Gupta [25] conducted a co-pyrolysis experiment utilising pinewood and mixed plastic wastes under different mass fractions. The study showed positive synergistic effects compared with individual components. The study carried out by Johansson et al. [26] showed the maximum production of hydrocarbons during co-pyrolysis. In this study, the addition of plastic waste to woody biomass significantly affected the product composition. Jin et al. [27] examined the synergetic effect during co-pyrolysis of wheat straw and plastic waste. The study also showed a positive synergistic effect on char yield. Oyedun et al. [28] demonstrated the quantity and properties of char and oil with respect to the amount of plastic during the co-pyrolysis process. Dewangan et al. [29] conducted co-pyrolysis studies on combined LDPE and

sugarcane bagasse. The study produced maximum liquid oil with 40 MJ/kg heating value.

In order to improve the quality of liquid oil, a large variety of nanobased catalysts are utilised. Many studies have reported catalytic pyrolysis processes with various catalysts, for instance ZSM-5 [30], HZSM-5 [31], zeolite [32], Cu-Al$_2$O$_3$ [33], and Fe$_2$O$_3$ [34]. These catalysts lower the energy inputs and increase the condensable liquid oil. Zhang et al. [35] conducted pyrolysis experiments on Douglas fir sawdust and HDPE in the presence of ZSM-5 catalysts. From the experimental results, it was understood that adding the HZSM-5 catalyst could decrease the activation energy. Copyrolysis of macroalgae and HDPE was done by Xu et al. [36] to analyse the synergistic effect towards enhanced biofuel production. This process showed that the catalytic process lowered the oxygen, nitrogen, and acid levels in the derived bio-oil. Furthermore, adding HZSM-5 with the feedstocks increased the reaction pathways and biofuel production as well as lowered the activation energy.

The goal of this work is to investigate the synergistic effects of agricultural residues and plastic during the co-pyrolysis process in the presence of HZSM-5 nanocatalysts. The synergistic effect on liquid oil yield was analysed using a batch type fixed bed reactor. The liquid oil yield and its compositions during thermal, co-pyrolysis, and catalytic co-pyrolysis were analysed based on synergistic effects.

2. Materials and Methods

2.1. Materials. CS and MPW were used for this study to analyse probable synergistic effects during their co-pyrolysis. The cotton shell used for this study is a typical lignocellulosic biomass and was collected from the local fields in and around Coimbatore. The city is generally called the cotton city of the state. The city has more than 100 spinning mills and produces a variety of cotton fabrics. The feedstocks for these industries are supplied by nearby agricultural farms. The climate in and around the city is more suitable for the cultivation of cotton. After eliminating cotton from the shells, they were thrown away and fired into the field itself. The open burning of these shells causes a severe effect on the environment. In order to avoid this and to find a suitable recycling method, this study focused on the utilisation of CS for the pyrolysis process. The municipal plastic wastes contains majority of PE, HDPE, and PET materials. Both the materials were completely screened and dried in the open sunlight for more than 15 days. They are converted into small particles with an average diameter of 0.5 mm to 1.0 mm. The elemental analysis of both the materials was analysed to find its suitability for the pyrolysis process. The proximate analysis was done to measure the volatile matters within it. All the analysis was performed by following ASTM protocols. Table 1 shows the proximate and ultimate analysis of the feedstock materials.

2.2. Thermogravimetric Analysis. Thermogravimetric analysis of the selected feedstock was performed to find thermal degradation properties using the TGA701 (LECO Corporation, St. Joe, Michigan, US) thermogravimetric analyser.

TABLE 1: Feedstock characteristics.

Parameters	CS	MPW
Proximate analysis (wt%)		
Volatile matter	61.60	89.40
Fixed carbon	26.06	0.42
Moisture content	9.52	0.35
Ash	2.81	9.83
Ultimate analysis (wt%) (ash free basis)		
Carbon	46.02	82.20
Hydrogen	4.91	15.65
Nitrogen	0.60	2.40
Oxygen[#]	48.46	0.30
Sulfur	0.01	1.45

[#]By difference.

The test was carried out in a nitrogen environment and its volume flow rate was maintained at 3.5 l/min. The dehydration and devolatilisation were done at the heating rate of 20°C/min. Before heating, the feedstocks were dried at 100°C. The analysis was done by heating the sample from atmospheric conditions to 600°C. For the analysis, 10 mg sample is loaded into the crucibles.

2.3. Material Characterisation. The collected feedstock material was subjected to proximate and elemental analysis. The 2400 CHNS Organic Elemental Analyzer (N2410650, Perkin Elmer Ltd, US) is employed to find the elements present in the samples. The same instrumentation is also used for liquid oil analysis. The FTIR analysis of the obtained liquid oil through catalytic co-pyrolysis was done with the aid of a FTIR (BRUKER Optik GmbH, TENSOR 27 Bruker Corporation) spectrophotometer with the support of OPUS version 6.5 in transmission mode. The analysis was done by collecting the spectrum between 400 and 4000 cm^{-1} with 4 cm^{-1} resolution. After the sample was disseminated over zinc selenide crystal, the spectrum was obtained in reflectance mode. The physical analyses of the liquid samples were investigated to determine their applicability for various uses. The physical properties of the oil were done in accordance with ASTM standards. Many physical characteristics such as density, kinematic viscosity, flash point, heating value, and pH value were considered for this analysis. The individual and catalytic pyrolysis oils used for physical analysis were collected under experimental conditions that yielded higher liquid oils.

2.4. Reactor Facility. Individual and co-pyrolysis experiments were performed using a batch type laboratory scale fixed bed reactor. The internal diameter and height of the reactor are 50 mm and 150 mm, respectively. The set-up consists mainly a reactor with an electrical heater, a condenser, and a liquid collection unit. The reactor is perfectly insulated with Mineral-Chromel and Alumel to avoid energy loss during pyrolysis. The temperature of the reactor is controlled by the PID controller and auto transformer. The temperature inside the reactor was measured by using K type
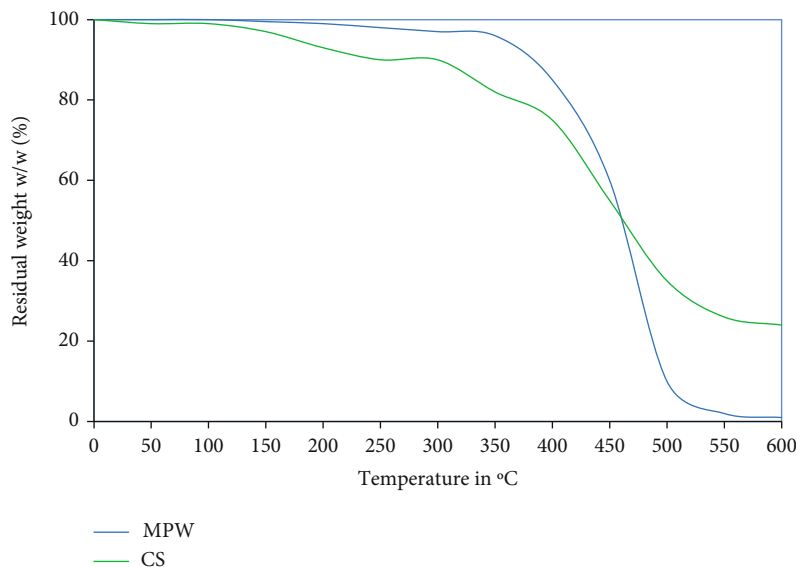
Figure 1: TGA analysis of CS and MPW.

thermocouples fixed at two locations inside the reactor. Once the reactor reached the desired temperature, it was maintained stable by auto cut-off unit. The outlet of the reactor pipe is connected to the series of two condensers. The ice water supplied to the condenser is kept at 5°C. The condensed liquid obtained from the condenser was collected in conical flasks and stored separately for further analysis. At the end of each experiment, the char was collected from the bottom of the reactor and weighed using an electronic weighing machine. The liquid oil obtained from the reaction was also collected and weighed. The weight percentage of uncondensable gas fractions was found by the remaining material balance.

2.5. Experimental Procedure. The effect of thermal, co-pyrolysis, and catalytic co-pyrolysis on liquid oil yields was investigated by four different phases. In the first phase, the thermal pyrolysis of CS was examined by changing process temperature from 350°C to 550°C. In the second phase, the thermal pyrolysis of MPW was also conducted by changing the temperature from 350°C to 550°C. The aim of the second phase is to find the optimum temperature for maximum liquid oil yield and the impact of process temperature on biofuel yield. The next phase of experiments was conducted on co-pyrolysis by changing the biomass and plastic blend ratios to 1:0, 2:1, 1:1, 1:2, and 0:1 at 500°C. The fourth phase of the experiments was carried out on catalytic co-pyrolysis at 1:2 blending ratio (biomass to plastic) by utilising HSZM-5 nanocatalysts supplied by Sri Aathi Vinayaga Industries, Tamil Nadu, India, to find the synergistic effect on liquid oil production.

3. Results and Discussions

3.1. Thermogravimetric Analysis. Figures 1 and 2 show the TGA and differential thermogram (DTG) of a CS and MPW. In the case of CS, there were no volatiles released

until it reached 200°C. According to d'Almeida et al. [37], the biomass is stable till it reaches 200°C, with negligible weight losses. This stage represents the drying and removal of extractives. The rapid pyrolysis occurred between 290°C and 450°C. The weight loss below 290°C represents the desertion of water molecules from CS. The first and second peaks developed in the experiment due to hemicellulose and cellulose breakdown [38]. Generally, decomposition of hemicelluloses into acetic acid, furfural, and furan occurs at temperatures between 200 and 260°C. The slow degradation rate after 420°C represents the breakdown of lignin. It is the main reason for the formation of phenolic compounds in the pyrolysis products [39]. The differences in thermal behaviour between CS and MPW in TGA analysis occur due to molecular arrangement and degradation rate. The degradation MPW occurs in single step between 340°C and 540°C. Comparing with biomass, the degradation of plastics takes place at elevated temperatures. MPW begins to degrade structurally at around 260°C. The single peak noticed in both the curves represents the weight loss owing to the temperature increase. At 350 to 500°C, the maximum degradation occurred (81.5%). Girija et al. [40] also represented the single stage degradation of PET material. It is also very difficult to explain the thermal disintegration mechanism of plastics due to their aromatic nature.

3.2. Thermal Pyrolysis of Cotton Shell. Figure 3 depicts the product distributions of the thermal pyrolysis of CS samples under different operating temperatures. The results reveal that when the pyrolysis temperature is increased, the char yield is reduced. This is owing to increased primary breakdown at higher temperatures [41]. The abrupt increase in gas fractions and the reduction in liquid oil products have been noticed as the temperature increased above 450°C. This could be due to secondary reactions of the pyrolysis liquid into noncondensable gases at elevated temperatures [42]. The results are also in good agreement with the previous
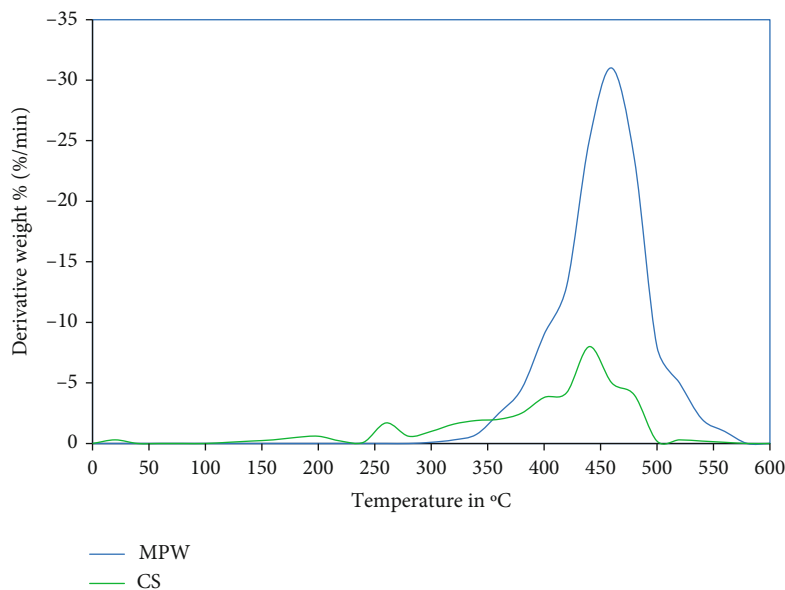
FIGURE 2: DTG analysis of CS and MPW.
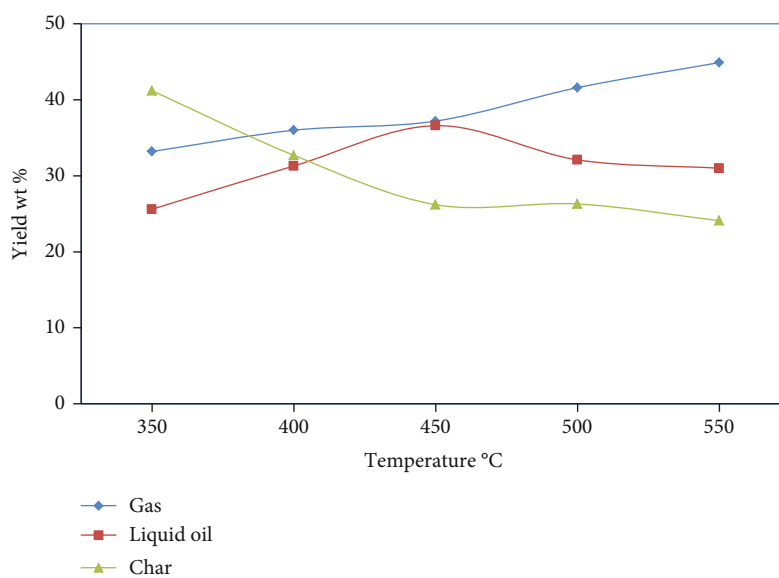
FIGURE 3: Product distributions during pyrolysis of CS.

literature conducted on different biomass materials such as rapeseed and soybean cake [43, 44]. The yield of liquid oil is lowered at lower temperatures and increased with increasing temperatures. The increased decreased pattern of the liquid oil yield with increased temperature is due to the higher decomposition of condensable volatiles at 450°C. The liquid oil production reached maximum at 450°C (36.6 wt%). With increasing temperatures, the yield of gas fractions also increases. At 350°C, the gas yield is 33.2 wt% and at 550°C, it reaches the maximum value up to 44.9 wt%. In most cases, the lower pyrolysis temperature favours a higher char yield and the higher temperature promotes gas yields. The same trend is also observed in the flash pyrolysis of CS [45].

3.3. Thermal Pyrolysis of Municipal Plastic Wastes.
Figure 4 demonstrates product distributions during the thermal pyrolysis of MPW at various temperatures. In this study, the yield of char products decreased with increased temperature. At 550°C, the char production is only 3.3 wt%. The reduction in char yield is attributed to secondary repolymerisation reactions [46]. When the temperature is changed from 350°C to 550°C, the yield of liquid oil changes from 62.4 wt% to 69.4 wt% and the maximum yield is recorded as 70.6 wt% at 500°C. The higher temperature of the reactor increases the gas yield and reduces the char production. When compared to biomass, the pyrolysis of plastics yields more liquid oil due to its structure. In plastic pyrolysis process, the stability of the benzylic radical favoured unzip
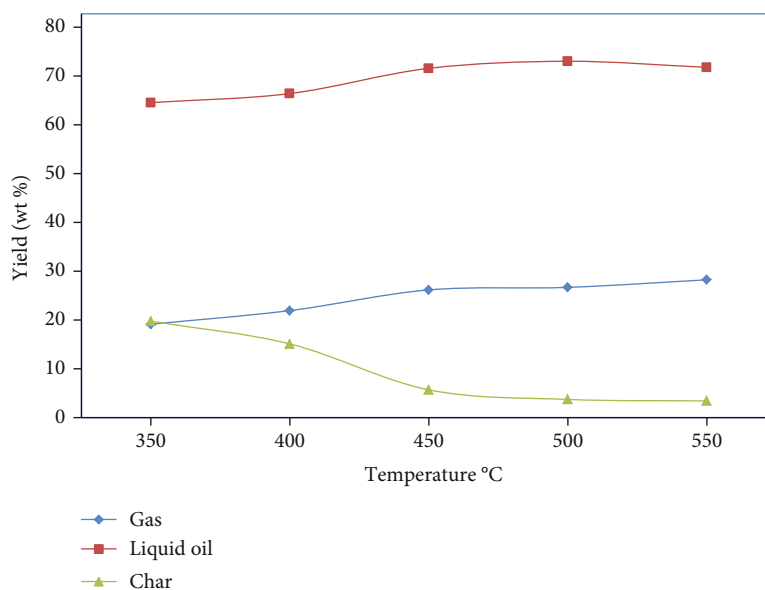
FIGURE 4: Product distributions during pyrolysis of MPW.
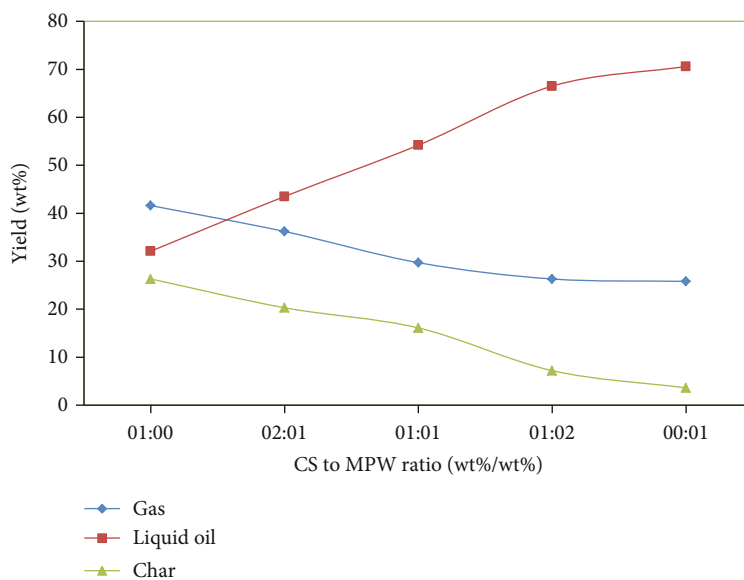
FIGURE 5: Product yield at different blend ratio.

reaction and restricted further cracking process. As a result, the main product of plastic pyrolysis was liquid oil.

3.4. Co-pyrolysis at Different Blend Ratio.

Figure 5 demonstrates product distributions during co-pyrolysis of CS and MPW under different blend ratios. The figure shows increased liquid oil production with respect to the increased amount of plastics in the feedstock. The aim of the experiments in this phase is to produce high-quality and large-quantity liquid oil. The liquid oil yield is increased to 66.5 wt% at 1 : 2 ratio. The increased yield at higher percentage of plastics in the feedstock is attributed to the presence of higher levels of hydrogen in the feedstock [47, 48]. During the co-pyrolysis process, polyolefin polymers in the plastics

can act as perfect hydrogen donors, resulting in higher oil production [49]. While biomass is reacting with plastics, a number of reaction radicals can be created. These radicals interact and favour the production of liquid oil without phase separation. A considerable increase in pyrolysis liquid output has been reported by many researchers, indicating synergistic impact [50, 51]. Furthermore, the reduction of char was found as the plastic ratio increased, indicating a higher degree of conversion.

3.5. Catalytic Co-Pyrolysis Process.

For the catalytic process, 30 grams of blended feedstock (1 : 2-CS:MPW) was mixed thoroughly with the catalyst (10% wt%/wt% of feedstock) and kept in the reactor. The temperature throughout this
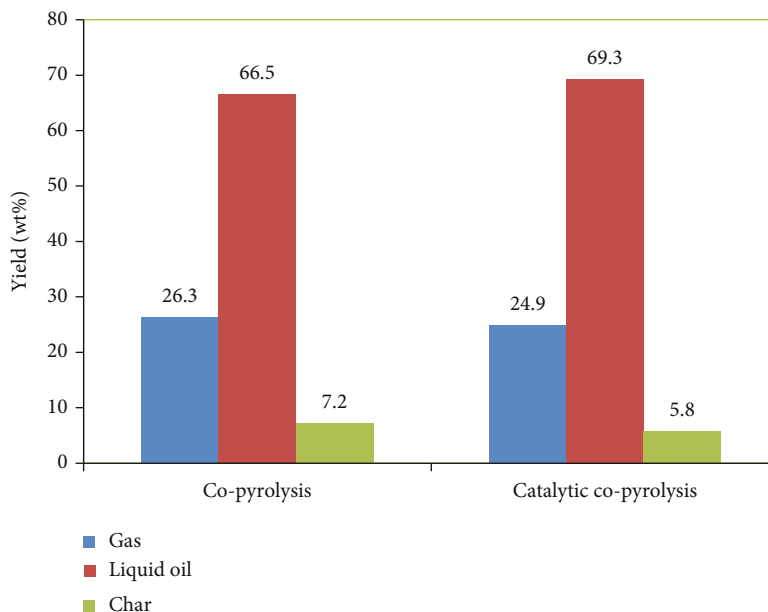
Figure 6: Comparison between catalytic and noncatalytic co-pyrolysis process.

Table 2: Physical characterisation of liquid oils.

Type of oil	Density in kg/m^3	Viscosity in cSt	Flash point in °C	pH	HHV in MJ/kg
CS pyrolysis oil	1005	7.7	160	3.4	17.65
MPW pyrolysis oil	935	2.6	95	6.2	41.6
Co-pyrolysis oil	980	5.7	110	4.8	34.1
Catalytic co-pyrolysis oil	980	5.6	105	4.6	34.6

phase of experiments is kept at 500°C. Figure 6 evaluates the yield of liquid oil, char, and gas obtained from co-pyrolysis and catalytic co-pyrolysis processes. From the figure, it can be understood that the catalytic co-pyrolysis process yields more liquid products than the co-pyrolysis process. At co-pyrolysis, the maximum liquid oil production was 66.5 w%. But through catalytic co-pyrolysis, the production of liquid was enhanced to 69.3 wt%. The catalytic process increased the yield by up to 4.21%. The increase in liquid oil production and the reduction in char residue showed a beneficial synergy between CS and MPW. The reaction between the catalyst and feed materials is quite complicated due to the complex structure of the materials [52]. But the main reason for the positive synergy effect on liquid yields is the relationship between biomass and plastic-derived olefins [53]. In the presence of the catalysts, it was found that the oxygenated components could react with olefins. Furthermore, it has also been shown that plastic-derived hydrocarbons can perform as hydrogen donors for biomass-derived oxygenates, reducing the formation of char in catalytic conversions [54].

3.6. Characterisation Study

3.6.1. Physical Analysis of Liquid Oils. Table 2 represents the physical characterisation of liquid oils obtained from this study. The table shows some of the basic fuel properties.

Table 3: Comparison of heating value of the liquid oils.

Source	Value in MJ/kg	Reference
MPW	41.6	This study
CS and MPW	34.6	This study
Napier grass	19.79	[55]
Pine seed	20.00	[56]
Ficus religiosa	18.30	[57]
Spirulina platensis	25.70	[59]
Hard wood	18.63	[60]
Palmyra fruit bunch	13.92	[61]

When compared with CS pyrolysis oil, the co-pyrolysis oil offers a higher heating value. The density of MPW pyrolysis oil was found to be lower than other pyrolysis oils. The heating value of the individual MPW oil is higher than other oils due to the absence of oxygenated elements. The comparison of MPW pyrolysis oil, co-pyrolysis oil, and bio-oil obtained from other samples is provided in Table 3. From the table, it can be understood that the MPW pyrolysis oil has a higher HHV than co-pyrolysis oil. The presence of lower oxygen molecules in the bio-oil is the main reason for the increased heating value. The addition of wood-based lignocellulosic material with plastic waste reduced the heating value to 34.6 MJ/kg. Furthermore, individual biomass pyrolysis oils
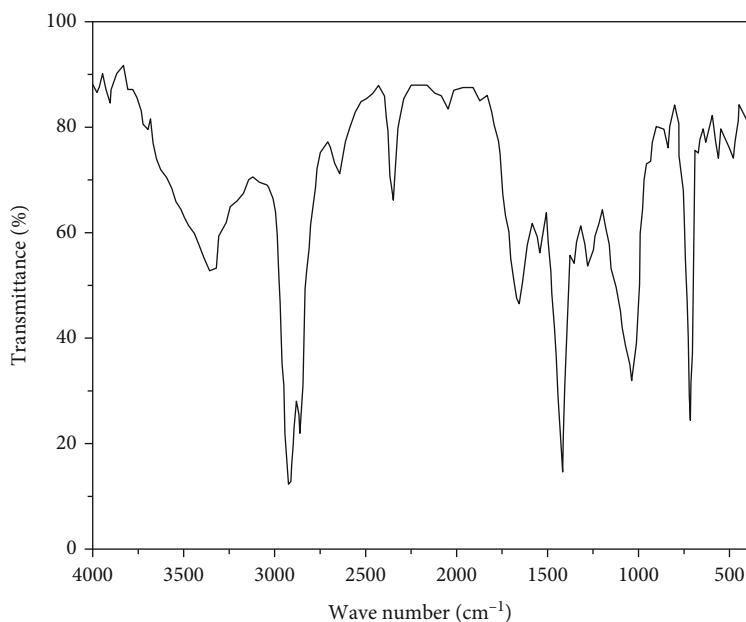
FIGURE 7: FTIR spectra of catalytic co-pyrolysis oil.

showed lower heating values than co-pyrolysis oils due to a higher fraction of oxygenated elements in the feedstock materiel. The pH value of the co-pyrolysis and catalytic pyrolysis oils is moderate in the range of 4.6-4.8. It is a representation of the corrosiveness of the oil. The value of pH indicates that the bio-oil has less corrosive properties than other bio-oils produced from other biomass materials [55–57]. Acids in the pyrolysis oils are mostly caused by the breakdown of hemicellulose present in the biomass material. The pyrolysis oil typically has a pH value of between 3 and 6 [58]. The lower pH value is naturally corrosive to steel, aluminum, and nickel-based materials.

3.6.2. FTIR Spectra. The FTIR spectrum of liquid oil obtained from the catalytic process derived at maximum yield conditions is shown in Figure 7. From the obtained spectra, it can be confirmed that the liquid oil is a combination of water, phenolic compounds, aromatic compounds, acids, alkenes, and nitrogenated elements. The existence of water and phenolic compounds in the oil is identified by O-H stretching vibration at 3200-3600 cm^{-1}. The same compounds were discovered and reported in the literature [62, 63]. The existence of aliphatic hydrocarbons is specified by C-H stretching and bending vibrations at 2900-3000 cm^{-1} and 1300-1450 cm^{-1}. The existence of alkenes is identified by the peak obtained at 675-900 cm^{-1}.

4. Conclusion

In this work, the synergistic effect of catalytic co-pyrolysis of cotton shell and municipal plastic wastes on liquid oil yield was analysed. The four-phase experimental study showed higher liquid oil yield during the catalytic co-pyrolysis process. During catalytic pyrolysis, a positive synergistic effect on liquid oil production was identified with reduced char

production. During the co-pyrolysis process, polyolefin polymers in the MPW act as perfect hydrogen donors, resulting in higher liquid oil products than biomass pyrolysis oil. On the other hand, the catalytic co-pyrolysis process increased the yield by up to 4.21% more than the co-pyrolysis process because of its positive synergistic effect. The relationships between biomass-derived oxygenated compounds and plastic-derived olefins were the main reason for the positive synergy effect. By the catalytic co-pyrolysis process, the maximum liquid oil yield of 69.3 wt% was acquired at 500°C with a CS/MPW ratio of 1 : 2. The physical analysis of the oil obtained at the maximum yield condition shows 34.6 MJ/kg. The obtained liquid oil can be tested as an alternative fuel for boilers and IC engines. Further research is also possible on kinetic studies of noncatalytic and catalytic pyrolysis reactions.

Data Availability

The data used to support the findings of this study are included within the article.

Conflicts of Interest

The authors declare that there is no conflict of interest regarding the publication of this article.

References

[1] X. Liu, K. R. G. Burra, Z. Wang, J. Li, D. Che, and A. K. Gupta, "Towards enhanced understanding of synergistic effects in co-pyrolysis of pinewood and polycarbonate," *Applied Energy*, vol. 289, p. 116662, 2021.

[2] M. Naushad, G. Sharma, and Z. A. Alothman, "Photodegradation of toxic dye using Gum Arabic-crosslinked-

poly(acrylamide)/Ni(OH)$_2$/FeOOH nanocomposites hydrogel," *Journal of Cleaner Production*, vol. 241, p. 118263, 2019.

[3] A. Azhar, Y. Yamauchi, A. E. Allah et al., "Nanoporous iron oxide/carbon composites through in-situ deposition of prussian blue nanoparticles on graphene oxide nanosheets and subsequent thermal treatment for supercapacitor applications," *Nanomaterials*, vol. 9, no. 5, p. 776, 2019.

[4] P. Madhu, T. Stephen Livingston, and I. N. Manickam, "Fixed bed pyrolysis of lemongrass (Cymbopogon flexuosus): bio-oil production and characterization," *Energy Sources, Part A: Recovery, Utilization, and Environmental Effects*, vol. 39, no. 13, pp. 1359–1368, 2017.

[5] S. N. Naik, V. V. Goud, P. K. Rout, and A. K. Dalai, "Production of first and second generation biofuels: a comprehensive review," *Renewable and Sustainable Energy Reviews*, vol. 14, no. 2, pp. 578–597, 2010.

[6] C. S. Dhanalakshmi, M. Mathew, and P. Madhu, "Biomass Material Selection for Sustainable Environment by the Application of Multi-Objective Optimization on the Basis of Ratio Analysis (MOORA)," in *Materials, Design, and Manufacturing for Sustainable Environment*, pp. 345–354, Springer, Singapore, 2021.

[7] N. H. Al-Shaalan, I. Ali, Z. A. ALOthman, L. H. Al-Wahaibi, and H. Alabdulmonem, "High performance removal and simulation studies of diuron pesticide in water on MWCNTs," *Journal of Molecular Liquids*, vol. 289, article 111039, 2019.

[8] I. Ali, O. M. Alharbi, Z. A. ALOthman, A. M. Al-Mohaimeed, and A. Alwarthan, "Modeling of fenuron pesticide adsorption on CNTs for mechanistic insight and removal in water," *Environmental Research*, vol. 170, pp. 389–397, 2019.

[9] S. M. Wabaidur, M. A. Khan, M. R. Siddiqui et al., "Oxygenated functionalities enriched MWCNTs decorated with silica coated spinel ferrite - a nanocomposite for potentially rapid and efficient de-colorization of aquatic environment," *Journal of Molecular Liquids*, vol. 317, p. 113916, 2020.

[10] Z. A. Alothman, A. H. Bahkali, M. A. Khiyami et al., "Low cost biosorbents from fungi for heavy metals removal from wastewater," *Separation Science and Technology*, vol. 55, no. 10, pp. 1766–1775, 2020.

[11] C. D. Nwani, W. S. Lakra, N. S. Nagpure, R. Kumar, B. Kushwaha, and S. K. Srivastava, "Toxicity of the herbicide atrazine: effects on lipid peroxidation and activities of antioxidant enzymes in the freshwater fish Channa Punctatus (Bloch)," *International Journal of Environmental Research and Public Health*, vol. 7, no. 8, pp. 3298–3312, 2010.

[12] K. Ravindra, T. Singh, and S. Mor, "Emissions of air pollutants from primary crop residue burning in India and their mitigation strategies for cleaner emissions," *Journal of Cleaner Production*, vol. 208, pp. 261–273, 2019.

[13] A. E. M. Fodah, M. K. Ghosal, and D. Behera, "Microwave-assisted pyrolysis of agricultural residues: current scenario, challenges, and future direction," *International Journal of Environmental Science and Technology*, vol. 19, pp. 2195–2220, 2022.

[14] Z. A. ALOthman, "A review: fundamental aspects of silicate mesoporous materials," *Materials*, vol. 5, no. 12, pp. 2874–2902, 2012.

[15] M. A. Khan, A. A. Alqadami, S. M. Wabaidur et al., "Oil industry waste based non-magnetic and magnetic hydrochar to sequester potentially toxic post-transition metal ions from water," *Journal of Hazardous Materials*, vol. 400, p. 123247, 2020.

[16] A. A. Alqadami, M. A. Khan, M. R. Siddiqui, and Z. A. Alothman, "Development of citric anhydride anchored mesoporous MOF through post synthesis modification to sequester potentially toxic lead (II) from water," *Microporous and Mesoporous Materials*, vol. 261, pp. 198–206, 2018.

[17] M. N. Nabi, M. M. Rahman, and M. S. Akhter, "Biodiesel from cotton seed oil and its effect on engine performance and exhaust emissions," *Applied Thermal Engineering*, vol. 29, no. 11-12, pp. 2265–2270, 2009.

[18] J. A. Onwudili, N. Insura, and P. T. Williams, "Composition of products from the pyrolysis of polyethylene and polystyrene in a closed batch reactor: effects of temperature and residence time," *Journal of Analytical and Applied Pyrolysis*, vol. 86, no. 2, pp. 293–303, 2009.

[19] M. S. M. Khan and Z. Kaneesamkandi, "Biodegradable waste to biogas: renewable energy option for the Kingdom of Saudi Arabia," *International Journal of Innovation and Applied Studies*, vol. 4, no. 1, pp. 101–113, 2013.

[20] N. Ágnes and K. U. T. I. Rajmund, "The environmental impact of plastic waste incineration," *AARMS–Academic and Applied Research in Military and Public Management Science*, vol. 15, no. 3, pp. 231–237, 2016.

[21] C. Vibhakar, R. S. Sabeenian, S. Kaliappan et al., "Production and optimization of energy rich biofuel through co-pyrolysis by utilizing mixed agricultural residues and mixed waste plastics," *Advances in Materials Science and Engineering*, vol. 2022, 9 pages, 2022.

[22] R. Verma, K. S. Vinoda, M. Papireddy, and A. N. S. Gowda, "Toxic pollutants from plastic waste- a review," *Procedia Environmental Sciences*, vol. 35, pp. 701–708, 2016.

[23] N. Kiran, E. Ekinci, and C. E. Snape, "Recyling of plastic wastes via pyrolysis," *Resources, Conservation and Recycling*, vol. 29, no. 4, pp. 273–283, 2000.

[24] S. Y. Oh and Y. D. Seo, "Polymer/biomass-derived biochar for use as a sorbent and electron transfer mediator in environmental applications," *Bioresource Technology*, vol. 218, pp. 77–83, 2016.

[25] K. G. Burra and A. K. Gupta, "Kinetics of synergistic effects in co-pyrolysis of biomass with plastic wastes," *Applied Energy*, vol. 220, pp. 408–418, 2018.

[26] A. C. Johansson, L. Sandström, O. G. Öhrman, and H. Jilvero, "Co-pyrolysis of woody biomass and plastic waste in both analytical and pilot scale," *Journal of Analytical and Applied Pyrolysis*, vol. 134, pp. 102–113, 2018.

[27] Q. Jin, X. Wang, S. Li et al., "Synergistic effects during co-pyrolysis of biomass and plastic: gas, tar, soot, char products and thermogravimetric study," *Journal of the Energy Institute*, vol. 92, no. 1, pp. 108–117, 2019.

[28] A. O. Oyedun, C. Z. Tee, S. Hanson, and C. W. Hui, "Thermogravimetric analysis of the pyrolysis characteristics and kinetics of plastics and biomass blends," *Fuel Processing Technology*, vol. 128, pp. 471–481, 2014.

[29] A. Dewangan, D. Pradhan, and R. K. Singh, "Co-pyrolysis of sugarcane bagasse and low-density polyethylene: influence of plastic on pyrolysis product yield," *Fuel*, vol. 185, pp. 508–516, 2016.

[30] A. López, I. De Marco, B. M. Caballero, M. F. Laresgoiti, A. Adrados, and A. Aranzabal, "Catalytic pyrolysis of plastic wastes with two different types of catalysts: ZSM-5 zeolite and Red Mud," *Applied Catalysis B: Environmental*, vol. 104, no. 3-4, pp. 211–219, 2011.

[31] M. del Remedio Hernández, A. Gómez, Á. N. García, J. Agulló, and A. Marcilla, "Effect of the temperature in the nature and extension of the primary and secondary reactions in the thermal and HZSM-5 catalytic pyrolysis of HDPE," *Applied Catalysis A: General*, vol. 317, no. 2, pp. 183–194, 2007.

[32] M. Syamsiro, H. Saptoadi, T. Norsujianto et al., "Fuel oil production from municipal plastic wastes in sequential pyrolysis and catalytic reforming reactors," *Energy Procedia*, vol. 47, pp. 180–188, 2014.

[33] J. Shah and M. R. Jan, "Polystyrene degradation studies using Cu supported catalysts," *Journal of Analytical and Applied Pyrolysis*, vol. 109, pp. 196–204, 2014.

[34] M. Sarker and M. M. Rashid, "Waste plastics mixture of polystyrene and polypropylene into light grade fuel using Fe2O3 catalyst," *International Journal of Renewable Energy Technology Research*, vol. 2, no. 1, pp. 17–28, 2013.

[35] X. Zhang, H. Lei, L. Zhu et al., "Thermal behavior and kinetic study for catalytic co-pyrolysis of biomass with plastics," *Bioresource Technology*, vol. 220, pp. 233–238, 2016.

[36] S. Xu, B. Cao, B. B. Uzoejinwa et al., "Synergistic effects of catalytic co-pyrolysis of macroalgae with waste plastics," *Process Safety and Environmental Protection*, vol. 137, pp. 34–48, 2020.

[37] A. L. F. S. d'Almeida, D. W. Barreto, V. Calado, and J. R. M. d'Almeida, "Thermal analysis of less common lignocellulose fibers," *Journal of Thermal Analysis and Calorimetry*, vol. 91, no. 2, pp. 405–408, 2008.

[38] H. Yang, R. Yan, H. Chen, D. H. Lee, and C. Zheng, "Characteristics of hemicellulose, cellulose and lignin pyrolysis," *Fuel*, vol. 86, no. 12-13, pp. 1781–1788, 2007.

[39] Y. K. Park, M. L. Yoo, H. W. Lee et al., "Effects of operation conditions on pyrolysis characteristics of agricultural residues," *Renewable Energy*, vol. 42, pp. 125–130, 2012.

[40] B. G. Girija, R. R. N. Sailaja, and G. Madras, "Thermal degradation and mechanical properties of PET blends," *Polymer Degradation and Stability*, vol. 90, no. 1, pp. 147–153, 2005.

[41] J. Ábrego, M. Atienza-Martínez, F. Plou, and J. Arauzo, "Heat requirement for fixed bed pyrolysis of beechwood chips," *Energy*, vol. 178, pp. 145–157, 2019.

[42] M. B. Pecha, J. I. Montoya, F. Chejne, and M. Garcia-Perez, "Effect of a vacuum on the fast pyrolysis of cellulose: nature of secondary reactions in a liquid intermediate," *Industrial & Engineering Chemistry Research*, vol. 56, no. 15, pp. 4288–4301, 2017.

[43] O. Onay and O. M. Koçkar, "Fixed-bed pyrolysis of rapeseed (_Brassica napus_ L.)," *Biomass and Bioenergy*, vol. 26, no. 3, pp. 289–299, 2004.

[44] A. E. Pütün, E. Apaydin, and E. Pütün, "Bio-oil production from pyrolysis and steam pyrolysis of soybean-cake: product yields and composition," *Energy*, vol. 27, no. 7, pp. 703–713, 2002.

[45] P. Madhu, H. Kanagasabapathy, and I. Neethi Manickam, "Cotton shell utilization as a source of biomass energy for bio-oil by flash pyrolysis on electrically heated fluidized bed reactor," *Journal of Material Cycles and Waste Management*, vol. 18, no. 1, pp. 146–155, 2016.

[46] A. López, I. De Marco, B. M. Caballero, M. F. Laresgoiti, and A. Adrados, "Influence of time and temperature on pyrolysis of plastic wastes in a semi- batch reactor," *Chemical Engineering Journal*, vol. 173, no. 1, pp. 62–71, 2011.

[47] L. Zhou, Y. Wang, Q. Huang, and J. Cai, "Thermogravimetric characteristics and kinetic of plastic and biomass blends co-pyrolysis," *Fuel Processing Technology*, vol. 87, no. 11, pp. 963–969, 2006.

[48] J. Guo and A. C. Lua, "Kinetic study on pyrolytic process of oil-palm solid waste using two-step consecutive reaction model," *Biomass and Bioenergy*, vol. 20, no. 3, pp. 223–233, 2001.

[49] Z. Ding, J. Liu, H. Chen et al., "Co-pyrolysis performances, synergistic mechanisms, and products of textile dyeing sludge and medical plastic wastes," *Science of the Total Environment*, vol. 799, p. 149397, 2021.

[50] J. D. Martínez, A. Veses, A. M. Mastral et al., "Co-pyrolysis of biomass with waste tyres: upgrading of liquid bio-fuel," *Fuel Processing Technology*, vol. 119, pp. 263–271, 2014.

[51] G. Su, H. C. Ong, Y. Y. Gan, W. H. Chen, C. T. Chong, and Y. S. Ok, "Co-pyrolysis of microalgae and other biomass wastes for the production of high-quality bio-oil: progress and prospective," *Bioresource Technology*, vol. 344, no. Part B, p. 126096, 2022.

[52] X. Zhang, H. Lei, S. Chen, and J. Wu, "Catalytic co-pyrolysis of lignocellulosic biomass with polymers: a critical review," *Green Chemistry*, vol. 18, no. 15, pp. 4145–4169, 2016.

[53] X. Li, H. Zhang, J. Li et al., "Improving the aromatic production in catalytic fast pyrolysis of cellulose by co-feeding low-density polyethylene," *Applied Catalysis A: General*, vol. 455, pp. 114–121, 2013.

[54] H. Zhang, J. Zheng, R. Xiao et al., "Co-catalytic pyrolysis of biomass and waste triglyceride seed oil in a novel fluidized bed reactor to produce olefins and aromatics integrated with self-heating and catalyst regeneration processes," *RSC Advances*, vol. 3, no. 17, pp. 5769–5774, 2013.

[55] R. Suntivarakorn, W. Treedet, P. Singbua, and N. Teeramaetawat, "Fast pyrolysis from Napier grass for pyrolysis oil production by using circulating Fluidized Bed Reactor: improvement of pyrolysis system and production cost," *Energy Reports*, vol. 4, pp. 565–575, 2018.

[56] M. N. Islam, M. U. H. Joardder, S. N. Hoque, and M. S. Uddin, "A comparative study on pyrolysis for liquid oil from different biomass solid wastes," *Procedia engineering*, vol. 56, pp. 643–649, 2013.

[57] Y. K. Rao, C. S. Dhanalakshmi, D. K. Vairavel et al., "Investigation on forestry wood wastes: pyrolysis and thermal characteristics of Ficus religiosa for energy recovery system," *Advances in Materials Science and Engineering*, vol. 2022, Article ID 3314606, 9 pages, 2022.

[58] A. Oasmaa, D. C. Elliott, and J. Korhonen, "Acidity of biomass fast pyrolysis bio-oils," *Energy & Fuels*, vol. 24, no. 12, pp. 6548–6554, 2010.

[59] S. Jamilatun, R. Budhijanto, and A. Budiman, "Non– catalytic slow pyrolysis of Spirulina platensis residue for production of liquid biofuel," *International Journal of Renewable Energy Technology Research*, vol. 7, no. 4, pp. 1901–1908, 2017.

[60] Y. Solantausta, N. O. Nylund, M. Westerholm, T. Koljonen, and A. Oasmaa, "Wood-pyrolysis oil as fuel in a diesel-power plant," *Bioresource Technology*, vol. 46, no. 1-2, pp. 177–188, 1993.

[61] P. Madhu, M. I. Neethi, and H. Kanagasabapathy, "Parametric analysis of cotton shell and Palmyra palm fruit bunch for bio oil in fixed bed pyrolysis system," *International Journal of*

Applied Environmental Sciences, vol. 9, no. 5, pp. 2427–2436, 2014.

[62] E. R. Kenawy, A. A. Ghfar, S. M. Wabaidur et al., "Cetyltri-methylammonium bromide intercalated and branched poly-hydroxystyrene functionalized montmorillonite clay to sequester cationic dyes," *Journal of Environmental Management*, vol. 219, pp. 285–293, 2018.

[63] A. Mittal, M. Naushad, G. Sharma, Z. A. ALothman, S. M. Wabaidur, and M. Alam, "Fabrication of MWCNTs/ThO2 nanocomposite and its adsorption behavior for the removal of Pb(II) metal from aqueous medium," *Desalination and Water Treatment*, vol. 57, no. 46, pp. 21863–21869, 2016.

Retraction

Retracted: Athletes' Ankle Injury Features and Rehabilitation Methods Based on Internet Big Data

Journal of Nanomaterials

This article has been retracted by Hindawi following an investigation undertaken by the publisher [1]. This investigation has uncovered evidence of one or more of the following indicators of systematic manipulation of the publication process:

(1) Discrepancies in scope

(2) Discrepancies in the description of the research reported

(3) Discrepancies between the availability of data and the research described

(4) Inappropriate citations

(5) Incoherent, meaningless and/or irrelevant content included in the article

(6) Peer-review manipulation

The presence of these indicators undermines our confidence in the integrity of the article's content and we cannot, therefore, vouch for its reliability. Please note that this notice is intended solely to alert readers that the content of this article is unreliable. We have not investigated whether authors were aware of or involved in the systematic manipulation of the publication process.

In addition, our investigation has also shown that one or more of the following human-subject reporting requirements has not been met in this article: ethical approval by an Institutional Review Board (IRB) committee or equivalent, patient/participant consent to participate, and/or agreement to publish patient/participant details (where relevant).

Wiley and Hindawi regrets that the usual quality checks did not identify these issues before publication and have since put additional measures in place to safeguard research integrity.

We wish to credit our own Research Integrity and Research Publishing teams and anonymous and named external researchers and research integrity experts for contributing to this investigation.

The corresponding author, as the representative of all authors, has been given the opportunity to register their agreement or disagreement to this retraction. We have kept a record of any response received.

References

[1] X. Li and M. Kang, "Athletes' Ankle Injury Features and Rehabilitation Methods Based on Internet Big Data," *Journal of Nanomaterials*, vol. 2022, Article ID 7904739, 9 pages, 2022.

Research Article

Athletes' Ankle Injury Features and Rehabilitation Methods Based on Internet Big Data

Xinke Li[1] and Meisheng Kang [ID][2]

[1]School of Physical Education&Health, Yulin Normal College, Yulin, 537000 Guangxi, China
[2]Business School, Yulin Normal College, Yulin, 537000 Guangxi, China

Correspondence should be addressed to Meisheng Kang; kangmeisheng@ylu.edu.cn

With the development of science and technology and the improvement of living standards, people are paying more and more attention to sports and health. However, the foot joints are very important joints in the human body and are one of the most vulnerable parts in sports. Foot joint sprain is a common clinical disease in orthopedics, accounting for the first place of joint ligament sprain. If the treatment is not timely or appropriate, it often leaves pain and joint instability, followed by osteoarthritis. The rate of repeated injuries after the first injury is very high. Due to the rapid development of visual sensing technology, computer technology, and image processing technology, Internet big data has been widely used in food, medical treatment, construction, chemical industry, electronics, packaging, automobile, and other fields. This article mainly studies the characteristics and rehabilitation methods of athletes' ankle injuries based on Internet big data. Based on Internet big data, this paper studies the function and structural stability of the foot joints and analyzes the causes of gymnast foot joint injuries. On this basis, this paper puts forward the treatment method of ankle joint injury. In this paper, 20 male competitive bodybuilders with ankle joint injury on one side were randomly divided into experimental group and control group. The experimental group received proprioception recovery training, and the control group received normal functional recovery training. Experimental results show that the proprioception training of foot joint can improve the dynamic balance ability of gymnasts and effectively prevent the occurrence of foot joint injury. In this paper, the stability of the anterior and posterior foot joints was measured by comparing the control group with the experimental group. After 6 weeks of proprioception training, there was no significant difference between the static balance ability of one foot and the healthy part of the injured side foot joints ($P > 0.05$).

1. Introduction

With the advent of the cloud era, big data has also attracted more and more attention. Big data, also known as massive data, refers to the collection of massive data, which can be retrieved, managed, processed, and sorted out in a reasonable time to help enterprises make business decisions. The analyst team believes that big data is usually used to describe a large amount of unstructured data and semistructured data created by a company. These data will spend too much time and money when downloaded to a relational database for analysis [1–3].

Foot joint injury is one of the most common sports injuries, accounting for 10 to 30 percent of the total sports injuries. The ankle joint is the flexion and garrison joint with the largest load on the human body. When standing, the whole body weight falls on the ankle joint, and the load value when walking is 5 times of the body weight. Therefore, ankle sprain is the most prone trauma in daily life. The most important technique in aerobics is jumping. The movement of a series of calisthenics basically depends on the ankle, and the knee, of wide bone flex stretch cushion, reduces the impact that moves to joint and reduces the harm to human body. Therefore, this study clarified the effects of aerobic training on the muscle strength, muscle strength perception, and joint motion perception of the participants' foot joints, providing a reference basis for improving the stability of foot joints and preventing and reducing foot joint injuries.

In terms of theoretical research, experts and scholars at home and abroad have done relevant research on the causes and treatment and rehabilitation methods of sports injury. Hunt et al.'s team believes that injury to the distal ligaments of the tibia and fibula heralds long-term ankle dysfunction. Mild and moderate maxillary joint injuries are difficult to stratify, and the impact of joint mandibular injuries on the size and distribution of ankle strength during physical activity is unclear. Significant changes in ankle kinematics and contact mechanics may explain why moderate comorbidities injuries take longer to heal and are more likely to develop long-term dysfunction and may lead to ankle arthritis [4]. Janssen et al.'s team describes the relationship between the potential predictor variables related to participants and the cumulative compliance of interventions to prevent sprained ankles. They randomized controlled trials (RCT) of the secondary analysis of compliance data and compared measures to prevent ankle ligament injury. They found that participation in high-risk sports was significantly associated with lower compliance of each group receiving NM training [5]. De Castro et al.'s team believes that current-limit strength training or KAATSU training has been proven to be as effective as traditional strength training, which can promote muscle strength and hypertrophy. Metabolic stress plays an important physiological role and may affect the training adaptability in question. In addition, the hypoxia generated by this technique may change the pattern of nerve recruitment. The implementation of this method will lead to an increase in the concentration of growth hormone (GH), which may lead to an increase in the plasma, or even muscle insulin-like growth factor 1 (IGF-1) [6].

Based on the theoretical basis of the treatment of ankle injury, this article randomly selected 20 male competitive aerobic athletes with lateral ankle injury as the research object and randomly divided them into training group and control group. The two groups were trained in rehabilitation for six weeks. The experimental group received ankle proprioceptive rehabilitation training, while the control group received general functional rehabilitation training. Experimental results show that ankle proprioceptive training can improve the dynamic and static balance of gymnasts and can effectively prevent the occurrence of ankle joint injuries.

2. Proposed Method

2.1. Ankle

2.1.1. Physiological and Anatomical Characteristics of Ankle. The ankle is a saddle joint with a wide front and narrow back of the talus. When the foot is in the flexion position of the sole, there is a large number of varus gap, which is easy to cause varus and damage the lateral collateral ligament during exercise. In aerobics, the ankle is mostly used, and excessive fatigue is the external factor leading to the injury [7, 8]. In the ankle joint, the foot is at right angles to the normal position of the lower leg. The increase in the angle between the lower leg and the back of the foot during exercise is called toe flexion, and vice versa. In the normal position,

the ankle joint is not easy to move laterally through the reinforcement of the surrounding ligaments, but easy to bend and extend. Ankle joint is often sprained in training, most of which are foot flexion, which suddenly turns inward, resulting in strong traction and injury of lateral ankle ligament [9, 10]. Valgus causes damage to the medial collateral ligament, also known as the deltoid ligament. The medial ligament of the ankle is very strong. When the medial collateral ligament is damaged, it is easy to be combined with avulsion fracture. But when the occurrence of medial injury, it is easy to combine the fracture, the formation of compound injury. Figure 1 shows the CT image of the ankle joint.

2.1.2. Structural Stability of the Ankle. In order to understand the proprioception and muscular strength characteristics of the foot joints, it is necessary to first understand the components of the foot joints. Ankle joint is one of the most important joints in human body, and it is the basis to guarantee the normal life of human body [11]. Anatomically, the ankle joint is the joint from the bone to the thigh, also known as the gauntlet joint. The fossa consists of the inferior tibial articular surface, the medial side of the fibula leg joint, the lateral side of the fibula foot joint, and the distal articular head. The foot joint package can be relaxed back and forth, retractable, with ligaments on both sides. These ligaments are the medial deltoid ligaments, which fan down from the medial malleolus and rest on the shoulder bone, the distance bone, and the heel bone. There are three lateral ligaments: anterior ligament of the calf, medial ligament of the ankle, and posterior ligament of the calf. All three ligaments begin laterally and stop at the anterior, inferior, and posterior ends of the distance bone and the heel bone. In the ankle ligament injury, the most common is the lateral injury, especially fibula ligament injury. The major muscles of the foot joint are the triceps, tibialis posterior, long neck, and long neck muscles. Fibula has long tendons and short tendons on the outside of the lower leg: the tibial tendon of the foreleg, extensor tendon of the sole of the foot, extensor tendon, and the third peroneal muscle [12, 13]. In fixing these muscles, the foot joints act as fulcrum for movement. In the distal fixation, the thigh is moved with the foot joint as the fulcrum. The ligaments around the foot joint participate in the movement of the foot joint. Before the foot touches the ground, the relaxation of the ligaments around the foot joint is conducive to the integration of the bones of the foot joint. After the foot touches the ground, it can induce the stabilization of the foot joint and the movement of the distance from the bone.

Therefore, the physiological anatomic structure of the ankle is the basis of ankle function and stability. The strength of ankle joint is directly related to the stability of supporting the whole body when completing the action. In aerobics, there are many jumps, and athletes need to control the height, distance, speed, and ankle force of the jump, which requires the athlete's vision, body, and balance to work together. On the other hand, the instability of ankle function sex can make athletic result drops.
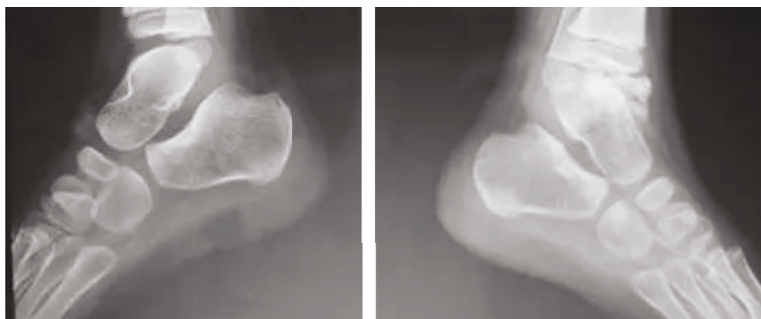
Figure 1: CT image of ankle joint.

2.1.3. Functional Stability of the Ankle. The mechanical function of the ankle joint is mainly the stabilization function of the ligaments around the foot joint and the joint package. The motor function mainly includes foot sole bending and dorsiflexion movement and varus valgus movement, and the neutral position of the internal and external rotation of the ankle refers to the angle perpendicular to the finger. The coordinated movement of the ankle, that is, the correctness of the so-called ankle posture, is mainly reflected in maintaining the stability of the foot below the center of gravity through the force in the opposite direction and eversion. Around the front axis of the foot joint, the foot is flexed and stretched (foot flexion or sole flexion; upward extension or dorsiflexion). The foot joint is basically a one-way joint, and the distance from the bone is mainly along the horizontal axis to represent the sagittal plane movement, which deviates from the coronal plane and promotes dorsolateral and sole flexion. The foot joint and the distance bone joint complement each other, forming a functional complex like the universal joint. The function of the foot joint is mainly in the sagittal plane, and the function of the subosseous joint is mainly in the coronal plane. In dorsiflexion of foot joint with external roll and plantar flexion with internal rotation, the subtalar joint may be combined with dorsiflexion, valgus, and varus. Plantar flexion incorporates internal and external rotation. When walking, the foot joint movement is almost always accompanied by the movement of the subosseous joint. On the contrary, the subosseous joint and the subosseous joint complement each other and move continuously.

2.2. Causes and Preventive Measures of Ankle Injury. The basic steps of calisthenics are alternating system, step system, ground system, foot lifting system, and leg system. Most of these technical movements are mainly based on the spring technique and carried out through the flexion and extension of the foot joints [14, 15]. Body sensation and strength play an important role in everything from body balance to ankle control. When the body and strength feel poor, the ankle is relatively unstable, and the possibility of sports injury increases, which directly affects the training and sports performance. The ankle joint technique of competitive calisthenics runs through the whole movement, and the difficulty of gymnastic movement and jumping rotation increases gradually.

2.2.1. More Difficult Movements. The calisthenic movement is a very difficult item and needs the superb technique for the performance, many difficult moves consist of support, jumps, and turns. These difficult movements will inevitably add to the load on the ankle, especially if the ankle is suddenly thrown into an explosive jump, and the ankle will bear two to four times the weight of the body. When athletes do not have good basic physical quality but are force to learn more difficult and complex technical movements, artificially, they will lack the necessary foundation and cannot complete the difficult technical movements. Therefore, these difficult movements will inevitably increase the possibility of ankle injury.

2.2.2. Too Long Training Time. Calisthenics training time is also the cause of ankle injuries. Because of the long training, the ankle is always under strain. Long-term training and the pressure on the ankle joint is too great, so that the ankle joint is constantly subjected to friction and compression, resulting in excessive fatigue of the ankle joint and resulting in ankle joint injury.

2.2.3. Weak Local Forces. Weak ankle and leg strength is another cause of ankle injuries. In aerobics, there are many jumping movements. Athletes need to fall from heights for a long time, such as kneeling and jumping and splitting in the air. At that time, the strength of the ankle joint was relatively weak, and the buffering effect could not be well controlled when landing, resulting in a short extension, flexion, and valgus of the ankle joint during landing and resulting in ankle joint injury. On the other hand, due to the weak force, some technical movements will be due to their own quality errors, resulting in irregular movements and deformation and resulting in ankle joint injury. It requires that the ankle joint must be strengthened in training or practice to meet the requirements of high-intensity sports.

2.2.4. Insufficient Preparatory Activities. In normal teaching and training, teachers generally pay more attention to the learning of teaching content and technical action. They do not pay enough attention to the lesson preparation activities, resulting in too short lesson preparation time, leading to students in the lesson preparation activities perfunctory. Ankle injuries are caused by intense training, especially aerobic exercise, because of their own characteristics, is more prone

to injury. Winter is the season for ankle injuries. As a result of this period of time, the temperature is lower, the human body capillary contracts, the muscle elasticity decreases, and the viscosity increases; therefore, the leg can cause ankle joint pain and sprain because of insufficient preparation for the movement. Preparatory activities mainly play the following three roles: first, improve muscle temperature and increase the elasticity and extension of muscles and ligaments, second is to improve the skill level of physical participation in sports internal organs, and third is to regulate the psychological function.

2.3. Treatment of Ankle Injury

2.3.1. Routine Treatment. Following, an ankle injury is the "price" principle of the usual treatment in the acute phase, which is the initial braking rest to avoid load, to eliminate swelling, and to allow the tissue to repair itself. Within 48 hours, ice compress was performed on the ankle joint to reduce bleeding and pain then wrapped with a small amount of tape, and finally, the injured ankle was raised higher than the heart to achieve analgesia, cooling, and hemostasis. In severe cases, the stent should be fixed. After receiving basic protection, go to the hospital to take X-ray photos as soon as possible to rule out the possibility of fracture. The basic pain symptoms in the acute phase are relieved, and traditional Chinese medicine is usually used. Athletes' injured ankles are treated with massage, acupuncture, electrotherapy, and rehabilitative practitioners. In the course of treatment, it is necessary to ensure the range of motion of the ankle joint to prevent joint adhesion and the decrease of the range of motion of the ankle joint of the new fibrous tissue. Usually the treatment of ankle injury site is mainly to prevent the injury of the patient to prevent adverse effects to play a certain amount of protection. But the main use of human physiology knowledge of this method of hemostasis and cooling, the lack of clinical effect of rehabilitation, the need to relieve pain and other normal function of the ankle muscle strength training, make their ankle joint get sufficient exercise.

2.3.2. Muscle Strength Training. An injury is accompanied by pain, swelling, effusion, and other symptoms. Braking and physical therapy are carried out in the pretreatment, and muscle strength training is carried out before the joint movement area is recovered and the pain is reduced or disappeared. The purpose of muscle strength training after foot joint injury is to recover the muscle dysfunction caused by motion brake reduction, such as incapacitated tendon atrophy, and to recover the articular tendon weakness caused by foot joint injury. Muscle training to increase muscle strength of the associated muscles around the foot joint is considered an important means to improve joint stability and prevent reinjury. However, the report showed that the negative effects of ligament damage were more significant than the functional changes in muscle strength in motor disorders such as closed soft tissue injuries and joint sprains. Although the muscle tissue around the foot joint was not damaged and muscle strength did not decline, the function of the foot joint was limited. Although the muscle strength of the ankle's associated tendons is strengthened, the ankle can also facilitate recovery and prevent repeated injuries. Some of the findings suggest that the increased muscle strength around the ankle, ankle safety, and ankle stability no longer reduce the risk of injury.

How important muscle strength training is to the rehabilitation treatment of ankle injury, the physiological system of the effect of muscle strength training on ankle rehabilitation still needs further research, and maybe because of the muscle machine, the muscle strength training that leads to the increase of muscle function has the effect of promoting the rehabilitation of ankle. Therefore, in the current research results, muscle strength training is considered to be the first treatment method to consider in the early rehabilitation training of foot joint injury.

2.3.3. Neuromuscular Control. Proprioception training is not a specific training method, but through different training methods, the body's main body fully elicits the sensory acceptor and proprioception to judge the body's shape, and after the perception of the movement process, the unit seeks the comprehensive adjustment of nerve and muscle activity activation. In rehabilitation training after a sprained ankle, as a balance of choice, many therapists restore the function of the ankle to train the nerves; muscle control function is one of the important methods. According to research, there is a certain signal after an ankle sprain, but the relevant empirical research is not very clear. In training, in order to maintain the stability of the ankle joint, its rehabilitation balance function plays a great role. It is usually necessary to train the patient to balance on the uneven plane, such as rotating plate, foam material, special ankle movement balance training machine, standing on the adjustable imbalance plane, by the ankle receptor around the agent to participate in the exercise of the adjustment, which helps improve the stability of the ankle. This balance training has been studied in different sports to improve joint proprioception and reduce the risk of reinjury. The training does to some extent increase the stability of the foot joint and reduce the risk of recurrent sprain, but it is necessary to investigate whether there is a potential association with the physiological mechanism and the enhanced neural control function of the surrogate receptors around the foot joint.

2.4. Big Data. Big data, or huge amount of data, refers to the amount of data involved is so large that it is impossible to capture, manage, process, and organize within a reasonable time through the current mainstream software tools to help enterprises make business decisions more positively. Big data has the characteristics of large scale, fast flow speed, and rich forms. Big data has been widely used and developed in aviation, e-commerce, and other fields, making up for the previous data acquisition methods and expanding the breadth and depth of data utilization. Figure 2 shows the application areas of big data.
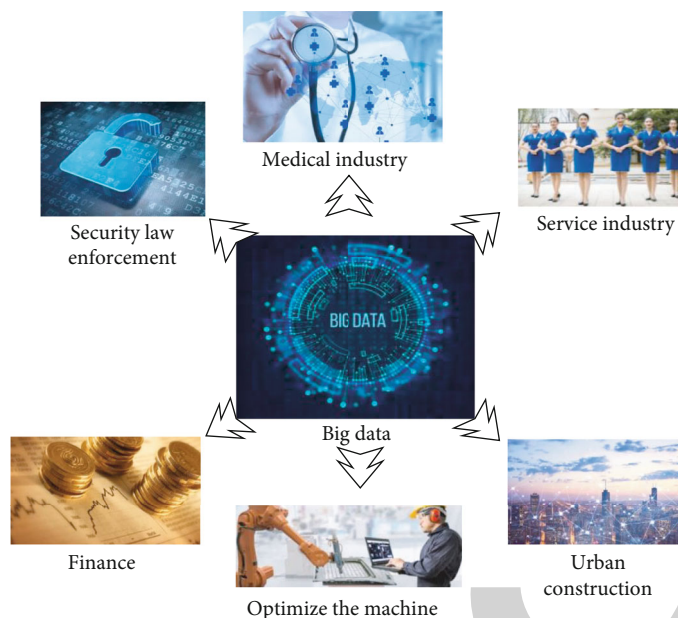
FIGURE 2: Application areas of big data.

3. Experiments

3.1. Data Collection. In this paper, 20 male competitive calisthenics players with ankle joint injury of only one foot were randomly selected as the research object: experienced unilateral ankle joint sprain within half a year, no ankle joint sprain in the last month, no history of lower limb fracture or operation, and the other side of the foot joint was not injured. The pretensile test and range bone tilt test were negative. According to the basic conditions of the research subjects' age, height, weight, etc., this article randomly divided 10 subjects into the experimental group and the control group in order to compare the damage of knee and ankle muscle strength and function of injured athletes and the degree of recovery after training. The age distribution is shown in Table 1. There was no significant difference between the two groups ($P > 0.05$), which could be compared. All subjects fully understood the purpose and process of the experiment and spontaneously participated in the experiment. The specific conditions of the two groups are shown in Table 2.

3.2. Experimental Method. In this paper, all the experimental intervention and data mining processes were completely completed in a professional sports rehabilitation training hall, and the whole process of the experimental process was monitored, so as to achieve timely adjustment and authenticity of the experimental data. The experimental group received proprioception recovery training, and the control group received normal functional recovery training. The experimental group and the normal training group were given 6 weeks, 3 times a week, of about 40 minutes of exercises on foot joint function. The experimental intervention was performed once a day for 1 test subject, and the same training could not be performed more than twice a day. Intervention sessions are held Monday through Friday from

TABLE 1: Age distribution table of the two groups.

Age	20	21	22	23	24
Test	2	1	4	1	2
Control	1	1	5	2	1

TABLE 2: Details of the two groups.

Group	Height	Weight	Diseased side Right	Left	Age
Test	173	68	4	6	22
Control	174	68	5	5	22

9 a.m. to 12 a.m. and from 2 p.m. to 5 p.m. Experimental interventional rehabilitation training was carried out on 6 persons in the experimental group and the normal training group each day. During the experiment, this study tried to create an atmosphere consistent with the usual training, so as to ensure that each subject's lifestyle did not need to change, and they would not receive any other rehabilitation training and physical sensory training. At the same time, there was no uncomfortable stimulation.

3.3. Test Index

3.3.1. Ankle Stability Test. Overall static parameters reflect the ability of the ankle joint to balance and stabilize. Front and rear axial static parameters reflect the ability of the ankle joint to balance and stabilize in the front and back directions. Left and right axial static parameters reflect the ability of the ankle joint to balance and stabilize in the left and right directions.

3.3.2. Ankle Proprioception Test. The overall stability index (SI) reflects the overall average swing angle or swing of the subject when standing. The anterior-posterior stability index

TABLE 3: Test results of the static balance ability of the affected ankle on one foot.

	Test group		Control group	
	Before	After	Before	After
Overall static parameters	3.7	2.7	3.7	2.8
Front and rear axial static parameters	2.5	2.1	2.5	2.3
Left and right axial static parameters	3.4	2.6	3.4	2.4
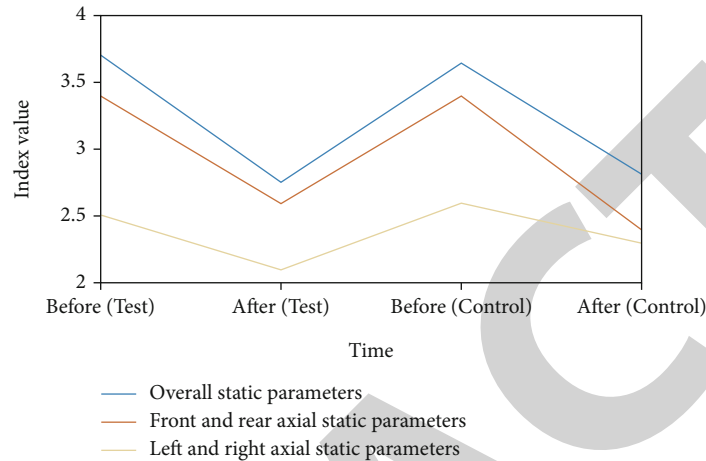
FIGURE 3: Test result of the static balance ability of the affected ankle.

(A/PSI) reflects the average swing angle or swing of the subject on the sagittal plane when standing. The left-right stability index (M/LSI) reflects the average swing angle or swing of the subject on the frontal plane when standing. The lower the above value, the smaller the degree of body shaking, indicating that the balance ability is stronger.

3.4. Statistics. This article uses Excel2010 to process the data before and after the experiment. All parameters are expressed in the form of mean ± standard deviation. SPSS18.0 software is used for mathematical statistical analysis. The test method is multivariate analysis of variance and paired sample T test. The significance level is 0.05.

4. Discussion

4.1. Test Results and Analysis of Injured Ankle Balance Function

4.1.1. The Static Balance Ability of the Affected Ankle Joint. Before and after the experiment, the experimental group and the control group were tested on the balance of the ankle. In this article, we tested each study object using the one-legged static balance test feature of the pro-kin system. Each subject was tested according to standard procedures, using the same test instrument. After the completion of the test, the test results of 20 subjects were collected and counted. Then, the three important indexes of stability of ankle joint in one-foot static balance function test system were analyzed. Then, the three indexes are calculated as the mean and standard deviation. The results of one-foot static balance test of the affected ankle joint are shown in Table 3 and Figure 3.

As we can see from Table 2 and Figure 1, intervention before the experiment, according to the control group and experimental group of ankle joint parts of a single static balance test results, can be seen, and after an ankle injury, ankle joint parts of the overall static parameters than health intactness of the overall static significantly increased ($P < 0.05$), especially front axle static parameters are significantly different ($P < 0.05$), and the difference of front axle static parameter is not obvious ($P > 0.05$). That is to say, the stability of the foot joint changes after the injury, especially the static parameters of the left and right axis direction are significantly different, and the potential risk of unstable reinjury of the foot joint is significantly increased. After 6 weeks of ankle function recovery training, the two groups of affected ankle joints were tested on the static balance function of one foot. There was a significant difference between the experimental group and the experimental group ($P < 0.05$). There were significant differences in the foot joints of the training group compared with those before the experiment ($P < 0.05$). This suggests that six weeks of training in the ankle function recovery system can effectively improve the stability of the damaged ankle joint.

4.1.2. Healthy Ankle Joint Static Balance Ability of One Foot. The main foot joint is the foundation and key to complete the new gymnastic balance movement. The balance pose requires not only the strength of the flexor muscles but also the strength of the muscles to be extended by combining with the ankle to achieve the balance. The quality of the balance movement is mainly determined by the development balance of the conventional ankle joint force and the joint

TABLE 4: One-leg static balance ability of the healthy ankle.

	Test group		Control group	
	Before	After	Before	After
Overall static parameters	2.9	2.8	2.7	2.7
Front and rear axial static parameters	2	2.1	2.1	2.1
Left and right axial static parameters	2.4	2.5	2.2	2.3
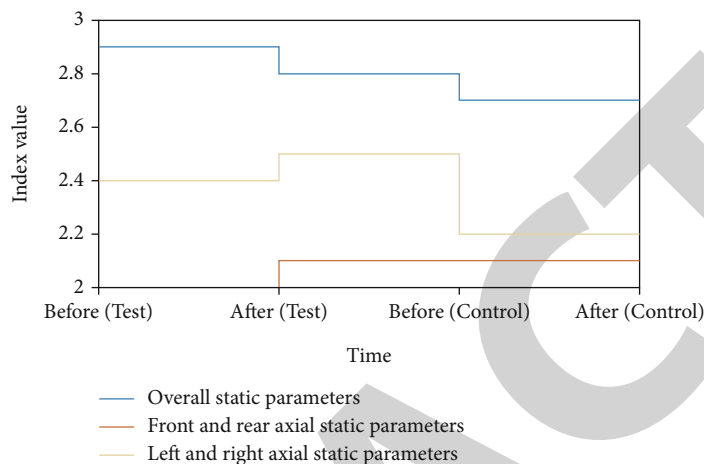
FIGURE 4: One-leg static balance ability of the healthy ankle.

TABLE 5: Test results of dynamic balance ability with both eyes open and standing on both feet.

	Before (test)	After (test)	Before (control)	After (control)
Overall static parameters	0.237	0.136	0.321	0.246
Front and rear axial static parameters	0.189	0.067	0.241	0.193
Left and right axial static parameters	0.104	0.069	0.133	0.127

improvement of flexion and extension. Low-level athletes spontaneously teach the foot joint force imbalance, and the stability of the balance movement is poor. Therefore, in the balance movement of the new gymnastics to the strength of the ankle joint, the main demand is the strength of the flexion and extension group of the coordination of balanced development and common improvement. The results of static balance ability test of healthy ankle joint are shown in Table 4 and Figure 4.

As shown in Table 3 and Figure 2, according to the results of measuring the static balance ability of one foot in the experimental group and the normal training group before the experimental intervention, the overall static parameters of the healthy foot joints in the experimental group were not significantly different from those in the control group ($P > 0.05$). After 6 weeks of training on the recovery of foot joint function, the static balance function of one foot in two groups of healthy joints was tested again. After the experiment, there was no significant difference in the static balance ability of one foot in the affected side foot joint compared with that before the experiment ($P > 0.05$), and there was no significant difference between the affected side foot joint in the comparison group and before the experi-

FIGURE 5: Test results of dynamic balance ability with eyes open and standing on both feet.

ment ($P > 0.05$). The comparative analysis of relevant data between the experimental group and the comparison group showed no significant difference, indicating that the

Table 6: Test results of standing dynamic balance ability with closed eyes and feet.

	Before (test)	After (test)	Before (control)	After (control)
Overall static parameters	0.224	0.331	0.097	0.241
Front and rear axial static parameters	0.186	0.217	0.034	0.231
Left and right axial static parameters	0.113	0.142	0.020	0.167

magnitude of foot joint load did not affect the functional training of injured foot joint balance.

4.2. Test Results and Analysis of Ankle Joint Function with Standing Feet

4.2.1. Dynamic Balance Ability when Standing with Eyes and Feet Open. In general, the lower the balance index, the less the body shakes and the higher the balance. In this paper, the results of proprioception test of ankle joint when standing with eyes and feet open were analyzed by multifactor dispersion analysis: gender: male and female; combination: experimental group and control group; test cycle: six weeks. It had a significant impact on the overall stability index (SI) and the left and right stability index (M/LSI) of open eyes before and after the test and had a significant difference in the SI and M/LSI values after 6 weeks of training ($P < 0.05$). The stability index (A/PSI) was lower after training than before, but there was no significant difference ($P > 0.05$). The results of the dynamic balance test when standing with both eyes and feet are shown in Table 5 and Figure 5.

We can see from Figure 3 that the different value of the overall stability index before and after the experiment is more significant than that of the control group. In this paper, professional sample T test was used for data analysis, and the analysis index was the anteropositive stable index (a/psi) and the left and right stable index (m/lsi). In this paper, it was found that when standing with the eyes open, the change of the stability index was greater than that of the left and right stability index, and the difference was significant ($P < 0.05$).

4.2.2. Dynamic Balance Ability when Standing with Eyes Closed and Feet Closed. In this paper, the dynamic balance ability of the experimental group and the control group was measured before and after the experiment. There was no significant difference in the dynamic balance ability of the two groups before the experiment, and the left and right stability index (M/LSI) of the experimental group was obvious after the experiment, that is, the left and right stability index of the experimental group was significantly smaller than that of the control group after the experimental training. There was a significant difference in the left and right eye closure stability index (M/LSI) before and after training, and the index test value decreased significantly after the training. In terms of overall stability index and before and after stability index, compared with before training, the value after training tends to decrease, but there is no signific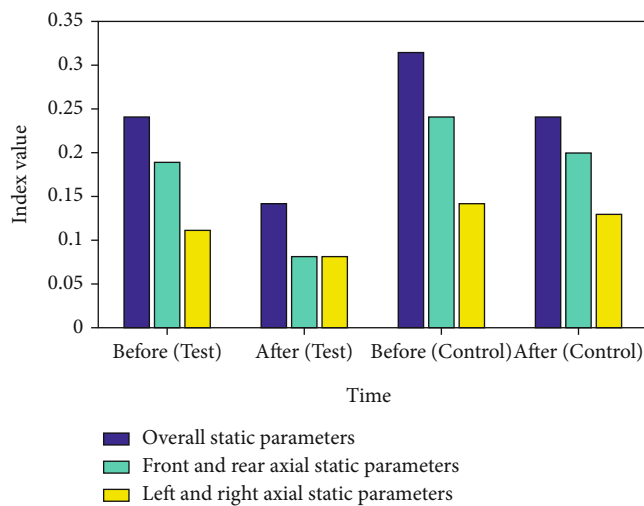ant difference. Table 6 and Figure 6 show the test results of standing dynamic balance ability with closed eyes and feet.
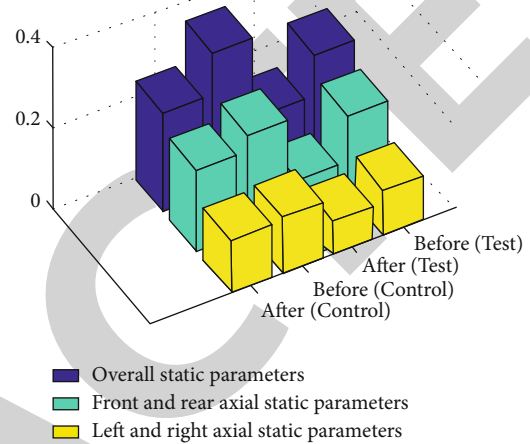
Figure 6: Test results of dynamic balance ability with eyes closed and standing on both feet.

As can be seen from Figure 4, for the left-right stability index when standing with eyes closed and feet closed, the posttest index value of the experimental group and the comparison group was smaller than the pretest value. The left and right eye closing stability index and right and right foot stability index of the experimental group with proprioception training were significantly reduced compared with the control group with normal rehabilitation training, which also indicated that the balance stability of proprioception training was better. After the anteroposterior stability index and the left and right stability index were analyzed by the corresponding sample T test, the anteroposterior stability index was significantly larger than the left and right stability index under the two-vertical condition of eye closure ($P < 0.05$).

5. Conclusions

(1) The experiment in this study shows that after the foot joints are damaged, the proprioception of the foot joints of competitive aerobic players will be affected and their ability will be reduced. Normal functional recovery training for damaged foot joints can help restore proprioception. Under the reduced condition, the proprioceptive function of the foot joint did not change, although the load was reduced. Therefore, weight loss training can be applied in the early stage of foot joint injury to help competitive bodybuilders recover the function of damaged foot joint

Hindawi

Research Article

Application of Nanoporous Super Thermal Insulation Material in the Prevention and Control of Thermal Hazards in Deep Mining of Metal Mines

Yigai Xiao [iD],[1,2] **Hongwei Deng,**[1] **Zhimou Xie,**[2,3] **and Wei He**[2]

[1]*School of Resources and Safety Engineering, Central South University, Changsha, 410083 Hunan, China*
[2]*Sinosteel Maanshan General Institute of Mining Research Co., Ltd., Maanshan, 243000 Anhui, China*
[3]*Sinosteel Nanjing Huaxin Technology Co., Ltd., Nanjing, 211100 Jiangsu, China*

Correspondence should be addressed to Yigai Xiao; xiaoyi421@csu.edu.cn

As an important energy material, mineral resources have an important role in the rapid growth of the national economy. In recent years, with the enhancement of mining strength and the improvement of mechanized production level, the depth of mining has also increased year by year. Therefore, the number of heat hazards in deep mine mining has increased year by year, and the problem of heat loss in deep mines has become increasingly prominent, which has seriously affected the safe and efficient production of mines. In this paper, the application of nanoporous super insulation materials in the prevention of thermal damage in deep mining of metal mines is studied, and the related theories of nanoporous super insulation materials and the prevention of thermal damage in deep mining of metal mines are understood on the basis of literature data. Nanoporous thermal insulation materials refer to thermal insulation materials with pore diameters in the nanometer range. This material can effectively prevent the collision of gas molecules and prevent the heat conduction of the gas. Then, the application experiment of nanoporous super thermal insulation materials in the prevention and control of heat damage in deep mining of metal mines is carried out. Through experiments, it is concluded that the room temperature thermal conductivity of the experimental material decreases with the increase of the addition of SiO_2 aerogel, and the downward trend is linear, and when the heat source temperature is 200°C, the coating surface temperature of the thermal insulation material (excluding aerogel) is 100°C, and the thermal insulation temperature difference is 100°C, while when the coating surface temperature of the aerogel thermal insulation coating is only 60°C, the thermal insulation temperature difference is 140°C. From these data, it can be seen that the thermal insulation performance of nanoporous super thermal insulation materials is better, which verifies the feasibility of its application in the prevention of heat damage in metal mine mining.

1. Inductions

Mineral resources, as one of the main energy consumed by the current social development, have played a vital role in the progress of social development. The mines in the central and eastern mining areas have introduced deep mining before, and the current mining depth of deep mines is still expanding [1, 2]. However, due to the expansion of mining depth, the temperature of deep mine shafts continues to rise, which seriously affects normal safe production [3, 4]. Thermal damage

in deep mine development is an objective reality, and creating a cool working environment is also an issue that needs to be improved in China's domestic mine development [5, 6]. Since China is the world's largest mineral resources producer, 95% of its mineral resources come from wells. In-depth study of mine utilization methods in order to obtain more mineral resources to support national construction and many mines in China have been developed at depths of more than 900-1300 meters, so high temperature heat loss in mines is an urgent need to solve the problem [7, 8].

In order to meet the high demand for mineral resources in the rapid development of society, it is necessary to increase the exploitation of mineral resources in the deep part of the earth. Solving the problems of ventilation difficulties and high temperature heat damage encountered in the process of deep well mining will greatly reduce the difficulty of mining mineral resources deep in the earth, improve the availability of underground energy, and promote the rapid development of society [9].

Regarding the investigation of thermal damage in mines, some scientific researchers pointed out that ventilation and refrigeration is the most common nonfreezing cooling method at present, which can be used to cool, dehumidify, and increase air concentration on the surface of hot mines. Mine ventilation can bring enough air to underground workers, and it can also reduce the content of harmful gases, thereby reducing the high temperature in the basement, but by increasing the ventilation, the pressure increases linearly, and the output of the fan is increased by three times, so mine ventilation alone cannot effectively alleviate the thermal hazards of high temperature mines. Therefore, the conventional coal mine ventilation principle cannot completely alleviate the thermal damage of high temperature coal mines [10]. Relevant researchers believe that the temperature of the original rock rises with the expansion of the mining depth, and the heat release of the original rock is also one of the main heat sources in the deep mine. In the tunnel under the hot mine, because the temperature of the cold air rises, the cold air inevitably conducts countercurrent heat exchange with the hot tunnel wall. If heat insulation materials are used to isolate the heated road wall from the cooling flowing air, the high temperature of the hot mine can be significantly reduced, similar to the thermal insulation of the building facade, which can prevent the facade from interacting with each other in summer and winter. The air between the inner walls performs countercurrent heat exchange, which has a cooling effect in summer, and a heat preservation effect in winter [11]. In the research of nanoporous insulating materials, some scholars have pointed out that SiO_2 and its composite aerogel have the characteristics of extremely low density, large specific surface area, and high porosity. They are suitable for many fields, and many unknown fields have great applications. Especially in the field of private thermal insulation, with the progress of economic growth, the world pays more and more attention to energy issues, and daily energy saving is particularly important. Due to the special pore structure characteristics of aerogel, it has an excellent thermal insulation effect. Compared with other insulation materials such as cotton insulation and polyurethane insulation, it has the advantage of better insulation performance and makes up for the disadvantage of poor thermal stability, so it has good potential application value [12]. To sum up, the research on the prevention and control of heat damage in mines has attracted much attention, but most of the studies have focused on artificial cooling measures, and few scholars have studied the use of heat insulation materials to control the generation of heat sources.

The innovations of this paper are as follows: (1) The application of nanoporous super insulation materials in the prevention and control of heat damage in deep mining of metal mines is studied. (2) The thermal damage in deep mining of metal mines and the thermal insulation principle of nanoporous super insulation materials are analyzed. (3) The feasibility of applying nanoporous super insulating materials in the prevention and control of heat damage in deep mining of metal mines is analyzed. (4) The application test of nanoporous super insulating material in the prevention and control of heat damage in deep mining of metal mines was carried out, and the feasibility of the method was verified by experiments.

2. The Prevention and Control of Thermal Damage in Deep Mines in Metal Mines and Nanoporous Super Thermal Insulation Materials

2.1. Analysis of Thermal Hazards in Deep Mine Mining in Metal Mines. The mining depth is more than 800 m, which is a deep well mining. Rocks with type II deformation characteristics at this depth will experience frequent rockbursts, which will affect the safety of the operation. The factors that cause thermal damage to deep wells include geothermal heat (mainly hot water produced by surrounding rocks and wells) and air compression heat entering the well (mainly air intake wells, inclined wells, etc.), ore oxidation, and thermal diffusion of underground electromechanical equipment, heat dissipation, explosive heat, and underground heat [13]. The mining methods of deep well mines are basically the same as those of shallow well mining, including three categories: open field method, filling method, and caving method. However, its structural parameters, mining sequence, and mining process should be adjusted according to the characteristics of deep mines, and due to the particularity of deep mines, the backfill mining method will become the mainstream mining method. Among them, the problems faced in deep well mining include deep well heat damage, ventilation and cooling problems, high ground pressure, and deep well water inflow. As the mining depth and lifting height increase, the weight of the lifting wire rope increases, and the ineffective energy consumption caused by the dead weight of the wire rope in the lifting operation becomes more and more prominent.

The heat of blasting is released instantaneously and plays a major role in the instantaneous rise of the temperature in the well, but the heat in the mine does not rise because of the short duration. Especially the underground DC ventilation can effectively prevent the accumulation of shock waves and quickly dissipate heat. Generally speaking, iron ore requires staff to clean up the site before organizing ore mining and blasting. After blasting, ventilation is required for a period of time before personnel can enter. Therefore, it is not necessary to consider the super position of blast heat as a cooling system to improve the working environment of underground workers [14]. Among them, deep well mining has the following main characteristics: high ground pressure, high ground temperature, and large mine gas.

2.1.1. Geothermal (Wall Stone). For deep iron ore, the initial rock temperature is very high, which is usually the main

reason for the high temperature of the mine. The heat transfer between hot wall rock and airflow is a complex and unstable heat transfer process. The airflow is very active in the mine. The walls and roads of the mine are convex. The thermal energy on its surface releases heat to the wind flow, thereby transferring the heat from the original rock to the cold mine wall and driveway. At the same time, the deep rocks are also cooled to form a cooling zone, and the temperature rises after heating. With the extension of the aeration time (generally one year later), the expansion of the cooling zone begins to weaken after the surrounding rock and the airflow have fully heat exchanged [15].

2.1.2. Thermal Oxidation.
Sulfur and iron in iron ore may undergo an exothermic oxidation reaction when they encounter oxygen in the air, leading to an increase in soil temperature. The heat released by oxidation is generated by the ore exposed to wind currents. After the connecting strips of the iron ore vein road, all the walls of the road surface are fixed with concrete mortar, so the oxidation heat release is mainly carried out in the vein tunnel and mining [16].

2.1.3. Heat Dissipation of Electromechanical Equipment.
With the increase in the degree of mechanization of production links such as underground mining, tunnel boring, and iron ore transportation, the installed capacity of electromechanical equipment has grown rapidly. The installed power of tunnel surface is above 1000 kW. The electrical energy consumed by underground electromechanical equipment is either used to increase the kinetic energy of materials or liquids (the kinetic energy changes very little, usually negligible), or it is converted into heat energy, and almost all of the heat energy generated is diffused into the air [17].

2.1.4. The Surface Atmosphere Brings Heat.
Air flows from the surface to the wellhead, and the temperature and humidity of the surface atmosphere inevitably affect the temperature and humidity of the air in the well. The moisture content of the surface atmosphere changes very little every day, showing a pattern of high at noon and low at night. Although the daily temperature fluctuates greatly, when it flows into the well, due to the heat exchange with the rocks in the surrounding tunnel, the fluctuation of the air temperature in the well gradually becomes smaller, and this change is basically not felt in operation. The main influence of downhole air temperature by climate is the seasonal variation of surface temperature, especially water content. This is because the latent heat of water vaporization is much greater than the specific heat of air. In summer, the surface temperature and humidity are relatively high, which is one of the factors that affect the increase in temperature and humidity of downhole air flow [18].

2.2. Thermal Insulation Principle of Nanopore Super Thermal Insulation Material

2.2.1. Principle of Heat Conduction.
The essence of heat conduction is the process of transferring energy from the high temperature part of the object to the low temperature part, or from the high temperature object to the low temperature object, by the collision of a large number of molecular thermal motions in the material. A porous material is a material with a network structure composed of interconnected or closed pores [19]. For porous materials, the gas thermal conductivity measured experimentally is often greater than the sum of the gas thermal conductivity and the gas thermal conductivity. The gas-solid combined thermal conductivity is the increase in thermal conductivity caused by the gas-solid interaction. In the process of transferring heat to the porous material, some gas molecules are placed in the small holes, which can be used as a shortcut for heat transfer to create new heat transfer channels. Compared with continuous medium materials, porous materials generally have the advantages of low relative density, high specific strength, high specific surface area, light weight, sound insulation, heat insulation, and good permeability. If the material contains many channels, it can conduct gaseous heat, which will make the gaseous heat have a more obvious effect (as shown in Figure 1). This heat transfer process is carried out with gas molecules as the carrier, so it is related to the number of gas molecules (gas pressure). The greater the difference between the thermal conductivity of solid and the thermal conductivity of gas, the more obvious the bonding effect, and the greater the thermal conductivity of gas-solid bonding. If the pore size is very small, the gas molecules transfer heat in a manner similar to the lattice vibration, which can produce a very obvious gas-solid bonding thermal conductivity [20]. In the industry, there are many heat transfer processes dominated by heat conduction, such as heating and vulcanization of rubber products and heat treatment of steel forgings. The law of heat conduction plays an important role in the design and calculation of kilns, heat transfer equipment, and thermal insulation and in the analysis of temperature distribution of catalyst particles [21].

2.2.2. Characteristics of Nanoporous Thermal Insulation Materials.
Nanoporous thermal insulation materials refer to thermal insulation with pore diameters in the nanometer range. This material can effectively prevent the collision of gas molecules and prevent the heat conduction of the gas. The thermal conductivity of the nanoporous thermal insulation material under normal temperature and pressure can be lower than that of static air. Therefore, nanoporous thermal insulation materials and vacuum thermal insulation materials are also called super thermal insulation materials. At present, nanoporous insulating materials are mainly composed of aerosol and nanopowder insulating composite materials. Table 1 shows the density and thermal conductivity of many nanoporous insulating materials. It can be seen that the thermal conductivity of nanoporous insulating materials is relatively low. Nano-microporous thermal insulation materials mainly include thermal insulation materials such as nanoinsulation boards and nanoaerogel felts, and Jinshi nano-microporous thermal insulation materials. According to the particularity of thermal motion, it uses the unique thermal conductivity of nanoporous materials and the heat reflection function given by functional
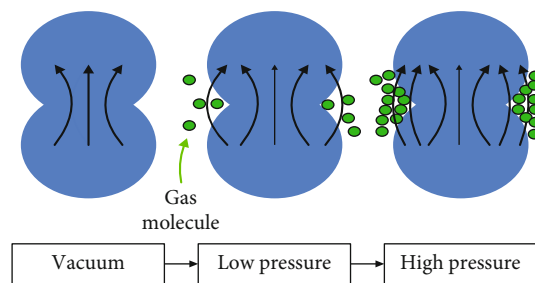
FIGURE 1: Schematic diagram of gas-solid combined thermal conductivity.

materials and is suitable for binders and various inorganic elements. A low thermal conductivity thermal insulation material is produced by a synthetic process, which is actually smaller than the thermal conductivity of still air.

2.2.3. Reasons for Heat Insulation

(1) The pore size of the nanoaerogel is below 100 nm, which effectively increases the reflective interface. If the particle size of the material is in the same order of magnitude as the incident wavelength, the incident electromagnetic wave will be affected by the scattering effect, and the transmittance of the incident electromagnetic wave will decrease. The ability of the material to absorb heat radiation significantly achieves the purpose of heat insulation

(2) Since the air is mainly composed of nitrogen and oxygen, its mean free path of thermal motion is about seventy nanometers. The pore size of nanoinsulating materials is basically no more than fifty nanometers, which is much lower than the mean free path of thermal motion between molecules in the air, so it is in a condition similar to that of a vacuum. Gas molecules cannot enter the nanopores at will. When the gas adheres to the pore wall, the pores no longer conduct heat energy, thereby effectively reducing the thermal conductivity of the material. There are many performance indicators of insulating materials, and the characteristics of various insulating materials are also different. The main performance indicators of commonly used insulating materials include breakdown strength, heat resistance, insulation resistance, and mechanical strength

(3) Due to the low bulk density of nanogels and a large amount of air inside, the thermal conductivity of air at room temperature is the lowest, which effectively improves the thermal insulation performance of the material

Nanoaerogel thermal insulation coating is a kind of composite thermal insulation coating, which combines the characteristics of thermal insulation coating and radiation thermal insulation coating. The thermal insulation principle of the two works together [22].

2.3. The Application of Nanoporous Super Thermal Insulation Materials in the Prevention and Control of Thermal Hazards in Deep Mining of Metal Mines

2.3.1. Preventive and Management Measures against High Temperature Hazards. Nonartificial cooling measures mainly include optimizing the development system and road layout during mine development and development, optimizing extraction and filling methods, strengthening ventilation, adopting controllable circulation, and taking personal protective measures by workers [23].

(1) The development system and road layout are optimized. The mining development system should consider separate development methods as much as possible, and try to use a hybrid or lateral ventilation system with a short air inlet path to reduce heat absorption

(2) Optimize the fixing method and filling method, and adopt the post-fixing sequence. Under the same conditions, the air volume and wind speed of the work surface is higher than that of the front support, which helps to reduce the temperature, which can improve the air circulation and heat dissipation conditions of the mine. Compared with the cavitation method, the filling method increases the effective air volume of the mine and solves the basic problems of hot water leakage, residual combustible ore and surrounding rock in the hole, roof heat, and floor heat diffusion. Lower filling materials will also absorb a lot of heat

2.3.2. Application of Nanoporous Thermal Insulation Materials. According to the above analysis, the nanoporous super insulating material has excellent thermal insulation performance, so this feature can be used to control the heat dissipation of the deep well heat source. The following are the nanoporous thermal insulation measures.

(1) Laminated Insulation. The method of laminated insulation is relatively simple. Insulating laminate materials are usually filled with materials with low thermal conductivity and rolled onto the surface where insulation is required. There are three types of laminated insulation: foam type, powder type, and fiber type [24]. In addition to the average temperature of the insulation layer, the thermal conductivity of the foam insulation material also depends on the material and density of the foam gas. Therefore, the insulation laminate should be made of as dense material as possible, because the low density will reduce the heat in the solid. The main disadvantage of dust and fiber insulation is the penetration of water vapor and air through the insulating layer to the cold surface. This problem can be solved by installing a moisture-proof layer. In order to prevent the condensation and solidification of the gas in the insulation material space and ensure good insulation performance, it is necessary to fill and accumulate gas with low thermal conductivity, and the condensation temperature of this gas should be lower than that of the cold surface. Generally, cold

TABLE 1: Density and thermal conductivity of nanoporous insulating materials.

Materials	Composition	Density (g/cm^3)	Thermal conductivity (W/(m:k))	Maximum service temperature (°C)
	Cellulose	0.056-0.098	0.031-0.034	-270
	Polyimide	0.11	0.031	350
Aerogel	Phenolic aldehyde	0.19	0.011	-250
	SiO$_2$	0.16	0.01 3	800
	Carbon	0.052-0.183	0.020-0.037	≥2000

surface temperatures above 77 K are filled with nitrogen, and cold surface temperatures below 77 K are filled with argon.

(2) Vacuum (or Fiber) Heat Insulation. Vacuum heat preservation is to fill the insulating intermediate layer with porous insulating material and at the same time evacuate the space of the insulating intermediate layer to a specific vacuum. The heat conduction of gas is the main way of heat transfer between porous media. Filling the vacuum interlayer with dust can reduce the distance between the radiation surfaces and reduce the thermal conductivity of the gas. Dust particles can reflect and scatter radiation and reduce the heat transfer of radiation. At the same time, the contact area between the dust particles is small, the thermal resistance is high, and the thermal conductivity of the solid is low.

2.4. Preparation of Nanoporous Super Insulation Material. The silicon aerogel manufacturing process includes three basic steps: sol-gel process, aging process, and drying process. The possible uses of silica aerogels depend to a large extent on the microstructural properties of the 3D framework and the nanostructured surfactant group. These special surface structures can generally be obtained by adjusting the sol-gel process parameters and modified silica aerogels, and the process parameters can be used to obtain bubbles with different characteristics. Therefore, it is very important to select a suitable composition and processing method to prepare silica aerogel to meet the performance required by bubbles in various applications. Figure 2 summarizes the existing aerogel manufacturing process and some synthesis parameters. These parameters affect the formation of the gel network, which in turn affects the performance and application of aerogels. Almost all aerogels can be prepared by liquid chemistry (sol-gel method). During the preparation process, changes in several parameters such as the type and quantity and type and concentration of precursors will affect the evolution of the microstructure of the aerogel network. The chemical reaction process of the aerogel composition used to prepare the aerogel material, such as the type of solvent, reaction temperature, and pH value, should be designed according to the desired yield.

In the process of silicon aerogel forming colloidal gel with lattice structure, the alkoxide-forming aerogel can ionize the precursor through hydrolysis or acid-catalyzed reaction and then alkali-catalyzed dehydration and condensation. In the reaction, the two -OH remove a H$_2$O molecule to form a siloxane bond. During the aerogel preparation process, the condensation polymerization reaction and hydrolysis reaction of the silane precursor and the alkoxide

solvent proceed simultaneously, continue to exist in the entire colloidal gel process, and eventually lead to gel after the reaction.

The sol-gel reaction process has many parameters that affect its structure. The three-dimensional structure of the gel can be adjusted by adjusting the basic parameters of the reaction, and ultimately determine the nanostructure of the network and the properties of the final material, which is controlled. These parameters usually include precursor concentration, relative precursor and solvent concentration, solvent type, relative water and precursor concentration, temperature, and pH. In addition, organic molecular groups or nanoscale organic groups can be added during the sol-gel reaction process to give the gel network a specific function. Generally speaking, suitable alkoxide derivatives containing organic functional groups can be added by chemical reactions, or additives can be used in the porous network by natural methods. For example, it can be used in liquid gels to obtain hydrophobic aerogels, and the surface of the network structure is introduced by chemical reaction to introduce methyl functional groups to obtain a hydrophobic structure. It can also increase the mechanical strength of polymer mixtures and gels. In addition, catalysts, nanoparticles, magnetic, or titanium oxide nanoparticles can be added to the gel network structure to obtain new aerogel properties such as catalytic properties, optical properties, mechanical strength, and magnetic properties.

3. Application Experiment of Nanoporous Super Thermal Insulation Materials in the Prevention and Control of Heat Damage in Deep Mining of Metal Mines

3.1. Preparation of Experimental Materials

3.1.1. Experimental Materials. The materials used in the experiment are 45% concentration silica solution, solidified magnesium oxide, Portland P. C 32.5R initial strength silicate composite cement, White Soot 2000 mesh, foaming agent, pore former, and other additives.

3.1.2. Additives. The additives used were pore-forming agent and foaming agent obtained from Chengdu Kelong Chemical Reagent Factory.

3.1.3. Reinforced Materials. Glass fiber was obtained from Chengdu Kelong Chemical Reagent Factory. The chemical composition is shown in Table 2.
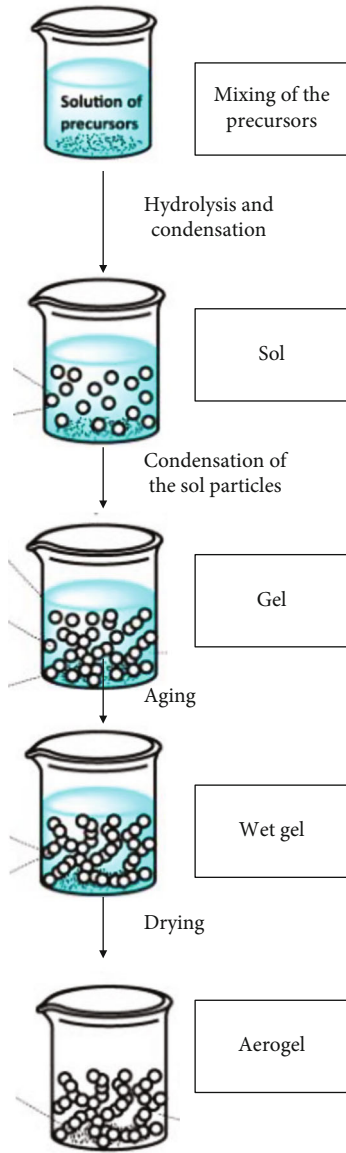
FIGURE 2: Aerogel manufacturing process.

TABLE 2: Chemical composition of glass fiber.

	SiO$_2$	Al$_2$O$_3$	MgO	Li$_2$O	Fe$_2$O$_3$	B$_2$O$_3$	CeO$_2$
%	51-59	24.5-26.5	11-20	0-0.9	0.6-1.5	1-4	0.6-0.8

3.1.4. Formation Mechanism of Stomata Structure. Weigh cement-based materials, fillers, pore formers, etc. According to a certain mixing ratio, pour into a container and mix into a liquid slurry. After the blowing agent is injected, gas is generated and formed during the continuous expansion of the gas-wet interface. When gas passes through the liquid, the surface of the liquid shrinks automatically due to the action of surface tension, and the gas is wrapped by a layer of liquid film to form bubbles. At the same time, the added surfactant contains a large number of anionic groups, these anion groups are compressed into a gas absorption layer, and some of the remaining groups diffuse around the colloid or silicone beam particles, thereby producing surface micelles. The gas acts as a "coating" that sticks the bubbles to the system. The solid particles adhere to the vicinity of the bubble under the action of the initiator, thereby effectively preventing the precipitation of solid particles, and a uniform and stable three-phase power source "solid-liquid-gas" coexistence system is established near the bubble. When the solid phase is condensed, the liquid phase separates, and the solid phase closely surrounds the bubbles, thereby producing a porous silica-based porous insulator with closed pores.

3.1.5. Process Flow. Figure 3 shows the manufacturing process flow of a porous insulating material based on silicon dioxide. Cement-based materials, fillers, air trapping agents, surfactants, and fibers are weighed in a certain proportion, mixed with the cement-based materials, and then the fillers, fibers, and surfactants are added to the container and stirred for about 40 seconds to form a uniform slurry. Then, add the air-entraining agent and stir evenly, and then quickly pour the slurry into the mold. The porous material is formed by on-site self-assembly technology and dried under natural conditions, and then, the experimental sample is cast.

3.2. Experimental Method

3.2.1. Thermal Conductivity Test. There are different thermal conductivity methods for measuring thermal conductivity according to measuring different types of materials, working temperature, and thermal conductivity materials. The method of measuring thermal conductivity can be classified according to the mechanism of thermal conductivity, the shape of the sample, and the direction of heat flow. According to the macroscopic mechanism of thermal conductivity, it is divided into steady method and unsteady method. According to the shape of the sample, it is divided into plane method, rod method, cylindrical method, and ball method. According to the direction of heat flow, it can be divided into longitudinal heat flux method and radial heat flux method. Usually laser method, hot cable method, heat flow method, protective hot plate method, etc. are used.

In this paper, the thermal conductivity of the insulating protective layer is measured by the protective plate method. The protective plate method is measured according to the basic principle of the steady-state differential equation of thermal conductivity. By installing the same two samples between the two cooling plates and the concentrated heating plate of the thermal conductivity meter, a laminated structure of cooling plate, sample, hot plate, sample, and intercooling plate can be produced. In order to ensure the same direction of heat flow through the two specimens, the structure is equipped with a heat preservation structure around the specimen and the heating plate to avoid radial heat transfer and conform to the characteristics of axial one-dimensional heat conduction. After waiting for the temperature distribution of the test sample to balance, a constant temperature δT ($\Delta T = T2 - T1$) is formed on the top and bottom of the sample. By measuring the direction of the temperature flow of the sample and the temperature step
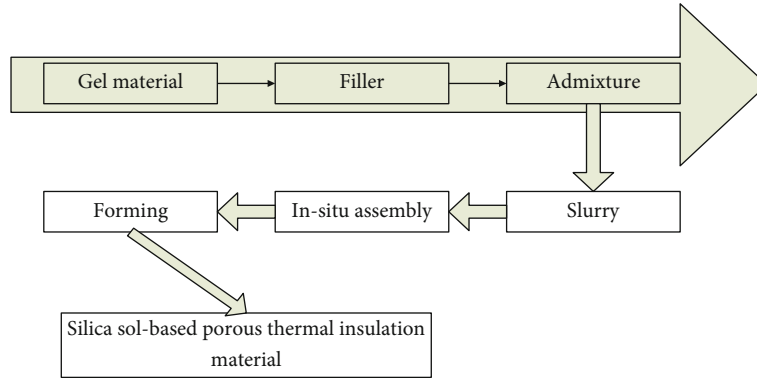
FIGURE 3: Manufacturing process flow of porous insulating material of silicon dioxide.

along it, the direction of the temperature flow and the thermal conductivity of the sample can be obtained using the following heat equation. The test principle of the protection board method is simple and the measurement accuracy is high.

$$\Delta T(\tau) = \left[\frac{p_0}{\pi^{3/2} kr}\right] f(\tau). \tag{1}$$

In the formula, p is the output power of the catheter, the unit is W, r is the radius of the catheter, the unit is m, and $f(\tau)$ is a dimensionless transient function. Here,

$$\tau = \sqrt{\frac{\alpha t}{r^2}}. \tag{2}$$

In the formula, τ is the test time, the unit is s; a is thermal diffusivity.

In this experiment, the Swedish thermal constant analyzer HotDisk TPS250 was used to determine the thermal conductivity of the coating. The sensor placed between the two materials acts as the heat source and temperature sensor of the device and generates specific output energy by introducing current pulses. Since the temperature rise of the catheter is proportional to the voltage, the thermal conductivity of the material can be calculated from the temperature data that changes over time, and the average value of each sample group is measured 3 times.

3.2.2. High Temperature Insulation Performance Test.
Dry the $15\,\text{cm} \times 15\,\text{m} \times 3\,\text{cm}$ sample to be tested, and then place it on a constant temperature hot stage with ceramic digital display to ensure that a stable and uniform air flow can be formed on the heated surface of the sample. Due to the temperature change on the back and the heat-resistant ceramic fiber insulation blanket around the thermocouple, the temperature error caused by the air flow moving on the back of the sample is reduced. Through the three detection points on the front and back of the sample, the temperature evaluation test is carried out within 30 minutes of data. For samples with good high temperature insulation, the lower the front and back temperature, the better the effect of the high temperature insulation system of the sample.

3.3. Establishment of Thermal Conductivity Model.
According to Fourier's law, the thermal conductivity of randomly distributed nanowires is

$$k_{eff} = -\frac{Q_z}{A_z VT}. \tag{3}$$

In the equation, Q_z is the heat flow through the cross section, and VT is the temperature difference in the direction of the heat flow. This is because the pores of the fibrous porous material are very small, and the filling stage is air. Therefore, in the model, the contribution of air to the thermal conductivity of the fibrous porous material is negligible. Therefore, Q_z is the sum of the heat flux of each nanowire passing through the cross section, which can be written as

$$Q_z = \sum_{\alpha=1}^{n_s A_z} Q_\alpha. \tag{4}$$

In the formula, Q_α is the average heat flow through a single nanofiber, the negative sign indicates that the direction of the heat flow is opposite to the z-axis direction, and Q_α is the areal density of the nanowire. Assuming that the contact points of all nanofibers have the same contact thermal resistance, and when the heat passes through the contact points, half of the heat flow flows into or out of a single nanofiber, so we get the heat flow of a single fiber as

$$Q_\alpha = k_0 A_0 \frac{N_c}{2} Bi \frac{\Delta T_{\alpha\beta}}{L}. \tag{5}$$

In the formula, k_0 represents the thermal conductivity of a single nanofiber, $\Delta T_{\alpha\beta}$ represents the temperature difference between contacting nanofibers, and Bi represents the biological number. The formula is

$$Bi = \frac{HL}{k_0 A_0}. \tag{6}$$

In the equation, H is the thermal conductivity of the

nanowire contact, which is the reciprocal of the contact thermal resistance.

Therefore, for randomly distributed nanowires, according to geometric parameters such as the volume fraction, size, and orientation distribution of the nanofibers, the effective thermal conductivity of the porous fiber material can be expressed as follows.

$$k_{eff} = \phi \frac{Bi}{o(4.55 + Bi_T)} k_0. \tag{7}$$

In the formula, φ is the filling rate of fibers in the fibrous porous material, and k_{eff} and k_{eff} respectively, represent the effective thermal conductivity of the fibrous porous material and the thermal conductivity of the fibrous material.

4. Experimental Results

4.1. Thermal Conductivity Test Results. The thermal insulation coatings with different addition amounts of SiO_2 aerogel (as shown in Table 3) were prepared into $15 \, cm \times 15 \, m \times 3 \, cm$ samples, and the thermal conductivity of the coatings at room temperature was tested after drying. The results are shown in Figure 4.

It can be seen from Figure 4 that the room temperature thermal conductivity of the experimental material decreases with the increase of the SiO_2 aerogel addition, and the downward trend is linear.

4.2. High Temperature Insulation Performance Test. In order to investigate the influence of aerogel on the thermal insulation temperature difference, the test results of the thermal insulation temperature difference between the aerogel-free experimental material and the aerogel thermal insulation material were compared, and the results are shown in Figure 5.

It can be seen from Figure 5 that the surface temperature of the aerogel insulation material is generally lower than the surface temperature of the non-silica-based insulation material. This shows that SiO_2 aerogel can effectively enhance the thermal insulation effect of thermal insulation coatings. When the heat source temperature is 200°C, the surface temperature of the material of the thermal insulation layer (without aerogel) is 100°C, and the thermal insulation temperature difference is 100°C, but when the surface temperature of the aerosol thermal insulation material is 60°C, the insulation temperature difference is 140°C. Compared with the nonaerogel thermal insulation material, the temperature of the silica-based thermal insulation material is reduced by 42.3%, and the thermal insulation temperature difference is increased by 42.9%. In contrast, silica-based thermal insulation materials have excellent thermal insulation effects.

Figure 6 is a graph showing the temperature change with time of a silica-based insulation material and a silica-based insulation material-free material.

TABLE 3: Addition of SiO_2 aerogel.

Sample no.	The volume fraction of aerogel in the mixture (%)	The volume fraction of closed pores in the mixture (%)
QY-1	49	4
QY-2	44	4
QY-3	41	4
QY-4	39	4
QY-5	34	4
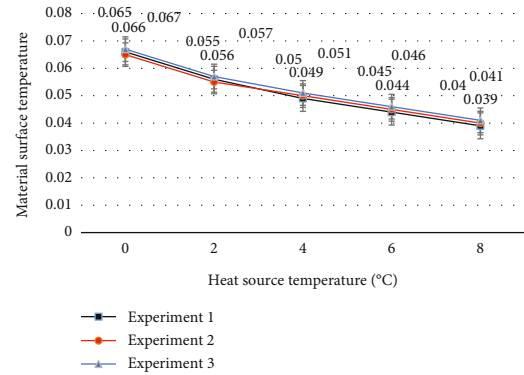
FIGURE 4: Thermal conductivity of paint at room temperature.

It can be seen from Figure 6 that as time goes by, the temperature of the backside of the silica-based insulating material gradually increases. The heating rate is very fast in the first 20 minutes, and the temperature on the back of the sample rises linearly, rising by 7-8°C every minute. After 20 minutes, the growth rate began to slow down. This is mainly due to the fact that as the silica aerogel starts to function and decomposes at high temperatures, the reaction begins to absorb part of the heat. The addition of aerogel powder increases the porosity of the material, resulting in most pores with a diameter of less than 50 nm, which actually eliminates the transfer of heat in the material.

4.3. Fire Performance Analysis. In this part of the experiment, closed pores and air-entraining agents introduced by aerogel powder were used to form a complex insulation system. The aerosol content puts different volume fractions of closed pore gas into the slurry while maintaining its raw material ratio unchanged. Finally, it is possible to produce high-fire performance composite materials with closed porous aerogel material powders with different bulk densities. At the same time, considering the bursting of the foam during the adding or mixing process, the amount of foam added can be adjusted by adjusting the volume density of the mixture. The closed pores refer to the air bubbles sucked by chemicals from the air, except for cement concrete, excess water and other pores produced by cement hydration. In the test, a reference sample with the same composition and no insulation component is usually used as the reference
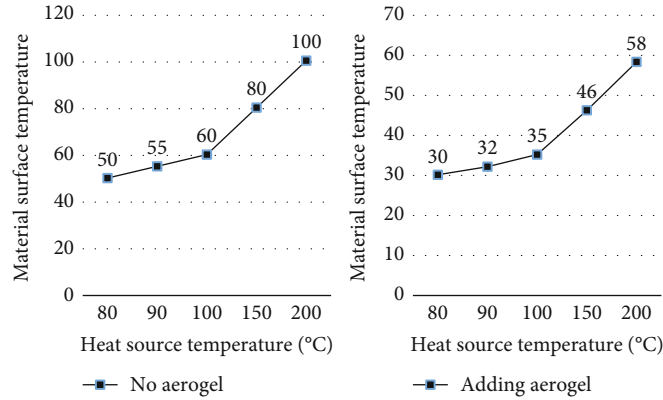
Figure 5: Insulation temperature difference test result.
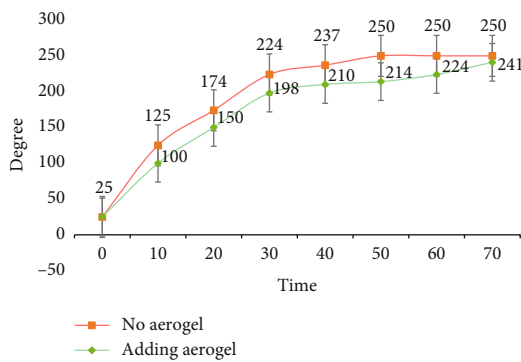
Figure 6: Temperature vs. time curve.
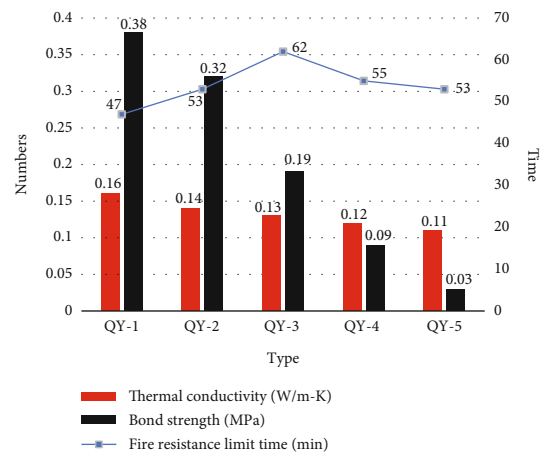
Figure 7: Sample thermal conductivity, fire resistance, and adhesive strength test results.

Table 4: Composition ratio of closed-cell aerogel powder composite coating.

Sample no.	The volume fraction of aerogel in the mixture (%)	The volume fraction of closed pores in the mixture (%)
QY-1	53	0
QY-2	53	4
QY-3	53	7
QY-4	53	10
QY-5	53	13

material, and the relative density between the insulation component sample and the control sample is used to express the porosity. Table 4 shows the composition ratio of the closed-cell aerogel material and the powder composite coating. In the course of the experiment, the corresponding error is allowed according to the adjustment of the bulk density of the mixture.

The samples QY-1 to QY-5 that reached the 28th curing period were tested for thermal conductivity, fire resistance, and adhesive strength. The test result is shown in Figure 7.

It can be seen from Figure 7 that both the thermal conductivity of the composite coating and the thermal conductivity of the aerogel coating gradually decrease with the decrease of the volume density of the closed-cell gas.

5. Conclusions

This article focuses on the application of nanoporous super insulation materials in the prevention of heat damage in deep mining of metal mines. After understanding the relevant theories, the application experiments of nanoporous super insulation materials in the prevention of heat damage in deep mining of metal mines are carried out. According to the experimental results, in the heat insulation test experiment, the temperature of the back surface of the experimental material gradually increases with the increase of time. The temperature rises quickly in the first 20 minutes, and the temperature on the back of the sample rises linearly, rising by 7-8°C every minute. After 20 minutes, the growth rate begins to slow down. This is mainly due to the addition of aerogel powder and the increase in the porosity of the coating, which reduces the pore size inside the coating, most of which is less than 50 nanometers, which effectively eliminates the increase in heat transfer inside the coating. However, due to the limitation of time and technology, we have not carried out in-depth research on it, so we will further explore other aspects of nanoporous insulating materials in the follow-up.

Data Availability

No data were used to support this study.

Conflicts of Interest

The authors declare that there are no conflicts of interest regarding the publication of this article.

Acknowledgments

References

[1] X. Zhao, Y. Pan, J. Jiang, S. Xu, J. Jiang, and L. Ding, "Thermal hazard of ionic liquids: modeling thermal decomposition temperatures of imidazolium ionic liquids via QSPR method," *Industrial & Engineering Chemistry Research*, vol. 56, no. 14, pp. 4185–4195, 2017.

[2] N. Zang, X. M. Qian, Z. Y. Liu, and C. M. Shu, "Thermal hazard evaluation of cyclohexanone peroxide synthesis," *Journal of Thermal Analysis & Calorimetry*, vol. 124, no. 2, pp. 1131–1139, 2016.

[3] X. Zhai, X. U. Yu, and Y. U. Zhijin, "Design and performance simulation of a novel liquid CO_2 cycle refrigeration system for heat hazard control in coal mines," *Journal of Thermal Science*, vol. 28, no. 3, pp. 585–595, 2019.

[4] R. Zhao, D. Muzzio, T. Vickery et al., "Thermal hazard investigation of a pharmaceutical intermediate," *Process Safety Progress*, vol. 37, no. 2, pp. 263–267, 2018.

[5] Y. Liu, X. Wang, C. M. Shu et al., "Thermal hazard evolution on guanidine nitrate," *Journal of Thermal Analysis and Calorimetry*, vol. 133, no. 2, pp. 1–13, 2018.

[6] H. Qiaoyun, Z. Yi, L. Kongqing, and Z. Shenghua, "Computational evaluation of cooling system under deep hot and humid coal mine in China: a thermal comfort study," *Tunnelling & Underground Space Technology*, vol. 90, pp. 394–403, 2019.

[7] H. Yin, Y. Shi, H. Niu et al., "Characteristics, detection, and prevention of karst sinkholes: a case study in Laiwu iron ore mine areas, Shandong Province, China," *China. Environmental Earth ences*, vol. 77, no. 4, pp. 1–12, 2018.

[8] Q. Wang, X. Wang, X. Liu et al., "Prevention of groundwater disasters in coal seam floors based on TEM of Cambrian limestone," *Mine Water and the Environment*, vol. 37, no. 2, pp. 300–311, 2018.

[9] P. Shan, X. Lai, and X. Liu, "Correlational analytical characterization of energy dissipation-liberation and acoustic emission during coal and rock fracture inducing by underground coal excavation," *Energies*, vol. 12, no. 12, article 2382, 2019.

[10] J. Wang, Z. Wan, H. Zhang et al., "Application of thermal insulation gunite material to the high geo-temperature roadway," *Advances in Civil Engineering*, vol. 2020, Article ID 3870, 12 pages, 2020.

[11] M. Oschatz and R. Walczak, "Crucial factors for the application of functional nanoporous carbon-based materials in energy and environmental applications," *C*, vol. 4, no. 4, pp. 56–56, 2018.

[12] B. David, "Application of nanotechnology-based thermal insulation materials in building construction," *Slovak Journal of Civil Engineering*, vol. 24, no. 1, pp. 17–23, 2016.

[13] J. P. Hidalgo, J. L. Torero, and S. Welch, "Experimental characterisation of the fire behaviour of thermal insulation materials for a performance-based design methodology," *Fire Technology*, vol. 53, no. 3, pp. 1–32, 2016.

[14] M. Noroozi, M. Panahi-Sarmad, M. Abrisham et al., "Nanostructure of aerogels and their applications in thermal energy insulation," *ACS Applied Energy Materials*, vol. 2, no. 8, pp. 5319–5349, 2019.

[15] H. Wang and Q. Zhou, "Finite element analysis of surrounding rock with a thermal insulation layer in a deep mine," *Mathematical Problems in Engineering*, vol. 2020, Article ID 1853, 11 pages, 2020.

[16] B. Gluch, "Equivalent climate temperature analysis as a criterion of climate hazard evaluation in polish underground mines," *Archives of Mining Sciences*, vol. 63, no. 4, pp. 975–988, 2018.

[17] W. Yu, F. Han, W. Liu, and S. A. Harris, "Geohazards and thermal regime analysis of oil pipeline along the Qinghai–Tibet Plateau Engineering Corridor," *Natural Hazards*, vol. 83, no. 1, pp. 193–209, 2016.

[18] C. S. Pathak and S. A. Mandavgane, "Application of recycle paper mill waste (RPMW) as a thermal insulation material," *Waste and Biomass Valorization*, vol. 10, no. 8, pp. 2343–2352, 2019.

[19] J. Zhao, J. Huang, R. Wang, H. R. Peng, and S. Ji, "Investigation of the optimal parameters for the surface finish of k9 optical glass using a soft abrasive rotary flow polishing process," *Journal of Manufacturing Processes*, vol. 49, pp. 26–34, 2020.

[20] S. M. Chen, A. X. Wu, and Y. M. Wang, "Analysis of influencing factors of pillar stability and its application in deep mining," *Journal of Central South University (Science and Technology)*, vol. 49, no. 8, pp. 2050–2057, 2018.

[21] P. Wang, S. Wang, X. Zhang et al., "Rational construction of CoO/CoF2 coating on burnt-pot inspired 2D CNs as the battery-like electrode for supercapacitors," *Journal of Alloys and Compounds*, vol. 819, article 153374, 2019.

[22] M. Kurimoto, Y. Yamashita, T. Yoshida, T. Kato, T. Funabashi, and Y. Suzuoki, "Influence of nanopore diameter on dielectric permittivity of epoxy/open nanoporous silica microcomposites," *IEEE Transactions on Dielectrics & Electrical Insulation*, vol. 25, no. 3, pp. 1022–1029, 2018.

[23] M. Sumislawska, K. N. Gyftakis, D. F. Kavanagh, M. D. McCulloch, K. J. Burnham, and D. A. Howey, "The impact of thermal degradation on properties of electrical machine winding insulation material," *IEEE Transactions on Industry Applications*, vol. 52, no. 4, pp. 2951–2960, 2016.

[24] S. Tsukada, Y. Nakanishi, T. Hamada, K. Okada, S. Mineoi, and J. Ohshita, "Ethylene-bridged polysilsesquioxane/hollow silica particle hybrid film for thermal insulation material," *RSC Advances*, vol. 11, no. 40, pp. 24968–24975, 2021.

Hindawi

Research Article

Theoretical Modeling of Composite Micro- and Nano-Fiber Devices and Electronic Information Application Research

Haibin Yang and Zhidong Liu [iD]

Electrical and Information Engineering College, Jilin Agricultural Science and Technology University, Jilin, 132101 Jilin, China

Correspondence should be addressed to Zhidong Liu; liuzhidong@jlnku.edu.cn

With the continuous development of information science and technology, micro- and nano-fiber optic sensing technology has been widely used in the fields of medicine, communication engineering, and environmental monitoring, and fiber optic devices are widely available in the market because of their advantages such as anti-magnetic interference, corrosion resistance, light weight, high sensitivity, and transmission bandwidth. The purpose of this paper is to investigate the intrinsic correlation between micro- and nano-optical fiber devices and electronic information, introduce the fabrication process of micro- and nano-optical fiber, numerical simulations, and corresponding magnetic field experiments, explore the effects of polarization dispersion and polarization-related dissipation on the system, and enhance the sensing characteristics of micro- and nano-optical fiber through experimental design to maximize its functionality. The experimental results show that the refractive index and magnetic field exhibit a linear relationship with correlation coefficients of 0.995 and 0.994, respectively, when the external magnetic field is between 70 Oe and 300 Oe.

1. Introduction

1.1. Background. Fiber optic technology began in the 1950s, the essence of the medium optical waveguide, while optical fiber is the study of the transmission and exchange of light, the emergence of low-loss optical fiber in the 1970s to promote the development of fiber optic technology [1, 2]. With the continuous progress of science and technology, the convenience of the use of tools has become the mainstream trend, but also continue to become the direction of the scientific community continue to research, the use of tools more and more integrated to meet the needs of the times, micro-fiber optic technology has become the subjects of research, in this context, micro- and nano-fiber optic technology into the field of vision, due to the continuous in-depth research found that micro- and nano-fiber optic technology can form different functions of micro- and nano-photonics devices. It has different degrees of impact on many modern industries, and from this perspective, there is a real need for the development of micro- and nano-fiber optic technology.

1.2. Significance. With the continuous development of micro- and nano-fiber technology, researchers have found that micro- and nano-fibers have many interesting properties [3, 4]. When the diameter of the fiber reaches the micro-nano-scale, the outer diameter of the optical fiber is generally 125-140 μm, and the core diameter is generally 3-100 μm and when the diameter is kept within a certain range, the binding of the optical field is stronger than that of an ordinary fiber, which can enhance the interaction between light and the medium and produce nonlinear effects at lower input power; it can transfer the energy force of the optical field to propagate outside the fiber, and this energy can be used as a sensitive sensor material for light coupling in certain cases.

1.3. Related Work. Micro- and nano-fiber optic technology is relevant in real life, but because of its late appearance, many functions are still being explored and have led to numerous studies. XIA presents different micro- and nano-structured fiber optic probes for biosensing, imaging, and stimulation applications and argues that modifications to the fiber can

extend the design freedom from waveguide optimization to functional material integration, and that fiber optic probes with optimized waveguide structure or integrated functional materials of fiber optic probes can achieve enhanced optical mode interaction with biological samples, leading to ultra-sensitive biosensors with significantly low detection limits [5]. Jiang J proposed an optical detection method based on micro- and nano-fiber (MNF) technology through a simple single-mode fiber. Theoretically, the evaporation field generated by MNF is calculated and its relationship with refractive index and water in oil is established, after which a MNF probe with a diameter of $800 - 125 \mu$m is fabricated and prepared by means of a home-made melt-tapered platform. The experimental results showed that the MNF-based optical sensor could achieve real-time measurement of moisture in transformer oil with a sensitivity of 1.8 ppm when the MNF diameter was 800 nm [6]. May-Arrioja D. A. presented experimental results of an optical fiber pressure sensor based on multimode interference effects (MMIs). The key component is a small multimode fiber (MMF) part without cladding, which is placed in direct contact with a polydimethylsiloxane polymer layer previously attached to a pressure-sensitive membrane. As the applied pressure increases, both the polymer contact area and the induced stress on the MMF increase in proportion to the applied pressure. The response of the sensor is highly linear over the pressure range of 0-960 kPa with a sensitivity of -0.145×10-3 mW/kPa. The main features of the MMI pressure sensor are its low cost and high repeatability [7]. Liu presented recent research advances in key devices and technologies for fiber optic sensor networks (FOSN). As the most important devices for FOSN, a variety of light sources have been developed, including broadband multi-wavelength fiber lasers operating in C-band, switchable tunable 2-μm multi-wavelength fiber lasers, ultrafast mode-locked fiber lasers, and optical broadband chaotic sources with very promising applications in FOSN [8]. Krehlik P. provided an overview of an electronically stabilized (ELSTAB) fiber time and frequency (T& F) distribution system, which is based on the idea of using variable electronic delay lines as compensation elements, describes various extensions of the basic system that allow the creation of a long-range multi-user network, discusses the fundamental limitations of the approach caused by fiber dispersion and system dynamics, and outlines the main hardware challenge of the system, which is the design of a pair of low-noise, precisely matched delay lines. Finally, experimental results of T&F distribution over a 615 km long fiber are presented, demonstrating an average frequency stability of 105 s and a time calibration well below 50 ps accuracy in the range of $1-7 \times 10$-17 [9]. Pimentel R presents a cost-effective bridge crane (B-WIM) system for identifying train loads using fiber optic technology. The system is capable of estimating the speed, geometry, and static axle loads of trains using an algorithm proposed by Moses. The algorithm involves solving a reverse identification problem where the measured structural response is known and the load scenario is unknown. The method relies on the concept of the influence line (IL), which is estimated from the passage of a calibrated vehicle with known characteristics

[10]. An innovative reversible data hiding (RDH) scheme is proposed which uses Lagrangian interpolation polynomials, secret sharing, and bit permutation to achieve electronic medical security. The covered medical images are subsampled into four shares, and cloud computing with Internet proves to be an important tool for providing better healthcare services. However, the maintenance, privacy, confidentiality, and security of electronic health information (EHI) pose a huge challenge for telemedicine. The scheme is used to expand subsamples to hide EHI, and secret information is processed using Lagrangian interpolation polynomials before being embedded in various cover images [11]. Wang presented the principle of holographic lithography and described its application in fabricating various micro- and nano-photonic structures such as 3D face-centered cubes, wooden piles, diamond-like photonic crystals, and quasi-crystalline structures, chiral metamaterials, and periodic defect mode structures, and holographic lithography is a low-cost, time-saving, and efficient microfabrication method with promising applications in making metamaterials and photonic crystal templates [12]. Micro- and nano-photonic structures are booming with a series of results in structural characterization, theory, and fabrication, but most of the high-quality photonic structures are artificial, and there are still some challenges in fabricating artificial large-area high-quality photonic materials.

1.4. Innovation Points. In this paper, we analyze the refractive index sensing characteristics of different types of single-mode fiber modes, think about the relationship between them in different cases, and verify the sensitivity of the refractive index through the experiment of interferometric instrumentation of different fibers; we propose a diameter-based fiber regulator to destroy the fiber by external force to change its original mode field distribution, and analyze its sensitivity in different cases through experiment. From this, the reasons for the change in transmission are explored.

2. Theoretical Modeling of Composite Micro- and Nano-Fiber Devices and Research Methods for Electronic Information Applications

2.1. Overview of Micro- and Nano-Optical Fibers. In the late 1870s, micro- and nano-fiber optic technology began to develop and was widely used in several fields, especially in the field of information applications [13]. Micro-nano-photonics mainly studies the law of interaction between light and matter at the micro-nano-scale and its applications in light generation, transmission, regulation, detection, and sensing. Micro-nano-photonics subwavelength devices can effectively improve the photonic integration, and it is expected to integrate photonic devices into a small single optical chip like electronic chips. Fiber optic technology is essentially a sensing technology, and the first controlled recordings appeared in the early 1990s, when some researchers proposed the use of glass fibers for medical
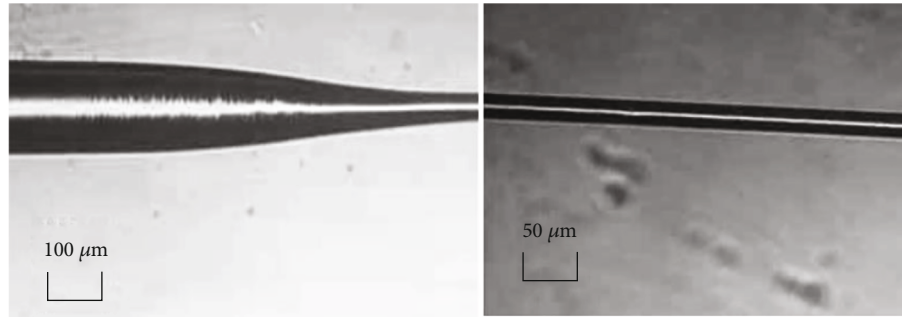
FIGURE 1: Micro-nano-area under optical microscope.

examinations, which led to the further development of micro- and nano-fiber optic technology in medicine. The difficulty of using light propagation is how to reduce transmission down loss and achieve optical communication. It was not until the continued maturation of fiber optic materials and wire drawing technology in 1972 that the low consumption of optical fibers was substantially advanced and successfully used to create a successful fiber optic communication system line, which laid the foundation for the practicalization of fiber optic communication [14].

Because fiber optic technology has many advantages such as high temperature and corrosion resistance and is widely used in real life, the survey data show that the global consumption of micro- and nano-fiber optic sensor market will grow at a rate of 20%, and the output value of about 5 billion U.S. dollars, in the Asia-Pacific region, China is the largest consumer and production market [15]. Photonic devices with many structures have been successfully made using micro- and nano-fiber technology, which have shown important research value in different fields such as communication and sensing, and more micro- and nano-fibers are designed and widely used. Microstructured fibers have been widely used in cutting-edge research in many fields such as optical communication, fiber sensing, and optical metrology, such as the generation of supercontinuum, high-power pulse transmission, ultra-low-power nonlinear effects, and tomography and remarkable results have been achieved in this research direction. Figure 1 shows the micro- and nano-regions under optical microscope.

2.2. Micro- and Nano-Fiber Mode Field Distribution. Micro- and nano-fibers are those whose diameters are infinitely converging to the micron or nanometer scale and whose refractive indices are relatively large. To explore the mode field distribution of micro- and nano-fibers, we first need to understand Maxwell's set of equations [16]. Figure 2 shows a schematic diagram of a micro- and nano-fiber.

First, we need to construct an ideal model of a micro- and nano-fiber, assuming that it can satisfy the following conditions.

(1) A diameter greater than 10 nm, which can respond to the optical field

(2) The micro-nano-fiber is relatively long, enough to establish a suitable mode field distribution

(3) The micro-nano-fiber indicates that it cannot be too coarse, but acceptable only to the extent that scattering of light is negligible

(4) The diameter of the micro-nano-fiber is uniformly distributed

Based on the above ideal state of the micro-nano-fiber, we can set the micro-nano-fiber as a cylinder, at which time the refractive index of the micro-nano-fiber can be segmented to represent.

$$t(a) = t_1, 0 < a < q, \tag{1}$$

$$t(a) = t_2, q < a < \infty. \tag{2}$$

In the above equation, q, t_1, and t_2 are the radius, core refractive index, and external ambient refractive index of the micro-nano-fiber, respectively. Fiber index of refraction generally refers to graded-index fiber. Graded-index fiber is also called self-focusing fiber. The center of refractive index of the fiber is the highest and decreases along the radial direction. The light beam propagates in the fiber and can be automatically focused without dispersion.

In general, neglecting their depletion, we express Maxwell's equations in the micro- and nano-fibers as follows: Maxwell's equations are a set of partial differential equations established by British physicist James Clark Maxwell in the 19th century to describe the relationship between electric and magnetic fields, charge density, and current density.

$$\left(\nabla^2 a^2 t^2 - \rho^2\right) \vec{b} = 0, \tag{3}$$

$$\left(\nabla^2 a^2 t^2 - \rho^2\right) \vec{k} = 0. \tag{4}$$

In the above expression, a is the refractive index of the point, $t = 2\pi\tau$, where τ is the wavelength and ρ is the wavelength propagation constant.
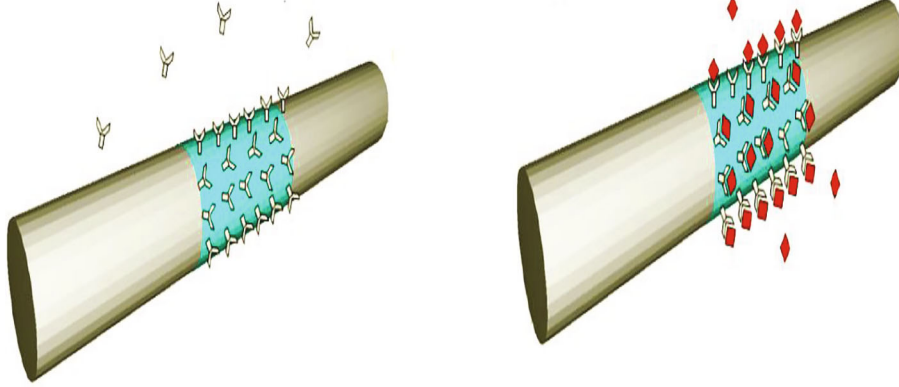
FIGURE 2: Schematic diagram of micro- and nano-fiber.

The eigenequation of the vector mode sum is expressed as:

$$
\begin{bmatrix} J'_Q(U)_+ k'_Q(W) \\ UJ'_Q(U)WK_Q(K) \end{bmatrix} \begin{bmatrix} J'_Q(U)_+ m^2{}_2 k'_Q(W) \\ UJ'_Q(U)m^2{}_1 WK_Q(K) \end{bmatrix} \\ = \left(\frac{v\alpha}{km_1} \right)^2 \left(\frac{V}{UK} \right)^4 . \tag{5}
$$

For PE$_{0M}$ mode, there exists:

$$
\frac{m_1{}^2 J_1(U)_+ m_2{}^2 T_1(W)}{UJ_0(U)WK_0(W)} = 0. \tag{6}
$$

For PN$_{0M}$ mode, there exists:

$$
\frac{J_1(U)_+ T_1(W)}{UJ_0(U)WK_0(W)} = 0. \tag{7}
$$

In the above equation, it denotes the Cybel function, $V = P_0 t(m_1^2 - m_2^2)/2$, $U = t(k_0^2 m_1^2 - \alpha^2)/2$, $W = t(\alpha^2 - k_0^2 m_2^2)/2$ where $t = 2b$.

Theoretically, optical fibers have many propagation modes, but only the transmission conditions and republican transmission modes can be propagated using optical fibers at the same time, and from this perspective, the propagation modes are not infinite. According to the number of transmission modes in the fiber, the fiber can be divided into multimode fiber and single-mode fiber. At a certain operating wavelength, multimode fiber is a dielectric waveguide that can transmit many modes, while single-mode fiber only transmits the fundamental mode. In micro- and nano-optics, the accommodation mode depends on the radius and refractive index of the micro- and nano-optics [17]. The expression for the refractive index of micro- and nano-optics medium is as follows:

$$
\Delta m = m_1 - m_2. \tag{8}
$$

The expression of the fundamental mode energy condition of the micro- and nano-fiber is:

$$
W = \pi \frac{f_{AZ}}{\mu_0} \left(m_1^2 - m_2^2 \right) \approx 2.40, \tag{9}
$$

where $f_{AZ} = 2b$ denotes the critical diameter of the micro- and nano-fiber.

The expressions for each component of the electric field transmitted in a micro- and nano-fiber can be expressed as:

$$
e_t = -\frac{c_1 J_0(UR) + c_2 J_2(UR)}{J_1(U)} f_1(u), \tag{10}
$$

$$
e_u = -\frac{c_1 J_0(UR) - c_2 J_2(UR)}{J_1(U)} g_1(u), \tag{11}
$$

$$
e_p = -i \frac{U J_1(UR)}{\mu \sigma J_1(U)} f_1(u), \tag{12}
$$

where $0 \leq c < q$;

$$
e_t = -\frac{U c_1 K_0(WR) - c_2 k_2(WR)}{W K_1(W)} f_1(u), \tag{13}
$$

$$
e_u = -\frac{U c_1 k_0(WR) + c_2 k_2(WR)}{W k_1(W)} g_1(u), \tag{14}
$$

$$
e_p = -i \frac{U k_1(WR)}{\tau \sigma k_1(W)} f_1(u). \tag{15}
$$

For a micro-nano-fiber with uniform diameter and no significant folding, the expression can be expressed as:

$$
T_{c1} = \frac{1}{2} \left(\frac{\gamma_0}{\pi_0} \right)^{0.5} \frac{l m_1^2}{\alpha J_1^2(R)} * \left[c_1 c_3 J_0^2(RF) + c_2 c_4 J_2^2(RF) \right. \\ \left. + \frac{1 - A_1 A_2}{2} J_0(RF) J_2(RF) \cos (2\theta) \right]. \tag{16}
$$
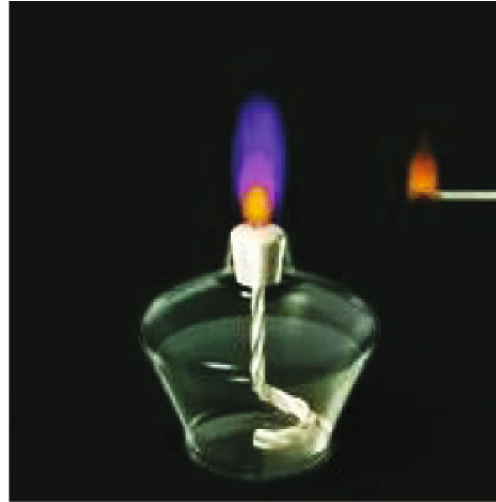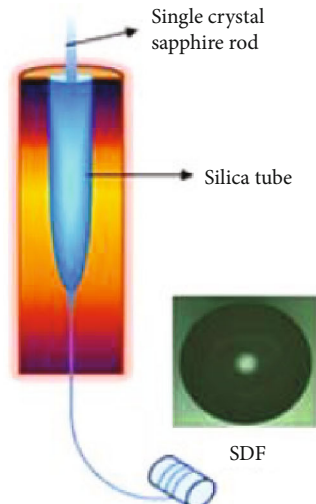
Figure 3: Machining tools and materials.

At this point, $0 \le c < q$.

$$T_{c2} = \frac{1}{2} \left(\frac{\gamma_0}{\pi_0} \right)^{0.5} \frac{l m_1^2 U^2}{\alpha L_1^2(W) W^2} * \left[c_1 c_5 l_0^2(WF) + c_2 c_6 l_2^2(WF) \right.$$
$$\left. + \frac{1 - 2\Delta - A_1 A_2^2}{2} L_0(WF) L_2(WF) \cos 2\theta \right].$$
(17)

At this point, $q \le c < \infty$.

2.3. Electronic Information. "Electronic information" is an informatics vocabulary, and its appearance is closely related to the rapid development of computer technology, communication technology, and high-density storage technology and its wide application in various fields. Electronic information engineering is a discipline that applies computer and other modern technologies for electronic information control and information processing. It mainly studies the acquisition and processing of information, and the design, development, application, and integration of electronic equipment and information systems.

2.4. Preparation Methods of Micro- and Nano-Optical Fibers. Micro- and nano-optical fibers are circular optical waveguides with diameters in the micron range. Since the introduction of micro- and nano-fiber technology, researchers have explored a variety of methods for fabricating micro- and nano-fibers. In terms of specific practice, there are only two methods to fabricate micro-nano-constructions: top-to-bottom and bottom-to-bottom. The process of making optical fiber by chemical growth method is a bottom-to-top process, and the micro-nano-fiber drawn from bulk glass is a top-to-bottom process. It is customary for us to refer to the process of fabricating micro- and nano-fibers using chemical techniques as bottom-up. Other technologies manufacture processes called top-to-bottom processes whose

main raw materials include, but are not limited to, block glass and single-mode fibers [18, 19].

2.4.1. Single-Mode Fiber Fabrication. The fabrication of micro- and nano-optical fibers using flame heating hair was first proposed in 2003. This method mainly uses an alcohol lamp for heating; first, a small section of fiber is heated until it melts, and then tension is applied to both ends of the fiber until the desired diameter of the micro-nano-fiber is obtained. If we want to make it very light, the heating and melting operation in the natural environment is very easy to be affected by the external environment; secondly, when applying tension to the micro-nano-fiber, we need to keep the tension constant, then there is a great limitation of this method when we need to make a finer diameter, and the micro-nano-fiber is easy to break if we are not careful, so this method is only applicable to the ideal state, and it is very difficult to do in practice [20, 21]. When heating the single-mode fiber, a certain stretching force is applied to both ends of the single-mode fiber, and the pulling force can be kept constant by controlling the stretching speed. Figure 3 shows the processing tools and materials:

2.4.2. Block Glass Fabrication. In addition to single-mode fiber fabrication, researchers have proposed that bulk glass can be used as a material for micro-nano-fiber preparation, and this method has a wide selection of materials, including sulfide glass, fluoride glass, and tellurite glass, among others, and the desired substances, such as ions, can be added to these materials, so that the fabricated micro-nano-fiber can be more complete during the fabrication process [22]. The steps are as follows.

(1) First, the micro-nano-fiber is heated, noting that the melting point at this point must be greater than that of the chosen glass material

(2) Contacting the bulk glass with the heated fiber while continuing to maintain the high temperature of the micro-nano-fiber
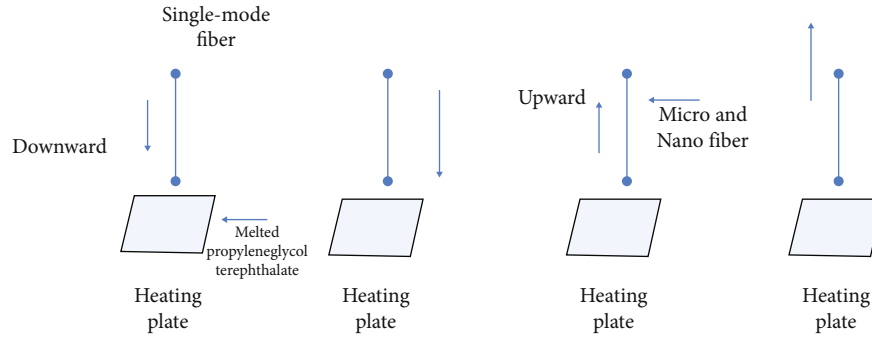
Figure 4: . Operation schematic.

(3) Take away the lump glass when the mutual contact appears to be melted, but it must be confirmed that there is a small portion of melted glass material on the micro-nano-fiber at this time

(4) Pacing the new micro-nano-fiber in contact with the heated micro-nano-fiber

(5) Lowering the heating temperature to cool down the glass between the two micro-nano-fibers

(6) The application of a certain rate of pulling from unheated micro-nano-fibers results in new micro-nano-fibers. Using this method of fabrication, micro-nano-fibers with different characteristics can be produced depending on the materials chosen

2.4.3. Polymer Fabrication. In addition to the above-mentioned raw materials, researchers have found that polymers can also be used to fabricate micro- and nano-fibers. In the early days, micro- and nano-optical fibers have been successfully fabricated using polypropylene terephthalate polymers. The low melting point, good flexibility, and fast crystallization rate of poly (propylene terephthalate) make it possess the requirements for fiber formation, and the refractive index of poly (propylene terephthalate) is only 1.638 when it is in the amorphous state, which possesses good optical confinement [23, 24]. The manufacturing steps are as follows.

(1) Firstly, poly (propylene terephthalate) is heated to a softened state in which the temperature is kept stable

(2) Contacting the melted poly (propylene terephthalate) with a single-mode optical fiber, at which point the single-mode fiber will have some residue of the poly material

(3) Lifting the single-mode fiber at this time at a certain speed

After lifting the single-mode fiber, an intuitively very fine micro-nano-fiber will appear, and it will rapidly cool down into an amorphous poly (propylene terephthalate) micro-nano-fiber. Figure 4 shows a schematic diagram of the operation:

2.4.4. Laser Preparation. Since the use of gas for heating is susceptible to interference from the external environment and can easily cause errors during preparation, researchers have worked to find fabrication methods that are free from interference from the external environment, and in 2006 successfully fabricated micro-nano-fibers using a carbon dioxide laser as a heating instrument, which uses a carbon dioxide laser to scan and heat a single-mode fiber [25]. The main principle is to adjust the output of the carbon dioxide laser with a total controller, and use a tool to focus the laser on a single-mode fiber, and the spot diameter matches the micro-nano fiber used. By controlling the angle of the tool, the entire light spot in the single-mode fiber can move axially, and the heating of the single-mode fiber needs to change the structure; the longer the micro-nano-fiber needed, then the higher the power output of the CO2 laser needs to be, but this method is not infinitely long, and the diameter of the pulled micro-nano-fiber is still said to be relatively large compared to other methods [27].

2.4.5. Electrode Heating Preparation. To understand the problem of interference from the external environment, in addition to using a CO2 laser, researchers have proposed to protest the use of electrodes for heating; the main steps of which are as follows.

(1) First fixing the single-mode fiber with one end placed in a heater

(2) Using a heater bar to press the single-mode fiber into the container, the heater bar needs to be connected to the electrode with a standard voltage of 250 V. The temperature of the heated container needs to reach 1600°C

(3) The other end of the micro-nano-fiber is fixed on the rotating platform, and the rotating platform is driven to rotate after reaching a certain temperature, and the heated single-mode fiber can be drawn out of the micro-nano-fiber during the rotation process

The micro-nano-fiber prepared using this heating method can reach 900 nm in diameter and several hundred mm in length, and the heating of the single-mode fiber using electrodes can provide a large heating area and make the

TABLE 1: Comparison of various micro- and nano-fiber drawing methods.

Preparation method	Two-part pulling method	Self-adjusting pulling method	Block glass drawing	Polymer drawing	Laser pulling	Electrode heating and drawing
Micro- and nano-fiber diameter (nm)	49	19	49	65	3000-39985	893
Transmission loss	0.008 dB/nm	*	0.01 dB/nm	0.01 dB/nm	0.06 dB/nm	0.01 dB/nm
Features	Easy and convenient	Minimal diameter	Multi-doped micro- and nano-fibers	Low melting point	Overcoming environmental interference	Longest length
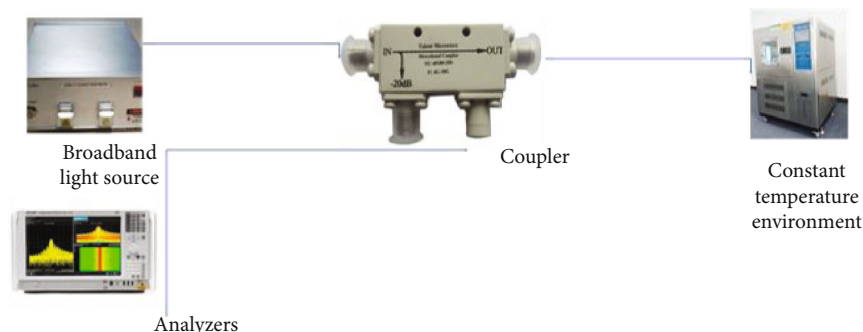
FIGURE 5: Schematic diagram of the test system.

TABLE 2: Relative humidity values of salt solutions.

Solution		Magnesium chloride	Lithium chloride	Potassium carbonate	Sodium chloride
Relative humidity (%)	26°C	32.3	11.1	43.5	75.1
	29°C	32.1	11.2	43.5	75.2
	30°C	32	11.2	43.5	75.2

single-mode fiber uniformly heated; in this process, the user can change the voltage as well as the rotating platform to change the length and diameter of the micro-nano-fiber [28]. Table 1 shows the comparison of various micro- and nano-fiber drawing methods:

3. Experiments on Theoretical Modeling of Composite Micro- and Nano-Fiber Devices and Electronic Information Applications

3.1. Experimental Environment. The micro-nano-fiber sensor is put into different humidity devices, and the data acquisition connector is connected to the broadband light source and the spectrum analyzer through a 3 dB coupler, and the humidity environment in the experiment uses a supersaturated solution, and we select different supersaturated solutions such as sodium chloride, potassium carbonate, magnesium chloride, and lithium chloride for the experiment, keeping the experimental temperature between 26°C and 29°C [29]. If the temperature of the chemical solution is too low or too high, a chemical reaction will occur, resulting in the deterioration of the solution, and deviations will occur in the experiment. The experimental setup is shown in Figure 5.

3.2. Experimental Data Acquisition. Table 2 shows supersaturated solutions with different humidity levels, and in our experiments, we passed sensors with different specifications through these supersaturated solutions in sequence, labeled separately, at different temperatures, and the wavelength of the micro-nano-fiber changed as the humidity of the solution varied [30]. The wavelength of magnesium chloride solution will shorten as the temperature increases, and other solutions will remain unchanged or elongated.

According to the data in Table 3, it can be seen that the wavelengths of the micro-nano-fibers were significantly shifted by adding them to different supersaturated solutions while keeping the experimental temperature constant, but they basically drifted toward the long wave direction. In addition, with the increase of ambient humidity, the center wavelength of the reflection spectrum of the humidity sensor shifts to the long wavelength direction.

According to the data in Table 4, it can be seen that different micro-nano-optical fibers change in different supersaturated solutions while keeping the experimental temperature constant, and overall, when the temperature is constant, the greater the relative humidity of the solution, then the greater the amount of drift to come, and according to the experiment, it can be seen that the larger drift occurs

TABLE 3: Wavelengths of saturated solutions with different humidity.

Solution	Magnesium chloride	Lithium chloride	Potassium carbonate	Sodium chloride
Temperature (°C)	25	25	25	25
Wave length (nm)	1530	1537	1538	1536
Loss (db)	50	35	45	40

TABLE 4: Wavelength drift.

Solution	Magnesium chloride	Lithium chloride	Potassium carbonate	Sodium chloride
Temperature (°C)	25	25	25	25
Wet relative humidity (%)	10	30	50	70
Wavelength drift amount (nm)	0	0.2	0.7	1.3

TABLE 5: Sensor corresponding parameters.

Sensors	Micro- and nano-fiber diameter (μm)	Sensitivity (pm/%)	Linearity (%)
Magnesium chloride	115	23.12	99.61
Lithium chloride	23	31.75	99.59
Potassium carbonate	17	32.18	99.29
Sodium chloride	14	35.46	99.73

in magnesium chloride, followed by sodium chloride solution, and the smallest drift occurs in lithium chloride solution [31].

According to the data in Table 5, it can be seen that the sensitivity of the sensors used in the experiments is above 99%, and most of the humidity sensors are higher than the sensitivity of ordinary optical fiber humidity sensors, so it can be concluded that the sensor sensitivity of micro-nano-fiber humidity sensitivity has been improved to a great extent compared with ordinary micro-nano-fiber. Combined with the above mentioned that within a certain humidity, the wavelength drift amount and humidity have a good linear relationship, so we believe that the humidity sensor has good detection effect in a certain acidic solution environment [32].

4. Theoretical Modeling and Electronic Information Application Research Analysis of Composite Micro- and Nano-Fiber Devices

4.1. Micro- and Nano-Optical Fiber Stability Characteristics. In the above experiments, we introduced that wavelength and refractive index are length dependent. If the length is simply changed, then the wavelength also changes, and in order to explore the relationship, we utilized an interferometer axial strain characteristic measurement instrument for detection (Figure 6 shows the interferometer axial strain system) each time the position is shifted and its length is changed, and the following data are obtained.

According to Figure 7, we can see that we have carried out the projection profiles during the changes of 80 μm,
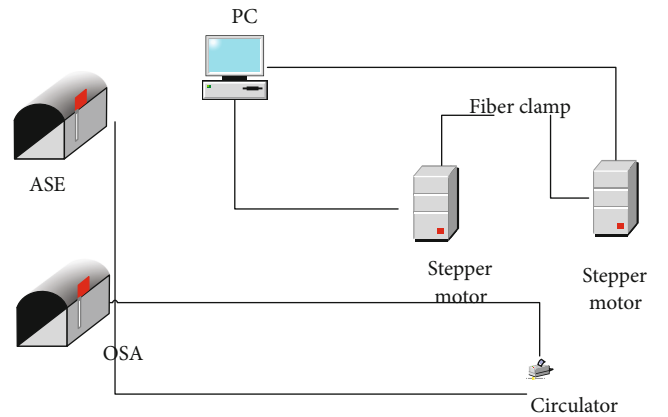
FIGURE 6: Interferometer axial strain system.

160 μm, 240 μm, and 320 μm, respectively, and from the data, we can see that the difference in the values of the spectral interference valley drift is relatively small in different length displacement changes, and overall it is still relatively stable and basically does not change much according to the valley comparison, so that it can be used as a strainer [33].

According to the data variation in Figure 8, we can find that analyzing the ratio of the length of the axial change to the length of the fiber can be derived from the microstrain of the fiber axially, and according to the recorded changes corresponding to the wavelengths shown in the figure, we can see that the reasonable sensitivity of the interferometer is around 0.55, while the sensitivity of the interferometer we obtained is around 0.6 and 0.61, so we can confirm that the sensitivity is reasonable at this time.
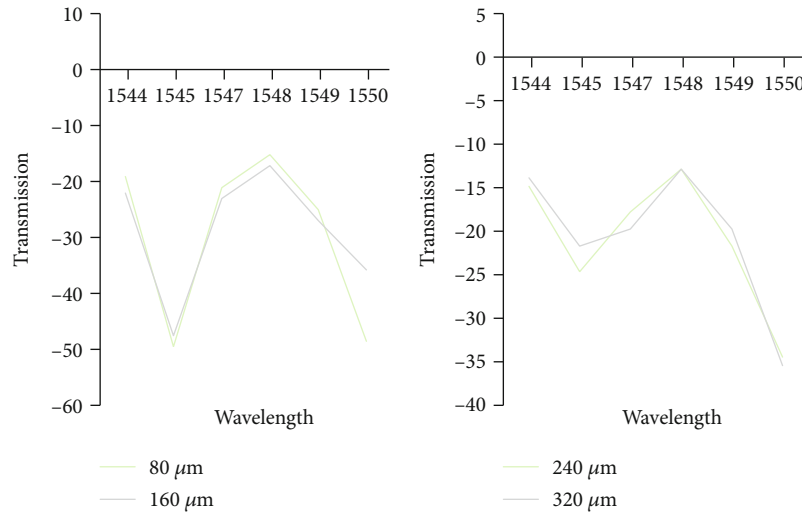
FIGURE 7: Microstrain measurement.
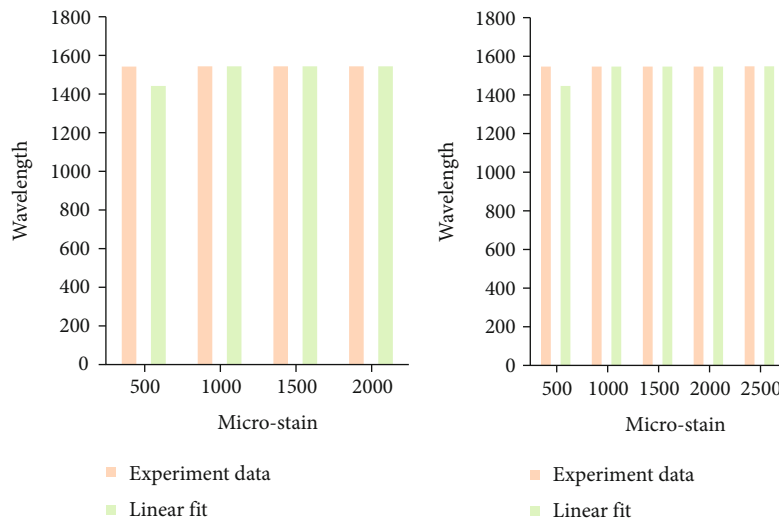
FIGURE 8: Relationship between wavelength and strain variation.

4.2. The Magnetic Field of Micro- and Nano-Fibers. As mentioned in the previous section, the magnetic field of micro-nano-fiber is closely related to the fiber diameter and core refractive index. According to the analysis in the study, chemical means can be used to change the diameter of the micro-nano-fiber as a way to change the whole magnetic field distribution, and in order to verify this conjecture, we conducted an experimental analysis and found that the diameter size of the micro-nano-fiber does have a large influence on the whole magnetic field [34].

According to Figure 9, when the corrosive solution is contacted with the micro-nano-fiber, it is found that it has a large impact on the diameter of the micro-nano-fiber, resulting in a higher loss of the micro-nano-fiber, so it can be seen that the difference between the wave and valley in the figure is large, and once the external interference is performed, it will lead to a large change in its magnetic field; when the corroded micro-nano-fiber is added to the magnetic fluid solution when there is no external magnetic influ-

ence, its refractive index size remains at 1.4. When we add the magnetic fluid, it is obvious that the wavelength of the micro-nano-fiber has changed and the frequency has shifted.

4.3. Relationship between Magnetic Field Strength and Transmittance of Micro- and Nano-Fibers. In the above, we mentioned that the size of external magnetic field will cause the micro-nano-fiber to change to different degrees, and by adding different properties of magnetic fluid can make the refractive index of the micro-nano-fiber change, and when the refractive index changes, its transmittance will also change, and the main changes are as follows:

From Figure 10, it can be seen that the influence of the magnetic field size on the transmittance, but according to the obtained data, we find that the transmittance presents a nonlinear relationship; when the external magnetic field is less than a certain data, the transmittance will remain unchanged, and when the external magnetic field reaches the degree of saturation, its transmittance does not change
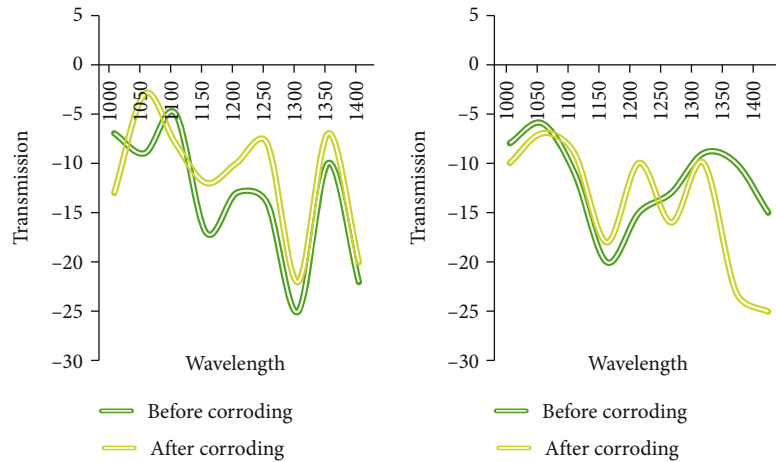
Figure 9: Comparison chart of corroded fiber.
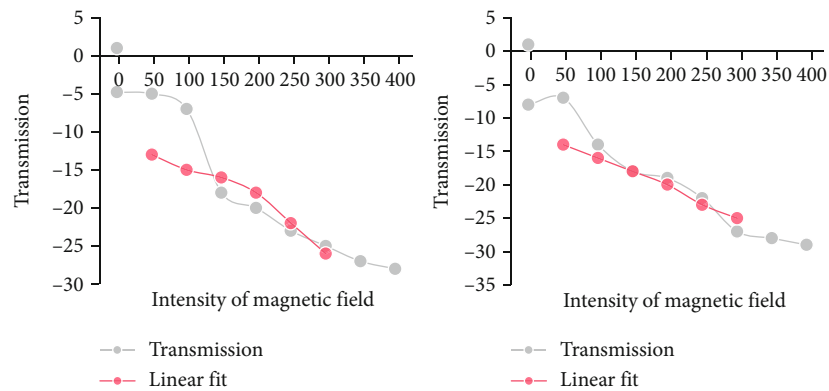
Figure 10: Comparison of magnetic field strength and transmittance.

significantly, but when the external magnetic field is between 70 Oe and 300 Oe. However, when the external magnetic field is between 70 Oe and 300 Oe, they show a certain linear relationship with correlation coefficients of 0.995 and 0.994, respectively. This data indicates that the relationship of the optical magnetic field can be adjusted by using different degrees of external magnetic field and can be applied in the communication magnetic field.

5. Conclusions

With the continuous development of micro- and nano-fiber technology, fiber optic devices are gradually adding to the convenience of miniaturization, and in the process of continuous miniaturization, micro- and nano-fiber technology is also developing, and micro- and nano-fibers of different structures, diameters, and lengths are being manufactured continuously, and at present, the academic exploration of the characteristics of micro- and nano-fibers with differences in fabrication and the application of devices in different fields has become the current fiber optic science and technology and scientific. In this paper, we will focus on the fabrication of micro- and nano-fibers. In this thesis, we have (1) investigated the fabrication methods of micro-

and nano-fibers in different transmission modes, and analyzed their physical significance, advantages, and disadvantages in the practical process, and their practical value; (2) explored the transmission characteristics of fine core micro- and nano-fibers with different diameters and their distribution characteristics, and simulated the transmission modes of different sizes of micro- and nano-fibers; (3) investigated the connection between the magnetic field of micro- and nano-fibers and fiber diameter, core refractive index, and found the connection between the magnetic field of micro- and nano-fibers. The larger the diameter of the micro-nano-fiber, the larger the wavelength shift, and the corresponding change in refractive index, thus changing the magnetic field; (4) to explore the correlation between the magnetic field and transmittance, it is found that when the external magnetic field is less than a certain data, the transmittance will remain unchanged, and when the external magnetic field reaches saturation, the transmittance does not change significantly, but when the external magnetic field is between 70 Oe and 300 Oe, the transmittance does not change significantly. However, when the external magnetic field is between 70 Oe and 300 Oe, they show a certain linear relationship. Although this paper has explored certain contents, there are still many shortcomings: (1) the operation

steps of the micro-nano-fiber research in this paper are all in the ideal experimental environment, the encapsulation technology of micro-nano-fiber needs a constant temperature environment, and due to this necessary condition, it cannot be utilized in a commercial environment on a large scale; (2) when using chemical technology for corrosion, it is easy to make mistakes, and the corrosion solution. We still need to find other relatively safe methods to fabricate micro-nano-fibers; (3) the techniques adopted in this paper are considered to be operational, which makes it difficult to ensure that the fabricated micro-nano-fibers are identical, which makes it more difficult to mass produce micro-nano-fibers.

Data Availability

The data that support the findings of this study are available from the corresponding author upon reasonable request.

Conflicts of Interest

The authors declared no potential conflicts of interest with respect to the research, authorship, and/or publication of this article.

References

[1] H. Song and M. Brandt-Pearce, "Range of influence and impact of physical impairments in long-haul DWDM systems," *Journal of Lightwave Technology*, vol. 31, no. 6, pp. 846–854, 2013.

[2] H. Song and M. Brandt-Pearce, "A 2-D discrete-time model of physical impairments in wavelength-division multiplexing systems," *Journal of Lightwave Technology*, vol. 30, no. 5, pp. 713–726, 2012.

[3] B. Gao, X. Ning, and P. Xing, "Shock wave induced nanocrystallization during the high current pulsed electron beam process and its effect on mechanical properties," *Materials Letters*, vol. 237, no. 15, pp. 180–184, 2019.

[4] G. Bo, L. Chang, H. Chenglong et al., "Effect of Mg and RE on the surface properties of hot dipped Zn–23Al–0.3Si coatings," *Science of Advanced Materials*, vol. 11, no. 4, pp. 580–587, 2019.

[5] X. Yu, S. Zhang, M. Olivo, and N. Li, "Micro- and nano-fiber probes for optical sensing,imaging, and stimulation in biomedical applications," *Photonics Research*, vol. 8, no. 11, pp. 104–125, 2020.

[6] J. Jiang, X. Wu, Z. Wang, C. Zhang, G. Ma, and X. Li, "Moisture content measurement in transformer oil using micro-nano fiber," *IEEE Transactions on Dielectrics and Electrical Insulation*, vol. 27, no. 6, pp. 1829–1836, 2020.

[7] D. A. May-Arrioja, V. I. Ruiz-Perez, Y. Bustos-Terrones, and M. A. Basurto-Pensado, "Fiber optic pressure sensor using a conformal polymer on multimode interference device," *IEEE Sensors Journal*, vol. 16, no. 7, pp. 1956–1961, 2016.

[8] D. Liu, Q. Sun, P. Lu, L. Xia, and C. Sima, "Research progress in the key device and technology for fiber optic sensor network," *Sensors*, vol. 6, no. 1, pp. 1–25, 2016.

[9] P. Krehlik, Ł. Śliwczyński, Ł. Buczek, J. Kołodziej, and M. Lipiński, "ELSTAB—fiber-optic time and frequency distribution technology: a general characterization and fundamen-

[10] tal limits," *IEEE transactions on ultrasonics, ferroelectrics, and frequency control*, vol. 63, no. 7, pp. 993–1004, 2016.

[10] R. Pimentel, D. Ribeiro, L. M. Matos, A. Mosleh, and R. Calçada, "Bridge Weigh-in-Motion system for the identification of train loads using fiber-optic technology," *Structure*, vol. 30, no. 1, pp. 1056–1070, 2021.

[11] R. F. Mansour and S. A. Parah, "Reversible data hiding for electronic patient information security for telemedicine applications," *Arabian Journal for Science and Engineering*, vol. 46, no. 9, pp. 9129–9144, 2021.

[12] X. Wang, H. Lü, Q. L. Zhao, S. Y. Zhang, and W. Y. Tam, "Application progress of holographic lithography in fabrication of micro-nano photonic structures," *Guang pu xue yu Guang pu fen xi= Guang pu*, vol. 36, no. 11, pp. 3461–3469, 2016.

[13] S. V. Kulakov, A. N. Yakimov, A. Bugaev, M. Postema, and V. B. Voloshinov, "Special issue: wave electronics and applications thereof in information and telecommunication systems," *Applied Acoustics*, vol. 112, p. 216, 2016.

[14] B. Wolf and C. Scholze, "Medicine 4.0: examples of applications of electronics, information technology and microsystems in modern medicine," *Medecine Sciences*, vol. 34, no. 11, pp. 978–983, 2018.

[15] G.-D. Peng, *Handbook of Optical Fibers*, Springer, Berlin/Heidelberg, Germany, 2018.

[16] Y. Qi, J. Zhang, Q. Feng, X. Zhang, Y. Liu, and Y. Han, "A novel high sensitivity refractive index sensor based on multicore micro/nano fiber," *Sensors*, vol. 9, no. 3, pp. 197–204, 2019.

[17] D. L. Costa, R. S. Leite, G. A. Neves, L. N. . L. Santana, E. S. Medeiros, and R. R. Menezes, "Synthesis of TiO_2 and ZnO nano and submicrometric fibers by solution blow spinning," *Materials Letters*, vol. 183, pp. 109–113, 2016.

[18] J. Amirian, S. Y. Lee, and B. T. Lee, "Designing of combined nano and microfiber network by immobilization of oxidized cellulose nanofiber on polycaprolactone fibrous scaffold," *Journal of Biomedical Nanotechnology*, vol. 12, no. 10, pp. 1864–1875, 2016.

[19] P. Carrera, P. J. Espinoza-Montero, L. Fernández, H. Romero, and J. Alvarado, "Electrochemical determination of arsenic in natural waters using carbon fiber ultra-microelectrodes modified with gold nanoparticles," *Talanta*, vol. 166, pp. 198–206, 2017.

[20] Y. Liu, A. Nguyen, A. Allen, J. Zoldan, Y. Huang, and J. Y. Chen, "Regenerated cellulose micro-nano fiber matrices for transdermal drug release," *Materials Science and Engineering C*, vol. 74, pp. 485–492, 2017.

[21] J. Han, D. Wang, and P. Zhang, "Effect of nano and micro conductive materials on conductive properties of carbon fiber reinforced concrete," *Nanotechnology Reviews*, vol. 9, no. 1, pp. 445–454, 2020.

[22] A. Kumar, M. P. Gupta, J. Banerjee et al., "Micro-welding of stainless steel and copper foils using a nano -second pulsed fiber laser," *Lasers in Manufacturing & Materials Processing*, vol. 6, no. 2, pp. 158–172, 2019.

[23] F. Xu, "Miniature function-integrated devices based on optical microfibers," *Yingyong Kexue Xuebao/Journal of Applied Sciences*, vol. 35, no. 4, pp. 469–502, 2017.

[24] F. P. Calmon, A. Makhdoumi, M. Medard, M. Varia, M. Christiansen, and K. R. Duffy, "Principal inertia components and applications," *IEEE Transactions on Information Theory*, vol. 63, no. 8, pp. 5011–5038, 2017.

[25] R. Zheng, Y. D. Liu, and H. Jin, "Optimizing non-coalesced memory access for irregular applications with GPU computing," *Frontiers of Information Technology & Electronic Engineering*, vol. 21, no. 9, pp. 1285–1301, 2020.

[26] T. R. Hu, J. B. Luo, H. Kautz, and A. Sadilek, "Home location inference from sparse and noisy data:models and applications," *Frontiers of Information Technology & Electronic Engineering*, vol. 17, no. 5, pp. 389–402, 2016.

[27] C. ILihong, "2 5- and 3-D TSV technology applications and failure analysis challenges," *Electronic Device Failure Analysis: A Resource for Technical Information and Industry Developments*, vol. 18, no. 3, pp. 54-55, 2016.

[28] Y. M. Yu and K. Kang, "Analysis and design of transformer-based CMOS ultra-wideband millimeter-wave circuits for wireless applications: a review," *Frontiers of Information Technology & Electronic Engineering*, vol. 21, no. 1, pp. 97–115, 2020.

[29] D. G. Nedumaran, M. A. Kumar, and M. Alaguraja, "Effect of mobile applications on farming in Virudhunagar District -a study," *SSRN Electronic Journal*, vol. 68, no. 1, pp. 12718–12727, 2020.

[30] W. B. Han, X. G. Chen, S. F. Li et al., "A novel non-volatile memory storage system for I/O-intensive applications," *Frontiers of Information Technology & Electronic Engineering*, vol. 19, no. 10, pp. 1291–1302, 2018.

[31] S. Khazaei and M. Rezaei-Aliabadi, "A rigorous security analysis of a decentralized electronic voting protocol in the universal composability framework," *Journal of Information Security and Applications*, vol. 43, pp. 99–109, 2018.

[32] R. A. Baryshev, S. V. Verkhovets, and O. I. Babina, "The smart library project: Development of information and library services for educational and scientific activity," *The Electronic Library*, vol. 36, no. 3, pp. 535–549, 2018.

[33] Y. C. Xie, H. Huang, Y. Hu, and G. Q. Zhang, "Applications of advanced control methods in spacecrafts:progress, challenges, and future prospects," *Frontiers of Information Technology & Electronic Engineering*, vol. 17, no. 9, pp. 841–861, 2016.

[34] M. B. Hariz and F. Bouani, "Synthesis and implementation of a fixed low order controller on an electronic system," *International Journal of System Dynamics Applications*, vol. 5, no. 4, pp. 42–63, 2016.

Research Article

A Smart Memory Controller for System on Chip-Based Devices

Mohammed Altaf Ahmed ⬤ and Jaber Aloufi

Department of Computer Engineering, College of Computer Engineering & Sciences, Prince Sattam Bin Abdulaziz University, Alkharj-11942, Saudi Arabia

Correspondence should be addressed to Mohammed Altaf Ahmed; m.altaf@psau.edu.sa

This research paper deals with a system-on-chip (SoC) architecture design where multiple processors are inbuilt with other blocks of memory and control logic developed by nanomaterials. The multiprocessing-based SoC architecture is commonly used in the latest electronic devices such as smartphones, tablets, and smart wristwatches with large memory sizes. The data handing in these highly memory-dense devices is a critical task, and it needs special attention for the smooth operation of the device. This research proposed a smart controller to exchange data between various processors and input-output devices to tackle this challenge. A proposed controller block controls the data flow between memory and different SoC components and processors. A memory access controller (MAC) is presented in this research study to manage and accelerate data transmission speed and reduce the processors' activity for SoC-based devices. The proposed MAC will integrate into the SoC with multiprocessing units, including gaming processors, at minimum hardware overhead and low power consumption. It improves the memory accessing efficiency and reduces the processors' activity of a system. As a result, the system's performance and power consumption improve at an acceptable level compared with the other conventional methods. This research is aimed at enhancing the performance of any SoC-based device where multiprocessing engines are inbuilt and flexible enough to serve various SoCs.

1. Introduction

In response to the rising demands of IoT devices, the 4G mobile phone devices cannot provide complete imminent services, which is required for the next-generation IoT-based system and other SoC-based systems [1, 2]. There is ample research conducted in this context of next-generation 5G mobile services [3, 4].

The traffic growth exponentially increases mobile phone networks from the generation of the cellular system 1G to 5G [5]. As per the survey of the CISCO Corporation, the data traffic on the mobile web becomes doubled from 2010 to 2011. They also stated that mobile traffic would increase by 1000x and above by 2021 compared to 2010 [6]. Due to this increased level of mobile traffic, the energy consumption of the mobile handset user increases with immense power. Therefore, it directly affects the expenditure. It is necessary to rethink the design to control these attributes and manage the network to reduce spending in a next-generation mobile

phone system called the 5G generation. There is a future prediction of a fully connected society where everybody and everything is interconnected, on a common platform of the Internet of Things (IoT)—where many devices serve a single person. Therefore, the forthcoming 5G cellular infrastructure for massive data support will enable smart cities. There will be a need for an intelligent SoC design to support these 5G features in next-generation mobile phone devices and other SoC-based devices. The SoC of these devices should compromise with a high-end processing unit with an intelligent memory controller inbuilt feature.

In this context, a low-power, high-performance SoC development approach is accessible [7] that deals with the power management in the SoC for IoT-based devices. This SoC approach was developed on 65 nm technology and occupied an area of $1.0 \times 1.7 \, \text{mm}^2$. Similarly, a method dealt with an adaptive power management (APM) design module that extensively supports learning techniques [8] and reduces power consumption in the IoT-SoC.

We are aware that the SoC is a single-chip integrated system and each block of it remains the intellectual property (IPs). The IPs are part of SoC, are available as processor core (one or more) peripheral devices, and are sometimes called macros. They are incorporated as per the requisition or demand of the SoC design. The SoC of these intelligent devices consists of some hardware and some software IPs. The hardware IPs are the processor, random access memory (RAM), and universal serial bus (USB) devices. The software IPs are the device drivers, the processor running algorithms, etc. IPs communicate together via specific channels called the on-chip bus, and it links all the IPs that belong to it [9]. This SoC bus works on a precise communication protocol containing various bus strategies. For instance, the IP begins communication to any other IP only when the bus is idle (not accessible by any further IPs). In this case, the IP with control over the bus is called the master, and other IPs responding to it are called slaves [10].

In case the master is accessing the SoC bus to convey their messages to other IPs at a particular instance, known as the active master. This SoC bus will remain idle during the absence of the active master. In recent times, multiprocessor systems have been drastically used to improve power performance compared to single processor systems in desktop segments. It caused the extensive application of multiple processor SoC cores, known as multiprocessor SoCs (MPSoCs) [11, 12]. These MPSoC cores are commonly available in the latest smartphone and other gaming devices. Therefore, some processors need to be offloaded to handle essential tasks and deal with such a high configurable multiprocessor-based SoC.

This paper is motivated by the future requirements of the SoC architecture of multiprocessor-based smart devices to fulfill consumers' demands. We cannot ignore the snapdragon SoC as it explicitly concerns multiprocessor-based devices [13]. The majority of the market for android-based devices uses Snapdragon SoC in their devices. The single snapdragon SoC contains many processing units based on the ARM instruction set. In this research study, we proposed a MAC unit to perform tasks in parallel with the processor to enhance the speed and performance of the processing engines. Memories generally occupy the majority area of SoC, and it motivates this research to choose the MAC unit as a research topic to improve the processor performance. SoC architectures of the majority of digital systems mainly consist of nanomaterial-based memories. For example, the SoC of mobile phone devices, smart wristwatches, and mobile tablets comprises large memory sizes. The International Technological Roadmap for Semiconductor (ITRS) report is available for reference [14, 33] to convey that the memories occupy most of the SoC area. The MAC unit is small in hardware and occupies a tiny space overhead when integrating with SoC design when manufacturing the nano-technological chip. Compared with the processor area (here, we consider a Snapdragon SoC), it holds a very thin area overhead of 0.0003% with low power consumption and a fast data transfer rate. Thus, the area overhead is negligible compared to a SoC area.
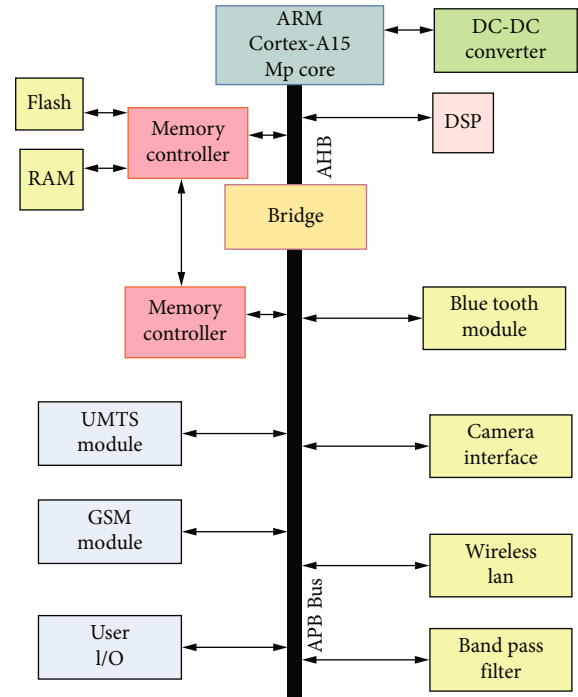
Figure 1: SoC architecture with multiprocessing units.
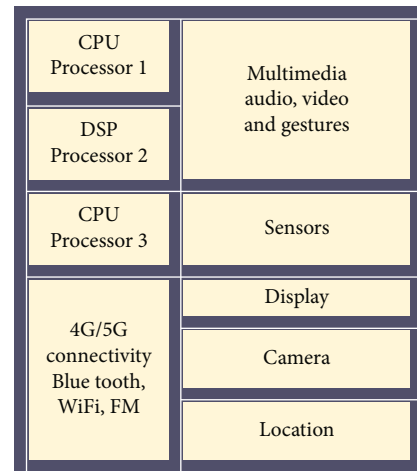
Figure 2: The Snapdragon multiprocessing is SoC.
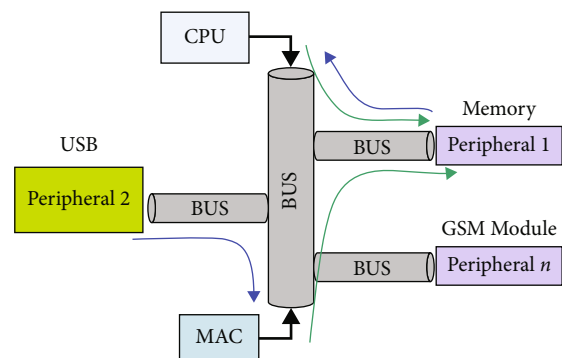
Figure 3: MAC data exchange principle.
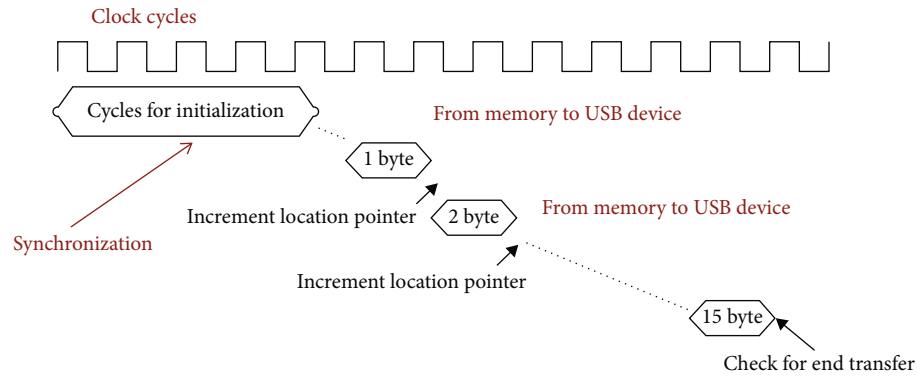
Figure 4: MAC transfer of data between peripheral and memory.

The authors' contributions to the article is noted as follows:

(i) Proposing a novel MAC unit architecture to perform memory accessing tasks while integrated with SoC at a fast transfer rate

(ii) Evaluate area overhead and power consumption and analyze the processor's performance with and without integrating the MAC unit into the SoC of the smart device

(iii) Reduces the processor's activity, and hence, it saves system power and temperature by integrating MAC unit into SoC

The paper is organized as follows: Section 2 outlines the SoC architecture of the mobile phone for previously available devices in terms of the services provided. Section 3 proposes the MAC architecture for mobile SoC. Simulation and ASIC Synthesis results are presented in Section 4. In this section, we have compared the area overhead of SoC by taking the example of Qualcomm's processor Snapdragon SoC. Finally, we conclude the paper in Section 5.

2. SoC Architecture with Multiprocessing Units

A generic SoC architecture with multiprocessing units with various IP blocks is depicted in Figure 1. This SoC architecture uses the ARM Cortex-A15 multicore processor with advanced microcontroller bus architecture (AMBA) [15]. There are two different processing cores included in this SoC, namely, ARM Cortex A15, also known as a general purpose multiprocessor (GPMCP), and digital signal processing (DSP) processor [12]. These GPMCP and DSP processors are coupled with the memory controller core, enabling them to collaborate with other external flash memory, and system memory with the help of a high-performance AMBA advanced high-performance bus (AHB). In addition to these IPs, there is additional peripheral IP in the system, which supports UTMS (universal mobile telecommunications system) and GSM (global system for mobile communication). The external IPs are connected with the system through the high-performance bus known as AMBA advanced peripheral bus (APB). Since every mobile phone SoC consists of these two
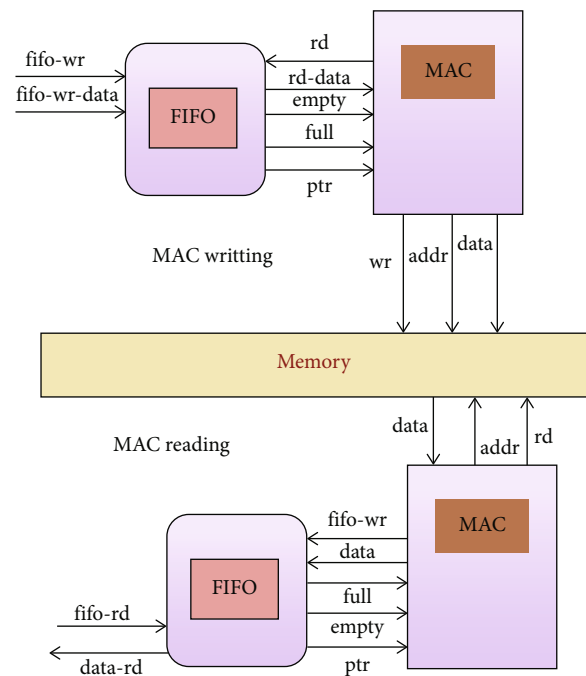
Figure 5: Proposed memory controller for multiprocessor-based SoC.

high-performance buses, AMBA-AHB and AMBA-APB [16], the system will work [17]. These two buses are responsible for data exchange between peripherals and processors. A bridge is used as an interface between the AMBA-AHB bus and the AMBA-APB bus to share information. A system architecture that uses AXI bus architecture is also available in recent research [18] for the FPGA-based dynamic partial reconfigurable security system for low area and power.

In SoC technology, trivial functions are conceived through the reusability of IPs. The reusability of IPs results in the rapidity of constructing a computer system based on a single-chip application. It is the root cause of the ever-growing fame of SoCs [19]. The constructional block diagram of a SoC is built up by reusing different modules. These reusable prevailing modules comprise an ARM processor core, peripherals modules like GSM and UMTS, memory controllers, etc. The precompiled libraries for the system-

TABLE 1: Signal description of memory controller for mobile SoC.

Pin	Description
rd	This signal enables the read operation when MAC wants to read data from FIFO.
rd_data	The data bus, which holds data, is read from FIFO to write into the memory through the state machine.
full	This input indicates to the MAC state machine about FIFO-full status.
empty	This input indicates that FIFO is empty to the MAC state machine, with no further data available to read.
ptr	There are two FIFO pointers to indicate reading and writing location and decide between empty and full status.
wr	wr is a write-enabled signal to memory, indicating writing operation.
addr	Addr signal indicates the exact location of memory to write/read data from or into it.
Data	It is a data bus that carries data to write into and read from memory.
rd	Read enable to indicate read operations from memory.
fifo_wr	Enable signal from MAC state machine to write into the FIFO.
fifo-rd	Request from the peripheral to read data from FIFO.
Data-rd	Data bus carrying the data read from FIFO for any external device.

level programmer are also available in the form of software drivers. The multiprocessor SoC system is flexible to extend by adding new IPs.

The IP configuration in SoCs always describes the formal models. The multiprocessor SoC incorporates many IPs like different peripherals, processors, and memory cores. These IPs perform various functions at various speeds and work at different data exchange behaviors. Due to their unusual behavior, their interconnections have to be comprehensive enough to handle the individual IP smoothly. Also, they must provide a standard approach to connect with all such IPs.

Usually, in the typical SoC architecture, all the IPs are connected with a common bus called a SoC bus. This SoC bus is linked with all the IPs of that particular SoC. Therefore, it has to set up a single platform for every IP connected to it, and the design is consequently called the platform-based design. This platform builds by integrating generic hardware (buses, processors, memory, etc.) and software (microcontroller code), and it can be remodeled to obtain differentiated products. Presently the typical SoC buses include Altera Avalon [20], IBM Core Connect, IDT IP Bus [21], Open Core Protocol [22], and Wishbone. This research work analyzes the AMBA [15] in detail, as it is the industry standard for creating SoCs. For example, AMBA is being used by many corporations like NVidia, Qualcomm, and Actel [23, 24] in their products.

The standard AMBA is rendered by ARM, which elucidates as a generalized set of useful buses and is used in system-based integrated circuits (ICs). These system-based ICs are known as SoCs, traditional microcontrollers, and application-specific integrated circuits (ASICs). In 1996, the first time the ARM-based processors used this standard (AMBA) in their SoCs. Internally, AMBA consists of two types of buses: high-performance system buses to connect core IPs and a flexible peripheral bus to join many input outputs devices and the components. The AMBA-AHB connects various IPs, for example, a processor, a DSP, and advanced memory controllers as shown in the SoC architecture.

Similarly, the AMBA-APB (advanced peripheral bus) connects various peripheral IPs dedicated to that system.

Additionally, AMBA provides the flexibility of upgrading the SoC. The SoC upgradation is possible by replacing some IPs with advanced versions (like the Bluetooth IP module) and adding IPs to enhance the functionality of the existing design (for example, adding an FM receiver, etc.). There is a bridge between the AHB and APB buses which is also shown in the multiprocessor SoC. This bridge is a standard bus-to-bus interface that provides communication between the IPs connected to different buses in a standardized way.

In this research, we are focused on specialized processing and integration. We know that the building of multiprocessor SoC requires many particular processing engines, which are custom designed to provide the user with the lowest power and higher performance [25]. A notable example is the Qualcomm Snapdragon (Snapdragon) [26, 27]. The SoC of Snapdragon processing is shown in Figure 2. The SoC consists of typical processing engines that integrate into a single piece of silicon [28]. There is a trend towards integrating more and more onto the SoC. The integration capabilities depend on the silicon traders' IP technology and design abilities.

The benefits of integration result includes being cost-effective, low area, lower power, and low temperature. The SoC architect will make the appropriate design decisions and trade-offs among the many dependencies throughout the system. This insight gives the right system view and the ability to propagate features, accurately simulate use cases, and quickly respond to market demands. This research takes a step to enhance the system performance and speed of the devices using multiprocessing units to accept the consumers' challenges and needs. The proposed MAC unit is an independent entity. It can easily integrate with the SoC with a reasonable transfer rate to get these features at low power consumption and a lite area overhead.

3. Implementation of Proposed MAC for SoC

The processor does intelligent operations like arithmetic and managerial processes. The real-time mobile systems incorporated today are built up with multiprocessors. These processors performed various functions by interacting with any
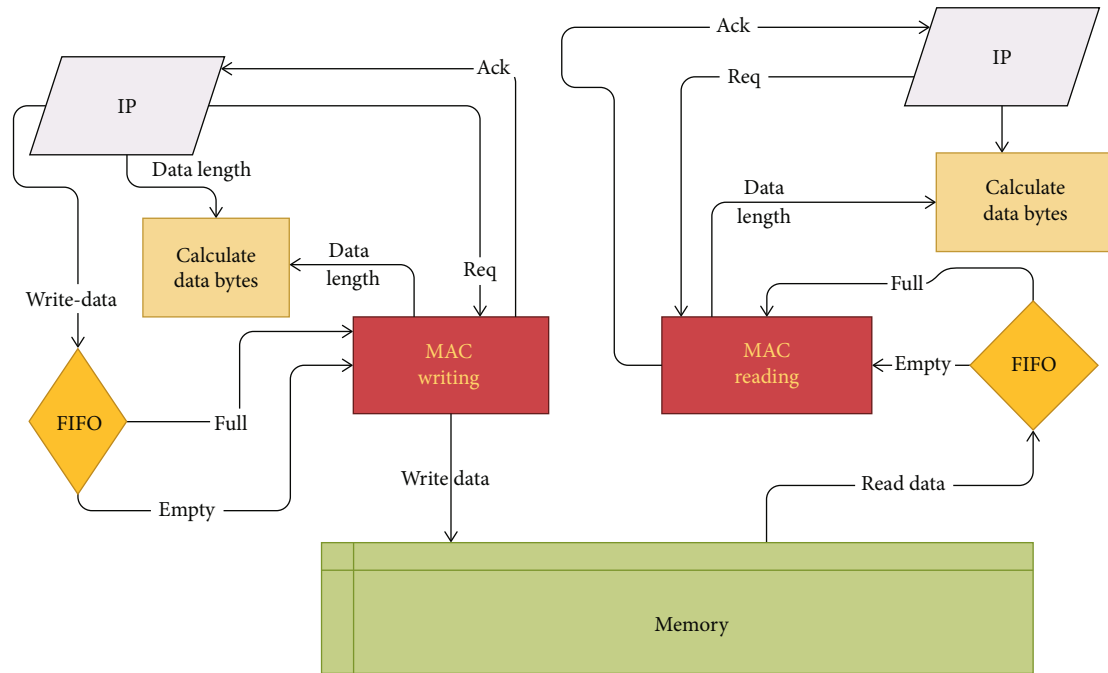
FIGURE 6: MAC flow chart.

Simulator is doing circuit initialization process.
Finished circuit initialization process.
Reset issued...   10
Reset deasserted...   30
Req issued with Dword count = 05   70
fifo_wr_ptr = 05, fifo_empty = 0   70
Memory write at addr = 00, data = 6c0895e81   150
Memory write at addr = 01, data = 28484d609   170
Memory write at addr = 02, data = 0b1f05663   190
Memory write at addr = 03, data = 506b97b0d   210
Tx ACK asserted, total mem wr count = 00   210
Memory write at addr = 04, data = 506b97b0d   230

External IP request for 5 writers into memory

On the request of device 5 times writing
into memory at address 00 to 04

The data at 00 to 03

At time scale in ns
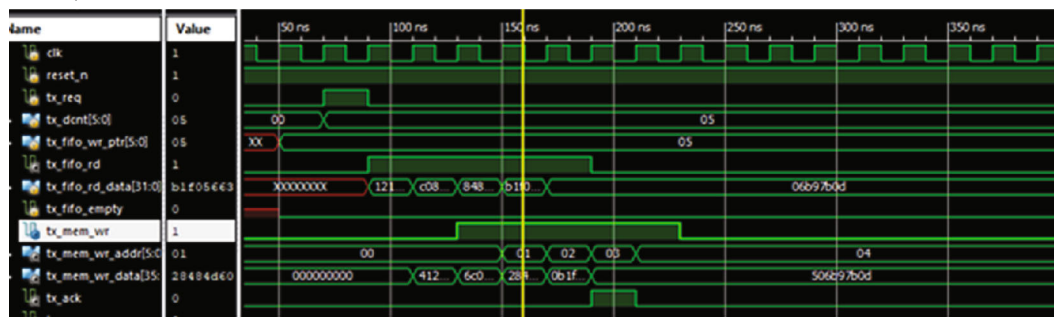
FIGURE 7: MAC read from FIFO and write into the memory on the request of the device.

other processor in the same SoC. By doing this on one side, adding many processors to share the load on the other side. The processors waste their time by transferring data between themselves. Therefore, this research introduces the MAC to avoid this labor work of data transmission performed by any specialized processing engine in SoC-based devices. The MAC is a separate entity, and it integrates into SoC to perform such tasks. The research presents a real-time embedded system with fast data accessing support. It is known for its processor multitask support to achieve better yield and less power consumption while supporting future expansions. The system is called intelligent when it integrates the memory access controller for accessing the data between IP devices and memory, including cache. Hence, it can increase processing speed and reduce processing activity to save power. The active processor, among other processors in a specific SoC, excessively uses the memory while in use. Therefore, the MAC unit plays a significant role while the processor offloads memory accessing tasks in any specific SoC-based device.
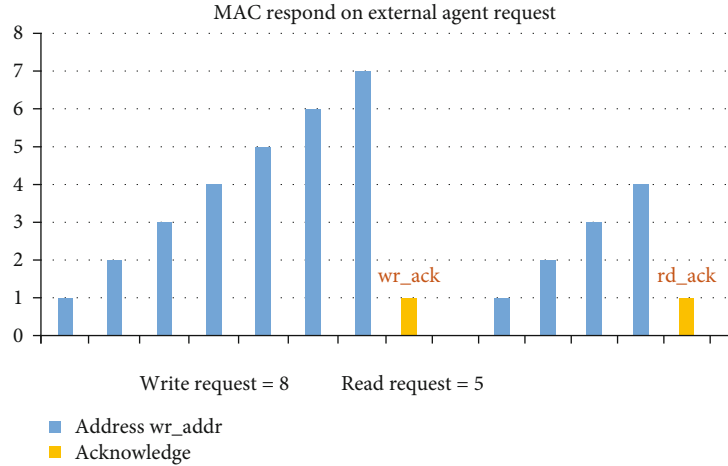
FIGURE 8: MAC responds to an external agent's request to access the memory.

Today, high-end smart processors are used in sophisticated real-time systems such as automotive, avionics, and some medical equipped devices where this MAC unit can be used for integration. The use of MAC in the systems provides CPU usage and high system throughput. Before the MAC application was narrow to computers, servers, etc., but now it has become an integrated system entity in a new generation system. The MAC unit can transfer data between the entities as follows:

(i) Between two memories

(ii) Between memory and IPs

(iii) Between two IPs

(iv) Between two processing systems

The MAC handles all data transfer tasks, freeing the processor to manage other essential functions for any selected embedded systems [28].

How data exchange between peripherals (together with memory blocks) and processors by using these buses in SoC as indicated in Figure 3. There are two masters over the bus, the CPU and MAC. Once the data is accessed from memory by either of these two masters, the appropriate memory address information is updated. It works in two modes. The first mode CPU is the master, and the second mode MAC will be the master over the bus. The CPU sends the request to the bus for access in the first mode. A bus will grant access to the CPU in response to this request. The CPU will operate on data accessing by updating data into an appropriate memory location after getting a permit on a bus. On another side, when MAC is master over a bus, it can access any peripheral and memory connected to the bus in the second mode.

3.1. Case when MAC in SoC. There is an example of a case when MAC is in the SoC.

Example 1. For example, when MAC transfers the data between UART and memory. It reads the UART registers

TABLE 2: External agents request to access the memory.

Request	Address	Data	Acknowledge
Write Request-8	wr_addr	—	—
	0	6c0895e81	—
	1	28484d609	—
	2	0b1f05663	—
	3	306d7cd0d	—
	4	c46df998d	—
	5	4b2c28465	—
	6	e89375212	—
	7	300f3e301	1
Read Request = 5	rd_addr		
	0	c46df998d	—
	1	4b2c28465	—
	2	e89375212	—
	3	300f3e301	—
	4	306d7cd0d	1

and appropriate memory locations through the bus and released the bus grant once the operation finished. If the processor alone performs this operation, it requires more instruction cycles. This way, it needed more time to transfer the data between a memory and an external peripheral connected. Instead, the MAC engine handles this transfer operation by offloading the processor for sharing of data. An arbitration mechanism is used to grant access between the processor and MAC. The data transfer procedure is represented in Figure 4 by the MAC unit between peripherals and memory, data copied from memory and transferred to the USB by MAC itself. The data length of 15 bytes is considered.

Benefits of being MAC in multiprocessor-based devices:

(i) The power consumption reduces to a great extent. If the CPU runs for longer, it consumes more power, which the presence of the MAC will overcome by offloading the CPU
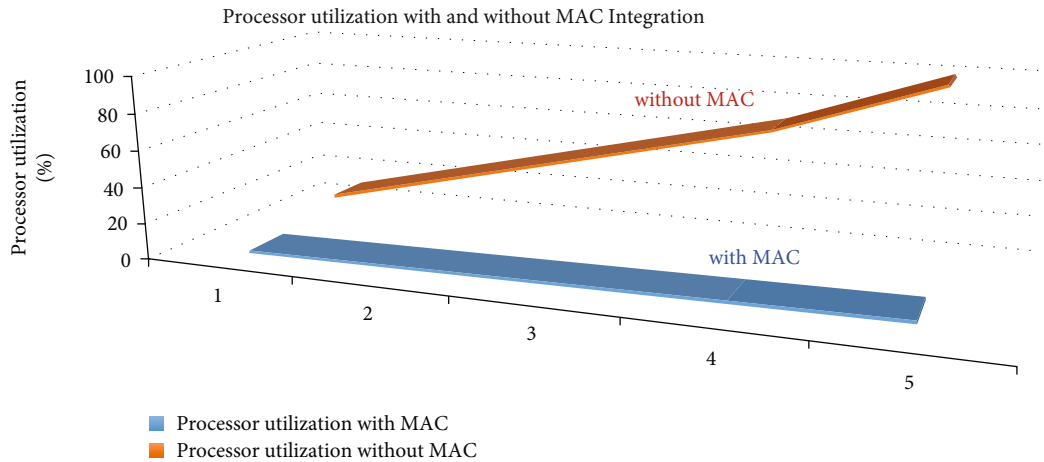
FIGURE 9: Processor utilization comparison with and without MAC.

(ii) MAC is an individual entity, and it performs data transfer operations individually in parallel to CPU operation. Thereby, it may be used in the simulation of a multiprocessing environment and helps in improving the processor's bandwidth

(iii) It makes the CPU idle for more time and frees up the processor to perform a more advanced task in future product improvement

3.2. Proposed MAC Architecture. The proposed memory access controller for multiprocessor-based SoC is shown in Figure 5. The MAC engine with first-in-first-out (FIFO) handles the extra load of the multiprocessing units to free the individual processor to perform another essential task in parallel. This offloading of the processing units in smartphone devices takes place by MAC's proposed design method. The architecture consists of MAC in the writing mode and MAC in the reading mode, and a FIFO block on both sides is used for synchronization. In the first part, the MAC performs reading operations for any IP (peripheral) from FIFO. Similarly, the MAC performed writing operations into the FIFO for any external IP (peripheral) in the second part.

Once the writing or reading operation is complete, the data will be available for any external device or IP to read or write from FIFO. The external device then accesses the data from FIFO.

Two memory controllers are implemented in Verilog hardware description language for accessing the data. The buffer memories (FIFO) on both sides are used to store the data temporarily to avoid data loss and mismatches. Hence, it synchronizes the speed of the peripheral and controller. The MAC signals and the description are summarized in Table 1. The external IP will write the data into the FIFO in writing mode. This data is then read by MAC and stored in the memory. The status of available data in FIFO will be updated by the pointer signal 'ptr.' Therefore, the MAC engine will read the appropriate data from FIFO and write it into the memory. Thus, the memory contains the data by writing any external IP into it.

TABLE 3: ASIC area report for proposed MAC.

Design	Cell	Cell area (nm^2)	Net area (nm^2)	Total area (nm^2)
Proposed MAC unit	2201	31272	16220	67497

TABLE 4: Area comparison between the proposed MAC and the other existing approaches.

Design	Cell	Cell area (nm^2)	Net area (nm^2)	Total area (nm^2)
Proposed MAC	2201	31272	16220	67497
DMA [30]	3901	56179	21237	99417
DMA [31]	3637	48312	25177	93289
DMA [32]	4637	62749	30256	101389
DMA [33]	4213	56274	28096	10017

Writing of memory is carried out as follows:

(i) The experiment results are taken by considering 8 K of memory

(ii) Memory size (Mem-array) = 8 K

(iii) Each location of memory contains 64-bit data = 8 bytes

(iv) Total location required for 8 K data (max-add) = 210

(v) Address location will vary from zero '0' to the 2^{10}

The data is written into the memory for all 1000 address locations, and each address location contains 8 k of data. If 64-bit is the data line, it requires 2^{10} address locations. Max-add is indicating as 2^{10}. The writing operation can be performed and expressed in equation (1).

$$MEMORY[Add] < Data\_wr. \qquad (1)$$
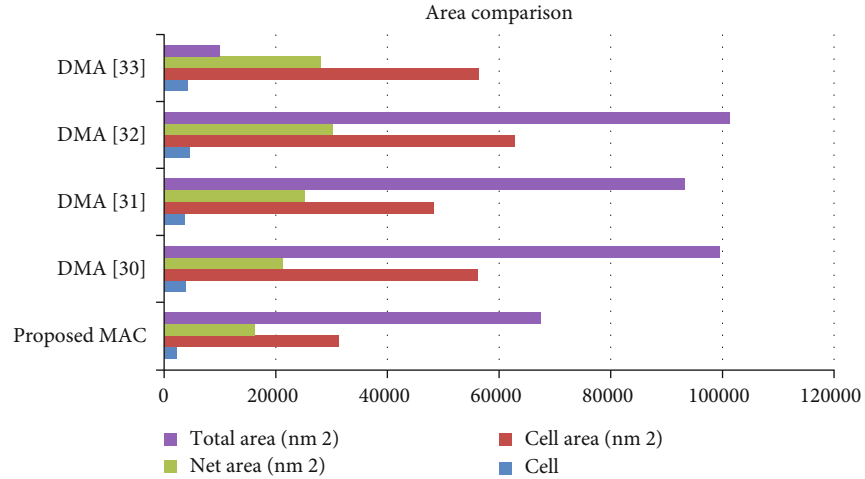
Figure 10: Area comparison graph.

The data is already available in the memory on the other side of the MAC reading operation. The MAC engine will read it from memory and write it into the FIFO for any connected external IP. Once the data is available in FIFO, the external IP will come and read it. The MAC reads the status of FIFO by pointer 'ptr' signal. The reading operation can be performed and expressed in equation (2).

$$Data\_rd <\ = Memory\ [Address]. \tag{2}$$

The IP request for accessing the memory decides that MAC has to work in writing or reading mode. If the request is for writing to the memory, the MAC first checks for the data request is for how many bytes (length), and then it grants writing into the FIFO to the requested IP. The MAC continuously checks the full-empty status of FIFO and depends on the availability of data in FIFO. MAC will write the data into the memory on the availability of data in FIFO. Whereas if the request is to read the data from memory, the MAC first checks the IP request, calculates the bytes, and allows the IP to read the data from FIFO. The data in the FIFO is available by the MAC after reading it from memory. The flow of reading and writing data for any requested IP is shown in Figure 6. Multiple requests and reading writing operations can perform in parallel by the proposed MAC unit in any SoC-based system.

4. Results

Verilog HDL is used to design the MAC unit. The simulation and synthesis are performed on the EDA tool. The top-level Verilog module includes two-part transmitting (writing) and receiving (reading) parts, and each part uses a MAC unit with a FIFO block. The simulation is performed on the Xilinx simulator. A case where an external device is writing data into the memory is shown in Figure 7. In this case, the external IP wants to write into the memory by sending a write request. It writes data into the FIFO on the approval of its request by a grant signal. Once the data is

Table 5: Data transfer rate for the proposed MAC and other existing methods.

Design	Max frequency (MHz)	Mega cycles per sec	Transfer rate (Mbytes/sec)
Proposed DMA	350	350	1400
DMA [30]	320	320	1200
DMA [31]	320	320	1200
DMAC [32]	250	250	1000
DMA [33]	250	250	1000

available in FIFO, the MAC will read it and write it into the memory. The MAC unit continuously reads the FIFO pointer to act during this process. On the other side, when external IP wants to read data from memory, the MAC unit will read data from memory and write it into the FIFO for any requested external IP. The read-write request handled by the MAC unit itself to offload the processor is shown in the graph in Figure 8 and Table 2.

FIFO pointer in each operation increments and appropriate information about data availability is communicated with the MAC. Depending on the pointer location, MAC will perform operations. We consider 64 as the FIFO depth for both the reading and writing sides. In this research, we implement a controller that can allow multiple IPs to access the memory without any involvement of the processors. As a result, processor performance and speed will increase drastically, and it can only concentrate on its operations other than memory access.

The developed MAC unit can integrate into mobile phone SoC to perform enhanced features data accessing memory to offload the processor. Hence, it increases the processing speed and power optimization of any processor. It can merely be understood by considering an example of wave generation. In a wave generation process for SoC, the MAC will perform a data exchange operation instead of a

FIGURE 11: Data transfer rate comparison.

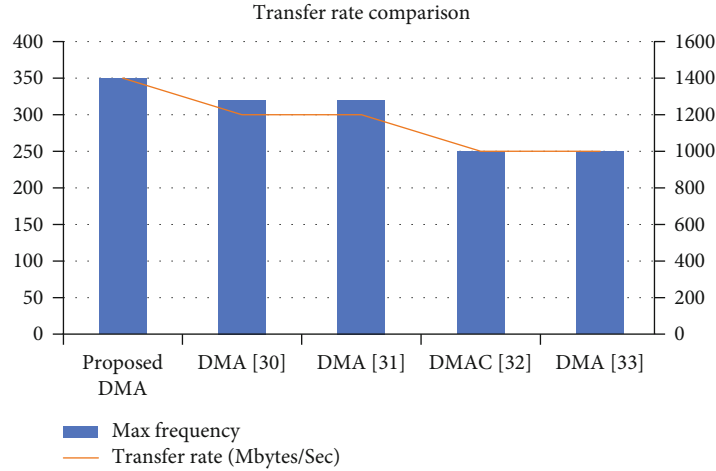processor. As a result, processor utilization will reduce drastically, directly affecting processor speed and power consumption. The purpose of a wave generator is to generate waves continuously [29]. The continuous stream will create without interruption by continually accessing the data from the look-up-table (LUT) to the digital-to-analog converter (DAC) data register. If there is a MAC unit available in the SoC architecture, the updating of data from LUT to the DAC register will take place by the MAC unit, and hence processor activity reduces significantly.

Large processor bandwidth and power are required when the wave's frequency and the number of samples increase. In case of the absence of the MAC unit in mobile device SoC, it forces the processor to perform this hectic task of data updating into the DAC register. Therefore, in this way, the processor consumes many instruction cycles to copy the data from LUT to the DAC register, affecting its performance significantly.

Instead, the MAC unit can easily do this task of data accessing from memory to the DAC register at the required time interval. Additionally, the MAC is not interrupt-driven like a processor. In this case, the processor does not need to do anything as long as the wave generates. As a result, a large amount of power will save because, generally, the processor consumes more energy than the MAC unit. The processor acts in power-down mode if it is not in use for data transfer operation, and hence, there will be a reasonable saving of static and dynamic power consumed. Thus, the MAC helps optimize the system's power consumption where a significant portion of work is to transfer data. The comparison graph between processor utilization with and without MAC is plotted and shown in Figure 9, and it is not scaled. We can see from the chart how speed and power performance affect any mobile phone SoC when the MAC unit is integrated.

The synthesis process of the MAC unit is performed on the ASIC platform. The ASIC synthesis results are received on the synopsis tool design compiler with $32 \, nm^2$ technology. The MAC unit is implemented on ASIC to calculate the area overhead and to integrate with Qualcomm's Snapdragon SoC. The design of MAC uses only 2201 cells with a cell area of $31272 \, nm^2$, a net area of $16220 \, nm^2$, and a total

TABLE 6: Power consumption of proposed and other methods.

Design	Leakage power (μW)	Dynamic power (μW)	Total power (μW)
Proposed DMA	1.67	194	196
DMA [30]	2.09	246	248
DMA [31]	2.90	233	236
DMAC [32]	2.07	252	356
DMA [33]	2.72	230	333

area of $67497 \, nm^2$. The synthesis result for area calculation is tabulated in Table 3. The design frequency, the power consumption, and the data transfer rate of the MAC block are computed. The existing approaches of the MAC are also implemented, and the obtained results are compared with the proposed MAC unit. The area comparison is tabulated in Table 4 and indicated in the graph in Figure 10.

The design frequency and the data transfer rate of the proposed MAC unit and the other available conventional methods of memory access controller are tabulated in Table 5. The comparison graph is shown in Figure 11.

The power consumption comparison for the proposed and other approaches are listed in Table 6 and the graph in Figure 12.

The commercially available SoC having the transistor count, including only the processing units, is 32 billion MOSFETs by 2019. For example, Qualcomm's Snapdragon processor gate count is more than 3 billion transistors [34, 35]. If we consider one cell having four gates or 16 transistors (4-transistors per logic gate), three billion transistors have 187 million cells.

The proposed design in this research used only 2201 cells with $32 \, nm^2$ technology. Therefore, integrating this controller with the Snapdragon SoC results in negligible area overhead with enhanced power optimization and speed features. The processor activity reduces to a great extent, and hence, it optimizes the system's power consumption. The result of the
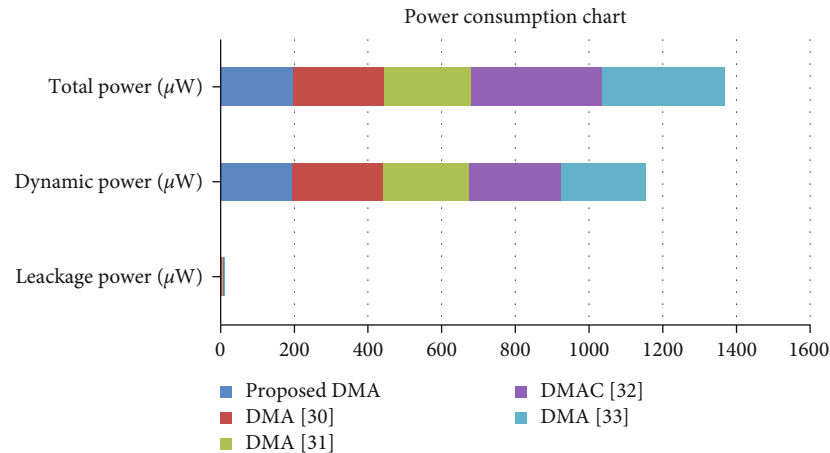
Figure 12: Power consumption comparison.

Table 7: Comparison of area overhead.

Design	Cell	Overhead
Proposed MAC unit	2201	0.0011%
Snapdragon SoC	187 million	—

SoC area = 187 million cells, MAC area = 2201 cells, and area overhead = 0.0011%.

comparison of area overhead is tabularized in Table 7. The results show that integrating a MAC unit with SoC increases the area to just 0.0011%. Some SoC-based systems are available in the research study [36–40] for our notice.

5. Conclusion

A memory access controller for the multiprocessor-based SoC devices is proposed in the presented research. The architecture of a memory controller is proposed to fulfill the consumer's demands for IoT devices. The SoC consists of a multiprocessing unit, and MAC integration decreases the processing activity and power consumption by offloading processors from the memory-accessing task. As a result, it increases the speed of the processors to perform more essential tasks. The processor performance comparison is noticed with and without integrating a memory controller into the SoC while developing this nanomaterial-based product. It has been seen that the memory controller's presence will drastically affect processing speed and the power consumption of the processing units. The MAC unit is minimal, and it takes a low area overhead at low power consumption and fast data rate transfer. The hardware overhead is only a limitation. The MAC unit is a separate entity, and therefore, it may use for any future enhancement of SoC design with a lite area overhead.

Data Availability

The simulation screen results and excel file graphs data used to support the findings of this study are included within the article.

Conflicts of Interest

The authors declare no conflicts of interest to report regarding the present study.

Acknowledgments

References

[1] H. Rahimi, A. Zibaeenejad, and A. A. Safavi, "A novel IoT architecture based on 5G-IoT and next generation technologies," in *2018 IEEE 9th Annual Information Technology, Electronics and Mobile Communication Conference (IEMCON)*, Vancouver, BC, Canada, 2018.

[2] S. Mei, J. Chai, S. B. Wang, C. H. Ng, G. S. Ungvari, and Y. T. Xiang, "Mobile phone dependence, social support and impulsivity in Chinese university students," *International Journal of Environmental Research and Public Health, MDPI*, vol. 15, no. 3, 2018.

[3] M. Agiwal, A. Roy, and N. Saxena, "Next generation 5G wireless networks: a comprehensive survey," *IEEE Communications Surveys & Tutorials*, vol. 18, no. 3, pp. 1–1, 2016.

[4] A. O. Alkhamisi, S. M. Buhari, G. Tsaramirsis, and M. Basheri, "An integrated incentive and trust-based optimal path identification in ad hoc on-demand multipath distance vector routing for MANET," *International Journal of Grid and Utility Computing*, vol. 11, no. 2, pp. 169–184, 2020.

[5] J. Rodriguez, *Fundamentals of 5G Mobile Networks*, John Wiley Publisher-2015, 2015.

[6] "The Zettabyte Era – trends and analysis," 2019, http://www.cisco.com/en/US/solutions/collateral/ns341/ns525/ns537/ns705/ns827/VNI_Hyperconnectivity_WP.html.

[7] H. Jeong, J. Lee, H. Yoo, and I.-C. Park, "A low-power high-performance SoC platform for IoT applications," *IDEC Journal of Integrated Circuits and Systems*, vol. 2, no. 1, pp. 37–45, 2016.

[8] Y. Debizet, G. Lallement, F. Abouzeid, P. Roche, and J. Autran, "Q-learning-based adaptive power management for loT system-an-chips with embedded power states," in *2018 IEEE International Symposium on Circuits and Systems (ISCAS)*, pp. 1–5, Florence, Italy, 2018.

[9] A. Goel and W. R. Lee, "Formal verification of an IBM core connect processor local bus arbiter core," in *In DAC '00: Proceedings of the 37th Conference on Design Automation (ACM)*, pp. 196–200, New York, 2000.

[10] R. J. Gutmann, "Advanced silicon IC interconnect technology and design: present trends and RF wireless implications," *IEEE Transactions on Microwave Theory and Techniques*, vol. 47, no. 6, pp. 667–674, 1999.

[11] W. O. Cesario, D. Lyonnard, G. Nicolescu et al., "Multiprocessor SoC platforms: a component-based design approach," *IEEE Design & Test of Computers*, vol. 19, no. 6, pp. 52–63, 2002.

[12] M. Baklouti, H. Krichene, and M. Abid, "Synchronous communication-based Many-core SoC," *Arabian Journal for Science and Engineering*, vol. 42, no. 2, pp. 845–857, 2017.

[13] "Device specification Snapdragon 820E processor (APQ8096SGE)," 2018, https://developer.qualcomm.com/download/sd820e/qualcomm-snapdragon-820e-processor-apq8096sge-device-specification.pdf.

[14] I T R S, "System design source," 2011, http://www.itrs.net.

[15] A R M, "AMBA Specification (Rev 3.0)," 2007, http://infocenter.arm.com/help/index.jsp?topic=/com.arm.doc.set.amba/index.html.

[16] M. Posner and D. Mossor, *Designing Using the AMBA™ 3 AXI Protocol—Easing the Design Challenges and Putting the Verification Task on a Fast Track to Success*, Synopsys, Inc, industry article, 2020.

[17] K. Sekar, K. Lahiri, A. Raghunathan, and S. Dey, "Dynamically configurable bus topologies for high-performance on-chip communication," *IEEE Transactions on Very Large Scale Integration (VLSI) Systems*, vol. 16, no. 10, pp. 1413–1426, 2008.

[18] R. Saravana Ram, M. L. C. Prabhaker, K. Suresh, K. Subramaniam, and M. Venkatesan, "Dynamic partial reconfiguration enchanced with security system for reduced area and low power consumption," *Microprocessors and Microsystems*, vol. 76, 2020.

[19] W. Savage, J. Chilton, and R. Camposano, "IP reuse in the system on a chip era," in *In ISSS '00: Proceedings of the 13th International Symposium on System Synthesis (IEEE)*, pp. 2–7, Madrid, Spain, 2000.

[20] N. Xu and Z. Zhou, "Avalon bus and an example of SOPC system," *Semiconductor Technology*, vol. 28, no. 2, pp. 17–20, 2003.

[21] I D T, "Idt peripheral bus. White Paper (IDT, Santa Clara)," 2004, IEC, Iec61508 - functional safety standard for electrical/electronic/programmable electronics systems, http://www.iec.ch/functionalsafety.

[22] W. D. Weber, "Enabling reuse via an IP core-centric communications protocol: open core protocol tm," *Proceedings of the IP*, pp. 20–22, 2000.

[23] K. Huang, J. Lu, J. Pang et al., "FPGA prototyping of an AMBA-based windows-compatible SoC," in *In Proceedings of the 18th Annual ACM/SIGDA International Symposium on Field Programmable Gate Arrays (ACM*, pp. 13–22, New York, 2010.

[24] P. Ateshian and D. Zulaica, *ARM synthesizable design with Actel FPGAs: with mixed-signal SoC applications (set 3)*, McGraw-hill Inc., New York, 2010.

[25] Qualcomm Technologies Incorporated Design document, "Designing mobile devices for low power and thermal efficiency," 2013, https://www.qualcomm.com/media/documents/files/designing-mobile-devices-for-low-power-and-thermal-efficiency.pdf.

[26] J. Osborne, "Qualcomm snapdragon 1000 for laptops could pack 8.5 billion transistors," *Tech Radar*, vol. 2018, 2018.

[27] "Qualcomm product specification," 2019, https://www.qualcomm.com/products/snapdragon-835-mobile-platform.

[28] T. Risset, "SoC (system on Chip)," in *Encyclopedia of Parallel Computing*, D. Padua, Ed., Springer, Boston, MA, 2011.

[29] S. Gupta, Applications Engineer Sr, and L. Natarajan, "Optimizing embedded applications using DMA," *Applications Engineer Sr, Cypress Semiconductor Corp. Published in EE Times Design*, 2010, http://www.eetimes.com.

[30] M. A. Ahmed, A. Aljumah, and M. G. Ahmad, "Design and implementation of a direct memory access controller for embedded applications," *International Journal of Technology*, vol. 10, no. 2, pp. 309–319, 2019.

[31] S. Ma, L. Huang, Y. Lei, Y. Guo, and Z. Wang, "An efficient direct memory access (DMA) controller for scientific computing accelerators," *IEEE International Symposium on Circuits and Systems (ISCAS)*, vol. 2019, pp. 1–5, 2019.

[32] Y. J. M. Shirur and K. M. Sharma, "Design and implementation of efficient direct memory access (DMA) controller in multiprocessor SoC," in *2018 International Conference on Networking, Embedded and Wireless Systems (ICNEWS)*, pp. 1–6, Bangalore, India, 2018.

[33] Y. Wang, T. Wang, P. Zhou, and X. Wang, "Design and implementation of a flexible DMA controller in video codec system," in *2014 19th International Conference on Digital Signal Processing*, pp. 78–82, Hong Kong, China, 2014.

[34] "Qualcomm Snapdragon Processor datasheet.Qualcomm Snapdragon 835 (8998)," 2019, https://www.notebookcheck.net/Qualcomm-Snapdragon-835-SoC-Benchmarks-and-Specs.207842.0.html.

[35] D. Takahashi, "Qualcomm's Snapdragon 835 will debut with 3 billion transistors and a 10 nm manufacturing process," *VentureBeat*, 2017, https://venturebeat.com/2017/01/03/qualcomms-snapdragon-835-will-debut-with-3-billion-transistors-and-a-10nm-manufacturing-process/.

[36] M. R. Yahya, N. Wu, G. Yan, and Y. Yasir, "Review of photonic and hybrid on chip interconnects for MPSoCs in IoT paradigm," in *2018 21st Saudi Computer Society National Computer Conference (NCC)*, Riyadh, Saudi Arabia, 2018.

[37] S. Kumar, S. Sahoo, A. Mahapatra, A. Kanta Swain, and K. K. Mahapatra, "Security enhancements to system on chip devices for IoT perception layer," in *2017 IEEE International Symposium on Nano electronic and information Systems (iNIS)*, pp. 151–156, Bhopal, India, 2017.

[38] I. Al-Darraji, D. Piromalis, A. A. Kakei et al., "Adaptive robust controller design-based RBF neural network for aerial robot arm model," *Electronics*, vol. 10, no. 7, p. 831, 2021.

[39] G. Tsaramirsis, M. Papoutsidakis, M. Derbali, F. Q. Khan, and F. Michailidis, "Towards smart gaming olfactory displays," *Sensors*, vol. 20, no. 4, p. 1002, 2020.

[40] S. Alnatheer and M. A. Ahmed, "Optimal method for test and repair memories using redundancy mechanism for SoC," *Micromachines*, vol. 12, no. 7, p. 811, 2021.

Research Article

Nanomaterials and Research on the Repair of Basketball Sports Ligament Injury

Zhongyou Xing [ID]

College of Physical Education, Xuchang University, Henan 461000, China

Correspondence should be addressed to Zhongyou Xing; 11992005@xcu.edu.cn

Sports ligament injury refers to muscle or joint injury caused by excessive use of limbs or long-term use of wrong training methods. This is a very common sports disease, and the body's ability to heal itself is poor. At present, the clinical methods to treat this disease mainly include autologous structure transplantation, allogeneic structure transplantation, and artificial ligament reconstruction. Nanomaterials refer to materials made of them as basic units. Transplantation of homologous and allogeneic structures may cause immune rejection in the human body. Therefore, the use of nanomaterials to reconstruct artificial ligaments is the current research hotspot of sports injury repair. This article mainly studies the repair effect of nanomaterials on basketball sports ligament injuries. In this paper, by implanting nanofiber scaffolds in sports-injured rabbits, observing and comparing the healing, growth, and proliferation of damaged cells after implantation, and the compatibility of nanofibers with cell tissues, so as to determine that nanomaterials have an impact of lion sports injury repair and the interaction between nanomaterials and cells. According to the experimental results, the implantation of nanofiber scaffolds can greatly accelerate cell proliferation and differentiation and promote the healing of sports-damaged tissues; nanofiber scaffolds have good histocompatibility, so the use of nanomaterials can promote the repair of sports ligament injury in basketball sports.

1. Introduction

Partial ligament injury without dislocation of the joint is called transition ligament itself complete fracture, it can also be attached to the bone avulsion, so as to form a potential joint dislocation subluxation or even complete dislocation. The main types of ligament injury are lacerations or ruptures. This is a very common sports disease, and the human body has very poor self-healing ability to this disease. The current clinical methods to treat this disease mainly include autologous structure transplantation, allogeneic structure transplantation, and artificial ligament reconstruction. Artificial ligaments have a long history of repairing sports ligament injuries. As early as the 1970s, artificial ligaments have been used in clinical research. These artificial materials have carbon fiber and other synthetic materials that are well described with human cells. For fibers, the treatment effect is not very good because these materials generally produce great friction with the tissue cells of the body, and even produce some debris, which has a great impact on the body's

movement function. Today, with the development of nano-technology, nanomaterials such as inorganic nanomaterials, polymer organic nanomaterials, nanocomposites, and bionic nanomaterials have been continuously developed, which have been used in the field of biomedicine. In 2007, Qin Ruiyun and others developed nanobone, which has a great effect on repairing damaged tissue cells. The porous structure of the nanomaterial is conducive to cell metabolism, because the effect of nanomaterials on cell structure and function determines the cytotoxicity and application value of nanomaterials, but it will not cause immune rejection in the body, so it has high compatibility with cells [1].

At present, homologous structural transplantation and allogeneic structural transplantation that can repair the ligament injury caused by dragon dance and lion dance may cause immune rejection in the body. Therefore, the use of nanomaterials for artificial ligament reconstruction is the current research hotspot of sports injury repair. This article is studying the effect of nanomaterials on the repair of ligament injury caused by dragon dance and lion dance.

Nanomaterials have many excellent structural characteristics, like nanomaterials that can be applied to infrared sensor materials because of their high optical absorption. The size of this material is on the order of nanometers. Due to the reduction of its particle size, nanomaterials have a large proportion of surface atoms and strong adsorption capacity, so they have high chemical reaction activity. This feature can regulate cell adhesion, proliferation, and differentiation. In addition, there are interactions and connections between nanometer units of nanomaterials. Many artificial synthetic materials used to treat sports ligament injuries have many shortcomings, such as low compatibility, which causes tissue inflammation, and too long use-time that may cause breakage. These problems will cause poor treatment effects. With the development and progress of nanotechnology, nanomaterials have gradually overcome these shortcomings, so nanomaterials will be widely used in the field of biomedicine, especially in the treatment of sports ligament injuries in recent years. This article uses experiments to explore the impact of nanofiber scaffold implantation on the repair of sports ligament injury [2, 3].

In this paper, by implanting nanofiber scaffolds into rabbits with sports injuries, the author observed and compared the healing, growth, and proliferation of damaged cells after implantation, and the compatibility of nanofibers with cell tissues, so as to judge the sports injury caused by nanomaterials. The effect of repair and the interaction between nanomaterials and cells. In the experiment, 20 healthy rabbits were selected; all artificially created sports ligament injuries and epidermal wounds. Then, 10 of them were implanted with nanofiber scaffolds as the experimental group, and the remaining 10 were left untreated as the control group. In the following three days, seven days, and ten days, the wound healing of the rabbits was observed, and samples were collected for H&E staining, flow cytometry, and scanning electron microscopy, and corresponding charts were made based on the test results. Implanting nanofiber scaffolds in the body is a very effective method for judging the compatibility of materials and cell tissues. This method can directly observe the body's response to nanomaterials, and this experiment further studies nanomaterials and nanomaterials through slicing and the relationship between tissue cells. In the experiment, we will also observe the rabbit's mental state, eating, and wound changes to judge the effect of nanomaterials on wounds and the effect on cell tissue. HE staining in this experiment can clearly observe the state and number of cells, and flow cytometry can count the proliferation and differentiation of cells [4].

Sports ligament injuries are often caused by strenuous exercise or external forces, which are mainly divided into lacerations or ruptures. The human body has a poor self-healing ability for this disease. The current clinical treatment of this disease mainly has its own structure. Transplantation, allogeneic structure transplantation, and artificial ligament reconstruction; the first two treatments may cause immune rejection in the human body. Therefore, this article is studying the role of nanomaterials on the repair of ligament damage caused by dragon dance and lion dance. In this paper, by implanting nanofiber scaffolds into rabbits with sports inju-

ries, the author observed and compared the healing, growth, and proliferation of damaged cells after implantation and the compatibility of nanofibers with cell tissues, so as to judge the sports injury caused by nanomaterials. The effect of repair and the interaction between nanomaterials and cells. The experimental results in this paper show that the porous structure of nanomaterials can promote the metabolism of cell tissues. Since the material has no biological activity, it will not cause immune rejection in the body. The implantation of nanofiber scaffolds has a certain promotion effect on wound healing and improves the healing rate of wounds. According to H&E staining tests, nanomaterials can promote cell proliferation and differentiation, and it can be intuitively observed that nanomaterials such as tissue cells have good compatibility which reduces the inflammation caused by the dragon dance and lion dance motor ligament injury, so the use of nanomaterials can promote the repair of the dragon dance and lion ligament injury [5, 6].

2. Preparation and Performance of Nanofiber Scaffold

2.1. Preparation Method of Nanofiber Scaffold

2.1.1. Weaving. The three-dimensional nanofiber scaffold is a kind of collector that uses a high-speed rotating shaft to prepare a unidirectionally arranged nanofiber mat. The first single-circle-oriented nanofiber scaffold used a high-speed rotating mandrel as a collector, and then cut into thin strips along the direction of fiber arrangement. And then using lasso technology, a relatively good structure nanofiber scaffold can be prepared. Using this principle in the same way, weaving and other textile techniques can be used in the preparation process to prepare PLA, PCL, and other nanomaterials into various specific structures [7].

2.1.2. Gas Foaming. The chemical foaming method uses a chemical method to generate gas to make the plastic foam; heat the chemical foaming agent added to the plastic to decompose it to release the gas and foam. In addition, it can also use the chemical interaction between the plastic components, reacting with the released gas and foam. The gas foaming method can maintain the shape of nanomaterials during the preparation of nanofiber scaffolds. Xie et al. developed another more advanced gas foaming method, which requires the generation of bubbles in aBH4 aqueous solution and then rapid freeze drying. The NaBH4 aqueous solution will quickly penetrate into the nanofiber membrane. In addition, the customized mold combination can optimize the gas foaming method. Based on the predesigned glass cover, the thickness of the expanded nanofiber scaffold can be adjusted [8].

2.1.3. 3D Printing. 3D printing is a technology that uses adhesive materials such as powdered metal or plastic to construct objects layer by layer on the basis of digital model files. 3D printing is a kind of rapid prototyping technology, also known as additive manufacturing. It is a technology that uses powdered metal or plastic and other bondable materials

to construct objects based on digital model files by printing layer by layer. 3D printing technology is realized through a printer, so the computer can precisely control the shape and structure of the nanofiber scaffold. Due to the high precision of this technology, it is very suitable as a new way to prepare the nanofiber scaffold. The nanofiber scaffold prepared by 3D printing has a porous structure and the internal network is built by nanofibers. At present, many nanofiber scaffolds at home and abroad are prepared by using 3D printing technology. It is believed that with the further development of this technology, its role in preparing nanofiber scaffolds will become more and more important [9].

2.1.4. Self-Assembly.

Self-assembly is a phenomenon in which the constituent elements of the system gather and organize themselves into a regular structure without the intervention of human external forces. For example, the crystallization of molecules is a self-assembly phenomenon. Self-assembly generally exists in nature. For example, the cells of organisms are self-assembled by various biological molecules; and the self-assembly of various molecules is also a very important method to construct nanomaterials. This so-called bottom-up method is currently widely used to prepare nanomaterials with optical, electrical, magnetic, sensing, and catalytic functions. According to the current research status at home and abroad, molecular self-assembly is a new way to prepare nanomaterials. Generally, the structural units of molecular self-assembled nanomaterials are macromolecular substances such as polypeptides and proteins. Molecular self-assembly is currently widely used in spacecraft at home and abroad. Nanofiber scaffolds prepared by this method have very good performance and are widely popular in domestic and foreign research fields. Therefore, this method has become a research hotspot [10, 11].

2.1.5. Freeze-Drying.

Freezing prevents further agglomeration, and vacuum-dried particles tend to agglomerate and grow larger. Freeze-drying uses the principle of sublimation of ice crystals. In a high vacuum environment, the moisture of frozen food materials is directly sublimated from ice solids to steam without melting of ice. Generally, the moisture in vacuum-dried materials is converted in liquid form. The food is dried in the vapor state, so freeze-drying is also called freeze sublimation drying. Freeze-drying technology can not only dry the material quickly but also not destroy the original material structure of the material. This dehydration method is very convenient, efficient, and safe. Therefore, it is often used in two fields of food and materials. It has a wide range of applications, welcomed by everyone. Three-dimensional porous nanofiber refers to the preparation of the scaffold which requires this method. Ding et al. first studied the use of a high-speed homogenizer to break the electrospun nanofiber membrane, and then freeze-dry the material to obtain a nanofiber scaffold. The nanofiber scaffold prepared in this way has a wide range of applications and can be applied to a variety of different tissues, because it is a nanofiber scaffold with a specific shape and function that can be 3D printed using a computer [12].

2.2. Performance of Nanofiber Scaffold.

Nanofiber scaffolds with good performance need to be able to simulate the natural extracellular matrix environment and need to have the following advantages: high compatibility, certain mechanical strength, biodegradability, hydrophilicity, large specific surface area, and highly penetrating porous structure. The characteristics of nanofiber scaffolds need to enable cell adhesion, migration, differentiation, and proliferation, as well as the transmission of nutrients and metabolism. Therefore, most of the materials of nanofiber scaffolds are three-dimensional nanofiber porous structures, because this nanomaterial has good compatibility with cell tissues, and its structure not only meets the requirements, but also promotes cell proliferation and differentiation. At present, the preparation process of nanofiber scaffolds at home and abroad includes weaving, gas foaming, 3D printing, self-assembly, freeze-drying and other steps. After being made, they are mostly used to lead the way in biomedicine. This article is about nanofiber scaffolds for dragon dance and lion dance sexual injury. Of course, there are many other preparation methods. Compared with other methods, this method is cheaper and easier to operate and is suitable for large-scale production. At present, nanofiber scaffolds such as PLLA, PCL, and PLAG have been prepared by this method at home and abroad [13].

The crystallinity and hydrophobicity of PCL are stronger than those of PLLA. PLLA and PCL are two kinds of nanomaterials that are widely used. They have good compatibility and are biodegradable. However, if PLLA is not easy to be implanted in the body, it may break due to too long usetime. On the contrary, a good PCL can make up for the shortcomings of PLLA. The material has good toughness and strong plasticity but insufficient mechanical strength. Therefore, mixing the two materials can improve each other's shortcomings. The performance of the new mixed material is very outstanding, and it overcomes the insufficient toughness of PLLA and the insufficient strength of PCL. The mixed material is very popular in clinical medical research [14]. About 72 hours after injury, platelet and multi potential mesenchymal cells began to appear in the wound. At this time, macrophages devoured necrotic tissue and released growth factors including FGF, TGF, and PDGF, which stimulated the proliferation of fibroblasts and the synthesis of collagen I, III, and V and noncollagen egg white, and induced vascularization and granulation tissue formation, which we call the proliferation period. In the proliferation stage, fibroblasts produce compact and porous connective tissue with collagen characteristics and are combined in the ligament fracture area, which we call scar tissue. The scar tissue was irregular in shape at the beginning of formation, rich in collagen of type 3 and type 5, and began to form a small diameter collagen fiber bundle, followed by the remodeling and maturity of the tissue, and finally the ligament healing was realized. During the process of regeneration ligament maturation, the porosity of tissue gradually decreases and extracellular matrix gradually enriches and grows along the axial direction. The new tissue begins to have a stable directionality, which lasts for at least one year.

If ionomer treatment is performed on the fiber scaffold, the surface of the nanofiber scaffold can be changed for a long time, and the water contact angle of the nanofiber scaffold can be reduced, thereby improving the hydrophilicity of the nanofiber scaffold, and this operation can also improve the nanofiber scaffold biocompatibility, so the performance of the nanofiber scaffold can be improved through this treatment. The hydrophilicity of the nanofiber scaffold increases with the increase of plasma treatment time, and the function of the nanofiber scaffold to promote cell proliferation after plasma treatment is also improved. However, plasma treatment can also damage the fiber structure of the nanofiber scaffold, and the longer the time, the more serious the structure damage, which leads to the destruction of the performance of the nanofiber scaffold. Therefore, when performing plasma treatment on the nanofiber scaffold, it is necessary to strictly follow the steps to control the time within the effective time range that can improve the performance of the nanofiber scaffold without damaging the structure of the nanofiber scaffold. In the preparation of nanofiber scaffolds, it is necessary to change the force applied to the fibers to change the performance of the nanofiber scaffolds [15].

2.3. Prospect of Nanomaterials in the Ligament Injury of Basketball Sports. Research on the use of nanofibers in tissue engineering started late and is still in its infancy, especially in the field of biomedicine. There are fewer studies on fusion of nanomaterials. Many domestic and foreign studies have not entered the stage of clinical experimental research, so nanomaterials are used in dragon dance and lion dance. There is little experience in sexual ligament injury, and the related safety and reliability performance still need a lot of experiments to further improve. At present, nanomaterials are still facing many problems when used for sports ligament injuries, such as how to construct the cell-nanomaterial interface, how to reduce the body's immune rejection caused by nanofiber scaffolds, and how to improve the compatibility of nanomaterials. With the advancement of tissue engineering technology, the second generation of biomaterials began to develop into the third generation of activated bionic materials. Therefore, it is necessary to develop a nanobionic material with repair function in sexual ligament injury and reduce complications such as inflammation caused by immune rejection reaction [16].

With the further development of nanotechnology, nanobiology, nanomaterials, nanomedicine, and other disciplines have also developed and progressed. Especially in recent years, these disciplines have gradually begun to merge and penetrate, and there has also been an in-depth integration between the biological field and nano materials. Research has brought new treatment methods and ideas, and the application of nanomaterials in medicine has opened up many new research directions. At present, new nanomaterials will be developed for ligament injuries [17].

With the further development of nanotechnology, nanomaterials have begun to merge with the biological. This trend has also provided new ways and methods for the treatment of ligament injury caused by dragon dance and lion dance. Over the years, nanomaterials have made great achievements in the treatment of ligament injuries. Big research results and applications have gradually increased and become research hotspots. However, the application of nanomaterials in various aspects is still insufficient, especially in the biological field. There are fewer studies on fusion of nanomaterials. Many domestic and foreign studies have not entered the stage of clinical experimental research. If nanomaterials are required to be integrated and used more widely in the biological field, it will take a long time to strengthen the research and cooperation of personnel in related fields to develop more useful bionanomaterials and integrate nanomaterials into medical treatment more deeply. We believe that with the further development of nanotechnology and the development of more nanomaterials, there will be progress in disease diagnosis and drug treatment. This material will be used to treat more diseases and bring new hope to more patients [18].

3. Experimental Steps

3.1. Experimental Materials and Instruments. The materials and instruments used were 20 healthy male and female rabbits, PCL nanofiber scaffold, physiological saline, test tube, surgical instrument, pipette, 75% ethanol solution, 30% supersaturated sodium sulfide solution, flow cytometer, microscope, and centrifugal precipitator.

3.2. Experiment Method

3.2.1. Experimental Grouping. In the experiment, 20 healthy rabbits were selected, all artificially created sports ligament injuries and epidermal wounds. Then, 10 of them were implanted with nanofiber scaffolds as the experimental group, and the remaining 10 were left untreated as the control group. In the following three days, seven days, and ten days, the wound healing of the rabbits was observed, and samples were collected for H&E staining, flow cytometry, and scanning electron microscopy, and corresponding charts were made based on the test results.

3.2.2. Preparation of Animal Models and Wound Treatment. Shave the hair beside the spine of the healthy rabbit, then gently wipe the rabbit's back with a 30% supersaturated sodium sulfide solution, and clean it after a few minutes. Subsequently, the rabbit was injected with 3% pentobarbital solution, and then the rabbit's skin was cut and separated to the deep fascia. Then, 10 rabbits were randomly selected to be implanted with nanofiber scaffolds as the experimental group, and the remaining 10 rabbits were dipped in gauze and wrapped in saline to wrap their wounds as the control group.

3.2.3. Collection of Animal Model Specimens. In three days, seven days, and ten days after the sports ligament injury, the specimens were collected according to the steps. Collect specimens at each observation time node, then fix the specimens with formalin for 48 hours, then dehydrate with ethanol and embed the sections with paraffin, so that the sections are ready.

3.2.4. TUNEL Test. According to the established observation time node, collect the required specimens, follow the detection steps of TUNEL detection, complete the detection step by step, and then carefully observe the number of apoptotic cartilage cells and the spatial distribution characteristics and distribution range under the microscope. Under the microscope, it can be observed that the nucleus of the apoptotic cartilage cells is brown, and their morphology and size are different. Compared with normal cells, the nuclear phase is more compact, and even some cytoplasms may be positive and stained. The apoptotic cells in the late stage will be further broken up, and there are apoptosis cells with different nuclear fragments. Some apoptotic chondrocytes were positive, but the color was very light. The nuclei of normal cargo cells are stained blue, and the nuclei are similar in shape and size. The nucleus is larger than the apoptotic nucleus.

3.2.5. Observation by Transmission Electron Microscope. Take 2 days, 7 days, and 10 days after the injury of the motor ligament, and 2 samples from the control group, then soak the samples in glutaraldehyde phosphate solution, and then put the samples in the refrigerator for two days. After the specimen is processed, it is trimmed into a neat long strip, and then placed in osmic acid and fixed for 2 hours. Then, follow the conventional steps of making slices, process the collected specimens step by step, and finally observe the cell status carefully under the microscope to observe the number of apoptotic cells and the characteristics and range of their distribution locations.

4. Results Analysis

4.1. H&E Staining. After H&E staining, it can be seen that there are a few scattered apoptotic and necrotic cells around the ligament injury area and articular cartilage. The color of the nucleus is very prominent after staining, and it can also be seen that the cell membrane is not broken. Two days after ligament injury, more apoptotic ligament cells can be observed. On the fourth day after injury, the number of apoptotic ligament cells that can be observed reaches a peak and is distributed everywhere. Compared with the control group, after the nanofiber scaffold was implanted in the treatment group, the number of apoptotic ligament cells was much less than that in the control group on the second day, and the rate of cell apoptosis was also greatly delayed.

As shown in Figure 1, within ten days after the ligament injury, the ligament injury gradually healed over time. Three days after ligament injury, the healing rate of the control group without any treatment was very low, only 25%. On the contrary, the wound healing rate of the experimental group implanted with nanofiber scaffolds was nearly twice as that of the control group, as high as 40%. Seven days after the ligament injury, the wound healing rate of the experimental group soared to 70%. Although the control group also increased slightly, it was still much less than the experimental group, only 57%. Ten days later, the wound healing rate of both groups increased, but because the wounds were basically close to healing, the increase in the experimental group was only 20%, while the increase in the control group

was as high as 30%. It can be seen that implanting nanomicroscopic scaffolds in the body can help promote wound healing.

In Figure 2, the number of normal ligament cell apoptosis is generally very small, while the number of ligament apoptotic cells after ligament injury increases significantly. Two days after the ligament injury, the number of ligament injury cells in the experimental group was 23, while the control group had 62 cells under the microscope. Four days after the ligament injury, the number of apoptotic cells in the ligament reached its peak. There were 117 in the control group, while the experimental group had 78 in comparison. Then, until the fourth week, the apoptotic cells in the ligament began to decline gradually, and the decline in the experimental group was more rapid than the decline in the control group. On the tenth day, the experimental group dropped to 42, while the control group had a little more, down to 59. And then in the fourth week, the two groups' costs fell to the same level. It can be seen that implanting nanofiber scaffolds in the body can reduce the apoptosis of ligament cells and promote the healing of ligament injuries.

According to the analysis of this experiment, it can be concluded that implanting nanofiber scaffolds in rabbits can promote cell metabolism, accelerate wound healing, and reduce the apoptosis of ligament damaged cells. According to the experimental results, no complications such as inflammation and immune rejection occurred, indicating that the nanofiber scaffold has good compatibility with the cells in the body, and promoting wound healing indicates that nanomaterials can increase cell metabolism and accelerate cell proliferation and differentiation.

4.2. Flow Cytometry Detection. After implanting the nanofiber scaffold in the experimental group, after the ligament cells reacted with type II collagenase at each observation time node, the collected samples were made into cell suspension, and then tested by flow cytometry. The test results show that compared with the control group and normal ligaments, the apoptosis rate of ligament cells and the number of ligament cells in the treatment group are greatly reduced at each time node. This is for future research on nanomaterials. The relationship with cells plays an important role.

The results of flow cytometry can see the proliferation of ligament cells. Figure 3 shows the proliferation of ligament cells after ligament injury. It can be seen from the figure that the number of ligament proliferating cells that can be observed under the microscope under normal circumstances is certain. After ligament injury, ligament cells begin to proliferate in large numbers. In the four days after ligament injury, the ligament cells of the experimental group and the control group increased significantly, and the experimental group increased by 10 more than the control group. After the fourth day, the proliferation rate of ligament cells increased. By the seventh day, the number of ligament cells increased, reaching 55 in the control group and 68 in the experimental group. In the next few days, the number of ligament cell proliferation in the experimental group and the control group began to decline, while the control group declined even faster, and it dropped to 20 on the 14th day,
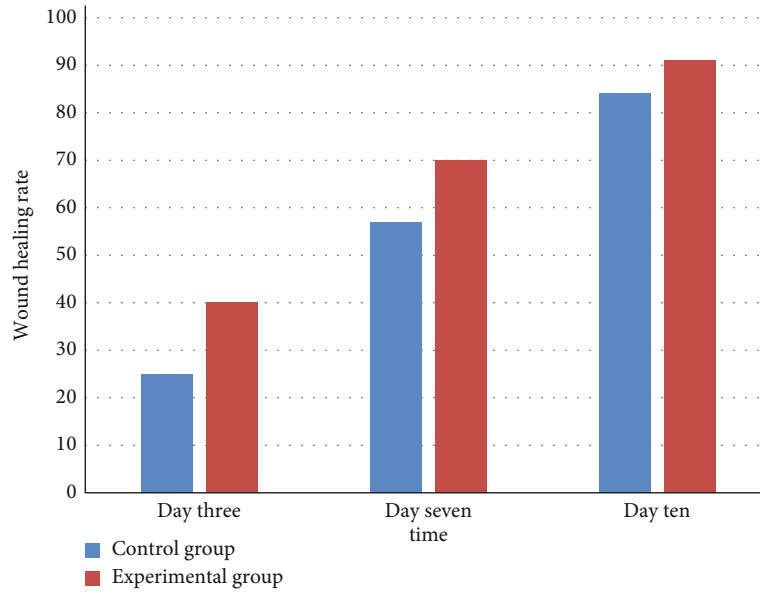
FIGURE 1: Comparison of wound healing rate.
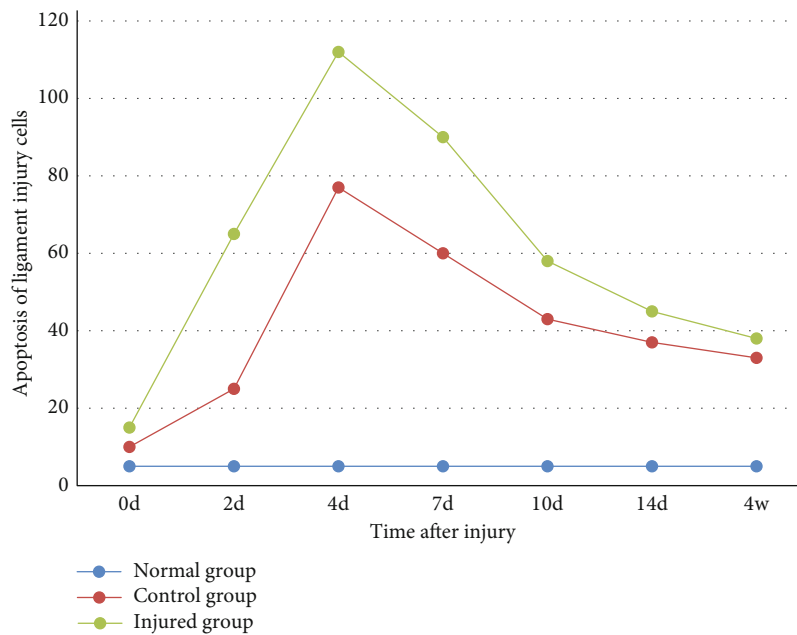
FIGURE 2: Comparison of changes in apoptosis of ligament injury.

while the experimental group dropped to 28. Four weeks later, the number of ligament cell proliferation in the experimental group and the control group was basically the same as the normal group. Figure 3 illustrates that implanting nanofiber scaffolds in rabbits can promote the proliferation and differentiation of ligament cells after ligament injury, so as to promote the healing of ligament injury.

In this experiment, the state of the cells can be observed under a microscope, and it can be judged that after ligament injury, there will be ligament cell apoptosis. According to Figure 4, in the control group, the apoptotic rate of ligament cells continued to rise within four days after injury, reaching

a peak on the fourth day, and then the apoptotic rate decreased. It can be seen that when the ligament is damaged, the ligament cells will continue to undergo apoptosis and necrosis. Within a short time after the ligament is injured, a small amount of apoptosis appears in the surface layer of the ligament. In the following two days, this kind of apoptosis begins to move to the middle layer. After days, apoptotic cells are more widely distributed and the damage is more serious. After 14 days, the damage was reduced and the wound began to recover. Four weeks later, the damage was basically healed, and the cells no longer continued to apoptosis. After the experimental group was implanted with
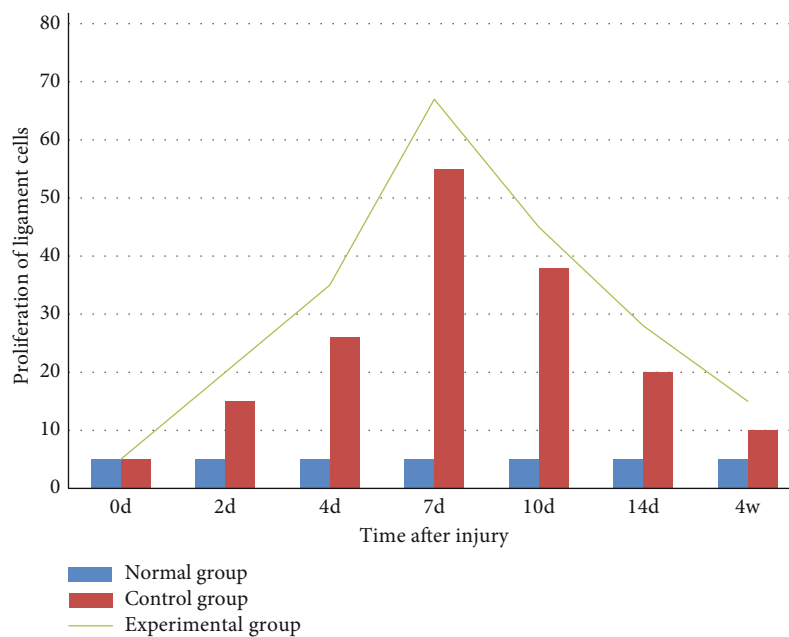
FIGURE 3: Ligament cell proliferation.
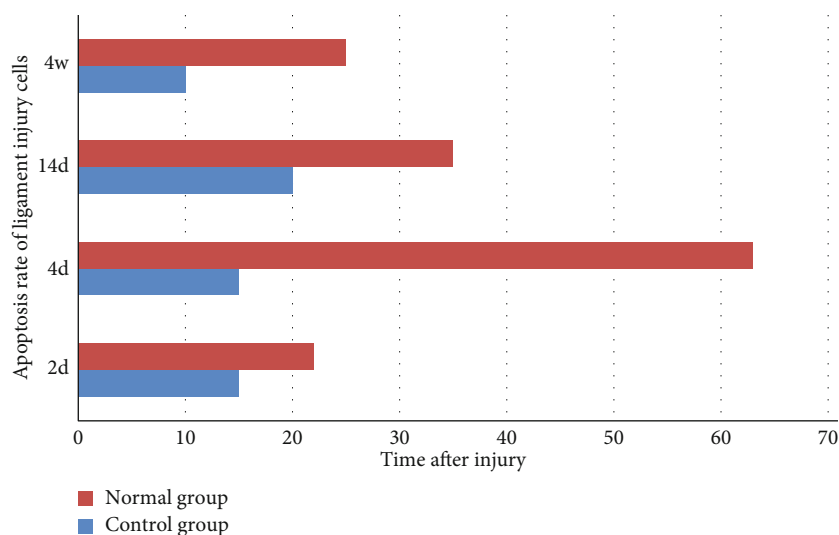
FIGURE 4: Comparison of changes in apoptosis rate of ligament cells.

the nanofiber scaffold, although the trend was similar to that of the control group, the cell apoptosis rate was much smaller in comparison. On the second day after ligament injury, the apoptosis rate of ligament cells in the experimental group was 5% lower than that of the control group. On the fourth day of the peak apoptosis rate, the experimental group was 50% lower than that of the control group. After 14 days, the experimental group was 50% lower than that of the control group. The control group was 15% lower than that of the control group on the fourth day, and the rate of difference between the two groups began to drop. Figure 4 shows that implanting nanofiber scaffolds in rabbits can inhibit ligament cell apoptosis and reduce the rate of ligament cell apoptosis.

The above two figures show that the implantation of nanofiber scaffolds in rabbits can promote the division of ligament cells and inhibit the apoptosis of ligament cells. Promoting cell division can prove that the porous structure of nanofibers can promote cell metabolism, and the relatively large surface area is conducive to cell adhesion, which can promote the proliferation of ligament cells. In addition, nanomaterials can also inhibit cell apoptosis, indicating that nanomaterials have good compatibility with ligament cells, which can avoid immune rejection and reduce complications such as inflammation.

5. Conclusions

The degree of differentiation of ligament cells is high; the proliferation is slow in vivo, and it is difficult to self-heal for sports ligament injuries. Therefore, the use of nanomaterials in the treatment of sports ligament injuries has become

a current research focus. In this paper, nanofiber scaffolds are implanted in rabbits with sports injuries. By observing the results of H&E staining, flow cytometry, and e-sports scanning, the healing and cell organization of damaged wounds before and after nanofiber scaffolds can be compared. The healing rate of serotonin, as well as the cell growth and proliferation after sports ligament injury and the compatibility of nanofibers with cell tissues can be judged, so as to determine the effect of nanomaterials on sports injury repair and the mutual influence between nanomaterials and cells. The experimental results in this paper show that the porous structure of nanomaterials can promote the metabolism of cell tissues. Since the material has no biological activity, it will not cause immune rejection in the body. The implantation of nanofiber scaffolds has a certain promotional effect on wound healing and improves the healing rate of wounds. According to H&E staining tests, nanomaterials can promote cell proliferation and differentiation, and it can be intuitively observed that nanomaterials such as tissue cells have good compatibility and reduces inflammation caused by motor ligament injury. With the development of nanotechnology, nanoelectronics, nanobiology, nanomaterials science, nanomedicine, and other subdisciplines have been established and developed. What is particularly important is that these disciplines are merging and penetrating into each other. The combination of materials science and biomedicine is more and more close, and various materials with specific functions will be more and more applied to biomedicine. In the next few years, nanoceramics in biomaterials will play a leading role in artificial bones. Inorganic and organic composite nanomaterials with various characteristics will also play an important role in the interventional repair of ligament injury. By pretreating OA chondrocytes with mgf-c24e in vitro, the therapeutic effect of mgf-c24e on the complications of ligament injury was studied. It was found that mgf-c24e could inhibit the spontaneous apoptosis of OA chondrocytes and promote the proliferation, migration, mechanical properties recovery, and extracellular matrix synthesis of OA chondrocytes. It was found that mgf-c24e regulated endoplasmic reticulum stress through endoplasmic reticulum membrane protein perk and inhibited cartilage degradation in the pathogenesis of OA.

Data Availability

The data that support the findings of this study are available from the corresponding author upon reasonable request.

Conflicts of Interest

The author declares that he has no conflicts of interest.

References

[1] M. Askenberger, E. Bengtsson Moström, W. Ekström et al., "Operative repair of medial patellofemoral ligament injury versus knee brace in children with an acute first-time traumatic patellar dislocation: a randomized controlled trial," *American Journal of Sports Medicine*, vol. 46, no. 10, pp. 2328–2340, 2018.

[2] M. Askenberger, E. Bengtsson Moström, W. Ekström et al., "Operative repair of medial patellofemoral ligament injury versus knee brace in children with an acute first-time traumatic patellar dislocation: a randomized controlled trial," *The American Journal of Sports Medicine*, vol. 25, no. 1, pp. 122–132, 2018.

[3] B. Gao, N. Xu, and P. Xing, "Shock wave induced nanocrystallization during the high current pulsed electron beam process and its effect on mechanical properties," *Materials Letters*, vol. 237, no. 15, pp. 180–184, 2019.

[4] J. Macossay-Torres, "Methods for making artificial ligaments and tendons," vol. 37, no. 7, pp. 131–140, 2015.

[5] F. Alaee, J. Apostolakos, H. Singh et al., "Lateral clavicle fracture with coracoclavicular ligament injury: a biomechanical study of 4 different repair techniques," *Knee Surgery, Sports Traumatology, Arthroscopy*, vol. 25, no. 7, pp. 2013–2019, 2017.

[6] Y. Zhao, H. Li, S. Wan et al., "Knowledge-aided convolutional neural network for small organ segmentation," *IEEE Journal of Biomedical and Health Informatics*, vol. 23, no. 4, pp. 1363–1373, 2019.

[7] L. I. Bo, "Repair of ankle fracture combined with triangular ligament injury," *Biped and Health*, vol. 89, no. 5, pp. 1827–1833, 2019.

[8] S. Guo-Tao and L. Jing, "Analysis on status quo, focus and frontier of domestic sports injury research based on mapping knowledge," *Modern Preventive Medicine.*, vol. 38, no. 9, pp. 3305–3312, 2017.

[9] L. Nazarenko, S. Bargmann, and H. Stolarski, "Energy-equivalent inhomogeneity approach to analysis of effective properties of nanomaterials with stochastic structure," *International Journal of Solids and Structures*, vol. 59, no. 2, pp. 183–197, 2015.

[10] T. Shigeta, S. Sakamoto, X. K. Li et al., "Luminal injection of hydrogen-rich solution attenuates intestinal ischemia-reperfusion injury in rats," *Transplantation*, vol. 99, no. 3, pp. 500–507, 2015.

[11] G. Bo, L. Chang, H. Chenglong et al., "Effect of Mg and RE on the surface properties of hot dipped Zn–23Al–0.3Si coatings," *Science of Advanced Materials*, vol. 11, no. 4, pp. 580–587, 2019.

[12] B. Wang and A. Walther, "Self-assembled, iridescent, crustacean-mimetic nanocomposites with tailored periodicity and layered cuticular structure," *ACS Nano*, vol. 9, no. 11, pp. 10637–10646, 2015.

[13] M. N. Sundaram, S. Sowmya, S. Deepthi, J. D. Bumgardener, and R. Jayakumar, "Bilayered construct for simultaneous regeneration of alveolar bone and periodontal ligament," *Journal of Biomedical Materials Research Part B: Applied Biomaterials*, vol. 13, no. 4, pp. 912–925, 2015.

[14] E. Naghashzargar, S. Farè, V. Catto et al., "Nano/micro hybrid scaffold of PCL or P3HB nanofibers combined with silk fibroin for tendon and ligament tissue engineering," *Journal of Applied Biomaterials & Functional Materials.*, vol. 16, no. 1, pp. 156–166, 2018.

[15] M. Askenberger, E. Bengtsson Moström, W. Ekström et al., "Microfiber-reinforced nanofibrous scaffolds with structure and material gradients to mimic ligament-to-bone interface," *Journal of Materials Chemistry B, 5(43).*, vol. 29, no. 3, pp. 705–718, 2017.

[16] A. G. Bajpayee, E. Rodolfo, M. Scheu et al., "Sustained intra-cartilage delivery of low dose dexamethasone using a cationic

carrier for treatment of post traumatic osteoarthritis," *European Cells & Materials*, vol. 34, no. 2, pp. 341–364, 2017.

[17] M. Spoliti, A. Giai Via, J. Padulo, F. Oliva, A. Del Buono, and N. Maffulli, "Surgical repair of chronic patellar tendon rupture in total knee replacement with ipsilateral hamstring tendons," *Knee Surgery, Sports Traumatology, Arthroscopy*, vol. 24, no. 10, pp. 3183–3190, 2016.

[18] E. Naghashzargar, S. Farè, V. Catto et al., "Nano/micro hybrid scaffold of PCL or P3HB nanofibers combined with silk fibroin for tendon and ligament tissue engineering," *Journal of Applied Biomaterials*, vol. 26, no. 9, pp. 649–655, 2015.

Research Article

Therapeutic Effect of Nanotitanium Oxide Combined with Exercise Rehabilitation Training on Wrist Joint Injury of Boxers

Xiaohua Li,[1] **Jianbo Li** ⓘ**,**[2] **and Meifang Zhang**[2]

[1]*School of Physical Education, Hunan University of Arts and Science, Changde, 415000 Hunan, China*
[2]*Computer Application Research Center, Hunan Applied Technology University, Changde, 415000 Hunan, China*

Correspondence should be addressed to Jianbo Li; ljbtom@huas.edu.cn

The rapid development of society promotes the rapid improvement of science and technology. On this basis, the development of nanotechnology has also made great achievements and has been applied to all walks of life. Among them, nanotitanium oxide provides favorable conditions for the medical treatment of various joint injuries. And sports rehabilitation training also plays an irreplaceable role in the treatment of joint injury, promoting the rapid recovery of joint injury. Boxing is a sport in which boxing gloves are worn for fighting. It has both amateur and professional competitions. The purpose of this paper is to study the therapeutic effect of nanotitanium oxide combined with sports rehabilitation training on the wrist joint injury of boxers. According to the therapeutic effect of the research, it can provide useful treatment basis for clinical treatment and help boxers recover wrist joint injury, so as to carry out boxing training later. The method adopted in this paper is as follows: first, the subjects were randomly divided into nanotitanium oxide combined with sports rehabilitation training group, nanotitanium oxide treatment group, sports rehabilitation training treatment group, and control group. Then, the subjects were tested with the score table, and the score data were recorded. Finally, chi-square test was used to test the experimental results. In conclusion, through the research and comparison, it is found that nanotitanium oxide combined with sports rehabilitation training can reduce the pain of boxers' wrist joint injury; after the treatment of wrist joint injury of boxers by nanotitanium oxide combined with sports rehabilitation training, the pain score decreased, and the daily function was improved; the PT score before the experiment was 15%, and the peak torque score after the experiment was 26%. The Pt/BW score was 22% before the experiment and 37% after the experiment. This reflects the strength of wrist muscle contraction, judging that the stability of wrist joint is enhanced after the experiment; nanotitanium oxide combined with exercise rehabilitation training can increase the sensitivity of wrist joint after the treatment of boxer wrist joint injury.

1. Introduction

Boxing [1] is a competitive sport with strong antagonism. Boxing was introduced into China in the 19th century. However, due to various reasons, boxing was not carried out in China until 1986 and gradually embarked on the road of standardization. It is a contest between two athletes in terms of physical fitness, skills, psychology, and agility. It is also a sport to test the comprehensive ability of athletes. It can improve and cultivate people's agile, calm, brave, and indomitable spirit. Boxing in China is gradually developing. The goal of boxing is to win more points than the other

party to win or knock the other party down. At the same time, the competitor should try to avoid the attack of the other party. Although China's boxing has made a breakthrough, there is still a considerable gap between the overall level and the high-level countries. Compared with boxing developed countries, China does not have its own boxing culture, and China's professional boxing has no echelon construction. One of the most important reasons is sports injury. To improve boxing level, not only from the boxing training process, but also from the recovery of the body after training, is a very important aspect. Through stretching training, the recovery after exercise and the causes of boxing

injury are comprehensively and systematically studied in order to reduce sports injury [2] and promote the vigorous development of boxing in China. Boxing started late in China, and from the development trend in recent years, the state pays attention to training methods and means and attaches importance to the physical training of athletes. How to maximize the performance of athletes has become the primary task, but the research on muscle recovery and injury prediction after training is not enough. Injury is an important factor that affects boxing performance. Body pulling training can improve the flexibility of the body, relieve the pain of skeletal muscle, increase the elasticity of skeletal muscle, reduce the hardness of foot, and prevent sports injury. The reason why rehabilitation training is necessary in training is that after high-intensity training, the energy reserve in the body will inevitably be consumed, leading to fatigue and functional decline. According to the principle of recovery and over recovery, it is necessary to recover and over recover the energy and material of the body after the exercise, so as to improve the functional level of the body and create material conditions for the improvement of sports performance.

Nanoparticle is a kind of nanomaterial [3], also known as ultrafine particle, which refers to the size of 1-100 nm particles. Nanoparticles are located in the transition zone between atomic clusters and macroobjects and between microsystems and macrosystems. They are a group composed of a small number of atoms or molecules. Therefore, they are both atypical microsystems and atypical macrosystems. It has small size effect, surface effect, quantum size effect, and macroquantum tunneling effect, which makes it present the characteristics of magnetic, optical, and electrical sensitivity that traditional materials do not have. Therefore, it has different toxicological characteristics from micron and conventional particles. In the field of drug therapy and molecular imaging, nanoparticles have become potential new drug carriers due to their special chemical structure, surface properties, and small particle size [4], which provides new prospects for drug delivery and targeted therapy at specific sites. Among the nanomaterials, nanotitanium dioxide (TiO_2) [5] is the most widely used. Because of its small particle size, it has been industrialized and widely used in coatings, pigments, ceramics, sunscreen cosmetics, antiaging, air purification, sewage treatment, antibacterial detoxification, food packaging, antistatic, and other fields. Adding nano-TiO_2 powder to cosmetics in a certain proportion can effectively shield ultraviolet rays. At the same time, nanotitanium oxide has a certain role in promoting the treatment of boxer wrist joint injury [6].

In the process of human activities, the original components and energy materials of human tissues and cells need to be continuously decomposed to release energy to meet the needs of human activities. In the process of decomposition of energy materials, the synthesis of energy materials was also carried out. According to the principles of recovery and over recovery, restorative training can realize the recovery and storage of basic energy materials and create material conditions for improving the physical level of the body. After high load training, athletes will have the feeling of

muscle "compression" and often feel heavy leg, even pain. If massage, bath, application of some drugs or jogging, and other means of recovery will speed up the blood circulation in the muscle, the muscle will return into a relaxed state as soon as possible. After high load training and competition, the nervous system remains normal in activity. Rehabilitation training [7] can affect this complex functional system, fixing the control path between the central nervous system and the surrounding organs dominated by random control. Long-term and systematic rehabilitation training can not only improve the interaction between vegetative organs and motor organs but also improve the interaction between organs around the central nervous system and central organs [8]. Rehabilitation training can adjust the long-term tension of the striated muscle to moderate relaxation, thus forming a strong connection and making the muscle work actively in the next step; it can also change the cross-section and tension of blood vessels, capillaries, arterioles, and venules. In relaxation training, the tension and contraction of blood vessels can be relaxed and the tension can be relieved. As a result, dilated blood vessels can contract and become normal medium tension. The human body's response to movement, especially the training of tissues and organs caused by the changes of morphological structure and function, is conducive to maintaining the relative stability of the internal environment, so as to achieve the purpose and function of protecting the human body from injury, and further expanding the production capacity, that is to say, human adaptability. When the body adapts to a certain level after training, the body is in a relatively stable state and needs to provide new stimulation, that is, a higher level of training. Break the original stable state and make the body adapt to the new training load.

An excellent athlete often works out a reasonable recovery method after training or before training, which can lay the foundation for athletes to maintain good competitive state for a long time and obtain the best sports results. Through literature retrieval and analysis, it is found that in China, the research on wrist joint injury of boxers [9] mainly focuses on the proportion of wrist joint injury, injury site, simple factors of injury, and some simple prevention and treatment measures. This paper mainly studies the therapeutic effect of nanotitanium oxide combined with sports rehabilitation training on boxer wrist joint injury. In this study, the subjects were randomly divided into nanotitanium oxide combined with sports rehabilitation training group, nanotitanium oxide treatment group, sports rehabilitation training treatment group, and control group. Then, the subjects were tested with the score table, and the data obtained from the score were recorded. Finally, the experimental results were tested by chi-square method. The innovation of this paper is to compare the treatment scores of nanotitanium oxide combined with sports rehabilitation training group, nanotitanium oxide treatment group, sports rehabilitation training treatment group, and control group without treatment. The experiment proves that nanotitanium oxide combined with sports rehabilitation training has a positive effect on the treatment effect of boxing athletes' wrist joint injury, which provides some useful for clinical treatment basis.

2. Nanotitanium Oxide and Wrist Joint Injury of Boxers

2.1. Nanotitanium Oxide.
A nanometer is a unit of length, one billionth of a meter. When the size of the material reaches the nanometer level, the material will have many different characteristics, thus showing its unique effect and function. Nanomaterials refer to materials with one or more components and at least one dimension in the range of 1-100 nanometers, including nanoparticles, nanofibers, nanotubes, and nanosynthetic materials. Nanoparticle is a kind of nanomaterial, which means that the single particle size is less than 100 nm. The physical properties of nanomaterials [10] mainly depend on the size, composition, and surface properties of nanomaterials, while the biological effects of nanomaterials are closely related to the physical and chemical properties of nanomaterials. Due to their unique small size effect, surface effect, quantum size effect, and macroscopic quantum tunneling effect, nanomaterials have electrical, optical, mechanical, and magnetic properties different from ordinary materials [11, 12].

Nanotitanium oxide (TiO_2) is a new inorganic chemical material. In recent years, due to its special performance, wide application, and broad market prospect, it has become a research hotspot. Nano-TiO_2 has large specific surface area and surface atomic number; the surface energy and surface tension increase rapidly with the decrease of particle size; the thermal, magnetic, optical, and sensitive properties and surface stability of nanoparticles are different from those of traditional particles due to small size effect, surface effect, quantum size effect, and macroscopic quantum tunneling effect. As a new photocatalyst [13], UV-resistant agent, and photoelectric effect agent, it is widely used in coatings, pigments, ceramics, sunscreen cosmetics, antiaging, air purification, sewage treatment, antibacterial detoxification, food packaging, antistatic, and other fields. Different orders of nano-TiO_2 enter some specific parts of the human body in different ways and produce inherent toxic effects. At present, the research of nano-TiO_2 is mainly focused on animal experiments, such as tissue effect, cytotoxicity [14], effect on the molecular structure and expression of genetic material DNA, and the influence on other biological macromolecules.

2.2. Boxing.
Boxing is a highly confrontational sport, which belongs to the skill type combat project. The project is characterized by technology led. Physical fitness and tactics play a decisive role in this project. The characteristic of boxing match is that under the same rules, both players wear protective gloves and hit each other's effective scoring position with their fists. The confrontation between the two sides is the external performance of the project, and obtaining effective scores is the ultimate goal. The two players in the designated area competition hit each other but also need to be prepared for defense and counterattack this high-intensity confrontation; the athletes' physical requirements are very high but also determine the core role of health in this project. There are four rounds in each round of women's boxing, and each round is 2 minutes, with an interval of 60 seconds. The uniqueness of boxing lies in people's different views on box-

ing. Boxing is a person-to-person competitive event. Therefore, the beating and being beaten in the competition, as well as the injury consequences, especially the scene of being knocked down and unable to stand up in professional boxing, have great objections in many people's thoughts.

2.3. Wrist Joint Injury.
Wrist joint, also known as radial wrist joint, is an important part of hand joint. The wrist is the connection between the hand and the forearm. It is an important part of the upper limb and bears a large load in the support and thrust of the upper limb. In addition to the distal radius [15] and ulna, there are eight carpal bones of different shapes. Due to the complex structure of wrist joint, more joints, and ligaments, it has higher flexibility. The anatomical features of the wrist allow it to move in two planes: radial ulnar deviation in the frontal plane (abduction adduction) and sagittal flexion and extension (palmar flexion and dorsiflexion). As far as wrist joint is concerned, it should include radial and ulnar joints. Intercarpal joint consists of adjacent carpal bones. The bone and bone are intertwined, and they are connected by complex ligaments and tendons in varying degrees of motion.

Wrist injury has great influence on fine motion of hand and upper limb. It is necessary to define the types of wrist joint disorders and take effective rehabilitation guidance in time. Wrist rehabilitation medicine involves many aspects; rehabilitation evaluation and rehabilitation treatment are the core. Correct rehabilitation assessment is the premise of effective rehabilitation treatment, and the functional recovery under ideal state depends on effective rehabilitation treatment [16].

For wrist rehabilitation assessment, the clinical is mainly evaluated by the pain, motion dysfunction and other subjective assessment indicators of the wrist [17]. ROM, also known as ROM, refers to the maximum motion curve of the joint, that is, the normal range of motion from the beginning to the end of the joint, usually expressed in degrees. It is one of the important indexes to evaluate the range and degree of joint motor function injury. First of all, it is the preferred evaluation method for physical dysfunction diseases with limited joint activity such as fracture and arthritis. It is suitable for joint movement disorders caused by various reasons, such as joint fixation, trauma, and surgery. The range of motion can be divided into active range and passive range. Active range of motion (AROM) refers to the arc of joint movement when muscles contract actively; passive range of motion (PROM) refers to the arc movement of joints without muscle contraction under the action of external force. It can be seen that the range of motion of the joint is the activity behavior of patients, which can be used to evaluate the influence of muscle contraction force on joint range of motion. The range of passive joint motion refers to the passive behavior under the action of external force, which can evaluate the limited degree of joint activity of examiners. Due to the different anatomical structure and physiological mechanics of each joint, the active and passive range of motion of the same joint is also different. The range of motion of the joint is also affected by race, gender, age, and examination position. Taking the normal range of

ROM in rehabilitation medicine as reference value, the differences of rehabilitation goals were analyzed and compared.

3. Exercise Rehabilitation Training

3.1. Rehabilitation. The World Health Organization defines rehabilitation as through various measures to reduce the impact of disability and to reintegrate the disabled into society. These include the use of training to promote the adaptation of persons with disabilities to their surroundings and the adjustment of their surroundings and social conditions to facilitate their social integration. Therefore, rehabilitation refers to the comprehensive and coordinated use of various measures to reduce the mental, social, and physical barriers of the disabled, so as to make them play their full potential and return to society.

Rehabilitation medicine [18] is a medical application subject with independent theoretical basis and functional evaluation method, with large application scale and high treatment technology. Its purpose is to speed up the rehabilitation process of human injury, prevent and reduce the degree of disability, and help the disabled return to society. Rehabilitation treatment is a variety of measures taken by people to reduce the disability of the disabled, train the disabled to acquire knowledge and skills, and improve their ability of self-care and social participation. Rehabilitation treatment can be generally divided into the following categories: (1) physical therapy (PT); (2) occupational therapy (0t); (3) speech therapy; (4) psychotherapy; (5) recreational therapy; and (6) traditional Chinese medicine. Physical therapy includes exercise therapy and physical factor therapy: physical factor therapy, also known as "physical therapy," is a method to prevent and treat diseases by using physical factors such as electricity, light, sound, magnetism, water, cold, and heat; occupational therapy is a process of applying purposeful and selected occupational activities to evaluate, treat, and train patients who have lost their ability to take care of themselves and work in varying degrees due to physical, mental, and developmental dysfunction or disability. It is a rehabilitation treatment method. Exercise therapy refers to active or passive movement of patients with bare hands or with the aid of instruments and improves functions and promotes rehabilitation through the effect of force, which is a widely used treatment. Entertainment therapy is a psychotherapy method to cultivate temperament and improve physical and mental health through various entertainment activities (such as listening to music, learning singing, watching movies, watching TV, watching drama performances, dancing, games, playing chess, and visiting the garden).

3.2. Exercise Rehabilitation Training. In the rehabilitation of wrist injury, early and correct exercise is very important. For professional athletes, once the injury occurs, it will directly affect the play of skills and tactics and sports life in the competition. Therefore, it is very important to protect the wrist. Through muscle movement, promote blood circulation, accelerate metabolism, prevent muscle atrophy, and enhance muscle strength. It is necessary to make short-term functional rehabilitation plan and long-term ADL rehabilitation plan according to the course of disease and the severity of the disease.

Common rehabilitation methods are as follows: physical therapy such as external application (external application of drugs can promote good blood circulation and prevent inflammation), acupuncture, and moxibustion (which can improve local pain valve and gradually improve mechanical balance of muscles), by promoting blood circulation, improving the nutrition of local tissues, improving the vitality of cell tissues, accelerating the absorption or elimination of pathology and metabolites, promoting wound healing and eliminating inflammation, and injection therapy (which can promote local blood circulation and prevent joint adhesion). Exercise therapy, also known as therapeutic exercise [19, 20], is one of the basic treatment methods of rehabilitation medicine, according to the characteristics of patients' life to improve the function of patients.

The general principles of wrist rehabilitation training are as follows:

(1) Early principle: the structure of wrist joint is complex; the recovery time is long after injury. When wrist ligament injury or fracture occurs, early medical treatment can seize the best treatment opportunity to prevent cartilage wear and tear, ligament aging and joint pain, joint relaxation, and instability caused by improper movement during the injury; when wrist joint dysfunction caused by stroke, timely and effective treatment can avoid the occurrence of joint deformity, so as to ensure the normal range of motion of the joint. At the same time, by stimulating the activity of brain cells, it can promote the occurrence of compensatory function of brain tissue in corresponding regions, so as to reduce the degree and rate of disability

(2) Moderate principle: although increasing the number and frequency of rehabilitation training is helpful to the recovery of motor function, blind pursuit of progress may lead to secondary injury of injured joints. If the swelling and pain of the affected joint is aggravated, it should be stopped immediately, and the treatment should be evaluated after the tissue pain disappears

(3) Sufficiency principle: on the premise of following the moderate principle, the range of motion of each joint should reach or be as close as possible to the normal range of motion of each joint

(4) Progressive principle: in rehabilitation training, it should be carried out step by step, and the training form and exercise amount should be adjusted according to the special pathological conditions of joints in each rehabilitation stage

(5) Gentle principle: in passive exercise training, we should pay attention to observe the expression changes and reactions of patients and try to avoid the pain of patients and the soft tissue injury of affected limbs and joints

TABLE 1: Pain scale sheet.

Pain grading	No pain									The most painful
At rest	1	2	3	4	5	6	7	8	9	10
Repetitive wrist movement	1	2	3	4	5	6	7	8	9	10
When lifting weights	1	2	3	4	5	6	7	8	9	10
Frequency of pain	1	2	3	4	5	6	7	8	9	10
The most painful time		2	3	4	5	6	7	8	9	10

TABLE 2: Functional difficulty scale.

Pain grading	No pain									The most painful
Daily life	1	2	3	4	5	6	7	8	9	10
Housework	1	2	3	4	5	6	7	8	9	10
Work	1	2	3	4	5	6	7	8	9	10
Recreational activities	1	2	3	4	5	6	7	8	9	10

(6) Self-help principle: many patients cannot fully recover after discharge, and most patients need long-term rehabilitation training after discharge. Therefore, it is necessary to have a kind of portable and convenient rehabilitation training assistant device anytime and anywhere

(7) Rehabilitation training needs the principle of individual treatment. According to different age, condition and functional state, exercise means, preparation posture, and amount of exercise are selected to develop and improve muscle function (strength, speed, and endurance) and joint activity

4. Therapeutic Effect of Nanotitanium Oxide Combined with Exercise Rehabilitation Training on Wrist Joint Injury of Boxers

4.1. Experimental Materials. The total number of patients in this study was 80, aged 16-47 years, with an average of 25.6. They were randomly divided into four groups: nanotitanium oxide treatment group, rehabilitation exercise training treatment group, nanotitanium oxide combined with rehabilitation exercise training treatment group as the experimental group, and wrist joint injury natural healing as the control group, with 20 cases in each group, 11 males and 9 females. The injury treatment study lasted from 1 to 30 days. All patients were provided by the department of orthopedics and traumatology, the first hospital of D province.

4.2. Experimental Methods. Random grouping method: random number method was used in this experiment. Nanotitanium oxide treatment group, rehabilitation exercise training group, and nanotitanium oxide combined with rehabilitation exercise training group were the experimental group, and the wrist joint injury natural healing was the control group

Case shedding and treatment: automatic use of other methods during the treatment process or accidental death (except for complication death) cases decreased. Treatment: follow-up, registration, and analysis

Case exclusion criteria: the clinical data records were found to be wrong, incomplete, or completely missing before statistical analysis, which affected the statistical analysis

Efficacy criteria: pain and function: the pain and function during the 5-week treatment were scored by PRWE score standard, and the score results were recorded

Safety assessment criteria: level 1: safety, no adverse reactions. Level 2: relatively safe. If adverse reactions occur and no treatment is needed, the trial can continue. Grade 3: safety problems, moderate adverse reactions, can continue to test after treatment. Grade 4: the test was stopped due to adverse reactions

4.3. Data Processing. Observation time and index record: the observation records were made before and after treatment at three time points (the first day, the seventh day, and the 35th day).

Chi-square test was used for counting data, and t test was used for measurement data. Take $p > 0.05$ as no statistical significance, no difference; take $0.01 < p < 0.05$ as the difference has statistical significance; $p < 0.01$ as the significant statistical significance, the difference is significant.

4.4. Scoring Table. Pain score table:

As shown in Table 1, please evaluate your average wrist pain in the past week on a 0-10 scale. 0 means that there is no pain at all, (0-10) indicates that the pain is increased once, and 10 means that the pain has never stopped, or dare not move because of the pain.

Function score table:

As shown in Table 2, please circle the most difficult movements in the past week on a scale of 0-10. 0 means there is no difficulty, (0-10) indicates that the activity difficulty increases in turn, and 10 means that the activity is very difficult and cannot do these daily activities.
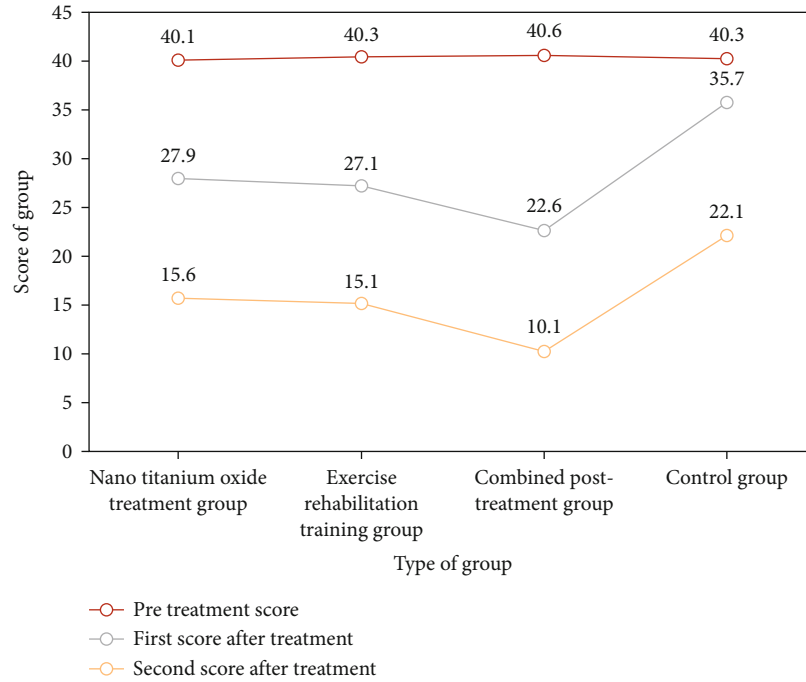
Figure 1: Comparison of pain between the four groups.
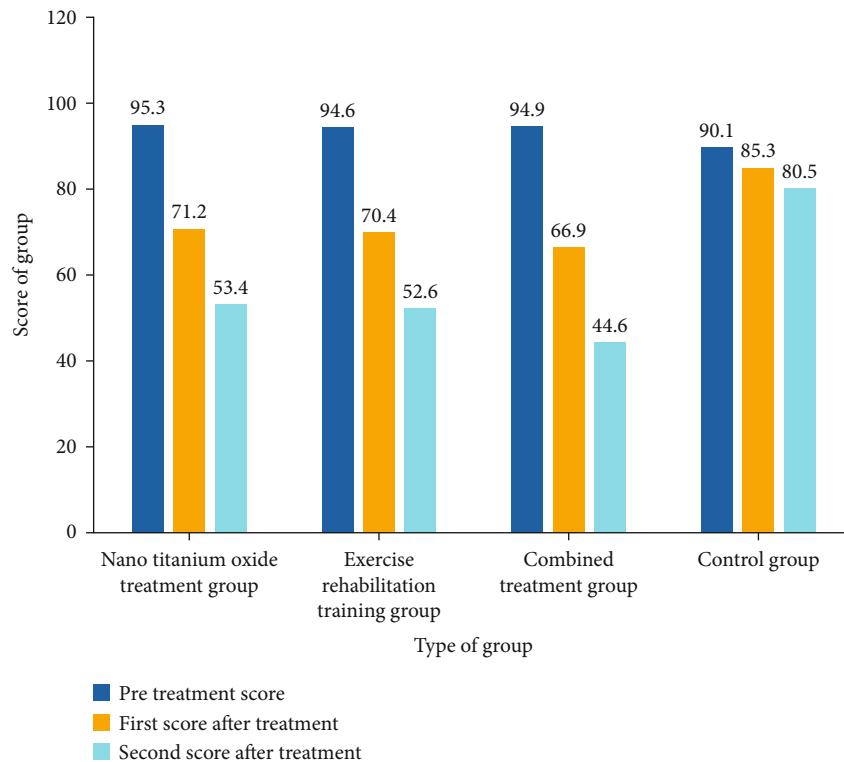
Figure 2: Functional comparison between the four groups.

5. Results and Discussion

5.1. Comparative Analysis of Pain. As shown in Figure 1, before treatment, the scores of nanotitanium oxide treatment group, rehabilitation exercise training treatment group,

nanotitanium oxide combined with rehabilitation exercise training treatment group, and control group were 40.1, 40.3, 40.6, and 40.3, respectively. Pain comparison was made for the first time after treatment in nanotitanium oxide treatment group, rehabilitation exercise training treatment group,

Measurement of wrist internal rotation velocity
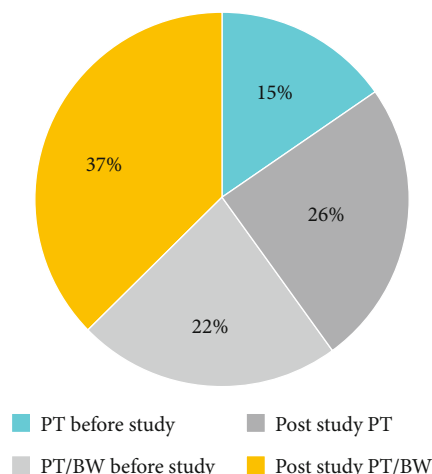
Figure 3: Measurement of wrist internal rotation velocity.
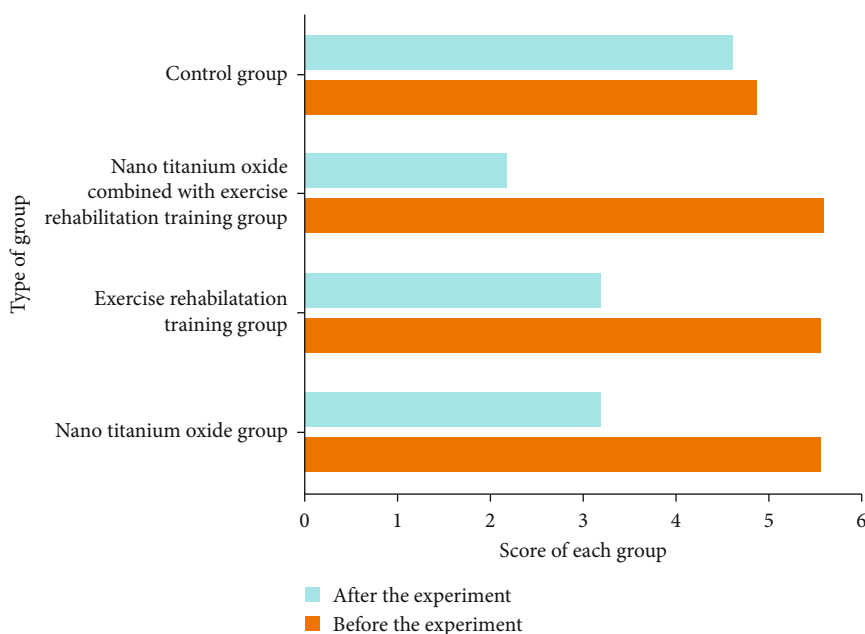
Figure 4: Treatment effect of three groups of treatment on boxer wrist joint.

nanotitanium oxide combined with rehabilitation exercise training treatment group, and control group. The scores were 27.9, 27.1, 22.6, and 35.7, respectively; the scores of nanotitanium oxide treatment group, rehabilitation training group, nanotitanium oxide combined with rehabilitation exercise training group, and control group were 15.6, 15.1, 10.1, and 22.1, respectively, after the second treatment; through comparison, it was found that nanotitanium oxide combined with rehabilitation exercise training could reduce the pain of wrist joint injury of boxers.

5.2. Function Comparison Analysis. As shown in Figure 2, before treatment, the functional scores of nanotitanium oxide treatment group, rehabilitation exercise training treatment group, nanotitanium oxide combined with rehabilitation exercise training treatment group, and control group

were 95.3, 94.6, 94.9, and 90.1, respectively. The first functional scores of nanotitanium oxide group, rehabilitation training group, nanotitanium oxide combined with rehabilitation exercise training group, and control group were 53.4, 52.6, 44.6, and 80.5, respectively. Before treatment, there was no significant difference among the groups. After treatment, the score of nanotitanium oxide combined with exercise rehabilitation training decreased significantly. Through comparison, it was found that after the treatment of wrist joint injury by nanotitanium oxide combined with sports rehabilitation training, the functional score decreased, and the daily function was improved.

5.3. Analysis of Peak Torque Comparison. As shown in Figure 3, the peak torque (PT) reflects the maximum muscle strength produced by muscle contraction. The maximum

torque output produced by muscle contraction, namely, peak torque to body weight ratio (Pt/BW), refers to the peak torque value per unit weight. The relative muscle strength reflecting muscle contraction can be used for the peak torque ratio between active muscle and antagonistic muscle of individuals or people of different weights. It can reflect the balance of muscle strength and judge the stability of joints in a certain sense. In Figure 3, the PT score before and after the experiment was 15%, 26%, 22%, and 37%, respectively. Therefore, nanotitanium oxide combined with sports rehabilitation training has a great role in promoting the treatment of boxing wrist joint injury.

5.4. Sensitivity Comparison Analysis. As shown in Figure 4, the sensitivity score of nanotitanium oxide treatment group before treatment was 5.59 and after treatment was 3.22; the sensitivity score of exercise rehabilitation training treatment group before treatment was 5.61 and after treatment was 3.21; the sensitivity score of nanotitanium oxide combined with exercise rehabilitation training before treatment was 5.63 and after treatment was 2.19; the sensitivity score of control group before treatment was 4.91 and after treatment was 4.65. It can be seen that there is no significant difference between the two groups. The scores of nanotitanium oxide treatment group and exercise rehabilitation training treatment group were significantly reduced by 2.37 and 2.40, respectively, but the effect of nanotitanium oxide combined with exercise rehabilitation training treatment group was more obvious. It shows that nanotitanium oxide combined with exercise rehabilitation training has a great role in promoting the sensitivity of wrist joint injury treatment of boxers.

6. Conclusion

China's boxing is gradually developing. Compared with developed countries, there is a big gap between China and developed countries. One of the most important reasons is sports injury. Wrist injury is a very common kind in life; especially when exercising, it is easy to cause wrist injury. To improve boxing level, not only from the boxing training process, but also from the recovery of the body after training, is a very important aspect. This paper mainly studies the therapeutic effect of nanotitanium oxide combined with exercise rehabilitation training on wrist joint injury in boxing, which provides some beneficial basis for clinical treatment. By studying the therapeutic effect of nanotitanium oxide combined with sports rehabilitation training on Boxers' wrist joint injury, it is found that nanotitanium oxide combined with sports rehabilitation training can reduce the pain of boxers' wrist joint injury; after the treatment of wrist joint injury of boxers by nanotitanium oxide combined with exercise rehabilitation training, the pain score decreased and daily work decreased. The Pt/BW score before and after the experiment was 15% and 26% and 22% and 37%, respectively. The relative muscle strength reflecting muscle contraction can be used for the peak torque ratio between active muscle and antagonistic muscle of individuals with different weights. It can reflect the balance of mus-

cle strength in a certain sense and judge the stability of wrist joint after nanotitanium oxide combined with exercise rehabilitation training.

Data Availability

The data that support the findings of this study are available from the corresponding author upon reasonable request.

Conflicts of Interest

The authors declared no potential conflicts of interest with respect to the research, authorship, and/or publication of this article.

Acknowledgments

References

[1] J. Xing, G. Wang, J. Zhao et al., "Toxicity assessment of perfluorooctane sulfonate using acute and subchronic male c57bl/6j mouse models," *Environmental Pollution*, vol. 210, no. 3, pp. 388–396, 2016.

[2] D. Forsdyke, A. Smith, M. Jones, and A. Gledhill, "Infographic: psychosocial factors associated with outcomes of sports injury rehabilitation in competitive athletes," *British Journal of Sports Medicine*, vol. 51, no. 7, pp. 561–561, 2017.

[3] C. Yin, F. R. Negreiros, G. Barcaro et al., "Alumina-supported sub-nanometer pt10 clusters: amorphization and role of the support material in a highly active co oxidation catalyst," *Journal of Materials Chemistry A*, vol. 5, no. 10, pp. 4923–4931, 2017.

[4] M. Z. Ahmad, S. A. Alkahtani, S. Akhter et al., "Progress in nanotechnology-based drug carrier in designing of curcumin nanomedicines for cancer therapy: current state-of-the-art," *Journal of Drug Targeting*, vol. 24, no. 4, pp. 273–293, 2016.

[5] M. Shakeel, F. Jabeen, S. Shabbir, M. S. Asghar, M. S. Khan, and A. S. Chaudhry, "Toxicity of nano-titanium dioxide (TiO$_2$-NP) through various routes of exposure: a review," *Biological Trace Element Research*, vol. 172, no. 1, pp. 1–36, 2016.

[6] A. Relyea-Chew and F. S. Chew, "Multiple open wrist fractures and dislocation of the distal radioulnar joint from a dog bite injury," *Radiology Case Reports*, vol. 14, no. 7, pp. 837–841, 2019.

[7] K. Lo, M. Stephenson, and C. Lockwood, "Effectiveness of robotic assisted rehabilitation for mobility and functional ability in adult stroke patients: a systematic review protocol," *Jbi Database of Systematic Reviews & Implementation Reports*, vol. 15, no. 1, pp. 39–48, 2017.

[8] A. P. D. Silva, F. C. Sassi, and C. R. F. D. Andrade, "Oral-motor and electromyographic characterization of patients submitted to open and closed reductions of mandibular condyle fracture," *Codas*, vol. 28, no. 5, pp. 558–566, 2016.

[9] L. M. Romero-Muñoz, A. Segura-Fragoso, F. Talavera-Díaz, J. Guimbard-Pérez, D. Caba-Mora, and A. Barriga-Martín, "Neurological injury as a complication of spinal surgery:

incidence, risk factors, and prognosis," *Spinal Cord*, vol. 58, no. 3, pp. 318–323, 2020.

[10] H. M. Saleh, F. A. El-Saied, T. A. Salaheldin, and A. A. Hezo, "Macro- and nanomaterials for improvement of mechanical and physical properties of cement kiln dust-based composite materials," *Journal of Cleaner Production*, vol. 204, no. 1, pp. 532–541, 2018.

[11] Y. Tang, "combined effects of nano-silica and silica fume on the mechanical behavior of recycled aggregate concrete," *Nanotechnology Reviews*, vol. 10, no. 1, pp. 819–838, 2021.

[12] P. Wang, S. Wang, X. Zhang et al., "Rational construction of CoO/CoF2 coating on burnt-pot inspired 2D CNs as the battery-like electrode for supercapacitors," *Journal of Alloys and Compounds*, vol. 819, article 153374, 2019.

[13] Y. Shiraishi, S. Kanazawa, Y. Sugano et al., "Highly selective production of hydrogen peroxide on graphitic carbon nitride (g-c3n4) photocatalyst activated by visible light," *ACS Catalysis*, vol. 4, no. 3, pp. 774–780, 2014.

[14] D. Tibullo, I. Barbagallo, C. Giallongo, L. Vanella, and G. L. Volti, "Heme oxygenase-1 nuclear translocation regulates bortezomib-induced cytotoxicity and mediates genomic instability in myeloma cells," *Oncotarget*, vol. 7, no. 20, pp. 28868–28880, 2016.

[15] S. H. Ang, S. W. Lee, and K. Y. Lam, "Ultrasound-guided reduction of distal radius fractures," *American Journal of Emergency Medicine*, vol. 28, no. 9, pp. 1002–1008, 2010.

[16] T. Y. Kim, S. H. Kim, and H. Ko, "Design and implementation of BCI-based intelligent upper limb rehabilitation robot system," *ACM Transactions on Internet Technology*, vol. 21, no. 3, 2021.

[17] U. Woehlbier, A. Colombo, M. J. Saaranen et al., "Als-linked protein disulfide isomerase variants cause motor dysfunction," *EMBO Journal*, vol. 35, no. 8, pp. 845–865, 2016.

[18] J. Kim, S. Yoon, J. J. Kang, K. Han, S. K. Kim, and S. K. Kim, "Research designs and statistical methods trends in the annals of rehabilitation medicine," *Annals of Rehabilitation Medicine*, vol. 41, no. 3, pp. 475–482, 2017.

[19] B. Matthew, "Optimising the late-stage rehabilitation and return-to-sport training and testing process after ACL reconstruction," *Sports Medicine*, vol. 49, no. 7, pp. 1043–1058, 2020.

[20] G. H. Choi, H. Ko, W. Pedrycz, A. K. Singh, and S. B. Pan, "Recognition system using fusion normalization based on morphological features of post-exercise ECG for intelligent biometrics," *Sensors*, vol. 20, no. 24, p. 7130, 2020.

Hindawi

Research Article
Application of New Energy Composites in Sports Facilities and Fitness Equipment

Jiejian Zhang[1,2] **and Yang Mi**[ID][3,4]

[1]*Department of Physical Education, Science and Technology College Gannan Normal University, Ganzhou, 341000 Jiangxi, China*
[2]*Department of Leisure Sports, Jungwon University, Chungbuk 28024, Republic of Korea*
[3]*School of Sports and Health, Linyi University, Linyi, 276000 Shandong, China*
[4]*Department of Physical Education, Woosuk University, Jeonju 55069, Republic of Korea*

Correspondence should be addressed to Yang Mi; miyang@lyu.edu.cn

New energy composite is an advanced material that can replace the traditional single metal material, especially the newly developed or developed material with superior performance. At present, the material is widely used in automobile manufacturing and other fields, but there is a lack of development and application of the material in the field of sports. To solve these problems, this paper puts forward the application of new energy composites in sports facilities and fitness equipment. In this paper, the testing methods of new energy materials, including thermoelectric testing method and energy absorption testing method, can quantitatively evaluate the properties of a kind of new energy composites and point out the direction for the development of materials with high thermoelectric properties and high-energy absorption and consumption properties. Then, through the preparation experiment of new energy materials, this paper studies the preparation process and self-shrinkage test of carbon nanomaterials. Finally, it is proposed to use carbon nanomaterials in the sensor design of health monitoring data acquisition system. The experimental results show that when the water ash ratio is low, the self-shrinkage value of carbon nanomaterial slurry is 74.68% lower than that under the original conditions. In the experimental study of omnidirectional monitoring characteristics, through the repeated tensile tests of rectangular sensor and omnidirectional sensor at different temperatures, it is found that the sensitivity coefficient of the sensor made of carbon nanomaterial is between 55.8 and 60.4, and the maximum fluctuation is only 5. This fully proves that the carbon nanotube omnidirectional sensor has omnidirectional detection ability.

1. Introduction

1.1. Background. Since the birth of human civilization, material has been closely related to human life. There are generally three forms of matter in nature, namely, solid, liquid, and gas. With the development and progress of science and technology, materials not only penetrate into people's daily life, but also are widely used in aerospace, marine engineering, biomedical engineering, optoelectronics, and other fields. This article observes that new energy materials may also be applicable to the field of sports. New materials refer to some newly developed or under research and development materials with excellent performance, mainly including superconducting materials, solar cell materials, hydrogen storage materials, solid oxide cell materials, intelligent materials, magnetic materials, nanomaterials, high-temperature structural ceramics, amorphous materials, and high-density energy storage materials. Composite material refers to the new material composed of material components of different properties by using advanced material preparation technology.

1.2. Significance. Under the background of global fossil energy shortages and environmental pollution, the development of high-performance thermoelectric materials and efficient new energy technologies has attracted extensive attention in the industry. The composite material not only

maintains the advantages of the material properties of each component, but also obtains the comprehensive performance that cannot be achieved by a single component material through the complementarity and correlation of the properties of each component. Human beings also need to systematically study the durability of carbon nanomaterials and other cement-based composites. The unique one-dimensional structure of carbon nanotubes and nanofibers and the two-dimensional structure of graphene, as well as the advantages of compact structure, large specific surface area, and high strength of carbon nanomaterials, can effectively transport water in cement through the landfill matrix and holes in the matrix, improve the compactness of cement materials, and further improve the durability such as impermeability and corrosion resistance. On the basis of improving the self-shrinkage properties of carbon nanomaterial and cement-based composites, other durability properties of carbon nanomaterial and cement-based composites can be systematically studied to improve their safety and service life, which is of great engineering significance and value. With the popularization of high-performance concrete with low ratio of water and binder, the crack phenomenon caused by early automatic shrinkage of concrete is becoming increasingly obvious. Adding carbon nanomaterials into cement materials can not only effectively fill the pores of the cement matrix, but also increase the content of hydration products, to improve the density of matrix.

1.3. Related Work. The role of new energy and composite material, materials, and sports equipment in human life is becoming increasingly obvious, and many scholars have carried out research on these two topics. Wang Q believes that, under the background of establishing emerging engineering education, the content of organic chemistry of material engineering needs innovation. He strives to improve the application effect of organic chemistry from the aspects of material preparation and material application, selection, process, method reform, improvement of evaluation system, and optimization of organic chemistry experiments. His research focuses on the application expansion of materials, but ignores the detailed manufacturing innovation of materials [1]. Martinho F pointed out that the monolithic series integration of third-generation solar materials on silicon has broad prospects in the fields of photoelectrochemistry and photovoltaics. However, this may be challenging when involving the high-temperature reaction process, which may damage the bottom cell of photovoltaic equipment. They have proved that the protection of the bottom cell of photovoltaic equipment largely depends on the barrier layer engineering at the device level, but their research has not produced several single-chip series solar cells, which is limited to the application of new energy materials [2]. Mansurov Z A studied the effect of activated carbon with multilayer graphene (three layers and more sheets) on the thermal decomposition of substances based on hydroxyammonium nitrate and carboxymethyl cellulose. His results showed that the addition of activated carbon with multilayer graphene could increase the combustion rate of hydroxyammonium nitrate by up to four times; however, in the exper-

iment, the addition of activated carbon in the thermal decomposition stage reduced the temperature and time of chemical reaction, resulting in some deviations in the experimental results [3]. Paben J believes that the flexible packaging material will not disappear soon, and the upcoming pilot project aims to ensure that it will not enter the landfill. He proposed a material recycling facility, which will install additional sorting equipment. The transformation will enable the facility to start producing postconsumer flexible packaging bags, which are defined as single-layer or multilayer material films, expanding the source mode of new energy materials. However, he did not explain the defects of materials made from recycled raw materials [4]. Tao Kunwei studied the compact materials project, which will provide a high-energy, high-throughput neutron source for material irradiation research, which is essential for advanced nuclear energy projects driven by China's long-term accelerators. He introduced a numerical study of a particle beryllium targets using inclined particle flow as the target and heat carrier. To study the heat treatment capacity of the target as a sports facility, the heat deposition and transfer in the target were numerically simulated. However, his research damaged the back plate of the experimental material in terms of heat dissipation and radiation [5]. Lee J Y evaluated the function of a dual water supply system operating in sports facilities based on technical, quantitative, and financial data, including the collection and use of rainwater for nonpotable purposes. Analysis was conducted to determine the water-saving efficiency and cost reduction of the facility within 3 years. The results show that rainwater can be managed for the benefit of the environment, and economic benefits can be obtained by saving the water cost of municipal water supply and sewage treatment. However, the results of this study are not encouraged because of the overexploitation of groundwater [6]. Sukiri's research aims to determine customer satisfaction with the services and fitness equipment of the academic gymnasium of the School of Sports Science, Jakarta State University. He made a questionnaire and published it using Google forms. His research used survey and descriptive analysis. According to the data returned by the interviewees, the average interviewee was satisfied with the facility, but did not pay attention to the interviewee's satisfaction with the facility [7]. Thakur T S believes that cycling and other sports activities are a healthy, interesting, and low impact way of exercise, which is suitable for people of all ages. His research paper covers the evolution of sports facilities from ancient times to modern times. Through this study, he has tried to study the transformation of sports facilities through a wide range of technical applications to improve and enhance their functions, but his research focuses on the improvement of bicycles and does not extend the research results to other fitness equipment [8]. The deficiency of these studies is that the research methods and perspectives are still not novel and comprehensive enough.

1.4. Innovation Points. This paper boldly puts forward the application of new energy materials in the field of sports and expands the application scope of new energy materials. The most representative carbon nanomaterials in new

energy materials are used to prepare motion monitoring sensors, which expands the new idea of sensor design.

2. Performance Test Methods of New Energy Materials

2.1. Thermoelectric Test Method for New Energy Composites. New energy composites are made by combining two or more fibers in a matrix. New energy composites have the characteristics of high strength, elastic modulus, and excellent mechanical properties. Mechanical characteristics are also relatively good, which can fully meet the requirements and make them a popular choice for light weight and high-performance applications. Because the cost of carbon fiber is too high, the combination of glass fiber and carbon fiber is needed to obtain reliable mechanical properties [9]. The new energy composites with mixed carbon fiber and glass fiber have a good balance in mechanical properties; that is, the disadvantages of one fiber can be offset by the advantages of another fiber [10]. In addition to the mixed structure, the strength, damage resistance, and service life of new energy composites can be improved by changing the microstructure of materials. However, the mixing and aggregation of fibers have a significant impact on the elastic properties of the composites. On the one hand, it is the microstructure characteristics of fibers, namely, the aggregation of fibers and the distribution of fibers in the aggregation area, a small amount of bonding between the foundation and fibers, bending effect, and unevenly distributed fibers, that will weaken the mechanical properties of composites [11]. On the other hand, it is generally believed that the experimental mechanical properties of new energy composites are far from the theoretical prediction results. Therefore, it is of great significance to determine the influence of these defects on the effective properties of new energy composites.

The content of the experimental method is the thermoelectric test of materials. Firstly, the key technical indexes of thermoelectric performance test are analyzed. All relevant metrics were analyzed in detail. According to the thermoelectric performance test principle, the signal acquisition circuit required for corresponding parameter measurement is designed, and the thermoelectric performance test platform is built to realize the automatic measurement of thermoelectric performance parameters of new energy materials [12].

Seebeck coefficient is the ratio of voltage to temperature difference generated by Seebeck effect, which represents the ionization impurity scattering coefficient [13]. Assuming that only the electric field and temperature gradient of the material are in a stable state, and the material is a nondegenerate semiconductor, the relaxation time is approximately obtained according to the Boltzmann equation. Then, the Seebeck coefficient of the material is shown in

$$A = \pm \frac{k_B}{e} \left[b - \left(s + \frac{5}{2} \right) \right], \qquad (1)$$

where s is the scattering coefficient and B is the reduced Fermi level. Therefore, if semiconductor thermoelectric

materials are doped, the ionized impurity concentration increases, and the ionized impurity scattering coefficient increases [14]. If the large ionized impurities are scattered (high concentration of ionization impurities), the Seebeck coefficient corresponding to the specified carrier concentration is greatly improved, and the thermoelectric performance is improved. If the material is a single band nondegenerate semiconductor, the Seebeck coefficient of the material can be expressed by

$$A = \pm \frac{k_B}{e} \left[b - \left(s + \ln \frac{N}{n} \right) \right] \qquad (2)$$

Therefore, the Seebeck coefficient of materials is related to carrier concentration, state density, Fermi energy level, scattering coefficient, and other physical quantities. In formula (2), n is the state density, and N is the carrier concentration.

When calculating the conductivity of materials, the expression of conductivity q is Q = neu. In the formula, n is the carrier concentration, and u is the error rate.

$$n = \frac{2(2\pi m^* k_B T)^{1.5}}{h^{1.5}} F_{s+0.5}(b), u = \frac{4e}{3\pi^{1/2}} (s + 1.5)(k_B T)^s \frac{t_0}{m^*}, \qquad (3)$$

where $m*$ is the effective mass of the carrier, h is the Planck constant, and t0 is the relaxation time. Formula (3) shows that the conductivity is affected by the scattering coefficient, effective mass, Fermi level, and other factors, and the carrier concentration and mobility do not necessarily increase at the same time. When the effective mass of the material increases, the carrier concentration increases, and the mobility decreases [15]. If the mobility decreases, the conductivity and thermal conductivity decrease at the same time.

From the microscopic point of view, the transmission process of heat energy is mainly realized by carrier motion and lattice vibration. In the case of semiconductor materials in the intrinsic state and semiconductor materials in the exogenous excitation region, only the contribution of carrier and lattice phonons to the thermal conductivity must be considered [16]. In other words, $k = k_{ph} + k_c$, where k_{ph} is the phonon thermal conductivity and k_c is the thermal conductivity of the carrier. General thermoelectric materials are applicable in the exogenous excitation stage. Therefore, only the contribution of carrier thermal conductivity and phonon thermal conductivity to thermal conductivity must be considered [17]. At the beginning of the twentieth century, Altengilsch of Germany put forward the analysis of three important parameters affecting thermoelectric properties and put forward the thermoelectric performance index Z to measure the thermoelectric properties of materials.

$$Z = \frac{A^2 Q}{k}, E = A^2 Q, \qquad (4)$$

where a is the Seebeck coefficient, K is the thermal conductivity, q is the conductivity, and E is the power factor. This formula can be used to reflect the comprehensive

thermoelectric properties of materials. The larger the Z value, the higher the thermoelectric properties of the material. Therefore, for materials with good thermoelectric characteristics, the Seebeck coefficient is large; that is, the obvious thermoelectric effect requires the conductivity Q to be as large as possible, and the thermal conductivity must be K small with less Joule heat. Materials with high thermoelectric properties point out the direction for the production of new energy composites [18].

2.2. Test Method for Energy Absorption of Materials.
Sports facilities and fitness equipment have high mechanical requirements for materials, and the manufacturing materials must have strong energy absorption capacity in order to meet the sports facilities and fitness equipment for the material strength requirements. This paper has mentioned that the new energy material absorber achieves impedance matching conditions by adjusting the electromagnetic parameters, to reduce reflection and achieve high absorption, because the reflection is actually caused by the impedance mismatch with the material surface. However, the use of impedance matching theory means that new energy materials need to be regarded as a whole; that is, their optical properties can be described by macroscopic optical parameters impedance Z and refractive index n [19]. According to the equivalent media theory (theory of composite properties), the structural unit of new energy materials is a subwavelength size smaller than its working wavelength, so they can be regarded as a whole. Moreover, their electromagnetic characteristics can be expressed by the equivalent permeability Ueff and equivalent dielectric constant Eeff [20].

In free space, the impedance Z, refractive index n, dielectric constant e, permeability u, and reflectivity R are assumed. If a uniform plate with thickness D, when the electromagnetic wave with angular frequency w is vertically incident on one side of the material plate, its transmission performance can be expressed by the reflection coefficient F and transmission coefficient T [21]. The expression is as follows:

$$\frac{f}{t} = -\frac{i}{2}\left(Z - \frac{1}{Z}\right)\sin nkd, \tag{5}$$

$$t^{-1} = \left[\sin(nkd) - \frac{i}{2}\left(Z - \frac{1}{Z}\right)\cos(nkd)\right]e^{ikd}. \tag{6}$$

The principle of magnetic wave vertical incidence is shown in Figure 1.

Under the condition of impedance matching, it can be seen that the reflection coefficient r tends to 0, while the transmission coefficient T can be reduced to the exponential form:

$$t^{-1} = e^{-i(n_1-1)kd} * e^{n_2kd}. \tag{7}$$

At this time, there are two limit cases for the transmittance of the material $t = |t|2$. In the first case, when the transmittance T and reflectivity R are both 0, the absorbance A is 1, and the electromagnetic wave is completely absorbed. The second case is that the reflectivity R and absorptivity a are 0 and the transmittance t is 1. At this time, the material neither
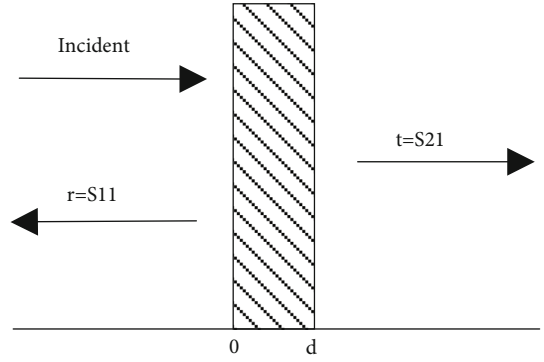

Figure 1: Schematic diagram of scattering parameters of electromagnetic new energy materials.

reflects nor absorbs electromagnetic waves, realizing perfect stealth [22]. For energy absorption by new energy materials, only the first case is considered in this paper. At this time, there are

$$\lim_{n2\to\infty} T = |t|^2 = \lim_{n2\to\infty} e^{-2n_2kd} = 0. \tag{8}$$

Since t only tends to 0 in the actual structure, $N2$ usually shows a large peak. It can be seen that the design of new energy materials to absorb energy is actually to design a structure with appropriate dielectric constant Eeff and permeability Ueff to meet the impedance matching conditions, reduce the reflectivity r to 0, reduce the transmittance t as much as possible, and consume the energy of electromagnetic wave inside the structure as much as possible, to obtain high absorption [23].

3. Preparation, Experiment, and Application of New Energy Materials

3.1. Preparation of Carbon Nanomaterials.
In this paper, the representative carbon nanomaterials in new energy materials are selected to study their preparation and application process. The preparation and application of carbon nanomaterials are beneficial to improve the material quality of exercise equipment. In this paper, the effects of different carbon nanomaterial content, water-cement ratio, and test age on the self-shrinkage properties of cement paste samples were studied: (1) three water-cement ratios of 0.25, 0.30, and 0.35 were selected to study the changes of self-shrinkage properties of carbon nanomaterial cement paste with water-cement ratio. (2) Six contents of 0.05 wt%, 0.075 wt%, 0.1 wt%, 0.12 wt%, and 0.15 wt% were selected to study the effects of different carbon nanomaterial contents on the self-shrinkage properties of cement paste composites. Choosing different doses of nanomaterials for research allows for a full understanding of carbon nanomaterials properties. (3) The self-shrinkage values of three kinds of carbon nanomaterial and cement-based composites were measured every 1 min by self-shrinkage tester to study the self-shrinkage characteristics of carbon nanomaterial and cement paste composites. To ensure the good workability of the specimens with low water-cement ratio, a certain

amount of polycarboxylic acid water reducer was added in the preparation process.

The dispersant of multilayer carbon nanotubes is gum Arabic, and the mass ratio of multilayer carbon nanotubes to gum Arabic is 1 : 6. In addition, a certain amount of defoamer needs to be added to the prepared multiwall carbon nanotube suspension [24]. Through experimental exploration, it is determined that the addition of 0.13 wt% tributyl phosphate defoamer can eliminate the bubbles generated in the ultrasonic process of multiwall carbon nanotube suspension. The mix proportion design of high-performance multiwall carbon nanotube cement-based composites is shown in Table 1.

The dispersant of carbon nanofibers is methylcellulose, and the two mass ratios are 1 : 2. Moreover, a certain amount of defoamer must be added to the prepared carbon nanofiber suspension. The experimental investigation results show that if 0.15 wt% tributyl phosphate defoamer is added, the bubbles generated by the carbon nanofiber suspension can be removed in the ultrasonic process [25].Table 2 shows the ratio of basic composites to high-performance carbon nanofiber products.

The dispersant of graphene (GNP) is polyethylene vinyl phenyl ether (co 890), and the mass ratio of GNP to co 890 is 1 : 5. In addition, a certain amount of defoamer must be added to the prepared graphene suspension. The experimental investigation shows that the addition of 0.20 wt% three-phosphate butyl defoamers can eliminate the foam [26] formed by the suspension of graphene in an ultrasonic process.

3.2. Self-Shrinkage Test Results of Carbon Nanomaterials. The effects of multiwalled carbon nanotube content, water-cement ratio, age, and surfactant Arabic gum on the self-shrinkage of cement paste that were studied here are some results from the above tests.

(1) Under the same water-cement ratio, the self-shrinkage of multiwalled carbon nanotube cement paste changes with age.

Under the condition of the same water-cement ratio, the change of self-shrinkage performance of multiwall carbon nanotube cement paste with age is shown in Figure 2.

It can be seen from these four figures that when the water-cement ratio is 0.30 and 0.35, the automatic shrinkage value of multilayer carbon nanotube cement paste test piece first decreases and then increases with the increase of age. When the water-cement ratio is 0.25, the autogenous shrinkage value of the specimen increases with age, especially from the initial setting time to the first day of the test time. When the test age increases to 7 days (w/C =0.35 and 0.30) or 14 days (w/C =0.25), the growth rate of self-shrinkage value of MWCNT cement paste is very small, the growth rate of self-shrinkage value is slow, and the self-shrinkage curve tends to be stable. Because the reaction between cement and water is heating, the temperature of the sample increases, resulting in thermal expansion. The early heating reaction of cement is intense, and the hydration reaction will release a lot of heat, causing the thermal expansion of the

Table 1: Mix proportion of high-performance multiwall carbon nanotube cement-based composites.

Sample serial number	Water-cement ratio W/C	MWCNTs/ wt%	GA/ wt%	TBP/ wt%	PS/ wt%
S25-A-0	0.25	0.00	0.00	0.13	0.60
S25-A-1	0.25	0.05	0.30	0.13	0.60
S25-A-2	0.25	0.07	0.45	0.13	0.60
S25-A-3	0.25	0.10	0.60	0.13	0.60
S25-A-4	0.25	0.12	0.72	0.13	0.60
S30-A-0	0.30	0.00	0.00	0.13	0.20
S30-A-1	0.30	0.05	0.30	0.13	0.20
S30-A-2	0.30	0.07	0.45	0.13	0.20
S30-A-3	0.30	0.10	0.60	0.13	0.20
S30-A-4	0.30	0.12	0.72	0.13	0.20
S35-A-0	0.35	0.00	0.00	0.13	0.00
S35-A-1	0.35	0.05	0.30	0.13	0.00
S35-A-2	0.35	0.07	0.45	0.13	0.00
S35-A-3	0.35	0.10	0.60	0.13	0.00
S35-A-4	0.35	0.12	0.72	0.13	0.00

Table 2: Mixing ratio of high-performance nanocarbon fiber cement-based composites.

Sample serial number	Water-cement ratio W/C	CNTs/ wt%	MC/ wt%	TBP/ wt%	PS/ wt%
S25-B-0	0.25	0.00	0.00	0.15	0.60
S25-B-1	0.25	0.05	0.10	0.15	0.60
S25-B-2	0.25	0.10	0.15	0.15	0.60
S25-B-3	0.25	0.12	0.20	0.15	0.60
S25-B-4	0.25	0.15	0.24	0.15	0.60
S30-B-0	0.25	0.00	0.00	0.15	0.20
S30-B-1	0.25	0.05	0.10	0.15	0.20
S30-B-2	0.25	0.10	0.15	0.15	0.20
S30-B-3	0.25	0.12	0.20	0.15	0.20
S30-B-4	0.25	0.15	0.24	0.15	0.20
S35-B-0	0.25	0.00	0.00	0.15	0.00
S35-B-1	0.25	0.05	0.10	0.15	0.00
S35-B-2	0.25	0.10	0.15	0.15	0.00
S35-B-3	0.25	0.12	0.20	0.15	0.00
S35-B-4	0.25	0.15	0.24	0.15	0.00

cement, to offset part of the self-shrinkage. The self-shrinkage value at this time is actually the combined result of thermal expansion and self-shrinkage. When the water-cement ratio is 0.3 and 0.35, respectively, on the first day of measurement, the expansion value caused by thermal expansion is greater than the self-shrinkage value, resulting in the decline of the self-shrinkage curve, and the self-shrinkage value is negative [27]. Then, with the increase of age, the hydration reaction of cement slows down gradually, which weakens the thermal expansion phenomenon, and the self-shrinkage value is gradually greater than the expansion value, which makes the self-shrinkage curve rise and the

(a) W/C = 0.35

(b) W/C = 0.30

(c) W/C = 0.25

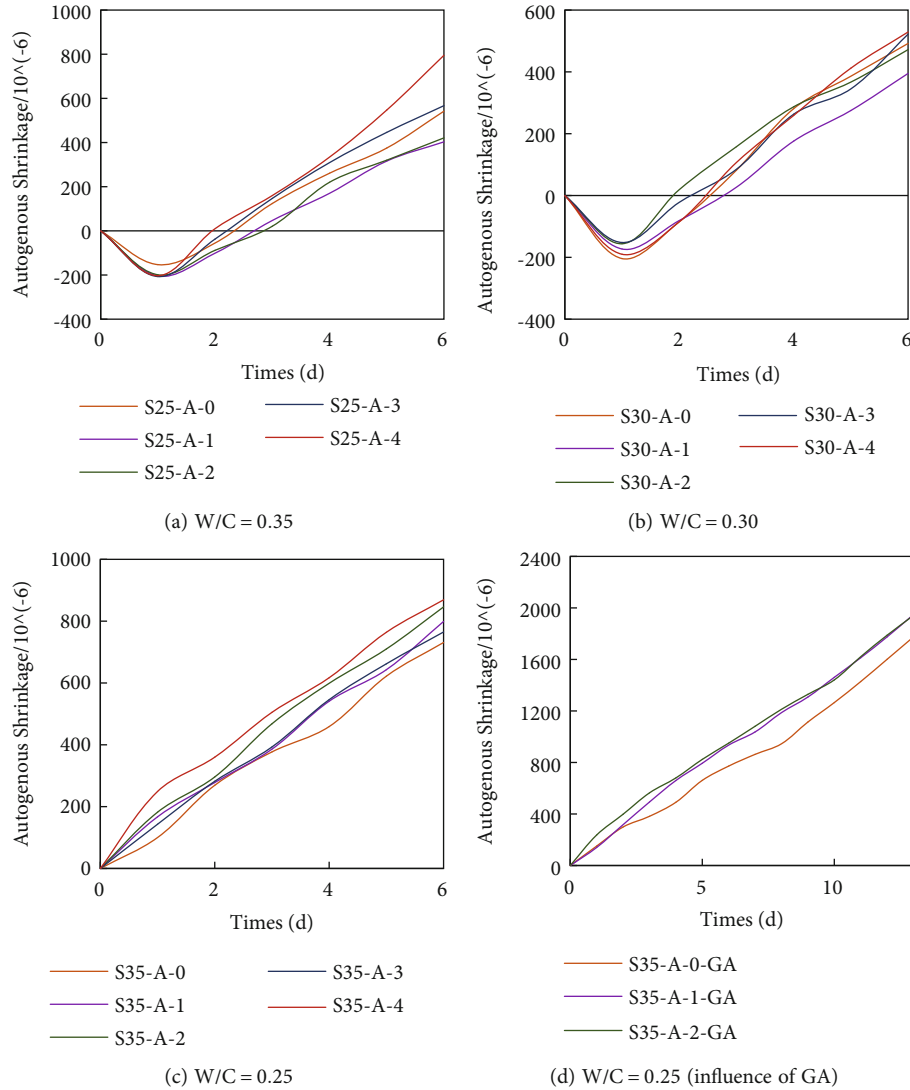(d) W/C = 0.25 (influence of GA)

FIGURE 2: Self-shrinkage changes of new energy materials with different nano and lime ratios.

self-shrinkage value presents a positive value. However, when the water-cement ratio is 0.25, even on the first day of measurement, the self-shrinkage value of the specimen is much greater than the thermal expansion value, so the self-shrinkage value of the specimen increases with the increase of age.

(2) Under the same water-cement ratio, the self-shrinkage of multiwalled carbon nanotube cement paste changes with the change of carbon nanotube content.

It can be seen from these four figures that, under the condition of a certain water-cement ratio, with the increase of the content of multiwalled carbon nanotubes, the self-shrinkage value of multiwalled carbon nanotube cement paste first decreases and then increases. When the water-cement ratio is 0.35 and the test age is 7 days, the self-shrinkage value of cement paste containing 0.05 wt% MWCNTs is the smallest, which is 46.74% lower than that of the blank sample. In addition, when the water-cement

ratio is 0.30 and the measurement age is 7 days, the optimum content of multiwalled carbon nanotube cement paste is 0.075 wt%, and the reduction rate of self-shrinkage value is 45.37% compared with the blank specimen under the same conditions. When the water-cement ratio is 0.25 and the measurement age is 7 days and 14 days, respectively, the optimum content of multiwalled carbon nanotube cement paste sample is 0.075 weight, and the self-shrinkage value is reduced by 9.32% and 11.54%, respectively, compared with the blank sample. It can also be observed from the figure that when the doping amount of multiwall carbon nanotubes reaches 0.12 wt%, the self-shrinkage value of the cement paste specimen containing multiwall carbon nanotubes is greater than that of the reference sample. It can be inferred that the high content of multiwalled carbon nanotubes limits the dispersion of multiwalled carbon nanotubes in the cement matrix, resulting in poor dispersion and aggregation of multiwalled carbon nanotubes in the cement matrix. This not only fails to give full play to the advantages of multiwalled carbon nanotubes, but also causes interface

(a) W/C = 0.35 (7 d)

(b) W/C = 0.30 (7 d)

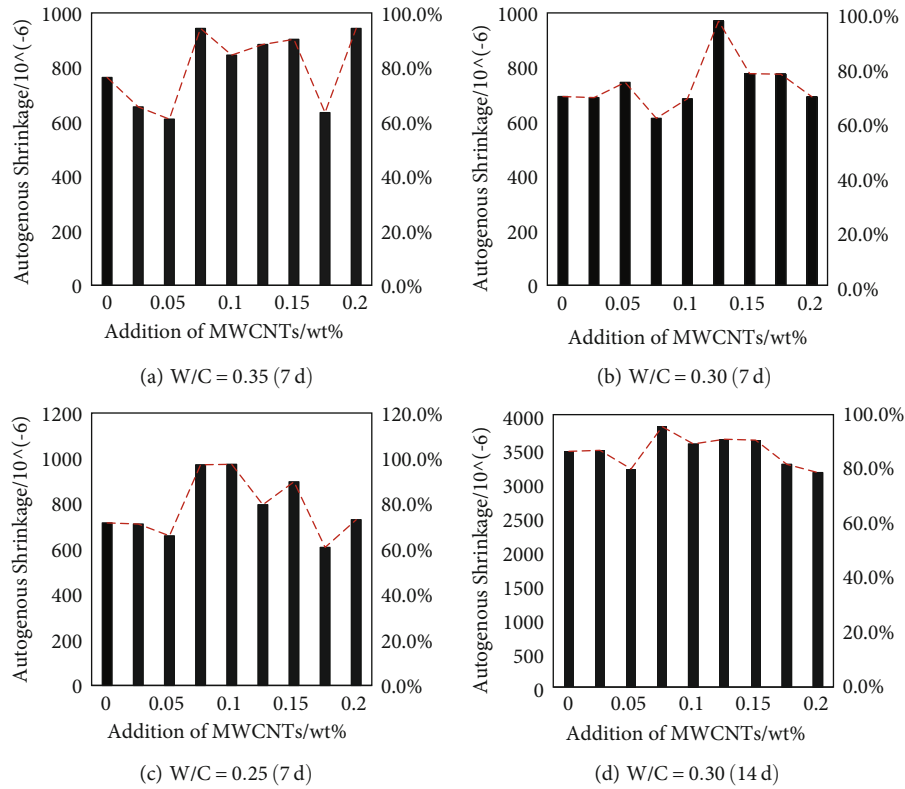(c) W/C = 0.25 (7 d)

(d) W/C = 0.30 (14 d)

FIGURE 3: Variation of self-shrinkage value of nanomaterials under different water-cement ratio.
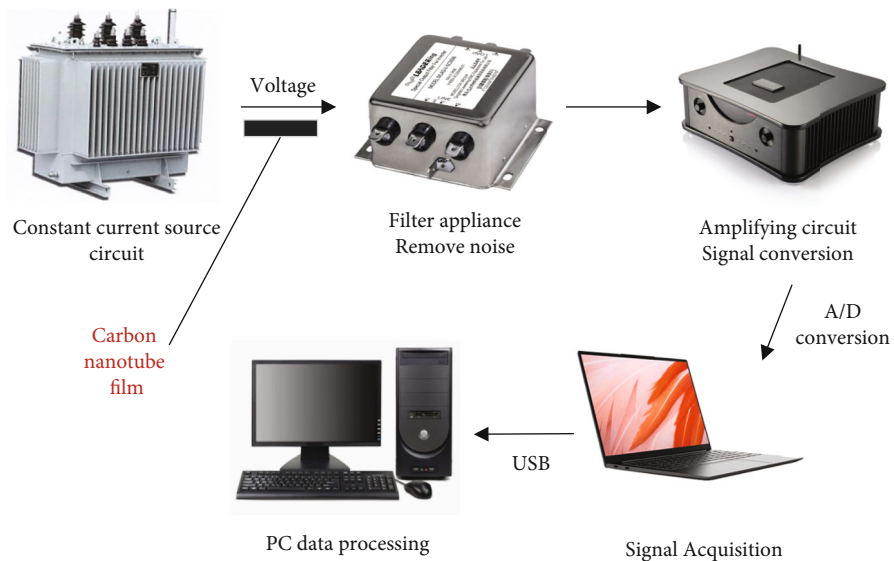
FIGURE 4: Hardware circuit design block diagram.

defects between multiwalled carbon nanotubes and cement matrix, which brings harm to cement-based materials and increases the self-shrinkage value of specimens [28]. Under a certain water-cement ratio, the auto-shrinkage performance of the multiwalled carbon nanotube cement slurry varies with its content, as shown in Figure 3.

The experimental results of self-shrinkage of carbon nanomaterials are as follows. When the ratio of water to cement is 0.3 and 0.35, the self-shrinkage value of carbon nanomaterial cement paste first decreases and then increases with the increase of age. When the ratio of water to cement is 0.25, the self-shrinkage value of the test piece increases with the increase of age, especially from the initial setting time to the second day of the test age. When the test age increases to 7 d (w/C =0.35 and 0.30) or 14 d (w/C =0.25), the growth rate of autogenous shrinkage value of carbon

FIGURE 5: Simulation diagram of third-order Butterworth filter.
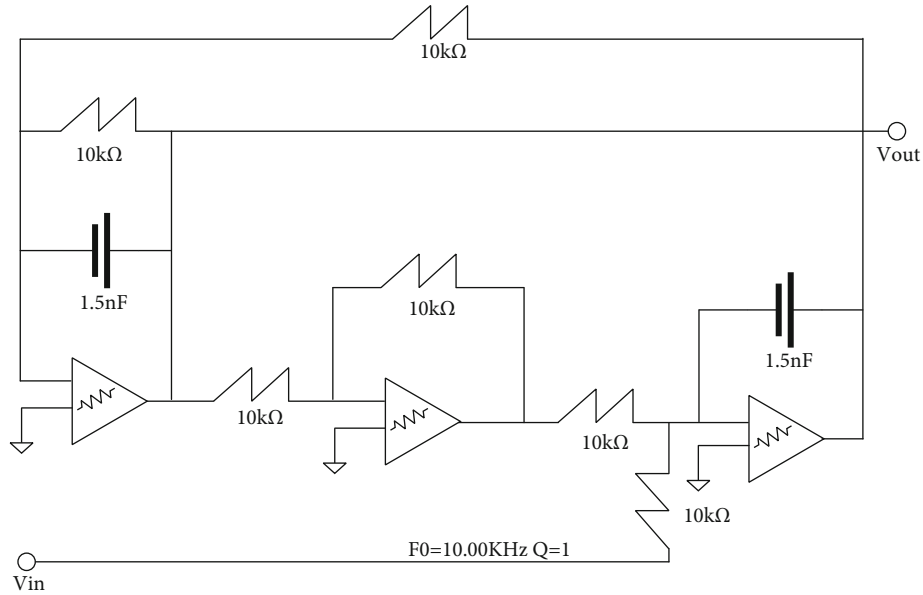
nanomaterial cement paste will decrease, but the growth rate of autogenous shrinkage value is slow. Under the same water-cement ratio, with the increase of carbon nanomaterial content, the self-shrinkage value of carbon nanomaterial cement paste first decreases and then increases [29]. When the water-cement ratio is 0.35 and the test age is 7 days, the self-shrinkage value of cement paste containing 0.05 wt% carbon nanomaterial is the smallest, which is 46.74% lower than that of the blank sample. When the content of carbon nanomaterial reaches 0.12 wt%, the self-shrinkage value of carbon nanomaterial cement paste sample is greater than that of the blank sample. The greater the content of carbon nanomaterial, the greater the self-shrinkage value of cement paste.

3.3. Application of Carbon Nanomaterials. This part mainly studies the hardware circuit design of polymer-based composite health monitoring data acquisition system based on carbon nanotube thin film sensor. The system is mainly composed of power supply circuit, constant current source circuit, filter circuit, amplification circuit, data acquisition circuit, and main computer. The communication circuit is composed of real-time online detection of basic parameters such as resistance value, film temperature, and film distortion state of the film sensor during composite deformation [30]. The block diagram of hardware design is shown in Figure 4.

Compared with other filters, the amplitude characteristic curve in the passband of Butterworth filter is almost parallel, there is no obvious fluctuation, and the useful signal can pass through almost without attenuation. For the clutter signal above this frequency, the amplitude curve shows a strict downward trend, the interference with the signal is stronger and stronger, and the filtering accuracy is higher and higher. However, the transition band is long, and the clutter signal processing effect near the cut-off frequency is not obvious. After filter simulation, the circuit design scheme and spec-
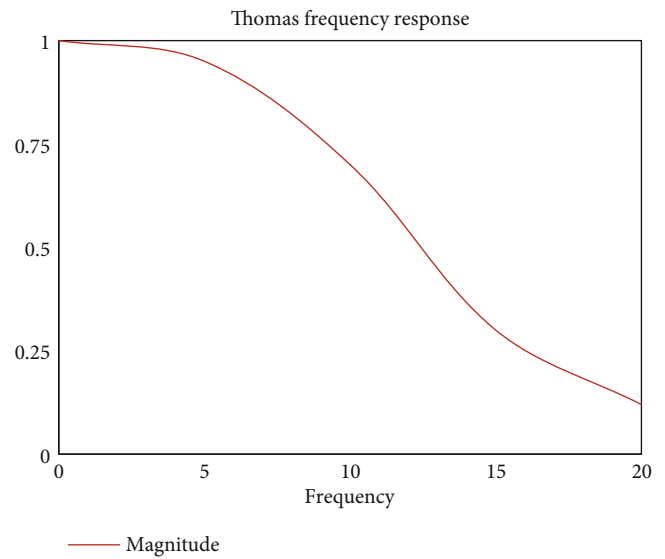
FIGURE 6: Amplitude frequency diagram of third-order Butterworth filter.

trum diagram of the curve are obtained, as shown in Figure 5 and Figure 6.

It can be seen from the amplitude-frequency diagram of Butterworth filter that the curve is strictly monotonically decreasing. When the amplitude is -3 dB, the passband gain is 0.7, and the corresponding cut-off frequency is 9.982 khz, which is a little different from the ideal value of 10 kHz. However, the transition band is relatively flat, and the filter gain corresponding to 12.5 k frequency is as high as 0.5, which has no obvious effect on the clutter near the cut-off frequency.

Generally, the damage mode of large structural members has the following two characteristics: the uncertainty of damage location and the randomness of damage direction, which poses a great challenge to the current real-time

FIGURE 7: Multiangle tensile comparison test of rectangular sensor and omnidirectional sensor.

FIGURE 8: Tensile test results of rectangular sensor at 0° and 90°.

condition monitoring method of large structural members. In view of this situation, this paper puts forward the following design scheme. Traditional rectangular sensors are distr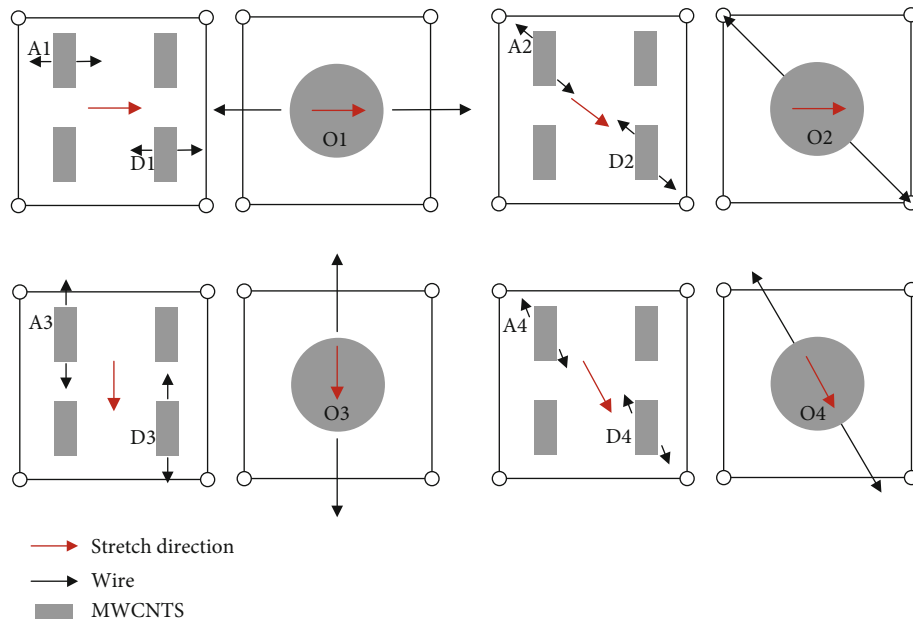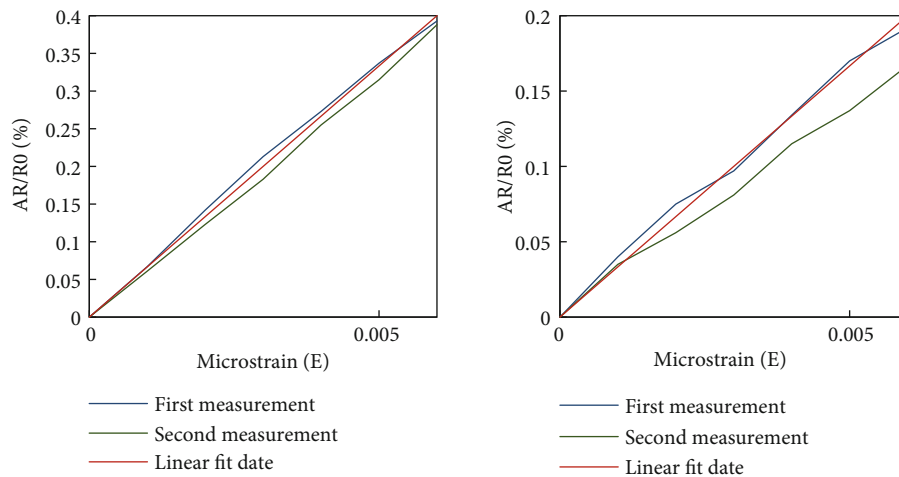ibuted in matrix composites in an array manner to detect different areas of the structure online and in real time. The scheme is shown in Figure 7.

For the first scheme, when the composite substrate is locally bent and deformed, four rectangular sensors with different orientations will produce different strain characteristics, resulting in some differences in the fluctuation value of the resistance change rate. By comparing the data fluctuation, the position of bending deformation can be preliminarily determined. However, because the sensor pasting method of the traditional rectangular sensor is synchronized with the fiber direction of the tested polymer matrix composite, the rectangular sensor can collect the change value of resistivity

in the fiber direction in real time. However, when the fission direction of the composite substrate is in the vertical direction or any angle of the optical fiber, there is a certain measurement error in the distribution mode of the rectangular sensor array. The measured resistance value is only the vertical component of the optical fiber direction, which cannot well reflect the strain state of the material. Therefore, in the comparative test of this paper, this paper will further verify whether the rectangular sensor has omnidirectional characteristics and test whether the rectangular sensor has omnidirectional monitoring capability of composite materials.

The experimental results of data processing are shown in Figure 8. Because the four sensors are symmetrically distributed in the array, their deformation states are completely consistent. This paper takes the sensor in the upper left corner as a representative for real-time data analysis. It is found

that there is always a strict linear relationship between the resistance change rate of the film sensor and the tensile stress whether the film detection direction is along the horizontal or vertical direction. In the range of 0-6000ue, with the increase of tensile stress, $\triangle$ R/R0 increases linearly. Carbon nanotube films are very sensitive to small strains. During the loading process, the change rate of resistance is positively correlated with the increase of tensile strain. Through the linear fitting of the least square method, the tensile strain sensing equation of the rectangular thin film sensor is $\triangle R/R0 = 70e - 0.5$ along the optical fiber direction and $\triangle R/R0 = 40e - 0.1$ along the vertical direction of the optical fiber. The sensitivity coefficients of the two directions are quite different, and the feedback damage information of the same material in different directions is different, so there is a certain measurement error.

4. Discussion

With the diversification of application fields, materials are often affected by complex mechanical loads, multiphysical field coupling, and even corrosive environment. The research of carbon nanomaterials, carbon nanofibers, and graphene-based composites is still in the exploratory stage, and further research is needed in many aspects. This paper needs to further study the total shrinkage of carbon nanomaterial and cement-based composites. The shrinkage of cement materials also includes drying shrinkage, plastic shrinkage, carbonization shrinkage caused by carbonization, chemical shrinkage, and cold shrinkage caused by temperature reduction. The conditions can further test the total shrinkage value of carbon nanomaterials and cement-based composites and study the effects of carbon nanomaterials, carbon nanofibers, and graphene on the total shrinkage properties of cement-based materials.

5. Conclusions

With the increase of water-cement ratio, the self-shrinkage of cement paste specimen decreases clearly. When the water-cement ratio is 0.25, the self-shrinkage value of 0.05% carbon nanomaterial cement paste is 74.68% lower than that when the water-cement ratio is 0.30. In the experimental study of omnidirectional monitoring characteristics, through the repeated tensile tests of rectangular sensor and omnidirectional sensor at 0℃, 30℃, 60℃, and 90℃, it is found that the sensitivity coefficient of rectangular sensor is quite different from the short side, but the sensitivity coefficient of omnidirectional sensor fluctuates slightly in different directions, ranging from 55.8 to 60.4, and the maximum fluctuation is only 5. This fully proves that the carbon nanotube omnidirectional sensor has omnidirectional detection ability.

Data Availability

The data underlying the results presented in the study are available within the manuscript.

Conflicts of Interest

The authors declare that they have no conflicts of interest.

References

[1] Q. Wang, "Teaching reform of organic chemistry in new energy materials and devices specialty under the background of establishing the emerging engineering education," *University Chemistry*, vol. 34, no. 7, pp. 42–46, 2019.

[2] F. Martinho, A. Hajijafarassar, S. L. Marino et al., "Nitride-based interfacial layers for monolithic tandem integration of new solar energy materials on Si: the case of CZTS," *ACS Applied Energy Materials*, vol. 3, no. 5, pp. 4600–4609, 2020.

[3] Z. A. Mansurov, M. K. Atamanov, Z. Elemesova, B. T. Lesbaev, and M. N. Chikradze, "New nanocarbon high-energy materials," *Combustion Explosion and Shock Waves*, vol. 55, no. 4, pp. 402–408, 2019.

[4] J. Paben, "How a materials recovery facility will sort flexible plastics," *Resource Recycling*, vol. 38, no. 1, pp. 11–11, 2019.

[5] K. W. Tao, A. L. Zhang, A. J. Cai et al., "Simulation studies of the granular flow beryllium target for the compact materials irradiation facility," *Nuclear Instruments and Methods in Physics Research*, vol. 942, pp. 162401.1–162401.6, 2019.

[6] J. Y. Lee, Y. C. Choi, and J. W. Lee, "The effect of participation motivation in the university sports facility users on Servicescape: differences in students and local residents," *Korean Journal of Sports Science*, vol. 29, no. 5, pp. 463–474, 2020.

[7] I. Setiawan and T. Anggah, "Customer satisfaction with fitness services and equipment facilities in gym academic faculty of science of science, Jakarta State University[j]," *Gladi Jurnal ILMU Keolahragaan*, vol. 12, no. 1, pp. 42–47, 2021.

[8] T. S. Thakur and P. M. Babu, "Evolution of bicycles and their utility as fitness aids -a review," *Nursing and Health Sciences*, vol. 8, no. 3, pp. 19–23, 2019.

[9] L. Zhou, F. Li, L. Wang, Y. Wang, and G. Wang, "A new energy consumption model suitable for processing multiple materials in end milling," *The International Journal of Advanced Manufacturing Technology*, vol. 115, no. 7-8, pp. 2521–2531, 2021.

[10] E. K. Jang, J. Im, J. Ahn, S. Yoon, and K. Y. Cho, "Layer design and approach in new energy storage materials," *ECS Meeting Abstracts*, vol. 2, 2020.

[11] B. Gao, X. Ning, and P. Xing, "Shock wave induced nanocrystallization during the high current pulsed electron beam process and its effect on mechanical properties," *Materials Letters*, vol. 237, no. 15, pp. 180–184, 2019.

[12] P. Wang, S. Wang, X. Zhang et al., "Rational construction of CoO/CoF2 coating on burnt-pot inspired 2D CNs as the battery-like electrode for supercapacitors," *Journal of Alloys and Compounds*, vol. 819, p. 153374, 2019.

[13] C. M. Lampert, G. Smestad, K. L. Chopra, A. Roos, and H. Takakura, "Smestad and solar energy materials and solar Cells," *Solar Energy Materials and Solar Cells*, vol. 194, pp. A1–A3, 2019.

[14] N. Navarro, R. Kajiura, A. Miura, and K. Tadanaga, "Organic–inorganic hybrid materials for interface design in all-solid-state batteries with a Garnet-type solid electrolyte," *ACS Applied Energy Materials*, vol. 3, no. 11, pp. 11260–11268, 2020.

[15] Y. Tang, Z. Chen, W. Feng, Y. Nong, C. Li, and J. Chen, "Combined effects of nano-silica and silica fume on the mechanical behavior of recycled aggregate concrete," *Nanotechnology Reviews*, vol. 10, no. 1, pp. 819–838, 2021.

[16] C. Giannoulakis, "Sport facility & event management," *International Journal of Sport Communication*, vol. 12, no. 4, pp. 606–609, 2019.

[17] W. Suk and J. Y. Han, "impact of a new sport facility for urban regeneration: a case of DGB Daegu Bank Park," *Korean Journal of Sport Management*, vol. 26, no. 3, pp. 52–69, 2021.

[18] T. Kim and S. K. Min, "A comparative advantage analysis of regional leisure sport facility industry," *Korean Journal of Sport Management*, vol. 25, no. 4, pp. 113–124, 2020.

[19] G. Oseghale, "Sports facilities condition assessment in selected universities in south western Nigeria," *IOSR Journal of Sports and Physical Education*, vol. 8, no. 2, pp. 1–07, 2021.

[20] P. R. Milton, L. M. Williamson, K. Brubaker, and M. Papania, "Recreate and retain: how entrance into a campus recreation facility impacts retention," *Recreational Sports Journal*, vol. 44, no. 2, pp. 89–98, 2020.

[21] L. Capasso, D. D'Alessandro, V. I. Popov, I. I. Libina, and I. I. Torubarova, "Hygienic requirements for the construction and operation of sports facilities in the Russian Federation and Italy," *Review Manuscrip. Gigiena i Sanitariia*, vol. 99, no. 1, pp. 20–25, 2020.

[22] G. Grossman, V. Beck, W. Dan, E. Toklu, and M. El-Sayed, "Application of a continuously active antimicrobial surface coating in two professional sports training facilities," *Infection Control and Hospital Epidemiology*, vol. 41, no. 1, pp. s440–s440, 2020.

[23] A. A. Kim, Y. Sunitiyoso, and L. A. Medal, "Understanding facility management decision making for energy efficiency efforts for buildings at a higher education institution," *Energy and Buildings*, vol. 199, pp. 197–215, 2019.

[24] M. Parrott, J. Ruyak, and G. Liguori, "The history of exercise equipment: from sticks and stones to apps and phones," *ACSM s Health & Fitness Journal*, vol. 24, no. 6, pp. 5–8, 2020.

[25] A. Freitas and T. S. Lacerda, "Fitness centers: what are the most important attributes in this sector?," *International Journal for Quality Research*, vol. 13, no. 1, pp. 177–192, 2019.

[26] Z. Arifin, S. D. Prasetyo, S. Suyitno et al., "Rancang Bangun Alat elliptical trainer outdoor," *Mekanika Majalah Ilmiah Mekanika*, vol. 19, no. 2, pp. 104–112, 2020.

[27] B. Gopi, M. Di Canio, N. Chintalapudi, F. Amenta, and G. Nittari, "Development of physical training smartphone application to maintain fitness levels in seafarers," *International Maritime Health*, vol. 70, no. 3, pp. 180–186, 2019.

[28] X. Zhao, Y. Dong, X. Yuan, J. Li, Y. Zhao, and Z. Bao, "Improvement of unmanned aerial vehicle cluster atmospheric monitoring algorithms," *Journal of Environmental Protection and Ecology*, vol. 20, no. 3, pp. 1068–1075, 2019.

[29] J. Eickhoff-Shemek, "HIIT for clinical populations: safety and legal liability issues for community fitness facilities," *ACSM s Health & Fitness Journal*, vol. 25, no. 5, pp. 65–67, 2021.

[30] F. Qian, "State council: strengthen the construction of public fitness venues and facilities to develop mass sports," *China City Planning Review*, vol. 29, no. 4, pp. 6–6, 2020.

Research Article

Mechanical Properties of Graphene Composite Materials and Mesonumerical Experiments on the Mechanical Properties of Unsaturated Soil-Rock Mixtures

Qinghai Zhang [ID],[1] Lihua Wu,[1] and Jianfei Li[2]

[1]*College of Agriculture and Hydraulic Engineering, Suihua University, Suihua, 152000 Heilongjiang, China*
[2]*Northeast Forestry University, School of Civil Engineering, Harbin, 150040 Heilongjiang, China*

Correspondence should be addressed to Qinghai Zhang; zqh464354668@163.com

Graphene, as an emerging two-dimensional carbon nanomaterial, has attracted widespread attention and in-depth research by domestic and foreign researchers. With its excellent mechanical properties, graphene is used as a reinforcing material in polymers, ceramics and rubber, and other matrices, which can significantly improve the toughness of the matrix. However, under the action of natural factors such as continuous rainfall or heavy rain, the accumulation layer landslide is often in an unsaturated state, which is very easy to induce disasters. Based on this background, we use micronumerical simulation methods and graphene composite materials to study the mechanical properties of unsaturated soil-rock mixtures to understand the mechanical properties of unsaturated soil-rock mixtures and evaluate and predict its stability. This paper takes the soil of a landslide zone in a certain city as the numerical test object. Through the automatic generation technology of the mesostructure model of the soil-rock mixture, a series of numerical experiments were carried out on the random mesostructure model of the soil-rock mixture, and the gravel content was analyzed in depth. Experiments show that the model can reasonably describe the volume expansion of the soil-rock mixture under low confining pressure, the volume compression under high confining pressure, and the phenomenon that the peak strength of the soil-rock mixture increases with the increase of confining pressure, which verifies that the model is simulating soil and rock. This shows that the stress-strain relationship curves of different soil-rock interface parameters, rock content, saturation, and the number of wet and dry cycles all show obvious nonlinear characteristics and strain hardening. This shows that graphene composites can be used in the study of the mechanics of unsaturated soil-rock mixtures, which is of great significance for improving the landslide environment and enhancing its mechanical properties.

1. Introduction

With the development of the national economy, in engineering practice, foundation resistance problems exist in UHV transmission line foundations, underground space foundations, high-rise building foundations, and marine construction foundations. Therefore, geotechnical scholars have more research on the resistance of foundations. More and more, it has gradually become a popular direction. In many engineering constructions, there are very high requirements

on the mechanical properties of soil-rock mixtures. Most of the natural shallow soils exist in unsaturated forms, with less overall water content, and have good shear resistance [1–3]. The increase of water content will weaken its performance, so the change of water content will have a greater impact on the mechanical characteristics of natural unsaturated soil. Of course, it is not the only influence. Therefore, the mechanical research on the properties of this kind of media, as well as the stability analysis, deformation and instability prediction, and prevention of the common accumulation

layer slopes and other slopes containing soil-rock mixed media in engineering construction in my country. It has good application value.

The rapid development of nanotechnology is continuously expanding the application of traditional materials such as soil and rock, bringing new opportunities and hopes to the development and transformation of mixed soil composite materials [4]. Nanomaterials are ultrafine materials with a particle size on the order of nanometers. Combining them with mixed soil can successfully enhance the mechanical strength of the mixed soil. Graphene, as a 2D layered inorganic nanomaterial with a periodic structure, is currently the strongest material known in the world [5, 6]. Due to its excellent mechanical properties, it can act in a polymer matrix like other nanomaterials, to nanoenhancement. At the same time, due to the physical properties of graphene itself, it can also be widely used in composite materials.

In the past ten years, scholars at home and abroad have conducted a large number of pioneering and fruitful researches on soil-rock mixtures and have accumulated rich research results and research experience. Qin et al. studied the preparation and mechanical properties of graphene and multiwalled carbon nanotube reinforced composite ceramic coatings. Use infrared spectroscopy (FTIR analysis) to identify the structure of functionalized and hybrid functionalized carbon nanotubes. The coating is brushed on the substrate and then cured at a temperature below 250°C. The morphological and cross-sectional features were studied by scanning electron microscopy (SEM). The experimental results show that the composite coating has a compact structure, and the graphene and the mixed-treated carbon nanotubes are well dispersed. The addition of 0.2 wt% graphene and 0.2 wt% hybrid functionalized carbon nanotubes resulted in a significant increase in hardness and fracture toughness. At the same time, due to the high tensile strength of graphene and carbon nanotubes, the bonding strength between the composite coating and the metal substrate is improved. Compared with pure alumina coating, the friction coefficient, wear depth, and wear width of composite coating are much lower. However, the experimental conclusions are not suitable for application to unsaturated soil-rock mixtures [7]. Lei et al. studied the characteristics of the shear strength parameters of the rock and soil aggregates in the embankment slope of the reservoir, gave the law of the shear strength of the rock and soil aggregates, and proposed the characteristics of the rock and soil aggregates considering the influence of suction and saturation. The unsaturated shear strength formula studies the physical mechanism of sliding or failure of such slopes under rainfall infiltration conditions. Based on the analysis of the slope rainfall infiltration process, a 3D unsaturated saturated-unsaturated seepage field and its finite element solution model were established. Studies have shown that the minimum safety factor of accumulated rock and soil aggregates is not reached when the rainfall stops, but occurs several hours after the rainfall stops. This phenomenon is consistent with the destruction process of the actual slope engineering, but its overall research lacks data support, and more data is needed to support its conclusions [8]. In order to obtain the mechanical properties of the weathered soil-rock mixture at the edge of a highway landslide in western China, Jin needed to perform large and medium-sized triaxial shearing on the three weathered rock-soil mixtures on site due to the reduction of sample size and particle size test. The effects of particle size and sample size were analyzed. The results show that it has a strong scale effect: mechanical properties are closely related to particle size, sample size, and sample classification. As the particle size increases, the internal friction angle increases first and then decreases. At the same time, the reasons for these differences are analyzed. The experimental results lack more data to support the trend of internal friction angle changes [8].

This paper uses the FORTRAN language program to realize the method of establishing the soil-rock mixture numerical model by the indoor test gradation, and with the help of the mesonumerical simulation method and the implicit integration algorithm, the finite element program is used to surround the seepage mechanics response of the soil-rock mixture of the accumulation layer landslide. And the mechanism of deformation and failure carries out a series of biaxial tests of unsaturated soil-rock mixed media under different soil-rock interface parameters, rock content, and saturation, and different numbers of dry and wet cycles, using soil mechanics, rock mechanics, seepage mechanics, and elastoplastic mechanics obtain the influence law of soil-rock interface parameters, rock content, saturation, number of dry-wet cycles, and other factors on the deformation and strength characteristics of soil-rock mixture to reveal its seepage mechanism and deformation and failure characteristics.

2. Mechanical Properties of Unsaturated Soil-Rock Mixture and Graphene Composite Materials

2.1. The Structure and Properties of Graphene. Since Professor N and Professor G successfully prepared single-layer graphene, graphene has attracted more and more attention and research from all walks of life. Graphene is the basic unit of other carbon materials in various dimensions. Currently, members of the carbon family include the following: zero-dimensional fullerenes, one-dimensional carbon nanotubes, and two-dimensional graphene to three-dimensional diamond and graphite. Graphene has a six-membered ring arranged in a periodic honeycomb structure, in which C atoms are connected to adjacent C atoms by sp^2 hybrid orbitals, the bond angle of the C-C bond is 120°, and the bond length is 0.142 nm. This stable structure gives graphene ultrahigh strength, with Young's modulus of 1.1 TPa and a breaking strength of 125 GPa. Each C atom of graphene has 4 valence electrons. When 3 electrons form an sp^2 bond, there will be an unbonded electron forming a large π bond above and below the plane of the graphene. At this time, the π bond is half-filled. The state allows electrons to move freely in it, and the large π bonds between layers form π orbitals perpendicular to the graphene plane. These π orbitals are effective channels for free electrons to shuttle

through the two-dimensional structure of graphene. Give graphene excellent electrical and thermal conductivity. The electron migration rate of graphene in a single atomic layer reaches $10000\,cm^2/v$, and the thermal conductivity is 3000-$5000\,wm^{-1}/k$. Theoretically, the specific surface area of a single-layer graphene can reach $2630\,cm^{-2}/g$, which not only further increases the electrical and thermal conductivity of graphene but also provides a larger contact area for its surface functionalization. In addition, the unique energy band structure of graphene also enables it to possess electromagnetic properties such as quantum Hall effect, quantum tunneling effect, and quantum Hall ferromagnetism. With its excellent properties in terms of force, light, electricity, and magnetism, graphene is widely used to enhance and improve the mechanical, electrical and electromagnetic shielding properties of composite materials.

Strictly speaking, there is thermodynamic instability in the two-dimensional crystal structure, and there is no long-range ordered two-dimensional crystal in nature. That is to say, if in a free state, the graphene sheet will curl into carbon nanotubes or stacked into graphite, which also makes graphene easy to agglomerate in a macroscopic state, and it is difficult to exist as a single layer.

Professor A added the original graphene and the functionalized graphene treated with nitric acid to the cement-based material to test its mechanical properties and explored the influence of the incorporation of graphene on calcium silicate hydrate. Atomic force microscope observations found that in cement-based materials mixed with graphene, graphene is present in the generated calcium silicate hydrate, and the content of high-density calcium silicate hydrate increases, and the overall mechanical properties of the composite material are enhanced. Molecular dynamics shows that the addition of functionalized graphene improves the interface strength and the integrity of cement-based composites. In addition, phase analysis shows that the incorporation of graphene and functionalized graphene can affect the phase composition and surface toughness of the product, which is the reason why the overall toughness and plasticity of graphene cement-based composites are improved.

2.2. Simulation Method of Soil-Rock Interface.
In a soil-rock mixture, the existence of soil-rock interface has an important influence on its mechanical properties and deformation and failure characteristics [9, 10]. The contact of the soil-rock interface is a typical nonlinear problem. In the numerical calculation, the contact surface element is generally introduced to simulate the contact problem. When there are many contact surfaces, the calculation is often not easy to converge [11, 12]. Therefore, for materials with a large number of discontinuous surfaces on the mesoscale, such as soil-rock mixture, the use of conventional contact surface elements to simulate the soil-rock interface has obvious limitations.

2.2.1. Master-Slave Interface Model.
The master control plane can invade the slave plane between the nodes of the slave plane, as shown in Figure 1(a) [13]. This regulation can well realize the simulation of the mechanical behavior of the soil-rock interface, because in the soil-rock mixture, the stiffness and strength of the rock are generally much greater than those of the soil, and the rotation and translation of the rock under the external load will affect it. The surrounding soil produces contact force, and the sharp corners of the rock passing through the soil will cause the deformation and failure of the soil, which is consistent with the mechanical mechanism of the interaction between soil and rock [14, 15].

In order to obtain the best simulation results, when simulating the soil-rock interface, the pair of surfaces in contact between the rock and the soil is defined as the contact pair in the calculation model. The soil surface is the subordinate contact surface, and the rock surface is the dominant contact surface shown in Figure 1(b) [16].

2.2.2. Friction Model.
When simulating the contact characteristics of soil and boulders, the Coulomb friction model should be used as the soil-rock interface contact model, and the friction factor is used to characterize the friction behavior between two surfaces. The relationship between stress and shear displacement on the contact surface is shown in Figure 2.

The solid line in the figure is the ideal friction behavior. The default friction factor is 0 (the contact surface is completely smooth). Before the stress at the contact surface reaches the maximum stress τ_{max}, the tangential slip is 0 until the stress between the contact surfaces is equal to the relative sliding of the contact surface which will occur only when the ultimate stress μp is [17, 18], namely,

$$\tau_{max} = \mu p. \tag{1}$$

In the formula, μ is the friction factor, and p is the normal contact force between the two contact surfaces.

2.3. Unsaturated Soil Seepage and Strength

2.3.1. Unsaturated Seepage.
The flow of liquid pores into unsaturated soils follows Darcy's law or Forchheimer's law, and the expressions are as follows:

$$V = -K\,grad H = KJ, \tag{2}$$

$$snV_f\left(1 + \beta\sqrt{V_f \cdot V_f}\right) = -K\frac{\partial H}{\partial X} = -K\,grad H, \tag{3}$$

where V is the seepage velocity, J is the hydraulic gradient, H is the piezometric head, snV_f is the seepage velocity through the unit area in a certain direction, and K is the permeability coefficient [19, 20].

According to Darcy's law, there are

$$k = \frac{v}{gK}. \tag{4}$$

According to Forchheimer's law, there are

$$k = \frac{v}{g + g\beta\sqrt{V_f \cdot V_f}}K. \tag{5}$$

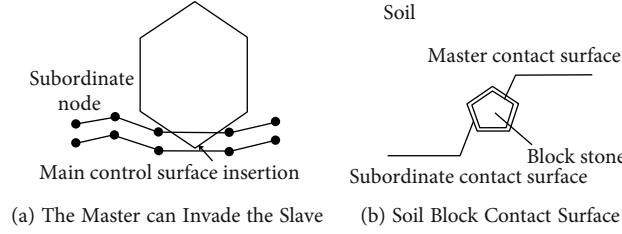(a) The Master can Invade the Slave   (b) Soil Block Contact Surface
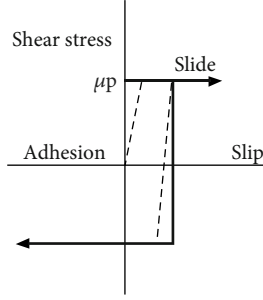
Figure 1: Simulation method of soil-rock interface.

Figure 2: Schematic diagram of Coulomb friction model.

In the formula, v is the dynamic viscosity coefficient. For unsaturated soil, since liquid and gas coexist, the degree of saturation directly affects the permeability resistance, so at this time, k or K is a function of the degree of saturation S, so it is uniformly written as

$$k = k_s(S)K. \qquad (6)$$

In the formula, $k_s(S)$ is the saturation correlation coefficient, and for isotropic materials, K is a scalar.

2.3.2. Unsaturated Soil Strength. An important factor in the instability of the soil-rock mixture slope caused by rainfall is that the rainfall causes the reduction of the matrix suction in the shallow unsaturated soil-rock mixture, resulting in loss [21, 22]. The influence of unsaturated characteristics on soil-rock mixture is mainly reflected in the influence of matrix suction on its shear strength, namely,

$$\tau_f = c' + (\sigma - u_a) \tan \phi' + (u_a - u_w) \tan \phi^b. \qquad (7)$$

In the formula, τ_f is the shear strength of unsaturated soil, σ is the normal stress, and $\sigma - u_a$ is the net normal stress.

2.4. Automatic Generation Technology of Soil-Rock Mixture. With the rapid development of digital graphics processing technology, remarkable results have also been achieved in the mesostructure of soil-rock mixtures. However, digital image processing technology largely relies on the acquired cross-sectional images of all the soil-rock mixtures in the study area, so this method has certain limitations [23–26]. The main function of the preprocessing program of the soil-rock mixture numerical model is to generate a certain amount of rock in a specific research area, so that the parti-

cle size distribution of the rock system itself conforms to a specific gradation curve. Furthermore, it is possible to make the generated discrete stone system have statistical self-similarity properties, that is, fractal [27].

2.4.1. Random Number. The stochastic simulation method is used to simulate the size, orientation and spatial distribution of the blocks in the soil-rock mixture, namely,

$$R_i = \text{mod} \, (2053 R_{i-1} + 13849, m), \qquad (8)$$

$$\text{RND}_i = \frac{R_i}{m}. \qquad (9)$$

Among them, R_{i-1} is the seed number that triggers the random number generator input from the outside.

2.4.2. The Shape of the Block Stone in the Soil-Rock Mixture. In order to simulate boulders objectively, arbitrary random polygons are used in the program to simulate boulders. The maximum and minimum number of sides of the boulders is put from the outside [28]; then,

$$L(x, \lambda) = f(x) - \lambda^T c(x). \qquad (10)$$

Among them,

$$c((x)) = (c_1(x), \cdots, c_p(x))^T, \qquad (11)$$

$$\varphi(x, u) \equiv f(x) + \frac{1}{\mu} \|c(x)\|_1. \qquad (12)$$

Among them, μ is called the penalty factor, and $\|c(x)\|_1$ is the l_1 norm of the vector function $c(x) = (c_1(x), \cdots, c_p(x))^T$. In the specific simulation process, as needed, the concave polygon is not needed for artificial control [29, 30].

2.4.3. Determination of the Spatial Position and Orientation of Block Stones in Soil-Rock Mixture. First, create the center of the rock, and then multiply the random number by the width of the sample to get the coordinate value of the center of the rock in the sample [31, 32]. Before determining the vertex coordinates of the polygon, a random number must first be created as the angle of deflection of the side of the polygon. After determining the deflection angle, since the number of sides of the polygon has been determined, the deflection angle required to generate a polygon radius can

be calculated as

$$\beta = a + (i - 1) \cdot \frac{2\pi}{n}. \tag{13}$$

Then, generate a random number and combine the boundary diameter of the polygon with the maximum and minimum radius to determine the radius of the polygon at this time. After the polygon radius is determined, since the angle between the polygon side and the x-axis is known, multiply the angle by the angle. The cosine and sine values of can get the vertex coordinates of the polygon [33, 34].

2.4.4. Determination of the Area of Block Stone in Soil-Rock Mixture. This type of polygon is decomposed into multiple triangles, and the area of the polygon is calculated by calculating the area of the triangle separately. The formula used is as follows:

$$\text{Area} = \frac{1}{2} \sum_{i=1}^{n} \begin{vmatrix} x_0 & x(i) & x(i+1) \\ y_0 & y(i) & y(i+1) \\ 1 & 1 & 1 \end{vmatrix}. \tag{14}$$

Among them, (x_0, y_0) is the coordinate of the center of the polygon; $(x(i), y(i))$ is the coordinate of the vertices of the polygon.

2.4.5. Determination of rock content in the model. In the established two-dimensional model, the size of the stone content is defined as the ratio of the area occupied by the boulders in the model to the total area of the model. The specific formula is as follows:

$$e = \frac{\sum A_i}{A}. \tag{15}$$

In the formula, e is the stone content rate, A_i is the area of a single stone, and A is the total area of the model.

2.5. Mechanical Safety of Unsaturated Soil-Rock Mixture. Since the mechanical properties of the unsaturated soil-rock mixture effectively inherit the advantages of steel and concrete, it has good plasticity and adjustability and can form a beautiful structure. It has high strength and rigidity and can be built into a larger span structure. Good integrity, good ductility, and the structure can better resist external disasters, such as earthquakes and hurricanes; good durability and fire resistance can be applied to many characteristics such as harsh environments and widely used in construction and other civil engineering.

3. Experimental Design of Mechanical Properties of Unsaturated Soil-Rock Mixture

3.1. Test Subject. Taking the landslide zone soil in a landslide area of this city as the object of numerical experiment, through the automatic generation technology of the mesostructure model of the soil-rock mixture, a series of numerical experiments were carried out on the random mesostructure

model of the soil-rock mixture, and the gravel content, the soil-rock contact characteristics, saturation, dry-wet cycle, and many other factors affect the macromechanical properties and deformation failure of unsaturated soil-rock mixtures. The material composition of the landslide accumulation body and the sampling point diagram of the accumulation body are shown in Figure 3.

3.2. Content of Numerical Experiment

3.2.1. Mechanical Properties of Unsaturated Soil-Rock Mixture under Different Rock Contents. The unsaturated soil-rock mixture consists of soil and crushed stone. The different content of crushed stone will change the internal structure of the soil-rock mixture, which will inevitably affect its mechanical deformation properties. Based on the landslide zone test ground gradient in a landslide-prone area of this city, the random soil-rock mixture intermediate generation system is used to create numerical experimental geometric models with different rock contents and the corresponding unsaturated soil-rock mixture. They are determined in the ABAQUS test model, perform a biaxial compression test, and study the effect of the content of crushed rocks on the stress-stress ratio and volume-axial stress curve of the unsaturated soil-rock mixture.

3.2.2. Mechanical Properties of Unsaturated Soil-Rock Mixtures under Different Saturations. As a typical heterogeneous bulk material, unsaturated soil-rock mixture has a large internal porosity and is affected by saturation. This paper uses the ABAQUS program as a platform to combine mechanical calculations and seepage calculations to conduct biaxial tests of unsaturated soil-rock mixture samples under different saturation conditions. Study the mechanical properties and failure mechanism of soil-rock mixture samples under different saturations.

3.3. Numerical Test Model Establishment. The numerical test refers to the indoor triaxial shear test of a sliding body in a landslide area in this city for sample preparation. The indoor test is scaled according to the original gradation of the sliding body at the landslide site. The particle size of the sample is above 60 mm, accounting for 5.22%. The particle size of 20 mm or more accounts for 25.52%, and the content of fine particles smaller than 5 mm is 35.84%. Therefore, the equivalent replacement method is used to scale the ultraparticle size part, and the ultraparticle size part ($d_{\max} = 60$ mm) is 60-5 mm. Perform equivalent substitutions, and the gradation composition is shown in Table 1.

3.3.1. Determination of Minimum Particle Size. This frequency value test adopts a 30 cm ∗ 60 cm biaxial test. The minimum particle size of the numerical biaxial test is determined by the soil-rock threshold combined with the original gradation of the landslide body to be 1 cm.

3.3.2. Model Establishment. This paper simulates the five sets of gradation curves of the indoor triaxial test. Within the range of 30 cm ∗ 60 cm, the self-developed random stone generation system is used to automatically generate crushed

Material composition of
deposits before landslide

Material composition of
deposits after landslide

Exposed section of bedrock
and accumulation body
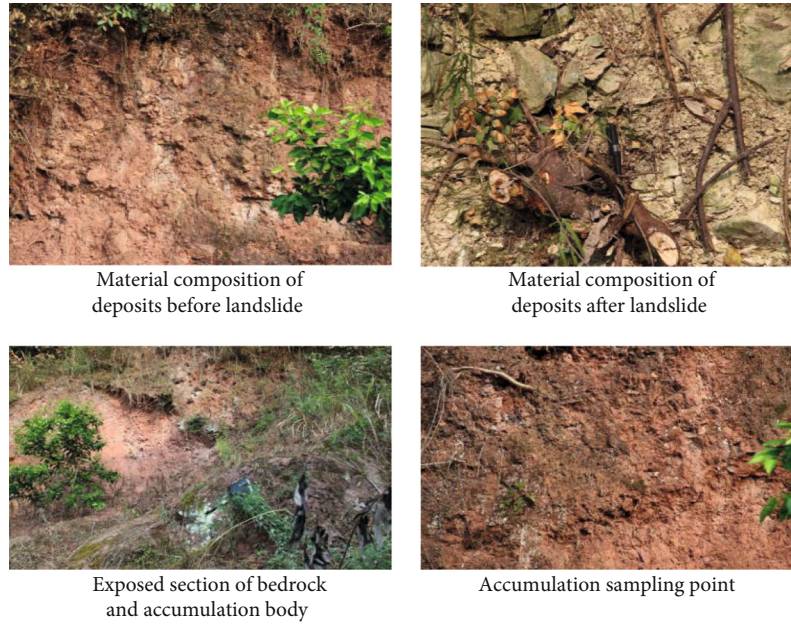

Accumulation sampling point

FIGURE 3: Material composition of the landslide accumulation body and the sampling point map of the accumulation body.

TABLE 1: Test grading of rock and soil slide.

| Test gradation | Percentage of each granule group | | | | | | | | | |
| | 60-40 | 40-20 | 20-10 | 10-5 | 5-2 | 2-1 | 1-0.5 | 0.5-0.25 | 0.25-0.1 | <0.1 |
						(mm)				
1	0	0	20.18	21.41	15.60	8.41	8.67	6.35	6.05	10.32
2	0	13.50	24.20	19.30	12.50	8.80	7.20	3.70	3.70	7.10
3	5.27	17.43	26.19	16.23	10.79	7.56	5.82	2.68	2.76	5.27
4	8.50	22.50	25.00	17.00	9.00	6.00	4.00	3.00	3.00	1.00
5	15.76	26.83	23.55	14.32	9.43	3.36	4.56	2.19	0	0

stones and soil, and then, the corresponding nonstandards are established in ABAQUS.

3.3.3. Crushed Stone Content.
According to the grading curve, the rock content is 32%, 38%, 47%, 56%, and 65%, and then, the geometric model of the soil-rock mixture is generated according to the random generation system of the block stone, and the corresponding geometric model is established in ABAQUS. Divide the grid, as shown in Figure 4, and set the initial conditions and boundary conditions of the soil-rock contact characteristics of the unsaturated soil-rock mixture to prepare for the next biaxial numerical test.

3.4. Statistical Processing.
Statistical analysis was performed with SPSS 13.0 statistical software. The significance test of the difference was performed by one-way analysis of variance, the difference between the two groups was tested by LSD-t, and the statistical results of the mechanical properties of the unsaturated soil-rock mixture were performed by the group t-test. $P < 0.05$ is considered to be statistically significant.

4. Mechanical Properties of Unsaturated Soil-Rock Mixture

4.1. Verification of Numerical Model Test.
Take the indoor triaxial test of gravel soil with 47% gravel content as an example to verify the rationality of the random soil-rock mixture model. The parameters of the biaxial numerical model are shown in Table 2.

The size of the model is 30 cm ∗ 60 cm from the previous three-axis test. The vertical displacement of the bottom boundary is constrained, the surrounding stress boundary conditions are used, and the top of the model is servo controlled to apply axial load. Confining pressures of 0.4 MPa, 0.8 MPa, 1.2 MPa, and 1.6 MPa were, respectively, applied in the calculation of the biaxial test. The calculation results of the biaxial test mainly analyze the relationship between deviatoric stress and axial strain and the relationship between volume and axial strain. At the same time, it is compared with the indoor test results, as shown in Figures 5 and 6.

Figures 5 and 6 show that the normality of the calculated value of the model and the measured value of the test are the same whether it is the voltage-voltage ratio curve or the

Stone content 32%   Stone content 38%   Stone content 47%   Stone content 56%   Stone content 65%
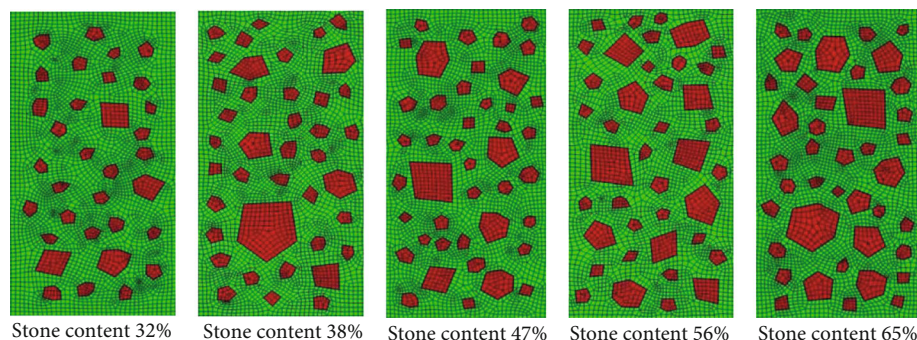
FIGURE 4: Soil-rock mixture samples of different rock block contents in FEM.

TABLE 2: Table of physical and mechanical parameters of soil-rock mixture test.

Material type	Density ($kg \cdot m^{-3}$)	Elastic modulus (MPa)	Poisson's ratio	Internal friction angle (°)	Cohesion (kPa)
Clod	2000	50	0.38	28	50
Block stone	2800	17500	0.20	41	12000

volume-axis voltage ratio curve, which shows the adaptability of the model to different pressure situations. It shows that the model can reasonably describe the volume expansion of the soil-soil mixture at low constraint pressure, the compression of the volume under high constraint pressure, and the increase of the maximum strength of the soil-rock mixture with the increase of the constraint pressure, which confirms that the model simulates a soil-rock mixture.

4.2. Deformation Characteristics of Unsaturated Soil-Rock Mixture under Different Soil-Rock Interface Parameters. Using the unsaturated numerical test model, the biaxial consolidation drainage test was carried out under the confining pressure of 0.4 MPa, 0.8 MPa, 1.2 MPa, and 1.6 MPa, respectively. During the loading process, the confining pressure is kept stable by the strain servo control, and the speed of the upper loading plate is controlled to apply the axial force to obtain the stress-strain relationship curve and the volume-axis strain relationship curve of the corresponding confining pressure under different soil-rock interface contact parameters, such as shown in Figures 7 and 8.

It can be seen from Figures 7 and 8 that the stress-strain relationship curves of the unsaturated soil-rock mixture with the same rock content show obvious nonlinear characteristics. The initial linear segments coincide, and the peak principal stress difference increases with the increase of confining pressure. The five types of samples with rock content all show the characteristics of strain hardening, and with the increase of confining pressure, the phenomenon of strain hardening becomes more significant. From the volumetric strain-axial strain relationship curve, it can be seen that at low confining pressure, the specimens have undergone a deformation process from shear shrinkage to dilatancy. As the confining pressure increases, the dilatancy

deformation of the specimen gradually weakens at high confining pressure. During compression, the specimen basically exhibits shear deformation, and with the increase of strain, the growth rate of shear deformation tends to decrease. Under the same confining pressure, the larger the rock content of the unsaturated soil-rock mixture, the higher the peak strength value. The smaller the axial strain when the peak strength is reached, the more rock content and the greater the initial elastic modulus of the sample, which will enter the plasticity. After the deformation stage, the strain hardening characteristics are more pronounced.

4.3. Failure Mechanism of Unsaturated Soil-Rock Mixture under Different Soil-Rock Interface Parameters. Under various soil-rock interface parameters, the mesoscopic failure morphology of each sample during each axial strain process under confining pressure is shown in Figure 9.

It can be seen from Figure 9 that when the friction coefficient of the soil-rock interface is small, the unsaturated soil-rock mixture appears as a loose failure mode, with obvious open cracks, and when the friction coefficient is large, it appears as an overall failure. This is due to the broken stones and the soil. During the loading process, the gravel inside the soil-rock mixture moves and rotates. When there is no friction between the soil and the boulder or the friction is small, the movement of the boulder cannot drive the surrounding soil. The coordinated deformation of the body will leave a large gap behind it. When the soil behind it reaches a plastic state, the crushed stones can not play a restraint, making the shear failure zone of the soil-rock mixture extremely irregular and appearing to be circumscribed. When the interface friction coefficient is very large, the greater the occlusion between the rock and the surrounding soil, the more coordinated the deformation of the rock and the surrounding soil; the friction required for basic rotation and translation of the rock is very large, so only translation and dislocation occur. So the shear failure zone basically passes through the sharp corners of the rubble and seldom branches and bypasses the previous rubble.

4.4. Mesopermeability Test Analysis. In order to study the influence of the rock content of the soil-rock mixture on the macroscopic permeability, the test selects the rock content of 32%, 38%, 47%, 56%, and 65% and five conditions, respectively. When the crushed stone is in close contact with
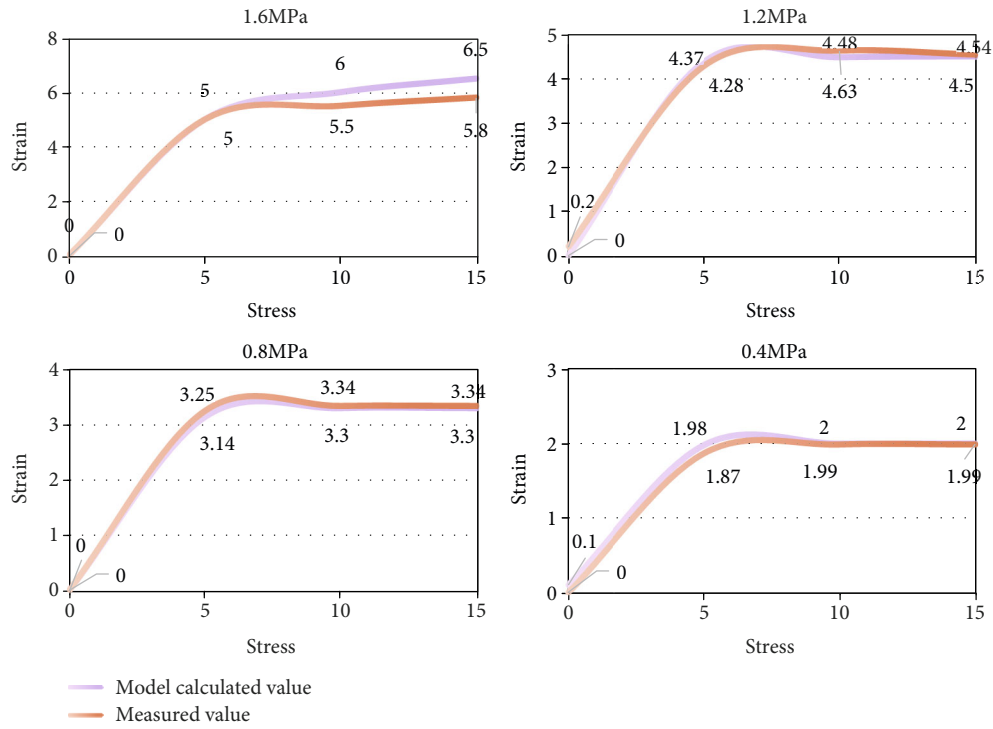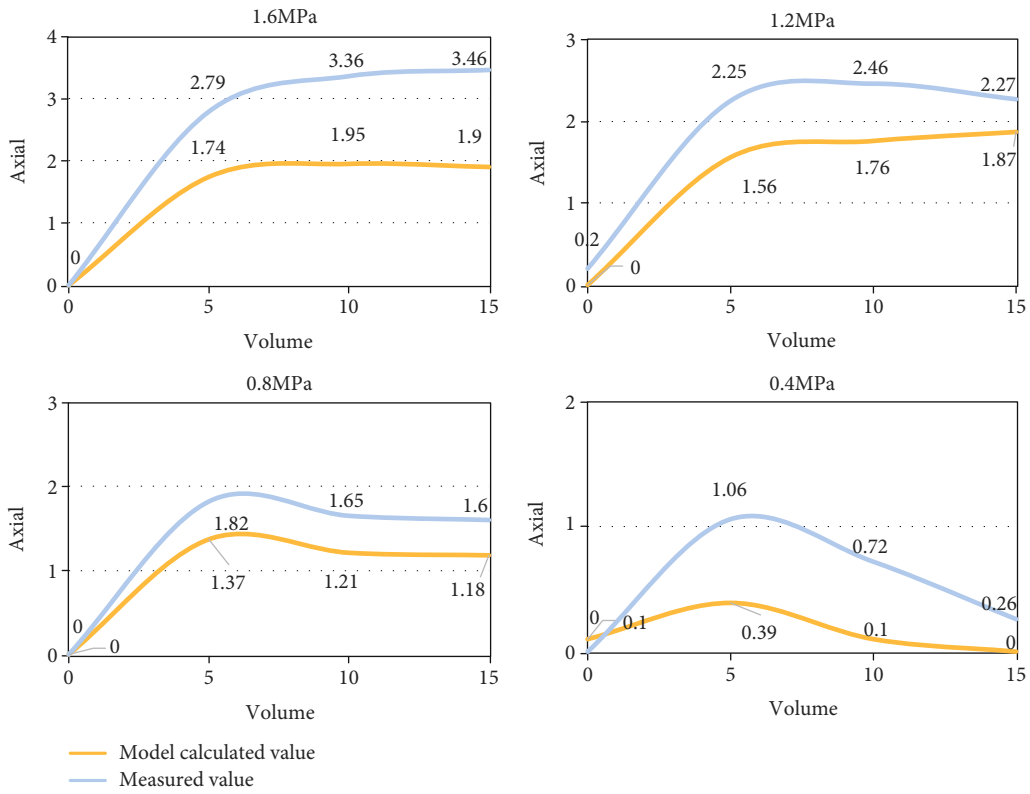
Figure 5: Stress-strain relationship curve.

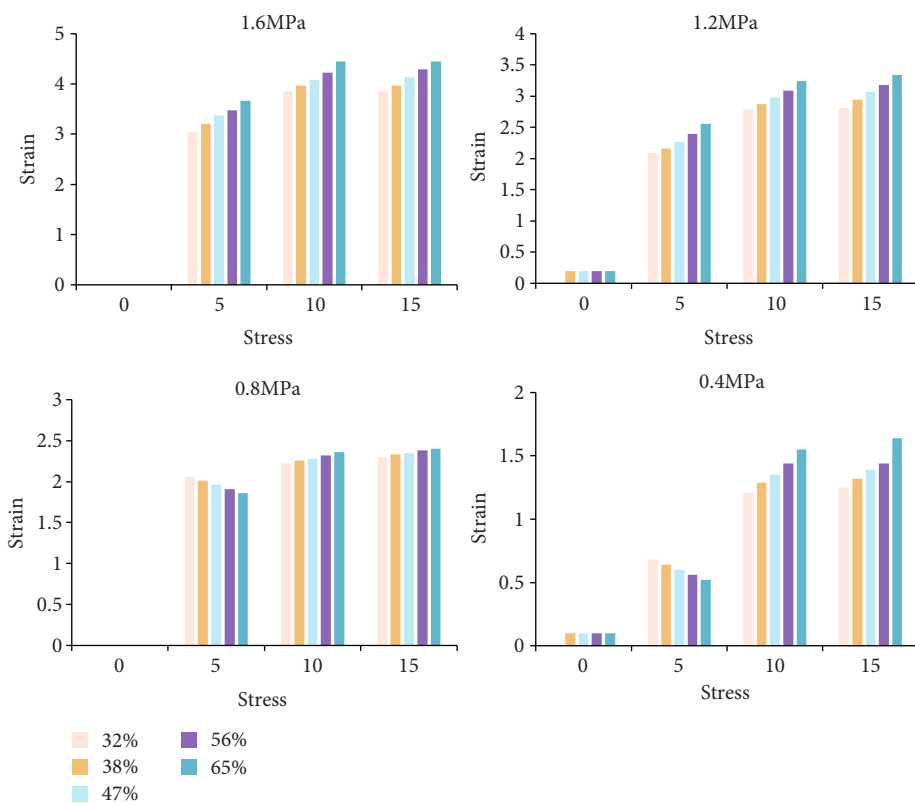Figure 6: Volume-axial strain relation curve.

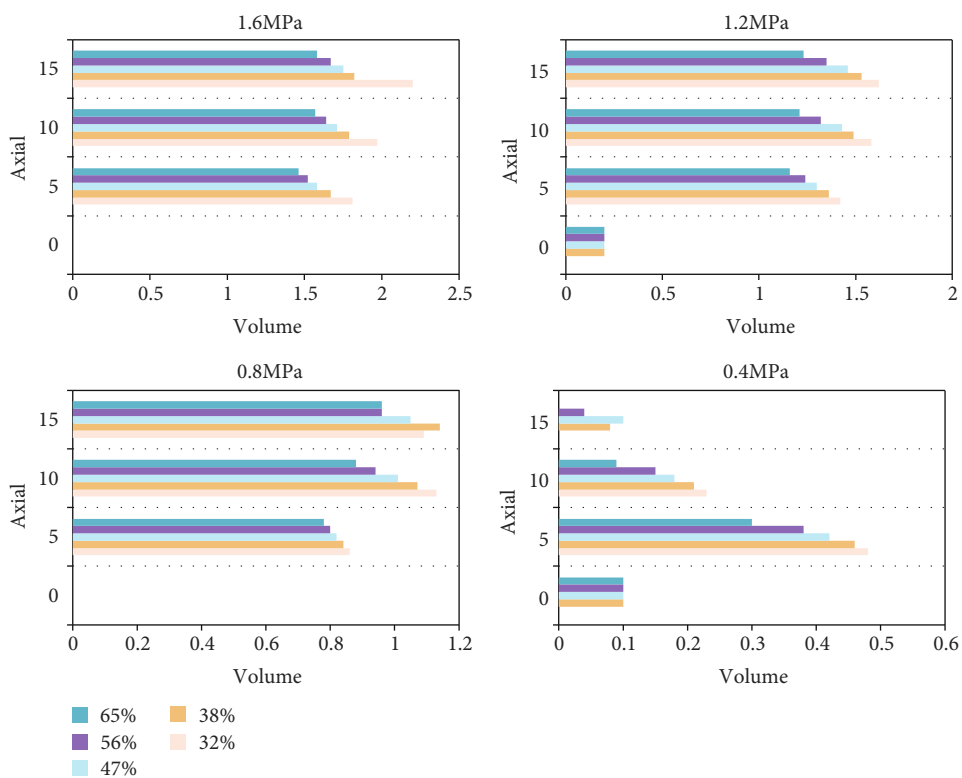Figure 7: Stress-strain relationship curve of different rock content under the same confining pressure.

Figure 8: Volume-axial strain curve of different rock content under the same confining pressure.
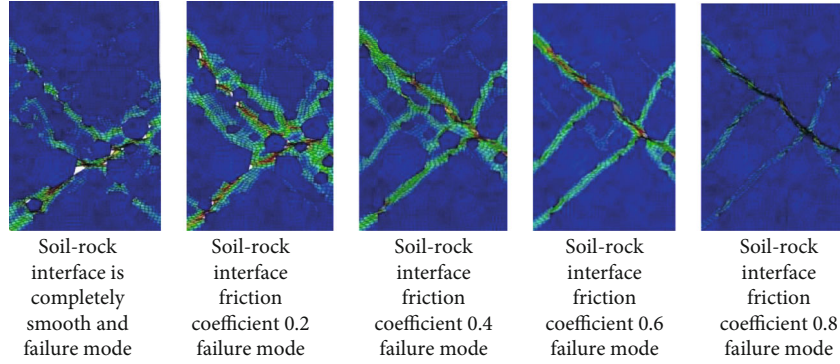
| Soil-rock interface is completely smooth and failure mode | Soil-rock interface friction coefficient 0.2 failure mode | Soil-rock interface friction coefficient 0.4 failure mode | Soil-rock interface friction coefficient 0.6 failure mode | Soil-rock interface friction coefficient 0.8 failure mode |

FIGURE 9: Final failure form of unsaturated soil-rock mixture.
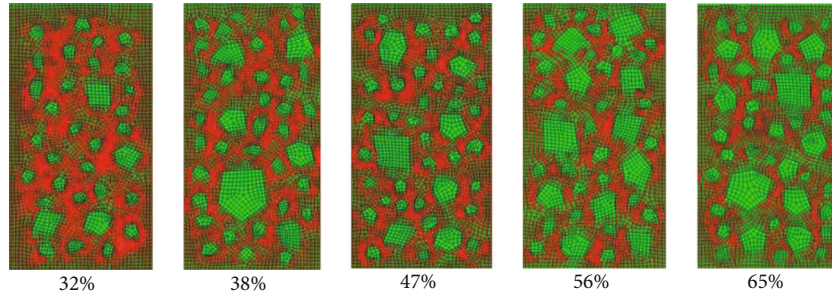

| 32% | 38% | 47% | 56% | 65% |

FIGURE 10: Characteristics of mesolevel seepage field of unsaturated soil-rock mixture with different rock content.

TABLE 3: Relationship curve between permeability coefficient and rock content of unsaturated soil-rock.

Osmotic pressure (MPa)	0	20	40	60	80
0.1	0.095	0.082	0.078	0.074	0.069
0.2	0.098	0.087	0.085	0.083	0.080
0.3	0.101	0.095	0.098	0.101	0.103
0.4	0.105	0.107	0.118	0.129	0.139

the soil and the permeability of the stone is not considered, the mesoseepage field distribution of each sample obtained through the numerical permeability test is shown in Figure 10.

According to the results of numerical experiment analysis, the relationship between the macropermeability coefficient of the soil-rock mixture and the rock content of the soil-rock mixture is drawn as the ordinate. The results are shown in Table 3.

It can be seen from Table 3 that the macroscopic permeability coefficient of soil-rock mixture changes with rock content obtained from the prediction of each mesostructure model and numerical experiment. It can be seen that when the rock is in close contact with the soil, when the pore water passes through the broken rock in the narrow soil between the rocks, the seepage rate is relatively large, and the pore water pressure contours are densely distributed. The pore water pressure of these parts on the surface drops faster. The narrower the channel, the denser the value, and the faster the pore water pressure drops. The permeability before and after the block rock is very small. Under the same seep-

age pressure, the macroscopic permeability coefficient of the unsaturated soil-rock mixture decreases with the increase of the rock content. This is mainly because the pore water flows through the pores in the unsaturated soil between the crushed stones. The increase in the rock content of the soil and the narrowing of the spacing between the crushed stones makes the soil more discontinuous, and the flow of pore water is more difficult.

5. Conclusions

In this paper, the purity, crystallinity, chemical structure, and micromorphology of graphene are characterized and analyzed at multiple levels through comprehensive testing methods such as microscopy, providing a reliable basis and basic guarantee for subsequent testing. Based on the random rock generation system, the corresponding unsaturated soil-rock mixture ABAQUS finite element program was compiled. Using the master-slave contact algorithm, the characteristics of the soil-rock interface, rock content, saturation, and dry humidity were proposed. After fusing the graphene composite material into the unsaturated soil-rock mixture, starting from the difference in circulation, the biaxial numerical test method is used to deeply analyze the influence of various factors such as soil-rock interface parameters, rock content, saturation, and dry and wet cycles. Study its mechanical properties and the microscopic damage mechanism and macroscopic mechanical behavior of unsaturated soil-rock mixtures. From the shape of the stress-strain relationship curve, the stress-strain relationship curves of different soil-rock interface parameters, rock

content, saturation, and the number of wet and dry cycles all show obvious nonlinear characteristics and strain hardening. As the confining pressure increases, the hardening becomes more obvious. The shear strength parameters of unsaturated soil-rock mixtures increase with the increase of soil-rock interface parameters. Finally, there is a comprehensive use of various microtesting methods to study the microscopic mechanism of graphene in the soil-rock mixture. When the soil-rock interface is completely smooth, the unsaturated soil-rock mixture sample is broken in bulk, with obvious open cracks and obvious dilatancy. When the interface parameter increases to a certain extent, the unsaturated soil-rock mixture is destroyed as a whole, and the dilatancy phenomenon is not very obvious. Both the constitutive model and the yield criterion of the numerical experiment in this paper adopt the Mohr Coulomb model, which has a certain gap with the results of the indoor experiment. Therefore, it is necessary to strengthen the theoretical research.

Data Availability

The data that support the findings of this study are available from the corresponding author upon reasonable request.

Conflicts of Interest

The authors declared no potential conflicts of interest with respect to the research, authorship, and/or publication of this article.

Acknowledgments

References

[1] S.-B. Tsai, R. Saito, Y.-C. Lin, Q. Chen, and J. Zhou, "Discussing measurement criteria and competitive strategies of green suppliers from a green law perspective," *Proceedings of the Institution of Mechanical Engineers, Part B: Journal of Engineering Manufacture*, vol. 229, 1_suppl, pp. 135–145, 2015.

[2] S.-B. Tsai, Y.-C. Lee, and J.-J. Guo, "Using modified grey forecasting models to forecast the growth trends of green materials," *Proceedings of the Institution of Mechanical Engineers, Part B: Journal of Engineering Manufacture*, vol. 228, no. 6, pp. 931–940, 2014.

[3] S. B. Tsai, Y. Z. Xue, P. Y. Huang et al., "Establishing a criteria system for green production," *Proceedings of the Institution of Mechanical Engineers, Part B: Journal of Engineering Manufacture*, vol. 229, no. 8, pp. 1395–1406, 2014.

[4] Y. Tang, Z. Chen, W. Feng, Y. Nong, C. Li, and J. Chen, "Combined effects of nano-silica and silica fume on the mechanical behavior of recycled aggregate concrete," *Nanotechnology Reviews*, vol. 10, no. 1, pp. 819–838, 2021.

[5] P. Wang, T. Yao, Z. Li et al., "A superhydrophobic/electrothermal synergistically anti-icing strategy based on graphene composite," *Composites Science and Technology*, vol. 198, article 108307, 2020.

[6] L. Zeng, J. Shi, J. Luo, and H. Chen, "Silver sulfide anchored on reduced graphene oxide as a high -performance catalyst for CO_2 electroreduction," *Journal of Power Sources*, vol. 398, pp. 83–90, 2018.

[7] L. Qin, D. Bian, Y. Zhao, X. Xu, and Y. Guo, "Study on the preparation and mechanical properties of alumina ceramic coating reinforced by graphene and multi-walled carbon nanotube," *Russian Journal of Applied Chemistry*, vol. 90, no. 5, pp. 811–817, 2017.

[8] L. Jin, Y. Zeng, L. Xia, and Y. Ye, "Experimental and numerical investigation of mechanical behaviors of cemented soil–rock mixture," *Geotechnical & Geological Engineering*, vol. 35, no. 1, pp. 1–18, 2016.

[9] P. Shan and X. Lai, "Influence of CT scanning parameters on rock and soil images," *Journal of Visual Communication and Image Representation*, vol. 58, no. 1, pp. 642–650, 2019.

[10] P. Shan and X. Lai, "Mesoscopic structure PFC~2D model of soil rock mixture based on digital image," *Journal of Visual Communication and Image Representation*, vol. 58, pp. 407–415, 2019.

[11] H. Xing, L. Liu, and Y. Luo, "Water-induced changes in mechanical parameters of soil-rock mixture and their effect on talus slope stability," *Geomechanics and engineering*, vol. 18, no. 4, pp. 353–362, 2019.

[12] M. Gao, H. Wang, Y. Wang, T. Shen, and W. Wu, "Flame retardancy and mechanical properties of a novel intumescent flame- retardant unsaturated polyester," *Journal of Vinyl and Additive Technology*, vol. 22, no. 3, pp. 350–355, 2016.

[13] X. H. Yang, Y. P. Zhu, N. Guo, Z. B. Shi, and G. L. Ran, "Research on effects of compactness and matric suction on strength deformation characteristics of soil-rock aggregate mixture," *Rock and Soil Mechanics*, vol. 38, no. 11, pp. 3205–3214, 2017.

[14] J. Peranic and Z. Arbanas, "Impact of the wetting process on the hydro-mechanical behavior of unsaturated residual soil from flysch rock mass: preliminary results," *Bulletin of Engineering Geology and the Environment*, vol. 79, no. 2, pp. 985–998, 2020.

[15] H. Z. Wei, W. J. Xu, C. F. Wei, and Q. S. Meng, "Influence of water content and shear rate on the mechanical behavior of soil-rock mixtures," *SCIENCE CHINA Technological Sciences*, vol. 61, no. 8, pp. 1127–1136, 2018.

[16] W. Tun Tun, T. Sato, H. Saito, and Y. Kohgo, "Mechanical properties and stress–dilatancy relationships of unsaturated soil under various cyclic loading conditions," *Acta Geotechnica*, vol. 15, no. 7, pp. 1799–1813, 2020.

[17] H. Toyota, S. Takada, and A. Susami, "Rate dependence on mechanical properties of unsaturated cohesive soil with stress-induced anisotropy," *Soils and Foundations*, vol. 59, no. 4, pp. 1013–1023, 2019.

[18] H. Toyota, S. Takada, and A. Susami, "Mechanical properties of saturated and unsaturated cohesive soils with stress-induced anisotropy," *Geotechnique*, vol. 68, no. 10, pp. 883–892, 2018.

[19] P. B. Xu, H. Xu, and H. M. Wen, "3D meso-mechanical modeling of concrete spall tests," *International Journal of Impact Engineering*, vol. 97, pp. 46–56, 2016.

[20] Y. Li, Z. Guan, Z. Wang et al., "3D meso-scale finite element modelling on cement paste corroded in sodium sulfate with X-ray CT technique," *Construction and Building Materials*, vol. 202, pp. 727–737, 2019.

[21] J. Suchorzewski, J. Tejchman, M. Nitka, and J. Bobiński, "Meso-scale analyses of size effect in brittle materials using DEM," *Granular Matter*, vol. 21, no. 1, pp. 9–15, 2019.

[22] D. Ghosh and E. M. Constantinescu, "Well-balanced, conservative finite difference algorithm for atmospheric flows," *AIAA Journal*, vol. 54, no. 4, pp. 1370–1385, 2016.

[23] J. Hajrasouliha, R. J. Nedoushan, M. Sheikhzadeh, and T. Dastan, "Meso-macro numerical modeling of noncircular braided composite parts based on braiding process parameters," *Composite Structures*, vol. 224, p. 111065, 2019.

[24] J. Chen and L. Wang, "Mechanical parameters of wheat in triaxial compression tests and meso-mechanics simulation," *Journal of Computational and Theoretical Nanoscience*, vol. 13, no. 9, pp. 6387–6394, 2016.

[25] P. F. Shan, "Image segmentation method based on K-mean algorithm," *EURASIP Journal on Image and Video Processing*, vol. 2018, no. 1, 9 pages, 2018.

[26] M. Abdolmaleky, M. Naseri, J. Batle, A. Farouk, and L. H. Gong, "Red-green-blue multi-channel quantum representation of digital images," *Optik*, vol. 128, pp. 121–132, 2017.

[27] M. Márton, F. Markolt, L. Szabó et al., "Den site selection of the European badger,Meles melesand the red fox,Vulpes vulpesin Hungary," *Journal of Vertebrate Biology*, vol. 65, no. 1, pp. 72–79, 2016.

[28] G. Okuma, D. Kadowaki, Y. Shinoda, T. Akatsu, O. Guillon, and F. Wakai, "Determination of the size of representative volume element for viscous sintering," *Journal- Ceramic Society Japan*, vol. 124, no. 4, pp. 421–425, 2016.

[29] W. Kim and S. Y. Choi, "An improved implicit time integration algorithm: the generalized composite time integration algorithm," *Computers & Structures*, vol. 196, pp. 341–354, 2018.

[30] Z. Wang, B. Wu, G. Xu, and O. S. Bursi, "An improved equivalent force control algorithm for hybrid seismic testing of nonlinear systems," *Structural Control & Health Monitoring*, vol. 25, no. 2, 2018.

[31] J. Li and K. Yu, "An alternative to the Bathe algorithm," *Applied Mathematical Modelling*, vol. 69, no. MAY, pp. 255–272, 2019.

[32] S. Ma and H. Yuan, "A continuum damage model for multiaxial low cycle fatigue of porous sintered metals based on the critical plane concept," *Mechanics of Materials*, vol. 104, pp. 13–25, 2017.

[33] L. I. Jian, S. Chen, and L. Jiang, "On implicit integration of the bounding surface model based on swell-shrink rules," *Applied Mathematical Modelling*, vol. 40, no. 19-20, pp. 8671–8684, 2016.

[34] J. F. Chen and E. V. Morozov, "A consistency elasto-viscoplastic damage model for progressive failure analysis of composite laminates subjected to various strain rate loadings," *Composite Structures*, vol. 148, no. Jul., pp. 224–235, 2016.

Research Article

Optimization of Flocculation and Sedimentation Parameters of Total Tailing Filling Material Based on Response Surface Method

Gang Li [iD],[1,2] **Dengpan Qiao** [iD],[1] **and Jincheng Xie**[1]

[1]*College of Land and Resources Engineering, Kunming University of Science and Technology, Kunming, 650000 Yunnan, China*
[2]*Guizhou Coal Mine Design Research Institute Co., Ltd, Guiyang, 550000 Guizhou, China*

Correspondence should be addressed to Dengpan Qiao; 20030033@kust.edu.cn

Using sulfide ore and oxide ore tailings of a tin mine in Yunnan as raw materials, 17 groups of flocculation settling tests were designed by Box-Behnken in Design-Expert software, and the settling velocity and underflow concentration of mixed tailings with sulfur/oxygen ratio of 5 : 5 were studied. The effects of volume concentration, flocculant unit consumption, and flocculant concentration on settling velocity and underflow concentration were explored, and the optimal parameters of settling velocity and underflow concentration were obtained. *Results*. The best mixing parameters of mixed tailings are volume concentration of 17.66%, flocculant unit consumption of 39.589 g/t, and flocculant concentration of 0.195%. At this time, the settling speed is 2.231 mm/s and the underflow concentration is 65.289%. The flocculation settling velocity under this parameter condition was tested, and the experimental results were consistent with the predicted results of the model. This surface method can be used to design the flocculation and settlement test of mine tailings, which has certain guiding significance for the selection of parameters in actual production of mines.

1. Introduction

With the continuous development of social economy, people's demand for mineral resources is higher and higher. The deepening of resources and the large-scale stacking of solid waste have become the difficult problems facing the development of mining industry. Filling method is widely used as a clean and efficient mining method, which can solve the stacking of surface tailing waste [1–3].

The filling method needs to make tailings and other solid wastes into slurry and transport them to the goaf. The thickening and dehydration of tailings is the premise of the filling pulping process. The traditional tailing dewatering method is natural sedimentation, which can improve the sedimentation efficiency by increasing the sedimentation area. However, with the progress of beneficiation technology, the particle size of tailings becomes smaller and smaller, and the tailings become finer and finer. There are some problems in the use of natural sedimentation, such as serious fine particle overflow and slow sedimentation speed [4]. Adding flocculant to the tailing slurry can improve the settling velocity of tailings and reduce

the overflow concentration [5]. Therefore, many scholars have carried out a lot of research work on the process of flocculation sedimentation. By studying the settling velocity of muddy liquid surface, based on the settling time, unit consumption of flocculant, and settling velocity of muddy liquid surface, the action mechanism of unit consumption of flocculant in different settling stages was obtained [6]. The law of multifactor flocculation and sedimentation is studied, and the important factors affecting flocculation and sedimentation are selected by the Design-Expert software, and the parameters are optimized [7]. Through the static flocculation sedimentation test of total tailings, the solid flux model of total tailing flocculation sedimentation is established, and the influence law of different feeding speed on sedimentation in the process of dynamic flocculation sedimentation is explored [8]. The support vector machine (SVM) regression prediction model is established, and the model parameters are optimized by genetic algorithm to predict the settlement velocity [9]. A simple regression model of sedimentation rate was obtained by fitting the static flocculation sedimentation test according to the feed concentration and unit consumption of flocculant [10].

It can be seen from the above reference that a series of tests are needed to determine the parameters of flocculation and sedimentation. Summarize the rules from the experiment, and finally determine the addition range of parameters. The surface response method has some advantages in this process. The test scheme can be designed by determining the variation range of independent variables, and the overall test can be simplified, and at the same time, the optimization scheme within the variation range of independent variables can be obtained.

In this paper, aiming at the two kinds of tailings of sulfide ore and oxide ore of a tin mine, the indoor static flocculation sedimentation test of sulfide ore tailings, oxide ore tailings, and three mixed tailings with different sulfur oxygen ratio are carried out to study the influence of different particle size composition of tailings on the sedimentation rate. For the mixed tailings with sulfur oxygen ratio of 5 : 5, the response surface method is used to design the test, explore the influence law of various parameters on flocculation sedimentation effect, and optimize the feeding parameters.

2. Experimental Materials

2.1. Basic Physical Parameters of Total Tailings. There are mainly two kinds of tailings of a tin mine in Yunnan: oxidized ore tailings and sulfide ore tailings. Specific parameters are shown in Table 1.

As shown in Table 1, the apparent density of sulfide tailings is 3042 kg/m^3. The apparent density of oxidized tailings is 2861 kg/m^3. The density of sulfide tailings is higher. The loose density of sulfide tailings is 1365 kg/m^3. The loose density of oxidized tailings is 1245 kg/m^3. The stacking compactness of sulfide tailings is 0.449, and the porosity is 0.551. The stacking compactness of oxidized tailings is 0.435, and the porosity is 0.565. In terms of loose density, packing compactness, and porosity, they are relatively close.

From Table 2, showing the mineral composition analysis, it can be seen that the main components of the tailings are calcite and mica, accounting for 40–50% and 23–35%, respectively. The chemical properties of the tailings are relatively stable, and there is no chemical reaction with water.

2.2. Tailing Grading. The two kinds of tailings are obviously different in appearance, gradation, and basic physical parameters. The grading analysis of two kinds of tailings is carried out. The detailed results of tailings grading are shown in Figure 1.

It can be seen from the figure that the tailings of sulfide ore are mainly distributed below -500 mesh, accounting for 40.87%. The average particle size of sulfide tailings is 84 μm. The median particle size was 40 μm. The particle size of 60% tailings is 53 μm. Oxidized tailings are mainly distributed below -500 mesh, accounting for 46.11%, and the median particle size is 31 μm. 60% of oxidized ores is below 40 μm. The average particle size and median particle size of oxidized ore tailings are smaller than sulfide ore tailings, which shows that in morphology, oxidized ore tailings are finer than sulfide ore tailings. Both kinds of tailings are distributed below -500 mesh. Generally speaking, the particle size of the two filling

TABLE 1: Basic physical parameters of sulfide ores.

Type	Apparent density/ (kg/m^3)	Loose density/ (kg/m^3)	Packing compactness	Porosity
Sulfide ores	3042	1365	0.449	0.551
Oxidized ores	2861	1245	0.435	0.565

TABLE 2: Analysis results of mineral composition of tailings.

Mineral name	Mineral content of sulfide ores (%)	Mineral content of oxidized ores (%)
Calcite	40–50	35–40
Mica	25–35	25–40
Fluorite	5–10	5–10
Dolomite	5–10	5–15
Amphibole	1–5	5-10

tailings is too fine [11, 12]. If natural settlement is adopted, it will cause problems such as too slow speed, insufficient underflow concentration, and high overflow concentration. Therefore, it is necessary to adopt flocculation settlement method to improve the settlement effect of tailings and realize stable sand discharge of sand bin.

3. Flocculation Sedimentation Mechanism

The polymer flocculant aggregates the particles through "bridging action" to form flocculation groups [13, 14]. The action mechanism is that some active groups in the molecules are adsorbed on the surface of the particles, the rest extend into the solution to form unstable molecules, and the particles with vacancies on other surfaces contact these extended parts to form aggregates, so as to complete the "bridging" between the particles. If the flocculant is excessive and the polymer active group completely wraps the particles, there is no other vacancy on the particle surface for the extended active group to contact, and the bridging action will not be completed. Therefore, the addition amount of flocculant has a reasonable range, and the larger the flocculant is, the better the flocculation effect is. Different flocculant types will produce different effects. Polymer flocculants can be generally divided into anionic, cationic, and nonionic types. Because different types of flocculants have different molecular composition and flocculation structure, and their action forms and effects are significantly different in solution environments with different pH values and different charges, the polymer flocculant rt301 with polyacrylamide model is selected for flocculation sedimentation test in this test.

4. Flocculation Sedimentation Test of Mixed Tailings

4.1. Experimental Design. In order to study the interaction between flocculant and tailing slurry sedimentation velocity and underflow concentration, a tailing flocculation sedimentation test was designed. Considering that in the actual
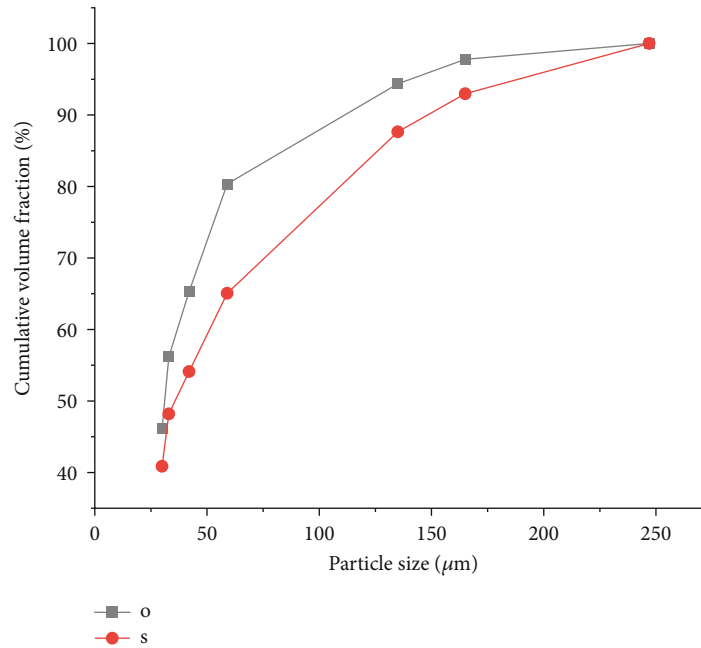
FIGURE 1: Grain size composition of full tailings.

production and application of the mine, sulfide tailings and oxidized tailings will be mixed and discharged in the proportion of 5 : 5 in most cases. The volume concentration range of the mixed slurry discharged by the concentrator is 15%-21%. Most research results believe that the main influencing factors of flocculation sedimentation are slurry volume concentration, flocculant unit consumption, and flocculant solution concentration. Therefore, based on the above conditions, the volume concentration of test slurry is designed to be 15%~21%, the unit consumption of flocculant is 20~60 g/T, and the flocculant concentration is 0.1~0.3%.

Response surface method [15, 16] can intuitively optimize the feeding parameters and predict and analyze the objectives. It can not only conduct single-factor analysis but also consider the impact of parameter interaction on the objectives. The volume concentration X_1 of tailing slurry, unit consumption X_2 of flocculant, and flocculant concentration X_3 were selected as independent variables, and the sedimentation velocity Y_1 and underflow concentration Y_2 were selected as response values. Box-Behnken in the Design-Expert software is used to design the test scheme of three factors and three levels and analyze the influence law of the interaction of various variables on sedimentation velocity and underflow concentration. The levels of various factors are shown in Table 3.

4.2. Test Result.
In the settlement test, the settlement velocity of solid particles in the slurry is mainly determined by observing the position of the solid-liquid interface, as shown in the figure. The settling velocity and underflow concentration of solid particles are calculated by recording the height and time of solid-liquid interface.

Figure 2 shows the settlement process of tailings with the passage of time. With the passage of time, the height of settlement interface is getting lower and lower. The settlement

TABLE 3: Factors and levels of response surface methodology.

Independent variable	Horizontal coding		
	-1	0	1
Volume concentration $(X_1)/(\%)$	15	18	21
Unit consumption of flocculant $(X_2)/(g/t)$	20	40	60
Flocculant solution concentration $(X_3)/(\%)$	0.1	0.2	0.3

speed of tailings can be calculated by reading the height of settlement interface.

The specific test scheme and results are shown in Table 4. The multiple regression equations of response value, sedimentation velocity (Y_1), and underflow concentration (Y_2) are obtained by multiple fitting of the test results with design expert:

$$Y_1 = -0.63 + 0.35X_1 + 0.02X_2 + 1.94X_3 - 1.25 \\ \times 10^{-4}X_1X_2 - 0.067X_1X_3 - 7.5 \times 10^{-3}X_2X_3 \quad (1) \\ - 0.012X_1^2 - 2.19 \times 10^{-4}X_2^2 - 1.525X_3^2,$$

$$Y_2 = 7.197 + 4.07X_1 + 0.48X_2 + 47.42X_3 - 1.125 \\ \times 10^{-3}X_1X_2 + 1.09X_1X_3 - 0.18X_2X_3 - 0.096X_1^2 \quad (2) \\ - 5.34 \times 10^{-3}X_2^2 - 149.9X_3^2.$$

During the experiment, the experimental concentration, flocculant unit consumption and flocculant concentration can be determined. However, the granularity of tailings in each experiment has a small amount of uncertainty. Therefore, under the same experimental conditions, there will be some differences in the experimental results, but these
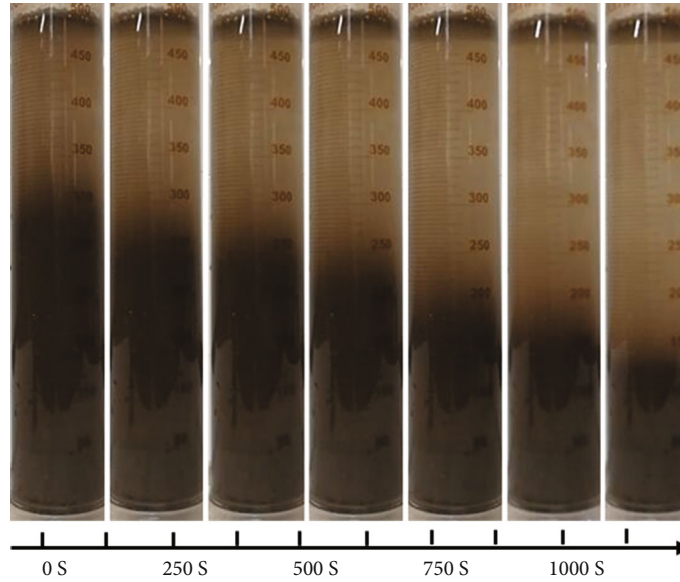
0 S 250 S 500 S 750 S 1000 S

Figure 2: Schematic diagram of settlement test.

Table 4: Response surface test design and results.

Number	Code value			Actual value		Predicted value	
	X_1	X_2	X_3	Y_1	Y_2	Y_1	Y_2
1	0	0	0	2.21	65.76	2.20	65.58
2	-1	0	1	2.38	60.66	2.37	60.47
3	1	0	-1	1.81	65.12	1.82	65.31
4	0	0	0	2.18	65.38	2.20	65.58
5	-1	1	0	2.28	60.41	2.28	60.28
6	0	-1	1	2.11	62.12	2.11	62.26
7	0	-1	-1	2.12	61.88	2.12	61.56
8	0	0	0	2.19	65.81	2.20	65.58
9	1	-1	0	1.74	64.89	1.73	65.02
10	1	0	1	1.74	66.22	1.74	65.95
11	0	1	1	2.04	61.29	2.04	61.61
12	-1	0	-1	2.37	60.87	2.37	61.14
13	1	1	0	1.68	65.01	1.68	64.96
14	0	1	-1	2.11	62.49	2.11	62.35
15	0	0	0	2.22	65.75	2.20	65.58
16	0	0	0	2.19	65.19	2.20	65.58
17	-1	-1	0	2.31	60.02	2.31	60.07

differences are very small, and there will be no serious deviation from the correctness of the experimental results.

4.3. Reliability Test of Regression Model Based on Response Surface Method. The model reliability of multiple regression equations of sedimentation velocity (Y_1) and underflow concentration (Y_2) is tested. Figure 3 shows the comparison between the predicted values of the sedimentation velocity and underflow concentration model and the test values. It can be seen from Figure 3 that the test values are evenly distributed on the fitting line and both sides. It can be seen that

the error between the two is small, which proves that the sedimentation velocity and underflow concentration model are reliable.

Goodness of fit (R^2) represents the difference between the measured value and the regression value, and the value is between 0 and 1. The closer R^2 is to 1, the higher the reliability of the model is. The R^2 values of sedimentation velocity and underflow concentration are 0.998 and 0.99, respectively, which are close to 1, which means that the model is very reliable. The p value of the model represents the significance of each factor, and the p value less than 0.05 represents the significance of the model. The p values of the regression models of sedimentation velocity and underflow concentration are less than 0.0001, and the residuals of the two regression models are not significant, which represent that the model is very significant.

5. Influence of Response Surface Parameters on Flocculation Sedimentation

5.1. Effect of Single Factor of Response Surface Parameters on Flocculation Settlement of Mixed Tailings. It can be seen from Figure 4 that the influence law of various factors on flocculation sedimentation is as follows:

(1) Keeping the unit consumption of flocculant and flocculant concentration unchanged, with the increase of volume concentration, the sedimentation rate gradually decreases and the impact is more intense. The underflow concentration first gradually increases and then tends to be flat, which indicates that the impact of the continuous increase of the initial feed volume concentration on the underflow concentration is decreasing

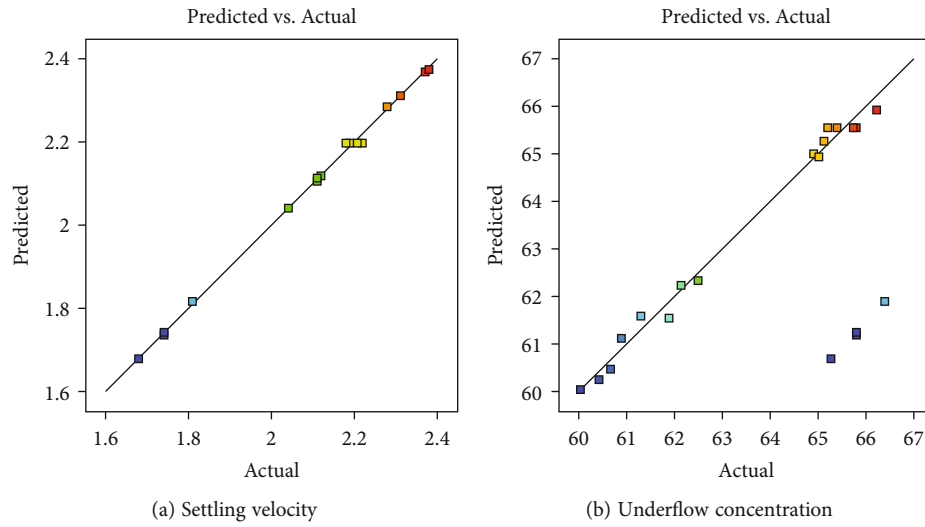(2) Keep the volume concentration and flocculant concentration unchanged. With the increase of

(a) Settling velocity

(b) Underflow concentration

FIGURE 3: Comparison between experimental value and predicted value.

(a) Settling velocity
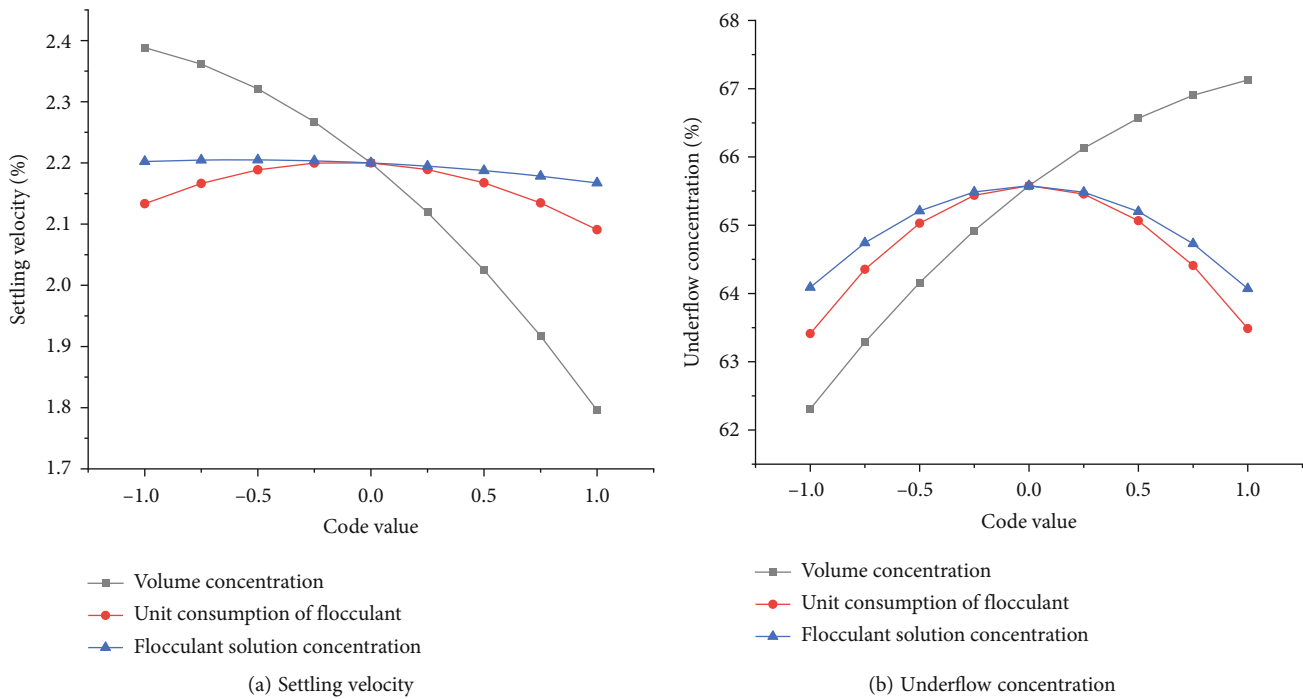
(b) Underflow concentration

FIGURE 4: Single-factor analysis of response surface.

flocculant unit consumption, the sedimentation velocity and underflow concentration increase first and then decrease and reach the maximum in the range of 37-41 g/T. This shows that if the unit consumption of flocculant exceeds the optimal action range, the sedimentation effect will become worse. This is because the fine tailings adsorb a large number of flocculating molecules to produce too much floc water, which will worsen the driving effect of coarse particles on fine particles. The steric effect of a large number of polymer adsorption membranes makes the tailing particles

repel each other; the siltation layer occupying the bottom space hinders the downward sedimentation of particles and worsens the compaction and dehydration process in the later stage, and too much flocculation structure reduces the underflow concentration

(3) Keep the volume concentration and unit consumption of flocculant unchanged. With the increase of flocculant concentration, the sedimentation velocity changes little, and the underflow concentration increases first and then decreases, reaching the maximum at about 0.2%.

TABLE 5: Variance analysis of settlement velocity model.

Source	Sum of square	df	Mean square	F value	p value	
Model	0.7995	9	0.0888	495.5	<0.0001	Significant
A-volume concentration	0.7021	1	0.7021	3916.17	<0.0001	
B-unit consumption of flocculant	0.0036	1	0.0036	20.15	0.0028	
C-flocculant solution concentration	0.0025	1	0.0025	13.67	0.0077	
AB	0.0002	1	0.0002	21.25	0.2996	
AC	0.0016	1	0.0016	8.92	0.0203	
BC	0.0009	1	0.0009	5.02	0.06	
A^2	0.0489	1	0.0489	272.66	<0.0001	
B^2	0.0324	1	0.0324	180.84	<0.0001	
C^2	0.001	1	0.001	5.46	0.0521	
Residual	0.0013	7	0.0002			
Lack of fit	0.0002	3	0.0001	0.216	0.8807	Not significant

TABLE 6: Analysis of variance of underflow concentration model.

| Source	Sum of square	df	Mean square	F value	p value	
Model	82.37	9	9.15	78.59	<0.0001	Significant
A-volume concentration	46.46	1	46.46	399.01	<0.0001	
B-unit consumption of flocculant	0.0105	1	0.0105	0.0903	0.7726	
C-Flocculant solution concentration	0.0006	1	0.0006	0.0053	0.9442	
AB	0.0182	1	0.0182	15.33	0.7042	
AC	0.429	1	0.429	3.68	0.0964	
BC	0.5184	1	0.5184	4.45	0.0728	
A^2	3.12	1	3.12	26.84	0.0013	
B^2	19.17	1	19.17	164.66	<0.0001	
C^2	9.46	1	9.46	81.25	<0.0001	
Residual	0.8152	7	0.1165			
Lack of fit	0.5089	3	0.1696	2.22	0.2288	Not significant
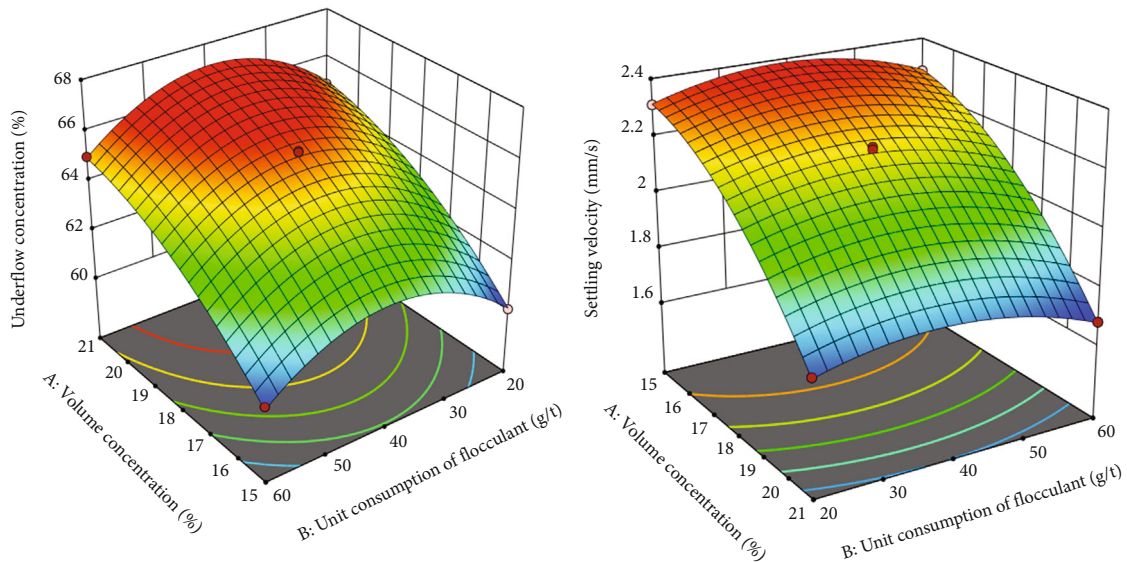
FIGURE 5: Interaction analysis of response surface factors.

5.2. Effect of Interaction of Response Surface Parameters on Flocculation and Sedimentation of Mixed Tailings. From the variance analysis of sedimentation rate and underflow concentration (as shown in Tables 5 and 6), it can be seen that the *F* value of volume concentration and flocculant unit consumption AB is the largest, which means that the interaction between them has the most significant impact on the flocculation and sedimentation of mixed tailings. Keep the flocculant concentration unchanged at 0.2%. Analyze the impact of volume concentration and flocculant unit consumption on sedimentation rate and underflow concentration, as shown in Figure 5. It can be seen from the figure that the sedimentation rate and underflow concentration are affected by the unit consumption of flocculant, and both increase first and then decrease. The best unit consumption of flocculant is in the range of 37-41 g/T. The increase of volume concentration makes the sedimentation velocity gradually smaller. The volume concentration increases from 15% to 18%, the velocity decrease range is about 7.9%, the volume concentration increases from 18% to 21%, and the velocity decrease range is about 18.36%, which indicates that the influence on the sedimentation velocity becomes more and more intense with the continuous increase of volume concentration. The underflow concentration increases with the increase of volume concentration, the volume concentration increases from 15% to 18%, the increase range of underflow concentration is about 5.2%, while the volume concentration increases from 18% to 21%, and the increase range of underflow concentration is about 1.8%, which indicates that the influence on underflow concentration decreases with the increase of volume concentration. With the increase of volume concentration, the influence of unit consumption of flocculant on sedimentation velocity and underflow concentration is decreasing, which proves that the influence of volume concentration on sedimentation effect is greater than that of unit consumption of flocculant.

5.3. Parameter Optimization. The Design-Expert software is used to optimize the results of flocculation sedimentation test. The underflow concentration and sedimentation velocity are the largest. The best parameters calculated by the model are feed volume concentration 17.66%, flocculant unit consumption 39.589 g/t, and flocculant concentration 0.195%. The sedimentation velocity is 2.231 mm/s, and underflow concentration is 65.289%. Taking the volume concentration of 17.7%, the unit consumption of flocculant 39 g/T, and the flocculant concentration of 0.2% as the actual test parameters, a flocculation and sedimentation test was designed.

The settling velocity is 2.247 mm/s, and the underflow concentration is 65.77%, which is basically consistent with the optimization results. The test results prove the correctness of the optimization model.

6. Conclusion

In this paper, the slurry flocculation sedimentation tests under different slurry volume concentration, flocculant unit consumption, and flocculant solution concentration are designed, and the test results are analyzed and studied by response surface method. The following conclusions are drawn:

(1) The effect of flocculation and sedimentation is not only affected by single factors, but also by the interaction between factors, especially the interaction of volume concentration and unit consumption of flocculant

(2) Based on the research results of response surface method, the optimal mixing parameters of mixed ore tail mortar with sulfur oxygen ratio of 5 : 5 are predicted. The volume concentration is 17.66%, the unit consumption of flocculant is 39.589 g/t, the flocculant concentration is 0.195%, the settlement velocity is 2.231 mm/s, and the underflow concentration is 65.289%

Data Availability

The data that support the findings of this study are available from the corresponding author upon reasonable request.

Conflicts of Interest

The authors declared no potential conflicts of interest with respect to the research, authorship, and/or publication of this article.

Acknowledgments

References

[1] W. Aixiang, Y. Ying, C. Haiyong, C. Shunman, and H. Yue, "Development status and trend of paste technology in China," *Journal of Engineering Science*, vol. 40, no. 5, pp. 517–525, 2018.

[2] W. Aixiang, W. Yong, and W. Hongjiang, "Present situation and trend of paste filling technology," *Metal Mine*, vol. 7, pp. 1–9, 2016.

[3] Q. Dengpan, C. Weihua, Z. Lei, Y. Weixin, W. Xianlai, and H. Wang, "Modern mining concept and filling mining," *Science and Engineering of Nonferrous Metals*, vol. 2, no. 2, pp. 7–14, 2011.

[4] H. Hua and S. Henghu, "Development of mine filling technology and new paste like filling technology," *China mining*, vol. 6, pp. 49–52, 2001.

[5] S. Xiuzhi, H. Haiyan, L. M. Du Xianghong, and W. Huaiyong, "Experimental study on flocculation settlement of mortar liquid at the end of vertical sand bin. Mining and Metallurgy," *Engineering*, vol. 30, no. 3, pp. 1–3+11, 2010.

[6] Z. Qinli, W. Shi, and W. Xinmin, "Influence law of unit consumption of flocculant on settling velocity of muddy liquid surface of full tail mortar," *Chinese Journal of nonferrous metals*, vol. 27, no. 2, pp. 318–324, 2017.

[7] W. Aixiang, Z. Liang, Y. Shenghua, and W. Leiming, "Influencing factors of flocculation settlement of full tailings,"

Chinese Journal of Nonferrous Metals, vol. 26, no. 2, pp. 439–446, 2016.

[8] S. Caixing, G. Lijie, and C. Xin, "Static and dynamic flocculation sedimentation characteristics of total tailings," *Chinese Journal of nonferrous metals*, vol. 31, no. 1, pp. 194–202, 2021.

[9] X. Wang, Z. Jianwen, and Z. Deming, "Optimal prediction model of flocculation settling velocity of full tailings," *Chinese Journal of Nonferrous Metals*, vol. 25, no. 3, pp. 793–798, 2015.

[10] J. Huazhe, W. Wang Hongjiang, J. X. Aixiang, Y. Qingwen, and L. Xiang, "Law and mechanism of flocculation and sedimentation of total tailings," *Journal of Beijing University of science and technology*, vol. 32, no. 6, pp. 702–707, 2010.

[11] Y. Fa and Z. Lin, "Experimental study on filtration of Meishan fine tailings," *Journal of Anhui University of Technology (NATURAL SCIENCE EDITION)*, vol. 27, no. S1, pp. 94–97, 2010.

[12] F. Xiangjun, *Hydraulics of Slurry and Granular Material Transportation*, Tsinghua University Press, Beijing, 1994.

[13] Z. Jun, R. Junpeng, Z. Jinkang, and M. Xiaoyun, "Research progress of polymer flocculants," *Chemical Technology and Development*, vol. 50, no. 7, pp. 35–37, 2021.

[14] W. Hong-Jiang, P. Qing-Song, Y. Ying, and G. Jia-Bin, "Research status and prospect of thickening technology for metal tailings," *Chinese Journal of Engineering*, vol. 1, 2022.

[15] F. Ziguo, Q. Dengpan, G. Zhonglin, X. Jincheng, H. Fei, and W. Jiaxin, "Experimental study on mix proportion and strength of waste rock aeolian sand cement based on RSM-BBD," *Journal of coal*, vol. 43, no. 3, pp. 694–703, 2018.

[16] Q. Gao, X. Yang, W. Zhenjiang, C. Dexin, and H. Jianyuan, "Optimization of mixed aggregate filling slurry ratio based on RSM-BBD," *Journal of Hunan University (NATURAL SCIENCE EDITION)*, vol. 46, no. 6, pp. 47–55, 2019.

Research Article

Construction of MPEG-PCL Nanomicelle Ocular Drug Delivery Vector and Its Application in the Treatment of Hypertensive Fundus Disease

Hongxiao Xu,[1] **Jingxing Liu,**[2] **Zhaoxia Teng,**[3] **Ming Ru,**[1] **Zhaoping Wang** ,[4] **and Yingcui Wang** [1]

[1]*Department of Cardiology, Qilu Hospital (Qingdao), Cheeloo College of Medicine, Shandong University, Qingdao, 266035 Shandong, China*

[2]*Emergency Department, Qingdao Municipal Hospital (Group), Qingdao NO.9 People's Hospital, Qingdao, 266000 Shandong, China*

[3]*Department of Endocrinology, Qingdao Municipal Hospital (Group), Qingdao NO.9 People's Hospital, Qingdao, 266000 Shandong, China*

[4]*Department of Emergency, Qilu Hospital (Qingdao), Cheeloo College of Medicine, Shandong University, Qingdao, 266035 Shandong, China*

Correspondence should be addressed to Zhaoping Wang; wang_zp2008@163.com
and Yingcui Wang; 199462000803@email.sdu.edu.cn

With the continuous development of society and the continuous development of technology, people's living standards have gradually improved, and the development of new things has gradually entered a new agenda. Alcoholism has gradually taken over most people's lives. Excessive drinking can lead to excessive alcohol content in the body, which is harmful to the liver. The stomach and other organs are affected, and the formation of high blood pressure is directly related to excessive drinking. And hypertensive patients are prone to have some adverse reactions and cause other more serious diseases. Hypertensive ocular fundus disease is one of its complications. Hypertensive ophthalmopathy is caused by abnormal changes in the retina, which can be very harmful. Patients with low rates and blindness can cause vision loss. Such diseases must be treated in time to allow patients to get rid of the troubles of the disease as soon as possible and restore their quality of life. In the treatment of hypertensive fundus disease, low-intensity laser radiation combined with nanomicelle ocular drug delivery carrier treatment has achieved a relatively ideal treatment effect. This article adopts the comparative treatment method and selects 120 patients with hypertensive ocular fundus disease admitted to X Hospital from 2018 to 2020 and evenly distributes them into the experimental group and the control group for comparative treatment experiments. Conclusions are obtained based on the analysis of treatment data. Related factors analyzed include age, gender, whether retinal laser photocoagulation has been performed before, and whether anti-VEGF treatment has been performed before surgery. The experimental results proved that there was no difference in the overall quality of life between the two groups before the treatment and at the end of the first course of treatment ($P > 0.05$), and the overall quality of life of the experimental group was higher than that of the control group until the end of the second course of treatment ($P < 0.05$). Hypertensive fundus disease is very harmful. If it is not treated in time, it will cause blindness in patients. In the treatment of hypertensive fundus disease, the use of low-intensity laser irradiation combined with MPEG-PCL nanomicelle therapy is beneficial to the recovery of vision and blood flow. The change index can guarantee the safety of treatment at the same time, which is worthy of clinical promotion.

1. Introduction

Ophthalmic diseases have more complex causes, more different diseases, and more variable conditions and belong to clinical ophthalmic diseases. It will seriously affect the vision of the patient and may even cause blindness. Therefore, in order to effectively improve the vision of patients, the above-mentioned various consequences must be effectively prevented. Effective treatment of patients with bottom disease is very important. The traditional method of administration can make the drug concentration in the retina reach a higher level, but the half-life of the drug in the vitreous is shorter. Therefore, chronic uveitis requires repeated injections and patient compliance is poor. In order to solve the above problems, nanomaterials have emerged as different carriers for drugs. Compared with traditional drug delivery methods, the use of nanomaterials to distribute drugs to treat eye diseases has great advantages. Drug nanoformulations can target drug delivery, extend the time of drug action, improve drug bioavailability, and reduce drug dosage and side effects.

Researchers at home and abroad have conducted a lot of research on the problem of blood vessel retrieval in retinal images, and new methods are constantly emerging. Foreign scholars are interested in classifier methods [1, 2]. The classifier method is mainly applied in two stages. First, perform spatial connection region segmentation through a basic algorithm, and then use peripheral features to divide the selected region into blood vessels and nonvessels. The classifier design only uses the gray matter information of blood vessels, and the influence of external conditions on the segmentation results cannot be excluded. The proportion information of the segmented object can only be obtained after the segmentation is completed, and must be used in combination with other methods, and cannot be directly used in the application field of the basic segmentation algorithm. Fengping and Weixing cited the filter operator used in air road detection and designed a classifier for blood vessel segmentation [3]. GeethaRamani and Balasubramanian use teaching samples to perform machine learning to segment samples and unknown objects [4]. Rodrigues and Marengoni divided 12 groups by calculating the average value and change of the gray pixel value under the line segment with an interval of $\pi/12$ and divided into the final blood vessel segmentation method by the support vector machine method [5].

With the rapid development of the Internet of Things technology in China, various hospitals have also accelerated the construction of medical intelligence and built a hospital information system under the new situation to realize the sharing of medical information and resources, and at the same time carry out the reasonable allocation of medical resources in hospitals and communities [6–9]. The image of the retinal fundus is often affected by external conditions, resulting in problems such as uneven light, uneven contrast, and weak contrast between blood vessels and the collected image, making it difficult to remove retinal blood vessels. Haythornthwaite combines the connectivity of the blood vessel network to monitor the top line of the blood vessel to execute the structure of the blood vessel network [10],

Zhang et al. proposed a segmentation threshold exploration method based on local and global features, which combines window matching and dynamics Monitoring technology is used to extract blood vessels, and iterative rules are designed, and the adaptive threshold method is further used to segment the blood vessel region. This method has achieved a good export effect [11]. Takahashi et al. monitor blood vessels by detecting the connection points and connection points of blood vessels, so as to realize network extraction [12].

The existing extraction methods are mainly aimed at normal retinal images, which are not universal. Under ideal conditions, such as uniform light distribution, less noise interference, and no disease, they can basically extract the structure of blood vessel contours correctly when diseases appear in the image, especially in large damaged areas and vascular area. This article focuses on the method of extracting blood vessels from retinal images. The purpose is to eliminate noise interference and diseases and to obtain a complete retinal blood vessel network structure. This article deeply studies the retinal blood vessels under the disease. A new technique for suppressing lesions based on a filtering method is proposed, combined with the technique of restoring the binary image of the vascular network structure, to complete the segmentation of the retinal vessel structure, thereby extracting the structure of the vessel.

2. Application of Nanomaterial Drug Delivery System in the Treatment of Hypertensive Fundus Disease

2.1. Research Content and Methods. This article first uses the literature survey method to query a large amount of data, gives a brief introduction to the preparation and characterization of nanomicelles, explains and elaborates the application of nanomaterials in medicine, and analyzes the nanomaterial drug delivery vehicle in ophthalmology treatment, the application of nanomaterials in the treatment of glaucoma, and the application of nanomaterials loaded with drugs in uveitis. After that, the method of comparative treatment was adopted, and the experimental group and the control group were compared with two different treatment methods. Here, we use the method of limiting single-factor analysis and regression analysis to analyze the influence of each factor on this experiment. Finally, based on the regression results, the construction of MPEG-PCL nanomicelle ocular drug delivery vector and its application in the treatment of hypertensive fundus disease is put forward corresponding suggestions. The article structure is shown in Figure 1.

2.2. Nanomaterials

2.2.1. Characteristics of Nanomaterials. Nanomaterials are generally very small in size, large in specific surface area, and high in surface energy. The number of surface atoms accounts for a high proportion of the total number of atoms. When the particle size is less than 10 nm, the percentage of surface atoms increases sharply, and these surface atoms
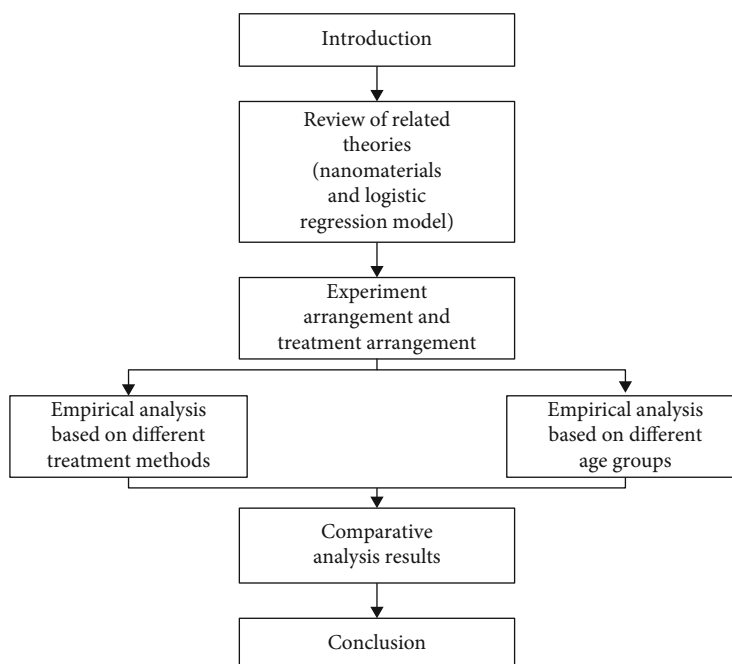
FIGURE 1: Research flow chart.

are in a very empty state. They have extremely high activity and are very unstable [13, 14]. Once you encounter other atoms and combine them to stabilize themselves, this effect is called surface effect.

In nanomaterials, when the particle size reaches a certain physical characteristic size, the energy levels of electrons adjacent to the metal Fermi plane change from an almost continuous state to a discrete state, while the nanoparticles have discontinuous, higher-occupancy molecules. The orbital and lower molecular orbital are asymmetry, and the energy gap is the quantum size phenomenon of nanomaterials [15].

The ability of tiny particles to pass through the dam is called the tunnel effect. When a dielectric layer with a small dielectric constant is modified on the surface of a nanomaterial, it is related to the rest of the medium surrounding the unmodified nanomaterial [16, 17]. Compared with bare nanomaterials, this will cause greater changes in its optical properties. This phenomenon is called the dielectric confinement phenomenon.

(1) Application of Nanomaterials. Throughout the scientific frontier literature and books on nanoelectrocatalysts, the most mentioned word is energy. Energy is no longer a problem of a certain country but has become a problem of global concern. When a crisis occurs, there is no one. The country can take care of itself. The vast number of scientific researchers is working against clean energy. Nanoelectrocatalysts, as a very important role in clean energy, are attracting widespread attention. Regardless of whether the heat increases or decreases, nanoelectrocatalysts will become a solution. The key to the energy problem, nanomaterials have attracted great attention since their birth [18, 19]. With the continuous advancement of science and technology, the research on nanoelectrocatalysis by scientific researchers has become more

and more in-depth, and it has played its own application value in many aspects, such as hydrogen and oxygen evolution electrocatalyst, electrocatalytic carbon dioxide reduction catalyst, and microbial fuel cell electrocatalyst.

2.3. Logistic Regression Model. Regression accounting model is a two-type model, as long as the vector $x = (x_1, x_2 \cdots x_n)$ has n independent variables and the ratio coefficient is p $(y = 1|x) = p$, it can be represented by the conditional probability distribution $p(y = 1|x) = p$ of partial logistic distribution [14]. Show the observed value of $p(y = 1|x) = p$ probability. Therefore, the logistic regression model can be expressed as

$$p(y = 1 \mid x) = \pi(x) = \frac{1}{1 + e^{-g(x)}}. \tag{1}$$

Usually $f(x) = 1/1 + e^{-g(x)}$ is called the logistic function and

$$g(x) = w_0 + w_1 x_1 + \cdots + w_n x_n. \tag{2}$$

The probability that y; does not occur under the condition of x is

$$p(y = 0 \mid x) = 1 - p(y = 1 \mid x) = 1 - \frac{1}{1 + e^{-g(x)}} = \frac{1}{1 + e^{g(x)}}. \tag{3}$$

Therefore, the ratio of the probability of y occurring to not occurring is

$$\frac{p(y=1 \mid x)}{p(y=0 \mid x)} = \frac{p}{1-p} = e^{g(x)}. \quad (4)$$

This ratio is called the occurrence ratio of the event and is recorded as odds. Take the logarithm of odds to get

$$\ln\left(\frac{p}{1-p}\right) = g(x) = w_0 + w_1 x_1 + \cdots + w_n x_n. \quad (5)$$

Usually use maximum likelihood estimation to find the parameters of the classification model:

$$L(w) = \prod_1^n (\pi(x_i))^{y_i} (1 - \pi(x_i))^{1-y_i}. \quad (6)$$

The maximum likelihood estimation is to find the parameter $w_0, w_1, \cdots, w_n$ so that $L(w)$ takes the maximum value [20].

In the same way, the basic idea of the logistic regression model is applied to personal credit risk assessment: Given the sample data $(X_{i1}, X_{i2}, \cdots, X_{in} : Y_i)(i = 1, 2, \cdots, k), X_i \in R^p$ of n groups of loan application customers is an indicator variable, $y_i \in [0, 1]$ is a 0-1 variable, where $y_i = 0$ indicates that the credit category of the i customer is a bad customer, $y_i = 1$ indicates that the credit category of the i customer is a good customer [21]. The relationship between Y_i and X_{i1}, $X_{i2} \cdots X_{in}$ is as follows:

$$E(Y_i) = P_i = f(\beta_0 + \beta_1 X_{i1} + \beta_2 X_{i2} + \cdots + \beta_n X_{in}). \quad (7)$$

Among them, $f(X)$ is a monotonically increasing function in [0,1].

$$P_i = f(X) = \frac{e^x}{1 + e^x}. \quad (8)$$

Y_i is the 0-1 distribution of the mean $P_i = f(\beta_0 + \beta_1 X_{i1} + \beta_2 X_{i2} + \cdots + \beta_n X_{in})$, the probability function:

$$\begin{aligned} P(Y_i = 1) &= P_i \\ P(Y_i = 0) &= 1 - P_i \end{aligned} \quad (9)$$

Then, the logistic regression equation is

$$P_i = \frac{\exp(\beta_0 + \beta_1 X_{i1} + \beta_2 X_{i2} + \cdots + \beta_n X_{in})}{1 - \exp(\beta_0 + \beta_1 X_{i1} + \beta_2 X_{i2} + \cdots + \beta_n X_{in})}. \quad (10)$$

The above equation can be linearly transformed, so

$$\ln\left(\frac{P_i}{1-P_i}\right) = \beta_0 + \beta_1 X_{i1} + \beta_2 X_{i2} + \cdots + \beta_n X_{in}, i = 1, 2, \cdots, n. \quad (11)$$

$Y_1, Y_2, \cdots, Y_n$ is an independent binary variable, $f_i(Y_i)$ represents the probability of Yi = 1 or 0. And the likelihood function is

$$L(\beta) = f(Y_1, Y_2, \cdots, Y_n) = \prod_1^n f_i(Y_i) = \prod_1^n P_i^{Y_i} (1 - P_i)^{1-Y_i}. \quad (12)$$

Both sides of Formula (12) take the natural logarithm and the log-likelihood function:

$$\ln f(Y_1, Y_2, \cdots, Y_n) = \sum_1^n \left[Y_i \ln\left(\frac{P_i}{1-P_i}\right) \right] + \sum_1^n [\ln(1 - P_i)]. \quad (13)$$

Bringing Formula (10) into Formula (13) is

$$\begin{aligned} \ln f(Y_1, Y_2, \cdots, Y_n) &= \sum_1^n Y_i(\beta_0 + \beta_1 X_{i1} + \cdots + \beta_n X_{in}) \\ &- \sum_1^n \ln\left[1 + e^{(\beta_0 + \beta_1 X_{i1} + \cdots + \beta_n X_{in})}\right], i = 1, 2, \cdots, n. \end{aligned} \quad (14)$$

2.4. Application of Nanomaterial Drug Delivery Carrier in the Treatment of Ophthalmopathy

2.4.1. Application of Nanomaterial Drug Delivery Carrier in the Treatment of Glaucoma. Surgical filtration is a common method of clinical treatment. The main reason is the increase in intraocular pressure caused by conjunctival fibrosis and drainage tract contraction [22, 23]. The advantages are high drug loading and good biocompatibility. Targeted liposome-polypeptide-siRNA nanoparticles as an effective and safe nonviral gene delivery system can be used to prevent conjunctival fibrosis after glaucoma infiltration surgery and other fibroblast-induced ophthalmology.

2.4.2. Application of Drug-Loaded Nanomaterials in Uveitis. Uveitis is a general term for inflammation of the iris, ciliary body, and choroid tissue and is also a chronic inflammation. At present, glucocorticoids, nonsteroidal, anti-inflammatory drugs and immunosuppressive agents can effectively treat uveitis, but these drugs have difficulty reaching the retina to achieve a complete therapeutic effect [24, 25]. Therefore, treating uveitis remains a challenge. Recent studies have shown that nanocells can improve the solubility of drugs and increase the permeability of conjunctival epithelial cells through good hydrophilicity and high drug encapsulation potential.

(1) Application of Drug-Loaded Nanomaterials in Retinal Diseases. By activating specific promoters to reduce the loss of photoreceptor cells, reduce the cavity between the plexus layer and bipolar cells, increase the thickness of the outer nuclear layer of the retina [26, 27], and promote the growth of the retina. And improve the structure of the retina. Therefore, solid lipid nanoparticles gene replacement therapy can restore the retinal structure of mice with retinal protein deficiency.

(2) Application of Nanomaterial Drug Delivery Carrier in the Treatment of Hypertensive Fundus Disease. Through the mutual transformation of the primary and secondary structure of the polypeptide and the self-assembly behavior, among them, polypeptide hydrogel is a self-assembled nanomaterial with nanofiber structure. The hydrogel polypeptide has good biocompatibility and controlled degradation. As a controlled drug delivery system, it has the advantages of high drug loading and smart drug release [28, 29]. Therefore, the gel based on nanofiber polypeptide can prevent the occurrence of hypertensive bottom disease by affecting the proliferation and differentiation of LEC, so as to achieve a better therapeutic effect.

2.5. Drug Delivery Vehicle

2.5.1. Drug Delivery Nanocarrier. With the development of new drug delivery systems, it has become a research hotspot to keep the therapeutic activity of drugs to the maximum while reducing the side effects of drugs. In recent decades, amphiphilic block copolymer drug carriers that can form nanomicelle structures through self-assembly in the water phase have received extensive attention. The amphiphilic block polymer as a drug carrier can physically encapsulate hydrophobic drugs in the core of the micelle, increasing the water solubility of poorly soluble drugs, and the hydrophilic layer formed by the hydrophilic segment of the amphiphilic polymer material can protect the drug carrier from passing through. Pass the biological barrier to enter the diseased site and achieve drug delivery [30, 31]. The chemical composition, molecular weight, and hydrophilic-hydrophobic block ratio of the amphiphilic polymer can be flexibly changed according to the required micelle particle size and morphology. As a drug carrier, nanomicelles can not only extend the time of drug circulation in the body and improve the shortcomings of poor solubility and low stability of the drug but also enrich the drug in the diseased site through the EPR effect and increase the uptake of the drug by cells and tissues.

2.5.2. Characterization of Polymer Materials

(1) NMR Ammonia Spectroscopy. The polymer material was vacuum dried in advance and then analyzed by H-NMR. Weigh 5-10 mg of the sample to be tested and transfer it to a clean NMR tube, add $500\,\mu\mathrm{L}$ of deuterated chloroform or deuterated DMSO to fully dissolve it, use tetramethylsilane as the internal standard, and detect the displacement of ammonia protons in each sample by a nuclear magnetic resonance spectrometer. Analyze the chemical structure of the sample to be tested [32].

(1) Fourier transform infrared spectroscopy

The polymer material is vacuum dried in advance. Take about 200 mg of potassium bromide (KBr) and use a grinding rod to fully grind into ultrafine powder, weigh 2 mg of the sample to be tested and potassium bromide to fully grind

and mix, and then make it into potassium bromide tablets for detection by infrared spectroscopy [33–36].

2.5.3. Preparation and Characterization of Micelles

(1) Preparation of Polymer Micelles. The polymer material is prepared by solvent evaporation method to make micelles. The method is briefly described as follows: weigh 10 mg polymer powder and dissolve it in 5 ml tetrahydrofuran, ultrasonically make it fully dissolved, and then add the solution dropwise to 10 ml deionized water at a rate of 1 second/drop through the 21-gauge needle of a glass syringe. During the process, keep the stirring speed at 500 r/min. After the addition is completed, continue to stir until the tetrahydrofuran is fully volatilized to obtain the polymer micelle solution. Before the particle size and morphology of the micelle solution are tested, use a 450 micron filter to filter out impurities and collect it in a container store in a refrigerator at 4°C.

2.5.4. Characterization of the Particle Size and Morphology of Micelles. The dynamic light scattering method is used to detect the average particle size and polydispersity index of the prepared nanomicelles. The abovementioned micelle preparation method is used to prepare a polymer micelle solution with a concentration of 1 mg/ml, and it is detected by a dynamic laser scattering nanoparticle sizer. The test temperature is 25°C. A transmission electron microscope was used to observe the morphology of the prepared nanomicelles. Use the abovementioned micelle preparation method to prepare a nanomicelle solution with a concentration of 1 mg/ml, drop a drop of the micelle solution to be tested on the surface of the carbon film copper mesh, keep it for 90s, absorb the remaining liquid with filter paper, and add a drop of phosphonic acid. (2.5 wt%) aqueous solution for negative dyeing. After dyeing for 60 seconds, the residual dye is absorbed and the surface of the copper mesh is fully evaporated before observation by transmission electron microscope.

3. Experimental Study on the Application of Nanomaterial Drug Delivery System in the Treatment of Hypertensive Fundus Disease

3.1. Test Subject. The main data source of this study is the 120 patients with hypertensive fundus disease who visited the hospital from 2018 to 2020 in X Hospital. These 120 patients with hypertensive fundus disease are the subjects of our study. We obtained the patient's willingness to participate in this study anonymously. The 120 volunteers were divided into groups by random grouping, 60 people in each group. In the experimental group, there were 35 males and 25 females, aged between 37 and 65, with an average age of 44.5 years and a course of 1 year to 3.5 years, with an average of 2.2 years; the control group, 37 males and 23 females, were between 38 and 62 years old, with an average age of about 45.2 years, and the course of disease was 1 to 3 years, with an average of 2 years. The 120 volunteers suffered from hypertensive ocular fundus disease after examination, and

there was no interference from other diseases, and there were no symptoms of drug allergy, and the kidneys and other organs were functioning normally. The three doctors with rich work experience in this hospital are comprehensively judged for judging the degree of treatment. If there is a dispute, the result can be selected through discussion.

3.2. Efficacy Judgment and Index Observation Analysis. The BCVA levels of the patients before treatment, 1 month after treatment, 2 months after treatment, and 3 months after treatment were detected by the eye chart. The BCVA levels of the two groups of patients were compared and statistically recorded. Comparison of the clinical treatment effects of the two groups of patients. According to the degree of recovery of clinical symptoms such as eye pain, swelling, congestion, and the degree of improvement in vision, the level of treatment effect is judged.

3.3. Experimental Method

3.3.1. Preparation Before Treatment. Before treatment, the two groups of patients were tested for vision, and the blood pressure and hemorheology indexes of the two groups of patients were measured at the same time. Provide psychological care to patients, mediate their psychological pressure, and reduce their psychological burden. Try to meet the needs of patients, avoid patients from being left out, and keep patients warm. Introduce the possible reactions of such symptoms to the patient and the cases that have been successfully treated, improve the patient's self-confidence, and help improve the treatment effect.

3.3.2. Treatment. The control group was given low-intensity laser irradiation treatment, using a low-intensity laser with a power of 300 mW to irradiate the eyes of the patient, 2 times/d, 30 min/time, a week as a course of treatment, lasting for two courses; after each irradiation, the patient's eyes were protected by dripping levofloxacin hydrochloride gel. The experimental group was combined with nanotherapy on the basis of the control group. One week was a course of treatment and lasted for two courses. After treatment, the patient's vision, blood pressure, and blood rheology were tested again.

3.4. Gather Data. In order to obtain accurate data to compare and analyze the feasibility and effectiveness of this experiment, this paper uses the Cora dataset and the IMB dataset. The statistical data used in this article has a different unit dimension for each index data. After calculating the data in the previous steps, we can get the similarity between users and select several users closest to the interests and preferences of user u_a to form set N_a. Then, calculate the score of user u_a on j according to the score of the user in the set N_a on the unrated item j, the prediction formula is shown in Formula (15):

$$p_{a,i} = \frac{\sum_{b \in N_a} sim_{u_a,u_b} r_{b,i}}{\sum_{b \in Na} | sim_{u_a,u_b} |}, \tag{15}$$

where $p_{a,i}$ is the predicted score of user a on the unrated item i. In the recommendation system, user scoring preferences are

sometimes different. For example, some users are accustomed to giving higher ratings to items, while some are accustomed to giving lower ratings. In order to reduce the difference between users scoring preferences and improve the accuracy of rating prediction, the method of Formula (16) introduces the users average rating $\bar{r}$, and the specific form is shown in Formula (16):

$$p_{a,i} = \overline{r_a} + \frac{\sum_{b \in N_a} sim_{u_a,u_b} (r_{b,i} - \overline{r_b})}{\sum_{b \in N_a} | sim_{u_a,u_b} |}. \tag{16}$$

There are many data standard processing methods, but different data standardization methods will have a certain impact on the evaluation results of the system. For the positive indicator standardization method:

$$y_{ij} = \frac{x_{ij} - \min \{x_{ij}\}}{\max \{x_{ij}\} - \min \{x_{ij}\}}. \tag{17}$$

For negative index standardization methods:

$$y_{ij} = \frac{\max \{x_{ij}\} - x_{ij}}{\max \{x_{ij}\} - \min \{x_{ij}\}}. \tag{18}$$

After standardizing the data, using the principal component analysis of nonlinear logarithmic centering, the processing steps of logarithmic transformation and row vector centering are

$$z_{ij} = \ln y_{ij} - \sum_{i=1}^{m} \ln y_{ij}/m. \tag{19}$$

3.5. Statistical Methods. SPSS23.0 software was used for data processing, and the count data was expressed as a percentage (%), k is the number of data in this experiment, σ^2 is the variance of all survey results, and $P < 0.05$ indicates that the difference is statistically significant. The formula for calculating reliability is shown in equation (20).

$$a = \frac{k}{k-1} \left(1 - \frac{\sum \sigma_i^2}{\sigma^2}\right). \tag{20}$$

4. Experimental Analysis of the Application of Nanomaterial Drug Delivery System in the Treatment of Hypertensive Fundus Disease

4.1. Evaluation Index System Based on Index Reliability Testing. Reliability refers to the stability and reliability of the questionnaire. This article adopts the α coefficient method created by L.J. Cronbach. The α coefficient can be obtained by Reliability Analysis in SPSS software. It is generally believed that the α coefficient above 0.8 indicates that the effect of the index setting is very good, and above 0.7 is also acceptable. Here, we analyze the reliability of each type of object, and the reliability index we choose for each type of object is slightly different. The results are shown in Table 1.

TABLE 1: Summary Table of Reliability Test Results.

Group	Index combination	Alpha coefficient (α)
Control group	The effect is obvious Partial relief Stable Invalid Deterioration	0.7932
Experimental group	The effect is obvious Partial relief Stable Invalid Deterioration	0.8226

TABLE 2: Quality of life data analysis table.

	Control group	Test group	Time (t)	Significant difference (P)
0 day	7.832	7.742	0	1
1-2 days	7.952	7.952	0.85	1.202
3-4 days	8.189	8.256	2.132	1.503
5-6 days	8.426	8.628	5.292	2.232
7-8 days	8.827	9.125	8.513	3.273
9-10 days	8.869	9.256	9.952	1.469
11-12 days	8.912	9.389	11.692	0.662
13-14 days	8.982	9.537	13.5	0.001
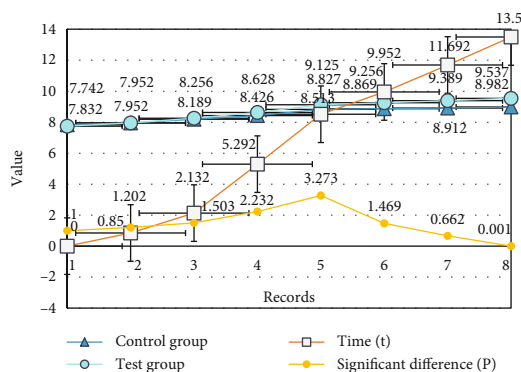
FIGURE 2: Comparison of the overall quality of life between the two groups of patients before and after intervention.

It can be seen from Table 1 that the influence of the data obtained by the control group and the study group on this experiment is acceptable ($\alpha > 0.7$), and the influence caused by the environment and living habits is within the acceptable range, satisfying the experiment prerequisites to start.

4.2. Based on the Quality of Life and Complications of the Two Groups of Patients during Treatment

4.2.1. Comparative Analysis of the Quality of Life of the Two Groups of Patients. We first compare and analyze the quality of life of the two groups of patients. We choose to conduct surveys and process data for analysis every two days before

TABLE 3: Anxiety data analysis table.

	Control group	Test group	Time (t)	Significant difference (P)
0 day	17.000	17.000	0.074	0.984
1-2 days	15.521	15.387	0.241	0.821
3-4 days	14.127	13.124	1.121	0.234
5-6 days	12.682	11.486	2.012	0.112
7-8 days	11.020	9.264	2.982	0.004
9-10 days	8.869	7.132	3.125	0.003
11-12 days	6.852	4.162	3.632	0.002
13-14 days	3.326	1.521	4.437	0.001

treatment. When we conduct data collection and analysis, we ask three doctors with extensive work experience to participate in this experiment, the overall quality of life of the patients was comprehensively scored to calculate the significant difference, and the results are shown in Table 2. We make a scatter plot based on this result, as shown in Figure 2.

It can be seen from Figure 2 that there was no difference in the overall quality of life of the two groups before the treatment and at the end of the first course of treatment ($P > 0.05$), until the end of the second course of treatment, the overall quality of life of the experimental group was higher than that of the control group ($P < 0.05$). That is to say, when the treatment is completed, the overall life treatment of the experimental group is higher than that of the control group. This conclusion is reliable and there is no significant difference.

4.2.2. Comparative Analysis of Anxiety Degree between Two Groups. We compare and analyze the anxiety of the two groups of patients. We choose to conduct surveys and process data for analysis every two days before treatment. When we conduct data collection and analysis, we asked three doctors with extensive work experience participating in this experiment, the patients' anxiety level was comprehensively scored to calculate the significant difference, and the results are shown in Table 3. We make a bar graph based on this result, as shown in Figure 3.

It can be seen from Figure 3 that there was no difference in anxiety between the two groups of patients before the first use of targeted drugs ($P > 0.05$). The two groups of patients were compared at the end of the first course of treatment and at the end of the second course of treatment. The score of the experimental group was low. Compared with the control group ($P < 0.05$), that is to say, the anxiety level of the experimental group is lower than that of the control group during half of the treatment. This conclusion is reliable and there is no significant difference.

4.2.3. Comparative Analysis of Depression Degree of Two Groups of Patients. We made a comparative analysis of the depression levels of the two groups of patients. We chose to conduct surveys and process data for analysis every two days before treatment. When we collected and analyzed data, we asked the three doctors who participated in this experiment with extensive work experience, the degree of

depression of the patients was comprehensively scored to calculate the significant difference, and the results are shown in Table 4. We make a line chart based on this result, as shown in Figure 4.

It can be seen from Table 4 that there was no difference in the degree of depression between the two groups of patients before the first use of targeted drugs and at the end of the first course of treatment ($P > 0.05$), and until the end of the second course of treatment, the degree of depression in the experimental group was higher than that in the control group ($P < 0.05$). That is to say, the degree of depression in the experimental group is higher than that in the control group when the treatment is completed. This conclusion is reliable and there is no significant difference.

4.3. Based on Single-Factor Comparison. First, through univariate analysis, all the above possible factors are studied to initially screen out the relevant factors. Among them, the chi-square test is used for categorical factors, and the independent sample T test is used for data factors. The results are shown in Table 5.

(1) Analyze the treatment effects of different genders

We analyzed the treatment effect of patients according to different gender groups at the same time and judged the treatment effect level according to the degree of recovery of clinical symptoms such as eye pain, swelling, congestion, and the degree of improvement in vision. Let the three doctors with extensive work experience participating in this experiment calculate the significant difference by comprehensively scoring the patient's overall quality of life, as shown in Figure 5.

It can be seen from Figure 5 that the cure rate for men is 93.05%, and the cure rate for women is 89.58%. At the same time, whether it is completely cured or completely ineffective, there is no correlation between gender and ERD ($P > 0.05$). That is to say, the probability of suffering from hypertensive fundus disease is not related to gender. This conclusion is reliable and there is no significant difference.

4.3.1. Analyze According to whether Cataract Surgery Has Been Done. We divided patients into groups according to whether they had undergone cataract surgery and analyzed their treatment effects. We judged the level of treatment effect according to the degree of recovery of clinical symptoms such as eye pain, swelling, and congestion, and the degree of improvement in vision. Let the three doctors with extensive work experience participating in this experiment calculate the significant difference by comprehensively scoring the patient's overall quality of life, as shown in Figure 6.

It can be seen from Figure 6 that the cure rate of patients who have undergone cataract surgery is 83.33%, and the cure rate of patients who have not undergone cataract surgery is 91.22%. At the same time, whether it is completely cured or completely ineffective, gender is related to the occurrence of ERD. Sex ($P < 0.05$). That is to say, the probability of suffering from hypertensive fundus disease is related to whether
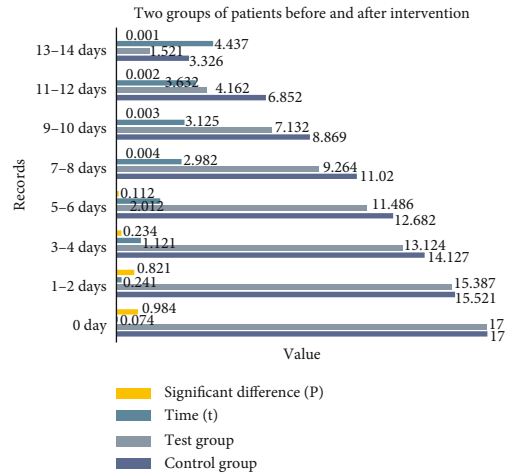

FIGURE 3: Comparison of anxiety between the two groups of patients before and after intervention.

TABLE 4: Depression data analysis table.

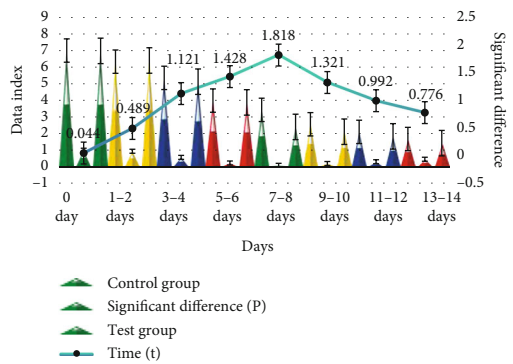|	Control group	Test group	Time (t)	Significant difference (P)
0 day	7.00	6.98	0.044	0.984
1-2 days	6.33	6.40	0.489	0.922
3-4 days	5.35	5.12	1.121	0.552
5-6 days	3.98	3.87	1.428	0.213
7-8 days	3.42	2.39	1.818	0.073
9-10 days	2.55	2.10	1.321	0.182
11-12 days	2.09	1.82	0.992	0.289
13-14 days	1.66	1.41	0.776	0.44

FIGURE 4: Comparison of depression between two groups of patients before and after intervention.

or not cataract surgery has been done. This conclusion is reliable and there are significant differences.

4.3.2. Analyze According to whether PRP Surgery Has Been Done. We grouped patients according to whether they had undergone PRP surgery and analyzed their treatment effects at the same time. According to the degree of recovery of clinical symptoms such as eye pain, swelling, congestion, and the degree of improvement in vision, the level of treatment

TABLE 5: Categorical independent variable and dependent variable assignment table.

Assignment variable		Category	Number	Proportion
Dependent variable	Result	ERD	10	8.3%
		NO ERD	110	91.7%
Independent variable	Gender	Male	72	60%
		Female	48	40%
	History of cataract surgery	Yes	6	5%
		No	114	95%
	PRP treatment history	Yes	22	18.3%
		No	98	81.7%
	History of anti-VEGF treatment before surgery	Yes	30	25%
		No	90	75%
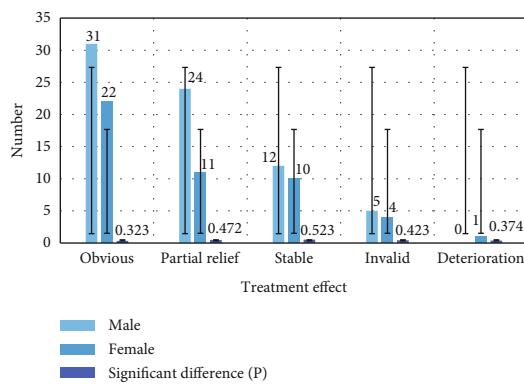
FIGURE 5: Analyze the treatment effect of different genders.
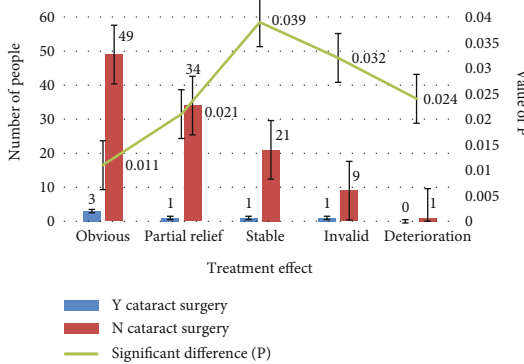
FIGURE 6: Analysis diagram of environmental pollution caused by three kinds of cars driving the same distance.
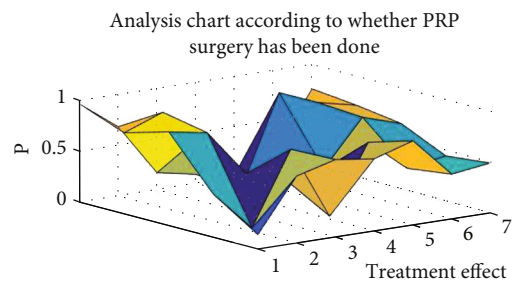

FIGURE 7: Analysis chart according to whether PRP surgery has been done.

FIGURE 8: According to whether there is a history of anti-VEGF treatment before surgery.

effect was evaluated. Let the three doctors with extensive work experience participating in this experiment calculate the significant difference by comprehensively scoring the patient's overall quality of life, as shown in Figure 7.

It can be seen from Figure 7 that the cure rate of patients who have undergone PRP surgery is 86.36%, and the cure rate of patients who have not undergone cataract surgery is 92.85%. At the same time, whether it is completely cured or completely ineffective, there is no correlation between gender and ERD. Sex ($P > 0.05$). That is to say, the probability of suffering from hypertensive fundus disease has noth-

ing to do with whether or not PRP has been performed. This conclusion is reliable and there is no significant difference. Because it is impossible to count the number of treatment points of patients undergoing PRP before surgery in this study, this may have a certain impact on this result.

4.3.3. Analyze According to whether There Is a History of Anti-VEGF Treatment before Surgery. We grouped patients according to whether they had a history of anti-VEGF treatment before surgery and analyzed their treatment effects. We judged the treatment effect according to the degree of recovery of clinical symptoms such as eye pain, swelling, and congestion, and the degree of visual improvement. Let the three doctors with extensive work experience participating in this experiment calculate the significant difference by comprehensively scoring the patient's overall quality of life, as shown in Figure 8.

It can be seen from Figure 8 whether the cure rate of patients with a history of preoperative anti-VEGF therapy is 90%, and the cure rate of patients who have not undergone cataract surgery is 92.22%. At the same time, whether it is completely cured or completely ineffective, it is all gender and ERD. There is a correlation ($P < 0.05$). That is to say, the probability of suffering from hypertensive fundus disease is related to whether there is a history of anti-VEGF treatment before operation. This conclusion is reliable and there are significant differences. In this study, due to the fact that there are many new blood vessels in the fundus of some patients, in order to smooth the operation and achieve better results after the operation and reduce the occurrence of rebleeding, anti-VEGF treatment is used within 3-7 days before the operation, and the drug is selected according to the patient's own wishes. All patients in this group who received anti-VEGF treatment before surgery did not develop ERD.

5. Conclusion

The use of nanocarriers for drug delivery can significantly improve the bioavailability of the drug, reduce the dosage and frequency of administration, increase the residence time of the drug in the local tissue, and reduce the side effects of the drug, overcoming many of its shortcomings. Traditional methods of administration can improve ocular tissue disease. At present, the ophthalmic drug delivery system is still in the process of continuous improvement. Therefore, it is a huge challenge to develop a drug delivery system for the back of the eye that results in a sustained and controlled release, is noninvasive, and can be self-administered by the patient. Advances in nanodrug delivery systems and drug delivery technologies have greatly promoted the development of ophthalmic drug delivery and provided broad prospects for the treatment of ophthalmic diseases. However, there are few reports on the quality control and safety assessment of the drug distribution system, so further research and exploration are needed. It is believed that with the continuous deepening of related research, nanodrug delivery systems will be more used in clinical treatment during the administration of ophthalmic drugs, which will bring good news to patients with ophthalmological diseases.

At present, most retinal blood vessel extraction methods are mainly used for normal retinal images. Therefore, when applied to a large range of lesion images, it is difficult to accurately extract blood vessels due to the interference of lesions and other nonvascular structures, and a large number of nonvascular structures cannot be filtered. In addition, this article focuses on vascular bone extraction and vascular structure segmentation methods suitable for retinal imaging. At the same time, in order to further eliminate the residual nonvascular pixels, a multiple hysteresis threshold method based on dilution of the standard hysteresis threshold is proposed. On this basis, a method suitable for fundus was proposed. The method of extracting the vascular skeleton of the nonvascular structure of the diseased image is suppressed. This method filters the nonvascular structures in the patient image to a large extent and can keep the blood vessel skeleton relatively complete.

This study investigated the effect of the combination of low-intensity laser radiation and traditional Chinese medicine treatment on hematological indicators of patients with hypertension. It can be seen from the results that at different times after treatment, the BCVA of the study group was significantly higher than that of the control group. Recovering vision can obviously help. In the treatment process, the combined treatment of the two methods did not increase the incidence of side effects but reduced the incidence of side effects. At the same time, the results of the two bleeding groups showed that the bleeding index of the study group was better than that of the control group. The treatment effect is ideal. In addition, doctors must continue to strengthen research to provide patients with more effective treatment methods and drugs to accelerate the recovery of vision.

Although the use of MPEG-PCL nanomicelle ocular drug delivery carrier has carried out in-depth research on the treatment of hypertensive fundus diseases, there are still many shortcomings. The depth and breadth of this research are not enough. In the process of this research, the experimental data, the selection and acquisition of the test were carried out under absolutely ideal conditions, and the completeness and effectiveness were not enough. Some interfering factors involved in the experiment were not taken into account, and the patient's condition tracking was also restricted by many factors. The research on the academic level is also limited, and the treatment of hypertensive fundus diseases is still in the preliminary stage. In the future work, appropriate treatment methods and means will be studied from more perspectives based on the existing technology and level, and the quality of medical treatment will be continuously improved.

Data Availability

The data that support the findings of this study are available from the corresponding author upon reasonable request.

Conflicts of Interest

The authors declared no potential conflicts of interest with respect to the research, authorship, and/or publication of this article.

Acknowledgments

References

[1] H. Wei, A. Sehgal, and N. Kehtarnavaz, "A deep learning-based smartphone app for real-time detection of retinal abnormalities in fundus images," *Real-Time Image Processing and Deep Learning*, vol. 10996, 2019.

[2] K. Shankar, Y. Zhang, Y. Liu, L. Wu, and C. H. Chen, "Hyperparameter tuning deep learning for diabetic retinopathy fundus image classification," *Access*, vol. 8, pp. 118164–118173, 2020.

[3] W. Fengping and W. Weixing, "Road extraction using modified dark channel prior and neighborhood FCM in foggy aerial images," *Multimedia Tools and Applications*, vol. 78, no. 1, pp. 947–964, 2019.

[4] R. Geetha Ramani and L. Balasubramanian, "Retinal blood vessel segmentation employing image processing and data mining techniques for computerized retinal image analysis," *Engineering*, vol. 36, no. 1, pp. 102–118, 2016.

[5] L. C. Rodrigues and M. Marengoni, "Segmentation of optic disc and blood vessels in retinal images using wavelets, mathematical morphology and Hessian-based multi-scale filtering," *Biomedical Signal Processing & Control*, vol. 36, pp. 39–49, 2017.

[6] Y. Zhang, L. Sun, H. Song, and X. Cao, "Ubiquitous WSN for healthcare: recent advances and future prospects," *IEEE Internet of Things Journal*, vol. 1, no. 4, pp. 311–318, 2014.

[7] J. Choi, C. Choi, S. Kim, and H. Ko, "Medical Information Protection Frameworks for Smart Healthcare based on IoT," in *Proceedings of the 9th International Conference on Web Intelligence, Mining and Semantics (WIMS 2019)*, pp. 1–5, Seoul, Korea, 2019.

[8] Z. Lv and H. Ko, "Introduction to the special issue on recent trends in medical data security for e-health applications," *ACM Transactions on Multimidia Computing Communications and Applications*, vol. 17, 2021.

[9] A. K. Singh, A. Anand, Z. Lv, H. Ko, and A. Mohan, "A survey on healthcare data: a security perspective," *ACM Transactions on Multimedia Computing Communications and Applications*, vol. 17, no. 2s, pp. 1–26, 2021.

[10] C. Haythornthwaite, "Learning, connectivity and networks," *New Library World*, vol. 120, no. 1/2, pp. 19–38, 2019.

[11] M. Zhang, X. Cao, L. Peng, and R. Niu, "Landslide susceptibility mapping based on global and local logistic regression models in Three Gorges Reservoir area, China," *Environmental Earth Sciences*, vol. 75, no. 11, pp. 1–11, 2016.

[12] R. Takahashi, Y. Hatanaka, T. Nakagawa et al., "Automated analysis of blood vessel intersections in retinal images for diagnosis of hypertension," *Medical Imaging Technology*, vol. 24, no. 4, pp. 270–276, 2016.

[13] J. D. Benck, T. R. Hellstern, J. Kibsgaard, P. Chakthranont, and T. F. Jaramillo, "Catalyzing the hydrogen evolution reaction (HER) with molybdenum sulfide nanomaterials," *ACS Catalysis*, vol. 4, no. 11, pp. 3957–3971, 2014.

[14] J. O. Tijani, O. O. Fatoba, O. O. Babajide, and L. F. Petrik, "Pharmaceuticals, endocrine disruptors, personal care products, nanomaterials and perfluorinated pollutants: a review," *Environmental Chemistry Letters*, vol. 14, no. 1, pp. 27–49, 2016.

[15] K. Rasmussen, M. González, P. Kearns, J. R. Sintes, F. Rossi, and P. Sayre, "Review of achievements of the OECD working party on manufactured nanomaterials' testing and assessment programme. From exploratory testing to test guidelines," *Regulatory Toxicology and Pharmacology*, vol. 74, no. 11, pp. 147–160, 2016.

[16] M. Hu, Z. Yao, and X. Wang, "Graphene-based nanomaterials for catalysis," *Industrial & Engineering Chemistry Research*, vol. 56, no. 13, pp. 3477–3502, 2017.

[17] D. Bozyigit, N. Yazdani, M. Yarema et al., "Soft surfaces of nanomaterials enable strong phonon interactions," *Nature*, vol. 531, no. 7596, pp. 618–622, 2016.

[18] K. Garner, S. Suh, and A. A. Keller, "Response to comments on "assessing the risk of engineered nanomaterials in the environment: development and application of the nanoFate Model"," *Environmental Science & Technology*, vol. 52, no. 9, pp. 5511–5511, 2018.

[19] N. B. Raja, I. Çiçek, N. Türkoğlu, O. Aydin, and A. Kawasaki, "Correction to: landslide susceptibility mapping of the Sera River Basin using logistic regression model," *Natural Hazards*, vol. 91, no. 3, pp. 1423–1423, 2018.

[20] L. Jianfeng, L. Zhiyong, Z. Yan, Z. Wei, and G. Maolong, "Analysis of factors affecting the prognosis of ICU patients by multiple logistic regression model: a retrospective cohort study of 1 299 patients in 12 consecutive years," *Zhonghua wei Zhong Bing ji jiu yi xue*, vol. 29, no. 7, pp. 602–607, 2017.

[21] L. Y. Sun, C. L. Miao, and L. Yang, "Ecological environmental early-warning model for strategic emerging industries in China based on logistic regression," *Ecological Indicators*, vol. 84, no. JAN., pp. 748–752, 2018.

[22] L. Essa, D. Laughton, and J. S. Wolffsohn, "Can the optimum artificial tear treatment for dry eye disease be predicted from presenting signs and symptoms?," *Contact Lens and Anterior Eye*, vol. 41, no. 1, pp. 60–68, 2018.

[23] J. Qian, "The stepwise establishment of standardized treatment for the thyroid eye disease," *Zhonghua Yan Ke Za Zhi*, vol. 53, no. 6, pp. 404–407, 2017.

[24] S. Fraser-Bell, R. Symes, and A. Vaze, "Hypertensive eye disease: a review," *Clinical & Experimental Ophthalmology*, vol. 45, no. 1, pp. 45–53, 2017.

[25] S. Jun, "Definition and diagnostic criteria of dry eye disease: historical overview and future directions," *Investigative Ophthalmology & Visual Science*, vol. 59, no. 14, pp. DES7–DES12, 2018.

[26] N. Itoh, E. Yamamoto, T. Santa, T. Funatsu, and M. Kato, "Effect of nanoparticle surface on the HPLC elution profile of liposomal nanoparticles," *Pharmaceutical Research*, vol. 33, no. 6, pp. 1440–1446, 2016.

[27] P. L. Lam, W. Y. Wong, Z. Bian, C. H. Chui, and R. Gambari, "Recent advances in green nanoparticulate systems for drug delivery: efficient delivery and safety concern," *Nanomedicine*, vol. 12, no. 4, pp. 357–385, 2017.

[28] A. C. Fortes, V. D. N. Bezzon, G. L. B. de Araújo, C. O. P. Santos, and H. G. Ferraz, "Preparation and physicochemical characterization of drug loaded in castor oil-based polyurethane," *Journal of Thermal Analysis and Calorimetry*, vol. 139, no. 3, pp. 1949–1957, 2020.

[29] J. Zhou, S. Chen, P. Luo, B. Du, and H. Yao, "A "submunition" dual-drug system based on smart hollow NaYF4/apoferritin nanocage for upconversion imaging," *RSC Advances*, vol. 6, no. 40, pp. 33443–33454, 2016.

[30] V. Agrahari, V. Agrahari, and A. K. Mitra, "Nanocarrier fabrication and macromolecule drug delivery: challenges and opportunities," *Therapeutic Delivery*, vol. 7, no. 4, pp. 257–278, 2016.

[31] Q. B. Wang and X. L. Wang, "Advances in designation of targeting nanocarrier-drug delivery systems for pancreatic cancer. Fudan University," *Journal of Medical Sciences*, vol. 45, no. 1, 2018.

[32] T. Buttersack, P. E. Mason, R. S. McMullen et al., "Valence and core-level X-ray photoelectron spectroscopy of a liquid ammonia microjet," *Journal of the American Chemical Society*, vol. 141, no. 5, pp. 1838–1841, 2019.

[33] S. H. Eom, S. Senthilarasu, P. Uthirakumar et al., "Preparation and characterization of nano-scale ZnO as a buffer layer for inkjet printing of silver cathode in polymer solar cells," *Solar Energy Materials & Solar Cells*, vol. 92, no. 5, pp. 564–570, 2008.

[34] A. K. Sood, Pritambir, and M. Aggarwal, "A mathematical approach to a more accurate determination of critical micelle concentration and other thermodynamic parameters of 14-2-14 gemini surfactant in water–organic solvent mixed media at variable temperatures," *Journal of Surfactants and Detergents*, vol. 20, no. 1, pp. 297–305, 2017.

[35] S. Wang and K. Zhao, "Dielectric analysis for the spherical and rodlike micelle aggregates formed from a gemini surfactant: driving forces of micellization and stability of micelles," *Langmuir*, vol. 32, no. 30, pp. 7530–7540, 2016.

[36] B. Xue and Z. Wu, "Key technologies of steel plate surface defect detection system based on artificial intelligence machine vision," *Wireless Communications and Mobile Computing*, vol. 2021, Article ID 5553470, 12 pages, 2021.

Hindawi

Retraction

Retracted: Garment Digital Design Method Oriented to the Production Process of Graphene-Modified Nylon Knitted Fabric

Journal of Nanomaterials

This article has been retracted by Hindawi following an investigation undertaken by the publisher [1]. This investigation has uncovered evidence of one or more of the following indicators of systematic manipulation of the publication process:

(1) Discrepancies in scope

(2) Discrepancies in the description of the research reported

(3) Discrepancies between the availability of data and the research described

(4) Inappropriate citations

(5) Incoherent, meaningless and/or irrelevant content included in the article

(6) Peer-review manipulation

The presence of these indicators undermines our confidence in the integrity of the article's content and we cannot, therefore, vouch for its reliability. Please note that this notice is intended solely to alert readers that the content of this article is unreliable. We have not investigated whether authors were aware of or involved in the systematic manipulation of the publication process.

Wiley and Hindawi regrets that the usual quality checks did not identify these issues before publication and have since put additional measures in place to safeguard research integrity.

We wish to credit our own Research Integrity and Research Publishing teams and anonymous and named external researchers and research integrity experts for contributing to this investigation.

The corresponding author, as the representative of all authors, has been given the opportunity to register their agreement or disagreement to this retraction. We have kept a record of any response received.

References

[1] Z. Zhou, "Garment Digital Design Method Oriented to the Production Process of Graphene-Modified Nylon Knitted Fabric," *Journal of Nanomaterials*, vol. 2022, Article ID 6114483, 13 pages, 2022.

Research Article

Garment Digital Design Method Oriented to the Production Process of Graphene-Modified Nylon Knitted Fabric

Zhiya Zhou [ID]

School of Preschool and Art Education, Xinyang Vocational and Technical College, Xinyang, 464000 Henan, China

Correspondence should be addressed to Zhiya Zhou; 171849163@masu.edu.cn

Graphene is a single-atom-thick layer of carbon atoms, the thinnest material ever discovered. The special single atomic layer structure of graphene makes it have many unique physical and chemical properties, and these excellent properties make graphene have a bright application prospect in the field of composite materials. The use of modern digital production technology to coordinate the management of various production departments of an enterprise can greatly reduce the input of human resources and improve the utilization of materials and equipment resources. In the process of caprolactam monomer polymerization, adding filler is a common method to strengthen and toughen nylon. The main fillers are powder fillers and fibrous materials. In order to make the fillers denatured, the fillers are usually pretreated with a silane coupling agent before modification. This research mainly discusses the digital clothing design method oriented to the production process of graphene-modified nylon knitted fabric. The color of graphene-modified cotton fiber is gray and black. With the increase of graphene content, the color becomes darker. Graphene has become a hotspot in materials science due to its unique two-dimensional crystal structure and excellent mechanical, thermal, and electrical properties. In this paper, the preparation and organic modification of graphene oxide and its application in cast nylon are mainly studied. Therefore, when designing graphene-modified cotton fiber jacquard graphene knitted fabric, the color matching has certain restrictions. The shrinking is to reduce the friction between the fibers through the appropriate concentration of the shrinking agent and improve the stretching and shrinking ability of the wool fiber. The fabric feels plump after shrinking, forming fluff, and improving the warmth retention performance. Due to the different design of the veil material, ground yarn material, and organizational structure of the fabric sample, the basic parameters of the fabric are directly different. Therefore, first perform the width, density, areal density, thickness, and raw material content ratio of the blank sample of the fabric. And wait for testing. In order to realize the digitization of styles, this research has developed a drawing system, which provides a large number of drawing tools to enable designers to draw clothing styles more accurately. The system for digital realization consists of six parts, including desktop environment, drawing tools, linear settings, curve drawing, data storage, and user interface. There are a variety of curves to choose from in computer graphics. The B3 spline curve has become the first choice due to its smoothness, no Runge phenomenon, and few saved data. When the mass fraction of graphene-modified nylon was reduced to 18%, the inhibitory rate of *Staphylococcus aureus* and *Escherichia coli* was still greater than 80%. Nylon/modified graphene oxide nanocomposites with different filler contents were prepared by in situ polymerization with modified graphite oxide as modified filler. The effects of modified graphene oxide on the mechanical properties, wear resistance, and thermal properties of the composites were investigated. This research will promote the development of a customized platform for apparel collaborative management.

1. Introduction

Nylon has the advantages of high strength and good wear resistance and has a wide range of applications in clothing and industrial fields. At present, through the differentiation, higher performance, and multifunctionalization of nylon, it is the trend of nylon development to consolidate and deepen the application of nylon in high-end fields. Graphene is a simple substance formed by the ordered arrangement of carbon on a two-dimensional plane. This unique layered structure

enables graphene to have many excellent properties, enabling graphene to be used in various fields. With the continuous development of thermal clothing, the use of new thermal fiber to improve the thermal performance of clothing has become a main development direction. The new graphene-modified fabric is prepared by mixing the graphene and polymer slices to cut the mother particles and then adding the polymer melt spinning fluid. The thermal function of graphene-modified cotton fiber has become a concern.

As the most common material on earth, carbon material is even more wonderful in itself. It is the fundamental material that constitutes the hardest diamond and the softest graphite. Since the appearance of fullerenes and carbon nanotubes, researchers from all over the world have shown great interest in the study of carbon materials. The electrical properties of graphene-modified cotton fiber can reduce the harm of static electricity of woolen products to the human body, while the antibacterial performance is more healthy and hygienic. Relatively speaking, graphene-modified cotton fiber makes the development of multifunctional light knitting fabric have a new exploration direction. In this study, graphene knitted fabrics are more useful by combining with graphene-modified cotton fibers.

These unique properties of graphene make it have a broad application prospect in the fields of field effect devices, sensors, transparent electrodes, photodetectors, solar cells, energy storage devices, polymer composites, nanocomposites, etc. Graphene has a wide range of uses. Bo reported on the design and implementation of multimode optical fiber sensing technology for displacement sensing. Multimode fiber speckle pattern sensor with different core fiber structure is used for sensing spatial information content. The sensor is highly sensitive to the geometry change of the sensing part by using the inner product of the speckle field of multimode fiber. The sensitivity and dynamic range of displacement sensor of heterocore fiber speckle pattern sensor and straight multimode fiber speckle pattern sensor are studied. It is found that the sensitivity of the FSS is as high as $0.1\,\mu$m, and the dynamic range is about $3\,\mu$m, which is better than the FSS of the straight structure multimode fiber. The dynamic response of noncore FSS displacement was also studied [1]. Liu believes graphene has become a hot topic in the material world. Many applications of graphene have already been produced, including gas sensors, photovoltaics, and field effect transistors. He demonstrated that graphene sheets can be used as an ideal inorganic ingredient to build hybrid polymer hydrogels via supramolecular pathways, which have not yet gained the same popularity as other applications. GO nanosheets were first modified by grafting β-cyclodextrin to chemically transformed graphene (CCG) and then noncovalently functionalized by inclusion complexation of block copolymer Azo-PDMA-B-PNIPam [2]. Modern techniques for using monocrystalline silicon are based on growing high-quality ingots of monocrystalline silicon up to 12 inches in diameter or more. For many applications of graphene, large areas of high-quality (preferably single crystal) materials will be possible. Since it was first grown on copper foil a decade ago, inch-sized single crystal graphene has been achieved. Here, he showed graphene

films grown in 20 minutes (5×50) cm^2 size, with >99% ultrahigh oriented grains. This growth is achieved by synthesizing a single crystal Cu(11 11) foil of the size of a meter as the substrate. Graphene islands were epitaxial grown on Cu(11 11) surface. The graphene islands merge seamlessly into graphene films with high single crystallinity and ultrafast growth of graphene films. These achievements were achieved through temperature gradient-driven annealing techniques for the production of single crystal Cu from industrial polycrystalline copper foils and the wonderful effect of continuous oxygen supply from adjacent oxides [3]. Khan presents a novel method for the formation and deposition of copper nanocube-decorated reduced graphene oxide (RGO-CUNCs) nanosheets on indium tin oxide (ITO) electrodes using a very simple method. Cubic copper nanocrystals have been successfully prepared on RGO by chemical reduction at low temperature. He characterized the morphology of the synthesized materials by UV-vis spectroscopy, scanning electron microscopy (SEM), Fourier transform infrared spectroscopy (FTIR), and atomic force microscopy (AFM). He found that the CuNCs formed were uniformly and evenly decorated on the RGO nanosheets. This novel ITO/RGO-CUNCs represents a promising platform for future device manufacturing and electrocatalytic applications [4]. Cao believes that van der Waals heterostructures are an emerging class of metamaterials, consisting of vertically stacked two-dimensional building blocks, which provide a huge tool set to design their properties on top of the already rich tunability of two-dimensional materials [5]. Chen studied the binary language multiattribute group decision-making problem for evaluating the design effect of clothing and accessories with incomplete weight information and introduced some basic concepts and operation rules of binary language variables. He established a model based on entropy weight method to determine attribute weight. According to the traditional idea of gray relation analysis (GRA), he determines the optimal alternative by calculating the linguistic degree of each alternative and the gray relation between the positive and negative ideal solutions of binary language. Finally, he gives an illustrative example for evaluating the design effect of clothing and accessories to validate the developed method [6]. According to the current market and research status, there are two types of new fiber: active and passive thermal insulation. The passive thermal fibers are mainly hollow thermal fibers. Many research teams load graphene on textiles through dip rolling, coating, UV curing, and other methods to obtain textiles with far-infrared and antistatic properties, but the durability of the textiles prepared is poor. The graphene surface has no functional groups, so it has limited dispersibility in organic solvents, which severely limits the application prospects of graphene in the preparation of functional materials. Graphene oxide has abundant oxygen-containing functional groups and also has the excellent performance characteristics of graphene.

The exfoliation of graphite oxide in the polymer matrix is a prerequisite for the preparation of nanocomposites with well-dispersed graphite oxide fillers. Therefore, exfoliation treatment of graphite oxide is crucial. At present, solvent-based exfoliation and thermal exfoliation have become the

main methods to obtain single-layer graphite oxide. The color of graphene-modified cotton fiber is gray and black. With the increase of graphene content, the color becomes darker. Therefore, when designing graphene-modified cotton fiber jacquard graphene knitted fabric, the color matching has certain restrictions. The shrinking is to reduce the friction between the fibers through the appropriate concentration of the shrinking agent and improve the stretching and shrinking ability of the wool fiber. The fabric feels plump after shrinking, forming fluff, and improving the warmth retention performance. Due to the different design of the veil material, ground yarn material, and organizational structure of the fabric sample, the basic parameters of the fabric are directly different. Therefore, first perform the width, density, areal density, thickness, and raw material content ratio of the blank sample of the fabric. In recent years, seamless knitted fabrics have become the trend of fashion underwear because of their comfort, body sculpting, beauty, fashion, and changing characteristics and are more and more favored by consumers. However, the current seamless knitted fabrics on the market generally use some common materials, and the use of functional fibers is less, so it is difficult to meet people's requirements for healthy and functional clothing fabrics. Graphene composite fiber is a new type of functional fiber, which not only has the conventional characteristics of general fibers but also has far-infrared, antistatic, antiultraviolet, and other properties.

2. Research Methods

2.1. Graphene-Modified Cotton Fiber Jacquard Knitted Fabric Design

2.1.1. Product Weaving Process.
The graphene composite fiber is applied to the field of seamless knitting, and the seamless knitted product obtained can not only reflect its inherent comfort and beauty but also endow it with far-infrared, antistatic, antiultraviolet, and other characteristics. The color of graphene-modified cotton fiber is gray and black. With the increase of graphene content, the color becomes darker. Therefore, when designing graphene-modified cotton fiber jacquard graphene knitted fabric, the color matching has certain restrictions. In addition to the white, gray, and black combination of the above-mentioned plain products, in order to have a certain breakthrough in color, a combination of gray and pink is used, and black tops are used to wrap the pattern. The gray yarn is a graphene-based top, and the pink yarn is a conventional top. The graphene-based top is a graphene-based polyester top, and the conventional top uses a mixed top of 60% wool and 40% acrylic. The jacquard pattern and jacquard machine are shown in Figure 1. The main pattern color of the jacquard knitted fabric is red, the edging is black, and the background is gray. The jacquard pattern is shown in Figure 1(a). As a textile tool, the jacquard machine is an important invention in ancient China. Ordinary looms can only weave plain weave fabrics, and fabrics with complex patterns can only be woven by jacquard looms.

The equipment used is a computer jacquard antiair blower artificial fur machine, as shown in Figure 1(b). This machine is a stepper motor controlled top feeding circular knitting machine. It can be used for jacquard and plain color. The pattern capacity is more than 8 million pixels. When designing jacquard fabrics, it can be used for fixed-point jacquard according to various parts of the human body. The artificial fur machine has 18 routes, the machine number is E6, the needle diameter is 27 inches, the total number of needles is 1184, the rated speed is 35 r/min, and the number of knitting colors is 2-8, which is the top of the machine. The number of carding devices, the large cylinder carding head can card the fiber length range of 38~200 mm, the small cylinder carding head can card the fiber length range of 26~127 mm. The positive blowing device is installed on the sinker triangle seat platform, and its main function is to blow the top fiber straight and smooth through the high-pressure fan to weave a plush fabric. On this basis, an antiblowing device is added, which is installed on the edge of the suction hood, and its main function is to blow the top fiber into the knitting needles and knit to form a flat graphene knitted fabric.

The calculated weights form a set of weighted numbers:

$$\beta = \frac{1}{n-1}\sum_{i=1}^{n}(x - x_1)^2 + \frac{1}{n+1}\sum_{i=1}^{n}(y - y_1)^2, \tag{1}$$

$$\overline{\phi} = \sqrt{\phi}. \tag{2}$$

For numerical attributes, the similarity calculation method is

$$\mathrm{sim}(f_1, f_2) = 1 - \frac{|f_1 - f_2|}{1 + |f_1 - f_2|}. \tag{3}$$

Further give the following similarity calculation formula:

$$\mathrm{sim}(f_1, f_2) = \frac{1}{1 + |f_1 - f_2|}. \tag{4}$$

The similarity is as follows:

$$\mathrm{sim}(X_0, X_1) = \frac{\mathrm{count}(x_0, x_1)}{\mathrm{count}(x_0) + \mathrm{count}(x_1)}. \tag{5}$$
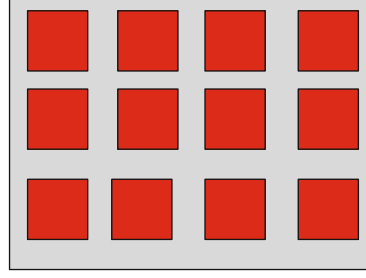
Among them, $\mathrm{count}(x_0)$ is the number of fabric elements [7].

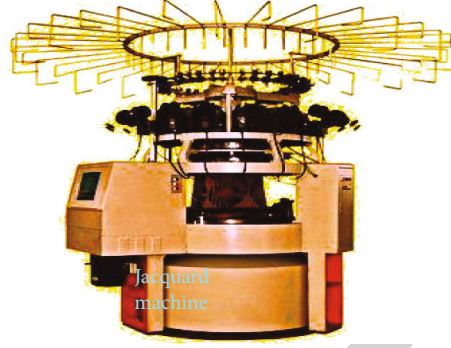Obtain the preferential membership degree matrix r [8, 9]:

$$r_{i,j} = \frac{(x_{i,j} - x_{\min})}{(x_{i,j} - x_{\max})}. \tag{6}$$

The similarity of fabric nodes can be calculated using the following formula [10]:

$$\mathrm{sim}(f_1, f_2) = \frac{\sum_{k=1}^{l} s(f_1, f_2)}{z}. \tag{7}$$

(a) Jacquard pattern

(b) Computer jacquard antihair faux fur machine

FIGURE 1: Jacquard type and jacquard machine.

Multiply the weight of the attribute w_i by the above formula [11]:

$$\text{sim}(f_1, f_2) = \frac{\sum_{k=1}^{l} sw_i(f_1, f_2)}{zw_i}. \tag{8}$$

From the definition of cubic spline function, the i-th segment spline function can be expressed as [12, 13]

$$y(x) = \left[(x_1 - x_t)^2, (x_1 - x_t)^3, 1\right] \begin{bmatrix} \dfrac{2}{h} & \dfrac{2}{h^2} & \dfrac{1}{h^3} \\ \dfrac{2}{h} & 0 & \dfrac{2}{h} \\ \dfrac{1}{h^3} & \dfrac{2}{h^2} & 0 \end{bmatrix}. \tag{9}$$

You can use the condition that the second derivative of the front and back two curve segments is continuous at the type value point to list an equation [14]:

$$\beta m + 2m + \chi m = C. \tag{10}$$

Among them, $\beta = 1/h$.

Need to construct three interpolated cubic splines on the parameter U [15]:

$$\begin{aligned} x &= x(U), \\ y &= y(U), \\ z &= z(U). \end{aligned} \tag{11}$$

The cumulative chord length corresponding to the given value point P is [16]

$$S = \sum_{j=1}^{k} |P_j - P_i| = \sum_{j=1}^{k} \sqrt{(x - x_i)^2 + (y - y_i)^2}, \tag{12}$$

$$Q(m, n) = Q(m, n) + K(m, n)N(m, n). \tag{13}$$

Take the scale factor at the above feature size as [17]

$$S(m, n) = N(m, n)r * t(m, n). \tag{14}$$

N is the number and S is the area.

Import the pattern into the Design Star artificial fur design system, and set the corresponding flower width and height. This pattern has a flower width of 1184 and a flower height of 210. After the import is successful, carefully check the details of the pattern, such as different colors and misalignment. The colors are arranged in the order of feeding, which are gray tops, pink tops, and black tops. During the feeding process, the gray bottom is fed with graphene-based polyester gray tops, the red part is fed with pink wool and acrylic blended tops, and the black part is fed with black wool and acrylic blended tops. At this time, the system will automatically calculate the ratio of excellent yarns, which is gray, respectively, tops : pink tops : black tops are 43.8% : 27.8% : 28.4%.

After processing the pattern diagram, export the pattern diagram (BMP format), the wool feeding program (WM format), and the needle selection program (XZ format) from the system and import them to the U disk. Copy the three files and transfer them to the control panel. Set the rotation speed to 25 r/min. When the number of cycles (the number of cycles is the total number of yarns plus 1) is 4, the total number of revolutions Z is set to 11318 [18, 19].

$$Z = \left(\frac{x_m}{0.0254}\right) \times \frac{Z_m}{x_L}. \tag{15}$$

Among them, x_m is the number of meters under the cloth. x_L is the number of loops. Z_m is longitudinal density [20].

Calculation of elastic elongation [21]:

$$S = \frac{D_2 - D_1}{D_1} \times 100\%. \tag{16}$$

Air permeability T calculation [22]:

$$T = \frac{Q}{A} \times 167. \tag{17}$$

Q represents the average airflow, and A represents the study area [23].

Moisture permeability calculation [24]:

$$WV = \frac{\Delta m}{A \cdot t}. \tag{18}$$

2.1.2. Product Finishing Process. The general finishing process after the forward and reverse blowing graphene knitted fabric off the machine is gray cloth $\longrightarrow$ shrinking $\longrightarrow$ washing $\longrightarrow$ dehydration $\longrightarrow$ opening $\longrightarrow$ shaping $\longrightarrow$ shearing $\longrightarrow$ steaming $\longrightarrow$ finished product.

Shrinking is to reduce the friction between the fibers through the appropriate concentration of the shrinking agent and improve the stretching and shrinking ability of the wool fiber. The fabric feels plump after shrinking, forming fluff, and improving the warmth retention performance. This product uses a weakly acidic surfactant with a pH between 5.5 and 6.0 and calcium chloride with a concentration of 5%. Calcium chloride improves the separation of wool fibers and prevents excessive felting of wool fibers, thereby obtaining better shrinkage. With acid shrinking, the shrinking effect is better when the temperature is higher, so the temperature is set to 42°C.

The setting equipment is a hot air setting machine with a setting speed of 13 m/min, a steam pressure of 4 kg/cm^2, a cloth drop speed of 12.2 m/min, and a post-overfeeding speed and a cold water roll speed of 12.4 m/min.

Shearing adopts the method of moving cloth forward and round knife forward rotation, and the rotation speed of the round knife is set to 1000 rpm/min. Shearing makes the surface of the fabric more uniform and has a better gloss.

The steaming equipment is XHL-1900 continuous steaming machine, the steaming temperature is set to 130°C, and the speed is 20 m/min.

2.2. Finishing Process of Graphene-Modified Cotton Fiber Knitted Fabric

2.2.1. Experimental Fabric Design. Design a thin graphene knitted fabric with wool, polyester, and nylon in raw materials. The two sides of the fabric formed by the double-sided structure can show different properties and styles through different materials, and the fabric is richer and has a certain fluffy feeling. Four ways are 55dtex nylon filaments, 5 ways are blended yarns of 20% wool and 80% polyester, and 6 ways are 55ditex graphene-modified nylon filaments. The knitting result of the thin knitted fabric is shown in Figure 2. The equipment is E 40 double-sided circular knitting machine.

2.2.2. Finishing Process Design. Boiling it can make the thin woolen cloth smooth and dense, stiff, smooth, and elastic. The setting is to stabilize the performance of polyester and nylon filaments, thereby improving the dimensional stability of thin wool. The effect of steaming on the structure and style of thin woolen cloth is similar to the cooking process, which makes the woolen cloth smoother and the body bones more elastic. Therefore, the postfinishing process of formulating thin knitted fabrics is gray cloth $\longrightarrow$ cooking $\longrightarrow$ dehydration $\longrightarrow$ opening $\longrightarrow$ wet inspection $\longrightarrow$ shaping $\longrightarrow$ shearing $\longrightarrow$ steaming $\longrightarrow$ finished product.

(1) Cook It. In order to make the fabric smooth and compact and obtain a crisp feel, it is necessary to carry out the cooking process. The cooking process parameters are set to a temperature of 90 degrees Celsius and a time of 50 minutes, and softener is added when the temperature is slowly cooled to below 40 degrees Celsius by adding cold water.

(2) Finalize. In order to make the surface of the fabric smooth and prevent the fabric from wrinkling, it is necessary to shape and finish the sample. The shaping process parameters are temperature 160 degrees Celsius, speed 30 m/min, and width 160 cm.

(3) Steaming. Steaming is to improve the stability and flatness of the cloth surface, while improving the gloss and feel of the cloth surface. Because the fabric is light and dense, in order to improve the feel of the fabric as much as possible, the feeding speed should be reduced. The setting parameters of the steaming process are temperature 170 degrees Celsius, speed 5 m/min, and tension 80 N.

2.3. Basic Parameter Test of Rough Sample. The structural parameters of the fabric have a certain influence on the wearability of the fabric. Due to the different design of the veil material, ground yarn material, and organizational structure of the fabric sample, the basic parameters of the fabric are directly different. Therefore, first perform the width, density, areal density, thickness, and raw material content ratio of the blank sample of the fabric. Then, wait for testing. The basic parameters of the blank sample are shown in Table 1.

(1) Fabric density test: place the sample flat on the table without stretching or widening. The Y51IB fabric density mirror was used to measure the longitudinal density and lateral density of different samples from the warp and weft directions of the sample. The unit is circle/cm

(2) Fabric thickness test: the YG(B)141D digital fabric thickness meter with an accuracy of 0.01 mm is used, and the standard used is GB/T 3820-1997 "Determination of Thickness of Textiles and Textile Products"

(3) Fabric surface density test: a FA1004 electronic balance with an accuracy of 0.0001 g is used to weigh the mass of the sample. The experimental procedure is in accordance with FZ/T 70010-2006 "Determination of the Dry Weight of Knitted Fabrics in Square Meters"

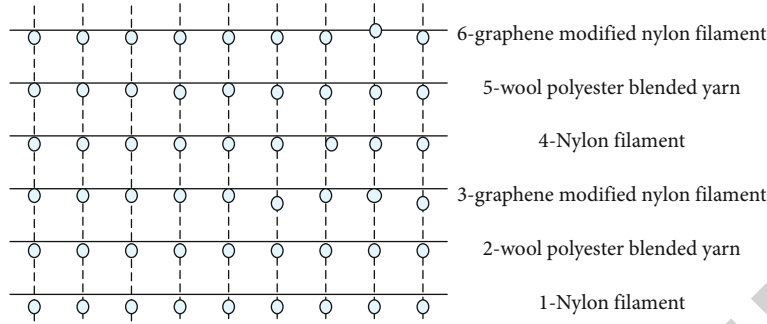(4) Spandex content test: the veil, ground yarn, and spandex are detached from the fabric manually and

6-graphene modified nylon filament

5-wool polyester blended yarn

4-Nylon filament

3-graphene modified nylon filament

2-wool polyester blended yarn

1-Nylon filament

Figure 2: Knitting results for thin knit woolen fabric.

Table 1: Basic parameters of the blank test samples.

Sample number	Areal density (g/m^2)	Thickness (mm)	Spandex content (%)	Width (m)
		0.829	5.87	0.228
#1	256.20	2.222	5.72	0.225
#2	285.97	2.422	6.25	0.225
#3	226.89	2.272	6.22	0.220
#4	206.27	0.882	6.22	0.220
#6	262.54	2.202	5.64	0.226
#7	277.57	2.252	5.82	0.228
#8	282.52	2.472	5.92	0.220
#9	225.26	0.864	6.22	0.225

then dried and cooled before being weighed. Finally, calculate the spandex content Q:

$$Q = \frac{P}{M + N + P} \times 100\%. \tag{19}$$

M is the veil, N is the ground yarn, and P is the spandex.

If the total time used to produce a suit jacket is T_1, the total time used for each machine position is

$$T = \frac{T_1}{N}. \tag{20}$$

2.4. Digitization of Clothing Styles. There are many commonly used drawing software, such as Photoshop, Adobe-image, and AutoCAD. In order to realize the digitization of styles, this research has developed a drawing system, which provides a large number of drawing tools so that designers can more accurately complete the drawing of clothing styles. After the styles are drawn, they will be stored in the library for recall. This can not only improve the efficiency of designing clothing but also save the designed clothing according to the parts, so as to provide nonprofessional designers for selection, splicing, modification, and other recreation. The digital processing plan of clothing is shown in Figure 3.

2.4.1. Basic System Environment. Hardware environment is Pentium 4 PC, color laser printer.

Software environment is Win2000 Server operating platform, Microsoft SQL Server 2000 database management system.

Development tools are Microsoft Visual c++6.0, Access 2000, Adobe Photoshop, CorelDRAW.

For users and fashion designers, there are mainly the following requirements:

(1) Each clothing style is uniformly divided into collars, pieces, sleeves, pants, or skirts. Designers must strictly follow this order when drawing styles

(2) The software should provide designers with enough drawing tools so that they can input clothing styles more accurately, including the elimination tool and the tool to get the mirror image of the drawing about the axis of symmetry of the screen

(3) After the designer finishes drawing a garment part, he must save it before he can continue drawing the next part. After saving a part, the part will be displayed in gray, indicating that the part has not been placed

(4) When inputting detailed points and lines, the software provides the designer with abbreviated display of each detail for his selection

2.4.2. Curve and Its Storage Method. There are a variety of curves to choose from in computer graphics, and B3 spline is preferred due to its smoothness everywhere, no lattice phenomenon, and less data.

In the course of the work, the junction of the curve is uncertain, so the chain table is used to store the curve.

2.4.3. Digital Realization. The system for digital realization consists of six parts, including desktop environment, drawing tools, linear settings, curve drawing, data storage, and user interface.

Among them, the desktop environment module contains two classes: COMyBitmap and CWorkEnviroment. The former is a simple encapsulation of the functions of the CBit map class. It can display a bitmap with a transparent background. In the graphics input system, the ClyBit map class is used to display the entry and other details of the clothing as a template for drawing clothing. The latter saves all the
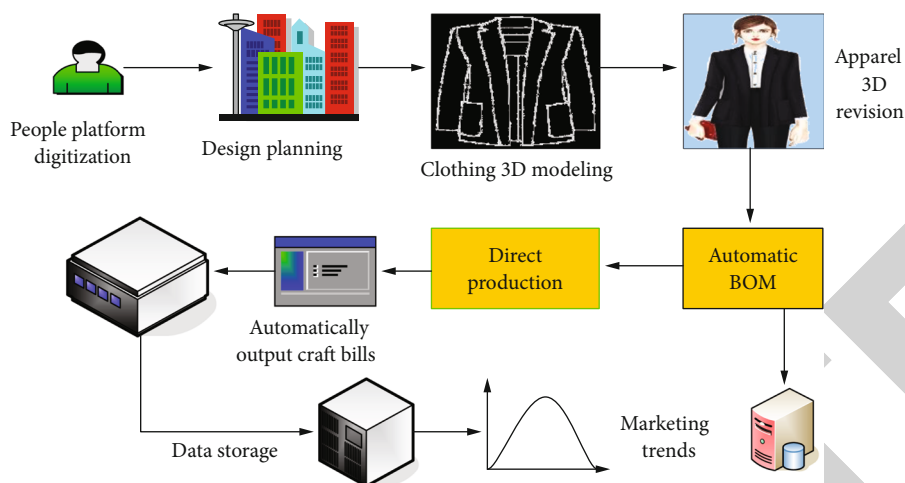
FIGURE 3: Clothing digital processing scheme.

environment parameters of the desktop, including the color of the current brush, the display ratio, and the height and width of the desktop.

The database has established three tables for each part, which are used to store the information of the points on the curve, the information of the curve, and the information of the parts.

When saving clothing parts, select the point selection tool, click the node or line with the right mouse button to display its number, and, at the same time, you can save the details of the selected point and line. This is an important step in the digitization of clothing styles. The correct and detailed definition of key points or lines is the basis for intelligent transformation of clothing. Figure 4 shows the digital intelligent design of clothing.

3. Results

Without instructions, the customer will study the details according to his selected style or sample style. The production process sheet is a guiding document for the workshop workers to process and make garments. Therefore, these contents need to be recorded in the customer-specific RFID tags. Clothing customization needs to redesign the process according to the customer's requirements. In order to reduce the operation time of the personnel, the basic craft sheet can be made in advance. After the system reads the customer style information, it will automatically jump out modification of the craft list which can form a customer's personalized craft list. This method of making documents greatly reduces the time to remake the craft sheet, and the technicians only need to click to select or input a few sentences to complete the production. The content of the subpage of the "production" link of the digital production process sheet is shown in Figure 5.

Click to enter the production sheet section, the production sheet that has been made will display "modify," and the customer column that has not been made will display the "make" link. The homepages of production sections such as production notices, production process sheets, production

processes, and RFID tags are all in tabular form, as shown in Table 2.

Set up a buffer zone for the stock of flour and accessories, and set a red line for the stock volume to ensure the stability of the buffer stock. When the inventory is below the red line, the management staff immediately contact the supplier to supplement the materials, instead of waiting until the surface accessories have been consumed. The traditional inventory only needs to keep the noodles and accessories. When the production department needs the materials, the outbound management is done. The material management under the digital collaborative management requires the management personnel to prepare in advance based on the daily fabric sales data and the inventory balance. This mechanism can ensure that as long as the fabric is displayed at the front end of the sales, the production department can provide enough processing materials, and the overall production process will not be affected by the lack of stock. At the same time, we can arrange customized production sequence and adjust production technology according to the availability of surface accessories. In the material management module, it is possible to know the inventory situation at any time and, according to the sales situation of last week, combined with the inventory red line, determine whether to request replenishment. Material management is shown in Table 3.

According to 50% calculation, the lowest market price and garment price are shown in Table 4. The cost of the vest is lower, and the use of yarn replacement to keep warm can also reduce a certain cost. The thicker the fabric weave, the greater the cost. Because the factory's products need to maintain a 15% profit, agents and shopping malls also have a certain profit, so the sales price is generally more than 50% of the cost. The retail price of the clothing is 198 yuan, and the actual purchase price is 89 yuan. Therefore, the clothing designed in this study is moderately priced in the market and has a certain market potential.

The fabric comparison of different samples is shown in Table 5. It can be seen from Table 5 that the ground yarns of the fabrics of the 9 samples are all nylon, so the antipilling performance is the same for the inside of the fabric. The veil
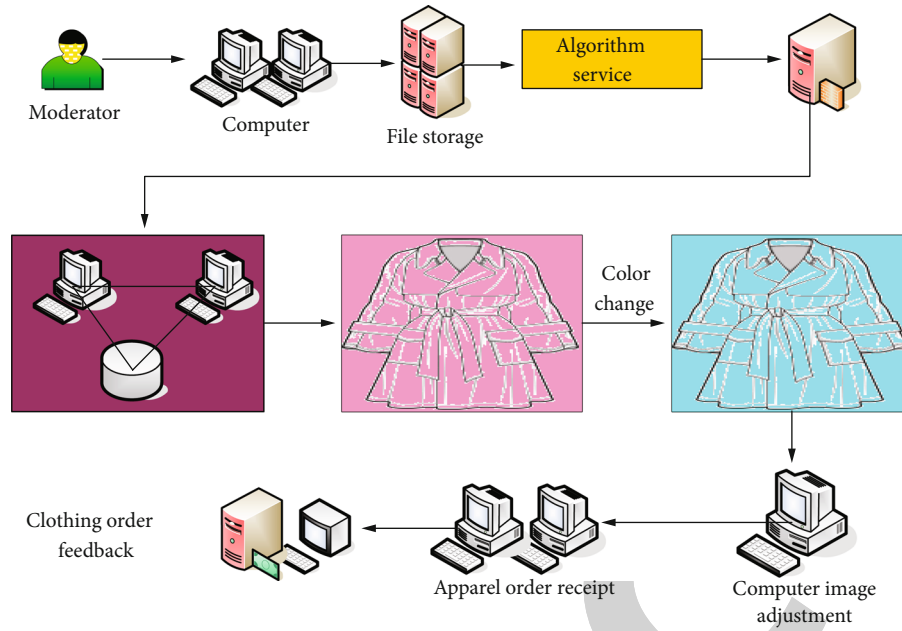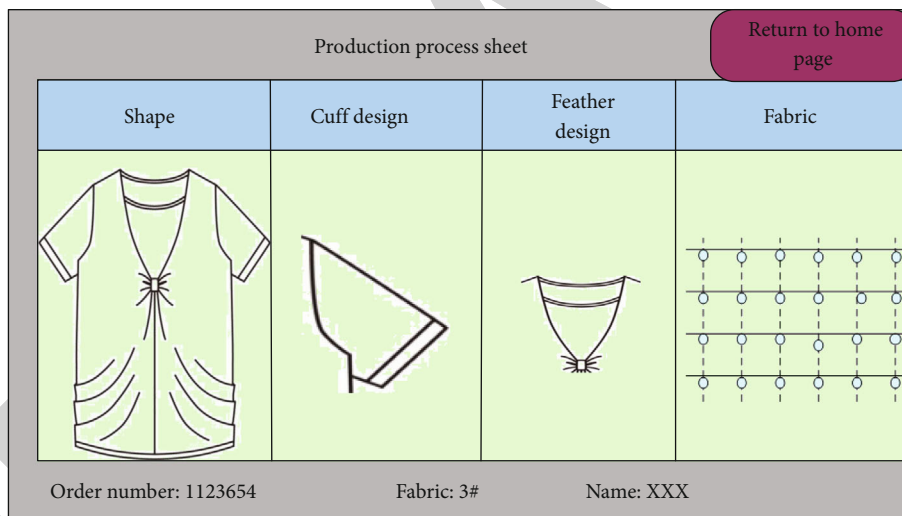
FIGURE 4: Digital and intelligent design of clothing.

FIGURE 5: Subpage content of the digital production process list.

TABLE 2: Home table form.

Customer serial number	Order number	Notice/process/ process/RFID
1	2222356	Make
2	2222357	Make
3	2222358	Make
4	2222359	Make
5	2222360	Revise
6	2222362	Revise
7	2222362	Revise

of the fabric is different, and the antipilling performance is different. The veil is nylon, which has a high resistance to pilling, and there is almost no pilling after rubbing for 7000. The antipilling performance of the fabric using viscose is relatively low. After 2000, serious pilling has been produced on the surface of the fabric. Experiments show that the fuzzing and pilling resistance of the veil made of nylon is better than that of the veil made of viscose. Nylon is not easy to fuzz and pill, which has little effect on the appearance of the fabric.

After the fabric was irradiated with a full-spectrum UVB metal halide solar lamp for 10 minutes, samples 1-6 rose to the highest temperature, and samples 2 and 5 were higher than other fabrics. Turn off the metal halide solar lamp, and each sample undergoes a 10-minute cooling process.

Table 3: Material management.

Type code	Style description	Last week's sales	Inventory balance	Inventory red line
#1	6% cotton, 94% polyester	11 meters	345	300 m
#3	Oxford fabric	23 meters	128	150 m
#4	2% chemical fiber, stripes	168 meters	456	400 m
#2	Pure cotton red	123 meters	785	200 m

Table 4: The minimum market price and ready-to-wear price are calculated at 50%.

Clothing style	$X1$	$X2$	$X3$	$Y1$	$Y2$
Cost price (yuan)	22	22	41	42	30
Lowest market price (yuan)	34	67	62	63	45

Table 5: Fabric comparison for different samples.

Clothing style	#1	#2	#3	#4	#5	#6	#7	#8
125	4.7	4	4.7	3.7	4	4.7	7	4
500	4	3	3	3.7	7	3	3.7	3
1000	7	3	3	3	3.7	3	3.7	3
2000	7	1.7	3.7	1	1	1	7	1
5000	7	1.1	3	1	3	1.7	7	1
7000	4.7	1	3.7	1.7	3.7	1.7	7	1.7

The final temperature of sample 2 is close to sample 1 and higher than sample 3, and the temperature of sample 5 is close to sample 4 and higher than sample 6. It can be seen that when graphene-modified nylon is on the surface of the fabric, the fabric has better heat storage performance. Graphene-modified nylon heat storage performance is shown in Figure 6.

The test results of the fabric's thermal insulation performance are shown in Figure 7. The veil of sample 2 uses graphene-modified nylon, and the heat preservation rate is higher than that of other fabrics. Judging from this, when the coverage of the graphene-modified nylon on the surface of the fabric increases, the warmth retention of the fabric is improved. The main reason is that the surface of the graphene-modified nylon has particulate matter, which increases its specific surface area and has more voids in the composition. The formation of still air is relatively more.

The mass fraction of graphene-modified nylon of sample 1 is 40%, and the corresponding *Staphylococcus aureus* and *Escherichia coli* have the highest antibacterial rate. When the mass fraction of graphene-modified nylon is reduced to 18%, *Staphylococcus aureus* has antibacterial rate of bacilli which is still greater than 80%. Graphene-modified nylon makes knitted fabrics have longer-lasting antibacterial properties, and when the mass fraction of graphene-modified nylon reaches 18%, the antibacterial properties of knitted fabrics can meet the standard. The antibacterial effect is shown in Figure 8.

Orthogonal experiment to explore the relationship between temperature, time, and expansion rate is shown in Figure 9. As the temperature increases, the expansion rate increases and then decreases. The longer the time, the greater the expansion rate, which will decrease after 30 s.

Fourier transform infrared spectroscopy is used to study the chemical structure of fibers. It can be seen that fiber 1 and fiber 2 have weak amide characteristic peaks around 1720 cm (respectively, -CO-NH- stretching vibration and bending vibration), while the modified graphene fiber does not show corresponding characteristics. Peak, which shows that during the formation of fiber 1 and fiber 2, the carboxyl groups on the modified graphene sheet are ionized and form noncovalent ionic bridges with the coupling agent. During the fiber drying process, in the process, with the volatilization of the solvent between the sheets, the distance between the modified graphene sheets decreases so that the ion bridge can be further reacted into a covalent bond form. The transition from ionic bridges to covalent bonds can enhance the mechanical properties of the fibers. Among them, such a transformation is more significant in fiber 2. Fourier transform means that a function that satisfies certain conditions can be expressed as a trigonometric function (sine and/or cosine function) or a linear combination of their integrals. In different research fields, Fourier transform has many different variants, such as continuous Fourier transform and discrete Fourier transform.

The mechanical properties of the fiber can be characterized by a tensile machine. In the characterization, the original size of the fiber is 1 cm, and the stretching rate is 10%/min. The final value obtained is the average value obtained by testing at least 10 samples of each fiber. Dried fiber 1 and fiber 2 prepared by this method have good mechanical strength. The mechanical strength of fiber 2, fiber 1, and modified graphene fibers can reach 356 MPa, 296 MPa, and 148 MPa, respectively, and their mechanical strength is comparable to modified graphene fibers and CNTs obtained by other wet spinning methods. At the same time, the fiber is also flexible and can be bent into different shapes or spun into a textile structure. High bulk density and large ion accessible surface area are two prerequisites for supercapacitor electrodes to achieve high volume capacity. The infrared spectra and tensile properties of fiber 1, fiber 2, and modified graphene fibers are shown in Figure 10.

4. Discussion

At present, the main types of thermal underwear on the market include pure cotton underwear, cashmere thermal underwear, and wool thermal underwear. The advantages of pure cotton underwear are breathable, moisture-permeable, soft, and comfortable, but its disadvantages are easy
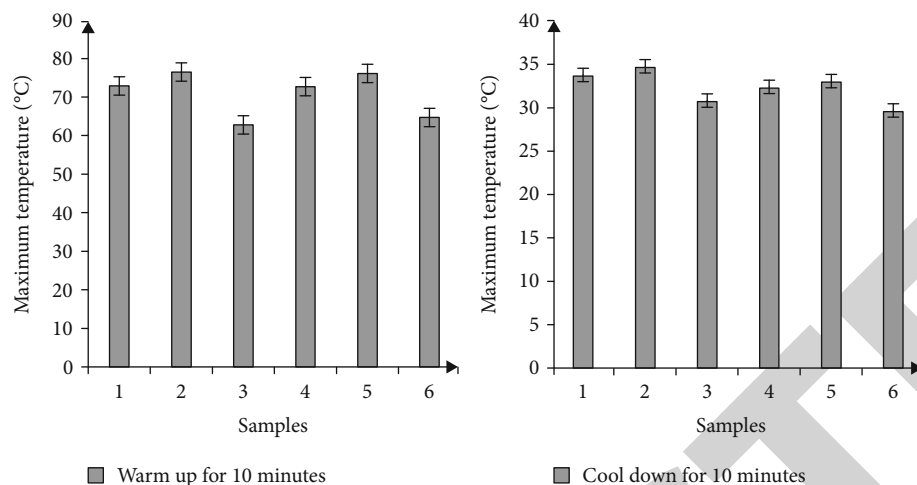
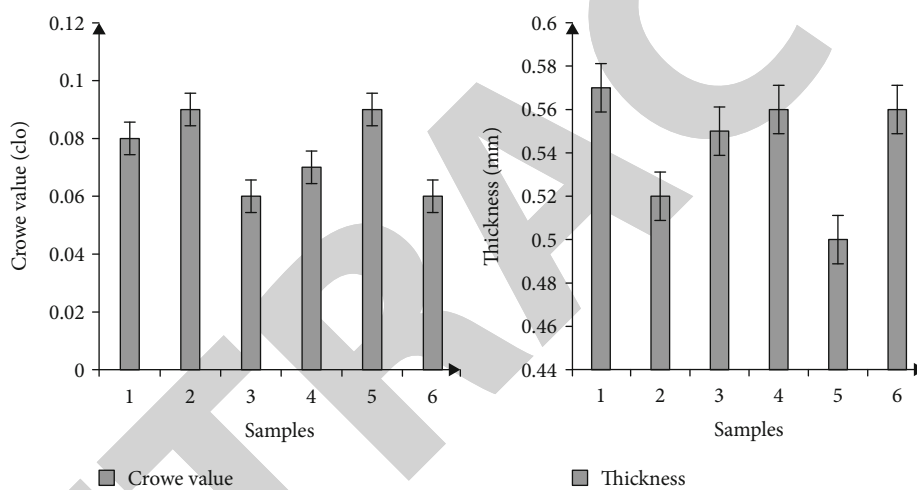Figure 6: Thermal storage properties of graphene-modified nylon.

Figure 7: Test results of the insulation performance of the fabric.
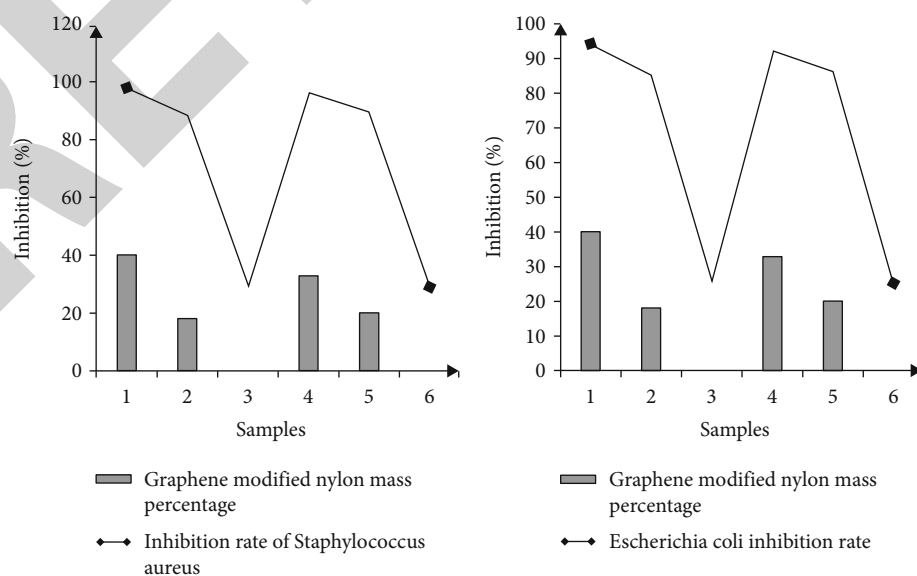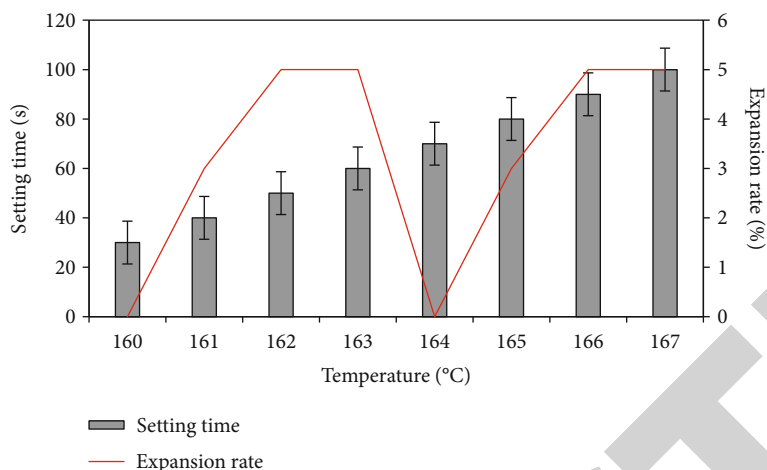

Figure 8: Antibacterial effect.

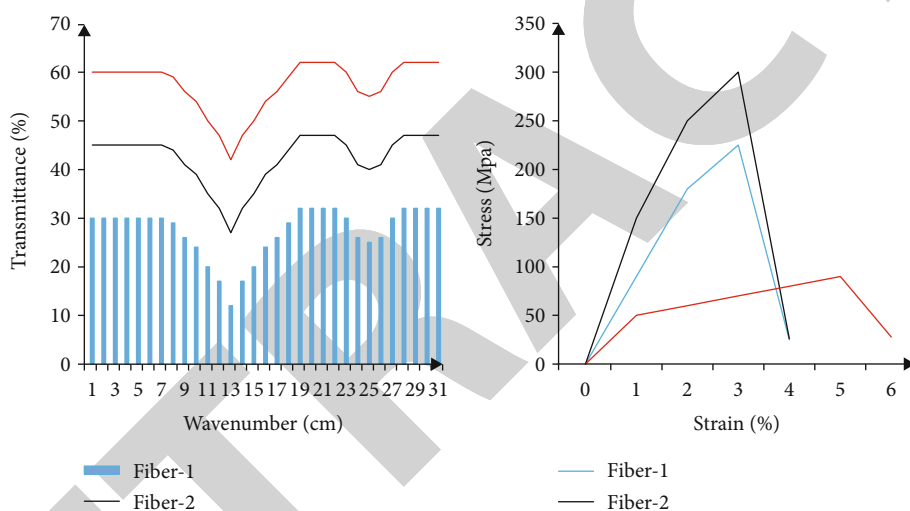Figure 9: The relation between the time and the amplification rate.

Figure 10: Infrared map and tensile properties of fiber 1, fiber 2, and modified graphene fibers.

to shrink, easy to deform, and not close to the body; cashmere thermal underwear has the advantages of soft, slippery, comfortable, and dry. There is a high content of still air inside the fabric, and the curled fluff on the surface of the fabric also enhances the fabric's elasticity, warmth retention, and bulkiness, making the underwear more elastic. Cashmere fabric can also quickly discharge sweat and quickly adjust the temperature to make people feel comfortable according to the external environment. However, the output of cashmere is relatively rare, and its price is relatively high; most of the wool used in wool thermal underwear is merino wool. Merino wool has delicate fabrics and has the advantages of being comfortable to wear next to the body, without any irritation. In addition to its good heat retention and moisture absorption, it also has a more comfortable stretch tension. In China, in the 1950s, a method of adding warmth to people with warm colors was adopted. Long ago, thermal underwear used was mostly cotton wool, which is comfortable and warm, and by increasing its thickness to reduce heat loss, thereby improving the thermal effect of underwear.

However, the thickness of the clothing is not linearly related to the warmth retention effect, and the warmth retention effect will decrease when it is thicker to a certain stage. In addition, the continuous increase in the thickness of underwear also seriously affects people's free movement and beauty. In order to make thermal underwear not only have good thermal insulation properties but also reduce the thickness of clothing, people have introduced various thermal underwear [25, 26].

The preservation of key lines and key points of components is the more cumbersome part of the digital preservation process, but it is also the basis for the intelligent realization of the software, because only the definition of each key line and each key point can be used to make these inputs The lines are no longer ordinary drawing lines, but smart lines that can be changed according to the requirements of the designer and can be combined and transformed in place according to instructions. The digital realization of clothing styles is the basic part of the entire clothing design software, and the purpose is to serve the display and changes

of subsequent clothing styles. Since the display of clothing styles requires a large number of fully defined original clothing styles as a basis, professional designers need to draw the required styles into the library. This drawing and storage of the digital clothing design system research process is the digital process of styles [27, 28]. How to enable professional designers to input styles accurately and as easily as possible has become the most important problem in the design process of this research [29].

With the development of industrialization, in order to reduce the cutting and stitching process in the traditional knitting process, seamless knitting technology has begun to be developed. Seamless garments can be woven not only on circular knitting machines but also on flat knitting machines. Seamless flat knitting machines can weave multiple tubular fabrics at the same time and connect them directly in the production process. The intelligence of a computer is given by people. When the designer enters the style into the computer, the computer does not know that the input line is the neckline, which is the neckline, or the combination of these lines is a collar, it just records the entire line in a picture format just the picture. Therefore, simply using the brush to draw how many styles on the computer can not realize the future intelligent call, so assigning values to the drawn lines and points has become a prerequisite for achieving intelligence [30, 31].

5. Conclusion

This research mainly discusses the digital clothing design method oriented to the production process of graphene-modified nylon knitted fabric. The color of graphene-modified cotton fiber is gray and black. With the increase of graphene content, the color becomes darker. Therefore, when designing graphene-modified cotton fiber jacquard graphene knitted fabric, the color matching has certain restrictions. The fabric feels plump after shrinking, forming fluff, and improving the warmth retention performance. Due to the different design of the veil material, ground yarn material, and organizational structure of the fabric sample, the basic parameters of the fabric are directly different. Therefore, first perform the width, density, areal density, thickness, and raw material content ratio of the blank sample of the fabric. The customization system platform was developed in research and changed the custom model of customers in the store to try on clothes in the past. Consumers can choose suitable products according to the clothing categories, styles, fabrics, etc. provided on the corporate website and can discuss the details of clothing with the designer. Designs such as embroidery and logo, while saving customers' time, meet customer's personalized clothing design. The follow-up work can further optimize the production process sheet and production notice. In the later stage of the article, different fabrics can be studied, combined with ergonomics, to design and develop a set of graphene composite fiber seamless underwear.

Data Availability

The data that support the findings of this study are available from the corresponding author upon reasonable request.

Conflicts of Interest

The author declared no potential conflicts of interest with respect to the research, authorship, and/or publication of this article.

References

[1] W. Bo, Y. Fu, Y. Liu, R. Guo, and T. S. Francis, "Displacement sensing with hetero-core fiber specklegram," *Journal of Holography and Speckle*, vol. 1, no. 1, pp. 53–57, 2017.

[2] J. Liu, G. Chen, and M. Jiang, "Supramolecular hybrid hydrogels from noncovalently functionalized graphene with block copolymers," *Macromolecules*, vol. 44, no. 19, pp. 7682–7691, 2011.

[3] X. Xu, Z. Zhang, J. Dong et al., "Ultrafast epitaxial growth of metre-sized single-crystal graphene on industrial Cu foil," *Science Bulletin*, vol. 62, no. 15, pp. 1074–1080, 2017.

[4] M. Khan, M. A. Rahman, P. Yasmin et al., "Formation and characterization of copper nanocube-decorated reduced graphene oxide film," *Journal of Nanomaterials*, vol. 2017, no. 4, 6 pages, 2017.

[5] Y. Cao, V. Fatemi, A. Demir et al., "Correlated insulator behaviour at half-filling in magic-angle graphene superlattices," *Nature*, vol. 556, no. 7699, pp. 80–84, 2018.

[6] J. Chen, "Research on evaluating the design effect of clothing and accessories with 2-tuple linguistic information," *Journal of Intelligent & Fuzzy Systems*, vol. 37, no. 2, pp. 2059–2066, 2019.

[7] P. Wang, T. Yao, Z. Li et al., "A superhydrophobic/electrothermal synergistically anti-icing strategy based on graphene composite," *Composites Science and Technology*, vol. 198, p. 108307, 2020.

[8] X. Xu and T. Li, "Design and implementation of hand-held electrocardiogram monitor," *Shengwu yixue gongchengxue zazhi*, vol. 34, no. 6, pp. 895–899, 2017.

[9] Y. Su, X. Wang, Y. Li, Z. Pan, and Z. Liu, "Analysis of the conductivity property of live working shielding clothing," *Journal of Industrial Textiles*, vol. 48, no. 3, pp. 643–659, 2018.

[10] A. Ambrosetti and P. L. Silvestrelli, "Adsorption of Rare-Gas Atoms and Water on Graphite and Graphene by van der Waals-Corrected Density Functional Theory," *The Journal of Physical Chemistry C*, vol. 115, no. 9, pp. 3695–3702, 2011.

[11] X. Zhang, Z. Li, X. Wang, and J. Yu, "The fractional Kelvin-Voigt model for circumferential guided waves in a viscoelastic FGM hollow cylinder," *Applied Mathematical Modelling*, vol. 89, pp. 299–313, 2021.

[12] F. Giubileo and A. D. Bartolomeo, "The role of contact resistance in graphene field-effect devices," *Progress in Surface Science*, vol. 92, no. 3, pp. 143–175, 2017.

[13] N. Yoshikawa, T. Tamaya, and K. Tanaka, "High-harmonic generation in graphene enhanced by elliptically polarized light excitation," *Science*, vol. 356, no. 6339, pp. 736–738, 2017.

[14] D. G. Papageorgiou, I. A. Kinloch, and R. J. Young, "Mechanical properties of graphene and graphene-based nanocomposites," *Progress in Materials ence*, vol. 90, no. 90, pp. 75–127, 2017.

[15] N. S. Fa, Y. Zhang, S. H. Li, T. Y. Lan, and J. L. Xu, "Hollow selenium encapsulated into 3D graphene hydrogels for lithium–selenium batteries with high rate performance and

Hindawi

Retraction

Retracted: Facile and straightforward synthesis of Hydrazone derivatives

Journal of Nanomaterials

This article has been retracted by Hindawi following an investigation undertaken by the publisher [1]. This investigation has uncovered evidence of one or more of the following indicators of systematic manipulation of the publication process:

(1) Discrepancies in scope

(2) Discrepancies in the description of the research reported

(3) Discrepancies between the availability of data and the research described

(4) Inappropriate citations

(5) Incoherent, meaningless and/or irrelevant content included in the article

(6) Peer-review manipulation

The presence of these indicators undermines our confidence in the integrity of the article's content and we cannot, therefore, vouch for its reliability. Please note that this notice is intended solely to alert readers that the content of this article is unreliable. We have not investigated whether authors were aware of or involved in the systematic manipulation of the publication process.

Wiley and Hindawi regrets that the usual quality checks did not identify these issues before publication and have since put additional measures in place to safeguard research integrity.

We wish to credit our own Research Integrity and Research Publishing teams and anonymous and named external researchers and research integrity experts for contributing to this investigation.

The corresponding author, as the representative of all authors, has been given the opportunity to register their agreement or disagreement to this retraction. We have kept a record of any response received.

References

[1] N. U. Ain, T. M. Ansari, M. R. H. Shah Gilani et al., "Facile and straightforward synthesis of Hydrazone derivatives," *Journal of Nanomaterials*, vol. 2022, Article ID 3945810, 6 pages, 2022.

Research Article

Facile and straightforward synthesis of Hydrazone derivatives

Noor ul Ain,[1] Tariq Mahmood Ansari,[1] M. Rehan H. Shah Gilani ⬤,[1,2,3] Guobao Xu,[3] Gaolin Liang,[2] Rafael Luque ⬤,[4] Mabkhoot Alsaiari ⬤,[5,6] and Mohammed Jalalah ⬤[5,7]

[1]*Institute of Chemical Sciences, Bahuddin Zakariya University, Multan 60800, Pakistan*

[2]*CAS Key Laboratory of Soft Material Chemistry, Department of Chemistry, University of Science and Technology of China, 96 Jinzhai Road, Hefei, Anhui 230026, China*

[3]*State Key Laboratory of Electroanalytical Chemistry, Changchun Institute of Applied Chemistry, Chinese Academy of Sciences, Changchun, Jilin 130022, China*

[4]*Departamento de Quimica Organica, Universidad de Cordoba, Campusde Rabanales, Edificio Marie Curie, CtraNnal IV, Km. 396, E-14014 Cordoba, Spain*

[5]*Promising Centre for Sensors and Electronic Devices (PCSED), Advanced Materials and Nano-Research Centre, Najran University, P.O. Box: 1988, Najran 11001, Saudi Arabia*

[6]*Empty Quarter Research Unit, Department of Chemistry, College of Science and Art in Sharurah, Najran University, Sharurah, Najran 11001, Saudi Arabia*

[7]*Department of Electrical Engineering, Faculty of Engineering, Najran University, Najran 11001, Saudi Arabia*

Correspondence should be addressed to Rafael Luque; luquerfl@gmail.com and Mabkhoot Alsaiari; mabkhoot.alsaiari@gmail.com

This study was undertaken to report the swift, facile and convenient synthesis of novel hydrazones obtained by condensation reaction between 2-Amino-3-formylchromone and hydrazine derivatives. Various characterization techniques such as MALDI Mass, FTIR, ^{1}HNMR and ^{13}CNMR spectrum analysis was done to determine the chemical structure of these novel six hydrazones. Furthermore, UV-Vis and fluorescence spectra was studied to calculate λ_{max} and ε_{max}. These hydrazones are quite useful for their facile synthesis and chemical structure. Such hydrazones require separate clinical research to find their applications in biomedical fields.

1. Introduction

Hydrazones are special organic compounds derived from the Schiff-base family and comprising of $\diagup_{C}{=}_{N}{-}_{N}{=}_{C}\diagdown$ bonds with additional donor sites. The donor sites make hydrazones more flexible and versatile for their structural and functional properties [1]. For instance, hydrazones are very significant reactants in different reactions such as hydrazone iodination, Shapiro and Bamford-Stevens reaction. On the other hand, hydrazones act as intermediates in Wolff-Kishner reaction. The C and H atoms in hydrazones tend to react with organometallic nucleophiles. Due to its highly acidic nature, the alpha-hydrogen atom of hydrazones is comparatively more nucleophilic than that of ketones [2]. Different studies have reported the biological importance of trigonal hybridized nitrogen atom in azomethine group of hydrazones which is remarkable for having one pair of electrons in its either π or sp^2 orbitals [3, 4]. Their hetero atomic nature and specific electronic properties make them very important structural compounds [5]. One of the most promising organic hole transporting materials are aromatic hydrazones. Recently, some researchers have reported the synthesis of polymeric hydrazones with remarkable properties such as high glass transition temperatures, good film-formation and moderate charge transport [6].

The ligation of hydrazones with surface immobilized hydrazines and aldehydes-modified antibodies can be used to anchor captured proteins on oxide coated biosensor substrates [7]. Hydrazones are also being used as inhibitors such as strong poly (ADP-ribose) glycohydrolase (PARG) [8].

Aroyl hydrazones have been reported to use in clinical theranostic applications due to their ferric ion scavenging activities [9]. The role of N, O and S in metal coordination at the active sites of numerous metallobiomolecules is also well known for various industrial, antimicrobial, anticancer and herbicidal applications [10, 11]. The chelating ligands get coordinated with metal ions by N, O or S as donor atoms. They have been found to show a wide variety of biological applications and are becoming a hotspot of research [12, 13]. The coordination of metal ions with the biologically active compounds can enhance their potential [14]. The polymeric hydrazones and their coordination in polymer drug conjugates is involved in hydrolysis. The rate of hydrolysis is significantly faster at acidic pH as compared to those of carbamates [15]. Hydrazone linkers are stable only in physiological conditions (pH 7.4) but they are prone to get cleaved under acidic conditions such as the intracellular conditions of endosomes and lysosomes protects them by forming micelle around. The hydrophobic drugs are hence gets protected from the host defense system in the body [16]. For instance, the anticancer drug DOX is released at higher rate under acidic conditions due to the nature of linkage between the DOX and micelles [17]. Chromone derivatives have received great attention of researchers for their applications. These compounds show wide spectrum of biological activities such as antimicrobial, antitumor, anti-allergic, antiviral, anti-inflammatory and anticancer activities [18].

Due to the aforementioned applications of hydrazones, herein we have reported the quick, facile, and convenient synthesis of six novel hydrazones containing N, O, or S atoms derived from Chromone. Hopefully, the combination of the chromone moiety with hydrazides may provide more biologically active resulting compounds. The typical synthesis of hydrazones can be described as follows:

$$2 - \text{Amino-3-formylchromone} + \text{Hyadrazide} \xrightarrow[\text{Reflux}]{\text{Acetic Acid}} \text{Hydrazone}$$

(1)

2. Materials and Methods

2-Amino-3-formylchromone, 2-hydroxybenzhydrazide, 3-hydroxy-2-napthoic acid hydrazide, isonicotinic acid hydrazide, 2-picolinyl hydrazide, thiophene-2-carboxylic hydrazide, and 2-furoic acid hydrazide were purchased from TCI (Japan) or J&K (China) with purity higher than 98% and used without further purification. UV-Vis spectra were recorded by using a UV-1000 spectrophotometer of Techcomp (China). Fluorescence spectra were recorded on F-7 Fluorescence spectrophotometer (Hitachi, Japan). MALDI mass spectra were obtained on time-of-flight Ultrflex II mass spectrometer (Bruker Daltonics). ^{1}H and ^{13}CNMR spectra of hydrazones in DMSO-d6 solutions were recorded on a 300 MHz Bruker AV 300 spectrometer and chemical shifts are indicated in ppm.

The equimolar mixture of 2-amino-3-formylchromone and hydrazine derivative (i.e., 2-hydroxybenzhydrazide, 3-hydroxy-2-napthoic acid hydrazide, isonicotinic acid hydrazide, 2-picolinyl hydrazide, thiophene-2-carboxylic hydra-

TABLE 1: Reaction conditions for the 6 hydrazones.

No.	Compd.	Solvent	Time(min)	Color	Yield (%)
1	CBH	Acetic acid	9	White	72
2	CNH	Acetic acid	1	Yellow	81
3	CISNH	Acetic acid	25	Yellow	69
4	CPH	Acetic acid	25	Yellow	73
5	CTPH	Acetic acid	25	Yellow	65
6	CFH	Acetic acid	25	Yellow	70

TABLE 2: MALDI mass data of the six synthesized hydrazones.

Serial no	Compd.	Calculated molecular mass	Observed molecular mass
1	CBH	323.302	323.592
2	CNH	373.360	373.531
3	CISNH	308.291	308.676
4	CPH	308.291	308.457
5	CTPH	313.331	313.487
6	CFH	297.265	297.280

TABLE 3: Fluorescence data of the 6 hydrazones.

No.	Compd.	Solvent	Conc. (μM)	Excitation (nm)	Emission (nm)
1	CBH	DMSO	100	374.0	458.0
2	CNH	DMSO	10	374.0	458.0
3	CISNH	DMSO	10	373.0	459.0
4	CPH	DMSO	10	390.0	458.2
5	CTPH	DMSO	10	374.0	456.4
6	CFH	DMSO	100	273.0	455.8

zide, or 2-furoic acid hydrazide) in acetic acid was refluxed for a certain time (Table 1). After reflux, the solution was cooled to room temperature, poured into ice-water and stirred. When the precipitates started to appear, the reaction mixtures were allowed to stand for an hour to afford maximum precipitates. Detail reflux times, colors of the precipitates, and yields of the hydrazones are shown in Table 1. MALDI mass, Fluorescence, FTIR, and ^{1}HNMR data of the 6 hydrazones are shown in Tables 2–5. UV-Vis and fluorescence spectra of the 6 hydrazones are shown in Figures 1 and 2, respectively.

3. Results

In this study, different hydrazides were used such as 2-hydroxybezhydrazide (CBH), 3-hydroxy-2-napthoic acid hydrazide (CNH), isonicotinic acid hydrazide (CISH), 2-picolinyl hydrazide (CPH), thiophene-2-carbhydrazide (CTPH), and 2-fouric acid hydrazide (CFH) for synthesis of hydrzones. The results of the study have revealed that it took only 9 min for CBH to obtain maximum white precipitates of the reaction mixture. On the other hand, the

TABLE 4: FTIR data of the 6 hydrazones.

No.	Compd.	C=O	C=N-	-NH-	-OH	NH-C=O	-NH2
1	CBH	1641	1605	3080	3500	1550	3284
2	CNH	1646	1606	3083	3437	1554	3270
3	CISNH	1650	1605	3292		1550	3434
4	CPH	1675	1606	3293		1535	3439
5	CTPH	1652	1607	3272		1551	3404
6	CFH	1655	1606	3291		1551	3411

TABLE 5: ^{1}HNMR data of the 6 hydrazones (ppm).

No.	Compd.	Deuterium Solvent	CH=N-	-NH-	-OH	-NH2
1	CBH	DMSO	8.96	12.15	11.98	9.70,9.36
2	CNH	DMSO	8.94	12.12	11.50	9.71,9.38
3	CISNH	DMSO	8.96	12.12	…….	9.68,9.38
4	CPH	DMSO	9.08	12.34	…….	9.88,9.28
5	CTPH	DMSO	8.91	11.94	…….	9.65,9.31
6	CFH	DMSO	8.92	11.93	…….	9.68,9.30
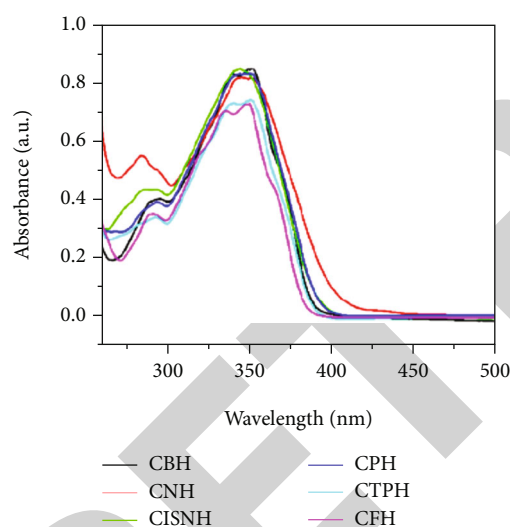
FIGURE 1: UV-Vis spectra of the 6 hydrazones in DMSO. The concentration of all hydrazones in μM are shown in Table 3.

hydrazones through CNH was appeared with greenish precipitates in the reaction flask within one minute. The stirring of reaction mixture on heat was done to obtain maximum precipitates for few minutes. But it was not happened during the synthesis of hydrazones of CISNH, CPH, CTPH, and CFH. The precipitates were not appeared during reflux. In these reactions, a clear solution was observed for 25 min.

After reflux, the solutions were cooled at room temperature, poured into ice-water, and stirred. When the precipitates started to appear, the reaction mixtures were allowed to stand for an hour to afford maximum precipitates. The precipitates were then filtered, dried, and characterized. Structures of the precursors and synthesized hydrazones are listed in Table 6.
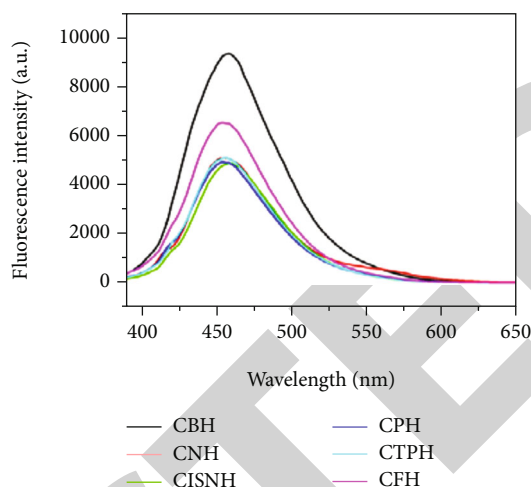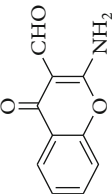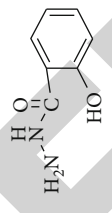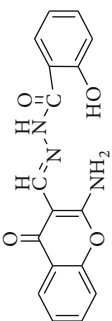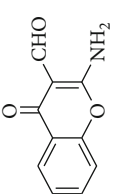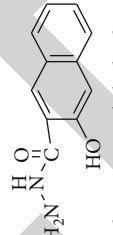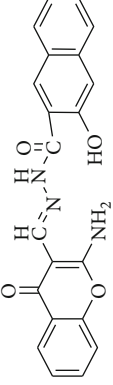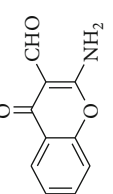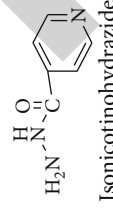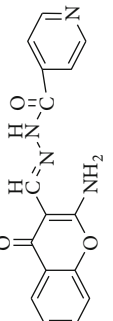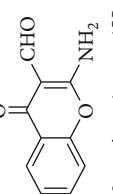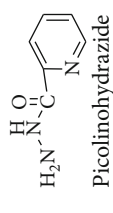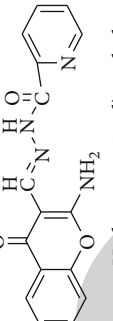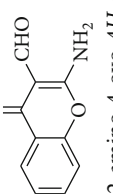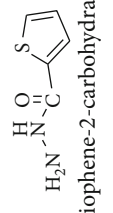

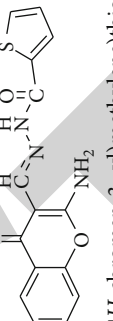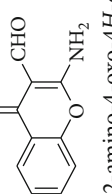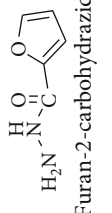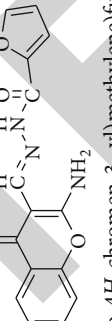FIGURE 2: Fluorescence spectra of the 6 hydrazones in DMSO. The concentration of CBH and CFH is 100 μM, while the concentration of other 4 hydrazones is 10 μM.

The results obtained through MALDI mass are well consistent with the molecular weights of these six hydrazones, as shown in Table 2. The λ_{max} and ε_{max} values of these six hydrazones were calculated according to their UV-Vis spectra. Fluorescent properties of the hydrazones were also studied and their excitation and emission wavelengths are mentioned in Table 2. Furthermore, FTIR, ^{1}H and ^{13}CNMR spectral data of the hydrazones confirmed the proposed structures of hydrazones.

4. Discussion

Detailed principle peaks on the FTIR and ^{1}HNMR spectra are listed in Tables 4 & 5, respectively. The signal at chemical shifts (δ, ppm) of 11.93-12.34 in ^{1}HNMR spectra are assigned to the –NH group, concomitant with the observation of rapid loss of these signals. Same is the case with -NH$_2$ groups whose peaks of both protons signals at chemical shifts of 9.28-9.88. The signals at δ of 11.98 ppm and 11.50 ppm are assigned to the aromatic –OH protons of CBH and CNH, respectively. The resonance peaks between 8.91 ppm to 9.08 ppm in the spectra are assigned to the azomethine (-CH=N-) of these hydrazones. Signals at δ 6.70-8.79 are assigned to the aromatic protons. In 13CNMR spectra of these hydrazones, four key resonance signals were observed. These are δ 153.0-153.4 for azomethine (-CH=N-), carbonyl carbon of chromone ring roughly at δ 162.9-165.0, carbon of chromone ring attached to carbon of azomethine at δ 92.6-92.8, and δ 173.3-173.7 for the carbon (–C-NH2) on the chromone ring in all hydrazones. The signals of carbonyl carbons from hydrazine motifs were observed roughly at δ 162.9, 160.7, 150.4, 160.1, 157.3, and 145.7 from CBH, CNH, CISNH, CPH, CTPH, and CFH, respectively. The detail of other carbons in all hydrazones is described as following: Six carbons on the benzene ring of chromone of CBH are shown at δ 145.6, 133.9, 128.1, 125.3, 121.8, and 117.6. Three carbons on chromone ring are δ 173.7, 165.0, and 92.6. Six carbons on the benzene ring having –

TABLE 6: Chemical structures of reactants and hydrazones in this work.

Reactant	Hydrazide	Product
2-amino-4-oxo-4H-chromene-3-carbaldehyde	2-hydroxybenzohydrazide	(E)-N′-((2-amino-4-oxo-4H-chromen-3-yl) methylene)-2-hydroxybenzohydrazide
2-amino-4-oxo-4H-chromene-3-carbaldehyde	3-hydroxy-2-naphthohydrazide	(E)-N′-((2-amino-4-oxo-4H-chromen-3-yl)methylene)-3-hydroxy-2-naphthohydrazide
2-amino-4-oxo-4H-chromene-3-carbaldehyde	Isonicotinohydrazide	(E)-N′-((2-amino-4-oxo-4H-chromen-3-yl)methylene)isonicotinohydrazide
2-amino-4-oxo-4H-chromene-3-carbaldehyde	Picolinohydrazide	(E)-N′-((2-amino-4-oxo-4H-chromen-3-yl)methylene)picolinohydrazide
2-amino-4-oxo-4H-chromene-3-carbaldehyde	Thiophene-2-carbohydrazide	(E)-N′-((2-amino-4-oxo-4H-chromen-3-yl)methylene)thiophene-2-carbohydrazide
2-amino-4-oxo-4H-chromene-3-carbaldehyde	Furan-2-carbohydrazide	(E)-N′-((2-amino-4-oxo-4H-chromen-3-yl)methylene)furan-2-carbohydrazide

OH were shown at δ 160.1, 133.9, 125.3, 119.0, 116.9 and 115.2. Six carbons on the benzene ring of chromone of CNH are shown at δ 150.4, 133.4, 129.0, 121.1, 121.1, and 117.1. Three carbons on chromone ring are at δ 173.5, 163.9, and 92.6. Ten carbons on the naphthyl ring are shown at δ 145.7, 129.0, 127.1, 125.9, 125.2, 125.2, 125.2, 125.2, 124.1, and 110.9. Six carbons on the benzene ring of chromone of CISNH are shown at δ145.7, 128.7, 126.9, 125.0, and 116.8. Three carbons on the chromone ring are at δ 173.5, 163.0, and 92.6. Five carbons on the isonicotinic ring are shown at δ133.6, 125.0, 125.0, 121.5, and 121.5. Six carbons on the benzene ring of chromone of CPH are shown at 150.0, 135.2, 127.1, 125.0, 122.2, and 117.1. Three carbons on chromone ring are at δ 173.4, 163.1, and 92.8. Five carbons on the pyridine ring are shown at δ 148.9, 146.1, 134.9, 125.0, and 122.2. Six carbons on the benzene ring of chromone of CTPH are shown at δ 144.2, 128.5, 125.3, 125.3, 121.8, and 117.1. Three carbons on the chromone ring are at 173.4, 162.9, and 92.8. Four carbons on the thiophene ring are shown at δ 138.1, 133.5, 131.6, and 128.5. Six carbons on the benzene ring of chromone of CFH are shown at δ 133.4, 125.2, 125.2, 125.2, 121.7, and 116.8. Three carbons on the chromone ring are at δ 173.3, 163.0, and 92.8. Four carbons on the furan ring are shown at δ145.7, 145.7, 114.5, and 112.2. These spectroscopic data confirmed the successful syntheses of the 6 hydrazones mentioned above. The λ_{max} (nm) and εmax values of these six hydrazones were calculated according to their UV-Vis spectra, the λ_{max}, are in the range of 344 to 351 nm and ε_{max} was from 1.50 x 10^4 to 3.26 x 10^4 cm^{-1} M^{-1}.

5. Conclusions

This study highlighted the synthesis and spectroscopic characterization of 6 novel hydrazones. The hydrazones were quickly synthesized through convenient and facile approach. This study reported the synthesis of CBH in 9 min. On the other hand, CNH was synthesized in 1 min only. After the reflux of 25 min, other 4 hydrazones were synthesized. The importance of these hydrazones can be realized in live cell imaging for detection of metal ions. These compounds are quite beneficial for their role as chemo sensors. As a future perspective of this study, these hydrazones containing oxygen, sulfur, and nitrogen atoms may lead biologists for its applications in biomedical fields.

Data Availability

No data were used to support this study.

Conflicts of Interest

There is no conflict of interest.

Funding

Acknowledgments

References

[1] P. G. Avaji, C. H. V. Kumar, S. A. Patil, K. N. Shivananda, and C. Nagaraju, "Synthesis, spectral characterization, in-vitro microbiological evaluation and cytotoxic activities of novel macrocyclic bis hydrazone," *European Journal of Medicinal Chemistry*, vol. 44, no. 9, pp. 3552–3559, 2009.

[2] G. Uppal, S. Bala, S. Kamboj, and M. Saini, "Therapeutic review exploring antimicrobial potential of Hydrazones as promising Lead," *Der Pharma Chemica*, vol. 3, no. 1, pp. 250–268, 2011.

[3] O. Pouralimardan, A. C. Chamayou, C. Janiak, and H. Hosseini-Monfared, "Hydrazone Schiff base-manganese(II) complexes: Synthesis, crystal structure and catalytic reactivity," *Inorganica Chimica Acta*, vol. 360, no. 5, pp. 1599–1608, 2007.

[4] H. G. Li, Z. Y. Yang, B. D. Wang, and J. C. Wu, "Synthesis, crystal structure, antioxidation and DNA-binding properties of the ln complexes with 1-phenyl-3-methyl-5-hydroxypyrazole-4-carbaldhyde-(benzoyl)hydrazone," *Journal of Organometallic Chemistry*, vol. 695, pp. 412–422, 2010.

[5] M. Al-Nuri, A. Haroun, I. Warad, M. Mahfouz, and S. Al-Resayes, "Synthesis and characterization of some antifungal active hydrazones from combined of several functionalities hydrazides with di-2-pyridyl ketone," *Journal of Saudi Chemical Society*, vol. 11, pp. 313–318, 2007.

[6] R. Laurinaviciute, J. Ostrauskaite, J. V. Grazulevicius, and V. Jankauskas, "Synthesis, properties, and self-polymerization of hole-transporting carbazole- and triphenylamine-based hydrazone monomers," *Designed Monomers and Polymers*, vol. 17, no. 3, pp. 255–265, 2014.

[7] J. Y. Byeon, F. T. Limpoco, and R. C. Bailey, "Efficient bioconjugation of protein capture agents to biosensor surfaces using aniline-catalyzed Hydrazone ligation," *Langmuir*, vol. 26, no. 19, pp. 15430–15435, 2010.

[8] R. Islam, F. Koizumi, Y. Kodera, K. Inoue, T. Okawara, and M. Masutani, "Design and synthesis of phenolic hydrazide hydrazones as potent poly (ADP-ribose) glycohydrolase (PARG) inhibitors," *Bioorganic & Medicinal Chemistry Letters*, vol. 24, no. 16, pp. 3802–3806, 2014.

[9] J. X. Yu, V. D. Kodibagkar, R. R. Hallac, L. Liu, and R. P. Mason, "Dual 19F/1H MR gene reporter molecules for in vivo detection of β-galactosidase," *Bioconjugate Chemistry*, vol. 23, no. 3, pp. 596–603, 2012.

[10] S. J. Peng, "Synthesis, crystal structures, and antibacterial activity of two Hydrazone derivatives 3-Methoxy-N'-(3,5-Dibromo-2-Hydroxybenzylidene)Benzohydrazide methanol solvate and 3-Methoxy-N'-(2,4-Diclorobenzylidene)Benzohydrazide," *Journal of Chemical Crystallography*, vol. 41, no. 3, pp. 280–285, 2011.

[11] J. Wu, B.-A. Song, D.-Y. Hu, M. Yue, and S. Yang, "Design, synthesis and insecticidal activities of novel pyrazole amides

Hindawi

Research Article

Nanomaterials Combined with Sports Rehabilitation Therapy in the Treatment of Shoulder Arthritis of Volleyball Players

Jie Cui ⬤

Department of Sports and Arts, Bengbu Medical College, Bengbu, 233030 Anhui, China

Correspondence should be addressed to Jie Cui; 0200047@bbmc.edu.cn

Shoulder arthritis is one of the most common injuries of professional volleyball players. It needs shoulder force to buckle, block, and bounce, which leads to frequent shoulder injuries. In addition, the late rehabilitation treatment is not in place, which will seriously affect the performance of volleyball players' skills. Periarthritis of the shoulder is referred to as frozen shoulder, commonly known as congealed shoulder and fifty shoulder. The shoulder pain gradually develops, worse at night, and gradually increases, and the shoulder joint movement function is limited and increasingly aggravated. After reaching a certain level, it gradually relieves and finally fully recovers as the main manifestations of the shoulder joint capsule and its surrounding ligaments and tendons. Shoulder periarthritis is a common condition in which shoulder pain and inconvenience are the main symptoms. This paper studies the application of nanomaterials combined with sports rehabilitation therapy in the treatment of shoulder arthritis of volleyball players. We selected 50 volleyball players with shoulder arthritis injuries, randomly assigned nanomaterials combined with sports rehabilitation therapy as the experimental group and traditional sports rehabilitation therapy as the control group, 25 cases in each group. The experimental group was treated with nanomaterials combined with sports rehabilitation, while the control group was treated with traditional sports recovery methods for 5 weeks. Nanomaterials have a certain uniqueness. When the scale of matter is small to a certain extent, quantum mechanics must be used instead of traditional mechanics to describe its behavior. When the particle size of the powder is reduced from 10 microns to 10 nanometers, its particle size is 1000 times, and when converted into volume, it will be 10 times the 9th power, so there will be obvious differences in the behavior of the two. The physical examination of the two groups of volleyball players' shoulder joint visual analogue scale (VAS) pain score and shoulder joint isokinetic detection (including shoulder joint extension and adduction, shoulder joint flexion and extension, and shoulder joint movement to 90° shape) is compared. The results showed that the VAS score of the experimental group was significantly lower than that of the control group ($P < 0.05$), and the isokinetic test of the experimental group was better than that of the control group ($P < 0.05$). After exercise rehabilitation training for shoulder joint dysfunction, the average strength and activation of 10 muscles were improved, among which the lower trapezius, the middle trapezius, and the serratus anterior were significantly improved. It can be seen that as an effective treatment of shoulder arthritis, nanomaterials combined with sports rehabilitation therapy can not only accelerate the rapid recovery of volleyball players after injury but also effectively prevent the occurrence of arthritis symptoms, so that volleyball players can give full play to their skills on the court.

1. Introduction

Under coach Lang Ping's leadership, the Chinese women's volleyball team won the World Cup in 2015 and the Rio Olympics in 2016. In 2018, China once again dominated Asia and became the champion of the Jakarta Asian Games. It stands at the top of the world again, and Chinese volleyball has entered a new stage of development. Volleyball is a kind

of competitive sport which is dominated by technology [1]. It usually takes a long time and repeated training to improve skills. Long-term, high-load training is easy to make athletes' muscles and joints suffer from chronic injury or strain. If we do not pay attention to it, the condition will appear repeatedly or even worsen, and it will not be easy to cure completely. Sports training, competition practice, and sports injury are inseparable. Training can improve the athletes'

sports level. Competition is one of the standards to test athletes' sports ability. But at the same time, unreasonable, overload training or incorrect technical movements will also cause sports injury, affecting the normal training and the improvement of competition results. Therefore, it is one of the necessary conditions for volleyball players to know the common sports injuries, preventive measures, and rehabilitation means. Shoulder arthritis is very common in sports, especially in badminton, volleyball, swimming, baseball, and other items; because of the retrograde movement of athletes' upper limbs, it is easy to produce the symptoms of shoulder joint pain. In 2016, the National Training Bureau also carried out statistics on athletes' rehabilitation injuries. The main injuries of shoulder joint were subacromial impact syndrome, rotator cuff injury, and Meng lip injury.

Shoulder joint injury [2] is one of the most common injuries of volleyball players, which is an important reason to affect the training and competition performance of volleyball players. In volleyball, shoulder joint is used in defense, block, spike, and serve. Therefore, volleyball technique depends on the function of shoulder. In the process of spiking, the strength is transferred from the body, shoulder, elbow, and wrist to the end of the upper limb. When it is transferred to the end of the upper limb, it needs to reach a higher speed to catch a high-quality ball. When you swing your arm, you need to overcome a lot of resistance and a lot of spiking. Shoulder joint, as an important part of the upper limb and body power transmission, needs to bear high exercise load. Therefore, if the athletes continue to carry out high-load training under the condition of insufficient preparation or irregular technical movements, they may damage the shoulder joint. Shoulder joint is the largest and most flexible joint of the upper limb. The articular surface is large, the glenoid is shallow and small, the joint capsule is loose, and the ligament is weak. These physiological characteristics determine that the shoulder joint has good flexibility and poor stability. In the volleyball injury technique, the shoulder joint injury caused by impact is the most likely. The common cause of shoulder pain caused by shoulder joint injury is subacromial impact syndrome, and the nature of the injury is mainly chronic injury. In daily training and competition, due to the need for multiple swing arm strokes, high-intensity, long-term exercise on the shoulder is easy to make the impact of the coracoacromial arch, leading to subpeak mucositis, and more serious will lead to shoulder sleeve tissue degeneration or tear, leading to shoulder pain and obstacles. The method of adding vibration stimulation to conventional strength training can more effectively improve the effect of volleyball players' shoulder joint strength training.

When spiking the ball, the abduction angle of the upper arm is less than 120°, and the flexion of the arm to hit the ball forward and downward at a high speed is the most important factor leading to shoulder injury of the players. Secondly, because these young players started the college entrance examination for sports from the second and third year of high school, and the training time was tight, so the exercise load and amount of exercise were not reasonable enough. In recent years, semiconductor polymer nanoparti-

cles with strong near-infrared absorption and good biocompatibility have attracted people's interest in biosensors, fluorescence imaging, photoacoustic imaging, and photothermal therapy. There are three commonly used methods for preparing conjugated polymer nanoparticles: nanoprecipitation, microemulsion, and self-assembly. However, these conjugated polymer nanoparticles with hydrophobic surfaces are not stable in themselves, and their surfaces do not further couple the functional groups of biomolecules. In general, amphiphilic polymers or phospholipids can be coated on the surface of conjugated polymer nanoparticles to improve their biocompatibility and provide further modified functional groups. Therefore, most of the existing conjugated polymer nanoparticles have the problems of easy dissociation and poor structural stability, which hinder their application in biomedicine. In recent years, it has been reported that hydrophilic polyethylene glycol (PEG) [3] is grafted onto the main chain of semiconductor polymer to prepare nanoparticles with stable structure. However, the synthesis of amphiphilic semiconductor oligomers requires a time-consuming and laborious process. Each modification is specially designed for each different semiconductor-conjugated polymer. Therefore, it is necessary to prepare semiconductor polymer nanoparticles with stable structure, surface functional groups, excellent imaging, and therapeutic properties [4]. This paper studies the treatment of volleyball players' shoulder arthritis with nanomaterials combined with exercise rehabilitation therapy [5, 6]. Badminton is an indoor sport that uses a long-handled mesh racket to hit a small ball made of feathers and cork across the net. The badminton game is played on a rectangular field with a net in the middle of the field. The two sides use various techniques and tactics such as serving, hitting, and moving the ball to hit the ball back and forth on the net so that the ball does not fall within the effective area of its own side or make the opponent miss the ball to win.

In volleyball, serving and spiking are the two most lethal techniques in volleyball, and they are also the basic techniques that are mainly controlled by the shoulder joint, using the most and deepest techniques of the shoulder joint. The joints have certain physiological and anatomical weaknesses, and if they are not well adjusted in the teaching and training, sports injuries will be caused. Shoulder injury will not only disrupt the daily training rhythm of volleyball players but also reduce their competitive level and performance and even end their career in advance. On this basis, this study compared the characteristics of athletes with or without shoulder arthritis in the school of education, Nanjing University of Physical Education, and the observation of shoulder pain, the impact of stability and flexibility syndrome peak, and the peak of power sequence and arm swing to complete the mobilization and recruitment of dynamic chain muscle strength are different from the normal shoulder joint function of athletes. On the one hand, through the timely evaluation and detection of the shoulder function of volleyball players, functional training is carried out for the weak points of the shoulder to prevent injuries. On the other hand, after the occurrence of mild injury, timely targeted training should be carried out to find and correct wrong

movements, strengthen weak muscle strength, reduce the chance of injury recurrence, and improve sports performance and competitive ability. Through the application of nanomaterials combined with sports rehabilitation therapy in the experimental group and the traditional treatment in the control group for 5 weeks, respectively, the physical examination of the two groups of volleyball players' visual analogue scale (VAS) pain score and shoulder joint isokinetic test (including shoulder joint extension and adduction, shoulder joint extension and adduction, and shoulder joint isokinetic test) was carried out. The results show that the viewpoint put forward in this paper is conducive to the recovery of shoulder arthritis [7]. The results can provide a reference for the scientific training and rehabilitation of volleyball players and provide suggestions for the treatment and prevention of shoulder arthritis of volleyball players. Visual analogue scale (VAS) is a simple method for measuring pain intensity in clinical practice. The basic method is to use a walking scale about 10 cm long, with 10 scales on one side, and two ends, respectively. Among them, the "0" score indicates no pain, and the "10" score indicates the most severe pain, which is unbearable. In clinical use, turn the scale side away from the patient and let the patient stand on the ruler; the corresponding position that can represent the degree of pain is marked on the top, and the doctor assigns the score according to the position marked by the patient. In daily training and competition, volleyball players with subacromial impact syndrome will have pain in their shoulder when they repeatedly serve and spike for a long time, which will negatively affect their shoulder function, competitive ability, and psychological state.

2. Preparation of Conjugated Polymer Nanomaterials

The conjugated polymer system [8] of the molecular main chain contains large delocalized π bond. The most important characteristics of them are that they have three unsaturated carbon bonds, double space carbon bonds, or single structure bonds intersecting with aromatic rings. This property is conducive to the delocalization of free electrons and carriers in the polymer. The delocalization and delocalization polarization of the internal structure of the conjugated polymer directly affect the luminescence of the conjugated polymer. Because of the long-range shift and large π bond, the gap between the molecular energy level becomes smaller and smaller, and the free electron can move freely along the main chain of the main chain-conjugated polymer, that is, the so-called "molecular line" effect. Conjugated polymers have excellent electrical signal conductivity, excellent energy transfer rate can achieve the effect of signal amplification, and fluorescence resonance energy transfer (FRET) [9] can achieve significant enhancement of fluorescence signal. Nanomaterials refer to materials that have at least one dimension in the three-dimensional space at the nanometer size (1-100 nm) or are composed of basic units, which are approximately equivalent to the scale of 10 to 1000 atoms tightly packed together.

2.1. Synthesis Methods of Common Conjugated Polymer Nanomaterials

2.1.1. Suzuki Coupling Reaction. The early Suzuki coupling reaction [10], sometimes called Suzuki Miyagi coupling reaction, was named after scientists Suzuki Chang and Miyagi. Suzuki's reaction mechanism consists of three steps in the catalysis and circulation, which has been widely used at present.

The first step is oxidation addition reaction. As a catalyst, LNPD and electrophilic RX have oxidative addition, and the product is a transition compound. The first step is the most important. PEG is a series of products that are nontoxic, nonirritating, and slightly bitter in taste, have good water solubility, and have good compatibility with many organic components. They have excellent lubricity, moisture retention, dispersibility, adhesive, antistatic agent and softener, etc. and are widely used in cosmetics, pharmaceuticals, chemical fibers, rubber, plastics, paper, paint, electroplating, pesticides, metal processing, and food processing. There are a wide range of applications in the industry.

The second step is transfer metallization. Under the action of alkaloids, organic borides are first transformed into negatively charged substances and then metallized with the products.

The third step is reduction and elimination of reaction. Product R is formed by transfer metallization and elimination process $R_1 - R_2$. The FLIR E40 touchscreen user interface is designed to be intuitive, taking full advantage of the full 3.5-inch display and providing easy access to all analytical tools. The 3 movable detection points can accurately and perfectly analyze three-phase electrical problems. By viewing the automatically calculated temperature difference, you can instantly grasp the crux of the problem. The temperature range and image can be fine-tuned. Various suitable color palettes are available to enhance detection. Thermal images are superimposed with visible light images for easy and clear positioning.

2.1.2. Heck Reaction [11]. Palladium is used as catalyst to catalyze the cross-coupling reaction of halogenated aromatics, haloalkenes, and vinyl compounds, which is called Heck reaction. It is worth mentioning that β-hydrogen, a free halogenated hydrocarbon, can also trigger the ghost alkylation reaction.

First of all, halogenated products have oxidation and replenishment; the matrix is coordination and transfer, carbon bond rotation, palladium and β hydrogen removal sequence, and catalyst deoxidation and elimination cycle.

2.1.3. Sonogashira Cross-Coupling Reaction. The synthesis of aryl halides and alkenyl halides with palladium or copper as catalyst under the catalysis of terminal alkynes is called the Sonogashira cross-coupling reaction. Transition metal catalysis is one of the most commonly used methods for the synthesis of carbon triple bonds. The Sonogashira reaction is widely used in material synthesis, natural material purification, active intermediate catalysis, and other fields. Due to the high price of palladium, copper catalyst is usually used.

The Sonogashira coupling reaction has been developed and improved by a large number of chemical researchers. On the one hand, the cost of the reaction process is low and the conditions for chemical synthesis are mild. On the other hand, a large number of novel green reaction conditions are used in the Sonogashira cross-coupling reaction, which has far-reaching significance in the field of chemistry and great potential in the development and application of real life. At present, the main problem is that the activity of copper salt as catalyst is not enough, and no efficient and cheap copper salt ligand has been found.

2.1.4. Glaser Polymerization. The oxidative stress polymer reaction with copper as catalyst is called the Glaser polymer reaction. The Glaser coupling reaction is also an important reaction to construct C-C single bond, which plays a key role in the synthesis of natural compounds, drugs, and optoelectronic information materials. In recent years, there are many reports about catalytic coupling reactions, mainly focusing on the search for new catalysts, new ligands, and new catalytic systems.

In recent years, the coupling reaction between polyethylene glycol and ionic liquid has been widely used in chemical industry. At present, polyethylene glycol and ionic liquid are the green media studied by many researchers. Compared with the Glaser reaction method using traditional organic solvent, the first two methods have simple conditions and high yield. On the other hand, reactants can be recycled and reused, thus greatly improving the utilization of atoms from the point of view of atoms in the chemical synthesis process. In addition, the odor of traditional basic organic amines can be rejected in the reaction process. In the process of chemical synthesis of Glaser in the medium of PEG, the effects of different molecular weight of PEG, different catalysts, different copper ligands, and different temperatures on Glaser reaction were studied. The best reaction conditions were selected, and the catalytic coupling of terminal alkynes with different properties was realized under the best reaction conditions. RX reacts with a non-transition metal-organic compound RM under the catalysis of transition metal complexes to form carbon-carbon bonds. The cross-coupling reaction has high efficiency, good selectivity, and mild reaction conditions and is an effective means of modern organic synthesis.

2.2. Preparation of Instruments. The distribution of nanomaterials in the cells and the production of ROS were studied by fluorescence imaging of Olympus IX81 laser scanning confocal microscope [12]. The cytotoxicity test and analysis were carried out by Casey cell count, enzyme-linked immunosorbent assay, and Sch RFE system. The temperature change of photothermal test was monitored by FLIR E40 thermal infrared imager; PerkinElmer used the new K-series III small animal internal imager to image the human shoulder.

2.3. Preparation Method of Polymer Nanoparticles. At present, the three methods most widely used in the field of conjugated polymer nanoparticles are nanoprecipitation, microemulsion, and self-assembly.

2.3.1. Nanoprecipitation Method. Nanoprecipitation is also called reprecipitation. The main step is to inject the hydrophobic conjugated polymer organic solution into the weak solvent represented by ultrapure water under the condition of ultrasound with certain power intensity. Under the hydrophobic action, the solubility of conjugated polymer in two solvents is very different. Once the conjugated polymer molecules extend in organic solvent, they will gradually agglomerate in ultrapure water and finally form spherical nanoparticles. In addition to the coupling polymer itself, the size of nanoparticles is also affected by their high concentration in the initial organic solution. Then, the organic solvent and excess water were removed by rotary evaporation apparatus, and finally, the conjugated polymer nanoparticles with good stable distribution were obtained.

2.3.2. Microemulsion Method. Compared with the nanoprecipitation method, the biggest difference between the microemulsion method is that the solvent phase is composed of acetone, dichloromethane, tetrahydrofuran, and other organic solvents and is insoluble in water. The most important thing is to add surfactants as stabilizers in the process of microemulsion preparation. The main function of surfactants is to prevent the aggregation of conjugated polymers. Firstly, the organic semiconductor polymer is dissolved in the organic phase and then injected into the super pure water mixed system containing surfactant. In the high-power water bath ultrasonic state, the organic phase in the conjugated polymer is dispersed slowly in the aqueous phase, and finally, the emulsion is formed. Finally, we can turn on the rotary evaporator, evaporate the excess organic solvent and ultrapure water, and finally form the nanosolution we need. In this process, the emulsion forms four conjugated polymer nanoparticles through nucleation, coalescence, agglomeration, and heat treatment. Microemulsions typically consist of surfactant, cosurfactant, solvent, and water (or aqueous solution). In this system, two immiscible continuous media are divided into tiny spaces by surfactant amphiphilic molecules to form a microreactor, the size of which can be controlled in the nanometer range, and the reactants react in the system to form solid phase particles. Because microemulsion can precisely control the particle size and stability of nanomaterials, it limits the nucleation, growth, agglomeration, and other processes of nanoparticles. The resulting nanoparticles are coated with a layer of surfactant and have a certain amount of condensed matter structure.

2.3.3. Self-Assembly Method. Compared with the former two methods, the self-assembly method is relatively simple. Its main step is to suspend or completely dissolve the conjugated polymer and coassembly materials with positive and negative charges in ultrapure water. They vibrate violently in a certain proportion, and then, we can directly get the nanoparticles we need through the centrifugal process at a certain speed.

3. Research on the Combination of Nanomaterials and Rehabilitation Therapy of Shoulder Joint Injury

3.1. Causes of Shoulder Joint Injury. The shoulder joint injuries of 75 volleyball majors in the Nanjing Institute of Physical Education were investigated by questionnaire and observation. It is found that the key to shoulder joint injury in volleyball is serve and spike. The main reason for the injury is that the athlete's technical mastery is not comprehensive and the standard and warm-up are not enough. Excessive shoulder abduction angle is the key to shoulder injury. The average abduction angle of attacker with shoulder joint injury was 146.51° and that without injury was 117.23°. The results show that the optimum temperature range is between 105° and 130°. In addition, the reason of shoulder injury is that the swing sequence of the upper limb is not the swing time and the front limb is too long. When smashing, the abduction angle of the upper arm is less than 120°. At the same time, the arm bends to hit the ball forward and down at high speed, which is the most important factor leading to the shoulder injury of small players. Because of the structural attribute of shoulder joint and the high requirement of hitting speed due to the action range and explosive force in volleyball match, students are easy to cause shoulder joint injury under the premise of nonstandard and uncoordinated volleying. The second important reason is the shoulder injury caused by the difference of preparation and physical fitness. In addition to the weakness of the anatomical results of the shoulder joint itself, the technical links leading to the shoulder joint injury include the following: due to the rigidity of the limbs, unable to understand the flogging action, directly press the upper arm down to hit the ball; the force sequence is wrong, and the elbow joint is dominant; the shoulder is not relaxed enough, and the arm is in the leading stage; the whole body lacks the process of coordination force, and the coordination force is just the local force of the shoulder; the jump time is not correct, and the ball is not buckled or missed.

To sum up, the causes of shoulder injury of volleyball players can be started from internal and external factors. The internal reason is that the shoulder joint is composed of humeral head and scapula, which is a typical ball and socket joint. The joint capsule is thin and loose, the joint basin is shallow, and the shoulder joint is flexible but unstable. Its stability mainly depends on the dynamic balance of shoulder joint muscle strength. If the amplitude and speed of the upper limb movement are too large and too fast, the imbalance of muscle strength between the protomyo and the antagonistic muscles is easy to cause damage. The external reason is in all volleyball techniques, serve and spike are the two techniques with the highest score. If the team wants to win, they will do these two exercises over and over in their daily training. Jumping and spiking refers to that when the human body is in the air, the strength of the trunk is transferred to the shoulder to drive the arm to swing and hit the ball. The damage caused in this process can be divided into two situations: one is that there is a mistake in the take-off process, and then, the ball is hit into the air; the other is that

the technical action at the moment of hitting is not standardized, which is easy to cause shoulder damage.

3.2. Sports Rehabilitation Therapy for Shoulder Joint Injury. It has been reported that Bobath handshake weightlifting training is mainly used for active and passive sports, lasting for 10-20 minutes, 4-6 times a day; the second is the centripetal winding method, 3-4 times a day. The research adopts a group of dumbbell strength training methods, which consist of eight movements, including shoulder bending 90 degrees and 180 degrees, 90 degrees abduction, push up, rotation, neck rear arm flexion and extension, and neck rear arm flexion and extension+rotation of the forearm internal and external rotation, easy to pull, basically including most of the shoulder joint function training mode; each group of dumbbell maintains 10 weeks through weekly incremental training. Rehabilitation training program is designed for patients with rotator cuff injury 3 weeks after surgery, with a total of four stages: in the first stage, shoulder joint fixation, elbow bending and expansion function, hand grip strength, wrist, rowing, and other exercises. The intensity of training develops gradually according to the patient's bearing range. The shoulder muscles perform long contraction movement, and the shoulder joints perform passive movement. In the second stage, the movement pain should be avoided as much as possible. The shoulder joint should carry out active and passive activities, just as it is assisted by pulley, shoulder ladder, and other equipment. The range of motion is controlled under the scapula to ensure no pain; while performing isometric contraction exercise, the muscles at different angles start to exercise the hand resistance function scapula movement, 20 times/time, 2 times/day. In the third stage, the glenohumeral joint and scapula are trained, and the stability of tendon sleeve training is ensured. According to the adaptation, the shoulder abduction activity plan is made by me. Gradually, return to the normal range of activity and continue to carry out posture correction training; muscle strength increased. Attach a low weight sandbag to the arm to enhance the stability of the joint, 40 times/time, 3 times/day. In the fourth stage, the resistance training should continue to recover the upper limb movement function, increase the strength training of the rotator cuff muscles as much as possible, then expand the rotation muscle tension, and enhance the muscle strength, proprioception, and flexible coordination training, which can improve the throwing, skills, and other training methods, 40 minutes/time, 3 times/day.

Some scholars have designed similar rehabilitation training programs: the first stage lasts for one week, mainly using grip strength training, elbow flexion and extension training, joint capsule tension training, neck extension training, and vertical swing training; the second stage lasts for five weeks, mainly using shoulder bending movement, external and internal rotation movement, and cuff muscle tissue, 10 times/group of exercise load. In the third stage, horizontal bending, large external rotation, shoulder bending forward, back pulling towel, and straight arm lifting were used. The results show that the rehabilitation training program can accelerate the relief of pain, shoulder joint movement

limitation, and other symptoms, reduce the dependence of anti-inflammatory analgesic drugs and local block drugs, and significantly improve the shoulder joint movement function.

There are also scholars who have studied a rehabilitation training program for excellent high-level volleyball players with shoulder arthritis. Rehabilitation training emphasizes the accuracy of the movement, based on the principle of small intensity and multiple times. Exercises include the following: (1) strengthening the stability of shoulder muscle group, upper limb stability exercise, and ball holding stability exercise of locking power chain, which are 30-40 seconds/ group and 3 groups/day, respectively. (2) The weight was small (3 kg), 20 times/group, 3 groups/day for the whole pot exercise, straight elbow rowing exercise, bird bending exercise, dumbbell shoulder turning exercise, shrug exercise, and dumbbell resistance exercise. (3) Elastic belt strength exercise includes abduction pull-up, forward pull-up, back pull, chest extension, front pull, forearm internal rotation, and forearm external rotation, 20-30 times/group, 3 groups/day. (4) The elastic rope mimics the forehand and backhand movements. The results showed that after 4 weeks of rehabilitation training, the angle expansion increased significantly, the pain of expansion and kidnapping disappeared, the strength of rotating muscle increased, the strength and stability of shoulder increased significantly, there was no pain, no soft feeling, fear disappeared, and no need for muscle paste protection.

3.3. Nanomaterials and Rehabilitation Therapy for Shoulder Joint Injury. Phototherapy with conjugated polymer nanomaterials is mild and will not cause obvious damage to normal tissue cells. Because the light source is absorbed by the photosensitizer gathered around the shoulder cells by the external light source, the external light source should have strong tissue penetration ability, and the near-infrared light is generally selected as the external light source [13]. At present, photodynamic therapy mainly includes PDT [14] and PTT [15]. Photodynamic therapy uses photosensitizers to capture light sources and then act on oxygen to produce monooxygen or reactive oxygen radicals. It uses the strong oxidation of singlet oxygen or reactive oxygen radicals to cause irreversible damage to biological cells and kill the pathogenic cells. Photodynamic therapy is a kind of treatment method that photosensitizers absorb near-infrared light to penetrate biological tissues, convert light energy into heat energy, and make the inflammatory cells of local shoulder joint reach high temperature and then kill the inflammatory cells.

(1) Photodynamic therapy (PDT) [16] is a kind of treatment method that uses photosensitizers to absorb light, produce single oxygen or reactive oxygen free radicals, kill inflammatory cells of shoulder joint, and treat shoulder injury. The basic reaction process is that when the photosensitive substance in biological tissue is illuminated, it absorbs photon energy and changes from ground state (S0) to excited state (S1). The excited photosensitive material is very

unstable, and it will emit energy back to the ground state (S0) by emitting fluorescence or system crossing into the three states (T1). Generally speaking, most photodynamic reactions involve the triplet state of photosensitizer. Triplet photosensitizers transfer the light of oxygen molecules under the condition of energy and produce singlet oxygen (type II). Photodynamic therapy (PDT) is a method that uses photosensitizer molecules to gather in the inflammatory cells of shoulder joint and then irradiates the inflammatory cells of shoulder joint with external light source to produce singlet oxygen or active oxygen free radicals, killing the inflammatory cells of shoulder joint. Photodynamic therapy has been widely used in the treatment of skin diseases and superficial tissue diseases because of its mild conditions and no damage to normal tissue cells

(2) Photothermal therapy [17] is a therapeutic method to kill inflammatory cells of shoulder joint by using heat generated by photothermal converter. The main working principle of photothermal therapy is as follows: under the action of photothermal conversion agent, the near-infrared light which has good penetrability to biological tissue is used as the excitation light source to improve the local temperature, so as to achieve the treatment method of killing inflammatory cells of shoulder joint. This kind of local treatment is simple and effective without obvious side effects. In recent years, photothermal therapy has been greatly developed, because light source and photosensitizer only need two basic conditions. However, because these photosensitizers need to penetrate tissues, they also need to have good ability to absorb near-infrared light. In addition, PTT can be used for deep treatment of shoulder inflammation because of its strong tissue-penetrating ability

Conjugated polymer nanomaterials combined with sports rehabilitation therapy can effectively cure the athlete's shoulder arthritis, relieve the athlete's pain, and quickly treat and prevent the recurrence of inflammation. In the case of conjugated polymer nanomaterials, photodynamic therapy or photothermal therapy can reduce the pain of patients with shoulder joint inflammation.

4. Results and Discussion

4.1. Comparison of Gender, Age, and VAS Score before Treatment between the Two Groups. Shown as Table 1, there were 50 volleyball players with shoulder arthritis. During the follow-up, 4 cases were excluded and 2 cases were dropped. Finally, 23 cases in the experimental group and 21 cases in the control group were followed up. There were 13 males and 10 females in the experimental group and 9 males and 12 females in the control group. There was no significant difference in gender between the two groups ($P > 0.05$).

Shown as Table 2, there was no significant difference in age between the two groups ($P > 0.05$).

Table 1: Comparison of gender differences between the two groups.

	Total/case	Male/case	Female/case
Experience group	23	13	10
Control group	21	9	12
X^2		0.004	
P		0.963	

Table 2: Comparison of age distribution between two groups ($\bar{x} \pm s$, year).

	Number/case	Age
Experience group	23	59.36 ± 4.35
Control group	21	62.27 ± 5.84
t		1.237
P		0.238

Table 3: VAS score before treatment in two groups ($\bar{x} \pm s$, min).

	Number/case	Age
Experience group	23	5.35 ± 0.35
Control group	21	6.34 ± 1.34
t		0.446
P		0.563

Table 4: Comparison of VAS scores of two groups at different time points after operation ($\bar{x} \pm s$).

	12 h	24 h	48 h
Experience group	3.02 ± 1.27	2.23 ± 0.65	2.79 ± 0.54
Control group	4.53 ± 0.84	3.61 ± 0.26	3.02 ± 0.82
t	-1.271	-1.029	-0.472
P	0.324	0.023	0.628

Shown as Table 3, there was no significant difference in VAS score between the two groups before treatment ($P > 0.05$).

4.2. Comparison of VAS Scores of Two Groups in Different Time Periods. Shown as Table 4, there was no interaction between time and group in repeated measurement of variance statistical analysis; VAS scores of the two groups at different time points had time effect; VAS scores of the two groups at different time points had group effect. It can be seen from Table 4 that the pain score of the experimental group is better than that of the control group at 12 h, 24 h, and 48 h, but the difference is not statistically significant ($P > 0.05$).

Shown as Figure 1, VAS scores of the two groups had grouping effect at different time points. As shown in Figure 1, there may not be any change at the beginning,

but after the method of the experimental group, the VAS score began to produce a qualitative change. The pain score of the experimental group was better than that of the control group at 3 weeks, 6 weeks, and 12 weeks, and the difference of VAS score from 4 days to 3 weeks was statistically significant ($P < 0.05$).

Shown as Figure 2, the number of compressions between the test group and the control group was 0-12 h, 12-48 h, 48-96 h, and 96-156 h, and the average number of compressions in the four time periods in the experimental group was smaller than that in the control group, with statistical difference ($P < 0.05$).

4.3. Adverse Effects of Analgesia in the Experimental Group within Two Days. Shown as Figure 3, the incidence of adverse reactions in the experimental group was 23.0%, among which nausea accounted for 30% and dizziness and headache accounted for 30%. The incidence of adverse reactions in the control group was 36.4%, including 4 cases of nausea, 2 cases of vomiting, and 5 cases of dizziness and headache. The incidence of adverse reactions in the experimental group was significantly lower than that in the control group ($P < 0.05$).

4.4. Shoulder Isokinetic Test. Shown as Figure 4, there was no interaction between the two groups through repeated measurement of variance statistical analysis; there was time effect in the constant Murley score of the two groups; there was grouping effect in the constant Murley score of the two groups. There was no significant difference in pronation and abduction scores between the two groups, but there was significant difference in the scores of 1 week and 3 weeks ($P < 0.05$). At 6 weeks, the scores of entropion and abduction in the experimental group were slightly higher than those in the control group, but the difference was not statistically significant ($P > 0.05$).

5. Conclusion

The stability and flexibility of the shoulder joint and the muscle control ability of the shoulder joint are decreased in patients with shoulder joint dysfunction. It is easy to cause injury; the activation sequence of shoulder muscles for those with shoulder joint dysfunction is inconsistent with the requirements of the volleyball spiking action, which is easy to cause injury and affect the spiking effect. The biological structure of human shoulder joint is complex. It consists of muscle group, skeleton, ligament, tendon, surrounding soft tissue, and skin. There are nerves and blood vessels in the muscle structure of the shoulder joint, which provide power for the movement of the shoulder joint. Volleyball players need to spike, serve, and release the ball in training and competition engineering, which is easy to cause shoulder injury and inflammation. In order to catch the ball with quality and strength, it is necessary to overcome the huge resistance when swinging the arm. If the shoulder causes sports injury, it will seriously affect the play of skills on the field, resulting in the decline of competition results. In order to avoid the occurrence of such events, this paper proposes the
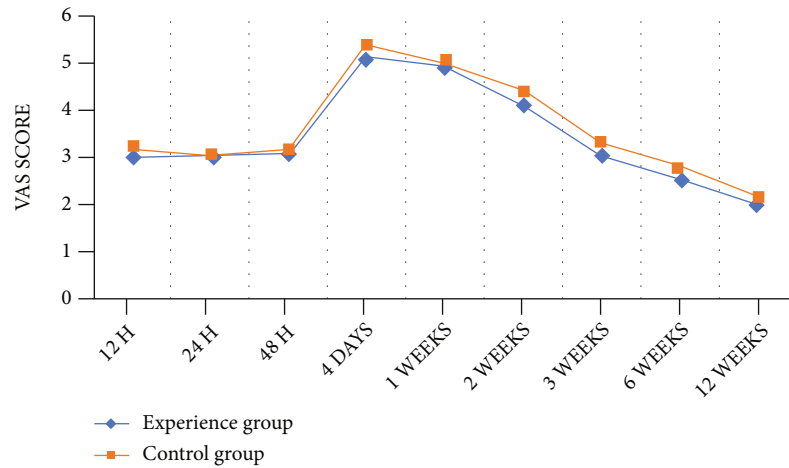
Figure 1: VAS score trend chart of two groups at different time points after operation.
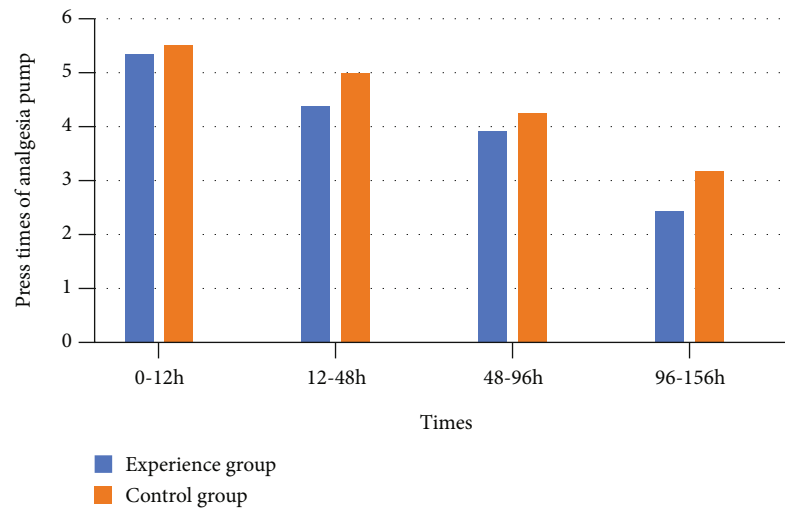

Figure 2: Comparison of compression times of analgesia pump between the two groups in different time periods within two days after operation ($\bar{x} \pm s$).
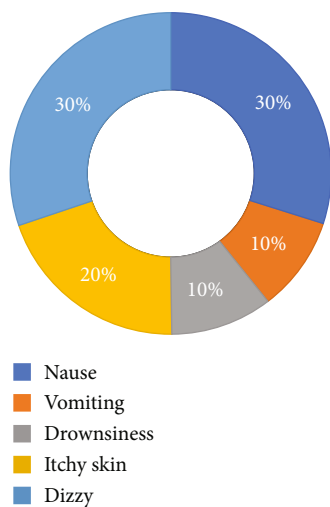

Figure 3: Comparison of analgesic adverse reactions between the two groups within two days after surgery.

application of nanomaterials combined with sports rehabilitation therapy in the treatment of volleyball players' shoulder arthritis. Firstly, the preparation of conjugated polymer nanomaterials is studied, which can be used in photodynamic therapy or photothermal therapy to treat the shoulder inflammation of volleyball players. Therefore, the experimental group and the control group are divided into different treatment methods. The results show that the experimental group is better than the control group in VAS pain analysis, and the pain score is significantly lower than the control group. The number of times of the experimental group and the control group are the same as the control group in the comparison of the number of times of pressing. The adverse reaction rate of the control group is 36.4% in the test of adverse reactions of analgesia; the score of varus and abduction in the experimental group was slightly higher than that in the control group. It can be seen that the nanomaterials combined with sports rehabilitation therapy proposed in this paper have a very good effect on
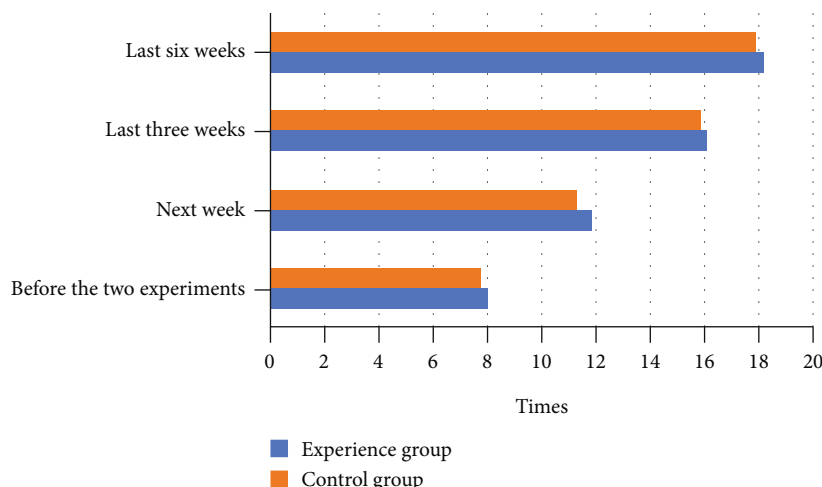
FIGURE 4: Perioperative abduction scores were obtained before and after surgery at 3, 6, and 12 weeks ($\bar{x} \pm s$).

the shoulder arthritis of volleyball players, and there is a great market space in the future. Exercises to improve shoulder mobility are suggested to be added to the preparatory activities for daily training. During the intensive spike training week, more attention should be paid to activating weak small muscle groups and improving their strength, so as to keep the strength of the shoulder muscles balanced, so as to prevent shoulder joint injuries and improve sports performance.

Data Availability

The data that support the findings of this study are available from the corresponding author upon reasonable request.

Conflicts of Interest

The author declared no potential conflicts of interest with respect to the research, authorship, and/or publication of this article.

References

[1] H. D. O. Castro, G. M. Praça, G. D. C. T. Costa, G. F. Pedrosa, and P. J. Greco, "Visual behavior and the quality of decision-making on volleyball," *Revista Brasileira de Cineantropometria & Desempenho Humano*, vol. 18, no. 6, pp. 638–647, 2017.

[2] Y. Wang, C. Wang, H. Chen, and X. Ye, "Shoulder joint pain of rotator cuff injury treated with electroacupuncture and Mulligan's mobilization: a randomized controlled trial," *Chinese Acupuncture & Moxibustion*, vol. 38, no. 1, pp. 17–21, 2018.

[3] T. Kanazawa, M. Kaneko, T. Niide et al., "Enhancement of nose-to-brain delivery of hydrophilic macromolecules with stearate- or polyethylene glycol-modified arginine-rich peptide," *International Journal of Pharmaceutics*, vol. 530, no. 1-2, pp. 195–200, 2017.

[4] I. M. Alibe, K. A. Matori, H. A. A. Sidek et al., "Effects of polyvinylpyrrolidone on structural and optical properties of willemite semiconductor nanoparticles by polymer thermal treatment method," *Journal of Thermal Analysis and Calorimetry*, vol. 136, no. 6, pp. 2249–2268, 2019.

[5] Y. Tang, Z. Chen, W. Feng, Y. Nong, C. Li, and J. Chen, "Combined effects of nano-silica and silica fume on the mechanical behavior of recycled aggregate concrete," *Nanotechnology Reviews*, vol. 10, no. 1, pp. 819–838, 2021.

[6] B. Gao, X. Ning, and P. Xing, "Shock wave induced nanocrystallization during the high current pulsed electron beam process and its effect on mechanical properties," *Materials Letters*, vol. 237, no. 15, pp. 180–184, 2019.

[7] H. Zhu, H. Wei, B. Li, X. Yuan, and N. Kehtarnavaz, "Real-time moving object detection in high-resolution video sensing," *Sensors*, vol. 20, no. 12, p. 3591, 2020.

[8] D. Liu, B. Yang, B. Jang et al., "Molecular design of a wide-band-gap conjugated polymer for efficient fullerene-free polymer solar cells," *Energy & Environmental Science*, vol. 10, no. 2, pp. 546–551, 2017.

[9] F. Tian, J. Lyu, J. Shi, and M. Yang, "Graphene and graphene-like two-denominational materials based fluorescence resonance energy transfer (fret) assays for biological applications," *Biosensors and Bioelectronics*, vol. 89, Part 1, pp. 123–135, 2017.

[10] Z. He, F. Song, H. Sun, and Y. Huang, "Transition-metal-free suzuki-type cross-coupling reaction of benzyl halides and boronic acids via 1,2-metalate shift," *Journal of the American Chemical Society*, vol. 140, no. 7, pp. 2693–2699, 2018.

[11] N. Arsalani, A. Akbari, M. Amini, E. Jabbari, S. Gautam, and K. H. Chae, "Poss-based covalent networks: supporting and stabilizing pd for heck reaction in aqueous media," *Catalysis Letters*, vol. 147, no. 4, pp. 1086–1094, 2017.

[12] G. M. R. De Luca, E. Desclos, R. M. P. Breedijk et al., "Configurations of the re-scan confocal microscope (rcm) for biomedical applications," *Journal of Microscopy*, vol. 266, no. 2, pp. 166–177, 2017.

[13] B. Wang, B. F. Zhang, X. W. Liu, and F. C. Zou, "Novel infrared image enhancement optimization algorithm combined with DFOCS," *Optik*, vol. 224, article 165476, 2020.

[14] M. M. Kim, A. A. Ghogare, A. Greer, and T. C. Zhu, "On the in vivo photochemical rate parameters for PDT reactive oxygen species modeling," *Physics in Medicine and Biology*, vol. 62, no. 5, pp. R1–R48, 2017.

[15] J. S. Mandlate, B. M. Soares, T. S. Seeger et al., "Determination of cadmium and lead at sub-ppt level in soft drinks: an efficient

combination between dispersive liquid-liquid microextraction and graphite furnace atomic absorption spectrometry," *Food Chemistry*, vol. 221, no. APR.15, pp. 907–912, 2017.

[16] C. A. Morton and L. R. Braathen, "Daylight photodynamic therapy for actinic keratoses," *American Journal of Clinical Dermatology*, vol. 19, no. 5, pp. 647–656, 2018.

[17] L. Shao, R. Zhang, J. Lu, C. Zhao, X. Deng, and Y. Wu, "Mesoporous silica coated polydopamine functionalized reduced graphene oxide for synergistic targeted chemo-photothermal therapy," *ACS Applied Materials & Interfaces*, vol. 9, no. 2, pp. 1226–1236, 2017.

Hindawi

Research Article

Construction and Research of Amorphous Alloys and Ferroelectric Materials in the Digital Logistics Platform

Zhi Chen and Ying Wang (ID)

College of Economics and Management, The Open University of Guangdong, Guangzhou, 510091 Guangdong, China

Correspondence should be addressed to Ying Wang; ywang@gdrtvu.edu.cn

People have higher and higher requirements for the size, sensitivity, measurement range, repeatability error, and power consumption cost of sensors and memories in the field of electronic information technology. "Logistics" as another new industry in the modern social division of labor is showing its infinite vitality, and the rise of digital logistics is the use of network technology to meet the development of this era. Based on the application of amorphous alloys and ferroelectric materials to the construction of logistics digital platform, this paper is aimed at demonstrating the function of nonstatic alloys and ferroelectric materials to promote the data storage of logistics digital platform and other aspects from multiple perspectives. This article is mainly divided into two general directions. The first is to study the physical and chemical properties of amorphous alloys and ferroelectric materials separately. The content of the article is more complete by referring to relevant research literature or obtaining relevant targeted information; the basic structure of the digital logistics platform is modeled, and the application of amorphous alloys and ferroelectric materials is mainly applied to the two parts of the data service composition and the data layer. This arrangement is based on the sensor as the key to data processing. Location is of great significance to the entire platform system. The experimental results show that the digital logistics platform constructed in this paper can reach a score of 7.75 in terms of data security and 7.39 in terms of flexibility. It also increases the efficiency of the entire operation process.

1. Introduction

With the rapid development and rapid popularization of computer network application technology, electronic trading platforms have gradually increased. After development, a comprehensive trading system with a complete logistics system, financial services, and platform technology has been gradually formed [1, 2]. E-commerce is in a stage of rapid growth with strong growth, and many companies are approaching the direction of e-commerce, and modern logistics systems must rely on efficient modern logistics information platforms [3, 4]. In the traditional transaction mode, it is difficult for the demand side to know all the conditions of the materials, which is not conducive to the sale of the supplier, and it is not conducive to the purchase of the demand side. Because the concept of logistics is highly valued in the rise of e-commerce and the development of modern logistics relies greatly on the construction of information, information technology in logistics is another important application industry in

the future information industry. Utilizing the accuracy, speed and openness brought by information technology greatly facilitate both supply and demand, better adapt to the needs of social and economic development, and promote the transformation of material transactions from traditional models to electronic transaction models [5].

In the customer-centric era, time and information efficiency are of the utmost importance. The efficiency of logistics management directly determines the efficiency of the entire supply chain [6]. With the application of the sharing economy, human logistics has become an emerging industry, and only logistics-based management platforms can show its efficiency and flexibility. Through the standardization of company logistics and warehousing, further improve the management process of warehousing logistics, so that the company has the ability to provide logistics public services. With the help of the R&D platform, the synchronization area of the business center is developed to reduce the loss of income caused by internal use and to increase

the integration of the sources of all parties and strengthen the source [7].

Due to the wide practicability of amorphous alloys and ferroelectric materials, researchers at home and abroad have paid a lot of attention. Lee et al. at home and abroad have prepared a Zr-based amorphous alloy-based composite material reinforced by continuous fibers of tungsten (W) or tantalum (Ta) by liquid pressing technology. The relationship between their tensile strength properties, microstructure, and mechanical deformation was studied using the Hopkinson split tie rods. The dynamic tensile test results show that the maximum strength of W fiber-reinforced composites (757 MPa) is much lower than the quasistatic measured strength, while the maximum strength of Ta fiber-reinforced composites (2129 MPa) is very high, but it is not yet widely used [8]. Lesz and Dercz have prepared binary Ni-Nb amorphous alloy ribbons by melt spinning technology. Melt spinning, a forming method using polymer melt as raw material, is spun using a melt spinning machine. Any heating can melt or turn into a viscous flow state without significant degradation of the polymer and can be spun using melt spinning method. Differential scanning calorimetry was used to study the glass transition and crystallization phenomena of the alloy, and the thermal properties of the binary Ni-Nb tape during heating and cooling were analyzed by DTA. The structure and fracture morphology of the belt were examined by X-ray diffraction and scanning electron microscopy [9]. Kulikova et al. studied the crystallization process and determined the structure and thermal properties of the Al86Ni8Ho6 amorphous alloy in a wide temperature range. It found the three-stage nature of the crystallization process when heated to 700 K. According to the high temperature X-ray diffraction analysis data, the three-stage kinetic model of the crystallization process has a reaction sequence based on the calculation of multiple nonlinear regressions [10]. In Rajaei et al.'s research, Ni-Mo and Ni-Mo-P alloy coatings were electrodeposited on AISI304 stainless steel samples as metal bipolar plates to improve the corrosion resistance, hydrophobicity, and conductivity of the samples. Scanning electron microscope (SEM) micrographs show that the prepared coating is uniform and dense. Potentiodynamic and potentiostatic polarization tests carried out in a simulated PEMFC cathode environment show that the corrosion resistance of the coated sample is significantly improved compared with that of the bare sample [11]. Barrett et al. reviewed the application of light emission electron microscopy (PEEM) and low energy electron microscopy (LEEM) in the study of the electronic and chemical structure of ferroelectric materials. Both PEEM and LEEM can be used for direct and reciprocal space imaging. Together, they provide access to surface charge, work function, topography, chemical mapping, surface crystallinity, and band structure. The application examples of ferroelectric thin film and single crystal research are introduced [12]. Fedeli et al. use the (vector) phase-field model description of ferroelectric domain evolution coupled with electroelastic equations to establish a simulation framework for electromechanical active materials. Several numerical experiments were performed to test the behavior of the adopted simulation framework. They proposed equal geometric collocation as a cheap but very accurate alternative to standard finite element discretization, which is also suitable for complex coupling problems [13]. Gorodetsky et al. proposed the conceptual model of the digital platform for cyber-physical management of manufacturing enterprises in the industry 5.0, proposed the types of basic platform services, listed the minimum service set of each type, and described their functions. It confirmed the leading role of multiagent system as the basic software architecture and technology, developing digital ecosystem applications. Examples of digital platforms and smart service ecosystems are provided to manage the cargo transportation of Russian railways in accordance with the principle of "Uberization." Ubiquitization means transforming existing work and services into tasks that are independent of each other and assigning them when needed [14]. Obviously, these studies are aimed at any aspect of amorphous alloys, ferroelectric materials, and logistics digital platforms. However, there is a relative lack of research that combines the two of them or even studies based on these three subjects. In terms of methods, these studies are relatively singular, so that the experimental results have certain limitations.

The main innovations in the construction of amorphous alloys and ferroelectric materials in the digital logistics platform studied in this paper are as follows: (1) By studying the interaction between defects and microstructures in ferroelectric materials, in-depth exploration of the failure mechanism of ferroelectric materials has better theoretical guiding significance for the reliability design of smart components. (2) By studying the interaction between electrical inclusions and microstructures, the hysteresis loops of different electrical inclusion models are given, so that the dielectric constant of electrical inclusions can be controlled to improve material properties or prevent material performance degradation. (3) The phase field method is used to study the stress field and microstructure evolution process of the electrode tip in MFA under different applied electromechanical loads and different temperature environments. The main consideration is the effect of temperature changes on the stress concentration area. (4) The temperature change of a substance is often closely related to the change of the microstructure and macroscopic properties. Through thermal analysis, accurate thermodynamic data related to the chemical reaction or physical process of the substance can be directly obtained.

2. Theoretical Analysis of Amorphous Alloys and Ferroelectric Materials

2.1. Ferroelectric Materials. In the past few decades, low-dimensional ferroelectric materials such as ferroelectric thin films, ferroelectric nanowires, and ferroelectric nanopillars have been widely used in the development of micronano devices due to their various excellent physical properties [15]. The preparation technology of ferroelectric materials is also more and more developed. Ferroelectric materials developed by the combination of thin ferroelectric thin films and microelectronics technology have become the most

active field of ferroelectric research in the world. Ferroelectric materials have a thermoelectric effect [16]. Ferroelectrics belong to pyroelectric crystals, but the crystal structure is more special. With its inherent characteristics of low energy consumption and fast response, it is widely used in the preparation of microfunctional components and has become a hot research object. Density functional theory does not care about the specific configuration of electrons. Its central goal is to find the space distribution of charges corresponding to the ground state of the system and to describe the physical state and chemical properties of particles, materials and solids through corresponding particle density functions. Multiferroic materials with ferromagnetic and ferroelectric properties are mainly concentrated in transition metal (rare-earth element) oxides, mainly due to their complex electronic structures and competing interactions. The mechanism of electric polarization is very complicated, and the corresponding multi-iron mechanism is also different. Ferroelectric materials can be applied to data storage [17]. Under the action of the stronger alternating electric field, the polarization intensity P of the ferroelectric body varies nonlinearly with the external electric field, and in a certain temperature range, P behaves as a double-valued function of the electric field E, showing a hysteresis phenomenon, and this P-E return line is the electric hysteresis return line. The hysteresis line is able to visually reflect the magnitude of the maximum polarization strength, residual polarization strength, coercivity field, etc., and the energy storage density of the material can be calculated from the hysteresis line integral. Due to the hysteresis loop of ferroelectric materials and the polarization reversal properties produced in the hysteresis loop, ferroelectric materials are widely used in ferroelectric memory (FRAM). Integrated ferroelectric materials are used in storage, infrared detection and imaging devices, ultrasonic and surface wave devices, and optoelectronic devices. In fact, under the action of external mechanical-electric load, the electric field near the crack is strengthened, which causes the electrical domain structure near the crack to reverse, that is, domain change [18, 19]. Since the accumulation of charge in the crack indicates that the electric field is concentrated in the crack, the formation of high-energy electric inclusions is formed. The crack tip produces high tensile stress concentration, which eventually leads to device failure. The digital oscilloscope completes the work of the acquisition card and does not require a voltage automatic attenuation module and a frequency measurement circuit, which greatly reduces the complexity of the circuit, while the operation is simple, and the integration and safety of the system are also improved [20].

2.2. Amorphous Alloy.

The amorphous alloy is solidified by ultrarapid cold solidification, the alloy solidifies when the atoms are too late to orderly arrangement of crystallization, the solid alloy obtained is a long-range disordered structure, the molecules (or atoms, ions) that make up its material are not spatially regular periodic, there is no grain, and grain boundaries of crystalline alloys exist. The best properties of amorphous materials are directly related to their unique atomic properties. Therefore, studying the atomic system

of amorphous materials is of great significance for understanding the properties of amorphous materials [21, 22]. A large number of scientists gradually discovered the insignificant value of these materials and supported their enthusiasm for the research of amorphous materials. The continuous grid accident model is used to describe the structure of metal-like amorphous alloys. The structural units of these amorphous alloys are random, and they are randomized in the form of copoint, collinear, and coplanar in a three-dimensional space. The connection forms a long-range disordered amorphous alloy. The structure of the amorphous alloy is isotropic, there are no line and surface crystal defects, and the metal bonding characteristics between atoms are maintained [23]. Compared with crystalline materials, amorphous alloy materials have a similar collision process. Considering the microstructure of amorphous alloys, the vacancies, interstitial atoms, and atom-depleted regions formed by it can exist instantaneously, but over time, these defects are impossible to stably exist in the amorphous alloy body. Related experimental studies have found that adding a certain number of large-scale atoms to the amorphous alloy will change its close packing mode, thereby reducing the corresponding diffusion coefficient and affecting its structural changes [24]. Many atoms show a certain state of coordination unsaturation, which makes the free energy of the system higher, which makes it have better mechanical properties and unique physical and chemical properties than traditional crystal alloys [25, 26]. The choice of opposing interaction forces in the system has a significant impact on the accuracy of molecular energy simulation results. Under low temperature or high pressure conditions, the tensile strength between the atomic plane of the amorphous alloy and the surrounding atoms is very strong, which is likely to cause a large amount of local plastic damage. However, large local atoms will not undergo plastic deformation due to local fatigue at high temperature or low pressure but will flow in a diffusion configuration [27]. The plastic deformation state of amorphous alloy is shown in Figure 1.

The energy saving and economic advantages of amorphous alloys are expected to be a reasonable and efficient evaluation method [28]. Amorphous alloys are widely used in distribution transformers, high power switching power supplies, pulse transformers, magnetic amplifiers, medium frequency transformers, and inverter cores, suitable for frequencies below $10\,\mathrm{kHz}$. Amorphous alloys are prepared by the powder solidification and direct solidification methods. At present, the structure determination technology of amorphous materials also shows certain application limitations in this aspect, and it is unable to accurately detect the atomic arrangement. Study the internal molecular dynamics of amorphous alloys, and use formulas to derive this process:

$$
R_\alpha = \sum_l Q_l(\delta_{l,k}(a)) + \frac{1}{2}\sum_{li}\varphi_{li}(a_{li}) - \sum_{i\neq l}\delta_i^x(a_{il}),
$$

$$
\varphi(a) = \left\|1 + \chi\left(\frac{a}{a_h}\right)\right\| \exp\left[-\varphi\left(\frac{a}{a_h - 1}\right)\right]. \tag{1}
$$

Among them, Q_l is the energy required for atomic

Compression   Ball punching

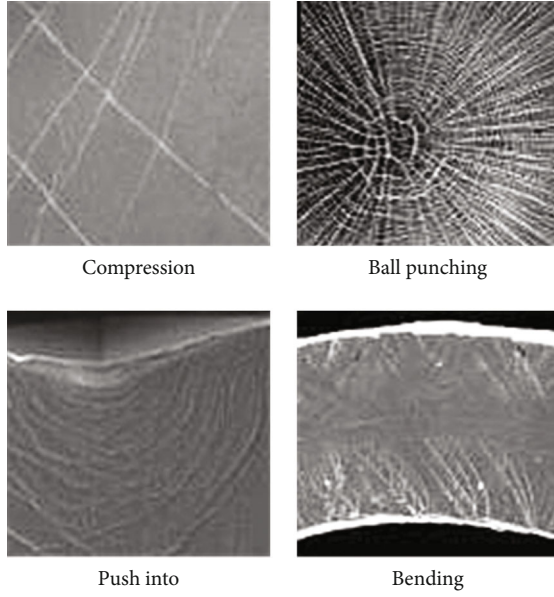Push into   Bending

FIGURE 1: Plastic deformation state of amorphous alloy.

movement, $\delta_{l,k}$ is the electron density, and the distance between adjacent atoms is represented by a_{il}. According to the mechanical properties of the material, the multibody potential φ_{il} is simulated [29], and the density of the boundary structure can be calculated as

$$\delta(a) = \delta_o f(a-1) = \frac{1}{m-1} \left(\sum_{il} \chi(a - a_{il}) \right) \lim_{l \longrightarrow \nabla}(a),$$

$$[a_l(s+s_i) - a_l(s_0)]^2 = \lim_{l \longrightarrow \nabla} \frac{\|\bar{a}(s) - \bar{a}(s)\|}{s-1}. \qquad (2)$$

$\lim_{l \longrightarrow \nabla}$ represents the diffusion coefficient, s is the square of the average displacement, $\bar{a}$ is the position of the atom, m is the free volume, and the surrounding volume is represented by $f(a-1)$. After measuring the macroscopic hardness of the material with a Vickers hardness tester, it is found that the general hardness of the material has not changed. This is caused by the combined effect of hardness and elasticity, that is,

$$\iint s = \frac{R}{(3\pi)^{1.2r}} * \frac{1}{(Li)^{1.2}} \exp\left(-\frac{l^2}{3Li}\right),$$

$$\eta_{il} = \eta_{i0} = \frac{1}{3}\eta_{l1} = -\frac{\delta \forall r}{2(1-a)^2}. \qquad (3)$$

Since there is not enough time to make a specific dynamic system $\iint s$, the flow of the amorphous alloy is accompanied by an increase in its internal free volume content $\forall r$, to identify the enriched area and the sparse area, expressed by the following formula:

$$Q = \left(\frac{h_1}{\kappa}\right) \exp\left[-\frac{ya^3\alpha}{G(\nabla G)^2}\right]. \qquad (4)$$

The collision will change the trajectory of the particle. The particle moves along a broken line κ inside the material, constantly changing the direction of travel, and there is a complex cascade rotation outside [30, 31]. After the particle leaves, an empty space ∇G surrounded by a large number of oxides is formed.

3. Practical Application Data and Experiments of Materials in the Digital Logistics Platform

3.1. Properties of Amorphous Alloys. The storage system has become the bottleneck of data system performance improvement. In essence, intensive data computing poses unprecedented problems for the speed of storage systems. However, most storage systems, especially those that require high-speed data processing, are also built on custom magnetic hard drives. Because flash hard disks are completely built on semiconductor chips and do not have mechanical transmission functions, this different feature makes flash hard disks an efficient storage medium, which can improve the storage efficiency of mass systems [32, 33]. In the storage system, it is necessary to find a suitable location for the flash drive to achieve the proper balance between performance and cost. The existing method considers the difference of storage media, but does not consider the difference between the four functions. At this stage, magnetic hard drives are still very important in storage systems. Therefore, for most storage systems, flash drives should not be as easy to plan as replacing existing magnetic hard drives but should be a way to improve storage system performance. Many amorphous alloy materials have excellent corrosion resistance, which greatly promotes their practical applications in various technical fields. Because no matter what kind of product, its corrosion resistance is an important index to measure its quality; especially for sensor technology, this is even more important. The basic structure of the sensor provides the material basis for its work. But the sensor's sensitive components usually need energy while realizing its sensitive functions. And energy is basically provided by the appropriate form of circuit. In some important areas, it performs search operations better than other applications. The physical properties of amorphous alloys are shown in Table 1.

The breakthrough in the preparation process has enabled more and more millimeter-level bulk amorphous alloys and centimeter-level bulk amorphous alloys to be successfully prepared. Through some chemical theories, we have known that the activation point of chemical reaction is the defect in the material structure, and the reason for the formation of the galvanic cell in the electrochemical corrosion process is the fluctuation of the composition. Through industrial technology, we can deliberately introduce defects into the material to realize this material and analyze the mechanism and original elements of several

TABLE 1: Main physical properties of amorphous alloys.

Performance	Amorphous alloy
Saturation magnetic induction	1.539
Coercivity	<4.0
Unit loss	0.17
Density	7.20
Hardness	855
Saturation magnetostriction coefficient	35
Maximum permeability	>200
Thickness	0.03

commonly used amorphous alloy materials preparation methods, as shown in Figure 2.

Amorphous alloys have a very unique microstructure. The magnetostriction of amorphous alloy materials has become an important reason that affects its magnetic properties because there is no obvious macroscopic magnetic anisotropy in amorphous alloys. It is the existence of this excellent characteristic that makes amorphous alloy materials become excellent high-resistance materials and precision resistance materials. To this end, research is carried out on the correlation between physical characteristics and performance, as shown in Figure 3.

Due to the existence of alloy composition, preparation process, heat treatment, and other methods when preparing amorphous alloys, amorphous alloys can also exhibit unique dynamic characteristics according to different production methods. The paper value of similar amorphous materials has little effect on the statistical results; but the effect of specific heat on the statistical results is more significant. Measuring pressure not only is a very important issue in various fields of production and scientific research but also has a very important meaning in people's daily life. By picking up the signal in the induction coil and processing the signal data, the changed voltage and frequency signals are finally obtained, and the relationship between the output voltage and the vibration frequency is explored, as shown in Figure 4.

The above figure is a data analysis of the correlation between the expansion voltage and the output voltage and the vibration frequency in different regions of different turns. On the whole, the output voltage expands with the continuous expansion of the voltage, respectively, when the voltage is 1.1 and 2.25 reaching the maximum value; and the relationship between vibration frequency and voltage is generally negative. When the temperature is constant, it decreases with the increase of the compressive stress, and when the compressive stress is constant, it increases linearly with the vibration frequency. Whenever a new type of functional material appears, people will try their best to apply this material to sensor technology and try to explore the advantages of these functional materials to serve the development of sensor technology. The output voltage increases monotonously with the increase of distance and pressure, and the oscillation frequency decreases monotonously with the increase of distance and pressure. It can effectively hinder the rapid expansion of the shear band, overcome the shortcomings of catastrophic fracture and no macroscopic plasticity of metallic glass materials during tensile deformation, and make the composite material on the basis of maintaining the high elasticity and high strength of the amorphous alloy. It has large compressive plasticity and hardness.

3.2. Ferroelectric Materials. Ferroelectric materials are indispensable electrodes and have been extensively studied. It has a variety of polarization conditions. At different frequencies, multiple polarization conditions will produce different effects, so the dielectric appearance of different materials is very different. And the higher the polarization strength and electrical distribution of the dielectric material is, the greater the possibility that the material size will be uniform. The ferroelectric crystal maintains the ferroelectric phase below the Curie temperature and has ferroelectricity. When the temperature exceeds the Curie temperature, the ferroelectric crystal undergoes a phase change from a tetragonal crystal level to a rectangular energy level and transforms into a paraelectric body, which causes the spontaneous polarization of the ferroelectric material. The refrigeration mechanism of the ferroelectric card is shown in Figure 5.

The microstructure of ferroelectric materials determines the macroscopic properties of ferroelectric materials to a certain extent, and the simulation of the microstructure is very important in material design. It is difficult for ferroelectric bulk materials to control the crystal orientation, but the crystal orientation also has a negligible effect on the physical properties of the bulk material. If a compact block is used as an active amplifier, the response speed of the composite block is low and the oscillator is high. As regards frequency characteristics, design curve is impossible. We know that under the excitation of the alternating electric field of the probe, the surface of the sample is deformed due to the inverse piezoelectric effect, specific to the local area of the sample surface touched by the probe which may produce a slope. The records of the data statistics of the electric card effect under different electric inclusion situations are shown in Table 2.

Most ferroelectric applications have a phase transition temperature from a high paraelectric temperature to a low ferroelectric temperature. The ferroelectric vibration theory proposed on the basis of the elastic state theory considers the participation of the electric field, which can fully explain the purpose of spontaneous polarization. The increase of the external electric field within a certain range can make the temperature environment generated by the giant electric card effect more biased towards room temperature and thus form a more friendly experimental temperature. As the temperature increases, the ferroelectricity of the ferroelectric single crystal becomes smaller and smaller, but the high electric energy generated by the concentration of the electric field at the electrode tip keeps the domain structure active.

3.3. Construction of Digital Logistics Platform. Digital logistics is a system provider, optimizer, and combiner. We combine all aspects of logistics chain information operations for customers, provide customers with operational solutions, collect real-time information, provide a platform for
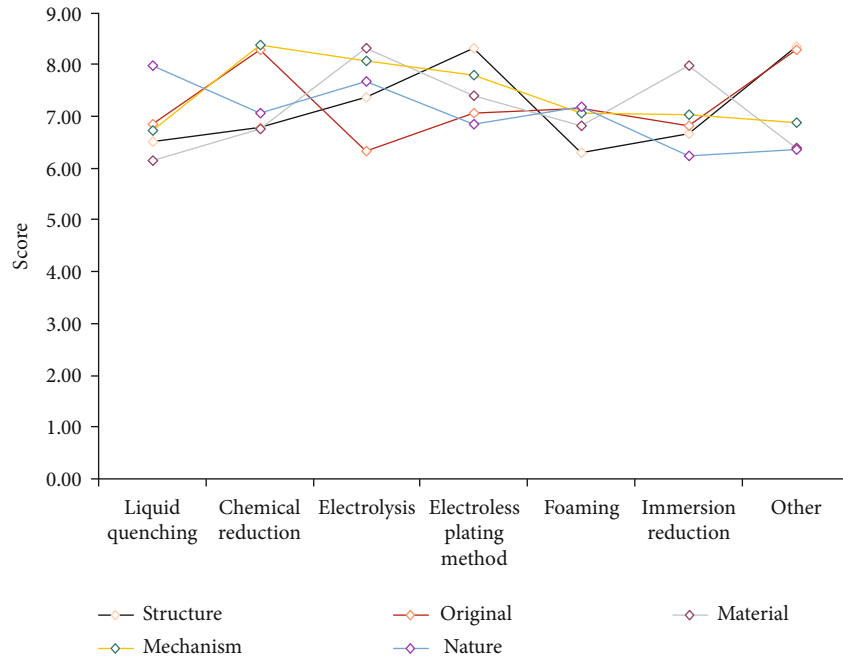
Figure 2: The impact of different methods on different elements.
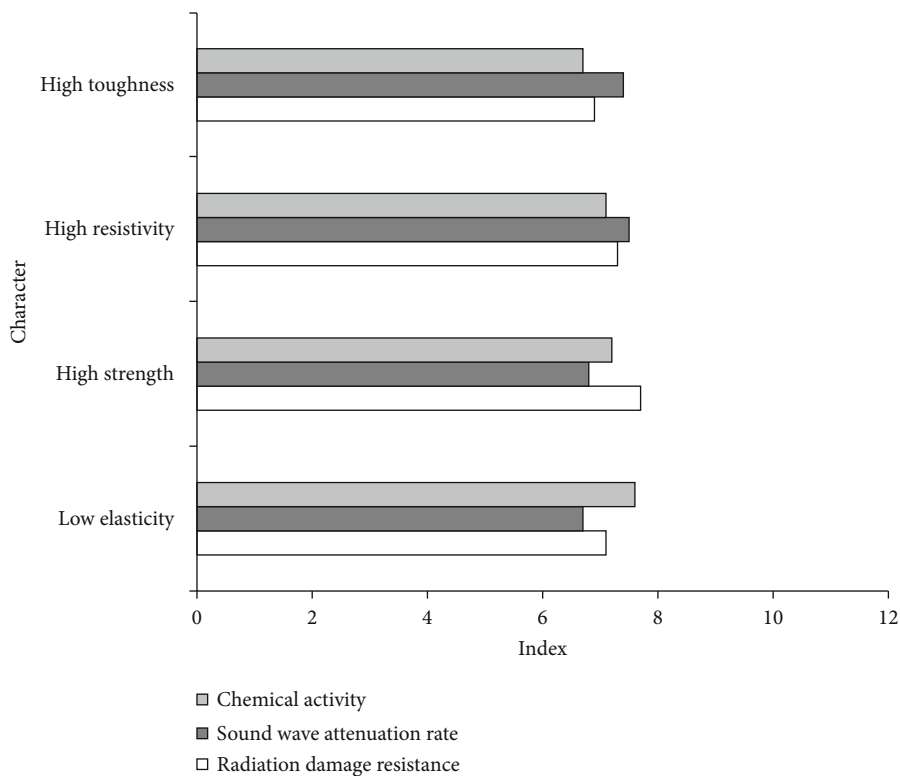

Figure 3: The correlation between physical characteristics and performance.

operational operations, promote the realization of logistics standardization, and constitute a multi-interface, multiuser, cross-regional, time-free macrologistics service platform. Nowadays, distribution and multitasking and manufacturing activities put forward requirements for the construction of

store systems and logistics platforms required by logistics companies, requiring logistics companies' applications and materials used in logistics to be more integrated, modern, and diversified. The logistics cost advantage is the core competitiveness of every logistics company. The logistics
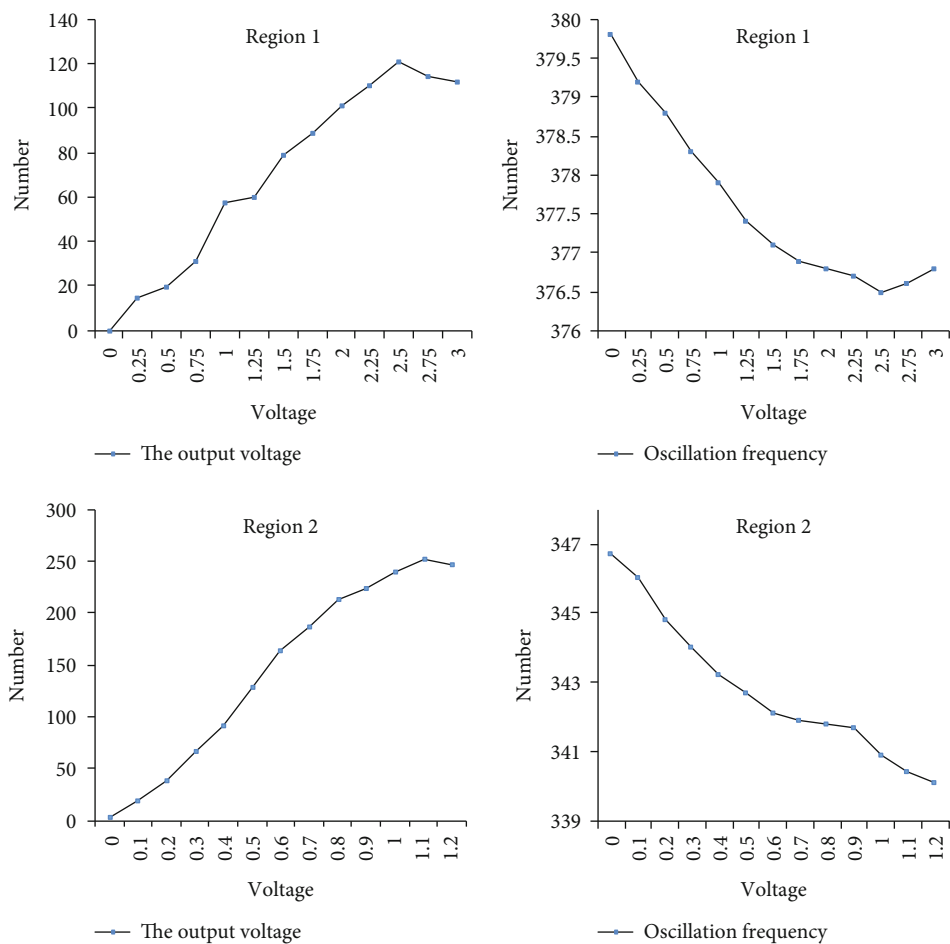
Figure 4: The relationship between output voltage and vibration frequency.
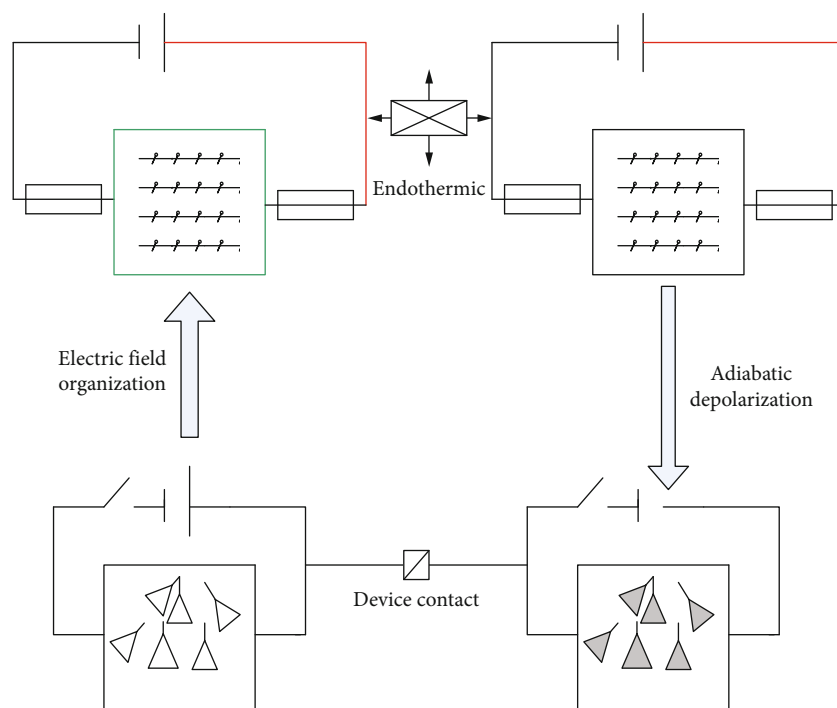
Figure 5: Ferroelectric card refrigeration mechanism.

TABLE 2: Data related to the electrical card effect under different electrical inclusions.

Electric inclusion mode	Temperature	Average temperature	Electric card
Air	200	-8.7	0.117
Air	450	16.01	0.023
Silicone oil	150	-18.3	0.372
Silicone oil	350	6.24	0.417
Water	100	-4.72	0.81
Water	240	6.26	0.216

information platform of logistics enterprises can use this series of feedback data to carry out effective analysis and improvement, and at the same time, it can also strengthen the communication and cooperation between logistics enterprises and goods suppliers and subordinate agent distributors. Because of the impressive use of a large number of inactive resources in society, the economic distribution system has taken root in all walks of life, and the concept of distribution is deeply ingrained. The current network platform includes the field of live broadcast services. Digital logistics has no time and space constraints and can complete logistics tasks with high quality within the specified time. The platform architecture is shown in Figure 6. For suppliers or digital logistics platforms with multiple distribution centers, when selecting a distribution center, they often agree on the service scope of the distribution center.

Use these controls repeatedly on multiple pages. Compared with user controls, custom controls are another step forward. Collect multisource data through the data augmentation system. Firstly, it is integrated, sorted, and saved to the data system level and then transmitted through the data call bar. Filter out the appropriate data information according to the corresponding database table, and then return to the front-end interface for display. It provides a robust functional system and is very suitable for large-scale applications that require reasonable unit testing, such as a digital logistics information platform that can carry multiple systems. The first appearance of the system is the database operation interface. Users can click on the table to be modified in the navigation bar on the left side of the interface. When the database model changes, just change the mapping object of the model. Due to information asymmetry and information barriers, it will lead to waste of resources on both sides of the supply and demand. In the process of loss, the profits of each party cannot be maximized, and some even cause serious economic losses, which seriously disrupt the normal order of social and economic activities. Therefore, it is necessary for us to digitize logistics management. Part of the logistics and distribution data of a certain company is selected, as shown in Table 3.

System functional requirement analysis is to describe all the functional submodules of the system from the user's point of view, and it needs to reflect the function and operation process of each module. Analyze the characteristics of digital logistics, as shown in Figure 7.

The data in the above figure shows that the digital logistics platform constructed in this article can reach a score of 7.75 in terms of data security and up to 7.39 in terms of flexibility. The logistics information management platform uses the power of the Internet to develop a network system based on logistics information and improve information exchange. Part of the multihoming phenomenon caused by platform differentiation is normal behavior. The multilayer system structure can provide more complete components for the logistics information platform, which not only improves the stability of the system performance, power consumption, and reusability but also saves a lot of system development costs; the currently widely used electronic authentication technology has passed. The identification of the user's identity and effectively prevent illegal users from entering is an effective method for scientific management and control of the system. In this system, the number of people used is relatively large, and the data involved is also a lot, which has higher requirements for the accuracy and completeness of the data.

In the case of low cost of multihoming behavior of bilateral users of logistics platforms, logistics platforms need to face the problem of the scale of bilateral users in the market. The logistics platform's product differentiation product service strategy determines the transfer barrier of the logistics platform. Platforms with differentiated services can often lock users more stably in market competition. Logistics platform companies use advanced GIS geographic information system navigation and GPS transportation and vehicle tracking systems to provide optimized route services for cargo transportation on the platform and vehicle safety supervision during driving. Perform data evaluation on the four aspects of basic management, business management, supervision management, and decision-making management of three different logistics management modes: visual logistics, bilateral logistics, and traditional logistics, as shown in Figure 8.

Compared with the traditional logistics management system, the digital logistics platform based on virtual simulation technology of logistics services can enhance the intuitiveness of river basin information expression and improve the system's display and processing ability of multi-dimensional and massive logistics data. The test of the system is not only a test for the function of the system, but also the operating environment of the system must be tested. Data owners need a set of effective data management and maintenance methods, and data users also need to understand the data and discover the data. In the process of data access, high efficiency, availability, and stability meet the development requirements. The scale of the data is conducive to the use
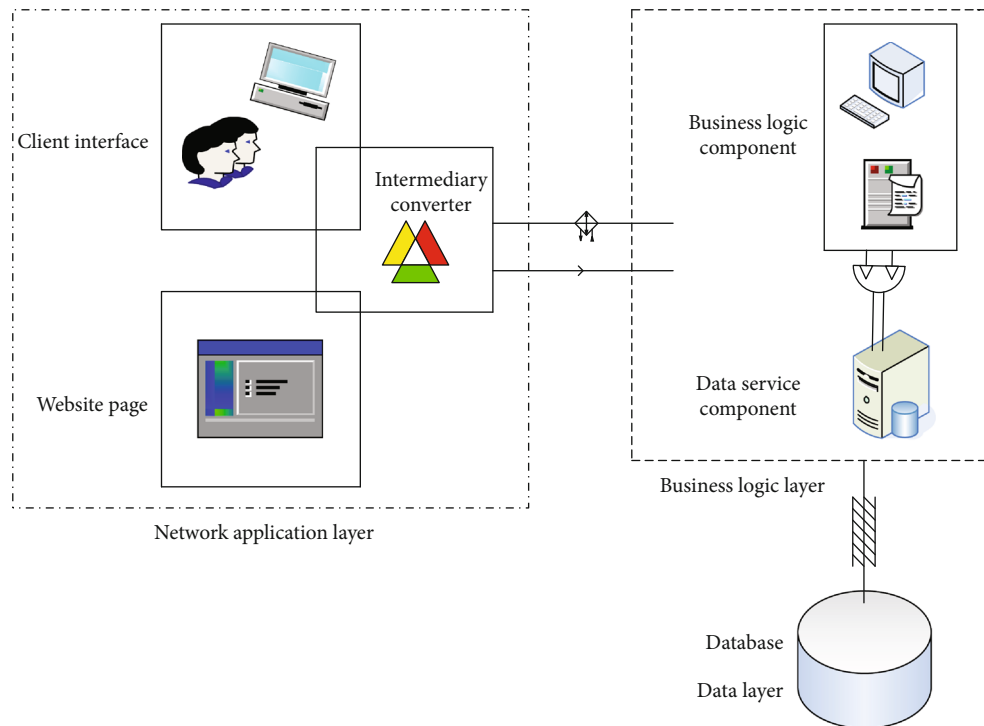
FIGURE 6: Platform architecture.

TABLE 3: One day's delivery data on a company's logistics platform.

Serial number	Longitude	Dimension
120	117.213	33.217
121	117.214	33.682
122	117.013	33.465
123	117.467	33.816
124	117.287	33.247
125	117.257	33.812
126	117.634	33.497
127	117.446	33.681
128	117.771	33.589

of users and ensures the security and stability of the data. Digital logistics can help Chinese transport enterprises to improve the efficiency of transport operations and the quality of logistics services. It is an indisputable fact in the industry that the operation of logistics needs to be networked.

4. Discussion

With the rise of the global Internet of Things technology boom in recent years, sensors, as the core component of the Internet of Things technology, have received unprecedented attention. The sensitive function of amorphous alloy material means that when this alloy is used as a sensor's sensitive material, it can convert the detected nonelectricity into a signal that is easier to pick up and process according to a certain rule. In some special occasions, it can also exert

unimaginable positive and effective effects. Therefore, when studying the use of amorphous alloy materials, the mechanical functions should be used properly and flexibly. So far, bulk amorphous alloys have significant tensile strength and value as advanced materials. The polarization time of amorphous materials is slower than that of thin film materials. Therefore, the result cannot indicate the exact location. In the whole process, the shape of the amorphous alloy material does not change. The magnetic properties of the amorphous alloy material are mainly used, and it is difficult to measure the pressure. Comprehensive utilization of various properties of amorphous alloy materials is for achieving the purpose of pressure measurement.

There are abundant material expectations for ferroelectric applications, especially in small sensors and transducers. Nowadays, more and more experts and scholars are beginning to use ferroelectric testing devices in a multiphysics coupling environment to explore the richer information of ferroelectric materials in a multiphysics coupling environment. Due to its own characteristics, in actual service, ferroelectric materials are affected not only by the electric field but also by the interaction and influence of the stress field and the temperature field. Ferroelectric materials often exhibit richer physical properties in a multi-physics coupling environment, thus expanding their application fields. The ferroelectricity of ferroelectric crystals is the result of the movement of electric domains on the microscopic level, and the hysteresis loop and electrostriction of ferroelectric materials are the result of the movement of electric domains. This research content is relatively small in this article, and follow-up work will conduct more detailed research on this.
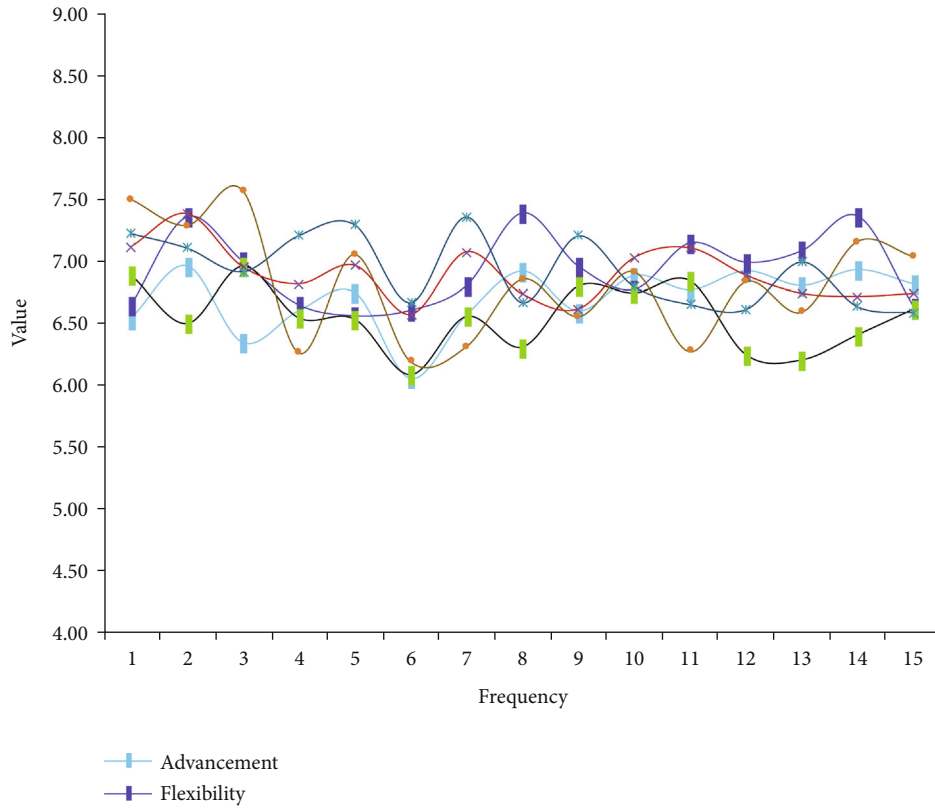
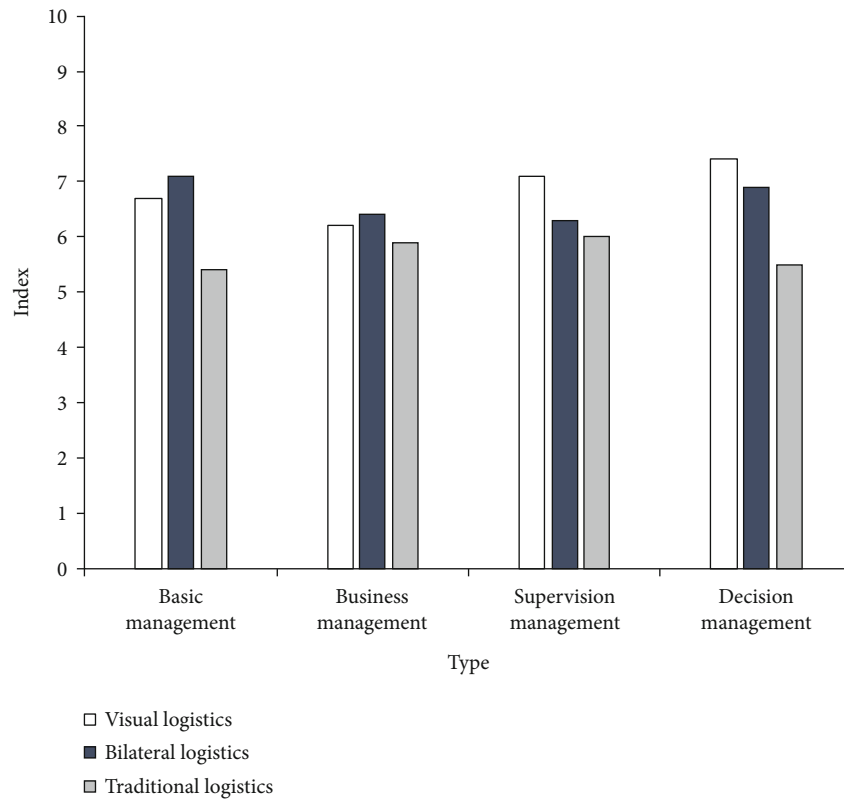Figure 7: Characteristic analysis of digital logistics.

Figure 8: Corresponding score values of each management part of different logistics.

5. Conclusion

Logistics distribution is an important part of modern logistics management, especially suitable for objects with a large number of workplaces, such as companies with thousands of customers. Many logistics companies have begun to explore the logistics platform model, hoping to achieve cost reduction and efficiency enhancement, transformation, and improvement through the construction of logistics platform, and significantly enhance their competitiveness. Warehousing is one of the most important links in the supply chain. The efficiency and cost of the warehousing system also directly affect the efficiency and cost of all logistics. In the available logistics and collection process, the incompetence of the distribution chain supply chain is often caused by the inaccuracy or poor visibility of information in the logistics process. The integration of internal logistics sources, the planning and optimization of supply logistics, production logistics, and sales logistics systems through centralized management and innovative services are in full swing, and some results have been achieved. The lack of data measurement and exchange methods has a significant impact on all aspects of storage, such as storage and messaging, and there is also a lack of supporting information to identify macro and micro decision-making. Track the location through the specific positioning of the logistics location, to realize the storage of commodity data and the process of emergency adjustment of orders when it is out of storage and real-time monitoring of the path of the outgoing process to realize visualization. These links have extremely high requirements for data processing technology.

Data Availability

The data that support the findings of this study are available from the corresponding author upon reasonable request.

Conflicts of Interest

The authors declared no potential conflicts of interest with respect to the research, authorship, and/or publication of this article.

References

[1] W. Sima, M. Zou, M. Yang, Q. Yang, and D. Peng, "Modeling of grain-oriented Si-steel and amorphous alloy iron core under ferroresonance using Jiles–Atherton hysteresis method," *AIP Advances*, vol. 8, no. 5, pp. 56608–56608, 2018.

[2] S. B. Tsai and K. Wang, "Using a novel method to evaluate the performance of human resources in green logistics enterprises," *Ecological Chemistry and Engineering S*, vol. 26, no. 4, pp. 629–640, 2019.

[3] Y. Chen, W. Zheng, W. Li, and Y. Huang, "The robustness and sustainability of port logistics systems for emergency supplies from overseas," *Journal of Advanced Transportation*, vol. 2020, Article ID 8868533, 12 pages, 2020.

[4] R. Tang, W. Tong, and X. Han, "Overview on amorphous alloy electrical machines and their key technologies," *Chinese Journal of Electrical Engineering*, vol. 2, no. 1, pp. 1–12, 2017.

[5] Y. F. Ma, B. Z. Tang, L. Xia, and D. Ding, "Outstanding magneto-caloric effect of a Gd60Ni37Co3 amorphous alloy," *Chinese Physics Letters*, vol. 33, no. 12, pp. 101–104, 2016.

[6] H. F. Tan, B. Zhang, Y. K. Yang, X. F. Zhu, and G. P. Zhang, "Fracture behavior of sandwich-structured metal/amorphous alloy/metal composites," *Materials & Design*, vol. 90, pp. 60–65, 2016.

[7] E. V. Ubyivovk, E. V. Boltynjuk, D. V. Gunderov, A. A. Churakova, A. R. Kilmametov, and R. Z. Valiev, "HPT-induced shear banding and nanoclustering in a TiNiCu amorphous alloy," *Materials Letters*, vol. 209, pp. 327–329, 2017.

[8] H. Lee, G. S. Kim, C. Jeon et al., "Dynamic tensile deformation behavior of Zr-based amorphous alloy matrix composites reinforced with tungsten or tantalum fibers," *Metals & Materials International*, vol. 22, no. 4, pp. 707–713, 2016.

[9] S. Lesz and G. Dercz, "Study on crystallization phenomenon and thermal stability of binary Ni–Nb amorphous alloy," *Journal of Thermal Analysis & Calorimetry*, vol. 126, no. 1, pp. 19–26, 2016.

[10] T. V. Kulikova, V. A. Bykov, A. A. Belozerova, A. M. Murzakaev, and R. E. Ryltsev, "Crystallization kinetics of Al86Ni8Gd6 amorphous alloy," *Journal of Surface Investigation. X-ray, Synchrotron and Neutron Techniques*, vol. 10, no. 2, pp. 356–360, 2016.

[11] V. Rajaei, H. Rashtchi, K. Raeissi, and M. Shamanian, "The study of Ni-based nano-crystalline and amorphous alloy coatings on AISI 304 stainless steel for PEM fuel cell bipolar plate application," *International Journal of Hydrogen Energy*, vol. 42, no. 20, pp. 14264–14278, 2017.

[12] N. Barrett, J. E. Rault, J. L. Wang et al., "Full field electron spectromicroscopy applied to ferroelectric materials," *Journal of Applied Physics*, vol. 113, no. 18, pp. 136–240, 2018.

[13] P. Fedeli, A. Frangi, F. Auricchio, and A. Reali, "Phase-field modeling for polarization evolution in ferroelectric materials via an isogeometric collocation method," *Computer Methods in Applied Mechanics and Engineering*, vol. 351, pp. 789–807, 2019.

[14] V. I. Gorodetsky, V. B. Laryukhin, and P. O. Skobelev, "Conceptual model of a digital platform for cyber-physical management of a modern enterprises. Part 2. Digital Services," *Mekhatronika Avtomatizatsiya Upravlenie*, vol. 20, no. 7, pp. 387–397, 2019.

[15] Y. Zhang, W. Ni, and Y. Li, "Effect of siliconizing temperature on microstructure and phase constitution of Mo–Mosi$_2$ functionally graded materials," *Ceramics International*, vol. 44, no. 10, pp. 11166–11171, 2018.

[16] S. Qiu, J. Huang, F. Shen et al., "Ternary Co–Ni–B amorphous alloy with a superior electrochemical performance in a wide temperature range," *International Journal of Hydrogen Energy*, vol. 41, no. 6, pp. 3955–3960, 2016.

[17] L. Zhu, J. Zhu, W. Tong, and X. Han, "Analytical method of no-load iron losses of axial flux amorphous alloy permanent magnet motor," *Zhongguo Dianji Gongcheng Xuebao/proceedings of the Chinese Society of Electrical Engineering*, vol. 37, no. 3, pp. 923–930, 2017.

[18] B. Gao, X. Ning, and P. Xing, "Shock wave induced nanocrystallization and its effect on mechanical properties," *Materials Letters*, vol. 237, no. 15, pp. 180–184, 2019.

[19] H. Guo, H. Zhang, W. Tang et al., "Furfural hydrogenation over amorphous alloy catalysts prepared by different reducing agents," *BioResources*, vol. 12, no. 4, pp. 8755–8774, 2017.

[20] Y. Deng, Y. Yang, L. Ge, W. Yang, and K. Xie, "Preparation of magnetic Ni-P amorphous alloy microspheres and their catalytic performance towards thermal decomposition of ammonium perchlorate," *Applied Surface Science*, vol. 425, pp. 261–271, 2017.

[21] F. Qiang, M. Fu, W. Chao, T. Zhiwei, L. Xumin, and C. Bin, "Effects of Sn and B on thermal stability of Fe based amorphous alloy ribbons," *Heat Treatment of Metals*, vol. 41, no. 3, pp. 159–162, 2016.

[22] P. Wang, S. Wang, X. Zhang et al., "Rational construction of CoO/CoF$_2$ coating on burnt-pot inspired 2D CNs as the battery-like electrode for supercapacitors," *Journal of Alloys and Compounds*, vol. 819, article 153374, 2019.

[23] X. L. Wang, Y. X. Zheng, M. L. Jia, L. S. Yuan, C. Peng, and W. H. Yang, "Formation of nanoporous NiCuP amorphous alloy electrode by potentiostatic etching and its application for hydrazine oxidation," *International Journal of Hydrogen Energy*, vol. 41, no. 20, pp. 8449–8458, 2016.

[24] O. M. Hertsyk, L. M. Boichyshyn, M. O. Kovbuz, Y. O. Kulyk, and V. K. Nosenko, "Corrosion resistance of the Fe 68.93 Mn 1 Mo 4 Cr 2 C 7 P 10 B 5 Si 2 (Cu, W,Al) 0.07 amorphous alloy in media with different aggressiveness," *Materials Science*, vol. 51, no. 5, pp. 1–8, 2016.

[25] B. Chen, H. Guo, Z. Wan et al., "Efficient catalytic hydrogenation of butyl levulinate to γ-valerolactone over a stable and magnetic CuNiCoB amorphous alloy catalyst," *Energy & Fuels*, vol. 32, no. 4, pp. 5527–5535, 2018.

[26] X. Li, F. Lv, Y. X. Geng et al., "Preparation and corrosion property of (Cu$_{50}$Zr$_{50}$, 100-x)Ndx amorphous Alloy," *International Journal of Electrochemical Science*, vol. 12, no. 1, pp. 726–732, 2017.

[27] P. Wang, T. Yao, Z. Li et al., "A superhydrophobic/electrothermal synergistically anti-icing strategy based on graphene composite," *Composites Science and Technology*, vol. 198, article 108307, 2020.

[28] C. Jie and Z. Zhu, "The study on surface chemical modification of Fe$_{71.5}$Cu$_1$Nb$_3$Si$_{13.5}$B$_9$V$_2$ amorphous alloy ribbons and its piezomagnetic effect," *Journal of Magnetism & Magnetic Materials*, vol. 419, no. dec., pp. 451–455, 2016.

[29] C. Liu, P. Lu, Z. Z. Gu, J. Yang, and Y. Chen, "Bidirectional tuning of thermal conductivity in ferroelectric materials using E-controlled hysteresis characteristic property," *The Journal of Physical Chemistry C*, vol. 124, no. 48, pp. 26144–26152, 2020.

[30] Y. Zhang, H. Dan, J. Chen et al., "Evaluation of energy storage performance of ferroelectric materials by equivalent circuit model," *Ceramics International*, vol. 47, no. 14, pp. 20512–20518, 2021.

[31] C. Lian, Z. A. Ali, H. Kwon, and B. M. Wong, "Indirect but efficient: laser-excited electrons can drive ultrafast polarization switching in ferroelectric materials," *Journal of Physical Chemistry Letters*, vol. 10, no. 12, pp. 3402–3407, 2019.

[32] Y. Zhang, H. Huang, L. X. Yang, Y. Xiang, and M. Li, "Serious challenges and potential solutions for the industrial Internet of Things with edge intelligence," *IEEE Network*, vol. 33, no. 5, pp. 41–45, 2019.

[33] O. I. Khalaf and G. M. Abdulsahib, "Optimized dynamic storage of data (ODSD) in IoT based on blockchain for wireless sensor networks," *Peer-to-Peer Networking and Applications*, vol. 14, no. 5, pp. 2858–2873, 2021.

Research Article

Preparation Method of High Resilience Nonslip Basketball Sole Composite Material

Zheng Wang,[1] **Yihe Liu,**[2] **and Shuang Zhang** [2]

[1]*College of Sport, Neijiang Normal University, Neijiang, 641100 Sichuan, China*
[2]*School of Artificial Intelligence, Neijiang Normal University, Neijiang, 641100 Sichuan, China*

Correspondence should be addressed to Shuang Zhang; zhang.s@njtc.edu.cn

Today, with the gradual improvement of material living standards, basketball is becoming more and more popular, and the pursuit of sports protection and shoes performance is also getting higher and higher. A good pair of basketball shoe soles can help athletes solve these problems. This article is aimed at studying the preparation of basketball shoe soles made of high resilience and nonslip composite materials. Under this research topic, this paper proposes a method for the design of shoe sole antislip pattern and the measurement method of composite material's resilience performance and a 3D printing method based on FDM technology to print the shoe sole. At the same time, an experiment was designed to explore the high resilience and antislip performance of the sole. And the stability of printing technology is analyzed to ensure the quality of sneaker printing. The experimental results in this article show that the antislip performance of the sole printed by the above method design has been improved by 31%, and the rebound capacity has been improved by 44%. At the same time, the rebound time is significantly shorter than that of several common basketball shoes on the market.

1. Introduction

The correct selection of sports shoes with appropriate functions is an important link that sports enthusiasts should not ignore. The structural design and material function of sports shoes play a very important role in protecting the human body and improving sports performance. The basketball population in China is increasing day by day, and there is a great demand for basketball shoes. Various manufacturers compete with each other for the research and development of basketball shoes. The functionality and professionalism of basketball shoes are the main considerations for fans. In a fierce basketball game, if a person's foot touches the ground, it will receive an impact from the ground to the human body. The impact of the impact can cause various damages to all parts of the human body. For example, if you twist your feet hard, your ankle will be sprained, your feet will be swollen, and pain will occur. At the same time, in basketball, excessive footsteps will move laterally, putting a burden on muscles and bones, and eventually, joint skills will decline, and tendons may become stiff. Basketball players will exercise their knees after a lot of sports. Injuries, ankle and middle finger injuries, are very common. At the same time, the antiskid of basketball shoes is also extremely important, which can effectively prevent athletes from slipping and causing ankle injuries.

However, there are two problems with the slip resistance and high elasticity of current basketball shoes. First of all, companies have exaggerated the antislip and elastic functions of basketball shoes, causing people to misunderstand the understanding and consumption of basketball shoes; second, as the basic performance of basketball shoes, the antislip and rebound ability has not received full attention from basketball shoe manufacturers. Most basketball shoes are designed with nonslip mode, and the structure is more beautiful than the actual function. The problem of ankle sprain caused by basketball foot slip cannot be solved at all. With this in mind, we believe that the study of the sole pattern and resilience of basketball shoe soles has important value and importance.

The sole design of basketball shoes is the focal point of the entire sports shoe. Basketball shoes are a prerequisite

for excellent performance. Basketball shoes provide excellent protection and elasticity, and most of these basketball shoes have excellent bottom design. With the increasing influence of basketball, more and more people have begun to devote themselves to the design of high resilience and nonslip performance of the soles of basketball shoes. Liang et al. proposed a feasible method to select the material of the beam collector in the HPM device. First, he compared the elasticity of several metals to strong relativistic electron beam (IREB) bombardment. This resilience is mainly determined by the density and melting point of the material. Compared with stainless steel, copper, molybdenum, and tungsten, titanium shows good resilience. Therefore, the theoretical results indicate that titanium is a promising material that can be used in HPM equipment [1]. However, this research is only an analysis based on theoretical research, and no experiment is used to verify the conclusion. Kakunuri et al. use the controlled pyrolysis of electrospun SU-8 photoresist nanofibers to fabricate a binder-free carbon nanofiber mesh on a stainless steel wafer collector. The electrochemical performance of the prepared carbon nanofiber mesh was studied by conducting charge and discharge experiments under different current densities. This excellent electrochemical performance can be attributed to the smaller lithium-ion diffusion length and the elasticity in the entangled carbon nanofibers to adapt to the volume changes during charging and discharging [2]. However, under different current densities, the charging and discharging experiments did not compare the performance under low current and high current, and there are still some deficiencies. Han et al. proposed that in order to make the structural noise of ship-borne equipment reach the prescribed standards, the excitation force of the equipment should be limited, and antivibration devices such as elastic supports and bellows should be added. Since structural noise depends on the design of the equipment base, it is important to achieve a low-vibration base design. In his research, the typical pump base was optimized using design of experiment (DOE) and computer-aided engineering (CAE) techniques to minimize the vibration transmitted from the equipment base to the ground [3]. However, there is still no clear statement on how to achieve a certain degree of antivibration through the structure of the material. Ju et al. conducted a parametric study on field data of more than 100 locations measured under two heavy object impact sources. The results show that the size of the room and the dynamic stiffness of the elastic floor mat material are the main factors affecting the impact noise of the floor. According to the analysis results, a simple regression equation of the impact noise of the heavy hammer is proposed. These formulas are expected to guide engineers to consider floor impact noise levels in the early design stage before construction [4]. Among them, the elasticity of the elastic floor mat material can be well used in our design. Xiao et al. tested the 4% cement stabilized base mixture in different system laboratories, including unconfined compressive strength and splitting strength of curing time, 90 d compression and splitting elastic modulus, erosion resistance, freeze-thaw resistance, dry shrinkage, and temperature shrinkage. And he conducted a comparative analysis of the test results [5].

We can use its experimental experience on elastic modulus for reference in our material elasticity experiment. Kim et al. believe that recycled synthetic resin materials produced from waste vinyl and waste plastics contain many foreign substances. Such plastic products made of recycled resin materials containing foreign matter are of poor quality, and their strength and rigidity are reduced. Foreign objects include heavy metals, cement, foil, dyed paper, and dust. After installing the manufactured equipment, recycled resin is produced, and its heavy metal content is evaluated. Recycled synthetic resin materials are also used in plastic products, and their strength is evaluated. In addition, changes in production are also evaluated [6]. For the preparation of PVC synthetic resin, we can use it in the preparation of shoe soles. Sun et al. modified the surface of iron-rich sludge with silane coupling agent KH550 to prepare modified iron-rich sludge, which was then filled into polyvinyl chloride to prepare PVC/KH550-FeS composite materials [7]. By modifying FeS, its heat resistance, stretchability, and other related properties can be improved very well, and the same can be done in the preparation of sneaker sole material PVC. By blending or adding various additives (such as antioxidants, etc.) to improve to enhance functional performance, Shen et al. classify polymer-based building materials into three categories: substrates, coatings, and adhesives according to their uses. And he carefully demonstrated the latest progress in their preparation and application [8]. Most of the appeal literature is about the consideration of elasticity, and the experimental analysis of the specific parameters of elasticity has not been explored in detail. The experimental part is also researched on the basis of theory, and the external environment factors in the actual use process are not taken into consideration. The innovation of this article lies in the theoretical support of the pattern design and antiskid design of basketball shoes. This article designs its antiskid pattern and resilience ability and designs experiments to analyze and compare its antiskid ability and resilience ability. At the same time, 3D printing technology is used as technical support to print the soles of sneakers in batches. The quality problems of sneakers that may be caused by parameter problems in the 3D printing process are also analyzed, and the influence of irrelevant factors is excluded, which can ensure the performance of sneakers while ensuring the output.

2. Sole Performance Design Method

2.1. Shoe Sole Antislip Pattern Design. The characteristics of the outer layer of the venue, such as material, reinforced hardness, and microhardness, will greatly affect the performance of antislip and wear resistance. In the link where the field and the pattern maintain continuous friction, due to the action of force and heat, the outer layer of contact has obvious changes (the antiskid pattern of the sole is worn, the sole is deformed, etc.), and such changes also affect the performance of friction loss. The outer morphology and microscopic contact of the field and the pattern continue to change during the friction process [9]. In addition, the microscopic components of the friction outer layer will also

appear to be cracked and transferred and then act on the shape of the contact outer layer, so that the antislip and abrasion performance of the outsole pattern will be significantly changed. Therefore, the status of the venue will be directly related to the functional attributes of the outsole pattern (floor humidity, antiskid ability, and floor material of the arena, etc.). When there are differences in venues, different outsole patterns should be designed (square, dotted, and divergent). The study of different sole patterns plays a vital role in the antislip performance of the soles. A good and suitable sole pattern can greatly improve the antislip properties of the soles [10].

The shoe soles with square pattern and small dot pattern have the best slip resistance on asphalt pavement and the second place on cement pavement. This is because both cement roads and asphalt roads are rough surfaces, and the soles are in surface contact when they are in contact with them. The contact area between the small dot pattern soles and the cement roads and asphalt roads is obviously smaller than that of the square pattern soles. Therefore, the test results of cement pavement and asphalt pavement are consistent. In other words, the sliding resistance of the sole of the square pattern is greater than the sliding resistance of the sole of the small dot pattern. The type of friction surface is an external factor and cannot be controlled. DuShaxun [11] of Shaanxi University of Science and Technology and others used two continuous, four continuous, and sliding block samples to study the antiskid properties of wood, cement, and marble on three different pavements. The double-sided continuous mode is composed of one or more decorative elements, and a specific curve is used as the skeleton to form a unit mode, which is arranged continuously according to a specific space, distance, and direction to form a regular pattern. The square continuous pattern is a pattern that uses one or more decorative elements to form a basic unit. It is repeatedly configured in a specific space according to a specific bone structure, and it can be expanded and continued indefinitely (it stretches through infinite stacking and cascading). In the experiment, the marble surface is the smoothest, the pattern that touches the ground is the largest, the adsorption between molecules is the strongest, so the friction between the ground and the sole of the shoe is the largest, and the sliding performance is the highest. However, due to the different places where various types of shoes are used (concrete road, indoor court, outdoor plastic court, etc.), that is, the road conditions are different, the pattern design is not single (zoomair, get, regular pattern, and chevron), it needs to be designed according to the external environment and different uses of the sole. The analysis of the foundation state of the basketball court mainly focuses on its surface shape. The characteristics of the foundation shape have a great influence on the movement function of the sole and the pattern design of the sole. The contact surface between the pattern of the shoe sole and the ground is composed of tiny raised peaks and valleys of various shapes. The shape of the thick peak of the contact surface between the outer Tor and the field is usually an ellipsoid. Since the contact size of the ellipsoid is much smaller than its own radius of curvature, it can almost be regarded as a sphere. The contact of two planes can be regarded as the contact of uneven spheres, which simulates the contact of rough surfaces in the ideal state [12].

2.1.1. Basketball Shoes. In the main distribution map of plantar pressure under different walking postures, the main force area and sliding trend of the stressed foot pressure are analyzed by measuring the plantar pressure of different adults' bare feet under different walking postures (duck gait, scissor gait, rooster gait, jumping gait, etc.). This coincides with the design of the circular pattern on the inner side of the forefoot of the basketball shoe. According to Figure 1 (measured gait is scissor gait), the analysis of the sliding trend of the stressed foot under different walking postures can also be used to design soles with different pattern directions for shoes of different purposes [13].

The circular outsole pattern is mostly used in basketball shoes (as shown in Figure 2). The outer sole pattern is usually the center of the circle on the inner side of the front sole. Because when a basketball player turns around while holding the ball, with one foot as the axis, the center of gravity of the body will fall on the inner side of the forefoot (resulting in larger hands on the forefoot of the sole, increased wear and tear, and easy to cause pattern wear). Designing a pattern with a heart shape here can make it easier for basketball players to do this technical action, turning more sensitive and saving effort. This pattern is especially suitable for big players.

2.2. Determination of Elastic Properties of Shoe Sole Composite Materials

2.2.1. Determination of Poisson's Ratio. Poisson's ratio is used to express the elastic properties of materials. (Poisson's ratio refers to the ratio of the absolute value of the transverse normal strain to the axial normal strain when the material is in unidirectional tension or compression, also known as the transverse deformation coefficient, which is an elastic constant that reflects the transverse deformation of the material). Poisson's ratio is defined as the absolute value of the ratio of the transverse strain A caused by the uniformly distributed longitudinal stress to the corresponding longitudinal strain B within the proportional limit of the material, namely,

$$\mu = \frac{-\varepsilon_x}{\varepsilon_y}. \tag{1}$$

At the same time, Poisson's ratio can be described by material performance parameters such as elastic modulus E, bulk modulus K, and shear modulus G [14]. For linear materials, the following relationships exist:

$$\mu = \frac{1}{2}\frac{(3K - 2G)}{(3K + 2G)},$$

$$\mu = \frac{E}{2G - 1},$$

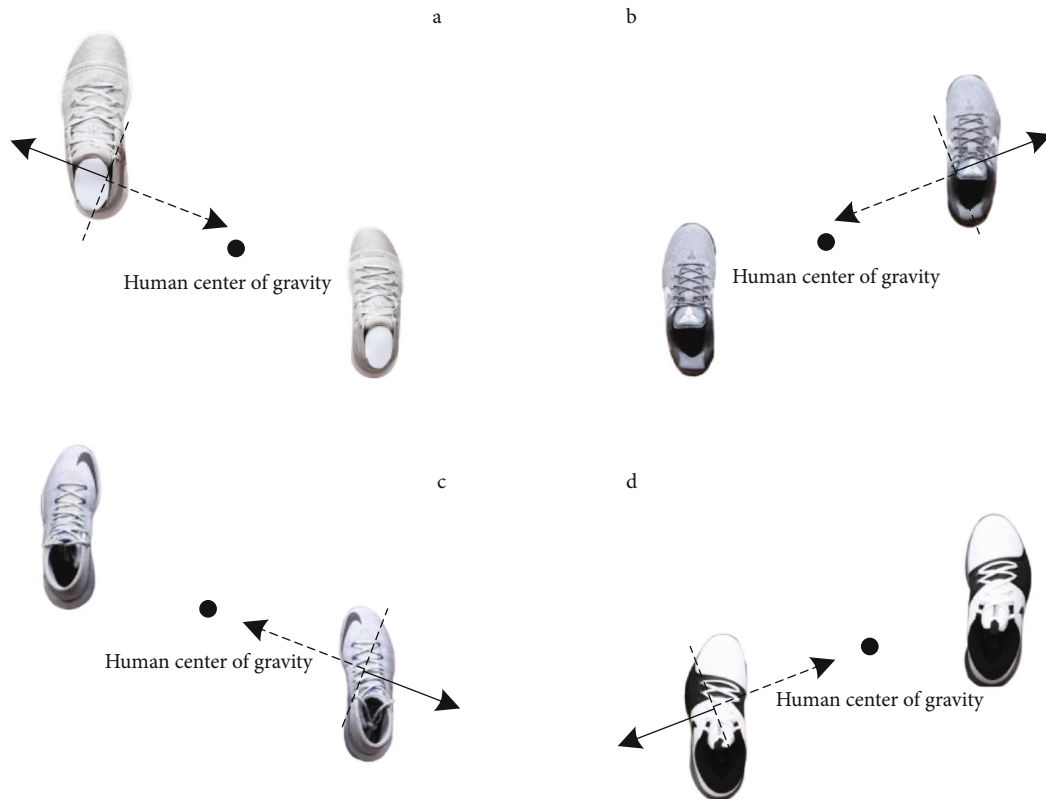$$\mu = \frac{1 - E/3K}{2}. \tag{2}$$

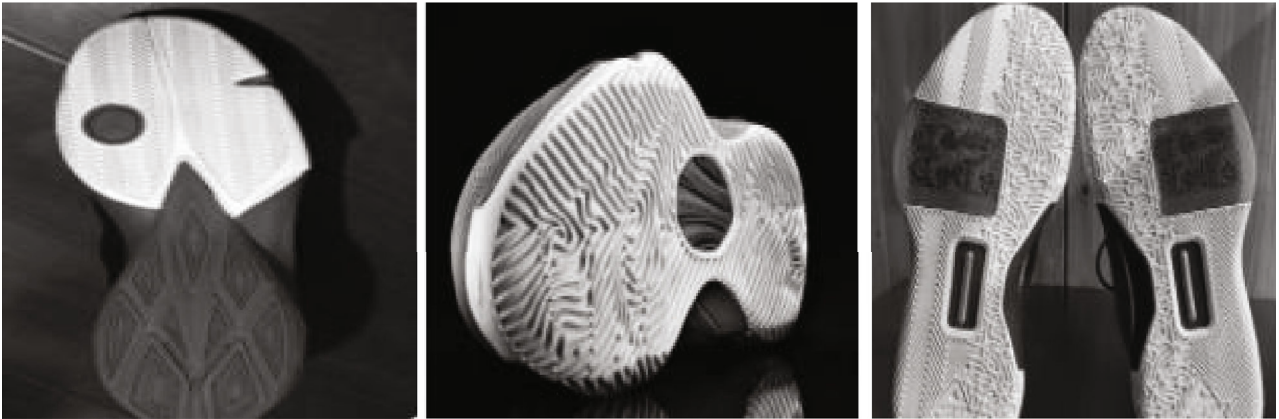Figure 1: Analysis of the sliding trend of the stressed foot in different walking postures.

Figure 2: Basketball shoes with nonslip patterns.

When two of the three quantities of the material's elastic modulus E, shear modulus G, and bulk modulus K are known, the Poisson's ratio can be calculated.

For the Poisson's ratio of isotropic linear elastic materials, expression (1) is fully applicable. In the case of viscoelastic materials, Poisson's ratio is a parameter related to both temperature and load time. According to the nature of the load, it can be divided into static viscoelastic Poisson's ratio and dynamic viscoelastic Poisson's ratio [15, 16]. The former represents the transverse strain response to longitudinal strain under static load conditions, and the latter represents the transverse strain response to longitudinal strain.

Under dynamic load conditions, it represents the response to longitudinal strain. According to the viscoelastic properties of the material, the distortion has hysteresis. Therefore, we have sufficient reasons to believe that the Poisson's ratio of viscoelastic materials is more complicated.

Starting from the definition of Poisson's ratio, this article uses a static strain gauge to determine the Poisson's ratio of the resin matrix according to the full-bridge connection method, as shown in Figure 3. R1, R2, R3, and R4 are resistance strain gauges, R1 and R3 measure longitudinal strain, R2 and R4 measure lateral strain, and RL is a temperature compensation sheet. The full bridge approach we use can

efficiently utilize the concept of double differential. Therefore, the output voltage can reach as much as 4 times of the single-arm output voltage, which can greatly improve our measurement sensitivity in the actual measurement [17].

The measurement of Poisson's ratio is carried out under relaxed conditions, that is, the strain of pure resin material is compressed by 2%, and the change process of Poisson's ratio with time in 100 minutes is measured. Among them, the proportion of the test piece is 1 : 1 according to the volume ratio of resin to curing agent, and the plasticizer is 5% volume fraction of dibutyl phthalate and xylene agent, pouring the test piece in a 50 ml syringe and cutting it according to a certain size. The measurement result is shown as the solid line in Figure 4.

It can be found from Figure 4 that the Poisson's ratio of pure resin material also has relaxation characteristics, gradually decreasing until it stabilizes. The Poisson's ratio under relaxation conditions of viscoelastic materials is similar to the relaxation modulus, and the expression of attenuation series can also be used to approach the experimental data [18–20]. Using the origin curve fitting function, the result of Poisson's ratio can be fitted to the dashed line in the figure above, and the fitting curve expression is:

$$\mu(x) = 0.419 + 0.059e^{-1008x} - 0.054e^{-0.031x} + 0.062e^{-0.022x}.$$
$$(3)$$

2.2.2. Calculation of the Relaxation Modulus of the Combined Unit.
For a completely elastic material, there is such a relationship between the shear modulus and the elastic modulus and Poisson's ratio:

$$G = \frac{E}{2(1 + \mu)}.$$
$$(4)$$

But for linear viscoelastic materials, the relationship between shear modulus and elastic modulus and Poisson's ratio is related to time, and there is such an implicit relationship:

$$\int_0^t G(x - \tau) \frac{\partial \mu(\tau)}{\partial x} = \frac{E(x)}{2 - G(x)} [1 + \mu(0)].$$
$$(5)$$

Differentiate both sides of formula (5) to get:

$$G(0) \frac{\partial \mu(x)}{\partial x} = \frac{\partial E(x)}{\partial x} - \frac{\partial G(x)}{\partial x} [1 + \mu(0)],$$
$$(6)$$

where:

$$G(0) = \frac{E(0)}{2(1 + \mu(0))}.$$
$$(7)$$

$E(0)$ and $\mu(0)$ are directly determined from the experiment:

Solutions have to:

$$\frac{\partial G(x)}{\partial x} = \frac{((\partial E(x)/\partial x) - G(0)(\partial \mu(0)/\partial x))}{[1 + \mu(0)]}.$$
$$(8)$$

2.3. 3D Printing Process Based on FDM Technology.
According to the different printing methods of each layer in the molding process, the mainstream methods of 3D printing currently include fused deposition modeling (FDM), SLS, LOM, and SLA. However, the layered printing methods and materials used in the above technologies are quite different, and they all have their own advantages and disadvantages, and the fields of use are also different. In this paper, here's the advantage: additive manufacturing industry advances FDM 3D printers are feature-rich and can manufacture durable parts from your computer-aided design documents (CAD files). The parts are so robust that they can be used as high-level concept models, functional prototypes, manufacturing tools, and production parts. Engineers can produce a variety of products simply by loading different files and materials, which no other traditional machining process can do. FDM technology is used to 3D print the soles of sneakers to prepare the high-resilient nonslip sneakers we need [21].

2.3.1. Fused Deposition Modeling (FDM).
In fused deposition modeling (FDM), the thermoplastic material is melted by a heated nozzle, and the molten material is extruded from the nozzle by extrusion and friction, and it is coated on the worktable according to the slice model, and the parts are layer by layer [22].

The principle of FDM is shown in Figure 5, which shows a dual-nozzle printer. The filamentous prototype material (typically 1.75 mm or 3 mm in diameter) and the support material are printed by different nozzles. Usually, the support material will be made of characteristic materials (such as water-soluble materials), so that it can be removed by the corresponding method after printing. The coiled wire-like prototype material and supporting material pass through the wire feeding structure, and the wire is sent to the nozzle to be heated to a molten state. Then, according to the distribution data of the slice model on this layer, the corresponding prototype or supporting material is squeezed at the corresponding position, and it is coated on the workbench to gradually complete an entire layer. When a layer is completed, the nozzle rises a layer height distance. Then, the next layer is melted, and the newly coated layer is bonded to the previous layer, and so on, until the entire preliminary solid shape is completed. After the overall modeling is completed, the supporting materials are removed, the rough burrs on the solid surface are trimmed and then painted, polished, and colored as needed. Single-jet printing means that the prototype and supporting materials use the same material and the same nozzle [23].

The principle of fused deposition molding is easy to understand, simple in structure, and convenient to operate. PLA (polylactic acid) and various ABS plastics are often used. The materials are mostly in rolls and filaments, which are easy to carry and replace. At the same time, the overall
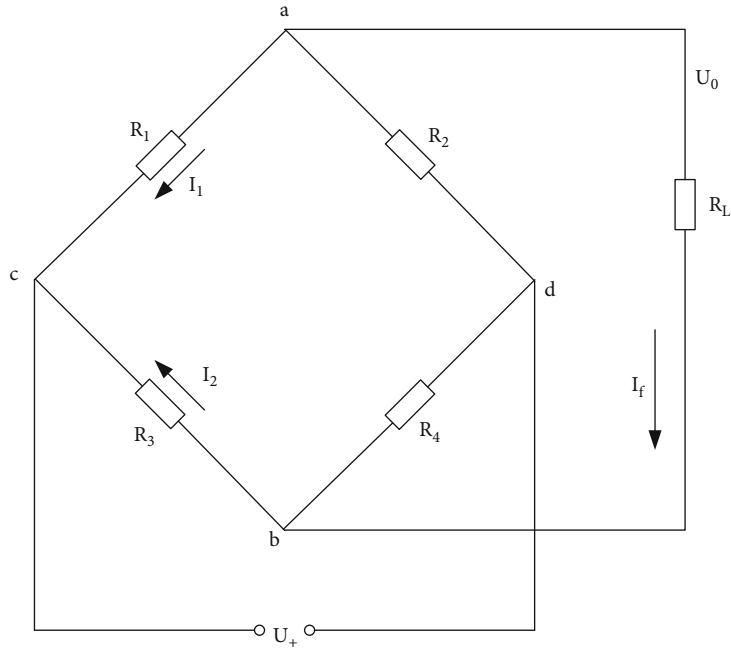
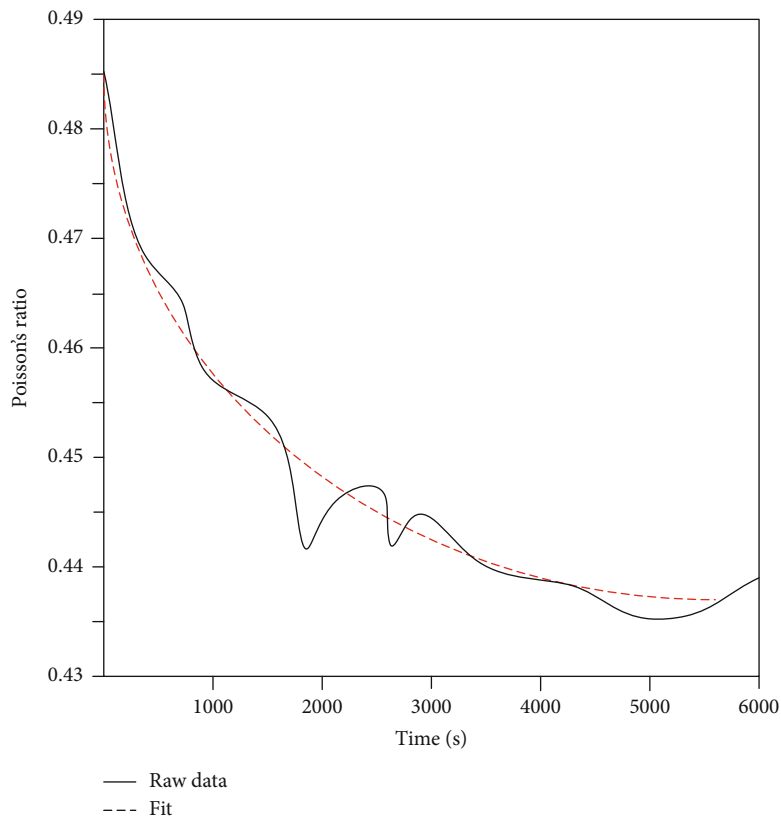Figure 3: Full bridge circuit connection.

Figure 4: Poisson's ratio measurement results.

price of equipment and materials is relatively cheap (FDM, SLA, 3DP, SLS, LOM, and PCM). It is the most commonly used and popular 3D printing method in the current market. It has impressive performance in desktop and industrial printing. The disadvantage is that supporting materials are required, and the printing speed of the mechanical nozzle is slow, and the accuracy is slightly insufficient when making high-precision parts.
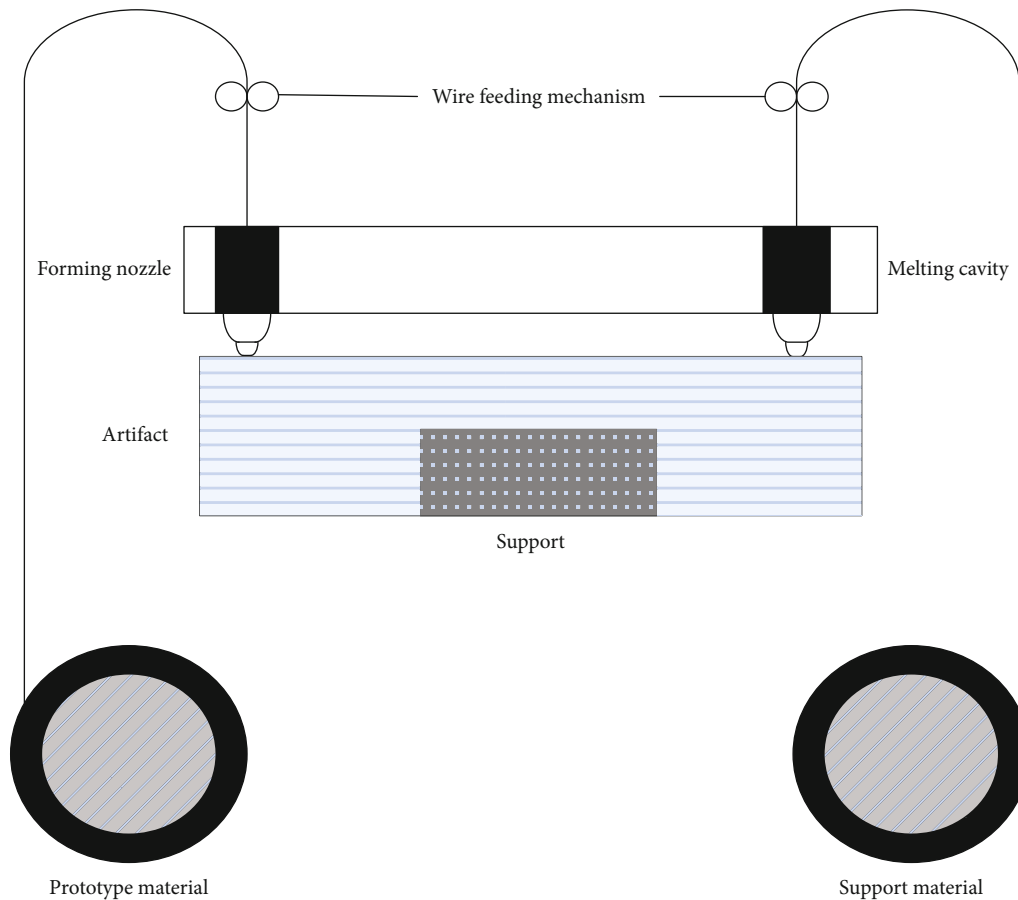
FIGURE 5: Fused deposition molding method.

3. Experiment

3.1. The Antiskid Performance of the Sole of Basketball Shoes. According to the test data information given by "Underwriters Laboratories (UL)" and other institutions, when the friction coefficient does not exceed 0.4, it corresponds to a very dangerous interval, that is, it is extremely easy to slip. The friction coefficient is in the range of 0.5 to 0.6, which is the basic safety range. The friction coefficient $p > 0.6$, which is in a very safe range. This experiment is to use this standard as the antiskid performance standard of sneakers to conduct experimental investigations. The objects of investigation are 6 common antiskid basketball shoes on the market and experimental shoes printed by FDM technology combined with 3D printing technology (30 pairs of shoes of each brand were sampled for experimental investigation). The relevant parameters of the experimental objects are shown in Table 1.

As shown in Table 2, there are seven groups of test subjects. Let them move on the relatively dry-pressed ceramic floor, keeping the moving direction to slide forward horizontally. The antiskid friction coefficient of ordinary sports shoes is 0.73~1.25 (the average value is 0.98). Sliding the heel forward on the dry-pressed ceramic floor tiles, the antiskid friction coefficient of ordinary sports shoes is 0.67~0.98 (average value is 0.80). It can be seen that under dry conditions, the friction coefficients of ordinary sports shoes sliding forward horizontally and the heel sliding forward are both

greater than 0.6. It is in a very safe range, and the sole has excellent antislip properties.

As shown in Table 3, we moved seven groups of test subjects on the pressed ceramic floor filled with distilled water, keeping the direction of movement as horizontal and sliding forward. The antiskid friction coefficient of ordinary sports shoes is 0.59~0.75 (average value is 0.65), which is between the basic safe range and the very safe range. Sliding forward on the heel of pressed ceramic floor tiles with distilled water, the anti-skid friction coefficient of ordinary sports shoes is 0.37~0.58 (average value is 0.47). The average value of friction coefficient is in the range of 0.5 to 0.6, which is in the basic safe range. Only sample no. 2 has a sole friction coefficient of 0.37, which is in a very dangerous range.

From this, we can get the size of the forward horizontal sliding friction coefficient, which depends on the friction between the entire sole and the tile surface. The contact friction part between the heel and the tile surface is also another key factor that affects the friction coefficient of the forward horizontal sliding.

3.2. Resilience Performance Test of Composite Materials for Preparing Shoe Soles

3.2.1. Experimental Method. The tensile performance test of the composite material for preparing shoe soles is carried out in accordance with GB/T14337-2008.

Table 1: Related parameters of experimental sneakers.

Group	Brand	Price	Antislip parameters
1	Nike	1299	0.71
2	Adidas	2499	0.74
3	Anta	599	0.68
4	Li Ning	899	0.64
5	Jordan	800	0.66
6	Peak	500	0.65
7	FDM	—	—

Table 2: Sliding condition of shoe soles on dry-pressed ceramic floor tiles.

Sliding direction	Slide forward	Swipe back
1	1.1	0.98
2	0.8	0.7
3	0.73	0.67
4	0.8	0.72
5	0.86	0.76
6	1.13	0.89
7	1.05	0.85

Table 3: Sliding condition of shoe soles on pressed ceramic floor tiles with distilled water.

Sliding direction	Slide forward	Swipe back
1	0.66	0.4
2	0.61	0.37
3	0.59	0.58
4	0.6	0.41
5	0.61	0.54
6	0.7	0.53
7	0.71	0.5

Table 4: Elastic performance test results of different brands of sole composite materials.

Group	Breaking strength	Elastic modulus
1	5.34	1002
2	5.11	854
3	4.79	762
4	4.36	694
5	4.23	652
6	4.02	669
7	5.97	1283

First, equilibrating the prepared shoe sole composite material sample in a test environment with a temperature of $20 \pm 3°C$ and a humidity of $65 \pm 5\%$ for 24 hours.

Table 5: Test results of resilience performance of different brands of sole composite materials.

Group	Height before pressing	Height after pressing	Rebound time
1	2.3	2.28	8.6 s
2	2.5	2.47	7.8 s
3	2.8	2.75	9.1 s
4	2.3	2.29	8.8 s
5	2.5	2.5	7.9 s
6	2.2	2.19	8.2 s
7	2.4	2.39	7.1 s

Adjusting the electronic multifunction strength machine to the normal state, setting the pretension to 0.5 cN, the pull-up force value of 1 cN, the clamping distance of 20 mm, and the stretching speed of 10 mm/min. Tensile tests were carried out on the composite materials of the soles of seven groups of different brands from 1 to 7, respectively, and the number of experiments was 50 times in total.

3.2.2. Experimental Results. Table 4 shows the average experimental results of the composite materials of seven groups of different brands of shoe soles.

From the data in Table 4, we can see that the elastic parameters of several common brands on the market have reached a relatively excellent range, and the elastic modulus of the sole prepared in this experiment is 1283, and the breaking strength is 5.97. In that respect, they are significantly better than the shoes on the market. But at the same time, the resilience performance of sneakers is also more important. Now, we will explore its resilience performance and reflect the strength of its resilience performance through the resilience time. The specific data is shown in Table 5.

From the data in Table 5, it is not difficult to see that the resilience performance of several common brands of basketball shoes on the market is still good. The modulus of resilience of the soles prepared in this experiment differed by 0.1, which is considered to be an excellent price comparison. The rebound time is also far ahead of other brands of basketball sneakers. The time is only 7.1 s, which is 0.7 s faster than the second-placed 7.8 s.

4. The Influence of Sole Printing Parameters on Sole Performance

4.1. 3D Printing Impact Analysis. This section mainly selects 4 factors of layer height, thickness, printing speed, and nozzle temperature as independent variables. The single factor of KES style and stiffness are tested and orthogonally tested, respectively. This paper analyzes the relationship between 3D printing parameters and the surface, compression, and tensile properties measured in KES, as well as the influence of printing parameters on the stiffness of the printed sample, and obtains the best combination of process parameters for the corresponding performance. After measuring the bending length and the mass per unit area, the relationship between the printing parameters of the single factor
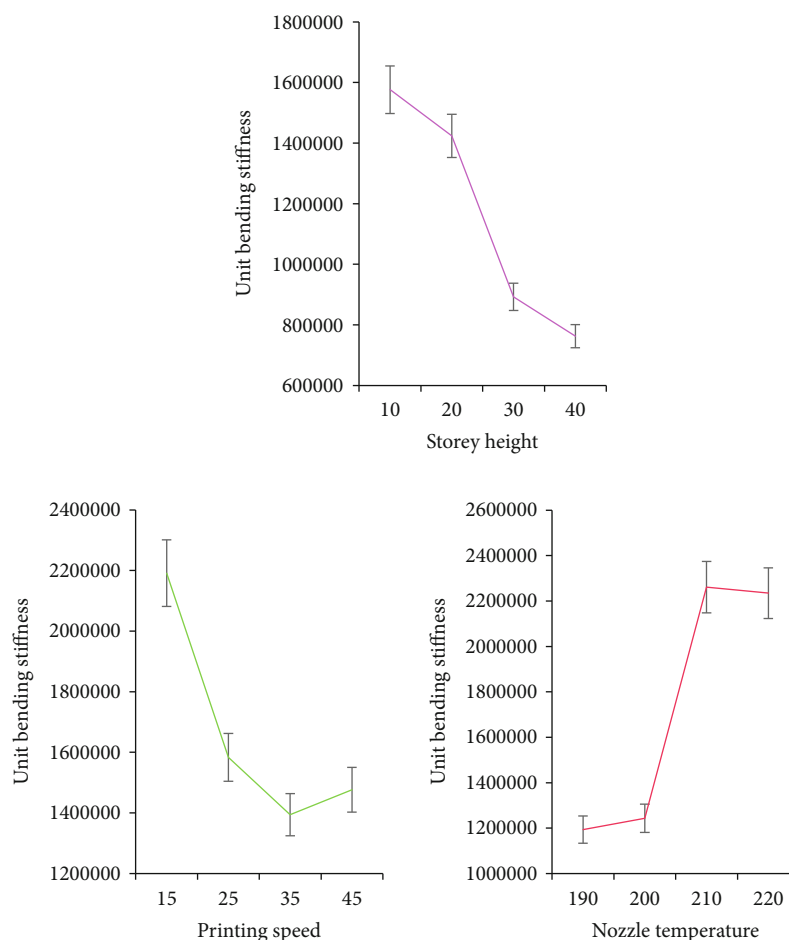
FIGURE 6: The relationship between each single-factor printing parameter and the bending stiffness per unit width.

experiment and the bending stiffness per unit width is shown in Figure 6.

From the Figure 6, we can see that in the range of 0.1 mm to 0.4 mm, the flexural rigidity per unit width decreases as the layer height increases. That is, the bending deformation ability of the printed sample increases with the increase of the layer height. In the thickness range of 0.5 mm to 1.0 mm, as the thickness increases, the bending stiffness per unit width increases. That is, the bending deformation ability of the printed sample decreases as the thickness of the printed sample increases. In the printing speed range of 15 mm/s to 45 mm/s, as the printing speed increases, the bending stiffness per unit width decreases first, and the trend tends to be flat around 35 mm/s. The overall trend is that the bending stiffness per unit width decreases with the increase of printing speed. That is, the bending deformation ability of the printed sample increases as the printing speed increases. In the nozzle temperature range of 190°C to 220°C, as the nozzle temperature increases, the bending stiffness per unit width increases, and the trend gradually becomes gentle. That is, the bending deformation ability of the printed sample decreases with the increase of the temperature of the nozzle. Overall, it has little effect on the antiskid and high resilience performance of sneakers.

5. Conclusions

This article mainly studies the preparation of sneaker soles made of high-resilient nonslip composite materials. First, this article analyzes the formula for high resilience. Through formula calculation, by comparing the suitable high resilience interval of the shoe sole, in terms of antislip performance, the pattern of the shoe sole is also analyzed, and the pattern with the best antislip ability is obtained by comparing several patterns. This article mainly studies the preparation of sneaker soles made of high-resilient nonslip composite materials. First, this article analyzes the formula for high resilience. This article uses formula calculations to compare the suitable high resilience interval of the shoe sole. In terms of antislip performance, the pattern of the sole is also analyzed, and the pattern with the best antislip ability is obtained by comparing several patterns.

Data Availability

The data that support the findings of this study are available from the corresponding author upon reasonable request.

Conflicts of Interest

Acknowledgments

References

[1] Y. Liang, J. Sun, S. Huo et al., "Exploration of collector materials in high-power microwave sources," *IEEE Transactions on Plasma Science*, vol. 46, no. 2, pp. 384–389, 2018.

[2] M. Kakunuri, S. Kaushik, A. Saini, and C. S. Sharma, "SU-8 photoresist-derived electrospun carbon nanofibres as high-capacity anode material for lithium ion battery," *Bulletin of Materials Science*, vol. 40, no. 3, pp. 435–439, 2017.

[3] H. S. Han, K. H. Lee, and S. H. Park, "Naval-vessel on board equipment base to minimize structure-borne noise," *Journal of Mechanical Science & Technology*, vol. 30, no. 12, pp. 5371–5379, 2016.

[4] H. K. Ju, D. H. Mun, G. C. Jeong, and H. G. Park, "Influence of floor dimension and resilient material on heavy impact noise of floating floor system," *Transactions of the Korean Society for Noise & Vibration Engineering*, vol. 27, no. 4, pp. 434–443, 2017.

[5] J. Xiao, C. F. Wu, Z. H. Zhan, X.-G. Ta, and W.-J. Do, "Research on performances of cement stabilized brick and concrete recycled aggregate base," *Zhongguo Gonglu Xuebao/ China Journal of Highway and Transport*, vol. 30, no. 2, pp. 25–32, 2017.

[6] J. H. Kim, C. S. Cha, J. Y. Kim, and J. H. Kim, "Development of a process technique for heavy metal removal in the production of recycled synthetic resin materials," *Journal of the Korean Society of Manufacturing Process Engineers*, vol. 17, no. 4, pp. 137–142, 2018.

[7] Y. Sun, D. Li, J. Wang, D. Gong, and F. Wang, "Preparation of PVC/Fe-rich sludge composites," *Hecheng Shuzhi Ji Suliao/ China Synthetic Resin and Plastics*, vol. 35, no. 4, pp. 24–27, 2018.

[8] J. Shen, J. Liang, X. Lin, H. Lin, J. Yu, and Z. Yang, "Recent progress in polymer-based building materials," *International Journal of Polymer Science*, vol. 2020, Article ID 8838160, 15 pages, 2020.

[9] N. Pittala, F. Thétiot, S. Triki, K. Boukheddaden, G. Chastanet, and M. Marchivie, "Cooperative 1D triazole-based spin cross-over FeII material with exceptional mechanical resilience," *Chemistry of Materials*, vol. 29, no. 2, pp. 490–494, 2017.

[10] X. Ge, J. Yang, H. Wang, and W. Shao, "Research on resilience model of emergency material distribution network," *Journal of Wuhan University of Technology (Transportation Science and Engineering)*, vol. 42, no. 5, pp. 727–731, 2018.

[11] B. Sprecher, I. Daigo, W. Spekkink et al., "Novel indicators for the quantification of resilience in critical material supply chains, with a 2010 rare earth crisis case study," *Environmental Science & Technology*, vol. 51, no. 7, pp. 3860–3870, 2017.

[12] C. Yang and P. Okumus, "Ultrahigh-performance concrete for posttensioned precast bridge piers for seismic resilience," *Journal of Structural Engineering*, vol. 143, no. 12, p. 04017161, 2017.

[13] S. S. Shyu, E. Fu, and E. C. Shen, "Clinical and microcomputed topography evaluation of the concentrated growth factors as a sole material in a cystic bony defect in alveolar bone followed by dental implantation: a case report," *Implant Dentistry*, vol. 25, no. 5, pp. 707–714, 2016.

[14] J. H. Zhao and Y. C. Chang, "Alveolar ridge preservation following tooth extraction using platelet-rich fibrin as the sole grafting material," *Journal of Dental Sciences*, vol. 11, no. 3, pp. 345–347, 2016.

[15] X. Zhang, Z. Li, X. Wang, and J. Yu, "The fractional Kelvin-Voigt model for circumferential guided waves in a viscoelastic FGM hollow cylinder," *Applied Mathematical Modelling*, vol. 89, pp. 299–313, 2021.

[16] Y. Tang, W. Feng, Z. Chen et al., "Fracture behavior of a sustainable material: recycled concrete with waste crumb rubber subjected to elevated temperatures," *Journal of Cleaner Production*, vol. 318, article 128553, 2021.

[17] S. Aisawa, C. Nakada, H. Hirahara, N. Takahashi, and E. Narita, "Preparation of dipentaerythritol-combined layered double hydroxide particle and its thermostabilizing effect for polyvinyl chloride," *Applied Clay Science*, vol. 180, no. Nov., p. 105205, 2019.

[18] Y. Wu, H. Qiao, Y. Ding et al., "Properties of pigmented antistatic PVC paste," *Hecheng Shuzhi Ji Suliao/China Synthetic Resin and Plastics*, vol. 35, no. 3, pp. 17–20, 2018.

[19] Y. Zhang, W. Ni, and Y. Li, "Effect of siliconizing temperature on microstructure and phase constitution of Mo-MoSi$_2$ functionally graded materials," *Ceramics International*, vol. 44, no. 10, pp. 11166–11171, 2018.

[20] Y. Zhang, Y. Li, and C. Bai, "Microstructure and oxidation behavior of Si-MoSi$_2$ functionally graded coating on Mo substrate," *Ceramics International*, vol. 43, no. 8, pp. 6250–6256, 2017.

[21] Indian, Leather, Group, "China (Wenzhou) Int'l leather, shoe material & shoe machinery fair, your first choice!," *Indian Leather*, vol. 49, no. 12, pp. 217–217, 2016.

[22] K. Lawinska, W. Serweta, I. Jaruga, and N. Popovych, "Examination of selected upper shoe materials based on bamboo fabrics," *Fibres & Textiles in Eastern Europe*, vol. 27, no. 6(138), pp. 85–90, 2019.

[23] Z. Czaplicki, Z. Olejniczak, and W. Serweta, "Investigation into the shoe sole materials for the persons over 60 years old," *Przeglad Wlokienniczy*, vol. 73, no. 5, pp. 29–32, 2019.

Hindawi

Research Article

Flame Resistance Characteristics of Woven Jute Fiber Reinforced Fly Ash Filled Polymer Composite

G. Sakthi Balan,[1] **R. Balasundaram,**[2] **K. Chellamuthu,**[3] **S. Nandha Gopan,**[3] **S. Dinesh** (ID)**,**[4] **V. Vijayan** (ID)**,**[4] **T. Sathish** (ID)**,**[5] **and S. Rajkumar** (ID)[6]

[1]*Research Scholar, School of Mechanical Engineering, Vellore Institute of Technology, Vellore, Tamil Nadu, India*
[2]*Department of Mechanical Engineering, SRM Institute of Science and Technology, Tiruchirapalli Campus, Tamil Nadu, India*
[3]*Department of Mechanical Engineering, K. Ramakrishnan College of Engineering, Trichy, India*
[4]*Department of Mechanical Engineering, K. Ramakrishnan College of Technology, Samayapuram, Trichy, 621112 Tamil Nadu, India*
[5]*Department of Mechanical Engineering, Saveetha School of Engineering, SIMATS, Chennai, 602 105 Tamil Nadu, India*
[6]*Department of Mechanical Engineering, Faculty of Manufacturing, Institute of Technology, Hawassa University, Ethiopia*

Correspondence should be addressed to S. Rajkumar; rajkumar@hu.edu.et

Due to their unique characteristics, natural fiber reinforced polymer composites have recently been increasingly utilised to replace traditional materials. Fire retardant resins can increase flammability, and they have a deleterious influence on the mechanical properties of the material (Fan et al., 2020). As a result, this experiment examined the flammability of woven jute fiber reinforced with fly ash. The specimens were created by hand layup using a L9 orthogonal array and varying ratios of jute fiber, fly ash, and time for chemical fiber treatment. Vertical and horizontal flammability tests are conducted in accordance with ASTM D635 and ASTM D3801, respectively. According to the test results, the inclusion of fly ash significantly reduces flammability. In this work, 5 wt% inclusion of the jute fiber, 15 wt% addition of the fly ash, and with 10 hours, NaOH treatment produces a composite with minimum burning rates of 10.2 mm/min in horizontal UL-94 tests. To determine the link between input and output characteristics, various regression models from machine learning are used. Multilayer perception produced a stronger association in both horizontal and vertical testing, according to the models.

1. Introduction

Numerous plants and animals are naturally exploited to obtain fibers. Apart from this, numerous synthetic fibers are manufactured and reinforced. The shelf life and degree of biodegradability of fibers are determined by their physical and chemical structure. Synthetic fibers have superior mechanical properties over natural fibers since they are manufactured specifically for their intended use. Due of their unique characteristics and abundant availability, natural fibers are frequently used as reinforcement in polymer composites. Salem et al. examined the fundamental features of jute fiber reinforced composites and discovered that by increasing the interfacial bonding between the fiber and matrix, and the thermomechanical properties can be enhanced [1]. Ashraf et al. conducted a critical analysis and addressed recent advances in jute-based composites. Additionally, they illustrated the various issues associated with the excessive use of synthetic composites [2]. Saravanan et al. and Dinesh et al. discussed the challenges associated with developing composites reinforced with jute fiber using a variety of manufacturing techniques and reported on their mechanical properties. They discussed the mechanism through which the material degrades using scanning electron microscopy [3, 4]. Roya et al. investigated the fire resistance of jute cloth treated with flame retardants and

discovered that the treated specimens developed char and contained minimal volatiles [5]. Zaman et al. examined the challenges associated with developing natural fiber-reinforced composites with superior mechanical characteristics and chemical and flame resistance. They used a variety of treatments on natural jute fibers to strengthen the interfaces with resins [6]. Wang et al. conducted a characterisation study on silane-treated jute fabric and evaluated its thermal and surface properties, concluding that the treated fibers demonstrated increased stability in hot conditions due to the structures, as well as improved tensile characteristics [7]. Khalili et al. developed biodegradable composites by using flax fibers with hydroxyapatite nanoparticles. They discovered that the addition of flax fiber enhances the flexural and tensile modulus, whereas the presence of nano-HA reduces the strength and increases the water intake [8]. Sonnier et al. investigated the differences in fire retardancy between natural, glass, and carbon fiber reinforced composites and discovered that, when compared to natural fibers, carbon and glass fibers exhibit greater resistance to flame [9]. Shah et al. evaluated the flame resistance capabilities of numerous natural fiber composites and concluded that the inclusion of appropriate additives increases the natural fibers' flame resistance. He demonstrated that silicon-based additives perform better [10]. Oktem et al. enhanced the fire resistance and mechanical capabilities of hybrid jute/flax composite buildings while maintaining their attractive appearance. They enhanced these properties by a variety of chemical treatments [11]. Rashid et al. investigated the flame resistance of green composites and discovered that the synergistic technique significantly reduces the peak temperature rate while silane treatment enhances the decomposition temperature [12]. Mathubala and Nandhini synthesised jute fiber composites and investigated their heat and fire resistance properties, concluding that fiber adherence and bonding to the matrix improve the composites' fire resistance properties [13]. Latif et al. concentrated on the production of nanocomposites utilising vinyl ester as the matrix and jute cloth as the reinforcement. Additionally, they concentrated on organo-modified montmorillonite (OMMT), which has a high aspect ratio and a low surface charge density [14]. Shahinur et al. investigated the thermal properties of composites reinforced with jute fiber and discovered that fiber that had been chemically treated absorbed less heat than untreated samples [15]. Salimov et al. investigated the flammability and fire resistance of certain natural fiber and textiles in order to safeguard them from fire. Additionally, they provided the findings of their investigation [16]. Ribeiro et al. investigated the flame resistance of jute fiber reinforced epoxy composites intended for tile applications and discovered that the incorporation of jute fiber had no effect on the fire resistance [17].

Sakthi Balan et al. incorporated waste plastics and eggshells into composites along with jute and bahunia racemose fiber reinforcement and evaluated the composites' moisture absorption. They concluded that the addition of particulates and fillers reduces the composites' water absorption more than fiber do. Fibers promote moisture absorption because they are hydrophilic [18, 19]. Sakthi Balan et al and Nava-neethakrishnan et al. improved the composite's mechanical properties to make it more resistant to environmental influences. They examined critical parameters such as tensile strength, hardness, and resistance to moisture absorption and optimised the data to determine which factor had the most influence on mechanical properties [20, 21]. Nava-neethakrishnan et al. created an epoxy-based composite reinforced with MWCNTs/g-C3N4 and investigated the composite's water absorption and wear properties [22]. The properties that can be altered in the polymer composites make them versatile for applications in various fields, such as constructions, microelectronics, and biomedical fields. Devastations due to building fire stress the importance of flame-retardant polymer composites, since they are directly related to human life conservation and safety [23]. The flammability of a composite formed by reinforcing woven jute fiber with waste fly ash is investigated in this work. The data are optimised in order to determine the most significant element affecting flammability. The low-flammability specimen is recommended for usage in roofing materials as well as vehicle and airplane structures.

2. Materials and Methods

A composite is composed of a matrix as a base and a reinforcement to enhance the strength and some physical and mechanical properties. The physical and other composite characteristics can also be improved by choosing proper chemical treatment. On the whole, the strength of the polymer composite can be improved by proper chemical treatment of the fibers and by producing defect-free composites. Defects are mostly produced during the manufacturing of the composites, and proper measures have to be taken to minimize or avoid the common defects. In this work, natural fiber jute is chosen for reinforcement, a filler of fly ash is used, and its flammability studies are carried out as per the standards. Normally, fibers are used in many forms such as short fibers, long fibers, and woven fabric. When using the short and long fibers, orientation of the fibers and fiber density plays a major role. During the usage of natural fibers, the fibers have to be treated chemically to improve the bonding between the matrix and the fibers. In this work, the woven jute fabric is used which is chemically treated before usage. NaOH treatment is well suited for jute fibers.

Fly ash is used as filler material which is obtained from the thermal power plant which burns lignite-type coal. Generally, fillers are used to improve the surface and hardness properties of the composite. In this composite, the main purpose of using the filler is to reduce the pore formation during the production of the composite and to suppress the flame propagation during the flammability test. Normally, jute fiber is flammable, but if it is reinforced into a polymer matrix along with nonflammable filler powders, the flammability property of the material changes. Three factors are chosen as important and varied during the manufacturing of the composite as per Taguchi's experimental design. Percentage of fiber addition, percentage of filler addition, and the chemical treatment are chosen as the input factors, and the composites are manufactured. After curing, the

TABLE 1: Orthogonal array experimental design with burning rate UL-94 results.

Percentage of jute fiber	Percentage of fly ash	NaOH chemical treatment time in hours	Burning rate (mm/min)		Cotton ignition	Classification
			Horizontal UL-94 test	Vertical UL-94 test		
5	5	0	13.4	14.5	No	v0
5	10	5	10.8	12.3	No	v0
5	15	10	10.2	11.2	No	v0
10	5	5	17.1	19.4	No	v1
10	10	10	13.9	15.3	No	v1
10	15	0	11.8	13.1	No	v0
15	5	10	22.5	24.3	No	v1
15	10	0	19.9	21.2	No	v1
15	15	5	18.7	20.5	No	v1

composites are tested for their flammability by following the standard procedure as per ASTM standards. The jute fibers are chemically treated with NaOH with fixed concentrations. One set of fibers is used as untreated, and another set is treated for 5 hours and another set for 10 hours. After chemical treatment, the fibers are flushed with ordinary water and dried in an oven. Then, the filler powder fly ash is collected from the thermal power plant is sieved to remove the foreign particles and particles of varying sizes. The fly ash filler must be of the same size and as it is collected from the cyclonic separator and water scrubber, and the fly ash is also dried in the oven and then used. As the fiber and fillers are added in weight percentages, both are weighed before adding to the composite.

The composites are manufactured by compaction process using mild steel mold. The traditional hand layup process is used for making the composite. The epoxy is mixed in an equal ratio with the hardener, and the filler powder is also mixed along with resin and layered on the surface of the mold. Then, the woven jute fabric fiber which is chemically treated is stacked over the resin-filler mixture and then again a layer of resin and filler is layered. The process is repeated until the required thickness is obtained and then the composite is closed with a top cover and tightened using bolts and nuts. The whole setup is kept in the compression molding machine and given pressure so that the excess resin can be removed, and this compression removes the air trapped inside the composite stacking. Then, the setup is left undisturbed for 12 hours for curing, and then the composite is removed from the mold. The mold is then cleaned and used for stacking the next set of composite with different input factors.

3. Flammability Studies

Flammability tests on polymer composite materials are conducted according to the ASTM D635 protocol for horizontal UL–94 testing and ASTM D3801 process for vertical UL–94 testing. A specimen size of 1251333 mm is required to complete a flammability test. The test is carried out by fixing the specimen in horizontal and vertical directions with the help of a stand. Below the specimen, the base must be filled with a layer of cotton to check the dripping from the specimen. A

Bunsen burner is used to fire the specimen. The fire is introduced at the open end of the specimen for 10 seconds and then removed and allowed to propagate along the length of the specimen. A stopwatch has to be used for calculating the time taken for the specimen to burn from 25 mm to 100 mm. This process is repeated for all nine specimens, and the burning rate of the material is calculated using the following equation.

$$\text{Rate of Burning (mm/min)} = 60 \times \frac{\text{Length of the sample burnt (mm)}}{\text{Sample burning time (Seconds)}}. \tag{1}$$

Based on the time taken for the specimen to burn, the specimens are classified under v0, v1, and v2 classes. If the burning time is less than 10 seconds and without igniting the cotton, then, the specimen is classified under v0 category which has high flame resistance. If the specimen burns for less than 30 seconds and could not ignite the cotton at the bottom, then, it comes under v1 category. If the specimen burns less than 50 seconds and if the cotton underneath the specimen got ignited, then, it falls under v2 category which has less flame retardant. Some specimen burns completely and that falls under NC (no classification). The specimen without any dripping and has less burning time can be identified as a specimen with high flammable resistance.

4. Results and Discussion

Flammability tests were executed as per the standard procedure, and the cotton ignition was also checked for the dripping nature of the composite materials. The tested composites are categorized under three categories as v0, v1, and v2 based on the burning time of the composites. In Table 1, the parameters that are varied for the manufacturing of the composites and their different levels are listed along with the flammability test results. The results of the test were fed into MINITAB software for regression analysis and ANOVA table formation [24, 25]. Various plots are plotted during optimization to study the behavioral pattern of the results.
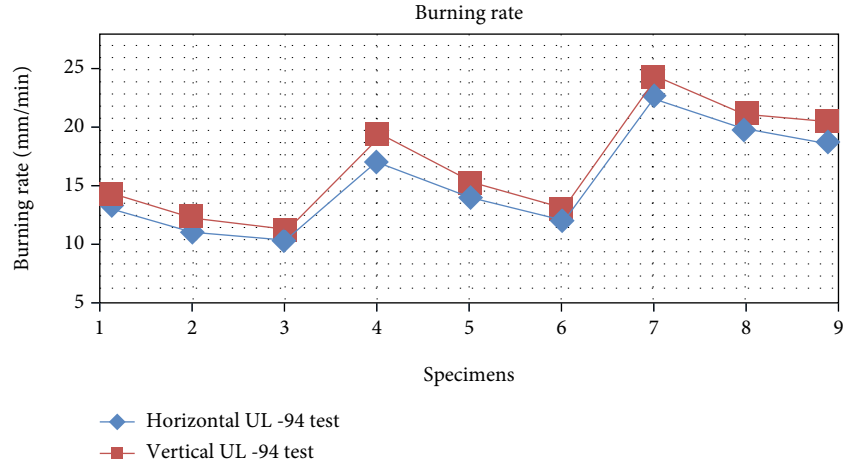
FIGURE 1: Burning rate—horizontal UL 94 vs. vertical UL 94 test results.

TABLE 2: Difference in values between horizontal and vertical UL-94 tests.

| Specimen number | Burning rate (mm/min) | | Difference in values |
	Horizontal UL-94 test	Vertical UL-94 test	
1	13.4	14.5	1.1
2	10.8	12.3	1.5
3	10.2	11.2	1
4	17.1	19.4	2.3
5	13.9	15.3	1.4
6	11.8	13.1	1.3
7	22.5	24.3	1.8
8	19.9	21.2	1.3
9	18.7	20.5	1.8

In Figure 1, the burning rate data for the nine specimens are presented alongside the results of the horizontal and vertical flame tests. The plot reveals that the test results are fairly similar and that the difference between them is very small. Table 2 indicates the difference in values between the horizontal and vertical UL-94 tests.

4.1. ANOVA for Horizontal Test. In Table 3, variance results for the flat test were mentioned, and the Fischer value suggests that the addition of jute fibers affects the firing ability of the material, and fly ash addition also suppresses the propagation of the fire. From the main effect plotting, as shown in Figure 2, the influence of the input parameters can be proved once again.

$$
\begin{aligned}
\text{Regression Equation for Horizontal UL} - 94 \text{ test} \\
= 10.32 + 0.8900 \text{ Composition of Jute fibers} \\
- 0.4100 \text{ Composition of Fly ash} \\
+ 0.0500 \text{ NaOH treatment.}
\end{aligned}
\tag{2}
$$

In Figures 3 and 4, the interaction between the input fac-

tors and the relation between the two most influencing factors were mentioned, respectively, through interaction and contour plots. From the contour plot observation, for minimum flammability, the inclusion of jute fiber must be 5 wt% and fly ash inclusion must be 15 wt%. From Figure 5, the contribution of factors can be understood. The equation for regression analysis of both the horizontal and vertical flammability tests was designated in equations (2) and (3).

4.2. ANOVA for Vertical Test. In Table 4, ANOVA results were tabulated, and the summary of the model is also tabulated.

$$
\begin{aligned}
\text{Regression equation for Vertical UL} - 94 \text{ test} \\
= 11.67 + 0.933 \text{ Composition of Jute fibers} \\
- 0.447 \text{ Composition of Fly ash} \\
+ 0.067 \text{ NaOH treatment.}
\end{aligned}
\tag{3}
$$

To know the significance of the model, the regression square value is verified. R-squared measures the strength of the relation between a model and the dependent variable on a convenient scale. After fitting a linear regression model, it determined how well the model fits the data. Based on the experimental results, the R squared value changes; in this work, we got the R-square value is 95.50% for vertical test and 95.10% for horizontal test, which indicates the significance of the model. Fischer's value from Table 4 indicates the influence of each input factor on the results. From the F value, the composition of the fibers was found to be the most influential factor and the addition of the fly ash to the composite also has some influence on the flammability property of the composite. The main effect plot shown in Figure 6 is plotted for signal-to-noise ratio with a smaller is better principle. The plot indicates the jute fiber addition influences the results more as that plot shows more deviation. As per the smaller is a better concept, the addition of the jute fiber must be minimum, the addition of the fly ash must be maximum, and the chemical treatment has a very negligible amount of contribution in deciding the flammability property.

The interaction plot in Figure 7 shows the interlinkage between the input factors. In Figure 8, the contour plot

TABLE 3: ANOVA results for horizontal test.

Source	DF	Adj SS	Adj MS	F value	P value
Regression	3	144.405	48.135	32.37	0.001
Composition of jute fibers	1	118.815	118.815	79.9	0
Composition of fly ash	1	25.215	25.215	16.96	0.009
NaOH treatment	1	0.375	0.375	0.25	0.637
Error	5	7.435	1.487		
Total	8	151.84			
S	R-sq	R-sq(adj)		R-sq(pred)	
1.21943	95.10%	92.17%		82.83%	
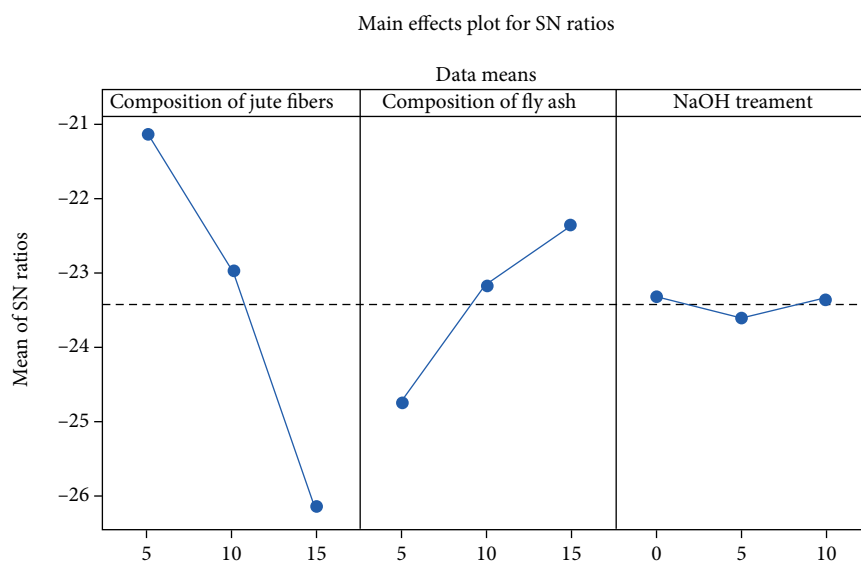
FIGURE 2: Main effect plotting for horizontal flame test.
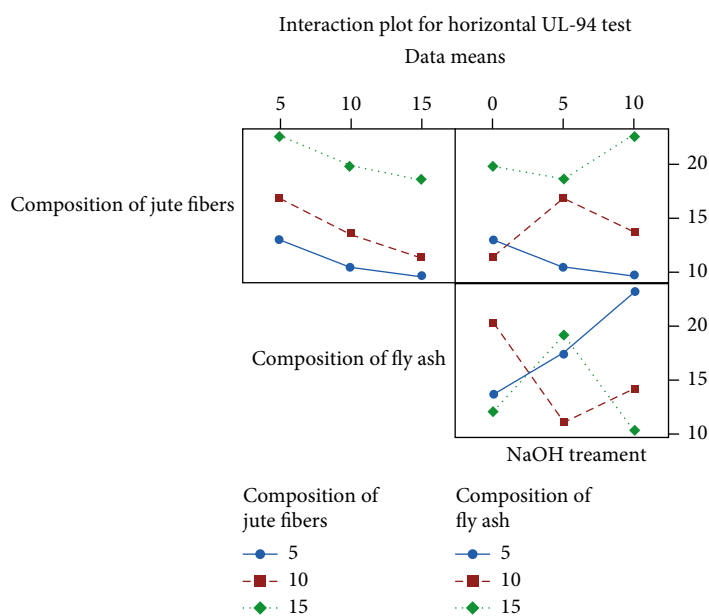
FIGURE 3: Interaction plotting for horizontal flame test.

Contour plot of horizontal UL-94 vs composition of J, composition of F

Horizontal UL -94 test

- < 12
- 12-14
- 14-16
- 16-18
- 18-20
- 20-22
- > 22
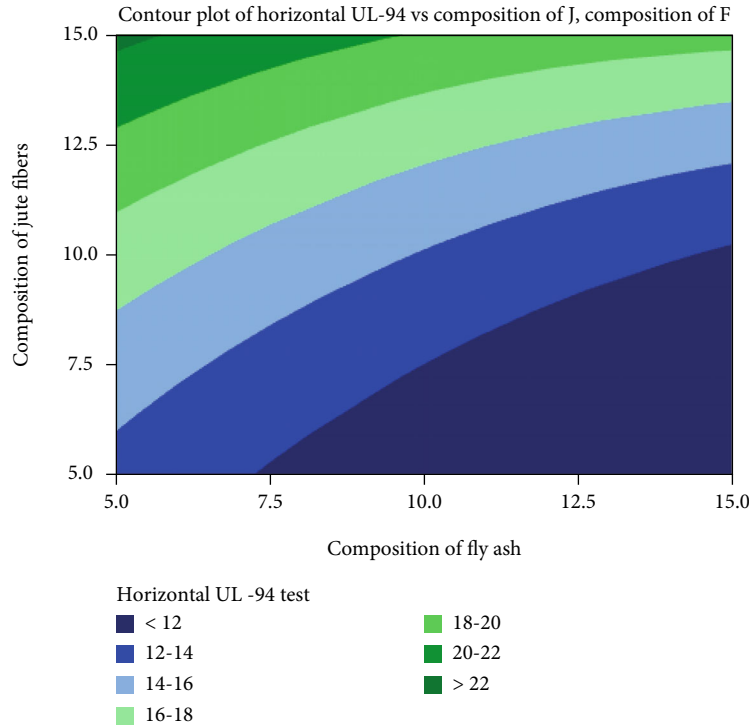
FIGURE 4: Contour plotting for horizontal flame test.

Contribution plot for horizontal flammability test

- Composition of jute fibers
- Composition of fly ash
- NaOH treament
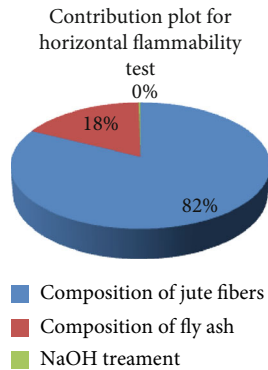
FIGURE 5: Contribution chart for horizontal flame test.

indicates the best optimum level to obtain minimum burning rates. From the contour plot, for getting lower burning rates, the inclusion of fiber should be minimized, and the addition of the fly ash must be increased. As the fiber used in this composite is a natural fiber, the tendency to catch fire is more and so if the percentage addition of the fiber is more, the burning rates are also found to be increased which is not advisable. The fly ash addition seems to lower the burning rates as it is already obtained from burning the coal. The ash will diminish the fire and tends to form char, which will stop the propagation of the fire throughout the material. As the fly ash was added in powder form, it reduces the defects formed during the production of the composite. The major defect formed in a polymer composite during the production is the formation of blowholes and surface cracking. The fly ash fills the holes formed in the core and surface of the composites and also improves the surface properties and reduces

the microcracks formed during curing. The NaOH chemical treatment has no contribution in determining the burning properties of the composite. Maybe it can influence the strength and other properties of the composite. The addition of the jute fiber increases the burning rate by 81%, and the fly ash addition minimizes it by 19% which can be understood by the contribution plot shown in Figure 9.

4.3. Regression from Machine Learning. Regression analysis is performed to forecast the value of yield values from the set of independent variables. In addition, it is used to find the effect of input data on the dependent variable. Recently, many researchers are using machine learning models that are capable of analyzing complex data with more accurate results. Navaneethakrishnan et al. [22] used linear regression, MLP, and SVR in addition to ANOVA to find the best regression model to predict the output parameters. Hence, in this work also, various regression models from machine learning are applied. To apply these algorithms, WEKA open source software is used. Tables 3 and 4 show the regression models for both horizontal and vertical tests. Figure 10 shows the difference between various output parameters.

In Table 5, output data of the machine learning analysis were tabulated, the difference between the actual value and linear regression, MLP, and SVR was plotted, and the error bars indicate the levels of variation between the regression values and actual burning rate values of the horizontal test. Table 6 shows the error values between the actual value and the three regression analysis values. Error value 1 shows the difference between actual value and linear regression values, error value 2 shows the difference between actual

TABLE 4: ANOVA results for vertical test.

Source	Degrees of freedom	Adjacent sum of squares	Adjacent mean sum of squares	Fischer value	P value
Regression	3	161.26	53.753	35.36	0.001
Composition of jute fibers	1	130.667	130.667	85.96	0
Composition of fly ash	1	29.927	29.927	19.69	0.007
NaOH treatment	1	0.667	0.667	0.44	0.537
Error	5	7.6	1.52		
Total	8	168.86			
S	R-sq	R-sq(adj)		R-sq(pred)	
1.23288	95.50%	92.80%		86.31%	
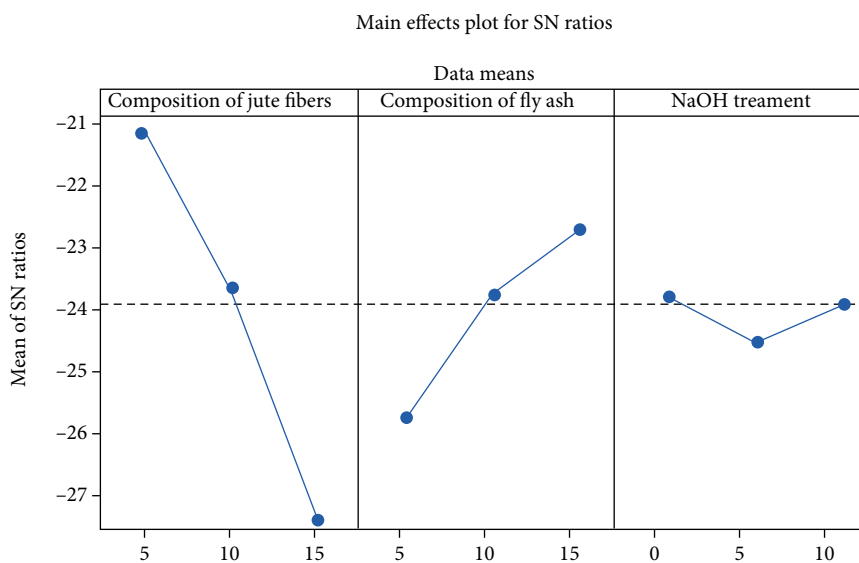
FIGURE 6: Main effect plot for SN ratios.
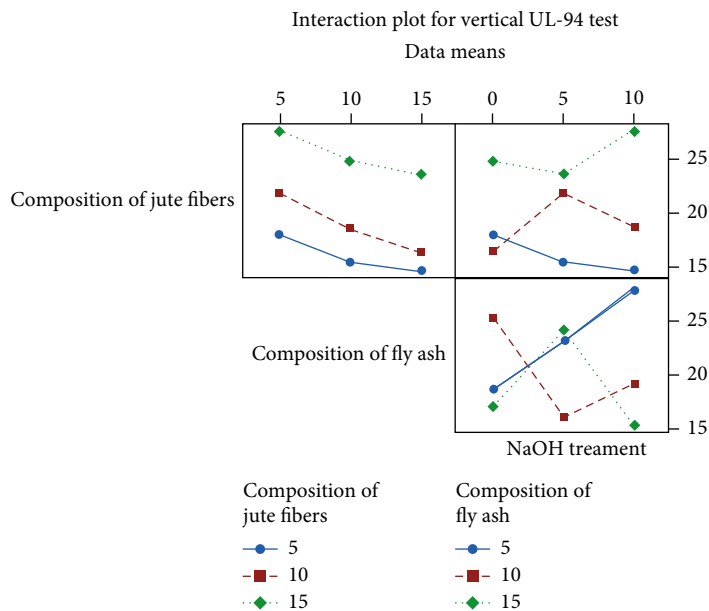
FIGURE 7: Interaction plot for vertical UL-94 test results.

Contour plot of vertical UL-94 t vs composition of J, composition of F

vertical UL -94 test

■ < 12
■ 12-14
■ 14-16
■ 16-18
■ 18-20
■ 20-22
■ 22-24
■ > 24
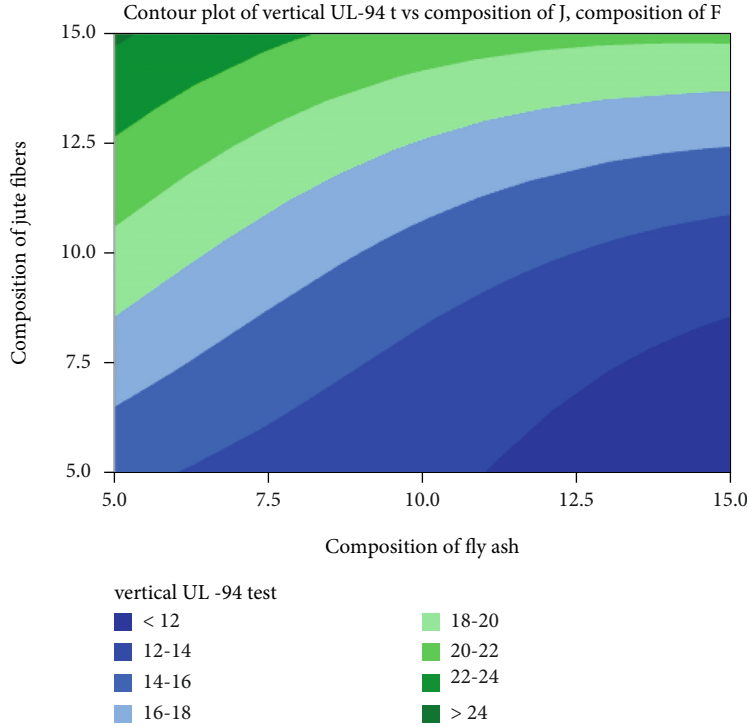
FIGURE 8: Contour plot for vertical UL-94 test results.

Contribution plot for vertical flammability test

■ Composition of jute fibers
■ Composition of fly ash
■ NaOH treament
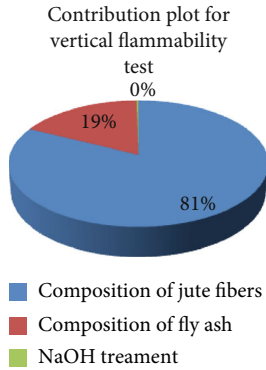
FIGURE 9: Contribution chart for vertical UL-94 test results.

values and multilayer perception values, and error value 3 indicates the difference between actual and support vector regression values for horizontal tests. The regression equations of linear, MLP, and SVR are mentioned in equations (4), (5), and (6), respectively. Table 7 shows the machine learning analysis results for vertical test.

LR:

$$\text{Burning rate} : 0.2249 + 0.7236 \, x \, \text{Jute fiber} - 0.333 x \text{Fly ash}. \tag{4}$$

MLP:

$$\begin{aligned} \text{Burning rate} : &-0.86728 \, (\text{Threshold}) + 2.853 x (\text{Jute fiber}) \\ &- 0.4437 x (\text{fly ash}) + 0.1025 x (\text{NaOH}). \end{aligned} \tag{5}$$

SVR:

$$\begin{aligned} \text{Burning rate} : &0.1932 + 0.7309 \, (\text{jute fiber}) - 0.271 \, x (\text{fly ash}) \\ &+ 0.0759 \, x (\text{NaOH}). \end{aligned} \tag{6}$$

Table 8 shows the error values between the actual value and the three regression analysis values. Error value 1 shows the difference between actual value and linear regression values, error value 2 shows the difference between actual values and multilayer perception values, and error value 3 indicates the difference between actual and support vector regression values for vertical tests. From Figure 11, the contrast between the actual burning rates of the specimen and the machine learning outputs were studied. Specimens 5, 6, and 9 show some deviation, and other values are nearer to the machine learning results. Based on the below-mentioned equations (7), (8), and (9), the regression analysis was carried out using machine learning.

LR:

$$\text{Burning rate} : 0.2468 + 0.7125 \, x \, \text{Jute fiber} - 0.341 \, x \, \text{Fly ash}. \tag{7}$$

MLP:

$$\begin{aligned} \text{Burning rate} : &-0.514 \, (\text{Threshold}) + 3.477 \, x \, (\text{Jute fiber}) \\ &- 0.496 \, x \, (\text{fly ash}) - 0.2931 \, x \, (\text{NaOH}). \end{aligned} \tag{8}$$
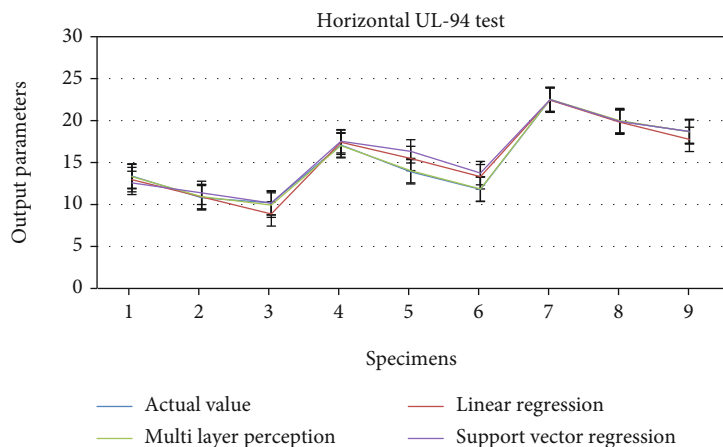
Figure 10: Difference between various output parameters.

Table 5: Machine learning analysis results for horizontal test.

Sl. no.	Input parameters			Output parameters (burning rate)			
	Jute fiber %	Fly ash %	NaOH treatment time in hours	Actual value	Linear regression	Multilayer perception	Support vector regression
1	5	5	0	13.4	12.9675	13.3242	12.5739
2	5	10	5	10.8	10.9134	10.938	11.3808
3	5	15	10	10.2	8.8716	9.9294	10.1754
4	10	5	5	17.1	17.4201	17.0142	17.5431
5	10	10	10	13.9	15.489	14.0376	16.3377
6	10	15	0	11.8	13.3119	11.8605	13.7424
7	15	5	10	22.5	22.4372	22.5246	22.5
8	15	10	0	19.9	19.8186	19.9908	19.9047
9	15	15	5	18.7	17.7645	18.6747	18.6993
		Correlation coefficient			0.9739	0.9995	0.9713
		Root mean square error			0.0757	0.011	0.0895

Table 6: Error values between actual and various regression values for horizontal test.

Sl. no.	Output parameters (burning rate)						
	Actual value	Linear regression	Error value 1	Multilayer perception	Error value 2	Support vector regression	Error value 3
1	13.4	12.9675	0.4325	13.3242	0.0758	12.5739	0.8261
2	10.8	10.9134	-0.1134	10.938	-0.138	11.3808	-0.5808
3	10.2	8.8716	1.3284	9.9294	0.2706	10.1754	0.0246
4	17.1	17.4201	-0.3201	17.0142	0.0858	17.5431	-0.4431
5	13.9	15.489	-1.589	14.0376	-0.1376	16.3377	-2.4377
6	11.8	13.3119	-1.5119	11.8605	-0.0605	13.7424	-1.9424
7	22.5	22.4373	0.06273	22.5246	-0.0246	22.5	0
8	19.9	19.8186	0.0814	19.9908	-0.0908	19.9047	-0.0047
9	18.7	17.7645	0.9355	18.6747	0.0253	18.6993	0.0007

SVR:

$$\text{Burning rate} : 0.2516 + 0.6748\,(\text{jute fiber}) - 0.3267\,\text{x}\,(\text{fly ash}) + 0.0733\,\text{x}\,(\text{NaOH}). \tag{9}$$

From Tables 3 and 4, it is evident that all the regression models have a correlation coefficient of more than 0.97, and its mean square value is less than 0.07. This shows a strong association among parameters of both input and output. From the equations, it is also understood that jute fiber has a positive correlation, and fly ash has a negative correlation. It shows that by addition of fly ash reduces the burning rate and the effect of NaOH is very less. These results were confirmed with the ANOVA test.

TABLE 7: Machine learning analysis results for vertical test.

Sl. no.	Input parameters			Output parameters (burning rate)			
	Jute fiber %	Fly ash %	NaOH treatment time in hours	Actual value	Linear regression	Multilayer perception	Support vector regression
1	5	5	0	14.5	14.4357	14.4357	14.5012
2	5	10	5	12.3	12.1956	12.7196	12.8375
3	5	15	10	11.2	9.9686	11.1214	11.1738
4	10	5	5	19.4	19.0993	19.3744	19.4006
5	10	10	10	15.3	16.8723	15.523	17.7369
6	10	15	0	13.1	14.6322	13.3353	14.6322
7	15	5	10	24.3	23.7629	24.3262	24.3
8	15	10	0	21.2	21.5359	21.4442	21.1953
9	15	15	5	20.5	19.2958	20.501	19.5316
	Correlation coefficient				0.9752	0.9993	0.9767
	Root mean square error				0.0732	0.0152	0.0785

TABLE 8: Error values between actual and various regression values for vertical test.

Sl. no.	Output parameters (burning rate)						
	Actual value	Linear regression	Error value 1	Multilayer perception	Error value 2	Support vector regression	Error value 3
1	14.5	14.4357	0.0643	14.4357	0.0643	14.5012	-0.0012
2	12.3	12.1956	0.1044	12.7196	-0.4196	12.8375	-0.5375
3	11.2	9.9686	1.2314	11.1214	0.0786	11.1738	0.0262
4	19.4	19.0993	0.3007	19.3744	0.0256	19.4006	-0.0006
5	15.3	16.8723	-1.5723	15.523	-0.223	17.7369	-2.4369
6	13.1	14.6322	-1.5322	13.3353	-0.2353	14.6322	-1.5322
7	24.3	23.7629	0.5371	24.3262	-0.0262	24.3	0
8	21.2	21.5359	-0.3359	21.4442	-0.2442	21.1953	0.0047
9	20.5	19.2958	1.2042	20.501	-0.001	19.5316	0.9684
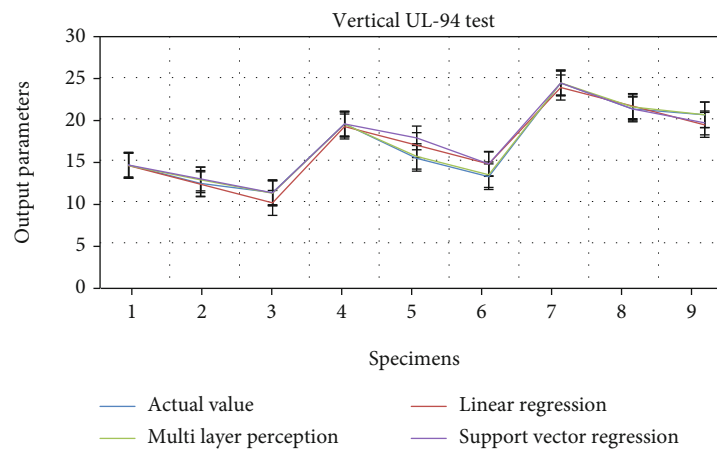
FIGURE 11: Difference between various output parameters for vertical test.

5. Conclusion

Flammability tests are done especially for the composites manufactured with natural fiber reinforcement, as by nature natural fibers have high burning properties when compared to manmade fibers. The test carried out for flammability of polymers and plastic materials used in electronic devices is expressed as UL-94. The test results were rated as V0, V1, and V2 based on the extinguishing of the flames after removing the burner.

Thus, the natural fiber-reinforced composite with jute fiber reinforcement and fly ash filler addition was manufactured and tested for its flammability. From the results obtained from the testing and optimization, the addition of the jute fiber influences more and increases the flammability property of the composite, and the inclusion of the fly ash

reduces the burning rates of the composites. The results were verified by referring to various plots and graphs. The optimum levels obtained from the plot are with 5 wt% inclusion of the jute fiber, 15 wt% addition of the fly ash, and with 10 hours chemical treatment; minimum burning rates can be obtained. In horizontal UL-94 tests, 10.2 mm/min burning rate, and in vertical UL-94 tests, 11.2 mm/min burning rate was obtained. Validation tests were also carried out with these levels, and the results obtained show minimum deviation from the predicted values which are acceptable. To analyze the process parameters' effects on flammability, ANOVA, LR, MLP, and SVR were used.

The regression models also indicate that jute fiber induces the burning rate due to positive correlation and whereas fly ash reduces the burning rate due to negative correlation. The effect of NaOH is very less on the burning rate. In the future, fly ash could be added as a reinforcement agent to reduce the flammability for other natural fibers and greatly reduce the flammability affecting electronic parts. As it is self-extinguishable, it can be used in places where the material needs to be requiring more resistance to flames.

Data Availability

The data used to support the findings of this study are included in the article. Should further data or information be required, these are available from the corresponding author upon request.

Disclosure

It was performed as a part of the Employment Hawassa University, Ethiopia.

Conflicts of Interest

The authors of this article declare that we have no conflict of interests.

Acknowledgments

References

[1] T. F. Salem, S. Tirkes, A. O. Akar, and U. Tayfun, "Enhancement of mechanical, thermal and water uptake performance of TPU/jute fiber green composites via chemical treatments on fiber surface," *E-Polymers*, vol. 20, no. 1, pp. 133–143, 2020.

[2] M. A. Ashraf, M. Zwawi, M. T. Mehran, R. Kanthasamy, and A. Bahadar, "Jute based bio and hybrid composites and their applications," *Fibers*, vol. 7, no. 9, p. 77, 2019.

[3] C. Saravanan, S. Dinesh, and V. Vijayan, "Assessment on effect of silicon carbide and copper reinforcement on AL7075 alloy," *AIP Conference Proceedings*, vol. 2378, p. 020025, 2021.

[4] S. Dinesh, C. Saravanan, and V. Vijayan, "Fabrication and analysis of aluminium filled epoxy resin composites for mechanical properties," *AIP Conference Proceedings*, vol. 2378, p. 020026, 2021.

[5] P. K. Roya, S. Mukhopadhyaya, and B. S. Butolaa, "A study on durable flame retardancy of jute," *Journal of Natural Fibers*, vol. 15, no. 4, pp. 483–495, 2018.

[6] S. U. Zaman, S. Shahid, K. Shaker et al., "Development and characterization of chemical and fire resistant jute/unsaturated polyester composites," *The Journal of The Textile Institute*, pp. 1–10, 2021.

[7] X. Wang, L. Wang, W. Ji, Q. Hao, G. Zhang, and Q. Meng, "Characterization of KH-560-modified jute fabric/epoxy laminated composites: surface structure, and thermal and mechanical properties," *Polymers*, vol. 11, no. 5, p. 769, 2019.

[8] P. Khalili, X. Liu, Z. Zhao et al., "Fully biodegradable composites: thermal, flammability, moisture absorption and mechanical properties of natural fibre-reinforced composites with nano-hydroxyapatite," *Materials*, vol. 12, no. 7, p. 1145, 2019.

[9] R. Sonnier, A. Taguet, L. Ferry, and J.-M. Lopez-Cuesta, "Flame retardancy of natural fibers reinforced composites," *Towards Bio-based Flame Retardant Polymers*, vol. 73-98, pp. 73–98, 2018.

[10] A. U. R. Shah, M. N. Prabhakar, and J.-I. Song, "Current advances in the fire retardancy of natural fiber and bio-based composites – a review," *International Journal of Precision Engineering and Manufacturing-Green Technology*, vol. 4, no. 2, pp. 247–262, 2017.

[11] M. F. Oktem and B. Altintop, "Yüksek Sıcaklık Uygulamalarında Kullanılmak Üzere Kimyasal İşlemden Geçirilmiş Hibrit Jüt - Keten Doğal Kompozitlerin Geliştirilmesi," *Science*, vol. 8, no. 1, pp. 187–196, 2019.

[12] M. Rashid, K. Chetehouna, and N. Gascoin, "Analysing flammability characteristics of green biocomposites: an overview," *Fire Technology*, vol. 2020, pp. 31–67, 2021.

[13] G. Mathubala and M. Nandhini, "Flammability and thermal studies of jute fibre reinforced polymer composites," *Malaya Journal of Matematik*, vol. 5, no. 2, pp. 856–858, 2020.

[14] M. Latif, M. N. Prabhakar, G.-B. Nam, D.-W. Lee, and J.-I. Song, "Influence of organomodified nanoclay on the mechanical and flammability behavior of jute fabric/vinyl ester nanocomposites," *Composites Research*, vol. 30, no. 5, pp. 303–309, 2017.

[15] S. Shahinur, M. Hasan, Q. Ahsan, and J. Haider, "Effect of chemical treatment on thermal properties of jute fiber used in polymer composites," *Journal of Composites Science*, vol. 4, no. 3, p. 132, 2020.

[16] O. A. Salimov, O. Yuldasheva, A. Salimov, and A. A. Xamitov, "Research of the combustibility and fire resistance of some natural fibers and textile products," *Textile Journal of Uzbekistan*, vol. 9, no. 1, p. 5, 2020.

[17] A. Ribeiro, H. Mariot, E. Angioletto, and A. D. Noni, "Fire exposure behavior of epoxy reinforced with jute fiber applied to ceramic tiles for a ventilated facade system," *Materials Research*, vol. 22, suppl 1, 2019.

[18] G. Sakthi Balan and M. Ravichandran, "Study of moisture absorption characteristics of jute fiber reinforced waste plastic filled polymer composite," *Materials Today: Proceedings.*, vol. 27, pp. 712–717, 2020.

[19] G. Sakthi Balan, A. Mohana Krishnan, and S. R. Saravanavel, "Investigation on properties of bahunia racemosa fiber and

egg shell powder reinforced polymer composite," *Materials Today: Proceedings*, vol. 33, no. 7, pp. 4084–4089, 2020.

[20] R. Balachandhar, R. Balasundaram, and M. Ravichandran, "Analysis of surface roughness of rock dust reinforced AA6061 -Mg matrix composite in turning," *Journal of Magnesium and Alloys*, vol. 9, no. 5, pp. 1669–1676, 2021.

[21] G. Navaneethakrishnan, T. Karthikeyan, S. Saravanan et al., "Structural analysis of natural fiber reinforced polymer matrix composite," *Materials Today Proceedings*, vol. 21, no. 1, pp. 7–9, 2020.

[22] G. Navaneethakrishnan, T. Karthikeyan, V. Selvam, and S. Saravanan, "Effects of MWCNTs/g-C3N4 on mechanical and thermal properties of epoxy hybrid nanocomposites," *Journal of Engg. Research*, 2021.

[23] K. Babu, G. Renden, R. A. Mensah et al., "A review on the flammability properties of carbon-based polymeric composites: state-of-the-art and future trends," *Polymers*, vol. 12, no. 7, p. 1518, 2020.

[24] S. Srikanth, A. Parthiban, V. Vijayan, S. Dinesh, and S. Sathish, "Experimental investigation of Nd:YAG laser welding of inconel 625 alloy sheet," *Engineering*, vol. 1, pp. 377–386, 2021.

Research Article

Integrating Nanomaterial and High-Performance Fuzzy-Based Machine Learning Approach for Green Energy Conversion

A. V. L. N. Sujith,[1] **R. Swathi,**[2] **R. Venkatasubramanian,**[3] **Nookala Venu,**[4] **S. Hemalatha,**[5] **Tony George** [6] **A. Hemlathadhevi,**[7] **P. Madhu** [8] **Alagar Karthick** [9,10] **M. Muhibbullah** [11] **and Sameh M. Osman**[12]

[1]*Department of Computer Science and Engineering, Anantha Lakshmi Institute of Technology and Sciences, Ananthapuramu, Andhra Pradesh-515721, India*
[2]*Department of Computer Science and Engineering, Sri Venkateswara College of Engineering, Tirupati, Andhra Pradesh-517502, India*
[3]*Department of Electrical and Electronics Engineering, New Prince Shri Bhavani College of Engineering and Technology, Chennai, Tamil Nadu- 600073, India*
[4]*Department of Electronics and Communication Engineering, Balaji Institute of Technology and Science, Narsampet, Warangal, Telangana-506331, India*
[5]*Department of Computer Science and Engineering, Panimalar Institute of Technology, Chennai, Tamil Nadu-600123, India*
[6]*Department of Electrical and Electronics Engineering, Adi Shankara Institute of Engineering and Technology, Mattoor, Kalady, Kerala-683574, India*
[7]*Department of Computer Science and Engineering, Panimalar Engineering College, Chennai-600123 Tamil Nadu-600123, India*
[8]*Department of Mechanical Engineering, Karpagam College of Engineering, Coimbatore, Tamil Nadu-641032, India*
[9]*Renewable Energy Lab, Department of Electrical and Electronics Engineering, KPR Institute of Engineering and Technology, Coimbatore 641407, Tamil Nadu, India*
[10]*Departamento de Quimica Organica, Universidad de Cordoba, EdificioMarie Curie (C-3), Ctra Nnal IV-A, Km 396, E14014 Cordoba, Spain*
[11]*Department of Electrical and Electronic Engineering, Bangladesh University, Dhaka 1207, Bangladesh*
[12]*Chemistry Department, College of Science, King Saud University, P.O. Box 2455, Riyadh 11451, Saudi Arabia*

Correspondence should be addressed to M. Muhibbullah; m.muhibbullah@bu.edu.bd

Biomass is a renewable and sustainable green energy material. It is made up of lignin, cellulose, and hemicellulose with considerable amount of water, extractives, and inorganic chemical compounds. The use of biomass materials and other biogenic wastes for energy recovery represents an eco-friendly way. Biomass material selection is one of the most significant aspects for any energy conversion process, and it is a common outsourcing problem that includes material preparation, reactor performance, economic assessment, and calorific value of the products. Fuzzy systems can be quite useful in high-performance computing during the selection of biomass materials. In each engineering process, material selection is a crucial step since each material is having its own set of characteristics. This study presents the application of type-1 fuzzy set for the selection of suitable biomass material for yielding maximum bio-oil. This study focuses on seven locally available materials such as rice straw (M-1), sunflower shell (M-2), hardwood (M-3), wheat straw (M-4), sugarcane bagasse (M-5), corn cop (M-6), and palm shell (M-7). The study evaluated seven important properties of the materials such as lignin (P-1), cellulose (P-2), hemicellulose (P-3), volatile matter (P-4), fixed carbon (P-5), moisture content (P-6), and ash content (P-7). The findings demonstrated that sugarcane bagasse (M-5) is the best option for maximum bio-oil yield. Furthermore, the potential of nanoscale catalysts in improving the yield of bio-oil through real-time experiments was studied. The findings of this work add to our understanding of the application of fuzzy-based systems for energy applications.

1. Introduction

In recent years, the use of biomass materials for the production of valuable chemicals and biofuels has gained popularity as a way to minimise emissions of greenhouse gases emitted by the combustion of fossil diesel fuels [1]. It is an organic substance with a lot of chemical energy. It has traditionally been used for energy purposes through direct burning. The annual global biomass production is expected to be 146 billion metric tonnes. The current biomass availability in India is estimated as 500 million metric tonnes per year. According to the report received from ministry, biomass availability is expected to be between 120 and 150 million metric tonnes per year. Biomass presently accounts for 32% of the country's overall primary energy consumption. It is a renewable resource that appears to offer clear environmental benefits and lower greenhouse gas emissions. Wood chips and agricultural wastes are the examples for low-value biomass feedstocks. It comprises a wide range of chemical components. Alcohols [2], organic acids [3], formic acid, and furfurals [4] are among the compounds addressed. These chemicals are then transformed into a variety of derivatives that are employed in the chemical and pharmaceutical sectors. Many researchers have published data on chemicals extracted from a wide range of biomass feedstocks, as well as specific feedstocks including carbohydrates, triglycerides, cellulose, hemicellulose, lignin [5], and furfural [6]. Machine learning algorithms are designed to extract knowledge from data using classic approaches such as clustering, classification, and relationships. To create more flexible outcomes, fuzzy sets are used in combination with these approaches. In the construction of machine learning algorithms and models, fuzzy-based knowledge representation and reasoning are widely used. They gave a new-fangled life to the scientific truth of machine learning which have been in a hidden stage for a long period. Fuzzy sets are used throughout the data processing stage because it may simulate partial and inaccurate data representations. In the mapping of data representation, the fuzzy extension principle was used.

The effective handling of erroneous data and uncertainty is a critical phenomenon in any decision-making process. According to Lee et al. [7], if the imprecision of humanity's decision-making process is mishandled, the results could be perplexing. Fuzzy set theory is a wonderful tool for expressing human knowledge [8]. It is a formalised technique for scientifically conveying ambiguity and vagueness [9]. Zadeh proposed fuzzy sets theory in 1965 as an expansion of the classical notion of set [10]. Salii defined an L-relation, a more broad type of structure that he examined in an abstract algebraic framework [11]. Fuzzy relations are a type of fuzzy relation that is currently widely used in fuzzy mathematics and has applications in linguistics, decision-making, and clustering. Fuzzy set theory has been used by several researchers to deal with uncertainty in a range of decision-making problems [12]. Many literatures used fuzzy-based techniques for energy management system. Previously, Chehri and Mouftah [13] proposed this system for hybrid grid solar power energy management system. Samuel [14] proposed a home energy management system based on a multioutput adaptive neurofuzzy inference system. For a photovoltaic solar home, Chekired et al. [15] proposed a fuzzy logic energy management system. The main idea behind this study is to evaluate the biomass materials in order to get higher quantity and rich biofuel by evaluating the yield parameters. This can be attained with the aid of fuzzy logic and fuzzy inference systems, which have been shown to be useful tools. This system can identify, predict, and control the complex, nonlinear, and imprecise systems. This is very attractive technology that can solve any problems without any accurate mathematical models [16]. Typically, a fuzzy system is formed by collecting knowledge from subject experts and converting their tacit knowledge of the underlying process into linguistic variables and fuzzy rules. Previously, this approach was used for various decision-making processes such as identification of suitable distributor location [17], medicine [18], assessment of power transformer [19], employee performance [20], and hospital performance [21].

Pyrolysis is the method of thermochemical decomposition of organic compounds for the production of energy-rich biofuel in the absence of air at elevated temperatures. There are three different types of pyrolysis reactions differentiated based on the process temperature and reaction time. They are conventional slow pyrolysis, fast pyrolysis, and flash pyrolysis. In fast and flash pyrolysis, the biomass is heated rapidly up to the temperature of 500°C to 650°C. Among other thermochemical conversion processes, pyrolysis offers an innovative solution to problems with heat transmission, product quantity, and quality. In the point of environment considerations particularly emission and waste management, pyrolysis technologies for biomass conversion to energy generation have attracted more attention in recent years and are increasingly attaining advances [22]. Furthermore, for the pyrolysis reactors for biomass conversion into bio-oil, char gas offers various advantages, including improved product quality, reduced operating costs, higher liquid product yield, enhanced reaction speeds, and lower heat requirements. Catalytic pyrolysis is a potential technology for improving biomass-based materials into liquid fuel and other value-added products [23]. Use of nano-based catalysts enhances the pyrolysis process with lower activation energy by lowering the lowering pyrolysis temperature [24]. In catalytic process, the catalyst and feedstock materials are mixed together and kept inside the reactor for catalytic reforming and cracking. Various types of catalysts including nickel-based, metal-based, alkali-based, zeolite catalysts, and carbon-supported catalysts are used in various processes for the production of higher amount of volatiles [25]. For the catalytic pyrolysis conversion of wood-based biomass materials, ZSM-5 zeolite is the most commonly utilized catalysts. Because of the medium pore size and two-dimensional channel-like pore structure, these catalysts are widely used for increasing maximum fuel yield from biomass [26]. The ambient environment had a substantial impact on the catalytic pyrolysis effects particularly which could boost hydrogenation by increasing catalyst accessibility. The identification of suitable material for the yielding maximum biofuels and chemicals has not been

examined using analytical hierarchy process (AHP) and other multicriteria decision-making (MCDM) approaches.

This research focused on the use of fuzzy AHP to select suitable biomass materials for thermochemical conversion processes, specifically pyrolysis. Pyrolysis is a hopeful option for thermochemical conversion of lignocellulosic material. It is a method for converting organic molecules into energy-rich products. This method can produce carbon as a byproduct, which is referred to as carbonization. Pyrolysis, unlike other high-temperature processes such as hydrolysis and combustion, does not require the use of water, oxygen, or other reagents. It is a simple, inexpensive technology that can be used for variety of feedstocks. This process produces high-quality liquid oil and chemicals when compared to other conversion techniques. The qualities and requirements for selecting the best biomass material are examined using expert critiques and literature before selecting numerous materials for this study. The selected materials are available plenty and have no value. After the cultivation, these materials are burnt in open atmosphere in the field itself because of its low density. Open burning of these materials causes severe impact on the environment. So appropriate recycling of these materials is essential. In this context, this study selected seven alternatives out of available plenty in nature to produce maximum liquid oil through thermal and nano-catalytic pyrolysis by investigating its lignocellulosic and its components identified through proximate analysis. The developed fuzzy logic model predicted the yield for a given set of inputs. Finally, the prediction is validated with experimental study conducted by using specified set of input through thermal as well as catalytic pyrolysis.

2. Materials and Methodology

2.1. Materials. The raw biomass materials used for this study are collected from local agricultural field in Coimbatore, India. The raw wood is finely processed into particles having average diameter of less than 0.5 mm. For this form, the biomass materials are initially processed with ball mill and shieved using shieve shaker. To promote pyrolysis reaction and feedstock characterization, the particle size of the biomass materials is very important to prevent heat and mass transmission constraints. So the feedstock has been ground to below 0.5 mm. Before evaluating proper characteristic study, the biomass materials are dried in open sunlight for a week and further dried in an oven for 1 hr maintained at ±100°C. This process can considerably remove the moisture content in the biomass samples which affect the process as well as yield quantity.

2.2. Methods

2.2.1. Material Evaluation. Economic and environmental variables are the two most important elements that can influence biomass material choices. They are listed as follows. Various studies explain some parameters to consider in biomass selection. However, no study effectively specifies this information. Figure 1 shows the property evaluation of the biomass materials.
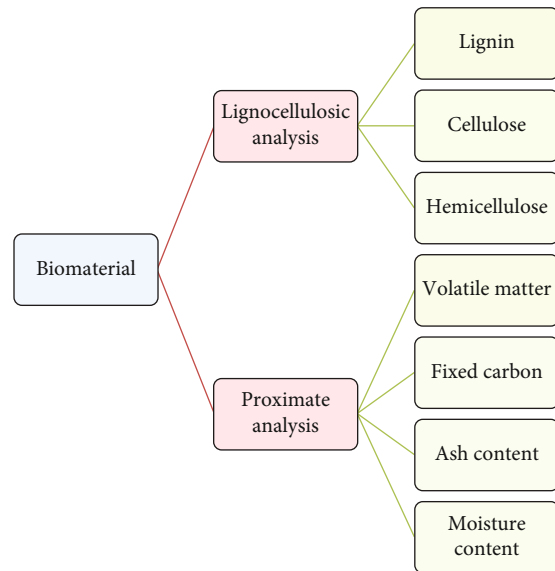
FIGURE 1: Biomass material property evaluation.

  (i) *Input.* Cost for production and storage

 (ii) *Output.* Yield of biofuel

(iii) *Conversion Rate.* Efficiency of conversion

(iv) *Emission.* Release of harmful gases

 (v) *Usage of Chemicals.* Properties of chemicals obtained from product

(vi) *Technological Development.* Gap between current stages

(vii) *Sustainable Energy.* Replacing fossil fuel

2.2.2. Type-1 Fuzzy Approach. Fuzzy sets were brought out by Zadeh in 1965 as the expansion of the conventional notion of set [10]. Here, each constituent has depicted with the help of membership function valued in the actual unit interval [0, 1]. Because of their ability to handle vagueness in preference values, fuzzy set theory has steadily gained favour in the selection of appropriate materials. This approach is frequently utilized in a variety of fields when data is partial or inaccurate [27]. The type-1 fuzzy set $\tilde{a}$ in X is a set of well-organized pair where $\tilde{a}$ is represented as $\tilde{a} = \{(x, \mu_{\tilde{a}}(x)) \mid x \in X\}$ where x represents the constituents of the set X and $\mu_{\tilde{a}}(x)$ is called the membership function or the degree of membership of x.

Suppose $\tilde{a}$ is a triangular fuzzy number (TFN) (a_l, a_m, a_u), where a_l, a_m, and a_u are the promising values of membership function shown in Figure 2.

Then the membership function is defined as

$$\mu_{\tilde{a}}(x) = \begin{cases} 1 - \dfrac{a_m - x}{a_m - a_l}, a_l \leq x \leq a_m, \\[2mm] 1 - \dfrac{x - a_m}{a_u - a_m}, a_m \leq x \leq a_u, \\[2mm] 0, \text{otherwise.} \end{cases} \tag{1}$$
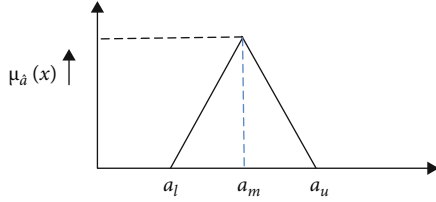
Figure 2: Illustration of triangular fuzzy set.

Suppose $\tilde{a} = (a_l, a_m, a_u)$ and $\tilde{b} = (b_l, b_m, b_u)$ are two triangular fuzzy numbers so the mathematics operations between two type-1 fuzzy sets are as follows:

$$
\begin{aligned}
\tilde{a} \oplus \tilde{b} &= (a_l + b_l, a_m + b_m, a_u + b_u), \\
\tilde{a} \ominus \tilde{b} &= (a_l - b_l, a_m - b_m, a_u - b_u), \\
\tilde{a} \otimes \tilde{b} &= (a_l \times b_l, a_m \times b_m, a_u \times b_u), \\
\frac{\tilde{a}}{\tilde{b}} &= \left(\frac{a_l}{b_u}, \frac{a_m}{b_m}, \frac{a_u}{b_l}\right), \\
\frac{1}{\tilde{b}} &= \left(\frac{1}{b_u}, \frac{1}{b_m}, \frac{1}{b_l}\right), \\
k \times \tilde{b} &= (k \times b_l, k \times b_m, k \times b_u),
\end{aligned}
\tag{2}
$$

where k is a crisp number.

The choice of material for thermochemical conversion to produce biofuels and chemicals is a strategic and critical decision for researchers. The evaluation of many parameters is part of this selecting procedure. This approach involves evaluating a number of factors to select the best biomass source. Some studies may consider higher profits and better outcomes; however, the evaluation should be focused on social and environmental issues. The majority of researchers are only interested in the biological composition of biomass. For 2nd-era ethanol, Kahr et al. [28] evaluated the lignocellulosic ethanol potential of wheat straw, rice straw, oat straw, and maize stover among other potential agricultural wastes. Ciancolini et al. [29] used agglomerative hierarchical cluster analysis to assess the biomass and polyphenol production of eight cardoon genotypes. Nine capacities are tested in this study in order to find significant differences. Vaezi et al. [30] developed a numerical set of rules for biomass material selection in the gasification process. Figure 3 shows the methodology adopted for this study.

2.2.3. Validation by Catalytic Pyrolysis Experiment

(1) Reactor Setup. The pyrolysis reactor is the heart of the pyrolysis process. In this study, the top two ranked biomass material suggested by fuzzy technique is utilized for fixed-bed pyrolysis in order to verify the reliability of the assessment. For this purpose, the reactor made up of stainless steel with inner diameter 100 mm and length 150 mm is utilized. The system consists of heating system, condenser unit, and liquid collection system. The reactor is heated with a 2 kW electrical resistance heater attached with ammeter and volt-

meter setup. A separate autotransformer is attached with the reactor to control the rate of heat input. For proper collection of bio-oil, the evolved gas generated from the reactor is allowed through the condenser, in which the ice water maintained at 0°C is supplied for the condensation process. The condensed liquid oil is then collected into the glass beaker and stored for further study. The char generated during the pyrolysis process was collected from the bed directly at the end of each run. The uncondensable gases produced from the reactor are collected by using gas balloon system.

(2) Reaction Process. ZSM-5 is selected for this study due to its higher activity and stability, as well as its good selectivity, metal tolerance, and flexibility, especially when used as an additional catalyst [31]. Zeolites can be shape-selective catalysts through transition state selectivity or molecular diameter-based exclusion of competing reactants. These catalysts can be utilized for oxidation. The processes can take place within the pores of the zeolite. Desilication of ZSM-5 with NaOH solution produced HZSM-5 for the catalytic process. For this, 25 grams of zeolite is combined with a 250 mL of 0.3 M NaOH and maintained at 75°C. After that, the mixture is filtered and dried in an oven by keeping the temperature not less than 100°C. The dried sample was changed to hydronium form with a 0.2 M NH_4NO_3 solution at 80°C for 24 hours and then again dried at 100°C and calcined at 500°C for almost 6 hours, yielding 0.3 HZSM-5 as the final product. On the reactor, 100 grams of powdered biomass was combined with catalyst and reaction was carried out at by keeping the bed temperature of 500°C. The evolved gases coming out from the reactor are allowed to condenser unit, and the condensed vapour is collected in the form of bio-oil. The weight of the bio-oil is measured directly with the help of weighing machine. Each experiment is conducted till no volatile matter is released from the reactor. For that purpose, minimum of 45 min is maintained for each run. In catalytic pyrolysis process, two types of reactions are taken place inside the reactor. First is the formation of phenolic contents due to deoxygenation or the loss of one or two oxygen atoms. This stage is also the responsible for the formation of cyclopentadiene, fulvenone, and fulvene components. The process of deoxygenation is basically driven by the stability of the separation groups such as water, carbon monoxide, and carbon dioxide. Second is the formation of final products and transmethylation. This stage is responsible for the production of cresols and methyl components [32]. The yield of the desired product is found by the following formula.

$$
\text{Yield (wt\%)} = \frac{\text{Yield of oil/char/gas}}{\text{Biomass feed}}.
\tag{3}
$$

3. Results and Discussion

3.1. Material Selection.
Biomass material selection is mainly concerned with the biomass to biofuel conversion techniques in order to yield the maximum biofuels such as crude bio-oil, char, and gas to fulfil the future energy needs. In the world, there are plenty of materials available as a resource
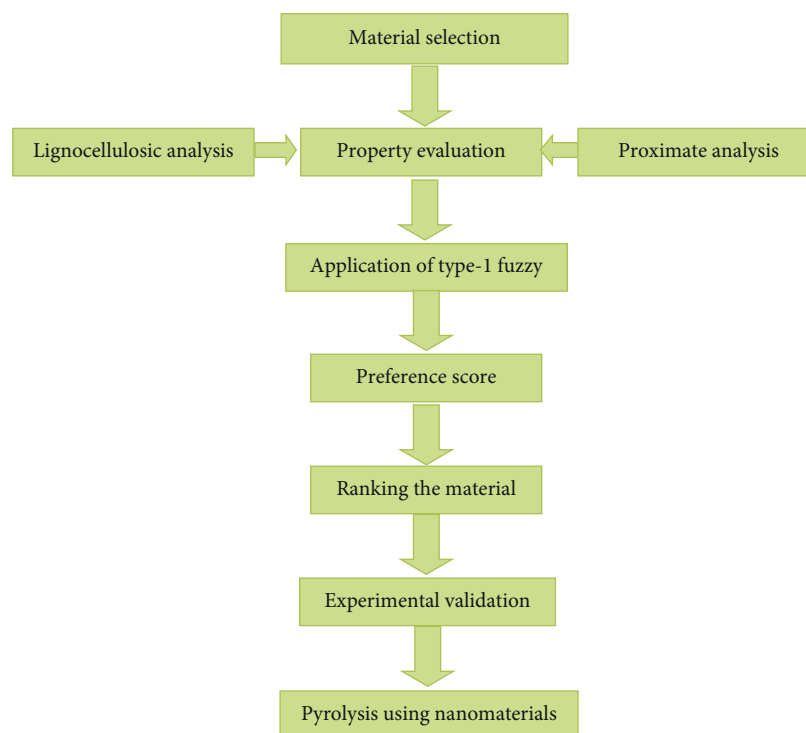
FIGURE 3: Methodology.

for various applications. Each material has its own unique characteristics, applications, advantages, and limitations. Earlier than the beginning of petro oil era, renewable feedstock materials were a major segment for total energy and chemical supplies. Biomass is a natural material supply chemicals and energy up to date. Among the other types of renewable materials, lignocellulosic biomass are available abundant, low-value materials utilized for fuels, chemicals, and energy to replace fossil resources [33]. They are composite material which has cellulose, hemicellulose, and lignin approximately at 50 wt%, 25 wt%, and 25 wt%, respectively [34]. The components are connected mutually to provide structural stability. It also contains reasonable amount of water, extractives with inorganic elements. Cellulose is a linear long-chain polymer that encircles mostly crystalline structures with tiny amorphous regions. They are structured in fibrils and then grouped together to form cellulose fibres, which are aware of the fibrous character of biomass cell walls. Hemicelluloses are also the amorphous polymers having shorter structure of five to six carbon sugars. It serves as a link between the cellulose and the lignin [35]. Lignin is a three-dimensional polymer made up of phenylpropane units linked together in a number of ways. The most prevalent outsourcing difficulty is material selection, which is the most important aspects of any biomass conversion process. Since different materials have some unique properties and value, the procedure for biomass material selection has a main role related to the conversion efficiency as well as the heating value of the biofuel [36]. This process of selection is identified to be the imperative decision-making process for biofuel conversion techniques which includes biomass preparation, performance of the reactor, economic evaluation, and heating value of the biofuel products.

3.2. Evaluation of the Material Properties. Different biomass materials have some unique characteristics. Analysis of material properties shown in Figures 4–10 is very important for the selection of best biomass material for pyrolysis. Chemical analysis biomass material is one of the most essential parts during the evaluation of reaction characteristics. In biomass, cellulose and lignin are often considered as the most important components [37]. The lignocellulosic content of materials is measured using the conventional wet chemistry technique. It is suggested as the best approach for analysis of lignocellulosic contents [38]. This method is a powerful and accurate method, whereas 0.50 grams of samples is analysed for each entry. Figure 4 shows the lignin content, and Figure 5 shows the cellulose content present in the materials 1 to 7. According to the data, the lignin content of the materials is varied from 13.4 wt% to 44 wt%. It can be clearly shown that M-5 has lower lignin content but M-7 has higher lignin concentrations. Generally, higher lignin contents of the material slower the pyrolysis reaction yielding maximum char. The presence of cellulose in the material enhances the thermochemical conversion yielding maximum liquid products [39]. The values of cellulose in the selected materials vary from 27.7 wt% to 52.5 wt%. The material M-6 contains the highest amount of cellulose content of all the samples, and M-7 has the lowest. With reference to lignin and cellulose contents, M-6 may be suggested as a suitable material, but the hemicellulose content of the material M-6 is lower than the M-2 and M-5.
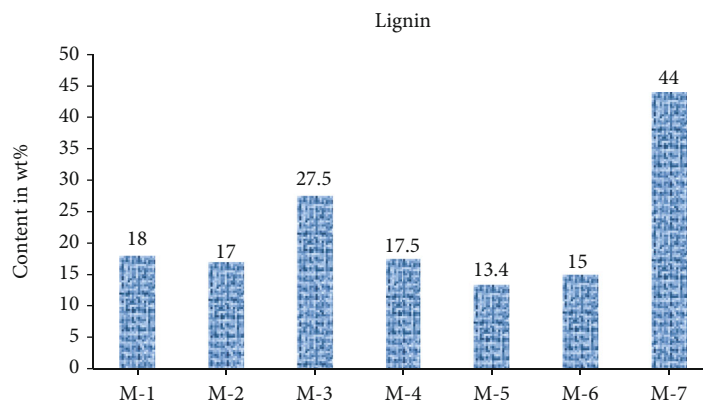
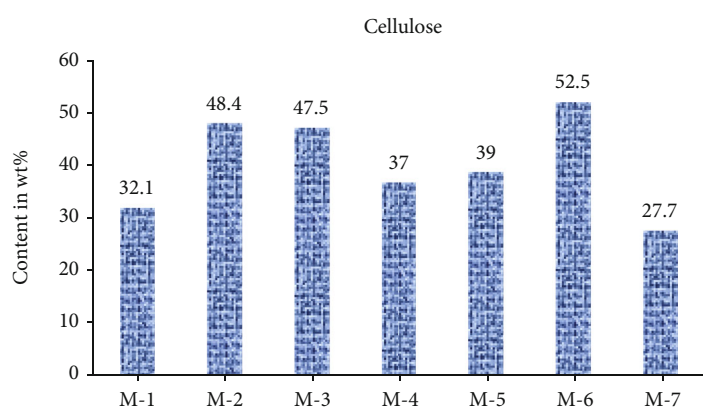Figure 4: Lignin contents of the selected materials.

Figure 5: Cellulose contents of the selected materials.
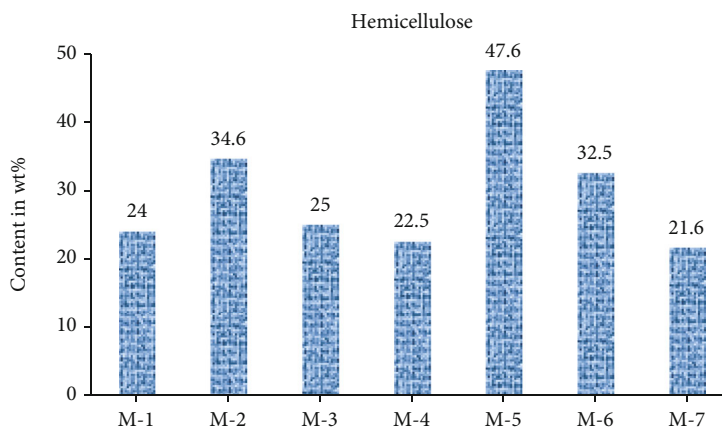

Figure 6: Hemicellulose contents of the selected material.

The presence of hemicellulose content of the material also enhances the conversion of material to biofuel during pyrolysis. The total content of the cellulose and hemicellulose is termed as holocellulose favour for the yield of biofuel. Based on the above said three properties, the favourable material for yielding maximum biofuel cannot be suggested without deep investigation. Material with more volatile contents produces more bio-oil and biogas, while material with higher fixed carbon yields more char particles. The selected sample is having more amount of volatile contents (58.8 wt% to

80.2 wt%). Based on volatile contents, M-5 can be suggested as the best one for maximum energy conversion. The presence of fixed carbon in the material is ranging from 6.54 wt% (M-6) to 21.0 wt% (M-4). The material's moisture content has an impact on the heat transfer phenomena during energy conversion [40]. The moisture content present in the feedstock might obviously reduce the reaction temperature. During conversion process, the initial heat applied to the process is used to evaporate the moisture content of the feedstock material. It also affects the heating value of
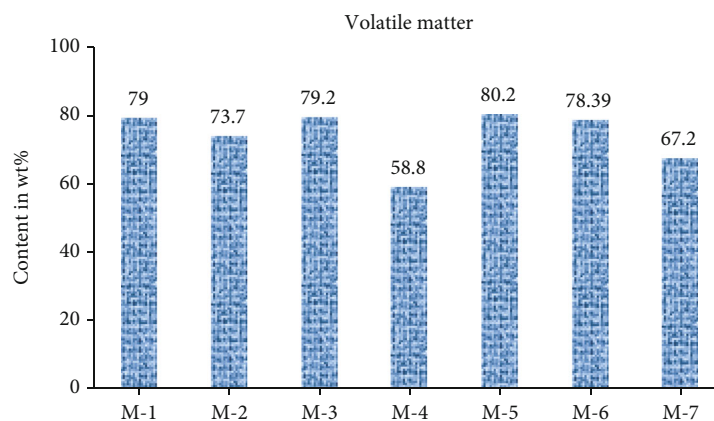
Volatile matter

FIGURE 7: Volatile matters of the selected materials.
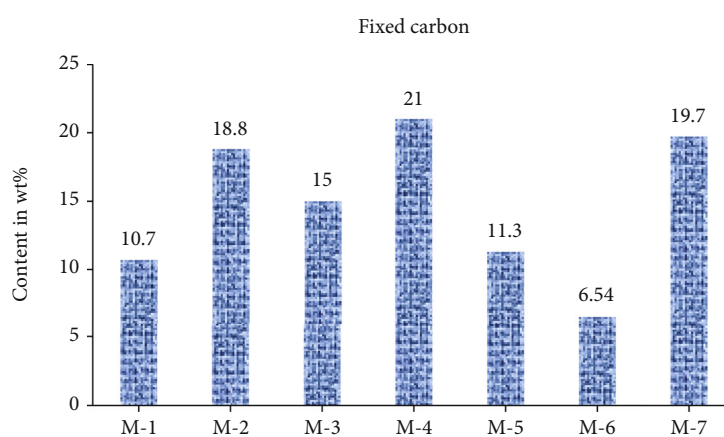
Fixed carbon

FIGURE 8: Fixed carbons of the selected materials.
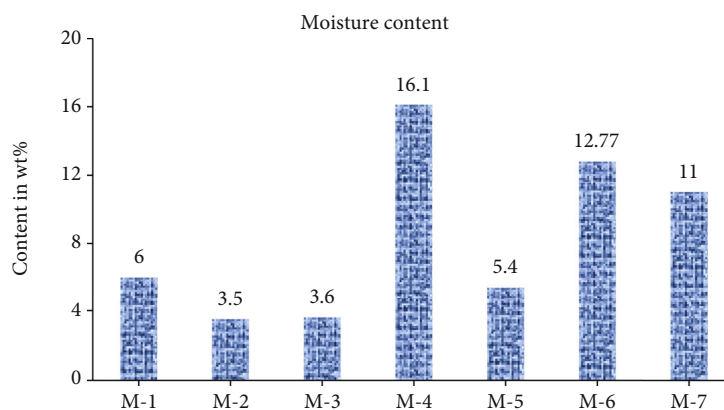
Moisture content

FIGURE 9: Moisture contents of the selected materials.

the reaction products. Previously, many studies have recommended the feed particles should have lower moisture content in order to favour for quality bio-oil yield [41, 42]. The material with lower moisture content always yields the fuel with higher energy content [43]. According to Figure 9, the moisture content of the materials is varied from 3.5 wt% to 16.1 wt%. From the figure, it can be shown that M-2 has lower moisture content whereas M-4 has more. The analysis was carried out in accordance with ASTM pro-

cedures to determine the proximate analysis (VM-ASTM D3175, FC-By difference, MC-ASTM D3173, and AC-ASTM D3174). The increased moisture content in the material significantly affects the oil quality. The influence of ash content during pyrolysis has been studied extensively. The amount of ash in the biomass sample has a direct impact on the yield and composition of the pyrolysis products. It also has an impact on the efficiency of the conversion process. As a result, one of the factors for selecting the best
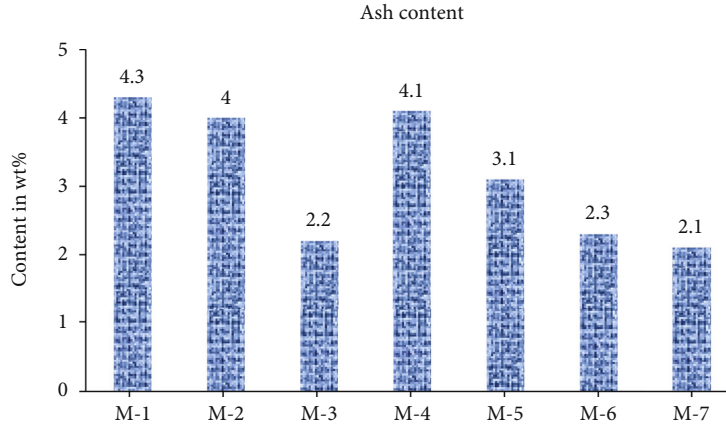
FIGURE 10: Ash contents of the selected materials.

TABLE 1: Type-1 fuzzy pairwise comparison matrix for weight calculation.

	P-1	P-2	P-3	P-4	P-5	P-6	P-7
P-1	(1,1,1)	$\left(\frac{1}{5},\frac{1}{4},\frac{1}{3}\right)$	$\left(\frac{1}{3},\frac{1}{2},\frac{1}{1}\right)$	$\left(\frac{1}{7},\frac{1}{6},\frac{1}{5}\right)$	$\left(\frac{1}{3},\frac{1}{2},\frac{1}{1}\right)$	(1,2,3)	$\left(\frac{1}{3},\frac{1}{2},\frac{1}{1}\right)$
P-2	(3,4,5)	(1,1,1)	(1,2,3)	$\left(\frac{1}{3},\frac{1}{2},\frac{1}{1}\right)$	(2,3,4)	(2,3,4)	(1,2,3)
P-3	(1,2,3;1),	$\left(\frac{1}{3},\frac{1}{2},\frac{1}{1}\right)$	(1,1,1)	$\left(\frac{1}{4},\frac{1}{3},\frac{1}{2}\right)$	(1,2,3)	(2,3,4)	(1,2,3)
P-4	(5,6,7;1)	(1,2,3)	(2,3,4)	(1,1,1)	(4,5,6)	(5,6,7)	(3,4,5)
P-5	(1,2,3;1)	$\left(\frac{1}{4},\frac{1}{3},\frac{1}{2}\right)$	$\left(\frac{1}{3},\frac{1}{2},\frac{1}{1}\right)$	$\left(\frac{1}{6},\frac{1}{5},\frac{1}{4}\right)$	(1,1,1)	(2,3,4)	$\left(\frac{1}{3},\frac{1}{2},\frac{1}{1}\right)$
P-6	$\left(\frac{1}{3},\frac{1}{2},\frac{1}{1}\right)$	$\left(\frac{1}{4},\frac{1}{3},\frac{1}{2}\right)$	$\left(\frac{1}{4},\frac{1}{3},\frac{1}{2}\right)$	$\left(\frac{1}{7},\frac{1}{6},\frac{1}{5}\right)$	$\left(\frac{1}{4},\frac{1}{3},\frac{1}{2}\right)$	(1,1,1)	$\left(\frac{1}{4},\frac{1}{3},\frac{1}{2}\right)$
P-7	(1,2,3)	$\left(\frac{1}{3},\frac{1}{2},\frac{1}{1}\right)$	$\left(\frac{1}{3},\frac{1}{2},\frac{1}{1}\right)$	$\left(\frac{1}{5},\frac{1}{4},\frac{1}{3}\right)$	(1,2,3)	(2,3,4)	(1,1,1)

biomass is the lower level of the samples. During pyrolysis, ash particles usually extinguish the vapour conversion. So for this process, the biomass with reduced ash content is often preferred. As a result, the best material for pyrolysis should have most of volatile matter, fixed carbon, and lowest moisture and ash contents. Based on the above characteristic study, the properties such as cellulose, hemicellulose, volatile matter, and fixed carbon are considered as beneficial (high are better) and lignin, moisture, and ash contents are considered as nonbeneficial (low are better).

3.3. Ranking of the Material. The fuzzy pairwise comparison matrix for weight calculation using type-1 fuzzy AHP is shown in Table 1. The weights are derived using geometric mean method [44]. The type-1 fuzzy weights are defuzzified to obtain the crisp numeric weights, which are further normalised to obtain the final weights of criteria. These values are reproduced by multiplication with the evaluation matrix to get preference score. Table 2 displays the weighted normalised evaluation matrix. The graphical representations of the ranks are also shown in Figure 11. It can be seen that sugarcane bagasse is the best alternative having rank 1. The

TABLE 2: Weighted normalised evaluation matrix.

	P-1	P-2	P-3	P-4	P-5	P-6	P-7
M-1	.0449	.1255	.0689	.3577	.0420	.0251	.0533
M-2	.0476	.1892	.0994	.3337	.0737	.0431	.0573
M-3	.0294	.1857	.0718	.3586	.0588	.0419	.1042
M-4	.0462	.1446	.0646	.2662	.0824	.0094	.0559
M-5	.0603	.1525	.1367	.3631	.0443	.0279	.0739
M-6	.0539	.2052	.0934	.3549	.0256	.0118	.0996
M-7	.0184	.1083	.0620	.3043	.0773	.0137	.1091

next best material is hardwood which is ranked 2. The ranks are obtained based on the preference score shown in Table 3, and Table 4 shows the ranks of the selected biomass materials based on the preference score. The lignin percentage of sugarcane bagasse is so low compared to other materials, and the lower lignin level of 13.4% and greater hemicellulosic content of 47.6% forecast the best option for optimum bio-oil production. The moisture level of the sugarcane bagasse is also quite low, at only 5.4 wt%. As a result, sugarcane bagasse provides greater quality and has a higher
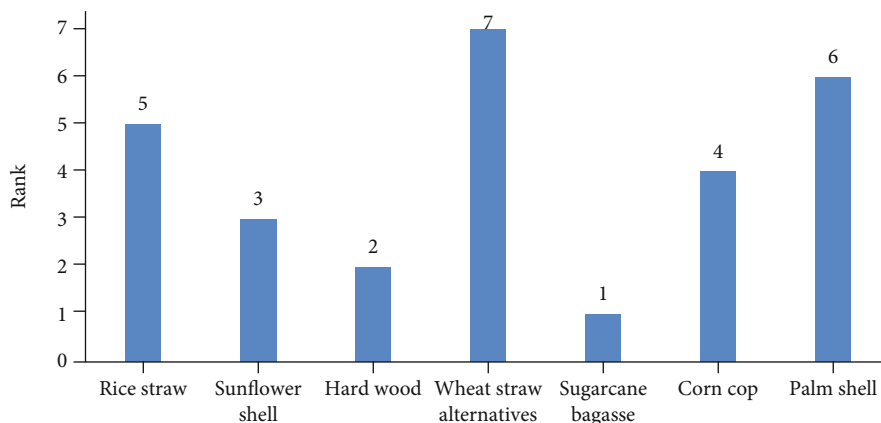
FIGURE 11: Rank of the biomass material.

TABLE 3: Preference score.

Alternatives	Preference score
M-1	0.7156
M-2	0.8433
M-3	0.8492
M-4	0.6690
M-5	0.8577
M-6	0.8429
M-7	0.6923

TABLE 4: Ranking of the material based on preference score.

Alternatives	Rank
RS (M-1)	5
SS (M-2)	3
HW (M-3)	2
WS (M-4)	7
SB (M-5)	1
CC (M-6)	4
PS (M-7)	6

TABLE 5: Yield of biofuel under selected operating condition.

Feedstock	Fuzzy-based rank	Bio-oil yield in wt%		Experimental rank
		Thermal pyrolysis	Catalytic pyrolysis	
Sugarcane bagasse	1	48.3	50.4	1
Hardwood	2	44.6	46.8	2

3.4. Experimental Validation. The yield of bio-oil with respect to biomass pyrolysis and catalytic pyrolysis is shown in Table 5. For thermal pyrolysis, the yield of bio-oil is 48.3 wt% for sugarcane bagasse and 44.6 wt% for hardwood material. At a catalyst loading of 2 wt%, the bio-oil yield is increased to 50.4 wt% and 46.8 wt% for sugarcane pyrolysis and hardwood, respectively. The yield of bio-oil from top-ranked sugarcane bagasse via thermal pyrolysis and catalytic pyrolysis is more when compared to second-ranked hardwood. When the experimental and theoretical findings were compared, they were virtually identical, indicating a strong correlation between them.

4. Conclusion

In this study, type-1 fuzzy set approach was used to design a mechanism for selecting optimal biomass material for the pyrolysis process for maximum bio-oil yield. The type-1 fuzzy set was suggested which helps in the process of selecting suitable biomass materials among a large number of available alternatives. By considering seven evaluation criteria, this study gives the ranking order of the materials based on the performance score, and the order was sugarcane bagasse>hardwood>sunflower shell>corn cop>rice straw>palm shell>wheat straw. For a particular biomass material selection problem, this method considers biomass material selection qualities and their interrelationships. This method yields significant results and also establishes a link between previous studies for appropriate material selection for optimal bio-oil yield. The results of this method are in good accord with those of experiments. Under the same experimental circumstances, the top-ranked material yielded 3.7 wt% and 3.6 wt% more liquid oil than the second-ranked

heating value. The quality of the oil is generally affected by the water content of the biomass feedstock [45]. Various researches have also confirmed this. One of the reasons for the superior quality of the bio-oil is the lower ash level of the sugarcane bagasse [46]. Wheat straw has higher moisture content than other biomass materials, as well as a lower cellulose content, which means it has a lesser chance of producing maximum bio-oil yield [47]. As a result, it was placed seventh among the other selected materials. During thermochemical conversion processes, there is a strong relation among the degradation of volatile contents and the rise in product yield [48]. The production of biofuels results in a 90% loss of their volatile constituents [49]. Even if rice straw and sugarcane bagasse have the same quantity of volatile matter, higher level of hemicellulose and lower ash content in sugarcane bagasse may be the key reason for its ranking among other biomass materials and for the prediction of acceptable biomass.

material during thermal and catalytic pyrolysis, respectively. The results provide confidence, and this approach can be applied for other thermochemical conversion processes in order to identify the best biomass material.

Data Availability

The data used to support the findings of this study are included in the article.

Conflicts of Interest

The authors declare that there is no conflict of interest regarding the publication of this article.

Acknowledgments

References

[1] P. V. Elumalai, M. Parthasarathy, J. S. Lalvani et al., "Effect of injection timing in reducing the harmful pollutants emitted from CI engine using N-butanol antioxidant blended eco-friendly Mahua biodiesel," *Energy Reports*, vol. 7, pp. 6205–6221, 2021.

[2] C. S. Dhanalakshmi and P. Madhu, "Recycling of wood bark of Azadirachta indica for bio-oil and chemicals by flash pyrolysis," *Indian Journal of Ecology*, vol. 46, no. 2, pp. 347–353, 2019.

[3] T. Werpy and G. Petersen, "Top value added chemicals from biomass NATO," *Advanced Science Institute*, vol. 1, no. 2, pp. 263–275, 2004.

[4] B. Agarwal, K. Kailasam, R. S. Sangwan, and S. Elumalai, "Traversing the history of solid catalysts for heterogeneous synthesis of 5-hydroxymethylfurfural from carbohydrate sugars: a review," *Renewable and Sustainable Energy Reviews*, vol. 82, pp. 2408–2425, 2018.

[5] P. Madhu, H. Kanagasabapathy, and I. N. Manickam, "Conversion of cotton residues to bio-oil and chemicals through flash pyrolysis in a fluidised bed reactor," *International Journal of Energy Technology and Policy*, vol. 14, no. 1, pp. 20–33, 2018.

[6] X. Li, P. Jia, and T. Wang, "Furfural: a promising platform compound for sustainable production of C4and C5Chemicals," *ACS Catalysis*, vol. 6, no. 11, pp. 7621–7640, 2016.

[7] A. H. Lee, H. Y. Kang, C. F. Hsu, and H. C. Hung, "A green supplier selection model for high-tech industry," *Expert Systems with Applications*, vol. 36, no. 4, pp. 7917–7927, 2009.

[8] D. Dubois and H. Prade, *Fundamentals of fuzzy sets (Vol. 7)*, Springer Science & Business Media, 2012.

[9] G. Büyüközkan, "An integrated fuzzy multi-criteria group decision-making approach for green supplier evaluation," *International Journal of Production Research*, vol. 50, no. 11, pp. 2892–2909, 2012.

[10] L. A. Zadeh, "Fuzzy sets," *Information And Control*, vol. 8, no. 3, pp. 338–353, 1965.

[11] V. N. Salii, "Relations Izv. Vysh. Uchebn. Zaved," *Matematika*, vol. 44, no. 1, pp. 133–145, 1965.

[12] M. Kilic and İ. Kaya, "Investment project evaluation by a decision making methodology based on type-2 fuzzy sets," *Applied Soft Computing*, vol. 27, pp. 399–410, 2015.

[13] A. Chehri and H. T. Mouftah, "FEMAN: Fuzzy-based energy management system for green houses using hybrid grid solar power," *Journal of Renewable Energy*, vol. 2013, Article ID 785636, 6 pages, 2013.

[14] J. S. GK, "MANFIS based SMART home energy management system to support SMART grid," *Peer-to-Peer Networking & Applications*, vol. 13, no. 6, 2020.

[15] F. Chekired, A. Mahrane, Z. Samara, M. Chikh, A. Guenounou, and A. Meflah, "Fuzzy logic energy management for a photovoltaic solar home," *Energy Procedia*, vol. 134, pp. 723–730, 2017.

[16] V. J. Manoj Praveen, R. Vigneshkumar, N. Karthikeyan, A. Gurumoorthi, R. Vijayakumar, and P. Madhu, "Heat transfer enhancement of air-concrete thermal energy storage system–CFD simulation and experimental validation under transient condition," *Proceedings of the Institution of Mechanical Engineers, Part E: Journal of Process Mechanical Engineering*, no. article 09544089211007370, 2021.

[17] C. T. Chen, "A fuzzy approach to select the location of the distribution center," *Fuzzy Sets and Systems*, vol. 118, no. 1, pp. 65–73, 2001.

[18] L. Todorova, K. Atanassov, S. Hadjitodorov, and P. Vassilev, "On an intuitionistic fuzzy approach for decision making in medicine: part 2," *International Journal Bioautomation*, vol. 7, pp. 64–69, 2007.

[19] R. Liao, H. Zheng, S. Grzybowski, L. Yang, Y. Zhang, and Y. Liao, "An integrated decision-making model for condition assessment of power transformers using fuzzy approach and evidential reasoning," *IEEE Transactions on Power Delivery*, vol. 26, no. 2, pp. 1111–1118, 2011.

[20] I. Ahmed, I. Sultana, S. K. Paul, and A. Azeem, "Employee performance evaluation: a fuzzy approach," *International Journal of Productivity and Performance Management*, vol. 62, no. 7, pp. 718–734, 2013.

[21] M. Amiri, M. Hashemi-Tabatabaei, M. Ghahremanloo, M. Keshavarz-Ghorabaee, E. K. Zavadskas, and J. Antucheviciene, "A new fuzzy approach based on BWM and fuzzy preference programming for hospital performance evaluation: a case study," *Applied Soft Computing*, vol. 92, article 106279, 2020.

[22] W. A. Rasaq, M. Golonka, M. Scholz, and A. Białowiec, "Opportunities and challenges of high-pressure fast pyrolysis of biomass: a review," *Energies*, vol. 14, no. 17, p. 5426, 2021.

[23] A. A. Lappas, K. G. Kalogiannis, E. F. Iliopoulou, K. S. Triantafyllidis, and S. D. Stefanidis, "Catalytic pyrolysis of biomass for transportation fuels," *Wiley Interdisciplinary Reviews: Energy and Environment*, vol. 1, no. 3, pp. 285–297, 2012.

[24] D. Pan, F. Su, H. Liu et al., "Research progress on catalytic pyrolysis and reuse of waste plastics and petroleum sludge," *ES Materials & Manufacturing*, vol. 11, no. 2, pp. 3–15, 2021.

[25] M. Hu, B. Cui, B. Xiao, S. Luo, and D. Guo, "Insight into the ex situ catalytic pyrolysis of biomass over char supported metals catalyst: syngas production and tar decomposition," *Nanomaterials*, vol. 10, no. 7, p. 1397, 2020.

[26] J. Chen, C. Liu, S. Wu, J. Liang, and M. Lei, "Enhancing the quality of bio-oil from catalytic pyrolysis of kraft black liquor

lignin," *RSC Advances*, vol. 6, no. 109, pp. 107970–107976, 2016.

[27] M. Jafarian and S. E. Vahdat, "A fuzzy multi-attribute approach to select the welding process at high pressure vessel manufacturing," *Journal of Manufacturing Processes*, vol. 14, no. 3, pp. 250–256, 2012.

[28] H. Kahr, J. Wimberger, D. Schürz, and A. Jäger, "Evaluation of the biomass potential for the production of lignocellulosic bioethanol from various agricultural residues in Austria and worldwide," *Energy Procedia*, vol. 40, pp. 146–155, 2013.

[29] A. Ciancolini, M. Alignan, M. A. Pagnotta, G. Vilarem, and P. Crinò, "Selection of Italian cardoon genotypes as industrial crop for biomass and polyphenol production," *Industrial Crops and Products*, vol. 51, pp. 145–151, 2013.

[30] M. Vaezi, M. Passandideh-Fard, M. Moghiman, and M. Charmchi, "On a methodology for selecting biomass materials for gasification purposes," *Fuel Processing Technology*, vol. 98, pp. 74–81, 2012.

[31] P. H. Schipper, F. G. Dwyer, P. T. Sparrell, S. Mizrahi, and J. A. Herbst, "Zeolite ZSM-5 in Fluid Catalytic Cracking: Performance, Benefits, and Applications," in *ACS Symposium Series*, pp. 64–86, ACS Publications, Washington, DC, 1988.

[32] P. Hemberger, V. B. Custodis, A. Bodi, T. Gerber, and J. A. van Bokhoven, "Understanding the mechanism of catalytic fast pyrolysis by unveiling reactive intermediates in heterogeneous catalysis," *Nature Communications*, vol. 8, no. 1, pp. 1–9, 2017.

[33] K. Senthilnathan, G. Suresh, S. Ilaiyavel, R. Ravi, and S. Srinivasan, "Experimental investigation of polymer matrix composites gears with different fiber proportions," *International Journal of Vehicle Structures and Systems*, vol. 12, no. 2, pp. 212–216, 2020.

[34] L. A. Costa, A. F. Fonseca, F. V. Pereira, and J. I. Druzian, "Extraction and characterization of cellulose nanocrystals from corn stover," *Cellulose Chemistry and Technology*, vol. 49, no. 2, pp. 127–133, 2015.

[35] Q. Yang and X. Pan, "Correlation between lignin physicochemical properties and inhibition to enzymatic hydrolysis of cellulose," *Biotechnology and Bioengineering*, vol. 113, no. 6, pp. 1213–1224, 2016.

[36] L. Ye, Y. Han, J. Feng, and X. Lu, "A review about GVL production from lignocellulose: focusing on the full components utilization," *Industrial Crops and Products*, vol. 144, article 112031, 2020.

[37] M. Hajaligol, B. Waymack, and D. Kellogg, "Low temperature formation of aromatic hydrocarbon from pyrolysis of cellulosic materials," *Fuel*, vol. 80, no. 12, pp. 1799–1807, 2001.

[38] X. Jin, X. Chen, C. Shi et al., "Determination of hemicellulose, cellulose and lignin content using visible and near infrared spectroscopy in *Miscanthus sinensis*," *Bioresource Technology*, vol. 241, pp. 603–609, 2017.

[39] A. Gani and I. Naruse, "Effect of cellulose and lignin content on pyrolysis and combustion characteristics for several types of biomass," *Renewable Energy*, vol. 32, no. 4, pp. 649–661, 2007.

[40] C. S. Dhanalakshmi, P. Madhu, A. Karthick, M. Mathew, and R. V. Kumar, "A comprehensive MCDM-based approach using TOPSIS and EDAS as an auxiliary tool for pyrolysis material selection and its application," *Biomass Conversion and Biorefinery*, pp. 1–16, 2020.

[41] S. Xiong, J. Zhuo, B. Zhang, and Q. Yao, "Effect of moisture content on the characterization of products from the pyrolysis of sewage sludge," *Journal of Analytical and Applied Pyrolysis*, vol. 104, pp. 632–639, 2013.

[42] K. Sudalaiyandi, K. Alagar, V. J. MP, and P. Madhu, "Performance and emission characteristics of diesel engine fueled with ternary blends of linseed and rubber seed oil biodiesel," *Fuel*, vol. 285, article 119255, 2021.

[43] R. Samuelsson, S. H. Larsson, M. Thyrel, and T. A. Lestander, "Moisture content and storage time influence the binding mechanisms in biofuel wood pellets," *Applied Energy*, vol. 99, pp. 109–115, 2012.

[44] N. Y. Pehlivan, T. Paksoy, and A. Çalik, "Comparison of Methods in FAHP with Application in Supplier Selection," in *Fuzzy Analytic Hierarchy Process*, pp. 67–98, Chapman and Hall/CRC, 2017.

[45] D. Carpenter, T. L. Westover, S. Czernik, and W. Jablonski, "Biomass feedstocks for renewable fuel production: a review of the impacts of feedstock and pretreatment on the yield and product distribution of fast pyrolysis bio-oils and vapors," *Green Chemistry*, vol. 16, no. 2, pp. 384–406, 2014.

[46] J. Zhang, J. Liu, and R. Liu, "Effects of pyrolysis temperature and heating time on biochar obtained from the pyrolysis of straw and lignosulfonate," *Bioresource Technology*, vol. 176, pp. 288–291, 2015.

[47] I. Petric, A. Šestan, and I. Šestan, "Influence of initial moisture content on the composting of poultry manure with wheat straw," *Biosystems Engineering*, vol. 104, no. 1, pp. 125–134, 2009.

[48] V. Balasundram, N. Ibrahim, R. M. Kasmani et al., "Thermogravimetric catalytic pyrolysis and kinetic studies of coconut copra and rice husk for possible maximum production of pyrolysis oil," *Journal of Cleaner Production*, vol. 167, pp. 218–228, 2017.

[49] Y. C. Chen and L. Y. Chen, "Pelleting spent coffee grounds by waste utensils as binders of biofuels," *Journal of Environmental Chemical Engineering*, vol. 9, no. 3, article 105006, 2021.

Hindawi

Research Article

Performance Evaluation of Cyclic Stability and Capacitance of Manganese Oxide Modified Graphene Oxide Nanocomposite for Potential Supercapacitor Applications

R. Ranjith Kumar,[1] **S. Thanigaivel,**[2] **Nibedita Dey,**[2] **A. K. Priya** ⓘ**,**[3] **Alagar Karthick** ⓘ**,**[4,5] **V. Mohanavel** ⓘ**,**[6] **S. Kannadhasan,**[7] **M. Muhibbullah** ⓘ**,**[8] **and Sameh M. Osman**[9]

[1]*Department of Civil Engineering, SRM Institute of Science and Technology, NCR Campus, Modinagar, -201204. Uttar Pradesh, Ghaziabad, Delhi, India*

[2]*Saveetha School of Engineering, Department of Biotechnology, Saveetha Institute of Medical and Technical Sciences, Thandalam, 602105, Chennai, Tamil Nadu, India*

[3]*Department of Civil Engineering, KPR Institute of Engineering and Technology, -641407, Coimbatore, Tamilnadu, India*

[4]*Renewable Energy Lab, Department of Electrical and Electronics Engineering, KPR Institute of Engineering and Technology, Coimbatore 641407, Tamil Nadu, India*

[5]*Departamento de Quimica Organica, Universidad de Cordoba, EdificioMarie Curie (C-3), Ctra Nnal IV-A, Km 396, E14014 Cordoba, Spain*

[6]*Chennai-Centre for Materials Engineering and Regenerative Medicine, Bharath Institute of Higher Education and Research, 600073 Tamilnadu, India*

[7]*Department of Electronics and Communication Engineering, Cheran College of Engineering, -639111, Karur, Tamilnadu, India*

[8]*Department of Electrical and Electronic Engineering, Bangladesh University, Dhaka 1207, Bangladesh*

[9]*Chemistry Department, College of Science, King Saud University, P.O. Box 2455, Riyadh 11451, Saudi Arabia*

Correspondence should be addressed to M. Muhibbullah; m.muhibbullah@bu.edu.bd

Supercapacitors are a revolutionary type of energy storage device. They must be able to charge and discharge quickly while maintaining a high energy density. A storage material's cyclic stability is a desirable feature. The type of electrode materials employed for the specific study design affects supercapacitor performance. Manganese dioxide has long been regarded as one of the best and most abundant materials in nature, having a potentially high specific capacitance. They also offer a wider potential range, more electroactivity, and are more environmentally friendly. However, because of its decreased volume expansion and low conductivity, it is difficult to use as a capacitor material. As a result, carbon-based porous films and supports can be employed to produce critical composites to overcome the current shortcoming. These nanoparticle-based materials will have improved electrical conductivity and a large surface area. Graphene oxide (GO) has a high surface area, thermal stability, and porosity. As an electrode material, many types of MnO2/carbon-based materials have been widely used in supercapacitors. Their overall performance is influenced by their construction processes, metal ratios, electrolyte medium, and voltage factors. Microwave technology was chosen as a cost-efficient and effective alternative to expensive and laborious techniques for fabricating MnO2/GO composites. The production procedure of a supercapacitor has been explored in this study using MnO2-GO composite materials. Using the electrochemical deposition process, the nanocomposite materials of MnO2-GO are significantly deposited on the stainless steel (SS) substrate material. Galvanostatic charge-discharge techniques and cyclic voltammetry (CV) analytical methods were used to investigate the storage and cycle ability of supercapacitors. The composite MnO2-GO supercapacitor has a higher electrochemical capacitance based on these findings.

1. Introduction

There is a great demand for both energy (conventional and nonconventional) resources due to the increase in living standards. For that reason, the electrochemical energy storages are obtained to be the substitute for this problem [1, 2]. A supercapacitor (SC), formerly electric double layer capacitor (EDLC), is the generic term for the electrochemical capacitor (ECs) family. A conventional solid dielectric is not present in SCs. Two storage principles determine the capacitance value of an EC, which both indivisibly contribute to the total capacitance [1, 3]. In this day and age, consumption of energy in the form of fossil fuels like oil, coal, and natural gas has drastically increased. This adversely affects the world and the environment in ways like global warming, ecological destruction, and endangering life forms. Utilization of renewable energy is the need of the hour as it is ecofriendly. Countries have allotted funds and manpower exclusively to develop ways to use and create energy. Solar, tidal, hydrothermal, geothermal, and wind energy have played their share in alleviating major problems related to energy and environmental conservation all around the world [3, 4]. However, clean energy is very limited and cannot be directly applied to many applications. This is due to the natural conditions and the shortfall of resources; it greatly depends on the types of sources used and causes poor stability as well as tunability with regard to electricity generation. Hence, trustworthy electrochemical systems are encouraged to address efficient conversion, utilization, and storage of above sources [4]. Supercapacitors also known as electrochemical capacitors are the next-generation storage devices. They are popular for their green and clean nature of fabrication and implementation [5]. They also have a greater capacitance potential with higher power output and shelf life when compared to lithium-ion batteries [6]. Along with simple structure, they possess faster charging and pollution free effects while manufacturing. They can be easily applied to portable electronics, hybrid electric locomotives, data backup, etc. [7].

Due to their compact structures, high surface area, unique chemical, physical, and mechanical capabilities, nanomaterials have gotten a lot of interest in recent years. The ability to produce and process NMs is the first milestone in nanotechnology for exploring novel physical features and understanding possible uses of NMs. The NMs are also epic in structure and have features that can be adjusted. As a result of this development, NM has been useful in real-world applications [2, 8].

Manganese oxide (MnO_2) offers the benefit of relatively cost-effective, high theoretical capacitance (~1300 F g^{-1}), and environmentally compatible [9]. MnO_2 is used for catalysts, sensors, lithium batteries, and alkaline MnO_2/Zn cell applications. The advancements required in generating active materials mainly concern with overall stability, high reversible capacitance, structural flexibility, improved cation diffusion rate under high charge-discharge condition, and environmental friendliness. The composition of MnO_2 materially changes the morphology of the surface and leads to an increase in the pseudocapacitive performance of MnO_2 as an increase in porosity [2]. The proposed theoret-

ical reasons for MnO_2 being a better alternative for electrode materials is its high theoretical capacity in reference to an individual electron-based redox potential reactions of each atom was observed in a wider potential window, electroactive in neutral electrolytes, etc. [10]. These lead to lower corrosion of the collector, and other benefits were incorporated in Figure 1. Improving the performance of electrode materials for the production of high-energy supercapacitors.

The availability of the material is also found to be in excess naturally, which decreases its price value. The crystal structure of the metal also forms crystallinity hence supporting charge storage and dissipation. It has been reported that tunnel or chain structure of alpha, beta, and gamma MnO_2 facilitates easier transfer of electrons with higher capacitance. Nanoranged MnO_2 has a larger reaction area for feasible and enhanced cation intercalation and deintercalation when compared to its amorphous form [11, 12].

In recent years, graphene attained huge interest especially in the fields of electric devices, energy storage applications, and sensors due to their unique property of physiochemical characteristics, such as high surface area, excellent conductivity, and mechanical stability. Structurally, graphene oxide (GO) has been visualized as a graphene sheet with its basal plane and edges filled with oxygen groups. Graphene hybridization with functional NMs enhances the component functional properties and even produces new properties through cooperative interaction.

GO has been an appropriate support material for MnO_2 loadings in electroactive materials for supercapacitors [13]. GO not only affords high surface area for MnO_2 nanosheets deposition but also provides to those nanostructures good adhesion. GO had a significant impression on the property of electrochemical in the GO-MnO_2 nanocomposites. Scheme of MnO_2 nanocomposites shown in Figure 2 mentioned with the application of supercapacitors made out of MnO_2 with optimizing parameters which helps in improving the capacitance, stability, and storage etc.

MnO_2 nanoparticles can be deposited uniformly on GO with high density. The high loading efficiency of MnO_2 and high surface area of MnO_2-GO increase the specific capacitance of MnO_2-GO [14].

This work is aimed at fabricating the composite of MnO_2-GO and achieving good conductivity in the charge storage process. The MnO_2 and MnO_2-GO composites were synthesized by the electrodeposition method. After electrodeposition, the galvanostatic charge-discharge analysis was performed to characterize the charge storage ability of the film from which we can find the ability of the composite as an electrode of a supercapacitor.

2. Materials and Method

2.1. Fabrication of MnO_2-GO Nanocomposite Supercapacitor. MnO_2 was synthesized using standard protocol reported previously in 2015 [15]. Graphene oxide was synthesized by modified Hummers method [16]. MnO_2 and MnO_2-GO NMs were coated on electricity collector substrates by constant potentiostat mode in the electrodeposition method. The SS substrate was cut and polished into
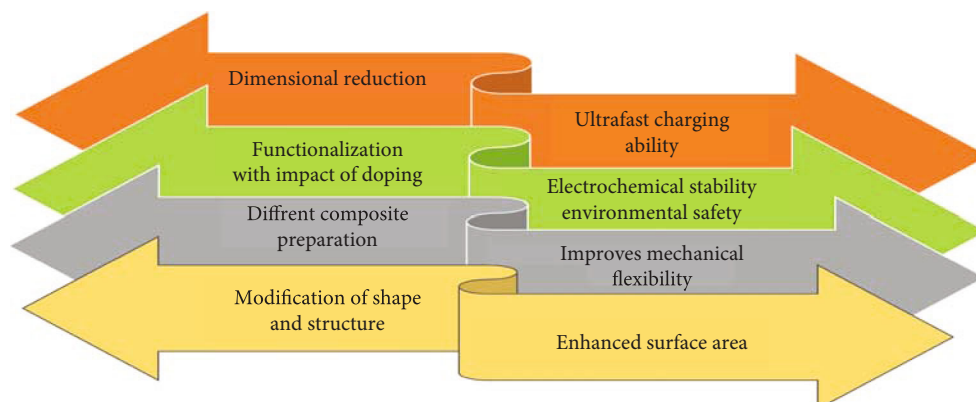
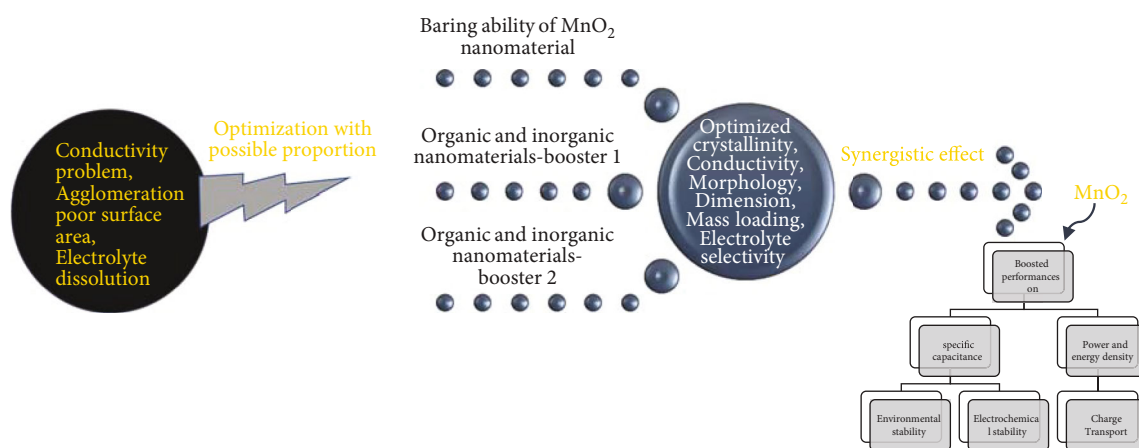FIGURE 1: Performance enhancement of electrode materials for high-energy supercapacitors.

FIGURE 2: Scheme of MnO$_2$ nanocomposites for the application of supercapacitors.

1×1 cm size and then washed for 15 min in deionized water by a bath sonicator.

The electrochemical deposition was performed for 30 min at 0.8 V using the as prepared SS substrate as the working electrode. Different concentrations of GO (10 mg, 15 mg, and 20 mg) with 25 ml DI water were dispersed by ultrasonication, and then 0.1 M of MnSO$_4$ solution was added to prepare the electrolyte solution. The pH of the electrolyte solution was maintained at 10 by adding 1 M NaOH. Ag/AgCl and Pt electrodes were used as reference and counter electrodes, respectively [17]. The resulting thin films were dried at room temperature after the process of rinsing in DI water. The overall process of synthesis was displayed in the scheme of Figure 3.

2.2. Electrochemical Analysis

2.2.1. Analyzing Setup.
For the electrochemical analyses 0.1 M of Na$_2$SO$_4$ dissolved in 50 ml of double-distilled water used as an electrolyte solution, Ag/AgCl was fixed as the reference electrode, whereas prepared MnO$_2$ electrodes made with thin films are considered as working electrodes, and electrodes made out of platinum wire are considered as a counter electrode. These three electrodes were immersed in the electrolyte solution the setup was connected to the BIO-

LOGIC Science SP-50 model Electrochemical Workstation for the analyses.

2.2.2. Cyclic Voltammetry.
The electrochemical characteristics of specified composites are typically measured using cyclic voltammetry, a standard technique. The potential scan starts at a point where there is no electrochemical reaction. The scan proceeds to the switching potential at a predetermined constant rate, then reverses direction and returns to the electrode as oxidation or reduction, accordingly. The formula below was used to compute the active material's specific capacitance.

$$\text{Specific capacitance} = C = \frac{I}{(mv(V_a - V_c))} \left(\frac{F}{g}\right). \quad (1)$$

I considered as applied current (A), where $(V_a - V_c)$ are considered as the potential of sweep window (V), m is known as mass of the active material (g), and v is the scan rate (V s^{-1}).

2.2.3. Galvanostatic Charge–Discharge.
The charge-discharge potential and cycle ability of prepared MnO$_2$-GO nanocomposite was measured using galvanostatic charge–discharge
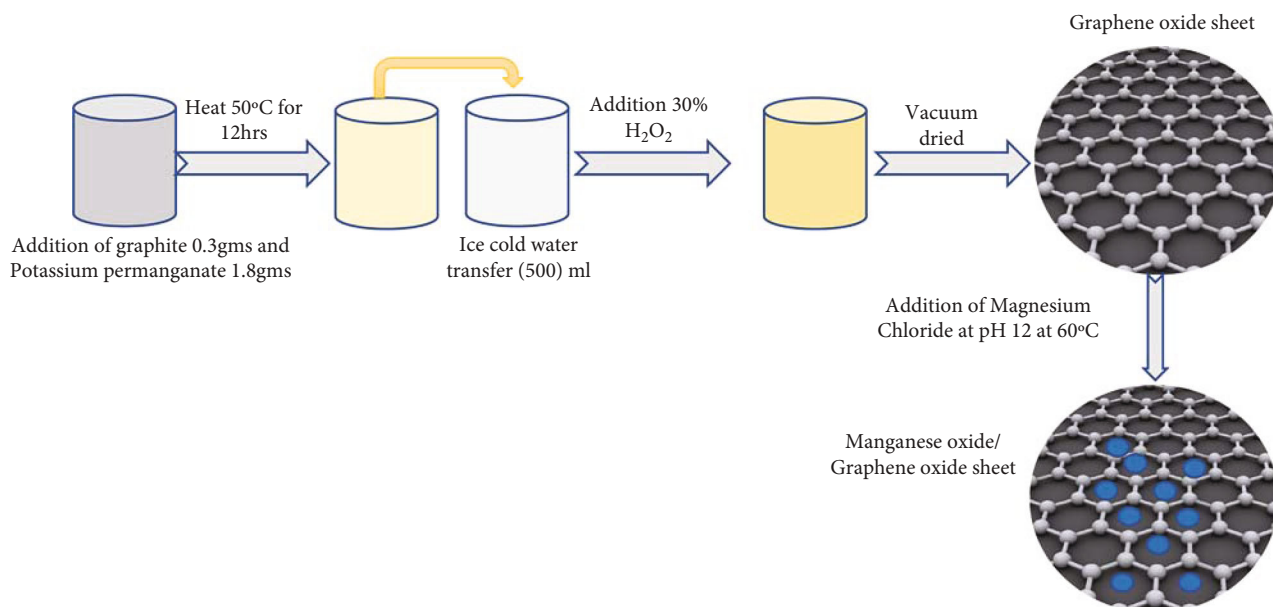
FIGURE 3: Schematic of GO sheets and formation of MnO2/GO nanocomposites.

(GCD) technique. It is necessary to conduct the charge and discharge at a constant current until a predetermined voltage is obtained. A cycle is a loop of charging and discharging that repeats over and over again. The time required to reach the set potentials for the applied current was plotted. In the charging process, the constant rate of increment in the potential and the discharge process the constant rate of decrement in the potential with time is the perfect behavior for the charge storage device.

Using the charge-discharge curve the capacitance and cycling behavior of the electrode material has been monitored, and also the charge density, energy density, and capacitance of the material were calculated from the following equations.

Specific Capacitance of the active material is $C = \dfrac{(IX\Delta t/\Delta VXm)F}{g}$.

(2)

3. Results and Discussions

3.1. Cyclic Voltammetry Studies. Cyclic voltammetry was performed using prepared MnO_2 and MnO_2-GO thin films. Here, prepared thin films were fixed as working electrodes whereas the platinum wire was considered as a counter electrode, and Ag/AgCl was a reference electrode, respectively, an aqueous solution of 0.1 M Na_2SO_4 as the electrolyte for different scan rates.

Figure 4 shows a cyclic voltammogram of MnO_2 and MnO_2-GO thin films by applying a scan rate of $5\,mV\,s^{-1}$ between the potential of 0 and 0.8 V. It shows the current density vs. potential curve of MnO_2: GO (different concentration) composites and pure MnO_2. From that, we found that MnO_2 has a low current density 10 mg MnO_2 added for GO composite which has high current density compared
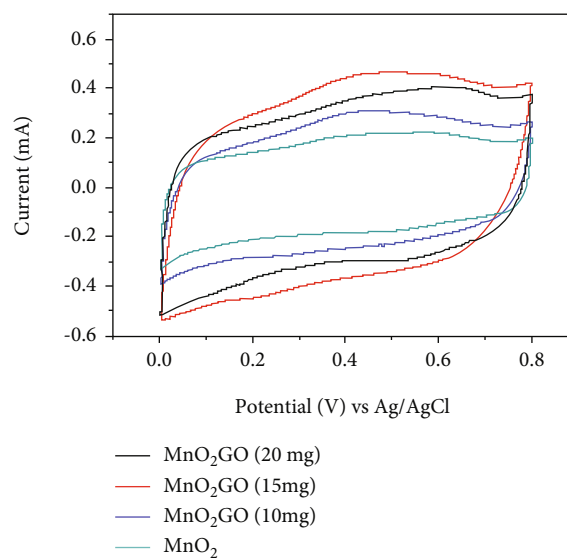
FIGURE 4: CV current density of MnO_2 and MnO_2-GO.

to pure MnO_2. Also, 15 mg MnO_2-GO composite has a high current density compared to 10 mg composite, and 20 mg MnO_2-GO composite has a low current density compared to 15 mg composite because further increment in GO tends to decrease the amount of MnO_2 on the surface of the electrode. Ding reported successful electrodeposition of manganese dioxide nanoparticles onto an indium tin oxide glass substrate using the cyclic voltammetry (CV) method, which was used to create an indium tin oxide glass substrate from an aqueous solution of 0.1 M Na_2SO_4 containing 5×10^{-3} M $MnSO_4$, and they achieved 294 Fg^{-1} [9].

3.2. Galvanostatic Charge-Discharge Technique. Galvanostatic charge/discharge experiments were performed to evaluate
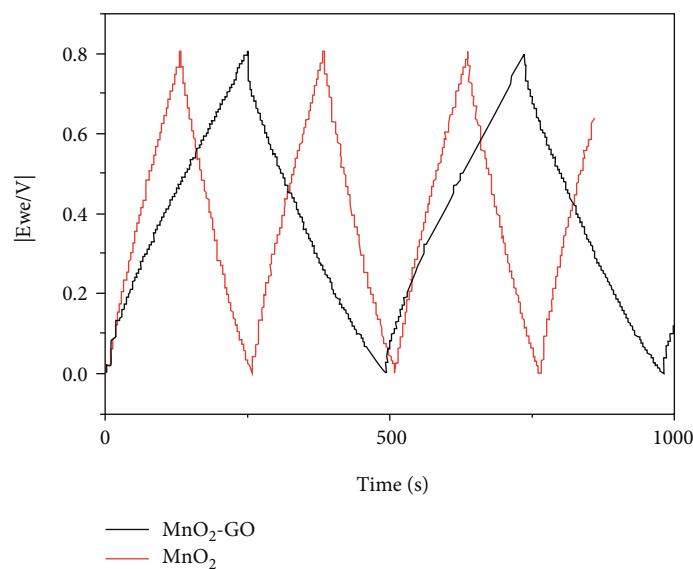
FIGURE 5: Charge and discharge times in MnO_2 and MnO_2-GO.

the specific capacitance and cycle ability of the developed MnO_2 and MnO_2-GO electrode materials. Further, the insight into the relationship between the specific capacitance of the different MnO_2 nanostructures has been studied. The galvanostatic charge-discharge is also performed using the biologic sp-50 electrochemical workstation. Figure 5 depicts the charge-discharge performance of the electrodeposited MnO_2 for the first few cycles.

The potential-time curve was measured from 0 to 0.8 V versus the reference electrode for more than 300 cycles, 0.1 M Na_2SO_4 was used at a current density of 0.5 mA cm^{-2}. The curves are almost linear and present in the form of typical symmetrical triangle shape which indicates the pseudocapacitance of MnO_2. The composition of MnO_2-GO has a high charge and discharge time compared to MnO_2. Thus, it reported to have increased specific capacitance of MnO_2-GO. Sebastin et al. have reported that multilayered film electrodes show good electrochemical properties [6]. Hence, the obtained results indicate that these newly synthesized films could be used as potential applications in electrochemical capacitors.

Figure 6 clearly shows the variation in specific capacitance with respect to the cycle number of MnO_2 and MnO_2-GO electrodes. In which MnO_2 has the specific capacitance of 80 F/g for the first cycle whereas MnO_2-GO has the specific rate of capacitance up to 140 F/g for first cycle. MnO_2-GO displays high specific capacitance compared with MnO_2. Furthermore, the linear line indicates the cycling performance of MnO_2 and MnO_2-GO. It shows the films have retained almost 95% of their specific capacitance even after 300 cycles. With these promising results, these materials can be used as an ideal material in supercapacitor applications.

Addition of MnO_2 to graphene oxide sheets addresses the low volumetric density of graphene-based electrodes. This would prevent the agglomeration of the sheets which happens due to Van der Waals attraction between the nano-
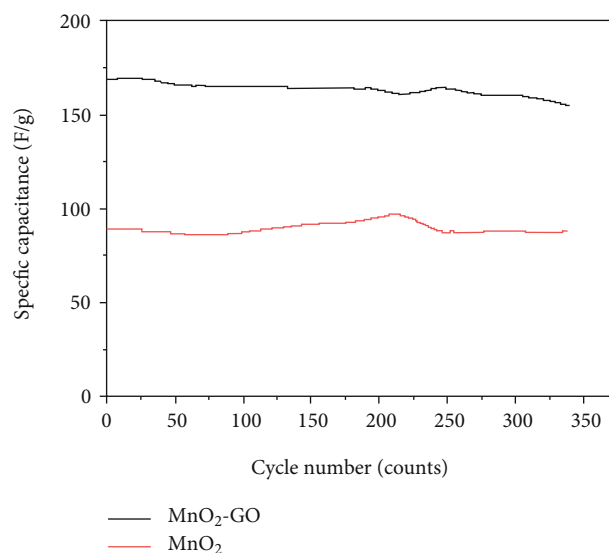
FIGURE 6: Cycling ability of MnO_2 and MnO_2-GO.

particle and the porous material [18]. Elastic constraint is provided by the carbon skeleton of GO. This avoids the dissolution of the electroactive property of MnO_2. A simple microwave-assisted technique can rapidly green synthesize MnO_2/GO composites by simple deposition of the nanoparticle onto the sheet [19]. Previous studies stated that doping of MnO_2 increases the specific capacitance by three times when compared to pure GO sheet or pure birnessite MnO_2 [19, 20].

The ratio of the MnO2 by weight plays a crucial role in the capacitance performance. With an increasing mass ratio, the specific capacitance tends to increase which coincides with the results we have obtained for the current study [21]. Composites tend to have higher diffusivity and mobility of charges than disordered MnO2. Changing the crystal structures and orientations of MnO2, it is suggested that

TABLE 1: Reported outcomes on MnO2/GO composites for supercapacitor applications.

Electrolyte	Crystal/porous material	Specific capacitance	Reference
1 M Na_2SO_4	Gamma MnO_2 crystal with graphene	270 (0.5 A g^{-1})	[24]
1 M KOH	MnO_2 or graphene	342.8 (0.5 A g^{-1})	[25]
1 M Na_2SO_4	N doped graphene/MnO_2	411.5 (0.5 A g^{-1})	[26]
Na_2SO_4 1 M	Graphene oxide/MnO_2	315 (0.5 A g^{-1})	[27]
Na_2SO_4 1 M	Graphene oxide/MnO_2	360.3 (0.5 A g^{-1})	[28]
Na_2SO_4 1 M	Reduced graphene oxide/MnO_2	759 (2 A g^{-1})	[29]
1 M Na_2SO_4	Graphene/MnO_2	234.8 (0.1 A g^{-1})	[30]
1 M Na_2SO_4	Graphene/MnO_2	255 (0.5 A g^{-1})	[31]
1MNa_2SO_4	Graphene/MnO_2	133 (0.5 mvs^{-1})	[32]
1 M Na_2SO_4	Graphene/CNT/MnO_2	372 (0.5 A g^{-1})	[33]
1 M Na_2SO_4	Sponge reduced graphene oxide/MnO_2	205 (0.1 A g^{-1})	[20]
—	Graphene/MnO_2	310 (2 mvs^{-1})	[34]
—	MnO_2/CNP/graphene	255 (2 mvs^{-1})	[35]
—	Graphene/MnO2/activated carbon fiber felt	∗ 1.516	[36]
—	Reduced graphene oxide-MnO_2	274 (10 mvs^{-1})	[37]
—	Mn_3O_4/rGO	∗∗ 52.2	[38]
1 M Na_2SO_4	GO/MnO_2	140 (0.5 A g^{-1})	Current study

GO/MnO2 performance as an active material can be greatly influenced. Eco-friendly techniques under milder conditions are found to be more feasible to control the shape and dimension of the nanoparticle [22]. Controlling oxygen functional moieties and doping of heteroatom on the GO sheets can aid in manufacturing hi-performance electrode materials.

Synthesis method has a great influence on the electrochemical performance of MnO_2/GO nanocomposites. The specific capacitance of current study is quite low when compared to previously reported nanocomposites. We infer that the microwave technique opted by might not have supported the formation of proper crystal formation in MnO_2. As it was already reported that crystal structure positively influences the specific capacitance of a capacitor material. The nanoparticle used in this study does provide high energy density to the porous GO, but the structure of the lattice might not be at its very best. GO ensures upgraded cyclic performance and stability. The microstructure of the sheets with functional groups portrays different properties in various orientations and dimensions for the given nanocomposite. This gives the rational feasibility to optimize this nanocomposite and maximize it to its potential. Nanotubes and nanofibers offer high and rapid diffusion due to its one dimensional orientation.

This shortens the ion diffusion pathway which leads to high conductivity and enhanced mechanical properties. Flexibility is also attained by the capacitor material. Similarly, two-dimensional GO is also regarded as an ideal conductive substrate with enhanced specific surface area, conductivity, and ultralow density. Compared to nanotubes, the diffusivity is quite low for GO. Activated form of carbon is mostly opted for fabrication of storage devices owing to its three-dimensional structure and rich functional groups. Although a rich porous support structure is provided in

the current study for the nanoparticle the performance yielded was quite less. Orderly channels without obstructions can further maximize the electrochemical performance of MnO_2. They accelerate the ion transport and make the diffusivity easier for MnO_2.

Hence, the current material can be experimented with by incorporating additional channels in the Go sheet to see if the performance could be improved. Even the graphitization of the sheet makes conducive improvement in the transfer of charge between the nanoparticle and the carbon base. Low graphitization of the sheet used in the current study might also be the reason for low performance of the capacitor material. In the previous years of effort has been taken to explore the potential of MnO_2/GO composites for their capacitance function. Exciting outcomes have been accomplished so far. There are still many drawbacks in the nanoparticle that hinder its electrochemical property if not set right. A few have already been discussed above [23]. Efforts need to be taken to focus on developing new generation nanoparticle combinations with potential doping to address all drawbacks mentioned above. Table 1 represents the previously reported outcomes on MnO_2/GO composites for supercapacitor applications.

4. Limitations and Future Scope

A greater amount of testing and research into MnO2-GO materials is required in order to produce better supercapacitors in the future. Aspects such as poor structural stability and reduced ion diffusion need to be addressed as well [38–44]. Researchers should look into and test high-capacitance materials that can be reversed and modified, when necessary, as well as rapid cation diffusion at high charging and discharging rates.

5. Conclusion

An electrochemical deposition approach was used to deposit MnO_2 and varied concentrations of MnO_2-GO composites on an SS substrate in this investigation. The CV curves depicted the electrochemical performance of pure and composite materials synthesized in various ratios. In comparison to pure, 10 mg, and 20 mg GO added MnO2 thin films, the 15 mg GO-MnO_2 electrodeposited film has a high current density. Because it covers the highest area of MnO2 in the composite, increasing the GO tends to lower the film's performance. The charge storage behavior of the films is demonstrated by galvanostatic charge-discharge analysis, galvanostatic charge-discharge curves have been conducted with different composition of GO to ensure the effective capacitance which shows that MnO2 and MnO_2-GO thin films have specific capacitances of 80F/g and 140F/g for the first cycle, respectively, and that the composite retains approximately 95 percent of capacitance after 300 cycles. When compared to previously published nanocomposites, the current study's specific capacitance is quite low. We deduce that the microwave approach used may not have promoted the creation of appropriate MnO_2 crystals. Despite the fact that the nanoparticle was given a rich porous support structure in the current work, the results were disappointing. MnO_2 electrochemical performance can be improved even further by having clean, unobstructed channels. Although the nanoparticle utilized in this study provides a high energy density to the porous GO, the lattice structure may not be optimal. Low graphitization of the sheet utilized in this investigation could possibly be a factor in the capacitor's poor performance.

Data Availability

The data used to support the findings of this study are included in the article.

Conflicts of Interest

The authors declare that there is no conflict of interest regarding the publication of this article.

Acknowledgments

References

[1] S. Chen, L. Qiu, and H. M. Cheng, "Carbon-based fibers for advanced electrochemical energy storage devices," *Chemical Reviews*, vol. 120, no. 5, pp. 2811–2878, 2020.

[2] D. Rajesh, M. K. Francis, P. B. Bhargav, A. Nafis, and C. Balaji, "2D layered nickel-cobalt double hydroxide nano sheets @ 1D silver nanowire- graphitic carbon nitrides for high performance super capacitors," *Journal of Alloys and Compounds*, p. 162803, 2021.

[3] N. Hemalatha, R. Saravanakumar, P. Veeramanikandan, and V. R. Kumar, "Evaluation of capacitance cycle ability with MnO2-go nanocomposite supercapacitor," in *2021 6th International Conference on Communication and Electronics Systems (ICCES)*, pp. 102–106, 2021.

[4] A. K. Priya, R. Gokulan, A. Vijayakumar, and S. Praveen, "Bio-decolorization of remazol dyes using biochar derived from ulva reticulata: isotherm, kinetics, desorption, and thermodynamic studies," *Desalination and Water Treatment*, vol. 200, pp. 286–295, 2020.

[5] V. Yogeshwaran and A. K. Priya, "Experimental studies on the removal of heavy metal ion concentration using sugarcane bagasse in batch adsorption process," *Desalination and Water Treatment*, vol. 224, p. 27160, 2021.

[6] S. Sebastin, A. K. Priya, A. Karthick, R. Sathyamurthy, and A. Ghosh, "Agro waste sugarcane bagasse as a cementitious material for reactive powder concrete," *Clean Technology*, vol. 2, pp. 476–491, 2020.

[7] D. Salinas-Torres, R. Ruiz-Rosas, E. Morallón, and D. Cazorla-Amorós, "Strategies to enhance the performance of electrochemical capacitors based on carbon materials," *Front. Mater.*, vol. 6, p. 115, 2019.

[8] B. E. Conway, *Electrochemical Supercapacitors: Scientific Fundamentals and Technological Applications*, Springer Science & Business Media, 2013.

[9] K. Q. Ding, "Cyclic voltammetrically prepared copper-decorated MnO2 and its electrocatalysis for oxygen reduction reaction (ORR)," *International Journal of Electrochemical Science*, vol. 5, pp. 72–78, 2009.

[10] Y. Xie, C. Yang, P. Chen, D. Yuan, and K. Guo, "MnO_2-decorated hierarchical porous carbon composites for high-performance asymmetric supercapacitors," *Journal of Power Sources*, vol. 425, pp. 1–9, 2019.

[11] M. Yang and K. L. Choy, "A nature-derived, flexible and three dimensional (3D) nano-composite for chronic wounds pH monitoring," *Materials Letters*, vol. 288, article 129335, 2021.

[12] J. R. Rajabathar, H. A. Al-lohedan, P. Arunachalam et al., "Synthesis and characterization of metal chalcogenide modified graphene oxide sandwiched manganese oxide nanofibers on nickel foam electrodes for high performance supercapacitor applications," *Journal of Alloys and Compounds*, vol. 850, article 156346, 2021.

[13] Y. Liu, D. Yan, Y. Li et al., "Manganese dioxide nanosheet arrays grown on graphene oxide as an advanced electrode material for supercapacitors," *Electrochimica Acta*, vol. 117, pp. 528–533, 2014.

[14] C. Ruttanapun, C. Phrompet, W. Tuichai, A. Karaphun, S. Daengsakul, and C. Sriwong, "Influence of free electron charge and free extra framework anions in calcium email protected rGO (email protected rGO) cement composites with enhanced dielectric and electrochemical properties," *Journal of the Taiwan Institute of Chemical Engineers*, vol. 127, pp. 334–348, 2021.

[15] H. Aminirastabi, Z. Weng, H. Xue et al., "Evaluation of nano grain growth of TiO_2 fibers fabricated via centrifugal jet spinning," *Nano-Structures & Nano-Objects*, vol. 21, article 100413, 2020.

[16] T. Nibedita Dey, "A Comparative evaluation of graphene oxide based materials for electrochemical non-enzymatic sensing of

curcumin," *Materials Research Express*, vol. 5, no. 2, article 025406, 2018.

[17] Suhasini, "Effect of deposition method and the surfactant on high capacitance of electrochemically deposited MnO_2 on stainless steel substrate," *Journal of Electroanalytical Chemistry*, vol. 690, pp. 13–18, 2013.

[18] L. Sheng, L. Jiang, T. Wei, and Z. Fan, "High volumetric energy density asymmetric supercapacitors based on well-balanced graphene and Graphene-MnO2Electrodes with densely stacked architectures," *Small*, vol. 12, no. 37, pp. 5217–5227, 2016.

[19] Z. Yang, J. Zhang, M. C. W. Kintner-Meyer et al., "Electrochemical energy storage for green grid," *Chemical Reviews*, vol. 111, pp. 3577–3613, 2011.

[20] J. Yan, Z. Fan, T. Wei, W. Qian, M. Zhang, and F. Wei, "Fast and reversible surface redox reaction of graphene-MnO2 composites as supercapacitor electrodes," *Carbon*, vol. 48, pp. 3825–3833, 2010.

[21] S. Saha, P. Maji, D. A. Pethsangave et al., "Effect of morphological ordering on the electrochemical performance of MnO2-graphene oxide composite," *Electrochimica Acta*, vol. 317, pp. 199–210, 2019.

[22] G. Zhu, Z. He, J. Chen et al., "Highly conductive three-dimensional MnO2-carbon nanotube-graphene-Ni hybrid foam as a binder-free supercapacitor electrode," *Nanoscale*, vol. 6, pp. 1079–1085, 2014.

[23] T. Wang, D. Song, H. Zhao et al., "Facilitated transport channels in carbon nanotube/carbon nanofiber hierarchical composites decorated with manganese dioxide for flexible supercapacitors," *Journal of Power Sources*, vol. 274, pp. 709–717, 2015.

[24] X. Wang, L. Chen, S. Zhang et al., "Compounding δ-MnO2 with modified graphene nanosheets for highly stable asymmetric supercapacitors," *Colloids and Surfaces*, vol. 573, pp. 57–66, 2019.

[25] H. Wang, Q. Fu, and C. Pan, "Green mass synthesis of graphene oxide and its MnO2 composite for high performance supercapacitor," *Electrochimica Acta*, vol. 312, pp. 11–21, 2019.

[26] Q. Le, M. Huang, T. Wang, X. Liu, L. Sun, and X. Guo, "Bio-template derived three dimensional nitrogen doped graphene@MnO2 as bifunctional material for supercapacitor and oxygen reduction reaction catalyst," *Journal of Colloid and Interface Science*, vol. 544, pp. 155–163, 2019.

[27] Z. S. Wu, W. Ren, D. W. Wang, F. Li, B. Liu, and H. M. Chen, "High-energy MnO2 nanowire/graphene and graphene asymmetric electrochemical capacitors," *ACS Nano*, vol. 4, pp. 5835–5842, 2010.

[28] K. Dai, L. Lu, C. Liang, J. Dai, Q. Liu, and Y. Zhang, "In situ assembly of MnO2 nanowires/graphene oxide nanosheets composite with high specific capacitance," *Electrochimica Acta*, vol. 116, pp. 111–117, 2014.

[29] S. Jadhav, R. S. Kalubarme, C. Terashima, B. B. Kale, V. Godbole, and A. Fujishima, "Manganese dioxide/reduced graphene oxide composite an electrode material for high-performance solid state supercapacitor," *Electrochimica Acta*, vol. 299, pp. 34–44, 2019.

[30] Y. Cheng, S. Lu, H. Zhang, C. V. Varanasi, and J. Liu, "Synergistic effects from graphene and carbon nanotubes enable flexible and robust electrodes for high-performance supercapacitors," *Nano Letters*, vol. 12, pp. 4206–4211, 2012.

[31] W. S. Li, M. L. Chang, K. C. Chuang, Y. S. Li, J. D. Luo, and H. C. Cheng, "Electrochemical properties of CNT/MnO2 hybrid nanostructure with low-temperature hydrothermal synthesis as high-performance supercapacitor," *Journal of the Electrochemical Society*, vol. 166, pp. A2194–A2198, 2019.

[32] R. Amade, A. Muyshegyan-Avetisyan, J. M. González, A. P. Pino, E. György, and E. Pascual, "Super-capacitive performance of manganese dioxide/graphene nano-walls electrodes deposited on stainless steel current collectors," *Materials*, vol. 12, p. 483, 2019.

[33] J. Ge, H. B. Yao, W. Hu, X. F. Yu, Y. X. Yan, and L. B. Mao, "Facile dip coating processed graphene/MnO2 nanostructured sponges as high performance supercapacitor electrodes," *Nano Energy*, vol. 2, pp. 505–513, 2013.

[34] Y. Xiong, M. Zhou, H. Chen et al., "Synthesis of honeycomb MnO_2 nanospheres/carbon nanoparticles/graphene composites as electrode materials for supercapacitors," *Applied Surface Science*, vol. 357, pp. 1024–1030, 2015.

[35] Q. Yang, L. Dong, C. Xu, and F. Kang, "High-performance supercapacitors based on graphene/MnO2/activated carbon fiber felt composite electrodes in different neutral electrolytes," *RSC Advances*, vol. 6, no. 15, pp. 12525–12529, 2016.

[36] G. Zhang, L. Ren, L. Deng, J. Wang, L. Kang, and Z.-H. Liu, "Graphene-MnO_2 nanocomposite for high-performance asymmetrical electrochemical capacitor," *Materials Research Bulletin*, vol. 49, pp. 577–583, 2014.

[37] T. Xiong, W. S. V. Lee, X. Huang, and J. M. Xue, "Mn3O4/reduced graphene oxide based supercapacitor with ultra-long cycling performance," *Journal of Materials Chemistry A*, vol. 5, no. 25, pp. 12762–12768, 2017.

[38] J. G. Wang, Y. Yang, Z. H. Huang, and F. Kang, "Effect of temperature on the pseudo-capacitive behavior of freestanding MnO2@carbon nanofibers composites electrodes in mild electrolyte," *Journal of Power Sources*, vol. 224, pp. 86–92, 2013.

[39] T. Yousefi, A. N. Golikand, M. H. Mashhadizadeh, and M. Aghazadeh, "Template-free synthesis of MnO2 nanowires with secondary flower like structure: characterization and supercapacitor behavior studies," *Current Applied Physics*, vol. 12, no. 1, pp. 193–198, 2012.

[40] Y. Qian, S. Lu, and F. Gao, "Preparation of MnO2/graphene composite as electrode material for supercapacitors," *Journal of Materials Science*, vol. 46, no. 10, pp. 3517–3522, 2011.

[41] Z. Li, Y. Mi, X. Liu, S. Liu, S. Yang, and J. Wang, "Flexible graphene/MnO2 composite papers for supercapacitor electrodes," *Journal of Materials Chemistry*, vol. 21, no. 38, pp. 14706–14711, 2011.

[42] J. Zhang, J. Jiang, and X. S. Zhao, "Synthesis and capacitive properties of manganese oxide nanosheets dispersed on functionalized graphene sheets," *The Journal of Physical Chemistry C*, vol. 115, no. 14, pp. 6448–6454, 2011.

[43] L. Zhang, R. Jamal, Q. Zhao, M. Wang, and T. Abdiryim, "Preparation of PEDOT/GO, PEDOT/MnO2, and PEDOT/GO/MnO2 nanocomposites and their application in catalytic degradation of methylene blue," *Nanoscale Research Letters*, vol. 10, no. 1, pp. 1–9, 2015.

[44] J. Wang, R. Zeng, D. Guodong et al., "Rapid microwave-assisted synthesis of various MnO_2 nanostructures and their magnetic properties," *Materials Chemistry and Physics*, vol. 166, no. 15, pp. 42–48, 2015.

Research Article

Fabrication of MnO$_2$ Nanocomposite on GO Functionalized with Advanced Electrode Material for Supercapacitors

R. Ranjith Kumar,[1] **S. Thanigaivel,**[2] **A. K. Priya** ⬤,[3] **Alagar Karthick** ⬤,[4,5]
Chandrabhanu Malla ⬤,[6] **P. Jayaraman,**[7] **M. Muhibbullah** ⬤,[8] **Razan A. Alshgari,**[9]
and Abdulnasser Mahmoud Karami[9]

[1]*Department of Civil Engineering, SRM Institute of Science and Technology, Delhi NCR Campus, Modinagar, Ghaziabad, 201204 Uttar Pradesh, India*
[2]*Saveetha School of Engineering, Department of Biotechnology, Saveetha Institute of Medical and Technical Sciences, Thandalam, Chennai, 602105 Tamil Nadu, India*
[3]*Department of Civil Engineering, KPR Institute of Engineering and Technology, Coimbatore, 641407 Tamil Nadu, India*
[4]*Renewable Energy Lab, Department of Electrical and Electronics Engineering, KPR Institute of Engineering and Technology, Coimbatore, 641407 Tamil Nadu, India*
[5]*Departamento de Quimica Organica, Universidad de Cordoba, EdificioMarie Curie (C-3), Ctra Nnal IV-A, Km 396, E14014 Cordoba, Spain*
[6]*Department of Mechanical Engineering, Radhakrishna Institute of Technology and Engineering, Bhubaneswar, 752057 Odisha, India*
[7]*Department of Mechanical Engineering, Prathyusha Engineering College, Aranvoyal Kuppam, Tiruvallur, 602025 Tamil Nadu, India*
[8]*Department of Electrical and Electronic Engineering, Bangladesh University, Dhaka 1207, Bangladesh*
[9]*Chemistry Department, College of Science, King Saud University, Riyadh 11451, Saudi Arabia*

Correspondence should be addressed to M. Muhibbullah; m.muhibbullah@bu.edu.bd

A new strategy for supercapacitor formation was carried out in the study using electrodes made of graphene oxide (GO) and manganese dioxide (MnO$_2$) nanocomposites. To the present knowledge, only a few investigations have been carried out concerning the synthesis of GO-MnO$_2$-based nanocomposites and their electrochemical properties, with varying mass ratios, as well as the change in electrochemical properties of their components as MnO$_2$ and GO were tested individually for the enhanced stability and performances. A synthetic method was performed successfully to manufacture MnO$_2$/GO nanocomposites. The findings of the present study show that the composites have a lot of potential as an effective conduction property. A composite of graphene oxide supported manganese dioxide nanocomposites fabricated with the simple soft chemical route. As-prepared nanocomposites can be improved in performance by the interactions between GO and MnO$_2$.

1. Introduction

In the last few decades, the importance of nanomaterials was enormously increased due to their unique features and mechanical properties. Various approaches have been implemented to develop a vast number of nanomaterials through the dedicated synthesis methods of top-down and bottom-up methods which are considered as the most common and commercial techniques for nanomaterial synthesis. Nanofragmentation is considered as one of the effective and most promising methods in the field of nanotechnology to generate and tune the nanomaterials into different unique
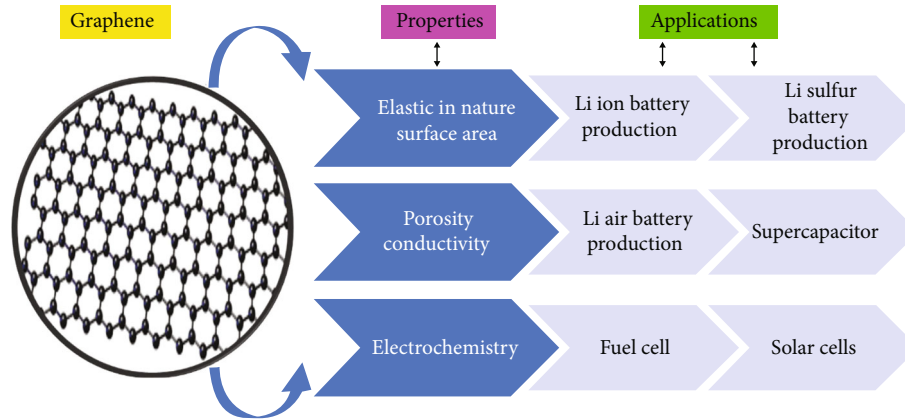
Figure 1: Mechanical and electrical properties and their applications of graphene.

nanostructures like nanotubes, nanofibers, and nanorods. This makes them valuable for real-world applications concerning its property which have also been discussed in Figure 1 with the various phenomena. Energy is considered to be one of the most significant needs in today's world, and it is used in various forms [1, 2]. Nonetheless, rising energy demand causes natural issues and the exhaustion of petroleum derivatives such as fossil fuels. Therefore, a serious examination of energy stockpiling and conversion has gotten a great deal of consideration as far as future innovation advancement. Due to its powerful thickness, long cycle life, and quick charging rate, supercapacitors are increasingly being used to supplement or even replace batteries in a variety of applications [2, 3]. The M_{30} electrode has the largest specific capacitance; they can be credited in the form of joined concepts to make MnO_2 as a redox potential of pseudocapacitance and reduced graphene oxide (rGO) as an electrical twofold layer capacitance. The M_{30} electrode's further developed performance could also be attributed to its high graphene carbon content, which helps in diminishing the cationic way into the terminal network that is electrode matrix and bringing down move obstruction which is transfer resistance.

There is a large demand for both conventional and nonconventional energy resources as there is a sudden rise in population and also an increase in living standards. There is a need for nonconventional renewable energy sources due to the increase in greenhouse gas and the depletion of fossil fuels. Therefore, electrochemical energy systems are found to be the alternative for this problem [4]. Recently, electrochemical capacitors like supercapacitors have been introduced over conventional energy stockpiling because of their powerful thickness and energy density when compared to the conventional and recent batteries in Figure 2. They have been used in dc motor drives, robots, electric vehicles, and even UPS (uninterruptable power supply) systems. Due to the charge capacitance, the storage of supercapacitors is subdivided into three different types such as electrical double-layer capacitors (EDLCs), psuedocapacitors, and hybrid or mixed electrodes; recent advancements in the supercapacitance are discussed in Figure 3. The best supercapacitors are the ones that should possess maximum energy
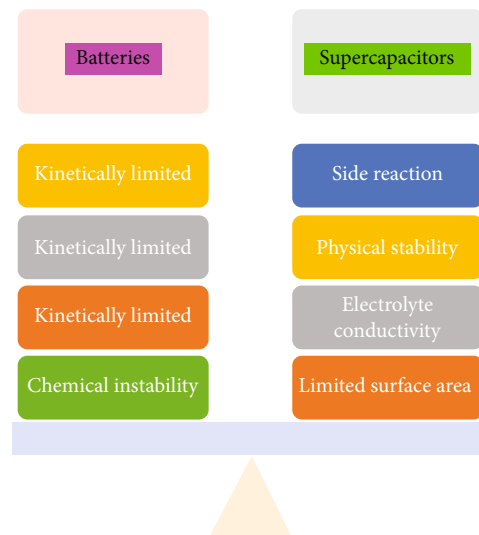

Figure 2: Comparison of batteries' and supercapacitors' performances.

storage capacitance. The supercapacitor capacitance value is decided by two storage principles, which both grant indivisibly to the total capacitance [5].

As an alternative to ruthenium oxide (RuO_2) (which is widely used in metal oxide supercapacitors), manganese oxide (MnO_2) offers the advantage in terms of high hypothetical capacitance, cost proficiency, and less toxicity as well as environmental safety [6, 7]. MnO_2 has been used for lithium batteries, sensors, catalysts, and alkaline Zn/MnO_2 cell applications; under ambient settings, MnO_2 is perhaps considered as the most steady manganese oxides, with remarkably strong physical and excellent compound properties. These mixtures' high polymorphism and underlying adaptability have given them a wide scope of uses, including catalysis, biosensors, and energy stockpiling. MnO_2 electrodes have set up themselves as a conceivably ideal terminal material for replacing RuO_2 in supercapacitors because of their high explicit capacitance, natural similarity, and cost viability [8–11].

The main concerns regarding for advancement of active materials in supercapacitor development were underlying
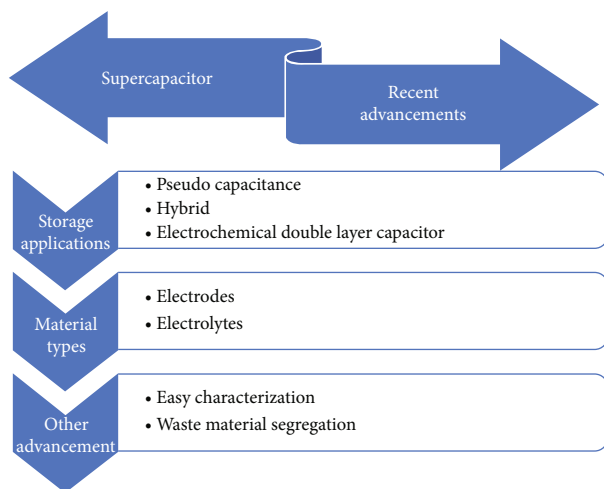
Figure 3: Recent advancements in supercapacitor.

adaptability and dependability, quick cation dissemination under high charge-release rates, high reversible capacitance, and natural friendliness. In general, manganese is a change metal component that can exist in different types of stable oxides, viz, MnO, Mn_3O_4, Mn_2O_3, and MnO_2, and crystallizes in different types of crystal structures [12, 13]. Usually, MnO_2 is amorphous. Deposition of Fe does not change the amorphous nature of MnO_2 but changes its surface morphology that results in increased porosity, increasing the pseudocapacitive performance of MnO_2 [1, 14, 15]. Both active and inert electrodes may be used in high surface area, conductive materials for capacitive supercapacitors that utilize infinitesimal charge partition, or quick, reversible redox responses in the active materials for pseudocapacitance [16, 17].

Graphene is a 2D (dimensional) single-layer hexagonal lattice closely packed by sp^2 carbon molecules with a carbon-based nanostructure, namely, carbon-carbon distances of 0.142 nm between the atoms. Over the most recent days, the emergence of graphene-mediated materials is used for the fabrications of graphene-based composites which are made a lot of consideration in the field of science and technology because of their novel properties like high mechanical strength, great thermal and electrical conductivity, innate adaptability, and good optical and electrochemical features. It is the first crystal that is steady at normal temperature conditions, especially at room temperature [17–20].

Since its experimental discovery in 2004 [18], graphene has been utilized in a variety of applications. In light of its uniqueness, it has piqued the interest and imagination of scholars. It has high surface region, great conductivity, and other unique qualities the ease with which it may be functionalized, the mechanical qualities that it has, and as a result, graphene nanosheets have gained a lot of attention. There is a lot of excitement about the possible applications in a variety of technology fields, nanoelectronics, batteries, and supercapacitors, to name a few sensors and field-effect transistors [21–23].

Graphene has high conductivity and surface area that can be considered as an ideal choice for use in supercapacitors because of its capacitance values in the selected mate-

rials which are directly proportional to its surface area. As surface area increases, its energy storage value also increases. The capacitance value of graphene materials varies and depends on how they have been stacked. If the surface area of the graphene sheet increases, it can easily be accessible to electrolytes and contributes to the capacitance. So improper stacking of graphene also leads to less capacitance. Hence, avoiding the inner or outer sheet restacking can help graphene in increasing the performance of energy storage. Thus, graphene-based nanomaterials provide an ideal platform to develop various potential materials in the branches of electronics, energy storage devices, and biosensors. The electrons are generally delocalized on either side of the single graphene sheet layer sheet which acts as a barrier and prevents the sheet from restacking; at the same time, these electrons can be useful for identifying other surfaces to bind. Oxidation and shedding of graphite lead to the development of hydrophilic graphite oxide known as graphene oxide. The single-layer oxide of graphene possesses several oxygen species in its structure and aids in various chemical modifications. Hence, numerous graphene-based functional nanomaterials can be generated according to their chemical modifications.

Graphene oxide possesses good mechanical stability and can act as appropriate support for stacking manganese oxide in electroactive materials for supercapacitor applications [24]. The single-layered graphene oxide gives a high surface region for the deposition of MnO_2 nanosheets without any restocking and helps in adhesion to other nanostructures. With the high surface region and high stacking effectiveness of the MnO_2-GO composite, the particular capacitance value increases [25].

The present study focuses on the development of a MnO_2GO-based supercapacitor that should attain good electric conductivity. MnO_2 and MnO_2-GO composite can be synthesized by a simple and economical electrodeposition method.

2. Materials and Methodology

2.1. Synthesis of MnO_2-GO Nanocomposites. Advanced Hummers and Offeman's method was used to synthesize GO. Approximately 10 milligrams of graphene oxide with MnO_2 was added and processed using an ultrasonicator after dispersion, after which the reaction mixture was boiled under the microwave; then, the reaction mixture was mixed into the solution of 10 ml of $FeCl_3$ and 1 M H_2SO_4; this solution was added for about 2 hours using the syringe. The sample mixture was then emptied into 20 ml of double-distilled water added after stirring. Centrifugation was used to obtain MnO_2/GO nanocomposites, which were then washed several times with water. The overall process has been schematically represented in Figure 4 [26–28].

2.2. Fabrication of MnO_2-GO Supercapacitor (SC). MnO_2-GO nanostructures were deposited on current collector substrates by the electrodeposition method by constant potentiostat mode. The stainless steel (SS) substrate was cut and polished into 1×1 cm and then washed by ultrasonication for 15 min in deionized water. Electrodeposition was carried
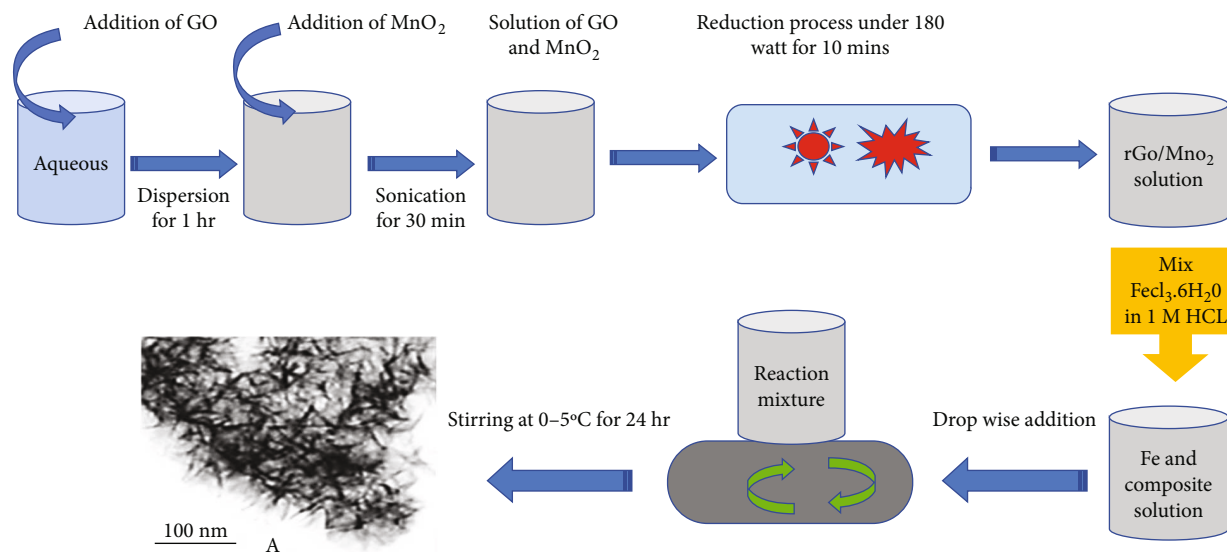
FIGURE 4: Schematic overview of nanocomposite formation under controlled conditions.
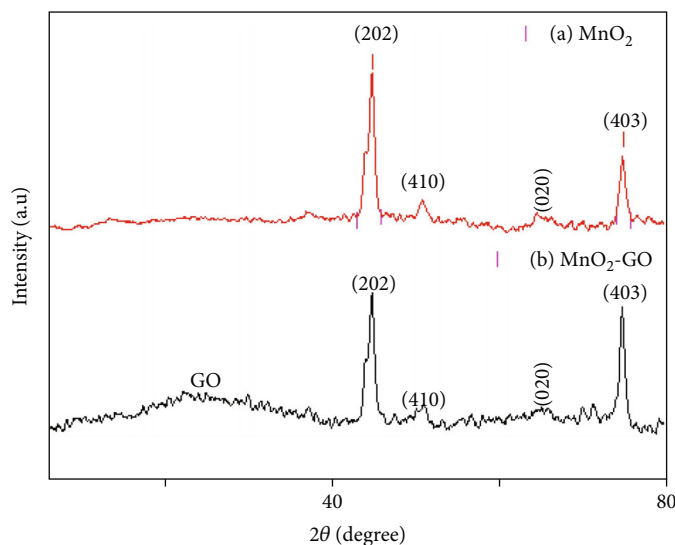

FIGURE 5: (a) MnO_2 and (b) MnO_2-GO substrate.

potentiostatically at 0.8 V for 30 min using the as-prepared SS substrate considering it as the testing electrode. Platinum and silver/silver chloride terminals were utilized as counter electrodes (reference), individually. The electrolyte was prepared by 20 mg of GO mixed with 25 ml deionized water and dispersed by ultrasonication; then, 0.1 M of $MnSO_4$ arrangement was added. The pH of the arrangement was made to 10 by adding 1 M NaOH. The resulting films were rinsed in deionized water and dried at room temperature [14, 27, 29].

2.3. Substrate Characterization. The construction of fabricated nanocomposite thin films was portrayed by powder XRD (Skillet logical XPert Pro MRD diffractometer, Amsterdam, Netherland), worked at 40 kV and 30 mA, and furnished with Cu radiation at a wavelength of 0.15406 nm. The functional groups of electrodeposited MnO_2-GO nanocomposites were analyzed by FTIR-ATR. The local type of

functional groups in the nanocomposite was recorded in the scope of 3000-500 cm^{-1} (Fourier transform infrared spectrometer, Shimadzu, Japan).

2.4. Transmission Electron Microscopic Analysis. Transmission electron microscopy was utilized to inspect the morphologies of as-obtained products to determine their shape, size, and dimensions (TEM). All experiments were conducted utilizing a three-anode framework comprising of a functioning electrode made of exposed or modified glassy carbon (GCE, 3 mm in width), a reference electrode made of saturated calomel (SCE), and an assistant electrode made of platinum wire.

3. Result and Discussion

3.1. XRD Analysis. Figure 5 shows the XRD pattern for the MnO_2 and MnO_2-GO deposited films, Figure 5(a)

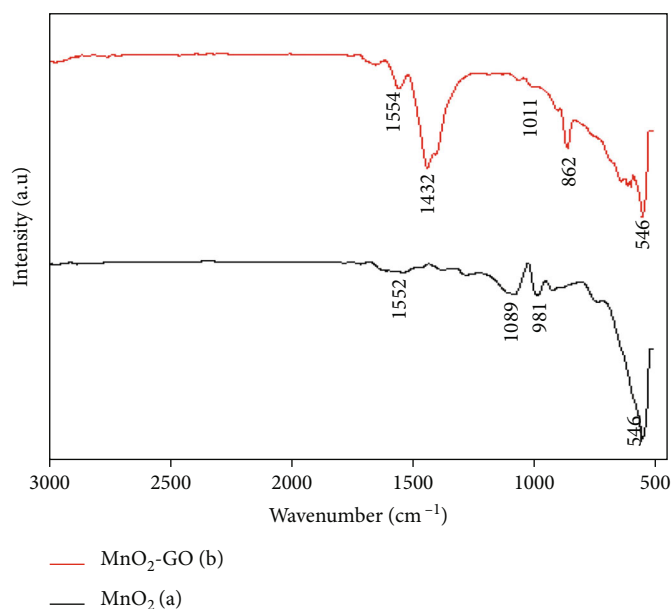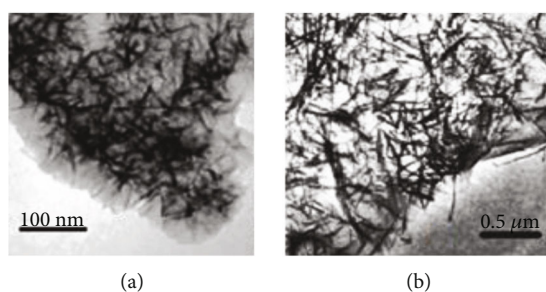FIGURE 6: (a) MnO$_2$ and (b) MnO$_2$-GO.

(a) (b)

FIGURE 7: TEM micrograph of nanocomposite morphology: (a) 100 nm magnification of nanostructure; (b) 500 nm-based magnification of nanostructure.

represents MnO$_2$, and Figure 5(b) represents MnO$_2$-GO substrate. All the diffraction peaks for the MnO$_2$ thin film have good agreement with the reference JCPDS (no. 65-1298), further indexed to orthorhombic MnO$_2$ (orthorhombic crystal structure). The sharp peak tends to the small grain size found as 12 nm by Scherer's formula. The diffraction pattern of MnO$_2$-GO composite also exhibits the same as MnO$_2$ except for the peak around 26° which is due to the presence of GO. It affirms the presence of MnO$_2$ and GO in the composite. The top at 26° weak and broad peak is referred from the research article of [24] The average XRD patterns and Raman spectra of chemically synthesized GO-MnO$_2$ nanocomposites were investigated when the MnO$_2$/GO feeding ratio was varied. As indicated by the report of the most concentrated GO peak around the 2 theta 10, 2°, the (001) reflection is comparative, and because of the introduction of oxygen-containing functional groups on the graphite sheets, the interlayer dividing (0.87 nm) was a lot bigger than the interlayer of pristine graphite (0.34 nm).

3.2. FTIR Analysis. FTIR analysis was carried out for SS modified MnO$_2$ and MnO$_2$-GO thin films; as shown in Figure 6, the results show several transmittance peaks for

MnO$_2$ thin films; it represents Figure 6(a) MnO$_2$ and Figure 6(b) MnO$_2$-GO. The strong peak at 546 cm^{-1} is given to the Mn-O stretching vibration of MnO$_2$, and the peaks at 981, 1089, and 1552 are due to the vibration of O-O and OH bending vibrations. For MnO$_2$-GO film, the peak at 546 cm^{-1} for MnO$_2$ and the peaks around 1554 cm^{-1} 1432 cm^{-1} are also found which are attributed to the C=C vibrations and O-H vibration of graphene oxide. It clearly shows the presence of MnO$_2$ and GO in the MnO$_2$-GO film. The functional group peaks of MnO$_2$ and GO have been crosschecked from the research publication of [30].

3.3. TEM Analysis. Image of graphene oxide nanosheets were viewed by transmission electron microscopy. The as-synthesized GO sheet is discovered to have a smooth surface. With generally high magnification, the manganese oxide nanoparticles were covered with nanosheets of graphene oxide nanoparticles, and more insights concerning the morphology of nanocomposites were investigated, in which GO nanosheets are made out of several layers and the length of each MnO$_2$ nanoparticle is cut formed as slice with scales going from 30 to 50 nm. Moreover, MnO$_2$/GO arrangement of nanocomposites can be ultrasonicated in ethanol for

about an hour with little deficiency of MnO_2 from GO, demonstrating that MnO_2 adsorption on the outside of GO is steady. These recently mentioned properties are those of manufactured MnO_2/GO nanocomposites.

TEM was used to examine GO/MnO_2-based nanocomposites, which were prepared straight from the reaction mixture with no contamination of the surface coating. The surface of the graphene oxide sheet was disordered. The dissolved nanoneedles are less ordered or unbounded as a result of the crystallization process. The sample's morphology was observed as heterostructure nanocomposites in Figure 7 with diameters ranging from 20 to 500 nm. Figure 7(a) shows the resolution of composites at 100 nm scale range where the clear observations of the nanostructure are observed. In Figure 7(b), the structure of nanocomposites was observed with a 500 nm scale range for the comparison in the morphology and shapes of the composites, which was further corroborated with [17, 26, 31]. According to the report of [27, 32], the less arranged precursors on GO sheets rapidly evaporated with the development of extra nanoneedles through a dissolution crystallization mechanism as the reaction advanced from 1 to 10 minutes. The morphology of samples with a more extended response time of 30 minutes showed no discernible differences, implying that the crystal formation process was nearly complete after that time [33, 34].

In this study, MnO_2/graphene oxide nanocomposites were effectively formed using a simple wet-chemical process. MnO_2 is completely covered on the outside of GO nanosheets, according to TEM investigations, and the elements and composition were confirmed by EDX and FT-IR. The content, as well as the crystal structure, was investigated using XRD.

4. Conclusion

In this work, pristine MnO_2 and MnO_2-GO composites were successfully coated on SS by the electrodeposition method. The obtained coatings were homogeneous and showed a very good adhesion on the metal substrate. The coated substrates were characterized using XRD and FTIR. The primary properties were examined utilizing the X-beam diffraction method. From the outcomes, we discovered the orthorhombic structure of MnO_2 with a molecule size around 12 nm. Besides, we conclude with the presence of MnO_2 and graphene sheets in the composite. FTIR spectrum confirmed the presence of Mn-O stretching vibration and bending vibration of graphene oxide in the composite.

Graphene has a distinct chemical makeup and a wide range of properties, including exceptional electrical, optical, thermal, and mechanical capabilities. To meet the increased demand for thin-film processing, composite-mediated integration has evolved in recent technologies, and a number of synthetic techniques, including chemical and physical methodologies, have been created for device integration as well. Graphene has been composited with polymers, semiconductor nanoparticles, metals, metal oxides, sulphides, alloys, carbon nanotubes, organic molecules, and other materials. The enhancement of the properties of these composited materials is based not only on the individual components but also on their interaction.

In this study, authors are experiencing the advantage of making novel and an innovative supercapacitor (SC) which was made out of nanocomposites, which had excellent advantages over other conventional capacitors and other electronic devices. The advantages include the following: they are most commonly used in electric hybrid vehicles, military types of machinery, communication devices for uninterrupted power supply in mobiles, and laser devices.

There are certain challenges to overcome; the supercapacitors are cost-effective and highly dense in energy. Recently, many initiatives have been started to overcome the problems associated with the low energy density developed by the SCs which are developed from nanostructure-mediated electrodes with enhanced capacitance. Higher operating voltages can help you save money on your energy bills. The energy density increases as the working potential window widens, needing less material, separator, and electrolyte to store the same amount of energy. A high cell voltage means that fewer cells must be connected in series to form a specific voltage system, reducing the load on external voltage-balance circuits, which are now widely utilized. Last but not least, electrode materials for SCs have sparked a lot of attention in recent years as a way to create cost-effective and high-performing energy storage devices. Waste materials are a cost-effective way to make supercapacitor electrodes for this purpose, albeit they still need a lot of work (fabrication methods, electrolyte selection, etc.) before they can be sold as raw electrode material in the commercial market.

Data Availability

The data used to support the findings of this study are included within the article.

Conflicts of Interest

The authors declare no potential conflict of interest.

Acknowledgments

References

[1] D. P. Dubal, W. B. Kim, and C. D. Lokhande, "Galvanostatically deposited Fe: MnO_2 electrodes for supercapacitor application," *Journal of Physics and Chemistry of Solids*, vol. 73, no. 1, pp. 18–24, 2012.

[2] Y. Liu, D. Yan, Y. Li et al., "Manganese dioxide nanosheet arrays grown on graphene oxide as an advanced electrode material for supercapacitors," *Electrochimica Acta*, vol. 117, pp. 528–533, 2014.

[3] Suhasini, "Effect of deposition method and the surfactant on high capacitance of electrochemically deposited MnO_2 on stainless steel substrate," *Journal of Electroanalytical Chemistry*, vol. 690, pp. 13–18, 2013.

[4] T. Yousefi, A. N. Golikand, M. H. Mashhadizadeh, and M. Aghazadeh, "Template-free synthesis of MnO_2 nanowires with secondary flower like structure: characterization and supercapacitor behavior studies," *Current Applied Physics*, vol. 12, no. 1, pp. 193–198, 2012.

[5] B. E. Conway, *Electrochemical Supercapacitors: Scientific Fundamentals and Technological Applications*, Springer Science & Business Media, 2013.

[6] H. Yang, J. Jiang, W. Zhou et al., "Influences of graphene oxide support on the electrochemical performances of graphene oxide-MnO 2 nanocomposites," *Nanoscale Research Letters*, vol. 6, no. 1, p. 531, 2011.

[7] Z. Li, J. Wang, X. Liu, S. Liu, J. Ou, and S. Yang, "Electrostatic layer-by-layer self-assembly multilayer films based on graphene and manganese dioxide sheets as novel electrode materials for supercapacitors," *Journal of Materials Chemistry*, vol. 21, no. 10, pp. 3397–3403, 2011.

[8] Z. Li, Y. Mi, X. Liu, S. Liu, S. Yang, and J. Wang, "Flexible graphene/MnO 2 composite papers for supercapacitor electrodes," *Journal of Materials Chemistry*, vol. 21, no. 38, pp. 14706–14711, 2011.

[9] J. Zhang, J. Jiang, and X. S. Zhao, "Synthesis and capacitive properties of manganese oxide nanosheets dispersed on functionalized graphene sheets," *The Journal of Physical Chemistry C*, vol. 115, no. 14, pp. 6448–6454, 2011.

[10] K. Q. Ding, "Cyclic voltammetrically prepared copper-decorated MnO_2 and its electrocatalysis for oxygen reduction reaction (ORR)," *International Journal of Electrochemical Science*, vol. 5, pp. 72–87, 2009.

[11] L. Zhang, R. Jamal, Q. Zhao, M. Wang, and T. Abdiryim, "Preparation of PEDOT/GO, PEDOT/MnO 2, and PEDOT/GO/MnO 2 nanocomposites and their application in catalytic degradation of methylene blue," *Nanoscale Research Letters*, vol. 10, no. 1, pp. 1–9, 2015.

[12] S. Chen, J. Zhu, X. Wu, Q. Han, and X. Wang, "Graphene Oxide–MnO2Nanocomposites for supercapacitors," *ACS Nano*, vol. 4, no. 5, pp. 2822–2830, 2010.

[13] A. L. M. Reddy, F. E. Amitha, I. Jafri, and S. Ramaprabhu, "Asymmetric flexible supercapacitor stack," *Nanoscale Research Letters*, vol. 3, no. 4, pp. 145–151, 2008.

[14] J. Lei, X. Lu, W. Wang et al., "Fabrication of MnO 2/graphene oxide composite nanosheets and their application in hydrazine detection," *RSC Advances*, vol. 2, no. 6, pp. 2541–2544, 2012.

[15] X. Yang, W. Tang, Q. Feng, and K. Ooi, "Single crystal growth of birnessite-and hollandite-type manganese oxides by a flux method," *Crystal Growth & Design*, vol. 3, no. 3, pp. 409–415, 2003.

[16] D. Zheng, Z. Yin, W. Zhang, X. Tan, and S. Sun, "Novel branched γ-MnOOH and β-MnO2Multipod nanostructures," *Crystal Growth & Design*, vol. 6, no. 8, pp. 1733–1735, 2006.

[17] M. Xu, L. Kong, W. Zhou, and H. Li, "Hydrothermal synthesis and pseudocapacitance properties of α-MnO2Hollow spheres and hollow urchins," *The Journal of Physical Chemistry C*, vol. 111, no. 51, pp. 19141–19147, 2007.

[18] S. Devaraj and N. Munichandraiah, "Effect of crystallographic structure of MnO2on its electrochemical capacitance properties," *The Journal of Physical Chemistry C*, vol. 112, no. 11, pp. 4406–4417, 2008.

[19] M. Toupin, T. Brousse, and D. Bélanger, "Influence of microstucture on the charge storage properties of chemically synthesized manganese dioxide," *Chemistry of Materials*, vol. 14, no. 9, pp. 3946–3952, 2002.

[20] Q. Li, J. B. Olson, and R. M. Penner, "Nanocrystalline α-MnO2Nanowires by electrochemical step-edge decoration," *Chemistry of Materials*, vol. 16, no. 18, pp. 3402–3405, 2004.

[21] R. Kötz and M. J. E. A. Carlen, "Principles and applications of electrochemical capacitors," *Electrochimica Acta*, vol. 45, no. 15-16, pp. 2483–2498, 2000.

[22] M. Kaempgen, C. K. Chan, J. Ma, Y. Cui, and G. Gruner, "Printable thin film supercapacitors using single-walled carbon nanotubes," *Nano Letters*, vol. 9, no. 5, pp. 1872–1876, 2009.

[23] Q. Wang, Z. H. Wen, and J. H. Li, "A hybrid supercapacitor fabricated with a carbon nanotube cathode and a TiO_2–B nanowire anode," *Advanced Functional Materials*, vol. 16, no. 16, pp. 2141–2146, 2006.

[24] P. Simon and Y. Gogotsi, "Materials for electrochemical capacitors," *Nanoscience and technology: a collection of reviews from Nature journals*, pp. 320–329, 2009.

[25] C. Xu, X. Wang, J. Zhu, X. Yang, and L. Lu, "Deposition of $_{Co3O4}$ nanoparticles onto exfoliated graphite oxide sheets," *Journal of Materials Chemistry*, vol. 18, no. 46, pp. 5625–5629, 2008.

[26] S. Chen, J. Zhu, Q. Han, Z. Zheng, Y. Yang, and X. Wang, "Shape-controlled synthesis of one-dimensional MnO2via a facile quick-precipitation procedure and its electrochemical properties," *Crystal Growth & Design*, vol. 9, no. 10, pp. 4356–4361, 2009.

[27] Z. Chen, I. Santoso, R. Wang et al., "Surface transfer hole doping of epitaxial graphene using MoO 3 thin film," *Applied Physics Letters*, vol. 96, no. 21, article 213104, 2010.

[28] C. Berger, Z. Song, T. Li et al., "Ultrathin epitaxial graphite: 2D electron gas properties and a route toward graphene-based nanoelectronics," *The Journal of Physical Chemistry B*, vol. 108, no. 52, pp. 19912–19916, 2004.

[29] Y. Wang, Z. Shi, Y. Huang et al., "Supercapacitor devices based on graphene materials," *The Journal of Physical Chemistry C*, vol. 113, no. 30, pp. 13103–13107, 2009.

[30] E. Yoo, J. Kim, E. Hosono, H. S. Zhou, T. Kudo, and I. Honma, "Large reversible Li storage of graphene nanosheet families for use in rechargeable lithium ion batteries," *Nano Letters*, vol. 8, no. 8, pp. 2277–2282, 2008.

[31] F. Schedin, A. K. Geim, S. V. Morozov et al., "Detection of individual gas molecules adsorbed on graphene," *Nature Materials*, vol. 6, no. 9, pp. 652–655, 2007.

[32] W. Yang, Z. Gao, J. Wang et al., "Synthesis of reduced graphene nanosheet/urchin-like manganese dioxide composite and high performance as supercapacitor electrode," *Electrochimica Acta*, vol. 69, pp. 112–119, 2012.

[33] L. Wang, Y. Zheng, S. Chen et al., "Three-dimensional kenaf stem-derived porous carbon/MnO2 for high-performance supercapacitors," *Electrochimica Acta*, vol. 135, pp. 380–387, 2014.

[34] W. Wei, X. Cui, W. Chen, and D. G. Ivey, "Manganese oxide-based materials as electrochemical supercapacitor electrodes," *Chemical Society Reviews*, vol. 40, no. 3, pp. 1697–1721, 2011.

Research Article

Use of Organic and Copper-Based Nanoparticles on the Turbulator Installment in a Shell Tube Heat Exchanger: A CFD-Based Simulation Approach by Using Nanofluids

Supat Chupradit [ID],[1] **Abduladheem Turki Jalil** [ID],[2,3] **Yulianna Enina,**[4] **Dmitriy A. Neganov,**[5] **Muataz S. Alhassan,**[6] **Surendar Aravindhan,**[7] **and Afshin Davarpanah** [ID][8]

[1]*Department of Occupational Therapy, Faculty of Associated Medical Sciences, Chiang Mai University, Chiang Mai 50200, Thailand*
[2]*Faculty of Biology and Ecology, Yanka Kupala State University of Grodno, 230023 Grodno, Belarus*
[3]*College of Technical Engineering, The Islamic University, Najaf, Iraq*
[4]*Department of Propaedeutics of Dental Diseases, Sechenov First Moscow State Medical University, Moscow, Russia*
[5]*Department of Legal Disciplines, Kazan Federal University, Russia*
[6]*Division of Advanced Nanomaterial Technologies, Scientific Research Center, Al-Ayen University, Thi-Qar, Iraq*
[7]*Department of Pharmacology, Saveetha Dental College and Hospital, Saveetha Institute of Medical and Technical Sciences, Chennai, India*
[8]*Young Elite Researchers, Science and Research Branch, Islamic Azad University, Tehran, Iran*

Correspondence should be addressed to Abduladheem Turki Jalil; abedalazeem799@gmail.com
and Afshin Davarpanah; afshindpe@gmail.com

Heat exchangers with unique specifications are administered in the food industry, which has expanded its sphere of influence even to the automotive industry due to this feature. It has been used for convenient maintenance and much easier cleaning. In this study, two different nanomaterials, such as Cu-based nanoparticles and an organic nanoparticle of Chloro-difluoromethane (R_{22}), were used as nanofluids to enhance the efficiency of heat transfer in a turbulator. It is simulated by computational fluid dynamics software (Ansys-Fluent) to evaluate the Nusselt number versus Reynolds number for different variables. These variables are diameter ratio, torsion pitch ratio, and two different nanofluids through the shell tube heat exchanger. It is evident that for higher diameter ratios, the Nusselt number has been increased significantly in higher Reynolds numbers as the heat transfer has been increased in turbulators. For organic fluids (R_{22}), the Nusselt number has been increased significantly in higher Reynolds numbers as the heat transfer has been increased in turbulators due to the proximity of heat transfer charges. At higher torsion pitch ratios, the Nusselt number has been increased significantly in the higher Reynolds number as the heat transfer has been increased in turbulators, especially in higher velocities and pipe turbulence torsions.

1. Introduction

The heat exchanger is used to transfer heat efficiently between two fluids (gas or liquid) to another [1–3]. The most common heat exchangers are car radiators and radiators [4–6]. Heat exchangers are used in various industries such as air conditioning [7–11], automobile, oil and gas, and many other industries [6, 12, 13]. Heating equipment

in process systems such as refineries is generally divided into two general categories of furnaces and heat exchangers [14–19]. The difference between a furnace and a heat exchanger is in the heating source [20–23], which means that the heating source is liquid and gas [24–29]. While in a heat exchanger, the heating source is a hot fluid. In the furnace, according to the type of heating source, the heat transfer mechanism in the form of convection and radiation

is combined [30–33], while the heat transfer mechanism in the heat exchanger is only convection [34–36]. In general, heat transfer calculations from high-temperature plates lead to the simultaneous creation of different effects of heat transfer mechanisms on the characteristics of heat exchangers and other heat transfer equipment [37–39].

On the other hand, forced displacement in the heated layers of nanofluid around a rotating axis is still a fundamental issue that needs further study [40–45]. Access to smaller, lighter, and more efficient devices for better heat transfer has always been desirable in industrial equipment such as electronic components and heat exchangers [46–48]. Since nanofluids have a higher thermal conductivity than normal fluids, they have always been of interest in recent years [49–53]. Ho et al. conducted a limited-volume numerical study to investigate the free heat transfer of water/aluminum oxide in a cylindrical chamber with insulated inner walls and hot and cold outer walls. Based on their findings, the choice of different models for viscosity predicts different values for the Nusselt number [54, 55]. Xu et al. and Dalkilic and Wongwises investigated the combined displacement of water/aluminum oxide nanofluids in a right-angled triangular chamber [56, 57]. According to their reports, with an increasing amount of nanoparticles, heat transfer occurs [58].

Jahanshahi et al. conducted an experimental and numerical study with a finite volume method to investigate the free heat transfer of water/silicon oxide in square chambers with hot and cold vertical walls and horizontal insulated walls. According to their findings, the average unsalted number in all Riley numbers increases with the increasing volume fraction of nanoparticles [59]. Aminossadati and Ghasemi numerically investigated the natural displacement of water/copper oxide nanofluids in Grashev numbers and different volume fractions in a square chamber with local heating. According to their results, with increasing Riley number and volume fraction of nanoparticles, the average Nusselt number increases [60]. Basak et al. numerically examined fluid flow and heat transfer in natural displacement in hot-bottomed triangular chambers and cold lateral walls in a porous medium. The average Nusselt number increases [61].

In the present study, two different nanomaterials, such as Cu-based nanoparticles and an organic nanoparticle of Chloro-difluoromethane (R_{22}), were used as nanofluids to improve the heat transfer efficiency of a turbulator. It is simulated by computational fluid dynamics software (Ansys-Fluent) to evaluate the Nusselt number versus Reynolds number for different variables. These variables are diameter ratio, torsion pitch ratio, and two different nanofluids through the shell tube heat exchanger. One of the reasons for this choice is the current applications of this geometry in thermal insulation processes, cooling of various rotating machine components, and energy management in general.

2. Materials and Methods

2.1. Materials

2.1.1. Cu-Based Nanoparticle. A copper-based nanoparticle is a type of copper-based particle between 1 and 100 nm.

Like many other nanoparticle forms, Cu-based nanoparticles could be formed by natural processes or through chemical synthesis.

2.1.2. R_{22}. Chloro-difluoromethane is a complex type of hydrochlorofluorocarbon (HCFC). This colorless gas is commonly known as R_{22}, which is used for refrigeration or propellant properties.

2.2. Mesh Convergence. To achieve a correct numerical solution in simulating single-phase fluid flows when accurate flow information is not available, it is necessary to use classical smooth flow equations within the Reynolds number range to ensure smooth flow. The equations of mass, momentum, and energy survival governing the displacement flow problem in cylindrical properties can be summarized as follows:

$$\frac{1}{r}\frac{\partial}{\partial r}\left[\left(\rho_{nf}V_r r\right)\Gamma_1 - \Gamma_2 r\frac{\partial r_1}{\partial r}\right] + \frac{1}{r}\frac{\partial}{\partial \theta}\left[\rho_{nf}V_\theta \Gamma_1 - \frac{\Gamma_2}{r}\frac{\partial \Gamma_1}{\partial \theta}\right]$$
$$+ \frac{\partial}{\partial z}\left[\rho_{nf}V_z \Gamma_1\right] = \Gamma_3,$$

(1)

where r_1 to r_3 is explicitly defined in Table 1 for various situations.

It is clear that to solve the set of Equation (1), it is necessary to introduce the fluid and thermal properties of nanofluids. These properties include conductivity, viscosity, density, coefficient of thermal expansion, and specific heat capacity. After reviewing a large number of theoretical and quasiexperimental models presented by researchers to model the thermal conductivity and effective viscosity of water-copper oxide nanofluids and compare their results with each other, it was decided to use the models presented by Corsion. These models are semiexperimental, and their results are very consistent with the experimental results of others. The corrosion model for the thermal conductivity is

$$\frac{k_{nf}}{k_f} = 1 + 4.4 \, \mathrm{Re}_b^{0.4} \, \mathrm{Pr}^{0.66} \left(\frac{T}{T_{fr}}\right)^{10} \left(\frac{k_p}{k_f}\right)^{0.03} \varphi^{0.66}, \quad (2)$$

where Pr is the Prandtl number for the base fluid and Re_b is the Reynolds number for the brown motion of the nanoparticles and is obtained from the following equation:

$$\mathrm{Re}_b = \frac{2\rho f k_B T}{\pi \mu_f^2 d_p}. \quad (3)$$

As given in the momentum survival equations, the density changes in the Boeing force term follow the Bozinsky approximation. The effective density of the nanofluid, the Bozinsky term coefficient, and the denominator of the thermal diffusion coefficient are also calculated using the mixing law:

$$\rho_{nf} = (1 - \varphi)_{\rho_f} + \varphi \rho_{np}, \quad (4)$$

TABLE 1: Calculation of various parameters.

Governing equations	Γ_1	Γ_2	Γ_3
Continuity	1	0	0
Momentum	V_r	μ_{nf}	$-\frac{\partial p}{\partial r} + (\rho\beta)_{nf} g(T - T_i)\cos\theta + \rho_{nf}\frac{V_\theta^2}{r} - \frac{2\mu_{nf}}{r^2}\frac{\partial V_\theta}{\partial_\theta} - \mu_{nf}\frac{V_\theta}{r^2}$
Momentum, θ	V_θ	μ_{nf}	$-\frac{1}{r}\frac{\partial p}{\partial\theta} + (\rho\beta)_{nf} g(T - T_i)\sin\theta + \rho_{nf}\frac{V_r V_\theta}{r} - \frac{2\mu_{nf}}{r^2}\frac{\partial V_r}{\partial_\theta} - \mu_{nf}\frac{V_\theta}{r^2}$
Momentum, z	V_z	μ_{nf}	$-\frac{\partial_p}{\partial Z}$
Energy	$C_{p_{nf}}T$	k_{nf}	0

$$\left(\rho c_p\right)_{nf} = (1 - \varphi)\left(\rho C_p\right)_f + \varphi\left(\rho C_p\right)_{np}, \tag{5}$$

$$(\rho\beta)_{nf} = (1 - \varphi)(\rho\beta)_f + \varphi(\rho\beta)_{np}. \tag{6}$$

The base fluid is specific heat density and capacity, in contrast to the conductivity, viscosity, and thermal expansion coefficient, which are considered during the numerical solution of the temperature variable, which is determined for the water-based fluid as the following correlation relations:

$$C_{pf} = 2 \times 10^{-6}T^4 - 3 \times 10^{-3}T^3 + 1.6T^2 - 357.7T + 342.82, \tag{7}$$

where $R^2 = 0.9995$ and $\rho_f = -0.0034T^2 + 1.7538T + 775.93$.

Although the above equations take more time to converge or so-called converge problem, it provides more accurate modeling results.

2.3. Computational Fluid Dynamics (CFD) Solver.

The nonlinear equation system is solved using the CFD solver in Ansys-Fluent software. This solver discretizes the equations by the volume control method but solves them in a coupled manner using the finite element method. The playback sentences are carefully double-discretized, and the Ray and Chou algorithm is used to couple the speed and pressure. Nonuniform networks network the computational domain with the organization. The criterion of $y^+ < 10$ is used for the boundary layer elements in all geometries that the size of the elements adjacent to the walls and the entrance grows with a ratio of 1.08. The minimum number of elements for the aspect ratio is 75 times 595428, and the maximum number of elements for the aspect ratio is 15 times 2530800. The output of the problem is calculated in the form of dimensionless Nusselt numbers and coefficient of friction in the inner and outer walls to express the amount of heat transfer from the walls and dynamic flow analysis using.

$$\mathrm{Nu}_i = \frac{\overline{h_i}D_h}{k_{nf}}, \tag{8}$$

$$\mathrm{Nu}_o = \frac{\overline{h_o}D_h}{k_{nf}}, \tag{9}$$

$$C_{f_i} = \frac{\tau_{w_i}}{0.5\rho_{nf}V_{in}^2}, \tag{10}$$

$$C_{f_i} = \frac{\tau_{w_o}}{0.5\rho_{nf}V_{in}^2}. \tag{11}$$

3. Results

3.1. Validation.

To determine the correct values of the variables and the accurate boundary layer modeling, the network independence test from numerical solution was performed using velocity and temperature profiles for different aspect ratios of the desired geometry. This test was performed for water fluid without considering nanoparticles. All networks have a boundary layer with the condition $y^+ < 10$, and the number of elements increases in both axial and radial directions. The criterion for selecting a network is to reach a single answer to increase the number of elements in all directions and the boundary layer. The results were validated by previous literature to continue the evaluations from simulations. It is depicted in Figure 1. As it is evident, the error percentage is negligible, and our simulations can be trusted.

3.2. Nusselt Number.

As shown in Figure 2, the effect of various diameter ratios (0.2, 0.15, 0.05, and 0) has been evaluated on the Nusselt number (Nu) in different Reynolds numbers. The Nusselt number has been increased for higher diameter ratios, especially in higher Reynolds numbers, as the heat transfer has been increased in turbulators.

As shown in Figure 3, the effect of various torsion pitch ratios (0.45, 0.30, 0.15, and 0) has been evaluated on the Nusselt number (Nu) in different Reynolds numbers. The Nusselt number has been increased for higher torsion pitch ratios, especially in higher Reynolds numbers, as the heat transfer has been increased in turbulators, especially in higher velocities and pipe turbulence torsions.

As shown in Figure 4, the effect of various R_{22} and Cu-based nanoparticles has been evaluated on the Nusselt number (Nu) in different Reynolds numbers. It is evident that for organic fluids (R_{22}), the Nusselt number has been increased, especially in higher Reynolds numbers, as the heat transfer has been increased in turbulators due to the proximity of heat transfer charges.
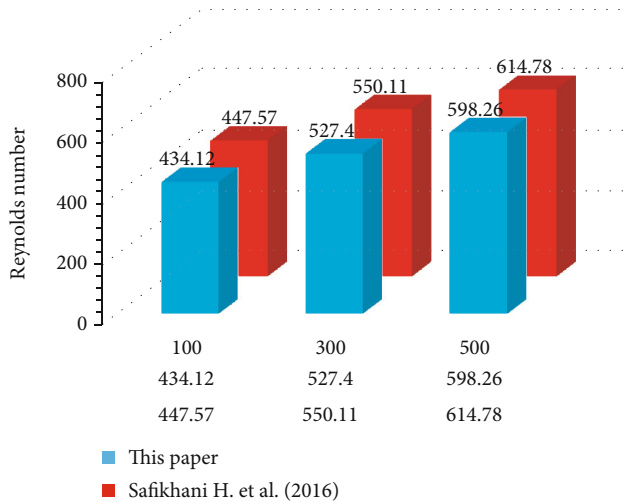
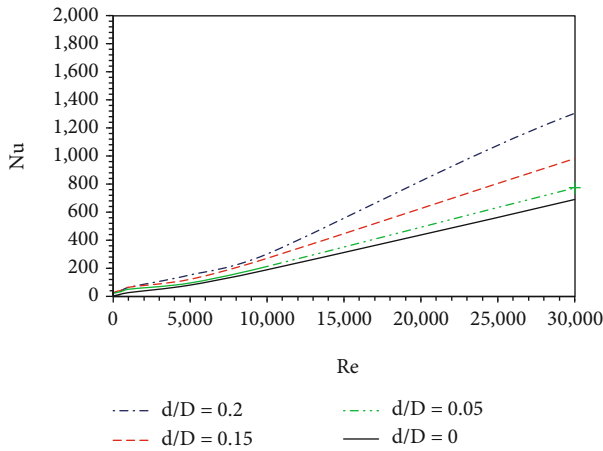FIGURE 1: Validation between our simulations and Safikhani et al. [62].

FIGURE 2: Effect of various diameter ratios on Nusselt number (Nu) in different Reynolds numbers.
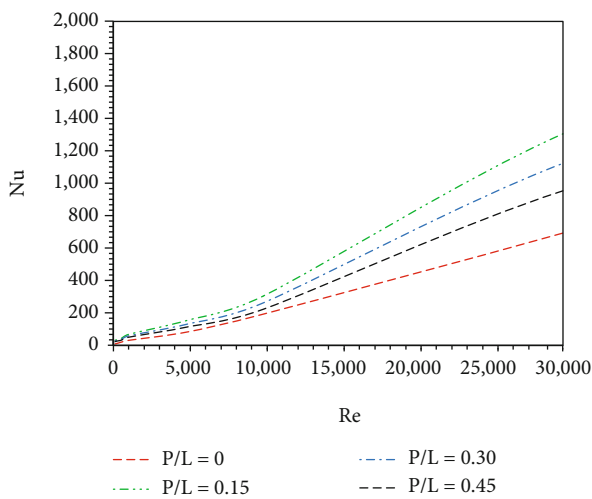

FIGURE 3: Effect of various torsion pitch ratios on Nusselt number (Nu) in different Reynolds numbers.
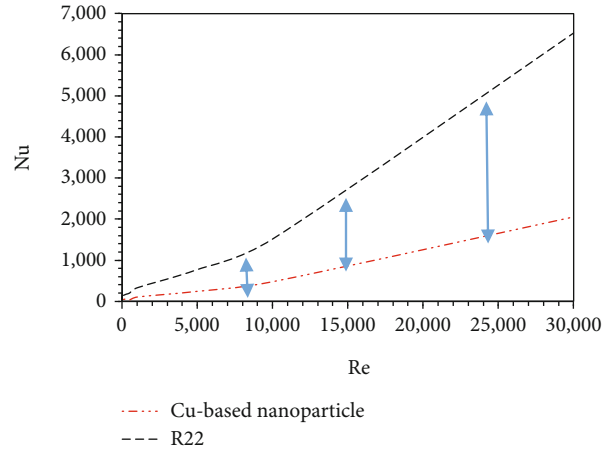

FIGURE 4: Effect of R_{22} and Cu-based nanoparticles on Nusselt number (Nu) in different Reynolds numbers.

4. Discussion and Conclusions

Despite the limitations of validating the problem, the correctness of the code can be ensured by solving classical governing equations for similar geometries, regardless of the rotation of the inner cylinder, and comparing the results of the present numerical solution with the work of others. Figure 1 shows a comparison between the present work results and the study of Safikhani et al. (2016), and there is an excellent correlation between these results for the two heat flux ratios of 0.5 and 2. The maximum numerical error for the Reynolds number is 9.2%. The amount of numerical error of the coefficient of friction between both numerical solutions in the inner and outer walls is negligible, which shows a good agreement between the results of these solutions.

Heat transfer media are usually composed of fluids such as water and oil with a lower thermal conductivity than these nanoparticles. For example, the thermal conductivity of copper is 700 times the thermal conductivity of water and 300 times the thermal conductivity of engine oil, or the thermal conductivity of copper oxide is about 60 times the thermal conductivity of water. Therefore, fluids containing fine particles of metal compounds, metal oxides, carbon nanotubes, graphene, or hybrids are expected to exhibit better thermal properties than pure fluids. The larger surface area of the nanoparticles increases the intensity of heat transfer from the fluid to the particles where the fluid is warmer than the nanoparticles and transfers heat from the particles to the fluid where the fluid is cold. To transfer heat by displacement, the particles must be easily displaced by the fluid. Due to technological problems, studies in this field have focused more on suspensions that include particulate matter suspended in millimeters and with a maximum of micrometers. Particles on this scale cause acute problems in the heat transfer equipment so that these particles quickly settle in the system and become clogged as they pass through the ducts, causing a significant pressure drop. In addition to the collision of these particles with each other and with the system's wall and equipment causing abrasion, it is theoretically determined that the smaller the particles, the higher their heat transfer level.

Power plants are considered one of the most important industrial centers of the country and have a particular sensitivity. This importance includes the various parts used in it, such as turbines, boilers, and converters. The transfer of thermal energy from one fluid to another in the industry is done by a heat exchanger device. There are two fluids with different temperatures in heat exchangers, which provide the conditions for heat exchange between the two fluids, usually exchangers. Thermals are used to cool a hot fluid, heat a fluid to a lower temperature, or both. The heat exchanger transfers energy between two fluids through an interface. Since nanoparticles affect the fluid's thermal properties, nanofluids in heat exchangers can be very efficient and helpful. Viscosity is the resistance to the relative motion of a fluid. This parameter plays a crucial role in momentum transmission between fluid layers, and its effect becomes more pronounced when there is movement between fluid layers. In liquids, viscosity is caused by the presence of van der Waals forces between molecules.

It should be noted that this simulation has been done with Ansys-Fluent software, and after designing the initial design using the study of existing articles and researches. Simulation is an educational technique that provides all or part of a clinical experience in a safe environment and helps a person learn without fear of personal weakness or fear of self-harm through interactive activities. The use of simulation in the industry is widely evolving worldwide. Its prevalence is influenced by technological advances, changes in ethical issues raised in learning industrial skills, the congestion of industrial environments for training, and the lack of manpower. Experts work in companies to help with the training process. Simulation has several benefits, including increasing personal safety, enhancing interactive and inclusive learning, helping to improve learners' problem-solving and critical thinking skills, and achieving self-regulated learning. However, despite all the mentioned advantages, it is noteworthy that due to the financial costs of providing simulation equipment and the need for proper cost management, especially in educational centers in the present era, the results of using similar types should be done through numerous researches. Instruments should be examined on learners' learning, and according to the effectiveness of different types of simulators, each of them was prepared and prepared for educating learners.

The main findings of this study are as follows:

(i) The Nusselt number has been increased for higher diameter ratios, especially in higher Reynolds numbers, as the heat transfer has been increased in turbulators

(ii) For organic fluids (R_{22}), the Nusselt number has been increased, especially in higher Reynolds numbers, as the heat transfer has been increased in turbulators due to the proximity of heat transfer charges

(iii) At higher torsion pitch ratios, the Nusselt number has been increased, especially in higher Reynolds numbers, as the heat transfer has been increased in turbulators, especially in higher velocities and pipe turbulence torsions

Abbreviations

Re: Reynolds number
Pr: Prandtl number
α: Twist angle (degree)
Nu: Nusselt number
μ: Viscosity (kg·m^{-1}·s^{-1})
f: Friction coefficient
D: Pipe diameter (m)
d: Wire diameter (m)
ρ: Density (kg/m^3)
h_f: Height (m)
g: Gravity (m·s^{-2})
h: Displacement heat transfer coefficient (W/K).

Data Availability

There is no available data for this paper.

Conflicts of Interest

The authors declare that they have no conflicts of interest.

References

[1] R. Andrzejczyk, T. Muszynski, and M. Gosz, "Experimental investigations on heat transfer enhancement in shell coil heat exchanger with variable baffles geometry," *Chemical Engineering and Processing - Process Intensification*, vol. 132, pp. 114–126, 2018.

[2] B. Esan and A. Hassan, "Nexus between carbon dioxide emission, energy consumption and economic growth in Nigeria," *International Journal of Sustainable Energy and Environmental Research*, vol. 9, no. 1, pp. 46–55, 2020.

[3] J. Ni, X. Zhuang, and M. A. Wahab, "Review on the prediction of residual stress in welded steel components," *Computers, Materials & Continua*, vol. 62, no. 2, pp. 495–523, 2020.

[4] A. Li, X. Mu, X. Zhao, J. Xu, M. Khayatnezhad, and R. Lalehzari, "Developing the non-dimensional framework for water distribution formulation to evaluate sprinkler irrigation," *Irrigation and Drainage*, vol. 70, no. 4, pp. 659–667, 2021.

[5] S. Kang and T. Park, "Detecting outlier behavior of game player players using multimodal physiology data," *Intelligent Automation and Soft Computing*, vol. 1, 2019.

[6] K. Valizadeh, S. Farahbakhsh, A. Bateni et al., "A parametric study to simulate the non-Newtonian turbulent flow in spiral tubes," *Energy Science & Engineering*, vol. 8, no. 1, pp. 134–149, 2020.

[7] D. Zhang, X. Chen, F. Li, A. K. Sangaiah, and X. Ding, "Seam-carved image tampering detection based on the cooccurrence of adjacent LBPs," *Security and Communication Networks*, vol. 2020, 12 pages, 2020.

[8] Y. Song, D. Zhang, Q. Tang, S. Tang, and K. Yang, "Local and nonlocal constraints for compressed sensing video and multiview image recovery," *Neurocomputing*, vol. 406, pp. 34–48, 2020.

[9] S. Zhou and J. Qiu, "Enhanced SSD with interactive multiscale attention features for object detection," *Multimedia Tools and Applications*, vol. 80, no. 8, pp. 11539–11556, 2021.

[10] Q. Tang, K. Wang, K. Yang, and Y. S. Luo, "Congestion-balanced and welfare-maximized charging strategies for electric vehicles," *IEEE Transactions on Parallel and Distributed Systems*, vol. 31, no. 12, pp. 2882–2895, 2020.

[11] J. Wang, W. Chen, Y. Ren, O. Alfarraj, and L. Wang, "Blockchain based data storage mechanism in cyber physical system," *Journal of Internet Technology*, vol. 21, no. 6, pp. 1681–1689, 2020.

[12] T. Tjahjono, M. Elveny, O. A. Ibrahim et al., "Role of cryogenic cycling rejuvenation on flow behavior of ZrCuAlNiAg metallic glass at relaxation temperature," *Transactions of the Indian Institute of Metals*, vol. 1, 2021.

[13] S. Kaur and V. K. Joshi, "Hybrid soft computing technique based trust evaluation protocol for wireless sensor networks," *Intelligent Automation and Soft Computing*, vol. 26, no. 2, pp. 217–226, 2018.

[14] "Mg-Cr layered double hydroxide intercalated oxalic anion to remove cationic dye solutions: rhodamine B and methylene blue," *Journal of Environmental Treatment Techniques*, vol. 9, no. 2, pp. 383–391, 2020.

[15] M. Sharma, H. Pham, and V. B. Singh, "Modeling and analysis of leftover issues and release time planning in multi-release open source software using entropy based measure," *Computer Systems Science and Engineering*, vol. 34, no. 1, pp. 33–46, 2019.

[16] M. Zarei, A. Davarpanah, N. Mokhtarian, and F. Farahbod, "Integrated feasibility experimental investigation of hydrodynamic, geometrical and, operational characterization of methanol conversion to formaldehyde," *Energy Sources, Part A: Recovery, Utilization, and Environmental Effects*, vol. 42, no. 1, pp. 89–103, 2020.

[17] K. Gu, L. Yang, Y. Wang, and S. Wen, "Traceable identity-based group signature," *RAIRO-Theoretical Informatics and Applications*, vol. 50, no. 3, pp. 193–226, 2016.

[18] B. Yin, S. Zhou, Y. Lin, Y. Liu, and Y. Hu, "Efficient distributed skyline computation using dependency-based data partitioning," *Journal of Systems and Software*, vol. 93, pp. 69–83, 2014.

[19] M. Long and X. Xiao, "Outage performance of double-relay cooperative transmission network with energy harvesting," *Physical Communication*, vol. 29, pp. 261–267, 2018.

[20] Y. Song, J. Li, X. Chen, D. Zhang, Q. Tang, and K. Yang, "An efficient tensor completion method via truncated nuclear norm," *Journal of Visual Communication and Image Representation*, vol. 70, p. 102791, 2020.

[21] J. Wang, W. Wu, Z. Liao, Y. W. Jung, and J. U. Kim, "An enhanced PROMOT algorithm with D2D and robust for mobile edge computing," *Journal of Internet Technology*, vol. 21, no. 5, pp. 1437–1445, 2020.

[22] D. Zhang, S. Wang, F. Li et al., "An efficient ECG denoising method based on empirical mode decomposition, sample entropy, and improved threshold function," *Wireless Communications and Mobile Computing*, vol. 2020, 11 pages, 2020.

[23] Q. Tang, K. Wang, Y. Song, F. Li, and J. H. Park, "Waiting time minimized charging and discharging strategy based on mobile edge computing supported by software-defined network," *IEEE Internet of Things Journal*, vol. 7, no. 7, pp. 6088–6101, 2020.

[24] "The impact of polluting sources on the physical-chemical properties of water in the Curved River in Kosovo," *Journal of Environmental Treatment Techniques*, vol. 9, no. 2, pp. 368–374, 2020.

[25] K. Li, W. Yang, and K. Li, "A hybrid parallel solving algorithm on GPU for quasi-tridiagonal system of linear equations," *IEEE Transactions on Parallel and Distributed Systems*, vol. 27, no. 10, pp. 2795–2808, 2016.

[26] F. Fan, C. Qi, J. Tang, Q. Liu, X. Wang, and Y. Yan, "A novel thermal efficiency analysis on the thermo-hydraulic performance of nanofluids in an improved heat exchange system under adjustable magnetic field," *Applied Thermal Engineering*, vol. 179, p. 115688, 2020.

[27] Z. Xu, W. Liang, K. C. Li, J. Xu, and H. Jin, "A blockchain-based roadside unit-assisted authentication and key agreement protocol for internet of vehicles," *Journal of Parallel and Distributed Computing*, vol. 149, pp. 29–39, 2021.

[28] W. Wang, Y. Yang, J. Li, Y. Hu, Y. Luo, and X. Wang, "Woodland labeling in Chenzhou, China, via deep learning approach," *International Journal of Computational Intelligence Systems*, vol. 13, no. 1, pp. 1393–1403, 2020.

[29] Y. Qu and N. Xiong, "RFH: a resilient, fault-tolerant and high-efficient replication algorithm for distributed cloud storage," in *the 41st International Conference on Parallel Processing*, pp. 520–529, Pittsburgh, PA, USA, 2012.

[30] J. Zhang, K. Yang, L. Xiang, Y. Luo, B. Xiong, and Q. Tang, "A self-adaptive regression-based multivariate data compression scheme with error bound in wireless sensor networks," *International Journal of Distributed Sensor Networks*, vol. 9, no. 3, 2013.

[31] J. Zhang, J. Sun, J. Wang, and X. G. Yue, "Visual object tracking based on residual network and cascaded correlation filters," *Journal of Ambient Intelligence and Humanized Computing*, vol. 12, no. 8, pp. 8427–8440, 2021.

[32] K. Gu, Y. Wang, and S. Wen, "Traceable threshold proxy signature," *Journal of Information Science & Engineering*, vol. 33, no. 1, 2017.

[33] W. Li, Y. Ding, Y. Yang, R. S. Sherratt, J. H. Park, and J. Wang, "Parameterized algorithms of fundamental NP-hard problems: a survey," *Human-centric Computing and Information Sciences*, vol. 10, no. 1, pp. 1–24, 2020.

[34] E. A. P. Akhir, R. Bachok, N. I. Arshad, and A. Aiman Zamri, "Conceptual framework for SIDS alert system," in *2018 4th International Conference on Computer and Information Sciences (ICCOINS)*, Kuala Lumpur, Malaysia, 2018.

[35] K. Li, X. Tang, B. Veeravalli, and K. Li, "Scheduling precedence constrained stochastic tasks on heterogeneous cluster systems," *IEEE Transactions on Computers*, vol. 64, no. 1, pp. 191–204, 2015.

[36] Y. Cui, W. Wang, B. Li, and D. Zuo, "Numerical study on the thermal-hydraulic performance of a circular-arc-wavy helically coiled heat exchanger developed based on chaotic advection," *International Journal of Heat and Mass Transfer*, vol. 159, p. 120084, 2020.

[37] M. Hemmat Esfe, S. Saedodin, E. Hasani Malekshah, A. Babaie, and H. Rostamian, "Mixed convection inside lid-driven cavities filled with nanofluids," *Journal of Thermal Analysis and Calorimetry*, vol. 135, no. 1, pp. 813–859, 2019.

[38] J. Mgm, M. S. A. Yajid, and A. Khatibi, "A situation analysis of integrated logistics Berhad Malaysia," *Syst Rev Pharm.*, vol. 11, no. 1, pp. 734–741, 2020.

[39] W. Yang, K. Li, Z. Mo, and K. Li, "Performance optimization using partitioned SpMV on GPUs and multicore CPUs," *IEEE Transactions on Computers*, vol. 64, no. 9, pp. 2623–2636, 2015.

[40] M. Kalteh, K. Javaherdeh, and T. Azarbarzin, "Numerical solution of nanofluid mixed convection heat transfer in a lid-driven square cavity with a triangular heat source," *Powder Technology*, vol. 253, pp. 780–788, 2014.

[41] "Heat transfer and fluid flow analysis of a novel micro-miniature cryocooler model," *Advanced Journal of Chemistry-Section A*, pp. 32–38, 2018.

[42] J. Mei, K. Li, A. Ouyang, and K. Li, "A profit maximization scheme with guaranteed quality of service in cloud computing," *IEEE Transactions on Computers*, vol. 64, no. 11, pp. 3064–3078, 2015.

[43] W. Fang, X. Yao, X. Zhao, J. Yin, and N. Xiong, "A stochastic control approach to maximize profit on service provisioning for mobile cloudlet platforms," *IEEE Transactions on Systems, Man, and Cybernetics: Systems*, vol. 48, no. 4, pp. 522–534, 2018.

[44] R. Shirmohammadi, A. Aslani, R. Ghasempour, L. M. Romeo, and F. Petrakopoulou, "Process design and thermoeconomic evaluation of a CO_2 liquefaction process driven by waste exhaust heat recovery for an industrial CO_2 capture and utilization plant," *Journal of Thermal Analysis and Calorimetry, pp.*, vol. 145, no. 3, pp. 1585–1597, 2021.

[45] A. Davarpanah, M. Zarei, K. Valizadeh, and B. Mirshekari, "CFD design and simulation of ethylene dichloride (EDC) thermal cracking reactor," *Energy Sources, Part A: Recovery, Utilization, and Environmental Effects*, vol. 41, no. 13, pp. 1573–1587, 2019.

[46] K. Li, W. Yang, and K. Li, "Performance analysis and optimization for SpMV on GPU using probabilistic modeling," *IEEE Transactions on Parallel and Distributed Systems*, vol. 26, no. 1, pp. 196–205, 2015.

[47] P. Saravana Bhavan and J. Selwin Rajadurai, "Investigation on helical coiled tube heat exchanger for parallel and counter flow using CFD analysis," *Lecture Notes in Mechanical Engineering*, 2020.

[48] M. Farsi, M. Khoshvaght-Aliabadi, and A. Alimoradi, "A parametric study on heat transfer and pressure drop characteristics of circular tube with alternating flattened flow path," *International Journal of Thermal Sciences*, vol. 160, p. 106671, 2021.

[49] K. Li, W. Ai, Z. Tang et al., "Hadoop recognition of biomedical named entity using conditional random fields," *IEEE Transactions on Parallel and Distributed Systems*, vol. 26, no. 11, pp. 3040–3051, 2015.

[50] R. Syah, A. Davarpanah, M. Elveny, and D. Ramdan, "Natural convection of water and nano-emulsion phase change material inside a square enclosure to cool the electronic components," *International Journal of Energy Research*, 2021.

[51] D. Yang, T. S. Khan, E. Al-Hajri, Z. H. Ayub, and A. H. Ayub, "Geometric optimization of shell and tube heat exchanger with interstitial twisted tapes outside the tubes applying CFD techniques," *Applied Thermal Engineering*, vol. 152, pp. 559–572, 2019.

[52] A. Davarpanah, "Parametric study of polymer-nanoparticles-assisted injectivity performance for axisymmetric two-phase flow in EOR processes," *Nanomaterials*, vol. 10, no. 9, p. 1818, 2020.

[53] J. Gujar, B. Londhe, R. Zambare, R. Kavade, and M. Shingare, "Glycine: an efficient catalyst for the synthesis of tetra-substituted imidazole derivatives in aqueous medium," *Journal of Applied Organometallic Chemistry*, vol. 1, no. 3, pp. 134–142, 2021.

[54] Y. Xuan and Q. Li, "Investigation on convective heat transfer and flow features of nanofluids," *Journal of Heat Transfer*, vol. 125, no. 1, pp. 151–155, 2003.

[55] C. J. Ho, M. W. Chen, and Z. W. Li, "Numerical simulation of natural convection of nanofluid in a square enclosure: effects due to uncertainties of viscosity and thermal conductivity," *International Journal of Heat and Mass Transfer*, vol. 51, no. 17-18, pp. 4506–4516, 2008.

[56] Y. Xu, K. Li, L. He, L. Zhang, and K. Li, "A hybrid chemical reaction optimization scheme for task scheduling on heterogeneous computing systems," *IEEE Transactions on Parallel and Distributed Systems*, vol. 26, no. 12, pp. 3208–3222, 2015.

[57] A. S. Dalkilic and S. Wongwises, "Intensive literature review of condensation inside smooth and enhanced tubes," *International Journal of Heat and Mass Transfer*, vol. 52, no. 15-16, pp. 3409–3426, 2009.

[58] B. Ghasemi and S. M. Aminossadati, "Mixed convection in a lid-driven triangular enclosure filled with nanofluids," *International Communications in Heat and Mass Transfer*, vol. 37, no. 8, pp. 1142–1148, 2010.

[59] M. Jahanshahi, S. F. Hosseinizadeh, M. Alipanah, A. Dehghani, and G. R. Vakilinejad, "Numerical simulation of free convection based on experimental measured conductivity in a square cavity using water/SiO_2 nanofluid," *International Communications in Heat and Mass Transfer*, vol. 37, no. 6, pp. 687–694, 2010.

[60] S. M. Aminossadati and B. Ghasemi, "Natural convection of water-CuO nanofluid in a cavity with two pairs of heat source-sink," *International Communications in Heat and Mass Transfer*, vol. 38, no. 5, pp. 672–678, 2011.

[61] T. Basak, S. Roy, and S. Krishna Babu, "Natural convection and flow simulation in differentially heated isosceles triangular enclosures filled with porous medium," *Chemical Engineering Science*, vol. 63, no. 13, pp. 3328–3340, 2008.

[62] H. Safikhani, A. Zare Mehrjardi, and M. Safari, "Effect of inserting coiled wires in tubes on the fluid flow and heat transfer performance of nanofluids," *Transport Phenomena in Nano and Micro Scales*, vol. 4, no. 2, pp. 9–16, 2016.